

## **Portable Spectroscopy and Spectrometry 1**

# **Portable Spectroscopy and Spectrometry 1**

Technologies and Instrumentation

*Edited by*

*Richard A. Crocombe*

Crocombe Spectroscopic Consulting  
Winchester  
MA, USA

*Pauline E. Leary*

Federal Resources  
Stevensville  
MD, USA

*Brooke W. Kammrath*

Department of Forensic Science  
Henry C. Lee College of Criminal Justice and Forensic Sciences  
University of New Haven  
West Haven  
CT, USA

and

Henry C. Lee Institute of Forensic Science  
West Haven  
CT, USA

**WILEY**

This edition first published 2021  
© 2021 John Wiley & Sons Ltd

All rights reserved. No part of this publication may be reproduced, stored in a retrieval system, or transmitted, in any form or by any means, electronic, mechanical, photocopying, recording or otherwise, except as permitted by law. Advice on how to obtain permission to reuse material from this title is available at <http://www.wiley.com/go/permissions>.

The right of Richard A. Crocombe, Pauline E. Leary and Brooke W. Kammrath to be identified as authors of the editorial material in this work has been asserted in accordance with law.

*Registered Offices*

John Wiley & Sons, Inc., 111 River Street, Hoboken, NJ 07030, USA  
John Wiley & Sons Ltd, The Atrium, Southern Gate, Chichester, West Sussex, PO19 8SQ, UK

*Editorial Office*

The Atrium, Southern Gate, Chichester, West Sussex, PO19 8SQ, UK

For details of our global editorial offices, customer services, and more information about Wiley products visit us at [www.wiley.com](http://www.wiley.com).

Wiley also publishes its books in a variety of electronic formats and by print-on-demand. Some content that appears in standard print versions of this book may not be available in other formats.

*Limit of Liability/Disclaimer of Warranty*

In view of ongoing research, equipment modifications, changes in governmental regulations, and the constant flow of information relating to the use of experimental reagents, equipment, and devices, the reader is urged to review and evaluate the information provided in the package insert or instructions for each chemical, piece of equipment, reagent, or device for, among other things, any changes in the instructions or indication of usage and for added warnings and precautions. While the publisher and authors have used their best efforts in preparing this work, they make no representations or warranties with respect to the accuracy or completeness of the contents of this work and specifically disclaim all warranties, including without limitation any implied warranties of merchantability or fitness for a particular purpose. No warranty may be created or extended by sales representatives, written sales materials or promotional statements for this work. The fact that an organization, website, or product is referred to in this work as a citation and/or potential source of further information does not mean that the publisher and authors endorse the information or services the organization, website, or product may provide or recommendations it may make. This work is sold with the understanding that the publisher is not engaged in rendering professional services. The advice and strategies contained herein may not be suitable for your situation. You should consult with a specialist where appropriate. Further, readers should be aware that websites listed in this work may have changed or disappeared between when this work was written and when it is read. Neither the publisher nor authors shall be liable for any loss of profit or any other commercial damages, including but not limited to special, incidental, consequential, or other damages.

*Library of Congress Cataloging-in-Publication Data*

Names: Crocombe, Richard A., editor. | Leary, Pauline E., editor. |  
Kammrath, Brooke W. editor.

Title: Portable spectroscopy and spectrometry 1: technologies and instrumentation / edited by Richard A.  
Crocombe, Pauline E. Leary, Brooke W. Kammrath.

Description: First edition. | Hoboken, NJ : Wiley, 2021. | Includes  
bibliographical references and indexes. | Contents: v. 1. Technologies  
and instrumentation.

Identifiers: LCCN 2020042686 (print) | LCCN 2020042687 (ebook) | ISBN  
9781119636366 (v. 1 ; hardback) | ISBN 9781119636335 (v. 1 ; adobe pdf) |  
ISBN 9781119636410 (v. 1 ; epub)

Subjects: LCSH: Spectrometer. | Spectrum analysis.

Classification: LCC QC373.S7 P67 2021 (print) | LCC QC373.S7 (ebook) |  
DDC 621.36/1-dc23

LC record available at <https://lccn.loc.gov/2020042686>

LC ebook record available at <https://lccn.loc.gov/2020042687>

Cover Design: Wiley

Cover Image: Hand © Artem Furman/Shutterstock;

Infrared Spectrum: Courtesy of Pauline Leary and Brooke Kammrath

Set in 9.5/12.5pt STIXTwoText by SPi Global, Chennai, India

*To my parents, my family, and all those in spectroscopy I've worked with, and learned from, over the years.*

Richard A. Crocombe, Ph.D.

*This book is dedicated to **John A. Reffner**. Everyone needs someone in their life like you are to me: A **teacher** to provide them guidance when needed, a **mentor** to help them see what they can achieve, and a **friend** to talk to when they need to know it will all work out.*

Pauline E. Leary, Ph.D.

*The dedication of this book is shared amongst all of the members of my family. To my mother Shirley and late father Milton, I am grateful for all of the many life lessons you taught me and your encouragement to pursue a career that I love. To my twin sister Lindsey, I appreciate having you as my forever best friend, partner in crime, and womb-mate. To my husband Matt, a choice in a life partner is the most important decision a person can make, and I chose very wisely. You are my biggest champion, and I am yours – together we can accomplish anything. And to my children Riley and Grayson, I love you so much. I hope you always stay curious because curiosity is the best teacher, the mother of invention, the cure for boredom, the key to creativity, the engine of achievement, and the beginning of science.*

Brooke W. Kammrath, Ph.D.

## Contents

**List of Contributors** *xiii*

**Foreword** *xvii*

**Preface for Volume 1** *xix*

**Acknowledgements** *xxi*

### **1 Introduction to Portable Spectroscopy 1**

*Pauline E. Leary, Richard A. Crocombe and Brooke W. Kammrath*

- 1.1 Introduction 1
- 1.2 Defining Portable Spectrometers 1
- 1.3 Performance 2
- 1.4 History and Availability 4
- 1.5 Instrument Design and Enabling Technologies 7
- 1.6 Producing Results 8
- 1.7 Outline of These Volumes 9
- Acronyms and Abbreviations 11
- References 12

### **2 Engineering Portable Instruments 15**

*Terry Sauer*

- 2.1 Size/Weight 15
- 2.2 Sample Interface 16
- 2.3 Embedded Computer vs. External Personal Computer (PC) 16
- 2.4 Reduced Feature Set 17
- 2.5 Target of Non-Spectroscopist 17
- 2.6 Power Budget 18
- 2.7 Voltage Conversion 18
- 2.8 Decon/Ingress Protection (IP) Rating 19
- 2.9 Testing the Seal 20
- 2.10 Gloved Operation 20
- 2.11 Display 21
- 2.12 Thermal Concerns 23
- 2.13 Optical Elements 27
- 2.14 Interferometer Optical Design 27
- 2.15 Interferometer Bearings 29
- 2.16 Vibration 30

2.17	Shock	30
2.18	Battery	31
2.19	Electrostatic Discharge (ESD)	32
2.20	Ergonomics	34
2.21	Laser Safety	34
2.22	Stability	35
2.23	Service	38
2.24	Communications/Wireless	38
	References	38

### **3 Design Considerations for Portable Mid-Infrared FTIR Spectrometers Used for In-Field Identifications of Threat Materials 41**

*David W. Schiering and John T. Stein*

3.1	Introduction and Background	41
3.2	FTIR System Components	44
3.3	FTIR Spectrometer Performance Attributes	53
3.4	Modeling and Simulation Guide to Portable Instrument Design and Development	55
3.5	Portable FTIR Performance Benchmarks	60
3.6	Conclusion	62
	Abbreviations and Acronyms	62
	References	63

### **4 PAT Applications of NIR Spectroscopy in the Pharmaceutical Industry 67**

*Pierre-Yves Sacré, Charlotte De Bleye, Philippe Hubert and Eric Ziemons*

4.1	Introduction	67
4.2	Continuous Manufacturing and Real-Time Release Testing	67
4.3	PAT Implementation of Near-Infrared Spectroscopy	73
4.4	Conclusion	79
	Glossary	81
	References	82

### **5 MOEMS and MEMS – Technology, Benefits & Uses 89**

*Heinrich Grüger*

5.1	Introduction	89
5.2	Grating-Based Spectrometers	92
5.3	Fourier Transform Spectrometer	101
5.4	Tunable Fabry-Perot Interferometer	104
5.5	Integration Strategies for MEMS-/MOEMS-Based Spectrometers	106
5.6	Use of MEMS-Based NIR Spectrometers	108
	Acronyms and Abbreviations	109
	References	110

### **6 Portable Raman Spectroscopy: Instrumentation and Technology 115**

*Cicely Rathmell, Dieter Bingemann, Mark Zieg and David Creasey*

6.1	Introduction	115
6.2	The Case for Raman: Capabilities and Scope	115
6.3	The Theory of Raman Spectra	116

6.4	Basics of a Raman System	119
6.5	“Portable” Versus “Handheld” Versus “Mini”	119
6.6	Performance Needs in Portable Raman Instruments	120
6.7	Excitation Laser	122
6.8	Optical Filters and Sampling Optics	125
6.9	Spectrometer Design	127
6.10	Sample Interface and Accessories	134
6.11	Spectral Processing and Analysis	135
6.12	Special Cases	138
6.13	Conclusion	140
	Acronyms and Abbreviations	141
	References	141

## 7 Optical Filters – Technology and Applications 147

*Oliver Pust*

7.1	Overview on the Use of Optical Filters in Spectroscopy	147
7.2	Optical Filters as Auxiliary Filters	154
7.3	Optical Filters as Complementary Filters	159
7.4	Optical Filters as Wavelength Selective Element	161
7.5	Conclusion and Outlook	175
	References	176

## 8 Portable UV–Visible Spectroscopy – Instrumentation, Technology, and Applications 179

*Anshuman Das*

8.1	Introduction	179
8.2	Typical Instrumentation of a Portable UV–Vis Spectrometer	180
8.3	Measurement Configurations	183
8.4	Types of Instrumentation Used in UV–Vis Spectroscopy	187
8.5	Applications	193
8.6	Challenges for Portable Spectrometers	202
8.7	Outlook	204
	References	204

## 9 Smartphone Technology – Instrumentation and Applications 209

*Alexander Scheeline*

9.1	Introduction and Context	209
9.2	Challenges of Smartphone Spectrometry	210
9.3	Progress to Date	213
9.4	Conclusion and Prospective	230
	References	230

## 10 Portable Standoff Optical Spectroscopy for Safety and Security 237

*Matthew P. Nelson and Nathaniel R. Gomer*

10.1	Introduction	237
10.2	Portable Standoff Optical Instrument Types	240
10.3	Portable Standoff Optical Instrument Technologies	242
10.4	Portable Standoff Optical Spectroscopy Sensor Selection	248

10.5	Portable Standoff Optical Spectroscopy Sensors and Applications	253
10.6	Conclusions and Future Direction	269
	Acronyms and Abbreviations	269
	References	270

## **11 Microplasmas for Portable Optical Emission Spectrometry 275**

*Vassili Karanassios*

11.1	Introduction	275
11.2	A Brief Review of the Portable Microplasma Literature	276
11.3	Conclusion	284
	Acronyms	284
	Abbreviations	284
	Acknowledgments	285
	References	285

## **12 Portable Electro-Optical-Infrared Spectroscopic Sensors for Standoff Detection of Chemical Leaks and Threats 289**

*Hugo Lavoie, Jean-Marc Thériault, Eldon Puckrin, Richard L. Lachance, Alexandre Thibeault, Yotam Ariel and Jean Albert*

12.1	Introduction	289
12.2	A Differential FTIR Approach for Standoff Gas Detection	289
12.3	iCATSI Sensor	297
12.4	Active FTIR for Ground Contamination Detection	299
12.5	Signature Collection: Broadband Portable Field Spectral Reflectometer	303
12.6	Imaging Gas Filter Correlation Radiometry	308
12.7	Conclusion	317
	References	317

## **13 Handheld Laser Induced Breakdown Spectroscopy (HHLIBS) 321**

*David Day*

13.1	Introduction	321
13.2	Handheld LIBS-Enabling Technologies	323
13.3	Commercial HHLIBS Specifications	337
13.4	HHLIBS Applications	337
13.5	Summary and Future Expectations	341
	References	341

## **14 Miniaturized Mass Spectrometry – Instrumentation, Technology, and Applications 345**

*Dalton T. Snyder*

14.1	Introduction	345
14.2	Instrumentation	346
14.3	Applications	358
14.4	Summary and Outlook	364
	Acronyms	364
	Further Reading	365

<b>15</b>	<b>Portable Gas Chromatography–Mass Spectrometry: Instrumentation and Applications</b>	<b>367</b>
	<i>Pauline E. Leary, Brooke W. Kammrath and John A. Reffner</i>	
15.1	Introduction	367
15.2	History of Portable GC–MS	368
15.3	Critical Components for Portability	370
15.4	Applications	379
15.5	The Future of Portable GC–MS	384
	Acknowledgments	385
	References	385
<b>16</b>	<b>Development of High-Pressure Mass Spectrometry for Handheld and Benchtop Analyzers</b>	<b>391</b>
	<i>Kenion H. Blakeman and Scott E. Miller</i>	
16.1	Introduction	391
16.2	Ion Trap Development for HPMS	392
16.3	Commercialization and Applications	401
16.4	Conclusions	408
	References	408
<b>17</b>	<b>Key Instrumentation Developments That Have Led to Portable Ion Mobility Spectrometer Systems</b>	<b>415</b>
	<i>Reno F. DeBono and Pauline E. Leary</i>	
17.1	Background and History	415
17.2	Principles of Ion Mobility Spectrometry	417
17.3	Current Innovations and Future Directions	439
17.4	Conclusions	441
	Acronyms	442
	Abbreviations and Symbols	443
	References	444
<b>18</b>	<b>X-Ray Sources for Handheld X-Ray Fluorescence Instruments</b>	<b>449</b>
	<i>Sterling Cornaby</i>	
18.1	Background	449
18.2	The Miniature X-Ray Source	450
18.3	The Selection of a Target Anode Material for XRF	455
18.4	Functionality of X-Ray Sources for HHXRF	461
18.5	Conclusion	472
	References	473
<b>19</b>	<b>Semiconductor Detectors for Portable Energy-Dispersive XRF Spectrometry</b>	<b>475</b>
	<i>Andrei Stratilatov</i>	
19.1	Introduction	475
19.2	Semiconductor Detector Fundamentals: Signal Formation	476
19.3	Detectors for Portable Spectrometers: Design and Performance	486
19.4	Silicon Drift Detectors	489

19.5	Si Detectors' Quantum Efficiency: X-Ray Entrance Windows	491
19.6	Conclusion	498
	Acronyms and Abbreviations	499
	References	499
<b>20</b>	<b>Field-Deployable Utility of Benchtop Nuclear Magnetic Resonance Spectrometers</b>	<b>501</b>
	<i>Koby L. Kizzire and Griffin Cassata</i>	
20.1	Introduction	501
20.2	NMR Theory	503
20.3	Magnet Miniaturization	505
20.4	Improvements in Sensitivity and Resolution	506
20.5	Current bNMR Spectrometers	507
20.6	Applications	509
20.7	Conclusion	510
	References	511
<b>21</b>	<b>Rapid DNA Analysis – Need, Technology, and Applications</b>	<b>515</b>
	<i>Claire L. Glynn and Angie Ambers</i>	
21.1	Need for Speed	515
21.2	Technology	518
21.3	Applications	529
21.4	Limitations and Important Considerations	538
21.5	Future Considerations and Conclusions	539
A	Appendix	540
A.1	Acronyms	540
	References	541
<b>22</b>	<b>Portable Biological Spectroscopy: Field Applications</b>	<b>545</b>
	<i>Brian Damit and Miquel Antoine</i>	
22.1	Introduction	545
22.2	Organization of This Chapter	547
22.3	Attributes of Field-Portable Spectroscopy Systems	547
22.4	Field Applications	548
22.5	Summary, Challenges, and Outlook	558
	Acknowledgements	558
	List of Acronyms	559
	References	559
	<b>Index</b>	<b>565</b>

## List of Contributors

***Jean Albert***

Bluefield Technologies Inc.  
San Francisco  
CA, USA

***Angie Ambers***

Department of Forensic Science  
Henry C. Lee College of Criminal Justice  
and Forensic Sciences  
University of New Haven  
West Haven  
CT, USA

***Miquel Antoine***

Johns Hopkins Applied Physics Laboratory  
Laurel  
MD, USA

***Yotam Ariel***

Bluefield Technologies Inc.  
San Francisco  
CA, USA

***Dieter Bingemann***

Wasatch Photonics, Inc.  
Logan  
UT, USA

***Kenion H. Blakeman***

908 Devices Inc.  
Boston  
MA, USA

***Griffin Cassata***

Department of Forensic Science  
Henry C. Lee College of Criminal Justice  
and Forensic Sciences  
University of New Haven  
West Haven  
CT, USA

***Sterling Cornaby***

Moxtek, Inc.  
Orem  
UT, USA

***David Creasey***

Wasatch Photonics, Inc.  
Logan  
UT, USA

***Richard A. Crocombe***

Crocombe Spectroscopic Consulting  
Winchester  
MA, USA

**Brian Damit**

Johns Hopkins Applied Physics Laboratory  
Laurel  
MD, USA

**Anshuman Das**

Labby Inc.  
Cambridge  
MA, USA

**David Day**

Scips Incorporated  
Woburn  
MA, USA

**Charlotte De Bleye**

Department of Pharmacy  
University of Liege  
Liege, Belgium

**Reno F. DeBono**

Trace Detection Scientist  
Formerly of Barringer Instruments  
Warren  
NJ, USA

and

Smiths Detection  
Edgewood  
MD, USA

**Claire L. Glynn**

Department of Forensic Science  
Henry C. Lee College of Criminal Justice  
and Forensic Sciences  
University of New Haven  
West Haven  
CT, USA

**Nathaniel R. Gomer**

ChemImage Corporation  
Pittsburgh  
PA, USA

**Heinrich Grüger**

Fraunhofer Institute for  
Photonic Microsystems  
Dresden, Germany

**Philippe Hubert**

Department of Pharmacy  
University of Liege  
Liege, Belgium

**Brooke W. Kammrath**

Department of Forensic Science  
Henry C. Lee College of Criminal Justice and  
Forensic Sciences  
University of New Haven  
West Haven  
CT, USA

and

Henry C. Lee Institute of Forensic Science  
West Haven  
CT, USA

**Vassili Karanassios**

Department of Chemistry and  
Waterloo Institute for Nanotechnology  
University of Waterloo  
Waterloo  
ON, Canada

**Koby L. Kizzire**

Department of Forensic Science  
Henry C. Lee College of Criminal Justice  
and Forensic Sciences  
University of New Haven  
West Haven  
CT, USA

**Richard L. Lachance**

Bluefield Technologies Inc.  
San Francisco  
CA, USA

**Hugo Lavoie**

Defence R&D Canada – Valcartier Research Center  
Quebec  
QC, Canada

**Pauline E. Leary**

Federal Resources  
Stevensville  
MD, USA

**Scott E. Miller**

908 Devices Inc.  
Boston  
MA, USA

**Matthew P. Nelson**

ChemImage Corporation  
Pittsburgh  
PA, USA

**Eldon Puckrin**

Defence R&D Canada – Valcartier Research Center  
Quebec  
QC, Canada

**Oliver Pust**

Delta Optical Thin Film A/S  
Hørsholm, Denmark

**Cicely Rathmell**

Wasatch Photonics, Inc.  
Logan  
UT, USA

**John A. Reffner**

John Jay College of Criminal Justice  
City University of New York  
New York  
NY, USA

**Pierre-Yves Sacré**

Department of Pharmacy  
University of Liege  
Liege, Belgium

**Terry Sauer**

Presco Engineering  
Woodbridge  
CT, USA

**Alexander Scheeline**

Department of Chemistry  
University of Illinois at Urbana-Champaign  
Urbana  
IL, USA

and

SpectroClick Inc.  
Savoy  
IL, USA

**David W. Schiering**

RedWave Technology  
Danbury  
CT, USA

**Dalton T. Snyder**

Resource for Native Mass Spectrometry Guided  
Structural Biology  
The Ohio State University  
Columbus  
OH, USA

**John T. Stein**

JTS Consultancy  
Ashburn  
VA, USA

**Andrei Stratilatov**

Moxtek, Inc.  
Orem  
UT, USA

**Jean-Marc Thériault**

Defence R&D Canada – Valcartier Research Center  
Quebec  
QC, Canada

***Alexandre Thibeault***

Bluefield Technologies Inc.  
San Francisco  
CA, USA

***Eric Ziemons***

Department of Pharmacy  
University of Liege  
Liege, Belgium

***Mark Zieg***

Wasatch Photonics, Inc.  
Logan  
UT, USA

## Foreword

When I first learned that Richard Crocombe, Pauline Leary, and Brooke Kammrath were editing a two-volume series of books that cover the development of field-portable analytical technologies and the numerous applications of these technologies, I was excited because I knew that these scientists had the experience, knowledge, and energy to produce a great product, books that I will immediately add to my library.

So, who am I to make such a bold evaluation of these books? My name is John A. Reffner and I am currently a tenured full Professor of Forensic Science at the City University of New York's John Jay College of Criminal Justice. I have also received several distinguished awards including some for developments that enabled portable spectroscopic instruments. After graduating from Akron University in 1956, I joined the "Works Technical Analytical Laboratory" at the B.F. Goodrich Tire and Rubber Company. This experience taught me the valuable lesson that chemistry is essential for a major corporation to be successful, a lesson which was continually reinforced throughout my almost 65 years of professional experiences. I have had the good fortune of working with many prominent scientists and business leaders. I have seen how science and chemistry change the world. I have also seen how consumer demands drive technology and innovation, leading us to where we are today, immersed in essential portable technologies that have changed the world.

A short story that exemplifies my passion for the field of portable instruments is the introduction of the DuraScope at the Pittsburgh Conference in 1998, and the subsequent development of the TravelIR portable infrared spectrometer. Our SensIR Technologies team, which included the likes of Don Sting, Jim Fitzpatrick, Don Wilks, and Bob Burch, introduced this new micro-ATR (Attenuated Total Reflection) accessory for FT-IR (Fourier transform infrared) spectrometers. While it might not seem that such an accessory could make a system portable, a scientist from a major supplier of chemicals was very excited about the product. In his work, he traveled to paper companies to resolve customer complaints. While he didn't need an ATR accessory, what he did need was a small FT-IR, possibly an ATR-based infrared system, that could fit in the overhead storage compartment of a commercial airplane. As a result of these conversations, the TravelIR was born. The TravelIR was the first portable infrared spectrometer delivered to the market, enabling the identification of an infinite number of samples at the sample site.

The novelty of the TravelIR attracted a lot of interest, but portability was low on the list of requirements by a majority of end users. That was, of course, until 11 September 2001. One week after the 9/11 terrorist attacks, letters containing anthrax spores were delivered to members of the news media, and to United States Senators Tom Daschle and Patrick Leahy. A total of five people died from exposure to these spores, and seventeen others were infected. These terrorist events had a significant impact on field-portable analytical instruments. There became an immediate need to identify dangerous chemicals, including white powders, quickly and reliably at the sample site. This need catalyzed the portable-spectroscopy market.

Infrared spectrometers like the TravelIR were well-suited as a chemical identifier and could meet the analytical needs of field users, but it was clear that simply having a small footprint capable of providing reliable answers to a

trained scientist was not enough. Systems for deployment needed to endure the rough handling and environmental conditions required of a valid field-portable analytical device. In addition, it was necessary for these systems to collect spectral data and translate that data into actionable results in real time by a nonscientist operator with minimal training. SensIR's follow-up to the TravelIR was a product known as the HazMatID. This system was ruggedized to meet aggressive military specification standards including those for ruggedness and total immersion in decontamination solution. The "genie was out of the bottle" and the need for field-portable instruments exploded.

As you read the 45 chapters of these books, you will see the versatility in both the instrumentation and technologies, as well as the tremendous impact these systems have upon our society. Whether considering how portable spectrometers are used in hazmat and military operations to assess safety and defense concerns, by archaeologists and other cultural historians to help understand artwork and ancient civilizations, or the value these systems offer to practitioners of the forensic, pharmaceutical, and geological sciences, the reader will appreciate the challenges to their development, the breadth of their applicability, and the irreplaceable value they afford to the end user.

November 2020

*John A. Reffner*

Professor of Forensic Science  
at the City University of New York's  
John Jay College of Criminal Justice

## Preface for Volume 1

There have been tremendous developments in portable spectroscopy and spectrometry instrumentation over the last several decades resulting in their use in a variety of applications. However, portable spectroscopic instruments have not had significant visibility within the scientific community when compared with the current generation of high-performance laboratory spectrometers. This is attributable to a number of factors, including their very applied (as opposed to research) nature, which has resulted in their predominant use by non-scientists and a dearth of publications in the refereed literature. The numbers of these instruments deployed today can therefore come as a surprise. For instance, as early as the 1990s over 60 000 ion mobility spectrometer (IMS) systems were deployed worldwide; in 2019, a single model of an IMS detector had deployments from the previous 14 years of over 90 000; cumulative handheld x-ray fluorescence (XRF) shipments today total more than 100 000; and portable Raman shipments number in the tens of thousands. For these, and some other portable spectrometers, there are more instruments in the field than there are in laboratories.

One of us (RAC) published a review article in late 2018 on portable spectroscopy, covering optical and elemental (XRF and laser-induced breakdown spectroscopy (LIBS)) instruments and applications. Just covering those areas required 50 printed pages. Two of us (RAC and PEL) have also taught day-long short courses on this topic, and realized that we were barely scratching the surface of this field. It therefore became apparent that this field could benefit from comprehensive coverage in a book. The editors bring different backgrounds to this: from instrumentation and applications development (RAC), training on instrumentation and applications in safety and security, the military, and pharmaceuticals (PEL), and teaching instrumentation and forensic applications (BWK). As a result of this, our original concept expanded from one book to two volumes. Here, in Volume 1, we focus on the instrumentation itself and enabling technologies. Volume 2 focuses on the myriad of applications of portable instrumentation.

Volume 1 starts with a chapter on engineering portable spectrometers in general, and then proceeds through the electromagnetic spectrum covering XRF, ultraviolet (UV)-visible, near-infrared, mid-infrared and Raman spectroscopies. Microplasmas and LIBS areas are addressed, nuclear magnetic resonance (NMR), and also a number of portable mass spectrometry instrument types are described. Some special topics include smartphone spectroscopy, optical-filter technology and micro-electromechanical systems/micro-opto-electromechanical systems (MEMS/MOEMS) (key to many very small spectrometers and hyperspectral imagers) and stand-off detection. And as we write this, under coronavirus lockdown, the volume also includes chapters on DNA instrumentation and biological analyzers.

We hope that the combination of Volumes 1 and 2 provides thorough coverage of the whole field, with chapters written by technical experts with hands-on expertise. The authors have a range of experiences, from working in instrument companies, universities, and research institutes, to those intimately involved with the military and hazardous-material teams, drawn from North America, Europe, Asia, and Australia. These authors have made efforts for their chapters to cover the field up to early 2020, and we thank all the authors for their contributions. In

addition, most of the chapters were also reviewed by third-party experts to ensure their quality and completeness, and we thank the reviewers for their helpful suggestions.

June 2020

*Richard A. Crocombe*

Crocombe Spectroscopic Consulting

Winchester, MA, USA

*Pauline E. Leary*

Federal Resources

Stevensville, MD, USA

*Brooke W. Kamrath*

Department of Forensic Science

Henry C. Lee College of Criminal Justice and Forensic Sciences

University of New Haven

West Haven

CT, USA

and

Henry C. Lee Institute of Forensic Science

West Haven

CT, USA

## Acknowledgements

The editors would like to thank and acknowledge the following scientists and subject matter experts for their willingness to review the chapters within these volumes.

### Volume 1

Katherine Bakeev  
Sheldon Brunk  
Michael Burka  
Cecil Dybowski  
Peter Griffiths  
Michael Kessler  
Richard Lareau  
Christopher Palmer  
Alexander Scheeline  
Ken Schreiber  
Dalton Snyder  
Mazdak Taghioskou

### Volume 2

Jose Almirall  
Paul Bartholomew  
Amy Bauer  
Lucia Burgio  
Craig Gardner  
Richard Jackson  
Lena Kim  
Larry McDermott  
Ellen Miseo  
John A. Reffner  
Luis Rodriguez-Saona  
Shiv Sharma  
Brandye Smith-Goettler

# 1

## Introduction to Portable Spectroscopy

Pauline E. Leary<sup>1</sup>, Richard A. Crocombe<sup>2</sup> and Brooke W. Kammrath<sup>3,4</sup>

<sup>1</sup>Federal Resources, Stevensville, MD, USA

<sup>2</sup>Crocombe Spectroscopic Consulting, Winchester, MA, USA

<sup>3</sup>Department of Forensic Science, Henry C. Lee College of Criminal Justice and Forensic Sciences, University of New Haven, West Haven, CT, USA

<sup>4</sup>Henry C. Lee Institute of Forensic Science, West Haven, CT, USA

### 1.1 Introduction

In this book, we regard a portable spectrometer as an analytical instrument, which generates clear answers for its operator, when it is carried to the sample, i.e., spectrometer to the sample rather than sample to the spectrometer. The instrument ideally will operate in point-and-shoot mode, or at least minimize sampling handling, and the primary output is not *a spectrum* but rather *a result*. In some cases, the result might be a sample identification; in others it may be a pass/fail visual or audible alarm (green light/red light). The operators of these instruments are rarely scientists, but may instead be hazardous-material technicians, armed-services personnel, or even scrap-metal dealers. These spectrometers may have to conform to regulatory standards such as Title 21 CFR Part 11, which governs electronic records and signatures within the pharmaceutical industry in the United States, or legal standards for the admissibility of scientific evidence, such as Daubert and Frye [1, 2], which govern the admissibility of scientific evidence in all United States Courts. The environments within which they may be used can be life threatening, such as when dealing with improvised explosive devices (IEDs), to analyze suspicious white powders, during kinetic military action, or chemical spills. When performing analytical testing in these situations, reliable, rapid results that are easy for the operator to interpret, understand, and act on are critical.

### 1.2 Defining Portable Spectrometers

The definition of a portable spectrometer can be quite variable. In some instances, portable simply means the instrument can be moved to the sample location, even if the instrument is large and cumbersome; in some cases even a laboratory-based system that is built into a fixed mobile laboratory is considered portable. In other instances, and what seems to be more the expectation from today's users, a portable spectrometer should be small, lightweight, and capable of running on battery power for a reasonable duration of time. These instruments are intended for use in the field and, therefore, must perform well outside the climate-controlled environment of a laboratory. They must operate and maintain their calibration over wide ranges of temperature and humidity. They are usually dust and water resistant, if not waterproof, and capable of withstanding physical shocks, for instance, being dropped onto a hard surface from a few feet off the ground. If used for the detection and identification of hazardous materials, they must be able to withstand decontamination procedures, which can involve being scrubbed down with a solution of bleach.



**Figure 1.1** One of the earliest “portable” LOPAIR spectrometers, left (Source: Image courtesy of the United States Army), alongside a modern portable ATR FTIR (right). Source: Thermo Fisher Scientific.

Frequently, the first iterations of a portable spectrometer are not truly portable from a size, weight, and power (SWaP) perspective, but rather are considered portable because the spectrometer is taken to the sample. Over time, though, as the technology evolves, a greater degree of SWaP friendliness is usually achieved. As an example, Figure 1.1 shows one of the earliest (if not *the* earliest) “portable” infrared (IR) spectrometers, which was based upon long-path IR (LOPAIR) technology, alongside a modern portable IR attenuated total reflection (ATR) spectrometer. In 1954, the United States military began development of this LOPAIR system for the detection of chemical warfare agents (CWAs). The principle behind this device was that the G-series nerve agents absorb radiation in certain portions of the IR spectrum. Such a device would scan the atmosphere continuously in advance of troops and give a warning alarm when G-series agents were detected. The prototype model, designated the E33 Area Scanning G-Agent Alarm, performed satisfactorily up to about 300 yards, but weighed over 250 lbs and used too much electrical power [3]. In contrast, a large percentage of today’s portable IR systems are Fourier transform IR (FT-IR) systems that weigh only a few pounds and operate for hours on an internal battery with no external computer or sampling accessories required. It is important to note that modern portable FT-IR instruments, using an ATR sample interface, are typically deployed to perform single-measurement analysis and not scan environments continuously as was the intention of the original E33 LOPAIR system. There are some modern portable FT-IR systems that scan continuously to monitor environments (see the Chapter 12 in this volume by Lavoie et al.), but these generally employ transmission sampling, rather than ATR, and tend to be larger and heavier than portable FT-IR ATR spectrometers. They also require significantly more computer processing power since they scan and provide results continuously, performing identifications in seconds, and running 24/7/365. Examples include the Gasmet Technologies Oy DX4000, which is used to monitor stack emissions and can monitor up to 50 gases simultaneously [4, 5], as well as the MKS Instruments, Inc. AIRGARD®, which is used to monitor environments for CWAs and toxic industrial chemicals (TICs) [6, 7]. Although individual chapters in this book may use slightly different definitions, the authors of this chapter have provided a general classification scheme of portable spectrometers in Table 1.1 based upon SWaP expectations.

### 1.3 Performance

When judged against its laboratory counterpart, a portable spectrometer, evaluated strictly on typical laboratory specifications for analytical performance, usually will not perform as well. Laboratory-based systems attempt to

**Table 1.1** General classification of portable spectrometers.

Class	Size	Weight	Power	Examples
Vehicle mounted and transported				Military application (see chapter by Samuels [Volume 2])
Vehicle transportable	Much greater than $40 \times 35 \times 35$ cm ( $16 \times 14 \times 14$ in.)	>20 kg >44 lbs	May require shore power with no battery option and external computing accessories	First-generation portables; installs in fixed mobile laboratories
Person portable	$\sim 40 \times 35 \times 35$ cm ( $\sim 16 \times 14 \times 14$ in.)	$\sim 3-20$ kg $\sim 7-44$ lbs	May run for a limited duration on battery with hot-swappable battery replacement option	Portable GC-MS systems; IMS systems used in aviation security for passenger screening
Handheld	$\sim 30 \times 15 \times 7$ cm ( $\sim 12 \times 6 \times 3$ in.)	$\sim 0.5-3$ kg $\sim 1-7$ lbs	Self-contained, battery-powered, embedded data system	Portable XRF, FTIR, Raman, and LIBS
Wearable	$\sim 10 \times 20 \times 5$ cm ( $\sim 5 \times 10 \times 2$ in.)	$\sim 0.5$ kg $\sim 1$ lb	Some visible region instruments	IMS-based CWA-monitoring devices; some visible-region instruments
Smartphone-based	$\sim 4 \times 4 \times 4$ cm ( $\sim 1.5 \times 1.5 \times 1.5$ in.)	$\sim 0.5$ kg $\sim 1$ lb	Visible region only, using the smartphone camera as the sensor	See chapters by Scheeline (Volume 1), and by Peveler and Algar (Volume 2)

Sizes and weights are approximate, and some instruments in each class may be smaller and lighter.

achieve optimal performance in terms of criteria such as resolution, signal throughput, and signal-to-noise ratio (SNR). They frequently have great flexibility in their data acquisition parameters, in their sample introduction or sampling accessories, and even in the spectral range over which they operate. Portable systems tend to have poorer performance in terms of these types of criteria. The spectral range and resolution of portable instruments is usually either fixed, or predetermined by the manufacturer's hardware and engineering choices, and in many cases the measurement time is automatically determined as the spectral data are collected, ensuring that the spectrum has a sufficient SNR for the type of analysis, but not necessarily an optimal SNR. Frequently, only one sampling method is provided, with an emphasis toward point-and-shoot capability over versatility in sampling approach.

While all of this discussion of performance implies that portable instruments are inferior to their laboratory-based counterparts, raw spectroscopic performance is only part of the rationale for using portable spectrometers and, therefore, only part of the criteria that should be used to establish performance of a portable spectrometer. The fit-for-purpose operational requirements, including deployment potential, that are critical for a field instrument must also be considered. An instrument's deployment potential is impacted by items such as required accessories, SWaP, software interface, training requirements, ability to be used when the operator is encumbered by required personal protective equipment (PPE), and the ability of the operator to achieve results (not data) in the field. If these factors are not appropriate for use in the intended environment, the system would offer no value in the field.

With regard to deployment potential, requirements for storage and use in extreme environmental conditions are normal. It is common for portable spectrometers to rate themselves against aggressive standards such as MIL-STD-810, the Test Method Standard for Environmental Engineering Considerations and Laboratory Tests

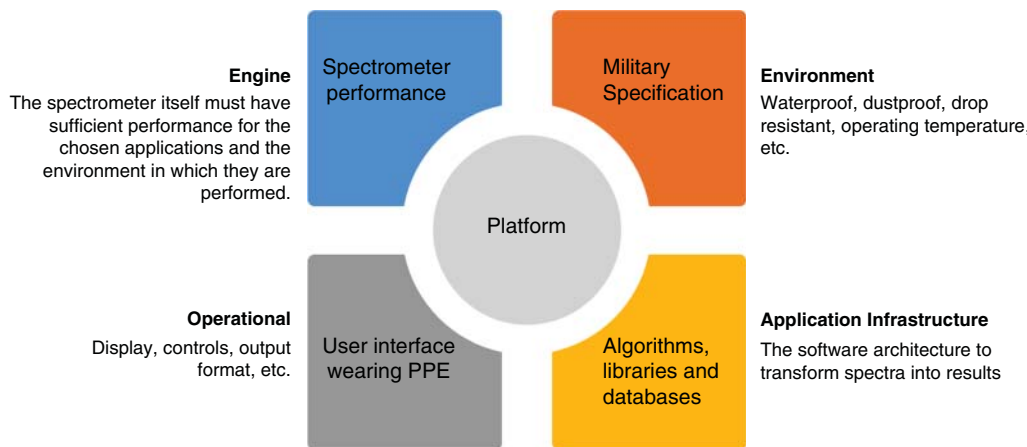


**Figure 1.2** Main components of a successful portable spectroscopy platform.

of the United States Department of Defense. This Standard contains materiel acquisition program planning and engineering direction for considering the influences that environmental stresses have on materiel throughout all phases of its service life [8]. The ability of a system to function under variable environmental conditions including temperature, humidity, and altitude as well as endure and remain functional after exposure to drops and vibrations is evaluated. Even in situations where portable systems may not be intended for use by the military, comparison with this standard is sometimes made and referenced, so that an evaluation of overall ruggedness and deployment potential of a system can be easily assessed. When both analytical performance and operational requirements are considered, the true value of a portable spectrometer can be effectively assessed for a specific application. Figure 1.2 summarizes the main components for consideration during the design and development of a portable spectroscopy platform.

The ability of a portable system to meet these reconciled goals between analytical and operational performance is variable, and frequently dependent upon the technology. For instance, portable IR and Raman instruments generally achieve many of them, and instruments of this type that offer good analytical performance, and are easy to deploy, have been available from a number of vendors for the past 15 years. Portable gas chromatography–mass spectrometry (GC–MS) systems, on the other hand, frequently perform well from an analytical perspective, but offer deployment challenges due to SWaP, their need to perform under vacuum, use of compressed gases, and the complexity of data generated which is not always easily converted to results. These requirements add deployment challenges. The smallest portable GC–MS that is currently commercially available is significantly larger and heavier than even a combined portable IR/Raman system.

## 1.4 History and Availability

For many of the spectroscopic techniques, the availability of portable spectrometers was driven by safety, security, terrorism, and military concerns. The major exceptions to this are handheld X-ray fluorescence (XRF), laser-induced breakdown spectroscopy (LIBS), and near-infrared (NIR) spectroscopy systems, where field instrumentation has been driven almost exclusively by commercial reasons. Figure 1.3 shows a time line of critical events that have transpired over the past century and have contributed either critically or peripherally to the need for and subsequent development of portable spectrometers. Figure 1.4 details the initial portable-instrument deployments based upon technology for systems capable of being hand carried to the scene and operating at the sample site using battery power.

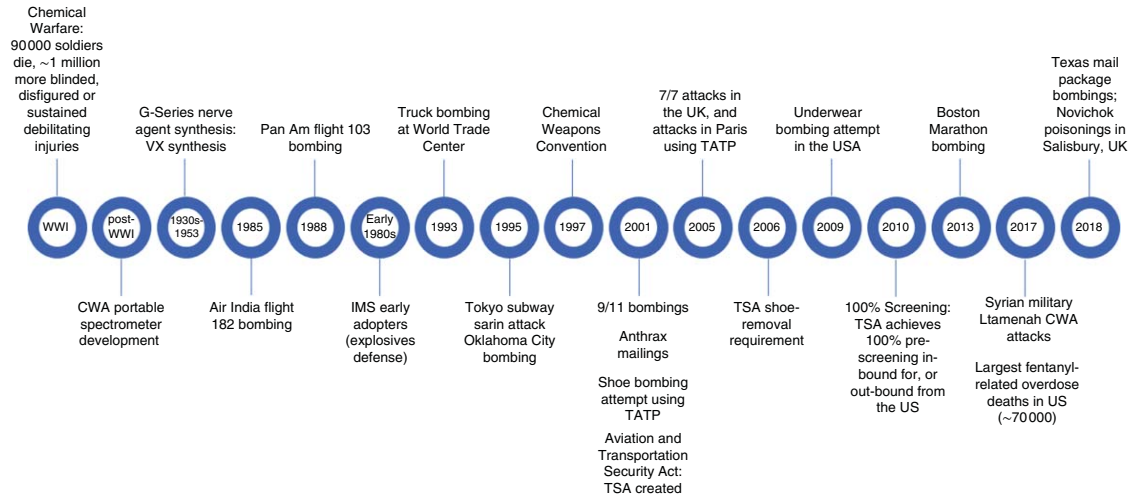


**Figure 1.3** Time line of events of importance to the development of portable spectrometers.

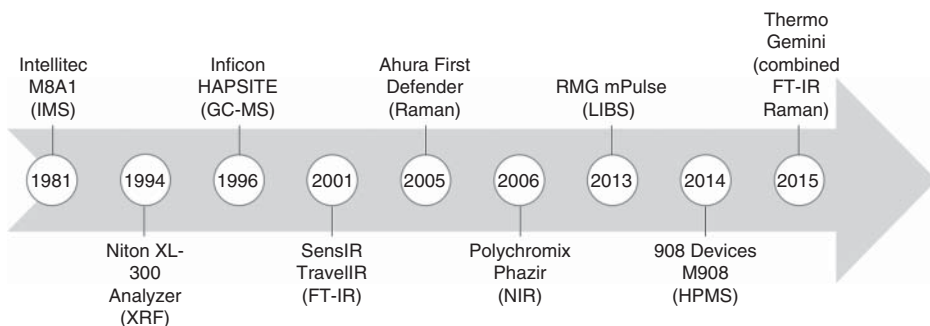


**Figure 1.4** Initial technology deployments for portable spectrometers capable of being carried to the scene and operated on battery.

While the consequences of 9/11 have certainly been a driving force for innovation in technology, and were instrumental in the development of many modern portable platforms including IR, Raman, and high-pressure mass spectrometry (HPMS) systems, the use of portable instruments at the sample site, and the value this type of analysis provides, began much further back in our history. Jeffery Smart, Command Historian at Aberdeen Proving Ground, in his summary entitled “History of Chemical and Biological Detectors, Alarms, and Warning Systems” reviewed military-related chemical detectors used throughout the twentieth century [3]. The earliest detectors he describes are vapor field detectors used to replace the “sniff test” used during World War I to detect and identify dangerous chemicals. There, troops learned that German mustard agents indeed smelled like mustard, while the allied mustard agent smelled like garlic. These observations were used by trained gas scouts, positioned to provide advance warning to the main trench line of an incoming gas cloud, but had serious negative consequences for those with continued exposure to dangerous chemicals at low concentrations, and much more significant consequences when concentrations were high. Vapor field detectors did not require troops to remove their protective masks to identify these dangerous substances. Some of the vapor field detectors that served as sniff-test replacements included instruments based upon a copper flame test lantern, a selenious acid field detector, an iodine pentoxide test, an iodic acid test field detector, and a hydrogen sulfide field detector [3].

The military were not the only early users of portable spectrometers. Kammrath et al. in their chapter on the applications of portable spectrometers to the field of forensic science (Volume 2) discuss the use of a portable spectrometer called a Drunkometer in the 1930s to measure breath-alcohol levels. This system was developed at Indiana University and relied on the colorimetric reduction of potassium permanganate by ethyl alcohol. These authors report the most recent developments in breath-alcohol instruments combine electrochemical sensors and IR spectrometers in a single platform.

With regard to portable GC-MS, the first truly portable GC-MS system was introduced in 1996 for the analysis of hazardous air pollutants at the sample site [9]. Earlier attempts to take the GC-MS instrument to the sample, which happened to be on the planet Mars, were successful when GC-MS was deployed on the Viking voyage in 1976 [10], but the GC-MS technology used was not as much *portable* as it was *transportable*; the system was designed specifically for the mission and was, essentially, part of a fixed mobile laboratory [11].

Some of the first ion mobility spectrometers (IMSs) were deployed to the military in the early 1980s for detection of CWAs [3]. The United States Federal Bureau of Investigation (FBI) has deployed IMS systems, at least since 1991, for use in a wide variety of drug-interdiction missions, as well as for post-blast forensic analysis in the World Trade Center, Oklahoma City, and Atlanta Olympics incidents [12]. These systems were ultimately deployed extensively within the aviation security market for the detection of explosives (see Chapter 8 by Leary and Joshi in Volume 2). Military interest in the ability to detect CWAs in theater is long-standing, but interest in the detection of explosives within the aviation security market is more recent. In 1986, the United States Bureau of Alcohol, Tobacco and Firearms (ATF) reported that between the years 1977 and 1986, of the nearly 12 000

bombings reported, only about 100 considered either military bases or airports as the primary target [13]. Since this time, there has been significant interest in explosives detection within the aviation security market, which, as Leary and Joshi describe in their chapter on the applications of IMS, was critically impacted by terrorist bombings of Air India Flight 182 in 1982, Pan Am flight 103 in 1988, and American Airlines flights 11 and 77 as well as United Airlines flights 175 and 73 on 11 September 2001. The three days in history on which these acts of terrorism transpired mark the deadliest terror attacks in the histories of Canada, the United Kingdom, and the United States, respectively, and were integral to the development of particle explosives detection systems using IMS. During the late 1980s, the Canadian government funded development of a high-speed IMS-based explosive particle detection system, which formed the basis of the Barringer Instruments, Inc. (now Smiths Detection) IONSCAN 150 and subsequent Barringer IMS platforms. Prior to this, the focus for explosives detection capabilities using IMS had been on detecting volatile explosives such as nitroglycerin (NG), dinitrotoluene (DNT), and ethylene glycol dinitrate (EGDN) in the vapor phase. This vapor-phase approach did not allow for the detection of low-volatility explosives such as trinitrotoluene (TNT), pentaerythritol tetranitrate (PETN), and Research Department Explosive (RDX) [14]. In 1996 the Federal Aviation Administration (FAA) of the United States Department of Transportation established the qualification process for checkpoint screening [15]. In November 2001, the Aviation and Transportation Security Act was signed into law in the United States, and the Transportation Security Administration (TSA) was created to oversee security in all modes of transportation [16]. IMS has been an integral part of the aviation security market for detection of particulate residues of explosives since its initial introduction to it in the early 1990s.

As noted above, handheld XRF and LIBS developments have been commercially driven, primarily by the metals markets, from field geology and mining, through fabrication and inspection, to recycling. The history of portable XRF analyzers was summarized in a 2012 symposium [17] and started with an isotope-source lead paint analyzer in the early 1990s, followed by alloy analyzers in the mid-1990s, and later converting almost exclusively to instruments using miniature X-ray tube sources. Key enabling technologies specific to XRF were the development of thermoelectrically cooled silicon PIN-diode (p-type-intrinsic-n-type) detectors, [18] and miniature X-ray tubes [19, 20]. Handheld LIBS instruments are a much more recent development, and have been applied in essentially the same areas as handheld XRF with each having its advantages and limitations (e.g., LIBS is capable of lighter element analysis however is minimally destructive).

Although NIR spectroscopy is widely used in the food, feed, and agriculture sectors, and also in pharmaceutical manufacturing, the adoption of portable instruments has been much slower for NIR as compared with Raman instruments. This may be because there has not been a single “killer app” – there are a multitude of individual applications, each requiring its own validated database or calibration. This is due to the somewhat nonspecific nature of NIR spectra, especially at shorter wavelengths, in that there are no bands that are highly characteristic of individual compounds.

## 1.5 Instrument Design and Enabling Technologies

The design and manufacture of portable systems is not a simple task. When an outsider first peers into the world of portable spectrometers, they frequently consider them to be simplified versions of laboratory systems. This impression is misguided, though, because from their theoretical inception to their manifestation in the final product, these instruments are fundamentally different from their equivalent laboratory-based counterparts, in both hardware and software. Historically, and even in laboratories today, almost naturally, a spectroscopist’s concern is optimizing analytical performance. What can be done to get the most signal with the least noise, improve the resolution, and offer the most versatile sampling options? When developing portable technologies, though, this approach must be abandoned. The question that needs to be answered is not, “What product offers the best performance at an affordable price?”, but rather, “What product or technology successfully integrates sufficient certainty

**Table 1.2** Enabling technologies for portable spectrometry.

All portables	Optical	XRF	MS and GC-MS
Mobile computing power: processors, memory	Optical telecom	Miniature X-ray sources	Miniature ion traps
Consumer electronics: user interfaces	Diode lasers	X-ray detectors (PIN, silicon drift detectors [SDD])	Pump technology
Communications: Wi-Fi, Bluetooth	Fiber optics	Pulse-counting electronics	Narrow-bore GC columns
MEMS and MOEMS technologies	Cameras, sensors, and array detectors	Fundamental parameter theory and calculations	MS sampling and sample introduction
Battery power and power management	Compact spectrographs		Ionization methods
Chemometrics and algorithms	Holographic filters (Raman)		
“The cloud”	ATR technology (IR)		

of results while meeting operational requirements, especially deployment potential, for the task at hand?” The answers to the different facets of this question are frequently at odds with each other, but a portable platform will thrive when the right balance has been struck among them. For this reason, it is critical that an instrument developer understands not only the technology, but also the application, the end user, and the deployment environment.

Design of a system is fundamentally limited by the availability of enabling components and technologies. All portable spectrometers have benefitted from the developments in computing power and consumer electronics, but there are other advances that have also been integral to the development of these systems. A short list of these includes low-power-consumption processors, low-cost/high-capacity memory, compact displays, mobile user interfaces, power management, battery capacity, Wi-Fi, Bluetooth, and cameras. Table 1.2 details some of the enabling technologies that have been important to the development of portable platforms.

## 1.6 Producing Results

While some portable spectrometers may be employed primarily to collect spectra for further analysis (e.g., see Chapters 21 by Pozzi et al. and 22 by Donais and Vandenebeele in Volume 2), the majority are designed to produce actionable results at the time of analysis. To generate these actionable answers, the developers of these instruments have put extensive resources into reliable identification algorithms, spectroscopic libraries or databases, and qualitative and quantitative calibrations. Real-life samples are most often mixtures, and this has been addressed with a combination of calibration, library, and algorithm development. These issues are addressed in the Chapters 2 and 3 by Zhang and Schreyer in Volume 2. This work has been done by the established large instrument companies, but there are new companies marketing devices in the visible-to-1000 nm region directly to the public, making wide claims about their analytical capabilities, and potentially relying on crowd-sourced data. This is a cause for concern in the scientific community and is explored in Chapter 23 by Crocombe in Volume 2. Figure 1.5 shows the primary contributing factors that enable a successful portable spectroscopy product.

Applications are critical for the success of portable spectrometers. An overview of the role applications development plays in the development and deployment of portable instruments is presented in the “Preface” for Volume 2.

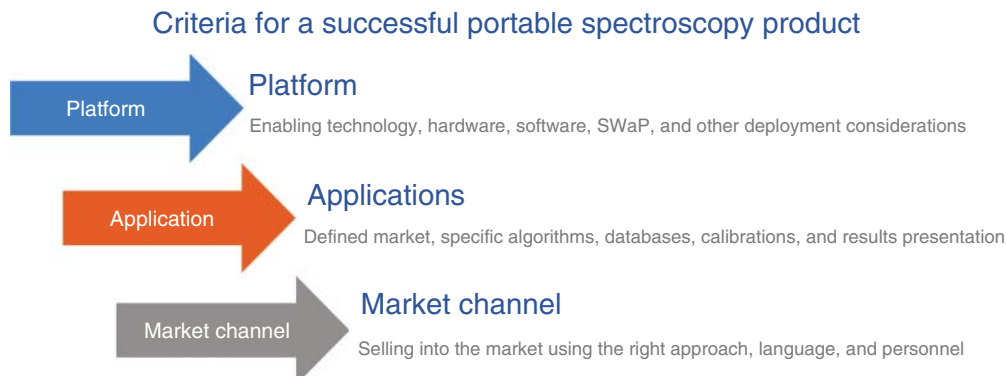


**Figure 1.5** Criteria for a successful portable spectroscopy product.

## 1.7 Outline of These Volumes

This book, in two volumes, seeks to cover today's portable spectroscopy instrumentation and markets. We have also included chapters on biological analyzers and DNA instrumentation, which, while not strictly spectroscopic in nature, complement the other technologies, and are of particular interest as this book is compiled in 2020, in the midst of the COVID-19 pandemic. Due to the size of this project, a small number of portable spectroscopic instruments is not covered, one of which is portable radiation detectors.

It seemed the best way to begin these volumes was with a discussion of the role engineering plays in the development of portable systems. A spectrometer is truly a system, including elements designed by mechanical, electrical, optical, and software engineers. To fit all of this together into a small, light, rugged, simple-to-operate instrument requires a conscious effort at systems engineering. In an optimal design, each of these elements will impact the others, as discussed by Sauer in Chapter 2 of this Volume. For instance, in an integrated handheld instrument, issues like noise pickup, power management, and heat dissipation are all greatly magnified as compared with laboratory instruments. In addition, the use of PPE limits the ability to use touch screens and small physical controls. This chapter describes these details and considers approaches to options that address these challenges. This discussion is then followed by in-depth reviews of both the established and emerging portable technologies, as well as some of the critical components that continue to enable them. Whether it be optical methods like IR and Raman that underwent a revolution after 9/11, or methods including ion mobility, MS, GC-MS, and HPMS that are capable of detecting and quickly identifying invisible threats in dangerous environments, these chapters provide in-depth coverage of these systems, components, and the critical applications that have driven their success. Volume 1 ends with discussions of both DNA (deoxyribonucleic acid) and biological technologies; these analyzers and their use in industries such as defense, medicine, food and agriculture, as well as the environmental and forensic sciences, are considered.

Volume 2 demonstrates why portable spectrometers have become so successful. Due to an inherent need for reliable detection and identification at the sample site, this volume begins with a discussion by these editors regarding the impact of applications on the development of portable spectrometers. This is followed by chapters describing algorithm and library development for portable systems; both are critical to the success of a portable platform and the applications that drive them. Portable systems must provide answers without requiring complex data interpretation or assessment on the part of the operator. As such, a significant amount of energy is spent developing proprietary search algorithms with the goal of requiring no input from the user to successfully identify the sample components, even at low concentrations. Algorithms designed to identify individual components in mixture samples are becoming more common and are described during this discussion. Electronic libraries for spectral matching are also critical. Instrument vendors will frequently reference the size of their onboard libraries, but it is

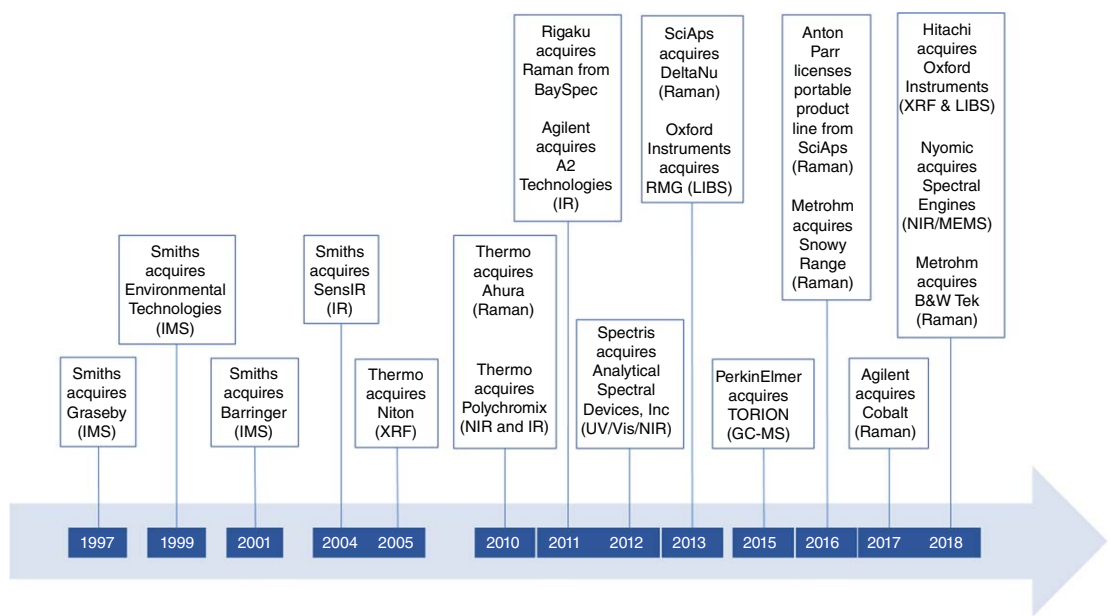


**Figure 1.6** Acquisitions/consolidations in the portable spectroscopy industry.

clear that having the right library of reference data can be more important than having a large number of library entries. Target libraries focused on specific applications are important, and help improve automatic-identification accuracy.

Some of the major applications that have relied heavily upon portable spectroscopy are then reviewed from the perspective of the end user. These chapters are presented by expert users that not only understand the technologies, but the advantages and limitations when they are applied in the real world. There is an impressive diversity in these applications. When warranted based upon the extensive breadth of applications, some chapters cover a variety of applications for a specific technology; others approach the chapter from an industry or application field perspective, and demonstrate how different portable technologies are used within a specific industry. The reader will not only be able to appreciate how critical these portable systems have become within these industries, but also understand how they are successfully deployed. We end with a look to the future and how things will likely continue to evolve as we move ahead in a world of ever-changing needs. It is interesting to note that the growth in portable spectroscopy sales has spurred a wave of acquisition and consolidation in the industry (Figure 1.6). The first wave of acquisitions, between 1997 and 2010, appears to have been driven by a desire to access the safety, security, and military markets, and the second, from 2010 until now, to access the growing commercial/civilian markets. It will be interesting to see how this evolves in the coming years.

## Acronyms and Abbreviations

ATF	Bureau of Alcohol, Tobacco and Firearms
ATR	Attenuated total reflection
CFR	Code of federal regulation
COVID-19	Coronavirus disease of 2019
CWA	Chemical warfare agent
DNA	Deoxyribonucleic acid
DNT	Dinitrotoluene
EGDN	Ethylene glycol dinitrate
FAA	Federal Aviation Administration
FBI	Federal Bureau of Investigation
FT-IR	Fourier transform infrared
GC-MS	Gas chromatography-mass spectrometry
HPMS	High-pressure mass spectrometry
IED	Improvised explosive device
IMS	Ion mobility spectrometry
IR	Infrared
kg	kilogram
lb	Pound
LIBS	Laser-induced breakdown spectroscopy
LOPAIR	Long-path infrared
MEMS	Microelectromechanical systems
MIL-STD-810	Test Method Standard for Environmental Engineering Considerations and Laboratory Tests of the United States Department of Defense
MOEMS	Micro-opto-electromechanical systems
MS	Mass spectrometry
NG	Nitroglycerin
NIR	Near infrared

nm	Nanometer
PETN	Pentaerythritol tetranitrate
PIN	p-type-intrinsic-n-type
PPE	Personal protective equipment
TIC	Toxic industrial chemical
TNT	Trinitrotoluene
TSA	Transportation Security Administration
SDD	Silicon drift detector
SNR	Signal-to-noise ratio
SWaP	Size, weight, and power
XRF	X-ray fluorescence

## References

- 1 D.C. Circuit Court (1923). *Frye v. United States*. 293 F. 1013.
- 2 United States Supreme Court (1993). *Daubert v. Merrell Dow Pharmaceuticals, Inc.* 509 U.S. 579.
- 3 Smart, J. (2009). *History of U.S. Army Research & Development, Chemical and Biological Detectors, Alarms, and Warning Systems*. Aberdeen Proving Ground: U.S. Army Research, Development and Engineering Command.
- 4 Gasmet Technologies Oy. *Gasmet Portable Gas Analyzers, DX4000*. Gasmet [Online]. <https://www.gasmet.com/products/category/portable-gas-analyzers/dx4000> (accessed 24 May 2020).
- 5 Gasmet Technologies Oy. *Gasmet Portable FTIR Gas Analyzer, DX4000*. Gasmet [Online]. <https://www.gasmet.com/wp-content/uploads/2018/01/Product-Prochure-DX4000-2020-web.pdf> (accessed 24 May 2020).
- 6 MKS Instruments, Inc (2010). *Application Note, CWA/TIC Detection (App Note 1/10-8/13)*. MKS Instruments [Online]. [https://www.mksinst.com/mam/celum/celum\\_assets/resources/AIRGARD-CWA-TICDetection-AppNote.pdf?1](https://www.mksinst.com/mam/celum/celum_assets/resources/AIRGARD-CWA-TICDetection-AppNote.pdf?1) (accessed 16 September 2020).
- 7 MKS Instruments, Inc *Ambient FTIR Air Analyzer AIRGARD*. MKS Instruments [Online]. <https://www.mksinst.com/p/AIRGARD-CWA> (accessed 16 September 2020).
- 8 United States Department of Defense (2019). *Department of Defense Test Method Standard Environmental Engineering Considerations and Laboratory Tests*. United States Department of Defense.
- 9 Crume, C. (2009). *History of Inficon HAPSITE: Maintenance Management, Support, and Repair*. KD Aanalytical [Online]. <http://www.kdanalytical.com/instruments/inficon-hapsite-history.aspx> (accessed 16 September 2020).
- 10 Biemann, K., Oro, J., Toulmin, P. III, et al. (1977). The search for organic substances and inorganic volatile compounds in the surface of Mars. *Journal of Geophysical Research* 82: 4641–4658.
- 11 Leary, P.E., Kammerath, B.A., and Reffner, J.A. (2018). *Field-Portable Gas Chromatography-Mass Spectrometry*. Wiley Encyclopedia of Analytical Chemistry.
- 12 Wood, K. (1998). Statement Submitted to the House Committee on Transportation Subcommittee on Public Buildings and Economic Development Relative to Technological Solutions to Federal Building Security, June 4.
- 13 Nyden, M.R. (1990). *A Technical Assessment of Portable Explosives Vapor Detection Devices*. United States Department of Justice NIJ Report 300-89.
- 14 DeBono, R. (2020). Personal Communication, May 25.
- 15 Kraus, T.L. (2008). *The Federal Aviation Administration: A Historical Perspective, 1903–2008*. Washington, DC: United States Department of Transportation.
- 16 United States Transportation Security Administration. *Transportation Security Timeline*. Transportation Security Administration [Online]. <https://www.tsa.gov/timeline> (accessed 30 March 2020).
- 17 Bosco, G.L. (2013). Development and application of portable, hand-held X-ray fluorescence spectrometers. *TrAC Trends in Analytical Chemistry* 45: 121–134.

- 18** Pantazis, T., Pantazis, J., Huber, A., and Redus, R. (2010). The historical development of the thermoelectrically cooled X-ray detector and its impact on the portable and hand-held XRF industries. *X-Ray Spectrometry* 39: 90–97.
- 19** Cornaby, S. and Kozaczek, K. (2016). X-ray sources for handheld X-ray fluorescence instruments. In: *Encyclopedia of Analytical Chemistry*. Wiley.
- 20** Crocombe, R.A. (2018). Portable spectroscopy. *Applied Spectroscopy* 72: 1701–1751.

## 2

### Engineering Portable Instruments

Terry Sauer

Presco Engineering, Woodbridge, CT, USA

In the past two decades, spectrometers have moved out of the laboratory and into a wide variety of portable applications. Designing portable spectrometers requires a change in the mindset for product managers and engineers alike. Traditional spectrometer systems are judged on performance and on flexibility. They are designed to support a broad range of applications typically without a dedicated purpose in mind. This makes it difficult to specify how much performance is adequate, or “good enough,” so the designers are tasked with making performance as good as possible, within the constraints of budget and size. Portables, by contrast, are typically designed for a fixed task, or, at most, a limited set of purposes, such as unknown material identification or quality control. The metric of instrument quality is likely to be something completely different from signal to noise or stability over time. The end user is likely not to be a spectroscopist, and cares only about whether the instrument works and gives the right answer. Users do not care about whether a portable Fourier transform infrared (FTIR) system supports four different methods of apodization; they want a simple user interface and consistent performance.

While the user desires a system that is simple to use, there are many features that require significant thought and design effort for such a system to be successful. Obvious concerns are size, weight, and power. We will explore these and many other considerations which are important for portable spectroscopy systems. The focus of this chapter will be on engineering aspects for FTIR and Raman systems. The chapter will address a range of aspects which are all necessary for the design and manufacture of a successful spectrometer. A spectrometer is truly a system, including elements designed by mechanical, electrical, optical, and software engineers. To fit all this together into a small, light, rugged, simple-to-operate instrument requires a conscious effort at systems engineering. In an optimal design, each of these elements will impact the others.

#### 2.1 Size/Weight

For a system to be easily portable, it must be relatively small and lightweight. As with many electronic devices, systems continue to get ever smaller and faster. In 2001, SensIR Technologies won an R&D 100 award for the TravelIR (The Free Library 2019). This “portable” system was an FTIR instrument which by itself weighed 26 pounds. The instrument required a separate power supply and laptop computer. To operate it away from a wall socket required a “Portawattz” portable battery and inverter. The entire system with computer and Portawattz weighed over 50 pounds. By contrast, newer handheld FTIR instruments (Smiths’ HazMatID Elite and ThermoFischer Scientific’s TruDefender FTX) weigh in the range of 3–5 pounds complete with built-in computer and lithium-ion rechargeable battery. Handheld Raman systems can be even smaller, with the Metrohm Raman Mira DS weighing in at 1.5 pounds.

*Portable Spectroscopy and Spectrometry 1: Technologies and Instrumentation*, First Edition.

Edited by Richard A. Crocombe, Pauline E. Leary and Brooke W. Kammrath.

© 2021 John Wiley & Sons Ltd. Published 2021 by John Wiley & Sons Ltd.

## 2.2 Sample Interface

Laboratory spectrometers have a wide variety of available accessories to support sampling of liquids, solids, and powders. A typical spectrometer has a sample compartment with a defined beam path. Accessories are mounted into this compartment and can be used to make a variety of measurements including transmission, diffuse or specular reflectance, grazing angle or ATR (attenuated total reflection). Samples may need to be prepared in particular ways in order to be measured.

Portable instruments will likely be used outside of a laboratory, without access to sample preparation equipment. The ability to analyze neat samples, or to provide specialized simple sample prep, is key to being useful in the field.

Many portable spectrometers provide a single, permanently mounted sample interface. For FTIR systems, a diamond ATR element is a popular choice as it is extremely durable and versatile. Raman systems typically have a single fixed-focus lens. There are exceptions to both of these generalizations. The Agilent 4300 portable FTIR instrument has clip-on front ends to provide diffuse reflectance, grazing angle, external reflectance options along with both diamond and germanium ATR elements. The Metrohm Raman Mira system has several different focal length lenses, calibration standards, and specialty sampling accessories which attach to the output aperture of the system.

External sampling accessories enable a reduced overall size for the instrument. There is no need for a compartment large enough to contain all sizes of accessory. Handheld instruments favor accessories which require no alignment after installation.

## 2.3 Embedded Computer vs. External Personal Computer (PC)

Laboratory spectrometers have traditionally been coupled to external computers. In the early eighties, these were proprietary devices built by the instrument makers. Nicolet Instruments developed a dedicated 20-bit computer, the Nicolet 1080, to allow higher precision arithmetic than the 16-bit computers prevalent at the time. The computer filled a 19-in. rack and had a small monochrome oscilloscope-type display.

In the mid-1980s, the IBM personal computer (PC) and its clones took over the laboratory. Instruments connected to the PC using proprietary interface cards. The PC enabled more standardized software, migrating over time from Microsoft disk operating system (MS-DOS) to Microsoft Windows and providing increasingly complex display and analysis capabilities.

TravelIR continued this path, connecting to a standard Windows laptop using a parallel interface provided by a third-party data acquisition company.

Despite the success of the TravelIR, separate PCs were not ideal for portable instruments, and designers started to integrate computers into the instruments themselves. HazMatID included a PC-on-a-card. It was an industrial computer in the PC-104 form factor, about 4 in. by 4 in. The portable device operated with Windows XP Embedded, and included a 6.4-in. touchscreen as a user interface.

Even this embedded computer proved too large for a true handheld instrument, and subsequent generations of the instrument moved to personal digital assistants, or PDAs, as the control and interface device. These devices often operated using versions of consumer-operating systems, such as Microsoft Windows CE.

The next step in size reduction required the design of specialized PC boards for embedded control. The embedded processors in these systems are designed for low power and to support advanced power management enabling extended battery life. Some instruments incorporated credit card-sized or smaller “systems on module” or SOMs. These SOMs are computing engines which include the tightly coupled elements required for a computer to operate. The main central processing unit (CPU), random access memory (RAM), permanent storage, and display drivers are all laid out efficiently. These high-speed signals can be tricky to arrange properly, as they may require low capacitance, controlled impedance, and path length matching for parallel signals. An instrument designer can purchase all of this demanding work in a predesigned module, reducing time and cost of getting to market.

The SOM has an additional advantage when it comes to creating the software to operate the instrument. The SOM manufacturer will generally provide a BSP, or Board Support Package. This pre-built software image will support the processor and set of peripherals on the SOM. BSPs can support a number of operating systems, including Linux and embedded Windows. Typical BSPs include features, such as display drivers for the integrated video electronics, touchscreen or keyboard support, a boot loader to start the board from power on, and management tools for volatile and nonvolatile memory.

SOMs are often designed to support easily connecting them to a custom-printed circuit board which has the dedicated components required to operate the spectrometer. This connection may take the form of mezzanine connectors which allow boards to stack in layers. SOMs often connect with a single inline memory module (SIMM) socket, which is familiar as the connector used to install RAM into personal computers.

For the ultimate in size reductions, designers place processors and support chips directly on a PC board which drives the instrument. This approach provides the most control over shape of the board as well as removing the need for connectors between a SOM and a carrier board. Removing these connectors reduces system volume and can improve system reliability.

The trade-offs among these approaches allow the designer to optimize for instrument size, development cost, reuse of existing software, and instrument bill of material cost.

## 2.4 Reduced Feature Set

Laboratory instruments are like Swiss Army knives. Their owners expect them to have a wide variety of uses. As capital equipment in an applications lab, they must justify their cost by being able to address a range of analyses. Bench space in labs is inevitably at a premium, so each instrument must provide flexibility. This can take the form of a sample compartment supporting many accessories, an external port for larger accessories, and flexible software with many choices to optimize performance for each desired analysis.

By contrast, portable instruments are typically targeted at a single problem or a small set of problems. Many of the instruments sold to Emergency Responders are designed simply to identify unknown materials. The operators of these identifiers may be under a great deal of stress as they work to find out whether the suspect material is a threat to life or health. It is critical for these operators that the instrument be simple to operate, with no unnecessary settings which could confuse the operator or be accidentally left in the wrong position, potentially impacting the results.

Laboratory instruments are often sold based on their broad feature set, with the thought that each additional feature or setting may be the one which causes a potential customer to select this instrument over a competitor. Portable instrument designers must adapt a new mindset which values simplicity and reliability over complexity and adaptability.

## 2.5 Target of Non-Spectroscopist

Users of benchtop instruments are often spectroscopists. In routine analysis, a technician may operate the system on a daily basis, but the analytical methods are generally developed and maintained by a supervisor with an understanding of spectroscopy. By contrast, nonscientists operate many handheld systems. This further reinforces the requirement that the software in particular be simple and intuitive to operate, including all maintenance and administrative functions as well as the execution of sample measurement and analysis. Wherever possible, software engineers should consider preselecting values or lumping them into groups. For example, instead of asking a method developer to enter a numeric value for the number of scans to collect, provide “sensitivity” options of low, medium and high, which the system will translate into appropriate values for the particular spectrometer design.

## 2.6 Power Budget

Portable systems are often expected to operate on a rechargeable battery. Battery technology continues to evolve, but it is almost always a limiting factor in the operation of a spectrometer. There are several concerns related to battery power as contrasted to an alternating current (AC) supply. The user is most concerned with operating lifetime as measured in hours. The designer must also plan for a limited amount of current, a safe shutdown when the battery charge runs out, and the ability to operate consistently over a range of voltages over the charge cycle of the battery.

Establishing a power budget for the system is important before selecting a battery. Every electronic component will consume power. The first step in the power budget is to add up the current used by each consumer. This may be more complicated than reading values from a data sheet, particularly with microprocessors whose current requirements may vary significantly depending on what they are doing. As an example, an NXP i.MX6ULL (NXP 2019) lists current draw ranging from 500  $\mu$ A to 750 mA. The processor has four different power modes to allow the system to conserve energy whenever possible. Several microprocessor manufacturers provide tools to estimate power draw for their CPUs based on configuration and activity. An example is Silicon Labs' AppBuilder, part of their Precision32<sup>TM</sup> development suite. AppBuilder provides a Power Estimator function (Silicon Labs 2019).

Because the device may have components operating at a variety of voltages, it can be simpler to compute the power budget in Watts rather than in Amps. The power requirement for each component is the product of voltage and current.

$$P = IV$$

where:

$P$  = Power in Watts

$I$  = Current in Amps

$V$  = Voltage

The current drawn from the battery is important to calculate using the battery voltage. This is likely to differ from the voltage required by the components. Every conversion to a different voltage is less than 100% efficient. Losses in voltage conversion can be significant. So, it is important to categorize them as well.

With information about the end power consumer's current requirements and the voltages of both battery and device, the total power for the device can be calculated by summing the power for each component and the loss for each voltage conversion.

In some situations, the power budget is too large for the preferred battery. Increasing the size of the battery can negatively impact the overall size and weight of the instrument. This can be mitigated by balancing the use of components, and not turning multiple power consumers on at the same time. An example would be a Raman spectrometer, where the laser consumes hundreds of milliwatts when it is on, and a search processor also requires hundreds of milliwatts. By powering the processor down until the laser is turned off, the system can avoid consuming too much current for a limited-capacity battery.

## 2.7 Voltage Conversion

The integrated circuits within a spectrometer may require a set of power supplies at different voltages, known as power rails. With a single battery as a power source, the designer must provide voltage conversion to generate the necessary rails. Logic circuitry generally operates with voltages which are positive relative to system ground. However, the first stage of analog circuits, such as the preamplifier for an optical detector, often requires symmetric voltages above and below ground. Charge coupled device (CCD) detectors, such as those used in Raman spectrometers, may require several voltage rails. The Hamamatsu S11850-1106 (Hamamatsu 2019) is a CCD array detector with 2060  $\times$  70 pixels. It requires voltage supplies of +24 VDC, +12 VDC, +5 VDC, and -8 VDC.

These voltages are typically generated from the battery voltage within the instrument by the use of DC/DC converters, also known as switching power supplies. The detailed design of a DC/DC conversion circuit is beyond the scope of this work. However, there are some key attributes worth considering for the implementation of voltage conversion within a battery-powered device.

Despite the DC (for Direct Current) in the name, DC/DC converter circuits operate internally at high switching frequencies. These frequencies can be a source of electronic noise, which can cause problems with noise in the instrument's internal signal circuitry and can lead to radiated electric field emissions which may appear when the instrument is tested for regulatory compliance. Switching frequencies can range from hundreds of kHz to several MHz. Selection of operating frequencies for the DC/DC converters can have a significant impact on instrument size as well as performance.

DC/DC converters are available in chip packages. They generally require a few external components, typically capacitors, resistors and inductors. As the switching frequency increases, the size of the external components gets smaller. EE Times magazine performed a set of tests in which they found that moving the switching frequency from 350 kHz to 1.6 MHz reduced the board space of their DC/DC converter by 35% (Nowakowski and King 2006).

A downside to higher frequency conversion is a decrease in efficiency. The same EETimes experiment found that the efficiency of the converter dropped from 91% at 350 kHz to just under 87% at 1.6 MHz.

DC/DC converters are constant power output devices. As their input voltage lowers, they will pull more and more current at the supply voltage in order to provide the desired output power. It is important to consider this for battery-powered devices. As the battery discharges, the supplies will draw more current to satisfy their power needs. This becomes a downward spiral. Higher currents through a battery's internal resistance will lower the effective output voltage even more. It is wise to consider the battery's operational voltage range and not just its nominal rating. The design should include a means to monitor the battery voltage and to provide a graceful shutdown before the system enters the spiral caused by low voltage and increasing current.

## 2.8 Decon/Ingress Protection (IP) Rating

Portable systems are likely to be used outdoors in inclement weather. In addition, systems may be exposed to harmful materials, including toxic industrial chemicals, biological threats, or chemical weapons or their precursors. Systems must be capable of withstanding the sample materials as well as the cleaning solutions required to decontaminate them.

### 2.8.1 Ingress Protection

Systems which need to be decontaminated require a degree of liquid-tightness. This is often specified using an IP (Ingress Protection) rating. IP ratings are defined by IEC (International Electrotechnical Commission) Standard 60529 (IEC 1989). IP ratings are two-digit codes. The first digit refers to mechanical ingress, such as objects or dust. The second digit refers to liquid ingress. The letter X is often used as a wildcard to allow a single number to cover a range of ratings. For example, IP6X includes both IP67 and IP68 products. This is not an official designation per IEC 60529. Typical IP ratings for portable instruments are provided in Table 2.1.

### 2.8.2 Sealing an Enclosure

Achieving IP67 and IP68 is challenging. The number of seams must be minimized. Seals for X7 and X8 are typically achieved using O-rings. Compression of the O-ring should follow the manufacturer's recommendation. Compressing an O-ring over a large panel opening may require a large number of fasteners to ensure even compression. Using hollow O-ring cord can dramatically reduce the force needed to achieve a good seal. Screws holding the

**Table 2.1** IP ratings.

Rating	Solid particle	Liquid
40	No particle or wire greater than 1 mm in size can enter enclosure.	No liquid protection.
50	Dust protected – ingress of dust is not completely eliminated, but not enough dust can enter to prevent system from operating.	No liquid protection.
51	Dust protected – ingress of dust is not completely eliminated, but not enough dust can enter to prevent system from operating.	Protected against dripping water. Water is dripped for 10 min vertically at the flow rate of 1 mm/min.
52	Dust protected – ingress of dust is not completely eliminated, but not enough dust can enter to prevent system from operating.	Protected against dripping water while tilted. Unit is tilted 15° with water dripping for 10 min at 3 mm/min.
67	Dust tight – no ingress of dust.	Immersion in water up to 1 m of depth for 30 min.
68	Dust tight – no ingress of dust.	Immersion in water of 1 m or more, duration specified by the manufacturer.

case parts together must be outside the seal and threaded into blind holes or must have a gasket under the head to prevent leaks along the threads. APM Hexseal Seelscrew™ screws (APM Hexseal, APMhexseal.com) have an integrated O-ring in a groove under the head.

## 2.9 Testing the Seal

Seal testing can be performed in several ways. On a new instrument design, it may require several iterations to attain a reliable seal. The simplest starting position is an (empty) instrument housing. Dunk the instrument at a defined distance for a defined time. After removing the instrument from the tank, all external water must be removed before opening the instrument for inspection.

In production, this dunk, remove, inspect test is not practical. How do we know that we have not introduced a new leak when we reseal the instrument after inspection? A more reliable means of testing for water ingress is to use an accurate balance to weigh the instrument before and after dunking. The outside of the instrument must be thoroughly dried, and the balance must both support the mass of the instrument and have the precision to detect the change in mass caused by a few drops of water.

Better yet, a pressure or vacuum tester can evaluate seals without the risk of filling a valuable instrument with water because an assembly technician missed torqueing a single screw. The design engineer must include a connection port in the housing; this can be as simple as a sealing screw which is installed after the test is complete. Commercial testers are available which can connect to this port. They create a pressure differential between the inside of the case and the ambient air. The test setup monitors the decay in this pressure differential over a defined period to identify any leaks. Manufacturers of pressure and vacuum decay testers include Cincinnati Test and Uson.

## 2.10 Gloved Operation

Instruments used by hazardous materials teams are subject to a special set of requirements for user interface. The suits worn by the teams include several layers of gloves. An example of an external glove is shown in Figure 2.1,

**Figure 2.1** HazMat gloves.



with a standard nitrile glove for comparison. These gloves obviously impair the dexterity of the operator. Systems for this type of use require large controls with good separation between buttons to reduce the chance of pressing more than one button at a time. Raised molded buttons on a keypad help to ensure the operator can easily locate the button through the glove.

Capacitive touch screens are popular on consumer handheld devices, but are incompatible with many gloves. Thin nitrile gloves used in medical applications will often work with capacitive screens. Resistive touch screens work with any glove material. Drawbacks to resistive screens are that they are typically not multitouch, and that they require a flexible membrane on the outside surface. These membranes are more susceptible to physical or chemical damage than the glass one can use with capacitive screens.

It can be difficult to touch a small icon with a bulky glove. Potential solutions include ensuring that icons and all software controls are scaled as large as possible. Using a stylus can help. Typical styli for electronic devices are too small to grasp easily in these gloves. HazMatID used a specially designed large diameter stylus with a tether to prevent loss. This stylus was turned from a solid piece of acetyl with a rounded point to activate the screen.

## 2.11 Display

Another key piece of the user interface is the display. There are many aspects of the display for a handheld instrument which deserve special consideration.

### 2.11.1 Content

Traditional spectrometers are all about the spectrum. Users want to be able to see and manipulate them and to perform analysis, such as baseline correction, smoothing, etc. For most smaller portable spectrometers, this is too much capability. Spectral display and manipulation are challenging to implement with a restricted user interface. Users are looking to answer, typically “what is this sample?” or “what are the components of this mixture?” Designers should consider limiting the display to information which is useful to the intended user. Method development and detailed spectral analysis can be migrated to a PC-based application.

### 2.11.2 Brightness

Sunlight legibility can be extremely important and challenging to achieve. Liquid crystal display (LCD) panels, commonly used for portable displays, are available in a range of brightnesses, measured in nits (a nit is 1 candela per square meter). A survey of LCD panels for Original Equipment Manufacturer (OEM) use shows a range from 300 to 850 nits (Sharp Electronics Corporation 2019). High-brightness LCD panels can reach as high as several thousand nits. Several manufacturers of LCD panels suggest that a minimum of 700 nits should be specified for a display to be sunlight readable.

Organic light-emitting diode (OLED) displays are an alternative which features daylight readability and requires no separate backlight, as the pixels are light-emitting. OLEDs are available in a much more limited range of sizes in the form factors required for portable equipment.

### 2.11.3 Legibility

HazMat operators may wear multiple face shields while operating equipment in their personal protective gear. The shields may cause distortion due to curvature or condensation. This can make it difficult to read the detailed text or graphics on small screens. User displays should be designed with this in mind, using large, highly contrasting text and controls.

### 2.11.4 Guidance

Operators of this equipment may not be trained spectroscopists and may not operate the equipment every day. Providing cartoons or videos illustrating the next step in the analysis process can assist the operator in getting better results.

### 2.11.5 Display Power

Backlights for LCD panels are often one of the larger consumers of power. The Sharp LQ035Q3DG05 display draws up to 238 mW (Sharp Electronics 2009). Power draw for backlights is generally proportional to the surface area of the display. A 6.4 in. display will draw approximately four times as much backlight power as a 3.1 in. display of the same technology. Transflective displays are able to reflect ambient light from the rear of the panel and can reduce the amount of light required from the backlight.

### 2.11.6 Temperature Range

LCD panels have operational ranges which may be limited relative to the environments in which portable equipment is operated. At cold temperatures, the response time of the liquid crystals slows down, and below a threshold, the display will cease to operate. Display manufacturers continue to extend these ranges. The Sharp LQ035Q3DG05 is a 3.5 in. diagonal display which can operate over a temperature range from  $-30$  to  $+80^{\circ}\text{C}$ . In extreme situations, heaters can be added to displays to increase their low-temperature capability.

### 2.11.7 Ruggedness

Like a cell phone, handheld portables are prone to being dropped. Landing on a display or a corner of a case can place large sudden stresses on a display. Laminated displays can be custom-fabricated to greatly enhance the durability of LCD panels. Optically bonding a window to the front of the display using an index-matching adhesive can improve the display's apparent brightness as well as its mechanical robustness (General Digital 2019). This process must be started early in the development cycle, as lead times on these custom-assembled displays can be extensive.

## 2.12 Thermal Concerns

Temperature control is essential for operation and performance of optical spectrometers. Changes in temperature can affect optical alignment through expansion or contraction of support materials. Detectors have performance curves which vary with temperature and may stop working entirely if they get too warm. This is the case with DTGS (deuterated tryglycine sulfate) pyroelectric detectors, which have a Curie point above which they de-pole and no longer function. Newer versions of these pyroelectrics are doped with L-alanine to form deuterated L-alanine doped triglycine sulphate (DLATGS), which are self-poling, and recover when temperatures are returned below the Curie point.

Spectrometer instruments almost invariably contain sources of heat. The most obvious source is the optical energy source, particularly in the case of an incandescent filament or globar. In some laboratory instruments, the source generates enough heat to require liquid cooling. Less obvious sources of heat include the various electronic components, such as power supplies, batteries, and the motors or drive electronics used to control moving parts within the system. Some optical benches include heaters on the spectrometer's optical assembly or on components, such as gas cells. These heaters are used to provide a controlled, stable temperature. The heaters themselves and the control electronics driving them provide additional heat load to the instrument.

In a laboratory system, it is common to provide vents in the enclosure, and a cooling fan to ensure airflow through the system. In some systems, the speed of the fan is controlled electronically to assist with temperature control of the overall system. In these systems, as the interior temperature rises the fan's speed is increased to provide additional cooling.

### 2.12.1 Cooling Performance of a Ventilated System

Systems with vents and fans cool the internal components by transferring their heat to air, which is then exhausted from the enclosure by a fan or blower. As the warm air is forced out of the enclosure, it is replaced by fresh air at ambient temperature. With sufficient airflow, components inside the enclosure can be kept within a few degrees of ambient temperature. This cooling efficiency depends on the surface area available to transfer the component heat to the moving air. Hot components, such as power transistors can be coupled to extruded heatsinks with fins running parallel to the air motion.

### 2.12.2 Sealed Systems

A portable system faces further challenges with respect to remaining cool. These systems are typically designed to work in less well-controlled environments. The potential presence of dust, moisture, or even rain suggests that the enclosure should be sealed from the environment. This precludes the option of blowing air through the enclosure. At the same time, the instrument is likely to be moved outside of the climate-controlled laboratory, and may face temperatures ranging from below freezing to as high as 50 °C. Furthermore, portable instruments may be housed

**Table 2.2** Detector performance at temperature.

Cooling	Operating temperature (°C)	D*
Two-stage TEC	-40	≥4.0 E10
Three-stage TEC	-65	≥6.0 E10
Four-stage TEC	-75	≥6.0 E10
LN <sub>2</sub>	-196	≥1.0 E11

in plastic enclosures. Molded enclosures provide advantages over metal enclosures with respect to cost, weight, and ergonomics. However, in general, plastics are far worse conductors of heat than metal, such as aluminum.

### 2.12.3 Detector Cooling

Detectors in both Raman and FTIR instruments are generally temperature sensitive.

- Dark current in CCD array detectors used in Raman systems doubles with every increase of 2–5 °C. (Hamamatsu 2015)
- DLATGS detectors are sensitive to temperature in a non-monotonic way. The D\* (a measure of performance for optical detectors) of Leonardo's Series 99 detector has a maximum value between 35 and 40 °C. By the time the temperature reaches 50 °C, the D\* is only 80% of the maximum (Leonardo 2017). The same detector's responsivity drops as temperature rises, resulting in a desired operating point on the lower side of the D\* peak.
- Mercury cadmium telluride (MCT) detectors operate best at liquid nitrogen temperatures, but can also be operated using multistage thermoelectric coolers. Some examples from Infrared Associates' website show some relative performance values for 1 mm by 1 mm square detectors (Infrared Associates n.d.) (Table 2.2):

Any of the thermoelectric means of stabilizing or lowering temperature requires a heatsink. The thermoelectric cooler (TEC) moves heat from the detector into its opposing side. This hot side of the TEC must be cooled, usually using ambient air.

### 2.12.4 Moving Heat to Ambient Air

In a sealed system, forced air is not an option for cooling local hot spots, such as the high temperature side of the TECs often used for controlling detector temperatures. With semiconductors, a designer can often locate the hot component on a wall of the enclosure, allowing direct conduction to fins on the outside of the enclosure for ambient convection cooling. The location of detectors is dictated by the optical design, and the TEC may not be conveniently located at the outside wall. Conduction is generally the most efficient means of moving heat within an enclosure, but there are several options for conduction. Once the heat reaches the outside wall, there are further considerations on how to dissipate it in a way which does not negatively impact the instrument design. Adding external fins may not fit with the instrument aesthetic, may provide a means for mechanical shock and/or electrical disturbances to be coupled directly to the sensitive detector, and, in extreme situations, may cause risk of operator discomfort or injury due to elevated temperatures. In the next section, we will calculate temperature rise at the hot side of a hypothetical TEC with a selection of thermal approaches. For our input, we will assume we are operating a four-stage TEC to cool an MCT detector in a TO66 can. The approximate power draw of such a TEC is 0.6 A at 8.25 VDC, for a power of about 5 W. (Note that far less power is actually removed from the detector itself.) We will explore three scenarios.

#### 2.12.4.1 Direct Coupling to Heatsink Convection Cooling

For all the scenarios, we will work with a Wakefield–Vette 396-1AB heatsink. This is an extruded aluminum form with ten fins. Its base measures  $127 \times 76.2$  mm, and the fins are 35.1 mm tall. Wakefield–Vette's data sheet lists a thermal resistance of  $1.85^\circ\text{C}/\text{W}$  with natural convection, and  $1.07^\circ\text{C}/\text{W}$  with forced air at 500 LFM (linear feet/minute).

For our first scenario, we will couple the hot side of the TEC directly to the heatsink. (For all the scenarios, we are assuming perfect coupling at junctions between components. In reality, there will be additional temperature rise at these interfaces. This rise can be minimized using thermal pads or compounds). We are injecting 5 W into the heatsink, with a thermal resistance of  $1.85^\circ\text{C}/\text{W}$ . The temperature rise of the heatsink above ambient  $T_{hs}$  is then simply:

$$\Delta T_{hs} = QR_{tc} = 5(1.85) = 9.25^\circ\text{C}$$

where

$Q$  = Heat flow

$R_{tc}$  = Thermal resistance of the heatsink under convection

If our ambient temperature  $T_a$  is  $25.0^\circ\text{C}$ , the temperature  $T_c$  of the hot side of the TEC will be:

$$T_c = T_a + \Delta T = 25.0 + 9.25 = 34.25^\circ\text{C}.$$

#### 2.12.4.2 Direct Coupling to Heatsink-Forced Air Cooling

If we want to provide more efficient cooling, which may be required if the ambient air temperature is higher than  $25^\circ\text{C}$ , we can compute the effect of adding a fan. This fan is forcing air over the heatsink, and can be outside our sealed enclosure. We simply substitute the forced air thermal resistance  $R_{tf}$  for the convection thermal resistance  $R_{tc}$ .

$$\Delta T_{hs} = QR_{tf} = 5(1.07) = 5.35^\circ\text{C}$$

This change has reduced the temperature rise from 9.25 to  $5.35^\circ\text{C}$ .

#### 2.12.4.3 Remote Heatsink with Aluminum Bar

As described above, sometimes we do not have the option of locating the TEC directly on the wall of our enclosure. If the TEC is in the center of the instrument, we can couple it to an outside heatsink by means of an aluminum bar. Let us assume a bar which is a rectangular prism, 2 cm square in cross-section by 10 cm long. Fourier's Law of steady state conduction tells us that:

$$q = KA\Delta T/L$$

where

$q$  = Heat flow

$K$  = Material's conductivity

$A$  = Surface area of conductor

$i$  = Length of conductor

$\Delta T$  = Temperature difference from inside to outside enclosure

Solving for  $\Delta T$  gives:

$$\Delta T = qL/KA$$

A representative value for  $K$  for aluminum is 236 W/(m-K). Our temperature rise through the length of the aluminum bar  $\Delta T_{ab}$  can be calculated by substituting:

$$\Delta T_{ab} = \frac{qL}{KA} = \frac{5(\text{W}) * 0.1(\text{m})}{236 \left( \frac{\text{W}}{\text{mK}} \right) * (0.02 \text{ m}) * (0.02 \text{ m})} = 5.3^\circ\text{C}$$

This temperature rise is almost as much as we observe between the heatsink and ambient with forced air cooling. We can add this temperature rise to that of the heatsink to find  $T_c$ :

$$T_c = T_a + \Delta T_{ab} + \Delta T_{hc} = 25.0 + 5.3 + 9.25 = 39.5^\circ\text{C}.$$

#### 2.12.4.4 Remote Heatsink with Heatpipe

Between the heatsink-air interface and the aluminum bar's resistance, we have a temperature rise of almost 15 °C at the high side of the TEC. Transferring heat from one location to another can be done extremely efficiently by replacing our aluminum bar using a heatpipe. See Figure 2.2 for examples of heatpipes. Heatpipes are partially evacuated hollow tubes containing a heat transfer fluid and a wicking material. The fluid undergoes a phase change when one end of the tube is heated. The vapor moves to the other end of the tube where it condenses. The liquid then wicks back to the hot end to repeat the cycle. The resulting flow results in the equivalent of a thermal conductivity in the range of 30 000–40 000 W/mK, hundreds of times higher than that of aluminum. If we use 30 000 as our value for a 6 mm-diameter heatpipe in the equation above, our new temperature rise becomes:

$$\Delta T_{hp} = \frac{qL}{KA} = \frac{5(\text{W}) * 0.1(\text{m})}{30\,000 \left( \frac{\text{W}}{\text{mK}} \right) * \pi * (0.003 \text{ m})^2} = 0.59^\circ\text{C}$$

The TEC hotside temperature  $T_c$  is now:

$$T_c = T_a + \Delta T_{hp} + \Delta T_{hc} = 25.0 + 0.59 + 9.25 = 34.8^\circ\text{C}.$$

Thus, we see that a heatpipe of 5 mm diameter can replace a 2 cm square bar and reduce the thermal rise by a factor of 10. The heatpipe requires less space and weighs significantly less than the aluminum bar.

Heatpipes can be bent following the manufacturer's guidelines. Advanced Thermal Solutions (ATS) recommends a minimum bend radius at least three times the heatpipe's diameter.



**Figure 2.2** Heatpipes.

## 2.13 Optical Elements

Laboratory instruments are able to take advantage of infrastructure within the facility. As well as AC power sources, this can include a source of dry gas for purging optical systems. This constant supply of desiccated gas protects optics from moisture, allowing the use of hydrophilic materials, such as KBr, a standard material for beamsplitters and optical windows used in the mid-infrared. These materials are easily damaged by the presence of moisture in the atmosphere, and can quickly become cloudy or completely destroyed if they are exposed to excess water vapor. KBr is frequently used in general-purpose instruments because it has a wide transmission window, allowing spectroscopy over the range of 48 800–345 cm<sup>-1</sup> (Spectral Systems n.d.).

In portable instruments, KBr is not a suitable choice. Other materials are more appropriate, though they can limit the available spectral window. Given the general assumption that the portable instrument is more limited in purpose, it is often possible to select a material which is transparent over an adequate spectral range for the application. Zinc Selenide, ZnSe, is a frequent choice for portable FTIR systems. It has a transmission range of 18 000–461 cm<sup>-1</sup>.

Zinc Selenide is commonly available as a window material with two flat, parallel surfaces. It can also be diamond-turned into relatively complex shapes to be used as focusing elements where appropriate.

## 2.14 Interferometer Optical Design

Portable FTIR spectrometers face several restrictions with respect to their laboratory counterparts. These constraints should be considered when selecting the optical layout of the interferometer itself. This section will review three interferometer topologies and provide comments regarding the tradeoffs made for portability.

### 2.14.1 Traditional Michelson

A standard Michelson interferometer consists of two flat reflective surfaces and a beamsplitter. See Figure 2.3. The angle between the two beams may be 90°, though other angles are also frequently used. One mirror is fixed, and the second is translated with motion parallel to the optical beams. These mirrors must be aligned to be perpendicular to their respective beams. In particular, the moving mirror must maintain its alignment to within a fraction of a wavelength over its entire range of motion. The allowed deviation from perpendicularity is a function of the required wavelength resolution of the instrument. The offset in beampath caused by a given angular misalignment

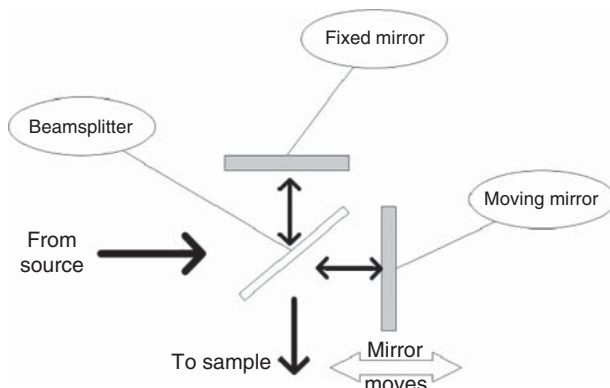


**Figure 2.3** Michelson interferometer.

is proportional to the diameter of the beam. As the beam travels out and back, the beampath error is double that of the mirror error. Smaller beams are more forgiving of angular misalignment than larger beams. The mechanism used to align these assemblies generally tilts either the fixed mirror or the beamsplitter itself. HazMatID and GasID are examples of portable FTIR systems using flat mirrors in Michelson interferometers.

### 2.14.2 Michelson with Cube-Corner Reflectors

Cube corners are optical constructions with three orthogonal reflective surfaces. These structures are familiar from the “cat’s eye” reflectors common on bicycles. Any beam of light which enters the acceptance angle of the cube corner will be returned parallel to the axis upon which it arrived. The beam will be translated by a distance which depends upon the distance from the optical center of the cube corner. The chief advantage of cube corners in interferometers is that they are insensitive to angular misalignment. Aligning a cube-corner interferometer does not require a tilt to any optical component; rather the fixed cube corner is translated in X and Y axes until its return beam is satisfactorily aligned to superpose itself over the beam returning from the moving mirror. TravelIR used a cube-corner Michelson interferometer.

### 2.14.3 Dual-Pendulum

A dual-pendulum interferometer uses two cube-corner reflectors mounted to a two-armed rotating yoke. See Figure 2.4. This type of interferometer was first described by Rippel and Jaacks (Rippel and Jaacks 1988). The entire yoke assembly is rotated over a small angle about an axis. The two reflectors move in opposite directions relative to the beamsplitter; as one moves closer, the other moves farther away. This has the effect of doubling the change in relative pathlengths, allowing a smaller displacement for a given resolution. The rotation is achieved by a magnet and coil assembly similar to that used to move the heads of a magnetic disk drive. A major advantage for a portable interferometer is that the entire rotating assembly, including mirrors, arms, and drive components, can be balanced with its center of mass aligned with the pivot point. This balance reduces the interferometer’s sensitivity

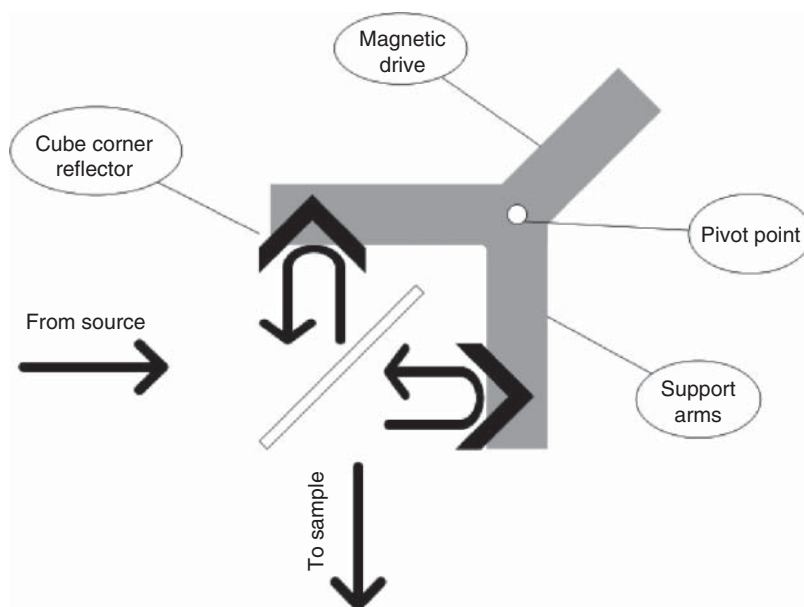


**Figure 2.4** Dual-pendulum interferometer.

to shock or vibration, as any force imparted to the moving assembly by the axle will not impart any rotational moment to the assembly. A dual-pendulum design is used in the ABB-Bomem line of process instruments. It was also included in the Smiths Detection HazMatID Elite handheld FTIR system.

## 2.15 Interferometer Bearings

Moving mirrors and their supports must move accurately and reliably over the life of the instrument. As we have seen, the tolerances on this motion are measured in fractions of wavelengths. In many instruments, the mirror is moving anytime the instrument is powered on. This results in tens or hundreds of thousands of mirror strokes. The motion of the mirror must be constrained by bearings, but typical bearings used in mechanical devices are not adequate for our purposes. Tolerances on pins and leaves in a hinge mechanism are not typically tight enough to provide rotation while not allowing sideways motion.

Many interferometers rely on flexing steel members for joints. Nicolet's 5-series interferometer used a "porch swing" mechanism including four rigid arms with a pivot at each end of each arm. See Figure 2.5. Each of the pivot points was a small piece of spring steel which would bend to allow the arm to move like a classic porch swing. See Figure 2.5. The assembly maintained the alignment of the carriage, which, in turn, supported the moving mirror in a constant orientation throughout the stroke. The flexible elements, known as pivot bearings, can be purchased in a cylindrical format. The assembly includes two spring steel leaves coupling two aluminum cylinders. One cylinder is pressed into the fixed structure, and the second is pressed into the moving arm. As long as the movement is constrained to within the pivot's design limit, its life is essentially infinite. Typical angular limits range from  $\pm 3.7$  to  $\pm 15^\circ$ , depending on the bearing's size, material of construction, and load limit (C-Flex Bearing Co 2015).

As instruments get smaller, the size and number of components in a porch swing become problematic. The design team at SensIR Technologies combined the flex pivots and rigid arms of a porch swing design into two flat spring-steel leaves, one at each end of the moving mirror assembly. See Figure 2.6. These leaves were cut as a stack of material to ensure the shape of all leaves is identical. The length of the leaf must be adequate compared with the desired stroke of the moving mirror, in order to ensure the steel is not flexed beyond its fatigue limit. This design is inherently self-centering. With no power applied, the moving assembly rests in the center of the stroke. The SensIR design included mechanical end-of-travel limits to prevent the spring steel from being over-flexed as the instrument is subjected to vibration or shock in transit.

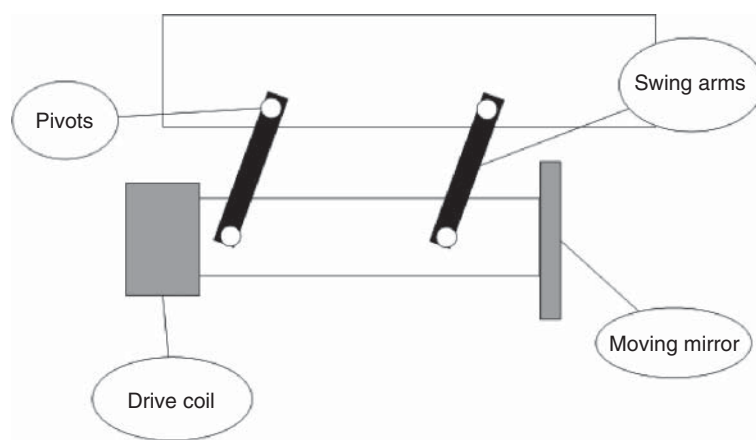


**Figure 2.5** Porch swing bearing.

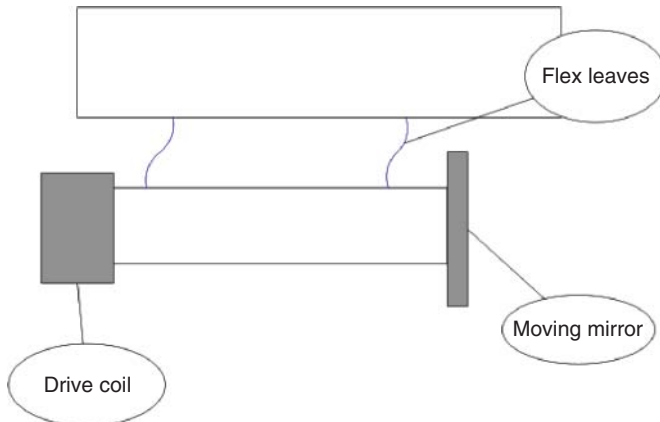


**Figure 2.6** Flex-leaf bearing.

Instruments using cube-corner reflectors are more tolerant of angular movement during scanning. The TravelIR instrument took advantage of this by using a high-precision ball bearing linear slide to provide motion for the moving mirror. This slide provided low friction and was simple to assemble into the interferometer. Because the slide is not self-centering, TravelIR included a solenoid-operated brake which would lock the sliding mechanism whenever power was removed from the system. TravelIR was prone to dust or rough spots in the slides, sometimes caused by drops of the instrument. These small sticking points in the travel would cause nonconstant motion of the moving mirror, which resulted in distortions in the spectrum.

Rotational scanning interferometers, such as the dual-pendulum design described above, can take advantage of the flex pivot components to provide both movement and a self-centering design. Placing two flex pivots in the same line allows stability about the axis while providing for adequate rotation.

## 2.16 Vibration

Vibration is a concern for both bench and portable devices. Bench devices are often mounted on damping feet to reduce transmission of vibration from the bench into the device. FTIR systems are particularly susceptible as they collect data at frequencies in the audible spectrum and are, therefore, sensitive to noises. They also incorporate a moving mirror whose motion can be disturbed by impact or system vibration. This problem is worse for handheld devices as users cannot hold them perfectly still during sampling.

Various instrument designers have incorporated feedback loops from the FTIR metrology laser to the servo drive on the moving mirror within the Michelson interferometer. The Smiths Detection HazMatID Elite instrument uses a Phase Locked Loop (PLL) to tie the frequency of the interference pattern of the metrology laser to a crystal oscillator. The error signal from the PLL is fed back into the drive voltage for the servo drive. This ensures the mirror moves at a constant velocity. A paper presented at the May 2012 SPIE conference describes an experiment in which the resulting disturbance rejection dramatically reduces the noise present in a spectrum of caffeine acquired while the instrument is rocked at approximately 10 Hz (Arno et al. 2012).

## 2.17 Shock

Portable instruments are much more likely than benchtop systems to be subjected to rough handling or dropping. In addition to issues with data collection during a shock event, the systems are likely to be damaged. Shock

**Figure 2.7** Smiths detection ACE-ID.



exposure can be minimized by the application of elastomeric bumpers on corners or surrounding the entire instrument. Arno et al. describe a means of designing “smart bumpers” with optimized durometer and shape to minimize the G forces experienced by the instrument when dropped. The Smiths Detection ACE-ID Raman spectrometer fits into a molded rubber jacket which cushions all corners of the instrument while leaving exposed metal surfaces to allow component cooling. See Figure 2.7.

## 2.18 Battery

Most portable instruments are battery-powered. Battery technology improves every year, increasing power density and battery lifetime. Specifying and maintaining the battery and its associated system is a complex task. In addition to engineering issues, batteries can impose regulatory restrictions with respect to travel or shipment. It is important to understand these implications early in the design cycle. Some larger capacity lithium-ion batteries require special paperwork to ship.

### 2.18.1 Primary vs. Rechargeable Batteries

In general, systems are designed for exclusive use of specialty rechargeable batteries. Some smaller handheld systems have requirements for using commonly available primary (non-rechargeable) cells, usually for ease of availability. When operating in the field, it is often easier to locate a pack of three cells in a local store than it is to find or recharge a special lithium-ion battery pack.

### 2.18.2 Charge Management

The user of an instrument will expect to have some information about how much charge is left in the battery. Over time, users have raised expectations due to their experience with devices, such as cell phones, which constantly display percent charge remaining. There are a number of ways to compute the remaining battery life, depending on the battery configuration. The most obvious means is to measure the voltage provided by the battery. As the battery is depleted, its output voltage drops following a curve which varies depending on battery chemistry. Issues with this means of measurement include the variation of voltage as a function of instrument current draw, and the shape of the curve for some chemistries. Lithium-ion batteries maintain an almost constant voltage for much of their discharge cycle. When the voltage starts to drop, it falls steeply. This makes it easy to judge when a battery is 90% discharged, but difficult to establish when it reaches 50 or 75%.

### 2.18.3 User-Replaceable Batteries

Replaceable batteries provide flexibility in use. They allow the user to maintain a stock of ready-to-use batteries and minimize the downtime when an instrument is discharged. Replaceable batteries are commonly used in cordless tools. Allowing the user to replace a battery can add significant complexity for instrument designers. From a mechanical perspective, the instrument needs a door or other means of inserting and removing the battery. It requires robust yet easy-to-operate connections, and the battery itself must be packaged in a way to survive outside the instrument. This adds extra volume and weight for the battery case. These are among the drivers in the consumer lines of phones and tablets which have manufacturers moving away from user-replaceable batteries. Electrical designers also have reason to avoid replaceable batteries. User-replaceable batteries make it harder for the system to know the state of charge through coulomb counting, as the system loses all known history whenever the battery is removed from the instrument. On the positive side for electrical design, if the battery is chargeable only outside the instrument, then the instrument does not need to provide support for charging circuitry, reducing the component count and worst-case heat load.

### 2.18.4 Smart Batteries

A means of delegating the battery state-of-charge calculation is to employ a “smart battery.” These battery backs incorporate one or more integrated circuits specifically to manage the state of charge of the battery. Most of these smart battery packs comply with the System Management Bus, or SMBus protocols. SMBus is based on the I2C hardware definition. I2C is a two-wire bidirectional serial bus. The SMBus protocol was originally defined by Intel in 1995. The specification is maintained by the Smart Battery System Implementers Forum (System Management Interface Forum 2013).

The Smart Battery contains nonvolatile memory. The built-in battery circuitry uses this memory to log important parameters. The instrument can query the battery to learn about its present voltage, state of charge, time to empty at current discharge rates, and the number of charge/discharge cycles the battery has experienced. The instrument’s internal charging circuitry can work with the smart battery to provide optimal control over charge rate. Specialized charger chips have been developed to support smart battery management. Chip families, such as TI’s BQ25000 series, list over 250 different specialized parts for managing rechargeable batteries (TI 2019). External smart chargers are also commercially available to support charging smart batteries outside the instrument.

## 2.19 Electrostatic Discharge (ESD)

Electronic devices are subject to disturbance from Electrostatic Discharge, or ESD. Almost all devices sold in the European Union must be certified to meet CE requirements. CE certification requires that devices survive static

discharges as specified in EN61000. ESD compliance is tested using an ESD simulator, a piece of test equipment which injects a spark at known voltage to critical parts of the device. The EUT, or Equipment Under Test, is placed on an insulted sheet on top of a grounded reference surface prior to the test. The ESD simulator has a pointed tip which is placed on or near the EUT. The tip is then pulsed to high voltage, typically in the range of 2–15 kV. The tip is moved to a number of locations selected on the outside surface of the EUT.

For traditional line-powered equipment, the standard defense against ESD is to provide a low-resistance path from any exterior surface to earth ground via the device's line cord. Handheld and portable devices often have no line cord or may have it only during the time they are being charged. This presents a different challenge to the portable equipment designer. Without the “infinite drain” of earth ground into which to dump the sudden influx of ESD-generated charge, what can we do to mitigate problems caused by ESD?

ESD damage in circuits is not caused by an elevated voltage over the entire circuit, but rather by the large difference in voltages across the circuit, or an individual component, caused by the many-kilovolt level discharge into a single point in the instrument. This near-instantaneous injection of charge can cause extremely high currents to flow for short periods of time. In a battery-powered device, we cannot shunt these currents around our circuits to earth ground. The charge in the end will equilibrate across the instrument, bringing the entire device to a new voltage potential. What we can do is to provide paths for the equilibrating currents which do not flow through our delicate electronic circuits.

Bill Jackson of TI published a white paper in 2008 describing means of mitigating ESD and radio frequency (RF) issues in battery packs themselves (Jackson 2008). These techniques are also valid for reducing the impact of ESD on our handheld devices.

ESD mitigation recommendations include:

- Minimize entry of charge via an insulated case. The ESD tester generates a 15 kV voltage at its tip. This voltage is looking for its easiest path to ground. A plastic case with adequate thickness can prevent the voltage from “breaking through” to conductors inside the instrument. The thickness required can be calculated from the breakdown voltage (also known as dielectric strength) of the material used for the case. Nylon 6 has a breakdown voltage of between 10 and 25 kV/mm depending on temperature and humidity (Unitika 2019). A case thickness of 2 mm would provide a minimum breakdown voltage of 20 kV, more than the 15 kV required for ESD. Different plastics have different breakdown voltages. The value is typically listed on a material data sheet from the plastic supplier. This strategy can defend most of the instruments; however, certain controls, screws, and connectors for power and communications can still be vulnerable.
- Provide voltage clamps on communication lines. Universal serial bus (USB) connectors are subject to frequent user interaction and are, therefore, likely areas for ESD events. Standard practice is to include a diode-based voltage clamp component as close as possible to the connector itself. These are simple six- or ten-lead devices which connect between the USB D+ and D– pins and ground. In use, they limit the ability of the data lines to move away from ground.
- Understand the surge path. The true key to minimizing ESD disturbance is to recognize the path which the surge in voltage will take as it translates to current. In a line-powered instrument, the obvious strategy is to create what Jackson calls a high-current ground path, which couples all exposed conductive surfaces to earth ground. This high-current ground path is intentionally separated from the low-current ground path, which is used for signals and more sensitive internal components. These two separate ground paths should be connected at a single point to prevent voltage gradients along the high-current path from being transmitted to the low-current path. Physical separation is also important, as the sudden current surge caused by an ESD event will create magnetic fields which can transmit the surge into adjacent traces. ESD current sources, such as the ground points in the USB transient suppressors, should be connected to the high-current ground path. The use of ground planes and ESD spark gaps within the printed circuit board layers can help minimize injection of ESD events into sensitive circuitry.



**Figure 2.8** Printed handgrip.

## 2.20 Ergonomics

Portable equipment is by its nature handheld or at the minimum transportable. Transportable equipment must have well-defined lift points and be within weight limits for users to move and carry. Handheld equipment has much more stringent requirements. An instrument which will be carried and used throughout the day must be comfortable to operate for users across a wide range of sizes and strengths.

A key goal for the design of a handheld device is to provide grips and controls which fit comfortably in a range of hand sizes. The range of hand sizes has been extensively studied by a wide range of organizations. The National Institutes of Health (NIH) published a paper studying the hand size of firefighters (Hsiao 2015). The document includes several key dimensions, listing the range for each.

It is often extremely useful to create a three-dimensional model of the proposed handheld design, or at least of some key sections. These models may be sculpted from clay or foam. It is now easy to design the model using CAD (Computer Aided Design) and to 3D print an assortment of shapes. These shapes can be evaluated by users with a range of hand sizes to determine the best shape and size for comfort, ease of grip, and access to key controls. Figure 2.8 shows a sample 3D-printed handgrip used for user review.

## 2.21 Laser Safety

Many spectrometers contain lasers. For Raman systems, the laser is the excitation source for the measurement. FTIR systems almost always include a laser used as a reference to measure travel of the moving mirror.

In the US, laser safety is enforced by the CDRH, the Center for Devices and Radiologic Health, a division of the FDA (Food and Drug Administration). In Europe, laser products are certified according to EN-60825. Manufacturers of laser devices are required to file reports with the CDRH certifying the class and safety aspects of the lasers they produce (US FDA 2018).

Lasers are divided into safety classes, which are similar, if not identical, between the CDRH and EN-60825 nomenclature. Most handheld spectrometers include lasers in the classes between 1 and 3R or 3B. Class 1 lasers are considered eye-safe and need no special handling or safeguards. They can still be hazardous if viewed using optical aids, such as magnifiers or telescopes. Class 3R or 3B lasers are considered hazardous to eyes and/or skin depending on exposure time. The classification of a laser depends on several factors, including its wavelength, power, and angle of divergence (21 CFR 1000.40 2019).

The laser classification of a device is based on the amount of laser energy which is accessible to the user; thus, a device may contain a class 3 laser, but still be a class 1 device if the energy is prevented from leaving the confines of the device. Benchtop FTIR systems including Helium Neon lasers often provided beam-blocking mechanisms to prevent laser energy from escaping; thus, allowing the instrument to be listed as a Class 1 device despite its internal Class 3 laser. Portable FTIR systems are much more likely to use a diode laser as a reference. With proper design to limit power output, these diode lasers can be constructed as Class 1 modules in their own right. This ensures that laser safety is not compromised when the instrument cover is opened.

Lasers for Raman systems pose more issues. The power level required to excite a sample is generally high enough to prevent it from being a Class 1 laser. Typical Raman handheld systems deliver approximately 100 mW of laser power at wavelengths of 785 or 1064 nm. Handheld Raman systems frequently have lasers rated class 3B.

Bench Raman spectrometers generally require the user to place the sample into a light-tight compartment with a laser interlock switch. This system prevents the laser light from escaping to a point where it could cause harm to the user.

Some portable Raman systems have small vial holder compartments which allow the sampling of liquid samples in glass vials. These compartments have sensors to determine that they are closed, providing a safety interlock which allows the system to operate as a Class 1 device.

However, one of the key advantages of a handheld Raman system is that it allows a user to analyze a sample without removing it from its container. This container may be a large reservoir of unknown liquid found in a suspected clandestine drug lab. Opening the container may pose a different risk to the operator. It is safer and easier to measure the spectrum through the wall of the container. This requires that the laser be accessible outside the instrument.

A key value for determining eye safety is the Nominal Ocular Hazard Distance, or NOHD. The NOHD is the distance from the laser at which the beam no longer exceeds the Maximum Permissible Exposure, or MPE. The calculation of the NOHD is beyond our scope. The MPE is expressed in irradiance, or power density as  $\text{W/m}^2$ . The faster a laser beam diverges, the more rapidly its power density will decrease and the shorter the NOHD. Using a fast optic at the exit of the Raman system creates a focal point close to the laser exit, after which the beam will diverge rapidly. The Thermo Scientific TruScan RM's Statement of Compliance states that it is eye-safe at a distance greater than 14 cm (Thermo Scientific 2016).

## 2.22 Stability

Many spectroscopic techniques are ratiometric. They measure a sample spectrum by computing the ratio between measurements with and without a sample present. These two separate measurements are often known as single-beams. The measurement taken with no sample present, known as the "background" or "reference," is used to characterize the current line-shape of the spectrometer system, including the source, alignment, and all optics in the light path. The measurement with a sample present includes all the instrument information as

well as new information provided by the sample itself. Dividing the sample measurement by the background measurement cancels the instrument line-shape, leaving only sample information in the form of a spectrum.

The preceding statement assumes that the instrument line-shape has not changed significantly in the time between measuring the background and the sample single-beams. If there has been a significant change, then that change will show up in the ratioed spectrum.

Stability for FTIR instruments is generally measured and specified by collecting two background single-beams separated by a defined time period, often measured in hours. These two single-beams are ratioed, resulting in a “100 percent line.” In a perfect instrument with no noise and no instability, the result would be a straight line with the value of 1.00, or 100%. As time is increased in our imperfect real-world instruments, the line will become fuzzy as a result of noise, and will tilt or bend as a result of instability. Instrument makers specify stability as the maximum amount of deviation over a defined time at a particular wavelength or wavelengths. Agilent’s Cary 630 FTIR Spectrometer Preventive Maintenance Checklist (Agilent Technologies 2016) specifies comparing the values at 1000 and 3000 cm<sup>-1</sup> over a 30-minute period.

Changes in line-shape are principally results of four causes:

- Thermal expansion, which causes the optical elements to move relative to each other. If these movements happen within the interferometer, they will be wavelength dependent, seen as a tilt in the spectrum from one end to the other.
- Mechanical misalignment, caused by optical components shifting due to shock or vibration.
- Interferents in the beam path including changes in moisture or CO<sub>2</sub> content.
- Temperature changes in thermally sensitive components.

In benchtop instruments, designers use a number of techniques to ensure minimal change in instrument line-shape over time. Unfortunately, many of these techniques are not easily available to designers of portable instruments. Some of the common approaches and their applicability to portables include:

### 2.22.1 Mass

High-resolution, high-performance bench instruments use massive metal baseplates, often cast from aluminum. The large mass helps stabilize the optical path thermally and mechanically. The mass will be slow to respond to changes in temperature. The large mechanical size of the baseplate can also provide increased rigidity, reducing susceptibility to motion due to shock or vibration. Adding mass to a portable instrument is problematic as one of the primary requirements is typically to keep the weight as low as possible.

### 2.22.2 Active Thermal Control

Laboratory instruments often incorporate electric heating elements coupled to the spectrometer body. These heaters keep the instrument or subsystem at a constant temperature slightly above ambient. By minimizing temperature change with time, the instrument can minimize thermal motion and associated changes in optical alignment. This strategy is difficult to implement in a portable instrument because of the increased power requirement to operate the heaters, which significantly reduces battery life.

### 2.22.3 Long Warm-Up Time

When an instrument is powered on from a cold start, it undergoes significant thermal change. Every power-consuming element generates heat. This heat is not evenly distributed throughout the instrument. So, some parts will rise in temperature faster than others. The change in temperature causes thermal stresses and movement within the optical structures. In a benchtop instrument, the operator can “wait this out,” leaving the

instrument powered on for several hours to stabilize prior to making measurements. In a portable instrument, this is not an option for two reasons. First, the battery life is limited and the user does not want to waste a good portion of the battery just coming to thermal equilibrium. Second, and more importantly, the portable instrument is probably being deployed to generate time-sensitive information, such as the identity of a potentially hazardous material. Operators of portable spectrometers are almost always in a hurry, and cannot afford to wait for systems to stabilize thermally before making a measurement.

#### 2.22.4 Dry-Gas Purge

As mentioned above, dry-gas purges can extend the life of hydrophilic optical elements. They can also reduce or eliminate the presence of light-absorbing moisture and CO<sub>2</sub> in the beam path. Dry gas is typically provided in the form of compressed Nitrogen, boil-off from a liquid Nitrogen dewar, or compressed air which has been desiccated using an air dryer. All of these options require some combination of volume, weight, or power which is not present in a portable system.

The above techniques are challenging or impossible to apply to portable spectrometers. We need to find some new approaches. Several successful techniques include:

#### 2.22.5 Minimize Beam Path

Spectral components caused by moisture or CO<sub>2</sub> in the beam path are predictable using Beer's Law. The amount of signal is proportionate to three things:

1. The spectral absorptivity of the material.
2. The concentration of the material.
3. The path length of interaction between the material and the light beam.

We cannot control the absorptivity of the material, but we can minimize the concentration and the path length of interaction. Designing a system with a short beam path is consistent with our goal of making the instrument as small and light as possible. Because materials change size thermally as a percent of their original size, smaller components will exhibit less absolute movement for the same temperature change.

#### 2.22.6 Seal and Desiccate

The other component of Beer's law that we can control is the concentration of interferents. The most common problems are seen from H<sub>2</sub>O and CO<sub>2</sub>, which are present in varying concentration in the atmosphere, and may change rapidly in the presence of human operators due to water vapor and carbon dioxide in their breath.

The obvious way to prevent change in the level of gas or vapor interferents is to seal the system, or as much of the optical path as is practical. It is important to provide a means to purge the system with dry gas before sealing it. A desiccant will absorb whatever moisture penetrates the seal. Dessicants are often considered user-replaceable, and the design should provide for this if it is felt to be necessary. A molecular sieve is a class of desiccant which can trap molecules other than water, including CO<sub>2</sub>.

Because FTIR spectroscopy is a ratiometric technique, we can tolerate some degree of interference, as long as it is constant. The sealed design and presence of a dessicant or molecular sieve will stabilize the concentrations of CO<sub>2</sub> and water vapor, allowing them to ratio out of the sample spectrum.

#### 2.22.7 Collect Backgrounds Frequently

Spectrometers change over time. This is particularly true at startup as the system temperature is changing rapidly. The more closely in time we can collect our background and sample single-beams, the less the instrument line-shape will change between the two measurements. Software in portable instruments is often structured to

force the user to collect a background immediately prior to collecting the sample single-beam. This background single-beam can be scanned automatically for unusual spectral features and, thereby, be used to establish system cleanliness before allowing the user to place the sample.

## 2.23 Service

Portable instrumentation is subject to rough handling, from unintentional banging against furniture to operators who throw the instrument into the back of a pickup truck before heading out to the field. Despite every effort to design robustness into the system, it will eventually need to be serviced. Traditional laboratory instruments are usually serviced on site by a visiting service technician.

## 2.24 Communications/Wireless

As mentioned above, portable spectrometers often lack full-size display screens, keyboards, and mice. This can impose challenges in analyzing data on the device itself. It is often practical to move the data onto a PC for analysis or onto a network for archiving. Almost every modern portable device includes a USB port for this purpose. In a production or hot zone environment, having wireless communications can significantly reduce the amount of time and effort required to get data from the portable equipment to a fixed computer. In an office or lab environment, this may be as simple as adding a Bluetooth or Wi-Fi module to the system. For a hazardous materials team, the range of these technologies may not be adequate to reach from the operator to the command vehicle, which is typically outside the hot zone. A range of proprietary radio modems is available for this type of communications. Using a commercial module with Federal Communications Commission (FCC) approval can reduce the certification burden compared to designing a solution using component parts.

## References

- 21 CFR 1000.40 (April 2019). Title 21 – Food and Drugs. *21 CFR 1000.40*.
- Agilent Technologies (2016). *Cary 630 FTIR Spectrometer Preventive Maintenance Checklist – Standard*. Agilent Technologies.
- Arno, J., Cardillo, L., Judge, K. et al. (2012). Advances in hand-held FT-IR instrumentation. In: *Proceedings of the SPIE 8374, Next-Generation Spectroscopic Technologies V*, 837406 (17 May 2012). Baltimore, MD: SPIE.
- C-Flex Bearing Co (2015). <https://c-flex.com/pivot-bearings/life-projections> (accessed 17 September 2019).
- General Digital (2019). *Optical Bonding of Flat Panel Displays*. General Digital. <https://www.generaldigital.com/optical-bonding-of-flat-panel-displays> (accessed 17 September 2019).
- Hamamatsu (2015). *Back-thinned TDI-CCD Technical Information*. Hamamatsu. [https://www.hamamatsu.com/resources/pdf/ssd/tdi-ccd\\_kmpd9004e.pdf](https://www.hamamatsu.com/resources/pdf/ssd/tdi-ccd_kmpd9004e.pdf) (accessed 20 September 2019).
- Hamamatsu (2019). *Line Sensors for Spectrophotometry*. Hamamatsu. [https://www.hamamatsu.com/resources/pdf/ssd/s11850-1106\\_kmpd1132e.pdf](https://www.hamamatsu.com/resources/pdf/ssd/s11850-1106_kmpd1132e.pdf) (accessed 20 September 2019).
- Hsiao, H. (2015). Firefighter hand anthropometry and structural glove sizing: a new perspective. *Hum. Factors*: 1359–1377.
- IEC (1989). *ANSI Web Store*. ansi.org. <https://webstore.ansi.org/Standards/IEC/IEC60529Ed1989> (accessed 19 September 2019).
- Infrared Associates (n.d.). *Infrared Associates HgCdTe (MCT) Detectors*. Infrared Associates. <http://irassociates.com/index.php?page=hgctde> (accessed 20 September 2019).

- Jackson, B. (2008). *ESD and RF Mitigation in Handheld Battery Pack Electronics*. TI.
- Leonardo (2017). *Leonardo DLATGS IR Detector*. Leonardo. [https://www.leonardocompany.com/documents/20142/3151790/DLATGS\\_IR\\_Detectors\\_for\\_Instrumentation\\_LQ\\_mm08096\\_b.pdf?t=1538987888860](https://www.leonardocompany.com/documents/20142/3151790/DLATGS_IR_Detectors_for_Instrumentation_LQ_mm08096_b.pdf?t=1538987888860) (accessed 20 September 2019).
- Nowakowski, R. and King, B. (2006). Choosing the optimum switching frequency of your DC/DC converter. *EE Times*. [https://www.eetimes.com/document.asp?doc\\_id=1272335#](https://www.eetimes.com/document.asp?doc_id=1272335#) (accessed 17 September 2019).
- NXP (2019). *NXP Processors and Microcontrollers*. NXP. <https://www.nxp.com/docs/en/data-sheet/IMX6ULLIEC.pdf> (accessed 15 September 2019).
- Rippel, H. and Jaacks, R. (1988). Performance data of the double pendulum interferometer. *Mikrochim. Acta [Wien]* II: 303–306.
- Sharp Electronics (2009). Device Specification for TFT-LCD Module Model No. LQ35Q3DG03 (30 October).
- Sharp Electronics Corporation (2019). *Sharp Electronics Corporation Device Division*. Sharp Electronics Corporation. [https://www.sharpsma.com/products?sharpCategory=Industrial%20LCD&p\\_p\\_parallel=0](https://www.sharpsma.com/products?sharpCategory=Industrial%20LCD&p_p_parallel=0) (accessed 17 September 2019).
- Silicon Labs (2019). *Precision32 32-bit Microcontroller Development Suite*. Silicon Labs. <http://www.ti.com/tool/TIDA-00285?keyMatch=POWER%20TOOL&tisearch=Search-EN-everything&usecase=part-number> (accessed 15 September 2019).
- Spectral Systems (n.d.). *Properties of Materials for Spectroscopy*. Spectral Systems. [https://www.spectral-systems.com/wp-content/uploads/2014/04/Properties-Chart\\_L.pdf](https://www.spectral-systems.com/wp-content/uploads/2014/04/Properties-Chart_L.pdf) (accessed 30 September 2019).
- System Management Interface Forum (2013). *SMBus*. System Management Interface Forum. <http://www.smbus.org> (accessed 15 September 2019).
- The Free Library (2019). 39th Annual R&D 100 Awards (October 2019). *The Free Library*. <https://www.thefreelibrary.com/39th+Annual+R%26D+100+Awards.-a079197011> (accessed 15 September 2019).
- Thermo Scientific (2016). *Thermo Scientific TruScan RMUnited States Pharmacopeia (USP)Chapter <1120> — Raman Spectroscopy Statement of Compliance*. Tewksbury, MA: Thermo Scientific.
- TI (2019). *Battery Charger ICs*. TI. <http://www.ti.com/power-management/battery-management/charger-ics/products.html> (accessed 15 September 2019).
- Unitika (2019). *Nylon Resin (Nylon 6) General Properties*. Unitika. <https://www.unitika.co.jp/plastics/e/nylon/nylon6/03.html> (accessed 15 September 2019).
- US FDA (2018). *Radiation Safety Report*. US Food and Drug Administration. <https://www.fda.gov/media/72606/download> (accessed 13 September 2019).

## 3

# Design Considerations for Portable Mid-Infrared FTIR Spectrometers Used for In-Field Identifications of Threat Materials

*David W. Schiering<sup>1</sup> and John T. Stein<sup>2</sup>*

<sup>1</sup>*RedWave Technology, Danbury, CT, USA*

<sup>2</sup>*JTS Consultancy, Ashburn, VA, USA*

## 3.1 Introduction and Background

The use of chemical weapons on civilians by the Iraqi military, the World Trade Center terrorist attacks of 11 September 2001, the anthrax letters sent through the US Postal Service mail system, and threats to military assets and civilian populations due to the use of improvised explosive devices (IEDs) have served to significantly change the capabilities of teams charged with ensuring safety and responding to chemical, biological, radiological, nuclear, and explosives (CBRNE) threats. The most sophisticated response teams, for example, the combating Weapons of Mass Destruction Civil Support Teams (WMD-CST), the New York City Fire Department (FDNY) Hazmat Team, the Chemical Biological Incident Response Force (CBIRF), or the US Army 20th CBRNE Command, are outfitted with mobile platforms containing the most advanced, in-field analyses technologies for detecting a broad range of CBRNE threats. The nature of the threat is continually changing due to the imagination and innovation of the terrorist adversaries. The evolving threat has created an environment for innovation in the scientific, technology development, and engineering communities charged with bringing improved capabilities to these sleuths and responders.

What are the needs of the responder or sleuth working in the field with instrumentation to identify threats and provide safety and security to the population? The responder desires solutions, not technology. The instrumentation must be easy to use and useable in the hot zone, where the threat is located. The operator wants actionable intelligence, not only a chemical or product name. The instrument should be lightweight, but rugged, durable, and dependable. It should identify multiple threats, have an easily expandable library, and the ability to analyze dirty samples. The instrument should be safe to use and useable by an operator encumbered by personal protective equipment (PPE). Preferably, there should be no consumables and the instrument should use commonly available, commercial-off-the-shelf batteries. Managing size, weight, and power (SWaP) while maintaining acceptable analytical performance is perhaps the dominant design driver for a portable device, one not appearing in the design trade space for the previous generation of laboratory, benchtop instruments.

Infrared (IR) spectroscopy is a mainstay analytical method for the identification and characterization of materials. The absorption bands in the IR spectrum arise from vibrational transitions in molecules and, therefore, the overall spectrum is very sensitive to changes in molecular structure. Coblenz [1] is generally credited with first understanding that the observed bands in the IR spectrum are associated with molecular bonds and atomic groupings, and the structural properties of molecules. Most of the IR absorption bands associated with fundamental vibrational modes are observed in the mid-IR region from 4000 to 400 cm<sup>-1</sup>. Characteristic frequencies of IR absorption bands associated with molecular functional groups provide a basis for interpreting

IR spectra and classifying materials [2, 3]. Since the vast majority of covalently bonded molecules give rise to IR absorption, IR spectroscopy may be applied across many industries and disciplines, including criminalistics and forensic science. IR spectroscopy has been categorized as among “Category A” techniques, having “maximum potential discriminating power” by the Scientific Working Group for the Analysis of Seized Drugs (SWGDRUG) [4]. The IR absorption spectrum is related to the complex refractive index, a physical constant for a molecule. The IR spectrum is essentially a fingerprint of a molecule and can be used to identify unknowns when many candidates are possible. The identification is directed by digital comparison with a database of spectra of known materials. An example of identification from a portable spectrometer is illustrated in Figure 3.1, a screen capture of a threat analysis. Ammonium nitrate is a common oxidizer used by terrorists in homemade explosives (HMEs). In this software implementation, the threat spectrum can be viewed and overlaid with the spectral library data. A similarity score indicating the goodness of fit between the threat and library spectra, and threat chemical and safety data may also be displayed. Different portable spectrometers have different software implementations, but a common feature is the reliance on spectral matching. Spectral matching is challenged with samples that are mixtures or materials that are not represented in the library. Most commercial portable Fourier transform infrared (FTIR) instruments also employ some type of automated mixture analysis method.

The development of portable IR spectrometers initiated significant growth in the use and applications of spectroscopy systems, including both IR and Raman. Small, hardened, and tailored instruments found their way into the hands of many professionals who had no prior experience with sophisticated scientific instrumentation. This discussion shall be concerned with the instrumental aspects of portable FTIR spectrometers used in condensed-phase sample analyses, with particular focus placed on aspects that challenge portability and use in the field. We will confine the discussion to mid-IR FTIR instruments and fabrication methods currently employed for commercial instrumentation. A few groups have reported FTIR instrumental developments based on micro-electromechanical systems (MEMS) fabrication methods [5–7]; see the chapter in Volume 1 of this text by Grüger for a discussion of MEMS technology. A commercial MEMS FTIR spectrometer product is available that operates in the near-IR spectral region. While MEMS methods offer unparalleled potential for reducing the size and power requirements for the optical and mechanical elements of an FTIR platform, the current state of the art for IR sources, detectors and sample interfaces limit the reduction in overall instrument size that could be realized through the incorporation of MEMS technology. Also, current MEMS structures are so small that

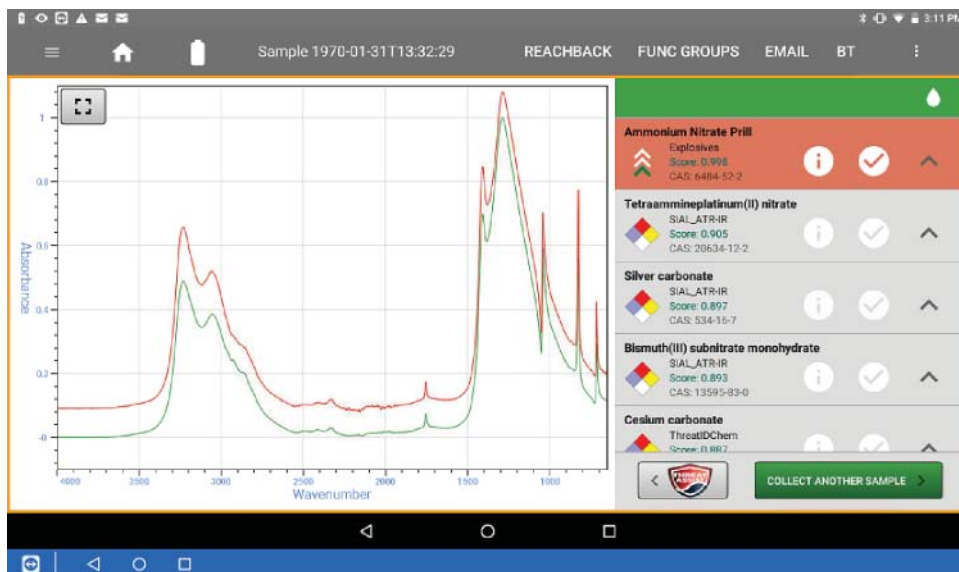


**Figure 3.1** Analysis software screen for the identification of a homemade explosive (HME) component, ammonium nitrate. Source: Courtesy of RedWave Technology.

the reduction in the mid-IR signal is such that currently available, uncooled detectors do not provide sufficient signal-to-noise ratio (SNR) for practical use.

The first commercial portable FTIR spectrometer was the *TravelIR*<sup>TM</sup> (SensIR Technologies, LLC, Danbury, CT) introduced in 2000. One of the first applications of this spectrometer was in the mitigation of clandestine drug laboratories, collecting on-site evidence and chemical hazard data for site safety and remediation. The customers were US federal drug enforcement agencies. After the events of 2001, particularly the anthrax letters, field responders looked for better tools for responding to chemical incidents, providing immediate on-site intelligence and capability to address chemical, biological, and explosive threats. By 2002, the *TravelIR* was deployed into many response teams [8]. Early on, the limitations of the *TravelIR* became apparent. The size and weight were too large. The instrument was not waterproof nor could it be decontaminated, precluding its use where exposure to biological or chemical warfare agents (CWA) was a possibility. Although battery operation was possible, the instrument was almost always used with mains AC power as the battery was very heavy and cumbersome. The *SensIR* team immediately began development of a portable FTIR spectrometer that would address these shortcomings. In July 2003, the *HazMatID*<sup>TM</sup> (SensIR Technologies, LLC, Danbury, CT) was first shipped – more than 80 units to a Department of Defense (DoD) entity for use in base protection. The *HazMatID* was a small, suitcase-mounted FTIR spectrometer that was size reduced and hardened specifically for field response applications [9]. The instrument was submersible and fabricated of materials that would withstand corrosive decontamination fluids. Importantly, the instrument would operate greater than two hours using an integrated battery. These developments were firsts for any FTIR spectrometer. The *HazMatID* was marketed until 2018 by *Smiths Detection, Inc.* Several thousand were shipped and many are still in use.

Subsequent to these initial efforts, several companies have developed portable FTIR systems [10–12]. Current models of portable FTIR spectrometers are indicated in Figure 3.2, with some of their pertinent specifications. Suitcase-portable instruments provide a higher level of optical and computational performance, more software features, and larger screen size, while handhelds provide the ultimate in portability – size and weight reduction.



Year of introduction	2019	2014	2012	2010
Company	Redwave Technology	Agilent Technologies	Smiths Detection	Thermo Scientific
Size	14" x 10.6" x 6.12"	4" x 7.5" x 13.6"	10.6" x 5.6" x 3.1"	7.8" x 4.4" x 2.1"
Weight	15 lb	4.4 lbs	5 lbs	3 lbs
Spectral range	650 – 4000 cm <sup>-1</sup>			
Resolution	4 cm <sup>-1</sup>	4 cm <sup>-1</sup>	4 cm <sup>-1</sup>	4 cm <sup>-1</sup>
Battery life	>4 h	3 h	>5 h	>2 h
Operational temperature	−10 to + 50°C	0 to + 50°C	−20 to + 50°C	−25 to + 40°C

**Figure 3.2** Current models of portable FTIR spectrometers. Source: RedWave Technology, © Agilent Technologies, Inc., Image used with permission © Smiths Detection, and © Thermo Fisher Scientific.

Numerous in-field applications of portable FTIR spectrometers have been reported and include identification or analysis of CWA [13, 14], biological toxins [15], narcotic drugs [16], explosives [17], cultural heritage materials [18, 19], geologic materials [20], counterfeit pharmaceuticals [21], and regulated plasticizers in polymer products [22].

## 3.2 FTIR System Components

### 3.2.1 Interferometer Overview

The heart of an FTIR spectrometer is the interferometer. An absorption spectrum is not directly recorded. The recorded signal in an FTIR spectrometer is an optical interference signal called an interferogram. The IR spectrum is obtained by computation, transforming the time-based interferogram to a frequency-based spectrum, using a Fourier transform algorithm. Many of the details of this process are omitted in this discussion; the reader is directed towards several excellent descriptions [23–26]. We will be concerned primarily with instrumental aspects that impact miniaturization and field-use of FTIR systems and will discuss interferograms and spectra largely without connecting them.

A diagrammatical representation of a Michelson interferometer [27, 28] is shown in Figure 3.3. The IR source emission is directed towards and split by a beamsplitter into reflected and transmitted beams. The reflected and transmitted beams impinge onto fixed and moving mirrors, plane mirrors in this example. Ideally, the beamsplitter is 50% reflective and 50% transmissive. The beamsplitter is fabricated by coating an IR-transparent substrate that is very flat, typically  $<1/20$  of the highest wavelength of interest. The beamsplitter coating can be multilayered and use different materials, but in the mid-IR region, germanium (Ge) is a significant component in the beamsplitter composition. To compensate for refraction and beam shifts in the beamsplitter substrate, an IR plate of equal

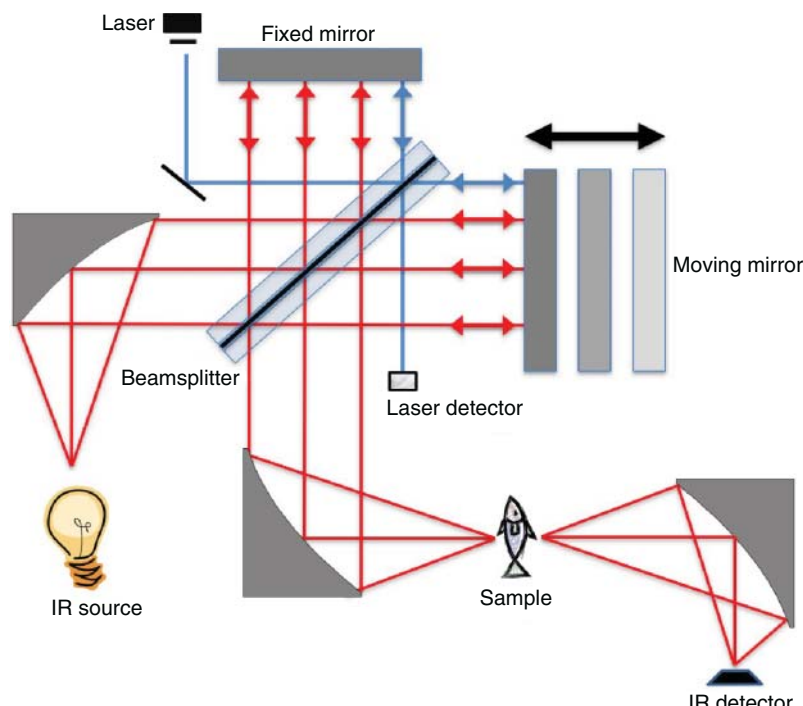


**Figure 3.3** The Michelson interferometer configuration used for FTIR spectrometry.

thickness and flatness is placed over the beamsplitter. This is the compensator plate. The beamsplitter substrate, beamsplitter coating, and compensator plate comprise the beamsplitter assembly.

An optical interference signal is generated by varying the optical path difference (OPD) between the fixed and moving arms of the Michelson interferometer. The interferogram represents the intensity of this signal as a function of the OPD. The easiest way to visualize this is to first consider a monochromatic light source.

In an FTIR spectrometer, a laser reference system is used to ensure the sampling accuracy of the measured IR interferogram points. The laser has an essentially monochromatic output. The laser is directed to the same optics as the IR radiation, but uses a different beamsplitter coating and detector. The moving mirror is scanned continuously, but it is instructive to consider the laser interferogram construction in specific increments of the laser wavelength. When the distance between the fixed and moving mirror and beamsplitter is the same, the laser beam wavefronts at the beamsplitter are in phase and the two beams constructively interfere, yielding an intensity maximum measured at the detector. At a moving mirror position of  $\frac{1}{4}$  the laser wavelength, the two beams are  $\frac{1}{2}$  wavelength out of phase, complete destructive interference results, and zero signal is measured at the detector. In this condition, all of the laser intensity is directed back towards the laser head. Since the beam travels twice the distance between the fixed and moving mirrors and the beamsplitter (forwards-backwards), the OPD is twice ( $2\times$ ) the difference between the distance between the beamsplitter and fixed and moving mirrors. At a moving mirror position of  $\frac{1}{2}$  the laser wavelength, the wavefronts at the beamsplitter are again in phase, constructive interference results, and a maximum signal is measured at the detector. At OPD that are integral multiples of the laser wavelength ( $n * \lambda$ ), a signal maximum is measured; at OPD that are  $n/2 * \lambda$ , no signal is measured at the detector. The monochromatic signal intensity varies between zero and a maximum between  $n/2 * \lambda$  and  $n * \lambda$ . Thus, the intensity of a monochromatic light source varies sinusoidally; it is a cosine wave. The interferometer modulates the beam at a frequency (in Hz),  $f = 2Vv$  where  $V$  is the mirror velocity in cm/s and  $v$  is the spectral frequency in  $\text{cm}^{-1}$ . The situation is more complicated when the broadband IR source output is considered. When the OPD is zero, all IR wavelengths are in phase and constructively interfere; the IR interferogram signal intensity is the maximum. This is the centerburst of the interferogram, observed at zero optical path difference (ZPD). As the moving mirror is scanned, the IR wavelengths recombining at the beamsplitter undergo various degrees of constructive and destructive interference. This leads to a characteristic appearance of a polychromatic source with a high signal at ZPD and much lower signal on the wings of the interferogram away from ZPD. Each frequency in the IR spectrum is encoded by the interferometer in the audio frequency range by the relation  $2Vv$ . The Fourier transformation process decodes this time-based frequency information into the spectrum.

In an FTIR spectrometer, a laser reference system is used to measure the OPD corresponding to each sample of the IR interferogram. The laser is directed to the same optics as the IR radiation, but uses a different beamsplitter coating and detector suitable for the laser wavelength, see Figure 3.3. As the laser has an essentially monochromatic output, the output produced by the laser detector is a cosine wave as described above. Sampling of the IR interferogram is typically performed at the zero crossings of the laser interferogram.

A benefit of an FTIR spectrometer is that the spectral resolution is constant over the spectral range and is determined by the maximum OPD. In the theoretical case, where the IR beam passing through the interferometer is perfectly collimated (beam divergence is zero), the achievable spectral resolution is  $1/\text{OPD}_{\max}$ , e.g.  $0.25 \text{ cm OPD}$  for  $4 \text{ cm}^{-1}$  spectral resolution. In this report, our interest is in condensed-phase applications where moderate spectral resolutions ( $4-8 \text{ cm}^{-1}$ ) will suffice. This is a benefit to the developer since the moving mirror will not be moved nor control required over larger distances, and allows some interferometer size reduction.

### 3.2.2 Optics

Brief mention can be made of the optics in the spectrometer. More detailed descriptions regarding the source, detector, metrology laser, and sample interface are made below. The intended field application for portable FTIR spectrometers limits the choice of transmission optics in the system. Most laboratory-based FTIR instruments

operating in the mid-IR use potassium bromide (KBr) optics for the beamsplitter substrate, compensator plate, detector window, and sample compartment windows. KBr provides good spectral range coverage; however, the material is hygroscopic and must be protected from atmospheric humidity either by flushing the instrument with dry air or nitrogen, or by sealing and desiccating the spectrometer enclosure. Due to high humidity that can be encountered outdoors, KBr optics are not suitable for portable FTIR systems used for chemical defense or field forensics. Zinc selenide (ZnSe), a non-hygroscopic material, is used for the beamsplitter assembly and IR detector window. ZnSe suffers from high reflection losses; therefore, the surfaces are coated with a broadband antireflection coating to improve efficiency. ZnSe optics yield a mid-IR spectral range of 4000–650 cm<sup>-1</sup>. Aspheric reflective focusing optics in the system, ellipsoids and paraboloids, are typically fashioned in aluminum (Al) by diamond turning machining, leading to a very precise optical figure, then overcoated with gold (Au) or Al for the reflective surface. The sample interface optics are discussed below.

Most portable FTIR interferometers use a Michelson configuration very much as illustrated in Figure 3.3. The *HazMatID* and *ThreatID*<sup>TM</sup> (RedWave Technology, Danbury, CT) employ a 60° beamsplitter orientation that provides greater throughput. Maintaining optical alignment is an important factor particularly for in-field units that may experience severe random vibration and shock environments. Software-actuated precision alignment is afforded by suitcase models. The motors used to align the fixed mirror require some space to integrate and contribute to the power budget, but can ensure that the interferometer is always aligned. The operator is alerted when alignment is needed and may be required to intervene.

Handheld units are permanently aligned by bonding or mechanically fixing the optics. Eliminating provisions for in-field alignment simplifies the optical system and aids miniaturization but at the expense of spectroscopy performance as the instrument must operate with some level of misalignment present. The *HazMatID Elite*<sup>TM</sup> (Smiths Detection, Inc., Edgewood, MD) design utilizes a double pendulum interferometer with cube corner optics [29, 30]. The double pendulum interferometer is a symmetric rotary mechanism and provides some optical compensation for misalignment during the course of a scan [23, 24, 31].

### 3.2.3 Interferometer Scanning System

Precise control of the interferometer moving mirror motion and sampling of interferogram points is a significant contributor to acquiring good-quality analytical data. The interferometer scanning control and signal digitization require significant engineering design and development expertise and effort, to realize the flawless integration of optics, electronics, and software. FTIR spectrometers universally use a voice coil actuator to drive the moving mirror. Most of the systems in Figure 3.2 utilize a blade flexure attached to the moving mirror assembly, the assembly then is attached to the actuator. These flexures are very durable and reliable in the field. The *HazMatID Elite* rotary interferometer utilizes crossed pair of flexures, a flex pivot, that constrain translation while providing the desired single rotational degree of freedom. Another type of interferometer moving mirror assembly is the tubular, “syringe” type [32]. In the syringe-type assembly, a circular moving mirror, attached to the voice coil actuator, moves within an outer tube that can be constructed of glass. This design inhibits tilting of the moving mirror during a scan. To reduce friction, the moving mirror is attached to a graphite piston that slides within the tube. Apparently, Thermo Scientific (previously Ahura Scientific) uses an interferometer of this type in its handheld spectrometers, even proposing a liquid material like silicon oil to reduce friction [33].

As discussed above, the interferogram of a monochromatic light source, a laser, is a sinusoidal signal, a cosine wave. As with their laboratory-based counterparts, portable FTIR spectrometers use a laser fringe-referencing method to control scanning and digitization of the IR interferogram. It is instructive to reference Figure 3.4 to understand the process. On the left of the figure are full-scale representations of the laser interferogram, the voice coil drive current, and a double-sided IR interferogram for a single stroke of the moving mirror assembly. The sloping, increasing coil current is the shape observed for a drive with a restoring force as with spring flexures or flex pivots. At the right in Figure 3.4 is a magnified view of a portion of the scan that allows visualization of the

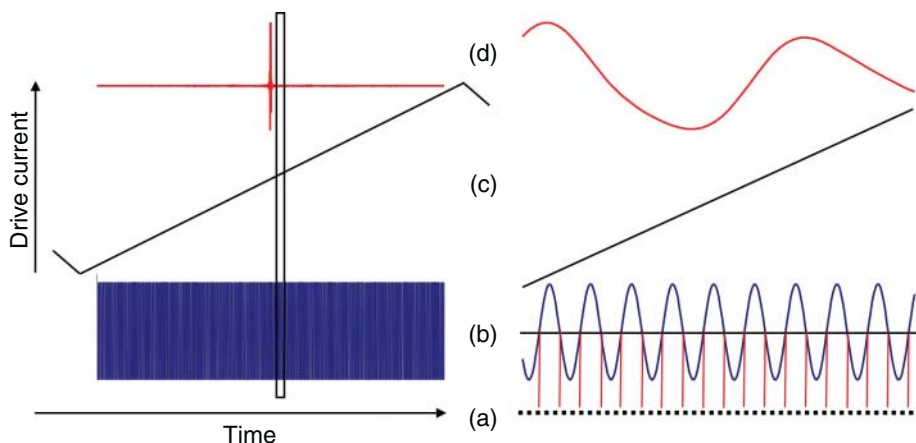


**Figure 3.4** Interferometer control and interferogram digitization. (a) Delta sigma digitizer clock. (b) Laser interferogram with zero crossings indicated. (c) Voice coil drive current. (d) IR interferogram trace.

laser fringe spacing, zero crossings of the laser fringes, and the IR interferogram. In this illustration, every laser fringe zero crossing is indicated. One method of sampling the interferogram is to use the laser zero crossings to trigger the analog-to-digital converter (ADC) sample and hold circuit to digitize an IR interferogram datum. In this method, the laser interferogram is a continuous analog signal and only the IR signal points are digitized. In portable spectrometers, the wavelength of a 1310 nm diode laser yields a Nyquist frequency of  $7633 \text{ cm}^{-1}$ , if the interferogram is sampled at every fringe. The *HazMatID* and *HazMatID Elite* instruments generate multiples of the laser zero crossings by using electrical circuits and sample the IR interferogram at fractions of zero crossings using the ADC triggering mode. As suggested by Minami and Kawata [34], portable FTIR spectrometers developed by RedWave Technology and Agilent Technologies (formerly A2 Technologies) use delta-sigma ADCs and high-precision digital methods to sample the IR interferogram.

Delta-sigma ADCs were developed for digital audio applications and are relatively inexpensive since they are used in consumer products. Additionally, they are 24-bit precision and have multiple signal inputs. However, they do not incorporate sample-and-hold circuits so there is no triggering of the ADC; a different method of fringe referencing is required. The laser interferogram is digitized using one of the delta-sigma ADC inputs. These converters incorporate clocks with speeds  $>100 \text{ kHz}$ . The bandwidth of a portable FTIR spectrometer is  $3.8 \text{ kHz}$  (Nyquist frequency) when running with a 1310 nm near-IR laser and OPD velocity of  $0.5 \text{ cm/s}$ . The delta sigma ADC provides significant oversampling of the laser interferogram, in equal time increments provided by the clock. Using digital processing techniques [35, 36], the laser zero crossing points are located very precisely by interpolation of clock sampling points on the interferogram. Delta sigma ADCs offer several advantages – high dynamic range, relaxed requirements for hardware band-limiting filters as the interferogram is sampled many times greater than the Nyquist limit, more forgiveness for velocity errors as the laser zero crossings are accurately located via interpolation and processing the interferogram, and changes and improvements can be made in software rather than necessitating hardware changes [37].

Another important function of laser fringe referencing is moving mirror velocity control. The control electronics of FTIR spectrometers include a proportional–integral–derivative (PID) servo controller that makes real-time adjustments to the voice coil drive current, keeping the laser fringes at constant separation in both OPD and time (constant frequency). This results in enhanced immunity to mechanical vibration as would occur in a moving vehicle and allows the bandwidth of the signal conditioning amplifier to be minimized without incurring phase errors. In early portable instruments, the PID servo was implemented as an analog circuit. In later instruments, the PID servo was coded in firmware in a field-programmable gate array (FPGA) integrated circuit. Current portable

instruments integrate as much electronic function as feasible into FPGAs to reduce size by eliminating hardware circuits and because changes and improvements are easier to make, effectively requiring changes in software, not hardware changes.

### 3.2.4 Infrared Radiation Sources

Radiation sources for FTIR spectrometers emit broadband IR radiation when heated by passing a current through a resistive material; by definition, they are incandescent sources. These broadband IR radiation sources approximate the output of an idealized blackbody radiator where the spectral distribution of output brightness is determined by the temperature of the radiator, via Planck's Law, and the source emissivity. To realize high brightness and, therefore, higher SNR, increasing the source temperature as high as possible is warranted. In practice, there are limitations to increasing source temperature and brightness. Planck's Law, expressed in terms of spectral density as a function of frequency in  $\text{cm}^{-1}$  and temperature, is expressed in Eq. (3.1).

$$U_v(v, T) = \frac{2hc^2v^3}{\exp(hcv/kT) - 1} \quad (3.1)$$

There is significant diversity in the availability of IR source components. Examples of IR sources that have been used or investigated for use in portable FTIR spectrometers are shown in Table 3.1 with their nominal operating temperatures and operating power requirement. The first three (3) sources in Table 3.1 have been used in commercial instruments and the fourth source has at the minimum been investigated for use. The computed blackbody spectral brightness of these four sources is shown in Figure 3.5.

The most common IR source in laboratory-based FTIR spectrometry is the air-cooled silicon-carbide (SiC) ceramic, sometimes called the *Globar*. When operated with the recommended voltage, the source temperature is 1035 °C (1308 K). It should be emphasized that the values in Table 3.1 are nominal. These sources can be operated within a voltage range. Higher voltages will result in higher color temperatures and higher spectral density at the expense of source lifetime. At the recommended voltages, the sources in Table 3.1 exceed 20,000 operating hours and rarely need replacement. *TravelIR*, the first portable FTIR spectrometer for condensed-phase threat assessment [8], was configured with a SiC source as in Table 3.1, operated at 10 V DC. This instrument was primarily powered with a mains AC power supply or a rather bulky, heavy DC battery power source.

The IR source is the most significant element in the power budget for a portable FTIR spectrometer and in subsequent instrument designs, focus was placed on this component for power reduction, reducing SWaP, and increasing battery charge life, albeit with a concomitant tradeoff in lower SNR. Reduction in power budgets for battery operation and reduced SWaP are not the greatest concern for laboratory instruments operating on mains power.

The *HazMatID* and subsequent commercial portable FTIR instruments utilized lower power wire sources fashioned from *Kanthal*® or other proprietary materials. As can be seen from Figure 3.5, there is as much as a 30%

**Table 3.1** IR source choices for portable FTIR spectrometers.

Source type	Nominal operational temperature (°C)	Nominal operational power (W)
SiC ceramic (air-cooled)	1035	10.2
Kanthal® wire	950	4.2
Proprietary wire	900	2.1
2-D MEMS emitter	650	0.18

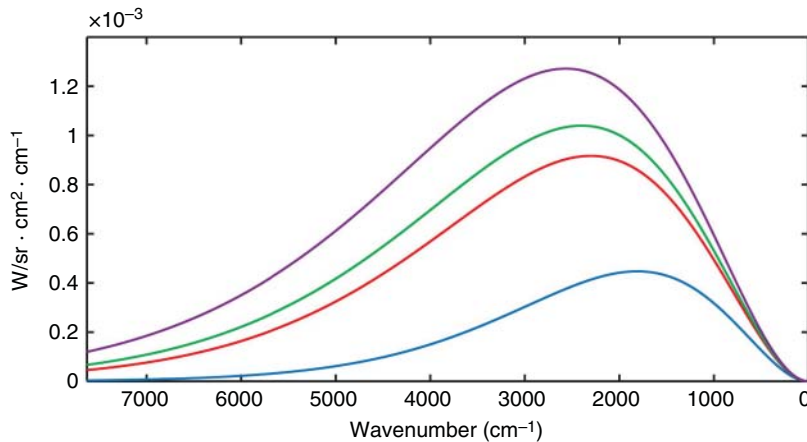


**Figure 3.5** IR source brightness computed from Planck's Law (Eq. (3.1)) for sources in Table 3.1. Blue: Film 2D source; red: proprietary wire; green: Kanthal wire; purple: SiC ceramic.

reduction in peak signal with the wire sources compared to the *Globar*. However, the power reduction afforded by wire sources allowed further miniaturization and development of handheld FTIR spectrometers.

More reduction in source operating power may be gained by using thick film sources produced using MEMS manufacturing methods [38, 39]. Using such automated production methods, these components can be produced in great volumes and at low cost. These types of sources are available from several producers and their primary application has been for use in low-cost, single-purpose nondispersive IR (NDIR) analyzers. There are numerous designs available, but a common feature is the formation of a resistive element on a planar substrate. The resistive element is formed by thick film deposition techniques. These sources have low thermal mass, allowing the element to be heated and cooled rapidly to realize pulsed operation with an attendant reduction in power dissipation. The benefits accruing from this are manifold, as the reduced power dissipation reduces the burden placed on the thermal management structures required to reject the heat to the ambient as well as reduces the volume and weight of the battery. The performance cost is in SNR. Because they are operated at lower color temperatures, 2D sources generate less brightness and, therefore, less signal.

### 3.2.5 Infrared Detectors

IR radiation detectors convert photon energy to a voltage or current proportional to the IR energy flux. Detectors for FTIR spectroscopy fall into two (2) classes, thermal detectors or photon detectors. Typical detectors used for mid-IR spectroscopy are indicated in Table 3.2 with representative detector performance metrics. The specific detectivity,  $D^*$ , is a measure of the intrinsic sensitivity of the IR detector and is expressed in Eq. (3.2), below.  $D^*$  is the reciprocal of the noise equivalent power, NEP, normalized to the square root of the detector area,  $A_d^{1/2}$ . NEP is a measured quantity that is the ratio of the noise spectral density (V/Hz<sup>1/2</sup>) to the detector responsivity (V/W), a measure of the SNR due to the detector element.

$$D^* = \frac{A_d^{1/2}}{\text{NEP}} \quad (3.2)$$

Mercury–Cadmium–Telluride (MCT) detectors are photon detectors that are commonly used in a photoconductive mode. These detectors operate by taking advantage of the intrinsic electro-optical properties of the MCT semiconductor. The band gap of this material is such that a mid-IR photon can promote an electron in the semiconductor from the valence band to the conduction band, increasing conductance and lowering resistance. A current

**Table 3.2** Typical mid-IR detectors for FTIR spectrometry with operational metrics.

Detector element	Detector type	Spectral range <sup>a),b)</sup> (cm <sup>-1</sup> )	Operating temperature	$D^*$ (cm Hz <sup>1/2</sup> /W)
DLATGS	Pyroelectric	ca. 15 000–650	−20 to +55 °C	$5.2 \times 10^8$
PbZrO <sub>3</sub> –PbTiO <sub>3</sub> (PZT)	Pyroelectric	ca. 15 000–650	−20 to +70 °C	$1 \times 10^7$
LiTaO <sub>3</sub>	Pyroelectric	ca. 15 000–650	−20 to +70 °C	$2 \times 10^8$
NB HgCdTe	Photoconductive	ca. 15 000–830	−78 °C	$\geq 4.0 \times 10^8$
NB HgCdTe	Photoconductive	ca. 15 000–750	77 K	$4 \times 10^{10}$

a) Pyroelectric spectral response is limited by ZnSe optics.

b) Photoconductive detector high-frequency spectral response is limited by ZnSe optics.

is biased through the detector and the change in conductance induces a change in voltage developed across the detector that is proportional to IR flux. MCT detectors have the advantage of high intrinsic responsivity and low noise and are the most sensitive detectors (highest SNR) used in FTIR spectrometry for mid-IR applications. However, these detectors must be cooled and yield the best performance at cryogenic temperatures. MCT detectors can be cooled by using liquid N<sub>2</sub>, a Stirling refrigerator, or a four-stage thermoelectric cooler (TEC). Although the SNR performance of MCT detectors cannot be approached with thermal detectors, the practical limitations imposed by cryogenic cooling, including access to cryogenic fluids, high power requirements and volume associated with mechanical refrigeration or multistage TECs, make MCT devices unsuitable for portable instruments.

To the knowledge of these authors, all commercial portable and handheld FTIR spectrometers employ deuterated L-alanine-doped triglycine sulfate (DLATGS) thermal detectors. DLATGS is a ferroelectric material that exhibits pyroelectric behavior. At temperatures below their Curie point, pyroelectric crystals are spontaneously electrically polarized. Under illumination by IR radiation, the extent of the electrical polarization of the crystal is thermally altered. This alteration of the electrical polarization state can be measured as an electrical signal when electrodes are attached to the faces of the pyroelectric crystal. The choice of DLATGS is due to its higher  $D^*$  and concomitant higher SNR performance than other thermal, pyroelectric detectors, such as lithium tantalate (LiTaO<sub>3</sub>) or lead zirconate : lead titanate (PZT), see Table 3.2. DLATGS does present a challenge to the developer, however. The Curie point of DLATGS is 59 °C; at higher temperatures, the crystal “de-poles,” and the detector does not respond to IR radiation. For portable in-field FTIR instruments, the operational temperature requirement can be as high as 50 °C ambient, and under a solar load with additional heat from the internal source and electronics, the internal temperature can be as high as 60 °C. Therefore, it becomes necessary to stabilize the DLATGS temperature using an integrated single-stage TEC. The power usage of the TEC must be considered in the context of heat rejection from the instrument, battery size and weight. In instrument designs employing thermoelectrically cooled detectors, the power demands of the TEC are often second only to those of the IR source. The temperature set point of the TEC can be programmed and in the *HazMatID Elite* instrument is held near 32 °C [30]. To reduce power consumption and battery size and mass, thermal management (heat dissipation) and its impact on the design of the spectrometer case and heat sinks have been considered and modeled using Finite Element Analysis [30].

The proximity of the TEC to the IR detector element allows mechanical noise produced within the TEC assembly to couple to the IR detector. As pyroelectric materials are typically piezoelectric as well, this results in the degradation of the signal developed by the IR detector. Strobing TEC operation in a manner synchronous with the interferometer scanning or other strategies may be effective in reducing this effect.

Detectors for FTIR are operated in an AC-coupled mode; the analog electronics that process the electrical signal only respond to the modulated component of the IR signal. As indicated above, the IR radiation is modulated in the audio frequency range by the interferometer. Ideally, the modulation frequency range should be matched to

the optimum responsivity band of the detector. There are limitations to perfectly matching the optimum detector frequency response. Generally, the responsivity of the pyroelectric detector increases with decreasing frequency ( $1/f$ ), with greater  $D^*$  at  $<100$  Hz. To produce such a low modulation frequency, the moving mirror must scan extremely slowly, resulting in an undesired, long scan time. Slower optical velocities lead to poorer baseline stabilities in transformed spectra and the dynamic range of the ADC might be exceeded at the interferogram centerburst. A compromise in optimum responsivity is made for DLATGS detector operation. The interferometer scanning mechanism is generally operated at  $\sim 0.5$  cm/s OPD velocity. This leads to a modulation frequency bandwidth of 325–2000 Hz in the spectral range of interest.

### 3.2.6 Metrology Laser

A key enabling technology for practical FTIR spectrometry is the reference laser metrology system and servo control of the mirror drive voltage, maintaining uniform velocity and fringe spacing during the scan. A separate but coincident laser interferometer is universal in FTIR spectrometers. As previously presented, the laser interferogram consists of a cosine wave whose period is precisely known. By sampling the IR interferogram at the zero crossings of this waveform, this precision is transferred to wavenumber axis of the spectrum derived from the IR interferogram.

Until the advent of portable FTIR spectrometers, the helium–neon (HeNe) gas laser was universally employed as the reference laser. The *TravelIR* used an HeNe laser, but, as mentioned above, did not provide usual operations under battery power. Gas lasers provide narrow output linewidths and wavelength stability. These properties are excellent benefits for a laser metrology system for FTIR spectrometry. However, HeNe lasers employ a high voltage power source for the discharge tube; therefore, their operating powers are  $>10$  W for the models used in FTIR spectrometry. As with the IR source, the HeNe reference laser is a significant consumer of power and inhibitor to reducing SWaP. In addition, the HeNe laser and its associated power supply are quite bulky and heavy, adversely contributing to size and mass. In developing battery-integrated portable FTIR systems, a lower power reference laser was required.

The telecommunications industry has been a boon to the development of photonics systems, including low-power, rugged, small, solid state communications lasers. The *HazMatID* was the first commercial FTIR spectrometer to replace the HeNe reference laser with a solid state laser. Most of the commercial, portable FTIR spectrometers use a distributed feedback (DFB) telecommunications laser that operates in the near-infrared (NIR). This type of laser typically employs an InGaAsP/InP diode fabricated in quantum well structure. The power required to operate the diode laser is 0.024 W, a significant reduction in required operational power. Additionally, the size and mass of the diode assembly are minuscule in comparison to the HeNe laser and power supply. Performance compromises are made with diode lasers relative to HeNe. The output bandwidth of diode lasers is significantly greater than HeNe. NIR diodes have a specified output bandwidth of  $>5\text{ cm}^{-1}$ , much greater than HeNe which are better than  $0.05\text{ cm}^{-1}$ . In practice, the NIR diode laser exhibits significantly narrower linewidths than specified, yielding measured IR spectral bandwidths of  $2\text{ cm}^{-1}$ ; however, they are only to be used for applications where moderate spectral resolution ( $4\text{--}8\text{ cm}^{-1}$ ) will suffice, as in the case of condensed-phase unknown identification. The output wavelength will drift with temperature with the diode laser, causing a spectral shift in the recorded spectra. Manufacturers have employed temperature-stabilizing hardware in the diode assembly or spectral calibration methods to correct for these temperature-induced wavelength shifts.

### 3.2.7 Internal Reflection Sample Interface

The placement and removal of the unknown threat sample are important user-interface attributes in a portable FTIR system. Indeed, the first portable FTIR instrument was very much designed around its sample interface,

which predated the spectrometer by a couple of years. A rugged, chemically resistant and optically transparent interface is required for portable FTIR instruments used in condensed-phase unknown analysis. Traditional IR analyses of liquids and solids were accomplished by transmission spectroscopy, requiring some degree of sample preparation and the use of alkali halide crystal materials, such as NaCl, KBr, or KCl. These materials are far less than optimum for field use as they are brittle, hygroscopic, and highly water soluble. Attenuated total reflection (ATR) IR spectroscopy is well known and has been used for analytical IR spectroscopy since the 1960s. ATR spectroscopy relies on the phenomenon of internal reflection. The theory and experimental aspects of ATR spectroscopy were developed by Harrick [40, 41] and Fahrenfort [42]. In this report, we shall not address many of the details of the theory and the reader is encouraged to consult the referenced literature. ATR spectroscopy requires an internal reflection element (IRE), an IR-transmitting crystal prism that is optically dense (higher refractive index than the samples analyzed). The IREs used for traditional ATR optics were most commonly Ge, ZnSe, and KRS-5 (ThI : ThBr). Incident IR radiation illuminates the sample through the crystal at an incident angle,  $\theta_i$ , from normal. Radiation reflected from the internal surface of the prism exits at an equal reflection angle  $\theta_r$ . If  $\theta_i, \theta_r \geq \theta_c$ , the critical angle as defined in Eq. (3.3) below, total internal reflection at the IRE/sample interface occurs.  $n_2$  is the refractive index of the sample; and  $n_1$  is the refractive index of the IRE. For a sample with a refractive index,  $n_2$ , of 1.5, a good estimate for many samples encountered, and an IRE refractive index,  $n_1$ , of 2.4, the critical angle,  $\theta_c$ , is  $39^\circ$ . To satisfy this condition, most ATR interfaces are designed with a nominal angle of incidence,  $\theta_i$ , that is  $45^\circ$  or slightly greater.

$$\theta_c = \sin^{-1} \left( \frac{n_2}{n_1} \right) \quad (3.3)$$

At the reflection interface between the IRE and sample, the incident IR radiation electric field extends some distance beyond the interface and into the sample material. This nonzero electric field amplitude extending into the sample is called the *evanescent wave* and it is this evanescent wave that interacts with the molecules comprising the sample, leading to the observed IR absorption spectrum. Equation (3.4), below, describes the depth of penetration for the evanescent wave for a sample in contact with an IRE where radiation undergoes total internal reflection. The refractive indices are defined as above.

$$d_p = \frac{\lambda}{2\pi n_1 \sqrt{(\sin^2 \theta - (\frac{n_2}{n_1})^2)}} \quad (3.4)$$

$\theta$  is the angle of incidence relative to the normal of the IRE surface;  $\lambda$  is the wavelength of the incident IR radiation. For IR radiation in the mid-IR region ( $4000\text{--}650\text{ cm}^{-1}$  or  $2.5\text{--}15.4\text{ }\mu\text{m}$ ), the penetration depth,  $d_p$ , varies from ca. 0.5 to 3  $\mu\text{m}$  across the spectral range. At these pathlengths, all IR bands are observed at <1 absorbance unit (AU), in the linear regime. As the total quantity of material sampled is ca. 2.3  $\mu\text{g}$ , small quantities are required for high-quality spectra, and these instruments can be considered as micro-sampling tools.

ATR spectroscopy has practical advantages over transmission spectroscopy because (i) little or no sample preparation is required; the sample is measured by contact with the IRE; and (ii) the optical pathlength is reproducible and controlled for a given sample and is determined by the ratio the refractive index of a sample in good contact with the IRE and the refractive index of the IRE, both constants.

The traditional IRE crystals are not water soluble, but generally are not physically durable enough for use in austere environments in the field. Wilks [43] first reported the use of a diamond prism for use as an IRE. These early diamonds were natural Type-IIA, extremely expensive, and due to cost, generally not practical or commercially viable. Optical-grade, synthetic diamond, first produced in the mid-1990s [44], provided an optimum sample interface for instruments used in the field for condensed-phase sample analysis. The availability of highly pure, single crystal, Type-IIA synthetic diamonds has served to transform qualitative IR spectroscopy methods. Now, most qualitative IR analyses are performed with ATR methods using diamond IREs. All currently available, portable FTIR instruments use some type of diamond ATR sample interface.

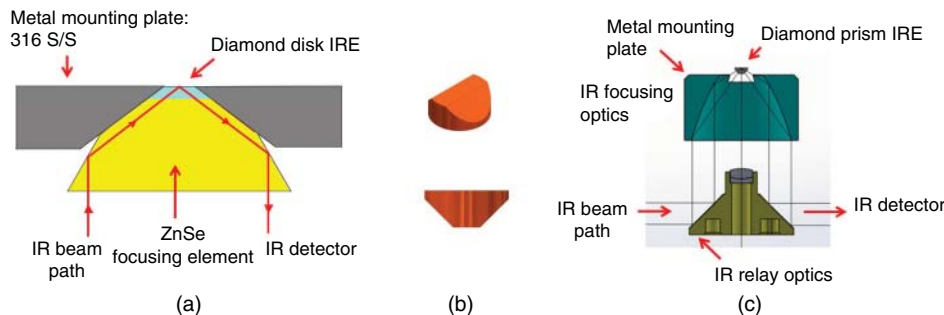


**Figure 3.6** Single-reflection diamond ATR optics employed in portable FTIR systems. (a) Diamond disk IRE optically contacted with ZnSe. (b) “Rooftop” diamond IRE typical in prism configuration. (c) Diamond prism IRE with associated optics.

What makes diamond material, specifically Type-IIA diamonds, one of the best choices for IR spectroscopy and specifically in-field IR spectroscopic analyses? Type-IIA diamonds are free from nitrogen and other impurities that limit optical transmission. Type-IIA diamonds are optically transparent from the ultraviolet (UV) to the far-IR. Diamond is the hardest known substance. The Knoop hardness index for diamond is  $9000 \text{ kg/mm}^2$ . This hardness property makes diamond impervious to scratching and optical performance degradation, providing a rugged surface for hard, abrasive samples and ease in cleaning. Diamond is chemically resistant. Diamond will not react with encountered chemicals, including caustic materials and will withstand decontamination by common decontamination fluids including hypochlorite solutions. Finally, diamond has a relatively high refractive index, ca. 2.4, that makes it a good candidate for an IRE for IR spectroscopy.

There are two general ATR optical designs employed for field-portable FTIR spectrometers, as shown in Figure 3.6. All instruments used in threat identification use single-reflection ATR optics. Early instruments, including the *TravelIR* and the *HazMatID*, employed the configuration as shown in Figure 3.6a. This arrangement, referred to as a *DuraDisk™* (SensIR Technologies, LLC, Danbury, CT), used a ZnSe-focusing crystal shaped with aspheric surfaces, optically contacted to a synthetic diamond disk that served as the sample interface [45, 46]. The ZnSe–diamond assembly is mechanically fixed into a stainless steel (in some cases Hastelloy®) disk that is integrated into the instrument top plate. As the refractive indices of ZnSe and diamond are nearly identical, nominally 2.4, there are no reflective losses at the ZnSe–diamond interface and the optical efficiency is very high. At the time, 1995–2002, this configuration was more cost-effective to produce than is the case today. Greater availability of cheaper, single-crystal synthetic diamonds caused designers to shift to prism IRE designs as shown in Figure 3.6c. Some variation of this design is employed in all portable ATR FTIR spectrometers today. The diamond IRE is an inverted “rooftop” that is fashioned from a truncated cylinder as illustrated in Figure 3.6b. The diamond is a single crystal with a circular sample-contacting surface that is 2–2.5 mm in diameter. The modulated IR source radiation is introduced into the crystal face by an aspheric-focusing reflector, either Al- or Au-coated. The detector-return-focusing optic is also an aspheric reflector. In either configuration (Figure 3.6a or c), a small amount of sample is brought into contact with the diamond and the IR spectrum is recorded in an ATR mode. For solids, an integrated press applies 15–50 lbs force to the sample, ensuring good contact with the diamond surface and spectra with maximized absorbances.

### 3.3 FTIR Spectrometer Performance Attributes

FTIR spectrometry has inherent advantages over other infrared instrumental methods, such as scanning monochromator or spectrograph instruments. For the most part, these advantages readily translate to portable or handheld applications. The first advantage to discuss is the *multiplex advantage*, or Fellgett’s advantage. In an

FTIR spectrometer, all wavelengths are measured simultaneously. In comparison with a scanning monochromator, this leads to an SNR advantage or time advantage. All other parameters being equal, the FTIR instrument yields spectra with  $M^{1/2}$  better SNR for equal scan times or  $M^{1/2}$  faster acquisition for equal SNR, where  $M$  is the number of resolution elements, the spectral range divided by the spectral resolution,  $\Delta\nu$ . Spectrograph monochromator instruments are also multiplexing spectrometers. However, it is not possible to cover the mid-IR range with a single grating in a spectrograph without significantly degrading resolution. Spectrographs are not presently adequate for broad threat, in-field identifications based on spectral comparison methods.

The second advantage enjoyed by FTIR spectrometry is the *throughput advantage*, or the Jacquinot advantage. Throughput (or étendue),  $\Theta$ , is a constant for radiometric optical systems and is the geometric light-gathering power, equal to the product of the area and solid angle,  $A * \Omega$ , at any focus. As FTIR spectrometers do not employ a slit, as do scanning or spectrograph monochromator systems, the throughput and, therefore, the signal, is higher for FTIR instruments operating at equal resolution. As we will discuss below, throughput is an important trade-off for portable instruments. Higher throughput translates to larger optics and larger instruments.

The last advantage of FTIR instruments that we will discuss is the *wavelength precision* or Conne's advantage. The wavelength accuracy and reproducibility of an FTIR instrument is far better than a dispersive spectrometer due to the laser-referencing interferometer control and accurate tracking of mirror position by using the laser interferogram fringes. This is quite important for the in-field identification of threats based on spectral comparison methods. Wavelength shifts between the sample and library spectra would degrade the comparison metrics and, therefore, the accuracy of identifications. Although the wavelength accuracy and reproducibility of portable FTIR spectrometers are not as high as HeNe-referenced instruments, it is good enough that spectral library reference spectra recorded on different models of FTIR spectrometers, including laboratory systems, can be used on the portables with good success in threat identifications in the field.

### 3.3.1 Trading Rules for FTIR Spectrometry

In an ideal scenario, the developer of an instrument would like to maximize all of performance attributes that are important for the intended applications of the instrument, SNR and spectral resolution frequently being the most important applications attributes. In a radiometric instrument, the signal amplitude is a function of IR source power and optical parameters, noise originates from the detector, associated electronics, and uncertainty in the OPD at which the interferogram is sampled.

$$\frac{\text{Signal}}{\text{Noise}} = \frac{U_v(T)\Theta\Delta\nu t^{1/2}\epsilon}{\text{NEP}} = \frac{U_v(T)\Theta\Delta\nu t^{1/2}D^*\epsilon}{A_d^{1/2}} \quad (3.5)$$

The SNR of an FTIR spectrometer can be estimated from Eq. (3.5) above. This relation ties together many of the physical attributes that we have discussed. For in-field threat identification, the SNR and wavelength precision are the two of the most important characteristics for analytical performance. Maximizing SNR allows more precise spectral comparisons and identification of minor components in mixtures, an important requirement, since many field samples are impure.

Equation (3.5) reflects the so-called “trading rules” for FTIR spectrometry. These physical parameters require balancing in design decisions for portable spectrometers, perhaps more so than in laboratory-based systems for which the management of SWaP is not a factor. The acquisition time,  $t$ , is the total integration time during data collection including signal averaging of scans. The acquisition time is an operator-selectable parameter, and of small consequence to design. The OPD velocity determines the time per scan and is usually selected to yield interferogram modulation frequencies that are compatible with the detector frequency response. Depending on the manner that interferograms are collected, the acquisition time per scan is typically in the range from one to four seconds. Typical default total acquisition times (signal averaging multiple individual scans) are 30 seconds to record the spectrum of the unknown threat.

Perhaps the easiest design parameter to balance is the best spectral resolution,  $\Delta\nu$ , expressed in  $\text{cm}^{-1}$ . The majority of portable and handheld FTIR spectrometers are targeted toward condensed-phase unknown identifications, not quantitative analyses of gas-phase molecules where higher spectral resolutions yield more accurate concentration determinations. For condensed-phase samples, the IR spectral linewidth is determined by intermolecular interactions and generally exceeds moderate instrumental spectral resolutions. Field-portable spectrometers have instrumental spectral resolutions no better than  $4\text{ cm}^{-1}$ . Decreasing resolution to  $8\text{ cm}^{-1}$  would improve SNR and not degrade identification accuracy. Defining  $4\text{ cm}^{-1}$  as the best spectral resolution design specification somewhat simplifies the interferometer requirements, optical design, and size.

$U_s(T)$  is the IR source brightness, estimated by Planck's Law and expressed in Eq. (3.1) above. The design trade-off with higher source brightness (higher signal) is higher operating power and, therefore, larger SWaP. Optical throughput,  $\Theta$ , should be conserved in the optical system from the source element to the detector. The typical DLATGS detector element size is 1 mm square. The diamond ATR element is  $\sim 2$  mm at the sample. Beamsplitter diameters (apertures) are 25 mm for suitcase instruments and 12.5 mm for handheld instruments. The larger beamsplitters in suitcase-portable instruments, like *HazMatID* and *ThreatID*, yield significant SNR advantages over handhelds, albeit at the expense of SWaP. The final signal-related parameter,  $\varepsilon$ , is the optical efficiency. The detected IR signal amplitude is reduced by losses in the optical system. Fifty percent of the IR radiation is directed back towards the source by the beamsplitter, only 50% travels towards the sample. Most mirrors in the optical system are aluminum coated with reflectivity of 98.7% at  $1000\text{ cm}^{-1}$  resulting in 1.3% signal loss per reflection. The diamond ATR element has both reflection losses and absorptive losses. As refractive index of diamond is relatively high, 2.4, the reflection losses on the prism faces are 17% per face, leading to an efficiency of 69%. However, the transmission through the diamond prism can be increased as much as 30% through application of a broadband antireflection coating to the prism faces [47]. Two-phonon absorption of diamond is observed near  $2000\text{ cm}^{-1}$  [48] leading to significant absorption loss (and reduced signal) in this region of the spectrum. Fortunately, few chemical compounds exhibit fundamental IR absorption bands in this range, the exceptions being triple-bonded compounds, such as nitriles, cyanides, and alkynes, or cumulated double-bonded compounds, such as isocyanates and thioisocyanates. The beamsplitter substrate, compensator plate, and detector window are composed of ZnSe and comprise six (6) optical surfaces. Since the refractive index of ZnSe is also 2.4, the transmission efficiency through these optics is expected to be  $(1 - 0.17)^6$ , or 33%. Again, through the application of a broadband antireflection coating to the ZnSe surfaces, the transmission efficiency is significantly improved.

Equation (3.5) provides an SNR estimate presuming that the instrument is detector-noise limited. The NEP and corresponding  $D^*$  values are measured quantities for a given detector. In reality, there are noise sources that do not originate in the detector that can be manifested in the signal train and cause the real SNR performance to be less than detector-noise limited (the measured noise is greater than the detector noise). Potential noise sources include radiated energy picked up by the analog electronics on the preamplifier and filtering circuits, variations in the source intensity, and the TEC on the DLATGS detector. Through good engineering design and testing practice, these noise sources are minimized to the degree possible. Another noise source is due to sampling error caused by velocity jitter that can arise through external perturbations to the interferometer scanning mechanism. This is a particularly nettlesome problem for a handheld or portable field instrument used in uncontrolled environments. With modern FTIR technology, these scan errors may be compensated by signal-processing methods when the digitized laser interferogram is available for post processing with the IR interferogram [30].

## 3.4 Modeling and Simulation Guide Portable Instrument Design and Development

In this section, we discuss ways in which a simulation model can be used during the technology development and product definition phase of a new portable FTIR spectrometer development.

The first step in the design process for a new instrument is product definition, the object being to specify the instrument's capabilities in a way that best aligns with the perceived needs. The metrics used to specify these capabilities fall into two general categories: "performance" metrics, such as SNR and spectral resolution which the designer typically strives to maximize, and "cost" metrics which should be minimized. Cost metrics refer to parameters in limited supply; in the case of a portable instrument, the most expensive of these is frequently SWaP.

Performance metrics are generally interrelated by reciprocal functions where the designer may improve one aspect of instrument performance by accepting a reduction in another, an example being spectral resolution and SNR. The relationships linking performance and cost metrics are generally direct, i.e. improved performance implies a greater cost.

In the past, when the term "FTIR" implied a large instrument operating in the controlled environment of a laboratory and tethered to the power grid, the designer's task during product definition was to best balance the performance metrics. Cost metrics, particularly SWaP, were of little importance as the market placed no premium on minimizing these. To assist in balancing the performance metrics, "trading" rules, each of which defines the reciprocal relationship between a pair of performance metrics, were used.

The appeal of the trading rule lay in the insight it provided to the designer as the various aspects of instrument performance were balanced. The relationships were readily illustrated as curves in 2D spaces, and significant features, such as maxima or inflection points were readily identifiable.

### 3.4.1 The Need for a New Tool

As FTIR spectrometers shrunk from benchtop box to case-mounted portable units and handheld devices and the operating venue moved from the lab to the field, SWaP became a significant cost metric. Market demand for portability dictated smaller and lighter products, while the limited energy storage capacity of battery technology made reducing power consumption a critical factor.

Also accompanying the new generation of portable instruments were new performance metrics, such as run-time, robustness to thermal and vibratory environments, compatibility with decontamination procedures and user interface ergonomics. Many of these new metrics are strongly linked to SWaP.

The greater number of metrics implied more complex trading rules whose results could no longer be displayed in easily visualized two- or three-dimensional spaces. The inability to display the results in an intuitive format reduced the usefulness of the trade rule to the designer.

### 3.4.2 System Simulation as a Multiple-Dimension Trade Rule

A system-level math model may be viewed as the general case of a trading rule. The model represents the complete set of metrics, and the results set generated when one or more of the model parameters are varied represents the complete set of functional relationships present between the metrics. The model's usefulness during product definition lies in the ability it provides to the designer to extract subsets of the results suitable for display in an insightful format.

Such a model is extensible to accommodate any number of cost or performance metrics. Synthetic figures of merit (FOMs), e.g. run-time/watt-hour, may be defined and subsequently displayed and traded just as metrics corresponding to directly observable characteristics, e.g. spectral range.

### 3.4.3 Simulation Model Architecture

Because it provides easily visible linkages between the elements of a physical instrument and those of the simulation model, a model that is functionally partitioned by clearly defined interfaces and in a fashion similar to that of the physical instrument facilitates development, troubleshooting, and validation. Figure 3.7 illustrates a

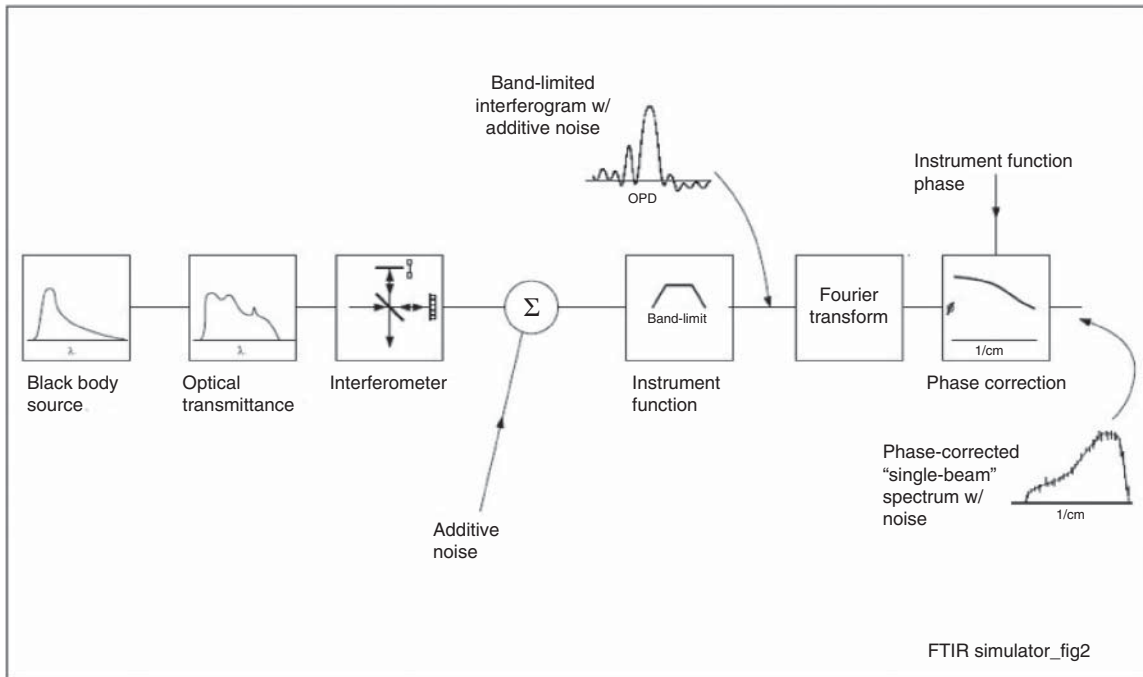


**Figure 3.7** Functional partitioning of the modelling simulator. The system provides good visibility into the system operation by allowing observation of intermediate results, such as the interferogram or the power spectral density entering the interferometer.

model architecture that closely mirrors that of a physically realizable system. The presence of internal nodes corresponding to observable points in the actual instrument, e.g. the interferogram observed at the output of the IR preamplifier, facilitates validation of the model against actual hardware. This level of visibility also makes the model a useful tool for isolating faults occurring in an actual instrument.

The complexity of the simulation model and the level of fidelity of its results are functions of its intended application. If the model is to be used during requirements definition or anomaly investigation, it must provide accurate, precise results and provide good visibility into internal nodes implying a detailed, complex model. If the model will be used only as a guide during product definition, a lower level of performance and fewer inputs are required, and a simpler model may suffice.

Fortunately, the physics underlying FTIR is well understood and documented in the literature and the mathematics is general in nature and robust, factors which reduce the burden of developing a suitable model. A more detailed summary of the elements of an FTIR spectrometer system that can be modeled by the simulator and their pertinent inputs are presented in Table 3.3. The model is detailed, adhering to the parameters of Eq. (3.5), and includes signal elements as well as noise contributions from the detector and electronics, as well as phase contributions.

The design of the user interface is a strong determinant of the model's ease-of-use. A "dashboard" metaphor on which all user-definable parameters, salient results, and other "system-state" variables are displayed is an efficient interface design. Inclusion of some form of progress indicator to assure the user that the simulation has not "hung" is useful, particularly if the time required to execute a simulation exceeds a few seconds, which is often the case.

General-purpose script-based software tools, such as *MATLAB®*, are well-suited to performing the required mathematical operations. The requirement to generate textual scripts and the lack of a convenient method for incorporating blocks of explanatory text and comments are significant shortcomings of the tool.

**Table 3.3** Simulation model elements and their corresponding elements of a physically realizable instrument.

Model element	Physical element	Domain	User-specified parameters
Foreoptics	IR source	Phys. optics	Color temp., Phys. dimensions
	Collimator	Geo optics	Phys. dimensions, Beam divergence
	Optical coatings	Phys. optics	Spec. transmittance
Sample	Sample	Phys. optics	Spec. transmittance
	ATR	Phys. optics	Spec. transmittance, dispersion
Interferometer	OPL modulator	Phys. optics	Stroke, pitch, Jitter, Mirror quality, Dispersion
Detector	Detector and FET	Complex freq.	Spec. responsivity, Freq. resp., Johnson & 1/f noise
Signal channel electronics	Preamplifier, freq. equalization, ADC	Complex freq.	Gain, Freq. resp., Johnson & quantization noise
Signal processing	Fourier transform, phase correct	Numerical processing	Phase correction strategy

The rightmost column of the table lists some of the parameters specified by the user during simulation.

Interpreted coding languages, such as *Python*, are also capable of performing the calculations but exhibit the same shortcomings. Also, as the graphics capability of most such languages is much less developed than that of *MATLAB®*, a user will most likely have to export the simulation results to another package for formatting and display.

Numerical word processors, such as *MathCAD®* and *SMath Studio*, produce “live” note sheets incorporating both text and familiar mathematical symbology. The word-processor paradigm makes incorporating textual notes and comments easy and the note sheet format executes as it is typed eliminating the need to develop scripts. The mathematical and graphics capabilities of *MathCAD* are sufficient for the task, although not as well-developed as those of *MATLAB*.

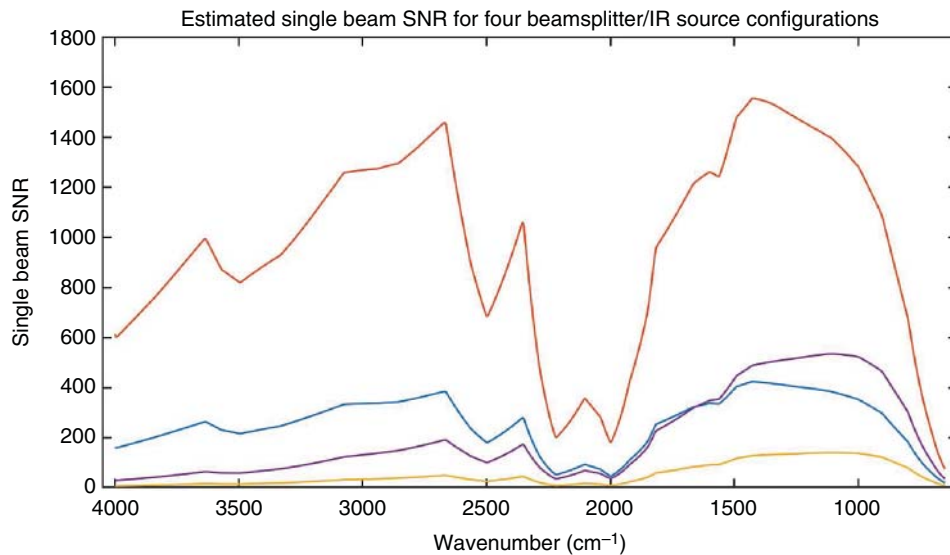
#### 3.4.4 An Example – Optics and Source Trade Study

Figure 3.8 illustrates the use of a simulation model to identify which of the four candidate instrument configurations will meet a specified single scan, peak SNR requirement of 400 : 1 while minimizing unit size and power demands.

The simulation was set up to display single scan, single beam SNR as the performance metric. The diameter of the optical beam (beamsplitter) and the temperature of the IR source were defined as cost metrics serving as surrogates for instrument size and power, respectively. Two options for each of the cost metrics were assessed, resulting in the four simulation cases shown.

Three of the cases satisfy the SNR requirement. The large margin between the performance and the requirement seen in the high-power/large-beam example indicates a design significantly exceeding the stated target, and that the required performance could most likely be achieved at lower “cost.”

This is borne out by the models that incorporate a larger beamsplitter with a lower power source and a smaller beamsplitter with a higher power source, Figure 3.8, middle, indicating that the requirement can be met with either of the cost metrics at the smaller of the possible values. The availability of two compliant configurations rather than just one provides the designer additional freedom during subsequent trades.



**Figure 3.8** Single beam SNR, single scan simulation results for hypothetical miniaturized FTIR spectrometers with different beamsplitter diameters (throughput) and source color temperatures. Orange: 12.5 mm-diameter beamsplitter and 1176 K source color temperature; blue: 6.25 mm-diameter beamsplitter and 1176 K source color temperature; purple: 12.5 mm-diameter beamsplitter and 730 K source color temperature; yellow: 6.25 mm-diameter beamsplitter and 730 K source color temperature.

### 3.4.5 Power Budget Simulation

As mentioned previously, instrument size, weight and power are significant “cost” factors driving the design of a battery-powered portable FT instrument. The power demanded by the instrument will directly impact the size and weight of the battery, as both the volumetric power density (watt-h/in.<sup>3</sup>) and the gravimetric power density (watt-hour/kg) of the battery are limited by the chemistry employed. As the battery is often the largest and heaviest single component in the instrument, its size and mass will significantly impact those of the instrument.

Increased power demand will also impact the instrument volume and weight indirectly through the increased complexity of the thermal management structures needed to reject the greater heat produced. Consequently, the power demand posed by a prospective instrument design can serve as a representative surrogate for all three elements of SWaP.

Estimating the power demanded by a prospective instrument design is readily accomplished through simulation. As the instrument performs a defined sequence of operations a defined number of times, while recording a spectrum, the instrument may be modeled as a set of discrete states, each representing a specific function, e.g. increment scanning mirror position, and search library for spectrum match. In operation, the instrument follows a path passing through all states, in some cases, revisiting a state repeatedly. The states are characterized by a common set of state variables, each of which indicates the condition assumed by a given hardware element and its power demand or the power required to execute a software process while in that state.

Summing the power values over the set of state variables and multiplying by the dwell time spent in the state yields an estimate of the total energy dissipated by the instrument while in the given state. Summing the energy values over the trajectory followed during the process yields an estimate of the total energy required to execute the process.

As the IR radiation source is frequently the single largest power dissipator in the instrument, the choice of technology utilized for this component will strongly affect the rate at which the battery is depleted, and, consequently, the number of spectra that may be acquired between battery replacement or re-charge.

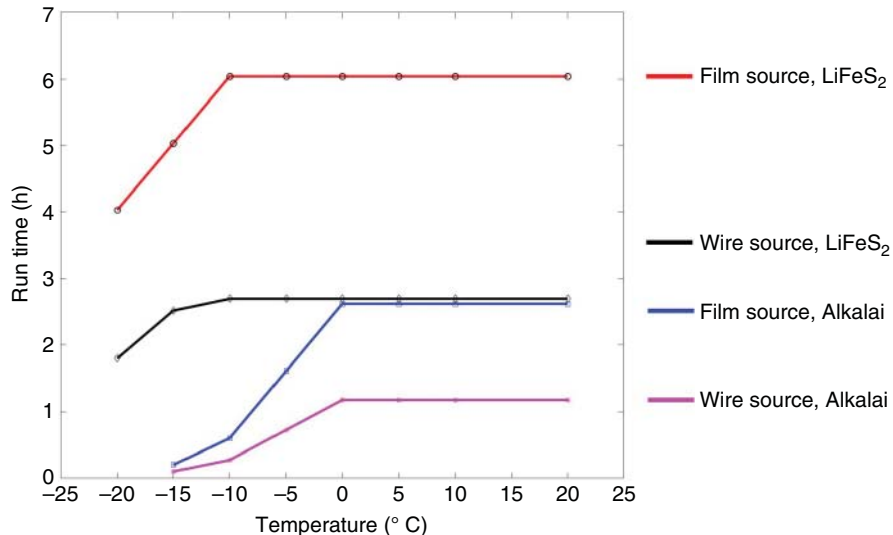


**Figure 3.9** Simulator-estimated battery run-time vs. operating temperature for a hypothetical FTIR spectrometer configuration for two (2) IR source types and two (2) battery chemistries.

Shown in Figure 3.9 are the estimated battery-charge run-times for four hypothetical spectrometer hardware configurations – two IR source types and two battery technologies. The reduction in run-time with falling temperature is a consequence of the diminishing battery capacity in cold environments that is typical of most battery chemistries. As indicated by the red plot, the low power requirements posed by a power-strobed thick-film IR source coupled with the high capacity of lithium batteries result in an estimated run-time in a “warm” ambient environment of six hours. As a hypothetical FTIR instrument design matures and the power metrics are updated to better reflect the actual instrument design, the precision of the estimates improves.

It must be borne in mind that the selection of battery chemistry may not be made based solely on the run-time provided. The allowed thermal environments, the level of “care” demanded during recharge, possibility of spontaneous combustion, and transport limitations imposed on some battery chemistries are all factors that influence the selection of battery chemistry, in addition to device price.

### 3.5 Portable FTIR Performance Benchmarks

The SNR of a portable FTIR spectrometer is an important analytical performance attribute relative to the ability to identify unknowns. As we have discussed, SNR should be maximized, but achieving high SNR is counter to miniaturization. Representative measured absorbance noise for portable suitcase and handheld FTIR systems are shown in Figure 3.10. These data were recorded with DLATGS detectors in the mid-IR region from 4000 to  $650\text{ cm}^{-1}$  for a one-minute acquisition using  $4\text{ cm}^{-1}$  spectral resolution. The spectra are plotted on a common scale; the handheld data is offset for clarity. In both the cases, the absorbance noise is  $<0.001\text{ AU}$  across the mid-IR range (significantly less for the suitcase model) except in the diamond absorption region near  $2000\text{ cm}^{-1}$  and in the low-frequency region where the source emission and optical efficiency fall off. The maximum sample absorbances for single-reflection diamond ATR measurements fall in the range from 0.15 to 0.5 AU; therefore, the peak-to-peak absorbance-to-noise ratios exceed 150 : 1. The noise for the suitcase-portable unit is ca. 4× less than the handheld, and even better than this in the high-frequency region. The major contributor is optical throughput. Also, the

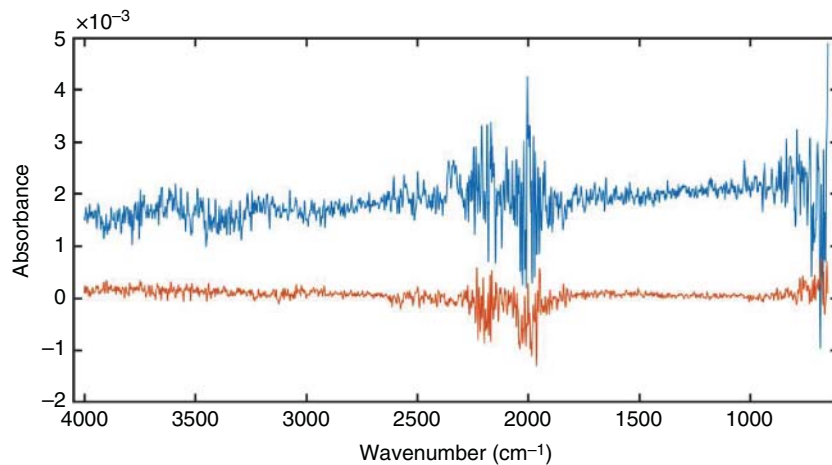


**Figure 3.10** Representative absorbance noise recorded from handheld (blue) and suitcase-portable (orange) spectrometers. Measurement conditions – one minute acquisition,  $4\text{ cm}^{-1}$  spectral resolution, single reflection diamond ATR, and DLATGS detector.

source color temperature is higher in the case of the suitcase-portable instrument resulting in higher signal in the high-frequency region of the spectrum in comparison with the handheld. Note that these observations are consistent with the SNR plots generated by simulation and presented in Figure 3.8.

The absorbance and wavenumber reproducibility are also important metrics for ATR spectroscopy systems. While providing ease in sampling and a rugged sample interface, there is more instrument-to-instrument variability in ATR spectroscopy when compared to transmission spectroscopy. Since library spectra are not always recorded on the same instrument as the unknown sample, this instrument-to-instrument variability can be important, particularly when analyzing for minor components in mixtures. It is possible that library spectra are recorded with completely different ATR optics than on the instrument used for analyses. As shown in Eq. (3.4), the penetration depth and, therefore, the absorbances of ATR spectra are dependent on the angle of incidence and the refractive index ratio of the sample and the IRE. Observed ATR spectra are sensitive to angle-of-incidence variations, particularly when close to the critical angle. Also, band shifts due to dispersion in the real part of the refractive index are observed in spectra when closer to the critical angle. The alignment of the ATR optics is not exact across instruments and this leads to small, effective incident-angle variations. These angle variations can contribute to both variation in absorbance intensity and shifts in the indicated wavenumber.

Representative instrument-to-instrument variation is shown in Figure 3.11 in which 2-propanol spectra were recorded in single-reflection mode with diamond ATR optics on 70 different instruments and are overlaid. It should be mentioned that there might also be some sample placement variation in these data; the diamond surface might not be completely covered in all cases. Also shown is the standard deviation over the spectral range from 4000 to  $650\text{ cm}^{-1}$ . In this case, the variation appears to be intensity differences primarily. The ratio of the mean IR spectrum standard deviation to the standard deviation across all samples is 29 : 1. The instrument-to-instrument variation due to the ATR sample interface exceeds the instrumental noise contribution. This variation does not impact the major component identification, but can place a limit on fractional concentration limits of identification (LOI) for minor components in mixtures. Currently, minor components in mixtures can be identified at concentrations of ca. 10% or greater using automated software methods, lower if using expert operator-guided spectral interpretation skills.

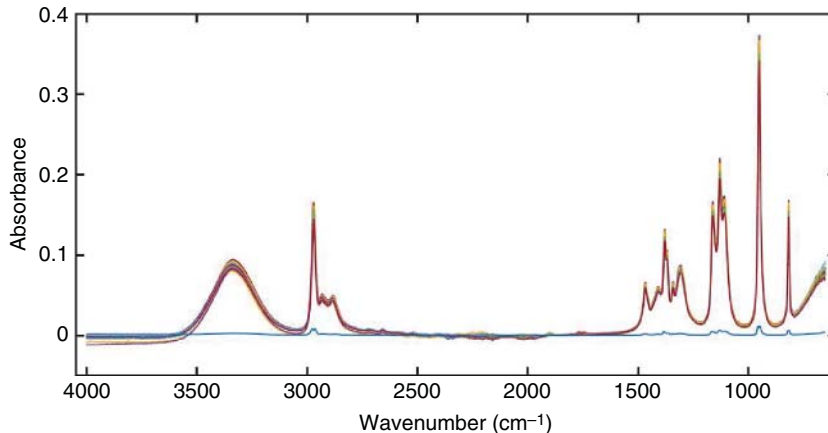


**Figure 3.11** 2-propanol (liquid) recorded on 70 different portable FTIR instruments. Also shown (blue) is the standard deviation at each spectral frequency. Measurement conditions: 30 seconds acquisition,  $4\text{ cm}^{-1}$  spectral resolution, single reflection diamond ATR, and DLATGS detector.

### 3.6 Conclusion

The needs of the responder who is called to analyze chemical threats, for example, chemical warfare agents, toxic industrial chemicals, explosives, and narcotic drugs, drove the technology development of portable FTIR spectrometers. This led to a revolution in miniaturizing and hardening vibrational spectroscopy instrumentation in general. The footprint of laboratory systems has also been reduced, due to the performance and commercial success that portable spectrometers have enjoyed. In this report, we have discussed the technologies that have enabled the development of portable FTIR spectrometers and the performance tradeoffs faced in developing these instruments. The size reduction and performance of portable FTIR spectroscopy have relied on technology advances in numerous fields. Continued developments in the integrated circuit design and miniaturization of computers have provided smaller platforms while concomitantly increasing computational speed and solid-state memory capacity. Materials development, primarily made for abrasives, led to affordable, single crystal, synthetic diamond optics. The availability of embedded systems, e.g. FPGAs, digital signal processors (DSPs), has allowed the reduction in parts count and allotted volume for electronic hardware components. The development of Li-ion battery technology for portable computers provided a higher energy density needed to achieve acceptable run-time from a portable FTIR spectrometer. The telecommunications revolution provided small, low-power, solid state lasers, optical coatings, and fabrication methods. The digital electronics, multimedia industry provided low-cost, high-precision ADCs. Improvements in electronics-manufacturing methods, including multilayered printed circuit board (PCB) manufacture and flex circuits, also minimized the size contribution of electronics.

### Abbreviations and Acronyms

2D	two-dimensional
ADC	analog-to-digital converter
ATR	attenuated total reflection
AU	absorbance unit
CBIRF	Chemical Biological Incident Response Force

CBRNE	Chemical, Biological, Radiological, Nuclear, and Explosives
CWA	Chemical Warfare Agents
DFB	distributed feedback
DLATGS	deuterated L-alanine-doped triglycine sulfate
DoD	Department of Defense (USA)
DSP	digital signal processor
FDNY	New York City Fire Department
FOM	figure of merit
FTIR	Fourier transform infrared
FPGA	field-programmable gate array
HME	homemade explosive
IED	improvised explosive device
IR	infrared
IRE	internal reflection element
LOI	limit of identification
MCT	mercury–cadmium–telluride
MEMS	micro-electromechanical systems
NDIR	nondispersive infrared
NIR	near-infrared
OPD	optical path difference
PCB	printed circuit board
PID	proportional-integral-differential
PZT	lead zirconate titanate ( $\text{PbZrO}_3\text{-PbTiO}_3$ )
SNR	signal-to-noise ratio
SWaP	size, weight, and power
SWGDRUG	Scientific Working Group for the Analysis of Seized Drugs
TEC	thermo electric cooler
WMD-CST	Weapons of Mass Destruction Civil Support Team (USA)
ZPD	zero-path difference

## References

- 1 Coblenz, W.W. (1905). *Investigations of Infra-red Spectra*, Publication No. 35. Washington, DC: Carnegie Institution of Washington.
- 2 Colthup, N.B., Daly, L.H., and Wiberley, S.E. (1990). *Introduction to Infrared and Raman Spectroscopy*, 3e. St Louis, MO: Academic Press.
- 3 Bellamy, L.J. (1975). *The Infra-red Spectra of Complex Molecules*. Dordrecht: Springer.
- 4 Scientific Working Group for the Analysis of Seized Drugs (2019). *Scientific Working Group for the Analysis of Seized Drugs (SWGDRUG) Recommendations, Version 8*. [http://www.swgdrug.org/Documents/SWGDRUG%20Recommendations%20Version%208\\_FINAL\\_ForPosting\\_092919.pdf](http://www.swgdrug.org/Documents/SWGDRUG%20Recommendations%20Version%208_FINAL_ForPosting_092919.pdf) (accessed 3 March 2020).
- 5 Khalil, D., Omran, H., Medhat, M., and Saadany, B. (2010). Miniaturized tunable integrated Mach-Zehnder MEMS interferometer for spectrometer applications. *Proc. SPIE* 7594: 75940T-1–75940T-13. <https://doi.org/10.1117/12.843658>.
- 6 Deutsch, E.R., Reyes, D., Schildkraut, E.R., and Kim, J. (2009). High resolution miniature FTIR spectrometer enabled by a large linear travel MEMS pop-up mirror. *Proc. SPIE* 7319: 73190J-1–73190J-8. <https://doi.org/10.1117/12.818862>.

- 7 Tortschanoff, A., Kenda, A., Kraft, M. et al. (2009). Improved MOEMS-based ultra-rapid Fourier transform infrared spectrometer. *Proc. SPIE* 7319: 73190I-1. <https://doi.org/10.1117/12.818646>.
- 8 Schiering, D.W. (2003). The TravelIR Haz-Mat Chemical Identifier. *Fire Eng.* 98: 98–99.
- 9 Norman, M.L., Gagnon, A.M., Reffner, J.A. et al. (2004). An FT-IR sensor for identifying chemical WMD and hazardous materials. *Proc. SPIE* 5269: 143–149.
- 10 Mukhopadhyay, R. (2004). Portable FTIR spectrometers get moving. *Anal. Chem.* 76: 369–372A.
- 11 Sorak, D., Herberholz, L., Iwascek, S. et al. (2012). New developments and applications of handheld Raman, mid-infrared, and near-infrared spectrometers. *Appl. Spectrosc. Rev.* 47 (2): 83–115. <https://doi.org/10.1080/05704928.2011.625748>.
- 12 Crocombe, R.A. (2018). Portable spectroscopy. *Appl. Spectrosc.* 72 (12): 1701–1751. <https://doi.org/10.1177/0003702818809719>.
- 13 Bryant, C.K., LaPuma, P.T., Hook, G.L., and Houser, E.J. (2007). Chemical agent identification by field-based attenuated total reflectance infrared detection and solid-phase microextraction. *Anal. Chem.* 79: 2334–2340.
- 14 Ong, K.Y., Baldauf, F.C., Carey, L.F., and St. Amant, D.C. (2003). Domestic preparedness program: evaluation of the TravelIR HCl™ HazMat chemical identifier. *ECBC-TR-355. DIR, ECBC, ATTN: AMSSB-RRT-AT, APG, MD 21010-5424.* <https://apps.dtic.mil/dtic/tr/fulltext/u2/a421836.pdf> (accessed 3 March 2020).
- 15 Schiering, D.W., Walton, R.B., Brown, C.W. et al. (2004). Towards the characterization of biological toxins using field-based FT-IR spectroscopic instrumentation. *Proc. SPIE* 5585: 21–32.
- 16 Manali, D. and Seelenbinder, J. (2016). Automated fast screening method for cocaine identification in seized drug samples using a portable fourier transform infrared (FT-IR) instrument. *Appl. Spectrosc.* 70 (5): 916–922.
- 17 Arnó, J., Frunzi, M., Weber, C., and Levy, D. (2013). Advanced sampling techniques for hand-held FT-IR instrumentation. *SPIE Proc. Vol. 8726, Next-Gen. Spectrosc. Technol. VI:* 87260U-1–87260U-8. <https://doi.org/10.1117/12.2016148>.
- 18 Vagnini, M., Gabrieli, F., Daveri, A., and Sali, D. (2017). Handheld new technology Raman and portable FT-IR spectrometers as complementary tools for the in situ identification of organic materials in modern art. *Spectrochim. Acta A* 176: 174–182.
- 19 Bell, J., Nel, P., and Stuart, B. (2019). Non-invasive identification of polymers in cultural heritage collections: evaluation, optimisation and application of portable FTIR (ATR and external relectance) spectroscopy to three-dimensional polymer-based objects. *Herit. Sci.* 7 (95): 1–18. <https://doi.org/10.1186/s40494-019-0336-0>.
- 20 Tang, P.L., Alqassim, M., Daé, N.N. et al. (2016). Nondestructive handheld Fourier Transform Infrared (FT-IR) analysis of spectroscopic changes and multivariate modeling of thermally degraded plain portland cement concrete and its slag and fly ash-based analogs. *Appl. Spectrosc.* 70 (5): 923–931.
- 21 Bansal, D., Malla, S., Gudala, K., and Tiwari, P. (2013). Anti-counterfeit technologies: a pharmaceutical industry perspective. *Sci. Pharm.* 81 (1): 1–14. <https://doi.org/10.3797/scipharm.1202-03>.
- 22 Higgins, F. (2013). *Rapid and reliable phthalate screening in plastics by portable FTIR spectroscopy – application note. Agilent Technologies Publication number: 5991-3649EN*, 1–8. Agilent Technologies.
- 23 Griffiths, P.R. and DeHaseth, J.A. (2007). *Fourier Transform Infrared Spectrometry*, 2e. New York: Wiley-Interscience.
- 24 Jackson, R.S. (2002). Continuous scanning interferometers for mid infrared spectrometry. In: *Handbook of Vibrational Spectroscopy*, vol. I (eds. J.M. Chalmers and P.R. Griffiths), 264–282. New York: Wiley.
- 25 Sumner, P.D., Abrams, M.C., and Brault, J.W. (2001). *Fourier Transform Spectrometry*. San Diego, CA: Academic Press.
- 26 Griffiths, P.R., Foskett, C.T., and Curbelo, R. (1972). Rapid-scan infrared Fourier transform spectroscopy. *Appl. Spectrosc. Rev.* 6 (1): 31–78.
- 27 Michelson, A.A. (1891). Visibility of interference-fringes in the focus of a telescope. *Philos. Mag., Ser. 5* 31: 256–259.

- 28** Michelson, A.A. (1903). *Light Waves and their Uses*. Chicago: University of Chicago Press.
- 29** Schiering, D.W., Arnó, J., Messerschmidt, R.G., and Zou, P. (2010). Performance trade-off modeling for a hand-held FTIR spectrometric vapor identifier. *Proc. SPIE* 7680: 76800R1-10.
- 30** Arnó, J., Cardillo, L., Judge, K. et al. (2012). Advances in handheld FT-IR instrumentation. *Proc. SPIE* 8374: 837406-837414. <https://doi.org/10.1117/12.921052>.
- 31** Rippel, H. and Jaacks, R. (1988). Performance data of the double pendulum interferometer. *Mikrochem. Acta (Wein)* II: 303–306.
- 32** Coffin, J. (1999). *Interferometer Having Glass Graphite Bearing*, US Patent No. 5,896,197. Washington, DC: US Patent and Trademark Office.
- 33** Azimi, M., Bibby, A., Brown, C.D. et al. (2011). *Handheld Infrared and Raman Measurement Devices and Methods*, US Patent No. 7,928,391 B2. Washington, DC: US Patent and Trademark Office.
- 34** Minami, K. and Kawata, S. (1993). Dynamic range enhancement of Fourier transform infrared spectrum measurement using delta sigma modulation. *Appl. Optics* 32 (25): 4822–4827.
- 35** Brault, J.W. (1996). New approach to high precision Fourier transform spectrometer design. *Appl. Optics* 35: 2891–2896.
- 36** Turner, A., Hoult, R.A., and Forster, M.D. (1999). *Digitisation of Interferograms in Fourier Transform Spectrometry*, US Patent No. 5,914,780. Washington, DC: US Patent and Trademark Office.
- 37** Brault, J.W. (1997). New developments in FT-IR spectrometer design. *Mikrochem. Acta (Suppl.)* 14: 121–124.
- 38** Hildenbrand, J., Kürzinger, A., Peter, C., et al. (2008). Micromachined mid-infrared emitter for fast transient temperature operation for optical gas sensing systems. *IEEE SENSORS 2008 Conference Proceedings*, Lecce, Italy (26–29 October 2008), pp. 297–300.
- 39** Sebastian Weise, S., Bastian Steinbach, B., and Steffen Biermann, S. (2016). MEMS-based IR sources. *Proc. SPIE* 9752: 97521E-1–97521E-7. <https://doi.org/10.1117/12.2208410>.
- 40** Harrick, N.J. (1960). Surface chemistry from spectral analysis of totally internally reflected radiation. *J. Phys. Chem.* 64 (9): 1110–1114.
- 41** Harrick, N.J. (1967). *Internal Reflection Spectroscopy*. New York: Wiley.
- 42** Fahrenfort, J. (1961). Attenuated total reflection – a new principle for the production infra-red reflection spectra of organic compounds. *Spectrochim. Acta A* 17: 698–709.
- 43** Wilks, P.A. Jr., (September, 1977). Use of diamonds in internal reflection spectroscopy. *Am. Lab.* 79–83.
- 44** Harris, D.C. (1994). Development of chemical-vapour-deposited diamond for infrared optical applications – status report and summary. *Office of Naval Research: NAWCWPNS TP 8210*. <https://apps.dtic.mil/sti/pdfs/ADA282999.pdf> (accessed 3 March 2020).
- 45** Sting, D.W. and Milosevic, M. (1997). *Optical Sensing with Crystal Assembly Sensing Tip*, US Patent No. 5,703,366. Washington, DC: US Patent and Trademark Office.
- 46** Milosevic, M., Sting, D., and Rein, A. (1995). Diamond composite sensor for ATR spectroscopy. *Spectroscopy* 10: 44–49.
- 47** Spectral-Systems. *Application Note: Diamond Anti-Reflection Coating*. Hopewell Junction, NY: Spectral-Systems. [www.spectral-systems.com](http://www.spectral-systems.com) (accessed 3 March 2020).
- 48** Wehner, R., Honk, H., and Kress, W. (1967). Lattice dynamics and infra-red absorption of diamond. *Solid State Commun.* 5: 307–309.

## 4

### PAT Applications of NIR Spectroscopy in the Pharmaceutical Industry

*Pierre-Yves Sacré, Charlotte De Bleye, Philippe Hubert and Eric Ziemons*

*Department of Pharmacy, University of Liege, Liege, Belgium*

#### 4.1 Introduction

This chapter covers applications of small, miniature, and portable near-infrared (NIR) spectrometers in process analytical technology (PAT) in pharmaceutical manufacturing. Many of the unit processes in secondary pharmaceutical manufacturing employ mobile, moving and/or high-vibration processing equipment, and, in addition, the space available for an analyzer is often very small. These factors lead to the use of miniature and portable spectrometers, sometimes battery-powered, and communicating via wireless.

The technologies employed in these spectrometers are described elsewhere in these volumes, for instance, in the chapter by Pust on optical filter technologies, and by Grüger et al. on micro-electro-mechanical systems (MEMS) and micro-opto-electro-mechanical systems (MOEMS) spectrometers. Other applications of portable NIR instruments are covered by Siesler and colleagues (materials analysis in general), Miseo, Meyer and Ryan (food) and Beć, Grabska and Huck (food, feed and agriculture).

#### 4.2 Continuous Manufacturing and Real-Time Release Testing

##### 4.2.1 Continuous Manufacturing

Fifteen years ago, in the launch of the PAT initiative by the Food and Drug Administration (FDA), the pharmaceutical industry was asked to continue to improve the quality of the manufactured pharmaceuticals [1]. The pharmaceutical industry mainly works in a batch release manner; that is to say that a final drug product is the result of several independent production steps. These may also take place in different geographical areas, leading to the shipping and storage of the different intermediates in containers to the next manufacturing facility. This increases the risk of degradation over time, or due to environmental conditions (light, humidity, etc.). Therefore, increasing the quality of pharmaceutical manufacturing will both decrease the risks for the patients, and the costs for the manufacturer linked to the destruction of out-of-specification batches.

One way to tackle this issue is to move from a batch release to a continuous release paradigm, and towards continuous manufacturing in the pharmaceutical industry, is supported by the emerging technology program of the FDA [2]. Emerging technologies are defined as innovative or novel: (i) product-manufacturing technology; (ii) manufacturing process; and/or (iii) testing and monitoring technology [3]. Continuous manufacturing is not a new concept, and is already implemented in other industries, but very few pharmaceutical processes are actually continuous [1]. This may be partially explained by the costs needed for a continuous manufacturing implementation, and the relatively low actual level of knowledge within the pharmaceutical industry of continuous manufacturing processes. A continuous process is one in which materials are ceaselessly charged

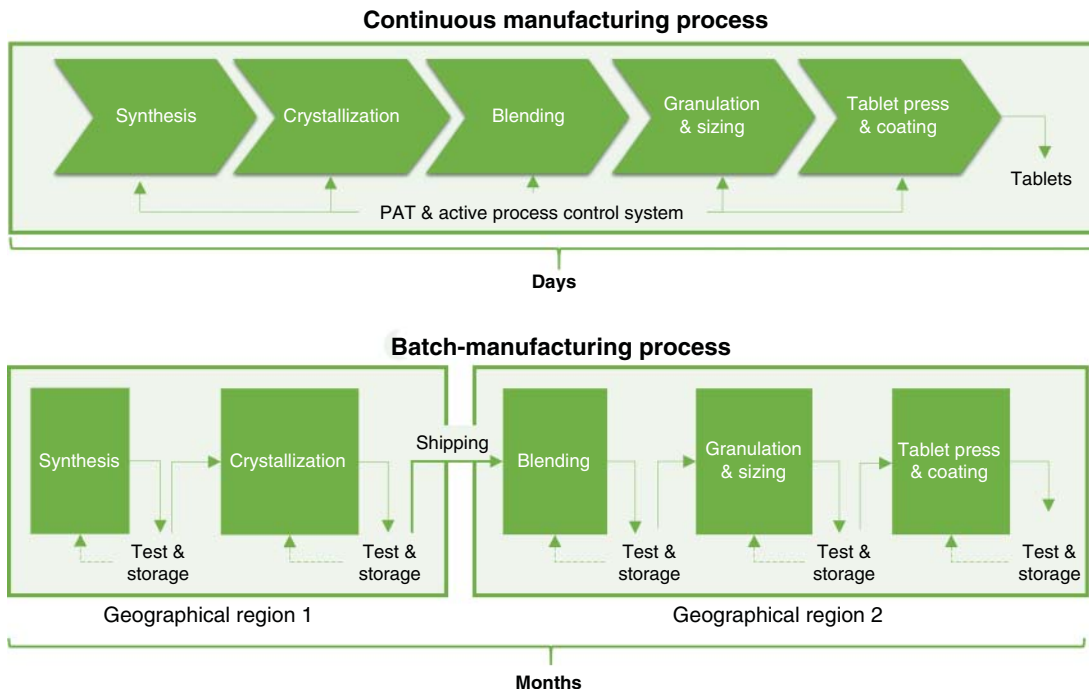


**Figure 4.1** Comparison between continuous manufacturing and batch manufacturing.

into the system, while the final product is continuously discharged [4]. The opposite of batch release, this concept implies the full connection of the production units, with the use of PAT systems, together with process-control systems to monitor and control the integrated manufacturing plant (see Figure 4.1). The continuous process units are generally more efficient, more reactive, reduced in volumes, and have an augmented yield and fewer wastes compared to classical process units. These types of production units may, therefore, respond faster to a drug shortage or sudden changes in demand or need (such as in epidemic outbreak). Furthermore, their reduced size enables their transport directly to places where the drugs are needed [5].

However, continuous manufacturing needs the process to be designed and conceived as a single system. It is, therefore, necessary to have a thorough understanding of the process including the different connections between their process units. This understanding is achieved through the use of the concepts of Quality by Design (QbD) [6, 7]. The QbD concept implies the definition of the quality target drug product profile (QTTP) that identifies the critical quality attributes (CQAs) of the drug product (e.g. active pharmaceutical ingredient – API – content, pH, moisture, flowability, or particle size). Once these CQAs are defined, the critical process parameters (CPPs; e.g. screw speed, solid feed rate, and liquid feed rate), and the critical material attributes (CMAs; e.g. particle size, particle shape, cohesive/adhesive properties, and electrostatic properties) are identified, and the links between these CMAs and CPPs to the CQAs are elucidated using a design of experiments (DoE) (see Figure 4.2). This understanding of the process leads to the development of a control strategy to ensure that the CMAs and CPPs are within the appropriate (and previously defined) ranges of the design space (DS), ensuring the final product quality [8–11]. This real-time monitoring of the process, and the insurance of the quality of the final product through the design of the process itself, naturally lends itself to real-time release testing (RTRT) of the final product. Another important regulatory aspect associated with the definition of a DS is that modifying the operating conditions, while staying within the limits of the design space, is not considered as a change, and does not require a regulatory

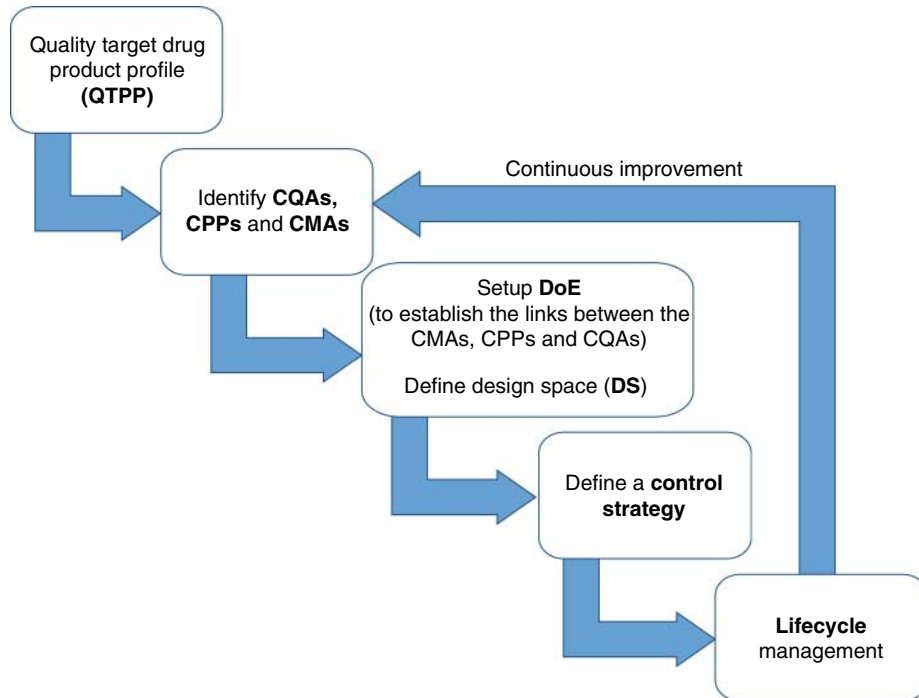


**Figure 4.2** QbD typical flowchart. CQA: critical quality attributes; CMA: critical material attributes; CPP: critical process parameters; DoE: design of experiments.

post-approval change [12]. A nice example of the whole QbD continuous manufacturing in a good manufacturing practice (GMP) environment has recently been reported by Roggo et al. [13].

These concepts are already implemented in the International Council for Harmonisation of Technical Requirements for Pharmaceuticals for Human Use (ICH)<sup>1</sup> via quality guidance documents ICH Q8/Q9/Q10/Q11 and Q13 [14]. However, there are very few continuous manufacturing processes actually working. Indeed, only five drug products manufactured in this way are actually in the market: Orkambi® and Symdeko® (Vertex); Prezista® (J&J); Verzenio® (Eli Lilly); and Daurismo® (Pfizer) [14]. Many reasons may explain this, but one of these is that the transfer of active process control from development to manufacturing is not straightforward. Indeed, most units of production are still controlled one at a time. Therefore, once a disturbance is detected, the adjustment of the CPP variable takes a long time, resulting in a long period of generation of nonconforming products. Therefore, the recently introduced concept of quality by control (QbC) insists on the need for “an active process control system based on a high degree of quantitative and predictive product and process understanding,” enabling real-time and automated adjustment of the CPPs [14]. This automated adjustment is part of the “smart factories” concept. This relatively new concept pushes forward all the previously described initiatives with a virtual twin of the factory using artificial intelligence to anticipate each adjustment of the process and its consequences. This virtualization of the manufacturing plant is the future of PAT strategies, called cyber-physical-based PAT [15]. Another issue is the definition of “batch,” and the raw material traceability required by regulatory agencies. These items may be addressed by the use of residence time distribution (RTD). The RTD is used to describe how a material travels inside the unit operations of a continuous process system. It is also used to set the measurement frequency of sensors to ensure that any unacceptable content uniformity variations would be detected [16–18].

1 <https://www.ich.org/page/quality-guidelines>.

All the above presented concepts and initiatives are based on computations and predictions obtained through statistical modeling of the process. However, to be able to obtain accurate modeling and control of the process, and, therefore, high-quality pharmaceutical products, the statistical models have to be fed with high-quality data coming from sensors. These sensors are very different by nature depending on the CPPs to monitor (temperature, speed, etc.), or the CQAs of the by-products (assay, humidity, particle size, etc.) [19]. NIR spectroscopy is part of the family of soft sensors frequently used in continuous manufacturing, since it is able to assess both physical (particle size, tensile strength, and powder density) and chemical information (API content, blend homogeneity, and water content) in a single analysis [20–23]. However, to be efficient, the sensing device should be representative of both the material, the process, and the analyte [24–26].

#### 4.2.2 Analytical Sensors and Their Positioning

To ensure this representativity, the analyst has several possibilities, among which are the selection of the appropriate location of the probe, and the selection of the adequate device properties.

The appropriate location will obviously depend on the considered process. For a tableting process, two main locations have been reported in the literature: the transition chute during the material discharge [27, 28], and the tablet-press feed frame before the dies [29–31]. The chute is the easiest location to place the probe, since there is a lot of room, and it allows the rejection of the blend if it is out of the specifications. The feed frame on the other side is more difficult to access, but is more representative of the final tablet. Indeed, Sierra-Vega et al., among others, showed that there was an additional mixing effect in the feed frame [32]. To do so, they used the miniature MicroNIR™ spectrophotometer, and compared both the chute and the feed-frame locations. Their results demonstrated that the drug concentration in the chute was not representative of the final drug concentration in the tablets, contrarily to the feed-frame-acquired spectra. Furthermore, the relative standard deviation in the feed frame was 60% lower than that in the chute. The feed frame seems, therefore, to be the best location for the assessment of drug concentration in the final product, while allowing rejecting (and reprocessing) the nonconforming blends. In this example, the authors used a dispersive miniature device. However, this choice is not obvious since many options exist: dispersive vs. Fourier transform (FT), transmission vs. reflection, single-point vs. multipoint measurements, etc.

The choice of dispersive vs. FT devices was investigated by Shi et al. [33] in a continuous tableting process. Contrary to the preconceived idea that dispersive is better than FT for monitoring blend homogeneity, because the movement of the mirror in the interferometer would lead to the detection of different flowing powder sections in the blending process, they showed a more contrasted picture. They tested several spectral resolutions with the FT device and different co-adds for both devices. The dispersive spectrophotometer outperformed the FT when the measurements were performed without co-adds. However, when performing co-adds, the FT outperformed the dispersive device for sensitivity and selectivity, while being equivalent for other tested parameters. They concluded that FT systems might be of interest depending on the process analyzed and the measurement time available.

Most PAT NIR measurements are performed in diffuse reflectance mode because of the ease of implementation and the various interfaces available: large scanning area (e.g. Bruker's Matrix Probe head), specific cleaning systems for blending monitoring (e.g. GEA's Lighthouse probe) or small size probes (e.g. Sentronic's SentroPAT). Another possibility offered by reflectance NIR measurements is the use of multifiber probes to perform real-time fast hyperspectral imaging measurements. One of these systems called spatially resolved spectroscopy (SRS) has been successfully used to detect and reject tablets with a wrong API content, or nonhomogenous distribution of API right after tableting. The 26 NIR spectra were collected simultaneously using an integration time of 1 ms [34].

Nevertheless, NIR transmittance measurements are also very interesting. Indeed, they allow measuring a larger and more representative volume of the sample. Sánchez-Paternina et al. [35] were able to measure through a 5.6 mm-thick sample that is considerably more than the 1.7–2.9 mm depth of penetration of NIR radiation in

the diffuse reflectance mode reported by Iyer et al. [36]. The root mean square error of prediction (RMSEP) values obtained in transmittance mode were 2.35–5.61 times less than the ones obtained in reflectance. However, transmittance measurements also suffer from limitations. Alam et al. [37] investigated the implementation of NIR transmittance measurements in a chute of powder. The quantitation of the API in the flowing powder was affected by the flow rate changes and the thickness of the powder stream. The quantitation of the API was only possible through a powder stream thickness of 1–2 mm. This constitutes a challenge to implement NIR transmission measurements in continuous manufacturing since the powder flow rate is subject to variations depending on the production needs.

#### 4.2.3 Chemometric Modeling of the Data

These changes in powder flow rate and, more generally, the fact that the materials to be investigated are flowing at relatively high speeds, constitute a major challenge to the modeling of NIR data. Indeed, traditionally, calibration and validation samples (powder mixes, granulates, tablets, etc.) are prepared off-line at several concentration levels to avoid a too high consumption of raw materials, and to be able to correctly correlate the NIR spectrum to the sample [38]. However, this way of calibrating NIR quantitative models often leads to discrepancies and bad results due to lack of correspondence between laboratory spectra and process spectra [39, 40]. To get around this difficulty, Blanco et al. tried to compute a process spectrum ( $S_p$ ), and then multiply the laboratory spectra by a determined factor to increase their correspondence [41]. The main advantage of this strategy is that it does not need a reference method. Figure 4.3 shows the principal components score plot of tablets produced on an industrial manufacturing line, and powder blends mixed in laboratory used to build the regression model. As one can see on the left figure, the two blends are spectrally different, but once the laboratory blends are multiplied by the process spectrum, the two sets of spectra overlap, indicating a closer spectral similarity. The higher the similarity, the more accurate the regression model to predict manufactured tablets.

Other teams have used chemometrics tools to remove the physical influence of the samples on the NIR spectra. Pauli et al. [42] used independent component analysis (ICA) to dissociate information from the concentration and from the speed of the powder stream in a continuous manufacturing process. First, they reduced the spectral range to avoid high-noise spectral regions, and then they added a derivative preprocessing step to reduce the influence of speed. Using ICA, they were able to have an accurate qualitative monitoring of the API content. However, when quantitative values are needed, quantitative regression models are necessary, but are more difficult to set up, especially due to the different tablet speeds. They recommended developing quantitative models only for production in routine production, and not during the development of the process because of the huge workload. This consideration is a common limitation of multivariate statistical process control (MSPC) strategies. Indeed, MSPC strategies are based on the projection of the measured data (e.g. the NIR spectrum) onto a small number of new dimensions (e.g. principal components), and the assessment that they are below statistical control thresholds (e.g. Hoteling's  $T^2$  or  $Q$  residuals) [43]. Nevertheless, these thresholds have to be set, and, generally, this is done with limited calibration sets that may not capture all the future variability of the process. This may lead to biased decisions and under optimal process control during the development stages.

Colón et al. [44] investigated the use of NIR in a continuous manufacturing process. They observed issues using NIR sensor due to solvate exchange with water in the environment that induced a change in NIR spectrum (but not in final product quality), and issues due to the relaxation of tablets. To handle these differences, they updated the calibration model using both laboratory tablets (for the complete set of concentration levels), pilot scale tablets at 100% of label claim, and tablets at 90, 100, and 110% of the label claim coming from the continuous manufacturing process. This augmentation of the calibration dataset allowed the incorporation of as much variability as possible to increase the robustness of the prediction to changes in the process. They also identified and removed the spectral ranges that were the most impacted by changes in humidity.

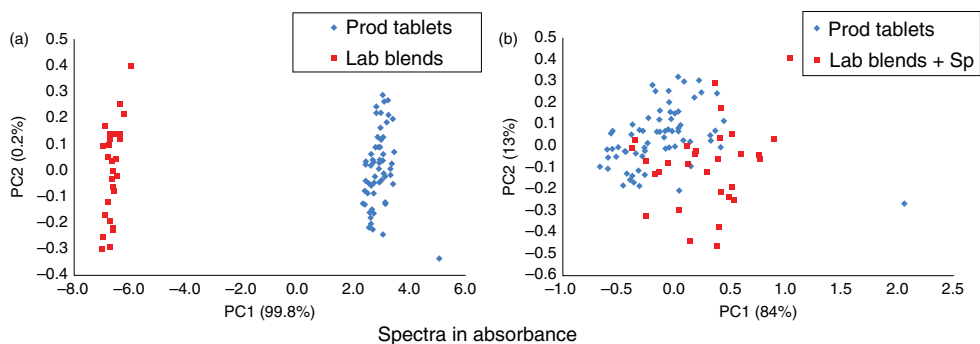


**Figure 4.3** Scatter plot of PCA scores from absorbance spectra over the wavelength range 1100–2300 nm for: (a) laboratory blends and production tablets and (b) laboratory blends +  $S_p$  and production tablets. Source: Blanco et al. [40] © 2011, Elsevier.

Using spectroscopic sensors to monitor CQAs also affects the control of the process because of its inherent difference of uncertainty, compared to CPP measurements. Indeed, spectroscopic measurements are altered by the imperfect interfacing with the sample, and the need to use a statistical modeling of the measurement, while CPPs are often measured by mechanical or electrical sensors. Therefore, adjusting CPPs using noisy CQA measurements may potentially amplify variations and influence the final product quality. In this framework, Su et al. propose to use the concept of data reconciliation [45]. Data reconciliation explicitly uses process knowledge by combining measurement data with a process model. This “ensures that the reconciled measurements are consistent with the known relationships between process variables with minimum adjustment of the measurement data.” This approach was shown to be superior to conventional MSPC approach in a rotary tablet press process. Another aspect to keep in mind while developing NIR spectroscopy methods to monitor processes is the maintenance of the chemometric model [46, 47]. Although some *qualitative* models are developed for each production and are *de facto* maintenance free [48], most of the *quantitative* models need to be maintained through time in order to ensure their accuracy from production to production. Several maintenance strategies have been proposed to tackle this issue [49, 50].

## 4.3 PAT Implementation of Near-Infrared Spectroscopy

Besides these challenges and limitations, NIR spectroscopy is one of the most used PAT techniques [51, 52]. The sections below will make a nonexhaustive demonstration of the possible implementations of NIR as PAT sensor in the manufacturing of solid pharmaceutical dosage forms. Although presented separately, the different process operations are intended to be interconnected in a continuous manufacturing line [53]. The monitoring of bio-processes is out of the scope of the present chapter. The interested reader may find relevant information in the following papers [54, 55].

### 4.3.1 Raw Material Identification

Raw material identification (RMID) is a routine task in the pharmaceutical industry. These tests are performed before processing the materials, in order to avoid mistakes as much as possible, and, therefore, saving time and money. This material verification applies not only to both purchased materials (e.g. excipients), but also to some internal transfers of materials, for instance, APIs manufactured at another plant. In particular, if RMID can be performed on the loading dock, it means that samples do not have to be taken, and analyzed in a laboratory setting, while the materials are quarantined in a warehouse.

Originally, these tests were performed in laboratories using destructive tests, such as liquid chromatography. Nowadays, thanks to the recent developments of handheld and portable spectroscopic devices, these identification tests may be performed in the warehouse even directly through the packaging [56, 57]. Both Raman and NIR spectroscopies are used in this task for both active ingredients and excipients [58–60]. While Raman spectroscopy is gradually expanding its capabilities and applications, NIR spectroscopy still has its advantages when examining fluorescent materials, and many “small-molecule” APIs are conjugated molecules (aromatics), leading to the high probability of being fluorescent. NIR spectroscopy also presents a strong advantage for the characterization of physical parameters of pharmaceutical powders (e.g. particle size, moisture, etc.) [61] (see Figure 4.4). A detailed review of the NIR spectroscopy applications in pharmaceutical particle technology may be found elsewhere [62]. These physical parameters may also be very important to monitor since they may be key quality attributes for the subsequent processes. Therefore, a fast and nondestructive analysis of the incoming raw materials may ensure their future processability or even allow adjustments of the process parameters according to the defined QbD strategy.

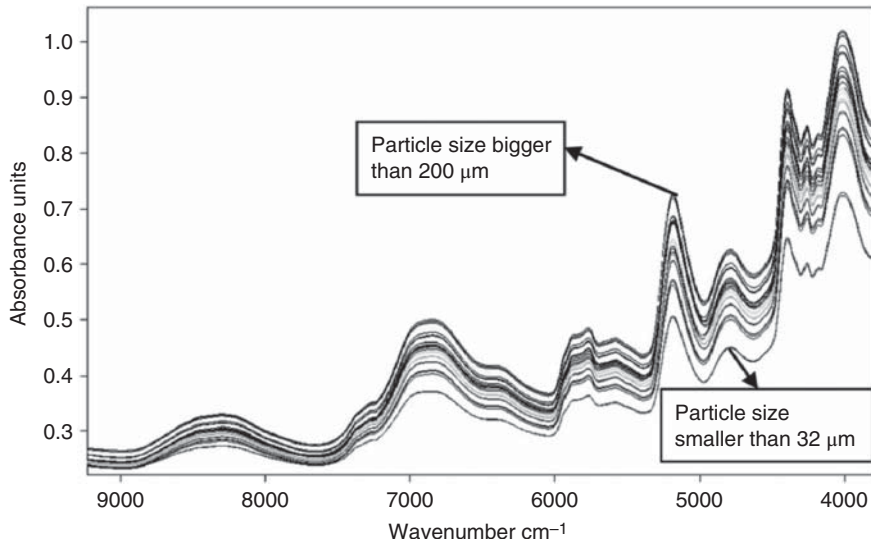


**Figure 4.4** Original NIR spectra of different particle size fractions of HPMC. Source: Devjak Novak et al. [61] © 2012, Elsevier.

### 4.3.2 Blending

Once identified and weighed, the raw materials often require a blending step to ensure the homogenous mixing of the different powders. This is a critical step of the pharmaceutical solid-state products manufacturing since it has a direct impact on the final product quality and homogeneity. The blending process is affected not only by several physical properties of the powders, such as particle size, shape, and density, but also by process parameters, such as blender size, shape, fill level, and blend time [63–65]. Those parameters/properties may lead to nonhomogenous blends if not correctly monitored. Most of the actual techniques to assess blend homogeneity are based on the manufacturer's experience and on physical sampling, using thieves, despite the demonstrated drawbacks [66]. Indeed, physical sampling disturbs the powder flow, and the sampling is often nonrepresentative due to the uneven flow of particles of different shapes. Therefore, the possibility to monitor the blending process noninvasively is a natural implementation of the PAT technique. Among these, NIR has been the most used one because of the influence of both physical and chemical information [20, 67–69]. The sensors used to monitor blending processes are mostly wireless MEMS-based devices (e.g. SentroPAT™ BU from Sentronic or MicroNIR™ from Viavi). However, several practical issues may arise, such as the fouling of the measurement window due to powder deposition. In order to circumvent this issue, manufacturers developed more complex measurement systems (e.g. Lighthouse Probe™ from GEA) with an integrated cleaning system of the probe. Other kinds of sensors, such as chemical imaging devices, have also been successfully used to monitor and evaluate blending operations in order to increase the sampling representativity [64, 70, 71].

The analysis of the spectral data may be qualitative or quantitative. Quantitative monitoring of the blending process monitors content variations and assumes the end point as being a constant content. It may be the most accurate approach [72–74], although discrepancies between calibration and routine measurements may appear due to the powder flow [75]. El-Hagraspy and Drennen [76] found that multivariate linear regression (MLR) was more efficient to follow the blending process than principal component regression (PCR) or partial least squares (PLS), due to the fact that it considered a reduced spectral range and was, therefore, more robust to process variations. Similarly, Nakagawa et al. showed that the locally weighted PLS (LW-PLS) improved by 38.6% (in root mean squared error of prediction) the conventional PLS calibration [77, 78]. However, quantitative calibration is

time and resource consuming, and, therefore, requires an important effort that is not feasible during the development stage of a new process. Moreover, the robustness, transfer and scale-up of the models are also important limitations.

On the other hand, qualitative analysis considers spectral variance, and the blend is said to be optimal once a stable or desired spectral profile is reached. Several statistical methods have been successfully applied among which are moving block standard deviation (MBSD) [67], principal component score distance analysis (PC-SDA) [63], soft independent modeling of class analogy (SIMCA) [79], or moving F-test [48, 80]. These approaches are easily deployed, and may be used during the development of a new process while providing information on the evolution of ingredient properties, process settings and environmental conditions, but no insight into the final quantitative composition of the blend. Nevertheless, the obtained information may be used to adapt subsequent operations, such as granulation.

### 4.3.3 Granulation and Sizing

Sometimes, due to their physical properties, the different ingredients of the pharmaceutical formulation do not mix well, and segregate during the blending operation. Therefore, it is appropriate to granulate powdered ingredients through compression, dry granulation, or in the presence of a binder under wet conditions; this is wet granulation. Granulation ensures the homogeneity and downstream processability of the blend (e.g. improved powder flow and compressibility). The granulated material is eventually dried, if wet granulation was used, blended, and compressed.

Although reviewing the different granulation possibilities is out of the scope of the present chapter, most of the spectroscopic investigations are focused on the determination of water during wet-granulation or post-granulation drying. Although our attention is centered on NIR applications, it is important to keep in mind that other kinds of sensors may also be envisaged. For example, microwave sensors may advantageously replace NIR probes for moisture determination, thanks to the highest penetration depth (2–5 cm compared to 0.5–2.5 mm for NIR reflection), with a significant reduction of effort for the development of the quantitative regression model [81].

Gavan et al. [82] developed a QbD strategy for a fluidized bed granulation process of two APIs, and used a portable NIR sensor to monitor the moisture content during the process with an orthogonal-PLS model in order to ensure the necessary robustness regarding changes in the process parameters. Fonteyne et al. [83, 84] used both NIR and Raman spectroscopy to follow up the polymorphic forms of theophylline during a continuous drying process together with the moisture content. Although the results were relatively accurate, they emphasized the fact that “care should be taken when evaluating the average moisture content and solid-state values obtained on the total granule load, since significant differences between the different sieve fractions of the granules were observed.”

More recently, Pauli et al. [85] used NIR spectroscopy to monitor in-line the particle size distribution (PSD) of the granules during a GMP continuous granulation process. They used three PLS models to predict, respectively, the size range of 20–234 µm (X10), 98–1017 µm (X50), and 748–2297 µm (X90), respectively. They obtained RMSEP values of 17, 97, and 174 µm for PSD X10, X50, and X90, respectively that were sufficiently accurate to monitor changes and take adequate dispositions to adjust the process. This application is somewhat challenging since the correlation of particle size-related information to variances in NIR spectra is mainly based on changes in spectral slope and baseline offset, but water content and other sample variations due to the continuous processing context disturbed these factors.

### 4.3.4 Extrusion

Besides granulation operations, other processing tools may also be envisaged to ensure a homogenous mixture of the component while increasing the bioavailability of poorly soluble drugs. One of these tools is the hot melt extrusion (HME). Extrusion is the process of shaping a material (extrudate) by forcing the material through an orifice

(die) using pressure. This process consists of the mixture of the active ingredients with a meltdown water-soluble polymer. It allows obtaining a molecular dispersion of the API within the matrix, increasing its solubilization in the gastro-enteral fluids. NIR spectroscopy has been extensively used in HME experiments to monitor both the API content, the solid state of the extrudates and elucidate the interactions between the ingredients [86–89].

Baronsky-Probst et al. [90] used NIR spectroscopy to monitor the homogeneity of the incoming materials, and the strand after cooling to assess the API content and the solid state in the final product. They preferred these locations to the more conventional position in the die to avoid pressure and temperature effects on the sample, and, therefore, obtain a more robust model. Wahl et al. [91] paid particular attention to the location of the NIR probe regarding the theory of sampling (TOS) precepts, and decided to place the NIR probe close to the die after the mixing screws. The connector to the die was modified to force the melt into an annular flow with high shear rates ensuring representative sampling. The developed PLS model was able to quantify the API, and changes in screw speed from 150 to 250 rpm did not affect the predictions much. Saerens et al. [92] used NIR spectroscopy in an HME process to get insights into the types of interactions between the API and the polymer together with the assay of the API. They elucidated that the interactions are manifested as hydrogen bonds between Kollidon® SR and metoprolol tartrate molecules. These findings were confirmed off-line using ATR-FTIR and Raman spectroscopy and differential scanning calorimetry (DSC). However, interpretation of NIR spectra remains complicated, and is often advantageously replaced by Raman spectroscopy when the purpose is the elucidation of interaction mechanisms.

#### 4.3.5 Tableting

Once the homogenous mixing of ingredients is obtained (via direct blending, granulation or HME), the natural next step is tableting. This step may appear less important to monitor considering that homogeneity of powders has been ensured during the previous steps [93]. However, this step of the process is the closest one to the final product. Therefore, it is sometimes easier to monitor the quality of the product directly in the press, especially if there is a following coating step.

Dalvi et al. [94] compared the quantitative performances of a portable NIR spectrophotometer (Viavi MicroNIR™), placed directly in the feed frame with in-line measurements of the resulting tablets (Visiotec VisioNIR™), and at-line measurements with a benchtop spectrophotometer (Bruker MPA™). Good agreements were found between these three measurements. However, discrepancies were observed between NIR measurements and ultraviolet (UV) assay possibly due to nonrepresentative surface distribution of API, together with spectral variations resulting from dynamic sample presentation. The same team also combined results from NIR spectroscopy and NIR chemical imaging (NIR-CI) in the feed frame [95]. The main advantage was that the NIR-CI approach had a sampling volume five times higher than the NIR probe alone, and allowed an image of the distribution of the ingredients in the feed frame to be obtained. These insights might be valuable when developing a new process.

Durão et al. [96] monitored five components during the tableting process of a multivitamin formulation (31 components) using NIR spectroscopy, light-induced fluorescence (LIF) spectroscopy and red, green and blue (RGB) color imaging together. They used multiblock PLS (mb-PLS) that combines the scores obtained by separate PLS models for each block (one block per PAT sensor) in a single model. Therefore, they were able to use information coming from the different sensors, which allowed better predictions than the NIR sensor alone. Figure 4.5 shows the predicted concentration of ferrous fumarate in the blend using NIR only (Figure 4.5a), or all the sensors (Figure 4.5b). A sensible improvement may be observed when all sensors were used compared to NIR alone.

Pauli et al. [42] placed two NIR probes at different locations of a continuous tableting process: in the feed frame, and in the press just before tablet ejection. They were able to analyze 100% of the produced tablets (70 000 tablets/h), but the spectra were highly impacted by process parameters and, therefore, PLS models developed with off-line spectra were not suitable for the analysis of in-line measurements. They also observed a time-shift between the predictions of the two probes. This reflects the mixing phase inside the feed frame,

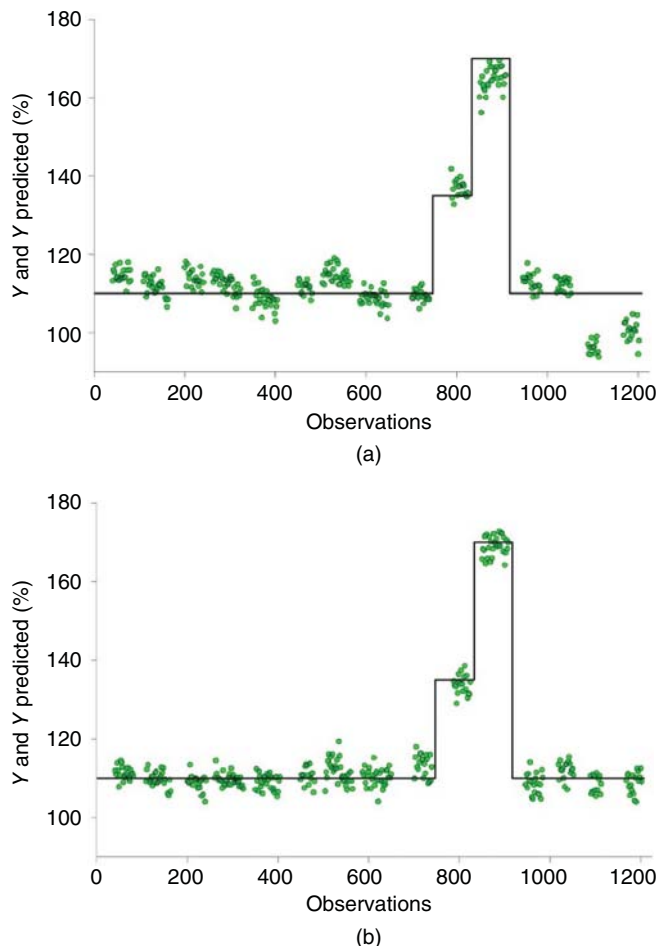


**Figure 4.5** Predicted value of Ferrous Fumarate with a PLS model using data from (a) NIR and (b) all tools. The dark line represents the theoretical  $Y$  value. Source: Durão et al. [96] © 2017 Elsevier.

implying a recycling loop of the excessive granules, estimated at one minute in the present case. Therefore, they emphasized in the necessity to have several sensors at different locations to get better knowledge on the process and the different residence times. Indeed, these phenomena may have a direct impact in the management of process adjustments based on the information provided by the different sensors, especially if they are placed at different locations.

NIR spectroscopy may also be used to understand the powder behavior in the tablet press. He et al. [97] used quantitative NIR models to gain knowledge on powder segregation phenomenon inside a tablet press. The use of spectroscopic tools allowed fast, nondestructive analysis at several places of the process.

#### 4.3.6 Coating

The coating process is a crucial step of oral solid preparations manufacturing. Indeed, the coating may act as a physical screen to avoid the effects of oxidation, humidity and illumination conditions in order to improve the stability of the final product or process intermediates. It is sometimes used to protect workers avoiding the generation of toxic dusts of intermediate products. The coating may also play an active role in the protection (gastro-resistant)

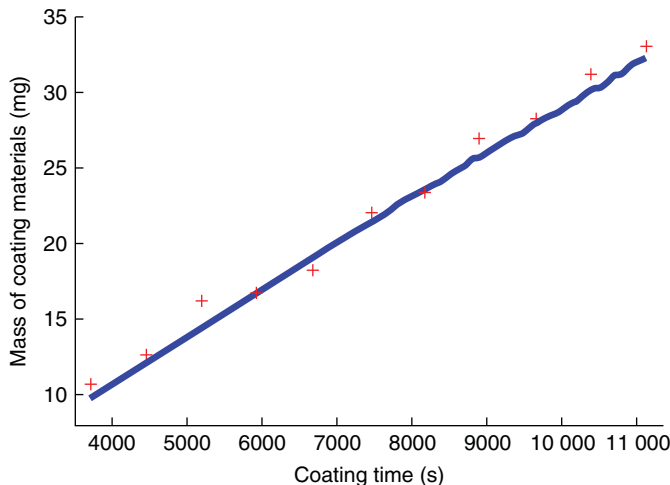


**Figure 4.6** Real-time monitoring of coating deposit mass: (\*) real-time NIR predictions during the pan-coating operation and (+) experimental results obtained by weighing. Source: Gendre et al. [100] © 2017, Elsevier.

and liberation (modified release) of the drug *in vivo*. The coating homogeneity and thickness are important to control the timing of the drug-release. Many off-line techniques exist to monitor the coating thickness, such as the changes in the weight, height or diameter of the pellet/tablet cores coated during the process [98]. Other more advanced techniques, such as Terahertz 3D imaging, are also used [99]. These techniques necessitate a sampling step during the process, and the measure of several samples to be representative, which is time consuming, and neither allows a fast and accurate adjustment of the process, nor an accurate end-point detection. Therefore, these off-line tools are advantageously replaced by in-line sensors among which NIR probes especially for aqueous-based coatings [100–103]. Figure 4.6 shows an example of coating deposition monitoring using NIR spectroscopy (blue stars) versus the weighing off-line reference method (red crosses). Compared to weighing, NIR spectroscopy allows a noninvasive (and nondisturbing) follow-up of the process at a higher sampling rate. Bogomolov et al. [104] compared NIR spectroscopy, Raman spectroscopy, and their combination, to follow up a coating process. Their findings suggest that both techniques may provide interesting insights, and offered comparable performances depending on the nature of ingredients to follow. Wahl et al. [105] decided to compare optical coherence tomography (OCT) and NIR spectroscopy as in-line PAT tools for a coating process. They used an NIR contact probe, highlighting the fact that the distance of the sample to the probe is crucial. Therefore, they applied a filter based on the absorbance ratio at  $I_{1634\text{ nm}}/I_{2030\text{ nm}}$  ensuring that the spectra eventually analyzed with the PLS model are effectively tablet spectra. They compared off-line and in-line NIR measurements and obtained satisfactory results of RMSEP: 7.8 and 7.2  $\mu\text{m}$  for off-line and in-line measurements, respectively and a final coating thickness of 70  $\mu\text{m}$ . NIR and OCT results were consistent and well correlated to each other. However, the method development effort was significantly smaller for OCT since it directly provides a thickness measurement, while chemometrics are necessary for NIR spectra interpretation.

Igne et al. [106] studied the influence of the sampling frequency on the analysis of a coating process. They compared several combinations: with and without co-adds (1–64 co-adds), and spectral sampling over time (from 1 to 15 pan rotations). They found that the sampling frequency had a significant impact on the spectral data quality and the resulting quantitative analyses. A single co-add is noisier (smaller signal/noise ratio) than a 64 co-adds spectrum; however, it is less sensitive to the averaging of disturbances due to the dynamic nature of the process. In conclusion, they argued that a single co-add provides information on the process (bed height variations) and the tablet-to-tablet variations. The 64 co-adds-based predictions were more focused on the variability amongst the tablets; this time-dependent averaging improved up to 4 averages, but then stabilized. They concluded that if

the sought information is the tablet-to-tablet variability, then averaging may be limited to one spectrum, and the number of co-adds adapted to the process variability. Another important finding was that the correlation between measured spectra and the reference data was not obvious. Indeed, the matching of physical sample collection and spectral acquisition is not the optimal modeling approach due to the slow phenomenon of the coating process. In their case, a temporal offset up to 60 seconds was less biased and had comparable RMSEP. This emphasizes once again the complexity of correlating spectral data of dynamic processes with reference values to build robust quantitative models.

Another important aspect associated with the coating process is the curing stage consisting of a post-coating drying step during which the polymer is exposed to a high temperature. This step changes the structure of the film influencing mechanical properties of the film, film–tablet adhesion, and the dissolution profiles of coated substrates [107].

Gendre et al. [108, 109] used X-ray micro-diffraction (X $\mu$ CT), NIR and Raman spectroscopies to gain insights into the curing process and structures of the film coating. It allowed them to compare both dynamic and static curing conditions, and determine the end point of the processes, leading to similar dissolution profiles of the drugs. They were then able to demonstrate that a 24-hour static curing led to the same results as a 4-hour dynamic curing process. Korasa et al. [110] used NIR spectroscopy to monitor the curing process of pellets. They had reliable results predicting the coating thickness, but discrepancies appeared when predicting the drug-release rate because the pellet moisture content disturbed the PLS model at high moisture content.

#### 4.3.7 End-Product Testing

Once the pharmaceutical product has completed all the processing steps, a last step of verification may ensure that only “good-quality” or conforming products are packaged and marketed. Application of NIR spectroscopy in the quality control of pharmaceutical preparations will not be extensively reviewed in this chapter, and detailed applications may be found in recent reviews [111–113].

Nevertheless, some interesting applications may be pointed out, such as the prediction of dissolution profiles. Pomerantsev et al. [114] used NIR spectroscopy, together with PLS and dynamic modeling, to predict the dissolution profiles of pH-sensitive coated pellets. Pawar et al. [115] were also able to predict the dissolution of immediate release tablets at-line, on a continuous manufacturing plant, using transmission NIR (see Figure 4.7). They included several variables, such as API concentration, blender speed, feed frame speed and compaction force to build a multilinear regression model using the principal component scores.

Other, more specific, applications are related to the new axes of research in the pharmaceutical field, such as the printing of tablets or oral films. These drugs may be printed on demand with a personalized composition [116, 117]. However, it is almost impossible to imagine coupling these manufacturing techniques with a destructive technique, such as high-pressure liquid chromatography (HPLC), in a drug store or even at the patient’s home. Therefore, it might be interesting to use nondestructive portable systems, such as NIR spectrophotometers or NIR-chemical imagers, to perform the quality control of such drugs [118, 119].

Another important part of the end-product quality control covers the analysis of substandard and falsified medicines [120]. In this context, NIR spectroscopy has already proven its usefulness [121–124] and the development of low-cost handheld devices is already demonstrating its applicability [57, 125–128]. See the chapter by Leary, Crocombe and Kalyanaraman in these volumes for more details.

## 4.4 Conclusion

NIR spectroscopy is a light-based technique enabling the remote and nondestructive analysis of samples, providing both physical and chemical information. These characteristics may explain that NIR spectroscopy is one of

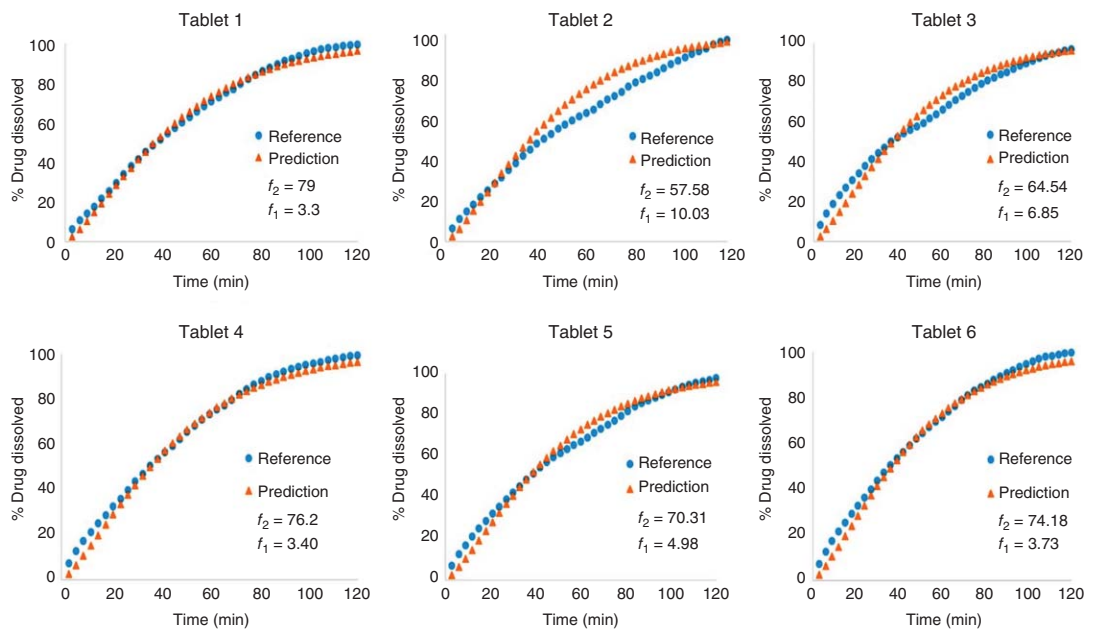


**Figure 4.7** Predicting individual dissolution profile from model-dependent approach. The similarity factor is greater than 50 indicating a good agreement between the observed and predicted results. *Source:* Pawar et al. [115] © 2016, Elsevier.

the emerging technologies recommended by the regulatory agencies to monitor continuously the pharmaceutical processes. Nevertheless, its characteristics may also constitute a limitation to its implementation. Indeed, the spectra are hardly interpretable and must be processed by advanced machine learning tools in order to obtain meaningful usable information. The building of a robust quantitative model is not straightforward. It needs a lot of time and effort to be applicable in routine. One of the major gaps is the correlation of the spectra obtained in a dynamic environment with reference values obtained off-line with reference methods. Therefore, several strategies have been exposed in the beginning of the chapter to handle this issue.

Nevertheless, the amount of research and application papers in the pharmaceutical field demonstrates once more that NIR spectroscopy has a bright future ahead.

## Glossary

**Continuous Manufacturing (CM):** CM of pharmaceutical drug products is a new approach within the pharmaceutical industry, opposing traditional batch-manufacturing processes based on its potential to increase manufacturing flexibility and efficiency. In CM, all process units are directly connected to each other. The starting material is continuously charged into the first process unit at the beginning of the line, while the final product is simultaneously discharged at the end [13].

**Critical Process Parameter (CPP):** CPPs are process inputs that have a direct and significant influence on critical quality attributes when they are varied within regular operation range [6].

**Critical Quality Attribute (CQA):** CQAs are physical, chemical, biological, or microbiological properties or characteristics that must be controlled directly or indirectly to ensure the quality of the product [6].

**Design of Experiments (DoE):** A DoE is a structured, organized set of experiments used to determine, model and quantify the relationship between factors affecting a process and the output of that process.

**Design Space (DS):** The DS is the multidimensional combination and interaction of input variables (e.g. material attributes) and process parameters that have been demonstrated to provide assurance of quality. Working within the DS is not considered as a change (see also ICH Q8 R2 [12]).

**Dissolution profile:** Graphical representation in terms of concentration vs. time of the release of an active pharmaceutical ingredient from a dosage form in an appropriate selected dissolution medium. It is used to verify that the drug will be correctly released in the patient's body ensuring its safety and biological activity.

**High Pressure Liquid Chromatography (HPLC):** HPLC is used to separate, identify and quantify each substance present in a mixture. It is composed of a solid stationary phase and a liquid mobile phase. The separation occurs because of differences of affinity of the components of the mixture towards the stationary and the mobile phase. Several types of detectors may be used to analyze the substances after their physical separation, such as ultraviolet spectroscopy, mass spectrometry, and fluorescence spectroscopy.

**Partial Least Squares (PLS):** PLS is a variable reduction technique which reduces the number of variables by making linear combinations of the original variables. These combinations are called PLS factors. The PLS factors are defined in such a way that they maximize the covariance with the response variable. This way latent variables are more directly related to the response variable than, for example, those obtained in PCA. PLS may be applied as a regression or a classification algorithm.

**Polymorphism:** In crystalline solids, the polymorphism is the ability of a substance to exist in different molecular arrangements and/or different molecular conformations. The polymorphic behavior of pharmaceutically active substances can affect their therapeutic efficacy and safety.

**Principal Component Analysis (PCA):** PCA is a variable reduction technique which reduces the number of variables by making linear combinations of the original variables. These combinations are called the principal components and are defined in such a way that they explain the highest (remaining) variability in the data and are by definition orthogonal. The importance of the original variables in the definition of a principal component

is represented by its loading and the projections of the objects on to the principal components are called the scores of the objects.

*Process Analytical Technology (PAT)*: PAT is defined by the US FDA as “a system for designing, analyzing, and controlling manufacturing through timely measurements (i.e., during processing) of critical quality and performance attributes of raw and in-process materials and processes, with the goal of ensuring final product quality. It is important to note that the term analytical in PAT is viewed broadly to include chemical, physical, microbiological, mathematical, and risk analysis conducted in an integrated manner. The goal of PAT is to enhance understanding and control the manufacturing process”.

*Quality by Design (QbD)*: The QbD concept implies that the final product quality is built in the conception (the design) of the process itself. It necessitates a deep understanding of the process and the product with the definition of CPPs influencing the CQAs of the product.

*Quality by Testing (QbT)*: QbT is an actual system implemented in the pharmaceutical industry ensuring the quality of the final product by following a sequence of testing steps. These may include, but are not limited to, testing of incoming raw materials, in-process control and final product testing. The QbT approach is not dynamic by essence.

*Residence Time Distribution (RTD)*: RTD is a term coming from the chemical engineering field. It is defined as “the probability of time that a solid or fluid material stays inside one or more unit operations in a continuous system.” [17] It is a crucial information to better understand and model the material flow in the process. It is also used to define the “batch” notion in CM.

*Root Mean Square Error (RMSE)*: This measure is frequently used in multivariate data analysis to evaluate the goodness of fit of a regression model. It may be applied on the calibration samples (RMSEC), on the cross-validation samples (RMSECV) or with the predictions of an external set of validation (RMSEP). It is computed as follows:

$$\text{RMSE} = \sqrt{\sum_{i=1}^n \frac{(\hat{y}_i - y_i)^2}{n}}$$

where  $\hat{y}_i$  is the value of the sample predicted by the model,  $y_i$  is the actual value of the sample, and  $n$  is the total number of samples.

*Target Product Quality Profile (TPQP)*: It consists of the characteristics that the drug product should possess in order to reproducibly deliver the therapeutic benefit promised. The TPQP guides formulation scientists to establish formulation strategies and keep the formulation effort focused and efficient. TPQP is related to identity, assay, dosage form, purity, and stability in the label [6].

*Theory of Sampling (TOS)*: The theory of sampling is theorization of the sampling process enabling a representative sampling. It focuses only on the sampling process and not on the sample itself [129].

## References

- 1 Yu, L.X. and Kopcha, M. (2017). The future of pharmaceutical quality and the path to get there. *Int. J. Pharm.* 528 (1–2): 354–359.
- 2 FDA and CDER (2017). Advancement of emerging technology applications for pharmaceutical innovation and modernization guidance for industry. *FDA-2015-D-4644*.
- 3 O'Connor, T. and Lee, S. (2017). Emerging technology for modernizing pharmaceutical production. In: *Developing Solid Oral Dosage Forms*, 2ee (eds. Y. Qiu, Y. Chen, G. Zhang, et al.), 1031–1046. Elsevier.
- 4 Lee, S.L., O'Connor, T.F., Yang, X. et al. (2015). Modernizing pharmaceutical manufacturing: from batch to continuous production. *J. Pharm. Innov.* 10 (3): 191–199.
- 5 Adamo, A., Beingessner, R.L., Behnam, M. et al. (2016). On-demand continuous-flow production of pharmaceuticals in a compact, reconfigurable system. *Science* 352 (6281): 61–67.

- 6 Yu, L.X. (2008). Pharmaceutical quality by design: product and process development, understanding, and control. *Pharm. Res.* 25 (4): 781–791.
- 7 Zhang, L. and Mao, S. (2017). Application of quality by design in the current drug development. *Asian J. Pharm. Sci.* 12 (1): 1–8.
- 8 Lebrun, P., Krier, F., Mantanus, J. et al. (2012). Design space approach in the optimization of the spray-drying process. *Eur. J. Pharm. Biopharm.* 80 (1): 226–234.
- 9 Singh, B.N. (2019). Product development, manufacturing, and packaging of solid dosage forms under QbD and PAT paradigm: DOE case studies for industrial applications. *AAPS PharmSciTech* 20 (8): 313.
- 10 Ziemons, E., Hubert, C., and Hubert, P. (2019). Process analysis – overview. In: *Encyclopedia of Analytical Science*, 3e, vol. 8, 396–402. Oxford, UK: Academic Press.
- 11 Yu, L.X., Amidon, G., Khan, M.A. et al. (2014). Understanding pharmaceutical quality by design. *AAPS J.* 16 (4): 771–783.
- 12 International Conference on Harmonization (2009). *ICH Q8(R2) Pharmaceutical Development*. [https://database.ich.org/sites/default/files/Q8\(R2\)\\_Guideline.pdf](https://database.ich.org/sites/default/files/Q8(R2)_Guideline.pdf).
- 13 Roggo, Y., Pauli, V., Jelsch, M. et al. (2020). Continuous manufacturing process monitoring of pharmaceutical solid dosage form: a case study. *J. Pharm. Biomed. Anal.* 179: 112971.
- 14 Su, Q., Ganesh, S., Moreno, M. et al. (2019). A perspective on quality-by-control (QbC) in pharmaceutical continuous manufacturing. *Comput. Chem. Eng.* 125: 216–231.
- 15 Barenji, R.V., Akdag, Y., Yet, B., and Oner, L. (2019). Cyber-physical-based PAT (CPbPAT) framework for Pharma 4.0. *Int. J. Pharm.* 567: 118445.
- 16 Engisch, W. and Muzzio, F. (2016). Using residence time distributions (RTDs) to address the traceability of raw materials in continuous pharmaceutical manufacturing. *J. Pharm. Innov.* 11 (1): 64–81.
- 17 Gao, Y., Muzzio, F.J., and Ierapetritou, M.G. (2012). A review of the residence time distribution (RTD) applications in solid unit operations. *Powder Technol.* 228: 416–423.
- 18 Bhaskar, A. and Singh, R. (2019). Residence time distribution (RTD)-based control system for continuous pharmaceutical manufacturing process. *J. Pharm. Innov.* 14 (4): 316–331.
- 19 Ierapetritou, M., Muzzio, F., and Reklaitis, G. (2016). Perspectives on the continuous manufacturing of powder-based pharmaceutical processes. *AIChE J.* 62 (6): 1846–1862.
- 20 Nagy, B., Farkas, A., Magyar, K. et al. (2018). Spectroscopic characterization of tablet properties in a continuous powder blending and tableting process. *Eur. J. Pharm. Sci.* 123: 10–19.
- 21 Pestieau, A., Krier, F., Thoorens, G. et al. (2014). Towards a real time release approach for manufacturing tablets using NIR spectroscopy. *J. Pharm. Biomed. Anal.* 98: 60–67.
- 22 Rehrl, J., Karttunen, A.-P.P., Nicolaï, N. et al. (2018). Control of three different continuous pharmaceutical manufacturing processes: use of soft sensors. *Int. J. Pharm.* 543 (1–2): 60–72.
- 23 Rehrl, J., Kruisz, J., Sacher, S. et al. (2016). Optimized continuous pharmaceutical manufacturing via model-predictive control. *Int. J. Pharm.* 510 (1): 100–115.
- 24 Petersen, L., Minkkinen, P., and Esbensen, K.H. (2005). Representative sampling for reliable data analysis: theory of sampling. *Chemom. Intel. Lab. Syst.* 77 (1–2): 261–277.
- 25 Sánchez-Paternina, A., Sierra-Vega, N.O., Cárdenas, V. et al. (2019). Variographic analysis: a new methodology for quality assurance of pharmaceutical blending processes. *Comput. Chem. Eng.* 124: 109–123.
- 26 Esbensen, K.H., Friis-Petersen, H.H., Petersen, L. et al. (2007). Representative process sampling – in practice: variographic analysis and estimation of total sampling errors (TSE). *Chemom. Intel. Lab. Syst.* 88 (1): 41–59.
- 27 Vargas, J.M., Nielsen, S., Cárdenas, V. et al. (2018). Process analytical technology in continuous manufacturing of a commercial pharmaceutical product. *Int. J. Pharm.* 538 (1–2): 167–178.
- 28 Vargas, J.M., Roman-Ospino, A.D., Sanchez, E., and Romañach, R.J. (2017). Evaluation of analytical and sampling errors in the prediction of the active pharmaceutical ingredient concentration in blends from a continuous manufacturing process. *J. Pharm. Innov.* 12 (2): 155–167.

- 29** Li, Y., Anderson, C.A., Drennen, J.K. et al. (2019). Development of an in-line near-infrared method for blend content uniformity assessment in a tablet feed frame. *Appl. Spectrosc.* 73 (9): 1028–1040.
- 30** Harms, Z.D., Shi, Z., Kulkarni, R.A., and Myers, D.P. (2019). Characterization of near-infrared and raman spectroscopy for in-line monitoring of a low-drug load formulation in a continuous manufacturing process. *Anal. Chem.* 91 (13): 8045–8053.
- 31** Gosselin, R., Durão, P., Abatzoglou, N., and Guay, J.-M. (2017). Monitoring the concentration of flowing pharmaceutical powders in a tableting feed frame. *Pharm. Dev. Technol.* 22 (6): 699–705.
- 32** Sierra-Vega, N.O., Román-Ospino, A., Scicolone, J. et al. (2019). Assessment of blend uniformity in a continuous tablet manufacturing process. *Int. J. Pharm.* 560: 322–333.
- 33** Shi, Z., McGhehey, K.C., Leavesley, I.M., and Manley, L.F. (2016). On-line monitoring of blend uniformity in continuous drug product manufacturing process – the impact of powder flow rate and the choice of spectrometer: dispersive vs. FT. *J. Pharm. Biomed. Anal.* 118: 259–266.
- 34** Boiret, M. and Chauchard, F. (2017). Use of near-infrared spectroscopy and multipoint measurements for quality control of pharmaceutical drug products. *Anal. Bioanal. Chem.* 409 (3): 683–691.
- 35** Sánchez-Paternina, A., Román-Ospino, A.D., Martínez, M. et al. (2016). Near infrared spectroscopic transmittance measurements for pharmaceutical powder mixtures. *J. Pharm. Biomed. Anal.* 123: 120–127.
- 36** Iyer, M., Morris, H.R., and Drennen, J.K. (2002). Solid dosage form analysis by near infrared spectroscopy: comparison of reflectance and transmittance measurements including the determination of effective sample mass. *J. Near Infrared Spectrosc.* 10 (4): 233–245.
- 37** Alam, M.A., Shi, Z., Drennen, J.K., and Anderson, C.A. (2017). In-line monitoring and optimization of powder flow in a simulated continuous process using transmission near infrared spectroscopy. *Int. J. Pharm.* 526 (1–2): 199–208.
- 38** Dal Curtivo, C.P., Funghi, N.B., Tavares, G.D. et al. (2015). The critical role of NIR spectroscopy and statistical process control (SPC) strategy towards captopril tablets (25 mg) manufacturing process understanding: a case study. *Pharm. Dev. Technol.* 20 (3): 345–351.
- 39** Blanco, M. and Peguero, A. (2010). Influence of physical factors on the accuracy of calibration models for NIR spectroscopy. *J. Pharm. Biomed. Anal.* 52 (1): 59–65.
- 40** Blanco, M., Cueva-Mestanza, R., and Peguero, A. (2011). NIR analysis of pharmaceutical samples without reference data: improving the calibration. *Talanta* 85 (4): 2218–2225.
- 41** Blanco, M. and Peguero, A. (2010). Analysis of pharmaceuticals by NIR spectroscopy without a reference method. *TrAC – Trends Anal. Chem.* 29 (10): 1127–1136.
- 42** Pauli, V., Roggo, Y., Pellegatti, L. et al. (2019). Process analytical technology for continuous manufacturing tableting processing: a case study. *J. Pharm. Biomed. Anal.* 162: 101–111.
- 43** Bro, R. and Smilde, A.K. (2014). Principal component analysis. *Anal. Methods* 6 (9): 2812–2831.
- 44** Colón, Y.M., Vargas, J., Sánchez, E. et al. (2017). Assessment of robustness for a near-infrared concentration model for real-time release testing in a continuous manufacturing process. *J. Pharm. Innov.* 12 (1): 14–25.
- 45** Su, Q., Bommireddy, Y., Shah, Y. et al. (2019). Data reconciliation in the Quality-by-Design (QbD) implementation of pharmaceutical continuous tablet manufacturing. *Int. J. Pharm.* 563: 259–272.
- 46** European Medicines Agency (2014). Guideline on the use of Near Infrared Spectroscopy (NIRS) by the pharmaceutical industry and the data requirements for new submissions and variations. *Guideline-EMEA/CHMP/CVMP/QWP/17760/2009* 44: 1–28.
- 47** Food and Drug Administration (2015). *Development and Submission of Near Infrared Analytical Procedures Guidance for Industry*. Food and Drug Administration.
- 48** Fonteyne, M., Vercruyse, J., De Leersnyder, F. et al. (2016). Blend uniformity evaluation during continuous mixing in a twin screw granulator by in-line NIR using a moving F-test. *Anal. Chim. Acta* 935: 213–223.
- 49** Miyano, T., Nakagawa, H., Watanabe, T. et al. (2015). Operationalizing maintenance of calibration models based on near-infrared spectroscopy by knowledge integration. *J. Pharm. Innov.* 10 (4): 287–301.

- 50 Wise, B.M. and Roginski, R.T. (2015). Model maintenance: the unrecognized cost in PAT and QbD. *Chim. Oggi-Chem. Today* 33 (2): 38–43.
- 51 Jamrógiewicz, M. (2012). Application of the near-infrared spectroscopy in the pharmaceutical technology. *J. Pharm. Biomed. Anal.* 66: 1–10.
- 52 De Beer, T., Burggraeve, A., Fonteyne, M. et al. (2011). Near infrared and Raman spectroscopy for the in-process monitoring of pharmaceutical production processes. *Int. J. Pharm.* 417 (1–2): 32–47.
- 53 Singh, R., Velazquez, C., Sahay, A. et al. (2016). Advanced control of continuous pharmaceutical tablet manufacturing processes. In: *Process Simulation and Data Modeling in Solid Oral Drug Development and Manufacture. Methods in Pharmacology and Toxicology* (eds. M. Ierapetritou and R. Ramachandran), 191–224. New York, NY: Humana Press.
- 54 Classen, J., Aupert, F., Reardon, K.F. et al. (2017). Spectroscopic sensors for in-line bioprocess monitoring in research and pharmaceutical industrial application. *Anal. Bioanal. Chem.* 409: 651–666.
- 55 Rathore, A.S., Bhambure, R., and Ghare, V. (2010). Process analytical technology (PAT) for biopharmaceutical products. *Anal. Bioanal. Chem.* 398 (1): 137–154.
- 56 Mansouri, M.A., Sacré, P.-Y., Coic, L. et al. (2020). Quantitation of active pharmaceutical ingredient through the packaging using Raman handheld spectrophotometers: a comparison study. *Talanta* 207: 120306.
- 57 Deidda, R., Sacre, P.-Y., Clavaud, M. et al. (2019). Vibrational spectroscopy in analysis of pharmaceuticals: critical review of innovative portable and handheld NIR and Raman spectrophotometers. *TrAC Trends Anal. Chem.* 114: 251–259.
- 58 Sun, L., Hsiung, C., Pederson, C.G. et al. (2016). Pharmaceutical raw material identification using miniature near-infrared (MicroNIR) spectroscopy and supervised pattern recognition using support vector machine. *Appl. Spectrosc.* 70 (5): 816–825.
- 59 Calvo, N.L., Alvarez, V.A., Lamas, M.C., and Leonardi, D. (2019). New approaches to identification and characterization of tioconazole in raw material and in pharmaceutical dosage forms. *J. Pharm. Anal.* 9 (1): 40–48.
- 60 Diehl, B., Chen, C., Grout, B. et al. (2012). Non-destructive material identification. *Eur. Pharm. Rev.* 17 (5): 3–8.
- 61 Devjak Novak, S., Šporar, E., Baumgartner, S., and Vrečer, F. (2012). Characterization of physicochemical properties of hydroxypropyl methylcellulose (HPMC) type 2208 and their influence on prolonged drug release from matrix tablets. *J. Pharm. Biomed. Anal.* 66: 136–143.
- 62 Razuc, M., Grafia, A., Gallo, L. et al. (2019). Near-infrared spectroscopic applications in pharmaceutical particle technology. *Drug Dev. Ind. Pharm.* 45 (10): 1565–1589.
- 63 Puchert, T., Holzhauer, C.-V., Menezes, J.C. et al. (2011). A new PAT/QbD approach for the determination of blend homogeneity: combination of on-line NIRS analysis with PC Scores Distance Analysis (PC-SDA). *Eur. J. Pharm. Biopharm.* 78 (1): 173–182.
- 64 Bakri, B., Weimer, M., Hauck, G., and Reich, G. (2015). Assessment of powder blend uniformity: comparison of real-time NIR blend monitoring with stratified sampling in combination with HPLC and at-line NIR Chemical Imaging. *Eur. J. Pharm. Biopharm.* 97: 78–89.
- 65 Anderson, C.A. and Velez, N.L. (2018). Blending and characterization of pharmaceutical powders. In: *Particles and Nanoparticles in Pharmaceutical Products. AAPS Advances in the Pharmaceutical Sciences Series*, vol. 29 (eds. H.G. Merkus, G.M.H. Meesters and W. Oostra), 233–275. Cham: Springer.
- 66 Muzzio, F.J., Robinson, P., Wightman, C., and Brone, D. (1997). Sampling practices in powder blending. *Int. J. Pharm.* 155 (2): 153–178.
- 67 Sekulic, S.S., Ward, H.W., Brannegan, D.R. et al. (1996). On-line monitoring of powder blend homogeneity by near-infrared spectroscopy. *Anal. Chem.* 68 (3): 509–513.
- 68 Ma, H. and Anderson, C.A. (2008). Characterization of pharmaceutical powder blends by NIR chemical imaging. *J. Pharm. Sci.* 97 (8): 3305–3320.

- 69** Chavez, P., Lebrun, P., Sacré, P.-Y. et al. (2015). Optimization of a pharmaceutical tablet formulation based on a design space approach and using vibrational spectroscopy as PAT tool. *Int. J. Pharm.* 486 (1–2): 13–20.
- 70** Wu, Z., Tao, O., Dai, X. et al. (2012). Monitoring of a pharmaceutical blending process using near infrared chemical imaging. *Vib. Spectrosc.* 63: 371–379.
- 71** Li, W., Woldu, A., Kelly, R. et al. (2008). Measurement of drug agglomerates in powder blending simulation samples by near infrared chemical imaging. *Int. J. Pharm.* 350 (1–2): 369–373.
- 72** Blanco, M., Cueva-Mestanza, R., and Cruz, J. (2012). Critical evaluation of methods for end point determination in pharmaceutical blending process. *Anal. Methods* 4 (9): 2694–2703.
- 73** Palmer, J., O'Malley, C.J., Wade, M.J. et al. (2018). Opportunities for process control and quality assurance using online NIR analysis to a continuous wet granulation tableting line. *J. Pharm. Innov.* 1–15.
- 74** Corredor, C.C., Lozano, R., Bu, X. et al. (2014). Analytical method quality by design for an on-line near-infrared method to monitor blend potency and uniformity. *J. Pharm. Innov.* 10 (1): 47–55.
- 75** Momose, W., Katz, J.M., Drennen, J.K., and Anderson, C.A. (2015). Development of NIR methods for blend analysis using small quantities of materials. *J. Pharm. Innov.* 10 (1): 36–46.
- 76** El-Hagrasy, A.S. and Drennen, J.K. (2006). A process analytical technology approach to near-infrared process control of pharmaceutical powder blending. Part III: quantitative near-infrared calibration for prediction of blend homogeneity and characterization of powder mixing kinetics. *J. Pharm. Sci.* 95 (2): 422–434.
- 77** Kim, S., Kano, M., Nakagawa, H., and Hasebe, S. (2011). Estimation of active pharmaceutical ingredients content using locally weighted partial least squares and statistical wavelength selection. *Int. J. Pharm.* 421 (2): 269–274.
- 78** Nakagawa, H., Kano, M., Hasebe, S. et al. (2014). Verification of model development technique for NIR-based real-time monitoring of ingredient concentration during blending. *Int. J. Pharm.* 471 (1–2): 264–275.
- 79** El-Hagrasy, A.S., Delgado-Lopez, M., and Drennen, J.K. (2006). A process analytical technology approach to near-infrared process control of pharmaceutical powder blending: part II: qualitative near-infrared models for prediction of blend homogeneity. *J. Pharm. Sci.* 95 (2): 407–421.
- 80** Besseling, R., Damen, M., Tran, T. et al. (2015). An efficient, maintenance free and approved method for spectroscopic control and monitoring of blend uniformity: the moving F-test. *J. Pharm. Biomed. Anal.* 114: 471–481.
- 81** Corredor, C.C., Bu, D., and Both, D. (2011). Comparison of near infrared and microwave resonance sensors for at-line moisture determination in powders and tablets. *Anal. Chim. Acta* 696 (1–2): 84–93.
- 82** Gavan, A., Iurian, S., Casian, T. et al. (2020). Fluidised bed granulation of two APIs: QbD approach and development of a NIR in-line monitoring method. *Asian J. Pharm. Sci.* 15 (4): 506–517.
- 83** Fonteyne, M., Vercruyse, J., Díaz, D.C. et al. (2013). Real-time assessment of critical quality attributes of a continuous granulation process. *Pharm. Dev. Technol.* 18 (1): 85–97.
- 84** Fonteyne, M., Gildemyn, D., Peeters, E. et al. (2014). Moisture and drug solid-state monitoring during a continuous drying process using empirical and mass balance models. *Eur. J. Pharm. Biopharm.* 87 (3): 616–628.
- 85** Pauli, V., Roggo, Y., Kleinebudde, P., and Krumme, M. (2019). Real-time monitoring of particle size distribution in a continuous granulation and drying process by near infrared spectroscopy. *Eur. J. Pharm. Biopharm.* 141: 90–99.
- 86** Vo, A.Q., He, H., Zhang, J. et al. (2018). Application of FT-NIR analysis for in-line and real-time monitoring of pharmaceutical hot melt extrusion: a technical note. *AAPS PharmSciTech* 19 (8): 3425–3429.
- 87** Kelly, A.L., Halsey, S.A., Bottom, R.A. et al. (2015). A novel transreflectance near infrared spectroscopy technique for monitoring hot melt extrusion. *Int. J. Pharm.* 496 (1): 117–123.
- 88** Kelly, A.L., Gough, T., Dhumal, R.S. et al. (2012). Monitoring ibuprofen–nicotinamide cocrystal formation during solvent free continuous cocrystallization (SFCC) using near infrared spectroscopy as a PAT tool. *Int. J. Pharm.* 426 (1–2): 15–20.

- 89** Islam, M.T., Scoutaris, N., Maniruzzaman, M. et al. (2015). Implementation of transmission NIR as a PAT tool for monitoring drug transformation during HME processing. *Eur. J. Pharm. Biopharm.* 96: 106–116.
- 90** Baronsky-Probst, J., Möltgen, C.-V., Kessler, W., and Kessler, R.W. (2016). Process design and control of a twin screw hot melt extrusion for continuous pharmaceutical tamper-resistant tablet production. *Eur. J. Pharm. Sci.* 87: 14–21.
- 91** Wahl, P.R., Treffer, D., Mohr, S. et al. (2013). Inline monitoring and a PAT strategy for pharmaceutical hot melt extrusion. *Int. J. Pharm.* 455 (1–2): 159–168.
- 92** Saerens, L., Dierickx, L., Quinten, T. et al. (2012). In-line NIR spectroscopy for the understanding of polymer–drug interaction during pharmaceutical hot-melt extrusion. *Eur. J. Pharm. Biopharm.* 81 (1): 230–237.
- 93** Järvinen, K., Hoehe, W., Järvinen, M. et al. (2013). In-line monitoring of the drug content of powder mixtures and tablets by near-infrared spectroscopy during the continuous direct compression tableting process. *Eur. J. Pharm. Sci.* 48 (4–5): 680–688.
- 94** Dalvi, H., Langlet, A., Colbert, M.-J. et al. (2019). In-line monitoring of Ibuprofen during and after tablet compression using near-infrared spectroscopy. *Talanta* 195: 87–96.
- 95** Dalvi, H., Fauteux-Lefebvre, C., Guay, J.-M. et al. (2018). Concentration monitoring with near infrared chemical imaging in a tableting press. *J. Spectr. Imaging* 7 (1): a5.
- 96** Durão, P., Fauteux-Lefebvre, C., Guay, J.-M. et al. (2017). Using multiple process analytical technology probes to monitor multivitamin blends in a tableting feed frame. *Talanta* 164: 7–15.
- 97** He, X., Han, X., Ladyzhynsky, N., and Deanne, R. (2013). Assessing powder segregation potential by near infrared (NIR) spectroscopy and correlating segregation tendency to tabletting performance. *Powder Technol.* 236: 85–99.
- 98** Knop, K. and Kleinebudde, P. (2013). PAT-tools for process control in pharmaceutical film coating applications. *Int. J. Pharm.* 457 (2): 527–536.
- 99** Brock, D., Zeitler, J.A., Funke, A. et al. (2012). A comparison of quality control methods for active coating processes. *Int. J. Pharm.* 439 (1–2): 289–295.
- 100** Gendre, C., Genty, M., Boiret, M. et al. (2011). Development of a Process Analytical Technology (PAT) for in-line monitoring of film thickness and mass of coating materials during a pan coating operation. *Eur. J. Pharm. Sci.* 43 (4): 244–250.
- 101** Moltgen, C.V., Puchert, T., Menezes, J.C.C. et al. (2012). A novel in-line NIR spectroscopy application for the monitoring of tablet film coating in an industrial scale process. *Talanta* 92: 26–37.
- 102** Liu, R., Li, L., Yin, W. et al. (2017). Near-infrared spectroscopy monitoring and control of the fluidized bed granulation and coating processes – a review. *Int. J. Pharm.* 530 (1–2): 308–315.
- 103** Korasa, K. and Vrečer, F. (2018). Overview of PAT process analysers applicable in monitoring of film coating unit operations for manufacturing of solid oral dosage forms. *Eur. J. Pharm. Sci.* 111: 278–292.
- 104** Bogomolov, A., Engler, M., Melichar, M., and Wigmore, A. (2010). In-line analysis of a fluid bed pellet coating process using a combination of near infrared and Raman spectroscopy. *J. Chemometr.* 24 (7–8): 544–557.
- 105** Wahl, P.R., Peter, A., Wolfgang, M., and Khinast, J.G. (2019). How to measure coating thickness of tablets: method comparison of optical coherence tomography, near-infrared spectroscopy and weight-, height- and diameter gain. *Eur. J. Pharm. Biopharm.* 142: 344–352.
- 106** Igne, B., Arai, H., Drennen, J.K., and Anderson, C.A. (2016). Effect of sampling frequency for real-time tablet coating monitoring using near infrared spectroscopy. *Appl. Spectrosc.* 70 (9): 1476–1488.
- 107** Felton, L.A. (2013). Mechanisms of polymeric film formation. *Int. J. Pharm.* 457 (2): 423–427.
- 108** Gendre, C., Genty, M., da Silva, J.C. et al. (2012). Comprehensive study of dynamic curing effect on tablet coating structure. *Eur. J. Pharm. Biopharm.* 81 (3): 657–665.
- 109** Gendre, C., Genty, M., Fayard, B. et al. (2013). Comparative static curing versus dynamic curing on tablet coating structures. *Int. J. Pharm.* 453 (2): 448–453.

- 110** Korasa, K., Hudovornik, G., and Vrečer, F. (2016). Applicability of near-infrared spectroscopy in the monitoring of film coating and curing process of the prolonged release coated pellets. *Eur. J. Pharm. Sci.* 93: 484–492.
- 111** Görög, S. and Szántay, C. (2017). Spectroscopic methods in drug quality control and development. In: *Encyclopedia of Spectroscopy and Spectrometry*, 3e (eds. J.C. Lindon, G.E. Tranter and D.W. Koppenaal), 178–187. Academic Press.
- 112** Singh, R. (2018). Implementation of control system into continuous pharmaceutical manufacturing pilot plant (powder to tablet). In: *Computer Aided Chemical Engineering*, vol. 41, 447–469.
- 113** Román-Ospino, A.D., Cárdenas, V., Ortega-Zuñiga, C., and Singh, R. (2018). PAT for pharmaceutical manufacturing process involving solid dosages forms. In: *Computer Aided Chemical Engineering*, vol. 41, 293–315. Elsevier.
- 114** Pomerantsev, A.L., Rodionova, O.Y., Melichar, M. et al. (2011). In-line prediction of drug release profiles for pH-sensitive coated pellets. *Analyst* 136 (22): 4830.
- 115** Pawar, P., Wang, Y., Keyvan, G. et al. (2016). Enabling real time release testing by NIR prediction of dissolution of tablets made by continuous direct compression (CDC). *Int. J. Pharm.* 512 (1): 96–107.
- 116** Rantanen, J. and Khinast, J. (2015). The future of pharmaceutical manufacturing sciences. *J. Pharm. Sci.* 104 (11): 3612–3638.
- 117** Awad, A., Trenfield, S.J., Gaisford, S., and Basit, A.W. (2018). 3D printed medicines: a new branch of digital healthcare. *Int. J. Pharm.* 548 (1): 586–596.
- 118** Trenfield, S.J., Goyanes, A., Telford, R. et al. (2018). 3D printed drug products: non-destructive dose verification using a rapid point-and-shoot approach. *Int. J. Pharm.* 549 (1–2): 283–292.
- 119** Khorasani, M., Edinger, M., Raijada, D. et al. (2016). Near-infrared chemical imaging (NIR-CI) of 3D printed pharmaceuticals. *Int. J. Pharm.* 515 (1–2): 324–330.
- 120** WHO (2018). *Substandard and Falsified Medical Products – Fact Sheet*. WHO.
- 121** Rebiere, H., Guinot, P., Chauvey, D., and Brenier, C. (2017). Fighting falsified medicines: the analytical approach. *J. Pharm. Biomed. Anal.* 142: 286–306.
- 122** Been, F., Roggo, Y., Degardin, K. et al. (2011). Profiling of counterfeit medicines by vibrational spectroscopy. *Forensic Sci. Int.* 211 (1–3): 83–100.
- 123** Zontov, Y.V., Balyklova, K.S., Titova, A.V. et al. (2016). Chemometric aided NIR portable instrument for rapid assessment of medicine quality. *J. Pharm. Biomed. Anal.* 131: 87–93.
- 124** Mbinze, J.K., Sacré, P.-Y., Yemoa, A. et al. (2015). Development, validation and comparison of NIR and Raman methods for the identification and assay of poor-quality oral quinine drops. *J. Pharm. Biomed. Anal.* 111: 21–27.
- 125** Crocombe, R.A. (2018). Portable spectroscopy. *Appl. Spectrosc.* 72 (12): 1701–1751.
- 126** Ciza, P.H., Sacré, P.-Y., Waffo, C. et al. (2019). Comparing the qualitative performances of handheld NIR and Raman spectrophotometers for the detection of falsified pharmaceutical products. *Talanta* 202: 469–478.
- 127** Vickers, S., Bernier, M., Zambrzycki, S. et al. (2018). Field detection devices for screening the quality of medicines: a systematic review. *BMJ Glob. Health* 3 (4): e000725.
- 128** Roth, L., Biggs, K.B., and Bempong, D.K. (2019). Substandard and falsified medicine screening technologies. *AAPS Open* 5 (1): 2.
- 129** Esbensen, K.H. and Wagner, C. (2015). Theory of sampling (TOS) – fundamental definitions and concepts. *Spectrosc. Eur.* 27 (1): 1–4.

# 5

## MOEMS and MEMS - Technology, Benefits & Uses

*Heinrich Grüger*

*Fraunhofer Institute for Photonic Microsystems, Dresden, Germany*

### 5.1 Introduction

#### 5.1.1 Definitions

The term MEMS – micro-electromechanical systems – has shifted in its meaning through the last decades. Today, relevant characteristics are considered to be “a microscopic device” featuring “electrical functionality” and “moving parts” [1]. The definition includes sensors where a movement or displacement is converted into an electric signal [2], actuators where electrical driving principles are used to initiate motion or rotation of a deflectable part [3], as well as combinations of both, e.g. in ultrasonic transducers [4], accelerometers [5] and gyroscopes [6].

Most commercial MEMS are produced on silicon wafers, but other materials have been used as well, e.g. “Diamond MEMS” [7]. Mechanical motion is actuated by means of electrical driving principles, which can be electrostatic, magnetic or piezoelectric. For proper operation, MEMS need matching drive electronics, often operated in a close loop mode [8]. Ultracompact outlines can be achieved by the combination of MEMS and complementary metal-oxide-semiconductors (CMOS) in chip-scale assembly, or in selected cases, MEMS on top of CMOS [9].

The combination of electrical and mechanical functions enables devices, like microphones [10, 11], loudspeakers [12, 13], ultrasonic transducers [4, 14], pressure sensors [2], acceleration sensors [5, 15–17], gyroscopes [6, 18, 19], and many more. MEMS devices can be found in consumer electronic devices, like mobile phones, tablets, digital or video cameras, toys, entertainment equipment, drones, but also in more critical applications. For instance, in automobiles, a steadily increasing number of MEMS devices takes care of safety and comfort; tire pressure sensors are the most obvious example.

Optical MEMS are a specific class of actuators featuring interaction of MEMS actuation and light. Examples are scanner mirrors in rotational<sup>1</sup> [20–24] or piston-type configurations [25, 26], spatial light modulators [27, 28], also tiltable gratings [29], more complex devices [30], and optical MEMS systems in a chip [31]. Bulk silicon micro-machined scanner mirrors have been used for applications, like laser light deflection, from bar code scanning to projection, microscopy and spectroscopy [32]. Future systems, like LIDAR (light detection and ranging) are being developed [33]. Surface micro-machined mirror arrays in digital light processors [34] are used in digital cinema projectors and similar applications.

Optical MEMS contribute significantly to the development of systems for portable spectroscopy. The term “MOEMS” – “micro-opto-electromechanical systems” – is used for combinations of MEMS and micro-optics (see preface in [35]), but does not define a class of special MEMS. In the following, all devices are simply named MEMS.

1 <https://www.hamamatsu.com/eu/en/product/type/S12237-03P/index.html>.

Some devices which are fabricated using typical MEMS technologies, but lacking selected features of the MEMS definition, have been called “MEMS” or “MEMS technology-based” as well. Phrases like “no moving parts” are in contradiction to the basic MEMS definition. Nonetheless, devices based on such technologies have been used for spectrometer systems successfully and will be discussed here as well.

### 5.1.2 Brief History of MEMS

Microelectronic devices fabricated in CMOS technologies have changed the world since the detection of the rectifier effect by Ferdinand Braun in 1874. Today, multibillion transistors can be integrated in a single chip, and structures have feature sizes down to seven nanometers.

The availability of large wafer substrates and reliable process technology initiated the invention of devices which are not mainly electronics, but featuring electrically driven micro-mechanics. The term “Micro-electromechanical Systems – MEMS” was used first in a proposal to US Defense Advanced Research Projects Agency (DARPA) in July 1986. Details of the invention and history have been summarized in literature [35]. Here some relevant milestones shall be mentioned briefly. A special kind of silicon wafer substrate provides a lateral structure of silicon and silicon oxide. SOI – silicon on oxide – wafers have a top layer in the range from  $\frac{1}{4}$  to 150  $\mu\text{m}$  active silicon on 1–2  $\mu\text{m}$  silicon oxide and a few hundreds of microns of silicon as handle layer. The advantage of this structure is the application of deep etch processes [36] which are extremely selective between silicon and silicon oxide. Thus, the oxide layer can be used as etch stop from top and bottom. The anisotropic deep etching, either wet, using fluid acids, or gas phase based, e.g. plasma etch or reactive ion etch (RIE), became the key to MEMS production. Much effort has been put into the optimization of anisotropic etch steps. Most relevant was the invention of the deep reactive ion etch (“DRIE”) in the 1990s, often named “Bosch process” due to the inventing company [37]. The Bosch process has become the standard process for MEMS production. High aspect ratios can be achieved, which are used to realize MEMS structures with deep and steep trenches, or even complex 3D structures.

The continuous shift to larger substrates in microelectronics came later for MEMS, but high-volume production has been established long ago (Figure 5.1).<sup>2</sup>

The invention of optical MEMS devices followed the general MEMS technology development. Optical surfaces, e.g. mirrors, were integrated on moving parts. The main increase in complexity was in the field of optical

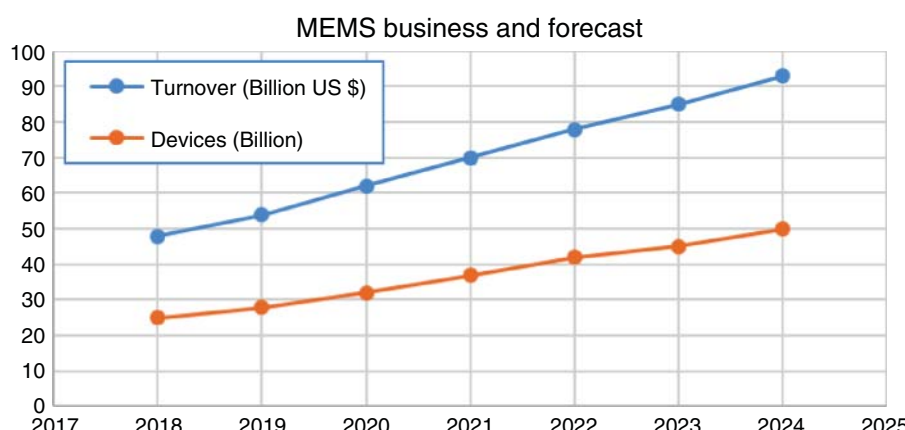


**Figure 5.1** Development of the annual MEMS production volume. Source: Based on New market perspectives for the MEMS & Sensors. [http://www.yole.fr/iso\\_upload/News/2017/PR\\_STATUSMEMSINDUSTRY\\_NewMarketPerspectives\\_YOLE\\_June2017.pdf](http://www.yole.fr/iso_upload/News/2017/PR_STATUSMEMSINDUSTRY_NewMarketPerspectives_YOLE_June2017.pdf).

<sup>2</sup> [http://www.yole.fr/iso\\_upload/News/2017/PR\\_STATUSMEMSINDUSTRY\\_NewMarketPerspectives\\_YOLE\\_June2017.pdf](http://www.yole.fr/iso_upload/News/2017/PR_STATUSMEMSINDUSTRY_NewMarketPerspectives_YOLE_June2017.pdf).

MEMS assembly. The optical areas must be accessible. Thus, the assembly technology must be adapted to optical requirements like openings or windows.

A prominent example for optical MEMS-based systems were projectors for commercial and later private use. From cinema to meeting rooms and private entertainment, the use of a digital light processor, a MEMS device with a very high number of individually actuated mirrors [27], provided a significant increase in image quality compared to the earlier transmission panel based on liquid crystal displays (LCDs). The MEMS device was originally invented by Texas Instruments in 1987, and projectors based on digital light processing (DLP) entered the market in 1997.

Since the 1990s, monolithic MEMS scanner mirrors have been developed for applications, like barcode scanning and laser projection. The recent demand for LIDAR systems in automotive applications may lead to an increased demand for scanning mirrors from the automotive sector.

### 5.1.3 Basics of MEMS Technology

Pattern generation for MEMS devices on the wafer uses the same lithographic technology as used for CMOS components. A photoresist is applied, which is exposed to ultraviolet (UV) light through a mask bearing the structural information (e.g. chromium on glass, using 10 $\times$  magnification). The structural information is transferred to the resist on the wafer before different deposition or etch steps is/are applied. These steps are repeated several times until the device is finished [38].

Typically, MEMS devices feature much wider structural feature sizes than CMOS devices. This is due to the fact that mechanical interaction, e.g. force sensing in acceleration or gyro sensors, as well as optical applications, require significant mass or optical active area to operate properly.

Characteristics for MEMS technologies are deep etch process steps with high aspect ratios. To realize MEMS structures, deep but narrow trenches have to be etched from the front side. For instance, the mirror plate of a bulk silicon microscanner mirror may be 150  $\mu\text{m}$  thick, but the trenches should be only 2  $\mu\text{m}$  wide. In turn, deep etch optimization reached aspect ratios up to 1 : 1000.

Freestanding structures formed by the front side trenches are released by first backside cavity etch, stopping on the buried oxide, and a final buried oxide removal. The main issue is the realization of deep trenches in silicon stopping on silicon oxide (Figure 5.2).

For 3D optical MEMS using the vertical areas of the etch structures or trenches, it is important to consider the so-called scallops originating from the repeated etch and deposition steps of the Bosch process. There are process options available to reduce the formation of these scallops.

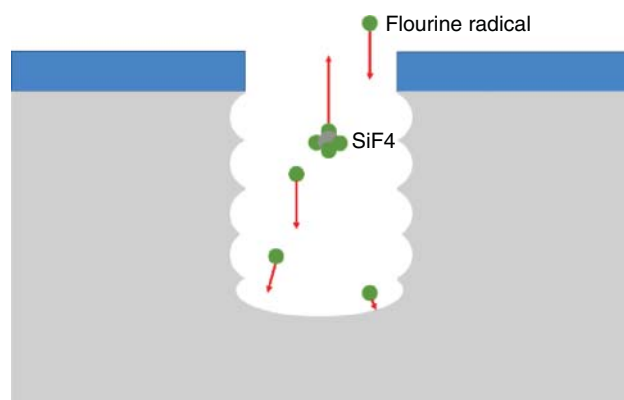


**Figure 5.2** Anisotropic gas phase etch of silicon with photoresist.

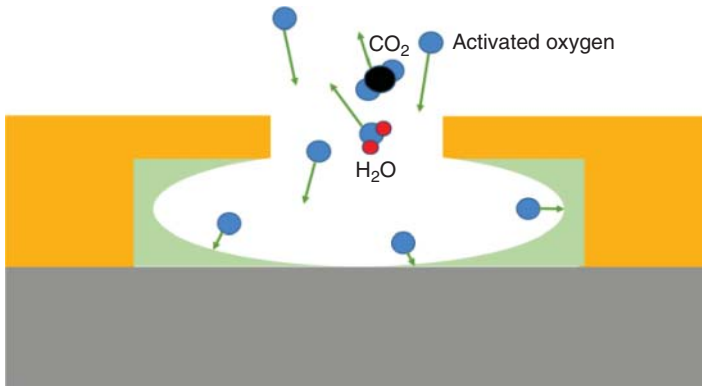


**Figure 5.3** Removal of sacrificial layer by plasma etch.

Surface micro-machined MEMS differ in the etch process. Here a sacrificial layer is deposited and planarized [39]. Holes are etched into the sacrificial layer for the realization of hinges, before the surface MEMS material, typically a metal or alloy, is deposited. Applying another photolithography process step, the lateral MEMS structures and the etch holes are generated. Afterward, the sacrificial layer is removed by gas phase etching and the surface MEMS structures (Figure 5.3) are released.

MEMS devices are extremely reliable and robust: their small size means that they are very “stiff” with resonant frequencies much higher than found in ambient vibrations. Especially for bulk silicon micro-machined devices, the properties of the monocrystalline material leads to favorable system capabilities, while reproducibility ensures high standards for the systems based upon MEMS devices.

Once designed, the production of MEMS can easily be scaled up to high-volume production. The initial development requires an initial effort for setup, chip design, lithography mask manufacturing and process implementation. The process, consisting of hundreds of individual steps, may take multiple weeks to a month’s time. Finally, production on the 200 or 300-mm wafers used today provides a low cost for the individual chip in volume production, which offers market opportunities for MEMS-based systems.

#### 5.1.4 NIR Analysis

MEMS-based systems mostly enable small outline, high-volume and low-cost applications. For portable spectroscopy, this shifts the focus for MEMS-based systems toward the field of near-infrared (NIR) analysis, where the spectrometer and a light source will be the main components. The light source, e.g. a small halogen bulb, can be cost-efficient as well. No complex laser system is required as compared with Raman spectrometers. The potential for high-volume production addresses users of mobile devices. NIR spectroscopy, because both organic and inorganic matter can be analyzed, opens day-to-day applications in life, like food, dermatology, and medical. Furthermore, inorganic applications are possible in the geology, i.e. minerals.

For solid organic matter, the penetration depth of NIR radiation can be up to several millimeters, and, thus, more than the surface layers can be analyzed. The combination and overtone bands of organic molecules are used in both qualitative and quantitative analyses using chemometrics-based mathematical models based on reference data.

Requirements for different spectrometers or spectral analyzers are summarized in Table 5.1.

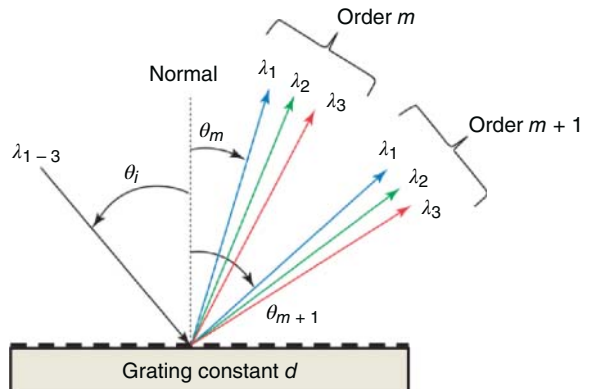
## 5.2 Grating-Based Spectrometers

Historically, prism-based spectrosopes, invented in 1814 by Joseph von Fraunhofer, were the first spectral analyzers used for scientific applications – the evaluation of the sun’s spectrum. Dispersive gratings were invented

**Table 5.1** Requirements for multipurpose spectral analyzers.

	Portable desktop	Handheld	Mobile phone add-on	Mobile phone integrated
Size	<100 × 100 × 100 mm <sup>3</sup> <4" × 4" × 4"	<75 × 50 × 25 mm <sup>3</sup> <3" × 2" × 1"	<50 × 25 × 15 mm <sup>3</sup> <2" × 1" × 0.6"	<10 × 10 × 4.5 mm <sup>3</sup>
Range	950–1900 nm/ 1250–2500 nm	950–1900 nm	1000–1850 nm	1000–1850 nm
Resolution	<10 nm	10 nm	12 nm	15–18 nm
Stability	0.1–0.5 nm	0.5 nm	0.5 nm	0.5–1 nm
SNR	1 : 4096	1 : 1024	1 : 1024	1 : 256 (512)

Devices with defined uses may differ mainly in their spectral ranges.

**Figure 5.4** Reflection grating.

by David Rittenhouse in 1785 [40, 41]. Compared to prism-based systems, they have a higher dispersive power and, if used in reflection, there is no absorption through the material. Important spectrometer designs were presented by Otto von Littrow in 1862, H. Ebert [42] in 1889, followed by the work of Monk and Gillieson [43, 44], Czerny and Turner [45, 46], and the improved Ebert–Fastie [47, 48]. Other less prominent configurations have been published [49].

Grating-based spectrographs became the dominant technology in the NIR as soon as gratings with sufficient quality became available. The reproduction technologies to realize numerous gratings from a single master device were key to their commercial success. The diffraction pattern of a grating is based on the geometric path difference (Figure 5.4).

The grating equation (Eq. (5.1)) describes the mathematics criteria for constructive interference. Intensity maxima for a given wavelength will occur if the path difference,  $d_n$ , matches an integer multiple of the wavelength, including higher positive ( $n > 1$ ) and negative ( $n \leq -1$ ) diffraction orders.

$$d_n = n \lambda = g (\sin \alpha - \sin \beta) \quad (5.1)$$

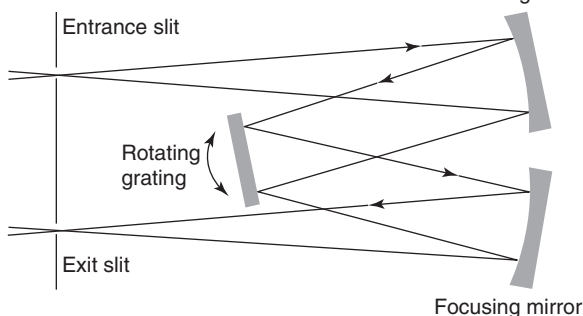
The resolving power of a grating  $\lambda/\Delta\lambda$  is depending on the number of elements  $N$  and the diffraction order  $n$  (Eq. (5.2)).

$$\lambda/\Delta\lambda = n N \quad (5.2)$$

The characteristic setup of a Czerny–Turner-type grating spectrometer is shown in Figure 5.5. The five major components of such a spectrometer are (i) entrance aperture – usually a slit, but could be a pinhole or the end

Collimating mirror

Figure 5.5 Czerny–Turner setup for a NIR spectrometer.



of an optical fiber as well, (ii) collimating mirror, (iii) grating, (iv) refocusing mirror, (v) exit aperture – slit and screen or detector behind it.

Today, scientific instruments are available either in the classic design with rotating gratings and flexible mounts for selected detectors, or small-sized systems using fixed gratings and detector arrays. Over the past few decades, significant work was put into miniaturization and efficient production of these spectrometers. Similar to digital photography, this may lead to their application in numerous fields, many of which are yet to be developed. The main reason is that spectroscopy is a very capable technique for the analysis of organic matter; its capabilities will be advantageous in an increasing field of applications.

Diffraction at a grating only occurs if the d-spacing is wider than half of the wavelength, which limits the resolution of grating-based spectrometers. The NIR bands of organic molecules in the condensed phase are typically wide, and, thus, the resolution required is not challenging. So, there is a growing market for NIR analysis.

### 5.2.1 Fixed Grating-Based Spectrometer

The first miniature spectrometer entered the market in 1992 from Ocean Optics, founded in 1989, now known as Ocean Insight. Based on a detector array, and applying a crossed Czerny–Turner configuration, the trend to miniaturization was initiated. Silicon detectors enable low-cost systems, but are limited to a long wavelength cutoff around 1100 nm. Similar systems have been developed for NIR applications using InGaAs detector arrays, which are still quite expensive. The slogan “no moving parts” has been used to characterize these systems. Thus, they do not exactly meet the MEMS definition.

Fixed grating spectrometers have been realized by applying MEMS technologies, i.e. reactive silicon deep etching of the slits, and the same chip housing the detector array. Hamamatsu has presented a “thumb size” spectrometer,<sup>3</sup> using a chip assembled with a concave grating, which was fabricated on a quartz body (Figure 5.6).

The first design with an outline of  $27.6 \times 16.8 \times 13 \text{ mm}^3$  offered either a spectral range from 340 to 750 nm with 14 nm resolution or 640–1050 nm with 20 nm resolution. The second generation with a reduced outline of  $20.1 \times 12.5 \times 10.1 \text{ mm}^3$  featured a detector with 256 elements each  $12.5 \mu\text{m}$  wide and addressed a spectral range from 340 to 780 nm with 15 nm resolution.

New in 2019<sup>4</sup> was an ultracompact design optimized for the use in mobile phones with  $11.5 \times 4.0 \times 3.5 \text{ mm}^3$  announced to be the world’s smallest spectrometer for NIR (640–1050 nm, 17–20 nm resolution).

In the end, the miniaturization of detector-array-based spectrometers faces limitations. The number of detector elements cannot be reduced without affecting either range or resolution. In the NIR region, the element size strongly correlates with the detector noise. Ultracompact systems, i.e. below 10 mm size, require the reduction of the array outline to 256 elements, which may be only  $25 \mu\text{m}$  wide. In turn, to cover a spectral range of 1000 nm,

<sup>3</sup> <https://www.hamamatsu.com/us/en/product/type/C12666MA/index.html>.

<sup>4</sup> <https://www.hamamatsu.com/us/en/product/type/C14384MA-01/index.html>.

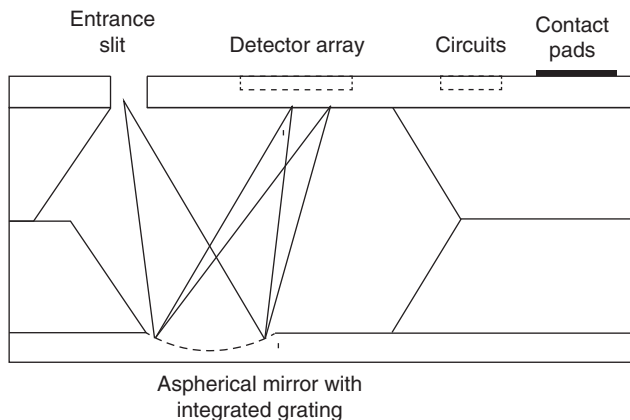


**Figure 5.6** Chip for miniaturized spectrometer with slit and detector array.

each element has to cover 4 nm. This affects already the theoretical limits for resolution, and the stability of the wavelength scale as well.

### 5.2.2 MEMS Scanning Grating

Standard scanning monochromators use a mechanical drive to rotate the grating and thereby control which wavelength falls on the exit slit. Considering this, it became clear that a grating structure on a deflectable MEMS scanner device (Figure 5.7) could be used to realize a similar monochromator setup [29, 50].

Researchers at Fraunhofer IPMS initiated the development of MEMS scanning-grating devices based upon an existing 1D scanner mirror device with a resonant drive. This mirror is based on bulk silicon micro-machining, with typical device silicon thicknesses ranging between 30 and 90  $\mu\text{m}$ . The grating is fabricated on the front side of the vibrating silicon plate by a wet anisotropic etch, using an additional mask for the grating structure, and is generated as grooves along the 111 crystal faces. Thus, the grating facets are atomically smooth, but the angle is given by the crystal orientation of the wafer used. Regular 100-oriented wafers result in facets along the 111 direction in an angle of 54.7°. Specific blazes are possible applying BSOI wafers with tilted crystal orientations for

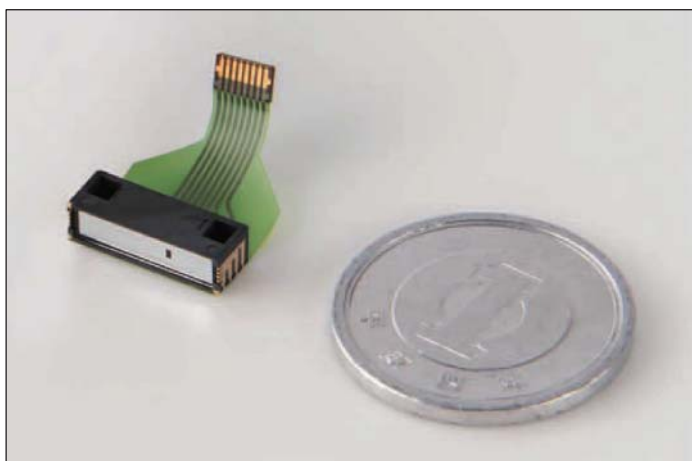


**Figure 5.7** Ultracompact outline spectrometer (Hamamatsu). Source: Hamamatsu Photonics K.K.

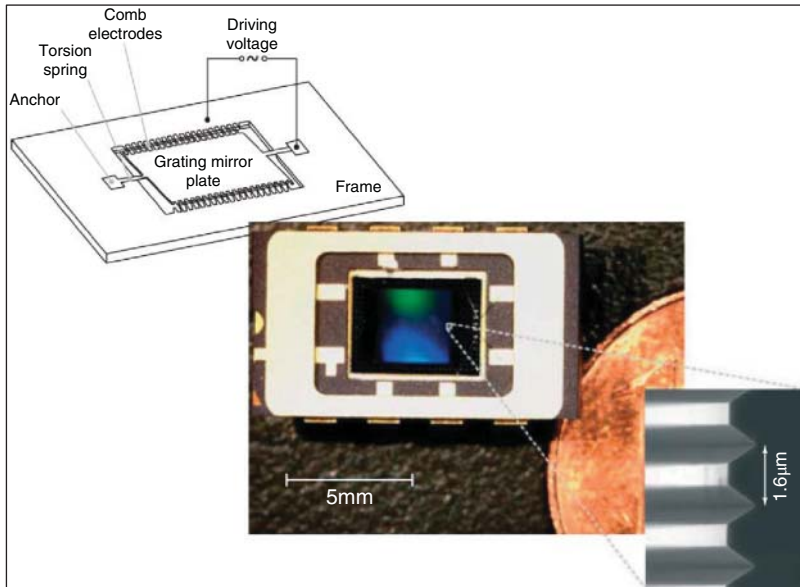


**Figure 5.8** 1D MEMS scanner device with grating. Source: Fraunhofer IPMS.

the active layer, but the huge effort is not justified by the results. For NIR applications, sufficient efficiency in a broad range is more relevant than highest efficiency at a single small band.

Different grating structures have been investigated (Figure 5.8), including refill process steps, leading to sinusoidal structures. Each structure has its specific advantages and disadvantages, but, in the end, the v-grooves have been selected for the system implementation [51].

Based on the MEMS scanning grating device, a spectrometer for NIR was developed (Figure 5.9). It features a Czerny–Turner configuration with an SubMiniature version A (SMA) coupler to connect standard optical fibers. An entrance slit can be added, and then an ultraprecision off-axis mirror is used for collimation. The grating is mounted on an adjustable stage, including a position readout sensor. The diffracted light is collected by a refocusing second mirror, and then captured by a standard single-element indium gallium arsenide (InGaAs) photodiode detector behind an exit slit. The signals are amplified by a three-stage transimpedance amplifier. A digital control unit computes the spectra from the intensities captured, and the grating position information. The sinusoidal movement, or an improved motion model, are used for highly accurate wavelength information and stability. A resonant MEMS device opens the option for long-term MEMS motion detection, or even active control in a close loop configuration, resulting in very accurate wavelength stability (Figure 5.10).

This device may be suitable for initial portable applications, but for real mobile use, a more miniaturized design would be advantageous. This, and a demand for high-volume capabilities, was the motivation for further research work. Size reduction is limited by the need for component alignment, but a promising option is the integration of more functions into the MEMS chip. Besides the grating, both slits can be integrated into the MEMS chip design, with the alignment determined by the lithographic accuracy of the MEMS process. In classic Czerny–Turner designs, the grating must be tilted out of the plane of grating and slits. However, this is difficult in a MEMS chip, and requires a more complex design [52]. A solution is the use of the first negative diffraction order. The entrance and exit slits were placed on one side of the grating, and the so-called *W*-configuration shifted to a folded double-V. For the realization, a new MEMS chip was fabricated. The weak point of this design is the need for complex off-axis mirrors; both mirrors were fabricated by ultraprecision micro-machining (UPM) in one aluminum substrate. The spectrometer is the size of a sugar cube (Figure 5.11), and was integrated by stacking the mirror substrate, a space

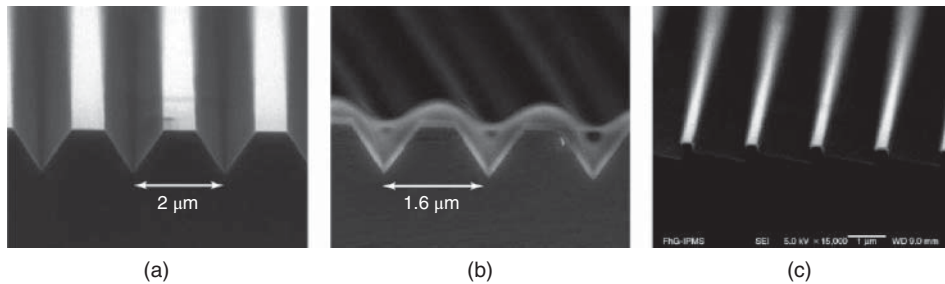


**Figure 5.9** SEM images of different grating structures etched into silicon. (a) V-grooves etched into silicon. (b) Glass refill resulting in sinusoidal surface structures. (c) Blaze gratings realized using wafers with  $4^\circ \dots 11^\circ$  angle misfit of the 111 orientation. Source: Fraunhofer IPMS.

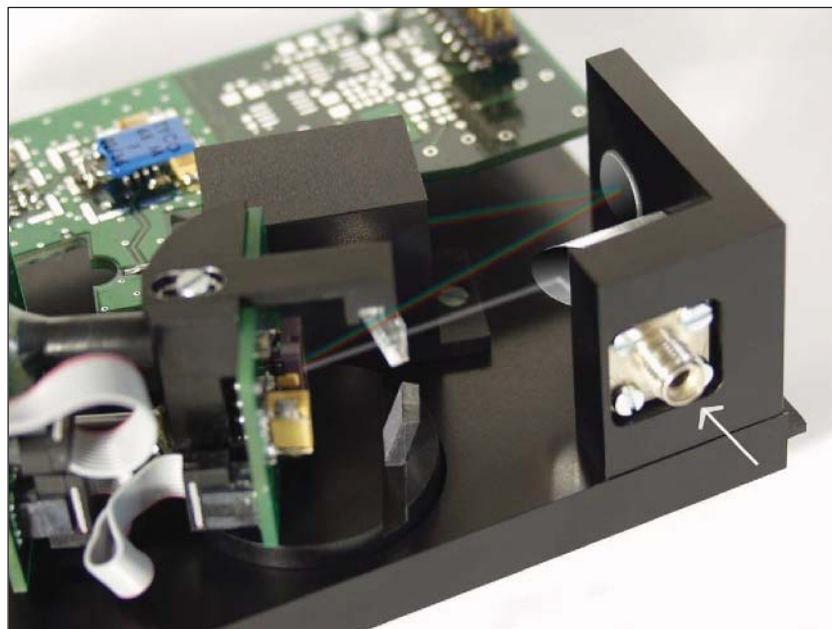


**Figure 5.10** SGS 1900 MEMS-based scanning grating spectrometer. Source: Fraunhofer IPMS.

including structures for stray light suppression, and the MEMS board with a bar die detector chip, placed in a cavity in the MEMS chip [53].

The sugar cube-sized spectrometer achieved performance close to the existing SGS 1900 system. Besides this, some major disadvantages came up. The mirrors are complex and no technology was available for the production in volume and on large substrates. Stacking a huge number of spectrometers from a few large substrates and dicing afterward turned out to be complex too, as no reliable technology for dicing this stack could be found. Thus, the further development of a more miniaturized MEMS-based spectrometer, which would fit into mobile phones, had to be based on a different approach. The availability of a high throughput assembly tool that could put optical elements into selected places of complex 3D bodies was key. This next crossed Czerny–Turner design was further miniaturized. Spherical mirrors with rotation symmetric surfaces would be sufficient, if the astigmatism and coma could be controlled by the optic design. In the end, longer slits and a larger detector turned out to be advantageous.

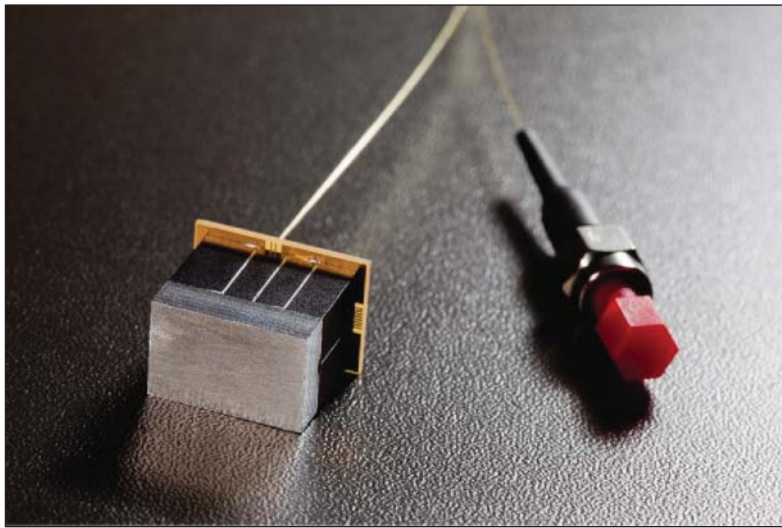


**Figure 5.11** MEMS scanning grating spectrometer in sugar cube size. *Source:* Fraunhofer IPMS.

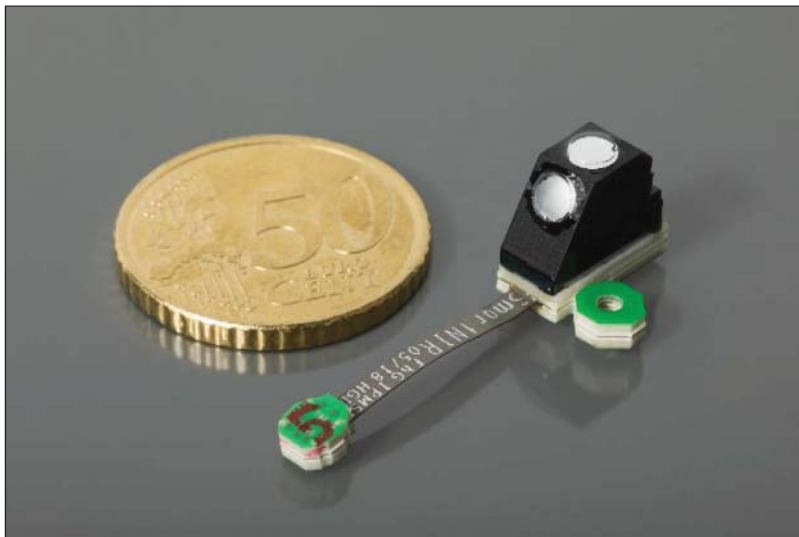


**Figure 5.12** Ultracompact MEMS scanning grating spectrometer. *Source:* Fraunhofer IPMS.

Based on the optic design, a spectrometer body was fabricated by means of 3D printing. Both mirrors and the entrance slit were assembled to the body, which was then placed on the MEMS board containing the MEMS scanning grating device, exit slit and detector (Figure 5.12).

### 5.2.3 DLP-Based Spectrometers

A different kind of deflectable mirror device can be realized using surface micro-machining. A thin material – most often a metal alloy – is deposited on a sacrificial layer which is removed afterward to generate free-standing structures. Due to the thickness limit of the sacrificial layer, the size of these types of MEMS mirrors must be

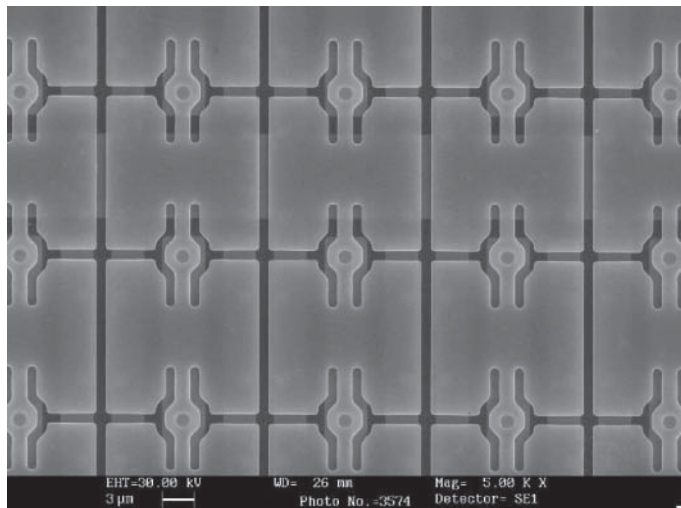


**Figure 5.13** SEM image of a surface micro-machined spatial light modulator. *Source:* Fraunhofer IPMS.

**Figure 5.14** Design of a fixed grating and DLP spectrometer (InnoSpectra). *Source:* InnoSpectra Corporation.



small, typically in the tens-of-micrometers range. High numbers of individual mirrors can be realized on one device. The freestanding structures can be deflected by means of electrostatic drive (Figures 5.13 and 5.14).

DLPs enable different spectrometer concepts and designs [54].<sup>5</sup> The most relevant types are a fixed grating spectrometer with DLPs for the selection of a pass wavelength to a single detector element and Hadamard spectrometers.

In fixed grating spectrometers, the detector array used in the image plane can simply be replaced by a tilting element light processor which deflects the light of one selected wavelength onto a single detector device, and the rest into an optical stop. This is advantageous if the detectors array is more expensive than the DLP and a single element detector.<sup>6</sup>

A weak spot of the grating spectrometers discussed previously is the very low signal level and the strong influence of noise in the electronic readout system. Here, Hadamard systems offer an alternative approach with similar components in the setup. The basic idea of a Hadamard transform spectrometer [55, 56] is to put half of the wavelengths of light on the single detector and then scan the change of the individual wavelengths within that half, instead of scanning small wavelength intervals. Afterward, the spectrum is calculated. The advantage is much higher flux on the detector, and, thus, less influence of detector noise. As compared with conventional array read-out, a higher resolution analog-to-digital conversion is necessary. Based on this basic idea, much more complex approaches have been realized, which can also be used for more sophisticated spectral imaging systems.

5 <http://www.ti.com/lit/wp/dlpa048a/dlpa048a.pdf>

6 [http://www.inno-spectra.com/index\\_en](http://www.inno-spectra.com/index_en)

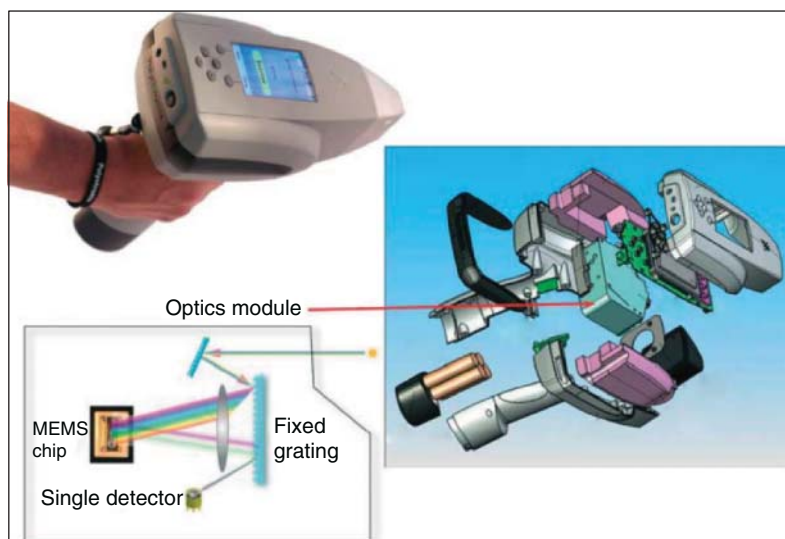


**Figure 5.15** PAHZIR. Source: Encyclopedia of Analytical Chemistry in 2013 by John Wiley & Sons, Ltd. DOI: 10.1002/9780470027318.a9376

One of the first systems for portable spectroscopy was the “PHAZIR,” developed by Polychromix which became part of Thermo Fisher Scientific later. A MEMS chip using surface micro-machining was realized by MEMS provider Boston Micromachines. It was operated as a programmable mask in a Hadamard-type configuration. A handheld system (Figure 5.15) was applied in handheld field applications, like recycling of carpet, which requires discrimination of carpet fiber materials, typically wool, nylon, polyethylene terephthalate, etc. the database and matching algorithm was stored in the system’s memory.

#### 5.2.4 Scanner Mirror-Based Micro-Spectrometer

Technically, there is no need to realize a grating structure on a MEMS scanner device to build a monochromator or spectrometer. Applying a simple scanning mirror device, and illuminating a grating mounted in an appropriate direction, also enables a monochromatic optical setup (Figure 5.16). The scanner essentially changes the incident angle of the collimated beam onto the grating. This design needs the grating as an additional component, but it offers advantages as well. The technology for the scanner is simplified, and the deflection required is only half of a scanning grating device which addresses the same spectral range. This contributes to possible cost reduction on the electronic side for the driver, but potentially the MEMS itself is less demanding too.

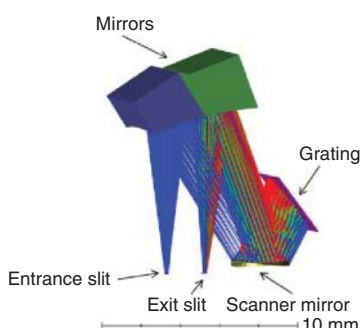


**Figure 5.16** Optic design for a scanner mirror micro-spectrometer. Source: Grüger et al. [57]. © 2019, Society of Photo-Optical Instrumentation Engineers.

There are some more advantages of this concept. The grating can be simply changed, which opens flexibility for different  $d$ -spacing and blaze, and modular approaches may be possible. There are also no limitations from wet etching in silicon. Thus, the same basic system concept can be modified to fit the requirements of different applications.

Fraunhofer ENAS presented an early version of this kind of spectrometer. A system was realized that operates in the 1100–2100 nm range with a resolution of 12 nm [58].

A highly integrated spectrometer, based on resonant 1D scanner mirrors, was presented in 2019 [57]. The system is aimed at a 950–1900 nm wavelength range, addressable with uncooled extended InGaAs detectors. An ultracompact setup, in  $25 \times 15 \times 15$  mm<sup>3</sup> outline, includes the optical bench, MEMS, slits and detector on a printed board. The MEMS deflection can be reduced to  $\pm 5^\circ$  instead of  $\pm 9.6^\circ$ , used for the previous scanning grating approach, without decrease in the spectral range. The resolution is still slightly below 10 nm.

### 5.3 Fourier Transform Spectrometer

Fourier transform (FT) or FT infrared (FTIR) spectrometers use interference in an interferometer instead of diffraction at a dispersive element. While scanning the interferometer, the signal is captured by a detector in the image plane, and then converted to a spectrum via a Fourier transformation.

FTIR spectrometers are the most accurate general-purpose devices for infrared spectroscopy [59]. Besides the use in laboratories, extremely miniaturized systems are now available for the mobile device market.

The reason for the success of FTIR spectrometers are the well-known advantages of the approach:

“Fellgett advantage”: Multiplex operation, i.e. all wavelengths are captured simultaneously;

“Jacquinot advantage”: High optical throughput as no slits limit the aperture, resulting in a good signal-to-noise ratio (SNR); “Connes advantage”: Linearity of the wavelength scale can easily be calibrated, e.g. using a reference laser.

FTIR spectrometers can address a broad spectral range limited by their detector’s sensitivity only. No higher diffraction orders, or related complications, appear. For proper operation, FTIR spectrometer-based systems need a highly stable light source because fluctuations of the illumination will generate noise across all the wavelengths. Sufficient computation power is required for the Fourier transform itself, but today this is no longer a real concern.

The most common option to realize an FT spectrometer is the use of a Michelson interferometer. The central part is the beam splitter, which divides the incident radiation into two beams. The reference beam is reflected by a fixed mirror, and the second beam by a moveable mirror (Figure 5.17). After recombination of both beams, the interference can be observed at the image plane.

To acquire spectroscopic information, the interferometer is scanned by translating the movable mirror. A detector in the image plane captures the signal. The mirror path  $L$  is the only parameter which limits the spectral resolution (Eq. (5.3)) [59].

$$\Delta v = 1/L \quad (5.3)$$

However, in a practical FTIR spectrometer, the beam angles cannot be limited to infinite. Thus, diameter of source and detector as well as the focusing optics will reduce the resolving power beyond the theoretical limit [59].

The interferogram pattern is captured as a function of the mirror position, digitized at regular optical retardation intervals. Afterward, it is converted to spectrum (linear in frequency – usually units of reciprocal centimeters) by a Fourier transformation (Eq. (5.4)).

$$F(w) = \frac{1}{\sqrt{2\pi}} \int_{-\infty}^{\infty} f(t)e^{iwt} dt \quad (5.4)$$

The fast Fourier transform (FFT) algorithm computes frequency domain information from time domain information. Historically, the basic algorithm was already used by Carl Friedrich Gauss in 1805. For implementation on a digital computer, one of the most prominent contributions was given by James Cooley and John W. Tukey in 1965 [60].

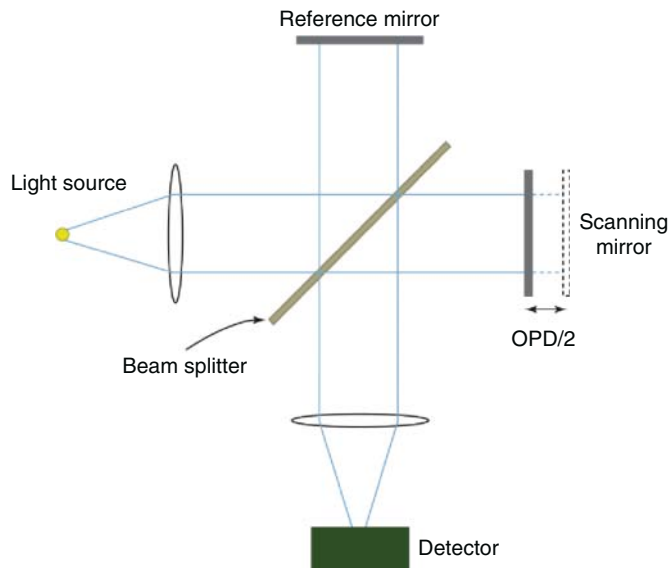


**Figure 5.17** Michelson interferometer for an FT spectrometer setup.

### 5.3.1 MEMS Piston Mirror-Based FTIR Spectrometer

Different kinds of piston-type MEMS scanner mirror devices have been fabricated. The main difference is the deflection of the mirror planes. These can either be actuated in the chip plane or perpendicular out of the chip plane.

In an early stage, the University of Neuchatel group [61, 62] fabricated mirrors actuated in plane. The mirror plate had a size of  $75 \times 500 \mu\text{m}$ , and a Michelson interferometer was realized based upon this device. The displacement reached  $80 \mu\text{m}$  by applying a driving voltage of  $\pm 10 \text{ V}$ . This was a demonstration that the MEMS FTIR spectrometer concept had been realized. For commercial use, this MEMS device is too large for low cost, and the mirror plane is too small for adequate performance.

Piston-type MEMS mirrors, moving in the out-of-plane direction, have been developed and fabricated by Fraunhofer IPMS. The first trials were performed with bending springs [25] before the development of pantograph bearings (Figure 5.18) took place [26]. The mirror diameters reached up to 5 mm.

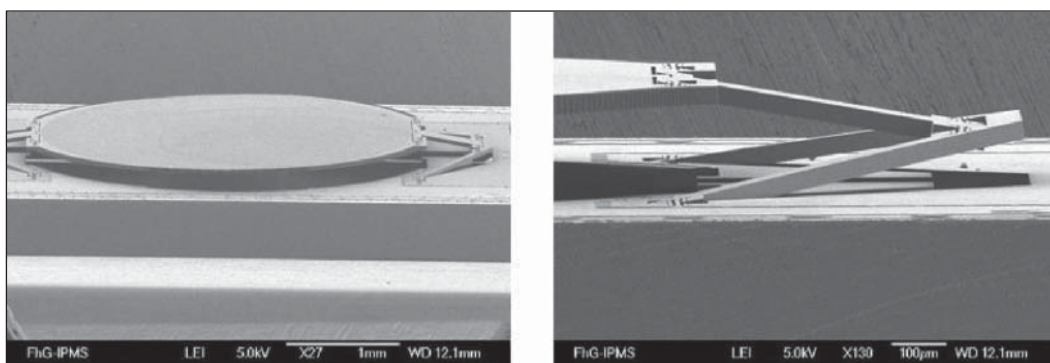


**Figure 5.18** MEMS piston scanner mirror with pantograph bearings. Source: Fraunhofer IPMS.

**Figure 5.19** Hamamatsu FTIR spectrometer. Source: Hamamatsu Photonics K.K.



Air damping (i.e. air resistance to motion of the mirror) is a serious issue for these devices. Applying reduced air pressure (10 Pa), the driving voltage can be as low as 10 V, while under normal atmospheric pressure, more than 100 V are necessary. Deflections can reach up to  $\pm 600 \mu\text{m}$ .

Using the mirrors with pantograph design, FTIR spectrometers have been developed [63–66]. The systems were operated in a spectral range between 2.5 and 16  $\mu\text{m}$  and a resolution of 8  $\text{cm}^{-1}$  has been achieved. The commercialization of the FTIR spectrometer build around this MEMS device faced drawbacks however; no product is available yet.

Recently, new and promising work was presented by Hamamatsu.<sup>7,8</sup> Based on a resonant piston-type MEMS scanner mirror, with a mirror plate diameter of 3 mm, vibrating in a frequency range of  $275 \pm 50 \text{ Hz}$  with an amplitude of 160–180  $\mu\text{m}$ , a compact FTIR spectrometer has been realized (Figure 5.19). Applying a drive voltage of up to 80 V, a spectral range of 1100–2500 nm is covered, using an extended range InGaAs detector. The spectral resolution reached 5.7 nm, together with a favorable SNR of 7 500–55 000. The system offers an SMA fiber coupler with an incident focal distance of 6.24 mm, and a numerical aperture (NA) of 0.4.

### 5.3.2 Monolithically Integrated Interferometers

Extremely small outlines can be achieved when the entire systems is integrated monolithically. MEMS chip-integrated FTIR spectrometers, based on the Michelson interferometer, have been realized [67]. The optical path inside the chip plane requires the mirrors to be etched vertically into the active silicon layer of the MEMS substrate. A limiting factor is the quality of the reflecting surfaces, and for a long time, scallops inhibited sufficient planarity. With the availability of improved etch steps, the Egypt-based company Si-Ware realized monolithically integrated MEMS-based interferometers successfully (Figure 5.20).

The beam splitter, fixed mirror and moveable mirror have been fabricated in the same chip. Simple external mirrors or reflecting prisms can be adapted for optical coupling into the cavity, and to the detector.

The system based on this chip was called NeoSpectra Micro.<sup>9</sup> The outline is  $32 \times 32 \times 22 \text{ mm}^3$ , and the weight is 17 g. It addresses a wavelength range from 1350 to 2500 nm, and offers a resolution of 16 nm; wavelength accuracy is stated to be  $\pm 1.9 \text{ nm}$ , and repeatability  $\pm 0.35 \text{ nm}$ , respectively. The SNR is in a 1 : 1500–2000 range. Besides the ultrasmall interferometer chip, the detector requires thermoelectric cooling which affects the detector size. In the end, the system is available as a handheld with approximately 1 kg weight. It is battery operated for 1000 s of measurements per battery charge [68].

<sup>7</sup> [https://www.hamamatsu.com/resources/pdf/ssd/ftir\\_engine\\_kacc9012e.pdf](https://www.hamamatsu.com/resources/pdf/ssd/ftir_engine_kacc9012e.pdf).

<sup>8</sup> [https://www.hamamatsu.com/resources/pdf/ssd/c15511-01\\_kacc1294e.pdf](https://www.hamamatsu.com/resources/pdf/ssd/c15511-01_kacc1294e.pdf).

<sup>9</sup> <https://www.neospectra.com/our-offerings/neospectra-micro/neospectra-micro-development-kit>

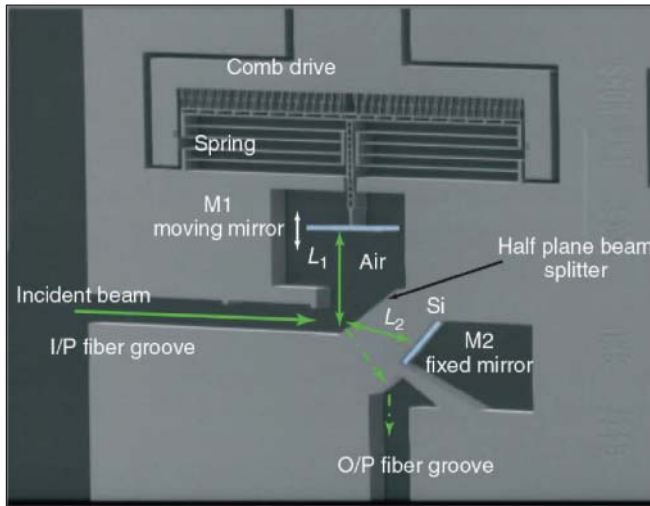


**Figure 5.20** Monolithically integrated Michelson interferometer.

## 5.4 Tunable Fabry–Perot Interferometer

The Fabry–Perot Interferometer (FPI), as realized first in 1897 by Charles Fabry and Alfred Pérot, is an optical bandpass filter made through a cavity formed between two reflecting surfaces [69, 70]. Inside the interferometer, optical waves can propagate, and those matching the resonance criteria are enhanced, the others interfere destructively and vanish. Technically, two partially transparent mirrors are adjusted with a well-defined air gap. If the width of the gap can be varied, a tunable filter is realized. Deflectable MEMS mirrors can be employed, which is a very promising option to construct spectroscopic equipment. An advantage of the FPI approach is that no beamsplitter or reference system is necessary for operation, which makes the setup simple, thus cost efficient and compact.

The incident radiation is reflected multiple times between the two mirrors (Figure 5.21). To simplify the considerations, it shall be assumed that the reflectivity of both mirrors is identical, which is reasonable for most cases.

Depending on the geometry ( $l, \alpha$ ) a path difference  $\delta$  is generated (Eq. (5.5)).

$$\delta = (2\pi/\lambda) 2n l \cos \alpha \quad (5.5)$$

The transmitted intensity  $T_e$  can be calculated if the reflectance  $R$  is known.

$$T_e = (1 - R)^2 / (1 - 2R \cos \delta + R^2) = 1 / (1 + F \sin^2[\delta/2]) \text{ considering } F = 4R / (1 - R)^2 \quad (5.6)$$

$T_e$  is shown graphically in Figure 5.22. It becomes 1 for  $2 n l \cos (\alpha) = m \lambda$

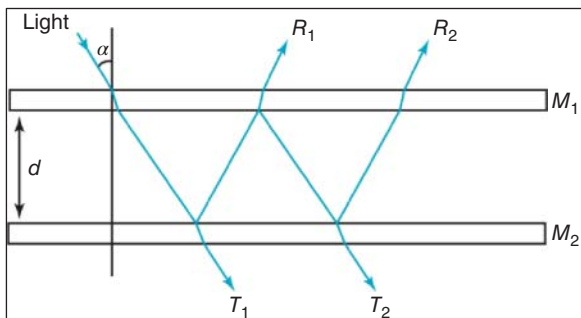
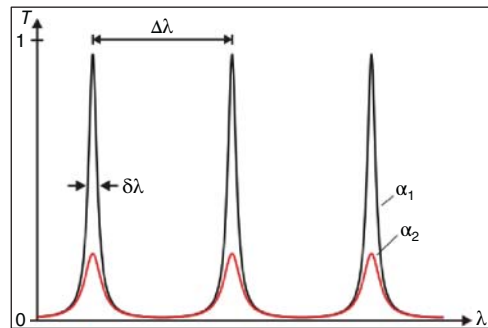


**Figure 5.21** Multiple reflection between two mirrors.

**Figure 5.22** Transmission  $T_e$  of an FPI.



The resolution strongly depends on the number of passes inside the interferometer. Close to infinite passes, the filter function becomes very sharp. Depending on the reflectivity of the mirrors, the number of reflections in a real FPI can be very high, up to  $\approx 10^5$  and the transmittance peaks become very narrow. There is a simple relationship between the free spectral range ( $\Delta\lambda$ ) and the resolution ( $\delta\lambda$ ), expressed as the Finesse ( $\mathcal{F}$ ). The simplification is justified for  $R > 0.5$ .

$$\mathcal{F} = \Delta\lambda/\delta\lambda = \pi/(2 \arcsin(1/\sqrt{\mathcal{F}})) \approx \pi \sqrt{\mathcal{F}}/2 = \pi \sqrt{R}/(1-R) \quad (5.7)$$

MEMS-based system designs are very promising for a tunable FPI. The setup is simple, and does not require complex optical alignments, as needed for FTIR or grating spectrometers. Nonetheless, there are some general limitations. The free spectral range is limited by principle, and additional bandpass filters are required.

For proper operation, some requirements must be fulfilled, and the stability of the actuated mirror plate during movement is the most relevant one. No tilting of the actuated mirror plane is tolerable: the mirror plate must remain planar with a  $\lambda/50$ – $\lambda/100$  planarity requirement. The alignment of both mirrors must be accurate in this range as well.

Three examples described here show different implements of FPIs: bulk micro-machined silicon, surface micro-machined silicon and piezo drive-based systems.

A bulk silicon micro-machining device, similar to piston-type scanner mirrors, can be used to design an FPI. In particular, Fraunhofer ENAS [71] has presented a specific design in bulk micro-machined silicon, featuring double bearings for more stability. The MEMS chip has a size of  $5 \times 5 \text{ mm}^2$  with an optical aperture measuring  $1.8 \times 1.8 \text{ mm}^2$ . The FPI spectrometer is realized in TO 39 outline. Applying driving voltages in a 15–60 V range, a bandwidth of 50–200 nm was achieved. The spectral ranges in the 3–11  $\mu\text{m}$  field can be selected 3–5, 5–8 or 8–11  $\mu\text{m}$ . The transmittance of the filter itself is higher than 70%. A consortium of InfraTec and Jenoptic Optical Systems has commercialized this technology.

A surface micro-machined MEMS device, using sacrificial layer technology, has been fabricated by Hamamatsu.<sup>10</sup> The device is mounted to a TO 5 carrier. The weight of the system is only 1 g. An InGaAs detector with 0.3 mm diameter is used, with an integrated bandpass filter. Driving voltages between 10 and 50 V are necessary. The FPI transmittance is around 60%. The system can address short-wave infrared (SWIR) ranges 1350–1650 nm with 18 nm resolution, 1550–1850 nm with 20 nm resolution, or 1750–2150 nm with 22 nm resolution.

The piezoelectric-driven FPI systems have been launched by VTT for SWIR systems and imagers [72, 73]. InGaAs detectors enable a spectral range from 1100 to 1600 nm. The piezo-driven FPI is using three actuators, and both mirrors use dielectrical layers for enhanced reflectivity. An example for an imager features  $256 \times 320$  pixels. The field of view is  $30^\circ$ , focal length  $f = 12 \text{ mm}$ , the opening offers  $F = 3.2$ , and the spectral resolution is 15 nm.

A spectral sensor was developed. The product NIRONE was launched through the VTT spin-out “Spectral Engines” (now part of Nynomic). The system has an outline of  $25 \times 25 \times 17.5 \text{ mm}^3$ , and a weight of 15 g. Using a

<sup>10</sup> <https://www.hamamatsu.com/eu/en/product/optical-sensors/spectrometers/mems-fpi-spectrum-sensor/index.html>.

single-element InGaAs detector, an SNR between 1 500 and 15 000 has been achieved. Different spectral ranges can be addressed with slightly varying resolution: 1.1–1.35 µm @ 12–16 nm/1.35–1.65 µm @ 13–17 nm/1.55–1.95 µm @ 15–21 nm/1.75–2.15 µm @ 16–22 nm/2.0–2.45 µm @ 18–28 nm.

## 5.5 Integration Strategies for MEMS-/MOEMS-Based Spectrometers

Any spectroscopic device has high requirements for precision. The accuracy of the alignment of the optical components inside must be adjusted during production, and has to remain constant throughout its entire lifetime. Deviations affect the spectral range, the dispersion, the resolution or the optical throughput. Two different kinds of deviation may occur: some may be compensated by calibration, for example, if the wavelength range shifts. This is solvable, but requires undesired effort. Other deviations affect the system performance, and must be controlled by the accuracy of the assembly process.

In the past, benchtop spectrometers typically used alignment structures as micrometer screws and elongated holes, which enabled a sub-micrometer precision of the alignment of the individual components, albeit in a time-consuming procedure. The alignment accuracy reaches in the same range as the thermal expansion of a macroscopic system for just a few Kelvin temperature change.

Miniaturization reduces the options for manual alignment, and, thus, increases the complexity of the procedure. MEMS-based systems have specific requirements: the MEMS device must be assembled to a carrier or directly on a printed circuit board and electrical contacts must be connected. The aim is always an ultracompact system. There are some options for the integration of such optical systems. The design choices depend on the number of systems which will be produced. High-volume integration typically requires individually designed components, which may result in high initial effort, but low cost per piece.

### 5.5.1 Classic System Assembly for MEMS-Based Systems

The basic integration procedure for spectroscopic equipment can be adopted for MEMS-based systems as well. The core element is a chassis or baseplate, mounted in either a floor frame or a case, where bearings or assembly structures are designed at the right positions. All relevant components can be manually mounted and systematically adjusted in all six degrees of freedom. This manual process could be very accurate, but it is time-consuming, and the miniaturization options are limited. Furthermore, the production volume may be limited as well by the efficiency of the integration procedure, i.e. the manual alignment time required.

An example for this integration approach is the scanning grating spectrometer SGS 1900. The MEMS component and the detector are assembled in carriers. The MEMS in package grants access to the grating as optical active area from the front side, and an optical position readout from the backside. Wire bonds onto pads on the chip front side realize electrical contacts. Both mirrors are mounted on adjustable stages. The slits are placed at the fiber optical entrance stage and in front of the detector.

It is clear that here limitations for size reduction arise. Even if optical components are directly integrated into the housing, e.g. by LIGA (lithography, electroplating and molding) technology for mirrors and gratings, the alignment is critical, due to the complex assembly, and limits any reduction in size before optical limitations arise.

### 5.5.2 Stacking

Stacking components is a very efficient and well-established way to integrate axial optical systems. Lenses for cameras are a prominent example, where even multiple elements are integrated with high accuracy. MEMS-based Fabry-Perot interferometer represent axial optical systems for spectroscopic applications. Here stacking works fine.

For the realization of complex off-axis systems, like spectrometers or Michelson interferometers, stacking becomes quite complex. In principle, components could be stacked, but the alignment in 3D will make the situation complicated and the alignment tricky.

An idea for the efficient integration of miniaturized systems was the use of large substrates which bear components for a high number of systems, stack those and dice them afterward into the individual systems. Thus, a single alignment step could enable many devices.

This works especially fine if a lot of functionality can be integrated in each of the substrates. For a MEMS-based scanning-grating spectrometer, it is possible to integrate both slits into the same chip using the accuracy of the lithographic technologies. As the grating is not deflected in the rest position, changes to the normal Czerny-Turner have to be applied. Instead of a tilt of the grating to adjust the wavelength [53] of the W-configuration of the spectrometer, here the first negative diffraction order has been used to shift the configuration toward a folded double-V. An appropriate design is possible without predeflection of the grating. A small drawback is the complexity of the mirrors, which have to be off-axis and should have bi-conic areas. These mirrors could be realized by ultraprecision surface micromaching, and it is possible to realize both in a single substrate. Thus, the alignment task is reduced to two components only.

Grating spectrometer requires a focal length to operate properly; thus, between the MEMS and the mirror substrate, a space has to be implemented. The thickness is in a 6–8 mm range: shorter focal distances would result in a strongly reduced resolution for the NIR, which cannot be compensated through higher line densities, due to the  $d < \lambda/2$  limitation. Direct wafer stacking using a wafer bond process, thus, is not an option. In-plane integration of a MEMS-based optical path is not possible, as no technology is available today that can realize appropriate mirrors, or grating structure, in vertical integration in silicon.

### 5.5.3 Place and Bend

A new integration concept was invented recently [74]. A need for high production volume of complex off-axis optics arises if a spectrometer is integrated into a mobile phone. This cannot be satisfied efficiently by existing integration technologies. Either new tools for high-volume 3D integration will have to be designed, or new concepts enabling integration with existing equipment, i.e. highly efficient and accurate 2D assembly tools, need to be developed.

This concept is based on the Japanese art “Origami,” where a complex 3D body is folded from a planar “substrate” – a simple sheet of paper. The idea of “Place and Bend” assembly employs a substrate that features bending structures along designated lines. The substrate can be made from a plastic material by means of additive manufacturing (3D printing), casting, injection molding or other technologies. The electronic and optical components are placed in 2D assembly technology (“place”), afterward the walls are folded (“bend”), and the body with the optical path inside forms automatically if the accuracy is high enough. The concept was proven [75] and first spectrometers (Figure 5.23) have been realized using this “place and bend” assembly [57]. Further work on materials [76], process technology optimization and system design is planned. Fabrication of an FTIR spectrometer might be possible as well, and there are ideas how to design an interferometer efficiently.

### 5.5.4 Chip-Scale Integration

The highest level of MEMS integration can be reached by putting the entire optic design directly into the MEMS chip. A lot of limitations have to be faced, but if successful, the miniaturization will reach the highest level possible and production will be efficient and scalable up to any number. Up to now, this was shown successfully for FTIR spectrometer using Michelson interferometers by the scientists of Si-Ware Systems [67, 68, 76].

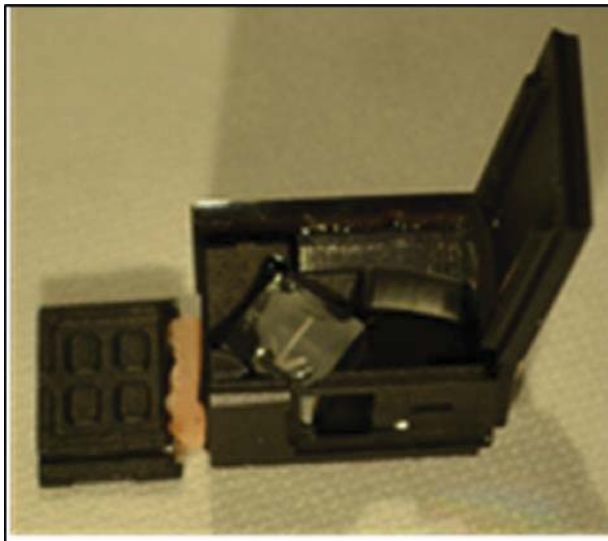


**Figure 5.23** NIR spectrometer realized by “Place and Bend Assembly.” *Source:* Fraunhofer IPMS.

## 5.6 Use of MEMS-Based NIR Spectrometers

The actual interest in miniaturized spectrometers, especially for NIR applications, is based on the possibilities for material analysis. In combination with the availability of access to data by mobile Internet services, the evaluation of measurements in the field in real time becomes possible. In principle, as a mobile phone add-on, or integrated to such a device, everybody would be able to perform composition analysis of solid objects, especially organic matter like food, cloth, and skin. Fluids in containers could be treated in a similar way if the container is sufficiently transparent. Liquid analysis requires different sample preparation, for example, cuvettes, and measurements in transmission instead of diffuse reflection.

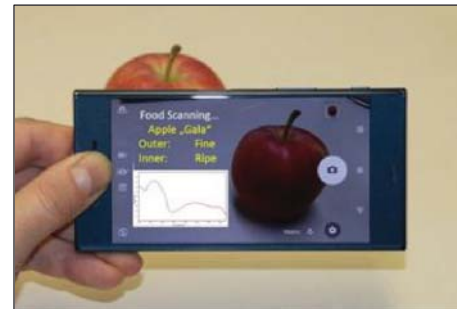
The potential of mobile spectral analysis has attracted the attention far beyond the spectroscopic system providers. Mobile phone manufacturers, service providers and also user groups are seeking solutions suitable for use in the field.

NIR offers a good balance of effort of measurement and quality of the results. As noted above, the penetration depth gives an insight into an objects bulk composition, not just the surface. The broad structure of partially overlapping overtone and combination bands in the NIR require mathematical methods for the evaluation (chemometrics), and access to a database service with reference data that has been obtained using standard laboratory methods. Today, mobile devices offer sufficient computation power, and both access to online data (“the cloud”) or storage on the device itself.

The general setup of a mobile spectral analyzer consists in a light source with illumination optics, optics for signal acquisition, the spectroscopic device, processing unit and data storage, and optionally online data access components (Figure 5.24). Besides this, a user interface (screen, indicator lamps, keyboard, etc.) is necessary. Furthermore, measurements in reflection require that a white standard be measured for reference from time to time. Results may also be communicated through a data interface.

The evaluation is based on chemometrics, which uses reference data from previous measurements of known samples, or samples which have been analyzed by reference methods. In the future, this may become simplified by the use of artificial intelligence methods and the possibility to include feedback and statistics from many measurements in the field. There will be a huge volume of information available if everybody is analyzing everything with an individual mobile spectral analyzer, and this may open options for the future of reference data.

**Figure 5.24** Sketch of a spectral analyzer. Source: Fraunhofer IPMS.



Systems for either a selected single purpose or for multipurpose measurements will be designed. They may differ in the spectroscopic setup, especially range and resolution. The user could be a professional, or even an expert, but also nonscientific people may use those systems. In the second case, guidance will be mandatory to achieve valuable results. Software “Apps” will lead the user through the measurement procedure. A combination of a spectral analyzer, and a camera integrated in one device, looking along the same optical axis, opens the option to guide the user by using the display, which may serve to initiate the measurement at the right spot and in the correct distance by showing crosshairs and color indicators for distance [77]. Also, image evaluation may provide collection of additional information about the object under test, e.g. specify kind (“apple”) or sort (“Elstar apple”), and select an optimized reference database.

In the end, the results of the material analysis, solids and fluids, especially organic matter, can be evaluated and relevant information extracted. The user is interested in this compositional information, or data correlated to the composition, and the displayed result could be just one bit of information like “pass” and “fail” or “buy” – “not buy.”

## Acronyms and Abbreviations

CMOS	Complementary metal-oxide-semiconductor
BSOI	Bonded silicon on insulator
DARPA	Defense Advanced Research Projects Agency
DLP	Digital light processing
DRIE	Deep reactive-ion etching
InGaAs	Indium gallium arsenide
LCD	Liquid crystal display
LIGA	German acronym for “ <b>Lithographie, Galvanoformung, Abformung</b> ” (lithography, electroplating and molding)
MEMS	Micro-electromechanical systems
MOEMS	Micro-opto-electromechanical systems
NIR	Near infrared
FPI	Fabry–Pérot interferometer
FT	Fourier transform
FTIR	Fourier transform infrared
RIE	Reactive-ion etching
SMA	SubMiniature version A
SNR	Signal-to-noise ratio
SOI	Silicon on insulator

TO	Transistor outline
UPM	Ultraprecision machining/ultraprecision micromachining
UV	Ultraviolet

## References

- 1 Rai-Choudhury, P. (ed.) (2000). *MEMS and MOEMS Technology and Applications*, SPIE Press Monograph, vol. PM85, preface, IX, ISBN 9780819437167. SPIE.
- 2 Clark, S.K. and Wise, K.D. (1979). Pressure sensitivity in anisotropically etched thin-diaphragm pressure sensors. *IEEE Transactions on Electron Devices* 26 (12): 1887–1896.
- 3 Schenk, H., Wolter, A., Dauderstädt, U. et al. (2005). Micro-opto-electro-mechanical systems technology and its impact on photonic applications. *Journal of Microlithography, Microfabrication and Microsystems* 4 (4): 041501–041511.
- 4 Ladabaum, I., Jin, X.C., Soh, H.T. et al. (1998). Surface micromachined capacitive ultrasonic transducers. *IEEE Transactions on Ultrasonics, Ferroelectrics and Frequency Control* 45 (3): 678–690.
- 5 Roylance, L. and Angell, J. (1979). A batch-fabricated silicon accelerometer. *IEEE Transactions on Electron Devices* 26: 1911–1917. <https://doi.org/10.1109/T-ED.1979.19795>.
- 6 Bernstein, J., Cho, S., King, A. et al. (1993). A micromachined comb-drive tuning fork rate gyroscope. *Proceedings of IEEE Micro Electro Mechanical Systems Workshop (MEMS '93)*, Fort Lauderdale, FL, pp. 143–148.
- 7 Kohn, E., Gluche, P., and Adamschik, M. (1999). Diamond MEMS – a new emerging technology. *ELSEVIER Diamond and Related Materials* 8 (2–5): 934–940, ISSN 0925-9635, [https://doi.org/10.1016/S0925-9635\(98\)00294-5](https://doi.org/10.1016/S0925-9635(98)00294-5).
- 8 Tortschanoff, A., Holzmann, D., Lenzhofer, M., and Sandner, T. (2013). Closed-loop control for quasi-static MOEMS mirrors. *Proceedings of SPIE*, vol. 8252, *MOEMS and Miniaturized Systems XI*, 82520T. <https://doi.org/10.1117/12.907825>.
- 9 Fischer, A.C., Forsberg, F., Lapisa, M. et al. (2015). Integrating MEMS and ICs. *Microsystems & Nanoengineering* 1: 15005. <https://doi.org/10.1038/micronano.2015.5>.
- 10 Scheper, P.R., van der Donk, A.G.H., Olthuis, W., and Bergveld, P. (1994). A review of silicon microphones. *Sensors and Actuators A: Physical* 44 (1): 1–11. [https://doi.org/10.1016/0924-4247\(94\)00790-X](https://doi.org/10.1016/0924-4247(94)00790-X).
- 11 Lee, S.S. and Lee, W.S. (2008). Piezoelectric microphone built on circular diaphragm. *Sensors and Actuators A* 144 (2): 367–373. <https://doi.org/10.1016/j.sna.2008.02.001>.
- 12 Cheng, M.C., Huang, W.S., and Huang, S.R.S. (2004). A silicon microspeaker for hearing. *Journal of Micromechanics and Microengineering* 14: 859–866. <https://doi.org/10.1088/0960-1317/14/7/004>.
- 13 Kaiser, B., Langa, S., Ehrig, L. et al. (2019). Concept and proof for an all-silicon MEMS micro speaker utilizing air chambers. *Microsystems & Nanoengineering* 5: 43. <https://doi.org/10.1038/s41378-019-0095-9>.
- 14 Amelung, J., Klemm, M., Elsäßer, L. et al. (2016). Back end of line integration technology of capacitive micromachined ultrasonic transducers (CMUT). *Proceeding of the Smart Systems Integration 2016*, Munich (9–10 March 2016).
- 15 Drabe, C., Schenk, H., Roscher, K. U. et al. (2004). Accelerometer by means of a resonant micro actuator. *Proceedings of SPIE*, vol. 5344, *MEMS/MOEMS Components and their Applications*. doi: <https://doi.org/10.1117/12.524130>.
- 16 Lee, I., Yoon, G.H., Park, J. et al. (2005). Development and analysis of the vertical capacitive accelerometer. *Sensors and Actuators A* 119: 8–18. <https://doi.org/10.1016/j.sna.2004.06.033>.
- 17 Amarasinghe, R., Dao, D.V., Toriyama, T., and Sugiyama, S. (2007). Development of miniaturized 6-axis accelerometer utilizing piezoresistive sensing elements. *Sensors and Actuators A: Physical* 134: 310–320. <https://doi.org/10.1016/j.sna.2006.05.044>.

- 18** Palaniapan, M., Howe, R.T., and Yasaitis, J. (2002). Integrated surface-micromachined z-axis frame microgyroscope. In: *International Electron Devices Meeting 2002*, 203–206. IEEE <https://doi.org/10.1109/IEDM.2002.1175813>.
- 19** Park, S., Horowitz, R., and Tan, C.W. (2008). Dynamics and control of a MEMS angle measuring gyroscope. *Sensors and Actuators A: Physical* 144 (1): 56–63. <https://doi.org/10.1016/j.sna.2007.12.033>.
- 20** Schenk, H., Sandner, T., Drabe, C. et al. (2009). Single crystal silicon micro mirrors. *Physica Status Solidi C* 6 (3): 728–735. <https://doi.org/10.1002/pssc.200880714>.
- 21** Schenk, H., Wagner, M., Grahmann, J., and Merten, A. (2018). Advances in MOEMS technologies for high quality imaging systems. *Proceedings of SPIE 10587, Optical Microlithography XXXI*, 1058703. doi: <https://doi.org/10.1117/12.2297399>.
- 22** Kurth, S., Kaufmann, C., Hahn, R. et al. (2005). A novel 24-kHz resonant scanner for high-resolution laser display. *Proceedings of SPIE* 5721: 23–33.
- 23** Senger, F., Hofmann, U., Wantoch, T. et al. (2015). Centimeter-scale MEMS scanning mirrors for high power laser application. *Proceedings of SPIE* 9375: 9375\_7. <https://doi.org/10.1117/12.2079600>.
- 24** Kasturi, A., Milanovic, V., Hu, F. et al. (2019). MEMS mirror module for programmable light system. *Proceedings of SPIE 10931, MOEMS and Miniaturized Systems XVIII*, 109310L. <https://doi.org/10.1117/12.2511074>.
- 25** Kenda, A., Drabe, C., Schenk, H. et al. (2006). Application of a micromachined translatory actuator to an optical FTIR spectrometer. *Proceedings of SPIE 6186, MEMS, MOEMS, and Micromachining II*, 618609, pp. 1–11.
- 26** Sandner, T., Grasshoff, T., Schenk, H., and Kenda, A. (2011). Out-of-plane translatory MEMS actuator with extraordinary large stroke for optical path length modulation. *Proceeding sof SPIE 7930, MOEMS and Miniaturized Systems X*, 79300I-1-9. doi: <https://doi.org/10.1117/12.879069>.
- 27** Oden, P.I. (2008). Texas instruments' DLP products massively paralleled MOEMS arrays for display applications: a distant second to mother nature. *Proceedings of the SPIE 6959, Micro (MEMS) and Nanotechnologies for Space, Defense, and Security II*, 69590D. doi: <https://doi.org/10.1117/12.778499>.
- 28** Gehner, A., Durr, P., Kunze, D. et al. (2018). Novel  $512 \times 320$  Tip-Tilt Micro Mirror Array in a CMOS-Integrated, Scalable Process Technology. *IEEE Proceedings of the International Conference on Optical MEMS and Nanophotonics*, Lausanne Switzerland (29 July–2 August 2018). doi: <https://doi.org/10.1109/OMN.2018.8454624>.
- 29** Schenk, H. and Grüger, H. (2003). Spektrometer. Patent WO 002003069289.
- 30** Wang, Y., Kanamori, Y., Sasaki, T., and Hane, K. (2009). Design and fabrication of freestanding pitch-variable blazed gratings on a silicon-on-insulator wafer. *Journal of Micromechanics and Microengineering* 19: 025019. <https://doi.org/10.1088/0960-1317/19/2/025019>.
- 31** Saadany, B., Omran, H., Medhat, M. et al. (2009). MEMS tunable Michelson interferometer with robust beam splitting architecture. *IEEE Proceedings of the International Conference on Optical MEMS and Nanophotonics*, Cleanwater, FL, USA (17–20 August 2009). doi: <https://doi.org/10.1109/OMEMS.2009.5338601>.
- 32** Zimmer, F., Grüger, H., Heberer, A. et al. (2005). Scanning Micro-Mirrors: From bar-code-scanning to spectroscopy. *Proceedings of SPIE*, vol. 5873, *Optical Scanning*, 5873, pp. 84–94. doi: <https://doi.org/10.1117/12.614895>.
- 33** Sandner, T., Grasshoff, T., Wildenhain, M., and Schenk, H. (2010). Synchronized microscanner array for large aperture receiver optics of LIDAR systems. *Proceedings of the SPIE*, vol. 7594, *MOEMS and Miniaturized Systems IX*, 75940C. doi: <https://doi.org/10.1117/12.844923>.
- 34** Hornbeck, L. J. (1996). Digital light processing and MEMS: reflecting the digital display needs of the networked society. *Proceedings of SPIE*, vol. 2783, *Micro-Optical Technologies for Measurement, Sensors, and Microsystems*. doi: <https://doi.org/10.1117/12.248477>.
- 35** Motamedi, M.E. (2005). *MOEMS Micro-Opto-Electro-Mechanical Systems*. Bellingham Washington, USA: SPIE Press.

- 36** Liebermann, M.A. and Lichtenberg, A.J. (2003). *Principles of Plasma Discharges and Material Processing*, chapter 5, 2ee. Wiley-VCH <https://doi.org/10.1002/0471724254>. ISBN: 0-471-72001-1.
- 37** Inventors Franz Laermer and Andrea Schlip (1996). Method of anisotropically etching silicon. US Patent 5,501,893, filed 5 August 1994, published 26 March 1996.
- 38** Hilleringmann, U. (2014). *Silizium-Halbleitertechnologie*, 6ee. Wiesbaden: Springer Vieweg Verlag. ISBN: 978-3-8348-1335-0.
- 39** Krishnan, M., Nalaskowsk, J.W., and Cook, L.M. (2010). Chemical mechanical planarization: slurry chemistry, materials, and mechanisms. *Chemical Review* 110: 178–204. <https://doi.org/10.1021/cr900170z>.
- 40** Loewen, E.G. and Popov, E. (1997). *Diffraction Gratings and Applications*. New York: Marcel Dekker.
- 41** Palmer, C. (2014). *Diffraction Grating Handbook*, 7ee. Rochester, NY: Richardson Gratings.
- 42** Ebert, H. (1889). Zwei Formen von Spectrographen. *Annalen der Physik* 274: 489–493.
- 43** Monk, G.S. (1928). A mounting for the plane grating. *Journal of the Optical Society of America* 17: 358–362.
- 44** Gillieson, A.H.C.P. (1949). A new spectrographic diffraction grating monochromator. *Journal of Scientific Instruments* 26: 334–339.
- 45** Czerny, M. and Turner, A.F. (1930). Über den Astigmatismus bei Spiegelspektrometern. *Zeitschrift für Physik* 61: 792–797.
- 46** Czerny, M. and Pletti, V. (1930). Über den Astigmatismus bei Spiegelspektrometern II. *Zeitschrift für Physik* 63: 590–595.
- 47** Fastie, W.G. (1952). A small plane grating monochromator. *Journal of the Optical Society of America A* 42: 641–647.
- 48** Fastie, W.G. (1952). Image forming properties of the Ebert monochromator. *Journal of the Optical Society of America A* 42: 647–650.
- 49** Neumann, W. (2014). *Fundamentals of Dispersive Optical Spectroscopy Systems*. SPIE Press Book. ISBN: 9780819498243.
- 50** Grüger, H., Wolter, A., Schuster, T. et al. (2003). Realization of a spectrometer with micromachined scanning grating. *Proceeding of Photonics West 2003*, San Francisco CA, USA.
- 51** Zimmer, F., Grüger, H., Heberer, A. et al. (2006). Development of high-efficient NIR-scanning gratings for spectroscopic applications. *Proceedings of SPIE*, vol. 6114, *MOEMS Display, Imaging, and Miniaturized Microsystems IV*, 611407. doi: <https://doi.org/10.1117/12.644481>.
- 52** Grüger, H., Knobbe, J., and Pügner, T. (2019). Optical arrangement for a spectral analysis system, method for its production and spectral analysis system. US Patent 10,247,607 granted 2 April.
- 53** Pügner, T., Knobbe, J., and Grüger, H. (2016, 2016). Near-infrared grating spectrometer for Mobile phone applications. *Applied Spectroscopy* 70 (5): 734–745.
- 54** Pruitt, E. (2015). Latest developments in Texas Instruments DLP near-infrared spectrometers enable the next generation of embedded compact, portable systems. *Proceedings of SPIE Vol. 9482, Next-Generation Spectroscopic Technologies VIII*, 94820C. doi: <https://doi.org/10.1117/12.2177430A>.
- 55** Harwit, M. and Sloane, N.J.A. (1979). *Hadamard Transform Optics*. New York: Academic Press.
- 56** Treado, P.J. and Morris, M.D. (1989). A thousand points of light: the Hadamard transform in chemical analysis and instrumentation. *Analytical Chemistry* 61: 723A–734A.
- 57** Grüger, H., Knobbe, J., and Pügner, T. (2019). MEMS based NIR spectrometer with extended spectral range. *Proceeding of Photonics West*, San Francisco, CA, USA.
- 58** Otto, T., Saupe, R., Weiss, A. et al. (2006). Principle and applications of a new MOEMS Spectrometer. *Proceedings of SPIE*, vol. 6114, *MOEMS Display, Imaging, and Miniaturized Microsystems IV*.
- 59** Griffiths, P.R. and De Haseth, J.A. (2007). *Fourier Transform Infrared Spectrometry*, 2ee. Hoboken, NJ: Wiley.
- 60** Cooley, J. and Tukey, J. (1965). An algorithm for the machine calculation of complex Fourier series. *Mathematics of Computation* 19: 297–301.

- 61** Manzardo, O., Herzig, H.P., Marxer, C.R., and de Roonij, N.F. (1999). Miniaturized time-scanning Fourier transform spectrometer based on silicon technology. *Optics Letters* 24 (23): 1705–1707. <https://doi.org/10.1364/OL.24.001705>.
- 62** Montgomery, P.C., Montaner, D., Manzardo, O. et al. (2004). The metrology of a miniature FT spectrometer MOEMS device using white light scanning interference microscopy. *Thin Solid Films* 450: 79–83. <https://doi.org/10.1016/j.tsf.2003.10.055>.
- 63** Sandner, T., Kenda, A., Drabe, C. et al. (2007). Miniaturized FTIR-spectrometer based on optical MEMS translatory actuator. *Proceedings of SPIE*, vol. 6466, *MOEMS and Miniaturized Systems VI*, 646602.
- 64** Sandner, T., Kenda, A., Scherf, W. et al. (2008). Translatory MEMS actuators for optical path length modulation in miniaturized Fourier-transform infrared spectrometers. *Journal of Micro/Nanolithography MEMS and MOEMS* 7 (2).
- 65** Kenda, A., Kraft, M., Tortschanoff, A. et al. (2014). Development, characterization and application of compact spectrometers based on MEMS with in-plane capacitive drives. *Proceedings of SPIE*, vol. 9101 *Next-Generation Spectroscopic Technologies VII*, 910102. doi: <https://doi.org/10.1117/12.2053347>.
- 66** Sandner, T., Gaumont, E., Grasshoff, T. et al. (2018). Translatory MEMS actuator with wafer level vacuum package for miniaturized NIR Fourier transform spectrometers. *Proceedings of SPIE 10545, MOEMS and Miniaturized Systems XVII*, 105450W. doi: <https://doi.org/10.1117/12.2290588>.
- 67** Ghoname, A. O., Sabry, Y. M., Anwar, M. et al. (2019). Ultra wide band MIR MEMS FTIR spectrometer. *Proceedings of SPIE 10931, MOEMS and Miniaturized Systems XVIII*, 109310Z. doi: <https://doi.org/10.1117/12.2509378>.
- 68** Fathy, A., Sabry, Y. M., Amr, M. et al. (2019). MEMS FTIR optical spectrometer enables detection of volatile organic compounds (VOCs) in part-per-billion (ppb) range for air quality monitoring. *Proceedings of SPIE 10931, MOEMS and Miniaturized Systems XVIII*, 1093109. doi: <https://doi.org/10.1117/12.2508239>.
- 69** Hernandez, G. (1986). *Fabry-Perot Interferometers*. Cambridge, UK: Cambridge University Press.
- 70** Vaughn, J.M. (1989). *The Fabry-Perot Interferometer: History, Theory Practice and Applications*. Bristol, UK: Adam Hilger.
- 71** Ebermann, M., Neumann, N., Hiller, K. et al. (2016). Tunable MEMS Fabry-Pérot filters for infrared microspectrometers: a review. *Proceedings of SPIE 9760, MOEMS and Miniaturized Systems XV*, 97600H.
- 72** Mannila, R., Holmlund, C., Ojanen, H. J. et al. (2014). Short-wave infrared (SWIR) spectral imager based on Fabry-Perot interferometer for remote sensing. *Proceedings of SPIE 9241, Sensors, Systems, and Next-Generation Satellites XVIII*. doi: <https://doi.org/10.1117/12.2067206>.
- 73** Rissanen, A., Guo, B., Saari, H. et al. (2014). VTT's Fabry-Perot interferometer technologies for hyperspectral imaging and mobile sensing applications. *Proceedings of SPIE 10116, MOEMS and Miniaturized Systems XVI*, 101160I, doi: <https://doi.org/10.1117/12.2255950>.
- 74** Grüger, H., Knobbe, J., and Pügner, T. Bendable substrate with a device. Patent application US 2019/0250032.
- 75** Grüger, H., Knobbe, J., Pügner, T. et al. (2017). Concept for a new approach to realize complex optical systems in high volume. *Proceeding of Photonics West*, San Francisco, CA, USA.
- 76** Grüger, H., Knobbe, J., and Sabiha, M. (2019). Investigation of mechanical and optical properties of 3D printed materials serving as substrate for place and bend assembly. *Proceeding of Photonics West*, San Francisco, CA, USA.
- 77** Grüger, H., Knobbe, J., and Pügner, T. System und entsprechendes Verfahren zur Vermessung eines Objekts. Patent DE102017204740.2.

## 6

### **Portable Raman Spectroscopy: Instrumentation and Technology**

*Cicely Rathmell, Dieter Bingemann, Mark Zieg and David Creasey*

*Wasatch Photonics, Inc., Logan, UT, USA*

#### **6.1 Introduction**

Nearly one century ago, C.V. Raman discovered that light scattered from molecules contained a “feeble fluorescence” that carried information about the vibrational states of those molecules [1]. Upon further study, the source was discovered to be a new form of inelastic scattering of light that is rich in chemical information. The field of Raman spectroscopy was born.

The initial experiments performed by Raman and a parallel team in Russia required exposure times on the order of hours for crystals, and up to 180 hours for gases [2]. Thanks to decades of technological advancements, Raman spectra of many solids and liquids can now be collected using a handheld device in just seconds. This chapter explores the current state of that technology, and the many competing factors and tradeoffs that must be considered when designing a portable Raman instrument for applied use. First, we will look at the benefits of Raman spectroscopy as an analytical technique, and review the theory behind the Raman effect so as to better understand the demands on the instrumentation required, then delve deeper into the pertinent aspects of portable system design.

#### **6.2 The Case for Raman: Capabilities and Scope**

Raman spectroscopy’s greatest strength is its ability to rapidly provide a fingerprint representative of the chemical structure of a material. This fingerprint can be used for identification with high chemical specificity, and may be applied to solids, liquids, and gases. Modern-day portable Raman instruments are noncontact, easy to use, require no special sample preparation, and often employ straightforward point-and-shoot operation. They are available with flexible sample interfaces, and can be configured for through-barrier measurements to enable detection of substances in bags, vials, and even colored or opaque bottles.

In contrast to infrared spectroscopy, Raman spectroscopy is insensitive to water content, eliminating a major source of interference, and allowing direct analysis without sample preparation. When configured with robust analysis software and appropriate sampling accessories, a portable Raman instrument need not be operated by an expert, vastly increasing the applications in which this powerful technology can be used. Simply put, portable Raman has the ability to provide answers at the point of use.

These benefits have propelled the use of portable Raman instruments into several fields spanning quality, safety, and health. In the pharmaceutical industry, the technology allows for easy identification of materials on site, from incoming inspection to outgoing quality control. Here, a portable Raman instrument allows the user to bring the

instrument to the sample when the sample cannot easily or should not be moved, and provides instant answers without disrupting the flow of inventory and operations. In security and forensics, portable Raman instruments offer rapid substance identification in the field, providing the instantly actionable information needed by first responders and security personnel.

In the medical field, portable Raman facilitates use at point-of-care, allowing immediate patient diagnostics and monitoring throughout the course of treatment to improve clinical outcomes. It expands the reach of quality diagnostics to remote and under-resourced settings, as well as facilitating in-home use for medical conditions which require frequent monitoring.

It is important to note that the use of Raman is not limited only to the classification of bulk materials or Raman-active compounds. Raman-active markers or tags extend the use of the technique for identification or validation in authentication or process-monitoring applications. Raman tags may also be functionalized to bind to specific chemicals or biological compounds and agents for use in assays, expanding the potential of Raman in point-of-care settings. Specific applications are discussed in the chapter in Volume 2 of this book by Hargreaves.

While the benefits of Raman are many, the technique comes also with limitations. Raman spectroscopy can struggle to measure low concentrations, samples prone to fluorescence (particularly complex organic molecules and geological samples containing trace amounts of transition metal ions), and dark-colored, easily ignited, or delicate materials. Reliance on laser excitation requires attention to eye safety through sampling accessories or protective gear. Special techniques and operating conditions have been developed to mitigate each of these circumstances, and will be discussed in a “Special Cases” section near the close of this chapter.

None of these capabilities or applications could have progressed beyond the laboratory without significant evolution of the supporting technology. Before Raman spectroscopy could become more widely used as an analytical technique, it needed to become smaller, lighter, and easier to use. The past 25 years have seen advances in the hardware to achieve greater sensitivity in a smaller footprint, allowing Raman to escape the lab. It has also seen advances in science as regards our understanding of **how** to use Raman spectroscopy to answer key problems. As a result of this progress, many new application spaces and use cases have emerged in which portable Raman can be applied.

### 6.3 The Theory of Raman Spectra

Raman spectroscopy is an analytical technique based upon the Raman effect, in which light is scattered inelastically from a molecule, yielding information about its vibrational states. As the theory has been treated exhaustively by others [3–5], we will provide only a brief overview, focusing on those aspects most pertinent to applied use.

In classical terms, when light interacts with molecules, the electron cloud resonates with the incident light. This light will almost always be scattered unaltered, but there is a probability of one part in a million that the photon will lose energy to (or even more rarely, gain energy from) a vibration that couples strongly to the polarizability of the molecule. This causes light of a different wavelength to be emitted, an effect known as Raman scattering.

Raman spectroscopy is complementary to infrared spectroscopy, in which light couples to the molecular dipole moment (light couples to the polarizability of the molecule in Raman spectroscopy). Both techniques provide information about vibrational states, but differ in their sensitivity to specific molecular vibrations. Water, for example, with its strong dipole moment and low polarizability, has a strong infrared absorbance, but a very small Raman resonance.

In theory, Raman scattering can be achieved with any wavelength of light, provided it is of sufficient intensity. As described previously, the vast majority of the incident photons will be elastically scattered – a phenomenon known as Rayleigh scattering. Of the inelastically scattered photons, many will have lost energy, yielding longer wavelength photons (Stokes radiation), and a smaller fraction will have seen an increase in energy, yielding shorter wavelength photons (anti-Stokes radiation), as shown in Figure 6.1.

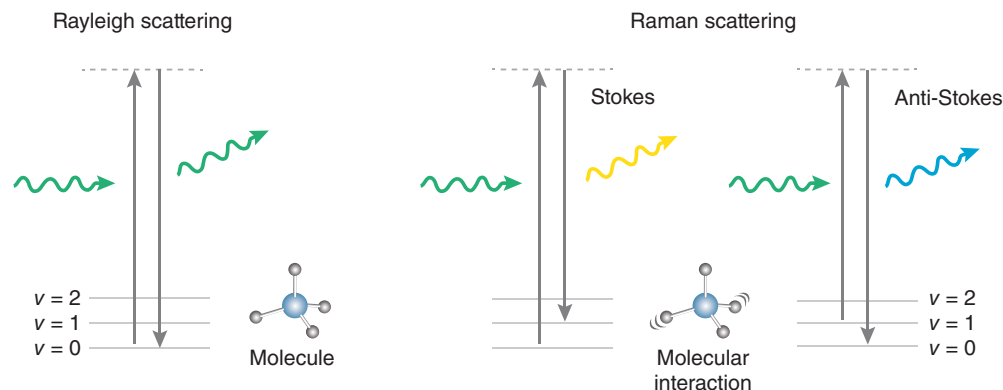


**Figure 6.1** In Rayleigh scattering, the molecule returns to the same state, resulting in no change in energy for the scattered photon. In Raman scattering, the molecule returns to a different state, either losing energy (resulting in a Stokes shift, to longer wavelength) or gaining energy (resulting in an anti-Stokes shift, to shorter wavelength). Source: Courtesy of Wasatch Photonics.

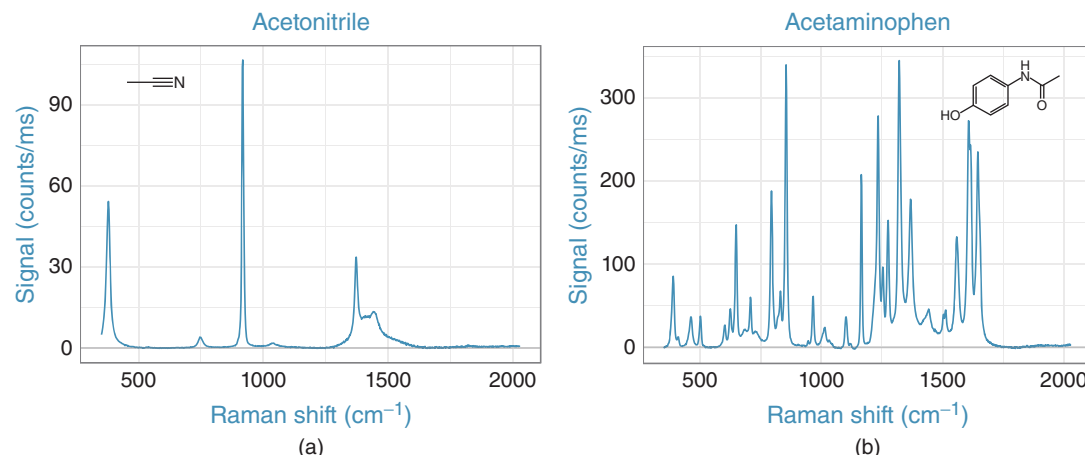


**Figure 6.2** (a) Acetonitrile and (b) Acetaminophen as measured using 785 nm Raman. Source: Courtesy of Wasatch Photonics.

Information is contained in the frequency shifts of the emitted photons relative to the input light; each frequency shift or peak observed maps to one of the vibrational frequencies in the molecule. A typical Raman spectrum consists of several to many peaks. For simple molecules, like acetonitrile, the Raman spectrum may feature narrow and well-separated peaks, while for complex organics, like acetaminophen, the Raman peaks are often more frequent and closely spaced and/or overlapping, as shown in Figure 6.2.

The pattern of peaks composing a Raman spectrum is very specific to the material being interrogated, providing a unique fingerprint by which it can be identified. The lower frequency range up to  $1500 \text{ cm}^{-1}$  Raman shift is often sufficient to confirm identity, and, for this reason, is called the “fingerprint” region. Valuable information is also found in the “functional” region, out to  $3600 \text{ cm}^{-1}$  Raman shift, as shown in Table 6.1. As the name indicates, the frequencies in this extended range primarily indicate the presence of specific functional groups in a molecule; they represent local molecular information, rather than information about the overall molecular structure.

**Table 6.1** Raman frequencies of common chemical functional groups.

Functional group	Position (cm <sup>-1</sup> )	Remarks
>S-S<	500–550	
C-C	~1060 and 1127	Polyethylene
C-C	700–1260	Highly mixed in complex molecule
Aromatic ring	~1000	Monosubstituted
Aromatic ring	~1000	1,3 disubstituted
Aromatic ring	~1000	1,3,5 trisubstituted
Aromatic ring	~860	1,4 disubstituted
CH <sub>3</sub> umbrella mode	~1375	
CH <sub>3</sub> and CH <sub>2</sub> deformations	1410–1460	
>C≡C<	~1650	
>C≡C<	~1623	Ethylene
>C≡O mixed with NH deformation	1620–1690	Amide I
>C≡O	1710–1745	Changes for ketone, aldehyde, and ester
C≡C	2100–2300	
SH	2540–2600	
>CH <sub>2</sub>	2896 and 2954	Ethane
>CH <sub>2</sub>	2845 and 2880	Polyethylene
CH <sub>3</sub>	2870 and 2905	Polypropylene
R <sub>1</sub> R <sub>2</sub> R <sub>3</sub> CH	2880–2890	Methine CH
CH	~2900	Cellulose
CH	~3015	Olefinic CH
CH	~3065	Aromatic CH
CH	3280–3340	Acetylenic CH
NH	3150–3340	Broadened and shifted by H-bonding
OH	3000–3600	Broadened and shifted by H-bonding

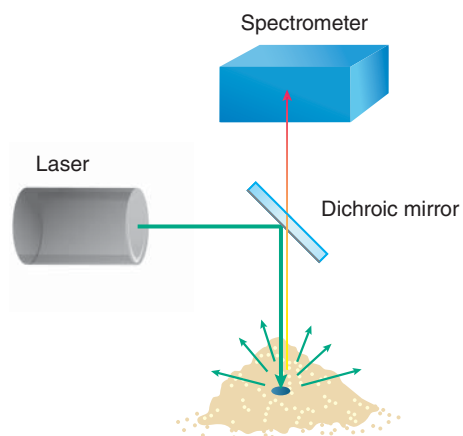
Source: Adar [6]. © 2016, UBM.

A Raman spectrum displays the intensity of the Raman emission as a function of the frequency shift relative to the incoming light frequency. Raman spectra are reported in terms of the “Raman shift,” the frequency difference relative to the excitation source. This is reported in wavenumbers (cm<sup>-1</sup>), a frequency space convention adopted in IR spectroscopy, and one which allows the two complementary techniques (infrared and Raman) to speak a common language for the identification and study of molecules. Raman shift may be calculated using the following equation, where  $\nu_{\text{Raman}}$  signifies the Raman shift, and  $\lambda$  signifies wavelengths of the excitation laser and the Raman emission, as indicated by the subscript:

$$\nu_{\text{Raman}} = \frac{1}{\lambda_{\text{Excitation}}} - \frac{1}{\lambda_{\text{Raman}}}$$

By working in frequency space, Raman spectra measured with different excitation sources may be directly compared; each peak marks the frequency of molecular vibration, independent of the excitation wavelength.

**Figure 6.3** Epi-illumination optical configuration, typical in handheld Raman systems. Source: Courtesy of Wasatch Photonics.



## 6.4 Basics of a Raman System

A portable Raman system consists of three main functional units: a laser, a sample interface, and a spectrometer. For now, these three main components will be described only briefly to provide an overview of the whole system; each element will be discussed in more detail in the sections to follow.

The laser acts as the excitation source, providing the high intensities needed to balance the low probability of Raman scattering and yield sufficient Raman signal for detection. The laser beam is focused onto the sample to achieve better imaging of the resulting Raman emission into the spectrometer.

The sample interface provides delivery of the laser light to the sample, and collection of the Raman emission. In portable Raman instruments, the emission is most often detected as backscattered light in an “epi-illumination” arrangement (also termed 180° collection), as shown in Figure 6.3, with added sampling optics to both focus the laser and collect the Raman emission. A longpass dichroic mirror typically reflects the shorter wavelength laser onto the main beam path, then transmits the Raman-scattered light for routing to the spectrometer (note: some portable systems may use a different optical configuration). An additional longpass filter integrated into the sampling optics or spectrometer performs further rejection of the laser light and passes the Raman signal. The sample optics may be contained within the body of a fiber-coupled probe for increased flexibility, but more often are integrated with the laser and spectrometer as a single unit.

The spectrometer performs detection of the Raman signal; an array detector is used to capture all wavelengths simultaneously. As only one in  $10^6$  of the incident photons will be returned as Raman scatter, an extremely sensitive spectrometer is needed; high throughput is mandatory. The spectrometer reports a spectrum, which is translated in software to a Raman shift relative to the laser frequency.

These three components may be designed and integrated differently depending on system size and operational constraints, performance requirements, application, and sampling optic needs. Even within the subset of compact Raman instrumentation, a variety of form factors exist.

## 6.5 “Portable” Versus “Handheld” Versus “Mini”

When considering “portable” Raman systems, the first form factor that comes to mind is a handheld system, epitomized by early designs like the Ahura First Defender (acquired by ThermoFisher Scientific) [7] and Snowy Range CBEx [8], acquired by Metrohm Raman [9]. Handheld Raman instruments are roughly the size of a digital multimeter, with an integrated processor, user interface, and display screen, as shown in Figure 6.4. They run on



**Figure 6.4** Handheld Raman systems: (a) Vaya Raman Raw Material Identity Verification System. *Source:* © Agilent Technologies, Inc. Reproduced with permission of Agilent Technologies, Inc. (b) Mira DS Flex. *Source:* Metrohm AG. Reproduced with permission of Metrohm AG.

battery power, are operated in “point and shoot” mode, and provide answers in minutes or less using onboard or cloud-based library matching software. More than a dozen vendors on the market provide solutions in this form factor for material identification in pharma, hazmat, and authentication [7–26].

At a slightly larger size are “portable” Raman systems – too large to be operated handheld, but still small, lightweight, and robust enough to be easily moved from one location to another, as shown in Figure 6.5. These have footprints ranging in size from roughly half to a full sheet of letterhead or A4 paper, and may be packaged for transport in a hard, waterproof case containing specialized sample chambers, or have a fiber-coupled sample interface. They may be operated as field analyzers, or deployed for use in the clinic or the plant. Power may be provided by a battery, mains power (i.e. cabled), or a combination of both. A laptop or tablet may be used for data processing and analysis, or all functions may be integrated and accessible via a user interface and display screen. A number of the handheld Raman system vendors also offer systems in this form factor, as do many application-specific vendors and compact spectrometer providers [27–33].

At the other extreme would be “mini” or pocket-sized Raman systems small enough to fit in the palm of your hand. While several companies offer mini-spectrometers [34–36], work in this area has not yet progressed to a fully integrated “mini” Raman system design capable of displacing the current generation of handheld Raman instruments. Industry focus has instead been on application optimization and sample interfaces, software graphical user interfaces (GUIs), and library matching/analysis, but will surely come back to miniaturization in the very near future.

## 6.6 Performance Needs in Portable Raman Instruments

Having developed a general understanding of the theory, basic system design, and possible form factors pertinent to portable Raman spectroscopy, we can now address its performance needs. Some are dictated by the technique

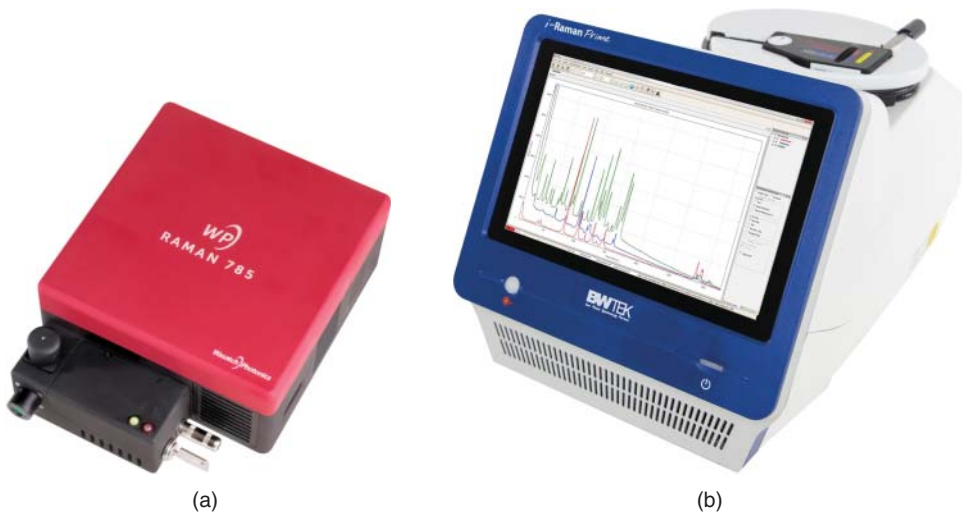


**Figure 6.5** Portable Raman systems: (a) WP 785L, an integrated Raman system designed for use with external data processing. *Source:* Courtesy of Wasatch Photonics. (b) i-Raman Prime 785H, an integrated Raman system including onboard user interface screen. *Source:* Metrohm AG. Reproduced with permission of Metrohm AG.

itself, while others are imposed by the required form factor, use case, or operating environment. All of these factors compete when designing a portable Raman instrument, and a general design principle of “good enough” for the application must be ruthlessly applied. In portable Raman systems, the goal is to generate an accurate answer at the required confidence level, in the smallest footprint and measurement time, and at the lowest cost and power draw possible. In doing so, one must also consider whether the answer must be qualitative (identification) or quantitative (how much), as a portable Raman instrument is most often used for identification, but is also capable of identifying components in mixtures and assessing relative concentrations.

As a technique, Raman spectroscopy requires extremely high sensitivity, and depends on highly blocking filters to reject Rayleigh scatter from the excitation laser. Even still, there is the potential for fluorescence to interfere – from the sample itself, and from optical components in the system; this must be minimized through a choice of excitation wavelength or other special configurations, which we will touch on near the close of this chapter.

The system as a whole must offer sufficient spectral range and optical resolution to acquire the peaks needed for analysis, and good signal strength across the full spectrum. Most portable Raman instruments cover  $200\text{--}2400\text{ cm}^{-1}$ , with optical resolution from  $6$  to  $15\text{ cm}^{-1}$  FWHM (full-width at half-maximum), depending on the application space. The spectra generated must be stable over time and temperature to allow for consistent spectral substance identification against a general library; even more so when quantitative answers are needed. Low unit-to-unit variation is desirable to facilitate matching against a master library, with as little correction as possible.

Portable operation introduces its own requirements, both in ruggedization and reduction of SWaP (Size, Weight, and Power). Operating environments may span indoor and outdoor operation, and the mechanical design must be robust against shock and vibration. Some degree of self-calibration is needed to validate the operation and minimize downtime, and spectral processing and analysis must be integrated to yield immediate answers.

Handheld operation takes these needs a step further, as the instrument must be smaller and lighter, with low power draw to allow for battery operation. The instrument must be even more sturdy, possibly water-resistant, and temperature-insensitive to handle field operation by a nonexpert. A specific IP (ingress protection) rating may be required to guard against intrusion from dirt, dust, other foreign bodies, and moisture [37]. Measurement times must be a few seconds or less when the user is holding the instrument against the sample, both for operator

convenience and to minimize power draw. Lower power lasers are attractive not only to extend battery life, but also to avoid burning of high value, fragile, or explosive samples; the consequently reduced signal generated by lower laser powers underscores the need for highly sensitive detectors. Miniaturized, phone-sized screens typically require simplified software interfaces, providing conclusive answers in a minimum number of steps.

With these general performance needs in mind, we can now look at each component in the system individually to see how they contribute, consider the relevant design factors and options, and explore the current state of the art in portable Raman instrument design.

## 6.7 Excitation Laser

While any laser, in theory, can be used to generate a Raman spectrum, the choice of wavelength is the greatest factor in determining the strength and quality of that spectrum. The intensity of the Raman signal scales proportionally with the intensity of excitation light, and inversely with its wavelength to the fourth power:

$$I_{\text{Raman}} \propto \frac{I_{\text{laser}}}{\lambda^4}$$

Shorter laser wavelengths thus yield far more Raman signal, but also generate more autofluorescence background in organic and biological samples due to the excitation of electronic transitions. This fluorescence appears as a broad background, but can be significantly reduced by working at longer excitation wavelengths, particularly in the near infrared (NIR), as shown in Figure 6.6. Working in the NIR comes at the expense of Raman signal, however, and results in higher cost, lower sensitivity, and increased size, weight, and power draw due to the need for cooled indium gallium arsenide (InGaAs) detectors.

There is also a window in the ultraviolet (UV) prior to the onset of fluorescence yet within the sensitivity range of silicon detectors, shown in Figure 6.7. This is accessible with some limitations: UV laser sources offer lower power, have limited lifetimes, and are inconvenient from a size and power draw standpoint. UV Raman spectroscopy also places more stringent requirements on longpass filter performance and the spectrometer (including the grating), to achieve equivalent optical resolution and starting wavenumber. In addition, glass becomes opaque in the UV range, and portable UV Raman instruments are, thus, reserved for specialized applications, such as standoff spectroscopy.

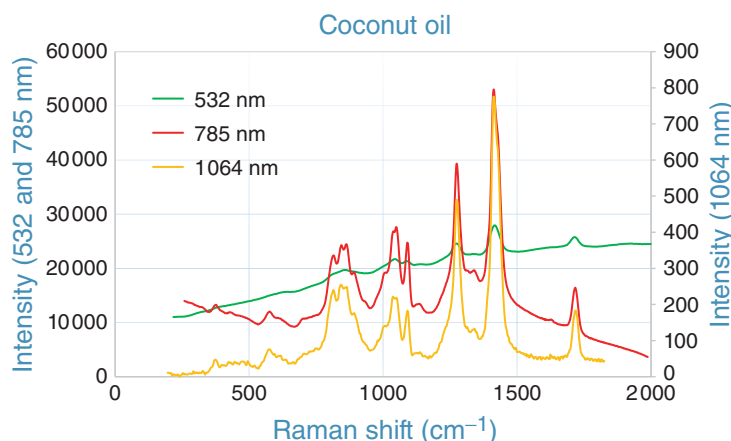


**Figure 6.6** Choice of excitation wavelength can help to mitigate fluorescence background, as observed when comparing Raman spectra for coconut oil using 532, 785, and 1064 nm excitation. *Source:* Courtesy of Wasatch Photonics.

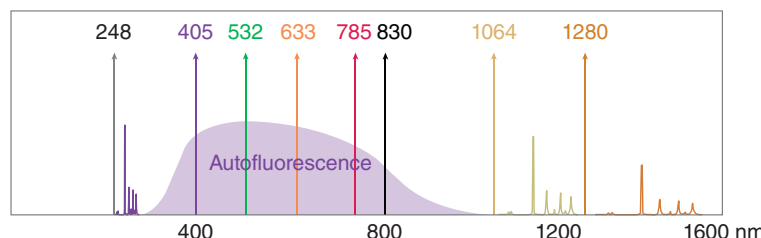


**Figure 6.7** Plotting some typical Raman excitation wavelengths together with the autofluorescence band generated by intense excitation light illustrates the benefits of working at both UV and IR wavelengths for Raman spectroscopy. *Source:* Courtesy of Wasatch Photonics.

The development of stable, compact laser sources for nonspectroscopy applications has been a key enabling technology in the evolution of portable Raman instruments [38, 39], and has determined the specific wavelengths across the spectrum that have become easily accessible using commercial off-the-shelf (COTS) components. Blu-ray disc players gave us 405 nm diode lasers, solid state Yttrium Aluminum Garnet (YAG) lasers used in materials processing yielded 1064 nm and its doubled 532 nm wavelength, and 633 nm diode lasers have replaced the ubiquitous helium-neon (He-Ne) laser used in research and industry. Optical storage applications drove the development of 785 nm lasers, while 830 nm is a common diode pump laser wavelength.

Of these, the most popular wavelength used for handheld Raman instruments is 785 nm, as it yields the best trade-off between Raman signal strength and fluorescence background for the widest range of samples, with minimal sample heating. It allows measurement of Raman-active materials with Raman shifts to  $3500\text{ cm}^{-1}$  using a silicon detector, reducing cost and power draw while yielding good signal strength.

As the calculation of Raman shift is predicated on accurate knowledge of the excitation wavelength, laser wavelength purity, stability, and repeatability are key requirements. The laser linewidth is typically  $<3\text{ cm}^{-1}$  to avoid line-broadening of Raman peaks, and a wavelength-selective element may be integrated into the laser or at its output to ensure consistent center wavelength and suppression of sidebands; a volume Bragg grating and/or dichroic laser line filter may be used. Minimal thermal drift, excellent mechanical ruggedness, and short warmup times help support the generation of consistent spectra in portable Raman instruments, where the laser may be switched on and off for each measurement and encounter a wide variety of operating environments.

Portable Raman instruments generally offer 10–499 mW of output laser power (Class 3B), focused to a spot size 50–200  $\mu\text{m}$  in diameter. Laser safety must be considered in instrument design, whether in the form of a mechanical interlock at the sample interface or physical shielding, particularly for longer operating focal lengths. Handheld Raman systems generally have fixed laser power, but portable systems may offer adjustable output laser power for better control in avoiding sample damage or ignition of explosives. The laser may also be rastered across the sample, linearly or in an orbital pattern, to minimize heating of any single location. This has the added advantage of providing a more representative view of the sample, particularly for crystalline or inhomogeneous samples and mixtures.

The intensity stability of the laser's output is important for quantitative measurements, and calibration is needed when comparing answers from multiple units. A good beam profile, or spatial mode quality (as measured by the  $M^2$  factor, or beam quality factor) is also very important to ensure the quality of focus on the sample at the desired operating distance.

Raman instruments use either single-mode (SM) or multimode (MM) lasers, where “mode” refers to the spatial mode or beam profile, as shown in Figure 6.8. SM lasers are lower in output power, typically up to 100 mW at 785 nm and  $<300\text{ mW}$  at 1064 nm; however, they offer the ability to focus the laser spot to a tighter spot due to their Gaussian beam profile. Typical SM lasers have an  $M^2 < 1.1$  and a spectral bandwidth  $<100\text{ kHz}$ .

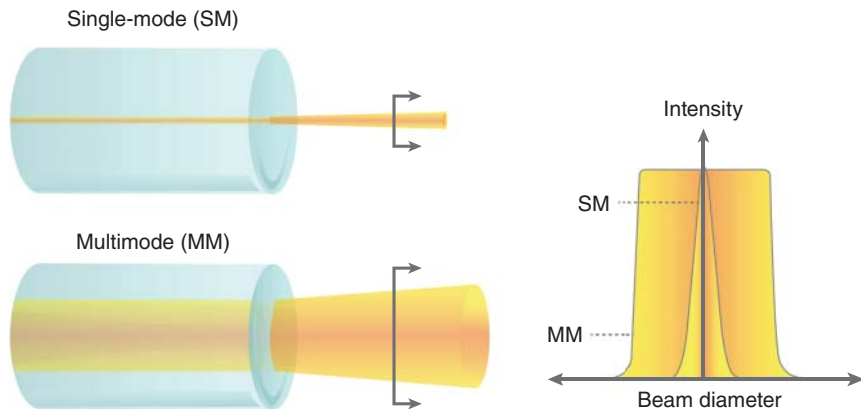


**Figure 6.8** Single-mode and multimode lasers differ in both beam size and spatial intensity distribution profile. The radial distribution of a Gaussian beam can be more tightly focused to generate greater power density at the sample. *Source:* Courtesy of Wasatch Photonics.

MM lasers offer the user more output power, typically greater than or equal to 500 mW at 785 nm and up to 800 mW at 1064 nm, and are less susceptible to mode hopping. However, MM lasers cannot be focused as tightly as SM lasers due to lower native beam quality. Also, the use of the highest MM laser power levels may be limited in portable Raman systems by regulatory compliance, operator safety, and sample preservation.

### 6.7.1 Laser Packaging

Raman systems based on SM lasers traditionally use a small, monolithic TO-56 can in open beam format or the larger 14-pin butterfly package as shown in Figure 6.9, in either a fiber-coupled or open beam configuration. The TO-56 packaged product delivers a collimated output beam in a very compact package, making it ideal for integration into lightweight instrumentation. The SM laser 14-pin butterfly package is available at wavelengths ranging from 405 to 1064 nm for Raman spectroscopy. In this form factor, the laser is wavelength stabilized and delivers output power with ultranarrow spectral bandwidth and a diffraction-limited output beam. TO-56 SM lasers are less thermally stable than equivalent butterfly packages, and can suffer greater intensity fluctuations.

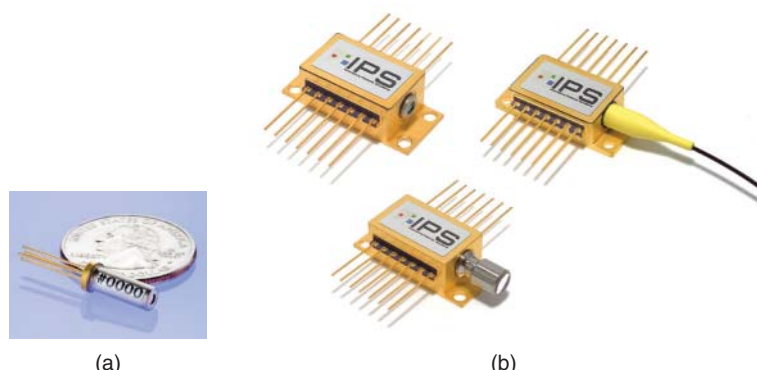


**Figure 6.9** Laser packages used for Raman spectroscopy: (a) TO-56 can and (b) 14-pin butterfly packages with different coupling options (going clockwise, fiber-coupled, beam shaping and homogenizing STUB output, and open beam output). *Source:* Innovative Photonic Solutions. Reproduced with permission of Innovative Photonic Solutions.

Raman instrumentation using MM lasers also uses a 14-pin butterfly package (open-beam or fiber-coupled). These multimode spectrum-stabilized lasers offer high wavelength stability over time, temperature and vibration. MM lasers are available from 532 to 1064 nm and feature side mode suppression techniques to ensure the laser's stabilized central peak wavelength remains "locked" regardless of case temperature (15–45 °C). Other telecom industry diode lasers have been used in research applications, notably at 1280 and 1550 nm.

In general, MM lasers have the additional benefit of higher mean time before failure (MTBF) and typical lifetimes exceeding 10 000 hours, with exact lifetime and operating parameters being dependent upon the manufacturer, wavelength, model, and output power.

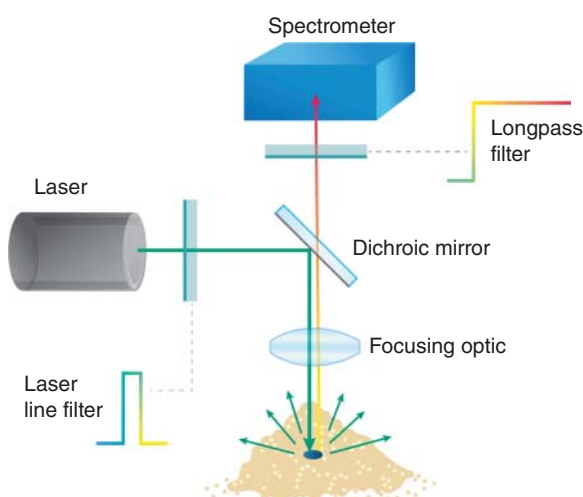
## 6.8 Optical Filters and Sampling Optics

The next elements in the optical path of a portable Raman instrument are the optical filters and sampling optics sometimes referred to together as the "probe." These probe elements may be housed separately via fiber coupling for some larger portable systems, but are always fully integrated into the unit in handheld Raman spectrometers. Together, they route clean laser light to the sample, and isolate Raman signal from Rayleigh scatter for delivery to the spectrometer (see Figure 6.10).

The first of these elements is a laser line cleanup filter. It can serve two purposes, both with the same goal of achieving the cleanest laser line possible, with no extraneous wavelength emission to cloud the Raman spectrum. A laser line cleanup filter is a narrow bandpass filter with a FWHM of 1.5–4 nm, with OD 5–OD 6 of blocking at shorter and longer wavelengths (OD = optical density). It may be used at the output of a multimode diode laser to block side modes and clean up laser output, removing the broadband amplified spontaneous emission (ASE). When used in a fiber-coupled Raman system, it also targets Raman scattering from the delivery fiber itself – background signal generated due to propagation of the intense laser light. By applying a laser line filter to the output of the laser routing fiber inside the probe head, this background can be stripped away [40].

The second element is the dichroic mirror used for laser and Raman signal routing. It is typically oriented at 45° to the laser, reflecting laser light to route it to the sample, and passing the longer wavelength Stokes emission (Raman signal) for routing to the spectrometer. While it is also possible to instead transmit the laser and reflect the Raman signal in a shortpass configuration, it is much easier to manufacture longpass dichroic mirrors than shortpass dichroic mirrors, particularly when broad bandwidths are desired.

**Figure 6.10** Epi-illumination schematic typical in a portable Raman system, with all the optical filters shown.  
Source: Courtesy of Wasatch Photonics.



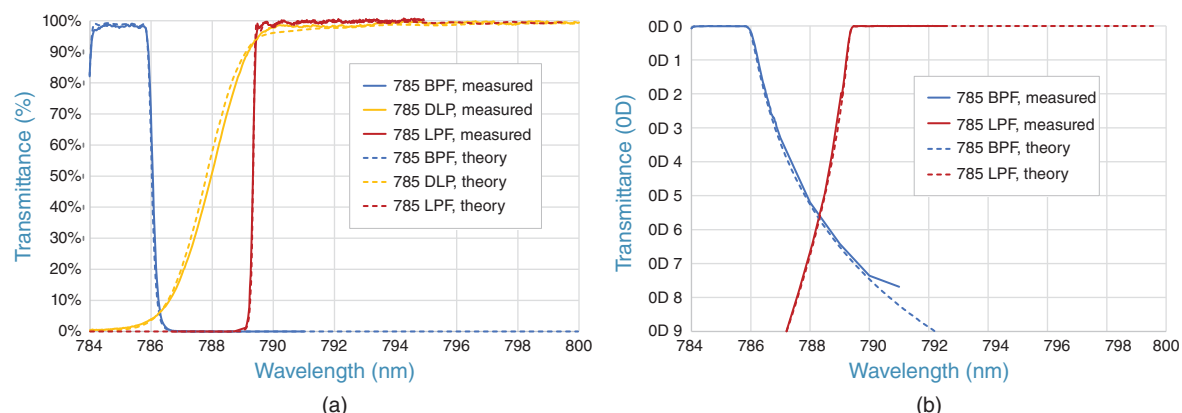


**Figure 6.11** A matched 785 Raman filter set composed of a bandpass filter for laser line cleanup (BPF), a dichroic longpass mirror (DLP), and longpass filter (LPF), showing both theoretical and measured curves. (a) Transmittance curves plotted in percentage show the steep edges used to isolate the 785 nm laser line and Raman signal, while (b) transmittance curves plotted on an OD scale illustrate the deep blocking required to obtain good SNR. Source: 785 Raman filter. © 2020, Iridian Spectral Technologies Ltd.

The third element is the focusing optic, which both focuses the laser light onto the sample and collects the resulting Raman emission. This will be addressed at a later point when discussing the sample interface, once the groundwork for all considerations in its design has been laid. At this point, it is sufficient to say that these optical elements should be made of low fluorescence glass to avoid the addition of background.

The final element in the filtering and sampling optics is the longpass or “edge” filter used to reject the otherwise overwhelming Rayleigh scatter. A minimum of OD 6 absolute blocking at the laser wavelength is required (with OD 5 average blocking over a broader band to address any other background). Optical densities greater than this are difficult to manufacture, even more difficult to measure accurately, and of no benefit in the “good enough” philosophy of portable Raman.

Longpass edge filters come in a variety of grades, commensurate with the edge steepness, aka “transition width” or “cutoff.” This may be quantified in percentage relative to the laser wavelength, or in  $\text{cm}^{-1}$  for more direct comparison between wavelengths. Edge steepness is determined by the application, though very few key Raman peaks lie close to the laser in typical portable applications.

Achieving a given edge steepness in  $\text{cm}^{-1}$  is more difficult at shorter excitation wavelengths, and can lead to excessively thick filter coatings in the NIR. These considerations favor the use of shortwave infrared longpass filters, as the most common 250–400  $\text{cm}^{-1}$  edge transitions can easily be achieved to match 785 or 830 nm lasers, and are sufficient for the needs of handheld Raman.

It is also important that all three filters in use work together to achieve the needed OD and passband. Off-the-shelf Raman filters often come matched to one another in terms of edge location, steepness, and combined laser and autofluorescence blocking, as shown in Figure 6.11. These three are often designed together for original equipment manufacturer (OEM) applications to achieve peak performance, particularly if uncollimated light is used anywhere in the system.

Dichroic filters exhibit a blue shift with increasing angle of incidence, which is compounded with polarization splitting for angles above  $\sim 10^\circ$ , and, thus, a steep edge designed for collimated light can quickly become washed out when used with a range of input angles. This is one of the most common sources of laser bleedthrough, which manifests itself as a trailing background in the first  $\sim 200 \text{ cm}^{-1}$  of a Raman spectrum.

## 6.9 Spectrometer Design

All the optical elements described to this point have concentrated on the generation and collection of clean, stable Raman-scattered light. A Raman spectrometer is then required to capture the spectrum with sufficient range, optical resolution, signal strength, and consistency to allow analysis and the generation of robust answers. We call out a Raman spectrometer specifically, as the consequences of tradeoffs between range, optical resolution, and optical throughput are unique to this technique; it is not sufficient to repurpose an off-the-shelf broadband spectrometer when designing for the needs of portable Raman instruments. First, we shall look at the performance requirements of the Raman spectrometer as a whole, then at the options for bench design and optical elements within, as well as how each impacts performance.

While the specific application will dictate the requirements for range, optical resolution, and optical throughput, handheld Raman spectrometers typically measure the fingerprint region and beyond to  $2400\text{ cm}^{-1}$  Raman shift, with  $<15\text{ cm}^{-1}$  FWHM optical resolution; they are designed with the aim of acquiring data in under five seconds. Depending on the materials to be identified, better optical resolution or an extended range to capture functional-group information may be required. Spectral bandwidth, optical resolution, and throughput are determined by the focal length of the spectrometer, its dispersion, slit width, and the numerical aperture (NA), combined with the array detector's pixel count and pitch. These are the dials to be turned, and their interdependencies must be managed in designing for “good enough” performance with the aim of robust library matching and/or quantification [41].

Additional constraints on the spectrometer design may also be imposed by the choice of laser wavelength, as mentioned previously. Excitation laser wavelengths longer than  $\sim 850\text{ nm}$  require the use of an InGaAs detector, while shorter excitation wavelengths require better optical resolution (in nm space) to achieve the same optical resolution in  $\text{cm}^{-1}$ . For example,  $10\text{ cm}^{-1}$  resolution when using  $830\text{ nm}$  excitation equates to a spectrometer resolution of  $0.74\text{ nm}$ , while  $0.29\text{ nm}$  spectrometer resolution is needed to maintain the same  $10\text{ cm}^{-1}$  resolution using  $532\text{ nm}$  excitation (taking a peak located, for example, at  $400\text{ cm}^{-1}$  from the excitation laser). Since we are working in frequency space, instrument optical resolution also varies across a Raman spectrum, improving toward the long-wavelength end. Some manufacturers specify an average resolution, while others quote guaranteed resolution over the full operating bandwidth.

When manufacturing portable Raman systems, it is preferable to minimize unit-to-unit variability, though the spectral-response function of each unit must still be corrected for prior to library matching. The spectral-response function is the product of the efficiency of each individual optical component within the full system, and is heavily dependent on the spectral response of the spectrometer.

Finally, thermal and mechanical stabilities of the spectrometer are of utmost importance for portable or handheld Raman instruments, both as regards wavelength calibration (key for identification applications) and spectral sensitivity (essential for quantitative work).

As we consider each aspect in the optical design of a Raman spectrometer, we will refer back to the abovementioned requirements to inform our discussion of the available design options and constraints.

### 6.9.1 Optical Bench Design

The general design for any Raman optical bench includes an input slit, collimation optics, a dispersive element, and focusing optics for imaging onto a detector. The fundamental question in optical bench design is then whether to use reflection or transmission optics, illustrated in Figure 6.12. This choice has a number of impacts, played out through (and resulting from) the optical elements employed in each case.

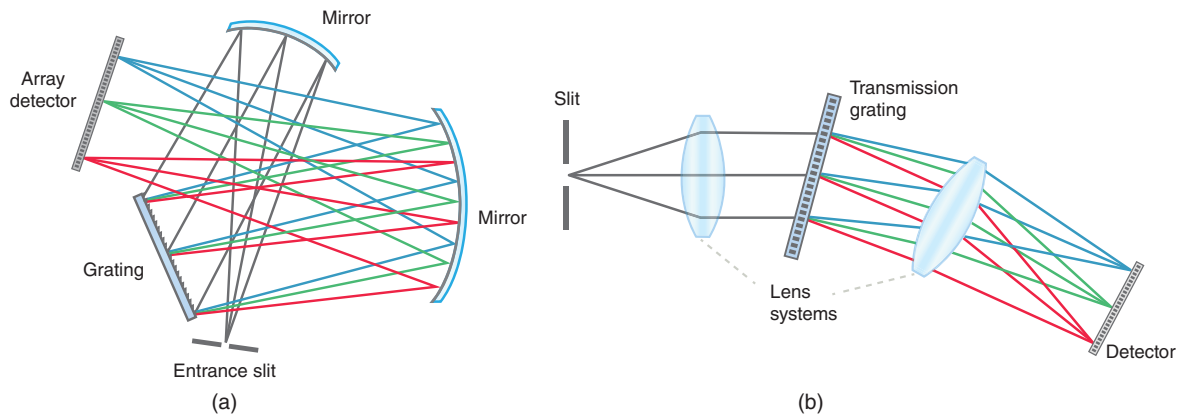


**Figure 6.12** Two typical optical bench designs used in portable Raman spectrometers: (a) Reflective grating and optics in a crossed Czerny–Turner configuration, and (b) Transmissive grating and optics in a Littrow configuration. Source: Courtesy of Wasatch Photonics.

Reflective designs often use a Czerny–Turner optical bench geometry, with a reflective grating and concave focusing mirrors forming a W-shaped optical path. If the beam path is folded (as shown in Figure 6.12a), a compact optical bench is created that can be manufactured using readily available, low-cost optics. This approach epitomizes the “good enough” philosophy, yielding adequate signal in a compact footprint at low cost. It does, however, come with trade-offs. The folded design adds astigmatism, and any angle shift in the optics due to misalignment leads to a wavelength shift, impacting calibration.

Transmissive designs most often employ a Littrow configuration, with lens sets for collimation and focusing, and dispersion provided by a transmission grating. This on-axis approach minimizes astigmatism and other aberrations, the balance of which can be compensated through careful optical design. Transmissive designs are far less angle sensitive than reflective designs, and, thus, are much more robust against vibrations or temperature changes. This same property makes them easier to align, and spectral-response functions are more consistent from unit to unit. Edge filters may also be integrated directly into the design in the collimated space between the first lens set and grating (a design option which is far more challenging to implement in a reflective design).

While these factors are important, the primary design criterion for a portable Raman spectrometer must be sensitivity. Overall light collection power is dominated by the NA, the range of angles over which the system can accept the light. Put simply, the more light collected by the spectrometer, the more light can be detected, allowing for shorter measurement times. The throughput of a spectrometer (or étendue,  $G$ ) scales with slit area ( $A_{\text{slit}}$ ) and  $NA^2$ :

$$G = A_{\text{slit}} \times NA^2 \quad [\text{mm}^2 \times \text{sr}]$$

The light collection power of a spectrometer may also be expressed in terms of *f*-number (*f*/#). A high NA equates to a low *f*-number, and, thus, more throughput.

$$f/\# \approx \frac{1}{2NA}$$

Coming back to our two geometries, lenses allow for a higher NA than mirrors of the same size, favoring a transmissive design when greater collection efficiency is needed. They also win on the preservation of light within the optical bench as lenses with antireflection (AR) coatings offer higher efficiency than metallic mirrors. Though this comes with some increase in cost, it is often merited when overall performance to price ratio is considered.

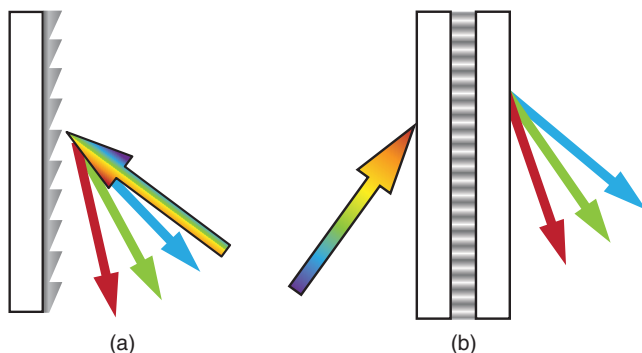


**Figure 6.13** (a) Diffraction from a surface relief grating in reflection, (b) diffraction from a volume phase holographic grating in transmission. *Source:* Courtesy of Wasatch Photonics.

### 6.9.2 Diffraction Grating

The diffraction grating serves to provide the needed dispersion for the spectrometer using interference from a periodic structure. Diffraction gratings may operate in reflection or transmission as shown in Figure 6.13, and, thus, the choice may be dictated by preferred optical bench geometry. Understanding the performance of each can influence the choice of geometry, however.

Reflection gratings are manufactured either by ruling parallel grooves in a metallic coating or are replicated (pressed) from a master. This allows them to be mass produced at low cost, but the use of a mechanical process results in lower reproducibility and eventual deterioration of the master. This impacts unit-to-unit variability, with further risk to spectral response consistency in volume if the master must be replaced.

The efficiency of a ruled reflection grating tends to peak at the blaze wavelength, then fall off to either side and may vary widely over the operating bandwidth. The diffracted light is also split across multiple orders, and, thus, typical efficiency curves for first-order diffracted light range from 25 to 60% over the bandwidth [42]. This may be further decreased by dust, fingerprints, or damage to the grating surface; while the reflection grating will remain operational, it cannot be cleaned, and efficiency is permanently reduced. The presence of ghost images and scattered light can add noise to spectra, which is undesirable in Raman spectroscopy, especially given the low signal levels which are typically measured.

Transmission gratings may be manufactured by etching a periodic structure into a transmissive substrate, with similar efficiency curve challenges as ruled reflection gratings. If manufactured holographically, however, the grating can be designed so as to divert the majority of transmitted light into the first order for greater efficiency. Holographic gratings are all originals, and as such, have high reproducibility, but are more expensive than ruled gratings.

Surface-relief holographic gratings are etched, while volume phase holographic (VPH) gratings are created by imaging an index of refraction variation into gelatin film capped with glass. VPH gratings offer the additional benefit of being easy to handle and clean and are AR-coated to further reduce loss. Holographic transmission gratings, in general, offer good efficiency over a broad range as shown in Figure 6.14 ( $>70\text{--}80\%$  is typical), and display far less polarization dependence than ruled reflection gratings. When applied to Raman instruments, these benefits increase sensitivity and reduce signal dependence on the orientation of sample crystals, respectively.

### 6.9.3 Stray Light

Stray light is an excess of light of a given wavelength in regions on the detector intended to sense other wavelengths. It arises due to scattering from optical components or surfaces within the spectrometer, focusing limitations, and

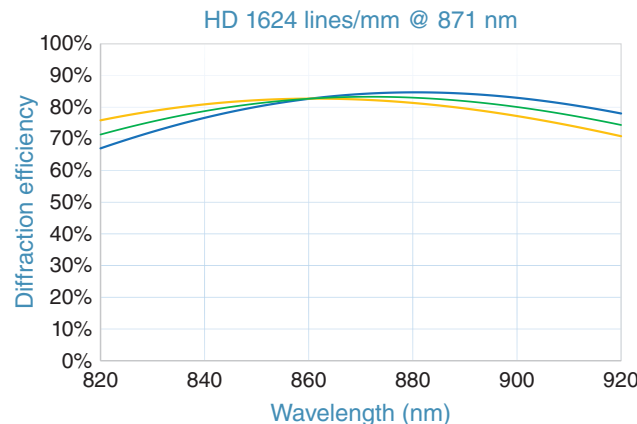


**Figure 6.14** A volume phase holographic (VPH) transmission grating for Raman, 1624 lines/mm @ 871 nm. Source: Courtesy of Wasatch Photonics.

diffraction from higher orders in the grating. This often takes the form of spillover to wavelengths close by, but some light is scattered at larger angles, and, hence, over larger wavelength differences. In Raman instruments, stray light can lead to a slight broadening of a peak, formation of a pedestal on a peak, or a raised baseline. Use of low-scatter optics, careful correction for aberrations in focusing, and use of adequate, well-placed baffles within the optical design can help mitigate stray light.

#### 6.9.4 Detectors

The detector in a portable Raman spectrometer converts photons into electrons, as measured over a period of time (the “integration time”). Portable Raman spectrometers use a linear array detector to read out the entire spectrum simultaneously using 512–4096 pixels. Each pixel generates an analog voltage output which is digitized to yield a raw intensity spectrum of “counts” versus pixels. This data can then be translated into a Raman spectrum using the wavelength calibration coefficients of the instrument and the Raman shift equation described earlier.

A detector used for portable Raman spectroscopy must be sensitive and have low inherent dark noise to yield the required signal-to-noise ratio (SNR). In practical terms, it must be relatively low-cost, consume less power than detectors used in larger instruments, and fit within a miniaturized bench. This combination of attributes could not have been imagined possible prior to the adoption of low-cost commercial array detectors by spectroscopy in the 1990s [43–45]. Used in devices like photocopies, these commercial charge coupled device (CCD) detector arrays, based on silicon technology, offered reasonable sensitivity and SNR across the visible and short-wave infrared (SWIR) at a much lower price point than traditional scientific-grade detectors – the epitome of “good enough” technology. This, in turn, inspired detector manufacturers to expand the selection of lower cost array detectors for applied spectroscopy, optimizing factors like spectral-response curve, dark noise, speed, power consumption, size, cooling, and number of pixels to suit different applications and price points [46].

Raman spectrometers typically use either a CCD or complementary metal-oxide semiconductor (CMOS) linear array detector to collect and read out a spectrum, similar to the examples shown in Figure 6.15. Some detectors consist of a 2D array of pixels, designed to be summed vertically (known as “binning”) to produce a final 1D array of higher sensitivity than would otherwise be possible. Most sensors deployed in portable Raman instruments are based on silicon technology; InGaAs technology is used for >1064 nm Raman signals. The exact sensor choice is based upon excitation wavelength, desired optical resolution, instrument sensitivity, application or use case, and cost [47].

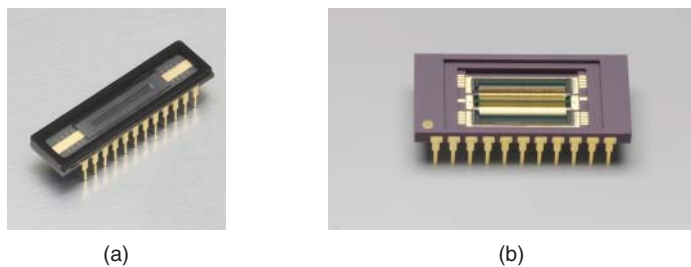


**Figure 6.15** Examples of linear array detectors used in portable Raman: (a) Hamamatsu S10420 series back-thinned type CCD area image sensor, (b) Hamamatsu G9214 series InGaAs linear image sensor. *Source:* Hamamatsu Corporation. Reproduced with permission of Hamamatsu Corporation.

The sensitivity of a detector is gauged by its quantum efficiency (QE), the ratio of electrons produced versus incident photons. Most sensor manufacturers supply a graph of the relative sensitivity versus wavelength to help designers choose the correct detector for each specific application, as different fabrication methods can be used to optimize QE for specific wavelength ranges. Back-thinned detectors take this a step further, thinning the silicon wafer and reversing its orientation relative to the electrodes so as to increase interaction with light. This method greatly improves quantum efficiency, but can lead to etaloning, a sinusoidal modulation in the detector response that can be detrimental to low-signal applications, like Raman, especially when looking at highly fluorescent samples.

The most common CCD used for 633, 785, and 830 nm excitation has been the back-thinned NIR-enhanced S1151× series from Hamamatsu, offered in 1024 and 2048 pixel formats. The post-processing method used in the manufacture of this particular back-thinned sensor served to not only increase the native QE above 750 nm, but also reduced the fringing or etalon characteristics of the sensor, an ideal combination for 633–830 nm Raman. Due to recent litigation [48], however, these sensors are no longer commercially available, and, as such, instrument providers are evaluating new, alternate sensors with a view to minimizing the impact on Raman performance. Shorter wavelength excitation Raman, e.g. 532 nm, often utilizes non-NIR-enhanced sensors or front-illuminated CCD detectors.

Most 1064 nm-excitation-based instruments use either 512-pixel or 1024-pixel linear photodiode InGaAs arrays [49, 50]. These sensors are typically cooled to below  $-10^{\circ}\text{C}$  to offer optimal SNR. InGaAs sensors have a higher power draw due to the high demands of the thermoelectric coolers (TECs) used to lower the detector temperature and are considerably more expensive than silicon sensors. As such, they place additional constraints on portable Raman instrument design and performance. InGaAs linear detectors also have unique gain/offset correction requirements, as each pixel can be considered an independent photodiode. Due to the interleaved array design often used to control alternating pixels, multiple calibrations may be required to produce a smooth spectrum.

Detector technology continues to evolve to support the next generation of portable Raman instruments. Uncooled InGaAs sensor availability is on the rise, driven by technology advancements in other sectors, such as night vision and security. These offer some interesting avenues for 1064 nm Raman development, especially when used with high throughput optical benches. In the silicon region of the spectrum, new and novel sensors are also gaining in prevalence, largely through markets like consumer electronics. Here, CMOS-based sensors from Hamamatsu (S11639) and Sony (IMX series) show promise for sensors that could enable more compact and cost-effective Raman instrumentation in the coming years.

### 6.9.5 Electronics Design

Although scientific-grade detectors and digital camera sensors have improved immensely in recent years, they still require a significant amount of custom electronics to be used optimally for Raman spectroscopy. In addition,

portable Raman spectrometers incorporate a variety of other components requiring electrical power and control, all of which must be integrated together in a low-power, miniaturized set of boards and interface cards.

Typically, the electrical design will start (or end, depending on your perspective) with a “daughtercard” holding the detector itself. This daughtercard will often have tight dimensional and mechanical requirements, as the detector will need to be mounted and aligned with great precision at the end of the optical collection path. Ambient light leakage at this terminus can be ruinous for acquisition, so various gaskets and optical baffles may be introduced. The detector itself will likely be thermally cooled, meaning a TEC, thermistor and heatsink will be competing for direct access to the detector’s surface. Any heat or electrical noise generated by other electrical components can potentially degrade the raw signal generated by the sensor, and, thus, power-hungry components should be kept as far from the detector as possible.

All of these are reasons for the detector daughtercard to be as small and minimal as possible, typically containing only the basic analog front-end (AFE) needed to digitize the pixel voltage into digital intensity counts through a carefully gained and filtered analog-to-digital converter (ADC). The ADC bit-resolution will determine the detectable dynamic range (vertical extent in counts) of the system. For instance, a 12-bit ADC can only report 4 096 different levels ( $2^{12}$ ) of intensity, regardless of the detector sensitivity, while a 16-bit ADC supports a much richer scale of 65 536 intensity levels ( $2^{16}$ ). The daughtercard then passes the integral intensities back to a “main-board” for processing and communications.

The daughtercard will also be responsible for the various clocks and control signals used to drive the detector acquisition. For deterministic high-speed timing, these clocks are typically generated by a field-programmable gate array (FPGA) which will often read out the digitized intensity values from the ADC. While FPGAs provide robust and reliable timers, they can be complicated to design and maintain, so once a spectrum of intensity values has been read out from the daughtercard, it may be passed straight to a standard microcontroller or microprocessor for disposition.

There are many types of microcontrollers and microprocessors in use for portable Raman spectrometers, but most are converging on the ARM family of processors [51] to leverage the broad commercial and open-source toolchains supporting that platform. The choice of a processor will largely depend on (or drive) the determination of the types of spectral processing which can be applied, and where those processes will occur. A low-power microcontroller may serve primarily as a communications gateway to offload the raw data as expediently as possible (indeed, such could be provided by the FPGA alone); or a more powerful microprocessor may elect to provide significant post-processing and even Raman matching internally.

Beyond the basic collection and routing of spectral data, there are many other functions which the spectrometer’s electrical design needs to support. It will be responsible for distributing and level-shifting clean power on various “rails,” often including 12, 5, 3.3 V and other voltages in a single system. It must also power and control TECs on detectors and/or lasers. It will control the lasers themselves, including safety interlock and status LEDs. Battery subsystems will require charging electronics, possibly during measurement operations, and provide “gas gauge” status indicators to monitor charge state. Communication subsystems can be extensive, depending on the variety of communication buses and protocols supported, from low-level I<sup>2</sup>C or serial peripheral interface (SPI) hooks to power-hungry USB 3.0, Wi-Fi and Ethernet ports.

Medical Raman systems may include integrated photodiodes for laser power monitoring, and advanced instruments may include articulated motors to raster the laser beam or offset the optical path between measurements. Fully handheld devices will need electrical control of the user keypad and display screens. Consideration must be made toward external connectors if required for firmware or library updates, factory maintenance or cables for triggering or standoff operation. Nonvolatile storage must be provided via electrically erasable programmable read-only memory (EEPROM) or similar to store configuration and calibration data specific to the device.

All of the above electrical functions need to be integrated into as few boards as possible, occupying as little real estate as possible. It is clear, therefore, that careful consideration of the specific requirements for a given application is merited to ensure that a sufficient and complete, yet minimal, set of features are implemented in any particular

design to optimize performance and operational runtime for the specified use case. Given the above, the electrical design of portable Raman systems will particularly benefit from attention to the following areas.

Low-noise electronics are desirable for the highest SNR, to yield the best analytical sensitivity. In most cases, electronic noise is significantly lower than other noise contributions, and, thus, should only be noticeable when looking at very small signals on a very low dark-current background.

The primary driving factor in electronics design for portable Raman systems is the need for low power consumption to maximize battery life. This also enables the use of a smaller battery, which results in a smaller form factor overall. To reduce the proportion of space taken up in the instrument by the battery, and to prolong the time between charges, the microprocessor firmware can be programmed with sleep options to conserve power. The measurement cycle can also be designed to preserve power by turning off the laser diode and TECs when not in use, as these represent major power draws within the instrument.

Communication options may include wireless protocols, such as Bluetooth, Wi-Fi, or similar to parlay with a phone app or the cloud [26]; low-power Bluetooth (BLE) is attractive as regards power consumption, but can be slow for spectral acquisition. If a laptop is used for analysis, USB or Ethernet connection is typical.

### 6.9.6 Mechanical Design

The mechanical demands on Raman instrumentation have never been greater, with a wider range of environmental operational requirements than ever before. A cursory glance at manufacturer datasheets shows the importance of shock, drop, and vibrational specifications tested to international and military standards along with IP ratings, like IP67 [37], which describes ingress protection against dust and water. Size and weight are minimized, as the lower the size and mass, the more user-friendly and more likely the acceptance in certain operational environments. The specifications also show the wide-ranging temperature and humidity conditions expected from Raman instrumentation.

All of this means that a Raman instrument needs to be designed with mechanical and thermal stability in mind from the beginning, selecting key components, like excitation laser, optical bench design, sample interface, power management, and display so as to withstand these demands individually as well as at the system level. Achieving this level of mechanical stability means unit-to-unit reproducibility is maximized, and material identification via library matching is less arduous due to improved spectroscopic data integrity on all platforms in the same product family.

There are various mechanical features and accessories of particular use in portable Raman instruments, though the convenience and value of each must be weighed against all critical cost and SWaP goals for inclusion in any particular system. Integrated mechanical shutters allow “dark” or “laser-off” measurements to be taken at any point (and automated by software) to help normalize spectra and improve library matching; however, holding shutter arms in fixed positions (independent of orientation and gravity) represents a minor but constant power draw, and incorporation of a rarely articulated component represents opportunity for breakage under stress.

High-availability applications may require a replaceable battery to minimize downtime when the charge runs low, adding requirements for a housing door or removable lid to accommodate hot-swapping of batteries. Various external connectors may require IP ratings, often leading to bulkier and more expensive ports. Even nominally handheld devices may include provisions for mounting on tripods or unmanned platforms. Field calibration standards can be built into lens caps, and standoff aides, like removable nosecone guides, can simplify measurement uniformity against different samples. Minor amenities like lanyard rings may be included to ease operator workflow.

A comprehensive thermal model of the system using computational fluid dynamics (CFD) may be required to balance the various thermal sources within the housing (e.g. processors and TECs) and ensure the heat they produce flows consistently and predictably away from thermally sensitive electro-optical components (detector

and laser). A systematic thermal design will account for the thermal design power (TDP) of electrical components under load across a range of battery states and ambient environmental conditions and may involve Monte Carlo simulation to cover all the corner cases. Simulation results can advise the placement of fans, vents and heatsinks to direct stray heat and minimize overall system thermal noise.

## 6.10 Sample Interface and Accessories

Our earlier discussion of the excitation laser, sampling optics, and spectrometer took us as far as the dichroic for routing laser light to the sample and Raman signal to the spectrometer, with only brief mention of the optics to focus light onto the sample and collect the resulting Raman emission. This is an extremely important aspect of design for portable Raman, as the sample interface and accessories must be tailored to the specific application and/or sample type so as to produce a high level of sample signal, with the lowest level of background signal arising from the container or ambient light. For quantitative work, it is important to achieve highly reproducible alignment of optics to the sample.

For portable applications, it is strongly preferred to measure the sample in its native container, without transfer to a sample vial. Noncontact examples include white powder in plastic bags, chemicals inside a polyethylene container or an amber glass bottle (through-barrier), or identification of medication in a blister pack. For a bulk liquid or powdered sample, a dip probe in direct contact may be used. In either case, ambient light should be minimized – the sample interface and coupling optics should be designed with shielding, backed by the common practice of recording an ambient light signal under the same ambient conditions to account for both dark current and ambient light levels.

In the typical epi-illumination setup discussed under sampling optics, a lens is used to focus the collimated laser beam onto the sample, and to collect the Raman emission into a collimated beam. The beam is focused with a second lens onto the spectrometer slit (in a fully integrated system configuration) or a fiber (in case of an external probe). This second lens needs to be matched in NA to the input of the spectrometer (or spectrometer-coupling fiber, when an external probe is used). In the case of clear liquids, a higher NA sample lens is ideal to collect a larger solid angle of Raman emission, but from a shorter focal depth. In the case of solid samples, the imaged focal volume is shortened due to scatter, but the imaged area increases through backscatter. These counteracting effects mostly cancel, which opens up some flexibility for adjusting the working distance to the sample without loss of signal.

When deciding between a fiber-coupled probe and direct coupling via “integrated probe” (free-space optics), the direct coupling approach is chosen most often. It is more integrated, more compact, offers greater efficiency by using less optics, and can image a taller emission area from the sample onto the full slit. Fiber-coupled sample optics provide flexibility for instruments that cannot be held against a sample, as shown in Figure 6.16. The disadvantages of this flexible sample interface are the potential for fiber breakage, additional losses from fiber coupling, and the sacrifice of signal when the circular fiber is imaged onto a rectangular slit.

Working through a barrier for analysis of powders or liquids as described above is possible because most barriers allow a surprising degree of transmission of laser light into the container, and of Raman signal back to the system, particularly at NIR wavelengths beyond the range of our vision. Also, as the container and sample working distances are different, a long-working-distance lens can be made to focus deep inside the container to increase the proportion of Raman signal from the target material relative to the container emission. See the discussion on spatially offset Raman spectroscopy (SORS) below, and also in the chapter in Volume 2 by Hargreaves.

Handheld Raman instruments often come with useful accessories, as illustrated in Figure 6.17, to facilitate measurement of different sample types. These may include lenses of different focal length, a vial holder, or reader for slides used in surface-enhanced Raman scattering (SERS), to be discussed later. Portable Raman instruments may be configured with various probe options, including dip probes for process applications.

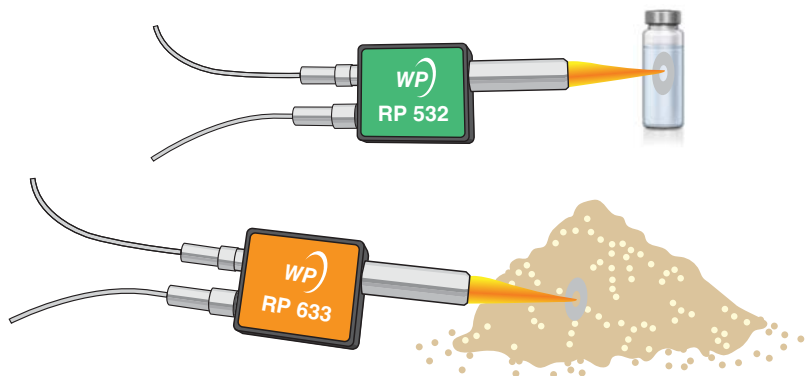


**Figure 6.16** Probe-based portable Raman systems can work through-barrier to probe materials in containers, or sample powders directly. *Source:* Courtesy of Wasatch Photonics.



**Figure 6.17** Some handheld Raman systems like the Mira DS are offered with a variety of attachments for measurement of powders, liquids, solids, and SERS substrates. *Source:* Metrohm AG. Reproduced with permission of Metrohm AG.

Sampling accessories are also important to ensure compliance with pharmacopeia standards. Wavelength calibration is typically performed using ASTM method E1840, which uses a standard compound with Raman signal across the full spectral range, such as a mixture of acetonitrile and toluene [52]. Raman shift accuracy may then be validated via a recommended reference standard, such as polystyrene, in compliance with United States Pharmacopeia (USP) chapter <1120> or European Pharmacopeia (EP) chapter <2.2.48> [53, 54].

The final point of consideration in the discussion of sample interface is the need for laser safety to be integrated into the sample interface, as most portable Raman systems utilize a Class 3B laser. It should only be possible to fire the laser if the laser is in a closed beam path when working distances are long. A short-focal-length lens may also be deemed adequate to ensure safe laser operation. In all cases, laser safety warning labels must be clearly visible on the instrument, and guidelines for safe operation and use cases included in the manual.

## 6.11 Spectral Processing and Analysis

Beyond the acquisition of a Raman spectrum in a portable Raman instrument lies the computer hardware, software, spectral processing, and libraries needed to generate answers from the data. In this section, we will discuss each, focusing on the aspects most pertinent to portable Raman spectroscopy.

### 6.11.1 Processing Hardware

Converting the many peaks of a Raman spectrum into an actionable answer requires more powerful hardware than is convenient to package inside a miniaturized optical bench. Commercial Raman systems have, therefore, converged around two basic configurations: either integrating an embedded computer alongside the spectrometer within a shared housing or performing processing and user interface on a physically separate phone or laptop which communicates with the spectrometer through wired or wireless protocols. In the ubiquitous “Internet of Things” (IoT), either option can be backed by cloud-based services if communication options allow.

Full integration of computer hardware onto the instrument adds size, weight, power consumption, and, of course, cost. Matching libraries must be stored or at least cached on the instrument, requiring additional storage and periodic updates, and causing security concerns for some applications. These are far outweighed, however, by the benefits of having all elements integrated into one compact package with push-button control; this is the standard for the many handheld Raman instruments deployed in the field.

Use of separate processing on a phone, tablet, or laptop allows COTS hardware to be used, is more easily updated, and allows additional flexibility and options in the user interface versus buttons or touchscreens. Communication between the instrument and remote processor can utilize a variety of consumer and industrial standards, like USB, Bluetooth, or Wi-Fi; data may be stored (or even processed) remotely in the cloud. This multiple-device approach, however, complicates measurement operation and makes the system susceptible to all the information technology (IT) vulnerabilities that come with nightly updates, operating system upgrades, and the like. The necessity to transmit spectral data between devices can also present a security issue for some applications.

### 6.11.2 Spectral Processing

A key step in the analysis of the acquired spectrum is post-processing to prepare the data and remove instrument variability. Library matching and quantitative analysis are both sensitive to spectral response mismatches between the portable instrument used in the field and the benchtop equipment used to establish the sample library (or determine calibration). Third-party or legacy Raman libraries may have been collected at a different laser wavelength, a different spectral resolution and range, or with different optics, which impacts the spectral shape and consequently matching accuracy. It is, thus, necessary to correct for as many of these differences as possible after acquisition of sample measurements in the field, and before comparing spectra via library matching [55].

An important step in most spectroscopic measurements is the subtraction of an ambient signal (laser-off) measurement, which must be taken at the same integration time and ambient conditions as the sample measurement. Also, many spectra may be averaged together over time to improve SNR and reduce spurious noise peaks. Linearity correction may be needed to account for varying detector sensitivity as pixels near saturation. Gain and offset corrections may also be needed in post-processing if not automated within the spectrometer.

As detectors can develop “bad pixels” over time (similar to LCD screens), the software may need to average or interpolate across gaps in the input data. High-frequency noise may be removed through simple convolutions, such as “boxcar averaging” of adjacent pixels. The sequencing of these steps is important and worthy of careful consideration, but will vary depending on what features are integrated into spectrometer hardware, versus what remains to be done in software.

Beyond standard spectral cleanup, there are other operations which can improve matching results against a particular library or sample type, depending on the particulars of an application. Sample or library spectra may need to be interpolated against a common  $x$ -axis, or normalized in intensity. Intensity correction can be applied with a calibration generated against a Raman intensity standard to account for overall system spectral response of the field instrument (as per ASTM E2911-13 [56]).

Baseline correction can be used to eliminate any remaining sample fluorescence, for which a number of methods have been developed [57, 58]. Finally, a Raman shift calibration of the field instrument against a Raman standard

sample (see, for example, ASTM E1840-96 [52]) is typical to account for environmental effects and ensure proper calibration in  $\text{cm}^{-1}$  space [55, 59].

Raman signal quality may degrade at either end of the Raman shift detection range, due to laser blooming, detector response roll-off, filter cutoff edges, and general vignetting by the optics. Therefore, matching results may further improve through careful trimming of the spectrum to an optimal detector ROI (region of interest).

With all corrections complete, the Raman spectrum can then be presented to the source library for matching. In-house library development is a significant investment for Raman providers, particularly as they must be both comprehensive and targeted in order to meet the needs of a specific industry. Specialist companies who provide Raman libraries are on the increase, helping to bridge the gap between spectrum and answer for OEMs and researchers alike [60, 61]. Two possible use cases for libraries are described below.

### 6.11.3 Analysis: Identification Using Libraries

The primary goal of many handheld Raman instruments is to determine the identity of unknown substances and/or validate their identities. This is done via matching of the spectral profile against a library of known substances. This requires access to an existing, validated library, or the ability for a user to create her, his, or their own library. The option of creating a dedicated user-defined library is popular, as samples under test may be very specialized, and this ensures the direct comparison of known substances against unknowns for the particular use case. This also allows the user to ensure the library spectra were collected under similar conditions and equipment to what will be used in the field; this flexibility is balanced against the cost in time and materials to generate such measurements.

Library matching may be performed using a number of possible methods. (See the chapter in Volume 2 by Zhang, Lee and Shreyer for a discussion of algorithms, and the chapter in Volume 2 by Schreyer for a discussion of libraries.) One simple method is correlation analysis, in which the two spectra are compared wavenumber for wavenumber on a common (usually interpolated) scale to determine the degree of correlation between the two spectra. Another method uses peak identification, looking at position and relative intensity to generate and compare peak lists for the unknown versus a library.

Mixture analysis is somewhat more complex, but is a valuable tool given that it can identify adulteration or improperly prepared materials, as well as aid identification of samples in a container or deliberately concealed materials by removing the container signal [62]. Mixture analysis is an iterative process: in simple terms, the closest first match is subtracted from the spectrum and the remaining difference spectrum is used to search the library for a second match. The spectrum is then reconstructed as the best linear combination of these first two matches and the routine repeated for additional matches using proprietary algorithms [63].

### 6.11.4 Analysis: Quantification Using Chemometrics

Some handheld Raman instruments, and many application-specific portable instruments, seek to answer the question “how much?” for evaluation of purity, process analytics, or diagnostics. This adds a need for access to spectral response calibration parameters for the instrument to produce an intensity-corrected spectrum. As the Raman peak intensities will be proportional to the analyte’s concentration, it is possible to develop a predictive model for concentration based on the evaluation of a series of standards across the concentration range of interest.

One approach to this is to look at the integrated peak intensity for one or more characteristic Raman peaks. As the relationship between signal and concentration is known, the user can rely on a limited calibration set and interpolate between calibration points. The downside of this method is that it is sensitive to cross talk from substances with overlapping Raman spectral peaks. This risk can be reduced by analyzing multiple characteristic peaks.

An alternative approach uses multivariate analysis (chemometrics) to look at the spectrum as a whole [64]. By using the entire spectrum rather than just individual peaks, it is possible to automatically account for cross-sensitivities and overlapping peaks. Development and execution of the model, however, are less transparent and requires much more extensive calibration effort to guard against interferences.

### 6.11.5 User Software

Above the spectral processing and identification or quantitative analysis algorithms lies the user interface – the software employed by the user to yield an answer. User software in portable Raman is almost always application specific to reduce the need for user training, knowledge, and support. On the simplest level, it must cover auto-settings, like integration time adjustment, background subtraction, and prompts for calibration against standards. It must also have built-in safeguards to identify when poor-quality data have been acquired, or when the instrument requires service.

For portable devices, the user software must make operation as simple as possible, from spectrum to identification or quantification with the push of a button. Results are displayed with the greatest clarity possible: yes/no, pass/fail, identity and confidence level, identities and concentrations, etc. The operating software may interface to a cloud analysis routine or feed into a global database for record-keeping. As libraries may evolve over time, either with added compounds or improved algorithms, mobile software should be easily updatable by end users.

Applications supporting identification or authentication will often include privacy or security aspects which must be carefully considered in software design, especially with regard to data storage and transmission. As part of application-specific support, requirements may be placed on data acquisition and storage to comply with Food and Drug Administration (FDA) regulations for electronic record-keeping (FDA 21 CFR Part 11) [65]. This is common for medical and pharmaceutical applications to ensure data integrity.

Given the inherent potential for injury with any laser-based system, Raman system software must be designed to minimize the opportunity for accidental exposure to laser radiation (FDA CFR 21.I.J.1040.10-11) [66]. While a comprehensive laser-safety protocol cannot be completely implemented in software, a well-designed user interface and rigorous use of watchdogs, timeouts, and conservative defaults will reduce chances for accidental laser exposure.

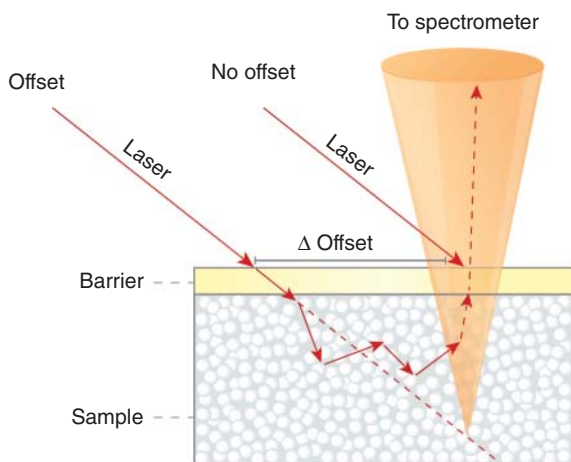
The needs for user software in handheld and portable Raman can vary widely depending on the application and operating environment, but all share a common baseline of requirements: ease of use, clear communication, and robust answers.

## 6.12 Special Cases

### 6.12.1 Fluorescence Mitigation

Although fluorescence background can be reduced through the use of excitation at wavelengths shorter than (<250 nm) or longer than (1064 nm) the autofluorescence region, it is not always practical. As such, alternative techniques have been developed to post-process data to reduce the broadband fluorescence signal and allow discrete Raman lines to be viewed [67, 68]. John Cooper et al. demonstrated in their work at Old Dominion University how multiple excitation wavelengths can be used to this effect [69]. This approach has been taken up commercially by Bruker in their Bravo instrument [21]. Recently, IPS/Metrohm presented a dual-wavelength excitation and deployment of their own mathematical algorithm to this effect also [70]. Further developments are underway at other Raman instrument vendors, and more are expected in this area in the near future.

**Figure 6.18** Representation of an SORS geometry showing “zero offset” versus “offset” laser excitation relative to the detector, with a separation distance  $\Delta S$ .



### 6.12.2 Through Barrier

Sample preparation is time consuming and can sometimes even be dangerous (as in hazmat) or costly (as in pharma), so it is highly advantageous to be able to provide reliable material identification through barriers to avoid the time or risk associated with removing a sample from its container. Matousek et al. first developed the SORS approach [71] subsequently implemented by Cobalt Light Systems [72] and acquired by Agilent, who have deployed the technology in several of their instruments [73]. By comparing measurements in which a single excitation laser at 830 nm is spatially offset to a measurement with no offset as shown in Figure 6.18, it is possible to differentiate the Raman signal of the material under investigation from the barrier or barriers in the near field. Similar approaches involving manually or dynamically adjusting laser spot size and focus distance with respect to the barrier and sample are deployed by other vendors.

In the medical field, Raman measurements through skin or tissue are gaining prevalence, with imaging geometry and excitation wavelength being tailored to the application. One such example of this is RSP Systems’ GlucoBeam technology, whereby they are able to reproducibly and accurately determine glucose concentrations through all skin tones [74].

### 6.12.3 Standoff and Proximity

Traditional Raman instrumentation are point detectors; however, for safety purposes, it may be a requirement to sample at a longer, safer working distance. With this in mind, Pendar has developed a handheld Raman instrument which provides sensing up to 1 m [75], reputed to offer limited fluorescence interference and lower laser energy than many other commercially available options. Metrohm also offers the Mira DS with an attachment designed for remote Raman identification up to 1.5 m [9]. With the increase in unmanned aerial vehicle (UAV) technology and the potential reduction in the payload of miniature Raman instrumentation, future advancements in standoff Raman are possible.

### 6.12.4 SERS

The intensity of Raman scattering is prohibitively low for a number of desired applications, including the detection of low concentrations in liquid, and of trace materials on surfaces. This limitation may be overcome using SERS, a technique which uses noble metal nanostructures to enhance the Raman signal by a factor of  $10^6$ – $10^8$  or more [76]. It requires molecules to be adsorbed on a metal surface or “captured” between coalescing nanoparticles in

a solution, but has the benefit of minimizing acquisition time and reducing the amount of sample needed [77]. Most portable Raman instruments offer a substrate accessory or can be quite easily adapted for the measurement of SERS-based materials.

One of the challenges in deploying SERS commercially is reproducibility, as the strength of the SERS signal depends strongly on the geometric characteristics of the nanostructures. This necessitates very tight control over fabrication, and the resulting properties, in order to ensure consistent answers and reliable calibration curves for quantitative measurements [78]. SERS materials must be cost-effective and easy to fabricate, or at least reusable so as to keep the cost of assay low. Commercial SERS materials must also be highly stable over time, temperature, and humidity to be a viable solution for mission-critical applications in medicine and defense.

SERS can be performed using solid substrates or colloidal nanoparticles (NP) in solution. Solid substrates are fabricated using lithography, chemical etching, or plasma deposition, and may be composed of very well-defined geometric structures or deposited nanoparticles [79–83]. These substrates offer a general enhancement in signal (the magnitude of which may vary), but are generally not fabricated to look for a specific analyte.

Colloidal NPs offer benefits in reproducibility, tunability of optical properties via particle shape and size, and the benefit of optional surface functionalization to allow use in different environments and for specific proteins, nucleic acids, bacteria, and other biological markers. The ability to conjugate NPs to be specific to a biological target also facilitates multiplexing, as has been demonstrated for bacterial pathogens using a portable Raman system [84]. They can be fabricated cost-effectively and with high reproducibility, showing promise for applications in biomedical, environmental, and food quality applications. As yet, however, few commercial suppliers of colloidal SERS sensors have emerged, though we expect significant growth in this area in the coming years [85].

## 6.13 Conclusion

Raman spectroscopy has come a long way since C.V. Raman's early experiments hinted at its existence. Seeing how far the technique has come and what it is now able to accomplish, it seems quite incredible that Raman was able to see this "feeble fluorescence" at all.

Bit by bit, technological advances have broken down the barriers to the technique's widespread application, so that the evolution of portable Raman technology reads much like an anthology of the history of applied photonics itself. Each borrowed technology has helped make Raman smaller, more powerful, and more accessible, from lasers developed for Blu-ray players to ion beam-sputtered (IBS) filter technology perfected for telecom, gratings manufactured holographically, and detectors evolved from photocopiers.

In its current incarnation, Raman spectroscopy is capable of yielding definitive answers about identity and even concentration in critical aspects of security, pharma, and health – and the possible applications are only increasing. There will always be tradeoffs between size, cost, sensitivity, and power consumption, but each new appropriation of technology and optimization of design erodes those barriers further, allowing Raman to find its way into new use cases and new fields.

This is important, as the greatest potential for the expanded use of Raman lies in its increased use by nonexperts at the point of need or the point of care. To fully harness the potential of the technique, it is important that we continue to lift the current limitations on sensitivity, fluorescence mitigation, and power levels, while simultaneously driving for even smaller point-and-shoot devices geared to the specific needs of each new application and user base.

What will this look like? It may be a smartphone with integrated Raman, or a device the size of a deck of cards interfaced with cloud computing. One thing is for certain – it will take advantage of the latest technology to deliver "good enough" performance with better-than-ever fit, form, and function.

## Acronyms and Abbreviations

ADC	Analog-to-Digital Converter
AFE	Analog Front End
ASE	Amplified Spontaneous Emission
BLE	Bluetooth Low Energy
CCD	Charge Coupled Device
CFD	Computational Fluid Dynamics
CMOS	Complementary Metal Oxide Semiconductor
COTS	Commercial Off-The-Shelf
EEPROM	Electrically Erasable Programmable Read-Only Memory
FDA	US Food and Drug Administration
FPGA	Field Programmable Gate Array
FWHM	Full Width Half Maximum
GUI	Graphical User Interface
IBS	Ion Beam Sputtering
I <sup>2</sup> C	Inter-Integrated Circuit protocol for microprocessors
IoT	Internet of Things
IP	Ingress Protection
LCD	Liquid Crystal Display
LED	Light Emitting Diode
$M^2$ factor	Beam quality factor
MM	Multimode (fiber)
MTBF	Mean Time Between Failure
NA	Numerical Aperture
NP	Nanoparticles
OD	Optical Density
OEM	Original Equipment Manufacturer
QE	Quantum Efficiency
SERS	Surface-Enhanced Raman Spectroscopy
SM	Single-Mode (fiber)
SNR	Signal-to-Noise Ratio
SORS	Spatially Offset Raman Spectroscopy
SPI	Serial Peripheral Interface
SWaP	Size, Weight and Power
TDP	Thermal Design Power
TEC	Thermoelectric Cooler
USB	Universal Serial Bus

## References

- 1 Raman, C.V. (1927). A new radiation. *Journal of Physics* 2: 387.
- 2 Singh, R. (2002). CV Raman and the discovery of the Raman effect. *Physics in Perspective* 4 (4): 399–420.
- 3 Koningstein, J.A. (2012). *Introduction to the Theory of the Raman Effect*. Dordrecht: Springer Science & Business Media.

- 4 Long, D.A. (2002). *The Raman Effect: A Unified Treatment of the Theory of Raman Scattering by Molecules*. Chichester: Wiley.
- 5 Ferraro, J.R., Nakamoto, K., and Brown, C.W. (2003). *Introductory Raman Spectroscopy*. USA: Elsevier Science.
- 6 Adar, F. (2016). Introduction to interpretation of Raman spectra using database searching and functional group detection and identification. *Spectroscopy* 31: 16–23.
- 7 ThermoFisher Scientific. *FirstDefender™ RMX Handheld Chemical Identification* [online]. <https://www.thermofisher.com/order/catalog/product/FIRSTDEFENDERRMX#/FIRSTDEFENDERRMX> (accessed 13 March 2020).
- 8 CBEx. *Snowy Range Instruments* [online]. <http://www.wysri.com/cbex> (accessed 13 March 2020).
- 9 Metrohm AG. *Mira Handheld Raman Analyzers* [online]. <https://www.metrohm.com/en-us/products-overview/spectroscopy/mira-handheld-raman-spectrometers> (accessed 13 March 2020)
- 10 ThermoFisher Scientific. *TruScan™ RM Handheld Raman Analyzer* [online]. <https://www.thermofisher.com/order/catalog/product/TSRMTRUTOOLS#/TSRMTRUTOOLS> (accessed 13 March 2020).
- 11 Chemring Group PLC. *PGR-1064® Handheld Raman Spectrometer* [online]. <http://www.chemringds.com/what-we-do/sensors-and-information/chemical-and-biological-detection/chemical-detection> (accessed 13 March 2020).
- 12 Field Forensics. *HandyRam II™ Handheld Raman Spectrometer* [online]. <https://www.fieldforensics.com/introducing-handyram-ii> (accessed 13 March 2020).
- 13 Smiths Detection. *ACE-ID Hand-Held Non-contact Chemical Identifier* [online]. <https://www.smithsdetection.com/products/ace-id> (accessed 13 March 2020).
- 14 Serstech AB. *Serstech 100 Indicator* [online]. <https://serstech.com/our-offer/serstech-100-indicator> (accessed 13 March 2020).
- 15 Coda Devices. *CDI 2 Handheld Raman Analyzer* [online]. <https://codadevices.com/cdi2> (accessed 13 March 2020).
- 16 All Safe Industries Inc. *ChemPro 100 Indicator Handheld Raman Spectrometer* [online]. <https://www.allsafeindustries.com/chempro-100i-handheld-chemical-detector.aspx> (accessed 13 March 2020).
- 17 Rigaku. *Advanced 1064 nm Handheld Raman Spectrometer for Raw Material Identification* [online]. <https://www.rigaku.com/products/raman/progeny> (accessed 13 March 2020).
- 18 B&W Tek. *Handheld Raman Spectrometers* [online]. <https://bwtek.com/technology/handheld-raman> (accessed 13 March 2020).
- 19 Agiltron. *PinPointer™ Handheld Raman Spectrometer* [online]. <https://agiltron.com/product/handheld-raman-spectrometer> (accessed 13 March 2020).
- 20 Anton Paar. *Handheld Raman Spectrometer: Cora 100* [online]. <https://www.anton-paar.com/us-en/products/details/handheld-raman-spectrometer-cora-100> (accessed 13 March 2020).
- 21 Bruker. *BRAVO Handheld Raman Spectrometer* [online]. <https://www.bruker.com/products/infrared-near-infrared-and-raman-spectroscopy/raman/braovo.html> (accessed 13 March 2020).
- 22 Agilent. *Resolve Handheld Through-Barrier Identification System* [online]. <https://www.agilent.com/en/products/raman-spectroscopy/raman-spectroscopy-systems/handheld-chemical-identification/resolve> (accessed 13 March 2020).
- 23 Agilent. *RapID Raw Material ID Verification System* [online]. <https://www.agilent.com/en/products/raman-spectroscopy/raman-spectroscopy-systems/pharmaceutical-analysis/rapid> (accessed 13 March 2020).
- 24 SciAps. *CHEM-200 Raman Analyzer* [online]. <https://www.sciaps.com/raman-spectrometers/chem-200> (accessed 13 March 2020).
- 25 Optosky. *What is Handheld Raman?* [online]. <https://optosky.com/handheld-raman.html> (accessed 13 March 2020).
- 26 CloudMinds. *Smart Raman XI* [online]. <http://airaman.com> (accessed 13 March 2020).

- 27 Wasatch Photonics. *High Performance Raman* [online]. <https://wasatchphotonics.com/product-category/spectrometers/raman> (accessed 13 March 2020).
- 28 B&W Tek. *Portable Raman Spectrometers* [online]. <https://bwtek.com/raman-technology/portable> (accessed 13 March 2020).
- 29 Horiba Scientific. *AnywhereRaman* [online]. <https://www.horiba.com/us/en/scientific/products/raman-spectroscopy/raman-spectrometers/benchtop-and-portable-raman/details/anywhereraman-tm-33805> (accessed 13 March 2020).
- 30 Agiltron. *Benchtop Raman Spectrometers* [online]. <https://agiltron.com/category/raman-chemical-detection-spectrometers/benchtop> (accessed 13 March 2020).
- 31 StellarNet Inc. *Raman Spectrometers Lasers and Probes* [online]. <https://www.stellarnet.us/systems/raman-spectrometers-lasers-and-probes> (accessed 13 March 2020).
- 32 Tornado Spectral Systems. *HyperFlux™ PRO Plus Raman Spectroscopy System* [online]. <https://tornado-spectral.com/solutions/hyperflux/> (accessed 13 March 2020).
- 33 Ocean Insight. *QE Pro Raman Series* [online]. <https://www.oceaninsight.com/products/spectrometers/raman-qepro-raman-series> (accessed 13 March 2020).
- 34 Hamamatsu. *Mini-spectrometers* [online]. <https://www.hamamatsu.com/us/en/product/photometry-systems/mini-spectrometer/index.html> (accessed 13 March 2020).
- 35 Ibsen Photonics. *FREEDOM Raman* [online]. <https://ibsen.com/products/oem-spectrometers/freedom-spectrometers/freedom-raman> (accessed 13 March 2020).
- 36 Imec. *Handheld Raman Spectrometer Technology* [online]. <https://www.imec-int.com/en/imaging-vision-systems/handheld-raman-spectrometer-technology> (accessed 13 March 2020).
- 37 IECEE (1989). *Degrees of Protection Provided by Enclosures (IP Code)*. <https://www.iecee.org/certification/overview/> (accessed 22 September 2020).
- 38 Angel, S.M., Carrabba, M., and Cooney, T.F. (1995). The utilization of diode lasers for Raman spectroscopy. *Spectrochimica Acta Part A: Molecular and Biomolecular Spectroscopy* 51 (11): 1779–1799.
- 39 Pan, M.-W., Benner, R.E., and Smith, L.M. (2006). Continuous lasers for Raman spectrometry. In: *Handbook of Vibrational Spectroscopy*. Chichester: Wiley.
- 40 Carrabba, M.M. and Rauh, R.D. (1992). Apparatus for measuring Raman spectra over optical fibers. United States Patent 5,112,127, 12 May.
- 41 Scheeline, A. (2017). How to design a spectrometer. *Applied Spectroscopy* 71 (10): 2237–2252.
- 42 Newport Corporation. *Richardson Gratings™: Plane Ruled Reflection Gratings* [online]. [https://www.gratinglab.com/Products/Product\\_Tables/T2.aspx](https://www.gratinglab.com/Products/Product_Tables/T2.aspx) (accessed 13 March 2020).
- 43 Kruschwitz, J.D. (2006). From small fish to oceans of opportunity: the story of Ocean Optics Inc. *Optics & Photonics News* 17 (2): 10–11.
- 44 Williamson, J.M., Bowling, R.J., and McCreery, R.L. (1989). Near-infrared Raman spectroscopy with a 783-nm diode laser and CCD array detector. *Applied Spectroscopy* 43 (3): 372–375.
- 45 Wang, Y. and McCreery, R.L. (1989). Evaluation of a diode laser/charge coupled device spectrometer for near-infrared Raman spectroscopy. *Analytical Chemistry* 61 (23): 2467–2651.
- 46 Pommier, C.J., Walton, L.K., Ridder, T.D. et al. (2006). *Array Detectors for Raman Spectroscopy*. Chichester: Wiley.
- 47 Heintz, R. (2019). *Back Illuminated vs. Front Illuminated CCD-Based Imaging Sensors and How it Impacts Raman Spectra, White Paper WP53197*. ThermoFisher Scientific.
- 48 Saylor, J. (2019). *SiOnyx, LLC v. Hamamatsu Photonics K.K.*, No. CV 15-13488-FDS (D. Mass. 25 July 2019). <https://www.jdsupra.com/legalnews/massachusetts-patent-litigation-wrap-up-48739>.
- 49 Hamamatsu. *InGaAs Linear Image Sensors* [online]. <https://www.hamamatsu.com/us/en/product/optical-sensors/image-sensor/ingaas-image-sensor/ingaas-linear-image-sensor/index.html> (accessed 13 March 2020).

- 50** Sensors Unlimited. *Linear Photodiode Arrays* [online]. <http://www.sensorsinc.com/products/focal-plane-arrays> (accessed 13 March 2020).
- 51** Arm Limited. *Arm Processors for the Widest Range of Devices – from Sensors to Servers* [online]. <https://www.arm.com/products/silicon-ip-cpu> (accessed 2 April 2020).
- 52** ASTM E1840-96 (2014). *Standard Guide for Raman Shift Standards for Spectrometer Calibration*. West Conshohocken, PA: ASTM International.
- 53** The United States Pharmacopeia Convention (2020). *USP 43-NF 38 General Chapter <1120>*.
- 54** European Directorate for the Quality of Medicines & Healthcare (2016). *European Pharmacopeia 8.7 Edition 2016, Chapter 2.2.48*.
- 55** Rodriguez, J.D., Westenberger, B.J., Buhse, L.F. et al. (2011). Standardization of Raman spectra for transfer of spectral libraries across different instruments. *Analyst* 136 (20): 4232–4240.
- 56** ASTM E2911-13 (2013). *Standard Guide for Relative Intensity Correction of Raman Spectrometers*. West Conshohocken, PA: ASTM International.
- 57** Cadusch, P.J., Hlaing, M.M., Wade, S.A. et al. (2013). Improved methods for fluorescence background subtraction from Raman spectra. *Journal of Raman Spectroscopy* 44: 1587–1595.
- 58** Chi, M., Han, X., Xu, Y. et al. (2019). An improved background-correction algorithm for Raman spectroscopy based on the wavelet transform. *Applied Spectroscopy* 73 (1): 78–87.
- 59** McCreery, R.L. (2006). Photometric standards for Raman spectroscopy. In: *Handbook of Vibrational Spectroscopy*. Chichester: Wiley Online Library. <https://onlinelibrary.wiley.com/doi/abs/10.1002/0470027320.s0706>.
- 60** S.T. Japan USA LLC. *Spectra Databases* [online]. <http://www.stjapan-usa.com/spectradb.html> (accessed 13 March 2020).
- 61** Wiley Science Solutions. Know It All Spectroscopy Edition Software [online]. <https://sciencesolutions.wiley.com/knowitall-spectroscopy-software/> (accessed December 2020).
- 62** Wilcox, P.G. and Guicheteau, J.A. (2018). Comparison of handheld Raman sensors through opaque containers. *Proceedings of SPIE 10629 Chemical Biological Radiological Nuclear and Explosives (CBRNE) Sensing XIX*, Orlando, FL (16 May 2018).
- 63** Yaghoobi, M., Wu, D., Clewes, R.J. et al. (2016). Fast sparse Raman spectral unmixing for chemical fingerprinting and quantification. *Optics and Photonics for Counterterrorism, Crime Fighting, and Defence XII, International Society for Optics and Photonics*, vol. 9995.
- 64** Varmuza, K. and Filzmoser, P. (2016). *Introduction to Multivariate Statistical Analysis in Chemometrics*. Boca Raton, FL: CRC press.
- 65** U.S. FDA (2003). CFR part 11: electronic records. *Electronic Signatures* 21: 1–12.
- 66** U.S. FDA (2019). 21CFR1040.10, performance standards for light emitting products. *Code of Federal Regulations* 8.
- 67** Wei, D., Chen, S., and Liu, Q. (2015). Review of fluorescence suppression techniques in Raman spectroscopy. *Applied Spectroscopy Reviews* 50 (5): 387–406.
- 68** Winfield, G. (2019). *Over the Spectral Rainbow: Christina Baxter, CEO at Emergency Response TIPS, Talks to Gwyn Winfield about the Road to Raman Riches*. CBRNe World. [https://cbrneworld.com/index.php?option=com\\_content&view=article&id=1335%3Aover-the-spectral-rainbow&catid=22%3AJuly-2019](https://cbrneworld.com/index.php?option=com_content&view=article&id=1335%3Aover-the-spectral-rainbow&catid=22%3AJuly-2019) (accessed 13 March 2020).
- 69** Cooper, J.B., Abdelkader, M., and Wise, K.L. (2013). Sequentially shifted excitation Raman spectroscopy: novel algorithm and instrumentation for fluorescence-free Raman spectroscopy in spectral space. *Applied Spectroscopy* 67 (8): 973–984.
- 70** Chimenti, R. (2017). *Dual Wavelength Applications in Portable Raman Spectroscopy*. Reno, NV: SciX.
- 71** Matousek, P., Clark, I.P., Draper, E.R. et al. (2005). Subsurface probing in diffusely scattering media using spatially offset Raman spectroscopy. *Applied Spectroscopy* 59 (4): 393–400.
- 72** Parker, W. (2018). Scanner for spatially offset Raman spectroscopy. US Patent 9,880,099.

- 73** Agilent. *Spatially Offset Raman Spectroscopy (SORS)* [online]. <https://www.agilent.com/en/technology/spatially-offset-raman-spectroscopy> (accessed 13 March 2020).
- 74** Lundsgaard-Nielsen, S.M., Pors, S.M., and Banke, S.O. (2018). Critical-depth Raman spectroscopy enables home-use non-invasive glucose monitoring. *PLoS One* 13 (5): 1–11.
- 75** Pendar Technologies. *Pendar X10* [online]. <https://www.pendar.com/products/pendar-x10> (accessed 13 March 2020).
- 76** Haynes, C.L., McFarland, A.D., and Van Duyne, R.P. (2005). Surface-enhanced Raman spectroscopy. *Analytical Chemistry* 77 (17): 338A–346A.
- 77** Langer, J., Jimenez de Aberasturi, D., Aizpurua, J. et al. (2020). Present and future of surface-enhanced Raman scattering. *ACS Nano* 14 (1): 28–117.
- 78** Fan, M., Andrade, G.F., and Brolo, A.G. (2019). A review on recent advances in the applications of surface-enhanced Raman scattering in analytical chemistry. *Analytica Chimica Acta* 1097: 1–29.
- 79** Silmeco. *SERS Substrates – SERStrate* [online]. <https://www.silmeco.com/products/sers-substrate-serstrate> (accessed 13 March 2020).
- 80** Hamamatsu. *SERS Substrate J12853* [online]. <https://www.hamamatsu.com/us/en/product/type/J12853/index.html> (accessed 13 March 2020).
- 81** Integrated Optics UAB. *SERS Substrates* [online]. <https://integratedoptics.com/products/sers-substrates> (accessed 13 March 2020).
- 82** SERSitive. *SERSitive Substrates* [online]. <https://www.sersitive.eu> (accessed 13 March 2020).
- 83** Ocean Insight. *SERS Substrates* [online]. <https://www.oceaninsight.com/products/sampling-accessories/raman-sers> (accessed 13 March 2020).
- 84** Kearns, H., Jamieson, L., Graham, D. et al. (2019). Rapid portable pathogen detection with multiplexed SERS-based nanosensors. *Spectroscopy Raman Technology* 34: 20–31.
- 85** Real-Time Analyzers. *SERS Products* [online]. <http://www.rta.biz/products/sers-products> (accessed 13 March 2020).

# 7

## Optical Filters – Technology and Applications

*Oliver Pust*

*Delta Optical Thin Film A/S, Hørsholm, Denmark*

### 7.1 Overview on the Use of Optical Filters in Spectroscopy

As the title of this chapter suggests, we look at the use of optical filters in spectroscopy. The use of optical filters includes spectrometers that detect electromagnetic radiation from the ultraviolet (UV) to the mid-infrared (MIR) part of the spectrum. It excludes gamma-ray spectrometers, X-ray spectrometers, and microwave spectrometers but also mass spectrometers. Sometimes, the term *optical* is used as a synonym for light that is visible to the human eye (380 to 780 nm)<sup>1</sup>. However, this definition seems too narrow, and we want to consider the above-mentioned larger part of the electromagnetic spectrum. Another method that we do not consider here is polarisation spectroscopy. Although such spectrometers might contain filters, they are not elemental to the method.

#### 7.1.1 Types of Spectrometers

Spectrometers can be differentiated using different parameters. One of these parameters is size or portability. The use of optical filters in large or small spectrometers can be very different. For this reason, we divide spectrometers into three categories: bench-top, portable, and hand-held spectrometers. As the book focuses on portable spectroscopy, the use of optical filters in bench-top spectrometers will be discussed only briefly. Portable spectrometers inherently comprise hand-held spectrometers as well. However, the type and purpose of optical filters in these two types of spectrometers are typically very different. For this reason, they will be discussed in different sections.

##### 7.1.1.1 Bench-top Spectrometers

Bench-top spectrometers are large, complex instruments that are designed for high performance and high flexibility. Typically, they can perform both excitation and emission scanning. For an emission scan, the excitation or illumination wavelength is kept fixed and the emission wavelength of the sample is recorded over a wider spectrum of interest either by a rotating grating or other filtering devices. For an excitation scan, this procedure is repeated for many different excitation wavelengths that are either originating from a number of discrete laser lines or light-emitting diodes (LEDs), or by filtering a broadband light source such as halogen or deuterium lamps or more recently supercontinuum lasers or laser-ignited plasma sources.

<sup>1</sup> There are many species such as birds, bees, or mantis shrimps that can see UV radiation invisible to the human eye.

### 7.1.1.2 Portable Spectrometers

Portable or miniature spectrometers are certainly the most used spectrometer types and are produced in quantities of many ten thousands per year worldwide (Tematsys reports 40,000 U sold in 2016 and projects 170,000 U in 2021, [16]). They are most often fibre-coupled, use a grating as dispersive element and a charge-coupled device (CCD) or complementary metal–oxide–semiconductor (CMOS) line scan array as detector. Miniature spectrometers can be used as stand-alone systems connected to a personal computer (PC) or laptop or as integrated part of a larger spectrometer system. The key in both cases is that there are no moving parts and that the spectrum is measured instantaneously without scanning.

### 7.1.1.3 Hand-held Spectrometers

Hand-held or micro-spectrometers are the latest step in miniaturisation. Their volume is only of the order of a few cubic centimetres or even smaller. These days they find their way into smartphones and wearables for consumer applications. Possible use cases are checking the ripeness of fruit, the freshness and unaltered condition of meat or the blood oxygen concentration.

## 7.1.2 Types of Optical Filters

Optical filters are often overlooked but nevertheless important or even crucial key components in every optical instrument – especially in spectrometers. Out of personal experience working in an optical filter company, the author can confirm that there is a widespread and increasing tendency to consider optical filters at late stages during the development process of a new optical instrument, only to find out that filters with the desired requirements cannot or can only be designed or produced at prohibitive cost.

A good optical measurement almost always starts with a high-performance optical filter.<sup>2</sup> Therefore, it is necessary to understand optical filters and consider them in the design process from the very beginning. It is also a good idea to involve the filter manufacturer of choice early on. They might have valuable insight and tips to prevent blind roads and unnecessary cost.

Not unexpectedly, there are several types of optical filters. And each type has its own features, benefits, and disadvantages. In the following, we will consider coloured glass or absorptive filters, liquid crystal tunable filters (LCTFs), acousto-optic tunable filters (AOTFs), and thin-film or interference filters. Our focus will lie on thin-film filters because they are by far the most used filters.

### 7.1.2.1 Coloured Glass Filters

The oldest type of filters are coloured glass filters. These consist of glass that is on purpose doped with metallic salts. These absorb certain wavelengths, which makes the glass appear in the complementary colour when a white light source such as the sun is viewed through the glass. It is not known who invented (coloured) glass, but it is known that production of glass including colouring was known in ancient Egypt and Phoenicia. There is evidence, which suggests that glass was already in use as far back as the fourteenth century BC [6].

The major advantage of coloured glass filters is their insensitivity to the angle of incidence (AOI) of incoming light. The spectral characteristic does not change with AOI or opening angle (OA). This makes them ideal for applications with large angles or a large field of view (FOV). Another advantage is that undesired radiation is absorbed in the filter and not reflected within the instrument, where it could propagate uncontrolled and decrease the quality of the measurement signal. At the same time, the fact that undesired light is absorbed limits the use of coloured glass filters to low light intensities. They cannot be used as filters for strong light sources because they might heat up and be destroyed quickly.

Another drawback is their low resistance to temperature and humidity. Colored glass filters degrade over time and compromise the instrument's performance. Even protective coatings cannot fully prevent this process. As

<sup>2</sup> Just consider the path of light or radiation into and through an optical instrument.

degradation is a slow and creeping process, it is typically only discovered when the adverse effects become strong. As opposed to instruments equipped with modern hard-coated thin-film interference filters, instruments with coloured glass filters require regular check-ups and periodic exchange of the filters, which incurs increased cost of ownership and potentially negative user experience.

While coloured glass filters can have deep blocking depending on their thickness, it is not possible to freely design their spectral performance. Deeper blocking goes hand in hand with reduced transmission. Their cut-on or centre wavelengths are determined by the metal salts, and the selection is limited. Last but not least, some materials of coloured glass filters are covered by RoHS<sup>3</sup> (Restriction of Hazardous Substances) regulations, and although there are exemptions for now, this might not be the case in the future. Many manufacturers of optical instruments have preemptively begun to exchange coloured glass filters with thin-film filters. This is not always possible without at least a partial redesign of the instrument due to the different characteristics of the two filter types.

#### 7.1.2.2 Liquid Crystal Tunable Filters

LCTFs use electrically controlled liquid crystal elements to select a specific wavelength of light for transmission through the filter while excluding others based on wavelength-dependent polarisation created in birefringent crystals. This type of filter is ideal for use with imaging devices, because it offers a large clear aperture, excellent imaging quality, and a simple linear optical path. A typical LCTF is constructed from a stack of fixed filters consisting of interchanging birefringent crystal/liquid crystal combinations and linear polarisers. The spectral region passed by LCTFs depends on the choice of polarisers, optical coatings, and the liquid crystal characteristics.

#### 7.1.2.3 Acousto-optic Tunable Filters

An AOTF uses an acousto-optical crystal that consists of an optically anisotropic crystal of tellurium dioxide, lithium niobate, or quartz that is coupled to a piezoelectric crystal that acts as an acoustic transducer. When a radio frequency (RF) signal in the range of 150–300 MHz is applied to the piezoelectric crystal, an ultrasonic sound wave is generated that travels through the optical crystal and changes its refractive index. The change in refractive index changes the angles in which light rays are diffracted. Different wavelengths can be selected at different angles at the exit side of the crystal.

#### 7.1.2.4 MEMS-based and Piezo-Actuated Fabry–Perot Tunable Filters

VTT has developed tunable filters that are based on the Fabry–Perot interferometer principle [2]. The length of a cavity (here air gap) between two mirrors determines the wavelength that is transmitted through the Fabry–Perot interferometer. When the cavity length is changed, the transmitted wavelength changes as well and a tunable filter is achieved. The micro-electro-mechanical systems (MEMS)-based Fabry–Perot tunable filter can be mass-produced and is applicable to small sensors such as point detectors or imaging sensors in smart phones, while the piezo-actuated Fabry–Perot tunable filter can be produced with larger clear apertures. A general limitation of the Fabry–Perot approach is the small tuning range of the filters. In the first case, it is limited by the free spectral range and in the latter case to approximately  $\pm 10\%$  around the centre wavelength.

#### 7.1.2.5 Thin-Film Filters

While the phenomenon of constructive and destructive interference of light waves at the surfaces of thin films has been known for several centuries, it was only in 1939 that Walter H. Geffcken created the first interference filters using dielectric coatings [8].

<sup>3</sup> Restriction of the Use of certain Hazardous Substances in Electrical and Electronic Equipment (RoHS-Directive 2011/65/EU).

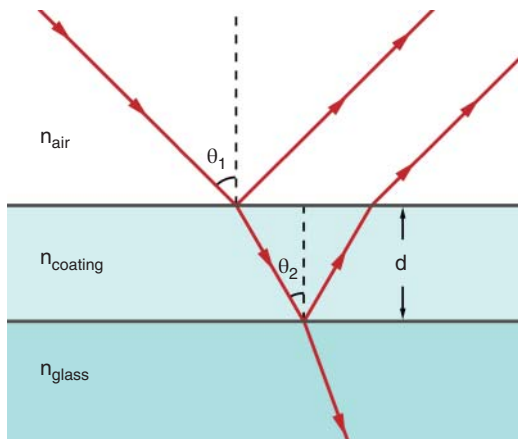


**Figure 7.1** A wave of light reflecting off the upper and lower boundaries of an anti-reflection coating on glass. The reflected waves interfere with one another.

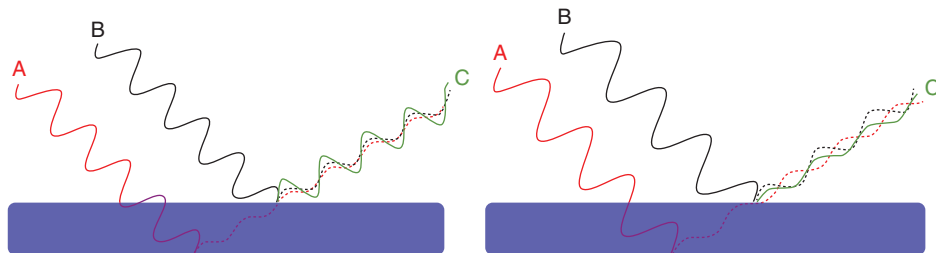


**Figure 7.2** Constructive and destructive interference of two light waves that are partially reflected at the interfaces of a thin film. (Jhbde [BY-SA <https://creativecommons.org/licenses/by-sa/3.0/>]).

#### 7.1.2.5.1 Principle of Thin-Film Interference

Thin-film interference occurs when light waves reflected off boundaries between thin films of materials with different refractive indices interfere with one another (see Figure 7.1). In this process, the intensity of the resulting light wave can either be enhanced (constructive interference) or attenuated (destructive interference).

When the film thickness is an odd multiple of one-quarter wavelength of the light wave, the reflected waves from both surfaces interfere destructively (see Figure 7.2 right). As the wave can no longer be reflected, it is completely transmitted through the thin film. When the film thickness is a multiple of a half-wavelength of the light, the two reflected waves interfere constructively, enhancing the reflection and attenuating the transmission (see Figure 7.2 left).

An odd-numbered sequence of layers of quarter-wave thickness with alternating high and low refractive index is called a quarter-wave stack and is the basic building block of any filter type. The structure reflects strongly over a region around that wavelength for which the layers are quarter waves, usually known as the reference wavelength. By combining quarter-wave stacks with different reference wavelengths and modifying them by modern methods such as the needle optimisation technique [17], it becomes possible to design filters with almost any desired spectral performance – manufacturability, especially economical, is a separate topic though and the subject of ongoing research and technical development. For an in-depth discussion of thin-film filter technology, refer to [12].

#### 7.1.2.5.2 Angular Sensitivity of Thin-film Filters

A well-known but nevertheless often neglected inherent property of thin-film filters is their angular sensitivity. The wavelengths, at which constructive and destructive interference occurs, depend on the optical path lengths through the media or the phase thicknesses in a multilayer coating. It is obvious that the phase thickness  $\Phi$  changes

with the AOI:

$$\Phi = \frac{2\pi}{\lambda} n(\lambda) d \cos \theta \quad (7.1)$$

where

- $\lambda$  is the wavelength of light,
- $n(\lambda)$  is the refractive index of the layer,
- $d$  is the physical thickness of the layer,
- $\theta$  is the angle of light propagating in the layer.

The angle of light in the layer is linked to the AOI in air  $\gamma$  by Snell's law:

$$n \sin \theta = \sin \gamma \quad (7.2)$$

Hence,

$$\cos \theta = \sqrt{1 - \left( \frac{\sin \gamma}{n} \right)^2} \quad (7.3)$$

The coating mostly consists of a high number of layers, alternating between two materials with a high refractive index  $n_H$  and low refractive index  $n_L$ . However, it is acceptable to introduce an effective refractive index, representing the whole multilayer structure:

$$n_{\text{eff}} \approx \sqrt{n_H \times n_L} \quad (7.4)$$

The coating treated in Figure 7.3 is made of  $Ta_2O_5$  and  $SiO_2$ . At a wavelength of 720 nm, those materials have refractive indices of approximately 2.1085 and 1.4771, giving an effective refractive index of 1.7648.

Assuming a wavelength of 721.5 nm at normal incidence (the black curve at the  $T = 50\%$  point), we may calculate the following values for the rest of the angles shown in Figure 7.3 with the formula:

$$\lambda_\theta = \lambda_0 \frac{\sqrt{n^2 - \sin^2 \theta}}{n} \quad (7.5)$$

$$\begin{aligned} \lambda(\theta = 5^\circ) &= 720.6 \text{ nm}, & \lambda(\theta = 10^\circ) &= 718.0 \text{ nm}, \\ \lambda(\theta = 15^\circ) &= 713.7 \text{ nm}, & \lambda(\theta = 20^\circ) &= 707.8 \text{ nm}, \\ \lambda(\theta = 25^\circ) &= 700.5 \text{ nm}, & \lambda(\theta = 30^\circ) &= 691.9 \text{ nm}. \end{aligned}$$

The values fit the curves quite well. However, polarisation effects clearly cause a severe distortion of the edge at angles of incidence larger than  $20^\circ$ . It is recommended to keep angles of incidence lower than  $15^\circ$ . The curves shown in Figure 7.3 tell why.

A similar effect is caused by cone half-angle (CHA) or OA, where  $OA = 2 \text{ CHA}$ . The effects of a non-collimated beam passing through an interference filter can be considered as averaging the effects of angles of incidence across a certain angular range. Figure 7.4 shows the passband of a nominally 17-nm-wide (full width at half maximum (FWHM)) bandpass filter. With increasing OA, the centre wavelength shifts toward shorter wavelengths, the edges of the passband become less steep, and as a consequence peak transmission drops because the edges cross each other earlier. It is noteworthy though that FWHM increases only slightly from 17 to 20 nm. It is not recommendable to use an OA larger than  $\pm 16^\circ$  in most cases, as the effects of increasing OAs grow progressively. The same is true for the effects of AOIs.

The blue-shift with increasing AOI can be exploited to achieve wavelength tunability in an optical system. By tilting the filter in the beam path, a bandpass filter can be tuned to a different centre wavelength.<sup>4</sup> However, as

<sup>4</sup> This effect is also used to compensate for the production tolerances within a batch of extremely narrow bandpass or Raman long-wave pass filters.

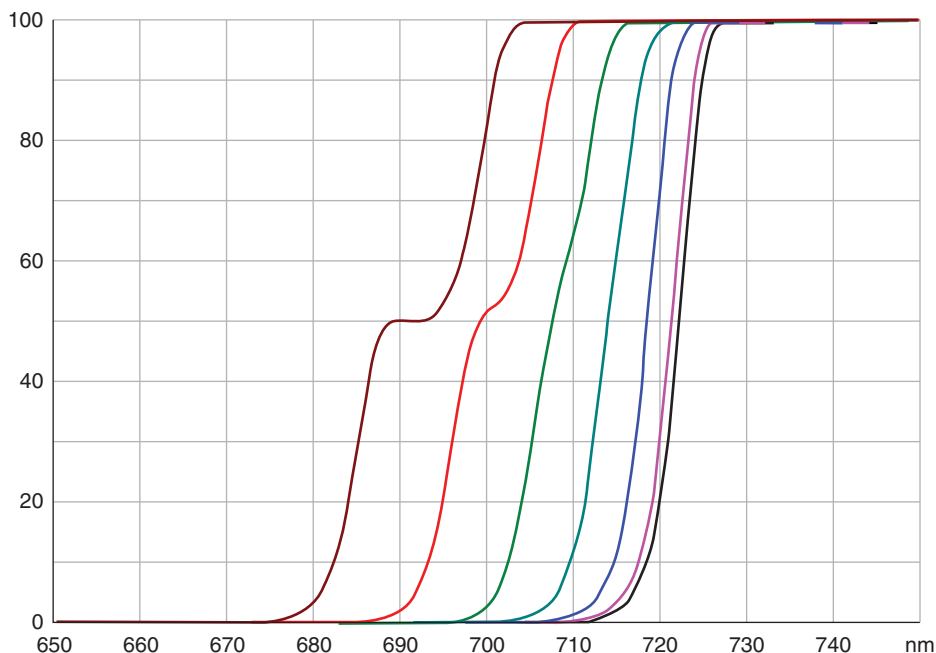


**Figure 7.3** Angular dependency of a long-wave pass filter in steps of  $5^\circ$  from  $\text{AOI} = 0^\circ$  (black curve) to  $\text{AOI} = 30^\circ$  (brown curve). Source: Courtesy of Delta Optical Thin Film A/S.

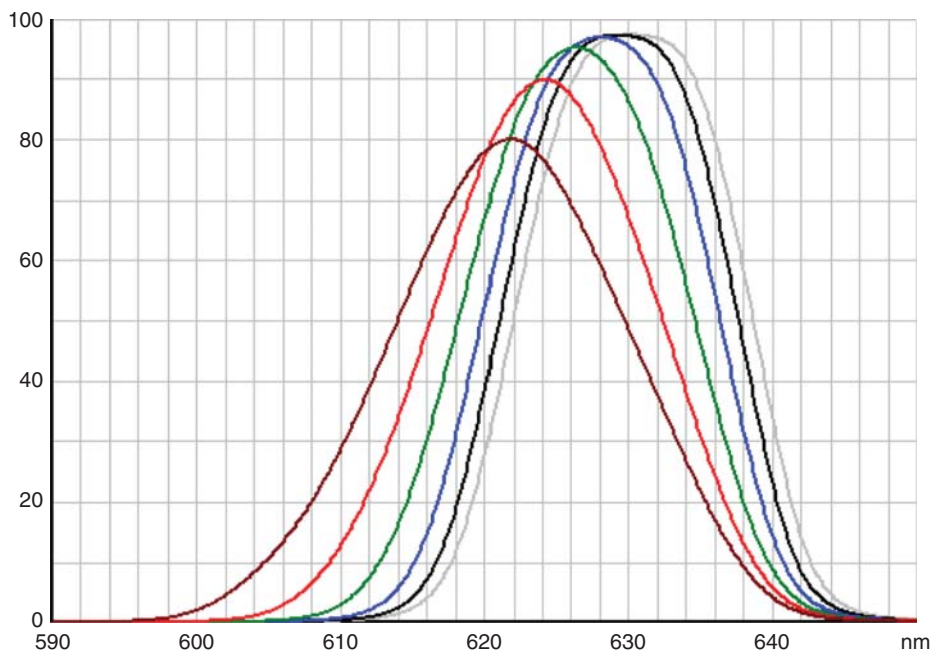


**Figure 7.4** Predicted bands formed for opening angles (OA) of  $\pm 0^\circ$  (light-grey),  $\pm 8^\circ$  (black curve),  $\pm 12^\circ$  (blue),  $\pm 16^\circ$  (green),  $\pm 20^\circ$  (red),  $\pm 24^\circ$  (brown). The centre wavelength of the band shifts toward shorter wavelengths as the OA increases, and the band becomes less box-shaped. Source: Courtesy of Delta Optical Thin Film A/S.

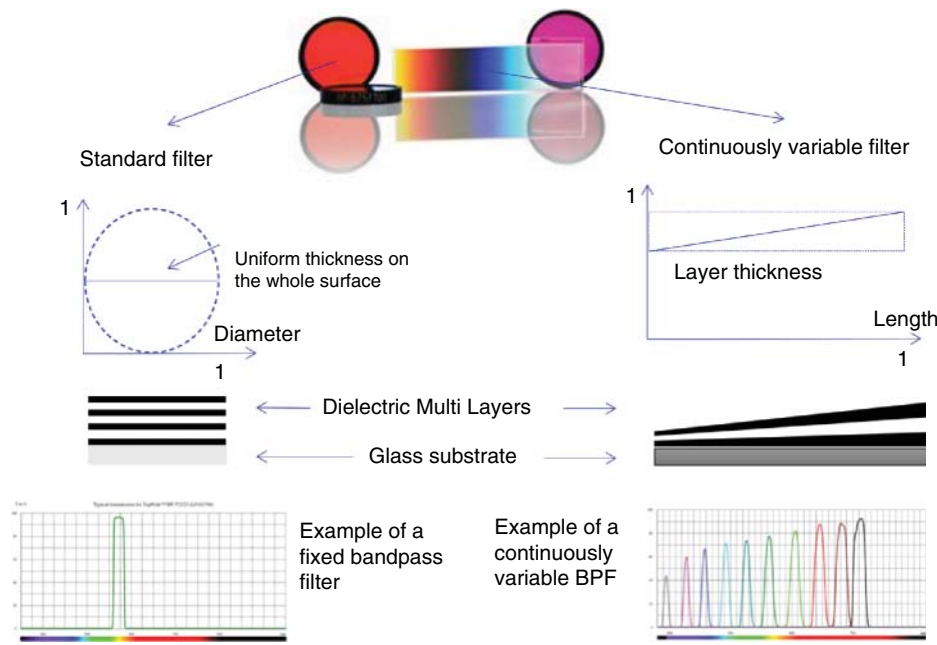


**Figure 7.5** Construction principles of standard fixed and continuously variable filter.

shown above, the tuning range is limited to a few tens of nanometres before the adverse effects become too large. An elegant and purposeful way of realising tunable filters is described in the next paragraphs.

#### 7.1.2.5.3 Continuously Variable Filters

For many years, interference filters were produced as fixed wavelength, that is spatially homogeneous filters. Irrespective of the specific type of filter (short-wave pass, long-wave pass, or bandpass filter), the goal of filter production was and is to yield filters that have a uniform spectral characteristic across their clear aperture and a high percentage of identical filters within a batch.

The centre wavelength of a bandpass filters depends on the optical thickness of the individual thin-film layers within the coating stack. As such, it is an obvious idea to create a variable filter by changing the total thickness of the stack continuously in one spatial dimension of a filter (Figure 7.5).

The thickness and wavelength gradients can be established along a circle segment (circular variable filter) or a straight line (often called linear variable filter). In both cases, the spectral characteristics change *continuously* along one spatial dimension of the filter. These filters are not segmented (butcher block filters) but are truly continuous. The word *linear* in linear variable filter must not be confused with the property of wavelength dispersion. The dependency between wavelength and position on the filter is not necessarily linear but can, for example, also on purpose be exponential (see Figure 7.6).

Like traditional filters with fixed wavelength characteristics, continuously variable filters (CVFs) can be produced as edge or bandpass filters and as dichroic beamsplitters as well. Although CVFs have been known and manufactured for more than a couple of decades, their spectral performance reached the necessary level for spectroscopic applications and durability for use with strong light sources only in recent years. Early CVFs were often produced with coloured glass or included thin metal layers (induced transmission filters) to achieve out-of-band blocking. This limited transmission, lifetime, and laser-induced damage threshold (LIDT).

Advances in design and production technology made it possible to produce CVFs that reach the same spectral performance as traditional fixed-wavelength filters. Modern CVFs reach transmission and blocking levels, and

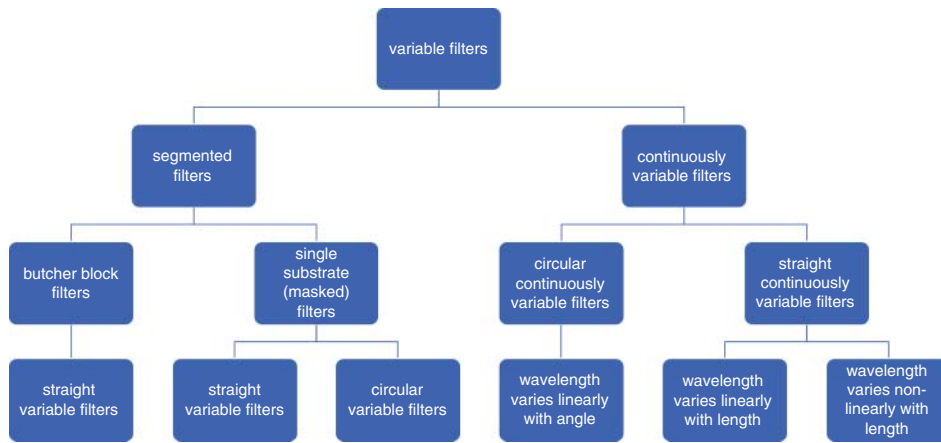


**Figure 7.6** Classification and nomenclature of variable filters (author's suggestion).

edge steepness that are sufficient for demanding fluorescence measurements. Figures 7.7 and 7.8 show the performance of continuously variable long-wave pass filters (CVLWPs) and continuously variable short-wave pass filters (CVSWPs). Each of the filters can be used separately. Combining CVLWPs and CVSWPs enables the construction of bandpass filters that can be tuned continuously with centre wavelengths across several hundred nanometres, with the added benefit of tunable bandwidth. As CVF monochromators, these filters are for example used in fluorescence microplate readers or laser scanning microscopes.

The filters offer blocking better than OD<sup>5</sup> over the complete reflection range of several hundred nanometres. It is possible to increase the blocking to beyond OD6 by placing two identical CVF in series. The filters are coated on single fused silica substrates for minimal autofluorescence and high LIDT, which makes it possible to use them as wavelength selector for high-power broadband light sources such as supercontinuum lasers. Examples of the use of CVFs will be described in Sections 7.2.3, 7.3, 7.4.3, 7.4.4.

## 7.2 Optical Filters as Auxiliary Filters

Optical filters have two main uses in spectroscopy. They can either be the primary wavelength-selective elements or serve as auxiliary filters for different purposes. In the latter use case, they do not replace gratings but still perform important additional functions in a spectrometer.

### 7.2.1 Neutral Density Filters

Neutral density (ND) filters are used to control the light's intensity before it reaches the detector. Sometimes, the light intensity is too high and will saturate the sensor. To prevent saturation, an ND filter is inserted into the light path to decrease the light intensity to a level close to the saturation level. This is achieved by selecting the ND filter that has the optimal extinction ratio from a series of different filters, or using a variable ND filter. The word neutral refers to the ideal property of an ND filter to offer a constant extinction ratio across a certain wavelength range. However, in practice, there will be some variation of the extinction ratio with wavelength that should be taken into account.

<sup>5</sup> OD stands for optical density and is a quantitative measure expressed as a logarithmic ratio between the radiation falling upon a material  $I_0$  and the radiation transmitted through a material  $I_1$ , more specifically  $OD = -\log_{10}(I_1/I_0)$ .

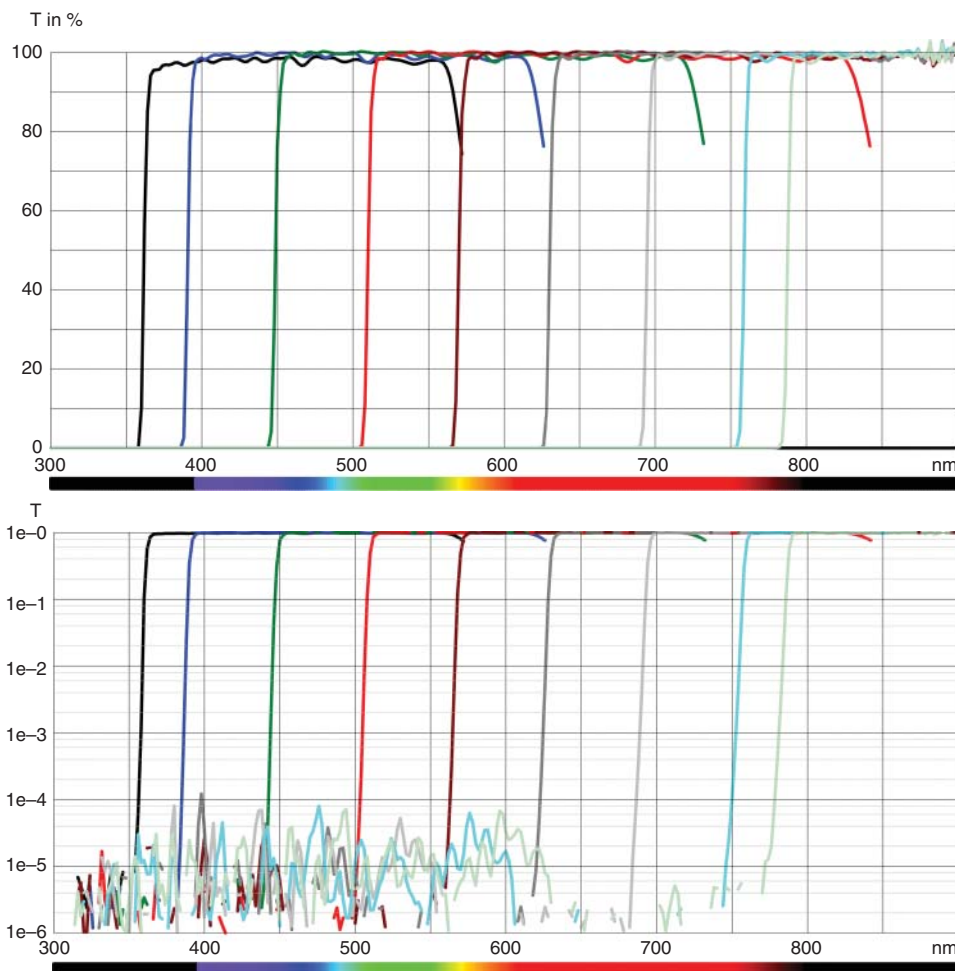


**Figure 7.7** Measured transmission and blocking performance of modern continuously variable long-wave pass filter. The spectra were measured with a PerkinElmer 900 spectrophotometer using a 200  $\mu\text{m}$  narrow slit at nine discrete locations to demonstrate the spectral properties. Given the continuous nature of the filter, any other cut-on wavelength can be found at intermediate positions. Source: Courtesy of Delta Optical Thin Film A/S.

### 7.2.2 Optical Filters as CCD/CMOS Equalizer Filters

Silicon-based photo detectors detect radiation between approximately 200 and 1200 nm with their maximum sensitivity between 500 and 600 nm. The spectral sensitivity curve can be optimised for high UV or near-infrared (NIR) sensitivity at the expense of the overall sensitivity or sensitivity in other wavelength ranges. For many applications, it is desired to work with a spectral sensitivity curve that spectrally is as flat as possible. This can be achieved by equaliser filters, also called gain flattening filters.

Figure 7.9 shows a typical curve of such a filter. In wavelength regions where the detector has low sensitivity (UV and NIR), the filter has high transmission. As the sensitivity of the detector increases from UV and NIR toward its maximum, the transmission level of the filter gradually decreases, so that the product of sensor sensitivity and filter transmission becomes flat.

Ideally, the filter curve would follow the inverse of the sensor sensitivity curve (see Figure 7.10, orange curve). The result would be a combined response curve that is flat in the whole specified wavelength range (see Figure 7.10,

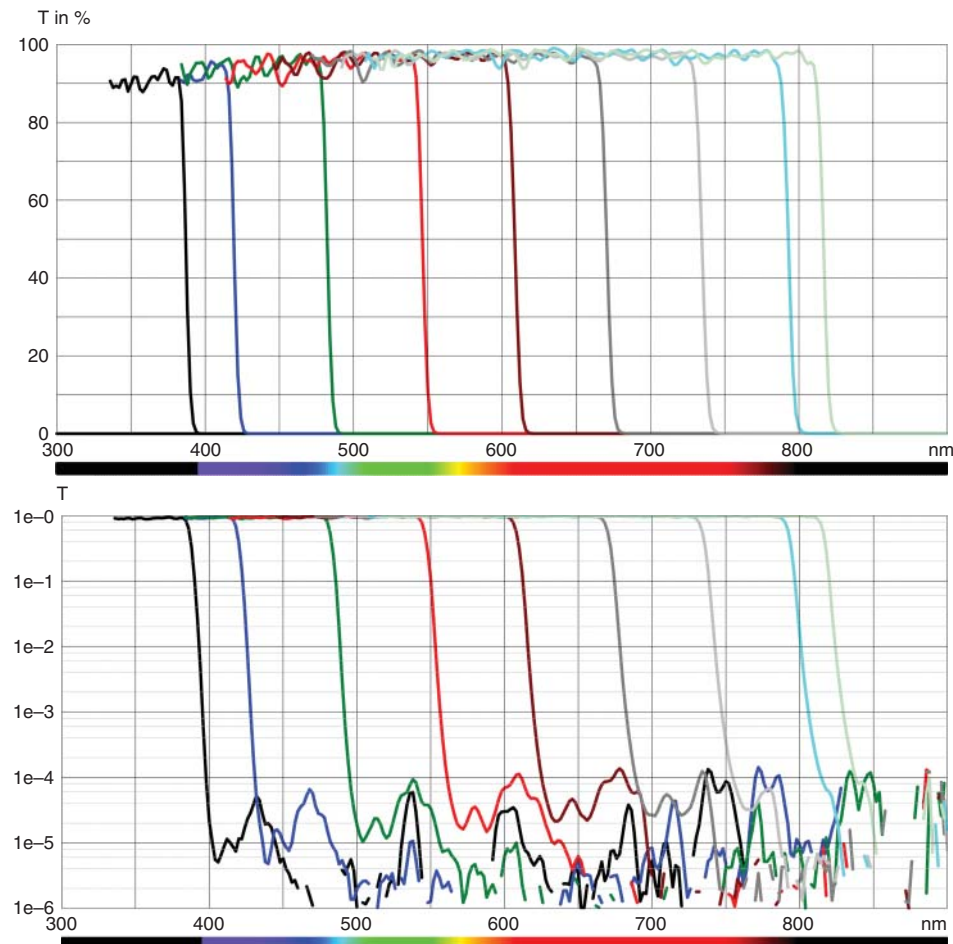


**Figure 7.8** Measured transmission and blocking performance of modern continuously variable short-wave pass filter. The spectra were measured with a PerkinElmer 900 spectrophotometer using a 200  $\mu\text{m}$  narrow slit at nine discrete locations to demonstrate the spectral properties. Given the continuous nature of the filter, any other cutoff wavelength can be found at intermediate positions. Source: Courtesy of Delta Optical Thin Film A/S.

green curve). An undesired consequence would be that the filter transmission would drop below 10 % where the sensor sensitivity is high to compensate for the low sensitivity in UV and NIR.

In practice, a compromise is made between overall flatness and combined response level (see Figure 7.11). The filter transmission remains high where the sensor sensitivity has its highest gradients. In the example shown here, the filter transmission is allowed to drop to 30 %, which in turn keeps the combined response flat between 240 and 950 nm. Other compromises are possible with different filter designs. It is noteworthy that this approach requires that arbitrary filter transmission characteristics can be designed and produced. Both has become possible in recent years with new design techniques for synthesising filter performance, and coating technologies that allow very accurate control of the thickness of individual coating layers.

### 7.2.3 Optical Filters as Order-Sorting Filters

The wavelength dispersive element in most mini-spectrometers is a grating. Besides the primary wavelengths ( $\lambda_0$ ) that are to be detected, gratings also generate wavelengths at higher orders  $n$ . These higher-order wavelengths are

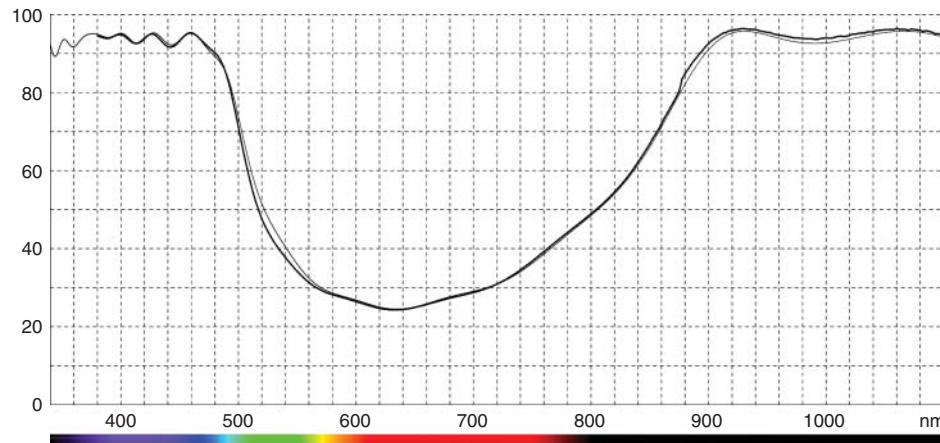


**Figure 7.9** Spectral curve of a realised equaliser filter. Source: Courtesy of Delta Optical Thin Film A/S.

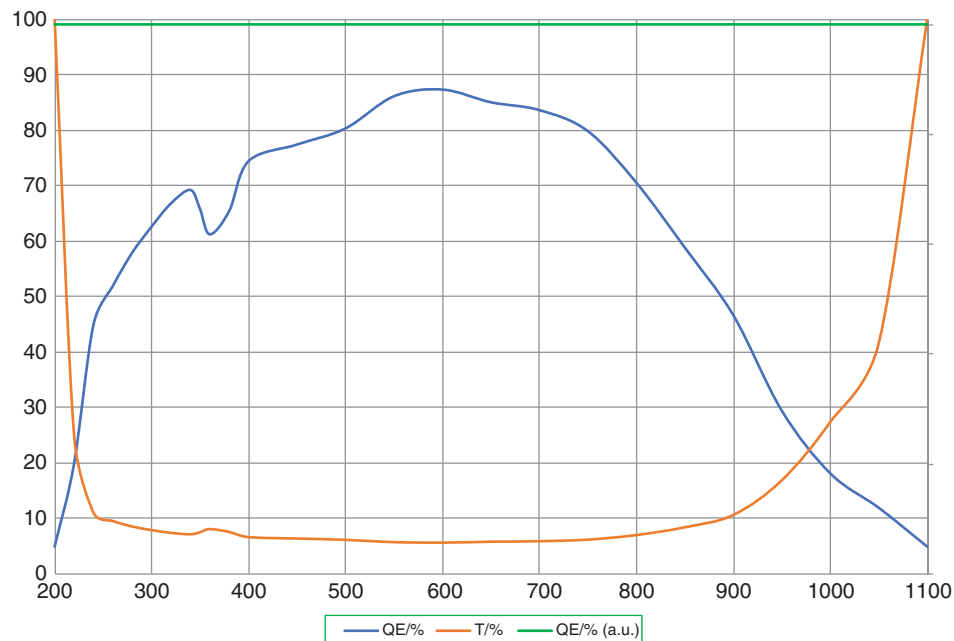


**Figure 7.10** Ideal equaliser filter: quantum efficiency curve (blue), filter curve (orange), combined response (green).

fractions of the primary wavelength ( $\lambda_n = \lambda_0/n$  with  $n = [2, 3, 4, \dots]$ ). These higher orders are spatially separated by angle, if the spectrometer covers less than one octave ( $\lambda_2/\lambda_1 < 2$ ). If  $\lambda_2/\lambda_1$  exceeds a factor of 2, the orders begin to overlap (see Figure 7.12) and need to be removed or *sorted out* before they reach the detector. For spectrometers that cover less than one octave, this can easily be done by a simple long-wave pass filter with a fixed cut-on wavelength. In this case, the cut-on wavelength must just be a little smaller than the lower wavelength of the spectrometer.

For spectrometers that cover more than one octave, a more advanced order-sorting filter is needed. Traditionally, segmented order-sorting filters were used. These could either be different segments of glass with long-wave pass filters of different cut-on wavelengths that were glued together, or a single substrate that was coated with areas

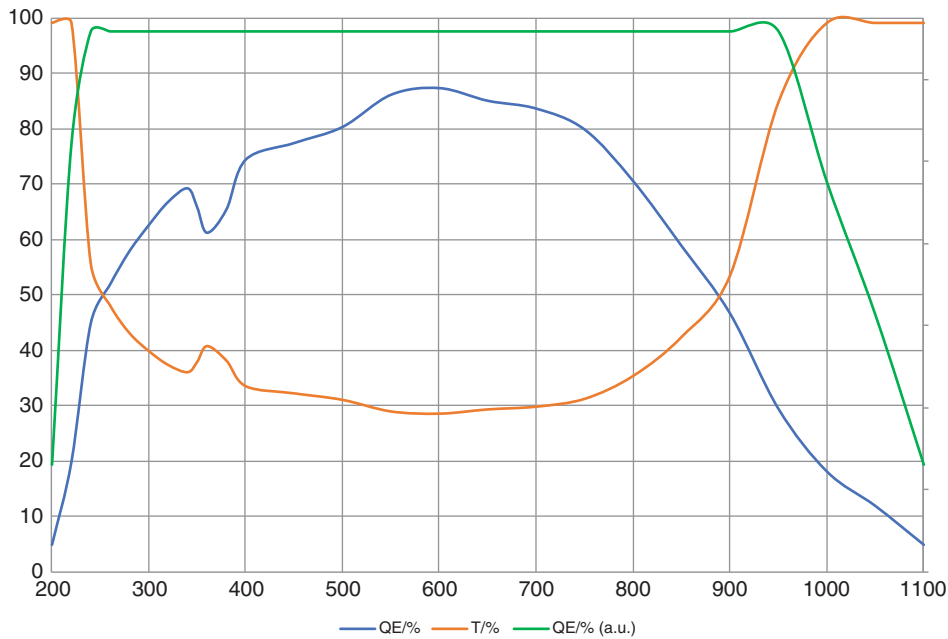
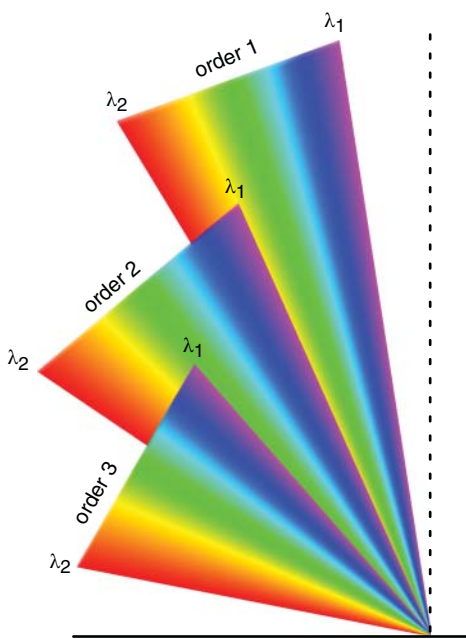


Figure 7.11 Real equaliser filter: quantum efficiency curve (blue), filter curve (orange), combined response (green).

Figure 7.12 Overlapping orders in a grating spectrometer.



with long-wave pass filters of different cut-on wavelengths (see red curve in Figure 7.13). In either case, there are discontinuities where the glass segments or filter coatings meet. These discontinuities can also be seen in measured spectra, typically as dips. For a standard UV–NIR spectrometer that makes use of the sensitive wavelength range of silicon-based detectors (200–1100 nm), three segments are needed.



**Figure 7.13** Comparison of segmented and continuously variable order-sorting filters (horizontal axis: detector length in mm, vertical axis: wavelength in nm): first order (orange curve), second order (yellow curve), third order (green curve), cut-on wavelength of segmented order-sorting filter (red curve), cut-on wavelength of continuously variable order-sorting filter (blue curve).

A more advanced and elegant way are continuously variable order-sorting filters (CVOSFs) because their coating is continuous, and the long-wave pass cut-on wavelength changes continuously along the filter (see blue curve in Figure 7.13). Furthermore, a CVOSF suppresses more stray light because the cut-on wavelength moves together with the dispersion of the grating, whereas with segmented filters the distance from the cut-on wavelength to the first-order one wants to transmit gradually increases and allows more stray light to pass through the filter.

Another advantage of CVOSFs is their insensitivity to misalignment with respect to their intended position in front of the detector. In Figure 7.13, misalignment can be seen as a horizontal shift of the filter curve. It is obvious that the red curve will quickly intersect with either the first-order curve or the second-order curve. A segmented order-sorting filter that is less sensitive to misalignment eventually requires a fourth segment. The CVOSF on the other hand can be misaligned by several millimetres before the curves intersect. However, for both filter types, an additional safety margin needs to be kept because of the finite steepness of the filter edge. If the nominal  $\lambda_{50\%}$  wavelength<sup>6</sup> is positioned too close to the first order, the filter transmission has not yet reached its maximum and signal strength is lost. If the nominal  $\lambda_{50\%}$  wavelength is positioned too close to the second order, the blocking has not yet reached its maximum and higher-order radiation will reach the detector.

### 7.3 Optical Filters as Complementary Filters

Gratings are today the standard component in spectrometers to analyse light by its spectral content. They can be used in a fixed configuration with linear arrays in mini-spectrometers (as described in the previous subsection) or as rotating elements with collimated light sources (excitation monochromator) and with point detectors (emission monochromators) in larger spectrometers.

<sup>6</sup> There are two definitions of  $\lambda_{50\%}$ : (a)  $\lambda_{50\%}$  is the wavelength at which transmittance has reached 50% or (b) where the filter achieves 50% of the maximum transmission. For the discussion of CVOSF, this distinction is not critical because CVOSFs have approximately 95% transmission and because the safety margin of CVOSF is large.

In principal, the quality of spectral measurements is affected by two factors: the occurrence of second- and higher-order reflections from the grating, and scattered light reaching the detector. Inaccuracies in a variety of measurements between 1 and 10% are typical without proper calibration and suppression of stray radiation. This scattered light can arise from any optical surface, from light leaks, and insufficient baffles, but the dominant source of scattered light is the diffraction grating itself.

Optical bandpass filters that are centred at the selected wavelengths of the excitation or emission gratings can help suppress most of the scattered light. During a wavelength scan, a series of bandpass filters needs to be moved sequentially into the beam path – either on a slider or filter wheel. The more the scattered light needs to be suppressed, the narrower the filters need to be, the more filters are needed to cover a given wavelength range. In practice, a compromise is chosen to keep the spectrometer feasible.

Another way of reducing scattered light is a second monochromator stage. For applications requiring the highest levels of performance, a double grating is used whereby the light from the first grating is passed through a second unit, reducing scatter and giving even greater resolution. However, each optical unit which the incident light impinges on results in a loss of energy. Hence, there is a trade-off between wavelength resolution and the intensity of the emitted light. In addition, the second grating makes the spectrometer bulky, expensive, prone to misalignment, and reduces its sensitivity because of the loss in signal strength.

Edinburgh Biosciences has developed an alternative approach using a pair of continuously variable edge filters to form a fully tunable bandpass filter – both in centre wavelength and bandwidth. Although the described solution is not applied in a portable instrument, it is mentioned here to demonstrate the usefulness of CVF in spectroscopy.

Figure 7.14 shows the typical setup of a single-monochromator spectrometer that is complemented with additional tunable bandpass filters. The tunable bandpass filters consist of a pair of a CVLWP filter and a corresponding CVSWP filter with spectral properties as shown in Figures 7.7 and 7.8. The filters are mounted on computer-controlled linear drives and placed in series in the beam path of the spectrometer. The rising and the falling edges of the edge filters form a bandpass filter whose centre wavelength and bandwidth can continuously and independently be tuned by either moving the filters in the same direction or in opposite directions. The centre wavelength can be adjusted across several hundred nanometres, and the bandwidth can be as narrow as a few nanometres or as wide as several dozens of nanometres. A full wavelength scan can automatically be performed by automatically tuning the centre wavelength to those of the grating and selecting a bandwidth that is appropriate for the measurement, and scattered light can be suppressed while the signal can be maximised.

The advantage of this approach over both a single- and a double-monochromator is clearly demonstrated at the example of the cyclohexane Raman spectrum that was measured with the EI FLS920 single monochromator fluorescence spectrometer (Figure 7.14). The measurement of high-resolution Raman scattering requires very high sensitivity and a clean background level as the probability for a Raman scattering event is only in the order of  $10^{-6}$ . Cyclohexane exhibits several Raman peaks between 509.8 and 586.1 nm (Raman shift between 384.1 and  $2938.3\text{ cm}^{-1}$ ) when excited at 500 nm.

A high level of background is observable in the spectrum measured without filters (Figure 7.14, red/upper curve), and noise renders the weak peaks almost unobservable. The introduction of the synchronously tuned variable bandpass filters shows a significant reduction of the background noise (Figure 7.14, green/middle curve) by one order of magnitude (because of the deep broadband blocking of the CVFs) without compromising the signal strength (because of the high transmittance in the passband of the CVFs). The resulting reduction in photonic noise makes the weak peaks observable (see e. g. the weak peak at 576.8 nm). The signal-to-noise ratio (SNR) improves by a factor of 3.4 for the strongest peak. Obviously, even better ratios are achieved for the weaker peaks. For comparison, the same experiment was repeated on a double-monochromator system (Figure 7.14, blue/lower curve). The use of two additional diffraction gratings in the beam path severely reduces the signal strength which – despite the reduction in background levels – renders the weaker peaks unobservable (for more details refer to [14]) (Figure 7.15).

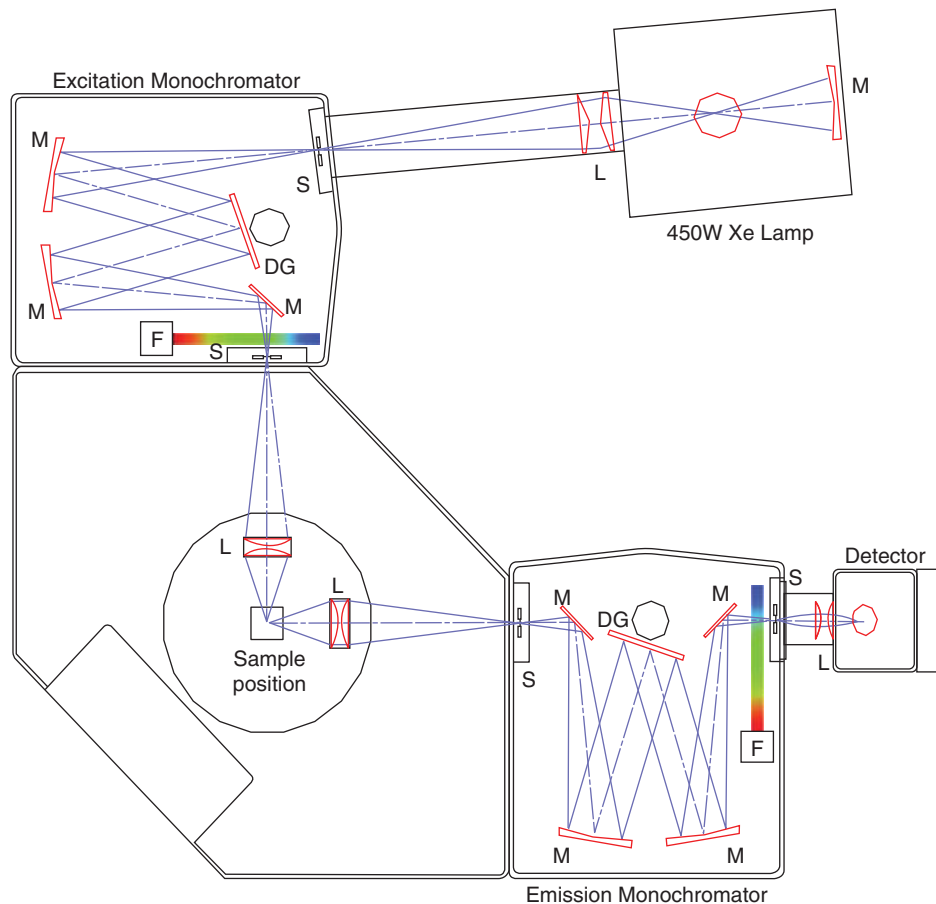


**Figure 7.14** Typical setup of a spectrometer with single excitation and emission monochromators complemented with additional tunable bandpass filters. M: Mirror, L: lens, S: slit, DG: diffraction grating, F: new continuously variable filter stages. Source: Courtesy of Edinburgh Biosciences.

## 7.4 Optical Filters as Wavelength Selective Element

Optical filters are often found in bench-top spectroscopic instruments, such as micro-plate readers, as wavelength-selective elements. They are mounted on sliders or in filter wheels to facilitate wavelength selection in the excitation or emission channel. Even though filters have advantages over gratings because of their potentially much higher light grasp (for definition and details see [12] pp. 659), only a limited number of fixed filters can be installed in an instrument at a time. This limits the flexibility of the instruments and makes signal optimisation very difficult and time-consuming. BMG Labtech has developed a new generation of multi-mode micro-plate readers that use CVF and offer the high light grasp and thus sensitivity of filter-based micro-plate readers and at the same time full tunability of a grating-based instrument with the added benefit of narrow and wider passbands, which allows collection of a stronger signal. In addition to the tunable bandpass filters described in the previous section, the reader also includes a continuously variable dichroic (CVD) mirror that separates the excitation from the emission light in an epifluorescence setup (see Figure 7.16).

In hand-held spectrometers on the other hand, there is not enough space for a filter solution with moving parts. For this reason, hand-held spectrometers were until recently only based on gratings. Recent developments in the

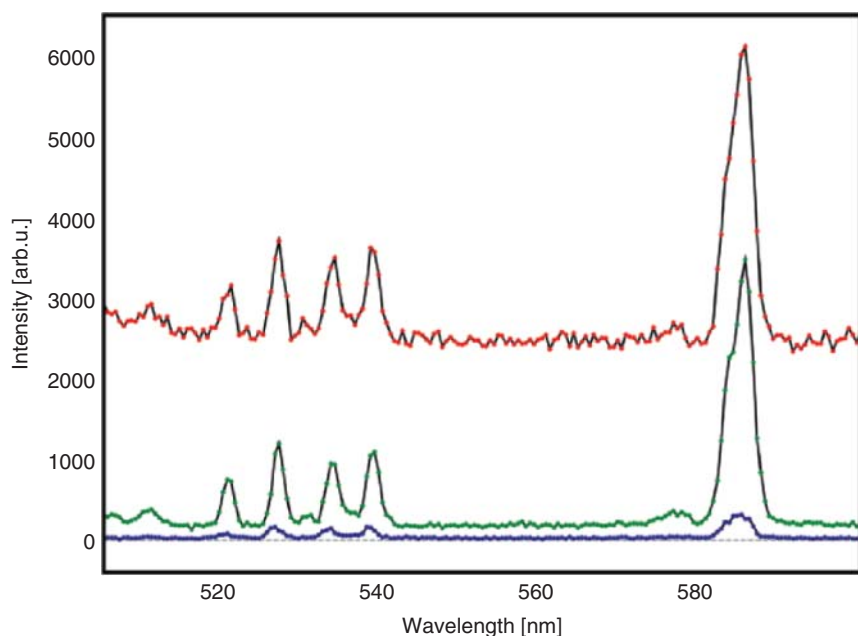


**Figure 7.15** Raman spectra of cyclohexane measured at an excitation wavelength of 500 nm. The red curve (upper) denotes a spectrum taken at 1 nm spectral resolution without the use of variable filters. The green spectrum (middle) is taken with the variable filters in place. For comparison, the same measurement was repeated on a double-monochromator spectrometer (blue curve – lower). The signal is severely reduced. Source: Courtesy of Edinburgh Biosciences.

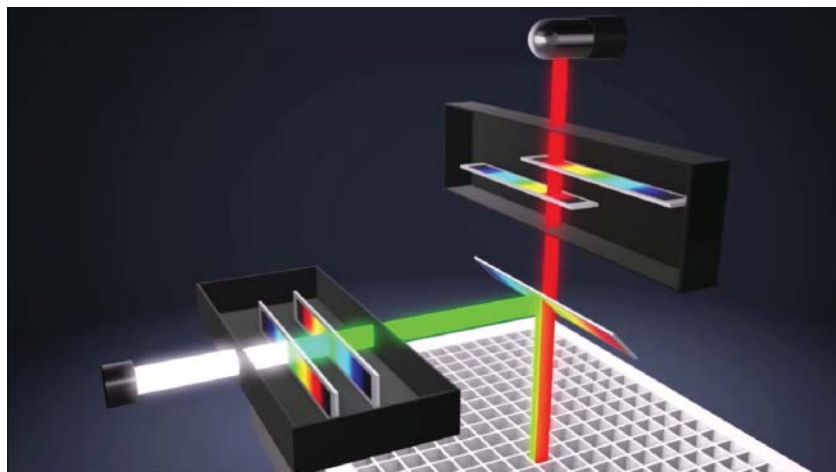


**Figure 7.16** Optical engine of a CVF-based multi-mode micro-plate reader. To the left, the light from a Xenon flash lamp is filtered by a CVF monochromator to the optimal excitation wavelength range of the fluorophore in the micro-plate well. The filtered beam is reflected by the CVD into the well. The red-shifted fluorescence emission passes the CVD and is filtered by a second CVF monochromator to the optimal emission wavelength range of the fluorophore before it reaches the detector at the top of the image. Source: Courtesy of BMG Labtech GmbH.

field of continuously variable bandpass filters (CVBPF) enabled completely new spectrometer designs. Previous CVBPF – for example SCHOTT'S Veril filter<sup>7</sup> – were not designed for general purpose spectroscopic use and are typically too big for hand-held instruments. Another limiting factor is the fact that the blocking range does not cover the complete wavelength range in which silicon-based detectors are sensitive to radiation (typically from 200 to 1200 nm).

Newer generations of CVBPF overcome these limitations. Figures 7.17 and 7.21 show two CVBPF for the NIR, respectively, Visible/NIR (VIS/NIR) wavelength range. Common to these and similar filters is that they provide OD4 blocking or even better in the sensitive wavelength range of silicon-based detectors (CCD or CMOS).<sup>8</sup> This provides a high signal to background ratio without the need of any additional filters and allows the use of the detector in sunlight or other uncontrolled ambient light situations.

Besides their blocking capabilities, modern CVBPFs feature passbands that are narrow and steep enough for many spectroscopic applications (for example, fluorescence or colour measurements) and high transmission levels. Their size has shrunken so much that they now can be combined with typical line or array sensors. The combination with a line sensor enables point measurements and is described in the next section. Combining a CVBPF with an array sensor opens up for novel designs of multi- or hyperspectral cameras and is described in Section 7.4.4.

An important parameter of any spectrometer is its wavelength resolution. In case of diffractive spectrometers, it is mainly defined by the size of the slit and can achieve sub-nanometre resolution in exchange of optical throughput. For spectrometers that are based on CVBPFs, the spectral resolution is a combination of several factors. The dominating factor is the optical design bandwidth of the CVBPF. It is a theoretical value that is defined for collimated light with an infinitely small spot size on the filter, and which is the result of the bandpass layer structure of the filter. Typically, a multi-cavity design is used that naturally exhibits narrow bands with steep edges. The bandwidth is directly proportional to the centre wavelength in the first approximation (see for example Figure 7.21; the measured curves shown there are very close to the design performance).

When a CVBPF is coupled to a pixel-based sensor, the spectral performance is no longer defined by the slit size in the spectrometer but by the pixel size of the sensor, which is typically a few micrometres. For all practical purposes, this means that a single pixel receives light of a spectral width that corresponds to the design bandwidth of the CVBPF, which is typically several nanometres wide. The spectral resolution then is a combination of the filter's bandwidth, the filter's wavelength gradient, and the sensor's pixel pitch. As an example let us look again at the filter from Figure 7.21: its bandwidth is approximately 2% of its centre wavelength, i. e. 14 nm at 700 nm. Its wavelength gradient is  $(880-450 \text{ nm})/35 \text{ mm} = 12.3 \text{ nm/mm}$ . With a pixel pitch of say  $10 \mu\text{m}$ , the change of peak wavelength between neighbouring pixels becomes  $12.3 \text{ nm/mm} \times 10 \mu\text{m} = 0.123 \text{ nm}$ .

It is obvious that in this example, the spectra are oversampled by a factor of 100. This allows for pixel binning to enhance signal and reduce noise at the same time. It also makes it possible to apply post-processing methods that are known from classical spectroscopy – such as spectral deconvolution – to enhance apparent spectral resolution beyond that of the filter's optical bandwidth. However, typically, it will not be possible to reach sub-nanometre spectral resolution as with spectrometers that employ a slit. On the other hand, the light throughput or light grasp can be considerably higher, and the spectral resolution is still high enough for applications like fluorescence or colour measurement. As such both methods can be considered complementary and have their optimal applications in their own right. In a real optical instrument, more factors such as AOI and OA that were discussed in Section 7.1.2.5 and distance of filter to sensor surface need to be considered to assess final spectral resolution.

#### 7.4.1 Point-of-Care Instruments

Point-of-care (PoC) instruments are the subject of research and development worldwide. The goal is to bring medical diagnostic and treatment methodologies from large central laboratories and operation theatres to local

<sup>7</sup> [https://www.schott.com/advanced\\_optics/english/products/optical-components/optical-filters/interference-filters/bandpassfilter.html](https://www.schott.com/advanced_optics/english/products/optical-components/optical-filters/interference-filters/bandpassfilter.html).

<sup>8</sup> It is noteworthy that all side bands, that narrow bandpass filter designs typically exhibit, are suppressed.

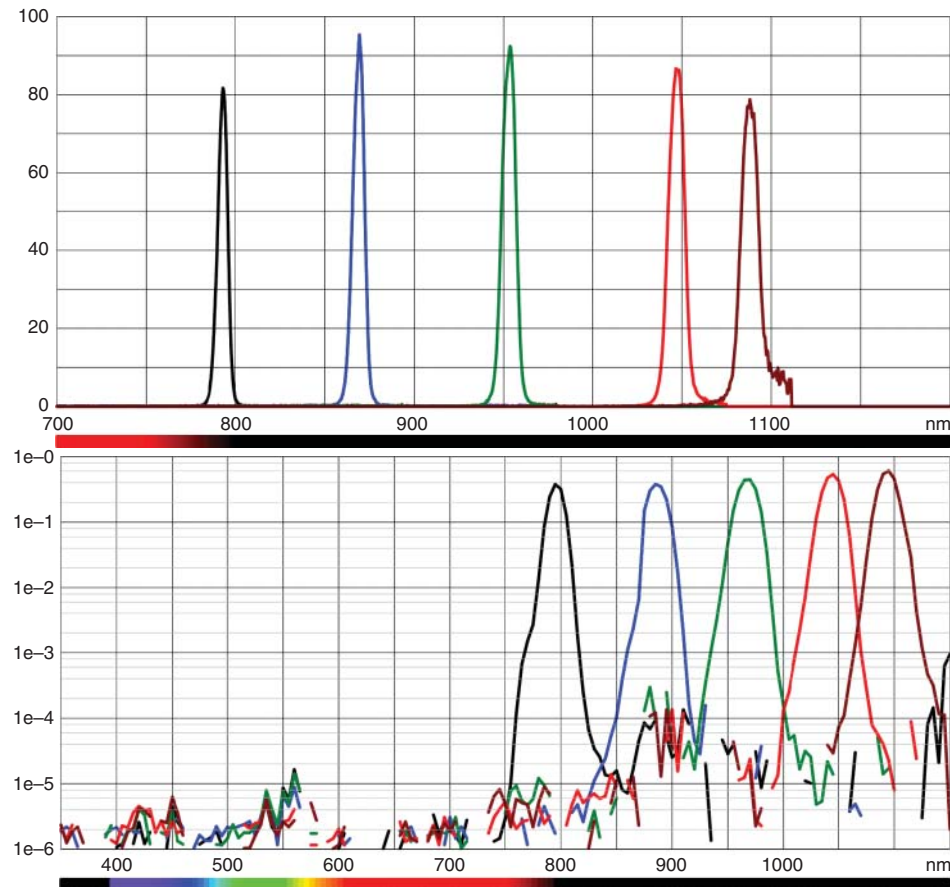


**Figure 7.17** Measured transmission and blocking characteristics of continuously variable NIR bandpass filter covering 800–1100 nm along 18.5 mm. The spectra were measured with a PerkinElmer 900 spectrophotometer using a 200  $\mu\text{m}$  narrow slit at five discrete locations to demonstrate the optical bandwidth. Given the continuous nature of the filter, any other peak wavelength can be found at intermediate positions. Source: Courtesy of Delta Optical Thin Film A/S.

physicians and to patients' beds or homes. Nowadays blood or other body liquids are sampled in the doctor's office and sent to a central laboratory. This causes a time delay of several days that can make the difference between life and death, but at least puts psychological stress on the patient. PoC also has the prospect to make advanced diagnostics available for patients in remote locations or developing countries.

PoC medical technologies require portable, small, and robust instrumentation for practical implementation. Most of the potential applications of PoC technology require a detection sensitivity at least equivalent to existing methods. This means that the optics in this system need to be at least as good as in larger equipment. The challenge is to reduce the size of all optics without compromising the optical output. Hand in hand with the size reduction of the instrument, often OAs increase to collect a sufficient signal. This has potentially adverse effects on filter performance as discussed in Section 7.1.2.5. These need to be managed by modern design and production technology. Moreover, small PoC instruments that are based on fluorescence detection typically do not have enough space to accommodate a dichroic beamsplitter (that helps suppress the excitation light in the emission channel) to separate the excitation from the emission channel. This puts higher blocking requirements on the bandpass filters in the instrument.

A good example for successful miniaturisation of a diagnostic method previously only available in large desktop instruments is Cepheid's GeneXpert Omni. It provides portable clinical molecular diagnostic polymerase chain reaction (PCR) testing using cartridge technology. The cartridge's microfluidics regulate all aspects of the testing process from sample preparation, nucleic acid extraction, amplification, and fluorescence-based detection. The instrument itself contains a large number of custom-designed bandpass filters that enable more tests beyond the initially planned human immunodeficiency virus (HIV) viral load test.<sup>9</sup>

#### 7.4.2 Cataract Diagnosis and Treatment

Cataracts are a large and growing problem with a globally ageing population. The demand for cataract operations creates major stress on medical services worldwide (20 million surgeries per year). Future requirements of 44 million surgeries per year are projected for 2030.

The cloudiness of a cataractous eye lens limits visual diagnostic decisions on the extent of a cataract. Edinburgh Biosciences has shown that fluorescence emission from the eye can solve this problem quantitatively [7]. The fluorescence spectrum from a healthy lens changes significantly during cataract formation. This allows early diagnosis and permits more quantitative measurement of the cataract development.

Currently, the replacement of the lens is a plastic implant in the course of a major surgery. This is highly successful but demands full operating theatre resources and highly trained surgeons. The capsule retaining the lens is necessarily opened to allow insertion of the plastic lens. Such treatments can cause opacity of the capsule that reaches around 30% after three years and 50% after five years. It is treated by capsulotomy creating an aperture with a high-powered laser. Fragility of the capsule sometimes indicates a non-recommendation for this procedure.

Edinburgh Biosciences has developed a photobleaching treatment method of the cataract that retains the natural lens. This also allows the accommodation of the human lens to be preserved. The photobleaching process needs to be closely monitored. The process returns the lens spectrum to that of a healthy lens. Therefore, a PoC instrument was developed that contains both the tryptophan fluorescence-based detection and monitoring, and the photobleaching treatment module (see Figure 7.18).

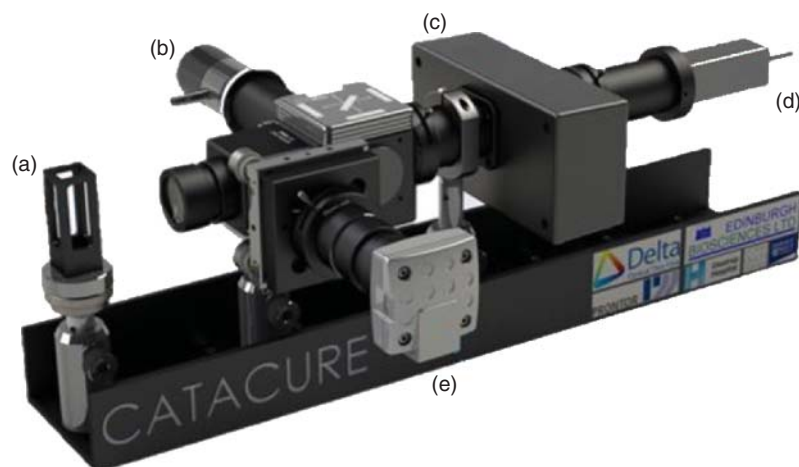


**Figure 7.18** Functional prototype of a combined cataract diagnostic, monitoring, and treatment of PoC instrument with (a) sample (eye) location, (b) LEDs for excitation of fluorescence and photobleaching, (c) spectrometer based on continuously variable bandpass filter, (d) single photon-counting photomultiplier tube, (e) sample (eye) imaging system. Source: Courtesy of Edinburgh Biosciences.

<sup>9</sup> <https://www.cepheid.com/en/component/phocadownload/category/6-press-releases?download=132:2016-september-8-press-release>.



**Figure 7.19** Hand-held NIR spectrometer for quality control of grain. Source: Courtesy of GrainSense Oy.

At the heart of the monitoring module is a CVBPF on a linear drive. The spectrum is collected with a single photon-counting photomultiplier. The compact optical system which together with LED excitation, treatment sources, photomultiplier, and phase-sensitive electronics is 95% smaller in volume than today's instruments while retaining high light grasp and operation in ambient lighting conditions.

#### 7.4.3 Point Measurements – Hand-Held NIR Spectrometer for Quality Control of Grain

The device shown in Figure 7.19 is a portable NIR spectrometer with integrated integration sphere that analyses protein, moisture, carbohydrates, and oil contents – the key constituents of crop value – in grain and other crops. Only a few kernels are needed, and results are obtained in a few seconds. The device applies a new method of NIR spectroscopy. As mentioned above, wavelength dispersion is not achieved with a grating but with a CVBPF that was specifically designed for this application (see Figure 7.17). The filter has an active length of 18.5 mm (in the wavelength direction) and a height of 3 mm. It is mounted flush with a custom photodiode array of 64 rectangular pixels that discretises 800–1100 nm into 64 spectral channels.

As the kernels are placed in the mid-cross-section of a small integration sphere, their orientation does not matter. Another advantage of this design is the improvement of both signal strength and SNR. In traditional NIR absorption spectrometers, the light passes the sample only once. By illuminating the kernels in the integration sphere, the light bounces back and forth and passes through the kernels several times before it reaches the detector. This also reduces the measurement time.

The new device allows farmers, cereal seed producers, and plant breeders for the first time to control the quality of their products in the field before and during harvest without needing to rely on large laboratories or the quality and price assessment by the buyers, because this new spectrometer is robust and easy to use. The device also helps meat producers monitor and adjust the protein content of feed in real time during the growth of their livestock. This has a major impact on the profitability of meat production.

#### 7.4.4 Imaging Applications – Continuously Variable Bandpass Filters for Hyperspectral Imaging

Hyperspectral imaging (HSI) has been used for a couple of decades in applications such as satellite imaging, air reconnaissance, and other not overly price-sensitive markets. Still, there is no clear definition of the term *hyperspectral* imaging. Sometimes techniques that produce 2D images with more than the typical three RGB colours (or spectral channels) – for example by inclusion of a NIR channel – are already called hyperspectral. Mostly though, this is not considered sufficient. Typically, even 10 spectral channels are still to be called multispectral rather than hyperspectral. In the following, we require that certain criteria are fulfilled for an imaging technique to be called hyperspectral:

- For every pixel in the image, we measure the spectrum of the incident light or radiation.
- The measured spectrum is continuous and not discretised to a limited number of channels or bands.
- The spectrum covers more than one sub-wavelength range, for example, UVA, visible, and NIR, or NIR and SWIR.

The advent of alternative approaches makes HSI attractive for volume markets or even consumer products, for example, cancer detection, precision farming with unmanned aerial vehicles (UAVs) or directly at the plant, food testing in supermarkets, and many more. Alternative approaches comprise sensors that are coated at wafer level with fixed wavelength bandpass filters (e. g. PIXELTEQ or imec). Common are also thin-film coatings on glass substrates that can be patterned during deposition (*in situ*), or using a photolithographic process over the coating to block the addition or subtraction of materials deposited on the substrate surface (e. g. Materion). These micro-patterning techniques allow (a) filters that have a staircase of different centre wavelengths in one direction (also called stepped filters, suited for the so-called push-broom technique) or (b) 2D mosaics (suited for the so-called snapshot technique).

However, according to the above criteria, strictly speaking these solutions do not provide hyperspectral capability but are inherently multispectral due to their discrete changes in centre wavelength. Typically, between 10 and 100 different wavelengths or channels are offered. A truly hyperspectral sensor offers a continuous change in centre wavelength and as such a virtually unlimited number of channels.

A different approach to filters for HSI is followed with CVBPFs. They are fabricated for mid-size and full-frame CCD or CMOS sensors (e. g. 25 mm × 25 mm or 24 mm × 36 mm). These filters offer very high transmission levels and are fully blocked in the light-sensitive wavelength range of silicon-based detectors (200–1150 nm or higher). The combination of CVBPFs with silicon detectors allows the design of very compact, robust, and affordable HSI detectors (see Figure 7.20) that offer several advantages and benefits over conventional approaches:

- Large aperture compared with grating and prism,
- higher transmission than grating and prism,
- short measurement time,
- high suppression of stray light and
- excellent signal to background ratio.

These thin-film filters are coated with silicon dioxide and metal oxides on a single fused silica substrate without the use of glue, coloured glasses, or thin metal layers. The resulting filters are very robust against environmental conditions like temperature and humidity, and spectrally and mechanically stable. The filters are ideally suited for long-term use in airborne or space applications without any degradation. They are produced in coating chambers that are specifically modified to create a thickness gradient of the deposited coating material along one direction of the filter substrates. As the centre wavelength of a bandpass filter depends on the optical thickness of the interference layers, the thickness gradient creates a filter, whose centre wavelength changes continuously along the filter length.

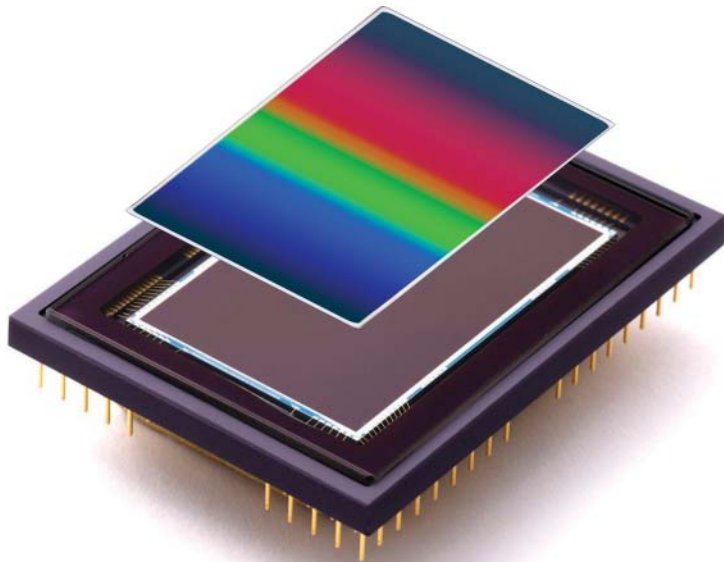


**Figure 7.20** Continuously variable filter based hyperspectral imaging detector.

Figure 7.21 shows the transmission characteristics of a CVBPF that covers a centre wavelength range from 450 to 880 nm with a bandwidth of approximately 2% of its centre wavelength. In a wide wavelength range, the transmission is higher than 90%. The transmission below 550 nm is underestimated due to the limited ability of the spectrophotometer to resolve narrow bands. But even more important than the peak transmission is that all undesired light from 200 to 1150 nm is suppressed better than OD4.

#### 7.4.4.1 Comparison with Grating and Prism-Based Systems

Due to the diffractive nature of gratings and prisms, their use requires a certain large distance between sensor and diffractive element. This results in a large instrument that is prone to misalignment due to mechanical influences. Furthermore, a slit is needed to obtain high spectral resolution (see Figure 7.22). The slit limits the light throughput. The SNR level is typically not better than 200 : 1 [3].

CVBPFs, on the other hand, can be mounted directly on top of or close to the sensor. Options include gluing onto the sensor surface, replacing the cover glass with the filter or a mechanical holder. The resulting detector is very compact and robust at the same time. The optical design does not require the use of a slit. Light is collected through the full aperture of the lens. Together with the high transmission and the optical bandwidth of the filter, the HSI camera becomes very light efficient. The deep broadband blocking of the filter ensures a high SNR and minimises spectral crosstalk.

Without a slit, every acquired image shows the complete scene. This makes it possible to use the so-called windowing technique. It allows to arbitrarily image the scene from different positions without the need for precise synchronisation of lateral movement and image acquisition like with the push-broom technique. With the windowing technique, it is possible to construct the hyperspectral data cube using image pattern recognition techniques (see Figure 7.23). Another advantage is that 3D height information is readily available with standard stereoscopic reconstruction techniques because the objects in space are imaged from different angles throughout the image sequence (see Section 7.4.4.3).

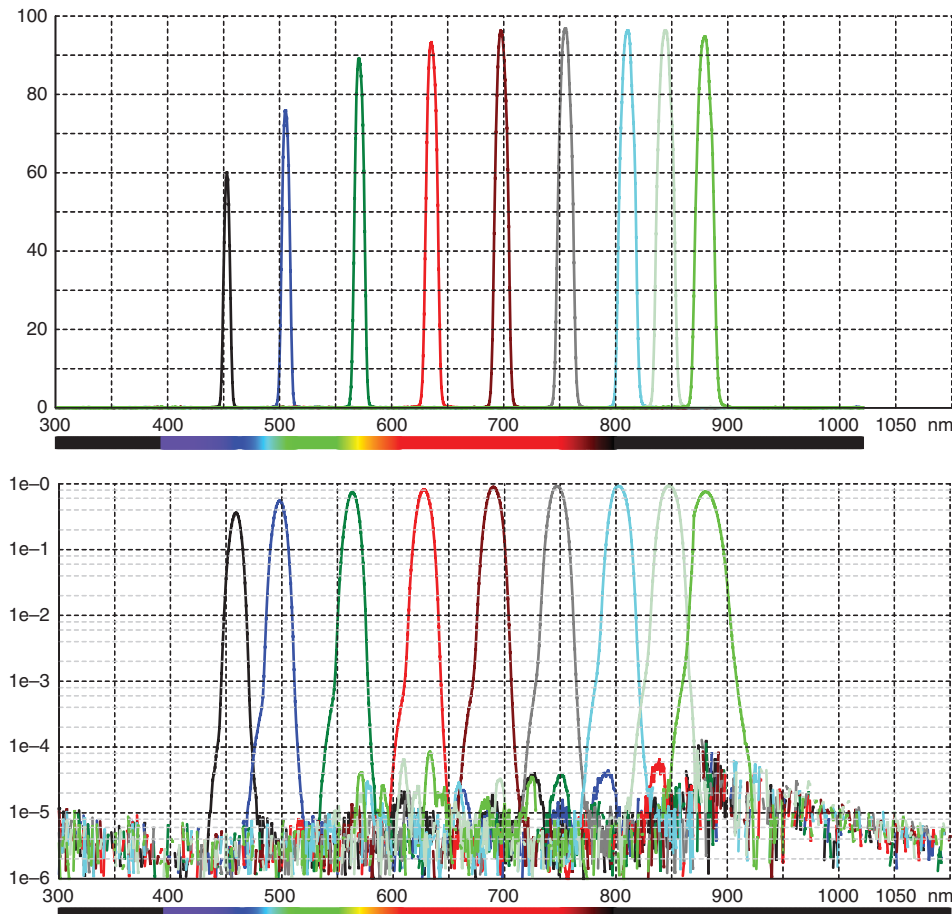


**Figure 7.21** Measured transmission and blocking characteristics of a continuously variable bandpass filter covering 450–880 nm along 35 mm. The spectra were measured with a PerkinElmer 900 spectrophotometer using a 200  $\mu\text{m}$  narrow slit at nine discrete locations to demonstrate the optical bandwidth. Given the continuous nature of the filter, any other peak wavelength can be found at intermediate positions. Source: Courtesy of Delta Optical Thin Film A/S.

#### 7.4.4.2 Comparison with Wafer-level-Coated Detectors

What makes wafer-level-coated detectors (also known as filter-on-chip) attractive is the possibility to coat filters in arbitrary patterns also on small imaging sensors. Small size can be a crucial factor in certain applications. The same is true for snapshot capability (acquisition of the hyperspectral data cube with only one image). In this case, the sensor is coated with a 2D pattern of bandpass filters with different but constant centre wavelengths. The snapshot capability of course comes at the cost of reduced spatial resolution. Another typical trade-off of coating at wafer level is the limited spectral complexity of the filters. Imec, for example, offers simple Fabry-Perot filters that do not create sharp bands and have strong side bands that limit the overall free spectral range and the obtainable SNR.

CVBPFs are suited for larger sensors. To maintain their high performance and large wavelength range, the filters cannot be made much smaller than 20 mm in the variable direction with current production technology. An approach to enable snapshot HSI with CVBPFs was demonstrated by Fraunhofer IOF and recently commercialised by Cubert GmbH. It makes use of 2D lens arrays (plenoptics cameras) that are, for example, used in light field cameras [18]. A more detailed discussion takes place in Section 7.4.4.4 below.

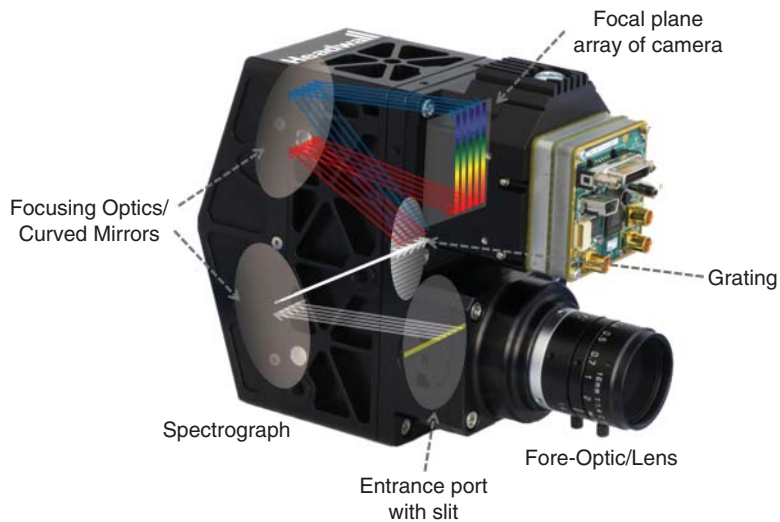


**Figure 7.22** Design of a classical hyperspectral imaging camera with grating. Source: Courtesy of Headwall Photonics.

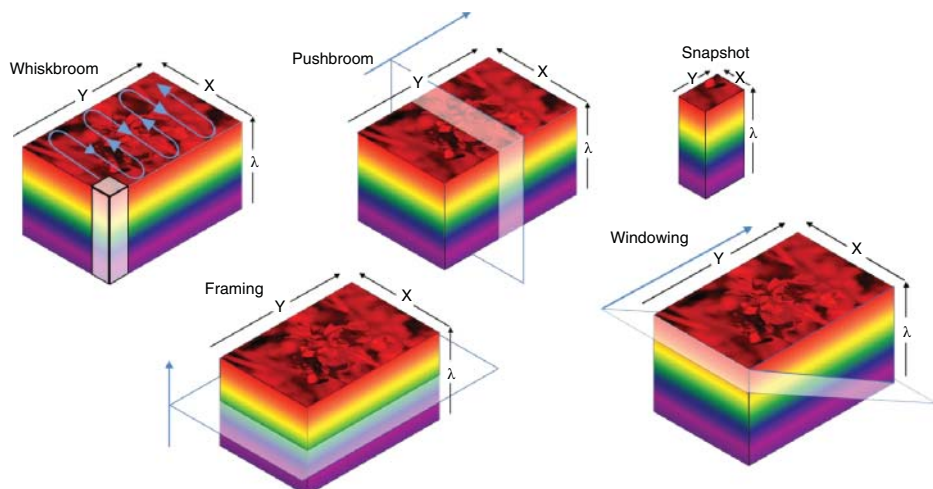


**Figure 7.23** Different modes of acquiring the hyperspectral data cube. Source: Courtesy of Matt Gunn, Aberystwyth University.

#### 7.4.4.3 3D Hyperspectral Imaging

For some applications, for example, precision farming or quality control of manufactured components, it is advantageous to combine hyperspectral data with 3D surface information [1]. In precision farming, this provides information on both nutrition and health of crop as well as its height and growth. However, it is not possible to extract the height information from traditional hyperspectral cameras that use slits and therefore only image a narrow slice of the object, especially under imaging conditions in which the relative movement between camera and object cannot be precisely controlled like with UAVs. Even with snapshot cameras, this is difficult because of their limited spatial resolution that typically is not sufficient for 3D reconstruction.

On the other hand, hyperspectral cameras using a CVBPF have superior spatial resolution that allows 3D reconstruction of the imaged scene by standard stereoscopic image processing [1]. This makes use of the fact that each object in the scene is viewed from different angles while passing by.

#### 7.4.4.4 Snapshot Hyperspectral Imaging

The acquisition of the whole hyperspectral data cube with just one instantaneous image acquisition or measurement is not possible with classical push-broom or framing hyperspectral cameras. One approach to snapshot HSI was presented and discussed earlier with filters coated directly at wafer level in a mosaic pattern. Another approach to enable snapshot HSI combines 2D lens arrays with CVBPFs. Several groups have demonstrated prototypes ([9, 13, 15]). In the following, we discuss Fraunhofer IOF's solution [9] that was recently commercialized by CubertGmbH [11].

In order to overcome the restrictions of using scanning techniques or wafer-level-coated detectors, Fraunhofer IOF Jena proposes a multispectral imaging concept based on a multi-aperture system approach using a customised microlens array (MLA) combined with a CVBPF and a silicon-based image sensor (see Figure 7.24). In addition, a tailored baffle array is utilised for preventing optical crosstalk between adjacent optical channels. A customised multispectral analysis tool features the capabilities for advanced object classification.

The main advantage of choosing a micro-optical imaging system in combination with a CVBPF is the simultaneous capturing of spectral and spatial information in a single shot due to distinct spectrally coded channels. The multi-aperture principle allows one degree of freedom between the spectral and spatial sampling according to the

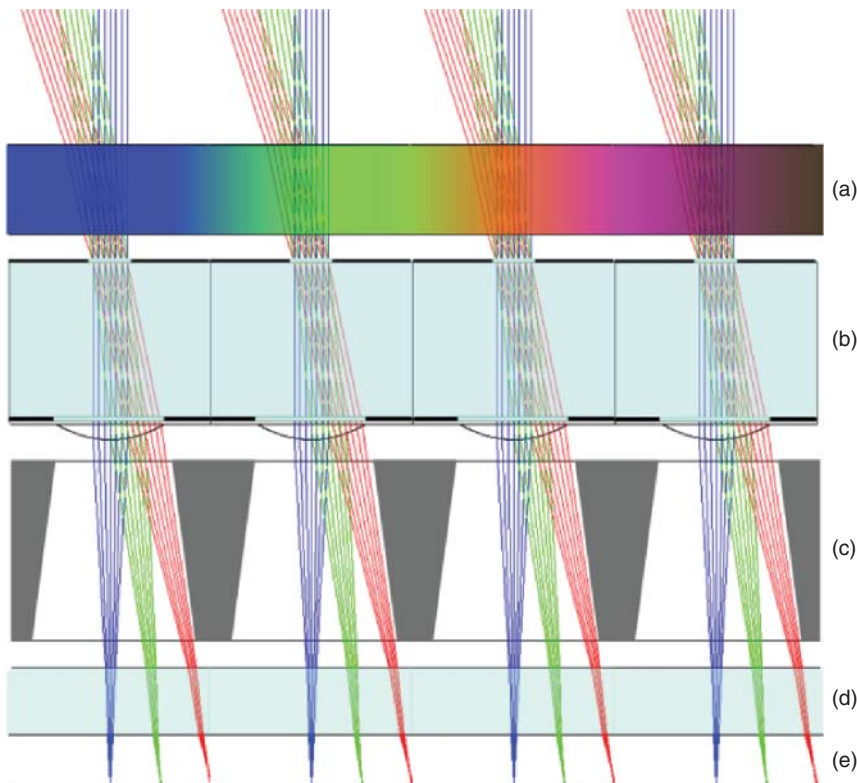


**Figure 7.24** Cross section through Fraunhofer IOF's camera. The main elements are (a) continuously variable bandpass filter, (b) microlens array (MLA), (c) baffle array, (d) cover glass, and (e) image sensor. The light ray angles are color-coded. The colours do not represent wavelengths. Source: Courtesy of Fraunhofer IOF.

**Table 7.1** Overview of system parameters of the snapshot multispectral camera.

System parameter	Value
Channels	11 × 6 (on Cartesian grid)
Optical path length	7.2 mm
f-Number	(F/#) 7
Field of view (FOV)	68° (diagonal)
Image resolution	400 × 400 pixels (per channel)
Spectral range	450–850 nm
Spectral sampling	6 nm (linear)

constraints of the CVBPF and the size of the image sensor. The number of spectral channels is therefore equal to the number of microlenses. As a proof of concept, the optical design of the MLA employs a single microlens surface. The optimisation yields the system parameters that can be seen in Table 7.1. The CVBPF is slightly rotated around the optical axis with respect to the MLA in order to achieve a linear spectral sampling over the extended spectral range (see Figure 7.25). If the filter was not tilted, all lenses in one specific column would be exposed to the same wavelength.

The ultra-compact micro-optical system comprises microlenses in an array within diameters and sag heights in the range of hundreds of micrometres. Hence, the fabrication of the MLA was performed by the state-of-the-art wafer-level optics technologies. A spherical microlens master is fabricated by UV lithography and reflow of photoresist. A replication tool is created and used for moulding of the final lens elements. The CVBPF, the MLA, and the Baffle array were mounted in a mechanical holder, actively aligned to the image sensor and fixed to the housing. The snapshot multispectral camera demonstrator has an overall size of only 60 × 60 × 28 mm<sup>3</sup>.

The spectral response of each individual pixel depends on the bandwidth of the CVBPF and the AOI on the filter. A spectral calibration corrects these effects using a tunable light source. The multispectral camera enables the

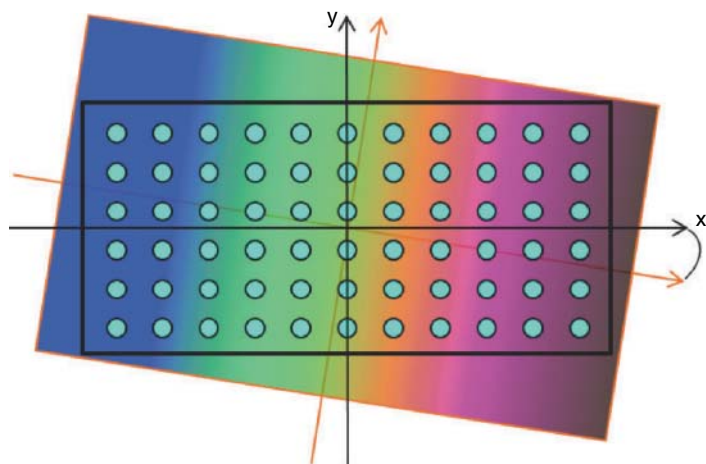


**Figure 7.25** By tilting the filter axis with respect to the lens array axis, a simultaneous acquisition of 66 spectrally equidistant channels is possible.



**Figure 7.26** Raw image of an extended scene in the lab (right, the red square shows an enlarged subimage) and in comparison, an image captured with a standard RGB camera (left). Source: Courtesy of Fraunhofer IOF.

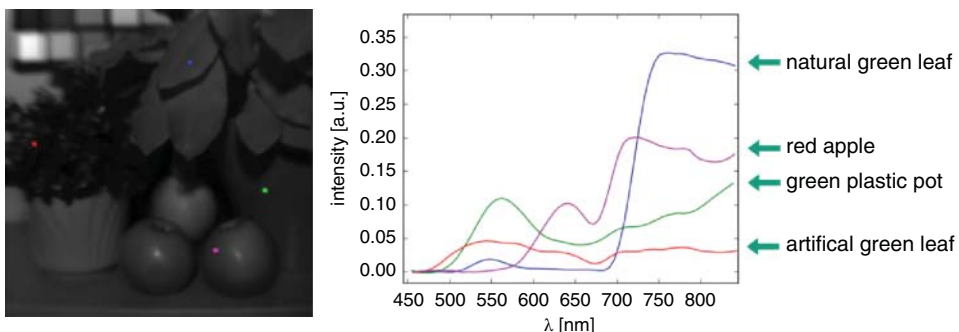


**Figure 7.27** Test scene in the lab (left) and spectra extracted from the four marked objects (right). Source: Courtesy of Fraunhofer IOF.

snapshot acquisition of 66 spectral channels with a linear spectral sampling of approximately 6 nm over a wavelength range of 450–850 nm with a spectral resolution between 10 and 16 nm. In addition, an object distance dependent spatial calibration of the channels provides an accurate overlay of the individual sub-images in the data cube.

Figure 7.26 depicts the raw image of an extended scene in the lab (right) and in comparison, an image captured with a standard RGB camera (left). Due to the short focal length of the microlenses, the imaging module exhibits a large depth of field and therefore every object in the subimage is in focus (red square). The custom-developed software tool allows for a comprehensive analysis of spectra of objects in the scene as seen in Figure 7.27. For example, four processed and corrected spectra provide detailed object information, which constitutes the basis for an advanced object classification.

The camera demonstrator combines state-of-the-art micro-optical manufacturing methods and a multi-aperture imaging principle with a commercial CVBPF. It enables the realisation of highly compact and cost-efficient devices, capable of capturing spectrally resolved, extended object fields in a single shot with high resolution. Moreover, the proposed system concept provides a high flexibility with respect to spatial and spectral resolution by tailoring the number of spatial and spectral channels. The prospective fields of application of the developed system include environmental and agriculture monitoring, industrial surveillance and sorting, as well as biomedical imaging.

#### 7.4.4.5 Spectral Quality of the Different Approaches

Cubert GmbH compared their three generations of hyperspectral video cameras side by side in an identical setup. The FireflEYE Q285 was, at the time of its launch, the first hyperspectral camera that could acquire a complete

hyperspectral data cube ( $x, y, \lambda$ ) with one single image shot. The prism-based sensor technology offered light efficiency of up to 70%. With 125 spectral channels (450–950 nm) and an image size of  $50 \times 50 \text{ px}^2$ , 2500 spectra were recorded simultaneously. With just  $50 \times 50 \text{ px}^2$ , it is difficult to resolve spatial structures in the image. Therefore, a second image sensor with only one band (panchromatic) was integrated into the camera, imaging the same view with  $1000 \times 1000 \text{ px}^2$ . With this additional information, the users can perform pan-sharpening of the spectral data that transform the final data cubes to a maximum size of  $1000 \times 1000 \times 125$ .

The multispectral ButterflEYE camera is based on the filter-on-chip technology. The number of spectral channels decreased to 16 or 25 depending on sensor type. The combined model ButterflEYE X2 provides an image resolution of  $512 \times 272 \text{ px}^2$ .

The Ultris camera was developed based on the light field technology described above. The camera reaches a native image resolution of  $400 \times 400 \text{ px}^2$  with 100 spectral channels that consecutively cover the wavelength range from 450 to 850 nm. This means that the previously unheard number of 160 000 spectra is acquired simultaneously. The 12-bit sensor of the camera makes it possible to detect minute intensity differences in the spectral content while keeping the noise level very low. The dual GigE camera interface guarantees an image frame rate of up to 6 Hz.

Looking at the distribution of the spectral channels across their respective wavelength ranges between the three cameras, the improvements become obvious. Due to its prism-based optics, the Q285 has a nonlinear<sup>10</sup> but steady distribution of the channels. The camera based on a filter-on-chip sensor suffers additionally from the fact that the distance and position of the spectral channels cannot accurately be determined because of the complicated production process. The channels of the Ultris on the other hand are spaced equidistantly with a bandwidth (FWHM) of 2% of the centre wavelength.

The three cameras (ButterflEYE X2, FireflEYE Q285, and Ultris Q20) were installed in the same setup for a comparison. The exposure time was optimised with the help of a white reference to derive the maximum dynamics. As illumination, a stabilised tungsten light source (50 W) was used with exposure times of 10 ms (Q285), 16 ms (Ultris), and 120 ms (x2). The reflectance properties of the test samples were calculated by subtracting the dark current image from the measurement image and subsequently dividing it by the image of a calibrated 95% white reference (Zenith Lite). The dark current measurement and the white reference were averaged 20 times to achieve a good noise reduction.

The measurement, however, was acquired without any averaging and post-processing in order to faithfully represent the inherent noise. The data are presented in their original form without averaging, sharpening, or smoothing to show the true spectral quality of each sensor. Figure 7.28 (right side) shows quantities derived from the hyperspectral data cubes. The first line shows typical RGB representations (true colour), the two bottom lines show typical indices that are used for vegetation analysis. Each pixel of the different images represents one spectral curve of the respective sensors.

In the case of the FireflEYE Q285, the low spatial resolution is obvious. The colour representation on the other hand is very clear, which is also confirmed by the noise-free images of the vegetation indices. The filter-on-chip camera X2 has a higher spatial resolution but exhibits the typical high noise level of this type of sensor. Especially, the vegetation indices can only be used after intensive post-processing. The new Ultris combines high spatial resolution with low noise levels. Both the image quality and the spectral quality are excellent. The image noise is on a comparable level with the FireflEYE Q285.

Figure 7.28 (left side) shows the spectral signature of the sensors using three differently coloured paper samples. The spectra of all pixels in a predefined area with homogeneous colour were averaged. Because the standard deviation represents the noise equivalent of the sensors, it is used as error bars for each channel. The result shows clearly that the new Ultris can easily level with the spectral quality of the FireflEYE even though the Ultris has a tremendously higher spatial resolution.

---

<sup>10</sup> The refractive index of the prism material increases with decreasing wavelength.

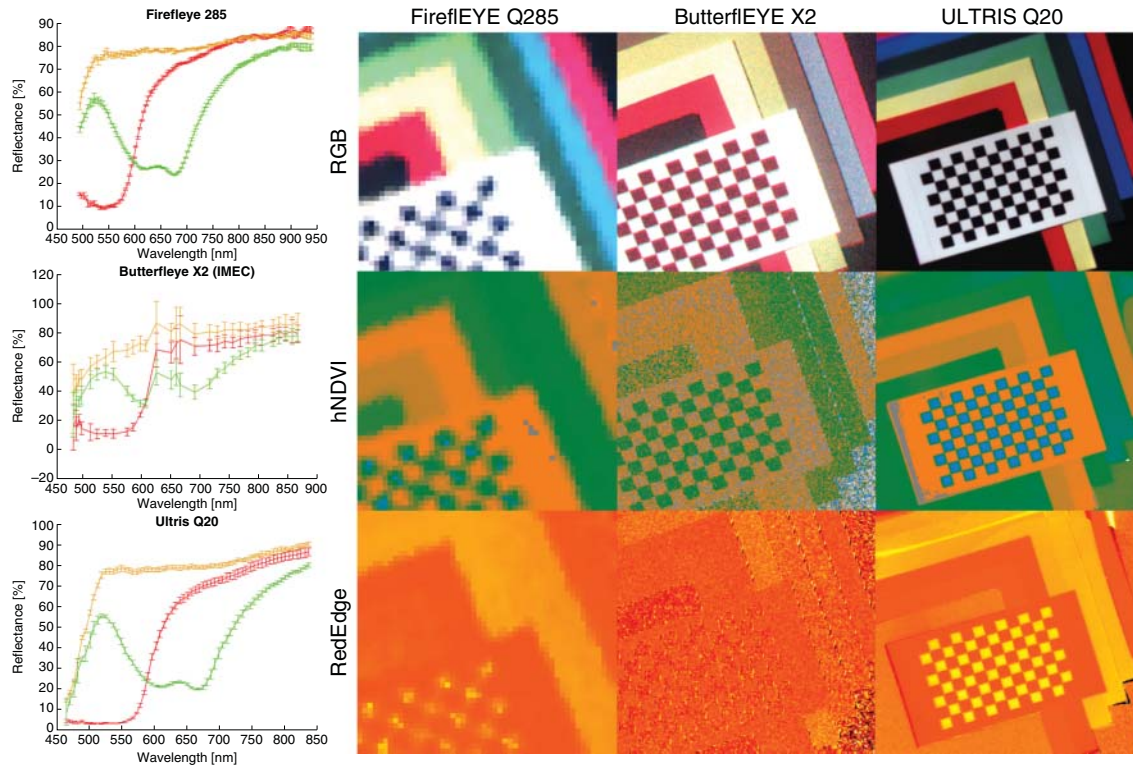


**Figure 7.28** Comparison of the spectral quality of the three hyperspectral video cameras. For each camera, the spectra of the red, green, and yellow samples are shown along with the respective noise indicating standard deviation (left). Image comparison of the three hyperspectral video cameras FireflEYE Q285, Butteflye X2 und Ultris Q20. For each camera, an RGB image (true colour) and two vegetation indices (hNDVI and RedEdge) are shown (right). Source: Courtesy of Cubert GmbH.

## 7.5 Conclusion and Outlook

All three approaches have their specific strengths. Classical hyperspectral cameras with gratings and prisms achieve the highest spectral resolution and are well suited for demanding applications in research. Sensors that are coated at pixel level allow the most compact cameras, offer total flexibility with respect to filter pattern, and are readily suited for snapshot imaging. Cameras based on CVBPFs combine high light efficiency, high SNR, and high spectral resolution with compactness and robustness. An in-depth discussion is made available by Renhorn et al. [4].

Although some of the filters that are discussed above are usually called linear variable filters, they are typically not perfectly linear with respect to centre wavelength versus position on the filter. This can easily be compensated for by a calibration curve or a one-time calibration of the assembled detector. However, there are good reasons for designing filters that deliberately are nonlinear.

As can be seen from the transmission curves in Figure 7.21, the bandwidth is proportional to the centre wavelength. This is a natural property of the multi-cavity design that is used in the filters. Consequently – if we for example compare light with 450 and 900 nm – there are twice as many neighbouring pixels on the sensor that see light of 900 nm as there are pixels that see light of 450 nm. This can be compensated for with an exponential relation between centre wavelength and its spatial position on the filter. Other design targets are possible. Desirable are filters that cover a larger wavelength range over a shorter length. Recently, filter designs were realised that, for example, cover 450–950 nm over 35 mm with an exponential dispersion function (see Figure 7.29).

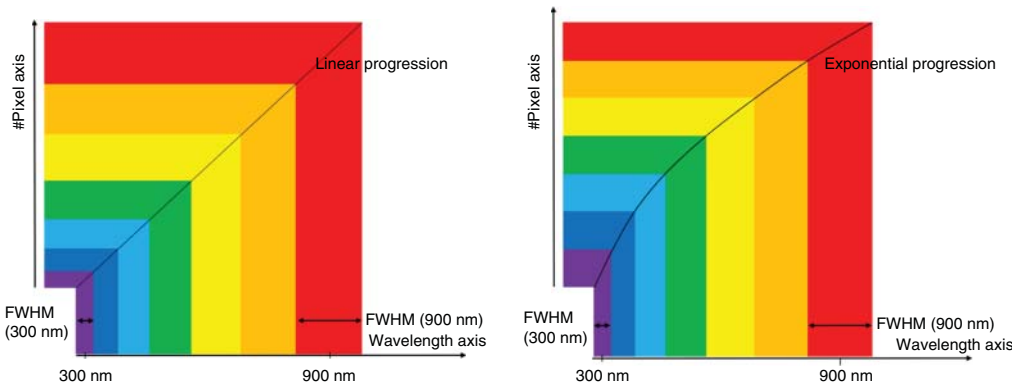


**Figure 7.29** Comparison of CVBPF with linear and exponential dispersion.

Although the emphasis of this section lies on HSI, it should be mentioned that the same technology can be used to replace gratings in compact spectrometers – making them even more compact. Produced with ultra-hard coating technology, the filters can be diced to very narrow stripes that can be mounted in front of a line scan detector. This concept is, for example, used in wearable devices to measure the oxygen content of blood. Another promising application is the fusion of fluorescence microscopy and HSI as hyperspectral fluorescence microscopy. The technology is applicable to both laser scanning microscopy and wide-field microscopy [5, 10].

## References

- 1 Ahlberg, J., Renhorn, I.G., Chevalier, T.R., Rydell, J., and Bergström, D. (2017). Three-dimensional hyperspectral imaging technique. *SPIE Proceedings Volume 10198, Algorithms and Technologies for Multispectral, Hyperspectral, and Ultraspectral Imagery XXIII*, San Francisco (5 May 2017), Bd. 1019805. doi:10.1117/12.2262456.
- 2 Antila, J., Miranto, A., Mäkinen, J. et al. (2010). MEMS and piezo actuator based Fabry–Perot interferometer technologies and applications at VTT. *Proceedings of the SPIE Defense, Security, and Sensing, 2010*, Orlando, FL, USA (27 April 2010). 7680, 04, S. 76800U. doi:10.1117/12.850164.
- 3 Bachmann, C.M., Eon, R.S., Lapszynski, C.S. et al. (2019). Foote: a low-rate video approach to hyperspectral imaging of dynamic scenes. *J. Imag.* 5 (6): 119. doi:10.3390/jimaging5010006.
- 4 Renhorn, E.I., Bergström, D., Hedborg, J., Letalick, D., and Möller, S. (2016). High spatial resolution hyperspectral camera based on a linear variable filter. *Opt. Eng.* 55 (11). doi:10.1117/1.OE.55.11.114105.
- 5 Favreau, P.F.U.A. (2014). Excitation-scanning hyperspectral imaging microscope. *J. Biomed. Opt.* 19(4). doi:10.1117/1.JBO.19.4.046010.
- 6 Fleming, S.J. (1999). *Roman Glass: Reflections on Cultural Change*. Philadelphia, PA: University of Pennsylvania Museum. ISBN 9780924171727.
- 7 Gakamsky, D.M., Dhillon, B., Babraj, J., Shelton, M., and Smith, S.D. (2011). Exploring the possibility of early cataract diagnostics based on tryptophan fluorescence. *J. R. Soc. Interf.* 8. doi:10.1098/rsif.2010.0608.
- 8 Geffcken, W. (1942). *Interferenzlichtfilter*. German Patent 742 463, filed 15 July 1942.
- 9 Hubold, M., Berlich, R., Gassner, C., Brüning, R., and Brunner, R. (2018). Ultra-compact micro-optical system for multispectral imaging. In: *MOEMS and Miniaturized Systems XVII* Bd. 10545 (ed. P., Wibool, P., Yong-Hwa, and Z., Hans), 206–213. International Society for Optics and Photonics, SPIE, Hrsg.
- 10 Gao, L. and Smith, R.T. (2015). Optical hyperspectral imaging in microscopy and spectroscopy – a review of data acquisition. *J. Biophoton.* 8 (6): 441–456. doi:10.1002/jbio.201400051.
- 11 Locherer, M. (2019). Lichtfeld für HSI. <https://www.invision-news.de/download/ausgabe-3-2019-september/>.

- 12** Macleod, H.A. (2010). *Thin-Film Optical Filters*. Boca Raton: CRC Press. ISBN 978-1-4200-73027.
- 13** Mu, T., Han, F., Bao, D., Zhang, C., and Liang, R. (2019). Compact snapshot optically replicating and remapping imaging spectrometer (ORRIS) using a focal plane continuous variable filter. *Opt. Lett.* 44 (5): 1281–1284. doi:10.1364/OL.44.001281.
- 14** Smith, S.D., Kerr, A., Shelton, M., and Fenske, R. (2012). Upgrade of diffraction grating spectrometers for multiple purposes. [edinburghbiosciences.com/wp-content/uploads/2013/04/Upgrade-of-diffraction-grating-spectrometers.pdf](http://edinburghbiosciences.com/wp-content/uploads/2013/04/Upgrade-of-diffraction-grating-spectrometers.pdf).
- 15** Stanley, R.P., Chebira, A., Ghasemi, A., and Dunbar, A.L. (2017). Hyperspectral imaging using a commercial light-field camera. In: *Proceedings Volume 10110, Photonic Instrumentation Engineering IV*; 1011013, SPIE OPTO, San Francisco, CA, USA (28 April 2017). doi:10.1117/12.2253599.
- 16** Tematys (2016). Miniature and micro spectrometers: end-user needs, markets and trends. <https://tematys.fr/Publications/en/spectroscopy/42-miniature-and-micro-spectrometers-end-user-needs-markets-and-trends-.html>. Version: 2016.
- 17** Tikhonravov, Alexander V., Trubetskoy, M.K., DeBell, G.W. (1996). Application of the needle optimization technique to the design of optical coatings. *Appl. Opt.* 35 (28): 5493–5508. doi:10.1364/AO.35.005493.
- 18** Zhou, Z., Yuan, Y., and Xiangli, B. (2010). Light field imaging spectrometer: conceptual design and simulated performance. *Frontiers in Optics 2010/Laser Science XXVI OSA Technical Digest*. Rochester, NY, USA (2428 October 2010). doi:10.1364/FIO.2010. FThM3.

**8**

## **Portable UV–Visible Spectroscopy – Instrumentation, Technology, and Applications**

*Anshuman Das*

*Labby Inc., Cambridge, MA, USA*

### **8.1 Introduction**

Spectroscopy instrumentation is transforming, thanks to developments in advanced manufacturing techniques in the integrated circuits (IC) and optical components (Crocombe 2013, 2018). With better lithographic methods, such as nanoimprint lithography (Chou et al. 2014; Mohamed 2019) and extreme ultraviolet lithography (Ogletree 2016; Radamson et al. 2018), it is now possible to pack millions of electronic components within a single chip and even embed optical functionality. This has led to the realization of faster and powerful on-chip computing, for instance, in our smartphones. High demand for these computing devices has driven down costs and paved the way for field-level applications in virtually every industry. Whether it is in the form of distributed sensing networks or *Internet of Things* (IoT) (Karanassios and Fitzgerald 2018)-based approaches (Gubbi et al. 2013; Zanella et al. 2014), field-level instrumentation has dramatically changed over the last decade.

Although spectrometers are routinely used in material analysis today, they have been more suited to controlled laboratory environments (Nelson 2019). Several factors are responsible for this trend including the cost of the instrument, need for an expert for interpretation, need for sample preparation, noise from ambient light sources, and sensitivity to ambient conditions, among others. Among all the different spectral ranges for spectrometers, from ultraviolet-visible (UV-Vis), near infrared (NIR), shortwave infrared (SWIR), mid-infrared (MIR) and far infrared (FIR), the most successful field deployments have been possible for the UV-Vis instruments. By far, instrumentation costs have limited the use of other optical spectrometers. Silicon (Si)-based sensors and devices are low-cost, while those based on Germanium (Ge) and Indium–Gallium–Arsenide (InGaAs) are expensive, and do not scale as well as Si. As a result, linear or image (2D) sensors based on these detectors are not field-compatible due to much higher costs. Hence, innovative single-detector approaches have been the focus of recent developments (Gelabert et al. 2016), although the principles behind these techniques (e.g. Hadamard transform) have been known for many years. Due to these constraints, UV-Vis spectrometers have been more successfully demonstrated in portable configurations, although for a limited range of applications, such as water quality analysis (Langergraber et al. 2004).

In this chapter, the basic instrumentation configurations for portable UV-Vis spectrometers will be introduced. This will be followed by an in-depth review of various approaches for achieving spectral acquisition from digital micromirror devices (DMD) to do-it-yourself (DIY) approaches for teaching or hobby to smartphone spectrometers. Finally, some applications and challenges of portable UV-Vis spectrometers will be discussed, followed by challenges and future prospects.

## 8.2 Typical Instrumentation of a Portable UV–Vis Spectrometer

Although technically the UV–Vis spectrum spans from around 190–800 nm, most spectrometers will offer a higher wavelength limit up to 1100 nm. This is because Si has an appreciable responsivity into the NIR region (Pavesi et al. 2013). However, most common spectrometer configurations will not operate over this entire wavelength range. There is generally a tradeoff between spectral bandwidth and wavelength resolution. So, manufacturers will offer spectral ranges that are a subset of 190–1100 nm. Additionally, there are no light sources that have such a broad emission spectrum. Generally, a combination of two or more light sources is needed to achieve coverage from 190 to 1100 nm. Finally, most applications typically do not require their entire bandwidth along with a high resolution. Due to these factors, spectrometers operate in limited spectral bandwidths within the entire UV–Vis–NIR spectrum.

### 8.2.1 Basic Configuration of UV–Vis Spectrometers

A UV–Vis spectrometer, like most other spectrometer technologies (James 2007), comprises a broadband light source, a dispersing element like a prism or grating, slits and a detector (Ball 2006; Milton et al. 2009), as shown in Figure 8.1. Depending on the arrangement, the detector could be a point detector or a linear array. Incident light is either focused or directed through a narrow slit on to the dispersing element, which spatially separates the spectral components. These components are either directly collected at a detector or pass through the test sample before being received at the detector. Depending on the instrumentation, the spectrum could be captured sequentially by rotating the dispersing element or using a linear detector array.

### 8.2.2 Light Sources

Traditionally, Deuterium lamps are used as the excitation source in the UV spectrum with an emission in the range of 190–400 nm. Xenon (Xe) lamps are also used in the 200–1000 nm range, sometimes in flash mode, as opposed to continuous mode, but they have intense peaks in the NIR region. More recently, a range of UV light-emitting diodes (LEDs) have also been used although with lower bandwidths. Tungsten lamps are by far the most common Vis–NIR sources with emissions in the 350–2500 nm. Again, broadband Vis LEDs are also available with various phosphors to extend emission bandwidths. Although Tungsten and Xe lamps require cooling in order to dissipate excess heat, they can be made quite compact and designed for portable spectrometers. A comparison of emission spectra of various sources is shown in Figure 8.2.

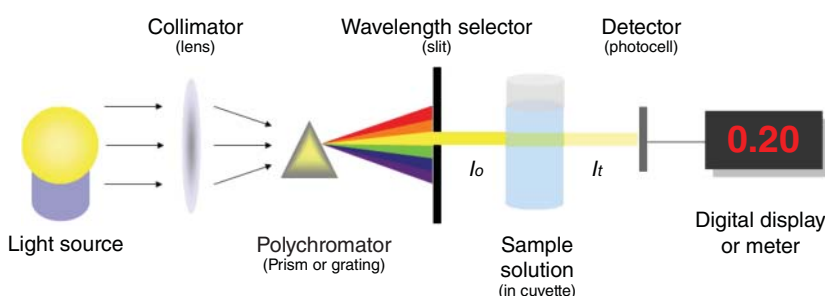


**Figure 8.1** Typical spectrometer instrumentation.

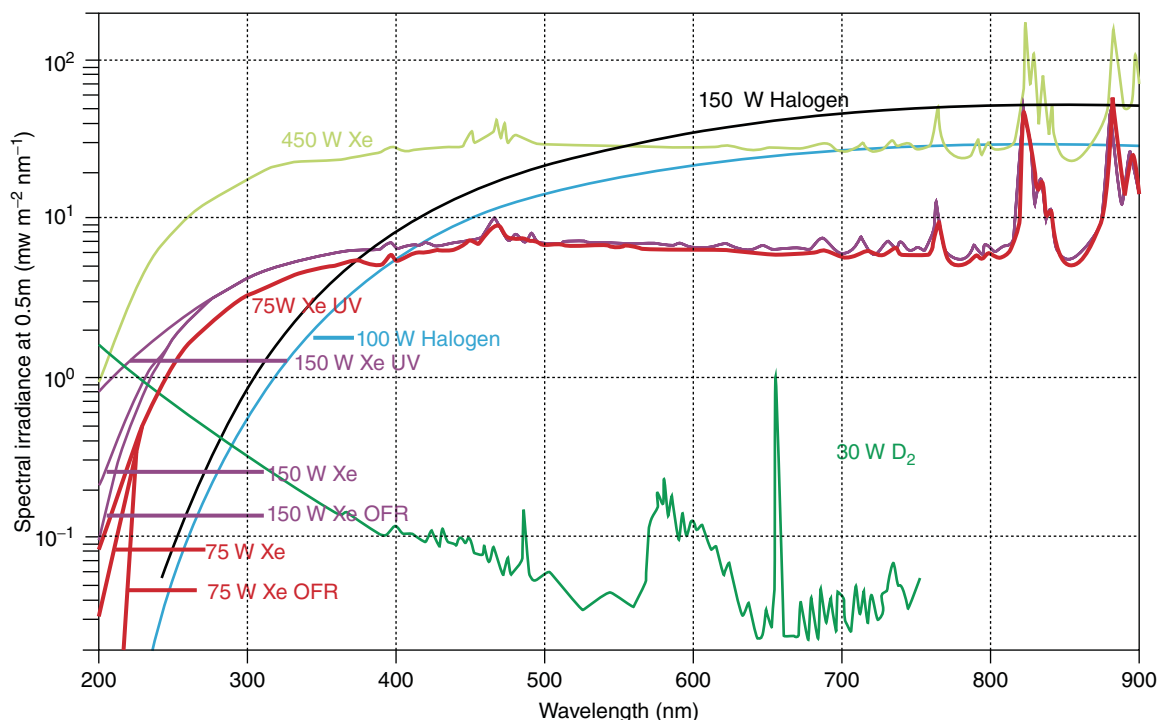


**Figure 8.2** Spectra of common UV-Vis light sources. Source: Spectroscopy Instruments Catalog, Zolix. © Zolix Instruments Co.,Ltd.

### 8.2.3 Dispersing Elements

Although early designs of spectrometers involved prisms, most modern configurations have gratings (James 2007; Loewen and Popov 2018). Compared to prisms, gratings are lighter, more compact and offer flexibility in terms of resolution, size and bandwidth. Typically, ruled gratings are used in spectrometers with high diffraction efficiency, customizable coatings and a choice of blaze parameters. A typical diffraction grating is shown in Figure 8.3.

**Figure 8.3** Gratings as dispersing elements. Source: Photo courtesy of Newport Corporation.



Recently, there have been demonstrations of spectrometers without a traditional dispersing element. Configurations involving a miniature 2D sensor with suitable filters over each pixel have shown limited applicability due to low spectral resolution (Oliver et al. 2013). However, they offer a simpler approach to achieve wavelength separation and may find niche applications.

In many benchtop configurations, these gratings are mounted on precision rotation stages for wavelength selection. Although this approach offers very high spectral resolution, it is complex to implement and sensitive to vibrations. Therefore, they are not generally suited for portable spectrometers. There are two most commonly used grating mount configurations. One is a Czerny–Turner configuration, where a plane grating is used with two concave mirrors. Light is incident from an entrance slit on to one of the concave mirrors that collimates the beam on to the grating. The diffracted light from the grating is focused by the second concave mirror on to the detector. The other is an aberration-compensated Paschen mount configuration, where the grating is etched on a concave surface that acts as a dispersing and focusing element, as shown in Figure 8.15. The Paschen configuration has fewer optical components and can be monolithically integrated on a chip. However, such gratings are challenging to fabricate and less flexible to employ.

#### 8.2.4 Detectors

Almost all spectrometers that operate in the UV–Vis region have Si detectors (Acree 2006). Si has an excellent responsivity over the entire UV–Vis–NIR range; and it is readily available and customizable into regular photodetectors, avalanche detector or photomultiplier tubes, depending on the sensitivity required. Most portable UV–Vis spectrometers today use diode arrays in the complementary metal oxide semiconductor (CMOS) or charge coupled device (CCD) configurations and can have several thousands of pixels for high-resolution applications, as shown in Figure 8.4. These arrays are compact with fast readout times and can have inbuilt high-resolution analog-to-digital (A/D) converters.

#### 8.2.5 Interfaces, Displays, and Data Storage

Depending on the application, benchtop and portable spectrometers can have their own display. Although several general-purpose spectrometers may require a desktop computer, there are scenarios where some amount of computing is done on the spectrometer itself and results are displayed on a built-in display unit. There is a range of portable spectrometers that require universal serial bus (USB) interfaces and work with laptops or desktop computers, while others have wireless capabilities to transmit data to a *Bluetooth*- or *Wi-Fi*-enabled device. Hence, a

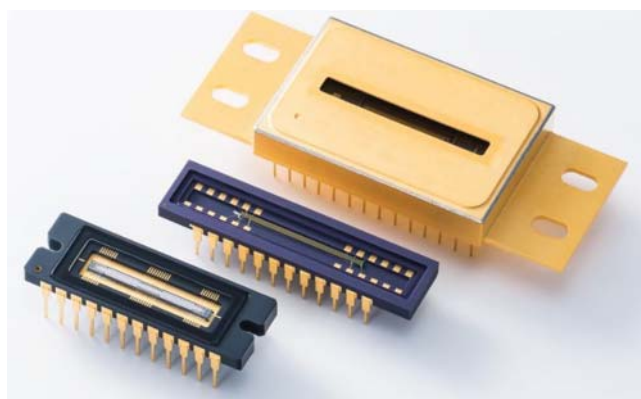


**Figure 8.4** Photodiode arrays used in portable UV–Vis spectrometers. *Source:* Photo courtesy of Hamamatsu Photonics.



**Figure 8.5** (a) Standalone spectrometer with display. Source: Permission from Sekonic. (b) Typical USB-type spectrometer. Source: USB4000 Fiber Optic Spectrometer, Ocean Optics. © 2006 Ocean Optics, Inc.

distinction can be made that portability always does not imply field compatibility. Several popular spectrometers like the one shown in Figure 8.5, do offer portability but their interface is USB-based, which means they require an external laptop or desktop computer to visualize and process data. This does not support standalone operation and is generally suited to lab-based studies. Standalone spectrometers with inbuilt displays have local data storage and can have secure digital (SD) cards or USB storage capability for portability of data.

### 8.2.6 Other Instrumentations

In addition to the basic instrumentation, portable spectrometers have circuitry to convert incident analog signals into digital signals for storage and postprocessing. A/D converters are usually present on the spectrometer board itself along with microcontrollers, buffers, and other control circuits. If some computing is done locally on the spectrometer, additional circuitry involving field-programmable gate arrays (FPGAs) could be present as well. Finally, data transfer circuitry in the form of USB, local area network (LAN), or Bayonet Neill-Concelman (BNC) ports may be found on spectrometers. In wireless devices, transmitting and receiving antennae will be present.

## 8.3 Measurement Configurations

A spectrometer is always used in a specific configuration depending on the sample state (solid, liquid, or gas), material interaction, and type of assay among other factors. For instance, liquid samples are typically examined using a transmission or absorption arrangement where the illuminating light source and detector are on either side of the sample. A few common illumination-collection geometries are presented in this section.

### 8.3.1 Reflection

In a reflection arrangement, the light source and detector are on the same side of the sample that is being examined. Upon illumination, the sample reflects certain wavelengths, which are collected by the detector. Depending

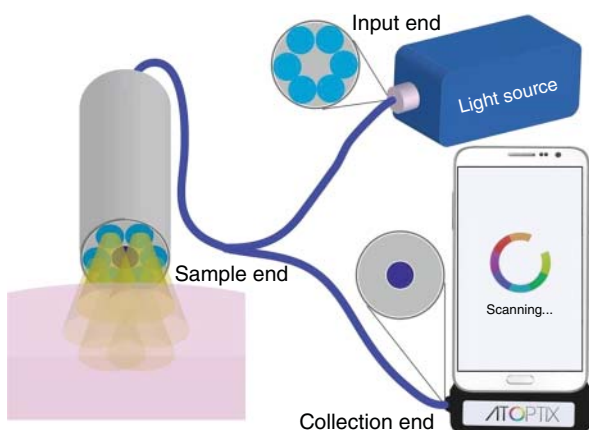


**Figure 8.6** Typical setup for reflection spectroscopy using optical fibers. Creative Commons license. Source: Edwards et al. (2017). Licensed under CC BY 4.0.

on the sample surface, there can be diffuse and/or specular components. In some cases, an integrating sphere may be required to capture both the diffuse and specular components simultaneously. Figure 8.6 shows a typical reflection arrangement using optical fibers. A fiber bundle with six illuminations and one centrally placed collection fiber is used as the probe. The sample is illuminated by the six fibers on the periphery and the reflected light is guided to the spectrometer using a splitter arrangement. This is a common reflection configuration in portable spectrometers and the use of optical fibers minimizes any alignment issues. A similar setup can be realized in a free-space arrangement without optical fibers.

This configuration is most commonly used for color-sensing applications, where the reflection spectrum of a sample needs to be determined. Color measurements are used across several industries to characterize and standardize paints, pigments, and displays among others. Section 8.5 will discuss specific examples in color sensing.

### 8.3.2 Absorption

In an absorption measurement setup, the light source and detector are on either side of the sample, as shown in Figure 8.7. Light first passes through a reference, which is typically a nonabsorbing material like distilled water. The reference transmission spectrum is captured and saved. Next, the sample is introduced and another transmission spectrum is recorded. By assuming that there are no other interactions like scattering or reflection, the absorption spectrum can be deduced from the transmission spectrum by applying Beer–Lambert’s law. Benchtop spectrometers generally have a double beam configuration for measuring absorption, wherein the reference and sample measurements can be done simultaneously. However, in portable spectrometers, those are not feasible, and measurements for the reference and sample need to be done sequentially. In such cases, fluctuations in the light source limit the sensitivity of detection. An example of a portable absorption spectrometer is shown in Figure 8.7b.

### 8.3.3 Fluorescence

Another common configuration that is especially seen in biomedical applications involves detecting fluorescence (Lakowicz 2006). Depending on the use case and sample state, there are several geometries for detecting fluorescence from thin films, solutions, droplets to powders among others. Typically, a narrowband source is used for exciting the fluorophore and the wavelength of the source chosen such that it coincides with an absorption maximum of the fluorophore. In most cases, laser sources are used to obtain suitable signal strength, but high-intensity LEDs have also been used in recent implementations. On the detector side, longpass filters are generally used to reject the excitation wavelength and only transmit the fluorescence signal comprising longer wavelengths. This is a versatile configuration where the source and detector can be arranged in absorption or reflection-like geometries.

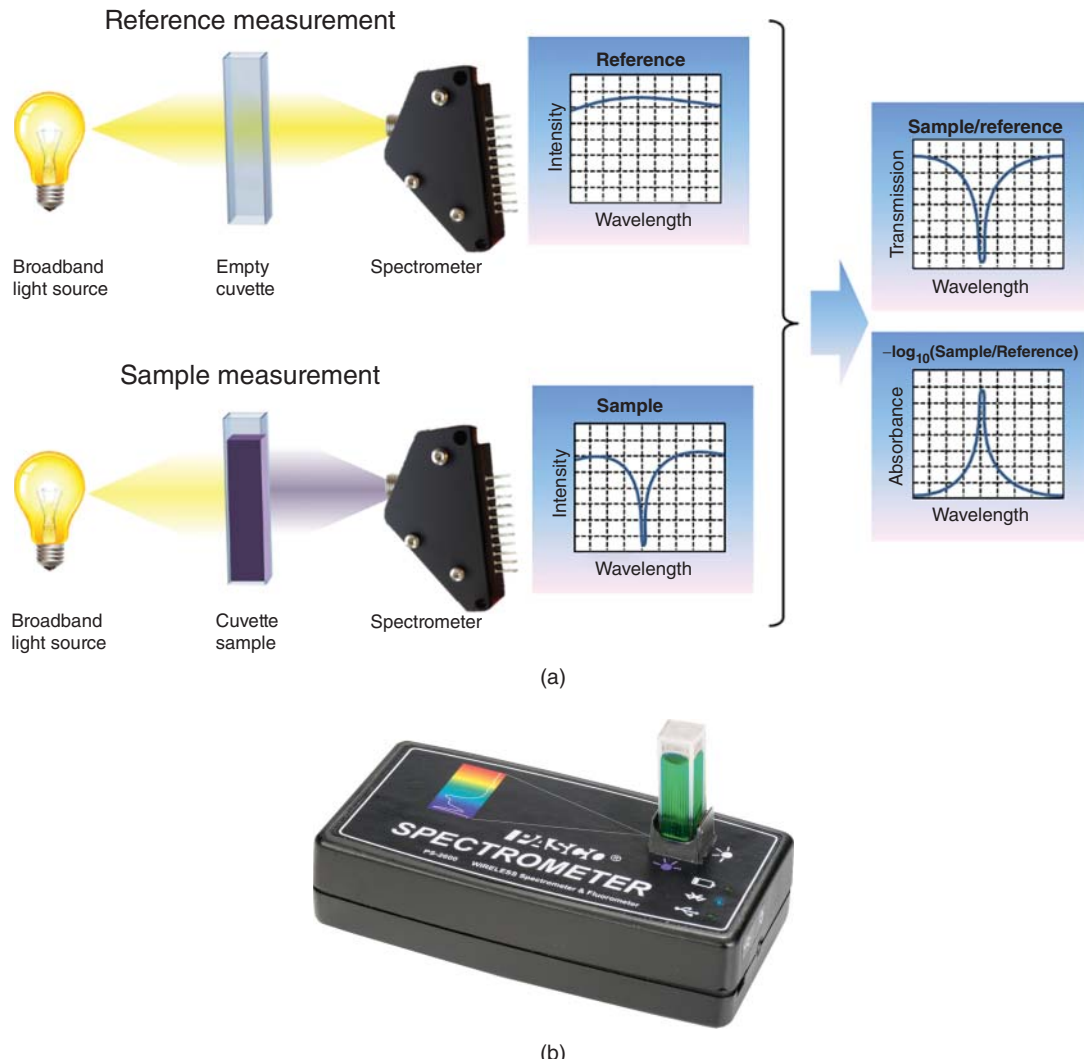


**Figure 8.7** (a) Absorption spectroscopy setup. *Source:* Permission from Ibsen Photonics. (b) Example of a portable absorption spectrometer. *Source:* Permission from PASCO.

In applications where the fluorophore has a weak fluorescence or exists in low concentrations, additional focusing optics are employed to increase the signal collected by the spectrometer. This geometry is routinely used in confocal microscopy where a spectrometer is coupled to the microscopy objective and fluorescence spectra are captured at each point as a raster scan is carried out. However, in portable fluorescence measurement configurations, optical fibers are typically used to minimize alignment errors. In some cases, a custom sample holder has been designed to house the filters and other optical components, as shown in Figure 8.8. Yu et al. demonstrated a smartphone-based spectrometer, where the fluorescence signal was incident on a grating placed at the camera of the smartphone that played the role of a detector (Yu et al. 2014). The image captured by the camera could be calibrated with known sources and a spectrum could be extracted based on that.

Although a spectrum can be obtained using the geometry shown in Figure 8.8, that is only the first step toward a usable device. Several questions need to be addressed regarding the stability of the wavelength calibration, the

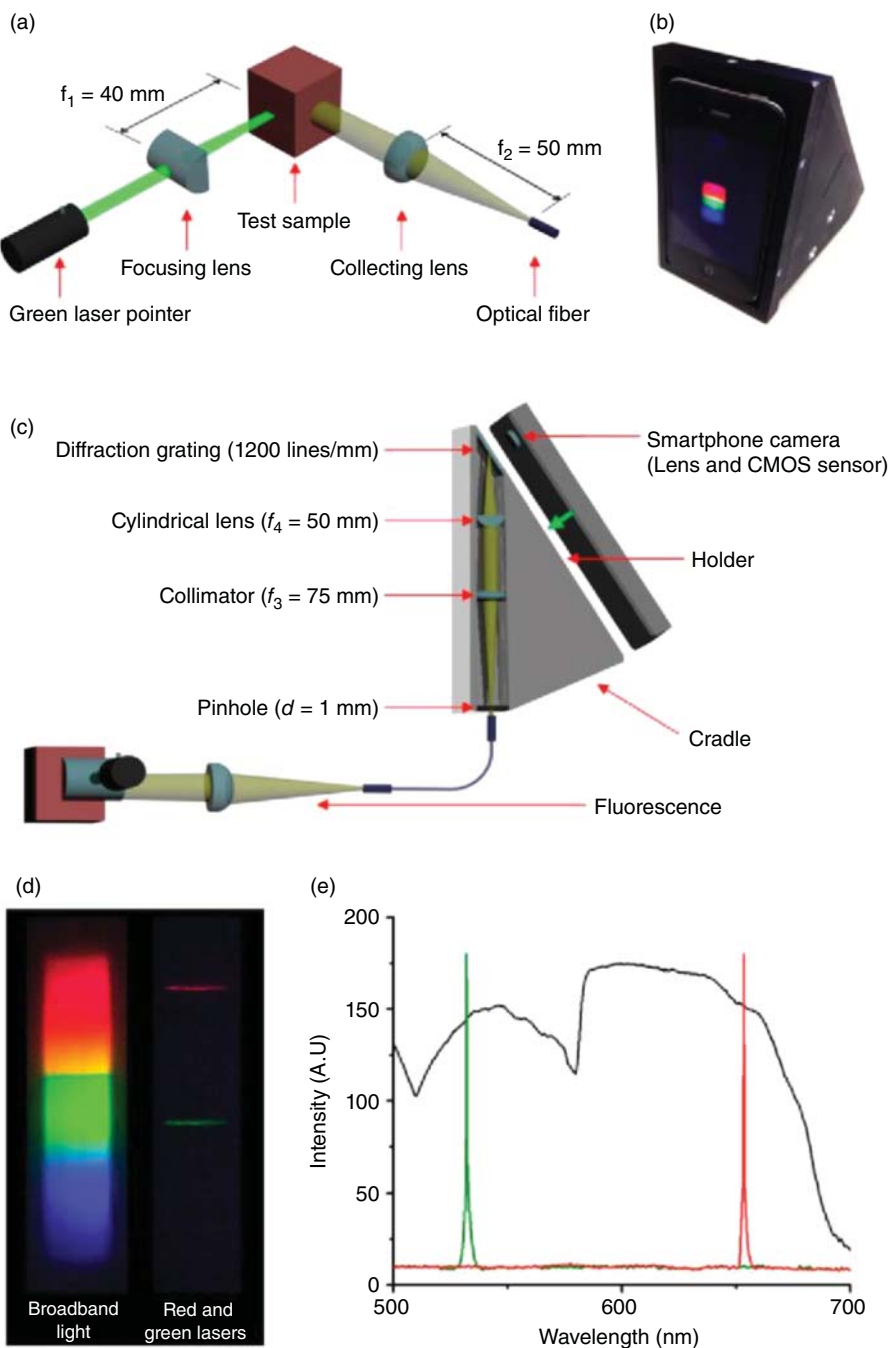


**Figure 8.8** Smartphone-based portable fluorescence spectrometer arrangement. Source: Yu et al. (2014). © 2014 American Chemical Society.

linearity of the response, effect of background noise, and summing of adjacent pixels. Without a complete understanding of the device performance and limitations, developing applications, particularly in the biomedical field can lead to low sensitivity and specificity of tests. Section 8.6 discusses some of the parameters to keep in mind when developing applications based on such spectrometer configurations.

## 8.4 Types of Instrumentation Used in UV–Vis Spectroscopy

Due to the need for robust field operation and cost constraints, several innovative designs have been demonstrated in portable UV–Vis spectrometers. Some of these are unique to portable spectrometers with marked differences compared to traditional spectrometer instrumentation. In general, the bulk of the instrumentation is focused on accurately converting an incident light signal into its spectral components. Light sources, guiding optics, A/D conversion and other peripheral electronic components are straightforward to implement. The process of reliably dispersing the incident light signal, capturing it with low noise and then converting it to a calibrated optical spectrum is a challenging aspect of spectrometer instrumentation. The accuracy of this process determines the eventual possible applications. For instance, a robust implementation allows for use of such devices in highly sensitive biomedical applications, whereas a basic lower quality version would be good for teaching purposes.

In this section, various approaches for achieving light dispersion and subsequent conversion to the light spectrum will be introduced.

### 8.4.1 Grating with Linear Detector Array

This approach can be considered as a compressed version of a traditional benchtop spectrometer. Almost all the instrumentation is identical except for a reduction in component size and distances involved. A diffraction grating is used to spatially disperse the incident light signal and a suitably placed linear detector array simultaneously captures its constituent spectral components, as shown in Figure 8.9a. Typically, the linear array is comprised of  $2^n$  ( $n = 8,9,10,11,12\dots$ ) CCD or CMOS pixels. The grating density, size, and the number of pixels determine the wavelength resolution of the spectrometer. Additionally, the input aperture diameter, optical magnification, and aberrations can affect the final spectral resolution. These spectrometers are also called array or grating spectrometers due to the instrumentation type, as shown earlier in Figure 8.5.

### 8.4.2 Digital Micromirror Devices

A major drawback of linear array-based spectrometers is the need for a sensor with multiple pixels or detectors. Typically, to achieve a wavelength resolution of around 1 nm or lower, 4096 pixels may be required. This is not a problem for Si-based detectors as image sensors in consumer cameras generally have a comparable number of pixels. However, if the detector is made from other materials like InGaAs or Ge in the case of NIR spectrometers, the cost of the device increases significantly. In such cases, single detector arrangements are desirable. An alternate approach involves using Fourier transform (FT)-based techniques. Although FT spectrometers are quite popular, they have some drawbacks. For instance, they do not directly measure spectra, but obtain interferograms, which need to be transformed into spectra by postprocessing. This enforces a higher requirement for computing power. In 2003, Spudich et al. came up with an innovative approach that eliminates linear arrays and addresses the drawbacks of FT-based systems (Spudich et al. 2003). They introduce a digital micromirror array where the orientation of the mirror can be digitally controlled. After a grating splits the incident light into the spectral components, each micromirror sequentially reflects light on to a single detector, almost behaving like a rotating grating. A spectrum can be generated after all the micromirrors have reflected their respective spectral components. Since these mirrors have a size of 10  $\mu\text{m}$  and a pitch of about 5.4  $\mu\text{m}$ , they can be operated at microsecond-switching speeds.

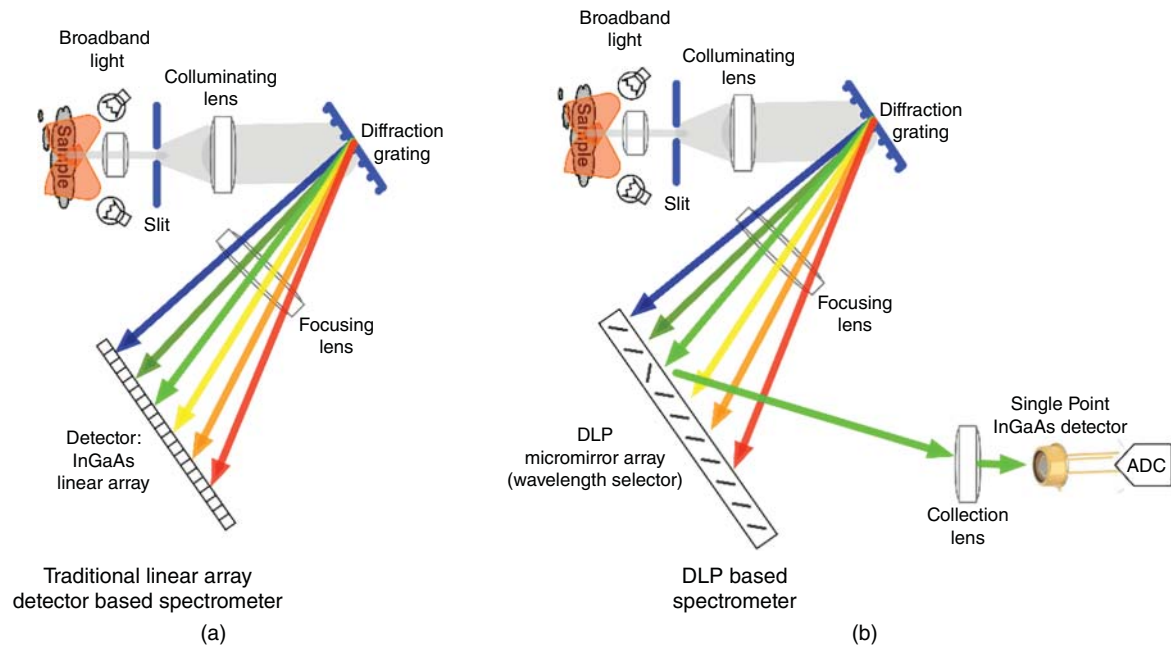


**Figure 8.9** (a) Traditional array-based spectrometer. (b) Micromirror-based spectrometer. Source: © Texas Instruments.

This allows for fast acquisition of spectra with minimal postprocessing requirements, based on a Hadamard transform. Recently, Texas Instruments (TI) commercialized micromirror-based spectrometers using their digital light projector (DLP) technology (Gelabert et al. 2016), as shown in Figure 8.9b. Figure 8.10 shows a micromirror-based spectrometer using the DLP2010NIR module, which can operate from 700 to 2000 nm.

#### 8.4.3 2D Filter Array-Based Devices

For grating-type spectrometers to be effective, there has to be a gap introduced between the grating and the linear detector array. A larger gap allows for better spatial separation of wavelengths, which results in higher resolution. Due to this inherent requirement, conventional grating-type spectrometers cannot be made into miniature chip-like devices unless monolithic fabrication is carried out. As a result, these portable grating-based spectrometers often have dimensions in the tens of centimeters. There are applications that require ultracompact spectrometers, where resolution can be traded for size. For instance, in space applications, there is a need for lightweight and compact sensors. In such scenarios, spectrometers fabricated with grating-free elements, such as filter arrays are more suitable (Oliver et al. 2013). In this approach, a filter array with varying transmission spectra is placed over a CCD image sensor, as shown in Figure 8.11a.

In this arrangement, the filters have a selective transmission spectrum that exclusively allows a narrow wavelength band. By designing several filters that cover a given spectral region, a spectrum can be reconstructed by analyzing the intensities obtained at individual pixels of the CCD. Wang et al. demonstrated a 128-channel filter array-based spectrometer with dimensions of  $12\text{ mm} \times 12\text{ mm} \times 5\text{ mm}$ , giving rise to a volume of  $1\text{ cm}^3$  (Wang et al. 2007). Although this technique yields extremely compact spectrometers, fabricating a 128-channel filter array with each pixel having a different transmission pattern is quite tedious.

On similar lines, quantum dots (QDs) have also been used as filters due to ease of manufacturing. Chemical approaches can be used to alter the transmission properties of QDs and create the desired filter array. Bao and Bawendi demonstrated a QD spectrometer (Bao and Bawendi 2015) comprising a filter with 195 unique QDs, as shown in Figure 8.12.

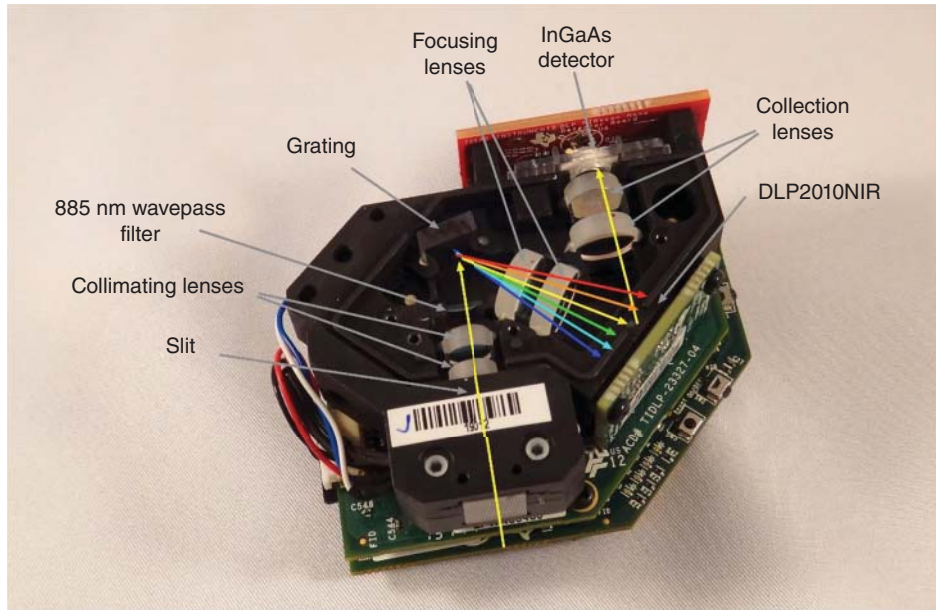


**Figure 8.10** Micromirror-based spectrometer developed by Texas Instruments. *Source:* Texas Instruments Incorporated.

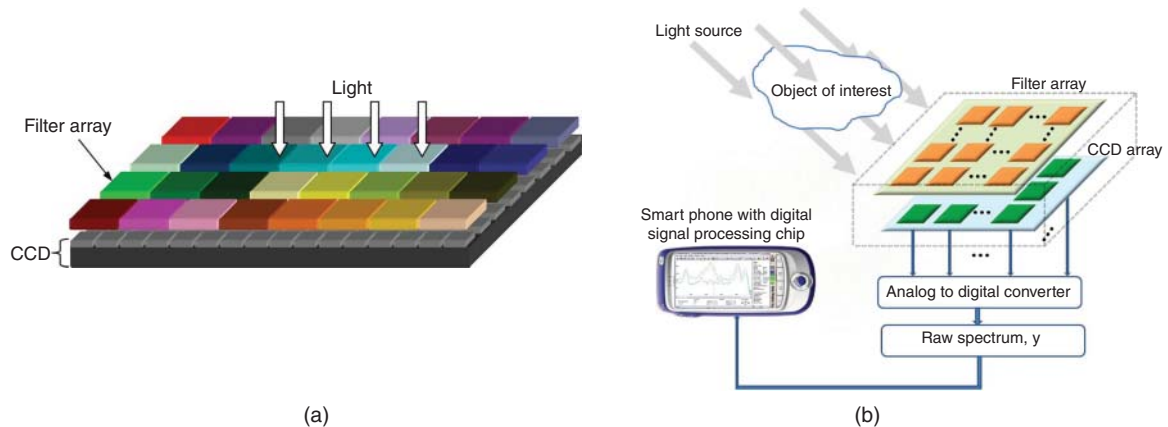


**Figure 8.11** (a) Filter array-based portable spectrometers. *Source:* Wang et al. (2007). © 2007 The Optical Society (b) Filter array with the random transmission. *Source:* Oliver et al. (2013). © 2013 The Optical Society.

Even though this approach is promising for realizing ultracompact spectrometers, most demonstrations have been shown in laboratories. There is one commercial instance of a spectrometer based on this approach called SCiO (SCiO n.d.). This product uses 12 filters in an array and operates from 700 to 1100 nm. Limited studies have shown reasonable prediction accuracy for measuring fat and moisture using this approach.

#### 8.4.4 Smartphone Camera-Based Approaches

In recent years, due to the ease of accessibility, high computational power and high-resolution cameras of smartphones, several groups have utilized smartphones as the central detection and computation module. This approach

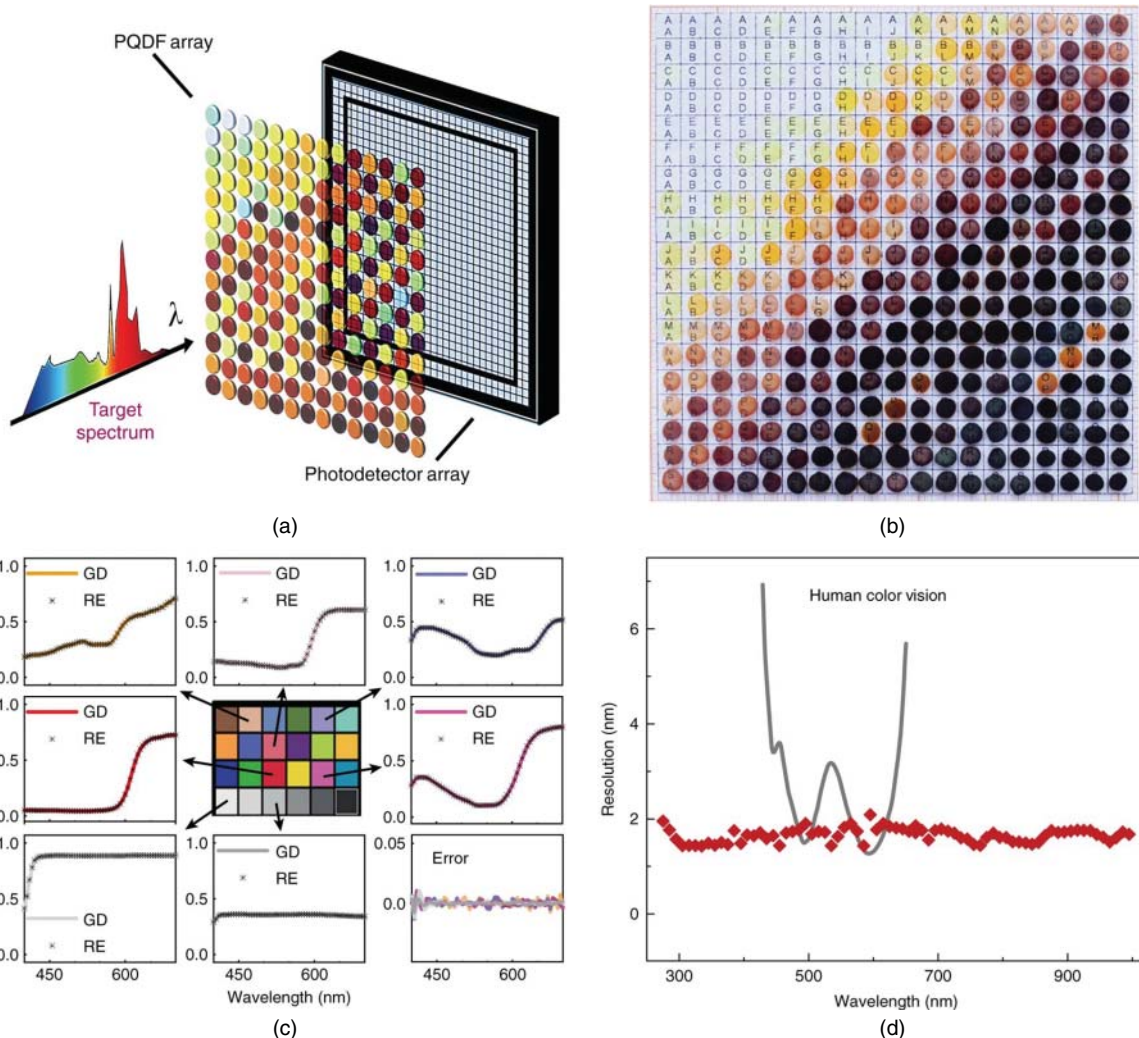


**Figure 8.12** Quantum dot spectrometer. (a) Schematic and (b) detailed configuration. Source: Bao and Bawendi (2015). © 2015 Springer Nature.

eliminates the need for components, like displays, A/D converters, and other peripheral communication circuitry (Long et al. 2014; McGonigle et al. 2018). An external battery-powered light source can be used with a grating directly in line with the smartphone camera, as shown in Figure 8.13. A test sample is introduced in this path and the spatially dispersed light is captured on the smartphone camera (de Oliveira et al. 2017). By accessing the raw optical data, the effect of Bayer color filters can be suppressed. Finally, using light sources with known wavelengths, a calibration can be set up.

This approach offers a cost-effective way to realize spectrometers without designing displays and other electronic components. However, not many commercial spectrometers based on this approach have reached the market, except for some do-it-yourself (DIY) kits that will be introduced in the next subsection. The technical details of smartphone-based spectrometers are described in the chapter in this Volume by Scheeline, and the field clinical applications in the chapter by Algar in Volume 2.

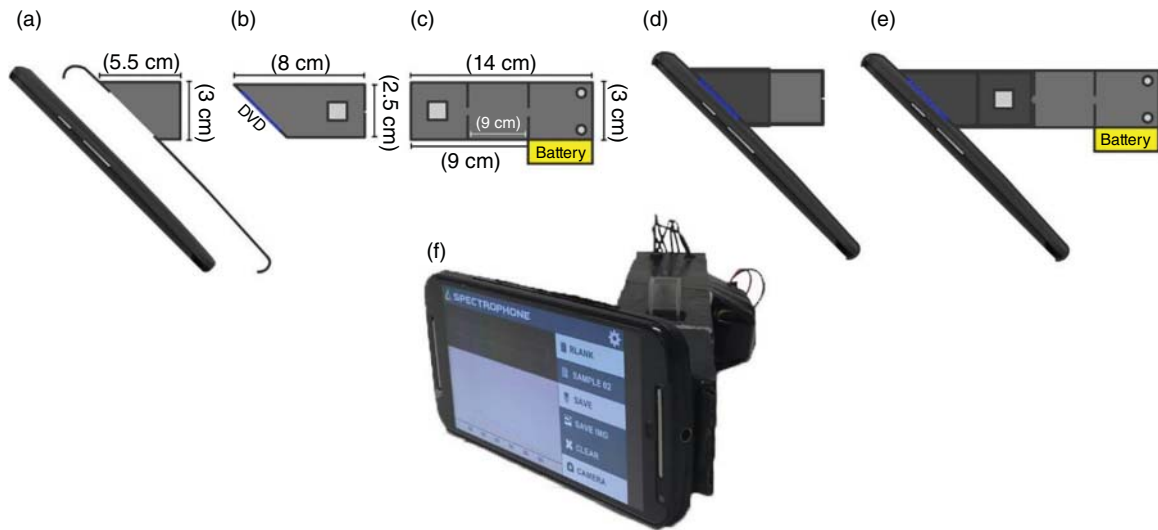


**Figure 8.13** Spectrometer design utilizing the camera of a smartphone as the detector. *Source:* Permission from Oliviera et al. (2017). © 2017 Elsevier.

#### 8.4.5 “DIY” Approaches

The emergence of rapid prototyping using 3D printers, laser cutters, and computer numerical control (CNC) machines has also ushered in DIY approaches for building spectrometers from readily available and inexpensive components (Hopkins 2014; Scheeline and Kelley 2013). For instance, Public Lab offers spectrometer kits for under \$10 consisting of a laser-cut cardboard attachment housing a DVD fragment that serves as the grating, as shown in Figure 8.14a. This attachment can be aligned with the camera of a smartphone to observe spectra using any camera app. This approach offers a great way to introduce spectroscopy into a teaching curriculum without the need for expensive spectrometers. Since these devices are suitable for education and hobby activities, they have



**Figure 8.14** DIY Spectrometer Kits. (a) Attachment for a smartphone. (b) Complete assembly. *Source:* Permission from Jeffrey Yoo Warren and Public Lab.

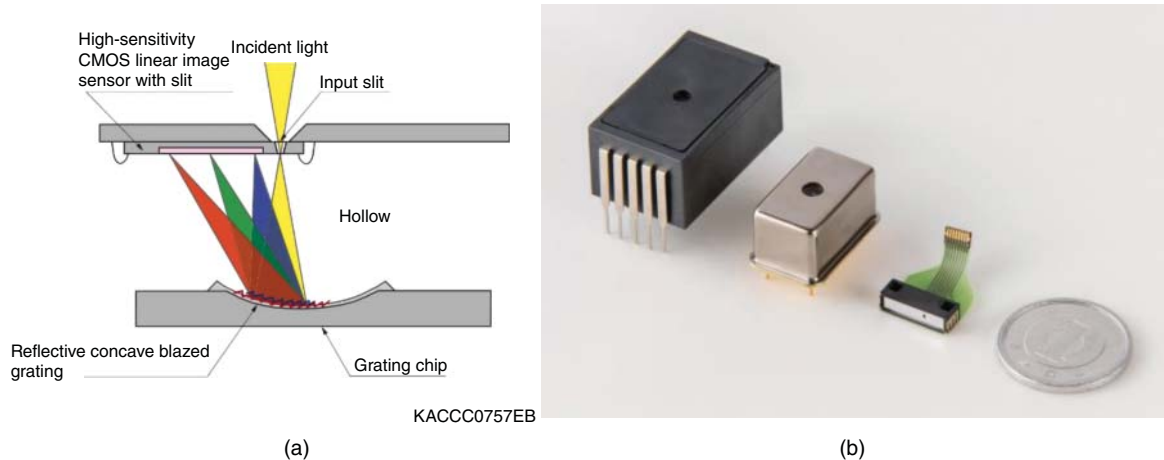


**Figure 8.15** (a) Architecture of MEMS-based spectrometer. *Source:* Structure/Technology | Mini-spectrometers, Hamamatsu. © Hamamatsu Photonics K.K. (b) Line of micro-spectrometers from Hamamatsu Photonics. *Source:* Photo courtesy of Hamamatsu Photonics.

limited applicability in scenarios that require high sensitivity and robust operation. In one instance, a webcam was modified with fiber optic cables to perform the action of an *n*-channel spectrometer (Sumriddetchkajorn and Intaravanne 2012).

#### 8.4.6 Compact Chip-Based Spectrometers

With the advent of advanced lithographic techniques for fabricating nanostructures, it is becoming possible to integrate optical assemblies at a chip level. For instance, Hamamatsu Photonics (Shibayama and Suzuki 2008) introduced a microspectrometer chip that had a blazed grating and CMOS linear sensor integrated into a single chip, as shown in Figure 8.15a. The spectrometer chip was fabricated using techniques commonly used in micro-electromechanical systems (MEMS) manufacturing. These chips only weigh about 5 g, have a wavelength resolution around 10–15 nm, and can operate from 340 to 840 nm. Recently, an SMD spectrometer chip (Figure 8.15b) was introduced that is designed to operate in the 640–1050 nm range and has a weight of 0.3 g, thereby making it suitable for applications where lightweight sensors are desirable.

#### 8.4.7 Standalone Smartphone Spectrometers

Smartphone-based spectrometers could be defined as devices where a significant process of the spectral conversion and postprocessing is carried out in a smartphone. This could be either using the phone's camera as an image sensor or capturing wireless spectral data followed by postprocessing on the phone through an app. Most examples introduced in previous sections used the camera of a smartphone and postprocessing to obtain a spectrum. In this subsection, some examples of standalone smartphone spectrometers are presented. Here, the spectrometer does not use the smartphone camera but has an inbuilt detector along with dispersing elements and other circuitry (Das et al. 2016). Most commonly, data captured from the sensor is transmitted using a wireless communication framework.

Bluetooth antenna and transmit/receive (Tx/Rx) protocols have been used in most such devices. An app on the smartphone is able to control the operation of the spectrometer, trigger data capture and Rx/Tx operations. Das et al. (2016) demonstrated a high-performance smartphone spectrometer design that used the Hamamatsu microspectrometer chip, as shown in Figure 8.16. They designed and fabricated all the wireless and control

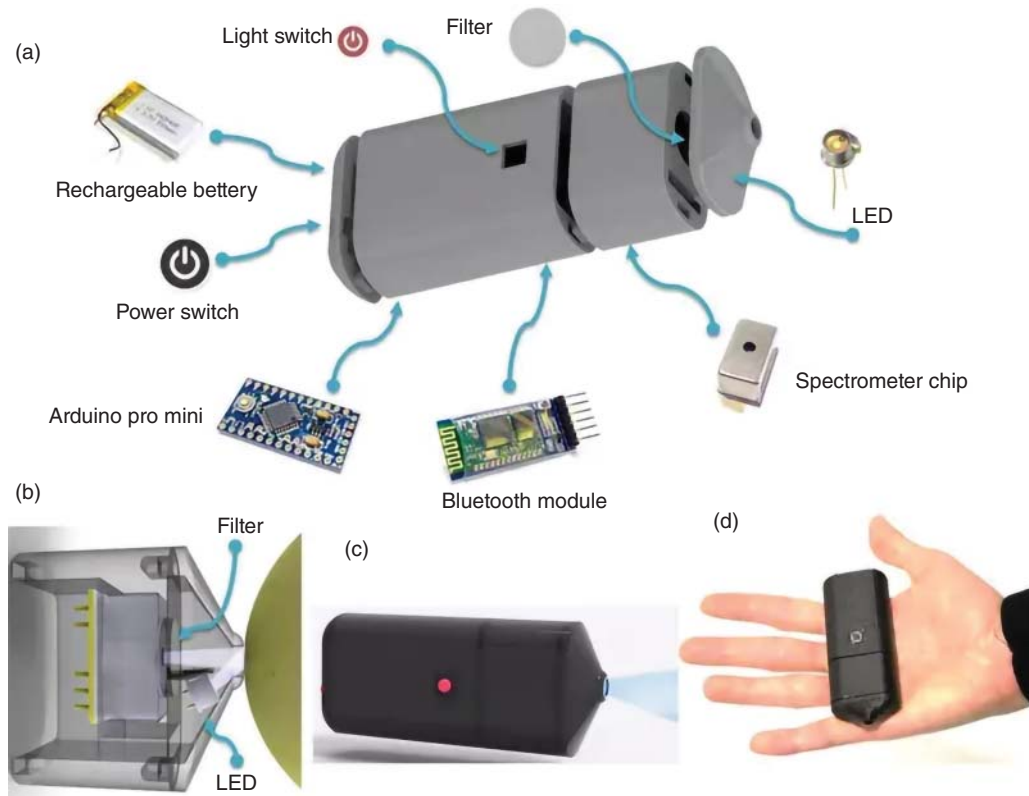


**Figure 8.16** Components involved in a standalone smartphone spectrometer developed by Labby Inc. Source: Das et al. (2016). Licensed under CC BY 4.0.

circuitry along with a customized smartphone app that could calibrate and process the data on the phone itself. This configuration is advantageous for remote operation where the smartphone needs to be at a distance from the spectrometer. Bluetooth antenna can communicate with the smartphone at a distance of up to 9–12 m for classic chips and beyond 100 m for low-energy chips. Additionally, it can work with any smartphone that has the app installed, without having to deal with specific camera configurations. However, they are more expensive mainly due to the chip.

## 8.5 Applications

In this section, various applications of portable UV–Vis spectrometers will be discussed.

### 8.5.1 Color Sensing

By far, the most common use of portable UV–Vis spectrometers is in color sensing (Giusti and Wrolstad 2001). The ability to quantifying color characteristics in terms of RGB, Lab, XYZ,  $\Delta E$  (color difference), and other metrics is central to several industries. Color matching is an important process for selecting paints in virtually any application that uses them. Portable color sensors are routinely used for color selection and matching in dentistry (Brewer et al. 2004; Sproull 1973), automotive (Streitberger and Dössel 2008), displays (Streitberger and Dössel 2008), food and



**Figure 8.17** Some portable color-sensing spectrometers. (a) Hach DR900. *Source:* Courtesy of Hach. (b) HunterLab Miniscan EZ 4500L. *Source:* Hunter Associates Laboratory, Inc. (c) Nix QC. *Source:* NIX SENSOR, LTD. (d) X-Rite eXact. *Source:* X-Rite, Incorporated.

beverage (Giusti and Wrolstad 2001), anthocyanins (Giusti and Wrolstad 2001), and textile (Berns 1992; Zhang and Li 2008) industries among many others. Spectrometers are used to obtain a calibrated reflection spectrum which is the first step in color measurement. Depending on the illuminant and International Commission on Illumination (CIE) color space, a reflection spectrum can be transformed to RGB, Lab, cyan, magenta, yellow, and key (CMYK), and other systems. Notable examples of portable color sensors are X-Rite, HunterLab, Nix, and Hach, as shown in Figure 8.17. Some color sensors, based on discrete filter sensors, are the size of a lipstick and can cost as low as \$59.

In addition to color systems like RGB and Lab, industrial applications have their own standards for quality control of oils, lubricants, beer, wine, etc. For instance, ASTM D1500D and D6045 are color-based methods for quantifying oil quality. ASBC 10 (standard reference method, SRM) is a standard for measuring beer color, whereas OIV-MA-AS2-07B is a standard for wine color (tone and intensity) using spectrophotometric methods (Streitberger and Dössel 2008).

### 8.5.2 Life Science Assays

Portable UV-Vis spectrometers have shown great potential in point-of-care (POC)-based assays, especially in enzyme-linked immunosorbent assay (ELISA) (Thiha and Ibrahim 2015). Most implementations of ELISA use either fluorescence or absorption spectroscopy in the UV-Vis spectrum, which makes UV-Vis spectrometers ideal for such applications (Schmid 2001). Long et al. demonstrated a smartphone-phone spectrometer-based ELISA for detecting peanut allergens (Long et al. 2014). They used the camera of the smartphone as the detector, earlier

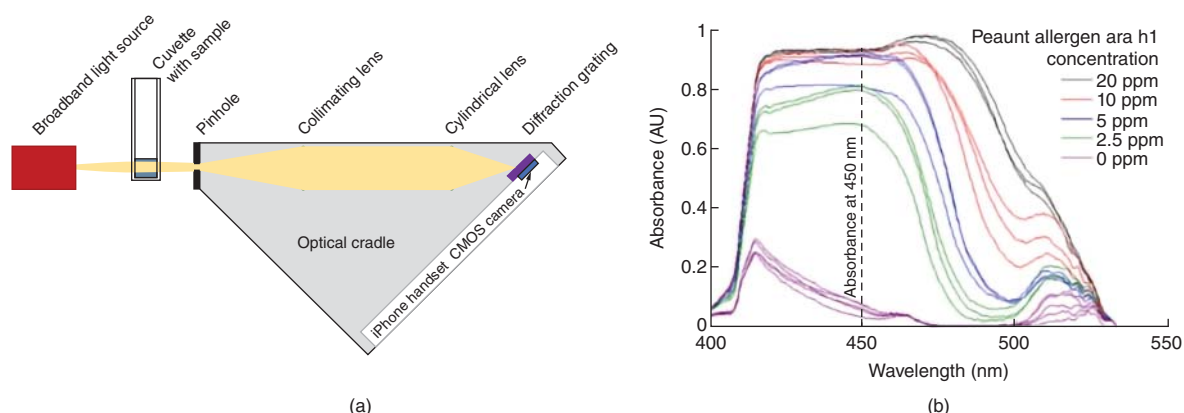


**Figure 8.18** (a) Smartphone spectrometer arrangement for ELISA. (b) Absorption spectra correlated to peanut allergen. Source: Long et al. (2014). © 2014 Optical Society of America.

described in Section 8.4.4. A schematic of their setup is shown in Figure 8.18a along with the absorption spectra in Figure 8.18b.

Nucleic acids like deoxyribonucleic acid (DNA) and ribonucleic acid (RNA) have a characteristic absorption peak at around 260 nm, which can be used to detect and quantify their concentration (Desjardins and Conklin 2010). Additionally, proteins have an absorption centered at around 280 nm. Portable UV spectrometers are well-suited for these applications. For instance, the NanoDrop™ is a portable spectrophotometer that only intakes 1–2  $\mu$ l of a sample and can analyze absorption or fluorescence spectra to detect concentrations of nucleic acids and proteins. Figure 8.19a shows the NanoDrop One/OneC spectrophotometer manufactured by Thermo Fisher. Another small-volume spectrometer is the UV5Nano from Mettler Toledo, as shown in Figure 8.19b.



**Figure 8.19** (a) NanoDrop One/OneC spectrophotometer. Source: Permission from Thermo Fisher. (b) UV5Nano small volume spectrometer. Source: METTLER TOLEDO.



**Figure 8.20** Smartphone-based fluorescence spectrometer for the screening of skin disease. Source: Poojary et al. (2019).

### 8.5.3 Biomedical Applications

Several molecules that constitute blood, urine, and skin have absorption or fluorescence in the UV–Vis spectrum. As a result, spectrometers operating in this spectral region can be used for not only detecting concentrations of chromophores like hemoglobin (Edwards et al. 2017), but also screen for any disease or abnormalities in a POC setting (Das et al. 2015). Wahi et al. (2018) demonstrated a smartphone spectrometer to excite fluorophores in the skin, such as collagen and NADH (nicotinamide adenine dinucleotide (NAD) plus hydrogen (H)) with 385 nm UV-A light for diagnostic applications. Poojary et al. (2019) used a portable smartphone spectrometer to screen for skin diseases like vitiligo by observing UV fluorescence, as shown in Figure 8.20. Their device was effective in detecting hyperpigmentation and hypopigmentation in the skin with the advantage of tracking variations over time. This could be useful in monitoring treatments of patients who are receiving different medications and determining efficacies (Figure 8.21).

Edwards et al. demonstrated a Grating-Fresnel (G-Fresnel) spectrometer design that could measure hemoglobin concentration from diffuse reflectance spectra from tissue phantoms (Edwards et al. 2017). They obtained errors under 10% for hemoglobin concentration, which establishes the efficacy of these devices for POC settings. In another study, Maity et al. developed a portable spectrometer for detecting malaria in blood samples (Maity et al. 2019). Thiha et al. demonstrated a portable absorption spectroscopy-based ELISA reader for diagnosing dengue fever (Maity et al. 2019). Although only a few of these devices have made it to the market, these studies point to the potential of the portable spectrometer for biomedical applications.

### 8.5.4 Water Testing

An established application of portable UV–Vis spectrometers has been in water quality testing, with several products available today in the market. Water quality analysis plays an important role in the individual- and community-level health. There is always a threat for water contamination from various sources, such as industrial waste, sewage (Langergraber et al. 2004), agricultural pollution among others. In such scenarios, a portable device can prove crucial for testing water quality from reservoirs and other sources. For instance, measuring the absorption spectrum of water can detect several colored materials like dyes (Antonov et al. 1999; Özdemir et al. 2017). Additionally, reagents can be used to bring about some kind of contrast to improve the detectability of trace or nonabsorbing contaminants. The Hach DR3900 is an excellent example of a portable water quality tester that has been used for detecting a host of contaminants, such as chromium, ammonium, and phosphorus, among others, as shown in Figure 8.22.

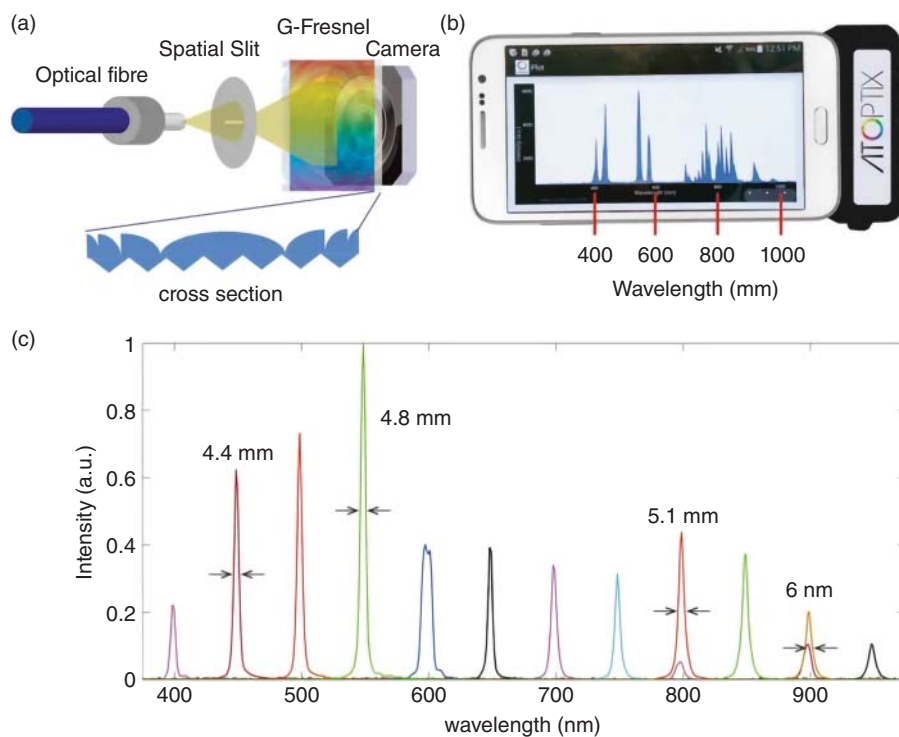


**Figure 8.21** G-Fresnel spectrometer for detecting hemoglobin concentration. Source: Edwards et al. (2017). Licensed under CC BY 4.0.



**Figure 8.22** Hach DR3900 spectrophotometer for water quality analysis. Source: Courtesy of Hach.

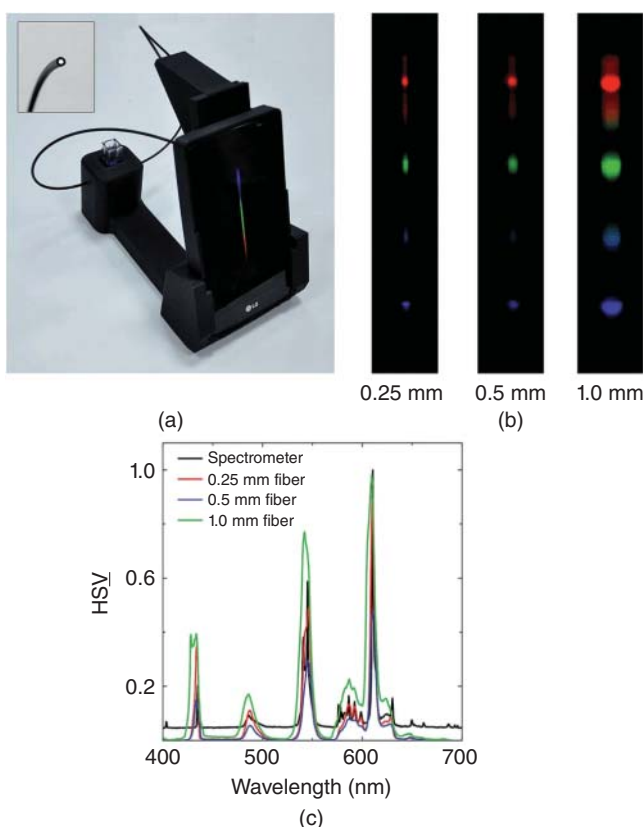


**Figure 8.23** Smartphone spectrometer for detecting methylene blue in the water. (a) Smartphone spectrometer prototype with an optical fiber coupled to the camera flash. (b) Images of light output from the fibers. (c) Spectra corresponding to the fibers compared with a standard spectrometer. *Source:* Özdemir et al. (2017). © 2017 Royal Society of Chemistry

In a recent study, Özdemir et al. (2017) demonstrated a smartphone spectrometer for detecting dyes like methylene blue by adsorbing dye molecules on polyacrylonitrile (PAN)/zeolite nanofibers, as shown in Figure 8.23. In another example, Wang et al. used a DVD grating-based smartphone spectrometer to detect neurotoxins in water (Wang et al. 2016).

### 8.5.5 Food and Beverage Applications

By far the most commonly researched application of portable spectrometers is in the space of food and beverage quality analysis. They have been used for a range of applications, such as detecting ripeness (Das et al. 2016), composition, chlorophyll content (Maxwell and Johnson 2000; Porra et al. 1989), anthocyanins (Boulton 2001; Giusti and Wrolstad 2001; Gupta et al. 2018), phenols (Acevedo et al. 2007; Martelo-Vidal and Vázquez 2014), and meat freshness (Boulton 2001; Giusti and Wrolstad 2001; Gupta et al. 2018), among others. This is attributed to the fact that fruits, vegetables, cheese, meats, and seafood all contain components that absorb, reflect, or fluoresce under UV-Vis light. Many of these components also change as foods age, and, hence, can be good indicators of ripeness or freshness. For instance, Das et al. (2016) developed a portable smartphone spectrometer that utilized a longitudinal variation of chlorophyll fluorescence to determine the ripeness of a variety of apples, as shown in Figure 8.24.

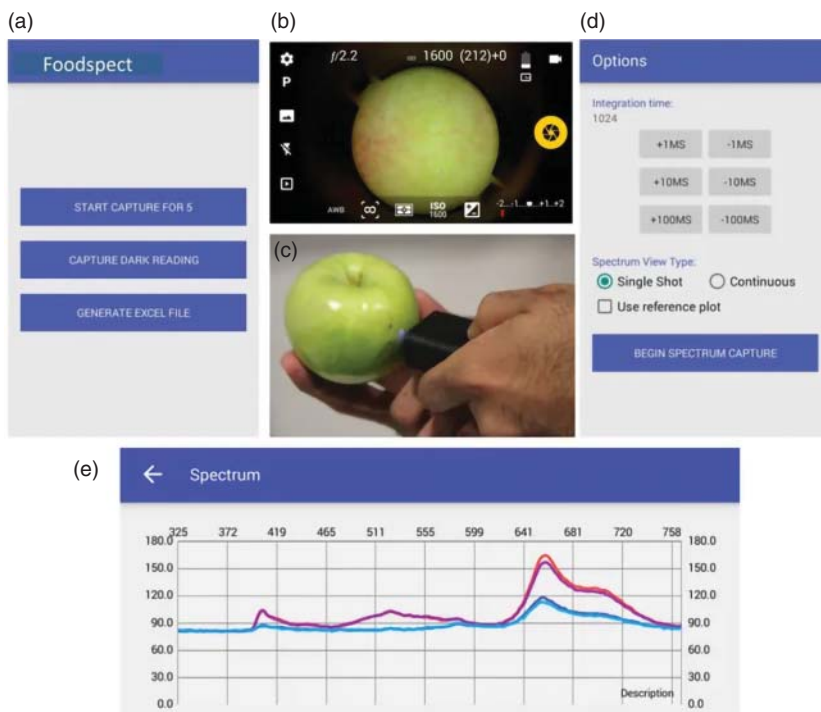


**Figure 8.24** Smartphone spectrometer for detecting ripeness of apples using chlorophyll fluorescence. *Source:* Permission from Das et al. (2016).



**Figure 8.25** Linksquare smartphone spectrometer being used in fruit freshness analysis. *Source:* Permission from Linksquare and You et al. (2017).

In this application space, there are a few commercial portable Vis spectrometers out in the market, such as Linksquare, which have shown some success in classifying food and detecting freshness, as shown in Figure 8.25a. You et al. (2017) used the Linksquare spectrometer to classify identical-looking food powders, like sugar, salt, rice, etc., using reflection spectroscopy, as shown in Figure 8.25b. They used machine learning algorithms for classification and achieved near 100% accuracy for eight different types of food powders.

In another report, Cai et al. (2017) demonstrated pencil-like spectrometer using a prism-grating configuration with an image sensor, as shown in Figure 8.26a. The spectrometer operated in the 400–675 nm region with a

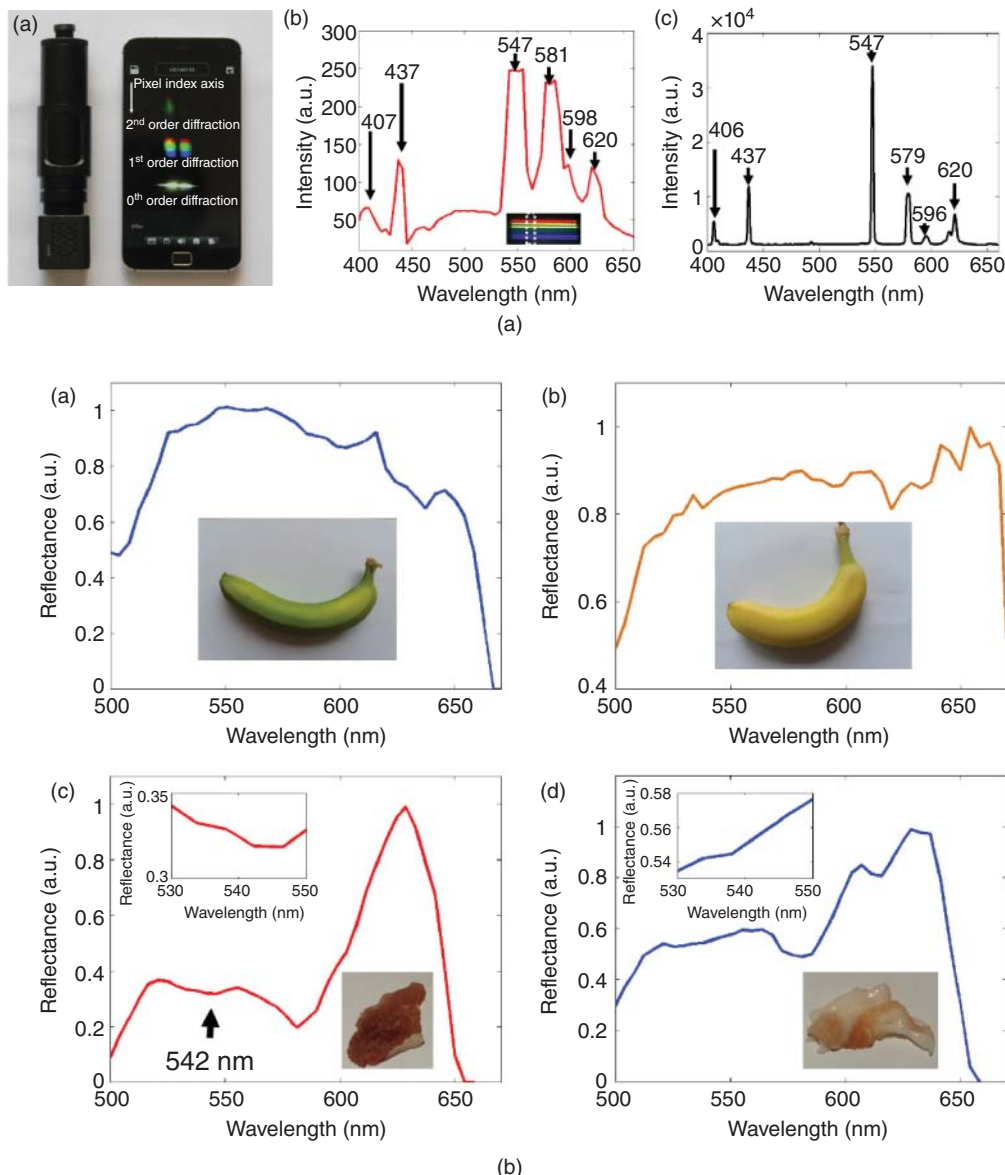


**Figure 8.26** Top. Panel A, Pencil-like smartphone spectrometer. Panel B, Mercury lamp spectrum captured by the pencil spectrometer. Panel C, Mercury lamp spectrum obtained using a commercial spectrometer. Bottom. Panel A, Reflectance spectrum of unripe banana. Panel B, Reflectance spectrum of ripe banana. Panel C, Reflection spectrum of pork muscle. Panel D, Reflection spectrum of pork fat. *Source:* Cai et al. (2017). © 2017 Optical Society of America.

resolution of 17 nm. The spectrometer was used for several applications including detecting ripeness of bananas and freshness of pork, as shown in Figure 8.26b.

### 8.5.6 Geosensing Applications

Spectroscopy has been a powerful technique for atmospheric and environmental remote sensing. In recent years, portable spectrometers have been increasingly used in volcanology, aerosol sensing, and detection of atmospheric

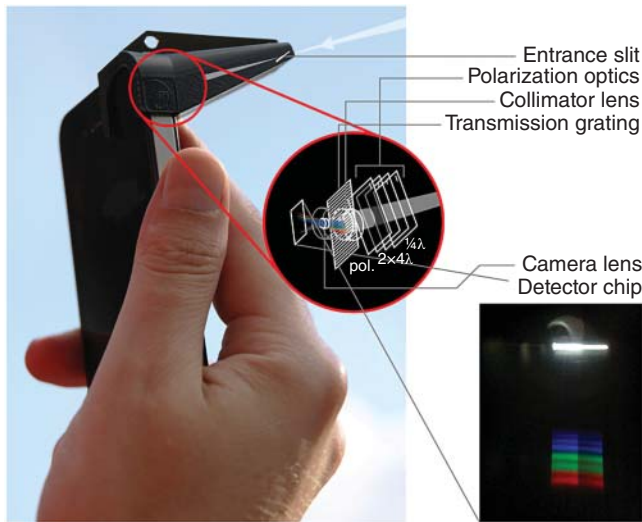


**Figure 8.27** Smartphone spectropolarimeter for sensing atmospheric aerosols. Source: Snik et al. (2014). © 2014 John Wiley & Sons

gases, like  $\text{SO}_2$ , among other applications. For instance, Snik et al. (2014) demonstrated a smartphone spectropolarimeter for aerosol mapping, which measured the degree of linear polarization as a function of wavelength, as shown in Figure 8.27. They designed a low-cost add-on comprising polarizers and a transmission grating, which was attached to the camera of the smartphone. Using this miniature arrangement, multiple (over 3000) measurements could be conveniently made by “citizen spectroscopists.” Reasonable agreement between ground-based spectrometers was observed, which establishes the potential of portable spectrometers for aerosol sensing.

Galle et al. (2003) developed a portable UV spectrometer for sensing  $\text{SO}_2$  emissions for applications in volcanic surveillance. The spectrometer had a Czerny–Turner configuration and operated in the 245–380 nm spectral range for achieving differential optical absorption. A telescope was used to capture the scattered UV light from aerosols, which was then coupled to the spectrometer using an optical fiber cable, as shown in Figure 8.28a. The telescope-spectrometer arrangement could be mounted on a car, a helicopter, or a tripod, such that measurements

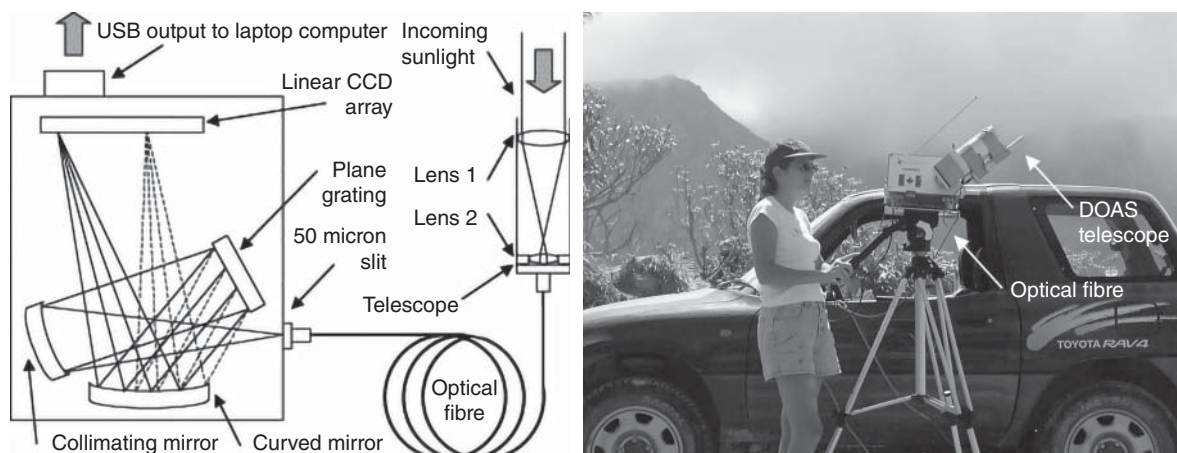


**Figure 8.28** Portable UV spectrometer for  $\text{SO}_2$  detecting during volcanic eruptions. (a) Spectrometer design. (b) Field implementation. Source: Permission from Galle et al.



**Figure 8.29** Ocean Optics STS spectrometer mounted on a drone. *Source:* Ocean Optics Inc. and VOXearch Inc.

could be made close to the site of the volcanic eruption, as shown in Figure 8.28b. Compared to the existing SO<sub>2</sub> detectors, this approach was attractive as the spectrometer could capture the entire UV spectrum, thereby providing greater flexibility to identify errors and apply better statistical methods. Furthermore, a good agreement was observed with a standard correlation spectrometer, which established the accuracy of their prototype.

### 8.5.7 Spectrometers on Drones and Aerial Platforms

Due to the recent availability of compact microcontrollers, like Raspberry Pi and Arduino, and the ease of interfacing with a host of peripheral components, it has become increasingly possible to integrate spectrometers on to unmanned aerial vehicles (UAVs) or drones and other aerial platforms (Dwight et al. 2018; Hakala et al. 2018). This allows for surveillance of vegetation and crops, forests, and other natural resources on a large scale. For instance, Ocean Optics has developed a spectrometer kit designed for drone applications, as shown in Figure 8.29. This spectrometer operates in three ranges – UV (190–650 nm), Vis (350–800 nm), and NIR (650–1100 nm). It has a 2.4 GHz Wi-Fi link that operates in a range of up to 150 m. Furthermore, the kit works on a Raspberry Pi microcontroller, which makes it straightforward to control and capture data. Due to this feature, it can work with most imaging and navigation systems. The drone-spectrometer has already been used by research groups for monitoring for pesticides and fertilizers in farms.

## 8.6 Challenges for Portable Spectrometers

### 8.6.1 Tools Versus Toys

Portable UV–Vis spectrometers have been in the market for decades now and have shown promise in a range of applications. However, with the emergence of new approaches, like filter arrays, chip-based sensors, micromirrors, and image-based spectrometers, there has been an explosion in researchers demonstrating proof-of-concept demonstrations. While this opens up new opportunities for applications, there are instances where there is not much focus on performance characterization. Just being able to detect a spectrum is not a sufficient criterion for the method to be applicable in a realistic application. Spectroscopic measurements go beyond mere spectral acquisition and involve several steps from sample information/preparation, dark and reference acquisition, sample

acquisition, spectral data conditioning, postprocessing, and, finally, interpretation. Without careful assessments at each stage, errors can propagate and result in less-effective measurements. A distinction should be made whether the spectrometer is a “toy” or a “tool.” A toy version would be great for educational and hobby use, whereas a tool version would be imposed with stringent performance requirements. The issues involved in the construction of appropriate libraries and calibrations are described in the chapter by Schreyer.

Although there are several approaches and reports of new spectrometer designs, only a few of them have made it to the market. Within them, a smaller subset has been commercially successful. By looking at established spectrometers in the market, it is possible to impose certain constraints, such as ease of manufacturing, scalability, robustness, among others, that will determine the successful deployment of newer portable spectrometer technologies. This section highlights a few aspects that will aid in the development of robust spectrometers.

### 8.6.2 Need for Robust Protocols

Establishing a protocol is critical for obtaining effective test results. A robust protocol starts with proper attention to the sample. Is there sample preparation needed? Is the sample contaminated? Is the sample homogenous? Are there relevant spectral changes in the region being measured? These are a few questions to ask before actually going ahead with tests. Unfortunately, there have been instances of commercial demonstrations where a portable spectrometer is shown to operate with random sample geometries, and accurate results are claimed. Materials like animal feed and hay are very inhomogenous, and a forage testing lab would make pellets out of them for accurate testing. Yet, we can see some portable spectrometers testing piles of hay in the field and claiming some kind of utility from that. This issue is explored in the context of NIR spectroscopy in the chapters in Volume 2 by Siesler and colleagues.

Additionally, if the same spectrometer is used for analyzing multiple materials, like produce, cheese, or meats, then there needs to be different protocols as the raw signal from them is different. The signal will have different noise characteristics, the texture of various materials can have different specular and diffuse reflection features, and the homogeneity may be different. In such cases, there is a need for customizing the protocol to suit each fruit, vegetable, meat type, etc. In general, without a robust testing protocol, it will not be feasible to obtain meaningful test information.

### 8.6.3 Noise Suppression

Since portable spectrometers are often operated in the field, there is a chance of noise entering the system from a range of sources. Unlike tests done in a controlled laboratory setting, noise plays a significant role in uncontrolled environments. Specifically, in the case of UV–Vis spectrometers, ambient light can be a source of the noise. Hence, care must be taken to isolate the sample from ambient noise, i.e. eliminate stray light. In reflection mode, the distance between the sample and spectrometer can increase the chance of stray light and hinder repeatability. The design and user protocol need to ensure that the distance remains fixed. Finally, noise can also originate from electronics. Dark noise subtractions must be performed routinely before testing samples. Additionally, light source fluctuations should be studied and their effect needs to be quantified on the accuracy of testing.

### 8.6.4 Calibration

Wavelength calibration is a critical process in spectroscopy and plays an important role in determining the accuracy of measurements. All factors that can affect calibration need to be considered, such that their effect can be quantified and minimized (Burggraaff et al. 2019). For instance, in camera-based spectrometers, internal Bayer filters in the image sensor can disrupt the calibration. The use of RAW format images has shown to minimize the effect of these filters. The positioning of the grating must be robust and not change, as that can affect the calibration. In the case of filter array-based spectrometers, the spectral overlap of the filters needs to be considered.

### 8.6.5 Device-to-Device Repeatability

As the fabrication method becomes more complex, device-to-device performance repeatability can become a challenge. For instance, filter array-based spectrometers require several hundreds of optical filters to achieve wavelength separation. Small changes in the spectral characteristics of these filters will change the calibration. In the case of chip-based spectrometers, small tolerances during fabrication can change the performance. Protocols for calibrating every unit are needed, such that their performance is identical.

## 8.7 Outlook

The notion of a “lab” is taking a new meaning thanks to new sensors, the increased computing power of smartphones and the emergence of cloud functionality. On the one hand, today’s smartphones boast of 6 GB random access memory (RAMs), 2 GHz processors, and a range of wireless communication approaches with the availability of programmable open source components. On the other hand, miniaturized spectrometers have been realized due to advanced fabrication approaches. The merger of these technologies offers promising opportunities for a range of applications that were not feasible earlier. Today, portable spectrometers can be seamlessly integrated into smartphones via apps and be made more effective through cloud computing and machine learning. It will be possible to generate large spectroscopic datasets for a range of food, beverage, and agricultural products that will pave the way for intelligent sensors that “learn” over time and enable new applications like counterfeit detection, predict harvest times, and improve the distribution of produce among other uses: so-called “smart agriculture.”

## References

- Acevedo, F.J., Jiménez, J., Maldonado, S. et al. (2007). Classification of wines produced in specific regions by UV–visible spectroscopy combined with support vector machines. *Journal of Agricultural and Food Chemistry* 55 (17): 6842–6849. <https://doi.org/10.1021/jf070634q>.
- Acree, W.E. (2006). Detectors, absorption and luminescence. In: *Encyclopedia of Analytical Chemistry*. John Wiley & Sons, Ltd <https://doi.org/10.1002/9780470027318.a5405>.
- Antonov, L., Gergov, G., Petrov, V. et al. (1999). UV-Vis spectroscopic and chemometric study on the aggregation of ionic dyes in water. *Talanta* 49 (1): 99–106. [https://doi.org/10.1016/S0039-9140\(98\)00348-8](https://doi.org/10.1016/S0039-9140(98)00348-8).
- Ball, D.W, Society of Photo-optical Instrumentation Engineers (2006). *Field guide to Spectroscopy*. SPIE.
- Bao, J. and Bawendi, M.G. (2015). A colloidal quantum dot spectrometer. *Nature* 523 (7558): 67–70. <https://doi.org/10.1038/nature14576>.
- Berns, R.S. (1992). Instrumental colour measurements and computer aided colour matching for textiles, by H. S. Shah and R. S. Gandhi, Forward, by Fred W. Billmeyer, Jr., Mahajan book distributors, Ahmedabad, India, 1990, 370 pp., 12 color plates, hardbound, \$60.00. *Color Research & Application* 17 (1): 62–62. <https://doi.org/10.1002/col.5080170111>.
- Boulton, R. (2001). The copigmentation of Anthocyanins and its role in the color of red wine: a critical review. *American Journal of Enology and Viticulture* 52 (2): 67–87.
- Brewer, J. D., Wee, A., & Seghi, R. (2004). Advances in color matching. *Dental Clinics of North America*, 48(2), v, 341–358. <https://doi.org/10.1016/j.cden.2004.01.004>
- Burggraaff, O., Schmidt, N., Zamorano, J. et al. (2019). Standardized spectral and radiometric calibration of consumer cameras. *Optics Express* 27 (14): 19075. <https://doi.org/10.1364/oe.27.019075>.
- Cai, F., Wang, D., Zhu, M., and He, S. (2017). Pencil-like imaging spectrometer for bio-samples sensing. *Biomedical Optics Express* 8 (12): 5427. <https://doi.org/10.1364/boe.8.005427>.

- Chou, S.Y., Krauss, P.R., Renstrom, P.J. et al. (2014). Nanoimprint lithography. *Nanoimprint Lithography* 4129 (1996): 9–14. <https://doi.org/10.1116/1.588605>.
- Crocombe, R.A. (2013). *Handheld Spectrometers: The State of the Art* (eds. M.A. Druy and R.A. Crocombe). SPIE <https://doi.org/10.1117/12.2017892>.
- Crocombe, R.A. (2018). Portable spectroscopy. *Applied Spectroscopy* 72 (12): 1701–1751. <https://doi.org/10.1177/0003702818809719>.
- Das, A., Swedish, T., Wahi, A. et al. (2015). *Mobile Phone Based Mini-Spectrometer for Rapid Screening of Skin Cancer* (eds. M.A. Druy, R.A. Crocombe and D.P. Bannon). SPIE <https://doi.org/10.1117/12.2182191>.
- Das, A.J., Wahi, A., Kothari, I., and Raskar, R. (2016). Ultra-portable, wireless smartphone spectrometer for rapid, non-destructive testing of fruit ripeness. *Scientific Reports* 6 <https://doi.org/10.1038/srep32504>.
- Desjardins, P. and Conklin, D. (2010). NanoDrop microvolume quantitation of nucleic acids. *Journal of Visualized Experiments* 45 <https://doi.org/10.3791/2565>.
- Dwight, J.G., Tkaczyk, T.S., Alexander, D. et al. (2018). Compact snapshot image mapping spectrometer for unmanned aerial vehicle hyperspectral imaging. *Journal of Applied Remote Sensing* 12 (04): 1. <https://doi.org/10.1117/1.JRS.12.044004>.
- Edwards, P., Zhang, C., Zhang, B. et al. (2017). Smartphone based optical spectrometer for diffusive reflectance spectroscopic measurement of hemoglobin. *Scientific Reports* 7 (1): 12224. <https://doi.org/10.1038/s41598-017-12482-5>.
- Galle, B., Oppenheimer, C. et al. (2003). A miniaturised ultraviolet spectrometer for remote sensing of SO<sub>2</sub> fluxes: A new tool for volcano surveillance. *Journal of Volcanology and Geothermal Research* 119, 1–4, 1.
- Gelabert, P., Pruitt, E., Perrella, G. et al. (2016). *DLP NIRscan Nano: An Ultra-Mobile DLP-Based near-Infrared Bluetooth Spectrometer* (eds. M.R. Douglass, P.S. King and B.L. Lee). SPIE <https://doi.org/10.1117/12.2231054>.
- Giusti, M.M. and Wrolstad, R.E. (2001). Characterization and measurement of Anthocyanins by UV-visible spectroscopy. *Current Protocols in Food Analytical Chemistry* 00 (1): F1.2.1–F1.2.13. <https://doi.org/10.1002/0471142913.faf0102s00>.
- Gubbi, J., Buyya, R., Marusic, S., and Palaniswami, M. (2013). Internet of things (IoT): a vision, architectural elements, and future directions. *Future Generation Computer Systems* 29 (7): 1645–1660. <https://doi.org/10.1016/j.future.2013.01.010>.
- Gupta, O., Das, A.J., Hellerstein, J., and Raskar, R. (2018). Machine learning approaches for large scale classification of produce. *Scientific Reports* 8 (1) <https://doi.org/10.1038/s41598-018-23394-3>.
- Hakala, T., Markelin, L., Honkavaara, E. et al. (2018). Direct reflectance measurements from drones: sensor absolute radiometric calibration and system tests for forest reflectance characterization. *Sensors (Switzerland)* 18 (5) <https://doi.org/10.3390/s18051417>.
- Hopkins, J.L. (2014). DIY Spectroscopy, Chapter 4. In: *Using Commercial Amateur Astronomical Spectrographs*, 101–123. Springer [https://doi.org/10.1007/978-3-319-01442-5\\_4](https://doi.org/10.1007/978-3-319-01442-5_4).
- James, J.F. (2007). Spectrograph design fundamentals. In: *Spectrograph Design Fundamentals*, vol. 9780521864. Cambridge University Press <https://doi.org/10.1017/CBO9780511534799>.
- Karanassios, V. and Fitzgerald, R. (2018). The Internet of Things (IoT) for a smartphone-enabled optical spectrometer and their use on-site and (potentially) for Industry 4.0. In: *Next-Generation Spectroscopic Technologies XI* (eds. M.A. Druy, R.A. Crocombe, S.M. Barnett, et al.), 4. <https://doi.org/10.1117/12.2305466>.
- Lakowicz, J.R. (2006). Principles of fluorescence spectroscopy. In: *Principles of Fluorescence Spectroscopy*. Springer <https://doi.org/10.1007/978-0-387-46312-4>.
- Langergraber, G., Fleischmann, N., Hofstaedter, F., and Weingartner, A. (2004). Monitoring of a paper mill wastewater treatment plant using UV/VIS spectroscopy. *Water Science and Technology* 49 (1): 9–14. <https://doi.org/10.2166/wst.2004.0004>.
- Loewen, E.G. and Popov, E. (2018). Diffraction gratings and applications. In: *Diffraction Gratings and Applications*. Taylor and Francis <https://doi.org/10.1201/9781315214849>.

- Long, K.D., Yu, H., and Cunningham, B.T. (2014). Smartphone instrument for portable enzyme-linked immunosorbent assays. *Biomedical Optics Express* 5 (11): 3792. <https://doi.org/10.1364/BOE.5.003792>.
- Maity, M., Gantait, K., Mukherjee, A., & Chatterjee, J. (2019). Visible Spectrum-based Classification of Malaria Blood Samples on Handheld Spectrometer. *2019 IEEE International Instrumentation and Measurement Technology Conference (I2MTC)*, pp. 1–5. <https://doi.org/10.1109/I2MTC.2019.8826860>.
- Marteló-Vidal, M.J. and Vázquez, M. (2014). Determination of polyphenolic compounds of red wines by UV-VIS-NIR spectroscopy and chemometrics tools. *Food Chemistry* 158: 28–34. <https://doi.org/10.1016/j.foodchem.2014.02.080>.
- Maxwell, K. and Johnson, G.N. (2000). Chlorophyll fluorescence – a practical guide. *Journal of Experimental Botany* 51 (345): 659–668. <https://doi.org/10.1093/jexbot/51.345.659>.
- McGonigle, A., Wilkes, T., Pering, T. et al. (2018). Smartphone spectrometers. *Sensors* 18 (2): 223. <https://doi.org/10.3390/s18010223>.
- Milton, E.J., Anderson, K., Kneubühler, M., and Fox, N. (2009). Progress in field spectroscopy. *Remote Sensing of Environment* 113: S92–S109. <https://doi.org/10.1016/J.RSE.2007.08.001>.
- Mohamed, K. (2019). Nanoimprint lithography for Nanomanufacturing. In: *Comprehensive Nanoscience and Nanotechnology*, 357–386. Elsevier <https://doi.org/10.1016/b978-0-12-803581-8.10508-9>.
- Nelson, D.L. (2019). Introduction to spectroscopy. In: *Spectroscopic Methods in Food Analysis*, 3–34. Taylor and Francis <https://doi.org/10.1201/9781315152769-1>.
- Ogletree, D. F. (2016). Molecular excitation and relaxation of extreme ultraviolet lithography photoresists. In *Frontiers of Nanoscience* (vol. 11, pp. 91–113). Elsevier. <https://doi.org/10.1016/B978-0-08-100354-1.00002-8>
- de Oliveira, H.J.S., de Almeida, P.L., Sampaio, B.A. et al. (2017). A handheld smartphone-controlled spectrophotometer based on hue to wavelength conversion for molecular absorption and emission measurements. *Sensors and Actuators B: Chemical* 238: 1084–1091. <https://doi.org/10.1016/J.SNB.2016.07.149>.
- Oliver, J., Lee, W.-B., and Lee, H.-N. (2013). Filters with random transmittance for improving resolution in filter-array-based spectrometers. *Optics Express* 21 (4): 3969–3989. <https://doi.org/10.1364/OE.21.003969>.
- Özdemir, G.K., Bayram, A., Kılıç, V. et al. (2017). Smartphone-based detection of dyes in water for environmental sustainability. *Analytical Methods* 9 (4): 579–585. <https://doi.org/10.1039/C6AY03073D>.
- Pavesi, L.V., Lorenzo, L., Vivien, L. et al. (2013). *Handbook of Silicon Photonics*. Taylor and Francis <http://books.google.com/books?id=lypGfgJqSM8C&pgis=1>.
- Poojary, S., Jaiswal, S., Wahi, A. et al. (2019). A portable fluorescence spectrometer as a noninvasive diagnostic tool in dermatology: a cross-sectional observational study. *Indian Journal of Dermatology, Venereology and Leprology* 85 (6): 641. [https://doi.org/10.4103/ijdvl.IJDVL\\_440\\_18](https://doi.org/10.4103/ijdvl.IJDVL_440_18).
- Porra, R.J., Thompson, W.A., and Kriedemann, P.E. (1989). Determination of accurate extinction coefficients and simultaneous equations for assaying chlorophylls a and b extracted with four different solvents: verification of the concentration of chlorophyll standards by atomic absorption spectroscopy. *BBA – Bioenergetics* 975 (3): 384–394. [https://doi.org/10.1016/S0005-2728\(89\)80347-0](https://doi.org/10.1016/S0005-2728(89)80347-0).
- Radamson, H.H., Simeon, E., Luo, J., and Wang, G. (2018). Scaling and evolution of device architecture. In: *CMOS Past, Present and Future*, 19–40. Elsevier <https://doi.org/10.1016/b978-0-08-102139-2.00002-1>.
- Scheeline, A., & Kelley, K. (2013). *Cell Phone Spectrometer*. [http://www.asplib.org/onlineArticles/elabware/Scheeline\\_Kelly\\_Spectrophotometer/index.html](http://www.asplib.org/onlineArticles/elabware/Scheeline_Kelly_Spectrophotometer/index.html).
- Schmid, F.-X. (2001). Biological macromolecules: UV-visible spectrophotometry. In: *Encyclopedia of Life Sciences*. John Wiley and Sons <https://doi.org/10.1038/npg.els.0003142>.
- SCIO (n.d.). SCiO – The World’s First Pocket Sized Molecular Sensor. <https://www.consumerphysics.com> (accessed 2 December 2019).
- Shibayama, K. and Suzuki, T. (2008). Patent No. US8027034B2. <https://patents.google.com/patent/US8027034>.
- Snik, F., Rietjens, J.H.H., Apituley, A. et al. (2014). Mapping atmospheric aerosols with a citizen science network of smartphone spectropolarimeters. *Geophysical Research Letters* 41 (20): 7351–7358. <https://doi.org/10.1002/2014GL061462>.

- Sproull, R.C. (1973). Color matching in dentistry. Part II. Practical applications of the organization of color. *The Journal of Prosthetic Dentistry* 29 (5): 556–566. [https://doi.org/10.1016/0022-3913\(73\)90036-X](https://doi.org/10.1016/0022-3913(73)90036-X).
- Spudich, T.M., Utz, C.K., Kuntz, J.M. et al. (2003). Potential for using a digital micromirror device as a signal multiplexer in visible spectroscopy. *Applied Spectroscopy* 57 (7): 733–736. <https://doi.org/10.1366/000370203322102799>.
- Streitberger, H.J. and Dössel, K.F. (2008). Automotive paints and coatings. In: *Automotive Paints and Coatings*, 2e. John Wiley and Sons <https://doi.org/10.1002/9783527622375>.
- Sumriddetchkajorn, S. and Intaravanne, Y. (2012). Home-made N-channel fiber-optic spectrometer from a web camera. *Applied Spectroscopy* 66 (10): 1156–1162. <https://doi.org/10.1366/11-06522>.
- Thiha, A. and Ibrahim, F. (2015). A colorimetric enzyme-linked Immunosorbent assay (ELISA) detection platform for a point-of-care dengue detection system on a lab-on-compact-disc. *Sensors* 15 (5): 11431–11441. <https://doi.org/10.3390/s150511431>.
- Wahi, A., Jaiswal, S., Sahoo, A. et al. (2018). Smartphone-based fluorescence spectroscopy device aiding in preliminary skin screening (erratum). In: *Optics and Biophotonics in Low-Resource Settings IV*, vol. 10485 (eds. D. Levitz, A. Ozcan and D. Erickson), 21. SPIE <https://doi.org/10.1117/12.2289857>.
- Wang, S.-W., Xia, C., Chen, X. et al. (2007). Concept of a high-resolution miniature spectrometer using an integrated filter array. *Opt. Lett.* 32: 632–634.
- Wang, L.-J., Chang, Y.-C., Ge, X. et al. (2016). Smartphone optosensing platform using a DVD grating to detect neurotoxins. *ACS Sensors* 1 (4): 366–373. <https://doi.org/10.1021/acssensors.5b00204>.
- You, H., Kim, Y., Lee, J.H. et al. (2017). Food powder classification using a portable visible-near-infrared spectrometer. *Journal of Electromagnetic Engineering and Science* 17 (4): 186–190. <https://doi.org/10.26866/jees.2017.17.4.186>.
- Yu, H., Tan, Y., and Cunningham, B.T. (2014). Smartphone fluorescence spectroscopy. *Analytical Chemistry* 86 (17): 8805–8813. <https://doi.org/10.1021/ac502080t>.
- Zanella, A., Bui, N., Castellani, A. et al. (2014). Internet of things for smart cities. *IEEE Internet of Things Journal* 1 (1): 22–32. <https://doi.org/10.1109/JIOT.2014.2306328>.
- Zhang, B., & Li, H. (2008). Research on application for color matching in textile dyeing based on numerical analysis. *Proceedings – International Conference on Computer Science and Software Engineering, CSSE 2008*, 1, pp. 357–360. <https://doi.org/10.1109/CSSE.2008.609>

**9**

## Smartphone Technology – Instrumentation and Applications

Alexander Scheeline<sup>1,2</sup>

<sup>1</sup>Department of Chemistry, University of Illinois at Urbana-Champaign, Urbana, IL, USA

<sup>2</sup>SpectroClick Inc., Savoy, IL, USA

### 9.1 Introduction and Context

Array detectors have been a spectrometric tool for approximately half a century. In 1988, I obtained my first charge coupled device array (CCD), a Thomson CSF liquid nitrogen-cooled 586 by 384 pixels,  $26\text{ }\mu\text{m}^2$ -pixel device with a controller the size of a PC-AT, connected to a PC-XT that, in turn, could communicate with the rest of the world over a 1200-baud modem [1, 2]. This CCD allowed more measurements to be made in one hour than the technology it replaced, photographic plates, could make in a week, with greater convenience, linearity, and dynamic range. Dark current (when the CCD was below  $-110^\circ\text{C}$ ) was undetectable. Linear diode array spectrometers in the ultraviolet (UV) and visible were already common. What more could a spectroscopist desire?

In due time, the answer became clear: portability, lower cost, and less need for an expert user were all desirable. A variety of highly portable instruments have become available, some as small as a pack of playing cards. Still, spectrometry is typically carried out by skilled personnel. However, the populace at large has many measurement needs: medical tests, water quality tests, characterization of food, clothing, surface contamination, and a myriad of determinations that would be more timely and useful if made at a point of need rather than in a laboratory.

Thus, when cell phones appeared, it was a short extrapolation to think that cell phone spectrometry would soon become common. Everything that was part of a 1988 array spectrometry instrument, the detector, controller, computer, storage, and communications device, was an all-in-one package. In the Netherlands, an inexpensive spectropolarimeter attachment for iPhones was used to measure air quality in a large citizen science activity in 2013 [3, 4]. While numerous literature articles suggest such instruments are feasible, none are commonly available in the United States as of fall, 2019, and only two commercial cell phone spectrometers have come to the author's attention, one by Huawei in China [5] and one by AlphaNov in France [6]. One suspects they are unavailable in the United States for two reasons: (i) in the case of the Huawei device, a web search reveals it is only for sale in Burma, suggesting that the hopes of its designers were not met by the manufactured product and (ii) both devices would violate a foundational United States patent [7]. Samsung has filed a patent for a reflectance spectrometer built into a phone [8–10], though similarities to the SCIO device [11] and the Huawei offering are apparent. In addition to visible measurements, they suggest vibrational spectra will be obtained using the Si-Ware NeoSpectra infrared spectral engine[9].

One has two choices in describing cell phone spectrometry. One may report research to date for noncommercial systems, speculate on systems specifically designed to do spectrometry and small enough to fit into a cell phone along with the rest of the normal components, or discuss the challenges of working with devices engineered for taking selfies and landscapes when desiring output to have scientific merit. This chapter focuses on the

latter. Data processing takes place on the phone; this differs from an early approach by Whitesides and coworkers, where the camera transmitted a Joint Photographic Experts Group (JPG) to a central processing station for image correction and interpretation [12]. Such transmission avoided the need for on-site computation and was utterly dependent on web access. While 5G communications may someday make the web ubiquitous, there are still many places where cellular or Wi-Fi reception is slow or nonexistent.

Other recent reviews include [13–16], while the role of smartphone (or, equivalently, cell phone) spectrometry in contrast to other portable instruments is reviewed in [17]. Some authors focus on developing chemistry that is robust for use by nonprofessional analysts, but assume that high-quality spectrometry is readily achieved [18–20], a viewpoint rejected by the current author. Use of filters to turn cell phones into filter photometers or hyperspectral imaging cameras (with a series of filters) are not discussed here.

Additionally, this chapter does not focus on the use of a smartphone as a computer connected to an external, portable instrument. A handheld spectrometer connected to a laptop or smartphone will give identical results, absent software bugs. The design of portable standalone instruments, while having much in common with smartphone spectrometry, has the extra design freedom to employ a detector optimized for the measurement rather than for inclusion in a thin, lightweight device, can have an independent source of electrical power, and need not share detecting duties with a camera optimized for snapshots.

Furthermore, the emphasis is on quantitative measurement of the trace to minor components of specimens. Identification of major components is often most easily done with near-infrared spectrometry. Minor or trace components either do not have a spectrum of sufficient magnitude to sense against a fluctuating background (differences in lighting and major components), or require amplification of their optical properties to allow detection (colorimetric reactions, fluorescence excitation). In some cases, external reactant packages allow for semi-quantitative testing using cellcams without additional wavelength resolution other than the red, green, blue (RGB) pixel combination common in color cameras. For example, qualitative detection of psychoactive drugs can be performed with a “swipe card” and picture test [21]. Qualitative testing can be thought of as a binary test of whether the concentration of a sought-for-substance (or interferents) is above a threshold. This places negligible demands on a detector for linearity. Quantitative work does require a linear response, or nonlinear response sufficiently reproducible and smooth to allow linearization. Furthermore, because the resolution of most small, portable systems is 1 nm or coarser, atomic spectrometry is ignored.

We also note that smartphone spectrometry is a subset of smartphone chemical analysis. Separations, electrochemistry, and even mass spectrometry may someday be included in a cellular device, but that is beyond current technology and the scope of this chapter.

## 9.2 Challenges of Smartphone Spectrometry

Any spectrometer must produce a result that can be verified. This requires both precision and accuracy. Calibration is typically carried out under controlled conditions, yet a portable, citizen-science instrument must operate under conditions of temperature, humidity, dust, vibration, battery or power status, and human operation that often is not conducive to stability, reproducibility, and quality control. Let us contrast how a laboratory instrument and a putative cell phone spectrometer are designed, built, calibrated, maintained, and used. See Table 9.1.

To understand the engineering challenges of cell phone spectrometry, let us expand the information in Table 9.1. Power is an obvious problem. If wall socket power is available, it makes little difference whether an instrument requires milliwatts or hundreds of watts. Running from a battery, power consumption limits instrument and controller lifetime. If a cell phone battery stores 100 Ah of charge and can run the phone for 24 hours, then an instrument drain of 3 A (the upper limit for universal serial bus (USB) 2.0 [22] using microconnectors) could reduce battery lifetime by a factor of 2 (USB 3.0 supports higher currents, and, thus, is potentially even a greater strain on batteries). Since USB power is nominally at 5 V, maximum sustained power is limited to 15 W, with

**Table 9.1** Summary comparison of laboratory and cell phone spectrometer characteristics.

Characteristic	Laboratory instrument	Cell phone spectrometer
Power consumption	Minor consideration	Minimize to avoid battery load
Temperature stability	Lab temperature roughly constant; materials chosen to minimize performance change with temperature	Wide and unpredictable temperature range requires either extraordinary measures for stability or temperature-monitoring and real-time compensation for changes
Humidity	20–80% in air-conditioned spaces	0% – supersaturated
Optical train	Optimized for performance	Simplicity and light weight essential
Sample/spectrometer alignment	Rigid	Varies from rigid to arbitrary to random
Detector choice	Optimized for performance	Built-in camera or dedicated, microfabricated spectral engine
Wavelength range	Optimized for problem-solving	Limited by low-power light sources, built-in detector constraints
Intensity dynamic range	Limited by detector and stray light	Limited by detector, stray light, and access to raw detector data
Calibration: wavelength	At factory; reconfirmed intermittently	Must be confirmed at the time of use; alignment highly variable
Calibration: linearity	Detector and electronics ensure typically excellent	Must be characterized; typically quite nonlinear
Calibration: slope response	At factory; pattern noise removed in firmware or software	Must be characterized by an end user
Likely user expertise	Trained professional	Unknowable
Dominant source of variance	Typically sample	Ambiguous

lower power desirable. Such power levels preclude the use of many, if not most, arc lamps and blackbody radiators. Light-emitting diodes (LEDs) light sources, including use of the LED flash built into many, if not most, cell phones, are common. Note that this power limitation thus restricts wavelength range for luminescence and absorbance measurement, independent of detector characteristics. Even sunlight has been employed, though the variability of cloud cover and the earth's rotation present obvious challenges [23]. The authors of [23] confuse dispersion with resolution, and while they obtain linear working curves, slope and precision do not always match the performance of laboratory instruments for reasons discussed throughout the current chapter.

Any portable instrument must deal with temperature variations. Maintaining instrument stability even in laboratories is challenging, as materials change size with temperature, semiconductors change conductivity, light sources change steady state and noise behavior, and detectors shift dark current and shot noise levels. There are two ways to deal with temperature effects. One is to carefully engineer thermal expansivity and temperature response of components to minimize drift with temperature. The other is to allow the system to drift but to calibrate its behavior at the temperature, location, and time of employment. Both approaches are challenging, though the latter often allows a lighter instrument to be devised. Similarly, the humidity not only can lead to fogged optics (high humidity) and static damage to electronics (low humidity), but also varies the refractive index of air, subtly influencing wavelength calibration. Any material porosity can add hysteresis to responses to humidity changes, further complicating instrument stabilization.

Laboratory instruments can employ mirrors, prisms, gratings, lenses, and fiber optics in a wide range of geometries. Portable instruments typically use thin polymer optics (Fresnel lenses, transmission gratings, thin

film polarizers) to minimize mass. Such optics may limit image quality and, consequently, throughput, resolution, and channel crosstalk.

Spectrometers may have built-in sample holders or may be connected to samples with fiber optics or other relaying optics. Either of these is more stable than a handheld cell phone which is typically not equipped with a sample holder or a fiber optic connector [24]. It is common to place the phone in a frame [25–28] or to mount a sample holder and grating in front of the phone's camera [6, 29–31]. While such arrangements give adequate precision in short-term demonstrations, the author is not aware of any long-term stability characterization nor of interuser or interinstrument transferability studies.

Most daunting is detector choice. Laboratory instruments can be engineered with any detector that optimizes wavelength coverage, resolution, dynamic range, noise, and so on for a particular measurement. In cell phones, the most obvious detector is one of the built-in cameras, whose choice is forced on the spectroscopist and user by engineers optimizing for cost, the field of view, color balance, and “selfie” appeal. Often, the default behavior is to preprocess images for white balance, brightness, and hue, thus destroying any information on intensity. The wavelength range is limited by interposing a near-infrared filter to block light in the wavelength regions to which silicon most sensitively responds (750–950 nm).<sup>1</sup> Fortunately, both Android and iOS operating systems have system calls allowing control of exposure and gain and allow access to raw detector signal. One should never use JPG images for doing quantitative spectrometry; JPG is a lossy compression scheme that is guaranteed to distort working curves [33]. Whether the cost/performance benefits of adding dedicated spectrometric engines to phone detectors will prove to be commercially viable is unclear.

Phone cameras are naturally optimized for detection between 400 and 700 nm, though filters frequently reduce throughput past 650 nm to prevent excessive redness in images (silicon response increases in the near infrared while human response fades). Plastic lenses and other components cut off UV light below ~315 nm, and silicon has poor response below ~400 nm. A Nikon D50 single lens reflex (SLR) camera observing a high-pressure sodium vapor lamp through a diffraction grating easily sees the visible sodium emission and absorption lines (see Section 9.3.1.6 in this chapter) and the continuum between 420 and 685 nm. Observation of a mercury vapor lamp with an OmniVision OV5640 camera (a common 5 MPix cell phone camera) showed only the visible multiplets (404, 435, 546, 579 nm), not the 256 nm line. The wide availability of silicon detectors coated to allow UV detection contrasts the wavelength range restriction of cell phone cameras.

The aforementioned OV5640 chip has 10-bit on-chip digitization but typically reports 8-bit data to the observer. Digitization noise thus limits single-pixel precision to 1 part in 256 or 1 part in 1024 [34, 35]. Realistically, one cannot use the detector's entire dynamic range, as linearity suffers near pixel full well exposure [36]. As most CCD arrays have deep wells (holding over  $10^5$  electrons) and digitizers with 14-bit or 16-bit precision and some linear diode arrays have 20-bit dynamic range, the range available on a cell phone instrument will be challenging. A number of reported instruments appear to use large numbers of pixels, together with careful choice of exposure time, to allow dynamic range approaching three orders of magnitude [26–28, 33, 37, 38]. The author has championed the use of gratings that generate a large number of orders with varying throughput to broaden the dynamic range of an instrument beyond the dynamic range of the detector [30, 39–41]. An argument for the use of CCD or complementary metal oxide silicon (CMOS) arrays with narrowband filters overlaying the array as a separate spectral analyzer added to phone is that dynamic range would be higher [5, 42].

Calibration for wavelength requires a standard. If a mercury lamp or other line source is available, such calibration is straightforward and can use long-standing algorithms [43, 44]. Unfortunately, mercury lamps require high voltage, generate UV light, are fragile, and in many cases, are physically large, complicating alignment. Alternatively, neon bulbs or fluorescent lamps may be employed, as further discussed in Section 9.3.1.6. White LEDs show promise as continuum sources with known peak emission wavelength. However, peak wavelength varies

---

<sup>1</sup> Silicon wavelength response varies based on doping and thickness. See e.g. figure 1–11, p. 6 in [32] for examples of a range of responses. Since absent calibration, one rarely has knowledge of the wavelength response details of the sensor in a smartphone, generalizations above response beyond “visible region” are difficult.

with temperature [45] and even nominally identical LEDs have a range of peak wavelengths [46] that shift as the LED ages [47, 48].

Thanks to the Central Limit Theorem [49], massively parallel measurements have a higher precision in measuring a mean signal than individual detector measurements. When using a cellular camera as a detector, some subsets of the pixels are employed, so precision depends on camera size, pixel size, pixel-to-pixel variation, light flux, temperature (which influences dark current), and the optical train's uniformity in illuminating pixels. An excellent study of the relative importance of global and individual pixel response has recently been published, together with algorithms for calibrating spectroradiometric response of individual cellcams and classes of cellcams [33].

Not to be overlooked is that the typical cell phone user is not a trained spectroscopist. Regardless of the precision and accuracy of the cell-based spectrometer, the human user must prepare a specimen in a way that allows the instrument to function optimally. How can one ensure that a determination performed with a cellular spectrometer has validity if the performance of the user is unknown and unknowable? How many users will be interested in undergoing any level of training? If the operation is only feasible where user skill is minimal (as is currently the case for home pregnancy tests or the use of test strips for pH, blood glucose, and such), is there anything to be gained by adding spectrometric capability to the cell cam?

Finally, for a measurement to be useful, the dominant source of signal variance has to be the property that the user is trying to study. If an instrument's variance from all causes except the analyte is one order of magnitude lower than the variance due to the analyte, the instrument is good enough for semiquantitative work. If the instrument contributes variance as large as that of the analyte, no useful information can be obtained on a statistically sound basis. Every factor in Table 9.1 has to be understood, quantified, and validated for cell phone spectrometry to have a commercial future.

One thus sees that making a viable cell phone spectrometer is a daunting task. Many of the engineering choices one would like to have are unavailable. Essentially everyone on earth owns or knows someone who owns a smartphone [50]. While no statistics are available, personal experience strongly suggests that a much lower percentage of humanity is trained in chemical analysis. There is, thus, a danger in making cell phone spectrometers without adding a training and quality control component to the operating software. Without adequate guidance, the untrained user could easily generate meaningless data even from the best engineered device, but a cost-effective device will surely have performance trade-offs that will demand care in specific areas of sample preparation from the user.

## 9.3 Progress to Date

This chapter emphasizes device engineering, not applications, which are described in the chapter in Volume 2 by Peveler and Algar. Rather, we discuss aspects of instrument engineering which influence analytical performance, but which are not necessarily emphasized in some prior work.

### 9.3.1 Dispersion and Resolution

#### 9.3.1.1 Conventional Transmission Gratings

Undispersed, zero-order light transits transmission gratings undeviated, regardless of grating rotation. If one wishes 400–700 nm to display across the detector, the resolution is more than twice as high if zero order is not visible on the detector, so that the wavelength range observed is 300 nm, not 700 (or more) nm. Figure 9.1 shows the problem and a common solution.

In inset (a), the grating is interposed on incoming light just in front of the camera lens. When focused, zero order is approximately in the center of the scene. Plus and minus first order are dispersed across the camera field

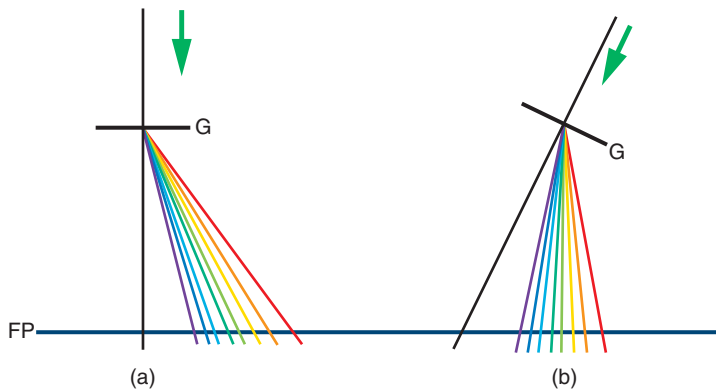


**Figure 9.1** Diffraction through transmission gratings. FP = focal plane, G = diffraction grating. Arrow indicates the direction of incoming light. (a) Grating normal to the entering light beam and parallel to the focal plane. (b) Focal plane normal to diffracted beam at some selected wavelength.

of view. Groove spacing on the grating is chosen so that the desired wavelength range appears between the edge of the visible field and the center of the camera, with the corresponding negative order on the other side of the grating normal (not shown) [51]. Geometry (a) is simple to align, but the resolution is typically poor. The range between 0 and 400 nm is typically devoid of information; for illustrative purposes, assume that red cutoff is at 700 nm and dispersion is linear. If the diffracted light covers 2100 pixels, then 450 are illuminated by  $-1$  order, 450 by  $+1$  order, and the remaining 1200 pixels are illuminated by zero order and the UV region to which native silicon is unresponsive (and low-power light sources provide negligible illumination). Dispersion is 0.66 nm per pixel, but optical aberrations (coma, spherical, chromatic, field curvature) typically limit resolution to significantly poorer values, especially if the incident light is incompletely collimated and the instrument entrance aperture is larger than one pixel. Geometry (b) disperses light only in a single order. While wavelength calibration is more difficult since zero order is not visible, the dispersion may place a 300 nm range across the same 2100 pixels, giving dispersion of 0.143 nm/pixel, thus improving dispersion, and potentially resolution, by about a factor of 4. A subtle additional limiting factor is that the maximum relative resolution possible from first-order diffraction,  $\lambda/\Delta\lambda = N$ , the number of grating grooves illuminated. Cell phone cameras typically have entrance apertures of the order of 2–3 mm, and coarse gratings suitable for low-resolution spectrometers have 200–600 grooves/mm. Thus, a 200-groove grating coupled to a 2 mm entrance aperture limits resolution to  $\sim 400$  (or 1 nm at 400 nm), while a 3 mm aperture and 600 groove grating could potentially have resolution  $\sim 1800$ . The imposition of a Bayer pattern (red/green pixels in even camera rows, green/blue pixels in odd rows) [52] further degrades resolution and data recovery (see also Section 9.3.3). When reviewing manuscripts, the author has seen numerous cases of others equating dispersion with the resolution, ignoring finite pixel size, aberrations, and so on. An example of geometry (b) can be seen in figure 1 of reference [27], with several more examples in figure 2 of reference [13].

### 9.3.1.2 Stacked, Mutually Rotated Gratings

Several of the problems of coupling linear gratings to areal detectors may be overcome, in principle, by averaging data over multiple orders. If orders are projected onto nonoverlapping regions of a multimegapixel array, then each of the orders may be independently examined, and the dynamic range of the instrument as a whole is the product of the dynamic range of the camera and the variable throughput of the multiplicity of orders. This is the basis of the author's developments in portable spectrometry [30, 40, 53]. Two or more gratings are positioned parallel to the focal plane, slightly separated along the light propagation direction, with the collimated illuminating beam centered on the camera, as in Figure 9.1a. The dispersion direction of one grating is rotated about the optical

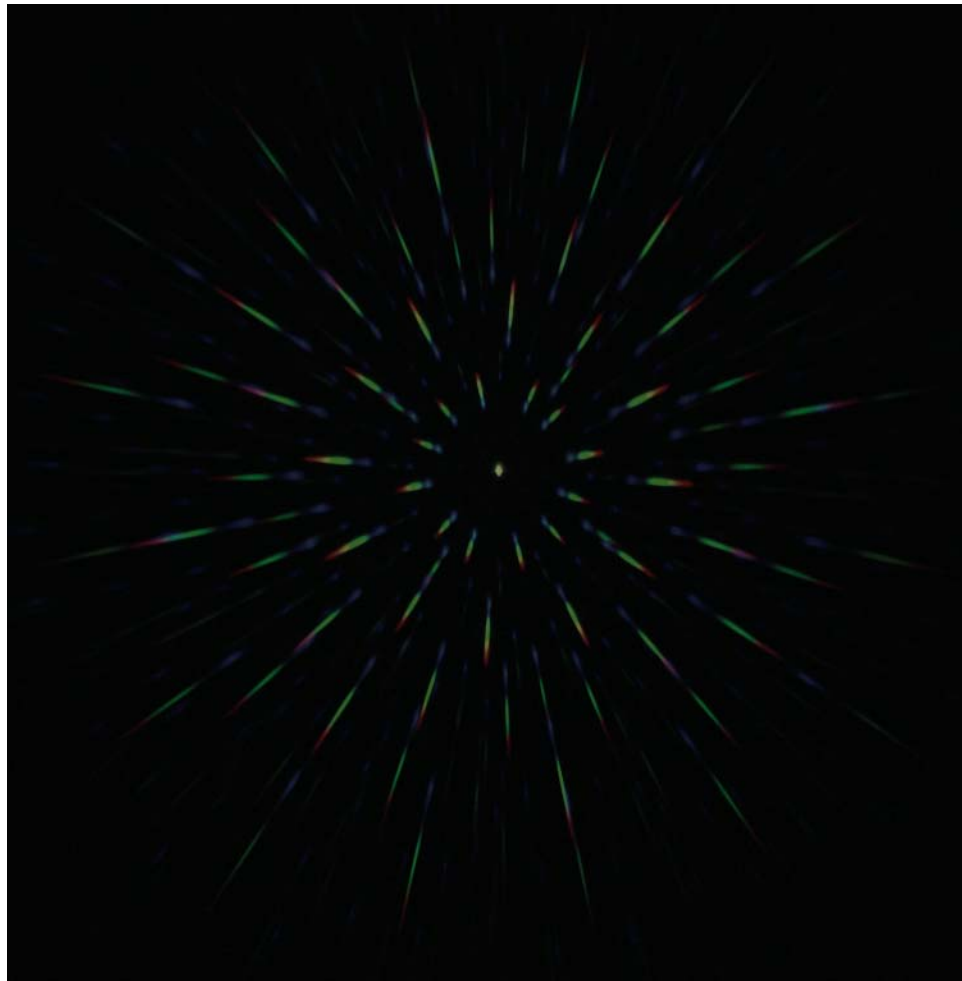


**Figure 9.2** An example of the many orders visible when stacked, double-axis diffraction gratings are illuminated with collimated light from a white LED. Zero order appears in the approximate center of the image.

axis so that orders are dispersed at a multiplicity of radii and angles. Particularly useful patterns appear when double-axis gratings [54] are employed.<sup>2</sup> An example appears in Figure 9.2.

The chief theoretical advantages of this grating arrangement are (i) the peak emission of the LED occurs at a known wavelength (slightly influenced by device temperature and LED fabrication precision [45]), allowing real-time wavelength calibration. The peak wavelength response of the camera may be different than peak emission output of the LED, so the LED must be taken as a secondary standard and the system initially calibrated using a source where wavelength information is not easily skewed by differences in camera sensitivity with wavelength. Atomic emission lines serve this purpose well, but are unlikely to be available in a safe, portable unit. Fluorescent lamps that emit mercury neutral atom lines are widely available and are discussed in Section 9.3.1.6. (ii) Different orders have strikingly different throughput, so, once calibrated, can be used to expand the dynamic range of the instrument beyond the dynamic range of the camera. The author has used an 8-bit camera to get 12 bits of dynamic

<sup>2</sup> Ordinary plane gratings are ruled with equally spaced, parallel grooves. Double axis gratings consist of a square (or, plausibly, rectangular) grid of bumps so that dispersion is in both  $x$  and  $y$  Cartesian directions [54].

range, as the various orders gave throughput differences of up to a factor of 20. Using a 2 mW 633 nm laser projected through a double axis grating and measuring throughput with a photodiode, observed power ranged from 869 μW (zero order) to 200 μW (first order) to 300 nW (third order), meaning that a single grating inherently has nearly three orders of magnitude dynamic range. Since, approximately, the throughput of a beam diffracted by two gratings is the product of the efficiency of each grating, it is clear that stray light rather than camera performance will limit the dynamic range of instruments with stacked, mutually rotated gratings. (iii) Resolution degrades gracefully as the amount of light available for a measurement decreases. At 100% transmittance, second-order spectra may be readily observed, while first-order spectra are saturated (as is the case of Figure 9.2). At lower flux, weak orders disappear into the background and strong orders come out of saturation. Lower orders have higher throughput and lower dispersion, so throughput/resolution tradeoff is readily evident. (iv) Signal averaging (to overcome shot noise and digitization granularity) and resolution are accommodated on a single detector, in contrast to using single axis gratings that give a single wavelength range and resolution. It is unclear whether processing data from the hundreds of thousands of usefully illuminated pixels will provide sufficient precision in contrast to employing the entire field of view (with a single axis grating) in which field curvature complicates both wavelength resolution and calibration.

The position of each order depends on the rotation of the gratings about their common normal, the rotation of the camera with respect to the grating rulings, the order of diffraction in  $x$  and  $y$  from each grating, and any off-axis illumination angle. For normal incidence, the relevant equations are:

$$n_{\text{eff}} \lambda = d_0 \sin \beta \quad (9.1)$$

$$n_{\text{eff}} = (n_{x1}^2 + n_{y1}^2 + n_{x0}^2 + n_{y0}^2 + 2((n_{x1} n_{x0} + n_{y0} n_{y1}) \cos \theta_g + (n_{y0} n_{x1} - n_{x0} n_{y1}) \sin \theta_g))^{1/2} \quad (9.2)$$

$$\theta_{n_{\text{eff}}} = \arctan \frac{n_{y1} \cos \theta_g + n_{x1} \sin \theta_g + n_{y0}}{n_{x1} \cos \theta_g - n_{y1} \sin \theta_g + n_{x0}} \quad (9.3)$$

where

$\lambda$  = Wavelength of interest (nm)

$d_0$  = Grating spacing (nm). If the spacing is different for  $x$  and  $y$  (i.e. if the diffracting regions on the double axis gratings form a rectangle rather than a square), one may readily revise Eqs. (9.2) and (9.3).

$n_{\text{eff}}$  = Effective order number. Counterintuitively,  $n_{\text{eff}}$  is not necessarily an integer. For example, for  $n_{x0} = n_{y0} = 1$ ,  $n_{x1} = n_{y1} = 0$ ,  $n_{\text{eff}} = \sqrt{2}$

$n_{wm}$  = Diffraction order with respect to a cardinal axis in a grating plane  $w$  is either  $x$  or  $y$ , Cartesian directions, and  $m$  is an integer order in the Cartesian direction specified.

$\theta_g$  = Angle between the  $x$  axes for the two double-axis gratings.

$\beta$  = Diffraction angle with respect to the grating normal, regardless of rotation from the reference  $x$  orientation

$\theta_{n_{\text{eff}}}$  = Rotation of the order from the  $x$ -axis, taken as the orientation of order (1,0,0,0).

Commercial implementations of this design are not yet widely used, in part because the software to implement all the calibrations required has proven difficult to write. If such calibration becomes facile, the match to typical cell phone cameras (3–15 MPix, 8–10 digitization bits per pixel) is excellent.

### 9.3.1.3 Polarization Sorting

Because light scattering is polarization dependent, skylight and scattering from aerosols are polarized. Combining a diffraction grating, quarter-waveplate, “ $2 \times 4\lambda$ ” phase retarder, and a thin film polarizer allows a cell phone camera to do spectropolarimetry in a single image [4]. The mass-produced instrument is shown in Figure 9.3.

As explained in [55], the relative intensity of  $x$  and  $y$  polarized light can be obtained by using wavelength-independent waveplates. Fresnel rhombs using total internal reflection for polarization come close to this ideal but

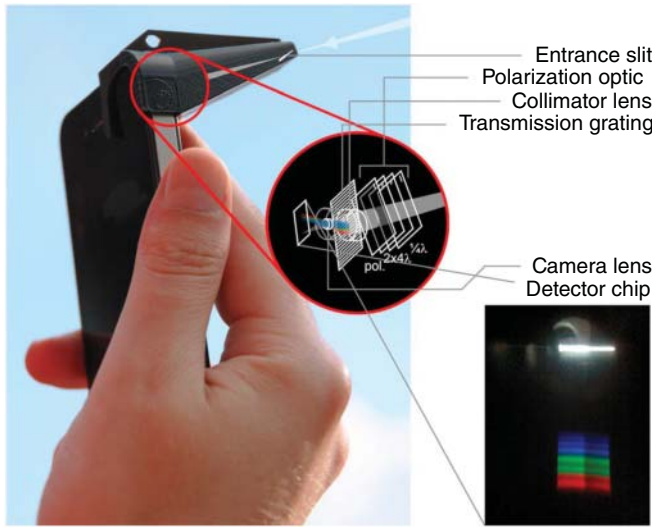


**Figure 9.3** Cell phone spectropolarimeter. Source: Sink et al. [4].

are ungainly for portable use. Thin film polarizers and waveplates are hardly achromatic, and temperature changes significantly influence retardance. However, for citizen science experiments, accuracy is good enough and nonidealities can either be compensated (by modeling) or averaged (central limit theorem). Thus, in Figure 9.3, intensity modulation is not cleanly periodic in either wavelength or wavenumber, but relative *p*- and *s*-polarization can be extracted throughout the visible. Based on an understanding of polarized light, Figure 9.3 appears to be slightly inaccurate. Instead of two “ $4\lambda$ ” waveplates, there are likely two  $\frac{1}{4}\lambda$  waveplates, giving a total of  $\frac{1}{2}$  wave phase shift. Those waveplates occlude only one half of the entering beam. Thus, the part of the beam that traversed only the correctly labeled quarter-waveplate shows linear polarization in one plane, while the portion of the beam that traverses three quarter-waveplates generates data in the plane perpendicular to that of the singly occluded beam. The linear polarizer ensures that the grating is illuminated by only one polarization, avoiding throughput differences for orthogonal polarizations as is common for diffraction gratings. Because the alignment of the phone with respect to reference directions is imprecise, errors in polarization  $\sim \cos \theta$  where  $\theta$  is the tilt of the phone from some reference direction can be anticipated. In general, one must presume that a cell phone camera has a random orientation with respect to the outside world, and so calibration algorithms must allow for arbitrary tilts.

#### 9.3.1.4 Fabry–Perot, Wedge Filtered, and Nanoarray Optical Sensors

Early cell phone cameras sensed radiation to  $\sim 1000$  nm. Near-infrared light made strong near-infrared emitters look violet in color images. Most current color cameras include a near-infrared blocking filter so that, other than at 940 nm, employed by devices, such as video remotes to communicate, smartphones no longer respond to infrared light. Prior to the advent of near-infrared filters, cellcams allowed measurement of such atmospheric constituents as ozone or water vapor [56].

Omitting USB-equipped instruments that can communicate with any USB-equipped device including cell phones, one thus expects few cell phone interferometric instruments. A visible instrument based on a wedge interferometer (linear variable filter) as in Ocean Optics’ (now Ocean Solutions’) discontinued Spark line of miniature spectrometers [57, 58] would be a possibility. Another, pursued by Consumer Physics [11] in the near infrared, is to make a thin film [59] array color-selective array sensor small enough to fit in a phone. Such sensors with 8–16 spectral bands are also available in the visible [60–62] from vendors who have had less publicity. Greater number of spectral bands may be available in planar arrays in the future. An early paper described how to extract

over 100 passbands with better than 1.5 nm resolution [63]. The Si-Ware NeoSpectra MEMS interferometer looks promising [9]. A Fabry–Perot interferometer [64–66] tuned to measure CO<sub>2</sub> is available in a size that could clamp onto a cell phone [67]. Precision is  $\pm 100$  ppm for CO<sub>2</sub> levels between 100 and 1000 ppm.

All the interferometric approaches are technically viable, but their routine use depends on reaching a scale where unit cost is acceptable. Most require that a detector other than the cell phone camera be employed.

An ingenious approach to absorbance measurement has been described by Ding et al. [68]. Broadband light is polarized, partitioned by a microlens array, and transmitted through a wedge interferometer (alternatively, a linear variable optical filter), the output of which is refocused through the smartphone camera's lens and projected onto the detector. Because each lens sends light through a small portion of the wedge interferometer, each spatial region provides intensity information over a small band of the spectrum. By averaging throughput over many pixels, the effect of pixel-to-pixel response variation is minimized. Resolution is set by the size of the wavelength range transmitted by each illuminated region of the wedge. Polarization is necessary to avoid chromatic aberration from wedge birefringence and the consequent difference in wavelength transmission at each *xy* location for different polarizations. The long-term viability of the approach depends on the economics of fabricating wedge filters, the stability of suitably mounted filters as a function of temperature, humidity, and aging, and the adequacy of wavelength resolution with this approach.

Another recent development is the fabrication of arrays of semiconducting sensors with differing wavelength response along the array [69]. Because sensors are about the size of camera pixels, one expects that noise characteristics can be made comparable to current cameras. However, signal averaging with multiple pixels requires more complicated geometry than reported as of September 2019. Reproducibility of wavelength response, with reproducible changes as a function of temperature, will also be critical. If microfabrication can be made sufficiently reproducible, then spectrometric sensors even less expensive than the interferometers described in the previous paragraph may be practical, at which point use of cameras for spectral parsing may be unnecessary.

### 9.3.1.5 Why Not Prisms or Conventional Instruments?

Prism spectrometers, while less common than grating instruments, are not unusual [70]. The nonlinear dispersion due to changes in refractive index with wavelength complicates wavelength calibration and compresses the spectrum in the red, but can be readily handled by fitting to an appropriate spline or polynomial function. However, prisms weigh more than transmission gratings and can be more challenging to align. However, use of a multi-component cemented cuboid prism has recently been reported, in which the prism and camera are colinear and parameters are designed specifically to minimize response differences from one device to another [71]. Optimally, the detector should be large compared to the prism, which means that many cell phone cameras are suboptimal for use with this approach. A separate, large, embedded CCD would be preferable.

Because most cell phones have a USB port, almost any conventional instrument could be interfaced to a phone if the instrument also is USB-compatible. One typically does not call such arrangements a cell phone spectrometer because the phone is acting purely as a computer and communications device, not a data collector. Only if the camera or some other sensor built into the phone is used to transduce light to numbers is the instrument a cell phone spectrometer. This is consistent with usage in the defining patent for the field [7].

Simply shrinking a conventional Czerny–Turner or Rowland circle instrument is conceivable and has been patented [72]. It is unclear whether such a device has ever been built or sold, or what resolution or throughput may have been realized. Narrower applicability, but simpler construction, has been reported for cell phone colorimeters [37, 73, 74]. Here, either LEDs provide wavelength selection or the color selection among red-, green-, and blue-responding pixels defines the spectral range. Because the wavelength range is often wider than the absorption feature being monitored, working curve nonlinearity is expected.

### 9.3.1.6 Wavelength Calibration Sources

Convenient calibration sources must be stable, encapsulated, safe, and readily available. There are numerous sources for atomic emission sources which work well in the laboratory but are not available in general commerce.

Portable, inexpensive wavelength calibration standards may include selected LEDs, but should not be random LEDs that are becoming common light sources, as precise values for peak emission wavelengths may vary. Neon lamps are simple line emission sources [75], emitting a dense set of lines in the yellow and red part of the spectrum, but providing few lines in the blue. If one can trust that calibration will be stable for days at a time, mercury vapor street lamps and sodium vapor lamps (either high-pressure or low-pressure) are widely observable after dark (though LED lamps are beginning to replace such vapor lamps for environmental reasons). Indoor fluorescent lamps are also common, but present additional difficulties. Laser pointers have two, likely insurmountable, problems. They are too intense for direct use, and, if based on diode lasers, have poor wavelength precision.

Examples of possible calibration sources are shown in Figures 9.4 and 9.5 (fluorescent light), Figure 9.6 (high-pressure sodium vapor lamp), and Figure 9.7 (simulation of a neon lamp). While the examples have been chosen to emphasize specific problems, in fact, all sources must be evaluated for such limitations.

Because fluorescent lights are common, mercury atomic emission is almost always present, and the phosphor composition often includes terbium- and europium-doped yttrium oxide, these sources might be considered universal transfer standards. If a fiber optic collects light from the lamp and sends the light to an entrance aperture of a spectrometer, this approach is plausible (although lamp aging may alter the relative intensity at various wavelengths). However, given the grating/phone camera geometry commonly employed as discussed in conjunction

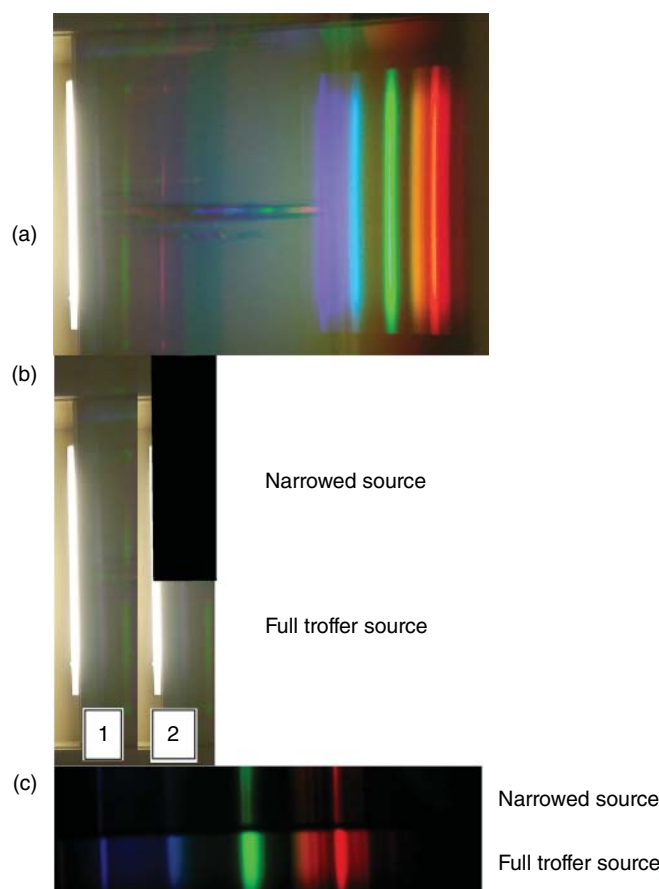


**Figure 9.4** Linear fluorescent bulb used as a reference. (a) Unmasked fluorescent troffer and full field spectrum. (b) Masking of lamp; inset 1 unmasked, inset 2 heavily masked. (c) Comparison spectra for masked and unmasked lamp.

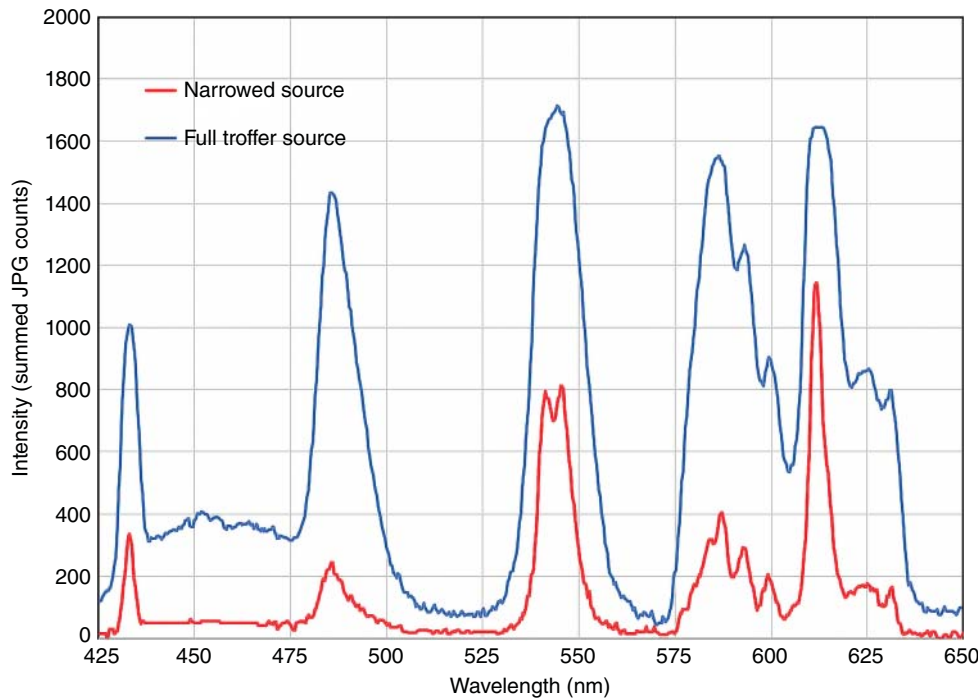


**Figure 9.5** Comparison of full height troffer spectrum with masked lamp spectrum. For line and band identification, see [76]. Source: Alexander Scheeline.

with Figure 9.1, one is tempted to point the phone at a fluorescent lamp through the diffraction grating and use the resulting image for calibration.

In Figure 9.4a, the 5 MPix camera in an LG 4S cell phone is used to observe a small fluorescent light in a compact troffer (rectangular, recessed light fixture) through a 600 line/mm transmission grating. The initial impression is that the fluorescent light could provide reference wavelength data. Inset (b) sketches how the troffer was masked for the remaining images in Figure 9.4, with inset (b).1 showing the unmasked troffer (in fact, the same image as in inset A), while inset (b).2 shows how the troffer was masked with black paper (a drawing of the masking, rather than a photo, is used for clarity). Spectra of the partially masked troffer are photographed in Figure 9.4c and plotted in Figure 9.5, the latter extracted using software available online [77, 78]. The extracted spectra sum the 8-bit signals in selected regions of the JPG image in Figure 9.4c over a height of 9 pixels. Lines and bands are identified in [76]. Because the center of the illuminated pixels in zero order (white band of the troffer image) is 29 pixels wide in the unmasked area and 13 pixels wide in the masked area, a shift of 8 pixels to align wavelengths was necessary for generating the blue trace in Figure 9.5 compared to the red trace. Such shifting due to the size of the source is a general feature of spectrometers without fixed entrance apertures and limits the wavelength calibration precision, whether the instrument is portable or fixed. In addition, barrel or pincushion distortion in the camera and the nonlinear relationship between angle and distance on the focal plane of any camera complicates fitting of wavelength to a position in the camera. Image curvature, common to any spectrometer where the illumination is off axis, may further compromise the uniformity of calibration as a function of height in the image. In Figure 9.4a, the green band top and bottom ends are 8 pixels to the right of the center of the band over an image height of 980 pixels. Since the dispersion is about 0.71 nm/pixel, this corresponds to an apparent wavelength range along a single column of the image of 5.6 nm. Of course, data processing can compensate for such curvature, provided it is noticed, characterized, and employed.

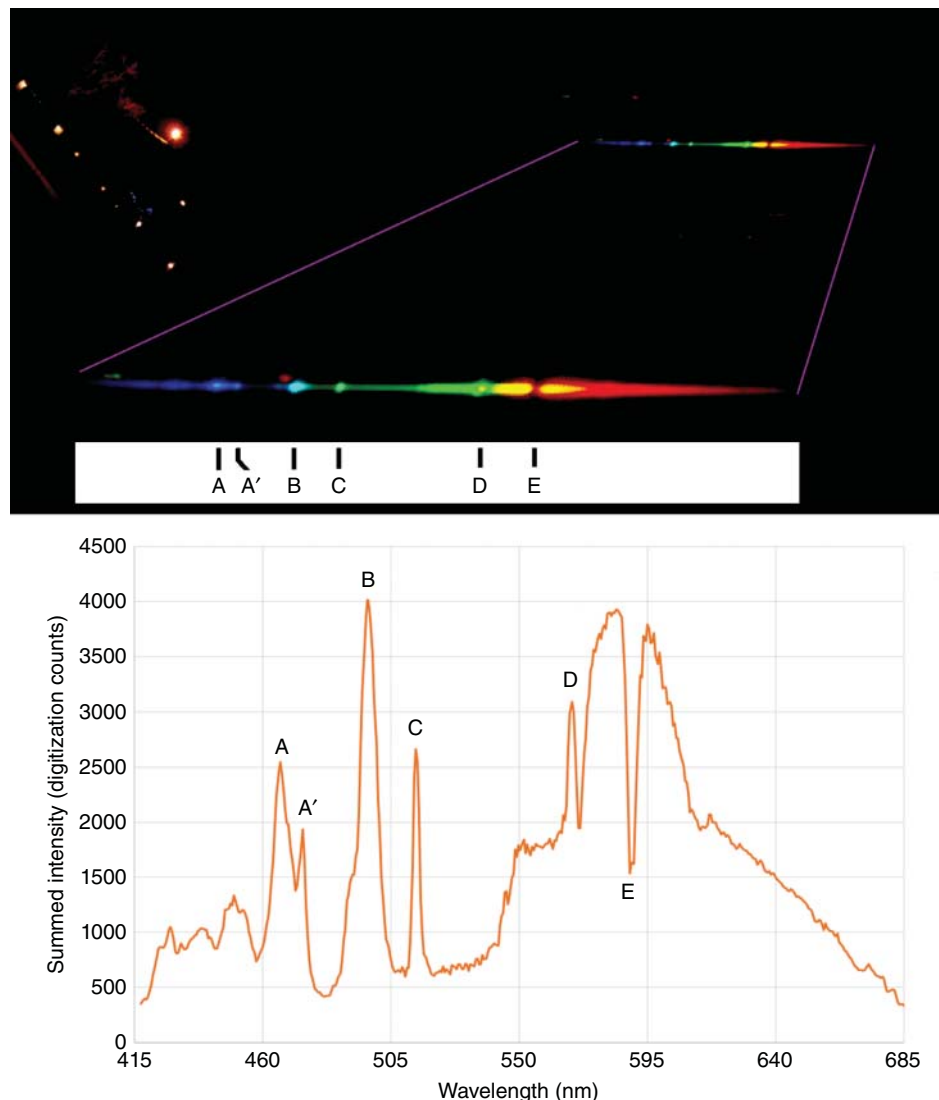


**Figure 9.6** High-pressure sodium vapor lamp spectrum, annotated.

Figure 9.5 also shows how source size can obscure spectral structure and, thus, mislead one as to the wavelength of a particular line or band. When viewing the full troffer height, the band near 550 nm appears to be a single entity, most likely due to the 546 nm Hg I line. When the troffer is masked, it becomes evident that two transitions are present, one due to Hg I emission, and the other due to Te<sup>3+</sup> phosphorescence or the cluster of Hg I lines emitting near 579 nm.

Figure 9.6 shows emission from a high-pressure sodium vapor lamp street light, taken with the same 600 line per mm grating as used for the fluorescent lamp spectrum and using the same Nikon D50 camera employed for the calibration image in Figure 9.4c. The top of the image shows the lamp at left and dispersed spectrum stretching to the right. An enlarged rendering of the spectrum is shown below, with violet guidelines superimposed on the figure. Atomic absorption by the ~589 nm sodium D lines is evident as feature E ( $2p^2S_{1/2} - 2p^2P_{1/2,3/2}^o$ ). Feature D is easy to mistake for the Hg I 546 nm line (plausibly from a NaHg amalgam), but is, in fact, a sodium line

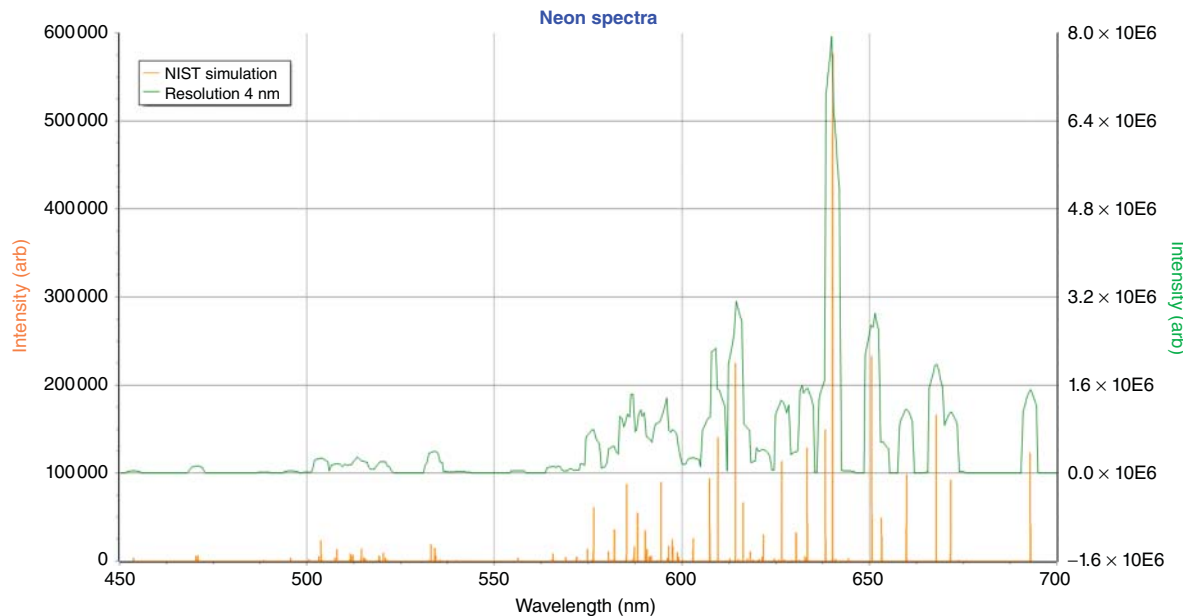


**Figure 9.7** Simulated neon atomic emission and effect of low resolution on observations.

( $3p^2P_{1/2,3/2}^0 - 4d^2D_{3/2}$ ) at 568 nm. Other features are: A ( $3p^2P_{1/2,3/2}^0 - 6d^2D_{3/2,5/2}$ ) (466 nm), A' ( $3p^2P_{1/2,3/2}^0 - 7s^2S_{1/2}$ ) (475 nm), B ( $3p^2P_{1/2,3/2}^0 - 5d^2D_{3/2}$ ) (498 nm), and C ( $3p^2P_{1/2,3/2}^0 - 6s^2S_{1/2}$ ) [79–81].

Last, in Figure 9.7, we show the spectrum expected from a neon bulb. Data were simulated using National Institute of Standards and Technology (NIST's) atomic spectral database, assuming a temperature of 2 eV, with Doppler broadening, and electron density of  $10^{14} \text{ cm}^{-3}$  [81]. The orange trace shows what a high-resolution spectrometer might observe – a spectrum dense in red and yellow lines, but weak in the blue and green, thus forcing the use of the frequently poor assumption of linear dispersion across the wavelength range. The green trace simulates the appearance with a spectrometer with 4 nm resolution, using pixels spaced every 0.5 nm. Offsets from expected bright-line wavelengths and blurring of adjacent lines are readily seen.

In short, calibration with any portable light source or handheld instrument is difficult, of limited precision, and a likely source of measurement error.

### 9.3.2 Focus

Most smartphone cameras have lenses that are focused for distant objects. Field of view ranges from a few degrees in zoom or telephoto mode to quite wide angles (the author has seen up to  $60^\circ$ ) for group selfies. Accurate wavelength calibration requires constant zoom, and optimum resolution requires tight, consistent focus. Fortunately, both iOS and Android operating systems include commands to set focus and zoom. In neither case, however, can one be confident of the stability or reproducibility of the zoom and focus functions. In the author's experience, autofocus is the least controllable parameter of the camera modules commonly found in phones.

One common camera, available from OmniVision since at least 2012, is the OV5640,  $2592 \times 1944$  pixels, approximately 4 mm focal length, and  $\pm 22.5^\circ$  field of view in the x (wide) direction. For an ideal planar detector, distance from scene center,  $r$ , and off-axis angle of the object viewed,  $\beta$ , are related by

$$r = r_0 \tan \beta \quad (9.4)$$

where  $r_0$  is a scaling constant. For this particular detector, when  $r = 1296$  pixels (half the width of the detector) and  $\beta = 22.5^\circ$ ,  $r_0 = 3129$  pixels. If the small-angle approximation applied, each pixel would subtend  $22.5^\circ/3129 = 0.0072^\circ = 26''$ , but, in fact, differentiation of Eq. (9.4) shows

$$\frac{dr}{d\beta} = r_0 \sec^2 \beta \quad (9.5)$$

Since pixel size is constant ( $dr = 1$ ), the angle subtended by each pixel scales as

$$d\beta = \frac{\cos^2 \beta}{r_0} \quad (9.6)$$

Thus, in the limit that pixels are large compared to the resolution set by the rest of the instrument, wavelength range per pixel appears to improve as  $\cos^2 \beta$ , or by a factor of 0.85 at  $22.5^\circ$ . In the real world, pixel-limited resolution is uncommon. Almost always, pixels are small compared to the optical blur generated by the rest of the optics [82]. Under these circumstances, a fixed  $d\beta$  is stretched across a region scaling as  $\sec \beta$ . Given the commonly derived dispersion of a spectrograph,

$$\frac{d\lambda}{dx} = \frac{d \cos \beta}{nf} \quad (9.7)$$

where  $n$  is the grating diffraction order,  $f$  the spectrometer camera mirror or lens focal length, and  $d$  (other than when meant as differential operator) the grating spacing, an image of width  $w$  at the center of the detector blurs to width  $w \sec \beta$ . The off-axis blurring exactly compensates for the increase in dispersion with angle, so that resolution,  $\lambda/\Delta\lambda$ , scales as

$$\frac{\lambda}{\Delta\lambda} = \frac{\frac{d \sin \beta}{n}}{\frac{\Delta x_{\text{eff}} d}{nf}} = \frac{f \sin \beta}{\Delta x_{\text{eff}}} = k \lambda \quad (9.8)$$

Independent of diffraction order, resolution increases with wavelength, with a scaling constant dependent on camera focal length and the effective size of the entrance aperture image in zero order. Since focus adjustments change  $f$  and  $\Delta x_{\text{eff}}$ , image blur influences resolution as well as throughput, but the dependence is hidden from the casual user.

### 9.3.3 Pixel-to-Pixel Uniformity

Even the most uniform detectors have some response variation from pixel to pixel. As almost all cell phone cameras are color cameras, the variation in color filter transmission and blocking from pixel to pixel multiplicatively increases pixel response variance. Because human eyes compensate for minor variations in image quality, a good selfie camera may display significant nonuniformity, untroubling to humans, but entirely inadequate for spectrometry. Quantum efficiency and slope response (change in signal per unit light flux) vary across the detector not only because of changes in dopant levels in the semiconductor but also because of vignetting (variation in light transmission efficiency across a scene) by the lens. Such variation was recently characterized [33] for two common cellular phones as shown in Figure 9.8.

Two characteristics are evident. First, the distributions in detector response are different for the two cameras; the iPhone camera has a nearly Gaussian distribution with gain  $\sim 1.75 \pm 0.25$  digitization units per electron (with slight bimodality for the green channel), while the Samsung Galaxy response is non-Gaussian and averages 1 count per electron. Human vision responds approximately logarithmically to light intensity, so the camera variations are irrelevant for their intended use. However, for spectrometry, the errors may be catastrophic. If  $I_0$  in Beer's Law is measured by a different pixel than  $I$ , the transmittance is meaningless unless pixel response has been calibrated. This problem has rarely been noted in enthusiastic papers on the possibilities of cell phone spectrometry, as averaging over thousands of pixels has concealed the problem. The problem of transferring a method from one phone to

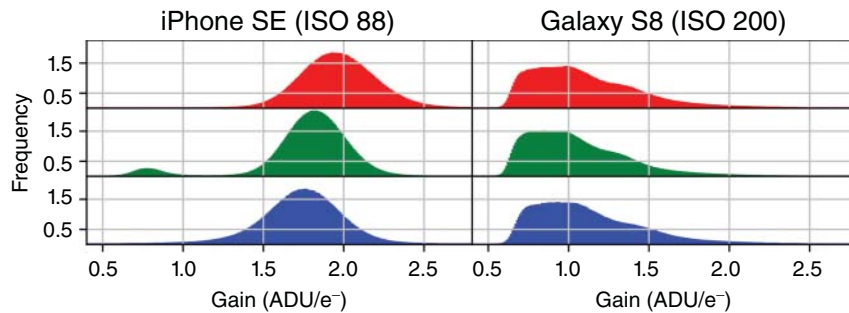


**Figure 9.8** Burggraaff's original caption: "Histogram of gain values in the R (top), G and  $G_2$  (middle), and B pixels (bottom) in the iPhone SE (left; ISO speed 88) and Galaxy S8 (right; ISO speed 200) sensors. The vertical axes were normalized to account for the different amounts of pixels." Source: Burggraaff et al. [33]. Licensed under CC BY 4.0.

another, given the variation in camera response, is obvious. While standardizing color correction between Bayer pattern color cameras has received significant attention, e.g. [83], such standardization is most useful for optimizing human perception of pictures, not for standardizing wavelength-dependent slope response, as the relative sensitivity within a particular color range (e.g. red, green, or blue) is not addressed when balancing perception color response.

Further complicating use of cell phone cameras is pixel response nonlinearity, shown, for example, in [84] or, unrecognized in turbidimetric measurement, in [85]. At some level of exposure, usually above 2/3 of pixel full well capacity, charge accumulation is sublinear, leading to saturation (no increase in signal for increasing exposure). The cited reference shows how to linearize the data. Excessive exposure leads to blooming, where adjacent pixels register signal from light not incident on that pixel. Such blurring is common to many array detectors; for low dynamic range cameras, the problem is exacerbated. To some degree, a nonlinear response can be compensated through the use of appropriate chemometrics, for example, classification and cluster analysis of RGB signals rather than fully dispersed spectra [74].

Alternatives to Bayer pattern sensing have been developed. Direct detection of red, green, and blue in a single pixel occurs in Foveon's chips [86]. Postprocessed to a JPG, bitmap (BMP), or tagged image file format (TIFF) image, a human might not, at first glance, see the difference from photos taken using a Bayer pattern. Firmware in most cameras depixelates images, thus destroying intensity data while improving perceived snapshot quality. The last thing a spectroscopist wants is any processing that destroys absolute intensity information or blurs information from adjacent pixels of different wavelength response. Getting useful information in the presence of pattern noise, shot noise, and varying responsivity is hard enough. "Helpfully" synthesizing composite colors by blurring data compounds calibration difficulties and increases the likelihood of artifact generation that is analyte dependent.

The nature of the pixelation problem is illustrated in Figure 9.9. We posit an atomic emission line and spectrometer such that the line spreads over 3 pixels in a Bayer pattern. Perhaps it is the mercury 546.1 nm line which is sensed with relative response 0.01 for blue, 1 for green, and 0.05 for red (not the values seen in measurement the author made on one particular camera, but similar). The figure shows where the image falls with respect to the pixels (ignoring curvature as discussed in conjunction with Figure 9.4) and assumes that any charge in excess of 255 counts spills into adjacent pixels. The model ignores nonlinearity short of saturation, and so more precisely shows where saturation occurs than is seen in real cameras. Precision is shot noise limited with noise just short of saturation of  $\pm 8$  counts ( $\pm 3\sigma$ ).

Despite such simple geometry and spectroscopy, the plot is rich with measurement artifacts. When the green pixels become saturated, adjacent pixels begin showing the signal from the overflow. The solid lines in the plot show data that would be obtained if exposures were taken once per arbitrary exposure time unit. However, most calibration schemes sample only a few exposure times, then fit the data to a regression line. The dashed lines are

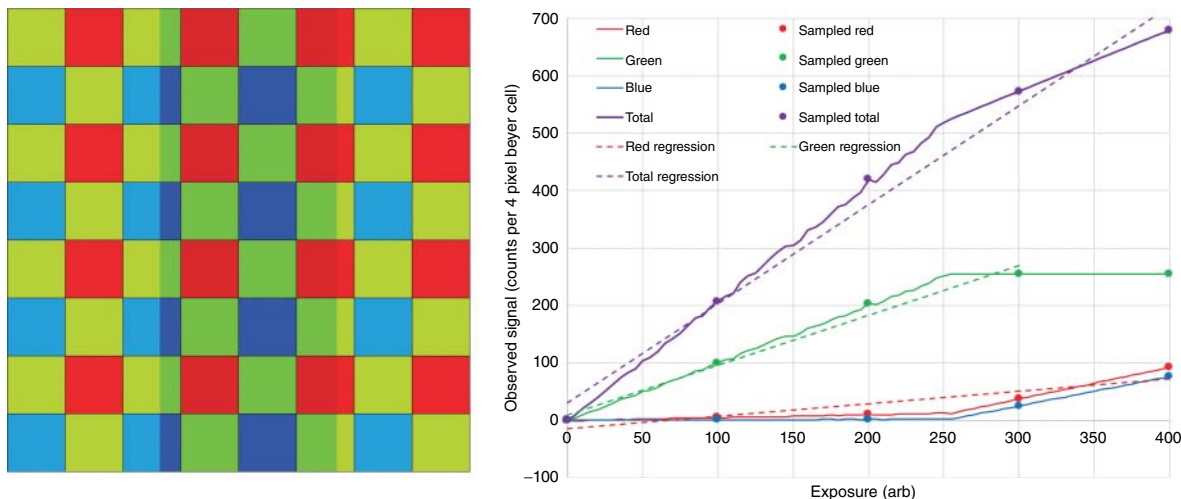


**Figure 9.9** Bayer pattern, showing illumination by a green atomic emission line spanning three columns. Related growth curves as a function of exposure shown in the plot. See text for explanation.

examples of regression fits (no blue data regression was performed to avoid clutter in the figure). “Obviously,” the saturation of the green data would be recognized by any competent measurement scientist, so regression would halt at the point where saturation is observed. Perhaps one would interpret the red (or blue) data as having a small slope that only rises above baseline at high exposure, not recognizing that blooming from overflowing green pixels is the cause. Simply summing across all pixel colors, ignoring the masking by the Bayer pattern has its own pathology. Unless one recognizes that the noise level is much lower than the fitting precision, there is little reason not to accept the regressed calibration line. Even if one knows the noise is small compared to the fitting error, it is unclear how to interpret the summed data. Add to this the pixel-to-pixel variations, focus limitations, and the impossibility of measuring the transmission profiles of the Bayer filters outside the camera, and clearly, the use of consumer-grade cameras presents severe problems for performing scientific measurements.

### 9.3.4 Coupling Cellular Cameras to Sample Holders

Already cited have been cell phone spectrometers that observe ambient light. Any instrument that has an entrance aperture can be coupled to a fiber optic, the distal end of which may observe any specimen as if the cell phone spectrometer were any benchtop or portable instrument. Thus, within this section, what is of interest is specimen holders other than fiber optic couplers that place the sample and cell phone spectrometer in close proximity or in contact so that the design is specific to the constraints of portability, size, cost, and repeatability of such instruments.

The most common sample holders are 1-cm cuvettes and 96-well plates. In addition, colorimetric test strips may be employed. We discuss each in turn.

#### 9.3.4.1 1-cm Cuvettes

For path length through a cuvette to be uniform, collimated light must impinge thereupon. Collimated light is also optimal for grating illumination. Benchtop instruments separately collimate light for the cuvette and grating, avoiding distortion from refraction and scattering/light diffusion in the cuvette. Scattering not only offsets the absorbance baseline but degrades wavefront planarity essential for grating performance. Using single collimation thus risks spectral blurring and dramatic increases in the background, but simplifies the optical system when scattering is only minor. Such an approach has been used in the handheld instruments the author

has employed, where the camera is the OmniVision unit previously cited. Light is collimated with an off-axis parabolic mirror, passed through the cuvette and grating stack, then observed with the camera module. The slight wedging of cuvette walls (draft) necessary to allow cuvettes to be removed from their forming molds means that the spectrum seen through the cuvette is translated on the camera from that seen for an air path spectrometer. The prior discussion of pixel-to-pixel variation indicates why this is problematic: different pixels measure  $I$  and  $I_0$  [30, 39–41, 53].

A 3D-printed dual-beam sample and grating holder that clips onto a phone were recently reported [31]. Two raw spectra are dispersed across the cell camera focal plane. While such geometry compensates for variance in light source output, it exacerbates problems in wavelength calibration, field curvature, and pixel-to-pixel response variance. The authors discuss none of the precision or accuracy problems of this geometry.

The sunlight-source spectrometer of reference [23] uses a 1-cm cuvette. Light is partially collimated and refocused with biconvex lenses. While light traversing the cuvette is close to collimated, spherical aberration makes the collimation imperfect. In contrast, an adapter for a cell phone that uses the cell phone's flash LED as the light source illuminates a cuvette with uncollimated light [87]. Here, too, working curve slopes are less than those from a multiwell plate reader, and working curve nonlinearity is evident. A spectrometer appropriate for classrooms, where light is dispersed with a fragment of a DVD and the predispersed, uncollimated light passed through a cuvette and into the cell camera gives linear working curves over narrow concentration ranges, but also displays background absorbance, at least at blue wavelengths [88]. Seemingly better performance with a 1-cm cuvette is obtained if an LED is used as light source, narrowing the spectral range but simplifying optics, wavelength selection, and signal averaging [73].

#### 9.3.4.2 96-Well Plates

Running samples in parallel allows for greater throughput but complicates instrument design. Should a single wavelength be passed through the wells, and then perform assays by averaging signal over those pixels observing a particular well? Should each well have white light passed through it, after which the signal is dispersed? Or should a dispersed spectrum illuminate each well, after which an image of the dispersed illumination provides a spectrum, spatially resolved within the image of each well? Postdispersion is the only one of these options which does not appear in the literature, and, probably, for good reason. Adequate precision would be difficult to obtain.

The previously cited chemometric data reduction has been performed on multiwell plates. The only wavelength resolution is in the RGB color separation of the camera pixels [74]. The wavelength precision is, thus, set by the camera manufacturer and the temperature sensitivity of the individual pixel bandpasses.

A well-developed approach to the use of multiwell plates comes from Ozcan's group [89]. Rather than trying to image the entire plate, a fiber optic bundle routes light from each well to a compact header readily photographed by the cellcam. A bank of LEDs illuminate all 96 wells at a putatively identical wavelength. One can imagine interchangeable LED banks to allow different wavelengths to be used, or the use of multicolor LEDs with appropriate diodes turned on for each determination. The use of white LEDs for tri-channel measurement is reported. This colorimeter does not permit resolution better than the LED's bandwidth, nor does it solve the limited digitization precision problem except by allowing signal averaging. LED wavelength precision is adequate for screening.

Glucose monitoring with accuracy comparable to an electrochemical blood glucose meter uses immobilized horseradish peroxidase (HRP) and colorimetric reactants in a 96-well format [90]. The light source is a tablet computer with a uniformly illuminated display, while the detector is a cellcam. The software selects for portions of the field of view not biased by line-of-sight obscuration. Neither the influence of off-axis viewing nor characterization of a reference light intensity is discussed; the authors use  $I_0 = 255$ , regardless of the actual backlight level. As long as the backlight intensity is constant and a reference sample is available for each experiment, this should not pose a problem. Instead of  $A = -\log_{10}(I/I_0)$ , one is essentially saying  $A = k - \log_{10}(I)$ , with the value of  $k$  implicit in the intercept of the working curve. It appears that the authors were focused on the chemistry of the glucose-selective reaction more than the quality and complexity of the spectrometry.

### 9.3.4.3 Test Strips

Test strips have been among the earliest analytical approaches employed with cellular telephone cameras. Whitesides developed an elaborate, low-cost test system using wax-impregnated paper and colorimetric reactions for Third World chemical and biomedical testing [12, 91–94]. Because calibration was so challenging, images were sent to a central computer for processing, rendering of diagnoses, and return to the user. A decade later, were the work to be repeated, it is likely that all processing would occur on the smartphone. Imaging has been augmented with electrochemical measurements [95, 96]. A fully optical pH meter, using only images of dye-embedded test strips, is now available [97]. Whitesides has opined (and the author concurs) that what most limits the development of inexpensive chemical and biomedical tests is that the areas that have the greatest need for such capabilities are least able to afford them, so that financing, rather than science or technology, impedes the broad dissemination of autonomous phone/test strip technology. One can imagine making tests that cost pennies apiece, but commercial investors are more interested in tests with healthy profit margins. Development of such tests will require support from non-governmental organizations (NGOs), governments, and foundations.

Suslick has championed the use of colorimetric arrays for “smell seeing,” sensing airborne species by quantifying patterns in color changes of porphyrins and other organometallics upon exposure [98, 99]. His group has used flat-bed scanners, cell cams, digital single-lens reflex cameras, and dedicated spectrometers for quantifying the patterns. Because signal averaging is most easily achieved and digitization bit depth greatest for the dedicated spectrometer, precision is highest. While “color depth” is 12 bits, this amounts to 4 bits each of red, green, and blue. As shown in figure 3 of [100], the authors distinguish the effect of averaging over multiple pixels within a color spot from the precision of a single pixel but do not characterize photometric precision of any individual pixel. For an 8-pixel diameter image, an iPhone 5S gave precision of 18 counts out of 4095, while a linear CCD, with optics optimized to match the test strip geometry, gave precision of 2 counts. While such practical contrasts are useful for comparing specific devices or measurement conditions, a more fundamental view of precision is needed for adequately designing and contrasting cell phone spectrometers in general.

### 9.3.5 Precision and Error Propagation

Without adequate precision, linearity, and accuracy, a cell phone spectrometer is worse than useless – it may be misleading. The formalism for explicating spectrophotometric precision has been developed for laboratory instruments. Selected overviews can be found in [34, 35, 101–108], and authors who have significantly contributed to such thinking include Winefordner, Crouch, Ingle, and Tellinghuisen. We will not derive quantitative expressions here but rather will highlight areas that are of significant concern, frequently with higher variance for a cell phone instrument than for common laboratory instruments. Some noise sources may also be related to deterministic as well as random errors, and some errors are cross-correlated.

- i. Digitization quantization noise: The charge stored in each camera pixel is converted to an integer before any signal processing can be done. For an  $N$ -bit converter, the minimum relative uncertainty for each digitization is 1 part in  $2^N$  or  $2^{-N}$ .
- ii. Shot noise in signal and dark current: While there are a few situations where shot noise can be suppressed, typical incoherent light has Poisson noise and so for  $M$  detected photons has uncertainty  $M^{1/2}$  for a signal-to-noise ratio of  $M^{1/2}$ . Bigger pixels can store higher charges and, thus, show lesser shot noise. For a typical cell cam with  $\sim 1.4 \mu\text{m}^2$  pixels, full well capacity is  $\sim 2 \times 10^4$  electrons. Maximum precision at the full well is, thus,  $\sim 140$ , which explains why 8-bit precision, as is common in JPG files, fits well with camera performance. Some cameras have 10-bit digitizers, and so generate 1 count for every 20 electrons at full scale. However, the last 2 bits fluctuate due to shot noise. The example in Figure 9.8 suggests one count approximately equals one electron. In such cameras, one requires 15-bit digitization to be able to quantify full well charge. Alternatively, for 11-bit digitization, a full well would hold only 2000 electrons, for a maximum

signal-to-noise ratio of 45. The author has not yet figured out how to resolve the discrepancies among these calculations, although one suspects that the digitization ratio (counts/electron) is some multiple of that shown in Figure 9.8.

- iii. Flicker noise: Even when power or current to a light source is precisely controlled, the output often fluctuates at low frequency (thus having a noise power spectrum  $\sim 1/f^\alpha$ ,  $f$  = frequency in Hertz,  $0 < \alpha < 2$ ). Flicker noise is commonly minimized by using dual-beam measurements. Few cell phone instruments are capable of instantaneous double beam measurement, so flicker noise is high in such systems. The flash LED is used as a light source for some spectrometers, and that LED is controlled only sufficiently to provide pleasing snapshots, not for high precision photometry. Electronic flash, either white LEDs or xenon flashlamps, are also possible. Without careful characterization, their precision is suspect, again requiring dual-beam operation.
- iv. Sample cell positioning noise: This is perhaps the most difficult noise source to control in portable instruments loosely attached to cell phones. Any change in position or angle of the sample-holder changes throughput and path length of light from the source to sample and sample to camera/sensor. If the flash LED in the cell phone is used as the light source, then the movement of a sample holder changes not only sample/camera alignment but also light source/sample alignment. Cuvettes and multiwell plates have strains, dust, and other imperfections whose position challenges precision measurement even in the lab. In portable settings, there is no way to identify, much less stabilize, their influence. To make meaningful measurements, sample cell positioning error must be small compared to the variance caused by the analyte. When such problems are ameliorated using a rigid, precisely alignable stand, portability is often compromised. Any claim of detection limits or quantification limits should indicate how much of the degradation from such limits in the laboratory is due to imprecise alignment in field instruments.
- v. Thermal noise (electronics): Random motion of electrons in resistors (including wires) is called Johnson noise. The root mean square noise voltage,  $v_N$ , increases with temperature  $T$ , resistance  $R$ , and bandwidth  $\Delta f$ :

$$v_N = \sqrt{4kTR\Delta f} \quad (9.9)$$

Thus, noise depends on the environment and the temperature of individual components. If a camera is not properly heat sunk, then heavy use will gradually increase noise magnitude. If Wi-Fi coverage is poor so that transmitter amplitude must be high, or a battery is heavily loaded and releasing waste heat, phone temperature will increase. Without monitoring component temperature, noise amplitude becomes a significant, unquantified, drifting parameter. A  $1\text{ k}\Omega$  resistor at  $300\text{ K}$  and  $1\text{ kHz}$  bandwidth has an root mean square (RMS) noise amplitude of  $129\text{ nV}$  or, equivalently,  $129\text{ pA}$ . Bringing a pixel with  $20\text{ kiloelectron}$  capacity to saturation in  $1/30$  second is a current of  $0.1\text{ pA}$ . Clearly, noise suppression is critical to measurement quality, and more noise can be tolerated in selfie images than in scientific measurements.

- vi. Thermal noise (mechanical structure): Solid objects can appear to have the rigidity of gelatin as temperature changes. Consider the coefficient of linear expansion of common optical and instrument materials (Table 9.2): Clearly, materials commonly used in laboratory instruments are less subject to temperature-induced dimensional changes than are materials employed in cell phones, injection-molded accessories, and plastic optics. A grating made of Mylar®, as are many inexpensive transmission gratings, will have, e.g.  $600\text{ lines/mm}$  at  $25^\circ\text{C}$ ,  $600.9\text{ lines/mm}$  at  $0^\circ\text{C}$ , and  $599.3\text{ lines/mm}$  at  $45^\circ\text{C}$ . Mylar stretched flat at  $0^\circ\text{C}$  with an unsupported span of  $2\text{ cm}$  will expand to a length of  $2.003\text{ cm}$  at  $25^\circ\text{C}$ , allowing a departure from planarity of  $\sim 0.67\text{ mm}$ , corresponding to a departure from the desired mechanical plane of approximately  $5^\circ$  at the mounting points (assuming continued planarity of the supporting frame, with maximum displacement at the optical axis). For molecular absorbance or molecular fluorescence spectrometry, the change in grating  $d$  spacing is small, leading to less than a  $2\text{ nm}$  shift in calibration at any pixel if dispersion is  $1\text{ nm/pixel}$ , but the change in the angle of incidence at the edges of the grating may be significant. A  $1\text{ cm}$  plastic cuvette will change path length by  $0.2\%$  between  $0$  and  $25^\circ\text{C}$  (or any comparable temperature change). Refractive indices are also temperature

**Table 9.2** Common coefficients of thermal expansion [105] except as noted.

Material	Coefficient of thermal expansion ( $\Delta L/(L\Delta T)$ , $K^{-1}$ ) $\times 10^6$
Invar	1.5
Polystyrene	70
Polycarbonate	65–70
Polyolefins	32–108
Mylar	59.4
Aluminum	21–24
Titanium	8.5–9
Pyrex	4
Fused quartz	0.55
BK-7	7.1 [117]

Source: Based on Rieke [105].

dependent. Assembly of optical components using materials of different coefficients of thermal expansion may lead to alignment shifts. All these thermally driven distortions decrease precision.

- vii. Thermal noise (wavelength calibration): As already noted, gratings or prisms change dispersion with temperature. If peak emission of an LED is used as a calibration reference, that too changes with temperature. Atomic emission lines are reliable for setting calibration wavelengths, but portable, low-power atomic line sources are rare. It is unfortunate that plasma panels (<http://edenpark.com/products.html>) are not optimized for use in the visible, neon lights have few emission wavelengths in the blue or green, mercury lamps require high-voltage transformers that are heavy, and flame emission poses assorted hazards in addition to being inconvenient to align.
- viii. Thermal noise (chemistry): The position of chemical equilibrium and the rate of the chemical reaction are both temperature dependent. Thus, the slope of analytical working curves is temperature dependent, even for an instrument with thermostated optics. Further, if the specimen undergoes chemical reaction during measurement, the reaction may heat or cool the sample holder/cuvette, in turn, changing refractive index, optical path, reflection losses at interfaces, and (if illuminated off-normal) beam position.
- ix.  $1/f$  noise: light source aging: The color temperature of white LEDs shifts with age, generating a gradual drift in the wavelength dependence of  $I_0$  for absorbance measurements. While LEDs drift more slowly and more monotonically than hot filament incandescent bulbs or arc lamps, they are not perfectly stable and, thus, also have  $1/f$  noise. Gradual aging of camera response due to humidity, the decay of detector Bayer filters, and diffusion of semiconductor dopants contributes additional  $1/f$  drifts. Camera quantum efficiency, thus, has a  $1/f$  component. One may view the substitution of one camera model for another in a particular series of cell phones as a low-frequency but a high-amplitude event.

### 9.3.6 User Training and Method Validity

Even experts display limited precision in carrying out analytical procedures, and nonexpert users are unlikely to have instincts for detecting sample handling or preparation actions that could lead to invalid or inaccurate results. If cell phone spectrometry is to be useful for anyone but plaintiff's attorneys, the spectrometers, methods, and operating procedures must be coordinated using computer intelligence and real-time feedback. Measuring the contributions of instrument, environment, and user to measurement error will require at least a Gage Repeatability and Reproducibility study [109–111] and potentially error propagation modelling as well.

It is likely that most users will not want to see raw data, will not wish to perform calibration activities, and will be intimidated if they are informed they made an error [112, 113]. Thus, at each step of sample handling and measurement, data must be critically examined by software and the sequence of operations tuned to what users actually do as opposed to assuming they have proceeded in some desirable way. The Goedel Theorem [114, 115] ensures that no computer program can anticipate all the missteps of which analysts are capable, but ensuring that many anticipatable errors can be trapped and handled will be just as important as devising well-calibrated hardware if cell phone chemical analysis is to succeed. The structure of such variable path programming has much in common with programmed learning system units and their interconnection [116].

## 9.4 Conclusion and Prospective

Technical, business, and psychological barriers must be overcome if cell phone spectrometry is to be more than a chimera. The difference between qualitative and quantitative measurements, between instruments that report to a smartphone and instruments employing the phone as a measurement device needs to be clear to producers and consumers alike. Applications that seek to support human perception (color-matching) and those that seek to make scientific measurements (quantitative analysis) must be carefully distinguished, as the former must mimic the nonlinearities and tastes/biases of the user, while the latter must seek to be as linear and objective as possible. For quantitative measurements, as emphasized here, the environmental variability in which the systems will be used means that either instruments must be unrealistically stable, or they must be rapidly calibrated either autonomously or by unskilled personnel at nearly the moment of use. The technical sophistication required must be produced at an extremely low cost so that the potential mass market can be served, and distribution channels established that allow for reasonable profit margins. It is likely that niche markets requiring large numbers of determinations for a few analytes will seed this market; lead in drinking water, coliform bacteria in water, and nitrate or phosphate in agricultural runoff are likely possibilities. User psychology is also important. The potential user must not be intimidated, must be guided to perform operations adequately, and must get a satisfactory, actionable result without excessive effort or time investment. While such outcomes may be possible for assay of major components of materials by, e.g. Raman, infrared, or near-infrared spectrometers mated to cellular telephones, it will be considerably more challenging to devise instruments, reactant kits, and procedures for minor and trace components.

## References

- 1 Mork, B.J. and Scheeline, A. (1988). Wavelength-resolved single-spark emission images using a charge coupled device detector. *Appl. Spectrosc.* 42: 1332–1335.
- 2 Mork, B.J. and Scheeline, A. (1989). Observations of high-voltage atmospheric-pressure spark discharges in argon using a charge-coupled device detector. *Spectrochim. Acta A* 44B: 1297–1323.
- 3 Leiden University (2013). Measuring particulates with your smartphone. <http://www.research.leiden.edu/news/measuring-particulates-with-your-smartphone.html> (accessed 1 September 2019).
- 4 Snik, F., Rietjens, J.H.H., Apituley, A. et al. (2014). Mapping atmospheric aerosols with a citizen science network of smartphone spectropolarimeters. *Geophys. Res. Lett.* 41: 7351–7358.
- 5 Oswald, E. (2017). With a built-in molecular spectrometer, this phone can identify any material. *Digit. Trends*. <http://www.research.leiden.edu/news/measuring-particulates-with-your-smartphone.html> (accessed 6 September 2019).
- 6 GoSpectro Spectrometer for Smart Phone (2019). <https://www.alphanov.com/en/news/gospectro-power-spectroscopy-your-fingertips> (accessed 16 September 2019).

- 7 Wang, S.X. and Zhou, X.J. (2008). Spectroscopic sensor on mobile phone. U.S. Patent 7,420,663, issued 2008.
- 8 Levenson, J. (2019). Samsung Galaxy S11 has a secret weapon to take on the iPhone 12. *T3 Smart Living*. <https://www.t3.com/news/samsung-galaxy-s11-spectrometer> (accessed 7 October 2019).
- 9 NeoSpectra (2019). MEMS + FT-IR. <https://www.neospectra.com/our-offerings/neospectra-micro> (accessed 16 September 2020).
- 10 Kang, S., Son, D., and Park, J. (2019). Electronic device comprising plurality of light sources. US Patent Application 16/359,189, published 2019.
- 11 Consumer Physics (2019). SCIO by consumer physics. <https://www.consumerphysics.com> (accessed 1 September 2019).
- 12 Martinez, A.W., Phillips, S.T., Carrilho, E. et al. (2008). Simple telemedicine for developing regions: camera phones and paper-based microfluidic devices for real-time, off-site diagnosis. *Anal. Chem.* 80 (10): 3699–3707.
- 13 McGonigle, A.J.S., Wilkes, T.C., Pering, T.D. et al. (2018). Smartphone spectrometers. *Sensors* 18 (223): 1–15.
- 14 Dutta, S. (2019). Point of care sensing and biosensing using ambient light sensor of smartphone: critical review. *TrAC* 110: 393–400.
- 15 Rezazadeh, M., Seidi, S., Lid, M. et al. (2019). The modern role of smartphones in analytical chemistry. *TrAC* 118: 548–555.
- 16 Saini, S.S., Sridhar, A., and Ahluwalia, K. (2019). Smartphone optical sensors. *OPN* 30 (2): 34–41.
- 17 Crocombe, R.A. (2018). Portable spectroscopy. *Appl. Spectrosc.* 72 (12): 1701–1751.
- 18 Ross, G.M.S., Bremer, M.G.E.G., and Nielsen, M.W. (2018). Consumer-friendly food allergen detection: moving towards smartphone-based immunoassays. *Anal. Bioanal. Chem.* 410: 5353–5371.
- 19 Nelis, J., Elliott, C., and Campbell, K. (2018). “The smartphone’s guide to the galaxy”: in situ analysis in space. *Biosensors* 8 (4): 96–126.
- 20 Alawsi, T. and Al-Bawi, Z. (2019). A review of smartphone point-of-care adapter design. *Eng. Rep.* 1 (2): e12039.
- 21 DetectaChem. MobileDetect Pouches. <https://detectachem.com/products/mobiledetect-pouches> (accessed 22 November 2019).
- 22 USB Implementers Forum, Inc (2018). USB Power Delivery. <https://www.usb.org/document-library/usb-power-delivery> (accessed 16 September 2020).
- 23 Jian, D., Wang, B., Huang, H. et al. (2019). Sunlight based handheld smartphone spectrometer. *Biosens. Bioelectron.* 143: 111632.
- 24 Hossain, M.A., Canning, J., Cook, K., and Jamalipour, A. (2016). Optical fiber smartphone spectrometer. *Opt. Lett.* 41 (10): 2237–2240.
- 25 Hong, J.I. and Chang, B.-Y. (2014). Development of the smartphone-based colorimetry for multi-analyte sensing arrays. *Lab Chip* 14 (10): 1725–1732.
- 26 Yu, H., Tan, Y., and Cunningham, B.T. (2014). Smartphone fluorescence spectroscopy. *Anal. Chem.* 86 (17): 8805–8813.
- 27 Long, K.D., Yu, H., and Cunningham, B.T. (2014). Smartphone instrument for portable enzyme-linked immunosorbent assays. *Biomed. Opt. Express* 5 (11): 3792–3806.
- 28 Long, K.D., Yu, H., and Cunningham, B.T. (2015). Smartphone spectroscopy: three unique modalities for point-of-care testing. *Next-Gen. Spectrosc. Technol.* VIII: 94820J-1-94820J-8.
- 29 Mudanyali, O., Dimitrov, S., Sikora, U. et al. (2012). Integrated rapid-diagnostic-test reader platform on a cellphone. *Lab Chip* 12 (15): 2678–2686.
- 30 Scheeline, A. and Bui, T.A. (2014). Energy dispersion device. U.S. Patent 8,885,161, issued 2014.
- 31 Bogucki, R., Greggila, M., Mallory, P. et al. (2019). A 3D-printable dual beam spectrophotometer with multi-platform smartphone adaptor. *J. Chem. Ed.* 96 (7): 1527–1531.
- 32 Hamamatsu Corp (2019). Silicon photodiodes. [https://www.hamamatsu.com/resources/pdf/ssd/e02\\_handbook\\_si\\_photodiode.pdf](https://www.hamamatsu.com/resources/pdf/ssd/e02_handbook_si_photodiode.pdf) (accessed 22 November 2019).

- 33** Burggraaff, O., Schmidt, N., Zamorano, J. et al. (2019). Standardized spectral and radiometric calibration of consumer cameras. *Opt. Express* 27 (14): 19075–19101.
- 34** Rothman, L.D., Crouch, S.R., and Ingle, J.D. (1975). Theoretical and experimental investigation of factors affecting precision in molecular absorption spectrophotometry. *Anal. Chem.* 47: 1226–1233.
- 35** Ingle, J.D. and Crouch, S.R. (1988). *Spectrochemical Analysis*. Englewood Cliffs, NJ: Prentice Hall.
- 36** Holst, G.C. and Lomheim, T.S. (2007). *CMOS/CCD Sensors and Camera Systems*. Winter Park, FL: JCD Publishing.
- 37** Hussain, I., Ahamad, K.U., and Nath, P. (2017). Low-cost, robust, and field portable smartphone platform photometric sensor for fluoride level detection in drinking water. *Anal. Chem.* 89 (1): 767–775.
- 38** Das, A.J., Wahi, A., Kothari, I., and Raskar, R. (2016). Ultra-portable, wireless smartphone spectrometer for rapid, non-destructive testing of fruit ripeness. *Sci. Rep.* 6: 32504.
- 39** Scheeline, A. (2018). Progress towards low resolution visible spectrometry with COTS components. *Next-Gen. Spectrosc. Technol.* X: 10657-06-1-10657-06-8.
- 40** Scheeline, A. and Bui, T.A. (2016). Stacked, mutually-rotated diffraction gratings as enablers of portable visible spectrometry. *Appl. Spectrosc.* 70 (5): 766–777.
- 41** Scheeline, A. (2015). Is “good enough” good enough for portable visible and near-visible spectrometry? *Next-Gen. Spectrosc. Technol.* VIII: 94820H-1-94820H-9.
- 42** Zhu, W., Yi, S., Chen, A. et al. (2019). Single-shot on-chip spectral sensors based on photonic crystal slabs. *Nat. Commun.* 10 (1): 1020–1025.
- 43** Sadler, D.A., Littlejohn, D., and Perkins, C.V. (1995). Automatic wavelength calibration procedure for use with an optical spectrometer and array detector. *J. Anal. Atomos. Spectrosc.* 10 (3): 253–257.
- 44** Miller, D.L. and Scheeline, A. (1993). A computer program for the collection, reduction, and analysis of Echelle spectra. *Spectrochim. Acta A* 48B: E1053–E1062.
- 45** Cao, X.A., LeBoeuf, S.F., and Stecher, T.E. (2006). Temperature-dependent electroluminescence of AlGaN-based UV LEDs. *IEEE Electron. Dev. Lett.* 27 (5): 329–331.
- 46** OSRAM (2012). ChipLED 0603 datasheet version 1.0, 1–23.
- 47** Xie, R.-J. and Hiosaki, N. (2007). Silicon-based oxynitride and nitride phosphors for white LEDs – a review. *Sci. Technol. Adv. Mater.* 8: 588–600.
- 48** Wagner, M., Herzog, A., Ganev, H., and Khanh, T.Q. (2015). LED aging acceleration – an analysis from measuring and aging data of 14,000 hours LED degradation. *12th China International Forum Solid State Lighting*, Shenzhen, China (2–4 November 2015), pp. 75–78.
- 49** Routledge, R. (2019). Central limit theorem. <https://www.britannica.com/science/central-limit-theorem> (accessed 19 September 2019).
- 50** Taylor, K. and Silver, L. (2019). Smartphone ownership is growing rapidly around the world, but not always equally. <https://www.pewresearch.org/global/2019/02/05/smartphone-ownership-is-growing-rapidly-around-the-world-but-not-always-equally> (accessed 1 September 2019).
- 51** Hernandez, T.C.M., Gonzalez-Valencia, E., Torres, P., and Ramirez, D.L.A. (2017). Low-cost spectrometer for educational applications using mobile devices. *Opt. Pura Apl.* 50 (3): 221–228.
- 52** Bayer Filter (2019). [https://en.wikipedia.org/wiki/Bayer\\_filter](https://en.wikipedia.org/wiki/Bayer_filter) (accessed 3 October 2019).
- 53** Scheeline, A. (2019). Energy dispersion cuvette. U.S. Patent 10,324,023, issued 2019.
- 54** Plymouth Grating Laboratory (2019). Two-dimensional (2D) diffraction gratings. <https://www.plymouthgrating.com/product/two-dimensional-2d-diffraction-gratings> (accessed 22 November 2019).
- 55** Snik, F., Karalidi, T., and Keller, C.U. (2009). Spectral modulation for full linear polarimetry. *Appl. Optics* 48 (7): 1337–1346.
- 56** Raju, L. (2012). Development of a low cost infrared spectrophotometer and a Matlab program to detect terrestrial and extraterrestrial water vapor. *Cent. Alabama Reg. Sci. Eng. Fair* 2013.

- 57** Coates, J. (2010). New miniaturized spectral measurement platforms covering the visible to the mid-IR. PDF of PowerPoint on linear variable filter spectra (7 October 2013). [http://depts.washington.edu/cpac/Activities/Meetings/Fall/2010/documents/NeSSI\\_Workshop\\_November\\_2010\\_Coates.pdf](http://depts.washington.edu/cpac/Activities/Meetings/Fall/2010/documents/NeSSI_Workshop_November_2010_Coates.pdf) (accessed 21 October 2019).
- 58** Coates, J. (2011). Integrated sensing module for handheld spectral measurements. U.S. Patent 7,907,282, issued 2011.
- 59** Macleod, H.A. (2017). *Thin Film Optical Filters*. Boca Raton, FL: CRC Press.
- 60** PixelSensor™ Multispectral Sensors (2019). <https://pixelteq.com/pixel-sensor> (accessed 1 September 2019).
- 61** 11 Channel Spectral Color Sensor (2019). <https://ams.com/as7341> (accessed 1 September 2019).
- 62** LightShift (2019). <https://surfaceoptics.com/products/hyperspectral-imaging/lightshift> (accessed 1 September 2019).
- 63** Wang, S.-W., Xia, C., Chen, X. et al. (2007). Concept of a high-resolution miniature spectrometer using an integrated filter array. *Opt. Lett.* 32 (6): 632–634.
- 64** Hercher, M. (1968). The spherical mirror Fabry-Perot interferometer. *Appl. Optics* 7: 951–966.
- 65** Wikipedia (2019). The Fabry Pérot Interferometer. [https://en.wikipedia.org/wiki/Fabry-Pérot\\_interferometer](https://en.wikipedia.org/wiki/Fabry-Pérot_interferometer) (accessed 21 November 2019).
- 66** Vaughan, M. (1989). *The Fabry-Perot Interferometer: History, Theory, Practice and Applications*. Boca Raton, FL: CRC Press.
- 67** Mannila, R., Hyypio, R., Korkalainen, M. et al. (2015). Gas detection with microelectromechanical Fabry-Perot interferometer technology in cell phone. *Next-Gen. Spectrosc. Technol.* VIII: 94820P.
- 68** Ding, H., Chen, C., Zhao, H. et al. (2019). Smartphone based multispectral imager and its potential for point-of-care testing. *Analyst* 144 (14): 4380–4385.
- 69** Yang, Z., Albrow-Owen, T., Cui, H. et al. (2019). Single-nanowire spectrometers. *Science* 365 (6457): 1017 LP–1020.
- 70** Learner, J. (2019). PARISS® imaging spectrograph. <https://lightforminc.com/products/imaging-spectrograph> (accessed 4 October 2019).
- 71** Choi, S., Kim, Y., Lee, J.-Y. et al. (2019). Minimizing device-to-device variation in the spectral response of portable spectrometers. *J. Sensors* 2019 (8392583): 7.
- 72** Zhang, J. (2013). Spectrometer miniaturized for working with cellular phones and other portable electronic devices. U.S. Patent 8,537,343, issued 2013.
- 73** Hussain, I., Bora, A.J., Sarma, D. et al. (2018). Design of a smartphone platform compact optical system operational both in visible and near infrared spectral regime. *IEEE Sensors* 18 (12): 4933–4939.
- 74** Coleman, B., Coarsey, C., and Asghar, W. (2019). Cell phone based colorimetric analysis for point-of-care settings. *Analyst* 144 (6): 1935–1947.
- 75** International Light Technologies, Inc.(2019). Neon Lamps: Application and Technical Notes. <https://www.intl-lighttech.com/specialty-light-sources/neon-lamps> (accessed 7 October 2019).
- 76** Wikimedia Commons (2009). File:Fluorescent Lighting Spectrum Peaks Labelled.png. [https://commons.wikimedia.org/wiki/File:Fluorescent\\_lighting\\_spectrum\\_peaks\\_labelled.png](https://commons.wikimedia.org/wiki/File:Fluorescent_lighting_spectrum_peaks_labelled.png) (accessed 8 October 2019).
- 77** Kelley, K.D. and Scheeline, A. (2009). Cell phone spectrophotometer. *J. Anal. Sci. Digit. Lib.*, entry 10059. [https://www.asdlb.org/onlineArticles/elabware/Scheeline\\_Kelly\\_Spectrophotometer/index.html](https://www.asdlb.org/onlineArticles/elabware/Scheeline_Kelly_Spectrophotometer/index.html) (accessed 16 September 2020).
- 78** Scheeline, A. and Kelley, K. (2014). CellPhoneSpecIntEd. <http://scheeline.scs.illinois.edu/~asweb/CPS/CellPhoneSpecIntEd.exe> (accessed 8 October 2019).
- 79** PhysicsOpenLab (2017). Spectral Lines Broadening. <http://physicsopenlab.org/2017/09/07/spectral-lines-broadening> (accessed 2 October 2019).
- 80** Miokovic, Z., Balkovic, D., and Veza, D. (2010). Shift and broadening of sodium nS-3P and nD-3P transitions in high pressure NaCd and NaHg discharges. *Arxiv*. <https://arxiv.org/ftp/physics/papers/0410/0410146.pdf> (accessed 1 October 2019).

- 81** Kramida, A., Ralchenko, Y., and Reader, J. (2018). NIST atomic spectra database (Ver 5.6.1) [Online]. [https://physics.nist.gov/cgi-bin/ASD/lines1.pl?spectra=Na+I&limits\\_type=0&low\\_w=400&upp\\_w=600&unit=1&submit=Retrieve+Data&de=0&format=0&line\\_out=0&en\\_unit=0&output=0&bibrefs=1&page\\_size=15&show\\_obs\\_wl=1&show\\_calc\\_wl=1&unc\\_out=1&order\\_out=0&max\\_low\\_enrg=&s](https://physics.nist.gov/cgi-bin/ASD/lines1.pl?spectra=Na+I&limits_type=0&low_w=400&upp_w=600&unit=1&submit=Retrieve+Data&de=0&format=0&line_out=0&en_unit=0&output=0&bibrefs=1&page_size=15&show_obs_wl=1&show_calc_wl=1&unc_out=1&order_out=0&max_low_enrg=&s) (accessed 7 October 2019).
- 82** Scheeline, A. (2017). Focal point: how to design a spectrometer. *Appl. Spectrosc.* 71 (10): 2237–2252.
- 83** Zhao, Y., Elliott, C., Zhou, H., and Rafferty, K. (2019). Spectral illumination correction: achieving relative color constancy under the spectral domain. *IEEE Int. Symp. Signal Process. Inf. Technol.* 2018: 690–695.
- 84** Ding, H., Chen, C., Qi, S. et al. (2018). Smartphone-based spectrometer with high spectral accuracy for mHealth application. *Sens. Actuat. A Phys.* 274: 94–100.
- 85** Bayram, A., Yalcin, E., Demic, S. et al. (2018). Development and application of a low-cost smartphone-based turbidimeter using scattered light. *Appl. Optics* 57 (21): 5935–5940.
- 86** Fovean Corp (2010). X3 technology direct image sensors. <http://www.foveon.com/article.php?a=67> (accessed 7 October 2019).
- 87** Wang, Y., Liu, X., Chen, P. et al. (2016). Smartphone spectrometer for colorimetric biosensing. *Analyst* 141 (11): 3233–3238.
- 88** Hosker, B.S. (2018). Demonstrating principles of spectrophotometry by constructing a simple, low-cost, functional spectrophotometer utilizing the light sensor on a smartphone. *J. Chem. Ed.* 95 (1): 178–181.
- 89** Berg, B., Cortazar, B., Tseng, D. et al. (2015). Cellphone-based hand-held microplate reader for point-of-care testing of enzyme-linked immunosorbent assays. *ACS Nano* 9 (8): 7857–7866.
- 90** Pla-Tolós, J., Moliner-Martínez, Y., Molins-Legua, C., and Campíns-Falcó, P. (2018). Solid glucose biosensor integrated in a multi-well microplate coupled to a camera-based detector: application to the multiple analysis of human serum samples. *Sens. Actuat. B Chem.* 258: 331–341.
- 91** Carrilho, E., Phillips, S.T., Vella, S.J. et al. (2009). Paper microzone plates. *Anal. Chem.* 81 (15): 5990–5998.
- 92** Ellerbee, A.K., Phillips, S.T., Siegel, A.C. et al. (2009). Quantifying colorimetric assays in paper-based microfluidic devices by measuring the transmission of light through paper. *Anal. Chem.* 81 (20): 8447–8452.
- 93** Whitesides, G.M. (2009). Paper diagnostics – using first world science in developing economies. *Pittsburgh Conf. Anal. Chem. Appl. Spectrosc.* 12.
- 94** Martinez, A.W., Phillips, S.T., Whitesides, G.M., and Carrilho, E. (2010). Diagnostics for the developing world: microfluidic paper-based analytical devices. *Anal. Chem.* 82 (1): 3–10.
- 95** Christodouleas, D.C., Nemiroski, A., Kumar, A.A., and Whitesides, G.M. (2015). Broadly available imaging devices enable high-quality low-cost photometry. *Anal. Chem. (Washington, DC, United States)* 87 (18): 9170–9178.
- 96** Ainla, A., Mousavi, M.P.S., Tsaloglou, M.-N. et al. (2018). Open-source potentiostat for wireless electrochemical detection with smartphones. *Anal. Chem.* 90 (10): 6240–6246.
- 97** Gotor, R., Ashokkumar, P., Hecht, M. et al. (2017). Optical pH sensor covering the range from pH 0–14 compatible with mobile-device readout and based on a set of rationally designed Indicator dyes. *Anal. Chem.* 89 (16): 8437–8444.
- 98** Rakow, N.A. and Suslick, K.S. (2000). A colorimetric sensor array for odor visualization. *Nature* 406 (6797): 710–713.
- 99** Suslick, K.S. and Rakow, N.A. (2001). A colorimetric nose: “smell – seeing”. *Proc. Electrochem. Soc.* 2001–15 (A): 8–13.
- 100** Askim, J.R. and Suslick, K.S. (2015). Hand-held reader for colorimetric sensor arrays. *Anal. Chem.* 87 (15): 7810–7816.
- 101** Ingle, J.D. and Crouch, S.R. (1972). Evaluation of precision of quantitative molecular absorption spectrometric measurements. *Anal. Chem.* 44: 1375–1386.
- 102** Galbán, J., de Marcos, S., Sanz, I. et al. (2007). Uncertainty in modern spectrophotometers. *Anal. Chem.* 79: 4763–4767.

- 103 Winefordner, J.D., Svoboda, V., Cline, L.J., and Fassel, V.F. (1970). A critical review of atomic emission, atomic absorption, and atomic fluorescence flame spectroscopy. *Crit. Rev. Anal. Chem.* 1 (1): 233–272.
- 104 Tellinghuisen, J. (2000). Statistical error calibration in UV-visible spectrophotometry. *Appl. Spectrosc.* 54 (3): 431–437.
- 105 Rieke, G. (2003). *Detection of Light: From the Ultraviolet to the Submillimeter*. Cambridge: Cambridge University Press.
- 106 Sweedler, J.V., Ratzlaff, K., and Denton, M.B. (1994). *Charge Transfer Devices in Spectroscopy*. New York: VCH.
- 107 McCreery, R.L. (2000). *Raman Spectroscopy for Chemical Analysis*. New York: Wiley-Interscience.
- 108 Tellinghuisen, J. (2019). Calibration: detection, quantification, and confidence limits are (almost) exact when the data variance function is known. *Anal. Chem.* 91 (14): 8715–8722.
- 109 Quality-One International (2019). Gage repeatability & reproducibility (Gage R&R). <https://quality-one.com/grr> (accessed 22 November 2019).
- 110 Peralta, M. (2012). *Measurement System Error Analysis: Analyzing and Reducing Measurement Errors in Test Systems*. CreateSpace Independent Publishing Platform.
- 111 Gupta, S.V. (2012). *Measurement Uncertainties: Physical Parameters and Calibration of Instruments*. Springer GmbH.
- 112 Scheeline, A. (2011). Democratization of Detection: Every Citizen a Sensor? *An Integr. Water Secur. Summit Dedic. to Defense-in-Depth*, University of the Pacific.
- 113 Scheeline, A. and Bui, T.A. (2014). *Millions of Shallow CMOS Pixels and the Art of Spectroscopy*. Pittcon.
- 114 Raatikainen, P. (2018). Gödel's incompleteness theorems. *Stanford Encycl. Philos.* (Fall 2018 Ed.) (accessed 21 October 2019). <https://plato.stanford.edu/archives/fall2018/entries/goedel-incompleteness> (accessed 16 September 2020).
- 115 Hofstadter, D. (1979). *Gödel, Escher, Bach: An Eternal Golden Braid*. New York: Basic Books.
- 116 Sherwood, B.A. (1977). *The Tutor Language*. Minneapolis, MN: The Control Data Education Co.
- 117 Glass Dynamics LLC. (2015). BK-7 optical glass. <http://www.glassdynamicsllc.com/bk7.html> (accessed 5 October 2019).

# 10

## Portable Standoff Optical Spectroscopy for Safety and Security

Matthew P. Nelson and Nathaniel R. Gomer

ChemImage Corporation, Pittsburgh, PA, USA

### 10.1 Introduction

#### 10.1.1 Motivation

In today's world, biological, explosive, chemical, and narcotic threats are a constant worry, with the number of incidents on the rise. Military, law enforcement, first responders, public health officials, and civilians alike are facing this new reality that has forever changed the way we live our lives. Post-9/11 biological threats emerged in the form of anthrax being sent through mail, while improvised explosive devices (IEDs) became the weapon of choice for Al-Qaeda and Islamic State of Iraq and Syria (ISIS) terrorist groups during the post-9/11 wars in Iraq and Afghanistan, and continue to be prevalent even today. In 2018, chemical attacks were reported to have taken place in Syria, resulting in the deaths of 40–50 people and potentially injuring more than a hundred (Anon 2020a). Abuse of opioids has rapidly become epidemic, being responsible for 68% of drug overdose deaths nationally in 2017 (Scholl et al. 2019). Even more recently, the COVID-19 pandemic has sickened millions and claimed the lives of hundreds of thousands of people around the globe (Anon 2020b).

As threat prevalence grows, so does the need for technological advancements that counter these dangers to society, whether through intelligence gathering, threat detection and identification, or obliteration of the hazard. In recent years, optical spectroscopy has demonstrated that it plays a role in addressing the problem since it has the potential to address a number of unmet needs associated with practical concepts of operation (CONOPS).

An ideal portable, standoff, optical spectroscopic sensor has several distinct characteristics. Most CONOPs demand that sensors be capable of real-time, or near real-time, measurements so as not to interrupt the flow of established procedures. Sensors need to be standoff in nature to increase the safety of operators/bystanders and equipment. Specific performance requirements are generally CONOPs-driven, but all demand high sensitivity and high specificity. Threat *identification* is often necessary in addition to *detection* alone. Given the broad range of end users, sensors need to be highly automated, and with easy-to-use user interfaces. Since the location of a threat in an area of interest is often unknown, sensors also need to be capable of wide-area scanning. Portability to enable ease in fielding, operating and supporting is often important, as well as the sensor being affordable, in terms of both acquisition and maintenance costs.

#### 10.1.2 Definitions

In order to set the stage for this chapter, we first need to define a few key terms in the context of portable standoff optical spectroscopic sensors for safety and security.

*Portable Spectroscopy and Spectrometry 1: Technologies and Instrumentation*, First Edition.

Edited by Richard A. Crocombe, Pauline E. Leary and Brooke W. Kammrath.

© 2021 John Wiley & Sons Ltd. Published 2021 by John Wiley & Sons Ltd.

**Table 10.1** Optical radiation wavelength regions and applicable detector technologies.

Optical radiation region	Wavelength range ( $\mu\text{m}$ )	Common detector technologies
Ultraviolet (UV)	0.010–0.35	PMT, vacuum phototube, UV-CCD, Si photodiode, UV-CMOS
Visible (VIS)	0.35–0.770	PMT, vacuum phototube, CCD, Si photodiode, CMOS
Near-infrared (NIR)	0.77–1	PMT, vacuum phototube, CCD, Si photodiode, CMOS
Shortwave-infrared (SWIR)	1–3	InGaAs, HgCdTe, InSb
Midwave-infrared (MWIR)	3–8	HgCdTe, InSb, PbSe
Longwave-infrared (LWIR)	8–15	HgCdTe, Microbolometers
Far-infrared (FIR)	15–1000	Doped silicon

The first term we will define is “portable” or “portability.” In the context of this chapter, we consider sensors that may be moved from one location to another by vehicle, or by man, to be portable. There are varying degrees of portability. Portability, as we define it here, will span vehicle-/robot-integrated, to man-portable (1 or 2 man-carry), to handheld (1–2 hand-carry), to wearable (heads-up display, cell phone-integrated, etc.).

Another term we will define is “standoff.” Although the majority of sensing technologies in this chapter fall in the meter-to-kilometer standoff range, our simplest definition of standoff is noncontact.

In the following sections, we will frequently refer to specific optical radiation regions. There is little agreement in the literature (Byrnes 2009; Henderson 2007; Ingle and Crouch 1988; IPAC 2012) on specific starting and ending points of each of these spectral regions. Therefore, it is prudent we define the spectral regions, associated wavelength ranges, and applicable detector technologies (see Table 10.1).

Related to the optical radiation region definitions is the associated detector terminology. When using the term “camera,” we will be referring to a device that acquires a digital record in the visible portion of the spectrum. “Charge coupled device (CCD)” and “complementary metal-oxide-semiconductor (CMOS)” detectors will generally be associated with the ultraviolet (UV), visible (Vis) and near-infrared (NIR) spectral regions. The use of the term “focal plane array (FPA)” detector will commonly be used to describe how the imaging detector technology is associated with the infrared (IR) spectral regions.

The final sets of terms we will define are single point vs. multipoint spectroscopy (multispectral, hyperspectral). Single-point spectroscopy refers to single spectral measurements acquired from a target of interest. Multipoint spectroscopy (also known as spectral imaging) describes multiple spectral measurements acquired from a target of interest, often resulting in an image where each pixel has an associated spectrum. There are two general classes of multipoint spectroscopy, namely multispectral and hyperspectral. We define multispectral as spectral information containing 2–10 bands, and images captured within discrete wavelengths and/or wavelength ranges of the electromagnetic spectrum. Multispectral measurements take advantage of the fact that many material characterization applications need only a small number of spectral bands to provide the desired analytical information for the analyte(s) of interest. A reduced number of spectral bands enables faster speeds (near real-time), and less data, and, therefore, computational burden. Finally, “hyperspectral” describes spectral information containing many 10s to 100s or even 1000s of bands. In hyperspectral imaging (HSI), a plurality of images are captured at discrete wavelengths, and/or wavelength ranges of the electromagnetic spectrum. Alternatively, hyperspectral images are obtained by the acquisition of full sets of spectra. These methods take advantage of full spectral library searching algorithms, but at a cost of sacrificing speed of acquisition and analysis. These full hypercube methods can also be computationally burdensome, due to large amounts of data.

### 10.1.3 Chapter Scope

The scope of this chapter is portable standoff optical spectroscopy for safety and security applications. We will focus primarily on optical absorbance-based sensors ([NIR], shortwave-infrared [SWIR] and midwave-infrared [MWIR]), and Raman sensors. There are many other technologies (UV/Vis absorbance, millimeter wave, terahertz, fluorescence, photoacoustic, and laser-induced breakdown spectroscopy [LIBS]) that also play an important role in standoff sensing capabilities, but will not be covered extensively in this chapter.

### 10.1.4 Portable Standoff Optical Spectroscopy History

#### 10.1.4.1 Standoff Optical Sensing Origins

In the broadest sense, the first standoff optical spectroscopic sensors were biological in origin: the eyes. The first proto-eyes evolved among animals 600 million years ago (Jones 2014). Like most standoff optical spectroscopic sensors, the eyes contain a light-gathering subsystem (i.e. lens and iris), a wavelength-selection device (i.e. the cone cells which distinguish color, along with rod cells which provide low-light contrast) and a detection subsystem (i.e. the retina which converts the collected light into a visual signal which is sent to the brain through the optic nerve for processing).

#### 10.1.4.2 Standoff Optical Spectroscopic Instrumentation Origins

Astronomy was the first field to utilize and develop standoff sensing instrumentation that enhanced what the human eye was able to sense. The most important development being the telescope, which was first credited to Hans Lippershey, an eyeglass-maker from the Netherlands in 1608. A year later, Galileo refined the design and used it for astronomy, which he used to discover four satellites of Jupiter and to discover sunspots. Since then, numerous improvements to the design have improved its use and performance (Editors 2008; King 2011).

The advancement of telescopes led to the first standoff spectroscopic measurements made from celestial objects, including planets and stars in order to determine properties such as chemical composition, mass, or temperature. In the mid- to late 1600s, Isaac Newton used a prism to look at the refractive properties of light. In the early 1800s, Joseph von Fraunhofer, using Newton's work and theories of wavelength dispersion, replaced the prism with a diffraction grating to improve the spectral resolution, and allow for the more accurate accounting of the dispersed wavelengths. The distinct black lines in emission spectra of the sun became known as Fraunhofer lines. Fraunhofer used this approach to collect spectral information from Venus, the Moon, and Mars (Hearnshaw 1986). Today, our knowledge of the composition of the sun and planetary atmosphere is based on standoff optical spectroscopy (Hanel et al. 1980).

Long-range optics, inclusive of the contemporary telescope, along with advancements in light sources, wavelength selection devices and detector technologies, have been key enablers that have led to modern standoff optical spectroscopic instrumentation. Standoff Raman and IR sensors are two categories of such sensor technologies that have benefited immensely from these developments.

#### 10.1.4.3 Standoff Raman Spectroscopic Instrumentation

Raman spectroscopy has long been a valuable technique for standoff and remote applications due to its ability to provide *in situ* analysis and a near unambiguous chemical fingerprint for a target. The first standoff Raman experimentation was performed by Tomas Hirschfeld in the 1970s, where long-range atmospheric measurements were made (Hirschfeld 1974). Hirschfeld paved the way for the development of smaller standoff-capable systems in the late 1900s and early 2000s for a wide range of applications (Angel et al. 1992), including explosive detection (Carter et al. 2005), mineral and organic compound analysis (Sharma et al. 2006), and planetary exploration (Angel et al. 2012).

#### 10.1.4.4 Standoff Infrared Spectroscopic Instrumentation

Development of standoff Fourier transform (FT)-based IR spectroscopic instrumentation for condensed phase samples has been encumbered by atmospheric interference and the necessity for moving parts and sample contact. The more recent development of quantum cascade lasers (QCLs) and supercontinuum laser sources (Dupont et al. 2012) has advanced the use of MWIR and longwave-infrared (LWIR) sensors for standoff sensing capabilities. QCLs have been widely used for gas-sensing applications (Pecharromán-Gallego 2017). Experimentation done by Thériault et al. (2004) showed the potential for passive IR to detect chemical warfare agents (CWAs) on surfaces.

NIR- and SWIR-based standoff sensors have seen faster implementation into standoff configurations, compared to MWIR and LWIR, due, in part, to their more robust performance under varied atmospheric conditions and cost-effective components and system design. Solar illumination and/or inexpensive broadband incandescent lighting may be used for source illumination and detectors can be uncooled.

#### 10.1.4.5 Portable Standoff Optical Spectroscopy Instrumentation

Historically, spectroscopic sensing instruments have been large, costly, and difficult to implement in field-based applications. These impediments to portability are largely due to the maturity of the required components, typically the illumination source (i.e. laser) or spectral analysis system (i.e. spectrometer and detector). Recent technological advances have reduced the size, weight, and power consumption requirements for system components, which has allowed a tremendous rise in the implementation and production of portable sensors.

The development of smaller, more durable IR and Raman handheld spectrometers came out of the post-9/11 war effort, as they were used in Iraq and Afghanistan to detect IEDs and other hazardous threats or materials. The first modern, practical NIR handheld was introduced in 2005 by a company called Polychromix (now Thermo Fisher Scientific). The first MWIR sensor was developed by SensIR (now Smiths Detection), which was FT-based and the size of a suitcase. The first fully capable portable Raman system was developed by Ahura Scientific (now Thermo Fisher Scientific) (Crocombe 2018).

## 10.2 Portable Standoff Optical Instrument Types

Portable standoff optical spectroscopic sensors fall into three main categories based on the method of operation. The following section will introduce each method and associated subcategories of sensors.

### 10.2.1 Point Measurement Sensors

The first category of sensors are the point measurement sensors. These instruments focus the illumination source onto the target surface, followed by the collection of a full spectrum using a spectrometer or interferometer. This approach is the simplest overall approach, and provides a full spectrum that may be searched against a spectral library. The downside of this approach, as it relates to portable standoff sensors, is that it requires knowledge of where to scan, often requiring the aid of a supplemental targeting or cueing sensor.

### 10.2.2 Spatial Scanning (Mapping) Sensors

The second general category of sensors are the spatial scanning (also known as mapping) sensors. Two main subcategories of spatial scanning sensors include point-by-point (Boogh et al. 1992) and line-mapping (Bowden et al. 1990; Jestel et al. 1998, “push-broom”) sensors.

Point-by-point sensors produce chemical “maps” by first focusing a light source (when using active illumination) onto a surface, followed by the collection of one or more spectra at each desired spatial location, using a spectrometer or interferometer. Spatially accurate chemical (spectral) images may be generated by acquiring

spectra with regular  $x$ ,  $y$ -coordinated collection of spectra. These sensors provide a full image and full spectra, but at the cost of lengthy acquisition times where the point measurement time,  $T_p$  is proportional to the number of measurements, “ $n$ .”

Line-scanning sensors are the second subcategory of spatial scanning sensors. Line scanning is an extension of point-by-point mapping. “Maps” of the sample surface are generated by focusing an elongated illumination beam (when using active illumination) in one dimension (using a cylindrical lens or a scanning mechanism such as a moving mirror) with the target oriented parallel to the entrance slit of a dispersive spectrograph equipped with a two-dimensional FPA detector. Each row of the detector provides a means to generate a full spectrum at each spatial location along the length of the illumination source. Line-scanning approaches have the advantage of being full image- and full spectrum-capable. Compared to point-by-point scanning, line-scanning acquisition times,  $T_L$ , are reduced as defined by the following:

$$T_L = (1/\sqrt{n}) * T_p \text{ (single point)}$$

However, the spatial resolution differs for  $x$ - and  $y$ -axes where the parallel direction is determined by optical properties of the collection optics, while the perpendicular direction is determined by the precision of the sampling mechanism.

### 10.2.3 Wide-field Imaging (Staring) Sensors

The third category of sensors is the wide-field or global imaging sensors. When applications demand rapid, accurate and more comprehensive characterization of target morphology and composition over a large area, wide-field imaging approaches are typically sought out. Advancements in the past 25 years have made wide-area, real-time spectroscopic imaging a reality.

Wide-field imaging sensors operate by illuminating the entire field-of-view, while images are captured at discrete wavelengths, and scanning portions of the spectrum (discrete waveband imagers), or by capturing all spatial and spectral information simultaneously (snapshot imagers). Discrete waveband imagers use imaging spectrometers (i.e. acousto-optical tunable filters (AOTFs) (Goldstein et al. 1996; Schaeberle et al., 1995, 1996; Treado et al. 1992), rotating dielectric filters (Batchelder et al. 1991), Fabry–Perot interferometers (Cristensen et al. 1995; Vaughn 1989) and liquid crystal tunable filters (LCTFs) (Morris et al. 1994, 1996; Turner and Treado 1997)) to scan through discrete wavelengths interleaved with image captures at each step. Alternatively, discrete waveband imagers can utilize source tuning (i.e. QCLs (Faist et al. 1994; Schlossberg and Kelley 1981) or light-emitting diodes (LEDs) (Schubert 2003) to illuminate the field-of-view one waveband at a time, while capturing images at each step. Snapshot imagers, on the other hand, operate using wavelengths/waveforms designed with a particular end use in mind ((i.e. snapshot (West et al. 2018), multivariate optical elements (MOEs) (Nelson et al. 1998b) or conformal filters (CFs) (Nelson et al. 2019, 2018, 2017, 2016)) or by using devices that enable multipoint full spectral image captures (i.e. fiber array spectral translators (FAST) – also known as dimension reduction arrays and fiber image compression devices) (Nelson et al. 1996, 1998a; Nelson and Myrick 1999a, b; Ma and Ben-Amotz 1997; Wentworth et al. 2007).

Advantages associated with wide-field imaging approaches include unparalleled speeds [near real-time ( $<10$  s) and real-time ( $>10$  detection frames/s)]. The disadvantage of wide-field imaging is that active source architectures require high source illumination power to achieve comparable illumination power densities, and, hence, signal levels, compared to point or line approaches.

For discrete wavelength imagers, the experiment time ( $T_{DW}$ ) is proportional to the number of spectral channels “ $m$ ” instead of the number of measurements, “ $n$ ”:

$$T_{DW} = (m/n)T_p \text{ or } T_W = (m/\sqrt{n}) * T_L$$

The experiment time for snapshot imagers ( $T_{SS}$ ) is proportional to the time to acquire a single point measurement, since there is not scanning of spectral channels (i.e.  $m = 1$ ), and all spatial measurements are being acquired simultaneously (i.e.  $n = 1$ ):

$$T_{SS} = (T_p/n)*ROI; T_{SS} = (T_L/\sqrt{n})*ROI; T_{SS} = (T_{DW}/m)*ROI$$

## 10.3 Portable Standoff Optical Instrument Technologies

This section is not meant to be a comprehensive treatment of technology approaches. We discuss the most common architectures in use by end users for each of the three standoff portable instrument types discussed in the previous section.

### 10.3.1 Point and Spatial Scanning

Point and spatial scanning instruments typically use either a dispersive-based optical spectrometer (Ingle and Crouch 1988) or an interferometer. Dispersive-based optical spectrometers are devices that measure light as a function of wavelength. Today, most devices are based on diffracted light produced through the use of a diffraction grating, in combination with a linear array or two-dimensional array detector. Point and spatial scanning devices use light-gathering optics to capture a portion of the photons emitted, scattered or reflected from a target surface, and direct it through the entrance slit of the spectrometer. A detector captures the dispersed light diffracted by the grating, and converts the photons to electric charge, which is read out by an analog-to-digital converter and computer, ultimately producing a single spectrum or multiple spectra of the target.

Two common interferometer-based spectrometers are the continuous-wave Michelson or FT interferometer (Ingle and Crouch 1988) and the spatial heterodyne spectrometer (SHS) (Gomer et al. 2011a, b, 2019).

Michelson or FT interferometers operate by splitting the light from a source into two beams by a half-silvered mirror to one fixed return mirror and one movable return mirror (introducing a time delay). The split light beams interfere producing a temporal-based interferogram. Subjecting the interferogram to an FT produces a frequency-based spectrum of the light.

SHS interferometers are fundamentally a Michelson interferometer with return mirrors replaced by fixed diffraction gratings oriented at particular angles. The return wavefronts produce wavenumber-dependent crossing angles resulting in a superposition of Fizeau fringes, containing spatial frequencies. A two-dimensional FPA records the fringe pattern. Applying an FT again produces a frequency-based spectrum of the light.

### 10.3.2 Wide-field Imaging

Wide-field imaging architectures are more diverse than the point- and line-scanning approaches. The following section discusses four main classes of wide-field architectures, namely fixed bandpass filter-based, tunable bandpass filter-based, optical fiber-based and source tuning-based.

#### 10.3.2.1 Fixed Bandpass Filter-Based

Fixed bandpass filter-based architectures include dielectric interference filter wheels, rotating dielectric filters, snapshot imagers, and MOEs. Optical filter technology and its applications are described in detail in the chapter in this Volume by Pust.

Dielectric interference filter (Baillard et al. 2006) sensors typically use a wheel or linear translation stage incorporating optical filters that reflect one or more spectral bands and transmit others. Interference filters consist of

multiple thin layers composed of dielectric material having different refractive indices. Placing a series of filters in a motorized filter wheel, in front of a two-dimensional detector array, and sequentially capturing images as the filters are mechanically moved in front of the imaging detector, enables a hyperspectral data cube to be collected. This approach is simple, and low cost, with good spatial resolution, and is high in optical throughput. Disadvantages of this approach include image shift from mechanical motion of filters, limitations around the number of filters used (i.e. wavelengths), slow speed and low spectral resolution.

Rotating dielectrics involve the mechanical rotation of dielectric filters (Batchelder et al. 1991), enabling tuning of the center bandpass. Like dielectric filter wheels, rotating dielectric designs are generally simple, of low cost and high spatial resolution and provide high optical throughput. Drawbacks of this approach include image shift from mechanical motion of filters and inhomogeneity of the bandpass across the field of view.

Snapshot architectures enable a method for capturing hyperspectral images during a single integration time of the camera (Figure 10.1). Most notable is the Bayer pattern approach (Bayer 1976) in which filters are fabricated onto a grid of detector pixels using common lithographic techniques (Buchsbaum and Morris 2000; Kutteruf et al. 2014). The grid is either applied to wafer-level glass and bonded to the sensor, or is deposited directly onto the semiconductor substrate of the sensor. Filter designs come in a variety of patterns including area (Bayer-like), row (stripe), per-pixel (Mosaic), wedge (line scan), or custom. Advantages of the snapshot design include high spatial resolution, real-time compatible, high throughput, no moving parts, the potential to be made to be very small, and environmental robustness. However, snapshot imagers lack reconfigurability. In other words, the snapshot technology cannot be field-upgraded to incorporate new threats, or to improve classification and false alarm performance. Since the filter array is bonded directly onto the FPA, upgrading the system not only likely requires new software and a new algorithm, but it also involves designing a new FPA if new or different wavelengths are necessary for detection. In addition, the fabrication time and cost of the snapshot's pixel-level filter array may be prohibitive at low production volumes. Other limitations include having a limited number of wavelength

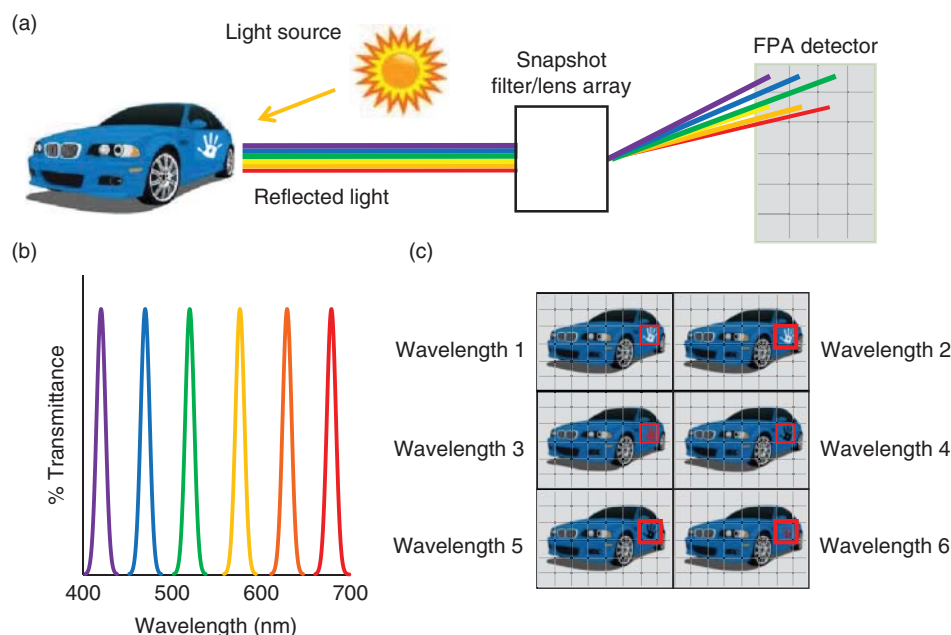


**Figure 10.1** Snapshot sensor concept illustration. (a) Light captured from a targeted scene is filtered at the pixel level on the focal plane array. (b) Example transmittance spectral profiles associated with coated pixels. (c) Reconstructed wavelength-resolved images.

bands, susceptibility to image artifacts (i.e. edge effects, etc. due to spatially offset pixel patterns), reduced spatial resolution and manufacturing difficulties depending upon filter design patterns and transmittance properties. With snapshot imagers, a trade between spatial resolution and spectral resolution is often a consideration.

MOEs (Nelson et al. 1998b) are the key elements of a multivariate optical computer. Traditional methods use multivariate or chemometric methods, such as multivariate calibration, classification, etc. to extract analytical information through generation of a regression vector from data collected at many wavelengths spanning the analytical measurement of interest (i.e. concentration). Multivariate optical computing encodes the regression vector optically into the transmission function of the optical element, i.e. the MOE. Light from a sample contains the spectral information of the samples. The normalized light detected after passing through the MOE is proportional to the dot product of the regression vector with that spectrum, and from this, the analytical measurement of interest may be obtained. MOE benefits include high spatial resolution, real-time compatibility, high optical throughput, no moving parts, a low size and weight. Shortcomings of MOEs include lack of reconfigurability, large upfront development effort, and susceptibility to changing conditions that have the potential to compromise measurement robustness.

### 10.3.2.2 Tunable Bandpass Filter-Based

Tunable bandpass filter-based architectures include LCTFs, AOTFs, and Fabry–Perot interferometers.

LCTFs are composed of a series of stages consisting of fixed retardance birefringent elements, bonded to a nematic liquid crystal waveplate, and sandwiched between linear polarizers (Morris et al. 1994, 1996; Turner and Treado 1997). Narrow bandpasses of light are achieved by controlling the voltages applied across the liquid crystal waveplate, resulting in constructive and destructive interference. Tuning is achieved via varying the applied voltages in a controlled way with a computer. Common LCTF types include the Lyot, Solc, Evans Split-Element, Multiconjugate Filter (MCF), and CF designs (Lyot 1944).

The Lyot design exhibits a bandpass and free spectral range determined by thickest and thinnest birefringent elements. Overall transmittance is a sinc function. The design suffers from poor optical throughput due to large numbers of highly absorbing polarizers.

The Solc (1965) filter has a fanout and folded filter design that improves optical throughput using only two polarizers, at a cost of poorer out-of-band rejection efficiency. The Evans split-element design (Evans 1949; Evans and Solc 1958) provides a better balance of throughput and sidelobe characteristics, and also reduces the number of polarizers to approximately half of the Lyot design.

The MCF design (Wang et al. 2006; Figure 10.2) addresses the need for improved optical throughput and thermal stability by combining the high transmittance of Solc and the high out-of-band rejection efficiency of Lyot. Its finesse (number of passband widths in a spectral period) is 1.5X of Evans and 2.0X of Lyot, allowing manufacturing with fewer stages.

The CF is a multivariate HSI architecture that uses a subset of elements of commercial-grade MCFs (Lyot 1944). CF is engineered to transmit multiband waveforms as opposed to single. Selection of passbands is CONOPs-specific and is optimized for maximum discrimination between target and background/interferents. CF-imaging exploits concepts of compressive sensing and multivariate optical computing in that it allows collection of imagery approximating detection response of conventional HSI with only two discrete measurements (i.e. filter-tuning states), rather than hundreds. Real-time (>10 detection frames per second, fps) detection imagery is achieved using an approach called dual-polarization conformal filter (DP-CF) imaging by the simultaneous collection of two tuning states. DP-CF sensors divide light captured by the sensor's light-gathering optics into two optical paths using a polarizing beam splitter, such that each path respectively preserves the parallel and perpendicular polarizations of light. Light from each path is then optically filtered by two discrete CFs tuned to target/background discrimination optimized voltage states. Filtered images are then captured onto one or two cameras. Images are ultimately cropped, co-registered, and mathematically manipulated to produce a score image that is further processed to provide streaming detection imagery.

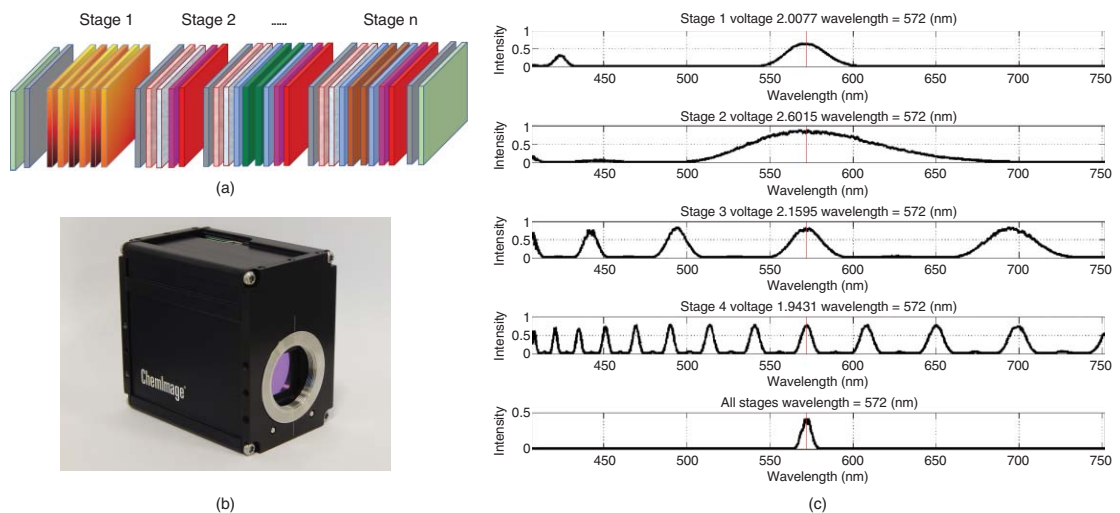


**Figure 10.2** Multiconjugate filter (MCF) design. (a) Series of stages consisting of polarizers, quartz retarders, and liquid crystal waveplates. (b) Photograph of assembled filter. (c) Transmittance spectral profiles of individual stages (top four) and combined (bottom). *Source:* Picture and data courtesy of ChemImage Corporation.

Strengths of the LCTF approaches include real-time compatibility (DP-CF), reconfigurability/adaptability, near-diffraction-limited spatial resolution, high out-of-band rejection efficiency and no moving parts. The main weaknesses of the LCTF architectures are inefficient full spectral data collection (except CFs), and low-to-moderate optical throughput depending on the design and restrictive storage temperature limits (i.e. approximately  $-15$  to  $+55^{\circ}\text{C}$ ).

AOTFs are solid-state, no-moving-parts tunable filter devices, based on the interaction of light with a traveling acoustic sound wave in an anisotropic crystal medium (Treado et al. 1992; Goldstein et al. 1996; Schaeberle et al. 1995, 1996). The devices are based on changes in the refractive index of a medium when sound waves are present, producing a refractive index grating that is “seen” by the light propagating through it. A narrow bandpass of light is created by applying a radio frequency (RF) signal to the AOTF. Tuning is achieved by changing the applied RF signal frequency and power.

AOTF advantages include relatively high optical throughput compared to LCTFs ( $\sim 40\%$  for unpolarized light), broad spectral coverage (UV to MWIR) and rapid tuning speeds ( $\sim 100\ \mu\text{s}$ ). Disadvantages include inefficient full spectral data collection, incompatibility with real-time imaging, broad spectral bandpass, a spatial resolution that is  $5\times$  worse than diffraction limits, and nonuniform spectral bandpass across the field of view.

Fabry–Perot interferometers (Cristensen et al. 1995; Vaughn 1989) (also known as etalons) incorporate an optical cavity made from two parallel reflecting surfaces with an air gap. Multiple instances of light interferences occur in the cavity. Light passes through the optical cavity when in resonance with the optical cavity, i.e. multiples of  $\lambda/2$  fit exactly within the cavity. Tuning is achieved by changing the distance or refractive index between the two surfaces. Fabry–Perot interferometers boast high image quality and high finesse. The devices are limited in that they provide moderate spectral resolution, low out-of-band rejection, limited free spectral range, small acceptance angle, and require extensive thermal management to reduce passband drift.

### 10.3.2.3 Fiber Optic-Based

Fiber optic-based approaches utilize the flexibility that optical fibers provide to physically reduce the dimensionality of data via FAST, enabling simultaneous capture of spectral and spatial data. FAST may be coupled to a traditional dispersive spectrometer, or an SHS.

FAST-dispersive devices (Figure 10.3) operate by global or wide-field illumination of a target area (Nelson and Myrick, 1999a, 1999b; Nelson et al., 1996, 1998a, 1998b; Wentworth et al. 2007). A portion of the light is gathered from the target area and projected in the form of an image onto the two-dimensional proximal end of the fiber bundle. Fibers are reordered in a specific pattern to the one-dimensional end, which is inserted in parallel into the entrance slit of a dispersive spectrometer equipped with an imaging format FPA detector. Spatial information is preserved in the  $y$ -axis while spectral information is in the  $x$ -axis. A single snapshot contains two spatial and one spectral dimension of data. The system software reconstructs the hypercube from the focal plane image and the known configuration of fibers at the 2D end of the bundle, providing position-specific spectra and wavelength-specific images. FAST-dispersive device’s main advantage is the speed for applications that are not light-limited. FAST provides a good balance between image fidelity and spectral information for certain applications where high image fidelity is not necessary. FAST also provides full spectral coverage. FAST disadvantages include low image fidelity (limited by the magnification of fibers and number of FPA rows).

FAST may also be coupled with an SHS (Figure 10.4) to enable wide-field HSI (Gomer et al. 2011a, b, 2019). Similar to FAST-dispersive, the target area is illuminated in a wide-field manner – i.e. laser for Raman measurements. The scattered light is collected, filtered with an appropriate collection optic and Rayleigh-rejection filter(s) and focused onto a FAST bundle. The output of FAST is collimated and directed into the SHS, and the output of each fiber is spatially dispersed onto a two-dimensional CCD. A single CCD image contains the spatially resolved interferograms which are transformed to the associated Raman spectra via an FT. SHS requires no moving parts and may be made to be very small. Unlike traditional dispersive spectrometers that require long focal lengths to achieve high spectral resolution, SHS is slitless, making it well-suited for wide-field illumination and functions

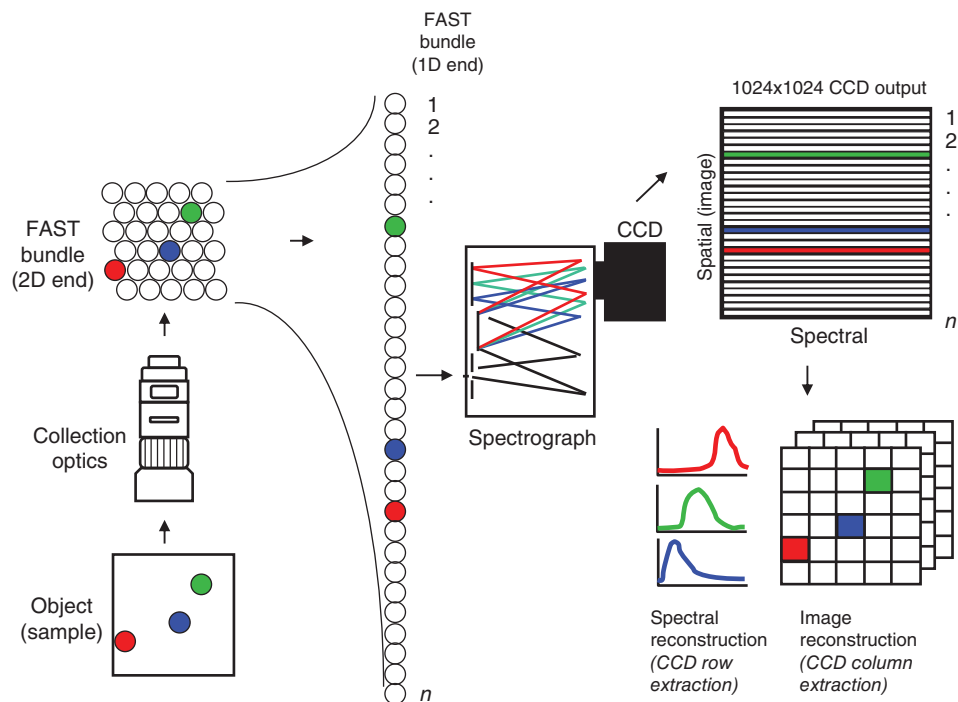


**Figure 10.3** Fiber Array Spectral Translator (FAST) concept illustration. Light from target is captured and projected onto the 2D end of fiber array, which is reordered distally into a linear array at the entrance slit of a dispersive spectrograph equipped with a 2D FPA detector. A single snapshot image captures two spatial and one spectral dimension of data simultaneously.

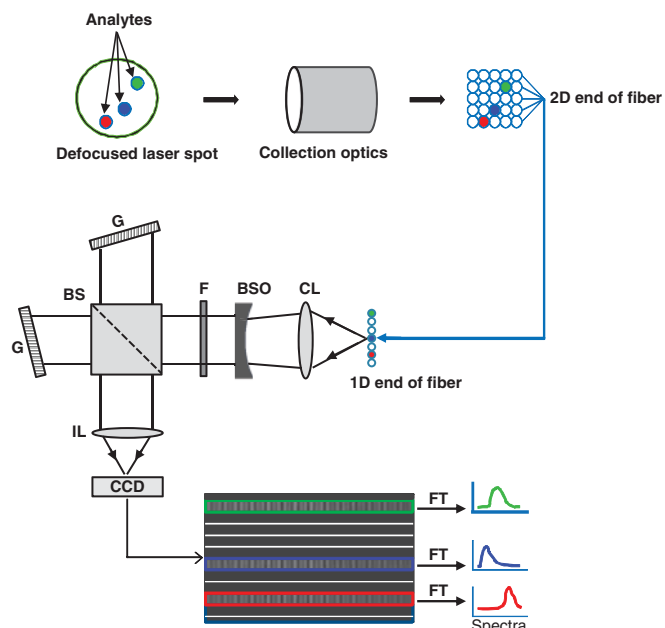


**Figure 10.4** Fiber Array Spectral Translator-Spatial Heterodyne Spectrometer (FAST-SHS) concept illustration. Light captured and propagated through the FAST bundle is imaged by the SHS producing an interferogram on detector rows that can be mapped back to specific spatial locations on the target. A Fourier transformation and image reconstruction produces spatially resolved spectra and spectrally resolved images.

CL, Collimating lens; BSO, beam shaping optics; F, optical filter; BS, beamsplitter; G, grating; IL, imaging lens; CCD, charge couple device; FT, Fourier transform.

like an interferometer – capable of very high resolving powers. SHS is relatively inexpensive and exhibits a large étendue. FAST-SHS requires tight control of alignment and is susceptible to vibrations and manufacturing difficulties. However, recent advances in monolithic SHS designs have largely addressed these limitations (Waldron et al. 2020).

#### 10.3.2.4 Source Tuning-Based

Up to this point, wide-field HSI techniques have been operating on the detection side. Alternatively, source tuning provides a means to achieving a similar result. Two popular source-tuning architectures are tunable QCLs and LEDs.

Tunable QCLs consist of semiconductor lasers emitting in the mid- to far-IR or terahertz region (Faist et al. 1994; Schlossberg and Kelley 1981). Laser emission is achieved through the use of inter-sub-band transitions in a repeated stack of semiconductor multiple quantum well heterostructures. QCLs operate in a fundamentally different mode than conventional laser diodes. They are comprised of dozens of alternating layers of semiconductor materials, which form quantum energy wells that confine the electrons to particular energy states. As electrons traverse the lasing medium, they transition from one quantum well to the next driven by the applied voltage. Photons are emitted as the electrons transition one valence band energy to a lower one. Output wavelengths are determined by the structure of the layers rather than the lasing material. Tuning may be achieved by varying temperature or through rotation of an external grating (external cavity design). Benefits of tunable QCLs include wide tuning range, fast response time, and compatible with operation in the spectral range associated with fundamental IR bands, where specificity and sensitivity are very good. Drawbacks include standoff range limits due to output power bounds as well as spectral range limitations in some cases.

LEDs are semiconductor light sources that emit light when current flows through them (Schubert 2003). Electrons in the semiconductor medium recombine with electron holes, releasing photons. The color (i.e. wavelength) emitted is determined by energy required to cross the bandgap of the semiconductor. Tunability is achieved by using a collection of LEDs with varying spectral outputs. LED advantages include low power consumption, long lifetime, small and fast switching speeds. Unfortunately, output power restricts standoff distance to just a few meters. LED availability outside the visible range is currently somewhat limited. Furthermore, output spectral profiles are relatively broad, and applications have the practical limitation of reliance on approaches to remove ambient light when used in outdoor, lighted conditions. This approach has been used in cultural heritage studies, where high-intensity, broadband, illumination of the sample is undesirable (Christens-Barry et al. 2009).

Table 10.2 summarizes the portable standoff optical spectroscopy technologies covered in this section. In the following section, we provide some direction on how to determine which technology is best suited to meet your application needs.

## 10.4 Portable Standoff Optical Spectroscopy Sensor Selection

With so many sensor and underlying technology options, selecting the most appropriate portable standoff optical spectroscopy sensor can be a daunting task. The answer to which option most often resides in the requirements governing the intended use scenarios. Primary factors that must be considered include the appropriateness of the underlying phenomenology and the spatial, spectral, and temporal measurement needs. Other important factors include environmental needs, size, weight, power and cost concerns and whether or not there is a need for reconfigurability.

### 10.4.1 Phenomenology Considerations

Having a sound understanding of the underlying spectral properties of the targets and backgrounds relevant to your application will go a long way in helping to select the most appropriate sensor. Knowing which spectroscopic

**Table 10.2** Portable, standoff, optical instrument technologies summary.

Portable instrument category	Portable instrument type	Wavelength selection device	Principle of operation	Capabilities	Challenges
Point and spatial scanning	Dispersive-based	Diffraction grating	Spectra generated by diffraction grating spatially separating incoming light into component frequencies onto a 1D or 2D detector	<ul style="list-style-type: none"> <li>• High spectral resolution</li> <li>• Full spectral coverage</li> </ul>	<ul style="list-style-type: none"> <li>• Inefficient image acquisition</li> <li>• Low area search rate</li> <li>• Poor spatial resolution</li> </ul>
	Interferometer-based	Fourier transform (FT) interferometer	Spectra obtained by measuring the coherence of a light source, using time-domain or space-domain measurements	<ul style="list-style-type: none"> <li>• High spectral resolution</li> <li>• Full spectral coverage</li> </ul>	<ul style="list-style-type: none"> <li>• Inefficient image acquisition</li> <li>• Low area search rate</li> <li>• Poor spatial resolution</li> </ul>
		Spatial heterodyne spectrometer	Similar to FT interferometer, but with no moving parts. For each wavenumber in the wavefront entering the interferometer, two wavefronts exit with a wavenumber-dependent crossing angle that produces an interference pattern that is mathematically deconvolved to a spectrum	<ul style="list-style-type: none"> <li>• High spectral resolution</li> <li>• Full spectral coverage</li> </ul>	<ul style="list-style-type: none"> <li>• Inefficient image acquisition</li> <li>• Low area search rate</li> <li>• Poor spatial resolution</li> </ul>
Wide-field imaging	Fixed bandpass filter-based	Dielectric interference filter wheels	Hyperspectral images are generated by capturing images sequentially for a series of discrete wavelengths defined by the dielectric interference filters used	<ul style="list-style-type: none"> <li>• Simple design</li> <li>• Low cost</li> <li>• High spatial resolution</li> <li>• High optical throughput</li> </ul>	<ul style="list-style-type: none"> <li>• Image shift artifacts</li> <li>• Limited number of wavelengths</li> <li>• Poor spectral resolution</li> <li>• Slow speed</li> </ul>
		Rotating dielectric filters	Hyperspectral images are acquired sequentially as a dielectric filter is mechanically rotated	<ul style="list-style-type: none"> <li>• Simple design</li> <li>• Low cost</li> <li>• High spatial resolution</li> <li>• High optical throughput</li> </ul>	<ul style="list-style-type: none"> <li>• Image shift artifacts</li> <li>• Limited number of wavelengths</li> <li>• Poor spectral resolution</li> <li>• Slow speed</li> </ul>
		Snapshot imagers	Filters are fabricated onto a grid of detector pixels using common lithographic techniques. A single image captures all wavelengths simultaneously	<ul style="list-style-type: none"> <li>• Real-time compatible</li> <li>• Moderate cost in high volumes</li> <li>• High optical throughput</li> <li>• No moving parts</li> </ul>	<ul style="list-style-type: none"> <li>• Image shift artifacts</li> <li>• Limited number of wavelengths</li> <li>• Moderate spatial resolution</li> <li>• Lack reconfigurability</li> </ul>

(Continued)

**Table 10.2** (Continued)

Portable instrument category	Portable instrument type	Wavelength selection device	Principle of operation	Capabilities	Challenges
	Multivariate optical elements		Fixed filter with regression vector associated with a particular chemical or physical measurement optically encoded into the transmission function	<ul style="list-style-type: none"><li>• Real-time compatible</li><li>• Moderate cost in high volumes</li><li>• High optical throughput</li><li>• No moving parts</li><li>• Small size, weight</li></ul>	<ul style="list-style-type: none"><li>• High upfront development cost and time</li><li>• Lacks reconfigurability</li><li>• Susceptibility to changing conditions</li></ul>
Tunable filter-based	Single-passband liquid crystal tunable filter (LCTF)		Construct consists of fixed birefringent retarders, polarizers, and liquid crystal waveplates. Hyperspectral images obtained by applying prescribed voltages to LC waveplates in a sequential fashion	<ul style="list-style-type: none"><li>• Near real-time compatible</li><li>• Reconfigurable</li><li>• High spatial resolution</li><li>• No moving parts</li></ul>	<ul style="list-style-type: none"><li>• Inefficient full spectral acquisition</li><li>• Low-to-moderate optical throughput</li><li>• Limited storage/operation temperature ranges</li></ul>
	Multipassband LCTF		Multipassband hyperspectral imaging architecture using a subset of elements of sequential LCTF. Two filters can be used in tandem to approximate a full hyperspectral image in only two measurements	<ul style="list-style-type: none"><li>• Real-time compatible</li><li>• Reconfigurable</li><li>• High spatial resolution</li><li>• No moving parts</li></ul>	<ul style="list-style-type: none"><li>• Susceptibility to motion-induced edge artifacts</li><li>• Limited storage/operation temperature ranges</li></ul>
	Acousto-optical tunable filter (AOTF)		Hyperspectral images achieved based on the interaction of light with a traveling acoustic sound wave in an anisotropic crystal medium. Tuning is achieved by changing the applied RF signal frequency and power	<ul style="list-style-type: none"><li>• High optical throughput</li><li>• Broad spectral coverage</li><li>• Rapid tuning speeds</li></ul>	<ul style="list-style-type: none"><li>• Inefficient full spectral acquisition</li><li>• Broad spectral bandpasses</li><li>• Moderate spatial resolution</li><li>• Nonuniform spectral bandpass across FOV</li></ul>
	Fabry-Perot interferometer		Hyperspectral images obtained by sequentially collecting images as the distance or refractive index between two parallel reflecting surfaces are changed resulting in wavelength-dependent optical interference	<ul style="list-style-type: none"><li>• High image quality</li><li>• High finesse</li></ul>	<ul style="list-style-type: none"><li>• Moderate spectral resolution</li><li>• Low out-of-band rejection</li><li>• Limited free spectral range</li><li>• Small acceptance angle</li></ul>

Fiber-based	Fiber array spectral translator (FAST)	Captured light is projected onto the 2D array of optical fibers rearranged distally into a 1D array and inserted in parallel into the entrance slit of a dispersive spectrometer or SHS equipped with an imaging format FPA detector. Single image contains two spatial and one spectral dimensions of data from which software reconstructs hyperspectral imagery	<ul style="list-style-type: none"> <li>• Near real-time compatible</li> <li>• Full spectral coverage</li> </ul>	• Low image fidelity
Source-tuning based	Quantum cascade lasers	Source modulation achieved with tunable laser source comprised of dozens of alternating layers of semiconductor materials that are tuned by varying temperature or through the grating rotation	<ul style="list-style-type: none"> <li>• Wide tuning range</li> <li>• Fast response time</li> <li>• Compatible with fundamental IR</li> </ul>	<ul style="list-style-type: none"> <li>• Limited standoff range</li> <li>• Limited number of wavelengths</li> </ul>
	Light-emitting diodes (LEDs)	Source modulation achieved by sequentially applying current to an array of semiconductor light sources that emit light of unique wavelengths	<ul style="list-style-type: none"> <li>• Low power consumption</li> <li>• Fast switching speeds</li> </ul>	<ul style="list-style-type: none"> <li>• Limited standoff range</li> <li>• Limited commercially available LEDs outside the visible range</li> <li>• Limited number of wavelengths</li> </ul>

technique is compatible with, and will provide the greatest potential for detecting analytes of interest in relevant amounts, and distributions among applicable backgrounds, is extremely beneficial. Not all sensing technologies are compatible with every spectroscopic phenomenology. For instance, LCTFs are not compatible with MWIR measurements due to the highly absorptive nature of the polarizers beyond the SWIR spectral range. With any phenomenology, there will inevitably be tradeoffs between sensitivity and selectivity. Be sure to select a technique that will provide a suitable level of detection performance. If identification is necessary, a technique that has a high degree of specificity (i.e. Raman or MWIR) should be pursued.

#### 10.4.2 Spatial, Spectral, and Temporal Considerations

It is important to know whether or not the application requires imaging. When sample heterogeneity is not a concern and the operator knows where the target of interest is located, a point-sensing strategy may suffice. Real-world targets and surfaces more often than not, however, are inherently heterogeneous in their composition and distribution. Further, many applications demand looking for the proverbial “needle in a haystack.” In other words, the sensor must locate a target of interest that is not readily visible to the naked eye. In these situations, scanning or imaging-based approaches may be most appropriate.

When imaging is required, knowing the spatial resolution, image fidelity, and area coverage requirements is important. Wide-field imaging approaches that use high-fidelity staring FPA detectors tend to provide the best spatial metrics performance. When the technique requires illumination with a laser source, one must choose point, scanning, or wide-field illumination approaches. This inevitably brings into play considerations, such as measurement time, eye safety, measurement uniformity across the field-of-view, and factors impacting data signal-to-noise ratios (SNR).

Laser sources contain etalons that give rise to temperature-dependent fringes in the output spectra, degrading data SNR. Speckle is another property exhibited by laser sources with which instrument platforms must contend. Approaches such as the use of rotating roughened silica for direct beam instruments, or integration of fiber agitators for fiber-delivery-based laser systems, have been used to mitigate speckle (Crocombe 2018). Eye safety and skin safety are other concerns that must be considered in the decision. Choice of laser wavelength, laser energy, or power density, and duration of exposure are all factors that go into computing key safety metrics, such as the maximum permissible exposure (MPE) values (Anon 2007; Schröder 2000).

If the measurement speed and the number of spectra are not large drivers in the decision, then a point or spatial scanning approach may be most appropriate since illumination may be confined to a small, localized area, limiting the opportunity for secondary scattering. However, if measurement speed and area search rate are critical drivers, then wide-field methods may be preferred.

Having knowledge of the spectral range and the number of spectral channels required to make the desired measurement is also important in sensor selection. The phenomenology often dictates the spectral range. To answer how many spectral channels are needed often requires subsetting high-resolution data, and modeling the outcome should a smaller number of wavelengths be used in the measurements. If a small number of spectral wavebands (i.e. <10) is sufficient, then fixed bandpass, tunable filter and source tuning-based instruments may be viable options. If the nature of the threat is likely to change spectrally, and sensor reconfigurability becomes necessary, then tunable filter-based or source-tuning-based approaches are good options to consider.

#### 10.4.3 Size, Weight, Power, and Cost (SWaP-C) Considerations

Sensor size, weight, power and cost (SWaP-C) concerns are also important factors to evaluate when selecting a portable sensor. Often, performance is traded to some degree in order to meet SWaP-C requirements of the end user. For example, it is not practical for a soldier to carry a high-resolution, 25-pound spectrometer on his/her person for extended periods of time. Fortunately, the trend in all portable instrument types discussed in this chapter

is toward lower SWaP-C options. Many of these technologies have or are undergoing miniaturization efforts in order to broaden market prospects and make portability and routine use more practical.

#### 10.4.4 Environmental Considerations

A final key category of considerations is environmental. Portability implies field use which often requires survival through rough use and exposure to the elements. Not all sensors are equal in this respect, and becoming familiar with the environmental specifications (i.e. temperature, humidity, shock and vibration, drop, etc.) is advisable in the selection of a standoff sensor. All optical-based sensors are susceptible to vibration-induced misalignments and damage, and many are also susceptible to temperature-induced spectral drift. Be sure to inquire about built-in temperature compensation routines. Also, know the temperature limits for both storage and operation of the device and ensure that they meet the needs of the intended use.

### 10.5 Portable Standoff Optical Spectroscopy Sensors and Applications

#### 10.5.1 Biothreat Detection and Identification

Rapid, reagentless detection and identification of biological threat organisms within complex backgrounds have long been an unmet need. Microbiology, immunoassays, genetic and molecular-based approaches for identification of bio-organisms require long analysis times for culturing, deoxyribonucleic acid (DNA) extraction and use of reagents. Reagentless optical methods, such as fluorescence or LIBS lack robust identification capability. Mass spectrometry is susceptible to false alarms due to background clutter and lack of signature robustness. Raman spectroscopy addresses a number of these deficiencies, but Raman alone is also susceptible to matrix effects. Bio-organism growth media and natural environmental contamination introduce signal-masking fluorescence, and nonagent Raman bands, into the measurement, resulting in low signal-to-background data. Raman imaging, however, provides a means to largely address the signal-to-background challenge by providing a means to efficiently generate “pure pixel” Raman spectra in the presence of clutter at a single-organism level.

Post-9/11, ChemImage Corporation led the development of an all-optical spectroscopic detection methodology and database of Raman signatures of biological threats, near-neighbors and confusants (Kalasinsky et al. 2007). The work was performed in collaboration with the former Armed Forces Institute of Pathology (AFIP) using a Falcon Raman Chemical Imaging Microscope platform equipped with red, green, blue (RGB) video, fluorescence chemical imaging, Raman chemical imaging and dispersive Raman spectroscopy. An extension of the initial signature work in collaboration with AFIP was the development of a portable FAST Raman and broadband fluorescence microscope platform called Eagle (Figure 10.5a).

##### 10.5.1.1 Hardware

Eagle uses RGB video and broadband fluorescence for targeting suspected biological material. Fluorescence imaging provides a reasonably good discriminator between biological and nonbiological material. A mercury arc lamp provides illumination for both visible brightfield reflectance and UV-excited fluorescence-imaging modes. In UV-fluorescence mode, sample fluorescence is induced using a 365 nm filtered mercury arc lamp in combination with a dichroic beam splitter, in an epi-illumination configuration, to direct UV light to the sample. Sample fluorescence is recovered in a back-scattered configuration through the dichroic beam splitter and an emission filter. Brightfield reflectance images are obtained with the use of a 50/50 beam splitter in place of the dichroic. In FAST Raman mode, the mercury lamp light is blocked using mirrors, allowing the beam from a 532 nm laser (frequency-doubled, diode-pumped neodymium-doped yttrium aluminum garnet (Nd:YAG) laser) to engage the sample. The resulting Raman radiation is split between LCTF and dispersive Raman channels. Eagle provides 13 mW of power (3000 W/cm<sup>2</sup>) over the field-of-view of the imaging optics. The FAST Raman

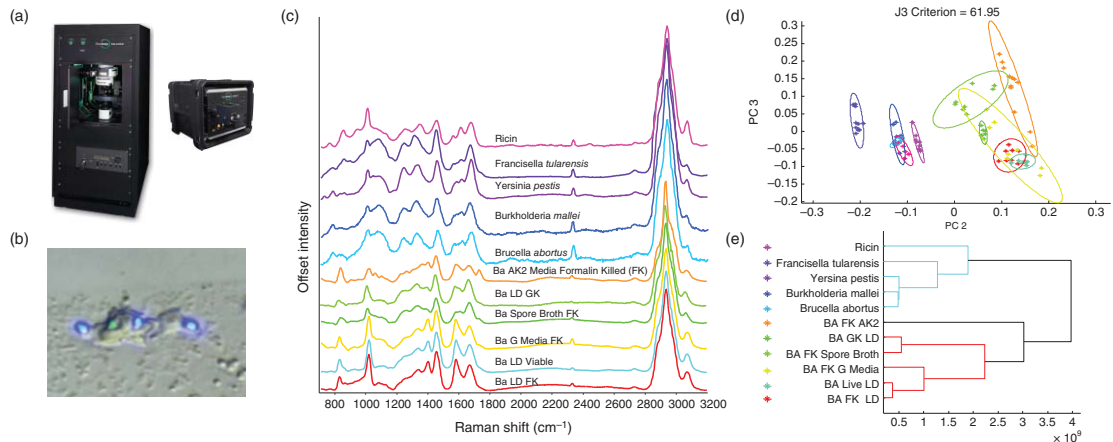


**Figure 10.5** Raman-based biothreat detection and identification. (a) Falcon Raman Chemical Imaging Microscope (left) and Eagle Transportable Raman Microscope system (right). (b) Raman (green) and fluorescence (blue) overlays onto differential image contrast image revealing bacterial spores. (c) Representative Raman spectra of Centers for Disease Control and Prevention (CDC) category A/B pathogens. (d) Principle component analysis (PCA) score plots revealing underlying pathogen spectral groupings. (e) Dendrogram showing taxonomic relationships of pathogens. Source: Pictures and data courtesy of ChemImage Corporation.

dispersive channel is equipped with a dispersive spectrometer, equipped with a thermoelectrically cooled CCD FPA, providing a full spectrum signature, with  $12\text{ cm}^{-1}$  spectral resolution.

#### 10.5.1.2 Software and Algorithms

ChemImage Xpert™ software provides acquisition control as well as data processing for the Falcon and Eagle instrument platforms. FAST Raman spectral data is typically corrected for instrument response using a National Institute of Standards and Technology (NIST) standard reference material and sample fluorescence. The spectra are then truncated to a usable Raman spectral range, followed by the application of a polynomial baseline correction. Common data analysis tools applied to the preprocessed data include Principal Component Analysis (PCA) for cluster analyses, Mahalanobis distance to evaluate the identity of agents, dendograms to visualize hierarchical cluster analysis of ranked similarity of spectra with associated agent class, and confusion matrices to quantify the degree of specificity inherent in the analysis. LCTF Raman image processing includes cosmic ray removal, instrument response correction, Gaussian blurring (for high-frequency noise removal), application of a Euclidean Distance classifier trained against known organism spectral responses, and fusion of video, fluorescence and/or Raman image data.

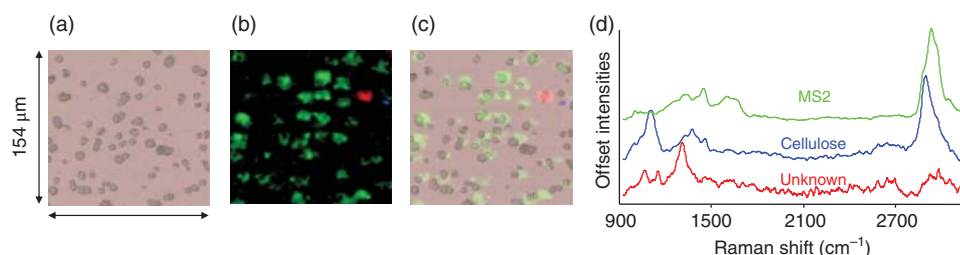
#### 10.5.1.3 Example Results

Figure 10.5c shows dispersive Raman spectra of pure Centers for Disease Control and Prevention (CDC) Category A/B pathogens along with an associated PCA scatter plot (Figure 10.5d), and dendrogram (Figure 10.5e). The Raman/fluorescence/brightfield differential interference contrast (DIC)-fused image (Figure 10.5b) shows the detection of bacillus globigii (Bg) spores in a complex background. A Bg suspension was intentionally added to outdoor ambient particulate matter collected into the aqueous collection fluid buffer by a Joint Biological Point Detection System (JBPD) sensor. The sample was subsequently deposited in droplet form onto a microscope slide, and imaged using the Falcon equipped with a  $100\times$  magnification objective. Bg spores are evident with both fluorescence and Raman imaging mode. However, due to the excitation wavelength, the Raman image reveals spores that are embedded deeper into the background clutter.

Figure 10.6 shows a FAST Raman result from a virus-simulant MS2 bacteriophage sample mixed with cellulose. The color-coded underlying Raman spectra reveal the spatial locations of the MS2 bacteriophages, cellulose and an unknown contaminant.

#### 10.5.2 Condensed Phase CWA Contamination Detection/Avoidance and Surveying/Mapping

In the event of a CWA attack, there is a need to be able to detect contamination on surfaces (ground, equipment, etc.) to avoid exposure to military personnel and civilians. A sensor addressing this need must operate in near to real time, and be capable of detecting CWAs, toxic industrial chemicals (TICs), nontraditional agents (NTAs), and



**Figure 10.6** FAST Raman chemical imaging example for biothreat detection and identification. Brightfield reflectance image (a), color-coded Raman chemical image (b), Raman/brightfield overlay (c), and underlying Raman spectra (d) of MS2 and cellulose mixture. Source: Pictures and data courtesy of ChemImage Corporation.

other chemical agents in solid and liquid forms while on the move. Such a sensor would provide advanced notice to warn personnel of potential threats, as well as ensure that military equipment is free of contamination since the availability of water on the battlefield is often limited for decontamination purposes.

#### 10.5.2.1 Sensor Type I: SWIR HSI LCTF

In 2014, ChemImage developed a SWIR HSI sensor called the VeroVision® Chemical Detector (VVCD). SWIR HSI requires no laser and can operate in an eye-safe manner, in a true standoff mode, using sunlight and/or onboard halogen lighting.

##### 10.5.2.1.1 Hardware

VVCD incorporates an LCTF coupled to an InGaAs FPA detector. The filter is tuned through computer control and the operator can either collect a series of images at specific wavelengths or acquire sequential images over a preprogrammed wavelength range. These images form a hypercube of data, which provides a SWIR reflectance spectrum at every image pixel.

##### 10.5.2.1.2 Software and Algorithms

The detection algorithms and software operate on the captured wavelength images to produce a detection image showing pseudocolored areas of contamination overlaid on a monochrome image of the detection scene.

##### 10.5.2.1.3 Example Results

Figure 10.7 shows a photograph of the VVCD prototype and detections of droplets applied using a spray bottle of CWA-simulant dimethyl methylphosphonate (DMMP) sprayed onto a scene featuring paint cans and containers at a 1 m standoff distance.

#### 10.5.2.2 Sensor Type II: SWIR HSI Snapshot

To mitigate storage temperature and motion sensitivity risks of the LCTF-based instrument, a SWIR snapshot imager called VVCD-S was also developed and evaluated. In order to implement this approach, ChemImage worked with Pixelteq, a manufacturer of micropatterned bandpass filter arrays.

##### 10.5.2.2.1 Hardware

The snapshot imager incorporates a  $3 \times 2$  filter-pixel pattern tessellated over a  $640 \times 512$ , 25  $\mu\text{m}$  pixel pitch InGaAs FPA, resulting in an effective FPA format of  $213 \times 256$  pixels.



**Figure 10.7** Shortwave-infrared hyperspectral imaging (SWIR-HSI) detection of chemical warfare agent (CWA) simulant at 1 m standoff using a liquid crystal tunable filter (LCTF)-based sensor. (a) LCTF-based standoff SWIR sensor (ChemImage's VeroVision® Chemical Detector [VVCD]). (b) Digital photograph of a real-world scene with a complex 3D structure that has been sprayed with CWA simulant. (c) SWIR detection image of CWA simulant (red) overlaid with SWIR pass-through image. Source: Pictures and data courtesy of ChemImage Corporation. Used with the permission of the Joint Program Executive Office for Chemical, Biological, Radiological and Nuclear Defense (JPEO-CBRND) – Approved for Public Release, Distribution Unlimited.

### 10.5.2.2.2 Software and Algorithms

Spectral Kitchen software was used to acquire image frames. Factory corrections were applied to correct for bad pixels and flat fielding. Wavelength image frames were reconstructed from the raw snapshot frame by extracting the intensity information from the pixels corresponding to each respective wavelength. Math operations were applied to the imagery to generate score imagery followed by spectral, spatial and temporal filters similar to the LCTF variant. Further, VVCD used ANNs (artificial neural networks) as the basis of the detection algorithm.

### 10.5.2.2.3 Example

Figure 10.8 shows representative SWIR snapshot detection images at a 1 m standoff distance of scenes containing CWA-simulant diethyl phthalate (DEP) deposited onto various surface types. Figure 10.8a shows a digital photograph of the VVCD-S sensor. Figure 10.8b shows detections in the green of 1  $\mu$ l depositions of DEP on linoleum (left), Formica® (middle), and drywall (right). Figure 10.8c shows a volume study of DEP-simulant on drywall (left), Formica® (middle) and soapstone (right) surface at concentrations between 0.2 and 1  $\mu$ l drops (i.e. left to right on surface – 1.0, 0.8, 0.6, 0.4, 0.2  $\mu$ l). While the snapshot imager readily detects the DEP droplets on drywall and Formica®, no detections were made on the soapstone due to the highly absorptive properties of the substrate.

### 10.5.2.3 Sensor Type III: LWIR QCL

LWIR standoff detection systems have also emerged in response to a need for detection and identification of CWA hazards. Both passive and active illumination architectures exist. Pendar Technologies developed a detector that addresses the challenges of laser packaging and optical design, integrated laser electronics, statistically robust decision algorithms and deep chemical knowledge for QCL-based LWIR sensing of CWAs.

#### 10.5.2.3.1 Hardware

The sensor utilizes a quantum cascade laser array (QCLA) source that provides a near-continuous, fully monolithic tunable source, ideal for field and handheld applications requiring speed, ruggedness and stability. The current design incorporates four 32-element QCLAs, with each array covering a distinct LWIR band within the 6.5–10.5  $\mu$ m region ( $1540\text{--}950\text{ cm}^{-1}$ ). This spectral range is particularly useful for sensitive and specific detection of CWAs. The emitted light in these four bands is then spectrally beam-combined, using dielectric mirrors and polarization techniques. The entire sensor is in an  $8 \times 8 \times 81.5\text{ cm}$  package.

#### 10.5.2.3.2 Software and Algorithms

The software provides control of these lasers in pulsed mode, projecting a 2 mm focused spot on targets. Speckle is mitigated by dithering the combined beams pointing angle slightly, resulting in a  $2 \times 2\text{ cm}$  illumination area

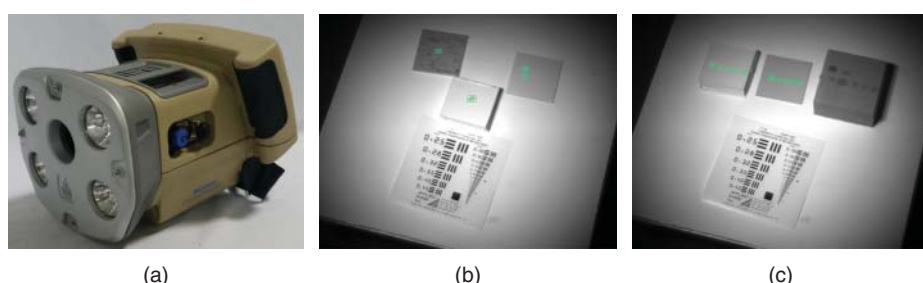


**Figure 10.8** SWIR HSI detection of CWA simulant at 1 m standoff using a snapshot imager-based sensor. (a) Snapshot imager-based standoff SWIR sensor (ChemImage's VeroVision® Chemical Detector-Snapshot [VVCD-S]). (b) SWIR detection image of 1  $\mu$ l droplets of diethyl phthalate (DEP) deposited on various substrate types (detection in green). (c) Limit-of-detection study showing varying volumes of DEP (i.e. left to right on surface – 1.0, 0.8, 0.6, 0.4, 0.2  $\mu$ l) on various surface types. Source: Pictures and data courtesy of ChemImage Corporation. Used with the permission of JPEO-CBRND – Approved for Public Release, Distribution Unlimited.

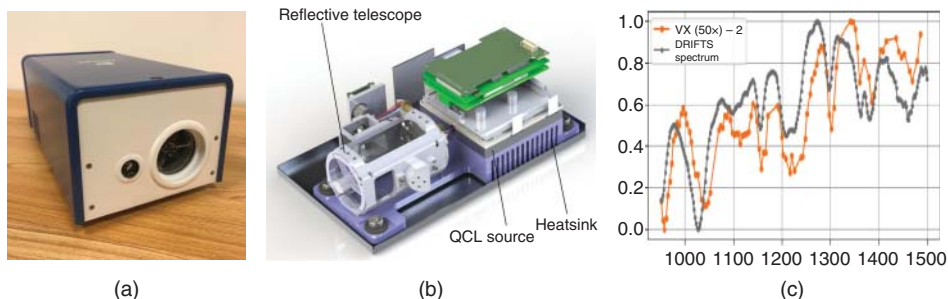


**Figure 10.9** Quantum Cascade Laser Array (QCLA)-based longwave infrared (LWIR) detection of CWA. (a) Integrated Pendar Technologies QCLA sensor (2.25 L volume, 4.5 lbs). (b) Drawing of the instrument overall architecture, showing the QCLA source, Reflective telescope used to emit and receive the LWIR light, and system electronics. (c) Example of a spectrum measured at the Defence Science and Technology Laboratory (Dstl, UK) of VX deposited on sandblasted stainless steel at  $500 \mu\text{g}/\text{cm}^2$  loading, acquired at 1.3 m standoff distance. The spectrum is compared to a reference acquired using a Bruker LUMOS FTIR microscope. *Source:* Pictures and data courtesy of Pendar Technologies. Used with the permission of the Defence Science and Technology Laboratory (Dstl, UK). Licensed under OGL v3.0.

at  $\sim 1.3$  m. Taking into account scan time, duty cycle, scan repetition and processing times, a total acquisition time of 3.3 seconds was achieved.

#### 10.5.2.3.3 Example

Figure 10.9a shows a photograph of the integrated QCLA system. Figure 10.9b shows the system architecture. Figure 10.9c shows a measurement taken at the Defence Science and Technology Laboratory (Dstl, UK) of VX deposited on sandblasted stainless steel at  $500 \mu\text{g}/\text{cm}^2$  loading, acquired at 1.3 m standoff distance (Blanchard and Vakhshoori 2020). This measurement was obtained by scanning the IR beam across a deposited VX droplet ( $25 \times 25$  measurements) to acquire a hyperspectral image ( $\sim 5$  minutes acquisition time), and then segmenting the image between background vs. contaminated pixels. The spectrum shown in Figure 10.9c is obtained by dividing the mean signal across the assumed contaminated pixels by the mean signal across the assumed clean pixels.

### 10.5.3 Gas-Phase Remote Chemical Cloud, CWA, TICS, and Detection

Gas-phase chemical releases threaten life, whether a release from an industrial accident or intentional terrorist release. Detection and monitoring of organic and inorganic gases and vapors (i.e. chemical cloud) from a remote distance are critical in this situation in order to provide advanced notice to warn personnel. Standoff IR sensors – either active or passive – are well-suited for this application given the high sensitivity and specificity of the available measurement tools. LWIR is relevant because the most condensed-phase and gas-phase materials exhibit unique and intense spectral features in the LWIR due to the fundamental vibrational bands in this part of the spectrum. LWIR provides near real-time detection and identification of CWAs, TICs, NTAs and other chemical agents in gas form.

There are numerous vendors and sensors available with capabilities that range in degree of specificity (specific chemical vs. general chemical family), sensitivity (from ppb-meter to hundreds of ppm-meter), spectral region ( $1.5\text{--}14.5 \mu\text{m}$ ), measurement type (filter-based vs. interferometer-based), weight ( $\sim 2\text{--}65 \text{ kg}$ ), data output (single-pixel spectrum vs. single/multi/hyperspectral image), range (2 m–10 km) and price (\$100–\$600 K) (National Security Technologies, LLC 2016). We report here on one handheld unit from Block Engineering called PORTHOS™.

#### 10.5.3.1 Hardware

Porthos is an FTIR-based LWIR sensor that operates in the  $7.5\text{--}13 \mu\text{m}$  spectral band. Single-pixel spectra are produced with a selectable resolution between 4 and  $8 \text{ cm}^{-1}$ . Images are created by point scanning and overlaying on

a visual image for analysis. The 7.7 kg sensor detects and alarms in a little at 2 seconds over a standoff range of 0.1–5 km. The sensor has two field-of-view options (i.e. 1.5° vs. 5°) and is capable of being powered on battery for up to 4 hours of operation under passive illumination mode.

#### **10.5.3.1.1 Software and Algorithms**

The Porthos can be operated from an external host computer using remote interface software to analyze spectral data with complete identification capability. The Porthos detects certain chemicals of interest and displays the chemical type, intensity, and records the information on an internal hard-drive. The supplied detection processing program can read the data, process the data, and create results.

The data output file of the Porthos instrument is read by proprietary software which shows the detection levels on the instrument display. The detection levels are overlaid at the bottom of the image collected by the monochrome video camera. The information collected and interpreted by the Porthos is performed in real time.

#### **10.5.3.1.2 Example**

Figure 10.10 shows the operation of Porthos portable standoff chemical detection system.

### **10.5.4 Explosives Detection and Identification**

IEDs are a real threat to military personnel and civilians, and detection of such devices is critical. Explosive Ordnance Disposal (EOD) technicians are trained to detect and remove IEDs. There is a need for mobile, standoff sensors with high area search rate (near real-time) and high specificity/sensitivity to keep technicians at safe distance from explosive threats. Detecting explosive residues associated with the emplacement or manufacturing of IEDs is one approach to countering IEDs.

#### **10.5.4.1 Sensor Type I: Deep-UV Raman Point Sensor**

To address the need for standoff detection and identification of explosive residues associated with the emplacement of IEDs, Alakai Defense Systems developed a standoff deep-UV Raman sensor called the Portable Raman Improvised Explosive Detector (PRIED).



**Figure 10.10** Fourier transform infrared (FTIR)-based LWIR sensor, PORTHOS in operation. *Source:* Pictures courtesy of Block Engineering.

#### 10.5.4.1.1 Hardware

PRIED is a deep-UV (262 nm excitation) portable Raman sensor, capable of up to 50 m standoff for homemade explosives (HMEs), and 10 m for most other chemicals. PRIED delivers a 0.5 cm diameter laser spot to excite the sample. Material amounts as little as 10s of  $\mu\text{g}/\text{cm}^2$  at 1 m, and higher amounts at 10 m, are detectable. It consists of a wand (5"  $\times$  7"  $\times$  15") and backpack (17"  $\times$  12"  $\times$  7"), and, when combined, weighs 31 lbs (short mission mode), or 38 lbs (extended mission).

Eye-safe operation is achievable in two operating modes: "Eyesafe" and "Max Detect." The system powers up in eye-safe mode. In this mode, the overall system is rated as a Class II laser system. To accomplish this, the PRIED system utilizes Alakai's patented stimulated aversion technology (Pohl et al. 2012) that results in a Class II system even though the sensor contains a Class III UV laser. In many applications, users wish to either acquire results faster or to interrogate lower concentration samples. In these cases, assuming they have the proper laser training and can control the nearby area around them, they can turn up the laser power by entering Max Detect Mode. To enter this mode, the user enters a password and the laser power is increased and the PRIED sensor operates with faster integration times, at farther detection distances or at lower detection capabilities.

#### 10.5.4.1.2 Operation

An operator pulls the wand trigger in half-way, points the visible targeting beam at the intended target, and then pulls the trigger all the way to start the Raman analysis. The operator holds the beam on target until the unit produces a red light (threat) or green light (no-threat) result.

#### 10.5.4.1.3 Example

Figure 10.11 shows photographs of PRIED in operation (Figure 10.11a), subsystem components (Figure 10.11b) and 50 m range Raman data of a potassium chlorate target at various collection times (Figure 10.11c).

#### 10.5.4.2 Sensor Type II: FTIR-Modulated Supercontinuum Laser

To exploit benefits of working with the fundamental infrared vibrational modes, Leidos developed a standoff FTIR-based instrument called the Supercontinuum Wide-band Infrared Fourier Transform (SWIFT) sensor.

#### 10.5.4.2.1 Hardware

SWIFT uses supercontinuum laser pulses modulated by an FTIR spectrometer and captured with high-speed detectors. A standoff distance of up to 15 m has been demonstrated for trace material identification on surfaces and air. SWIFT produces an active IR beam in the 2–11  $\mu\text{m}$  spectral region and captures data from a  $\sim 2^\circ$  angular field-of-view on the target. Material amounts as little as 10s of  $\mu\text{g}/\text{cm}^2$  for solids and liquids and 1 ppm for vapors have been demonstrated. SWIFT consists of a (24"  $\times$  18"  $\times$  18") sensor head atop a tripod with a combined weight

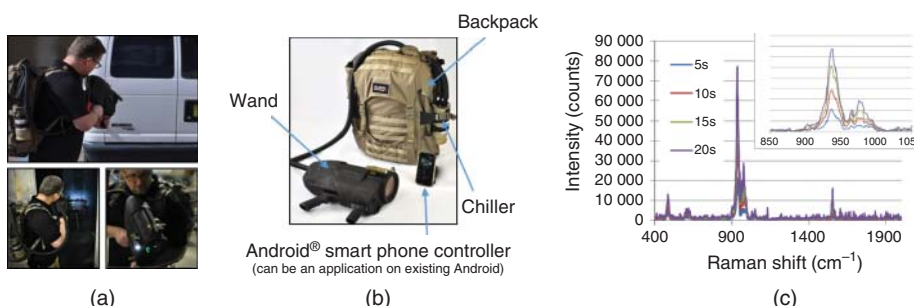


**Figure 10.11** Raman-based standoff detection of explosive threats. (a) Alakai Defense System's Portable Raman Improvised Explosive Detector (PRIED) sensor in operational use case scenarios. (b) PRIED subsystem components – backpack with a chiller (top), wand (bottom, left), and Android® smartphone controller (right). (c) Raman spectra of potassium chlorate at variable detector integration times. Source: Pictures and data courtesy of Alakai Defense Systems, Inc.

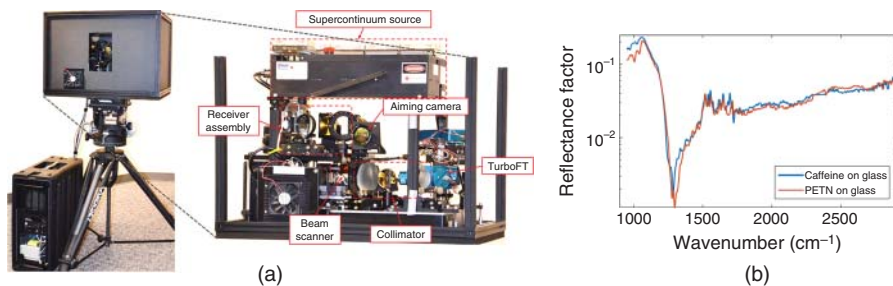


**Figure 10.12** FTIR supercontinuum laser-based standoff detection of explosive threats. Leidos' SWIFT sensor (a) performs direct reflectance measurements (b) on surfaces up to 15 m away for automated detection and identification of trace material contamination. The  $4\text{ cm}^{-1}$  spectral resolution enables discrimination of harmful materials from harmless ones. Source: Pictures and data courtesy of Leidos.

of 165 lbs. SWIFT currently is at a technology readiness level (TRL) of 5 for indoor applications and TRL 4 for outdoor applications. SWIFT is considered an eye-safe sensor having a Class 1 laser designation.

#### 10.5.4.2.2 Operation

SWIFT uses a built-in aiming camera to establish the measurement location. A pushbutton operation follows that generates FTIR spectra of the reflected light from the target that may be searched against a spectral library.

#### 10.5.4.2.3 Example

Figure 10.12a shows a photograph of the SWIFT sensor along with subsubsystem components (inset) and reflected light FTIR signatures of caffeine and pentaerythritol tetranitrate (PETN) on glass, respectively (Figure 10.12b).

#### 10.5.4.3 Sensor Type III: SWIR HSI LCTF

SWIR HSI sensors provide wide-area imaging at near real-time speeds. They overcome two obstacles present in Raman detection sensors – slow area search rate (due to small laser spot sizes), and eye safety concerns. SWIR HSI sensors may be integrated into mobile, robotic and handheld variants for detection of chemical, biological, explosive (CBEs) and narcotics. To address the shortcomings of current generation systems, ChemImage developed the VeroVision™ Threat Detector (VVTD).

##### 10.5.4.3.1 Hardware

VVTD is a portable, tripod-mounted sensor that utilizes LCTF-based SWIR technology. In operation, solar or supplemental broadband radiation illuminates the surface of interest. Photons are absorbed or reflected by materials depending on their composition. Threat detection and classification are facilitated through the multispectral acquisition of the target(s) at key wavelengths. VVTD is equipped with eight 35 W halogen light bulbs to provide close-range ( $<2.5\text{ m}$ ) standoff detection capabilities. Greater distances are achieved with the use of at-target lighting and/or reliance on solar illumination. Light-gathering optics with continuous  $2\times$  optical zoom and focus capture a portion of the reflected light, which is, in turn, directed to an LCTF coupled to an InGaAs FPA detector. RGB video is also included to provide for enhanced situational awareness. A power control module provides power distribution to the sensor as well as provides a housing for a lithium-ion battery capable of 2–4 hours of life depending on duty cycle.

##### 10.5.4.3.2 Software and Algorithms

VVTD's software is used to rapidly capture an abbreviated hyperspectral data cube, containing spatially resolved SWIR spectral signatures that may be compared to a SWIR-spectral library using pattern-matching algorithms to locate and identify threats in the scene. Once a threat is detected, higher resolution hyperspectral data may be acquired and autonomously processed to presumptively identify the threat component.

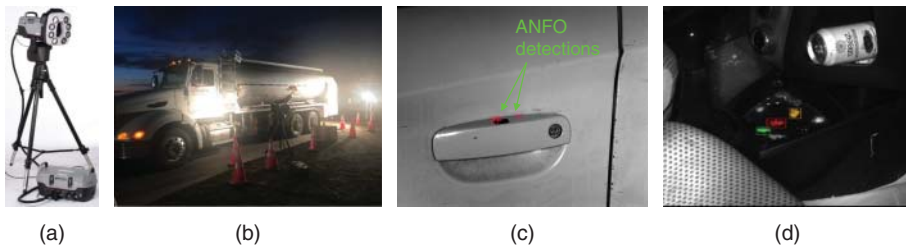


**Figure 10.13** SWIR-HSI-based standoff detection of explosive threats. (a) ChemImage VeroVision® Threat Detector (VVTD) in use screening vehicles for explosive residues at the 2019 US Open Championship (Pebble Beach, CA). (b) Ammonium nitrate fuel oil (ANFO) prill detection on a car door handle. (c) Narcotics detection in a vehicle console. *Source:* Pictures and data courtesy of ChemImage Corporation.

#### 10.5.4.3.3 Example

Figure 10.13 shows a photograph of the VVTD sensor (a), VVTD in operation at the 2019 US Open in Pebble Beach, CA (b) and representative threat material detection results associated with an entry control point (ECP) screening CONOPs (c and d).

#### 10.5.4.4 Sensor Type IV: Combined SWIR HSI LCTF/Raman FAST HSI Dispersive

In order to combat the threat of emplaced explosives (land mines, etc.), while ensuring the safety of military and civilian bystanders, ChemImage developed a multisensor, robot-mounted sensor capable of identification and confirmation of potential threats. The system, known as the Shortwave-infrared Targeted Agile Raman Robot (STARR), utilizes SWIR spectroscopy for the identification of potential threats, combined with a visible short-range standoff Raman FAST HSI system for material confirmation. The entire system is mounted onto a Talon UGV (Unmanned Ground Vehicle), giving the sensor an increased area search rate and reducing the risk of injury to the operator.

##### 10.5.4.4.1 Hardware

STARR incorporates LCTF-based SWIR HSI, offering wide-area surveillance, for autonomous near real-time detection, and FAST Raman to provide rapid multipoint Raman spectral analysis as a confirmation tool. The robot may be operated remotely wirelessly at distances up to 70 m from the operator, and STARR is capable of a 1–3 m sensor to target standoff range operation. STARR is integrated on a TALON UGV from Foster-Miller Inc. (part of Qinetiq North America) for high mobility and remote, wireless control, enabled through an 802.11n link. TALON features two-stage gripper arm, four cameras for area surveillance, and is controlled by an operator control unit through a two-way RF or fiber optic protocol.

In operation, a video RGB camera provides real-time situational awareness, guiding operator control to suspicious locations. The SWIR subsystem consists of light-gathering optics, coupled to an LCTF operating from 900 to 1700 nm and an InGaAs FPA. Images are captured at discrete wavelength characteristics of explosives within the SWIR library. STARR's Raman subsystem incorporates a 532 nm pulsed laser (5 mJ/pulse, 20 Hz rep rate), a 100-fiber ( $10 \times 10$ ) FAST bundle coupled to a dispersive spectrometer equipped with a  $1024 \times 1024$  intensified charge-coupled device (ICCD). Time gating of the ICCD allows reasonable Raman signals to be captured synchronously with the high-energy laser pulses in the presence of ambient light, while maintaining a moderate average power.

##### 10.5.4.4.2 Software and Algorithms

STARR software provides acquisition controls for the RGB video, SWIR and Raman subsystems. The SWIR subsystem has two operating modes: near real-time (a small number of wavelengths), and full spectral mode for greater spectral information. SWIR wavelengths are mathematically processed to generate a score image, with pixel intensities corresponding to the degree of match with library signatures. Additional spectral, spatial, and temporal filters are applied to the score imagery, overlaid onto the passthrough SWIR image, to generate a detection image revealing the location of potential threats in the scene.

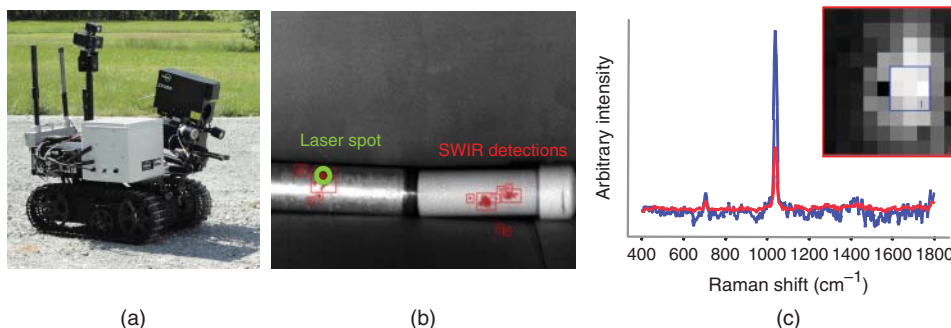


**Figure 10.14** Hybrid Raman and SWIR standoff detection of explosive threats. (a) Robot-integrated ChemImage Shortwave-infrared Targeted Agile Raman Robot (STARR) sensor. (b) SWIR-HSI detection image revealing suspected explosive residues on a pipe bomb. (c) FAST Raman image and spectra provide confirmation of explosive composition for an area indicated by the “laser spot” in Figure 10.13b. *Source:* Pictures and data courtesy of ChemImage Corporation. Used with the permission of the Navy Explosive Ordnance Disposal Technology Division (EODTECHDIV) – Approved for Public Release, Distribution Unlimited.

If detections are observed in the SWIR mode, the operator may then “click” on potential threats enabling FAST Raman targeting. In Raman mode, 100 spatially resolved spectra collected simultaneously, reconstructed into a Raman FAST image and analyzed using partial least squares discriminant analysis (PLSDA) database of known Raman threat signatures. The operator is notified by visual and audible alarms for any confirmed threats.

#### 10.5.4.4.3 Example

Figure 10.14 shows a photograph of the STARR system integrated on a TALON robot (Figure 10.14a), SWIR detection showing candidate threat locations (Figure 10.14b) and FAST-Raman confirmation of ammonium nitrate fuel oil (ANFO) residues on the exterior of simulated pipe bomb (Figure 10.14c).

### 10.5.5 Narcotics Detection and Identification

Today’s intensifying opioid crisis presents challenges to law enforcement as well as public safety. Sensors having standoff capability are increasingly important, considering the increased presence of synthetic opioids, such as fentanyl, that are leading to an ever-increasing number of deaths. Federal, state and local law-enforcement agencies require standoff sensors for border patrol, hazmat, crime scene investigation, clandestine laboratory cleanup and venue security.

#### 10.5.5.1 Sensor Type I: SWIR HSI LCTF

VVTI (described previously) offers additional capabilities for narcotics detection applications. Figure 10.15 shows standoff detection results from a simulated clandestine drug-manufacturing laboratory containing illicit narcotic simulants. The figure shows two images taken with VVTI of a scenario featuring illicit drug stimulants in plastic bags and glass containers, from a standoff distance. Figure 10.15a shows the scene acquired with the RGB camera, while Figure 10.15b shows the detection image generated by the SWIR HSI sensor and SWIR HSI software. The detection image highlights the potential threat detections using colored boxes, with each color unique to a specific class of compounds. The detections in the image are represented by red, green, and yellow boxes, indicating that three different classes of illicit narcotic stimulants are present. Since RGB imagery is collected simultaneously, it can provide additional information to confirm which containers have a potential threat and clarify any peculiarities in a SWIR region image by displaying the scene in the visible region.

#### 10.5.5.2 Sensor Type II: SWIR CF Imaging – ChemImage VeroVision™ Moving Target (VVMT)

With few exceptions, all inbound international airmails are subject to inspection at International Mail Facilities (IMFs) by US Customs and Border Protection (CBP), part of the US Department of Homeland Security (DHS). International mail has been identified as a well-used distribution system for illicit opioids entering the United



**Figure 10.15** SWIR HIS-based standoff detection of narcotics in a simulated clandestine laboratory scene. (a) Digital photograph of the scene containing a variety of material types including narcotic simulants. (b) SWIR chemical image revealing the location of various narcotic simulant types (red, green, and yellow false colors). *Source:* Pictures and data courtesy of ChemImage Corporation.

States. The CDC has published reports showing that overdose deaths involving any opioid – prescription opioids (including methadone), synthetic opioids, and heroin rose to nearly 50 000 in 2017 (Scholl et al. 2019). However, many of these fatal overdoses are driven by the combination of traditional opioids with extremely small amounts of the extremely potent Fentanyl and Carfentanil. Consequently, large-scale drug trafficking, coinciding with this serious health epidemic in the United States population, can occur via very small packages sent in the mail. As stated by the DHS Office of Inspector General (OIG) in the Customs and Border Protection (CBP) Audit at JFK International Airport from 2018: “CBP actions to address identified deficiencies and more effectively inspect international mail will be essential to winning the war on opioids and countering their devastating impact on the nation’s population.”

In response to a need to address limitations of current sensors for high throughput mail screening, ChemImage is developing a sensor called VeroVision® Moving Target (VVMT) which is based on real-time, reconfigurable SWIR DP-CF technology.

#### 10.5.5.2.1 Hardware

The VVMT prototype is a fully contained, portable (hand-carried – i.e. gripped and held with two hands) sensor. Illumination is provided by four (4) 35 W lamps for short standoff distance illumination. Light-gathering optics provide a 12° field-of-view (i.e. ~3.4 mm/pix at 10 m). An RGB video camera is incorporated for situational awareness. Other features include an integrated display with push-button, easy-to-use operational interface, a rechargeable battery and an optional tripod-mounting capability.

#### 10.5.5.2.2 Software and Algorithms

Conformal Training Software (CFTS) was used for voltage selection optimization based on target vs. background discrimination, and Spectral Kitchen Software provides real-time autonomous detection imagery.

#### 10.5.5.2.3 Example Results

Figure 10.16 shows a photograph of VVMTS in use (left) and representative feasibility results (right) for CWA surveying and mapping, high throughput mail screening and person-borne IED (PBIED) screening applications.

Table 10.3 provides a summary comparison of several portable standoff optical spectroscopy sensors that are in use for safety and security applications. Although far from being a comprehensive listing, the table provides the same perspective of key characteristics of a variety of instrument types.

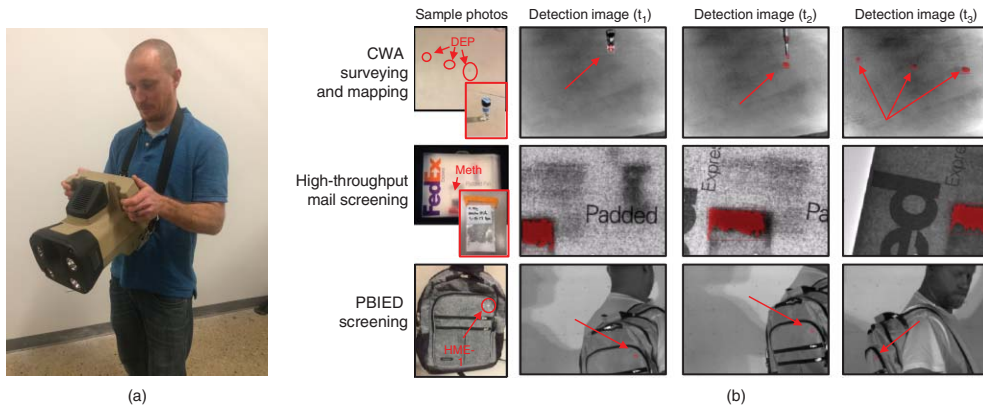


**Figure 10.16** Real-time SWIR-HIS-based standoff detection of CWA, narcotic, and explosive threats. (a) The handheld, real-time, reconfigurable Conformal Imaging sensor (ChemImage VeroVision® Moving Target [VVMT]) sensor. (b) Digital photographs and representative time-sequenced SWIR detection images of a CWA threat simulant (top), narcotic threat (middle), and explosive threat (bottom). *Source:* Pictures and data courtesy of ChemImage Corporation. Used with the permission of the Defense Advanced Research Projects Agency (DARPA) – Approved for Public Release, Distribution Unlimited.

**Table 10.3** Portable standoff optical spectroscopy instrument comparison.

No.	Parameter	Alakai defense systems PRIED	Block engineering LASERWARN™	Block engineering PORTHOS™	ChemImage VeroVision®	Leidos SWIFT	Photon systems STANDOFF 200
1	Name of product or technology	PRIED – portable Raman improvised explosive detection system	LASERWARN™	PORTHOS™	VeroVision® product family	Supercontinuum wide-band infrared Fourier transform (SWIFT)	STANDOFF 200
2	Model(s)	N/A	• Indoor • Outdoor models	N/A	<ul style="list-style-type: none"> <li>• VeroVision® Chemical Detector (VVCD)</li> <li>• VeroVision® Chemical Detector Snapshot (VVCD-S)</li> <li>• VeroVision® Moving Target (VVMT)</li> <li>• VeroVision® Threat Detector (VVTD)</li> </ul>	N/A	N/A
3	Manufacturer	Alakai defense systems	Block engineering	Block engineering	ChemImage Corporation	Leidos	Photon Systems, Inc.
4	Technology	Deep UV Raman	QCL and active IR absorption spectroscopy	Passive FTIR spectroscopy	SWIR-HSI	FTIR modulated supercontinuum laser	Deep UV Raman and fluorescence spectroscopy
5	Intended application	Standoff detection of threat chemicals	Fenceline, environmental, and leak detection gas monitoring	Military CWA and TIC gas detection	<ul style="list-style-type: none"> <li>• VVCD, VVTD – near real-time standoff detection of threats</li> <li>• VVCD-S, VVMT – real-time standoff detection of threats</li> </ul>	Trace material identification on surfaces and air	Real-time standoff CBE detection for first responders
6	Detected threat materials	CRNE/related materials, TICs/TIMs, narcotics/precursors	Most gases except symmetric and diatomic molecules	Military CWA and TIC gases	<ul style="list-style-type: none"> <li>• VVCD, VVCD-S – priority CWAs</li> <li>• VVMT, VVTD – priority explosive, narcotic and CWA threats</li> </ul>	Solid, liquid, and gas state threats	Broad range of CBE detection and classification
7	Identification capability	Yes	No	No	Presumptive ID capable	Yes	Yes

8	Time for detection (or identification)	3–30 s depending on range and concentration	2 s (typical), sub-second readings for rapid detection and immediate warning alerts	Seconds	• VVCD – <30 s • VVCD-S, VVMT – 0.1 s • VVTI – <10 s	15 s	<1 s to max about 10 s dependent on mode of detection, standoff, and concentration of target
9	Standoff distance range	Up to 50 m for HME's and 10 m for most other chemicals	250 m	0.1–5 km	• VVCD, VVCD-S – 1 m • VVMT, VVTI – 1–20+ m	15 m	0.6–5+ m
10	Optimum standoff distance	1–10 m	N/A	N/A	• VVCD, VVCD-S – 1 m for droplets • VVMT, VVTI – 1–3 m for residues	5–10 m	2 m
11	LOD at optical standoff distance	Trace concentrations at 1 m (10 s $\mu\text{g}/\text{cm}^2$ ) and residues at 10 m (100 s $\mu\text{g}/\text{cm}^2$ )	Varies with gas and standoff distance (e.g. Sarin at 10 ppb over 500 m)	Not available	• VVCD, VVCD-S – Sub-microliter droplets • VVMT, VVTI: $\mu\text{g}/\text{cm}^2$ at short distances to bulk at long distance	10 $\mu\text{g}/\text{cm}^2$ for solids/liquids; 1 ppm for vapors	< 1 $\mu\text{g}/\text{cm}^2$ of C&E materials and < ~60 bacterial spores
12	Angular FOV	0.06° starting with a 0.5 cm diameter spot size	Low-cost retroreflectors and mirrors for large area coverage	0.5 and 1.5°	• VVCD – 17° • VVCD-S – 17° • VVMT – 12° • VVTI – 10–20° (continuous zoom)	~2°	Point detector
13	Size (external dimensions)	Wand: 5" × 7" × 15", Backpack: 17" × 12" × 7"	18" × 14" × 6" inches (indoor); 37" × 14" × 10" inches (outdoor)	13.4" × 10.7" × 6.6"	• VVCD: 14.3" × 9.9" × 10.2" • VVCD-S: 10.5" × 9.4" × 8.2" • VVMT – 14.0" × 9.8" × 11.0" • VVTI – 18.5" × 7.9" × 9.4" (sensor head)	24" × 18" × 18"	7" × 12" × 17"

**Table 10.3** (Continued)

No.	Parameter	Alakai defense systems PRIED	Block engineering LASERWARN™	Block engineering PORTHOS™	ChemImage VeroVision®	Leidos SWIFT	Photon systems STANDOFF 200
14	Weight	<ul style="list-style-type: none"> <li>• Short mission mode: 31 lbs</li> <li>• Extended mode: 38 lbs</li> </ul>	<ul style="list-style-type: none"> <li>• 32 lbs (indoor)</li> <li>• 55 lbs (outdoor)</li> </ul>	17 lbs	<ul style="list-style-type: none"> <li>• VVCD, VVMT – 15 lbs</li> <li>• VVCD-S – 9.9 lbs</li> <li>• VVTD – 94 lbs (sensor, tripod, power box, computer)</li> </ul>	165 lbs	10 lbs
15	Battery or line powered?	Both	Line	Battery	Both	Line	Onboard battery
16	Is the system eye safe?	Yes – two operating modes Eyesafe and Max detect	Yes	Yes	Yes	Yes	Yes
17	Degree of autonomy	None yet but capability could be added if desired	Fully automated operation	Fully automated operation	Can be fully autonomous	Pushbutton after targeting	Can be fully autonomous
18	Reconfigurable for new materials (targets)	Yes	Yes	Yes	Yes	Yes	Yes
	Form factor(s)	Handheld wand with portable backpack	Fixed or portable	Handheld, UAV, tripod	<ul style="list-style-type: none"> <li>• VVCD, VVCD-S – handheld or tripod-mounted</li> <li>• VVMT – handheld, tripod-mounted, vehicle-mounted</li> <li>• VVTD – tripod-mounted</li> </ul>	Fixed, tripod-mounted	Handheld and adaptable to robot-mounted

## 10.6 Conclusions and Future Direction

Portable standoff spectroscopy has advanced significantly since the first portable standoff optical spectroscopic sensors became commercially available in the early 2000s. Substantial improvements have been made in point scanning, spatial scanning and wide-field imaging platform designs. Instrumentation has branched out from breadboarded components on an optical table to robust, fieldable units that have moved the technology far beyond the research laboratory setting. Along with these developments has come the expansion of the technology, and associated applications, ranging from close standoff, submicron Raman imaging of biological spores, to multikilometer standoff IR imaging of CWA clouds. Significant advances in the underlying instrument technologies have now made real-time, autonomous, wide-area, standoff spectroscopic imaging a reality. Combining multiple spectroscopic imaging modalities has dramatically increased what is possible from a structural, elemental composition, and molecular composition materials characterization standpoint.

Future trends will inevitably continue to push the capabilities of instrumentation in areas, such as reduced SWAP-C, increased autonomy, and increased utilization of artificial intelligence and machine learning methods. Application and market demands will propel Raman instrumentation development to enable greater area coverage, increased data acquisition rates, through-barrier capabilities, improved data SNR and increased instrument stability and ease-of-use. Sensor and data fusion methods will become more widely used to improve overall sensor performance. Algorithm advancements including mixture analysis methods and fluorescence mitigation or avoidance will be necessary. With the realization of these continual enhancements in portable, standoff spectroscopic instrumentation, new applications and uses of these technologies will inevitably prove beneficial to mankind.

## Acronyms and Abbreviations

AFIP	Armed Forces Institute of Pathology
ANFO	Ammonium Nitrate Fuel Oil
ANN	Artificial Neural Network
AOTF	Acousto-Optic Tunable Filter
CBE	Chemical, Biological, and Explosive
CBP	US Customs and Border Protection
CCD	Charge-Coupled Device
CDC	Centers for Disease Control and Prevention
CF	Conformal Filter
CMOS	Complementary Metal-Oxide-Semiconductor
CONOPS	Concept of Operations
CWA	Chemical Warfare Agent
DEP	Diethyl phthalate
DHS	Department of Homeland Security
DIC	Differential Interference Contrast
DMMP	Dimethyl methylphosphonate
DP-CF	Dual Polarization Conformal Filter
DRS	Diffuse Reflectance Spectroscopy
EOD	Explosive Ordnance Disposal
FAST	Fiber Array Spectral Translator
FPA	Focal Plane Array
fps	frames per second
FT	Fourier Transform

FTIR	Fourier Transform Infrared
HME	Homemade Explosive
HSI	Hyperspectral Imaging
ICCD	Intensified Charge-Coupled Device
IED	Improvised Explosive Device
JBPDS	Joint Biological Point Detection System
IMF	International Mail Facility
LCTF	Liquid Crystal Tunable Filter
LOD	Limit-of-Detection
LWIR	Longwave Infrared
MCF	Multiconjugate Filter
MOE	Multivariate Optical Element
MWIR	Midwave Infrared
NGCD	Next Generation Chemical Detector
NIR	Near-Infrared
NIST	National Institute of Standards and Technology
NTAs	Nontraditional Agents
OIG	Office of Inspector General
PCA	Principal Component Analysis
PETN	Pentaerythritol tetranitrate
PLSDA	Partial Least Squares Discriminant Analysis
PRIED	Portable Raman Improvised Explosive Detector
RGB	Red, Green, Blue
QCL	Quantum Cascade Laser
QCLA	Quantum Cascade Laser Array
SHS	Spatial Heterodyne Spectroscopy
SNR	Signal-to-Noise Ratio
SWaP-C	Size, Weight, Power and Cost
SWIR	Shortwave Infrared
TIC	Toxic Industrial Chemical
TRL	Technology Readiness Level
UAV	Unmanned Aerial Vehicle
UGV	Unmanned Ground Vehicle
UV	Ultraviolet
VIS	Visible
VVCD	VeroVision® Chemical Detector
VVMT	VeroVision® Moving Target
VVTD	VeroVision® Threat Detector

## References

- Angel, S.M., Kulp, T.J., and Vess, T.M. (1992). Remote-Raman spectroscopy at intermediate ranges using low-power CW lasers. *Appl. Spectros.* 46: 1085.
- Angel, S.M., Gomer, N.R., Sharma, S.K., and McKay, A.C. (2012). Remote Raman spectroscopy for planetary exploration: a review. *Appl. Spectrosc.* 66: 137–150.

- Anon (2007). *Safety of Laser Products – Part 1: Equipment Classification and Requirements*, 2ee. International Electrotechnical Commission.
- Anon (2020a). Wikipedia [Online]. en.wikipedia.org/wiki/Douma\_chemical\_attack (accessed 6 April 2020).
- Anon (2020b). Worldometer [Online]. www.worldometers.info/coronavirus (accessed 6 April 2020).
- Baillard, X., Gauguet, A., Bize, S. et al. (2006). Interference-filter-stabilized external-cavity diode lasers. *Opt. Commun.* 266 (2): 609–613.
- Batchelder, D., Cheng, C., Muller, W., and Smith, B. (1991). A compact Raman microprobe/microscope: Analysis of polydiacetylene Langmuir and Langmuir-Blodgett films. *Makromol. Chem. Macromol. Symp.* 46: 171.
- Bayer, B.E. (1976). Color imaging array. US Patent No. 3,971,065A.
- Blanchard, R. and Vakhshoori, D. (2020). Standoff detection of chemicals using infrared hyperspectral imaging and Raman spectroscopy. *Proc. SPIE Def. Sec. CBRNE Sensing XXI* 114160C: 114160C-1–114160C-10.
- Boogh, L., Meier, R., and Kausch, H. (1992). A Raman microscopy study of stress transfer in high-performance epoxy composites reinforced with polyethylene fibers. *J. Polym. Sci. B* 30: 325–333.
- Bowden, M., Gardiner, D.J., Rice, G., and Gerrard, D.L. (1990). Line-scanned micro Raman spectroscopy using a cooled CCD imaging detector. *Raman Spectros.* (21): 37–41.
- Buchsbaum, P.E. and Morris, M.J. (2000). Method for making monolithic patterned dichroic filter arrays for spectroscopic imaging. US Patent No. US6638668B2.
- Byrnes, J. (2009). *Unexploded Ordnance Detection and Mitigation*. Dordrecht: Springer.
- Carter, J.C., Angel, S.M., Lawrence-Snyder, M. et al. (2005). Standoff detection of high explosive materials at 50 meters in ambient light conditions using a small Raman instrument. *Appl. Spectrosc.* 59: 769–775.
- Christens-Barry, W.A., Boydston, K., France, F.G. et al. (2009). Camera system for multispectral imaging of documents. *Electronic Imaging* 7249: 8–18.
- Cristensen, K., Bradley, N., Morris, M., and Morrison, R. (1995). Raman imaging using a tunable dual-stage liquid crystal Fabry-Perot interferometer. *Appl. Spectrosc.* 49: 1120–1125.
- Crocombe, R.A. (2018). Portable spectroscopy. *Appl. Spectrosc.* 72 (12): 1701–1751.
- Dupont, S., Petersen, C., Thøgersen, J. et al. (2012). IR microscopy utilizing intense supercontinuum light source. *Opt. Express* 20 (5): 4887–4892.
- Editors, E.B. (2008). *Cassegrain reflector astronomical instrument* [Online]. <https://www.britannica.com/science/Cassegrain-reflector> (accessed 6 April 2020).
- Evans, J. (1949). The birefringent filter. *J. Opt. Soc. Am.* 39: 229–237.
- Evans, J. and Solc, I. (1958). Birefringent filter. *J. Opt. Soc. Am.* 48: 142–143.
- Faist, J., Capasso, F., Sivco, D. et al. (1994). Quantum cascade laser. *Science* 264 (5158): 553–556.
- Goldstein, S.K., Kidder, L., Herne, T. et al. (1996). The design and implementation of a high-fidelity Raman imaging microscope. *J. Microsc.* 184: 35–45.
- Gomer, N.R., Gordon, C.M., Lucey, P. et al. (2011a). Raman spectroscopy using a fixed-grating spatial heterodyne interferometer. *Spectroscopy* 26: 29.
- Gomer, N.R., Gordon, C.M., Lucey, P. et al. (2011b). Raman spectroscopy using a spatial heterodyne spectrometer: proof of concept. *Appl. Spectrosc.* 65 (8): 849.
- Gomer, N.R., Lamsal, N., Sun, H. et al. (2019). Explosive detection and identification using a wide-area hyperspectral raman imaging sensor. *Proc. SPIE Def. Sec. CBRNE Sensing XX* 110100H: 110100H-1–110100H-9.
- Hanel, R., Crosby, D., Herath, L. et al. (1980). Infrared spectrometer for Voyager. *Appl. Opt.* 19: 1391–1400.
- Hearnshaw, J. (1986). *The Analysis of Starlight*. Cambridge: Cambridge University Press.
- Henderson, R. (2007). *Wavelength considerations* [Online]. [web.archive.org/web/20071028072110/info.tuwien.ac.at/iflt/safety/section1/1\\_1\\_1.htm](http://web.archive.org/web/20071028072110/info.tuwien.ac.at/iflt/safety/section1/1_1_1.htm) (accessed 6 April 2020).
- Hirschfield (1974). Range independence of signal in variable focus remote Raman spectrometry. *Appl. Opt.* 13: 1435–1437.
- Ingle, J. and Crouch, S. (1988). *Spectrochemical Analysis*. Prentice Hall.

- IPAC, N. (2012). *Near, mid and far-infrared* [Online]. archive.is/20120529003352/http://www.ipac.caltech.edu/Outreach/Edu/Regions/irregions.html (accessed 6 April 2020).
- Jestel, N.L., Shaver, J.M., and Morris, M.D. (1998). Hyperspectral Raman line imaging of an aluminosilicate glass. *Appl. Spectrosc.* 52: 64–69.
- Jones, B.W. (2014). *Evolution of site in the animal kingdom* [Online]. https://webvision.med.utah.edu/2014/07/evolution-of-sight-in-the-animal-kingdom (accessed 6 April 2020).
- Kalasinsky, K., Hadfield, T., Shea, A. et al. (2007). Raman chemical imaging spectroscopy reagentless detection and identification of pathogens: signature development and evaluation. *Anal. Chem.* 79: 2658–2673.
- King, H.C. (2011). *The History of the Telescope*. New York: Courier Dover Publications.
- Kutteruf, M.R., Yetzbacher, M.K., Deprenger, M.J. et al. (2014). 9-band swir multispectral sensor providing full-motion video. *Proc. SPIE Airborne Intelligence, Surveillance, Reconnaissance (ISR) Systems and Applications XI* 9076.
- Lyot, B. (1944). The birefringent filter and its application in solar physics. *Astrophysics* 39: 229–242.
- Ma, J. and Ben-Amotz, D. (1997). Rapid micro-Raman imaging using fiber-bundle image compression. *Appl. Spectrosc.* 51: 1845–1848.
- Morris, H., Hoyt, C., and Treado, P. (1994). Imaging spectrometers for fluorescence and Raman microscopy: acousto-optic and liquid crystal tunable filters. *Appl. Spectrosc.* 48: 857–866.
- Morris, H., Hoyt, C., Miller, P., and Treado, P. (1996). Liquid crystal tunable filter Raman chemical imaging. *Appl. Spectrosc.* 50: 805–811.
- National Security Technologies, LLC (2016). *Passive Infrared Systems for Remote Chemical Detection Market Survey Report*. https://www.dhs.gov/sites/default/files/publications/PIS-RCD-MSR\_0716-508.pdf.
- Nelson, M. and Myrick, M. (1999a). Fabrication and evaluation of a dimension-reduction fiberoptic system for chemical imaging applications. *Rev. Sci. Instrum.* 70: 2836–2844.
- Nelson, M. and Myrick, M. (1999b). Single-frame chemical imaging: dimension reduction fiber-optic array improvements and application to laser-induced breakdown spectroscopy. *Appl. Spectrosc.* 53: 751–759.
- Nelson, M., McLestar, M., Aust, J., and Myrick, M., 1996. Distributed sensing of fiber optic arrays. The Pittsburgh Conference and Exposition on Analytical Chemistry and Applied Spectroscopy, Chicago, IL, March 1996.
- Nelson, M., Bell, W., McLester, M., and Myrick, M. (1998a). Single-shot multiwavelength imaging of laser plumes. *Appl. Spectrosc.* 52: 179–186.
- Nelson, M.P., Aust, J.F., Dobrowolski, D.J.A. et al. (1998b). Multivariate optical computation for predictive spectroscopy. *Anal. Chem.* 70: 73–82.
- Nelson, M.P., Shi, L., Zbur, L. et al. (2016). Real-time short-wave infrared hyperspectral conformal imaging sensor for the detection of threat materials. *Proc. SPIE Def. Sec.* 9824 (42): 982416-1–982416-9.
- Nelson, M.P., Tazik, S.K., Bangalore, A.S. et al. (2017). Performance evaluation and modeling of a Conformal Filter (CF) based real-time standoff hazardous material detection sensor. *Proc. SPIE Def. Sec. Next Gen. Spectros. Technol. X* 10210: 102100L-1–102100L-10.
- Nelson, M.P., Tazik, S.K., Treado, P.J. et al. (2018). Real-time short-wave infrared hyperspectral conformal imaging sensor for the detection of threat materials. *Proc. SPIE Def. Comm. Sens. Next Gen. Spectros. Technol. XI* 106570U: 106570U-1–106570U-10.
- Nelson, M.P., Tazik, S.K., and Treado, P.J. (2019). Real-time, reconfigurable, handheld molecular chemical imaging sensing for standoff detection of threats. *Proc. SPIE Def. Sec. CBRNE Sensing XX* 1101005: 1101005-1–1101005-10.
- Pecharrón-Gallego (2017). An overview on quantum cascade lasers: origins and development, quantum cascade lasers. *InTechOpen* https://doi.org/10.5772/6500.
- Pohl, K.R., Ford, A.R., Waterbury, R.D., Vunck, D., and Dottery, E.L. (2012). Optical hazard avoidance and method. US Patent No. US8724097B2.
- Schaeberle, M., Karakatsanic, C., Lau, C., and Treado, P. (1995). Raman chemical imaging: noninvasive visualization of polymer blend architecture. *Anal. Chem.* 67: 4316–4321.

- Schaeberle, M., Kalasinsky, V., Luke, J. et al. (1996). Raman chemical imaging: histopathology of inclusions in human breast tissue. *Anal. Chem.* 68: 1829–1833.
- Schlossberg, H. and Kelley, P. (1981). Infrared spectroscopy using tunable lasers. In: *Spectrometric Techniques* (ed. G. Vanesse), 161–238. New York: Academic Press.
- Scholl, L., Seth, P., Kariisa, M. et al. (2019). *Drug and opioid-involved overdose deaths – United States, 2013–2017. MMWR Morb. Mortal. Wkly Rep.* 2019 67: 1419–1427.
- Schröder, K. (2000). *Handbook on Industrial Laser Safety*. Technical University of Vienna.
- Schubert, E.F. (2003). *Light Emitting Diodes*. Cambridge, UK: Cambridge University Press.
- Sharma, S.K., Misra, A.K., Lucey, P.G. et al. (2006). Remote pulsed raman spectroscopy of inorganic and organic materials to a radial distance of 100 meters. *Appl. Spectrosc.* 60: 871–876.
- Solc, I. (1965). Birefringent chain filters. *J. Opt. Soc. Am.* 55: 621–625.
- Thériault, J.-M., Puckrin, E., Hancock, J. et al. (2004). Passive standoff detection of chemical warfare agents on surfaces. *Appl. Opt.* 43: 5870–5885.
- Treado, P., Levin, I., and Lewis, E. (1992). High-fidelity Raman imaging spectrometry: a rapid method using an acousto-optic tunable filter. *Appl. Spectrosc.* 46: 1211–1216.
- Turner, J.I. and Treado, P. (1997). LCTF Raman chemical imaging in the near infrared. *Proc. SPIE – Infrared Technol. Appl.* XXIII (3061): 280–283.
- Vaughn, J.M. (1989). *The Fabry–Perot Interferometer: History, Theory Practice and Applications*. Bristol, UK: Adam Hilger.
- Waldron, A., Allen, A., Colón, A., Carter, J.C., and Angel, S.M. (2020). Monolithic spatial heterodyne raman spectrometer: preliminary characterization results. *Appl. Spectrosc.*
- Wang, X., Voigt, T., Bos, P. et al. (2006). *Evaluation of a High-Throughput Liquid Crystal Tunable Filter for Raman Chemical Imaging of Threat Materials*, 637808. Boston: SPIE – The International Society of Optical Engineering.
- Wentworth, R., Neiss, J., Nelson, M., and Treado, P. (2007). Standoff Raman Hyperspectral Imaging Detection of Explosives. *2007 IEEE Antennas and Propagation Society International Symposium*, 4925–4928.
- West, M., Grossman, J., and Galvan, C. (2018). *Commercial Snapshot Spectral Imaging: The Art of the Possible. Mitre Technical Report*. McLean, VA: Mitre Corporation.

# 11

## Microplasmas for Portable Optical Emission Spectrometry

Vassili Karanassios

*Department of Chemistry and Waterloo Institute for Nanotechnology, University of Waterloo, Waterloo, ON, Canada*

### 11.1 Introduction

According to the Merriam Webster dictionary, a portable *object* is one “capable of being carried or moved about,” likely because it is smaller or lighter or because it requires lower amounts of consumables for operation as compared to its original counterpart. In terms of small-sized plasmas (in the form of microplasmas), numerous examples have been described in the literature [1–12]. To provide a basis for comparison, an original plasma-based *object* relevant to this work is an inductively coupled plasma, or ICP for short. To further provide an idea of average size, an ICP is formed on top of a torch with typical dimensions of about 25 cm in length and 2 cm in diameter. The widely used atmospheric pressure plasma-torch is powered by a relatively heavy and bulky (and, thus, not a person-portable) radiofrequency (RF) generator, typically the size of an office laser printer. For chemical analysis, atmospheric pressure operation is preferred because there is no need to use power-consuming and heavyweight vacuum pumps, as these disable portability. Furthermore, during the operation, an ICP torch becomes hot, so much so that the torch requires water-cooling. Cooling or other thermal management adds weight and complexity, thus also disabling portability. In terms of consumables required for operation, an ICP of the type described above uses a total of about 20 l/min of expensive argon gas and requires about 1.5 kW of electrical power. In addition to adding to operating costs, the need to carry such large amounts of consumables clearly disables portability. One way of addressing plasma portability is to use small-sized, lightweight plasmas with low requirements for consumables in the form of a microplasma [2–12].

A microplasma has been arbitrarily defined as a quasineutral electrical discharge (i.e. an ensemble of ions and electrons) with one critical dimension (such as height, width, radius) of 1000 µm or less [2, 3]. But, as the dimensions are reduced and approach the micrometer range, in addition to becoming small-sized and lightweight (thus enabling portability), microplasmas also become nonequilibrium and nonthermal. By being nonthermal, they do not require cooling or other thermal management, thus enabling portability. In addition, due to their small volume, a power density per unit volume equal to (or larger than) that obtained by an ICP can be obtained using lower input power (e.g. as little as a few Watts). And, due to their small size, they also require small flow rates of inert gas, with some of them operating using freely available air.

To be useful in portable chemical analysis applications (i.e. for use out of a laboratory), microplasmas must be a part of an instrument that also includes a portable spectrometer [13, 14]. A block diagram of such a system is shown in Figure 11.1. For such applications, a portable sample processor (often including sample preparation, sample separation, and sample introduction) is required [15]. Low-power operation (e.g. requiring less than 100 W of continuous operation) is essential [16–18]. The somewhat arbitrary 100 W limit is set by current battery technology; for example, state-of-the-art laptops use anywhere between about 50 and 100 W. Actual electrical power

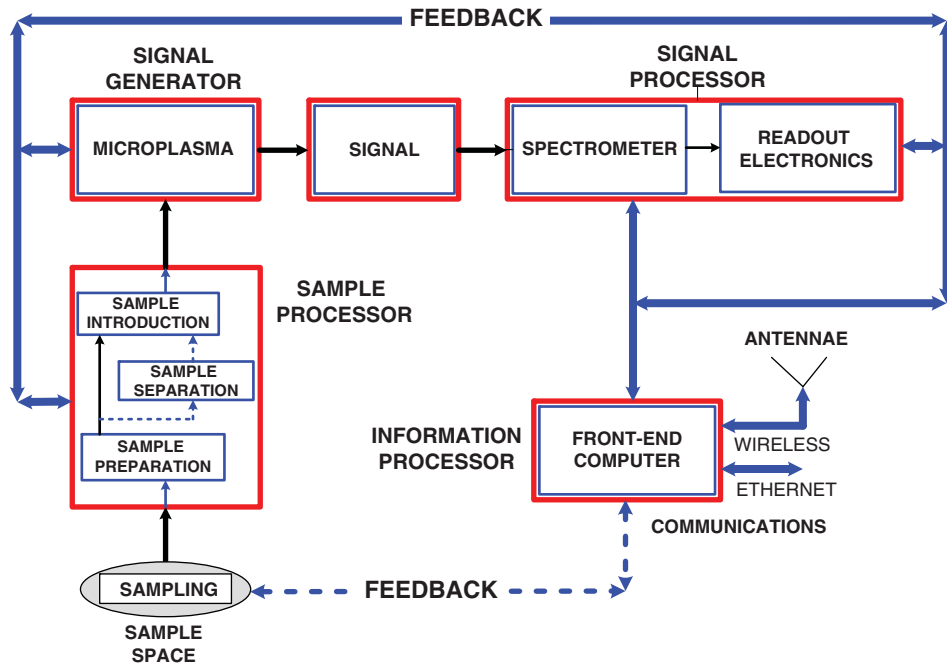


**Figure 11.1** Block diagram illustrating a portable microinstrument that includes a microplasma as a “signal generator” and it has associated processors, such as a sample processor, a signal processor, and an information processor. By analogy to the definition used for a microplasma, a microinstrument has at least one critical component (or subsystem or processor) in the microregime. *Source:* Based on Karanassios [2].

usage depends on the number of software applications running concurrently. A portable signal processor is also essential, and it involves a spectrometer along with its associated readout electronics. Most attempts at implementing a microinstrument of the type shown in Figure 11.1 involve the inclusion of a portable optical spectrometer [13, 14]. The brief review included in this chapter primarily involves optical spectrometers because many types of such spectrometers are commercially available, while, at present, portable mass spectrometers are not widely commercially available. (See the chapters by Snyder, Blakemen and Miller, and Leary et al. in this Volume for discussions of portable mass spectrometry, high-pressure mass spectrometry, and gas chromatography–mass spectrometry systems, respectively.) However, in the literature, many nonportable, lab-based mass spectrometers have been evaluated using a microplasma as an ion source. Microplasma–mass spectrometry combinations are mentioned not because they are portable, but because they demonstrate that microplasmas can be useful ion sources for mass spectrometry. To convert data into useful information, an information processor is also required. To reduce complexity and weight, the front-end processor (Figure 11.1) can be replaced by a smartphone [19–21]. And, to address power requirements, a variety of energy-scavenging and energy-harvesting approaches have been described [16–18].

## 11.2 A Brief Review of the Portable Microplasma Literature

### 11.2.1 Micro ICPs (Micro Inductively Coupled Plasmas)

Hopwood and coworkers have pioneered the development of miniaturized ICPs or mICPs as they call them [22–26]. These were primarily developed for operation in vacuum. Initially, one of the first examples involved the

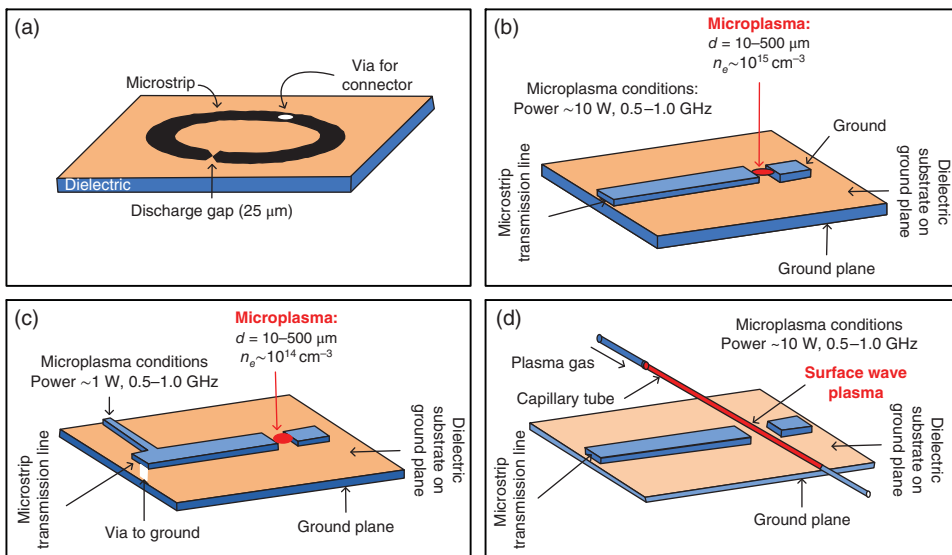


**Figure 11.2** (a) Microwave-induced microplasma (with a  $25\text{ }\mu\text{m}$  discharge gap); (b) a single transmission line microplasma; (c) a microwave plasma obtained using a microwave resonator; and (d) a surface wave microplasma [22, 23]. Source: Hopwood et al. [22]. Licensed under CC BY 3.0.

use of induction coils with diameters of 5, 10, and 15 mm. Following this initial implementation, the authors described various “plasmas-on-a-chip” designs operating using microwave frequencies. Using such frequencies, lightweight, inexpensive, and commercially available amplifiers could be used. Example designs are summarized in Figure 11.2. To put things in a scale-perspective, the traditional, widely used, lab-scale, ICPs operate at atmospheric pressure, they have a typical frequency of operation of 27 MHz (and sometimes 40 MHz or even 100 MHz), they require 1–2 kW of electrical power, and they use about 20 l/min of argon gas. Unlike the widely used lab-sized ICPs mentioned above, mICPs operate at low pressures (0.1–10 Torr), have frequencies ranging between 100 and 500 MHz (some more than that), and require less than 4 W of electrical power. A good analytical example of their application involves the determination of  $\text{SO}_2$  using molecular emissions, using a 5 mm (diameter) mICP and an optical multichannel analyzer (OMA). Despite their lightweight and use of low electrical power, low-pressure operation limits their portability and use in the field. However, due to their operation at low pressure, they are very well-suited as diagnostic tools for the semiconductor industry, and, in fact, they are commercially available for this purpose. They have been included here because they have been commercialized for use in the vacuum chambers employed by the semiconductor industry [25, 26].

### 11.2.2 Electrolyte Cathode Discharge (ELCAD)

In electrolyte cathode discharges (ELCADs), as their name implies, one of the electrodes (the cathode) contains a liquid electrolyte, obtained by adjusting the pH anywhere between 1 and 2 [27–35]. Electrolyte cathode direct current (DC) glow discharges were primarily developed to address the introduction of liquid samples into a glow discharge. To provide a bit of a perspective here and regardless of plasma-size, the question of how to introduce an initially ambient-temperature liquid sample into a gas-phase plasma continues to be an active area of research. In ELCADs, a nebulizer (as required for use in conventional flames and plasmas) is not necessary because sample introduction is facilitated due to use of a sample mixed with a liquid electrolyte in the cathode (Figure 11.3).

Historically, ELCADs are considered an outgrowth of glow discharge electrolysis (GDE), originally described in 1887. An example of a GDE cell is shown in Figure 11.3a. In this case, the plasma is formed between an electrode

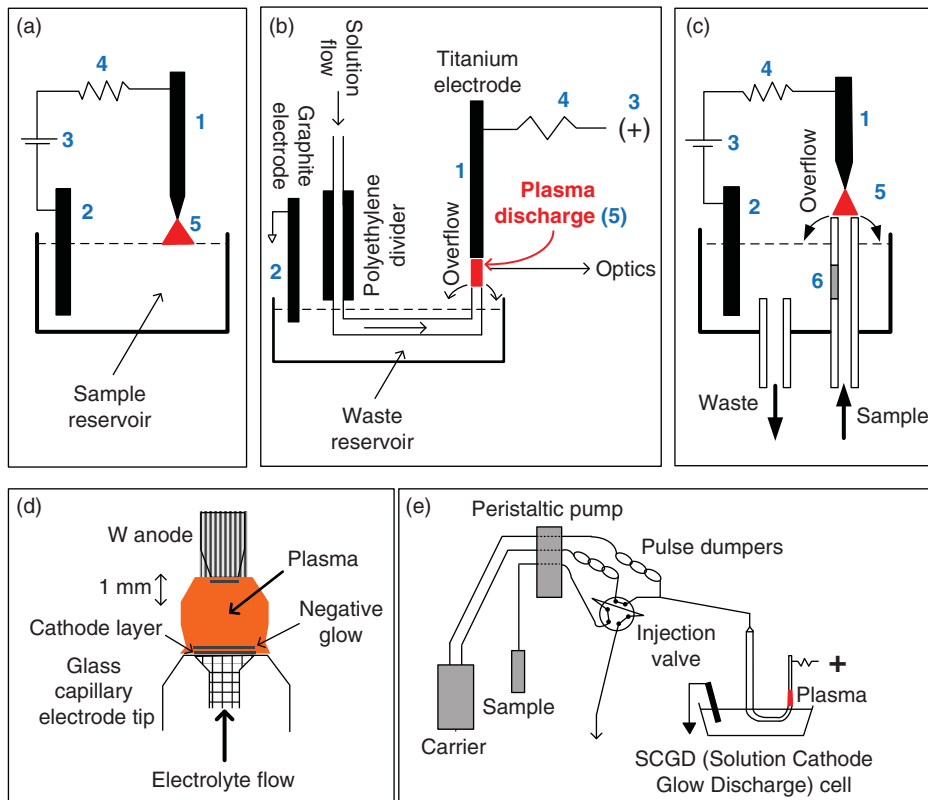


**Figure 11.3** Simplified illustrations for (a) glow discharge electrolysis (GDE) cell; and (b) electrolyte cathode discharge (ELCAD) systems. In all cases, the solution level is marked using a dashed line. (c) There is a continuous flow of sample. Source: Webb and Hieftje [30]. © 2009 American Chemical Society. (d, e) The inner diameter of the sample tube can be less than 1 mm. (1) Metal electrode; (2) solid counter electrode; (3) high-voltage dc power supply; (4) current-limiting resistor; (5) plasma; (6) glass frit or cotton fiber (generally a diaphragm, but not always present). Source: Webb et al. [31]. © 2007 American Chemical Society.

(often made of titanium), and the surface of a sample (buffered using an appropriate electrolyte). The distance between the tip of the electrode and the surface of the liquid (labeled sample reservoir in Figure 11.3a) varies, but it typically is a few mm. This is true for all configurations shown in Figure 11.3a–e. A resistor is used to ballast the discharge (item 4 in Figure 11.3a). Typical operating values are: open circuit output voltage of about 1200 V (typically less), current that can be adjusted to between 30 and 100 mA, and the ballast resistor which is variable to between 1.5 and 6.0 kΩ, and a discharge gap between 1 and 4 mm. Although the maximum electrical power is 120 W, typical operating powers are about 70 W. A graphite electrode (item 2 in Figure 11.3a) is immersed into the sample reservoir to complete the circuit.

For ELCADs, there is typically a continuous flow of sample (Figure 11.3b and c). The inner diameter of the sample tube is a few mm, and flow rates range between 8 and 10 ml/min. In some of the most recent miniaturized ELCAD designs, the inner diameter of the sample tube (Figure 11.3d and e) was less than 1 mm (e.g. 380 µm), and the flow rate ranged between 2.5 and 3.5 ml/min. In addition to continuous flow, a multiport valve (Figure 11.3d) was used for transient sample introduction (25 µl injection). In such a configuration (Figure 11.3d), an ELCAD can be used for chromatographic applications. The detection limits were impressive for 25 µl volume samples, ranging from 5 pg (0.2 ppb) for lithium to 6 ng (270 ppb) for mercury.

Because the surface must be covered with the solution for stable operation, a large volume of sample is used, and, thus, a significant volume of waste is produced. For example, typical flow rates in the range of 8–10 ml/min have been reported for most of the early ELCAD designs. More recent designs, however, operate at much lower flow rates, for instance, between 2.5 and 3.5 ml/min. Despite the simplicity of the ELCAD designs, the discharge performs well. Detection limits for most metals tested, as reported in the literature, typically range in the 10s of ppb, and short-term precision was reported to be around 1%, obtained using 1 ppm single-element solutions.

### 11.2.3 Liquid Sampling-Atmospheric Pressure Glow Discharge (LS-APGD)

This atmospheric pressure discharge is similar to an ELCAD and, as its name implies, it also incorporates liquid sample introduction (Figure 11.4) [36–41]. Specifically, a conductive tube delivers the sample, typically 5  $\mu$ l, to the discharge. The small amount of sample makes this discharge ideal as a detector for liquid chromatography. In addition, and unlike the ELCAD, a waste reservoir is unnecessary because the discharge is operated in total consumption mode. The typical 0.1–0.3 ml/min flow rate of the solution sample makes this parameter a key aspect of liquid sampling-atmospheric pressure glow discharge (LS-APGD), especially when used as a detector for liquid chromatography. Due to the low flow rate, a He-gas sheath (Figure 11.4) is necessary to reduce (or eliminate) signal fluctuations. Injection-to-injection, or sample-to-sample, precision of <10% RSD has been reported for concentrations in the range of hundreds of ppm. Relative unit-concentration detection limits have been reported to be in the 1–2 ppm range. Absolute unit (mass) detection limits of 5–10 ng have been reported for many elements across the periodic table. Remarkably, very little variation in detection limits has been reported for many of the elements tested.

### 11.2.4 Liquid Electrode Plasma (LEP)

A liquid electrode plasma (LEP)-optical emission spectrometry system (Figure 11.5) is described in a series of papers [42–46]. This system involves a combination of a quartz chip and sample flow system. In this system, an electroconductive solution sample is pumped into a microfluidic channel whose center is narrow ( $\sim$ 100  $\mu$ m wide). A pulsed, high voltage (about 1500 V) is applied at the opposite and wide ends of the channel, and a plasma is formed inside the narrow part of the channel. The sample that resides inside the narrow part of the channel

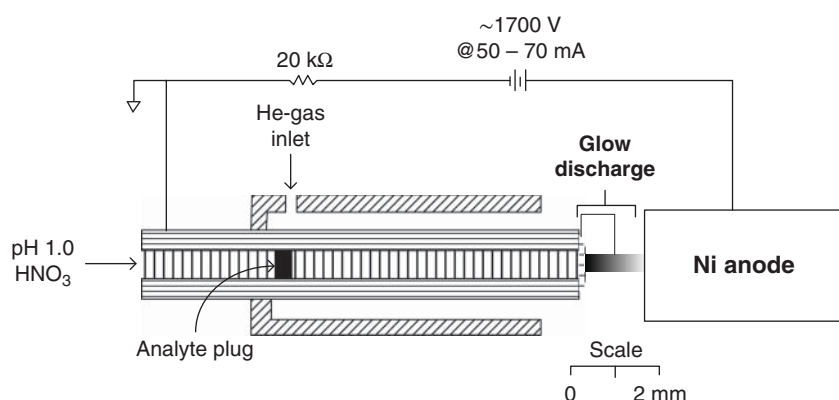


**Figure 11.4** Illustration of a liquid sampling-atmospheric pressure glow discharge (LS-APGD). A high voltage is applied between a conductive capillary and an Ni anode. Typical voltages and currents are shown in the figure. A glow discharge is formed between the solution emerging from the capillary and the anode. A flow of He-gas, running concentric to the solution, is used to stabilize the solution-delivery, especially when low solution flow- rates are utilized. Source: Modified from Marcus et al. [36].

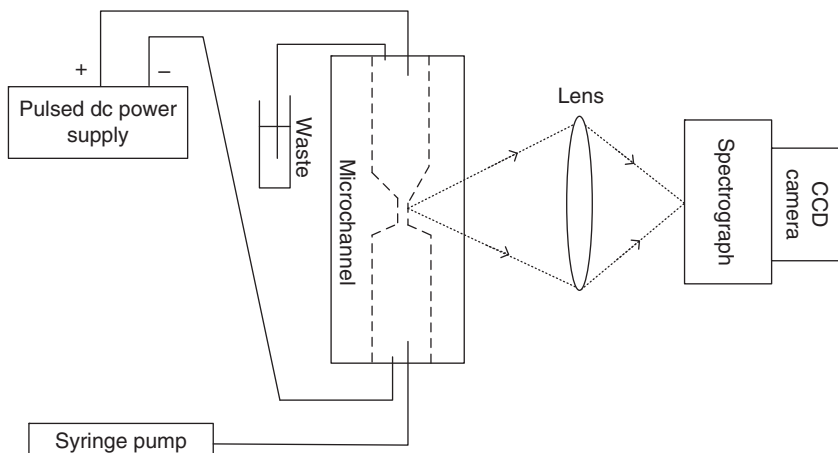


**Figure 11.5** Instrumentation setup for measurement by a liquid electrode plasma (LEP). Source: Kohara et al. [42]. © 2015 Royal Society of Chemistry.

is vaporized, and its interaction with the microplasma generates atomic emission. Spectral lines so generated are used for the construction of calibration curves. The limits of detection were reported to be 0.52 µg/l for cadmium and 19.0 µg/l for lead. There is a commercially available system based on this design [46].

### 11.2.5 Postage Stamp Microplasmas on Polymeric Substrates

To reduce costs (e.g. those associated with ownership, operation, and fabrication), we developed and characterized many designs of microplasmas on polymeric substrates, and some examples are shown in Figure 11.6. For the microplasmas of the type shown in Figure 11.6, although their critical plasma dimension was in the µm regime, they were formed inside millifluidic channels (e.g. ~2 mm wide or less). This was done for rapid prototyping [47] and to avoid accidental contact of the microplasma with the channel walls, which is important during testing. Once prototypes were produced, the channel width was never revisited. Although polymeric substrates have high dielectric strength, to address poor transmission of polymers in the ultraviolet (UV), the channels were fitted with a quartz plate (Figure 11.6).

### 11.2.6 3D-Printed Microplasmas

To reduce fabrication costs, we used an inexpensive 3D printer to rapidly prototype 3D chips in a few hours or less [47–49]. This approach eliminated the need for cleanrooms and lithography. The 3D chips on the polymeric substrate were fitted with a quartz plate to obtain transparency in the UV. An example of a 3D-printed microplasma is shown in Figure 11.7.

To provide some operation details, a microsample (e.g. 3 µl) containing an analyte (i.e. the species of interest) was introduced into the microplasma using the sample introduction system shown in Figure 11.8. This microsample introduction system consists of a coil filament made of rhenium (Re). Briefly, the assembly carrying the recoil filament is retracted from the vaporization chamber (Figure 11.8), which is connected to an external power supply. Typically, 3 µl of a sample or of a diluted standard solution (e.g. 500 ppb of Zn) is deposited on the filament, and the coiled-filament assembly is reinserted into the vaporization chamber. Using the external power supply, low electrical power (e.g. 0.85 W) is applied to the coil to vaporize the solvent of the microsample that was deposited on

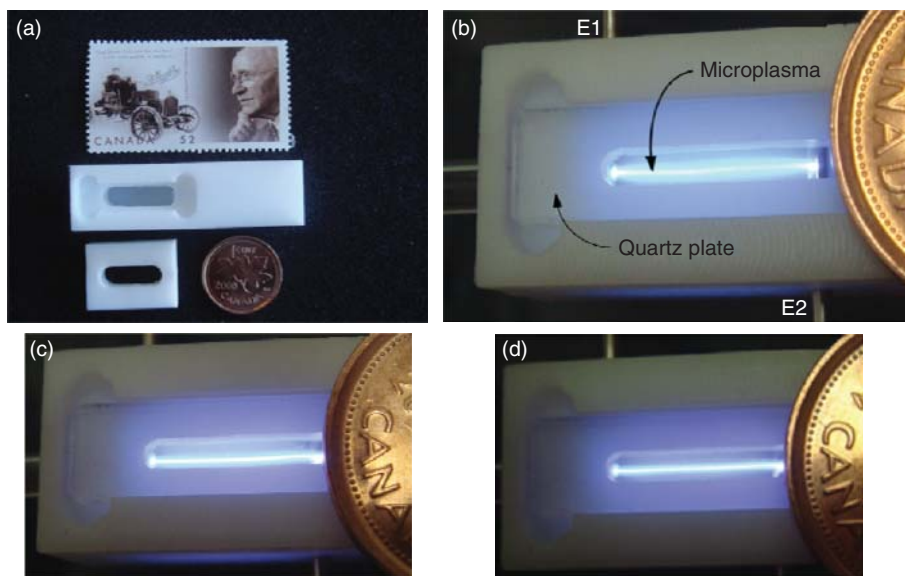
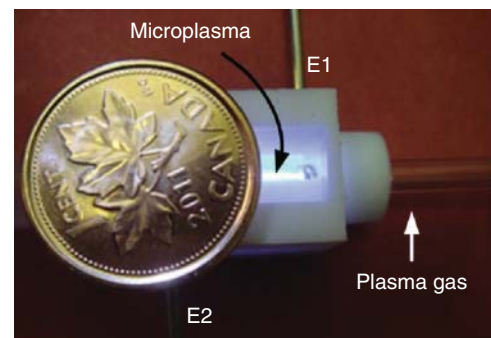


**Figure 11.6** (a) Postage stamp-sized polymeric 3D-chips used for microplasma formation, and (b) microplasma formed between electrodes E1 and E2. The critical microplasma dimension depended on operating conditions. For example, microplasmas with diameters of (b)  $\sim 750 \mu\text{m}$ , (c)  $\sim 400 \mu\text{m}$ , and (d)  $\sim 200 \mu\text{m}$  were formed. In these photographs, a one-cent coin was included for size. It is worth noting that the microplasma fits inside the letter A of the coin.

**Figure 11.7** 3D-printed microplasma fabricated on a hybrid 3D-chip. The microplasma is formed between electrodes E1 and E2. A one-cent coin has been included for size, the microplasma fits inside the letter A of the coin.



the coil. When the sample is dry, after about two minutes, the dried solution residue that remained on the coil was vaporized from the coil by applying higher electrical power to the coil (e.g.  $\sim 25 \text{ W}$ ). As shown in Figure 11.8, the outlet of the vaporization chamber of this sample introduction system is connected to the inlet of the microplasma. The sample vaporized from the coil was routed to the microplasma where it interacted with the microplasma, thus generating characteristic optical emission of the analyte present in the sample. Using the fiber-optic cable, optical emission was guided to the portable spectrometer, which could be controlled by a smartphone. An example of the signal so obtained is shown in Figure 11.9. The required signal processing, due to the transient nature of the signal generated by the recoil microsample introduction system, is briefly described in the caption of Figure 11.9.

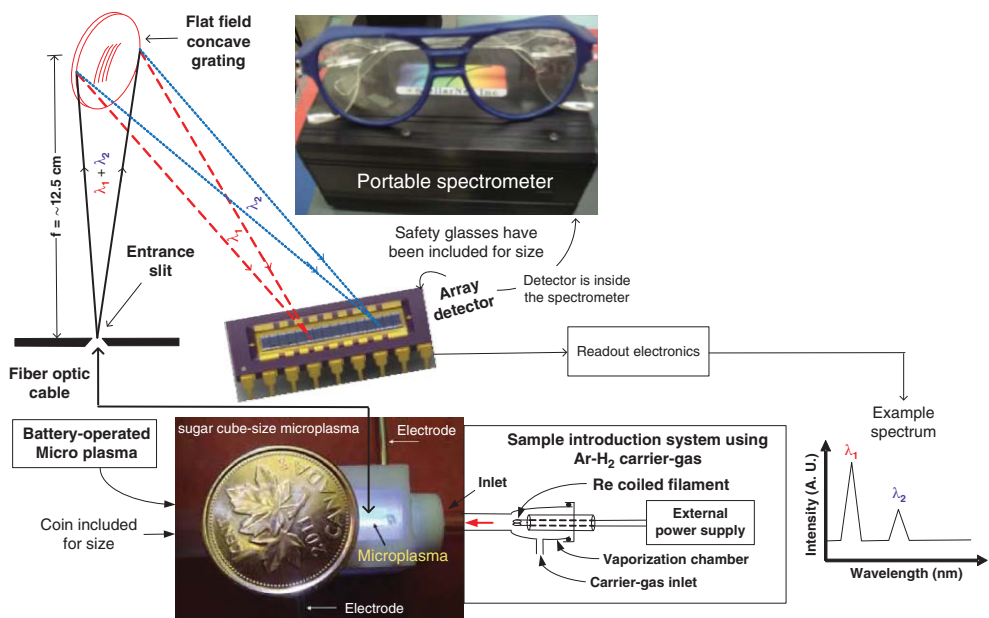


**Figure 11.8** Example of the experimental setup showing the sample introduction system and one of the varieties of microplasma devices (MPDs) we designed, fabricated, and evaluated. The microsample introduction system we used is shown in the center frame of this figure.

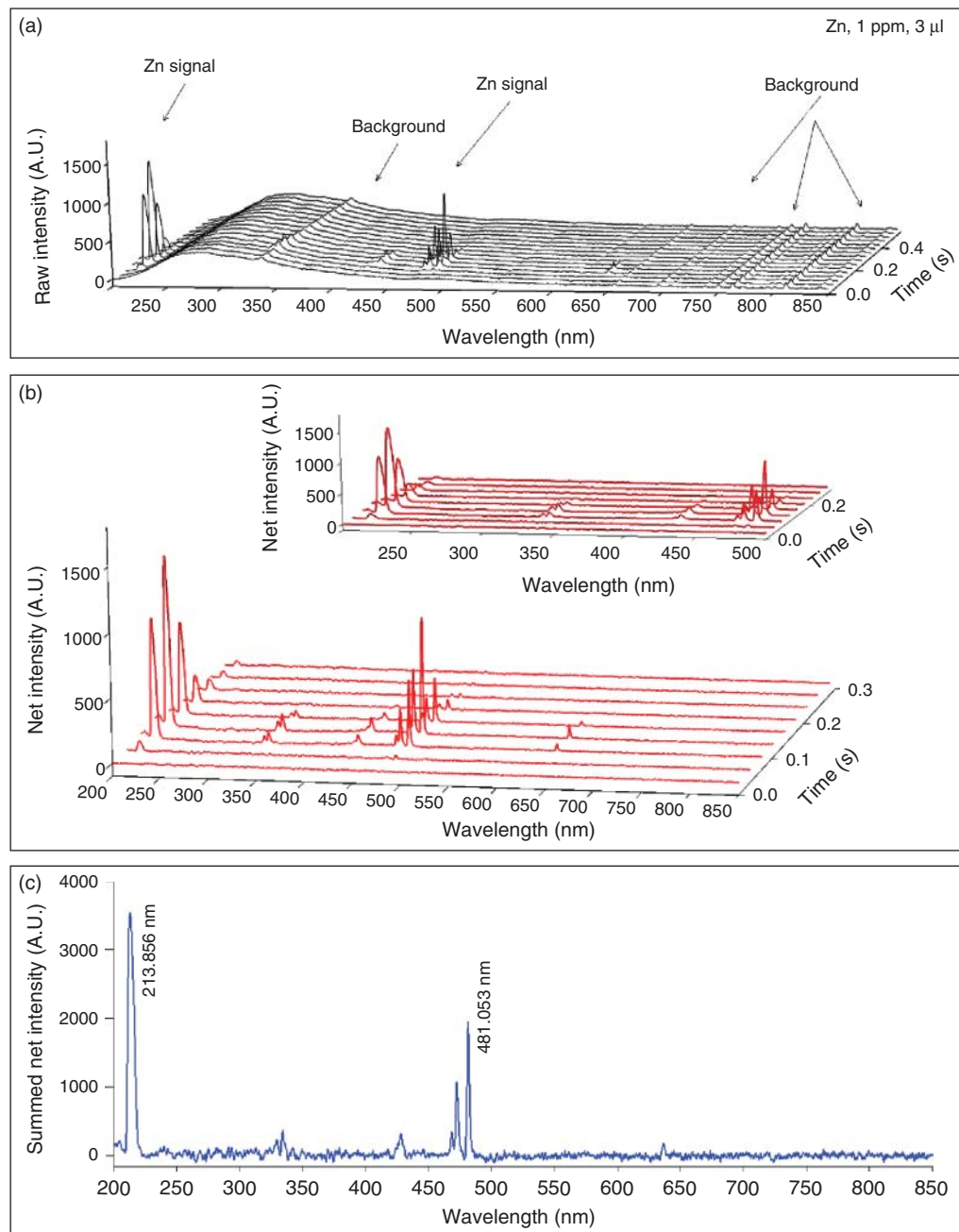


**Figure 11.9** (a) Raw signal, (b) background-subtracted signal, and (c) 2D-signal obtained by summing only the spectra that contained a signal in (b).

### 11.3 Conclusion

Over the last several years, a variety of microplasmas have been described in the literature. For use outside of a laboratory, the low power consumption of microplasmas is one of their key characteristics. Many of the microplasmas described in the literature can also be used with portable, optical emission spectrometers, so that the entire, portable, microplasma-based spectrometer systems can be developed for use in chemical analysis *on-site* (i.e. in the field). In the future, it would be interesting to see further development in portable microplasma designs, develop their fundamental microplasma characteristics and apply them to a variety of anticipated applications.

### Acronyms

3D	Three-dimensional
dc	Direct current
ELCAD	Electrolyte cathode discharges
GDE	Glow discharge electrolysis
ICP	Inductively coupled plasma
LS-APGD	Liquid sampling-atmospheric pressure glow discharge
mICP	Micro inductively coupled plasma
MPD	Microplasma devices
OMA	Optical multichannel analyzer
ppb	Parts per billion
ppm	Parts per million
RF	Radiofrequency
RSD	Relative standard deviation

### Abbreviations

kΩ	kilo-ohm
kW	kilowatt
L/min	Liters/minute
MHz	Megahertz
mA	Milliamp
mL/min	Milliliters/minute
mm	Millimeter
ng	Nanogram
pg	Picogram
µg/l	Micrograms/liter
µl	Microliter
µm	Micrometer
V	Volt
W	Watt

## Acknowledgments

Financial assistance from the Natural Sciences and Engineering Research Council of Canada (NSERC) and from Waterloo's Institute for Quantum Computing via a CFREF (Canada First Research Excellence Fund) is gratefully acknowledged.

## References

- 1** Crocombe, R.A. (2018). Portable spectroscopy. *Applied Spectroscopy* 72 (12): 1701–1751. <https://doi.org/10.1177/0003702818809719>.
- 2** Karanassios, V. (2004). Microplasmas for chemical analysis: analytical tools or research toys? *Spectrochimica Acta Part B* 59 (7): 909–928. <https://doi.org/10.1016/j.sab.2004.04.005>.
- 3** Karanassios, V. (2018). Microfluidics and nanofluidics: science, fabrication technology (from cleanrooms to 3D printing) and their application to chemical analysis by battery-operated microplasmas-on-chips”, Chapter 1. In: *Microfluidics and Nanofluidics* (ed. M.S. Kandousi), 1–34. InTech Publishing <https://doi.org/10.5772/intechopen.74426>.
- 4** Becker, K.H., Schoenbach, K.H., and Eden, J.G. (2006). Microplasmas and applications. *Journal of Physics D: Applied Physics* 39 (3): R55. <https://doi.org/10.1088/0022-3727/39/3/R01>.
- 5** Franzke, J., Kunze, K., Miclea, M., and Niemax, K. (2003). Microplasmas for analytical spectrometry. *Journal of Analytical Atomic Spectrometry* 18: 802–807. <https://doi.org/10.1039/B300193H>.
- 6** Janasek, D., Franzke, J., and Manz, A. (2006). Scaling and the design of miniaturized chemical-analysis systems. *Nature* 442: 374–380. <https://doi.org/10.1038/nature05059>.
- 7** Bruggeman, P. and Brandenburg, R. (2013). Atmospheric pressure discharge filaments and microplasmas: physics, chemistry and diagnostics. *Journal of Physics D: Applied Physics* 46: 464001. <https://doi.org/10.1088/0022-3727/46/46/464001>.
- 8** Yuan, X., Tang, J., and Duan, Y. (2011). Microplasma technology and its applications in analytical chemistry. *Applied Spectroscopy Reviews* 46: 581–605. <https://doi.org/10.1080/05704928.2011.604814>.
- 9** Luo, D. and Duan, Y. (2012). Microplasmas for analytical applications of lab-on-a-chip. *Trends in Analytical Chemistry* 39: 254–266. <https://doi.org/10.1016/j.trac.2012.07.004>.
- 10** Tachibana, K. (2006). Current status of microplasma research. *IEEJ Transactions* 1: 145–155. <https://doi.org/10.1002/tee.20031>.
- 11** Becker, K., Kersten, H., Hopwood, J., and Lopez, J.L. (2010). Microplasmas: scientific challenges and technological opportunities. *European Physical Journal D: Atomic, Molecular, Optical and Plasma Physics* 60 (3): 437–439. <https://doi.org/10.1140/epjd/e2010-00231-4>.
- 12** Chiang, W.-H., Mariotti, D., Sankaran, R.M. et al. (2020). Microplasmas for advanced materials and devices. *Advanced Materials* 32: 1905508. <https://doi.org/10.1002/adma.201905508>.
- 13** Weagant, S. and Karanassios, V. (2009). Helium-hydrogen microplasma device (MPD) on postage-stamp-size plastic-quartz chips. *Analytical and Bioanalytical Chemistry* 395: 577–589. <https://doi.org/10.1007/s00216-009-2942-2>.
- 14** Weagant, S., Dulai, G., Li, L., and Karanassios, V. (2015). Characterization of rapidly-prototyped, battery-operated, argon-hydrogen microplasma on a chip for elemental analysis of microsamples by portable optical emission spectrometry. *Spectrochimica Acta Part B* 106: 75–80. <https://doi.org/10.1016/j.sab.2015.01.009>.
- 15** Badiei, H.R., Stubley, G., Fitzgerald, R. et al. (2018). Computational fluid dynamics (CFD) applied to a glass vaporization chamber for introduction of micro- or nano-size samples into lab-based ICPs and to a

- CFD-derived (and rapidly prototyped via 3D printing) smaller-size chamber for portable microplasmas, Chapter 8. In: *Computational Fluid Dynamics: Basic Instruments and Applications in Science* (ed. A. Ionescu), 187–215. InTech Publishing <https://doi.org/10.5772/intechopen.72650>.
- 16 Trzciński, P., Nathan, A., and Karanassios, V. (2017). Approaches to energy harvesting and energy scavenging for energy autonomous sensors and micro-instruments. *Proceedings of SPIE* 10194: 1019431-1. <https://doi.org/10.1117/12.2262949>.
  - 17 Illar, J.A., Gao, Z., Sivoththaman, S., and Karanassios, V. (2019). From nanoenergy harvesting to self-powering of micro- or nano-sensors for measurements on-site or for IoT applications. *Proceedings of SPIE* 109831BA <https://doi.org/10.1117/12.2519939>.
  - 18 Lim, N., Millar, J.A., and Karanassios, V. (2020). Triboelectric nanogenerators for powering fieldable sensors and systems. *Proceedings of SPIE* 11390, *Next-Generation Spectroscopic Technologies XIII* 113900T <https://doi.org/10.1117/12.2559159>.
  - 19 Fitzgerald, R., Wang, E., and Karanassios, V. (2019). Smartphone-enabled data acquisition and digital signal processing: from current-output or voltage-output sensors for use on-site, to their use in IoT, in Industry 4.0 and (potentially) in Society 5.0. *Proceedings of SPIE* 1098304 <https://doi.org/10.1117/12.2519941>.
  - 20 Fitzgerald, R. and Karanassios, V. (2018). The internet of things (IoT) for a smartphone-enabled optical spectrometer and their use on-site and (potentially) for industry 4.0. *Proceedings of SPIE* 10657: 1065705. <https://doi.org/10.1117/12.2305466>.
  - 21 Fitzgerald, R., Wang, E., and Karanassios, V. (2018). Fast fourier transform of non-periodic signals generated from a microplasma: migrating from a desktop computer to an IoT-connected Smartphone. *Proceedings of SPIE* 10657, *Next-Generation Spectroscopic Technologies XI* 1065703: 7pp. doi: <https://doi.org/10.1117/12.2305462>.
  - 22 Hopwood, J., Hoskinson, A.R., and Gregorio, J. (2014). Microplasmas ignited and sustained by microwaves. *Plasma Sources Science and Technology* 23: 064002. <https://doi.org/10.1088/0963-0252/23/6/064002>.
  - 23 Minayeva, O.B. and Hopwood, J.A. (2003). Microfabricated inductively coupled plasma-on-a-chip for molecular SO<sub>2</sub> detection: a comparison between global model and optical emission spectrometry. *Journal of Analytical Atomic Spectrometry* 18: 856–863. <https://doi.org/10.1039/b303821a>.
  - 24 Hopwood, J. and Iza, F. (2004). Ultrahigh frequency microplasmas from 1 pascal to 1 atmosphere. *Journal of Analytical Atomic Spectrometry* 19: 1145–1150. <https://doi.org/10.1039/B403425B>.
  - 25 Verionix commercialized microplasma optical emission technology as a process or residual gas analyzer. <http://verionix.com> (accessed 1 June 2020).
  - 26 Inficon. <https://jusmundi.com/en/document/decision/en-verionix-inc-n-k-a-k1tech-ventures-inc-v-inficon-inc-opinion-of-the-united-states-district-court-of-the-southern-district-of-new-york-thursday-21st-april-2016> (accessed 22 October 2020).
  - 27 Webb, M.R., Andrade, F.J., Gamez, G. et al. (2005). Spectroscopic and electrical studies of a solution-cathode glow discharge. *Journal of Analytical Atomic Spectrometry* 20: 1218–1225. <https://doi.org/10.1039/B503961D>.
  - 28 Webb, M.R., Andrade, F.J., and Hieftje, G.M. (2007). Use of electrolyte cathode glow discharge (ELCAD) for the analysis of complex mixtures. *Journal of Analytical Atomic Spectrometry* 22: 766–774. <https://doi.org/10.1039/B616989A>.
  - 29 Cserfalvi, T. and Mezei, P. (2003). Sub-nanogram sensitive multi-metal detector with atmospheric electrolyte cathode glow discharge. *Journal of Analytical Atomic Spectrometry* 18: 596–602. <https://doi.org/10.1039/b300544p>.
  - 30 Webb, M.R. and Hieftje, G.M. (2009). Spectrochemical analysis by using discharge devices with solution electrodes. *Analytical Chemistry* 81: 862–867. <https://doi.org/10.1021/ac801561t>.
  - 31 Webb, M.R., Andrade, F.J., and Hieftje, G.M. (2007). High-throughput elemental analysis of small aqueous samples by emission spectrometry with a compact, atmospheric-pressure solution-cathode glow discharge. *Analytical Chemistry* 79: 7807–7812. <https://doi.org/10.1021/ac0707885>.
  - 32 He, Q., Zhu, Z., and Hu, S. (2014). Flowing and non-flowing liquid electrode discharge microplasma for metal ion detection by optical emission spectrometry. *Applied Spectroscopy Reviews* 49: 249–269. <https://doi.org/10.1080/05704928.2013.820195>.

- 33** Wu, J., Yu, J., Li, J. et al. (2007). Detection of metal ions by atomic emission spectroscopy from liquid-electrode discharge plasma. *Spectrochimica Acta Part B* 62 (11): 1269–1272. <https://doi.org/10.1016/j.sab.2007.10.026>.
- 34** Manjusha, R., Shekhar, R., and Kumar, S. (2019). Direct determination of impurities in high purity chemicals by electrolyte cathode discharge atomic emission spectrometry (ELCAD-AES). *Microchemical Journal* 145: 301–307. <https://doi.org/10.1016/j.microc.2018.10.052>.
- 35** Zhao, M., Peng, X., Yang, B., and Wang, Z. (2020). Ultra-sensitive determination of antimony valence by solution cathode glow discharge optical emission spectrometry coupled with hydride generation. *Journal of Analytical Atomic Spectrometry* <https://doi.org/10.1039/D0JA00009D>.
- 36** Marcus, R.K., Paing, H.W., and Zhang, L.X. (2016). Conceptual demonstration of ambient desorption-optical emission spectroscopy using a liquid sampling-atmospheric pressure glow discharge microplasma source. *Analytical Chemistry* 88 (11): 5579–5584. <https://doi.org/10.1021/acs.analchem.6b00751>.
- 37** Venzie, J.L. and Marcus, R.K. (2006). Effects of easily ionizable elements on the liquid sampling atmospheric pressure glow discharge. *Spectrochimica Acta Part B* 61 (6): 715–721. <https://doi.org/10.1016/j.sab.2006.02.005>.
- 38** Marcus, R.K., Manard, B.T., and Quarles, C.D. Jr., (2017). Liquid sampling-atmospheric pressure glow discharge (LS-APGD) microplasmas for diverse spectrochemical analysis applications. *Journal of Analytical Atomic Spectrometry* 32: 704–716. <https://doi.org/10.1039/C7JA00008A>.
- 39** Quarles, C.D. Jr., Manard, B.T., Burdette, C.Q., and Marcus, R.K. (2012). Roles of electrode material and geometry in liquid sampling-atmospheric pressure glow discharge (LS-APGD) microplasma emission spectroscopy. *Microchemical Journal* 105: 48–55. <https://doi.org/10.1016/j.microc.2012.01.012>.
- 40** Paing, H.W. and Marcus, R.K. (2017). Parametric evaluation of ambient desorption optical emission spectroscopy utilizing a liquid sampling-atmospheric pressure glow discharge microplasma. *Journal of Analytical Atomic Spectrometry* 32: 931–941. <https://doi.org/10.1039/C7JA00035A>.
- 41** Lu, Q., Feng, F., Yu, J. et al. (2020). Determination of trace cadmium in zinc concentrate by liquid cathode glow discharge with a modified sampling system and addition of chemical modifiers for improved sensitivity. *Microchemical Journal* 152: 104308. <https://doi.org/10.1016/j.microc.2019.104308>.
- 42** Kohara, Y., Terui, Y., Ichikawa, M. et al. (2015). Atomic emission spectrometry in liquid electrode plasma using an hour glass microchannel. *Journal of Analytical Atomic Spectrometry* 30: 2125–2128. <https://doi.org/10.1039/C5JA00059A>.
- 43** Khoai, D.V., Kitano, A., Yamamoto, T. et al. (2013). Development of high sensitive liquid electrode plasma - atomic emission spectrometry (LEP-AES) integrated with solid phase pre-concentration. *Microelectronic Engineering* 111: 343–347. <https://doi.org/10.1016/j.mee.2013.02.086>.
- 44** Khoai, D.V., Yamamoto, T., Ukita, Y., and Takamura, Y. (2014). On-chip solid phase extraction–liquid electrode plasma atomic emission spectrometry for detection of trace lead. *Japanese Journal of Applied Physics* 53: 05FS01. <https://doi.org/10.7567/JJAP.53.05FS01>.
- 45** Kitano, A., Liduka, A., Yamamoto, T. et al. (2011). Highly sensitive elemental analysis for Cd and Pb by liquid electrode plasma atomic emission spectrometry with quartz glass chip and sample flow. *Analytical Chemistry* 83: 9424–9430. <https://doi.org/10.1021/ac2020646>.
- 46** Commercialized by MICRO EMISSION (Japan). <http://www.micro-emission.com/products/papers.html>. (accessed 10 October 2020).
- 47** Weagent, S., Li, L., and Karanassios, V. (2011). *Rapid prototyping of hybrid, plastic-quartz 3D-chips for battery-operated microplasmas*, 209–226. InTech Publishing, Chapter 10. <https://doi.org/10.5772/24994>.
- 48** Shatford, R. and Karanassios, V. (2016). 3D printing in chemistry: past, present and future. *Proceedings of SPIE* 9855: 98550B–98560B. <https://doi.org/10.1117/12.2224404>.
- 49** Rue, W., Afzal, D., and Karanassios, V. (2020). An overview of 3D printing in chemistry. *Proceedings of SPIE* 11390: 1139016. <https://doi.org/10.1117/12.2559157>.

## 12

# Portable Electro-Optical-Infrared Spectroscopic Sensors for Standoff Detection of Chemical Leaks and Threats

Hugo Lavoie<sup>1</sup>, Jean-Marc Thériault<sup>1</sup>, Eldon Puckrin<sup>1</sup>, Richard L. Lachance<sup>2</sup>, Alexandre Thibeault<sup>2</sup>, Yotam Ariel<sup>2</sup> and Jean Albert<sup>2</sup>

<sup>1</sup>Defence R&D Canada – Valcartier Research Center, Quebec, QC, Canada

<sup>2</sup>Bluefield Technologies Inc., San Francisco, CA, USA

## 12.1 Introduction

For several decades, the advancement of spectroscopic technology has yielded systems more rugged and smaller than ever. This advancement has permitted the technology to leave the traditional laboratory setting and become usable in the field. Infrared (IR) spectroscopy and its corresponding technology that includes electric cryocoolers, rugged spectrometers or modulators and optical coatings contribute to the more prevalent use of the technology in the field. The development of detection, identification, and monitoring sensors has provided options for first responders, the military and environmental agencies to improve their threat-detection capabilities. Many materials of chemical interest (gas, liquid, or solid), such as greenhouse gases, air pollutants, or ground contaminants, possess good and discriminative signatures in the IR region. The present chapter will provide an overview of four IR spectroscopic techniques developed for the standoff detection and monitoring of various chemicals of interest. Three Fourier transform spectrometer (FTS)-based systems and one gas-filter correlation radiometric sensor will be discussed. The popular use of these technologies is on the near horizon.

## 12.2 A Differential FTIR Approach for Standoff Gas Detection

### 12.2.1 Background

Fourier transform infrared (FTIR) spectroscopy is a well-established technique for the passive remote monitoring of chemical vapors. There are several applications for which this technique is particularly well-suited, such as the remote monitoring of air pollutants and greenhouse gases, as well as the passive standoff detection and identification of toxic industrial compounds (TICs) and chemical warfare agents (CWAs). In this context, DRDC (Defence R&D Canada) Valcartier has been developing and optimizing a sensor technology for differential detection. This optimized configuration exploits the optical subtraction capabilities of a double-beam Michelson interferometer which provides an efficient means for the real-time suppression of the spectral background, which overlays the desired spectral signature, and the suppression of the internal IR emission contributions arising from the spectrometer itself. These subtraction attributes represent a definite advantage for portable spectroscopy. A review of the differential detection concept and its validation steps based on the double-beam Michelson FTIR spectrometer is given below.

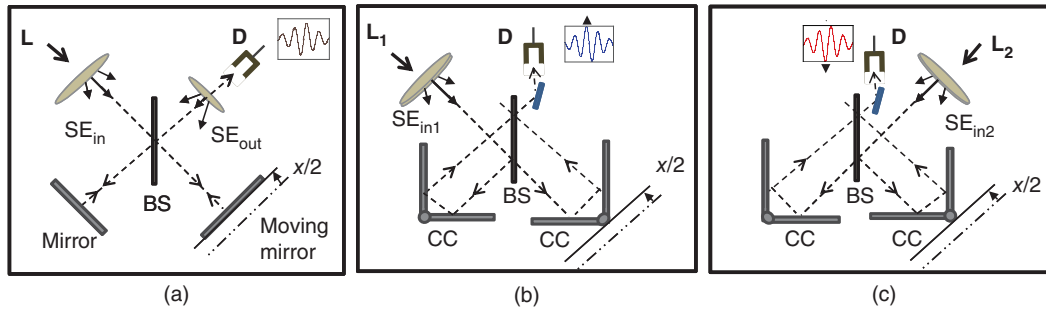


**Figure 12.1** Schematic views of a single-input port FTIR Michelson interferometer (a) and a double-input port FTIR Michelson interferometer (b and c) with their associated self-emission contributions; where *cc*, *SE*, and *BS* stand for corner-cube reflector, self-emission, and beamsplitter, respectively.

### 12.2.2 FTS Background

The basic principle of an FTS is that a Michelson interferometer modulates the incident beam intensity according to the wavelength of the radiation. As shown in Figure 12.1a, the beam from the source is divided by a beamsplitter (BS) into two separate components which are recombined after traveling different optical path lengths. In an FTS, the Michelson interferometer is designed in such a way that one or both of its mirrors can move periodically around a mean position creating a periodic optical path difference between the two interfering beams. In this case, when a monochromatic source of unit amplitude is incident on the interferometer, the emergent amplitude  $A(x)$  is given by

$$A(x) = (rt) + (tr)e^{i2\pi\nu x} \quad (12.1)$$

where  $\nu$  is the wavenumber (inverse of the wavelength,  $1/\lambda$ ),  $x$  is the optical path difference between the two interfering beams, and  $r$  and  $t$  represent the amplitude reflection and transmission coefficients of the beamsplitter, respectively. By definition, the emerging intensity  $F(x)$  is found by the multiplication of the amplitude  $A(x)$  with its complex conjugate  $A(x)^*$  yielding

$$F(x) = A(x)A(x)^* = 2RT + RT(e^{i2\pi\nu x} + e^{-i2\pi\nu x}) \quad (12.2)$$

where the beamsplitter reflection and transmission in intensity,  $R$  and  $T$  are given by  $(r \times r^*)$  and  $(t \times t^*)$ , respectively. The interferogram  $I(x)$  is defined as the modulated component of the above intensity where

$$I(x) = RT(e^{i2\pi\nu x} + e^{-i2\pi\nu x}) \quad (12.3)$$

and  $RT$  acts as the optical responsivity for this simplified design. Equation (12.3) represents the interferogram obtained from a monochromatic source passing through an ideal interferometer. When a polychromatic beam of spectral intensity  $S(\nu)$  (raw spectrum) propagates inside a Fourier transform (FT) interferometer, it generates an interferogram that can be represented by the continuous summation of individual modulations associated with each spectral element, i.e.

$$I(x) = \int_0^{\infty} S(\nu)(e^{i2\pi\nu x} + e^{-i2\pi\nu x}) d\nu \quad (12.4)$$

Using a mathematical workaround (it does not affect the physical representation) which consists in extending the domain of integration to include the negative values of  $\nu$  and assuming a symmetric spectrum such that  $S(-\nu) = S(\nu)$ , we find, after rearrangement, an interferogram expression more appropriate for processing. In this case and by application of the basic FT property, we have

$$I(x) = \int_{-\infty}^{\infty} S(\nu)e^{i2\pi\nu x} d\nu \quad (12.5)$$

$$S(v) = \int_{-\infty}^{\infty} I(x) e^{-i2\pi vx} dx \quad (12.6)$$

Equation (12.5) states that the interferogram generated by a Michelson interferometer is given by the inverse FT of the raw spectrum  $S(v)$ . Conversely, the raw spectrum  $S(v)$  is given by the FT of the interferogram (Eq. 12.6), which represents the foundational result of Fourier spectrometry.

### 12.2.3 Standard FTIR Spectrometer

The schematic of the instrument shown in Figure 12.1a corresponds to a standard single-input beam Michelson FTIR interferometer. For a real instrument of this type, the output signal is actually composed of radiation from different origins. An important part of this radiation comes from the external source,  $L$ , under study. The remaining contributions are generated by the instrument itself. This parasite radiation is due to gray body emissions and stray light reflections from the interferometer components (lenses, mirrors, inner walls, and others). It is referred to as the self-emission of the instrument. Figure 12.1a identifies the various sources of radiation intervening in a single measurement:  $L$  is the spectral radiance of the external source (target source),  $\mathbf{SE}_{in}$  and  $\mathbf{SE}_{out}$  represent the self-emissions (raw spectra) generated by the input and the output optics, respectively, and  $\mathbf{SE}_{BS}$  represents the beamsplitter self-emission (raw spectrum). In the IR, the self-emission terms mainly depend on the temperature of the intervening components. It is quite significant especially for an instrument operated at or near room temperature. Taken separately, each of these radiation sources generates a specific interferogram and, consequently, a corresponding raw spectrum. The sum of these individual raw spectra is given by

$$\mathbf{S} = (\mathbf{K} L) + \mathbf{SE}_{in} + \mathbf{SE}_{out} + \mathbf{SE}_{BS} \quad (12.7)$$

Equation (12.7) represents the usual way to link the complex raw spectrum  $\mathbf{S}$  to the target spectrum  $L$  (the one to be evaluated) taking into account the instrument characteristics which are the complex spectral responsivity  $\mathbf{K}$  and the complex spectral offset. The complex spectral offset of the instrument is a rather complicated expression involving the three different self-emission ( $\mathbf{SE}$ ) terms that are theoretically difficult to evaluate particularly for this type of instrument (single-beam). Usually, the self-emission terms are not stable in time due to thermal variations of instrument components. For this reason, the best way to acquire radiometrically accurate target spectra is by doing frequent calibration measurements. Ideally, this calibration is performed concurrently with each source measurement. The current method used for the accurate calibration (radiometric) of interferometric spectra is known as the two-temperature calibration method. In this method, two reference blackbodies of known radiances are required to solve the two unknowns, i.e. the spectral responsivity and the spectral offset of the instrument. Often for FTIR work in the long wave infrared (LWIR), the reference blackbodies are set to be close to the environmental temperature conditions; for instance, the hot reference blackbody is kept at a constant temperature near 60 °C, and the second one is at an ambient temperature near 20 °C.

The above discussion illustrates the usual attributes encountered with most standard FTIR instruments, i.e. the presence of variable and uncontrolled self-emissions, which necessitates three consecutive measurements (target and two references) for obtaining a single calibrated spectrum  $L$ . This represents a burden, especially for the real-time applications. In order to make the instrument more stable radiometrically and, consequently, more simple to calibrate, we have proposed to exploit and optimize certain attributes of the double-input beam interferometer design. As seen below, this type of interferometer is also suited for developing an FTIR spectrometer adapted for differential detection.

### 12.2.4 Double-Input Beam Interferometer

Among the few number of double-beam interferometers, the modified Michelson with corner-cube (CC) retroreflectors represents a relevant design from the point of view of its optimization for self-emission suppression.

Figure 12.1b and c give a schematic view of the double-beam Michelson interferometer. Note that both light sources  $L_1$  and  $L_2$  are actually installed in the same double-input-port interferometer. The use of two schematics (Figure 12.1b and c) is intended to simplify the ray tracing associated with each light source. The use of CC reflectors rather than standard flat plate mirrors has two main advantages for our application. First, the reflected beams from corner reflectors are offset laterally from the incident beams. This has the great advantage of decoupling input and output channels, as opposed to the standard single-beam interferometer where incident and reflected beams are superimposed. This attribute makes it possible to adjust independently the self-emission of each of the input ports without affecting in any way the output optics, which is not possible with the single-beam configuration. With this type of interferometer, the two beams from the two inputs are optically combined such that the two self-emission terms from each input port fully cancel out by optical subtraction, i.e. when the two self-emission terms are equal in intensity and  $180^\circ$  out of phase leading to a theoretically perfect cancellation.

The following equations serve to establish the expected attributes of the optimized instrument. A more complete analysis can be found in [1]. For an FTIR spectrometer based on a double-input port interferometer, the total signal  $\mathbf{S}$  represents the sum of two individual complex raw spectra,  $\mathbf{E}_1$  and  $\mathbf{E}_2$ , associated with each input. If input-1 and input-2 aim at target sources of radiance  $L_1$  and  $L_2$  (see Figure 12.1b and c), respectively, the resulting raw spectrum is given by

$$\mathbf{S} = \mathbf{E}_1 + \mathbf{E}_2 + \mathbf{SE}_{BS} \quad (12.8)$$

with

$$\mathbf{E}_1 = \mathbf{K}_1(L_1 + \mathbf{SE}_{in1}) \quad (12.9)$$

$$\mathbf{E}_2 = \mathbf{K}_2(L_2 + \mathbf{SE}_{in2}) \quad (12.10)$$

where  $\mathbf{K}_1$ ,  $\mathbf{K}_2$  and  $\mathbf{SE}_{in1}$ ,  $\mathbf{SE}_{in2}$  are defined as the responsivities and the self-emissions associated with input-1 and input-2, respectively, and  $\mathbf{SE}_{BS}$  represents the self-emission from the beamsplitter. The total self-emission contributions can be minimized to zero by the fulfillment of the three following conditions:

$$\text{Balanced responsivities : } \mathbf{K}_1 = \mathbf{K}_2(e^{i\pi}) = -\mathbf{K}_2 \quad (12.11)$$

$$\text{Balanced self-emissions : } \mathbf{SE}_{in1} = \mathbf{SE}_{in2} \quad (12.12)$$

$$\text{Beamsplitter transparency : } \mathbf{SE}_{BS} = 0 \quad (12.13)$$

By application of these three conditions, the resulting raw spectrum derived from Eqs. (12.8)–(12.10) reduces to

$$\mathbf{S} = \mathbf{K}_1(L_1 - L_2) \quad (12.14)$$

And, consequently, the differential radiance,  $L_1 - L_2$ , which represents the physical parameter of interest, is given by

$$\delta L = (L_1 - L_2) = \mathbf{S}/\mathbf{K}_1 \quad (12.15)$$

Equations (12.11)–(12.13) define in a mathematical sense the three conditions for an optimized FTIR spectrometer which does not contain any self-emission terms from the instrument itself. The resulting raw spectrum  $\mathbf{S}$  is directly proportional to the difference between the two source radiances  $L_1 - L_2$ .

### 12.2.5 CATSI Prototype

DRDC Valcartier has developed a passive FTIR sensor for the differential detection and identification of chemical vapor clouds at long standoff ranges [2]. The sensor is based on a double-input beam FTIR interferometer optimized for self-emission cancellation. This proof-of-concept sensor developed between 1995 and 2008 is referred to as the Compact Atmospheric Sounding Interferometer (CATSI). With this configuration, the two probed scenes

are optically combined onto a single detector resulting in a real-time optical subtraction. This yields a cloud vapor spectrum minimally perturbed by the background radiation. More precisely, the CATSI sensor consists of two identical 4-inch diameter Newtonian telescopes optically coupled to the dual-beam interferometer. Each telescope can be independently rotated to the selected scene. Figure 12.2a and b summarize the optical design and show the instrument mounted on a tripod.

An important design effort was done to optically balance the two input ports to achieve the optimization conditions (Eqs. 12.11 and 12.12). The CATSI system allows measurements of spectra according to the following specifications: scene fields of view (FOVs) from 4 to 11 mrad, spectral coverage from 3 to 18  $\mu\text{m}$ , and spectral resolution of  $1\text{ cm}^{-1}$  or greater. A double pendulum-scanning mechanism controls the periodic displacement of the two CC reflectors that generates the interferogram. The beamsplitter, which satisfies the third optimization condition (Eq. 12.13), consists of a thin air gap ( $\lambda/4$  at 7  $\mu\text{m}$ ) squeezed between two identical zinc selenide (ZnSe) plates having identical antireflection coatings on their external faces [1]. In practice, the beamsplitter assembly is made of two ZnSe plates separated by a thin circular ring made of hard material and having a thickness of approximately 2  $\mu\text{m}$ . For most of the work done in standoff chemical detection, the CATSI interferometer was optimized for the LWIR with a modulation efficiency (4RT) of 0.7 at 10  $\mu\text{m}$  and an mercury cadmium telluride (MCT) detector having a peak  $D^*$  of approximately  $4 \times 10^{10}$  Jones at 10  $\mu\text{m}$ . With this instrument, two scenes coming from adjacent FOVs are optically combined at the detector level yielding the spectral residual,  $\delta L$ , of the scenes. In its usual configuration of operation, the FOV of CATSI is set to 10 mrad and the angular tilt between the two FOVs is  $2^\circ$  (34.9 mrad). For instance, at a standoff range of 1 km, the distance between the two probed regions is 35 m and the diameter of the region is 10 m. Usually, this angular separation ( $2^\circ$ ) is sufficient to ensure that the gas cloud occupies partially only one FOV, the other being gas-free. However, in some field tests, we observed that the angular separation was too small to avoid cross contaminations, but the concentration variations induced by turbulence always yield a concentration differential that is easily detected by the differential detection with CATSI.

### 12.2.6 Target Gas Detection

In our approach, the passive remote monitoring of chemical vapors is based on the differential radiance equation (Eq. 12.15). Remote gas detection is performed from the optical subtraction of the radiance spectra received in each port (Figure 12.2c). The differential radiance is defined as the radiance of the scene containing the gas ( $L_{\text{gas}}$ ) minus the radiance of the adjacent same scene without the gas ( $L_{\text{clear}}$ ). With this condition, it can be verified [3] that for horizontal path scenarios and for a vapor cloud filling the entire FOV of the receiver, the differential radiance is simply given by

$$\delta L_{\text{calc}} = L_{\text{gas}} - L_{\text{clear}} = \Delta L_{\text{clear}} + (1 - \tau_{\text{gas}})(B_{\text{air}} - F_{\text{far}})\tau_{\text{near}} \quad (12.16)$$

Equation (12.16) gives the calculated differential radiance ( $\delta L_{\text{calc}}$ ) of a vapor cloud with a provision for handling a possible background variation ( $\Delta L_{\text{clear}}$ ) between the two adjacent scenes.  $\tau_{\text{near}}$  is the atmospheric transmittance between the gas and the sensor. The radiation source term ( $B_{\text{air}} - F_{\text{far}}$ ) represents the radiative contrast between the Planck radiance of the gas assumed to be at the same temperature as the air ( $B_{\text{air}}$ ) and the radiance of the background ( $F_{\text{far}}$ ). The term  $(1 - \tau_{\text{gas}})$  denotes the vapor cloud spectral emissivity where  $\tau_{\text{gas}}$  is defined by

$$\tau_{\text{gas}} = \exp[-\alpha(\nu)CL] \quad (12.17)$$

and  $\alpha(\nu)$  is the spectrally dependent absorption coefficient (1/ppm-m) of the compound obtained from a spectral library. The column density (CL), the parameter to be estimated, is given here in ppm-m. A general procedure of radiometric monitoring adapted for differential detection with a double-input beam FTIR interferometer was developed and tested. To exploit the attributes of this differential detection method, a processing algorithm called

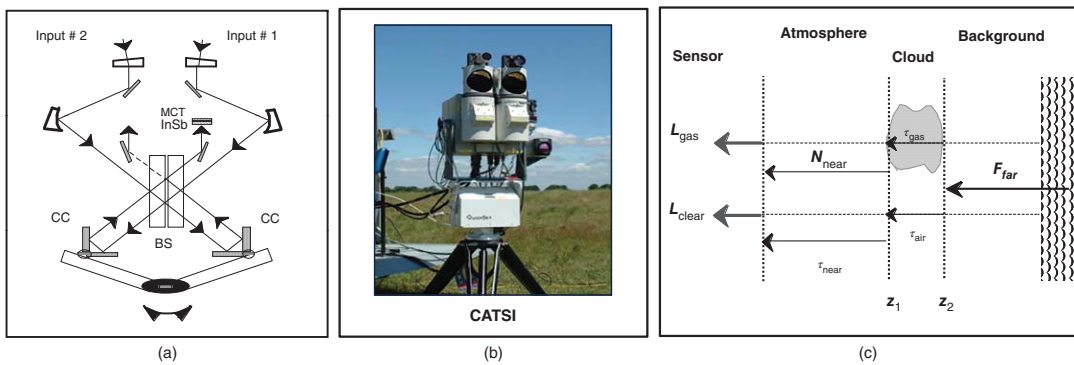


**Figure 12.2** Schematic of CATSI optical design (a) and a picture of the instrument mounted on a tripod (b). (c) Schematic diagram and related terminology defining the three-layer geometry for differential detection.

GASEM (Gaseous Emission Monitoring) was developed. GASEM was built to control the interferometer acquisition and to perform the online fitting that yields in real time the CL of the probed chemical target vapor [3]. The greatest advantage of this differential detection approach is to provide, in the field, a spectrally relatively clean signature of the remote chemical plume which facilitates its processing in real time. Figure 12.3 gives typical examples of the standoff detection and monitoring with the CATSI-GASEM capability. Figure 12.3a shows the measured and the GASEM best-fit spectra for a gas mixture of DMMP-SF<sub>6</sub> (dimethyl methylphosphonate–sulfur hexafluoride) released from a well-controlled stack situated at a distance of 1.5 km from the sensor. For this case, the best-fit spectrum was obtained using the CL reference estimates of 92 ppm-m for DMMP and 56 ppm-m for SF<sub>6</sub> as inputs for the GASEM model with  $T_{\text{FIT}}$  as the fitting parameter. In this case, the fitted plume temperature

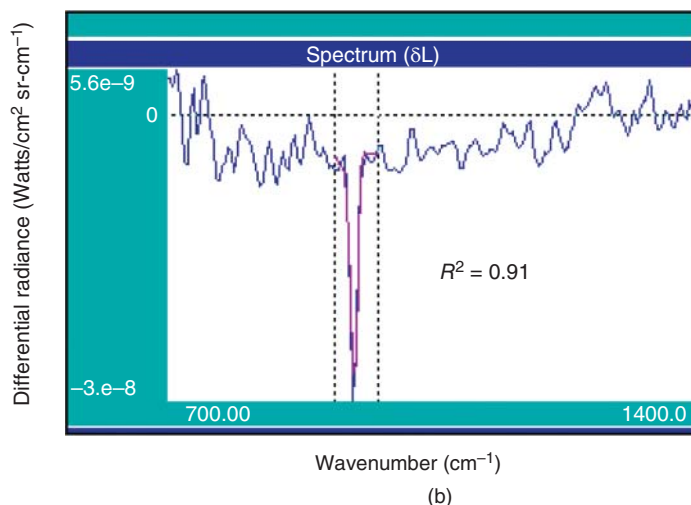
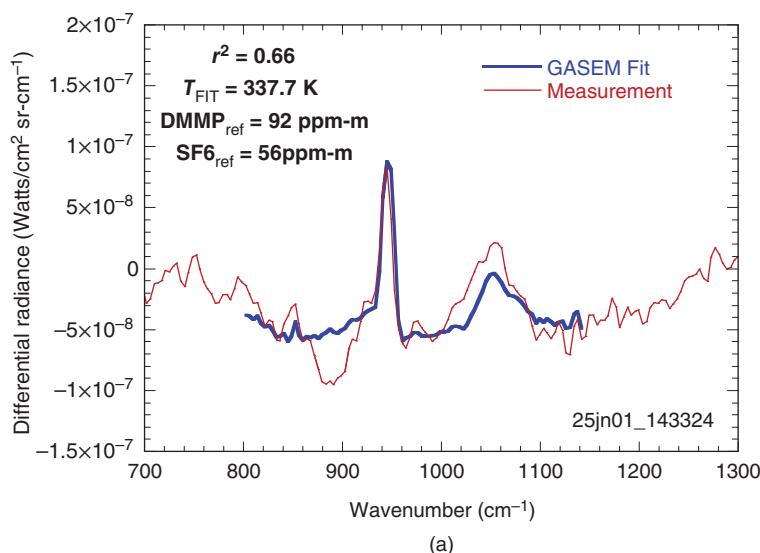


**Figure 12.3** Examples of monitoring results: (a) GASEM output showing the result of the best-fit DMMP-SF<sub>6</sub> spectrum (blue curve) with the measured differential radiance spectrum (red curve) at a standoff distance of 1.5 km; (b) GASEM result for the best-fit SF<sub>6</sub> spectrum (red curve) at a standoff distance of 5.7 km.

was determined to be 337.7 K (more details in ref. [3]). Figure 12.3b shows results for the standoff detection of SF<sub>6</sub> vapor released at a distance of 5.7 km from the CATSI sensor. For this case, the SF<sub>6</sub> was released from a tank connected to a 3 m aluminum pipe having a series of 5 mm holes linearly distributed along the pipe. The pipe

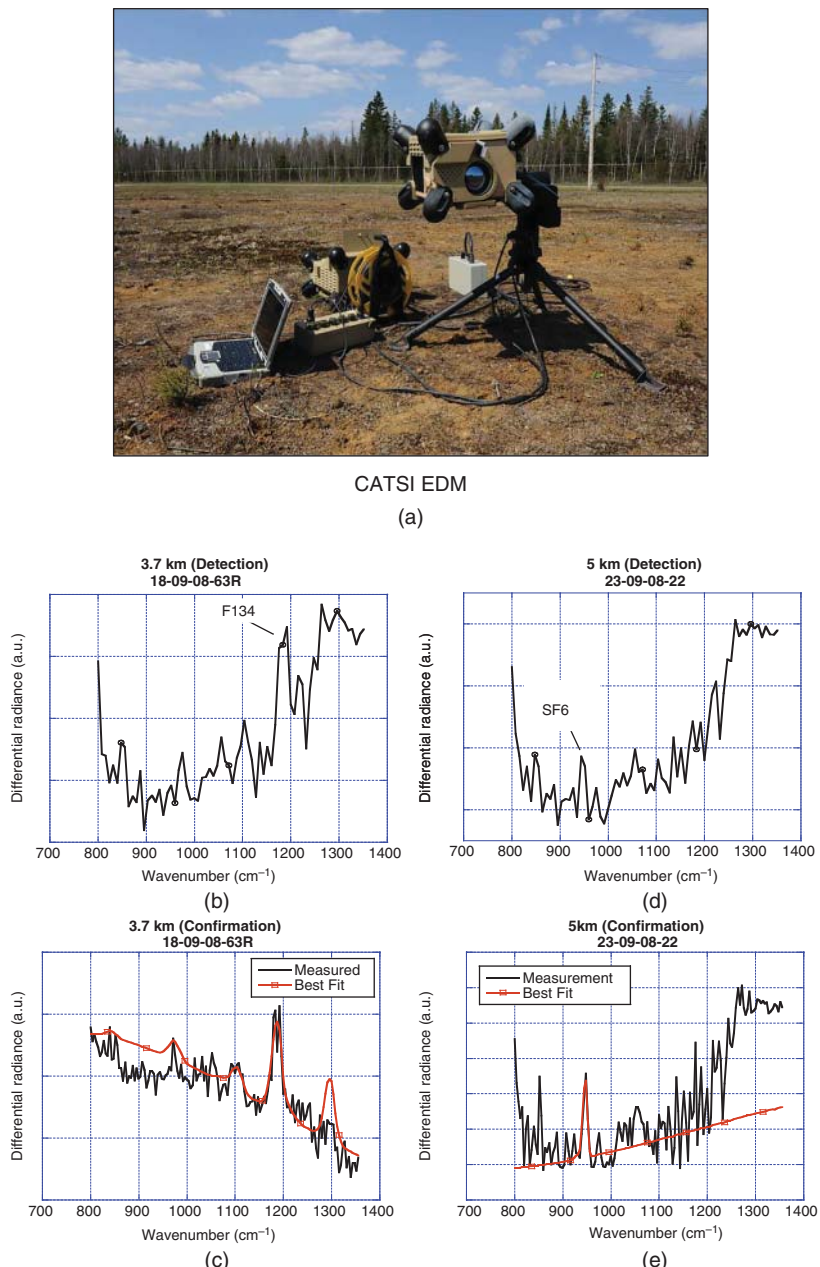


**Figure 12.4** (a) Picture of the CATSI EDM with its hardware; (b) Example of spectral radiance measurement at 3.7 km for a release of F134 recorded in the detection mode, and (c) in the confirmation mode; (d) Example of spectral radiance measurement at 5 km for a release of SF<sub>6</sub> recorded in the detection mode, and (e) in the confirmation mode.

was mounted vertically on the roof of the source-site building. The result of Figure 12.3b illustrates an example of the differential radiance measured (blue curve) with CATSI together with the GASEM best-fit calculation (red curve). In this case, the coefficient of determination ( $r^2$ ) between the measured and the best-fit spectra is better than 0.9 indicating a very good agreement between the measured and modeled SF<sub>6</sub> absorption bands. More results are available elsewhere [4, 5].

From 2004 to 2010, DRDC Valcartier also completed the development and validation of a ruggedized sensor for the detection and identification of gaseous CWAs and TICs. It is referred to as CATSI EDM (Compact Atmospheric Sounding Interferometer Engineering Model). The CATSI EDM sensor uses a well-balanced passive IR double-beam FTS with two adjacent FOVs to optically suppress the instrument self-emission and background spectrum [6]. As opposed to the original CATSI, the EDM uses only one telescope (see Figure 12.4a) to perform the differential sensing.

In this case, the two adjacent FOVs are defined by two fixed circular pupils located in the focal plane of the telescope which generate two scenes having an angular separation of 2° and where each scene (beam) is sent to its dedicated input port of the double beam interferometer. When combined with the Chemical Agent Spectral SIgnature Detection and Identification (CASSIDI, [6]) algorithm, CATSI EDM provides autonomous real-time detection and identification of CWAs and TICs at distances up to 5 km. CASSIDI performs three distinct functions: detection, confirmation, and alarm. Figure 12.4 presents results for two typical cases recorded during the performance field tests for standoff detection at 3.7 km (b, c) and at 5 km (d, e). In both cases, CATSI EDM autonomously detects, identifies, and alarms the actual target gas. Figure 12.4b shows the differential spectral radiance (resolution of 16 cm<sup>-1</sup>) recorded in the searching mode when the system detects the spectral signature of the target gas, F134 (1,1',2,2'-tetrafluoroethane). At this point, the gas location is recorded and the current searching pattern of the sensor is automatically changed to the confirmation mode. In the confirmation mode, the spectral resolution of the sensor is changed to 8 cm<sup>-1</sup> and the sensor concentrates its scanning and acquisitions to regions immediately surrounding the point of detection. This mode allows the collection of radiance spectra with sufficient signal-to-noise ratio (SNR) and spectral resolution to perform a spectral best fit that yields an estimate of the CL of the detected gas. This estimate is then used to make a decision to declare an alarm if the CL is above a reference threshold. Figure 12.4c presents the differential radiance measurement with the corresponding best fit obtained in the confirmation mode for the F134 gas. Figure 12.4d and e present the same type of results, but for the detection, confirmation, and alarm of SF<sub>6</sub> recorded during the 5 km segment of the performance field tests. In summary, over the 203 valid runs performed during the two weeks of field test evaluations, the CATSI EDM sensor successfully performed at both distances. In both cases, it exceeded the test performance requirement of a probability of detection of 80% with a 95% confidence level.

## 12.3 iCATSI Sensor

### 12.3.1 Background

The iCATSI (Figure 12.5a) is an adaptation from the ABB MRi imaging spectroradiometer that includes a symmetrical dual input–dual output optical system and an MCT photodiode linear array (16 by 1 pixel) [7–9]. As in the case for the original CATSI, the optimized configuration of iCATSI also exploits the optical subtraction capabilities of a double-beam Michelson interferometer, but with some major design improvements. iCATSI is a completely modular and configurable instrument where the input optics (reflective or refractive telescope), and the two detector modules (one per output) can be easily changed. The iCATSI was developed over the period from 2008 to 2010 and is still used as an R&D sensor today.

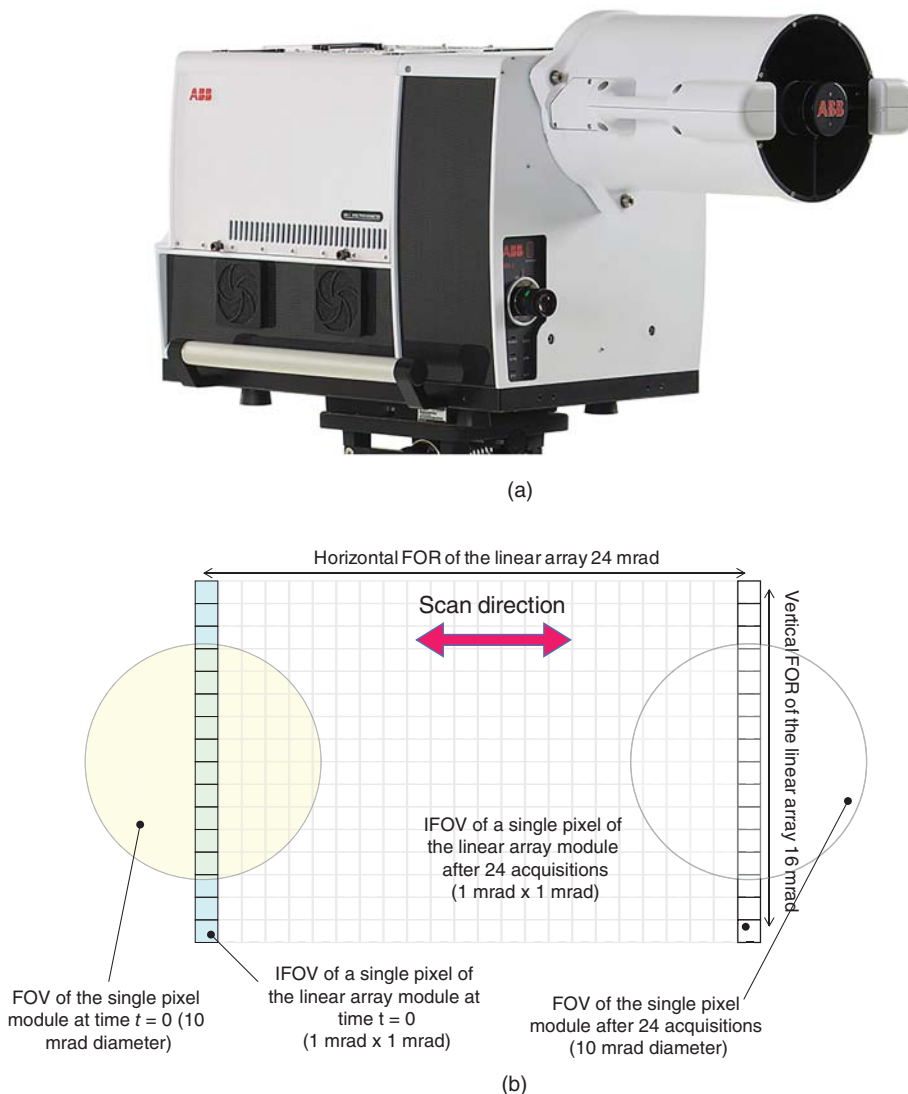


**Figure 12.5** Picture of the iCATSI sensor with both mono- and multipixel (right) detector and the scanning telescope (a). Field of regard (FOR) and field of view (FOV) of iCATSI and the scanning strategy (b).

### 12.3.2 System Configuration and Design

The iCATSI interferometer output ports are both configured to focus the beam onto their respective detectors. Stirling cycle coolers cool both detectors. The signals from the detectors are amplified and digitalized by electronics placed close to the detectors. The digital signals are then sent through the control electronics to the remote computer. There is a single telescope common to both input ports. At the output of the telescope, a reflecting prism splits the FOV of the scene into two parts. Each part feeds one input port of the interferometer. The angular separation between both input ports is set to two degrees. The spectrometer of the iCATSI is built around a double pendulum Michelson interferometer with CC reflectors [7–9]. Both CCs are mounted on the two tips of a V-shaped scan arm which rotates back and forth around a ZnSe beamsplitter. The motion of the scan arm is

monitored in real time by measuring the interference pattern of a helium-neon (He-Ne) laser that travels into the interferometer. The optical path difference (OPD) of the interferometer is approximately 1 cm. With this OPD, the highest spectral resolution achieved with a Boxcar-truncated spectral resolution (full width at half maximum [FWHM]) is approximately  $0.8 \text{ cm}^{-1}$  at  $8 \mu\text{m}$  and  $1.0 \text{ cm}^{-1}$  at  $3 \mu\text{m}$ .

The instrument is field deployable and can be considered as weatherproof. Thermal load, heat evacuation, and protection against the direct Sun and light rain are all implemented. The principal iCATSI configuration uses two MCT photodetectors, i.e. a monopixel detector with 10 mrad FOV and a 16-pixel linear array with 1 mrad/pixel FOV. The system generates a  $16 \times 24$  mrad field of regard (FOR) image of the scene using a scanning mechanism in the telescope [7–9]. Figure 12.5b summarizes the scanning strategy of iCATSI.

### 12.3.3 Results with the iCATSI

Detection tests were performed with iCATSI at a 500 m range. Initial tests were performed with a Freon-type refrigerant (F-152a) released from a laboratory fume hood. Figure 12.6 shows a sequence of screenshots recorded with iCATSI for the real-time detection and identification of the gas plume release. The colored pixels represent the detection score processed in real time with the gas detection algorithm of iCATSI. Six images are shown at various times over a period of one minute in which 50 l of gas were released. Each screenshot shows the visible image on which are superimposed two IR images (mosaic) resulting from the differential mode FOR of iCATSI. The system provides the same algorithm output for both FORs. Even with a low spatial resolution (1 mrad/pixel), the evolution and the release origin of the plume are easily identified. The color code goes from light blue to red where red shows the higher detection ratio. The iCATSI also has been validated against several other threats like acetone, methanol, and other TICs.

## 12.4 Active FTIR for Ground Contamination Detection

### 12.4.1 The Active iCATSI

The second application discussed in this chapter is the standoff detection, identification, and monitoring of ground contamination. The first responder and environment protection agencies need detection systems to rapidly find and segregate leaks and contaminated terrain for avoidance and decontamination purposes. In this respect, a detection system was proposed and built around an active compact FT interferometer. The system uses a graphite Globar heated to approximately  $1000^\circ\text{C}$  as an IR source to irradiate the interrogated surface. The system was optimized for the LWIR band ( $8\text{--}12 \mu\text{m}$ ) because many ground contaminants of interest have significant and discriminative signatures in this band.

### 12.4.2 System Configuration and Design

The system (Figure 12.7) was built with two optional configurations, one for active and the other for passive sensing. These two configurations are interchangeable by swapping the Globar source with the detector. For both configurations, the optical design is based on a Michelson double pendulum single-input and single-output port configuration with an optical velocity of 1 cm/s. The modulator provides a spectral resolution between 1 and  $32 \text{ cm}^{-1}$  (FWHM) over an optimized spectral range of  $8\text{--}13 \mu\text{m}$ .

The source illumination is optimized to produce a uniform illumination spot size of 10 cm at 5 m (20 mrad). The collection port has a slightly smaller spot size than the illumination at 5 m to avoid the collection of parasite radiation from the background. To maximize the overlap between the illumination and the collection spots, two 650 nm Picotronic laser diodes were installed on top of the telescope mount to help manually align the two beams. Finally,

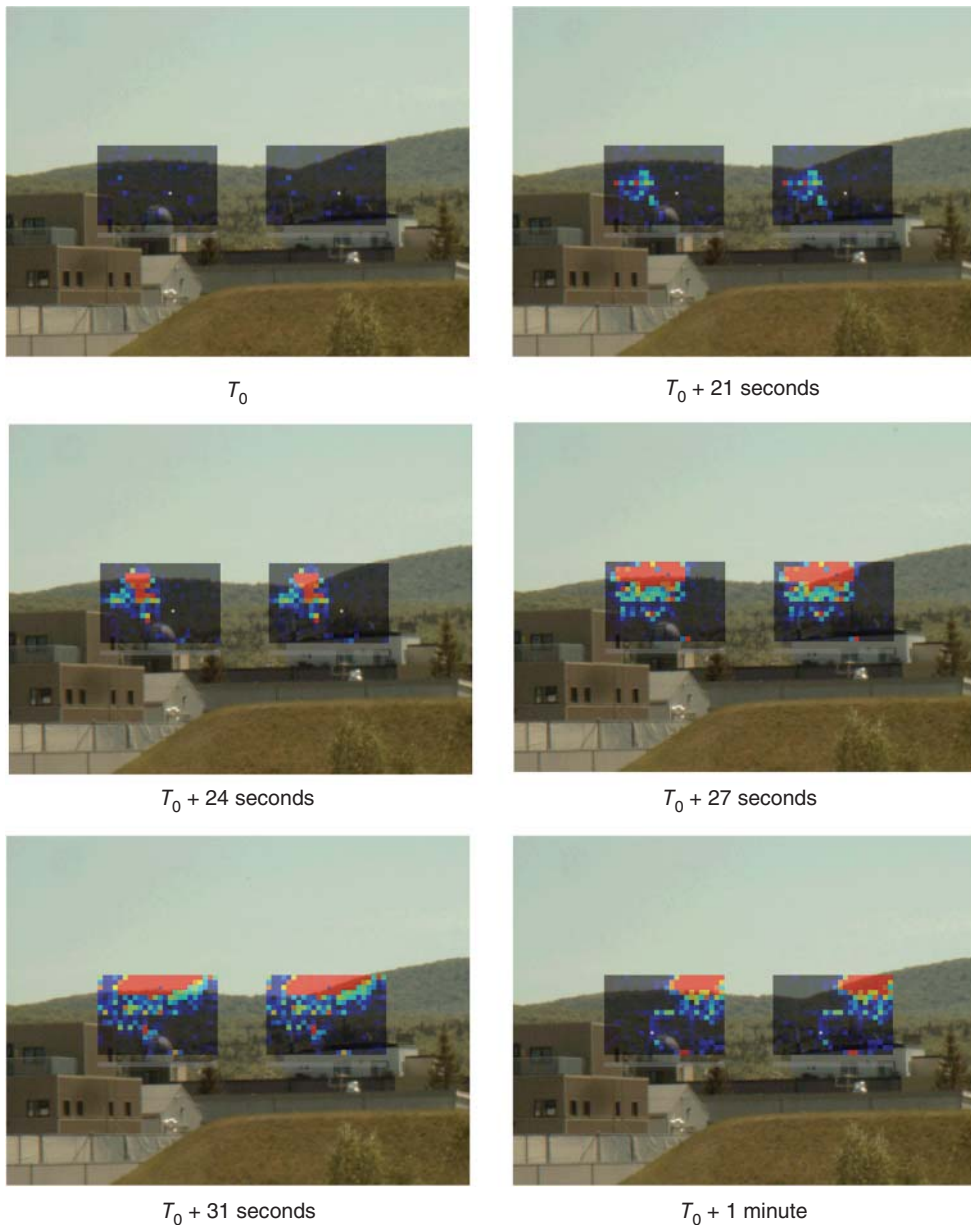


**Figure 12.6** Evolution of a Freon gas plume over a period of one minute measured with iCATSI.

the system can be battery-powered with an autonomy of a few hours when used with a commercial-off-the-shelf (COTS) battery belt.

The innovation behind the system is the use of a modulated source to reduce and filter the effect of the background radiation. In this system, the FTS itself modulates the source prior to irradiating the surface. With this strategy, the collected background radiation is not modulated yielding a direct-current (DC) level at the detector that is rejected by the fast Fourier transform (FFT). This results in a real-time subtraction of the natural/environmental background emission radiance.



**Figure 12.7** Picture of the active iCATSI from the front of the instrument.

### 12.4.3 Results with the Active iCATSI

Two main attributes can significantly affect the signal reflected from clean surfaces, i.e. the surface type and the surface reflection angle. As an example, Figures 12.8 and 12.9 show results for various surface types and the effect on the angle of incidence, respectively.

Comparison of the reflected signals from a Lambertian surface (Infragold), an aluminum mirror, a brushed aluminum panel, a piece of wood, and a piece of sandpaper demonstrate a large variability of reflected signal intensities. As expected, the brushed aluminum reflector and the aluminum mirror gave the highest reflected signal intensities, characterized by a fairly flat response between  $800$  and  $1400\text{ cm}^{-1}$ . The Lambertian surface shows a reflected intensity with the same spectral characteristics, but two orders of magnitude lower than the flat mirror result. The wood and the sandpaper have a signal reflectance one order of magnitude lower than the Infragold with some spectral features. These results demonstrate the difficulties and constraints that the surface type will generate for the detection and identification of ground contaminants.

Moreover, the reflected signal will be affected by the angle of incidence and the bidirectional reflectance distribution function (BRDF) of the surface. Figure 12.9 shows the signal reflected from two clean surfaces, Infragold and aluminum mirror, as a function of the angle of incidence relative to the surface normal. These measurements show that the angle of incidence on the Infragold surface is less critical than on a pure reflective surface: the reflection on Infragold is reduced by an order of magnitude from  $0$  to  $15^\circ$  relative to the surface normal while the reflection on a flat mirror is dramatically reduced by four orders of magnitude for only a one-degree tilt from the surface normal.

The above results show how sensitive the sensor could be to misalignment and how the detection sensitivity can be affected by the surface type and the angle of incidence.

Figure 12.10 shows detection results for the sensor (active configuration) located  $2\text{ m}$  away from a surface covered with SF96, a surrogate that acts as a liquid contaminant. The selected test surface is wood because it represents a difficult detection scenario due to its low reflectance. Figure 12.10 shows detection results of SF96 on wood at different concentrations ( $1\text{ ml}$  [ $0.0025\text{ ml/cm}^2$ ],  $5\text{ ml}$  [ $0.0125\text{ ml/cm}^2$ ], and  $10\text{ ml}$  [ $0.025\text{ ml/cm}^2$ ]) and angles of incidence ( $0$ – $15^\circ$  relative to surface normal). The results of Figure 12.10a can be understood based on the

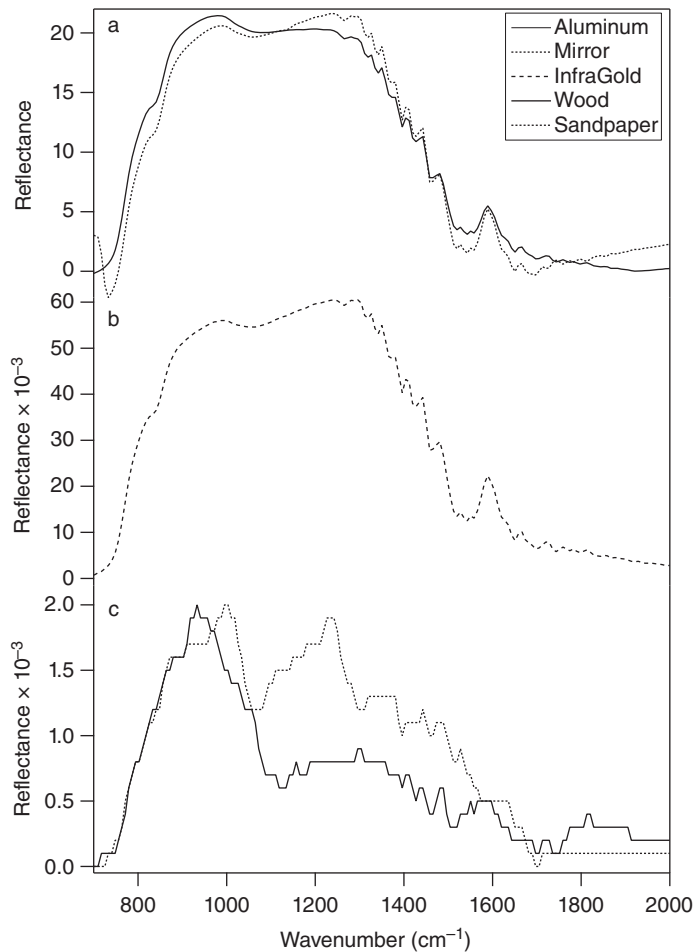


**Figure 12.8** Reflective signal as a function of surface type, aluminum plate, and mirror (a), Infragold (b), wood and sandpaper (c).

reflection phenomenology associated with rough surfaces, such as clean or covered plywood. The reflection from a rough surface can be divided into two main components, i.e. the specular reflection component which is parallel to the surface normal and the diffuse component scattered off normal. A large portion of the reflected beam is lost by scattering because the collection angle of the sensor is too small and only the specular component is detected. Overall, the intensity of the specular reflection component increases with the SF96 coverage because the effective surface (a mixture of SF96 and plywood) appears smoother yielding a larger specular reflection component. The system shows detection sensitivities down to 1 ml spread on a 20 × 20 cm<sup>2</sup> wood surface. Moreover, for Figure 12.10b, the system shows the detection of 0.025 ml/cm<sup>2</sup> of SF96 at an angle of incidence up to 15°. The SNR starts to become too low for detection around 15° and higher in this scenario.

In addition, DRDC Valcartier also developed a passive sensing technique for ground contamination using hyperspectral polarimetry. More information about this capability can be found in references [10, 11]. The system demonstrates a capability to detect and identify contamination on the ground and several surface types, such as metal, wood, and sandpaper at a standoff distance of up to 2 m. This technique could provide first responders with a new capability to identify and, hence, protect themselves against ground contamination.

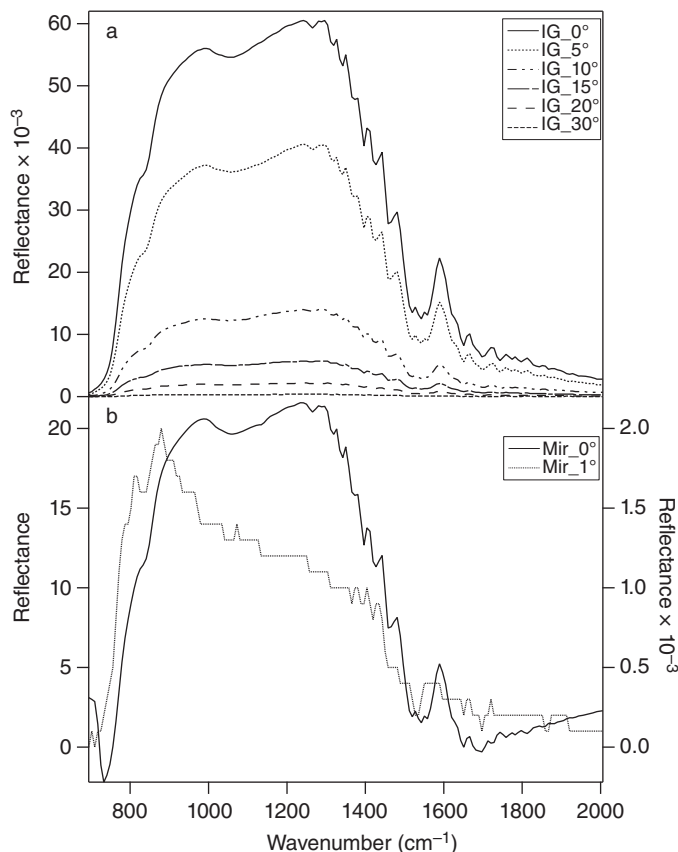


**Figure 12.9** Reflective signal collected at different angles on two different surfaces: Infragold (a) and mirror (b).

## 12.5 Signature Collection: Broadband Portable Field Spectral Reflectometer

### 12.5.1 Background

Diffuse spectral reflectance measurements in the field are a common and important endeavor in the areas of mineral and geological analysis [12], crops and agriculture characterization [13], and ground-truthing for spectral remote sensing applications [14], which includes the development of spectral libraries used in remote sensing exploitation algorithms. To carry out these measurements, field-deployable reflectometers have been used in the solar-reflective region (visible, near-infrared [NIR] and shortwave infrared [SWIR]) for more than 20 years. However, relatively few field-portable sensors exist for measuring reflectance in the emissive part of the spectrum that includes the longwave and midwave infrared (MWIR) regions (3–14 μm). Even fewer, if any, sensors exist that are capable of measuring reflectance across the entire IR spectrum from the NIR to the LWIR (0.7–14 μm). One such technology, a full spectrum reflectometer (FSR), has recently been fabricated by ABB to address the requirement of providing highly sensitive measurements of diffuse reflectance from 0.7 to 13.5 μm with a lightweight portable instrument, which is battery-powered and simple to operate in the field.

### 12.5.2 Design Overview

The FSR is based on a FTIR spectrometer design in which an IR source is collimated and sent through a Michelson interferometer. The optical path difference between the arms of the interferometer varies in time so that the beam

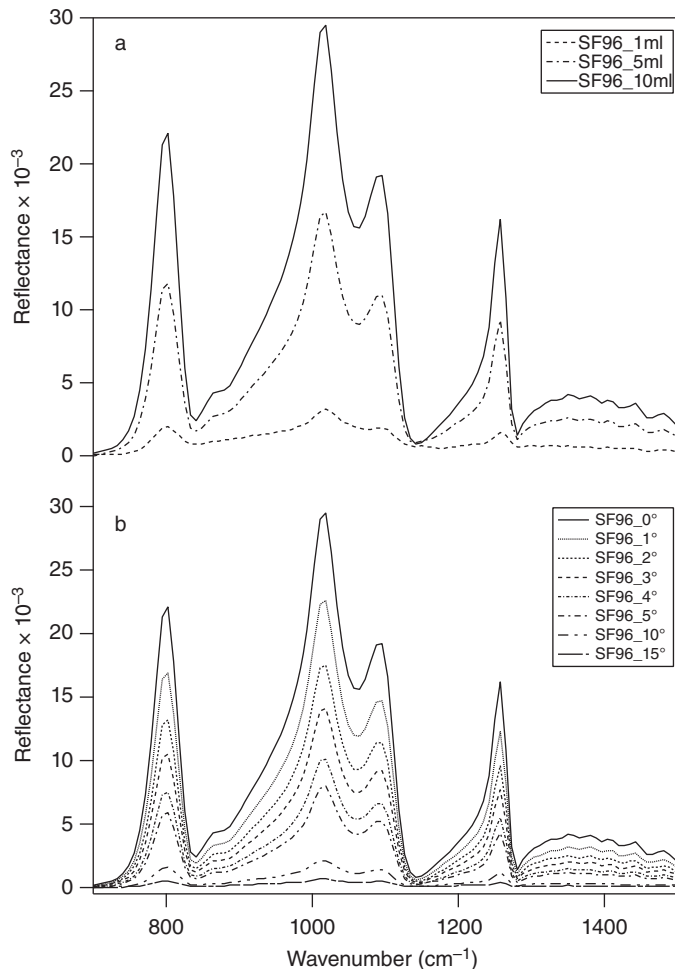


**Figure 12.10** Reflective signal with contamination of SF96 on wood at different concentration (a) and at different angle of incidence (b).

at the output of the interferometer has an amplitude that is modulated in time, as described in detail in Section 12.2.2. The modulated output radiation,  $I(x)$ , is then focused on a target consisting of a sample or appropriate reference material. The radiation,  $\rho I(x)$ , reflected by the target is collected and focused on to the detector, which measures it as an interferogram of the spectral radiance reflected by the target, as described by Eq. (12.5). The interferogram is subsequently converted to a spectrum,  $S(\nu)$ , by a FFT, as given by Eq. (12.6). The IR radiation,  $L_{\text{sample}}$ , emitted by the target does not contribute to the interferogram since it is not modulated by the interferometer. This process is shown by the schematic diagram in Figure 12.11.

The diffuse spectral reflectance,  $\rho(\nu)$ , is simply given by the ratio of the spectrum measured for the sample and reference targets:

$$\rho(\nu) = R_{\text{ref}} S(\nu)_{\text{sample}} / S(\nu)_{\text{reference}} \quad (12.18)$$

where  $R_{\text{ref}}$  is the absolute reflectance of the reference target that accounts for its spectral features. If required, the absolute reflectance of the reference material can be determined in principle using an independent technique

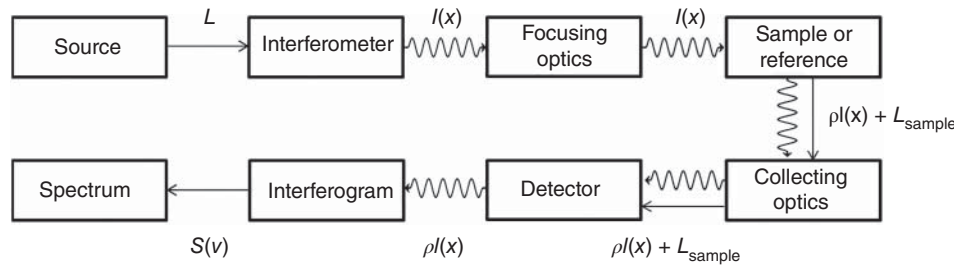


**Figure 12.11** Schematic diagram of the radiation flow in a broadband spectral reflectometer.

such as that offered by the National Institute of Standards and Technology (NIST), or a NIST-traceable calibration facility.

In practice, Infragold and Spectralon reference targets are used for the 2–13.5 and 0.7–3.3  $\mu\text{m}$  bands, respectively. Similarly, two IR sources are required to cover the large band; a silicon-carbide Globar for the 2–13.5  $\mu\text{m}$  region, and a quartz-tungsten-halogen lamp for the 0.7–3.3  $\mu\text{m}$  region. In addition, two detectors are required; a Stirling-cooled MCT detector for the 2–13.5  $\mu\text{m}$  region, and a thermoelectrically cooled indium-arsenide detector for the 0.7–3.3  $\mu\text{m}$  region, although there is a significant overlap of responsivity in the 2–3.3  $\mu\text{m}$  region.

The Michelson-type interferometer module is rugged and compact, measuring 6 cm  $\times$  12 cm  $\times$  14 cm and weighing less than 900 g, and incorporates CC reflectors in each arm of the interferometer. The modulated beam can be focused on the reflectometer's input port for a measurement of the sample target, or switched by a movable mirror to measure the internal reference targets. The radiation reflected by the sample and reference targets is collected at an angle that minimizes the specular reflection component.

The reflectometer is portable, weighing less than 13 kg, and can function on standard alternating current (AC) (110 or 220 V) or a low-voltage (9–36 V) battery that can last for up to three hours.

### 12.5.3 Main Operating and Performance Parameters

The main operating and performance parameters of the reflectometer are listed in Table 12.1.

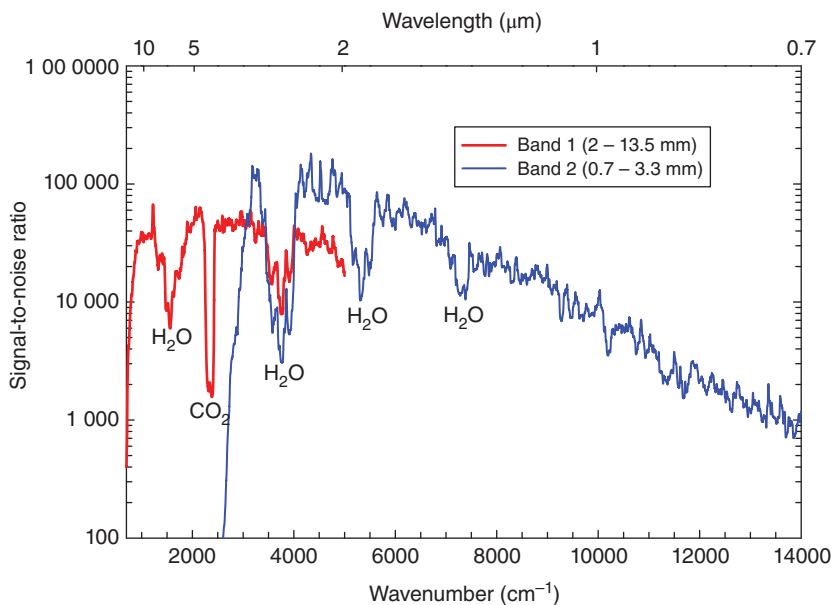
A measurement of the SNR for the two bands is shown in Figure 12.12. The measurement was obtained by averaging several individual spectra of the reference target (Infragold or Spectralon) and dividing the mean by the root-mean-square (RMS) noise of the measurements. An integration time of one minute was used at a spectral resolution of 16  $\text{cm}^{-1}$ .

### 12.5.4 Example Measurements Obtained with the Broadband Portable Field Spectral Reflectometer

The FSR has been deployed in the field on several occasions since its development in 2010. An example includes reflectance measurements of soil samples of the former distant-early-warning (DEW) radar site at Cape Dyer, Nunavut. The DEW line radar sites were created in the Canadian Arctic during the 1950s to provide the first line of protection during the Cold War [15]. Since 1990, the 21 sites were no longer required and the task of cleaning up the sites became an important environmental issue. The possible types of contamination that may be present on these sites include metals, paints, fuel, batteries, and electrical equipment. Due to the difficulty in accessing these very remote sites, one effective way to monitor the contamination could be with an airborne remote-sensing platform. To verify if the contamination could be characterized through measurements of the spectral reflectance, the FSR was deployed to one of the former radar sites (Dye-Main) located on Cape Dyer on the eastern coast of Baffin Island.

**Table 12.1** FSR operating parameters.

Characteristics	Values
Instrument type	Active reflectometer based on Michelson interferometer
Spectral resolution (cosine apodized)	4, 8, 16, and $32\text{ cm}^{-1}$
Spectral range	Band 1 : $740\text{--}5\,000\text{ cm}^{-1}$ ( $2\text{--}13.5\text{ }\mu\text{m}$ ) Band 2 : $3\,000\text{--}14\,000\text{ cm}^{-1}$ ( $0.7\text{--}3.3\text{ }\mu\text{m}$ )
Spectral instability	Less than 1% over 15 minutes
Diameter of the sensed spot	4 mm at 30 cm from the interferometer
Signal-to-noise ratio (when looking at the built-in references, at $16\text{ cm}^{-1}$ resolution setting, for one minute of observation time)	Band 1: >10 000 (see Figure 12.12) Band 2: >500 (see Figure 12.12)
Mass	12.25 kg (excluding batteries)
Dimensions	$30\text{ cm} \times 35\text{ cm} \times 43\text{ cm}$
Operating temperature	Tested from 0 to $35\text{ }^{\circ}\text{C}$

**Figure 12.12** SNR of the FSR for the  $2\text{--}13.5$  and  $0.7\text{--}3.3\text{ }\mu\text{m}$  bands. Absorption features associated with atmospheric water vapor and carbon dioxide within the instrument are present, as indicated in the graph (SNR measurements provided by ABB).

Some examples of reflectance measurements from areas contaminated with fuel and heavy metals are shown in Figures 12.13–12.15. Figure 12.13a shows a patch of ground, exposed for remediation, which smelled strongly of diesel fuel. The FSR was placed on the ground in various locations, as shown in Figure 12.13b, to obtain good-quality spectral reflectance measurements from  $0.7\text{--}13.5\text{ }\mu\text{m}$ , as shown in Figure 12.13c. Soil samples sent to the Royal Military College in Ottawa for chemical analysis were also measured with the FSR. Figure 12.14 shows

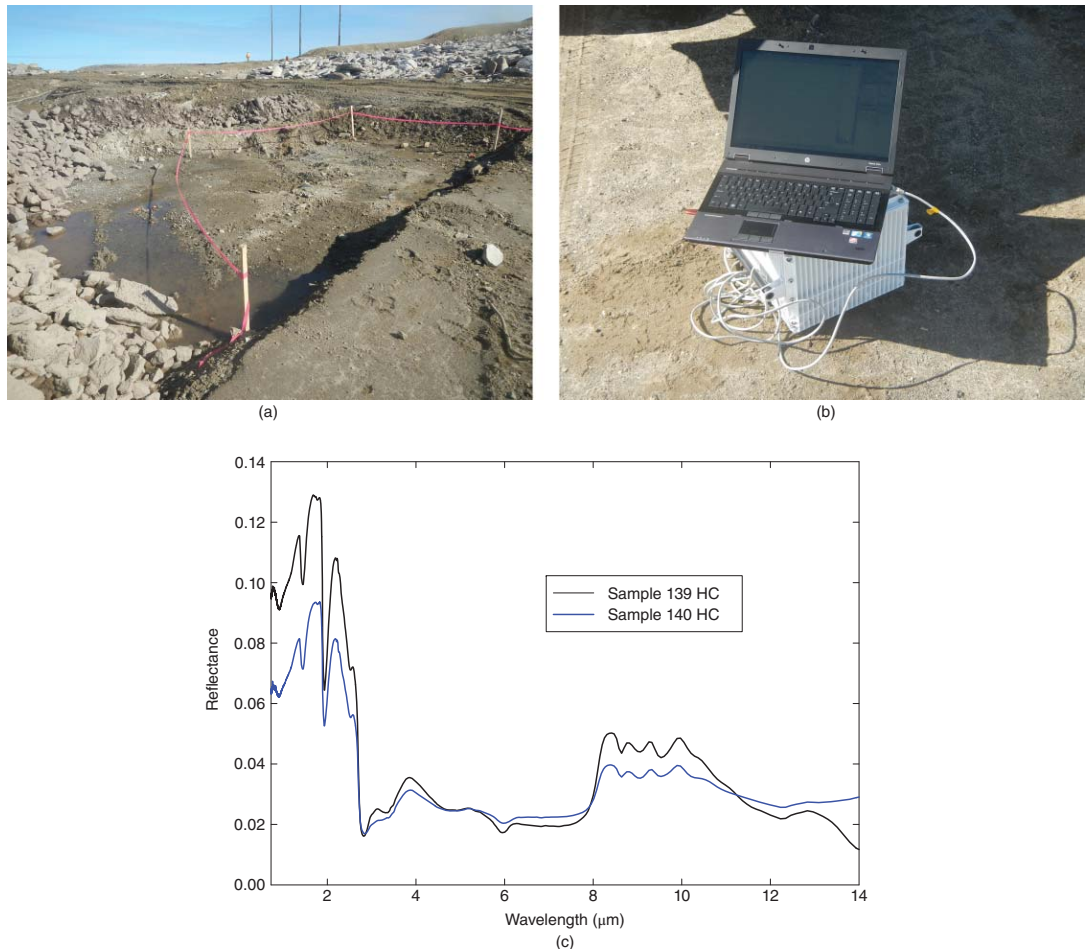


**Figure 12.13** (a) Region of Dye-Main contaminated with fuel (hydrocarbons). (b) FSR positioned to measure soil reflectance. A computer is connected to make use of full software capability. (c) Spectral reflectance measurements made with the FSR.

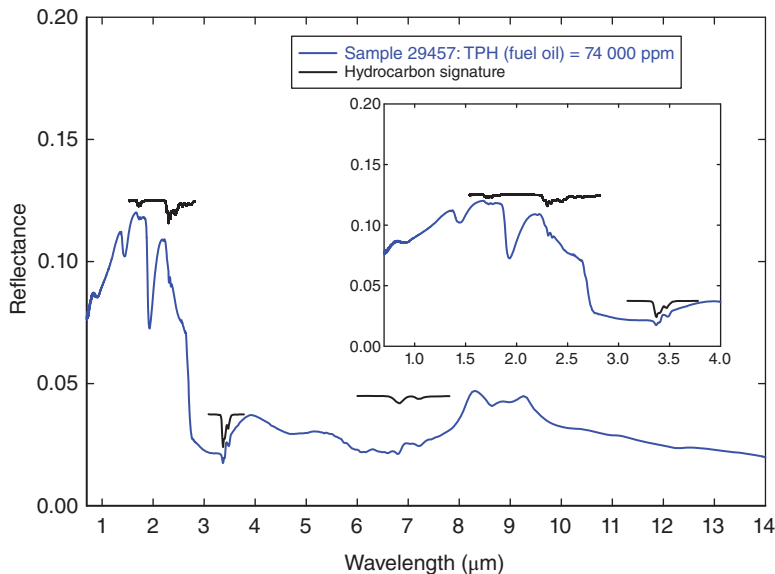


**Figure 12.14** Reflectance of the soil sample from Dye-Main containing a high concentration of hydrocarbon. The spectral features associated with hydrocarbons are observed in the spectrum displayed in the inset view expanded over the  $0.7\text{--}4\,\mu\text{m}$  region. The reference hydrocarbon absorption features (black line) are derived from a reflectance spectrum of diesel fuel.

examples of the reflectance results from one sample containing 74 000 ppm of hydrocarbons. The spectral features associated with hydrocarbons are observed in the spectrum at 1.7, 2.4, 3.3, and 7  $\mu\text{m}$ . Analysis of other soil samples showed that these features persisted for samples containing as little as 1000 ppm of hydrocarbons. Unfortunately, there were not any samples containing quantities of hydrocarbon in the 100 ppm range.

Figure 12.15a shows stains that were formed from the runoff from a pond that was contaminated with heavy metals from old equipment left on the site. Oxides of these metals formed from weathering processes may potentially be detected, thereby identifying the presence of the metal. The corresponding spectral measurements of these stains are shown in Figure 12.15b, which may be useful in identifying the contaminant.

## 12.6 Imaging Gas Filter Correlation Radiometry

### 12.6.1 Background

Gas Filter Correlation Radiometry (GFCR), a form of nondispersive IR spectrometry, has long been established as a simple, but efficient, means of detecting trace gas emissions, in terms of both sensitivity and selectivity levels. Taking advantage of the banded nature of gas-phase IR spectra, it is well-adapted to measuring target gas concentration in the section of the atmosphere located within the line of sight of an instrument focused on a given light source [16–18].

GFCR is an attractive technique for sensing applications. It combines the attributes of optical and mechanical simplicity, allowing the use of small, robust, low-powered and lightweight instruments with no moving parts, for improved durability and resistance to vibrations. GFCR detects target gases by using a bandpass filter to isolate measurements to a unique resonance band and comparing this with a gas cell that correlates to all of the absorption lines of a specific molecule within that band (Figure 12.16). The measured SNR is enhanced by the effect of the combined high spectral resolution (resolving power  $\lambda/\Delta\lambda > 20\,000$ ) and increased sensitivity due to the large

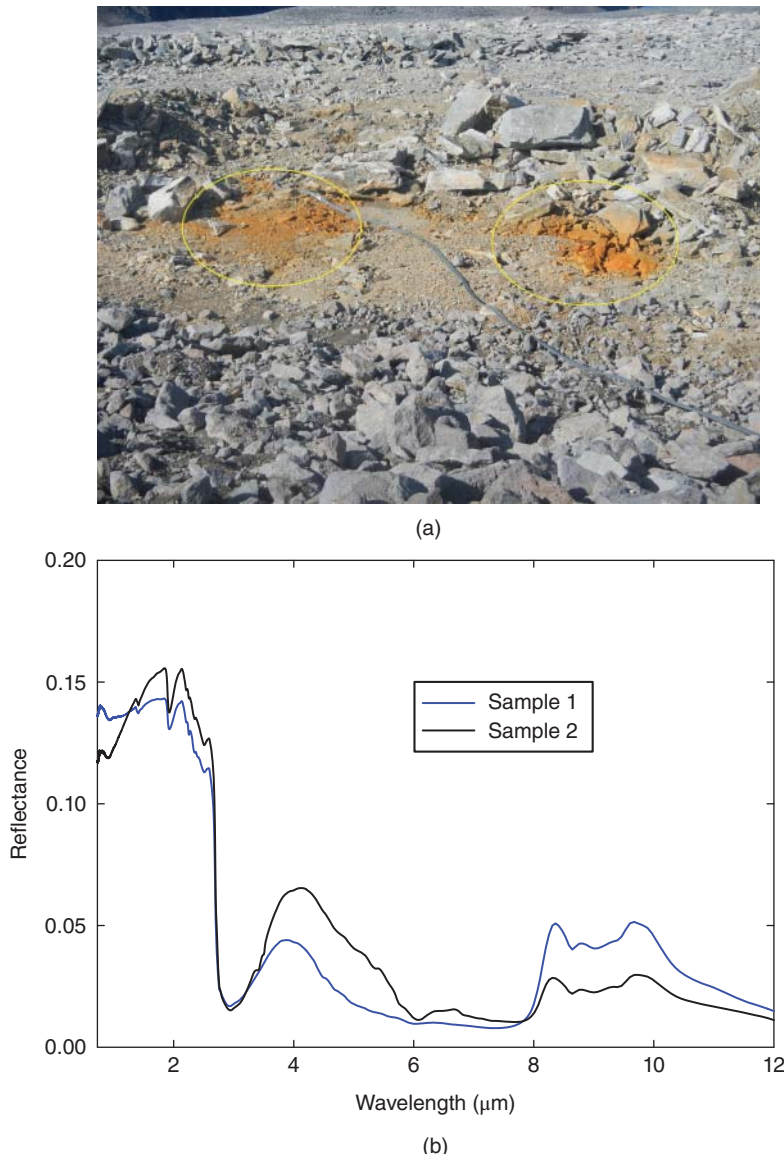


**Figure 12.15** (a) Region of Dye-Main contaminated with heavy metals (stains encircled). (b) Spectral reflectance measurements of the stains made with the FSR may be useful in identifying the associated metal oxide.

optical throughput. The resulting enhancements in target gas selectivity and high rejection of contaminant gases and interferences compares favorably with conventional radiometers. Moreover, since recording, reconstruction and analysis of spectral information are done by optical correlation, the SNR is greatly improved and data analysis simplified; the electrical signal recorded at the focal plane arrays (FPAs) level is already proportional to the CL of the target gas in the FOV.

Figure 12.17 illustrates the gas correlation measurement principle, well-adapted to detect trace gas leaks from portable platforms.

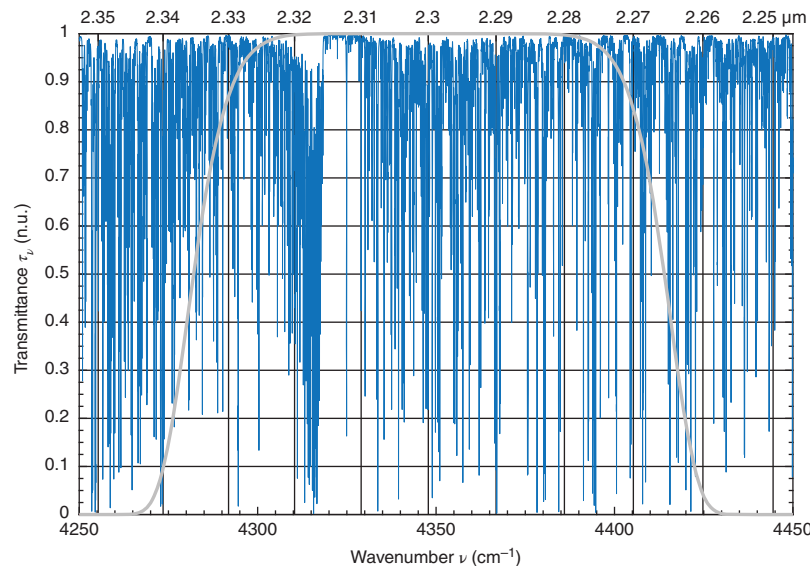


**Figure 12.16** Methane lines ( $\approx 20\,000$ ) within the bandpass at  $2.3\,\mu\text{m}$ .

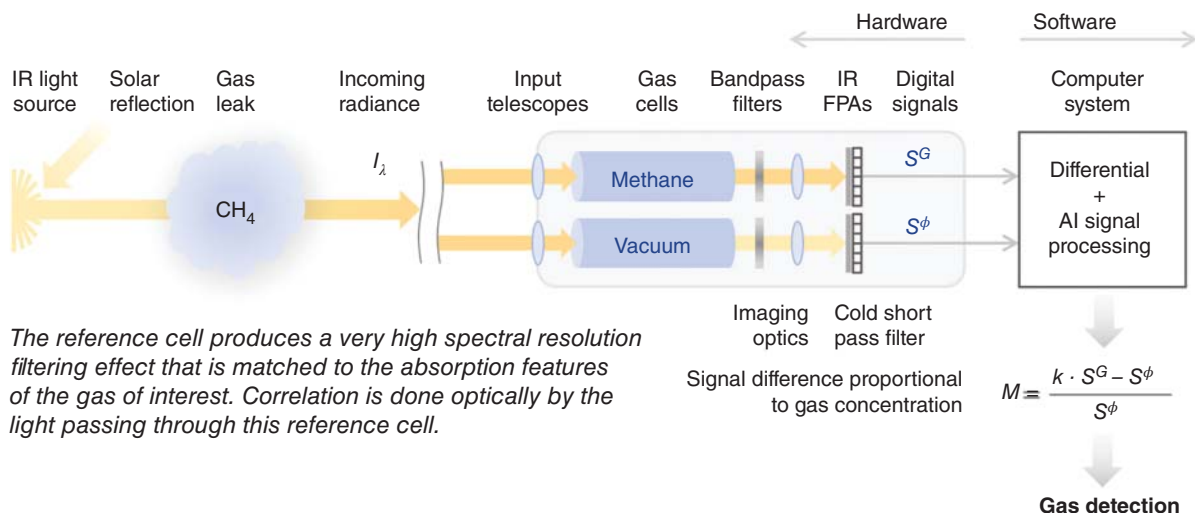


**Figure 12.17** Gas Filter Correlation Radiometry (GFCR) general operation concept (imaging synchronized views' implementation).

Using an advanced GFCR-imaging version, Bluefield's sensor identifies gases, visualizes quantity distribution over terrain maps and estimates concentrations in two-dimensional images. Its synchronized-view imaging system can locate and quantify specific emitters to an unprecedented sensitivity level and spatial resolution.

The synchronized view implementation (where the two FPA image acquisitions are triggered simultaneously) allows the readings to be correlated temporally *and* spatially, where every snapshot contains the complete spectral content for every scene location, making the GFCR differential image proportional to the absorption of the target gas only, nulling correlated noise (to first order) in the two images. This eliminates problems induced by scanning or modulation techniques, minimizing influence by geospatial variations in the background surface albedo or any other variations in the scattering characteristics.

## 12.6.2 Advanced Image Analysis and Artificial Intelligence Techniques

To fully leverage the GFCR method and attain unprecedented sensitivity levels, Bluefield created and implemented innovative techniques. Original GFCR systems used the analog electrical difference at the electronic amplifiers level on single-pixel detectors. Only recently has the system been digitalized with straightforward computer image analysis of recorded 2D frames captured with a small number of pixels.

Bluefield brings this to the next level. Its cutting-edge technology employs massive oversampling and a full range of advanced image processing and signal analysis tools, complemented by machine learning (ML) and artificial intelligence-based data-mining techniques. This approach makes the most out of every recorded photon to achieve unprecedented detection levels. This results in the automated processing of large amounts of high frame rate recorded data from the platform (similar to the space sensor presented in Section 12.6.5).

## 12.6.3 Experimental Prototypes (Ground, Helicopter, and Balloon)

Bluefield's prototype sensor is a first-generation, advanced GFCR instrument, and field-portable, built using a broadband MWIR detector. This configuration was chosen to detect gases in the SWIR ( $\text{CH}_4$  @  $2.3\ \mu\text{m}$ ) as well as in the MWIR regions ( $\text{CH}_4$  @  $3.4\ \mu\text{m}$  and  $\text{SO}_2$  @  $4.0\ \mu\text{m}$ ), which was successfully demonstrated in the field. However, this broadband configuration increases detrimental self-emission effects. Further, if using a single-gas configuration with a fixed cold filter at the Dewar level optimizes performance, it also limits operation to a single gas (as chosen for a mission-specific detection shown in Section 12.6.5).

Figure 12.18 shows the compact prototype sensor configured with methane and nitrogen (acting as the empty channel) closed cells during an outdoor field campaign. This was built by Bluefield with support from NovaSyst/AIWorx (now Bentley Systems) and Opto-Mécanique de Précision (OMP).

As discussed with GFCR, correlation is directly done at the optical level. Even if the subsequent different calibrations and advanced gas-detection algorithms to be applied are complex, they are not computationally heavy compared with FFT analysis associated with classical FTIR spectrometers. Currently, the prototype sensor operates at a frame rate enabling 30–50 ms computation time per frame, allowing both real-time processing and gas plume display. Additional sensor details are presented in Table 12.2.



**Figure 12.18** Bluefield's prototype sensor operating from a helicopter. Source: Bluefield Technologies Inc.

**Table 12.2** Bluefield's prototype sensor configuration.

Parameter	Values	Comments
Wavelength range (@ 50%)	$\approx 2.5\text{--}5.5\text{ }\mu\text{m}$	Broadband integrated Dewar and cooler assemblies covering both SWIR and MWIR
Detector array size and pitch	$640 \times 512, 15\text{ }\mu\text{m}$	MCT (HgCdTe), cryo-cooled to 90 K
Dark current density	$1.5\text{ nA/cm}^2$	Not a dominant noise source at short exposure time
Gas cells' length and pressure	10 cm, 760 Torr	Sealed $\text{CH}_4$ SWIR; refillable for other gases
Aperture diameter and FOV	35 mm, $11^\circ \times 8.8^\circ$	Stingray SR0955 broadband, 50 mm focal length
Instantaneous FOV (IFOV)	0.3 mrad	<Optical resolution
Spectral resolution	N/A ("infinite")	GFCR instrument uses all spectral lines in optical passband at native resolution (undigitized analog mode)
Temporal measurements per acquisition and frame rate	10–20 ms, $\leq 100$ fps	Depends on scene illumination conditions (background reflectance, cloud cover, Sun angle, etc.)
Digital data interface	Camera link, 14 bits	Through a single USB-3 connection to the laptop computer
Operation modes	Solar reflected <i>and</i> thermal (absorption and transmission)	
Operational distances	15 m–1000+ m	FOV = $1.9\text{ m} \times 1.5\text{ m}$ @ 10 m; FOV = $193\text{ m} \times 154\text{ m}$ @ 1000 m

#### 12.6.4 Laboratory Demonstration and Field Testing

Extensive experimental testing campaigns were performed at DRDC laboratories and outdoor test sites to study and demonstrate the prototype's ability to detect  $\text{CH}_4$  and  $\text{SO}_2$  under solar reflected and thermal modes with blackbodies in the background, as shown in Figure 12.19.

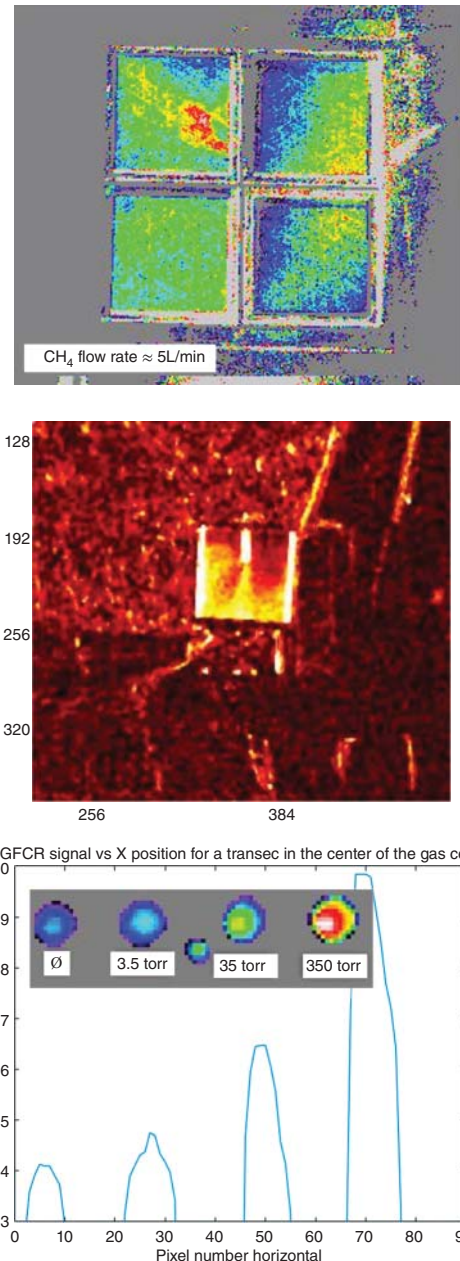
Controlled-release experiments were also performed during April 2019 at the Stoneham fire station, a secure facility located north of Québec City, Canada. Bluefield collaborated with an independent party, Flux Lab [19], to validate the results. Blind-test scenarios were used to evaluate the Bluefield technology detection capacity to transient methane plumes in realistic weather conditions and to determine the system's sensitivity when exposed to different methane flow rates. The prototype sensor threshold detection limit was evaluated at 0.1 kg/h (2 l/min) when measured horizontally on the ground at a 15 m distance, as shown in Figure 12.20. Blind tests from a helicopter showed a capacity to detect the presence of methane gas at release flow rates of 0.6 kg/h (14 l/min) at 100 m altitude, at wind speeds of about 16 km/h (10 mph) and varying amounts of sunlight and suboptimal cloud conditions. The sensor detected methane released at a flow rate of 12 kg/h from an altitude of more than 1.1 km (3000 ft) with similar wind speed levels.

To prepare for space flight and evaluate key components of the instrument (e.g. camera registration and gas cell behavior under low pressure and temperature environments), two high-altitude balloon tests were performed by Bluefield during summer 2019 to evaluate key components of the instrument (e.g. camera registration and gas cell behavior under low pressure and temperature environments). A "selfie" of the experiment can be seen in the bottom image of Figure 12.21.

#### 12.6.5 Space Mission

Prior NASA missions, starting in the 1970s, validated the GFCR approach, including the Halogen Occultation Experiment (HALOE) [20] on the Upper Atmosphere Research Satellite (UARS) and the MOPITT instrument [21] on the *Terra* spacecraft. The development of microsatellites makes  $\text{CH}_4$  monitoring from space affordable.

**Figure 12.19** Thermal mode CH<sub>4</sub> plume detection (top,  $L = 12$  m) and SO<sub>2</sub> plume flow visualization (middle and bottom,  $L = 10$  m) (SO<sub>2</sub> sensitivity of 110 ppm-m from the 10 cm 0.5 Torr cell). Source: Bluefield Technologies Inc.



Bluefield is developing a space-grade version of its sensor to fit into compact 20 kg microsatellites for monitoring CH<sub>4</sub> from low Earth orbit at 530 km altitude (Figure 12.22). The orbit will be Sun-synchronous with a local nodal crossing time of noon  $\pm 90$  minutes (optimized for Sun illumination and cold radiator orientation). Each satellite will carry and point sensors capable of detecting methane ground leaks at a fine spatial resolution of 20 m  $\times$  20 m (for more information see [22]). Satellites will measure nadir along the orbital track with a 13 km  $\times$  11 km FOV. An off-nadir pointing capacity of a  $\pm 25^\circ$  angle with a 500 km FOR allows additional coverage and increased capacity for cloud avoidance.

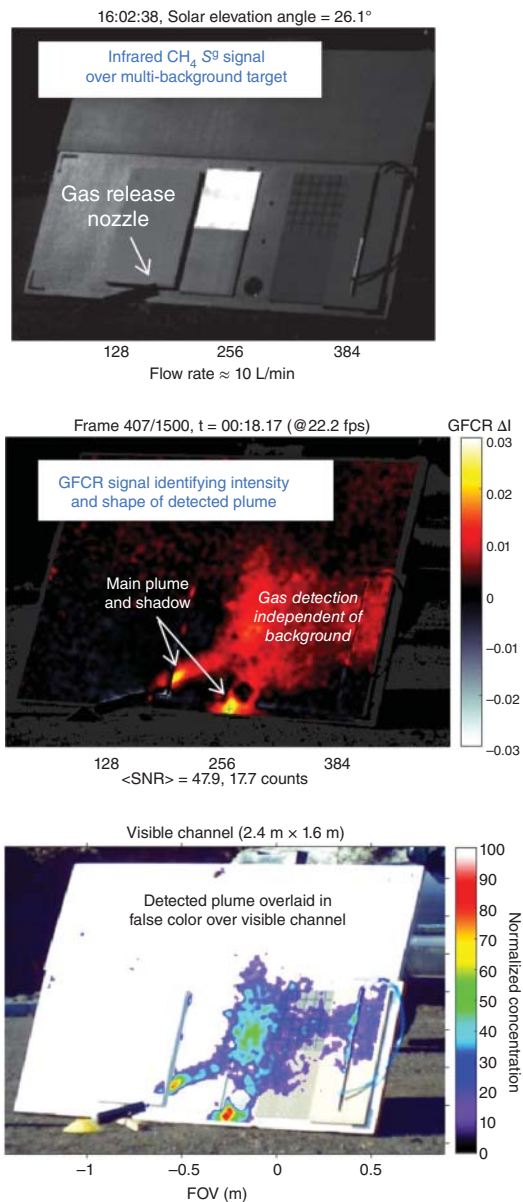


**Figure 12.20** Sun-reflected mode example of CH<sub>4</sub> plume detection ( $L = 15$  m) over a multialbedo background. Source: Bluefield Technologies Inc.

Maps of surface methane plumes (through column-averaged dry-air mixing ratios of CH<sub>4</sub>) will be produced by measuring solar backscattered radiation in the SWIR over the whole globe.

The CH<sub>4</sub> passband at 2.3 μm was also chosen because it delivers excellent sensitivity to atmospheric methane (factor 3–5 stronger absorption compared with 1.6 μm), and, therefore, shorter cells can be used. Further, this wavelength is nearly immune to interference from water and N<sub>2</sub>O contamination, as well as to changing Earth albedo, essential conditions for plume signature identification using GFCR back-reflected sunlight. Moreover, at 2.3 μm, the thermal emission components are at least three orders of magnitude less than the reflected solar signal, and the scattered downwelling radiation is relatively negligible, allowing quality illumination at low Sun angles and moderate cloud cover.

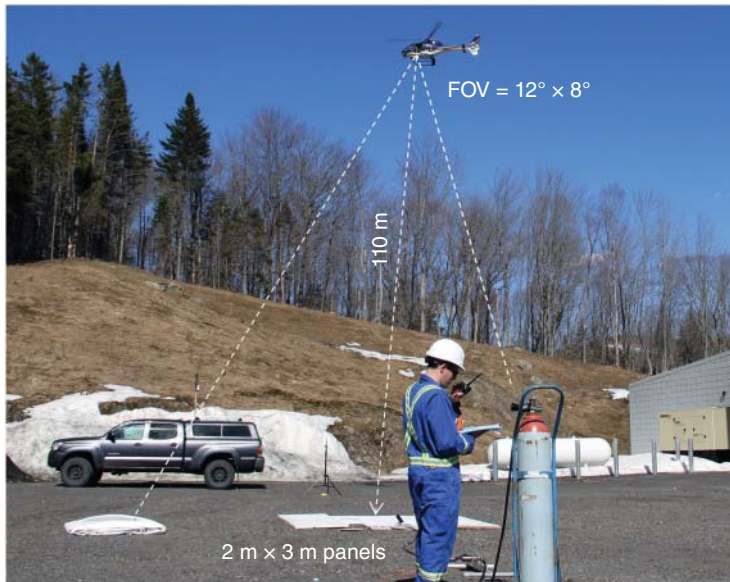


**Figure 12.21** Bluefield's prototype sensor helicopter flight test campaigns (top) and Bluefield test instrument during high-altitude balloon ascent (bottom). *Source:* Bluefield Technologies Inc.

In addition, while imaging spectrometers traditionally use a “whiskbroom” (with a point detector) or a “push-broom” (with a linear detector array) observation method to generate images as they progressively move along, limiting photon throughput, Bluefield’s sensor makes it straightforward to implement a spectral imaging method using FPAs, by operating in a “push-frame” observation mode, as shown in Figure 12.23 [23, 24]. In such a staring imaging mode, no FPA dimension is sacrificed to spectra creation (unlike standard diffractive or interferometric methods).

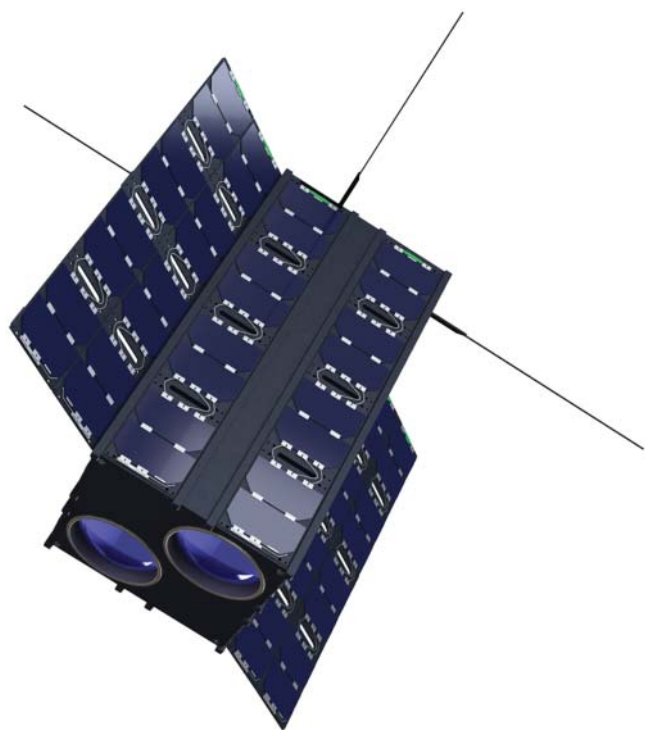


**Figure 12.22** Bluefield microsat early design.

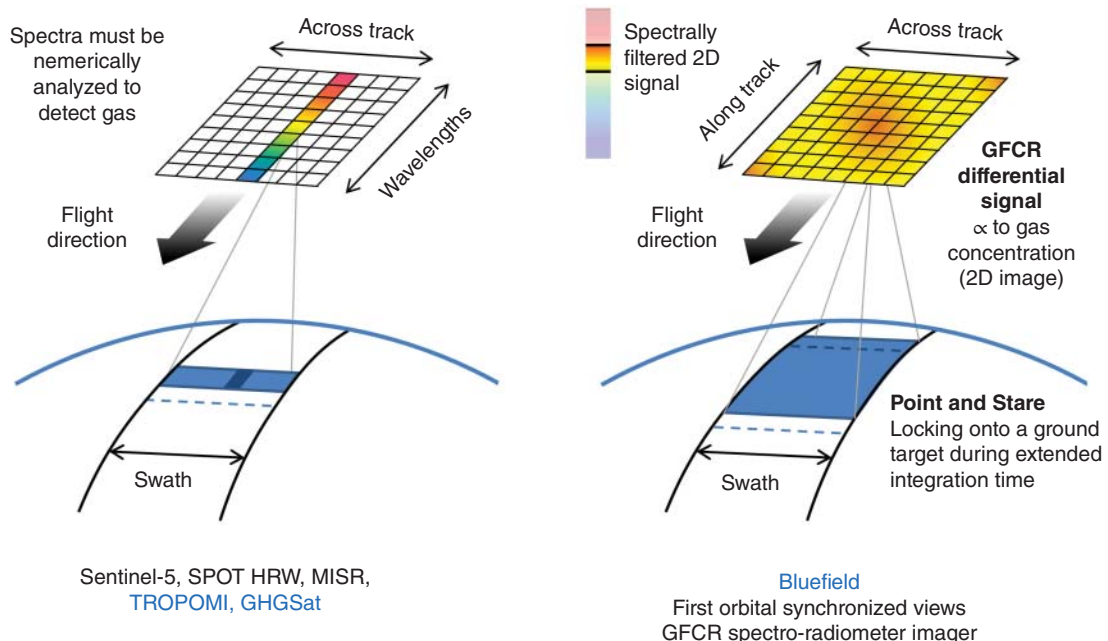


**Figure 12.23** Push-broom (left) and push-frame (right) observation methods.

Finally, to achieve unprecedented levels of stability and accuracy and limit system complexity by the addition of a pointing mirror mechanism, an Attitude Determination and Control Subsystem (ADCS) is used to perform lock-on-and-stare maneuvers for about 5–10 s on each ground target as it passes within their FOV.

Based on laboratory tests and data modeling, Bluefield satellites will detect methane at concentrations of <0.5% natural abundance (100 ppm-m integrated concentration threshold, or 65 kg/m<sup>2</sup>), corresponding to leak flow rates below ≈75 kg/h (3σ). Such a detection level achieves main point emission sources detection under the 2016 EPA Greenhouse Gas Reporting Program which contribute to >92% of total US point source emissions.

The goal of this satellite deployment is to ensure the levels of accuracy and precision required to address GHG inventories. This is achieved through adequate spatial and temporal resolutions and the coverage needed to track weak anthropogenic individual point sources, which tend to be relatively small and spatially clustered (e.g. oil and natural gas operations, livestock operations, landfills, coal mine vents, etc.).

## 12.7 Conclusion

In the last 20 years, DRDC Valcartier has developed a standoff differential detection method that exploits the attributes of dual-input beam interferometer systems for background and instrument self-emission suppressions. The greatest advantage of this approach is to provide, in the field, a spectrally clean signature of the remote chemical plume, which facilitates its processing in real time. The original CATSI and its subsequent militarized version (CATSI EDM) have clearly demonstrated the capability of the differential radiometric approach for the detection and identification of chemical vapor clouds located at large standoff distances. More recently, the CATSI family technology has expanded to include imaging capabilities for gas mapping (iCATSI) and a compact portable version for active sensing (AC-iCATSI).

A broadband portable field spectral reflectometer has also recently been developed for making contact surface measurements using active sources. The instrument is sensitive over the 0.7–13.5 μm region and permits the acquisition of signatures in the field to properly consider the chemical mixing and morphology of the surfaces encountered.

GFCR is another remote-sensing technique well-adapted for measuring trace gases on compact and portable instruments, outperforming classic spectrometers that cannot reach the required size to be practically implemented in a small platform without substantial performance loss. In that case, the GFCR technique is particularly well-adapted to reveal tenuous amounts of a selected target gas.

## References

- 1 Thériault, J.-M. (1999). Modeling the responsivity and self-emission of a double-beam Fourier-transform infrared interferometer. *Applied Optics* 38: 505.
- 2 Thériault, J.-M. (2001). Passive standoff detection of chemical vapors by differential FTIR radiometry. *DREV Technical Report, TR-2000-156*.
- 3 Thériault, J.-M., Puckrin, E., Bouffard, F., and Déry, B. (2004). Passive remote monitoring of chemical vapours by differential FTIR radiometry: results at a range of 1.5 km. *Applied Optics* 43: 1425–1434.
- 4 Lavoie, H., Puckrin, E., Thériault, J.-M., and Bouffard, F. (2005). Passive standoff detection of SF6 at a distance of 5.7 km by differential FTIR radiometry. *Applied Spectroscopy* 59 (10): 1189–1193.
- 5 Thériault, J.-M. and Puckrin, E. (2005). Remote sensing of chemical vapours by differential FTIR radiometry. *International Journal of Remote Sensing* 26: 981–995.

- 6 Thériault, J.-M., Lacasse, P., Lavoie, H. et al. (2010). CATSI EDM: a new sensor for the real-time passive stand-off detection and identification of chemicals. *Proceedings SPIE 7665, Chemical, Biological, Radiological, Nuclear, and Explosives (CBRNE) Sensing XI*, 766513 (5 May 2010).
- 7 Moreau, L., Prel, F., Lavoie, H. et al. (2010). A novel multi-pixel imaging differential standoff chemical detection sensor. *Proceedings of SPIE 7660*: 76602C.
- 8 Moreau, L.M., Prel, F., Lavoie, H. et al. (2011). iCATSI: a multi-pixel imaging differential standoff chemical detection sensor. In: *SPIE Defense Security and Sensing* (27 April 2011). Orlando, USA: SPIE Defense.
- 9 Prel, F., Moreau, L., Lavoie, H. et al. (2011). iCATSI, Multi-pixel imaging differential spectroradiometer for standoff detection and quantification of chemical threats. In: *SPIE Defense, Security & Sensing* (20 September 2011). Prague: SPIE Defense. (12 pages, 28 Slides).
- 10 Thériault J.-M., Fortin, G., Bouffard, F. et al. (2013). Hyperspectral gas and polarization sensing in the lwwr: recent results with moddifs. *Proceeding of 2013 5th Workshop on Hyperspectral Image and Signal Processing: Evolution in Remote Sensing (WHISPERS)*, Gainesville, FL, USA (26–28 June 2013). <https://ieeexplore.ieee.org/document/8080742> (accessed September 2020).
- 11 Thériault, J.-M., Fortin, G., Lavoie, H. et al. (2011). A new imaging FTS for LWIR polarization sensing: principle and application. In: *Imaging and Applied Optics, OSA Technical Digest*. Optical Society of America, paper FTuD2.
- 12 Bonifazi, G., Picone, N., and Serranti, S. (2013). Ore minerals textural characterization by hyperspectral imaging. *Proceedings of SPIE 8655, Image Processing: Algorithms and Systems XI*, 865510 (19 February 2013). doi: <https://doi.org/10.1117/12.2003054>.
- 13 Thenkabail, P.S., Smith, R.B., and De Pauw, E. (June 2002). Evaluation of narrowband and broadband vegetation Indices for determining optimal hyperspectral wavebands for agricultural crop characterization. *Photogrammetric Engineering & Remote Sensing* 68 (6): 607–621.
- 14 Kumar, A., Lee, W.S., Ehsani, R.J. et al. (2012). Citrus greening disease detection using aerial hyperspectral and multispectral imaging techniques. *Journal of Applied Remote Sensing* 6 (1) <https://doi.org/10.1117/1.JRS.6.063542>.
- 15 Lackenbauer, P.W., Farish, M.J., and Arthur-Lackenbauer, J. (2005). The distant early warning (DEW) line: a bibliography and documentary resource list. *The Arctic Institute of North America*, ISBN 1-894788-01-X.
- 16 Sandsten, J., Edner, H., and Svanberg, S. (1996). Gas imaging by infrared gas-correlation spectrometry. *Optics Letters* 21 (23): 1945–1947.
- 17 Chambers P. (2005). A study of a correlation spectroscopy gas detection method. Ph.D. Thesis. Faculty of Engineering, Science and Mathematics Optoelectronics Research Centre, University of Southampton, October 2005.
- 18 Mercier J.A., Smith M.W., Hunt J.P., and Ison A.M. (2012). *Modeling, sensor design, and performance predictions for gas filter correlation radiometers*. Sandia National Labs Report, SAND2012-7985, September 2012.
- 19 <http://fluxlab.ca>.
- 20 Russell, J.M. et al. (1993). The halogen occultation experiment. *Journal of Geophysical Research-Atmospheres* 98: 10 777–10 797.
- 21 Drummond, J.R. and Mand, G. (1996). The measurements of pollution in the troposphere (MOPITT) instrument: overall performance and calibration requirements. *Journal of Atmospheric and Oceanic Technology* 13: 314.
- 22 <http://Bluefield.co>.

- 23** L3Harris. Different types of scanning sensors. <http://www.harrisgeospatial.com/Support/Self-Help-Tools/Help-Articles/Help-Articles-Detail/ArtMID/10220/ArticleID/16262/Push-Broom-and-Whisk-Broom-Sensors> (accessed September 2020).
- 24** Fialka (2018). Meet the Satellites That Can Pinpoint Methane and Carbon Dioxide Leaks: European and Canadian orbiters can work together to catch wayward emissions. *Scientific American*. <http://www.scientificamerican.com/article/meet-the-satellites-that-can-pinpoint-methane-and-carbon-dioxide-leaks> (accessed September 2020).

# 13

## Handheld Laser Induced Breakdown Spectroscopy (HHLIBS)

*David Day*

*Sciaps Incorporated, Woburn, MA, USA*

### 13.1 Introduction

The Laser Induced Breakdown Spectroscopy (LIBS) measurement technique has similarities to other Optical Emission Spectroscopy (OES) methods in that it excites electrons in atoms and small molecules within a sample and then monitors the decay of those electrons back to lower energy states (Cremers and Radziemski 2006; Miziolek et al. 2006; Musazzi and Perini 2014). By analyzing the emitted light during the decay process, both the elements present and their concentrations may be determined. The element is determined from the unique electron transition energy, which yields specific emission wavelengths, and concentration is derived from the intensity of that emission.

However, unique to LIBS is that a short-pulsed laser with energies ranging from microjoules to 100s of millijoules is used to heat a sample surface, vaporize a small amount of the material, and excite electrons all at the same time. As with other OES methods, the emitted light is collected and analyzed with one or more spectrometers. Due to the very short duration of the emission event, multichannel spectrometers are typically used as opposed to scanning monochromator methods. Figure 13.1 shows a simplified schematic of a typical LIBS instrument.

The LIBS technique began in earnest in the early 1980s with scientific publication increasing nearly exponentially since that time (Noll 2012, p. 4). After the year 2000, several groups worked on making “transportable” and “portable” LIBS instruments ranging from backpack-based units to small suitcase-sized units. These typically used an umbilical cable containing fiber optic cables for delivering signals back to a spectrometer and either laser pulse delivery optics or power cables to a remote laser in the measurement head. As of 2013, there were several such research and commercial instrument producers which included Applied Photonics, Berlin Technologies, Iveya-Solution, StellarNet (Rakovsky et al. 2014).

In the spring of 2013, RMG Technology introduced the first self-contained truly handheld LIBS instrument which utilized a microjoule ( $\mu\text{J}$ ) laser. In early 2014, TSI (Shoreview, MN, USA) and SciAps (Woburn, MA, USA) both introduced LIBS handhelds with millijoule (mJ) lasers. In subsequent years, several more handheld LIBS instruments appeared from various companies including Rigaku (Wilmington, MA, USA), B&W TEK (Newark, DE, USA), Hitachi (formerly Oxford, formerly RMG) (Westford, MA, USA), Thermo Fisher (Tewsbury, MA, USA), and Vela (Burlington, MA, USA) (Figure 13.2).

All these handhelds are self-contained with no umbilical cables. However, they have many feature and capability differences. The variety of the basic components required for handheld LIBS and the technologies behind them are discussed in this chapter.

Traditional laboratory OES and LIBS instrumentation enjoy the luxury of being used in a stationary location and controlled temperature environment. Handheld LIBS (HHLIBS), on the other hand, must be capable of operation under variable thermal conditions, in any orientation, and must also be able to withstand various

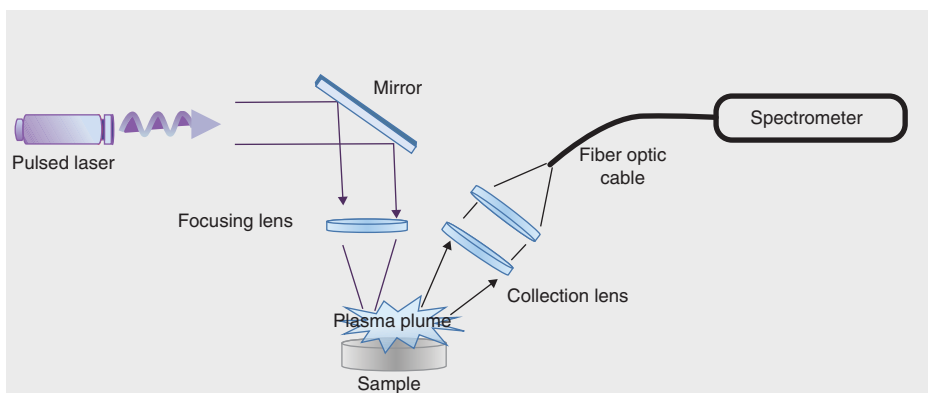


**Figure 13.1** Schematic diagram of the laser-induced breakdown spectroscopy measurement.



**Figure 13.2** Examples of commercially available HHLIBS clockwise from the upper left: TSI-ChemLite (Source: Courtesy of TSI), BWTEK-NanoLIBS (Source: Courtesy of BWTEK), Rigaku-Katana (Source: Courtesy of Rigaku), SciAps-Z (Source: Courtesy of SciAps), and Vela-A1 (Source: Courtesy of Vela).

environmental situations including dust, rain, mild vibration and shock. It is very difficult to design lasers and spectrometers that are entirely temperature-stable and so designers must be careful to apply some form of thermal compensation or utilize thermoelectric devices to keep instrument components at a constant temperature. The drawback of precise temperature control is that it can consume a good deal of electrical power, lowering battery life. Additionally, any form of temperature control produces heat, especially for thermoelectric cooling which is

very inefficient. The more heat that needs to be expelled from an instrument, the heavier and larger the outer cooling surfaces must be. A successful HHLIBS design becomes a sensitive balancing act between performance stability, power consumption, and instrument size and weight.

## 13.2 Handheld LIBS-Enabling Technologies

The technologies that enable handheld LIBS include:

- 13.2.1. Compact pulsed lasers
- 13.2.2. Compact spectrometers
- 13.2.3. Laser delivery optics, detection optics, and plasma containment
- 13.2.4. Beam rastering (in some instruments)
- 13.2.5. Gas purging (in some instruments)
- 13.2.6. Detector temporal gating (in some instruments)
- 13.2.7. Calibration (wavelength, intensity, and application)
- 13.2.8. Compact electronics and power supply

All of the above technologies have been evolving over the last several decades. However, it has really been during the last decade that miniaturization has progressed to the point of enabling all of them to be contained together in a fully standalone handheld instrument. In the following sections, these various components are reviewed.

### 13.2.1 Compact Pulsed Lasers

As of this writing, there are two types of pulsed lasers being utilized in commercially available fully self-contained HHLIBS instruments. These are microchip lasers, which are highly integrated with less than 1 mJ pulse energy, and lasers made from individual components with pulse energies from 100  $\mu$ J to 15 mJ. Both classes of lasers are Diode-Pumped Solid-State (DPSS) pulsed lasers with pulse energies limited to less than 15 mJ. “Transportable” LIBS systems with more powerful flashlamp-driven lasers in the 50 mJ range are available, such as Applied Photonics LIBSCAN 25 ([www.appliedphotonics.co.uk/products\\_services/libscan\\_25.htm](http://www.appliedphotonics.co.uk/products_services/libscan_25.htm) [accessed 1 November 2019]), but these systems are not fully self-contained handhelds and not covered in this chapter.

Microchip lasers, first reported in 1989 (Zayhowski and Mooradian 1989), are capable of pulse energies up to several hundred microjoules and pulse rates of up to several kHz. These lasers contain a resonant cavity consisting of an optical gain medium, a saturable absorber (SA or Q-Switch) and reflective coatings on each end (Aubert 2001). These components are fabricated as a single part with a total volume of only a few cubic millimeters. A pump diode is added to this which injects higher energy light into the gain medium through the back-mirror coating which is designed to be reflective at the laser output wavelength, but transparent at the pump diode wavelength. While there are various construction variations, Figure 13.3a shows a schematic diagram of a typical microchip laser. Further, output optics may be added either internally or externally to the laser package.

Microchip lasers are often associated with “micro-LIBS,” which is roughly defined as a measurement regime utilizing laser pulse energies less than 1 mJ, typically in the 10s–100s of microjoules and with pulse frequencies up to several kHz. Microjoule lasers may be constructed with a microchip or individual optical components.

Higher power ( $>1$  mJ), lower frequency lasers ( $<100$  Hz) are used in some HHLIBS instrumentation (SciAps, Thermo Fisher, TSI) that are constructed from individual components which include pump diodes, crystal gain media, cavity mirrors, and either a saturable absorber (passive Q-switch) or an active electronically controlled Q-switch. As a result of the larger size of the gain medium, more energy can be stored and then quickly released with each pulse. Pulse frequencies must be held to lower rates due to the high amounts of power dissipated internally per pulse. Optical pumping (excitation) of the crystal gain medium can be carried out in a similar fashion to the microchip laser by “end pumping” through one of the cavity mirrors or by “side pumping” (Figure 13.3b).

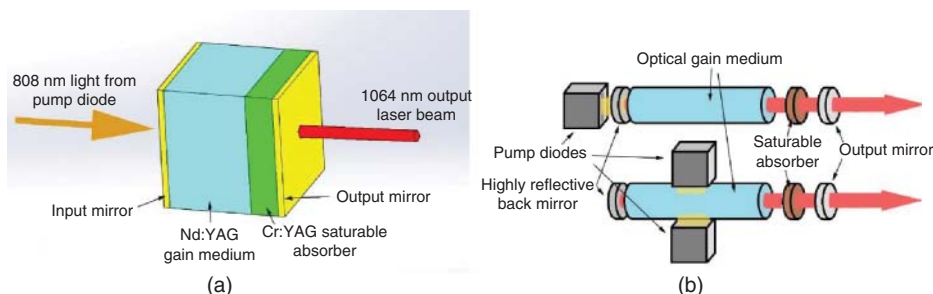


**Figure 13.3** (a) Nd:YAG microchip laser diagram. Input mirror is transparent to pump light at 808 nm, but highly reflective to laser 1064 nm light. Output mirror is partially reflective to laser 1064 nm light. Total volume  $0.03 \text{ cm}^3$  not including pump diode; (b) Diode-pumped solid-state laser. Top shows “end-pumped” configuration and bottom shows “side-pumped” configuration. Total volume  $25\text{--}100 \text{ cm}^3$ . Key components include pump diodes, gain media, mirrors, and the saturable absorber or “Q-switch.” Source: Mukhopadhyay (2011). © 2011 Lambert Academic Publishing.

There are several issues that must be considered in designing and utilizing small compact lasers in HHLIBS instruments. Typical efficiencies are on the order of a few percent. The average optical power output of a laser firing at 20 Hz and 10 mJ is 200 mW. With a 2% input-to-output power efficiency, the power consumption in this case would be 10 W average during pulsing. If an instrument design utilizes thermoelectric cooling to stabilize the laser temperature, the power consumption increases from there significantly. Fortunately, the laser is not firing continuously; however, in some applications, such as metal analysis, the duty cycle can be quite high. It is quite difficult to design any handheld instrument to dissipate 10 W of average power without an external fan, and so the main options left for thermal management are total external surface area and thermal conductivity to that surface, both of which must be maximized for thermal dissipation, but minimized for reasonable overall size and weight. Thus, the laser alone has a very important influence on final product ergonomics, which must be carefully considered in the design.

The technology is still evolving on DPSS lasers. There are many lasers commercially available from companies, such as Quantel (Bozeman, MT, USA), RPMC (O’Fallon, MO, USA), Coherent (Salem, NH, USA), Kigre (Hilton Head, SC, USA), and Thorlabs (Newton, NJ, USA) for example. However, due to the fact that most of the commercial lasers are not quite suitable for HHLIBS due to either large size, large power consumption, poor output power/rep rate, or cost, most commercial HHLIBS vendors are currently using their own proprietary technologies with the components finely tuned for the LIBS application. For the HHLIBS application, the optical components are often being pushed to the limits just within damage thresholds for pump diodes, gain media, and optical coatings. Antireflective coatings and mirror coatings are still evolving and so it is expected improvement in this field will be an enabling technology for even higher power DPSS lasers in the future (Lyngnes et al. 2006 and [https://www.photonics.com/Articles/High-Energy\\_Laser\\_Optics\\_Require\\_Coatings\\_in/p5/vo61/i482/a44258](https://www.photonics.com/Articles/High-Energy_Laser_Optics_Require_Coatings_in/p5/vo61/i482/a44258) [accessed 1 November 2019]).

The most common laser gain media used for HHLIBS microjoule and millijoule lasers are neodymium-doped yttrium aluminum garnet (Nd:YAG) or a neodymium-doped yttrium orthovanadate (Nd:YVO<sub>4</sub>) due to their relatively high efficiency and good thermal conductivity (Mukhopadhyay 2011, p. 70). A saturable absorber of chromium YAG (Cr:YAG) is typically used with 1064 nm emitting gain media. Other similar gain media materials producing output wavelengths from 800 to 1340 nm (Nd:YLF, Yb:YAG, Cr:LiSAF) have also been used to produce DPSS lasers (Noll 2012, p. 49).

At the power and repetition rate that HHLIBS 1064 nm lasers are operated, they all have a rating of Class 3B and are eye hazards. The HHLIBS from TSI and some first-generation SciAps instruments produce laser wavelengths in the range of 1500–1600 nm. TSI HHLIBS patents describe a laser that utilizes an Nd:YAG DPSS laser coupled with an Optical Parametric Oscillator (OPO) crystal which converts the 1064 nm light into two

lower energy (longer wavelength) outputs, one of which is at 1574 nm (Quant et al. 2016). The first-generation SciAps instrument utilized a Kigre laser with an erbium-doped phosphate laser gain medium and output wavelength of 1535 nm ([https://www.kigre.com/products/laser\\_glass.htm](https://www.kigre.com/products/laser_glass.htm) [accessed 1 November 2019]). Output wavelengths longer than 1500 nm are far safer because the light entering the human eye is highly absorbed by the intraocular fluid and reduces or prevents focused light from ever reaching the retina. This enables instrument laser safety classification of such long-wavelength instruments (>1500 nm) of Class 1 M (<https://www.tsi.com/products/metal-analyzers/chemelite-laser-aluminum-analyzer-4235> [accessed 1 November 2019]) depending on laser power levels and beam divergence conditions. However, since all HHLIBS produce plasmas regardless of the laser wavelength, safety features for sample presence detection are typically incorporated into the instrument-operational features. Reported examples of sample presence detection schemes include both plasma chamber pressure and light/dark sensor (Thermofisher 2020) (<https://www.thermofisher.com/order/catalog/product/NITONAPOLLO#/NITONAPOLLO> [accessed 2 March 2020]), both video analysis and light-emitting diode (LED) spectrum sample reflection (Day 2018), and real-time “per shot” spectral analysis (Day and Sackett 2017). With such safety features and proper training, a laser safety officer may allow class 3B laser instruments to be used under class 1 M laser conditions.

### 13.2.2 Compact Spectrometers

Compact spectrometers have been around since the early 1990s and were first sold by Ocean Optics (<https://oceanoptics.com/25-years-amazing-sensing-solutions> [accessed 1 November 2019]). Since that time, several other companies, Avantes (Apeldoorn, Netherlands) and Stellar Net (Tampa, FL, USA) for example, offer similar and ever smaller products. These types of spectrometers have found their way into numerous handheld technologies including Raman, near infrared (NIR), ultraviolet-visible (UV-Vis), and LIBS (Croccombe 2018). HHLIBS vendors generally do not disclose many details about the spectrometers they have either designed or purchased; however, the general basics of compact spectrometer design are covered in this section.

#### 13.2.2.1 Linear Detector Arrays

Key to the original Ocean Optics spectrometer’s operation were front-illuminated linear CCD (charge coupled device) detector arrays, developed originally for bar code scanners and produced by companies, such as Sony, Hamamatsu, and Toshiba. In more recent times, back-thinned CCDs (BT CCDs) and complementary metal-oxide semiconductors (CMOS) photodetector arrays have also been introduced, each with their own advantages and disadvantages. BT CCDs have a higher sensitivity than standard CCDs but also have a higher cost, due to more difficult processing. They also can have a periodic wavelength response function, known as “etaloning,” due to interference of internal surface layer reflections from the detector’s thinned layers. Another advantage of BT CCDs is that they are sensitive into the deep UV (<200 nm), whereas traditional CCDs lose sensitivity below 400 nm due to reduced photon penetration depth into silicon at short wavelengths (Darmont 2009). Traditional CCDs and some CMOS devices must be coated with an appropriate photon down-converting phosphor, such as Lumogen (<https://www.teledyne-e2v.com/content/uploads/2017/08/ccdttn103.pdf> [accessed 1 November 2019]) or Metachrome (<https://www.actonoptics.com/products/metachrome-coatings> [accessed 1 November 2019]) for sensitivity into the deep UV.

The linear array detectors typically have between 1024 and 4096 individual detector elements (pixels), spanning approximately 30 mm, that all collect photons simultaneously and are then read out after a fixed amount of integration time (Figure 13.4). This type of operation is key for LIBS measurement because the signal is only present for 10s of microseconds or less. It is for this reason that scanning monochromator spectrometers are not appropriate for LIBS spectral measurement.

Larger and more expensive benchtop LIBS systems often utilize an intensified CCD (ICCD) which incorporates an image intensifier mounted to the front of the CCD. Not only does the ICCD intensify the signal, but it also allows very precise electronics shuttering or “time gating,” i.e. the ability to start and stop collecting photons at

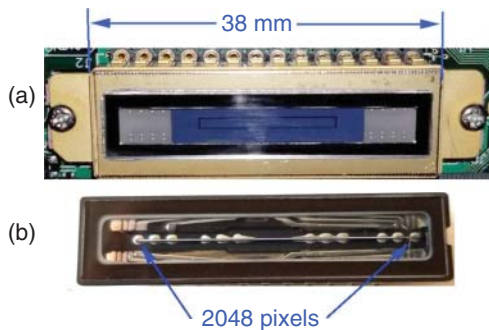


**Figure 13.4** Examples of two linear detector arrays: (a) Hamamatsu S11511-1006; and (b) Sony ILX511B charge coupled devices. Both sensors are shown on the same scale.

very precise and very short microsecond time scales. For HHLIBS, ICCDs are impractical because of their cost and drive electronics. Fortunately, some standard linear detector arrays have various degrees of electronic shuttering capabilities. HHLIBS instruments employing higher power lasers ( $>1\text{ mJ}$ ) benefit from electronic shutter control (temporal gating) so that the initial plasma continuum radiation can be rejected. For microjoule laser-based HHLIBS, electronic shuttering is not used or needed because continuum background is much reduced, and the laser repetition rate is much faster than the combined shutter speed and readout time of any available detector. For this reason, the detector specifications must be carefully reviewed and selected depending on how it will be used. A good example of some available detectors and specification can be viewed in the Avantes spectrometer catalog (ref. <https://www.avantes.com/catalog/19/#zoom=z> [accessed 1 November 2019]). See Section 13.2.6 for more details and examples of temporal gating with millijoule lasers.

### 13.2.2.2 Spectrometer Optics

Several current commercial HHLIBS utilize a spectrometer layout known as Czerny–Turner (CT) (Czerny and Turner 1930). The basic CT design incorporates in the order encountered along the optical path: an entrance slit, a collimating mirror, a diffraction grating, a refocusing mirror, and an exit slit. In the original CT design, the grating was slowly rotated so that the appropriate wavelength could be selected at the exit slit. For HHLIBS, the exit slit is replaced with the linear detector array and the different wavelengths impinge upon different pixels along the length of the array. In the classical CT design shown in Figure 13.5a, aberrations caused by the first off-axis collimating mirror 1 are partially compensated by the second refocusing mirror 2. A CT variant known as Crossed Czerny–Turner (Figure 13.5b) loses the aberration correcting feature, but gains an advantage in reduced overall size. Both types of spectrometers are currently used in commercial HHLIBS. Alternate forms of the CT design include the usage of transmission gratings (Quant et al. 2016), and lenses instead of mirrors. Figure 13.6 shows a commercial Avantes spectrometer that is used in some larger commercial LIBS instruments.

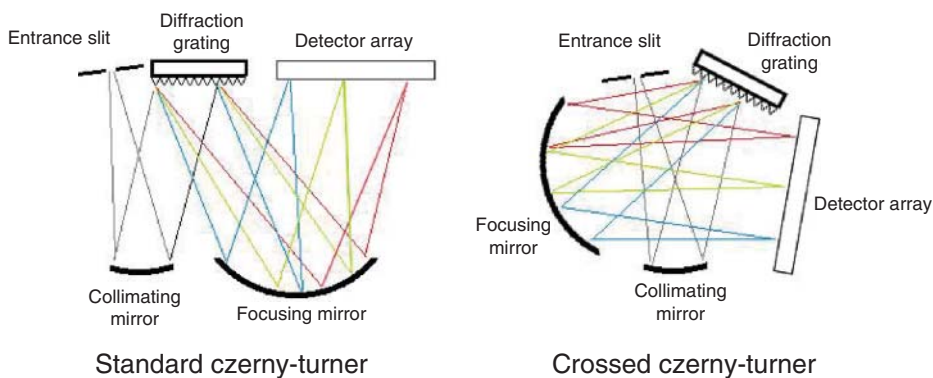


**Figure 13.5** Classical Czerny–Turner (a) and crossed Czerny–Turner (b) spectrometer configurations, both with linear detector arrays replacing the exit slit. Source: Based on Czerny and Turner (1930).

**Figure 13.6** Example of a small Avantes spectrometer that utilizes the standard CT configuration. 1, detector; 2, fiber optic connector; 3, diffraction grating; 4, input slit; 5, filter; 6, collimating mirror; 7, focusing mirror; 8 and 9, light traps. Source: Courtesy of Avantes.



Important to HHLIBS is the spectral resolution and spectral band needed to distinguish elemental emission lines. Factors that influence resolution and the spectral band are the diffraction grating and the mirror focal lengths. Higher diffraction grating groove densities and longer focal lengths both lead to a higher resolution. While detailed spectrometer design (Scheeline 2017) is beyond the scope of this chapter, suffice it to say that for spectrometer sizes that reasonably fit a handheld instrument and with current diffraction grating technology, the maximum resolution obtained in current commercial instrumentation is just below 0.1 nm. While this high resolution is not needed for most LIBS applications, it is important and utilized for certain applications such as carbon emission line quantification at 193.1 nm for better separation from neighboring lines (Section 13.4.2).

Another factor that must be considered is the spectral band or range captured by the linear detector. There is a trade-off between the desired resolution and range. HHLIBS designers carefully consider the resolution needed and where the elemental emission lines are for a given application and try to design a spectrometer that can meet both requirements. Several of the commercial HHLIBS used for metal alloy determination and sorting use a single spectrometer in the approximate range of 230–450 nm because most of the standard alloy base and alloying element emission lines can be found within that range. If we assume a detector with 2048 pixels, then the pixel resolution of the spectrometer would be  $(450 - 230 \text{ nm}) / 2048 \text{ pixels} = 0.108 \text{ nm/pixel}$ . However, for accurate peak location detection and quantification, the optical resolution must be about a factor of 2.5 lower (broader) than the pixel resolution, ensuring that the peak is spread over several pixels. It may seem counterintuitive, but by spreading the peak out over several pixels, the peak center can be located to better than a tenth of a pixel, whereas if the emission line were located entirely within one pixel, the location would only be known to the width of one pixel. Thus, the common resolution for these single-spectrometer HHLIBS units is on the order 0.2–0.3 nm. At least four commercial HHLIBS instruments use multiple spectrometers to get increased resolution and range (B&WTEK “NanoLIBS” utilizes two, Thermo Fisher “Apollo” utilizes two, TSI “ChemLite” utilizes two, and SciAps “Z” has various models with two, three, and four spectrometers) to open up the capability of more applications, such as carbon in steel, and a wider element suite including fluorine, lithium, sodium, potassium, and sulfur in geochemical analyses. Figure 13.7 shows an example of a spectrum from the SciAps Z300 which utilizes three spectrometers for a spectral range of 188–950 nm and resolution ranging from 0.15 to 0.35 nm.

### 13.2.3 Laser Delivery Optics, Detection Optics, and Plasma Containment

Laser delivery optics and plasma detection optics are implemented in different ways by the various HHLIBS manufacturers and not fully disclosed. Several of the basic methods are described.

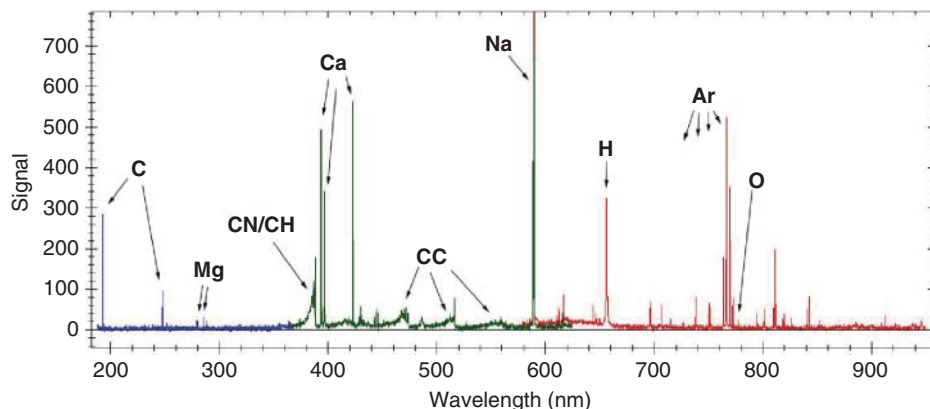


**Figure 13.7** LIBS spectrum exported from SciAps Z300 wide spectral range instrument with three spectrometers. Sample: human fingernail under argon purge, 5 mJ laser, 650 ns gate delay.

### 13.2.3.1 Laser Delivery Optics

Most DPSS lasers are designed to emit collimated or near-collimated light. This is convenient as it enables the HHLIBS design to incorporate some distance between the laser exit window and the focusing optic. A focusing optic, either a lens or a concave mirror, is used to bring the collimated laser beam to a small spot on the sample surface. In order to induce plasma on aluminum, the beam must be concentrated to a power density of  $\sim 10^7\text{--}10^8 \text{ W/cm}^2$  during the laser pulse (Noll 2012, p. 20). Materials with lower absorption coefficients require more power, with gas plasmas requiring on the order of  $10^{11} \text{ W/cm}^2$  (Cremers and Radziemski 2006, p. 40). Considering a laser with 100  $\mu\text{J}$  and a 2 ns pulse width as an example, there is 50 kW present during the pulse period. If that is focused on a 100  $\mu\text{m}$  spot, it yields roughly  $5 \times 10^8 \text{ W/cm}^2$  and will result in plasma on aluminum and most other metals. However, it will often not be enough to create plasmas on lower absorbance materials. Conversely, a 10 mJ laser with a 2 ns pulse width will have two orders of magnitude more power density per pulse and, in some cases, using slightly tighter focusing to 50  $\mu\text{m}$ , can create plasmas in air.

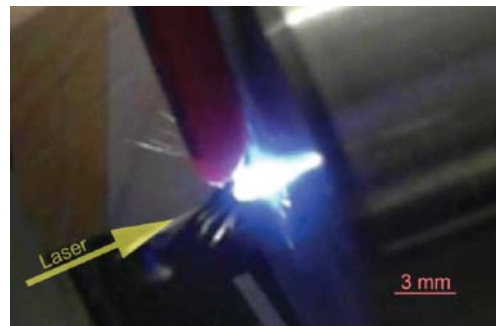
Optics must, therefore, be chosen to adequately focus to a spot small enough to reach sufficiently high-power densities during the pulse. The ultimate spot size is a function of beam diameter before the focusing optic, the focal length of the optic, and the laser beam quality. The interrelationships between these properties are beyond the scope of this chapter; however, the end result is that current HHLIBS instruments with the pulse energies described earlier utilize focusing optics with focal lengths on the order of 5–20 mm and attain power densities of  $10^8 \text{ W/cm}^2$  or higher.

### 13.2.3.2 Plasma and Particulate Containment

The distance from the plasma to the focusing optic is critical not only for obtaining enough power density (shorter is better), but also for keeping optics clean (longer is better). LIBS plasmas often emit small molten particles of the material under test (Figure 13.8). The higher the power the laser has, the further these particles can travel while remaining hot. If a molten particle reaches the focusing optics, it can become welded to it and only be removed by polishing or replacement.

The Thermo Fisher Apollo HHLIBS has a cleaning/polishing kit and procedure that is recommended every 1000 measurements ([https://players.brightcove.net/665001591001/dae1816b-a958-4ec8-b102-253bcd5c7d2a\\_default/index.html?videoId=5997407365001](https://players.brightcove.net/665001591001/dae1816b-a958-4ec8-b102-253bcd5c7d2a_default/index.html?videoId=5997407365001) [accessed 1 November 2019]). The SciAps Z models all have a disposable drop-in window placed between the focusing lens and plasma that is wiped off or replaced when necessary (Day et al. 2016). Similarly, a BWTek patent (Wang 2017) describes a protective window combined with an air-curtain to minimize buildup.

**Figure 13.8** Plasma with molten incendiaries resulting from a 10 mJ laser pulse (1064 nm) on steel. The red object is an argon delivery tube.



### 13.2.3.3 Plasma Light Collection Optics

Light collection from the plasmas and delivery to the spectrometer(s) are accomplished by a variety of means. In the simplest case, an optical fiber tip can be located near the plasma and off to the side of the incoming laser light with the fiber then delivering light directly to the spectrometer(s). In other designs, a refocusing lens or mirror can be used to collect more light from the plasma and match it to numerical aperture input cone of the optical fiber. In another HHLIBS design, a single lens is used for both laser focusing and plasma light collection (Figure 13.9). Advantages of this configuration are the alignment of the laser light path to the plasma light collection path is more easily maintained and only one optic need be moved to raster the beam (see Section 13.2.4).

### 13.2.4 Beam Rastering

Several HHLIBS models (Bruker-EOS500, BWTEK-NanoLibs, Rigaku-Katana, Hitachi-Vulcan, SciAps-Z, Vela-A1) implement some form of beam rastering. Beam rastering has been classically used in benchtop systems for the purposes of better averaging of sample inhomogeneities and, in some cases, for elemental mapping. In the case of HHLIBS microjoule lasers, rastering is a necessity because stationary beams stop creating plasmas after a few shots and, thus, must be constantly scanned. This behavior has been attributed to a change in surface reflectivity after the first pulse (Tashuk et al. 2007, p. 187) and to the presence of melted material after the first few shots if the sample is not moved (Rakovsky et al. 2014, p. 280). Regardless, the moving laser spot serves to effectively average inhomogeneity concentration variation across a sample surface (Figure 13.10). Multiple passes over the same line

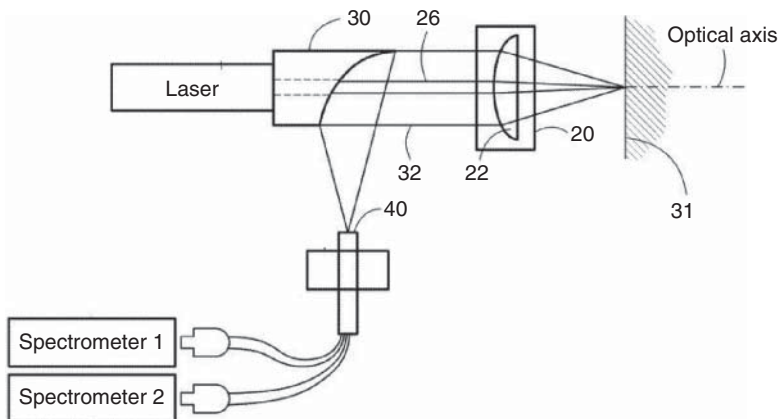


**Figure 13.9** Multispectrometer HHLIBS optical configuration enabling beam rastering through the movement of a single lens (22). Collected plasma light passes through the laser-focusing lens (22), then reflected off a parabolic mirror (30), and refocused on to a fiber optic cable (40). *Source:* Day (2018).

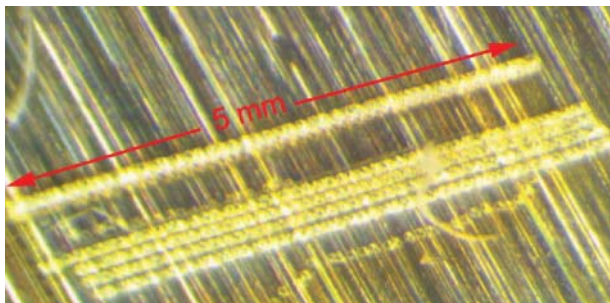


**Figure 13.10** Microjoule laser one-dimensional surface scans.

are used by some microjoule instruments to preclean a location before valid data are collected for analysis (Noll et al. 2018, table 3) and are described as “drill down” technology in Rigaku Katana literature (<https://www.rigaku.com/en/kt100s> [accessed 1 November 2019]) or “preburn” in Hitachi Literature (<https://hha.hitachi-hightech.com/assets/uploads/downloads/handheld-analysers/vulcan/LIBS-Analyser-For-QA-QC.pdf> [accessed 1 November 2019]).

When higher power lasers are used ( $>1\text{ mJ}$ ), LIBS plasmas can be consistently created from the same location without having to move the laser. This can be quite useful as initial laser shots can be used very effectively for “cleaning” the sample surface and burning through contamination and oxidation layers. TSI and Thermo Fisher units operate in this fashion using a single location. The SciAps HHLIBS not only uses cleaning shots, but also implements user-controlled two-dimensional rastering settings for the number of X- and Y-direction locations, the spacing between locations, number of cleaning shots per location, and number of data shots per location. While for alloy analysis, multiple locations are used for better averaging of inhomogeneities, in some geochemical applications, multiple sample locations are used to map out elemental distributions (Figure 13.11).

### 13.2.5 Gas Purging

Traditional benchtop LIBS systems incorporate the ability to purge samples with inert gases for the purposes of enhancing signal from the plasma. Gases with higher densities and lower thermal conductivity tend to keep the plasma localized, with higher plasma density and temperatures, which further results in more light emission (Noll 2012, p. 29). Argon is by far the most common purge gas used and has been shown to increase light output by more than a factor of 10 in some cases. Purge gas ionization energy can also play a role in transferring energy to the vaporized sample elements in certain cases. Fluorine, with an ionization potential of 17.4 eV, is a poor LIBS

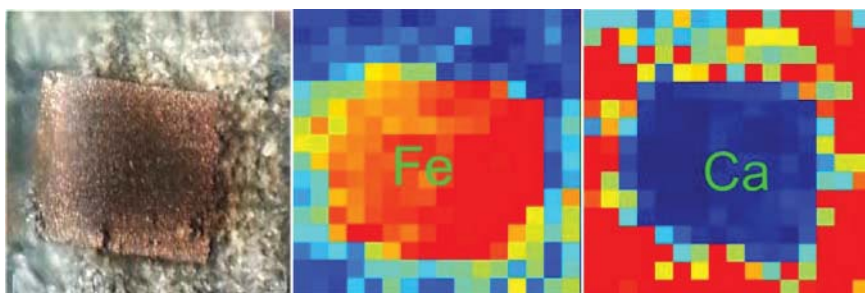


**Figure 13.11** Left: photo of iron pyrite inclusion in rock sample; middle and right:  $16 \times 16$  raster grid showing iron and calcium LIBS intensities or “heatmap” from the same sample. Grid-spacing  $120\text{ }\mu\text{m}$ , full image width  $1.8\text{ mm}$ . Source: Connors et al. (2016).

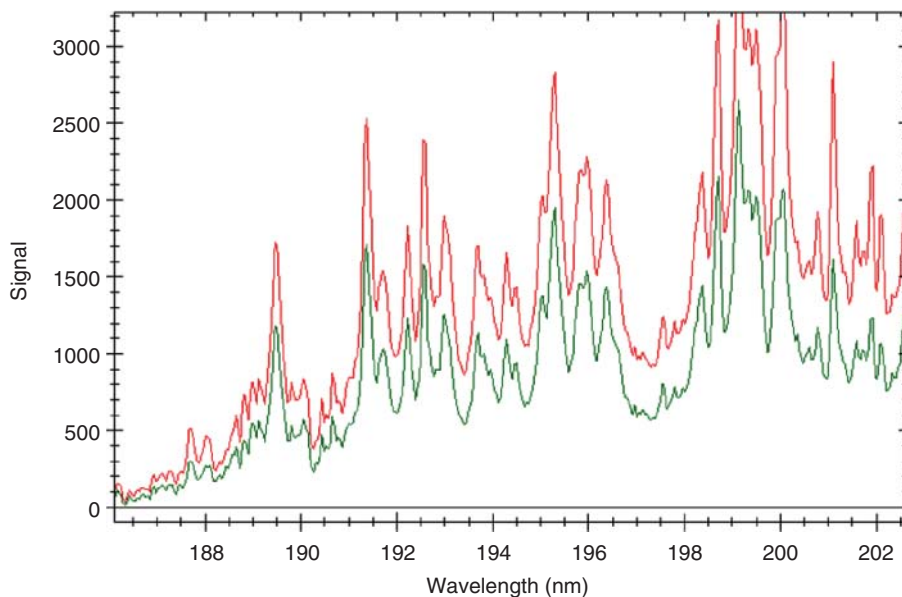


**Figure 13.12** LIBS spectrum (1050 Carbon Steel) from  $270\text{ }\mu\text{J}$  laser,  $1064\text{ nm}$  laser,  $140\text{ Hz}$ ,  $300\text{ mS}$  data collection window, no gating (green = air, red = argon purge).

emitter; however, it can be enhanced with a helium purge gas due to its high ionization potential (24.6 eV) relative to that of argon (15.8 eV) resulting in lower background and lower plasma-shielding effects (Asimellis et al. 2005; Cremers and Radziemski 1983). The helium enhancement has been used in HHLIBS to detect relative amounts of fluorine in fast food packing (Connors and Day 2018).

While the argon enhancement is beneficial for laser pulse energies greater than 1 mJ, it has been shown that for microjoule lasers, there is very little effect from a purge gas. Figure 13.12 shows an example of the LIBS signal from a steel sample (SRM 1050) in an air and argon environment using a  $270\text{ }\mu\text{J}$  pulse energy. While the signal was slightly higher for argon, there was no significant signal-to-noise enhancement. The insensitivity of microjoule laser plasmas to the gas environment is not well-understood, but may be related to the very short plasma lifetimes and dominance of substrate thermal conductivity.

As with high laser power benchtop LIBS systems, higher power HHLIBS laser plasmas ( $>1\text{ mJ}$  laser pulse) exhibit significant signal enhancement in the presence of argon (Figure 13.13).

The SciAps “Z” and Thermo Fisher “Apollo” HHLIBS models (5 and 10 mJ, respectively) both utilize argon purge for signal enhancement, and have shown that it is absolutely necessary for low carbon concentration measurement in carbon steels and L-grade stainless steels. In both cases, argon cartridges are enclosed within the instrument and flow is carefully controlled to last for hundreds of measurements. While noncarbon alloy analysis can be carried without argon on  $>1\text{ mJ}$  laser HHLIBS, the use of argon leads to higher signal levels and better precision for all elements.

### 13.2.6 Detector Temporal Gating

In the typical higher energy plasma excitation process ( $>1\text{ mJ}$ ), there is enough excitation to ionize a large percentage of the atoms (Noll 2012, pp. 146–149). Shortly after the laser pulse, which is typically a few nanoseconds in duration, the emitted light is observed over a large range of wavelengths with continuous broadband emission. This initial radiation is known as “continuum radiation” or “bremsstrahlung” (or braking light) and results from free electrons with random energies returning to vacant atomic energy levels. As a result of the free

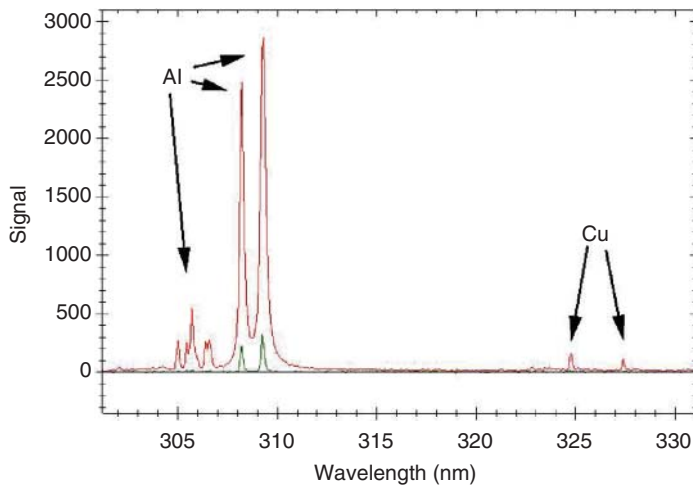


**Figure 13.13** HHLIBS spectra of aluminum foil in AIR ambient (green) and ARGON ambient (red) under otherwise identical conditions: 5 mJ laser pulse, 650 nS gate delay.

electrons having a distribution of energies, this initial radiation has no specific emission wavelength and results in broadband white light.

The initial continuum radiation decays on a time scale of 100s of nanoseconds to a few microseconds depending on experimental conditions (laser power, purge gas, energy density). After this point, there still exists both excited neutral atoms and excited ions. While some of the excited states decay during the initial continuum radiation, many excited states still exist well beyond this period and the narrow emission lines can be observed as they decay. Figure 13.14a shows an example of observed temporal emission of a liquid lithium chloride solution at three wavelengths (Hydrogen 656 nm, Lithium 671 nm, and 665 nm where there are no specific element emission lines). The continuum radiation is observed at all three wavelengths and is nearly gone by 0.5  $\mu$ s. The 665 nm emission falls to zero shortly thereafter. The 656 nm wavelength shows additional emission beyond 0.5  $\mu$ s and this is due to the H- $\alpha$  decay of excited hydrogen electrons. The hydrogen emission is mostly gone under these conditions (5 mJ laser, 80  $\mu$ m spot focus, 2 nS pulse duration, air ambient) by 1  $\mu$ s. The 671 nm emission line, due to Lithium de-excitation, has a longer lifetime than hydrogen and persists out to 3  $\mu$ s.

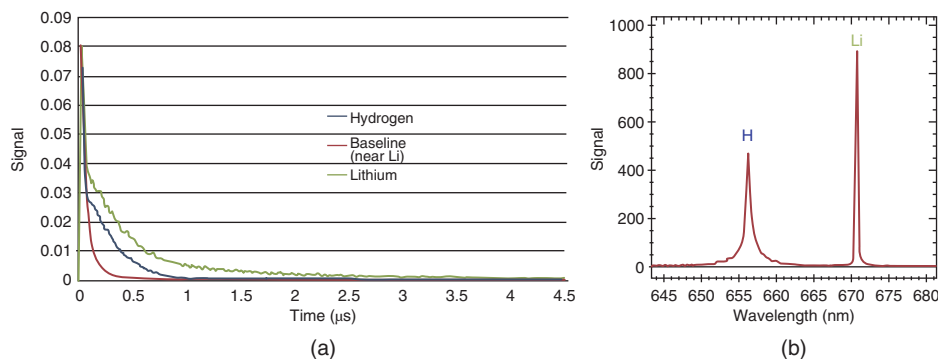


**Figure 13.14** (a) Temporal emission from lithium chloride solution using silicon photomultiplier detectors located at three specific wavelengths: hydrogen at 656 nm, lithium at 671 nm, and baseline at 665 nm; (b) resulting HHLIBS spectrum using 250 ns gate delay under identical conditions: (5 mJ 2 ns 1064 nm laser pulse at solution surface, air ambient).

It is, thus, the nature of  $>1$  mJ pulse energy LIBS that short lifetime states can be difficult to observe due to the initial continuum radiation masking them, and other longer lifetime states are easily observed. While it is not absolutely necessary, most benchtop and higher laser energy HHLIBS instruments incorporate “time-gated” spectrometer detectors which can block the initial continuum light through the use of high-speed electronic shutters. The advantages of doing so remove unwanted continuum background and, in many cases, yield narrower emission lines resulting from the lower plasma temperatures and electron densities at longer gate delay times. An example of this is shown in Figure 13.14b which utilized a 250 ns gate delay to eliminate continuum background; however, short lifetime species may be entirely lost by time-gating. This may be a disadvantage if their observation is desired, or it can be an advantage if there are nuisance short lifetime lines superimposed on other longer lifetime species. Figure 13.15 shows the influence of gate delay on the resulting spectrum.

In the lower energy pulse regime of microjoule lasers, the plasma behavior is somewhat different. The broadband continuum emission is much smaller than for the higher power lasers and the emission lifetimes are extremely short (Tashuk et al. 2007, p. 180). At low pulse energies below several 10s of microjoules, the plasma emission duration is similar to the length of the laser pulse itself (Gornushkin et al. 2004). In the several hundred microjoules range, plasma light emission durations are on the order of 10–100 ns, still about two orders of magnitude shorter than the higher energy pulsed lasers (Häkkänen and Korppi-Tommola 1995). At these short lifetimes, gating is simply not possible with standard CCD or CMOS detectors. However, as previously mentioned, the continuum radiation is very low with microjoule lasers and good spectra are obtained without gating. The pulse repetition rate of these lasers is often in the multiple kHz regime and so data are typically collected with the detector shutter left open over hundreds of pulses. This enables a significant amount of light to be accumulated within one detector integration lasting several hundred milliseconds and yields a good signal to noise ratio (SNR). Figure 13.16 shows an example of spectra collected from the same sample (86L20 Steel) and the same HHLIBS spectrometer using an ungated microjoule laser and a gated millijoule laser. In the region near 225 nm, which is dominated by ionic iron emission lines, the resulting spectra are very similar with some continuum and line broadening observed from the ungated microjoule laser.

In the region near 193 nm, where the critical carbon emission line is for steel analysis, there is a larger difference between the two techniques. The microjoule laser exhibits some line broadening and large emission peaks that do not appear in the gated millijoule laser spectrum. Carbon concentration in this steel is near 0.2%. The millijoule

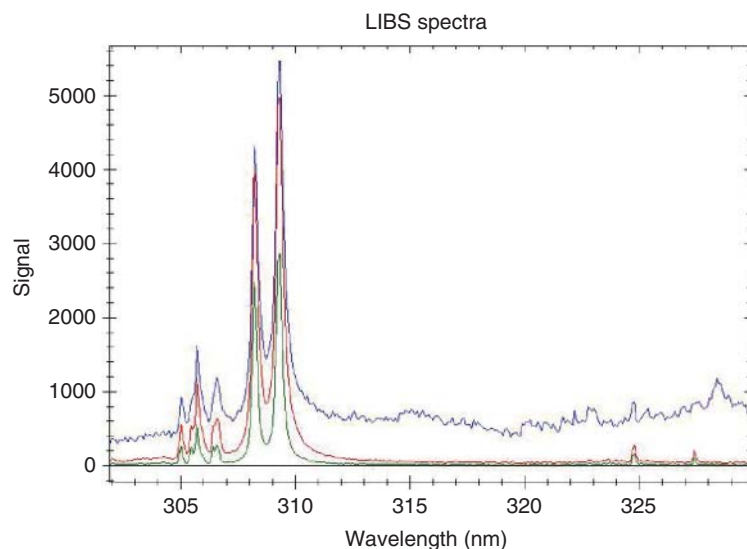


**Figure 13.15** HHLIBS spectrum of aluminum foil with various gate delays (green = 650 nS, red = 250 nS, blue = 0 nS) (5 mJ pulse, 2 nS pulse, argon ambient).

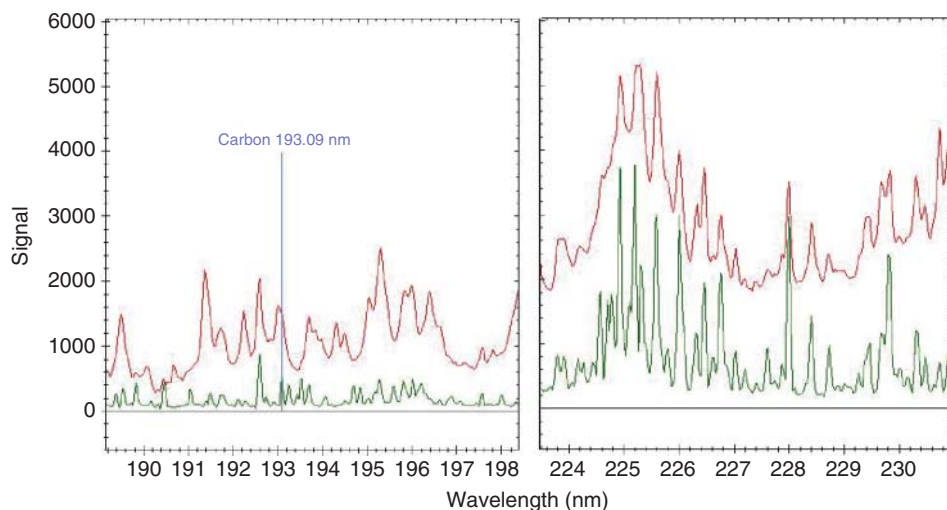


**Figure 13.16** LIBS spectra of 86L20 steel, argon environment, using an ungated laser (red,  $270\ \mu\text{J}$ , 140 Hz, 300 mS integration), and gated laser (green, 5 mJ, 650 nS gate delay).

laser spectrum exhibits a carbon emission line that is reasonably isolated from neighboring peaks while the microjoule laser spectrum exhibits a shoulder to the left of the carbon emission line. Both techniques are capable of measuring differences in carbon concentrations in steel, but the shoulder in the nongated microjoule laser spectrum makes it difficult to analyze lower concentration levels. The lowest carbon concentration shown in Figure 13.17 for the ungated microjoule laser was for 304H stainless near 0.05% carbon concentration. The smallest carbon peak from the gated millijoule laser was observed from the certified reference material “CP-Iron/IARM 27E” with a carbon concentration of 0.002% (<https://www.armi.com/hubfs/Certificates%20of%20Analysis/IARM-27E.pdf>).

### 13.2.7 Calibration

HHLIBS “calibration” can refer to spectrometer wavelength or intensity, and it can also refer to a particular application algorithm that yields elemental concentrations based on the observed emission lines in the LIBS spectrum.

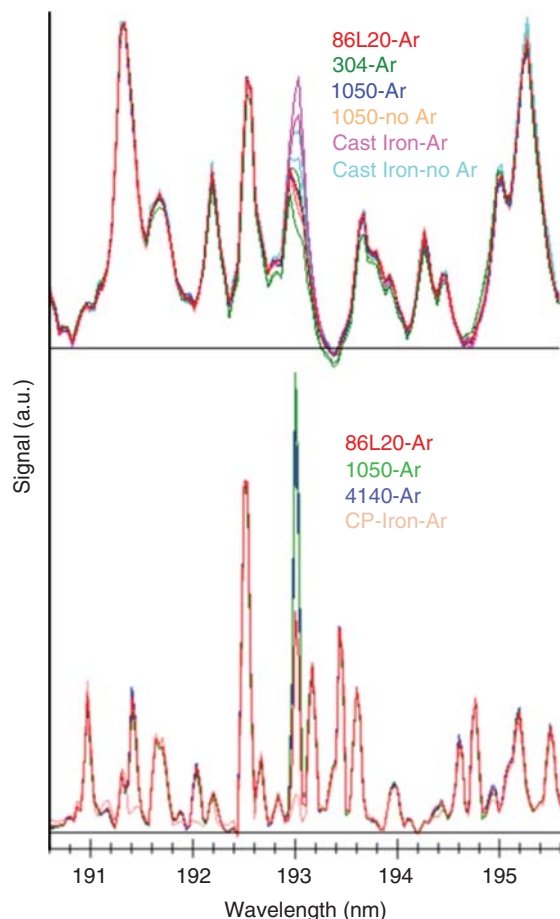
#### 13.2.7.1 Wavelength and Intensity Calibration

For HHLIBS to function well, the wavelength calibration (wavelength vs. pixel number) and intensity response (digital-to-analog converter [DAC] counts/photon vs. pixel number) must either remain stable over time and temperature, or the instrument must have some method to compensate for temperature-related drifts. All spectrometers experience a temperature-dependent shift in wavelength simply due to thermal expansion. To first order, this can be calibrated and built into the software while at the factory. However, in practice, manufacturers typically use known material standards that can be tested in the field. Through measurement of standard’s emission line locations and intensity values, corrections can be applied to the factory stored wavelength/intensity calibration. The correction values are, thus, updated every time the reference standards are checked. At least, one commercial HHLIBS can make measurements from an internal calibration surface at the desired intervals based on time or temperature, which frees the user from needing an external calibration standard. These techniques can result in wavelength reproducibility to approximately 0.01 nm despite large temperature changes or severe instrument shock.

#### 13.2.7.2 Application Calibration

The term “calibration” also refers to the algorithm by which LIBS spectral data is converted into elemental concentration results. Calibration techniques include traditional univariate methods, such as those used by OES

**Figure 13.17** Comparison of carbon emission peak at 193.09 nm of various steels. Data processed for baseline removal and normalization to 192.5 nm iron peak. Top: 270  $\mu$ J, ungated, 140 Hz, 300 ms integration, argon and no argon (labeled); bottom: 5 mJ, gated, 650 ns gate delay, argon.



(ASTM 1996) and more modern multivariate methods utilizing chemometric modeling (Guang et al. 2015; Zhang et al. 2018) and artificial neural networks (D'Andrea et al. 2014).

The most common method of application calibration in current HHLIBS is similar to conventional OES which creates a linear or polynomial function that relates an element's emission line intensity to the element's concentration. One difficulty with LIBS is that overall plasma intensity can vary significantly from laser shot to shot depending on the material under test. In these cases, to compensate for intensity variation, a matrix element which makes up the bulk of the material is often used as an internal standard. For example, when analyzing copper in steel, the copper emission line intensity will be divided by a nearby iron (matrix element) emission line intensity. The calibration that results is a polynomial that predicts elemental concentration based on that element's "intensity ratio." Another method for intensity compensation is to use the entire integrated spectrum over a selected region as an internal standard rather than a single matrix element peak.

Figure 13.18 shows a typical calibration in this case for molybdenum in iron. In this example, two Mo peaks (553.3 and 550.7 nm) were summed and referenced to the iron line at 537.1 nm. In addition to the straight summing of multiple peaks, signed multiplication factors may be applied to compensate for certain matrix effects or interference effects resulting from an overlapping peak, all techniques common to traditional OES.

Chemometric and machine learning algorithms (Kramer 1998; Mark and Workman 2018) are a rich area for LIBS data analysis. In recent years, some papers using HHLIBS-collected data have been published on PCA (principal component analysis), PLS (partial least squares) and PLS-DA (partial least squares discriminant analysis). PCA

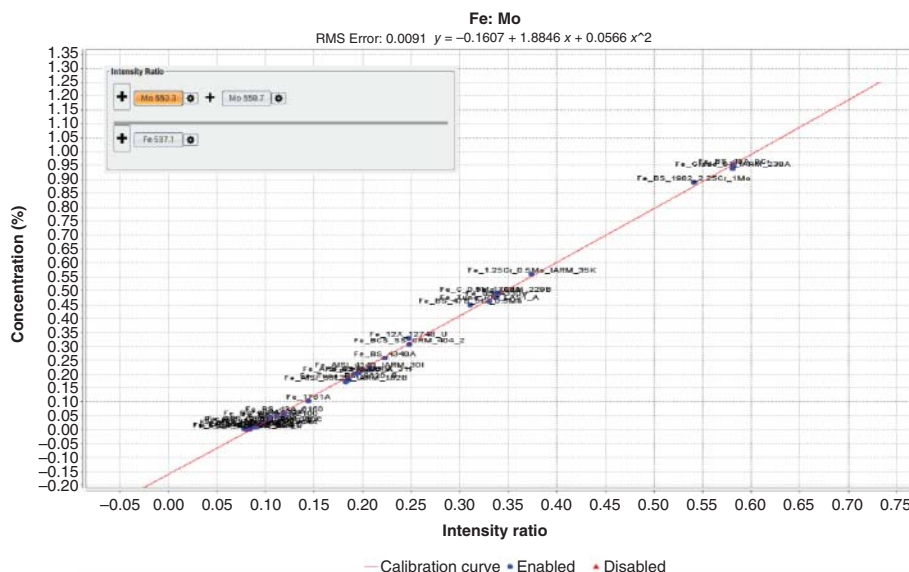


**Figure 13.18** Second-order polynomial calibration curve for prediction of molybdenum in iron based on measurement of assayed standards. The intensity ratio on the horizontal axis is calculated from the peak ratios defined in the upper left equation.

and PLS-DA are utilized for material classification and several examples of their use with HHLIBS data applied to geochemical materials have been demonstrated (Harmon et al. 2017, 2018). PLS is a quantitative prediction technique, and its use with HHLIBS data for determining elemental concentrations in steel has been successfully demonstrated (Afgan et al. 2017). Artificial neural network algorithms have also successfully extracted accurate elemental concentration in steels from HHLIBS data (X. Tan, personal communication).

There can be several drawbacks to chemometric and machine learning calibration methods. The data sets required for accurate classification or calibration can be quite large, and, thus, time-consuming to create. A second classical issue is that the models are only as good as the data contained within the model data set and, thus, predictions made on samples falling outside the model data set can yield erroneous results. Finally, chemometric model transfer between instruments is extremely difficult for any measurement technology, but especially so for LIBS due to the large range of variables associated with the LIBS technique (absolute laser power, optics and spectrometer transfer function, detectors) that are difficult to reproduce exactly between instruments.

Improved calibration transfer algorithms for both univariate and multivariate calibration schemes are needed for HHLIBS. Future developments along these lines should contribute significantly to HHLIBS performance enhancement and cost reduction for market-driven commercial applications.

### 13.2.8 Compact Electronics and Power Supply

Cell phone technology evolution is largely responsible for the availability of small powerful processors, high-capacity memory, high-resolution displays, Wi-Fi–Bluetooth–universal serial bus (USB) communications, global positioning system (GPS), and miniature cameras. All of these subunits are now incorporated in most HHLIBS as well as other handheld analyzers, such as X-ray fluorescence (XRF), Raman, NIR, and mid-infrared (MIR) instrumentation. These off-the-shelf components are combined with custom electronics for spectrometer communication, laser drive, and motor drive submodules.

Lithium-ion batteries are used to power HHLIBS instruments. With current battery technology, a 230 g battery yields 50 Wh of energy. Depending on operating characteristics, a 5 or 10 mJ DPSS laser will consume on the

order to 10–15 W average while firing. The rest of the HHLIBS system might continuously consume several watts, depending on implemented options. An HHLIBS under heavy usage might run the laser with a 40% duty cycle. Assuming around 8 W of average power consumption, a single 50 Wh 230 g battery can run for about six hours which is more than adequate for normal applications. Various operation times are listed by the different vendors, which obviously depends on actual battery size and internal electronics; however, they are all along these lines. All current commercial HHLIBS enable quick battery change-out in the event that even longer run times are required.

### 13.3 Commercial HHLIBS Specifications

The currently available commercial HHLIBS have a variety of capabilities and features, many of which have been described in this chapter. The differences arise from the technology utilized, features included, and desired applications for which the products are intended. Table 13.1 shows a brief summary of the basic HHLIBS features.

### 13.4 HHLIBS Applications

Completely untethered HHLIBS have now been in use for over five years and they have found their way into a variety of diverse application areas (David and Omenetto 2012). The main market-driving application for HHLIBS is metal analysis in the areas of positive material identification (PMI), nondestructive testing (NDT), scrap sorting, and quality control. A secondary market has also been recently developing for a variety of geochemical applications.

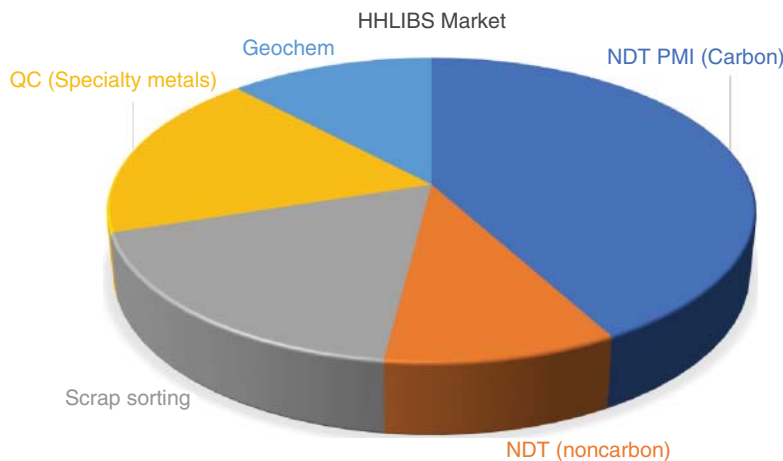
Applications just starting or still in development, but not yet driving the HHLIBS market cover a wide range of areas including lithium brine analysis ([https://www.sciaps.com/wp-content/uploads/2016/07/SciAps-ApNote-Lithium-Concentrations-in-Brines\\_Feb2017.pdf?x24702](https://www.sciaps.com/wp-content/uploads/2016/07/SciAps-ApNote-Lithium-Concentrations-in-Brines_Feb2017.pdf?x24702)), monoatomic salt PMI (<https://www.clinicaltrialsarena.com/products/nanolibs-handheld-labs-analyzer>), organic carbon in soils ([https://www.sciaps.com/wp-content/uploads/2018/12/SciAps\\_ApNote\\_Carbon-in-SoilsFinalRGB.pdf?x24702](https://www.sciaps.com/wp-content/uploads/2018/12/SciAps_ApNote_Carbon-in-SoilsFinalRGB.pdf?x24702)), soil contamination (Kumar et al. 2019), archeological analysis (Botto et al. 2019), and forensic analysis (Hark and East 2014), as a few examples.

Figure 13.19 shows a rough breakdown of the current HHLIBS market, several examples of which are described herein.

**Table 13.1** Commercial HHLIBS instrument characteristics as compiled from Noll et al. (2018), information generally available on the Internet, and personal communications.

	BRUKER	BWTEK	Hitachi	RIGAKU	SCIAPS	THERMO	TSI	VELA
Laser pulse energy	<1 mJ	<1 mJ	<1 mJ	<1 mJ	5 mJ	10 mJ	>5 mJ	up to 200 μJ
Laser pulse rep rate (Hz)	5000	1000–5000	7500	–	50	20	–	up to 4000
Laser ave range power (mW)	100	<200	<450	–	250	200	–	Up to 400
Laser wavelength (nm)	1064	1064	1064	1064	1064	1064	1574	1064
Raster	1D	1D	1D	1D	2D	No	No	1D
Argon purge	No	No	No	No	Yes	Yes	No	No
Detector gating	No	No	No	No	Yes	Yes	–	No
Spectral range (nm)	170–720	200–800	240–510	220–480	188–950	186–420	–	–
Weight (kg, with battery)	2.4	1.8	1.5	1.5	2.2	2.9	–	1.2
Measurement speed (s)	–	0.3	1	~2	2–3, ~10 carbon	~10 carbon	1–3	1

Source: Based on Noll et al. (2018).



**Figure 13.19** Estimated market breakdown of current handheld LIBS sales (D. Sackett and K. Smith, personal communications).

### 13.4.1 Scrap Sorting

For the last two decades, handheld XRF (HHXRF) has been the dominant instrument of choice for scrap sorting and it continues to be. HHLIBS, however, has found its way into certain scrap applications where HHXRF has a difficulty – for example, where measurement of lighter elements, such as silicon, magnesium, lithium, beryllium and boron are required. Aluminum is the largest scrap-sorting application for LIBS, and can differentiate the aluminum series from 1000 to 8000. One example of this is for scrap produced from the use of 5000 and 6000 series aluminum alloys in the automotive industry where magnesium and silicon concentrations are measured to determine the alloy type (<https://www.recycling-magazine.com/2016/10/17/new-sorting-system-for-separating-aluminium-alloys>, TSI: [https://www.tsi.com/getmedia/859f93cc-4296-46be-a81d-f048d7788a64/LIBS\\_Automated\\_Aluminum\\_Scrap\\_Sorting\\_LIBS-028-US?ext=.pdf](https://www.tsi.com/getmedia/859f93cc-4296-46be-a81d-f048d7788a64/LIBS_Automated_Aluminum_Scrap_Sorting_LIBS-028-US?ext=.pdf)).

HHLIBS can also differentiate between grades within a series including 6061/6063, 3003/3004, and 7050/7075 alloys (<https://hha.hitachi-hightech.com/en/blogs-events/blogs/2019/05/30/identify-aluminium-lithium-alloys-in-a-second-with-the-new-vulcan-optimum-handheld-libs-analyser>). The differentiation of these very similar alloy pairs relies on HHLIBS ability to make accurate measurements of Cu, Mg, Si, Zn, Zr, and Cr which may only be present in a few percent down to several tenths of a percent ([https://en.wikipedia.org/wiki/Aluminium\\_alloy](https://en.wikipedia.org/wiki/Aluminium_alloy)). However, the recent improvement in X-ray detection technology, specifically for Mg and Si, are moving several of these tough differentiations back into the HHXRF application arena (<https://www.sciaps.com/aluminum-sorting-with-x-ray-or-lbs-sciaps-has-the-answers>).

The aircraft/aerospace industry makes use of lithium-containing aluminum for the combined purpose of lower density by up to 10% and higher stiffness by up to 15% (Prasad et al. 2014). Lithium is an extremely bright LIBS emitter, and can easily be detected to less than 10 ppm levels making the technique very useful for these types of alloy separations.

Other HHLIBS-sorting applications claimed by the various manufacturers include Co, Cu, Fe, Mg, Ni, Pb, Sn, Ti, and Zn alloys. Most HHLIBS manufacturers list scrap-sorting as a major application for their commercial instruments:

<http://mhmp.bruker.com/acton/attachment/18602/f-0036/1/-/-/-/EOS%20500%20HH-LIBS%20brochure.pdf>

<https://hha.hitachi-hightech.com/en/product-range/products/handheld-xrf-lbs-analysers/handheld-lbs-analysers>.

<https://www.rigaku.com/en/products/libs/kt100s/app-scrapmetal>.

<https://tsi.com/solutions/solutions-by-application/scrap-metal-sorting-and-recycling>.

<https://www.sciaps.com/industries/scrap-metal-and-alloys>.

<https://www.thermofisher.com/us/en/home/industrial/spectroscopy-elemental-isotope-analysis/portable-analysis-material-id/industrial-elemental-radiation-solutions/niton-apollo-handheld-libs-analyzer.html>.

<http://velalibs.com/index.php?lang=en>.

### 13.4.2 Carbon Analysis

One of the most important examples for HHLIBS NDT and PMI is for carbon analysis in low alloy and stainless steels, which previously could only be done by larger arc/spark OES instrumentation. L-grade stainless steels, used in critical applications for petrochemical, food processing, pharmaceutical, and medical equipment, can have carbon concentrations as low as 100 ppm. Improvements in HHLIBS capabilities just during the last three years have yielded limits of detection (LODs) down to 80 ppm (SciAps 2018) enabling the differentiation of L-grade (<300 ppm carbon) and H-grade (>400 ppm carbon) stainless steels (<https://www.astm.org/Standards/A240.htm>), which is critical for correct material confirmation in these various applications that require either high temperature or high strength operation.

Making measurements of such low carbon concentrations can be difficult due to contamination on the sample surface. Just as in classical OES methods of carbon measurement, HHLIBS steel samples are typically ground to remove any dirt and corrosion buildup. Figure 13.20 shows an example of an HHLIBS stainless-steel calibration which utilizes the 193 nm carbon emission line ratioed to a nearby iron emission line.

### 13.4.3 Equivalent Carbon for Weldability

Another sizable NDT application is the measurement of Carbon Equivalents (CE), which is related to “weldability” of the material and is obviously important to know or confirm before pipes are welded or repaired. There are several

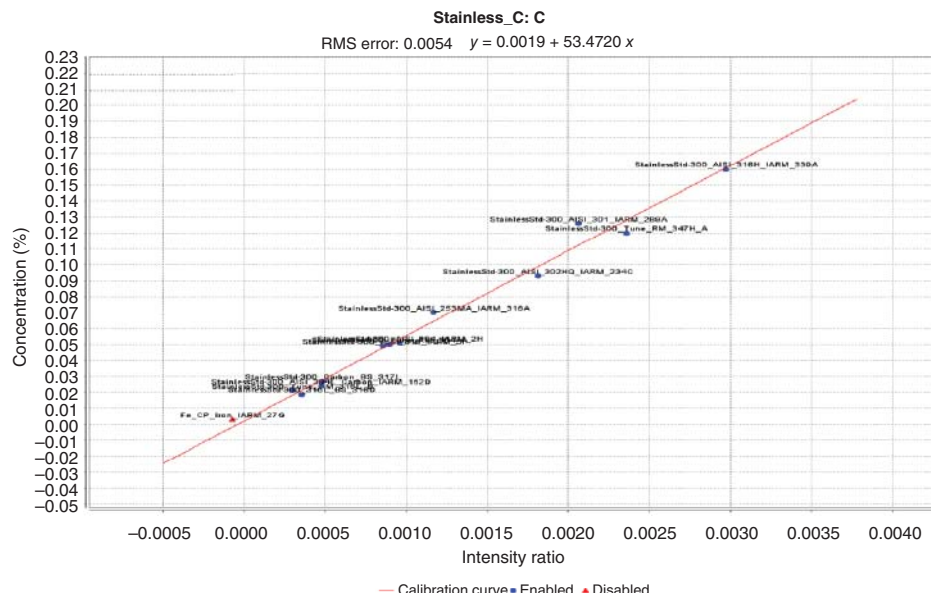


**Figure 13.20** Carbon in stainless calibration data and fitted calibration equation. Assayed concentration vs. HHLIBS intensity ratio of carbon 193.1 nm peak intensity to nearby iron emission line. Error bars represent  $\pm$  one standard deviation of the mean of five measurements.

formulas used for CE, but one example specified by the International Institute of Welding, or IIW, is:

$$CE = \%C + \frac{\%Mn + \%Si}{6} + \frac{\%Cr + \%Mo + \%V}{5} + \frac{\%Cu + \%Ni}{15}$$

All of these elements can be analyzed with HHLIBS, enabling CE determination and verification that the resulting value is less than the IIW threshold of 0.40%, thus reducing the risk of future cracking near the weld joint.

#### 13.4.4 Corrosion

Flow-accelerated corrosion (FAC) in carbon steels from water flow is of large concern in nuclear power plants and highly dependent on chromium concentrations in steel (Poulson 2014). If the chromium concentration decreases to below 0.1%, the rate of corrosion in carbon steel flow systems increases rapidly. HHLIBS can make the required measurement within three seconds to a confidence level of 0.015% Cr, making it a desirable alternative to the HHXRF and the radiation hazards associated therewith (SciAps 2016). Figure 13.21a shows a plot of HHLIBS measured versus assayed chrome content.

Sulfidic corrosion in refineries results from naturally occurring sulfur found in crude oil. Greatly accelerated at temperatures above 260 °C, pipes and pressure vessel walls are slowly thinned over time. The sulfidic corrosion rate is related to several factors including sulfur content, temperature, and silicon content of the carbon steel in use (<https://inspectionengineering.com/airs/2017-02-13/6123/a-primer-on-sulfidation-corrosion> [accessed 1 November 2019]). The American Petroleum Institute's (API's) guidance on avoiding sulfidation corrosion in oil-refining operations is to confirm the silicon content of piping and pressure vessels is above 0.1% (API RP 939-C 2009). HHLIBS testing of silicon on a variety of refinery components is shown in Figure 13.21b with a working LOD of 0.02% and an accuracy of 0.02–0.03% using spark-OES as a reference.

#### 13.4.5 Additional Positive Material Identification (PMI) Applications

PMI is critical for the aerospace, petrochemical and power-generation industries (Rigaku Inc. 2018; SciAps 2019). While HHXRF has traditionally been used for this application, HHLIBS excels in cases where light elements are involved, such as B, Be, Li, Si, and Mg. HHLIBS is particularly well-suited for measurement of Be in Bronze, Si and Mg in Al, and Al and Mg in Ti alloys (Patterson 2015). Measurement of boron-containing nickel and stainless aerospace alloys is also well-suited for HHLIBS. Li, B, and Be measurement down to 10 ppm in Aluminum alloys is also possible (SciAps 2019).

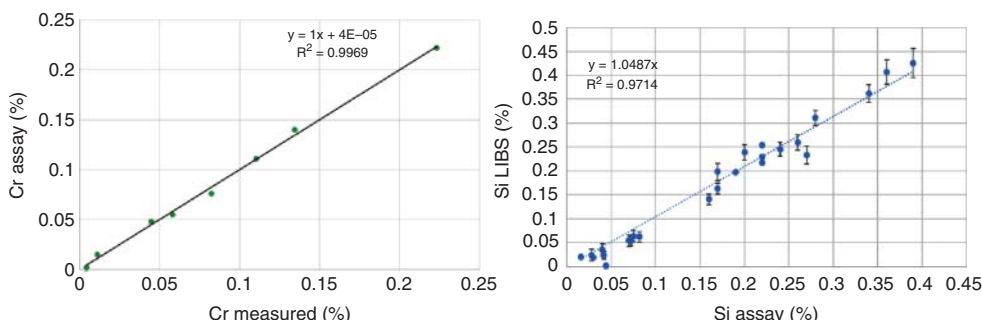


**Figure 13.21** (a) Chrome assay vs. HHLIBS-measured values in various carbon steels for flow-accelerated corrosion threshold (0.1% Cr) evaluation; (b) HHLIBS silicon concentration vs. assay made on various refinery components for sulfidic corrosion threshold (0.1% Si) evaluation using the Si 212.4 nm emission line.

### 13.4.6 Other Applications

There are other applications for HHLIBS, some of which were mentioned in Section 13.4 and many that were not mentioned, too numerous to list here. Some of these are covered elsewhere in this book. While they do not yet account for significant commercial sales, there is a great potential for many of them to become commercially significant in the coming years as technology and algorithms develop further.

## 13.5 Summary and Future Expectations

Technology advances and size reductions in pulsed lasers, high-power drive electronics, spectrometers, and data processing/communication components over the last decade have led to the current revolution in handheld LIBS instrumentation. It is expected that there is still progress to be made with laser size reduction and pulse power enhancement through improved optical components and optical coating technology. Along with continued spectrometer size reduction, there are new technologies in development, such as spatial heterodyne spectroscopy (Allen and Angel 2018) enabling very small and very high-resolution instruments and which should work well for laser ablation molecular isotopic spectrometry or LAMIS (Bol'shakov et al. 2016). Echelle spectrometers, with recent modeling showing miniature HHLIBS size-compatible versions are possible, are also an excellent candidate for future HHLIBS enabling very large spectral range and extremely high-resolution measurements (B. Beardsley, personal communication). As data processing power continues to increase, advanced chemometric algorithms, neural network and machine learning algorithms should also find their way into standard commercial products. While the current market-driving applications are mainly in metals analysis, the future looks bright for a large host of other applications that can benefit from this exciting field.

## References

- Afgan, M.S., Hou, Z., and Wang, Z. (2017). Quantitative analysis of common elements in steel using a handheld  $\mu$ -LIBS instrument. *Journal of Analytical Atomic Spectrometry*. <https://doi.org/10.1039/C7JA00219J>.
- Allen, A. and Angel, S. (2018). Miniature spatial heterodyne spectrometer for remote laser induced breakdown and Raman spectroscopy using Fresnel collection optics. *Spectrochimica Acta Part B: Atomic Spectroscopy*. <https://doi.org/10.1016/j.sab.2018.07.013>.
- API RP 939-C (2009). *Guidelines for Avoiding Sulfidation (Sulfidic) Corrosion Failures in Oil Refineries*, 1e. American Petroleum Institute.
- Asimellis, G., Hamilton, S., Giannoudakos, A., and Komitsas, M. (2005). Controlled inert gas environment for enhance chlorine and fluorine detection in the visible and near-infrared by laser-induced breakdown spectroscopy. *Spectrochimica Acta Part B*. <http://doi.org/10.1016/j.sab.2005.05.035>.
- ASTM E158-86 (1996). *e1 Standard Practice for Fundamental Calculations to Convert Intensities into Concentrations in Optical Emission Spectrochemical Analysis*. West Conshohocken, PA: ASTM International [www.astm.org](http://www.astm.org).
- Aubert, J.J. (2001). Microchip lasers. In: *Encyclopedia of Materials: Science and Technology*, 5594–5598. <https://doi.org/10.1016/B0-08-043152-6/00978-5>.
- Bol'shakov, A., Mao, X., Gonzalez, J., and Russo, R. (2016). Laser ablation molecular isotopic spectrometry (LAMIS): current state of the art. *Journal of Analytical Atomic Spectroscopy* <https://doi.org/10.1039/C5JA00310E>.
- Botto, A., Campanella, B., Legnaioli, S. et al. (2019). Applications of laser-induced breakdown spectroscopy in cultural heritage and archaeology: a critical review. *Journal of Analytical Atomic Spectrometry*. <https://doi.org/10.1039/C8JA00319J>.
- Connors, B. and Day, D. (2018). Screening food packaging for fluorinated compounds using laser-induced breakdown spectroscopy. *International LIBS Conference 2018*, Atlanta, GA (21–26 October 2018).

- Connors, B., Somers, A., and Day, D. (2016). Application of handheld laser induced breakdown spectroscopy (LIBS) to geochemical analysis. *Applied Spectroscopy*. <https://doi.org/10.1177/0003702816638247>.
- Cremers, D.A. and Radziemski, L.J. (1983). Detection of chlorine and fluorine in air by laser-induced breakdown spectroscopy. *Analytical Chemistry* <https://doi.org/10.1021/ac00259a017>.
- Cremers, D.A. and Radziemski, L.J. (2006). *Laser-Induced Breakdown Spectroscopy*. Chichester: Wiley.
- Crocombe, R.A. (2018). Portable spectroscopy. *Applied Spectroscopy* <https://doi.org/10.1177/0003702818809719>.
- Czerny, M. and Turner, A.F. (1930). Über den astigmatismus bei spiegelspektrometern. *Zeitschrift für Physik*. <http://dx.doi.org/10.1007/BF01340206>.
- D'Andrea, E., Pagnotta, S., Grifoni, E. et al. (2014). An artificial neural network approach to laser-induced breakdown spectroscopy quantitative analysis. *Spectrochimica Acta Part B: Atomic Spectroscopy* <https://doi.org/10.1016/j.sab.2014.06.012>.
- Darmont, A. (2009). Spectral response of silicon image sensors. White Paper. [https://britastro.org/sites/default/files/attachments/SpectralResponse\\_WhitePaper\\_April09.pdf](https://britastro.org/sites/default/files/attachments/SpectralResponse_WhitePaper_April09.pdf) (accessed 1 November 2019).
- David, H.W. and Omenetto, N. (2012). Laser-induced breakdown spectroscopy (LIBS), part II: review of instrumental and methodological approaches to material analysis and applications in different fields. *Applied Spectroscopy* 66 (4): 347–419.
- Day, D.R. (2018). Analyzer alignment, sample detection, localization, and focusing method and system. US Patent 9,939,383 B2, filed 5 February 2016 and issued 10 April 2018.
- Day, D.R., Sackett, D.W. (2017). Libs analyzer sample presence detection system and method. US Patent 9,664,565, filed 26 February 2015 and issued 30 May 2017.
- Day, D.R., Derman, K., Egan, J.E., and Soucy, P.E. (2016). Handheld libs analyzer end plate purging structure. US Patent 9,395,243 B2, filed 29 January 2015 and issued 19 July 2016.
- Gornushkin, I.B., Ampsonah-Manager, K., Smith, B.W. et al. (2004). *Microchip Laser-Induced Breakdown Spectroscopy: A Preliminary Feasibility Investigation*. <https://doi.org/10.1366/0003702041389427>.
- Guang, Y., Shujun, Q., Pengfei, C. et al. (2015). Rock and soil classification using PLS-DA and SVM combined with a laser-induced breakdown spectroscopy library. *Plasma Science and Technology*. <https://doi.org/10.1088/1009-0630/17/8/08>.
- Häkkänen, H.J. and Korppi-Tommola, J.E. (1995). UV-laser plasma study of elemental distributions of paper coatings. *Applied Spectroscopy* 49 (12): 1721–1728.
- Hark, R. and East, L.J. (2014). Forensic application of LIBS. In: *Springer Series in Optical Sciences*. <https://doi.org/10.1007/978-3-642-45085-3-14>.
- Harmon, R.S., Hark, R.R., Throckmorton, C.S. et al. (2017). Geochemical fingerprinting by handheld laser-induced breakdown spectroscopy. *Geostandards and Geoanalytical Research*. <https://doi.org/10.1111/ggr.12175>.
- Harmon, R.S., Throckmorton, C.S., Hark, R.R. et al. (2018). Discriminating volcanic centers with handheld laser-induced breakdown spectroscopy (LIBS). *Journal of Archaeological Science* <https://doi.org/10.1016/j.jas.2018.07.009>.
- Kramer, R. (1998). *Chemometric Techniques for Quantitative Analysis*. Marcel Dekker: Basel.
- Kumar, R., Devanathan, A., Mishra, N.L., and Rai, A.K. (2019). Quantification of heavy metal contamination in soil and plants near a leather tanning industrial area using libs and TXRF. *Journal of Applied Spectroscopy* <https://doi.org/10.1007/s10812-019-00919-w>.
- Lynges, O., Traggis, N., Dessau, K., and Myatt, C. (2006). Coating technologies for high-damage-threshold optics. *Optics & Photonics News* <https://doi.org/10.1364/OPN.17.6.000028>.
- Mark, H. and Workman, J. (2018). *Chemometrics in Spectroscopy*. <https://doi.org/10.1016/B978-0-12-805309-6.09994-3>
- Mizolek, A.W., Palleschi, V., and Schechter, I. (2006). *Laser Induced Breakdown Spectroscopy*. <http://dx.doi.org/10.1017/CBO9780511541261>.
- Mukhopadhyay, P. (2011). *Development and Characterization of Diode Pumped Solid State Lasers*. Saarbrücken, Germany: LAP LAMBERT Academic Publishing GmbH & Co. KG.

- Musazzi, S. and Perini, U. (2014). *Laser-Induced Breakdown Spectroscopy: Theory and Applications*. Berlin Heidelberg: Springer-Verlag.
- Noll, R. (2012). *Laser-Induced Breakdown Spectroscopy: Fundamentals and Applications*. Berlin Heidelberg: Springer-Verlag.
- Noll, R., Frick-Begemann, C., Connermann, S., and Sturm, V. (2018). LIBS analyses for industrial applications – an overview of developments from 2014 to 2018. *Journal of Analytical Atomic Spectroscopy* <https://doi.org/10.1039/c8ja00076j>.
- Patterson, J.I. (2015). *HH-XRF and HH-LIBS for Alloy Analysis: Choosing the Right Tool for the Right Job*. Portable Analytical Technologies <https://pdfs.semanticscholar.org/3346/41a9f180db4a11cb1ffbe6d59805e0be1923.pdf> (accessed 1 November 2019).
- Poulson, B. (2014). Predicting and preventing flow accelerated corrosion in nuclear power plant. *International Journal of Nuclear Energy*. <http://dx.doi.org/10.1155/2014/423295>.
- Prasad, N.E., Gokhale, A.A. and Wanhill, R.J. (2014). *Aluminum-Lithium Alloys: Processing, Properties, and Applications*. <https://doi.org/10.1016/C2012-0-00394-8>.
- Quant, F., Farmer, K.R., Tan, P.V. et al. (2016). Handheld laser induced breakdown spectroscopy device. US Patent 9,506,869 B2, filed 14 October 2014 and issued 29 November 2016.
- Rakovsky, J., Cermak, P., Musset, O., and Veis, P. (2014). *A Review of the Development of Portable Laser Induced Breakdown Spectroscopy and its Applications*. <http://dx.doi.org/10.1016/j.sab.2014.09.015>.
- Rigaku Inc. (2018). Positive Material Identification (PMI) of Metal Alloys. <https://www.rigaku.com/en/products/libs/kt100s/app003> (accessed 1 November 2019).
- Scheeline, A. (2017). How to design a spectrometer. *Applied Spectroscopy* 71 (10): 2237–2252.
- SciAps (2016). *Fast, Laser-Based Cr Analysis for Flow Accelerated Corrosion (FAC) Applications*. Application Note. <https://www.sciaps.com/fast-laser-based-cr-analysis-for-flow-accelerated-corrosion-fac-applications> (accessed 1 November 2019).
- SciAps (2018). *Carbon Analysis in Stainless and Carbon Steels with Handheld LIBS*. Application Note. [https://www.sciaps.com/wp-content/uploads/2018/04/SciAps\\_ApNote\\_LIBSCarbonMARCH2018.pdf?x24702](https://www.sciaps.com/wp-content/uploads/2018/04/SciAps_ApNote_LIBSCarbonMARCH2018.pdf?x24702) (accessed 1 November 2019).
- SciAps (2019). NDT and PMI. <https://www.sciaps.com/industries/ndt-pmi> (accessed 1 November 2019).
- Tashuk, M.T., Cravetchi, I.V., Tsui, Y.Y., and Fedosejevs, R. (2007). Micro-LIBS. In: *Laser-Induced Breakdown Spectroscopy* (ed. T. Page), 173–196. Amsterdam: Elsevier.
- Wang, S.X.. (2017). Laser induced breakdown spectroscopy (libs) apparatus based on high repetition rate pulsed laser. US Patent 9,797,776 B2, filed 27 May 2016 and issued 24 October 2017.
- Zayhowski, J.J. and Mooradian, A. (1989). *Single-Frequency Microchip Nd Lasers*. <https://doi.org/10.1364/OL.14.000024>.
- Zhang, T., Tang, H., and Hua, L. (2018). Chemometrics in laser-induced breakdown spectroscopy. *Journal of Chemometrics*. <https://doi.org/10.1002/cem.298>.

## 14

### Miniaturized Mass Spectrometry – Instrumentation, Technology, and Applications

Dalton T. Snyder

*Resource for Native Mass Spectrometry Guided Structural Biology, The Ohio State University, Columbus, OH, USA*

#### 14.1 Introduction

Mass spectrometry (MS) is a highly sensitive, selective, and versatile analytical tool for complex mixture analysis. Despite its overwhelming utility, mass spectrometry has usually been constrained to conventional analytical laboratories. Benchtop mass spectrometers are bulky, heavy, power-hungry, and expensive, akin to the first electronic computers of the mid-1900s or cell phones of the late twentieth century, which were not widely used, yet viewed promising. Even so, just as researchers and manufacturers reduced the size and power consumption of electronic devices while increasing their ease of use, so too is mass spectrometry being miniaturized to the point of portability, and so the scope of applications that can be investigated by mass spectrometry is being expanded.

At its core, mass spectrometry is the science and technology of ions, i.e. charged particles. The goal of most mass spectrometry experiments is to measure, ideally in an unbiased manner, the mass-to-charge ratios ( $m/z$ ) of ions generated from a particular sample, and, in doing so, deduce the chemical makeup of the sample's constituents. For example, mass spectrometry can determine whether an apple is organic by determining the presence or absence of pesticides, herbicides, and fungicides on the apple. Foliar phytochemicals can be monitored in response to some external stimulus, e.g. herbivory or volatile signaling cues from nearby plants. Trace amounts of explosives and narcotics can be detected from suspicious packages or residues during traffic stops or at an airport. Mass spectrometry can also detect chemical warfare agents CWAs on the battlefield in order to protect soldiers or civilians during times of war.

With conventional benchtop mass spectrometers, samples from each of these situations would have to be transported back to the lab for analysis. While there are many analytical questions that favor benchtop systems, which typically have higher sensitivity, resolution, and mass accuracy than their portable counterparts, in the cases listed above, portable mass spectrometers with modest performance would be more fitting. Removing suspicious packages from X-ray machines at the airport and moving or shipping them to a proper analytical laboratory is at best inconvenient and at worst logically impractical. If endogenous metabolites or externally applied chemicals (pesticides) are to be measured from plant foliage, the chemical makeup of the sample may change by the time it reaches the laboratory. In situations where lives are at risk – detecting CWAs or explosives, for example – the laboratory often *must* be brought to the sample rather than the sample being brought to the laboratory. There is, therefore, an increasing need and desire for portable analytical instrumentation, with mass spectrometry at the forefront as one of the most powerful tools in the analytical chemist's arsenal.

The first step in the mass spectrometry experiment is to produce ions from a sample of typically neutral molecules. Once ions are produced by the ionization source and transported to the mass analyzer in a vacuum, their  $m/z$  values can be measured with high accuracy and precision (indicating the molecular formulas of the

analytes) and, if coupled with tandem mass spectrometry, the arrangement of atoms of each of the sample's constituents can be determined. In order for the ion's  $m/z$  to be measured successfully by the analyzer, the ion must be transported from ambient air outside the vacuum chamber to the mass analyzer far below ambient pressure, either directly so through a capillary inlet or via an intermediate interface (e.g. a membrane inlet for the transport of dissolved gases and volatile organics). This represents a change in pressure of over seven orders of magnitude! While the ion is in vacuum, its trajectory can be controlled very precisely by electric (e.g. ion trap or quadrupole) and/or magnetic (e.g. magnetic sector) fields without substantial deviations in the ion motion that would otherwise be caused by collisions with background gas molecules. Vacuum systems are by far the most difficult subsystems to miniaturize and are usually the power and size bottleneck for portable MS systems.

## 14.2 Instrumentation

### 14.2.1 Ion Introduction and Vacuum Systems

The chemical makeup of a sample is determined by measuring the  $m/z$  values of the sample's components using a mass analyzer. In order for the ions' trajectories to be manipulated accurately, precisely, and *predictably*, the ions must be analyzed in a vacuum, normally at pressures where collisions with background gas have a negligible effect on ion motion. Generally, it is best if the mean free path of the ions is  $\sim$ 5–10 times the length of ion travel in the mass analyzer. For quadrupole ion traps, which can function at the highest pressure of all analyzers, the typical operating pressure is  $10^{-5}$  to  $10^{-3}$  Torr. In exceptional cases, ion traps can be operated at pressures around 1–10 Torr, but this is not typical and mass spectral resolution and sensitivity are severely compromised. Quadrupole mass analyzers operate at  $10^{-6}$ – $10^{-5}$  Torr, time-of-flight (TOF) mass analyzers require at most  $10^{-6}$  Torr, and sectors require similarly stringent pressure regimes. For TOF and sector mass analyzers, collisions are more detrimental toward resolution than for ion traps and quadrupoles. Orbitrap and Fourier transform ion cyclotron resonance mass analyzers are not discussed here as they are not appropriate analyzers for miniature systems due to their requirement for ultrahigh vacuum (problematic for terrestrial applications but feasible in space) and their complexity.

In order to achieve the necessary vacuum conditions for mass analysis, the mass analyzer needs to be seated in a vacuum chamber, typically a hollow block of stainless steel or aluminum. Various feedthroughs for vacuum pumps and control voltages are machined into a chamber that is otherwise sealed gas-tight with o-rings. A critical consideration in the design of a vacuum chamber is how ions will be introduced into the system. This decision determines which pumps are chosen to maintain the requisite mass analyzer pressure, and the size and power consumption of the pumps regulate the portability of the entire mass spectrometer.

In general, there are three strategies for ion introduction, shown in Figure 14.1. The first option (Figure 14.1a), which matches the strategy employed for benchtop mass spectrometers, is to couple differential pumping with a continuous atmospheric pressure interface (API). Ions from the ion source are introduced through an "inlet," usually a small hole in the vacuum chamber or a capillary that protrudes from the chamber, which allows the ions to pass from ambient pressure (760 Torr) to a first vacuum region at  $\sim$ 1–10 Torr. The modest pressure in the first region of differential pumping is often achieved in portable systems with a single diaphragm or scroll pump. The first region of differential pumping must usually have an ion optical element, such as an radio-frequency (RF) multipole or an ion funnel as well as a skimmer in order to keep the desolvating ions from being defocused as they undergo free jet expansion. In rare cases, e.g. Figure 14.1a, the inlet capillary stretches the length of the first pressure region. This strategy is simple but sacrifices sensitivity as ions are lost between the stages of differential pumping. The ions are then transported to the second stage of differential pumping which is held at high vacuum pressure and which houses the mass analyzer. Although differential pumping is ideal for benchtop systems, which do not have size and power constraints, it is challenging to implement effectively on portable spectrometers coupled with a continuous ion source due to the limitations in pumping capacity. Even so, a high acquisition rate

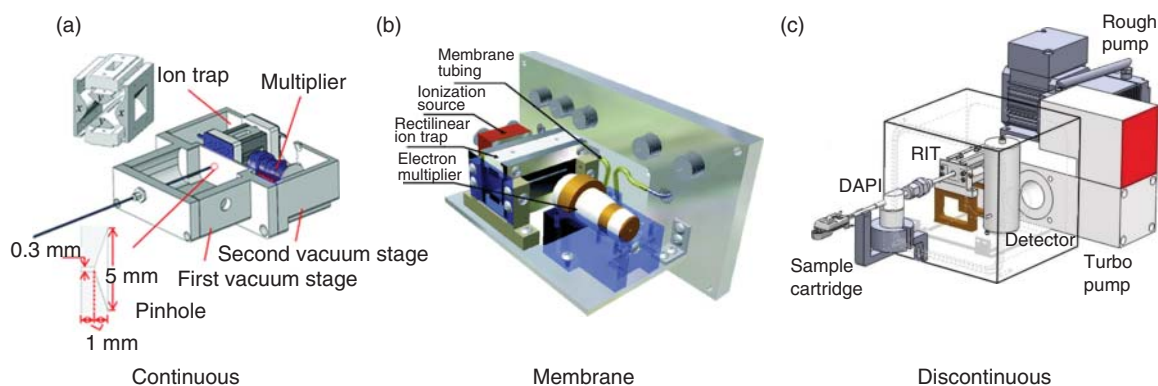


**Figure 14.1** Atmospheric pressure interfaces for portable mass spectrometers: (a) continuous atmospheric pressure interface (Source: Zhai, Y., Feng, Y., Wei, Y., Wang, Y., and Xu, W. (2015). Development of a miniature mass spectrometer with continuous atmospheric pressure interface. *Analyst* 140: 3406–3414. © 2015 Royal Society of Chemistry); (b) membrane inlet (Source: Gao, L., Song, Q., Patterson, G.E., Cooks, R.G., and Ouyang, Z. (2006). Handheld rectilinear ion trap mass spectrometer. *Anal. Chem.* 78: 5994–6002. © 2006 American Chemical Society); and (c) discontinuous atmospheric pressure interface (DAPI) (Source: Li, L., Chen, T.C., Hendricks, P.I., Cooks, R.G., and Ouyang, Z. (2014). *Anal. Chem.* 86: 2909–2916. © 2014 American Chemical Society).

(# of scans/second) is maintained because the ion source and mass analyzer can be operated continuously, and any external ionization source may be coupled with the system.

A second, particularly popular, option is to place the ion source inside the vacuum chamber (“internal” ionization) and introduce the sample through a membrane inlet (Figure 14.1b). The membrane, typically polydimethylsiloxane, limits gas conductance into the instrument and is simple to implement. Liquid and gas samples can both be introduced and heated so that volatiles and semivolatiles are desorbed and pass through the membrane and into the ionization region. Usually, the ion source is a variant of electron impact (EI) ionization, which generates molecular cations for mass spectrometry analysis. Like the continuous atmospheric interface, the system pressure is maintained throughout the analysis, and so the mass analyzer and ion source can be operated continuously, resulting in a high acquisition rate. The chemical composition of the membrane can be tailored for molecules of a particular size, polarity, or affinity; albeit, characteristics that increase the membrane’s selectivity also constrain its applicability (the main disadvantage). Membrane introduction mass spectrometry (MIMS) nonetheless remains a viable option for many targeted portable MS applications (e.g. monitoring volatiles in the environment), and the lax pumping requirements of MIMS systems are attractive for reducing system weight and power (SWaP).

The third API strategy is to pulse ions into the vacuum chamber, that is, implement a discontinuous atmospheric pressure interface (DAPI, Figure 14.1c). A compromise of sorts between the continuous and membrane interfaces, DAPI allows the use of smaller and lower power pumps while also maintaining compatibility with external ionization sources. Similar to the continuous API, ions travel through an aperture in the vacuum chamber or through a capillary inlet. However, in DAPI implementations, the ion introduction is pulsed rather than continuous. This is typically accomplished by replacing a portion of the metal inlet capillary with a soft silicone section that is constricted by a pinch valve. To introduce ions (and neutrals), the pinch valve is opened for ~10–20 ms, during which the pressure in the vacuum chamber increases by two to three orders of magnitude. Ions are trapped in the mass analyzer or some other trapping device while the neutrals are pumped away until the requisite pressure for mass analysis is attained, a period of time on the order of 500 ms. Mass analysis can then proceed as usual. The main compromise when using a discontinuous interface is the loss of acquisition rate. Because the mass analyzer must be pumped down to operating pressure after ions and neutrals are introduced, the typical acquisition rate of DAPI systems is ~1 Hz. The variable pressure in the vacuum chamber also limits DAPI systems to ion traps as mass analyzer candidates. Even so, DAPI is a promising ion introduction technology because the use of small vacuum

pumps enables greater portability and simplifies the MS design since a single vacuum stage is all that is needed, and the ability to couple with external ambient ionization sources is an attractive proposition.

The API design drastically affects both the size of the inlet aperture and the choice of backing and turbopumps. While a larger diameter inlet allows more ions into the mass analyzer per unit time, a greater number of neutral gas molecules are also introduced. Larger inlets, therefore, must also be accompanied by higher pumping capacity (read: bulkier and higher power pumps), which, in turn, limits instrument portability. So while a continuous API may seem the ideal option between the three choices discussed above, in practice, the apertures between pressure stages must often be made quite small to limit gas introduction, which limits ion fluence. For systems which use non-trapping mass analyzers (e.g. quadrupoles and magnetic sectors), it is usually not efficient to couple a DAPI interface with the analyzer without differential pumping, and so either the continuous or membrane API (or another API with limited gas conductance) is the only option.

The miniaturization of mass spectrometry would certainly not be possible without the ability to maintain a high vacuum with sufficiently small pumps. Figure 14.2 shows several of the most common backing and high vacuum pumps used in miniature and portable mass spectrometers, and Table 14.1 lists some of their specifications. KNF Neuberger, Pfeiffer, and Creare are the main manufacturers of small vacuum pumps. Usually, the pumping system of a miniature mass spectrometer consists of a ~10–80 L/s turbopump backed by a ~5 L/min diaphragm or scroll pump. The Pfeiffer line of high vacuum pumps includes the HiPace 10 (10 L/s), HiPace 30, HiPace 60 P, and HiPace 80, with higher capacity being accompanied by higher power consumption and instrumental bulk. For example, while the HiPace 80 specifications indicate a pumping capacity of up to 67 L/s (for nitrogen), its maximum 110 W power consumption and 2.4 kg mass are noticeably higher than the HiPace 10's 28.8 W maximum power consumption and 1.8 kg mass. Creare also manufactures specialized miniature vacuum pumps for portable mass spectrometers, including a 550 g turbopump and a 130 g drag pump. Both offer >4 L/s pumping capacity and a low power consumption of 12 W while maintaining a remarkably small footprint. Regardless of which high vacuum pump is chosen, it must be coupled with a backing pump, most often a ~5 L/min diaphragm pump akin

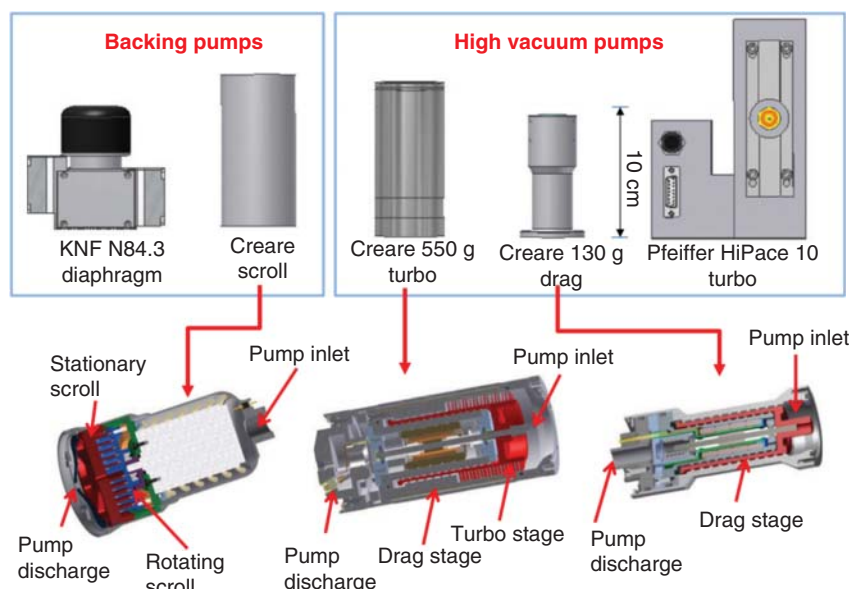


**Figure 14.2** Representative backing and high-vacuum pumps used in portable mass spectrometers. Source: Chen, C., Chen, T., Zhou, X., Kline-Schoder, R., Sorenson, P., Cooks, R.G., and Ouyang, Z. (2014). *J. Am. Soc. Mass Spectrom.* 26, 240–247. © 2014 American Chemical Society.

**Table 14.1** Characteristics of the vacuum pumps in Figure 14.2.

Pump	Weight (g)	Pumping speed	Compression ratio	Max. foreline pressure (Torr)	Max. power (W)	Rotor speed (rpm)	Inlet ID (mm)
KnF N84.3 diaphragm pump	900	5 L/min (at 1 atm)		760	18		
Creare 130 g scroll pump	350	1 L/min (at 1 torr)		760	6		
HiPace 10 turbopump	1800	10 L/s (at 0.1 mtorr)	$3 \times 10^6$	18	28	90k	24
Creare 550 g turbopump	550	>4 L/s (at 0.1 mtorr)	$1 \times 10^9$	10	12	100k	53
Creare 130 g drag pump	130	>4 L/s (at 0.1 mtorr)	$1 \times 10^5$	10	12	200k	25

Source: Chen, C., Chen, T., Zhou, X., Kline-Schoder, R., Sorenson, P., Cooks, R. G., and Ouyang, Z. Design of portable mass spectrometers with handheld probes: aspects of the sampling and miniature pumping systems. *J. Am. Soc. Mass Spectrom.* 26: 240–247. © 2014 American Chemical Society.

to the KNF N84.3, which weighs 900 g and consumes up to 18 W of power. KNF offers similar pumps with small variations in pumping capacity. The Pfeiffer MVP line of diaphragm pumps (not shown) consists of the MVP 010 which has a pumping capacity of up to 10 L/min and weighs only 2 kg. Meanwhile, Creare manufactures a 350 g scroll pump with a pumping capacity of 1 L/min and maximum power consumption of 6 W. The ultimate pressure of these backing pumps is usually on the order of ~1 Torr, with final pressures below  $10^{-5}$  Torr when coupled with a turbopump. This pressure is sufficiently low for quadrupole mass filters and ion traps which make up the majority of miniature mass analyzers.

### 14.2.2 Sampling and Ionization

Because mass spectrometry uses electric and magnetic fields to control the trajectories of charged particles in the gas phase, the first step in the analysis procedure is usually to generate ions from the corresponding neutral molecules that make up a sample and to transfer those ions into the vacuum chamber. If internal ionization is utilized instead of external ionization, then the neutral molecules are moved into the vacuum chamber and then ionized. Ionization and sampling are, therefore, critical steps to consider in the mass spectrometry workflow since they affect overall instrument design and can either limit or augment the capabilities of a portable mass spectrometer.

Ionization can be broadly classified as either external or internal, depending on where ions are generated from the corresponding neutral molecules. In the former case, sampling and ionization take place outside the vacuum chamber, and often sampling and ionization are conducted simultaneously (e.g. with ambient ionization sources). Sampling and external ionization can also be decoupled. One example is electrospray ionization (ESI), wherein the sample is dissolved in an ESI-compatible solvent to accomplish the sampling step. Ionization is effected by transporting the solution to the sharp end of a metal needle or glass capillary and applying a high potential difference between the solution and the inlet capillary of the instrument, generating a mist of charged droplets and eventually bare ions. In contrast, internal ionization is accomplished *inside the vacuum chamber*, and so the neutral sample (solid, liquid, or gas) must first be volatilized and transported into vacuum from atmospheric pressure. As discussed in the next paragraph, internal ionization is limited in scope, yet it remains a powerful tool in combination with well-established spectral EI ionization libraries.

*Internal ionization* occurs inside the vacuum chamber; the most common method is EI ionization in which an energetic (70 eV) electron beam from a resistively heated filament is directed at a volatilized sample. Figure 14.3a shows an arrangement of an EI ionization source coupled to a 3D ion trap. EI produces molecular cations (i.e. the neutral molecule loses an electron) but is also “hard” enough to cause fragmentation. As such, a single

analyte generally produces an array of mass spectral peaks including the molecular cations and fragments from unimolecular dissociation. Fortunately, EI is highly reproducible across instrument platforms and is ubiquitous. EI mass spectra acquired on a portable instrument can be directly compared to publicly available or internal databases – the National Institutes for Standards and Technology (NIST) EI database, for example – and sample components can be identified with high accuracy so long as they have undergone prior separation by gas chromatography (GC) to limit spectral contamination. Drawbacks of EI include limited filament lifetime at high pressure, especially in the presence of oxygen, and high power consumption. Glow discharge EI ionization can produce EI-like spectra without the use of a filament and at a fraction of the power consumption. A potential difference is applied between opposing plates in a pressurized (~0.5 Torr) region inside the vacuum chamber, generating cations, anions, and electrons. The electrons are then extracted through an aperture in one of the plates and are used for ionization.

As just described, for systems which use internal ionization, the sample must be converted to the gas phase (volatilized), moved inside the vacuum chamber, and finally ionized. Hence, the sample must be volatile, which severely limits the scope of molecular classes that can be observed to small, mostly nonpolar analytes such as volatile organic compounds (VOCs) and explosives. Even so, one of the primary benefits of internal ionization – often coupled with membrane inlets or other gas-constricting manifolds – is that less pumping capacity can be used to maintain vacuum compared to spectrometers that use external ionization. Several sampling methodologies can be happily married with internal ionization sources. Common suitors are headspace sampling, swabs, and solid-phase microextraction probes. Headspace sampling involves injecting a gaseous sample at equilibrium with its headspace and is particularly common for analysis of VOCs. Usually, internal ionization is coupled with GC to analyze headspace vapors. A drawback of this method is its limited sensitivity since the sample is not preconcentrated, yet its simplicity is attractive. Similarly, swabs made of paper, nylon, or other porous materials can also be used for sample collection. The swab is then inserted into a slot on the instrument and heated, thereby desorbing volatile and semivolatile analytes which are ionized and detected. Solid-phase microextraction (SPME) probes are common sampling devices (Figure 14.3b). Using SPME, analytes can instead be preconcentrated on a hydrophobic sorbent bed prior to injection onto a GC. SPME devices are typically fibers coated with liquid or solid polymeric films. The fiber is dipped into a sample of interest, wherein the sample adsorbs to the fiber material. The SPME probe is then inserted into the mass spectrometer and the sample-containing fiber is exposed and heated to desorb analytes from the fiber. SPME devices are small and convenient for trace sampling, are reusable (like some swabs), and have increased sensitivity due to sample concentration prior to injection into the instrument.

*External ionization* sources generate ions outside the vacuum chamber. Whereas for internal ionization sampling and ion generation are distinct, external ionization sources may entail only ionization or both ionization and sampling. The most common sources in which sampling and ionization are still distinct are ESI, nanoelectrospray ionization (nESI), and atmospheric pressure chemical ionization (APCI). To generate ions using ESI or nESI, a sample is dissolved in a solvent and the resulting solution is placed into a metal or glass capillary with a sharp tip. With the application of a high voltage between the solution and the instrument inlet (Figure 14.3c, voltage not shown), charged microdroplets are formed which eventually fission and desolvate to leave bare protonated or salt-adducted ions. Spray-based ionization is generally only suitable for polar analytes, yet it remains the most popular ionization source in mass spectrometry due to high sensitivity, ease of use at atmospheric pressure, and “softness” (i.e. very little fragmentation is induced in the source). APCI, another “soft” ionization source, uses a corona discharge to generate ions from a sample that has been heated and volatilized. APCI is suitable for polar and some nonpolar compounds so long as they are not thermally labile, and the ions observed are similar to those from ESI. In general, instruments which utilize external ion sources tend to have broader applicability in exchange for requiring higher pumping capacity to remove excess solvent and gas that is introduced through the instrument inlet. Matrix-assisted laser desorption/ionization (MALDI) and laser desorption ionization (LDI) are worth mentioning as alternative ion sources that use lasers to effect ionization. Because lasers increase overall

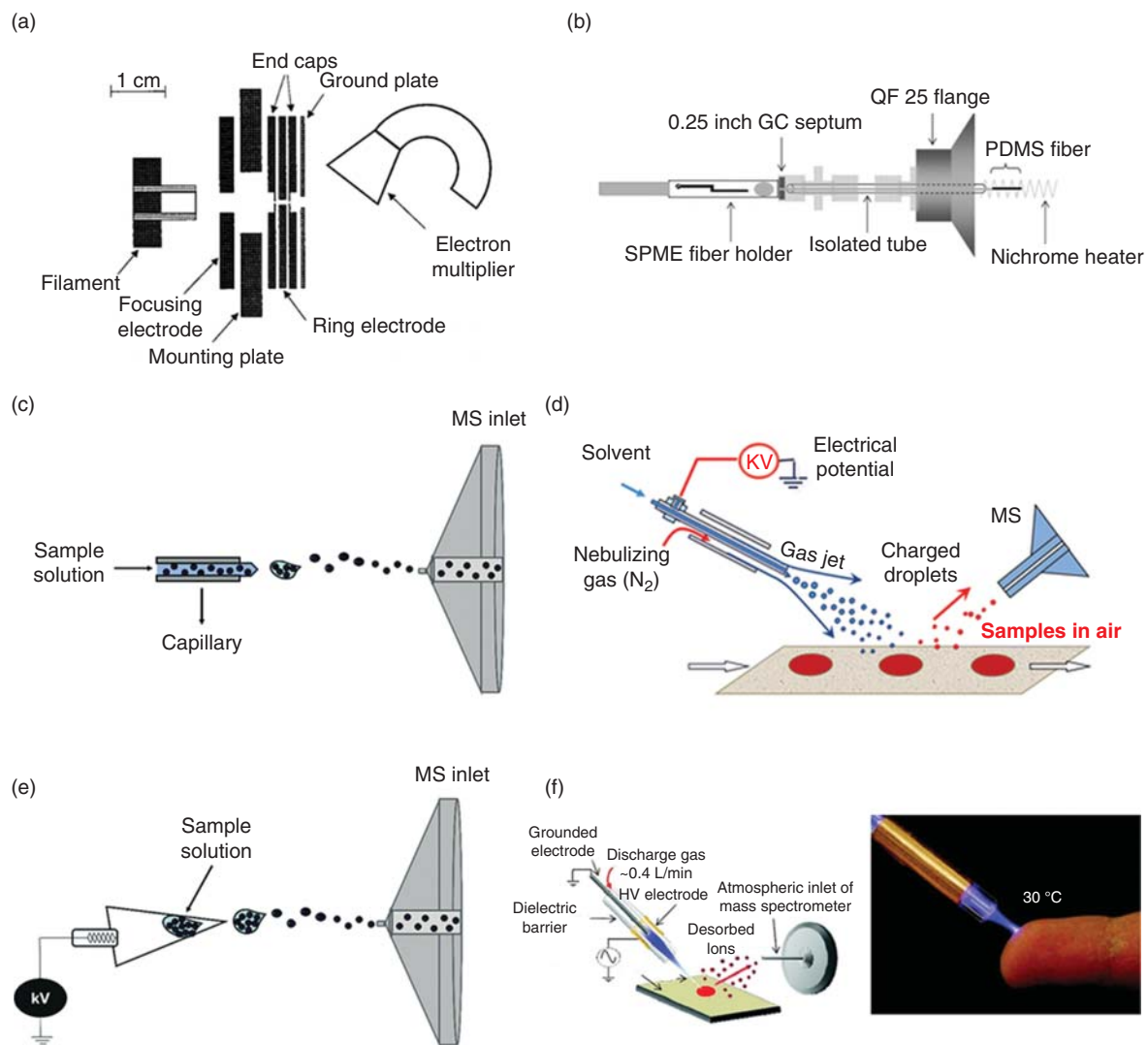


**Figure 14.3** Sample introduction and ionization for portable mass spectrometers. Samples can either be introduced to the vacuum chamber directly by thermal desorption [(b), solid-phase microextraction with thermal desorption] and ionized by (a) electron impact ionization; or analyzed directly using spray-based ionization [(c), electrospray ionization; (d) desorption electrospray ionization; (e), paper spray ionization] or plasma-based ionization [(f), low-temperature plasma]. Source: Panel (a) from Kornienko, O., Reilly, P.T.A., Whitten, W.B., and Ramsey, J.M. (1999). Electron impact ionization in a microion trap mass spectrometer. *Rev. Sci. Instrum.* 70: 3907–3909. © 1999 AIP Publishing. Panel (b) from Riter, L.S., Meurer, E.C., Cotte-Rodriguez, I., Eberlin, M.N., and Cooks, R.G. (2003). Solid phase microextraction in a miniature ion trap mass spectrometer. *Analyst* 128: 1119. © 2013 Royal Society of Chemistry. Panels (c) and (e) from da Silva, L.C., Pereira, I., de Carvalho, T.C., Filho, J.F.A., Romão, W., and Vaz, B.G. (2019). Paper spray ionization and portable mass spectrometers: a review. *Anal. Methods* 11: 999–1013. © 2019 Royal Society of Chemistry. Panel (d) from Ifa, D.R., Wu, C., Ouyang, Z., and Cooks, R.G. (2010). Miniaturized mass spectrometry – instrumentation, technology & applications. *Analyst* 135: 669–681. © 2010 Royal Society of Chemistry. Panel (f) reproduced from Harper, J., Charipar, N.A., Mulligan, C.C., Zhang, X., Cooks, R.G., and Ouyang, Z. (2008). Low-Temperature plasma probe or ambient desorption ionization. *Anal. Chem.* 23: 9097–9104. © 2008 American Chemical Society.

instrument volume and power consumption, they are not ideal for portable mass spectrometers, but they may be useful for targeted applications and for mass spectrometry imaging.

Ambient ionization is used to generate ions from samples in their native environment without any kind of sample pretreatment or preparation. Because sampling and ionization steps take place simultaneously, ambient ionization is the preferred method of ion generation for portable instruments. Ambient ionization was coined at the advent of desorption electrospray ionization (DESI), a technique in which a spray of charged microdroplets is aimed at a sample (Figure 14.3d). The sample is dissolved in a thin film of solvent and subsequently desorbed by further impacts of microdroplets. This generates a beam of fissioning/desolvating microdroplets that can be collected in the inlet of a mass spectrometer for analysis. The second ambient ionization technique reported in the literature was direct analysis in real time (DART), in which excited state gaseous species (helium, nitrogen, or argon) formed from exposure to a high potential difference cause a cascade of ion/molecule reactions which eventually produces pseudomolecular (protonated) ions. While DESI is most appropriate for polar analytes, DART is applicable to polar and some nonpolar analytes. Both DESI and DART use compressed gases, in DESI to generate the microdroplet spray and in DART to create excited-state atoms/molecules, which adds to overall SWaP. In addition, the extra gas load may increase system pressure, yet these drawbacks may be overshadowed by the versatility of combining sampling and ionization. Paper spray ionization is another ambient ionization source that replaces the glass or steel capillary of ESI with a simple paper triangle to which sample and high voltage are applied (Figure 14.3e). In this case, the paper substrate can also conveniently act as a swabbing material for sample collection. The paper can be modified in various ways to increase its sensitivity and/or selectivity (e.g. by increasing or decreasing its hydrophobicity) or to decrease the voltage needed to generate a spray (e.g. by doping in nanowires or carbon nanotubes). Other raw materials may be used as substrate, not just paper. For example, leaves and other plant material can be cut to a point and solvent and high voltage can be applied to generate ions (“leaf spray ionization”). Hence, paper spray is remarkably simplistic and easy to use, yet also quite versatile.

Plasma-based ambient ionization sources also abound. For example, a low-temperature plasma (LTP, Figure 14.3f) can be generated from an inert carrier gas (He, N<sub>2</sub>, Ar) at atmospheric pressure by applying a high alternating current (AC) voltage across a dielectric barrier. The plasma interacts directly with the sample for ionization and desorption. It is limited to analytes of low molecular weight (particularly those that are also volatile) but is applicable to both polar and nonpolar analytes and has low power consumption (~5 W). Many other plasma ionization sources exist, namely desorption atmospheric pressure chemical ionization (DAPCI), flowing afterglow atmospheric pressure glow discharge, plasma-assisted desorption ionization, and dielectric barrier discharge ionization. The differences in device configuration, AC vs. direct current (DC) discharge, gas substrate, plasma properties (e.g. temperature and “hardness”), flow rate, and power consumption are beyond the scope of this article.

### 14.2.3 Mass Analyzers

The mass analyzer is the heart of any mass spectrometer; its purpose is simply to measure the  $m/z$  values of the ions generated from a sample. There are several important mass analyzer figures of merit that must be considered: mass accuracy, mass resolution, mass range, sensitivity, dynamic range, acquisition rate, and pressure and electronic requirements. Mass accuracy describes the closeness of the measured mass to the exact theoretical (monoisotopic) mass, whereas mass resolution is a measure of mass spectral peak width, usually defined as  $m/\Delta m$  (where  $m$  is the measured  $m/z$  and  $\Delta m$  is the peak width measured as the full-width at half-maximum [FWHM] intensity). Sensitivity is the slope of the calibration curve (measured ion intensity plotted against concentration), dynamic range is a measure of the ratio of the highest concentration over the lowest concentration that can be measured simultaneously, and acquisition rate is the number of scans per second. Portable mass spectrometers should strive to achieve 10<sup>2</sup> ppm (parts per million) mass accuracy, unit mass resolution (i.e. resolving successive integer  $m/z$  values), ~10<sup>3</sup> dynamic range, and >1 Hz acquisition rate (maintaining compatibility with chromatographic methods).

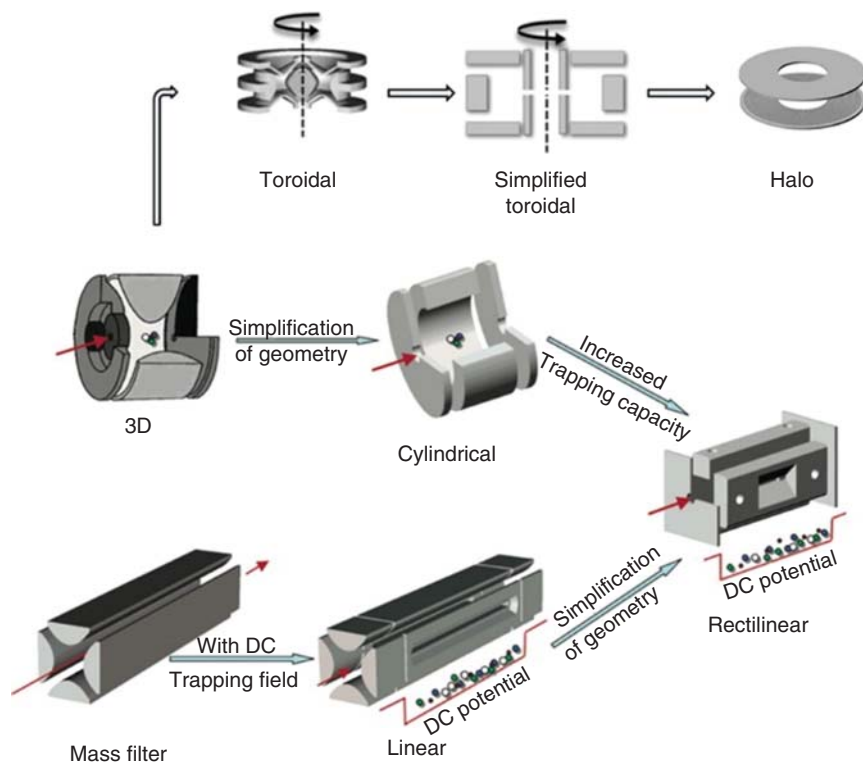


**Figure 14.4** Common mass analyzers in portable mass spectrometers. All are ion traps except for the quadrupole mass filter. Source: Snyder, D.T., Pulliam, C.J., Ouyang, Z., and Cooks, R.G. Miniature and fieldable mass spectrometers: recent advances. *Anal. Chem.* 88(1): 2–29. © 2015 American Chemical Society.

Due to the limitations imposed by the vacuum system, orbitrap, Fourier transform ion cyclotron resonance, and TOF mass analyzers – all of which function best at ultrahigh vacuum pressures ( $<10^{-7}$  Torr) – are generally not found in portable mass spectrometers. Instead, quadrupole ion traps and quadrupole mass filters operating at more modest pressure (ion trap:  $10^{-3}$ – $10^{-5}$  Torr; quadrupole mass filter:  $<10^{-5}$  Torr) are the practical choices. Notably, ion trap resolution and sensitivity conveniently benefit from the additional collision cooling at higher pressures! Figure 14.4 shows a sampling of the most prominent analyzer geometries. Quadrupole mass filters and ion traps satisfy the figures of merit qualifications listed above. They typically obtain mass errors  $<0.1$  Da as well as unit mass resolution and good dynamic range and sensitivity, all while having an acquisition rate on the order of 1–10 Hz.

A quadrupole mass filter consists of a set of four steel rods with hyperbolic cross-sections arranged in a square configuration. With the application of an RF voltage to one pair of rods opposite each other and the opposite phase of RF to the other pair of rods, a quadrupolar potential (or quadrupolar “field,” a common misnomer) is created inside the device. It is beyond the scope of this chapter to discuss the details of quadrupolar potentials and the Mathieu parameters that govern both quadrupolar mass filters and quadrupole ion traps, so only a brief description of the operation of these devices will be given here. If only an RF potential is applied to the quadrupole rods, then the quadrupole is said to be in “transmission” or “RF-only” mode, in which case ions of a large range of  $m/z$  values are transmitted. However, if a resolving DC is also applied (i.e. a positive DC potential on one pair of rods and the opposite polarity on the other pair), then the quadrupole mass filter is said to operate in “RF/DC” or “mass-selective stability” mode. That is, it is acting as an  $m/z$  resolving quadrupole by allowing only a small range

of  $m/z$  values through the device. If the RF and DC potentials applied to the rods are ramped simultaneously while keeping their ratio near-constant, then a mass spectrum may be obtained in order of increasing  $m/z$ .

A linear quadrupole ion trap can be thought of as a quadrupole mass filter with endcap electrodes whose applied DC potentials prevent ions from escaping from the device along its axis, thus trapping the ions. In contrast to the quadrupole which operates in mass-selective stability mode, the ion trap operates in “mass-selective instability” mode, wherein the ions are made unstable in order of  $m/z$  and are ejected toward an ion detector, generating a mass spectrum. To accomplish this task, only the RF voltage is applied to the trap rods, and the amplitude of the RF voltage is ramped linearly so as to make the trajectories of ions of successively higher  $m/z$  unstable so that they are ejected into a charged particle detector. The ions can be ejected at the Mathieu stability boundary at Mathieu  $q = 0.908$ , where

$$q = 4V_{RF}m/ze{r_0}^2\Omega^2 \quad (14.1)$$

$V_{RF}$  is the zero-to-peak amplitude of the RF voltage,  $e$  is the elementary charge,  $r_0$  is the inscribed radius of the device (half distance between opposite rods), and  $\Omega = 2\pi f$  is the angular RF frequency ( $f$  is the RF frequency in Hz). The ions can instead be ejected at any arbitrary Mathieu  $q$  parameter (frequency) by applying a supplemental dipolar AC frequency of low voltage to the ion trap rods, a method known as “mass-selective instability with resonance ejection.” This change in “operating point” can benefit resolution, sensitivity, and mass range, though the optimum ejection point must be carefully determined experimentally. Unlike the quadrupole mass filter, the ion trap’s performance metrics (save for dynamic range) fortunately do not inherently depend on device size, a characteristic also not shared by TOF and sector mass analyzers. Ion traps are thus the ideal candidates for portable mass spectrometers, with quadrupole mass filters coming in second place. Resolution and mass accuracy ought to be maintained in miniature versions of ion traps, and any loss in dynamic range can be compensated by making arrays of ion traps, as discussed below. As the size of an ion trap decreases, so does the path length of the ions, and so the analyzer can be operated at higher pressure while maintaining resolution. The drive RF frequency can be increased to compensate for any resolution losses since

$$m/\Delta m \propto \Omega_{RF}/P = \Omega_{RF}\tau/4\sqrt{(3)} \quad (14.2)$$

where  $m/\Delta m$  is the mass resolution,  $\Omega_{RF}$  is the angular RF frequency in radians/s,  $P$  is the buffer gas pressure, and  $\tau$  is the relaxation time of an ion caused by ion-neutral collisions.

The linear ion trap has evolved from the 3D quadrupole ion trap, which consists of a ring electrode and two endcap electrodes, all with hyperbolic cross-sections. The RF voltage is usually only applied to the ring electrode, and auxiliary resonance frequencies may be applied in a dipolar manner to the endcaps for resonance excitation or ejection. The 3D ion trap shares many of the same qualities of the linear ion trap, but the linear trap sports greater ion injection efficiency and trap capacity. As a result, 3D ion traps are becoming less prominent. Through the use of resonance excitation – applying a low-voltage auxiliary AC waveform with frequency matching an ion’s *secular frequency* (the ion’s  $m/z$ -dependent and, hence,  $q$ -dependent frequency of motion in the trap) – product ion MS/MS spectra may be generated. All types of quadrupole ion traps have the ability to perform single analyzer MS/MS experiments – tandem mass spectrometry – in which an ion is isolated, activated through collisions with intentionally introduced background gas molecules, and fragmented, and the fragments are subsequently mass analyzed. Product ion spectra can be used to confirm molecular identity through spectral library matching or to probe the connectivity of atoms in an ion whose structure is unknown and whose MS/MS spectrum is not already found in spectral libraries. Precursor ion scans, neutral loss scans, two-dimensional tandem mass spectrometry scans, and other unusual yet promising scanning methodologies are more recent innovations but have yet to see wide acceptance. Even so, the wide array of capabilities of quadrupole ion traps is yet another attractive feature for portable spectrometers.

Quadrupole ion traps come in many additional sizes and geometries in addition to the linear ion trap and 3D trap just described. For example, the cylindrical ion trap is a simplified 3D quadrupole ion trap in which

the cross-sections of the electrodes are rectangular and the edges are flat instead of hyperbolic. Similarly, the rectilinear ion trap is a simplified linear ion trap with rectangular cross-sections. While this electrode geometry compromises the quadrupolar character of the electric field, unit resolution and good mass accuracy can still easily be obtained in a package that is far easier to manufacture than traps designed with hyperbolic cross-sections. Moreover, quadrupole ion traps of all geometries are highly tolerant to electric field imperfections and to pressure variations, more so than other instruments. This is especially important as manufacturing tolerances become more stringent with smaller analyzer dimensions. The cylindrical ion trap and rectilinear ion trap retain all of the characteristics and capabilities of the 3D trap and linear trap, respectively, and they can be manufactured as serial or parallel arrays of mass analyzers that can enhance the capabilities of the analyzer, decrease power consumption by reducing the operating voltage, or increase the dynamic range. Maintaining consistency in size and electric field across the analyzers in the array remains a challenge and has prevented widespread adoption, yet arrays remain promising configurations.

The toroidal ion trap can be generated by rotating a 3D ion trap about an axis parallel to the line through the endcaps but tangent to the outside of the ring electrode. The result is a “donut” or toroidal shape, and the electric field inside the device is largely quadrupolar if an RF potential is applied. The main advantage of the toroidal trap in comparison to 3D and linear ion traps is the increase in dynamic range and sensitivity with a small increase in device size. The trapping capacity of the toroidal trap is perhaps orders of magnitude higher than a 3D trap of comparable inscribed radius. Like the cylindrical and rectilinear ion traps, toroidal traps with rectangular cross-sections have been investigated, and an elegant “halo ion trap” consisting of two ceramic plates with ring electrodes patterned on the plates has also been demonstrated. The toroidal traps have all the capabilities of other ion traps and portable versions have even been commercialized by TORION (now part of PerkinElmer). Improvements to the mass analyzer geometry are still ongoing, as the electrode curvature warps the electric field inside the device, which can have deleterious side effects.

While the main focus of this section has been quadrupole mass filters and quadrupole ion traps, by far the most common analyzers in portable mass spectrometers, there are other analyzers worth mentioning. Both sectors and TOF instruments suffer from performance degradation as the mass analyzer is shrunk, and so miniaturizing these devices comes at a steep cost in terms of mass spectral resolution. Even so, TOF instruments, which simply consist of plates with high voltages applied, offer theoretically unlimited mass range as well as excellent mass accuracy and resolution. Yet their requirement for ultrahigh vacuum limits their adoption in portable systems. Miniature magnetic sectors have been an interesting topic of research in recent years, with reports of coded aperture systems maintaining mass spectral resolution without sacrificing ion throughput at smaller dimensions. That is, the coded aperture design uses the Felgett advantage in a cycloidal mass analyzer geometry to increase signal-to-noise ratio without sacrificing resolution.

#### 14.2.4 Separations Prior to Mass Analysis

Analysis of samples with portable mass spectrometers is preferably conducted without any extraneous subsystems to minimize SWaP. The sampling interface, ion source, vacuum system, mass analyzer, detector, and data systems can all be considered essential. Separation capabilities prior to mass analysis, such as ion mobility (IM) spectrometry, gas or liquid chromatography (LC), and capillary electrophoresis (CE), which are auxiliary subsystems, can, however, be useful and sometimes essential for targeted applications or when the complexity of the sample is too high for unit resolution mass analyzers.

GC and LC, both conducted prior to analyte ionization, involve the injection of a sample into a “carrier” stream which pushes the sample components through a stationary phase (the “column”) where the constituents are separated in space and eluted usually in order of polarity. For GC, the carrier is an inert gas such as helium or nitrogen and the stationary phase is a polymer (e.g. dimethylsiloxane), whereas in LC, the carrier is a combination of polar and nonpolar solvents (water, methanol, acetonitrile, etc.) and the stationary phase consists of glass beads with a

polar or nonpolar (e.g. C<sub>18</sub>) coating. Because the stationary phase is generally nonpolar, sample constituents elute from the column starting with the most polar compounds. Both gas and liquid chromatography can be coupled to portable mass spectrometers and are useful for analyzing particularly complex mixtures where species overlapping in *m/z* space are problematic. GC is the more common method for portable systems and is usually coupled with internal EI ionization. Its most significant drawback is that only volatile and semivolatile analytes will be observed because the sample must be heated and vaporized prior to GC injection. In addition, only a few ionization sources can be coupled with GC, usually EI or glow discharge ionization. For LC, usually coupled with ESI, the analyte must be soluble in the mobile phase, and solvent reservoirs and liquid-handling systems add to SWaP.

Although CE has not been coupled with commercialized portable mass spectrometers, it is worth noting as an alternative to GC and LC. CE separates analytes by their electrophoretic mobility in an aqueous buffer. A potential difference is applied across some length of silica capillary tubing, and as the injected sample plug moves along the length of the capillary, the analytes separate by size and charge. In general, ions that are small and more highly charged will tend to migrate the quickest, and so they will be ionized (via ESI) and detected by the mass analyzer sooner than larger ions in low charge states, generating “chromatograms” similar to GC-mass spectrometry (GC-MS) and LC-MS. In contrast to GC, CE is an attractive separation technique for polar, nonvolatile analytes.

GC, LC, and CE are separations that are conducted prior to analyte ionization, whereas IM is a *post-ionization* separation scheme that takes place in the gas phase. IM involves the injection of ionized analytes into a drift gas with an electric field established across the pressurized IM chamber. The electric field pushes ions through the drift gas, but collisions between the ions and the drift gas cause the analytes to exit from the mobility cell in order of their gas-phase mobility. The ion’s mass, charge, size, and shape all affect the observed “drift time” (i.e. when the ions exit the cell). IM is most promising for larger molecules such as polypeptides and proteins, yet can also be useful for small molecules. For example, it can be used to distinguish isomeric species that are otherwise identical to the mass analyzer, though most IM systems do not have the resolution to do so. Like the other separation techniques, SWaP is increased by adding IM as a subsystem, and having a pressurized IM cell necessitates increased pumping capacity and likely more stages of differential pumping. Like TOFs and magnetic sector analyzers, the resolution of the IM separation depends on device size. As such, IM is rarely coupled to portable mass spectrometers (aside from the commercial Excellims MC3100 discussed later), but its adoption is likely to increase in the near future, particularly for forensic applications which often require two orthogonal dimensions of compound identification (e.g. IM and MS, GC and MS, or LC and MS).

#### 14.2.5 Detectors

After the ions are sorted into *m/z* bins by the analyzer, they must be converted into a measurable signal (a current or voltage) that is then digitized and processed by a computer. As the number of ions sorted by the mass analyzer per second is generally less than 100 000 ( $\sim 10^{-14}$  A), the signal must be amplified prior to digitization. The most common charged particle detectors in mass spectrometry are the electron multiplier, the Faraday cup, and the microchannel plate. An electron multiplier, the most common mass spectrometry detector, uses the kinetic energy of incident ions – accelerated to high energies via a large attractive voltage applied to the detector – to cause collision with a material having good secondary emission properties (e.g. Cu-BeO) and cause the release of secondary electrons. The electrons are then further accelerated and multiplied in stages, with each stage providing additional amplification. Typical gain is six to seven orders of magnitude. Discrete dynode detectors have 10–20 stages of amplification. A second type, the continuous dynode electron multiplier (or channeltron), uses a continuous lead-doped glass surface to generate secondary electrons from ion collisions. The channeltron device first converts incident positive or negative ions into electrons using a conversion dynode, and these secondary

electrons then proceed through the cascading effect of the multiplier. Overall, electron multipliers provide high gain (sensitivity) and dynamic range ( $10^4$ – $10^6$ ) with fast response time, though their lifetime is limited due to oxidation, surface contamination, and electron depletion. Mass discrimination is observed with these detectors since the gain is velocity dependent. Hence, lower  $m/z$  ions tend to generate larger signals due to their higher velocities, though this effect can be somewhat mitigated by increasing the voltage on the conversion dynode. A microchannel plate is a type of electron multiplier with many parallel channels. By biasing one side of the plate relative to the other, a cascading effect can be induced after a first collision of an analyte ion onto the device, generating amplification per channel of  $10^2$ – $10^4$  while ensuring fast rise times due to the minimal travel distance. Electron multipliers and microchannel plates can be made sufficiently small for most portable mass spectrometers and require high-voltage power supplies for operation.

In contrast to the cascading effects of electron multipliers, Faraday cups inherently provide no amplification, yet they also have less mass discrimination. A Faraday cup is simply a metal cylinder, cup, or plate onto which ions are neutralized. A current is generated which proceeds through a resistor and is amplified with external circuitry. Because there is no cascade of electrons within the detector, Faraday cups have much lower sensitivity than electron multipliers and their signals are more prone to be overwhelmed by background noise. They also provide slower rise times which can be improved by sacrificing sensitivity. As a result, these devices are not commonly used in portable mass spectrometers.

#### 14.2.6 Data Acquisition, Control, and Interpretation

After ions are sorted by the mass analyzer and converted to an amplified analog signal by the detector and its associated electronics, they must then be digitized, processed, and interpreted by a computer. For a portable system, the computer is ideally a rugged laptop or touchscreen tablet. Data processing can include signal averaging, background subtraction, peak annotation, molecular formula determination, MS/MS interpretation, isotope analysis, charge state assignment, quantitation (via internal or external standards), and more. The computer then displays the data to the user, who must either further interpret the data, act on it, or initiate further processing or mass spectrometry analyses.

The user interacts with the mass spectrometer through a GUI (graphical user interface), of which there are often “expert” and “novice” modes. Expert modes of operation may allow the user to redefine the instrument’s scan function, manually calibrate the  $m/z$  or intensity axis, and various other tasks. For most users, who are not likely to have backgrounds in mass spectrometry, a novice interface presents options to select particular analyses depending on the situation of interest and to optimize signal intensity through tuning of instrument parameters (e.g. timing, voltages, pressures, etc.). For example, the mass spectrometer can focus on detecting drugs, explosives, or VOCs, for which internal and external libraries of spectra are readily available. The instrument may guide these users through particular tasks such as calibration, sampling, ionization, and MS/MS analysis. Ideally, the instrument is capable of performing all of these tasks with minimal user intervention, and the instrument should identify the components in the mixture and also report a measure of confidence in the results. For most applications, the capabilities of the computer should be entirely internal and should not rely on external connections (e.g. the Internet) which are less reliable in unpredictable field environments. However, cloud integration presents a promising alternative for future data analytics in which data is acquired locally, processed in the cloud, and returned to be displayed to the user rather than being interpreted locally on the computer itself. Potential advantages of this methodology are access to faster and more sophisticated processing techniques which would otherwise be resource intensive on a local machine, comparison to a greater number of inhouse or Internet-accessible spectral libraries, remote instrument control, and the ability to monitor long-term instrument performance.

### 14.2.7 Commercially Available Systems

While miniature mass analyzers, new sampling and ionization strategies, and smaller and lower power vacuum pumps and electronics have been evolving over the course of several decades, only more recently have these technologies converged to a point where portable mass spectrometers could feasibly be commercialized. Table 14.2 lists currently available *portable* or *fieldable* mass spectrometers for which specifications are readily available from the manufacturers. Note that some systems which are *miniature* but not *fieldable* or *portable* have been excluded from this list, but are discussed briefly at the end of this section.

Three of the systems described in Table 14.1 contain quadrupole mass filters as analyzers, namely the FLIR G510, the Inficon Hapsite, and the Q Technologies AQUA MMS (miniature mass spectrometer). The G510 and the Hapsite both couple GC to EI ionization, with several auxiliary sampling strategies such as SPME, headspace sampling, a preconcentrator, and so on. They have relatively modest mass range that sufficiently covers volatile and semivolatile analytes compatible with these sampling methodologies, and they can operate on battery power for two to four hours. Intended applications of these devices include forensics, CWA and explosive detection, VOC monitoring, and more. The AQUA MMS similarly uses a quadrupole mass filter with EI ionization but has a more limited mass range that is suitable for detection of small organics and gases dissolved in water.

Most of the commercialized portable mass spectrometers understandably utilize ion traps as the mass analyzer. These include the 1st Detect TRACER 1000, the 908 Devices MX908, the Bayspec Continuity and Portability, Excelims' MC3100, the MassTech MT Explorer 50, the Torion (now PerkinElmer) T-9, and the Mini  $\beta$  from PURSPEC. Most of these systems use linear ion traps, with the exception of the MX908 which uses an unknown geometry, the MT Explorer 50 (which uses a 3D quadrupole ion trap), and the Torion T-9 (the only system to include a unique toroidal ion trap geometry). Many of these systems have atmospheric pressure interfaces that allow them to couple with ambient ionization sources, notably ESI, APCI, DART, MALDI, and/or paper spray. Like the FLIR and Inficon instruments, the T-9 has an internal ionization source and utilizes technologies such as SPME and GC. Most operate in both positive and negative ion modes, have upper  $m/z$  limits around  $m/z$  1000, and can operate on battery power for at least two hours. Common applications include explosive and CWA detection, narcotics analysis, and environmental monitoring.

There are other commercial systems that are *miniature* but not strictly portable. These include several single quadrupole mass spectrometers, including the 4500 MiD from Microsaic Systems, the DART QDa, ACQUITY, and SQ Detector 2 from Waters, and the Advion expression CMS (Compact Mass Spectrometer). Usually, these are intended as compact and simple benchtop detectors for pharmaceutical research, often coupled with LC. They are compatible with a variety of external ionization sources. Compact triple quadrupole systems do exist, e.g. the Agilent Ultivo and the Waters Xevo TQ-S micro, with sizes comparable to an LC stack. Lastly, TOFWERK develops custom-fieldable TOF mass spectrometers for a variety of purposes, including VOC detection and elemental analysis, and ZeteoTech has developed a “digital” MALDI-TOF platform for detection of high molecular weight biological species such as bacteria and proteins.

## 14.3 Applications

Portable instruments have expanded the utility of mass spectrometry beyond the analytical laboratory so that *in situ* measurements can be made in the field in real time. Though the virtually limitless potential of portable MS has yet to be realized in its entirety, several important applications have been described in detail in the literature and are emerging as practical cases.

Detection of illicit or dangerous substances is one case where it is logistically impractical or disadvantageous to collect the sample and bring it to a laboratory setting. Police officers, for example, have several tools at their

**Table 14.2** Commercially available miniature and portable mass spectrometers.

Instrument	Affiliation	Sample introduction	Ionization source(s)	Polarity	Analyzer	Mass range (m/z)	Resolution	MS/MS	Power	Mass (kg)	Intended application
TRACER 1000	1st Detect	Teflon-coated fiberglass swabs; sampling wand	CI	+/-	Linear ion trap	Unknown	Unknown	Unknown	110 VAC/230 VAC, 50 Hz/60 Hz	25	Explosives; Narcotics
MX908	908 Devices	Thermal desorption swab for solids/liquids; direct gas/vapor analysis	Internal	+/-	Ion trap	50–460	Unknown	Yes	>3 h of continuous operation	3.9	Chemical warfare agents; Narcotics; Emerging threats; Explosives; Precursors
Continuity	Bayspec	AI	TD-ESI; APCI; EI	+/-	Linear ion trap	50–1200	0.49 amu FWHM	Yes	72 W	20	Explosives; Narcotics; Pesticides; Mycotoxins
Portability	Bayspec	AI	TD-ESI; APCI; EI	+/-	Linear ion trap	50–650	0.49 amu FWHM	Yes	72 W	10	Explosives; Narcotics; Pesticides; Mycotoxins
MC3100	ExcellIMS	AI; Thermal desorption; Continuous liquid introduction	ESI; Corona + discharge		Linear ion trap + Ion mobility	20–2800	Unit	Yes	250 W	35	Narcotics; Food & Drug safety; Pharmaceuticals
G510	FLIR	Gas chromatography; Heated sample probe; Membrane introduction for vapors; Internal dual-bed preconcentrator with split/splitless injector port; direct liquid sampling via syringe; SPME; PSI	EI	+	Quadrupole mass filter	15–515	0.7 amu FWHM	No	2–4 h on battery	16.3	Narcotics; Explosives; Environmental contaminants
HAPSITE	Inficon	Gas chromatography; headspace sampling; SituProbe; SPME; Thermal desorption	EI	+	Quadrupole mass filter	41–300	Unknown	No	2–3 h on battery	19	VOCs; SVOCs; Chemical warfare agents; Toxic industrial materials

(Continued)

**Table 14.2** (Continued)

Instrument	Affiliation	Sample introduction	Ionization source(s)	Polarity	Analyzer	Mass range (m/z)	Resolution	MS/MS	Power	Mass (kg)	Intended application
MT Explorer 50	MassTech	Direct sampling	ESI, AP MALDI; APCI; sESI; DART	+/-	3D ion trap	30–2500	Up to 6000 @ 2000 Da	Yes	100–300 W	34	Narcotics; Explosives; Pesticides;
TORION T-9	PerkinElmer (Torion)	SPME; Needle trap; Gas chromatography	EI	+	Toroidal ion trap	41–500	Unit	Unknown	2.5 h on battery	14.5	Environmental volatiles and semivolatiles; Explosives; Chemical warfare agents; Hazardous substances; Food safety
Mini $\beta$	PURSPEC	AI (noncontinuous API)	AI (ESI, paper capillary spray)	+/-	Linear ion trap	50–2000	<1 amu	Yes	100 W	20	Narcotics; Food and drug regulation; Biomedical & clinical
AQUA MMS	Q Technologies	Membrane inlet	EI	+	Quadrupole mass filter	Up to 200	Unit	No	<50 W	Unknown	Oil/hydrocarbons in water; dissolved gases

APCI = atmospheric pressure chemical ionization; API = atmospheric pressure interface; AI = ambient ionization; CI = chemical ionization; DART = direct analysis in real time; EI = electron impact; ESI = electrospray ionization; FWHM = full-width at half-maximum; LTP = low-temperature plasma; PSI = prepass sample introduction; sESI = secondary electrospray ionization; SPME = solid-phase microextraction; TD = thermal desorption.

disposal for detection of illicit substances (drugs or alcohol), including chemical and electrochemical tests, but with the emergence of drug analogs and more potent alternatives (e.g. fentanyl and its derivatives), it is increasingly of value for officers to have immediate access to highly sensitive and selective, yet broadly applicable, analytical detectors. Figure 14.5a, for example, shows a mass spectrum of 10 ng each of three cathinones, 3,4-methylenedioxypyrovalerone ( $m/z$  276, MDPV), methylone ( $m/z$  208), and mephedrone ( $m/z$  178), deposited on a Teflon slide and detected using a Griffin AI-MS 1.2 cylindrical ion trap mass spectrometer. The analytes were sampled from the slide using DESI. This experiment demonstrates the high sensitivity and broad detection range that mass spectrometry brings to drug analysis in the field, as all three cathinones, though structurally diverse, can be detected in a single scan and in trace amounts. Portable mass spectrometers can be used for the detection of a range of nefarious substances, not just drugs. Figure 14.5b shows detection of gunshot residues methyl centralite ( $m/z$  241) and ethyl centralite ( $m/z$  269) via MS/MS, using rayon swabs to collect the material from a suspected shooter's hand and also to serve as the ionization substrate ("swab touch spray" ionization). A Mini 12 rectilinear ion trap mass spectrometer with DAPI was used for this experiment. This forensic application could provide an on-site test to determine whether a suspect has recently used a firearm.

Police officers are not the only public servants that may benefit from the adoption of MS as a primary field analytical methodology. Portable MS could be invaluable for warfighters who are constantly exposed to unknown, dangerous, and foreign substances. Figure 14.5c shows mass spectra of CWA VX ( $m/z$  267, ethyl ({2-[bis(propan-2-yl)amino]ethyl}sulfanyl)(methyl)phosphinate) and its degradation product ( $m/z$  175) recorded using a Griffin 450 GC-MS via EI ionization coupled to quadrupole mass analyzer detection, and Figure 14.5d shows detection of explosives Tetryl, TNT, and HMX collected using DESI on a Mini 10 mass spectrometer. One could imagine affixing a miniature mass spectrometer to a rover or drone that could be wirelessly controlled and driven to a sample for detection. This strategy would mitigate risk to personnel, particularly if the sample is believed to be acutely toxic, explosive, or otherwise dangerous. Even if personnel are directly involved in the mass spectrometry analysis rather than robots, in contrast to laboratory-based mass spectrometry, portable mass spectrometry offers immediate answers to pressing questions (is this substance dangerous?) in potentially life-threatening situations.

At the moment, the most common applications of portable mass spectrometry are related to first responders and warfighters, but there are other uses that have garnered interest, namely water quality monitoring and detection of VOCs. In both cases, the technologies of choice are membrane inlets (which gases and volatile analytes may freely diffuse through) combined with EI ionization and quadrupole mass detection. Single photon ionization (irradiating the sample with an ultraviolet laser) is another useful source for VOCs and can prevent spectral overlap (compared to EI) since fragments are not produced. Portable mass spectrometry can measure trace concentrations of dissolved gases, such as oxygen, carbon dioxide, and nitrogen, volatile organics, such as benzene and toluene, polycyclic aromatic hydrocarbons, polychlorinated biphenyls, and dioxins, to name a few. An example where these detection capabilities would be useful is the detection of oil or pharmaceutical contamination in water after an industrial disaster. The concentrations of VOCs in drinking water may also be monitored to ensure that chemical levels are below regulated levels. More generally, any form of environmental pollution monitoring can benefit from online or offline mass spectrometry detection, and onsite measurements necessitate portable instrumentation.

Though the current list of applications for portable mass spectrometry is somewhat limited, it is expanding quite rapidly as portability opens new avenues of analysis. Figure 14.6 illustrates several more recent demonstrations of portable mass spectrometry for food quality screening, point-of-care clinical analysis, and disease diagnostics. One could imagine a world in which supermarket shoppers use pocket-sized portable mass spectrometers to determine what chemicals (fungicides, pesticides, and herbicides) are on the produce they intend to purchase, answering questions such as "is this apple really organic?". The mass spectrum in Figure 14.6a results from detection of fungicide diphenylamine ( $m/z$  170) directly from the surface of an apple using LTP ionization coupled to a Mini 12 mass

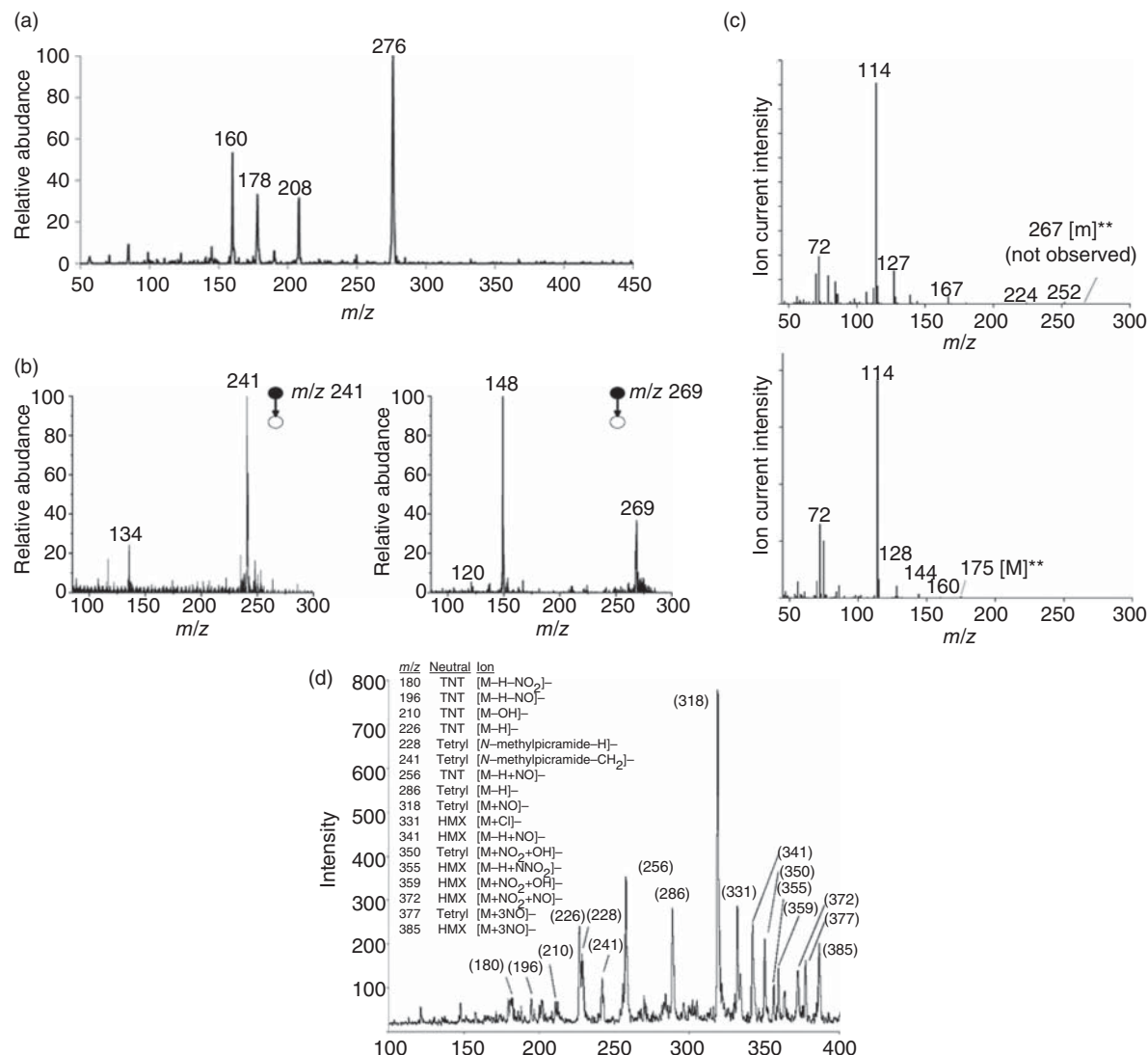


**Figure 14.5** Detection of narcotics, gunshot residues, chemical warfare agents, and explosives using miniature mass spectrometers: (a) desorption electrospray ionization mass spectrum of 10 ng each of 3,4-methylenedioxypyrovalerone ( $m/z$  276, MDPV), methylone ( $m/z$  208), and mephedrone ( $m/z$  178) on a Teflon slide using a Griffin Al-MS 1.2 cylindrical ion trap mass spectrometer; (b) swab touch spray product ion spectra of methyl centralite ( $m/z$  241) and ethyl centralite ( $m/z$  269) detected by a Mini 12; (c) quadrupole mass spectrum after electron impact ionization of chemical warfare agent VX ( $m/z$  267) and its degradation product ( $m/z$  175) recorded using a Griffin 450 GC-MS; and (d) negative ion mass spectrum of explosives Tetryl, TNT, and HMX collected using desorption electrospray ionization on a Mini 10 mass spectrometer. Source: Panel (a) from Vircks, K.E. and Mulligan, C.C. (2012). Rapid screening of synthetic cathinones as trace residues and in authentic seizures using a portable mass spectrometer equipped with desorption electrospray ionization. *Rapid Commun. Mass Spectrom.* 26: 2665–2672. © 2012 John Wiley & Sons. Panel (b) from Fedick, P.W., Bain, R.M. Swab touch spray mass spectrometry for rapid analysis of organic gunshot residue from human hand and various surfaces using commercial and fieldable mass spectrometry systems. *Forensic Chem.* 5: 53–57. © 2017 Elsevier. Panel (c) from Smith, P.A., Lepage, C.J., Lukacs, M., Martin, N., Shufutinsky, A., and Savage, P.B. Field-portable gas chromatography with transmission quadrupole and cylindrical ion trap mass spectrometric detection: chromatographic retention index data and ion/molecule interactions for chemical warfare agent identification. *Int. J. Mass Spectrom.* 295: 113–118. © 2010 Elsevier. Panel (d) reproduced from Sanders, N.L., Kothari, S., Huang, G., Salazar, G., Cooks, R.G. Detection of explosives as negative ions directly from surfaces using a miniature mass spectrometer. *Anal. Chem.* 82: 5313–5316. © 2010 American Chemical Society.

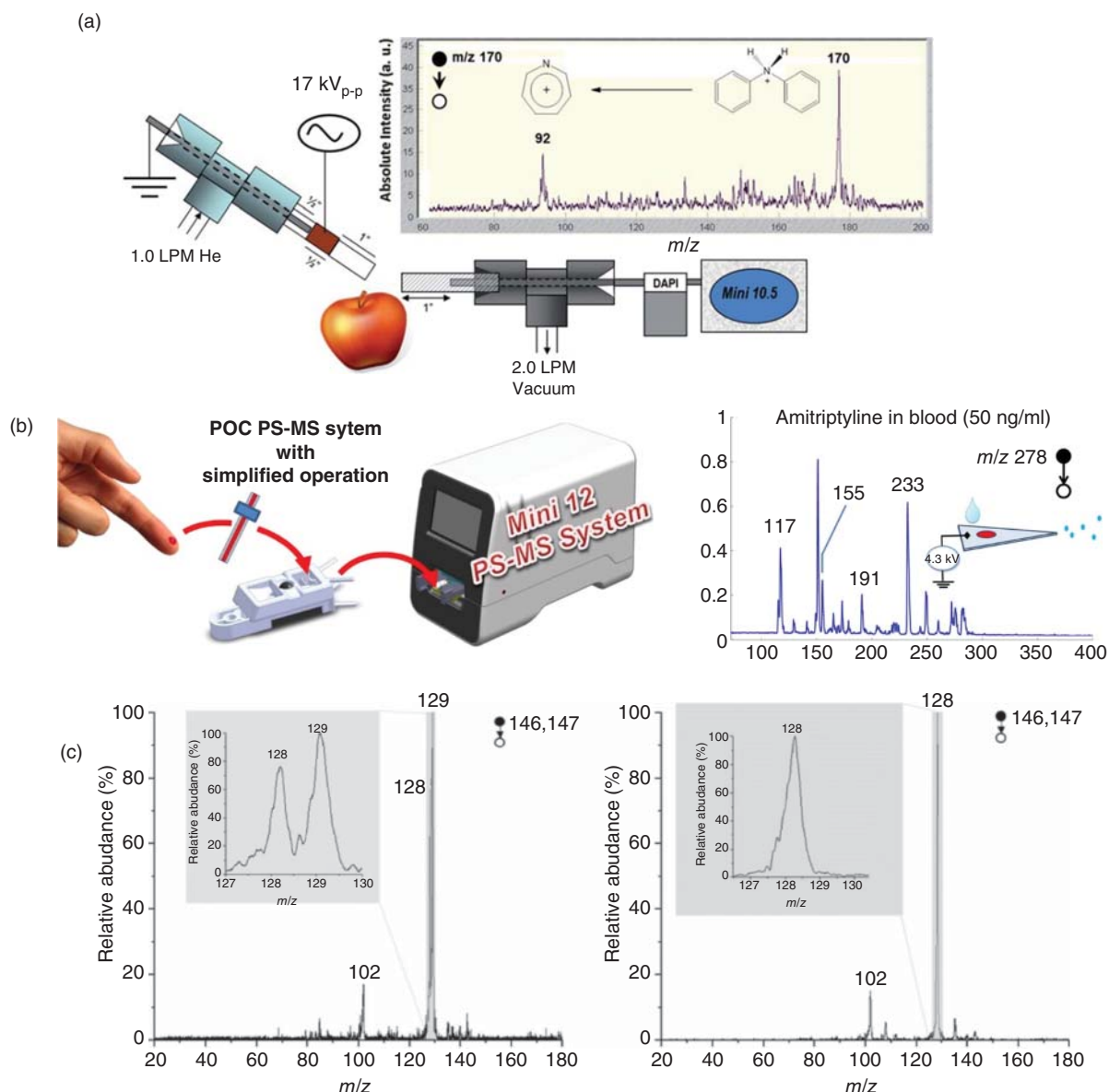


**Figure 14.6** Miniature mass spectrometers for detection of agrochemicals, point-of-care blood monitoring, and tissue analysis: (a) detection of fungicide diphenylamine directly from an apple using low-temperature plasma ionization on a Mini 10.5; (b) MS/MS spectrum of amitriptyline in blood using paper spray on a Mini 12; and (c) MS/MS spectra of deprotonated forms of 2-hydroxyglutarate ( $m/z$  146) and glutamate ( $m/z$  147) from an IDH (isocitrate dehydrogenase) mutant glioma (left) and IDH wild-type (right). The peak at  $m/z$  129 occurs only in the IDH mutant. Source: Panel (a) from Soparawalla, S., Tadjimukhamedov, F.K., Wiley, J.S., Ouyang, Z., and Cooks, R.G. In situ analysis of agrochemical residues on fruit using ambient ionization on a handheld mass spectrometer. *The Analyst* 136(21): 4392. © 2011 Royal Society of Chemistry. Panel (b) reproduced from Li, L., Chen, T.C., Hendricks, P.L., Cooks, R.G., and Ouyang, Z. (2014). Miniature mass spectrometer for clinical and other applications—introduction and characterization. *Anal. Chem.* 86: 2909–2916. © 2014 American Chemical Society. Panel (c) from Pu, F., Alfaro, C.M., Pirro, V., Xie, Z., Ouyang, Z., and Cooks, R.G. (2019). Rapid determination of isocitrate dehydrogenase mutation status of human gliomas by extraction nanoelectrospray using a miniature mass spectrometer. *Anal. Bioanal. Chem.* 411: 1503–1508. © 2019 Springer Nature.

spectrometer operated in the MS/MS mode. The product ion MS/MS scan of protonated diphenylamine is shown. Point-of-care analysis is a particularly promising direction, as it may offer money and time savings while providing immediate answers for many medical questions. It is reasonable to suppose that in the future, portable mass spectrometers would be used by doctors and nurses for drug and metabolite monitoring, early disease diagnosis, or bacteria detection onsite at the doctor's office. Figure 14.6b illustrates point-of-care drug-in-blood monitoring by paper spray mass spectrometry on a Mini 12 mass spectrometer. A drop of blood was placed on a paper triangle and solvent and high voltage were applied to generate ions that were detected by a rectilinear ion trap. Amitriptyline ( $m/z$  278, a prescription antidepressant) was detected via MS/MS at a concentration of 50 ng/mL. This experiment could be used to determine whether patients have been taking their prescribed mood-altering medications, and, because quantitative results can be obtained, to identify any changes in dosage that may be beneficial to them. This experiment may also be useful for therapeutic drug monitoring. Figure 14.6c shows negative ion mode MS/MS spectra of  $m/z$  146 and 147 (using a 2  $m/z$  wide isolation window), which correspond to deprotonated forms of 2-hydroxyglutarate and glutamate, respectively, from brain smears of (left) an isocitrate dehydrogenase (IDH) mutant glioma and (right) an IDH wild type. It is evident from the MS/MS spectra that only the IDH glioma gives the abundant product ion at  $m/z$  129 (a fragment of 2-hydroxyglutarate which has been shown to be indicative of glioma), whereas the wild type gives only fragments of glutamate, an indication of healthy tissue. In other words, MS/MS on a portable mass spectrometer can be used to detect cancerous tissues.

It is beyond the scope of this text to discuss every imaginable application of portable mass spectrometry. The field is advancing rapidly and new ideas are emerging every day; so, the topics included here should be understood as a subset of the applications that are either the most common or those which are exciting new developments. Space science, in particular, has been omitted from this text yet has been one of the primary drivers of miniature mass spectrometers and continues to push boundaries while also benefiting from new inventions. For those interested in the topic, reviews of extraterrestrial mass spectrometry are readily available in the literature.

## 14.4 Summary and Outlook

While mass spectrometry as a field has matured over the last several decades of research, only recently (~last 20 years) have portable mass spectrometers been the topic of intense research interest, culminating in the commercialization of several notable miniature and portable MS systems within the last decade. The advances in vacuum system, mass analyzer, sampling, ionization, and data acquisition/manipulation technologies will continue to drive mass spectrometry forward, resulting in substantially smaller, more power-efficient, and higher performing systems. As the overall system size decreases, the range of applications for portable MS will continue to increase rapidly, particularly if versatile methods of sampling and ionization (ambient ionization) are incorporated into newer designs. At the moment, internal ionization combined with membrane inlets (and often GC) and quadrupole mass filters remain popular choices for miniature systems, yet miniature ion traps coupled with ambient ionization and unique vacuum system configurations (e.g. DAPI) are emerging as the most sensible choice.

## Acronyms

AI	ambient ionization
APCI	atmospheric pressure chemical ionization
API	atmospheric pressure interface
CI	chemical ionization
CWA	chemical warfare agent

DAPI	discontinuous atmospheric pressure interface
DART	direct analysis in real time
DESI	desorption electrospray ionization
EI	electron impact (ionization)
ESI	electrospray ionization
FWHM	full-width at half maximum (a measure of mass spectral resolution)
GC	gas chromatography
IDH	isocitrate dehydrogenase
LDI	laser desorption ionization
LTP	low-temperature plasma (ionization)
MALDI	matrix-assisted laser desorption ionization
MS	mass spectrometry (or mass spectrometer, depending on context)
MS/MS	tandem mass spectrometry (two stages of mass selection and/or analysis, typically with an intermediate isolation and fragmentation step)
nESI	nanoelectrospray ionization
POC	point-of-care
PSI	prepless sample introduction or paper spray ionization, depending on the context
sESI	secondary electrospray ionization
SPME	solid-phase microextraction
TD	thermal desorption
Tetryl	2,4,6-trinitrophenylmethylnitramine (an explosive)
TNT	trinitrotoluene (an explosive)
HMX	1,3,5,7-tetranitro-1,3,5,7-tetrazoctane (an explosive)
VOC	volatile organic compound
VX	ethyl ({2-[bis(propan-2-yl)amino]ethyl}sulfanyl)(methyl)phosphinate (a chemical warfare agent, i.e. a nerve agent)

## Further Reading

- Blakeman, K.H., Wolfe, D.W., Cavanaugh, C.A., and Ramsey, J.M. (2016). *Anal. Chem.* 88: 5378–5384.
- Chen, C., Chen, T., Zhou, X. et al. (2015). *Journal of the American Society for Mass Spectrometry*. 26: 240–247.
- de Hoffman, E. and Stroobant, V. (2007). *Mass Spectrometry: Principles and Applications*, 3e. Wiley.
- Jiang, T., Zhang, H., Tang, Y. et al. (2017). *Anal. Chem.* 89: 5578–5584.
- Liu, X., Wang, X., Bu, J. et al. (2019). *Anal. Chem.* 91: 1391–1398.
- Snyder, D.T., Pulliam, C.J., Ouyang, Z.O., and Cooks, R.G. (2015). *Anal. Chem.* 88: 2–29.
- Tian, Y., Higgs, J., Barney, B., and Austin, D.E.J. (2014). *Mass Spectrom.* 49: 233–240.

## 15

# Portable Gas Chromatography–Mass Spectrometry: Instrumentation and Applications

*Pauline E. Leary<sup>1</sup>, Brooke W. Kammrath<sup>2,3</sup> and John A. Reffner<sup>4</sup>*

<sup>1</sup>*Federal Resources, Stevensville, MD, USA*

<sup>2</sup>*Department of Forensic Science, Henry C. Lee College of Criminal Justice and Forensic Sciences, University of New Haven, West Haven, CT, USA*

<sup>3</sup>*Henry C. Lee Institute of Forensic Science, West Haven, CT, USA*

<sup>4</sup>*Department of Sciences, John Jay College of Criminal Justice, City University of New York, New York, NY, USA*

### 15.1 Introduction

Gas chromatography–mass spectrometry (GC–MS) is a valuable laboratory method for the analysis of a wide range of analytes. It is extensively used and has even been called the gold standard for the identification of numerous chemical substances (Fogerson et al. 1997; Schecter et al. 1999; Tilstone et al. 2006). GC–MS systems integrate two independent technologies. Separation of mixtures into their components is performed using the GC; identification of these components is established based upon the GC and MS data. Independently, each method has value. GC is a premier analytical technique for the separation of volatile compounds. It combines rapid analysis, high resolution, excellent quantitative results, and moderate costs. MS systems are among the most information-rich detector types available. They require only micrograms or less of a sample, but provide data for both qualitative and quantitative analyses (McNair and Miller 2009). When combined, the value of the integrated system is dramatically increased over what either method can offer independently. For instance, the addition of MS detection to GC analysis enables confirmation of each chemical detected and presumptively identified in the GC. Likewise, the ability to separate complex mixtures on the front end using GC makes it possible to concentrate and purify components and then recover spectra of these purified components at low concentrations, even when masked within complex matrices.

There are many applications that benefit from the use of GC–MS in the field, but the development of portable versions of these systems has been relatively slow compared with the development of other types of portable spectrometers, such as infrared and Raman systems. Challenges faced when miniaturizing and extending GC–MS to field operators have been significant. In some instances, these challenges are based upon hardware limitations; in others, they are based upon challenges to the ability to effectively use these systems to generate results at the sample site. An example of the former is the need to use vacuum pumps. The availability of pumps to achieve the vacuum levels required to maintain good MS performance has been a limiting factor that continues to impact instrument design and portability. An example of the latter is the challenge of data interpretation in the field. GC–MS data are complex, and for many of the applications where portable GC–MS applications may have the largest potential benefit, operators frequently have a limited scientific and/or GC–MS background. As a result, extracting meaningful results from GC–MS data can be difficult and has limited the use of these systems in some applications. It seems fair to say that as the technology has progressed, vendors of these systems have worked to bridge the gap between generating powerful, but complex, GC–MS data and the translation of these data into meaningful results at the scene.

This chapter explores the current state of commercially available portable GC–MS technology. After a brief review of the history of these systems, the components critical to the performance of portable systems will be discussed followed by a review of the applications of this technology. The chapter will end with a discussion of what the future might hold for these systems as they continue to evolve to meet the needs of end users. This chapter is specific to integrated GC–MS systems. For a thorough discussion of standalone portable MS, see the chapter in this volume by Snyder; for a thorough discussion of standalone high-pressure MS, see the chapter in this volume by Blakeman and Miller.

## 15.2 History of Portable GC–MS

One of the earliest reports that demonstrate the value of being able to perform GC–MS analysis at the scene is the inclusion of GC–MS capability on the 1976 Viking voyage to Mars. Plans for the voyage were reported in 1969 (National Aeronautics and Space Administration 1970). By 1970, scientists were performing experiments to provide reference data intended to aid in the interpretation of soil-organics experiments planned for the voyage (Simmonds 1970). GC–MS was successfully deployed on the voyage in 1976 and the instrumentation details are documented (Biemann et al. 1977). The Viking voyage involved the deployment of GC–MS capability for field analysis, but the GC–MS technology used was not as much portable as it was transportable. The system was designed specifically for the mission and was, essentially, part of a fixed mobile laboratory.

Even by the year 2000, portable GC–MS instrumentation was still considered cumbersome and broadly categorized as either vehicle-portable or man-portable. Vehicle-portable GC–MS systems were described as transportable, fixed-laboratory systems, while man-portable systems were described as luggable (Meuzelaar et al. 2000). It seems the characteristics that made GC–MS instruments portable were not necessarily their size and weight, but rather their independent power and carrier gas supplies (Henry 1997). Today, it is reasonable to expect that portable systems offer weights that enable them to be hand-carried to the sample site.

The first truly portable GC–MS, the Inficon (East Syracuse, NY) HAPSITE was introduced in 1996. This system operated on a battery with an independent carrier gas supply. It offered a quadrupole MS and used a non-evaporative getter (NEG) pump to achieve vacuum. This product went through a series of iterations through the years. The most recent, the HAPSITE ER, was introduced to the market in 2008 and is designed to support the needs of the emergency-response community (Crume 2009). This system weighs 42 lbs (Inficon 2015). Most portable GC–MS competitors to the original HAPSITE, and for much of the life cycle of the HAPSITE product line, were either vehicle-portable or man-portable systems. In recent years, though, a number of vendors have presented alternatives to the HAPSITE family of products that are more comparable in size and weight. Today, the PerkinElmer (Waltham, MA) TORION T-9 and the FLIR (Wilsonville, OR) Griffin G510 are two such examples. The TORION T-9 uses a toroidal ion trap MS and weighs 32 lbs (PerkinElmer Inc 2020); the Griffin G510 uses a quadrupole MS and weighs 36 lbs (FLIR Systems, Inc. 2019). Details about the specifications of these systems and their intended applications are presented throughout this chapter. There are also vendors who provide GC–MS systems that are deployed to the sample site but are a bit heavier. One example is the Bruker (Billerica, MA) E<sup>2</sup>M which weighs 72 lbs (Bruker 2020). Another option for performing GC–MS at the sample site can occur when GC–MS systems that are not necessarily portable are taken to the sample site as part of a fixed mobile laboratory (Mississippi National Guard 2015; United States Environmental Protection Agency 2020). Figure 15.1 shows images of the HAPSITE ER, TORION T-9, and Griffin G510.

Aside from the reduction in size and weight, there are other aspects of portable GC–MS systems that have evolved and improved through the years that are making these systems more field-friendly. Some systems now offer software interfaces that are intuitive with easy-to-select options, even when the operator is wearing personal protective equipment. Modes of operation and required accessories are minimized. This is important not only for logistical



**Figure 15.1** Images of the Inficon HAPSITE ER (a) (Source: INFICON), PerkinElmer TORION T-9 (b) (Source: PerkinElmer Inc.), and FLIR Griffin G510 (c) (Source: FLIR Systems, Inc.).

reasons, but also because when GC-MS systems are used in the laboratory, it is typical for the operator to have some experience and educational background in the sciences. They also will likely have a general understanding of the fundamentals of the technology, as well as how it works. This is not always the case with field users. While some field users have formal education in the sciences, this type of background is not necessarily typical, nor is it always expected. Therefore, ease of use, library-search capabilities, data interpretation, and training requirements must be considered when the technology will be deployed for field use (Leary et al. 2016). In addition (and especially for many military and emergency-response applications), the end user will frequently be under considerable mission stresses and may have very little time to collect samples in an extremely tense, hostile, and dangerous environment. The instrumentation and software interface must be as simple and intuitive as possible so that the operator will have the best chance for success under these conditions.

The approach to deployment has also evolved and can impact whether the technology is successfully deployed by an organization. To relieve some of the burden of deploying portable GC-MS systems, an organization may focus the use of the technology on either a specific type of response or for detection, identification, and/or quantitation of a specific set of target chemicals. While this approach can limit the potential value of the technology that could be realized, it can significantly ease the burden of education and training users and significantly improve the chances for success in the field for the detection and identification of specific types of target chemicals.

## 15.3 Critical Components for Portability

During GC–MS analysis, a sample is introduced to the system using one of a number of different sample-introduction methods. The sample is vaporized and carried through the GC column in the presence of a carrier gas. During its transfer through the column, the individual components of the sample separate based, essentially, upon boiling point. As each purified chemical elutes from the GC column, it enters the MS where it is ionized, fragmented, and sorted based upon mass-to-charge ( $m/z$ ) value. By using a combination of both the GC and MS data, an identification of each chemical in the sample is made.

When designing portable GC–MS systems, the components that are important for the performance of lab-based GC–MS systems, such as sample collection and introduction, column and carrier gas, and mass analyzer and vacuum requirements, are also important for the performance of portable systems. When designing portable systems, though, optimization of performance is balanced with the goal of minimizing size, weight, and power consumption. Sample collection and introduction, GC (column and carrier gas), MS (mass analyzer, ionization source), and vacuum components will be considered separately.

### 15.3.1 Sample Collection and Introduction

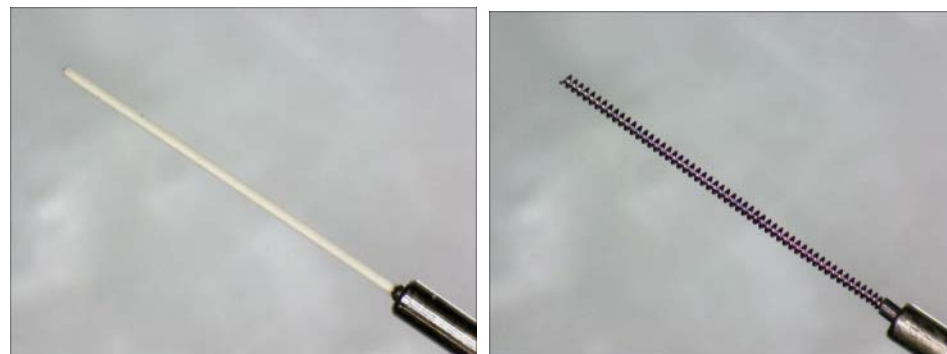
Sampling for portable GC–MS analysis is important. If an appropriate sampling method is not available for a specific analyte, the ability to analyze the sample at the scene may not be possible. Sampling devices are also important because they can increase instrument size, weight, and deployment logistics. Solid-phase microextraction (SPME) (Pawliszyn 1997) is commonly considered to be the easiest sampling method for field analysis. SPME provides a solvent-free method for sample collection. The SPME sampling device is small and weighs only a few ounces so it can be carried to the sample (Leary et al. 2016). It is, essentially, a cartridge containing a fiber coated with a polymer or sorbent onto which analytes selectively adsorb/absorb and concentrate. There are a variety of commercially available fibers that may be used. Fiber selection is based upon molecular weights and polarity of the intended analytes. Although useful in many applications, SPME is limited for a number of reasons including its selective sorption of chemicals which can significantly bias results, as well as its inability to sample solid samples. Other methods are routinely employed including direct and dynamic air sampling, headspace analysis, purge-and-trap options, and solid-sampling accessories. Different portable GC–MS systems offer different sampling options, and depending upon the application, one sampling method over another may be preferred. Factors that influence the desired sampling method include sample type, sample phase of matter, desired limits of detection, quantitative capabilities, and environmental conditions. Table 15.1 summarizes sampling options for some of the commercially available portable GC–MS systems.

Recently, PerkinElmer introduced coiled microextraction (CME) as a sampling method. The appearance of the device is similar to the SPME sampling device in size, weight, and appearance, but the internal SPME fibers are replaced by a CME insert. The insert is a treated wire that is finely coiled to trap liquid samples, including those with suspended solids, by capillary action. Once the solvent has dried, the dissolved compounds remain on the coiled wire ready for introduction into the heated injection port of the TORION T-9 for thermal desorption. The CME is intended to be a fast, easy, and reliable method for sample collection and introduction (PerkinElmer, Inc. 2018). Figure 15.2 shows a stereophotomicrograph of the sampling area of the CME insert and the SPME fiber. The length of the sampling area for both the CME and SPME devices is approximately 1 cm.

A device that has been used in the laboratory to improve sample collection and introduction and can be extended to use in the field is the MicroShot (see Figure 15.3) by Merlin Instrument Company (Centennial, CO). The MicroShot enables a simplified collection of samples for GC analysis. A GC syringe is mounted in the MicroShot injector and a spring-driven plunger slide holds and supports the syringe plunger, making it easy to rinse and fill the syringe without damaging the plunger. The sample volume is controlled by a calibrated

**Table 15.1** Sampling options for portable GC–MS systems.

Instrument	Sampling options
Hapsite ER	Air probe Headspace (option) SituProbe (option) SPME (option) Thermal desorption (option)
Torion T-9	SPME Coiled microextraction (CME) Air sampling with trap (option)
Griffin G510	Heated air probe Direct liquid sampling via syringe Liquid extraction via SPME fiber or PSI-Probe w/Gerstel Twister™ (option) Solid PSI-probe™ thermal separation via TAG™ (option)

**Figure 15.2** Sampling area of the CME (left) and the SPME fiber sampling area.

volume rod. When the injector is filled and armed, pushing the syringe needle into the injection port triggers the sample injection, reducing the injection process to a simple motion. Advantages to its use include improvement in injection precision, easy manipulation of the GC syringe plunger, fast injection (minimizing needle residence time in the injection port), and convenient sampling from a wide variety of sample containers (Merlin Instrument Company 2019).

### 15.3.2 Gas Chromatography

GC describes all chromatographic methods in which the mobile phase is a gas and may involve either a solid or liquid stationary phase retained on a solid sorbent or column wall. Gas–solid chromatography (GSC) comprises all techniques with an active solid as a stationary phase, while gas–liquid chromatography (GLC) is comprised of those techniques involving a liquid stationary phase. With the exception of a few specialized areas, such as the analysis of inorganic gases, GLC systems are more commonly used (Robards et al. 1994).

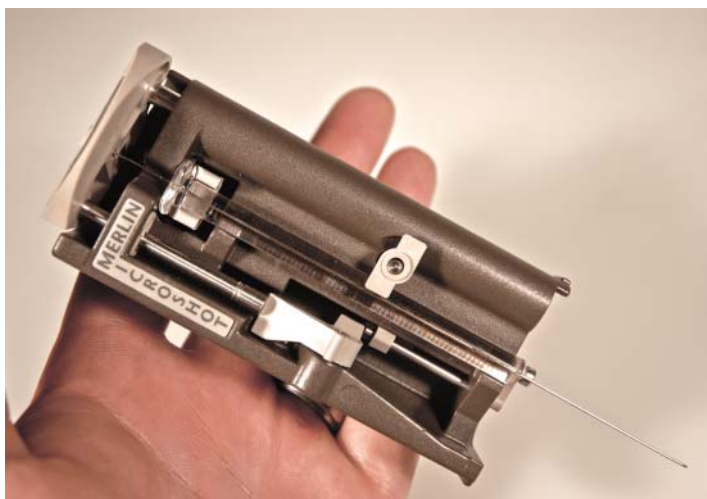


**Figure 15.3** MicroShot GC Sampling Device. Source: Merlin Instrument Company.

Chemicals travel through a GC at a rate that is characteristic of the chemical and based upon properties such as boiling point and vapor pressure. Separation of different chemicals occurs because each chemical partitions differently between the stationary and mobile phases. The time it takes for a chemical to travel through the GC at a specified flow rate is related to this partitioning behavior and is known as its retention time. Retention time can be used to identify a specific chemical within a mixture sample. Further analytical evaluation of each purified analyte that elutes from the GC may be performed when an MS is linked to the GC.

In addition to detecting and identifying a single analyte within matrices using GC, the chromatographic “pattern” generated when all of the chemicals in a sample elute from a column may also be used for identification, not of an individual analyte, but rather of the sample as a whole. This type of chromatographic-pattern analysis is frequently performed to identify ignitable liquids such as gasoline, diesel, and kerosene (Stauffer et al. 2008).

The two primary components of a GC that impact performance are the GC column and the carrier gas. Open-tubular (capillary) columns are the column of choice for the most portable GC–MS systems. These columns are well-suited for field-portable systems because the developments that led to the widespread adoption of open-tubular columns in the 1980s, primarily for chromatographic performance, coincidentally made this important component strong and lightweight. The low thermal mass of an open-tubular GC column allows for temperature-program analysis using relatively little power when heating is limited to the column itself. Using such a column assembly, aggressive temperature ramp rates are possible even when an instrument is operated using battery power. The resulting rapid analysis speeds improve the ability to quickly complete GC analyses in the field (Smith 2015). Open-tubular GLC columns with nonpolar stationary phases are the standard column option for most commercially available portable GC–MS systems. There have been portable systems that offer columns with alternative stationary phases to support specified applications such as those used in the cannabis and petrochemical industries (Restek n.d.), but these options are not widely available on most portable systems (Table 15.2).

Other properties of open-tubular columns that impact analytical performance include column length, stationary-phase film thickness, and diameter (Agilent Technologies Inc 2012). Increasing column length will increase resolution, column backpressure, and analysis time. Therefore, the choice of column length is a compromise between efficiency, operating pressure, and analysis time. The shortest column capable of generating the separating efficiency needed should be used (Robards et al. 1994). Stationary-phase film thickness has an

**Table 15.2** Summary of GC component types for portable GC–MS systems.

Instrument	Column	Length (m)	Film thickness ( $\mu\text{m}$ )	Stationary phase	Inner diameter (mm)	Temperature limit ( $^{\circ}\text{C}$ )	Carrier gas
Hapsite ER	DB-1MS	15	1	100% dimethylpolysiloxane (GLC)	0.25	200	Nitrogen
Torion T-9	MXT-5	5	0.4	Crossbond diphenyl dimethyl polysiloxane (GLC)	0.1	300	Helium
Griffin G510	DB-5MS	15	0.25	Phenyl arylene polymer (GLC)	0.18	300	Helium (hydrogen capable)

influence over retention, resolution, bleed, inertness, and capacity. Column diameter has an influence over efficiency, retention, pressure, carrier gas flow rate, and column capacity (Agilent Technologies, Inc. 2012).

The temperature limit of the column is also an important specification for portable GC–MS systems. Like with lab-based systems, a sample is amenable to GC analysis if it is thermally stable with an appreciable vapor pressure at the column temperature. This allows the sample components to vaporize in, and move with, the gaseous mobile phase (Robards et al. 1994). Some chemicals of interest to field-portable GC–MS users, such as low-volatility compounds, may need an elevated column temperature to achieve the vapor pressure required for GC–MS analysis. The temperature range of a system's GC column in these instances is an important consideration.

There are a number of different types of low-volatility chemicals of interest to users of portable GC–MS. Two examples include chemicals used in warfare, such as the V-series agents and incapacitating agents (Pitschmann 2014). The V-series agents are part of the group of persistent agents that can remain on skin, clothes, and other surfaces for long periods of time due to low-volatility characteristics (Keyes et al. 2015). A majority of V-series agents are listed in Schedule 1 of the Chemical Weapons Convention (CWC). Exposure to solids, liquids, or vapors from these agents can result in death within minutes (Ellison 2008). Military incapacitating agents are the third- and fourth-generation chemical warfare agents (CWAs) that became popular during the Cold War. In addition to military-specific agents, materials in this class encompass a wide variety of commercially available medicinal drugs that interfere with the higher functions of the brain, such as attention, orientation, perception, memory, motivation, conceptual thinking, planning, and judgment (Ellison 2008). BZ (3-quinuclidinyl benzilate) is an example of an incapacitating agent and is listed in Schedule 2 (Toxic Chemicals) of the CWC. It has a boiling point of  $320^{\circ}\text{C}$  (Incapacitating Agents 2007) and, like similar low-volatility compounds, can be a challenge for some GC–MS systems. The ability to run the column at higher temperatures makes analysis of this type of substance possible.

Not only is the ability to run at a higher column temperature important for some applications, but the system must also maintain good temperature control throughout the analysis path of the sample through the GC–MS. If good temperature control is not achieved across joints, such as between the GC and the MS, and transfer lines, such as in the sampling interface, analytes in the vapor phase may be lost during transfer through the system and will not be detected. For portable systems, the ability to heat the column to high temperatures and maintain good thermal control while minimizing power consumption so the system can run on battery is important.

Different portable GC–MS systems use different carrier gases. The carrier gas employed for use should be inert to analytes and compatible with other instrument components. Carrier gases selected for most GC applications include hydrogen, helium, and nitrogen. The choice of carrier gas among these three is important, primarily because it balances the column resolution required with analysis time. It impacts the resolution of a system

through its effect on column efficiency (Robards et al. 1994). Efficiency is observed chromatographically as narrow and well-resolved peaks. The efficiency of an open-tubular column, measured in plates (N) or plates per meter (N/m), increases as the inner diameter of the column decreases (Sigma Aldrich 2017). The efficiency a gas imparts upon column performance is exemplified in its van Deemter curve, which is a plot of the column efficiency as a function of the average linear velocity of the carrier gas. The most efficient separations, i.e., those with the lowest N values, are usually achieved with nitrogen as a carrier gas. However, nitrogen is only the most efficient gas at low flow rates. At higher flow rates, which are required for faster analysis and typical for open-tubular columns used in portable GC–MS systems, the efficiency of nitrogen drops off quickly. Both helium and hydrogen are significantly more efficient than nitrogen at higher flow rates.

When comparing hydrogen with helium, hydrogen is likely the best choice from a performance perspective for GC applications, especially with regard to speed of analysis under otherwise identical system configurations (de Zeeuw 2011). For mobile laboratories, hydrogen generators can be used to produce high-purity hydrogen which can be used as the carrier gas. However, helium is probably used in 90% of GC applications (Grob 1997). Leland Gas Technologies (South Plainfield, NJ) offers disposable helium canisters that are used for both the Griffin G510 and TORION T-9 systems. For both the systems, a single canister can perform over 100 analyses. There are logistics considerations since the canisters are compressed gases, but these canisters have extremely long shelf lives, which is a significant advantage when maintaining inventory.

### 15.3.3 Mass Spectrometry

Mass spectrometry is one of the most generally applicable of all the analytical methods, providing qualitative and quantitative information about the atomic and molecular composition of inorganic and organic materials. The MS produces charged particles that consist of the parent ion and ion fragments of the original molecule. It sorts these ions according to their *m/z* value. The mass spectrum is the record of the relative numbers of different kinds of ions and is characteristic of every compound, including isomers (Willard et al. 1988).

Primary components of an MS include the ionization source, mass analyzer, and detector. With regard to portable GC–MS systems, the use of pumps to achieve the required operating pressures is also an important consideration because this component limits the size and weight of handheld forms of the technology. It also drives the mass analyzer type and design used in a system. Table 15.3 summarizes mass analyzer details and specifications of commercially available portable GC–MS systems described within this chapter.

Once an analyte has been vaporized and successfully transported through the GC column, it enters the ion source of the MS. The ion source charges the molecule to form an ion. This process is required to control the path of the substance in a magnetic or oscillating electric field. Fragmentation of the species that enters the ion source is also expected to occur when electron ionization (EI) is used. This fragmentation is characteristic of the starting compound and the ionization conditions.

**Table 15.3** Mass analyzer details and specifications of portable GC–MS.

Instrument	Ion source	GC/MS interface	Mass analyzer	Mass range	Membrane-interfaced MS-only mode	Operating pressure (Torr)	Vacuum pump
Hapsite ER	EI	Membrane	Quadrupole	41–300	Yes	$\sim 10^{-6}$ or lower	NEG
Torion T-9	EI with dynamic ionization	Direct	Toroidal ion trap	41–500	Not available	$\sim 10^{-4}$	Turbomolecular (10 l/s)
Griffin G510	EI	Direct	Quadrupole	15–515	Yes	$\sim 10^{-6}$	Turbomolecular (80 l/s)

All portable GC-MS systems described within this chapter use EI. Unlike with other ionization methods, such as electrospray ionization (ESI), EI does not require the analyte to be polar. The success of EI for the ionization of organics led to its adoption as the standard ion source for use in organic mass spectrometry. The vapor pressure of many organic substances is sufficient, under the reduced pressure conditions of the MS source chamber, to require that the ion source act only as an ionizer, i.e., it does not have to volatilize the sample. This method was useful to replace gas-discharge sources for a number of reasons. First, gas-discharge sources (such as glow-discharge sources) operate at a higher pressure relative to the MS requirements, requiring heavy differential pumping. Second, the discharge, particularly the high-voltage type, can exhibit instability with a resultant fluctuating ion beam. Third, a critical factor of gas dischargers was the often-large ion-energy spread produced. Fourth, the energy of the ionizing electrons generated in the gas discharge is not always adequately controlled (Coburn and Harrison 1981).

EI is referred to as a hard-ionization method because it produces a substantial portion of the ionized molecules with such high energies that they fragment before leaving the ion source. The masses of these fragment ions provide the basic structural information used in interpretation (McLaffery and Turecek 1993). During EI, gas analyte molecules are bombarded by energetic electrons (typically 70 eV), which leads to the generation of a molecular radical ion ( $M^+$ ) that can subsequently generate the ionized fragments. EI spectra are highly reproducible and, therefore, can be compared with mass spectral libraries so identification of unknowns can be achieved (Santos and Galceran 2003). GC-MS systems that use EI are most popular because they frequently provide both of these molecular and fragment ions. All the commercially available portable GC-MS systems described within this chapter use EI as an ionization source.

Once ions are created, the ion beam can be separated according to the respective  $m/z$  values using a variety of mass analyzer types. Magnetic deflection, quadrupole filter, ion trap, orbitrap, time of flight, and cyclotron resonance are the separating techniques most commonly used in commercial MS systems (McLaffery and Turecek 1993). The list of MS types used in commercially available portable GC-MS systems is much smaller and primarily includes quadrupole filter and ion trap systems. It seems the greatest practical advantage of quadrupole mass analyzers when used in field-portable GC-MS systems is their ability to generate mass spectra that can be more easily interpreted to determine the identity of a true unknown. They also are usually directly comparable with spectra in the commercially available NIST (National Institute of Standards and Technology) MS database, which is an extensive collection of searchable MS data. With regard to field-portable ion trap systems, a significant benefit is that resolution does not inherently depend upon trap size. Also, they run at higher operating pressures than quadrupole systems so they require less aggressive pumping. Pumping requires a significant amount of power, which is not ideal for portable systems that need to operate on batteries and are intended to be small and lightweight. The need to pump aggressively challenges deployment of portable GC-MS in the field.

Quadrupole mass analyzers require high-vacuum (low-pressure) environments to achieve good performance and typically operate at vacuum levels on the order of  $10^{-6}$  Torr. They work by creating a quadrupole field using four electrically conducting parallel rods. Opposite pairs of electrodes are electrically connected. One diagonally opposite pair of rods is held at a positive direct-current (DC) potential, and the other is held at the negative of this DC potential. A radio-frequency (RF) oscillator supplies a specific signal to the first pair of rods, and an RF signal retarded by  $180^\circ$  to the second pair. The equipotential surfaces in the region between the four rods appear as oscillating hyperbolic potentials. Ions from the ion source are injected into the quadrupole array through an aperture. As the ions proceed down the longitudinal  $z$ -axis, they undergo transverse motion in the  $x$ - and  $y$ -planes perpendicular to the longitudinal axis. The DC electric fields tend to focus positive ions in the positive plane and defocus them in the negative plane. As the superimposed RF field becomes negative during part of the negative half-cycle of the alternating field, positive ions are accelerated toward the electrodes and achieve a substantial velocity. The following positive half-cycle has an even greater influence on the motion of the ion, causing it to reverse its direction (away from the electrode) and accelerate even more. The ions exhibit oscillations with increasing amplitudes until they finally collide with the electrodes and become neutral particles. The lighter the ion in

mass, the smaller the number of cycles before it is collected by the electrode. By controlling the ratio of DC/RF, the field can be established to pass ions of a narrow  $m/z$  range down the entire length of the quadrupole array (Willard et al. 1988). The smaller the range of stable  $m/z$  values, the better the resolution, but sensitivity is decreased. By simultaneously ramping the DC and RF amplitudes, ions of various  $m/z$  values are allowed to pass through the mass filter to the detector, i.e., mass-selective stability, and an entire mass spectrum can be recorded (Willard et al. 1988).

A benefit of using quadrupole mass analyzers in portable GC–MS systems is the ability of some of these systems to perform MS-only analysis. This is also sometimes referred to as survey mode. During GC–MS analysis, a sample is analyzed by separation through the GC, followed by the generation of mass spectra of each eluted sample component. During analysis in MS-only mode, the air sample collected bypasses the GC and enters the MS through a membrane that allows the MS system to, among other things, maintain the required vacuum for MS analysis. The instrument response is independent of the amount of time required for GC analysis and, therefore, is almost real time. The mass spectra of individual components are not separated and isolated for conclusive identification when using MS-only mode, so the data may be very complex. But there are some purported benefits of this capability. First, the intensity of the MS-only signal may be used to deduce an approximate concentration of volatile organic compounds (VOCs) at the point of sampling so that optimum positioning for GC–MS sampling can be determined. Once this optimum position is located, the system can then be switched to the standard mode and air sampling for GC–MS analysis can be performed (Inficon 2018). In systems that do not offer MS-only mode for analysis such as the TORION T-9, optimum sampling position for air samples can be determined by measuring the concentration at the anticipated sampling location using a photoionization detector (PID). PIDs are handheld devices commonly used by first responders and the military to measure the concentration of VOCs and other gases on scene. PIDs can reliably measure in the ppm (parts per million) and ppb (parts per billion) range (Rae Systems n.d.). A second purported benefit of MS-only analysis is that it may be used to detect ions associated with one or two specific target analytes (Beckley et al. 2013). A challenge to MS-only analysis is that some chemicals of interest are not of appropriate volatility for analysis in this mode. In addition, some chemicals of interest may be of appropriate volatility but are not detected because they cannot penetrate the membrane and enter the MS.

Ion trap mass analyzers are also used in portable GC–MS systems. The operating pressure for ion traps is higher than for other forms of MS systems such as quadrupoles, allowing for less stringent pumping requirements (Lammert et al. 2006). In addition, ion traps perform better at higher pressures due to collisional cooling (Tolmachev et al. 2000). This can be beneficial for portable systems. Commercially available ion trap mass analyzers employ three electrodes – two endcap electrodes that are normally at ground potential, and between them a ring electrode to which an RF voltage, often in the megahertz range, is applied – to generate a quadrupole electric field. This type of quadrupole ion trap was used to store ions and characterize their properties in the isolated state (Cooks et al. 1991). In addition to the confinement of ions, developments allowed for the ion trap to function as an MS in that the  $m/z$  values of the trapped ion species could be measured. The principal method for measuring the  $m/z$  values of confined ions is to tip the potential well of the ion trap so that the ions leave the ion trap in order of ascending  $m/z$  value, i.e., mass-selective instability (March 1997). Using mass-selective ejection, an ion trap MS takes a sample, ionizes it, and then traps ions over a large mass range of interest simultaneously. Once trapped, ions can be sequentially ejected in order of mass by adjusting the strength of the quadrupole field holding the ions. This is usually accomplished by ramping the RF voltage applied to the ring electrode. The ejected ions are detected by an external electron multiplier to produce a mass spectrum (Stafford Jr. 2002).

A primary challenge for these ion trap MS systems is the management of ion–ion repulsions in the trap. Ion trap repulsions can impact the mass spectrum due to space charge as well as ion–ion reactions and ion–molecule reactions. Space charge is a consequence of Coulomb's law, which quantifies the force ( $F$ ) between two point

charges ( $q$  and  $q'$ ) separated by a distance  $r$  as:

$$F = k \left( \frac{qq'}{r^2} \right)$$

When space charge occurs, shifts in  $m/z$  values may be observed in the spectrum, or sensitivity may be compromised (Busch 2004). Ion chemistry occurs when ions in the trap react with each other to form ion complexes such as dimers. Although this behavior is not always observed, when it is, it can challenge the library-search results of the system. For these chemicals, the resulting mass spectrum may not only contain fragments of the ions initially formed during ionization but may also contain fragment ions that are characteristic of the ion complexes. In extreme cases, all ions initially formed during the ionization process may be consumed during reactions in the trap due to ion chemistry. The mass spectrum, under these extreme conditions, may only contain fragments that are characteristic of the ion complexes.

It is usually possible to address space charge and minimize the occurrence of ion chemistry by controlling the number of ions in the trap. This may be achieved a number of different ways including (i) increasing trap volume, (ii) adjusting instrument settings such as filament current to reduce the number of ions created, and (iii) optimizing the number of ions generated in real time using dynamic ionization. While these approaches can help in controlled settings, in situations where the operator is under significant mission and time constraints analyzing samples of unknown identity and concentration, they are not always effective.

The TORION T-9 uses a toroidal ion trap MS. A primary benefit of the toroidal design is the increase in trapping volume achieved when compared with a conventional ion trap design of similar inscribed radius. This system also uses dynamic ionization to manage the number of ions entering the trap. Overloading the trap is the principal obstacle to obtaining reproducible spectra for an ion trap system (Adams 1989) and, therefore, it is critical that overload of the trap be prevented. Alternatively, too few ions in the trap will result in poor spectral quality. Optimizing the number of ions in real time is critical for good performance but can be challenging because the amount of analyte eluting from the column is continually changing. For these reasons, this toroidal ion trap system performs dynamic-ionization control which varies ionization time to control the trap's ion population. As the concentration entering the MS increases, the ionization time decreases; as the concentration entering the MS decreases, ionization time increases.

The TORION T-9 attempts to address the issue of ion chemistry using onboard library capabilities. During the development of its proprietary libraries, compounds of interest may be analyzed using the system under a variety of conditions, including at various concentrations. Then, library entries can be created in accordance with how the chemical behaves when analyzed by the system under these different conditions. For samples that behave differently at different concentrations, for example, more than one library entry may be present so that, regardless of the concentration of the sample encountered in the field, an identification will be made. This enables effective library-matching results when deployed in the field.

The TORION T-9 also addresses the issue of space charge during library searching. As previously mentioned, when space charge occurs, shifts in  $m/z$  values may be observed in the spectrum. For example, when too many ions of bromoform are generated in the trap, the 171 fragment that is expected may not be observed; it will shift to 172, or even 173 in extreme cases. If the potential of space charge is not accounted for during the library-search process, this behavior may result in a missed identification. Figure 15.4 shows the impact of space charge on the mass spectrum of bromoform. The top MS shows the fragments 171, 173, and 175 and their relative abundances when space charge does not occur during the analysis. The bottom MS shows what can happen to the mass assignment and relative abundance of these fragments when space charge occurs. In spite of the fact that space charge is evident in the bottom spectrum, this toroidal ion trap system will still accurately identify the substance, although the match factor is lower (88.2) than for the spectrum collected under normal conditions (99.6). The ability to

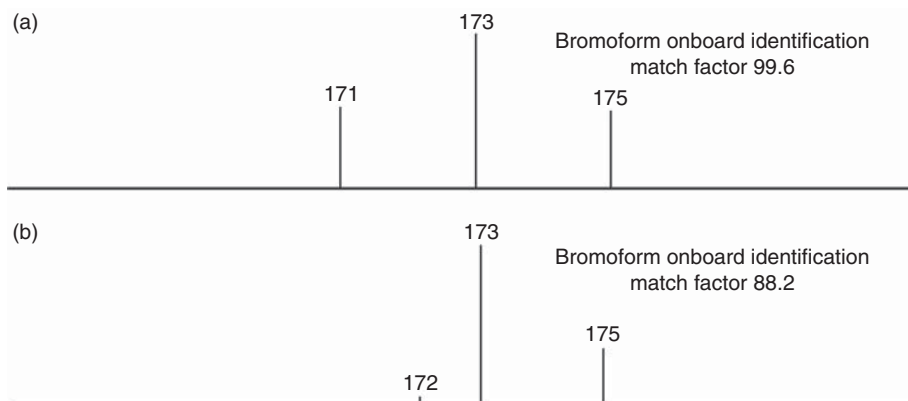


**Figure 15.4** The mass spectra of bromoform when it is free from space charge (a) and when space charge occurs (b).

identify the target chemical in the field, even in cases when space charge occurs, is important. This is because it is frequently difficult or even impossible for users to control the amount of sample introduced to the system when analysis is performed in the field. Therefore, the availability of libraries of ion trap spectra can be critical for these portable systems.

#### 15.3.4 Pumping and Vacuum Requirements

As previously mentioned, a primary challenge to the miniaturization of GC–MS systems is the need to achieve vacuum to perform the analysis. Pumps used to achieve vacuum may not only be bulky but may also be heavy. Depending upon the type of mass analyzer, the vacuum levels required for analysis may be high and, therefore, the performance requirements of pumps required to achieve such vacuum may be aggressive.

High vacuum is required for many portable GC–MS systems because the distance ions need to travel to reach the detector can be relatively large. These ions must reach the detector without undergoing collisions with other gaseous species along this path. The mean free path of the ion needs to be at least as large as the distance the ion must travel to reach the detector. Indeed, collisions would produce a deviation of the trajectory and the ion would lose its charge against the walls of the instrument before detection (de Hoffmann and Stroobant 2007).

The mean free path of the gas molecules can be calculated, and this parameter serves to define the conditions of viscous and molecular flow. When the mean free path of the gas molecules exceeds the dimensions of the vacuum container, the system is under molecular-flow conditions. Under such conditions, the residual gas molecules move without colliding with other gas molecules, instead ultimately colliding within the vacuum chamber (Busch 2001). The mean free path,  $\ell$ , of a particle is dependent upon pressure,  $p$ , in accordance with the equation:

$$\ell = \kappa T / (\sqrt{2} \pi d^2 p \pi)$$

where  $\kappa$  is the Boltzmann constant and  $d$  is the diameter of the particle. Depending upon the size and geometry of the mass analyzer used, i.e., the distance ions must travel to the detector, high vacuum may be a requirement for effective analysis. Due to the ability to miniaturize ion trap systems, the mean free path required for ions generated in ion trap systems can be lower than for quadrupole systems, i.e., the smaller the ion trap, the higher vacuum it can withstand to maintain unit-mass resolution. Therefore, pumping requirements for these systems are lower.

Pumping is accomplished when a net (nonrandom) direction to the movement of residual gas molecules in the vacuum chamber is attained (Busch 2001). Different pumps achieve this goal differently. There are a number of different types of pumps used to achieve vacuum in portable GC–MS systems. Historically, quadrupole field-portable systems required the use of a NEG pump to achieve the necessary vacuum required (Crume 2009).

Although quadrupole portable GC–MS systems like the HAPSITE ER that employ NEG pumps are still commercially available for sale and offer the advantage of lighter weight than other types of pumps, turbomolecular pumps capable of pumping 80 L/s are now available as an option for use with quadrupole systems. Ion trap systems use either diaphragm-backed turbomolecular pumps or even less aggressive pumps to achieve the required vacuum. Both the NEG and turbomolecular pump will be described in more detail as their use in field-portable systems is important.

NEG pumps remove or pump active gases by gettering (chemically combining) gases with metal alloys (Physical Electronics Inc. 2001). A primary advantage of the NEG pump, especially considering its ability to achieve the high vacuum required for quadrupole systems, is its lightweight (approximately 5 lbs) (Crume 2009). This feature is important for field-portable GC–MS systems. While the use of NEG pumps is important, especially considering they enabled the introduction of the field-portable (rather than transportable) quadrupole GC–MS systems to the field as far back as the year 1996 (Crume 2009), there are some challenges NEG pumps present when applied to field-portable GC–MS analysis. These challenges are both analytical and practical.

Analytically, the use of a NEG pump requires the placement of a membrane at the interface between the GC and MS. This membrane helps maintain vacuum while selectively allowing for the flow of organic compounds to the MS while blocking the flow of inorganic gases to the MS (Inficon 2008). In some instances, this membrane may also unwittingly prevent the introduction of some chemicals to the MS, challenging the ability of the system to analyze these substances (Bier and Cooks 1987). Practically, the NEG pump requires the use of a service module to activate the NEG pump (Inficon 2008). This activation process is required regularly in order for the NEG pump to remain functional, and can present logistical challenges for some field users. In addition, the service module itself is quite heavy (Crume 2009), including both a roughing pump and a turbomolecular pump to help achieve activation (Inficon 2016). While the service module is not required for analysis at the sampling point, it is required for sustainment of the portable GC–MS in the field. Activation is a process required for NEGs because when the getter material is exposed to air, the surface will “skin over” with reacted gases. This means the NEG will be totally enclosed in an envelope of oxides, nitrides, and other reacted gases. Additionally, the bulk of the material will be saturated with dissolved hydrogen gas. Since under these conditions, the getter material will be essentially inert, it will not provide an active getter-pumping surface. Activation, then, is the process to prepare the getter surface for pumping. This is done *in situ* by heating under vacuum (Danielson n.d.).

Turbomolecular pumps achieve vacuum by repeated collisions of residual gas molecules with rotating blades of a turbine motor. The edge speed of the rotors approaches the velocities of the residual molecules themselves. When a collision occurs, a direction is imparted to the motion of the residual gas molecules toward a region of higher pressure and toward the pump exhaust (a roughing pump) (Busch 2001). In portable GC–MS systems, the turbomolecular pump is frequently the limiting component that defines the ruggedness of the system.

Although the use of turbomolecular pumps may be considered generally advantageous, there are some disadvantages of turbomolecular pumps compared with NEG pumps. First, although these pumps are not necessarily large, they are heavy, which is undesirable in field-portable systems. In addition, they are sensitive to particulates and sediments and need to be protected from these contaminants. In modern field-portable GC–MS systems that are commercially available, pumps are contained within the system so that risk of exposure to particulates and sediments under normal wear-and-tear conditions is minimized.

## 15.4 Applications

Portable GC–MS is used to detect, identify, and quantify many different types of samples in many different industries. The value of being able to perform analysis at the scene is different for different applications. For instance, the ability to provide a confirmatory analysis of CWAs and other toxic industrial chemicals (TICs) during military operations is valuable because it allows the unit to independently maintain its initiative and momentum while at

the same time enabling adjustments to both operational and strategic decisions in real time (Leary et al. 2019). On the other hand, performing analysis of ignitable liquid residues (ILRs) at the scene of a fire investigation is valuable because it preserves sample integrity. ILRs are a mixture of volatile chemicals. By the time samples are received in the laboratory, a significant amount of the chemicals present in the ILR have likely evaporated (Lentini 2013). Analysis at the scene, therefore, provides a more accurate analysis of the sample at the time it was recovered.

There are a number of established applications where portable GC–MS is frequently used including environmental assessments for the analysis of both hazardous air pollutants and other VOCs, as well as for the analysis of CWAs and TICs. As the technology continues to evolve, the value of these systems within these disciplines continues to grow. In addition, there are a number of emerging applications where the technology offers value including for fire investigations, the analysis of illicit drugs, forensic investigations of explosives, cannabis analysis as related to medical marijuana, and the petrochemical industry. There are also a number of niche research projects that demonstrate the versatility of the application of this technology in the field.

#### 15.4.1 Environmental Applications

Portable GC–MS systems, at least historically, were most widely used in environmental applications (Henry 1997). There are a number of different types of environmental investigations where portable GC–MS analysis has value including site investigations for the analysis of ground contaminants, worker-safety assessments, and vapor-intrusion studies. Site investigations typically are performed by analyzing ground contaminants in soil, soil gases, or water. Worker-safety assessments might be undertaken if, for example, workers are digging in a known contaminated area where the air around the workers needs to be monitored to detect the off-gassing of dangerous chemicals. Vapor-intrusion studies are usually performed to verify contaminants in the ground are not penetrating a building structure (D. Schenk, 20 November 2019, personal communication). Regardless of the type of investigation, environmental assessments are usually focused on the analysis of hazardous air pollutants and other VOCs.

The first focused application for the use of portable GC–MS was for the analysis of hazardous air pollutants. In fact, the name HAPSITE is an acronym for Hazardous Air Pollutants on SITE (Crume 2009). The ability to detect and identify hazardous air pollutants is important because these chemicals can be dangerous, and amendments to the United States Clean Air Act (42 US Code §§7401-7671q 1970) make it a requirement that Environmental Protection Agency (EPA) regulate emissions of these pollutants. The original list included 189 pollutants. Since 1990, EPA has modified the list through rulemaking to include 187 pollutants. The hazardous air pollutants' list not only contains many VOCs, but also includes other hazardous compounds such as chlorine, titanium tetrachloride, and phosphorus (United States Environmental Protection Agency 2016).

VOCs are also detected and identified using portable GC–MS (Beckley et al. 2013; Eckenrode 2001; Fair et al. 2009; Gorder and Dettenmaier 2011; Henry 1997; Ho et al. 2001). These substances are members of a large group of organic chemicals that include any compound of carbon (excluding carbon monoxide, carbon dioxide, carbonic acid, metallic carbides or carbonates, and ammonium carbonate). Their detection and identification are important for a number of reasons. They participate in atmospheric photochemical reactions that contribute to ozone formation. They also play a role in the formation of secondary organic aerosols, which are found in airborne particulate matter. Finally, many individual VOCs are known to be harmful to human health (United States Environmental Protection Agency 2017).

#### 15.4.2 CWAs and TICs

As previously mentioned, the military's ability to detect and identify CWAs using a confirmatory method like GC–MS (Eckenrode 2001; Parrish 2005; Seto et al. 2005; Smith et al. 2004) is important because it enables the unit to independently maintain its initiative and momentum while at the same time enabling adjustments to both operational and strategic decisions in real time (Leary et al. 2019). Portable GC–MS systems are used for the detection

and identification of CWAs. A chemical agent is defined as a chemical substance that is intended for use in military operations to kill, seriously injure, or incapacitate mainly through its physiological effects (United States Department of Defense Joint Chiefs of Staff 2016). When these toxic chemicals and their precursors are prohibited under the CWC (Organisation for the Prohibition of Chemical Weapons n.d.), they are classified as CWAs. CWAs include choking, nerve, blood, blister, and incapacitating agents (United States Army, Marine Corps, Navy, Air Force 2005). Compared to conventional weapons, relatively small amounts of modern chemical agents may cause high number of casualties. Therefore, CWAs have been classified as weapons of mass destruction (WMD) (Szinica 2005).

Portable GC-MS systems are also used for the detection and identification of TICs (Bowerbank et al. 2009; Fair et al. 2009). TICs are industrial chemicals that when released into the atmosphere can have severe toxic effects on people and the environment. Examples include ammonia, chlorine, hydrogen chloride, hydrogen cyanide, and phosgene. The Occupational Safety and Health Administration (OSHA) of the United States Department of Labor classifies TICs into two groups, chemical and physical hazards, based on the type of risk they pose (Occupational Safety and Health Administration n.d.).

The military has spent significant resources to develop capabilities to detect and identify these dangerous chemicals. Ion mobility spectrometers continue to be a critical screening technology used by the military for exactly this purpose. (For a thorough discussion of portable ion mobility spectrometry, see the chapter in this volume by DeBono and Leary, and the chapter in volume 2 by Leary and Joshi.) However, ion mobility spectrometers are used for presumptive rather than confirmatory identifications. Before military units had the ability to perform confirmatory identifications of gases and vapors at the scene, it was necessary for them to operate under conditions that were not ideal. In most instances, tactics, techniques, and procedures dictated that decisions were made based upon information gathered using methods and instruments designed to classify or presumptively identify these substances. These methods included wet-chemical methods, colorimetric tests, electrochemical sensors, photoionization detectors, and ion mobility spectrometers (Detection and Measurement of Chemical Agents 1999; Murray 2013; Sun and Ong 2005). In other situations, samples were sent to remote laboratories, if access to such laboratories was available, for confirmatory testing. It could take days, weeks, or even months for results of testing to be returned. These limitations required that, in many instances, potentially critical intelligence be abandoned in theater with operations continuing as if the intelligence did not exist at all. In cases of personnel exposure to hazardous chemical agents, the inability to conclusively identify the agent causing the illness frequently required that the symptoms of the exposure be treated rather than the root cause (Leary et al. 2019).

Another benefit of portable GC-MS for this application is the large breadth of chemicals that can be characterized using this method. Even if a chemical has never been encountered or previously analyzed using GC-MS, the ability to interpret the GC-MS data collected in the field can help discern chemical identity and provide critical information about the threat. Essentially, the ability to analyze a substance using GC-MS is dependent upon (i) whether the chemical can be sampled and introduced to the system, (ii) has an appreciable vapor pressure at the column temperature so that it can pass through the GC, and (iii) whether the ionization method used in the mass analyzer is capable of generating ion fragments in the atomic-mass-unit (amu) range of the instrument. For modern portable GC-MS systems, this means that there are almost limitless numbers of chemicals that portable GC-MS systems can be used to help identify. In these situations, even though the sample will not alarm or be identified at the sample site, the data generated can be provided to scientific support teams for interpretation, providing potentially valuable intel. This is especially important as CWAs continue to evolve. New chemicals synthesized and developed for use in chemical warfare can be designed to circumvent detection and identification capabilities in the field, and the requirements of treaties like the CWC (Mirzayanov 2009). These substances can be tailored to meet toxicological or pharmacological goals. In addition, manufacturing, storage, transport, and delivery methods can be considered and optimized (Leary et al. 2019). The use of portable GC-MS is important in these situations because the data can be interpreted to identify new threats that might go undetected or uninterpreted using other methods.

The ability to analyze a sample using portable GC–MS is not possible if the sample cannot be introduced to the system. As such, the phase of matter of the sample can be critical. A portable GC–MS system capable of identifying chemicals in multiple phases of matter is currently under development through mid-2022. In October 2018, FLIR Systems, Inc. announced it had received an award from the United States Department of Defense (DOD) Joint Program Executive Office for Chemical, Biological, Radiological and Nuclear Defense (JPEO-CBRND) in support of the multiphase chemical agent detector (MPCAD) to develop a capability that will provide the ability to identify chemicals at low levels in aerosol, gas, liquid, and solid phases of matter. This instrument was proposed as a portable GC–MS solution that will provide the warfighter with field confirmation capabilities and better enable the Joint Forces to combat and interdict chemical weapons of mass destruction (WMD) (FLIR Systems, Inc. 2018).

#### 15.4.3 Fire Investigation

There are some emerging applications where industries will likely benefit from the use of portable GC–MS system including the field of fire investigation. The use and value of GC–MS for the analysis of fire debris to establish the presence and identity of ignitable liquids is well-established (ASTM International 2014; Newman 2004; Stauffer et al. 2008). More recently, this technology has been taken to the field so that analysis may be performed at the scene of a fire investigation (Visotin and Lennard 2016). This capability is important. Ignitable liquids are comprised of different mixtures of volatile chemicals. As a result, fire debris samples containing residues of these liquids may change over time, e.g., between sample collection in the field and analysis in the laboratory. Analysis in the field would, therefore, more accurately represent the chemical composition of the sample recovered at the scene rather than after some components may have evaporated during transport to and storage in the laboratory. In instances where analysis at a laboratory is required, portable GC–MS may be used to determine the best location from which to recover samples for laboratory submission. This helps minimize the potential of sending samples containing no residue of ignitable liquids to the laboratory. Negative samples not only cost money to perform the analytical testing, but also increase the potential for laboratory backlog.

The environmental and human health aspects of fire scenes were recently evaluated using portable GC–MS. Portable GC–MS was used for the on-site analysis of water samples for the identification of hazardous organic compounds at fire scenes. This research showed that portable GC–MS was capable of detecting and identifying a range of volatile and semivolatile organic compounds in fire water runoff, and could be used in conjunction with conventional laboratory analysis methods for a comprehensive understanding of hazardous organics released at fire scenes. Deployment of this portable instrumentation provides first responders with a rapid, on-site screening tool to appropriately manage the runoff water from firefighting activities. This ensures that environmental and human health is proactively protected (Lam et al. 2019).

#### 15.4.4 Illicit Drugs

The analysis of illicit drugs in the field by law enforcement and other first responders is an important capability that has become routine. An analytical scheme for such testing may include the use of colorimetric tests for screening, followed by either infrared or Raman spectroscopy for identification. Although portable GC–MS is more difficult to deploy than either of these methods, a primary advantage of using portable GC–MS for identification at the scene is that GC–MS can conclusively identify trace levels of drugs in street samples, even when these drugs are adulterated with large amounts of cutting agents. Figure 15.5 shows a chromatogram of an illicit drug sample recovered by law enforcement. Both portable infrared and Raman spectrometers identified this sample as quinine. Analysis of the sample using portable GC–MS (FLIR Systems, Inc. Griffin G510, Wilsonville, OR) showed the sample also contained the illicit drugs ketamine and fentanyl, as well as the drug levimasole.

These types of samples challenge other spectroscopic methods that struggle to detect drug samples at low concentrations, which is where GC–MS excels. This capability is especially advantageous in situations where high-potency opioids like fentanyl and its analogues are present at very low concentrations (Leary et al. 2017).

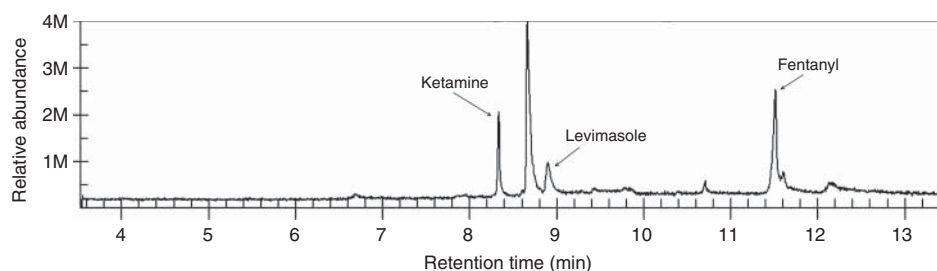


**Figure 15.5** Chromatogram of illicit drug substance (identified using portable infrared and Raman as quinine).

#### 15.4.5 Forensic Investigations of Explosives

The field of explosives analysis may also benefit from the use of field-portable GC-MS. Explosives are detected in the field using methods, such as ion mobility spectrometry, which can detect particulate residues of these substances at very low levels. While this type of analysis is important, the use of field-portable GC-MS can extend the analytical capabilities in the field to not only provide confirmation of initial ion mobility spectrometry and other testing results, but also to establish provenance of explosives when chemical markers used during explosive manufacture are detected and identified (Leary et al. 2016). Chemical markers may remain in a sample at trace levels and can be used as a point of differentiation among samples (Leary 2014). This is especially important in situations where homemade explosives such as hexamethylene triperoxide diamine (HMTD) and triacetone triperoxide (TATP) are analyzed. The ability to detect trace residues in these samples can provide insight into the history of the explosive sample including solvents and processes used for manufacture, providing useful investigative information in real time. Figure 15.6 shows a chromatogram of a sample of the explosive Composition C-4 tagged with DMNB (2,3-dimethyl-2,3-dinitrobutane) analyzed using portable GC-MS with SPME headspace analysis (Smiths Detection GUARDION, Edgewood, MD). The sample was purported to contain 0.1% DMNB which was automatically detected and identified using the system. Other advantages of performing GC-MS analysis of explosives at the scene of explosive events is because (i) it enables the development of render-safe procedures based upon real-time threat identification and assessment; (ii) intelligence turnaround time to support offensive operations is improved so Commanders are

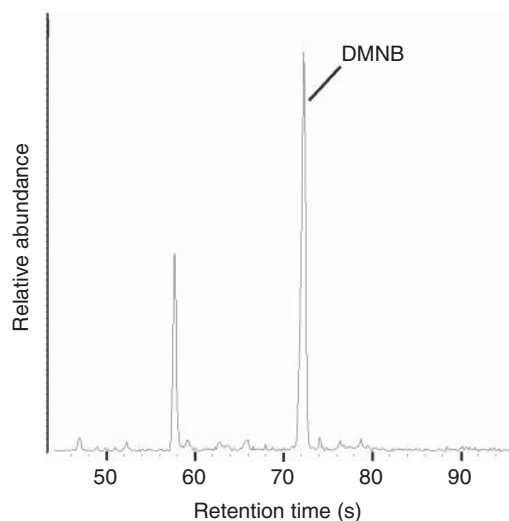


**Figure 15.6** Chromatogram of composition C-4 tagged with DMNB.

empowered to make actional decisions using reliable, confirmed information; (iii) real-time results help guide and optimize scene processing; and (iv) analysis at the scene enables the most accurate evaluation of the scene; results are representative of the scene at the time of analysis, not at some later time when samples are received and analyzed at the laboratory (Moquin et al. 2020).

#### 15.4.6 Cannabis Analysis

In 1970, the United States Congress placed marijuana (cannabis) into Schedule I of the Controlled Substances Act because they considered it to have “no accepted medical use.” As of December 2020, 33 of 50 states in the United States and Washington, D.C. have legalized the medical use of marijuana. Proponents of medical marijuana argue that it can be a safe and effective treatment for the symptoms of cancer, AIDS, multiple sclerosis, pain, glaucoma, epilepsy, and other conditions (ProCon.org n.d.). More than 60 cannabinoid species have been isolated from cannabis and identified (Brenneisen 2007). The ability to detect and identify some of these chemicals is important. For instance, Δ-9 tetrahydrocannabinol (THC) and cannabidiol (CBD) are used for determining a product’s total potency. In addition, the ratio of THC to CBD can determine the end usage of products as well as pricing and associated state tax revenue (908 Devices, Inc. 2017). For these and other reasons, the ability to detect, identify, and quantify these species in the field using portable GC–MS has become important.

#### 15.4.7 Petrochemicals

There are a number of different ways portable GC–MS systems may provide value to the petrochemical industry including the ability to establish the quality of crude oil coming from a well, as well as its use to troubleshoot processing. The composition of crude oil is never consistent, creating the opportunity for operational problems to arise, such as raw material feedstock changes between incoming crude oil batches. Production pressures require the source of the problem to be identified as quickly as possible. The best way to achieve this is often to use GC–MS to identify the presence and type of chemical responsible and determine at what point it entered the process (Harrison 2011).

#### 15.4.8 Others

There are other industries and applications that may benefit from the use of GC–MS in the field. A review of the literature shows a variety of different types of analysis that have already been attempted including the use of portable GC–MS to detect boar taint from samples on the slaughter processing line (Verplanken et al. 2015), to differentiate damaged and undamaged yellow Starthistle flower heads (Beck et al. 2015), and to detect and quantify munitions constituents in groundwater (Bednar et al. 2012). Portable GC–MS was also used to evaluate the volatility profiles from stockpiled almonds and compare results with data collected from benchtop systems. Despite the portable GC–MS system detecting fewer volatiles than the benchtop system, both systems resolved humidity treatments and identified potential fungal biomarkers at extremely low water activity levels. This ability to resolve humidity levels suggests that volatile profiles from germinating fungal spores could be used to create an early warning, nondestructive, portable detection system of fungal growth (Beck et al. 2016). While these applications and others that are currently being explored for viability may not be as widely deployed as others, the ability to perform these types of analyses in the field is testament to the ruggedness and versatility of modern portable GC–MS platforms.

### 15.5 The Future of Portable GC–MS

A primary value of portable GC–MS when compared with other field technologies is its ability to conclusively identify chemicals, even when present at low concentration within complex sample matrices. Depending upon the application, the features of a system that are important can be different. For instance, for military users “smaller,

lighter, faster" is a standard mantra and especially appropriate for field-portable GC-MS systems. These systems can be deployed to remote locations within hostile environments where they must be discretely hand-carried to the scene. In these situations, the addition of even a few ounces of weight can be critical. Further development to extend each system's current capabilities to be able to analyze a wider breadth of chemicals would be valuable. When deployed in other applications, though, development of flexibility in sampling methods and adding quantitative capabilities to a system may be more important than size and weight. These features may be important for applications such as environmental analysis, fire investigation, and illicit-drug analysis.

To achieve systems that are smaller, until the Griffin G510 was introduced to the market in 2017, innovation in mass analyzer design was the road taken. The use of ion trap designs has been important to achieving smaller and lighter systems due to the higher operating pressures of these systems. Vendors such as Smiths Detection and PerkinElmer developed portable ion trap GC-MS systems, while 908 Devices developed a variety of high-pressure MS products including standalone ion trap MS systems. For all of these ion trap systems, overcoming the consequences of trapping ions either through improvements in mass spectral design or in data processing capabilities would be beneficial. While not discussed in this chapter (see chapter in this volume by Blakeman and Miller), the high-pressure MS system by 908 Devices known as the MX908 has become an important capability that continues to grow into different markets. The ability to improve the spectral resolution of this high-pressure MS system and couple it with front end separation technologies like GC would provide an impressive portable capability that would be quite field-friendly.

## Acknowledgments

The authors would like to acknowledge Dalton T. Snyder for his review and suggestions for improvement to this chapter, and support provided by the Connecticut State Police K9 Unit, and specifically TFC Jon Naples and TFC Brian Faughnan for samples provided for analysis.

## References

- 42 US Code §§7401-7671q (1970). *United States Clean Air Act*. Office of the Law Revision Counsel of the U.S. House of Representatives.
- 908 Devices Inc. (2017). Application Note 1.0: Ultrafast Total Potency Analysis of Cannabindoids in Decarboxylated Oil Extracts Using G908. 908 Devices.com. [http://908devices.com/wp-content/uploads/2017/09/TotalPotency\\_AppNote\\_2017\\_v8.pdf](http://908devices.com/wp-content/uploads/2017/09/TotalPotency_AppNote_2017_v8.pdf) (accessed 28 October 2017).
- Adams, R.P. (1989). *Identification of Essential Oils by Ion Trap Mass Spectroscopy*. San Diego, CA: Academic Press, Inc.
- Agilent Technologies Inc. (2012). *Agilent J&W GC Column Selection Guide*. Agilent. [https://www.agilent.com/cs/library/catalogs/public/5990-9867EN\\_GC\\_CSG.pdf](https://www.agilent.com/cs/library/catalogs/public/5990-9867EN_GC_CSG.pdf) (accessed 4 October 2017).
- ASTM International (2014). *ASTM E1618-14, Standard Test Method for Ignitable Liquid Residues in Extracts from Fire Debris Samples by Gas-Chromatography-Mass Spectrometry*. West Conshohocken: ASTM International <https://doi.org/10.1520/E1618-14>.
- Beck, J.J., Porter, N., Cook, D. et al. (2015). In field volatile analysis employing a hand-held portable GC-MS: emission profiles differentiate damaged and undamaged yellow starthistle flowers. *Phytochem. Anal.* 26: 395–403. <https://doi.org/10.1002/pca.2573>.
- Beck, J.J., Willett, D.S., Gee, W.S. et al. (2016). Differentiation of volatile profiles from stockpiled almonds at varying relative humidity levels using benchtop and portable GC-MS. *J. Agric. Food Chem.* <https://doi.org/10.1021/acs.jafc.6b04220>.

- Beckley, L., McHugh, T., Gorder, K. et al. (2013). *Use of on-Site GC/MS Analysis to Distinguish between Vapor Intrusion and Indoor Sources of VOCs*. Environmental Security Technology Certification Program (ESTCP) <https://clu-in.org/download/issues/vi/VI-ER-201119-FR.pdf>.
- Bednar, A., Russell, A., Hayes, C. et al. (2012). Analysis of munitions constituents in groundwater using field-portable GC-MS. *Chemosphere* 87 (8): 894–901. <https://doi.org/10.1016/j.chemosphere.2012.01.042>.
- Biemann, K., Oro, J., Toulminn, P. III, et al. (1977). The search for organic substances and inorganic volatile compounds in the surface of Mars. *J. Geophys. Res.* 82 (28): 4641–4658. <https://doi.org/10.1029/JB082i028p04641>.
- Bier, M. and Cooks, R. (1987). Membrane interface for selective introduction of volatile compounds directly into the ionization chamber of a mass spectrometer. *Anal. Chem.* 59: 597–601. <https://doi.org/10.1021/ac00131a013>.
- Bowerbank, C.R., Lee, E.D., Sadowski, C.S. et al. (2009). Rapid field detection of chemical warfare agents and toxic industrial chemicals using a hand-portable GC-TMS system. *LCGC* 27 (4). <http://www.chromatographyonline.com/rapid-field-detection-chemical-warfare-agents-and-toxic-industrial-chemicals-using-hand-portable-gc?id=&sk=&date=&pageID=5> (accessed 18 April 2020).
- Brenneisen, R. (2007). Chemistry and analysis of phytocannabinoids and other cannabis constituents. In: *Marijuana and the Cannabinoids* (ed. M.A. ElSohly), 17. Totowa, NJ: Humana Press.
- Bruker (2020). *Technical Details of the Bruker E2M Mobile Gas Chromatograph Mass Spectrometer*. Bruker. <https://www.bruker.com/products/cbrne-detection/gc-ms/e2m/technical-details.html> (accessed 14 April 2020).
- Busch, K.L. (2001). High-vacuum pumps in mass spectrometers. *Spectroscopy* 16 (5): 14–18.
- Busch, K.L. (2004, June). Space charge in mass spectrometry. *Spectroscopy* 19 (6): 35–38.
- Coburn, J. and Harrison, W. (1981). Plasma sources in analytical mass spectrometry. *Appl. Spectros. Rev.* 17 (1): 95–164. <https://doi.org/10.1080/05704928108060402>.
- Cooks, R.G., Gilsh, G.L., McLuckey, S.A., and Kaiser, R.E. (1991). Ion trap mass spectrometry. *Chem. Eng. News (C&EN)* 69 (12): 25–41.
- Crume, C. (2009). *History of Inficon HAPSITE: Maintenance Management, Support, and Repair*. KD Analytical. <http://www.kdanalytical.com/instruments/inficon-hapsite-history.aspx> (accessed 5 June 2016).
- Danielson, P. (n.d.). How to use getters and getter pumps. R&D Magazine (February 2001). <http://www.normandale.edu/departments/stem-and-education/vacuum-and-thin-film-technology/vacuum-lab/articles/how-to-use-getters-and-getter-pumps> (accessed 9 November 2017).
- Detection and Measurement of Chemical Agents (1999). In *Chemical and Biological Terrorism: Research and Development to Improve Civilian Medical Response*. Washington, DC: National Academies Press.
- Eckenrode, B. (2001). Environmental and forensic applications of field-portable GC-MS: an overview. *J. Am. Soc. Mass Spectrosc.* 12 (6): 683–693. [https://doi.org/10.1016/S1044-0305\(01\)00251-3](https://doi.org/10.1016/S1044-0305(01)00251-3).
- Ellison, D.H. (2008). *Handbook of Chemical and Biological Warfare Agents*, 2e. Boca Raton, FL: Taylor & Francis Group, LLC.
- Fair, J.D., Bailey, W.F., Felty, R.A. et al. (2009). Method for rapid on-site identification of VOCs. *J. Environ. Sci.* 21 (7): 1005–1008. [https://doi.org/10.1016/S1001-0742\(08\)62375-X](https://doi.org/10.1016/S1001-0742(08)62375-X).
- FLIR Systems, Inc. (2019). *Person-Portable GC-MS Chemical Identifier FLIR Griffin™ G510*. FLIR Systems, Inc. <https://www.flir.com/globalassets/imported-assets/document/griffin-g510-datasheet.pdf> (accessed 14 April 2020).
- FLIR Systems, Inc. (2018). *FLIR Systems Receives Award Totaling \$28.7M for the Next Generation Chemical Detector (NGCD) from the United States Army*. FLIR Systems, Inc. <https://investors.flir.com/news-releases/news-release-details/flir-systems-receives-award-totaling-287m-next-generation> (accessed 16 April 2020).
- Fogerson, R., Schoendorfer, D., Fay, J., and Spiehler, V. (1997). Qualitative detection of opiates in sweat by EIA and GC-MS. *J. Anal. Toxicol.* 21: 451–458.
- Gorder, K.A. and Dettenmaier, E.M. (2011). Portable GC/MS methods to evaluate sources of cVOC contamination in indoor air. *Ground Water Monit. Remed.* 31 (4): 113–119. <https://doi.org/10.1111/j.1745-6592.2011.01357.x>.
- Grob, K. (1997). *Carrier Gases for GC*. Restek [http://www.restek.com/Technical-Resources/Technical-Library/Editorial/editorial\\_A017](http://www.restek.com/Technical-Resources/Technical-Library/Editorial/editorial_A017).

- Harrison, S. (2011). How gas chromatography-mass spectrometry can be utilised as a tool for forensic analysis. *Hydrocarbon Eng.* 16 (10): 33–36.
- Henry, C. (1997). Product review: take the show on the road: portable GC and GC/MS. *Anal. Chem.* 69 (5): 195A–200A. <https://doi.org/10.1021/ac9715682>.
- Ho, C.K., Itamura, M.T., Kelley, M., and Hughes, R.C. (2001). *Review of Chemical Sensors for in-Situ Monitoring of Volatile Contaminants*. Albuquerque and Livermore: Sandia National Laboratories.
- de Hoffmann, E. and Stroobant, V. (2007). *Mass Spectrometry: Principles and Applications*, 3e. West Sussex: John Wiley & Sons Ltd.
- Incapacitating Agents (2007). *Compendium of Chemical Warfare Agents* (ed. S.L. Hoenig). New York: Springer [https://doi.org/10.1007/978-0-387-69260-9\\_4](https://doi.org/10.1007/978-0-387-69260-9_4).
- Inficon (2015). *Specifications of the HAPSITE® ER Chemical Identification System*. Inficon.
- Inficon (2016). *Operating Manual, HAPSITE Service Module*. Inficon. <http://products.inficon.com/getattachment.axd/?attaname=service-module-operating-manual> (accessed 9 November 2017)
- Inficon (2008). *Hapsite Smart Plus Operators Manual*. Inficon. <http://products.inficon.com/GetAttachment.axd?attName=9243f3a0-981e-435b-aa6b-412124af0900> (accessed 11 March 2017).
- Inficon (2018). *HAPSITE ER Chemical Identification System*. Inficon. <http://products.inficon.com/GetAttachment.axd?attName=b0ddf534-db3e-4920-b9c1-ec872bc28a4d> (accessed 13 December 2020).
- Keyes, D.C., Benitez, F.L., Velez-Daubon, L.I., and Talavera, F. (2015). *E-Medicine Drugs and Diseases, Emergency Medicine*. CBRNE – Nerve Agents, V-series - Ve, Vg, Vm, Vx. <http://emedicine.medscape.com/article/831760-overview#showall> (accessed 9 March 2017).
- Lam, R.L., Kingsland, G., Johnstone, P. et al. (2019). Rapid on-site identification of hazardous organic compounds at fire scenes using person-portable gas chromatography-mass spectrometry (GC-MS) - part 2: water sampling and analysis. *Foren. Sci. Res.*: 1–15. <https://doi.org/10.1080/20961790.2019.1662648>.
- Lammert, S.A., Rockwood, A.A., Wang, M. et al. (2006). Miniature Toroidal radio frequency ion trap mass analyzer. *J. Am. Soc. Mass Spectrom.* 17 (7): 916–922. <https://doi.org/10.1016/j.jasms.2006.02.009>.
- Leary, P.E. (2014). Counterfeiting: a challenge to forensic science, the criminal justice system, and its impact on pharmaceutical innovation. Ph.D. thesis. Graduate Center of the City University of New York, New York.
- Leary, P.E., Kammrath, B.W., Lattman, K.J., and Beals, G.L. (2019). Deploying portable gas chromatography-mass spectrometry (GC-MS) to military users for the Identificaiton of toxic chemical agents in theater. *Appl. Spectrosc.* 73 (8): 841–858. <https://doi.org/10.1177/0003702819849499>.
- Leary, P.E., Dobson, G.S., and Reffner, J.A. (2016). Development and applications of portable gas chromatography-mass spectrometry for emergency responders, the military, and law-enforcement organizations. *Appl. Spectrosc.* 70: 888–896. <https://doi.org/10.1177/0003702816638294>.
- Leary, P.E., Gayle, B.A., Gross, D.L., and Frunzi, M. (2017). The fentanyl epidemic. *Fire Eng.* 170 (10): 26–32.
- Lentini, J.J. (2013). Analysis of ignitable liquid residues. In: *Scientific Protocols for Fire Investigation*, 2e (ed. J.J. Lentini). Boca Raton, FL: Taylor & Francis Group, LLC.
- March, R.E. (1997). An introduction to quadrupole ion trap mass spectrometry. *J. Mass Spectrom.* 32: 351–369.
- McLaffery, F.W. and Turecek, F. (1993). *Interpretation of Mass Spectra*, 4e. Sausalito, CA: University Science Books.
- McNair, H.M. and Miller, J.M. (2009). *Basic Gas Chromatography*, 2e. John Wiley & Sons, Inc.
- Merlin Instrument Company (2019). *Merlin Microshot*. Merlin Instrument Company. <https://merlinic.com/merlin-microshot> (accessed 17 April 2020).
- Meuzelaar, H.L., Dworanski, J.P., Arnold, N.S. et al. (2000). Advances in field-portable mobile GC/MS instrumentation. *Field Anal. Chem. Technol.* 4 (1): 3–13.
- Mirzayanov, V.S. (2009). *State Secrets: An Insider's Chronicle of the Russian Chemical Weapons Program*. Denver: Outskirts Press, Inc.
- Mississippi National Guard (2015). *Frequently Asked Question's*. Mississippi National Guard. <https://ms.ng.mil/aboutus/units/66tc/47cst/Pages/FAQs.aspx> (accessed 14 April 2020).

- Moquin, K., Higgins, A.G., Leary, P.E., and Kammrath, B.W. (2020, May). Optimized explosives analysis using portable gas chromatography-mass spectrometry for battlefield forensics. *Curr. Trends Mass Spectr.* 18 (2): 1–8.
- Murray, G.M. (2013). Detection and screening of chemicals related to the chemical weapons convention. *Encycl. Anal. Chem.*: 1–37. <https://doi.org/10.1002/9780470027318.a0403.pub2>.
- National Aeronautics and Space Administration (1970). *Astronautics and Aeronautics, 1969*. Washington, D.C.: Scientific and Technical Information Division, Office of Technology Utilization.
- Newman, R. (2004). Interpretation of laboratory data. In: *Fire Investigation* (ed. N. Nic Daéid). Boca Raton: CRC Press, LLC.
- Occupational Safety and Health Administration (n.d.). *Toxic Industrial Chemicals (TICs) Guide*. United States Department of Labor. <https://www.osha.gov/SLTC/emergencypreparedness/guides/chemical.html> (accessed 21 February 2020).
- Organisation for the Prohibition of Chemical Weapons (n.d.). *Genesis and History of the Chemical Weapons Convention*. Organisation for the Prohibition of Chemical Weapons. <https://www.opcw.org/chemical-weapons-convention/genesis-and-historical-development> (accessed 1 November 2016).
- Parrish, L.D. (2005). *Application of Solid Phase Microextraction with Gas Chromatography – Mass Spectrometry as a Rapid, Reliable, and Safe Method for Field Sampling and Analysis of Chemical Warfare Agent Precursors*. Bethesda: Dissertation – Uniformed Services University of the Health Sciences.
- Pawliszyn, J. (1997). *Solid Phase Microextraction*. Waterloo: Wiley-VCH, Inc.
- PerkinElmer Inc. (2018). *Product Note: Custodion CME Syringes for Easy Liquid Sample Collection and Injection*. PerkinElmer. [https://www.perkinelmer.com/lab-solutions/resources/docs/PRD\\_Custodion\\_CME\\_Syringe\\_014110\\_01.pdf](https://www.perkinelmer.com/lab-solutions/resources/docs/PRD_Custodion_CME_Syringe_014110_01.pdf) (accessed 25 April 2020).
- PerkinElmer Inc. (2020). *Torion T-9 Portable GC/MS*. PerkinElmer Inc. <https://www.perkinelmer.com/product/torion-t-9-portable-gc-ms-instrument-ntsst090500> (accessed 14 April 2020).
- Physical Electronics Inc (2001). *Technicians Non-Evaporative Getter Pump Component Manual*. Physical Electronics Inc. <http://www.pascaltechnologies.com/files/Pumps/Ion%20Pumps/Other%20Ion%20Pumps/Physical%20Electronics%20NEG%20Technicians%20Manual.pdf> (accessed 9 November 2017).
- Pitschmann, V. (2014). Overall view of chemical and biochemical weapons. *Toxins* 6: 1761–1784. <https://doi.org/10.3390/toxins6061761>.
- ProCon.org (n.d.). Should Marijuana Be a Medical Option? <https://medicalmarijuana.procon.org> (accessed 25 March 2018).
- Rae Systems (n.d.). *Photoionization Detectors (PIDs)*. Rae Systems: <http://www.raesystems.com/solutions/photoionization-detectors-pids> (accessed 25 March 2018).
- Restek (n.d.). *MXT-Msieve 5A Columns, Technical Description*. Restek. <http://www.restek.com/catalog/view/8578> (accessed 26 October 2017).
- Robards, K., Haddad, P.R., and Jackson, P.E. (1994). *Principles and Practice of Modern Chromatographic Methods*. London: Academic Press Limited.
- Santos, F. and Galceran, M. (2003). Modern developments in gas chromatography-mass spectrometry-based environmental analysis. *J. Chromatogr. A* 1000: 125–151. [https://doi.org/10.1016/S0021-9673\(03\)00305-4](https://doi.org/10.1016/S0021-9673(03)00305-4).
- Schechter, A.J., Sheu, S.U., Birnbaum, L.S. et al. (1999). A comparison and discussion of two differing methods of measuring dioxin-like compounds: gas chromatography-mass spectrometry and the calux bioassay - implications for health studies. *Organohalogen Compd.* 40: 247–250.
- Seto, Y., Kanamori-Kataoka, M., Tsuge, K. et al. (2005). Sensing technology for chemical-warfare agents and its evaluation using authentic agents. *Sens. Actuators B* 108: 1930197. <https://doi.org/10.1016/j.snb.2004.12.084>.
- Sigma Aldrich (2017). *How to Choose a Capillary GC Column*. Sigma Aldrich. <https://www.sigmaaldrich.com/analytical-chromatography/gas-chromatography/column-selection.html> (accessed 8 November 2017).
- Simmonds, P.G. (1970). Whole microorganisms studied by pyrolysis-gas chromatography-mass spectrometry: significance for extraterrestrial life detection experiments. *Appl. Microbiol.* 20 (4): 567–572.

- Smith, P.A. (2015). Portable gas chromatography. In: *Analytical Separation Science*, vol. 3 (eds. J. Anderson, A. Berthod, V. Pino and A.M. Stalcup). Wiley <https://doi.org/10.1002/9783527678129.assep031>.
- Smith, P.A., Jackson Lepage, C.R., Koch, D. et al. (2004). Detection of gas-phase chemical warfare agents using field-portable gas chromatography-mass spectrometer systems: instrument and sampling strategy considerations. *Trends Anal. Chem.* 23: 296–306. doi: 10.106/S0165-9936(04)00405-4.
- Stafford, G. Jr., (2002). Ion trap mass spectrometry: a personal perspective. *J. Am. Soc. Mass Spectrosc.* 13: 589–596.
- Stauffer, E., Dolan, J.A., and Newman, R. (2008). *Fire Debris Analysis*. Elsevier, Inc.
- Sun, Y. and Ong, K.Y. (2005). *Detection Technologies for Chemical Warfare Agents and Toxic Vapors*. Boca Raton, FL: CRC Press LLC.
- Szinica, L. (2005, October 30). History of chemical and biological warfare agents. *Toxicology* 214 (3): 167–181. <https://doi.org/10.1016/j.tox.2005.06.011>.
- Tilstone, W.J., Savage, K.A., and Clark, L.A. (2006). *Encyclopedia of Forensic Science: An Encyclopedia of History, Methods and Techniques*. Santa Barbara: ABC-CLIO, Inc.
- Tolmachev, A.V., Udseth, H.R., and Smith, R.D. (2000). Radial stratification of ions as a function of mass to charge ratio in collisional cooling radio frequency multipoles used as ion guides or ion traps. *Rapid Commun. Mass Spectrom.* 14 (20): 1907–1913. [https://doi.org/10.1002/1097-0231\(20001030\)14:20<1907::AID-RCM111>3.0.CO;2-M](https://doi.org/10.1002/1097-0231(20001030)14:20<1907::AID-RCM111>3.0.CO;2-M).
- United States Army, Marine Corps, Navy, Air Force (2005). *Potential Military Chemical/Biological Agents and Compounds*. <http://www.marines.mil/Portals/59/MCRP%203-37.1B%20z.pdf> (accessed 23 April 2016).
- United States Department of Defense Joint Chiefs of Staff (2016). Department of Defense Dictionary of Military and Associated Terms. [http://www.dtic.mil/doctrine/new\\_pubs/jp1\\_02.pdf](http://www.dtic.mil/doctrine/new_pubs/jp1_02.pdf) (accessed 23 April 2016).
- United States Environmental Protection Agency (2016). *Initial List of Hazardous Air Pollutants with Modifications*. United States Environmental Protection Agency. <https://www.epa.gov/haps/initial-list-hazardous-air-pollutants-modifications> (accessed 25 March 2018).
- United States Environmental Protection Agency (2017). Volatile Organic Compounds' Impact on Indoor Air Quality. <https://www.epa.gov/indoor-air-quality-iaq/volatile-organic-compounds-impact-indoor-air-quality> (accessed 11 December 2020).
- United States Environmental Protection Agency (2020). *EPA Region 9 Laboratory Field Services Summary*. United States Environmental Protection Agency. <https://www.epa.gov/regionallabs/epa-region-9-laboratory-field-services-summary#mobilelab> (accessed 14 April 2020)
- Verplanken, K., Wauters, J., Van Dirme, J. et al. (2015). Development and validation of a rapid detection method for boar taint by means of solid phase microextraction and a person-portable GC-MS. In: *Belgian Association for Meat Science and Technology (BAMST) Symposium*, 29–30. Belgium: Melle. <http://hdl.handle.net/1854/LU-7067733> (accessed 23 April 2016).
- Visotin, A. and Lennard, C. (2016). Preliminary evaluation of a next-generation portable gas chromatograph mass spectrometer (GC-MS) for the on-site analysis of ignitable liquid residues. *Aust. J. Forensic Sci.* 48 (2) <https://doi.org/10.1080/00450618.2015.1045554>.
- Willard, H.H., Merritt, L.L. Jr., Dean, J.A., and Settle, F.A. Jr., (1988). *Instrumental Methods of Analysis*, 7e. Belmont: Wadsworth Publishing Company.
- de Zeeuw, J. (2011). *Fast(Er) GC: How to Decrease Analysis Time Using Existing Instrumentation? Part IV: Using Hydrogen as the Carrier Gas*. doi: <https://blog.restek.com/?p=3520>

## 16

# Development of High-Pressure Mass Spectrometry for Handheld and Benchtop Analyzers

*Kenion H. Blakeman and Scott E. Miller*

*908 Devices Inc., Boston, MA, USA*

## 16.1 Introduction

Mass spectrometry (MS) is commonly referred to as the gold standard for chemical analysis, given its sensitivity, selectivity, and wide application ranges [1]. Single-molecule detection is possible for some applications and resolving powers in excess of 1 000 000 have been reported [2, 3]. While mass spectrometers can be extraordinarily powerful, they are typically large, complex, and expensive; require regular maintenance; have limited robustness; are confined to a laboratory environment; and require trained users to operate [4–6]. For decades, there has been strong interest in miniaturizing mass spectrometers, and in moving them outside the laboratory environment. A key set of parameters to consider for miniaturization and portability are size, weight, and power (SWaP) [7, 8]. A miniature mass spectrometer design must be robust enough to survive transport to a new location and operate on limited power supplies such as batteries or generators. Since mass spectrometers are classically optimized for performance in a particular location and only moved on the rarest of occasions by trained personnel, the design challenges are unique for portable instruments [9–11].

The transition from laboratory tool to field-portable mass spectrometer was first demonstrated by the Inficon HAPSITE system in 1996 [12]. While not intended to be a comprehensive list, several examples of field-portable mass spectrometers that have been released since then are summarized in Table 16.1. Some key differences include the type of mass analyzer that is used, including quadrupole mass filters (QMFs) and quadrupole ion traps (QITs). While a gas chromatograph can add additional analytical capabilities, it adds additional size, weight, and complexity to a system and may not be included depending on the intended use case. Despite multiple decades of field-portable MS development, considerable diversity in how systems are designed is seen.

As the mass spectrometer miniaturization has progressed, there has been a trend toward commercializing systems with weights in the 15–35 kg range. A key challenge for miniaturization has been the vacuum requirements associated with performing mass spectrometry. Vacuum requirements below  $<10^{-5}$  Torr are common for mass spectrometers and are typically achieved using large turbomolecular pumps that introduce considerable weight to the system. Ion trap mass analyzers can operate at higher pressures (e.g.  $10^{-3}$  Torr) but this is still well into the molecular flow regime [13, 14]. For technologies without such pumping requirements, such as ion mobility spectrometry (IMS) and optical methods, such as Fourier transform infrared spectroscopy (FTIR) and Raman, smaller analyzers have been commercialized [11, 15, 16]. For example, Smiths Detection released the LCD 3.3 handheld IMS in 2009, which has dimensions of  $10.54 \times 17.3 \times 4.65$  cm and weighs 0.65 kg [17]. The FirstDefender was a Raman spectrometer by Ahura Scientific, which was released in 2005 with dimensions of  $19.3 \times 10.7 \times 4.4$  cm and a weight of 1.8 kg [18].

**Table 16.1** Examples of commercially available field-portable mass spectrometers highlighting key specifications.

Name and developer	Year introduced	Mass analyzer	GC	Weight (kg)	Dimensions (cm)	Reference
Inficon HAPSITE	1996	QMF	Yes	19	46 × 43 × 18	[106]
Bruker E2M/MM2	2004	QMF	Yes	37.7	39 × 39 × 28	[107]
908 Devices M908	2014	QIT	No	2.0	22 × 18.5 × 7.6	[108]
Torion T-9	2015	QIT	Yes	14.5	47 × 36 × 18	[109]
Griffin G510	2017	QMF	Yes	16.3	33.7 × 33.7 × 40	[110]
908 Devices MX908	2017	QIT	No	3.9	29.8 × 21.6 × 12.2	[111]
Bayspec Continuity	2017	Dual QIT	No	20	33 × 33 × 43	[112]
1st Detect Tracer 1000 MS-ETDM	2019	QIT	No	24	36 × 45 × 53	[113]

The disparity between mass spectrometers in the 15 kg weight range at best and optical and IMS detectors in the 0.5–2 kg range leads to questions on how to bridge the weight gap. Since the late 1990s, one research approach has been to increase the operating pressure of an ion trap mass spectrometer. If the operating pressure was high enough (fractions of a Torr and above), the turbomolecular pump could be eliminated and only a highly miniaturized roughing pump would be required, a significant departure from conventional methods which utilize two large vacuum pumps.

In this chapter, the background of ion trap operation and its evolution over time will be summarized. Key developments on scaling an ion trap for higher pressure operation will be covered. Experimental results from high-pressure mass spectrometry (HPMS) experiments will be covered in detail. Finally, devices based on HPMS and their applications across different disciplines will be described.

## 16.2 Ion Trap Development for HPMS

### 16.2.1 Trapped Ion Motion Characterization

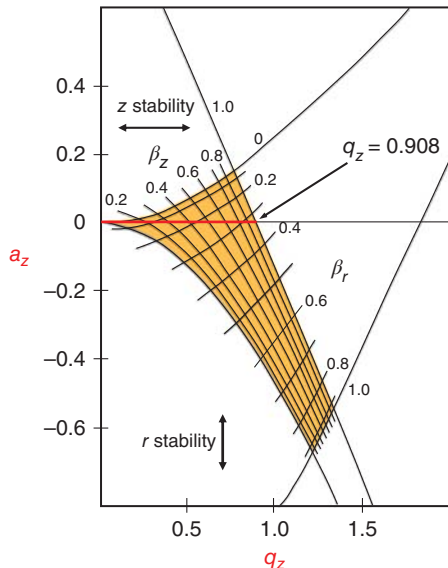
The development of HPMS analyzers centers on the development and analytical performance of QITs. The QIT mass analyzer was first reported by Paul and Steinwedel in 1953 [19]. It consisted of a central ring electrode separated from two endcap electrodes by insulating material. Trap dimensions are defined as the internal radius of the ring electrode ( $r_0$ ) and the distance from the center of the trap to the endcap electrodes ( $z_0$ ). Ions are introduced and ejected from the ion trap through apertures in the endcap electrodes.

Since the initial work by Paul and Steinwedel, there has been considerable research into understanding the motion of trapped ions. While a complete mathematical analysis is beyond the scope of this summary, several detailed analyses are cited here [20–22]. Central to the understanding of trapped ion motion are stability diagrams (Figure 16.1). Stability diagrams are determined by the Mathieu equation for ion motion and describe conditions where ions are stable in the ion trap based on dimensionless parameters  $a$  and  $q$ . The parameters  $a$  and  $q$  are further defined as  $a_z$  and  $q_z$  to define trajectories in the  $z$ -dimension, and  $a_r$  and  $q_r$  to define motion in the  $r$ -dimension. The equations for each of these dimensionless parameters are defined in Eqs. (16.1) through (16.4):

$$a_z = -\frac{16 \text{ eU}}{m(r_0^2 + 2z_0^2)\Omega^2} \quad (16.1)$$

$$a_r = \frac{8 \text{ eU}}{m(r_0^2 + 2z_0^2)\Omega^2} \quad (16.2)$$

**Figure 16.1** Stability diagram for a QIT. Ions are trapped with stable ion trajectories in the shaded orange regions. In typical mass-selective instability runs, no DC voltage is applied (red line) and ions are ejected when the RF voltage is tramped and  $q_z$  reaches 0.908.



$$q_z = \frac{8 \text{ eV}}{m(r_0^2 + 2z_0^2)\Omega^2} \quad (16.3)$$

$$q_r = \frac{-4 \text{ eV}}{m(r_0^2 + 2z_0^2)\Omega^2} \quad (16.4)$$

where  $U$  is the direct current (DC) voltage applied to the ring electrode,  $V$  is the zero-to-peak ( $0-p$ ) radio frequency (RF) voltage applied to the ring electrode,  $\Omega$  is the angular frequency of the RF signal applied to the ring electrode,  $e$  is the elementary charge,  $m$  is the mass of the ion,  $r_0$  is the trap radius, and  $2z_0$  is the distance between the two endcap electrodes. The coefficients assume a purely QIT geometry and are approximate values that will vary for different geometries [23, 24]. Theory predicts that areas of ion stability exist in both the radial and axial dimensions of the parameter space. Where these two regions overlap, the conditions are consistent with ions being stable in the ion trap [19, 22].

Additional insight into ion trap operation was gained through the work of Dehmelt, who modeled the frequency of motion of trapped ions as a simple harmonic oscillator in the  $z$ -dimension. The Dehmelt pseudopotential well depth ( $D_z$ ) approximates the maximum energy for an ion to remain stably trapped. Equation (16.5) defines  $D_z$  under the Dehmelt approximation conditions where  $q_z < 0.4$ .

$$D_z = \frac{eV^2}{4mz_0\Omega^2} = \frac{q_z V}{8} \quad (16.5)$$

Building off the  $D_z$  calculation, Dehmelt also described a relationship between the charge capacity of an ion trap ( $N_{\max}$ ) relative to  $D_z$  and the  $z_0$  critical dimension of the QIT (Eq. 16.6).

$$N_{\max} = 2.8 \times 10^7 D_z z_0 \quad (16.6)$$

Both the  $D_z$  and  $N_{\max}$  calculations proved critical in future decades when ion trap critical dimension scaling was investigated [25, 26].

## 16.2.2 Mass-Selective Detection

While the theoretical characterization of ion motion developed by Paul, Steinwedel, and March has proven robust, methods for mass analysis have significantly changed over time. Methods developed by Paul and Steinwedel

and then Dawson and Whetten were inefficient and limited to spectroscopy-type experiments [19, 27, 28]. Contemporary ion trap mass analysis is derived from mass-selective instability operation, developed by Stafford and coworkers at Finnigan MAT Corporation and the University of Kent in the early 1980s [29, 30]. In this mode of operation, ions are injected and trapped with a quadrupolar field for an indefinite time frame. Ions are ejected in order of increasing mass-to-charge ratio ( $m/z$ ) by ramping the RF voltage applied to the ring electrode with fixed  $\Omega$  until they are ejected when  $q_z > 0.908$ . Using this mode of operation, the mass range for an ion trap ( $m/e$ ) can be described on the basis of  $m/z$  by varying  $V$ ,  $\Omega$ , and the QIT dimensions until an unstable  $q_z$  value is reached (Eq. 16.7) [25].

$$\frac{m}{z} = \frac{8 V}{q_z(r_0^2 + 2z_0^2)\Omega^2} \quad (16.7)$$

While ion ejection could also be achieved by ramping the RF frequency in a similar fashion to the RF voltage, it has proven uncommon since resonant circuits are required to produce the 1–10 kV (p–p) RF voltages commonly used for this application [22].

The performance of mass-selective instability scans (mass range, sensitivity, and mass resolution) has been improved by introducing resonance ejection to the mass instability scans. Each  $m/z$  ion has a unique three-dimensional trajectory within the ion trap that occurs at a characteristic frequency, known as the secular frequency and defined in the  $z$ -dimension as ( $\omega_z$ ) [22]. The frequency of motion is commonly expressed by the trapping parameter  $\beta_z$ , which is a complex dimensionless function of the previously described  $a_z$  and  $q_z$  dimensional parameters when  $q_z$  is  $<0.4$  (Eq. 16.8).

$$\beta_z^2 \cong a_z + \frac{q_z^2}{2} \quad (16.8)$$

The  $\beta_z$  parameter can then be correlated back to the ion's real secular motion by Eq. (16.9).

$$\omega_z = \frac{\beta_z \Omega}{2} \quad (16.9)$$

Since the  $\beta_z$  value varies between 0 and 1 for a trapped ion, the ion's secular frequency is less than half of the drive RF frequency. During mass-selective instability scans with resonance ejection, an axial RF signal with a voltage on the order of hundreds of millivolts is applied across the endcap electrodes at the axial secular frequency of ion motion. This results in ions being ejected from the ion trap at a lower  $q_z$  and extends the mass range of the ion trap. The most common mode of operation uses a resonant RF frequency just below  $1/2$  of the drive RF frequency [22].

### 16.2.3 Mass Resolution for QITs

In all previously discussed methods of ion trap operation, the gas background pressures were maintained below  $10^{-5}$  Torr to minimize collisions between ions and neutral molecules, which are potentially detrimental to mass resolution and sensitivity [31, 32]. Commercial interest in the ion trap as a detector for gas chromatography led to experiments with the addition of helium buffer gas to the vacuum chamber. Stafford and coworkers increased the helium buffer gas pressure in their  $r_0 = 1$  cm (cm) ion trap from approximately  $10^{-6}$  to  $10^{-2}$  Torr and determined that optimal performance was achieved at a pressure near  $10^{-3}$  Torr [29]. Mass resolution was studied as a function of increasing helium pressure focusing on the PFTBA  $m/z$  69 and  $m/z$  502 peaks. The mass resolution ( $m/\Delta m$ ) at full-width at half-maximum (FWHM) for the  $m/z$  69 peak improved from 70 to 185 with the helium gas at  $10^{-3}$  Torr, while  $m/z$  502 was not detected without buffer gas but was detected at a mass resolution of 1700 with the buffer gas. They suggested that increased helium gas pressure caused collisional dampening of ion motion toward the center of the QIT, where the ions experience a more uniform trapping field, resulting in better defined secular motion of the trapped ions and ejection from the ion trap in a tighter time span, improving mass resolution. The performance in mass resolution and sensitivity of the relatively high operating pressure ( $10^{-3}$  Torr) opened the door for the ion trap to be used as a gas chromatography detector [33].

While the work by Stafford and coworkers significantly increased the operational pressure regime for ion traps, the vacuum requirements still confined these instruments to laboratory use. A theoretical breakthrough in ion trap scaling was realized by Goeringer and coworkers in 1992. While increasing the pressure from  $10^{-5}$  to  $10^{-3}$  Torr was successful, the ion neutral collisions with the buffer gas continued to be a concern due to their expected deleterious effect on resolution. Goeringer et al. created a model that assumed the motion of an ion could be approximated by a damped harmonic oscillator where the motion of the ion is determined from the RF frequency while being damped by ion neutral collisions. A dampening factor was added to the Mathieu equations for ion motion to account for these ion neutral collisions. They developed a new relationship (Eq. 16.10) for mass resolution ( $m/\Delta m$ ) as a function of buffer gas pressure ( $P$ ), collisional relaxation time ( $\tau$ ), and the RF frequency ( $\Omega$ ) [34].

$$\frac{m}{\Delta m} \propto \frac{\Omega}{P} = \frac{\Omega\tau}{4\sqrt{3}} \quad (16.10)$$

This relationship shows peak widths ( $\Delta m$ ) scale linearly with increased pressure and inversely with RF drive frequency. For a trap operated at a constant RF frequency, when pressure increases, the mean free path decreases proportionally, the ions experience more frequent ion neutral collisions, and mass resolution is reduced. However, if the RF frequency is scaled with the operating pressure, ions now experience more RF cycles per ion neutral collision and mass resolution can be maintained.

Building off the work by Goeringer et al., another model for ion trap motion was developed by Arnold and coworkers at the University of Utah [35]. Arnold et al. studied the dispersion of ions at the point of trap ejection rather than ions confined within a trap. They developed a relationship (Eq. 16.11) for a mass resolution that also includes additional variables including scan rate ( $a_m$ ), secular frequency ( $\omega_0 = 0.5\Omega$ ), thermal energy (kT), collisional relaxation time ( $\tau$ ), and neutral mass ( $M$ ).

$$\frac{m}{\Delta m} \leq \frac{\omega_0^2/2}{\sqrt{\frac{\pi a_m \Omega z_0}{m} + 8/\tau^2} \sqrt{\frac{kT}{mr_0^2 \omega_0^2} + \frac{1}{3} \frac{M}{m}}} \quad (16.11)$$

There are several significant differences between the models worth mentioning. The Arnold et al. mode assumes mass resolution scaled as scan rate to the  $1/2$  power under high scan speed conditions regardless of operating pressure. Since sensitivity and mass resolution are often a direct trade-off, this is a key consideration for detecting low-concentration analytes. The Goeringer et al. model did not consider the effect of scan rate on mass resolution. The Arnold et al. model predicts that mass resolution will be dependent on the relative masses of the analyte and neutral molecules, while the Goeringer et al. model does not explicitly consider these masses. However, consideration of the masses of the neutral molecules is important since there are multiple buffer gas options.

Whitten et al. addressed the possibility of scaling the RF frequency and trap size by a factor of 1000 to accommodate ion trap operation in the low-Torr pressure range [36]. They added a drag coefficient to the equations describing ion motion and investigated the effects on the ion trap stability diagram, concluding that mass resolution *could* be maintained at higher pressures, and discussed multiplexing ion traps for improved sensitivity and charge capacity at higher pressures.

#### 16.2.4 Ion Trap Dimensional Scaling and Simplified Geometries

Once the potential advantages of miniaturizing ion traps were recognized, the fabrication of small traps needed to be addressed. The hyperbolic QIT was developed with an emphasis on producing trapping fields that are as close to a pure quadrupole as possible [19]. However, higher order fields are created in ion traps by incorporating entrance and exit apertures required to introduce and detect the analyte. They are also introduced by any trap asymmetry, which becomes difficult to avoid as trap dimensions are reduced. The quadrupolar is the strongest field and dominates trap behavior by providing a linear restoring force for trapped ions with distance from the center of the trap. Higher order components such as hexapole, octapole, decapole, and dodecapole fields are strongest near

the boundaries of the trap and decrease nonlinearly with distance toward the center where ions predominantly reside [37, 38]. Since ions mainly reside close to the center of the ion trap, they mainly experience the quadrupolar fields, although the other field strengths are significant and must be addressed during trap development [24, 39].

While the hyperbolic electrodes of the QIT were effective at the 1 cm dimension scale, researchers quickly realized fabricating these precise features would become infeasible when trap dimensions were decreased in size. The cylindrical ion trap (CIT) design was introduced in 1977 by Bonner and coworkers [40]. The hyperbolic shapes of the three trap electrodes are replaced with cylindrical planar electrodes, which are amenable to both conventional machining and microfabrication techniques with miniaturized dimensions. Starting in the late 1990s, multiple groups studied the performance of miniaturized CITs operating in the  $10^{-3}$  Torr pressure regimes [5, 41–43]. Immediate concerns surrounded the performance of the CIT geometry, which simplifies fabrication but adds non-quadrupolar field characteristics to the ion trap geometry and influences performance [2, 44–46].

The challenges associated with nonideal ion trap geometries and higher order fields had been encountered in the earlier work by Finnigan Corporation. They noticed a mass shift in their mass spectra where ions were detected at the wrong  $m/z$  value depending on the chemical structure of the ion. They solved the problem extending the trap by 10.8% in the  $z_0$ -dimension to correct for field perturbations caused by apertures in the endcap electrodes used to inject and eject ions from the trap. They believed the endcap electrodes added an octapolar field component to the trapping fields and stretching the  $z_0$ -dimension offset the effect and corrected the mass shift [47]. Multiple groups have theoretically and experimentally studied the effects of changing CIT critical dimensions on ion trap performance [48–51]. While there are different trade-offs to consider, no set of critical dimensions for the CIT became standard as different groups prioritized different performance trade spaces depending on specific applications and system design requirements.

Another challenge of small ion traps is charge capacity. As noted earlier in Eq. (16.6), the charge capacity of an ion trap scales linearly with the  $z_0$ -dimension as charge repulsions limit the number of ions that can be stored in a trap. One potential solution is planar arrays of ion traps to maintain charge capacity [25, 26]. While charge capacity decreases linearly with the  $z_0$ -dimension, volume scales as  $z_0^3$ . Miniaturized ion trap arrays have the potential to maintain the charge capacity of a traditional 1 cm ion trap while storing that amount of charge in a lower volume of space. Early experiments into ion trap arrays focused on arrays of less than 10 individual traps with critical dimensions in the low mm dimensions [52–54]. The smallest trap arrays that have successfully performed mass analysis were reported by Pau and coworkers [51]. A trap consisting of  $r_o = 20 \mu\text{m}$  CIT arrays (256 and 2304 elements) was fabricated from p-doped polysilicon with silicon dioxide insulating layers. Xenon gas was detected at  $10^{-4}$  Torr of helium pressure with xenon concentration of 1%. Blaine and coworkers fabricated arrays with up to  $10^6$  elements of  $r_o = 1 \mu\text{m}$  CITs [48, 49]. However, when operated as a mass analyzer, the positively charged electrical current measured from the trap array could not be completely attributed to trapped ions and mass spectra were not presented. A major concern for ion trap arrays is uniformity across array elements that could result in a loss of mass resolution when the signals from multiple individual traps are detected simultaneously in time. Given this concern, there has been interest in developing ion trap designs that do not require multiple trap elements but still give the sensitivity benefits and high charge capacity that are predicted from trap arrays.

An alternative approach to limited charge capacity in miniature ion traps adapts linear ion trap (LIT) designs developed by Hager and Schwartz for miniature MS operation [55, 56]. The LIT consists of four hyperbolic rods similar to a QMF, except the rods are cut into three sections each set at unique DC potentials. Ions are contained along the length of the rods by applying carefully selected RF voltages to the rods. Trapping ions along the length of the rods improves charge capacity and minimizes space charge effects without loss in mass resolution. Similar to the QITs, the hyperbolic features of the LIT are not amenable to miniaturization. Ouyang and coworkers developed a simplified geometry based on the LIT where the four central hyperbolic rods are replaced with four planar electrodes and the two end segments of the LIT are replaced with two planar electrodes known as the rectilinear

ion trap (RIT) in 2004 [57]. The RITs have been fabricated with critical dimensions on the single mm scale in a variety of materials and their performance has been thoroughly characterized [58–60].

Another approach that uses elements of the LIT and CIT was demonstrated by Schultze and Ramsey in 2014 in the development of the stretched length ion trap (SLIT) [61]. The SLIT design replaces the cylindrical features found in CITs with a slot that stretches along the y-plane of the trap electrodes and increases sensitivity up to an order of magnitude compared to similarly sized CITs. Related designs such as a serpentine pattern along the y-plane of the trap electrodes have been investigated, demonstrating the versatility of this design. SLIT traps have been demonstrated with critical dimensions in the hundreds of  $\mu\text{m}$ , a size scale that is amenable to operating at pressures of up to 1 Torr [61].

Several additional simplified geometries that have been reported in the literature include multi-ring stacks [62], the coaxial ion trap [63], the toroidal ion trap [64–66], and the halo ion trap [67, 68]. Considerations for different trap designs include fabrication techniques, optimal critical dimensions, operating pressure, mass resolution optimization, and material selection.

### 16.2.5 Vacuum Pump Requirements for Miniature MS

There are multiple parameters related to the vacuum system that need to be jointly considered for a functional miniature mass spectrometer:

1. Minimize the power consumption of the pumping system for its intended operating pressure – this reduces the required battery payload (volume and weight) for useful uptime.
2. Maximize the pumping speed at operating pressure – the gas throughput of the mass spectrometer critically defines its response time, and the efficiency of ion transport from atmospheric ionization sources.
3. Minimize the time required to pump the MS down from atmospheric pressure – handheld tools are generally expected to be “shelf-ready” so time-to-readiness of a few seconds is ideal.
4. Minimize the cost of the pumping system – it is particularly critical to avoid exotic materials and eliminate extreme precision parts including precision bearings.
5. Minimize the size/weight of the pumping system.
6. Maximize the lifetime of the pumping system – eliminate high-loading bearings or wearing surfaces.
7. Ensure that the pumping system is capable of servicing the required vacuum and flow across the operating temperatures of interest in fieldwork (usually  $-20$  to  $50^\circ\text{C}$ ) and at different elevations.
8. The pumping system must survive and function through physical shock (e.g. drops) and vibration.

Among the groups who have investigated ion trap miniaturization, different approaches have been used to handle the vacuum requirements of the mass spectrometer. A typical mass spectrometer consists of at least two stages of pumping including a roughing pump and turbopump. Depending on inlet gas flow, the roughing pump can achieve pressures ranging from  $10^{-2}$  Torr to single-digit Torr values, while the turbopumps are backed by roughing pumps and reach operating pressures below  $10^{-2}$  Torr [69].

Sample introduction can take several forms. The simplest approach is to consistently sample an ambient environment through a restricted atmospheric inlet or capillary. This approach can provide fast response times but has high pumping requirements. A disadvantage is the potential for debris to obstruct the capillary, leading to significant downtime. Semipermeable membranes can be implemented to provide the needed pressure drop. These membranes may also be made selective to the analytes of interest while keeping other components outside of the mass spectrometer [70–72]. However, membrane inlets are typically considered a consumable and logistical burden, and in use can negatively impact response and cleardown time. An approach to minimize pumping requirements uses a valve to sample for a limited time, after which the valve closes, the vacuum pumps achieve the desired operating pressure, and the sample is mass analyzed. This method, known as discontinuous atmospheric pressure interface (DAPI), minimizes pumping requirements but increases analysis time since the sample is only being analyzed for a fraction of the total operational time, while also increasing mechanical complexity [73, 74].

### 16.2.6 High-Pressure Scaling Approaches

As noted above, almost all transportable mass spectrometers operate at pressures below  $10^{-3}$  Torr with turbomolecular pumping. Running at such low pressures means that no matter how much miniaturization of the mass analyzer is achieved, the SWaP and ruggedness of the overall instrument will be determined entirely by the pumping mechanism [36] – turbomolecular pumping is a catastrophe by every figure of merit. Accordingly, several efforts have been made to increase buffer gas pressure beyond the traditional molecular flow/ $10^{-3}$  Torr regime.

In one approach to high-pressure operation, Xu et al. used theoretical modes to study the effects of ion neutral collisions for ions trapped in air buffer gas up to 1 Torr operating pressure with a 5 mm RIT instrument operating at 1.1 MHz, matching the RF frequency regime used with traditional QIT instruments. Their theoretical model predicted that FWHM peak widths would increase from roughly 1 Da at  $4.1 \times 10^{-3}$  Torr to 9.5 Da at 0.25 Torr [75]. Experimental results by Song et al. using this RIT configuration did not investigate pressures above  $5 \times 10^{-2}$  Torr, but demonstrated FWHM peak widths of 0.98 Da at  $4.1 \times 10^{-3}$  Torr air buffer gas with an increase to 2.00 Da at  $5 \times 10^{-2}$  Torr [76]. Based on this FWHM vs. pressure trends, an FWHM of nearly 40 Da would have been projected at 1 Torr, making MS identifications quite difficult.

Jiang et al. developed a miniature mass spectrometer based on a 4 mm LIT and investigated several ion ejection methods as a function of air buffer gas pressure. Ions were trapped at an RF frequency of 1 MHz and then mass analyzed by two different ion trap modes known as dipolar resonance ejection and QE-dipolar resonance ejection modes where QE stands for quadrupole enhanced. Peak widths for a methionine–arginine–phenylalanine–alanine peptide (MRFA) peak at  $m/z$  524 were found to increase from 3.5 Da at  $2.95 \times 10^{-3}$  Torr to 4.23 Da at  $6.44 \times 10^{-3}$  Torr when the dipolar resonance ejection method was used. In comparison, the same peak widths increased from 1.58 Da at  $2.95 \times 10^{-3}$  Torr to 2.19 Da at  $6.44 \times 10^{-3}$  Torr with the QE-dipolar resonance ejection method. The pressure regime studied was limited by the operating pressure range of the electron multiplier detector [77].

Another approach to higher pressure operation was taken by Jiang et al. This group used a 1 cm CIT and two different RF frequency and pressure regimes. First, the CIT was operated at an RF frequency of 0.84 MHz and an operating pressure of  $5 \times 10^{-6}$  Torr to benchmark performance in the high-vacuum regime. Next, the operating pressure was increased to approximately  $1.5 \times 10^{-2}$  Torr and the RF frequency was increased to 2.4 MHz. Using this configuration, mass spectra of methyl salicylate were acquired. The pressure regime studied was limited by the operating range of the electron multiplier detector used [78].

Recent work by Decker and coworkers in 2019 has focused on miniaturizing a microscale planar ion trap (PLIT) for higher pressure operation. A microscale 800  $\mu\text{m}$  PLIT was fabricated with lithographic methods operated with an RF frequency of 2.71 MHz. Mass spectra of toluene were acquired from  $2.5 \times 10^{-3}$  to  $4.2 \times 10^{-2}$  Torr of helium buffer gas and peak widths at the highest pressure were estimated to be between 2.3 and 2.7 Da. Performance trade-offs such as power requirements for the RF driver, ion trap pseudopotential well depth, and mass resolution compared to a larger 2.5 mm critical dimension trap were also analyzed [79].

The elevated pressure operating strategies described so far focused on scaling RF frequency by less than a factor three compared to conventional ion traps. One challenge in the development of higher pressure MS is the generation of an appropriate RF waveform for driving the ion trap. The amplitude of the RF signal must be sufficiently stable to reliably eject ions without peak broadening. While the theory is clear that increasing the RF frequency should counteract increased RF collisions at higher pressures, increasing the RF frequency is not a trivial task. To produce an RF waveform used to trap and analyze ions, the required power scales as the RF frequency squared. Furthermore, power also scales with the capacitance squared. Smaller ion traps have smaller gaps between the electrodes, increasing the trap capacitance. Finally, electrical discharges must be avoided despite the presence of ions generated from the ionization source and the high voltages produced at high RF frequencies [80–82].

The approach of operating ion traps at higher RF frequencies was taken by Ramsey and coworkers starting in the late 1990s. In the seminal paper, a 500  $\mu\text{m}$  CIT was used to record the mass spectra of xenon atoms and PFTBA.

The RF frequency was 6.5 MHz for xenon and 5.0 MHz for PFTBA [42]. With the ion trap dimensions reduced by 20 times compared to conventional traps and the RF frequency increased by a factor of five and higher, this scaling method was unique and predicted to yield a high-quality mass spectra at higher pressures than had previously been achieved. Following the initial demonstration, several ion trap geometries were studied and used to measure the mass spectra of toluene, chlorobenzene, and 1-chloronaphthalene at nominally  $10^{-3}$  Torr helium [41].

Once the microscale ion trap operation was demonstrated, several methods for improving performance were characterized. To improve mass resolution and sensitivity of the microscale CITs, ions were ejected by mass-selective instability scans with resonance ejection utilizing nonlinear resonances. This method was termed double resonance ejection since trapped ions are resonant with both the quadrupolar (ion trapping) field, as well as the supplemental (axial) RF voltage applied to the endcap electrode at an RF frequency selected to match a nonlinear field resonance [83]. The axial RF voltage is applied during the RF ramp to eject the ions at a lower  $q_z$  value. Multiple resonance ejection techniques such as this are common in ion trap instruments; however, higher order field components are typically minimized or well-controlled [84]. Microscale CITs have large components of high-order field strength that are difficult to control because of their geometrical simplification and small critical dimensions [85, 86]. This presents a unique opportunity and need for methods such as using higher order field components to improve performance.

The large components of higher order fields in the microscale CIT designs revealed significant opportunities for performance improvements from nonlinear fields. The stability diagram was experimentally mapped out for six different resonances that demonstrated ions were ejected at a lower  $q_z$  value. Without the use of the double resonance ejection, the mass resolution ( $m/\Delta m$ ) for xenon atoms was found to be 44. With optimized double resonance ejection, mass resolutions up to 660 were measured for xenon atoms [83].

Since an obvious application for microscale traps was the analysis of volatile organic components in air (VOCs), a semipermeable membrane sample inlet was added to the MS instrument. Limit of detection (LOD) values were evaluated for six analytes and varied from 0.26 parts per million (ppm) for xylene to 13.8 ppm for acetone at operating pressures of  $1.5 \times 10^{-3}$  to  $3.8 \times 10^{-3}$  Torr in a helium carrier gas. Tandem mass spectrometry (MS/MS) was performed on chlorobenzene and improved the detection limit by a factor of 2.1 [87]. The effect of sample pressure on signal intensity was evaluated in the microscale CIT. Xenon peak intensities were characterized as a function of xenon pressure at different helium pressures. Increasing the helium pressure shifted the xenon concentration at which the signal strength was largest to a higher value, after which signal strength decays with pressure (all pressures below  $10^{-3}$  Torr). It was postulated that this effect was caused by scattering of xenon ions by xenon neutrals within the trap [88].

### 16.2.7 High-Pressure (~1 Torr) Trap Operation

Following optimization of the 500  $\mu\text{m}$  CIT in the low pressure ( $<10^{-3}$  Torr) regime, the focus turned to strategies for operating the microscale ion trap as a HPMS instrument, defined as pressures above 0.1 Torr. While Whitten et al. addressed the need to scale the ion trap to accommodate higher pressure operation, the next obstacle to higher pressure operation became the ion detector [36]. Electron multipliers are widely used in mass spectrometers due to their high sensitivity and sampling bandwidth [89–91]. However, they are pressure-intolerant due to their surface chemistry and even the most robust electron multipliers are only rated to approximately  $10^{-2}$  Torr.

Initial work separated the development of the ion source and microscale CIT from the detector by designing a differentially pumped mass spectrometer. The ionization source and microscale ion trap were housed in one chamber while the electron multiplier detector was housed in a separate vacuum chamber. The CIT and mounting scheme limited the gas flow between the two chambers – the CIT served as a small diameter orifice. The pressure drop inherent in this design made it possible to analyze ion source and trap performance at  $\approx 1$  Torr while still

using an electron multiplier at  $\approx 10^{-2}$  Torr. The two vacuum chambers were connected through a vacuum hose with an on/off valve to equalize the pressure between the two chambers when a high-pressure detector was being analyzed [92].

MS at approximately 1 Torr was demonstrated by Blakeman et al. in the early 2010s in helium buffer gas using a 500  $\mu\text{m}$  CIT operated in a differentially pumped mass spectrometer at RF frequencies ranging from 6.73 to 9.43 MHz. The ionization source was a thermionic filament (operated outside of the rated pressure range) while the detector was an electron multiplier operated around  $10^{-2}$  Torr. Filament parameters were optimized to detect xenon isotope peaks at a pressure of 1.2 Torr.

Three analytes were characterized over pressure ranges from approximately  $5 \times 10^{-2}$  Torr to 1 Torr, including xenon, 2-chloroethyl ethyl sulfide (CEES), and octane. Average peak FWHM for the five most abundant xenon isotopes were found to increase from 0.49 to 1.19 Da (an increase of 0.7 Da) when the pressure was increased from  $4.3 \times 10^{-2}$  to 1.0 Torr. Peak widths for CEES and octane were compared to a theoretical model [35]. Peak widths for CEES  $m/z$  75 peak were found to increase by  $0.52 \pm 0.02$  Da-Torr $^{-1}$  while the theoretical model predicted peaks to broaden by 0.60 Da-Torr $^{-1}$ . For octane  $m/z$  41, the peak widths increased by  $0.52 \pm 0.05$  Da-Torr $^{-1}$  compared to the theoretical mode of 0.55 Da-Torr $^{-1}$  [92].

Following the demonstration of HPMS with helium buffer gas operation, the focus moved toward HPMS operation with ambient air as the buffer gas. While helium is traditionally used in laboratories for its favorable collisional properties as a 4 Da species, a truly portable instrument would benefit from eliminating the need for a carrier gas, with the attendant gas cylinders, regulators, and logistical burden for users. The previous strategy of using a thermionic filament as an ionization source was not appropriate for use in ambient air, since filaments have poor tolerance to oxidation. Glow discharge ionization (GDI) was chosen as the replacement option since it operates well in the pressure regime around 1 Torr, draws low power (<0.5 W), and can be used as an electron or ion source. Emission currents for glow discharge as an electron source were characterized across a pressure regime from approximately 0.5 to 2 Torr of both nitrogen and air to ensure ionization stability when coupled to a microscale CIT at these operating pressures. While the target buffer gas was air, nitrogen was also characterized to confirm that additional air constituents did not detrimentally affect system performance [93].

In addition to ionization, air buffer gas operation presented new ion trap performance challenges since O<sub>2</sub> and N<sub>2</sub> have roughly seven times larger mass than helium, increasing the ion neutral collisional energy considerably. Mass spectra for *p*-xylene were compared between helium, nitrogen, and air buffer gases at 1 Torr buffer gas pressure for a 500  $\mu\text{m}$  CIT operated at 10 MHz RF frequency. Both the nitrogen and air mass spectra were acquired with the glow discharge electron source, while the helium mass spectra were acquired with a tungsten filament. Signal intensity was better for nitrogen and air since their ionization source was better suited for the high-pressure operation. Peak widths for *p*-xylene  $m/z$  91 and  $m/z$  106 peaks were compared between helium and air buffer gases as a function of operating pressure and are summarized in Table 16.2. Despite wider peak widths than traditionally observed with mass spectrometers at this mass range, each constituent of a four-component mixture of VOCs could be distinguished by the mass spectra acquired in 1 Torr of air [93].

**Table 16.2** Peak broadening vs. pressure for *p*-xylene in helium vs. air buffer gases.

<i>p</i> -Xylene peak	Peak broadening rate (Da-Torr $^{-1}$ )	Peak width at 1 Torr (Da)
<i>m/z</i> 91 in Helium	$0.51 \pm 0.07$	0.62
<i>m/z</i> 106 in Helium	$0.41 \pm 0.06$	0.62
<i>m/z</i> 91 in Air	$2.0 \pm 0.1$	4.78
<i>m/z</i> 106 in Air	$1.6 \pm 0.2$	5.04

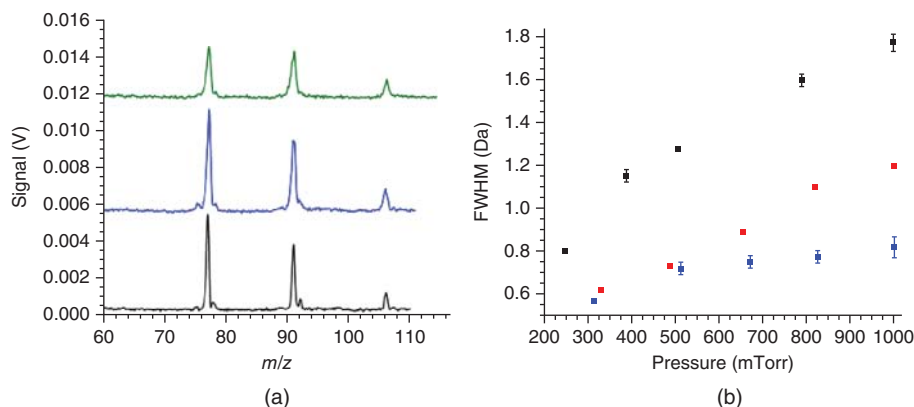


**Figure 16.2** (a) Mass spectra of *p*-xylene with  $r_o = 100 \mu\text{m}$  at an RF drive frequency of 59.44 MHz with ambient air pressures of 0.313 Torr (—), 0.672 Torr (—, red), and 1.02 Torr (—, green); and (b) peak widths for *p*-xylene 106 Da with increasing ambient air pressure for 30.34 MHz,  $r_o = 165 \mu\text{m}$  (■), 47.24 MHz,  $r_o = 100 \mu\text{m}$  (■, red), and 59.44 MHz,  $r_o = 100 \mu\text{m}$  (■, blue).

The Ramsey group followed the theoretical trends predicted by Goeringer and Arnold and worked to increase the frequency of the drive RF, and, thereby, the mass spectral resolution. CITs with critical dimensions between 500 and 100  $\mu\text{m}$  were analyzed (Figure 16.2). As the trap size decreased, higher RF frequencies could be evaluated while maintaining an operational mass range of approximately 140  $m/z$  using maximum RF voltage of approximate 1 kV (p–p). The same analyte *p*-xylene was used as the analyte for each CIT and the peak width for the  $m/z$  106 peak was quantitated. With an RF frequency of 59.44 MHz, the peak width was 0.8 Da and subunit resolution was achieved despite the elevated operating pressure. At 59.44 MHz, dropping the pressure from 1.02 Torr of ambient air to 0.313 Torr further improved peaks from 0.8 to 0.56 Da. Peak widths for a total of two traps and three RF frequencies are characterized to show the trade space between peak widths, RF frequency, and air buffer gas pressure [94].

With ionization and mass analysis demonstrated at 1 Torr of air, the last step to consider was ion detection. Previous work had been performed using electron multiplier detectors which are not compatible with operation above  $10^{-2}$  Torr. In contrast, Faraday cup detectors are capable of operation regardless of gas pressure, but do not offer the same sensitivity levels as electron multipliers. Two Faraday cup detectors were acquired and evaluated on HPMS platforms at pressures up to 1 Torr [95]. Mass spectra of four different aromatic benzene derivatives were acquired with these Faraday cup detectors in a series of experiments which demonstrated the full process of the mass spectrometer (ionization, mass analysis, detection) operated at 1 Torr of nitrogen buffer gas [96].

### 16.3 Commercialization and Applications

The first commercially available mass spectrometer operating at approximately 1 Torr came in 2014 with the launch of the M908 by 908 Devices, Inc. (Boston, MA). The M908 is a handheld mass spectrometer with dimensions of 22 cm  $\times$  18.5 cm  $\times$  7.6 cm and weighing 2.0 kg (Figure 16.3). It uses a GDI source, a microscale ion trap as the mass analyzer, and the detector is a Faraday cup [97]. Pumping is performed by a small, custom, mechanical scroll pump to achieve an operating pressure in the 1 Torr range in under 10 seconds. A notable feature of the M908 is the absence of an expensive, fragile, turbomolecular pump. The use of a mechanical pump as the sole source of vacuum increases the overall ruggedness of the device. The M908 is compliant with military (MIL-STD-810G) standards for shock/drop/vibration.

The miniature ion trap, ionizer, and Faraday cup are contained in an “MS core” (Figure 16.4). The core is user-replaceable in the event of severe contamination on-scene in order to reduce downtime to a few minutes (Figure 16.5). Post-event, the core can be easily cleaned and returned to service.



**Figure 16.3** M908 handheld mass spectrometer. Source: Figure courtesy of 908 Devices Inc.

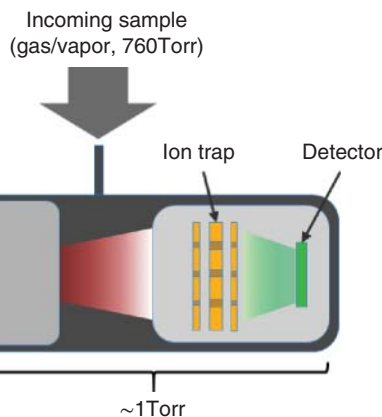


**Figure 16.4** Diagram showing the components of the M908 MS Core. The entire core is at a pressure of ~1 Torr.

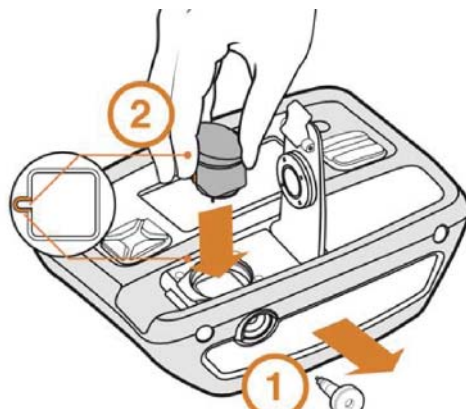


**Figure 16.5** The M908 MS core and inlet capillary (a). Source: Figure courtesy of 908 Devices Inc.. Replacement of the MS core (b).

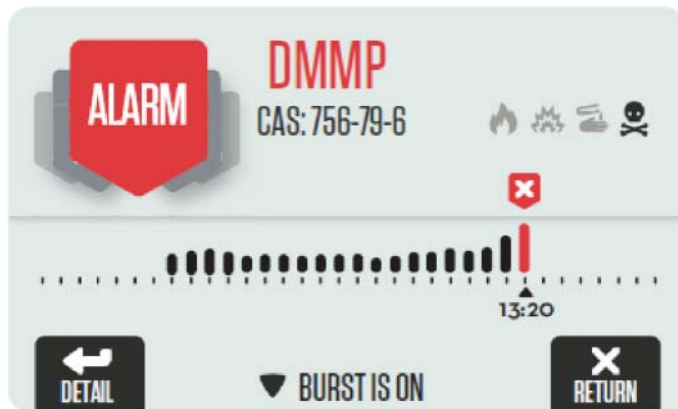


**Figure 16.6** M908 alarm screen in vapor mode. Each bar represents a mass spectrum – black bars indicate ion current detected, red bars indicate ion current detected and a match to the target library. Source: 908 Devices.

The M908 was designed specifically for the detection and identification of chemical threats at the point of need. It is battery operated, with a battery life of 2–4 hours depending on the mode of use. Vapor phase threats are detected by direct sampling through a small inlet capillary. The device measures ambient air directly and requires no additional carrier gas supply or dopant gas. The target library includes a variety of toxic industrial chemicals (TICs), solvents, and chemical warfare agents (CWAs).

Operationally, the M908 measures a mass spectrum of the surrounding air about once every second, detecting positively charged ions generated by the GDI. If the measured chemical signal (the total ion current) rises above a set threshold, the spectrum is automatically tested against the target library. If the spectrum matches one or more targets in the library, the M908 displays an alarm on the screen, along with the identity of the chemical or chemicals (Figure 16.6). All spectral analysis is done by the software. By design, the user is not required to assess the mass spectrum, making the M908 suitable for use by civilian users, first responders, and military teams.

Solid- and liquid-phase threats, as well as trace samples, are analyzed by swab sampling using a thermal desorption (TD) mode. Sampling swabs, made of Teflon-coated fiberglass, are used to deliver minute amounts of condensed phase material into the M908. The device rapidly heats the swab and any present threat material to over 200 °C, producing vapor which is measured by HPMS. TD mode targets include explosives and low-volatility CWAs, such as VX. Detection/identification limits vary by chemical: in the vapor phase ranging from sub-ppm for CWAs to 10s of ppm for some TICs, and in TD mode from sub-microgram to 10s of micrograms.

In 2017, a second-generation handheld mass spectrometer, the MX908 was launched by 908 Devices (Figure 16.7). The MX908 utilizes a dual-polarity atmospheric pressure chemical ionization (APCI) source driven by fast switching electronics that are capable of scanning both positive and negative mode polarities in approximately 0.1 seconds. The microscale ion trap design is optimized for the APCI source and the Faraday cup detector electronics are optimized for the fast switching dual-polarity MS scans (Figure 16.8). While slightly larger than the M908 with a weight of 3.9 kg and dimensions of 29.8 cm × 21.6 cm × 12.2 cm, the design updates improved the sensitivity of the platform by a factor of up to a thousand. The MX908 operates on battery power with a battery life of four hours and is MIL-STD 810G compliant.

The MX908 has both vapor and thermal desorption capability. The target library, which covers both positive- and negative-mode analytes, comprises over 100 threats, including TICs, CWAs, explosives, and narcotics (including fentanyl). Limits of detection/identification are summarized in Table 16.3.

Ionization via APCI is known to produce less fragmentation than the more common electron impact (EI) ionization [98–100]. Mass spectra produced by the MX908 exhibit large fractions of protonated molecules and higher *m/z* fragments. Additional fragments can be generated using the process of collision-induced dissociation (CID)



**Figure 16.7** MX908 handheld mass spectrometer. Source: Figure courtesy of 908 Devices Inc.

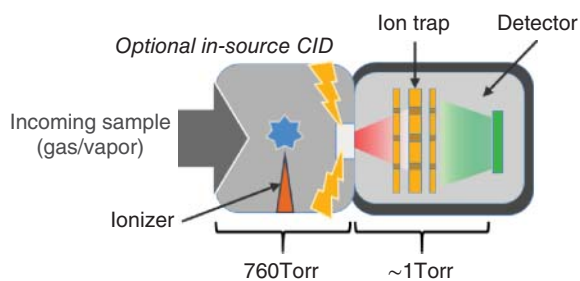


**Figure 16.8** Diagram showing the components of the MX908 MS Core. The ionization chamber on the left operates at atmospheric pressure. The chamber containing the ion trap and detector operates at  $\sim$ 1 Torr. A small aperture separates the two chambers.

**Table 16.3** Estimated LOD for key target classes in MX908.

Target class	Mode	Estimated LOD
Explosives – organonitrites	TD	<100 ng
Explosives – peroxides	Vapor/TD	<10 ppm/<3000 ng
Narcotics	TD	<100–1000 ng
Fentanyl	TD	<100 ng
CWA: nerve agents (G)	Vapor	<100 ppb
CWA: nerve agents (V)	Vapor/TD	<100 ppb/<100 ng
CWA: blister agents (HD)	Vapor	<2000 ng

[101, 102]. Ions generated in the ionization chamber (in-source CID) can be accelerated through the aperture with controlled levels of force, providing a well-defined amount of kinetic energy to the ions and fragmenting them to specific degrees. The MX908 uses multiple levels of CID to improve chemical specificity.

An example is shown in Figure 16.9. Two fentanyl analogs with identical molecular weights, 3-methylfentanyl and butyryl fentanyl (350.5 amu) are analyzed at low, medium, and high levels of CID voltage. At low CID voltage (left), no fragmentation is observed and the two fentanyls are indistinguishable. At a moderate CID voltage, two fragments are observed for both 3-methyl fentanyl (orange) and butyryl fentanyl (blue). The lower mass fragment is 105  $m/z$  for both targets, but the higher mass fragment observed is 189  $m/z$  for butyryl fentanyl and 202 for 3-methylfentanyl. The matching algorithms on the MX908 utilize both the mass/charge values of the ions observed

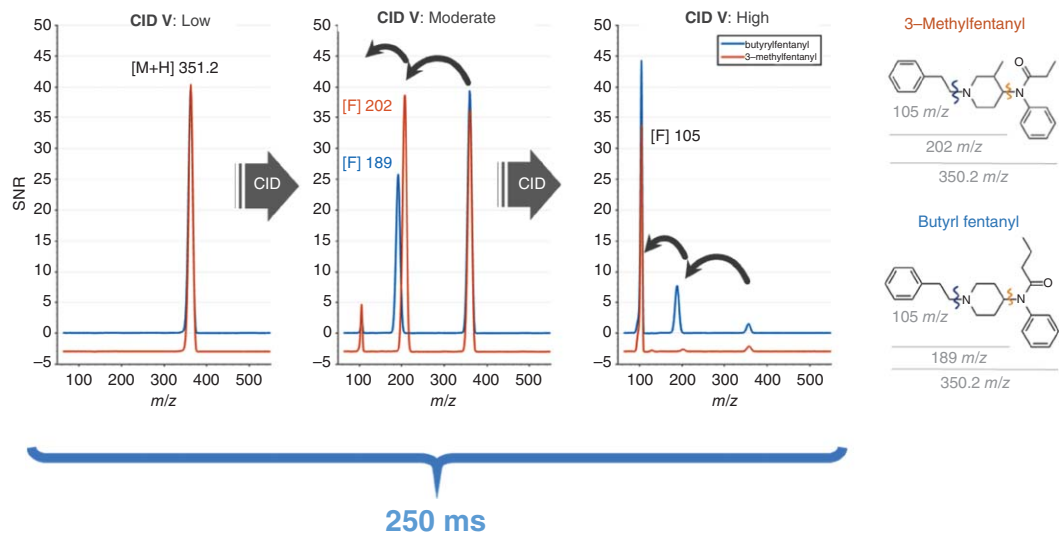


Figure 16.9 Use of CID to distinguish isobaric fentanyl analogs.



**Figure 16.10** The Rebel amino acid analyzer uses CE-ESI-HPMS to detect and quantify 33 metabolic targets from samples of cell culture media. Source: Figure courtesy of 908 Devices Inc.

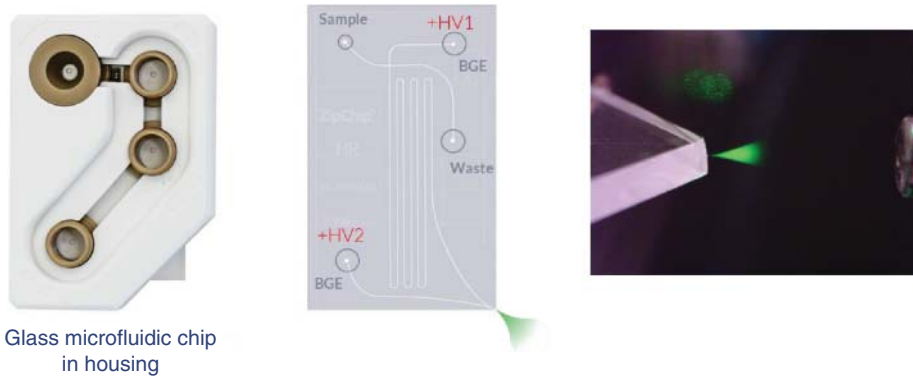
and the CID energy level at which they are observed to identify targets, reducing false alarm rates even in the presence of large amounts of cutting agents or other interferents [103].

HPMS has been used as the detector in conjunction with chemical separation techniques to improve the analysis of complex mixtures. An example is the recently released benchtop amino acid analyzer, the Rebel (Figure 16.10). Rebel was launched by 908 Devices in 2019, and utilizes HPMS detection in conjunction with a microchip-based capillary electrophoresis–electrospray ionization (CE-ESI) method to separate and quantify amino acids in complex biological samples, such as cell culture media [104, 105].

The Rebel's Spent Media assay is designed to automatically detect and quantify 33 metabolites, including the 20 common amino acids and 6 vitamins, in mammalian and fermentation media. The built-in autosampler gives the capability for running over 200 samples in a batch with no user intervention after initiating the batch. The entire process of analyzing a sample from the autosampler loading a sample through the separation, MS analysis, and automated data analysis takes under 10 minutes per sample. The separation and MS analysis itself take just under three minutes.

The Rebel is a benchtop instrument, not intended to be mobile. However, the use of HPMS as the detector provides considerable advantages over more typical liquid chromatography-MS (LC-MS) systems. Operating the system at  $\sim$ 1 Torr allows all vacuum pumps to be contained within the device so that the system sits entirely on the benchtop. No carrier or curtain gases are necessary. All of the required reagents are provided in the sample kit – no additional solvents are needed. The HPMS detector is essentially maintenance-free allowing the Rebel to be operated by analysts and biomanufacturing personnel, rather than analytical chemists.

The microfluidic chip used in Rebel is shown in Figure 16.11. The built-in autosampler delivers the sample and the background electrolyte (BGE) to the respective wells. A sequence of pneumatic pressures is applied to the wells to deliver a precise amount of sample into the separation channel. Typical volumes injected are around 4 nL. A sequence of applied high voltages induces an electrophoretic separation as the sample passes through the channel, and the sample is emitted from the corner of the chip as an electrospray. The chip is precisely positioned to deliver the sample to the inlet of the HPMS.



Glass microfluidic chip in housing

**Figure 16.11** (a) The Rebel microfluidic chip. Source: Figure courtesy of 908 Devices Inc. (b) Microfabricated glass layer of the chip showing sample and electrolyte wells, separation channel, and position of electrospray in green. (c) The positioning of the chip relative to the inlet of the HPMS. Source: Figure courtesy of 908 Devices Inc.

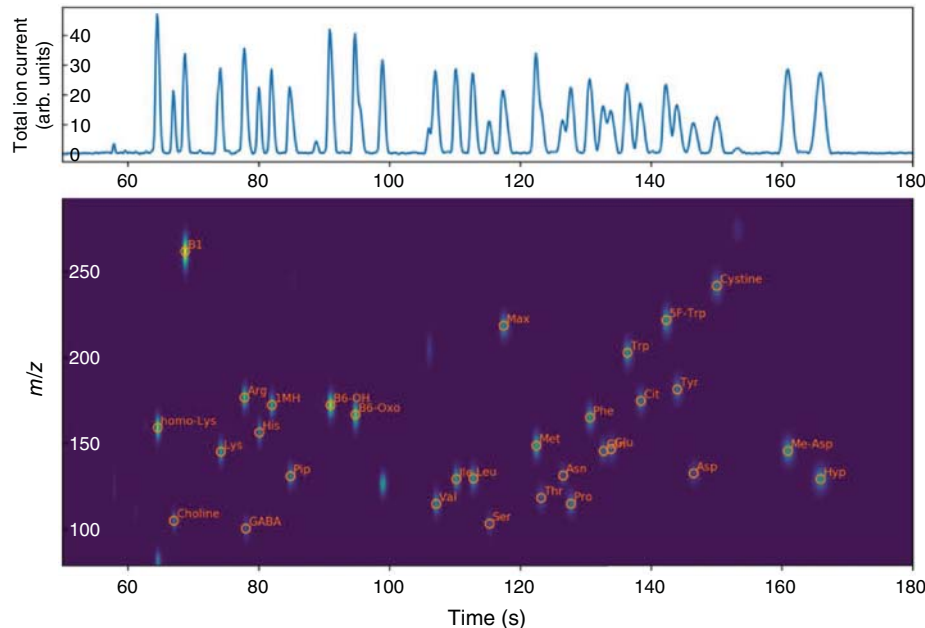


**Figure 16.12** Electropherogram and *m/z* map of the standard solution of analytes, all at a concentration of 25  $\mu\text{M}$ . Thirty-one components are identified and quantified in three minutes. The total ion current is shown in the top trace.

An example of Rebel data is shown in Figure 16.12. A mixture of amino acids, biogenic amines, and vitamins, all at concentrations of 25 micromolar ( $\mu\text{M}$ ), was analyzed. The sample volume injected was 3.6 nanoliters (nl). Thirty-one components were identified over a CE run of just under three minutes (min). The observed levels of total ion current signal for each component correspond to minute quantities of material: the electrospray contains 9 femtomoles of the component. The estimated limits of quantitation for Rebel are  $<5 \mu\text{M}$ , corresponding to below 1–4 pg (depending on the specific target) leaving the chip in the electrospray and demonstrating the sensitivity of the HPMS detector.

Applications for CE–ESI–HPMS include screening of raw materials and monitoring metabolite concentrations at different time points during cell culture growth. The separation and detection methods are tolerant to common

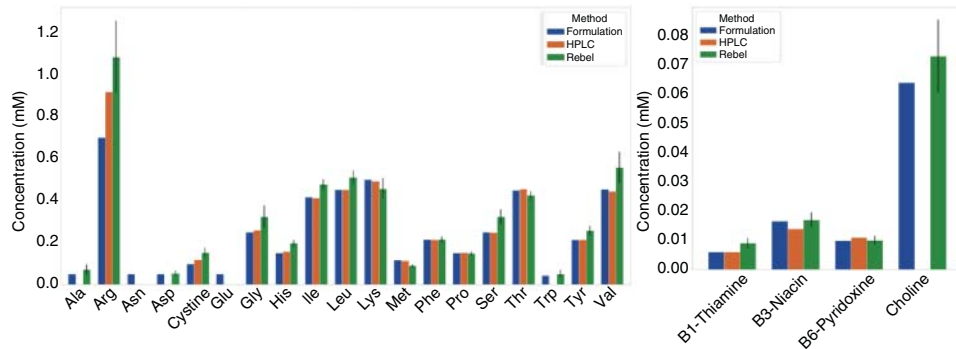


**Figure 16.13** Concentration values for amino acids and vitamins in DMEM-F12 cell culture media as determined by HPLC analysis ( $n = 1$ , orange) and Rebel analysis ( $n = 5$ , green). The manufacturer-reported values are shown in blue.

LC-MS interferences such as salts, sugars, antibodies, and proteins commonly found in cell culture media samples. Figure 16.13 shows the results of the analysis of fresh cell culture media (DMEM/F12, P/N D8437, Sigma-Aldrich). The media was run on both the Rebel and via HPLC, and the results were compared to the manufacturer's reported values. For the HPLC analysis, the sample was diluted 10×, then derivatized to add UV absorbent tags for detection. For the Rebel analysis, the sample was diluted 10× and analyzed directly.

The Rebel ran the sample and quantified all components in a single seven-minute run. The HPLC method required two separate runs – one for amino acids and one for vitamin analysis. Data were aligned very well between the Rebel ( $n = 5$ ) and HPLC ( $n = 1$ ). Note: the standard B vitamin method for HPLC did not cover choline; so, it was not detected.

## 16.4 Conclusions

Ion trap mass spectrometers have been workhorse instruments in laboratories since the 1980s. Miniaturization efforts have sought to move these mass spectrometers from laboratories where they are maintained and operated by trained personnel to portable units that no longer require advanced MS knowledge to operate. Ion traps have been miniaturized and analyzed using a variety of geometries by both academic and commercial groups. A key step toward truly handheld, portable units has been the introduction of HPMS. HPMS had led to MS instruments that no longer require turbomolecular pumps and can perform mass analysis with a single miniaturized roughing pump. The M908, MX908, and Rebel are all commercial instruments that utilize HPMS and perform analyses at the point of use for applications, such as TICs, CWAs, drugs, explosives, and metabolites.

## References

- Ouyang, Z., Noll, R.J., and Cooks, R.G. (2009). Handheld miniature ion trap mass spectrometers. *Anal. Chem.* <https://doi.org/10.1021/ac900292w>.
- Denisov, E., Damoc, E., Lange, O., and Makarov, A. (2012). Orbitrap mass spectrometry with resolving powers above 1,000,000. *Int. J. Mass Spectrom.* <https://doi.org/10.1016/j.ijms.2012.06.009>.
- Pelander, A., Decker, P., Baessmann, C., and Ojanperä, I. (2011). Evaluation of a high resolving power time-of-flight mass spectrometer for drug analysis in terms of resolving power and acquisition rate. *J. Am. Soc. Mass Spectrom.* <https://doi.org/10.1007/s13361-010-0046-z>.

- 4 Snyder, D.T., Pulliam, C.J., Ouyang, Z., and Cooks, R.G. (2016). Miniature and fieldable mass spectrometers: recent advances. *Anal. Chem.* <https://doi.org/10.1021/acs.analchem.5b03070>.
- 5 Badman, E.R. and Cooks, R.G. (2000). Miniature mass analyzers. *J. Mass Spectrom.* [https://doi.org/10.1002/1096-9888\(200006\)35:6<659::AID-JMS5>3.0.CO;2-V](https://doi.org/10.1002/1096-9888(200006)35:6<659::AID-JMS5>3.0.CO;2-V).
- 6 Verbeck, G.F. and Bierbaum, V.M. (2015). Focus on harsh environment and field-portable mass spectrometry: editorial. *J. Am. Soc. Mass Spectrom.* <https://doi.org/10.1007/s13361-014-1057-y>.
- 7 Palmer, P.T. and Limero, T.F. (2001). Mass spectrometry in the U.S. space program: past, present, and future. *J. Am. Soc. Mass Spectrom.* [https://doi.org/10.1016/S1044-0305\(01\)00249-5](https://doi.org/10.1016/S1044-0305(01)00249-5).
- 8 Ecelberger, S.A., Cornish, T.J., Collins, B.F. et al. (2004). Suitcase TOF: a man-portable time-of-flight mass spectrometer. *Johns Hopkins APL Tech. Dig. (Appl. Phys. Lab.)* 25: 14–19.
- 9 Gnyba, M., Smulko, J., Kwiatkowski, A., and Wierzba, P. (2011). Portable Raman spectrometer - design rules and applications. *Bull. Polish Acad. Sci. Tech. Sci.* <https://doi.org/10.2478/v10175-011-0040-z>.
- 10 Ho, C.K., Itamura, M.T., Kelley, M., and Hughes, R.C. (2001). Review of chemical sensors for in-situ monitoring of volatile contaminants. *Contract* <https://doi.org/10.2172/780299>.
- 11 Cottingham, K. (2003). Product review: ion mobility spectrometry rediscovered. *Anal. Chem.* <https://doi.org/10.1021/ac031304h>.
- 12 Harris, C.M. (2002). GC to go. *Anal. Chem.* 21: 585A–589A.
- 13 Glish, G.L. and Vachet, R.W. (2003). The basics of mass spectrometry in the twenty-first century. *Nat. Rev. Drug Discov.* <https://doi.org/10.1038/nrd1011>.
- 14 Haag, A.M. (2016). Mass analyzers and mass spectrometers. *Adv. Exp. Med. Biol.* [https://doi.org/10.1007/978-3-319-41448-5\\_7](https://doi.org/10.1007/978-3-319-41448-5_7).
- 15 Crocombe, R.A. (2018). Portable spectroscopy. *Appl. Spectrosc.* <https://doi.org/10.1177/0003702818809719>.
- 16 Sorak, D., Herberholz, L., Iwascek, S. et al. (2012). New developments and applications of handheld Raman, mid-infrared, and near-infrared spectrometers. *Appl. Spectrosc. Rev.* <https://doi.org/10.1080/05704928.2011.625748>.
- 17 Smiths Detection. LCD 3.3 Person worn CWA and TIC detector. <https://www.smithsdetection.com/products/lcd-3-3> (accessed 23 October 2019).
- 18 ThermoFisher Scientific. FirstDefender™ RMX Handheld Chemical Identification. <https://www.thermofisher.com/order/catalog/product/FIRSTDEFENDERRMX> (accessed 23 October 2019).
- 19 Paul, W. and Steinwedel, H. (1953). Ein Neues Massenspektrometer Ohne Magnetfeld. *Zeitschrift fur Naturforschung – Sec. A J. Phys. Sci.* <https://doi.org/10.1515/zna-1953-0710>.
- 20 March, R. E.; Todd, J. F. J. *Practical Aspects of Trapped Ion Mass Spectrometry*; 2016. <https://doi.org/10.1201/9781420083743>.
- 21 Bharti, A., Ma, P.C., and Salgia, R. (2007). *Mass Spectrom. Rev.* <https://doi.org/10.1002/mas.20125>.
- 22 March, R.E. (1997). An introduction to quadrupole ion trap mass spectrometry. *J. Mass Spectrom.* [https://doi.org/10.1002/\(SICI\)1096-9888\(199704\)32:4<351::AID-JMS512>3.0.CO;2-Y](https://doi.org/10.1002/(SICI)1096-9888(199704)32:4<351::AID-JMS512>3.0.CO;2-Y).
- 23 Drewsen, M. and Brøner, A. (2000). Harmonic linear Paul trap: stability diagram and effective potentials. *Phys. Rev. A – At. Mol. Opt. Phys.* <https://doi.org/10.1103/PhysRevA.62.045401>.
- 24 Alheit, R., Kleineidam, S., Vedel, F. et al. (1996). Higher order non-linear resonances in a Paul trap. *Int. J. Mass Spectrom. Ion Process.* [https://doi.org/10.1016/0168-1176\(96\)04380-7](https://doi.org/10.1016/0168-1176(96)04380-7).
- 25 Dehmelt, H.G. (1968). Radiofrequency spectroscopy of stored ions I: storage. *Adv. At. Mol. Opt. Phys.* [https://doi.org/10.1016/S0065-2199\(08\)60170-0](https://doi.org/10.1016/S0065-2199(08)60170-0).
- 26 Major, F.G. and Dehmelt, H.G. (1968). Exchange-collision technique for the RF spectroscopy of stored ions. *Phys. Rev.* <https://doi.org/10.1103/PhysRev.170.91>.
- 27 Dawson, P.H. and Whetten, N.R. (1968). Ion storage in three-dimensional, rotationally symmetric, quadrupole fields. II. A sensitive mass spectrometer. *J. Vac. Sci. Technol. A* <https://doi.org/10.1116/1.1492570>.

- 28** Dawson, P.H. and Whetten, N.R. (1968). Ion storage in three-dimensional, rotationally symmetric, quadrupole fields. I. Theoretical treatment. *J. Vac. Sci. Technol. A* <https://doi.org/10.1116/1.1492569>.
- 29** Stafford, G.C., Kelley, P.E., Syka, J.E.P. et al. (1984). Recent improvements in and analytical applications of advanced ion trap technology. *Int. J. Mass Spectrom. Ion Process.* [https://doi.org/10.1016/0168-1176\(84\)80077-4](https://doi.org/10.1016/0168-1176(84)80077-4).
- 30** Stafford, G. (2002). Ion trap mass spectrometry: a personal perspective. *J. Am. Soc. Mass Spectrom.* [https://doi.org/10.1016/S1044-0305\(02\)00385-9](https://doi.org/10.1016/S1044-0305(02)00385-9).
- 31** Dawson, P.H. (1977). The effect of collisions on ion motion in quadrupole fields. *Int. J. Mass Spectrom. Ion Phys.* [https://doi.org/10.1016/0020-7381\(77\)80082-X](https://doi.org/10.1016/0020-7381(77)80082-X).
- 32** Blatt, R., Schmeling, U., and Werth, G. (1979). On the sensitivity of ion traps for spectroscopic applications. *Appl. Phys.* <https://doi.org/10.1007/BF00894999>.
- 33** Borman, S.A. (1983). New gas chromatographic detectors. *Anal. Chem.* <https://doi.org/10.1021/ac00258a735>.
- 34** Goeringer, D.E., Whitten, W.B., Ramsey, J.M. et al. (1992). Theory of high-resolution mass spectrometry achieved via resonance ejection in the quadrupole ion trap. *Anal. Chem.* <https://doi.org/10.1021/ac00037a023>.
- 35** Arnold, N.S., Hars, C., and Meuzelaar, H.L.C. (1994). Extended theoretical considerations for mass resolution in the resonance ejection mode of quadrupole ion trap mass spectrometry. *J. Am. Soc. Mass Spectrom.* [https://doi.org/10.1016/1044-0305\(94\)85008-9](https://doi.org/10.1016/1044-0305(94)85008-9).
- 36** Whitten, W.B., Reilly, P.T.A., and Ramsey, J.M. (2004). High-pressure ion trap mass spectrometry. *Rapid Commun. Mass Spectrom.* <https://doi.org/10.1002/rcm.1549>.
- 37** Wang, Y., Franzen, J., and Wanczek, K.P. (1993). The non-linear resonance ion trap. Part 2. A general theoretical analysis. *Int. J. Mass Spectrom. Ion Process.*
- 38** Franzen, J., Gabling, R.H., Schubert, M., and Wang, Y. (1995). Nonlinear ion traps. *Pract. Asp. Ion Trap Mass Spectrom.*
- 39** Eades, D.M., Johnson, J.V., and Yost, R.A. (1993). Nonlinear resonance effects during ion storage in a quadrupole ion trap. *J. Am. Soc. Mass Spectrom.* [https://doi.org/10.1016/1044-0305\(93\)80017-S](https://doi.org/10.1016/1044-0305(93)80017-S).
- 40** Bonner, R.F., Fulford, J.E., March, R.E., and Hamilton, G.F. (1977). The cylindrical ion trap. Part I. general introduction. *Int. J. Mass Spectrom. Ion Phys.* [https://doi.org/10.1016/0020-7381\(77\)80034-X](https://doi.org/10.1016/0020-7381(77)80034-X).
- 41** Kornienko, O., Reilly, P.T.A., Whitten, W.B., and Ramsey, J.M. (1999). Micro ion trap mass spectrometry. *Rapid Commun. Mass Spectrom.* [https://doi.org/10.1002/\(SICI\)1097-0231\(19990115\)13:1<50::AID-RCM449>3.0.CO;2-K](https://doi.org/10.1002/(SICI)1097-0231(19990115)13:1<50::AID-RCM449>3.0.CO;2-K).
- 42** Kornienko, O., Reilly, P.T.A., Whitten, W.B., and Ramsey, J.M. (1999). Electron impact ionization in a microion trap mass spectrometer. *Rev. Sci. Instrum.* <https://doi.org/10.1063/1.1150010>.
- 43** Wells, J.M., Badman, E.R., and Cooks, R.G. (1998). A quadrupole ion trap with cylindrical geometry operated in the mass-selective instability mode. *Anal. Chem.* <https://doi.org/10.1021/ac971198h>.
- 44** Xu, W., Chappell, W.J., Cooks, R.G., and Ouyang, Z. (2009). Characterization of electrode surface roughness and its impact on ion trap mass analysis. *J. Mass Spectrom.* <https://doi.org/10.1002/jms.1512>.
- 45** Chaudhary, A., Van Amerom, F.H.W., and Short, R.T. (2014). Experimental evaluation of micro-ion trap mass spectrometer geometries. *Int. J. Mass Spectrom.* <https://doi.org/10.1016/j.ijms.2014.06.032>.
- 46** Lee, W.W., Oh, C.H., Kim, P.S. et al. (2003). Characteristics of cylindrical ion trap. *Int. J. Mass Spectrom.* <https://doi.org/10.1016/j.ijms.2003.08.001>.
- 47** Louris, J.N., Cooks, R.G., Syka, J.E. et al. (1987). Instrumentation, applications, and energy deposition in quadrupole ion-trap tandem mass spectrometry. *Anal. Chem.* <https://doi.org/10.1021/ac00140a021>.
- 48** Austin, D.E., Cruz, D., and Blain, M.G. (2006). Simulations of ion trapping in a micrometer-sized cylindrical ion trap. *J. Am. Soc. Mass Spectrom.* <https://doi.org/10.1016/j.jasms.2005.11.020>.
- 49** Cruz, D., Chang, J.P., Fico, M. et al. (2007). Design, microfabrication, and analysis of micrometer-sized cylindrical ion trap arrays. *Rev. Sci. Instrum.* <https://doi.org/10.1063/1.2403840>.
- 50** Tian, Y., Higgs, J., Li, A. et al. (2014). How far can ion trap miniaturization go? Parameter scaling and space-charge limits for very small cylindrical ion traps. *J. Mass Spectrom.* <https://doi.org/10.1002/jms.3343>.

- 51 Pau, S., Pai, C.S., Low, Y.L. et al. (2006). Microfabricated quadrupole ion trap for mass spectrometer applications. *Phys. Rev. Lett.* <https://doi.org/10.1159/000089267>.
- 52 Badman, E.R. and Cooks, R.G. (2000). A parallel miniature cylindrical ion trap array. *Anal. Chem.* <https://doi.org/10.1021/ac000109p>.
- 53 Tabert, A.M., Griep-Raming, J., Guymon, A.J., and Cooks, R.G. (2003). High-throughput miniature cylindrical ion trap array mass spectrometer. *Anal. Chem.* <https://doi.org/10.1021/ac0346858>.
- 54 Ouyang, Z., Badman, E.R., and Cooks, R.G. (1999). Characterization of a serial array of miniature cylindrical ion trap mass analyzers. *Rapid Commun. Mass Spectrom.* [https://doi.org/10.1002/\(SICI\)1097-0231\(19991230\)13:24<2444::AID-RCM810>3.0.CO;2-F](https://doi.org/10.1002/(SICI)1097-0231(19991230)13:24<2444::AID-RCM810>3.0.CO;2-F).
- 55 Hager, J.W. (2002). A new linear ion trap mass spectrometer. *Rapid Commun. Mass Spectrom.* <https://doi.org/10.1002/rcm.607>.
- 56 Schwartz, J.C., Senko, M.W., and Syka, J.E.P. (2002). A two-dimensional quadrupole ion trap mass spectrometer. *J. Am. Soc. Mass Spectrom.* [https://doi.org/10.1016/S1044-0305\(02\)00384-7](https://doi.org/10.1016/S1044-0305(02)00384-7).
- 57 Ouyang, Z., Wu, G., Song, Y. et al. (2004). Rectilinear ion trap: concepts, calculations, and analytical performance of a new mass analyzer. *Anal. Chem.* <https://doi.org/10.1021/ac049420n>.
- 58 Erickson, B.E. (2004). Miniaturized rectilinear ion trap. *Anal. Chem.* 17: 305A.
- 59 Hendricks, P., Duncan, J., Noll, R.J. et al. (2011). Performance of a low voltage ion trap. *Int. J. Mass Spectrom.* <https://doi.org/10.1016/j.ijms.2011.05.009>.
- 60 Wu, G., Cooks, R.G., Ouyang, Z. et al. (2006). Ion trajectory simulation for electrode configurations with arbitrary geometries. *J. Am. Soc. Mass Spectrom.* <https://doi.org/10.1016/j.jasms.2006.05.004>.
- 61 Ramsey, J.M. and Schultze, K.P. (2014). Miniature charged particle trap with elongated trapping region for mass spectrometry. US8878127B2.
- 62 Pau, S., Whitten, W.B., and Ramsey, J.M. (2007). Planar geometry for trapping and separating ions and charged particles. *Anal. Chem.* <https://doi.org/10.1021/ac0706269>.
- 63 Peng, Y., Hansen, B.J., Quist, H. et al. (2011). Coaxial ion trap mass spectrometer: concentric toroidal and quadrupolar trapping regions. *Anal. Chem.* <https://doi.org/10.1021/ac200600u>.
- 64 Lammert, S.A., Plass, W.R., Thompson, C.V., and Wise, M.B. (2001). Design, optimization and initial performance of a toroidal RF ion trap mass spectrometer. *Int. J. Mass Spectrom.* [https://doi.org/10.1016/S1387-3806\(01\)00507-3](https://doi.org/10.1016/S1387-3806(01)00507-3).
- 65 Lammert, S.A., Rockwood, A.A., Wang, M. et al. (2006). Miniature toroidal radio frequency ion trap mass analyzer. *J. Am. Soc. Mass Spectrom.* <https://doi.org/10.1016/j.jasms.2006.02.009>.
- 66 Higgs, J.M., Petersen, B.V., Lammert, S.A. et al. (2016). Radiofrequency trapping of ions in a pure toroidal potential distribution. *Int. J. Mass Spectrom.* <https://doi.org/10.1016/j.ijms.2015.11.009>.
- 67 Austin, D.E., Wang, M., Tolley, S.E. et al. (2007). Halo ion trap mass spectrometer. *Anal. Chem.*
- 68 Wang, M., Quist, H.E., Hansen, B.J. et al. (2011). Performance of a halo ion trap mass analyzer with exit slits for axial ejection. *J. Am. Soc. Mass Spectrom.* <https://doi.org/10.1007/s13361-010-0027-2>.
- 69 Chen, C.H., Chen, T.C., Zhou, X. et al. (2015). Design of portable mass spectrometers with handheld probes: aspects of the sampling and miniature pumping systems. *J. Am. Soc. Mass Spectrom.* <https://doi.org/10.1007/s13361-014-1026-5>.
- 70 Hoch, G. and Kok, B. (1963). A mass spectrometer inlet system for sampling gases dissolved in liquid phases. *Arch. Biochem. Biophys.* [https://doi.org/10.1016/0003-9861\(63\)90546-0](https://doi.org/10.1016/0003-9861(63)90546-0).
- 71 Davey, N.G., Krogh, E.T., and Gill, C.G. (2011). Membrane-introduction mass spectrometry (MIMS). *TrAC* <https://doi.org/10.1016/j.trac.2011.05.003>.
- 72 Giannoukos, S., Brkić, B., Taylor, S., and France, N. (2015). Membrane inlet mass spectrometry for homeland security and forensic applications. *J. Am. Soc. Mass Spectrom.* <https://doi.org/10.1007/s13361-014-1032-7>.
- 73 Gao, L., Cooks, R.G., and Ouyang, Z. (2008). Breaking the pumping speed barrier in mass spectrometry: discontinuous atmospheric pressure Interface. *Anal. Chem.* <https://doi.org/10.1021/ac800014v>.

- 74** Gao, L., Sugiarto, A., Harper, J.D. et al. (2008). Design and characterization of a multisource hand-held tandem mass spectrometer. *Anal. Chem.* <https://doi.org/10.1021/ac801275x>.
- 75** Xu, W., Song, Q., Smith, S.A. et al. (2009). Ion trap mass analysis at high pressure: a theoretical view. *J. Am. Soc. Mass Spectrom.* <https://doi.org/10.1016/j.jasms.2009.06.019>.
- 76** Song, Q., Xu, W., Smith, S.A. et al. (2010). Ion trap mass analysis at high pressure: an experimental characterization. *J. Mass Spectrom.* <https://doi.org/10.1002/jms.1684>.
- 77** Jiang, T., Xu, Q., Zhang, H. et al. (2018). Improving the performances of a “brick mass spectrometer” by quadrupole enhanced dipolar resonance ejection from the linear ion trap. *Anal. Chem.* <https://doi.org/10.1021/acs.analchem.8b03332>.
- 78** Jiang, P., Zhou, Z., Wu, Z., and Zhao, Z. (2018). Low-vacuum cylindrical ion trap mass spectrometry. *Instrum. Sci. Technol.* 46 (6): 614–627.
- 79** Decker, T.K., Zheng, Y., Ruben, A.J. et al. (2019). A microscale planar linear ion trap mass spectrometer. *J. Am. Soc. Mass Spectrom.* <https://doi.org/10.1007/s13361-018-2104-x>.
- 80** Jones, R.M., Gerlich, D., and Anderson, S.L. (1997). Simple radio-frequency power source for ion guides and ion traps. *Rev. Sci. Instrum.* <https://doi.org/10.1063/1.1148297>.
- 81** Schaefer, R.T., MacAskill, J.A., Mojarradi, M. et al. (2008). Digitally synthesized high purity, high-voltage radio frequency drive electronics for mass spectrometry. *Rev. Sci. Instrum.* <https://doi.org/10.1063/1.2981691>.
- 82** O'Connor, P.B., Costello, C.E., and Earle, W.E. (2002). A high voltage RF oscillator for driving multipole ion guides. *J. Am. Soc. Mass Spectrom.* [https://doi.org/10.1016/S1044-0305\(02\)00700-6](https://doi.org/10.1016/S1044-0305(02)00700-6).
- 83** Moxom, J., Reilly, P.T.A., Whitten, W.B., and Ramsey, J.M. (2002). Double resonance ejection in a micro ion trap mass spectrometer. *Rapid Commun. Mass Spectrom.* <https://doi.org/10.1002/rcm.635>.
- 84** Snyder, D.T. and Cooks, R.G. (2016). Successive resonances for ion ejection at arbitrary frequencies in an ion trap. *J. Am. Soc. Mass Spectrom.* <https://doi.org/10.1007/s13361-016-1473-2>.
- 85** Decker, T.K., Zheng, Y., McClellan, J.S. et al. (2018). Double resonance ejection using novel radiofrequency phase tracking circuitry in a miniaturized planar linear ion trap mass spectrometer. *Rapid Commun. Mass Spectrom.* <https://doi.org/10.1002/rcm.8267>.
- 86** Zhou, X., Liu, X., Chiang, S. et al. (2018). Stimulated motion suppression (STMS): a new approach to break the resolution barrier for ion trap mass spectrometry. *J. Am. Soc. Mass Spectrom.* <https://doi.org/10.1007/s13361-018-1995-x>.
- 87** Moxom, J., Reilly, P.T.A., Whitten, W.B., and Ramsey, J.M. (2003). Analysis of volatile organic compounds in air with a micro ion trap mass analyzer. *Anal. Chem.* <https://doi.org/10.1021/ac034043k>.
- 88** Moxom, J., Reilly, P.T.A., Whitten, W.B., and Ramsey, J.M. (2004). Sample pressure effects in a micro ion trap mass spectrometer. *Rapid Commun. Mass Spectrom.* <https://doi.org/10.1002/rcm.1389>.
- 89** Collins, R.D. (1969). The use of electron multipliers in mass spectrometry. *Vacuum* [https://doi.org/10.1016/s0042-207x\(69\)90023-2](https://doi.org/10.1016/s0042-207x(69)90023-2).
- 90** Dietz, L.A. (1965). Basic properties of electron multiplier ion detection and pulse counting methods in mass spectrometry. *Rev. Sci. Instrum.* <https://doi.org/10.1063/1.1719460>.
- 91** Tuithof, H.H., Boerboom, A.J.H., and Meuzelaar, H.L.C. (1975). Simultaneous detection of a mass Spectrum using a Channeltron electron multiplier array. *Int. J. Mass Spectrom. Ion Phys.* [https://doi.org/10.1016/0020-7381\(75\)87040-9](https://doi.org/10.1016/0020-7381(75)87040-9).
- 92** Blakeman, K.H., Wolfe, D.W., Cavanaugh, C.A., and Ramsey, J.M. (2016). High pressure mass spectrometry: the generation of mass spectra at operating pressures exceeding 1 Torr in a microscale cylindrical ion trap. *Anal. Chem.* <https://doi.org/10.1021/acs.analchem.6b00706>.
- 93** Blakeman, K.H., Cavanaugh, C.A., Gilliland, W.M., and Ramsey, J.M. (2017). High pressure mass spectrometry of volatile organic compounds with ambient air buffer gas. *Rapid Commun. Mass Spectrom.* <https://doi.org/10.1002/rcm.7766>.

- 94 Blakeman, K.H. (2015). *Development of high pressure mass spectrometry for handheld instruments*. The University of North Carolina at Chapel Hill.
- 95 Amptek. A250CF CoolFET® Charge Sensitive Preamplifier. <https://www.amptek.com/products/charge-sensitive-preamplifiers/a250cf-coolfet-charge-sensitive-preamplifier#Documentation> (accessed 31 October 2019).
- 96 Schultze, K.P. (2014). *Advanced System Components for the Development of a Handheld Ion Trap Mass Spectrometer*. The University of North Carolina at Chapel Hill.
- 97 Brown, C.D., Knopp, K.J., Krylov, E., and Miller, S. (2014). Compact Mass Spectrometer. US9099286B2.
- 98 Chen, H., Gamez, G., and Zenobi, R. (2009). What can we learn from ambient ionization techniques? *J. Am. Soc. Mass Spectrom.* <https://doi.org/10.1016/j.jasms.2009.07.025>.
- 99 Holčapek, M., Jirásko, R., and Lísá, M. (2010). Basic rules for the interpretation of atmospheric pressure ionization mass spectra of small molecules. *J. Chromatogr. A* <https://doi.org/10.1016/j.chroma.2010.02.049>.
- 100 Herrera, L.C., Grossert, J.S., and Ramaley, L. (2008). Quantitative aspects of and ionization mechanisms in positive-ion atmospheric pressure chemical ionization mass spectrometry. *J. Am. Soc. Mass Spectrom.* <https://doi.org/10.1016/j.jasms.2008.07.016>.
- 101 Marquet, P., Venisse, N., Lacassie, E., and Lachâtre, G. (2000). In-source CID mass spectral libraries for the “general unknown” screening of drugs and toxicants. *Analusis* <https://doi.org/10.1051/analusis:2000280925>.
- 102 Rodgers, M.T. and Armentrout, P.B. (1998). Statistical modeling of competitive threshold collision-induced dissociation. *J. Chem. Phys.* <https://doi.org/10.1063/1.476754>.
- 103 Falconer, T., Kern, S., and Voelker, S. (2018). Rapid, in situ detection of synthetic opioids. *66th ASMS Conference on Mass Spectrometry and Allied Topics*, San Diego, CA.
- 104 Gilliland, W.M., Mellors, J.S., and Ramsey, J.M. (2017). Coupling microchip electrospray ionization devices with high pressure mass spectrometry. *Anal. Chem.* <https://doi.org/10.1021/acs.analchem.7b03484>.
- 105 Gilliland, W.M. and Ramsey, J.M. (2018). Development of a microchip CE-HPMS platform for cell growth monitoring. *Anal. Chem.* <https://doi.org/10.1021/acs.analchem.8b03708>.
- 106 Inficon. HAPSITE® ER Chemical Identification System. <https://products.inficon.com/en-us/nav-products/product/detail/hapsite-er-identification-system> (accessed 23 October 2019).
- 107 Bruker. E<sup>2</sup>M the Mobile Enhanced Environmental Mass Spectrometer. <https://www.bruker.com/products/cbrne-detection/gc-ms/e2m/overview.html> (accessed 23 October 2019).
- 108 908devices. M908 Spec Sheet. [http://908devices.com/wp-content/uploads/2017/04/SpecSheet-908\\_2016\\_v3.pdf](http://908devices.com/wp-content/uploads/2017/04/SpecSheet-908_2016_v3.pdf) (accessed 31 October 2019).
- 109 PerkinElmer. Torion T-9 Portable GC/MS. <https://www.perkinelmer.com/product/torion-t-9-portable-gc-ms-instrument-ntsst090500> (accessed 23 October 2019).
- 110 FLIR. Person-Portable GC-MS Griffin G510. <https://www.flir.com/products/griffin-g510> (accessed 23 October 2019).
- 111 908devices. MX908 Spec Sheet. [https://908devices.com/wp-content/uploads/2017/09/MX908\\_SpecSheet\\_EOD\\_.pdf](https://908devices.com/wp-content/uploads/2017/09/MX908_SpecSheet_EOD_.pdf) (accessed 31 October 2019).
- 112 Continuity™ Transportable High-Sensitivity Mass Spectrometer. <https://www.bayspec.com/spectroscopy/continuity-transportable-high-sensitivity-mass-spectrometer> (accessed 23 October 2019).
- 113 TRACER 1000. <https://www.1stdetect.com/products/tracer-1000-ms-etc> (accessed 23 October 2019).

## 17

# Key Instrumentation Developments That Have Led to Portable Ion Mobility Spectrometer Systems

Reno F. DeBono<sup>1,3</sup> and Pauline E. Leary<sup>2</sup>

<sup>1</sup>Trace Detection Scientist, Formerly of Barringer Instruments, Warren, NJ, USA

<sup>2</sup>Federal Resources, Stevensville, MD, USA

<sup>3</sup>Smiths Detection, Edgewood, MD, USA

## 17.1 Background and History

Ion mobility spectrometry (IMS) is a gas-phase separation technique which works by predictably and reproducibly creating ions from neutral analyte molecules and separating these ions based on their size and shape under the influence of an electric field in the presence of a buffer gas. IMS is likely the most widely used trace detection method deployed in the field for testing of dangerous substances. It is selective, offers low detection limits, provides reliable identifications, and fast analysis times. IMS systems are size, weight, and power (SWaP) friendly, and perform at ambient pressure. These features are important for portability and amenable to miniaturization, with a robust deployment of portable and handheld systems in a variety of different markets. Systems have been extensively used by the military, as well as in aviation security, border inspection, and by first responders.

In chapter one of this volume, Leary, Crocombe, and Kammrath provide a general classification scheme of portable spectrometers in accordance with SWaP expectations. This classification scheme generally holds true for portable IMS systems and categorizes person-portable spectrometers as those that weigh between 3 and 20 kg, handheld systems as those that weigh between 0.5 and 3 kg, and wearable systems as those that weigh less than 0.5 kg. This chapter includes discussions of person-portable, handheld, and wearable IMS systems. Most of the largest portable IMS systems deployed would be classified as person portable; the smallest would be classified as wearable. For portable IMS systems, especially within markets, such as aviation security, where high sample throughput at a centralized location, such as a security checkpoint, is expected, end users are willing to accept person-portable systems that may not operate on battery power. These IMS systems, sometimes referred to as benchtop systems, are classified as portable since they are deployed to field users for analysis on site. On the other hand, users of the smallest IMS detectors have very strict requirements for battery operation. Therefore, significant resources are expended during design and development of handheld and wearable IMS systems like those used by the military to provide personal monitoring for chemical warfare agents (CWAs) and toxic industrial chemicals (TICs) to verify that these systems are as lightweight as possible and can run on commercial AA batteries for extended periods of time.

IMS is particularly effective at screening for the presence of hazardous chemicals, such as explosives, narcotics, TICs, CWAs, and opioids, including fentanyl analogs. IMS systems can be deployed either independently as a primary screening tool, or as a secondary complement to another screening method, such as X-ray, for alarm resolution or orthogonal detection. Targets that alarm using the initial screening method can be further interrogated using IMS. This two-tiered approach can be especially useful in situations where high throughput is required.

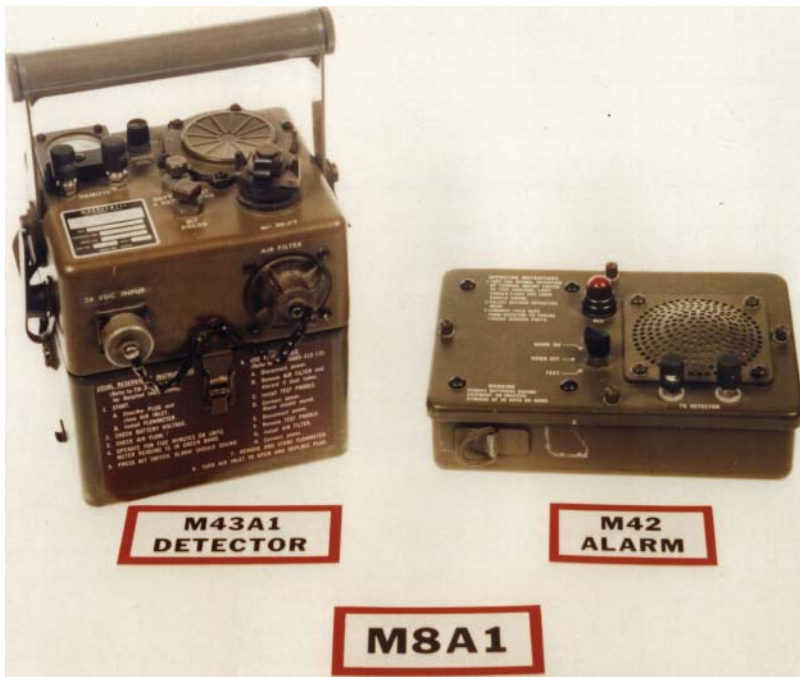


**Figure 17.1** M8A1 detector standardized by the United States Army in 1981. Source: Image courtesy of the United States Army.

Acceptance of IMS in the field is largely driven by its versatility regarding deployment, and the ease with which it fits within an organization's optimized concept of operations. Although IMS systems are deployed to a variety of different end users, the military and aviation industry have been critical to the success of portable IMS systems.

Initial development of portable IMS systems was due to military interest in the detection of CWAs. One of the earliest IMS detectors was a product manufactured by Intellitec [1] and known as the M8A1, which was standardized by the United States Army in 1981. The M8A1 was configured with an M43A1 ion detector linked with the standard M42 alarm. Figure 17.1 shows the configured M8A1 system. The M43A1 used an  $^{241}\text{Am}$  alpha radioactive ionization source. A pump drew air samples into the detector unit and then through a heater and filter. Contaminated air passed over the ionization source causing the ions of the chemical agent to cluster. A geometrically configured cell collected the clusters as electric current while a monitor sensed any voltage change which activated the alarm. The M43A1 detector could be placed up to 400 m from the M42 alarm to provide an early warning of a chemical cloud. The M8A1 alarm became the United States Army's single most important chemical detection capability, and by 1987, over 32 000 units were in the field. During Operation Desert Shield/Storm in 1990–1991, the United States Army used over 12 000 M8A1 systems as the main detection capability for chemical defense [2–5]. The military continues to actively support the development and deployment of IMS systems for CWA, TIC, and explosives detection. For instance, in 2019, Smiths Detection reported it provided more than 91 000 joint chemical agent detector (JCAD) units over the past 14 years [6].

The aviation industry has also been critical to the development of IMS detectors for the detection of explosives. In 2004, more than 10 000 explosives detectors based on IMS had been used at security checkpoints in airports worldwide [7]. Today that number is significantly higher due to the fact that over the last 25 years, IMS technology has sufficiently matured and continues to meet the well-defined and evolving aviation detection standards for explosives detection within regulatory bodies, such as the Transportation Security Administration (TSA) in the United States, the Department for Transport (DfT) in the United Kingdom, the Transport Canada in Canada, the European

Civil Aviation Conference (ECAC), and the Civil Aviation Administration of China (CAAC). Requirements of Customs, border control, correctional facilities, and law enforcement have been critical to the development of IMS detectors for trace narcotics detection, and more recently for detection of fentanyl and its analogs. For a thorough discussion on the applications of IMS, see chapter 8 in volume two of this text by Leary and Joshi.

## 17.2 Principles of Ion Mobility Spectrometry

Over the last 50 years, two variants of IMS systems have developed. The conventional form is based on a fixed-mobility property associated with the ion, which is not a function of the electric field. The second is based on changing ion mobility as a function of a changing electric field [8] (p. 1). The former is the basis of both drift-tube IMS (DTIMS) and aspiration IMS (AIMS), while the latter is the basis of differential mobility spectrometry (DMS). DMS is often referred to as field asymmetric waveform IMS (FAIMS), and over the years, has also been called other names including nonlinear drift spectrometry, differential IMS (DIMS), field ion spectrometry, and radio frequency IMS (RF IMS). Following brief discussions of AIMS and FAIMS systems, this chapter will focus on DTIMS.

### 17.2.1 Aspiration Ion Mobility Spectrometry

AIMS is based on the principle that ions move in air, and if an electric field is applied perpendicular to the flow of air through a drift tube, the ions will be pushed toward the walls of the drift tube [9]. In these systems, the ionization occurs at ambient conditions in the presence of a relatively high amount of water from the ambient environment, which affects the kinetics of ionization reactions [10]. At high-enough water-vapor concentrations, sensitivity can be compromised. Ions continuously enter the drift tube carried by a laminar flow of ambient air. No gating grid is used to pulse the ions, so instrument resolution is dependent on the inlet aperture dimensions. Theoretically, 100% of the ions are injected into the analyzer, so the signal-to-noise ratio (SNR) can be significantly improved compared with DTIMS systems [11] (p. 128). If the electric field polarity is switched, both positive and negative ions can be detected. A series of ion detectors, such as Faraday plates, are placed along the path of the deflected ions to generate the signal. For IMS detectors, ion detection is achieved by converting ions striking the detector into a current by neutralization at a collector electrode referred to as a Faraday plate [11] (pp. 155–156). As the ion swarm is neutralized, current flows in the metal Faraday plate: For positive ions, current flows to the plate and for negative ions, current flows away from the plate. If the electric field is fixed, then the distance the ions travel before they strike a detector is proportional to their mobility. In these fixed-field situations, ions of faster velocity collide with the detector earlier than ions with slower velocity. Poor spatial ion separation, due to space-charge effects and diffusion, results in poor resolving power. Both effects can be reduced by increasing the flow rate so that ion concentration and drift time decrease; however, the flow rate is limited since laminar flow is required.

Peaks associated with variable ion mobilities can be broad and overlapping. For this reason, the use of pattern recognition for detection algorithms in these systems is typical. Sensitivity is adjustable since ionization efficiency is flow-rate dependent [10]. AIMS is intrinsically more sensitive but less selective than DTIMS. AIMS systems are simple, offer high sensitivity, low cost, and are small. Figure 17.2 shows a schematic demonstrating the operating principle of an AIMS instrument that uses a radioactive  $^{241}\text{Am}$  ionization source. The pattern generated as the output signal is used for identification. Environics Oy (Finland) has been a primary manufacturer of AIMS systems.

### 17.2.2 Field-Asymmetric Ion Mobility Spectrometry

To separate ions, FAIMS exploits the differences in their mobilities in low and high fields. Separations performed based upon ion mobility are typically classified as low or high field depending upon whether the ion gains translational energy between collisions (high field) or achieves a steady-state drift velocity (low field) [12]. As previously

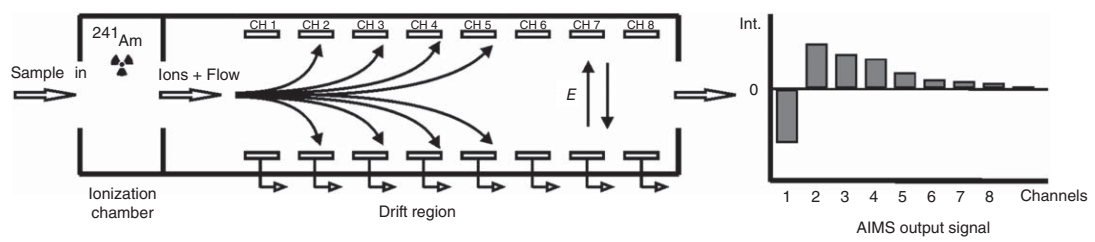


**Figure 17.2** Schematic demonstrating the operating principle of an AIMS instrument. Source: Mäkinen et al. [10]. © 2010, American Chemical Society.

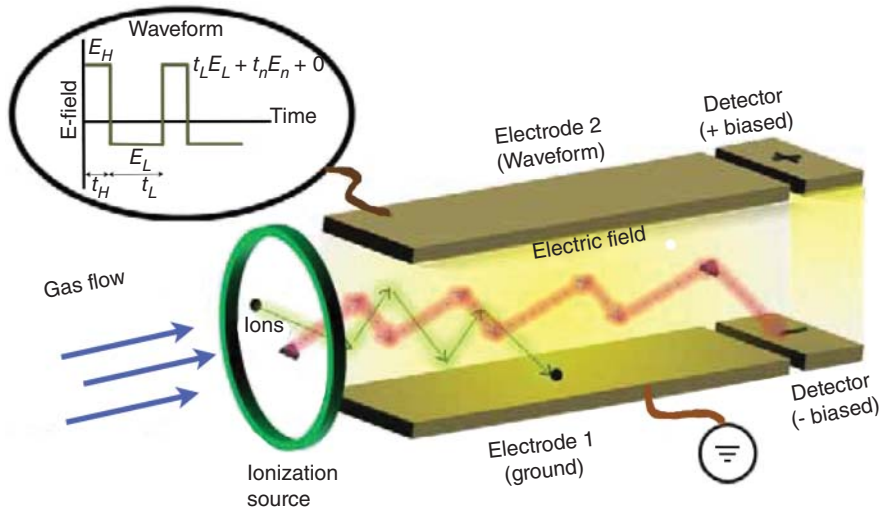


**Figure 17.3** Schematic demonstrating the operating principle of a FAIMS instrument. Source: Zrodnikov and Davis [13]. Licensed under CC BY 4.0.

described by Zrodnikov and Davis, during a FAIMS measurement, an electric field is created by applying a waveform between two electrodes; one that is grounded and one with an applied high-frequency alternating current (AC) square waveform. One cycle of the waveform induces an electric field which is an initially high strength, and it is then switched to a low-strength field in the opposite direction. Since an ion will have different mobility in the high- and low-strength regimes, the ion will have a net displacement toward one of the electrodes over each cycle of the waveform. This displacement is counterbalanced by the application of a direct current (DC) compensation voltage (CV). Each CV value allows ions with that corresponding specific differential mobility to pass through the drift region and reach the ion detector. The CV can also be specified to a value characteristic of a certain ion of interest to achieve an ion-filtering regime, or it can be swept across a range to record the abundance of all ion species that are present in a sample. Dispersion plots, which show ion abundance for scans of CV at different values of the asymmetric waveform amplitude, are commonly used to display sampled data [13]. The peak voltage of the waveform is referred to as the dispersion voltage (DV). Figure 17.3 shows a schematic demonstrating the operating principle of FAIMS.

FAIMS systems offer good separation power, but they have historically had power consumption issues associated with electric field requirements. High power consumption requirements are not a significant problem for lab-based systems connected to shore power, but are not well-suited for field instruments intended to operate on battery power. Recently, power issues have been resolved resulting in the development of a miniaturized, lightweight, handheld DMS system [14]. In the past 15 or so years, FAIMS has had some success penetrating security markets, but has not yet been widely adopted.

### 17.2.3 Drift-Tube Ion Mobility Spectrometry

#### 17.2.3.1 Theory

IMS works by predictably and reproducibly creating ions from neutral analyte molecules or atoms and separating these ions according to their size and shape. The first DTIMS, the configuration which formed the fundamental basis of current designs utilized in most field-deployed systems, was constructed about 50 years ago in 1970 [15] (p. 96). In this configuration, a neutral analyte is introduced to the system via a carrier gas and vaporized (if not already in the gas phase). The gas-phase analyte is then introduced to the ionization chamber where it is ionized,

usually in the presence of dopants, using atmospheric pressure chemical ionization (APCI). Ionization is selective producing either positive or negative ions which are injected into the drift tube via an ion shutter, which in most commercial IMS instruments is a gating grid. The ion shutter opens briefly for 50–200 µs and then closes, allowing a pulse of either positive or negative ions to enter the drift tube, depending on the drift-tube polarity. Ions travel the length of the drift tube, which is maintained at constant voltage and temperature, through a gas known as the buffer gas. In the drift tube, the ions separate based on their size, shape, and collisional cross-section, and are then detected using a Faraday plate. The amount of time it takes the ion to travel from the ion shutter to the detector is measured and used for identification (under specified operating conditions). Figure 17.4 shows the schematic of the operation of a typical DTIMS system. Figure 17.5 shows an IMS spectrum. Table 17.1 is a summary of many of the commercially available IMS systems currently on the market and widely deployed for the analysis of threats. Most of the deployed platforms are based on DTIMS due to their selectivity, which allows good material identification coupled with a low false-alarm rate.

Many factors impact the formation and movement of ions through an IMS. During the ionization process, dopants may be added to purposely form stable ion adducts or create weak interactions with the ion. The size and shape of the ions formed, to first order, are proportional to the molecular weight (MW) of the ion. However, the IMS signal also captures three-dimensional structural information from the average cross-sectional area. The average cross-sectional area is a function of the sweep volume of the ion as it rotates and vibrates. It enables the separation of structural isomers and ions of the same mass (isobaric ions). The ability to separate isobaric ions is particularly important since many lower MW compounds, those at less than about 600 atomic mass units (amu), have very similar masses, but are differentiable in IMS due to this capability. The basis of separation is a result of the interaction of the ion with the buffer gas. As a result, it is not surprising that properties of the buffer gas impact the effective cross-sectional area of the ion enabling separation of two ions of the same mass but different cross-sectional areas. Typically, for portable instruments, clean dry air, which is created in situ by drying ambient air and filtering organic material, is used as the buffer gas. The moisture content of the air is critical and must be taken into account by either controlling it or compensating for changes. Typically, water-vapor levels in the buffer gas are in the range of 1–10 parts per million (ppm).

The ions associated with field-deployed IMS platforms are generally molecular ions with either positive or negative charge. An electric field is applied to the drift tube to move an ion swarm from the ionization chamber through a buffer gas down the length of the drift tube. The buffer gas is typically air at atmospheric pressure. The buffer gas is at sufficiently high pressure ( $>\sim 1$  Torr, typically at atmospheric pressure for field-deployable platforms) that the ion mean free path is small and, therefore, the ions undergo multiple collisions and rapidly achieve a constant velocity. The velocity ( $v$ ) of the ion through the buffer gas is equal to the length of the drift tube ( $L$ ) divided by the time it takes an ion to move from the gating grid to the detector, which is known as its drift time ( $t_d$ ) (Eq. (17.1)).

$$v = \frac{L}{t_d} \quad (17.1)$$

An ion's drift velocity depends on the applied electric field strength,  $E$ , and its mobility constant,  $K$ . In the low-field regime of  $<\sim 500$  Volts/centimeter (V/cm), which is the regime within which most commercial DTIMS systems operate,  $K$  is essentially independent of  $E$  and can be treated as a constant [34]. The mobility  $K$  is a joint property of the ions and the buffer gas through which the motion occurs. Dividing  $v$  by  $E$  defines the mobility of the ion in terms of ion velocity per unit field ( $\text{cm}^2/\text{Vs}$ ), which normalizes the velocity of the ion to  $E$ .

$$K = \frac{v}{E} = \frac{L}{t_d E} \quad (17.2)$$

As air pressure increases, the number of collisions of the ion with neutral air molecules (78% N<sub>2</sub>, 21% O<sub>2</sub>) increases, and the mobility of the ion decreases. If the air is heated, air density decreases and mobility increases. As a result, reduced mobility,  $K_0$ , is typically used to account for changes in temperature ( $T$ ) and pressure ( $P$ ) by normalizing to 273 Kelvin and 760 Torr as shown in Eq. (17.3). To first order,  $K_0$  is independent of temperature

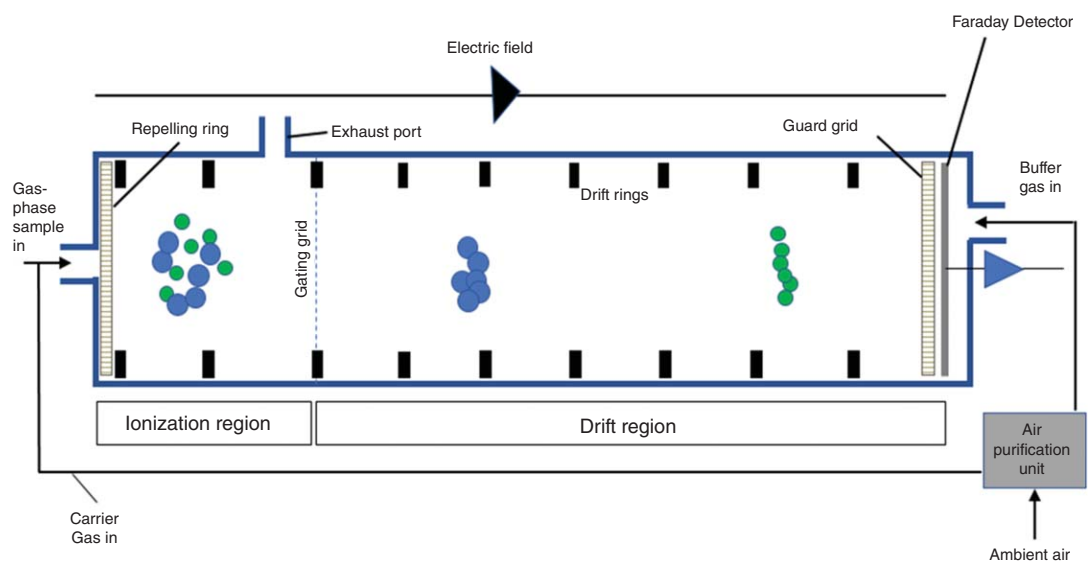


**Figure 17.4** Schematic of drift-tube IMS where the sample is brought in with a clean carrier flow.

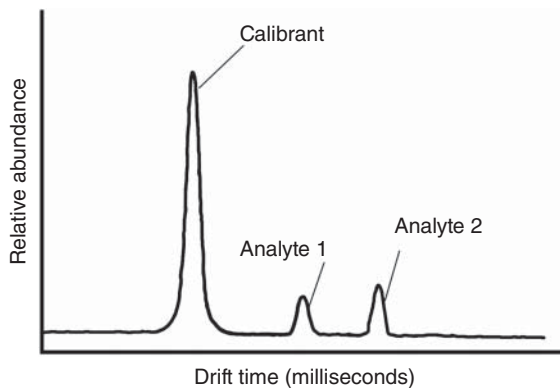


**Figure 17.5** IMS spectrum of a two-component sample.

and pressure.

$$K_0 = \frac{L}{t_d E} \left( \frac{P}{760} \right) \left( \frac{273}{T} \right) \quad (17.3)$$

As the ions travel through the drift tube, they are separated based upon their different mobilities which are a function of their size and shape. The greater the number of collisions and interactions the ion has with the buffer gas at a given electric field strength, the slower it will move. Larger ions move more slowly than smaller ions. IMS does not measure the properties of a single ion, but a group of gaseous ions referred to as a swarm [11] (p. 1). It is a swarm of ions with similar mobility that move through the drift tube with average mobility. The effective cross-sectional area is approximately proportional to the mass of the ion, and generally, a good correlation to first order is observed for  $1/K_0$  as a function of MW. Figure 17.6, which was compiled from data previously published by Karpas [35] and Metternich et al. [36], shows the relationship between  $1/K_0$  and MW. Linear regression was performed for the combined data sets as if they were one series, and the  $R^2$  value calculated was 0.9656. Since molecules with the same MW can have different average cross-sectional areas based on structure, it is not surprising that this relationship is not exactly one to one. Table 17.2 provides a general sense of how mobility scales with MW, detailing drift times measured for different substances along with their  $K_0$ ,  $1/K_0$  and MW. With regard to size and shape, reduced mobility coefficients are influenced by ion mass in cases in which a linear relationship exists within a homologous series. However, ions of the same mass but different functional groups, or ions of the same functional groups but different geometrical arrangements (isomers), often exhibit different  $K_0$  values, reflecting the influence of size and shape on mobility [15].

Ion swarm peaks will have a full width at half maximum (FWHM) of between 150 and 300  $\mu$ s for a gating pulse of 150  $\mu$ s. Figure 17.7 shows an IMS spectrum with three peaks with  $K_0$  values of 1.8000, 1.2000, and 1.000 associated with molecular ions with amu values of approximately ~121, 262, and 346, respectively. FWHM for the peaks are 200, 250 and 280  $\mu$ s, respectively.

The exact relationship between mobility,  $K$ , and chemical identity in IMS is not completely understood. So, the expected mobility of an ion cannot be accurately determined from first principles. The mobility of an ion is dependent on conditions used (electric field strength, pressure, temperature, buffer composition) while for mass spectrometry the mass-to-charge ratio ( $m/z$ ) is independent of measuring conditions. Historical attempts to apply theories regarding mobility indicated modifications to these theories were necessary. The evolution of many of these modifications, starting with Langevin's initial theoretical proposal in 1903 and leading to Eq. (17.4), which evolved from studies of mono- or diatomic ions in pure gases at subambient pressure, are summarized in Karasek's 1974 paper "Plasma Chromatography" [15, 37].

$$K = \frac{3e(2\Pi)^{\frac{1}{2}}(1 + \alpha)}{16N(\mu k T_{\text{eff}})^{\frac{1}{2}} \Omega_D(T_{\text{eff}})} \quad (17.4)$$

**Table 17.1** Field-deployed IMS systems categorized by IMS type and system weight.

IMS type	Vendor	$\leq 1.2 \text{ kg}$	$\leq 3.5 \text{ kg}$	$\leq 6 \text{ kg}$	$\leq 13 \text{ kg}$	$\leq 23 \text{ kg}$
DTIMS	Smiths Detection	LCD3.3 [16]	SABRE 5000 [17]	GID-3 [18]	IONSCAN 600 [19]	IONSCAN 500DT [20]
	Rapiscan			Hardened Mobile Trace [21]	Itemiser DX and Itemiser 4DX [22]	
	Leidos				H150 [23]	B220 [24]
	Bruker [25]	uRAIDplus	RAID M100 RoadRunner		DE-tector flex	DE-tector
	Nuctech			TR1000DB-A [26]	TR2000DB-A [27]	
	RAE Systems	ChemRAE <sup>a</sup> [28]				
AIMS	Environics Oy	ChemPro100i [29], ChemProX [30]				
	Owlstone Inc.			OwlSens-C [31]	OwlSens-T [32]	
FAIMS	Chemring Sensors and Electronic Systems	Juno [14]				

a) This product is an original equipment manufacturer version of the Environics ChemPro 100.  
*Source:* Based on MRIGlobal [33].

where,

$e$  = electron charge

$\alpha$  = correction factor

$N$  = number density of neutral gas molecules

$\mu$  = reduced mass ( $1/u = 1/m + 1/M$ ), where  $m$  is the mass of the ion,  $M$  is the mass of the neutral gas molecules

$k$  = Boltzmann constant

$T_{\text{eff}}$  = effective temperature of an ion based on thermal energy and energy acquired by an electric field

$\Omega_D(T_{\text{eff}})$  = effective cross-section of the ion which is a function of the  $T_{\text{eff}}$

Since drift velocities are sensitive to the exact identity of ions in the swarm, which is affected by the composition of the gas atmosphere and by changes in temperature, Eq. (17.4) is limited. Thus, the relationship between  $K$  and  $\Omega_D$  is inaccurately described or incomplete for large organic ions where  $\Omega_D$  is influenced by polar molecules or

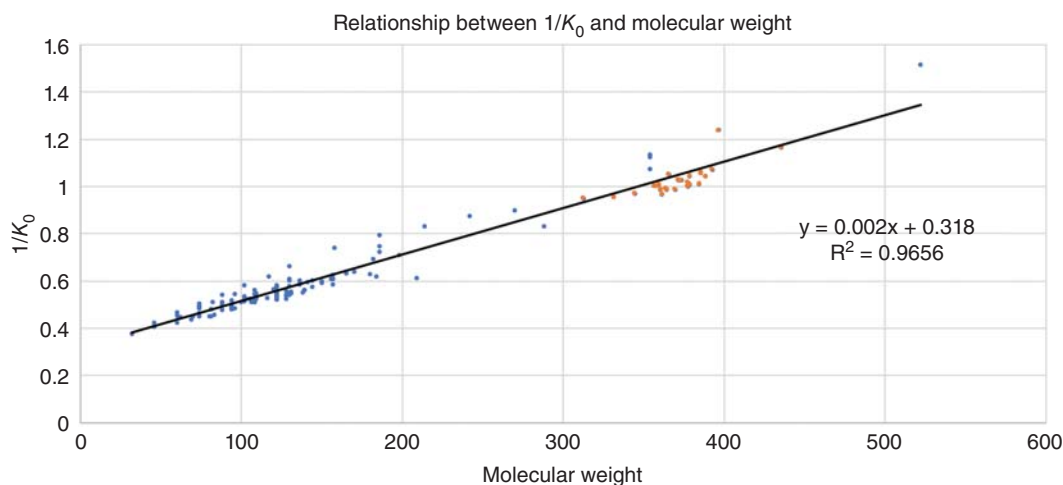


**Figure 17.6** Relationship showing the dependence of  $1/K_0$  on MW from previously published data for aliphatic/aromatic amines (blue) and synthetic cannabinoids (orange) in air or nitrogen between 150 and 250 °C. Source: Karpas [35]; Metternich et al. [36].

**Table 17.2** Drift times associated with  $K_0$  values for an 8-cm drift tube operated at 200 °C at atmospheric pressure in the air.

$K_0$	$1/K_0$	$t_d$ (ms)	~MW
2.400	0.4167	7.696	$50 \pm 8$
2.200	0.4545	8.395	$69 \pm 8$
2.000	0.5000	9.235	$92 \pm 9$
1.800	0.5556	10.261	$121 \pm 10$
1.600	0.6250	11.543	$156 \pm 11$
1.400	0.7143	13.192	$201 \pm 13$
1.200	0.8333	15.391	$262 \pm 15$
1.000	1.000	18.469	$346 \pm 18$
0.800	1.250	23.087	$473 \pm 22$

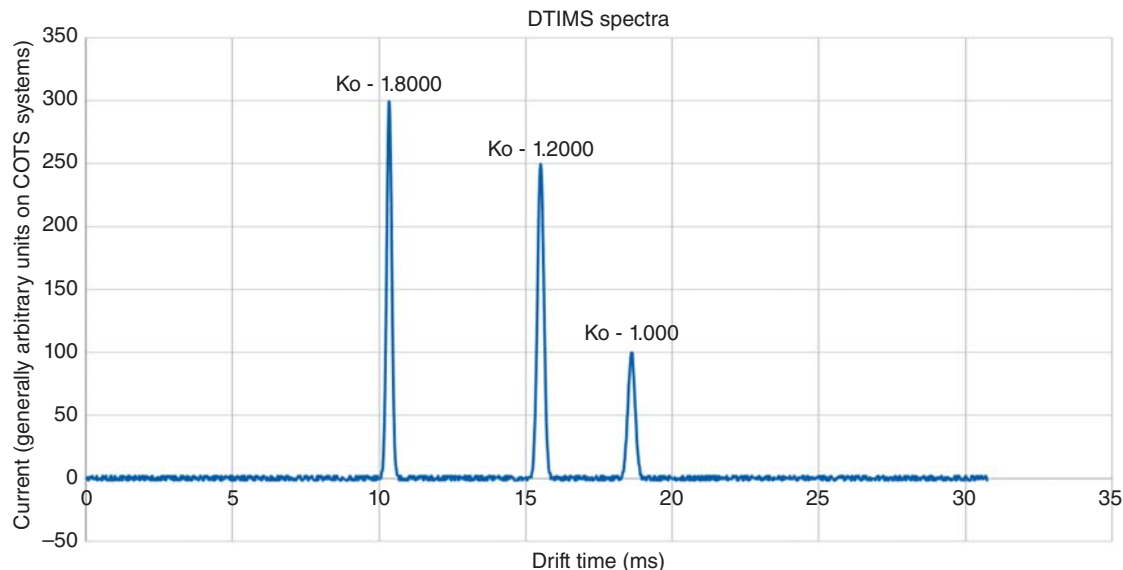


**Figure 17.7** Example IMS spectrum for ions with  $K_0$  values of 1.800, 1.200, and 1.000.

moisture in the drift region. There is no comprehensive model that includes ion-neutral associations in polarizable gas atmospheres and the role of temperature in controlling  $\Omega_D$  and, thus,  $K$ . The distribution of charge within a large organic ion also affects the observed mobility values, once again through the formation of clusters. This is not included in current formulas for mobility. Consequently, Eq. (17.4) and other formulas for mobility are incomplete descriptions of mobility measurements in the air at atmospheric pressure, and the correlation of ion structure, collision cross-section, and mobility over a range of experimental conditions should be considered an underdeveloped topic in IMS.

Electric field strength also has an impact on mobility, which is a function of the normalized field strength,  $E/N$ , where  $N$  is the gas number density. Field-deployable IMS systems operate at atmospheric pressure. So,  $N$  at 1 atm and 0 °C is approximately  $2.69 \times 10^{19} \text{ cm}^{-3}$  for an ideal gas at standard temperature and pressure. The units for  $E/N$  are Townsends (Td), where  $1 \text{ Td} = 10^{-17} \text{ Vcm}^2$ . This means for  $E = 250 \text{ V/cm}$  at STP,  $E/N = 0.93 \text{ Td}$ . The relationship between  $K_0$  and  $E/N$  is shown in Eq. (17.5) [8] (p. 57).

$$K_0 \left( \frac{E}{N} \right) = (K_0) \left( 1 + a \left( \frac{E}{N} \right)^2 + b \left( \frac{E}{N} \right)^4 + c \left( \frac{E}{N} \right)^6 \dots \right) \quad (17.5)$$

Why does  $E/N$  impact  $K_0$ ? Above a critical normalized field strength,  $(E/N)_c$ , the amount of energy imparted to the ion by the electric field due to collisions of the ions with the neutral buffer gas is non-negligible compared with the thermal energy of the buffer gas, and is not quickly dissipated. As a result, the effective temperature of the ion increases.  $(E/N)_c$  is dependent on the ion, the buffer gas, and temperature of the buffer gas. Under low-field conditions (at which most traditional DTIMS and AIMS systems operate ( $E < 500 \text{ V/cm}$ ,  $E/N < 3 \text{ Td}$ )),  $K_0$  is independent of  $E$  and  $E/N$ . Changes in temperature and pressure result in changes to  $N$ , which will result in variations of  $E/N$ . Table 17.3 shows a variation in  $E/N$  for  $E = 250 \text{ V/cm}$  for different temperatures and pressures. The Torr value of 760 corresponds to sea level and 525 Torr corresponds to 10 000 ft. For an IMS operating at 50 °C, the  $E/N$  field can vary from 1.10 to 1.59 Td when going from sea level to 10 000 ft. Since this is the low-field limit,  $K_0$  is not impacted.

Between  $(E/N)_c$  and about 100 Td (~20 000 V/cm at standard temperature and pressure), only terms up to  $(E/N)^4$  are significant [38]. Three possible behaviors are observed for  $K_0$  as a function of increasing  $E/N$ . These are

**Table 17.3** Variation in  $E/N$  (Td) as a function of temperature and pressure for  $E = -250 \text{ V/cm}$ .

Temperature (°C)	760 Torr	525 Torr
0	0.93	1.35
50	1.10	1.59
100	1.27	1.84

referred to in the literature as types A, B, and C behaviors. Type-A behavior is when  $K_0$  increases, i.e., the effective cross-sectional area of the ion decreases. This behavior is the most common and is where clustering of a component in the buffer gas, i.e., water or added modifier with the ion, is reduced with increasing electric field strength. Type-B behavior is when  $K_0$  first decreases and then increases. Type-C behavior is when  $K_0$  decreases, i.e., the effective cross-sectional area of the ion increases. The differences in mobilities at high and low electric field strength are used in FAIMS systems to differentiate between different types of ions. The design of field-deployable instruments requires an understanding of how  $K_0$  varies as a function of drift-tube conditions. Table 17.4 summarizes the impact of different operating conditions on mobility.

### 17.2.3.2 IMS Components

#### 17.2.3.2.1 Sample Introduction

Samples for IMS analysis are either collected as vapors or microscopic particles. In either case, the sample matrix can be complex, and most commercially available portable IMS systems do not offer front-end separation mechanisms to isolate the target analyte prior to introduction into the IMS. Therefore, both the analyte and the sample matrix are introduced to the system during analysis. The sample matrix has the potential to impact ion formation and detection results and may enhance or suppress the signal of the analyte. To prevent this from happening, dopants are used to control the ionization reactions so that reproducible, stable analyte ions are formed regardless of the sample matrix. Without the use of dopants, the matrix of the sample or trace contaminants in the buffer gas will control the ionization chemistry. Fortunately, most of the common chemicals detected by IMS are selectively and preferentially ionized compared to the common real-world background material encountered during analysis.

The sample matrix can also cause unwanted contamination of the system. IMS particle-detection systems which thermally desorb samples will typically have hot inlets and reaction regions which minimize dirt ingestion and maintain unit sensitivity. From a system-maintenance perspective, the IMS front end is ideally designed to minimize the accumulation of dirt and allow easy purging of the inlet and reaction region. This is particularly important for high throughput applications like those within the aviation-security industry, such as checkpoint and checked-baggage screening. Many systems used for high throughput swab analysis have built-in, automatic bake-out procedures which are executed during low-use periods. Bakeout for IMS systems is a term that is applicable to both vapor- and particle-detection systems and refers to a process where the temperature of the drift tube and other system components are increased for a specified time period to allow contamination and other debris to volatilize and pass through the system. Automatic bakeouts keep these systems working effectively at optimum sensitivity.

Sample introduction using vapor sampling is performed when the target analyte has a reasonable vapor pressure such that ppb (parts per billion) levels of material are introduced to the system during the sampling cycle. To prevent overload, some IMS systems offer a feature that causes automatic sampling to shut down if an overload is suspected. IMS systems are trace detectors with sensitivities in the low ppb range (low ng–pg range). In the real world where sample matrix and concentration are frequently unknown, the potential of the system analyzing high-concentration samples is real and can overload the system. Well-designed IMS systems have factored this in

**Table 17.4** Impact of conditions on IMS response for DTIMS and FAIMS systems.

Condition	DTIMS: Low field (<500 V/cm, @ 1 atm, <3 Td)	FAIMS: Electric field is switched between high- and low-field values during the analysis
Ion mobility ( $K_0$ )	Independent of E	The function of E, can increase, decrease or increase/decrease
Energy from an electric field	Negligible	Non-negligible, resulting in high effective temperature for ion during high-field condition which can decrease $K_0$ under high-field operation
Solvation by neutral gas molecules (water)	Increases effective cross-sectional area of the ion which will decrease $K_0$	Can help increase differences in $K_0$ between high and low electric fields
Temperature	Drift times of ions shift to lower values due to reduced air density as drift tube temperature increases. Reduced mobility may stay constant if there is no impact on clustering. Clustering is more significant at lower temperatures <150 °C	Can impact the differences in $K_0$ observed between high and low fields
Pressure	As pressure decreases, drift times of ions decrease	
Ion size	As ion size increases, $K_0$ decreases	With larger ions, a charge may be delocalized more and differences in $K_0$ may not be as large between high and low fields
Impact of clustering dopant	Ion size ↑ due to clustering and adduct formation, ↓ mobility	The ion charge is highly delocalized to minimize solvation effects; Declustering occurs which ↓ ion size and ↑ mobility
Adduct formation with ion (e.g., chloride or nitrate adduct formation)	Leads to new ion being formed, e.g., RDX*Cl <sup>-</sup> , RDX*NO <sub>3</sub> : ↑ ion size ↓ mobility	If electric field strength is high enough to dissociate adduct from the neutral analyte, then large mobility ↑. Otherwise, only minor changes to mobility are observed

during development. In these instances, the sampling cycle, which usually is preset for a specified amount of time for a given analysis, will automatically stop the sampling, but allow the IMS analysis to continue. Vapor sampling works well and is routinely deployed for the IMS detection and identification of both CWAs and TICs.

For semivolatile compounds, such as drugs and explosives, trace amounts of microscopic particles are collected by swabbing a surface. The swab substrate may be made of a number of different materials including paper, cotton, Nomex®, Teflon®-coated glass fiber, or other materials. The swab is heated at the IMS inlet to drive the sample into the vapor phase for analysis. Some modern IMS systems designed for trace-particle sampling use low-thermal-mass inlets with sophisticated inlet designs. These inlets and designs help minimize contact between the sample swab and the sample-inlet mechanism to reduce contamination, prevent system overload, and even lower power requirements. Some systems also offer variable-temperature desorption which can help optimize selectivity.

In most cases, with commercial portable IMS systems, sample flow into the system is performed either in the presence of ambient air or as a diluent in a clean carrier gas. Figure 17.4 shows a schematic of a single-tube DTIMS where a clean carrier gas is used. In this configuration, ambient air is dried and purified and it serves as both carrier

and buffer gas. If the water content in the sample stream is not controlled, variable sensitivity may be observed for some compounds.

#### 17.2.3.2.2 Ionization and Ionization Sources

**17.2.3.2.2.1 Ionization** All commercially available IMS systems use a soft ionization process based on APCI. When performing APCI, the sample enters the ionization region where primary reactant ions created by the ionization source in the presence of the carrier gas and chemical dopants selectively ionize the sample components. The carrier gas is typically clean dry air (<10 ppm H<sub>2</sub>O) which consists of nitrogen, oxygen, CO<sub>2</sub>, water vapor, and other trace gases. The selective and reproducible production of analyte ions in the air is critical to the success of IMS [39]. Also critical to its success is the ability to perform the analysis at ambient pressure with preferred ionization for analytes of interest over general interferences found in the sampling environment. Chemical dopants that enter the ionization chamber can be used to control the reaction chemistry by creating reproducible and stable analyte ion species and suppressing ionization of interferent species. They may also be used to create calibrant peaks.

To produce reproducible and stable ions, instruments have been designed to provide a controllable ionization environment. During the ionization process, the primary reactant ions formed depend on the ionization source and the composition of the carrier gas: Subsequently, the types of analyte ions produced depend on the nature of the primary reactant ions formed and dopants present. Of course, sample-matrix components are also part of the process. Dopant chemistry is a complicated but very significant aspect of instrument design and method development [39, 40]. Higher-proton-affinity dopants, such as ammonia [41], nicotinamide [42], or isobutyramide [43] can be added to suppress ionization of low-proton-affinity species so that selectivity is improved, and false alarms are minimized. The addition of high-electron-affinity chlorinated dopants, such as hexachloroethane and dichloromethane [41], are added to produce chloride ions to create an environment for the most effective ion chemistry. If dopants are not added to the system, reactant ions produced will be uncontrolled and what is present in the ambient background of the sample or the air stream. Typical ions formed in negative and positive modes along with relevant examples of ion complexes are shown in Tables 17.5 and 17.6, respectively. RDX, PETN, TNT, EGDN, and DNT are all explosive substances.

**Table 17.5** Typical ions formed in negative-ion mode.

Basis of formation	Short-form	Example	Comment
Dissociative charge transfer	X <sup>-</sup>	Cl <sup>-</sup>	
Adducts with react-ions (typically Cl <sup>-</sup> )	(M + Cl) <sup>-</sup>	(RDX + Cl) <sup>-</sup>	Source dopant added
Adducts with nitrates NO <sub>3</sub> <sup>-</sup>	(M + NO <sub>3</sub> ) <sup>-</sup>	(PETN + NO <sub>3</sub> ) <sup>-</sup> (HNO <sub>3</sub> + NO <sub>3</sub> ) <sup>-</sup>	Source typically ambient nitrates
Adducts with NO <sub>2</sub> <sup>-</sup>	(M + NO <sub>2</sub> ) <sup>-</sup>	(RDX + NO <sub>2</sub> ) <sup>-</sup>	
Adducts with O <sub>2</sub> <sup>-</sup>	(M + O <sub>2</sub> ) <sup>-</sup>	(RDX + O <sub>2</sub> ) <sup>-</sup>	Typically suppressed in the presence of nitrates and chlorides
Proton abstraction	(M - H) <sup>-</sup>	(TNT-H) <sup>-</sup> , (DNT-H) <sup>-</sup>	
Dimers	(M <sub>2</sub> + X) <sup>-</sup>	(2RDX + Cl) <sup>-</sup>	Unstable at higher drift tube temperatures
Decomposition	(NO <sub>3</sub> ) <sup>-</sup>	EGDN, NG	

Source: Based on Kozole et al. [43].

**Table 17.6** Typical ions formed in positive-ion mode.

Basis of formation	Short-form	Example	Comment
Protonated molecules	(M + H) <sup>+</sup>	(cocaine + H) <sup>+</sup>	Proton affinity
Adduct formation	(M + A) <sup>+</sup>	(tabun + NH <sub>4</sub> ) <sup>+</sup>	
Proton-bound dimers	(2M + H) <sup>+</sup>	(2 tabun + H) <sup>+</sup>	High temperatures can destabilize dimers

Source: Based on Puton and Namieśnik [44].

In addition to controlling reaction chemistry, when present in the ionization chamber, dopants may also be added to the buffer gas to modify its composition. As an example, although not commonly considered a dopant, water vapor is a chemical that is used to modify buffer-gas composition to optimize IMS analysis.

**17.2.3.2.2.2 Ionization Sources** Virtually, all IMS systems produced prior to the year 2000 used a radioactive source. These sources played an important role in the fundamental studies of IMS [15] (pp. 22–23, 38–39). Radioactive sources, such as the commonly used <sup>63</sup>Ni source, are regulated in the United States by the Nuclear Regulatory Commission (NRC), and in other countries by similar national organizations. Nonradioactive sources based on plasma discharge, photoionization, and high-energy photoionization (HEPI) have become more favorable options from regulatory and maintenance perspectives. Due to the ability to perform IMS without the use of a radioactive source, the burdens historically associated with the deployment of IMS systems containing a radioactive component have been removed.

**17.2.3.2.2.2.1 Radioactive Sources** Radioactive ionization sources, such as <sup>63</sup>Ni and <sup>241</sup>Am, used in IMS systems have many operational benefits. Typically, they are coated metal foils inserted into the reaction chamber: They are simple, stable, have long lifetimes, and require no power supply. They emit high energy particles, such as beta particles from <sup>63</sup>Ni, and alpha particles from <sup>241</sup>Am. The kinetic energy of these emitted particles exceeds the ionization thresholds of most analytes of interest and background air components [45–47]. These sources usually have high ionization efficiency, but low ionization selectivity [39, 40, 48, 49].

The most favored radioactive ionization source is 10 mCi of <sup>63</sup>Ni coated as a thin layer on a metal strip, generally nickel or gold. [50] The half-life of <sup>63</sup>Ni is about 100 years. The maximum energy of the electrons emitted from the <sup>63</sup>Ni is 67 keV, with average energy near 17 keV. Almost all the energy of this source is dissipated in the air at an ambient pressure within 10 to 15 mm from the surface of the metal. A common geometry of this source in IMS systems is cylindrical [15, 51] (p. 137). <sup>241</sup>Am has also been used as a source in IMS, usually in AIMS platforms. <sup>241</sup>Am was used as the ionization source in the M43A1 detector, one of the earliest portable IMS systems, which was deployed to military users for CWA detection [4]. Its half-life is about 432 years. Alpha particles emitted from <sup>241</sup>Am are highly energetic, with energies above 5.4 MeV. They have a short effective range in the air so that ionization is efficient in small-volume sources [52].

During the ionization process, beta particles emitted from the <sup>63</sup>Ni source collide with neutral molecules of O<sub>2</sub> and N<sub>2</sub> in the air causing electron ejections as they travel. This results in the formation of a plasma consisting of O<sub>2</sub><sup>+</sup>, N<sub>2</sub><sup>+</sup>, and thermalized electrons [15] (pp. 22–23, 38–39). Similar species are produced for <sup>241</sup>Am, except the high-energy alpha particles strip electrons from a large number of O<sub>2</sub> and N<sub>2</sub> molecules, producing a plasma consisting of thermalized electrons along its travel path, as well as N<sub>2</sub><sup>+</sup> and O<sub>2</sub><sup>+</sup>.

These primary reactant ion species then interact with air to create reactant ions as follows:

- (1) The thermalized electrons react with O<sub>2</sub> to create O<sub>2</sub><sup>-</sup>, which is hydrated as O<sub>2</sub><sup>-</sup>(H<sub>2</sub>O)<sub>n</sub>: The degree of hydration depends upon temperature and water-vapor levels.

**Table 17.7** Common ionization sources used in commercially available portable IMS systems.

Manufacturer	Instrument	Ionization source
All	Most pre-2000 instruments	Radioactive $^{63}\text{Ni}$
Bruker [53]	RAID-M	Radioactive $^{63}\text{Ni}$
Bruker [54, 55]	DE-tector, DE-tector-flex Raid-M <sub>NR</sub> , RoadRunner	High Energy Photoionization (HEPI)
Environics Oy	AIMS platforms	Radioactive $^{241}\text{Am}$
Leidos	B220	Photoionization (pulsed UV ion source, photonic ionization) [56]
Rapiscan	Itemiser DX	Radioactive $^{63}\text{Ni}$ [57]
Rapiscan	Itemiser 4DX	Photoionization (krypton lamp) [56, 58]
Smiths Detection	Ionscan 600	Dielectric barrier discharge [56]
Smiths Detection	LCD	Pulsed corona
Smiths Detection	Ionscan 500DT	Radioactive $^{63}\text{Ni}$

- (2) The positive ions  $\text{N}_2^+$ ,  $\text{N}_4^+$ ,  $\text{O}_2^+$ ,  $\text{O}_4^+$  are created and react with water vapor to generate  $\text{H}^+$  with water clusters of  $\text{H}^+(\text{H}_2\text{O})_n$ , where  $n = 1\text{--}10$ : The degree of clustering depends upon temperature and water-vapor levels.

Even though radioactive sources offer operational advantages, and the behavior of the radioactive sources used in IMS systems is well understood, the regulatory burdens associated with radioactive sources have resulted in the movement away from these sources and the development of nonradioactive sources for use in IMS systems.

**17.2.3.2.2.2 Nonradioactive Sources** Nonradioactive sources used in commercially available IMS systems include corona discharge and barrier discharge ionization sources, and photoionization sources. Table 17.7 details some of the available portable systems and the different radioactive and nonradioactive sources used in each. The details of the exact operation of these nonradioactive sources are usually not disclosed by the vendors beyond what is available in the patent literature. A few have been described below. It is important to recognize among instrument platforms that there may be minor-to-significant differences in performance based on the primary ionization source used.

**17.2.3.2.2.2.1 Corona Discharge** A corona discharge is, by definition, a gas discharge where the geometry confines the gas-ionizing processes to high-field ionization regions around the active electrode. To form a corona-discharge IMS source, a sharp needle or thin wire is placed 2–8 mm from a metal plate or discharge electrode with a voltage difference of 1–3 kV between the needle and the plate. An electric discharge develops in the gap between the needle or the wire and the opposing conductor [15] (p. 138).

Corona sources use a strong electric field to accelerate electrons toward the opposite electrode. The electrons collide with the neutral gas molecules, ejecting more electrons along the way, creating a plasma of  $\text{O}_2^+$ ,  $\text{N}_2^+$ , and thermalized electrons. In positive-ion mode, these primary reactant species subsequently form similar reactant ions to those formed when using a radioactive source ( $\text{N}_2^+$ ,  $\text{N}_4^+$ ,  $\text{O}_2^+$ ,  $\text{O}_4^+$ ), along with similar water clusters of  $\text{H}^+(\text{H}_2\text{O})_n$  [59]. In negative-ion mode, ionization behavior is different from that of radioactive sources due to the formation of  $\text{NO}_3^-$  [15, 60] (p. 137), [61]. To achieve a more similar ionization profile to that observed in radioactive sources, a pulsed voltage across the two electrodes is imposed, which causes an ion avalanche with enough

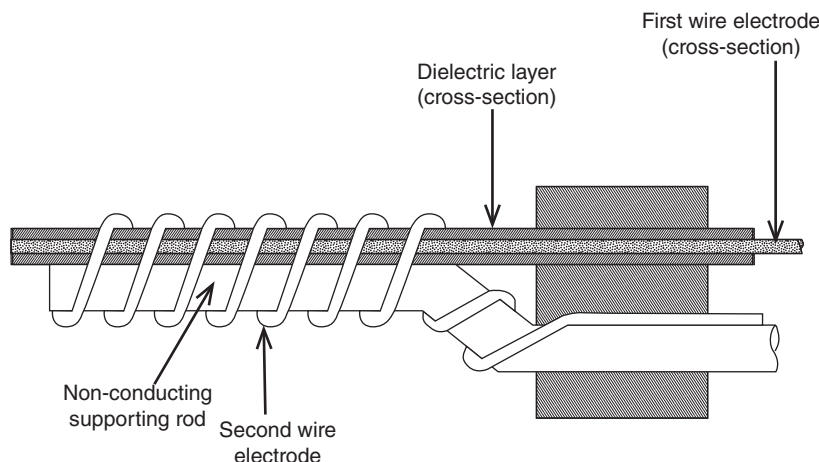


**Figure 17.8** Schematic of a DBD source. Source: Kubelik et al. [65].

energy to produce  $[(\text{H}_2\text{O})_n\text{O}_2]^-$  in analytically useful quantities, without producing significant levels of  $\text{NO}_2$ . Further, by pulsing the corona, the lifetime of the electrodes, and, hence, long-term stability of the system, is enhanced [61]. Commercially, corona discharge as an ionization source in field-deployed IMS was first proposed by Graseby Dynamics (now Smiths Detection) [62]. Subsequently, the first commercial IMS system using a corona discharge ionization source was likely the Smiths Detection LCD in 2002 for the government of the United Kingdom, and, subsequently, for the government of the United States as the JCAD in 2002 [11] (p. 28). There are some disadvantages to corona discharge sources including the need for an external power supply, corrosion of components, maintenance of the discharge, and the formation of corrosive chemical vapors, such as  $\text{NO}_x$  and ozone. Stability may be degraded by corrosion of the needle [62].

**17.2.3.2.2.2.2 Dielectric Barrier Discharge** Dielectric barrier discharge (DBD) sources are discharge ionization sources which have an insulating (dielectric) material in between metal electrodes, typically made from glass, quartz, ceramics, enamel, mica, plastics, silicon rubber, or Teflon with a gap distance between 0.1 and 10 mm [63, 64]. DBDs have low power consumption, long lifetimes, and work at ambient pressures. For these reasons, they are favorable for incorporation into field-deployable IMS instruments. The DBD source is inserted into the ionization region of the IMS.

DBDs are self-sustaining in electrode configurations containing an insulating material in the discharge path. This so-called dielectric barrier is responsible for a self-pulsing plasma operation and, thus, the formation of nonthermal plasma at normal pressure [64]. The discharge creates electrons with high average kinetic energy (1–10 eV), metastable species, and high energy photons. The ionization profile for DBDs is similar to that of corona discharge sources, and like with the corona, an advantage of pulsing is a reduction in production  $\text{NO}_3^-$ . A primary analytical benefit of a DBD ionization source is a larger and more controlled ionization region.

DBD ionization devices may come in planar and cylindrical configurations. With cylindrical configurations, the plasma can be generated in the volume between the electrodes or at the surface of the dielectric. With surface-based DBD sources, microdischarges are generated at the surface of the dielectric, resulting in a more homogenous plasma source than the volume-based DBD sources. A surface-based DBD source was recently proposed [65]. Figure 17.8 shows a schematic of this DBD which consists of a metal wire electrode coated with a dielectric layer and a second wire electrode wrapped around the coated metal wire electrode. Ionization starts with a short burst of a high-voltage pulse which initiates a plasma discharge.

**17.2.3.2.2.2.3 Photoionization** Most organic molecules will ionize when exposed to ultraviolet (UV) light in the photon range of 8–12 eV (155–103 nm) [49]. Application of an electrical discharge in the lamp in the presence of a noble gas at low pressure will result in the emission of photons. The formation of positive ions with photons has been described as direct ionization through the reaction described in Eq. 17.6 where  $h\nu$  is the photon energy and  $M$  is the neutral molecule.



The wavelength emitted by a UV lamp depends on the filler noble gas (Ar, Kr, H, Kr, or Xe) used and the lamp window material (LiF, MgF<sub>2</sub>, CaF<sub>2</sub>, CaF<sub>2</sub>, or Al<sub>2</sub>O<sub>3</sub>). The Kr-filled UV lamp (10.6 eV, 116 nm) with an MgF<sub>2</sub> window is the most common lamp with the strongest output and longest lifetime. A Kr lamp can ionize most hydrocarbons, alcohols, aldehydes, ketones, and esters if they do not contain chlorine, fluorine, or bromine. It can also ionize all amines and sulfides [66]. The probability of direct ionization is very low, especially for analytes present in a small proportion compared to other components of the carrier gas. Therefore, to promote the ionization efficiency of analyte molecules, a photoionization dopant, such as toluene or acetone, can be used. The Rapiscan Itemiser 4DX uses anisole as the photoionization dopant to create M<sup>+</sup> or MH<sup>+</sup> reactant ions in positive ion mode, and low energy electrons in negative mode. A metal surface can also be used with a UV lamp using the photoelectric effect to release low energy electrons from the metal surface. The major advantages of UV lamps are their small size, simplicity of use, and commercial availability. The disadvantage of UV lamps is a short operating lifetime. For instance, the Kr UV lamp used in the Itemizer 4DX offers a three-month lifetime [67]. These lamps also suffer a loss of 50% intensity through every 1.5 mm of purified air [68].

### 17.2.3.2.3 *Ion Injection*

In commercial DTIMS systems, ion injection is performed using gating-grid ion shutters. Ion gating currently is based on the presence of two closely spaced wire grids which span the cross-section between the ionization region and the drift tube. If the wire grids are in the same plane, this type of ion shutter is known as a Bradbury–Nielson (BN) gate. If the wire grids are in different planes, it is known as a Tyndall–Powel (TP) gate. The wire used in making BN and TP gates are typically less than 100 μm in diameter with wire spacing of ~1 mm. For the TP gate, this distance refers to the distance of the nearest wire in the adjacent plane. TP gates are typically used in commercial equipment due to their robustness as well as their ease and cost of manufacture.

Gate pulsing is important to system performance. Application of an electric field gradient across the wire grids results in an orthogonal force on the ions traversing the gating grids. This electric field is modulated to open or close the gate. In the closed state, the field gradient is strong enough to cause the ions to strike the gating grids; in the open state, the ions traverse the gate into the drift region. The gating pulse is a primary factor that impacts the FWHM of the ion peak which will be discussed later in the “Resolving Power, Resolution, Duty Cycle, and Coadding Scans” section of this chapter. In addition to the impact on FWHM, the timings of the opening and closing of the gate become important as ion mobility decreases because the slowest moving ions need to pass through the gate before it closes. As gate-pulse widths go below 100 μs, this can be a problem. For conventional gates and peak mobilities between 0.5 and 2.5 cm<sup>2</sup>/Vs, gating pulses should be 100 μs or greater. Otherwise, slower mobility ions will be filtered out resulting in very small ion signals [69]. Typically, ions are gated between 100 and 300 ms every 15–30 ms; hence, only ~1% of ions are injected into the drift tube. For AIMS and FAIMS systems, where ions are continuously injected, theoretically, 100% of the ions could be injected, depending on inlet aperture design.

### 17.2.3.2.4 *Drift Tube*

The drift tube is the most important part of the IMS; it is where separation occurs. The objective of the IMS design is to create a homogenous electric field inside the drift tube [70]. Ions enter the drift tube in the presence of a carrier gas, which in commercial instruments is typically clean dry air. In addition, in properly designed DTIMS

systems, a counterflow of clean dry air enters at the end of drift region near the detector to provide counterflow drift gas. The counterflow is used to ensure no neutral molecules from the ionization enter the drift tube. Prior to the introduction of air to the IMS, it is cleaned to remove volatile organics and reach water-vapor levels down to approximately 1–10 ppm. Control of air quality is important to ensure reliable ion formation and mobility. Air purification is one of the key development areas critical to portable systems and will be discussed later. It is also possible to use other carrier gases, such as nitrogen, helium, or argon, but their use requires the presence of a pressurized tank which is not desirable for field-portable systems. The drift tube is constructed of a series of ring electrodes creating a uniform field usually held between 200 and 300 V/cm. The positioning of the ring electrodes controls the uniformity of the field. The closer and greater the number of ring electrodes, the more uniform the field. Uniformity of the electric field is important because nonuniform fields act like a defocusing lens that degrades resolution. The mobility of the ion is dependent upon the electric field voltage in accordance with Eq. (17.7) [71] which shows the relationship among the ion mobility,  $K$ , the length of the drift tube,  $L$ , the electric field gradient  $E$ , and the measured drift time  $t_d$ . This relationship can also be stated in terms of the applied voltage ( $V$ ) across the drift tube.

$$K = \frac{L}{Et_d} = \frac{L^2}{Vt_d} \quad (17.7)$$

Typical drift tube lengths are 10 cm or less. Very short drift tube lengths require very fast ion shutters and amplifiers for acceptable separation capability. Typically, drift times for most commercial instruments with drift tubes between 4 and 10 cm is between 2 and 20 ms. The mobility of ions measured by field-portable equipment has molecular masses between 30 and 500 amu and mobilities between 2.5 and 0.8 cm<sup>2</sup>/Vs. Table 17.2 shows the expected drift times for peaks for  $K_0$  values between 2.4 and 0.8 cm<sup>2</sup>/Vs for an 8-cm drift tube at 200 °C with a gating pulse of about 150 μs.

#### 17.2.3.2.5 Guard Grid

The guard grid is located very close to the Faraday plate detector and has an applied potential such that the field gradient between the guard and detector is much higher than the drift tube field gradient. The guard grid is required to capacitively uncouple the approaching ion swarm from the Faraday plate. If the guard grid was not present, a current would be induced on the Faraday plate before the ion swarm came into contact with it, resulting in a non-Gaussian peak with tailing on the short-drift-time side. With the guard grid, the ion swarm is rapidly accelerated to minimize this effect resulting in Gaussian peak shape.

#### 17.2.3.2.6 Ion Detector – Faraday Plate

The ion detector at the end of the drift tube is a critical component of overall IMS sensitivity, and in portable IMS systems, it is a Faraday plate. A Faraday plate is used, as opposed to a Faraday cup, since the Faraday plate operates at atmospheric pressure. The detector converts the swarm of gas-phase ions into an electrical signal that provides both time and amplitude information. To ensure sharp and properly formed peaks, a guard grid is placed before the Faraday plate and held at the potential to quickly accelerate the ions to the plate, negating peak broadening due to capacitive charging.

The ion mobility spectrum is a plot of current as a function of time. Typical IMS peaks have FWHM values between 100 and 500 μs, and the Faraday plate offers a fast rise time (<10 μs), and fast recovery times, which are essential for minimizing peak broadening. Ion currents detected at the Faraday plate are on the order of a few nanoamps. For a typical IMS peak which is 200-μs wide, Johnson noise (~1 × 10<sup>-12</sup> A at 25 °C) limits the detection. For a single scan, 100 ions need to reach the detector to generate a signal [15] (pp. 155–158). The diameter of the Faraday plate, compared to the diameter of the drift tube, can impact peak width if the electric field near the outer diameter of the tube is not homogenous. This can be mitigated by using a Faraday detector with a smaller diameter than the drift tube. In these situations, a compromise between signal and resolution is required [70].

The Faraday plate is ideally designed and manufactured to have a long life and no maintenance issues. Some IMS systems will heat the Faraday plate to ensure neutralized ions are removed. Otherwise, samples which are thermally desorbed and release semivolatile species can condense on the detector degrading sensitivity over time. Instrument designers will put a lot of careful attention into the preamplifier electronics associated with the Faraday plate in order to reduce electronic noise and remove high-frequency noise. Care must also be taken to minimize any time delay introduced by the electronics or data processing which can artificially increase the measured drift time.

#### 17.2.3.2.7 Air-Flow and Air-Purification Systems

The key air flows in the IMS are the drift flow, sample flow, and exhaust flow. The drift flow should be countered to the ion flow in the drift tube to prevent neutrals in the ionization region from entering the drift tube. If neutrals do enter the drift tube, then uncontrolled ion clustering will occur which can result in unacceptable drift-time variability. The sample-flow medium must be clean and dry to prevent ion clustering and produce reliable and stable drift times. The exhaust flow is used to remove the unionized sample from the reaction region.

Clean, dry air is the primary support medium for these flows. Ambient air is typically pulled into the system and cleaned and dried internally. The ability to use ambient air is a very valuable field-deployment feature since gas accessories are, therefore, not required; however, keeping the airflow through the system clean and dry can be challenging. Medium- and high-performance IMS systems typically require water content to be <10 ppm for good performance. Ambient air water-vapor content can vary from 1000 to 40 000 ppm (0.02–36 g/m<sup>3</sup> of water vapor over the typical environmental conditions encountered from –20 to 50 °C).

To clean and dry the air, a variety of approaches are used. For small handheld systems, disposable molecular sieve packs are used and need to be replaced regularly. For these systems, regenerative air purification units currently are not an alternative due to power restrictions. Since most of the water vapor that enters the system will occur during sampling, disposable-sieve lifetime may be extended by minimizing the amount of external air which enters the system during sampling, or by recirculating the existing air supply. Historically, thin permeable membranes were used across the inlet to allow the sample to get through while minimizing water vapor ingress. Challenges to this approach, though, are that the membrane will create a delay in sample entry, and can also prevent some substances from entering the system. Smiths Detection developed an alternative method to limit the amount of water that enters the sample. In their LCD handheld IMS system, a small-volume pulse of sample vapor is pulled into the IMS through a pinhole [11] (pp. 48–49).

For larger systems, initially, charcoal and Drierite desiccant were used to clean and dry the ambient air. In these situations, the lifetime of the drying material could be extended by predrying the air using thermoelectric coolers or Nafion™ drying systems. Eventually, small regenerative air purification systems were developed. Typical regenerable systems have two sieve towers which can be operated in alternating sequence to provide clean air and to regenerate the sieve tower. This is particularly useful for systems which are used 24/7 at checkpoints, such as encountered in aviation security. Regenerable air purification systems also have the advantage of providing more consistent water-vapor levels, which reduces the width of detection windows, thus improving system performance.

#### 17.2.3.2.8 Outgassing

IMS systems are trace detection systems and very careful attention must be paid to ensure all the components used to build these systems are clean at the trace level. If not, volatile interferences can degas from these components, which can impact the ionization process and ion interactions in the drift tube. Introduction of trace levels of contamination can have significant impacts on performance. The ability to build such systems generally requires the development of cleaning processes for all components, which consist of washing, baking, and testing to ensure no outgassing of contaminants that degrade detection performance will occur. The cleaning processes that instrument manufacturers have developed are a critical core competency which is required for the mass production of portable systems.

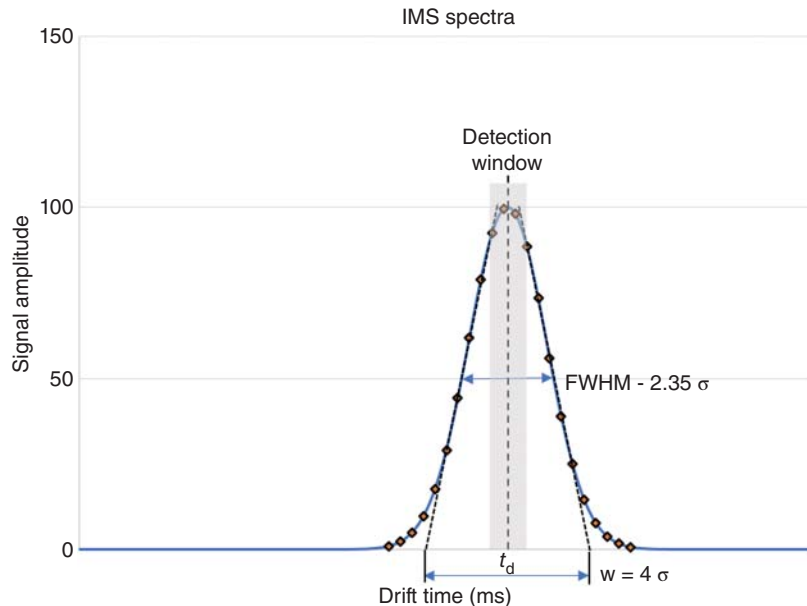


**Figure 17.9** IMS peak characteristics including drift time ( $t_d$ ), FWHM, sigma ( $\sigma$ ), peak width ( $W$ ) detection window, and digitization points.

### 17.2.3.3 Figures of Merit

#### 17.2.3.3.1 IMS Peaks, Peak Windows, Calibration, and Informing Power

An IMS peak is typically Gaussian in shape with a drift time associated with its maximum amplitude. A peak's FWHM, base width ( $\Delta W$ ), and standard deviation ( $\sigma$ ) are shown in Figure 17.9. During data acquisition, the analog signal is digitized based on the digitization rate of the instrument. Digitization is shown in Figure 17.9 as discrete points across the peak. The instrument can estimate the peak position by (i) using the digitization point at the maximum amplitude or interpolating the maximum based on the points around this maximum, or (ii) fitting the peak. Fitting the peak usually generates a more accurate peak-position value. Each instrument manufacturer uses its own method for determining peak position, which may be proprietary.

The expected peak position of the analyte peak is determined from the library  $K_0$  value. For DTIMS systems, this can be converted into drift-time space using two methods. In method 1, the system is designed to measure  $E$ ,  $P$ , and  $T$  in real time and calculate the expected drift time using Eq. (17.8).  $L$  is the length of the drift in cm,  $P$  is the pressure in Torr,  $T$  is temperate in K,  $t_d(\text{analyte})$  is the drift time of the analyte,  $K_0(\text{analyte})$  is the mobility of analyte, and  $E$  is the strength of the electric field.

$$\text{Method 1 : } t_d(\text{analyte}) = \frac{L}{K_0(\text{analyte})E} \left( \frac{P}{760} \right) \left( \frac{273}{T} \right) \quad (17.8)$$

Uncertainty in the drift time of the peak arises from the precision and accuracy of the sensors used to measure the values and the slight variations associated with the manufacture of the drift tube. Note this equation is valid for large variations of  $P$ , variations of  $E$  in the low-field limit, and a narrow range of temperatures for a fixed IMS drift-tube temperature. If the drift temperature is not fixed and is dependent on the ambient environment, which could range from  $-20$  to  $50$  °C, then the detection library will factor this into the  $K_0$  value used by the above equation to predict the expected ion peak drift time. This method has been used very effectively by some of the small handheld platforms with an acceptable false-alarm rate.

A more accurate method using an internal calibrant of defined  $K_0$  and measured drift time dispenses the need to measure  $T$ ,  $P$ , and  $E$ . This method is based on the use of Eq. (17.9) to predict the expected position of the analyte

peak. The  $t_d$ (calibrant) is the measured drift time of the calibrant,  $K_0$ (calibrant) is the known reduced mobility of the calibrant,  $K_0$ (analyte) is the known reduced mobility of the analyte peak and  $t_d$ (analyte) is the calculated expected position of the analyte.

$$\text{Method 2 : } t_d(\text{analyte}) = \frac{K_0(\text{calibrant})}{K_0(\text{analyte})} t_d(\text{calibrant}) \quad (17.9)$$

This is achieved typically by using either an external or internal calibrant substance to generate a calibrant peak to compensate for slight differences between manufactured instruments (drift-tube length, electric field, temperature) and ambient-pressure impacts. For a list of some internal calibrants used, see Kaur-Atwal; [72] these are typically specific to a manufacturer. A key criterion that must be considered when using this method is how often the calibration is performed. For some platforms, it is done constantly; for others, it may be done every 5–15 minutes or at even longer intervals. The interval which is chosen is determined by how much drift may occur in  $P$ ,  $T$ , and  $E$  and maintain an acceptable detection window.

There is sometimes a discrepancy between  $K_0$  values established using applied detection platforms and those established in academic settings. This is particularly true if the  $K_0$  value of the calibrant in the applied detection platform is different from the academic literature. The  $K_0$  values used by the field-deployable instrument will still be internally consistent, and it is possible to convert from an instrument's  $K_0$  scale to a literature-corrected  $K_0$  scale by using a well defined literature value, such as shown in Eq. (17.10).

$$K_0(\text{corrected}) = K_0(\text{vendor}) \times K_0(\text{TNT} - \text{litterature}) / K_0(\text{TNT} - \text{vendor}) \quad (17.10)$$

Once peak position is determined, the measured drift time is compared to the expected drift time of the peak from the detection library. All instruments have variability associated with the drift-time measurement, which creates variability in the peak-position measurement. This uncertainty is typically determined experimentally by characterizing the peak under a range of conditions, e.g., at different loading levels and environmental conditions at which the instrument will be operated in the field. In addition to individual instrument variability, unit-to-unit variability must be accounted for in the calibration and detection algorithm. This can be achieved in two ways. The first way is to optimize the calibration either during the calibration stage of manufacturing or during subsequent service. The second is to account for instrument-to-instrument variability, generally, by expanding detection windows slightly. This second method is preferred since this means a common detection algorithm can be loaded into every instrument and no additional unit calibration is required. It also makes library expansion much easier in the field.

The determined uncertainty is then used to define the detection-window width (shown in Figure 17.9). It is important to note that uncertainty is also dependent on instrument design. Although attempts are made to reduce the uncertainty during development to ensure a minimal variation of critical parameters that impact drift time, uncertainty is inevitable. Drift time of an IMS peak is a function of the drift-tube temperature, pressure, electric field, and water-vapor content. If the measured peak position is within the detection window, the first peak-alarm criterion is met. Detection-window width impacts the false-rate performance of the instrument which to a first order scales with detection-window size. It also impacts the ability to uniquely identify compounds with similar  $K_0$  values. For typical fixed-temperature commercial systems, detection width windows in the range of  $\pm 25\text{--}75 \mu\text{s}$ , or approximately  $\pm 0.001 K_0$  are expected. If the drift tube temperature is not fixed, then detection windows can be significantly larger. Alarm criteria will usually also consider other peak characteristics including amplitude and width.

Another measurement that helps establish a system's performance is informing power [73]. The informing power of an IMS correlates with false-alarm rate and the ability of the system under defined conditions to uniquely identify an analyte. Informing power of the scan period can be measured as the scan period divided by the average detection-window width associated with analyte peak position. For example, if the IMS system had a scan period of 20 ms and a typical peak window width of 0.100 ms, the informing power is  $20/0.1 = 200$ . If the system

is monitoring in both positive- and negative-ion modes, the overall informing power is 400. The informing power correlates inversely with false-alarm rate, i.e., the higher the information content, the lower the false-alarm rate. It is also a measure of the ability of the system to uniquely identify what was detected.

#### 17.2.3.3.2 Resolving Power, Resolution, Duty Cycle, and Coadding Scans

The resolving power,  $R_p$ , for a DTIMS is defined for a single peak as the ratio of the drift time ( $t_d$ ) to the FWHM [74]. Eq. (17.11) shows this relationship.

$$R_p = \frac{t_d}{\text{FWHM}} \quad (17.11)$$

We have discussed the measurement of drift time, but have not yet considered the FWHM measurement. The FWHM of the ion swarm is given by Eq. (17.12) where  $t_g$  is the gating pulse width and  $t_{\text{diff}}$  is diffusional broadening [74]. Diffusional broadening is a function of the temperature and is determined using Eq. (17.13), [74] where  $q$  is the charge on the ion. These equations are assuming a Gaussian shape of the ion swarm peak, which is a good assumption.

$$\text{FWHM} = \sqrt{t_g^2 + t_{\text{diff}}^2} \quad (17.12)$$

$$t_{\text{diff}} = \left[ \frac{16 kT \ln 2}{Vq} \right]^{\frac{1}{2}} \quad t_d = \left[ \frac{16 kT \ln 2}{Vq} \right]^{\frac{1}{2}} \frac{L^2}{KV} \quad (17.13)$$

The key takeaway points from these equations are that FWHM is controlled by the gating pulse width, while diffusional broadening is controlled by temperature, electric field strength, and drift-tube length. Other factors that can impact the FWHM of the ion through their effect on either drift time or diffusional broadening are columbic repulsion (space charge) for intense peaks and electric field inhomogeneities. For most field-portable IMS instruments, which have drift tube lengths in the range of 3–10 cm and electric field strengths in the range of 200–300 V/cm, pulse widths of 100–300  $\mu$ s are used with resolving power between 20 and 60 [75]. Resolving power can be increased by reducing the gating pulse width, but this reduces the signal. Therefore, a compromise between resolving power and sensitivity is necessary. Generally, a gating pulse of 200  $\mu$ s is used. When comparing resolving power of instruments, peaks with similar  $K_0$  values should be used. The higher the resolving power, the higher the ability of the instrument to resolve two closely spaced peaks. This ability can impact the false-negative rate of the instrument when complex spectra are present. Note that in the literature, there is a tendency to confuse terminology of resolving power and resolution, and, sometimes, resolving power is referred to as resolution.

Resolution (R) for an IMS is the ability to separate two peaks with drift times  $t_1$  and  $t_2$  and peak widths  $w_1$  and  $w_2$  as defined using Eq. (17.14). Resolution is particularly important when attempting to detect a peak in the presence of other peaks with similar drift times to minimize false negatives. There are mathematical tools which can be used to deconvolve closely overlapping peaks, but these can induce artifacts which must be considered when using this approach.

$$R = \frac{2(t_2 - t_1)}{(w_1 + w_2)} \quad (17.14)$$

The scan period for DTIMS systems is the time the signal is monitored after the gating grid is opened before opening the gate again. The scan period encompasses the range of mobilities in the detection library, which are characteristic of the mobilities of the detection substances over the anticipated operating environmental conditions. If the MW of the ions observed is less than 500 amu ( $K_0 \sim 0.80$ ), then for the DTIMS systems outlined in Table 17.1, scan periods are on the order of 23 ms. In order to improve the SNR, scans can be coadded. When scans are coadded, the signal increases with the number,  $n$ , of coadded scans. Noise, on the other hand, increases as a function of the square root of  $n$ . The anticipated SNR improvement as a function of the number of coadded

**Table 17.8** Anticipated signal-to-noise ratio improvement by coadding scans.

Number of scans coadded	1	2	4	16	32	100	256
Signal-to-noise (S/N) improvement	1.0	1.4	2.0	4.0	5.7	10.0	16.0

scans is shown in Table 17.8. Typically, the number of coadded scans required to achieve optimal results is determined during method development. The amount of time required to collect a spectrum is, therefore, equal to the scan period times the number of coadded scans. The total analysis time is equal to this value, times the number of spectra collected during the measurement. For the example of a 23-ms scan period with 20 added scans, an IMS spectrum is measured in 460 ms. Further, if the total analysis time is 10 seconds, ~22 average spectra each of 0.46 seconds duration would be measured during this analysis. To speed up processing, detection algorithms are typically applied to the IMS spectra rather than the individual scans.

The duty cycle of DTIMS system is the ratio of the gating pulse to the scan period. Typical gating-pulse widths of 0.200 ms are used. If the scan period is 23 ms, then the duty cycle is approximately 1%. When the gate is open, ions are injected into the drift tube; when closed, the ions generated in the reaction are neutralized when they strike the closed gate. From a practical perspective for DTIMS systems, 98–99% of ions are thrown away. For AIMs and DIMS, 100% of the ions are injected into the analyzer so the SNR can be improved by as much as 50 [11] (p. 128).

#### 17.2.3.3.3 Verification and Sensitivity Testing

It is typical for field-deployed IMS systems to provide a test sample referred to as either a verification sample or a confidence-test sample. Differently configured systems will use this sample to test different things, but generally, it will be used to establish that (i) the components required to get the sample into the ionization chamber of the system are functioning properly, (ii) the system is calibrated, and (iii) the detection algorithm is being applied properly and the system is alarming as intended. The verification sample should be different from the calibration sample in order to assure the system is properly calibrated.

#### 17.2.3.3.4 Sensitivity, Limit of Detection, and Limit of Alarm

IMS sensitivity is a function of many factors including sample introduction efficiency, sample ionization efficiency, gating efficiency, the efficiency of ion transfer through the drift tube, and conversion of the ions into an electronic signal as a function of its arrival time. The sample matrix can also impact sensitivity. For IMS platforms, there are generally two figures of merit used to evaluate sensitivity; (i) the limit of detection (LOD) which is usually calculated as baseline plus three times the instrument noise, and (ii) the limit of alarm (LOA) which is usually calculated as baseline plus ten times the instrument noise. LOA may be set higher if high background chemical noise is expected. To minimize false alarms, IMS platforms typically operate with detection libraries set at the LOA rather than the LOD.

#### 17.2.3.3.5 Battery Requirements

The battery lifetime of portable systems varies as a function of size and weight, i.e., systems that are smaller and lighter have longer lifetimes than those that are larger and heavier. Usually, attempts are made to minimize the use of components that consume power through engineering design. For small handheld detectors that may also be worn, expected battery life can be on the order of 75 hours. For handheld systems, battery lifetimes of four hours are reasonably expected and although hot-swappable batteries are frequently desirable for portable spectrometers, this is not usually a critical issue for IMS systems. Some modern benchtop systems can operate for up to one hour on battery. Since IMS systems perform at ambient pressure, they have an advantage with regard to battery life over other trace detectors, such as mass spectrometers, that require power-hungry and sometimes-difficult-to-maintain pumps to achieve vacuum.

## 17.3 Current Innovations and Future Directions

The current state and future direction of IMS seem to be focused in a few areas. Increasing the breadth of chemicals that can be detected in a single analysis is important, and is possible using modern systems capable of performing fast-switching polarities. The ability to detect both positive and negative ions simultaneously is important because there are many situations where screening for substances that generate both positive and negative ions is necessary. For example, standard military and commercial explosives are generally detected in the negative mode. However, homemade explosives, such as HMTD and TATP, that have become more commonly encountered in recent years, are detected in the positive mode. CWAs and TICs also fall into this category. For instance, many nerve agents generate positive ions, while blister agents, such as mustard gas, generate negative ions. The ability to screen for these different types of ions simultaneously in these situations is significant.

There are generally two approaches to performing simultaneous detection of positive and negative ions. The first is by polarity switching. Historically, switching polarities was slow – on the order of about ten seconds [76]. Fast stabilization of the electric field in the reaction and drift regions was difficult, but many of these stabilization challenges have been addressed. In 2001, Rapiscan (then GE Ion Track) developed a fast-switching-polarity IMS that detected both positive and negative ions by switching the drift tube at 20 Hz [77]. More recently, IMS systems capable of a 1–2 ms stabilization are achievable [78]. The second approach to simultaneous detection is the use of two drift tubes. An advantage to this approach is that the operating conditions, and specifically the drift-tube temperature, can be optimized for each mode of operation. A single sample enters the system and is split between two IMS systems – one run in the positive mode and one run in the negative mode. An example of this type of system is the Smiths Detection 500DT (DT being an acronym for dual tube). This product has been on the market since about the year 2005 and, although it is still a viable trace detection system that offers good performance, it is competing in today's market with systems that are cheaper, smaller, lighter, and require less power.

Improvement of detection algorithms is also an important area of interest and development for IMS systems. The size of detection libraries needs to increase due to an increasing breadth of threats, but these systems need to maintain or reduce false-alarm rates and minimize coalarms. Coalarms occur when two different threats are programmed into a detection library, but the presence of one may cause both threats to alarm. To date, very robust detection algorithms have been developed based on peak finding and/or the use of logic, which can be combined with desorption time for samples which use variable-temperature desorption profiles. Typically, a system's detection algorithm will look at a peak's position, width, amplitude, and desorption profile to generate an alarm. Some analytes may produce multiple ion peaks which can be helpful in reducing false positives. But there is information in peak shape, desorption profiles, and patterns associated with common interferences that cannot easily be used. This is where the use of artificial intelligence (AI) may help. Currently, none of the commercial platforms appears to be actively using this approach.

Other innovations look at improving resolving power and reducing drift-tube size. In 2013, Kirk et al. [79] published a paper which examined the use of increased electric field strength in the drift tube with short gating pulses to reduce diffusional broadening. This paper took an entirely different look at the fundamental equations of IMS and suggested a nonconventional way of operating the IMS, showing it was possible to develop short drift-tube systems that were capable of achieving better resolution than larger laboratory systems.

The authors of this chapter used the classical equations associated with IMS to examine three different scenarios to establish the potential for IMS performance improvement: Table 17.9 shows the results predicted for a conventional IMS configuration, a higher-resolution IMS configuration, and a shorter-drift-tube configuration with normal resolution. The impact on TNT peak of  $K_0$  1.54 is examined.

In scenario one, a drift tube of length 5 cm and gating pulse of 200  $\mu$ s was used. A TNT peak with  $K_0$  1.54 would have a drift time of 11.328 ms and FWHM of 266  $\mu$ s. The FWHM according to Eq. (17.12) is a function of the gating pulse and the diffusional broadening and both are comparable. The resolving power of the system is 43 and peaks

**Table 17.9** Impact of changing electric field and gating pulse on DTIMS performance.

	Variable	Scenario 1 <sup>a)</sup> (Conventional (normal) resolution)	Scenario 2 <sup>a)</sup> (Higher resolution)	Scenario 3 <sup>a)</sup> (Shorter drift tube with normal resolution)
IMS configuration ( $T = 40^\circ\text{C}$ , $P = 760 \text{ Torr}$ )	$E$ (V/cm)	250	2000	825
	E/N (Td)	1.06	8.5	3.5
	Length of drift tube (cm)	5	5	2
	Gating pulse (μs)	200	5	20
IMS peak at $K_0$ 1.54	Drift time (ms)	11.328	1.416	1.133
	Diffusional broadening (μs)	175	7.75	13.8
	FWHM (μs)	266	9.22	24.0
	Resolving power	43	153	46
Impact on # of coadded scans	Resolution (difference in $K_0$ required to fully resolve closely space peaks for $R = 1.0$ )	0.064	0.017	0.059
	Max scan period at $K_0$ 0.6 (ms)	21.81	2.726	2.181
	Signal: Max coadded scans in 0.50 s	18	147	183
	Noise: Square root of # of scans	4.3	12.1	13.5
	s/n improvement <sup>b)</sup>	1	2.83	3.16

a) Calculations based on  $T = 40^\circ\text{C}$ ,  $P = 760 \text{ Torr}$ .

b) Normalized to 1.

with differences greater than  $0.064 K_0$  can be fully resolved. The typical scan period is 22 ms. To improve the SNR, 18 scans could be coadded over 0.5 second.

In scenario two, the resolution of the system was improved by increasing the electric field from 250 to 2000 V/cm and reducing the gating pulse from 200 to 5  $\mu$ s. The TNT peak position shifted from 11.328 to 1.416 ms due to the much higher electric field, and  $E/N$  increased from 1 to 8.5 Td, outside the low-field limit. The overall FWHM is 9.22 ms which has increased the resolving power almost four times from 43 to 153. The resolution has also increased by  $\sim 4$ . In this scenario, peaks with  $\Delta K_0$  values greater than 0.017 can be fully resolved. This will help improve identification and minimize false negatives. With the much shorter scan period of 2.7 ms, 147 scans can be coadded over 0.5 second which improves the SNR over the conventional system by a factor of 2.83.

In scenario three, it was possible to reduce the length of the drift tube by 60% while maintaining the same performance as the conventional system. The drift-tube length is reduced from 5 to 2 cm, the electric field strength is increased from 250 to 825 V/cm, and the gating pulse is reduced from 200 to 20  $\mu$ s. The TNT peak position shifted from 11.328 to 1.133 ms due to the higher electric field and short drift-tube length.  $E/N$  increased from 1.05 to 3.5 Td. The overall FWHM is now 24  $\mu$ s for the TNT peak and the resolving power is 46. Resolution is similar to the conventional scenario, but the system is more compact. With the much shorter scan period of 2.1 ms, 183 scans can be coadded which improves the SNR over the conventional system by a factor 3.16.

Attempts at ion modification are another area of innovation. Mass spectrometry has always offered the ability to fragment ions to get an extra dimension of information about the analyte which can improve identification and reduce false alarms. Historically, it has been difficult to fragment ions at atmospheric pressure for IMS. With the advent of DMS and the ability to apply high AC fields between metal grids, high fields can be inserted into the reaction region or part way down the drift tube of an IMS. Terms such as ion modification and field-induced fragmentation (FIF) have been used to describe the results of this approach. Ions at ambient pressure can undergo fragmentation in high-frequency electric fields  $> 100$  Td ( $\sim 14\,000$  V/cm) [80]. Smiths Detection has described methods to combine ion modification with IMS drift tubes [81]. Gary Eiceman's group [80] has demonstrated the ability to cleave bonds for alcohols and six-member ring rearrangements for acetates. The ability to use new ionization process, such as electrospray ionization or derivatizations to ionize high-melting-point compounds that could not otherwise be desorbed and introduced to the system, is also an area of interest.

## 17.4 Conclusions

It is clear that IMS is a powerful analytical technique which has been used effectively in the field for many decades to assess dangerous threats including CWAs, TICs, drugs, and explosives. These systems are valuable to field users for a number of reasons, including their fast analysis times, simplified user interfaces that provide yes/no results, and sensitivity to threats of interest. Their relative ease of deployment is due, in part, to the fact that they operate at atmospheric pressure and use ambient air as both the carrier gas and buffer gas. The use of these systems by the military and within the aviation-security markets is extensive, and there are a number of other field applications where these systems have proven value. Recent attempts to extend the successful vapor-phase JCAD IMS system to the analysis of solids and liquids [82] is testament to the desire to even further expand the use of these systems to the adapting list of threats faced by the military and other security experts. Systems have evolved over the years to their current state where dual-ion-mode analysis is possible using lightweight battery-operated systems, and a review of the current innovations and future directions for this technology suggests they will continue to evolve to meet the ever-changing threat-detection needs.

## Acronyms

AC	Alternating current
AI	Artificial intelligence
AIMS	Aspiration ion mobility spectrometry
amu	Atomic mass units
APCI	Atmospheric pressure chemical ionization
BN	Bradbury–Nielson
CAAC	Civil Aviation Administration of China
CV	Compensation voltage
CWA	Chemical warfare agent
DBD	Dielectric barrier discharge
DC	Direct current
DfT	Department for Transport in the United Kingdom
DIMS	Differential ion mobility spectrometry
DMS	Differential mobility spectrometry
DNT	Dinitrotoluene
DTIMS	Drift-tube ion mobility spectrometry
DV	Dispersion voltage
ECAC	European Civil Aviation Conference
EGDN	Ethylene glycol dinitrate
FAIMS	Field asymmetric waveform ion mobility spectrometry
FIF	Field-induced fragmentation
FWHM	Full width at half maximum
HEPI	High-energy photoionization
HMTD	Hexamethylene triperoxide diamine
IMS	Ion mobility spectrometry
JCAD	Joint chemical agent detector
LOA	Limit of alarm
LOD	Limit of detection
MW	Molecular weight
NRC	National Regulatory Commission
ppb	Parts per billion
PETN	Pentaerythritol tetranitrate
ppm	Parts per million
SWaP	Size, weight, and power
RDX	Research department explosive
RF IMS	Radio frequency ion mobility spectrometry
TATP	Triacetone triperoxide
TIC	Toxic industrial chemical
TNT	Trinitrotoluene
TP	Tyndall Powell
TSA	Transportation Security Administration
UV	Ultraviolet

## Abbreviations and Symbols

$\alpha$	Correction factor
$^{241}\text{Am}$	Americium-241 radioactive ionization source
C	Celsius
cm	Centimeter
e	Electron charge
E	Electric field
$(E/N)_c$	Critical normalized field strength
eV	Electronvolt
g	Grams
Hz	Hertz
$h\nu$	Photon energy
k	Boltzmann constant
K	Mobility constant
$K_0$	Reduced mobility
keV	Kiloelectronvolt
kg	Kilogram
kV	Kilovolts
L	Length of the drift tube
m	Meters
mCi	Millicurie
mm	Millimeter
ms	Millisecond
N	Number density of neutral gas molecules
ng	Nanogram
$^{63}\text{Ni}$	Nickel-63 radioactive ionization source
$\Omega_D(T_{\text{eff}})$	Effective cross-section of the ion which is a function of the $T_{\text{eff}}$
P	Pressure
pg	Picogram
q	Ion charge
R	Resolution
$R_p$	Resolving power
$R^2$	Coefficient of determination
SNR	Signal-to-noise ratio
STP	Standard temperature and pressure
s	Seconds
$\sigma$	Standard deviation
T	Temperature
$T_d$	Townsend
$t_1$	Drift time analyte one (Eq. (17.14))
$t_2$	Drift time analyte two (Eq. (17.14))
$t_d$	Drift time
$t_{\text{diff}}$	Diffusional broadening

$t_g$	Gating pulse width
$T_{\text{eff}}$	Effective temperature of an ion based on thermal energy and energy acquired by an electric field
$\mu$	Reduced mass ( $1/u = 1/m + 1/M$ ), where $m$ is the mass of the ion, $M$ is the mass of the neutral gas molecules
$\mu\text{s}$	Microseconds
$\mu\text{m}$	Micrometers
$v$	Velocity
$V$	Volts
$w_1$	Peak width analyte one (Eq. (17.14))
$w_2$	Peak width analyte two (Eq. (17.14))
$\Delta W$	Base width

## References

- 1 Fatah, A.A., Barrett, J.A., Arcilesi, R.D. Jr., et al. (2000). *Guide for the Selection of Chemical Agent and Toxic Industry Material Detection Equipment for Emergency First Responders*, B1. Rockville: National Law Enforcement and Corrections Technology Center.
- 2 Smart, J. (2009). *History of U.S. Army Research & Development, Chemical and Biological Detectors, Alarms, and Warning Systems*. Aberdeen Proving Ground: U.S. Army Research, Development and Engineering Command.
- 3 Preparedness Directorate Office of Grants and Training (2007). *Guide for the Selection of Chemical Detection Equipment for Emergency First Responders*, 3rd. United States Department of Homeland Security.
- 4 Headquarters Department of the Army (1982. Change 2). *Technical Manual 43-0001-26-1, Change 2, 30 December 1985. Army Equipment Data Sheets: Chemical Defense Equipment*, 1-3. Headquarters, Department of the Army.
- 5 Office of the Special Assistant for Chemical Biological Defense & Chemical Demilitarization Programs (2006). *Department of Defense Chemical and Biological Defense Program Annual Report to Congress*, A3-A4. United States Department of Defense.
- 6 Galford, C. (2019). Smiths Detection Named Developer of DOD's Next Chemical Agent Detector. *Homeland Preparedness News* (16 January 2019).
- 7 Eiceman, G.A. and Stone, J.A. (2004). Ion mobility spectrometers in national defense. *Analytical Chemistry* 76: 390A-397A.
- 8 Shvartsburg, A.A. (2008). *Differential Ion Mobility Spectrometry: Nonlinear Ion Transport and Fundamentals of FAIMS*. CRC Press, Taylor & Francis Group 9781420051063, 1420051067.
- 9 Utriainen, M., Kärpänlöga, E., and Paakkanen, H. (2003). Combining miniaturized ion mobility spectrometer and metal oxide gas sensor for the fast detection of toxic chemical vapors. *Sensors and Actuators B: Chemical* 93 (1-3): 17-24.
- 10 Mäkinen, M.A., Anttalainen, O.A., and Sillanpää, M.E.T. (2010). Ion mobility spectrometry and its applications in detection of chemical warfare agents. *Analytical Chemistry* 82 (23): 9594-9600.
- 11 Eiceman, G.A., Zarpas, Z., and Hill, H.H. Jr., (2014). *Ion Mobility Spectrometry*, 3ee. Boca Raton: CRC Press, Taylor & Francis Group. ISBN: 978-1-4398-5997-1.
- 12 McDaniel, E.W. and Mason, E.A. (1973). *Mobility and Diffusion of Ions in Gases*, 372. John Wiley & Sons, Inc.
- 13 Zrodnikov, Y. and Davis, C.E. (2012). The highs and lows of FAIMS: predictions and future trends for high field asymmetric waveform ion mobility spectrometry. *Journal of Nanomedicine & Nanotechnology* 3: e109.
- 14 Chemring Sensors & Electronic Systems (2018). Juno point trace vapor detection of CWA and TICs. *Chemring Sensors & Electronic Systems* [Online]. [www.chemring.co.uk/~media/Files/C/Chemring-V3/documents/sensors/datasheet-junomar-2018.pdf](http://www.chemring.co.uk/~media/Files/C/Chemring-V3/documents/sensors/datasheet-junomar-2018.pdf).

- 15 Eiceman, G.A. and Karpas, Z. (2005). *Ion Mobility Spectrometry*, 2e. Boca Raton: CRC Press, Taylor & Francis Group. ISBN: 978-0-8493-2247-1.
- 16 Smiths Detection (2017). Technical Information, LCD 3.3, Compact Wearable CWA Identifier and TIC Detector. *LCD 3.3 Person Worn CWA and TIC Detector* [Online]. <https://www.smithsdetection.com/products/lcd-3-3> (accessed 26 December 2018).
- 17 Smiths Detection (2012). Technical Information SABRE 5000 Handheld Trace Detector for Explosives, Chemical Agents and Toxic Industrial Chemicals or Narcotics. *Smith Detection* (28 November) [Online]. <https://www.smithsdetection.com/products/sabre-5000> (accessed 26 September 2019).
- 18 Smiths Detection (2011). GID-3 Chemical Warfare Agent Detector. *Smith Detection* (15 August) [Online]. <https://www.smithsdetection.com/products/gid-3> (accessed 30 April 2020).
- 19 Smiths Detection (2017). *Technical Information – IONSCAN 600 Explosives and Narcotics Trace Detector*. Hemel Hempstead: Smiths Detection.
- 20 Smiths Detection (2011). *IONSCAN 500DT Explosives and Narcotics Trace Detection*. *Smith Detection* (15 February) [Online]. <https://www.smithsdetection.com/products/ionscan-500dt-2> (accessed 8 August 2013).
- 21 MRIGlobal (2018). CBRNE Tech Index Hardened Mobile Trace. *CBRNE Tech Index* [Online]. <https://www.cbrnetechindex.com/p/3330/Morpho-Detection-Inc/Hardened-MobileTrace-HMT> (accessed 30 April 2020).
- 22 MRIGlobal. CBRNE Tech Index Itemiser DX Series. *CBRNE Tech Index* [Online]. <https://www.cbrnetechindex.com/Print/3332/rapiscan-systems/itemiser-dx-series> (accessed 30 April 2020).
- 23 MRIGlobal (2018). CBRNE Tech Index H150 and H150E Handheld Trace Detectors. *CBRNE Tech Index* [Online]. <https://www.cbrnetechindex.com/p/6177/L3Harris/H150-and-H150E-Handheld-Trace-Detectors> (accessed 30 April 2020).
- 24 MRIGlobal (2018). CBRNE Tech Index B220 Series. *CBRNE Tech Index* [Online]. <https://www.cbrnetechindex.com/P/6179/L3Harris/B220-Series> (accessed 30 April 2020).
- 25 MRIGlobal (2018). CBRNE Tech Index Bruker IMS Compare. *CBRNE Tech Index* [Online]. <https://www.cbrnetechindex.com/Compare> (accessed 30 April 2020).
- 26 Nuctech Company Limited (2011). TR1000DB-A Handheld Explosives and Narcotics Trace Detector. *Nuctech* [Online]. <http://www.nuctech.com/en/SitePages/ThDetailPage.aspx?nk=PAS&k=BHFCEF&pk=FGAFHB> (accessed 30 April 2020).
- 27 Nuctech Company Limited (2017). Nuctech TR2000DB-A Desktop Explosives and Narcotics Trace Detector. *PT. Ekacitra Bumikarya* [Online]. <http://ekacitra.com/brosur/NUCTECH%20TR2000DB-A.pdf> (accessed 3 May 2020).
- 28 RAE Systems. ChemRAE Chemical Warfare Agent Detection. *RAE Systems* [Online]. [https://www.raesystems.com/sites/default/files/content/resource/FeedsEnclosure-ChemRAE\\_US\\_DS.pdf](https://www.raesystems.com/sites/default/files/content/resource/FeedsEnclosure-ChemRAE_US_DS.pdf) (accessed 29 April 2020).
- 29 Environics Oy (2019). ChemPro100i Handheld Chemical Detector. *Environics Oy* [Online]. [https://www.environics.fi/wp-content/uploads/2020/01/US\\_ChemPro100i-Handheld-Chemical-Detector.pdf](https://www.environics.fi/wp-content/uploads/2020/01/US_ChemPro100i-Handheld-Chemical-Detector.pdf) (accessed 29 April 2020).
- 30 Environics Oy (2019). ChemProX New Generation Handheld Chemical Detector. *Environics Oy* [Online]. [https://www.environics.fi/wp-content/uploads/2020/01/ChemProX\\_new\\_generation\\_handheld\\_chemical\\_detector-2.pdf](https://www.environics.fi/wp-content/uploads/2020/01/ChemProX_new_generation_handheld_chemical_detector-2.pdf) (accessed 29 April 2020).
- 31 Owlstone Inc (2017). OwlSens-C - Advanced Chemical Detector. *Owlstone Inc* [Online]. [https://www.owlstoneinc.com/media/uploads/files/OwlSensC\\_Slick\\_2017\\_FINAL.pdf](https://www.owlstoneinc.com/media/uploads/files/OwlSensC_Slick_2017_FINAL.pdf) (accessed 29 April 2020).
- 32 Owlstone Inc (2017). OwlSens-T - Advanced Chemical Sensing. *Owlstone Inc* [Online]. [https://www.owlstoneinc.com/media/uploads/files/OwlSensT\\_TIC\\_Slick\\_2017\\_FINAL.pdf](https://www.owlstoneinc.com/media/uploads/files/OwlSensT_TIC_Slick_2017_FINAL.pdf) (accessed 29 April 2020).
- 33 MRIGlobal. CBRNE Tech Index: ChemRAE. *CBRNE Tech Index* [Online]. <https://www.cbrnetechindex.com/Print/3422/rae-systems-inc/chemrae> (accessed 3 May 2020).
- 34 Prox, T., Prieto, M., Bryant, J. and Yost, R.A. (2012). Partial Ovoidal FAIMS Electrode. 8,237,118 B2. USA.
- 35 Karpas, Z. (1989). Ion mobility of aliphatic and aromatic amines. *Analytical Chemistry* 61: 684–689.

- 36** Metternich, S., Zörntlein, S., Schönberger, T., and Huhn, C. (2019). Ion mobility spectrometry as a fast screening tool for synthetic cannabinoids to uncover drug trafficking in jail via herbal mixtures, paper, food, and cosmetics. *Drug Test Analyst* 11 (6): 833–846.
- 37** Karasek, F.W. (1974). Plasma chromatography. *Analytical Chemistry* 46: 710A–720A.
- 38** Shvartsburg, A.A., Li, F., Tang, K., and Smith, R.D. (2006). High-resolution field asymmetric waveform ion mobility spectrometry using new planar geometry analyzers. *Analytical Chemistry* 78 (11): 3706–3714.
- 39** Puton, J., Nousiainen, M., and Sillanpää, M. (2008). Ion mobility spectrometers with doped gases. *Talanta* 76 (5): 978–987.
- 40** Waraksa, E., Perycz, U., Namieśnik, J. et al. (2016). Dopants and gas modifiers in ion mobility spectrometry. *TrAC Trends in Analytical Chemistry* 82: 237–249.
- 41** Kozole, J. et al. (2012). Characterizing the gas phase ion chemistry of an ion trap mobility spectrometry based explosive trace detector using a tandem mass spectrometer. *Talanta* 99: 799–810.
- 42** Keller, T. et al. (2006). Application of ion mobility spectrometry in cases of forensic interest. *Forensic Science International* 161 (2–3): 130–140.
- 43** Kozole, J. et al. (2015). Gas phase ion chemistry of an ion mobility spectrometry based explosive trace detector elucidated by tandem mass spectrometry. *Talanta* 140: 10–19.
- 44** Puton, J. and Namieśnik, J. (2016). Ion mobility spectrometry: current status and application for chemical warfare agents detection. *TrAC Trends in Analytical Chemistry* 85 (Part B): 10–20.
- 45** Karasek, F.W. and Denney, D.W. (1974). Role of nitric oxide in positive reactant ions in plasma chromatography. *Analytical Chemistry* 46 (6): 633–637.
- 46** Spangler, G.E. and Lawless, P.A. (1978). Ionization of nitrotoluene compounds in negative ion plasma chromatography. *Analytical Chemistry* 50 (7): 884–892.
- 47** Spangler, G.E. and Collins, C.I. (1975). Reactant ions in negative ion plasma chromatography. *Analytical Chemistry* 47 (3): 393–402.
- 48** Kim, S.H., Karasek, F.W., and Rokushika, S. (1978). Plasma chromatography with ammonium reactant ions. *Analytical Chemistry* 50 (1): 152–155.
- 49** Chuang, C., Dandan, J., and Haiyang, L. (2019). UV photoionization ion mobility spectrometry: fundamentals and applications. *Analytica Chimica Acta* 1077: 1–13.
- 50** Simmonds, P.G., Fenimore, D.C., Pettitt, B.C. et al. (1967). Design of a nickel-63 electron absorption detector and analytical significance of high-temperature operation. *Analytical Chemistry* 39 (12): 1428–1433.
- 51** Siegel, M.W. (1983). Rate equations for prediction and optimization of chemical ionizer sensitivity. *International Journal of Mass Spectrometry and Ion Physics* 46: 325–328.
- 52** Paakanen, H. (2001). About the applications of IMCELLTM MGD-1 detectors. *International Journal of Ion Mobility Spectrometry* 4: 136–139.
- 53** Bruker Daltonics (2016). Chemical Threat Mitigation, Compact of CWA/TIC Detector: Bruker μRAIDplus. *Bruker* [Online]. [https://www.bruker.com/fileadmin/user\\_upload/8-PDF-Docs/CBRNE\\_Detection/Literature/1815859\\_uRAIDplus.pdf](https://www.bruker.com/fileadmin/user_upload/8-PDF-Docs/CBRNE_Detection/Literature/1815859_uRAIDplus.pdf) (accessed 3 May 2020).
- 54** Bruker Daltonics (2015). Explosives Trace Detection, Explosives Threat Mitigation: Bruker RoadRunner. *Bruker* [Online]. [https://www.opcsystems.com/persistent/catalogue\\_files/products/brukerroadrunnerbrochure.pdf](https://www.opcsystems.com/persistent/catalogue_files/products/brukerroadrunnerbrochure.pdf) (accessed 3 May 2020).
- 55** Bruker Daltonics (2017). Explosives Trace Detection, Explosives Threat Mitigation: Bruker DE-tector flex. *Bruker* [Online]. [https://www.bruker.com/fileadmin/user\\_upload/8-PDF-Docs/CBRNE\\_Detection/Literature/1854797\\_DE-detector\\_flex\\_brochure.pdf](https://www.bruker.com/fileadmin/user_upload/8-PDF-Docs/CBRNE_Detection/Literature/1854797_DE-detector_flex_brochure.pdf) (accessed 3 May 2020).
- 56** Verkouteren, M. and Lawrence, J. (2017). IMS Measurements and Preliminary Peak Assignments for Trace Explosives in non-RAD ETDs. *Trace Explosives Detection (TED) Workshop*. Santa Fe, NM.
- 57** United States Regulatory Commission (2014). License Number 20-023904-01E. *Nuclear Materials License, NRC Form 274*.

- 58** Smiths, N., McLain, D., and Steeb, J. (2017). *Ion Mobility Spectrometer Field Test, Results from the Former New Brunswick Facility*. Argonne National Laboratory.
- 59** Dzidic, I., Carroll, D.I., Stillwell, R.N., and Horning, E.C. (1976). Comparison of positive ions formed in nickel-63 and corona discharge ion sources using nitrogen, argon, isobutane, ammonia and nitric oxide as reagents in atmospheric pressure ionization mass spectrometry. *Analytical Chemistry* 48 (12): 1763–1768.
- 60** Tabrizhi, M., Khayamian, T., and Taj, N. (2000). Design and optimization of a corona discharge ionization source for ion mobility spectrometry. *Review of Scientific Instruments* 71 (6): 2321–2328.
- 61** Hill, C.A. and Thomas, C.L.P. (2003). A pulsed corona discharge switchable high resolution ion mobility spectrometer-mass spectrometer. *Analyst* 128: 55–60.
- 62** Turner, R.B., Taylor, S.J., Clark, A. and Arnold, P.D. (2001). Corona Discharge Ion Source for Analytical Instruments. 6,225,623, USA.
- 63** Hu, J., Li, W., Zheng, C., and Hou, X. (2011). Dielectric barrier discharge in analytical spectrometry. *Applied Spectroscopy Reviews* 46 (5): 368–387.
- 64** Brandenburg, R. (2018). Dielectric barrier discharges: progress on plasma sources and on the understanding of regimes and single filaments. *Plasma Sources Science and Technology* 26 (5): 1–29.
- 65** Kubelik, I., Feldberg, S., Atamanchuk, B., et al. (2017). Dielectric Barrier Discharge Ionization Source for Spectrometry. 9,778,224 B2 USA.
- 66** TSI Incorporated (2013). Photoionization Detection (PID) Technology, Application Note TSI-147 Rev B. *TSI Incorporated* [Online]. [https://www.tsi.com/getmedia/e6812861-60a7-4dee-82a7-09b1ea9f734c/TSI-147\\_Photo\\_Ionization\\_Detection\\_Technology?ext=.pdf](https://www.tsi.com/getmedia/e6812861-60a7-4dee-82a7-09b1ea9f734c/TSI-147_Photo_Ionization_Detection_Technology?ext=.pdf) (accessed 1 May 2020).
- 67** TSA Trace (2020). Product Accessory Kit, with Lamps and Dopants, Itemiser 4DX. *TSA Trace* [Online]. [https://www.tsatrace.com/Product-Accessory-Kit-with-Lamps-and-Dopants-Itemiser-4DX\\_p\\_87.html](https://www.tsatrace.com/Product-Accessory-Kit-with-Lamps-and-Dopants-Itemiser-4DX_p_87.html) (accessed 3 May 2020).
- 68** Nazarov, E.G., Miller, R.A., Eiceman, G.A., and Stone, J.A. (2006). Miniature differential mobility spectrometry using atmospheric pressure photoionization. *Analytical Chemistry* 78 (13): 4553–4563.
- 69** Kirk, A.T. and Zimmermann, S. (2014). Bradbury-Nielsen vs. field switching shutters for high resolution drift tube ion mobility spectrometers. *International Journal of Ion Mobility Spectrometry* 17: 131–137.
- 70** Soppart, O. and Baumbach, J.I. (2000). Comparison of electric fields within drift tubes for ion mobility spectrometry. *Measurement Science and Technology* 11 (10): 1473–1479.
- 71** Davis, E.J., Grows, K.F., Siems, W.F., and Hill, H.H. Jr., (2012). Improved ion mobility resolving power with increased buffer gas pressure. *Analytical Chemistry* 84 (11): 4858–4865.
- 72** Kaur-Atwal, G., O'Connor, G., Aksenen, A.A. et al. (2009). Chemical standards for ion mobility spectrometry: a review. *International Journal of Ion Mobility Spectrometry* 12: 1–14.
- 73** Committee on Assessment of Security Technologies for Transportation (2004). *Opportunities to Improve Airport Passenger Screening with Mass Spectrometry*. Washington, DC: National Research Council of The National Academies.
- 74** Siems, W.F., Wu, C., Tarver, E.E. et al. (1994). Measuring the resolving power of ion mobility spectrometers. *Analytical Chemistry* 66 (23): 4195–4201.
- 75** Cottingham, K. (2003). Product review: ion mobility spectrometry rediscovered. *Analytical Chemistry* 75 (19): 435A–439A.
- 76** Jenkins, A. and McGann, W.J. (2004). Enhancements to Ion Mobility Spectrometers. 6,765,198 B2 USA.
- 77** McGann, W.J., Geodecke, K., Neves, J., and Jenkins, A. (2001). Simultaneous, dual mode IMS system for con-traband detection and identification. *International Journal of Ion Mobility Spectrometry*: 144–147.
- 78** Zaleski, H., et al. (2017). Fast-Switching Dual-Polarity Ion Mobility Spectrometry. 9,709,530 B2 USA.
- 79** Kirk, A.T., Allers, M. et al. (2013). A compact high resolution ion mobility spectrometer for fast trace gas analysis. *Analyst* 138 (18): 5159–5504.

- 80** Shokri, H. et al. (2020). Field induced fragmentation (Fif) spectra of oxygen containing volatile organic compounds with reactive stage tandem ion mobility spectrometry and functional group classification by neural network analysis. *Analytical Chemistry* 92 (8): 5862–5870.
- 81** Atkinson, J.R., Clark, A., Taylor, S.J., and Munro, W.A. (2011). Detection Apparatus. 7,932,489 B2 USA.
- 82** Smiths Detection Inc. (2018). *Smiths Detection Inc. to Develop Enhanced Chemical Explosives Detection Capability for United States Department of Defense*. Edgewood, MD: Smiths Detection.

## 18

### X-Ray Sources for Handheld X-Ray Fluorescence Instruments

Sterling Cornaby

*Moxtek Inc., Orem, UT, USA*

#### 18.1 Background

X-ray fluorescence (XRF) is used to identify elements within a sample, as well as quantify the amounts of each element from bulk percentages to parts per million. The major advantage of portable or handheld X-ray fluorescence (HHXRF) is that the instrument can be taken to the sample, rather than the sample to the instrument [1]. Portability has proven to be a very big advantage, demonstrated by the rapid growth of the HHXRF market in 2004–2020. HHXRF is taken directly to mines, on-site in mining investigations, used directly in scrap metal sorting yards, taken into homes to test lead in paint, to name just as a few examples. The development of miniature, lightweight X-ray sources was the critical component needed to shift XRF spectroscopy from the lab to the field. The X-ray source, within HHXRF instruments is small, on the order of 15 cm in length, lightweight on the order of 300 g, and low powered, consuming 5–10 W [2]. Additionally, all HHXRF instruments have single-element energy-dispersive (ED) detectors such as a silicon drift detector (SDD) or a PIN (p-type-intrinsic-n-type) diode. All of the qualities of these small components are needed to make the HHXRF instrument portable, battery powered, and about the size of a handheld cordless drill. The tube has to be very small, consume a small amount of power, and robust enough to withstand shocks from dropping and temperature extremes found in the field (Figure 18.1). These constraints made the miniature X-ray source what it is today, with an “X-ray source” defined to be composed of a miniature X-ray tube combined with a miniature high-voltage power supply (HVPS). The technical advancements in small X-ray sources are a major advancement that makes HHXRF possible.

Previously to about the year 2004, radioisotopes were used in the HHXRF instruments due to their lightweight, small size, and the monochromatic radiation with energies capable of exciting the K-lines in most materials of interest [3, 4]. The handling of radioactive materials severely limited HHXRF based on radioisotopes due to strict regulations on their handling and transportation.

In 1999, Moxtek developed its first few miniature X-ray tube-based X-ray sources, funded by a NASA SBIR for the CHEMIN XRD/XRF instrument for Mars missions [5]. This work developed into X-ray sources for HHXRF in the next few years. Having a miniature X-ray tube-based source was a huge advantage over radioisotopes, because it freed up legal restrictions, since in an X-ray source based on an X-ray tube, the radiation can be turned on and off. Other advantages included having the flux output level adjustable to maximize the signal from the detector, and the high voltage (HV) being adjustable, which is useful in changing the range of detected elements.

The rapid growth of the HHXRF market in 2004–2020 required that the X-ray sources be mass produced. In the second decade of the twenty-first century, the global demand for the miniature X-ray sources reached over 10 000 units per year level, far surpassing the market for the benchtop and laboratory analytical XRF instruments. Market-driven applications put HHXRF instruments in scrap yards, mines, deserts, high mountains, and arctic conditions in the hands of non-XRF experts.

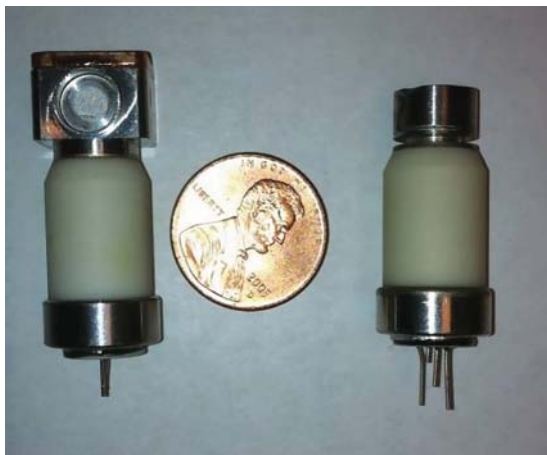


**Figure 18.1** Transmission window (right) and side window (left) tubes. The tube body is ceramic; the cathode and anode assemblies are metal alloys. *Source:* Courtesy of Moxtek, Inc.

Year	Weight	Voltage & Current	Tube Power
2001	(763 gm)	35 kV 100 $\mu$ A	3.5 W
2004	(320 gm)	40 kV 100 $\mu$ A	4 W
2006	(533 gm)	50 kV 200 $\mu$ A	10 W
2009	(335 gm)	50 kV 200 $\mu$ A	4 W
2012	(250 gm)	50 kV 200 $\mu$ A	4 W
2013	(750 gm)	70 kV 1000 $\mu$ A	12 W



**Figure 18.2** X-ray source weight and size reduction in 2001–2013 and a transition from cabled to monolithic design. The pen at the top of the image is shown as a size reference. *Source:* Courtesy of Moxtek, Inc.

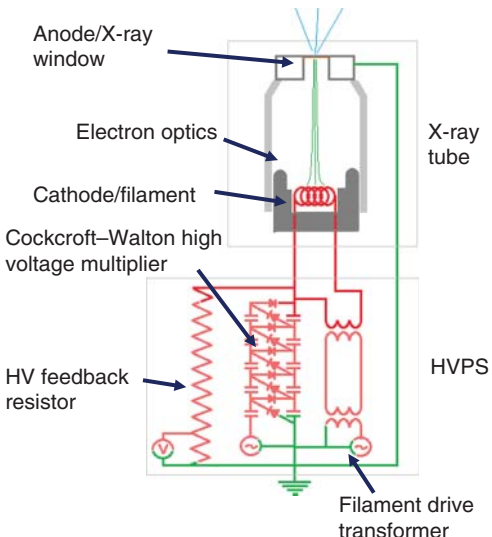
From the start, there has been a demand for reducing the size and weight of both the tubes and HVPSs. Figure 18.2 shows the reduction in size and weight over the period from 2001 until 2015. It also shows the increasing high voltage HV and power of the miniature X-ray sources. From about 2015 to today, miniature X-ray sources have stayed the same size. The emphasis on technological advances has currently shifted to performance enhancements.

Over the last five years, one major optimization desired by manufacturers of HHXRF instruments is possessing X-ray sources which are spectroscopically identical. A spectroscopically identical X-ray source allows one to switch out an X-ray source in an instrument with no other changes. For example, the MOXI™ source gives the same XRF spectra source-to-source with minimal or no recalibration of the instrument. This allows for swapping of X-ray sources in an instrument, without requiring instrument recalibration. This benefit is very much desired by HHXRF manufacturers because it reduces manufacturing complexity (the time required for calibration), and reduces service time for these instruments. This will be discussed in detail in Section 18.4.5.

## 18.2 The Miniature X-Ray Source

An X-ray source is composed of a miniature X-ray tube and a miniature HVPS; sometimes the HVPS is also called a generator. Figure 18.3 gives a schematic of the main parts of both an X-ray tube and the HVPS. The next two

**Figure 18.3** A schematic of an X-ray source with all its major parts labeled.



sections will describe the X-ray tube and the HVPS. In the final section, we will go over some specific examples of miniature X-ray sources.

### 18.2.1 The X-Ray Tube

The miniature X-ray tube used in HHXRF is more or less the standard hot-cathode tube design used since William Coolidge developed the original X-ray tube [6]. The main difference is the extremely small size achieved by the use of advanced materials and processing methods (Figure 18.1). The tube has a tungsten filament cathode which provides a source of electrons, an anode target for the electrons to decelerate in, which generates X-rays, and passive electron optics to guide the electron beam to the anode.

Some important aspects of the miniature tube include:

- A very small filament, which takes a low amount of input power to heat the filament to about 1800 °C. A low-power filament is needed to extend the time of battery operation in a portable instrument.
- A ceramic/metal vacuum envelope, providing robustness over a glass vacuum envelope. This helps to prevent the tube from breaking in the event of both mechanical and thermal shocks experienced by the instrument when used in the field.
- A “simple diode” or unipolar X-ray tube design, allowing for a single variable HV to run the X-ray tube. There are no other components, such as a “gate” for turning the tube on and off, or steering the electron beam, which are fairly common on many X-ray tubes [6]. The passive electron optics design is challenging, and is simply achieved by shaping of metal components of the tube. The passive electron optics need to work over a large range of 4–70 kV, and keep the electron beam at nearly the same location and size on the anode, with no active feedback. All of this effort simplifies the X-ray tube and the HVPS, so that the entire X-ray source can be smaller.
- The most popular “transmission-window” design combines the anode of the tube and the X-ray window of the tube into the same part. The beryllium window (usually 100–250 μm thick) is coated with a thin, ~1 μm, layer of the desired anode material. Details on the anode layer thickness are very application dependent. This allows for closer source-to-sample distance, which is a critical parameter for miniature X-ray sources in HHXRF.

All of these efforts result in a very small and robust miniature X-ray tube, well-suited for HHXRF.

Functionally, an X-ray tube produces X-rays with an electron beam impinging on the anode generating two general types of interactions: bremsstrahlung radiation and electron beam-induced characteristic X-ray radiation [7–11]. Bremsstrahlung radiation, also known as “braking” radiation, is caused by the impinging electrons interacting with the nucleus of an atom. As the electron approaches the atom, it is deflected and possibly stopped by the strong electric field surrounding the atom. This deceleration of the electron produces the bremsstrahlung radiation. This broadband radiation produces fewer photons at higher X-ray energies, with the intensity of bremsstrahlung X-rays approaching zero (in keV) at the tube’s HV setting (in kV).

Characteristic radiation is based on impinging electrons interacting with the electrons surrounding an atom. Kossel [8–11], Moseley [12, 13], and Barkla [14] presented the theoretical and experimental foundation for the quantum theory of producing characteristic X-rays. For induced characteristic radiation, an electron of high energy may ionize an atom by displacing an electron from one of the inner atomic shells. An electron from an outer shell may fall into the shell vacancy, emitting either another electron from the atom, or a photon, the photon being the desired reaction for the X-ray tube. The energy of the X-ray is dependent on the energy levels of the shells participating in the process, and therefore is “characteristic” to the material of the target.

The spectrum of X-rays from two different materials, which shows both bremsstrahlung radiation and electron-induced characteristic radiation, is shown in Figure 18.4, with no X-ray filters and a vacuum flight path. To tailor a spectrum for a specific XRF application, the HV setting on the tube is changed, or a variety of filters are put in front of the anode, to filter out lower energy X-rays from the source, and this is described in more detail below.

### 18.2.2 The High-Voltage Power Supply

The HVPS used is based upon the Cockcroft–Walton HV generator [15]. It generates the HV, and also provides the emission current needed to drive the electron current through the X-ray tube. It generates this DC HV based upon an oscillator, coupled with a ladder of capacitors and diodes (HV multiplier), using a half-wave rectifier design, as shown in Figure 18.3. To achieve the needed HV of 4 up to 70 kV, the input oscillating transformer has an HV oscillation amplitude of a few hundred volts to a few thousand volts, and a frequency of several kHz. The capacitor–diode ladder consists of between 8 and 15 stages.

The next critical component is the HV feedback resistor, which allows for monitoring the HV, and for controlling the HV on the Cockcroft–Walton HV generator. XRF requires a very stable high voltage, which in turn requires

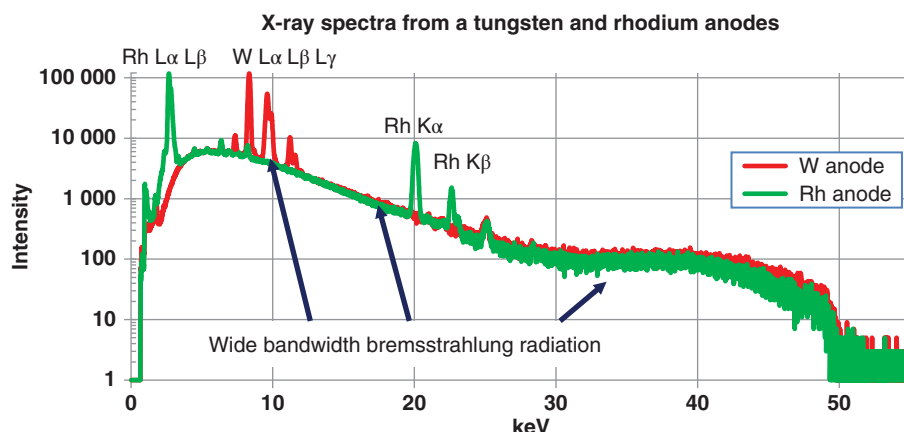
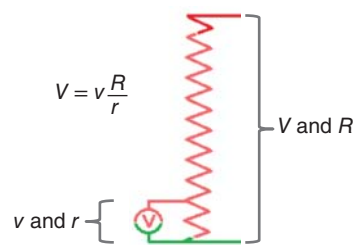


**Figure 18.4** An X-ray spectrum from both a tungsten and rhodium anode X-ray tube which shows both the bremsstrahlung and the characteristic X-ray radiation.

**Figure 18.5** A schematic of the HV feedback resistor. “ $V$ ” is the HV of the HVPS calculated by knowing “ $R$ ” the resistance of the entire resistor, “ $r$ ” is the resistance of the resistor subsection, and “ $v$ ” is the measured voltage of this resistor subsection.



having a very stable and a predictable HV feedback resistor. Figure 18.5 outlines the simple circuit that shows how the HV is measured, by a simple ratio of the resistance of the entire resistor to just a smaller subsection of the resistor.

The final component of the HVPS is the filament drive transformer. Miniature X-ray sources are run with the anode at ground, and the cathode is at HV. The filament is driven with an alternating current (AC) current provided by a series of transformers. Since the filament is at HV, the AC drive is achieved by a series of two or more transformers to isolate the HV.

One other critical design issue is achieving HV in small sizes without arcing. Both the tubes and the HVPSs are potted in a highly insulating material to prevent this. The layout of the HV components is also optimized to reduce the field gradients and provide enough HV standoff in the very small packages need for HHXRF.

### 18.2.3 Physical Examples of Miniature X-Ray Sources

Table 18.1 and Figure 18.6 show examples of some commercial X-ray sources currently being produced [10, 11]. The MOXI source, which is the latest design, is meant specifically for handheld applications, being very small, very light, and of lower power. The MAGPRO® X-ray source is meant for applications which need some more power, and are often put in small benchtop XRF instruments.

There are several characteristics of the X-ray source that are important. As mentioned earlier, for HHXRF the X-ray source has to be light and small, and consume low amounts of power. Other key properties described below include flux stability, target material selection, and source-to source spectra differences.

### 18.2.4 X-Ray Flux and Spectra

The flux coming from a tube-based X-ray source is often described by stating the highest operating voltage (spectral information), the emission current (flux information), and the anode material (spectral information),

**Table 18.1** This table shows the basic parameters of both the MOXI® and the MAGPRO X-ray sources.

Parameters	MOXI™	MAGPRO
HVPS output kV range (kV)	5–50	5–70
HVPS emission current range ( $\mu\text{A}$ )	5–200	10–1000
Anode material	W, Rh and others	W, Rh and others
HVPS power limit on X-ray tube (W)	4	12
HVPS power input voltage (VDC)	9	24
Total weight (g)	310	700



**Figure 18.6** Image of the MAGPRO (top) and MOXI (bottom) X-ray source.  
Source: Courtesy of Moxtek, Inc.

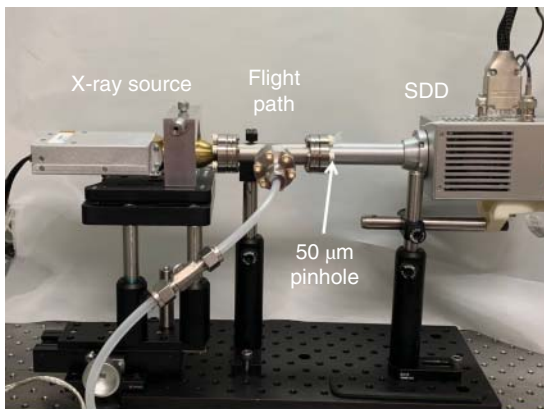


**Figure 18.7** This is an image of a setup to measure the flux. The vacuum flight path is specifically needed to eliminate air absorption for better detection of X-rays under about 5 keV. The windows on the flight path are 8  $\mu\text{m}$  thick, the flight path is 9.5 cm long. The pinhole was placed directly on the SDD window and has a 50  $\mu\text{m}$  diameter in a 0.5 mm thick tungsten foil. Source: Courtesy of Moxtek, Inc.

e.g. a 50 kV, 0.2 mA, tungsten anode X-ray source. This is sensible for many X-ray applications, but it is not as useful for comparing miniature X-ray sources to larger X-ray tubes [16].

One reasonably direct way to determine the X-ray radiation emitted from an X-ray source is with an ED detector, such as a PIN diode or a SDD. The radiation directly from an X-ray source is much too intense to measure the spectrum, but that can be overcome by putting a small pinhole of 10–200  $\mu\text{m}$  in front of the detector to decrease the flux hitting the detector. The flux measurement setup shown in Figure 18.7 gives results similar to the spectra shown in Figure 18.4.

It is exceedingly difficult to focus or collimate X-rays, especially in a handheld format. Therefore the designs of HHXRF instruments all feature the X-ray tube, the sample, and the detector in closest possible proximity to optimize the signal-to-noise ratio (SNR) of the spectra. The miniature sources shown in Figure 18.6 can get to within 2–3 cm from the sample. In this tight geometry, with just a few watts of tube power, the intensity of the emitted fluorescent X-ray radiation in most cases will reach the maximum count rate of a majority of existing SDDs [16]. This tight anode-to-sample distance is due to two major design features, the small X-ray tube size and the X-ray transmission anode on the X-ray tube.

### 18.2.5 Radiation Dose from Miniature X-Ray Sources

In an enclosed XRF system, the sample chamber is designed to be radiation-tight for radiation safety. Additionally, these instruments have interlocks which shut off the X-ray source if the sample chamber is opened to keep X-ray exposures from happening. For a HHXRF, there is more of a chance for X-ray exposure, since there is no radiation

**Table 18.2** Table of radiation dose from two tungsten anode miniature X-ray sources, at two different distances of 2 cm, and at 30 cm away.

Tube type	Radiation dose in mRem/s							
	No X-ray filter				1 mm Al filter			
	At 30 cm		At 2 cm		At 30 cm		At 2 cm	
	40 kV	60 kV	40 kV	60 kV	40 kV	60 kV	40 kV	60 kV
Magnum W anode at 4 W	18 at 100 µA	— —	3000 at 100 µA	— —	4 at 100 µA	— —	600 at 100 µA	— —
MAGPRO W anode at 12 W	55 at 300 µA	78 at 200 µA	9100 at 300 µA	12 500 at 200 µA	15 at 300 µA	20 at 200 µA	1800 at 300 µA	3100 at 200 µA

This is the dose with no additional filtration, just the native beryllium window.

enclosure, and they are open beam devices. Commercial instruments include a number of safety protocols, but they are not discussed here.

Focusing on just the X-ray source, it is considered radiation-safe if the radiation is strictly coming out of the window opening; radiation should not come out in other directions through other structures of the X-ray source. Repeating this in another way, if the window opening of the X-ray source is blocked from emitting radiation, the X-ray source will emit less than 0.2 mRem/h. (2 µGray/h) in any direction when turned on at the maximum kV and power. For reference, natural background radiation is about 0.01 mRem/h.

Another frequent question is “What is the radiation dose if the X-ray source window opening is not covered?” Table 18.2 outlines the radiation doses for both the Magnum® tube, used in the MOXI source, and the MAGPRO source. These values were measured with a Black Piranha radiation meter, which is a common radiation dose meter used in the medical field. At the distance of 30 cm, the dose rate is covering a circular area with a diameter of about 25 cm. Often, a filter is used in conjunction with the X-ray source. The table includes the radiation dose both with a 1 mm aluminum filter and without the filter.

The full body limit of radiation per year is less than 5000 mRem (50 mGray) for a radiation worker. An unfiltered miniature X-ray source can reach this limit in a localized area in just an hour or two at a 30 cm distance. At the distance of 2 cm, covering a very limited area of a few cm<sup>2</sup>, you could cause a very localized radiation burn on your skin if you held the tube right on your skin and left it on for a few seconds at full power. These small low-power X-ray sources need to be respected when it comes to radiation safety, especially at very close distances.

## 18.3 The Selection of a Target Anode Material for XRF

The basic premise of XRF is that high-energy X-rays are aimed at a sample and then the atoms in the sample may absorb an X-ray. This ionizes the atom by displacing an electron from one of the shells close to the atom. The next step is for an electron from an outer shell to fall into the shell vacancy, emitting the excess energy in the form of characteristic X-ray radiation. The energy of the X-ray is dependent on the energy levels of the shells participating in the process and therefore is “characteristic” to the material of the sample. More details in using XRF for material identification may be found in Van Grieken [3], Jenkins [17, 18].

A critical detail for the X-ray source used for XRF is that X-ray source needs to produce X-rays at energies higher than absorption edge of the element in order to ionize the atom. Every element has different absorption edges, just

as they have different characteristic X-ray lines. The X-ray source needs to be tuned in various ways for effective detection of different elements.

There are three basic methods for tuning the spectrum shape from the X-ray source:

- Setting the HV on the X-ray tube.
- Putting an X-ray filter between the X-ray source and the sample.
- Selection of the anode material on the X-ray tube.

The next few sections will go through these items in detail, especially on the selection of the anode material since this is a central aspect of the miniature X-ray source.

### 18.3.1 Setting the High Voltage on the X-Ray Tube

From an XRF instrument perspective, setting the HV on the X-ray source is an easy change to make by changing the HV setting on the source's HVPS. Therefore, for any particular application, the HV can be adjusted to optimize for an XRF application quite easily. Increasing the HV does reach a maximum; the X-ray sources in HHXRF are limited to 40 or 50 kV. This limit is partially due to the efficiency of the PIN detectors and SDDs, which get quite low above 20 keV. At higher energies, the X-rays are progressively not absorbed by the detector and are therefore not detected. At 20 keV, 0.50 mm thick silicon absorbs roughly 30% of X-rays at that energy, and the absorption gets lower at higher X-ray energies. Also, the HV limit on the X-ray source is influenced by radiation safety; it is increasingly difficult to shield X-rays at higher energies. Therefore X-ray sources for HHXRF are not capable of exciting the K emission lines of elements with larger atomic numbers than lanthanum ( $Z = 57$ ), and so in HHXRF the L emission lines (lower energy) are used to detect elements heavier than lanthanum.

In practice, HVs like 50 kV are used in the more expensive and versatile HHXRF instruments. The HVs in these higher end HHXRF instruments are used for applications such as detecting cadmium for hazardous element detection, or in mining applications, whereas 35 or 40 kV is a typical maximum voltage setting for alloy identification in scrap metal sorting. In these less expensive, single-application HHXRF instruments, the X-ray sources are typically fixed to a single voltage.

Lower voltage settings are a benefit for light element XRF detection. Often, for detecting light elements emitting fluorescent X-rays lower than 3 keV, the HV is set to a voltage from about 8 to 15 kV. These HV settings maximize the L-line X-ray intensity of the tube's Ag or Rh anode, both of which are close to 3 keV, which excites elements with an absorption edge lower than 3 keV. Additionally, keeping the voltage lower on the tube effectively turns off the detection of elements with characteristic X-ray lines above 10–15 keV, as well as reducing background at lower keV.

### 18.3.2 X-Ray Filters

The use of X-ray filters in front of the X-ray source is very application specific. The details for using a particular filter can be wide ranging, depending on exactly what element or elements are of interest. Most often the filter's main function is to eliminate lower energy X-rays from the spectrum, thereby improving the SNR. For example, in metal detection in scrap metal sorting, a filter such as a 0.5 mm filter of aluminum is often used. This filter eliminates most of the X-rays below about 10 keV from the X-ray source. This reduces the background between 4 and 15 kV, which is the range where fluorescence from common metals are like iron, nickel, copper, and zinc are located.

Another more complicated filter example is one used for the Restriction of Hazardous Substances (RoHS) application. RoHS specifically is looking for the elements Cr, Br, Hg, Pb, and Cd, whose fluorescence spans a wide range of X-ray energies from 5.4 keV for Cr to 23 keV for Cd. For this application, a tungsten anode on the X-ray source is desirable. A copper filter 270  $\mu\text{m}$  thick blocks all the energy X-rays just above 9.0 keV, reducing the background

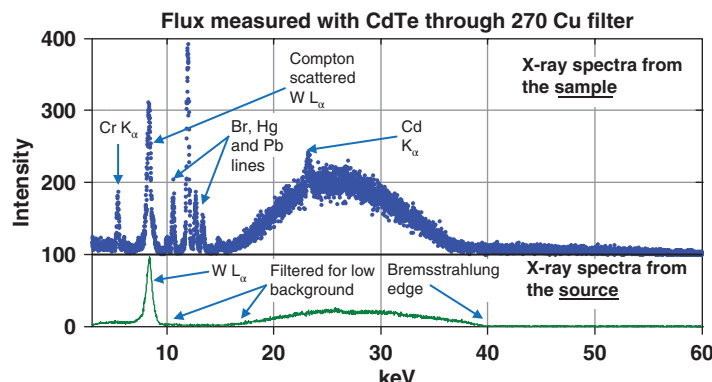


**Figure 18.8** This figure shows two resulting spectra using a tungsten anode source at 40 kV with a 270  $\mu\text{m}$  thick copper filter with a Cd–Te detector. The lower graph shows the spectrum from the X-ray source through 270  $\mu\text{m}$  filter combination. The upper graph shows the spectrum from a polyethylene sample with 750 ppm Cr, 400 ppm Br, 75 ppm Hg, 250 ppm Pb, and 100 ppm Cd. These figures show that the copper filter both lets the W  $L_\alpha$ -line from the source through to excite Cr, and suppresses the background under the Br, Hg, and Pd lines.

from 9 to about 15 keV, which is the region where the X-ray emission lines from Br, Hg, and Pb occur. Additionally, the tungsten  $L_\alpha$ -line from the X-ray tube is at 8.3 keV, which is just below the absorption edge at 9.0 keV of the copper foil; therefore, the sample is exposed to X-rays at 8.3 keV. The tungsten  $L_\alpha$ -line at 8.3 keV is effective at exciting the chromium  $K_\alpha$ -line at 5.4 keV, thereby enhancing the signal from the chromium in the sample. Figure 18.8 shows an example of using a copper filter for a (RoHS) XRF application.

From an XRF instrument perspective, changing the filter is independent from the X-ray source; therefore changing a filter is not too hard to do. Very often several filters are mounted on a wheel, after the X-ray tube, in the front of the instrument. Depending on the exact XRF application, the wheel is turned to the filter appropriate for that particular application. Often a filter selection is done simultaneously with a change in the X-ray source's HV for a particular XRF application.

### 18.3.3 X-Ray Anode Selection

Unlike the HV or the filter, the anode of the X-ray tube is fixed; you are unable to change an anode material due to this material being on the inside the vacuum of the X-ray tube. Getting the anode material correct is critical for both a single-XRF application instrument, as well as instruments for multiple XRF applications, because, in many ways, it defines the application capabilities of the instrument. Therefore, the choice of anode material strongly depends on the particular XRF application.

For HHXRF, there are two major classes of X-ray tube anode types: “light element” anodes, specifically for exciting light elements with absorption edges below about 3 keV, and “general use” anodes for exciting elements higher than about 3 keV. Each class of anode will be discussed in the two sections below.

#### 18.3.3.1 Anodes for Light Element XRF Detection

In HHXRF, light elements are defined as being from Mg ( $Z = 12$ ) to Cl ( $Z = 17$ ) in the periodic table. Light element XRF detection is a very technically demanding application, especially for HHXRF, and it determines most of the design limitations on X-ray sources for HHXRF, as well as on the X-ray detectors.

X-ray tube anodes for light element detection in HHXRF are most commonly made of either rhodium or silver. These elements are ideal for light element excitation in a sample because they both have L-lines which are near 3 keV: silver has L-lines between 2.9 and 3.4 keV and rhodium has L-lines between 2.7 and 3.0 keV. The L-line

strongly excites fluorescent lines just under 3 keV, such as from S, P, Si, Al, and Mg, which are the specific elements of interest for light element XRF. HHXRF X-ray sources designed for light element analysis use a very thin ( $\sim 125 \mu\text{m}$ , or thinner) beryllium window on the X-ray tube. This thinner window is for the purpose of minimizing X-ray absorption of the Rh or Ag L-lines in the X-ray window itself. In these light element applications, there is no X-ray filter. Air is often an unwanted filter, absorbing roughly 25% of the X-rays between 2.5 and 3 kV in about 1 cm of air (for reference, a 3 kV X-ray has a wavelength of about 0.4 nm). For lower energy X-rays subsequently emitted from the sample, the air absorption gets much stronger, and the air path is especially difficult to eliminate in HHXRF instruments. Some benchtop instruments used for light element XRF incorporate a helium purge, or a vacuum chamber, to eliminate absorption due to the air. These fundamental limitations of the HHXRF technique for light elements have led to the development of handheld laser-induced breakdown spectroscopy instrumentation – see the chapter in this volume by Day for details.

Often, X-ray sources used for light element detection are used for other XRF applications as well, which require running the X-ray source at a HV of 40–50 kV. This presents a design constraint in the X-ray source: a source optimized for 10–20 kV operation is not optimized for 40–50 kV. For HHXRF almost all the tubes are a transmission anode design, which consists of the target material deposited directly on the X-ray window with a thickness of about 1  $\mu\text{m}$ . The anode thickness is optimally set to be thick enough to stop the X-ray tube's electron beam, and then thin enough to not cause any additional filtering of the generated X-rays. In the design of the anode thickness, this optimum is specific for a single HV (Figure 18.9).

For light element detection, getting a large L-line from the X-ray source onto the sample to excite the light elements is paramount. Yet the same X-ray source is needed for XRF applications with higher voltages as well. This leads to a compromise in the design between the two applications.

The rhodium or silver anode layer has a few target thickness options for operation between 20 and 40 kV. This range of target thicknesses is split between the two application needs, for light element XRF and other XRF applications. An X-ray tube manufacturer will have a selection of proprietary thicknesses optimized over this range for HHXRF, with the exact target thickness picked by the instrument manufacturer (Tables 18.3 and 18.4). Figure 18.10 shows the X-ray flux advantage and disadvantage of three different rhodium anode thicknesses at different voltage settings. Since the light element XRF detection is so much more challenging, any HHXRF instrument made specifically for light element detection will almost always use the thinner rhodium target, RH3. The RH3 target thickness increases the L-line X-ray signal below 20 kV, which is exactly the reason that this thickness

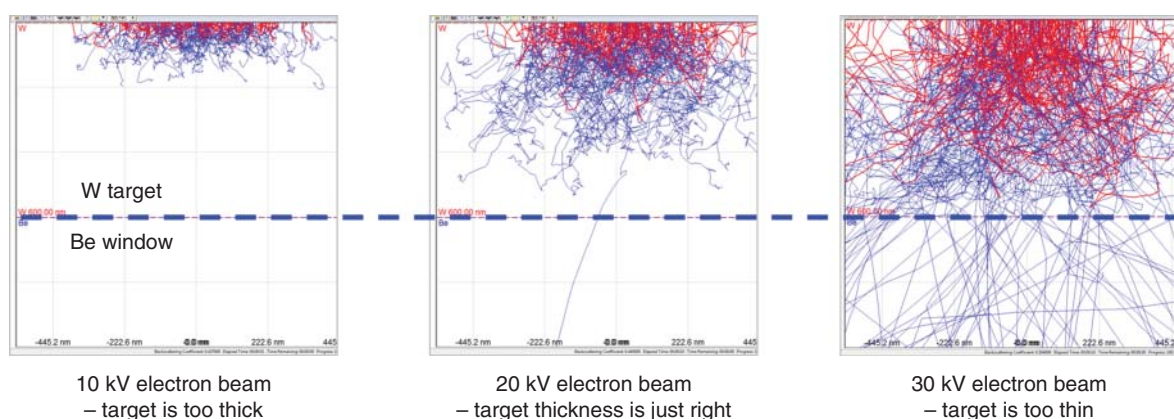


**Figure 18.9** This figure shows the electron interaction of a 1  $\mu\text{m}$  W foil with a 10, 20, and 30 kV electron beam. This thickness will have an optimal performance at 20 kV. Below 20 kV, the extra thickness of the foil acts as an X-ray filter, and above 20 kV, electrons get through the tungsten target into the beryllium window and do not generate the wanted X-rays. The electron interaction simulations are done in CASINO [19]. Source: Based on CASINO, Introduction to CASINO <https://www.gel.usherbrooke.ca/casino>.

**Table 18.3** This table gives the calculated and measured X-ray flux output of three Rh anode thicknesses produced and Moxtek, optimized for 20 kV (RH3), 25 kV (RH2), and 30 kV (RH7).

Target ID	Target material	Optimized kV		At 10 kV	At 20 kV	At 30 kV	At 40 kV	At 50 kV
RH3	Rh	20.0	e-Anode Sim.	0.95	1.00	0.87	0.62	0.38
			X-ray L-lines	0.58	1.00	0.81	0.53	0.36
RH2	Rh	25.0	e-Anode Sim.	0.90	0.99	0.99	0.90	0.70
			X-ray L-lines	0.45	0.84	1.00	0.82	0.60
RH7	Rh	30.0	e-Anode Sim.	0.87	0.99	1.00	0.96	0.82
			X-ray L-lines	0.43	0.77	1.00	0.85	0.63

For each anode thickness, the line labeled “e– anode Sim” shows the calculated emission of the X-ray L-lines from the anode. For each anode thickness, the line labeled “X-ray L-lines” shows the experimentally measured X-ray intensity in the L-lines, normalized to the X-ray tube power. The electron modeling trends line up well with the experimentally measured X-ray intensity. The differences between the two are due to the modeling not taking everything into effect such as self-anode absorption and X-ray window absorption.

**Table 18.4** This table gives the calculated and measured X-ray flux output of two Ag anode thicknesses produced and Moxtek, optimized for 20 kV (AG2) and 40 kV (AG1).

Target ID	Target material	Optimized kV		At 10 kV	At 20 kV	At 30 kV	At 40 kV	At 50 kV
AG2	Ag	20.0	e-Anode Sim.	0.94	1.00	0.91	0.70	0.45
			X-ray L-lines	0.56	1.00	0.82	0.53	0.36
AG1	Ag	40.0	e-Anode Sim.	0.83	0.98	0.97	1.00	0.93
			X-ray L-lines	0.36	0.70	0.95	1.00	0.83

For each anode thickness, the line labeled “e– anode Sim” shows the calculated emission of the X-ray L-lines from the anode. For each anode thickness, the line labeled “X-ray L-lines” shows the experimentally measured X-ray intensity in the L-lines, normalized to the X-ray tube power. The electron modeling trends line up well with the experimentally measured X-ray intensity. The differences between the two are due to the modeling not taking everything into effect such as self-anode absorption and X-ray window absorption.

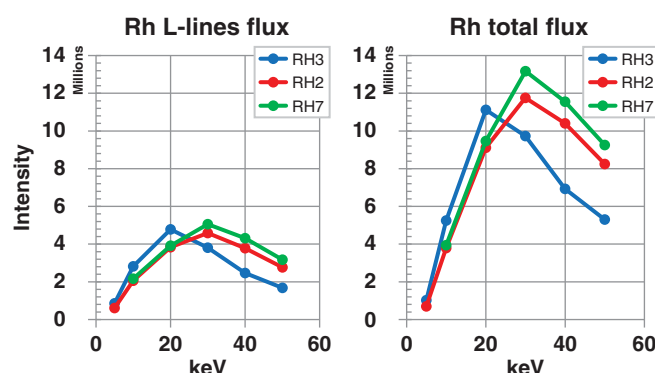


**Figure 18.10** The figure on the left shows the flux intensity for the Rh L-lines as a function of the voltage on an X-ray source, normalized to the X-ray tube power of 1 W. For light element detection, the target of choice is RH3, a thinner anode, which gives roughly a 20% increase in the L-line intensity at settings between 5 and 20 keV. The disadvantage of the RH3 anode thickness is that there is a loss in overall X-ray intensity of roughly 40% at settings between 30 and 50 kV at the high end, which most HHXRF manufacturers find acceptable.

is most often chosen. The X-ray flux drop-off for settings 30–50 kV is not wanted, but applications using the higher voltages still work reasonably well, even with the large reduction in X-ray intensity.

All the arguments for the rhodium anode apply equally well to the silver anode. The choice between the two target types is often to the decision of a particular instrument manufacturer. A downside to the rhodium target is the rhodium line at 2.70 keV is very close to the K-line for Cl at 2.62 keV. Several of the Rh L energies do not excite Cl, and the peaks are close together causing peak overlap with Cl. In this particular case of Cl detection, a silver anode is a better choice.

### 18.3.3.2 Anodes for Other XRF Applications

General use anodes for HHXRF are most commonly made of tungsten, and work with many XRF applications, with light element XRF being a notable exception. Tungsten anodes produce more flux per unit current, the reason being that the bremsstrahlung radiation production scales with the atomic number “Z” of the target [7]. Additionally tungsten is a very robust material, being a refractory metal with a high melting point, which often gives it the edge over other materials. Sources that have a tungsten anode have a beryllium window thickness of 250  $\mu\text{m}$  or more. Tungsten anodes are almost never used for light element XRF, so a thinner window is of no value. The tungsten anode thickness is optimized for the highest kV the source typically produces. For example an HHXRF instrument for scrap metal sorting has an X-ray source fixed at 35 kV. The tungsten anode thickness on the transmission anode source would likewise be optimized for 35 kV (Figure 18.11). Table 18.5 gives a list of typical tungsten anode thicknesses as well as the kV the anode is optimized for.

XRF applications that use a tungsten anode are very often used in conjunction with a filter exterior to the tube. Two notable filters are an aluminum filter of about 0.5 mm thickness for scrap metal sorting, and a copper filter for hazardous element detection (see Section 18.3.2).

For applications outside XRF, tungsten is the anode of choice for X-ray imaging due to tungsten’s mechanical robustness and higher X-ray output. For X-ray diffraction, a tight single energy of X-rays is desired. Common anode materials are chromium (5.4  $\text{K}_{\alpha}$ ), copper (8.0  $\text{K}_{\alpha}$ ), and molybdenum (17.5  $\text{K}_{\alpha}$ ). For X-ray diffraction, only a single characteristic line is desired, and the wide band of bremsstrahlung is not wanted because it contributes to the background noise. Often, sources for XRD are run at a kV that is three to four times the keV of the desired-ray emission line, so a copper source with a character line at 8 kV will be run at 30–40 kV on the X-ray tube.

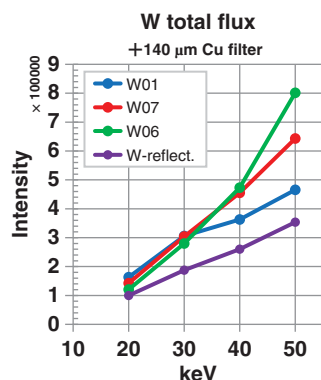


**Figure 18.11** This figure shows the X-ray intensity of several different tungsten anode types optimized for different high voltages, normalized to the X-ray tube power of 1 W. This is the flux through a copper filter, which is often how such a source would be used.

**Table 18.5** This table gives the calculated and measured X-ray flux output of 3 W anode thicknesses produced and Moxtek, optimized for 25 kV (W01), 40 kV (W07), and 60 kV (W06).

Target ID	Target material	Optimized kV								
			At 10 kV	At 20 kV	At 30 kV	At 40 kV	At 50 kV	At 60 kV	At 70 kV	
W01	W	25.0	e-Anode Sim.	0.88	0.97	0.96	0.82	0.58	0.39	0.26
			X-ray 3.5–10 keV	0.25	0.75	1.00	0.92	0.72	—	—
W07	W	40.0	e-Anode Sim.	0.77	0.87	0.98	0.99	0.95	0.78	0.58
			X-ray 3.5–10 keV	0.15	0.54	0.84	1.00	0.96	—	—
W06	W	60.0	e-Anode Sim.	0.37	0.69	0.90	0.96	0.98	1.00	0.94
			X-ray 3.5–10 keV	0.01	0.32	0.52	0.68	0.81	0.94	1.00
W-R	W	—	e-Anode Sim.	—	—	—	—	—	—	—
			X-ray 3.5–10 keV	0.37	0.79	0.95	1.00	0.83	—	—

W-R is a thick refection anode, like more traditional X-ray tube designs. For each anode thickness, the line labeled “e<sup>-</sup> anode Sim” shows the calculated emission of the X-ray L-lines from the anode. For each anode thickness, the line labeled “X-ray L-lines” shows the experimentally measured X-ray intensity between 3.5 and 10 kV, normalized to the X-ray tube power. The electron modeling trends line up well with the experimentally measured X-ray intensity. The differences between the two are due to the modeling not taking everything into effect such as self-anode absorption and X-ray window absorption.

## 18.4 Functionality of X-Ray Sources for HHXRF

X-ray sources for XRF have to be extremely stable and reproducible. More specifically, the **spectrum shape** (example in Figure 18.4) should not change in an XRF instrument for a particular HV setting over time, or any other variables like temperature. XRF manufacturers and XRF instrument users want their instrument to be repeatable. They all want the XRF instrument to give the same stoichiometric result each time it is used. If there is even a minor drift in the spectrum shape from the X-ray source, this has a good chance of likewise affecting the XRF stoichiometry results.

For many lab-based instruments, recalibration procedures are used to keep the results consistent over time, dealing with any drifts within the instrument, including the X-ray source over time. Recalibration can also be done within a HHXRF instrument, but in practice many instruments are calibrated a single time in production, and are never fully recalibrated again. Most HHXRF units do have a single reference sample to check the calibration, but the HHXRF device is more or less expected to give the same result in the stoichiometry for the lifetime of the device, without a full recalibration.

From an X-ray source perspective, this means that HHXRF manufactures want X-ray sources in which the spectrum shape, at a particular HV setting, is very repeatable and stable over the lifetime of the X-ray source. Keeping this spectrum shape the same over many different conditions for miniature X-ray sources for HHXRF is the major theme of the rest of this section. It is central to the design of sources for HHXRF.

From an X-ray source perspective, here is a list of major ways one can change the spectrum shape on an X-ray source:

1. **Change the HV:** This is very changeable, by design. The HV stability and repeatability are at the core of this section.

2. **Change the emission current:** This does change the X-ray intensity, but should not change the spectrum shape.
3. **Change the anode target material or the anode thickness:** The anode material and thickness are stable for a single X-ray source in normal operation.
4. **Change the X-ray filter:** In a HHXRF device the filters on the filter wheel are unlikely to change.

The HV stability of the X-ray source is extremely critical for XRF. Changing the HV on the X-ray source changes the spectrum shape, which changes the ratio of X-ray counts between each element's X-ray lines from a sample. The ratio between the different characteristic lines gives the stoichiometry of these elements, so if this ratio changes the XRF calibration is compromised (Figure 18.12). Because HV stability is so critical to the source's spectrum shape stability, and the spectrum shape stability is so critical to the XRF results, we look directly at the HV stability (see Section 18.4.1) from the spectrum from the source, by measuring the bremsstrahlung edge to insure the X-ray source has a stable HV (see Section 18.4.1).

The emission current changes the intensity of the X-rays from the source; it does not change the spectrum shape. Therefore, changing the emission current does not change the resulting ratios between X-ray lines in XRF from a sample. The emission current is important; setting it allows maximizing the counts on the XRF, and HHXRF manufacturers need the flux to be linear with the emission current (Section 18.4.4). But the emission current is not as nearly critical an issue, compared to a stable HV which affects the spectrum shape.

The anode thickness in the X-ray tube also affects the spectrum shape, in that the anode stops the electrons generating X-rays, and also acts as an X-ray filter for the generated X-rays. Tuning the thickness of the anode has several benefits needed for technically demanding applications such as light element XRF, as discussed in Section 18.3.3.1. Having tightly controlled thickness on the anode material is important to maintain an analogous spectrum shape between two different sources. Getting two different sources to have the same spectrum shape will be discussed below in Section 18.4.4.

Changing an X-ray filter also drastically changes the source's spectrum shape. In practice the filters are changed via a filter wheel on the front of the detector, based on the application (Section 18.3.2). If a HHXRF instrument is calibrated with a specific source and set of X-ray filters, the anode and filters for this instrument should not change, so the calibration should be stable. The designed filters will not change, but unwanted filters, such as

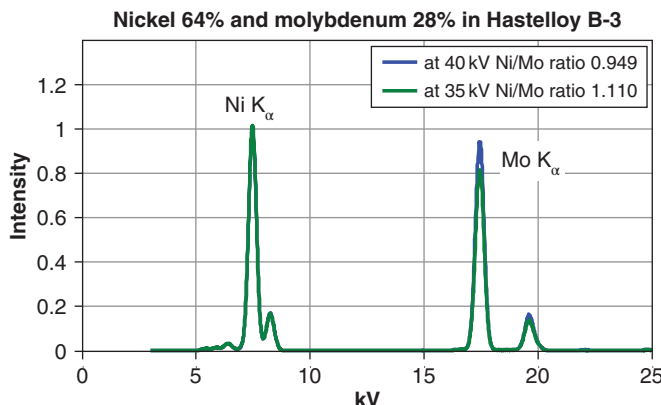


**Figure 18.12** This figure shows two resulting spectra from a Hastelloy B-3 sample excited with a silver anode tube with a  $70\text{ }\mu\text{m}$  Cu filter. The two spectra were taken with the tube set to 40 and 35 kV. This high-voltage shift changed the ratio between the peaks by 16%. In this setup, the nickel-to-molybdenum ratio can be changed by 0.5% by changing the voltage by just 200 V. This demonstrates that a stable high voltage is needed to maintain a consistent ratio between elemental X-ray lines, and to maintain a HHXRF calibration.

debris getting on the X-ray window, of the X-ray tube, or anywhere else along the beam path, can compromise the spectrum shape.

In the following sections, we will be exploring each of these factors, with a major emphasis on keeping the HV repeatable and stable over time and other variables. Substantial effort has been taken to fully characterize the miniature X-ray sources under these categories: environmental stress tests, X-ray flux and spot stability and repeatability tests, and multi-settings tests. The intent of this test is to provide confidence for those using these X-ray sources in HHXRF.

#### 18.4.1 Environmental Stress Testing

One consideration HHXRF has over lab-based XRF instruments is the environment [20]. HHXRF is meant to be used in a large range of field environments, and give the same stoichiometry in each of these environments. This translates into having the X-ray source functioning over an extended temperature range. Not only do the components need to stay operational, large efforts are made to keep the X-ray output stable over extended temperature ranges as well.

The typical temperature specification is a storage temperature range of  $-40$  to  $80$  °C and an operational range of  $-10$  to  $60$  °C. While developing a miniature X-ray source, the design is considered to be robust when the X-ray source can survive a 120 hour environmental test during which the temperature is ramped between the temperature extremes repeated 20 times. Each testing cycle is meant to find any weaknesses in the design, and when failure points are found they are fixed.

On recent X-ray source designs, the tests over these temperature ranges have also been done in conjunction with measuring the spectral output, in effort to minimize the spectrum shape changes over extended temperature ranges. Recent designs of the X-ray sources are made to vary less than 100 V in the HV over the operational temperature range of  $-10$  –  $60$  °C, to make the HHXRF system stable as possible, and give nearly identical results independent of the temperature of the environment.

#### 18.4.2 X-Ray High-Voltage Stability

Of all items on the list of ways to change the spectrum shape, the X-ray source's HV stability and repeatability are the most critical. This section's focus is on verifying and monitoring an X-ray source to make sure the HV is stable over time.

A stable spectrum shape from an X-ray source requires that the HV on that X-ray source must remain constant over time, hours to days to months, as well as over on and off cycles. Measuring the HV stability is accomplished by evaluating the X-ray spectrum directly, specifically the bremsstrahlung edge, over and over, in a setup like the one shown in Figure 18.7. A spectrum's bremsstrahlung edge is fit with a proprietary algorithm, giving the value of the bremsstrahlung edge in keV. This measurement provides the “spectroscopic” voltage in keV. The bremsstrahlung edge in keV coincides with the X-ray source's actual HV in kV (Figure 18.13).

If the bremsstrahlung edge moves over time, it means that the HV has shifted on the HVPS. Any changes in the HV over time in the X-ray source are very undesirable. The bremsstrahlung edge technique is very sensitive; changes in the HV on the order of 50–100 V can be seen. From an X-ray source's perspective, this measurement technique is extremely valuable because it detects voltage shifts semidirectly in units of keV, decoupling this key issue from other causes of flux drift, such as emission current changes or X-ray spot movement on the anode.

Figure 18.14 shows the results of the bremsstrahlung edge detection from a series of spectra measured every minute for eight hours. The HV stability results shown in Figure 18.12 are exactly what an XRF instrument needs from its X-ray source: the HV is stable to within  $\pm 100$  V for HHXRF over and extended time frame of hours to the life time of the source.

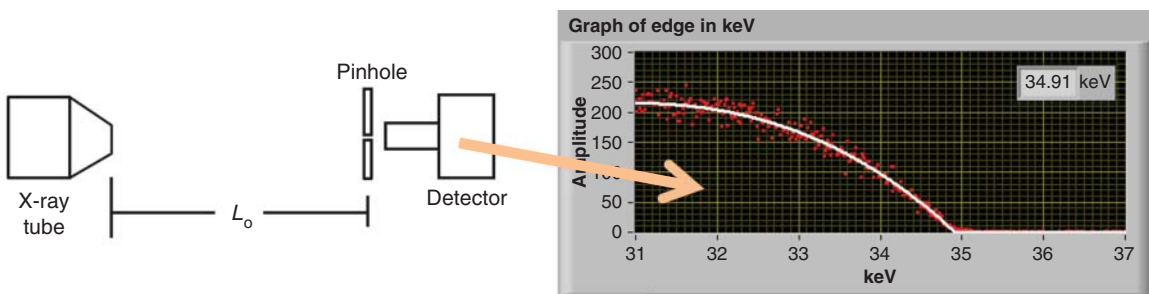


**Figure 18.13** A simple schematic on the right shows the setup used to measure the bremsstrahlung edge from an X-ray source. The graph on the right shows a spectrum measurement, zoomed in on the bremsstrahlung edge. In this case, the high-voltage calibrated source was set to 35 kV and the bremsstrahlung edge was measured to be at 34.9 keV, giving a small 0.10 kV offset between the two values.

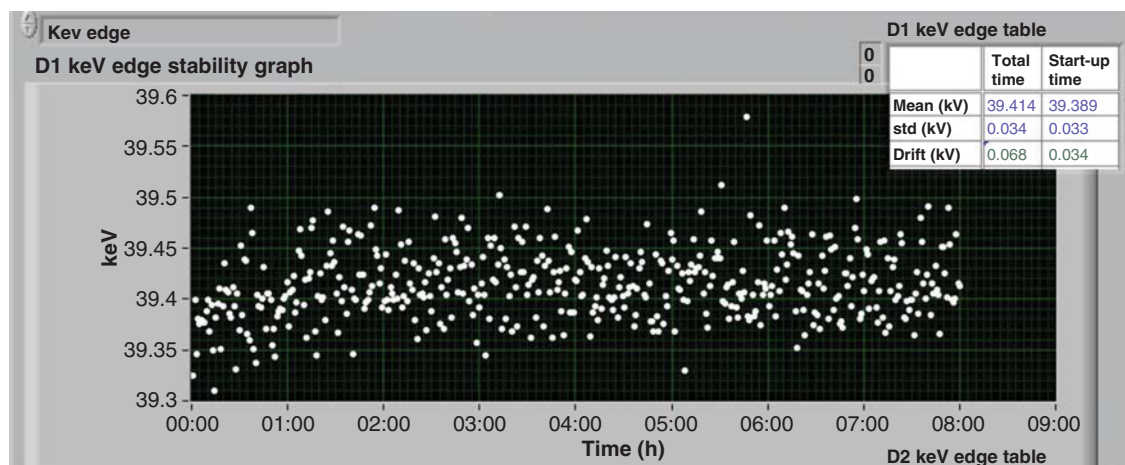


**Figure 18.14** A high-voltage repeatability test from a miniature X-ray source for HHXRF. An algorithm finds the bremsstrahlung edge in a spectrum, and records it for each of the spectra taken over eight hours. This source achieved a voltage of 39.4 kV (set at 40 kV), with a standard deviation of 34 V. This level of high-voltage stability is good for getting a stable HHXRF instrument.

### 18.4.3 X-Ray Flux Stability and Repeatability

The HV stability is just one of the most critical elements to having a stable flux, and having a stable and repeatable X-ray flux from the X-ray source is also needed for XRF. Types of issues that affect the flux stability are changes in the HV, spot movement on the X-ray tube, and changes in the emission current. As an X-ray source warms up when used, there are inevitable small changes in both the X-ray tube and the HVPS which will shift the X-ray flux around. The aim in designing these X-ray sources is to make the source as stable as possible throughout any changes.

The stability and repeatability test evaluates how the X-ray source operates over time. For the stability test, the X-ray source is left on for the entire test. For the repeatability test, the X-ray source is periodically cycled on and off: typical off cycles are 2–10 seconds, and typical on cycles are 30–120 seconds. The test durations can be from a time frame of several minutes to days. Testing the stability and repeatability source involves several detectors and instruments simultaneously measuring and evaluating the X-ray source, and Figure 18.15 shows an X-ray source testing setup, which incorporates several detectors. Having all these instruments evaluating the X-ray source simultaneously effectively pinpoints any issues on an X-ray source if the X-ray source is unstable.

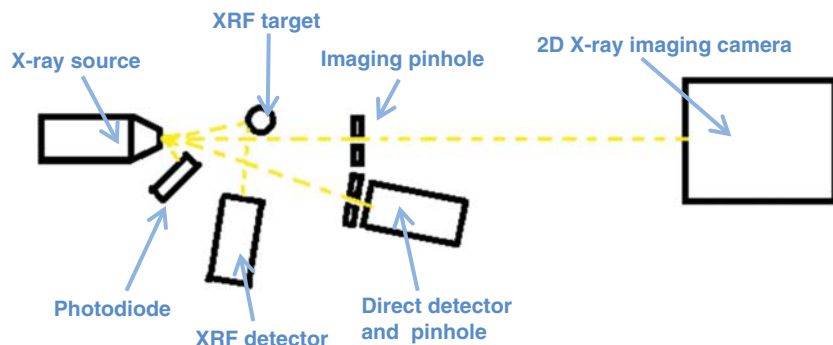


**Figure 18.15** A simple schematic of the stability and repeatability test showing all the major instruments, three flux detectors and an imaging detector, simultaneously measuring and evaluating the X-ray source. *Source:* Based on [10].

For both the stability and repeatability tests, the flux is measured directly from the source, which gives the flux stability (Figure 18.16), spectrum shape stability as well as the HV stability (Section 18.4.2). XRF flux is measured a second way using a secondary XRF target, simulating XRF instruments' stability. The flux output is measured a third way with a photodiode, which is very good for monitoring fast flux changes over tenths of a second. A time series of pinhole X-ray images of the X-ray tube's anode is also measured, which gives X-ray spot position stability (Figure 18.17). Each of these methods gives flux stability information, and differences between each measurement give vital clues as to what the causes any flux instability, if there is any. In addition to the four ways used to evaluate the flux from the source, several thermocouples are placed on different locations of the source's tube and HVPS,

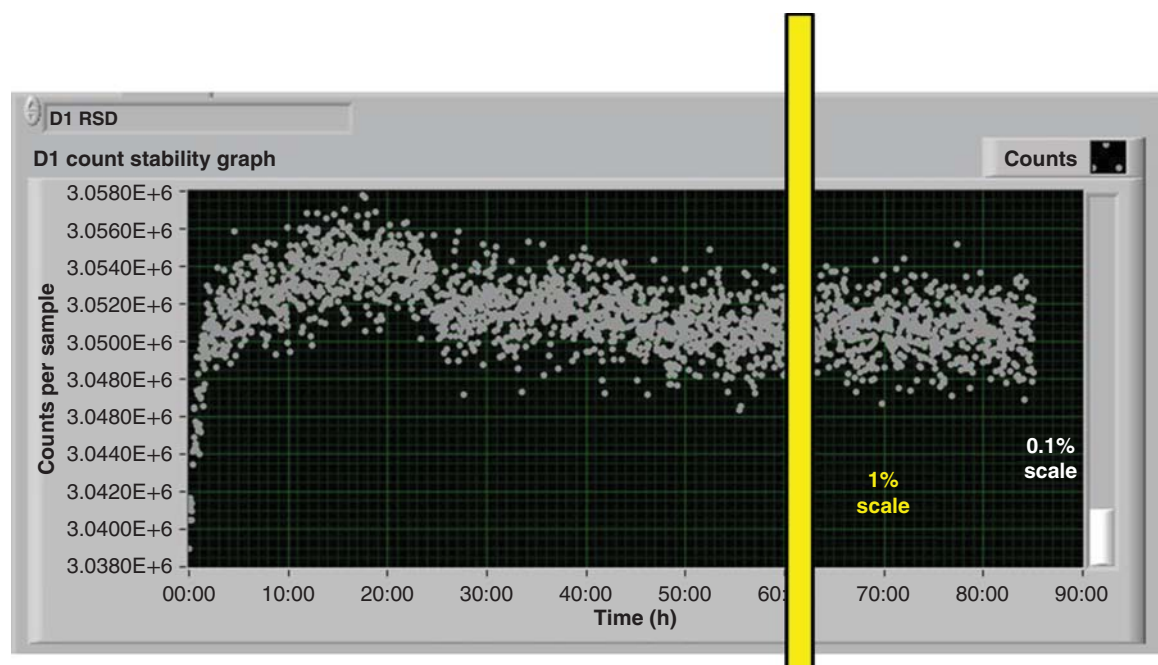


**Figure 18.16** An X-ray flux measured directly from ULTRA-LITE source, set at 50 kV and 80  $\mu$ A (the full 4 W) during a repeatability test, cycled on for 120 seconds and off for 5 seconds for 2400 cycles. This test measured an X-ray flux repeatability of 0.10% RSD over 85 hours. During the source's warm-up time of 30–45 minutes, the X-ray flux drifted by 0.45% [10].

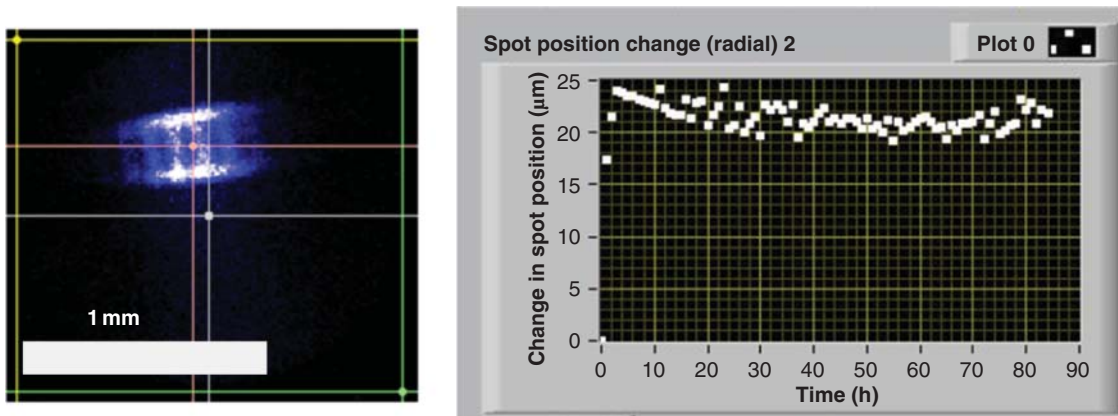


**Figure 18.17** An X-ray spot repeatability test from ULTRA-LITE source, taken simultaneously with information in Figures 18.16. To the left is a single pinhole camera image of the X-ray spot, with a spot size of  $390 \times 340 \mu\text{m}$  FWHM. The small white dot in the center of the image represents the physical center of the anode. The graph to the right shows the drift of the spot over time; it drifts  $\sim 20 \mu\text{m}$  as the source warms up over the first 30–60 minutes and has a constant position thereafter over 85 hours [21, 22].

and every signal and power line going into and out of the HVPS is monitored. Collecting all this information simultaneously permits finding correlations in the data, which is critical for troubleshooting issues, as problems are found. This stability and repeatability testing verifies that the X-ray source has a stable HV, a stable X-ray flux, and a stable X-ray spot needed for a HHXRF. At our company, this level of testing for sources has been used in development for several years [10]. The basics of this testing platform have also been moved to the production level, because it has been very effective at both detecting and diagnosing any issues in the X-ray sources produced.

#### 18.4.4 Multi-Settings Testing and Flux Linearity

The stability and repeatability testing verifies that an X-ray source is stable at one setting over time, and the multi-settings test determines the X-ray source functions over its entire range of voltage and emission current settings. In the multi-settings test, the X-ray source is turned on and off for a few seconds over a few hundred to thousands of different HV and emission current settings. The flux value is recorded with a photodiode, and every signal and power line going into and out of the HVPS is monitored. All of this information provides several ways to evaluate the X-ray source. Here we present data collected with the just photodiode which give information on:

- The flux turn-on time.
- The flux stability for a few seconds at each setting.
- The flux linearity over many settings.

For HHXRF, a quick turn-on time of under a second is desired. Figure 18.18 shows the signal flux, measured by the photodiode, as the X-ray source is turned on. The turn-on time can be measured over all the settings evaluated.

The flux stability for a few seconds at each setting is very valuable as well, showing if there are any settings that have an unstable flux. Figure 18.19 shows photodiode flux stability over a few seconds at each setting on an early prototype X-ray source. This was a very extensive test, with the source tested in  $1 \mu\text{A}$  steps (ranging from 0 to  $200 \mu\text{A}$ ) and  $0.5 \text{ keV}$  steps (ranging from 4 to 50 data  $\text{keV}$ ) resulting in data taken over 13 000 individual settings, with the entire test taking about 24 hours. A low standard deviation in the flux signal represents the desired stable flux output, and is represented in blue dots in the plot of Figure 18.19. A high standard deviation in the flux signal represents the undesired unstable flux output, and is represented in either red or yellow dots in the plot

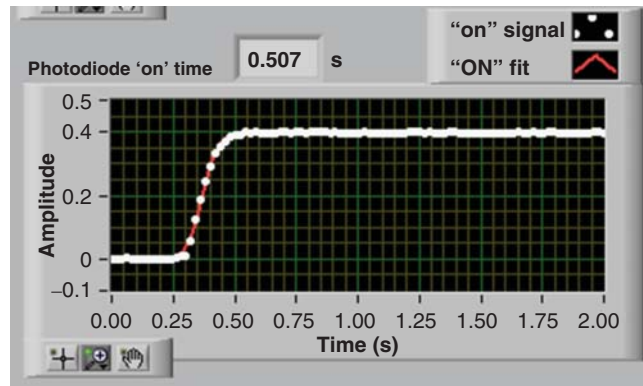
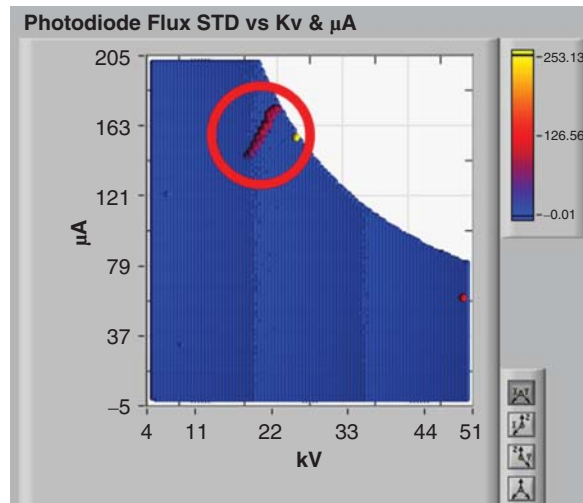


**Figure 18.18** This shows the X-ray flux signal measured over time by the photodiode as the source turns on. For this setting of 50 kV and 80  $\mu$ A, to the flux is fully on after 0.51 seconds [10].

**Figure 18.19** An example of data collected from the multi-settings test where the set voltage and the set current are plotted against the standard deviation of the X-ray flux measured, with a photodiode. An unstable flux output region is clearly seen inside the red circle [10].



of Figure 18.19. The settings with unstable flux stability are clearly identified in the region circled in red. This mapping procedure insures that the X-ray source is functional with a stable flux output over all the available HV and emission current settings that may be needed for a given XRF application.

Lastly, the flux linearity of the X-ray source is measured over several HVs. The flux output should be linear with the emission current on the source when the source is held at a constant HV (Figure 18.20). Measuring the X-ray flux at several emission current settings verifies this relationship. For HHXRF, flux linearity as a function of current is desired to insure the instrument's calibration.

#### 18.4.5 X-Ray Spectrum Stability Between Different X-Ray Sources

The previous sections focused on making sure the spectrum shape from a single X-ray source was stable and consistent over time and other variables. Spectrum shape stability is critical for an X-ray source within a HHXRF instrument, so the HHXRF instrument can maintain its calibration for months to years. In this section, the focus shifts from the same spectrum shape from over time on a single source, to obtaining the same spectrum shape across several different X-ray sources.

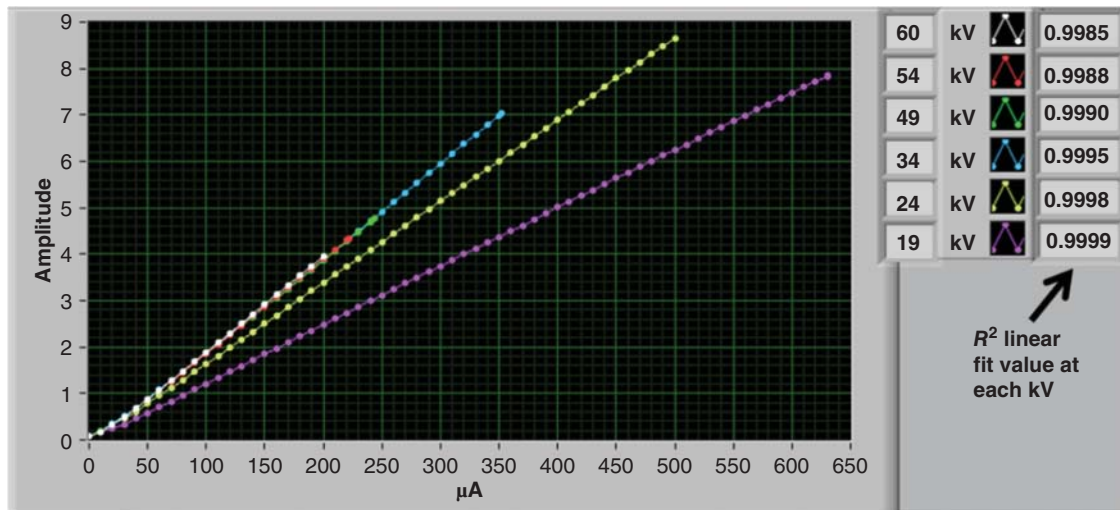


**Figure 18.20** The flux linearity from a tungsten X-ray source at a few selected high voltages. For settings from 60 to 19 kV the source flux is very linear, with  $R^2$  values all under 0.998. Several of the higher voltage linear curves are on top of each other due to the photodiode not detecting higher energy X-rays.

One feature desired by manufacturers of HHXRF instruments is having X-ray sources which are spectroscopically identical. A spectroscopically identical X-ray source allows one to switch out the source in an instrument with no other required changes: the new source will generate the same XRF spectra as the old source, with minimal or no recalibration of the instrument. This allows swapping of X-ray sources in an instrument, without requiring instrument recalibration, and is a major plus for instrument manufacturers, in both their manufacturing and service areas.

One of the major obstacles in making sources that are close to spectroscopically identical is having a tight and repeatable control over the voltage of the X-ray source's HVPS, which is discussed extensively in this section. A tight control is also needed within the anode thickness material, as well as any filters that are used. Controlling these features will allow for an XRF equivalent X-ray source with the same spectrum shape, so that one X-ray source can be exchanged for another X-ray source and the calibration on the XRF instrument is unaffected.

A proven solution for spectroscopically identical sources is the digitally controlled Moxi X-ray source. These handheld X-ray sources are spectroscopically identical for several XRF applications. Each digital X-ray source is calibrated to within  $\pm 250$  V over all settings between 4 and 50 kV, and this voltage accuracy is tight enough to allow for XRF equivalence for several XRF applications. We will outline how the new digital sources are HV calibrated, and then show how this calibration leads to a spectroscopically identical X-ray source.

#### 18.4.5.1 High-Voltage Calibration of X-Ray Sources

In order to calibrate the HV on an X-ray source, two basic requirements are needed:

- A meaningful and accurate way to measure the HV.
- A way for each X-ray source to store the HV calibration information, offsetting source-to-source differences due to variance in electrical components which make up the source.

The X-ray source's HV is measured by collecting a spectrum from the tube's anode, as discussed in Section 18.4.2. The bremsstrahlung edge measurement provides the “spectroscopic” voltage in keV, while the electronic monitors on the source's HVPS give an electronically measured voltage in kV (Figure 18.13). The difference between the two gives a correction factor, which can be used to tighten the accuracy between these two values.

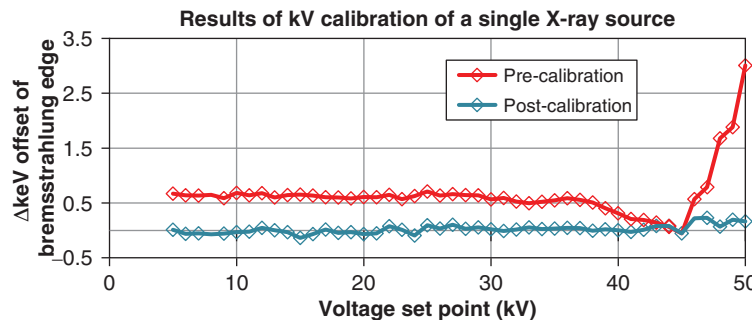


**Figure 18.21** This shows the offset between the tube's set voltage and bremsstrahlung edge measurements in 1 kV increments. The red line is the offset before the X-ray source is high-voltage calibrated, and the blue curve shows the offset after the digital X-ray source is high-voltage calibrated. Before calibration, the offset was close to 600 V, and gets as high as 3 kV at 50 kV. After calibration, the source is within  $\pm 250$  V, compared to the bremsstrahlung edge measurements.

The X-ray sources are designed to be operated over a range from 5 to 50 kV, and therefore spectra are taken at several HV. The bremsstrahlung edge is recorded over several tube voltage settings, generating a keV to kV offset for each voltage setting. In Figure 18.21, the red line shows the offset between the spectroscopically measured bremsstrahlung edge in keV and the pre-calibrated tube's set voltage in kV. One key idea is the pre-calibrated offset is nonlinear after about 40 kV. The electronic components do not have a strictly linear relationship with HV. This nonlinearity is due to variance in the HVPS board components, specifically the HV feedback resistor (Figure 18.5).

For an analog X-ray source, without any onboard memory, the variance in the electronic components in aggregate is the major driving factor for the HV offset of any particular X-ray source. This represents the limit in HV accuracy for an analog source. In a digital source, with onboard memory, a digital correction factor is stored for each kV setting, compared to bremsstrahlung edge. Most of the HV variance due to analog board component variations can be removed by the combination between measuring several bremsstrahlung edge spectra and storing a correction factor on the source's memory.

Manufacturers need every X-ray source produced to output the same tube spectrum shape to gain the benefits they want. Figures 18.22 and 18.23 show the HV offset between the bremsstrahlung edge measurement and the electronic HV setting over a 100 different X-ray sources. Figures 18.22 and 18.23, which intentionally have the same scale, show both the accuracy and precision of the HV between X-ray sources is drastically increased by the HV calibrating procedure. It is easily seen that the calibration done on the digital tube greatly reduces the voltage offset variation between multiple X-ray sources.

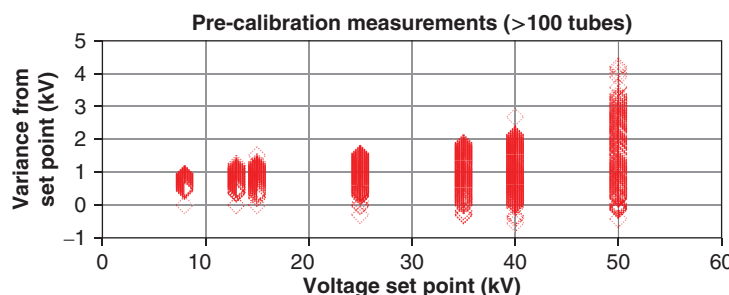


**Figure 18.22** This graph shows the offset between the tube's set voltage and bremsstrahlung edge over seven settings pre-calibration, on over 100 separate X-ray sources. This is the offset to be expected on a strictly analog X-ray source. Pre-calibration, the high voltage is typically offset by 800 V, and can vary by up to  $\pm 1000$  V (at 35 kV).

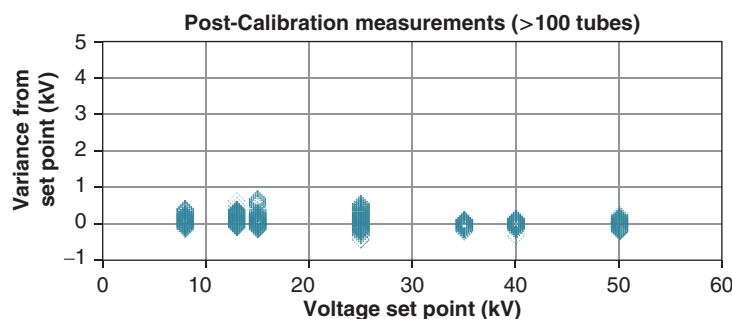


**Figure 18.23** This graph shows the offset between the tube's set voltage and bremsstrahlung edge over seven settings post-calibration, on over 100 separate X-ray sources. Post-calibration, the high voltage is typically offset by 100 V, and can vary by up to  $\pm 250$  V (at 35 kV).

The voltage accuracy and precision achieved in the digital X-ray source are much more tightly controlled. The benefit of this increased voltage accuracy has resulted in reducing manufacturing complexity in the calibration, and service time for XRF handheld instruments manufacturers. The next section will quantify what this voltage accuracy permits in terms of the resultant stoichiometry from an XRF instrument.

#### 18.4.5.2 X-Ray Source High-Voltage Dependence on XRF Stoichiometry

Several experiments were performed exploring how voltage variation on the X-ray source impacts the calculated stoichiometry from XRF for two different applications: nonaluminum metal sorting and aluminum metal sorting. The basic outline of the experiment is as follows:

- Five spectra were collected from a sample with over 800 k counts at a single HV setting.
- The spectra were then converted into elemental stoichiometry percentages with SinerX fundamental parameters software. The resulting stoichiometry percentages were averaged from the five spectra, giving a basic measurement variance.
- The HV of the tube was adjusted by a step size ranging from 200 to 500 V, depending on the sample, and another five spectra were collected.
- This was done over a range of voltage from 500 to 2000 V, depending on the sample.

Two samples were investigated:

- Hastelloy, with the tube nominally set to 35 kV to represent a “harder” case for nonaluminum metal alloy sorting (Figure 18.12). Hastelloy was chosen due to the Ni and Mo fluorescent peaks being far apart in energy. This large difference in the characteristic X-ray energies (7.4 keV K $\alpha$  for Ni and 17.4 keV K $\alpha$  for Mo) maximizes the change in the calculated stoichiometry when the tube’s voltage is changed.
- Al 7075, with the tube nominally set to 12 kV, to represent a “harder” case for aluminum metal alloy sorting. Al 7075 was chosen due to the Al and Zn peaks being far apart in energy. This large difference in the characteristic X-ray energies (1.5 keV K $\alpha$  for Al and 8.6 keV K $\alpha$  for Zn) maximizes the change in the calculated stoichiometry, when the tube’s voltage is changed.

From the data collected, the effects of changing the HV on the X-ray source on the stoichiometry could be quantified. As expected, as the voltage was changed the number of counts in the peaks nearest to the bremsstrahlung edge changed the most, Mo for the Hastelloy and Zn for the Al7075. The calculated Mo stoichiometry percentage was much more sensitive to tube voltage changes than the Ni percentage in the Hastelloy, and likewise with the Zn compared to the Al in the Al7075 sample.

If the Mo and Ni (or Al and Zn) calculated stoichiometry from an XRF spectra stays constant from a given XRF measurement, then we expect spectral XRF equivalence. The question becomes what X-ray source HV variance

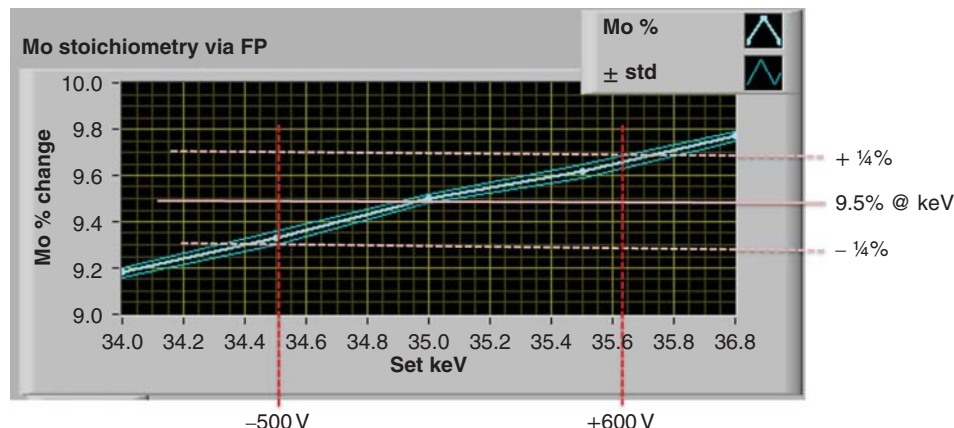


**Figure 18.24** This graph shows the stoichiometry change of the Mo as the high voltage of the tube is changed. The standard deviation of the measurements is represented by the thin lines just above and below the main center line. Holding the Mo peak stoichiometry to under  $\pm\frac{1}{4}\%$  error requires a high-voltage accuracy on the order of  $\pm 500$  V. Our current high-voltage calibration is under  $\pm 250$  V at 35 kV.

keeps the Mo and Ni (or Al and Zn) calculated stoichiometry small enough for XRF equivalence? To “quantify” this, if the stoichiometry of the elements stayed under 0.25%(0.5%), then the result is considered to be “XRF equivalent.” This quantification has been verified in practice, in that it works as intended in next-generation handheld X-ray sources sold today. Figure 18.24 shows the results for the stoichiometry of the Mo changing as a function of the tube’s HV for the Hastelloy sample at 35 kV, and likewise Figure 18.25 for the Zn lines for the Al7075 sample at 12 kV. From these graphs, it is fairly easy to see what the voltage range on the X-ray source needs to be to keep the calculated stoichiometry at or under  $\frac{1}{4}\%$  (Figures 18.24 and 18.25).

Nonaluminum metal sorting sources may have a  $\pm 500$  V variance in HV; this limit will produce “equivalent” sources, meaning that the stoichiometry should not vary more than  $\frac{1}{4}\%$ , tube-to-tube. The test case with the Hastelloy sample is a more demanding example for this application, due to the zinc and molybdenum lines being very far apart in X-ray energy. Therefore, with most other typical samples in which the element X-ray lines are closer in energy to each other, the difference a voltage change will have on the stoichiometry will tend to be lower.

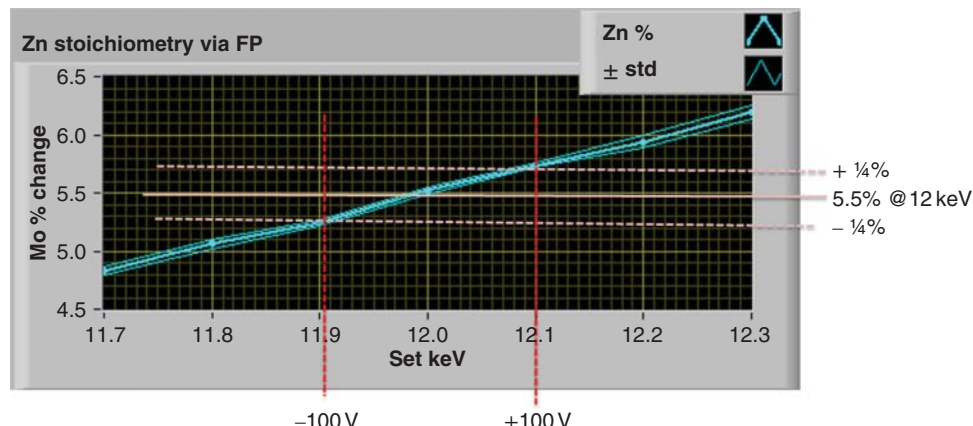


**Figure 18.25** This graph shows the stoichiometry change of the Zn as the high voltage if the tube is changed. Holding the Mo peak stoichiometry to under  $\pm\frac{1}{4}\%$  error requires a high-voltage accuracy on the order of  $\pm 100$  V. Our current high-voltage calibration is under  $\pm 250$  V at 12 kV.

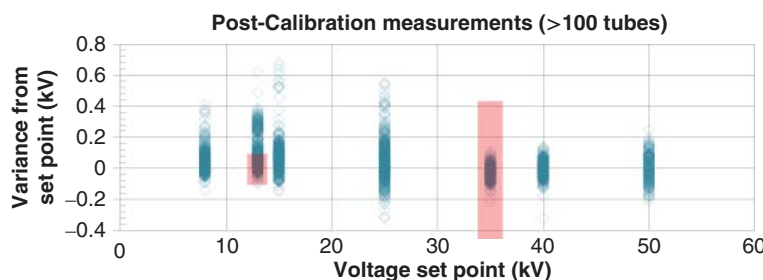


**Figure 18.26** This graph shows the offset between the tube's set voltage and bremsstrahlung edge over seven settings post-calibration, on over 100 separate X-ray sources. This is the exact same graph as Figure 18.23, with the y-axis zoomed in to show more detail. The red bars show the source's high-voltage accuracy needed to keep calculated stoichiometry from XRF spectra under  $\frac{1}{4}\%$ , for two different experimental setups, aluminum metal testing at 12 keV and nonaluminum metal sorting at 35 keV.

This test case can be extended to other XRF methods, such as ppm detection for RoHS/WEEE (waste electrical and electronic equipment), in which the X-ray source is at or above 35 kV. For these XRF techniques, keeping the voltage of the source to  $\pm 250$  V should keep the measurements very close to equivalent.

Aluminum metal sorting sources may have a  $\pm 100$  V variance in HV; this limit will produce “equivalent” sources, meaning that the stoichiometry should not vary more than  $\frac{1}{4}\%$ , tube-to-tube. Similarly, the test case with the Al7075 sample is a more demanding example for this application, due to the aluminum and zinc lines being very far apart in X-ray energy. Therefore, with most other typical samples in which the element X-ray lines are closer in energy to each other, the difference a voltage change will have on the stoichiometry will tend to be lower. For low-voltage XRF techniques, keeping the voltage of the source to  $\pm 250$  V is not enough to keep the stoichiometry to within  $\frac{1}{4}\%$ , but it is almost enough to keep it within  $\frac{1}{2}\%$ . Even so, this level of improvement in voltage variation is drastically smaller than for an analog X-ray source counterpart.

Figure 18.26 replots the variance of over 100 digitally calibrated sources, along with red bars giving the range of voltages required for “XRF equivalent,” keeping the stoichiometry variation under  $\frac{1}{4}\%$ . From this, we can see that the higher voltage XRF applications are well within the voltage tolerance needed to keep the voltage variance down to be “XRF equivalent.” For the more demanding XRF application at low kV, the control is not to the “XRF equivalent” level, but is closer to this ideal with the calibrated digital sources than without it.

## 18.5 Conclusion

The major advantage of portable or HHXRF is that the instrument can be taken to the sample, rather than the sample to the instrument. As a few examples, these instruments are taken directly to mines, on-site in mining investigations, used directly in scrap metal sorting yards, and taken into homes for lead in paint investigations. The development of miniature, lightweight, X-ray sources was the critical component needed to shift XRF spectroscopy from the lab to the field. This portability has proven to be a very big advantage, demonstrated by the rapid growth of the HHXRF market in 2004–2020.

For HHXRF, keeping the X-ray source small is very important, with a major emphasis on keeping the HV repeatable and stable over time and other variables (e.g. ambient temperature). Full characterization of these miniature X-ray sources provides confidence in the stability of the X-ray source within the HHXRF instrument, and therefore the qualitative and quantitative results the instrument produces.

“XRF equivalent” X-ray sources for HHXRF can be produced by careful HV calibration of the digital X-ray source. This HV calibration is achieved by bremsstrahlung edge measurements, and storing HV offset information on each source. The stored offset corrects for HV discrepancies due to the variance in the electronic components of the HVPS.

## References

- 1 Potts, P.J. and West, M. (eds.) (2008). *Portable X-Ray Fluorescence Spectrometry, Capabilities for in Situ Analysis*. Cambridge, UK: RSC Publishing.
- 2 Cornaby, S. and Kozaczek, K. (2016). Sources for handheld X-ray fluorescence instruments. In: *Encyclopedia of Analytical Chemistry* (ed. R. Meyers). John Wiley & Sons.
- 3 Van Grieken, R.E. and Markiwicz, A.A. (2002). *Handbook of X-Ray Spectroscopy*, 433. New York: Marcel Dekker.
- 4 Bosco, G. (2013). Development and application of portable, hand-held X-ray fluorescence spectrometers. *TrAC Trends Anal. Chem.* 45: 121–134.
- 5 Reyes-Mena, A., Knight, L.V., and Cornaby, S. (2000). *An XRD/XRF Instrument for the Microanalysis of Rocks and Minerals*. SBIR contract number NAS2-00010.
- 6 Coolidge, W.D. (1913). A powerful Röntgen ray tube with a pure electron discharge. *Phys. Rev.* 2: 409.
- 7 Lee, S.M. and McDonald, C. (2009). *Handbook of Optics*, 3e, vol. V (ed. M. Bass). New York: McGraw-Hill Companies, Inc., Chapter 54.
- 8 Kossel, W. (1916). Bemerkungen zum Seriencharakter der Röntgenspektren. *Verh. Deut. Phys. Ges.* 18 (339): 396.
- 9 Kossel, W. (1917). Zum Ursprung der Y-Strahlenspektren und Röntgespektren. *Phys. Z.* 18: 240.
- 10 Kossel, W. (1920). Zum Bau der Röntgespektren. *Z. Phys.* 1: 119.
- 11 Kossel, W. (1920). Über die Ausbildung der Röntgenserien mit wachsender Ordnungszahl. *Z. Phys.* 2: 470.
- 12 Moseley, H.J.G. (1913). The high frequency spectra of the elements part I. *Philos. Mag.* 26 (6): 1024.
- 13 Moseley, H.J.G. (1914). The high frequency spectra of the elements part II. *Philos. Mag.* 27 (6): 703.
- 14 Barkla, C.J. (1915). X-ray fluorescence and the quantum theory. *Nature* 95: 7.
- 15 Cockcroft, J.D. and Walton, E.T.S. (1932). Experiments with high velocity positive ions. (I) Further developments in the method of obtaining high velocity positive ions. *Proc. Roy. Soc. London Ser. A* 136: 619.
- 16 Cornaby, S. and Kozaczek, K. (2012). Flux comparisons of miniature X-ray source: XRF wattage-maps by application. *58th Denver X-Ray Conf. Adv. X-Ray Anal.* 56: 202–208.
- 17 Jenkins, R., Gould, R.W., and Gedcke, D. (1995). *Quantitative X-Ray Spectrometry*. New York: Marcel Dekker.
- 18 Jenkins, R. (1999). *X-Ray Fluorescence Spectrometry*, 2e. Chichester, UK: Wiley-Interscience.
- 19 CASINO. <https://www.gel.usherbrooke.ca/casino> (accessed 10 October 2020).
- 20 Cornaby, S., Morris, S., Smith, J. et al. (2012). Moxtek's new ultra-lite X-ray sources: performance characterizations. *58th Denver X-ray Conf. Adv. X-ray Anal.* 56: 202–208.
- 21 Caruso, D., Dinsmore, M., and Cornaby, S. (2009). Miniature X-ray sources and the effects of spot size on system performance. *58th Denver X-Ray Conf. Adv. X-Ray Anal.* 53: 228–233.
- 22 Uchida, H., Hasuike, K., Torii, K., and Tsunemi, H. (2006). Quantitative method of measuring spot size of microfocus X-ray generator. *Jpn. J. Appl. Phys.* 45 (6A): 5277–5279.

## 19

### Semiconductor Detectors for Portable Energy-Dispersive XRF Spectrometry

*Andrei Stratilatov*

*Moxtek, Inc., Orem, UT, USA*

#### 19.1 Introduction

Historically, the primary sensors used in energy-dispersive X-ray Fluorescence (EDXRF) spectrometers [1] were cryogenic cooled Si(Li) detectors. These detectors had a good energy resolution of 135 eV peak full-width at half-maximum (FWHM) using the 5.895 keV Mn-K<sub>α</sub> line emitted by an <sup>55</sup>Fe isotope source [2]. However, because of their size, cost, and complexity they are used only in analytical laboratories. Significant progress in semiconductor technology allowed silicon wafers of very low concentration of structural defects (dislocations) and impurities to be manufactured. That, together with planar technology introduced by J. Kremer [3], resulted in fabrication of Si detectors that do not require deep cryogenic cooling to achieve acceptable energy resolution. However, the fabrication of semiconductor detectors is a complex technology that uses multiple techniques, including doping, deposition, patterning, and surface passivation. The first thermoelectrically cooled Si-PIN detector developed at Amptek, Inc. in 1991 had a resolution of 850 eV [1]. Continuous refinement of planar technology, and progress in development of low noise front end electronics, led to significant improvements in the resolution of Si-PIN diodes over the following three decades. Today, the resolution of Si-PIN detectors with 10 mm<sup>2</sup> size, is about 150 eV at a temperature of -55 °C. This temperature is easily achieved with a cooling system based on a two-stage thermoelectric Peltier cooler (TEC), at a reasonable power consumption of ≤0.5 W. However, the resolution of Si-PIN detectors degrades rapidly with increasing sensitive area, because of the increased detector capacitance.

The revolutionary invention of silicon drift detector (SDD), made by Emilio Gatti and Pavel Rehak in 1982 [4], gave a new push to the development of semiconductor detectors for x-ray spectrometry, and provided remarkably better detector performance parameters than Si-PIN. The capacitance of SDDs is very small, and almost independent from detector sensitive area, which yields excellent energy resolution around 125 eV, a high counting rate, a peak-to-background ratio ≥ 10 000, and a higher working temperature up to -10 °C, or even higher, when high resolution is not a primary requirement.

Suitable low-noise-readout electronics have to be designed to exploit the SDD's intrinsic parameters, and to meet compactness requirements of portable XRF instruments. The integration of these electronics in custom application-specific integrated circuits (ASICs) was successful, and today readout ASICs for semiconductor detectors are commercially available [5].

The development of fast digital pulse processors (DPPs) played a significant role in the improvement of the performance of semiconductor detector systems. Today, DPPs have practically supplanted analog systems for output signal filtering and shaping. DPPs apply appropriate algorithms to filter the pulse and extract the pulse amplitude. DPPs offer several advantages over traditional analog systems: very high resolution (low signal-to-noise ratio), reduced ballistic deficit, higher throughput, and better stability.

All of these components, a PIN or SDD detector, cooled with a Peltier cooler, as well as the readout electronics, are small enough to easily fit on a small handheld XRF instrument. Let us briefly review the basic physical principles of semiconductor detectors.

## 19.2 Semiconductor Detector Fundamentals: Signal Formation

There are several fundamental textbooks which detail the relevant aspects of semiconductor detector physics and signal processing [2, 6, 7]. In addition, many research articles have been published over the decades of development of semiconductor detectors, fabrication technology, and associated electronics. Here we give just a brief review of the principles behind semiconductor detectors and readout electronics.

Semiconductor detectors are basically solid-state ionization chambers that have several advantages over gas ionization chambers.

- The average energy for creating electron–hole pair in Si is one order of magnitude (3.65 eV) smaller than those of gases ( $\approx 30$  eV).
- The high density ( $2.33 \text{ g/cm}^3$ ) of Si permits the construction of detectors of relatively low thickness with sufficient quantum efficiency (high stopping power).
- In Si, electrons and holes have high mobility ( $\mu_n = 1450 \text{ cm}^2/\text{V}\cdot\text{s}$ ,  $\mu_h = 450 \text{ cm}^2\text{s}\cdot\text{V}$ ), which leads to short collection time, i.e. high counting rate.
- Excellent mechanical rigidity simplifies a device design.
- Elements of front-end electronics and a detector can be integrated into a single device.

In the simplest configuration, an absorbing medium is capped by a pair of electrodes with an applied voltage, as illustrated in Figure 19.1. Absorbed radiation liberates charge in the form of electron–hole pairs.

$$Q_s = \frac{E}{E_i} e \quad (19.1)$$

where  $E$  is absorbed energy,  $E_i$  is the energy required to form a charge pair, and  $e$  is the electronic charge [6]. In the presence of electric field, carriers move (drift) parallel to the field. Due to interaction with crystal lattice, the velocity does not depend on the time during which the carrier is accelerated. This is because the carrier is always in equilibrium with the crystal lattice since the characteristic times of phonon excitation are much smaller than the transport time. So, the carrier velocity is only a function of electric field

$$\vec{v}(x) = \mu \vec{E}(x) \quad (19.2)$$

The moving charge induces an electrical current in the external circuit. It is important to understand that signal current begins instantaneously and reaches its maximum when electrons reach the anode. The instant current induced by moving charge is stated by Ramo's (or Ramo–Schokley) theorem [6].

$$i_k = -q\vec{v} \cdot \vec{E}_Q \quad (19.3)$$

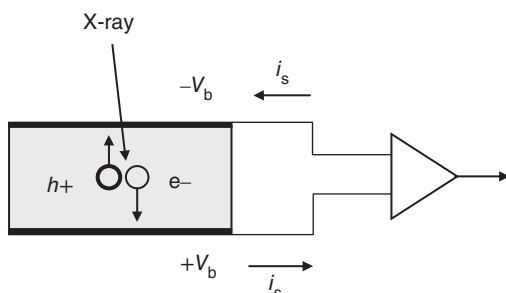


**Figure 19.1** The detector and amplifier.

Or, in scalar form, that current  $i$  induced on a given electrode due to the motion of a charge is given by:

$$i = E_v q v \quad (19.4)$$

where  $q$  is the moving electric charge;  $v$  is its instantaneous velocity, and  $E_v$  is the component of the electric field (weighting field) in the direction of  $v$  at the charge's instantaneous position, under the following conditions: charge removed, given electrode raised to unit potential, and all other conductors grounded.

### 19.2.1 Parallel Plate Geometry with Uniform Field

A semiconductor detector with very large overbias can be approximated by uniform field. The bias voltage  $V_b$  is applied across the electrode spacing  $d$ . The electric field

$$E = \frac{V_b}{d} \quad (19.5)$$

determines the motion of the charge carrier in the detector. The carrier's velocity

$$v = \mu E = \mu \frac{V_b}{d} \quad (19.6)$$

The weighting field is obtained by applying unit potential to the collection electrode and grounding the other:

$$E_v = \frac{1}{d} \quad (19.7)$$

So induced current

$$i = qvE_v = q\mu \frac{V_b}{d} \frac{1}{d} = q\mu \frac{V_b}{d^2} \quad (19.8)$$

Since the electric field and the weighting field are uniform throughout the detector, the current is constant until the charge reaches its terminal electrode.

Assume that the charge is created at the opposite electrode and transverses the detector thickness  $d$ . The required collection time, i.e. the time required to traverse the distance  $d$

$$t_c = \frac{d}{v} = \frac{d}{\mu \frac{V_b}{d}} = \frac{d^2}{\mu V_b} \quad (19.9)$$

The induced charge

$$Q = it_c = q\mu \frac{V_b}{d^2} \frac{d^2}{\mu V_b} = q \quad (19.10)$$

Next assume an electron-hole pair formed at coordinate  $x$  from the positive electrode. The collection time for the electron

$$t_{ce} = \frac{x}{V_c} = \frac{xd}{\mu_e V_b} \quad (19.11)$$

and the collection time for the hole

$$t_{ch} = \frac{d-x}{V_c} = \frac{(d-x)d}{\mu_h V_b} \quad (19.12)$$

Since electrons and holes move in opposite directions, they induce current of the same sign at a given electrode, despite their opposite charge. The induced charge due to the motion of the electron

$$Q_e = e\mu_e \frac{V_b}{d^2} \frac{xd}{\mu_e V_b} = e \frac{x}{d} \quad (19.13)$$

Correspondingly, the hole contributes

$$Q_h = e\mu_h \frac{V_b}{d^2} \frac{(d-x)d}{\mu_h V_b} = e \left(1 - \frac{x}{d}\right) \quad (19.14)$$

Assume that  $x = d/2$ . After the collection time for the electron

$$t_{ce} = \frac{d^2}{2\mu_e V_b} \quad (19.15)$$

The induced charge is  $e/2$ . At this time the hole, due to its lower mobility  $\mu_h \approx \mu_e/3$ , has induced  $e/6$ , yielding a cumulative induced charge of  $2e/3$ . After the additional time for the holes collection, the remaining charge  $e/3$  is induced, yielding the total charge  $e$ . The measured charge depends on the integration time. An integration time larger than the collection time of all charge carriers yields the full charge. A shorter integration time yields a fractional charge.

## 19.2.2 Detectors' Resolution: Physical Limit and Electronic Noise Influence

### 19.2.2.1 Fluctuation in Signal Charge: Fano Factor

A key characteristic of signal sensors is not just the magnitude of the signal, but also the fluctuation of the signal for a given absorbed energy. Both determine the minimum signal threshold and the relative resolution  $\Delta E/E$ . One of the remarkable features of the signal fluctuations in semiconductor detectors is that they are smaller than the simple statistical variance

$$\sigma_Q = \sqrt{N_Q} \quad (19.16)$$

A detailed calculation of this phenomenon is quite complicated, so the following derivation introduces some simplifications to illustrate the basic mechanism.

Two mechanisms contribute to the mean ionization energy. First, conservation of momentum requires excitation of lattice vibrations, and second, many modes are available for momentum and energy transfer with excitation energy less than the bandgap. Energy can be absorbed by either lattice vibration, i.e. phonon production without ionization (electron–hole pair production), or ionization, i.e. formation of a mobile charge pair. Let us assume that absorbed energy produced  $N_x$  excitations (phonons) and  $N_{ion}$  ionizations charge pairs. The sum of the energies going into excitation and ionization is equal to the energy deposited by incident radiation

$$E_0 = E_{ion} N_{ion} + E_x N_x \quad (19.17)$$

where  $E_{ion}$  and  $E_x$  are the energy required for a single ionization or excitation. In semiconductors,  $E_{ion}$  is the bandgap and  $E_x$  is the average phonon energy. Assuming Gaussian statistics, the variance in the number of excitations  $\sigma_x = \sqrt{N_x}$

and the variance in the number of ionizations  $\sigma_{ion} = \sqrt{N_{ion}}$ . For a single event, the energy deposited in the detector is fixed (although can vary from one event to the next). If the energy required for excitation is much smaller than required for ionization, sufficient degree of freedom will exist for some combination of ionization and excitation process to dissipate precisely the deposited energy. Hence, for a given energy deposited in the sample, a fluctuation in excitation must be balanced by an equivalent fluctuation in ionization:

$$E_x \Delta N_x + E_{ion} \Delta N_{ion} = 0 \quad (19.18)$$

If for a given event more energy goes into ionization, less energy will be available for excitation. Averaging over many events, this means that the variance in the energy allocated to the two types of processes must be equal:  $E_{ion} \sigma_{ion} = E_x \sigma_x$ , so,

$$\sigma_x = \frac{E_x}{E_{ion}} \sqrt{N_x} \quad (19.19)$$

From the total energy (19.18) we can extract

$$N_x = \frac{E_0 - E_{\text{ion}} N_{\text{ion}}}{E_x} \quad (19.20)$$

And insert this into (19.19) to obtain

$$\sigma_i = \frac{E_x}{E_{\text{ion}}} \sqrt{\frac{E_0}{E_x} - \frac{E_{\text{ion}}}{E_x} N_{\text{ion}}} \quad (19.21)$$

Overall, the number  $N_Q$  of charge pairs formed is the total deposited energy  $E_0$  divided by the energy deposition required to produce a charge pair. Since each ionization forms a charge pair that contributes to the signal,

$$N_{\text{ion}} = N_Q = \frac{E_0}{E_i} \quad (19.22)$$

Thus, the variance in ionization process

$$\sigma_{\text{ion}} = \frac{E_x}{E_{\text{ion}}} \sqrt{\frac{E_0}{E_x} - \frac{E_{\text{ion}}}{E_x} \frac{E_0}{E_i}} \quad (19.23)$$

which can be rewritten as

$$\sigma_{\text{ion}} = \sqrt{\frac{E_0}{E_i}} \sqrt{\frac{E_x}{E_{\text{ion}}} \left( \frac{E_i}{E_{\text{ion}}} - 1 \right)} \quad (19.24)$$

The second factor on the right-hand side is called the Fano factor  $F$ . Since  $\sigma_{\text{ion}}$  is proportional to the variance in signal charge  $Q$  and the number of charge pairs is  $N_Q = E_0/E_i$ ,

$$\sigma_Q = \sqrt{F N_Q} \quad (19.25)$$

In silicon  $E_x = 0.037$  eV,  $E_{\text{ion}} = E_g = 1.1$  eV, and  $E_i = 3.6$  eV for which the above expression yields  $F = 0.08$ , in reasonable agreement with the measured value  $F = 0.1$ . Thus, the variance of the signal charge is smaller than naively expected,  $\sigma_Q \approx 0.3 \sqrt{N_Q}$ .

A similar treatment can be applied if the degrees of freedom are much more limited, and Poisson statistics are necessary. However, when applying Poisson statistics to the situation of a fixed energy deposition, which imposes an upper bound on the variance, one cannot use the usual expression for variance:  $\text{var } N = N$ . Instead, the variance is  $(N - \bar{N})^2 = F\bar{N}$ , as shown by Fano in the original paper. An accurate calculation of the Fano factor requires a detailed accounting of the energy-dependent cross-sections and the density of states of the phonon modes. One can use this result to calculate the intrinsic resolution of semiconductor detectors

$$\Delta E_{\text{FWHM}} = 2.35 \cdot E_i \sqrt{F N_Q} = 2.35 \cdot E_i \sqrt{F \frac{E}{E_i}} = 2.35 \cdot \sqrt{F E E_i} \quad (19.26)$$

where in Si  $E_i = 3.62$  eV, and in Ge  $E_i = 2.9$  eV. For both the Fano factor  $F \approx 0.11$ . So, in well-designed detector systems, detectors have sufficiently small capacitance that, together with low noise readout electronics, allows electronic noise of  $\leq 80$  eV FWHM; so, the variance of the detector signal is a significant contribution. For example, Si detector intrinsic noise at 5895 eV (Mn K $\alpha$  line emitted by the  $^{55}\text{Fe}$  isotope source) is  $\Delta E = 114$  eV, which is the theoretical limit for detector system energy resolution at this X-ray photon energy.

### 19.2.2.2 Recombination and Trapping

One might expect that electrons and holes generated by absorbed X-ray photon will quickly recombine. However, it is not the case for Si (and Ge) because of several reasons. First, electrons and holes are dispersing by diffusion and second, they are separating by applied electric field. Furthermore, silicon is an indirect semiconductor

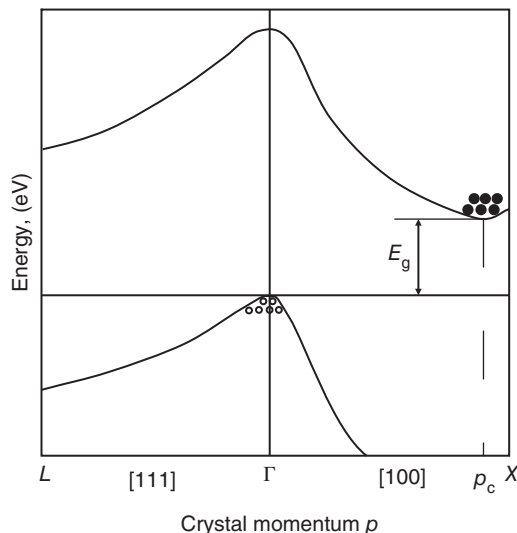


**Figure 19.2** Schematic presentation of the bond structure versus crystal momentum in indirect semiconductors (Si, Ge). In Si, the minimum bandgap associated with nonzero crystal momentum (wavevector).

and annihilation of electrons at the bottom of the conduction band and holes at the top of the valence band by direct transition is suppressed. This is because the bottom of the conduction band and the top of the valence band are offset in momentum space, and large momentum transfer to the crystal lattice is required for electron–hole annihilation to take place (see Figure 19.2).

This momentum offset needs to be found from another source, for example from lattice vibrations – phonons. Thus, in indirect semiconductors, annihilation is a two-step process. This leads to carrier's lifetime being significantly larger (ms) than collection time (ns). Impurities and crystal defects (vacancies, dislocations) can introduce additional energy levels (states) in the bandgap, which can trap charge. That drastically decreases the carrier's lifetime, and increases thermally generated current due to “stepping stone effect.” This leads to increased collected charge fluctuation and also increased background at low energy.

Impurities and crystal structure imperfections can act as traps for charge carriers. Traps can capture and remove mobile carriers available for signal formation. On the other hand, thermal excitation and applied electric field can release the carrier from the trap, resulting in delayed charge collection. In X-ray or gamma spectroscopy, these effects can lead to smear the signal distribution to lower energies. Even small amounts of trapping can lead to significantly low energy tails that adversely affect the ability to separate adjacent lines.

### 19.2.2.3 Thermal Noise

At any nonzero temperature, some thermal energy is shared by the electrons in the crystal. It is possible for a valence electron to gain sufficient thermal energy to be elevated across the bandgap into the conduction band, and leave a vacancy in the valence band, resulting in creation of the electron–hole pair. The motion of both of these charges contributes to the observed conductivity of the material. The probability per unit time that an electron–hole pair is thermally generated is given by

$$p(T) = CT^{3/2} \exp\left(-\frac{E_g}{2kT}\right) \quad (19.27)$$

where  $T$  is the absolute temperature,

$E_g$  is the bandgap energy,

$k$  is the Boltzmann constant,

$C$  is the proportionality constant characteristic of the material.

As reflected in the exponential term, the probability of the thermal excitation is critically dependent on the ratio of the bandgap energy and absolute temperature, and can be decreased drastically if the material is cooled.

Thermal excitations cause not only fluctuations in the number of electron–hole pair, but also charge carrier velocity fluctuations. The spectral density of the noise power caused by thermal fluctuations can be derived directly as the long wavelength limit of in Planck's theory of blackbody radiation.

#### 19.2.2.4 Leakage Current

PIN diodes and SDDs are reverse-biased devices. Ideally, reverse bias removes all mobile carriers from the junction volume, so no current can flow. However, thermal excitation can promote electrons across the bandgap, and a current flows even in the absence of radiation, hence the terms “dark current” or “leakage current.” The probability of electrons surmounting the bandgap is increased strongly by the presence of impurities in the lattice, as they introduce intermediate energy states in the gap that serve as “stepping stones,” as well as for recombination transitions. The reverse bias current depends exponentially on temperature

$$I_l \propto T^2 \exp\left(\frac{E_g}{2kT}\right) \quad (19.28)$$

where  $E_g$  is the bandgap energy and  $k$  the Boltzmann constant, so cooling the detector can reduce leakage substantially. The ratio of leakage currents at temperatures is:

$$\frac{I_l(T_2)}{I_l(T_1)} = \left(\frac{T_2}{T_1}\right)^2 \exp\left[-\frac{E_g}{2k} \left(\frac{T_1 - T_2}{T_1 T_2}\right)\right] \quad (19.29)$$

In Si ( $E_g = 1.12$  eV), this yields a 10-fold reduction in leakage current when the temperature is lowered by 14 °C from room temperature. In some situations surface leakage current can be as high as bulk leakage current or even greater. This can be prevented by use of guard rings. Leakage current is one of the most important factors that affect detectors resolution. So, only high-purity Si (low impurity and defect concentration) should be used for detector manufacturing. In general, in high-quality detectors, leakage current should not be higher than 1 nA/cm<sup>2</sup>.

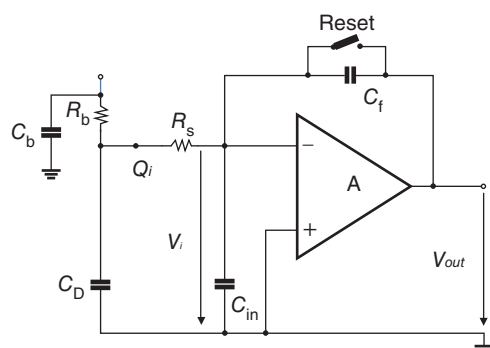
#### 19.2.2.5 Signal Formation and Energy Resolution

Once an X-ray photon is detected and current pulse is formed by sensor, it needs to be amplified. Several types of amplifiers can be used for this purpose. However, the most popular preamplifier which is used with semiconductor detectors in laboratory and portable spectrometers is the charge-sensitive preamplifier invented by Emilio Gatti in 1956. It is represented in Figure 19.3.

The basic building block is an inverting voltage amplifier with high input resistance. Typically in the first amplification stage, a junction gate field-effect transistor (JFET) or metal-oxide-semiconductor field-effect transistor (MOSFET) is used. For the inverting amplifier, the voltage gain is:

$$\frac{dV_{out}}{dV_i} = -A \text{ and } V_{out} = -AV_i. \quad (19.30)$$

**Figure 19.3** Principle of charge-sensitive amplifier.  $C_d$  represents a detector capacitance,  $R_s$  series resistance,  $C_{in}$  total input capacitance that includes amplifier input capacitance and stray capacitance, and  $C_f$  feedback capacitance. The reset switch is used for bringing the system into its operation condition.



Thus, the charge deposited on  $C_f$  is:

$$Q_f = C_f V_i = C_f(A + 1)V_i \quad (19.31)$$

We can assume an infinite input resistance, i.e. input current cannot flow into the amplifier, and all input current must charge up  $C_f$  and  $Q_f = Q_i$ . In this case the amplifier “dynamic” input capacitance is

$$C_i = \frac{Q_i}{V_i} = C_f(A + 1) \quad (19.32)$$

The voltage output per unit input charge

$$A_q = \frac{V_{\text{out}}}{Q_i} = \frac{AV_i}{C_i V_i} = \frac{A}{C_i} = \frac{A}{A + 1} \cdot \frac{1}{C_f} \approx \frac{1}{C_f} \quad (A \gg 1) \quad (19.33)$$

Or output voltage is

$$V_{\text{out}} \approx \frac{Q_i}{C_f} \quad (19.34)$$

Consequently, arriving X-ray photons will form a “step like” output signal until the reset switch brings the system back to its initial operational condition (when maximum output voltage will be reached), as in shown in Figure 19.4.

As already discussed above, the ionization process results in statistical signal peak broadening given by

$$\sigma_Q = \sqrt{FN_Q} \quad (19.35)$$

Repetitive measurements of the signal charge yields a Gaussian distribution, where standard deviation equals the root mean square (RMS) noise level. This allows calculation of the equivalent energy broadening (when the

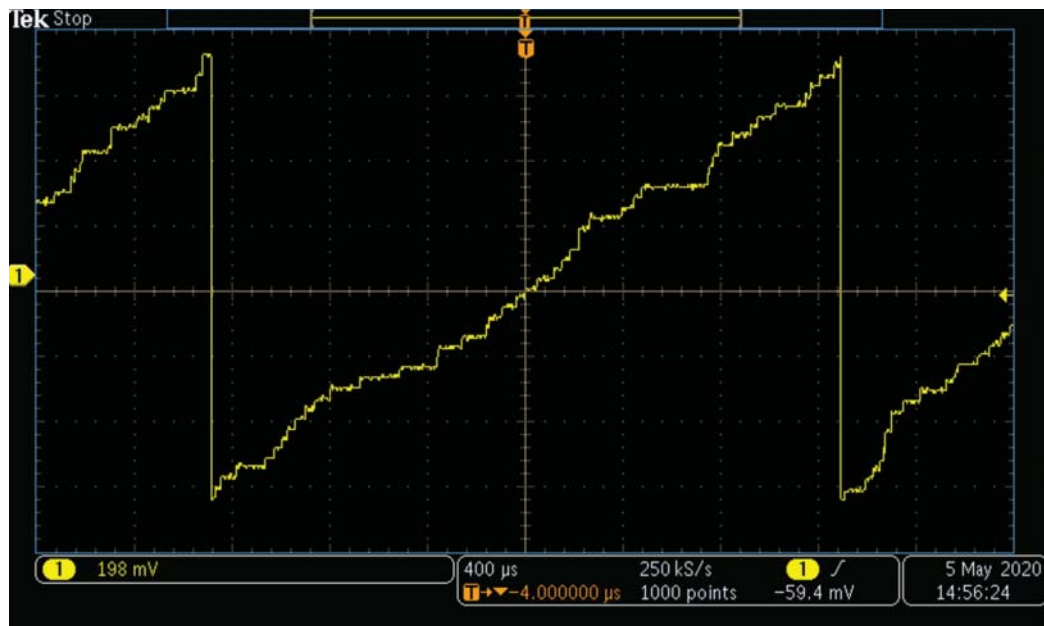


**Figure 19.4** Output signal of the charge-sensitive amplifier between two resets. Small steps correspond to X-ray photon detection events.

electronic noise is zero), which is known as detector dispersion or “Fano noise,” that is the detector resolution limit

$$\frac{\sigma(E)}{E} = \frac{\sigma(N_Q)}{N_Q} = \sqrt{\frac{F}{N_Q}} = \sqrt{\frac{FE_i}{E}} \quad (19.36)$$

$$\sigma(E) = \sqrt{FE_i E} \quad (19.37)$$

It is common practice to express energy peak broadening (“detector resolution”) in terms of the full-width at half-maximum (FWHM) as shown in Figure 19.5, although the correct definition for energy resolution is  $\Delta E/E$

$$R = \Delta E = 2.355\sigma(E) = 2.35 \sqrt{FE_i E} \quad (19.38)$$

In addition to signal fluctuations originating in the sensor, the detector resolution (and detection limit) is affected by fluctuations introduced by electronics. Electronics noise introduces baseline fluctuations, which are superimposed on the signal and alter the peak amplitude. Electronics noise and “Fano noise” are not correlated and they sum in quadrature

$$R^2 = \Delta E^2 + N_{el}^2 \quad (19.39)$$

The typical detector front-end equivalent scheme used for noise analysis is represented in Figure 19.6.

The detector is represented by capacitance  $C_D$ , the current noise generator  $i_{nd}$  models the “shot noise” caused by the detector leakage current. Resistors exhibit noise due to thermal velocity fluctuations of the charge carriers. This noise can be modeled as a voltage or a current generator. Resistors shunting the detector input act as a noise

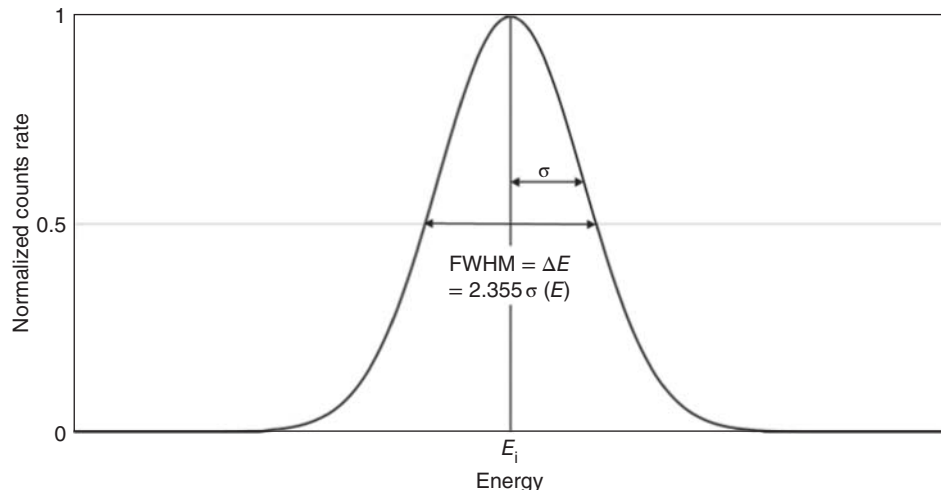


**Figure 19.5** Definition of resolution.

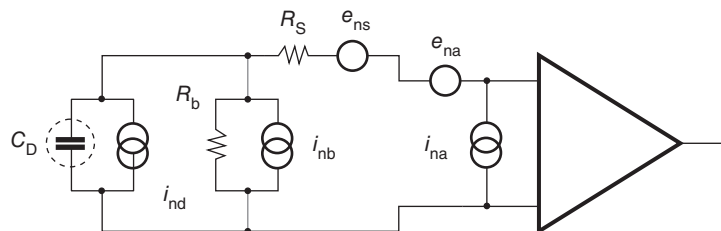


**Figure 19.6** An equivalent detector front end electronics circuit for noise calculations.

current generator, while resistors in series with the input act as voltage noise sources. Since the bias resistor effectively shunts the input because  $C_b$  (see Figure 19.3) passes current fluctuations to the ground, it acts as a current generator  $i_{nb}$ , and its noise has the same effect as the shot noise current from the detector. The series resistor  $R_s$  acts as a voltage generator. In-depth analysis of the detector's and preamplifier's noise is covered in several fundamental textbooks, for example [1, 4, 5]. Here we give a brief summary of different noise contributions, which are important for understanding of the detectors performance characteristics and their limitations.

#### 19.2.2.6 Johnson (Thermal) or Voltage Noise

When a current flows in resistors and semiconductors, electrons experience scattering on phonons (atomic vibrations), that leads to fluctuations in the electrons' velocities [8]. The degree of scattering depends on the energy  $kT$  of the vibrating atoms and one can write

$$e_n^2 = \frac{dV^2}{df} = 4kTR \quad (19.40)$$

Similarly, for the current

$$i_n^2 = \frac{di^2}{df} = \frac{4kT}{R} \quad (19.41)$$

The largest component of voltage noise is usually the JFET channel resistance, because of the coupling to the gate by gate-channel capacitance. This resistance is proportional to the inverse of the JFET transconductance,  $g_m$ , and RMS voltage noise density can be written as

$$e_n^2 = \frac{K4kT}{g_m} \quad (19.42)$$

Another contributor to thermal noise is a resistance of the back layer of the sensor and physical contact between the sensor and JFET gate that are in series with the JFET channel resistance. So,  $R_s$  will contribute to the voltage noise as

$$e_n^2 = 4kTR_s \quad (19.43)$$

#### 19.2.2.7 Current or Shot Noise

The current that flows in sensors is the result of many individual moving charges and experiences fluctuations due to different physical factors that result in noise. The spectral density of current or shot noise can be given as

$$i_n^2 = 2eI \quad (19.44)$$

where  $e$  is electronic charge and  $I$  is the average current.

Trapping and detrapping processes in resistors, dielectrics, and semiconductors can introduce additional fluctuations whose noise power frequently exhibits a  $1/f$  spectrum with spectral density of its voltage as:

$$e_{nf}^2 = \frac{A_f}{f} \quad (19.45)$$

The amplifier's noise is described fully by a combination of voltage and current sources at its input, shown in Figure 19.6 as  $e_{na}$  and  $i_{na}$ . So, for the circuit in Figure 19.6, one can write four noise components as

$$i_{nd}^2 = 2eI_d \quad (19.46)$$

$$i_{nb}^2 = \frac{di^2}{df} = \frac{4kT}{R_b} \quad (19.47)$$

$$e_{ns}^2 = 4kTR_s \quad (19.48)$$

$$e_{nf}^2 = \frac{A_f}{f} \quad (19.49)$$

Since individual noise contributions are random and uncorrelated, so that they add in quadrature.

### 19.2.2.8 Equivalent Noise Charge

Above, the noise contributions have been expressed in terms of voltage and current. It is often more useful to express them in the quantity to be measured. The noise level is then specified as the signal level for which the signal-to-noise ratio (S/N) equals one. So, detector systems that measure signal charge can be characterized in terms of equivalent noise charge (ENC). This is the signal charge that yields a signal-to-noise ratio (S/N) of one.

$$\text{ENC} = Q_n = \frac{Q_s}{\text{S/N}} \quad (19.50)$$

where  $Q_s$  is the signal charge. For a given detector material, the signal charge is determined by absorbed energy, then the noise also can be expressed in terms of energy – eV, keV, or in electrons. For example in Si  $Q_n = 1e$  corresponds to 3.64 eV. Then, energy resolution for ionization energy  $E_i$  is

$$\Delta E_n = E_i \cdot \text{ENC} \quad (19.51)$$

Equivalent noise charge is the most convenient measure of system noise when designing or characterizing detector systems. Nevertheless, in analyzing individual noise contributions, the basic noise parameters – voltage and current – are more useful.

The signal produced by the detector usually is not used directly; it is further amplified and shaped. The purpose of these procedures is to optimize the signal-to-noise ratio, to reduce interference between subsequent signals, to minimize the ballistic deficit effect, and to form signal shape for more accurate amplitude measurements. Mathematically, the pulse shaper can be presented in the form of a weighting function (see for details [6, 9]). In this case the ENC is given as

$$Q_n^2 = \frac{1}{2} i_n^2 \int_{-\infty}^{\infty} [W(t)]^2 dt + \frac{1}{2} C^2 e_n^2 \int_{-\infty}^{\infty} [W'(t)]^2 dt \quad (19.52)$$

The weighting function can be expressed in terms of characteristic time usually as “shaping time” or “peaking time.” This leads to a general formulation of the equivalent noise charge

$$Q_n^2 = i_n^2 F_i T_S + e_n^2 F_v \frac{C^2}{T_S} + F_{vf} A_f C^2 \quad (19.53)$$

where  $F_i$ ,  $F_v$ , and  $F_{vf}$  depend on the shape of the pulse determined by the shaper for a step unit and  $T_S$  is the characteristic time, whose choice, in general, depends on the type of the shaper.

For the circuit shown in Figure 19.6

$$Q_n^2 = \left( 2eI_d + \frac{4kT}{R_b} + i_{na}^2 \right) F_i \tau_S + (4kTR_s + e_{na}^2) F_v \frac{C_d^2}{\tau_S} + F_{vf} A_f C_d^2 \quad (19.54)$$

where  $e$  is the electronic charge;  $I_d$  is the detector leakage current;  $k$  is the Boltzmann constant;  $i_{na}$  is the JFET leakage current (typically negligible);  $R_b$  is the bias resistor;  $R_s$  is the total series resistance;  $C_d$  is the detector capacitance;  $e_{na}$  is the amplifier noise parameter;  $A_f$  is the device-specific noise parameter that determines 1/f noise contribution;  $F_i$ ,  $F_v$ , and  $F_{vf}$  are the shaper parameters; and  $\tau_s$  is the shaping time.

The typical dependence of the ENC as a function of shaping time and basic noise parameters is shown in Figure 19.7.

In real detector system analysis, the detector capacitance needs to be substituted with the sum of all capacitance shunting the input, i.e. the sensor capacitance, the preamplifier input capacitance, and stray capacitance (wire, etc.).

The summary:

- ENC strongly depends on leakage current that depends on temperature.
- ENC strongly depends on the capacitance at the preamplifier input.
- ENC strongly depends on voltage noise parameter of the preamplifier.

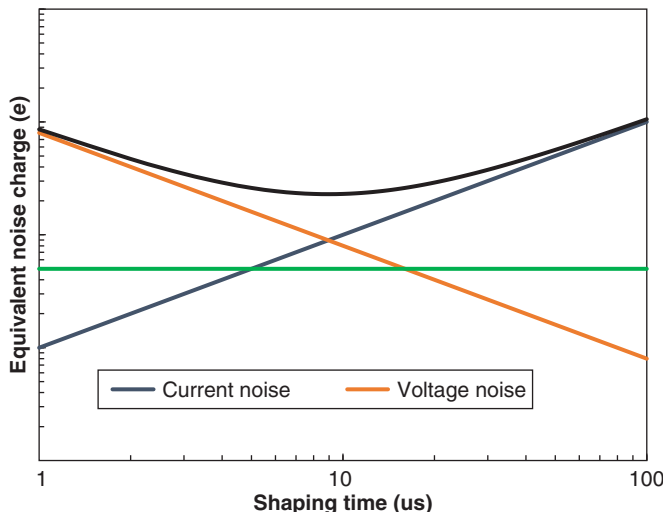


**Figure 19.7** Equivalent noise charge as a function of shaping time. The green line is  $1/f$  noise contribution and the black line is the resulting ENC.

- Signal-to-noise ratio can be improved by the optimal shaper design.
- The current and voltage contribution to ENC depend on shaping time: the current noise increases with shaping time, but the voltage noise decreases with  $\tau_s$ , and the optimal shaping time corresponds to the equal values of these contributions.
- The  $1/f$  noise contribution can be minimized by optimization of the shaper frequency band.

In general, to improve the detector system energy resolution, the developer should to strive to:

- Improve quality of start material and fabrication processes to decrease leakage current.
- Design the sensor and preamplifier with as low as possible capacitance.
- Design preamplifier with low voltage noise, mainly first amplification stage.
- Design an optimal shaper.

## 19.3 Detectors for Portable Spectrometers: Design and Performance

### 19.3.1 Si-PIN Diode Detectors

A silicon PIN diode, employing a simple planar geometry, is the basic style of semiconductor X-ray detectors. From the early 1980s until today, most have been produced using slightly n-doped, 400–5000  $\mu\text{m}$  thick,  $<111>$  silicon wafer, of  $5\text{ k}\Omega$  resistance. Figure 19.8 shows the cross-section of a typical PIN diode detector fabricated using the planar technology introduced by J. Kemmer in 1980. Typical wafer thickness is 400–625  $\mu\text{m}$  and resistance 5–10  $\text{k}\Omega$ .

The p+ and n+ layers are formed by introducing dopants. The similarly doped area shown on the left and right sides of the entrance window contact (“cathode”) forms a guard ring that isolates the detector diode from the edge of the chip. The guard ring is necessary because mechanical damage of the edge leads to unacceptably high leakage current. The guard ring can be grounded or floating. Electrical contacts are formed by deposited metal layers, typically aluminum. The intermediate surface between electrodes is protected by a dielectric layer of  $\text{SiO}_2$ .

When sufficient reverse voltage  $V_b$  is applied, the detector gets fully depleted. The depletion width is

$$w_d = \sqrt{\frac{2\varepsilon(V_b + V_{bi})}{Ne}} \quad (19.55)$$

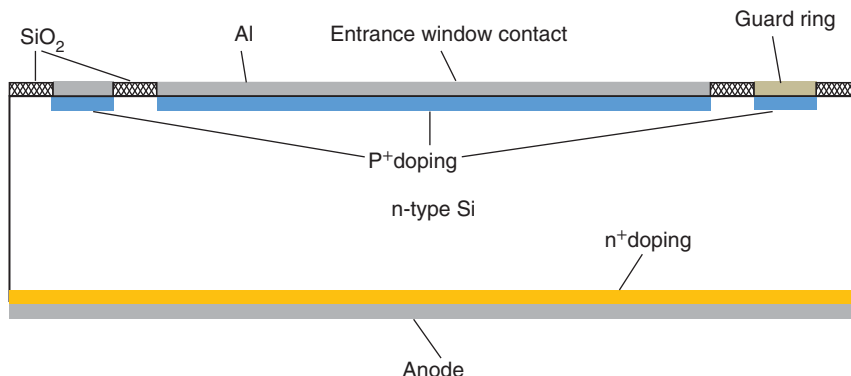


**Figure 19.8** Cross-section of a PIN-diode detector. Typically the entrance window connected to the gate electrode of the JFET.

where  $\epsilon$  is the dielectric constant (for Si  $11.9\epsilon_0$ ),  $V_{bi}$  is the inbuilt junction potential ( $\approx 0.5$  V for Si), and  $N$  is the dopant concentration. When the detector is fully depleted, the leakage current at given temperature and the detector capacitance

$$C = \epsilon \frac{A}{w_d} \quad (19.56)$$

is minimal. For example, the capacitance of the XPIN-6 detector from Moxtek, Inc., with  $6 \text{ mm}^2$  sensitive area, is about  $1.8 \text{ pF}$ .

Figure 19.9 presents the typical design of the PIN diode detector, packaged in a TO-8 can, which is the most common design for portable X-ray spectrometers. The sensor chip, together with JFET and thermistor (or a diode), is mounted on the ceramic substrate that is then placed on the two-stage Peltier TEC. The detector sensitive surface is apertured by an internal collimator to eliminate edge effects caused by incomplete charge collection. These affects can lead to poor peak-to-background ratio and formation of “ghost” peaks in the XRF spectra. All the necessary connections between metallized contacts and case pins are done by wire bonding. The detector assembly is protected with a nickel cap with a thin X-ray transparent window. The detector volume is evacuated and sealed. In most cases, manufacturers install getters inside of the sealed enclosure which allow the pressure inside to be kept low enough for several years.

The first amplification stage is typically a discrete JFET, with integrated feedback capacitor of about  $50 \text{ fF}$ , although several groups have reported fabrication of PIN diode detectors with integrated “on-chip” field-effect transistors (FETs) [10]. An example of the typical PIN diode detector design in TO-8 package is shown in Figures 19.9 and 19.10.

The entrance vacuum-tight and light-tight window is a very important part of the detector package. The window must provide good sealing and low absorption of the X-ray in a wide energy range. The most frequently used windows are made from vacuum-tight beryllium (Be) foils of  $8$  and  $25 \mu\text{m}$  thickness.

For better resistance to harsh environment, some manufacturers protect the Be window with a thin coating. For example, the DuraBerillium window from Moxtek is protected with DuraCoat® coat: a proprietary refractory material consisting of elements lighter than sodium that ensure beryllium windows stay vacuum tight in harsh environments. This product is highly resistant to moisture, chemicals, and abrasion, making it ideal for XRF applications. The Be window limits detector sensitivity at low energies, below  $1.5 \text{ keV}$ . When enhanced X-ray transmission at low energies is important, materials other then Be windows can be used, which will be discussed below.

The detectors for portable and handheld spectrometers are made as single modules together with a small low-noise preamplifier. The preamplifier is placed into aluminum housing that provides electromagnetic (EMI) shielding, and serves as a heatsink for the TEC’s hot side. The typical design of the detector for handheld EDXRF

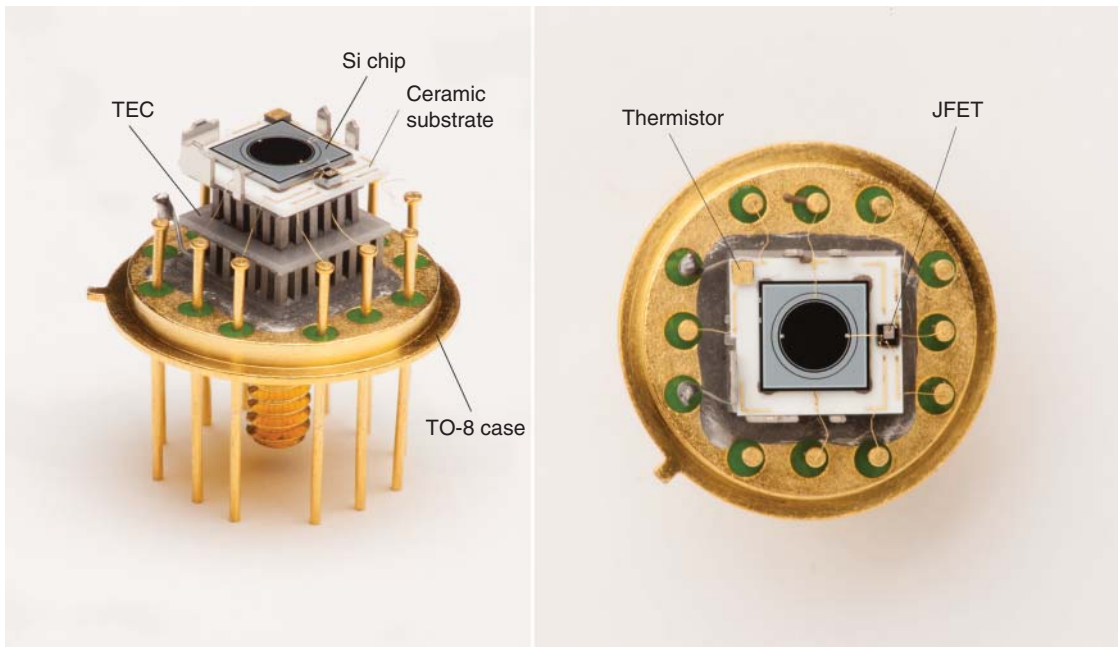


**Figure 19.9** Typical design of the Si-PIN detector in TO-8 case. Moxtek, Inc., XPIN-6 detector. *Source:* Courtesy of Moxtek, Inc.



**Figure 19.10** Typical design of the PIN diode detector module for handheld EDXRF spectrometer. XPIN-6 and XPIN-13 from Moxtek, Inc. *Source:* Courtesy of Moxtek, Inc.

spectrometers is presented in Figure 19.10. The two-stage TEC is effective enough to provide  $\Delta T$  between the detector chip and the detector housing up to  $80^\circ\text{C}$  at reasonable power consumption of about 0.5 W. So, the detector can operate at  $-35^\circ\text{C}$ , or even lower when higher resolution is required.

The typical resolution of PIN diode detectors lies within an interval of 150–200 eV at 5895 eV ( $\text{Mn K}_\alpha$  line obtained from  $^{55}\text{Fe}$  isotope source) and strongly depends on the detector sensitive area, i.e. the detector capacitance, as is shown in Figure 19.11. However, PIN diode detectors produce fast signals and demonstrate good stability with counting rate. The counting rate mainly is limited by shaping time of the pulse processor.

Despite the fact that SDDs today have better performance parameters, Si-PIN detectors are used in portable XRF spectrometers when price is the primary consideration, for example, in some handheld spectrometers from Bruker Nano Analytics and Olympus NDT. The major Si-PIN diode detector manufacturers are currently Moxtek, Inc., and Amptek, Inc.

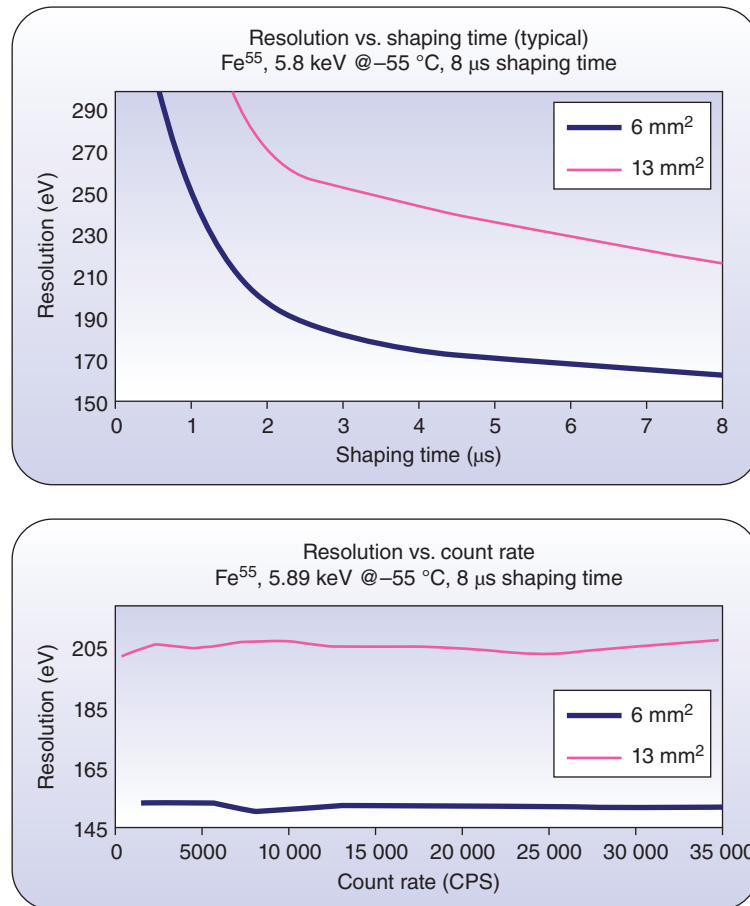


**Figure 19.11** Resolution of Si-PIN detectors as a function of peaking time, taken with detectors with different sensitive areas (upper part), and resolution stability against counting rate taken at a constant peaking time. XPIN-6 and XPIN-13 Si-PIN detectors from Moxtek, Inc.

## 19.4 Silicon Drift Detectors

In 1984 E. Gatti and P. Rehak presented a brilliant invention – a semiconductor drift chamber. Initially this device was designed and used as a particle-tracking position-sensitive detector. Later, the silicon drift chamber or SDD was optimized for X-ray spectrometry.

The main idea underlying the principle of the SDD is to create an electric field in a fully depleted bulk silicon wafer that drives electrons to the same small n+ doped electrode (anode), regardless of the position in which the electron was generated by thermal excitation or by X-ray ionization. In this case, the anode can be very small. In other words, in this structure the charge generated in a large area is collected in small collection electrode: the capacitance of this electrode can be very small (1–50 fF) and almost independent from the detector sensitive area. There are various drift detector topologies optimized for different detector applications [7]. Radial devices (Figure 19.12) are most suitable and interesting for energy measurements [11].

The cross-section of a drift detector is shown in Figure 19.13. The X-ray entrance detector window (top) is formed by a large, uniformly doped p+ area (diode). The opposite side (bottom) is segmented into concentric p+ doped rings (diodes), and at the center of the device there is small n+ doped anode. The drift field is formed by applying

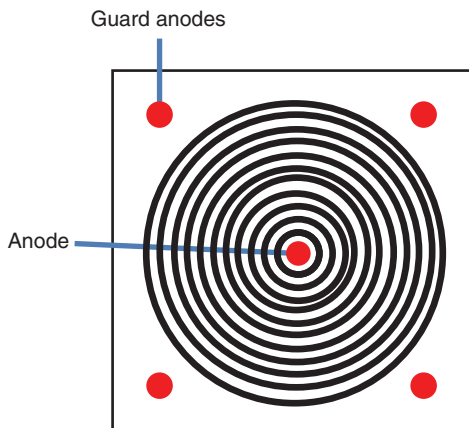


**Figure 19.12** Radial SDD with point-type anode in the center.

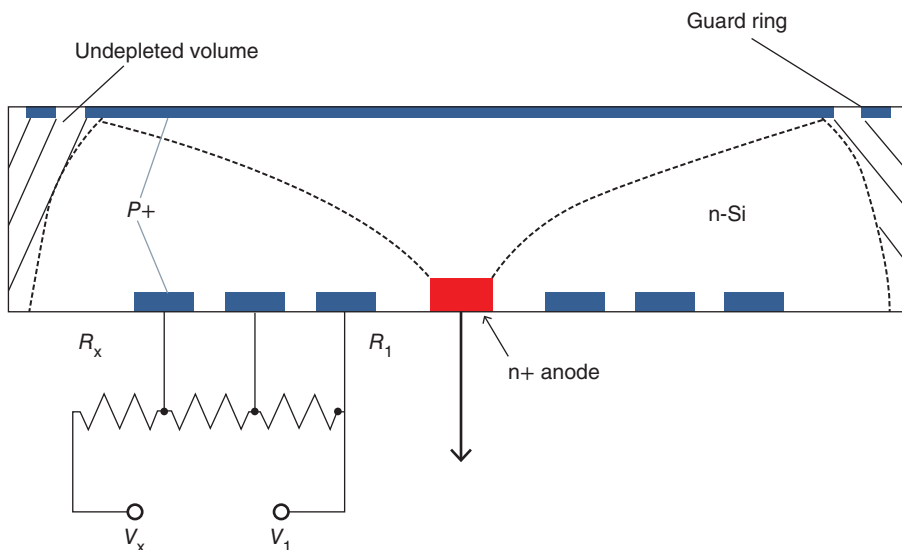


**Figure 19.13** Cross-section of a drift detector.  $R_1$  is the innermost ring,  $R_x$  is the outermost ring. The voltage of the drift rings  $V_1$ ,  $V_x$ , and X-ray entrance window is provided by an external source.

different voltages to n+ rings. By applying suitable voltages to the ring electrodes, one can create the drift field as a potential valley (or funnel) for majority carriers (electrons). So, the field continuously slopes down from the outer edge of the detector sensitive area on the top to the collecting electrode on the bottom.

Such a drift field can be formed by applying different voltages to each electrode from external power supply, but in most cases an integrated voltage divider is used to supply these voltages, which is more practical. However, other methods of rings biasing, for example “self-biasing,” can be used too [2].

The depletion in this type of SDD is achieved by applying voltage to the entrance window electrode that starts to deplete the bulk from the top to the bottom and to the concentric rings, which deplete the bulk from the ring toward the anode. There is a limitation on the attainable drift field, which comes from the condition that the voltage between diodes formed opposite each other on the two wafer surfaces has to be lower than the wafer’s full-depletion voltage. So, the maximum drift field is obtained when the voltage between  $R_1$  and  $R_x$  is slightly lower than the doubled depletion voltage, and the potential of the X-ray entrance window is about halfway in between. Another design replaces concentric rings with a continuous resistive spiral [12].

The anode can be connected to a discrete JFET transistor by a bond pad in the same way as a PIN diode. The negative side of this method is the added stray capacitance of bonding pad and flying wire. The detector with on-chip electronics was developed to overcome this problem [13]. The cylindrical geometry JFET was implanted into the center of the anode. However, the presence of the transistor in the center of the sensitive area leads to some problems with incomplete charge collection that decreases the peak-to-background ratio. To overcome this, perfect symmetry was sacrificed by moving the anode and the JFET to the edge of the device. In this design, the drift field forming electrodes have a droplet shape, and the anode and JFET are protected from X-ray exposure by an internal collimator [14].

Today, the most advanced detector readout electronics are amplifiers integrated in ASICs. ASICs have remarkably low ENC (1–3 electrons RMS) and very low input capacitance. That allows for very good resolution at low temperatures, down to 122 eV at 5895 eV X-ray photon energy, or good resolution <140 eV at moderate cooling or even at room temperature [5]. Improved semiconductor technology results in fabrication of wafers of very high quality. The current density at the anode of  $25 \text{ pA/cm}^2$  has been reported at room temperature. That results in resolution from 148 eV at  $+30^\circ\text{C}$ , down to 124 eV at  $-30^\circ\text{C}$  [15]. Using ASICs also enables low dead time and high count rate, since excellent resolution can be achieved at sub-microsecond peaking times [5, 16].

There are different types of commercially available SDDs for portable spectroscopy on today's market from different manufacturers, such as KETEK GmbH (Germany), PNDetector (Germany), XGLab-Bruker (Italy), and Amptek, Inc. (USA). They offer SDDs with different types of front-end electronics, different sensitive areas ranging from  $7 \text{ mm}^2$  up to  $150 \text{ mm}^2$ , and different shapes: round, droplet, hexagonal, and oval. Typical performance parameters are resolution better than 130 eV within temperature range from  $-60$  to  $-25^\circ\text{C}$ . Some detectors can be used at higher temperatures with a trade-off of poorer resolution. The maximum achievable counting rate is up to 2 Mcps, depending on peaking time.

Traditionally, Be windows of 8–25  $\mu\text{m}$  thickness were used in X-ray detector packages limiting detector sensitivity to low-energy X-rays (<1.5 keV). Now, practically all detector manufacturers have introduced SDDs with windows having good X-ray transparency down to sub-keV energies. Low-noise detector systems equipped with such windows allow detection of light elements.

## 19.5 Si Detectors' Quantum Efficiency: X-Ray Entrance Windows

The Si detectors' quantum efficiency  $I_{\text{reg}}/I_0$  is determined by absorption of X-rays in the detector volume that is given by

$$I = I_0 \exp(-\mu_a \rho x) \quad (19.57)$$

where  $I_0$  is the X-ray intensity at the surface,  $\rho$  is the Si density,  $\mu_a$  is the mass absorption coefficient that decreases generally with energy, and  $x$  is the penetration depth. So, Si detector's quantum efficiency is limited from the high energy side by a decreased value of  $\mu_a$  that can be compensated only by increased thickness of the detector, as is shown in Figure 19.14.

A second important part of semiconductor detector design that affects detector efficiency (or one can call it sensitivity since this parameter includes quantum efficiency of the detector and window transparency) is the entrance X-ray window. The detector X-ray entrance window for portable or handheld EDXRF spectrometers must satisfy following requirements:

- High X-ray transparency within the X-ray energy range of interest.
- Light-tightness.
- Vacuum-tightness.

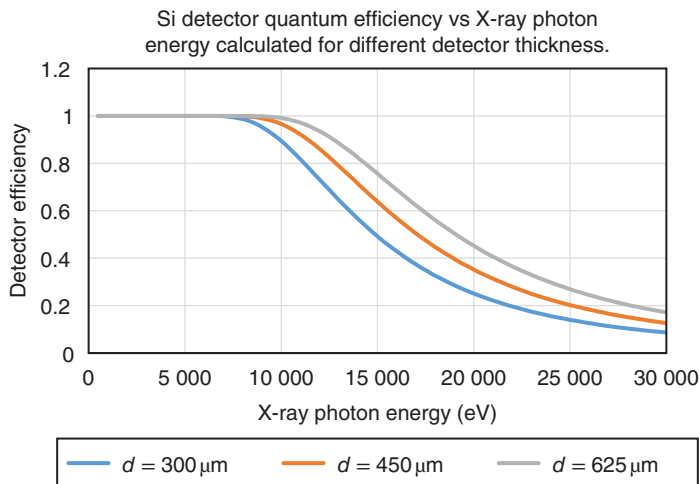


**Figure 19.14** Si detector quantum efficiency as a function of X-ray energy, calculated for detectors of different thickness.

- Must withstand a pressure difference of at least slightly higher than 1 bar and multiple pressure cycles.
- Must withstand multiple temperature cycles typically from approximately  $-20$  to  $+80$  °C.
- Should have a conducting layer for detector EMI shielding.

In many instances these requirements are in opposition to each other. For example, for high X-ray transparency, a window must be made from materials that consist of only light elements, have as low as possible density, and be very thin. Obviously these requirements can be satisfied only for the price of mechanical strength, i.e. can be more easily damaged by pressure differences.

The light-tightness often requires deposition of an additional light-absorbing layer, which also will attenuate low-energy X-rays. Thus, an optimal entrance window design can be achieved by series of reasonable compromises between different parameters. Today all major semiconductor detector manufacturers offer detectors with entrance window that provides enhanced sensitivity to low atomic number ( $Z$ ) elements down to lithium. Typically the low-energy window designs include support structures. Mechanically, the structure supports the film over pressure changes of up to 1.5 atm, and maintains the integrity of the film over thousands of pressure cycles. Optically, the support structure needs a large open area percentage, thereby maximizing the window's X-ray transmission. For example, Moxtek has traditionally made silicon rib support structures, made from silicon wafers. The silicon rib structures are available in an assortment of sizes ranging from 10 to 500 mm<sup>2</sup>.

PNdetector GmbH advertises “pnWindow” used in their SDD<sup>GL</sup> – Genius Line detectors, which allow detection of light elements down to Li with excellent peak-to-background information. The “pnWindow” design is kept as company proprietary information. Amptek, Inc., patented “C-Series” X-ray windows that utilize silicon nitride ( $\text{Si}_3\text{N}_4$ ) with an Al coating. This window extends SDD sensitivity range down to boron. The transparency of the C1 window is around 65% at 1000 eV, and 25% at 500 eV X-ray energy. In their VITUS product line, KETEK GmbH uses an ultrathin AP3.3 polymer window from Moxtek, Inc. Also, in 2015, KETEK reported successful development of a new window based on graphenic carbon [17].

Moxtek's AP3 X-ray windows are specifically made to transmit low-energy X-rays, from about 50 eV and above. This ultrathin polymer membrane allows for detection of X-ray fluorescence of light elements such as boron, carbon, nitrogen, and oxygen, as well as heavier elements. The windows are vacuum tight (less than  $5 \times 10^{-10}$  mbarL/s of He), and can withstand up to 1.5 atm of pressure without breaking. These windows are found in a variety of X-ray detectors throughout the world, including XRF detectors mounted in scanning electron microscopes (SEMs). The AP3 product line windows consist of an ultrathin polymer membrane of 3000 Å, layered with a proprietary

boron hydrate of about 200 Å, and coated with an Al layer of 300 Å thickness. The window's X-ray transmission was calculated and tested at the Advanced Light Source within an energy range of 108–1300 eV. Calculated and experimentally obtained X-ray transmission of the AP3 windows is presented in Figure 19.15. Moxtek has also developed hexagonal support structures for AP3 ultrathin films. Examples of both support structures are shown in Figure 19.16.

The calculated optical transmission of the silicon ribs support structure is 76.4%, and of the hexagonal diamond support structure is 72.2%. Unfortunately, the presence of support structures makes the optical transmission of the entrance window dependent on the incidence angle of incoming X-ray photon with regard to the window plane.

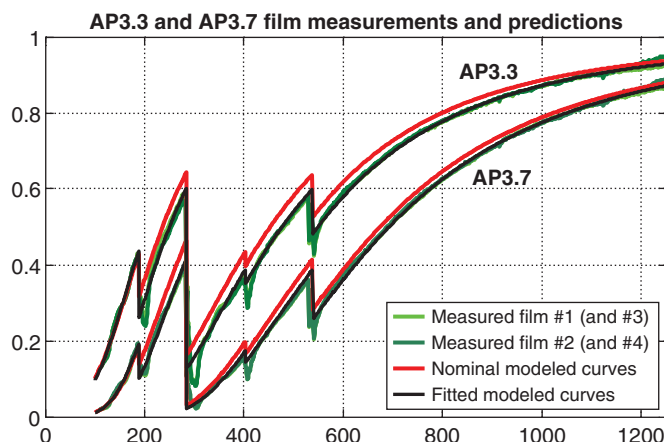


**Figure 19.15** This figure shows the measured and modeled X-ray transmission for both the AP3.3 and AP3.7 films, without any support structures. The light and dark green curves show the measured transmission for two AP3.3 films and two AP3.7 films. The red curves are modeled curves using the nominal film thicknesses for the AP3.3 and AP3.7 films. The black curves are also modeled, but using thicknesses which result from fits to the measured transmission curves. Discontinuities in these curves correspond to K-edges of windows material constituents.

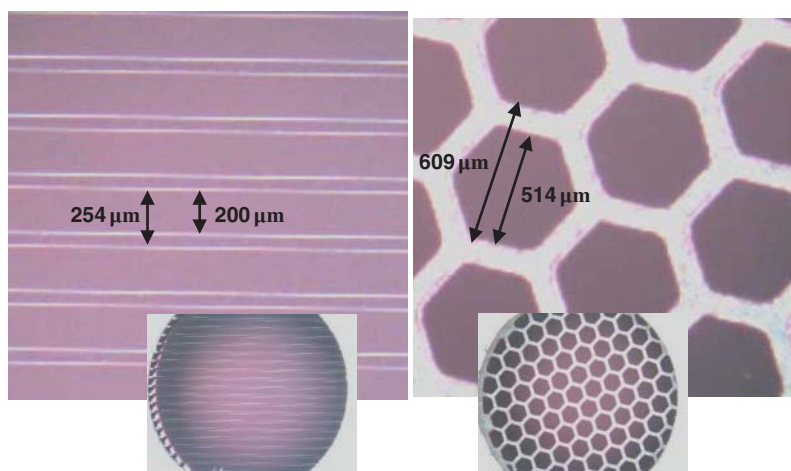


**Figure 19.16** Images of two different support structures. The images on the left show the traditional silicon rib structure. The silicon structure has a thickness of 381 μm, a rib width of 54 μm, a rib pitch of 254 μm, and a gap width of 200 μm. On the right is the hexagonal structure with a thickness of 90 μm, a rib width of 95 μm, a hexagonal pitch of 609 μm, and a gap width of 514 μm. Overall, both of these support structures have a 6.4 mm ID (32 mm<sup>2</sup> active area). *Source:* Courtesy of Moxtek Inc.

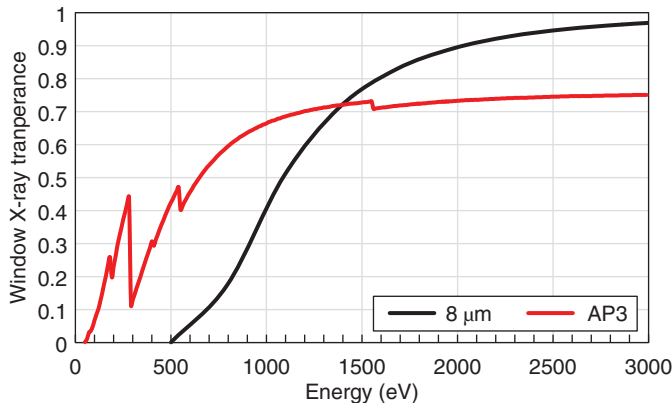


Figure 19.17 X-ray transmission of AP3 window and Be window of 8  $\mu\text{m}$  thickness within 50–3000 eV energy range.

That decreases X-ray transmission of the window at low energies for the fluorescence radiation emitted from a small irradiated point on a sample surface into a wide solid angle. The X-ray transmission of the AP3 window at normal beam incidence against those for the thinnest beryllium window (8  $\mu\text{m}$ ) is shown in Figure 19.17.

### 19.5.1 Influence of Environmental Noises on the Semiconductor Detector's Performance

A negative attribute of very sensitive detector electronics is that they can be easily affected by external disturbances, such as electromagnetic interference (EMI), microphonic effects caused by environmental electromagnetic fields, ground loops, and mechanical vibrations. These sources of disturbances are often encountered in close proximity to these semiconductor detectors, especially in portable energy-dispersive spectrometers, when the X-ray tube and detector are mounted very close to each other. In addition, handheld spectrometers are always at the risk of picking up environmental interference from vibrating equipment, cell phones, etc.

Different methods of the microphonic noise filtering have been proposed and analyzed in several publications [18, 19]. A study of the influence of these external interferences on the detector energy resolution was carried out by the Moxtek research group. This research work has been done focusing on periodic external interference disturbances associated with mechanical vibrations (microphonic noise), and electrical noise that affects the detector–preamplifier assembly. Because of this, we prefer to use term periodic “interference,” rather than “noise,” which implies a random disturbance.

All measurements were done using standard Moxtek PIN diode detectors, along with standard data acquisition electronics: charge-sensitive preamplifier and DPP. The external electrical disturbance was entered into the detector assembly by a simple connection of a function generator output and the detector housing, connected to the preamplifier’s ground. Mechanical vibrations were applied to the detector by a piezoelectric transducer connected to a function generator, with the transducer pressed to the detector housing for a good acoustic contact. All experiments were done by measuring the detector energy resolution as a function of the detector peaking time, within a peaking time range between 4 and 100  $\mu\text{s}$ , at different constant generator frequencies within 1–100 kHz range. The generator output signal amplitude was found experimentally, and the amplitude of the interference was set at a level high enough to observe the external disturbance in the detector, but without causing unreasonably high resolution degradation. The detector resolution measurements were done with 5895 eV X-ray photons, using a  $^{55}\text{Fe}$  isotope source. When either a mechanical or electrical periodic external interference is introduced to the detector, it drastically changes the resolution-peaking time dependence shape. The example of the resolution curve when the detector is under influence of the mechanical vibrations of 100 kHz is presented in Figure 19.18.

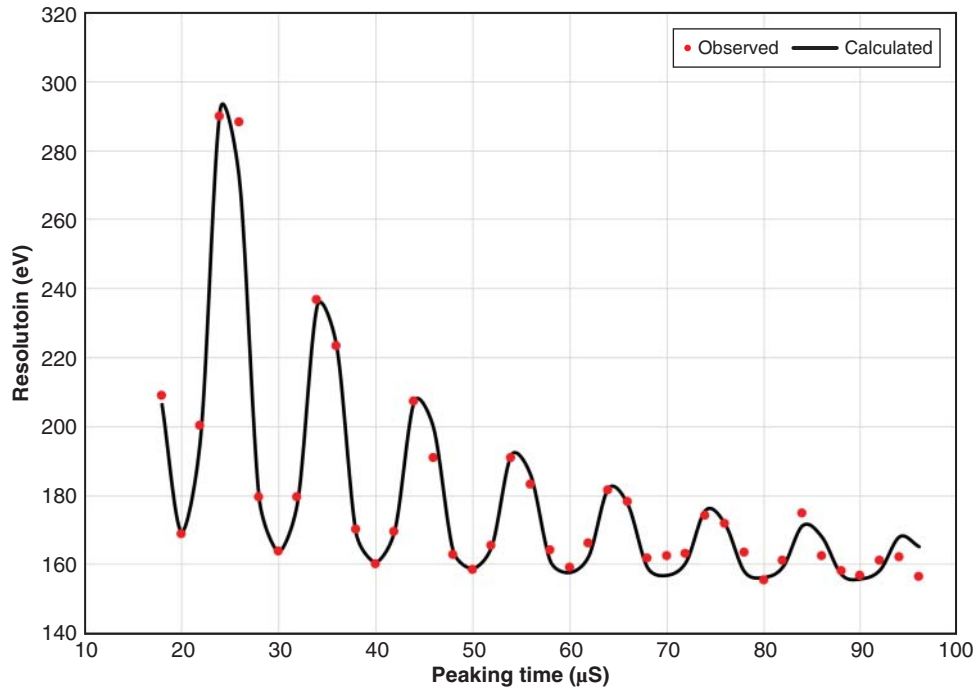


**Figure 19.18** The detector energy resolution as a function of the peaking time obtained with the PIN diode detector affected by the acoustic disturbance of 100 kHz. The experimental observations are shown as points. Solid line represents the best LMS fit obtained using (66).

As one can see, when the detector is affected by periodic interference, the resolution-peaking time dependence has several minimums and maximums, i.e. represented by the oscillating curve in Figure 19.18. As was expected, electrical and microphonic interference have the same effect on the resolution-peaking time dependence. That means the external interferences, regardless of if they affect the detector itself, or the detector's preamplifier, will result in adding a periodical wave into the preamplifier output signal (see Figure 19.19). Thus, when developing a mathematical model for the effect of the periodic interference influence on the detector resolution-peaking time dependence, we do not need to consider the interference nature, but the interference periodicity will play the key role in this model.

The full experimental peak width at half-maximum is given by the very well-known formula:

$$\text{FWHM} = \sqrt{\Gamma_{\text{Fano}}^2 + \Gamma_{\text{ENC}}^2 + \Gamma_{\text{others}}^2} \quad (19.58)$$

where:

$\Gamma_{\text{Fano}} = (2.35)\sqrt{\epsilon FE}$  is the Fano noise,

$\Gamma_{\text{ENC}}$  is the equivalent noise charge (ENC)

$\Gamma_{\text{others}}$  is any other factor that may affect resolution such as incomplete charge collection, traps concentration, etc.

The second term gives the dependence of ENC (random noise) from the peaking time (19.53). We can rewrite (19.53) in a form more convenient for the LMS fit:

$$Q_n^2 = A_1 \cdot \tau + A_3 \cdot \frac{1}{\tau} + A_3 \quad (19.59)$$

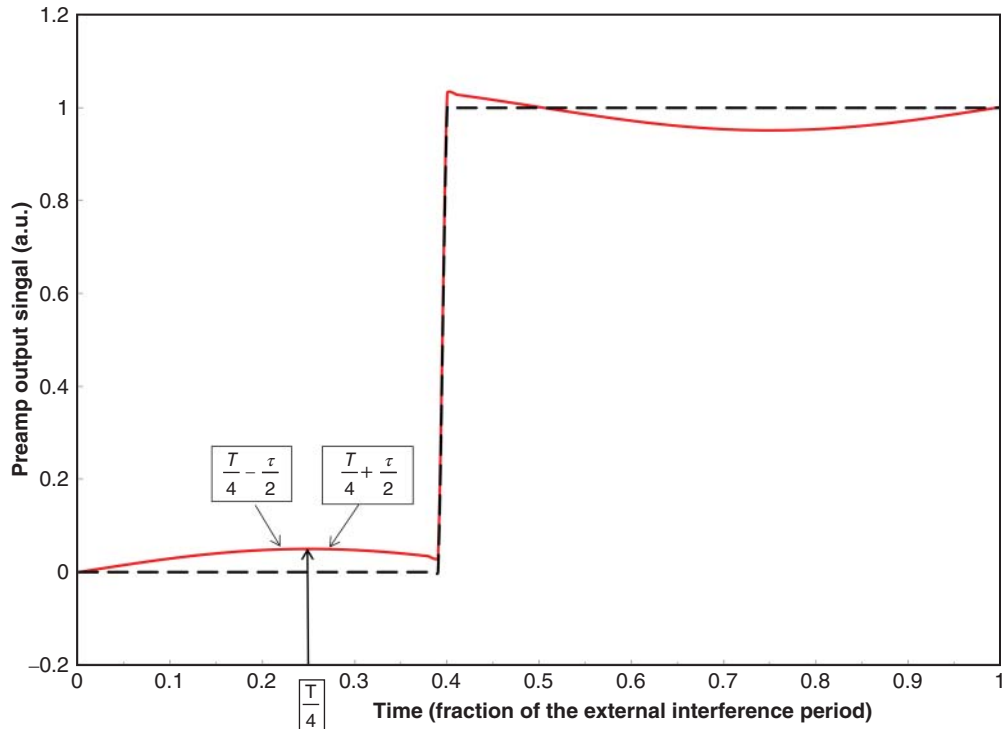


**Figure 19.19** Schematic presentation of the detector signal superimposed with the external periodical interference. Dashed line represents the detector signal as a step function, red solid line represents the sinusoidal wave that models the external interference.

where  $A_1 - A_3$  are parameters that will be refined during least median of squares (LMS) procedure. Let us assume that the detector works under the influence of some external periodic disturbance; that means, we have to add one more term into (19.58):

$$\text{FWHM} = \sqrt{\Gamma_{\text{Fano}}^2 + \Gamma_{\text{ENC}}^2 + \Gamma_{\text{Ext}}^2 + \Gamma_{\text{others}}^2} \quad (19.60)$$

Assuming the other noise sources and the external interference are significantly greater than  $\Gamma_{\text{others}}^2$ , we can omit this term. To find out the explicit form of  $\Gamma_{\text{Ext}}^2$ , let us consider the preamplifier output signal as a step function, corresponding to a detected X-ray photon, superimposed with a sinusoidal signal with frequency  $\omega$ , corresponding to a signal of external interference, as shown in Figure 19.4. Thus, for the external interference voltage, we can write down:

$$\langle U_t \rangle^2 = \frac{1}{T} \int_0^T D_m^2 \cdot \sin(\omega t)^2 dt \quad (19.61)$$

where  $D_m$  is the external disturbance signal peak amplitude,  $T$  is a period of external interference signal.

The DPP forms output trapezoidal pulse from moving average calculations as [6]:

$$S_0(n) = \sum_{k=0}^{N-1} W(k) \cdot S_i(n-k) \quad (19.61)$$

where  $S_0$  and  $S_i$  are the output and input signals, and  $W$  is the weighting function that yields the desired pulse shape. Therefore, the deviation from the average baseline value between two X-ray events, or deviation of the output signal from the true value caused by external interference, is equal to the external interference average

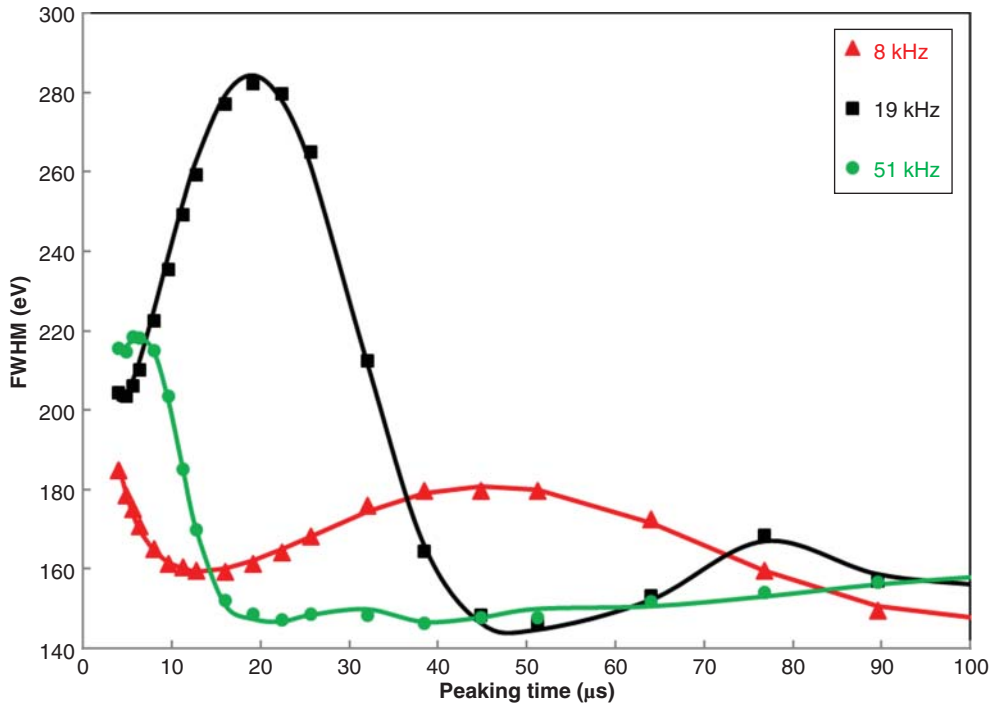


**Figure 19.20** The detector energy resolution-peaking time dependencies obtained when the detector was under influence of external interferences of different frequencies: triangles – 8 kHz, squares – 19 kHz, dots – 51 kHz. Solid lines correspond to the best LMS fits.

voltage calculated according to (19.61) within peaking time interval. The maximum amplitude of this deviation will be reached when the interval of averaging is centered around the maximum (or minimum) of the interference signal, as is shown in Figure 19.20. Thus, we can write down the deviation peak amplitude as:

$$D_m = \frac{1}{\tau} \int_{\frac{T}{4}-\frac{\tau}{2}}^{\frac{T}{4}+\frac{\tau}{2}} A_m \sin(\omega t) dt = A_m \frac{2 \cdot \sin\left(\frac{2\pi T}{4T}\right) \cdot \sin\left(\pi \cdot \frac{\tau}{T}\right)}{2\pi \cdot \frac{\tau}{T}} = A_m \frac{\sin(\pi \cdot p)}{\pi \cdot p} \quad (19.62)$$

where

$A_m$  is the external interference signal amplitude;

$T$  is the external interference period;

$\tau$  is the peaking time;

$$p = \frac{\tau}{T}.$$

One can note that when  $p = n$ , where  $n$  is an integer, the external interference will have no effect on the detector resolution, and its effect on the resolution will decrease with peaking time increase; this is exactly what we observe in experiment (Figure 19.20). Now, for the external interference, combining (19.61) and (19.62) and neglecting the integration on phase since the external interference is not correlated with photon detection events, we can write down:

$$\Gamma_{\text{Ext}}^2 = \langle U_t \rangle^2 = \sum_{k=0}^{N-1} [W(k)]^2 \left[ \frac{A_m}{\sqrt{2}} \cdot \frac{\sin(\pi p)}{\pi p} \right]^2 \quad (19.63)$$

and rewrite (19.58) in a form convenient for the LMS fit if the weighting function is known explicitly. Since in our work we used DPPs from different manufacturers, we did not know  $W(k)$  in explicit form. However, it was found

that the best agreement between the calculated dependence of FWHM as a function of the peaking time and the experimental observations can be reached when  $\Gamma_{\text{Ext}}^2$  is given as:

$$\Gamma_{\text{Ext}}^2 = K \cdot \frac{(\sin(\pi p))^4}{(\pi p)^2} \quad (19.64)$$

That can be explained by form of the weighting function that can vary from one DPP manufacturer to another, but we found that (19.64) works well for at least two DPPs from different manufacturers. Finally, the expression:

$$\text{FWHM} = \sqrt{((2.35)\sqrt{\varepsilon FE})^2 + \left(A_1 \cdot \tau + A_2 \cdot \frac{1}{\tau} + A_3\right) + \left(A_4 \frac{(\sin(\pi p))^4}{(\pi p)^2}\right)} \quad (19.65)$$

was used for LMS data fit, where coefficients A1–A5 were refining parameters. The results of the best fits of the resolution versus peaking time dependences are shown in Figure 19.20. As one can see, (19.65) gives an adequate description of the external interference effect on the detectors resolution regardless of the nature of this interference, and, we believe these considerations are applicable not only to PIN diode detectors, but to other types of detectors as well.

It was demonstrated that periodic interference and white noise that might influence the detectors in practice affect the detector energy resolution-peaking time dependence in different ways: white noise causes the energy resolution degradation within a wide range of the peaking times, but the periodic interference significantly changes resolution-peaking time dependence shape. Because of this, it is always useful to take measurements of the resolution-peaking time dependence in the wide range for proper detection system diagnostic, because just a single point measurement taken at one peaking time can lead to erroneous conclusion when the detector is under influence of the periodic interference. The detector resolution degradation depends not only on the external interference amplitude, but also on the peaking time-to-interference period ratio, i.e. on the interference frequency. Thus, the frequency of the external interference can be found from the resolution-peaking time dependence measurements using proposed model. That might help, for example, to develop proper digital filter when dealing with fixed frequency interference and not avoidable external disturbance.

## 19.6 Conclusion

Within the last decade, semiconductor detector technology has made significant progress. Currently, SDDs cooled with Peltier elements have a typical energy resolution between 125 and 140 eV, within detector temperature ranges between  $-35$  and  $15$  °C. The maximum count rate is about one million counts per second, and the detector sensitive area is up to  $150$  mm $^2$ . Modern detectors are compact, have low power consumption, and are mechanically robust and reliable devices, which can work within a wide range of ambient temperatures and under harsh conditions. They were successfully used, for example, in recent NASA missions on Mars. ASIC preamplifiers played a significant role in the improvement of detector performance parameters such as increased detector counting rate and improved sensitivity at low energies (below 1 keV). Thus, SDDs and (PIN diode detectors, when cost is the major concern) are the most suitable detectors for handheld XRF spectrometers, and their performance is equivalent to that of detectors made for in-lab use.

However, Si detectors have some fundamental limitations. They exhibit low quantum efficiency at high X-ray photon energy (above 15 keV), need to be cooled down, and their operational temperatures have to be stabilized. The demand for detectors with higher quantum efficiency at high energy, and with higher working temperatures (lower power consumption), will continue to increase for applications like basic research, for the space explorations, security, and medical industries, to name a few. Several research groups at universities and companies are working to satisfy this demand, not only by improving existing silicon detector technology, but also by engaging in a search for alternatives to silicon materials. Significant progress has been achieved in the development

of detectors based on cadmium telluride – CdTe (Amptek, Inc), and the cadmium zinc telluride CZT (Kromek Group), which have high quantum efficiency and good energy resolution at the incident photon energy up to 130 keV (see for example [20]). CdTe and CZT detectors are now commercially available. Another potential candidate for use in X-ray detectors is silicon carbide – SiC. Prof. G. Bertuccio and his group demonstrated that SiC detectors can operate at high and unstable temperatures up to 100 °C [21]. However, these types of detectors are still not being fully developed and more efforts are required to make them suitable for use in portable EDXRF spectrometers.

## Acronyms and Abbreviations

ASIC	application specific integrated circuit
CZT	cadmium zinc telluride
DPP	digital pulse processor
ENC	equivalent noise charge
EMI	electromagnetic interference
FWHM	full width half maximum
JFET	junction gate field-effect transistor
MOSFET	metal-oxide-semiconductor field-effect transistor
LMS	least median of squares
RMS	root mean square
SDD	silicon drift detector
Si(Li)	lithium-doped silicon detector
Si-PIN	silicon p-type–intrinsic–n-type detector
S/N	signal-to-noise ratio
TEC	thermoelectric cooler
TO-8	a specific metal can design, containing electronics

## References

- 1 Pantazis, T., Pantazis, J., Huber, A., and Redus, R. (2010). The historical development of the thermoelectrically cooled X-ray detector and its impact on the portable and hand-held XRF industries. *X-Ray Spectr.* 39: 90–97.
- 2 Lowe, B.G. and Saren, R.A. (2014). *Semiconductor X-Ray Detectors*. Taylor & Francis Group, Ltd.
- 3 Kemmer, J. (1984). Improvement of detector fabrication by the planar process. *Nucl. Instr. Methods Phys. Res. A* 226 (1): 89–93.
- 4 Gatti, E. and Rehak, P. (1985). Semiconductor drift chambers for position and energy measurements. *Nucl. Instr. Methods A* 235: 224–234.
- 5 Bombelli, L., Fiorini, C., Frizzi, T., Alberti, R., and Longoni, A. (2011). “CUBE”, a low noise CMOS preamplifier as alternative to JFET-nd for high-count rate spectroscopy. *Proceedings, 2011 IEEE Nuclear Science Symposium and Medical Imaging Conference (NSS/MIC 2011)*, Valencia, Spain (23–29 October 2011).
- 6 Spieler, H. (2005). *Semiconductor Detector Systems*, Series on Semiconductor Science and Technology (Book 12). Oxford University Press.
- 7 Lutz, G. (1999). *Semiconductor Radiation Detectors*. Springer.
- 8 Sze, S. and Kwok, K. (2007). *Physics of Semiconductor Devices*. John Wiley & Sons, Inc.
- 9 Radeka, V. (1972). Trapezoidal filtering of signals from large germanium detectors at high rates. *Nucl. Instr. Methods* 99 (3): 525–539.

- 10 Betta, G. and Dalla, F. (2000). Silicon PIN radiation detectors with on-chip front-end junction field effect transistors. *IEEE Trans. Nucl. Sci.* 47 (3): 829–833.
- 11 Rawlings, K. (1986). Radial semiconductor drift chambers. *Nucl. Instr. Methods* A256: 297–304.
- 12 Rehak, P., Gatti, E., Longoni, A. et al. (1989). Spiral silicon drift detector. *IEEE Trans. Nucl. Sci.* 36 (1): 203–209.
- 13 Hartmann, R., Hauff, D., Krisch, S. et al. (1994). Design and test at room temperature of the first silicon drift detector with in-chip electronics. *Proceedings of 1994 IEEE International Electron Device Meeting*, San Francisco, CA, USA, pp. 535–538. doi: <https://doi.org/10.1109/IEDM.1994.383476>.
- 14 Fiorini, C. and Longoni, A. (2008). Semiconductor drift detectors for X-ray and gamma-ray spectroscopy and imaging. *Nucl. Instr. Methods B* B266: 2173–2181.
- 15 Bertuccio, G., Ahangarianabhari, M., Graziani, C. et al. (2015). A silicon drift detector-CMOS front-end system for high resolution X-ray spectroscopy up to room temperature. *J. Instr.* 10: 001002.
- 16 Bombelli, L., Fiorni, C., Frizzi, T., et al. (2010). Low-noise CMOS charge preamplifier for X-ray spectroscopy detector. *IEEE Nuclear Science Symposium & Medical Imaging Conference*, Knoxville, TN, pp. 135–138. doi: <https://doi.org/10.1109/NSSMIC.2010.5873732>.
- 17 Huebner, S., Miyakawa, N., Kapser, S. et al. (2015). High performance X-ray transmission window based on graphenic carbon. *IEEE Trans. Nucl. Sci.* 62 (2): 588–593.
- 18 Fontanelli, F., Gatti, F., and Nostro, A. (1996). An adaptive system for the reduction of the microphonic noise in cryogenic detectors signal. *Nucl. Instr. Methods A* 370: 218–219.
- 19 Morales, J. and Garda, E. (1992). Filtering microphonics in dark matter germanium experiments. *Nucl. Instr. Methods Phys. Res. A* 321: 410–414.
- 20 Wilson, M.D., Cernik, R., Chen, H. et al. (2011). Small pixel CZT detector for hard X-ray spectroscopy. *Nucl. Instr. Methods Phys. Res. A* 652 (1): 158–161.
- 21 Bertuccio, G., Caccia, S., Puglisi, D., and Macera, D. (2011). Advances in silicon carbide X-ray detectors. *Nucl. Instr. Methods Phys. Res. A* 652 (1): 193–196.

## 20

### Field-Deployable Utility of Benchtop Nuclear Magnetic Resonance Spectrometers

Koby L. Kizzire and Griffin Cassata

*Department of Forensic Science, Henry C. Lee College of Criminal Justice and Forensic Sciences, University of New Haven, West Haven, CT, USA*

#### 20.1 Introduction

Soon after the close of World War II, Felix Bloch and Edward Purcell reported independent discoveries that demonstrated the absorption of radio frequency light by nuclei in a magnetic field [1, 2]. By the early 1950s, Varian produced the first commercially available instrument based on this principle [3], and by 1952, both investigators won the Nobel prize in physics [4]. The unconventional speed of these events demonstrated what most modern chemists will still affirm about nuclear magnetic resonance (NMR) – NMR spectroscopy is one of the most powerful analytical techniques for discovering and understanding inorganic and organic structures of compounds.

The physics of the NMR measurement favors higher magnetic fields and, thus, the subsequent pattern of instrument development led to a trend of bigger and better NMR spectrometers. Alongside advancements in user-friendly interfaces, instruments began gaining bulk quickly [5]. Larger magnets with greater magnetic fields were introduced to improve resolution and sensitivity and, in turn, the elucidative capabilities of the instrument. The fixed magnets of many of these instruments posed a restriction as the highest achievable homogeneous magnetic fields were quickly reached due to limitations in existing materials. However, after discoveries in superconductivity and the recent rise of hybrid instruments, this trend has continued into the present day [6]. Where instruments once routinely operated on as low as a 0.5 T magnet [6], company announcements are now reporting the release of instruments that operate at 28.2 T [7], and NMR spectroscopy experiments have been conducted in fields as high as 35.2 T [8].

While the capabilities of modern instruments are unquestionably incredible, they have come at substantial monetary cost. Prices vary depending on an overall package, but high-field NMR spectrometers (i.e. possessing field strengths of 7.05 T or greater) cost anywhere from \$100 000 USD to well over \$10 000 000 USD [9]. Rooms and even small buildings have been constructed or outfitted to receive new high-field NMR spectrometers, and the superconducting materials require continual replenishment of liquid He and N<sub>2</sub> over the lifetime of the instrument. Inevitable repairs or maintenance require the aid of a technician at the installation site and routinely cost thousands of dollars. The value of information gained from these instruments has clearly been worth the cost to those who can afford it.

In the face of these financial hurdles, it is not difficult to conceive of why the instruments of yesteryear are gaining attention. Scientists in the early decades of NMR were successfully utilizing data generated on instruments operating cryogen-free with field strengths of 1–2 T [10], and not every experiment requires high-resolution measurements. One notable company that moved to fill this niche, Anasazi Instruments, began producing 1.4 and 2.1 T fixed-magnet systems with a primary interest from academia. These instruments provide a superior affordability and ruggedness to modern high-field instrumentation that alleviate some concerns of allowing

inexperienced students to use them. However, they also contain traditional magnets of greater mass with the 2.1 T magnet weighing 918 kg [11].

Advances in several key components of NMR spectrometers have allowed a level of miniaturization of the modern versions of these units, and current commercial versions of these systems are often referred to as benchtop instruments. Although structural elucidation of simple molecules can be achieved by these lower field NMR spectrometers, the key uses of these instruments are often related to confirmation or quantitation of a known structure. Additional reasons for interest vary depending on the demands of various consumers. In addition to academia, marketing attention has especially focused on quality assurance and control, research, and the possibility of use in fieldwork [12]. The reduction in mass and external needs for some of these units has been so dramatic that they can be easily moved by one person to a site of greater benefit to the user.

The change in NMR spectrometer development trends toward instrumentation with lower field strengths has caused some understandable nomenclatural confusion. It is clear from a quick browse of review literature and manufacturer websites that there is no unified convention concerning what to call NMR spectrometers that have potential as field-deployable instruments for structure identification. Some common examples of descriptors include the more widely accepted benchtop [12–15] along with desktop [10, 16], portable [17–20], compact [21–23], and combinations of these and additional terms. The use of the term portable, which exists directly or in indirect public claims by manufacturers, must be approached carefully. While techniques like Raman and infrared spectroscopy (IR) have been reduced to a handheld scale, portable NMR spectroscopy is more akin to the development of the desktop computer versus the immovable, room-sized counterparts of the mid-twentieth century. A comparison of various NMR spectrometers is shown in Figure 20.1.

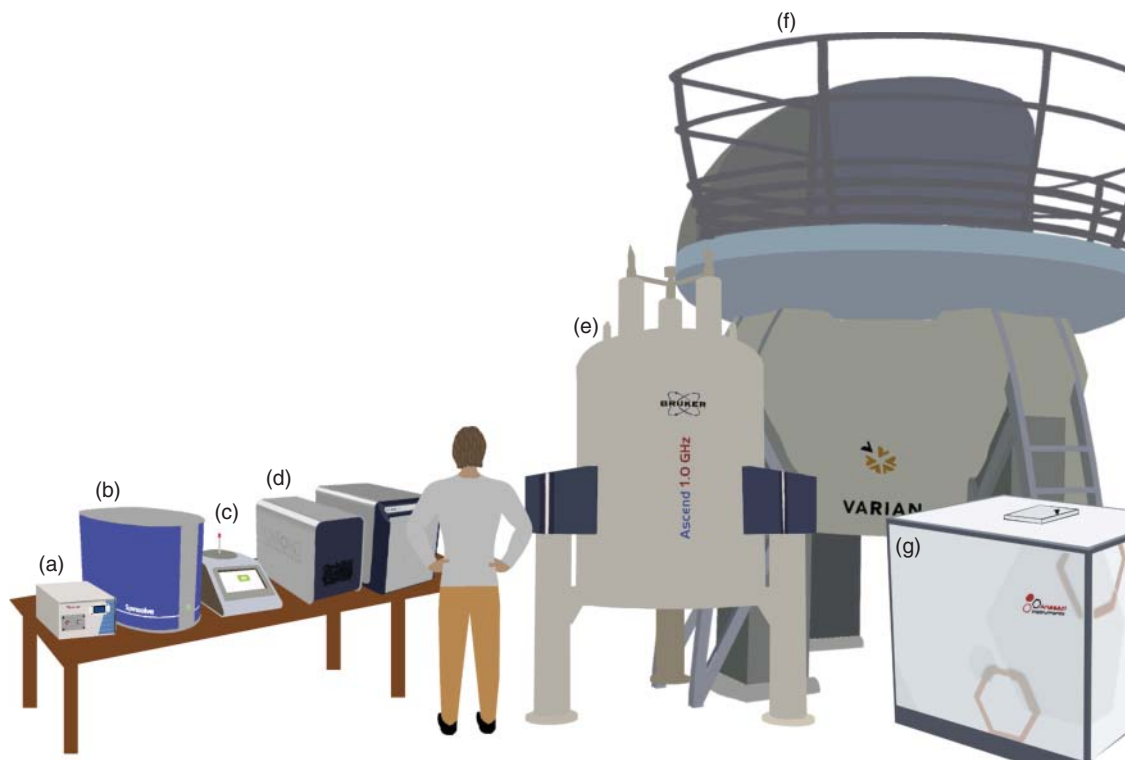


**Figure 20.1** Size comparison of various NMR spectrometers. These instruments are (a) Thermo Scientific's picoSpin 40, (b) Magritek's Spinsolve 60 Carbon, (c) Nanalysis' NMReady-60PRO, (d) Oxford Instrument's X-Pulse, (e) Bruker's Ascend 1.0 GHz spectrometer, (f) Vairan's Unity Inova a 900 MHz Spectrometer, and (g) Anasazi's Eft-90 NMR Spectrometer. Instruments (a–d) are bNMR spectrometers. Instrument (g) is a low-field NMR with similar capabilities to instruments (a–d), and instruments (e) and (f) are ultrahigh-field spectrometers.

For the sake of clarity, the instruments that will be addressed herein operate using permanent magnets of approximately 1.0–2.3 T, provide structural data useful for the identification of a substance, and are of a sufficiently small footprint and external power and/or resource requirement to allow potential field use. These instruments will be referred to as benchtop NMR (bNMR) spectrometers. In addition to the level of field-deployment capability achieved by these instruments, brief background of NMR theory and key advancements that have allowed the commercially available state of the art in bNMR spectrometers will be addressed.

## 20.2 NMR Theory

NMR is measured spectroscopically, and like other spectroscopic instruments, NMR instruments use electromagnetic waves to elicit a response from the analyte. More specifically, radio waves force some of the nuclei being measured to transition to higher energy states, and as nuclei return to states of lower energy, they release energy that is detected by the instrument. The detected energy is displayed on NMR spectra and analyzed for key structural elements in the analyte. NMR spectroscopy, however, requires the atom being analyzed to be NMR active. This intrinsic activity of certain atoms is directly associated with the quantum spin states of their respective nuclei.

Nuclear spin is the sole quality of a nucleus that leads to the possibility for NMR analysis. Spin is based on the electromagnetic principle that postulates that moving charges create magnetic fields. Taking the entire atom into consideration, the electrons circulate around the nucleus causing a magnetic field on the atom. Inside the nucleus, though, the protons and neutrons also have their own spin producing their own separate magnetic field. The magnetic field produced by these nuclear particles acts as any magnetic field would and can be manipulated with external fields. The term spin, describing movement in subatomic particles, is typically used in the classical descriptions of quantum physics. Subatomic particles do not spin as one would imagine a top or a coin to spin. Nuclear spin is more of an energy shift and a concentration of that energy throughout the particle.

The nuclear spin quantum number,  $I$ , is a measure of the magnetic properties of the particles in the nucleus. The  $I$  values possessed by an atom are interpretations of how the energy is concentrated in that atom, and the various energetic states the nucleus can occupy [24]. When  $I = \frac{1}{2}$ , the energy concentration is symmetrical and spherical about the particle. Because of this, the energy can only occupy one of two confirmations, either a (i) spin left or a (ii) spin right as described in the classical model of nuclear spin. NMR analysis of nuclei with  $I = \frac{1}{2}$  is simplified because of this limitation, and this accounts for most nuclei that are commonly investigated with this technique (e.g.  $^1\text{H}$ ,  $^{13}\text{C}$ , and  $^{19}\text{F}$ ).

When the atom is exposed to an external magnetic field, the nucleus' spin, which is magnetic, will either align with (i.e. parallel to) or against (i.e. antiparallel to) the magnetic field if it has  $I = \frac{1}{2}$ . Whether the spin is with or against the magnetic field, the resulting spin axis on the nucleus is never exactly parallel. The axis is always askew of true parallel to the magnetic field and instead precesses about the axis of the applied magnetic field. This precession is measured in terms of the Larmor frequency, which is different for each atom in each respective magnetic field [25]. Equation (20.1) shows the relationship of the Larmor frequency to the magnetic field.

$$\nu = \frac{\gamma}{2\pi} B_0 \quad (20.1)$$

In this equation,  $\nu$  is the Larmor frequency,  $\gamma$  is the gyromagnetic ratio of a given nucleus, and  $B_0$  is the strength of the magnetic field supplied by the instrument. The gyromagnetic ratio ( $\gamma$ ) can be thought of as the affinity of an atom to be manipulated by an applied magnetic field. The Larmor frequency needs to be matched by a radio frequency (RF) pulse in order to influence the nuclear precessional orientation. Because of its natural abundance relative to other isotopes, desirable spin state, ease of interpretation due to limited bonding, and prevalence in many organic and inorganic compounds, the  $^1\text{H}$  nucleus was most studied by NMR spectroscopy historically and is arguably still of greatest analytical interest. One common practice for classifying the performance of a given NMR spectrometer is the Larmor frequency of  $^1\text{H}$ . Most commonly encountered frequencies in bNMR spectrometers are

43, 60, 80, and 100 MHz corresponding to approximate magnetic field strengths of 1, 1.4, 2, and 2.3 T respectively.

The energy gap between spin states in a nucleus of  $I = \frac{1}{2}$  is quantized as indicated by the discussion above. Equation 20.2 shows the relationship of the energy separation between the spin states for these nuclei [24].

$$\Delta E = \gamma \hbar B_0 \quad (20.2)$$

Planck's constant,  $\hbar$ , divided by  $2\pi$  is  $\hbar$ . Given that the gyromagnetic ratio is an apparent constant inherent to each nucleus using standard operating conditions, it is clear that the magnetic field of the instrument is the manipulatable feature that can influence the magnitude of this gap.

To obtain a signal in NMR spectroscopy, the nucleus' spin must absorb and release energy as it transitions between spin states. Most common NMR active nuclei have positive spin quantum numbers. In these nuclei, the lower energy level is the one that aligns the nucleus' spin with the magnetic field, and the higher energy level is opposed to that field. There must be a greater number of nuclei attributed to the lower level than in the higher energy level in order to allow for a net absorption of energy from the RF pulse. This ratio of high-energy spin to low-energy spin at thermal equilibrium is called the Boltzmann distribution [26], which is defined in Eq. 20.3.

$$\frac{N_{\text{high}}}{N_{\text{low}}} = e^{-\frac{\Delta E}{kT}} = e^{-\frac{\gamma \hbar B_0}{kT}} \quad (20.3)$$

Boltzmann's constant is  $k$  and  $T$  is the temperature. Increasing the magnetic field strength of the instrument leads to an increase in the gap between spin states, and as expected, the Boltzmann distribution expressed here ( $N_{\text{high}}/N_{\text{low}}$ ) will decrease indicating a higher population of nuclei attributed to the lower energy state.

The movement of charged, subatomic particles produces a local spin-induced magnetic field. These subatomic magnetic fields are far weaker than the field produced by the instrument's magnet, but they are close enough to other subatomic magnetic fields in the molecule to show measurable effects. This effect is called shielding. When a nucleus of interest is surrounded by other nuclei and electrons producing magnetic fields, which is sometimes referred to as the magnetic environment, the overall magnetic field experienced by the nucleus is different from the one produced by the instrument's magnet, which is expressed in Eq. 20.4 [27].

$$\nu = \frac{\gamma}{2\pi} B_0 (1 - \sigma) \quad (20.4)$$

The shielding constant,  $\sigma$ , can be either positive or negative. The difference in magnetic field experienced by each nucleus occurs in a micro-environmentally dependent manner, which greatly aids the identification of structural features of compounds. As expressed in Eq. (20.1), the Larmor frequency will change based on the magnetic field experienced by the nucleus. The minor variations of the Larmor frequency lead to minor changes in signal output, which are expressed as parts-per-million shifts, or ppm shifts, relative to a standard signal (e.g. tetramethylsilane). Typically, on an NMR spectrum these shifts are represented as  $\delta$ . A more shielded nucleus will be shifted upfield and display a lower  $\delta$  than a nucleus that is deshielded and shifted downfield. Shift values reflect Larmor frequency differences as expressed in Eq. 20.5.

$$\Delta\nu = \frac{(\Delta\delta)\gamma B_0}{2\pi} \quad (20.5)$$

While the shifts of any two given signals are reported as the same ppm value between instruments of differing magnetic field strengths, the Larmor frequency difference of the signals is much greater on the instrument with the stronger field. Thus, stronger magnets not only mean stronger signal due to the population differences noted in Eq. 20.3 but also greater resolution.

The effect of magnetic field sensitivity of the instrument can also be approached by considering an approximation of the signal-to-noise ratio ( $S/N$ ), which is expressed in Eq. 20.6 [6].

$$\frac{\text{signal}}{\sqrt{\text{noise}}} \propto \frac{B_0^2}{\sqrt{\alpha B_0^{\frac{1}{2}} + \beta B_0^2}} \quad (20.6)$$

In this equation,  $\alpha$  and  $\beta$  relate to the cofactors of sample efficiency. If the RF coil is lossless, i.e. all input energy is converted to output energy, and the sample is conductive, then  $\alpha$  approaches zero. If the RF coil is lossy, i.e. some input energy is lost to other processes, then the sample is nonconductive, and  $\beta$  approaches zero. If  $\alpha$  is 0, the  $S/N$  is directly related to  $B_0$ , and if  $\beta$  is 0, the  $S/N$  is related to  $B_0^{\frac{7}{4}}$ . In either case, greater  $B_0$  results in higher  $S/N$  [6].

Even the most fundamental aspects of NMR theory presented here provide insight into the current state of NMR technology, especially with regard to the climb in magnetic field strength. Many of the aforementioned equations also indirectly hint at another vital need in any NMR spectrometer. Changes in  $B_0$  as a result of lack of homogeneity within the sample volume of the instrument's magnetic field would at the very least contribute to band broadening of signals.  $S/N$  and resolution are greatly improved by the homogeneity of the field, and the struggle to achieve both strength and homogeneity in a permanent magnet has characterized the development of today's bNMR spectrometers.

## 20.3 Magnet Miniaturization

When searching for literature on portable or mobile NMR spectrometers, one might be surprised to find decades-old examples. Many of these are based on earth's field NMR and include low-resolution techniques with very specialized uses (e.g. well logging) [28]. The magnets were often large, and creating a compact system was severely limited by the state of electronic components and computers. It was not until the mid-1990s that a truly compact and portable NMR spectrometer was developed – the NMR Mobile Universal Surface Explorer [29]. This instrument is used to make diffusion and relaxometry measurements as well as to develop images that provide information on surface characteristics of materials [10]. The low resolution of this instrument and others like it makes them unsuitable for spectroscopic measurements needed to identify substances and will not be further addressed in this chapter.

In the 2000s, intensive research efforts eventually culminated in the first commercially available bNMR spectrometer in 2009. Many technological hurdles were overcome by advancements in non-NMR technologies. The ever-improving abilities of the computer manufacturing industry to reduce the footprint of processors and storage hardware while improving data capacity provided an unarguable advantage in the reduction of the NMR spectrometer's size. Another marked improvement was the reduction in the size of RF coils thanks in part to the cell phone industry [26]. However, there is no question that the size of any NMR spectrometer is governed chiefly by the magnet. To achieve an acceptable volume of homogeneous magnetic field at a given field strength, large volumes ( $\sim 1 \text{ m}^3$ ) of heavy metallic material had to be used in permanent magnet systems of the 1960s and 1970s [5], and the field strengths and general properties of the materials used imposed severe limitations on the state and utility of NMR data [19].

In the search for magnetic materials with higher field strengths, two key properties are typically investigated – coercivity and remanence. Coercivity is the ability of a material to resist changes in its permanent magnetic field when an external magnetic force is applied. Remanence is the magnitude of a material's magnetic field in the presence of no applied magnetic force. In 1966, a rare earth cobalt alloy was found to have higher coercivity and remanence when compared with previous generations of alloys [30]. The continued research of rare earth alloys since that time has produced NdFeB-based materials, which are now commonly employed in many technological applications [31]. While NdFeB-based magnets have greatly increased the ability to achieve strong and highly stable magnetic fields, the amount of material required to make an effective NMR spectrometer using traditional magnet designs would be too heavy to achieve portability of any kind [5].

One key discovery reported in 1980 eventually led to the smaller magnetic systems of modern bNMR spectrometers. Following the development of rare earth cobalt magnets, Halbach reported that permanent magnets had the capability to generate strong, homogeneous fields when multiple magnets of a given shape and magnetization

orientation were properly arranged [32]. This discovery generated little interest in the NMR community for over a decade in part due to the interest in field strengths that far exceeded the use of this technique. However, the skyrocketing costs of high-resolution instrumentation and advancements made by the Blümich and Blümeler groups have made the Halbach-type array a staple of modern NMR spectrometer miniaturization efforts. The low cost of materials needed to produce these instruments has even led to a rise in researchers building their own units, which are sometimes referred to as “home-built” instrumentation [17, 19, 33].

Current use of the Halbach-type array coupled with improvements in modern magnetic alloys has resulted in experimental field strengths as high as 5.16 T [34], and the highest commercially available field strength currently used in bNMR spectrometers is ~2.3 T (~100 MHz). The exact arrangement, shape, and alloy composition of the components in the array vary between vendors, but in modern bNMR spectrometers, they generally consist of concentrically oriented magnetic units such that a high magnetic field is directed across a gap in the center of a cylindrical shape and very little stray field occurs externally [35]. Not only does this dramatically reduce the footprint of the magnetic system, but also it allows placement of the completed device near other magnetically sensitive laboratory equipment.

## 20.4 Improvements in Sensitivity and Resolution

The size of NMR spectrometers has been greatly reduced, and efforts to further minimize the instruments are ongoing, but as has been made clear in NMR theory, any NMR instrument based on permanent magnets cannot be expected to outperform high-field instrumentation in terms of sensitivity and resolution. Many researchers and manufacturers are currently more focused on improving the utility of data in order to broaden the capabilities and applications of low-field instruments. Additionally, the  $^1\text{H}$  shift range is one of the narrowest among commonly analyzed nuclei. For the relatively low fields of bNMR spectrometers, other nuclei have more desirable resolution in terms of frequency [26], which explains manufacturer interest in providing heteronuclear capabilities. These currently include  $^7\text{Li}$ ,  $^{11}\text{B}$ ,  $^{13}\text{C}$ ,  $^{15}\text{N}$ ,  $^{19}\text{F}$ ,  $^{23}\text{Na}$ ,  $^{29}\text{Si}$ , and  $^{31}\text{P}$  [36].

A notable technical hurdle for fixed magnetic materials operated at ambient temperatures is thermal drift, which can affect both resolution and sensitivity. While this has been mitigated in part by the development of new alloys, temperature fluctuations in a magnetic material can cause changes related to solid-state expansion, and these materials have coefficients that directly associate temperature changes with magnetic field strength [35]. As is demonstrated by Eq. 20.1, changes in field strength will cause proportional changes in the Larmor frequency, which will lead to broadening of the signal when the data of multiple acquisitions are averaged to improve S/N. This is especially true of spectra obtained over long periods of time. Thermal drift effects are less of a problem in superconducting instruments because the magnet temperature is maintained by boiling helium, but they have been observed immediately following helium fills or when data are collected over several weeks [37].

For low-resolution instruments, thermal drift presents a strong concern for lower concentration samples and many two-dimensional (2D) coupling experiments as these require longer acquisition periods. Many techniques used in high-resolution experiments can be utilized on these instruments. Field locking is performed using a signal related to a standard internal or external to the sample, and deuterated solvents are most typically used to this end [38]. Measurement of the fluctuation of this signal allows for drift adjustments to be made in the values observed in sample output prior to signal averaging.

Many modern bNMR spectrometer manufacturers have installed temperature control units to more directly address the environmental concern. Instead of modulating a near ambient temperature expected in most laboratories, bNMR spectrometers are designed to operate with a temperature in the magnetic environment around 30–40 °C. The internal temperature must remain relatively stable, and consequently, operating specifications recommend external environments of 18–26 °C with no more than 1.5 °C fluctuations per hour [39, 40]. As should be expected, operation of any of these instruments requires a minimum of 30 minutes to achieve a thermally

equilibrated readiness state. The level of thermal stability that would be required to obtain acceptable signal with sole use of environmental measures far exceeds the capacity of any temperature control units [41], so locking is used in conjunction with this method.

NMR spectrometry is a measurement of low sensitivity when compared with other forms of spectroscopy. Most measurements are performed at thermal equilibrium, where the gap induced in spin energy levels is known as polarization [42]. This leads to a defined nuclear population difference noted in Eq. 20.3. Sensitivity for these acquisitions is demonstrated in bNMR spectrometers by the need for either highly concentrated samples (e.g. 100 mM or greater concentrations for  $^1\text{H}$  experiments) or high acquisition times over which field drift can be of concern.

Hyperpolarization techniques have been investigated for decades and are now finding popularity in low-field measurements. As the name suggests, these methods are designed to induce greater differences in nuclear spin alignment than observed under thermal equilibrium alone [42], and have been shown to produce increases in signal that are orders of magnitude greater than thermally equilibrated acquisitions. Some of the most popular are varieties of dynamic nuclear polarization (DNP) and signal amplification by reversible exchange (SABER), but broad applicability of these techniques will require overcoming cost and the incorporation of complex equipment among other hindrances [15].

## 20.5 Current bNMR Spectrometers

The utility of today's bNMR spectrometers can be limited in a field setting. Original designs centered on the use of these instruments in academic, pharmaceutical, and quality control laboratory settings [12] where stable ambient conditions and limited movement of the device were expected. All bNMR spectrometer manufacturers have made claims of portability [43–46]. Before an examination of these claims, one should note that the term portability does not have a strict application or meaning even when applied to instruments, and there are no clear regulations or restrictions on the use of this term in the context of field instrumentation. This is due in part to the fact that each end user has unique needs that can be satisfied by various levels of instrument mobility.

All modern bNMR instruments can be operated solely on standard portable power supplies or generators without additional accessory needs. In the past, permanent magnet NMR spectrometers required sample spinning using air streams to provide ample homogeneity of the magnetic environment. These air streams would also be used to hold or transition a sample to the appropriate position for analysis. The air had to be supplied by portable tanks or a forced air line fitted at the site of installation. Due to the current state of autoshimming functions and other field homogeneity compensations and improvements, bNMR spectrometers do not have this requirement.

According to Gałuszka et al., instruments have been categorized for field use as transportable, portable, or handheld, where weight is one primary consideration in the division of these categories. Transportable instruments are recommended to be between 10 and 20 kg and portable instruments between 0.5 and 10 kg [47]. The United States' National Institute for Occupational Safety and Health (NIOSH) has similarly categorized field instruments as personal (i.e. wearable), portable, and transportable [48] but has not published weight ranges to accompany these terms. NIOSH does provide an ergonomic recommendation for the maximum weight of a single two-handed lift or carry at 23 kg, and additional movements and duration of the lift are expected to reduce that maximum [49]. While the size of bNMRs have been greatly reduced, most are still prohibitively heavy for a single individual to carry in view of these guidelines.

The current bNMR spectrometer market is dominated primarily by four manufacturers – Magritek, Nanalysis, Oxford Instruments, and Thermo Scientific. The differences in spectrometers supplied by each reflect slightly different capabilities and end user focus. Some specifications are listed in Table 20.1. Separate educational models of these instruments supplied by Magritek and Nanalysis have limited function and available nuclei

**Table 20.1** Instrument specifications of bNMR spectrometers.

Manufacturer and model	Field strength	Weight	Dimensions	Linewidth at % maximum peak height	Nuclei available <sup>a</sup>
Magritek [36, 50]					
Spinsolve 43	1 T	55 kg	58 × 43 × 40 cm	0.5 Hz at 50% and 20 Hz at 0.55%	<sup>1</sup> H, <sup>7</sup> Li, <sup>11</sup> B, <sup>13</sup> C, <sup>15</sup> N, <sup>19</sup> F, <sup>23</sup> Na, <sup>29</sup> Si, and <sup>31</sup> P
Spinsolve 60	1.4 T	60 kg	58 × 43 × 40 cm	0.5 Hz at 50% and 20 Hz at 0.55%	
Spinsolve 80	2 T	72.5 kg	58 × 43 × 40 cm	0.5 Hz at 50% and 20 Hz at 0.55%	
Spinsolve ULTRA	1 or 1.4 T	55 or 60 kg	58 × 43 × 40 cm	0.2 Hz at 50%, 6 Hz at 0.55%, and 12 Hz at 0.11%	
Nanalysis [40, 51]					
NMReady-60PRO	1 T	25 kg	30 × 28 × 49 cm	1.0 Hz at 50%	<sup>1</sup> H, <sup>7</sup> Li, <sup>11</sup> B, <sup>13</sup> C, <sup>19</sup> F, and <sup>31</sup> P
100PRO	2.3 T	97 kg	37 × 41 × 65 cm	1.0 Hz at 50%	
Oxford Instruments [39]					
X-Pulse <sup>b</sup>					<sup>1</sup> H, <sup>7</sup> Li, <sup>11</sup> B, <sup>13</sup> C, <sup>19</sup> F, <sup>23</sup> Na, <sup>29</sup> Si, and <sup>31</sup> P
Magnetic Unit	1.4 T	150 kg	39 × 54 × 43 cm	0.35 Hz at 50% and 10 Hz at 0.55%	
Electronics Unit		22 kg	30 × 61 × 42 cm		
Thermo Scientific [46, 52]					<sup>1</sup> H and <sup>19</sup> F
picoSpin 45	1.1 T	4.8 kg	18 × 15 × 29 cm	1.8 Hz at 50%	
picoSpin 80	2 T	19 kg	43 × 26 × 25 cm	1.8 Hz at 50%	

a) Listed nuclei are available for all models from a given manufacturer. Magritek, Nanalysis, and Oxford Instruments advise consultations for nuclei not listed.

b) The X-Pulse consists of two separate units. The units are separated to show weights and dimensions of each.

(i.e. <sup>1</sup>H and/or <sup>19</sup>F only). These instruments are not specifically addressed herein. Most of the units discussed here have masses greater than most would consider acceptable weights for portable instrumentation, but might be suitable for mobile laboratories. This is true of many bNMR spectrometers, but the focus herein will be on the previously mentioned manufacturers. The reader should be aware that other manufacturers of instrumentation with similar size and field strengths (e.g. Bruker's Fourier 60 and 80 models) to the largest of these are also available.

Of all bNMR manufacturers, Magritek presents the largest variety of optional accessories and instrument capabilities including a base educational model. Recent advances in shimming technology have led to the production of the Spinsolve ULTRA series of bNMRs, which possess line widths of less than 0.2, 6, and 12 Hz at 50, 0.55, and 0.11% peak heights, respectively [50]. These are the narrowest line widths of commercially available bNMRs and are achieved without the need for the resolution enhancement capability that Magritek provides on Spinsolve series instruments.

Nanalysis is recognized in the United States for its NMReady-60 professional and educational spectrometers, which offer similar nuclear and accessory capability to Magritek but with wider signal linewidths. The company is poised to have the highest field strength bNMR upon the release of the 100PRO [51], which also has a corresponding educational model, the 100e. Consequently, the 100 series instruments will have the highest signal resolution by virtue of the 2.3 T (100 MHz) field strength.

The X-Pulse by Oxford Instruments was also very recently announced and replaces the former Pulsar spectrometer [39]. Where Nanalysis' and Magritek's spectrometers allow the option of a probe for a single nucleus in addition to standard available nuclei, the X-Pulse's advantage is an optional broadband tuner that allows analysis of  $^7\text{Li}$ ,  $^{11}\text{B}$ ,  $^{13}\text{C}$ ,  $^{23}\text{Na}$ ,  $^{29}\text{Si}$ , and  $^{31}\text{P}$  without the need for multiple probes. The bulk of separate magnet and electronic units, which make this instrument the largest of bNMRs in both weight and volume, are a drawback in field use as they remove already limited space in mobile laboratories and may pose weight-related restrictions. However, the bulk of the magnet becomes an advantage for flow reaction monitoring at temperatures between 20 and 70 °C and provides a moderate level of thermal drift resistance relative to other spectrometers.

Thermo Scientific produces the picoSpin Series II spectrometers with 1.1 and 2 T field strengths, which are based on the first commercially available bNMR spectrometer. Developed originally for academic use, these instruments are limited in terms of multinuclear capabilities and, in contrast to their competitors, do not have 2D experiment options. The picoSpin instruments also use a less conventional capillary cartridge with sample injection via syringe in which sample viscosity and air introduction can be of some concern. This design allows small volumes of approximately 40  $\mu\text{L}$  to be sufficient for analysis [52]. There is also a soft-lock capability that allows acceptable performance of these instruments in relatively harsh environments. Manufacturer claims include the operation of the picoSpin 45 "on mountains and aboard NASA's Weightless Wonder zero-gravity aircraft" [53]. Of particular note, the limited consumable requirements and footprint, durability, and 5 kg mass of the picoSpin 45 allow classification of this instrument as portable, not simply field-deployable.

Overall, bNMR spectrometers allow a level of portability that is inconceivable in standard low-field instruments and any high-field instrument. If employed in a field setting, all of these instruments would be best suited to an environmentally controlled mobile laboratory in a context where time constraints are limited if turned on at the operational site. They perform best when infrequently moved or shut down. In terms of general portability, the picoSpin 45 most clearly fits constraints.

## 20.6 Applications

The data that a bNMR spectrometer can provide are similar in nature to what are gained from IR spectra. The signals can be compared to a library standard spectrum to identify a compound of interest and are related to the structural features of the compound analyzed. However, without a standard for comparison, the information that can be gleaned from spectra is somewhat limited. Some applications of Fourier transform-based experiments on higher field instruments apply to bNMR spectrometers. To a degree, a moderate level of structural elucidation can be achieved on these instruments. Structural elucidation is a process whereby NMR data, either alone or in conjunction with other forms of spectroscopy and/or mass spectrometry, allow an analyst to ascertain the chemical structure of a compound.

Elucidative capability may be generally defined by an estimated molecular weight maximum. However, even moderate signal overlap in compounds of lower molecular weight can greatly reduce the ability of bNMR units to identify an unknown compound for which no standard or library comparison can be made. Some manufacturers offer 2D capabilities, which correlate two 1D hetero- or homonuclear spectra shift patterns, in order to expand the capacity to solve structures. For example, an elucidation of strychnine on a 1.0 T (43 MHz) instrument has been reported and utilizes multiple 1D and 2D experiments [54]. This study was an analysis and assignment of peaks using purchased standards and comparisons to data generated on a 9.4 T (400 MHz) instrument. Although adulterant identification was claimed utilizing the 1.0 T instrument, some peak assignments made utilizing signals well below acceptable S/N were clearly informed by the foreknowledge of structures of the compounds involved.

The most promising qualitative and quantitative applications of bNMR instruments relate to analyses where the structure is known in whole or in part. Compound identifications are reasonably made in situations where reaction progress is being monitored or targeted analysis is performed. Synthetic processes are analyzed by examining the

loss and/or gain of expected signals in reagents and products. Recent developments in these methods center on the development of continuous flow techniques especially for monitoring changes in hazardous reagents within the confines of a fume hood [38]. These techniques have seen some success in specialized applications where few components are in the reaction mixture, but they are hampered by sensitivity issues previously discussed [15]. Targeted analysis, which is of greater importance in conventional use of field deployable instrumentation, relies on expectations of a limited number of structures and spectral library comparisons to achieve identification of an analyte.

Similar to other non-separatory techniques like IR, the success of identification or accuracy of quantitation is greatly aided by a sample where the target analyte is a major constituent or nearly pure. While targeted analysis with a bNMR spectrometer can have broad applications in materials [55], pharmaceuticals [56, 57], forensics [58–60], food [61], and fossil fuels [62] among others, the analysis of mixtures can pose limitations on its use as it does for high-field instruments. This is especially true for 1D-<sup>1</sup>H NMR, which has the greatest potential for rapid analysis in field situations.

A direct approach to the problem of mixtures is the use of hyphenated techniques. These have been conceived of for decades, especially with regard to liquid chromatography (LC)-NMR, but initially suffered from inherent difficulties related to sensitivity and interfering solvent signals. Advances in solvent suppression capabilities of NMR instruments in general have attracted new attention to liquid-based separations [63], but most reported applications still use high-field instrumentation. Successful separation and analysis of polymers has been reported using size exclusion chromatography and a 62 MHz bNMR spectrometer [64], but the general cost and expansion of the instrumental footprint of hyphenated instruments currently limits their utility in field settings.

The more conventional approach to the analysis of mixtures is the use of spectral deconvolution in 1D and 2D spectra. In addition to visual and manual approaches with reference spectra [60], several types of algorithms and methodologies are already available in high-field applications and are suitable for bNMR data. Deconvolution algorithms currently exist for many third-party NMR data processing programs such as Mestrelab's Mnova, ACD-Labs' ACD/NMR Workbook Suite, and Nucleomatica's iNMR. In bNMRs, deconvolution techniques have shown recent successes in the compositional analysis of fruit juices [65] and the differentiation of metabolites in urine and serum samples [66], and newer techniques like pure shift analysis have also been investigated [21]. As an alternative to deconvolution of acquired data, the measurement process can also be altered to improve deconvolution capabilities. An example of this approach is resolution enhancement, wherein the free induction decay signal is artificially enhanced to make spectral lines appear narrower [26].

## 20.7 Conclusion

While bNMR spectrometers cannot provide the sensitivity and resolution of high-field instruments, they excel in affordability, convenience, and relative mobility. These instruments already fill an important niche in academic, industrial, and government laboratory settings by making NMR spectroscopy a more accessible technique. Most facilities that use high-field NMR spectroscopy can only afford one instrument, which often means significant demand and delays in getting results. bNMR instruments are frequently advertised as a way to alleviate that burden and free up their high-field counterparts for experiments that actually need the resolution.

In recent years, efforts of further miniaturization have seen greatest success in instruments designed for relaxometric measurements, but current research in bNMR spectroscopy is largely focused on exploring current capability and improvements in data acquisition and processing. This trend is expected to continue as reduction in magnet volume necessitates a reduction in sample volume that reinforces sensitivity issues [67]. If broadly applicable versions of hyperpolarization techniques become available, it is possible that the next generation of bNMR spectrometers could all become feasible candidates for portable use. To date, only one can make that claim. Regardless, the small footprint and limited infrastructural needs of current bNMR spectrometers currently make them suitable for field use in mobile laboratories.

## References

- 1 Purcell, E.M., Torrey, H.C., and Pound, R.V. (1946). Resonance absorption by nuclear magnetic moments in a solid. *Physical Review* 69: 37–38.
- 2 Bloch, F. (1946). Nuclear induction. *Physical Review* 70: 460–474.
- 3 Rabenstein, D.L. (2001). NMR spectroscopy: past and present. *Analytical Chemistry* 73: 214A–223A.
- 4 NobelPrize.org (2019). The Nobel Prize in Physics 1952. *Nobel Media AB*. <https://www.nobelprize.org/prizes/physics/1952/summary> (accessed 14 September 2019).
- 5 Danieli, E., Perlo, J., Blümich, B., and Casanova, F. (2010). Small magnets for portable NMR spectrometers. *Angewandte Chemie International Edition* 49: 4133–4135.
- 6 Moser, E., Laistler, E., Schmitt, F., and Kontaxis, G. (2017). Ultra-high field NMR and MRI – the role of magnet technology to increase sensitivity and specificity. *Frontiers in Physics* 5: 33–47.
- 7 Wishart, D.S. (2019). NMR metabolomics: a look ahead. *Journal of Magnetic Resonance* 306: 155–161.
- 8 Gan, Z., Hung, I., Wang, X. et al. (2017). NMR spectroscopy up to 35.2 T using a series-connected hybrid magnet. *Journal of Magnetic Resonance* 284: 125–136.
- 9 Schwalbe, H. (2017). New 1.2 GHz NMR spectrometers – new horizons? *Angewandte Chemie International Edition* 56: 10252–10253.
- 10 Blümich, B. and Singh, K. (2018). Desktop NMR and its applications from materials science to organic chemistry. *Angewandte Chemie International Edition* 57: 6996–7010.
- 11 Anasazi Instruments. *The Eft-60 & Eft-90 Spectrometers*. Anasazi Instruments. <https://aiinmr.com/high-quality-durable-nmr-spectrometers-pmmr-instruments> (accessed 14 January 2020).
- 12 Frost & Sullivan (2018). *Benchtop NMR Spectroscopy Market Analysis: Ease of Use and Low Cost Boosts Growth*. [https://static1.squarespace.com/static/5707ede0d210b8708e037a1e/t/5b733ac14ae237dd6d8ede6e/1534278340205/FS\\_Benchtop-NMR-Nanalysis.pdf](https://static1.squarespace.com/static/5707ede0d210b8708e037a1e/t/5b733ac14ae237dd6d8ede6e/1534278340205/FS_Benchtop-NMR-Nanalysis.pdf) (accessed 11 July 2019).
- 13 Blümich, B. (2019). Low-field and Benchtop NMR. *Journal of Magnetic Resonance* 306: 27–35.
- 14 Gouilleux, B., Charrier, B., Akoka, S. et al. (2016). Ultrafast 2D NMR on a Benchtop spectrometer: applications and perspectives. *Trends in Analytical Chemistry* 83: 65–75.
- 15 Grootveld, M., Percival, B., Gibson, M. et al. (2019). Progress in low-field Benchtop NMR spectroscopy in chemical and biochemical analysis. *Analytica Chimica Acta* 1067: 11–30.
- 16 Zhong, Y., Huang, K., Luo, Q. et al. (2018). The application of a desktop NMR spectrometer in drug analysis. *International Journal of Analytical Chemistry* 2018: 3104569.
- 17 Louis-Joseph, A. and Lesot, P. (2019). Designing and building a low-cost portable FT-NMR spectrometer in 2019: a modern challenge. *Comptes Rendus Chimie* 22: 695–711.
- 18 Lei, K.M., Ha, D., Song, Y.Q. et al. (2020). Portable NMR with parallelism. *Analytical Chemistry* <https://doi.org/10.1021/acs.analchem.9b04633>.
- 19 Hugon, C., Aguiar, P.M., Aubert, G., and Sakellariou, D. (2010). Design, fabrication, and evaluation of a low-cost homogeneous portable permanent magnet for NMR and MRI. *Comptes Rendus Chimie* 13: 388–393.
- 20 Doğan, N., Topkaya, R., Subaşı, H. et al. (2009). Development of Halbach magnet for portable NMR device. *Journal of Physics: Conference Series* 153: 012047.
- 21 Cataing-Cordier, T., Bouillaud, D., Bowyer, P. et al. (2019). Highly resolved pure-shift spectra on a compact NMR spectrometer. *ChemPhysChem* 20: 736–744.
- 22 Halse, M.E. (2016). Perspectives for hyperpolarisation in compact NMR. *Trends in Analytical Chemistry* 83: 76–83.
- 23 Blümich, B. (2018). Beyond compact NMR. *Microporous and Mesoporous Materials* 269: 3–6.
- 24 Macomber, R.S. (1998). Chapter 2: Magnetic properties of nuclei. In: *A Complete Introduction to Modern NMR Spectroscopy*. New York: Wiley.

- 25** Warwick, A. (1993). Frequency, theorem and formula: remebering Joseph Larmor in electromagnetic theory. *Notes and Records of the Royal Society of London* 47: 49–60.
- 26** Blümich, B. (2016). Introduction to compact NMR: a review of methods. *Trends in Analytical Chemistry* 83: 2–11.
- 27** Harris, R.K., Becker, E.D., Cabral de Menezes, S. et al. (2001). NMR nomenclature: nuclear spin properties and conventions for chemical shifts (IUPAC recommendations 2001). *Pure and Applied Chemistry* 73: 1795–1818.
- 28** Blümich, B., Perlo, J., and Casanova, F. (2008). Mobile single-sided NMR. *Progress in Nuclear Magnetic Resonance Spectroscopy* 52: 197–269.
- 29** Eidmann, G., Savelsberg, R., Blümller, P., and Blümich, B. (1996). The NMR MOUSE, a Mobile universal surface explorer. *Journal of Magnetic Resonance, Series A* 122: 104–109.
- 30** Halbach, K. (1981). Physical and optical properties of rare earth cobalt magnets. *Nuclear Instruments and Methods in Physics Research* 187: 109–117.
- 31** Fischbacher, J., Kovacs, A., Gusenbauer, M. et al. (2018). Micromagnetics of rare-earth efficient permanent magnets. *Journal of Physics D: Applied Physics* 51: 193002.
- 32** Halbach, K. (1980). Design of permanent multipole magnets with oriented rare earth cobalt material. *Nuclear Instruments and Methods* 169: 1–10.
- 33** Yu, P., Xu, Y., Wu, Z. et al. (2018). A low-cost home-built NMR using Halbach magnet. *Journal of Magnetic Resonance* 294: 162–168.
- 34** Kumada, M., Iwashita, Y., Aoki, M., and Sugiyama, E. (2003). The strongest permanent dipole magnet. *Proceedings of the 2003 Particle Accelerator Conference*, vol. 3, 1993–1995. IEEE.
- 35** Blümller, P. and Casanova, F. (2016). Chapter 5: Hardware developments: Halbach magnet arrays. In: *Mobile NMR and MRI: Developments and Applications* (eds. M.L. Johns, E.O. Fidjonsson, S.J. Vogt and A. Haber). Cambridge: The Royal Society of Chemistry.
- 36** Magritek Ltd. *Spinsolve Benchtop NMR*. Magritek Ltd. <http://www.magritek.com/products/spinsolve> (accessed 15 January 2020).
- 37** Najbauer, E.E. and Andreas, L.B. (2019). Correcting for magnetic field drift in magic-angle spinning NMR datasets. *Journal of Magnetic Resonance* 305: 1–4.
- 38** Singh, K. and Blümich, B. (2016). NMR spectroscopy with compact instruments. *Trends in Analytical Chemistry* 83: 12–26.
- 39** Oxford Instruments PLC (2019). *X-Pulse: Benchtop NMR Spectrometer Technical Data Sheet*. Oxford Instruments PLC, xp-spec-09-19.
- 40** Nanalysis Corp (2019). *NMReady-60 User Manual*. Nanalysis Corp.
- 41** Manz, B. (2014). *The Lock and the Importance of Field Stability*. Magritek Ltd. <http://www.magritek.com/2014/08/12/the-lock-and-the-importance-of-field-stability> (accessed 27 December 2019).
- 42** Nikolaou, P., Goodson, B.M., and Chekmenev, E.Y. (2015). NMR hyperpolarization techniques for biomedicine. *Chemistry* 21: 3156–3166.
- 43** Magritek Ltd. *Magritek Home Page*. Magritek Ltd. <http://www.magritek.com> (accessed 15 September 2019).
- 44** Oxford Instruments PLC. *Pulsar*. Oxford Instruments PLC. <https://nmr.oxinst.com/products/nmr-spectrometers/pulsar> (accessed 15 September 2019).
- 45** Nanalysis Corp. *Nanalysis Home Page*. Nanalysis Corp. <https://www.nanalysis.com> (accessed 15 September 2019).
- 46** Thermo Fisher Scientific. *picoSpin 80 Series II NMR Spectrometer*. Thermo Fisher Scientific. <https://www.thermofisher.com/order/catalog/product/912A0832> (accessed 15 September 2019).
- 47** Gałuszka, A., Migaszewski, Z.M., and Namieśnik, J. (2015). Moving your laboratories to the field – advantages and limitations of the use of field portable instruments in environmental sample analysis. *Environmental Research* 140: 593–603.

- 48** DHHS (NIOSH) Publication (2012). *Components for Evaluation of Direct-Reading Monitors for Gases and Vapors*. DHHS (NIOSH) Publication, No. 2012-162. pp. 1–99.
- 49** Waters, T.R., Putz-Anderson, V., Garg, A., and Fine, L.J. (1993). Revised NIOSH equation for the design and evaluation of manual lifting tasks. *Ergonomics* 36: 749–776.
- 50** Magritek Ltd (2019). *Spinsolve Ultra* [Brochure]. Magritek Ltd.
- 51** Nanalysis Corp (2019). *100PRO* [Brochure]. Nanalysis Corp.
- 52** Thermo Scientific (2014). *picoSpin User Guide*. Thermo Scientific, No. 269–298002, Revision A.
- 53** Thermo Scientific (2016). *Thermo Scientific picoSpin Benchtop NMR Spectrometers* [Brochure]. Thermo Scientific, No. BR52832\_E 04/16M.
- 54** Singh, K. and Blümich, B. (2017). Desktop NMR for structure elucidation and identification of strychnine adulteration. *Analyst* 142: 1459–1470.
- 55** Pulst, M., Golitsyn, Y., Reichert, D., and Kressler, J. (2018). Ion transport properties and ionicity of 1,3-dimethyl-1,2,3-triazolium salts with fluorinated anions. *Materials* 11: 1723–1731.
- 56** Kern, S., Wander, L., Meyer, K. et al. (2019). Flexible automation with compact NMR spectroscopy for continuous production of pharmaceuticals. *Analytical and Bioanalytical Chemistry* 411: 3037–3046.
- 57** Assemat, G., Gouilleaux, B., Bouillaud, D. et al. (2018). Diffusion-ordered spectroscopy on a Benchtop spectrometer for drug analysis. *Journal of Pharmaceutical and Biomedical Analysis* 160: 268–275.
- 58** Duffy, J., Urbas, A., Niemitz, M. et al. (2019). Differentiation of fentanyl analogues by low-field NMR spectroscopy. *Analytica Chimica Acta* 1049: 161–169.
- 59** Antonides, L.H., Brignall, R.M., Costello, A. et al. (2019). Rapid identification of novel psychoactive and other controlled substances using low-field  $^1\text{H}$  NMR spectroscopy. *ACS Omega* 4: 7103–7112.
- 60** Pagès, G., Gerdova, A., Williamson, D. et al. (2014). Evaluation of a Benchtop cryogen-free low-field  $^1\text{H}$  NMR spectrometer for the analysis of sexual enhancement and weight loss dietary supplements adulterated with pharmaceutical substances. *Analytical Chemistry* 86: 11897–11904.
- 61** Chen, Y.F., Singh, J., Midgley, J., and Archer, R. (2020). Influence of time-temperature cycles on potato starch retrogradation *In Tuber* and starch digestion *In Vitro*. *Food Hydrocolloids* 98: 105240.
- 62** Voigt, M., Legner, R., Haefner, S. et al. (2019). Using fieldable spectrometers and chemometric methods to determine RON of gasoline from petrol stations: a comparison of low-field  $^1\text{H}$  NMR @ 80 MHz, handheld Raman and Benchtop NIR. *Fuel* 236: 829–835.
- 63** Bhavyasri, K., Sindhu, K., and Rambabu, D. (2019). A review: liquid chromatography-nuclear magnetic resonance spectroscopy (LC-NMR) and its applications. *IOSR Journal of Pharmacy* 9: 54–62.
- 64** Botha, C., Höpfner, J., Mayerhöfer, B., and Wilhelm, M. (2019). On-line SEC-MR-NMR hyphenation: optimization of sensitivity and selectivity on a 62 MHz Benchtop NMR spectrometer. *Polymer Chemistry* 10: 2205–2346.
- 65** Matviychuk, Y., Yeo, J., and Holland, D.J. (2019). A field-invariant method for quantitative analysis with Benchtop NMR. *Journal of Magnetic Resonance* 298: 35–47.
- 66** Percival, B.C., Grootveld, M., Gibson, M. et al. (2019). Low-field, Benchtop NMR spectroscopy as a potential tool for point-of-care diagnostics of metabolic conditions: validation, protocols and computational models. *High-Throughput* 8: 2.
- 67** Schwarz, I., Roskopf, J., Schmitt, S. et al. (2019). Blueprint for nanoscale NMR. *Scientific Reports* 9: 6938–6948.

## 21

### Rapid DNA Analysis – Need, Technology, and Applications

*Claire L. Glynn and Angie Ambers*

*Department of Forensic Science, Henry C. Lee College of Criminal Justice and Forensic Sciences, University of New Haven, West Haven, CT, USA*

#### 21.1 Need for Speed

##### 21.1.1 Addressing Industry Needs

The traditional forensic DNA (deoxyribonucleic acid) typing/profiling process involves a multistep procedure that includes DNA extraction, DNA quantitation, short tandem repeat (STR) amplification via polymerase chain reaction (PCR), separation and detection via capillary electrophoresis (CE), and profile interpretation (Figure 21.1). These processes, which technically could all be completed in 10–12 hours, realistically take weeks or months to complete in operational crime laboratories, depending upon the current backlog of the laboratory.

In order to expedite the process, integration of all traditional STR DNA profiling steps into a single instrument was conceived, and the development of Rapid DNA technologies emerged. While there are ongoing efforts to speed up the individual traditional in-laboratory processes, e.g. Rapid PCR protocols, there exists a need for portable, field-based Rapid DNA technologies whereby all the processes occur within one instrument, and which require reduced need for expert technical and scientific personnel. The hypothesis was that Rapid DNA technology could not only be an effective tool to eliminate DNA backlogs within accredited DNA laboratories, but also offer potential for application in field-based environments outside of the laboratory, including booking stations, border controls, disaster sites, and more.

Rapid DNA is defined by the Federal Bureau of Investigation (FBI) as follows: “Rapid DNA, or Rapid DNA analysis, is a term used to describe the fully automated (hands free) process of developing a DNA profile from a reference sample buccal (cheek) swab without human intervention” [1].

In 2010, under the direction of the FBI, the Rapid DNA Program Office was established in response to the growing need for the development and oversight of Rapid DNA technologies. The directive of this office was to strategize and facilitate research and development of Rapid DNA technology, with eventual integration, for use by law enforcement agencies. The Rapid DNA Program office brings together input and experts from a variety of agencies, some of which include the Department of Defense (DOD), the National Institute of Standards and Technology (NIST), the National Institute of Justice (NIJ), and other federal agencies.

The development of Rapid DNA technologies began with several aims:

- To establish a tool which could produce a DNA profile in a much-reduced time-period, as compared to current traditional DNA profiling methods employed in operational crime laboratories.
- To take this instrumentation out of the laboratory and into the field where it could be employed in field-based applications such as police booking stations, the battlefield, border controls, and disaster sites.
- To develop a technology that would be housed within one unit and could be operated by nontechnical users.

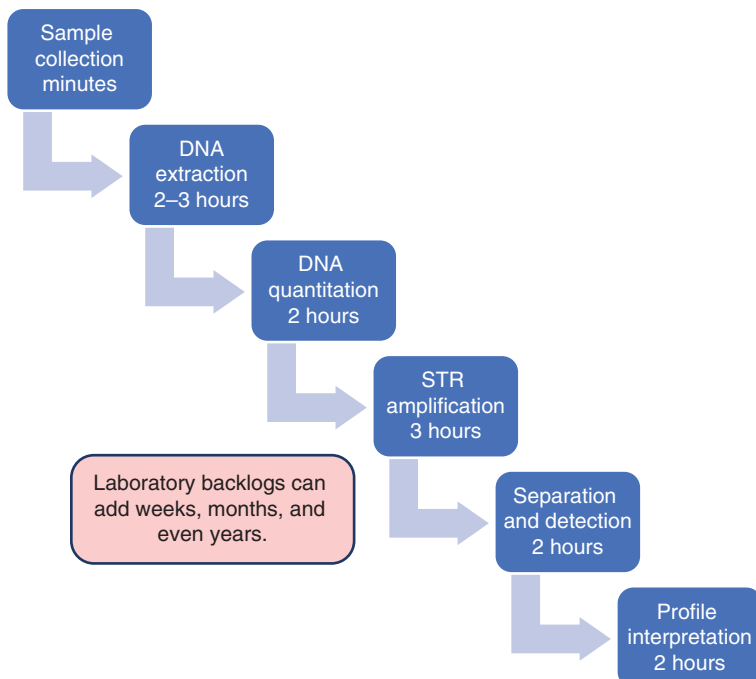


**Figure 21.1** Traditional forensic DNA profiling workflow.

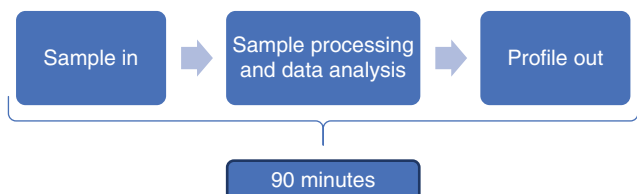


**Figure 21.2** Rapid DNA technology workflow.

Current Rapid DNA platforms combine the multistep process involved in traditional STR DNA profiling into one single instrument, with a “sample in, profile out” approach in design (Figure 21.2).

The platforms typically incorporate microfluidic and molecular biology technologies together to generate a DNA profile from a biological sample beginning with DNA purification, rapid thermal cycling, highly multiplexed amplification, focused DNA sequencing, optical detection of DNA sequences, and automated data analysis. The end result (the interpreted DNA profile/data) is simplified. The system first produces an indication of whether a full, partial, or no profile was obtained, and then subsequent built-in software analyses can compare Questioned versus Known samples and conduct kinship matching (if applicable). Rapid DNA policies have been developed by the National DNA Index System (NDIS) and the Scientific Working Group on DNA Analysis Methods (SWGDAM), and developmental validation studies were designed to ensure that Rapid DNA technologies generate results equivalent to those from an accredited DNA laboratory.

Within the last decade, there have been two companies that have emerged as the main players in the Rapid DNA technology market. These include ANDE® Corporation (Waltham, MA), and the Applied Biosystems division of Thermo Fisher Scientific (Waltham, MA) who acquired IntegenX (Pleasanton, CA).

### 21.1.1.1 ANDE (Accelerated Nuclear DNA Equipment) Corporation

The founding director of ANDE corporation, Dr. Richard Selden, established ANDE Corporation in 2004 in the Greater Boston area. Together with Dr. Selden, pioneering research was performed at MIT's Whitehead Institute to develop the first Rapid DNA platform. Following several years of successful pilot studies, in 2009 ANDE was awarded a competitive research and development grant which was sponsored by a variety of Federal agencies, including the DOD, FBI and the Department of Homeland Security (DHS). The ANDE Rapid DNA™ Identification System was the first to receive NDIS approval from the FBI. This approval represented a major milestone in the integration of Rapid DNA technology as it allows accredited NDIS laboratories to profile DNA samples with the ANDE Rapid DNA Identification System, and use the resulting profiles for upload to the FBI's Combined DNA Index System (CODIS), without the need for manual interpretation or technical review. ANDE's current platform, the ANDE 6C system utilizes a custom FlexPlex™ PCR chemistry, which produces a DNA profile generated from 27 STR loci within 94 minutes.

### 21.1.1.2 Applied Biosystems

In 2011, Northrop Grumman partnered with IntegenX, and was awarded a contract to produce a rapid human DNA identification system to the Army's Biometrics Identity Management Agency. In 2018, IntegenX was purchased by Thermo Fisher and now operates as part of the Applied Biosystems brand. Applied Biosystems produces the RapidHIT™ systems, including the RapidHIT 200 and RapidHIT ID platforms which utilize the GlobalFiler® Express PCR chemistry, and produces a DNA profile generated from 20 STR loci within two hours for the RapidHIT 200 platform, and 90 minutes for the RapidHIT ID platform. To date, the RapidHIT 200 System has been used to upload more than 1000 STR profiles into national DNA databases, both in the United States and in the United Kingdom.

It is of course essential that the evolution and ultimate integration of Rapid DNA technologies is closely monitored and overseen by organizations such as the NIST. NIST has been involved with the testing of various platforms since 2012.

In order for Rapid DNA technologies to be fully integrated into current forensic processes, it is necessary that the profiles produced be compatible with the original CODIS 13 core STR loci and the expanded CODIS 20 core STR loci (in effect as of 1 January 2017). This ensures that profiles generated with Rapid DNA instruments can be compared to those generated through traditional in-house DNA profiling methodologies. NIST has been performing maturity assessments since 2013 to assess the performance of these platforms (see Section 21.2.3).

## 21.1.2 The Rapid DNA Act of 2017

On 18 August 2017, the Rapid DNA Act (Public Law 115-50) was signed into US Federal law. The act was passed unanimously by the US House and Senate. The Rapid DNA Act amended the original DNA Identification Act of 1994, thereby allowing the DNA profiling of arrestees in booking station environments onsite using Rapid DNA technology platforms. The aim of this act was to: "establish a system for integration of Rapid DNA instruments for use by law enforcement to reduce violent crime and reduce the current DNA analysis backlog" [2]. With issuance of this law, US law enforcement agencies are given the "green light" by the Director of the FBI to process single-source reference buccal samples. There are two important features of the Rapid DNA Act. The first is that the generation and analysis must be fully automated, without human intervention or human data review. The second is that the FBI approves the Rapid DNA systems for use, and also that the FBI establishes the standards and procedures for use. Since 2017, the FBI has been preparing policies, the necessary Information Technology (IT) infrastructure, and modifications to CODIS in order to implement this new legislation. It is important to recognize that the Rapid DNA Act of 2017, the DNA Identification Act of 1994, and the FBI's Quality Assurance Standards only apply to those agencies and laboratories operating under the NDIS and CODIS agreements.

**Table 21.1** Comparison of Rapid DNA Analysis and modified Rapid DNA Analysis.

	Rapid DNA analysis	Modified Rapid DNA analysis
Defined as:	Automated extraction, amplification, separation, detection, and interpretation with <i>no human interpretation</i>	Automated extraction, amplification, separation, detection, <i>with human interpretation</i> and technical review
Instrumentation:	Rapid DNA system (includes interpretation software)	Rapid DNA instrument
Approval by:	FBI (referred to as NDIS-approved)	Formal approval not required if validated in accordance with the FBI Director's Quality Assurance Standards (QAS)
DNA profiles eligible for NDIS:	Yes, for accredited forensic DNA laboratories using an NDIS-approved Rapid DNA system	Yes, for accredited forensic DNA laboratories using Rapid DNA instruments

### 21.1.3 Rapid DNA Analysis

In December 2014, an addendum was issued to the FBI's Quality Assurance Standards (QAS) allowing the implementation of Rapid DNA technologies in accredited crime laboratories with single-source reference buccal samples. Two modalities of analysis were defined within the addendum Rapid DNA analysis and modified Rapid DNA analysis. The term "Rapid DNA analysis (RDA)" is defined as the fully automated process of developing a DNA profile *without* human intervention, while the term "modified Rapid DNA analysis (mRDA)" is defined as the fully automated process of developing a DNA profile, but *with* human interpretation and technical review of the resulting profile (Table 21.1).

## 21.2 Technology

### 21.2.1 ANDE Rapid DNA System

The first prototype Rapid DNA instrument was released in 2012 and is known as the DNAscan™ Rapid DNA Analysis System, from GE Healthcare Life Sciences and NetBio. NetBio later (in 2017) changed their name to ANDE Corporation. The DNAscan Rapid DNA Analysis System evolved into the ANDE 4C System, which was NDIS-approved by the FBI in 2016. The system has since undergone additional evolution, with the ANDE 6C System now being the latest generation platform.

#### 21.2.1.1 DNAscan™/ANDE® 4C Rapid DNA Analysis System

In order to satisfy the FBI's definition of Rapid DNA analysis, the DNAscan™/ANDE 4C system utilizes a fully automated profile interpretation and expert system software package (Figure 21.3).

The DNAscan™/ANDE 4C System consists of three primary components: the BioChipSet Swab, the BioChipSet Cassette, and the DNAscan™/ANDE 4C instrument. Within the BioChipSet cassette (Figure 21.4), DNA is purified, PowerPlex® 16 STR loci are amplified, and PCR products are separated by electrophoresis through a capillary system. All necessary reagents are preloaded onto the cassette, e.g. extraction reagents, STR amplification reagents, buffers, separation polymer. Within the cassette, there are electrophoretic channels molded into the cassette. Pneumatic pressure drives the reagents through the cassette, with a sophisticated thermal subsystem for multiplexed STR amplification [3].

**Figure 21.3** DNAscan™/ANDE 4C Rapid DNA System. Source: French et al. [3].

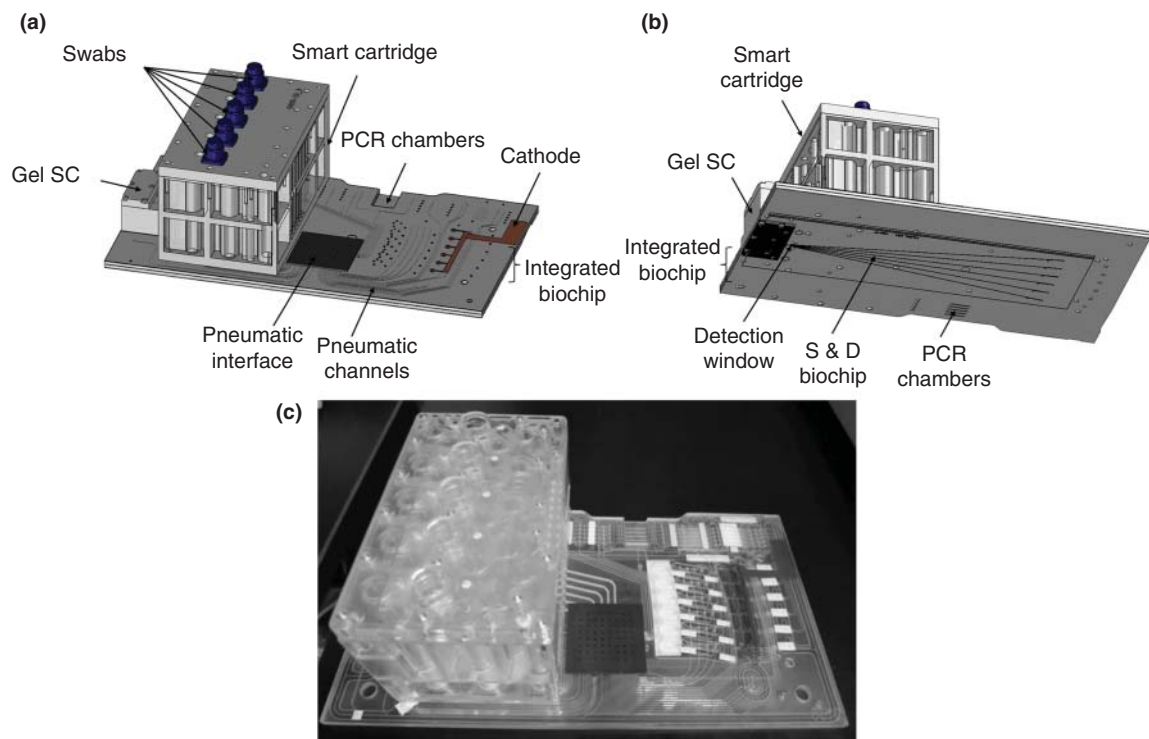


**Figure 21.4** Schematic of DNAscan™/ANDE® 4C BioChipSet Cassette (a: top view, b: bottom view, and c: photograph). Source: Tan et al. [4], 2020 Springer Nature. Licensed under CC BY 4.0.

While the PowerPlex 16 system had previously been approved by NDIS in a traditional laboratory setting, the use of the system in a Rapid DNA instrument required full developmental validation [3].

Integrated expert system software analyzes the data and provides the user with results via a checkmark system (depending on the user account type and security settings for each user). A green checkmark represents that a full profile was obtained and suitable for database searching. A red “X” represents that no profile was obtained.

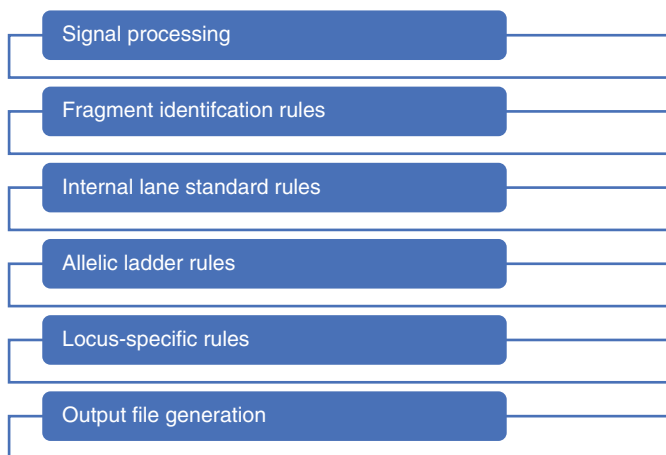


**Figure 21.5** Steps in DNAscan™/ANDE 4C expert system.

The expert system software processes the raw data, assigns allele designations, and interprets the DNA profiles. A series of steps are automatically followed within the expert software system (Figure 21.5).

If desired, the data can be reviewed by a forensic scientist and all raw data files can be exported. The genotypes are exported as CODIS Common Message Format (.cmf) files with allele tables listing all passing allele calls; the electropherogram is viewed as a bitmap; the .xml or .cmf file can be uploaded to CODIS; and the .fsa files are exported and can be analyzed in Genemapper® /Genemarker® STR analysis software.

The DNAscan™/ANDE 4C Rapid DNA Analysis System underwent extensive developmental validation, in collaboration with many external laboratories. The system provided high-quality, concordant results for reference buccal samples. The automated data analysis and the 2016 NDIS approval paved the way for its implementation in accredited DNA crime laboratories. The FBI Rapid DNA Program Office stated that “the system could confidently be used in an accredited laboratory for the rapid analysis of known exemplars and could be used by non-scientists in non-laboratory settings with appropriate protocols, quality assurance, and quality control measures in place” [5]. However, the increase of CODIS loci from 13 to 20 in 2017 caused the NDIS approval of the 4C system to be retracted by the FBI.

#### 21.2.1.2 ANDE 6C Rapid DNA Analysis System

On 1 January 2017, the original CODIS 13 core loci were updated and expanded to the new CODIS 20 core loci, in order to facilitate global data sharing efforts. While the ANDE 4C Rapid DNA System had proven successful for processing known buccal reference samples, it was hoped that other forensic specimens could also be processed using Rapid DNA technology. As a result, the ANDE 4C System underwent significant upgrades with expanded capabilities and resulted in the production of the ANDE 6C Rapid DNA System (Figure 21.6).

On 1 June 2018, the ANDE 6C System received NDIS approval for use in accredited DNA laboratories. The approval was granted following extensive multi-laboratory developmental validation studies [6]. The process is still based on the “Swab In, Profile Out” principle.

The ANDE 6C Rapid DNA System is based upon the same principles of previous generations with single-use microfluidic chips, rapid thermal cycling, and electrophoretic detection of fluorescently labeled PCR products, and automated data analysis, however with several enhancements made throughout the system. The instrument was specifically engineered for field deployment and on-site testing operations. In addition to its relatively small size (dimensions 75 cm × 45 cm × 60 cm) and weight (117 lbs), it is operational at altitudes as high as 3048 m (10,000 ft) and was ruggedized to account for vibration and shock during transportation, meeting the strict requirements of US Military Standard 810G (MIL-STD-810G) [7].



**Figure 21.6** ANDE 6C Rapid DNA System. *Source:* [www.ande.com](http://www.ande.com).

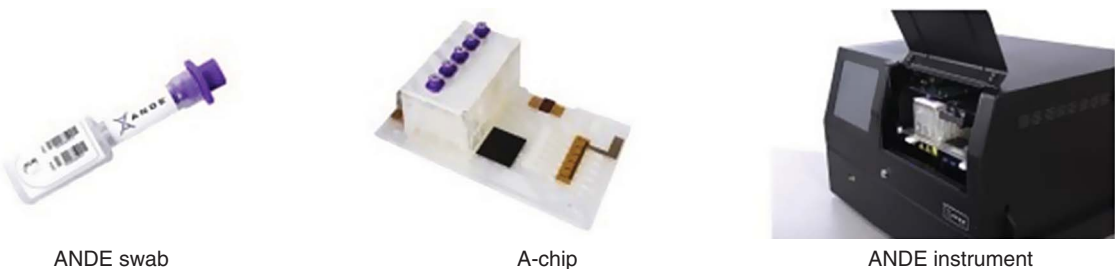


**Figure 21.7** ANDE 6C System components; swab, A-Chip, instrument. *Source:* Carney et al. [6].

The ANDE 6C Rapid DNA System consists of three components: the ANDE swab, the A-Chip or I-Chip, and the ANDE 6C Instrument (Figure 21.7). The automated Expert System software could be considered a fourth component.

The ANDE swab is a self-contained sterile swab loaded with a desiccant which facilitates sample drying and prevents sample degradation during storage. There is an embedded RFID tag on the top surface of the swab handle for sample tracking within the instrument.

The ANDE 6C System can be used with two different single-use microfluidic FlexPlex Chips. The A-Chip (A = Arrestee) and the I-Chip (I = Investigative). The A-Chip is used for known reference buccal samples, while the I-Chip is used for more challenging, lower DNA concentration samples such as blood, other forensically relevant body fluids, touch DNA, tissues, bone samples, etc. (Table 21.2).

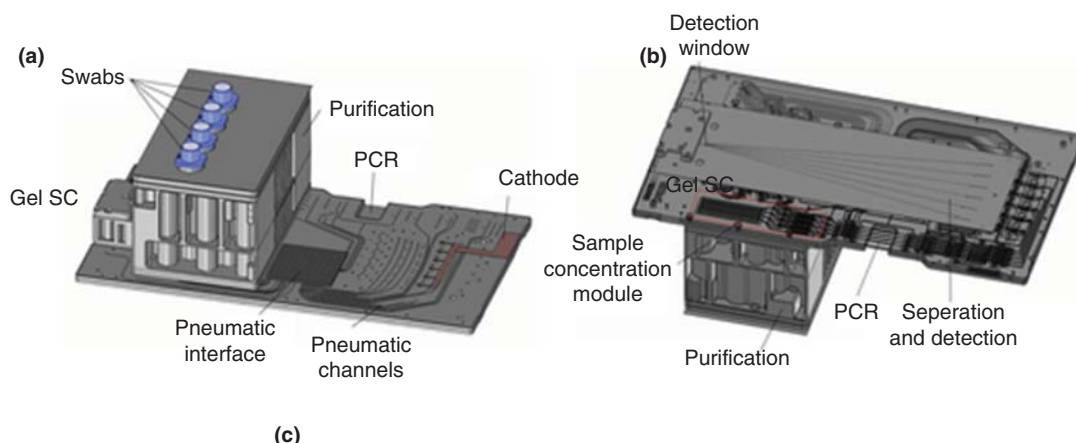
The major difference between the two chips is that the I-Chip runs four samples, while the A-Chip runs five samples. Within the I-Chip (Figure 21.8), a concentration step is performed after DNA purification in order to maximize the quantity of DNA for STR amplification.

The chips do not need to be refrigerated, and all reagents onboard the chip are stable for up to six months. The possibility of sample cross-contamination is eliminated as each chip has dedicated channels.

Within each chip, the DNA is extracted and purified using silica-based guanidinium salt extraction, 27 STR loci (including the CODIS 20 core loci) are PCR-amplified using a custom FlexPlex assay. The amplified PCR products, which are fluorescently tagged, are electrophoretically separated, and then detected using laser-induced fluorescence. The samples travel through the chip under pneumatic pressure.

**Table 21.2** Characteristics of A-Chips and I-Chips.

	A-Chip	I-Chip
Sample types	Buccal reference samples	Forensic samples (blood, semen, tissue, etc.)
Number of samples per run	five	four
Analysis time	94 minutes	106 minutes
Chip storage	Room temp (5–25 °C) for six months	
Operating conditions		10–40 °C 20–80% humidity

**Figure 21.8** Schematic of the ANDE I-Chip. Source: Turingan et al. [8]. © 2020, John Wiley & Sons.

The custom FlexPlex assay (based on the Promega Fusion 6C System) utilizes 27 STR loci and a six-dye fluorescent system (Figure 21.9). The assay contains:

- CODIS core 20 loci, plus Amelogenin (sex-determining marker)
- Y chromosome STRs (Y-STRs)
- Additional autosomal STRs (PENTA E, D6S1043, SE33).

The custom assay was created in order to allow the use of this assay on a global scale. The loci selected were chosen from the “cores” or “sets” used across the globe (Figure 21.10).

Therefore, the assay is compatible for comparisons with the CODIS 20 core loci (United States), the UK core set, the European Standard Set (ESS), Germany’s core loci, and the Australian core, in addition to the D6 locus, which is commonly used in China. The accuracy and precision of the allele calls made using the allelic ladder and the integrated expert system software in the ANDE 6C Rapid DNA System were investigated in several studies. Precision was determined by calculating the standard deviation of base pairs from each allele in the ladder and confirming that it was below the acceptable target value of 0.5 base pairs. Accuracy and precision of allelic calls was confirmed [6, 9].

At the end of the chip run, as the user need not be a technical expert, the integrated touchscreen will report the success of each sample via a simplified symbol system. A green checkmark signifies that the DNA profile obtained satisfies NDIS requirements for database searching. A yellow checkmark signifies that the DNA profile obtained

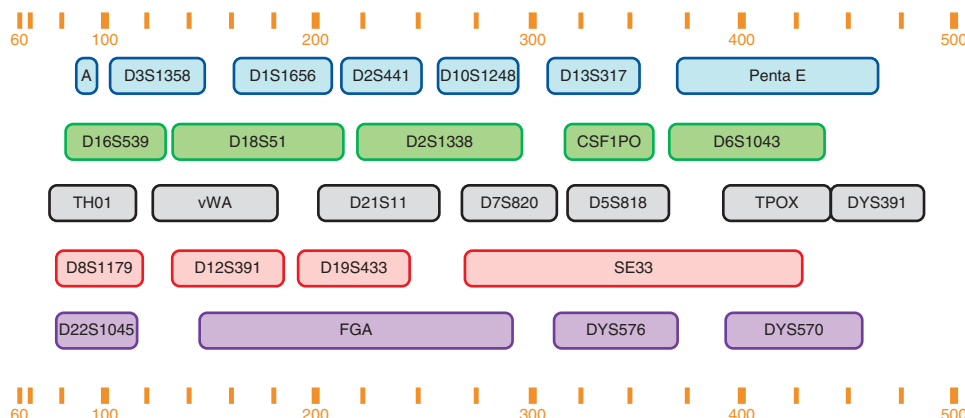


**Figure 21.9** Loci included in ANDE's FlexPlex assay. Source: Turingan et al. [8]. © 2020, John Wiley & Sons.

STR Loci	CODIS 20 core	European standard Set (ESS )	UK core	German core	Interpol standard set	PowerPlex® 16HS	FlexPlex assay	GlobalFiler® express
CSF1PO								
FGA								
TH01								
TPOX								
VWA								
D3S1358								
D5S818								
D7S820								
D8S1179								
D13S317								
D16S317								
D16S539								
D18S51								
D21S11								
D1S1656								
D2S441								
D2S1338								
D10S1248								
D12S391								
D19S433								
D22S1045								
Amelogenin								
Penta E								
Penta D								
D6S1043								
SE33								
DYS391								
DYS570								
DYS576								

**Figure 21.10** Global comparison of STR loci (green cells = included, red cells = not included).

satisfies NDIS requirements for database searching, but should be reviewed by a DNA analyst, or repeat the sample run. A red “X” signifies that the DNA profile obtained does not meet NDIS requirements for database searching and the sample run should be repeated.

The resulting electropherogram (EPG) for each sample can be exported and reviewed by a DNA analyst. All encrypted output files can be exported and decrypted using the FAIRS™ expert software package (ANDE Corporation). FAIRS allows the user to create and manage databases from both samples processed using the ANDE Rapid DNA System and conventionally produced DNA profiles that can be imported manually. The user can search and

match samples within the databases, and also perform kinship analysis. The FAIRS Export Service allows all run data to be exported to external sources. The following data can be exported:

- .xml and .cmf files for database searching.
- .png files of electropherograms.
- .fsa files of raw data for import into genotype software, e.g. GeneMapper® /GeneMarker®.

In 2019, a comprehensive developmental validation study was published investigating the ANDE 6C Rapid DNA System for use with arrestee and reference buccal swab processing. The study reported successful interpretation of over 2000 reference buccal samples tested, with 99.99% concordant alleles. Furthermore, the study evaluated several other important operational aspects of the system. Species specificity was investigated by testing 10 different species, some of which included micro-organisms found to be prevalent in the oral cavity, other commonly encountered micro-organisms, primates, and domestic animals. No DNA profiles considered “passing” or suitable for database searching were generated for any of the 10 species tested. Some peaks were detected in the mouse and primate samples, however, were failed by the expert system. The limit of detection was investigated by testing 30 reference swabs collected with one, three, or six swipes. All samples generated full profiles, with average peak height ratios of 82, 81, and 78%, for six swipes, three swipes, and one swipe, respectively. In addition, the researchers further investigated the use of already purified DNA as a starting sample and subjected it to a full Rapid DNA run. A range of quantities were evaluated which include 0.1, 0.25, 0.5, 1.0, and 2.0 µg. Only the 2.0 µg samples yielded full profiles. All others produced only partial profiles and were flagged/failed by the system.

Stability was investigated and demonstrated that freshly collected moist swabs could be stored at 4 °C or room temperature for seven days and would still produce full DNA profiles. During the collection of buccal reference samples, it is possible that other substances present in the mouth may also be collected on the swab which could act as PCR inhibitors. Ten potential PCR inhibitors were investigated, some of which included mint, beer, cigarette, coffee, gum, and mouthwash. All of the samples tested produced full profiles, and these inhibitors did not appear to have a negative impact on the PCR amplification.

The results of this comprehensive validation study reveal the ANDE 6C Rapid DNA System to provide results that are reliable, reproducible, and robust, therefore revealing its suitability for industry implementation.

## 21.2.2 Applied Biosystems Rapid DNA Systems

### 21.2.2.1 RapidHIT System/RapidHIT 200 System

In 2013, the first generation of the RapidHIT Human Identification System was developmentally validated [10]. Developmental validation studies demonstrated the system to have a high level of precision and accuracy. The system was reported to be “fit for purpose” with regard to the success rates, sensitivity, and robustness to PCR inhibitors. Further validation studies were soon after reported [11, 12]. The RapidHIT System is described as a fully integrated sample-to-profile system, which is capable of processing five samples, plus three controls, simultaneously (Figure 21.11).

The RapidHIT System uses PowerPlex 16HS chemistry and is also compatible with the GlobalFiler Express kit chemistry. Within the system, the traditional DNA laboratory workflow is housed within one single instrument, with DNA purification, PCR amplification, and fragment separation/detection occurring automatically, in approximately 90 minutes using the PowerPlex 16 chemistry, and 120 minutes using the GlobalFiler Express chemistry. The resulting DNA profiles are reviewed by DNA analysts and exported as CODIS searchable files. As the resulting profiles require manual review by a DNA analyst, this method falls under the modified Rapid DNA analysis method.

The RapidHIT System employs a single-use kit, which contains a series of individual cartridges: a sample cartridge (Figure 21.12), a control cartridge, an anode cartridge containing a linear polyacrylamide separation gel, and a buffer cartridge for CE separation. The system uses pneumatic pressure to drive the samples and reagents



**Figure 21.11** RapidHIT Human DNA Identification System. *Source:* Jovanovich et al. [11].

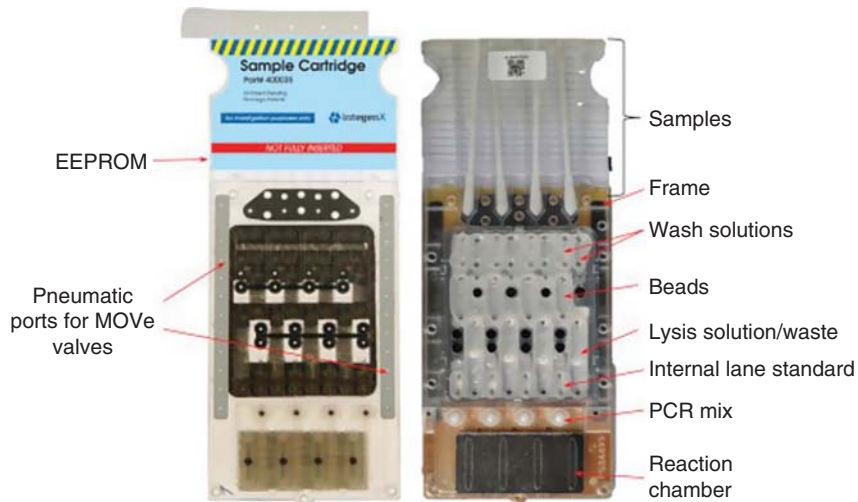


**Figure 21.12** RapidHIT system sample cartridge. *Source:* Jovanovich et al. [11].

through the cartridges. Up to four sample swabs are processed in the sample cartridge. One sample swab and three controls are processed in the control cartridge. The three controls are: a positive amplification control, a negative amplification control, and an allelic ladder.

The RapidHIT instrument is composed of four main subsystems which perform the required processes:

1. Sample preparation subsystem
  - The sample and control cartridges are inserted.
  - The samples are lysed, extracted, and purified using the DNA IQ System.
  - PCR amplification occurs using the PowerPlex 16 HS chemistry.
  - The Internal Lane Standard (ILS) is added (ILS 60, Promega).
2. Separation subsystem
  - Receives the STR amplified PCR products, plus the allelic ladder.
  - Eight separation capillaries are injected with the separation polymer.
  - The PCR products are injected into the capillaries using the separation buffer.
  - DNA fragments are separated by size via capillary array gel electrophoresis.
  - The capillaries are cleaned for the next sample run.

### 3. Detection subsystem

- The fluorescently labeled STR products are captured as they pass through the detection window.
- 20 mW, 488 nm solid-state laser is employed to excite the fragments.
- The excited fragments are detected using a CCD detector.

### 4. Control and analysis subsystem

- Utilizes an embedded computer system with the required processor and software.
- Image data from the CCD detector is captured.
- The data are processed and analyzed.

The RapidHIT System was shown to produce highly reproducible results with an 88% first pass success rate for buccal samples processed producing all 16 out of 16 loci called [11]. Other interlaboratory system studies were performed at the FBI laboratory, NIST, and the United States Army Criminal Investigation Laboratory (USACIL), which also produced full concordant profiles [13], while other internal validation studies produced similar results [14, 15]. The positive results generated from these studies encouraged further development of the system and revealed great potential for its use in both accredited DNA laboratories and booking stations for reference buccal reference sample processing. In 2014, IntegenX received approval from the FBI to upload directly to NDIS samples that have been processed using the RapidHIT System with the GlobalFiler Express Kits.

#### 21.2.2 RapidHIT ID System

In 2016, the next generation of RapidHIT System was developed, the RapidHIT ID System (Figure 21.13). This new system was generated to specifically meet the needs of a field-based, decentralized environment. Significant changes were made to the system to increase its efficiency, increase its capacity, reduce its footprint, and require less user intervention.



**Figure 21.13** RapidHIT ID System. Source: Salceda et al. [16].

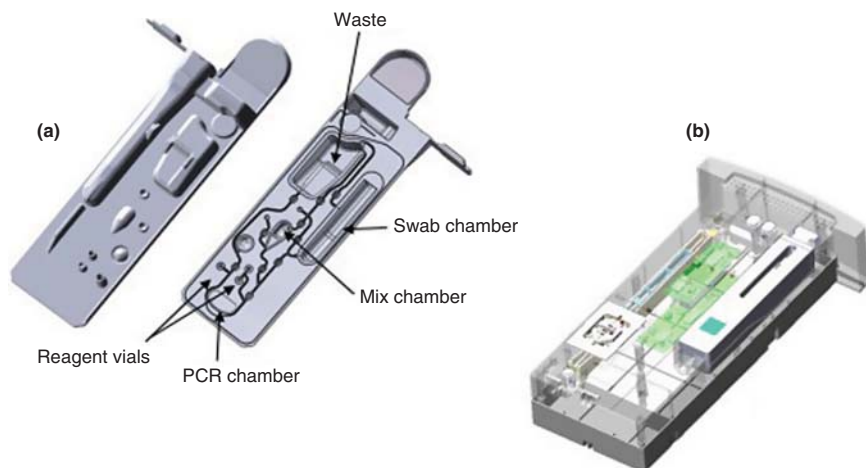


**Figure 21.14** RapidHIT ID (a) sample cartridge and (b) primary cartridge. *Source:* Salceda et al. [16], © 2017, Elsevier.

The previous cartridge, with a four subsystem configuration, was completely redesigned and replaced with a low-cost single-use cartridge for each sample, a control cartridge, and a primary cartridge housing the bulk reagents, and the capillary electrophoresis module suitable for running 150 samples (Figure 21.14).

The sample and primary cartridges are reported to have a reasonable shelf life and can be stored for six months at temperatures up to 25 °C. The sample cartridge contains the GlobalFiler Express primer set, master mix, and the size standard in separate vials. The primary cartridge contains the lysis buffer and electrophoretic reagents for 150 samples. After the DNA is extracted from the sample, the lysate moves from the swab chamber to the PCR chamber where the lysate is captured on a paper disc. The primer and master mixes then enter the PCR chamber, and thermal cycling occurs with 28 cycles, following the manufacturer's protocol. The size standard then enters the PCR chamber containing the PCR products causing them to flow into the mix chamber where the size standard and PCR products combine. This mixture is denatured and enters the primary cartridge for capillary electrophoresis to separate the DNA fragments, which are then optically detected. The raw DNA data are processed by the system with the resulting STR profile/electropherogram displayed on the screen. The .fsa files can be exported to GeneMarker HID for further analysis. An allelic ladder is not included in the sample processing, instead a “digital” allelic ladder is applied during the data analysis stages imported from a library of allelic ladders.

Another substantial upgrade and addition to the RapidHIT ID System was the development of the new RapidLINK software (IntegenX) for data analysis and DNA profile interpretation. The RapidHIT ID instruments transfer the output data to a central computer that operates the RapidLINK software. The RapidHIT ID System has a sophisticated security process with a fingerprint reader and camera for authenticating access. Furthermore, predictive analytics are utilized to monitor and manage consumable inventory across geographically distributed RapidHIT ID Systems.

### 21.2.3 Maturity Assessment

Since the release of the first prototype Rapid DNA instruments in 2012 (DNAscan Rapid DNA Identification System; ANDE Corporation/NetBio, and RapidHIT™® 200 Human Identification System; Applied Biosystems/IntegenX), the Applied Genetics Group of NIST has been investigating and evaluating their performance.

In August 2013, the first maturity assessment was performed across three federal laboratories [13]. This assessment investigated the DNAscan (ANDE/NetBio), and RapidHIT 200 (Applied Biosystems/IntegenX) instruments, using buccal reference samples. In this interlaboratory study, the success rate was measured by calculating the percentage of complete and correct/concordant profiles utilizing the CODIS 13 core loci. With the ANDE Rapid DNA instrument, the study reported 84% success, with 168 of 200 samples tested providing full concordant profiles. With the RapidHIT Rapid DNA instrument, the study reported 94% success, with 141 of 150 samples tested providing full concordant profiles. The combined results for both instruments report 88% success, with a total of 309 of 350 samples tested providing full concordant profiles. The results of this interlaboratory study provided the necessary success rates to further perform developmental validation studies.

In October 2014, the second maturity assessment was performed across seven independent laboratories, spanning US federal, state, and private laboratories [17]. The aim of this study was to assess the current state of the technology for the CODIS 13 core loci as software and hardware updates had been implemented. Both automated (Rapid DNA analysis) and manual (modified Rapid DNA analysis) review of the data sets were conducted. In addition, two STR PCR chemistries were employed: PowerPlex 16 (Promega Corporation, Madison, WI) and GlobalFiler Express (Applied Biosystems). The results of the study reported success for the CODIS 13 core loci ranged from 76% with automated data review to 80% with manual data review. The peak height ratios and stutter percentages were also found to be within observed developmental validation ranges using both PCR chemistries; PowerPlex 16 and GlobalFiler Express.

In January 2017, the original CODIS 13 core loci were expanded to 20. Therefore, a third maturity assessment was performed to assess the performance of Rapid DNA instruments with the expanded CODIS 20 core loci. In addition, there were significant updates to the existing platforms, and new platforms were developed. In 2018, the third, and most recent, maturity assessment was performed to evaluate the implementation of Rapid DNA outside of a laboratory environment for use only on single-source reference buccal samples [18]. This maturity assessment was performed using the ANDE 6C System, the RapidHIT 200 System, and the RapidHIT ID System. The participants in the study utilized the instruments in US federal, state, and local laboratories, police agencies, and commercial vendors. Each participant processed unknown buccal epithelial reference samples and sent the resulting data to NIST for evaluation. The success rate was measured by calculating the percentage of complete and correct profiles generated by the various Rapid DNA technologies, when compared to those generated using traditional STR DNA profiling methods in a laboratory environment. As the ANDE 6C system was the only platform at the time that was fully approved for NDIS upload, it was the only instrument eligible for Rapid DNA analysis. Therefore, the others underwent modified Rapid DNA analysis whereby the data were manually interpreted. The results of the study with the Rapid DNA analysis reported average success of 85% when analyzing the CODIS 20 core STR loci, ranging from 60 to 100% for the ANDE 6C instruments. The results of the study with the modified Rapid DNA analysis reported average success of 90% when analyzing the CODIS 20 core STR loci, ranging from 60 to 100% for all instruments. Remarkably, concordance between the different chemistries across the instruments (custom FlexPlex and GlobalFiler Express) was observed for 99.98% of the STR allele calls compared. A summary of the results from the three maturity assessments is provided in Table 21.3.

The continued efforts by NIST over the last eight years to support the development, validation, and implementation of Rapid DNA technologies has provided encouragement to law enforcement agencies that these instruments meet the standards and capabilities needed.

**Table 21.3** Summary of results from Rapid DNA maturity assessments.

Year	Instrument	STR typing chemistry	Samples tested per Lab	Total samples	Average % success
2013 [13]	ANDE 4C	PowerPlex® 16	200	350	88.3%
	RapidHIT 200		150		
2014 [17]	ANDE 4C	PowerPlex® 16	100	280	75.25%
	RapidHIT 200	PowerPlex® 16	60		
		GlobalFiler Express	120		
2018 [18]	ANDE 6C	FlexPlex™	100	240	87.5%
	RapidHIT 200	GlobalFiler® Express	60		
	RapidHIT™ ID	GlobalFiler® Express	80		

## 21.3 Applications

The potential applications of Rapid DNA technology are quite expansive and, while originally intended for use outside of the laboratory (i.e. portable field use), it also offers numerous advantages to being implemented within the laboratory environment.

### 21.3.1 Booking Station Use

A major goal of the development of Rapid DNA technologies was for the systems to be portable for use outside of the laboratory in a decentralized environment (e.g. booking stations, border control, etc.). The implementation of Rapid DNA technology in booking stations offers immense potential to expedite arrestee identification, and even link the arrestee to prior crimes (Figure 21.15).

When an arrestee is booked in at a booking station, numerous levels of information are collected/searched, including fingerprints, criminal history information, etc. With the advent of Rapid DNA technology however, even further levels of information can now be collected immediately by taking a known reference buccal sample from the arrestee, generating a CODIS searchable DNA profile onsite, and uploading the resulting profile to search for linkages to previous crimes. This allows the law enforcement agency to search unsolved crimes of special concern while an arrestee is still in custody, and before they are released in non-charging states.

This high-speed processing and interpretation could significantly increase the rate at which prior and current crimes are solved. By identifying arrestees that are wanted in connection with other crimes (e.g. murders, rapes, burglaries, etc.), there is potential to identify repeat criminals and prevent them from repeating their crimes again. In addition, potentially millions of arrestee DNA profiles could be generated continually with Rapid DNA instruments running 24/7. This would also positively impact the current backlog of reference sample processing experienced nationwide in accredited crime laboratories.

With the passing of the Rapid DNA Act in 2017, US law enforcement booking stations were now able to implement Rapid DNA technologies to type single-source reference buccal samples. This offers a rapid turnaround time

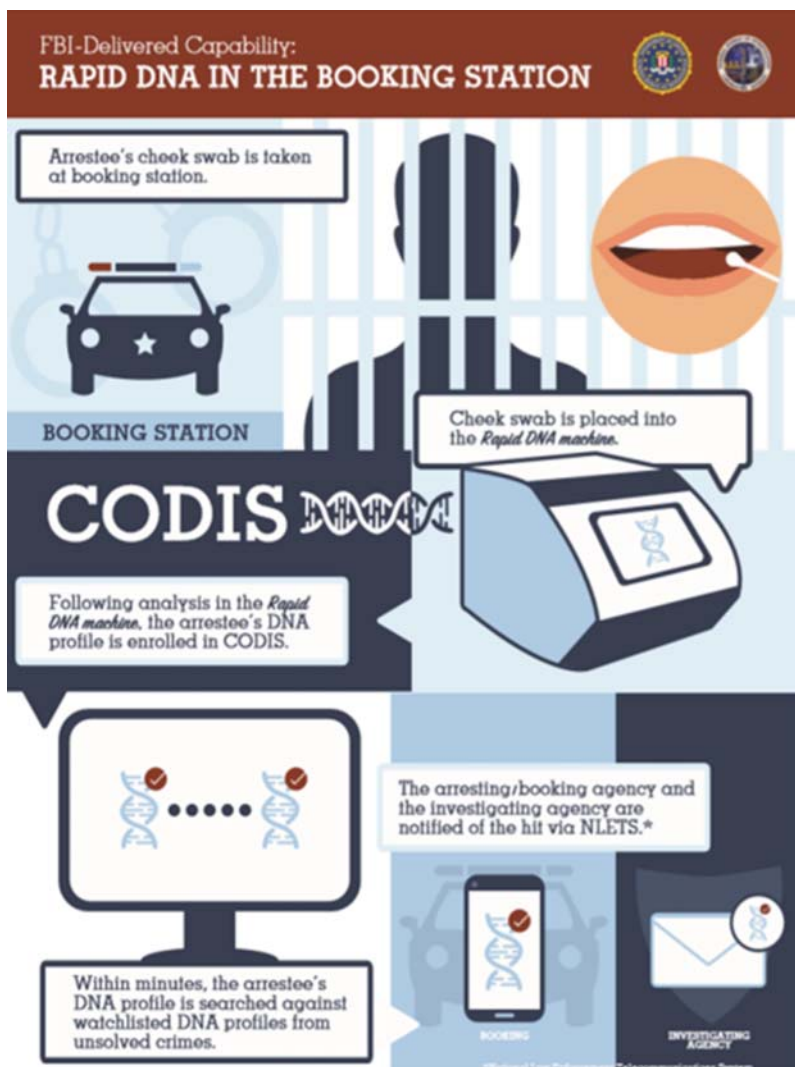


**Figure 21.15** Workflow of Rapid DNA in the booking station. Source: [www.fbi.gov](http://www.fbi.gov).

and can enhance an investigation by offering quick elimination of potential suspects, or indeed, by identifying perpetrators of previous crimes who had remained unknown.

Currently (March 2020), within the United States, there are five pilot sites utilizing Rapid DNA technologies in booking station environments. The implementation is not as simple as placing a Rapid DNA instrument into a booking station. Within the last two years, the FBI have been making updates to their IT infrastructure which includes new CODIS software and other necessary CODIS interfaces in order to allow the data generated with Rapid DNA technologies in booking station environments to communicate with CODIS. This includes the integration of criminal history information.

Further, there are a number of prerequisites for implementation into the booking station environment. In order for federal, state, or local booking agencies to be granted approval to introduce Rapid DNA technologies in their booking stations, they must meet the following criteria [19];

- The state must have implemented an arrestee DNA collection law that authorizes DNA analysis at the time of arrest. Federal booking agencies already meet this prerequisite.
- They must have Electronic Fingerprint (Live Scan) integration during the booking process for obtaining State Identification numbers (SID) (Universal Control Number [UCN] for federal booking agencies) from the State Identification Bureau (FBI for federal) in near real time.
- The booking agency must have network connectivity with the State Identification Bureau (SIB)/Criminal Justice Information Services (CJIS) Systems Agency (CSA).

It will be critical for booking agencies to work with their State CODIS Administrator to ensure all requirements are met for implementation of Rapid DNA technologies in their agencies.

### 21.3.2 Accredited DNA Laboratory Use

On 4 June 2018, the FBI granted ANDE Rapid DNA Systems with NDIS approval for the ANDE 6C system. This allows NDIS-accredited crime laboratories to implement ANDE Rapid DNA technology to process DNA samples and also to upload the resulting DNA profiles to CODIS. The traditional DNA profiling process performed in an accredited DNA laboratory is a multistep process that requires numerous forms of instrumentation, multiple individual lab spaces for each step, and highly skilled personnel. The DNA profiling process within an accredited laboratory can take days, weeks, and even months to obtain results. The advent and success of DNA profiling over the last 30 years, together with the positive outcomes it has brought to investigations, have encouraged investigators to submit more and more samples to the lab for testing and therefore causing higher demand for DNA testing to be performed, which can result in sizeable backlogs of samples to be processed.

While the analysis of forensic samples by a Rapid DNA system is not compliant with the FBI Director's QAS for Forensic DNA Testing Laboratories, Rapid DNA technology could alleviate some of the backlogs currently experienced. Within accredited DNA laboratories, Rapid DNA technologies could be used to process a wide range of sample types, some of which include:

- Known reference buccal samples submitted to the laboratory.
- Blood, other forensically relevant body fluids, and touch DNA sampled from evidence items examined in the laboratory.
- Sexual Assault Kits (SAKs) that are currently backlogged and remain untested.

Not only would the implementation of Rapid DNA technologies in accredited crime laboratories reduce the time it takes to produce results and therefore provide investigative leads quicker, but it would also reduce the amount of "hands on work" required by the lab staff, thereby allowing them time to work on other crimes.

#### 21.3.2.1 Known Reference Buccal Samples

Rapid DNA technologies have reported much success with the various platforms for use with single-source reference buccal samples. Reference buccal samples are collected from known individuals, including victims and suspects, from which an STR DNA profile is obtained and can be uploaded to a searchable database for matching. The reference buccal STR DNA profile can also be used to be compared against resulting DNA profiles from biological evidence recovered from evidence items, i.e. Questioned versus Known DNA profile comparison.

Much of the early studies investigating Rapid DNA technologies focused solely on their use with reference buccal samples, as the goal was to implement this technology in booking stations for arrestee identification purposes, and also in accredited DNA laboratories to alleviate the backlog of reference sample processing. Reference buccal samples typically contain high quantities of DNA and are not required to be quantified prior to STR Amplification, which is required for all other forensic samples by the FBI's DNA Advisory Board (DAB) QAS (Standard 9.3). The recommended best practice is the two-swab method: one swab for Rapid DNA profiling and one swab preserved for traditional DNA profiling.

Several studies have thoroughly validated the use of the current Rapid DNA systems with known reference buccal samples to assess limits of detection, species specificity, mixture implications, and susceptibility to PCR inhibition [6, 16]. Importantly, species specificity included interrogation of oral specific bacteria, which demonstrated limited cross reactivity.

### 21.3.2.2 Forensic Evidence Samples

#### 21.3.2.2.1 Bloodstains and Other Forensically Relevant Body Fluids

Witnessing the success of the RapidHIT System with reference buccal samples, IntegenX created a new protocol, called “Run Other Samples” to investigate the use of the system with samples other than reference buccal samples, such as blood and saliva (from cigarettes and drink containers), while using the same cartridges as those used for reference buccal sample processing. Both blood and saliva samples demonstrated 88% success rate, by yielding DNA profiles of sufficient quality for upload to a database. Furthermore, the researchers noted it was possible to retrieve the blood and saliva samples from the chambers after the full processing run, which were suitable for retesting using standard/traditional forensic STR profiling methods [20].

The ANDE 6C Rapid DNA System was also investigated for use with forensic evidence samples where the analysis of 1705 casework samples was found to be comparable to traditional laboratory methodologies [8]. Forensically relevant samples typically encountered in real forensic investigations were included in the study to interrogate the effectiveness of the ANDE 6C Rapid DNA System to recover full and concordant DNA profiles that are compliant with the FBI’s QAS and the NDIS operational procedures (although QAS standards require DNA quantitation for forensic samples that Rapid DNA systems do not perform). Sample types included dried blood on tile, blood on FTA paper, oral epithelial samples from drinking containers, saliva on non-FTA paper, saliva on FTA paper, neat semen, semen on fabric, blood recovered from a knife, blood on fabric, chewing gum, bone, and other Disaster Victim Identification (DVI) sample types. The results of the study demonstrated that the ANDE 6C Rapid DNA System and accompanying expert system produced reliable, reproducible, and robust results, demonstrating the capability of the system for automatic processing and interpretation of forensically relevant casework samples.

While the ANDE Rapid DNA System currently has NDIS approval for reference buccal sample processing, forensically relevant crime scene samples do not have approval for upload and searching in CODIS. However, until approval is granted, individual accredited forensic science laboratories can validate individual Rapid DNA technologies for use with casework samples comparison and searches within local and state databases (e.g. the state of Kentucky using Rapid DNA for Sexual Assault Kits).

#### 21.3.2.2.2 Touch DNA/Low-DNA Content (LDC) Samples

Touch DNA is DNA left behind when a person touches a surface or object and leaves behind sloughed epithelial skin cells. This type of “trace” evidence is often low in abundance of DNA and depends upon the surface characteristics and shedder status of the donor. The exact origin of touch DNA is not always certain but could be: shed keratinocytes or their constituent parts from outer layers, nucleated epithelial cells from other body fluids or body parts, cell-free DNA reserves endogenous to the hands (e.g. sweat), or cell-free DNA transferred from body fluids (e.g. saliva). The quantity of DNA recovered from touch DNA samples is highly variable, ranging from <6 to 100 ng. For context, 6 pg is approximately the quantity of genomic DNA in a single human cell. With regard to touch DNA samples and traditional STR profiling methods, considerable efforts have been made to improve the yield of probative information from these samples with regard to their collection methods, DNA extraction methods, and STR amplification methods.

In 2016, the ANDE platform was modified for use with low-DNA content (LDC) samples [21]. A modified BioChipSet (BCS) was produced, while the remainder of the platform and analysis were maintained (Figure 21.16).

The modification involved incorporating a microfluidic ultrafiltration (UF) module downstream from the purification, which essentially concentrates the extracted DNA following purification in order to maximize yield. The

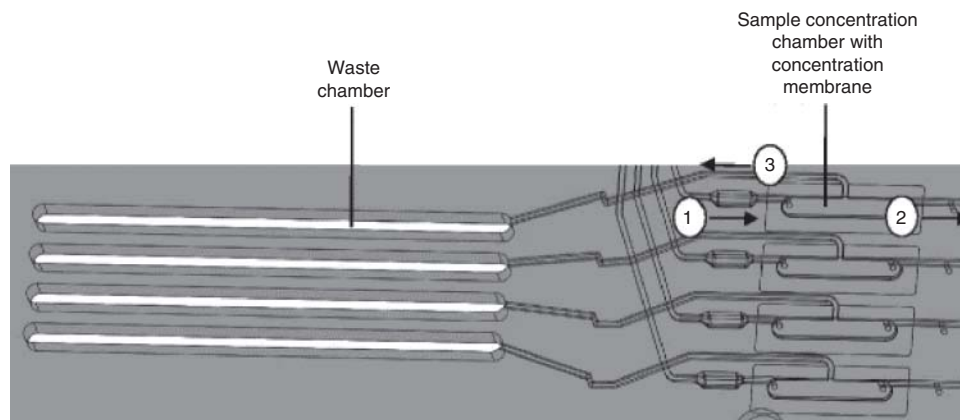


**Figure 21.16** BioChipSet concentration channels. *Source:* Turingan et al. [21], 2020 Springer Nature. Licensed under CC BY 4.0.

Smart Cartridge accepts four LDC samples and contains the liquid reagents required for sample processing. Fluids are transported throughout the biochip by pneumatic pressure – there are no moving parts. Essentially, using pneumatic pressure, the purified DNA moves toward a semipermeable UF membrane, which prevents the passage of the DNA fragments, but allows the elution solution to flow through to a waste chamber, resulting in concentrated DNA on the membrane.

The four concentration channels can be seen in Figure 18, one for each independent sample. Purified DNA solution flows into the concentration chamber (*arrow 1*) from the purification module. Concentrated DNA solution flows out of the concentration chamber (*arrow 2*) to the PCR chamber. The permeate is collected in the waste chamber (*arrow 3*). This modified method was tested with a large variety of sample types, including, oral epithelial cells from drinking containers, blood on FTA paper, blood on untreated paper, buccal cells on FTA paper, buccal cells on untreated paper, dried blood on ceramic tile, dried blood on clothing, dried semen on clothing, chewing gum, cigarette butts, swabs of cellphones, and bone fragments. This modified BCS for LDC analysis has a runtime of 102 minutes. The BCS utilizes the PowerPlex 16 HS assay.

#### 21.3.2.2.3 Tissue Samples

Exposure to harsh environmental insults can result in substantial degradation of human remains. With decomposed human remains, sometimes soft tissue samples are still viable for DNA testing. In other cases, the optimal sample types for DNA recovery are bones and teeth. In 2019, a study investigated the use of the ANDE 6C Rapid DNA System for use with buccal samples, teeth, bone samples, muscle tissue, liver tissue, and brain tissue [22]. The samples were exposed to aboveground decomposition at the Anthropology Research Facility (“Body Farm”) at the University of Tennessee. Some human donors were placed above ground immediately after collection, while another group were refrigerated in a morgue cooler for up to three months. The results of this study reported that exposed and refrigerated samples consistently produced partial or full concordant DNA profiles throughout the decomposition period that lasted one year. The results revealed buccal samples to be the “sample of choice” from remains which were exposed for up to 11 days, until maggot infestation interferes. Bone and tooth samples were the sample of choice for the one-year duration of the study. Muscle tissue produced full or partial profiles up to day 6 of exposure and, as expected, the profile generated deteriorated as time increased. It was observed that bicep samples and quadriceps produced similar results. Tissue samples produced full concordant profiles from the various tissue samples recovered from remains which had been refrigerated at the morgue over the three-month testing period. This study provides informative data to assist crime scene responders and medical examiners in their selection of samples which would likely yield identity information if Rapid DNA technologies are to be employed.

### 21.3.2.3 Sexual Assault Kits (SAKs)

The forensic investigation of sexual assault crimes can be challenging even in the most well-equipped crime laboratory. The analysis of Sexual Assault Evidence Kits or Sexual Assault Kits (SAKs) is time-consuming and labor intensive. The reality is that there are hundreds of thousands of backlogged SAKs spanning many years, across the globe, that have yet to be examined. Not only is this detrimental to the victims' right to justice, but it means the perpetrator of the crime remains free with the opportunity to reoffend.

The State of Kentucky in the United States was the first to adopt Rapid DNA technology for use in sexual assault investigations. In April 2019, Governor Matt Bevin announced the implementation of Rapid DNA technology, specifically, the ANDE 6C system, within the Kentucky State Police Forensics Laboratories and performed rigorous evaluation of the system. At the time a SAK is collected from a victim, all conventional samples are collected for traditional processing, however additional Rapid DNA swabs are collected also. Upon receipt of the SAK to the crime laboratory, the Rapid DNA swabs are processed immediately, while the remainder of the SAK is stored. The resulting DNA data generated within two hours are then searched against the local and state criminal databases. If a potential suspect is identified by the database, and apprehended by law enforcement within a short time period, it could also allow for the collection of trace evidence/biological fluids/DNA from the suspect, which perhaps would have been lost if it had taken weeks/months/years to identify the suspect. This would further strengthen the investigation and eventual outcome of the case.

By eliminating the backlog and testing all SAKs submitted to a crime laboratory, it will be possible to identify serial rapists, in both acquaintance and stranger rape cases. In addition, testing of SAKs could link different crimes. Sexual assault offenders typically engage in other criminal behavior such as burglary and homicide. Further to this, if a suspect/perpetrator is presented with DNA evidence linking them to a crime, the perpetrator often pleads out, resulting in earlier resolution of the case, saving the expense of a trial, and brings justice to the victim, which aids in their recovery. One in five women in America will experience rape or attempted rape at some point in their life. Currently, only 6 in 1000 sexual assault kits result in prosecution. The implementation of Rapid DNA technology has the ability to change that statistic.

#### Benefits of Testing all Sexual Assault Kits with Rapid DNA

- Quick apprehension eliminates opportunity to reoffend.
- Quick apprehension increases likelihood of recovery of forensic evidence from offender.
- Presenting the offender with DNA evidence linking them to the crime often leads them to confess or plead out.
- Identifies serial rapists.
- Identifies linkages to other crimes, e.g. burglary, homicide, etc.
- Knowledge of success of Rapid DNA may discourage offenders from offending.
- Knowledge that all kits will be tested will encourage victims to report these crimes.

### 21.3.3 Field Use

Outside of its use in booking stations and within an accredited crime laboratory, one of the major aims of the development of Rapid DNA technologies was to create ruggedized instruments suitable for field use in a wide variety of environments, e.g. mass disaster/mass casualty sites, battlefields, and border control stations, etc. This requires the instrument to be small in footprint, require no maintenance or optical calibration following transport, and the ability to operate using a standard power supply. Although traditional forensic DNA methods have been utilized for analysis of samples recovered from mass disaster/casualty events (including the 9/11 terrorist attacks [23–25], other terrorist attacks [26], natural disasters [27–29], and airplane crashes [30–32]), it can take many years (even decades) for all of the remains to be processed within an accredited crime laboratory. Victim remains from the 9/11 terrorist attacks in 2001 are still being analyzed by the Office of the Chief Medical Examiner (OCME) in New York, almost 20 years later. Therefore, there is great need and a wide scope of applications for Rapid DNA technology to be utilized to field uses.

### 21.3.3.1 Border Control, Immigration, and Human Trafficking Investigations

In May 2019, DHS announced the beginning of a pilot program to test the DNA of migrants arriving at the US border from Mexico who are suspected of fraudulent parentage or kinship claims. It was stated that the aim of this program was to utilize Rapid DNA technology as an investigative tool at the border to identify fraudulent cases of migrants claiming parentage or kinship with children that they are traveling with. It has been suggested that some migrants may be trying to take advantage of loopholes within the US Immigration System, whereby individuals arriving at the border with a child will avoid detention and can enter the asylum process more swiftly [33]. By identifying this type of fraudulent case, vulnerable children can be removed from potentially dangerous situations. Traditionally, the identification of this kind of fraudulent case has been performed using document screening and other investigative methods. Rapid DNA technology however offers a faster, more accurate method for parentage and kinship determination. ANDE Corporation has been contracted to perform the testing, at the border crossing, with results obtained within two hours. Homeland Security investigators from US Immigration and Customs Enforcement (ICE) can request to collect reference buccal samples from individuals, if they suspect a parent-child relationship is not legitimate. The resulting DNA profiles produced do not need to be uploaded to federal databases, reducing privacy and data storage concerns. Instead, within the FAIRS software package, parent and kinship verification can be performed.

There are some obvious limitations to this method, such as cases whereby parentage is through adoption, or indeed a parent may not be aware they are not the biological parent of the child. Other cases may include a family member, e.g. cousin, uncle, or aunt, traveling with the child. Nevertheless, if employed correctly and in tandem with other investigative methods to evaluate the full circumstances, the use of Rapid DNA technology at border crossings to stem fraudulent cases could prove very effective and reduce risk to vulnerable children.

While the use of Rapid DNA technology is being piloted in the United States only at this time, there is significant interest from other countries, particularly Eastern European and Asian countries, for the use of Rapid DNA technology at their border crossings to identify cases of human trafficking. Traditional DNA profiling has already been applied to combat human trafficking through victim identification, family reunification, and prosecution of human traffickers [34, 35]. In 2004, the DNA-PROKIDS program was established with the aim of combatting human trafficking using genetic identification of victims and their families, especially children. The program has successfully reunited illegally adopted and/or missing children with their families, and continues to do so. The program aims to establish a worldwide database of victims.

In 2014, a unique study was performed whereby covert investigators collected DNA samples using ANDE/NetBio sample swabs from individuals suspected of being victims of human trafficking [36] in Nepal and Costa Rica. Trained investigative personnel obtained samples during ongoing undercover investigative efforts. In circumstances where the collection of reference buccal samples was not practical to obtain, objects known to be in contact with the suspected human trafficking victim were sampled, e.g. cigarette butts, drink containers, etc. Objects located within the environment (e.g. brothels, locations suspected to house or transport victims) were also sampled, e.g. condoms and tissues. Objects located in public environments documented as areas where traffickers would congregate or engage were also sampled, e.g. cigarette butts and drink containers. All samples were processed using the DNAscan™/ANDE 4C Rapid DNA Identification System, with the modified low-DNA content (LDC) BioChipSet cassettes. A total of 50 samples were collected during the investigation. Nineteen of those samples were collected from known reference buccal samples of suspected human trafficking victims and yielded 95% success rate for obtaining full DNA profiles. The remaining 31 samples were collected from objects within the environment or in public places and produced 71% success rate for obtaining informative DNA profiles, with 23% full, 42% partial, and 6% mixture profiles. The results of this study provide evidence of immense support for the establishment of teams to implement the databasing of DNA profiles of suspected victims and perpetrators of human trafficking in an effort to combat the epidemic.

The identification of human trafficking remains to be a considerable challenge. The creation of a global database of human trafficking victims would offer effective evidence to support the identification of human trafficking

victims, family reunification, and prosecution of human traffickers. Traditional methods utilized within human trafficking investigations involve surveillance, use of informants, and interview and interrogation of both victims and perpetrators. These methods used in tandem with DNA profiling methods have proven useful to date. In this technological age, the sophistication of human trafficking crimes has evolved, and so must the investigative modes utilized to combat them.

#### **21.3.3.2 Disaster Victim Identification (DVI)**

There are numerous scenarios encountered in forensic casework that may result in mass fatalities, including bombings/explosions, natural disasters, fires, terrorist attacks, war conflicts, aviation crashes, and other mass transit accidents (e.g. high-speed passenger trains, subways). Human remains recovered in these situations often are severely damaged, dismembered, fragmented, commingled, in varying states of decomposition, or even skeletonized. Although many national, state, and regional crime laboratories exist throughout the country with extensive expertise and training in forensic DNA identification, these fixed “brick-and-mortar” laboratories are not amenable to field-based operations and testing. Hence, although these laboratories are willing partners in DVI efforts, the logistics of coordinating subcontracts and transporting biological samples long distances for genetic testing is tedious. Additionally, traditional DNA casework methods are both labor- and time-consuming, increasing the amount of time that families of decedents must wait for a positive identification.

Rapid DNA technology offers a potential solution to meet the high-throughput and onsite testing demand of mass fatality events. The ANDE 6C Rapid DNA System was specifically engineered for field deployment and onsite testing operations. In addition to its relatively small size and weight (as mentioned previously), it is operational at altitudes as high as 3048 m (10,000 ft) and was ruggedized to account for vibration and shock during transportation, meeting the strict requirements of US Military Standard 810G (MIL-STD-810G) [7]. Moreover, reagents are stable at room temperature for up to six months [8]. Complementing the ANDE 6C Rapid DNA instrument's compact size, fast runtimes, and temperature-stable reagents is kinship analysis software. This software, called FAIRS, has two secure modules which compare DNA profiles obtained from unidentified victims to direct reference samples or family member exemplars: (i) the Claimed Relationships module, and (ii) the Familial Search module. When algorithms embedded in the software determine a match, a formal report containing the decedent's genetic profile and the associated match statistic calculations are automatically generated for the case file. Hence, this comprehensive human identification system is particularly well-suited for location-based testing at accident sites, in disaster zones, and/or in temporary buildings or tents constructed by Disaster Mortuary Operational Response Teams (DMORTS).

DHS Science and Technology (S&T) Directorate is currently exploring the possibility of implementing Rapid DNA technology in mass fatality responses, especially since it is already being used to support immigration investigations and to combat transnational human trafficking [2, 6, 33]. DHS S&T has developed numerous drills and mock disaster victim identification exercises in order to: (i) assess if the instruments can be shipped in an expeditious and efficient manner for disaster response operations, and (ii) to identify and mitigate potential logistical challenges that might be encountered during complex deployments. Additionally, in 2019, the American Society of Crime Laboratory Directors (ASCLD) formed a Rapid DNA DVI Subcommittee, the goal of which is to determine best practices and develop policies for mass fatality applications ([www.ascld.org](http://www.ascld.org)). Although the SWGDAM has not yet developed formal guidelines for Rapid DNA analysis of DVI casework samples, the FBI has formed a working group to facilitate discussions on this issue.

Recent publicized successes using Rapid DNA technology in DVI cases likely will expedite discussions among the DHS S&T, ASCLD, SWGDAM, and FBI working groups, and may facilitate formal implementation of the technology in mass fatality response efforts. One of the aforementioned high-profile cases involved the 2018 “Camp Fire” in Paradise, California, which claimed the lives of 85 people and is the deadliest wildfire in California history. In collaboration with Butte County's Sheriff's Office and the California Department of Justice (DOJ),

ANDE Corporation deployed a team to assist with identification efforts. Remains from 69 victims were recovered; however, due to the intensity and duration of the fire, traditional methods of identification (e.g. fingerprints, odontology, surgical hardware) were only feasible for 22 of the decedents. Using a mobile (recreational) vehicle and three ANDE 6C Rapid DNA instruments, a variety of sample types from the victims' remains (e.g. bone, muscle, brain tissue, liver) and approximately 300 family reference samples were tested. DNA profiles were obtained from 62 of the 69 victims recovered (89.9% of samples tested). Of the 62 victims for whom DNA profiles were successfully generated, 58 victims (93.5%) were able to be positively identified via comparison to exemplars from biological relatives [37–45]. In 2019, less than a year after the wildfires, another tragedy struck in California. Thirty-three passengers and one crew member aboard the dive boat *Conception* perished when it caught fire off the coast of Santa Cruz Island. All 34 victims were identified within 10 days using ANDE Rapid DNA technology, much faster than the identification effort would have taken using traditional laboratory-based testing [22, 46].

In addition to the human remains from the California wildfires and the *Conception* boat fire that were successfully processed for DNA, the ANDE Rapid DNA platform has been subjected to extensive research with a broad spectrum of biological samples. During developmental validation, a total of 101 samples across seven different DVI-relevant tissue types were processed for accuracy and concordance. Included in the study were 18 bones (femora, humeri, ribs), 3 M teeth, 24 liver samples, 34 skeletal muscles, 2 brain cortices, 11 lung tissues, and 9 kidney samplings [8]. In another study, 10 deceased (donated) human subjects were exposed to the environment (surface deposition) at an approved outdoor research facility, and various tissue samplings were collected at regular time intervals over the course of a one-year study period. In general, successful DNA typing of soft tissues (brain, muscle, liver) was limited to relatively short postmortem time intervals (1–11 days), attributed to accelerated decomposition during environmental exposure compared to hard tissues. The majority of the bone/tooth samples tested yielded useful DNA profiles from the first day of collection through the end of the one-year experimental period [22]. Both of these research studies – as well as the casework performed during the California wildfires and the *Conception* boat fire – demonstrate proof-of-concept for DVI applications and support the use of this technology as a way to expedite human identification and family reunification efforts.

ANDE Corporation's Rapid DNA platform has already demonstrated robust and reliable forensic genetic testing of human remains with relatively short postmortem intervals (i.e. recent deaths ranging from one day to one year). However, human remains from mass fatality events are not always located and recovered within such short time frames. Victims of homicide, oppressive regimes, genocide, and war conflicts, for example, often are buried in clandestine graves and may not be discovered for many years (sometimes decades). These types of samples – which have been buried and have naturally skeletonized over time due to environmental insult – will pose additional challenges for rapid DNA platforms. Buried remains present an entirely different set of challenges compared to “fresh” bones that are recovered immediately or shortly after a fatality event has occurred. As the structural components of bone (i.e. calcium hydroxyapatite, collagen) decompose in a process called diagenesis, endogenous DNA molecules become far more susceptible to damage. Thus, buried bones typically yield much lower DNA quantities and present templates with a multitude of problematic lesions that can prevent successful profiling. Perhaps future research efforts could expand to include buried human remains. Successful application of Rapid DNA technology to naturally skeletonized remains which have been exposed to extended burial conditions or surface deposition across a broad range of climates and environments could dramatically expedite and change the landscape of forensic human identification casework.

#### 21.3.3.3 Enhancing Forensic Capabilities in Underdeveloped Countries

Rapid DNA technologies may represent an alternative mode of operation for the development of forensic science laboratories in underdeveloped countries. There are underdeveloped countries that do not have DNA profiling capabilities, and therefore could benefit from systems such as Rapid DNA technology whereby a more cost-effective, yet information-yielding approach could be employed. Within the United States, operational crime

laboratories are a huge expenditure. They require significant investment to build an entire DNA laboratory. The average DNA crime laboratory requires:

- Large equipment and infrastructure investments.
- Highly skilled technical and scientific personnel.
- Instrument maintenance and calibration.
- Freezer and cold storage.

For example, the DNA section of the Washington D.C. DNA crime laboratory in the United States endured initial setup costs of approximately USD \$22 million. They incur an annual DNA laboratory operating budget of about USD \$4 million. Other underdeveloped countries do not have this level of funding or budgetary capabilities. Rapid DNA technology, however, could represent an opportunity to apply DNA profiling to their investigations with a much-reduced initial setup cost and operational expenditure in underdeveloped countries.

## 21.4 Limitations and Important Considerations

There are some drawbacks and known limitations to this technology, and these should be considered prior to use or implementation.

### 21.4.1 Minute/Precious Samples

With multiple different Rapid DNA technologies available and ready for use, law enforcement agencies are eager to implement these technologies. With reference buccal samples and crime scene samples (e.g. blood, and other body fluids etc.), the recommended best practice is the two-swab method, whereby one swab is processed using Rapid DNA technology and the other is preserved for traditional DNA profiling in a laboratory. This ensures that if the Rapid DNA profiling fails for some reason, there is another available sample for testing. However, biological samples recovered from crime scenes or evidence items can often be minute in sample volume, i.e. trace biological evidence. Therefore, investigators must make the decision whether or not to consume the available sample using Rapid DNA profiling and retrieve results faster, or to preserve the sample and submit to the laboratory for traditional DNA profiling. In addition, when dealing with very minute samples within the DNA laboratory, standard operating procedures to enhance the recovery and yield of DNA from the samples are performed, in addition to methods to increase amplification of the PCR products. While systems such as the ANDE 6C Rapid DNA System with the I-Chip have added a concentration within their BioChipSet to increase yield, this may not be as effective as in-laboratory processes. Ultimately, there is a risk that potentially useful information could be lost due to the consumption of a trace sample when using Rapid DNA technologies, which might be prevented if submitted directly to the laboratory for processing. Because of this, it is recommended that minute or trace biological samples are preserved for traditional DNA processing.

### 21.4.2 Mixtures

With the current/most recent Rapid DNA technologies, the ANDE 6C Rapid DNA System, and the RapidHIT ID System, mixture resolution and interpretation within the systems are not possible. Both systems, however, will flag a sample run as possibly containing a mixture of DNA profiles.

DNA mixtures are profiles that are produced when a sample contains DNA contributions from two or more individuals. Mixed DNA profiles are failed by the system under one or more of the following conditions:

- Two or more heterozygous loci with three alleles.
- One or more heterozygous loci with four alleles.
- One or more hemizygous loci with two alleles.

In 2019, Carney et al. showed that the ANDE 6C Rapid DNA System could correctly identify mixed DNA samples from reference buccal samples that were created using a five different ratios of two-person mixed samples (19 : 1, 5 : 1, 1 : 1, 1 : 5, and 1 : 19) [6]. With the 19 : 1 and 1 : 19 samples however, the ANDE Expert System software ignores the minor contributors, which if reviewed manually by DNA analysts, in some cases, could yield probative information. In a separate study, the RapidHIT ID System correctly flagged mixture profiles that were processed using four different ratios of two-person mixed samples (1 : 1, 1 : 2.5, 1 : 4, and 1 : 9). Similar to ANDE, the RapidHIT systems are designed to flag DNA mixtures, however only once the data have been exported to GeneMapper<sup>TM</sup> or GeneMarker<sup>TM</sup>.

The ability to identify mixture samples quickly using Rapid DNA technology can aid an investigation by providing feedback to crime scene investigators who can then select other areas or stains to sample and improve or focus their collection. The ability to provide this type of strategy information is often lost, as it takes weeks or months to profile the sample using conventional methods.

## 21.5 Future Considerations and Conclusions

*Smaller and faster:* As with all field-based instrumentation, there is a continuous push to make the instruments smaller, and to produce results faster. The current Rapid DNA instruments are comparable in size to a large printer and produce results within approximately 90 minutes; however, this time frame includes a maximum of five samples per run. With future platforms, the time required to perform a run may not be amenable to faster run times, although they may be amenable to more samples per run.

*Cost:* As the technology advances and the demand increases, the cost of Rapid DNA technologies will be driven down. This cost will reduce not only the purchase of the instrument itself, but also the cost-per-sample to run.

*Standardization:* As there are just two major competing companies that produce Rapid DNA technologies at the moment, there is potential for other smaller companies to begin producing their own instruments, based on the success of the current two platforms. Inversely, there is also potential for the two major competing companies to join forces and merge to produce one super provider.

*Best practices:* Rapid DNA technologies were originally developed with the aim of using them in booking stations for arrestee profiling, requiring no technical expertise. The technology however has now expanded into more complex applications using crime scene and DVI samples, which can be low in DNA content and highly degraded. Therefore, best practices need to be developed to address the processing of individual evidence types, along with adequate training for these more complex sample types as they require technical expertise.

*Policies and legislation:* While the Rapid DNA Act of 2017 provided the springboard from which Rapid DNA technologies could truly be implemented into operational casework, it is crucial that new policies and legislation are continually being created and revised in order to keep up with technological advancements and as the methods are more broadly implemented. In addition, there needs to be buy-in from all parties involved where clear communication and agreement are maintained. This includes the instrument manufacturers, the law enforcement

agencies that bear the responsibility for the evidence handling, and the state prosecutors who will handle the cases in the courtroom and have to defend the use of these methods.

As technology advances, it is certain that further improvements will be made to existing platforms. Indeed, more platform providers may appear, or some existing providers may merge. The range of applications for both field-based and laboratory-based use will continue to grow as researchers refine the methodologies involved. Industry demand will undoubtedly grow as further successes are reported. Continued research and development will drive the technology forward and may ultimately lead to Rapid DNA technologies becoming a staple of crime laboratories across the world.

## A. Appendix

### A.1 Acronyms

A-Chip	Arrestee Chip
ANDE	Accelerated Nuclear DNA Equipment
ASCLD	American Society of Crime Lab Directors
BCS	BioChipSet
CCD	Charge Coupled Device
CE	Capillary Electrophoresis
CJIS	Criminal Justice Information Services
CODIS	Combined DNA Index System
CSA	CJIS Systems Agency
DAB	DNA Advisory Board
DHS	Department of Homeland Security
DHS S&T	Department of Homeland Security Science & Technology Directorate
DOD	Department of Defense
DOJ	Department of Justice
DMORT	Disaster Mortuary Operational Response Team
DVI	Disaster Victim Identification
EPG	Electropherogram
ESS	European Standard Set
FBI	Federal Bureau of Identification
FTA	Flinders Technology Associates
HID	Human Identification
ICE	Immigration and Customs Enforcement
ID	Identification
I-Chip	Investigative Chip
ILS	Internal Lane Standard
IT	Information Technology
LDC	Low DNA Content
mRDA	modified Rapid DNA analysis
NDIS	National DNA Index System
ng	Nanogram
NIJ	National Institute of Justice
NIST	National Institute of Standards and Technology

OCME	Office of the Chief Medical Examiner
PCR	Polymerase Chain Reaction
pg	Picogram
QAS	Quality Assurance Standards
RDA	Rapid DNA analysis
RFID	Radio Frequency Identification
SAK	Sexual Assault Kit
SIB	State Identification Bureau
SID	State Identification (number)
STR	Short Tandem Repeat
SWG DAM	Scientific Working Group on DNA Analysis Methods
UCN	Universal Control Number
UF	Ultra-Filtration
USACIL	United States Army Criminal Investigation Laboratory

## References

- 1 FBI.gov (2020). *FBI Webpage* [Internet]. <https://www.fbi.gov/services/laboratory/biometric-analysis/codis/rapid-dna> (accessed 1 April 2020).
- 2 Congress.gov (2017). *H. Rept. 115-117 – Rapid DNA Act of 2017* [Internet]. <https://www.congress.gov/congressional-report/115th-congress/house-report/117/1> (accessed 30 March 2020).
- 3 French, J.L., Turingan, R.S., Hogan, C., and Selden, R.F. (2016). Developmental validation of the DNAscan™ Rapid DNA analysis™ instrument and expert system for reference sample processing. *Forensic Science International: Genetics* 25: 145–156.
- 4 Tan, E., Turingan, R.S., Hogan, C. et al. (2013). Fully integrated, fully automated generation of short tandem repeat profiles. *Investigative Genetics* 4 (1): 16.
- 5 Moreno, L.I., Brown, A.L., and Callaghan, T.F. (2017). Internal validation of the DNAscan/ANDE™ Rapid DNA analysis™ platform and its associated PowerPlex® 16 high content DNA biochip cassette for use as an expert system with reference buccal swabs. *Forensic Science International: Genetics* 29: 100–108.
- 6 Carney, C., Whitney, S., Vaidyanathan, J. et al. (2019). Developmental validation of the ANDE™ rapid DNA system with FlexPlex™ assay for arrestee and reference buccal swab processing and database searching. *Forensic Science International: Genetics* 40: 120–130.
- 7 U.S. Department of Defense (2008). *Department Of Defense Test Method Standard: Environmental Engineering Considerations And Laboratory Tests Title* [Internet]. <https://www.atec.army.mil/publications/Mil-Std-810G/Mil-Std-810G.pdf> (accessed 12 April 2020).
- 8 Turingan, R.S., Tan, E., Jiang, H. et al. (2020). Developmental validation of the ANDE 6C system for rapid DNA analysis of forensic casework and DVI samples. *Journal of Forensic Sciences* 65 (4): 1056.
- 9 Grover, R., Jiang, H., Turingan, R.S. et al. (2017). FlexPlex27 – highly multiplexed rapid DNA identification for law enforcement, kinship, and military applications. *International Journal of Legal Medicine* 131 (6): 1489–1501.
- 10 Hennessy, L.K., Franklin, H., Li, Y. et al. (2013). Developmental validation studies on the RapidHIT™ human DNA identification system. *Forensic Science International: Genetics Supplement Series* 4: e7–e8.
- 11 Jovanovich, S., Bogdan, G., Belcinski, R. et al. (2015). Developmental validation of a fully integrated sample-to-profile rapid human identification system for processing single-source reference buccal samples. *Forensic Science International: Genetics* 16: 181–194.

- 12** Hennessy, L.K., Mehendale, N., Chear, K. et al. (2014). Developmental validation of the GlobalFiler® express kit, a 24-marker STR assay, on the RapidHIT® system. *Forensic Science International: Genetics* 13: 247–258.
- 13** Vallone, P.M. (2013). *Biometric Consortium Meeting, BCC, Tampa, FL, Sepember 2013*. NIST Rapid-DNA Inter-laboratory Study [Internet]. [https://strbase.nist.gov//pub\\_pres/Vallone\\_BCC\\_Talk\\_Sept2013.pdf](https://strbase.nist.gov//pub_pres/Vallone_BCC_Talk_Sept2013.pdf) (accessed 27 March 2020).
- 14** Larue, B.L., Moore, A., King, J.L. et al. (2014). An evaluation of the RapidHIT® system for reliably genotyping reference samples. *Forensic Science International: Genetics* 13: 104–111.
- 15** Holland, M. and Wendt, F. (2015). Evaluation of the RapidHIT™ 200, an automated human identification system for STR analysis of single source samples. *Forensic Science International: Genetics* 14: 76–85.
- 16** Salceda, S., Barican, A., Buscaino, J. et al. (2017). Validation of a rapid DNA process with the RapidHIT® ID system using GlobalFiler® express chemistry, a platform optimized for decentralized testing environments. *Forensic Science International: Genetics* 28: 21–34.
- 17** Romsos, E.L., Lembirick, S., and Vallone, P.M. (2015). Rapid DNA maturity assessment. *Forensic Science International: Genetics Supplement Series* 5: e1–e2.
- 18** Romsos, E.L., French, J.L., Smith, M. et al. (2020). Results of the 2018 rapid DNA maturity assessment. *Journal of Forensic Sciences* 65 (3): 953–959.
- 19** FBI.gov. *Rapid DNA* [Internet]. <https://www.fbi.gov/services/laboratory/biometric-analysis/codis/rapid-dna> (accessed 3 April 2020).
- 20** Gangano, S., Elliott, K., Anoruo, K. et al. (2013). DNA investigative lead development from blood and saliva samples in less than two hours using the RapidHIT™ human DNA identification system. *Forensic Science International: Genetics Supplement Series* 4: e43–e44.
- 21** Turingan, R.S., Vasantgadkar, S., Palombo, L. et al. (2016). Rapid DNA analysis for automated processing and interpretation of low DNA content samples. *Investigative Genetics* 7: 2.
- 22** Turingan, R.S., Brown, J., Kaplun, L. et al. (2019). Identification of human remains using Rapid DNA analysis. *International Journal of Legal Medicine* 134: 863–874.
- 23** Biesecker, L.G., Bailey-Wilson, J.E., Ballantyne, J. et al. (2005). DNA identifications after the 9/11 world trade Center attack. *Science* 310 (5751): 1122–1123.
- 24** Mundorff, A.Z., Bartelink, E.J., and Mar-Cash, E. (2009). DNA preservation in skeletal elements from the world trade center disaster: recommendations for mass fatality management. *Journal of Forensic Sciences* 54 (4): 739–745.
- 25** Holland, M.M., Cave, C.A., Holland, C.A., and Bille, T.W. (2003). Development of a quality, high throughput DNA analysis procedure for skeletal samples to assist with the identification of victims from the world trade Center attacks. *Croatian Medical Journal* 44 (3): 264–272.
- 26** Sudoyo, H., Widodo, P.T., Suryadi, H. et al. (2008). DNA analysis in perpetrator identification of terrorism-related disaster: suicide bombing of the Australian embassy in Jakarta 2004. *Forensic Science International: Genetics* 2: 231–237.
- 27** Prinz, M., Carracedo, A., Mayr, W.R. et al. (2007). DNA Commission of the International Society for forensic genetics (ISFG): recommendations regarding the role of forensic genetics for disaster victim identification (DVI). *Forensic Science International: Genetics* 1 (1): 3–12.
- 28** Deng, Y.J., Li, Y.Z., Yu, X.G. et al. (2005). Preliminary DNA identification for the tsunami victims in Thailand. *Genomics, Proteomics & Bioinformatics* 3 (3): 143–157.
- 29** Schou, M.P. and Knudsen, P.J.T. (2012). The Danish disaster victim identification effort in the Thai Tsunami: organisation and results. *Forensic Science, Medicine, and Pathology* 8 (2): 125–130.
- 30** Hsu, C.M., Huang, N.E., Tsai, L.C. et al. (1999). Identification of victims of the 1998 Taoyuan airbus crash accident using DNA analysis. *International Journal of Legal Medicine* 113 (1): 43–46.

- 31** Leclair, B., Frégeau, C.J., Bowen, K.L., and Fourney, R.M. (2004). Enhanced kinship analysis and STR-based DNA typing for human identification in mass fatality incidents: the Swissair flight 111 disaster. *Journal of Forensic Sciences* 49 (5): 939–953.
- 32** Piccinini, A., Betti, F., Capra, M., and Cattaneo, C. (2004). The identification of the victims of the Linate air crash by DNA analysis. *International Congress Series* 1261: 39.
- 33** Miroff, N. (2019). Homeland Security to test DNA of families at border in cases of suspected fraud. *Washington Post* [Internet]. [https://www.washingtonpost.com/immigration/homeland-security-to-test-dna-of-families-at-border-in-cases-of-suspected-fraud/2019/05/01/8e8c042a-6c46-11e9-a66d-a82d3f3d96d5\\_story.html](https://www.washingtonpost.com/immigration/homeland-security-to-test-dna-of-families-at-border-in-cases-of-suspected-fraud/2019/05/01/8e8c042a-6c46-11e9-a66d-a82d3f3d96d5_story.html) (accessed 3 April 2020).
- 34** Katsanis, S. and Kim, J. (2014). DNA in immigration and human trafficking. In: *Forensic DNA Applications: An interdisciplinary perspective*, Section 4, Chapter 22. Boca Raton: CRC Press, Taylor and Francis Group <https://www.routledge.com/Forensic-DNA-Applications-An-Interdisciplinary-Perspective/Primorac-Schanfield/p/book/9781466580220>.
- 35** Katsanis, S.H., Kim, J., Minear, M.A. et al. (2014). Preliminary perspectives on dna collection in anti-human trafficking efforts. *Recent Advances in DNA Gene Sequences* 8: 78–90.
- 36** Palmbach, T., Blom, J., Hoynes, E. et al. (2014). Utilizing DNA analysis to combat the world wide plague of present day slavery – trafficking in persons. *Croatian Medical Journal* 55 (1): 3–8.
- 37** Gin, K., Tovar, J., Bartelink, E.J. et al. (2020). The 2018 California wildfires: integration of Rapid DNA to dramatically accelerate victim identification. *Journal of Forensic Sciences* 65 (3): 791–799.
- 38** Department of Homeland Security (2019). Snapshot: S&T's Rapid DNA technology identified victims of California Wildfire. *DHS Science and Technology News* [Internet]. <https://www.dhs.gov/science-and-technology/news/2019/04/23/snapshot-st-rapid-dna-technology-identified-victims> (accessed 4 May 2020).
- 39** Border, G. (2018). California Taps War-Zone DNA Specialists After Wildfire. *Reuters* [Internet]. <https://www.reuters.com/article/us-california-wildfires-remains/california-taps-war-zone-dna-specialists-after-wildfire-idUSKCN1NK1EI> (accessed 3 April 2020).
- 40** Brown, K. (2018). California Turns to War-Zone DNA Test to ID Fire Remains. *Bloomberg* [Internet]. <https://www.bloomberg.com/news/articles/2018-11-19/dna-testing-company-gets-call-to-help-id-california-fire-victims> (accessed 3 April 2020).
- 41** Druga, M. (2019). No Rapid DNA Technology Identified Victims of California Wildfires. *Homeland Preparedness News* [Internet]. <https://homelandprepnews.com/stories/33583-rapid-dna-technology-identified-victims-of-california-wildfires> (accessed 3 April 2020).
- 42** Gin, K. (2019). California Wildfires: Rapid DNA and the Future of Mass Fatality Identification. *Forensic Science Executive* [Internet]. [www.forensicscienceexecutive.org](http://www.forensicscienceexecutive.org) (accessed 3 April 2020).
- 43** Evan Sernoffsky (2018). DNA Technology Helps Identify Camp Fire Victims; Challenge is Finding Family. *San Francisco Chronicle* [Internet]. <https://www.sfchronicle.com/california-wildfires/article/DNA-technology-helps-identify-Camp-Fire-victims-13406853.php> (accessed 3 April 2020).
- 44** Waitt, T. (2019). Rapid DNA. ID's deadly 'Camp Fire' Disaster Victims. *American Security Today* [Internet]. <https://americansecuritytoday.com/rapid-dna-ids-deadly-camp-fire-disaster-victims-see-how-video> (accessed 3 April 2020).
- 45** Zimmer, K. (2019). Rapid DNA Analysis Steps in to Identify Remains of Wildfire Victims. *The Scientist* [Internet]. <https://www.the-scientist.com/news-opinion/rapid-dna-analysis-steps-in-to-identify-remains-of-wildfire-victims-65156> (accessed 3 April 2020).
- 46** Woods, A. (2019). Officials Used "Rapid DNA" Tech to Identify California Boat Fire Victims. *The New York Post* [Internet]. <https://nypost.com/2019/09/05/officials-used-rapid-dna-tech-to-identify-california-boat-fire-victims> (accessed 3 April 2020).

## 22

### Portable Biological Spectroscopy: Field Applications

*Brian Damit and Miquel Antoine*

*Johns Hopkins Applied Physics Laboratory, Laurel, MD, USA*

#### 22.1 Introduction

Field uses for portable biological spectroscopy systems are highly diverse, ranging from biological defense to medical diagnostics, and even forensics. For some of these disciplines, application of portable spectroscopy is established, and represents either a primary or complementary tool for practitioners to analyze samples. In a field environment, where resources such as power, access to consumables, and analysis time can be limited, spectroscopy exhibits distinct advantages over other approaches (e.g. molecular assays) including near-instant feedback, simple operation and interpretation of data, and minimal or no need for consumables. Thus, demand for greater inclusion of portable spectroscopy into existing user workflows, especially in challenging field settings, is well deserved. Advances in fundamental spectroscopy research, ubiquity of smartphones, and world events (e.g. September 11) over the last several decades have expanded field applications for portable spectroscopy, irrevocably shaping the landscape of the discipline. Commercial off-the-shelf (COTS) portable spectroscopy technologies, which are systems users can deploy directly into the field, have evolved from requiring users to possess substantial technical background, to now exhibiting features like touchscreens, automated data interpretation, and requiring minimal user training. Separately, both academia and industry alike have reported headway in exploiting the smartphone, repurposing its onboard camera optics and software to perform spectroscopy; see the chapters by Scheeline in Volume 1 and Peveler and Algar in Volume 2. The promise of a “spectrometer in your pocket” may indeed represent an ideal embodiment of a portable system, further broadening the range of field applications for spectroscopic analysis in the future.

Table 22.1 provides an overview of this chapter, summarizing the range of field applications for portable biological spectroscopy. Key disciplines employing spectroscopy include biological defense, medical and healthcare settings, food and agriculture safety, environmental pollution monitoring, and forensics. The role of spectroscopy in these disciplines varies considerably, but retains the common theme of applying light, usually ultraviolet (UV), visible, and/or infrared, to probe for molecular structure or chemical composition, thereby supplying users with data regarding features of a biological sample. Figure 22.1 displays photos of commercial systems that have been designed for the specific purpose of field use. Within biodefense, portable spectroscopy systems maintain a critical function in early warning monitoring for an airborne biological attack, and detection of biothreat materials in solid-phase or liquid samples [1, 2]. Medical applications of portable spectroscopy are varied, spanning from analysis of human tissue to disease diagnostics [3, 4]. The use of portable spectroscopy systems in food and agriculture settings is similarly diverse, involving *in situ* use of spectroscopic techniques to rapidly identify biological contamination and analyze the welfare of crops. Growing environmental concerns in recent years have motivated on-site monitoring of biological pollutants in water, soil, and air [5, 6]. Finally, portable spectroscopy systems are

**Table 22.1** General overview of field applications of portable biological spectroscopy technologies.

Application area	Description	Spectroscopy types	Example usage
Biodefense	Detection of biological threats (solid, liquid, air phase)	Fluorescence, Raman, breakdown spectroscopy (LIBS)	Distribute portable detectors in area to monitor for airborne biological threats
Medical and healthcare	Assessment of tissue health and disease biomarkers	Infrared absorption, fluorescence, Raman	Attach infrared spectrometers to human subjects to measure tissue oxygenation
Food and agriculture	Monitoring of food contamination and welfare of crops and livestock	Fluorescence, visible, infrared, Raman	Measure the fluorescence spectra from meat surfaces to infer bacterial loading
Environmental pollution	Measurement of biological pollutants in water, soil, and air	Fluorescence, infrared absorption and reflectance	Assess water potability by measuring fluorescence from coliforms using a smartphone
Forensics	Identification of the presence of body fluids, bruises, and wounds	Fluorescence, visible absorption	Use portable light systems to locate blood at a crime scene to assist in sample collection by investigators

Biodefense

Camthrax  
(Source: Veritide Ltd.)Instantaneous biological analyzer and collector (IBAC)  
(Source: FLIR Systems, Inc.)

Food safety

SCiO  
(Source: Consumer Physics)

Water quality

Proteus  
(Source: Proteus Instruments)

Air quality

Wideband intensity bioaerosol sensor (WIBS)  
(Source: Droplet Measurement Technologies)

Forensics

Polilight  
(Source: Rofin Australia Pty Ltd.)**Figure 22.1** Photos of commercial portable biological spectroscopy systems developed for field use.

well established in the field of forensics, assisting crime scene investigators in locating and classifying biological samples like blood, other body fluids, and fingerprints present at a crime scene [7, 8]. This chapter reviews these disciplines, describing the use of portable biological spectroscopy from a field application perspective and providing practical considerations. To keep this chapter tractable, the scope of the discussions is constrained to reagentless spectroscopic detection approaches. This review also emphasizes technologies and concepts that are more mature, specifically those techniques that have been translated into practice, have demonstrated use in the field, and are integrated into the workflow of practitioners. However, less established, but notable advances that have potential to be transformative are referenced as well. This chapter concludes with a summary discussing challenges and outlook for portable biological spectroscopy in the coming years.

## 22.2 Organization of This Chapter

This chapter first describes the essential considerations for field-portable systems, namely the features that distinguish fieldable systems from their benchtop counterparts. The following discussion then summarizes specific field applications for portable spectroscopy: biological defense, medical and clinical, food and agriculture, environmental sciences, and forensics. These sections provide an overview of the field, and discuss specific applications, benefits, and limitations of portable spectroscopy in the respective field applications. The sections also introduce and describe several existing spectroscopy systems, as well as past systems to provide historical context to the reader. In addition to discussion of conventional technologies, this chapter includes discussion of other types of portable spectroscopy (e.g. smartphone), and their potential in future field applications.

## 22.3 Attributes of Field-Portable Spectroscopy Systems

Regardless of the specific field application, portable spectroscopy systems exhibit several important attributes that distinguish them from their benchtop counterparts. Paramount among these, portable systems must be transportable into their respective field setting, usually by a single user, which both limits the weight and form factor of a system. This limitation oftentimes results in sacrifice of features, reliability, and/or signal-to-noise ratio. Although “man portability” does not have a strict definition, portable systems are usually limited to a weight and size on the order of 14 kg and backpack sized ( $65\,000\,\text{cm}^3$ ) to be comfortably transported by a user. For many of the field scenarios described in this chapter, portable systems must include the capability to be battery powered, as users may not have access to wall or generator power. Ideally, field-portable spectroscopy systems do not consume reagents or other consumables since this requires users to transport additional supplies into the field. Depending on the specific field usage, other attributes of portable systems include onboard data analysis, robust wireless communications, minimal maintenance and calibration, and reliable operation in a range of environmental conditions (e.g. precipitation, wind, temperature, relative humidity, etc.). For example, portable spectroscopy systems used for environmental monitoring purposes may need to operate outdoors for extended durations and transmit data remotely to a user. Therefore, the properties of a portable spectroscopy system are dictated by its intended usage in a field setting.

For many field applications, a key consideration for a portable spectroscopy system is the user experience. User experience is a user’s perception or overall attitude toward a system – more precisely it refers to usability (ease-of-use), convenience, and even aesthetic of its hardware design or software interface. Although a largely subjective metric, a positive user experience is essential and dictates widespread adoption or rejection by practitioners. In challenging field environments, users prefer that interaction with the system be simple and intuitive, especially when users do not have expertise in the respective discipline. In general, it is desirable that these systems are accessible to a variety of users possessing both technical and nontechnical backgrounds. This characteristic empowers nonexperts like technicians, military personnel, law enforcement, volunteers, and citizen scientists

alike to confidently collect and analyze samples. Regardless of their background, users usually prefer simple formats like integrated touchscreens or connection to tablets or smartphones to operate a spectrometer in field environments. Single-button operation, where a user simply presses a button to begin analysis, acquire data, interpret data, and display results is also ideal. For technical users desiring in-depth details, for instance, those users wishing to view a spectral plot, some systems include an advanced-user mode that can be accessed. For these advanced users, impromptu customization of spectral libraries or adjustment of other data acquisition settings is also highly desirable. Another notable element of user experience is the analysis time or time-to-detect – essentially the time required for a system to analyze a sample. Optimally, analysis time is near instantaneous rather than on the scale of hours, allowing users to efficiently obtain results.

With regard to data collection in field settings, some spectroscopy systems require initial setup and then sample autonomously, whereas other systems require users to actively collect and manipulate samples. In the latter case, sample introduction workflow is a critical aspect of user experience, with complex, multistep procedures reflecting poorly on usability. In an ideal operation, a user simply points the system toward a sample, initiates a measurement, and then obtains results. A similar, but a more involved process necessitates users to physically collect a solid, liquid, or tissue sample, and transport the sample to a system for subsequent analysis. In general, fewer sample preparation steps and manipulations by a user yield fewer user errors and biases. Several field scenarios require users to be in personnel protective equipment (PPE) while performing analysis, thus for some systems, operation must be streamlined and accommodate users with limited finger dexterity and range of motion. After sampling is complete, contamination of the system, also referred to as carryover, is preferably minimal or easily removed either automatically or by a user.

## 22.4 Field Applications

### 22.4.1 Biological Defense

Application of portable spectroscopy systems in biological defense is well established, especially in comparison to other fields, with a range of technologies available for analyzing solid, liquid, and air-phase samples for biological threats. Commercial systems are widely adopted by militaries and biodefense agencies across the world; moreover, growing concerns about bioterrorism and new biological threats have precipitated development of new technologies. The following sections provide a summary of historical and existing portable biodefense spectroscopy systems with emphasis on higher maturity technologies.

#### 22.4.1.1 Biological Solid- and Liquid-Phase Detection

The 2001 anthrax letters incident (Amerithrax) motivated development of man-portable systems that can rapidly interrogate suspicious powders to detect biological materials without need for wet-chemistry preparation [9]. Marketed toward first responders, Hazmat teams, and military personnel, these handheld systems allow a user to load a powder sample into the system, press a button, and acquire results. Examples of such systems are the Camthrax and Ceeker (Veritide Ltd.). The Ceeker operates by measuring the fluorescence signature of dipicolinic acid (DPA), a compound uniquely present in *Bacillus* and *Clostridium* bacterial spores and responsible for the hardiness of the organisms. Due to the weakly fluorescing nature of DPA, the Ceeker applies a two-step analysis scheme: (i) 250 nm photodissociation of DPA to facilitate conversion of DPA to more fluorescent picolinic acid, and (ii) fluorescence measurement of picolinic acid with 350 nm excitation. After a 10-minute measurement and analysis period, the system alerts the user to the results by displaying a simple “yes” or “no” answer on a screen located on the instrument. Since the system does not provide species-level identification, detection is deemed presumptive as molecular biology techniques (e.g. polymerase chain reaction [PCR]) must confirm that the spore is a biological agent. Although the Ceeker targets bacterial spores, development efforts have investigated extending

these principles to detection of ricin and botulinum toxin – two proteins often implicated as biological weapons. A now defunct portable system, the Handheld Raman Imager (ChemImage) used Raman chemical imaging for the detection of both biological and chemical threats. The system combined molecular spectroscopy with digital imaging to analyze both powder/liquid samples and identify biological materials, especially those present in complex samples. In general, advances in assay technologies, particularly lateral flow assay (LFA) have largely superseded portable spectroscopy for field analysis of suspicious powder or liquid samples. These LFAs are simple nitrocellulose test strips in a pregnancy test-style format. In addition to offering species-level presumptive identification, LFA methods are less expensive, smaller, and provide more rapid results than portable spectroscopy systems.

#### 22.4.1.2 Biological Aerosol Detection

Portable spectroscopy systems are used extensively in the detection of biological aerosols (bioaerosols). Bioaerosols, defined as airborne particles of biological origin, can originate from natural sources or be released intentionally for the purpose of biowarfare. Since the late 1990s, biodefense programs have integrated portable spectrometers into their biodetection strategies to support early warning alarming of an airborne bioattack [1]. Operationally, users distribute these portable systems throughout a high-risk location, and the systems monitor air continuously for anomalous aerosols – these locations can include subway stations, sporting venues, tourist attractions, military bases, or other densely populated areas. Most systems use some variant of laser-induced fluorescence (LIF) spectroscopy as the detection mechanism, although several systems use other spectroscopic modalities (e.g. Raman scattering) to supplement or instead of LIF. LIF systems detect bioaerosols by sampling ambient aerosols, aerodynamically focusing these aerosols into a single file, and then interrogating each aerosol with laser light to measure its fluorescence signature; bioaerosols, which intrinsically contain fluorescent molecules, produce autofluorescence whereas nonbiological particles (e.g. road dust) yield minimal or no fluorescence signature. Thus, measurement of an abundance of fluorescent aerosols can indicate an airborne biological attack has occurred. As air-phase particles are analyzed in real time, these systems can automatically provide a warning alarm, promoting nearby personnel to seek immediate protective measures. A key caveat for LIF systems is that these technologies cannot discriminate between biological threats and more benign biological particles (e.g. pollen), and thus molecular assays are needed to confirm the bioaerosols indeed contain threat organisms. LIF systems range in dimensions from ruggedized handheld units ( $18 \times 15 \times 32$  cm) to larger units ( $90 \times 50 \times 75$  cm) that require vehicles for transport to a field site. For biodefense applications, these systems often contain wireless communications to enable networking and transmission of data and alarming status to users stationed at a command center. Some systems feature integrated aerosol collection modules that can be autonomously initiated to collect a bioaerosol sample. Within the biodefense community, portable real-time spectroscopy systems are often referred to as “triggers,” since they are operationally implemented to trigger aerosol collector systems that obtain an aerosol sample for subsequent processing with a molecular biology assay.

Portable LIF detectors are designed to target molecules naturally present in microorganisms and their growth media; the systems' excitation ( $\lambda_{\text{ex}}$ ) and emission ( $\lambda_{\text{em}}$ ) wavelengths overlap with the fluorescence spectra of high-intensity endogenous fluorophores in prokaryotic organisms. An exhaustive review of fluorophores and associated spectra for a variety of organisms is presented in Pöhlker et al. [10] Molecules specifically targeted by LIF systems include several amino acids (tryptophan, tyrosine, and phenylalanine), which have excitation and emission maxima of 260–280 nm and 280–350 nm respectively, and enzymes and coenzymes like nicotinamide adenine dinucleotide (NADH), which have excitation and emission of 290–450 nm and 440–535 nm, respectively [11]. Components of the cell wall, various pigments, and vitamins can also produce weak or moderate fluorescence signal. Nonvolatile constituents of cell-culture media, aerosolized with microorganisms, exist as residue on aerosols after a wet-dissemination, yielding exogenous autofluorescence. Lysogeny broth, for example, is comprised of tryptone and yeast extract, which contain fluorescent molecules like peptides and vitamins added to enhance microbial growth; indeed, these nonvolatile components can contribute significant fluorescence that is detectable by LIF systems.

Interest in portable LIF bioaerosol spectrometers for biodefense applications began in earnest with the Fluorescence Aerosol Particle Sensor (FLAPS, TSI Inc.), a design originally conceived by the Canadian Department of National Defence. Eventually adopted by the US military and Canadian biodefense programs, the FLAPS, later termed the Ultraviolet Aerodynamic Particle Sizer (UV-APS), employed laser excitation in the 340–360 nm range [1]. Nearly simultaneous investigations by the US Army Research Laboratory, White Sands Range, and Yale University were equally influential, establishing notable technological advancements and characterizing the spectroscopic properties of bioaerosols. Key contributions include experimental measurements of isotropy, yield, and degradation of bioaerosol fluorescence as well as introduction of sub-300 nm excitation laser configurations. Reduction in the form factor of portable LIF systems has benefited from semiconductors and light-emitting diode (LED) research supported through Defense Advanced Research Projects Agency (DARPA) funding [1].

As of 2020, a multitude of portable LIF bioaerosol systems exist, each possessing different features, optical configurations, and levels of maturity. Table 22.2 summarizes commercial detection systems and their distinguishing properties. Although these systems are available from different vendors, they fundamentally share an identical design – all systems contain some element for aerosol focusing, excitation lasers, photodetectors, signal-processing circuitry, algorithm, and user interface. The current trend in development of new LIF systems involves adding multiple excitation wavelengths and/or multichannel photodetectors to obtain spectrally resolved aerosol fluorescence signatures. These optical configurations enable real-time measurement of the excitation–emission matrix of single aerosols. Coupling these measurements with techniques in machine learning and pattern recognition to interpret the data can permit higher fidelity classification of aerosols, leading to better discrimination of threats to background aerosols [2]. Examples of such multichannel systems include two instruments developed by Droplet Measurement Technologies (DMT): the Wideband Integrated Bioaerosol Sensor (WIBS) and the Spectral Intensity Bioaerosol Sampler (SIBS). The WIBS is the first commercial aerosol LIF system to feature dual-wavelength excitation (280 and 370 nm), which is generated from two separate xenon flash lamps in the WIBS. The single-aerosol fluorescence is collected, filtered, and then detected by two detection channels, channel 1 (310–400 nm) and channel 2 (420–650 nm). Like the WIBS, the SIBS applies two excitation wavelengths, 285 and 370 nm, but it possesses greater spectral resolution, recording fluorescence emission over 16 channels in the range of 302–721 nm [12]. Both DMT systems are marketed for academic and environmental sampling, but will likely attract increasing attention from biodefense customers in coming years.

Besides LIF, other spectroscopic techniques like Raman, breakdown spectroscopy, and elastic light polarization have demonstrated potential in classifying threat bioaerosols. The Resource Effective Bioidentification System (REBS), introduced by Battelle, is a man-portable Raman spectrometer that provides autonomous identification of bacteria, spores, toxins, and viruses within 15 minutes or less. The REBS deposits aerosols onto a moving metallic collection tape, and then excites the aerosol sample using 643 nm beam that is shaped into a line geometry. A charged coupled device (CCD) measures the Raman spectra from positions on the line in approximately 1  $\mu\text{m}$  increments – afterward, the line is stepped across the tape to capture the spectra from all deposited particles on the tape, in a process referred to as line scanning. The REBS software algorithm then compares the measured spectra to known threat signatures for determination of a threat. Another portable system, the Rapid Agent Aerosol Detector (RAAD), combines LIF measurements with laser-induced breakdown spectroscopy (LIBS) to improve classification of an aerosol threat. RAAD employs three lasers: an 808 nm cueing laser, a 355 nm laser for elastic scattering and fluorescence measurement, and a 266 nm excitation laser for fluorescence measurement [2]. The system triggers LIBS on demand to obtain the elemental composition of single aerosols. Given the number of separate features measured during the analysis – two elastic scatter, two fluorescence, and a LIBS spectrum – data from the RAAD are well-suited to undergo statistical analysis to enhance discrimination of threat aerosols. An entirely non-LIF bioaerosol detector, the Polaron (ATI), relies on light polarization signatures of aerosols. The Polaron measures light depolarization upon interaction with an aerosol. After scattering, the degree of depolarization is measured by detection optics, and the data undergo analysis and comparison to a library of threat signatures. The Polaron is able to classify aerosols because different aerosol types have distinct chemical compositions and therefore uniquely

**Table 22.2** Summary of portable biological spectroscopy used primarily for aerosol biodefense applications.

Name	Developer/Vendor	Modality	Detection properties	Status (as of 2020)
Ultraviolet Aerodynamic Particle Sizer (UV-APS)	TSI Inc.	Aerodynamic sizing Fluorescence	Ex: 355 nm Em: 420–575 nm	Discontinued
Wideband Integrated Bioaerosol Sensor (WIBS)	Droplet Measurement Technologies	Optical sizing Fluorescence	Ex: 280 and 370 nm Em: 310–400 nm and 420–650 nm	Available
Spectral Intensity Bioaerosol Spectrometer (SIBS)		Optical sizing Fluorescence	Ex: 285 and 370 nm Em: 302–721 nm (16 channel resolution)	Available
Instantaneous Biological Analyzer and Collector (IBAC)	FLIR	Optical sizing Fluorescence	Ex: 405 nm	Available
TACBIO® Gen II	Chemical Biological Center	Optical sizing Fluorescence	Ex: 270 nm Em: 317–700 nm	Available
BioScout	Environics	Optical sizing Fluorescence	Ex: 405 nm	Available
Rapid Aerosol Agent Detector (RAAD)	MIT Lincoln Laboratory	Optical sizing Fluorescence Breakdown spectroscopy	Scattering: 808 nm Ex: 355 and 266 nm	Under development
Instantaneous Microbial Detection (IMD-A)	BioVigilant	Fluorescence	Ex: 405 nm	Available
Biological-Agent Warning Sensor (BAWS)	MIT Lincoln Laboratory	Fluorescence	Ex: 260 nm	Discontinued
Resource Effective Bioidentification System (REBS)	Battelle	Raman	Ex: 643 nm	Available
VeroTect	Biral	Optical sizing Particle asymmetry Fluorescence	Ex: 280 nm Em: 330–350 nm and 420–650 nm	Discontinued

This list represents only a fraction of the technologies that have been developed.

modify the polarization state of scattered light. Generally speaking, portable non-LIF systems are less mature than their LIF counterparts, but these approaches yield additional information about an aerosol, and can assist in better threat classification. Overall, wider adoption of these alternative spectroscopic techniques, combined with more spectrally resolved LIF measurements, holds promise in improving real-time detection capability in biodefense.

### 22.4.2 Medical and Healthcare

Portable spectroscopy technologies can potentially transform diagnostic approaches in the medical and healthcare fields. For practitioners, these technologies can potentially yield timely acquisition of quantitative, reliable, and objective data, supporting rapid assessment of patient health and well-being. Within the healthcare field, portable

spectroscopy systems, especially those used for on-site patient diagnosis and monitoring, are often referred to as point-of-care (POC) technologies [13]. As a whole, however, contemporary portable spectroscopy technologies are not widely commercialized or adopted in clinical settings due to their relative immaturity, requirement to meet stringent medical-device approvals, and challenges in educating medical professionals. The sections below detail the medical and healthcare areas that portable spectroscopy can contribute toward, offering researchers and healthcare workers unique tools that can complement their current approaches.

#### 22.4.2.1 Human Tissue

Portable spectroscopy has several benefits in the analysis of human tissue – the techniques give rapid output, are noninvasive to patients, reagentless, and provide a wealth of diagnostic information. As spectroscopy yields information on a molecular level, the data are invaluable in elucidating fundamental properties and composition, oxygenation, and differentiation and maturation of human tissue [14]. The near-infrared (NIR) region (650–1100 nm), often referred to as the “optical window” due to its minimal absorption by water and hemoglobin compared to other wavelengths, is applied for acquiring spectral measurements at the skin surface as well as penetration depths into tissue [15]. Specific applications of NIR spectroscopy in human tissue analysis include *in vivo* measurement of oxygen in muscle, study of skeletal muscle metabolism, and disease diagnosis. Using NIR light, users can measure an absorption spectrum and interpret peaks to infer details about the composition of a tissue sample [14]. Comparison of a measured NIR spectrum to the spectra from a normal sample provides information on the state of health of the tissue, and can guide further diagnostic decision-making.

In clinical settings, using portable NIR spectroscopy to measure the oxygenated and deoxygenated hemoglobin (Hb) and myoglobin (Mb) is commonplace. Contemporary portable NIR devices are smartphone-sized modules that attach to a human subject, collect spectra, and either store or transmit the data wirelessly [16]. These devices consist of an LED, photodiode, battery, microprocessor, and wireless networking module. *In vivo* measurements are achievable during human activity (i.e. locomotion), making NIR techniques especially attractive for studies in sports and exercise sciences. To calculate useful metrics (e.g. oxygenated Hb/Mb), raw data are processed with the Beer–Lambert equation [16]. Besides NIR spectroscopy, Raman spectroscopy and fluorescence spectroscopy of human tissue have been explored, but these techniques have not been translated into portable systems for clinical use. Although their prospects are promising, additional research is needed before adoption of these techniques to supplement conventional human tissue analysis.

#### 22.4.2.2 Disease Diagnosis

Spectroscopic approaches offer means to diagnose diseases in a POC manner by detecting the causative agent (i.e. pathogenic organism) or a biomarker of disease. On its own, spectroscopy largely does not have the fidelity to resolve specific identification of a target pathogen, protein, or other biomolecule. To gain specificity, a spectroscopy technique can be paired with a molecular biology assay that applies spectroscopy as means to report the detection of the target of interest. Among all the field applications discussed in this chapter, smartphone biosensing arguably holds the greatest potential, primarily due to both the ubiquity of the smartphone among the general public and widespread need for simple and rapid disease diagnosis. Indeed, academic literature contains numerous articles describing smartphone POC analysis, but these approaches remain immature and have not translated from basic research to practice [13]. Usually, these efforts have involved several key activities: (i) design of a custom smartphone cradle to house a sample, (ii) novel repurposing of smartphone optics, and (iii) development of software apps to process data and output a result; see the chapter in Volume 2 by Peveler and Algar. Proof-of-concept is then demonstrated by preparing and adding sample into the cradle, followed by recording readout from the smartphone setup [3, 4].

Examples of POC smartphone spectroscopy include detection of red and white blood cells, cholesterol, markers for hepatitis B and human immunodeficiency virus (HIV), syphilis antigens, and others [3, 4, 17, 18]. In many of these efforts, assays were immunoassay based, and used some form of colorimetric change or fluorescence

spectroscopy to detect binding of antibodies to the antigen target. In all studies, researchers used the optics of popular smartphones like the Apple iPhone or Samsung Galaxy iterations. Some concepts were moreover facilitated by microfluidics to reduce reagent consumption and further reduce the form factor of the smartphone setup to improve portability. Generally, future technical maturation of the referenced techniques, coupled with validation in clinical trials, will promote greater use of smartphone spectroscopy in disease diagnosis. As the scope of this chapter is related to reagentless spectroscopic detection, the reader is referred to the cited sources to gain greater perspective on pairing of portable spectroscopic techniques with biological assays, as this deserves a thorough treatment in its own right [19].

### 22.4.3 Food and Agriculture

Portable spectroscopy systems serve several roles in the food and agriculture industry: evaluation of product quality, determination of food safety, assessment of plant welfare, and others. The first section focuses on use of portable spectroscopy to monitor for microbial contamination of food. The following section briefly summarizes applications in spectroscopic characterization of crops and livestock. Use of these portable technologies directly at a field site (e.g. food processing line or farm settings) affords unique advantages including rapid turnaround in results and ease-of-use over conventional assay techniques, thereby improving decision-making by users.

#### 22.4.3.1 Food Safety and Hygiene

At food processing plants, the sanitation monitoring of food products, including meat, poultry, fruits, and vegetables is essential. Traditional techniques for analyzing foods for microbial contamination consist of coarse visual and odor inspection, and/or swabbing of the product and assaying the swab sample with plate counts or adenosine triphosphate (ATP) bioluminescence measurement [20]. Plate count or total viable count (TVC), which is reported in units of colony-forming units (CFU) per mL, g, or cm<sup>2</sup>, indicates the bacterial loading in the food, whereas ATP reflects the quantity of biomass and thus cleanliness – although ATP can also originate from the food as a nonmicrobial source. Performing conventional analysis, however, is time-consuming, laborious, and necessitates skilled workers to obtain a swab sample. As such, portable spectroscopic systems have emerged as alternatives to monitor spoilage, wherein the food product undergoes analysis through optical techniques during processing. Academic literature contains a wealth of studies documenting development and application of fluorescence, Raman, NIR, and visible spectroscopic approaches to monitor for food spoilage [21–28]. A variety of foods have been investigated: beef, fish, chicken, pork, milk, apple juice, ham, spinach, cabbage, and others. In these studies, researchers built portable systems, and then determined the correlation between measured spectral signatures and bacterial loading (e.g. CFU/g) on the food product. The spectral signature of interest depends on spectroscopic approach; for example, fluorescence-based systems usually probe for the presence of microbial tryptophan and/or other markers, whereas Raman systems scan for characteristic features in a measured Raman spectrum. The raw data are then processed with an appropriate data analysis method like partial least square (PLS) regression. As many foods exhibit heterogeneous compositions that interfere with discrimination, Raman spectra, which are inherently richer with information, must undergo data processing with more advanced multivariate techniques such as principal component analysis (PCA), neural networks, or other methods. In general, the studies have demonstrated that spectroscopy systems are indeed able to predict food contamination with reasonable accuracy – for instance, fluorescence techniques can achieve an  $R^2$  value that exceeds 0.80 for fluorescence signal vs. bacterial loading. Raman approaches may offer improved accuracy over fluorescence spectroscopy in estimating microbial contamination [27]. To further improve specificity, numerous authors have described the combination of biological assays with portable spectroscopy (e.g. smartphones); these approaches are described elsewhere [29].

In practice, several commercial systems are currently available for detection of microbial contamination across the food processing supply chain. The Bluline fecal detector (Veritide), a handheld system used for measuring contamination of beef, applies a fluorescence technique to detect chlorophyll molecules and associated metabolites on meat surfaces. Chlorophyll serves as an indirect marker of contamination because fecal matter of ruminants, like

cattle and sheep, characteristically contains an abundance of chlorophyll [30]. The Bluline enables a user to simply point-and-shoot at a meat target and receive results, facilitating rapid analysis of samples. Another handheld point-and-shoot system, the BFD-100 (FreshDetect GmbH), also based on fluorescence spectroscopy, measures spectra from a meat surface, analyzes data, and reports results within five seconds. An NIR-based device, the SCiO (Consumer Physics), records the NIR reflectance from a sample in the wavelength range of 760–1150 nm. Comparison of the NIR spectra of fresh food products to their aged counterparts allows a user to infer potential microbial spoilage of the product [31]. While it is unlikely that these devices will eclipse the gold standard of TVC in the near future, the convenience of these approaches is undeniable and deserving of continued attention within the food industry.

#### 22.4.3.2 Agriculture Applications

For farmers and ranchers, portable spectroscopy holds utility for *in situ* characterization of the crops and livestock during the product life cycle. In farming, portable systems can be deployed into a field to determine properties like plant growth, species and weed content. The resulting data can guide site-specific dispersal of fertilizer, water, or even herbicide to destroy the growth of undesirable species. Several studies have described the use of portable visible and NIR systems to differentiate crop from weeds by measuring the absorbance or reflectance spectra and analyzing data with PCA or other techniques [32, 33]. In these efforts, spectra were obtained using custom-built systems or commercial handheld spectroradiometers; these systems measure signatures originating from chloroplast-derived pigments, intercellular spaces, water, and cellulose. The accuracy of the classification by these techniques can depend strongly on data interpretation, but it is largely promising, demonstrating successful classification at a rate over 70% [33]. Another application for such technologies is in rapid extraction of information regarding the welfare of crops. For example, visible-light portable spectroscopy systems can detect chlorophyll content in leaves [34]. As chlorophyll is a marker of nutritional status and photosynthetic capacity, its detection can aid in quality assessment, and inform crop management. Uses of portable systems also extend to on-site quantification of biological contaminants like molds and mycotoxin on crops including maize, wheat, and peanuts [35, 36].

Within livestock science, portable spectroscopy has a unique role in profiling of livestock stool to predict forage quality of free-range animals. Characterizing the feces of the animals allows users to access diet and nutritional data in a rapid and noninvasive manner [37]. First introduced by Lyons and Stuth [32], and later adopted in numerous studies, this process consists of collecting fecal samples, performing an NIR reflectance measurement, and interpreting the data for dietary nutritional quality parameters like crude protein, digestible organic matter, and fiber [38]. Predictive models are developed beforehand by feeding animals known diets, recording the fecal spectra, and creating calibration equations; only 8–10 NIR wavelengths account for roughly 85–95% variation in diet [37]. The NIR spectra can reveal marked differences in fecal composition between animals possessing low-quality and high-quality diets for a variety of domesticated and even wildlife species. Continued progress in this area, especially in development of predictive models, will further improve the maturity of these techniques, enabling users to better monitor the health of livestock.

#### 22.4.4 Environmental Pollution Monitoring

Portable spectroscopy systems can detect biological pollution levels for a variety of environmental monitoring field applications. Microbial contamination of water, soil, and air can produce adverse effects to human health, animals, and agriculture, and so rapid biological pollutant monitoring through spectroscopic tools offers an attractive alternative to laborious culturing or and/or molecular assays. A key advantage of portable spectroscopy in microbial pollutant detection is that users can readily bring these systems to a site to analyze samples, or even install a system at the site for *in situ* and autonomous monitoring. These tools can then inform and facilitate immediate remedial activities to reduce the environmental impact. The sections below describe various applications of portable spectroscopy in biological pollutant monitoring for water, soil, and air.

#### 22.4.4.1 Water

Portable spectroscopy systems can assess microbial quality of wastewater and potability of water sources for rapid on-site analysis. Although Raman and other techniques have been investigated, academic literature has primarily emphasized fluorescence spectroscopy for measuring microbial properties of water [39]. Fluorescence originating from 280 nm excitation, referred to as tryptophan-like fluorescence (TLF) by the water quality community, is a marker of pathogenic microorganisms and anthropogenic organic matter, allowing a user to infer that the water is biologically contaminated. Numerous studies have described the development, characterization, or evaluation of compact handheld fluorimeters that measure TLF emission as a practical tool for pre-screening water to complement confirmatory culture and PCR techniques [40]. In general, these portable fluorimeters are technically simple, consisting of a water sample introduction port, UV-visible light source like an LED, light collection optics, photodetector, and associated software. Operation of the systems by a user is similarly straightforward, involving procurement of a water sample, insertion of the sample into the system, and interpretation of fluorescence results. This ease of operation is especially valuable as it is envisioned that these systems can be distributed to nonexperts in resource-limited settings for analysis of water quality. An example of a commercialized TLF detector is the Proteus Multiparameter Water Quality Meter (Proteus Instruments). Weighing 4.5 kg, the device measures fluorescence at 285 nm excitation, and outputs a real-time readout of coliform quantity and other water quality properties such as biochemical oxygen demand and total organic carbon.

Literature has established correlations of TLF intensity to coliform concentration (CFU/mL), obtaining log-linear correlation – shown over several logs – between the two types of measurements [41, 42]. This relationship was demonstrated for environmental water samples from multiple sites across several locales (United Kingdom, America, Africa, and China), although the correlation displays variability within a body of water, and TLF may overpredict coliform concentration compared to culturing measurements. Regardless, fluorescence measurements have potential use in predicting risk of microbial contamination, and improving prioritization of water samples that should undergo additional analysis [5]. At the moment, fluorimetry is not an established method for coliform analysis, but efforts to formalize it according to the World Health Organization (WHO) or other regulations are ongoing [43].

#### 22.4.4.2 Soil

Compared to water quality applications, development and use of portable spectroscopy systems in soil sciences remain less explored. Microbial biomass influences the biogeochemical equilibrium of soil, responsible for 80–90% of biotransformations – through organic matter decomposition and nutrient cycles – and consequently plant productivity and ecological sustainability [44]. Therefore, assessment of the microbial populations and their activity in soil is of key importance. Given that soil microbial biomass comprises only 5% or less of total organic carbon, spectroscopy cannot directly resolve its contribution to the soil spectra. Thus, researchers focus on indirect markers of microbial biomass, applying visible–NIR spectroscopy to analyze mineralization of soil organic matter (SOM) and soil organic carbon (SOC) since these components strongly absorb in these wavelengths.

Although traditional analysis includes extraction of soil core samples and analysis in the laboratory, mobile proximal soil sensing (PSS) has emerged as a concept to rapidly acquire spectral data of soil biota [45]. PSS involves affixing compact spectroscopy systems or other sensors to vehicles (e.g. tractor, all-terrain vehicles, etc.) so that the system is positioned adjacent to the soil surface. As the vehicle traverses the field, these systems record real-time measurements from soil immediately beneath the vehicle. Termed “on-the-go” analysis, this type of platform, when coupled with a global positioning system, provides spatial resolution mapping of the soil properties of an area of interest. Academic literature has reported on use of on-the-go technologies based on visible–NIR diffuse reflectance to measure SOM and SOC. [45] Setup and operation of such systems in the field requires consideration of distance from the sensor window to the soil surface, and presence of outlier materials like gravel. Notably, these

approaches have demonstrated moderate successes in showing a correlation between measured reflectance and SOM/SOC in the soil. Further field demonstrations and improvements to both hardware and data processing will facilitate broader adoption of these approaches by the soil science community.

#### 22.4.4.3 Air

Portable fluorescence-based spectroscopy systems, which were pioneered for military and biodefense purposes, have found select applications in civilian air quality monitoring of environmental airborne microorganisms, often referred to as primary biological aerosol particles (PBAPs) within the academic air quality community. As detailed in Section 22.4.1.2, these systems use LIF to excite biogenic fluorophores present in microorganisms to discriminate bioaerosols from nonbiological aerosols. Academic literature contains numerous field test campaign studies describing the use of these portable systems to measure the presence of pollutant bioaerosols in a diverse set of locales: Central Europe, the Amazon rainforest, China, and others [6, 46, 47]. In these campaigns, researchers installed systems at a field site, sampled ambient aerosols over timescales ranging from days to weeks, and interpreted the spatial, temporal, and spectral fluorescence patterns of the sampled bioaerosols. Early LIF studies, specifically those predating the development of the WIBS, focused on PBAPs exhibiting fluorescence emission of biogenic metabolic molecules (355 nm excitation), but advances in LIF bioaerosol technologies have enabled investigation into the multichannel fluorescence signatures of PBAPs. Greater spectral resolution in the fluorescence emission has allowed researchers to develop classification algorithms for PBAPs using statistical methods and machine learning approaches. These studies have demonstrated successes in combining multichannel LIF data with machine learning to classify PBAPs as bacteria, fungi, or other biogenic material, allowing moderate characterization of a biologically diverse air sample in real time [48]. Forthcoming LIF systems, which support even greater spectral resolution (see Section 22.4.1.2) and perhaps improved classification accuracy, can further establish the use of portable spectroscopy systems for monitoring of environmental bioaerosols.

#### 22.4.5 Forensics

Portable biological spectroscopy systems have expanded into the field of criminal forensics, providing investigators with compact tools to more thoroughly examine crime scenes and gather vital physiological evidence [7]. Spectroscopic approaches possess several essential attributes desired by the forensic community – the techniques are nondestructive, rapid, require no reagents or sample preparation, and involve a simple workflow that can be performed on site by a nonscientist; see the chapter by Kammrath et al. in Volume 2 of this book. In a field setting, such as a crime scene, portable spectroscopy systems can serve to locate the presence of secreted body fluids and stains that may not be visible to the naked eye, assisting investigators in collecting samples for subsequent extraction of genetic information from the sample. Spectroscopic analysis is presumptive, incapable of identification or connecting a body fluid sample to a specific individual. Several established uses of portable systems within forensics are described in the sections below.

##### 22.4.5.1 Detection of Body Fluids

Generally, the workflow for spectroscopic analysis at a crime scene setting consists of an initial assessment and proper documentation of the site. Afterward, investigators survey the area for biological evidence that includes body fluids like blood, saliva, sweat, semen, vaginal fluids, and urine. Some human and animal body fluids naturally fluoresce as these biological substances are comprised of fluorescent amino acids; semen for example is excited at 300–500 nm (UV–violet), emitting visible-light fluorescence in the 460–520 nm range [49, 50]. Within forensics, fluorescence-based spectroscopic searches, often referred to as Alternative Light Sources (ALSs),

colloquially termed blacklights or forensic light sources, involve illumination of areas suspected of containing biological fluids with an intense light source followed by visual observation of fluorescence emission [51]. Investigators are equipped with goggles to filter out scattered light and ambient light, improving their discrimination of fluorescence signal. ALS systems are highly portable, usually weighing less than 2 kg and can be carried with one hand. ALS systems are simple technologies containing only four major components: a broadband light source (e.g. xenon lamp), filters, light-shaping optics, and a flexible fiber-optic cable to allow the user to scan light across an area of interest. For some systems, excitation wavelength is selectable by the user; for example, Polilight (Rofin Forensic) systems generate light in 12 narrow wavelength bands ranging in color from UV to red, with the 415 nm band termed the “blood filter.”

Portable ALS systems, which have proven use in the detection of body fluids, feature coarse selectivity between biological fluid types. Proper selection of ALS wavelength and goggles by an investigator can improve contrast of a body fluid and/or stain, although the substrate containing the sample can also affect imaging. In one study, it was demonstrated that 450 nm excitation light combined with long-pass goggles enabled a user to visibly distinguish between dried urine, blood, and other fluids [51]. Compared to reference chemical-based screening tests like acid phosphatase and Phadebas paper, ALS systems have similar sensitivity to these assays, displaying a low incidence of false-negative results [51]. On the other hand, false-positive results, defined as ALS detection with a corresponding negative chemical test, are common due to the fluorescence properties of many nonbiological materials. Besides the use of fluorescence emission for locating body fluids at crime scenes, other approaches have been proposed for greater specificity in body fluid identification. This has mostly involved Raman spectroscopy due to its potential to identify chemical functional groups, but currently none of these approaches have been translated into portable systems for field use by crime scene investigators [52].

#### 22.4.5.2 Detection of Latent Fingerprints

Latent fingerprints, fingerprints that are undetectable by the naked eye, can also be located through use of spectroscopic approaches. Latent fingerprints are formed from residue of oil or perspiration deposited by an individual touching a solid surface with their finger. Several portable techniques have been proposed for detection and analysis of latent fingerprints: ALS, hyperspectral imaging, LIBS, and Raman [53, 54]. These spectroscopic approaches have considerable advantages over traditional methods for lifting fingerprints (i.e. dusting for fingerprints) since they can be performed rapidly and do not contaminate the fingerprint for further potential analysis. With ALS, investigators can scan surfaces, applying different light filters and optionally powders, and/or dyes to enhance imaging. Fingerprint evidence is then photographed and documented.

#### 22.4.5.3 Analysis of Bruises, Bite Marks, and Other Wounds

ALS approaches can afford enhanced visualization of bruises and other wounds, revealing features to forensic investigators that are otherwise unobservable with natural light. Bruises and similar injuries, which develop from blunt force trauma that causes dermal blood to leak into tissue, strongly absorb violet and blue light, producing high contrast when illuminated with these colors. Fluorescence from bruises is also observable though not as identifiable [8]. Spectrally, fresh blood exhibits two absorption peaks in the visible region: the Hb Soret peak at 415 nm, and a less intense peak between 520 and 590 nm attributed to oxyhemoglobin. Controlled experimental studies are largely lacking, but several laboratory investigations have reported on the effectiveness of ALS for forensic injury analysis, describing it as either vastly improving or no better than visualization with natural light [55–57]. Clinical studies have described benefits of portable ALS in revealing injuries in strangulation and possible child abuse victims [58, 59]. ALS can be useful in discerning fine features of bruises, deeper injuries, and enhancing contrast for subjects with darker complexions, although it does not appear to aid in determining the age of a bruise [60, 61].

## 22.5 Summary, Challenges, and Outlook

This chapter presented only a brief overview of field applications of portable biological spectroscopy. With future advances in basic spectroscopy research, smartphones, as well miniaturized technologies, field applications, and users of portable spectroscopy will only continue to expand. As witnessed from the last several decades, unexpected world events and increasing concerns about the environment, healthcare, disease transmission, or other areas, can prompt the growth of new and exciting analysis tools. The main obstacle for biological spectroscopy remains its inferior specificity compared to molecular biology assays, and in the context of its field applications, this concern is no different. In a field setting, spectroscopic techniques are limited to presumptive detection of a biological material, and generally lack species-level specificity to unequivocally identify or characterize a target. More robust or confirmatory techniques like PCR, immunoassay, or genome sequencing must complement spectroscopic analysis, requiring users to bring additional equipment, supplies, or consumables into the field. Developments in fundamental spectroscopy approaches, machine learning pattern recognition, and better integration with assays can improve specificity, accelerating greater adoption of portable spectroscopy within biology. Another facet for portable spectroscopy, which can be viewed as an opportunity, is the continued pursuit of miniaturization of optical components, control circuitry, and other hardware in order to reduce the form factor of these systems while preserving signal-to-noise ratio and user experience. Current developments in optics, materials science, and related disciplines can contribute toward achieving this goal.

While this chapter focused on several disciplines that maintain established uses for portable biological spectroscopy, these techniques may have unique utility in other nonconventional areas including astrobiology, anthropology, art history, and others. In these disciplines, portable biological spectroscopy can offer novel means to detect and classify biological materials in samples through a nondestructive process without need for wet chemistry. For example, several astrobiology studies have proposed a miniature Raman spectrometer to noninvasively probe for the existence of life, since Raman scattering is able to differentiate between spectral signatures from a sample containing both biological and geological constituents [62]. This type of system can be outfitted to a robotic lander or perhaps supplied to astronauts for analysis of samples; see the chapter in Volume 2 by Edwards et al. for more details. Within anthropology, archeologists have used portable systems to perform on-site identification of biomaterials present at historical burial sites; studies have reported on the Raman spectra of human and animal hair and skins cells dating back 4000 years ago found an Egyptian burial site [63]. Undoubtedly, portable biological spectroscopy will continue to find other meaningful applications as technologies improve and researchers desire to gather molecular description of their samples.

As stated in this chapter, smartphones, which already contain many of the necessary components for spectroscopic analysis, hold potential in transforming portable spectroscopy and, due to their ubiquity, even democratizing spectroscopy for citizen scientists (see the chapter in this Volume by Scheeline for more details). Clearly, as smartphone technologies undergo improvements to camera optics, their potential to perform a variety of biological spectroscopic analyses also grows. In the near future, smartphones can possibly serve as a generic spectrometer in any field application, with specific functionality being added by installing a relevant smartphone app. Furthermore, the existing ability of smartphones to upload real-time data that are rich in metadata like timestamps makes them well-suited to support the development of spectroscopic databases possessing spatial and temporal information. This capability can impact fields like environmental pollutant monitoring, where any individual with a smartphone can contribute high-fidelity environmental data at their specific location. With these advancements, the outlook for field-based portable spectroscopy is excellent, filled with exciting new possibilities and opportunities to improve practical biological detection.

## Acknowledgements

The authors acknowledge the Johns Hopkins Applied Physics Laboratory Janney Program for the funding support. The authors recognize Ms. Leah Carol and Dr. Jody Proescher for compiling references and reviewing this chapter, respectively.

## List of Acronyms

ALS	alternative light source
ARL	Army Research Laboratory
ATP	adenosine triphosphate
CCD	charged coupled device
CFU	colony-forming unit
COTS	commercial off-the-shelf
DARPA	Defense Advanced Research Projects Agency
DMT	Droplet Measurement Technologies
DPA	dipicolinic acid
FLAPS	fluorescence aerodynamic particle sizer
Hb	hemoglobin
LED	light-emitting diode
LFA	lateral flow assay
LIBS	laser-induced breakdown spectroscopy
LIF	laser- (or light)-induced fluorescence
NADH	nicotinamide adenine dinucleotide
Mb	myoglobin
NIR	near-infrared
PBAB	primary biological aerosol particles
PCA	principal component analysis
PCR	polymerase chain reaction
PLS	partial least squares
POC	point of care
PPE	personal protective equipment
PSS	proximal soil sensing
RAAD	Rapid Agent Aerosol Detector
REBS	Resource Effective Bioidentification System
SIBS	Spectral Intensity Bioaerosol Spectrometer
SOC	soil organic carbon
SOM	soil organic matter
TLF	tryptophan-like fluorescence
TVC	total viable counts
UV	ultraviolet
UV-APS	Ultraviolet Aerodynamic Particle Sizer
WIBS	Wideband Integrated Bioaerosol Spectrometer
WHO	World Health Organization

## References

- DeFreez, R. (2009). LIF bio-aerosol threat triggers: then and now. *Opt. Biol. Chem. Detect Def.* V. 7484 (September): 74840H. <https://doi.org/10.1117/12.835088>.
- Huffman, J.A., Perring, A.E., Savage, N.J. et al. (2019). Real-time sensing of bioaerosols: review and current perspectives. *Aerosol Sci. Tech.* 54 (5): 1–31. <https://doi.org/10.1080/02786826.2019.1664724>.
- Laksanasopin, T., Guo, T.W., Nayak, S. et al. (2015). A smartphone dongle for diagnosis of infectious diseases at the point of care. *Sci. Transl. Med.* 7 (273): 273re1. <https://doi.org/10.1126/scitranslmed.aaa0056>.

- 4 Giavazzi, F., Salina, M., Ceccarello, E. et al. (2014). A fast and simple label-free immunoassay based on a smartphone. *Biosens. Bioelectron.* 58: 395–402. <https://doi.org/10.1016/j.bios.2014.02.077>.
- 5 Sorensen, J.P.R., Lapworth, D.J., Marchant, B.P. et al. (2015). In-situ tryptophan-like fluorescence: a real-time indicator of faecal contamination in drinking water supplies. *Water Res.* 81: 38–46. <https://doi.org/10.1016/j.watres.2015.05.035>.
- 6 Yue, S., Ren, H., Fan, S. et al. (2017). High abundance of fluorescent biological aerosol particles in winter in Beijing, China. *ACS Earth Sp Chem.* 1 (8): 493–502. <https://doi.org/10.1021/acsearthspacechem.7b00062>.
- 7 Wee-chuen, L. and Bee-Ee, K. (2010). Forensic light sources for detection of biological evidences in crime scene investigation: a review. *Malaysian J. Forensic. Sci.* 1 (1): 20–30.
- 8 Lombardi, M., Canter, J., Patrick, P.A., and Altman, R. (2015). Is fluorescence under an alternate light source sufficient to accurately diagnose subclinical bruising? *J. Forensic. Sci.* 60 (2): 444–449. <https://doi.org/10.1111/1556-4029.12698>.
- 9 National Research Council (2011). *Review of the Scientific Approaches Used during the FBI's Investigation of the 2001 Anthrax Letters*. Washington, DC: The National Academies Press <https://doi.org/10.17226/13098>.
- 10 Pöhlker, C., Huffman, J.A., and Pöschl, U. (2012). Autofluorescence of atmospheric bioaerosols – fluorescent biomolecules and potential interferences. *Atmos. Meas. Tech.* 5: 37–71. <https://doi.org/10.5194/amt-5-37-2012>.
- 11 Ammor, M.S. (2007). Recent advances in the use of intrinsic fluorescence for bacterial identification and characterization. *J. Fluoresc.* 17 (5): 455–459. <https://doi.org/10.1007/s10895-007-0180-6>.
- 12 Könemann, T., Savage, N., Klimach, T. et al. (2019). Spectral intensity bioaerosol sensor (SIBS): an instrument for spectrally resolved fluorescence detection of single particles in real time. *Atmos. Meas. Tech.* 12 (2): 1337–1363. <https://doi.org/10.5194/amt-12-1337-2019>.
- 13 McCracken, K.E. and Yoon, J.Y. (2016). Recent approaches for optical smartphone sensing in resource-limited settings: a brief review. *Anal. Methods* 8 (36): 6591–6601. <https://doi.org/10.1039/c6ay01575a>.
- 14 Chiriboga, L., Xie, P., Yee, H. et al. (1998). Infrared spectroscopy of human tissue. I. Differentiation and maturation of epithelial cells in the human cervix. *Biospectroscopy* 4 (1): 47–53. [https://doi.org/10.1002/\(sici\)1520-6343\(1998\)4:1<47::aid-bspy5>3.3.co;2-1](https://doi.org/10.1002/(sici)1520-6343(1998)4:1<47::aid-bspy5>3.3.co;2-1).
- 15 Sakudo, A. (2016). Near-infrared spectroscopy for medical applications: current status and future perspectives. *Clin. Chim. Acta* 455: 181–188. <https://doi.org/10.1016/j.cca.2016.02.009>.
- 16 Hamaoka, T., McCully, K.K., Niwayama, M., and Chance, B. (2011). The use of muscle near-infrared spectroscopy in sport, health and medical sciences: recent developments. *Philos. Trans. R. Soc. A Math. Phys. Eng. Sci.* 369 (1955): 4591–4604. <https://doi.org/10.1098/rsta.2011.0298>.
- 17 Zhu, H., Sencan, I., Wong, J. et al. (2013). Cost-effective and rapid blood analysis on a cell-phone. *Lab Chip* 13 (7): 1282–1288. <https://doi.org/10.1039/c3lc41408f>.
- 18 Oncescu, V., Mancuso, M., and Erickson, D. (2014). Cholesterol testing on a smartphone. *Lab Chip* 14 (4): 759–763. <https://doi.org/10.1039/c3lc51194d>.
- 19 Kanchi, S., Sabela, M.I., Mdluli, P.S., and Inamuddin, B.K. (2018). Smartphone based bioanalytical and diagnosis applications: a review. *Biosens. Bioelectron.* 102 (August): 136–149. <https://doi.org/10.1016/j.bios.2017.11.021>.
- 20 Oto, N., Oshita, S., Makino, Y. et al. (2013). Non-destructive evaluation of ATP content and plate count on pork meat surface by fluorescence spectroscopy. *Meat Sci.* 93 (3): 579–585. <https://doi.org/10.1016/j.meatsci.2012.11.010>.
- 21 Schmidt, H., Sowoidnich, K., and Kronfeldt, H.D. (2010). A prototype hand-held Raman sensor for the in situ characterization of meat quality. *Appl. Spectrosc.* 64 (8): 888–894. <https://doi.org/10.1366/000370210792081028>.
- 22 Ye, X., Iino, K., and Zhang, S. (2016). Monitoring of bacterial contamination on chicken meat surface using a novel narrowband spectral index derived from hyperspectral imagery data. *Meat Sci.* 122: 25–31. <https://doi.org/10.1016/j.meatsci.2016.07.015>.

- 23** Saranwong, S. and Kawano, S. (2008). System design for non-destructive near infrared analyses of chemical components and total aerobic bacteria count of raw milk. *J. Near Infrared Spectrosc.* 16 (4): 389–398. <https://doi.org/10.1255/jnirs.807>.
- 24** Luo, B.S. and Lin, M. (2008). A portable Raman system for the identification of foodborne pathogenic bacteria. *J. Rapid. Methods Autom. Microbiol.* 16 (3): 238–255. <https://doi.org/10.1111/j.1745-4581.2008.00131.x>.
- 25** Sowoidnich, K., Schmidt, H., Kronfeldt, H.D., and Schwägele, F. (2012). A portable 671 nm Raman sensor system for rapid meat spoilage identification. *Vib. Spectrosc.* 62: 70–76. <https://doi.org/10.1016/j.vibspec.2012.04.002>.
- 26** Aït-Kaddour, A., Boubellouta, T., and Chevallier, I. (2011). Development of a portable spectrofluorimeter for measuring the microbial spoilage of minced beef. *Meat Sci.* 88 (4): 675–681. <https://doi.org/10.1016/j.meatsci.2011.02.027>.
- 27** He, H.J. and Sun, D.W. (2015). Microbial evaluation of raw and processed food products by visible/infrared, Raman and fluorescence spectroscopy. *Trends Food Sci. Technol.* 46 (2): 199–210. <https://doi.org/10.1016/j.tifs.2015.10.004>.
- 28** Liang, P.S., Park, T.S., and Yoon, J.Y. (2014). Rapid and reagentless detection of microbial contamination within meat utilizing a smartphone-based biosensor. *Sci. Rep.* 4: 4–11. <https://doi.org/10.1038/srep05953>.
- 29** Rateni, G., Dario, P., and Cavallo, F. (2017). Smartphone-based food diagnostic technologies: a review. *Sensors (Switzerland)* 17 (6) <https://doi.org/10.3390/s17061453>.
- 30** Oh, M., Lee, H., Cho, H. et al. (2016). Detection of fecal contamination on beef meat surfaces using handheld fluorescence imaging device (HFID). *Sens. Agric. Food Qual Saf. VIII.* 9864 (May): 986411. <https://doi.org/10.1117/12.2227184>.
- 31** Lee, S., Noh, T.G., Choi, J.H. et al. (2017). NIR spectroscopic sensing for point-of-need freshness assessment of meat, fish, vegetables and fruits. *Sens. Agric. Food Qual Saf. IX.* 10217 (May): 1021708. <https://doi.org/10.1117/12.2261803>.
- 32** Zhang, Y. and He, Y. (2006). Crop/weed discrimination using near-infrared reflectance spectroscopy (NIRS). *Fourth Int. Conf. Photon. Imaging Biol. Med.* 6047 (October): 60472G. <https://doi.org/10.1117/12.710957>.
- 33** Borregaard, T., Nielsen, H., Nørgaard, L., and Have, H. (2000). Crop-weed discrimination by line imaging spectroscopy. *J. Agric. Eng. Res.* 75 (4): 389–400. <https://doi.org/10.1006/jaer.1999.0519>.
- 34** Liu, B., Yue, Y.M., Li, R. et al. (2014). Plant leaf chlorophyll content retrieval based on a field imaging spectroscopy system. *Sensors (Switzerland)* 14 (10): 19910–19925. <https://doi.org/10.3390/s141019910>.
- 35** Sieger, M., Kos, G., Sulyok, M. et al. (2017). Portable infrared laser spectroscopy for on-site mycotoxin analysis. *Sci. Rep.* 7: 1–6. <https://doi.org/10.1038/srep44028>.
- 36** Levasseur-Garcia, C. (2012). *Infrared spectroscopy applied to identification and detection of microorganisms and their metabolites on cereals (corn, wheat, and barley)*. Agricultural Science, Godwin Aflakpui, IntechOpen. doi: 10.5772/34762. <https://www.intechopen.com/books/agricultural-science/infrared-spectroscopy-applied-to-identification-and-detection-of-microorganisms-and-their-metabolite>.
- 37** Stuth, J., Jama, A., and Tolleson, D. (2003). Direct and indirect means of predicting forage quality through near infrared reflectance spectroscopy. *F Crop Res.* 84 (1–2): 45–56. [https://doi.org/10.1016/S0378-4290\(03\)00140-0](https://doi.org/10.1016/S0378-4290(03)00140-0).
- 38** Lyons, R.K. and Stuth, J.W. (1992). Fecal NIRS equations for predicting diet quality of free-ranging cattle. *J. Range Manage.* 45 (3): 238. <https://doi.org/10.2307/4002970>.
- 39** Carstea, E.M., Bridgeman, J., Baker, A., and Reynolds, D.M. (2016). Fluorescence spectroscopy for wastewater monitoring: a review. *Water Res.* 95: 205–219. <https://doi.org/10.1016/j.watres.2016.03.021>.
- 40** Cumberland, S., Bridgeman, J., Baker, A. et al. (2012). Fluorescence spectroscopy as a tool for determining microbial quality in potable water applications. *Environ. Technol.* 33 (6): 687–693. <https://doi.org/10.1080/09593330.2011.588401>.

- 41** Baker, A., Cumberland, S.A., Bradley, C. et al. (2015). To what extent can portable fluorescence spectroscopy be used in the real-time assessment of microbial water quality? *Sci. Total Environ.* 532: 14–19. <https://doi.org/10.1016/j.scitotenv.2015.05.114>.
- 42** Baker, A., Ward, D., Lieten, S.H. et al. (2004). Measurement of protein-like fluorescence in river and waste water using a handheld spectrophotometer. *Water Res.* 38 (12): 2934–2938. <https://doi.org/10.1016/j.watres.2004.04.023>.
- 43** Nowicki, S., Lapworth, D.J., Ward, J.S.T. et al. (2019). Tryptophan-like fluorescence as a measure of microbial contamination risk in groundwater. *Sci. Total Environ.* 646: 782–791. <https://doi.org/10.1016/j.scitotenv.2018.07.274>.
- 44** Nannipieri, P., Ascher, J., Ceccherini, M.T. et al. (2003). Microbial diversity and soil functions. *Eur. J. Soil Sci.* 54: 655–670. <https://doi.org/10.1046/j.1365-2389.2003.00556.x>.
- 45** Dhawale, N.M., Adamchuk, V.I., Prasher, S.O. et al. (2015). Proximal soil sensing of soil texture and organic matter with a prototype portable mid-infrared spectrometer. *Eur. J. Soil Sci.* 66 (4): 661–669. <https://doi.org/10.1111/ejss.12265>.
- 46** Huffman, J.A., Sinha, B., Garland, R.M. et al. (2012). Size distributions and temporal variations of biological aerosol particles in the Amazon rainforest characterized by microscopy and real-time UV-APS fluorescence techniques during AMAZE-08. *Atmos. Chem. Phys.* 12 (24): 11997–12019. <https://doi.org/10.5194/acp-12-11997-2012>.
- 47** Toprak, E. and Schnaiter, M. (2013). Fluorescent biological aerosol particles measured with the waveband integrated bioaerosol sensor WIBS-4: laboratory tests combined with a one year field study. *Atmos. Chem. Phys.* 13 (1): 225–243. <https://doi.org/10.5194/acp-13-225-2013>.
- 48** Ruske, S., Topping, D.O., Foot, V.E. et al. (2018). Machine learning for improved data analysis of biological aerosol using the WIBS. *Atmos. Meas. Tech.* 11 (11): 6203–6230. <https://doi.org/10.5194/amt-11-6203-2018>.
- 49** Stoilovic, M. (1991). Detection of semen and blood stains using polilight as a light source. *Forensic Sci. Int.* 51 (2): 289–296. [https://doi.org/10.1016/0379-0738\(91\)90194-N](https://doi.org/10.1016/0379-0738(91)90194-N).
- 50** Nanda, K.D.S., Ranganathan, K., Umadevi, K.M., and Joshua, E. (2011). A rapid and noninvasive method to detect dried saliva stains from human skin using fluorescent spectroscopy. *J. Oral Maxillofac Pathol.* 15 (1): 22–25. <https://doi.org/10.4103/0973-029X.80033>.
- 51** Vandenberg, N. and Van Oorschot, R.A.H. (2006). The use of Polilights® in the detection of seminal fluid, saliva, and bloodstains and comparison with conventional chemical-based screening tests. *J. Forensic Sci.* 51 (2): 361–370. <https://doi.org/10.1111/j.1556-4029.2006.00065.x>.
- 52** Virkler, K. and Lednev, I.K. (2010). Raman spectroscopic signature of blood and its potential application to forensic body fluid identification. *Anal. Bioanal. Chem.* 396 (1): 525–534. <https://doi.org/10.1007/s00216-009-3207-9>.
- 53** Godwal, Y., Taschuk, M.T., Lui, S.L. et al. (2008). Development of laser-induced breakdown spectroscopy for microanalysis applications. *Laser Part Beams.* 26 (1): 95–103. <https://doi.org/10.1017/S0263034608000128>.
- 54** Nakamura, A., Okuda, H., Nagaoka, T. et al. (2015). Portable hyperspectral imager with continuous wave green laser for identification and detection of untreated latent fingerprints on walls. *Forensic Sci. Int.* 254: 100–105. <https://doi.org/10.1016/j.forsciint.2015.06.031>.
- 55** Trefan, L., Harris, C., Evans, S. et al. (2018). A comparison of four different imaging modalities – conventional, cross polarized, infra-red and ultra-violet in the assessment of childhood bruising. *J. Forensic Leg. Med.* 59 (April): 30–35. <https://doi.org/10.1016/j.jflm.2018.07.015>.
- 56** Nijs, H.G.T., De Groot, R., Van Velthoven, M.F.A.M., and Stoel, R.D. (2019). Is the visibility of standardized inflicted bruises improved by using an alternate ('forensic') light source? *Forensic Sci. Int.* 294: 34–38. <https://doi.org/10.1016/j.forsciint.2018.10.029>.

- 57** Olds, K., Byard, R.W., Winskog, C., and Langlois, N.E.I. (2016). Validation of ultraviolet, infrared, and narrow band light alternate light sources for detection of bruises in a pigskin model. *Forensic Sci. Med. Pathol.* 12 (4): 435–443. <https://doi.org/10.1007/s12024-016-9813-x>.
- 58** Holbrook, D.S. and Jackson, M.C. (2013). Use of an alternative light source to assess strangulation victims. *J. Forensic Nurs.* 9 (3): 140–145. <https://doi.org/10.1097/JFN.0b013e31829beb1e>.
- 59** Mimasaka, S., Ohtani, M., Kuroda, N., and Tsunenari, S. (2010). Spectrophotometric evaluation of the age of bruises in children: measuring changes in bruise color as an indicator of child physical abuse. *Tohoku J. Exp. Med.* 220 (2): 171–175. <https://doi.org/10.1620/tjem.220.171>.
- 60** Hughes, V.K., Ellis, P.S., and Langlois, N.E.I. (2006). Alternative light source (polilight®) illumination with digital image analysis does not assist in determining the age of bruises. *Forensic Sci. Int.* 158 (2–3): 104–107. <https://doi.org/10.1016/j.forsciint.2005.04.042>.
- 61** Owens, L., Warfield, T., Macdonald, R., and Krenzischek, E. (2018). Using alternative light source technology to enhance visual inspection of the skin. *J. Wound Ostomy Cont. Nurs.* 45 (4): 356–358. <https://doi.org/10.1097/WON.0000000000000448>.
- 62** Villar, S.E.J. and Edwards, H.G.M. (2006). Raman spectroscopy in astrobiology. *Anal. Bioanal. Chem.* 384 (1): 100–113. <https://doi.org/10.1007/s00216-005-0029-2>.
- 63** Edwards, H.G.M. and Munshi, T. (2005). Diagnostic Raman spectroscopy for the forensic detection of biomaterials and the preservation of cultural heritage. *Anal. Bioanal. Chem.* 382 (6): 1398–1406. <https://doi.org/10.1007/s00216-005-3271-8>.

## Index

### Symbols

<sup>9</sup>/<sub>11</sub> 237, 240, 253, 534  
<sup>241</sup>Am 416–418, 429–430, 443  
<sup>11</sup>B 260, 506, 508–509  
<sup>13</sup>C 503, 506, 508–509  
21 CFR Part 11 1, 138  
2-chloroethyl ethyl sulfide 400  
1-chloronaphthalene 399  
Δm 352, 354, 394–395, 399  
<sup>55</sup>Fe 475, 479, 488, 494  
<sup>1</sup>H 503, 506–508, 510  
2-hydroxyglutarate 363–364  
<sup>7</sup>Li 506, 508–509  
3-methylfentanyl 404  
<sup>15</sup>N 506, 508  
<sup>23</sup>Na 506, 508–509  
<sup>63</sup>Ni 429–430, 443  
<sup>31</sup>P 506, 508–509  
<sup>29</sup>Si 506, 508–509  
3D Ion Trap 349, 354–355, 360  
3D Printing 98, 107

### a

Acetone 299, 399, 432  
Acid Phosphatase 557  
Acquisition Rate 269, 347, 352–353  
Activation 379  
Active Pharmaceutical Ingredient 68, 81  
ADC (Analog to Digital Converter) 47, 51, 58, 62, 132, 140, 188, 242  
Advanced Light Source 493  
Aerodynamic Sizing 551  
Aerosol 200–201, 216, 380, 382, 549–551, 556  
Agriculture 67, 173, 303, 545–547, 553–554  
Agriculture Applications 554

AI (Artificial intelligence) 69, 108, 269, 311, 439, 442  
AIMS (Aspiration Ion Mobility Spectrometry) 417–418, 422, 425, 429–430, 432, 438, 442, 515, 534–535  
Airborne 167, 227, 305, 380, 545–546, 549, 556  
Airport 264, 345, 416  
Air Quality 209, 433, 546, 556  
Air Sampling 370–371, 376  
Alarm 1, 243, 253, 259, 263, 297, 381, 403, 406, 415–416, 428, 435–439, 441–442, 549  
Alcohol 361, 432, 441  
Allele 520, 522, 524, 528, 539  
Allelic Ladder 520, 522, 525, 527  
Allergen 194–195  
Alloy 92, 98, 327, 330–331, 338–340, 379, 450, 456, 470, 505–506  
Alloy Determination 327  
Alloy Identification 456  
Alloy Sorting 470  
Almonds 384  
ALS (Alternative Light Source) 557  
Ambient Ionization 348–349, 352, 358, 360, 363–364  
Ambient Pressure 346, 415, 428–429, 431, 438, 441  
Amelogenin 522–523  
Amino Acids 406–407, 549, 556  
Amitryptyline 364  
Analyte Peak 435–436  
Angular Frequency 393  
Animal Body fluid 556  
Animal Hair 558  
Anthrax 41, 43, 237, 548  
Anthropology 533, 558  
Antibodies 552  
Antigen 552  
Antigen Target 552

- APCI (Atmospheric Pressure Chemical Ionization) 350, 358–360, 364, 403, 428, 442  
 Apple iPhone 552  
 Application Calibration 334–335  
 Aqueous Buffer 356  
 Argon 275, 277, 328–335, 337, 352, 433  
 Army Research Laboratory 550  
 Arrestee Profiling 539  
 Art 42, 107, 122, 172–173, 275, 503, 558  
 Art History 558  
 ASCLD (American Society of Crime Laboratory Directors) 536, 540  
 ASIC (Application Specific Integrated Circuit) 475, 491, 498  
 Aspiration IMS 417  
 Atmospheric Pressure 103, 275, 277, 279, 284, 346–347, 349–350, 352, 358, 360, 364, 397, 403–404, 424–425, 433, 441–442  
 Atmospheric Pressure Interface 346–347, 358, 360, 364  
 ATP (Adenosine Triphosphate) 553  
 ATR (Attenuated Total Reflection) 16, 52–53, 55, 58, 60–62, 76  
 Autofluorescence 122–123, 126, 138, 154, 549  
 Automated Data Analysis 406, 516, 520  
 Aviation Security 415, 434
- b**
- Bacillus 255, 548  
 Background Spectrum 297  
 Background Subtraction 138  
 Backing Pump 348–349  
 Backlog 382, 515–517, 529, 531, 534  
 Bacterial Spores 254, 267, 548  
 Bakeout 426  
 Ballistic Deficit 475, 485  
 Bandgap 248, 478, 480–481  
 Base Pair 522  
 Batch Manufacturing 68  
 Battery Capacity 60  
 Battery Life 16, 32, 36–37, 43, 121, 133, 322, 403, 438  
 Battery Operation 43, 48, 121, 415, 451  
 Battery Powered 268, 449, 547  
 Battlefield 256, 345, 515, 534  
 Bayer Pattern 214, 224–225, 243  
 BCS (BioChipSet) 532–533, 540  
 Beam Rastering 323, 329  
 Beef 553  
 Beer 37, 184, 194, 223, 524, 552  
 Benchtop Spectrometer 106, 184, 187  
 Beryllium 338, 451, 455, 458, 460, 487, 494  
 Beverage 194, 198  
 Beverage Applications 198  
 BGE (Background Electrolyte) 406  
 Bioaerosol 546, 549–551, 556  
 Bioaerosol Fluorescence 550  
 Bioattack 549  
 Biodefense 545–546, 548–551, 556  
 Biodetection 549  
 Biogenic 407, 556  
 Biogeochemical Equilibrium 555  
 Biological Agent 548  
 Biological Analyzer 545–558  
 Biological Assay 553  
 Biological Contamination 545  
 Biological Defense 545, 547–548  
 Biological Pollutant 545, 554  
 Biological Pollution 554  
 Biological Sample 122, 406, 516, 536–538, 545  
 Biomedical Applications 184, 187, 196  
 Biometrics Identity Management Agency 517  
 Biomolecule 552  
 Biota 555  
 Bioterrorism 548  
 Biothreat 253–255, 545  
 Biotransformations 555  
 Biowarfare 549  
 Bite Mark 557  
 Blister Agent 404, 439  
 Blood 148, 164, 196, 213, 226, 363–364, 381, 521–522, 531–533, 538, 546–547, 552, 556–557  
 Blood Sample 196  
 Bluetooth 133, 136, 182, 192–193, 336  
 BN (Bradbury–Nielson) 432, 442  
 Boar Taint 384  
 Body Farm 533  
 Body Fluid 521, 531–532, 538, 546–547, 556–557  
 Body Fluid Sample 556  
 Boiling Point 370, 372–373  
 Boltzmann Constant 378, 424, 443, 480–481, 485  
 Boltzmann Distribution 504  
 Bone Sample 521, 533  
 Booking Station 515, 517, 526, 529–531, 534, 539  
 Border Control 417, 515, 529, 534–535  
 Border Inspection 415

- Border Protection 263, 269  
 Boron Hydrate 493  
 Botulinum toxin 549  
 Bragg Grating 123  
 Bremsstrahlung 331, 452, 457, 460, 462–464, 468–470, 472  
 Bremsstrahlung Radiation 452, 460  
 Bromoform 377–378  
 Bruise 546, 557  
 Buccal Sample 517, 520–521, 524, 526, 528–529, 531–533, 535, 538–539  
 Buffer Gas 354, 394–395, 398, 400–401, 415, 420, 423, 425–426, 428–429, 441  
 Butyryl Fentanyl 404  
 BZ (3-quinuclidinyl benzilate) 373
- C**
- C-4 (Composition C-4 Explosive) 383  
 CAAC (Civil Aviation Administration of China) 416, 442  
 Cadmium 24, 49, 280, 303, 456  
 Cadmium Telluride 24  
 Cannabis 372, 380, 384  
 Capillary Electrophoresis 355–356, 406, 515, 527, 540  
 Capillary Inlet 346–347  
 Carbohydrate 166  
 Carbon in Steel 327  
 Carbon Nanotubes 352  
 Carfentanil 264  
 Carrier Gas 352, 368, 370, 372–374, 399–400, 403, 419, 421, 427–428, 432, 441  
 Carrier Velocity 476, 481  
 Cathinone 361–362  
 Cathode 277–278, 284, 450–451, 453, 486, 519, 522  
 Causative Agent 552  
 CBD (Cannabidiol) 384  
 CBRNE (Chemical, Biological, Radiological, Nuclear, and Explosives) 41  
 CCD Detector (Charge coupled device) 131, 526  
 CE (Carbon Equivalents, or Capillary Electrophoresis) 16, 32, 339–340, 356, 406–407, 515, 524, 540  
 CE-ESI (Capillary Electrophoresis-Electrospray Ionization) 406  
 Cell Culture Media 406  
 Cellphone 209–229, 533  
 Cell Wall 549  
 CFU (Colony-Forming Units) 553, 555  
 Channeltron 356  
 Charge Capacity 393, 395–396  
 Charge Pair 476, 478–479  
 Chemical Agent 255, 258, 297, 381–382, 416, 442  
 Chemical Biological 41, 62, 551  
 Chemical Ionization 350, 352, 360, 364, 403, 442  
 Chemical Warfare Agent 43, 62, 240, 255–256, 269, 289, 297, 345, 358, 360–362, 364, 373, 403, 415, 442  
 Chemometrics 71, 78, 108, 137, 224  
 Chlorobenzene 399  
 Chlorophyll 198–199, 553–554  
 Choking 381  
 Cholesterol 552  
 Chromatogram 356, 382–383  
 CID (Collision-Induced Dissociation) 403–406  
 CIT (Cylindrical Ion Trap) 396–401  
 Citizen Science 209, 217  
 Citizen Spectroscopists 201  
 CJIS (Criminal Justice Information Services) 531, 540  
 Classification Algorithm 81, 556  
 Class 1 Laser 35, 261  
 Class 3 Laser 35  
 Clean Air Act 380  
 Clinical 116, 165, 190, 360–361, 363, 547, 552–553, 557  
 Clinical Applications 190  
 Clostridium 548  
 Cloud 108, 116, 120, 125, 133, 136, 138, 140, 211, 258, 269, 292–294, 312, 313, 314, 317, 357, 416  
 CME (Coiled Microextraction) 370–371  
 CMOS Detector (Complementary Metal-Oxide-Semiconductor) 333  
 CMS (Compact Mass Spectrometer) 358  
 Coaxial Ion Trap 397  
 CODIS (Combined DNA Index System) 517–518, 520–524, 528–532, 540  
 Coenzyme 549  
 Coiled Microextraction 370–371  
 Coliform 546, 555  
 Collisional Cooling 376  
 Collisional Cross-Section 420  
 Collisional Energy 400  
 Collisional Properties 400  
 Colorimeter 218, 226  
 Colorimetric 210, 225–227, 381–382, 552  
 Color Sensing 184, 193  
 Color Sensor 193–194  
 Column Backpressure 372

- Column Capacity 373  
 Column Diameter 373  
 Column Efficiency 374  
 Column Length 372–373  
 Confirmatory 379–381, 555, 558  
 Confirmatory Identification 381  
 Conformal Filter 241, 244, 269  
 Continuously Variable Filter 153, 161, 168  
 Continuous Manufacturing 67–71, 73, 79, 81  
 Conventional Ion Trap 377, 398  
 Copper 335, 456–457, 460  
 Corona Discharge 350, 430–431  
 Correction Factor 424, 443, 468–469  
 COTS (Commercial Off-The-Shelf) 136, 300, 425, 545  
 COVID-19 (Coronavirus Disease of 2019) 237  
 CQA (Critical Quality Attribute) 68–70, 73, 81  
 Crime Scene 263, 532–533, 538–539, 545, 547, 556–557  
 Crops 166, 202, 303, 545–546, 553–554  
 Crude Oil 340, 384  
 Cultural Heritage 44, 248  
 Current Noise 483, 486  
 Cutting Agent 382, 406  
 Cuvette 108, 180, 185, 225–226, 228–229  
 CV (Compensation Voltage) 419, 442  
 CWA (Chemical Warfare Agent) 43–44, 240, 255–258,  
     264–266, 269, 297, 358, 364, 373, 379–381,  
     403–404, 415–416, 427, 429, 439, 441–442  
 CWC (Chemical Weapons Convention) 373, 381  
 Cycloidal 355  
 Cylindrical Ion Trap 354–355, 361–362, 396  
 Cylindrical planar Electrode 396
- d**
- DAB (DNA Advisory Board) 531, 540  
 Dampening 394–395  
 DAPCI (Desorption Atmospheric Pressure Chemical  
     Ionization) 352  
 DAPI (Discontinuous Atmospheric Pressure Interface)  
     347–348, 361, 364, 397  
 DARPA (US Defense Advanced Research Projects  
     Agency) 90, 109, 265, 550  
 DART (Direct Analysis in Real Time) 352, 358, 360  
 Database 42, 100, 108–109, 138, 222, 253, 263, 350, 375,  
     517, 519, 522–524, 531–532, 534–535, 558  
 Data Collection 30, 54, 246, 331, 548  
 Data Conditioning 202  
 Data Processing 120–121, 210, 220, 255, 357, 434, 510,  
     553, 556  
 Daubert 1  
 DBD (Dielectric Barrier Discharge) 431, 442  
 Dead Time 491  
 Decapole 396  
 Decontamination 1, 43, 53, 56, 256, 299  
 Dehmelt Theory 394  
 Deoxygenated Hemoglobin (Hb) 552  
 Department for Transport 416, 442  
 Deployment 138, 179, 203, 317, 368–370, 375, 382,  
     415–416, 429, 434, 441, 503, 520, 536  
 Deposition 49, 74, 78, 91, 140, 167, 257, 475, 479, 492,  
     537  
 DESI (Desorption Electrospray Ionization) 352  
 Detection Limit 228, 278–279, 312, 399, 415, 483  
 Detector Array 94–95, 99, 130, 180, 187–188, 243, 312,  
     315, 325–326  
 Detector Capacitance 475, 481, 485, 487–488  
 Detector Cooling 24  
 Detector Quantum Efficiency 492  
 Detector Resolution 483, 494–495, 497–498  
 Detector Sensitive Area 475, 488–490, 498  
 Detector Window 46, 55, 489  
 DHS (US Department of Homeland Security) 263–264,  
     269, 517, 535–536, 540  
 Diamond 16, 27, 46, 52–53, 55, 60–62, 89, 493  
 Diaphragm 278, 346, 348–349, 379  
 Diaphragm Pump 348–349  
 Dichloromethane 428  
 Dichroic Filter 126  
 Dielectric Barrier Discharge Ionization 352  
 Diesel 306, 308, 372  
 Differentially Pumped Mass Spectrometer 399–400  
 Diffraction Grating 129, 160–161, 181, 186–188, 212,  
     214–217, 220, 239, 242, 249, 326–327  
 Digital Imaging 549  
 DIMS (Differential IMS) 417, 438, 442  
 Diode Laser 35, 47, 51, 123, 125, 219  
 Dipolar Resonance Ejection 398  
 Direct Liquid Sampling 359, 371  
 Disaster Victim Identification 536, 540  
 Discrete Dynode 356  
 Discrete Filter 194  
 Disease Biomarker 546  
 Disease Diagnosis 361, 364, 552–553  
 Disease Diagnostics 545

Dispersive Spectrometer 54, 246, 251, 255, 262, 494  
 DLATGS Detector (Deuterated L-Alanine Doped TriglycineSulphate) 24, 51, 55, 60–62  
 DLP (Digital Light Processor) 91, 98–99, 109, 126, 188  
 DMD (Digital Micromirror Device) 179  
 DMMP (Dimethyl Methylphosphonate) 256, 269, 296  
 DMORT (Disaster Mortuary Operational Response Team) 536, 540  
 DNA (Deoxyribonucleic acid) 515–540  
 DNA Advisory Board 531, 540  
 DNA Concentration 521  
 DNA Database 517  
 DNA Extraction 253, 515–516, 532  
 DNA Fragment 525, 527, 533  
 DNA Identification Act 517–518  
 DNA Mixture 539  
 DNA Policies 516  
 DNA Profiling 515–518, 520, 522–524, 527, 528, 529, 531–533, 535–539  
 DNA Purification 516, 521, 524  
 DNA Quantitation 515–516, 532  
 DNA Sequences 516  
 DNP (Dynamic Nuclear Polarization) 507  
 DNT (Dinitrotoluene) 428, 442  
 DOD (US Department of Defense) 43, 382, 515, 517, 540  
 Dodecapole Field 396  
 DOJ (US Department of Justice) 536, 540  
 Dopant 223, 229, 403, 420, 426–429, 432, 486–487  
 Doping 212, 352, 475, 487  
 Double Resonance Ejection 399  
 DPA (Dipicolinic Acid) 548  
 DPP (Digital Pulse Processor) 475, 494, 496–498  
 Drag Pump 348–349  
 Drift Flow 434  
 Drift Gas 356, 433  
 Drift Time 356, 417, 423–425, 427, 433–437, 439–440, 443  
 Drone 89, 202, 361  
 DTGS Detector (Deuterated TriglycineSulphate) 23  
 DTIMS (Drift Tube IMS) 417, 419, 420, 423, 425, 427, 432, 435, 437–438, 440, 442  
 Duty Cycle 258, 261, 324, 337, 432, 437–438  
 DVI (Disaster Victim Identification) 481, 532, 536–537, 539–540  
 Dynamic Ionization 377  
 Dynamic Range 47, 51, 132, 209, 211–212, 214–216, 224, 352–355, 357

**e**

Ease of Use 138, 345, 350, 369  
 ECAC (European Civil Aviation Conference) 416, 442  
 Edge Filter 126, 128, 160  
 EGDN (Ethylene Glycol Dinitrate) 428, 442  
 EI (Electron Impact) Ionization 356  
 Electromagnetic Wave 503  
 Electron Beam 349, 451–452, 458  
 Electron Charge 424, 443  
 Electron Ionization 374  
 Electron Multiplier Detector 398–399, 401  
 Electrophoresis 355–356, 406, 515, 518, 525, 527, 540  
 Electrophoretic Channels 518  
 Electrophoretic Mobility 356  
 Electrospray 349–352, 356, 360–362, 375, 406–407, 441  
 Electrospray Ionization 349–352, 356, 360–362, 375, 406, 441  
 ELISA (Enzyme-Linked Immunosorbent Assay) 194–196, 226  
 Emergency Responder 17  
 Emission Current 400, 452–453, 462–464, 466–467  
 Emission Line 215, 224–225, 229, 327, 332–335, 339–340, 456–457, 460  
 Emission Wavelength 147, 162, 212, 219, 229, 332  
 ENC (Equivalent Noise Charge) 485–486, 491, 495  
 Endcap Electrode 354, 376, 392–394, 396, 399  
 Endogenous Fluorophores 549  
 Energy-Dispersive 449, 475–476, 478, 480, 482, 484, 486, 488, 490, 492, 494, 496, 498  
 Energy-Dispersive XRF 475–476, 478, 480, 482, 484, 486, 488, 490, 492, 494, 496, 498  
 Environmental Applications 380  
 Environmental Conditions 67, 75, 134, 167, 370, 434, 436–437, 547  
 Environmental Pollution 361, 545, 554  
 Enzyme 194, 549  
 EPA (US Environmental Protection Agency) 317, 380  
 EPG (Electropherogram) 523, 540  
 Epithelial cell 532–533  
 Equilibrium 37, 229, 350, 476, 504, 507, 555  
 ESI (Electrospray Ionization) 349–350, 352, 356, 358–360, 375, 406–407  
 ESS (European Standard Set) 522–523, 540  
 Ethyl Centralite 361–362  
 Excitation Wavelength 118, 121–123, 126–127, 130, 138–139, 147, 162, 184, 255, 550, 557  
 Exhaust Flow 434

Exogenous Autofluorescence 549

Explosive Residues 259, 262–263

External Ionization 347, 349–350, 358

## f

Fabry-Perot 104–106, 109, 149, 169, 217–218, 241, 244, 246, 250

FAIMS (Field Asymmetric Waveform IMS) 417, 419, 422, 423, 426–427, 432, 442

False Alarm 243, 253, 406, 428, 438, 441

False Negative 437, 441

False Positive 439

Fano Factor 478–479

Fano Noise 483, 495

Faraday Cup Detector 401, 403

Faraday Plate Detector 433

Fat 189, 200

FBI (US Federal Bureau of Investigation) 515, 517–518, 520, 526, 530–532, 536, 540

FDA (US Food and Drug Administration) 35, 67, 138

Feces 554

Feed 67–68, 70, 76, 79, 138, 166, 203, 298

Felgett Advantage 355

Fenceline 266

Fentanyl 263–264, 361, 382–383, 403–405, 415, 417

Field Asymmetric Waveform IMS 417

Field Homogeneity 507

Field-Induced Fragmentation (FIF) 441–442

Field Strength 396, 399, 423, 425–427, 437, 439, 441, 443, 501–502, 504–506, 508–509

FIF (field-induced fragmentation) 441–442

Figure of Merit 398

Filament 23, 229, 280, 282, 349–351, 377, 400, 451, 453

Fire Debris 382

Fire Investigation 380, 382

First Responder 116, 237, 266, 299, 302, 361, 376, 382, 403, 415, 548

Fish 553

Fixed Magnet 501

FLIR 358–359, 368–369, 382, 546, 551

Flowing Afterglow 352

Flow Rate 20, 71, 275, 278–279, 312, 314, 317, 352, 372–374, 417

Fluorescence Spectra 185, 195, 549

Flux Linearity 466–468

Food 35, 67, 92, 108, 138, 140, 167, 193, 198–199, 209, 331, 339, 359–361, 510, 545–547, 553–554

Food Contamination 553

Food Processing Plants 553

Food Quality 140, 361

Food Safety 360, 546, 553

Food Spoilage 553

Forage 203, 554

Forensic Analysis 337

Forensics 46, 116, 358, 510, 534, 545–547, 556

Forensic Science 1, 42, 367, 501, 515, 532, 537

Fourier Transform 15, 42, 44, 58, 70, 101, 103, 109, 187, 240, 242, 247, 259–260, 266, 289–291, 295, 297, 299, 346, 353, 391, 509

Fourier Transform Ion Cyclotron Resonance 346, 353

FPI (Fabry-Perot Interferometer) 104–105, 109

Fragmentation 350, 374, 403–404, 441–442

Frequency Interference 498

Frye 1

FTIR (Fourier Transform Infrared) Spectrometer 27, 36, 41–66, 101–103, 107, 260, 289, 291–292

FTIR (Fourier Transform Infrared) Spectroscopy 37, 49, 62

Fungal Biomarker 384

Fungicide 345, 361, 363

Future 69, 71, 73, 81, 89, 108, 120, 138–139, 149, 165, 179, 213, 217, 269, 284, 324, 336, 340, 356–357, 364, 368, 384, 393, 439, 441, 537, 539, 545, 547, 553–554, 558

FWHM (Full-Width at Half-Maximum) 121, 125, 127, 151, 174, 297, 352, 359–360, 398, 400–401, 423, 432–433, 435, 437, 439–442, 466, 475, 479, 483, 495–498

## g

Gas Chromatography 276, 350, 355, 358–360, 362, 364, 367–368, 370–372, 374, 376, 378, 380, 382, 384, 394

Gas Detection 266, 289, 291, 293, 299, 310, 311

Gasoline 372

Gas Pressure 354, 394–395, 398, 400–401

Gas Sample 347

Gating Grid 417, 420, 423, 432, 437

Gating Pulse 423, 432–433, 437–441

Gaussian 123–124, 223, 255, 433, 435, 437, 478, 482

GC (Gas Chromatography) Column 370, 372–374

GDI (Glow Discharge Ionization) 400–401, 403

Genetic Profile 536

Genetic Testing 536–537

Genocide 537

Genotypes 520  
 Geochemical 327, 330, 336–337  
 Geology 92  
 Getter Pump 368  
 Glass Filter 148–149  
 GLC (Gas-Liquid Chromatography) Column 372  
 Glioma 363–364  
 Glutamate 363–364  
 Gold 46, 367, 391, 429, 554  
 Gold Standard 367, 391, 554  
 Grain 166  
 Growth Media 253, 549  
 Guard Grid 421, 433  
 GUI (Graphical User Interface) 120, 357  
 Gunshot residue 361–362  
 Gyromagnetic Ratio 503–504

***h***

Hadamard 99–100, 179, 188  
 Halbach 505–506  
 Halo Ion Trap 355, 397  
 Handheld Raman 15, 35, 119–120, 123, 125–127, 134–137, 139, 549  
 Handheld Spectrometer 35, 46, 119, 210, 240, 487–488, 494  
 Hazardous 1, 20, 35, 37, 149, 240, 360, 380–382, 415, 456, 460, 510  
 Hazmat 21–22, 41, 120, 138, 263, 548  
 Headspace Sampling 350, 358–359  
 Healthcare 518, 545–546, 551–552, 558  
 Helium 35, 51, 331, 352, 355, 373–374, 394, 396, 398–400, 433, 458, 506  
 Helium Gas 394  
 Hemizygous Loci 539  
 HeNe Laser 51  
 Hepatitis B 552  
 Herbicide 345, 361, 554  
 Heteronuclear 506  
 Heterozygous Loci 539  
 Hexachloroethane 428  
 Hexapole 396  
 HHXRF (Hand Held X-Ray Fluorescence) 338, 340, 449, 451, 453–454, 456–467, 469, 471–472  
 Higher Order Field 399  
 High Field 417, 427, 441  
 High Pressure 81, 350, 368

HME (Hot melt extrusion, or Homemade Explosive) 42, 75–76, 260, 267

HMTD (HexamethyleneTriperoxide Diamine) 383, 439, 442

HMX (1,3,5,7-tetranitro-1,3,5,7-tetraoctane) 361–362

Holographic Grating 129

HPLC (High Pressure Liquid Chromatography) 79, 81

HPMS (High Pressure Mass Spectrometry) 392–393, 395, 397, 399–401, 403, 406–407

Human Health 380, 382, 554

Human Remains 533, 536–537

Human Tissue 545, 552

Human Trafficking 535–536

Humidity 1, 33, 46, 67, 70–71, 77, 133, 140, 148, 167, 210–211, 218, 229, 253, 384, 522, 547

HVPS (High Voltage Power Supply) 449–453, 456, 468

Hyperbolic Electrode 396

Hyperbolic QIT (Quadrupole Ion Trap) 395

Hyperpolarization 507, 510

Hyperspectral Imaging 70, 167–168, 170–171, 210, 238, 244, 246, 248, 250, 256, 557

Hyphenated Techniques 510

***i***

ICE (US Immigration and Customs Enforcement) 535, 540

ICP (Inductively Coupled Plasma) 275–277, 284

IED (Improvised Explosive Device) 1, 41, 237, 240, 259, 264

Ignitable Liquid 372, 380, 382

Illicit Drugs 380, 382

ILR (ignitable liquid residue) 380

Imaging Sensor 149, 169, 241, 265

Immigration 535–536, 540

Immunoassay 253, 552, 558

IMS Drift Tube 441

Incapacitating Agent 373, 381

Induced Current 477

Informing Power 435–437

Infrared Detector 49, 311

Infrared Filter 212, 217

Infrared Radiation 48, 297

Infrared Source 297

Infrared Spectrometer 41–66, 166

Infrared Spectroscopy 73, 75, 77, 79, 101, 115–116, 166, 289, 391, 502

InGaAs(Indium Gallium Arsenide) Detector 94, 101, 103, 105–106, 122, 127, 188  
 Inhomogeneous Sample 123  
 Instantaneous Velocity 477  
 Intensity Calibration 334  
 Internal Ionization 349–350, 358, 364  
 Ion Chemistry 377, 428  
 Ion Complexes 377, 428  
 Ion Detector 354, 399, 416–417, 419, 433  
 Ion Ejection 394, 398  
 Ion Fragment 374, 381  
 Ion Funnel 346  
 Ion Injection 354, 432  
 Ionization Efficiency 417, 429, 432, 438  
 Ionization Energy 330, 478, 485  
 Ionization Source 345, 347–350, 352, 356, 358, 370, 374–375, 397–400, 416–417, 428–431, 443  
 Ion Mobility 355–356, 381, 391, 415–417, 419–438, 442  
 Ion Optical Element 346  
 Ion Size 427  
 Ion Swarm 417, 420, 423, 433, 437  
 Ion Trajectory 393  
 Ion Trap Array 396  
 Ion Trap Dimensions 399  
 Ion Trap Stability Diagram 395  
 IOT (Internet of Things) 136, 179  
 IP (Ingress Protection) Rating 19–20, 133  
 IRE (Internal Reflection Element) 52–53, 61  
 Iron 330, 333–336, 339, 456  
 ISO (International Standards Organization) 224  
 Isobutyramide 428  
 Isomer 374, 420, 423  
 Isotropy 550

**j**

JCAD (Joint Chemical Agent Detector) 416, 431, 441–442  
 JFET (Junction Gate Field-Effect Transistor) 481, 484–485, 487–488, 491  
 Johnson Noise 433

**k**

K Emission Line 456  
 Kentucky State Police Forensics Laboratories 534  
 Kerosene 372  
 Ketamine 382–383  
 kHz Regime 333

Kinship Analysis 524, 536  
 Known Sample 108, 516  
 KRS-5 (Thallium Bromide Iodide) 52

**l**

Larmor Frequency 503–504, 506  
 Laser Desorption Ionization 350  
 Laser Excitation 116, 139, 550  
 Laser-Induced Fluorescence 521, 549, 556  
 Laser Safety 34–35, 123, 135, 325  
 Latent Fingerprints 557  
 Lateral Flow Assay 549  
 LC (Liquid Chromatography) and MS (Mass Spectrometry) 356  
 Lead 19, 23, 33, 45, 50–51, 54, 61, 67–68, 70–71, 74, 91–92, 94, 109, 126, 128, 130–131, 187, 211, 224, 229, 280, 327, 331, 356, 375, 392, 427, 449, 458, 468, 472, 476, 480, 484–487, 491, 498, 503–504, 506–507, 531, 534, 540  
 Leaf Spray Ionization 352  
 Leakage Current 481, 483, 485–487  
 LED 62, 79, 132, 147, 165–166, 179–180, 184, 193, 211–213, 215, 218–219, 226, 228–229, 239, 241, 248, 251, 253, 325, 372, 375, 394, 415–416, 424, 426, 428, 430, 432, 434, 436, 438, 442, 458, 475, 501, 505–506, 508, 550, 552, 555  
 L Emission Line 456  
 Levimasole 382–383  
 LFA (Lateral Flow Assay) 549  
 LIBS (Laser Induced Breakdown Spectroscopy) 321–343  
 LIBS Plasma 328, 330  
 LIF (Laser Induced Fluorescence) 76, 432, 549–551, 556  
 Life Science 194, 518  
 Light Scattering 216  
 Limitations 43, 48, 50–51, 60, 71, 73, 75, 94, 101, 105–107, 116, 122, 129, 140, 163, 187, 219, 225, 243, 248, 264, 347, 353, 367, 381, 457–458, 484, 498, 501, 505, 510, 535, 538, 547  
 Limit Of Detection 399, 438, 442, 524  
 Linear Ion Trap 354–355, 358, 396  
 Linear Regime 52  
 Linear Variable Filter 153, 175, 217  
 Line Scanning 241, 550  
 Liquid Chromatography 73, 79, 81, 279, 355–356, 358, 371, 510  
 Liquid Residue 380  
 Liquid Sample 35, 183, 277, 279, 370, 545, 549

- LIT (Linear ion Trap) 99, 396–398  
 Lithium 15, 31–32, 50, 60, 149, 261, 278, 327, 332, 336–338, 492  
 Littrow 93, 128  
 Livestock Science 554  
 LOA (Limit Of Alarm) 438, 442  
 LOD (Limit Of Detection) 267, 339–340, 399, 404, 438, 442  
 Longpass Filter 119, 122, 125–126, 184  
 Lower Energy Pulse Regime 333  
 Low Field 417, 425, 427, 441, 506  
 Low Pressure 277, 312, 398–399, 432  
 Luminescence 211  
 Lysis Buffer 527  
 Lysogeny Broth 549
- m**
- Machine Learning 81, 199, 269, 311, 335–336, 550, 556, 558  
 Magnetic Field 33, 349, 501, 503–506  
 Magnetic Sector 346, 348, 355–356  
 Magnet Miniaturization 505  
 MALDI (Matrix-Assisted Laser Desorption Ionization) 350, 358, 360  
 MALDI-TOF (Time Of Flight) 358  
 Man-Portable 238, 368, 548, 550  
 Mapping 200, 240–241, 255, 264–265, 329, 467, 555  
 Mars 239, 368, 449, 498  
 Mass Accuracy 345, 352, 354–355  
 Mass Casualty 534  
 Mass Disaster 534  
 Mass Discrimination 357  
 Mass Filter 349, 353–355, 358–360, 364, 376, 391  
 Mass Range 352, 354–355, 358, 376, 394, 400–401  
 Mass Resolution 352–354, 378, 394–399  
 Mass-Selective Detection 393  
 Mass Spectrometry 345–364, 367–384, 391–407, 415–443  
 Mass Spectrum Due To Space Charge 376  
 Mathieu Equation 392, 395  
 Mb 76, 552  
 MCT (Mercury-Cadmium-Telluride) Detector 24, 50, 293  
 MDPV (3,4-methylenedioxypyrovalerone) 361–362  
 Mean Free Path 346, 354, 378, 395  
 Meat 148, 166, 198, 203, 546, 553–554  
 Medical Applications 21, 545  
 Membrane Inlet 346–347, 350, 360–361, 364, 397  
 MEMS (Micro-Electro-Mechanical-Systems) 42–43, 48–49, 67, 74, 89–109, 149, 192, 218  
 Mephedrone 361–362  
 Mercury Lamp 200, 212, 229, 253  
 Metabolite 345, 364, 406–407, 510, 553  
 Metabolite Monitoring 364  
 Metadata 558  
 Metal Analysis 324, 337  
 Methyl Centralite 361–362  
 Methyline 361–362  
 Methyl Salicylate 398  
 Michelson Interferometer 27–28, 30, 44–45, 101–104, 107, 242, 289–292, 303, 306  
 Microbial 549, 551, 553–555  
 Microbial Contamination 553–555  
 Microbial Pollutant 554  
 Microbial Properties 555  
 Microbial Spoilage 554  
 Microchannel Plate 356–357  
 Microchip Laser 323–324  
 Microfluidic Chip 406–407, 520  
 Micro Inductively Coupled Plasma 276, 284  
 Microorganisms 549, 555–556  
 Microplasma 275–284  
 Microscale Ion Trap 399, 401, 403  
 Microscopy 89, 185  
 Microshot 370, 372  
 Milk 553  
 MIL-STD-810G (Military Standard) 401, 520, 536  
 MIMS (Membrane Introduction Mass Spectrometry) 347  
 Minerals 92, 473  
 Miniature Ion Trap 351, 364, 396, 401  
 Mining 449, 456, 472  
 Mining Applications 456  
 Minute Sample 538  
 MIT (Massachusetts Institute of Technology) 473, 517, 551  
 Mixture Analysis 42, 137, 269, 345  
 Mixture Sample 372, 539  
 Mobile Phase 81, 356, 371–373  
 Mobile Phone 89, 93–94, 97, 107–108  
 MOEMS (Micro-Opto-Electro-Mechanical-Systems) 67, 89–109  
 Moisture 23, 27, 36–37, 68, 73, 75, 79, 121, 166, 189, 425, 430, 487  
 Molecular Assay 545, 549, 554

- Molecular Biology Assay 549, 552, 558  
 Molecular Cation 347, 349–350  
 Molecular Flow 378, 391, 398  
 Molecular Flow Regime 391  
 Molecular Ion 423  
 Molecular Radical 375  
 Molecular Sieve 37, 434  
 Molecular Weight 352, 358, 370, 404, 420, 424, 442, 509  
 Monochromator 53–54, 95, 154, 159–162, 321, 325  
 MOSFET (Metal-Oxide-Semiconductor Field-Effect Transistor) 481  
 mRDA (Modified Rapid DNA analysis) 518, 540  
 MS/MS (Tandem Mass Spectrometry) 354, 357, 359–361, 363–364, 399  
 Multichannel Spectrometer 321  
 Multimode Laser 124  
 Multiplex 53, 101  
 Multiplexed 516, 519  
 Multipoint 70, 238, 241, 262  
 Multispectral 167, 171–172, 174, 238, 261  
 Multispectral Imaging 171  
 Multivariate Analysis 137  
 Multivariate Optical Elements 241–242, 244  
 Munitions 384  
 Mustard 439  
 Mutant Glioma 363–364  
 Mycotoxin 359, 554
- n**
- Nanowires 352  
 Narcotics 261–264, 345, 358–360, 362, 403–404, 415, 417  
 NDIS (National DNA Index System) 516–520, 522–523, 526, 528, 531–532, 540  
 NDT (Non-Destructive Test) 337–339, 488  
 Nd:YAG (Neodymium-Doped Yttrium Aluminum Garnet) Laser 253  
 Near-Infrared Spectrometer 67–81, 166  
 Near-Infrared Spectroscopy 67–81, 166  
 Negative Ion 356, 358, 362, 364, 417, 420, 439  
 NEG (Non-Evaporative Getter) Pump 379  
 Nerve Agent 404, 439  
 Neural Network 257, 269, 335–336, 553  
 Neutral Density Filter 154  
 Neutral Mass 395  
 Neutral Molecule 345, 349, 394–395, 429, 432–433  
 NG (Nitroglycerin) 404  
 Nicotinamide 428, 549  
 NIJ (US National Institute of Justice) 515, 540  
 NIOSH (US National Institute for Occupational Safety and Health) 507  
 NIR (Near-Infrared) Bands 94  
 NIR Spectra 70–71, 74–76, 78, 554  
 NIR Spectrometer 94, 108–109, 158, 166, 187  
 NIR Spectroscopy 67–81, 92, 203, 552, 555  
 NIR Spectrum 71, 180, 552  
 NIST (US National Institute of Standards and Technology) 222, 255, 297, 350, 375, 515, 517, 526–528, 540  
 NMR (Nuclear Magnetic Resonance) Spectra 503  
 NMR Spectrometer 501–510  
 NMR Spectroscopy 501–510  
 Nondestructive Testing 337  
 Nonlinear Field 399  
 Nonradioactive Source 429–430  
 NRC (US Nuclear Regulatory Commission) 429, 442  
 NTAs (Non-Traditional Agents) 255, 258  
 Nuclear Spin 503, 507  
 Nuclear Spin Quantum Number 503  
 Nuclei 501, 503–504, 506–509  
 Nucleic Acid 140, 165, 195  
 Nucleus 452, 503–504, 509
- o**
- OCME (Office of the Chief Medical Examiner) 534  
 Octane 400  
 Octapolar Field 396  
 OES (Optical Emission Spectroscopy) 321, 334–335, 339–340  
 Open-Tubular Column 372, 374  
 Operating Pressure 346–347, 372, 374–376, 392, 394–395, 397–401  
 Opioids 237, 263–264, 382, 415  
 Optical Emission Spectrometer 284  
 Optical Emission Spectroscopy 321, 339  
 Optical Fiber 94, 96, 184–186, 198, 201, 242, 246, 251, 329  
 Optical Filter 67, 125, 147–174, 218, 242, 247  
 Optical Sizing 551  
 Optical Spectrometer 23, 179, 242, 276  
 Optical Spectroscopy 237–240, 242, 244, 246, 248, 252–253, 255–264, 266  
 Optical Transmission 53, 493  
 Optical Window 27, 552  
 Orbitrap 346, 353, 375

Order-Sorting Filter 156–157, 159  
 Outgassing 434  
 Oxygen 92, 148, 350, 361, 428, 492, 552, 555  
 Oxygenation 546, 552

## **p**

Paper spray ionization 351–352  
 Particle Asymmetry 551  
 Particle Sampling 427  
 Partition 372  
 PAT (Process Analytical Technology) 67–70, 73–78  
 Pathogen 140, 254–255, 552  
 Pathogenic Organism 552  
 Patterning 167, 475  
 Pattern Recognition 168, 417, 550, 558  
 PBAP (Primary Biological Aerosol Particles) 556  
 PCA (Principal Components Analysis) 72, 81, 254–255, 335, 553–554  
 PCR (Polymerase Chain Reaction) Amplification 524–525  
 PCR Inhibitors 524  
 Peak Annotation 357  
 Peak Position 435–436, 441  
 Peak Shape 433, 439  
 Peltier Cooler 475–476  
 Periodic Interference 495, 498  
 Permanent Magnet 503, 505–507  
 Person-Portable Spectrometer 415  
 Pesticide 202, 345, 359–361  
 PETN (Pentaerythritoltetranitrate) 261, 428, 442  
 Petrochemical 339–340, 372, 380, 384  
 Petroleum 340  
 PFTBA (Perfluorotributyl amine) 394, 399  
 Phadebas Paper 557  
 Pharmaceutical 1, 44, 67–70, 73–76, 78–79, 81, 115, 138, 339, 358–359, 361, 507  
 Pharmaceutical Manufacturing 67  
 Phenylalanine 398, 549  
 Phonon Energy 478  
 Phonon Excitation 476  
 Phosphorescence 221  
 Photodiode Detector 96  
 Photoionization 376, 381, 429–430, 432, 442  
 Photoionization Detector 376, 381  
 Photoionization Source 430  
 Picolinic Acid 548  
 PID (Photoionization Detector) 376

PID (Proportional-Integral-Derivative) 47  
 Pigment 184, 549, 554  
 Pinch Valve 347  
 PIN (p-type-intrinsic-n-type) Diode 454, 475, 481, 486–488, 491, 494–495, 498  
 Planar Electrode 396  
 Plastic 24, 33, 107, 134, 165, 173, 212, 228, 263, 431  
 Plate Count 553  
 PLIT (Planar ion Trap) 398  
 PLS (Partial Least Squares) 74–79, 81, 335–336, 553  
 PMI (Positive Material Identification) 337–340  
 Pneumatic Pressure 406, 519, 521, 524, 533  
 POC (Point Of Care) 163–165, 194, 196, 363, 552  
 Point and Shoot 119  
 Point Measurement Sensor 240  
 Point of Need 140, 209, 403  
 Polarization 50, 126, 129, 200–201, 216–218, 244, 257, 269, 507, 550–551  
 Polarization State 50, 551  
 Pollutant 289, 380, 545–546, 554, 556, 558  
 Polymer 44, 76, 79, 211, 280, 355, 370, 373, 492, 510, 518, 525  
 Polymorphic 75, 81  
 Positive Ion 375, 417, 430, 432, 439, 473  
 Poultry 553  
 Power Budget 18, 46, 48, 59  
 PPE (Personal Protective Equipment) 41, 548  
 ppm Shift 504  
 Precious Sample 538  
 Pressure Regime 346, 395–396, 398, 400  
 Presumptive 266, 381, 548–549, 556, 558  
 Presumptive Identification 549  
 Primary Biological Aerosol 556  
 Prism 25, 52–53, 55, 92–93, 103, 167–168, 174–175, 180–181, 199, 211, 218, 229, 239, 297  
 Probe 70, 74–76, 78, 119, 125, 134–135, 184, 349–351, 354, 359, 371, 509, 545, 553, 558  
 Product Testing 79  
 Program Office 515, 520  
 Prokaryotic Organism 549  
 Protein 140, 166, 195, 356, 358, 549, 552, 554  
 Prototype 165, 171, 191, 198, 202, 256, 264, 280, 292, 311, 312, 466, 518, 527  
 Pseudopotential Well 393, 398  
 PSS (Proximal Soil Sensing) 555  
 Pulsed Laser 262, 321–323, 333  
 Pumping Capacity 347–350, 356

Pumping Requirements 347, 376, 378, 391, 397  
p-xylene 400–401

***q***

QAS (US FBI's Quality Assurance Standards) 518, 531–532  
QCL (Quantum Cascade laser) 240–241, 248, 257–258, 266  
QE (Quantum Efficiency) 131, 157–158, 398, 477  
QE-Dipolar Resonance Ejection 398  
QIT (Quadrupole Ion Trap) 391–396, 398  
QMF (Quadrupole Mass Filter) 391–392, 396  
Quadrupolar Field 394, 396  
Quadrupole Ion Trap 346, 353–355, 358, 376, 391–392  
Qualitative Analysis 75  
Qualitative Models 73  
Quality 15, 46, 52, 58, 67–71, 73–74, 76, 78–79, 81, 91, 93, 103, 108, 115–116, 122–124, 137–138, 140, 148–149, 160, 166, 170, 173–175, 179, 187, 194, 196–198, 209–210, 212–213, 223–224, 226, 228, 246, 250, 297, 314, 328, 337, 354, 361, 377, 384, 399, 433, 449, 481, 486, 491, 502–503, 507, 518, 520, 531–532, 546, 553–556  
Quantitative Analysis 55, 78, 92, 136, 138, 367  
Quantitative Calibration 74  
Quantitative Models 71, 73, 79  
Quantum Cascade Laser 240–241, 248, 257–258  
Quantum Efficiency 131, 157–158, 223, 229, 476, 491–493, 495, 497–498  
Quantum Spin 503  
Quinine 382–383

***r***

Radiation Dose 454–455  
Radiation Safety 454–456  
Radioactive Ionization 416, 429, 443  
Radioactive Source 429–430  
Radio Frequency IMS 417  
Radioisotopes 449  
Raman Bands 253  
Raman Effect 115–116  
Raman Excitation 123  
Raman Scattering 116–117, 119, 125, 134, 139, 160, 549, 558  
Raman Spectra 115–118, 122, 162, 246, 253–255, 260, 546, 550, 553, 558

Raman Spectrometer 18, 31, 35, 92, 115–140, 382, 391, 546, 550, 558  
Raman Spectroscopy 73, 75–76, 78–79, 115–140, 239, 253, 382, 552, 557  
Raman Spectrum 117–118, 122, 125–127, 130, 135–137, 160, 553  
Rapid DNA 515–524, 526–540  
Rare Earth 505  
Rastering 323, 329–330  
Raw Material Identification 73  
Rayleigh Scattering 116–117  
RDA (Rapid DNA Analysis) 518  
Reactant Ion 428–430, 432  
Reaction Monitoring 509  
Reagent 196, 253, 406, 510, 518–519, 521, 524, 527, 533, 536, 547, 553, 556  
Rectilinear Ion Trap 347, 355, 361, 364, 397  
Recycling 77, 100, 338–339  
Reduced Mass 424  
Reduced Mobility 423, 427, 436, 443  
Reference Buccal 517–518, 520–521, 524, 526, 528–529, 531–532, 535, 538–539  
Reference Laser 51, 101  
Reflection Grating 93, 129  
Remote Instrument Control 357  
Resolution-Peaking Time 494–495, 497–498  
Resolving Power 93, 101, 248, 297, 391, 417, 432, 437, 439–441, 443  
Resonance Ejection 354, 394, 398–399  
Retention time 372, 383  
RF (Radio Frequency) Coil 505  
RF Frequency 354, 394–395, 398–401  
RF Frequency Regime 398  
RFID (Radio Frequency Identification) 521  
RF IMS 417, 442  
RF Pulse 504  
Rhodium 452, 457–458, 460  
Ricin 254, 549  
Ring Electrode 351, 354–355, 376, 392–394, 433, 490  
RIT (Rectilinear Ion Trap) 347, 397–398  
RMID (Raw Material identification) 73  
Robot 238, 262–263, 268, 361  
Rock 330, 473  
RoHS (Reduction of Hazardous Substances) 149, 456–457, 472  
Roughing Pump 379, 392, 397  
Rowland Circle 218

**S**

Safety and Security 41, 237–240, 242, 244, 246, 248, 252, 256, 258, 260, 262, 264  
 SAK (Sexual Assault Kit) 531, 534  
 Saliva 532, 556  
 Sample Collection 79, 350, 352, 370, 382, 516, 546  
 Sample Flow 279, 427, 434  
 Sample Holders 212, 225  
 Sample Interface 16, 42, 45–46, 51–53, 61, 115, 119–120, 123, 126, 133–135  
 Sample Introduction 275–282, 351, 359–360, 397, 426, 438, 548, 555  
 Sample Matrix 384, 426, 438  
 Samsung Galaxy 223, 553  
 Scan Rate 395  
 Scrap Metal 449, 456, 460, 472  
 Scroll Pump 346, 348–349, 401  
 SDD (Silicon Drift Detector) 449, 454, 456, 475–476, 481, 489–492  
 Secondary Electron 356  
 Sector 91, 131, 346, 348, 354–356  
 Secular Frequency 354, 394–395  
 Security 41, 116, 131, 136, 138, 140, 237–240, 242, 244, 246, 248, 252, 256, 258, 260, 262–264, 269, 415–416, 419, 426, 434, 441–442, 498, 517, 519, 527, 535–536, 540  
 Selectivity 70, 252, 297, 347, 352, 391, 420, 427–429, 557  
 Semen 522, 532–533, 556  
 Semiconductor Detector 475–486, 488, 490–492, 494, 496, 498  
 Semiconductor Laser 248  
 Semipermeable Membrane 397, 399  
 Semivolatile 347, 350, 356, 358, 360, 382, 427, 434  
 Semivolatile Analytes 350, 356, 358  
 Separations 210, 338, 355–356, 374, 417, 510  
 Separation Techniques 356, 406  
 SERS (Surface Enhanced Raman Spectroscopy) 134–135, 139–140  
 Service Module 379  
 Shaper 485–486  
 Shielding Constant 504  
 Shimming 508  
 Shock 1, 24, 29–30, 36, 46, 121, 133, 253, 322, 334, 397, 401, 449, 451, 520, 536  
 Shot Noise 211, 216, 224, 227, 483–484  
 SHS (Spatial heterodyne Spectrometer) 242, 246–248, 251

SIB (State Identification Bureau) 531, 550–551  
 SID (State Identification Number) 531  
 Si Detector 182, 475, 479, 491–493, 495, 497–498  
 Signal Averaging 54, 216, 218, 226–227, 357, 506  
 Signal Fluctuation 279, 478, 483  
 Signal Flux 466  
 Signal Processing 58, 189, 227, 281, 476, 520  
 Silicon Detector 94, 122–123, 167, 212, 498  
 Silicon Drift Detector 449, 475, 488–489, 498  
 Silicon PIN 486  
 Silver 457–458, 460, 462  
 Single mode 124  
 Single-mode 123–124  
 Site Investigations 380  
 Skimmer 346  
 Skin Cell 532  
 Smartphone Spectrometer 179, 192–193, 195–196, 198–200, 209–229  
 Smartphone Spectroscopy 52–53, 209–229  
 Snapshot Imaging 175  
 Soft Ionization 428  
 Soil Organic Carbon 555  
 Soil Organic Matter 555  
 Soil Surface 555  
 Solid Sample 134, 370  
 Soret peak 557  
 SORS (Spatially Offset Raman Spectroscopy) 134, 139  
 Space Charge 376–378, 396, 437  
 Spatially Offset Raman 134, 139  
 Spatial Resolution 169–171, 174, 241, 243–244, 246, 249–250, 252, 297, 310, 313, 555  
 Species 147, 227, 280, 333, 352, 356, 358, 374, 376, 378, 384, 400, 419, 428–431, 434, 524, 532, 548–549, 554, 558  
 Specifications 43, 70, 133, 253, 293, 326, 337, 348, 358, 368, 374, 392, 506–508  
 Spectral Interpretation 61  
 Spectral Library 42, 54, 238, 240, 261, 293, 297, 354, 357, 375, 510, 548  
 SPME (Solid-Phase Microextraction) Fiber 351, 370–371  
 SPME Sampling 370  
 Spore 254–255, 267, 269, 384, 548, 550  
 S&T (US Department of Homeland Security (DHS) Science and Technology Directorate) 536, 540  
 Standoff 122, 132–133, 139, 237–244, 246–249, 251–253, 255–269, 289–317, 453  
 Standoff Detection 237–269, 289–317

- Standoff Raman 139, 239, 262  
 Stationary Phase 81, 355–356, 371–373  
 Statistical Analysis 550  
 Steady State 25, 211  
 STR (short tandem repeat) Amplification 516, 518–519, 521, 531–532  
 Stray Field 506  
 STR DNA Profile 531  
 STR Loci 517–518, 521–523, 528  
 STR Profile 517, 527  
 Structural Elucidation 502, 509  
 Structural Isomers 420  
 Strychnine 509  
 Sugar 96–98, 199, 282  
 Supercontinuum Laser 147, 154, 240, 260–261  
 Surface-Enhanced Raman 134  
 Surface Passivation 475  
 Suspicious Powder 548–549  
 Swab 350, 359, 361–362, 403, 426–427, 515, 518–522, 524–525, 527, 531, 533–535, 538, 553  
 Swab Sampling 403  
 SWaP 41, 48, 51, 54–56, 59, 121, 133, 252–253, 269, 347, 352, 355–356, 391, 398, 415, 442, 521  
 Sweat 532, 556  
 SWGDAM (Scientific Working Group on DNA Analysis Methods) 516, 536
- t**
- Tandem Mass Spectrometry 346, 354, 399  
 Target Anode Material 455, 457, 459  
 Target Chemicals 369  
 Target Material 134, 453, 458–459, 462  
 TATP (Triacetone triperoxide) 383, 439, 442  
 TEC (Thermoelectric Cooler) 24–26, 50, 55, 132–133, 475, 487–488  
 Teeth 533, 537  
 Temperature Drift 427  
 Temperature Limit 246, 253, 373  
 Terminal Electrode 477  
 Tetryl (2,4,6-trinitrophenylmethylnitramine) 361–362  
 THC ( $\Delta$ -9 tetrahydrocannabinol) 384  
 Thermal Cycling 516, 520, 527  
 Thermal Desorption 351, 359–360, 370–371, 403  
 Thermal Drift 123, 506, 509  
 Thermal Energy 395, 424–425, 480  
 Thermal Excitation 480–481, 489  
 Thermal Noise 134, 228–229, 480, 484  
 Thermal Stability 133, 244, 507  
 Thermoelectric Cooler 24, 50, 131–132, 434, 487  
 Threat Identification 53–54, 237, 383  
 Threat signatures 263, 550  
 TIC (Toxic Industrial Compound) 255, 258, 266, 297, 379–381, 403, 415–416, 427, 439, 441–442  
 TIFF (Tag Image File Format) 224  
 Tissue Sample 533, 548, 552  
 TNT (Trinitrotoluene) 361–362, 428, 436, 439, 441–442  
 TO-8 Can 487  
 TOF (Time of Flight) 346, 356, 358  
 Toluene 135, 361, 398–399, 432  
 Toroidal Ion Trap 355, 358, 368, 377, 397  
 Touch DNA 521, 531–532  
 Touchscreen 16–17, 136, 357, 522, 545, 548  
 Toxic Industrial Chemical 19, 62, 255, 297, 379, 403, 415, 442  
 Toxin 44, 549–550  
 Toys 89, 202  
 Trace Detection 415, 434, 439  
 Trace Sampling 350  
 Trading Rule 54, 56  
 Training 138, 213, 229, 260, 264, 325, 369, 536, 539, 545  
 Trajectories 346, 349, 354, 392–393  
 Trajectory 59, 346, 378, 394  
 Transmission Grating 128–130, 200–201, 211, 213–214, 217–218, 220, 228, 326  
 Transportable 34, 254, 321, 323, 368, 379, 398, 507, 547  
 Transport Canada 416  
 Transport Time 476  
 Trap Electrode 396–397  
 Trapping Capacity 355  
 Trapping Device 347  
 Trapping Field 353, 394–396  
 Trapping Ion 396  
 Trapping Parameter 394  
 Trapping Volume 377  
 Tryptone 549  
 Tryptophan 165, 549, 553, 555  
 TSA (US Transportation Safety Administration) 416, 442  
 Tungsten 174, 180, 305, 400, 451–452, 454–458, 460, 468  
 Turbomolecular Pump 379, 391–392, 401  
 Turbo Pump 348

TVC (Total Viable Count) 553–554

Tyrosine 549

## **U**

UAV (Unmanned Aerial Vehicle) 139, 167, 170, 202, 268

UCN (Universal Control Number) 531

UF (Ultrafiltration) 532–533

Ultraviolet 53, 81, 147, 179, 212, 214, 238, 361, 432, 442, 545, 550–551, 557

United States Army 381, 416, 526

University of Tennessee 533

Unstable Flux 466–467

USACIL (United States Army Criminal Investigation Laboratory) 526

User Experience 149, 547–548, 558

UV Lamp 432

UV Light 91, 201, 253

UV-Visible Spectrometer 179–203

UV-Visible Spectroscopy 179–203

## **V**

Vacuum Chamber 277, 346–347, 349–351, 378, 394, 399–400, 458

Vacuum Pump 275, 346, 348–349, 358, 367, 392, 397, 406

Vacuum Requirements 370, 378, 391, 395, 397

Validation 56–57, 71, 116, 289, 297, 516, 519–520, 524, 526, 528, 537, 553

Van Deemter 374

Vapor Pressure 372–373, 375, 381, 426

Vapor Sampling 426–427

Verification 73, 79, 120, 340, 438, 535

Vibration 29–30, 36, 46–47, 67, 92, 116, 118, 121, 125, 128, 182, 210, 248, 253, 297, 322, 397, 401, 478, 480, 484, 494, 520, 536

Victim 531, 534–537, 540, 557

Victim Identification 535–536, 540

Virus 255

Visible 56, 130, 135, 147, 167, 179–180, 182, 184, 186, 188, 190, 192, 194, 196, 198, 200, 202, 209, 212–215, 217, 229, 238, 248, 251–253, 260, 262–263, 297, 299, 545–546, 553–557

Vitamins 406–407, 549

VOC (Volatile Organic Compound) 358–359, 361, 376, 380, 399–400

Volatile 17, 345–347, 350, 352, 356–358, 360–361, 367, 376, 380, 382, 384, 399, 433–434

Volatile Analytes 361

Voltage Noise 484–486

V-series Agent 373

VX (A thiophosphonate nerve agent) 258, 361–362, 403, 490

## **W**

Water Potability 546

Waterproof 1, 43, 120

Water Runoff 382

Water Testing 196

Wavelength Calibration 127, 130, 135, 185, 203, 211, 214–215, 218–220, 222, 226, 229, 334

Wavelength Dispersive 156

Weapons of Mass Destruction 41, 381–382

Wearable 148, 238, 415, 507

Weighting Field 477

Well Logging 505

White Blood Cell 552

Whitehead Institute 517

White Noise 498

White Powders 1, 134

White Sands Range 550

Wi-Fi 132–133, 136, 182, 202, 210, 228, 336

Wildfire 536–537

Wireless 67, 74, 133, 136, 182–183, 192, 262, 276, 547, 549, 552

WMD (Weapons of Mass Destruction) 41, 381–382

Wounds 546, 557

## **X**

Xenon Flash Lamp 162, 550

Xenon Gas 396

X-ray Anode 457

X-ray Detector 457, 475–498

X-ray Filter 452, 455–456, 458, 462

X-Ray Fluorescence 338, 449–450, 452, 454, 456, 458, 460, 462, 464, 466, 468, 470, 472–473, 475, 492

X-ray Flux 453, 458–461, 463–467

X-ray Radiation 452, 454–455

X-ray Source 449–473

X-ray Spectra 452, 457

X-ray Spectrum 452, 463, 467

X-ray Spot 463, 465–466

X-ray Transmission 454, 487, 492–494  
X-ray Tube 449–473, 494  
X-ray Window 451, 458–459, 461–462, 491–492  
XRF (X-Ray Fluorescence) Spectrometer 488, 498  
XRF Spectroscopy 449, 472  
Xylene 399–401

**y**

Yale University 550  
Yeast Extract 549

**z**

ZnSe (Zinc Selenide) 27, 46, 50, 52–53, 55, 293, 298

## **Portable Spectroscopy and Spectrometry 2**

# **Portable Spectroscopy and Spectrometry 2**

## **Applications**

*Edited by*

*Richard A. Crocombe*

Crocombe Spectroscopic Consulting  
Winchester  
MA, USA

*Pauline E. Leary*

Federal Resources  
Stevensville  
MD, USA

*Brooke W. Kammrath*

Department of Forensic Science  
Henry C. Lee College of Criminal Justice and Forensic Sciences  
University of New Haven  
West Haven  
CT, USA

and

Henry C. Lee Institute of Forensic Science  
West Haven  
CT, USA

**WILEY**

This edition first published 2021  
© 2021 John Wiley and Sons Ltd

All rights reserved. No part of this publication may be reproduced, stored in a retrieval system, or transmitted, in any form or by any means, electronic, mechanical, photocopying, recording or otherwise, except as permitted by law. Advice on how to obtain permission to reuse material from this title is available at <http://www.wiley.com/go/permissions>.

The right of Richard A. Crocombe, Pauline E. Leary and Brooke W. Kammrath to be identified as authors of the editorial material in this work has been asserted in accordance with law.

*Registered Offices*

John Wiley & Sons, Inc., 111 River Street, Hoboken, NJ 07030, USA  
John Wiley & Sons Ltd, The Atrium, Southern Gate, Chichester, West Sussex, PO19 8SQ, UK

*Editorial Office*

The Atrium, Southern Gate, Chichester, West Sussex, PO19 8SQ, UK

For details of our global editorial offices, customer services, and more information about Wiley products visit us at [www.wiley.com](http://www.wiley.com).

Wiley also publishes its books in a variety of electronic formats and by print-on-demand. Some content that appears in standard print versions of this book may not be available in other formats.

*Limit of Liability/Disclaimer of Warranty*

In view of ongoing research, equipment modifications, changes in governmental regulations, and the constant flow of information relating to the use of experimental reagents, equipment, and devices, the reader is urged to review and evaluate the information provided in the package insert or instructions for each chemical, piece of equipment, reagent, or device for, among other things, any changes in the instructions or indication of usage and for added warnings and precautions. While the publisher and authors have used their best efforts in preparing this work, they make no representations or warranties with respect to the accuracy or completeness of the contents of this work and specifically disclaim all warranties, including without limitation any implied warranties of merchantability or fitness for a particular purpose. No warranty may be created or extended by sales representatives, written sales materials or promotional statements for this work. The fact that an organization, website, or product is referred to in this work as a citation and/or potential source of further information does not mean that the publisher and authors endorse the information or services the organization, website, or product may provide or recommendations it may make. This work is sold with the understanding that the publisher is not engaged in rendering professional services. The advice and strategies contained herein may not be suitable for your situation. You should consult with a specialist where appropriate. Further, readers should be aware that websites listed in this work may have changed or disappeared between when this work was written and when it is read. Neither the publisher nor authors shall be liable for any loss of profit or any other commercial damages, including but not limited to special, incidental, consequential, or other damages.

*Library of Congress Cataloging-in-Publication Data*

Names: Crocombe, Richard A., editor. | Leary, Pauline E., editor. |  
Kammrath, Brooke W. editor.

Title: Portable spectroscopy and spectrometry 2 : applications / edited by Richard A.  
Crocombe, Pauline E. Leary, Brooke W. Kammrath.

Description: First edition. | Hoboken, NJ : Wiley, 2021. | Includes  
bibliographical references and indexes. | Contents: v. 2. Applications.

Identifiers: LCCN 2020042686 (print) | LCCN 2020042687 (ebook) | ISBN 9781119636403 (v. 2 ; hardback) |  
ISBN 9781119636427 (v. 2 ; adobe pdf) | ISBN 9781119636434 (v. 2 ; epub)

Subjects: LCSH: Spectrometer. | Spectrum analysis.

Classification: LCC QC373.S7 P67 2021 (print) | LCC QC373.S7 (ebook) |  
DDC 621.36/1-dc23

LC record available at <https://lccn.loc.gov/2020042686>

LC ebook record available at <https://lccn.loc.gov/2020042687>

Cover Design: Wiley

Cover Image: Hand © DenisNata/Shutterstock;

Mass Spectrum: Courtesy of NIST MS Spectral Database, adapted by Pauline Leary and Brooke Kammrath

Set in 9.5/12.5pt STIXTwoText by SPi Global, Chennai, India

*To my parents, my family, and all those in spectroscopy I've worked with, and learned from, over the years.*

Richard A. Crocombe, Ph.D.

*This book is dedicated to **John A. Reffner**. Everyone needs someone in their life like you are to me: A **teacher** to provide them guidance when needed, a **mentor** to help them see what they can achieve, and a **friend** to talk to when they need to know it will all work out.*

Pauline E. Leary, Ph.D.

*The dedication of this book is shared amongst all of the members of my family. To my mother Shirley and late father Milton, I am grateful for all of the many life lessons you taught me and your encouragement to pursue a career that I love. To my twin sister Lindsey, I appreciate having you as my forever best friend, partner in crime, and womb-mate. To my husband Matt, a choice in a life partner is the most important decision a person can make, and I chose very wisely. You are my biggest champion, and I am yours – together we can accomplish anything. And to my children Riley and Grayson, I love you so much. I hope you always stay curious because curiosity is the best teacher, the mother of invention, the cure for boredom, the key to creativity, the engine of achievement, and the beginning of science.*

Brooke W. Kammrath, Ph.D.

## Contents

**List of Contributors** xv

**Foreword** xix

**Preface for Volume 2** xxi

**Acknowledgements** xxiii

**1 The Role of Applications in Portable Spectroscopy 1**

*Richard A. Crocombe, Pauline E. Leary and Brooke W. Kammrath*

- 1.1 Introduction 1
- 1.2 The Evolution of Applications 1
- 1.3 What Defines an Application? 5
- 1.4 The Return on Investment for an Application 11
- 1.5 Preparing Samples in the Field 12
- 1.6 The Commercial Success of a Portable Spectrometer 15
- 1.7 Conclusions and Future Applications 16
- References 17

**2 Identification and Confirmation Algorithms for Handheld Analyzers 19**

*Lin Zhang, Lisa M. Lee and Suzanne K. Schreyer*

- 2.1 Introduction 19
- 2.2 Data Collection 22
- 2.3 Data Conditioning 26
- 2.4 Types of Algorithms 26
- 2.5 Display of Algorithm Results 34
- 2.6 Computational Considerations 37
- 2.7 Performance Characterization 39
- 2.8 Conclusion 40
- References 40

**3 Library and Method Development for Portable Instrumentation 43**

*Suzanne K. Schreyer*

- 3.1 Introduction 43
- 3.2 Instrument Use Overview 44
- 3.3 Library Development 45
- 3.4 Qualitative Model Development 48
- 3.5 Library Build 48

3.6	Case Study: Building a Polymorph Library	50
3.7	Case Study: Counterions and Effect on Selectivity	51
3.8	Case Study: Effect of Moisture on Peaks of Ammonium Nitrate	53
3.9	Case Study: Selectivity in an Explosive Sublibrary	54
3.10	Quantitative Method Development	55
3.11	Building Meaningful Predictive Models	58
3.12	Case Study: Prediction of Protein Levels in Flour Samples	58
3.13	Summary	61
	References	62
<b>4</b>	<b>Applications of Portable Optical Spectrometers in the Chemical Industry</b>	<b>65</b>
	<i>Xiaoyun Chen, Mark A. Rickard and Zhenbin Niu</i>	
4.1	Introduction	65
4.2	Review of Industrial Applications	67
4.3	In-Depth Examples	71
4.4	Conclusions and Prospects	80
	References	82
<b>5</b>	<b>The Value of Portable Spectrometers for the Analysis of Counterfeit Pharmaceuticals</b>	<b>85</b>
	<i>Pauline E. Leary, Richard A. Crocombe and Ravi Kalyanaraman</i>	
5.1	Introduction	85
5.2	Field Analytical Spectroscopy Methods	93
5.3	Deployed Systems	112
5.4	The Future	116
	Acknowledgments	117
	References	118
<b>6</b>	<b>Forensic Applications of Portable Spectrometers</b>	<b>125</b>
	<i>Brooke W. Kamrath, Pauline E. Leary and John A. Reffner</i>	
6.1	Breath Alcohol Testing	127
6.2	White-Powder Attacks	131
6.3	Illicit Drugs	134
6.4	Counterfeit Drugs	137
6.5	Explosives	138
6.6	Clandestine Labs	139
6.7	Ignitable Liquids	139
6.8	Future	140
6.9	Conclusions	142
	Acknowledgments	143
	References	144
<b>7</b>	<b>Military Applications of Portable Spectroscopy</b>	<b>149</b>
	<i>Alan C. Samuels</i>	
7.1	Introduction	149
7.2	Visible/Near-Infrared Hyperspectral Imaging for Bulk Explosive Material Detection and Camouflage Defeat Applications	150

7.3	Infrared Spectroradiometry for Remote Hazardous Vapor Detection and Early Warning	150
7.4	Infrared and Raman Spectroscopy for Condensed Phase Analysis (Energetics, Chemical Agents, Biological Agents)	151
7.5	Raman Spectroscopy for Surface Contamination Detection	153
7.6	Raman Spectroscopy for Presumptive Biological Hazard Classification and Early Warning of a Biowarfare Agent Attack	154
7.7	Fluorescence Spectroscopy as a Biological Detection “Trigger”	154
7.8	Networked Multimodal Sensors and Data Analytics and the Future	155
	References	156
<b>8</b>	<b>Applications of Ion Mobility Spectrometry</b>	<b>159</b>
	<i>Pauline E. Leary and Monica Joshi</i>	
8.1	Introduction	159
8.2	Applications	162
8.3	Conclusion	174
	References	175
<b>9</b>	<b>Portable Spectroscopy in Hazardous Materials Response</b>	<b>179</b>
	<i>David DiGregorio</i>	
9.1	The Hazmat Clinician	179
9.2	Defining the Mission: Meeting with the IC	180
9.3	Hazmat Huddle or Pre-Entry Brief	183
9.4	HPMS	190
9.5	Raman Spectroscopy	190
9.6	Fourier-Transform Infrared Spectroscopy (FT-IR)	191
9.7	IMS	191
9.8	GC-MS	192
9.9	Colorimetrics	193
9.10	Warranties and Reachback	193
9.11	Pitfalls	194
9.12	Complimentary Technologies	194
9.13	An Introduction to the Scientific Working Group for the Analysis of Seized Drugs (SWGDRUG)	194
9.14	SWGDRUG Recommendations: How They Related to the Hazmat Field	195
9.15	Ancillary Equipment	196
	References	198
<b>10</b>	<b>Toward Clinical Applications of Smartphone Spectroscopy and Imaging</b>	<b>199</b>
	<i>William J. Peveler and W. Russ Algar</i>	
10.1	Smartphone Imaging and Spectroscopy Capabilities: An Overview	200
10.2	Clinical Biomarkers Targeted for the Smartphone	203
10.3	Toward Clinical Applications of the Smartphone in Low-Cost and Point-of-Care Settings	207
10.4	Toward Clinical Applications in Primary Care or Pathology Laboratory Settings	211
10.5	Microscopy and Imaging on the Smartphone and the Potential Clinical Applications	218
10.6	Optical Measurements with Smartphones in the Clinic: An Outlook	219
	References	221

<b>11</b>	<b>Applications of Portable and Handheld Infrared Spectroscopy</b>	227
	<i>John A. Seelenbinder and Christina S. Robb</i>	
11.1	Rapid Response	228
11.2	Dispersed Samples	231
11.3	Nondestructive Testing	238
11.4	Conclusion	243
	References	243
<b>12</b>	<b>Spectra Transfer Between Benchtop Fourier-Transform Near-Infrared and Miniaturized Handheld Near-Infrared Spectrometers</b>	249
	<i>Uwe Hoffmann, Frank Pfeifer and Heinz W. Siesler</i>	
12.1	Introduction	249
12.2	Experimental Details	255
12.3	Results and Discussion	256
12.4	Summary of Transfer Strategy	262
12.5	Conclusions	265
	References	265
<b>13</b>	<b>Applications of Handheld Near-Infrared Spectrometers</b>	267
	<i>Hui Yan and Heinz W. Siesler</i>	
13.1	Introduction	267
13.2	Instrumentation	267
13.3	Applications	269
13.4	Qualitative Applications of Handheld NIR Spectrometers	269
13.5	Quantitative Analyses with Handheld NIR Spectrometers	276
13.6	Conclusions	294
	Acknowledgments	295
	References	295
<b>14</b>	<b>X-Ray, LIBS, NMR, and MS Applications in Food, Feed, and Agriculture</b>	299
	<i>Krzysztof Bernard Bec, Justyna Grabska and Christian Wolfgang Huck</i>	
14.1	Introduction	299
14.2	Applications of Transportable Spectroscopy and Spectrometry in Food, Feed, and Agriculture	301
14.3	Current Developments, Remaining Challenges, and Future Prospects	317
14.4	Concluding Remarks	319
	References	319
<b>15</b>	<b>Portable Near-Infrared Spectroscopy in Food Analysis</b>	325
	<i>Ellen V. Miseo, Felicity Meyer and James Ryan</i>	
15.1	Introduction	325
15.2	Spectroscopy	326
15.3	Analysis, Sampling, and Detection Limits	327
15.4	Use of Portable Near-Infrared Instruments in Food Analysis	332
15.5	Summary	336
	References	336

<b>16</b>	<b>Handheld Raman, SERS, and SORS</b>	<b>347</b>
	<i>Michael Hargreaves</i>	
16.1	Introduction	347
16.2	Raman Spectroscopy: Sampling Techniques, Technologies, and Considerations	347
16.3	Handheld Raman Devices	350
16.4	Sample Considerations	351
16.5	Usability Considerations	352
16.6	Surface-Enhanced Raman Spectroscopy (SERS)	352
16.7	Spatially Offset Raman Spectroscopy (SORS)	355
16.8	Standoff	358
16.9	Technology Combinations	358
16.10	Leveraging Data	359
16.11	Military Identification Applications	361
16.12	Pharmaceuticals	364
16.13	Narcotics	366
16.14	Novel Psychoactive Substances (NPS)	369
16.15	Summary	372
	Acknowledgments	372
	Images	372
	References	372
<b>17</b>	<b>Portable Raman Spectroscopy in Field Geology and Astrobiology Applications</b>	<b>377</b>
	<i>H.G.M. Edwards, J. Jehlička and A. Culka</i>	
17.1	Introduction	377
17.2	Dawn of Portable Raman Spectrometers	378
17.3	Conclusions	393
	Acknowledgement	395
	References	395
<b>18</b>	<b>Hyperspectral Proximal Sensing Instruments and Their Applications for Exploration Through Cover</b>	<b>401</b>
	<i>Carsten Laukamp, Monica LeGras and Ian Christopher Lau</i>	
18.1	Introduction	401
18.2	Field VNIR-SWIR Sensors	402
18.3	Field and Laboratory Fourier Transform Infrared Spectrometers	406
18.4	Hyperspectral Drill Core Sensing	408
18.5	Data Processing	408
18.6	Applications	412
18.7	Summary	416
	Acknowledgements	418
	References	418
<b>19</b>	<b>Handheld X-Ray Fluorescence (HHXRF)</b>	<b>423</b>
	<i>Stanislaw Piorek</i>	
19.1	Introduction – X-Ray Fluorescence	423
19.2	How Did We Get Here – Evolution of a Handheld XRF Analyzer	425

19.3	Contemporary HHXRF Analyzer: Construction and Operation	427
19.4	Calibration Methods	433
19.5	The Most Important Applications for HHXRF Analyzers	436
19.6	Remarks on Safety When Using HHXRF	448
19.7	Summary and Possible Future Developments for HHXRF	448
	References	449
<b>20</b>	<b>XRF and LIBS for Field Geology</b>	<b>455</b>
	<i>Bruno Lelière and Russell S. Harmon</i>	
20.1	Introduction	455
20.2	X-Ray Fluorescence Spectroscopy (XRF)	457
20.3	Laser-Induced Breakdown Spectroscopy (LIBS) for Field Geology	471
20.4	Current Potential and Future Developments of Field-Portable XRF and LIBS	486
	References	490
<b>21</b>	<b>Portable Spectroscopy for Cultural Heritage</b>	<b>499</b>
	<i>Federica Pozzi, Adriana Rizzo, Elena Basso, Eva Mariasole Angelin, Susana França de Sá, Costanza Cucci and Marcello Picollo</i>	
21.1	Introduction	499
21.2	Instrumentation	501
21.3	Applications to Cultural Heritage Research	503
21.4	Conclusions	516
	Acknowledgments	516
	References	517
<b>22</b>	<b>Portable Spectroscopy for On-Site and In Situ Archaeology Studies</b>	<b>523</b>
	<i>Mary Kate Donais and Peter Vandenabeele</i>	
22.1	Introduction	523
22.2	Molecular and Vibrational Spectroscopic Analysis	524
22.3	Atomic Spectroscopic Analysis	527
22.4	Case Study – Characterization of a Multiphased Stone Tower in Monterubliaglio, Umbria (Italy) by Portable X-ray Fluorescence Spectrometry	530
22.5	Conclusions	537
	Acknowledgements	538
	References	538
<b>23</b>	<b>The Future of Portable Spectroscopy</b>	<b>545</b>
	<i>Richard A. Crocombe</i>	
23.1	Introduction	545
23.2	Optical Spectroscopy	545
23.3	General Technology Improvements	546
23.4	Raman Spectrometers	548
23.5	XRF and LIBS	549
23.6	GC-MS and LC-MS	550
23.7	Ion Mobility Spectrometry (IMS) and High-Pressure Mass Spectrometry (HPMS)	550
23.8	NMR (Relaxometry, or Time-Domain NMR)	551
23.9	Hyphenation	551

- 23.10 Smartphone Spectrometers 552
- 23.11 Spectrometers Embedded in Consumer Goods 553
- 23.12 Spectrometers Marketed Directly to Consumers 555
- 23.13 Emerging Applications for Portable Spectrometers 557
- 23.14 Portable Hyperspectral Imaging 559
- 23.15 Biological Analyzers 560
- 23.16 Algorithms, Databases, and Calibrations 560
- 23.17 Conclusions 561
- Acknowledgements 561
- References 562

**Index 573**

## List of Contributors

***W. Russ Algar***

Department of Chemistry  
University of British Columbia  
Vancouver  
British Columbia  
Canada

***Eva Mariasole Angelin***

Department of Conservation and Restoration and  
LAQV-REQUIMTE  
NOVA School of Science and Technology  
NOVA University Lisbon  
2829-516 Monte da Caparica  
Portugal

***Elena Basso***

Department of Scientific Research  
The Metropolitan Museum of Art  
New York  
NY, USA

***Krzysztof Bernard Bac'***

Institute of Analytical Chemistry and Radiochemistry  
Leopold-Franzens University  
Innrain 80-82  
CCB-Center for Chemistry and Biomedicine  
Innsbruck  
Austria

***Xiaoyun Chen***

Analytical Science  
Core R&D  
Dow Chemical  
Midland  
MI, USA

***Richard A. Crocombe***

Crocombe Spectroscopic Consulting  
Winchester  
MA, USA

***Costanza Cucci***

“Nello Carrara” Institute of Applied Physics - National  
Research Council (IFAC-CNR)  
Via Madonna del Piano 10  
50019 Sesto Fiorentino (Florence)  
Italy

***A. Culka***

Institute of Geochemistry,  
Mineralogy and Mineral Resources  
Charles University  
Faculty of Science  
Prague 2  
Czech Republic

***David DiGregorio***

Hazardous Materials Emergency Response  
Massachusetts Department of Fire Services  
Stow  
MA, USA

***Mary Kate Donais***

Saint Anselm College  
Manchester  
NH, USA

**H.G.M. Edwards**

Centre for Astrobiology and Extremophiles Research  
School of Chemistry and Biosciences  
Faculty of Life Sciences  
University of Bradford  
Bradford  
West Yorkshire  
UK

**Justyna Grabska**

Institute of Analytical Chemistry and Radiochemistry  
Leopold-Franzens University  
Innrain 80-82  
CCB-Center for Chemistry and Biomedicine  
Innsbruck  
Austria

**Michael Hargreaves**

Rigaku Analytical Devices Inc.  
Wilmington  
MA, USA

**Russell S. Harmon**

Department of Marine  
Earth & Atmospheric Sciences  
North Carolina State University  
Raleigh  
NC, USA

**Uwe Hoffmann**

nir-tools  
Essen  
Germany

**Christian Wolfgang Huck**

Institute of Analytical Chemistry and Radiochemistry  
Leopold-Franzens University  
Innrain 80-82  
CCB-Center for Chemistry and Biomedicine  
Innsbruck  
Austria

**J. Jehlička**

Institute of Geochemistry,  
Mineralogy and Mineral Resources  
Charles University  
Faculty of Science  
Prague 2  
Czech Republic

**Monica Joshi**

Department of Chemistry  
West Chester University of Pennsylvania  
West Chester  
PA, USA

**Ravi Kalyanaraman**

Bristol Myers Squibb  
New Brunswick  
NJ, USA

**Brooke W. Kammerath**

Department of Forensic Science  
Henry C. Lee College of Criminal Justice  
and Forensic Sciences  
University of New Haven  
West Haven  
CT, USA

and

Henry C. Lee Institute of Forensic Science  
West Haven  
CT, USA

**Ian Christopher Lau**

CSIRO Minerals Resources  
Australian Resources Research Centre  
Kensington  
WA  
Australia

***Carsten Laukamp***

CSIRO Minerals Resources  
Australian Resources Research Centre  
Kensington  
WA  
Australia

***Pauline E. Leary***

Federal Resources  
Stevensville  
MD, USA

***Lisa M. Lee***

Thermo Fisher Scientific  
Tewksbury  
MA, USA

***Monica LeGras***

CSIRO Minerals Resources  
Australian Resources Research Centre  
Kensington  
WA  
Australia

***Bruno Lemi  re***

BRGM  
Orleans  
France

***Felicity Meyer***

TeakOrigin, Inc.  
Waltham  
MA, USA

***Ellen V. Miseo***

TeakOrigin, Inc.  
Waltham  
MA, USA

***Zhenbin Niu***

Dow Performance Silicones  
Dow Chemical  
Midland  
MI, USA

***William J. Peveler***

School of Chemistry  
University of Glasgow  
Joseph Black Building  
University Avenue  
Glasgow  
UK

***Frank Pfeifer***

Department of Physical Chemistry  
University of Duisburg-Essen  
Essen  
Germany

***Marcello Picollo***

“Nello Carrara” Institute of Applied Physics - National  
Research Council (IFAC-CNR)  
Via Madonna del Piano 10  
50019 Sesto Fiorentino (Florence)  
Italy

***Stanislaw Piorek***

Rigaku Analytical Devices  
Wilmington  
MA, USA

***Federica Pozzi***

Department of Scientific Research  
The Metropolitan Museum of Art  
New York  
NY, USA

***Mark A. Rickard***

Safety & Construction  
DuPont de Nemours, Inc.  
Wilmington  
DE, USA

***John A. Reffner***

John Jay College of Criminal Justice  
New York  
NY, USA

***Adriana Rizzo***

Department of Scientific Research  
The Metropolitan Museum of Art  
New York  
NY, USA

***Christina S. Robb***

The Connecticut Agricultural Experiment Station  
New Haven  
CT, USA

***James Ryan***

TeakOrigin, Inc.  
Waltham  
MA, USA

***Susana França de Sá***

Department of Conservation and Restoration and  
LAQV-REQUIMTE  
NOVA School of Science and Technology  
NOVA University Lisbon  
2829-516 Monte da Caparica  
Portugal

***Alan C. Samuels***

US Army Combat Capabilities Development  
Command  
Chemical Biological Center  
Aberdeen Proving Ground  
MD, USA

***Suzanne K. Schreyer***

Rigaku Analytical Devices  
Wilmington  
MA, USA

***John A. Seelenbinder***

PointIR Consulting LLC  
Watertown  
CT, USA

***Heinz W. Siesler***

Department of Physical Chemistry  
University of Duisburg-Essen  
Essen  
Germany

***Peter Vandenameele***

Gent University  
Gent  
Belgium

***Hui Yan***

School of Biotechnology  
Jiangsu University of Science and Technology  
Zhenjiang  
China

***Lin Zhang***

Thermo Fisher Scientific  
Tewksbury  
MA, USA

## Foreword

When I first learned that Richard Crocombe, Pauline Leary, and Brooke Kammrath were editing a two-volume series of books that cover the development of field-portable analytical technologies and the numerous applications of these technologies, I was excited because I knew that these scientists had the experience, knowledge, and energy to produce a great product, books that I will immediately add to my library.

So, who am I to make such a bold evaluation of these books? My name is John A. Reffner and I am currently a tenured full Professor of Forensic Science at the City University of New York's John Jay College of Criminal Justice. I have also received several distinguished awards including some for developments that enabled portable spectroscopic instruments. After graduating from Akron University in 1956, I joined the "Works Technical Analytical Laboratory" at the B.F. Goodrich Tire and Rubber Company. This experience taught me the valuable lesson that chemistry is essential for a major corporation to be successful, a lesson which was continually reinforced throughout my almost 65 years of professional experiences. I have had the good fortune of working with many prominent scientists and business leaders. I have seen how science and chemistry change the world. I have also seen how consumer demands drive technology and innovation, leading us to where we are today, immersed in essential portable technologies that have changed the world.

A short story that exemplifies my passion for the field of portable instruments is the introduction of the Dura Scope at the Pittsburgh Conference in 1998, and the subsequent development of the TravelIR portable infrared spectrometer. Our SensIR Technologies team, which included the likes of Don Sting, Jim Fitzpatrick, Don Wilks, and Bob Burch, introduced this new micro-ATR (Attenuated Total Reflection) accessory for Fourier transform infrared (FT-IR) spectrometers. While it might not seem that such an accessory could make a system portable, a scientist from a major supplier of chemicals was very excited about the product. In his work, he traveled to paper companies to resolve customer complaints. While he did not need an ATR accessory, what he did need was a small FT-IR, possibly an ATR-based infrared system, that could fit in the overhead storage compartment of a commercial airplane. As a result of these conversations, the TravelIR was born. The TravelIR was the first portable infrared spectrometer delivered to the market, enabling the identification of an infinite number of samples at the sample site.

The novelty of the TravelIR attracted a lot of interest, but portability was low on the list of requirements by a majority of end users. That was, of course, until 11 September 2001. One week after the 9/11 terrorist attacks, letters containing anthrax spores were delivered to members of the news media, and to United States Senators Tom Daschle and Patrick Leahy. A total of five people died from exposure to these spores, and 17 others were infected. These terrorist events had a significant impact on field-portable analytical instruments. There became an immediate need to identify dangerous chemicals, including white powders, quickly and reliably at the sample site. This need catalyzed the portable-spectroscopy market.

Infrared spectrometers like the TravelIR were well suited as a chemical identifier and could meet the analytical needs of field users, but it was clear that simply having a small footprint capable of providing reliable answers to a

trained scientist was not enough. Systems for deployment needed to endure the rough handling and environmental conditions required of a valid field-portable analytical device. In addition, it was necessary for these systems to collect spectral data and translate those data into actionable results in real time by a nonscientist operator with minimal training. SensIR's follow-up to the TravelIR was a product known as the HazMatID. This system was ruggedized to meet aggressive military specification standards including those for ruggedness and total immersion in decontamination solution. The "genie was out of the bottle" and the need for field-portable instruments exploded.

As you read the 44 chapters of these books, you will see the versatility in both the instrumentation and technologies, as well as the tremendous impact these systems have upon our society. Whether considering how portable spectrometers are used in hazmat and military operations to assess safety and defense concerns, by archaeologists and other cultural historians to help understand artwork and ancient civilizations, or the value these systems offer to practitioners of the forensic, pharmaceutical, and geological sciences, the reader will appreciate the challenges to their development, the breadth of their applicability, and the irreplaceable value they afford to the end user.

November 2020

*John A. Reffner*

Professor of Forensic Science  
at the City University of New York's  
John Jay College of Criminal Justice

## Preface for Volume 2

The rapid growth of portable spectroscopy and spectrometry technologies in the last 20 years can be attributed to their diverse applications in numerous scientific fields. The role applications play in instrument development will be discussed in depth in the Introduction chapter of this volume, as well as the reciprocating influence advancements in instrumentation have on creating new applications. While Volume 1 of this book focuses on the technologies of the portable spectrometers themselves, Volume 2 brings together 21 chapters on assorted applications. There are also two chapters at the start that focus on algorithm and spectral library development (by Zhang et al. and Schreyer, respectively), which are essential for successful applications of portable instruments. The editors feel that this fills a considerable void in the literature because much of the content contained herein has never been published, while the rest is spread out in a range of articles and instrument company application notes.

The application chapters are organized both by instrumentation type and also by scientific or technical disciplines. There are chapters devoted to applications of portable ion mobility spectrometry, infrared, Raman (including the surface-enhanced and spatially offset techniques), near-infrared (with a second chapter on spectral transfer from benchtop to handheld spectrometers), X-ray fluorescence, and smartphone spectroscopy. We also have chapters written on discipline-specific applications of portable instrumentation, specifically in the fields of Pharmaceuticals, Forensic Science, Military, HazMat, Clinical, Food Analysis, Field Geology and Astrobiology, Cultural Heritage, and Archaeology. Some disciplines that utilize portable instruments are not included in these specialty chapters because the editors feel that their content is comprehensively covered in other chapters. An example of this is Environmental applications, which are thoroughly represented in chapters devoted to portable instruments (i.e. GC-MS, Raman, and infrared).

From the inception of this book, it has been the intention of the editors to select recognized experts with hands-on experience to compose in-depth, authoritative chapters in their areas of expertise. The editors are grateful to the authors for their contributions, and also to the third-party experts who reviewed chapters to ensure their quality and completeness. The ultimate objective of this volume is to provide readers with a comprehensive collection of applications for portable spectrometers, which will be valuable for both their scientific knowledge and work.

It must be noted that in an edited book of this kind, in which the chapters come from varied authors with assorted backgrounds and fields of study, there will inevitably be heterogeneity in the arrangement and style of

each chapter. The editors hope that this will not detract from the usefulness of this book but instead reflect the diversity that is inherent in the myriad of applications of portable instrumentation.

June 2020

*Richard A. Crocombe*  
Crocombe Spectroscopic Consulting  
Winchester, MA, USA

*Pauline E. Leary*  
Federal Resources  
Stevensville, MD, USA

*Brooke W. Kammrath*  
Department of Forensic Science  
Henry C. Lee College of Criminal Justice and Forensic Sciences  
University of New Haven  
West Haven  
CT, USA

and

Henry C. Lee Institute of Forensic Science  
West Haven  
CT, USA

## Acknowledgements

The editors would like to thank and acknowledge the following scientists and subject matter experts for their willingness to review the chapters within these volumes.

### Volume 1

Katherine Bakeev  
Sheldon Brunk  
Michael Burka  
Cecil Dybowski  
Peter Griffiths  
Michael Kessler  
Richard Lareau  
Christopher Palmer  
Alexander Scheeline  
Ken Schreiber  
Dalton Snyder  
Mazdak Taghioskou

### Volume 2

Jose Almirall  
Paul Bartholomew  
Amy Bauer  
Lucia Burgio  
Craig Gardner  
Richard Jackson  
Lena Kim  
Larry McDermott  
Ellen Miseo  
John A. Reffner  
Luis Rodriguez-Saona  
Shiv Sharma  
Brandye Smith-Goettler

# 1

## The Role of Applications in Portable Spectroscopy

*Richard A. Crocombe<sup>1</sup>, Pauline E. Leary<sup>2</sup> and Brooke W. Kammrath<sup>3,4</sup>*

<sup>1</sup>*Crocombe Spectroscopic Consulting, Winchester, MA, USA*

<sup>2</sup>*Federal Resources, Stevensville, MD, USA*

<sup>3</sup>*Department of Forensic Science, Henry C. Lee College of Criminal Justice and Forensic Sciences, University of New Haven, West Haven, CT, USA*

<sup>4</sup>*Henry C. Lee Institute of Forensic Science, West Haven, CT, USA*

### 1.1 Introduction

As described in Volume 1 of this book, we regard a portable spectrometer as an analytical instrument that generates clear answers for its operator when it is carried to the sample, i.e. a spectrometer to the sample, rather than a sample to the spectrometer. The operators of these instruments are rarely scientists – although that is advantageous for several applications – but instead may be hazardous-material technicians, armed-services personnel, or even scrap-metal dealers. In many instances, level-A personnel protective equipment (PPE) must be worn during the analysis.

Operators rely on the instrument to obtain accurate and actionable information. In some cases, the result might be a sample identification; in others, it may be a pass/fail visual or audible alarm (green light/red light). In order to achieve this, the portable instrument has to process the spectrum or spectra to generate the result, without any intervention by the operator. Therefore, for identification, a combination of spectral libraries or databases is required, in conjunction with a suitable matching algorithm. For quantitation, a validated calibration is required, and again a suitable algorithm must have been used to generate that calibration. Consequently, considerations such as PPE, databases, calibrations, and algorithms are all essential components of the instrument (Figure 1.1).

### 1.2 The Evolution of Applications

The initial investigations and proof of concept of a new application for a portable spectrometer may be carried out using existing laboratory instruments, including determination of the spectral range, signal-to-noise ratio (SNR), and spectral resolution required. In general, though, it is best to develop the final application on the new product itself, because it will have an identical resolution, spectral range, etc., to the commercial product. Development of potential applications for a portable spectrometer typically begins as a response to an unmet market need. For instance, over many years, vendors of portable X-ray fluorescence (XRF) instruments were asked at trade shows whether their products could distinguish grades of stainless steel, especially “H” and “L” grades, differentiated based upon levels of carbon. H grades have between 0.04 and 0.1% carbon, while L grades have less than 0.03% carbon. The ability to distinguish these in the field is important because L grades, while more expensive, provide better corrosion resistance after in-situ welding where annealing is not possible. Handheld XRF is not sensitive to

### A successful portable spectroscopy platform

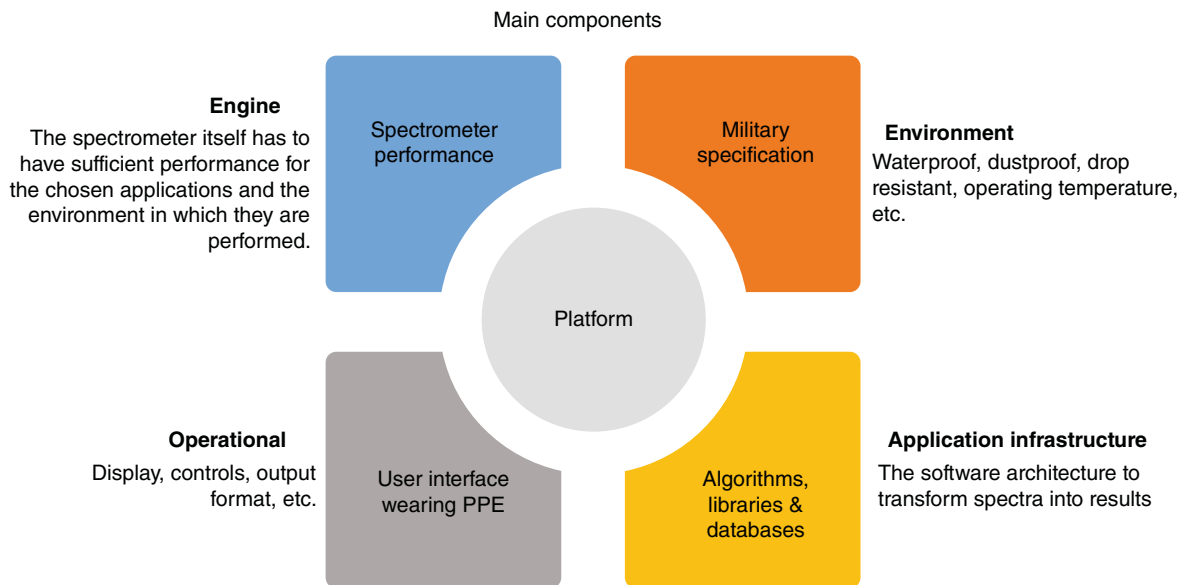


**Figure 1.1** A successful portable spectroscopy platform must extend beyond the spectrometer (engine) performance, and also include consideration of operational requirements, environmental conditions, and application infrastructure. The algorithm, database, and calibration required to process one or more spectra into results are key components.

carbon, so the enquiries spurred investigations and subsequent development of portable optical emission (OES) instruments, and, more recently, portable laser-induced breakdown spectroscopy (LIBS) systems.

In the government, safety, and security sectors, development may be spurred by real-world events that create new requirements. For example, the events of 9/11 and subsequent anthrax attacks in 2001 drove the requirement that response teams must be able to rapidly and reliably detect and identify white powders at the scene. As a result, many agencies issued solicitations looking for solutions that would help them achieve this goal. The development of portable infrared (IR) and Raman spectrometers thrived as a result since those methods worked well for this application.

A good example of an application-driven platform is the MX908 by 908Devices, which possesses different “modes” of operation, such as “drug-hunter,” “CWA-hunter,” and “explosives-hunter.” When operating in these different modes, the system uses the same hardware and software interface, but allows the user to, with the click of a button, select the analysis settings (i.e. search algorithm, sampling time, etc.) that will give them the best result for the type of sample being analyzed. These different configurations of the same base platform allow the end user to optimize the instrument at the time of analysis. The advantage is that the operator can carry one piece of optimized equipment for a number of different types of samples. XRF instruments are similar in that the same instrument can include calibrations for alloys, precious metals, consumer goods, etc. Selecting one of these calibrations sets will optimize the data collection parameters (including the tube voltage and current, x-ray filters and measurement time), and the algorithm used to generate the results.

In many cases, once a “platform” has been established for one application, it becomes apparent that it can be employed elsewhere. This is illustrated in Figure 1.2, where customers make requests because of marketplace exposure and experience. Subsequently, new application innovations take place, most likely involving the development of new or amended databases, algorithms, and calibrations, with the prospective customer possibly supplying or giving access to the samples of interest. This cycle has been most evident for portable XRF and Raman instruments and is illustrated in Figures 1.3 and 1.4.

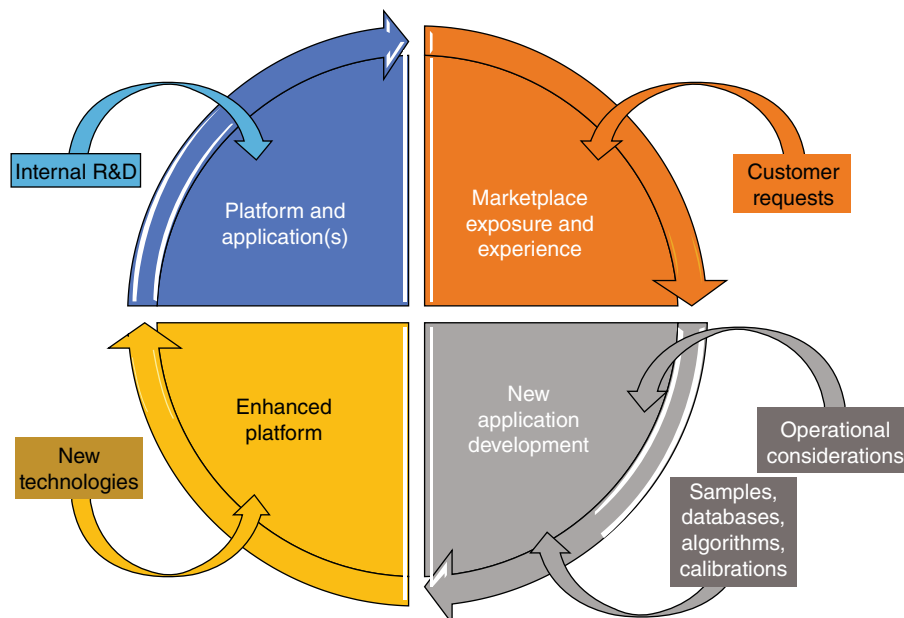


**Figure 1.2** The typical cycle of product and application developments.

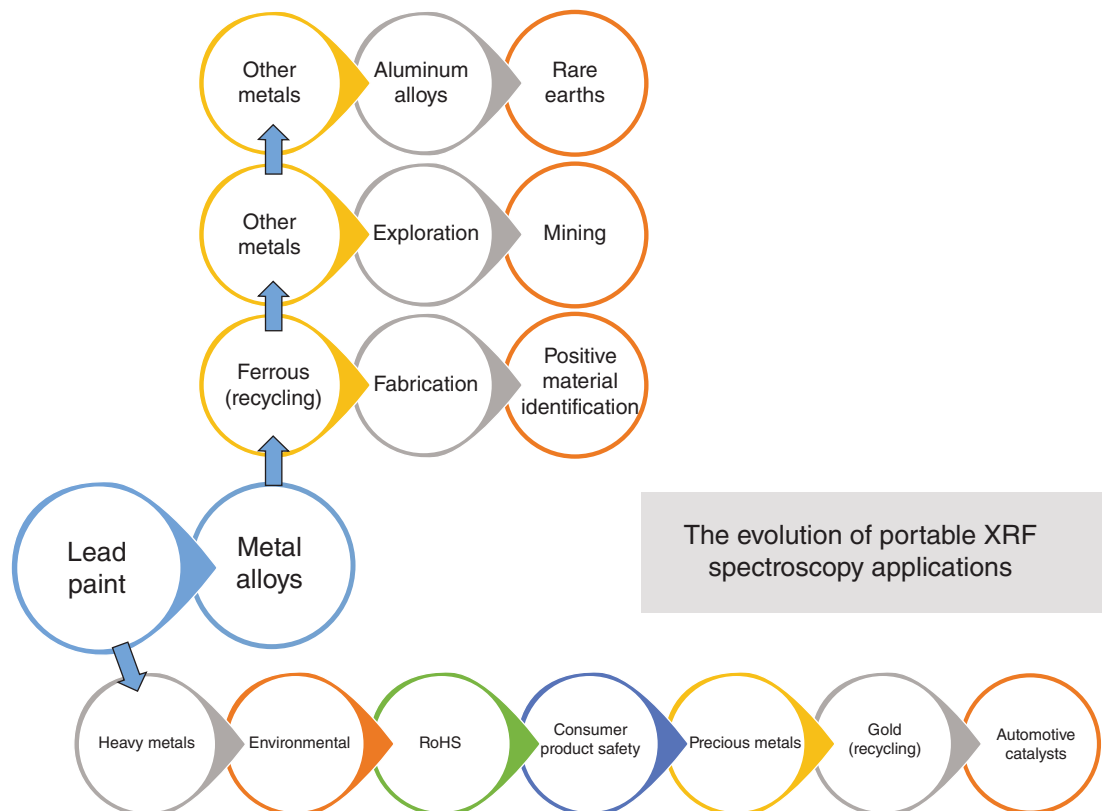


**Figure 1.3** The evolution of portable XRF spectroscopy applications. The first handheld XRF was developed for the detection of lead in paint and then applied to metal alloys. Applications in metal alloys spread to the whole of the metals “food chain.” Heavy metals remain an application area for consumer product safety, precious metal mining and recycling, and several other fields, as shown.

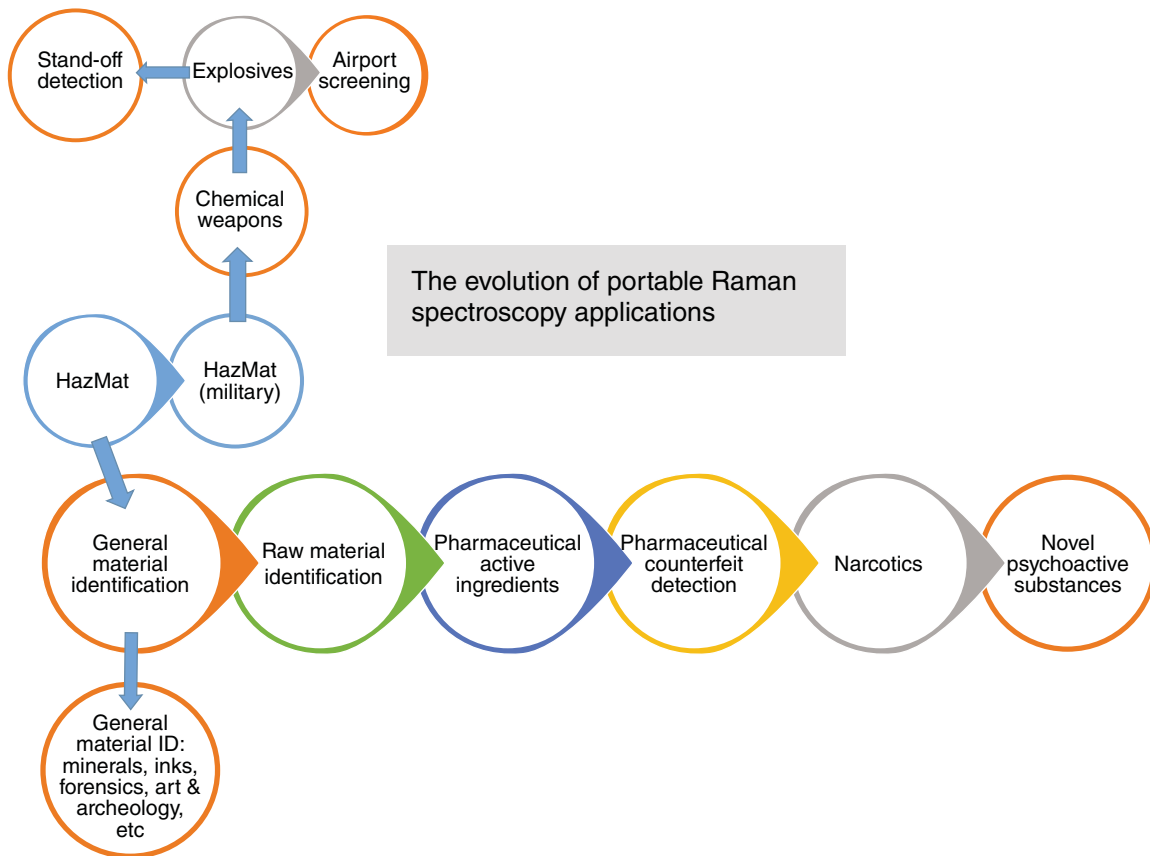


**Figure 1.4** The evolution of portable Raman spectroscopy applications. This starts with hazardous materials and moves into military applications. A separate thread takes the applications into general material identification, leading to chemical and pharmaceutical manufacturing. Street drugs emerged as a major application a few years ago, with the proliferation of synthetic narcotics and psychoactive substances.

Entry into a new market sector, although it may be “adjacent” in marketing terminology, is frequently very challenging. This is not always due to analytical performance requirements, but rather because of necessities regarding operational performance. In some instances, though, a follow-up product for a specific application is successful. This has been most evident for handheld XRF applications, as shown in Figure 1.3. Another example of this is the Thermo TruNarc product. The TruNarc, a handheld Raman spectrometer that is an iteration of the Thermo FirstDefender platform, is intended and optimized specifically for the on-scene narcotics market. Detection algorithms, onboard libraries, and other features of the TruNarc, including chain of custody and the inability of the operator to alter any data, are focused on providing the best results for drug samples in law enforcement settings.

In summary, we can see these cyclic portable spectroscopy development drivers:

1. Applications (user requirements) drive the development of instrumentation.
2. Available instrumentation drives the development of additional applications.

This is a theme common to many of the chapters in Volume 2. Algorithms, calibrations, and libraries are critically important for the success of applications and are discussed in detail in the next two chapters of this volume.

## 1.3 What Defines an Application?

It is usually true that when an application is well defined, a platform will have a greater potential for success. In these situations, awareness of specific challenges enables the manufacturer to address them throughout the product development lifecycle. The end user defines what the portable solution must be able to do in their requirements specifications, which will include specifications for both analytical and operational performance. Then the best solution to meet these requirements is selected for development and deployment. The detection of explosives at airports, which is governed by regulatory bodies such as the Transportation Security Administration in the United States, is an example of a situation where the application is very well defined. Interestingly, in many situations, the ability to develop an instrument is not limited by the analytical requirements of the platform, but rather the operational requirements.

Defining an application is not always easy, but some general items are important to consider. These include the nature of the sample and the sample matrix, e.g. (i) whether the sample is a mixture and if so, is the goal to identify all components, or just specific target chemicals; (ii) whether results must be qualitative or quantitative; (iii) operating space; and (iv) operational and sustainment requirements. In condensed phases, vibrational spectroscopic methods are limited in their application to mixtures to a few components in the percent concentration range. For complex mixtures and trace analysis, a separations method on the front end is required. The pre-eminent technique here is gas chromatography–mass spectrometry (GC–MS), covered in Volume 1. Ion mobility spectrometry (IMS) portable systems do not perform front-end separation but are widely used in airports for detection of trace amounts of explosives, as discussed both in Volume 1 (instrumentation) and Volume 2 (applications).

Hyperspectral instruments are widely used for the classification of terrain and vegetation. These instruments are described in the chapters by Nelson and Gomer, and Pust in Volume 1 and some applications by Laukamp, Legras, and Lau in Volume 2. The final chapter in Volume 2 also touches on these instruments. The algorithms used in hyperspectral data workup are beyond the scope of this book, and the reader is referred to that literature for details [1].

### 1.3.1 Mixtures

Once a technology platform is selected, a key next question is whether the sample is a pure material or a mixture. If the sample is a mixture, questions concerning homogeneity, sample matrix, concentration levels, and required detection limits must be considered. Most samples encountered in the field are, in fact, mixtures. Table 1.1 provides a high-level summary of technology platforms (by spectral range) as well as some important sample and analysis considerations for each. With that in mind, we will briefly highlight some of the issues, which are explored in the subsequent chapters.

Portable XRF and LIBS are both used to analyze metals and minerals. However, they have different characteristics, including the area interrogated and the sensitivity to surface coatings. Handheld XRF instruments usually interrogate a spot size with a diameter of about 8 mm, but this can be reduced to about 3 mm to examine smaller areas, for example, welds, whereas an individual LIBS “shot” may illuminate only 50–100  $\mu\text{m}$  in diameter, and, therefore, rastering of the excitation/collection optics is required for LIBS instruments. XRF is a surface technique, interrogating the first 500  $\mu\text{m}$  of thickness for alloys based on iron, nickel, or copper, and so surface cleaning or preparation is sometimes required. LIBS instruments can perform a “preburn” or “cleaning shots” to ablate the surface. Metallic samples are generally treated as homogeneous mixtures on the scale of the analytical area, but minerals are more heterogeneous, often with clearly visible grain structures. See the discussion below on preparing samples in the field.

When considering GC–MS, the value of this method for mixture samples is the ability to achieve very low limits of detection by separating each component of the sample and identifying each individually. This makes it possible to detect and identify some chemicals, even when the concentration of the analyte in the sample is small.

**Table 1.1** The applicability of handheld spectroscopic techniques to the analysis of mixtures.

Instrument technology	Target analyte	Typical sample phase	Sample type	Detection or identification limits
XRF and LIBS	Elements	Solids	For metals, mostly homogeneous mixtures (alloys) For minerals, typically heterogenous	High ppm to percentages
GC-MS	Molecules	Solid, liquid, gas (vapor)	Separates complex mixtures and enables individual analyte detection and identification	ppb and up; some ppt capabilities reported; ng levels
IMS	Molecules	Solid, gas (vapor)	Typically mixtures	ppb and up; low ng levels
Vibrational (IR and Raman)	Molecules	Solids and liquids	Pure compounds and mixtures; heterogeneous natural products	Single-digit percent

Some configurations also offer preconcentration methods during sample collection, which helps lower detection limits. Although very low limits of detection are possible for IMS, the sample matrix can interfere with the detection capabilities, usually by competing with the target analyte during the ionization process. If the matrix components preferentially ionize, they can suppress or even quench the analyte signal. However, in applications where IMS detectors have gained widespread acceptance, the target analytes tend to preferentially ionize, compared with commonly encountered matrix interferents.

In the near-infrared (NIR) and mid-IR trace detection in condensed phases would depend upon detecting small absorbances within a large and varying background. Therefore, in condensed phases, they are not trace techniques, as the SNR can be limited, and the spectra of the other components, or the matrix, are complex and overlapping. Because optical spectroscopy techniques generate a single ensemble spectrum from the sample with limited SNR, the detection limits tend to be in the three percent range at best, without enrichment or enhancement (such as surface-enhanced IR spectroscopy, SEIRS). A similar logic applies to Raman spectroscopy, although surface-enhanced Raman spectroscopy (SERS) is useful to lower detection limits, compared with bulk Raman analysis, when performing *qualitative* analysis. The enhancement is chemical dependent; for some applications such as for the identification of heroin, SERS improves the heroin signal while also reducing the fluorescence signal, which improves detection capabilities (see the chapter by Hargreaves in Volume 2).

### 1.3.2 Qualitative and Quantitative Analysis

Key to the success of a portable scientific instrument is the processing of spectra to give actionable results to non-scientists. This is slightly different for qualitative versus quantitative results. Qualitative analysis involves a spectral database or “library,” along with algorithms that give confident results, while quantitative methods require a validated calibration, with concentration data in the calibration samples obtained from a reference chemical method. The following discussion applies mainly to vibrational spectroscopy, but the principles can be applied to the other spectroscopies described in these volumes.

#### 1.3.2.1 Qualitative Analysis

In portable qualitative analysis, the goal is to identify an unknown. For a pure material (or which is homogeneous and can be identified via a product name or type, for instance, branded soft drinks), the usual procedure is to obtain the spectrum (frequently mid-IR or Raman) and compare it with spectra in a database (i.e. the spectral library).

There are two immediate questions: [a] what spectral library should be searched, and [b] what search algorithm should be used? The library should encompass all of the materials that might be encountered in the user scenario and not just the target chemicals. An example of this is when a suspected illicit drug is analyzed, the spectral library should not include just narcotics. If the library has limited content, then the “closest match” will always be a narcotic, even if it is an innocuous material, which would be a highly misleading result.

Consequently, a narcotics library should, at least, include a variety of non-narcotic “white powders,” for instance, pharmaceutical excipients such as lactose and mannitol, cutting agents commonly found in street-drug samples, flour, baking soda, infant formula, sugar, talcum powder, etc. Historically, vendors worked to expand the number of library entries; however, it is becoming more common to supply focused libraries for different applications (see the chapter by Schreyer in Volume 2). When appropriate libraries used for searching are coupled with search algorithms optimized for specific applications, i.e. sample types, satisfactory results are likely to be achieved at the sample site by non-scientists, with no operator intervention required.

When considering what search algorithm should be used, the choice can be critical. The most reliable qualitative or matching algorithms employ statistical-based or probabilistic approaches [2, 3]. They account for every feature in the spectrum, model noise, account for mixtures [4], and in the case of Raman spectra, also model fluorescence. The efficacy of these algorithms can be evaluated by examining the false-positive and false-negative rates, and using receiver operator characteristic (ROC) curves to model and visualize that data, as is done in clinical trials for diagnostic tests [5–7].

One of us has previously discussed [8] problems with search algorithms like Euclidean Distance (or a close relative, correlation) [9, 10]. These algorithms essentially square the spectrum, and emphasize broad, large area features, and de-emphasize narrower bands. But it may be the narrow bands that indicate some specific functional groups well. In addition, the Euclidean Distance algorithm does not perform well for mixtures and does not account for every feature in the spectrum. When applied to Raman spectra, any broad fluorescence background will be emphasized at the expense of the sharper Raman bands. Finally, these simple algorithms will always provide the *closest match*, whether or not it is a *correct match*. Using the calculated hit quality to determine a reliability metric may be useful for mitigating this problem, but it is not infallible, especially considering that when proprietary algorithms are used, understanding how hit values are calculated or even what they mean may not be possible. As an example, the SensIR TravelIR, which entered the market in 2001 and was the first portable Fourier transform IR (FT-IR) spectrometer, did not offer mixture analysis algorithms but used correlation-coefficient spectral processing. While this approach worked well for pure materials, the quality of “hits,” i.e. identifications, was significantly reduced for mixtures and required manual spectral interpretation from field operators, which was often difficult. Users were trained to look for a hit quality of 0.95 (1.0 being a perfect match) in order to have a high level of confidence in the result. Achieving such a high-quality match was not usually feasible for mixture samples, even when components were accurately identified by the system. The Ahura First Defender, which entered the market in 2005, and was the first portable Raman spectrometer specifically designed for hazardous-materials work, employed a mixture algorithm that claimed to identify up to five components in a mixture sample. Today, portable spectrometers frequently couple customized, focused libraries with optimized proprietary library-search algorithms for specific applications (see the chapter by Zhang, Lee, and Schreyer in Volume 2).

### 1.3.2.2 Quantitative Analysis

Quantitative analysis, by definition, is a technique for analyzing the composition of mixtures, and the following discussion applies mostly to portable NIR instruments. For quantitative models, analysis of calibration samples by standard (“reference”) methods is required: NIR is a secondary technique. It relies on the primary analysis of the samples using an established method, such as the Kjeldahl method for organic nitrogen, and combining that data in a chemometric method with the spectra of those samples. In addition, validation samples, similarly analyzed, confirm that the model works properly and is not using “accidental” correlations [11]. This procedure is illustrated in Figure 1.5. For natural products, because they vary significantly, and because NIR spectra are not very specific,

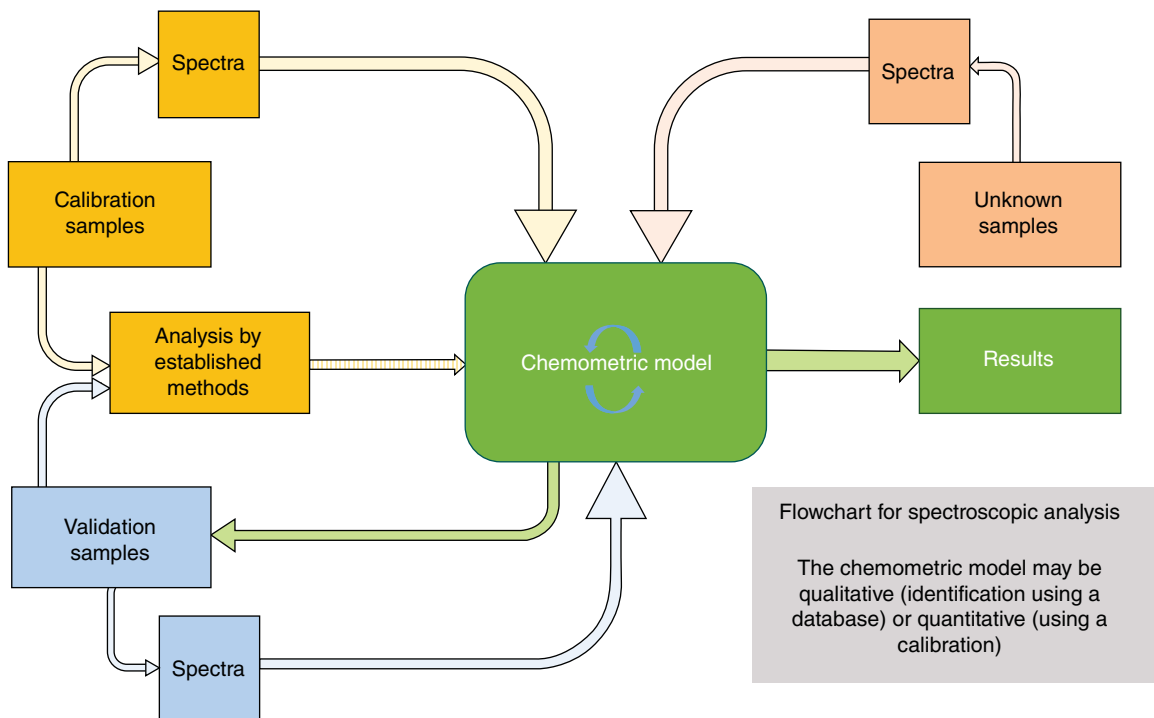


**Figure 1.5** A flowchart for the development of a spectroscopic analysis application. This especially applies to the vibrational spectroscopic analysis of mixtures.

a large number of calibration samples are required. In the case of the long-established grain analysis, this can be many thousands of calibration samples, collected over time, and updated yearly. Recommendations have been published outlining the items that should be reported in NIR calibration projects [12].

### 1.3.3 Operating Space

Just as in qualitative analysis, in quantitative analysis, an appropriate library should be used, its contents understood, and the valid operating space of the calibration appreciated. In a well-designed analysis, the initial spectrum will be run through a classifier, usually employing principal components analysis and a cluster-analysis algorithm. This will determine if the input spectrum is similar to those used for the calibration, and if it is not, the instrument should respond, “This is probably not what you said it was, do you want to proceed with predictions?” For example, using a combination of the visible and NIR regions, it is possible to determine the ripeness of a tomato spectroscopically. But what happens when the spectrum of a red rubber ball or green soap is input? As noted above, the software should flag the spectra as not being similar to the calibration set. However, a poorly designed calibration model, derived only from the visible region spectra, would likely indicate that the red rubber ball is a ripe tomato, and the green soap is an unripe one! This is because for devices operating in the visible region of the spectrum (approximately 400–700 nm), the main chemical constituents of food and produce – water, carbohydrates, proteins, fats – are all essentially colorless, i.e., they have no significant absorbances. Therefore, any matching for produce is done purely based on color. Silicon sensors are sensitive to approximately 1050 nm, and in the 700–1050 nm region, the very weak fourth overtone bands from C–H, N–H, and O–H bands of the colorless components can be detected, but the specific information is very limited. This may be a special concern with devices employing this region, which are marketed directly to consumers, when

**Table 1.2** The names of commercial paints identified by a color-matching spectrometer when analyzing various produce items.

Produce	Paint name 1	Paint name 2
Red apple	Red delicious	Apple-a-day
Green apple	Jalapeno pepper	Olive tree
Red tomato	Fire roasted	Old redwood
Grapefruit	Va-Va-Zoom	Curry sauce
Carrot	Brandywine	Clay pot
Parsnip	Burlap	Cool camel
Celery	Leafy Romaine	Sycamore tree

These names bear no relation to the chemical composition of the analytes because the color-matching spectrometer was used for an invalid application.

applying the spectrometer outside of the appropriate operating space, or when using crowd-sourced data. The potential caveats are explored in more detail in the final chapter of this Volume.

As an artificial example, we can look at using a commercial color-matching spectrometer outside of its operating space. A number of pieces of produce were scanned, and the names of the matching paint colors were recorded. Again, the paint colors identified were the best matches to the colors of the product measured. However, if taken literally, the names of the paint colors would be highly misleading for a consumer. Some of the “results” are shown in Table 1.2. The authors want to emphasize that this example is in no way critical of the performance of these spectrometers. These systems work very well for their intended application, i.e. generating CIE and RGB values and matching to commercial paints and standard colors (e.g. Pantone®), but it is intended to illustrate the perils of using a portable spectrometer outside its intended operating space (Figure 1.6).

### 1.3.4 Operational and Sustainment Challenges

There are two specific matters that must also be addressed regarding the implementation of portable spectrometers into the workflow. First, a special concern in some organizations, for instance, the military and airport security, is personnel turnover, leading to loss of knowledge and experience with these portable spectrometers. Turnover requires that new personnel have to be continually trained, which can be time-consuming for a complex instrument like a GC-MS. Second is understanding and implementing the requirements for instrument maintenance. The combination of these issues can lead to an instrument type, or platform, not being sustained. An example of this in recent years was the use of so-called “puffer” instruments in airport security, which worked well but were a challenge to service, leading to their withdrawal. In the military, a deployment team may have a regional logistics support system, which can help when there is turnover, leading to more frequent and effective usage of the portable instrument.

Operational and sustainment challenges are important considerations when determining the feasibility of an application for a portable spectrometer. From an operational perspective, we have previously described the need of some operators to perform analysis in high levels of PPE. For this reason, sampling procedures should be minimal, and the spectrometer’s interface must be easy to use. As an example of a system with an easy-to-use interface, Figure 1.7 shows the Smiths Detection HazMatID Elite portable FT-IR. The buttons used to operate the system are large, which makes them easy to select, and have a chemically resistant covering. In addition, they are backlit so that they are more easily seen in dark environments.

Another important operational consideration is the availability of live technical support to non-scientific operators in real time, frequently referred to as “Reachback.” In the military, this type of support is frequently offered by

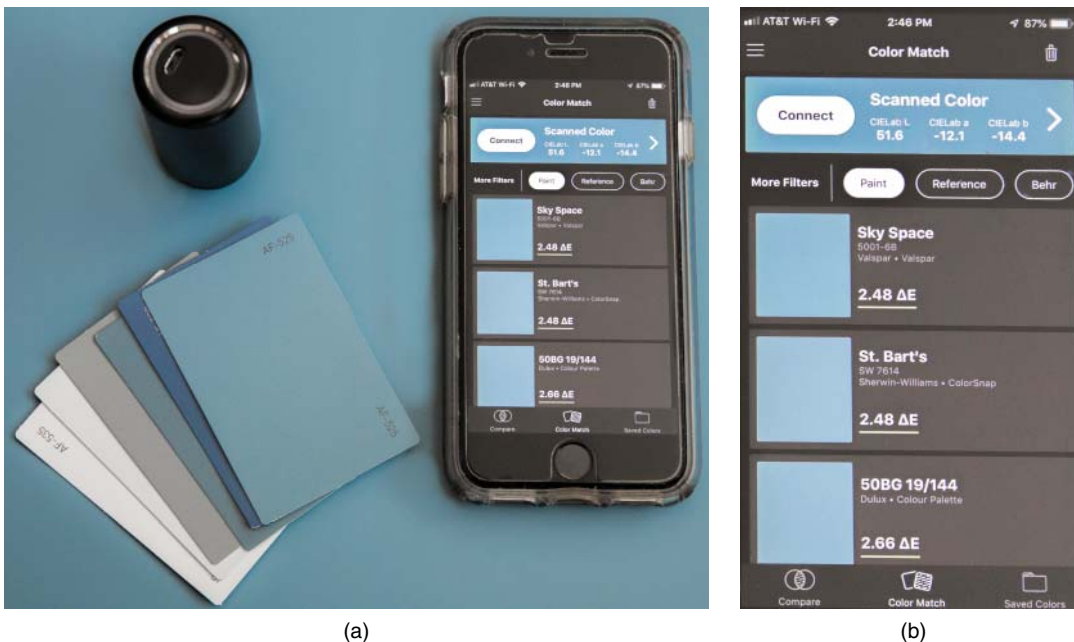


**Figure 1.6** Top left: A small, low-cost color-matching spectrometer, marketed directly to the public. Right: It is controlled by a smartphone app and can display paint matches. This is an example of a single-purpose device with an appropriate built-in algorithm and library. It does not claim to be a general-purpose analyzer. *Source:* Picture courtesy Eric Crocombe.



**Figure 1.7** Smiths Detection HazmatID Elite portable FT-IR, which uses large buttons for easy selection when encumbered by high levels of PPE. These buttons also are backlit for easy visualization when analysis is performed in dark environments. *Source:* Images used with permission. © Smiths Detection.

the organization's internal teams to their operators, but as hazmat and other civilian response teams such as those in the fire service began to routinely deploy portable spectrometers, instrument vendors began to offer live technical support 24/7/365 to help these responders interpret or confirm results at the scene. An operator emails the spectral result from the scene to the Reachback scientist, and the Reachback scientist interprets the spectral data in real time, and communicates his or her findings verbally and/or in writing to the end user. Today, these Reachback programs are an important consideration when purchasing a portable spectrometer because they affirm that reliable results can be generated at the scene. Reachback services are usually offered as options in service and warranty packages. Therefore, Reachback requires that the instrument be able to transmit the data and receive the feedback, preferably from within the "hot zone."

Sustainment challenges are also important considerations when deploying portable spectrometers. Fleet management, including the ability to perform regular firmware and software updates, especially when large numbers of systems are deployed across the globe, must be possible from a logistical perspective. This is especially important for instruments in a regulated industry (e.g. pharmaceutical manufacturing) so that quality supervisors are certain that the appropriate libraries and algorithms are used. It is also important to make sure that when a capability offered by a portable spectrometer is required for a military unit or command, instrument downtime is minimal and/or fully functioning backup systems are available. Also, considerations such as training required, availability of consumables and accessories, calibration requirements, and routine maintenance are all critical considerations. Some instruments, such as point-and-shoot Raman systems, attenuated total reflection (ATR)-based FT-IR spectrometers, and XRF instruments, are relatively easy to sustain. They have minimal requirements for routine maintenance, frequently are deployed with a calibration sample that does not expire, and have no significant accessories or consumables required for operation. On the other hand, portable GC-MS systems are more challenging to sustain in the field. Accessories such as required carrier gas and vacuum pumps make deployment more challenging, calibration samples are volatile and have expiration dates, and routine maintenance such as regular weekly or monthly startups may be required to help keep the system functional. Portable GC-MS offers unique capabilities that for some users are critical, but these systems are not as widely deployed as portable FT-IR, Raman, and XRF systems, and the reason is likely due to these operational and sustainment challenges.

## 1.4 The Return on Investment for an Application

Especially in a production environment, the return on investment (ROI) for an instrument purchase is a key consideration – production personnel will not purchase an instrument otherwise. For a pharmaceutical raw material identification (RMID) application, performed by handheld Raman or NIR, the benefits include ease of operation (use on the loading dock, in warehouse or inspection area with "point-and-shoot" sample interrogation through plastic liners), fast analysis (typically less than five seconds), accurate and reliable results (based on suppliers' barcode, built-in library, and algorithm), no waste, sample preparation or opportunity for contamination, and transferable methods. With the current RMID procedure, it is straightforward to calculate a hypothetical ROI, and this is laid out in Table 1.3. The assumptions here are relatively simple, and this ROI is based only on operator labor and time savings. The detailed assumptions include rapid FT-IR ATR laboratory methods, a laboratory technician's yearly salary of \$75 000 plus benefits cost, and analysis of only 1000 samples per month. Further benefits that could improve the ROI include, but are not limited to, increasing inventory turnover, improvements in operational areas such as warehouse space due to the reduction in inventory volumes, and reduced routine laboratory workload, which could enable scientists to focus on problem-solving instead of quality assurance/quality control (QA/QC). Comparison workflows for laboratory-based and portable instrument approaches are shown in Figure 1.8.

**Table 1.3** Comparing the cost of laboratory-based versus handheld raw material identification procedures.

Comparison of laboratory and handheld raw material identification procedure			
Conventional laboratory-based analysis		Handheld Raman or near-infrared spectroscopy approach	
Typical time to transport sample to central laboratory	45 min	Typical time to transport samples	4.75 min
Laboratory analysis time	2–30 min	Analysis time	0.25 min
Total	47–75 min	Total	5 min
Cost	\$33–\$53 per sample	Cost	\$3.55 per sample
Monthly cost on 1000 samples	\$33 000–\$53 000	Monthly cost on 1000 samples	\$3550
		Analyzer cost	\$20 000
		Return on investment	13–21 days

The return on investment for a handheld solution is quite evident.

## 1.5 Preparing Samples in the Field

Although much of the emphasis on portable spectroscopy is on “point-and-shoot” capabilities, this is not always possible. There are some areas where limited sample preparation is done in the field, and where sample introduction to the instrument is important. A classic example is water testing in the ultraviolet (UV)–visible region, where the addition of specific reagents for an analyte, and the use of cuvettes, is a long-established practice, and colorimetric tests have long been used for screening unknown drugs in the field [13]. A recent variant of this was introduced by DetectaChem [14], for the detection of narcotics and explosives, employing a consumable card containing a swipe patch and capsules of reagents; this has simplified the use of color tests at the scene (Figure 1.9). A number of different color-test cards are available based upon the target analyte(s), e.g. different cards for different drugs of abuse are available. The encapsulation of the reagent within the consumable card makes it easy to deploy and operate in the field. No weighing, measuring, or external accessories are required to create the color change. Either a dedicated “reader” instrument or a smartphone evaluates the resulting color and gives a simple positive/negative result. The use of the reader instrument or smartphone simplifies operation removing some of the subjectivity of the measurement since no “interpretation” is required by the operator.

It is important to highlight that recently, within the forensic science community, challenges to the use of colorimetric tests in the field have been described when applied in criminal cases [15–18]. This is specifically due to their misuse by attorneys and police investigators who encourage individuals to plead guilty to drug charges based on the results of these presumptive (not confirmatory) tests. As a result, several guilty pleas have been reversed due to subsequent laboratory testing where no illicit drug substance was detected during confirmatory analysis. Unfortunately, the frequency of this occurring is unknown because it is uncommon for forensic laboratories to perform testing on evidence items in cases that have already been adjudicated. These authors highlighted that from an analytical perspective, when applied properly and used to generate presumptive results, these color tests are valuable as part of an analytical workflow but recognize the additional legal issues surrounding the use of these color tests when deployed in criminal cases.

Other sample preparation and handling methods have been described in Volume 1, but a few will be highlighted here. Many techniques will probe the surface of a sample, and knowledge of the depth of penetration can be critical in understanding the result. Understanding whether this surface analysis represents the bulk or just a skin or surface layer is critical. An obvious example is in the NIR analysis of natural products, most of which will

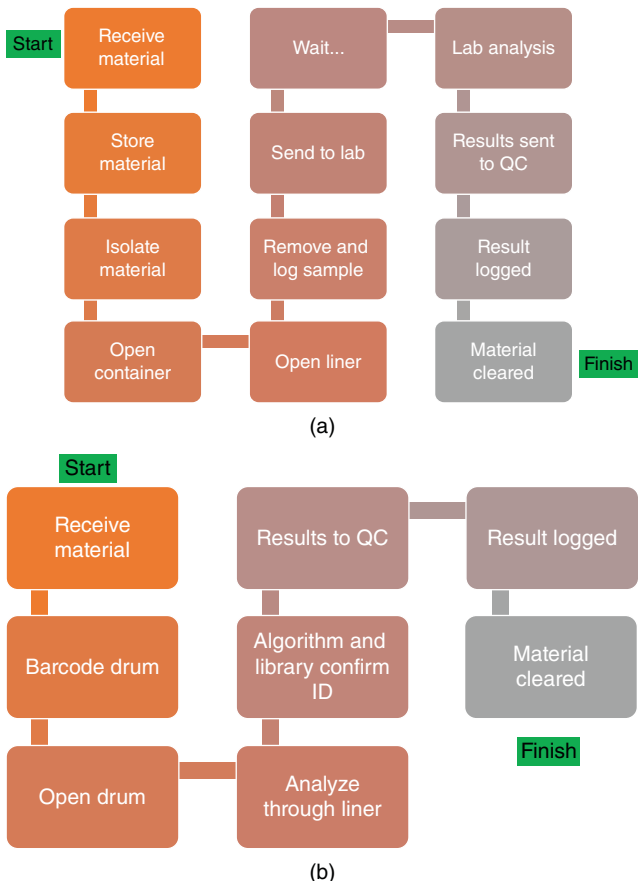


**Figure 1.8** Comparing the workflows for laboratory-based (a) and handheld (b) raw material identification processes. The handheld approach is clearly simpler and faster.

have a skin or husk, with a different chemical composition from the interior. Less obvious is a handheld XRF or LIBS examination of metallic samples. For alloys based on iron, copper, and nickel, XRF is a surface technique, interrogating approximately the top 500 µm of the sample. This implies that the operator may have to clean the sample to eliminate corrosion, paint, oils, etc. and should be alert to the possibility that the sample may be plated. Portable LIBS instruments have the capability of “drilling down” to some extent, but the same considerations apply. In field geology, rocks may be coated with regolith, essentially rock dust. Here, a quick field sample preparation tool may help quickly grind a sample and then compress it, so that the sample is more representative of the bulk.

For FT-IR spectroscopy, it is evident that one of the primary reasons for its success in portable form is due to the ability to perform ATR sampling. In order to collect a good-quality IR spectrum when using ATR, the primary requirements (assuming the sample is IR active) are that the sample must have a refractive index ( $n$ ) lower than, and make intimate contact with, the internal reflection element, which is usually diamond ( $n = 2.42$ ). If these two requirements can be met, the ability to reproducibly collect good-quality spectra is easily achieved. This is an important concept from a deployment perspective because sampling many technology platforms can significantly bias results. With portable FT-IR using ATR sampling, it is reasonable to expect that if a RMID method is developed using an instrument at a pharmaceutical manufacturing plant in New Jersey, transfer of this method to instruments of equivalent models in locations in other parts of the world, will be straightforward.



**Figure 1.9** DetectaChem's consumable card. The swipe patch is at the top center and the reagents on the rear of the card. This approach removes the need for an operator to handle reagents, and the use of a “reader” instrument removes subjectivity in the analysis of color. *Source:* From DetectaChem.

With regard to Raman spectroscopy, it does seem that most end users like this method best primarily due to its point-and-shoot sampling through containers such as glass vials, plastic drum liners, and baggies. This is of considerable importance for the on-scene analysis of illicit drugs in light of the rise of fentanyl, carfentanil, and other analogs, which pose considerable danger to first responders. There is one important consideration, though, which is that samples can burn, or even detonate in the case of an explosive, when exposed to the laser used to create the Raman scatter. In these situations, it is important to analyze a small portion of the sample using either a delay or a robot-mounted configuration with remote control of the instrument; classic samples that may detonate include “black” and “smokeless” powders, as well as some homemade explosives.

In addition, the SERS effect is being capitalized on for the analysis of street drugs by portable Raman spectroscopy (see the chapter in Volume 2 by Hargreaves). SERS has specific benefits for the identification of heroin, which is fluorescent under 785-nm excitation; the use of a SERS substrate not only quenches the fluorescence but also enhances the heroin Raman signal. A number of SERS sample devices have been developed by different instrument manufacturers, with emphasis on ease of use in the field and longevity of the substrate.

The requirement to prepare samples in the field for GC–MS analysis can be challenging. The concept of “dilute and shoot” is well-recognized and accepted by laboratory GC–MS analysts, but the need to dissolve, condense, derivatize, or somehow prepare a sample for analysis can be challenging for many portable GC–MS applications. From an operational perspective, GC–MS systems are commonly deployed to people working in hostile or dangerous environments, and analysis needs to be performed as quickly as possible, with as few steps as possible. In these situations, if there is not enough time, getting an analytical result will be aborted. In addition, it must be acknowledged that in most applications, these systems are not being used by scientists. The only training the operator may have is that provided at the time the equipment was received, and further, the operator may use the system very infrequently; the more complex the sample preparation requirements, the less chance for a successful result. It is important to recognize that GC–MS is a very valuable technique that can be applied to many different types of samples, but when applied in the field by non-scientific operators, it has the best chance for success when used for specific target chemicals using the most simplified methods for sample preparation and introduction.

From a sample preparation perspective, one of the easiest portable systems to deploy is an IMS. These systems operate in vapor or particle modes of operation. Vapor sampling is used if the target analyte has a reasonable vapor

pressure such that ppb (parts per billion) levels of material are introduced to the system during the sampling cycle. In this situation, the air containing the target analyte is pulled into the system under ambient conditions, so no carrier gas or significant pumping is required. If the target analyte does not have a reasonable vapor pressure, particle sampling is used, wherein the trace residues are swiped and then thermally desorbed from the swipe during the analysis. As mentioned previously, sample preparation is quite easy for IMS. Also, limits of detection can be quite low, down to low ppbs or single-digit nanograms, but the use of this method is limited to a relatively small number of target analytes such as select drugs, explosives, chemical warfare agents, and toxic industrial chemicals (see chapter by DeBono and Leary in Volume 1 and Leary and Joshi in Volume 2).

## 1.6 The Commercial Success of a Portable Spectrometer

### 1.6.1 Marketing

Marketing is not the focus of this book, but it is worth noting a few items pertaining to the commercial success of a portable spectrometer. Three main factors are required for that success (Figure 1.10): the platform itself, the application, and, finally, the channel to market. It is just not true that if you build it, they will come! An instrument company needs to understand that channel and employ personnel (domain experts) who understand it and can communicate in that market sector, using the local terminology and speaking the right language. For instance, the scrap-metal dealer will refer to his portable XRF instrument as a “gun,” which would be confusing to somebody coming from the military sector. Similarly, the ROI for portable XRF in scrap-metal dealing is so clear and immediate that this is almost a cash business. Again, this is a far cry from government and military procurement, where the timescale can be years.

It is also important to understand the whole environment in which a portable instrument will be used. Pharmaceutical manufacturing is highly regulated, and because of its international nature, the US Food and Drug Administration (FDA) and its regulations (e.g. 21 CFR (Code of Federal Regulations) Part 11 required for sale into the US market) have a worldwide influence. In addition, in that environment, documentation like

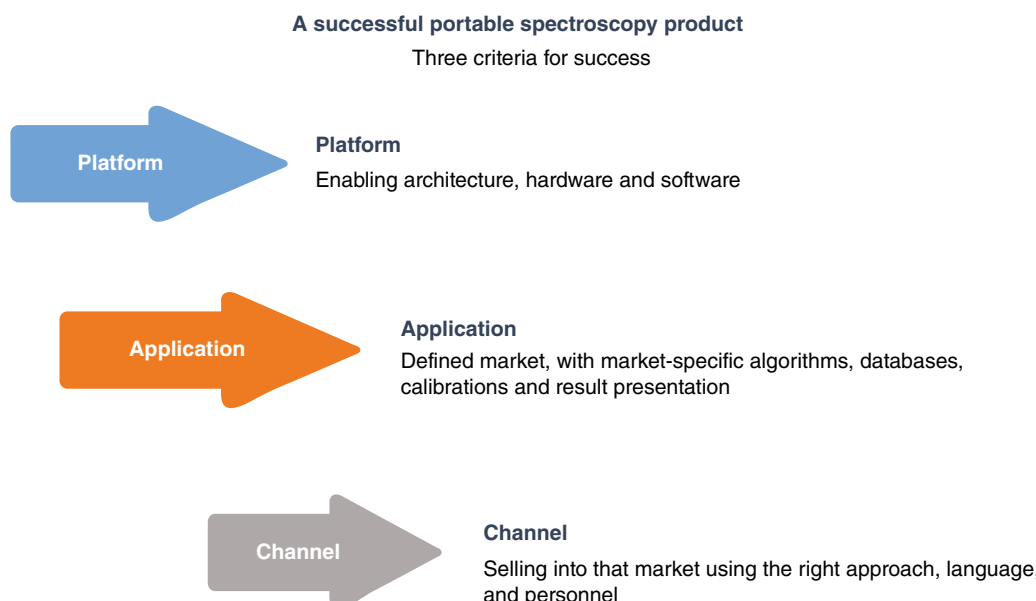


**Figure 1.10** For a portable spectrometer product to be successful, a developer or manufacturer has to pay attention to three distinct areas: the platform itself, its applications, and the channel to market.

DQ/IQ/OQ/PQ (design, instrument, operational, and performance qualification), as well as draft SOPs (standard operating procedures), will be required. A lack of knowledge of these requirements will instantly disqualify a vendor. In an area like illegal drugs, a company may be selling to an individual police force, but the deployment of the instrument has implications for others, including the magistrate, local prosecutor, or district attorney (DA), who would be responsible for presenting the results in court. In addition, a knowledge of funding cycles, procurement channels, and available grants is important.

## 1.7 Conclusions and Future Applications

One of the themes of this chapter has been how applications drive the development of instrumentation, and in turn, instrumentation drives the development of applications. Two key variants have emerged in recent years, described in the final chapter of this volume: the potential of very low cost of instruments operating using silicon-based detectors and sensors, and the influence of the consumer market and enhancement of consumer goods. These change the picture we have described of portable instrument and applications development, and a version incorporating these new drivers is shown in Figure 1.11. The possible application areas for spectroscopic devices for consumers are explored in the final chapter of this volume that includes food, personal fitness, personal care, identification and verification of household items, etc. Each of them would need its validated calibration and spectral database.

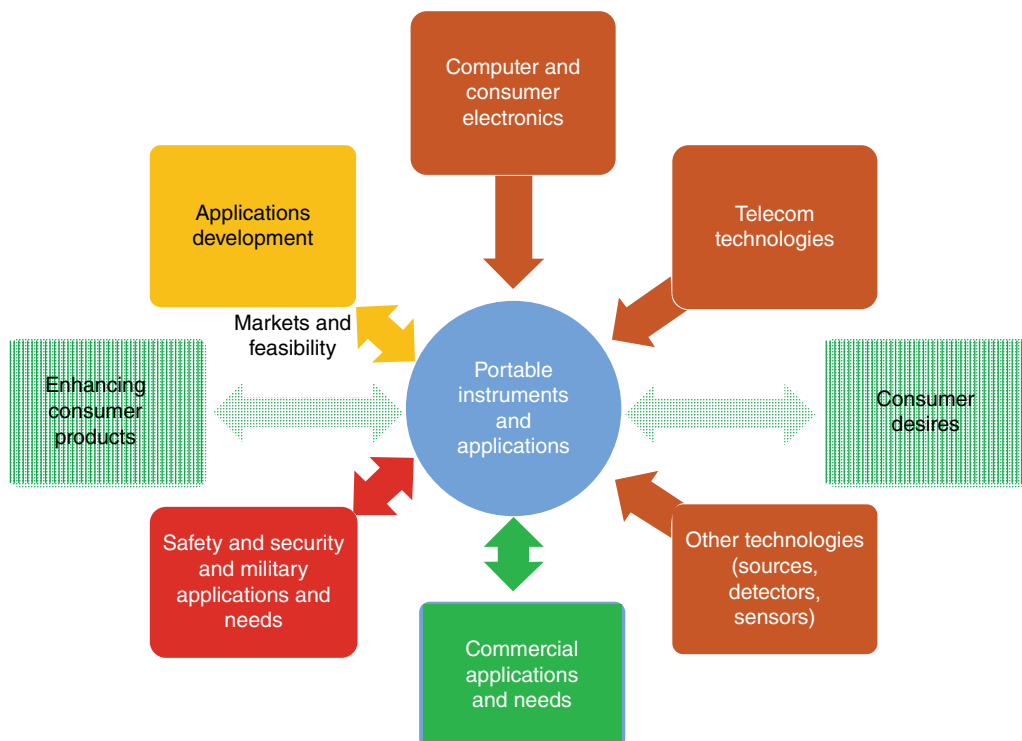


**Figure 1.11** As component costs are reduced, consumer-based drivers influence the development of portable spectroscopic instruments and their applications.

## References

- 1 Schowengerdt, R.A. (1997). *Remote Sensing: Models and Methods for Image Processing*, 2e. San Diego: Academic Press.
- 2 Brown, C.D. and Vander Rhodes, G.H. (2007) Spectrum searching method that uses non-chemical qualities of the measurement. US Patent 7,254,501 B1.
- 3 Green, R.L., Hargreaves, M.D., and Gardner, C.M. (2013). Performance characterization of a combined material identification and screening algorithm. *Proc. SPIE* 8726: 87260F.
- 4 Yaghoobi, M., Wu, D., Clewes, R.J., and Davies, M.E. (2016). Fast sparse Raman spectral unmixing for chemical fingerprinting and quantification. *Proc. SPIE* 9995: 99950E.
- 5 Swets, J.A. (1988). Measuring the accuracy of diagnostic systems. *Science* 240 (4857): 1285–1293.
- 6 Brown, C.D. and Davis, H.T. (2006). Receiver operating characteristics curves and related decision measures: a tutorial. *Chemom. Intel. Lab. Syst.* 80: 24–38.
- 7 Brown, C.D. and Green, R.L. (2006). Performance characterization of material identification systems. *Proc. SPIE* 6378: 637809.
- 8 Crocombe, R.A. (2018). Portable spectroscopy. *Appl. Spectrosc.* 72 (12): 1701–1751.
- 9 Duckworth, J. (1998). Spectroscopic qualitative analysis. In: *Applied Spectroscopy: A Compact Reference for Practitioners* (eds. J. Workman Jr. and A. Springsteen). Chestnut Hill, MA: Academic Press Chapter 5, 166–193.
- 10 Lowry, S.R. (2002). Automated spectral searching in infrared, Raman, and near-infrared spectroscopy. In: *Handbook of Vibrational Spectroscopy* (eds. J.M. Chalmers and P.R. Griffiths), 1948–1961. Chichester, UK: Wiley.
- 11 Burns, D.A. and Ciurczak, E.W. (2007). *Handbook of Near-Infrared Analysis*, 3e. Boca Raton, FL: CRC Press.
- 12 Williams, P., Dardenne, P., and Flinn, P. (2017). Tutorial: Items to be included in a report on a near infrared spectroscopy project. *J. Near Infrared Spectrosc.* 25 (2): 85–90.
- 13 Hafer, K.E. and Brettell, T.A. (2018). Presumptive color tests of seized drugs. In: *Encyclopedia of Analytical Chemistry* (ed. R.A. Meyers). Wiley.
- 14 DetectaChem. <https://www.detectachem.com> (accessed 23 June 2020).
- 15 Gabrielson, R. and Sanders, T. ProPublica, “BUSTED”. <https://www.propublica.org/article/common-roadside-drug-test-routinely-produces-false-positives> (accessed 3 July 2020). (Co-published with The New York Times Magazine.)
- 16 Kelly, J. Marijuana policy project. “False Positives Equal False Justice”. <https://www.mpp.org/issues/criminal-justice/false-positives> (accessed 3 July 2020).
- 17 Gabrielson, R. Since we reported on flawed roadside drug tests, five more convictions have been overturned. <https://www.propublica.org/article/since-we-reported-on-flawed-roadside-drug-tests-five-more-convictions-have-been-overturned> (accessed 3 July 2020).
- 18 Lieblein, D., McMahon, M.E., Leary, P.E. et al. (2018). A comparison of portable infrared spectrometers, portable Raman spectrometers, and color-based field tests for the on-scene analysis of cocaine. *Spectroscopy* 33 (12): 2–8.

## 2

### Identification and Confirmation Algorithms for Handheld Analyzers

*Lin Zhang<sup>1</sup>, Lisa M. Lee<sup>1</sup> and Suzanne K. Schreyer<sup>2</sup>*

<sup>1</sup>*Thermo Fisher Scientific, Tewksbury, MA, USA*

<sup>2</sup>*Rigaku Analytical Devices, Wilmington, MA, USA*

### Glossary

- y** vector of unknown spectrum, consisting of elements  $y_1 \dots y_i \dots y_n$ .
- x** vector of known library spectrum, consisting of elements  $x_1 \dots x_i \dots x_n$ .
- X** matrix of known library spectra, consisting of  $x_1 \dots x_k$ .
- b** vector of fitting (regression) coefficients, consisting of elements  $b_1 \dots b_k$ .

### Abbreviations and Acronyms

CCD	charge-coupled device
FIR	finite impulse response
FTIR	Fourier transform infrared
GC-MS	gas chromatography-mass spectrometry
HPMS	high pressure mass spectrometry
HQI	hit quality index
IMS	ion mobility spectrometry
LEL	lower explosive limit
LIBS	laser induced breakdown spectroscopy
MS	mass spectrometry
ROC	receiver-operator characteristic
SNR	signal-to-noise ratio
XRF	x-ray fluorescence

### 2.1 Introduction

Our lives have been redefined by the perpetual emergence of new products that are easier to use, smarter, and faster than their predecessors. Enabling this evolution are advances in miniaturization that have produced ever smaller mechanical, optical, and electronic products and devices. In the realm of analytical chemistry, portable and handheld devices are now commercially available for a range of spectroscopic techniques (e.g. infrared, Raman, x-ray fluorescence [XRF], mass spectrometry [MS], etc.) [1]. Not only is such instrumentation available, but also tens

of thousands of such devices have been deployed across the globe for application user groups spanning military, law enforcement, manufacturing industries (pharmaceutical, textiles, chemicals, etc.), environmental monitoring, and art historians.

Frequently, the field users of handheld spectrometers do not have extensive training in science or spectroscopy. While the spectroscopic “engine” may be considered the heart of a handheld spectrometer, the algorithms and associated software should certainly be considered the brains. The algorithms define the data collection protocol, how spectra are processed (frequently to overcome nonideal measurement conditions), and how the final data is converted into actionable information on behalf of the end user. The software user interface communicates this information to the end user in an interpretable format.

As noted above, the range of analytical applications served by handheld spectrometers is quite broad, and analytical and performance requirements can vary substantially from one application to another. Whereas laboratory instrumentation is typically a general purpose tool to be used by experts, handheld devices are often tailored to a specific application to enable use by nonexperts. The focus of this chapter is on handheld optical spectroscopy, and the examples given come from that field, although the principles and mathematical methods apply to other spectroscopies. The portable elemental techniques of XRF and laser-induced breakdown spectroscopy (LIBS) are only touched on briefly, and the reader is referred to chapters in these volumes that cover those topics for more details: by Cornaby for portable XRF sources, Piorek for XRF and Day for LIBS. Similarly, MS, high-pressure mass spectrometry (HPMS), gas chromatography-mass spectrometry (GC-MS), and ion mobility spectrometry (IMS) are not specifically addressed, and the reader should see the chapters by Snyder for MS, Blakeman and Miller for HPMS, Leary, Kammrath and Reffner for GC-MS, and De Bono and Leary for IMS.

In the next section, we provide additional detail on some of the most common use case scenarios and the associated instrument and algorithm design considerations.

### 2.1.1 Use Case Scenarios

As described above, users of handheld spectrometers include military, law enforcement, manufacturers, and others. These users employ handheld devices in an extreme range of environmental conditions (in the desert, on the trunk of a car, in a cold storage room, etc.). Accordingly, many handheld spectrometers are designed to operate over a wide range of temperature, humidity, lighting conditions, etc. While the instrumentation is designed to minimize variability in measured data associated with the ambient environment, such effects cannot be completely removed. Consider ambient temperature as an example. Some handheld devices have been certified to be functional over temperature ranges from  $-20$  to  $+40$  °C or more. From an instrumentation perspective, temperature changes of this magnitude can cause minor variations in a spectrometer’s optical path (temperature-induced shear), which can impact characteristics of the measurement such as apparent wavelength position. From a sample perspective, temperature differences can cause peak shifting and peak broadening or narrowing, due to variability in the local sampling environment caused by the degree of hydrogen bonding. A typical example would be in the case of mid-infrared spectroscopy where the O-H band could shift due to temperate change. Given the extreme conditions that these systems must operate under, a major design consideration is ensuring that the algorithms are capable of handling imperfect and variable input data.

Beyond a shared need to use handheld spectrometers under a wide range of conditions, the applications of the diverse user groups highlighted above might seem disparate. What could a soldier investigating a reported peroxide-based explosive possibly have in common with a warehouse worker evaluating an incoming raw material? In both cases, the end user has an expectation of what the material *should* be, and they need to verify whether it is what they think it is. Despite the very broad user groups who use handheld devices, the fundamental questions being asked frequently fall into one of the five following categories:

- 1) Is something present?
- 2) Is this material what I think it is?
- 3) What group does this belong to?

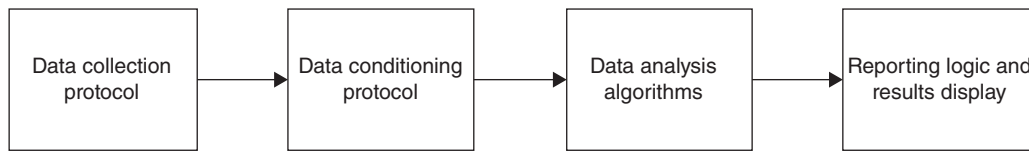


**Figure 2.1** System level block diagram representing major algorithm functions in handheld spectrometers.

- 4) What is this?
- 5) How much of this is present?

As discussed in Section 2.4, each one of these questions effectively represents a different type of algorithm. Specific aspects of the associated algorithms and examples are provided in more detail below.

### 2.1.2 System Level Overview

At the system level, the core algorithm components of a typical handheld spectrometer can be placed into discrete blocks. The algorithm functions highlighted in the block level diagram in Figure 2.1 are typically present in one form or another, independent of the final application the device is being used for.

The algorithm components in Figure 2.1 will be expanded on in further detail below; however, we will briefly touch on each functional block here as well.

As suggested by the heading, the data collection protocol represents the instructions by which the instrument collects a spectrum. In a typical laboratory setting, an analyst determines the optimal settings by which a particular substance will be measured. Measurement settings can change substantially from one substance to another and as such are typically included as part of an analytical method or standard operating procedure. To make the handheld technology accessible to nonexperts, the associated algorithms and embedded intelligence must automatically determine appropriate measurement settings (exposure time, laser power, number of scans to average, etc.). Considerations related to assignment of a data collection protocol are presented in Section 2.2.

The data conditioning step is performed to reduce unwanted variability in the measured data. Perhaps, the most common type of data conditioning is digital filtering applied to the measured spectrum in an effort to remove background baseline variation. In Raman spectroscopy, cosmic ray filtering is also frequently performed. It should be noted that data conditioning and data collection are not always completely independent. For example, in Fourier transform infrared (FTIR) measurements, a background spectrum is frequently collected in an effort to reduce variability due to changes in ambient atmospheric gas levels. Algorithm aspects related to data conditioning are reviewed in Section 2.3.

The data analysis algorithms are the calculations by which the data is converted into information for the end user. These are discussed in detail in Section 2.4.

Finally, the last system level processing block related to embedded algorithms for handheld devices are the reporting logic and results display. Once the measured data has been processed by the primary data analysis algorithms, a decision must be made regarding what to present to the end user. As an example, consider a material identification application where the end user wishes to answer: “what is this?” One approach is to present a rank-ordered list of the best matches to the user and allow them to determine which, if any, of the materials in that list represent a “match.” An alternate, more sophisticated approach is to evaluate the data against some sort of reporting threshold and report only the materials that represent a plausible match. Reporting logic and display of instrument results are considered in more detail in Section 2.5.

In addition to the sections related to the block diagram of Figure 2.1, we discuss strategies to implement algorithms on handheld instruments with limited processing power in Section 2.6. Finally, in Section 2.7, we describe methods to characterize identification performance in terms of accuracy and precision.

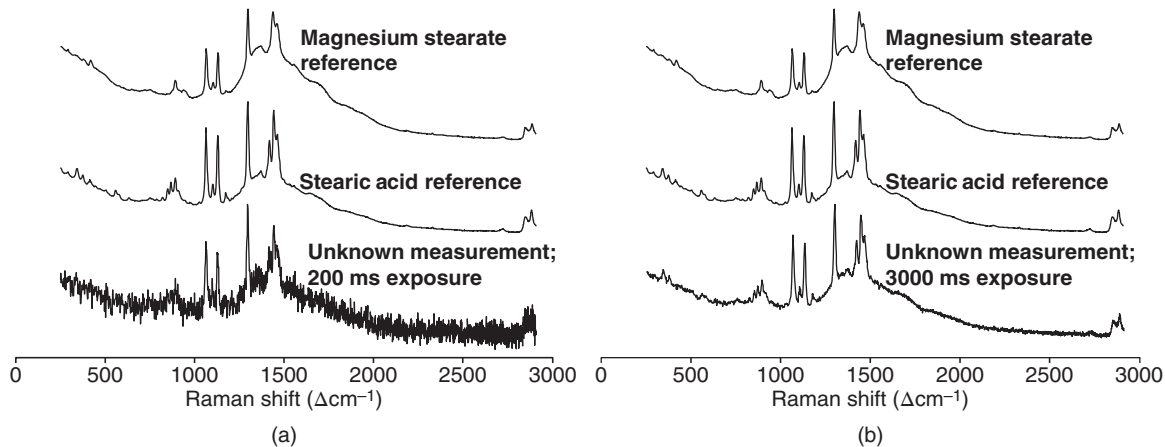


**Figure 2.2** Magnesium stearate verification example comparing the impact of measurement protocol on the selectivity of the end result. (a) Unknown spectrum was collected with a 0.2-s exposure time. (b) Unknown spectrum was collected with an exposure time of 3 s.

## 2.2 Data Collection

In an analytical laboratory environment, there is a hierarchy of objectives when considering the appropriate experimental conditions to utilize in a spectroscopic analytical method. At the highest level, the end goal of a method is to provide information that can be used to make an informed decision. Thus, prior to method development, consideration is made regarding what decision needs to be made. Review of the inputs necessary for decision-making will typically inform what properties of a sample need to be estimated and how well they need to be estimated (e.g. analytical performance requirements such as accuracy, precision, selectivity, etc.). Once “what” and “how well” have been defined, the method development process commences and effectively involves defining the details associated with the first three blocks in Figure 2.1. That is, method development involves defining the low-level protocols by which spectra should be collected (e.g. exposure time, number of co-adds per spectrum, etc.), the associated data conditioning, and the calculations (e.g. algorithms) that will be used to convert the collected, conditioned data into a result.

Consider an example where a pharmaceutical manufacturer needs to verify the identity of an incoming raw material. In this example, the certificate of analysis provided by the supplier indicates that the substance is magnesium stearate. Magnesium stearate is commonly present in tablet and capsule formulations to prevent other ingredients from sticking to manufacturing equipment during processing. Additionally, magnesium stearate suppliers often produce other chemically similar materials such as stearic acid (which can be used as a precursor in the production of magnesium stearate). Thus, one requirement of a magnesium stearate method is that it must be able to selectively distinguish between magnesium stearate and other chemically and spectroscopically similar materials.

Shown in Figure 2.2a are reference Raman spectra of magnesium stearate and stearic acid, along with an unknown test measurement that was acquired using a 0.2-seconds acquisition time. In this case, the signal-to-noise ratio (SNR) of the test measurement is poor enough that it is not possible to selectively distinguish whether the unknown material corresponds to magnesium stearate or stearic acid.

In Figure 2.2b, the reference spectra of interest are compared to a test measurement that was acquired using a longer, 3-seconds acquisition time. Under these conditions, the SNR has improved substantially, and inspection of the features near  $900\text{ cm}^{-1}$  reveals that the unknown measurement is consistent with stearic acid (e.g. the material is NOT magnesium stearate as labeled).

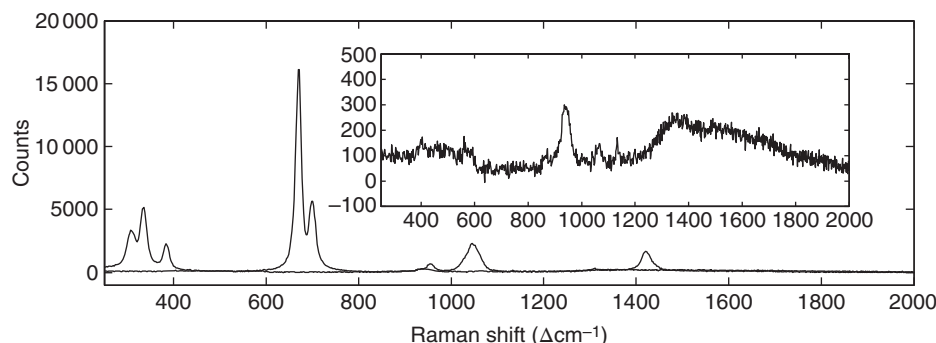


**Figure 2.3** Overlay of dimethyl sulfoxide and sodium phosphate dibasic Raman spectra. The measurements, both collected using a 0.05-s exposure time on the same handheld Raman system, illustrate the impact of Raman cross section on signal intensity. Inset contains an expanded view of sodium phosphate dibasic, which appears as a flat line in the larger figure.

At first pass, the example above may seem quite trivial. From the data in Figure 2.2, it is easy to verify that a 2-seconds data collection protocol is inadequate and that *an exposure time of 3 seconds is sufficient for magnesium stearate verification*. The caveat with the preceding italicized statement is that it is only known to be applicable for these specific substances (magnesium stearate and stearic acid) under the data collection conditions that were employed (temperature, humidity, ambient lighting, etc.). In a laboratory analytical method, such conditions are typically defined and fixed within a certain range. In contrast, field users of handheld spectrometers do not typically encounter problems that are so well bounded. In the following subsections, we will discuss various topics that make the data collection protocol such an important aspect of algorithms in handheld spectroscopic devices.

### 2.2.1 Sample Considerations

In handheld spectroscopy applications, samples corresponding to different materials of interest can have vastly different inherent signal intensities. The signal intensity depends on both the substance being measured and on the technique being used for the measurement. For example, water has a very high molar absorption coefficient and is very easily measured using infrared spectroscopy. In contrast, water has a small Raman cross section and may be unobservable in such measurements. This is especially true for portable Raman systems that do not measure the range above  $3000\text{ cm}^{-1}$ , which contains the most intense features corresponding to the  $\nu_1$  and  $\nu_3$  bands.

Different samples can produce very disparate signal intensities, even when using the same measurement technique. To illustrate this point, we have overlaid measurements of dimethyl sulfoxide and sodium phosphate dibasic in Figure 2.3.

The measurements shown in Figure 2.3 were collected on the same handheld Raman spectrometer under identical experimental conditions (exposure time, measurement geometry, etc.). The signal intensity for sodium phosphate dibasic is so much smaller than that of dimethyl sulfoxide (greater than 50 times difference) that the phosphate appears as a flat line in the larger figure and can only be seen clearly in the expanded view shown in the inset. Given that in many handheld applications the user does not know what substances may be encountered, this highlights the need for handheld devices to incorporate algorithms that are capable of adaptively setting measurement conditions such that a measurement with an appropriate SNR for the task at hand is obtained.

### 2.2.2 Environmental Considerations

Handheld devices are operated under a wide range of environmental conditions, and as already discussed in the introduction, this has the potential to impact sample analysis via spectroscopic effects such as peak shifting.

In addition, the ambient environment (temperature, lighting, etc.) can have a major impact on the SNR of a measurement for a given exposure time.

As an example of environmental conditions impacting spectroscopic analysis, we will highlight polystyrene Raman measurements performed under varying lighting conditions. In Raman spectroscopy, it is common to perform a background “dark” measurement that is subtracted from the “bright” (i.e. laser on) measurement in order to subtract out features related to ambient light. This process also allows features arising from detector dark current to be subtracted out. Shown in Figure 2.4 are individual bright and dark measurement pairs of polystyrene collected under different lighting conditions. Panel (a) shows the case where the sample is measured in the absence of ambient light. In this case, the bright measurement is dominated by Raman features, and the dark measurement is essentially a flat line containing a very low level of dark current detector counts. Additionally, panel (b) demonstrates a measurement of polystyrene collected in an indoor setting under fluorescent lighting. In this case, the bright measurement still contains the polystyrene Raman features, but it also contains several peaks in other areas due to ambient light (which are also seen in the dark measurements). These features correspond to atomic emission lines generated by elements present in the fluorescent lights. Finally, presented in panel (c) is

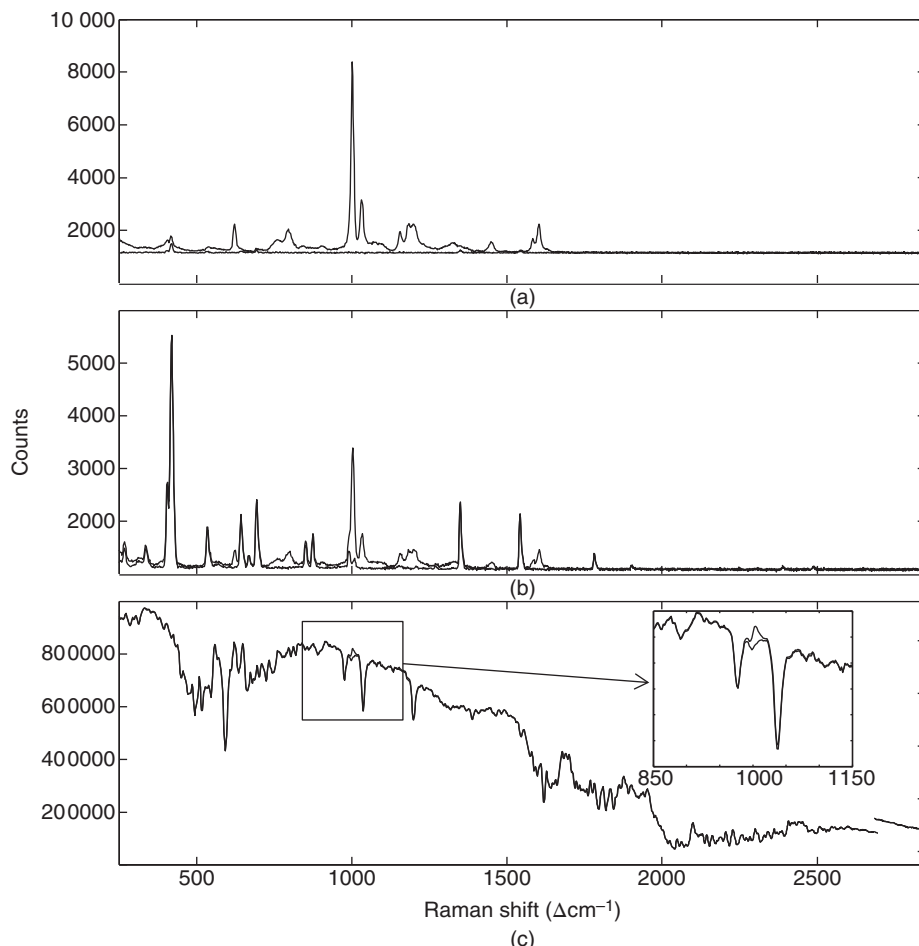


**Figure 2.4** Raman spectrum bright/dark scan pairs of polystyrene collected under different ambient lighting conditions. (a) No external ambient light: 0.025-s exposure. (b) Indoor measurement in the presence of fluorescent lighting: 0.025-s exposure. (c) Outdoor measurement in the presence of sunlight: 0.43-s total exposure.

a measurement of polystyrene that was collected in an outdoor setting. In this case, both the bright and dark are dominated by sunlight. The inset in panel (c) contains a zoom of the  $1000\text{ cm}^{-1}$  region to highlight that even in the presence of intense sunlight, the polystyrene Raman signal can be observed.

As described above, the final Raman spectrum is produced by subtracting the dark measurement from the bright measurement. Shown in Figure 2.5 are the final, dark subtracted, Raman spectra corresponding to the data in Figure 2.5.

A few interesting observations can be made by inspecting the data in Figure 2.5. Comparing the data from panel (a) with the data in panel (b) reveals that the SNR of the measurement collected in the presence of fluorescent lighting is perhaps slightly lower than what was achieved in “dark room” conditions (note that these measurements were both collected using a 25-ms exposure time). In contrast, evaluation of panel (c) reveals that the measurement collected in the presence of sunlight has much poorer SNR than either of the other two measurements, despite the fact that the total exposure time was 9 times longer. This can be explained by noting that the charge-coupled device (CCD) detector used to collect the data is subject to shot noise, which is Poisson distributed and proportional to the measured signal intensity.

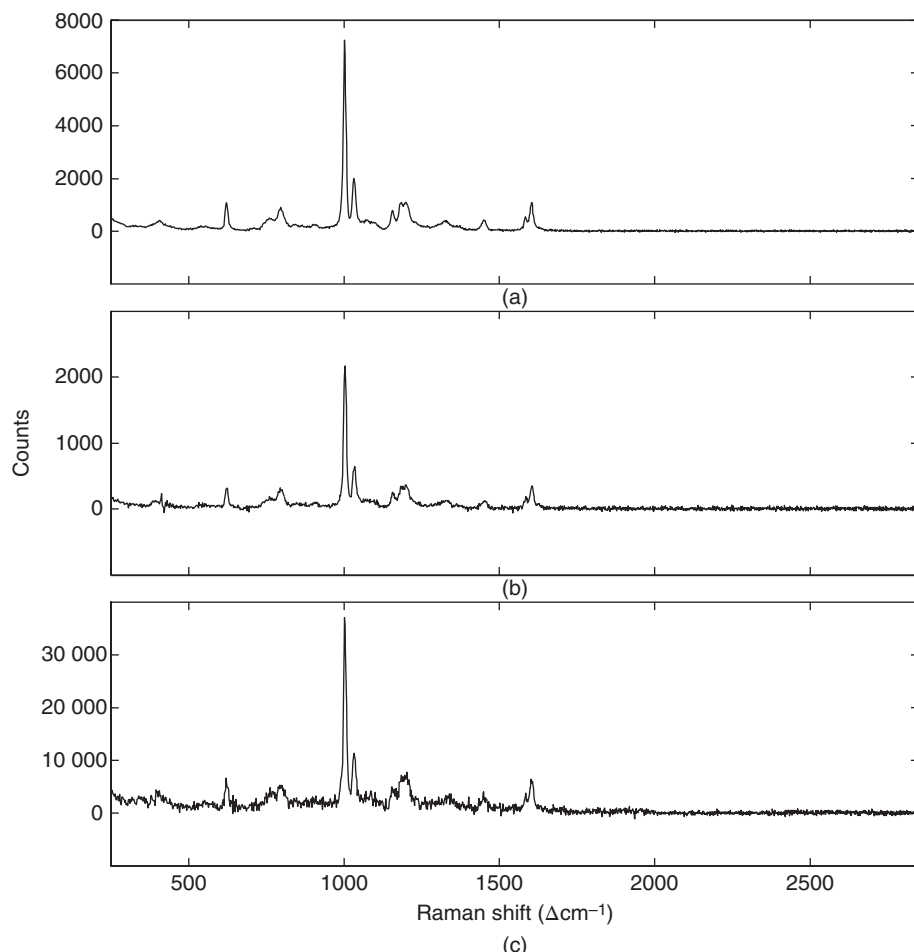


**Figure 2.5** Final, dark subtracted, Raman spectra collected under different ambient lighting conditions. (a) No external ambient light: 0.025-s exposure. (b) Indoor measurement in the presence of fluorescent lighting: 0.025-s exposure. (c) Outdoor measurement in the presence of sunlight: 0.43-s total exposure.

Thus, just as we demonstrated that attributes of the test material can drastically impact signal quality, so too can the measurement conditions at the time of data collection. While this example focused on ambient lighting, there are other environmental conditions such as temperature and humidity that can impact measurement quality. For the sake of brevity, no further examples of environmental impact on signal quality are presented.

## 2.3 Data Conditioning

As noted in Figure 2.1, once a measured spectrum has been collected, a data conditioning step typically takes place prior to evaluation by the final data analysis algorithms. Generally, the purpose of data conditioning, or signal processing, is to separate the desired part of the signal from the unwanted part of the signal (e.g. separate the pure signal from the noise). In the realm of analytical chemistry, digital filters are among the most widely used methods for signal processing. For a detailed introduction to digital filters and other forms of signal processing, we refer the interested reader to the encyclopedia article by Wentzell and Brown [2].

Briefly, a digital filter is an operation that is carried out on a contiguous subset of the original signal sequence to produce an estimated value in the filtered signal sequence. One such digital filter frequently used in spectroscopic applications is the non-recursive filter, also referred to as the finite impulse response (FIR) filter. Non-recursive filters operate by convolving a set of filter coefficients with the sequence of measurements to produce the filtered signal. Perhaps, the most familiar non-recursive filter to analytical chemists is the polynomial least-squares smoothing filter (e.g. Savitzky–Golay filters [3]). Such filters encompass both smoothing filters and derivative filters. Derivative filters can be useful for locating the position of a peak maximum or to highlight poorly defined features in a spectrum (e.g. the shoulder on a peak). In the context of handheld spectroscopy applications, slope and baseline offsets can sometimes pollute the signal. In Raman measurements, baseline differences can be caused by fluorescence contributions from the sample. In infrared measurements, sloping baselines are frequently observed for strongly absorbing samples such as dark-colored materials like rubber. Because the derivative of a function is unaffected by the addition of a constant, a first derivative is capable of eliminating scan-to-scan baseline offsets. Likewise, sample measurements plagued with a baseline that changes linearly with the ordinal variable (such as fluorescence) can make use of the second derivative to solve the problem.

In addition to the polynomial least-squares filters that are described above, another form of data conditioning sometimes applied to spectroscopic data is the median filter. The median filter is particularly useful for removing spikes or outliers from a measurement sequence. One example of such outliers impacting some handheld spectrometers arises from cosmic rays striking a photodetector [4]. While the median filter is effective at eliminating cosmic ray spikes, it represents a nonlinear transformation of the data and should be used with caution.

## 2.4 Types of Algorithms

The embedded algorithms running on handheld devices are used to convert the data collected by the device into an answer that will allow the user to take action. These algorithms can be grouped in different ways, and here, we group them by what question the user is asking when the device is used in the field. Table 2.1 lists the algorithm types discussed in this section. We attempted to present these in a hierarchical fashion; algorithms providing more detailed information about the sample under test can always be used to display less information to the user, but not vice versa. For example, a quantitative algorithm that determines the concentration of ammonium nitrate and diesel fuel in a sample can classify that sample as an improvised explosive device, but an algorithm that detects the presence of explosives cannot necessarily tell you how much ammonium nitrate is present.

**Table 2.1** List of algorithms that can be used with handheld spectrometers.

Type	Question
Detection	Is something present?
Confirmation	Is this what I think it is?
Classification	What group does this belong to?
Identification	What is this?
Quantitation	How much of this is present?

The algorithms are arranged in a hierarchical fashion (simplest to most complex), and the associated user question is listed.

### 2.4.1 Detection

Detection algorithms seek to determine if something is present. The simplest detection problem is to decide whether a signal is present or if a measurement represents only noise. An example of this is the detection of aircraft based on radar return. In the context of handheld spectroscopy, detection typically corresponds to the search for a material of interest that may be in the presence of interferences that are not specifically of interest. Most frequently, such analytes are of importance to health or human safety. Perhaps, the most familiar examples of detection in a portable instrument are ambient air “sniffer” systems designed to alarm when any one of a range of combustible hydrocarbon gasses is detected. The alarm detection threshold in this application is typically expressed as a fraction of a material’s lower explosive limit (LEL). As discussed in Section 2.6, the choice of this threshold effectively sets the tradeoff between detection rate and false alarm rate.

In addition to gas monitoring and sensing, detection algorithms also find use in applications spanning the other phases of matter. Examples of liquid detection problems frequently in the news include the screening of consumable liquids for poisonous materials (e.g. “methanol outbreaks” in liquors, glycerin tainted with diethylene glycol, etc.). Finally, a detection example involving solids can be found in airports wherein the surface of a backpack, handbag, or luggage is swabbed to pick up particulate matter that is subsequently analyzed for suspicious residues.

Most detection algorithms coupled to spectroscopic devices seek to detect trace amounts of something in or against an otherwise well-known background. They are also often just the first step in two or more measurements with analytical equipment to give the user suitable information about the situation. Because of these two factors, detection algorithms typically are allowed to have a higher false alarm rate than other algorithm types, as long as the detection rate for the lower limit of expected concentrations is acceptable.

If the background is well characterized, then the simplest and most sensitive detection algorithms seek to determine if the measured spectrum is different in any way from the expected background spectrum. For example, if a sample from a glass of water is measured using a Raman spectrometer, the presence of any Raman peaks with Raman shifts less than  $3000\text{ cm}^{-1}$  in the spectrum may indicate that the substance is not pure water, as water’s  $\nu_2$  vibrational mode (“scissoring bend”) at  $\sim 1650\text{ cm}^{-1}$  is typically too weak to be observed. If instead an FTIR spectrometer was used to measure the sample, the algorithm would fit the measured spectrum with a pure water spectrum at the correct temperature and analyze the spectral residual of the fit to the measured for any evidence of infrared absorption bands not due to water. Further discussion of detection algorithms is outside of the scope of this article.

## 2.4.2 Confirmation

Related to the detection problem are confirmation algorithms. Instead of knowing that the background is present and looking for any evidence of substances other than the background, the unknown measurement is assumed to be of a substance with known spectrum, and an assessment is performed to look for evidence that the measured spectrum contains something other than just the desired substance.

The most common fielded application using this general approach is identity testing of raw materials used in various pharmaceutical manufacturing processes. The manufacture of medicine is regulated worldwide to help ensure safety and effectiveness, with most countries requiring 100% identity testing of all raw materials used.

From a spectroscopic perspective, confirmation involves comparing the spectrum of an unknown material to a spectrum collected from a known material and looking for differences. Before the widespread use of computers, the spectra would be plotted on graph paper, and the confirmation would be made based upon a visual comparison of both the presence and absence of peaks in the spectra [5]. With the advent of computers, it has become feasible to mathematically compare spectrum  $\mathbf{y}$  corresponding to the unknown to spectrum  $\mathbf{x}$  of the known material. This involves the calculation of a metric relating to how similar the two spectra are to each other. As discussed in Section 2.3, the entire digitized spectra are typically preprocessed to minimize unwanted artifacts prior to assessing the data for similarity.

One common similarity measure is referred to as the hit quality index (HQI). Frequently, instrument manufacturers compute HQI as Pearson's correlation coefficient, which is written in scalar form as

$$\text{HQI} = r = \frac{\sum_{i=1}^n (x_i - \bar{x})(y_i - \bar{y})}{\sqrt{\sum_{i=1}^n (x_i - \bar{x})^2} \sqrt{\sum_{i=1}^n (y_i - \bar{y})^2}} \quad (2.1)$$

Here,  $\bar{x}$  and  $\bar{y}$  are the mean values of spectrum  $\mathbf{x}$  and  $\mathbf{y}$ , respectively, and  $n$  is the number of spectral elements in each. The HQI ranges from 1 (perfect correlation) through 0 (no correlation) to  $-1$  (the unlikely result that two spectra are perfectly anticorrelated). In addition to Eq. (2.1), a weighted version of correlation coefficient has been reported [6] and used for spectral matching, where more intense peaks receive more weight.

If we define  $\mathbf{u}$  as  $\mathbf{x}$  after it has been centered and normalized to have zero mean and unit length and likewise  $\mathbf{v}$  for a centered and normalized  $\mathbf{y}$ , then HQI can be written in vector form as

$$\text{HQI} = r = \mathbf{u} \cdot \mathbf{v}^T = \cos \theta \quad (2.2)$$

where  $\theta$  is the angle between the two unit vectors  $\mathbf{u}$  and  $\mathbf{v}$  in  $n$ -dimensional space.

As highlighted by Eq. (2.2), HQI corresponds to the angle between two spectra; however, another way to view the wavelength correlation is to plot the unknown and library spectra in  $(x,y)$  pairs, each pair corresponding to a particular wavelength. In order to illustrate the different representations and the utility of HQI, we consider the data in Figure 2.6, which shows an example of an unknown spectrum along with two known library spectra. Based on a visual assessment of this data, it can be seen that both library items contain features with significant overall similarity to the unknown spectrum. Figure 2.7 highlights the data in angular form as represented by Eq. (2.2) (plots a and c) as well as demonstrating the data in  $(x,y)$  pairs as discussed above (plots b and d). Based on the representation of the data in these ways, it becomes clear that the match to library item 1 is much better than the match to item 2.

While a correlation coefficient is a measure of how *similar* two spectra are (the higher the number, the more similar), distance metrics are sometimes used instead. Correlation distance and other distance metrics are an indication of how *different* two spectra are (the higher the number, the more different). The correlation distance metric is simply defined simply as  $1 - r$ , and other common distance metrics are listed in Table 2.2 and surveyed in the literature [7].

No matter which similarity metric is used, a threshold must be set to determine whether an unknown spectrum passes or fails the confirmation test. Obviously, an HQI of 1 is a pass, and an HQI of 0 is a fail, but what about other

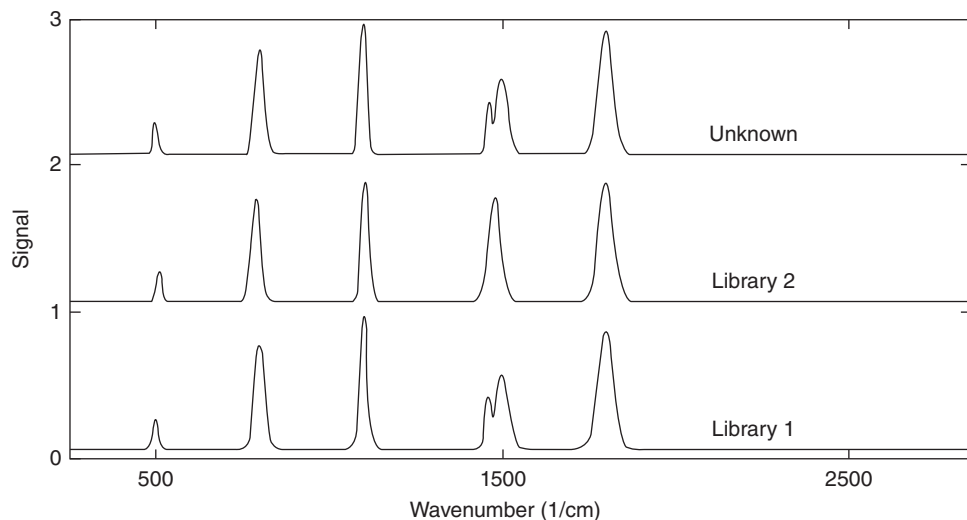


**Figure 2.6** Simulated vibrational spectra, plotted as signal intensity versus wavenumber (inverse wavelength).

values? While a correlation coefficient threshold of 0.95 is frequently used to determine whether two spectra are a match [8, 9], the correlation is merely an angle and not a probability. Thus, a threshold of 0.95 in no way means 95% likely, 95% confidence, or 95% agreement [10]. Further discussion regarding HQI threshold selection, as well as alternate statistical based measures are discussed in Section 2.5.

### 2.4.3 Classification

Beyond just detecting or confirming that something is present, the ability to classify an unknown material into a category may be all that is needed in order for the user to take the next action. Classifications such as “alarm vs. clear” or “pass vs. marginal vs. fail” often have more clear meaning to the user than other types of algorithm outputs, enabling more routine use by nonexperts at the point of need.

The classification task has the widest assortment of algorithms to choose from. When the task is well bounded in terms of sample composition and other factors affecting spectral variation and when samples of known identity can be obtained beforehand and at acceptable cost, a supervised classification method can be used. In these algorithms, the expert supervises development and optimization of the algorithm using this training set of reference information and spectra. Additionally, with special attention paid to overfitting the data, the training set can be used to assess performance using methods such as cross-validation and bootstrapping [11], although it is always preferable to have another separate data set for validation. When the boundedness and availability conditions cannot be met, the developer has to rely on unsupervised classification methods where no training or model optimization is performed before deployment. It is often difficult to give meaningful, actionable information to the user with unsupervised methods, however.

In either case, the task is to still classify the measured sample into a group, given the measured spectrum from the device. For classifiers using prior probability that is the probability that the sample belongs to a group without first measuring the spectrum, other information can also be collected from the sample and used. For example, if the sample is a dry white powder measured in an office environment, the prior probability that the sample is water or some other liquid at room temperature is very low. Algorithms ranging from the simple and intuitive k-nearest neighbors to the time-tested Fisher’s linear discriminant to the latest artificial neural network or support vector machine have been employed by algorithm developers and are discussed in detail outside of this article. Interested readers can find many excellent books and articles on classification algorithms, and as a starting place, we recommend books by Ripley [12] and Duda et al. [13] and the encyclopedia article by Lavine and Mirjankar [14].

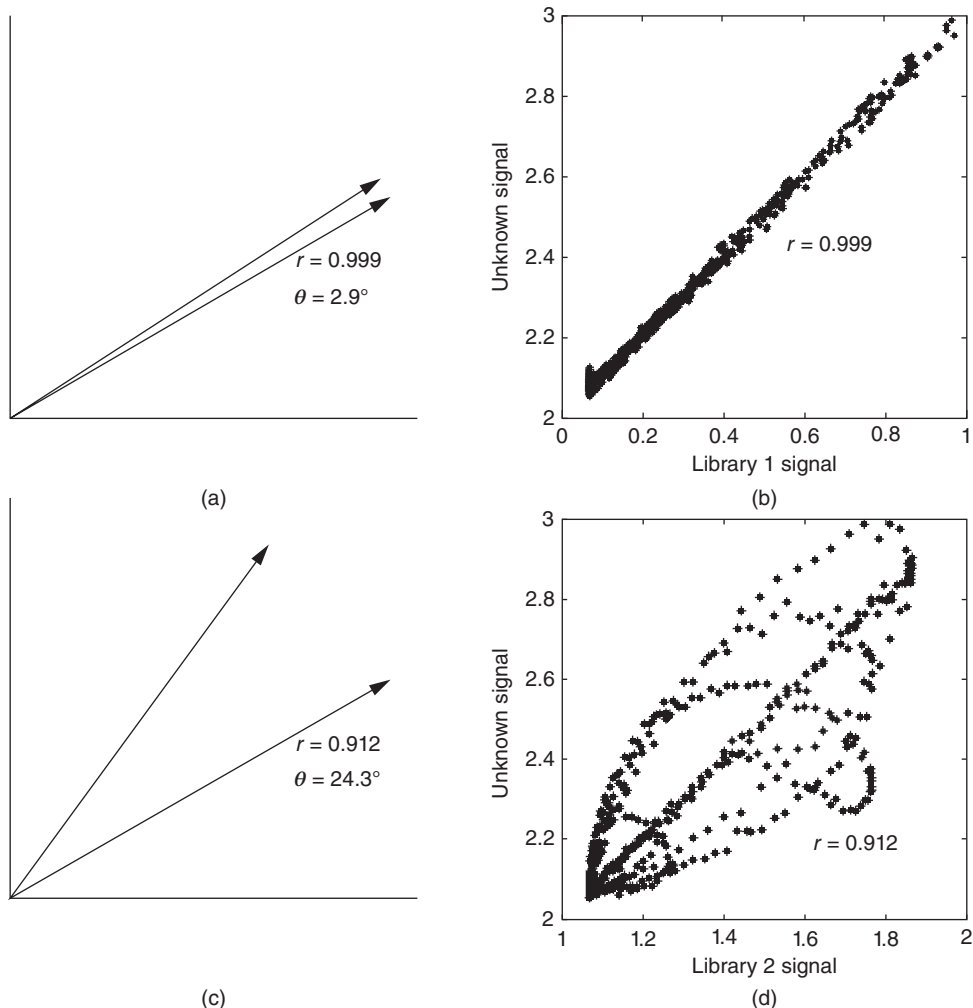


**Figure 2.7** Visualizing the correlation coefficient ( $HQI = r$ ) between the unknown and library spectra in two ways. (a) Unknown spectrum and library spectrum 1 plotted as unit vectors in  $n$ -dimensional space. (b) The same two spectra's signal intensities plotted as  $(x, y)$  pairs on a correlation plot. (c) Unknown spectrum and library spectrum 2 plotted as vectors. (d) The same two spectra plotted on a correlation plot.

#### 2.4.4 Identification

Identification algorithms should give the user enough information to determine what chemical or chemicals are in the scanned sample. As discussed further in Section 2.5, this can be in the form of a short list that an expert user can make a final determination from, or an unambiguous display naming only chemicals found by the algorithm with high confidence.

For samples composed of only one chemical, the algorithm task is similar to confirmation. The spectrum from the unknown material is compared to a library of known pure materials residing in the handheld unit's spectral database, one item at a time, using the similarity algorithms such as those described in Section 4.2. If the library is large, this process by itself can take too long for the user in the field. Methods to decrease the computation time without sacrificing detection performance too much are discussed in Section 2.6.

**Table 2.2** Distance metrics used to assess similarity between a spectrum  $\mathbf{x}$  with elements  $x_1 \dots x_n$  and a spectrum  $\mathbf{y}$  with elements  $y_1 \dots y_n$ .

Distance metric	Definition
Correlation distance	$1 - \frac{\sum_{i=1}^n (x_i - \bar{x})(y_i - \bar{y})}{\sqrt{\sum_{i=1}^n (x_i - \bar{x})^2} \sqrt{\sum_{i=1}^n (y_i - \bar{y})^2}}$
Minkowski distance City block, $p = 1$	$\sqrt[p]{\sum_{i=1}^n  x_i - y_i ^p}$
Euclidian, $p = 2$	
Chebyshev, $p \rightarrow \infty$	
Normalized Euclidian distance	$\sqrt{\sum_{i=1}^n \frac{(x_i - y_i)^2}{s_i^2}}$
Mahalanobis distance	$\sqrt{(\mathbf{x} - \mathbf{y})\mathbf{S}^{-1}(\mathbf{x} - \mathbf{y})^T}$

The variance of element  $i$  is  $s_i^2$ , and the inverse covariance matrix of  $\mathbf{x}$  and  $\mathbf{y}$  is  $\mathbf{S}^{-1}$ .

For samples composed of a mixture of two or more chemicals, the identification algorithm should seek to automatically identify all chemicals present. For both FTIR and Raman measurements, the unknown mixture  $\mathbf{y}$  can be modeled by a linear combination  $k$  known library spectra:

$$\mathbf{y} = b_1 \mathbf{x}_1 + b_2 \mathbf{x}_2 + \dots + b_k \mathbf{x}_k + \mathbf{e} = \mathbf{X}\mathbf{b} + \mathbf{e} \quad (2.3)$$

Here,  $\mathbf{b}$  are the fitting (regression) coefficients that describe how much of each library spectrum is in the unknown spectrum, and  $\mathbf{e}$  is the part of  $\mathbf{y}$  that is not fit perfectly by the linear model. We have omitted an offset term in the linear model, assuming that the preprocessing performed to  $\mathbf{y}$  and  $\mathbf{X}$  eliminates the need for it.

In addition to library spectra representing pure chemicals, other spectral shapes can also be included in the fit to model instrumental, environmental, and additional chemical terms. For example, offset and slope vectors can be used to model simple baseline drifts. Likewise, two interacting chemicals that cause the spectrum to not be modeled effectively with just a linear combination of their pure component spectra can still be modeled to the first approximation with an additional interaction spectrum, if it can be included beforehand in the library database.

Several commercial software packages allow the user to perform spectral subtraction in order to identify multiple components in a mixture spectrum. With this method, the user selects a first library spectrum ( $\mathbf{x}_1$ ) to subtract from the unknown spectrum. This item is selected from a rank-ordered list generated by the HQI metric, for example. Then, the user decides how much of this library spectrum ( $b_1$ ) to subtract from the unknown. To do this, they perform a visual assessment of the residual spectrum from the fitting procedure. Frequently, the scaling factor,  $b_1$ , is selected to minimize the resulting residual spectrum,  $\mathbf{y} - b_1 \mathbf{x}_1$ . Once a scaling factor has been chosen, the resulting residual spectrum is then compared with the remaining library spectra using the similarity metric method. This procedure can be repeated for more than two component fits.

In the best-case scenario, spectral subtraction requires an experienced spectroscopist to correctly perform the procedure. In scenarios where there is significant spectral overlap, it can be impossible to get an appropriate spectral residual (for use in fitting  $b_2$ ) without a-priori knowledge of an appropriate subtraction factor. To illustrate this point, consider the data displayed in Figure 2.8. For this example, component A and component B contain peaks in the same region with different relative intensities. Because of this, to fit either component individually and minimize the spectral residual will cause features from the other component to be eliminated. The only way to properly account for the contribution of components A and B is to fit both components simultaneously instead of one at a time.

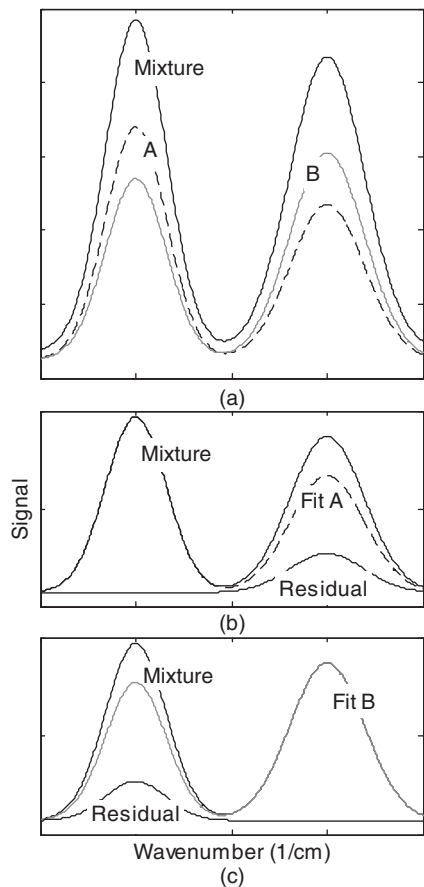


**Figure 2.8** Effect of fitting one component at a time. (a) Spectra of the measured mixture and components A and B. If both A and B are fit simultaneously, the fit would be perfect. (b) Fitting only component A results in a residual that will be impossible to fit with component B. (c) Fitting only component B results in a residual that will be impossible to fit with component A.

Simultaneous fitting of multiple components can be achieved using automated approaches to mixture analysis (e.g. stepwise regression [15]). With a large library of spectral candidates, the forward selection method is used, starting with fitting one component, then a linear combination of two components, etc., until some stopping criterion is met. A key difference between stepwise regression and manual spectral subtraction is that as the number of components is increased, the values for all  $b_1, b_2, \dots, b_k$  regression coefficients are reestimated. The stopping criterion can be based upon spectral similarity of the fit to the unknown or a maximum number of components to fit. After adding another component to the fit, the algorithm can look back at the other components used in the fit and decide whether or not to keep them, a procedure called elimination. How this type of mixture analysis can be performed on a handheld instrument with a large library in a reasonable amount of time is discussed in detail in Section 2.6.

Once the spectral shapes in the matrix  $\mathbf{X}$  to use in the linear model have been chosen, the fitting coefficients must be estimated. The simplest and most frequently used approach is called ordinary (or classical) least squares and seeks to minimize the sum of the squared residuals of  $\mathbf{y} - \mathbf{X}\mathbf{b}$ . This works well when the residuals at each element in the spectrum are normally distributed with the same variance. When the elements do not have equal variance and the variances are known, weighted least squares is a better approach. Here, the squared residuals at each element are weighted (multiplied) by the inverse of their variance, so that more uncertain portions of the spectrum are given less weight in estimating the fitting coefficients. Weighted least squares works well when there is not significant correlation between the residuals at each element. When there is significant correlation and the correlation is known in the form of a covariance matrix, then generalized least squares is the most appropriate

choice. Now, the fitting procedure is weighted by the inverse of the covariance matrix. Least squares regression is discussed in detail in many books, such as Mardia et al. [16] and Rencher and Christensen [17].

In matrix form, the estimate of the fitting coefficients for each of these least squares methods is computed using the general formula:

$$\mathbf{b} = (\mathbf{X}^T \mathbf{W} \mathbf{X})^{-1} \mathbf{X}^T \mathbf{W} \mathbf{y} \quad (2.4)$$

For generalized least squares,  $\mathbf{W}$  is the inverse of the covariance matrix of the residuals. Since the covariance matrix is often not known and because even when it is known the inverse is computationally expensive to compute, generalized least squares is difficult to implement in handheld instruments. For weighted least squares, this weighting matrix simplifies to a diagonal matrix with elements equal to the inverse of the variance of the residuals at each spectral element. And for ordinary least squares, the weighting matrix is simply a diagonal matrix of ones.

Once the fitting coefficients have been estimated, one of the similarity algorithms discussed in Section 4.2 can be used, with  $\mathbf{x}$  now replaced by  $\mathbf{Xb}$ . These similarity metrics describe how well the linear combination of library spectra matches the unknown spectrum. The partial correlation coefficient has also been used to determine how well each individual component matches the portion of the unknown spectrum that is orthogonal to the other components in the mixture [18].

There have been some recent efforts to implement machine learning to identify spectral data, using techniques such as genetic algorithms [19],  $k$ -nearest neighbors [19], and convolutional neural networks [20, 21]. However, the intensive computing power and memory required to train these machine learning techniques means that they are not feasible for deployment on portable handheld devices. A method by which to circumvent the memory and computational limitations of portable devices is to train a network beforehand and then upload the trained network to the instrument at manufacturer, although this implementation has not been reported by any vendor at this time. Another solution to the limitations is to perform the calculations on a separate, more powerful processor, which will be discussed in the later section “Off-line and cloud computing.”

#### 2.4.5 Quantitation

We briefly mention the final algorithm type here: estimating how much of a known substance is present in the sample under test. The same linear model assumption in Eq. (2.3) is usually used in quantitative algorithms. Unsupervised algorithms where the fitting coefficients are estimated given the unknown spectrum and known library spectra can be used to give quantitative estimates. The least squares methods described in Section 4.4 are also employed here. The library spectra themselves need to be quantitative in nature (e.g. molar absorptivity in units of  $\text{kg/l/m}$ ) for this method to be successfully used. Supervised algorithms are typically used though, when spectra of samples with known concentrations of the analyte of interest can be measured. These spectra and concentrations are then used to train the supervised algorithm, using quantitative algorithms such as inverse least squares, principal component regression, or partial least squares. Those interested in quantitative algorithms are referred to the encyclopedia article by Wold and Josefson [22].

Two elemental analysis techniques are available in a true handheld format: XRF and LIBS. XRF is a quantitative technique, and the primary method used is based on “fundamental parameters,” i.e. from XRF first principles, and this does rely on a factory-based calibration procedure for every instrument [23, 24]. In some cases, for instance, alloy identification, empirical calibrations are also used (see the chapter by Piorek [25]). Measurements of coatings and thin films may require some additional calculations [26].

Handheld LIBS devices [27], whose primary application is alloy sorting, have recently been commercialized (see chapter 13 in Volume 1 by Day). The results from these instruments require quantitative modeling approaches, which can be achieved via traditional univariate and multivariate chemometrics approaches as described above. Alternatively, a “calibration-free” method exists, which does not require empirical training data sets [28–33]. Rather than using samples of known concentrations, this method produces quantitative predictions based on first principles. The key to the successful implementation of this method in handheld LIBS systems is high spectral resolution in order to accurately remove unwanted interfering signals.

## 2.5 Display of Algorithm Results

As shown in Figure 2.1, once the data analysis algorithms have been executed, the final step is to apply reporting logic and display results to the user. For confirmation, what constitutes a pass or fail? For identification, how many similar items should be displayed and above what HQI value? The answers to these questions should be guided by what information will allow the user to infer the sample's identity and take the correct course of action.

### 2.5.1 User Inference

If the user is a spectroscopist, analytical chemist, or a well-trained expert user of handheld spectroscopy, then it makes sense to present them with detailed information and let them infer the answer from the information. For identification algorithms, a rank-ordered list of library items (or multiple items in the case of mixture analysis), together with HQI values, is a common approach. The user can then look through the chemical names on this list to rule out any that do not make sense given the ancillary information available to them (solid vs. liquid, pH, oxidizer test, etc.). The user can then also look through the list of HQI values, ruling out ones that are too low based upon training or experience, or looking for one or two that stand far above other values.

No hard rules have been established for when to accept or reject an HQI value. This is in part due to the fact that what is a “good enough” spectral match depends upon the situation. In a pharmaceutical manufacturing plant, incoming raw materials should match analytical standards to a very high degree in order to prevent errors in manufacturing. Furthermore, in this application, extensive method development and validation is performed, and an appropriate HQI is the subject of much consideration [34] and is extremely well defined. On the other hand, a much lower quality similarity metric value may suffice when a bomb squad technician observes a primary explosive on the handheld’s HQI list of potential matches. In this scenario, the end user is less concerned with knowing whether other items are also potentially present and also may be more accepting of false positives at the tradeoff of having excellent detection rates for explosive materials of interest.

In summary, rank-ordered information displays of candidate library matches not only provide the most information to the user but also put the most pressure on the user. Operators of field-based spectrometers are frequently under extreme duress, which further clouds decision-making. If the user is not familiar with spectroscopy or HQI, or is but uses the instrument infrequently, then it will be difficult for them to make an informed decision.

### 2.5.2 Statistical Inference

Statistical inference puts more of the decision-making responsibility on the algorithm. The term means drawing conclusions from data, which is exactly what the user wants from the handheld instrument. This method uses a metric as a test statistic, paired with a statistical distribution of that metric, to decide if the unknown spectrum is a match to a known spectrum (or linear combination of known spectra).

To illustrate the concept, consider the simple case of quality control at a thermometer manufacturer. When measuring temperature in a chamber controlled to 20 °C, a thermometer should read on average 20 °C. Suppose it is also known from an abundance of previous data that chamber readings from acceptable thermometers are normally distributed about 20 °C with a standard deviation of 0.2 °C. Suppose further that a newly manufactured thermometer reads 19 °C in the chamber. This is five standard deviations away from the expected value, so it is extremely unlikely that this is an accurate thermometer and just by chance it measured 1 °C low. By comparing the measured value to a probability distribution, the manufacturing test operator can easily reject this thermometer. Formally, we would have performed the steps in Table 2.3.

Statistical inference is used frequently in many different fields. Perhaps, the most widely known is for hypothesis testing in medicine. For example, a pharmaceutical company (and the regulating government) wishes to know if a new medicine produces better outcomes for the patients compared with the standard treatment. They formulate

**Table 2.3** An example procedure for developing a statistical inference algorithm.

Step	What this looks like for our thermometer example
Form a null hypothesis and an alternative hypothesis	$H_0$ : Thermometer is acceptable $H_A$ : Thermometer is not acceptable
Decide on what is an acceptable error rate for reaching the wrong conclusion (significance level)	It is acceptable if 5% of the time to incorrectly conclude that the thermometer is not acceptable
Choose a test statistic	Thermometer reading in 20 °C chamber
Determine what distribution the statistic follows	Thermometer readings are normally distributed with mean = 20 °C and standard deviation = 0.2 °C
Determine the probability that the test statistic value fits within the distribution given that the null hypothesis is true	Compute $Z = (19 - 20)/0.2 = -5$ and look up probability that $Z$ is less than $-5$ in $Z$ table: $p$ -value = 0.000 000 29
Accept or reject null hypothesis	0.000 000 29 is less than 0.05, therefore reject null hypothesis in favor of alternative

a hypothesis, define a test statistic, and test the hypothesis as part of the regulatory approval process. Outside of medicine, another example comes from the use of statistical process control in many different industries to determine if processes are within normal limits or not. As a final example from analytical chemistry, MS spectral searching algorithms use statistical inference to determine if the unknown compound matches anything in the library [35].

Returning to our concern, the null and alternative hypotheses to consider for a confirmation or identification algorithm are as follows:

$H_0$ : the sample measured in spectrum  $\mathbf{y}$  is consistent with the material in spectrum  $\mathbf{x}$ .

$H_A$ : the sample is not consistent with this material.

The acceptable error rate for the test depends on the application, as noted in the preceding section. Even within a given application, the acceptable error rate could vary by material. For example, in identifying chemical warfare agents, the user may wish to err on the side of caution and use a higher-than-normal error rate.

For a test metric, correlation coefficient or any of the distance metrics can be used. The key really is to understand what statistical distribution they follow and, if it is a parametric distribution, what the parameter values are. Otherwise, the distribution does not model the data well, and the inferences drawn can be erroneous.

As one example of a parametric distribution, consider the Mahalanobis distance defined in Table 2.1. When the residuals  $\mathbf{x} - \mathbf{y}$  are normally distributed about zero and when the library spectrum  $\mathbf{x}$  and covariance matrix  $\mathbf{S}$  are known without error, the square of the Mahalanobis distance is chi-squared distributed with degrees of freedom equal to the number of spectral elements [34]. When  $\mathbf{x}$  is known without error and  $\mathbf{S}$  is estimated from experimental samples, the squared distance follows the  $F$  distribution [34]. These various assumptions are often not all true in reality, and therefore, the actual statistical distribution may differ from chi-square or  $F$ , but nonetheless, they are good starting points when developing a statistical inference algorithm.

Shown in Figure 2.9 is an example of using inference to determine if the unknown matches the library spectrum of chloroform. You can see in Figure 2.9a that the two spectra look very similar by eye. The HQI (correlation coefficient) between the spectra is 0.99, a very high correlation. But careful examination of Figure 2.9a reveals that there are features in the unknown spectrum that are unaccounted for by the library spectrum of pure chloroform. In Figure 2.9b, the residual of the fit of pure chloroform to the unknown is plotted, along with the estimated uncertainty at each spectral element in the unknown spectrum, calculated according to the concepts presented in a patent [36]. Using this approach, the probability ( $p$ -value) that the unknown spectrum is actually pure chloroform

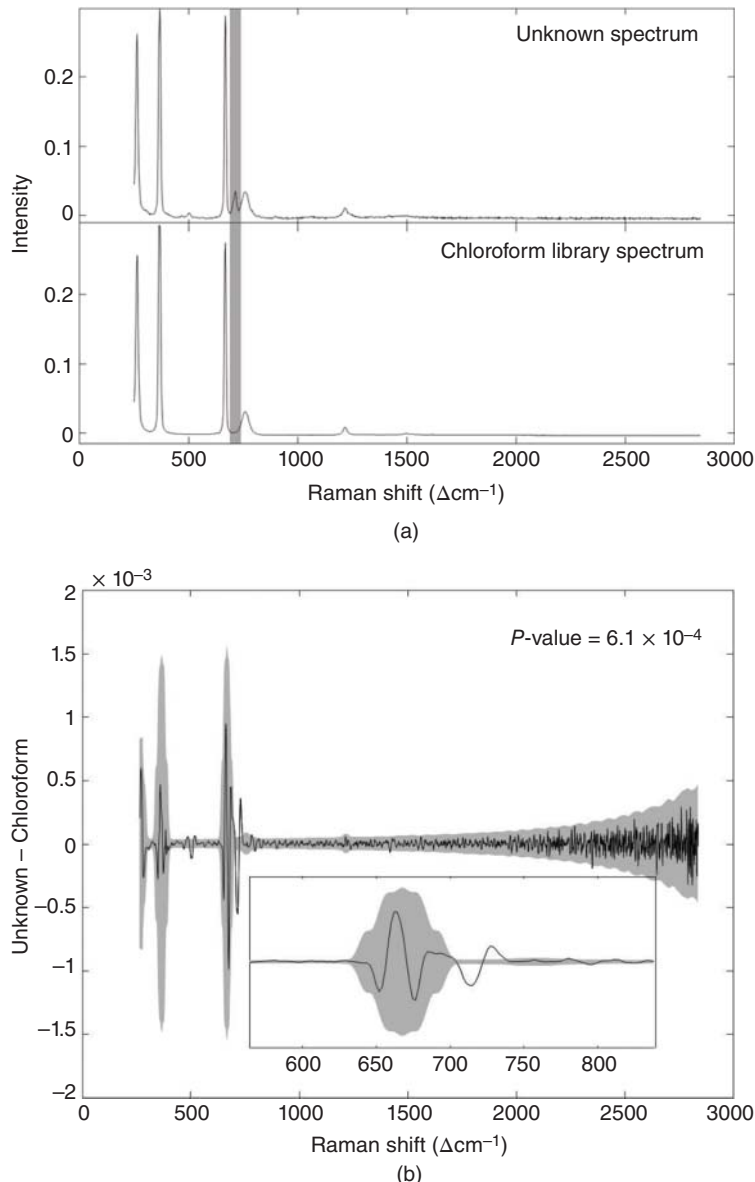


**Figure 2.9** Identification algorithm using statistical inference. (a) Raman spectra of an unknown and chloroform. (b) Residual of fit of chloroform to the unknown (black line) and uncertainty of unknown spectrum (gray shading,  $\pm 3$  standard deviations).

is  $6.1 \times 10^{-4}$ , and therefore, even though the HQI is high, the algorithm can confidently reject this hypothesis and continue on with a mixture analysis.

Another approach to using statistical inference centers on estimating a probability that  $\mathbf{x}$  matches  $\mathbf{y}$  using Bayes' theorem, shown in Eq. (2.5) using HQI as the test statistic:

$$P\{\mathbf{x} = \mathbf{y} \mid \text{HQI} = r\} = \frac{p \times g(r)}{p \times g(r) + (1 - p) \times f(r)} \quad (2.5)$$

Here,  $p$  is the prior probability that the unknown truly is  $\mathbf{x}$ ,  $g(r)$  is the probability density function for HQI values when the unknown is  $\mathbf{x}$ , and  $f(r)$  is the probability density function for HQI values when the unknown is *not*  $\mathbf{x}$ . As with hypothesis testing, the key is to accurately estimate the distributions of the test metric. This approach has been applied to identification of pure materials [37] and mixtures [18].

## 2.6 Computational Considerations

Analysis of unknown mixtures presents special computational challenges that cannot be ignored. Modern reference databases frequently contain in excess of 10 000 library spectra, and some mixture algorithms deployed on handheld devices attempt to simultaneously fit up to five mixture components. The number of potential mixture solution candidates that can be evaluated for a given library can be calculated using the following formula:

$$N = \frac{n!}{k!(n-k)!} \quad (2.6)$$

where  $N$  is the number of possible mixture candidates,  $n$  is the number of library reference spectra, and  $k$  is the maximum number of mixture components that are simultaneously fit. Based on the formula shown above, the number of possible mixture combinations scales rapidly with the number of components that are simultaneously fit, especially for large reference library databases. To illustrate this point, Table 2.4 captures the number of possible mixture candidates for a reference library containing 10 000 items as well as a smaller library containing only 100 items when two to four component solutions are considered.

From Table 2.4, it can be seen that with a 10 000 item library, there are  $10^7$  possible two component mixture candidates alone. Further complicating the issue is that handheld devices typically have limited on-board computing power. With the on-board processing capability available on portable devices today, it would take days to evaluate every potential mixture solution that could be generated from a large, modern reference database.

### 2.6.1 Off-Line and Cloud Computing

One approach to overcome the limitations of on-board memory and computational power is to take the data analysis to a more powerful computer. Some handhelds can operate as a data collection engine, with an export utility to move spectra to an external processor with faster and more parallel capabilities. There, these more powerful computers have the ability to quickly scour the library for matches, or run intensive machine learning algorithms to analyze the spectrum. Computational time can be further improved by splitting tasks into smaller parallel loops.

**Table 2.4** Number of potential mixture candidates ( $N$ ) as a function of the number of mixture components fit ( $k$ ) for 10 000 or 100 item ( $n$ ) libraries.

<b><math>N</math></b>	<b><math>k</math></b>	<b><math>N</math></b>
10 000	2	$4.9995 \times 10^7$
	3	$1.6662 \times 10^{11}$
	4	$4.1642 \times 10^{14}$
100	2	4950
	3	161 700
	4	3 921 225

Sometimes, it is not feasible to physically transport a powerful computer around with the portable handheld device during field analysis. In such cases, devices equipped with the proper wireless communication hardware and infrastructure can remotely upload data to a cloud network. Within the cloud architecture, more powerful processors can iterate through library matches or assign the data to deep learning models and perform identification analyses [38, 39]. The results can then be transmitted back to the device and reported to the user. In pharmaceutical and industrial applications, for example, method validation for sample authentication could be performed in the cloud instead of on the individual devices. Furthermore, the cloud could provide management platforms to manage and connect all cloud Raman devices, storing data, scientific analysis apps, and peer collaboration tools [40, 41]. The potential also exists for crowdsourcing spectra to enable the identification of many more substances [42], but this must be very carefully implemented to ensure that the spectra collected for the database meet certain standards.

Despite the potential for offline and cloud computing, there are limitations to its usage with handheld devices. For example, safety and security applications are often highly sensitive and require that all data reside locally or not be shared at all.

## 2.6.2 On-Board Identification with a Large Library and Mixture Analysis

As a result of the computational expense associated with the mixture problem, it is common for handheld identification devices to incorporate a rapid calculation that can be used to down select the library to a more manageable number of entries. Down selection can be performed prior to pure component assessment in order to speed even the analysis of pure materials, or it can be performed prior to the subsequent mixture analysis. The intention of this approach is to allow rapid analysis times for end users and ensure that the majority of computational time can be spent making a detailed assessment of the unknown sample against select library items of interest using the algorithms described above. Table 2.4 shows the drastic reduction in the number of possible computations of the mixture analysis is reduced from 10 000 to 100 candidates.

Rapid analysis time is achieved by reducing the amount of data needed to be analyzed. This is also referred to as dimensionality reduction, where the dimensions are the number of spectral elements. Two approaches to dimension reduction are feature selection and feature extraction. With feature selection, we try to choose important features from the spectra and analyze just these features. Because of their relationship to the unique vibrations of a molecule and small number compared to the number of spectral elements, Raman scattering and infrared absorption peak locations and intensities are used for feature selection in handheld spectrometers [43].

The other approach, feature extraction, reduces the dimensionality of the spectra by transforming the entire spectra to a new space with fewer dimensions. Principal component analysis has been employed, where, for example, 10 000 unique spectra can be represented with only 100 principal components while retaining 99.9% of the spectral variation in the original library.

Mathematically, the full set of library spectra  $\mathbf{X}$  are decomposed (via singular value decomposition) into a smaller set of spectral shapes ( $\mathbf{V}$ ) and spectral weights ( $\mathbf{T}$ ) as

$$\mathbf{X} = \mathbf{TV}^T \quad (2.7)$$

The weights of the unknown spectrum  $\mathbf{y}$  are computed using the stored library shapes as

$$\mathbf{t}_y = \mathbf{y}(\mathbf{V}^T)^{-1} \quad (2.8)$$

Now, we have reduced the problem from comparing  $\mathbf{y}$  to all possible combinations of  $\mathbf{X}$ , to instead comparing  $\mathbf{t}_y$  to all possible combinations of  $\mathbf{T}$ . This approach has been used in mixture analysis of infrared data by Lo and Brown [44].

Sparse approximation techniques can also be used to decompose the spectra using a reference library of spectra. By iteratively subtracting the contribution of selected spectra and updating the contribution of each spectrum,

chemical mixtures can be fingerprinted and quantified even when they contain relatively small chemical contributions [45].

### 2.6.3 Incorporation of User Input

Many of the algorithms highlighted thus far act in an independent, automated fashion without any input from the user. The minor exceptions to this are those that involve spectral subtraction (Section 4.4) and algorithm displays that provide a rank-ordered list of candidate solutions for the user to choose from (Section 5.1). As noted in Section 5.1, the perceived benefit of presenting a list to the user and allowing him or her to select the final answer is that they can make this decision in the context of other information available to them (solid vs. liquid, pH, color, etc.). As previously discussed, the disadvantage is that asking the user to make a final determination puts additional pressure on them in what is frequently an already stressful situation. An alternate approach that has recently been implemented in a commercial handheld spectrometer [46] is to allow the user to input a list of materials that they have reason to believe might be present. These materials are treated by the algorithms with special consideration where improved detection rates can be achieved. Further extending this approach would be algorithms capable of taking ancillary information from the user, such as physical state or pH, and utilizing that information when an unknown sample is assessed.

## 2.7 Performance Characterization

Referring back to Table 2.1, the user of the handheld analyzer wants to know if the material scanned is confirmed to be what it was presumed to be (confirmation algorithms) or if the material scanned can be identified as a single chemical or mixture of chemicals (identification algorithms). In either case, the algorithms are qualitative in nature, returning “what” is present rather than a quantitative “how much” result. To assess performance, it is therefore appropriate to compute true-positive and false-positive rates for a set of samples representative of what the user would encounter in the field.

True-positive rate is the fraction of times the device displayed the correct result, either confirming that the true material is present (confirmation) or correctly identifying the true material (identification). The true-positive rate can only be tested when the true material is represented in the analyzer’s library. False-positive rate is the fraction of times the device displayed the incorrect “positive” result, either confirming the incorrect material (confirmation) or identifying one or more materials that are not in the scanned sample (identification). In contrast to true-positive rate, false-positive rate can be tested using both materials that are and are not represented in the library.

Besides true-positive and false-positive rate, a parameter from information retrieval (web searching) algorithms called precision is useful for characterizing these qualitative algorithms. Precision is defined as the ratio of relevant results displayed to the total results displayed. For example, if the device displays a list of 10 items to the user and only two if those items are contained in the sample, the precision for this result is  $2/10 = 0.2$ .

Most handheld analyzers have a fixed algorithm, and performance assessment is therefore straightforward to carry out; a set of samples made from materials both represented and not represented in the library are scanned with several devices and several operators, and the three parameters described above are computed. But in the case when the user can vary a single threshold that controls what is displayed, the threshold setting will affect the true-positive rate, false-positive rate and precision of the analyzer. In this case, it makes more sense to use receiver-operator characteristic (ROC) curves to assess performance [47–49]. Details of how to use ROC curves for assessment of identification algorithms have been described elsewhere [50].

Several reports of detection performance for commercially available handheld devices exist in the literature. Brown and Green reported a ROC curve for identification of 261 materials measured on a Raman analyzer [50]. Bugay and Brush compared two confirmation algorithms operating on Raman spectral data from 18 common

pharmaceutical preparations [10]. Vignesh et al. analyzed 13 materials, including mixtures, scanned with a Raman spectrometer and identification algorithm [18]. Arno et al. reported on evaluation of an FTIR analyzer and its identification algorithm using 308 samples, including mixtures [51]. Green et al. studied 20 mixture systems with a Raman spectrometer and two identification algorithms and also analyzed 484 real-world samples using two identification algorithms [46]. More exhaustive testing has been carried out, but has not been published in peer-reviewed journals.

## 2.8 Conclusion

Algorithms for identification and confirmation on optical (Raman and infrared) handheld analyzers were first developed only 10 years ago and have undergone several generations of improvement. As evidence of their success in helping the user in the field, hundreds of thousands of handheld analyzers are in use today. Future developments to these algorithms will hopefully include the following:

- Improved performance in identifying complex mixtures.
- Lower limits of identification for minor components in mixtures.
- The ability to provide actionable information back to the user even when the sample cannot be identified (e.g. classifying the sample according to hazard for first responders).
- Incorporation of cloud computing.

One practical point is that instrument manufacturers may use proprietary algorithms. These should be disclosed to the purchaser and operator in sufficient detail so that they may judge the reliability of the results produced, for instance, identifications. In particular, the vendor should indicate the types and patterns of “scores” that represent a solid identification or detection.

With continued improvements in algorithms, along with hardware and other software components, handheld analyzers will continue to be an important tool for current users and are sure to find applications in other fields.

## References

- 1 Crocombe, R. (2018). Portable spectroscopy. *Appl. Spectrosc.* 72 (12): 1701–1751.
- 2 Wentzell, P. and Brown, C. (2006). Signal processing in analytical chemistry. In: *Encyclopedia of Analytical Chemistry* (ed. R.A. Meyers). American Cancer Society.
- 3 Savitzky, A. and Golay, M.J. (1964). Smoothing and differentiation of data by simplified least squares procedures. *Anal. Chem.* 36: 1627–1639.
- 4 McCreery, R.L. (2005). *Raman Spectroscopy for Chemical Analysis*, 1e. Wiley-Interscience.
- 5 Kendall, D.N. (1966). *Applied Infrared Spectroscopy*, 1e. Reinhold.
- 6 Griffiths, P.R. and Shao, L. (2009). Self-weighted correlation coefficients and their application to measure spectral similarity. *Appl. Spectrosc.* 63: 916–919.
- 7 Cha, S.H. (2007). Comprehensive survey on distance/similarity measures between probability density functions. *Int. J. Math. Model. Meth. Appl. Sci.* 1: 300–307.
- 8 Tanabe, K. and Saëki, S. (1975). Computer retrieval of infrared spectra by a correlation coefficient method. *Anal. Chem.* 47: 118–122.
- 9 Ulmschneider, M., Wunenburger, A., and Pénigault, E. (1999). Using near-infrared spectroscopy for the noninvasive identification of pharmaceutical active substances in sealed vials. *Analisis* 27: 854–856.
- 10 Bugay, D.E. and Brush, R.C. (2010). Chemical identity testing by remote-based dispersive Raman spectroscopy. *Appl. Spectrosc.* 64: 467–475.

- 11** Efron, B. and Gong, G. (1983). A leisurely look at the bootstrap, the jackknife, and cross-validation. *Am. Stat.* 37: 36–48.
- 12** Ripley, B.D. (2008). *Pattern Recognition and Neural Networks*, 1e. Cambridge University Press.
- 13** Duda, R.O., Hart, P.E., and Stork, D.G. (2012). *Pattern Classification*, 2e. Wiley-Interscience.
- 14** Lavine, B. and Mirjankar, N. (2012). Clustering and classification of analytical data. In: *Encyclopedia of Analytical Chemistry* (ed. R.A. Meyers). Wiley.
- 15** Draper, N. and Smith, H. (1998). *Applied Regression Analysis*, 3e. Wiley.
- 16** Mardia, K.V., Kent, J.T., and Bibby, J.M. (1979). *Multivariate Analysis*, 1e. Academic Press.
- 17** Rencher, A.C. and Christensen, W.F. (2012). *Methods of Multivariate Analysis*, 3e. Wiley.
- 18** Vignesh, T., Shanmukh, S., Yarra, M. et al. (2012). Estimating probabilistic confidence for mixture components identified using a spectral search algorithm. *Appl. Spectrosc.* 66: 334–340.
- 19** Madden, M. and Ryder, A. (2003). Machine learning methods for quantitative analysis of Raman spectroscopy data. *Proc. SPIE* 4876: 1130–1139.
- 20** Liu, J., Osadchy, M., Ashton, L. et al. (2017). Deep convolutional neural networks for Raman spectrum recognition: a unified solution. *Analyst* 142: 4067–4074.
- 21** Fan, X., Ming, W., Zeng, H. et al. (2018). Deep learning-based component identification for the Raman spectra of mixtures. *Analyst* 144: 1789–1798.
- 22** Wold, S. and Josefson, M. (2006). Multivariate calibration of analytical data. In: *Encyclopedia of Analytical Chemistry* (ed. R.A. Meyers). Wiley.
- 23** Markowicz, A. (2008). Quantification and correction procedures. In: *Portable X-ray Fluorescence Spectrometry, Capabilities for In Situ Analysis* (eds. P.J. Potts and M. West), 13–38. Cambridge, UK: RSC Publishing.
- 24** Jenkins, R. (1999). *X-Fluorescence Spectrometry*, 2e. Chichester, UK: Wiley.
- 25** Piorek, S. (2008). Alloy identification and analysis with a field-portable XRF analyser. In: *Portable X-ray Fluorescence Spectrometry, Capabilities for In Situ Analysis* (eds. P.J. Potts and M. West), 98–140. Cambridge, UK: RSC Publishing.
- 26** Piorek, S. (2008). Coatings, paints and thin film deposits. In: *Portable X-ray Fluorescence Spectrometry, Capabilities for In Situ Analysis* (eds. P.J. Potts and M. West), 56–82. Cambridge, UK: RSC Publishing.
- 27** Hahn, D. and Omenetto, N. (2012). Laser-induced breakdown spectroscopy (LIBS), part II: review of instrumental and methodological approaches to material analysis and applications to different fields. *Appl. Spectrosc.* 66: 347–419.
- 28** Ciucci, A., Corsi, M., Palleschi, V. et al. (1999). New procedure for quantitative elemental analysis by laser-induced plasma spectroscopy. *Appl. Spectrosc.* 53: 960–964.
- 29** Tognoni, E., Cristoforetti, G.L.S.P.V., Salvetti, A. et al. (2007). A numerical study of expected accuracy and precision in Calibration-Free Laser-Induced Breakdown Spectroscopy in the assumption of ideal analytical plasma. *Spectrochim. Acta B* 62 (12): 1287–1302.
- 30** Herrera, K., Tognoni, E., Gornushkin, I. et al. (2009). Comparative study of two standard-free approaches in laser-induced breakdown spectroscopy as applied to the quantitative analysis of aluminum alloy standards under vacuum conditions. *J. Anal. At. Spectrom.* 24: 426–438.
- 31** Herrera, K., Tognoni, E., Omenetto, N. et al. (2009). Semi-quantitative analysis of metal alloys, brass and soil samples by calibration-free laser-induced breakdown spectroscopy: recent results and considerations. *J. Anal. At. Spectrom.* 24: 413–425.
- 32** Bulajic, D., Corsi, M., Cristoforetti, G. et al. (2002). A procedure for correcting self-absorption in calibration free-laser induced breakdown spectroscopy. *Spectrochim. Acta B* 57 (2): 339–353.
- 33** Burakov, V., Kiris, V., Naumenkov, P., and Raikov, S. (2004). Calibration-free laser spectral analysis of glasses and copper alloys. *J. Appl. Spectrosc.* 71 (5): 740–746.
- 34** John, C.T. and Pixley, N.C. (2007). Methodology for NIR identification of pharmaceutical finished products with emphasis on negative controls and data driven threshold value selection. *Am. Pharm. Rev.* 10: 120–124.

- 35** Geer, L.Y., Markey, S.P., Kowalak, J.A. et al. (2004). Open mass spectrometry search algorithm. *J. Proteome Res.* 3: 958–964.
- 36** Brown, C.D. and Vander Rhodes, G.H. (2007). US Patent 7,254,501 B1.
- 37** Li, J. and Hibbert, D.B. (2005). Comparison of spectra using a Bayesian approach. An argument using oil spills as an example. *Anal. Chem.* 77: 639–644.
- 38** Liang, J. and Mu, T. (2019). Recognition of big data mixed Raman spectra based on deep learning with smartphone as Raman analyzer. *Electrophoresis* 41 (16–17): 1413–1417.
- 39** Chandler, L., Huang, B., and Mu, T. (2019). A smart handheld Raman Spectrometer with cloud and AI Deep learning algorithm for mixture analysis. *Proc. SPIE 10983, Next-Gen. Spectr. Technol. XII* 1098308: 1–9.
- 40** Thermo scientific introduces virtual app for handheld Raman Analyzer. The Science Advisory Board, 19 09 2019. [Online]. <https://www.scienceboard.net/index.aspx?sec=sup&sub=Drug&pag=dis&ItemID=358> (accessed 31 January 2020).
- 41** SCiO. SCiO by consumer physics 2017. [Online]. <https://www.consumerphysics.com/business/technology> (accessed 31 January 2020).
- 42** Mr. Spock's Smartphone: A spectrometer for your keychain. ZDNet 2014. [Online]. <https://www.zdnet.com/article/mr-spocks-smartphone-a-spectrometer-for-your-keychain> (accessed 31 January 2020).
- 43** Zürcher, M., Clerc, J.T., Farkas, M., and Pretsch, E. (1988). General theory of similarity measures for library search systems. *Anal. Chim. Acta* 206: 161–172.
- 44** Lo, S.C. and Brown, C.W. (1992). Near-infrared mixture identification by an automated library searching method: a multivariate approach. *Appl. Spectrosc.* 46: 790–796.
- 45** Yaghoobi, M., Wu, D., Clewes, R., and Davies, M. (2016). Fast sparse Raman spectral unmixing for chemical fingerprinting and quantification. In: *Proceedings of SPIE 9995, Optics and Photonics for Counterterrorism, Crime Fighting, and Defense XII*, 99950E. Edinburgh, UK: SPIE.
- 46** Green, R.L., Hargreaves, M.D., and Gardner, C.M. (2013). Performance characterization of a combined material identification and screening algorithm. In: *Proceedings of SPIE 8726, Next-Generation Spectroscopic Technologies V*, 87260F. Baltimore, MD: SPIE.
- 47** Swets, J.A. (1988). Measuring the accuracy of diagnostic systems. *Science* 240: 1285–1293.
- 48** Pepe, M.S. (2004). *The Statistical Evaluation of Medical Tests for Classification and Prediction*, 1e. Oxford University Press.
- 49** Brown, C.D. and Davis, H.T. (2006). Receiver operating characteristics curves and related decision measures: a tutorial. *Chemom. Intel. Lab. Syst.* 80: 24–38.
- 50** Brown, C.D. and Green, R.L. (2006). Performance characterization of material identification systems. In: *SPIE Proceedings of 6378, Chemical and Biological Sensors for Industrial and Environmental Monitoring II*, 637809. Boston, MA: SPIE.
- 51** Arno, J., Andersson, G., Levy, D. et al. (2011). Advanced algorithms for the identification of mixtures using condensed-phase FT-IR spectroscopy. In: *SPIE Proceedings of 8032, Next-Generation Spectroscopic Technologies IV*, 80320. Orlando, FL: SPIE.

# 3

## Library and Method Development for Portable Instrumentation

A Case Study Approach

Suzanne K. Schreyer

*Rigaku Analytical Devices, Wilmington, MA, USA*

### 3.1 Introduction

Portable instrumentation is employed in a variety of use scenarios, and diverse new use cases are rapidly developing. This chapter describes the most common cases of instrumentation in molecular spectroscopy that uses infrared (IR), Raman, or near-infrared (NIR) technology. By far the most common use case is the raw material identification (RMID) whereby an internal library is searched and compared to an unknown material. The result returned is from either a discovery search of the closest match in a library or, alternatively, a pass/fail result when part of a verification application. Classification of the material as part of a class or group is also a possibility. Most applications for portable instrumentation tend to fall into these categories. For these applications, speed and reliability tend to be the most valuable components as these types of applications tend to be used by nonexpert users to rapidly identify materials of interest. Typical use cases for these applications range from incoming inspection of pharmaceutical or warehouse materials to identification of unknown and potentially illegal or dangerous materials for safety and security applications.

Alternatively, a smaller set of applications utilize quantitative analyses where the instrument returns a material identification result and a quantitative value for a desired variable. Again, the user tends to be a nonexpert user, and the instrument may be used to rapidly give a quality result for incoming materials or to determine final component quality after a process mix. These types of applications build from a library and include further chemometric applications to classify including supervised methods such as soft independent modeling of class analogies (SIMCA) or unsupervised methods such as principal component analysis (PCA). Quantitative methods most commonly used are principal component regression (PCR) or partial least squares regression (PLSR). The cited methods (Massart et al. 1997) are the workhorses of chemometric analysis, but many other methods are available in commercial software packages.

While the uses for portable instruments are increasingly diverse, the case studies shown in this chapter will focus on the more common methods for library building and method development: the focus is on the major concerns involved in library building and model development. Since an instrument result is only as good as the data used to build a model or library, selection and robustness of the materials are important. A library build also should be fit for its intended use. Given the niche that portable instrumentation is used in, there are specific requirements for portable instrumentation that are not a major consideration in laboratory-based equipment. Method and library building for portable instruments requires not only that a match must be made of the sample to a library material but also that the results are returned quickly and reliably. In addition, ease of use and understanding to the user are also key components at this point. Results must be understandable to the nonexpert quickly, as time is often a key issue. This may include incoming inspection of pharmaceutical ingredients on a warehouse floor or rapid

threat detection by first responders. So another criteria for the portable instrument use is the ability to be used in a variety of scenarios and still be fit for use.

Short case studies, based on current applications for portable Raman, IR, and NIR instruments, are used to illustrate some points for consideration in building robust and reliable applications for material identification in pharmaceutical and safety/security applications. Quantitative applications are most commonly used in identification of key cost quality variables for the food and feed/agriculture users. These types of applications are generally performed by NIR instruments, being the most common workhorse technique in these industries. While the examples cited are of specific applications, the methods behind the library build and method development are applicable to any case or instrument where these are developed and used.

## 3.2 Instrument Use Overview

A full review of the applications of portable instruments is covered in other chapters in this volume, but a few citations are listed in order to illustrate the scope of use and instrumentation available. An overview of the techniques and uses of portable NIR (Pasquini 2018), mid-IR, (Sorak et al. 2012) and Raman spectrometers (Das and Agrawal 2011) shows the wide utility of these instruments in a range of applications in pharmaceutical (Deidda et al. 2019), quality control (da Silva et al. 2017), counterfeit drug detection (Ciza et al. 2019), archeological (Das and Agrawal 2011), forensic (de Araujo et al. 2018), and other sciences (Altinpinar et al. 2013; Farber et al. 2019). Applications of portable instruments in safety and security environments are also prevalent for ease of use and rapid response. The most common instruments for bulk analysis of materials in the forensics field are based on IR, and especially Raman spectroscopy for the identification of explosives (Fountain III et al. 2014; Lopez-Lopez and Garcia-Ruiz 2014) and other forensic materials of interest (Khandasammy et al. 2018). Raman spectroscopy is especially common for the identification of narcotics (de Oliveira Penido et al. 2016; Vítek et al. 2012), as it does not destroy the sample and analysis can be done through most packaging. Sampling through packaging is especially important in narcotics testing, due to the possibility of cross contamination and safety concerns for the first responder.

The most common instrumentation use for either Raman or IR spectroscopy is identification of materials – either in mixtures or as single components. As both techniques result in spectra that contain the fundamental frequencies of the sample, library building is mostly dependent on generating library quality spectra based on known and traceable standards. Material identification and model development is then focused on preprocessing methods (Zeaiter and Rutledge 2009) associated with noise reduction and spectral comparison to generate a best fit result of the sample to the library. Data pretreatment and preprocessing methods are integral to data selection for library build or calibration to reduce random noise and systematic variations. Once methods are built or a library is integrated, further examination is required to assess quality indices such as specificity, selectivity, and robustness. In addition to the previously cited references for preprocessing reviews, there are more focused references on algorithms for handheld spectrometers (Gardner and Green 2014) and examples of adapting laboratory spectrometer libraries to portable instrumentation (Weatherall et al. 2013). The latter is especially relevant, as many users have access to libraries on benchtop laboratory instruments that have been validated and would prefer to transfer these onto the portable instruments. Thus robust calibration transfer protocols may also be required in developing libraries on portable instruments.

Mixture analysis is an additional feature some instruments include, with varying degrees of success. For bulk analysis using molecular spectroscopy instruments, this usually involves deconvolutions based on spectral contribution of individual components and residual analysis as a determination of how many components are feasible to report. In general, most portable instruments can reliably report only two to three components of a mixture without delving into noise. Another limitation is that most of these instruments require components of a mixture to be present in the 5–10% range, due to detection limits of a bulk analytical technique. Some instruments may include complementary techniques to increase their limit of detection and expand their capability. An example of

this is surface-enhanced Raman spectroscopy (SERS) techniques offered with many portable Raman instruments (Alula et al. 2018; Mecker et al. 2012).

Data from mid-IR and NIR instrumentations (as well as Raman under certain conditions) can be expanded into the quantitative model development. A classic application for these techniques can be in process monitoring and in monitoring of moisture during lyophilization (Luypaert et al. 2007). These methods are more commonly seen with NIR, due to the ability of portable NIR instruments to scan through sample containers and the historic ability to readily integrate chemometrics with NIR. If the bulk analysis levels are adequate for the instrument, portable instruments can also do real-time checks on a process to ensure formulations are correct as part of a quality control (Roggo et al. 2007) or PAT process (De Beer et al. 2011). This may simply be a classification or verification method, or models can be built to return results of a component identification in a mix and/or quantitative measurement of a constituent or composition in a sample.

These examples are primarily focused on pharmaceutical applications, but the ability of portable instruments to monitor levels can also be expanded into the food, feed, and agricultural industries to report quality levels. Agricultural and feed analyses typically include protein, moisture, and fats but can be expanded to other quality levels (Modroño et al. 2017; Porep et al. 2015) with varying degrees of success. For example, in feed and agricultural monitoring, the most reliable and robust models tend to be the determination of moisture with NIR, followed by protein and fats. NIR monitoring of moisture is especially useful in pharmaceutical applications, for the quality control of moisture in a process application or finished formulation, and also for monitoring of lyophilization in retained samples.

Industrial process monitoring of food is another area that typically blends the use of spectroscopy methods (usually NIR) with quantitative analysis of chemical constituents and physical attributes (Grassi and Alamprese 2018) as these techniques give a rapid assessment of quality indices. While the use of spectroscopic instruments in the food/feed industries tend to be more in-line or laboratory analysis, the criteria to develop a quantitative model is similar to that required for at- or off-line instrumentation. The criteria for building quantitative models is more rigorous and involved than for material identification though and requires specialized knowledge and/or chemometric methods in order to develop and validate a robust model. These models require a traceable database for calibration development that should include variables that may be encountered in actual use. Spectral preprocessing is usually a standard step, followed by rigorous model development and testing before a model is validated and released for use. This type of method is generally much more time extensive than a qualitative or classification model and requires more extensive statistical analysis. While many chemometric packages are available as “black box” options to build these regression models, the danger lies in believing the software rather than applying knowledge and expert analysis to any proposed model.

The following sections will show case studies of building a qualitative library-based model for material identification on portable instruments and then expand into another case study showing some of the issues and strategies involved with developing and deploying a quantitative model on another portable instrument. While not comprehensive in its scope, these case studies highlight the common flow through of library building and model development, with a focus on building these models for portable instrumentation.

### 3.3 Library Development

All libraries and eventual models rely on high-quality data. It is often stated that a model (or library) is only as good as the data used to make it. High-quality data should represent the type of library: robust and reliable.

Data sets used for library building should be verified and traceable. If feasible, data should be obtained from a standard material with certificates of analysis, as for pharmaceutical grade materials. This ensures that a material in a library comes from a verified source. If this is not feasible due to the type of materials used, then the material should be verified by other means. This may involve verification by other types of analytical instrumentation (mass

spectrometry is the classic standard to use for verification, for example). Any data sent from a source can also be verified against external spectral libraries. For example, Raman spectra received from a source can be verified against external Raman libraries to ensure there is a match. In fact, before any spectrum is added to a molecular spectroscopic library, it is good practice to do an external validation with an external library search to ensure that no issue has occurred with the sample or spectrum. This provides an extra level of scrutiny that the proposed library material is of sufficient quality to return a correct result against a search of the external database.

Checking a spectrum against an external library is good practice, as the source material may have been contaminated or degraded, may not be of sufficient purity, or may have other quality issues. External checking of a material ensures that there is external verification and that the correct identification is applied to the spectra. Contamination is usually not an issue when the data comes from a reliable source and is a standard material; however, for many applications in safety and security where the users build their own libraries, this is not always the case. As an example, BioRad KnowItAll (Bio-Rad 2019) software contains extensive searchable libraries for a variety of spectroscopic instrument types in pharmaceutical and forensic applications. A comparison of the search results to the library spectra will quickly identify any spectral differences or issues with the spectra itself (baseline effects and noise). Conversely, a strong correlation between sample and the database and similar spectra gives an extra measure of security that the material is good enough to add to a library. Prior to adding materials to a library, it is good practice to ensure that the highest-quality spectra are generated.

The ideal is to generate robust spectra that have minimal noise and can be used to represent any future instances of this material. It is recommended that the library spectra be as noise free and “ideal” as can be reasonably achieved, because working scans generated in field use typically worse in quality. Common examples of some issues to be avoided in scanning materials is the presence of atmospheric water vapor and CO<sub>2</sub> bands in NIR and also interferences from bright light sources for Raman instruments. Other criteria to check are the sampling conditions – to ensure consistent sample presentation to the instrument. Examples include ensuring attenuated total reflectance (ATR) crystals for mid-IR are cleaned and appropriate pressure is applied on the crystal when scanning. In addition, ensure that laser and light sources in Raman and NIR are also cleaned and no contamination from previous samples or inadvertent thumbprints is present that can cause extra peaks or noise in the baseline. Most matching algorithms match the library spectra peaks to the unknown sample peaks and return a match criterion – examples are typically a correlation match or a probability match. Noise in the baseline or in the peaks reduces this match criterion and may obscure minor peaks. By allowing noise in the library spectra and not generating the highest-quality library scans, matching algorithms will compare random noise peaks to a user scan, and as the noise structure changes with instrument or other conditions, the match criteria worsen. Most instrument algorithms have a cutoff threshold, based on signal-to-noise ratio (SNR) or peak matching. If the SNR is below a predefined instrumental measurement as defined by the ratio of (commonly) the highest peak to the standard deviation of the baseline, then the spectrum is predominately noise. For peak matching, instruments may typically use a dot product of the sample spectra peaks and compare to the internal library. A correlation or hit quality index (HQI) is calculated between the sample and the library materials and rank ordered. A predefined threshold value for the correlation or other metric is defined in the instrument, and if the match threshold is not met, then no match is found. Hence it is important to ensure that the library quality is as ideal as possible. Noise will always be present, but it is important that it not obscure or change the spectral signal information to such a degree it is not reliable.

Library models are typically built by choosing the most reproducible spectra of a material based on standards or other traceable materials. Once built, a library should be tested using validation and other test materials. These typically include materials from different lots, batches, and manufacturers. For pharmaceutical materials, this should not present a problem in correctly identifying the material due to reproducibility of similar materials. Some issues that may reduce match quality in molecular spectroscopy instruments are often due to changes in physical properties, for example, differences in particle size. Gross differences in particle size change the shape of the spectral peaks, and depending on the type of material and the type of matching algorithm used, the match criteria may decline to a point that a match is not found. Most instruments using a light source (laser or tungsten

lamp) have the light trace a path through the sample and then return as spectral information. Particle size, packing density, or similar issues may change that pathlength and affect the match quality. It may be necessary to include spectra of the same material but in different particle sizes – often in a sublibrary to be searched as part of a cascade algorithm. An example of the physical changes that affect spectra is the effect of polymorphism in Raman spectra. Polymorphic forms are chemically identical but have more than one crystal structure. This in turn impacts the physical properties that may impact the resulting spectra.

Chemical changes as they relate to changes in counterions or hydration states may also affect resulting spectra. While resolution of portable instruments may not be sufficient to clearly differentiate small changes in hydration states, for example, any changes may impact the resulting crystal packing. Depending on these effects, spectral changes may be sufficient to differentiate the types. However, with small changes, the corresponding spectral change may also be small and difficult to selectively differentiate.

An understanding of the effect of these changes need to be considered prior to adding a material as the reference library spectra. Clearly they can be used to identify materials of undesired physical or chemical properties as part of incoming inspection but also need to be considered when building a library that may require the library to contain several variants of a given chemical.

One good example that illustrates how a parameter can affect spectra and library build is the effect of water. Both mid-IR and NIR are sensitive to water, and NIR is an excellent tool used to build libraries and models that can detect and monitor moisture. For example, NIR can be used to monitor lyophilization products that are retained to ensure that levels of moisture are within acceptable parameters. -OH bands are clear in both mid-IR and NIR spectra and can be utilized to develop moisture models. Conversely, any moisture in a material can overwhelm the spectra in the mid-IR and to a lesser extent in the NIR. Raman spectra are less sensitive to the effects of moisture, but spectral peaks will shift and/or broaden due to effects of hydrogen bonding, so in these cases we see the effect of moisture or water contamination on the resulting spectra. This is useful as an inspection method as the effects of water contamination may be evident. A hygroscopic material (i.e. starches) especially may fail incoming inspection if it has become water contaminated. Models can also be built (generally in NIR) to ensure that a material has a certain range of moisture. These are all parameters that affect the process and the final product and need to be accounted for in any library build.

While particle size and moisture are the most common variables that may affect a product and thus need to be accounted for in a library build, users may have other specific issues that are relevant to their end use to consider. Most portable instruments have factory libraries (i.e. libraries prepared and distributed by the manufacturer) included, but each user may need to tailor the instrument libraries to their own specific use. Therefore, the most useful portable instruments will allow users to create custom libraries or applications and provide scientific support for that process.

One common area of support in building custom libraries, and especially in building factory libraries, is to check for the selectivity and specificity of the library materials. Most instruments allow the user to set a cutoff criterion or will give the user a score that defines how selective a result is. There are publications that define the analytical figures of quality and the associated metrics used to evaluate them. These include USP chapters (US Pharmacopeia 2019, Chapter 1225, 1058, 197), ASTM Statistical procedures (ASTM 2019) (E1488-12, E300-03, E122-17), and a very good overview of the terminology available as a spectroscopy supplement (Workman 2019).

All the aforementioned criteria need to be defined and understood in any robust library build to ensure reliable results in the field or site where the instrument is used. For portable instrumentation, the building of the library is done by technical experts who are qualified to build the most robust library. Often – once a portable instrument leaves the laboratory or factory – the end user is not an expert and requires the instrument to give them a rapid and reliable result. These end users most likely will not interpret any response, so it is important that the results can be used as required and are reliable. One example would be a hazardous material technician or first responder, who needs reliable information to determine his immediate action. It is also the case that the end user may require the library developer to justify how the library was built and the accuracy of the result, either as part of an FDA audit for pharmaceutical libraries or as an expert witness in the safety and security sphere.

## 3.4 Qualitative Model Development

All spectroscopic models, whether they are qualitative classification methods, library-matching algorithms, or quantitative multivariate methods, follow a similar development cycle (Figure 3.1).

Library quality data is acquired, and library quality spectra are generated as described in the previous section. A model is defined and built. For many portable instruments, the model built is based on library matching of a user sample to the internal factory library and the return of an HQI (correlation or probability match). Another common type of qualitative method may be the use of classification or clustering algorithms. These can be used as part of a library build to assess the quality of the library, or they can be used to develop offline models. The most common and useful methods are unsupervised clustering such as PCA or hierarchical clustering (HCA) and supervised clustering (SIMCA, CART), distance metrics such as Euclidean or Mahalanobis distances, and hit quality matches such as correlation or HQI and probability analysis (Gardner and Green 2014). These are commonly used to return an instrument result to define a material (discovery library search), to verify that the material is what it is supposed to be (pass/fail result), or to classify a material into a category or group. Most portable instruments also include mixture analysis, which uses spectral matching and deconvolution to return possible spectral contributors to the sample spectrum. The result is often a percentage of spectral contribution and should not be mistaken for mixture component percentage.

For quantitative results, the most common method is PCR or PLSR. These two methods are the workhorses of multivariate regression analysis and will return results that indicate quantity of a given variable or component in a sample. Examples include both chemical (i.e. percent moisture or starch in a sample) and physical (particle size range of a sample) variables. These types of models typically require more extensive model development and expert use.

In all cases, the models are evaluated using both calibration and validation data sets (data used to build the model and similar data but in varying batches, lots, and vendors). Statistical analysis of these models with the calibration and validation data will give indications of the robustness and reliability of the model. This step generally requires refinement of the model and subsequent re-testing. The best test of any model though is actual use, and as the instruments with the models are put into play, user experiences and issues will determine how suited to use the resulting models are.

## 3.5 Library Build

A key first step toward library building involves the collection and scanning of appropriate library materials. Appropriate library materials are those that are defined as fit for use for the methods required. Thus a library may be a collection of pure standard materials that will form the basis of a discovery search of materials, or it may be a focused library consisting of key materials. In any case, the library materials are equivalent to the materials that will be scanned by end users. The materials to be scanned must also cover the range of materials in terms of variations in lots, batches, vendors, and physical or chemical conditions that will be part of the testing protocol. For pharmaceutical applications, the use of a USP standard or equivalent material is also required, as the

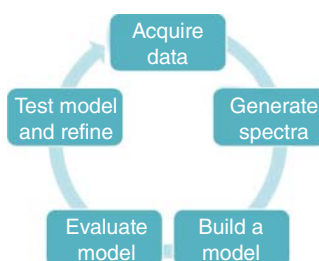


**Figure 3.1** Model development cycle overview.

library material requires a certificate of analysis or similar traceability. This is usually a pure material that will be used either for pure material verification or as a component in mixture analysis. For process control or testing, where mixtures are the result, a sublibrary of the mixture spectra can be used as verification. But in general, large libraries that are included in portable instrumentation contain only pure materials. It is also expected that these pure materials are added in as “best possible conditions” in order to generate the highest-quality spectra. Thus, pure materials are generally scanned in glass or quartz vials where the container materials do not contribute to any significance to the sample spectrum (Raman and NIR instruments). For mid-IR instruments, samples are usually run via ATR. Here it is essential that the ATR crystal be clean and that the surface of the crystal is covered by the sample. Liquids can be “dropped” onto the crystal, but solids need to be pressed down using an anvil with a standard pressure.

Once the highest-quality spectral scan is taken of a library material, the library materials need to be verified and validated. Verification is a multistep process and is generally considered an ongoing one as well. The first and easiest pass should be to scan using default settings (or normal operating conditions rather than library scan conditions). Scan the set of calibration materials used to build the library in the normal operating conditions. All these should return correct identifications with the appropriate matching statistics (common is the use of correlation scores, for example). The next step is using default conditions – rescan an alternative set of verification materials. Verification materials are the same type of materials as used in calibration but not part of the calibration set. So these may be samples from different lots, batches, or vendors. Again, these should pass the identification tests with appropriate statistics, and as well, any loss in statistical matching should not be too dissimilar. If a larger drop in correlation is noted in a sample between two vendors, for example, then spectra from both vendors’ material may need to be added to the library. The other criterion to test for in this round is to also scan through the sample’s common packaging materials. It is often the case that a library scan is taken of the material in a glass vial, but the ultimate user environment will be for an operator to test the material as it comes in receiving where the material is present in large drums and double bagged in plastic (often polyethylene). To avoid opening and potentially contaminating the incoming material, it is desirable to obtain confirmation of the material through the packaging. Thus scanning a material through the double bagging will be part of the verification process for that sample. Alternatively, many liquid samples arrive in large glass or amber bottles, and again verification testing should be done in the actual use conditions. Note that all these preceding examples are based on Raman and to a smaller extent on NIR instruments. For FTIR instruments, generating spectra requires the sample to be physically handled because of the instrument’s ATR method. Raman instruments have become increasingly useful because of the ability to scan through packaging and avoid any sample handling and potential contamination. NIR instruments were commonly used to scan materials whose Raman spectra could not be obtained due to fluorescence issues, but with the advent of lower fluorescing 1064 nm excitation instruments, the use of extra instrumentation is no longer as important. Raman instruments using 1064 nm excitation can be utilized with traditional Raman samples and also can be used for colored samples and materials that fluoresce with 785 nm excitation or materials that could previously only be scanned by FTIR.

In all cases, the order of library build should be summarized in the figure:

1. Acquire data: Use traceable standards if available (USP, JP, EP). Use external software or analytical instruments to verify the material if traceable standards are not available. Use pure materials for library build unless custom libraries for mixtures/process results/counterfeit are required.
2. Generate high-quality spectra: High signal, low noise. This represents your best spectrum of the material in question. Unless a custom mix/process library is being built, the spectrum should be of the pure material, without any peaks due to containers or packaging. For Raman or FTIR, one high-quality spectrum is often adequate for a library. NIR, due to its use of overtones or combination bands, may require multiple scans of the material.
3. Build a model: This is either a Discovery Library or Verification (Pass/Fail) Library for qualitative analysis. For quantitative analysis, the most common model is generally made using PCR or PLSR.

4. Evaluate the model: Other than generating the library scans, this is the most time intensive step as the model is verified using calibration and verification materials.
5. The model is constantly tested and refined with steps 4 and 5. If materials do not meet criteria set for match quality, then refining the model is required. In many cases this may involve reacquiring or adding data to meet the conditions. For qualitative library build, the most common requirement to acquire extra scans of a material may be due to physical or chemical changes that affect the reflectance path or change absorptivity of a material. These include particle sizes, counterion differences, crystallization changes (some due to waters of hydration), and polymorphism. Most pharmaceutical materials have strict criteria for any of these possible physical or chemical changes, so if the instrument can determine the difference, then this is another check for the sample not only to be the correct material but also to have the correct properties required.

The inherent variables to define and include in a library build are specified by each type of library built and may include any number of variables to consider. In the following case studies, one variable is used as an example of how this may impact a library build. The first case looks at the effect of including polymorph data into a custom pharmaceutical process library for a process input and resulting formulation. The second case study looks at the effect of counterions and their effect on selectivity for a series of common salts. While these case studies are focused on applications specific to Raman spectroscopy, a similar procedure would be used for FTIR or NIR data.

### 3.6 Case Study: Building a Polymorph Library

Ranitidine HCl exist in two forms – Form 1 and Form 2. The differences can be visualized in the Raman spectra (Figure 3.2) as the two forms differ in the small peaks present at 680, 1050, 1180, and 1650  $\text{cm}^{-1}$  and in the shape of the major peaks at 1250 and 1550  $\text{cm}^{-1}$ .

Overall, there is approximately 0.71 correlation between the two spectra. This is enough to separate the two spectra in a library, as a threshold cutoff (i.e. 0.80) can be set to return a pass for one form and a fail if the other form is present. In the example, one form is used exclusively in a formulation. Adding the two forms to a library will then be enough to ensure that the correct form is being added and also provide a check if the incorrect form is supplied.

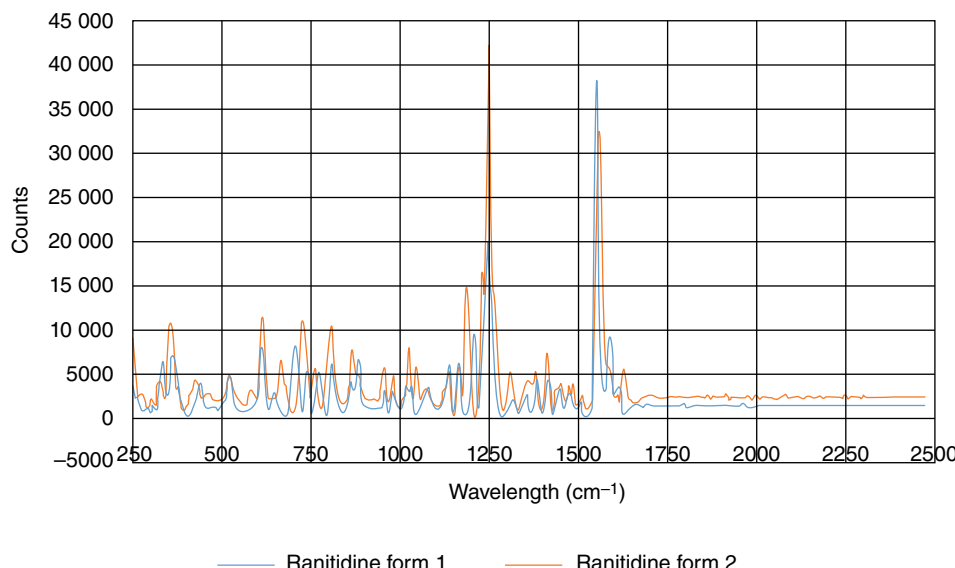


**Figure 3.2** Comparison of ranitidine Form 1 and 2 spectra.

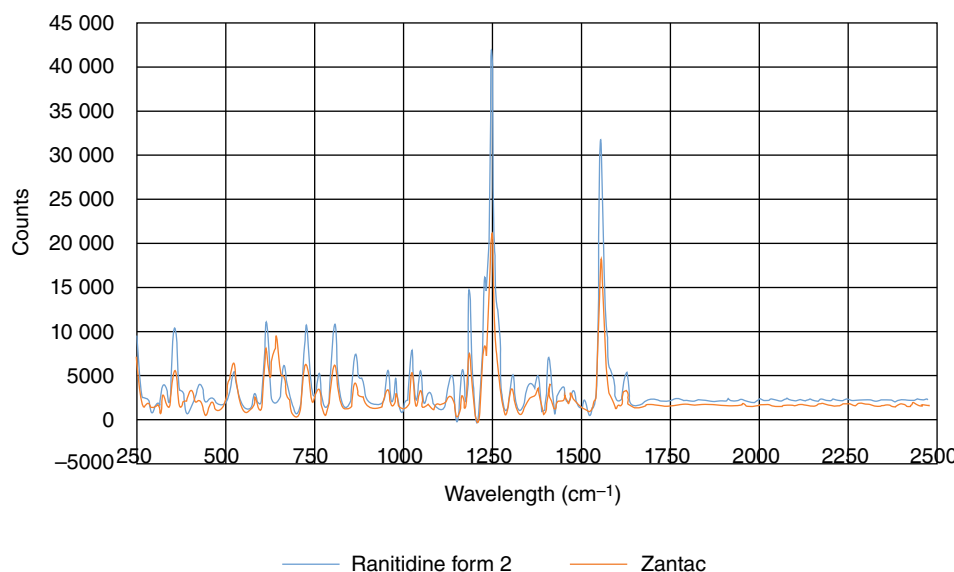


**Figure 3.3** Spectral overlay of Zantac and ranitidine Form 2 to show similar spectral features used to identify the form of ranitidine in Zantac.

Another check can also be added at the end of a process to ensure that the correct formulation used in a resulting product; in this case, Zantac contains ranitidine Form 2 and can be used to verify that the correct polymorph was added. A check of the spectra overlay of ranitidine HCl Form 2 with Zantac (Figure 3.3) shows good spectral overlay with the Form 2 features.

Since Zantac is a formulation, there are additional peaks present, due to the presence of other excipients. Comparison of Zantac with the two forms gives a correlation of 0.80 for Form 2 and 0.31 for Form 1, so there is a clear separation to show selectivity between the two forms.

Difference in polymorph types is important to characterize for any formulation as change in the polymorph will affect physical properties from solubility to bioavailability. In some cases, the incorrect polymorph form may cause product recall and extra expense to revamp process lines and ensure that the correct formulation is made.

## 3.7 Case Study: Counterions and Effect on Selectivity

Inorganic oxidizing salts are of especial interest in safety and security applications as they are both oxidizers and indicators of possible explosive mixtures. The primary salts of interest are anions such as nitrates, perchlorates, and chlorates. The most common cation salts are ammonium, potassium, magnesium, and sodium – although other metal cations can also be present.

It should be noted that the issues with selectivity of the counter cations raised by these other studies are common limitations for any portable Raman instrument. Portable instruments provide clear advantages in rapid response on-site in many hazardous situations, but as a trade-off to the speed and portability, these instruments do not have the resolution of bench-type instruments, and selectivity issues will be present in a greater amount for portable instrumentation.

### 3.7.1 Identification of Anionic Salts

The most common anionic salts of interest to safety and security applications are differentiation of nitrates, chlorates, and perchlorates. These are the main oxidizers as identified in CBRNE Tech Index (CBRNE 2019) and IABTI

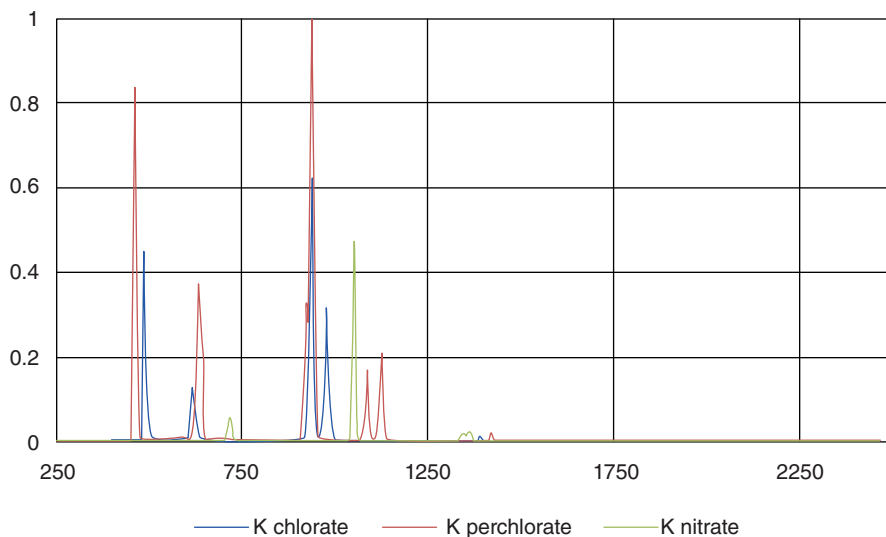


**Figure 3.4** Example of anionic forms of potassium salts.

lists. All these salts show characteristic spectra peaks that allow for differentiation in Raman spectra. Nitrates ( $\text{NO}_3^-$ ) can be differentiated from chlorates ( $\text{ClO}_3^-$ ) due to characteristic N–O bands. Chlorates can be differentiated from perchlorates ( $\text{ClO}_4^-$ ) due to the different number of oxygen atoms in these two anions, which gives them different molecular geometries: pyramidal for chlorates and tetrahedral for perchlorates. As an example, the Raman spectra of potassium chloride and potassium perchlorate are shown in Figure 3.4, where the red trace is from the chloride and black is from the perchlorate salt. There is sufficient peak separation and differences in the major peak to enable the differentiation of the chloride and the perchlorate. Similarly, spectra of nitrate and chloride anions also show sufficient differences in the peaks to enable these types of salts to be differentiated and identified.

Therefore even with the limitations of resolution present in portable Raman instrumentation, it is feasible to differentiate the most common types of anionic salts found in hazardous situations – nitrates, chlorates, and perchlorates.

### 3.7.2 Selectivity of the Cationic Salts

While the identification of the different anionic salts is relatively straightforward in most cases, the selectivity within each salt is inherently more difficult. Studies of bench-type instruments have shown that while the anion (nitrate, chloride, and perchlorate) is influenced by the cation type, this is a very slight effect that results in only a slight shift in the anion peak position. Figure 3.5 shows the Raman spectra of potassium, sodium, and magnesium nitrates. Note there are only slight differences in peak position for the main peak and slighter shifts for the smaller peaks. These small differences make selectivity very difficult for certain cation salts and preclude selectivity for a subset of cations. These findings were also reported in the cited reference (Zapata and Garcia-Ruiz 2018), which found that while the cation did influence the spectra so that a shift in the peak positions resulted, in some cases the shift was below the resolution limits of the instrument. The conclusion was that there were certain cation species that were not selective. Of course, identification of the cation is straightforward using portable elemental analyzers (e.g. X-ray fluorescence and laser-induced breakdown spectroscopy), and the reader is referred to those chapters for more details.

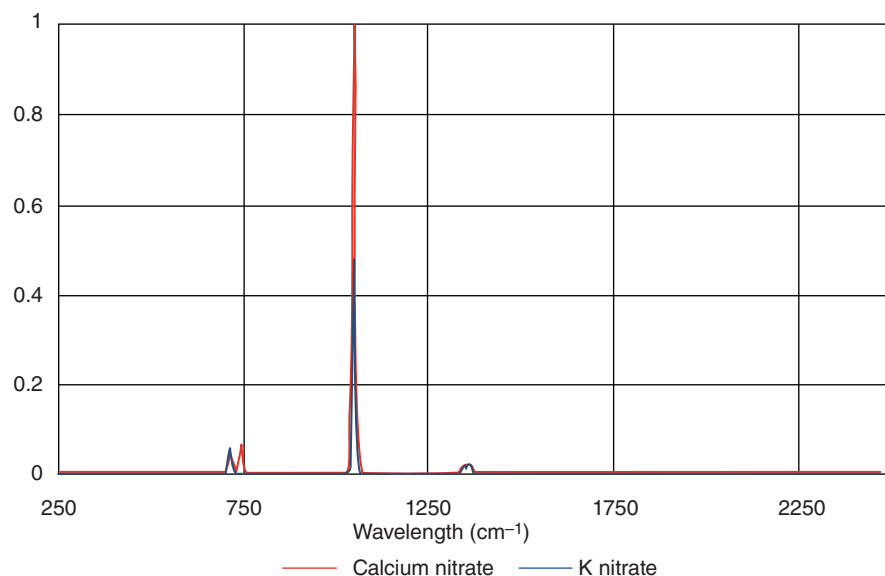


**Figure 3.5** Comparison of spectra for nitrate forms of calcium and potassium salts.

### 3.8 Case Study: Effect of Moisture on Peaks of Ammonium Nitrate

For ammonium nitrate, the N–H Raman bands of the ammonium cation are weak, and the dominant peaks in the spectra are due to the N–O stretching modes of the nitrate anion (Figure 3.6.). So little extra information is provided by the N–H bands.

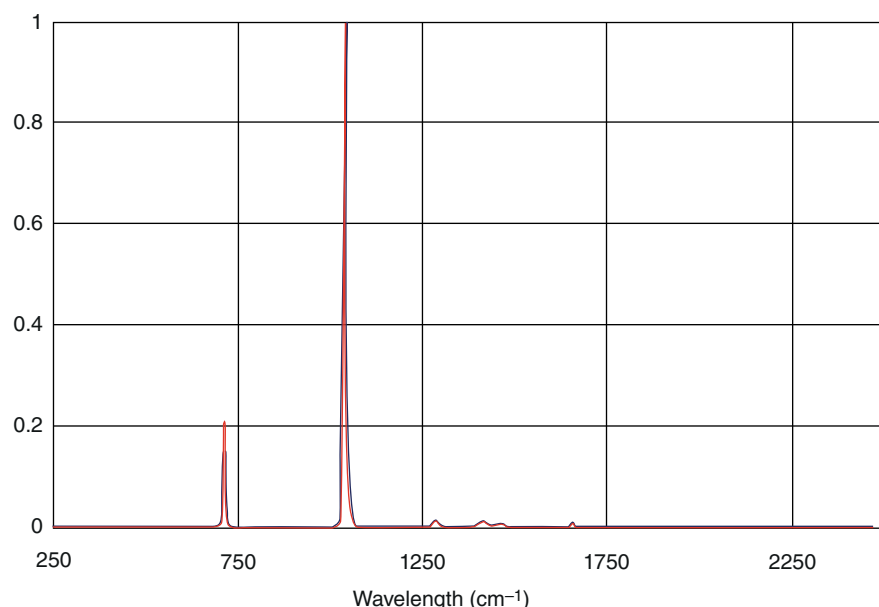


**Figure 3.6** Comparison of ammonium nitrate spectra and the peak broadening effect of moisture.

Therefore, any physical changes to the ammonium nitrate tends to offset the advantage of the extra information. The physical changes that can change a spectrum are typically particle size and changes in the peaks due to moisture. While water O–H peaks are not present in Raman spectra, the effects of moisture are. Peaks tend to broaden and shift in the presence of moisture especially as the water hydration spheres surround the ions.

This is a common effect for ammonium nitrate as it is hygroscopic (picks up moisture easily). This results in peak shifts that, while slight, are often enough to cause selectivity issues with other cation salts of nitrates. Since in some cases, the peak shifts due to different cation salts are between 6 and  $10\text{ cm}^{-1}$ , which tends to be less than the resolution of the majority of portable Raman instruments.

### 3.9 Case Study: Selectivity in an Explosive Sublibrary

Accepting and understanding the above conditions will determine the ultimate selectivity in a library that contains varying cation and anion types useful for an explosive library. It is suggested that after the spectra are collected so as to give the optimal spectrum for each material, further visualization and analysis of the data can be done to determine if there are any selectivity issues. Principal component (PC) plots (discussed in the next section) and correlation mapping are two valuable tools to determine if any library materials in a library may potentially misidentify as each other. For the cations and anions discussed, a simple correlation plot was made (Figure 3.7).

Areas off-center that may cause issues in selectivity are highlighted, based on the match threshold cutoff. For example, a default cutoff threshold of 0.80 will result in any of the yellow or red highlighted materials potentially causing false positives. By increasing the threshold to 0.90, only materials highlighted in red may cause selectivity issues. In this example, setting a threshold of 0.96 should be adequate to ensure that the library is selective for the materials tested. The correlation mapping can be expanded to include other materials (such as peroxides) in the library to identify (a) which materials may have selectivity issues with other materials and if so (b) then what should the cutoff threshold be set to avoid these issues. Note that if the materials are too similar to differentiate, then a custom application may need to be built to separate out just those materials of interest. This may involve selection of specific wavelengths that are distinct between the materials or tailored processing of the spectra.

In all the preceding cases, the important points are that both chemical and physical characteristics need to be accounted for in any library build, as these changes will affect spectra and the final library performance.

	Potassium chlorate	Potassium perchlorate	Ammonium nitrate	sodium nitrate	Calcium nitrate	Strontium nitrate	SPCAN	CAN	Potassium nitrate
Potassium chlorate	1.00	0.58	0.01	0.01	0.01	0.00	0.01	0.01	0.01
Potassium perchlorate	0.58	1.00	0.02	0.00	0.01	0.01	0.01	0.02	0.01
Ammonium nitrate	0.01	0.02	1.00	0.11	0.92	0.48	0.63	0.82	0.83
Sodium nitrate	0.01	0.00	0.11	1.00	0.05	0.02	0.01	0.26	0.02
Calcium nitrate	0.01	0.01	0.92	0.05	1.00	0.54	0.43	0.85	0.95
Strontium nitrate	0.00	0.01	0.48	0.02	0.54	1.00	0.03	0.74	0.38
SPCAN	0.01	0.01	0.63	0.01	0.43	0.03	1.00	0.21	0.30
CAN	0.01	0.02	0.82	0.26	0.85	0.74	0.21	1.00	0.75
Potassium nitrate	0.01	0.01	0.83	0.02	0.95	0.38	0.30	0.75	1.00

**Figure 3.7** Correlation map of common explosives and precursors to highlight potential selectivity of these materials.

## 3.10 Quantitative Method Development

Many of the procedures used to build quantitative models begin with qualitative or library development. Thus, while this section details the general steps for building a predictive model, the same sequence of steps is used to build classification or library models. Quantitative models then proceed into regression analyses, followed by more rigorous metrics to evaluate the model.

To begin, any model begins with the appropriate choice of instrument and a reliable source of data. For bulk analysis of materials (i.e. not trace analysis), FTIR, Raman, and NIR are appropriate choice of instruments provided the material has strong bands in the respective instrument choice. For instance, highly polar molecules (e.g. water, sugars) can be weak Raman scatterers but very strong absorbers in the IR region. Bulk analysis generally refers to a material that is present in greater than 5–10% of a mixture, although in certain instances the limit of quantitation is lower. An example of this is the detection of water in FTIR and NIR especially. However in general, as the levels present fall below 5% for a mixture component, the results become less robust.

The appropriate choice of data is also one of the most important criteria for how well a model or library performs. The data should cover the range of model required and account for similar variables to how and where the model is expected to perform; however, any model is only as good as the data that goes into it, so the appropriate acquiring of data cannot be stressed enough. No amount of preprocessing or massaging of data will compensate for poor or inappropriate data collection. It should also be stated that data to be used in library or model development is traceable and robust and should be the highest quality that can be obtained on that instrument. For library development, data is usually recommended to be obtained from a traceable source, and USP standard or equivalent materials are preferred. Unless this is part of the library design, there should not be any competing spectral features due to the container or other component interferences. Any data to be used in regression analysis must also be robust and reliable. Quantitative data should be obtained from verified and known methodology. Reference methods to obtain values are cited in several compendia (USP has a large number of references for methods and techniques, as does ASTM), and these have been previously cited as references for library build.

Overall, any data used in a model should be representative such that any variations are considered. Especially for quantitative models, variation in conditions may affect the scope of the predictions, for example, local data makes local models. To truly make a global model, variations in data conditions must be considered. This is especially important for any model for the food, feed, and agricultural data, as growing conditions and environments affect the resulting data used in the spectra. Another consideration to check is that the predictive value being measured is significant and not a series of random events. A model will collapse upon testing if there is not a relationship between spectra and an associated value.

### 3.10.1 Data Pretreatment

Once robust and reliable data is obtained, and prior to building models, most data undergoes some pretreatment steps (Figure 3.8).

A general illustration of common steps involves preprocessing of the data to remove baseline effects and to reduce noise or other variation and other common preprocessing steps. The net purpose of this step is to retain the significant information and reduce the noise. A minimalist approach is preferred as any data pretreatment has the side effect of changing the data and can remove information as well. The most common types of preprocessing are usually baseline correction using a first- or second-order derivative polynomial fit to reduce baseline effects and emphasize spectral differences. Library design often incorporates a normalization step in order to compare spectra. For NIR data, standard normal variate (SNV) pretreatment is also common due to the variation in the NIR spectra as replicates are taken. For further explanation of any of these methods, standard chemometric textbooks (Massart et al. 1997) are available.

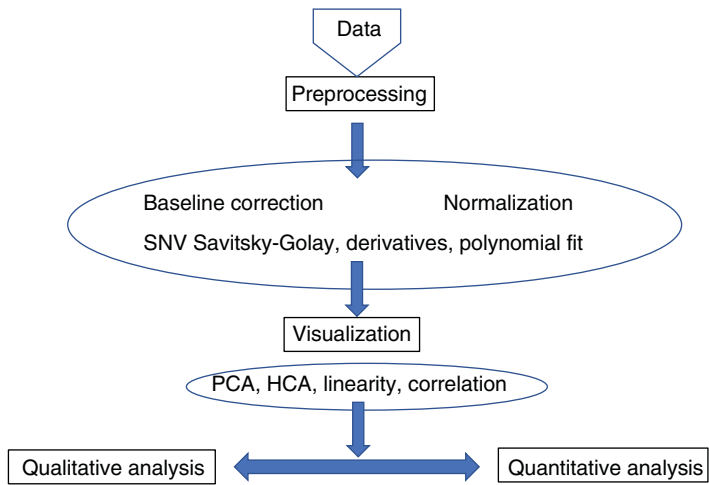


**Figure 3.8** Funneling of data through preprocessing and data visualization prior to analyses and method development.

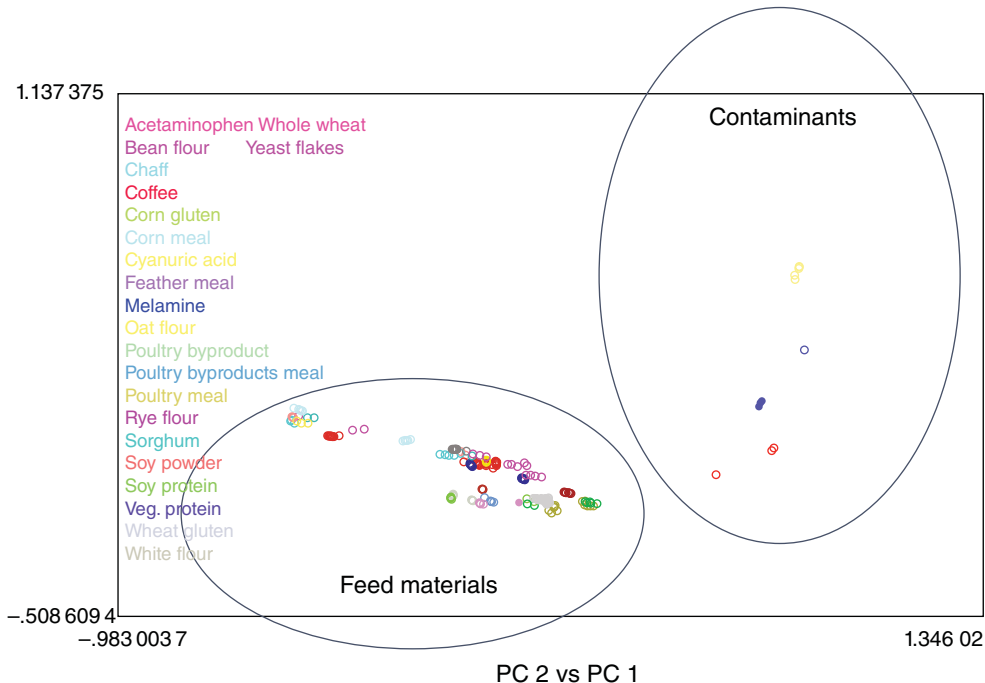


**Figure 3.9** Principal component plot shows clusters from contaminants and feed materials.

Next, the preprocessed data is often visualized in order to detect patterns or any anomalies. A common method is to use PCA to visualize natural groupings within data, as well as to provide a preliminary check on spectra and variable relationships. As an example of PCA used to evaluate natural groupings in data, the plot of PC1 and PC2 for a series of NIR spectra of feed ingredients and common feed contaminants is shown (Figure 3.9). The feed ingredients are separated from the common contaminants, and a gross differentiation of feed ingredients based on protein and carbohydrates is also visualized. This allows an indication of possible selectivity in any library build

as well. If materials are separated on a PC plot, then we can estimate that they are less likely to misidentify as other components in a library. Conversely if materials are not separable on the plot, then the potential for false-positive identification is possible, and other methods may need to be applied to separate the two components. A good check is that the material in question should cluster with “like” materials and be clearly separable from other groups. To fully utilize the clustering capability of PCA, it is best to have variants of a material and replicates. Clusters should be tight within replicates and similar materials and clearly separated from other clusters. A distance metric may be applied to define these cluster differences.

Especially relevant to selectivity issues is when replicate spectra are taken of a material and all replicates and materials are plotted on a PC plot. Potential selectivity issues are expected when the cluster of replicates have a larger cluster that may overlap that of competing materials.

For quantitative analysis, the use of a PC plot is also useful for estimating model viability. If the spectral data and the corresponding values are related and a regression model is possible, this is often reflected in a PC plot. For example, a plot of PC1 and PC2 (most common, though other PCs may be significant) may show a linear relationship that approximates the quantitative values. This may be an indication that the regression analysis will also be linear and a successful model can be built. Conversely, if there is an assumption of a linear relationship but the PC plot does not show this, then further evaluation of the data is required.

In the plot shown (Figure 3.10), it had been previously assumed that a feed sample could be monitored for protein, but the PC plot shows separation of the data into two clusters. These clusters are related to the source of the spectra, so what was driving the differences in the spectra was actually laboratory variability. When the resulting regression model was tested against external test samples, no predictive ability was found.

A common issue with not clearly understanding the data is this poor predictive ability. Most data models only rely on the use of correlation models, which are only useful for the prediction of linearity of the data (and any two points can make a line and a perfect correlation). That is why it is important to use other metrics and quick tools to visualize and assess data (such as PCA) prior to building any regression models or making assumptions about the data. If assumptions are made that the values and spectra are related when there is not a robust relationship, then the resulting model tends to predict to the mean of the data. So predictions tend to be the mean  $\pm$  standard deviation of the data, and while a number is returned, it is meaningless in its predictive ability. A good visualization

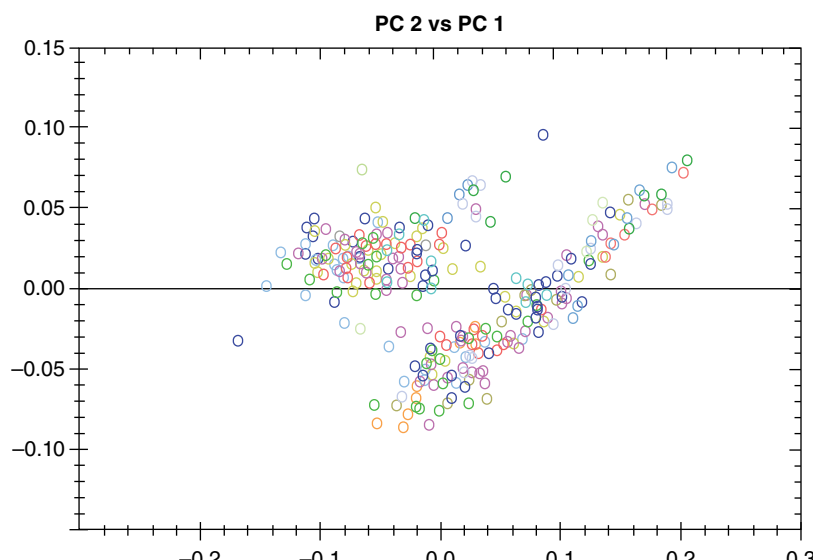


**Figure 3.10** Principal component plot gives clusters that indicate variability due to source rather than predictive ability for desired metric.

tool for this is to plot the data in PC space. A large “blob” of data indicates no variability has been found within the given PCs. Translated to a regression plot, what may be observed is a large “blob” of data centered about the mean of the values. Drawing a linear regression fit line through this data and returning a correlation metric will not make this type of model predictive for test data and ultimate end use.

## 3.11 Building Meaningful Predictive Models

As mentioned, predictive model building tends to require data that spans the possible conditions the model will be used for. As this tends to require a rather comprehensive data set, it is proposed that a smaller local model be built initially for proof of concept. This will give an estimation of whether the predictive measurements will work, and a larger global model will give robust and reliable results. A case study of the workflow for a proof of concept is given below.

## 3.12 Case Study: Prediction of Protein Levels in Flour Samples

NIR is a well-researched and utilized method for the determination of common parameters such as protein, moisture, and fats in food and feed analysis. Predictive models for protein and moisture especially tend to be robust and reliable. In this case study, a data set of 25 samples was used to build a predictive PLSR model for protein in wheat. This was a proof of concept study to show that the instrument can be used to predict on a local model. This was done prior to building a global model to ensure that this metric could be reliably predicted. Once proofed, the more extensive data collection and model building can be done for a global model. To begin, wheat samples were collected from a known source. All samples had reference values for protein levels obtained from a reference method (Kjeldahl measurement). The data was split into calibration data (used to build the PLSR models) and validation data. Data from both sets spanned the range of the protein measurements. Scanning with the NIR instrument was done in triplicate, and over triplicate positions, to account for scan and sample variations. Spectra were then evaluated for obvious anomalies such as outliers or noise.

Preprocessing of the spectra used SNV to offset particle inhomogeneities and packing differences and also Savitzky–Golay first-order derivative and second-order polynomial smoothing. The smoothing algorithm used a minimal point smooth (5 points) in order to reduce the noise but still retain features associated with changes in protein levels. Too high a smoothing will also smooth out small peak differences that are useful for protein differentiation. In this case there are small peak differences due to N–H overtone and combination bands over the effective wavelength ranges of 1700–1750 nm and 1960–2300 nm.

After preprocessing, the spectra were evaluated again to focus in on specific regions associated just with the protein differences. A comparison of the initial data and the preprocessed data is shown (Figure 3.11), with the preprocessed data focused in on the peaks that show variation due to the N–H overtone and combination regions.

After visualization inspection of the preprocessed data, a PLSR model is developed. This requires an examination of the scores (plot of latent variables or a PCA plot) to assess if there is inherent structure in the data and plots to determine the number of factors that are required for the resulting PLSR model. Recall that PLS is a data reduction method that determines the number of latent variables that contain information about the variable of interest (protein in this example) and then shifts noninformation-containing (noise) to higher latent variables. In this example, a plot of latent variables versus root mean square error (RMSE) showed that three latent variables are adequate to describe the information in the system. Thus the resulting PLSR model contains three variables. Adding any more will just result in adding back the noise into the system. This can also be seen in a plot of the loadings for each successive factor. The first loading plot is equivalent to the mean of the spectral plot, the next two loading plots encode spectral features important for the protein structure, and the subsequent loading plots just

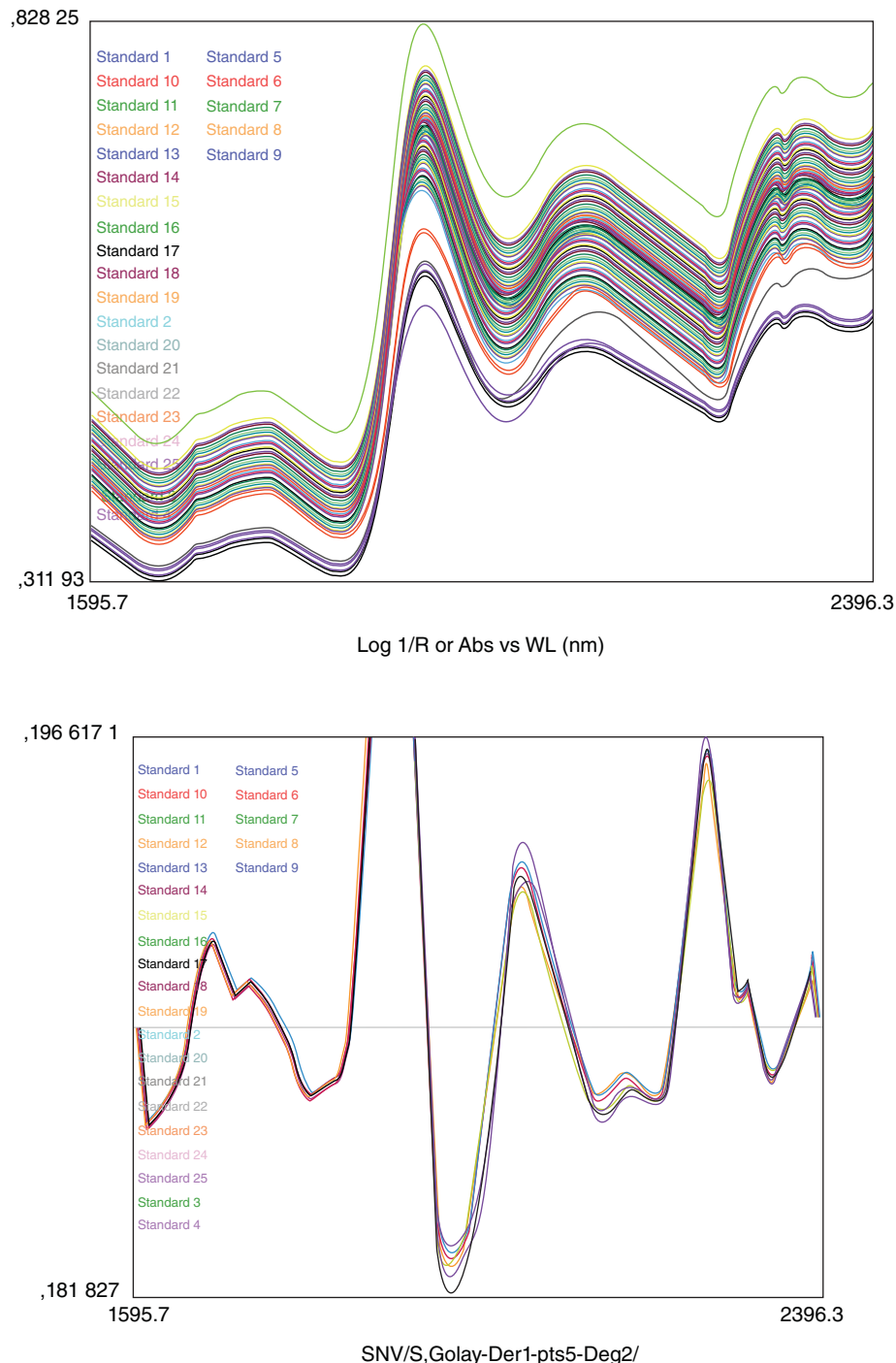


**Figure 3.11** Spectra of wheat samples with varying protein levels from instrument and after preprocessing. Spectral range is narrowed to focus on N-H regions.

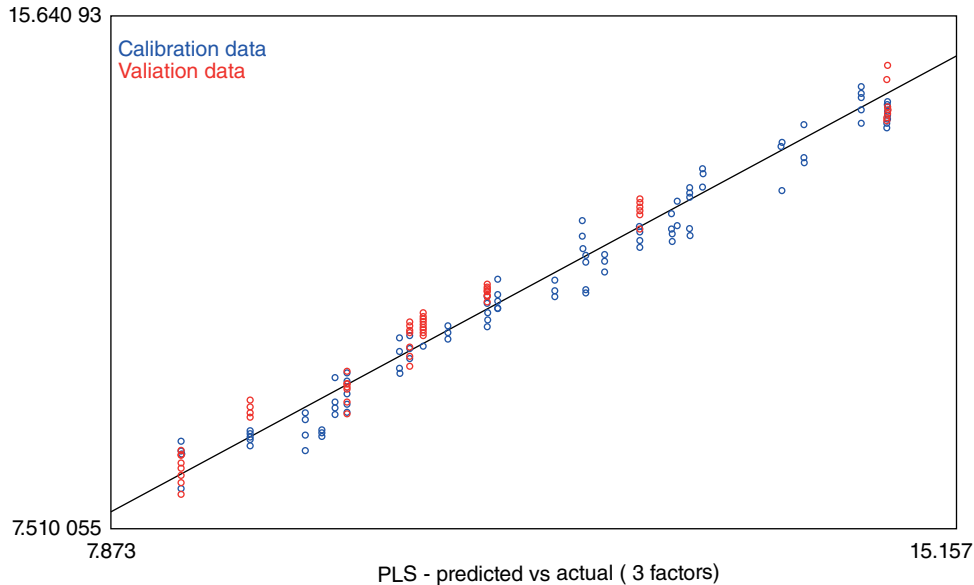


**Figure 3.12** PLS regression results for protein in wheat with calibration and validation predicted results.

show random variations, indicating a lack of useful signal. Thus, it was determined that 3 factors were optimal for the PLS model, based on the plot of factors and associated root mean square error of cross-validation (RMSECV), and past three-factor loading plots show increased loss of information and increased noise. The first three factors indicate the importance of the C–H combination bands at 1700 nm, the overtone bands at 2200–2300 nm, and the nitrogen overtone and combination bands at 2000–2200 nm regions.

The PLSR model for the prediction of protein in wheat was then built and evaluated using root mean square error of calibration (RMSEC) and RMSECV. A plot of the predicted versus the reference values also allows for the correlation result (Figure 3.12).

A further set of samples, not part of the initial data set used to build the model, is then tested, and a root mean square error of prediction (RMSEP) is made. There should be a clear consistent story for the data results. Any anomalies need to trigger an investigation into what is causing instability in the data. For example, examination of RMSEC, RMSECV, and RMSEP should show increasing but consistent errors. If RMSEP is much higher in error than using just the calibration and validation data, then the model may not be robust and could collapse predictive ability for data outside the model set. Examination of the residuals is also important information to assess the model. Residuals should be random and distributed about the zero, without any obvious pattern (Figure 3.13).

In all plots shown, both the data used in the calibration and any predictive data are included and should be consistent behavior between the calibration and prediction sets.

### 3.12.1 Further Steps for Building Up a Base Model

If the proof-of-concept local model gives reasonable results and is considered robust for prediction, then the next steps would use the model to predict on further external data. In building a global model, this may result in new data being added to the model and the model rebuilt with new RMSEs and analysis. This usually occurs when some variable not accounted for in the initial model is present in new data. It tends to arise in feed and related applications, because spectral changes may arise due to changes in growing conditions. So if the model is to be robust, it must include this type of data in the structure. Even after years of using a model successfully, there may arise conditions that result in the model being updated and revised. A good model will stand the test of time and

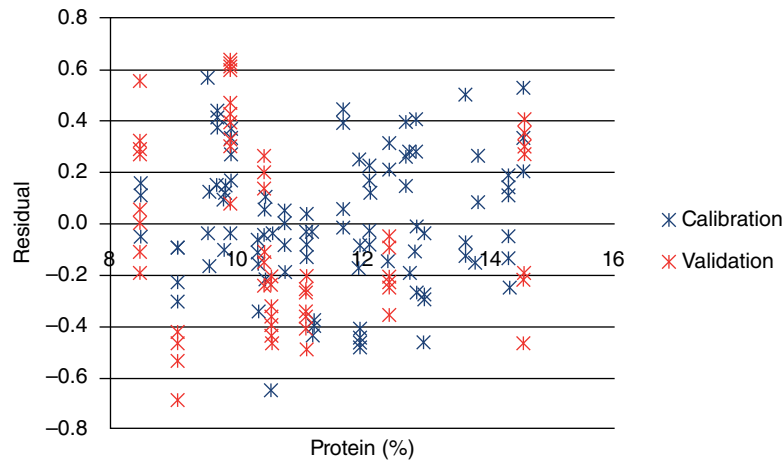


**Figure 3.13** Residual analysis of protein in wheat for calibration and validation data.

be flexible enough to allow for differing conditions without collapsing. Once a model is built, there will still be upkeep associated with it, as samples may change and new data and revisions need to be taken into account. That is why the model build process shown at the beginning of this chapter is cyclical.

One further criterion used to evaluate models built on portable instruments is to evaluate the transferability of the model from one instrument to another. The capability of cloning a model built on one instrument to a fleet of instruments is especially important for portable instruments. It is often the requirement that the predictive model and/or the library is developed at one location by an expert user. However, this model or library then needs to be transferred across multiple instruments in order to be used for the intended purposes.

Library transfer and model transfer may involve instrument standardization algorithms. A standardized library transfer procedure, for example, will involve comparison of test sample spectra between the parent and child instrument and subsequent adjustment of the calibration axes. Spectra are usually normalized, and baseline is corrected between instruments to allow for library transfer. For predictive models, there are additional steps beyond ensuring that spectra are similar between instruments. In predictive models, bias and slope adjustment may also be required. This can be tested by analyzing the bias and slope observed from a model on the parent and the child instrument. Bias adjustment is a rather straightforward process and is usually enough to adjust most models to give similar predictive abilities on both parent and child. Slope adjustment or any other requirements, if needed, will add increasing levels of difficulty in transferring models and require more expert correction. Testing across the fleet of instruments is usually performed on a common set of standards to evaluate the transferability of the models and libraries.

### 3.13 Summary

While not comprehensive, this chapter has presented some of the more general and commonly encountered issues in building libraries and models on portable instruments. The main driver for building both discovery libraries and predictive models is the generation of high-quality spectra from known and verified data, suitable to the requirements. This gives a solid foundation to any subsequent library analysis. Evaluation of a library then depends on selectivity testing to ensure that samples are correctly identified when present (true positives, true negative) and do not interfere in subsequent analysis (false positives, false negatives).

It is also obvious that any predictive models need to have data suitable for the prediction of a variable over the range desired. The model needs to be evaluated for its predictive ability using appropriate metrics – for linear

PLSR models, metrics include assessing the structure of the data (loadings, PCA plots, residuals), evaluating the predictive ability (RMSE, correlation plots), and testing the model against data both within and outside the model data set.

While only a few metrics and tools were covered in this chapter, there are many references that give details on model metrics and where to appropriately use them. The result of any of the described variables and those given in other test protocols is to increase the robustness of any library or model and ensure that these will be fit for use in appropriate user environments.

## References

- Altinpinar, S., Sorak, D., and Siesler, H.W. (2013). Near infrared spectroscopic analysis of hydrocarbon contaminants in soil with a hand held spectrometer. *Journal of Near Infrared Spectroscopy* 21: 511–521.
- Alula, M.T., Mengesha, Z.T., and Mwenesongole, E. (2018). Advances in surface-enhanced Raman spectroscopy for analysis of pharmaceuticals: a review. *Vibrational Spectroscopy* 98: 50–63.
- de Araujo, W.R., Cardoso, T.M.G., da Rocha, R.G. et al. (2018). Portable analytical platforms for forensic chemistry: a review. *Analytica Chimica Acta* 1034: 1–21.
- ASTM. (2019). Standard guide for statistical procedures for use in developing and applying test methods. ASTM E148-12, E300-03, E122-17.
- Bio-Rad (2019). *Bio-Rad KnowItAll Software*. California: Hercules www.bio-rad.com.
- CBRNE. (2019). CBRNETechIndex-Threat Card.
- Ciza, P.H., Sacre, P.-Y., Waffo, C. et al. (2019). Comparing the qualitative performances of handheld NIR and Raman spectrophotometers for the detection of falsified pharmaceutical products. *Talanta* 202: 469–478.
- Das, R.S. and Agrawal, Y.K. (2011). Raman spectroscopy: recent advances, techniques and applications. *Vibrational Spectroscopy* 57: 163–176.
- De Beer, T., Burggraeve, A., Fonteyne, M. et al. (2011). Near infrared and Raman spectroscopy for the in-process monitoring of pharmaceutical production processes. *International Journal of Pharmaceutics* 417 (1–2): 32–47.
- Deidda, R., Sacre, P.-Y., Clavaud, M. et al. (2019). Vibrational spectroscopy in analysis of pharmaceuticals: critical review of innovative portable and handheld NIR and Raman spectrophotometers. *Trends in Analytical Chemistry* 114: 251–259.
- Farber, C., Mahnke, M., Lee, S., and Kurouski, D. (2019). Advanced spectroscopic techniques for plant disease diagnostics. A review. *TrAC Trends in Analytical Chemistry* 118: 43–49.
- Fountain, A.W. III, Christesen, S.D., Moon, R.P., and Guicheteau, J.A. (2014). Recent advances and remaining challenges for the spectroscopic detection of explosive threats. *Applied Spectroscopy* 68 (8): 795–810.
- Gardner, C. and Green, R.L. (2014). Identification and confirmation algorithms for handheld spectrometers. In: *Encyclopedia of Analytical Chemistry* (ed. R. Meyers). New York: John Wiley & Sons, Ltd.
- Grassi, S. and Alamprese, C. (2018). Advances in NIR spectroscopy applied to process analytical technology in food industries. *Current Opinion in Food Science* 22: 17–21.
- Khandasammy, S.R., Fikiet, M.A., Mistek, E. et al. (2018). Bloodstains, paintings and drugs: Raman spectroscopy applications in forensic science. *Forensic Chemistry* 8: 111–133.
- Lopez-Lopez, M. and Garcia-Ruiz, C. (2014). Infrared and Raman spectroscopy techniques applied to identification of explosives. *Trends in Analytical Chemistry* 54: 36–44.
- Luypaert, J., Massart, D.L., and Heyden, Y.V. (2007). Near infrared spectroscopy applications in pharmaceutical analysis. *Talanta* 72: 865–883.
- Massart, D.L., Vandeginste, B.G.M., Buydens, L.M.C. et al. (1997). *Handbook of Chemometrics and Qualimetrics, Parts A and B*. Amsterdam: Elsevier.

- Mecker, L.C., Tyner, K.M., Kauffman, J.F. et al. (2012). Selective melamine detection in multiple sample matrices with a portable Raman instrument using surface enhanced Raman spectroscopy-active gold nanoparticles. *Analytica Chimica Acta* 733: 48–55.
- Modroño, S., Soldado, A., Martínez-Fernández, A., and de la Roza-Delgado, B. (2017). Handheld NIRS sensors for routine compound feed quality control: real time analysis and field monitoring. *Talanta* 162: 597–603.
- de Oliveira Penido, C.A.F., Pacheco, M.T.T., Lednev, I.K., and Silveira, L. Jr., (2016). Raman spectroscopy in forensic analysis: identification of cocaine and other illegal drugs of abuse. *Journal of Raman Spectroscopy* 47: 28–38.
- Pasquini, C. (2018). Near infrared spectroscopy: a mature analytical technique with new perspectives. *Analytica Chimica Acta* 1026: 8–36.
- Porep, J.U., Kammerer, D.R., and Carle, R. (2015). On-line application of near infrared (NIR) spectroscopy in food production. *Trends in Food Science & Technology* 46 (2): 211–230.
- Roggó, Y., Chalus, P., Maurer, L. et al. (2007). A review of near infrared spectroscopy and chemometrics in pharmaceutical technologies. *Journal of Pharmaceutical and Biomedical Analysis* 44: 683–700.
- da Silva, V.H., da Silva, J.J., and Pereira, C.F. (2017). Portable near infrared instruments: application for quality control of polymorphs in pharmaceutical raw materials and calibration transfer. *Journal of Pharmaceutical and Biomedical Analysis* 134: 287–294.
- Sorak, D., Herberholz, L., Iwascek, S. et al. (2012). New developments and applications of handheld Raman, mid-infrared and near-infrared spectrometers. *Applied Spectroscopy Reviews* 47 (2): 83–115.
- US Pharmacopeia. (2019). USP Chapter 1225, 1058, 197.
- Vítek, P., Ali, E.M.A., Edwards, H.G.M. et al. (2012). Evaluation of portable Raman spectrometer with 1064 nm excitation for geological and forensic applications. *Spectrochimica Acta Part A: Molecular and Biomolecular Spectroscopy* 86: 320–327.
- Weatherall, J.C., Barber, J., Brauer, C.S. et al. (2013). Adapting raman spectra from laboratory spectrometers to portable detection libraries. *Applied Spectroscopy* 67 (2): 149–157.
- Workman, J.J. (2019). The molecular spectroscopy terminology guide. *Spectroscopy* 34 (supplement s2): 8–38.
- Zapata, F. and Garcia-Ruiz, C. (2018). The discrimination of 72 nitrate, chlorate and perchlorate salts using IR and Raman spectroscopy. *Spectrochimica Acta Part A: Molecular and Biomolecular Spectroscopy* 189: 535–542.
- Zeaiter, M. and Rutledge, D. (2009). Preprocessing methods. In: *Comprehensive Chemometrics: Chemical and Biochemical Data Analysis* (eds. R.T. Steven and D. Brown), 121–231. Amsterdam: Elsevier.

## 4

### Applications of Portable Optical Spectrometers in the Chemical Industry

Xiaoyun Chen<sup>1</sup>, Mark A. Rickard<sup>2</sup> and Zhenbin Niu<sup>3</sup>

<sup>1</sup>*Analytical Science, Core R&D, Dow Chemical, Midland, MI, USA*

<sup>2</sup>*Safety & Construction, DuPont de Nemours, Inc., Wilmington, DE, USA*

<sup>3</sup>*Dow Performance Silicones, Dow Chemical, Midland, MI, USA*

#### 4.1 Introduction

Vibrational spectroscopy is a well-established technique widely found in analytical labs throughout the chemical, petrochemical, and materials industries [1]. Before the 1990s, vibrational spectroscopic analysis was typically practiced in analytical or quality control (QC) labs using benchtop instruments. Such instruments were not designed to be easily moved due to their large size and the potential to adversely affect the alignment of sensitive optical elements. In the 1990s, many groups reported the development of portable spectroscopy systems for Raman [2], near-infrared (NIR) [3], and mid-infrared (MIR), but they remained mostly research tools rather than robust tools ready to be deployed for general problem solving [4]. The convergence of many technologies paved the way for the commercialization of portable vibrational spectrometers in the 2000s [5]. This work focuses on providing a concise summary of recent examples of portable vibrational spectrometers in the chemical and petrochemical industry in the first part. In the second part, several recent examples from the authors are presented in detail to further illustrate the diverse and versatile applications of portable vibrational spectrometers. In this chapter, we will mainly focus on three vibrational spectroscopy techniques: infrared spectroscopy (IR), NIR spectroscopy, and Raman spectroscopy. There are several other optical spectroscopy techniques used in research and development (R&D) and QC labs, such as far-IR or Terahertz (THz) spectrometers, fluorescence spectroscopy, and ultraviolet-visible (UV-vis) spectroscopy. These techniques tend to provide more specific information for specialized applications than the chemical information provided by IR, NIR, and Raman spectroscopy. For the definition of portable spectrometers and handheld spectrometers, the reader is referred to a recent review article by Crocombe [6].

One general type of application that has been revolutionized by portable spectrometers is *in situ* reaction monitoring. There are numerous benefits of *in situ* monitoring of reactions with vibrational spectroscopy. (i) It enables the tracking of transient and labile intermediate species, which are intractable by *ex situ* analysis. (ii) It does not perturb the reaction, especially for reactions involving equilibria, small volumes, or sensitivities to air or moisture. (iii) It permits the study of fast reactions that are impractical for withdrawing samples for offline analysis. (iv) Real-time reaction information allows better decision-making. (v) No additional sample preparation is needed.

Monitoring reactions and processes in real time by *in situ* spectroscopy was demonstrated decades ago [7]. However, there had been many practical constraints that limited its broader application prior to the arrival of portable spectrometers. The high cost of *in situ* instruments (typically  $>\$100\,000$ ) limited the number of instruments an organization was willing to purchase. The size and weight of benchtop units often made it easier to set up a reaction next to the spectrometer rather than bring the spectrometer to the reactor. Even though this is not an

insurmountable challenge, setting up a reactor next to a spectrometer (often in an analytical lab) leads to barriers that may cause researchers to abandon an otherwise potentially fruitful *in situ* approach and to resort to the more tedious *ex situ* sampling approach.

The emergence of portable spectrometers has drastically reduced the barrier of implementing *in situ* reaction monitoring. First, the cost of ownership made it accessible to most laboratories. At the time of writing, portable spectrometers with *in situ* sampling capabilities can be purchased for \$20 000–\$30 000. For example, attenuated total reflection Fourier transform IR spectroscopy (ATR-FTIR) probes that are less than \$10 000 can be found from Art Photonics GmbH<sup>1</sup> and Axiom (now Hellma).<sup>2</sup> They can be coupled to portable spectrometers, such as the Thermo Scientific iS5 FTIR<sup>3</sup> and Bruker Alpha FTIR.<sup>4</sup> Well-packaged FTIR reaction monitoring systems are also available from Mettler Toledo<sup>5</sup> and ABB<sup>6</sup> though at a higher cost. In general, handheld spectrometers are not designed for reaction monitoring, and so they will not be discussed in this section. For Raman spectrometers, many new vendors have developed portable Raman systems suitable for reaction monitoring. For example, a B&W Tek i-Raman Plus system<sup>7</sup> costs slightly above \$20 000, which comes with a noncontact probe that can monitor a reaction mixture within a glass reactor by focusing the laser beam through the glass wall of a flask. More often, immersion optics are easier to use and can acquire high-quality spectra even from a turbid reaction mixture. NIR systems such as the Viavi MicroNIR<sup>8</sup> only cost about \$20 000, although in general, NIR is less frequently used for reaction monitoring in R&D projects and more frequently used for manufacturing processes. The improvement in portability means that all these instruments can now be readily shared by multiple projects at different labs as moving instruments and setting them up takes a matter of minutes instead of hours. It should be noted that while these portable instruments usually can start to function within minutes upon deployment to a new lab, for IR and NIR, a longer warm-up time (around 30 minutes to a few hours) is often necessary for the instrument to fully equilibrate with its environment to minimize potential CO<sub>2</sub> and water vapor absorbance. For portable Raman systems, the time is reduced to a few minutes.

Another important criterion to keep in mind during method development is long-term instrument and method support. It is important to account for potential instrument changes or have a procedure to recalibrate instruments for long-term projects. In addition, the analysis method may be impacted by instrument drift. For example, a peak area method based on stable baseline points may underperform a sophisticated chemometric method in the absence of instrument drift. However, the former may outperform the latter due to instrument drift. Compared to their benchtop counterparts, portable instruments may be more prone to instrument drift (e.g. shift in laser wavelength) due to their reduced thermal/environmental control and their more frequent in-field deployments typically subject to wider temperature ranges. For many R&D projects, the period during which *in situ* spectroscopy yields the most critical information is often only a few months. For example, once concentration profiles from multiple reactions are obtained by *in situ* spectroscopy, a kinetics model can be developed, and it may no longer be necessary to acquire *in situ* reaction data for future experiments. Under such circumstances, the long-term stability of instruments is generally not a problem as most of the portable spectrometers used by the authors exhibited no significant performance drift during a few months.

1 <https://artphotonics.com>

2 <https://www.hellma.com/en/laboratory-supplies/probes-for-laboratory-use/ir-products/axiot>

3 <https://www.thermofisher.com/order/catalog/product/IQLAADGAAGFAHDMAZA>

4 <https://www.bruker.com/products/infrared-near-infrared-and-raman-spectroscopy/ft-ir-routine-spectrometers/alpha/overview.html>

5 [https://www.mt.com/us/en/home/products/L1\\_AutochemProducts/ReactIR/attenuated-total-reflectance-atr.html](https://www.mt.com/us/en/home/products/L1_AutochemProducts/ReactIR/attenuated-total-reflectance-atr.html)

6 <https://new.abb.com/products/measurement-products/analytical/ft-ir-and-ft-nir-analyzers/laboratory-spectrometers/mb-rx>

7 <https://bwtek.com/products/i-raman-plus>

8 <https://www.viavisolutions.com/en-us/osp/products/micronir-spectrometers>

## 4.2 Review of Industrial Applications

### 4.2.1 Petrochemical and Fuel Applications

The petroleum industry extensively utilizes vibrational spectroscopy. For example, there have been numerous NIR applications for the online analysis of many properties of crude oil and its derivatives (e.g. composition, vapor pressure, viscosity, pour point, cloud point, solids, wax, etc.). Samples may be analyzed at oil platforms, oil wells, transfer pipes, or refineries. For such measurements, permanently installed analyzers are often used with various sampling accessories such as single-ended insertion probes (diffuse reflectance [DR] mode or transmission/transflectance mode) or a pair of probes mounted on opposite sides of a pipe. Such probes are engineered to withstand harsh conditions, such as high/low temperatures, high pressure, and corrosive environments. Dedicated spectrometers (often referred to as analyzers) are more commonly used than portable instruments. This is partly due to robustness requirements, and partly due to the various area classification requirements (i.e., safe use in areas where there might be explosive vapors present) that must be met by the instruments. However, as portable spectrometers become increasingly miniaturized, ruggedized, and wireless-enabled, they may become viable options for online applications.

For laboratory-based analyses, many studies have compared the performance of traditional benchtop spectrometers, which are generally not designed to be easily movable, to emerging portable spectrometers. In general, benchtop instruments offer higher spectral resolutions, larger spectral ranges, and higher signal-to-noise ratios. As many benchtop instruments have similar or even lower prices than portable instruments, there is usually no significant motivation to use portable instruments for laboratory-based analysis. This is especially true if the laboratory instrument is used as a general problem-solving tool applied to many different sample types, typically encountered in an analytical lab. The larger spectral range, higher spectral resolution of benchtop instruments, and the potential to use different sampling accessories make them more versatile. There are many exceptions to the generalizations above. For example, the portable Thermo Scientific Nicolet iS5 and Bruker Alpha FTIR spectrometers offer performance only slightly inferior to their high-end benchtop units but at a lower cost. Many new portable Raman systems (e.g. from B&W Tek and Marqmetrix) offer performance comparable to benchtop units and some at a lower cost as well.

Field applications are the primary motivation for portable instruments. Fuel samples are unstable over long periods and are also hazardous to transport, which makes portable instruments the method of choice for field analysis. Regardless of which technique is used, most of the published examples utilized a similar approach that involved the measurement of a large set of calibration samples with known properties and then relied on chemometrics (partial least squares regression [PLS] being the most frequently used method, but other methods such as multivariate curve resolution [MCR] were also used) to find the correlation between the measured spectra and the properties of interest. Very few studies used traditional univariate analysis based on simple peaks due to the highly complex composition and spectra of fuel samples. Benzene or other aromatic content analysis was one of the few analyses that could rely on this approach [8]. A surprisingly large number of fuel properties have been measured by portable spectrometers such as octane rating [2b, 8b, 9], density, viscosity, flash point, cloud point, and freeze point [10], adulteration by Methyl tert-butyl ether (MTBE) and benzene [8a] or by vegetable oils [11] and other adulterants [12].

Farquharson et al. demonstrated 22 correlation models in the 1000–1600 nm region (the second CH overtone and combination vibrational modes of hydrocarbons) for diesel, gasoline, and jet fuels using a portable fuel property analyzer (PFPA) with 10-mm path length with five-second acquisition time [13]. In general, the portable spectrometers' performance (with a spectral resolution of  $\sim 32\text{ cm}^{-1}$ ) was found to be only slightly inferior to the benchtop Fourier transform (FT) NIR instrument with  $4\text{ cm}^{-1}$  resolution. The PFPA offered sufficient performance for the purpose, often better than the incumbent American Society for Testing and Materials (ASTM) methods. The same group also developed a portable fuel analyzer based on a modified FT Raman spectrometer

using a 1064 nm ytterbium-doped Bragg fiber grating laser and an indium gallium arsenide (InGaAs) detector. The choice of 1064 nm was found to be critical for the particular fuels investigated. The instrument wavenumber stability and temperature stabilization (of both sample and instrument) were also critical for this application. After controlling these sources of variation, they successfully developed PLS models to Raman spectra for 500 fuel samples with eight different fuel properties such as viscosity, ignition timing, aromaticity, cloud point, flash point, and freeze point [14].

Clark et al. disclosed a potential for hydrocarbon analysis based on low-resolution Raman spectral analysis [2b]. The intensity ratio of specific Raman bands (e.g. 1006/1450 cm<sup>-1</sup>, the former mainly from aromatic ring modes, and the latter mainly from CH deformation modes) was shown to correlate with octane rating. In addition, the overall intensity of bands above 2000 cm<sup>-1</sup> ratioed to those of below 2000 cm<sup>-1</sup> was also found to correlate with octane rating. A low-resolution Raman spectrometer (model RH-3000 from Ocean Optics, with a range of 200–2700 cm<sup>-1</sup> and a spectral resolution of 10 cm<sup>-1</sup>) was also used in another study by Guzman et al. to study the oxidation status of olive oil. PLS models were proposed to correlate Raman spectra to primary and secondary oxidation parameters such as peroxide values and UV absorption at 232 and 270 nm. The Raman spectra were also proposed to offer more information regarding potential speciation changes (C=C, C=O, and peroxide) [15].

Zhang et al. reported using a portable Raman spectrometer with a 785-nm diode laser, 13 cm<sup>-1</sup> resolution, and a scanning range of 200–2000 cm<sup>-1</sup> for gasoline adulteration detection [8a]. Principle component analysis (PCA) was used to detect MTBE and benzene. A radial basis function neural network (RBFNN) approach was used to quantify the MTBE and benzene level, with a mean absolute percentage error (MAPE) reported to be 15.7 and 8.19%, respectively. A slightly longer spectral acquisition time (approximately one minute) was needed to acquire sufficient signal to noise than the several seconds typically used for NIR transmission spectra measurement.

Portable NIR was also employed to detect fuel adulteration. For example, Pimentel et al. compared the performance of a Viavi MicroNIR to a benchtop FT-NIR (ABB Bomem model MB 160D) to quantify vegetable oils in diesel/biodiesel blends using PLS analysis [11]. Similar to Farquharson's results, they reported overall comparable performance between the portable and benchtop instruments, though the latter did outperform the former slightly in accuracy and precision. A mid-IR system (Bruker VERTEX 70 ATR-FTIR) and a portable FT-NIR (ARCoptix) were also evaluated by de Carvalho et al. for vegetable oil adulteration in diesel [12a]. In addition to the frequently used PLS algorithm, they also tested MCR with alternating least squares (MCR-ALS) as an alternative algorithm. Similar performance was observed for the two algorithms, though MCR-ALS offered the advantage of potentially recovering the pure component spectrum of the adulterant. The choice between IR, NIR, or Raman partly depends on the spectral contrast of the adulterants in comparison to the matrix material.

Pimentel et al. further applied the Viavi MicroNIR as an offline simulator of octane number (based on PLS analysis) during the gasoline compounding processes [9a]. Simulated spectra were calculated as a linear combination of the feedstock hydrocarbon stream's spectra based on their concentrations, and the octane rating of such simulated spectra could be easily predicted, which removed the need to prepare actual mixture samples. It should be noted that this was a simulation, and the ability to computationally prepare calibration spectra as a general strategy remains to be further demonstrated for more real samples of complex mixtures. The same group also demonstrated standardization from a high-resolution benchtop instrument to the handheld MicroNIR using virtual standards as transfer samples [10b].

Jaeger et al. compared the performance of a low-field nuclear magnetic resonance (NMR) spectrometer (Thermo Scientific picoSpin80) and a handheld Raman (Ocean Optics IDRaman mini 2.0) to that of a FT-NIR Analyzer (Thermo Scientific Antaris II) in predicting the research octane number (RON) for gasoline samples. They applied multiple chemometric methods, including PCA, PLS, and support vector regression. The best predictions were achieved with NMR, followed by handheld Raman. It is interesting to note that the NIR prediction was found to

deviate the most from the existing methods in this study. The exact level of deviation is not always consistent, as it may depend on many factors such as the source of fuels, the type of instrument and sampling condition, and the preprocessing method and the chemometric model used [12b].

#### 4.2.2 Chemicals and Materials Applications

Portable spectrometers have been used in many industrial and materials-related applications. The key advantage of portable spectrometers is the ability to analyze samples outside of a lab environment, such as in a manufacturing plant or the field.

Carron et al. discuss the challenges of identifying materials, especially polymers and inorganic compounds, using portable Raman spectrometers [16]. They note that spectral preprocessing, such as the removal of a fluorescent background signal and baseline correction of a spectrum, is required to accurately match a spectrum of an unknown material to a spectral library of reference materials. The search algorithm is important when identifying similar materials, such as polystyrene (PS), styrene-butadiene (SB), styrene-acrylonitrile (SAN), and acrylonitrile-butadiene-styrene (ABS). A simple correlation algorithm that analyzed the full Raman spectrum failed to distinguish between these polymers, but a multi-tier correlation algorithm that compared selected spectral regions could identify them. In the field, portable Raman spectrometers can quickly identify classes of minerals and often speciate closely related ones. For example, Raman spectroscopy could distinguish between common types of carbonate minerals, including aragonite, calcite, and dolomite.

Kogler et al. used a portable B&W Tek Raman spectrometer to detect biofouling in a membrane filtration system in real time [17]. Biofouling of membranes is a major problem because it decreases the filtration capacity of the system and reduces its lifetime. The Raman signals of membrane foulants, which included adenine and bacteria, were enhanced using gold nanoparticles that were immobilized on the surface of the membrane. The nanoparticles enabled the measurement of low-concentration foulants and reduced interference from the strong Raman signal of the membrane.

Lopez-Lorente et al. used a portable B&W Tek Raman spectrometer to characterize mixtures of single- and multi-walled carbon nanotubes [18]. The authors dispersed the carbon nanotubes into water with a surfactant to prevent thermal damage during the analysis. They were able to identify and quantify single-walled nanotubes in a mixture of single- and multi-walled nanotubes using the Raman G and D bands.

A portable FTIR system was used in the DR mode to detect and discriminate between silicone and hydrocarbon oil on grit-blasted metal surfaces. A detection level approaching  $10 \text{ mg/m}^2$  was demonstrated [9b]. Karunathilaka et al. demonstrated that a portable Agilent FTIR with a single-bounce diamond ATR crystal could be used with PLS regression analysis to determine both major and minor fatty acid concentrations in marine oil omega-3 dietary supplements [19].

Corradini et al. used a portable ASD Products visible-NIR spectrometer to identify and quantify the concentration of microplastics in soil [20]. The key advantage of a portable spectrometer is its ability to analyze soil samples in reflectance mode without sample preparation or extraction of the microplastics. The authors were able to identify and quantify low-density polyethylene (LDPE), polyethylene terephthalate (PET), polyvinyl chloride (PVC), and mixtures of the polymers with a detection limit of  $\sim 15 \text{ g/kg}$ .

Lima built a portable NIR photometer using light-emitting diodes (LEDs) at 1300 and 1689 nm to measure benzene and toluene concentrations in water [21]. The aromatic hydrocarbons were extracted from water using a silicone material, then the transmittance of the silicone material was measured at 1300 nm for the reference signal and 1689 nm for the analyte signal. The detection limits of benzene and toluene were  $\sim 1 \text{ mg/L}$ , and the sensitivity of the NIR photometer was similar to a conventional FT-NIR instrument.

Li et al. used a portable B&W Tek Raman spectrometer combined with thin-layer chromatography (TLC) and surface-enhanced Raman spectroscopy (SERS) to measure sub-ppm concentrations of aromatic hydrocarbons in water [22]. The authors used a TLC plate to separate the contaminants from each other, and they added colloidal

silver particles to each contaminant spot on the TLC plate to enhance the Raman signal of the contaminants. This scheme enabled them to detect *p*-toluidine and *p*-nitroaniline in a wastewater sample at concentrations of 99 and 197 ppm, respectively. A similar approach was used by Yang et al. to measure the concentration of pentachlorophenol in water [23]. In this case, the Raman signal of pentachlorophenol was enhanced using cysteamine-modified silver nanoparticles. The detection limit was 0.20 µm. This approach was also used by Jiang et al. to measure the concentration of a 4,4'-dibromodiphenylether, which is a brominated flame retardant, in seawater. The Raman signal of 4,4'-dibromodiphenylether was enhanced using alkanethiol-modified silver nanoparticles. The detection limit was 120 µg/L.

Tang et al. used a handheld Agilent FTIR to nondestructively assess the extent of thermal damage to concrete, for example, concrete exposed to fire [24]. Thermal damage to concrete involves a variety of chemical reactions that can change its compressive strength. DR IR spectra of concrete samples were collected before and after thermal treatment of the concrete in a thermogravimetric analyzer. The spectra were analyzed with a partial least squares (PLS) model to predict the maximum temperature to which the sample had been exposed. The authors concluded that a handheld FTIR method could accurately and nondestructively measure thermal damage in concrete.

Gómez-Nubla et al. used a handheld B&W Tek Raman spectrometer to identify the mineral phases in black slag, a waste product of steel production [25]. The authors identified oxides and hydroxides of iron, silicates, ferrites, chromites, carbonates, magnesium oxides, sulfates, rutile, and amorphous carbon in the slag. They were able to identify treated slag by the presence of iron hydroxides formed from iron oxides. The handheld spectrometer identified all major components and a few minor components in the slag. In comparison, a lab-based Raman microscope identified all major and minor components.

Cheng et al. used a portable visible-NIR spectrometer from Spectral Evolution to differentiate between 5 phyllosilicate minerals (pyrophyllite, muscovite, talc, antigorite, and kaolinite) [26]. Reflectance spectra of mineral samples were collected from 350 to 2500 nm. Minerals absorb in three spectral regions: 400–1100 nm due to impurities, 1100–1700 nm due to overtones of OH stretching modes, and 1700–2500 nm due to combinations of the OH stretching and bending modes. The authors were able to identify the five minerals without sample preparation and concluded that this method is a promising way to quickly identify minerals in the field.

Lin et al. evaluated a handheld Thermo Scientific Raman spectrometer to analyze uranium ore concentrates and uranium dioxide in several forms [27]. The handheld Raman spectrometer could analyze uranium compounds but not darker powders like uranium dioxide and U<sub>3</sub>O<sub>8</sub>. In addition, the authors noted that the accuracy of the spectral searching algorithm could be improved.

Miller et al. used a Bruker Alpha FTIR in transmission mode to quantify the amount of silica dust on filter cassettes after exposure to mining environments [28]. Hase et al. used a portable Bruker EM27/SUN FTIR spectrometers to measure the greenhouse gas emissions of Berlin, Germany [29]. The concentrations of water, carbon dioxide (CO<sub>2</sub>), and methane in the atmosphere were measured over a three-week timeframe. NIR absorption spectra of the atmosphere were collected using the sun as a light source. The NIR measurements of water, CO<sub>2</sub>, and methane were referenced to the mole fraction of oxygen in the atmosphere, which is constant. Five instruments were placed around Berlin, and the results were used to determine that Berlin emits 800 kg CO<sub>2</sub> per second.

Suarez-Bertoa et al. used a portable MKS FTIR to measure the concentration of ammonia (NH<sub>3</sub>) emitted from gasoline and diesel vehicles [30]. Ammonia is a precursor of particulate matter (PM<sub>2.5</sub>) pollution. The portable FTIR was connected to the vehicle's exhaust system, and the NH<sub>3</sub> concentration, vehicle's speed, and other parameters were measured during on-road driving. The performance of the portable FTIR was similar to a conventional FTIR in lab emissions tests. The authors concluded that on-road NH<sub>3</sub> emissions of the gasoline vehicle were higher than the diesel vehicle and that NH<sub>3</sub> emission limits may need to be considered.

## 4.3 In-Depth Examples

### 4.3.1 Portable FTIR for Online Coating Characterization

Coating of polymeric films is a widely used process for making products, such as tapes, labels, release liners, and graphic arts, for many industrial and consumer applications. During the coating process, an online monitoring technique that provides real-time quality information about the coated film is highly desirable because it improves the production efficiency. Portable FTIR is a low-cost technique that can provide real-time information, such as film thickness and conversion of curing reactions. A representative example from the authors is the online FTIR analysis of silicone coatings applied to polymer substrates. This application has the potential to drastically shorten the test time and improve the production efficiency compared to widely used offline characterization techniques, such as an X-ray fluorescence (XRF)-based extraction method.

Release coatings are materials applied on substrates to prevent an adhesive surface from prematurely adhering to another surface. In addition, they must not contaminate or degrade the adhesion performance of the adhesive surface. Release coatings protect the adhesive layer on labels during label manufacturing, storage, and application and allow easy release of sticky materials. There are several types of release coatings, including polyacrylates, carbamates, polyolefins, fluorocarbons, chromium stearate complexes, and silicones. Silicone-based release coatings play a dominant role in their unique advantages, like low migration, low release forces, and relatively low cost [31]. At present, silicone-based release coatings are used extensively in tape, labeling, hygiene, medical and food industries. Generally, a two-part silicone formulation is mixed together and then applied to a polymer substrate, which then undergoes a thermal curing reaction by going through an oven. The curing reaction is based on hydrosilylation between a silane function group (Si-H) and a vinyl functional group catalyzed by Karstedt's catalyst.

To ensure optimal performance and minimize silicone migration, which causes cross contamination and degrades the adhesive performance, two important process variables need to be tightly controlled during the coating process of silicone release coatings: coat weight (which is equivalent to coating thickness) and conversion of the curing reaction. If the coat weight is too high or too low (i.e., too thick or thin), it may lead to high material consumption (high cost) or poor performance. If the curing is insufficient, then it causes cross contamination and deterioration of the adhesion performance; for example, the transfer of silicone material from the appropriately cured release liner to the adhesive layer of tape deteriorates the adhesion and tackiness of the tape. Both process variables can be measured through the use of portable FTIR.

A picture of a portable Bruker Alpha FTIR is shown in Figure 4.1. Since the film exits the oven in a horizontal orientation, the FTIR spectrometer was mounted on its side. A slot machined at the bottom of its transmission compartment allowing the film to pass through the compartment with the IR beam going through the film. It is important to point out that while it is certainly possible to use a conventional benchtop FTIR for this application, extensive modifications would have to be made to the instrument or production process. A portable FTIR significantly reduces the barrier to these types of applications. IR spectra were collected in the transmission mode at an interval of three seconds.

Figure 4.2 shows the reference spectra of several typical polymer substrates and silicone materials. Many strong bands had absorbances above 1.6 due to the thicknesses of the films and were considered saturated. These regions could not be used, and they are denoted by the colored bars at the top of the figure. PET had several saturated regions due to its many strong bands, while high-density polyethylene (HDPE) only exhibited saturated C-H stretch bands with the rest of the spectral range still useful. It is encouraging to note that one relatively well-resolved silicone band could always be found regardless of which polymer substrate was used.

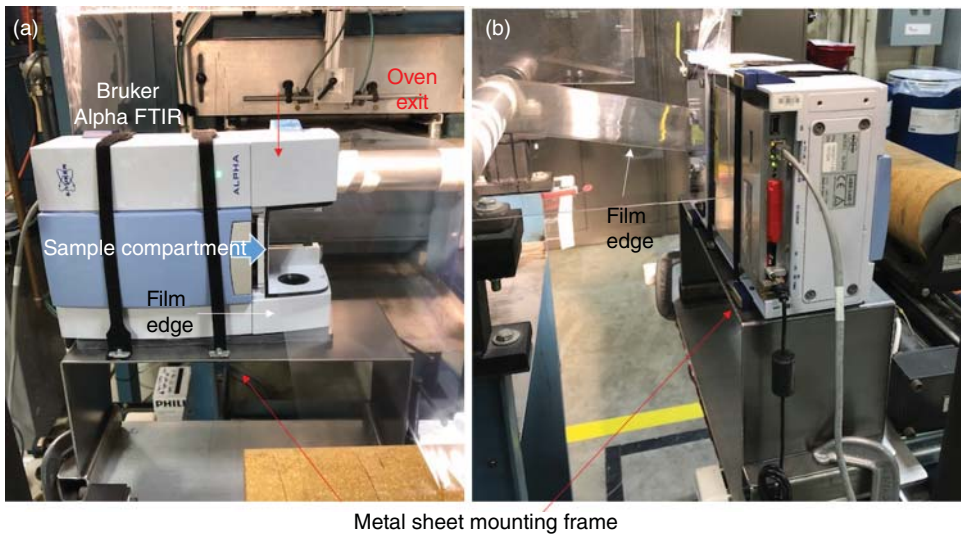


**Figure 4.1** Pictures of the online FTIR from two different angles. Source: The Dow Chemical Company.

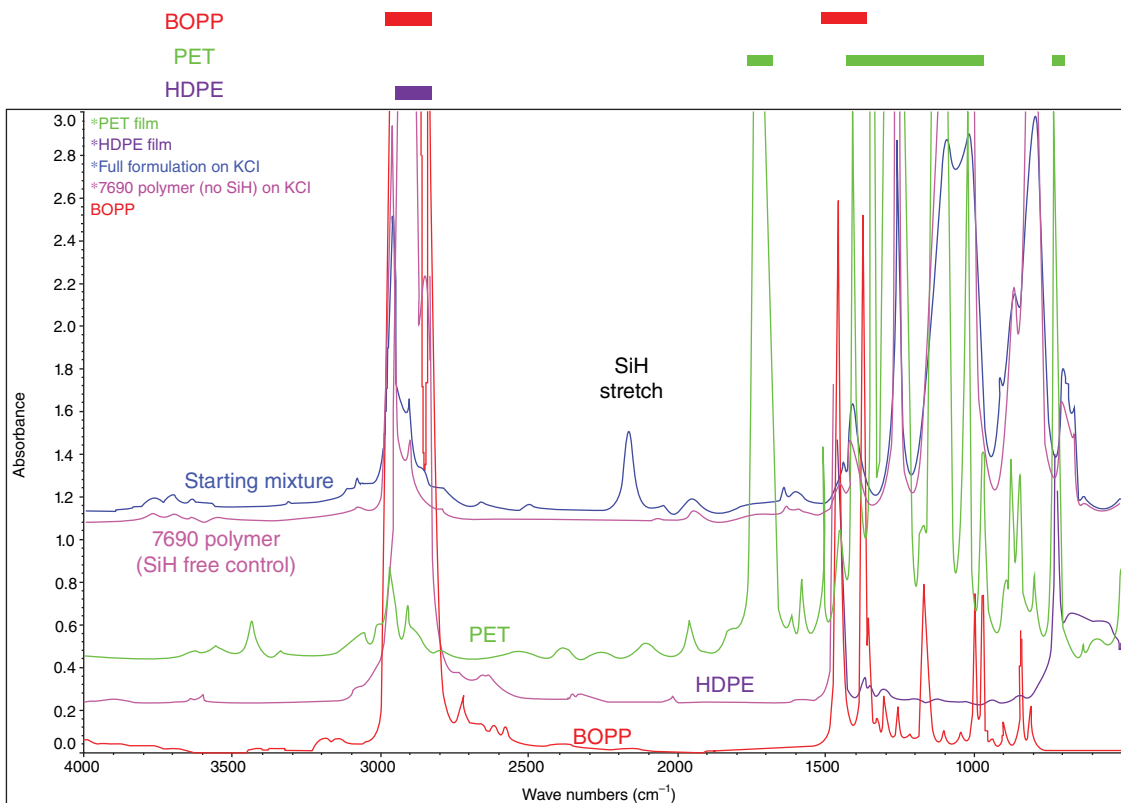


**Figure 4.2** Reference spectra of biaxially oriented polypropylene (BOPP), polyester terephthalate (PET), polyethylene (PE), and the starting coating mixture and its Si-H free control.

The top panel of Figure 4.3 shows an overlay of multiple spectra collected during a test when the coating thickness was intentionally varied, and the bottom panel shows the IR absorbance at  $1080\text{ cm}^{-1}$ , which was mostly due to the silicone coating. Four different coat weights were used, and they could be differentiated by their IR spectra. A good correlation was observed between the offline XRF results and the online FTIR results. It is also interesting to note that XRF could not differentiate between the two final conditions, while a discernible change was observed by IR.

In order to estimate the conversion of the hydrosilylation reaction, the Si–H absorbance at  $\sim 2160\text{ cm}^{-1}$  could be used (Figure 4.4). Even though PET did not have any fundamental modes around this region, it still contributed many features, presumably from its various overtones and combination bands. Their bands were stronger than the SiH band due to PET's higher concentration and greater thickness. Despite the overlap, the SiH absorbance in a cured film could still be clearly discerned upon spectral subtraction. Chemometric methods, such as classical least squares (CLS), could quantify the residual SiH groups.

In addition to online monitoring, the same portable FTIR was also employed to monitor the post-oven cure of a static film after it exited the oven. Figure 4.5 shows one example that was collected from a static film at the end of one trial. For the first 10 minutes, four scans were collected per spectrum. The number of scans was increased to 64 scans from the 12th minute until the end, which led to substantially improved signal to noise. A gradual decrease in the SiH absorbance was observed during this post-cure process. It is clear that even though the sample was simply sitting outside the oven at ambient conditions, the conversion continued with the SiH signal dropping by more than 25% over about one hour. The drop rate was higher in the first five minutes. Such results indicate that sample aging post-oven curing may be a significant source of variation for the incumbent XRF analysis if the elapsed time for each sample between its coming out of the oven and the actual analysis varies by only a few minutes. However, if a 20-minutes aging time is allowed before the analysis, then the error due to post-oven aging may be smaller.

### 4.3.2 Portable NIR for Polyurethane and Polyurea Foam

Polyurethane (PU) and polyurea foams are used in a wide range of applications, such as furniture, insulating materials in buildings and home appliances, and automotive. They are typically made by reacting isocyanate prepolymers and curatives such as polyols or polyamines [32]. Water is frequently used as a blowing agent because it generates  $\text{CO}_2$  *in situ* from its reaction with isocyanate (Figure 4.6).

When developing a foam formulation, there are many competing target properties that need to be met simultaneously, such as the rheology of the mixture, the gelling time and demolding time, porosity, and various mechanical properties. The fundamental reaction kinetics have a large impact on many of these properties, and therefore it is often desirable to understand the curing kinetics and the foaming rate. ATR-FTIR has been employed to follow PU foaming [33]. *In situ* ATR-FTIR offers many useful insights regarding reaction kinetics and detailed speciation due to its ability to monitor the entire reaction. As a result, the majority of the PU reaction kinetics studies have been carried out with ATR-FTIR and rarely with NIR due to NIR's more complicated spectral interpretation, especially when the cost of use became comparable for these two technologies [34].

The advent of portable NIR spectrometers resulted in new applications for several reasons. First, the NIR spectrometers are smaller than mid-IR spectrometers, making them easier to operate when space is limited, typically encountered in many lab fume hoods. Second, the DR mode is ideal for sampling polymer foam samples in the NIR range due to the right combination of scattering and absorption. For mid-IR, absorption tends to dominate over scattering, leading to poor quality DR spectra for polymer foams. It is interesting to note that this problem is reversed if the ATR sampling mode is used. For mid-IR, the ATR mode has an ideal penetration depth (on the order of microns), while the ATR penetration depth in the NIR is too short unless hundreds or thousands of bounces are used, which is not readily available using any commercial accessory. Note that in transmission mode, NIR generally has a much longer penetration depth than mid-IR. Another disadvantage of ATR sampling mode is that

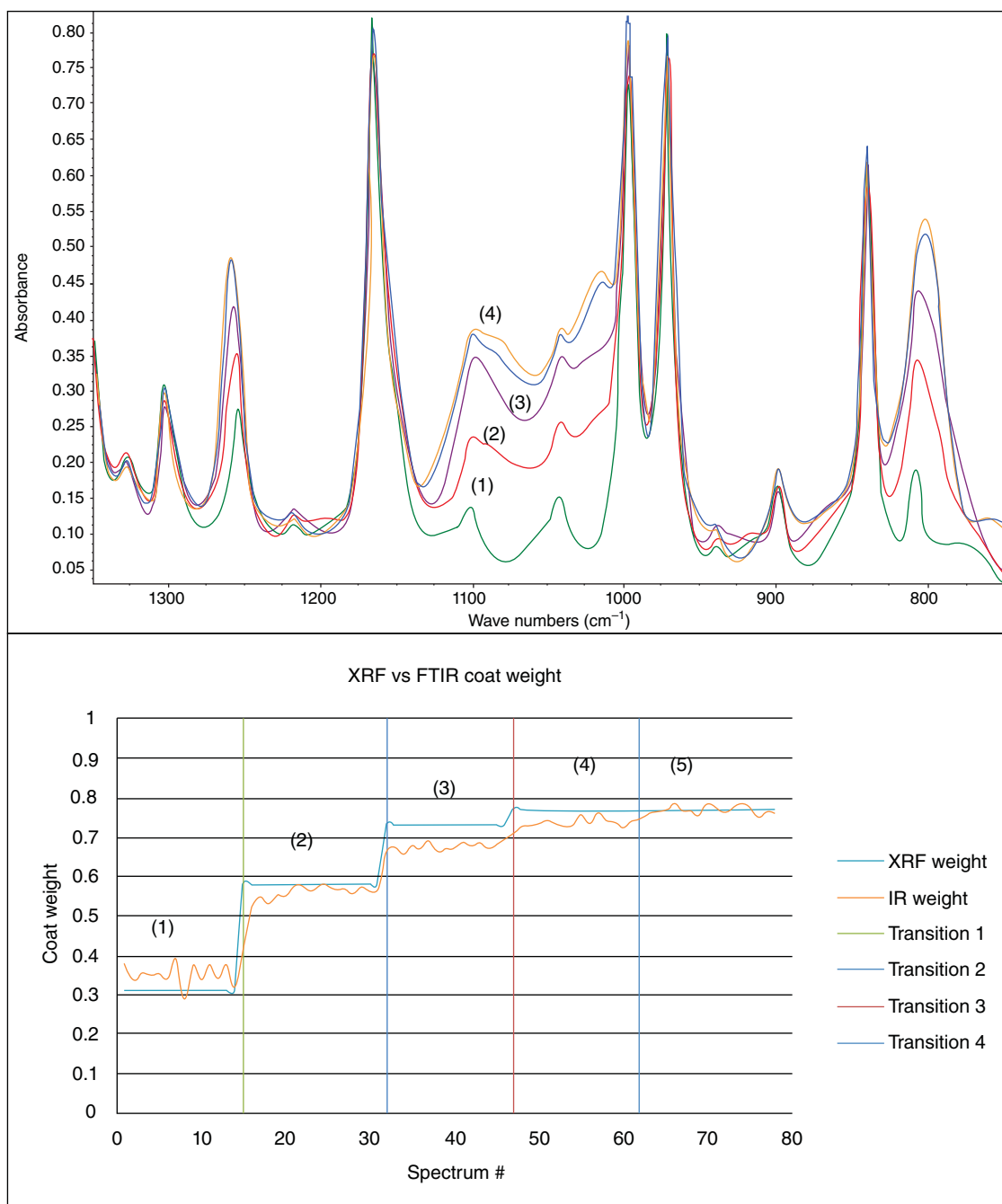


**Figure 4.3** Correlation between XRF coat weight (pounds/ream) and coat weight determined by IR.

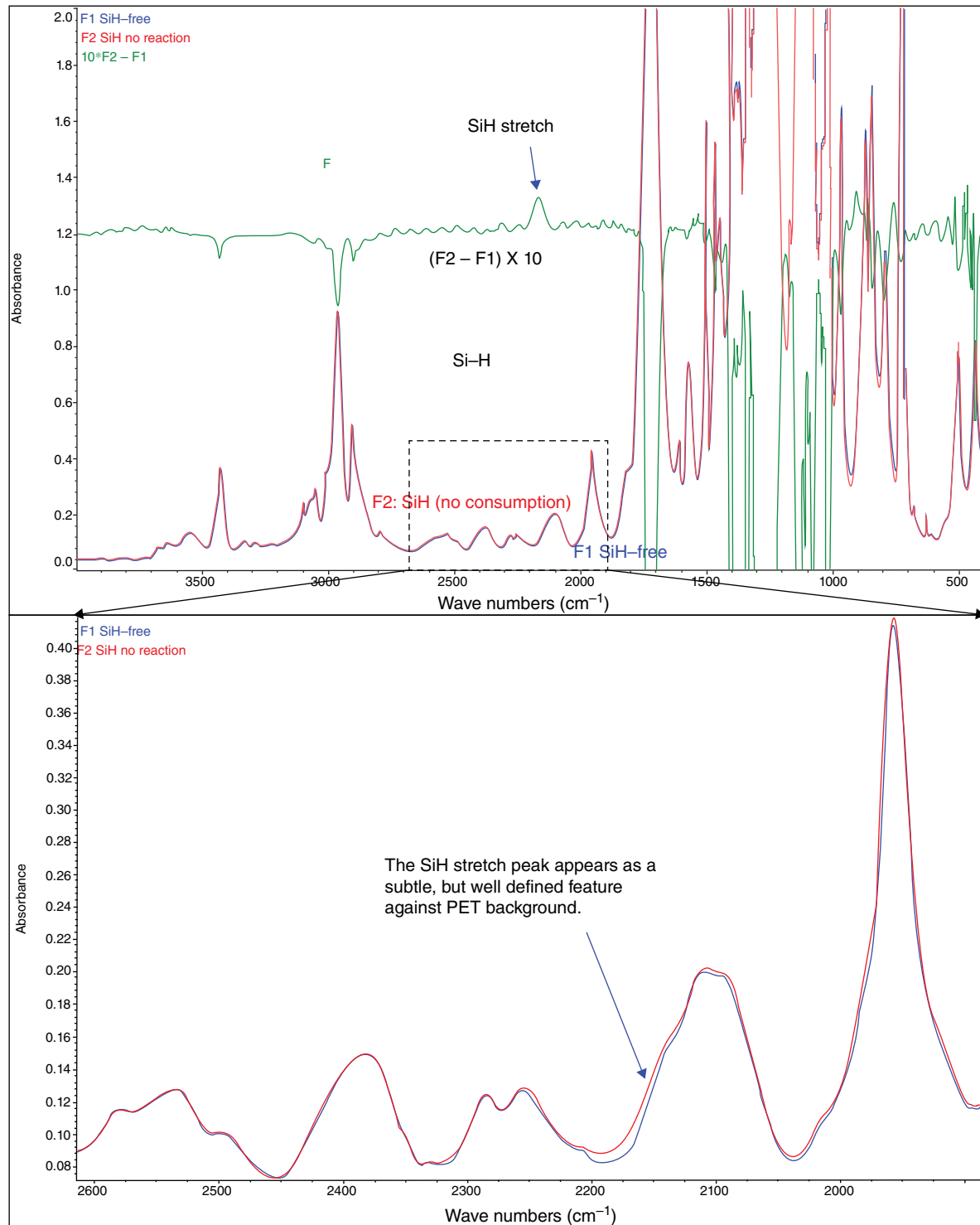


**Figure 4.4** Top: overlay of F1 and F2 coating spectrum, and their difference spectra. Bottom: enlarged view of the SiH stretch region.

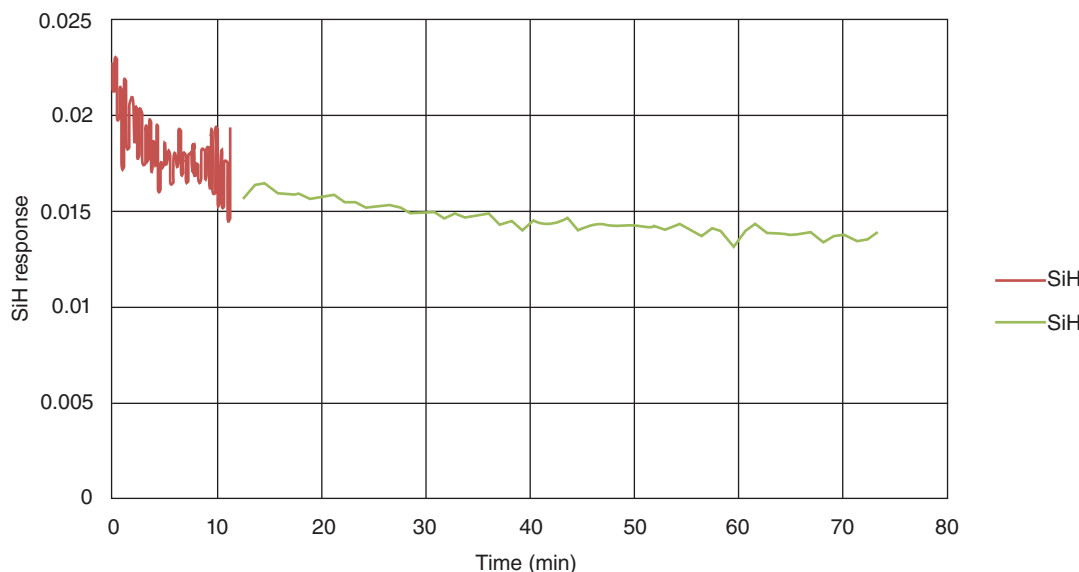


**Figure 4.5** Post-cure monitoring of the SiH response in a static film. Spectra were collected with shorter acquisition time at higher intervals for the first ~11 min and then with longer acquisition time and lower interval for the rest of the experiment.

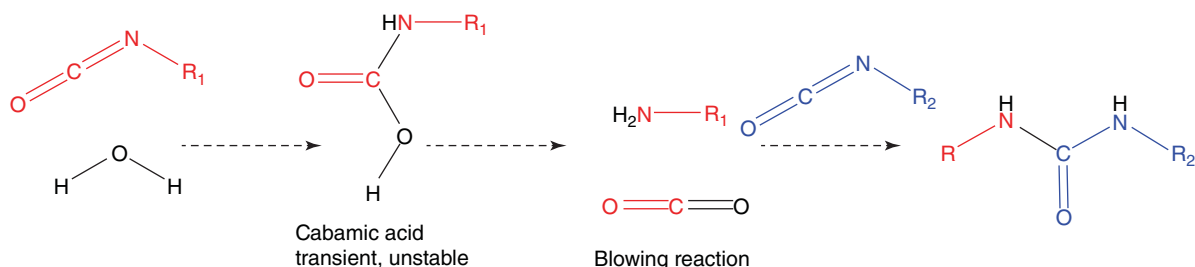


**Figure 4.6** Schematic reaction between water and isocyanates to form polyurea.

the ATR crystal needs to be in good contact with a sample. For exothermic systems, the ATR crystal may serve as a heat sink, which prevents the thin sample layer from heating up with the rest of the system and thus biasing the spectral results.

DR NIR also offers a noncontact sampling advantage, which makes it easy to sample a foam at different positions, as illustrated in Figure 4.7. Here we demonstrate the utility of portable NIR to investigate the curing reaction kinetics of a moisture curable PU system [35]. The lightweight nature of the Viavi MicroNIR even makes it easy to mount onto an automated and motorized arm so that it can point down toward a rising foam with the arm automatically keeping a constant gap between the sensor and the rising foam surface.

Two commercial one-part, moisture-cured, foam sealants were purchased and used for the following results. They are referred to as Foam 1 (intended for filling gaps and cracks) and Foam 2 (intended for larger gaps). Three reactions were carried out with Runs 1 and 2 using Foam 1 and Run 3 using Foam 2. Runs 1 and 3 were carried out on a dry day (humidity ~35%) and Run 2 on a humid day (humidity ~90%).

Raw spectra (see top panel of Figure 4.8) exhibited substantial baseline shifts as a result of the changing sample reflectivity during foaming. As the initial liquid mixture started to foam and became more porous, less light was reflected back to the sensor, which led to an increase in the baseline absorbance. It is worth noting that the change

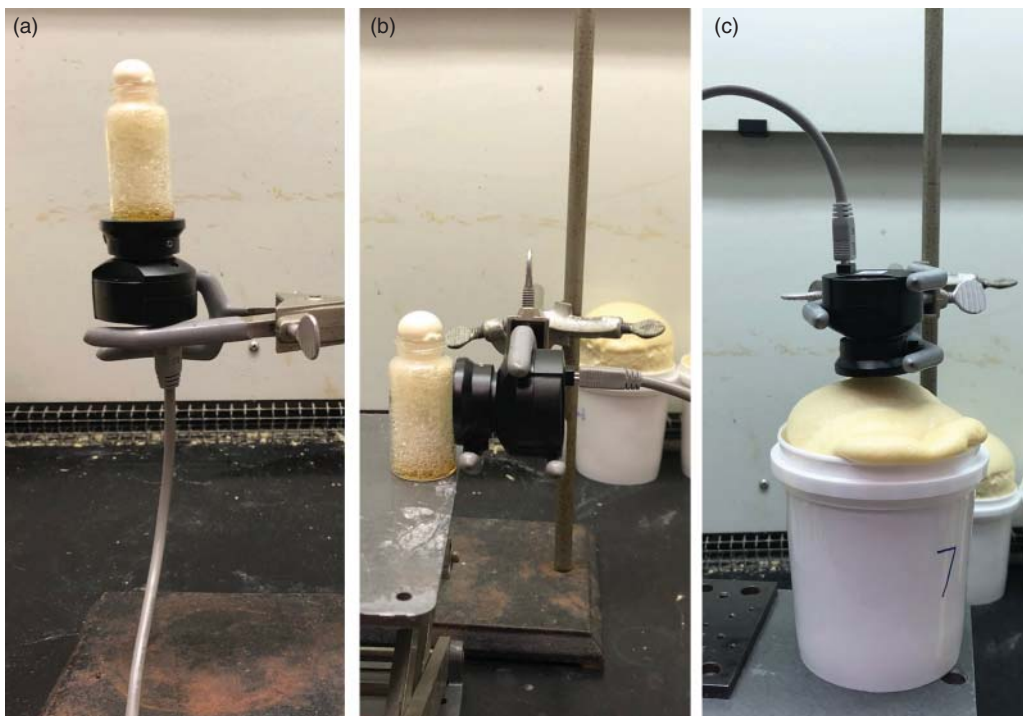


**Figure 4.7** Pictures of various geometries of MicroNIR sampling: (a) from bottom; (b) from side; (c) from top.  
Source: The Dow Chemical Company.

of baseline might also contain interesting physical information about the foam because the light loss is fundamentally determined by the foam porosity. However, the correlation may not be straightforward. The time-dependent baseline change at 1300 nm of the raw spectra is shown in Figure 4.9.

The baseline drift is effectively removed by preprocessing (carried out using PLS\_Toolbox 8.5, automatic weighted least squares with second-order basis filter, followed by multiplicative scatter correction), and the spectral changes due to the reaction can be clearly discerned as shown in the bottom panel of Figure 4.8. The absorbance peaks between 1300 and 1500 nm are from the second CH overtone, which remained more or less unchanged since the CH moiety did not participate in the curing reaction. The main change occurred at 1490 nm ( $6711\text{ cm}^{-1}$ ), due to the first overtone of NH from the polyurea product (see Figure 4.6). The absorbance at 1490 nm is overlaid with that of the baseline change in Figure 4.9. Based on the NH absorbance change, it is clear that the urea formation reaction was mostly completed within 20 minutes. However, the change in the baseline did not appear to slow down at that time, indicating that the bubble expansion continued to change the foam density even though the reaction was mostly complete. It is important to point out that the sample viscosity changed in a highly nonlinear fashion as a function of reaction conversion, which could explain the deviation.

Figure 4.10 overlays the reaction kinetics of the three runs. Runs 1 and 2 were carried out using the same foam but at low humidity for Run 1 and high humidity for Run 2. The humidity difference led to a slower reaction in Run 1 and a lower conversion to urea, as indicated by its lower 1490 nm absorbance. Run 2 and 3 were both carried out at high-humidity conditions, with Run 2 using Foam 1 intended for smaller gaps and Run 3 using Foam 2 intended for larger gaps. In order to fill larger gaps, Foam 2 cures more slowly to allow more expansion of the foam. Indeed Figure 4.10 clearly demonstrates the slower kinetics of Foam 2 (Run 3) than Foam 1 (Run 2) at identical conditions.

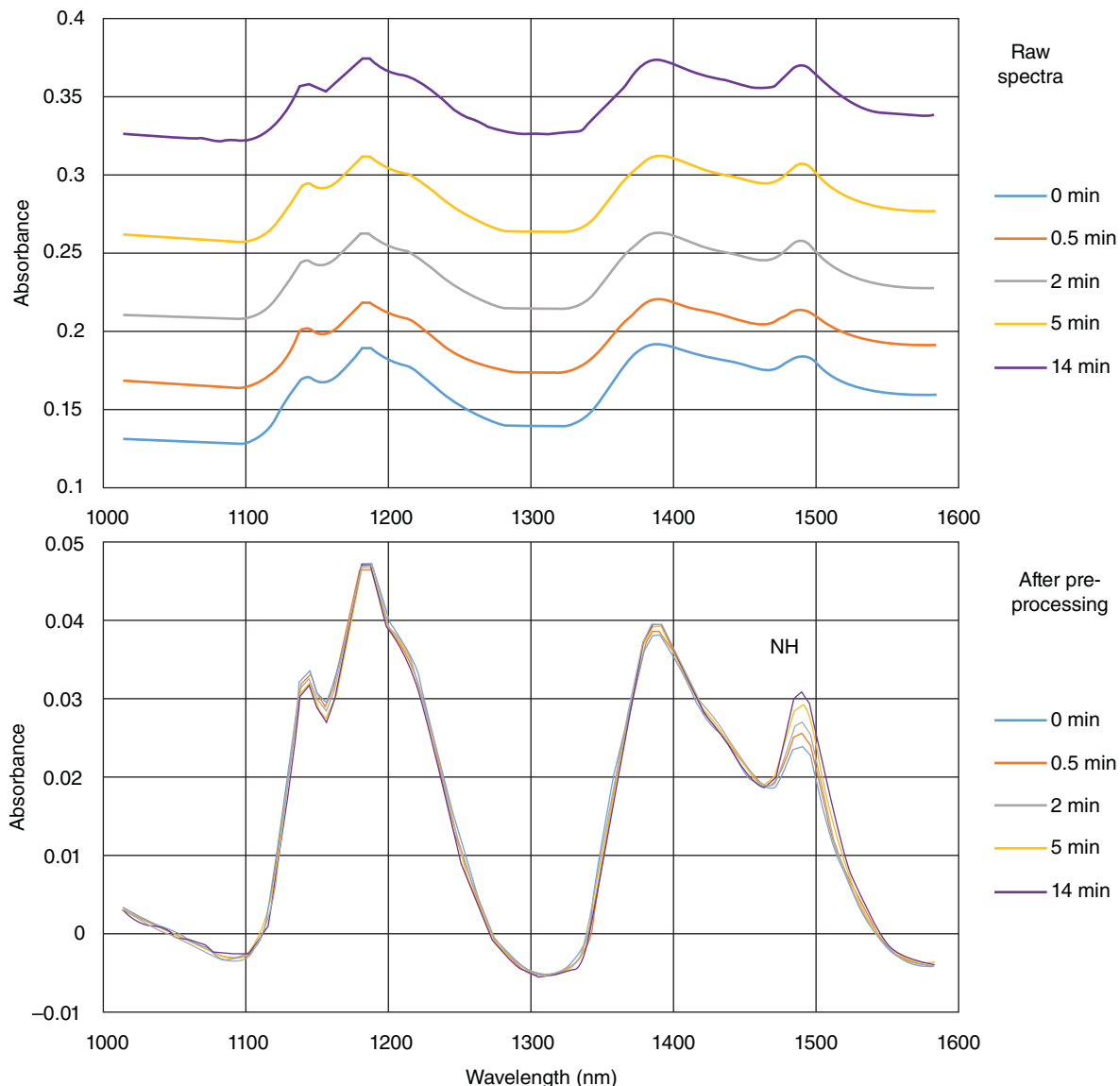


**Figure 4.8** Selected reaction spectra from Run 1. Top panel: the raw spectra; bottom panel: after preprocessing.

### 4.3.3 Portable Raman for Reaction Monitoring

There have been numerous case studies by the authors where *in situ* Raman was used to monitor reactions. Figure 4.11 shows a portable B&W Tek i-Raman Plus spectrometer (785 nm excitation) deployed to monitor a semi-batch emulsion polymerization reaction [36]. A short-focus immersion optic (from Kaiser Optical Systems, Inc.) was inserted through a rubber stopper into the reaction mixture. The turbidity of an emulsion polymerization may undergo significant changes throughout a reaction, and the raw Raman signal intensity can be influenced by many factors, including the emulsion particle size distribution. A CLS method was developed to quantify the spectral contribution of both monomers and polymers, which were used to serve as internal standards for each other. This approach enabled the extraction of quantitative reaction profiles, as shown in Figure 4.12. The different

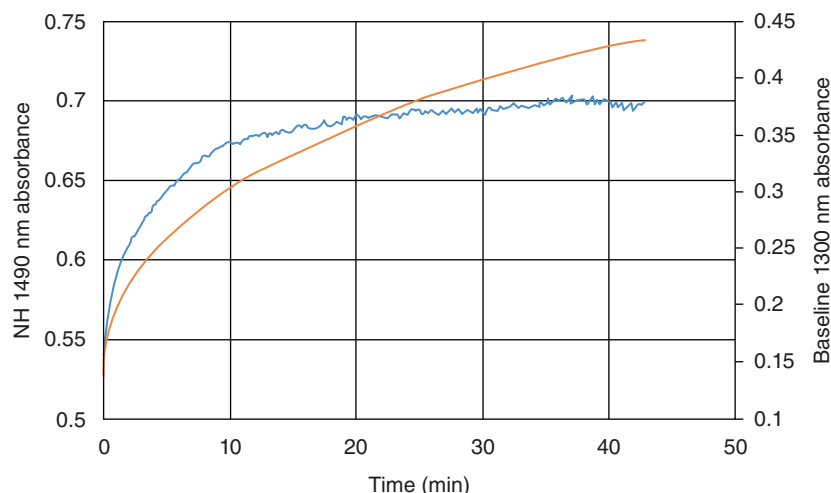


**Figure 4.9** Overlay of Run 1 baseline (orange) at 1300 nm (without preprocessing) and NH absorbance (blue, after preprocessing) at 1490 nm.

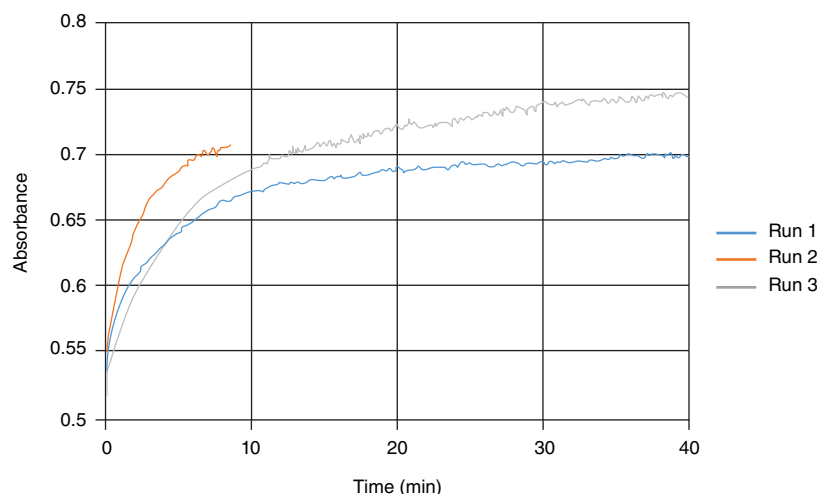


**Figure 4.10** Comparison of reaction kinetics of the two foaming reactions based on the normalized NH and OH absorbance.

reaction rates of methyl methacrylate (MMA) and butyl acrylate (BA) could be readily monitored and used to improve the process design. The multiple spikes after 130 minutes were validation experiments to demonstrate that when only one monomer was added, the correct response could be observed with minimal interference.

The i-Raman Pro system from B&W Tek includes an integrated touch screen computer so that the spectrometer can be operated without an external computer, further improving its portability. It was recently used to monitor the hydrolysis and condensation reactions of alkoxy silanes simultaneously with in situ IR and in-line NMR measurements [37]. The NMR measurements were not carried out within the reactor but by pumping the reaction mixture to the NMR magnet using a recirculation loop. The location of the NMR system dictated the location of the entire experiment setup, and the portable Raman and IR systems made it feasible to carry out this multi-analytical monitoring experiments. Multiple transient intermediate reaction intermediates were observed by both NMR and Raman, while in situ IR only tracked the overall functional group changes such as Si-methoxy and silanol groups.

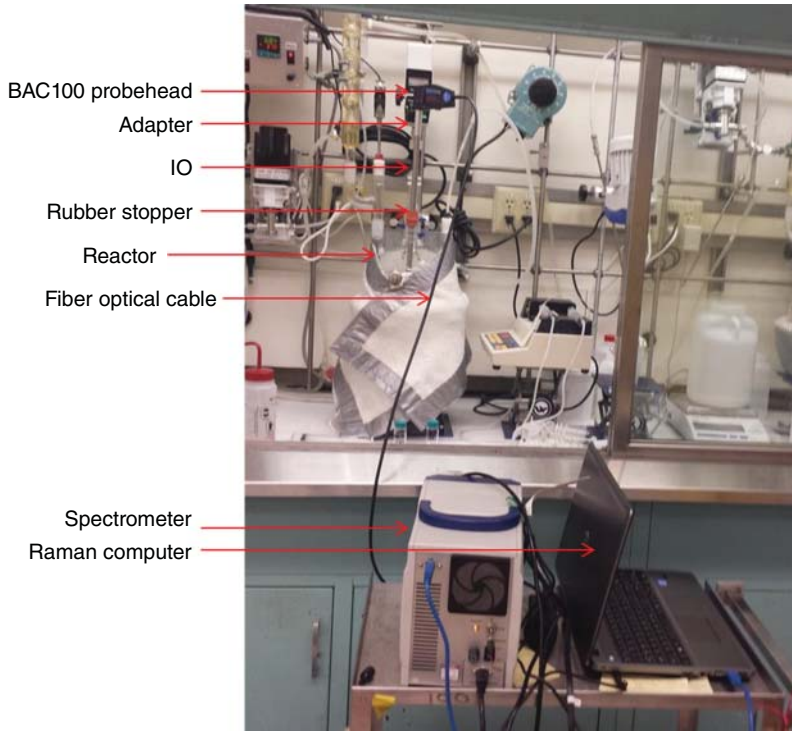


**Figure 4.11** A B&W Tek i-Raman Plus instrument is used to monitor a semi-batch emulsion polymerization reaction.  
Source: The Dow Chemical Company.

Determining the best technology for an application depends on what information is the most critical for process development.

In another study, the same i-Raman Pro system was used to monitor a two-phase hydrosilylation reaction [38]. A picture of the reactor with three immersion probes inserted is shown in Figure 4.13. The three probes were the ReactIR ATR probe, a short-focus Raman probe, and a long-focus Raman probe. While all three probes provided similar qualitative information regarding the consumption of the SiH and allyl C=C groups, substantially different quantitative results were obtained due to the sampling bias associated with each probe. It was found that Raman provided more representative sampling than ATR-FTIR for heterogeneous systems. In addition to the i-Raman systems from B&W Tek, Raman systems from Mettler Toledo and Marqmetrix have also been tested and showed good performance.

#### 4.4 Conclusions and Prospects

Portable Raman, IR, and NIR spectrometers have been successfully applied to numerous industrial applications. The applications of portable spectrometers to the chemical industry will continue to expand as they decrease in size and increase in performance. Their portability leads to many advantages over the conventional benchtop instruments. In-field applications such as gasoline testing at gas stations or oil fields, in situ reaction, and process monitoring at organic synthesis labs and pilot or production plants can now be routinely practiced with such portable instruments. The real-time analysis and result feedback enabled by such in-field analyses can greatly accelerate the decision-making process. Currently, the portable instruments' performances generally lag behind

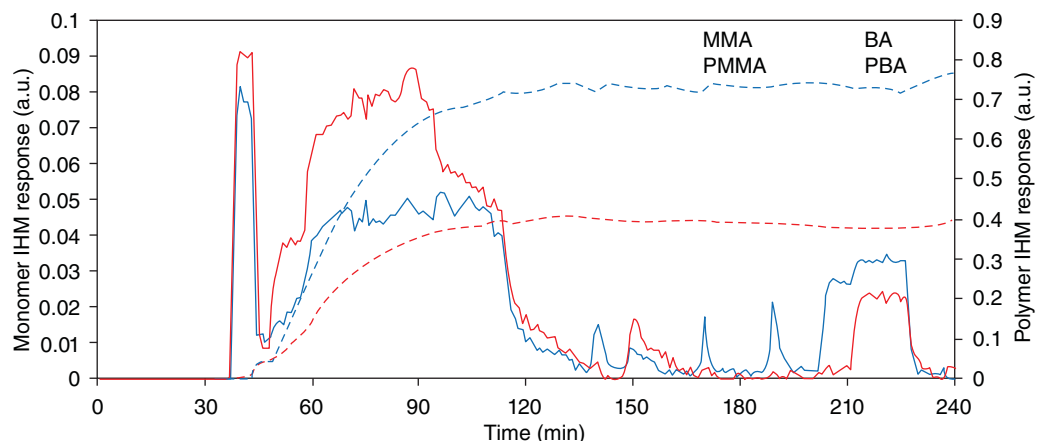


**Figure 4.12** Real-time concentration profiles of the two co-monomers and their incorporation into polymers could be monitored by in situ Raman. Source: Ref. [36]. © 2015, American Chemical Society.

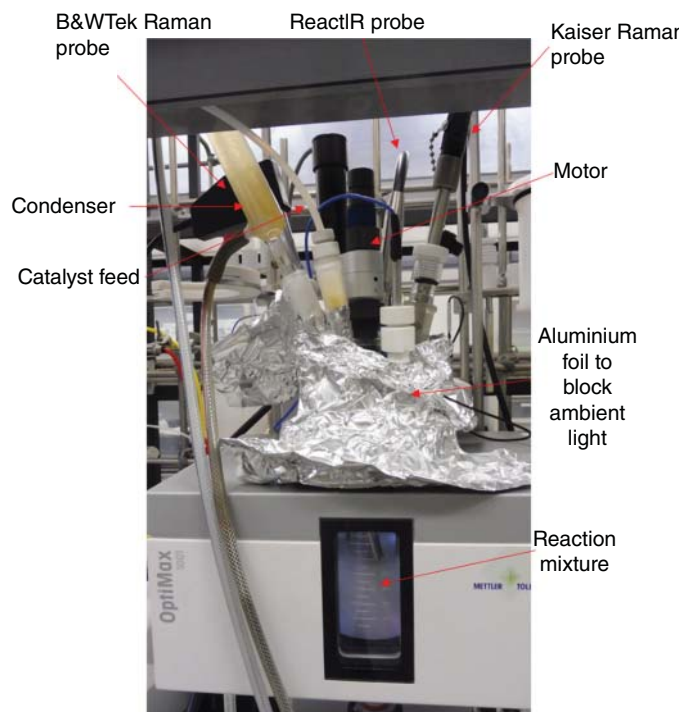


**Figure 4.13** A picture of the hydrosilylation reaction carried out in a Mettler Toledo OptiMax reactor with both in situ IR and Raman monitoring. Source: The Dow Chemical Company.

their benchtop counterparts in terms of spectral range, spectral resolution, wavelength stability, etc. However, as portable instruments and the associated data analysis methods are usually meant for specific tasks, they are often found to be fit for purpose. The need for portable vibrational spectrometers in the chemical industry will likely increase as the Industry 4.0 mega-trend<sup>9</sup> drives more and more process automation and optimization.

<sup>9</sup> [https://en.wikipedia.org/wiki/Industry\\_4.0](https://en.wikipedia.org/wiki/Industry_4.0)

## References

- 1** (a) Nyquist, R.A., Leugers, M.A., McKelvy, M.L. et al. (1990). Infrared spectrometry. *Anal. Chem.* 62 (12): 223–255. (b) Macho, S. and Larrechi, M. (2002). Near-infrared spectroscopy and multivariate calibration for the quantitative determination of certain properties in the petrochemical industry. *TrAC Trends Anal. Chem.* 21 (12): 799–806.
- 2** (a) Angel, S.M., Myrick, M.L., and Vess, T.M. (1991). *Remote Raman spectroscopy using diode lasers and fiber-optic probes*. SPIE 1435 <https://www.spiedigitallibrary.org/conference-proceedings-of-spie/1435/0000/Remote-Raman-spectroscopy-using-diode-lasers-and-fiber-optic-probes/10.1117/12.44232.short>. (b) Clarke, R. H. (1992). Hydrocarbon analysis based on low resolution raman spectral analysis. US Patent 5,139,334
- (c) Lewis, E.N., Treado, P.J., and Levin, I.W. (1993). A miniaturized, no-moving-parts Raman spectrometer. *Appl. Spectrosc.* 47 (5): 539–543. (d) Vess, T.M. and Angel, S.M. (1992). *Near-visible Raman instrumentation for remote multipoint process monitoring using optical fibers and optical multiplexing*, 118–126. Environmental and Process Monitoring Technologies, International Society for Optics and Photonics. (e) Farquharson, S. and Simpson, S.F. (1992). *Applications of Raman spectroscopy to industrial processes*. SPIE 1681 <https://www.spiedigitallibrary.org/conference-proceedings-of-spie/1681/0000/Applications-of-Raman-spectroscopy-to-industrial-processes/10.1117/12.137747.short>.
- 3** (a) Hyvarinen, T.S. and Niemela, P. (1990). *Rugged multiwavelength NIR and IR analyzers for industrial process measurements*. SPIE 1266. (b) Novinson, T. (1985). *Portable Infrared Spectrophotometer*. Google Patents.
- 4** Hassell, D.C. and Bowman, E.M. (1998). Process analytical chemistry for spectroscopists. *Appl. Spectrosc.* 52 (1): 18A–29A.
- 5** (a) Bakeev, K.A. (2010). *Process Analytical Technology: Spectroscopic Tools and Implementation Strategies for the Chemical and Pharmaceutical Industries*. Wiley. (b) Dent, G. and Chalmers, J.M. (2009). *Industrial Analysis with Vibrational Spectroscopy*. Royal Society of Chemistry. (c) Chalmers, J.M. (2000). *Spectroscopy in process analysis*, vol. 4. Taylor & Francis US. (d) Tschudi, J., O'Farrell, M., and Hestnes Bakke, K.A. (2018). Inline spectroscopy: from concept to function. *Appl. Spectrosc.* 72 (9): 1298–1309.
- 6** Crocombe, R.A. (2018). Portable spectroscopy. *Appl. Spectrosc.* 72 (12): 1701–1751.
- 7** (a) Williams, K. (1990). Remote sampling using a fibre-optic probe in Fourier transform Raman spectroscopy. *J. Raman Spectrosc.* 21 (2): 147–151. (b) Williams, K. and Mason, S. (1990). Future directions for Fourier transform Raman spectroscopy in industrial analysis. *Spectrochim. Acta Part A Mol. Spectrosc.* 46 (2): 187–196. (c) Mazzarese, D., Tripathi, A., Conner, W. et al. (1989). In situ FTIR and surface analysis of the reaction of trimethylgallium and ammonia. *J. Electron. Mater.* 18 (3): 369–377. (d) Blackmond, D.G., Goodwin, J.G. Jr., and Lester, J.E. (1982). In situ Fourier transform infrared spectroscopy study of HY cracking catalysts: coke formation and the nature of the active sites. *J. Catal.* 78 (1): 34–43. (e) Cavinato, A.G., Mayes, D.M., Ge, Z., and Callis, J.B. (1990). Noninvasive method for monitoring ethanol in fermentation processes using fiber-optic near-infrared spectroscopy. *Anal. Chem.* 62 (18): 1977–1982. (f) Kellar, J., Cross, W., and Miller, J. (1990). In situ near-infrared internal reflection spectroscopy for surfactant adsorption reactions using reactive internal reflection elements. *Appl. Spectrosc.* 44 (9): 1508–1512.
- 8** (a) Zhang, X., Qi, X., Zou, M., and Wu, J. (2012). Rapid detection of gasoline by a portable Raman spectrometer and chemometrics. *J. Raman Spectrosc.* 43 (10): 1487–1491. (b) Voigt, M., Legner, R., Haefner, S. et al. (2019). Using fieldable spectrometers and chemometric methods to determine RON of gasoline from petrol stations: a comparison of low-field 1H NMR@ 80 MHz, handheld RAMAN and benchtop NIR. *Fuel* 236: 829–835.
- 9** (a) da Silva, N.C., de Góes Massa, A.R.C., Domingos, D. et al. (2019). NIR-based octane rating simulator for use in gasoline compounding processes. *Fuel* 243: 381–389. (b) Powell, G., Hallman, R. Jr., and Cox, R. (1998). *Diffuse reflectance FTIR of stains on grit blasted metals*, 502–505. AIP Conference Proceedings, AIP.

- 10** (a) Smith, W. and Farquharson, S. (2006). *A portable fuel analyzer*. SPIE 6377. (b) da Silva, N.C., Cavalcanti, C.J., Honorato, F.A. et al. (2017). Standardization from a benchtop to a handheld NIR spectrometer using mathematically mixed NIR spectra to determine fuel quality parameters. *Anal. Chim. Acta* 954: 32–42.
- 11** Paiva, E.M., Rohwedder, J.J.R., Pasquini, C. et al. (2015). Quantification of biodiesel and adulteration with vegetable oils in diesel/biodiesel blends using portable near-infrared spectrometer. *Fuel* 160: 57–63.
- 12** (a) Câmara, A.B., de Carvalho, L.S., de Moraes, C.L. et al. (2017). MCR-ALS and PLS coupled to NIR/MIR spectroscopies for quantification and identification of adulterant in biodiesel-diesel blends. *Fuel* 210: 497–506. (b) Correia, R.M., Domingos, E., Cão, V.M. et al. (2018). Portable near infrared spectroscopy applied to fuel quality control. *Talanta* 176: 26–33.
- 13** Brouillette, C., Smith, W., Shende, C. et al. (2016). Analysis of twenty-two performance properties of diesel, gasoline, and jet fuels using a field-portable near-infrared (NIR) analyzer. *Appl. Spectrosc.* 70 (5): 746–755.
- 14** Smith, W. and Farquharson, S. (2006). *A portable fuel analyzer*, 63770E. Advanced Environmental, Chemical, and Biological Sensing Technologies IV, International Society for Optics and Photonics.
- 15** Guzmán, E., Baeten, V., Pierna, J.A.F., and García-Mesa, J.A. (2011). Application of low-resolution Raman spectroscopy for the analysis of oxidized olive oil. *Food Control* 22 (12): 2036–2040.
- 16** Carron, K. and Cox, R. (2010). *Qualitative Analysis and the Answer Box: A Perspective on Portable Raman Spectroscopy*. ACS Publications.
- 17** Kögler, M., Zhang, B., Cui, L. et al. (2016). Real-time Raman based approach for identification of biofouling. *Sens. Actuators B* 230: 411–421.
- 18** Lopez-Lorente, A., Simonet, B., and Valcarcel, M. (2013). Qualitative detection and quantitative determination of single-walled carbon nanotubes in mixtures of carbon nanotubes with a portable Raman spectrometer. *Analyst* 138 (8): 2378–2385.
- 19** Karunathilaka, S.R., Mossoba, M.M., Chung, J.K. et al. (2017). Rapid prediction of fatty acid content in marine oil Omega-3 dietary supplements using a portable Fourier transform infrared (FTIR) device and partial least-squares regression (PLSR) analysis. *J. Agric. Food Chem.* 65 (1): 224–233.
- 20** Corradini, F., Bartholomeus, H., Lwanga, E.H. et al. (2019). Predicting soil microplastic concentration using Vis-NIR spectroscopy. *Sci. Total Environ.* 650: 922–932.
- 21** de Lima, K.M.G. (2012). A portable photometer based on LED for the determination of aromatic hydrocarbons in water. *Microchem. J.* 103: 62–67.
- 22** Li, D., Qu, L., Zhai, W. et al. (2011). Facile on-site detection of substituted aromatic pollutants in water using thin layer chromatography combined with surface-enhanced Raman spectroscopy. *Environ. Sci. Technol.* 45 (9): 4046–4052.
- 23** Jiang, X., Yang, M., Meng, Y. et al. (2013). Cysteamine-modified silver nanoparticle aggregates for quantitative SERS sensing of pentachlorophenol with a portable Raman spectrometer. *ACS Appl. Mater. Interfaces* 5 (15): 6902–6908.
- 24** Leung Tang, P., Alqassim, M., Nic Daéid, N. et al. (2016). Nondestructive handheld Fourier transform infrared (FT-IR) analysis of spectroscopic changes and multivariate modeling of thermally degraded plain Portland cement concrete and its slag and fly ash-based analogs. *Appl. Spectrosc.* 70 (5): 923–931.
- 25** Gómez-Nubla, L., Aramendia, J., de Vallejuelo, S.F.-O. et al. (2013). From portable to SCA Raman devices to characterize harmful compounds contained in used black slag produced in electric arc furnace of steel industry. *J. Raman Spectrosc.* 44 (8): 1163–1171.
- 26** Cheng, H., Hao, R., Zhou, Y., and Frost, R.L. (2017). Visible and near-infrared spectroscopic comparison of five phyllosilicate mineral samples. *Spectrochim. Acta A Mol. Biomol. Spectrosc.* 180: 19–22.
- 27** Lin, D.H.M., Manara, D., Lindqvist-Reis, P. et al. (2014). The use of different dispersive Raman spectrometers for the analysis of uranium compounds. *Vib. Spectrosc.* 73: 102–110.
- 28** Miller, A.L., Drake, P.L., Murphy, N.C. et al. (2013). Deposition uniformity of coal dust on filters and its effect on the accuracy of FTIR analyses for silica. *Aerosol Sci. Tech.* 47 (7): 724–733.

- 29** (a) Hase, F., Frey, M., Blumenstock, T. et al. (2015). Application of portable FTIR spectrometers for detecting greenhouse gas emissions of the major city Berlin. *Atmos. Meas. Tech.* 8 (7): 3059–3068. (b) Frey, M., Hase, F., Blumenstock, T. et al. (2015). Calibration and instrumental line shape characterization of a set of portable FTIR spectrometers for detecting greenhouse gas emissions. *Atmos. Meas. Tech.* 8 (7): 3047–3057.
- 30** Suarez-Bertoa, R., Mendoza-Villafrerte, P., Riccobono, F. et al. (2017). On-road measurement of NH<sub>3</sub> emissions from gasoline and diesel passenger cars during real world driving conditions. *Atmos. Environ.* 166: 488–497.
- 31** Benedek, I. and Feldstein, M.M. (2008). *Technology of Pressure-Sensitive Adhesives and Products*. CRC Press.
- 32** Mascioli, R. L. (1986). Method for the preparation of semi-rigid polyurethane modified polyurea foam compositions. US Patent 4,568,702.
- 33** (a) Fernandez d'Arlas, B., Rueda, L., Stefani, P.M. et al. (2007). Kinetic and thermodynamic studies of the formation of a polyurethane based on 1,6-hexamethylene diisocyanate and poly(carbonate-co-ester)diol. *Thermochim. Acta* 459 (1): 94–103. (b) Li, S., Vatanparast, R., and Lemmetyinen, H. (2000). Cross-linking kinetics and swelling behaviour of aliphatic polyurethane. *Polymer* 41 (15): 5571–5576. (c) de Haseth, J.A., Andrews, J.E., McClusky, J.V. et al. (1993). Characterization of polyurethane foams by mid-infrared fiber/FT-IR spectrometry. *Appl. Spectrosc.* 47 (2): 173–179.
- 34** (a) DeThomas, F.A., Hall, J.W., and Monfre, S.L. (1994). Real-time monitoring of polyurethane production using near-infrared spectroscopy. *Talanta* 41 (3): 425–431. (b) Miller, C.E. and Eichinger, B. (1991). Analysis of reaction-injection-molded polyurethanes by near-infrared diffuse reflectance spectroscopy. *J. Appl. Polym. Sci.* 42 (8): 2169–2190. (c) Dupuy, J.; Benali, S.; Maazouz, A., Lachenal, G., and Bertrand, D. (2002). FT-NIR monitoring of a scattering polyurethane manufactured by reaction injection molding (RIM): univariate and multivariate analysis versus kinetic predictions. *Macromol. Symp.*, Wiley Online Library, pp. 249–260. [https://onlinelibrary.wiley.com/doi/10.1002/1521-3900\(200208\)184:1%3C249::AID-MASY249%3E3.0.CO;2-5](https://onlinelibrary.wiley.com/doi/10.1002/1521-3900(200208)184:1%3C249::AID-MASY249%3E3.0.CO;2-5) (d) Miller, C.E., Archibald, D., Myrick, M., and Angel, S. (1990). Determination of physical properties of reaction-injection-molded polyurethanes by NIR-FT-Raman spectroscopy. *Appl. Spectrosc.* 44 (8): 1297–1300.
- 35** Coyner, R. N. and Skujins, P. (1977). Moisture curable polyurethane systems. U.S. Patent No. 4,038,239.
- 36** Chen, X., Laughlin, K., Sparks, J.R. et al. (2015). In situ monitoring of emulsion polymerization by Raman spectroscopy: a robust and versatile chemometric analysis method. *Org. Process Res. Dev.* 19 (8): 995–1003.
- 37** Chen, X., Eldred, D., Liu, J. et al. (2018). Simultaneous in situ monitoring of trimethoxysilane hydrolysis reactions using Raman, infrared, and nuclear magnetic resonance (NMR) spectroscopy aided by chemometrics and Ab Initio calculations. *Appl. Spectrosc.* 72 (9): 1404–1415.
- 38** Chen, X., Cheng, Y., Matsuba, M. et al. (2019). EXPRESS: in situ monitoring of heterogeneous hydrosilylation reactions using infrared and Raman spectroscopy: normalization by phase-specific internal standards. *Appl. Spectrosc.* 73: 1299–1307. 3702819858916.

## 5

# The Value of Portable Spectrometers for the Analysis of Counterfeit Pharmaceuticals

*Pauline E. Leary<sup>1</sup>, Richard A. Crocombe<sup>2</sup> and Ravi Kalyanaraman<sup>3</sup>*

<sup>1</sup>*Federal Resources, Stevensville, MD, USA*

<sup>2</sup>*Crocombe Spectroscopic Consulting, Winchester, MA, USA*

<sup>3</sup>*Bristol Myers Squibb, New Brunswick, NJ, USA*

## 5.1 Introduction

Substandard and falsified medical products are recognized as a worldwide problem [1–3]. The World Health Organization (WHO) uses these definitions [4]:

- Substandard medical products
  - Also called “out of specification,” these are authorized medical products that fail to meet either their quality standards or their specifications, or both.
- Unregistered/unlicensed medical products
  - Medical products that have not undergone evaluation and/or approval by the national or regional regulatory authority for the market in which they are marketed/distributed or used, subject to permitted conditions under national or regional regulation and legislation.
- Falsified medical products
  - Medical products that deliberately/fraudulently misrepresent their identity, composition, or source.

In this chapter, we are largely concerned with falsified medical products, specifically counterfeit pharmaceutical products. In their 2017 report, the WHO notes that “Some 15 years ago, global sales of medicines rose above US\$500 billion for the first time. Since then, sales have doubled again, to approximately US\$1.1 trillion, with by far the largest growth occurring in middle-income markets [5, 6]. Unfortunately, this growth has opened the door not just to quality, safe and effective medicines, but also to medicines, vaccines and other products that do not meet quality standards and that are sometimes positively dangerous.” They further note, “It is very difficult to quantify the impact of substandard and falsified medical products. However there can be no doubt that substandard and falsified medical products:

- endanger health, prolong illness and even kill;
- promote antimicrobial resistance and the spread of drug-resistant infections;
- undermine confidence in health professionals and health systems;
- create distrust about the effectiveness of vaccines and medicines;
- eat into the limited budgets of families and health systems;
- provide income to criminal networks.”

The International Criminal Police Organization (INTERPOL) has reported that some organized criminal networks are using profits from falsified medicine operations to subsidize other clandestine activities [7, 8]. The WHO

report also notes that “substandard production and falsification affect all types of medical products. Much of the media coverage concerning ‘fake’ medicines, particularly those purchased over the internet, has focused on what are sometimes known as lifestyle medicines, such as slimming tablets and treatment for impotence. But over the past four years, the database has received notifications for everything from cancer medicines to contraception, from antibiotics to vaccines.” Malaria medicines [9], for example, account for nearly 20% of the falsified products reported, and antibiotics nearly 17%. So the threat to human life is obvious, and one of the latest cases is falsified chloroquine [10], approved as an antimalarial, and touted by some as effective against COVID-19. There are numerous publications detailing these cases, going back over 20 years [11–18]. Other international organizations have also documented the impact of these falsified products [19]; in addition to the effect on human health, there is overall economic damage, which is difficult to quantify but probably is at least tens of billions of dollars, maybe as high as \$200 billion [20–22].

In 2018, a comprehensive review of the literature from 1972 through 2017 regarding the acute health consequences of falsified medicines was published by Rahman et al. [23]. These authors identified 81 articles describing 48 incidents directly related to falsified drugs. These incidents resulted in approximately 7200 casualties, including 3604 deaths, and are summarized in Tables 5.1 and 5.2, showing the global extent of the immediate health consequences of these falsified drugs.

Pharmaceutical manufacturers are finding ways to fight counterfeit and substandard drugs by authenticating and identifying their products by various technologies, from manufacturing all the way through the supply chain. These include watermarks, barcodes, RFID tags, holograms, or covert patterns applied by special printing inks on packaging and on the pharmaceutical product [24–26]. Unfortunately, these measures, when applied to the packaging, have been forged, much like the pharmaceutical product itself [27]. Physical appearance is easily counterfeited, so robust chemical analysis must be used to distinguish between authentic and fake drugs. Sophisticated analytical methods can be carried out in a laboratory setting, but there is clearly a need for rapid assessment in the field, and a number of papers have surveyed the possible techniques [28–31].

### 5.1.1 Forensic and Legal Considerations

In developed countries, although counterfeit drugs are usually considered to be a problem for the pharmaceutical industry, frequently the challenges that need to be addressed are rooted in issues of public health, intellectual property (IP) rights, and law enforcement. These drug substances threaten public health and present unique challenges to the field of forensic science. These goods have caused sickness and death, and it is necessary that counterfeiters are identified and brought to justice. The Internet has caused a proliferation of counterfeit drugs because it is easy to reach the consumer directly, and many studies have shown that the incidence of counterfeit and nonauthentic drugs received from online purchases is high [32]. “Lifestyle” drugs like Viagra® are especially vulnerable in this forum because not only are authentic (noncounterfeit) versions of the drug usually more expensive than counterfeits but also the use of this medication as a treatment for erectile dysfunction may be a source of embarrassment to the patient. Ordering these drugs online makes it possible to purchase and receive the medication discreetly. Figure 5.1 shows an image of counterfeit Viagra along with an authentic tablet. Figure 5.2 shows an illegal imitation of Viagra along with an authentic tablet.

Many methods have been successfully used to classify a drug as counterfeit, including direct visual comparisons of microscopic and macroscopic features, infrared (IR) spectroscopy, Raman spectroscopy, and mass spectrometry (MS). Once it is determined that a drug is counterfeit, determination of source is important, which is more challenging than simply identifying a sample as counterfeit. Sourcing samples using analytical methods typically requires that counterfeit samples are further classified based upon chemical or physical markers present in the sample, and these can be detected and may be used to associate different samples with each other.

Clearly, detection and identification of counterfeit drugs are critical steps in the process of addressing the counterfeit-drug problem, and the scientific testing performed to achieve these goals must use methods that

**Table 5.1** Summary of incidents of falsified medicines causing health damage, including deaths or adverse reactions reported in the literature for incident years 1969–2005.

Year	Country	Health impact	Cause
1969	South Africa	Seven children died	Diethylene glycol poisoning from sedative mixtures
1982	USA	Seven people died	Cyanide-laced paracetamol
1986	India	14 patients died	Receiving doses of impure glycerin contaminated with diethylene glycol
1988	Nigeria	21-year-old woman died	Hyperglycemia due to fake insulin
1989	Haiti	89 people died	Paracetamol cough syrup prepared with diethylene glycol
1990	Nigeria	109 children died	Acute renal failure from diethylene glycol contaminated syrup/elixir
1990	Bangladesh	236 patients died including 51 children	Paracetamol syrup tainted with ethylene
1992	Argentina	26 people died	Consumption of a propolis syrup with a high level of diethylene glycol
1995	Haiti	85 children died	Ingestion of paracetamol syrup adulterated with diethylene glycol
1995	Niger	2500 people died	Falsified meningitis vaccine
1998	Brazil	200 unwanted pregnancies	Falsified contraceptive pill
1998	India	36 children suffered acute renal failure, 33 of them died	Cough expectorant contaminated with diethylene glycol
1998	Brazil	Several people died	Falsified anticancer drug
1998	Russia	1000 patients were hospitalized	Falsified insulin
1999	Cambodia	30 people died	Falsified artesunate prepared with sulfadoxine-pyrimethamine
1999	USA	17 deaths and 254 adverse effects	Falsified gentamicin
2001	USA	Several patients suffered tissue swelling or skin rashes	Injection of fake growth hormone
2002	USA	16-year-old boy suffered painful spasms	Injection of diverted drug containing very low amount of erythropoietin hormone
2002	USA	Death of a cancer patient	Falsified erythropoietin hormone
2004	Nigeria	Three hospitals reported cases of adverse reaction	Infusion contaminated with microorganism
2004	Canada	Four people died	Heart attacks and strokes after taking falsified amlodipine made from talc
2004	Argentina	Two women died and one gave birth to 26-week premature baby	Falsified iron injection for anemia
2005	USA	Five men died	Ingestion of misbranded dextromethorphan
2005	USA	Respiratory paralysis of several people	Fake version of Botox
2005	Myanmar	A 23-year-old man died from cerebral malaria	Artesunate tablet containing paracetamol as a main ingredient

Source: Rahman et al. [23] licensed under CC BY 4.0.

**Table 5.2** Summary of incidents of falsified medicines causing health damage, including deaths or adverse reactions reported in the literature for incident years 2006–2016.

Year	Country	Health impact	Cause
2006	Canada	Four people died	Unauthorized substitution of falsified Viagra containing talcum powder
2006	Panama	200 people died including more than 100 children	Paracetamol cough syrup contaminated with diethylene glycol
2007	Canada	58-year-old woman died	Falsified zolpidem and acetaminophen
2007	Hong Kong	Ten nondiabetic patients hospitalized due to hypoglycemia including one death and another taken to ICU	Herbal drug for erectile dysfunction containing glibenclamide
2008	China	12 patients died	Armillarisin manufactured with diethylene glycol as a solvent
2008	USA	785 adverse-reaction reports including 81 deaths	Falsified heparin contaminated with oversulfated chondroitin sulfate
2008	Singapore	150 patients hospitalized, seven remained comatose, and four subsequently died	Falsified Cialis, three herbal preparations, and sildenafil
2008	Norway	44 people suffered from poisoning	Fake flunitrazepam tablets containing scopolamine
2008	Nigeria	188 children died	Paracetamol teething mixture containing diethylene glycol
2009	China	Two people died	Falsified glibenclamide six times more potent than normal
2010	Australia	54-year-old man suffered from severe hypoglycemia	Ingestion of falsified tadalafil
2010	China	81 patients suffered from intraocular inflammation	Endotoxin-contaminated falsified bevacizumab
2013	Guinea-Bissau	75 patients had recurrence or increased frequency of seizures, two subsequently died	Falsified phenobarbital
2014	USA	65-year-old man suffered from hepatotoxicity	Chinese herbal medicine containing sildenafil
2014	Nigeria	105 patients had increased frequency of seizures	Falsified phenobarbital
2014	Congo	930 people suffered from dystonic reactions, 11 of them died	Falsified diazepam containing haloperidol
2014	USA	40 patients suffered from adverse events including one death	Nonsterile simulated IV fluids containing large amounts of endotoxin and significant bacterial contamination
2015	USA	Eight people suffered adverse effects	Ingestion of falsified alprazolam tablets found to contain fentanyl and, in some cases, etizolam
2015	India	15 patients suffered from intraocular inflammation	Injections of falsified bevacizumab
2016	USA	Seven people suffered adverse effects	Norco (acetaminophen and hydrocodone) containing fentanyl and promethazine
Unknown	UK	Acute lead intoxication of a man	Falsified ayurvedic drug for erectile dysfunction
Unknown	USA	Child complained of burning sensation after injection with human growth hormone	Human growth hormone containing inexpensive insulin
Unknown	Japan	39-year-old man suffered from hypoglycemia	Sexual-enhancement medication containing extremely large amount of glibenclamide and low amount of sildenafil

Source: Rahman et al. [23] licensed under CC BY 4.0.



**Figure 5.1** Counterfeit Viagra pills on the left (top and bottom) and authentic Viagra on the right (top and bottom).



**Figure 5.2** The tablet on the left is an illegal imitation (substandard) of the authentic Viagra tablet shown on the right.

work accurately and reliably. Analytical testing of counterfeit drugs *in the field* is usually performed to rapidly differentiate an authentic from a nonauthentic article and to classify these goods; this capability has value and may help determine source or origin. In situations where evidence will be used in court, the technologies and methods used must meet the standards of admissibility of scientific evidence in court. Historically, the results of tests performed using field instruments were used in a presumptive manner [33] to support investigations and

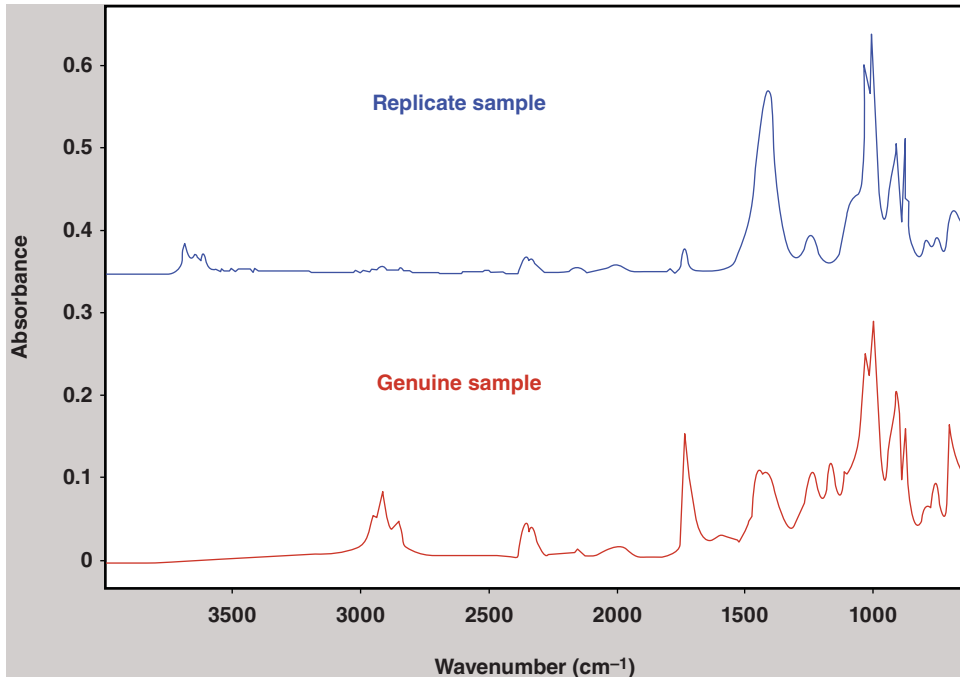


**Figure 5.3** IR spectra of the outside packaging of branded (genuine) and generic (replicate) over-the-counter medications analyzed using a portable IR spectrometer. These spectra can be used to quickly (within minutes) differentiate packaging. Source: Gabriele et al. [34]. © 2020 MJH Life Sciences.

for probable cause. More recently, the need to collect court-admissible data in the field is desirable because it may save time and money in the long term.

Analysis of counterfeits may begin with the evaluation of packaging used. Packaging for authentic medications is controlled, and, therefore, differences detected can be used for authentication purposes. For instance, a comparison of coatings on laminates used for both dosage form and bulk packaging may serve as a means for differentiation as may the adhesives used. Physical comparisons of markings and other sample features may also be used for this purpose. Once inside the packaging, physical and chemical characteristics of the dosage form may then be evaluated. Figure 5.3 shows the IR spectra collected using a portable IR spectrometer from the outside packaging of branded and generic over-the-counter medications. As shown here, the packaging from legal generics can be different from branded versions of a medication. This type of analysis is straightforward and, in many cases, can quickly and easily differentiate authentic from nonauthentic medications.

Analyzing packaging can be useful, but frequently analysis of the drug substance is required. When analyzing a drug in a pharmaceutical laboratory to confirm identity, IR or MS may be used for identification. An additional routine test (e.g. dissolution followed by liquid chromatography [LC]) may then be used to quantify the amount of drug present or establish its distribution throughout the final dosage form. Once the tablet is identified and quantified using standard test methods that were developed and validated during the drug-development and manufacturing processes, analysis is usually complete. When analyzing counterfeit drugs in a forensic setting, however, identification of the active pharmaceutical ingredient (API) is likely only one of many steps in the analytical workflow.

Counterfeits may have the proper API in the wrong dosage or solid-state form, and the solid-state form of the API is important for a variety of reasons [35, 36]. An example is polymorphism, where different polymorphs of the same chemical may exhibit different bioavailability [37]. The polymorphic form created during manufacture

may also have legal significance, because one polymorphic form may be covered under patent, whereas others may not [36]. In the case of different solid-state hydrates of the API, the wrong hydration level may result in underdosing tablets when hydration levels are too high or overdosing tablets when hydration levels are too low [38]. In addition, dosages and solid-state-form differences, particle size or distribution throughout the dosage form may be different, or residual solvents present may be different, which all may be used as points of comparison among samples. When evaluating counterfeits, the inactive ingredients may be different from the authentic versions of the drug and need to be identified and characterized. Foreign particles present in the counterfeit versions may serve as an additional feature for differentiation and identification. In these cases, nonroutine methods of pharmaceutical analysis need to be employed.

### 5.1.2 Field Analytical Overview

Different types of counterfeits present somewhat different analytical and legal challenges:

- True counterfeits, i.e. nonauthentic product, are intended to deceive and present public-health risks, are theft of IP rights, and result in monetary damage to the pharmaceutical innovator (and others in the retail chain). They also challenge brand management.
- Diverted authenticants create law-enforcement issues such as theft of property.
- Expired and otherwise substandard drugs, for instance, the case of antimalarials, are a public-health issue and in the long term can promote drug resistance.
- Imitations can include counterfeit generics and illegal generics. They can involve violations of law like those against the Hatch-Waxman Act in the United States intended to balance pharmaceutical innovation and development with the availability of affordable medicines.

It is worth noting that in the United States, one concern is public health, but control of supply chain is good, so frequently the discussion tends to focus on whether imported (i.e. purchased over the web) pharmaceuticals are authentic, along with violation of IP and other regulations. In developing countries, the concern is more in the public-health sector, although there have been cases in the United States where public health has been impacted [11–18].

Traditionally, qualitative and semiquantitative laboratory techniques – for example, disintegration, colorimetry, and thin-layer chromatography (TLC) – have been employed to determine if a pharmaceutical product is counterfeit. More sophisticated laboratory techniques include gas chromatography (GC) and LC [39]. Coupling MS to LC not only assists in authentication but also identifies even low concentrations of unknown ingredients in a counterfeit. Even in the lab, the drawback with such methods is the sample preparation and high lead time required for analysis. To overcome this, direct-ionization MS methods, such as direct analysis in real time (DART) and desorption electrospray ionization (DESI), are being used to eliminate sample preparation [40].

However, it is important that detection and identification of counterfeit drugs is performed *in the field*, using methods of analysis that are rapid and reliable. For instance, at Customs check points, the ability to detect and identify these goods quickly and accurately will prevent them from entering the local supply chain. It is not always practical or possible to delay entry of cargo to wait on results of laboratory testing. In fact, border agents typically will only have a few minutes to make a go/no-go decision under conditions of high stress. If detection and identification can occur in the field, law-enforcement organizations may take immediate action to prevent the infiltration of these goods into the market. It may also help to identify counterfeiters, establish provenance, and appropriately adjudicate these cases.

A field analog of traditional laboratory methods is the Global Pharma Health Fund “GPHF-Minilab,” a field test kit with simple disintegration, color-reaction tests, and easy-to-use TLC tests for rapid drug detection and drug potency verification [41]. It comprises four steps:

1. A physical inspection scheme of dosage forms and associated packaging material for an early rejection of the more crudely presented counterfeits

2. A quick check of the fill and total weight serves as an early indicator for the detection of false information related to the drug content
3. A simple tablet and capsule disintegration test in order to verify label claims on enteric coating and other modified-release systems
4. Easy-to-use TLC as chemical test for a rapid verification of label claims regarding drug identity and content

Supplies include sufficient quantities in order to perform about 1000 assays while ensuring that the total material costs for one test run do not exceed €3.

As noted in other chapters in this book, field-portable instruments need to be small, light, rugged, and easy to use, especially as they may be hand carried to the site where analysis will be performed. They are expected to experience significant wear and tear during transit and at the analysis scene. Frequently, specifications for drop testing and other ruggedization criteria are as critical as the specifications for the signal-to-noise ratio of the spectrometer. Due to the sometimes-precarious environments in which these instruments are expected to perform, they must have an easy-to-use software interface that generates result-driven answers rather than spectral displays requiring significant user interpretation. Automatic library searching, using algorithms tailored to optimize results in the field, is a significant aspect of these instrument designs. In addition, sampling and other accessories are sometimes required, but are not desirable. The more complex a field-portable instrument becomes, the less likely it will become a part of the routine on-scene workflow. There is also a need to minimize impractical consumables; in addition, the more gear that needs to be carried to make an instrument perform, the less likely the instrument will be successful in the field.

Given all of the above, one of the effective ways to authenticate and verify the identity of pharmaceutical products, in or out of the field, is by using vibrational spectroscopy techniques, such as IR and Raman spectroscopy, which obtain a unique spectral “fingerprint” of the drug product itself. These optical spectroscopic techniques possess a distinct advantage over chromatographic techniques in that they are nondestructive, require no reagents or supplies, and can rapidly characterize the suspect product in seconds and in some cases without the need to remove the drug from packaging. When a legitimate manufacturer receives a suspected counterfeit at a production or research facility, they can usually detect or differentiate it from authentic product using methods they deploy during development, manufacture, and release testing. But the challenge is making it possible to generate this type of result in the field. Over the past 15 years, great strides in the miniaturization and portability of optical spectroscopic instruments have been made. The technical details behind these advances are described in the chapters in Volume 1 of this book and will not be discussed in detail here.

These advances have enabled the “lab” to be brought closer to the arena where the counterfeit activities are taking place, such as deceitful manufacturing facilities, pharmacies, hospitals, warehouses, storage facilities, etc. This can provide a level of analytical control in the drug-distribution chain, from the manufacturing floor to the retail pharmacies. Pharmaceutical companies and local police and law-enforcement agencies can work together by using these portable devices to detect counterfeits in the field. Samples can be analyzed rapidly in a nondestructive manner on-location, and the results can be obtained within minutes, which can potentially help the operator take immediate follow-up steps in the form of seizures or to close down the counterfeit operations in a rapid manner. This is critical since the time taken for samples to be sent to remote testing facilities can be long enough to allow the unscrupulous counterfeiters to flee the site and reestablish operations elsewhere [42]. Portable optical spectrometers have made inroads into the pharmaceutical industry mainly in quality control for raw-material identification and in process analytical technology (PAT) [43]. Portable near-infrared (NIR) and Raman spectrometers were initially used for raw-material identification in the form of direct testing in warehouses or at incoming inspections [44, 45], so their extension into the field for the analysis of pharmaceuticals is natural.

## 5.2 Field Analytical Spectroscopy Methods

### 5.2.1 Vibrational Spectroscopy

As noted above, the technologies for portable NIR, mid-IR, and Raman instruments, as well as their (non-counterfeit-detection) applications, are described in other chapters in this book. A key ability of these instruments is their use by nonscientists, perhaps wearing personal protective equipment (PPE), to obtain actionable information, not just spectra. What is important to note about these three methods is that they perform analysis of the bulk product. What is meant by that in this chapter is that a visible amount of sample must be present in order for analysis to occur, and the resulting spectrum, although not always the case, is intended to be representative of the overall composition of the drug product. Sometimes different regions of the drug product may be analyzed using these three methods, but the intention is for the resulting spectrum to be representative of the area analyzed. For example, an analysis of the coating on a tablet will result in a different spectrum than when the core of the tablet is analyzed. The spectrum from the coating is intended to be representative of the coating, and the spectrum from the core is intended to be representative of the core.

Portable IR and Raman spectrometers have been deployed extensively to nonscientific users, such as law-enforcement personnel and hazardous-materials technicians, for the analysis of many types of illicit and authentic pharmaceuticals. Because these spectrometers provide specific chemical information about a sample, they can establish not only the chemical composition of the API, excipients, or drug product but also the solid-state form of the components such as salt form, polymorphic form, and hydration level [36]. They are also useful for the analysis of blister or other packaging. Generally, the applications where portable IR spectrometers may be useful are also those where Raman spectrometers may be applied, and these methods generally provide complimentary results. Due to differences in selection rules and relative band intensities, some samples may be more amenable to IR analysis while others are more amenable to Raman analysis.

Personnel using portable optical spectrometers need to be aware what portion of the sample under study is being interrogated, especially when samples are layered or otherwise heterogeneous, and as nonscientists, this may not be obvious to them. Some considerations are summarized in Table 5.3. Conventional Raman spectroscopy is a surface technique and, for a typical intact solid dosage form, will only interrogate the coating; the pill or tablet has to be broken open to interrogate its interior. The exciting radiation in a portable Raman instrument will also typically have a small spot size, typically from 30- $\mu\text{m}$  to 300- $\mu\text{m}$  diameter, and pharma solid dosage forms are not uniform. Spatially offset Raman spectroscopy (SORS) can give information about the bulk of the sample, and this is recently available as a handheld technique [46]. “Transmission Raman spectroscopy,” currently only available as a laboratory technique [47], can provide information about a whole tablet. Conjugated and aromatic molecules tend to be strong Raman scatterers, and many APIs fall into those classes. However, many APIs are also fluorescent under illumination with light at visible wavelengths, which can present problems. Most early handheld Raman spectrometers used 785-nm laser excitation, but several are now available using 1064-nm laser excitation, where the probability of fluorescence is reduced. Portable mid-IR instruments typically use an attenuated total reflection (ATR) sample interface, which requires intimate contact between the sample and an internal reflection element, sometimes referred to as the crystal. Not only does that mean the sample has to be handled, but this is also a surface technique, because only the top few microns are probed by the IR beam. Both Raman and mid-IR spectroscopies provide very specific information, as they give information about the fundamental molecular vibrations. NIR is not as specific, as only overtone and combination bands occur in that region of the spectrum. But because of lower extinction coefficients in the NIR, it offers greater depth penetration (greater as wavelengths are shorter), so NIR does sample the bulk as well as the surface, usually with a larger sampling diameter.

**Table 5.3** Some considerations for the use of vibrational spectroscopic methods for pharmaceutical dosage forms.

Technique	Conventional Raman	Mid-IR	NIR
Sample interrogated	Surface only	Surface only	Surface and bulk
Sample diameter	~1-mm spot size or less	Few mm for ATR sampling	~3–10-mm spot size
Sample handling required?	No sample handling	Requires sample handling for ATR	No sample handling
Can use with packaging?	Can sample through transparent packaging	No	Can sample through transparent packaging, but spectra will have contributions from the packaging
Sample fluorescence issues?	Samples may fluoresce	Fluorescence not an issue	Fluorescence not an issue
Sample heating issues?	Possible for dark samples	No	No
Specific chemical information?	Yes; fundamental vibrations	Yes; fundamental vibrations	Less; overtones and combinations
Most sensitive functional groups	Nonpolar groups (e.g. C=C) and skeletal or backbone groups tend to be stronger Raman scatterers	Polar functional groups (e.g. C=O, C-halogen) tend to have strong mid-IR bands	C—H, N—H, and O—H groups

From an analytical-testing perspective, there are other reasons aside from selection rules one might use IR over Raman, or vice versa. The use of IR over Raman may be preferred if the sample fluoresces during Raman analysis or if the sample burns when the laser, which is required to achieve sufficient Raman signal, heats the sample. As noted above, many substances of interest (typically aromatic APIs, but also some excipients like microcrystalline cellulose) within the pharmaceutical industry fluoresce. The development of portable Raman systems that use longer-wavelength laser excitation (1064 vs. 785 nm) is intended to address this issue of fluorescence, but it is frequently necessary to use portable IR if the fluorescence cannot be reduced during the optimized Raman analysis. Unlike with applications such as explosives or art conservation, burning (or even detonation) of a sample is usually not a problem when portable Raman systems are deployed for the analysis of pharmaceuticals. Raman spectroscopy is preferred to IR if the analyte is dispersed within water, as the Raman signal due to water is weak, so this can help detect and identify components within aqueous solutions. In the case of hydrates, though, the presence of stoichiometric water can provide an additional point of differentiation when using IR since the IR spectra of stoichiometric hydrates are usually different from each other and from its anhydrous form.

Aside from analytical considerations, there are also operational considerations that may dictate whether portable IR or portable Raman is used. Operationally, Raman has a significant advantage over FT-IR when deployed in the field; specifically, that it can “see through” transparent glass, clear blister packs, and plastic bags, so no contact with the sample is necessary. This can be especially important when the sample for analysis is hazardous. The ability to “point and shoot” [42] through packaging during a Raman analysis is a significant reason Raman is frequently favored over IR by field users. In order to collect an IR spectrum using an ATR system, a small amount of the sample must be transferred to the internal reflection element of the system. This requires not only that the drug or drug product be opened to perform the analysis but also that sampling of the material must occur. Aside from the potential hazards due to exposure to the sample, the need to open containers and sample the substance for analysis may also significantly increase the time required for an individual analysis and

therefore decrease overall sample throughout. Regardless of whether IR or Raman methods are performed in the field, analysis times are reasonably fast (on the order of seconds for the data collection). In some situations when analyzing counterfeit drugs, the drug substance itself is analyzed; in others, the packaging may be analyzed. Both approaches have been shown to be effective [48, 49].

It should be noted that for a sample in a clear plastic blister pack, the spectrum obtained by a Raman instrument will not contain significant contributions from the plastic, whereas the spectrum from a NIR instrument will. This is due to their fundamentally different modes of operation. Raman instruments are designed to be confocal, so that the exciting beam is focused on the sample (in this case a solid dosage form), and the scattered radiation is also collected from the same point. This discriminates against the spectrum of the clear blister pack. However, a NIR instrument is operating in diffuse-reflection mode, and the incident radiation passes through the plastic, suffering some absorption, is diffusely scattered by the sample, and passes through the plastic again, suffering further absorption, on its way to the detector. Therefore, the resulting spectrum is “contaminated” by the spectrum of the plastic. In some cases (e.g. polyethylene), the plastic spectrum is relatively simple, but in others (e.g. polymethylmethacrylate), it can be complex.

In a portable instrument, the spectrum is neither the final result nor the actionable information the operator desires. For counterfeit detection in the field, the sample spectrum needs to be compared with the spectrum of authentic material, bearing in mind that there may be slight differences between batches of authentic material, especially if they come from different manufacturing sites. This is explored in detail below, and chemometric comparison algorithms and library/database building are discussed in Volume 2 in chapters by Zhang et al., and Schreyer, respectively. Note that there is a clear distinction between proof of concept and development of a method versus deployment of that method on the portable instrument. Method development requires considerable skill and is usually done by an experienced scientist. However, once that method is deployed on a portable instrument, it can be operated by a nonscientist to give true/false, red-light/green-light, or genuine/counterfeit answers. But that type of method will be specific to one product; in other words, a method set up to detect fake Viagra will not work to detect fake Levitra® and vice versa. This also implies that the portable instrument should be capable of having many such stored “methods”, allowing the operator to choose (but not modify) which one should be used. This is in contrast to other uses of portable spectrometers in pharmaceutical manufacturing, for instance, in raw-material identification, where a single library and algorithm may be used for a wide variety of incoming materials.

In a broad generalization, two main algorithm types are used to detect counterfeits by vibrational spectroscopy. First, a spectral matching method can be used. Here a library of spectra of confirmed genuine products is created. The spectra of suspicious samples are compared against the appropriate library entries, and the quality of each match is evaluated. This was the method used in the 2010 and onward campaign in Nigeria, for example (see below for details). Second, a combination of principal component analysis (PCA) and cluster analysis is used. This has the advantage that genuine products from different manufacturing sites, and other genuine variances (e.g. storage conditions) are incorporated into the data set. Genuine products will cluster in a group in PCA space, whereas counterfeit products will tend to fall outside that cluster. Examples of this approach are also given below.

The following subsections describe counterfeit detection applications for Fourier transform IR (FT-IR), Raman, and NIR spectroscopies.

### 5.2.1.1 Fourier Transform Infrared (FT-IR) Spectroscopy

A majority of portable IR spectrometers are FT-IR systems, based upon ATR sample interface techniques and methods. Within the pharmaceutical industry, IR spectroscopy is used extensively for the identification of raw materials, excipients, drug substances, and drug products. In fact, the US Pharmacopeia (USP) in chapter <197> considers the IR absorption spectrum of a substance (when it is compared with a spectrum obtained concomitantly for the corresponding USP reference standard) to be, perhaps, the most conclusive evidence for the identification of a substance that can be realized from a single test [50]. It is no surprise, therefore, that the use of portable FT-IR

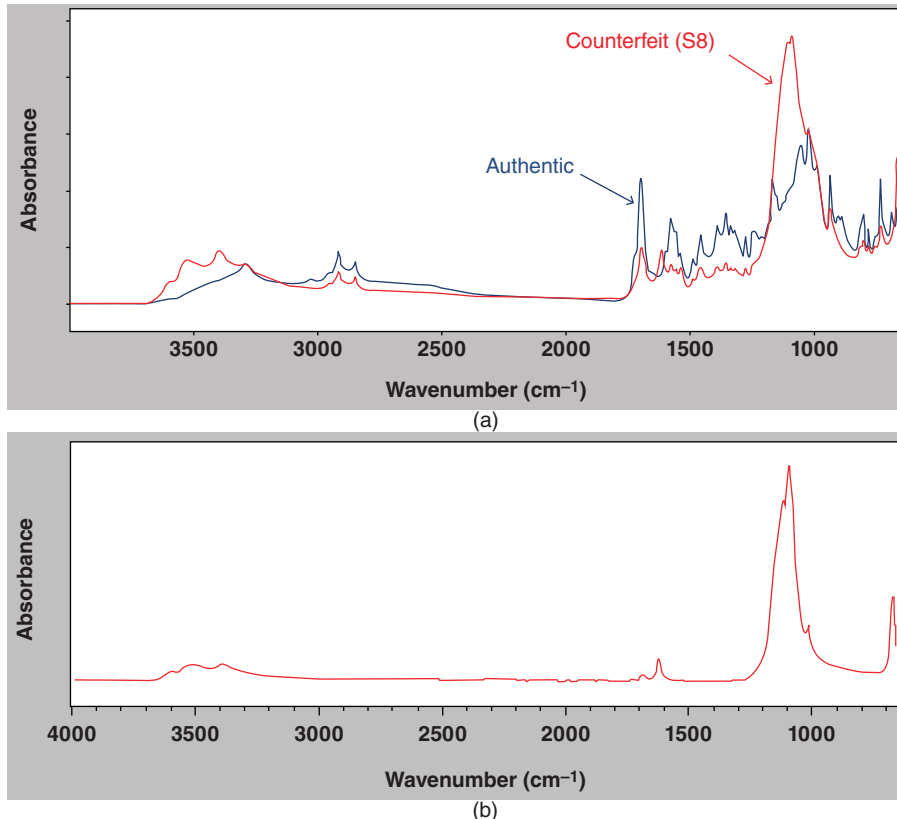


**Figure 5.4** (a) The average of 9 IR spectra of the core of 3 authentic tablets (blue) and the average of 21 IR spectra of the core of 7 tablets of a counterfeit lot (red). This example is interesting because not only does it show how portable FT-IR can be used to easily distinguish these samples from each other but it is also useful to establish chemical composition of the counterfeit product. In this example, the counterfeit-drug product has an IR spectrum that is similar to the authentic drug product but also has spectral features of calcium sulfate. (b) The IR spectrum of calcium sulfate, the absorption bands of which are observed in the spectrum from the counterfeit sample shown in figure 5.4a.

for the detection and identification of counterfeit drugs has value. As previously mentioned, the method can be applied for the analysis of the drug substance and/or its packaging. Regardless, it is both easy to perform and provides fast results.

As an example for using portable FT-IR analysis to analyze counterfeit drugs, Figure 5.4a shows an overlay of the average of nine spectra of the core of three tablets of an authentic drug product, as well as the average of 21 spectra from the core of seven tablets of a counterfeit version of the drug product; the spectra are area normalized. This example is interesting because not only does it show how portable FT-IR can be used to easily distinguish these samples from each other but also it is useful to establish chemical composition of the counterfeit product. In this example, the counterfeit-drug product has an IR spectrum that is similar to the authentic drug product but also has spectral features of calcium sulfate. Figure 5.4b shows the IR spectrum of calcium sulfate, the absorption bands of which are observed in the spectrum from the counterfeit sample.

Another significant potential value of portable FT-IR spectroscopy for counterfeit drugs is the ability to establish provenance of a sample. Counterfeit drugs may be chemically similar to the authentic product, but small differences in composition such as those due to different excipients may be observed in their IR spectra. Figure 5.5 shows a spectral overlay of an authentic tablet with a counterfeit version, as well as a spectral overlay of two

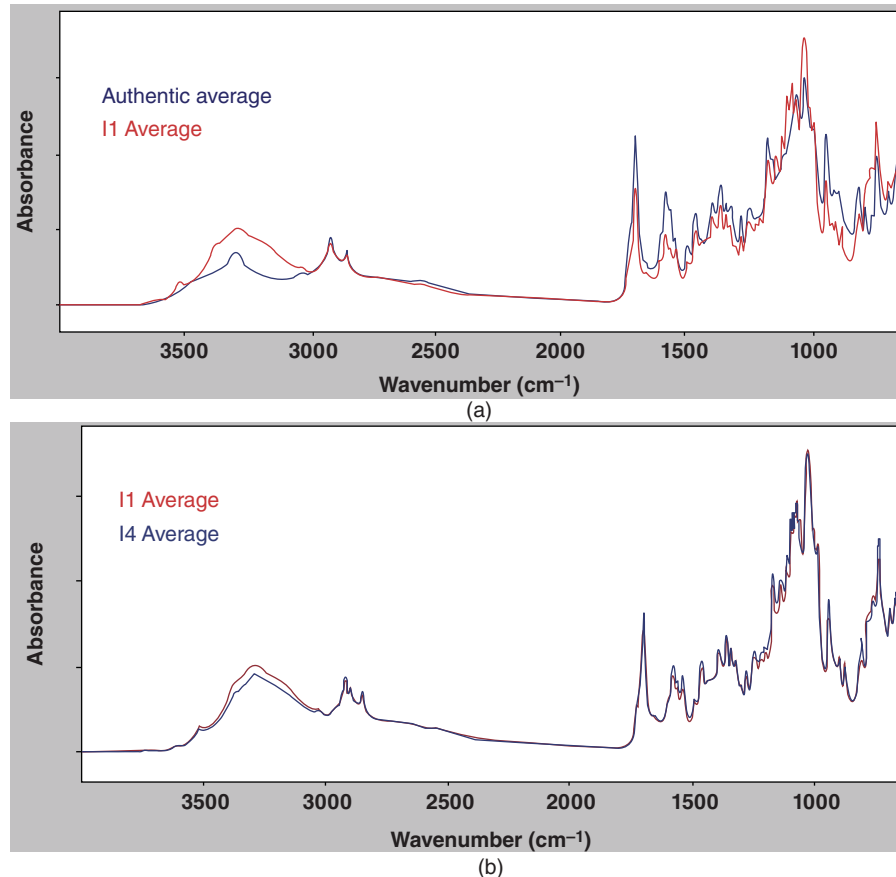


**Figure 5.5** (a) Spectral overlay of the average of 9 IR spectra of the core of 3 authentic tablets (blue) and the average of 21 IR spectra of the core of 7 tablets of a counterfeit lot (red). (b) Spectral overlay of the average of 21 IR spectra of the core for each of two different counterfeit drug samples expected to be of the same origin (all spectra area normalized). IR spectral analysis performed using a portable FT-IR (ATR).

different counterfeit-tablet samples expected to be from the same source. Note that based upon their IR spectra, the authentic and counterfeit samples are shown to be *chemically similar* to each other (Figure 5.5a). However, when spectra from different counterfeit samples expected to be from the same origin are evaluated (samples I1 and I4), the spectra are *almost identical* (Figure 5.5b). Please note that the “I” used as part of the sample names I1 and I4 indicates the origin of these samples is the country of India. The only differences are in the O–H stretching vibrations between 3000 and 3500  $\text{cm}^{-1}$ , which are due to differences in water content between the two samples. The average spectrum of sample I4 contains less water than the average spectrum of sample I1. This is an important observation because IR analysis is sensitive to water and drug tablets are known to sorb different amounts of water based upon many factors. Differences in water content may simply be due to storage conditions, e.g. humid versus dry environments, and water may also be present due to amorphous content of API or other components. Even small amounts of amorphous content can cause the sample to sorb more water than a crystalline form of the drug [51]. Amorphous content may be directly related to manufacturing process [52] and may provide insight as to the source of the tablets. Differences in water content may also be due to the presence of different stoichiometric hydrates. Since stoichiometric hydrates may have easily distinguishable IR spectra, the analysis of these types of samples can help samples of different origins from each other. It is important when interpreting data to consider all those factors before a conclusion about sample authenticity is made.

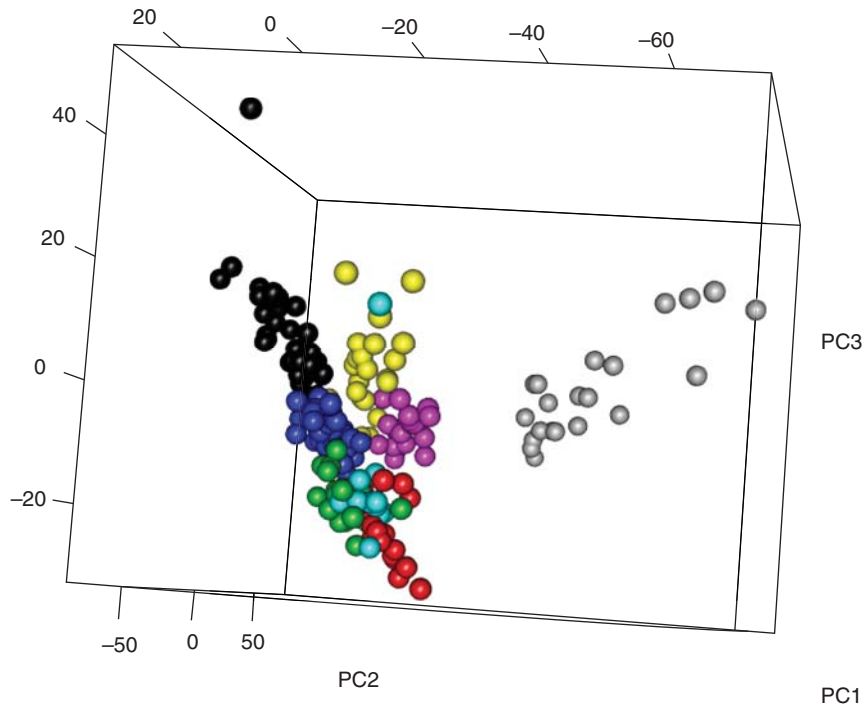


**Figure 5.6** 3-D score plot of IR spectra (auto scaled) from counterfeit and authentic pharmaceutical tablets. The variance values of PC1, PC2, and PC3 are 45.58, 27.47, and 12.16%, respectively.

Further attempts to differentiate samples from each other and establish provenance based upon IR spectral data are also possible using chemometrics [53, 54]. The spectra of seven counterfeit samples, including the two shown in Figure 5.5b, and the spectra of authentic drug product were evaluated using PCA-canonical variate analysis (PCA-CVA). PCA-CVA, using autoscaled data pretreatment, showed it was possible to classify these samples into eight groups (seven nonauthentic and one authentic). Hold-one-out cross-validation (HOO-CV) was used to determine an estimated error rate of 2.16% using 12 principal components (PCs). Figure 5.6 shows the three-dimensional (3-D) score plot. In this figure, each grouping is colored differently, and clustering based upon group assignment in three dimensions is evident.

The PCA-CVA HOO-CV confusion matrix is shown in Table 5.4. This confusion matrix visually shows the performance of the HOO-CV PCA-CVA model. Each row represents the predicted identity of the held-out sample while the columns show the actual identity. The number in each row shows the percentage of times the test algorithm placed the held-out sample in a given class (column). Thus, if all 10 replicates for all samples were correctly identified, then every cell in the diagonal would have a “100%”. This table shows that 86% of the time, I1 was accurately classified, but 14% of the time I1 was incorrectly classified as I4. It also shows that 95% of the time I4 was accurately classified, but 5% of the time it was incorrectly classified as I1. As previously mentioned, the primary difference between samples I1 and I4 as observed in the IR spectra is in the water content of the samples. It is possible when performing chemometrics analysis to remove the OH stretching region of the spectra prior to evaluation if desired, but that approach was not taken in this case.

### 5.2.1.2 Raman Spectroscopy

Portable Raman spectrometers have been commercially available since about 2005. These systems were initially intended for use by first responders for hazardous-material identification but gained acceptance within the

**Table 5.4** Confusion matrix for the HOO-CV PCA-CVA results for the IR data of counterfeit and authentic (A) tablets.

Prediction	Reference							
	I1	I2	I3 SINGS	I4	I5	S7	S8	A
I1	86%	0%	0%	5%	0%	0%	0%	0%
I2	0%	100%	0%	0%	0%	0%	0%	0%
I3 SINGS	0%	0%	100%	0%	0%	5%	0%	0%
I4	14%	0%	0%	95%	0%	0%	0%	0%
I5	0%	0%	0%	0%	100%	0%	0%	0%
S7	0%	0%	0%	0%	0%	95%	0%	0%
S8	0%	0%	0%	0%	0%	0%	100%	0%
A	0%	0%	0%	0%	0%	0%	0%	100%

This confusion matrix visually shows the performance of the HOO-CV PCA-CVA models. Each row represents the predicted identity of the held-out sample while the columns show the actual identity. The number in each row shows the amount of times the test algorithm placed the held-out sample in a given class (column). Thus, if all 10 replicates for all samples were correctly identified, then every cell in the diagonal would have a “100%”. This table shows that 86% of the time, I1 was accurately classified, but 14% of the time I1 was incorrectly classified as I4. It also shows that 95% of the time I4 was accurately classified, but 5% of the time it was incorrectly classified as I1.

Note: 12PCs were used, resulting in a 2.16% error rate (5 of 231 misclassified).

pharmaceutical industry for the identification of drug substance, drug products, excipients, and even product packaging. They frequently use 785-nm laser excitation, but instruments with longer-wavelength excitation (1064 nm) are now available.

There are a number of ways in which portable Raman systems can be used for the analysis of counterfeit pharmaceutical products [55]. Pattern matching can be used to *distinguish* one sample from another, but these instruments can also be used to *provide chemical information* about the sample. Figure 5.7 shows the average Raman spectra of two different samples of authentic drug product. For each sample, three Raman spectra were collected from different tablet-core locations for three different tablets of the sample, and the nine spectra were then averaged. Note that these average spectra are virtually indistinguishable from each other and they demonstrate how similar two spectra will be when the composition of the samples is the same. This type of analysis is quite straightforward and is, essentially, a pattern-matching exercise.

For comparison, Figure 5.8 shows the average Raman spectra of authentic product (three spectra from the core of three tablets), compared with the average spectra of the core of counterfeit versions of the authentic product. Note the similarity in the two spectra shown in Figure 5.8a, as well as the two spectra shown in Figure 5.8b. The similarity between the spectra shows that the counterfeit samples are chemically similar to, but not identical to, the authentic product. Even further, Figure 5.8a shows the average spectrum of counterfeit sample I1, while Figure 5.8b shows the average spectrum counterfeit sample I4. IR data of these samples was previously reviewed, and these two samples were shown to be of the same origin. Note that the Raman data supports this conclusion. The Raman spectra of these two samples are the same, and additional Raman bands present in I1 are also present in I4.

This same type of Raman analysis can be performed on capsule formulations. Figure 5.9 shows an overlay of the Raman spectra of an authentic and counterfeit capsule product. Although fluorescence is observed in both samples, Raman bands present in the authentic product are clearly absent from the counterfeit version. This data shows not only that these two samples are different from each other but also that drug substances present in the authentic product are not present in the counterfeit version [42].

As with IR data, Raman data can also be used to source samples when chemometrics methods are applied. The same samples whose portable IR data were evaluated using chemometrics in the previous section were analyzed using portable Raman, and chemometrics methods were applied in an attempt to establish source. PCA-CVA showed that it was possible to classify samples based upon their Raman spectra into eight groups (seven nonauthentic and one authentic). HOO-CV was used to determine an estimated error rate of 0.56% using 14 PCs. Figure 5.10 shows the 3-D score plot from PCA-CVA. In this figure, each group is colored differently, and, unlike with the IR spectra where clustering based upon group assignment was evident in three dimensions, no clustering is observed in the Raman data. However, Figure 5.11 shows the estimated error rates calculated as a

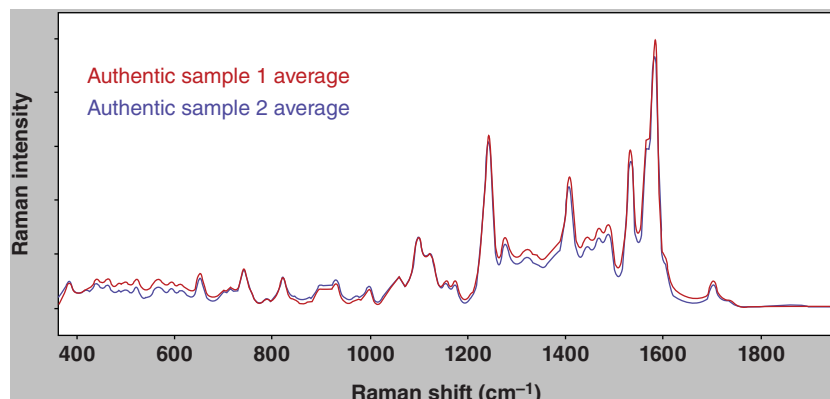


**Figure 5.7** The average Raman spectra of two different authentic product samples. Each Raman spectrum is the average of nine spectra of the core of three tablets for each authentic sample.

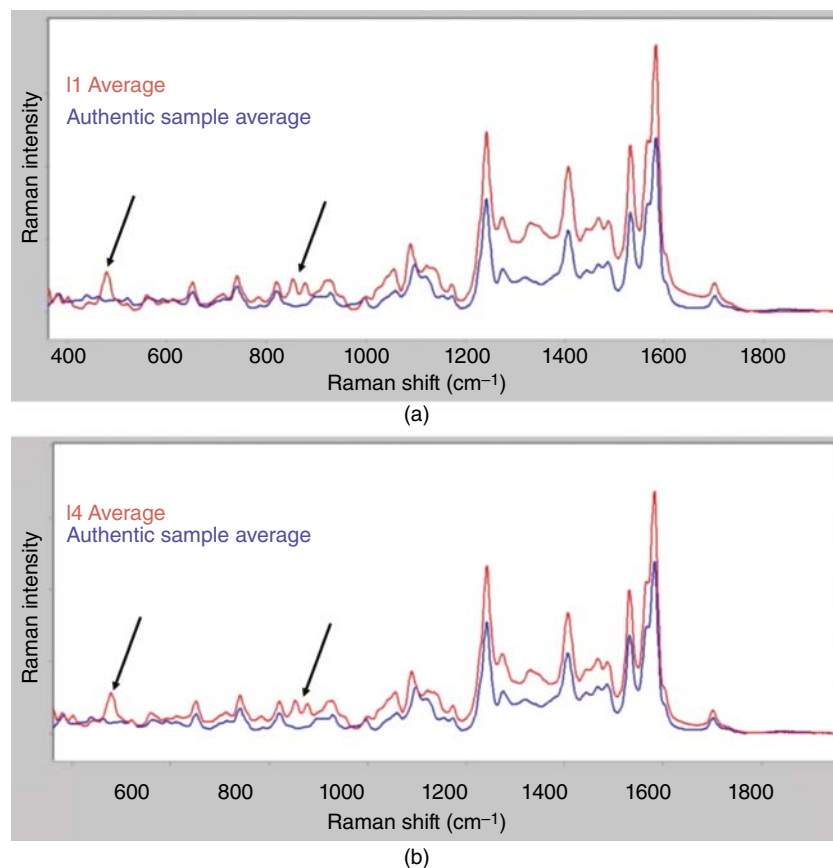


**Figure 5.8** (a) Spectral overlay of the average of nine Raman spectra of the core of 3 authentic tablets (blue) and the average of 18 Raman spectra of the core of 7 counterfeit tablets of the same lot (red). (b) Spectral overlay of the average of nine Raman spectra of the core of 3 authentic tablets (blue) and the average of 20 Raman spectra of the core of 7 counterfeit tablets of the same lot (red). The areas indicate regions of the spectrum that are similar to each other in samples I1 and I4 but different from the spectra of the authentic sample.

function of number of PCs for the Raman, and even though clustering is not evident in three dimensions, Raman spectroscopy was capable of successfully classifying most samples. This difference in clustering observed in the 3-D score plots between the IR (Figure 5.6) and the Raman data (see Figure 5.10) is interesting. It is possible the reason the separation was not evident in the 3-D score plot for the Raman data is because the Raman analysis spot size ( $50\text{ }\mu\text{m}$ ) is significantly smaller than it is for the IR analysis ( $1.3 \times 0.8\text{ mm}$ ). In addition, it is important to note that the spectral range of the Raman data is narrower, which could also contribute to this observation.

### 5.2.1.3 Near-Infrared (NIR) Spectroscopy

NIR radiation was discovered more than 200 years ago, but its practical use extends from the 1970s and 1980s and the work of Norris and Williams in the agricultural field [56–58]. These researchers were able to effectively predict the protein and moisture contents of ground wheat over a wide range of particle sizes. Benchtop grating and FT NIR instruments were commercially made available in the 1980s and 1990s and mainly used in the food and agricultural industry [59, 60], before being taken up in the pharmaceutical applications [61–63]. The capability of NIR spectroscopy to detect counterfeit drugs was realized by researchers at least 20 years ago [64–71], before the advent of portable NIR spectrometers.

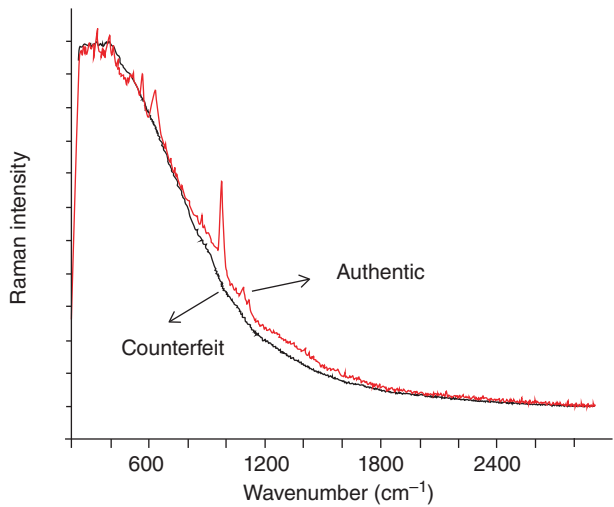


**Figure 5.9** Raman spectra from a portable spectrometer of counterfeit and authentic capsule formulations. Source: Kalyanaraman et al. [48]. © 2010 CompareNetworks, Inc.

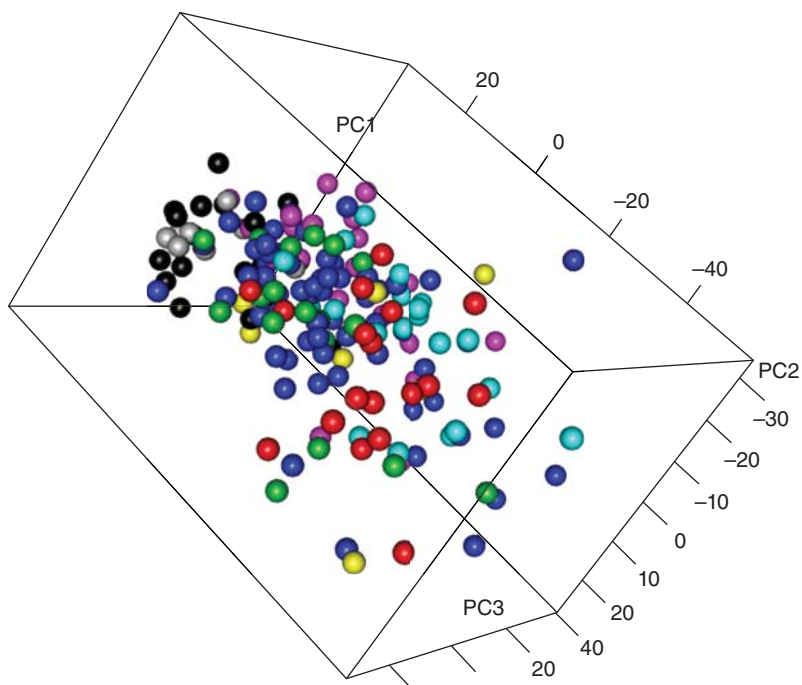


**Figure 5.10** 3-D score plot of Raman spectra (auto scaled) from counterfeit and authentic pharmaceutical tablets.

The commercial availability of portable NIR spectrometers began in 2006 with the introduction of the Polychromix “Phazir,” which was the size of a cordless drill. In the NIR region of the electromagnetic spectrum, a number of instruments were developed, especially in the short-wave NIR ( $<1\text{ }\mu\text{m}$ ) region, but did not achieve widespread adoption prior to the introduction of the Phazir [72]. Portable systems were mainly enabled due to technological advancement in micro-electro-mechanical systems (MEMS) and micro-opto-electro-mechanical

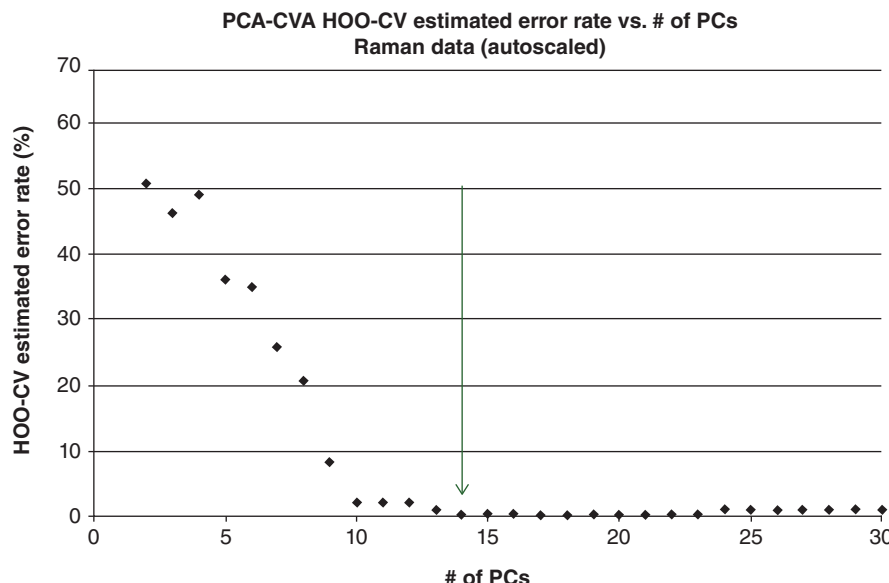


**Figure 5.11** PCA-CVA HOO-CV estimated error rate displayed as a function of the number of PCs. An estimated error rate of 0.56% was observed at 14 PCs.

systems (MOEMS), combined with rapid improvements in portable computing capabilities [73]. For a detailed discussion of MOEMS and MEMS, see the chapter by Grüger in Volume 1 of this book.

The change from benchtop to miniature and portable NIR spectrometers was encouraged by the pharmaceutical industry. With the stimulus of the US Food and Drug Administration's (USFDA's) "PAT Initiative" [74], miniature NIR instruments were used for process evaluation on equipment like blenders and dryers [75, 76], providing real-time analytical manufacturing process monitoring where a battery powered instrument with wireless communications is required, and in an environment that is very challenging for conventional spectrometers [77]. That was followed by on-site, in-the-field, and on-the-go capabilities for nondestructive testing for raw-material identification. In more recent years, even smaller NIR instruments that fit in the palm of the hand have become available, making it possible to take the "lab" to remote locations where the benefit of on-scene identification of counterfeits in real time could be realized, such as illicit manufacturing and storage sites, pharmacies, and hospitals.

NIR spectroscopy allows probing of overtone and combination bands of functional groups such as O–H, N–H, and C–H that are present in most pharmaceutical APIs and excipients [78]. Unlike Raman and mid-IR spectral bands, which are relatively sharp and may be used to assess chemical functional groups for molecular and structural identification, NIR spectral bands are weak and broad, and, as such, NIR raw spectra are initially noninformative [79]. When mathematical pretreatment is applied to the raw data, differences in the subtle features of the spectra may be used to differentiate samples such as counterfeit and authentic pharmaceuticals. The impact of different data pretreatment methods on spectra will be different and will impact results; therefore, pretreatment methods are an important part of the NIR method. Data pretreatment methods used for NIR spectra include baseline offset, baseline linear, normalize maximum, normalize range, normalize range center, normalize unit vector, derivative (Savitzky–Golay), standard normal variate (SNV), and multiplicative scatter correction [42].

The impact of data pretreatment on the NIR spectra of illicit drug substances using a narrow-range handheld NIR spectrometer was recently demonstrated by Kranenburg et al. [80], and their results are shown in Figure 5.12. The spectra on the left show the unprocessed raw data from multiple NIR scanners of the same make and model for an 86.6% cocaine HCl forensic case sample. Each colored line indicates five replicate spectra from a single scanner, and each color indicates data from a single scanner. Additive baseline shifts are clearly observed with most

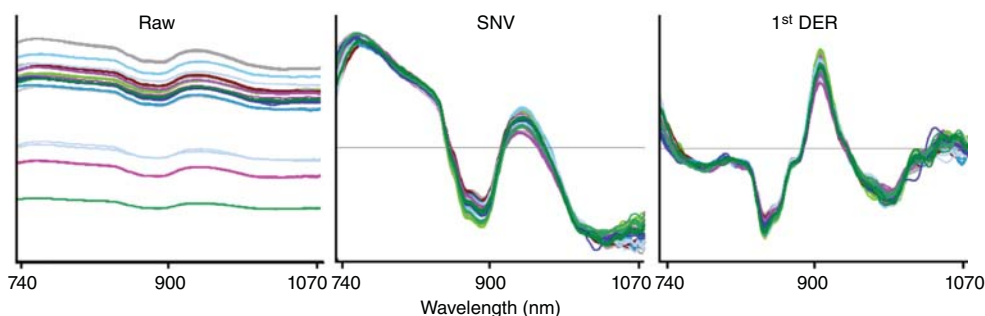


**Figure 5.12** The spectra on the left show the unprocessed raw data from multiple NIR scanners of the same make and model. Each colored line indicates five replicate spectra from a single scanner, and each color indicates data from a single scanner. The spectra in the middle of this figure show the raw data after applying standard normal variate (SNV) analysis, which addressed baseline issues. The spectra on the right show the first-derivative analysis of the SNV results, which was performed to put additional emphasis on the spectral differences. *Source:* Kranenburg et al. [80]. John Wiley & Sons. Licensed under CC BY 4.0.

scanners providing a similar intensity, while three individual scanners returned a notably less-intense signal. The authors attributed these baseline shifts to a number of potential factors commonly observed in diffuse-reflection spectra including scattering effects based upon differences in particle size. The spectra in the middle of this figure show the raw data after applying SNV analysis, which addressed baseline issues. The spectra on the right show the first-derivative (D1) analysis of the SNV results, which was performed to put additional emphasis on the spectral differences. Emphasizing spectral differences in different samples is a primary reason for applying pretreatment to otherwise noninformative NIR data.

When developing a NIR method, it is important to recognize that authentic pharmaceutical products may originate from different manufacturing sites and/or experience different storage and temperature conditions. These factors can impact the NIR spectrum of the sample. NIR methods must use data pretreatment and spectral-search methods that do not differentiate these authentic samples from each other while simultaneously differentiating these samples from counterfeit versions. Further, for successful deployment to be achieved, reliable and reproducible results must be evident across multiple instruments of a given platform.

As briefly noted above, a critical part of the method is the approach to spectral matching or spectral comparisons. Generally, when evaluating vibrational spectra for counterfeit detection, either a matching algorithm such as correlation or p-value or PCA and/or cluster analysis is performed. Generally, spectral matching compares the shape of each pretreated sample spectrum with each pretreated spectrum in the library that is created from the authentic samples and assigns a degree-of-match correlation value ranging from +1 (perfect match) to -1 (perfect antimatch) using chemometric algorithms. If an authentic product is tested and compared against the library spectrum, the match value should be close to +1 [42]. PCA is used in all the NIR examples within this chapter, as well as to evaluate some of the sample data presented in the mid-IR and Raman sections. PCA is a mathematical method of reorganizing information in a data set of samples such that new variables, referred to as PCs, are discovered. These PCs account for the majority of the variability in the data. In a spectrum, initially there may be hundreds or even thousands of variables; PCA reduces this number significantly, frequently to less than 20 [81]. Proper application of data pretreatment methods and other considerations for portable NIR spectral analysis and method development are outside the scope of this chapter but are considered by Sacré et al. in volume 1 of this book, and Hoffmann, Pfeifer, and Siesler in this volume of this book.

In an early example of NIR in drug product screening using laboratory equipment, PCA was performed on pretreated data to differentiate authentic 75-mg dosage Plavix® tablets from counterfeit versions. NIR spectra from ten intact authentic tablets were measured once on each side, and the mean SNV–second derivative (D2) spectrum was calculated for these 20 spectra. The NIR spectra from the counterfeit samples were also measured, and the data

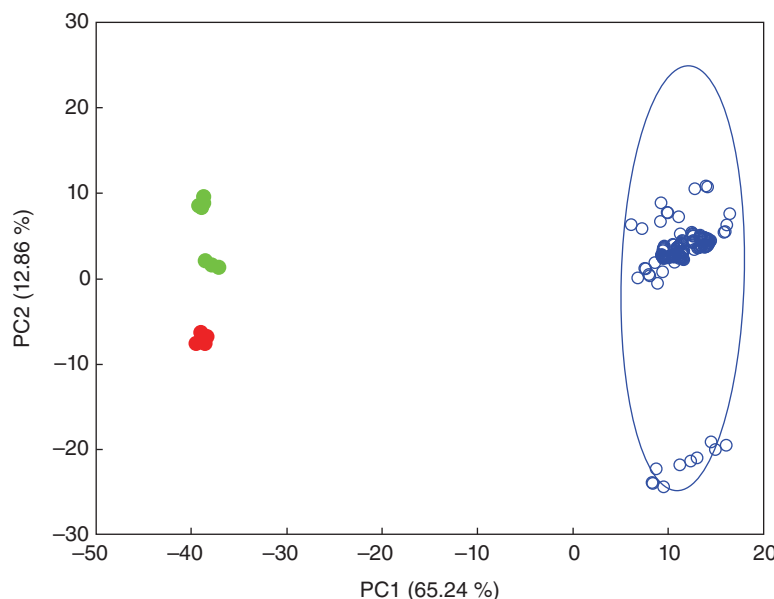


**Figure 5.13** PCA score plot of the SNV-D2 NIR spectral data of authentic 75-mg Plavix tablets (five batches, blue with the 95% equal frequency ellipse) and counterfeit versions from two different sources (red and green). *Source:* Moffat et al. [82].

was pretreated the same way. The SNV-D2 mathematical pretreatments removed the multiplicative combinations of the problems associated with the particle size, scatter, and other effects caused by the different orientations and sides of the tablets in the NIR spectrometer. Separate clustering for the two counterfeit samples from the authentic ones was observed in the PCA score plot shown in Figure 5.13 [82].

One of the first uses of portable NIR spectrometers to detect counterfeit pharmaceuticals was demonstrated by Kalyanaraman et al. for the analysis of capsule formulations with analysis performed through blister packaging [48]. The instrument used in this study had a spectral range of 1600–2400 nm and used a tungsten lamp for illumination. The system worked in diffuse-reflection mode, and, given the low NIR extinction coefficients, it probed both the surface of the capsule shell and the powder content. The raw data were pretreated by applying Savitzky–Golay D2 and unit-vector normalization, followed by smoothing. Identification and authentication of the capsule drug product using the pretreated NIR spectral data was performed using spectral-match correlation and PCA. These data are shown in Table 5.5 and Figure 5.14, respectively, and demonstrate that a portable NIR spectrometer, with  $20\text{--}40\text{ cm}^{-1}$  spectral resolution and a spectral D2 data pretreatment followed by normalization, is sufficient to differentiate between these authentic and counterfeit capsule products. The relatively low spectral resolution (as compared with portable Raman and mid-IR spectrometers) was found to not be a limiting factor due to the inherent broad spectral bandwidth of NIR bands.

The validation of NIR spectral signatures within the pharmaceutical industry is important. These signatures are intended to be representative of the authentic product, and spectra of test samples are compared against these spectral signatures to establish authenticity. An approach to validation of NIR spectral signatures using a portable NIR system for counterfeit-drug screening was performed by Kalyanaraman et al. [83]. Authentic samples from several different lots were used to develop an individual NIR spectral signature that would capture all the variations in physical properties of the drug product such as hardness, density, particle size, etc., which are critical parameters in NIR spectroscopy. Since the spectral signature for a given product using the portable spectrometer is validated for its intended use, which is to test and verify if a suspect product is counterfeit or authentic, as per ICH guidelines, this use may be viewed as a quality identity test requiring only validation for specificity [84]. However, these

**Table 5.5** NIR spectral match correlation values for authentic and counterfeit capsules analyzed through blister packaging using a portable NIR spectrometer.

Sample	Spectral match correlation
Authentic	0.973
Counterfeit 1	0.679
Counterfeit 2	0.700

Source: Kalyanaraman et al. [48]. © 2010 CompareNetworks, Inc.

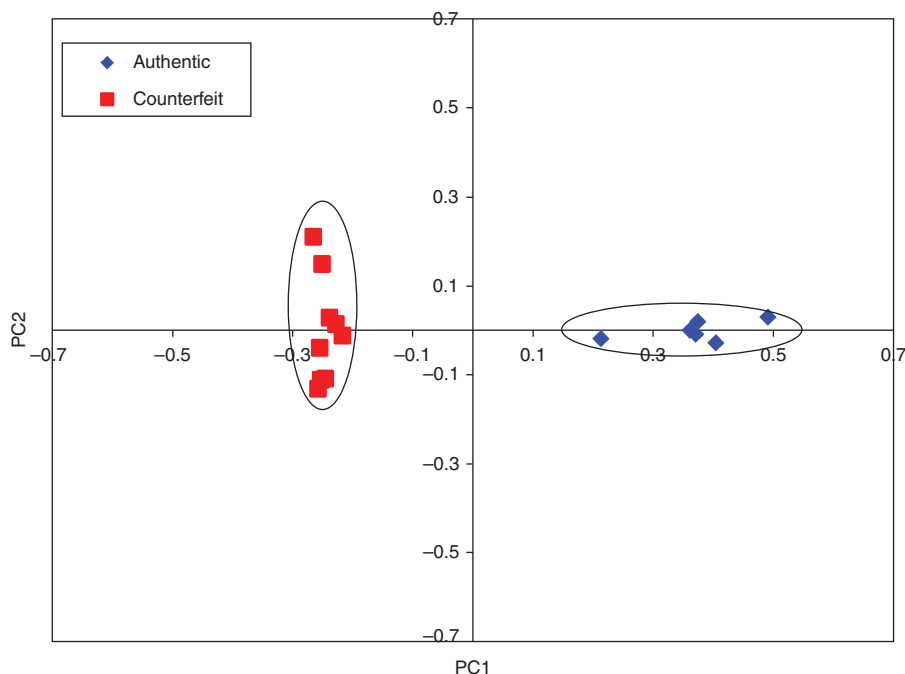


**Figure 5.14** PCA score plot of authentic and counterfeit capsules from portable NIR spectral data, with data pretreatment of Savitzky–Golay D2 and unit-vector normalization followed by smoothing. Source: Kalyanaraman et al. [48] © 2010 CompareNetworks, Inc.

authors also challenged the use of these NIR spectral signatures for ruggedness and robustness. This is important because these portable NIR units are intended to be used in the field where conditions such as humidity and temperature can affect the sample, the spectrometer, and, therefore, the results. In addition, when the units are deployed in the field, it is necessary that the method is rugged so that it performs the same way when applied to multiple systems.

For their study, authentic products under conditions of “extreme stress” including elevated temperature and humidity were used to mimic counterfeits. Counterfeit products are typically not manufactured using good manufacturing practices, so these authors noted that if authentic product under extreme stress conditions can be distinguished from the authentic product stored under unstressed conditions, the method could then be easily applied to screen counterfeit drugs. The specificity was examined by testing the authentic samples that were maintained at various stressed conditions such as different temperature and relative humidity values. The robustness

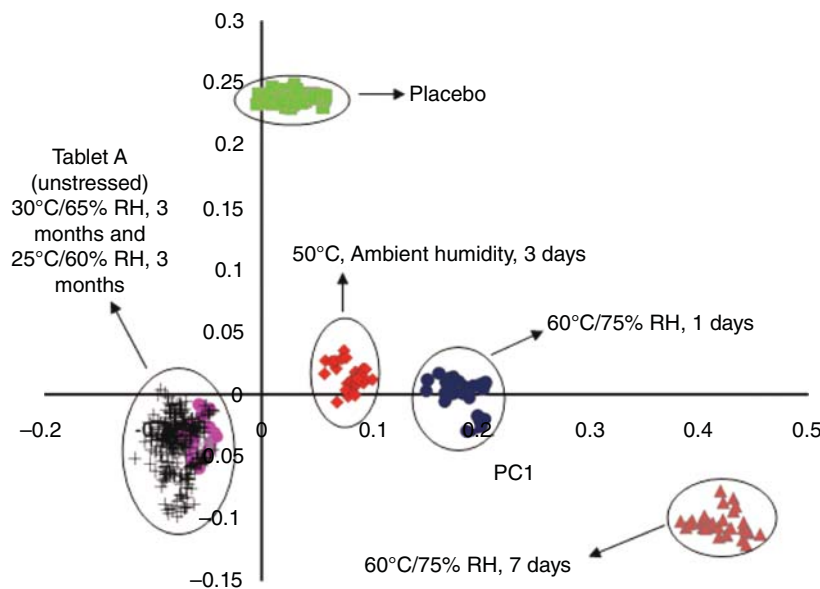


**Figure 5.15** PCA score plot for authentic tablets (tablet A under unstressed condition) along with placebo (no active ingredient) and stressed samples of authentic tablets. In this study, the placebo tablets are considered as counterfeit since they contain no active ingredient. Note that the authentic unstressed samples are well separated from both the stressed and placebo samples in the PCA score plot. Source: Kalyanaraman et al. [83]. © 2011 CompareNetworks, Inc.

of the spectral signature was performed by evaluating the impact of deliberate changes made to the portable NIR instrument – changes such as different instrument components, e.g. the source lamp, and data pretreatment processes. The ruggedness was tested by using a second analyst and a second spectrometer from the same vendor. Figure 5.15 shows the score plot that demonstrates the ability of the method to differentiate the stressed authentics from the nonstressed authentics.

### 5.2.2 Gas Chromatography–Mass Spectrometry (GC-MS)

The methods described so far to evaluate counterfeit pharmaceuticals have all been applied to bulk amounts of analyte. These methods are not intended to detect or identify trace levels of chemicals present within a sample. Pharmaceutical products, though, can frequently contain traces of chemicals such as residual solvents or volatile organic compounds (VOCs) that may be useful for differentiating samples from each other. GC-MS is commonly used within the pharmaceutical industry for the characterization of drugs and drug products and may be used to detect and identify these trace amounts of chemicals.

GC-MS is a reliable method used for the confirmatory identification of chemicals. Commercially available portable GC-MS systems have been on the market since the late 1990s [85] and, like portable IR and Raman spectrometers, are marketed and deployed to first responders and others attempting to detect and identify hazardous chemicals in the field. Portable GC-MS systems have detection limits in the parts-per-million (ppm) and parts-per-billion (ppb) ranges for many chemicals of pharmaceutical interest and can operate independently on battery using on-board disposable carrier-gas cartridges. Both ion-trap and quadrupole MS portable systems are currently available, each with its advantages and limitations. There is some variability in sampling options available for different portable systems. For instance, although most commercially available portable GC-MS systems offer vapor-phase sampling, not all allow for the introduction of liquid samples. As a result, sampling options may

limit the applicability of a system for a specific type of analysis. A detailed discussion of portable GC-MS and stand-alone MS instrumentation and technology is outside of the scope of this chapter, but both are covered in Volume 1 of this book in chapters by Leary, Reffner, and Kammrath, and Snyder, respectively.

### 5.2.2.1 Detection and Identification of Residual Solvents and Volatile Organic Chemicals (VOCs)

As mentioned, portable GC-MS may be useful to evaluate residual solvents or other VOCs present at trace levels within a drug product, even in samples where manufacturing is well controlled. These chemicals are introduced in a variety of ways. They may be present in the raw materials, they may be solvent residues remaining after manufacture of the drug product, or they may even be degradation products that develop during manufacture or storage. The chromatogram generated from these substances is a chemical profile that is representative of the sample and can provide insight about its manufacture and history including storage and transport conditions. The ability to reliably detect and identify differences in chromatographic profiles among different samples is useful when comparing authentic and counterfeit pharmaceuticals. Counterfeit versions of product are frequently not manufactured using the same method and solvents as the authentic product, so the chromatogram of the counterfeit will frequently be different from that of the authentic product. This chemical profile may also be used to classify counterfeit drugs into groups with similar profiles, providing investigative leads useful in establishing source or origin.

As with spectral-pattern comparisons performed using portable IR and Raman data, differentiation among samples can be performed simply by comparing chromatographic patterns. Figure 5.16 shows an overlay of chromatograms from the heated headspace of an authentic pharmaceutical tablet and of a counterfeit version. Each sample was collected using solid-phase microextraction (SPME) with a polydimethylsiloxane/divinylbenzene (PDMS/DVB) SPME sorbent. Note the significant differences between the chromatograms of the two samples indicating these two samples are different from each other. Each peak in a chromatogram is representative of a different chemical present in the sample. When performing a pattern comparison such as this to differentiate samples from each other, it is not necessary to identify each specific chemical present in the chromatogram. A comparison of the patterns created from each sample is usually sufficient.

SPME sampling is useful in field-portable settings because it provides an easy, solvent-free method for sample collection. The SPME sampling device is small and lightweight and can be carried to the sample with ease. The SPME sorbent selectively sorbs analytes from the sample based upon the SPME sorbent coating used, the chemical and physical properties of each analyte, and the mixture of analytes and their concentrations in the sample

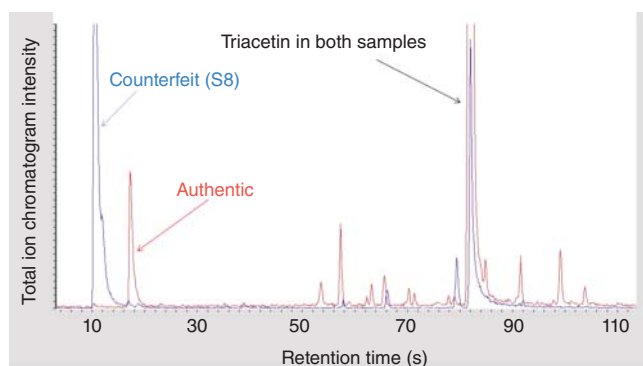


**Figure 5.16** Chromatograms from portable GC-MS of authentic and counterfeit pharmaceutical products. Sample preparation for each involved gentle crushing of the tablet and then heating to 60°C in a vial for headspace analysis. Chemicals collected on the PDMS/DVB SPME were thermally desorbed when injected into the GC-MS system.

matrix [86]. In many cases, this method removes the need to perform extensive extraction procedures that significantly complicate the analysis. During sample collection, the SPME sorbent is exposed to the sample until equilibrium has been achieved [87–89]. Determination of the equilibrium condition for a sample of unidentified chemical composition can be difficult, so optimal SPME sampling time in these situations is usually experimentally determined.

There are a number of different SPME fiber types available that offer sorbent phases engineered to ensure optimal extraction and desorption efficiency, limit sample carryover, and enable sampling of analytes over a wide molecular-weight range [90]. Chromatogram differences based upon SPME sorbent are expected. Different SPME sorbents, by design, selectively sorb different chemicals differently. This selective sorption accounts for the differences in chromatograms from the same sample analyzed at the same temperature using different SPME sorbents. Carboxen®-coated fibers offer the most efficient extraction of small volatile analytes (molecular weight <150). Due to the greater relative adsorptive strength of the Carboxen carbon molecular sieve for small molecules, compared with spherical graphitized polymer carbon or carbon black adsorbents, they can retain volatile analytes more strongly for increased sensitivity and reliable results. This characteristic can be attributed to the Carboxen tapered pore that results in enhanced thermodynamic properties and kinetics, enabling both efficient adsorption and desorption of low-molecular-weight or volatile compounds [87]. This type of fiber is useful for analyzing residual solvents and VOCs, especially for older samples or samples that have been exposed to high temperatures. In these situations, residual solvents may have already evolved from the sample by the time of analysis, so the ability to concentrate the remaining solvents onto the fiber may be critical for their detection in these situations. Figure 5.17 shows an overlay of chromatograms from the headspace of a counterfeit sample collected under identical conditions, except for SPME fiber sorbent. Note that the intensity of peaks, especially at the lower retention times, i.e. lower boiling points, is significantly higher when sampled using the Carboxen SPME.

A way to achieve further discrimination among samples is by adjusting the temperature of the headspace during sample preparation and collection. Differences in chromatograms based upon temperature are expected because the chemical composition of the headspace of the sample will change with temperature. Figure 5.18 shows the chromatograms from the heated headspace of a counterfeit sample collected and analyzed at different temperatures. Heating the headspace to a higher temperature enabled the detection of chemicals that exhibited higher retention times, i.e. higher boiling points. Both of these chromatograms are representative of the sample, but these

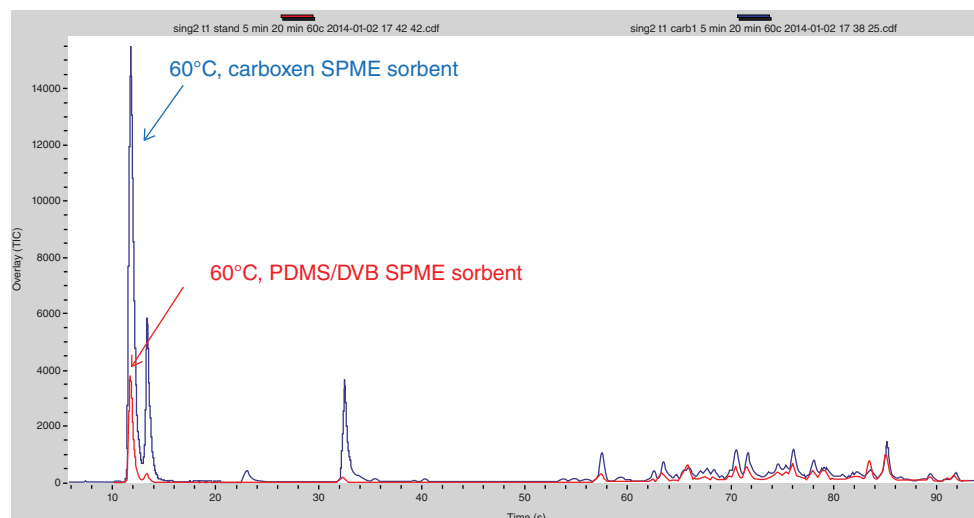


**Figure 5.17** Chromatograms of a counterfeit pharmaceutical analyzed at the same headspace temperature (60 °C) using two different SPME sorbents (Carboxen and PDMS/DVB).

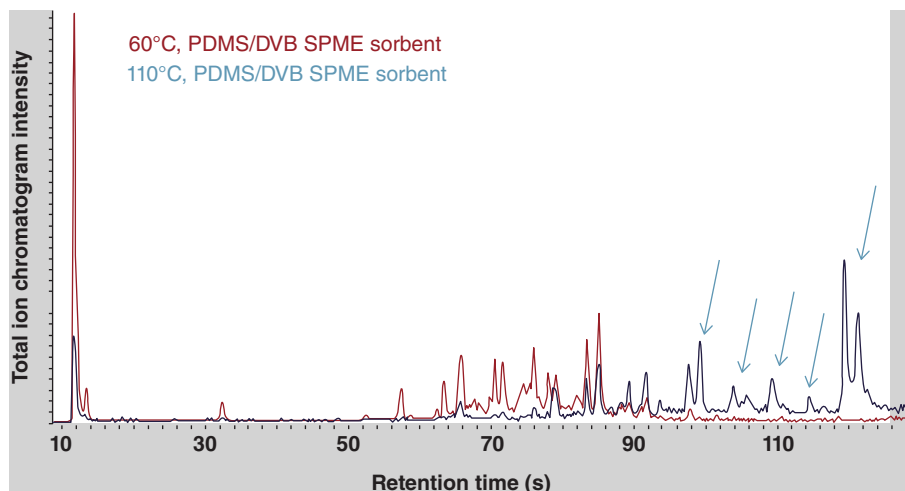


**Figure 5.18** Chromatograms of a counterfeit tablet analyzed at different headspace temperatures (60 and 110 °C) using the same type of SPME sorbent.

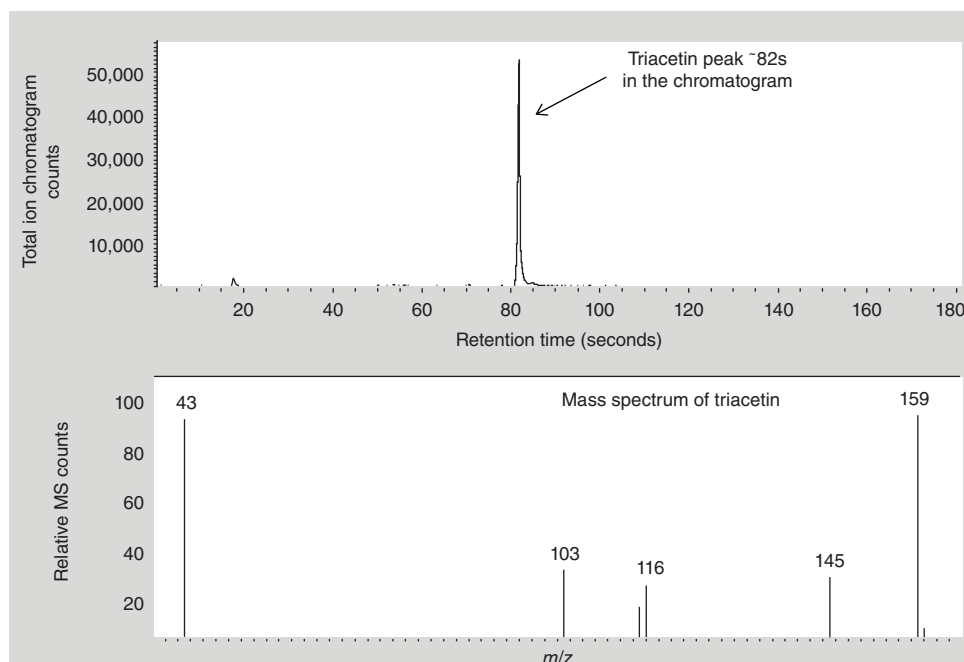


**Figure 5.19** Representative chromatogram of authentic tablet (top) along with the mass spectrum of triacetin (bottom). Triacetin is the primary chemical detected in the authentic tablets tested. Analysis performed using a PDMS/DVB SPME sorbent with headspace sample collection at 60 °C.

data demonstrate the reason comparisons of chromatograms of different samples should always be performed at the same preparation and collection temperatures for this type of analysis.

Identification of specific chemicals present in the sample may also provide useful information about the sample. Figure 5.19 shows the chromatogram from the heated headspace of an authentic pharmaceutical tablet, as well as the mass spectrum of triacetin. Triacetin was detected in all authentic tablets of this drug tested using this method.

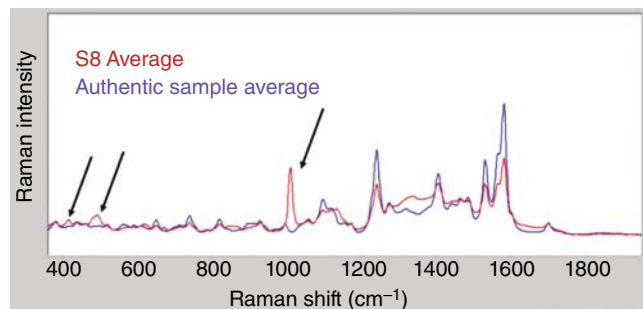


**Figure 5.20** Spectral overlay of the average of nine Raman spectra of the core of three authentic tablets (blue), and the average of nine Raman spectra of the core of three counterfeit tablets from sample S8.

Under the analysis conditions that included SPME sampling and portable GC–MS analysis, triacetin exhibits a chromatographic peak at about 82 seconds and ion fragments with  $m/z$  values of 159, 43, 103, 145, 116, and 115. Triacetin was also present in all tablets of counterfeit sample S8 that were analyzed (Figure 5.16). However, aside from the triacetin, virtually all other chemicals detected in the counterfeit sample at trace levels using this method were different from those detected in authentic samples. Although triacetin is present in the counterfeit sample, this GC–MS data indicates that these two samples are not from the same source. Further, the portable IR spectral data for this counterfeit sample, which was previously reviewed (Figure 5.4a), shows that this counterfeit sample (S8) contains calcium sulfate. Calcium sulfate was not detected in the IR spectra of any authentic versions of this drug product. Although not previously described, the portable Raman data for sample S8 was also different from that of authentic drug (Figure 5.20). Note that the additional Raman peaks present in the counterfeit sample at 415, 494, and  $1009\text{ cm}^{-1}$  are due to the presence of calcium sulfate in the sample.

### 5.2.2.2 Identification of Active Pharmaceutical Ingredient (API)

The portable GC–MS analysis described so far is specifically focused on the evaluation of trace levels of chemicals present in samples. Portable GC–MS may also be used to identify the API in a drug product. In instances where the API concentration in the drug product is relatively high, IR and Raman can be used for this purpose. In situations where the API concentration is low, however, a method like GC–MS may be necessary. An example where this type of evaluation is useful is for the identification of low doses of fentanyl in counterfeit drugs of abuse.

Overdose deaths due to fentanyl have become a significant problem in the United States [91, 92], and when the fentanyl concentration in the drug product is low, in-the-field detection of the fentanyl can be difficult. Fentanyl is approximately 100 times more potent than morphine, is abused for its intense euphoric effects, and can serve as a direct substitute for heroin in opioid-dependent individuals [93]. The lethal dose of fentanyl for an average adult is just 2 mg [94], and dilution of pure fentanyl into final dosage forms such as tablets that provide therapeutic dose (less than 1% for a 300-mg tablet) has occurred. “Mexican oxy” is one type of this illicit substance that has been mislabeled as oxycodone when sold [95]. Detection and identification of fentanyl in drug product using portable GC–MS is straightforward. Minimal sample preparation is required for drugs that are soluble in solvents compatible with the GC–MS instrumentation. Figure 5.21 shows the chromatogram of an illicit drug product containing fentanyl analyzed using a portable GC–MS system. No other illicit substance was detected in this drug product. To prepare the sample for analysis, a portion of the sample was dissolved in methanol, and 1  $\mu\text{L}$  of the solution was directly injected into the inlet. This preparation was minimal and enabled a confirmatory identification of fentanyl at the sample site.

These examples demonstrate the value of portable GC–MS for analysis in real time at the sample site. It is important, though, that differences in sampling conditions and sample history are considered when interpretations of

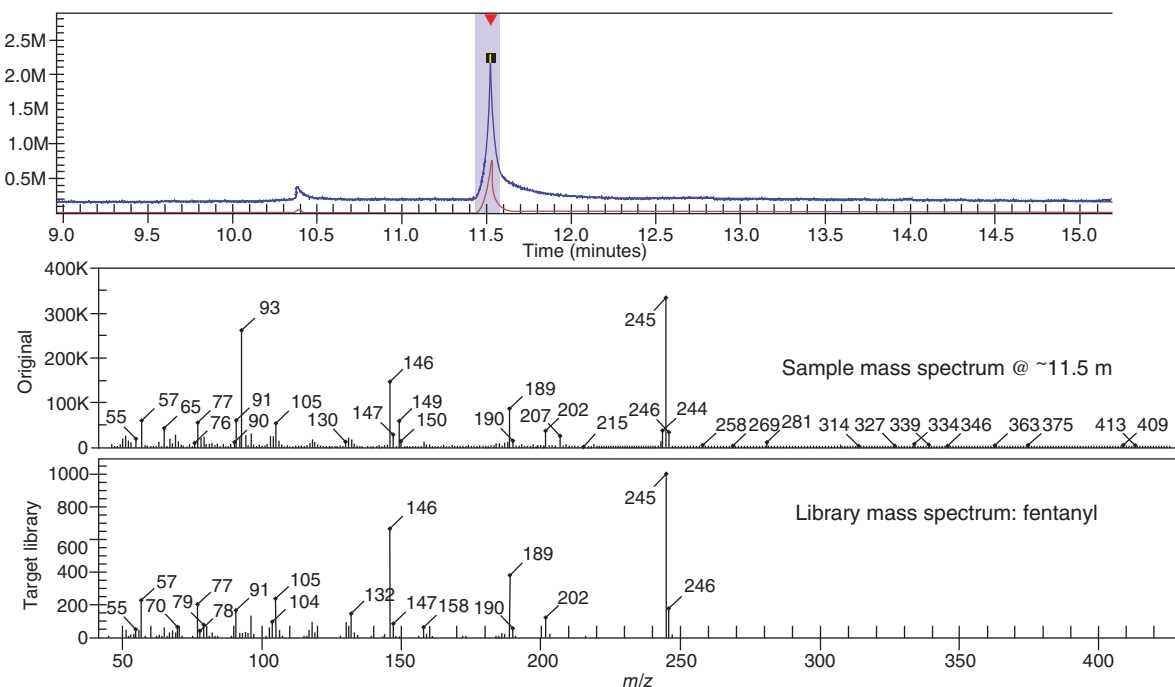


**Figure 5.21** (top) Chromatogram, (middle) mass spectrum of illicit drug product containing fentanyl, and (bottom) library mass spectrum of fentanyl. The sample was prepared by dissolving in methanol with a 1- $\mu$ L liquid injection.

any result, and especially GC–MS results, are performed. GC–MS is capable of detecting trace amounts of chemicals, but these chemicals may evolve from the sample during storage and transport. Sample history of a suspected counterfeit is frequently not known, so data interpretation should account for any potential differences in the sample’s chemical profile that may be due simply to storage or other valid explanation.

### 5.3 Deployed Systems

It is important to recognize that the problem of counterfeit pharmaceuticals is very complex and, in order to successfully address the problem, an integrated response from public-health officials, law enforcement, brand owners, regulatory agencies, and members of the supply chain is required. When considering the problem is global, and the types of drugs counterfeited in one region of the world may be quite different from drugs counterfeited in another, successfully addressing the challenges these goods present can be difficult. Counterfeit drugs are a particular problem in parts of Africa where unregulated outlets abound (Figures 5.22 and 5.23). There have been a number of studies recently published demonstrating the effectiveness of using portable spectrometers to detect and identify drugs [96–99], but these studies do not describe how well the systems perform when they are placed in the hands of the end user at the sample site, such as at a Customs check point or at a retail pharmacy. Recently, though, the successful use of portable technologies in the country of Nigeria has been reported to be integral to the improvement in the quality of pharmaceuticals available to Nigerian citizens.

In 2009, the National Agency for Food and Drug Administration and Control (NAFDAC), the Nigerian equivalent of FDA in the United States, deployed portable Raman spectrometers for the detection of counterfeit pharmaceuticals. NAFDAC used these systems at the sample site such as at border entries and retail pharmacies to



**Figure 5.22** Behind the counter of an unregulated medicine outlet in Africa. Source: Reproduced by permission from the World Health Organization, "WHO Global Surveillance and Monitoring System for substandard and falsified medical products", ISBN 978-92-4-151342-5, © World Health Organization 2017.



**Figure 5.23** Behind the counter of an unregulated medicine outlet in Africa. Source: Reproduced by permission from the World Health Organization, "WHO Global Surveillance and Monitoring System for substandard and falsified medical products", ISBN 978-92-4-151342-5, © World Health Organization 2017.

detect nonauthentic pharmaceuticals quickly and reliably [100]. The systems, which were TruScan Raman instruments from Ahura Scientific (now Thermo Fisher Scientific), were supplied to NAFDAC who, by working with authentic-drug manufacturers, created libraries of authentic medications, so the system generated pass/fail results (green screen/red screen) when suspicious drug products were tested [101]. As a result, the quality of drugs in the retail chain was improved. In a Nigerian case study, Bate and Mathur reported that for each of three drugs they

tested, a higher percentage passed sample testing after the deployment of the technology than before [102]. For instance, in 2007, only 57% of the artemisinin monotherapies passed the spectrometry test, whereas 88% passed in 2010. Within the artemisinin combination therapies, approximately 96% of the samples passed the spectrometry test in 2010 as opposed to 86% in 2007. Within the sulfadoxine–pyrimethamine pharmaceuticals, the success rate climbed from 50 to 85% between 2007 and 2010. These authors cite the use of the portable spectrometers as a primary reason for the improvement. In addition, Nigeria has also added other programs that work with the use of portable spectrometers to tackle the counterfeit-drug trade, including mobile authentication devices to protect the country's most heavily counterfeited drugs including vaccines, antibiotics, antimalarials, and diabetes medications. Figures 5.24 and 5.25 show examples of expired and counterfeit vaccines found recently in Niger. In Nigeria, NAFDAC reported that counterfeit antimalarial drugs went from 19.6% in 2012 to 3.5% in 2015 and attributed this decrease to both the authentication service and other NAFDAC strategies such as scanning drugs at ports with portable Raman spectrometers [103].

Despite improvement for some drugs, though, the counterfeit-drug problem in Nigeria is still significant. In Nigeria's predominantly informal distribution and retail networks, counterfeit and parallel medicines are often difficult to distinguish from the genuine article (see Figure 5.25 for an example from Niger) [100]. In these situations, additional methods available for testing might help provide further levels of discrimination of samples, but deployment of these technologies can be expensive and logistically difficult. In addition, estimates suggest that informal retail in Nigeria accounts for more than three-quarters of the value of the pharma market and parallel imports for up to half of drugs sold in some therapeutic areas. Several generics companies that have no commercial activities registered in Nigeria still have statin variants that are widely distributed and sold in country [104].



**Figure 5.24** Vials of meningitis vaccine found in Niger in 2015 had their expiry date manually extended by two years.  
Source: Reproduced by permission from the World Health Organization, "WHO Global Surveillance and Monitoring System for substandard and falsified medical products", ISBN 978-92-4-151342-5, © World Health Organization 2017.



**Figure 5.25** Falsified meningitis vaccine reported from Niger in 2017, in professionally printed packaging. *Source:* Reproduced by permission from the World Health Organization, "WHO Global Surveillance and Monitoring System for substandard and falsified medical products", ISBN 978-92-4-151342-5, © World Health Organization 2017.

This indicates that enforcement of IP rights is not effective in addressing the availability of these statin drugs. Since no generic statins are registered in Nigeria, any generic version should not be available, yet they are widely distributed. This is a significant violation of a brand owner's IP rights. It seems IP-rights enforcement related to pharmaceuticals in poor countries will not improve in the short term. Without the availability of nonauthentic drugs, no drugs at all would be available for these citizens, which can be considered a problem if government has a moral responsibility to guarantee its citizens a right to a healthy life [105]. Some researchers have proposed charging counterfeiters with manslaughter when a patient's death can be directly linked to performance of a counterfeit medication [106]. This approach may help curb the influx of counterfeit goods because it would increase the risk counterfeiters take when supplying these harmful drugs. Currently, the risk/reward ratio for counterfeiters in some regions of the world is so low that there is no incentive to deter these criminals from engaging in these activities [107]; whereas trafficking in heroin or cocaine can lead to severe penalties, including a death sentence in some countries, penalties for counterfeiting pharmaceuticals can be slight. There have been instances where safe medications have been delivered to these regions, but abuses in these situations are also a big problem that frequently lead to the diversion of these goods from their intended recipients [108].

Enforcement of IP rights is a complicated challenge that is burdensome to pharmaceutical manufacturers. NAFDAC recently announced a new partnership with the Pharmacists Council of Nigeria (PCN) to eradicate production and sale of counterfeit drugs in the country through enforcement [109]. John Clark, then Global Head of Security for Pfizer, in an interview with journalist Dan Rather in 2010, stated that his team at Pfizer will typically perform 80% of investigations required to bring charges against counterfeiters and will then turn their case over to authorities for ultimate prosecution [110]. As such, brand owners may work with local communities and authorities to help them secure their pharmaceutical supply chain. This can be very challenging and even dangerous in regions of the world where interruption of the counterfeit supply chain costs counterfeiter's business. The route from a counterfeit manufacturer to the intended customer can be very complex. This is illustrated in the WHO report for the 2012 case of counterfeit Avastin®, a trademarked brand of the cancer medicine bevacizumab. There was a tortuous roundabout trail: from Turkey to Egypt, to Switzerland, to Denmark, to the United Kingdom, and then to the United States (Figure 5.26) [111]. And the counterfeiting business is alive and well, even in the age of COVID-19, both inside the United States and around the world [112–115].

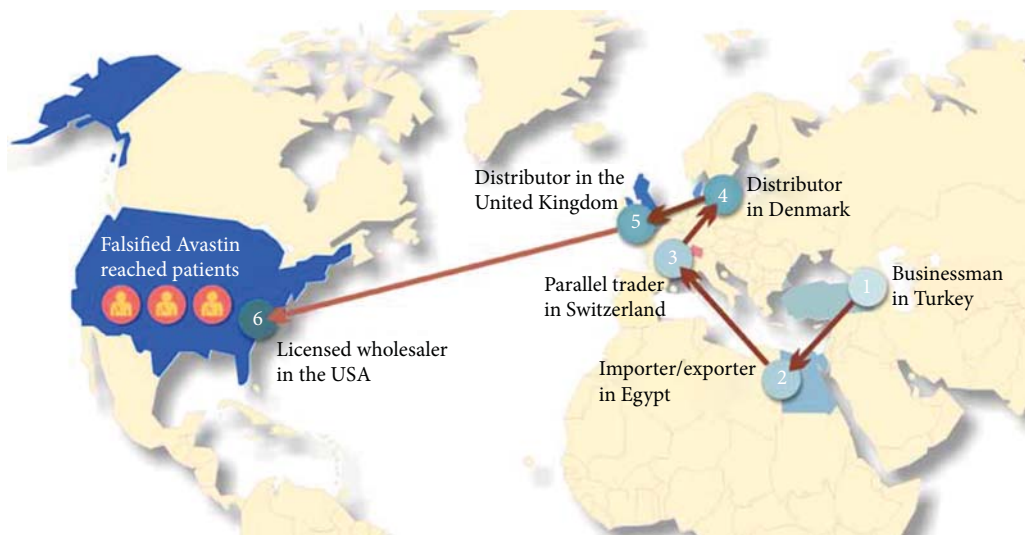


**Figure 5.26** Mapping the supply chain of falsified Avastin. Reproduced by permission from the World Health Organization. WHO global surveillance and monitoring system for substandard and falsified medical products. ISBN 978-92-4-151342-5, © World Health Organization 2017. Avastin is a registered trademark of Genentech USA, a member of the Roche Group.

## 5.4 The Future

It is clear that counterfeit drugs present a complex challenge to society locally, nationally, and globally. The ability to use portable spectrometers to address these challenges in detection and identification of these substances has been demonstrated. These instruments have been shown to provide accurate and reliable results that can be used at the sample site to quickly detect a counterfeit drug. Frequently, the spectrometers are used simply to screen the suspect drug product and determine whether the spectrum matches the spectrum of the authentic drug product. This type of evaluation is fast and simple. But there is a broader potential value this type of analysis offers, which is that the data from these spectrometers can be collected from different locations to provide meaningful information about the potential source of these goods. End users can share data with a central laboratory where scientists can review and process the data to look for similarities/differences in the chemistry being represented so that the value the data provides can be maximized.

In addition, a need for the future, especially in developing countries, is to bring down the price of these spectrometers so that they can be deployed. Frequently, the goal with development of portable spectrometers is smaller, lighter, and faster, but in many of the countries where the availability of counterfeit drugs is extensive, even the smallest, lightest, and fastest device may not be affordable. In these situations, considerations of price (both initially and for sustainment), training requirements, and power requirements are most critical. For example, (US \$2000) NIR spectrometers have emerged [116] that potentially make it more affordable for nonscientists to screen counterfeit and substandard drugs in the field.

It is also important to recognize that providing portable analytical capabilities is only part of the solution. These portable systems have been shown to reduce the availability of poor-quality drugs, but to permanently remove these drugs from the market, the response requires proactive support from public-health officials, law enforcement, brand owners, and others. Jurisdiction and sustained vigilance are also critical: counterfeiting operations are global in reach, and frequently these drugs originate from countries where IP rights are not valued.

## Acknowledgments

Part of this chapter is adapted from Pauline Elizabeth Leary, “Counterfeiting: A Challenge to Forensic Science, the Criminal Justice System, and Its Impact on Pharmaceutical Innovation”. A dissertation submitted to the Graduate Faculty in Criminal Justice in partial fulfillment of the requirements for the degree of Doctor of Philosophy, The City University of New York, 2014. © 2014 PAULINE ELIZABETH LEARY. The authors would also like to thank Professor Brooke W. Kammrath of the University of New Haven for her support with some of the chemometrics analysis of the mid-IR and Raman spectra.

## Acronyms and Abbreviations

D1	First derivative
D2	Second derivative
API	Active pharmaceutical ingredient
ATR	Attenuated total reflection
COVID-19	Coronavirus disease 2019
CVA	Canonical variate analysis
CWS	Correlation in wavenumber space
DART	Direct analysis in real time
DESI	Desorption electrospray ionization
FT	Fourier transform
FT-IR	Fourier transform infrared
GC	Gas chromatography
HOO-CV	Hold-one-out cross-validation
INTERPOL	International Criminal Police Organization
IP	Intellectual property
IR	Infrared
LC	Liquid chromatography
MEMS	Micro-electro-mechanical systems
MOEMS	Micro-opto-electro-mechanical systems
MS	Mass spectrometry
MSC	Multiplicative scatter correction
NIR	Near infrared
OECD	Organisation for Economic Co-operation and Development
PAT	Process analytical technology
PC	Principal component
PCN	Pharmacists Council of Nigeria
PDMS/DVB	Polydimethylsiloxane/divinylbenzene
PPE	Personal protective equipment
PCA	Principal component analysis
RFID	Radio frequency identification
SNV	Standard normal variate
SORS	Spatially offset Raman spectroscopy
SPME	Solid-phase microextraction

TLC	Thin-layer chromatography
USFDA	US Food and Drug Administration
VOCs	Volatile organic compounds
WHO	World Health Organization

## References

- 1 World Health Organization (2017). A study on the public health and socioeconomic impact of substandard and falsified medical products. Geneva, Switzerland. <http://www.who.int/medicines/regulation/ssffc/publications/Layout-SEstudy-WEB.pdf?ua=1> (accessed 15 July 2020). Licence: CC BY-NC-SA 3.0 IGO.
- 2 World Health Organization (2017). WHO global surveillance and monitoring system for substandard and falsified medical products. Geneva, Switzerland. Licence: CC BY-NC-SA 3.0 IGO.
- 3 OECD (Organisation for Economic Co-operation and Development) (1998). The economic impact of counterfeiting. Paris, France. <https://www.oecd.org/sti/ind/2090589.pdf> (accessed 20 October 2020).
- 4 Appendix 3 to Annex (2017). World Health Assembly document A70/23.
- 5 PWC (2012). From vision to decision: Pharma 2020. <https://www.pwc.com/gx/en/pharma-life-sciences/pharma2020/assets/pwc-pharma-success-strategies.pdf> (14 February 2021)
- 6 IMS Health (2015). IMS health forecasts global drug spending to increase 30 percent by 2020, to \$1.4 trillion, as medicine use gap narrows. <https://www.businesswire.com/news/home/20151118005301/en/IMS-Health-Forecasts-Global-Drug-Spending-to-Increase-30-Percent-by-2020-to-1.4-Trillion-As-Medicine-Use-Gap-Narrows> (accessed 14 February 2021).
- 7 INTERPOL (2014). *Pharmaceutical Crime and Organised Criminal Groups*. Lyon, France: INTERPOL.
- 8 OECD/EUIPO (2020). *Trade in Counterfeit Pharmaceutical Products, Illicit Trade*. Paris. <https://doi.org/10.1787/a7c7e054-en>: OECD Publishing [https://www.oecd-ilibrary.org/governance/trade-in-counterfeit-pharmaceutical-products\\_a7c7e054-en](https://www.oecd-ilibrary.org/governance/trade-in-counterfeit-pharmaceutical-products_a7c7e054-en) (accessed 1 November 2020).
- 9 Kaur, H., Clarke, S., Lalani, M. et al. (2016). Fake anti-malarials: start with the facts. *Malaria Journal* 15: 86. <https://doi.org/10.1186/s12936-016-1096-x>.
- 10 World Health Organization Medical product Alert No. 4/2020 (2020). *Falsified Chloroquine Products Circulating in the WHO Region of Africa*. Geneva, Switzerland: World Health Organization <https://www.who.int/news-room/detail/09-04-2020-medical-product-alert-n4-2020> (accessed 15 July 2020).
- 11 Mukhopadhyay, R. (2007). The hunt for counterfeit medicine. *Analytical Chemistry* 79: 2622–2627.
- 12 Everts, S. (2010). Fake pharmaceuticals – those fighting against counterfeit medicines face increasingly sophisticated adversaries. *C&E News* 88 (1): 27–29. <https://cen.acs.org/articles/88/i1/Fake-Pharmaceuticals.html>.
- 13 Hileman, B. (2003). Counterfeit drugs – Sophisticated technologies and old-fashioned fraud pose risks to the prescription drug supply in the U.S.. *C&E News* 81 (45): 36–43.
- 14 Hileman, B. (2001). Counterfeit Drugs – FDA battles growing global problem of fake, substandard pharmaceuticals in the U.S. *C&E News* 79 (44): 19–21.
- 15 Deisingh, A.K. (2005). Pharmaceutical counterfeiting. *Analyst* 2005 (130): 271–279.
- 16 Almuzaini, T., Choonara, I., and Sammons, H. (2013). Substandard and counterfeit medicines: a systematic review of the literature. *BMJ Open* 3: e002923. <https://doi.org/10.1136/bmjopen-2013-002923>.
- 17 Fahad, A., Alghannam, A., Aslanpour, Z. et al. (2014). A systematic review of counterfeit and substandard medicines in field quality surveys. *Integrated Pharmacy Research and Practice* 3: 71–88.
- 18 Institute of Medicine of the National Academies (2013). *Countering the Problem of Falsified and Substandard Drugs* (eds. G.J. Buckley and L.O. Gostin). Washington, DC: The National Academies Press. [https://www.ncbi.nlm.nih.gov/books/NBK202530/pdf/Bookshelf\\_NBK202530.pdf](https://www.ncbi.nlm.nih.gov/books/NBK202530/pdf/Bookshelf_NBK202530.pdf) (accessed 30 October 2020).

- 19 OECD/EUIPO (2020). *Trade in Counterfeit Pharmaceutical Products, Illicit Trade*. Paris, France: OECD Publishing <https://doi.org/10.1787/a7c7e054-en>.
- 20 Blackstone, E.A., Fuhr, J.P. Jr., and Pociask, S. (2014). The health and economic effects of counterfeit drugs. *American Health & Drug Benefits* 7 (4): 216–224.
- 21 Irish, J. (2010). Customs group to fight \$200 bln bogus drug industry. *Reuters* (10 June 2010). <https://www.reuters.com/article/us-customs-drugs/customs-group-to-fight-200-bln-bogus-drug-industry-idUSTRE65961U20100610> (accessed 29 October 2020).
- 22 Nayyar, G.M.L., Breman, J.G., Mackey, T.K. et al. (2019). Falsified and substandard drugs: stopping the pandemic. *The American Journal of Tropical Medicine and Hygiene* 100 (5): 1058–1065. <https://doi.org/10.4269/ajtmh.18-0981>.
- 23 Rahman, M.S., Yoshida, N., Tsuboi, H. et al. (2018). The Health consequences of falsified medicines – a study of the published literature. *Tropical Medicine and International Health* 23 (12): 1294–1303.
- 24 US Food and Drug Administration (2004). Combating counterfeit drugs. Rockville, MD, 18 February 2004. <https://www.fda.gov/media/77086/download> (accessed 29 October 2020).
- 25 The World Health Organization (WHO) (2010). Anti-Counterfeit Technologies for Protection of Medicines. March 2010. <http://www.who.int/entity/impact/events/IMPACT-ACTechnologiesv3LIS.pdf> (accessed 1 November 2020).
- 26 Davison, M. (2011). *Pharmaceutical Anti-Counterfeiting: Combating the Real Danger from Fake Drugs*. Hoboken, NJ: Wiley.
- 27 Donald G. McNeil Jr., (2007). In the World of Life-Saving Drugs, a Growing Epidemic of Deadly Fakes. *The New York Times* (20 February 2007). [http://www.nytimes.com/2007/02/20/science/20coun.html?\\_r=2&th&emc=th](http://www.nytimes.com/2007/02/20/science/20coun.html?_r=2&th&emc=th) (accessed 29 October 2020).
- 28 Vickers, S., Bernier, M., Zambrzycki, S. et al. (2018). Field detection devices for screening the quality of medicines: a systematic review. *BMJ Global Health* 3: e000725. <https://doi.org/10.1136/bmjgh-2018-000725>.
- 29 Roth, L., Nalim, A., Turesson, B., and Krech, L. (2018). Global landscape assessment of screening technologies for medicine quality assurance: stakeholder perceptions and practices from ten countries. *Globalization and Health* 14: 43. <https://doi.org/10.1186/s12992-018-0360-y>.
- 30 Bate, R., Tren, R., Hess, K. et al. (2009). Pilot study comparing technologies to test for substandard drugs in field settings. *African Journal of Pharmacy and Pharmacology* 3 (4): 165–170.
- 31 Martino, R., Malet-Martino, M., Gilard, V. et al. (2010). Counterfeit drugs: analytical techniques for their identification. *Analytical and Bioanalytical Chemistry* 398: 77–92. <https://doi.org/10.1007/s00216-010-3748-y>.
- 32 USFDA. Internet warning pharmacy letters. <https://www.fda.gov/drugs/drug-supply-chain-integrity/internet-pharmacy-warning-letters> (accessed 16 July 2020).
- 33 Fedchak, S. (2014). *Presumptive Field Testing Using Portable Raman Spectroscopy: Research and Development on Instrumental Analysis for Forensic Science*. Las Vegas Metropolitan Police Department. National Institute of Justice.
- 34 Gabriele, P.D., Reffner, J.A., and Leary, P.E. (2009). Detection and sourcing of counterfeit pharmaceutical products and consumer goods. *Spectroscopy, Special Issues*, August 1: 10–15.
- 35 United States Food and Drug Administration. Counterfeit medicine. <https://www.fda.gov/drugs/buying-using-medicine-safely/counterfeit-medicine> (accessed 21 July 2020).
- 36 Bucknell, D. (2008). Worldwide: pharmaceutical polymorphs & patent strategy. 21 May 2008. <https://www.mondaq.com/australia/patent/60884/pharmaceutical-polymorphs-patent-strategy> (accessed 25 July 2020).
- 37 Censi, R. and Di Martino, P. (2015). Polymorph impact on the bioavailability and stability of poorly soluble drugs. *Molecules* 20 (10): 18759–18776. <https://doi.org/10.3390/molecules201018759>.
- 38 Leary, P.E. (2005). The role of forensic science in drug development. Masters Thesis. John Jay College of Criminal Justice.

- 39** Fernandez, F.M., Green, M.D., and Newton, P.N. (2008). Prevalence and detection of counterfeit pharmaceuticals: a mini review. *Industrial and Engineering Chemistry Research* 47: 585–590.
- 40** Nyadong, L., Green, M.D., De Jesus, V.R. et al. (2007). Reactive desorption electrospray ionization linear ion trap mass spectrometry of latest-generation counterfeit antimalarials via noncovalent complex formation. *Analytical Chemistry* 79: 2150–2157.
- 41** Global Pharma Health Fund E.V (2020). *The GPHF-Minilab™ – Protection Against Counterfeit Medicines*. Giessen, Germany: Global Pharma Health Fund E.V <https://www.gphf.org/en/minilab> (accessed 29 October 2020).
- 42** Ellis, D.I., Muhamadali, H., Haughey, S.A. et al. (2015). Point-and-shoot: rapid quantitative detection methods for on-site food fraud analysis – moving out of the laboratory and into the food supply chain. *Analytical Methods* 7: 9401–9414.
- 43** Bakeev, K.A. (2010). *Process Analytical Technology*, 2nde. Chichester, UK: Wiley.
- 44** Diehl, B., Chen, C.S., Grout, B. et al. (2012). An implementation perspective on handheld Raman spectrometers for the verification of material identity. *European Pharmaceutical Review* 17: 3–8.
- 45** Jalenak, W., Brush, R., Green, R.L., and Brown, C.D. (2009). Verification methods for 198 common raw materials using a handheld Raman spectrometer. *Pharmaceutical Technology* 33 (10): 72–82.
- 46** Agilent. Resolve Handheld Raman Analyzer for Through-Barrier Chemical Identification. <https://www.agilent.com/en/product/molecular-spectroscopy/raman-spectroscopy/handheld-raman-chemical-detection-systems/resolve-handheld-raman-analyzer-for-through-barrier-chemical-identification> (accessed 14 February 2021).
- 47** Agilent. TRS100 Quantitative Pharmaceutical Analysis System. <https://www.agilent.com/en/product/molecular-spectroscopy/raman-spectroscopy/raman-pharmaceutical-analysis-systems/trs100-quantitative-pharmaceutical-analysis-system> (accessed 14 February 2021).
- 48** Kalyanaraman, R., Dobler, G., and Ribick, M. (2010). Portable Spectrometers for Pharmaceutical Detection. *American Pharmaceutical Review* 17 (5): 38–45.
- 49** Luczak, A. and Kalyanaraman, R. (2014). Portable and Benchtop Raman Technologies for Product Authentication and Counterfeit Detection. *American Pharmaceutical Review* 17 (6): 1–5.
- 50** United States Pharmacopeial Convention (2016). *United States Pharmacopeia and National Formulary (USP-NF)*. Rockville, MD: United States Pharmacopeial Convention.
- 51** Sacchetti, M. (2014). Thermodynamics of water-solid interactions in crystalline and amorphous pharmaceutical materials. *Journal of Pharmaceutical Sciences* 103 (9): 2772–2783. <https://doi.org/10.1002/jps.23806>.
- 52** Hancock, B.C. and Zografi, G. (1997). Characteristics and significance of the amorphous state in pharmaceutical systems. *Journal of Pharmaceutical Sciences* 86 (1): 1–12. <https://doi.org/10.1021/js9601896>.
- 53** Beebe, K.R., Pell, R.J., and Seasholtz, M.B. (1998). *Chemometrics: A Practical Guide*. Hoboken, NJ: Wiley.
- 54** Martens, H. and Næs, T. (1992). *Multivariate Calibration*. Hoboken, NJ: Wiley.
- 55** Handzo, B., Luczak, A., Huffman, S. et al. (2020). Benchtop and Portable Raman Spectrometers to Screen Counterfeit Drugs. *American Pharmaceutical Review* 23 (3): 38–43.
- 56** Norris, K.H. and Williams, P.C. (1984). Optimization of mathematical treatments of raw near-infrared signal in the measurement of protein in hard red spring wheat. I. Influence of particle size. *Cereal Chemistry* 61 (4): 158–165.
- 57** Norris, K.H. and Hart, J.R. (1996). Direct spectrophotometric determination of moisture content of grain and seeds. Proceedings of the 1963 International Symposium on Humidity and Moisture, Principles and Methods of measuring Moisture in Liquids and Solids, Volume 4. Reinhold Publishing Corporation, New York, pp. 19–25 (1965). Reprinted as. *Journal of Near Infrared Spectroscopy* 4: 23–30.
- 58** Williams, P. (2019). Karl H. Norris, the father of near-infrared spectroscopy. *NIR News* 30 (7–8): 25–27. <https://doi.org/10.1177/0960336019875883>.
- 59** Williams, P. and Norris, K. (eds.) (2001). *Near-Infrared Technology in the Agricultural and Food Industries*. St. Paul, MN: AACC Publications.

- 60 Roberts, C.A. , Workman Jr., J., Reeves III, J.B. et al. (2004). *Near-Infrared Spectroscopy in Agriculture*. Madison, WI: American Society of Agronomy, Crop Science Society of America, Soil Science Society of America.
- 61 Ciurczak, E.W. and Igne, B. (eds.) (2014). *Pharmaceutical and Medical Applications of Near-Infrared Spectroscopy*. Boca Raton, FL: CRC Press.
- 62 Burns, D.A. and Ciurczak, E.W. (2007). *Handbook of Near-Infrared Analysis*, 3rd. Boca Raton, FL: CRC Press.
- 63 Khan, P.R., Jee, R.D., Watt, R.A., and Moffat, A.C. (1997). The identification of active drugs in tablets using near infrared spectroscopy. *Pharmaceutical Sciences* 3: 447.
- 64 Scafì, S.H.F. and Pasquini, C. (2001). Identification of counterfeit drugs using near-infrared spectroscopy. *Analyst* 126: 2218. <https://doi.org/10.1039/b106744n>.
- 65 Ulmschneider, M. and Pénigault, E. (2000). Non-invasive confirmation of the identity of tablets by near-infrared spectroscopy. *Analisis* 28: 336. <https://doi.org/10.1051/analisis:2000124>.
- 66 Yoon, W.L. (2005). Near-infrared spectroscopy: a novel tool to detect pharmaceutical counterfeits. *American Pharmaceutical Review* 8: 115.
- 67 Olsen, B.A., Borer, M.W., Perry, F.M., and Forbes, R.A. (2002). Screening for counterfeit drugs using near-infrared spectroscopy. *Pharmaceutical Technology North America* 26: 62.
- 68 Rodionova, O.Y., Houmøller, L.P., Pomerantsev, A.L. et al. (2005). NIR spectrometry for counterfeit detection a feasibility study. *Analytica Chimica Acta* 549: 151. <https://doi.org/10.1016/j.aca.2005.06.018>.
- 69 Shin, M., Jee, R.D., Chae, K., and Moffat, A.C. (2005). Identification of counterfeit Cialis, Levitra and Viagra tablets by near-infrared spectroscopy. *The Journal of Pharmacy and Pharmacology* 57 (Supplement): S-11.
- 70 Yoon, W.L., Jee, R.D., Lee, G. et al. (2001). A non-destructive method to detect counterfeit medicines using near-infrared spectroscopy. *AAPS PharmSciTech* 3 (Supplement): Abstract 428.
- 71 O' Neil, A.J., Jee, R.D., Lee, G. et al. (2008). Use of portable near infrared spectrometer for the authentication of tablets and the detection of counterfeit versions. *Journal of Near Infrared Spectroscopy* 16: 327–333.
- 72 Saranwong, S. and Kawano, S. (2005). Commercial portable NIR instruments in Japan. *Near-IR News* 16 (7): 27–30.
- 73 Crocombe, R.A. (2018). Portable spectroscopy. *Applied Spectroscopy* 72 (12): 1701–1751. <https://doi.org/10.1177/0003702818809719>.
- 74 US Food and Drug Administration (2004). PAT — a framework for innovative pharmaceutical development, manufacturing, and quality assurance. <https://www.fda.gov/regulatory-information/search-fda-guidance-documents/pat-framework-innovative-pharmaceutical-development-manufacturing-and-quality-assurance> (accessed 20 July 2020).
- 75 Abatzoglou, N., Lapointe-Garant, P., and Simard, J. (2009). Real-time NIR monitoring of pharmaceutical blending processes with multivariate quantitative models. *European Pharmaceutical Review* 14 (5): 57–67. <https://www.europeanpharmaceuticalreview.com/article/732/real-time-nir-monitoring-of-pharmaceutical-blending-processes-with-multivariate-quantitative-models> (accessed 20 July 2020).
- 76 Parris, J., Airiau, C., Escott, R. et al. (2005). Monitoring API drying with NIR. *Spectroscopy* 20 (2): 34–41.
- 77 Sekulic, S.S., Ward, H.W., Brannegan, D.R. et al. (1996). On-line monitoring of powder blend homogeneity by near-infrared spectroscopy. *Analytical Chemistry* 68: 509–513.
- 78 Roggo, Y., Chalus, P., Maurer, L. et al. (2007). A review of near infrared spectroscopy and chemometrics in pharmaceutical technologies. *Journal of Pharmaceutical and Biomedical Analysis* 44 (3): 683–700.
- 79 Reich, G. (2005). Near-infrared spectroscopy and imaging: basic principles and pharmaceutical applications. *Advanced Drug Delivery Reviews* 57 (8): 1109–1143. <https://doi.org/10.1016/j.addr.2005.01.020>.
- 80 Kranenburg, R.F., Verduin, J., Weesepoel, Y. et al. (2020). Rapid and robust on-scene detection of cocaine in street samples using a handheld near infrared spectrometer and machine learning algorithms. *Drug Testing and Analysis* 12: 1404–1418. <https://doi.org/10.1002/dta.2895>.

- 81** Davies, A.M.C. and Fearn, T. (2004). Back to basics: The principles of principal component analysis. *Spectroscopy Europe* 16: 20–23.
- 82** Moffat, A.C., Assi, S., and Watt, R.A. (2010). Identifying counterfeit medicines using near infrared spectroscopy. *Journal of Near Infrared Spectroscopy* 18 (1): 1–15. <https://doi.org/10.1255/jnirs.856>.
- 83** Kalyanaraman, R., Dobler, G., and Ribick, M. (2011). *Near-Infrared (NIR) Spectral Signature Development and Validation for Counterfeit Drug Detecting Using Portable Spectrometer*, 98–104. American Pharmaceutical Review.
- 84** International Conference on Harmonisation of Technical Requirements for Registration of Pharmaceuticals for Human Use (2005). Validation of analytical procedures: text and methodology Q2(R1).
- 85** Crume, C. (2009). History of inficon HAPSITE: maintenance management, support, and repair. <http://www.kdanalytical.com/instruments/inficon-hapsite-history.aspx> (accessed 2 February 2018).
- 86** Leary, P.E., Dobson, G.S., and Reffner, J.R. (2016). Development and applications of portable gas chromatography-mass spectrometry for emergency responders, the military and law-enforcement organizations. *Applied Spectroscopy* 70 (5): 888–896. <https://doi.org/10.1177/0003702816638294>.
- 87** Pawliszyn, J. (1997). *Solid Phase Microextraction: Theory and Practice*. Wiley.
- 88** Zhang, Z., Yang, M.J., and Pawliszyn, J. (1994). Solid-phase microextraction. A solvent-free alternative for sample preparation. *Analytical Chemistry* 66 (17): 844A–853A. <https://doi.org/10.1021/ac00089a001>.
- 89** Reyes-Garcés, N., Gionfriddo, E., Gómez-Ríos, G.A. et al. (2018). Advances in solid phase microextraction and perspective on future directions. *Analytical Chemistry* 90 (1): 302–360. <https://doi.org/10.1021/acs.analchem.7b04502>.
- 90** Merck KGaA (2019). Sample smarter with automated SPME. [https://www.sigmaaldrich.com/content/dam/sigma-aldrich/docs/Sigma-Aldrich/General\\_Information/2/smart-spme-fibers-for-pal-ms.pdf](https://www.sigmaaldrich.com/content/dam/sigma-aldrich/docs/Sigma-Aldrich/General_Information/2/smart-spme-fibers-for-pal-ms.pdf) (accessed 12 July 2020).
- 91** Centers for Disease Control and Prevention (2020). Opioid Overdose, Fentanyl. <https://www.cdc.gov/drugoverdose/opioids/fentanyl.html> (accessed 22 July 2020).
- 92** Katz, J., Goodnough, A. and Sanger-Katz, M. (2020). In shadow of pandemic, U.S. Drug overdose deaths resurge to record. *The New York Times* (15 July 2020). <https://www.nytimes.com/interactive/2020/07/15/upshot/drug-overdose-deaths.html> (accessed 26 July 2020).
- 93** US Drug Enforcement Administration Division Control Division (2019). Fentanyl. [https://www.deadiversion.usdoj.gov/drug\\_chem\\_info/fentanyl.pdf](https://www.deadiversion.usdoj.gov/drug_chem_info/fentanyl.pdf) (accessed 4 June 2017).
- 94** DEA Strategic Intelligence Section (2019). 2019 National Drug Threat Assessment. [https://www.dea.gov/sites/default/files/2020-01/2019-NDTA-final-01-14-2020\\_Low\\_Web-DIR-007-20\\_2019.pdf](https://www.dea.gov/sites/default/files/2020-01/2019-NDTA-final-01-14-2020_Low_Web-DIR-007-20_2019.pdf) (accessed 8 March 2020).
- 95** Ramsdell, T. (2019). What is ‘Mexican oxy’ and why is it starting to spread in Mississippi?. *Sun Herald*. <https://www.sunherald.com/news/local/article227145934.html> (accessed 14 February 2021).
- 96** Dégardin, K., Guillemain, A., and Roggo, Y. (2017). Comprehensive study of a handheld Raman spectrometer for the analysis of counterfeits of solid-dosage form medicines. *Journal of Spectroscopy* 2017: 1–13. <https://doi.org/10.1155/2017/3154035>.
- 97** Wilson, B.K., Kaur, H., Allan, E.L. et al. (2017). A new handheld device for the detection of falsified medicines: demonstration on falsified Artemisinin-based therapies from the field. *American Journal of Tropical Medicine and Hygiene* 96 (5): 1117–1123. <https://doi.org/10.4269/ajtmh.16-0904>.
- 98** Dégardin, K., Desponds, A., and Roggo, Y. (2017). Protein-based medicines analysis by Raman spectroscopy for the detection of counterfeits. *Forensic Science International* 278: 313–325. <https://doi.org/10.1016/j.forsciint.2017.07.012>.
- 99** Kakio, T., Yoshida, N., Macha, S. et al. (2017). Classification and visualization of physical and chemical properties of falsified medicines with handheld Raman spectroscopy and X-ray computed tomography. *American Journal of Tropical Medicine and Hygiene* 97 (3): 684–689. <https://doi.org/10.4269/ajtmh.16-0971>.
- 100** Rather, D. (2010). The Mysterious Case of Kevin Xu, 14 September. *Dan Rather Reports*. AXS TV.

- 101 Sword, D. (2020). Personal Communication with R. A. Crocombe, 16–17 July.
- 102 Bate, R. and Mathur, A. (2011). The impact of improved detection technology on drug quality: a case study of Lagos, Nigeria. American Enterprise Institute economic policy working paper 2011-01 14 February 2011. <https://doi.org/10.2139/ssrn.2212974>.
- 103 Rotinwa, A. (2018). How Nigeria partners with tech companies to outwit drug counterfeiters. 10 July 2018. <https://www.devex.com/news/how-nigeria-partners-with-tech-companies-to-outwit-drug-counterfeiters-92953> (accessed 23 July 2020).
- 104 Holt, T., Millroy, L. and Mmopi, M. (2017). Winning in Nigeria: Pharma's new frontier. *McKinsey & Company* (12 May 2017). <https://www.mckinsey.com/industries/pharmaceuticals-and-medical-products/our-insights/winning-in-nigeria-pharmas-next-frontier#> (accessed 24 July 2020).
- 105 Gewertz, N. and Amado, R. (2004). Intellectual property and the pharmaceutical industry: a moral crossroads between health and property. *Journal of Business Ethics* 55 (3): 295–308.
- 106 Newton, P.N., McGready, R., Fernandez, F. et al. (2006). Manslaughter by Fake Artesunate in Asia – Will Africa Be Next? *PLoS Medicine* 3 (6): 0752–0755. <https://doi.org/10.1371/journal.pmed.0030197>.
- 107 Thomas, P. (2011). PharmaView: fake drugs: why business is booming. *PharmaView* (14 December 2011). <https://www.pharmamanufacturing.com/articles/2011/161> (accessed 26 July 2020).
- 108 Inciardi, J.A., Surratt, H.L., Kurtz, S.P., and Cicero, T.J. (2007). Mechanisms of prescription drug diversion among drug-involved club-and street-based populations. *Pain Medicine* 8 (2): 171–183. <https://doi.org/10.1111/j.1526-4637.2006.00255.x>.
- 109 Vanguard (2020). NAFDAC partners PCN in combating counterfeit drugs. 24 February 2020. <https://www.vanguardngr.com/2020/02/nafdac-partners-pcn-in-combating-counterfeit-drugs/> (accessed 24 July 2020).
- 110 This was featured in a 'Dan Rather Reports', first aired 14 September 2010. <https://m.youtube.com/watch?v=JL9iiyAx3Qw> (accessed 16 July 2020). This section begins at about six minutes into the report.
- 111 Reuters (2012). Egyptian middleman bought fake Avastin from Turkey. <https://www.reuters.com/article/usegyptian-avastin/egyptian-middleman-bought-fake-avastin-from-turkey-idUSTRE81R24120120228> (accessed 24 July 2020).
- 112 Europol (2020). Rise of Fake 'Corona Cures' Revealed in Global Counterfeit Medicine Operation. 21 March 2020. <https://www.europol.europa.eu/newsroom/news/rise-of-fake-%E2%80%98corona-cures%E2%80%99-revealed-in-global-counterfeit-medicine-operation> (accessed 16 July 2020).
- 113 Taylor, P. (2020). Fake versions of COVID-19 drug chloroquine seen in Africa. *Securing Industry* (3 April 2020). <https://www.securingindustry.com/pharmaceuticals/fake-versions-of-covid-19-drug-chloroquine-seen-in-africa/s40/a11544/#.XtKsLTzbDc> (accessed 24 July 2020).
- 114 United States Food and Drug Administration (2020). Beware of Fraudulent Coronavirus Tests, Vaccines and Treatments. 29 April 2020. <https://www.fda.gov/consumers/consumer-updates/beware-fraudulent-coronavirus-tests-vaccines-and-treatments> (accessed 24 July 2020).
- 115 BBC News (2020). Fake pharmaceutical industry thrives in West Africa. 14 July 2020. <https://www.bbc.com/news/world-africa-53387216#:~:text=The%20counterfeit%20pharmaceutical%20industry%20is,criminal%20syndicates%2C%20writes%20Emma%20Hooper>. (accessed 15 February 2021).
- 116 Wang, W., Keller, M.D., Baughman, T., and Wilson, B.K. (2020). Evaluating low-cost optical spectrometers for the detection of simulated substandard and falsified medicines. *Applied Spectroscopy* 74 (3): 323–333. <https://doi.org/10.1177/0003702819877422>.

## 6

### Forensic Applications of Portable Spectrometers

Brooke W. Kammrath<sup>1,2</sup>, Pauline E. Leary<sup>3</sup> and John A. Reffner<sup>4</sup>

<sup>1</sup>Department of Forensic Science, Henry C. Lee College of Criminal Justice and Forensic Sciences, University of New Haven, West Haven, CT, USA

<sup>2</sup>Henry C. Lee Institute of Forensic Science, West Haven, CT, USA

<sup>3</sup>Federal Resources, Stevensville, MD, USA

<sup>4</sup>John Jay College of Criminal Justice, New York, NY, USA

Forensic science, as defined by these authors, is the application of the scientific method to matters of the law. The law has several components that require the assistance of scientific analysis to aid in the administration of justice, such as criminal matters, civil cases, environmental regulations, patent litigations, and intellectual property disputes. Some of these will be interfaced with each other, such as in an automobile accident where there may be both civil and criminal actions pursued.

The foundation of forensic science was eloquently captured in the words of Dr. Paul Leland Kirk (1953) when he wrote of a criminal's actions:

Wherever he steps, whatever he touches, whatever he leaves—even unconsciously—will serve as silent evidence against him. Not only his fingerprints and his shoemarks, but also his hair, the fibers from his clothes, the glass he breaks, the tool mark he leaves, the paint he scratches, the blood or semen that he deposits or collects—all these and more bear mute witness against him. This is evidence that does not forget. It is not confused by the excitement of the moment. It is not absent because human witnesses are. *It is factual evidence.* Physical evidence cannot be wrong; it cannot perjure itself; it cannot be wholly absent. Only in its interpretation can there be error. Only human failure to find, study, and understand it can diminish its value.

The scientific method is a cyclic iterative process that is presented as a systematic series of steps that scientists use to logically and in an unbiased manner seek a solution to a problem. It includes observation and data collection, documentation, preservation, examination, contemplation, speculation (which includes hypothesis development), interpretation, verification, and the communication of results. The scientific method is employed for the analyses of physical evidence both in the field (e.g. at a crime scene) and in the forensic laboratory. The recent availability of field-friendly portable spectrometers is an important advancement for the successful implementation of the scientific method in the field.

There are numerous advantages of portable spectrometers in the forensic field. Portable spectrometers have detection, identification, and analysis capabilities that provide valuable investigative and adjudicative information about a sample. This data can be used on its own or to inform further evidence selection, preservation, and collection. It can provide real-time information that can help form investigative leads. The chance of loss or destruction of evidence is minimized with the use of portable spectrometers in the field. This is particularly important for delicate or unstable samples. For evidence that cannot be transported or is in a remote location, portable spectrometers provide their only method of chemical analysis. As can be observed by reading the various other chapters

in this book, the use of portable spectrometers in most industries is usually performed by nonscientist operators, frequently in a screening environment where a pass/fail result is the goal. In forensic science, though, portable spectrometers may serve a much different role. While in some instances they may be used by nonscientists, a significant value of these systems lies in their use by forensic scientists at the crime scene during the application of the scientific method to evaluate the scene.

Forensic scientists have long recognized the value of field tests for chemical detection and identification. These field tests have traditionally used non-spectrographic analytical methods. In 1881, Alexander Graham Bell built the first metal detector with the purpose of finding a bullet at autopsy in the body of President James Garfield, who had been shot in an assassination attempt (Detector Electronics Corp 2014). Metal detectors were later used to find bullets and cartridge casings at crime scenes. Colorimetric tests using Kitagawa tubes, invented in 1946, were used for the detection of invisible gases, including carbon monoxide and hydrogen sulfide in wrongful death cases and civil litigations of health and safety (Sensidyne® n.d.). Flame ionization detectors (FIDs) have been used since the 1960s for the identification of hydrocarbons (e.g. gasoline or other ignitable liquids) at suspected arson scenes. Today, colorimetric tests are commonly employed at the scene of a crime or suspected crime. Narcotics identification kits are presumptive field tests used by police officers or other response personnel, as they are inexpensive and readily available for purchase. The sodium rhodizonate and Griess color tests are used for the identification of lead and nitrites, respectively, which are characteristic components used in the detection of gunshot residue. There are also numerous color and fluorescence tests (e.g. Kastle Meyer or phenolphthalein, leucomalachite green, amido black, luminol) used for the presumptive identification of blood at crime scenes. There are also commercially available systems aimed at making the reading of colorimetric tests more objective by pairing them with cellular phones that photograph the results and digitally document them for chain-of-custody purposes (e.g. Detectachem's MobileDetect Pouches, <https://detectachem.com>; DetectaChem 2020). These examples demonstrate that the legal precedence of field testing in forensic science is well established.

There are special requirements for field testing instrumentation for forensic science applications. There are the “3 R’s” of forensic science methods: **rapid**, **reliable**, and create a **reviewable** record. Additionally, it must be accepted in a court of law; thus, the method must adhere to the appropriate rules of evidence. For US Federal Courts, evidence admissibility falls under Rule 702 (“Testimony by an Expert Witness”) in the Federal Rules of Evidence (2014) which states the following:

A witness who is qualified as an expert by knowledge, skill, experience, training, or education may testify in the form of an opinion or otherwise if:

- (a) the expert’s scientific, technical, or other specialized knowledge will help the trier of fact to understand the evidence or to determine a fact in issue;
- (b) the testimony is based on sufficient facts or data;
- (c) the testimony is the product of reliable principles and methods; and
- (d) the expert has reliably applied the principles and methods to the facts of the case.

In US State Courts, the rules of evidence admissibility depend on the state’s precedent case law, which are either based on the decisions in Frye v. United States (1923) or Daubert v. Merrell Dow Pharmaceuticals, Inc. (1993). The Frye standard of evidence admissibility is based on general acceptance by the relevant scientific community, while the original Daubert decision included the following four “prongs” or criteria: (i) the technique “can be (and has been) tested” meaning it has been subjected to significant hypothesis testing of the underlying principle, (ii) it has been “subjected to peer review and publication,” (iii) there is a “known or potential error rate... and the existence and maintenance of standards controlling the technique’s operation,” and (iv) it has gained “widespread acceptance within a relevant scientific community.” The third prong is generally split in two; thus, today, these are known as the five Daubert factors. They were intended as guidelines for good science and never intended to be a checklist, although in many courts they are mistakenly used as such. Other jurisdictions have similar

requirements for forensic evidence admissibility. For example, in the United Kingdom, the Crown Prosecution Service has guidelines for evidence admissibility, which has four guidelines based on (i) providing useful and specialized information outside the common knowledge of both judge and jury, (ii) the relevant and sufficient expertise of the expert, (iii) the impartiality of the expert, and (iv) the reliability of the evidence (The Crown Prosecution Service 2019). The development and use of portable technologies for forensic science applications must be completed in consideration of these conditional rules of evidence admissibility. Failure can result in the exclusion of the expert's testimony, and this could create a precedent that prevents the adoption of this technology's acceptance by the courts.

The power of portable spectrometers for field testing in forensic science is best demonstrated by its many applications. There are a number of different portable technologies that currently provide value to the field of forensic science. Table 6.1 summarizes some of the more commonly used methods along with applications, advantages, and limitations. (For more details on the technologies of these instruments, see Volume 1 of this text, Chapter 3 by Schiering and Stein, Chapter 6 by Rathmell, Bingemann, Zieg and Creasey, Chapter 14 by Snyder, Chapter 15 by Leary, Kammrath and Reffner, Chapter 16 by Blakeman and Miller, and Chapter 17 by DeBono and Leary.)

## 6.1 Breath Alcohol Testing

The analysis of breath alcohol content in the field is the foundation for all forensic on-scene testing. For as long as people have been driving automobiles, there have been concerns about alcohol impairment. The first law in the United States prohibiting alcohol-impaired driving with legal penalties was adopted in 1910 by New York State, with others following shortly thereafter in response to the rapidly growing popularity of automobile ownership (Schweir 2015). Initially, performance-based field sobriety tests were used to evaluate the intoxication state of a driver, but there was an urgent need for more objective and quantifiable on-scene testing due to public safety concerns.

The legal determination of driver impairment is based on the concentration of alcohol in the blood, not in the breath. However, because there is an established direct relationship between the concentration of alcohol in the blood and breath (2100:1), the breath alcohol concentration may be used for probable cause for arrest and/or as evidence of impairment at trials, depending on the laws of the jurisdiction. For example, in Canada, some field-deployable breath alcohol instrumentation is used for screening only, while other technologies, such as infrared (IR) spectroscopy, are also used for evidence in trial (Wigmore and Langille 2009). The legal limit for impairment also varies by country, with 0.08% weight per volume (i.e. 80 mg of alcohol in 100 mL of blood) being the legal limit in the United States, Canada, and most of the United Kingdom (it is 0.05% in Scotland), while the limit in China is 0.02%.

The history of field-portable breath alcohol instruments is well chronicled, with two excellent references available. Both are historical reviews, the first on blood and breath alcohol testing by Jones (1996) and the second focusing on the evolution of field instrumentation by Wigmore and Langille (2009) (Figure 6.1). The first field-portable breath alcohol instrument, the Drunkometer, was developed by R.N. Harger at Indiana University in the 1930s and relied on the colorimetric reduction of potassium permanganate by ethyl alcohol (Figures 6.2a and 6.3).

The Drunkometer employed mixed expired breath of the suspected drinking driver who provided it into a rubber balloon. The balloon was attached to a tube of purple liquid (potassium permanganate in sulphuric acid) and the breath was allowed to bubble through the solution. If there was alcohol in the breath there was a chemical reaction and the endpoint occurred when the purple colour of the solution turned into a yellowish brown colour. The amount of breath required to cause this colour change (and hence the blood alcohol concentration) could be gauged from what was left in the balloon or by connecting the apparatus to a water displacement gas meter or by measuring the weight of carbon dioxide collected in an Ascarite tube (Wigmore and Langille 2009).

**Table 6.1** Comparison of forensic applications of current portable spectroscopy and spectrometry instruments.

Spectrometer technology	Forensic applications	Advantages	Limitations
IMS	– Illicit drugs – Explosives	– Low LOD (ng) – Simple to operate – no sample preparation	– Presumptive identification due to the potential to co-alarm – Destructive – Direct sampling required – Long start-up time – Potential to overload the detector
FT-IR	– Breath alcohol – White powders – Illicit drugs – Counterfeit drugs – Explosives – Clandestine labs	– Nondestructive – Highly selective (molecular identification) – No sample preparation for ATR FT-IR analysis – Large commercial spectral libraries available – No consumables required – Simple to operate – Sealed cells available for hazardous materials	– Relatively high LODs (sample dependent) – No characteristic spectrum from most ionic or metallic materials – Complicated mixture interpretation – Not usually deployed for vapor/gas detection, although gas cells are commercially available
Raman	– White powders – Illicit drugs – Counterfeit drugs – Explosives – Clandestine labs	– Nondestructive – Highly selective (molecular identification) – No contact required – No consumables required – Analysis through some containers – Simple to operate	– Relatively high LODs (sample dependent; LODs reduced with SERS) – Fluorescence – Complicated mixture interpretation – Not capable of vapor/gas detection
GC-MS	– Illicit drugs – Counterfeit drugs – Explosives – Ignitable liquid residues – Clandestine labs	– Highly selective (molecular identification) – Low LODs – Mixture identification – Existence of large commercial quadrupole MS spectral libraries	– Destructive – Direct sampling required – Long start-up time – Difficult to distinguish isomers – More expensive than other portable technologies – Potential to overload the detector
MS	– Illicit drugs – Explosives	– Highly selective (molecular identification) – Low LODs	– Destructive – Direct sampling required – Difficult to distinguish isomers – Complicated mixture interpretation – Potential to overload the detector
HPMS	– Illicit drugs including fentanyl – Explosives	– Low LODs – Field friendly	– Presumptive identification – Non-interpretable data – Destructive – Direct sampling required – Potential to overload the detector

Generations of breath testing instruments and the principles of breath alcohol analysis employed, with one or more example of instruments per generation, especially those used in Canada

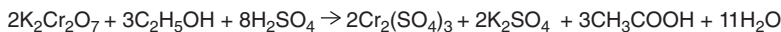
Time period	Generation	Instrument examples	Principles of breath alcohol analysis
1930-1953	First	Drunkometer Intoximeter Alcometer	Oxidation with potassium permanganate or iodide pentoxide
1954-1992	Second	Breathalyzer ( <b>Brokenstein Breathalyzer, 1969; 900A, 1974; 900B, 1992</b> ). Photo-electric intoximeter ethanograph	Oxidation with potassium dichromate and sulphuric acid contained in glass ampoules, colour change measured by visible photometry
1970-	Third	GC Intoximeter ( <b>Intoximeter Mk IV, 1978</b> )  Intoxilyzer 4011  ALERT Screener ( <b>J3A withdrawn in 1993</b> )  Alcometer ( <b>Alcolmeter AE-D1, 1982</b> )  <b>Alcosensor IV/RBT IV, 1995</b>  <b>Breathalyzer 7410 CDN with Printer (2002)</b>	GC separation with porapak Q column and FID or TC detectors  Single IR wavelength (3.4 microns)  N-type semiconductor (Taguchi cell)  Electrochemical sensor  Electrochemical sensor
1975-	Fourth	Intoxilyzer ( <b>4011AS, 1982</b> )  Intoxilyzer ( <b>5000C, 1992</b> )  BAC Datamaster ( <b>C, 1994</b> )  Datamaster ( <b>DMT-C, 2008</b> )	Dual IR wavelength at 3.39 and 3.49 microns  Multi IR wavelength (3.39, 3.48 and 3.80 microns)  Dual IR wavelength (3.37 and 3.48 microns)  Multi IR wavelength (3.37, 3.44 and 3.50 microns)
1985-	Fifth	Alcotest ( <b>7110, 1992</b> )  Intoxilyzer ( <b>8000 C, 2007</b> )	Single IR wavelength at 9.5 microns  Dual IR wavelength (3.4 and 9.4 microns)
1990-	Sixth	Alcotest ( <b>7110 MkII Dual C, 2002</b> )  Intox ( <b>EC/IR II, 2009</b> )  Alcotest (E-Pass) 8510 Alcosensor IV-XL POA	IR wavelength at 9.5 microns and electrochemical sensor  Dual IR wavelength (3.46 and 4.26 microns) and electrochemical sensor  Fuel cell based evidential instrument and screening device

**Figure 6.1** Wigmore and Langille's (2009) table showing the six generations of breath testing instruments and the principles of breath alcohol analysis employed. Source: Wigmore and Langille (2009). © 2009, Taylor & Francis.



Potassium permanganate      Ethyl alcohol      Sulfuric acid      Manganese (II) sulfate      Potassium sulfate      Acetic acid      Water

Mn(VII)



Potassium dichromate      Ethyl alcohol      Sulfuric acid      Chromium (III) sulfate      Potassium sulfate      Acetic acid      Water

Cr(VI) – absorbs at 420 nm

**Figure 6.2** The chemical reactions used in early breath alcohol devices, showing the oxidation of ethanol to acetic acid by (a) the reduction of the manganese ion from Mn(+7) to Mn(+2), resulting in a color change of purple to yellow-brown, and (b) the reduction of the chromium ion from Cr(+6) to Cr(+3), resulting in a loss of a yellow-orange color.



**Figure 6.3** Drunkometer product introduction at the Indiana State Fair, 1934. Image published with permission from the Indiana Historical Society. Source: Image published with permission from the Indiana Historical Society.

Due to the use of subjective visual assessment of color in this instrumentation, there was a need for more objective instrumental methods. The second-generation instruments incorporated a visible spectrometer to quantitatively measure the color change caused by the reduction of potassium dichromate by ethanol, thus decreasing the absorbance of light at 420 nm (Figure 6.2b). Figure 6.4 shows a breathalyzer in use.

Since the 1970s, two technologies emerged to improve the analysis of breath alcohol in field tests: electrochemical sensors (i.e. fuel cells) and IR spectroscopy. Electrochemical sensors are devices that convert a fuel and an oxidant into an electric current. In these field analyzers, alcohol is the fuel that is oxidized by atmospheric oxygen, and a current is generated that is proportional to the quantity of alcohol in the breath. IR sensors have improved over the years, beginning with single-wavelength spectrometers ( $3.4\text{ }\mu\text{m}$ ) which led to dual and now multiwavelength instruments. The evolution to dual-wavelength and multiwavelength spectrometers increased the specificity of breath alcohol instruments, eliminating acetone interference (which can be found in the breath of individuals, particularly those with diabetes). Additionally, in the 1980s, IR instruments increased ethanol specificity by employing a longer-wavelength ( $9.4\text{ }\mu\text{m}$ ) spectrometer, which corresponded to measuring absorbance of the C—O bond as opposed to the methyl symmetric and asymmetric stretching. The most recent developments in breath alcohol instruments combine electrochemical sensors and IR spectrometers in a single platform, which has increased their reliability. Ultimately, the motivation for the various advances of breath alcohol instruments is to improve their reliability and accessibility by the courts.

While these instruments have proven value, they must be operated by individuals with knowledge, training, and an understanding and appreciation for how the equipment should be deployed. When portable spectrometers are



**Figure 6.4** Dorothy Brengel helps W.D. Foden, Chairman of Statler Safety Committee, demonstrate the “Drunkometer,” on display at the Greater New York Safety Council, Hotel Statler, 28 March 1950. *Source:* Carl Nesenohn/AP/Shutterstock.

used by forensic scientists, there is an understanding by the operator of how to generate scientifically defendable data using the technology. The importance of training and education, instrument maintenance records, proper calibration, the use of appropriate standards/methods, etc. are fundamental to the training and education of a forensic scientist. However, when portable technologies are deployed by nonscientist operators, this is not usually the case. A significant challenge within the forensic science community comes when deploying portable technologies for field testing by nonscientists when the result of the field test will be used as part of a legal proceeding. A New York Times feature article from November 2019 entitled “These machines can put you in jail. Don’t trust them” (Cowley and Silver-Greenberg 2019) details some serious human failures with respect to the technology. The title for this article is a misnomer, as it is not the instruments but rather the operators who failed by not performing proper calibrations and instrument maintenance, etc. In addition, what these authors incorrectly attempt to establish is that the technology used is fundamentally flawed. It is not. When an appropriate technology is not properly applied, or the training, calibration, and method used in a specific case is not appropriate, as was the case in the situations detailed in this article, the result should be disregarded. What this article highlights, which was not addressed by these authors, is the need for a review of this type of evidence by a forensic scientist. If a field test is performed by a nonscientist, e.g. by a police officer at a suspected drunk-driver incident, and the testing result will be used as part of a legal proceeding, all aspects of the testing should be reviewed by a scientist to verify that the test results meets the standards for admissibility of scientific evidence in court.

## 6.2 White-Powder Attacks

A significant catalyst for the development of field-portable spectrometers was the 2001 anthrax white-powder attacks that began one week after 9/11. These events, also known as the Amerithrax attacks, occurred in two waves. The first wave involved five letters postmarked from Trenton, New Jersey, on 18 September to news media outlets in New York City and Boca Raton, Florida. The second wave included two letters sent to Democratic senators on 9 October. Ultimately, 5 people were killed and 17 hospitalized as a result of this exposure to weaponized anthrax. Subsequently, there were thousands of hoax white-powder attacks in the United States and around the world, with the goal of causing fear, chaos, and disruption. The primary recipients of these letters were politicians, journalists,

and celebrities. Highly publicized attacks on abortion clinics and religious institutions helped spread the anxiety to all. The mailrooms of many major companies and organizations were immediately challenged by the panic of white powder in envelopes and packages. Although the frequency of these white-powder attacks has declined significantly since 2001, these events continue.

Chemical detection and identification of these white powders at the scene were needed immediately. This was because upon receipt of a white-powder letter, buildings would be locked down and individuals hospitalized and quarantined. SensIR™ Technologies, Inc. (Danbury, CT) demonstrated the first field-portable Fourier transform IR (FT-IR) spectrometer in March of 2002 which they had introduced to the market in 2001. This portable spectrometer became a critical tool for identifying unknown materials at the scene of a suspected white powder attack.

It must be recognized that the majority of these white-powder incidents were hoaxes and did not contain chemical or biological threats. However, they did incite widespread fear and chaos. An example of the panic these hoax powder attacks caused was at the GE Capital Corporation in Stamford, CT. A worker reported finding a white powder in the mailroom near an existing incoming letter opening machine. Panic set in. The entire building was evacuated and shut down immediately. As a result of the fear of an anthrax attack, the building was closed for several days. At that time, no one knew exactly what to do or the best response approach to take for this type of call. The local Turner River emergency response team contacted SensIR and responded to the scene to investigate. They brought with them a SensIR scientist and a TravelIR™ field-portable IR spectrometer. Samples of the white powder were then identified by their IR spectra and found to be cellulose fibers resulting from paper envelopes being cut open. In this case, the on-scene IR spectral identification not only was able to diffuse the fear of poisoning but also was able to identify the source of the material. As a consequence of this white-powder panic, there were hundreds of thousands of dollars lost and fear perpetuated over what turned out to be only common paper dust. Additionally, the value of this technology was immediately recognized, with GE Capital Corporation subsequently purchasing three TravelIR instruments for the Turner River emergency response team: one for everyday use, one for training, and one as a back-up instrument that was kept in storage.

Another example occurred in 2002 when a group of first responders were meeting in Washington, DC, to evaluate portable IR technology for the on-site chemical analysis at white-powder events. During this meeting, a senior safety inspector for the US Postal Service was notified of a white-powder incident at the US Post Office in Washington, DC. Jim Fitzpatrick from SensIR was asked to join the inspector in going to this emergency situation. Upon arrival at the post office, a safety officer in a level-A hazmat suit approached Mr. Fitzpatrick who was awaiting a sample to analyze and was offered a simple face mask to protect himself. The irony of this was not lost, and he responded by asking “What’s wrong with this picture?” The TravelIR portable IR spectrometer was used to analyze a sample of the cream-colored powder material that was leaking from a package. An IR spectrum of the powder was recorded, and identification via the on-board spectral library resulted in a match to baby formula. Simultaneously, the mailer of the package was contacted by the Federal Bureau of Investigation (FBI) and asked what was in the package. Her reply was that her daughter had recently given birth to her first grandchild, and she was sending her powdered baby formula. In the minds of the first responders at this meeting, this served as confirmation of the value of this new portable technology for answering questions at an incident scene. Although this was exciting for the scientists, it also sent a false message about the potential information garnered from an IR spectrum. As seen in Figure 6.5, the IR spectrum of baby powder contains the strongly absorbing amide-I and amide-II bands, which are characteristic of proteins. The IR spectrum of anthrax also shows the presence of these protein bands. Thus, what the IR spectral library search algorithm hit on was the spectrum of protein, fats, and cellulose and not specifically baby formula. Thus, this had the potential to cause a false-negative response if anthrax had been present. As a result, the scientists at SensIR immediately modified the analytical detection process, so that if protein bands were identified in the IR spectrum, the sample must be further analyzed using a specific test for anthrax and other biological threats.

Innocuous white powders used to mimic threats, sometimes referred to as hoax powders, were frequently used by perpetrators causing these white powder events and, therefore, encountered by first responders called to the

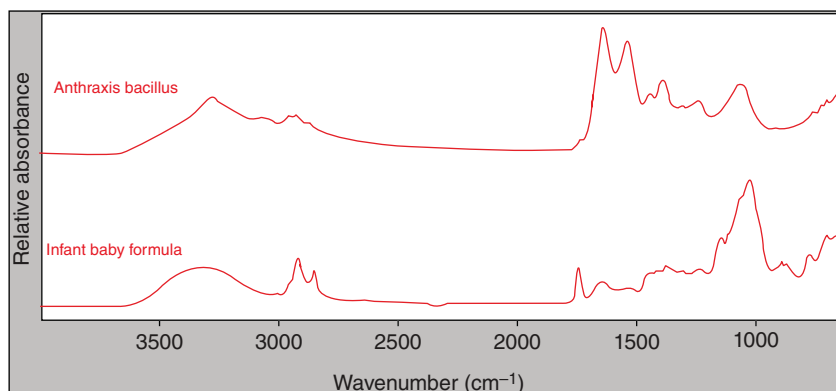


**Figure 6.5** IR spectra of *Bacillus anthracis* (top) and an infant baby formula (bottom), collected on a portable ATR FT-IR spectrometer, both containing the strongly absorbing amide I and II bands, which are characteristic of proteins.

scene. These powders could really be anything and included chemicals such as artificial sweeteners, baking soda, and baking powder (Kammrath et al. 2017). To perform an effective analysis of these chemicals, confirmatory methods such as FT-IR or Raman spectroscopy are necessary. Other field tests are often more limited in their applications or range of detections. They may identify a class of compounds but are usually not capable of confirmatory identification of a wide variety of analytes.

Portable FT-IR instruments are a valuable tool for the forensic identification of unknown materials in the field. Current instruments are handheld and rugged and offer several different options for sample analysis (e.g. internal reflection, diffuse reflection, specular reflection). FT-IR spectroscopy is capable of unequivocal chemical identification for a broad range of different materials. All methods have their limitations, with FT-IR's being its limit of detection (LOD), which is commonly estimated to be ~2–10% (depending on the material), its spectral properties (i.e. failure to detect some compounds like certain inorganics and symmetrical diatomic molecules), and difficulties detecting analytes in water due to water's strong absorption of IR radiation. Additionally, sample preparation is essential for good IR analysis. For transmission or reflection-absorption IR analysis, the sample must be sufficiently thin. For internal reflection spectroscopy, attenuated total reflection (ATR) spectra are obtained by reflection at the interface between the sample and the internal reflection element, and thus, the sample must be in contact with the internal reflection element. The result of this is that the ATR spectra are different from IR transmission spectra due to the wavelength dependence of the depth of penetration of the IR radiation during an ATR measurement. This can cause significant differences in absorption band intensities between ATR and transmission IR spectra. Additionally, minor shifts in peak positions may occur during an ATR measurement due to anomalous dispersion effects. Thus, it is essential when analyzing samples with internal reflection IR methods to compare and search using ATR spectral libraries. The same is true for transmission or any other spectral analysis because the method used to collect IR data imparts unique attributes to the spectrum.

Raman analysis produces molecular vibrational spectra that are complementary to those of IR spectra. These are generated by collecting the inelastically scattered radiation that is reflected from the sample and measuring the wavelength shift caused by the molecular vibrations of the sample from the monochromatic source. No contact is required, and analysis can be performed through some non-absorbing glass and plastic containers. Another Raman advantage is its use of visible-light radiation that enables instruments to employ conventional glass optics. It also has a wider spectral range, higher spectral resolution, and a higher LOD than IR for some analytes (e.g. pigments). One of the most significant limitations is the fluorescence that often occurs, which overwhelms the spectra and masks the weak Raman band. The occurrence of fluorescence can be minimized or eliminated by using a longer-wavelength laser source. Last, while Raman and IR are complementary, IR spectral databases are currently more extensive than Raman databases.

Today, when a white-powder event occurs, good analytical procedures begin with tests used to assess hazard level and other class characteristics, and then proceed to more sophisticated chemical analyzers. Next, if appropriate based upon the presence of amide absorption bands in the IR spectrum which indicate the presence of a potential biological substance, Prime Alert (GenPrime, Inc.), a broad-screen biodetection kit, is commonly used by first responders to identify the 13 most common weaponizable bioterrorist agents (e.g. anthrax, ricin, etc.). The kit contains five dye solutions that bind to microbes creating a specific detectable fluorescence. After the sample has been determined to not contain one of these biological terrorist agents, its evidential value as a hoax material is pursued. Ultimately, determining the identity of the white powder is essential for criminal investigations. This includes associating multiple hoax powder incidents together as well as determining the origin of the powder. The versatility of vibrational spectroscopy makes it a preferred analytical tool for forensic investigations of white powders.

### 6.3 Illicit Drugs

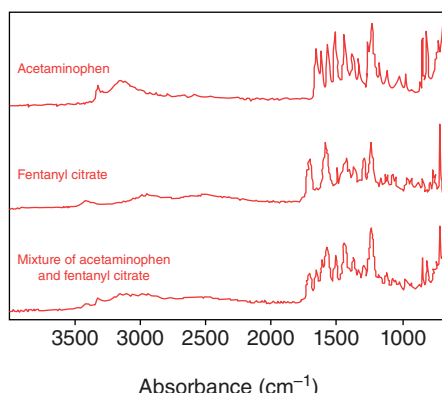
The illegal drug trade is one of the largest global businesses, with roughly 5.5% of the world population (271 million people, aged 15–64) having used a drug in 2016 (World Drug Report 2019). Consequently, most forensic laboratories (e.g. New York City Police Department Forensic Laboratory) devote a significant portion of their workforce allocation and financial resources to casework requiring illicit drug analysis. However, this is jurisdictionally dependent, because some states (e.g. Connecticut) do not test illicit drug evidence unless it is going to be used as evidence in trial. For these states, arrest warrants are achieved after a positive field test, most often a color test performed by a uniformed officer. With these results, many individuals are persuaded to accept plea deals rather than go to trial. Unfortunately, this has also caused considerable issues with wrongful convictions due to false-positive results (Bui 2019; Gabrielson and Sanders 2016; Jeong 2017; Kelly 2008; Lieblein et al. 2018; Peralta 2011; Report: Cocaine charges 2019). For example, innocuous items such as chocolate, teas, honey, blue cotton candy, tortilla flour, and bird droppings have all resulted in wrongful arrests due to the lack of specificity of these presumptive field tests. There is a need for accurate field tests for illicit drug identification, with many looking toward portable spectroscopy instruments as the alternative.

There is a false perception in the forensic community about portable spectrometers being cost prohibitive for field use when compared to traditional colorimetric presumptive kits. However, as described in a 2018 study by the National Institute of Justice's Forensic Technology Center of Excellence, the cost of portable instruments is comparable to that of the color field test kits (Forensic Technology Center of Excellence 2018). They reported that for a large metropolitan area, the cost of the color field tests is approximately \$30,000 per year ( $5,000 \text{ arrests} \times 2 \text{ tests per arrest} \times \$3 \text{ per test} = \$30,000$ ). However, this only addresses arrests and does not indicate the full scope of the required testing, which would include those analyses with negative results. This cost analysis also does not include either the need to stock separate tests for each drug class, or the shelf life of these chemical reagents. Thus, the \$30,000 per year cost is likely an underestimate of the total costs required by a police department for performing presumptive color field tests. In comparison, portable spectrometers currently have a range of prices (\$10,000–\$100,000) and thus require a relatively large up-front cost. It is hypothesized that the price of these instruments will decline as the technology matures and competition increases. It must be considered that each jurisdiction would need more than one portable spectrometer for field drug analysis, with at a minimum each first response evidence team requiring one. Ultimately, portable spectrometers do not have to be purchased yearly; thus, over a five-year period, they are quite cost effective. According to an article in PoliceOne, “For the Phoenix PD, the purchase of the handheld analyzer [a Raman spectrometer] delivered a strong return on investment, cutting the lab’s testing costs by a projected \$22,000 per month – a potential savings of \$1.3 million over a five-year period” (Planchet 2017).

Field-deployable ion mobility spectrometers (IMS) have been extensively used to screen for drugs at prisons and other locations of interest for decades (see Chapter 8 in Volume 2 by Leary and Joshi). Technological advancements have seen the development of handheld IMS, which makes them well equipped for the on-scene identification of illicit drugs. The major advantages of IMS for drug analysis include its rapid analysis, ease of use, the ability to perform mixture analysis, and its low LOD (i.e. single-digit nanogram level) for many analytes of interest. It is these capabilities that enable the IMS analysis of a swab from the outside of a suspicious package (Forensic Technology Center of Excellence 2018). Also, IMS methods can be applied at a crime scene where no visible presence of drugs or explosives are evident to establish whether trace levels of a drug or explosive substance are present and, therefore, bulk amounts of material were previously at the scene. The most significant disadvantages of IMS are as follows: it is not considered a confirmatory technique by forensic drug analysis standards (ASTM E2329-17 2017). Although there are many drugs that do not have known interferences, there are some drugs that have been known to co-alarm, such as carfentanil and oxycodone. Detection algorithms are continually refined to prevent co-alarms but can be challenging to separate for ions of virtually indistinguishable mobilities under a specified set of analysis parameters. The potential for false positives is significantly lower with IMS than with colorimetric testing. Additionally, its sensitivity means that it has the capability of being overloaded, which could result in delays with using the instrument with subsequent samples (Forensic Technology Center of Excellence 2018). Last, IMS has the potential for false-negative results due to the preferential ionization for certain components in a mixture, or even the sample matrix, which prevents the ionization and subsequent identification of other compounds. False-negative results may also occur due to sampling.

IR and Raman spectroscopy are considered confirmatory methods for drug identification by ASTM E2329-17, and thus, the use of these portable instruments in the field is highly favored. The advantages and limitations of both methods have been described above. Still, it is important to recognize that drugs are commonly found as mixtures, which complicate spectral interpretation. This is minimized by the availability of library search algorithms capable of multicomponent identification of mixtures (Figure 6.6). Lieblein et al. (2018) conducted a comparison study of cocaine mixture analysis by color-based field tests, IR, and Raman portable spectrometers. The authors “concluded that although portable spectrometers require a large initial financial investment, their high performance characteristics (e.g., ease of use, rapid analysis, non-destructive capability, acceptable LOD, minimal false positives and negatives) make them a superior tool to the color-based field tests for the on-scene presumptive analysis of cocaine HCl.” Additionally, it was determined that FT-IR spectroscopy is better suited for illicit drug analysis due to its lower detection limit, less interference from common adulterants, the potential for some drugs (i.e. heroin) to exhibit fluorescence during Raman analysis, and the greater number of spectra available in FT-IR spectral libraries. Currently, the fear by first responders of fentanyl toxicity and that of its more dangerous analogs (i.e. carfentanil) has promoted the need for noncontact analytical testing methods. Consequently, portable Raman

**Figure 6.6** IR spectra of acetaminophen (top), fentanyl citrate (middle), and a 50:50 mixture (bottom), collected on a portable ATR FT-IR spectrometer. Onboard instrument library search algorithms are capable of identifying both components of this mixture when they are both in relatively high proportions.



spectroscopy for illicit drug analysis at a scene is favored due to its ability to analyze samples through sealed transparent containers, thus limiting possible exposure and contamination.

Field-deployable gas chromatography-mass spectrometry (GC-MS) and MS instruments have been commercially available for over 20 years, with the HAPSITE® GC-MS debuting in 1996. However, they have not seen widespread adoption in the forensic field. These instruments have been used by the military and homeland security, but not commonly by local police officers for routine drug stops. These technologies are currently under development for this application (Forensic Technology Center of Excellence 2018). The potential of portable GC-MS or MS identification of illicit drugs is great, as it is the generally preferred method for drug analysis in a forensic laboratory. The major advantages of portable GC-MS and MS technologies are their ability to provide confirmatory identification of a wide range of samples, capacity for mixture analysis (in the case of GC-MS), high sensitivity, and multiple methods of sample introduction (e.g. solid-phase microextraction (SPME), direct injection, direct air sampling, etc.). The major limitations of portable GC-MS and MS are their destructive nature, the breakdown of thermally labile compounds during GC-MS (i.e. psilocybin, gabapentin,  $\gamma$ -hydroxybutyric acid) preventing their identification, the inability to distinguish between some isomers or polymorphs, and the potential to overload the system creating instrument downtime. Additionally, a GC-MS instrument will be able to identify the components of a mixture, but not provide the analysis to ascertain the identity of the sample. For instance, GC-MS will identify all the components of a gasoline sample, but not identify the sample as gasoline. Last, it is important to recognize that different ionization and mass analyzer configurations will result in differences in the mass spectra of samples. To account for this, it is essential to have mass spectral libraries (e.g. drugs and additives) created on similar instrumentation with which it will be tested. For example, as seen in Figure 6.7, the mass spectrum of heroin collected from a toroidal ion trap MS is significantly different from that collected on a quadrupole system due to space charge and ion-ion interactions that can occur during ion trapping (Leary et al. 2018). Consequently, a customized library for this type of field application is critical. As this technology advances, methods for field extraction are developed, and mass spectral libraries for drugs and additives on these instruments are created, portable GC-MS or MS instruments may become the preferred tool for on-scene drug analysis.

The emergence of commercially available portable high-pressure mass spectrometers (HPMSs) will likely have an impact on the on-scene detection of illicit drugs (see Chapter 16 in Volume 1 by Blakeman and Miller). The advantages of these instruments are that they use atmospheric pressure ionization and miniaturized ion trap mass spectrometers. This allows them to run at higher operating pressure, and therefore, they are more field-friendly. They also have low limits of detection for many drugs of interest, such as fentanyl and its derivatives. The primary disadvantage for portable HPMS is that its spectral resolution is compromised; thus, it is not considered to be a confirmatory method such as vacuum MS systems that achieve unit mass resolution. Furthermore, spectral interpretation is quite difficult, and library matching processes require complex algorithms.

Emerging synthetic drugs present an interesting challenge for field testing. Because of the constant evolution of new drugs such as bath salts (i.e. synthetic cathinones) and synthetic cannabinoids (e.g. K2), it is not possible for a spectral library to maintain or contain all imaginable compounds of interest for law enforcement. The contents of a spectral library are limited to those compounds that are characterized and tested. Clandestine laboratories do not necessarily conform to those known compounds when making a drug. Currently, if a material containing one of these uncharacterized synthetic drugs is analyzed, the library search would result in a “no match” or “unknown.” In such cases, it is recommended by these authors that the sample be referred to the forensic laboratory for further chemical analysis to prevent a false-negative conclusion. This also underscores the importance for an on-board spectral library to contain not only the classes of compounds of interest (i.e. drugs and additives) but also commonly encountered materials. Additionally, the ability to wirelessly transmit the data to a reachback chemist who can perform consultation and advanced spectral analysis in real time is essential.

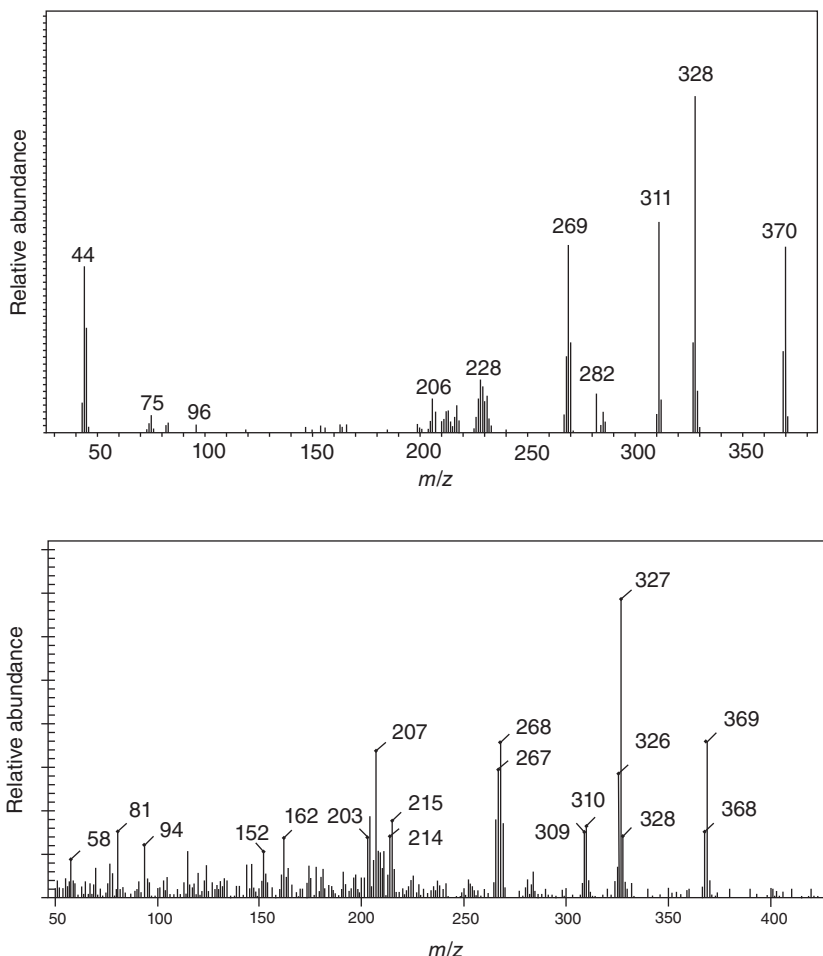


**Figure 6.7** Mass spectra of heroin collected on (a) a field portable ion trap MS and (b) a field portable quadrupole MS. The differences in  $m/z$  ratios are due to space charge and ion–ion interactions that occur in the ion trap, causing the peaks to have a  $+1m/z$  increase.

## 6.4 Counterfeit Drugs

Counterfeit pharmaceuticals are a significant problem not only for the pharmaceutical industry but also for the general population due to the health effects associated with taking unverified drugs. Leary (2014) provided an excellent analysis of the counterfeit drug problem and the use of portable spectrometers (IR, Raman, and GC-MS) for their identification and differentiation from genuine pills. There are both criminal and civil forensic issues when dealing with counterfeit pharmaceuticals. First, counterfeit medications can harm both the patient and the public at large. In addition, the violation of intellectual property rights is a civil matter that has considerable financial and societal implications.

Of particular interest to law enforcement officers and forensic drug chemists are recent advancements by counterfeit drug manufacturers that have enabled the production of illegal opiates that are identical in appearance (e.g. color, size, shape, mass, imprint) to genuine pills. This prevents their identification as counterfeits using the Drug Identification Bible (2015) or the Pill Identifier (<http://Drugs.com> 2020), which does not contain spectral

characteristics. After counterfeit pharmaceuticals are identified as non-genuine, they have the potential to be used to associate multiple counterfeit seizures or for source attribution. In order to identify a drug as counterfeit, there is a need to have an extensive collection of licensed pills representing all of the legitimate manufacturing facilities. These samples need to be analyzed to create libraries of genuine samples to which the suspect pills can be confirmed as counterfeit. Obtaining verified samples from the patent holders has proven to be the most significant barrier to creating these essential pharmaceutical spectral libraries.

## 6.5 Explosives

Explosives are a commonly used tool for destruction by domestic and international terrorists. They may also be used by other criminals for revenge killings or financial gain. Due to the extensive damage caused by the detonation of a bomb, when encountered, they receive considerable attention by both law enforcement and the media. There are a variety of bomb configurations, not only in the explosive chemicals used but also in the size of the explosive device and the magnitude of the resulting explosion. For example, package bombs are small explosive devices that are sent through the mail and subsequently initiated through a timer, tripwire, or other remote mechanism, such as those used in the Austin serial bombings in Austin, Texas, of May 2018. Alternatively, they can be large devices, such as the van used in the 1993 World Trade Center bombing or the truck used in the 1995 Oklahoma City bombing.

Explosive identification in the field has been the topic of research for more than 80 years. Walter McCrone, a pioneer of chemical microscopy, wrote his doctoral dissertation at Cornell University in the early 1940s on the microscopical identification of high explosives in the field. The purpose of this work was for intelligence analysis during World War II, thus making some of his results classified. McCrone's *Fusion Methods in Chemical Microscopy* (McCrone 1957) contains some of the procedures he developed for explosive field testing.

There is variation to which different agencies have incorporated portable spectrometers for explosive scene analysis. Some are early adopters of these technologies, while others have been reluctant to deploy these instruments into the field and instead prefer laboratory testing. While it may be important to perform testing in some instances in the laboratory, analysis at an explosive scene is an important capability for a number of reasons including its ability to enable the development of render-safe procedures based upon real-time threat identification and assessment (Moquin et al. 2020). The value of portable spectrometers for the on-scene analysis of explosives is also demonstrated by their use by the Australian Federal Police (AFP) who use portable instruments in their investigations (Besnon et al. 2011). The central laboratory of the AFP is an eight-hour flight from their territories in Indonesia, the Philippines, and Thailand; thus, portable instruments are used in the field to analyze pre- and post-explosion evidence collected at these remote locations (Besnon et al. 2011).

The broad range of detection capabilities of portable spectrometers is a necessity for the analysis of pre- and post-blast explosive materials. Explosive materials can be either organic or inorganic and may exist in any physical state (solid, liquid, or gas). They may also be either military-grade materials, commercially available, or homemade. For example, the Boston marathon bombing terrorism event (15 April 2013) used a pressure cooker bomb with a timer, and its explosive was purchased fireworks powder (black powder composed of charcoal, potassium nitrate, and sulfur) combined with metal balls and nails to increase damage. The Oklahoma City bombing was an act of domestic terrorism where a rental truck filled with a homemade ammonium nitrate–fuel oil (ANFO) improvised explosive devices (IED) was detonated in front of the Alfred P. Murrah Federal Building on 19 April 1995. The 1993 World Trade Center bombing was a terrorist attack where a homemade urea nitrate–hydrogen gas enhanced truck bomb was detonated below the North Tower. The terrorists responsible for the 7 July 2005 London Transit bombings used homemade triacetone triperoxide (TATP) IEDs. And the 2016 bombings in New York and New Jersey were composed of pressure cooker and pipe bombs containing an explosive similar to tannerite (a brand of binary explosive composed of aluminum powder mixed with ammonium nitrate and ammonium perchlorate)

that were detonated by small charges of hexamethylene triperoxide diamine (HMTD). Due to the diversity in the molecular and elemental composition of these materials, there is no single instrument capable of confirmatively identifying all possible explosive materials; thus, a suite of tools is necessary.

Colorimetric testing is a valuable tool for the field analysis of explosives because it can presumptively identify the explosive material or class of chemicals and inform subsequent testing via spectroscopic instruments. However, similar to when applied in illicit drug analysis applications, the results of colorimetric tests are not confirmatory and cannot stand alone. There are a variety of portable spectrometers that are used for the field identification of explosive materials, including IMS, IR, Raman, GC-MS, and MS (Besnon et al. 2011; Leary et al. 2019). The analytical approach differs for pre- and post-blast analysis, as well as by the agency in charge of an investigation. For undetonated explosives, the recovered bomb is first rendered safe and then analyzed to assess the severity of the threat using any combination of spectrometers mentioned above. For post-blast analysis, the dependence on residue recovery determines the protocol. For example, Raman or IR analysis are only completed if there is visible material of suspected residues. However, if a black powder or dark-colored residue is recovered, care must be taken when analyzing with Raman because dark samples have the potential to absorb the laser energy and detonate.

In the area of explosive analysis, the value of field testing is primarily for the assessment of the danger level and to provide potential investigative leads. Field-portable spectrometers for explosive analysis are commonly used by the military; however, there is often a different aim for forensic science applications, which ultimately must stand up in court. The capabilities of most portable spectrometers (i.e. sensitivity) have currently not yet matched those of their benchtop counterparts, and thus, laboratory analysis is preferred for litigation.

## 6.6 Clandestine Labs

The use of portable spectrometers at the scene of clandestine laboratories (clan labs) has proven to be essential for assessing safety and for providing both investigative and adjudicative information. Clan labs are secret or hidden spaces for the manufacturing of materials, commonly illegal drugs or explosives. Many of the materials used in the illicit production of explosives or drugs are hazardous, flammable, or toxic (e.g. ethers, acids, phosphorus, lithium, and magnesium metals, etc.), but they also have legitimate uses (Christian 2003). Anything in a clan lab, from residues in reactor vessels or garbage cans to the contents of sealed containers, must be chemically analyzed. This information is needed to develop safety and remediation plans as well as to provide information on the synthetic route used to manufacture the drug or explosive.

Safety is the highest priority when encountering a clan lab, both for the law enforcement and scientific personnel. Thus, identifying the components of unlabeled or falsely labeled containers is essential. The most versatile and generally useful tool for the identification of unknown materials at a clan lab scene is a portable IR spectrometer. It is often paired with non-spectrometry methods, such as wet chemistry tests (e.g. pH and colorimetric). Other instruments, such as portable Raman, GC-MS, and MS are used by some agencies for clan lab analyses but have not yet been as widely adopted for this purpose as portable IR technologies.

## 6.7 Ignitable Liquids

At fire investigation scenes, an important aspect of the event analysis is the detection and, if possible, identification of ignitable liquid residues. Ignitable liquids (e.g. gasoline, diesel, lighter fluid, alcohols, etc.) are volatile and flammable liquids commonly used by arsonists to initiate and/or accelerate the destruction caused by a fire.

Portable instruments have been used for this flammable gas analysis for decades, with hydrocarbon sniffers being commonly used to identify the location for subsequent sampling of debris to be sent for laboratory GC-MS analysis. These sniffers use a vacuum pump to draw air through a nozzle into a chemical detector, such as a

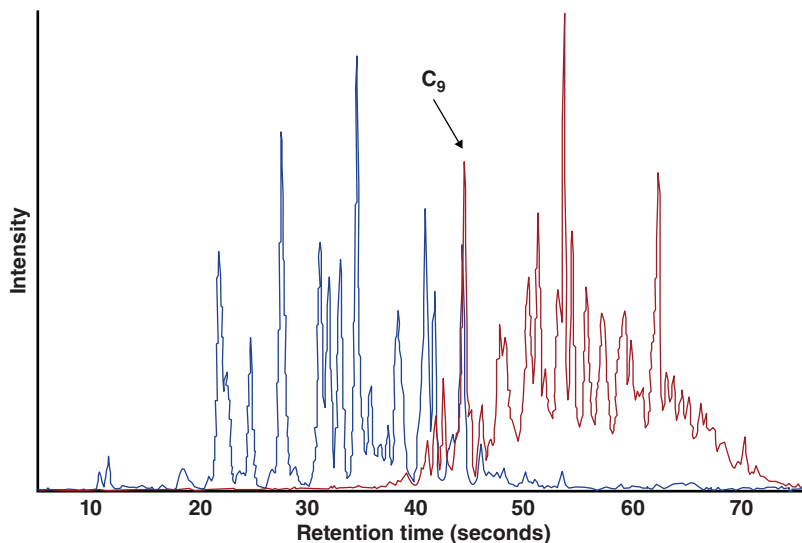


**Figure 6.8** Chromatograms collected by a field portable GC-MS of light (blue) and medium (red) petroleum distillates.  
Source: Leary et al. (2019).

catalytic bead sensor, FID, or solid-state detector (Furton and Harper 2004). Although sniffers equipped with a FT-IR spectrometer with a gas cell is possible, there is no commercially available system made with this technology. There are many materials (e.g. natural rubbers, some lacquers, carpets, etc.) that thermally decompose to generate flammable vapors that can trigger false-positive conclusions with these sniffers; thus, more specific analytical methods at the scene would be advantageous to prevent unnecessary analyses.

More informed sample selection can be achieved using portable GC-MS instruments, which are emerging as potential tools for fire investigations (Figure 6.8) (Leary et al. 2016, 2018, 2019; Visotin and Lennard 2016). SPME is a more sensitive sampling method than direct air sampling due to its ability to concentrate vapors for GC-MS analyses. However, during a SPME sampling, selective sorption of analytes is expected and can bias results. As this technology continues to improve, it is expected that portable GC-MS instruments will become the standard for arson investigations.

## 6.8 Future

The rapid advancements in technology and world events such as the consequences of 9/11 and explosions in the aviation industry have stimulated an expansive growth in the development of field-portable spectrometers. Many industrial applications exist for these tools, but the requirements for court acceptance have stunted their widespread adoption by the forensic science community. It can be expected that as these technologies continue to mature and are deemed reliable by practitioners of forensic science, these barriers will be breached and the full value of these instrumental methods will be recognized.

New applications of field-portable spectrometers will undoubtedly be discovered and validated for forensic analysis at the crime scene. For example, portable elemental analyzers, such as X-ray fluorescence (XRF) or laser-induced breakdown spectroscopy (LIBS) (see Chapter 13 in Volume 1 by Day, and Chapter 19 in Volume 2 by Piorek), could have value when analyzing unknown materials from clandestine laboratories. Portable LIBS could be used to analyze black sludge-like residues for the presence of lithium for the determination

of the methamphetamine synthetic route. Field-portable elemental, vibrational, and ultraviolet (UV)-visible spectrometers could provide useful investigative and adjudicative information at the scene of hit-and-run accidents in the analysis of paint chips, especially if paired with the paint database query (PDQ). Field-portable NIR instruments (see Volume 2, Chapter 12 by Hoffmann, Pfeifer and Siesler, and Chapter 13 by Siesler and Yan) are currently being used in the carpet recycling industry for fiber identification; in the future, this technology can be used for on-scene forensic fiber identification as well. Portable NIR spectrometers are also being widely embraced for the analysis of counterfeit pharmaceuticals (see Chapter 5 in Volume 2 by Leary, Crocombe and Kalyanaraman), which is also a forensic science issue and has the potential to be used for the scene identification of illicit drugs. As the technologies behind smartphone spectrometers continue to develop (see Chapter 9 in Volume 1 by Scheeline and Chapter 10 in Volume 2 by Peveler and Algar), it can be predicted that they too may see broad adoption by crime scene scientists. Another promising application is body-fluid identification by vibrational spectroscopy. There are numerous published research articles demonstrating the ability of benchtop Raman spectrometers to identify not only the type of body fluid and time since deposition but also the age, gender, and race of the donor (Virkler and Lednev 2008, 2009a, 2009b, 2010a, 2010b; Sikirzhytski et al. 2010, 2012a, 2012b, 2012c, 2013, 2017; Boyd et al. 2011; McLaughlin et al. 2013, 2014a, 2014b; Muro et al. 2016; Mistek et al. 2016; Muro et al. 2016; McLaughlin and Lednev 2015; Doty et al. 2016; Fujihara et al. 2017; Feine et al. 2017; Doty et al. 2017; Muro and Lednev 2017; Schlagetter and Glynn 2017; Schlagetter et al. 2017; Doty and Lednev 2018a, 2018b; Fujihara et al. 2018; Rosenblatt et al. 2019; Fikiet and Lednev 2019; McLaughlin et al. 2019). Many of these studies required chemometric methods for their successful application, which will need to be incorporated into portable instruments prior to their use in crime scene work for this type of analysis. One article by Fujihara et al. (2017) used a portable Raman spectrometer for blood identification and species discrimination. Currently, there is significant research in organic gunshot residue analysis using benchtop Raman spectroscopy (Bueno et al. 2012; López-López et al. 2013; Doty and Lednev 2018b; Khandasammy et al. 2019; Karahacane et al. 2019; Charles et al. 2020). As the sensitivities of portable Raman spectrometers improve, the on-scene identification of the organic component of gunshot residue could replace or complement colorimetric tests (e.g. the Griess and sodium rhodizonate tests). Last, questioned document analysis is a subdiscipline within forensic science that will benefit from field-portable spectrometers, such as for the analysis of suspected counterfeit banknotes and documents (Appoloni and Melquiades 2014; Oliveira et al. 2018; Rodrigues et al. 2019).

Potential improvements in the sensitivity of portable instruments will have major impacts on breath alcohol determinations and the detection of impaired driving. With advancements in portable FT-IR, GC-MS, and MS technologies, it is likely that these instruments will become the standard for on-scene breath alcohol testing. Driving under the influence of drugs (DUID), both legal (prescribed or over the counter) and illegal, is a serious global issue, and thus, its reliable detection in the field is imperative. A survey of over 9,000 drivers by the US Department of Transportation National Highway Traffic Safety Administration revealed that the total number of drug-positive nighttime weekend drivers was 20% in 2013/2014 (Berning et al. 2015). Currently, immunoassays are used for the on-scene screening of drugs in oral fluids, but these are only presumptive and suffer from inaccurate measurements that result in false negatives due to the hook effect. Field-portable spectrometers have excellent potential for the on-scene detection of drugs in breath and oral fluids; however, instrument improvements need to be made prior to acceptance by the forensic community and the courts. For portable Raman spectrometers, instrumental improvements in sensitivity and mixture interpretation would be required, while developments in a breath sample introduction device are needed to begin research on using portable GC-MS for this application. Additionally, although technologies are available, or will be in the near future, for DUID determinations, the greater need is for research to ascertain the relationship between drug concentrations in oral fluids and breath to driver impairment.

It is also inevitable that this miniaturization will impact other laboratory instruments, which could then be used in the field of forensic science. Field-deployable or portable capillary electrophoresis (CE) or liquid chromatography-mass spectrometry (LC-MS) instruments have been proposed and may prove useful for analysis of explosives, illicit drugs, and alcohol/drugs in oral fluids (Abonamah et al. 2019). Sophisticated laboratory

sample introduction ambient ionization methods, such as direct analysis in real time (DART), have become field deployable (e.g. “DART on a cart”), but further advancements are in development for use with portable instruments. There is also interest in capitalizing on enhanced Raman spectroscopy methods that improve detection limits and eliminate fluorescence interference, such as surface-enhanced and tip-enhanced Raman spectroscopy (SERS and TERS, respectively). Although SERS kits are commercially available for use with portable Raman spectrometers, there are reliability issues that have limited their acceptance by the forensic science community.

Rapid DNA technologies (see Chapter 21 in Volume 1 by Glynn and Ambers) are fully automated instruments capable of analyzing a sample and developing a DNA profile within 90–120 minutes. There are currently two manufacturers, and these transportable printer-sized instruments are being tested and evaluated by the FBI in the police booking stations of five states for use with known buccal swabs of arrestees (Federal Bureau of Investigation n.d.). There are considerable questions about the extent that this technology can be used in forensic case work, with issues being raised about potential problems regarding contamination and interpretation. Additionally, the legal community is concerned with the potential for complete sample destruction, which would not afford the defense the opportunity for subsequent laboratory testing. Ultimately, the ability to identify the source of a biological stain within a short period of time could be a meaningful advancement in forensic science and criminal justice due to its potential for swift identifications or exclusions.

It is inevitable that new spectrometer technologies will be developed in the future and then applied to analyzing samples of forensic interest. Some instruments, such as portable hyperspectral imaging and stand-off Raman (see Chapters 10 and 12 in Volume 1 of this text by Nelson and Gomer, and Lavoie et al., respectively), have only recently become commercially available. Although they have not yet been used for forensic analyses, there is unknown potential for these tools at a crime scene.

## 6.9 Conclusions

The availability of field-friendly portable spectrometers increases the need for having scientists at the crime scene. A crime scene is a complex environment, and a scientist is needed to make informed decisions on sample selection in order to maximize the information obtained from the scene. A scientist is needed in order to properly assess the scene, apply the scientific method, and use available instrumentation differently from the way these spectrometers are typically deployed to technicians or nonscientific operators. When used at a crime scene, a scientist is needed for proper use of the instrument, which is more than just operating the instrument in that it includes an expert evaluation of the scene and the data. Furthermore, it is the forensic scientist who is best suited for assessing the relevance of the results and holistically providing a meaningful interpretation of the evidence as it relates to questions at the crime scene. Last, an educated scientist is needed to effectively communicate the significance of the evidence to the triers of fact (i.e. the judge and/or jury).

Today’s portable spectrometers can be more sophisticated than the “go/no go” or “red light/green light” answer box results as applied in other industries. In the field of forensic science and specifically when used at crime scenes, they should be applied by scientists rather than operators or technicians. In situations where portable systems are used by law enforcement or other personnel and the data will be used as part of a legal proceeding, scientific review of the data and relevant circumstances must be performed by a scientist to verify the reliability of the data. Portable spectrometers are frequently developed for use by technicians who are trained to operate the instrument but allow the instrument to interpret the data. Historically, the courts have uncovered weaknesses in such a system and wisely recognized the need for expert analysis and interpretation of the evidence by a qualified scientist. Because of the technological advances in portable spectrometers and the need to verify the reliability of the evidence, there is a need to move away from the answer box to a knowledgeable scientific instrument to be used by scientists in the field.

As these technologies continue to advance, it is hoped that they can realize their full potential for crime scene implementation. Despite abundant research and validation, there has been reluctance to adopt these new scientific technologies. There are several barriers to their widespread adoption for crime scene investigations, including their high perceived costs and complexity, lack of adequate training, hesitancy to adopt new scientific technologies by law enforcement and the forensic science community, and reluctance to give up scientific evidence analysis by the laboratory scientists.

The primary goal of field-portable instruments within the field of forensic science is to improve the quality of forensic investigations. The most significant advantages of portable spectrometers over other field tests are their capabilities for providing confirmatory analyses that are rapid and reliable and create a reviewable record. The impact of the introduction of field-deployable spectrometers is documented over the past two decades by their rapid rate of growth, their successful adoption by some crime scene investigators, and acceptance by the courts. Continual instrumental improvements and application developments will advance the use of portable spectrometers by forensic science investigators to maximize the quality of information obtainable from physical evidence.

## Acknowledgments

The authors would like to extend our sincere appreciations to Jim Fitzpatrick (Red Wave Technology), Gina Guererra (Federal Bureau of Investigation), Alan Higgins (Federal Resources), Professor Koby Kizzire (University of New Haven), and Meghann E. McMahon (Wisconsin State Crime Laboratory) for sharing your experiences and/or engaging in thoughtful discussions on the uses of portable instruments in forensic science.

## Acronyms and Abbreviations

AFP	Australian Federal Police
ATR	Attenuated total reflection
CE	Capillary electrophoreses
DART	Direct analysis in real time
DUID	Driving under the influence of drugs
FBI	Federal Bureau of Investigation
FID	Flame ionization detector
FT-IR	Fourier transform infrared spectroscopy
GC-MS	Gas chromatography–mass spectrometry
HPMS	High-pressure mass spectrometry
IMS	Ion mobility spectrometry
IR	Infrared
K2	Common name applied to synthetic cathinones
LC-MS	Liquid chromatography–mass spectrometry
LOD	Limit of detection
MS	Mass spectrometry
ng	Nanogram
SERS	Surface-enhanced Raman spectroscopy
TERS	Tip-enhanced Raman spectroscopy

## References

- Abonamah, J.V., Eckenrode, B.A., and Moini, M. (2019). On-site detection of fentanyl and its derivatives by field portable nano-liquid chromatography-electron ionization-mass spectrometry (nLC-EI-MS). *Forensic Chemistry* <https://doi.org/10.1016/j.forc.2019.100180>.
- Appoloni, C.R. and Melquiades, F.L. (2014). Portable XRF and principal component analysis for bill characterization in forensic science. *Applied Radiation and Isotopes* 85: 92–95. <https://doi.org/10.1016/j.apradiso.2013.12.004>.
- ASTM International (2017). *ASTM E2329-17 Standard Practice for Identification of Seized Drugs*. ASTM International.
- Berning, A., Compton, R., and Wochinger, K. (2015). *Results of the 2013–2014 National Roadside Survey of Alcohol and Drug Use by Drivers*. Washington, DC: NHTSA National Center for Statistics and Analysis.
- Besnon, S., Speers, N., and Otieno-Alego, V. (2011). Portable explosive detection instruments. In: *Forensic Investigation of Explosions: International Forensic Science and Investigation*, 2ee (ed. A. Beveridge), 692–723. CRC Press.
- Boyd, S., Bertino, M.F., and Seashols, S.J. (2011). Raman spectroscopy of blood samples for forensic applications. *Forensic Science International* 208 (1–3): 124–128.
- Bueno, J., Sikirzhytski, V., and Lednev, I.K. (2012). Raman spectroscopic analysis of gunshot residue offering great potential for caliber differentiation. *Analytical Chemistry* 84: 4334–4339.
- Bui, L. (2019). Innocent man spent months in jail for bringing honey back to United States. *The Washington Post* (23 August). [https://www.washingtonpost.com/local/legal-issues/innocent-man-spent-months-in-jail-for-bringing-honey-back-to-united-states/2019/08/22/6c5c538c-71c3-11e9-9f06-5fc2ee80027a\\_story.html](https://www.washingtonpost.com/local/legal-issues/innocent-man-spent-months-in-jail-for-bringing-honey-back-to-united-states/2019/08/22/6c5c538c-71c3-11e9-9f06-5fc2ee80027a_story.html) (accessed 30 October 2020).
- Charles, S., Geusens, N., Vergalito, E., and Nys, B. (2020). Interpol review of gunshot residue 2016–2019. *Forensic Science International: Synergy* <https://doi.org/10.1016/j.fsisyn.2020.01.011>.
- Christian, D.R. (2003). *Forensic Investigation of Clandestine Laboratories*. CRC Press.
- Cowley, S. and Silver-Greenberg, J. (2019). These machines can put you in jail. Don't trust them. *The New York Times* (3 November). <https://www.nytimes.com/cdn.ampproject.org/c/s/http://www.nytimes.com/2019/11/03/business/drunk-driving-breathalyzer.amp.html>.
- Daubert v. Merrell Dow Pharmaceuticals, Inc. (1993). 509 U.S. 579, 589.
- DetectaChem (2020). Mobiledetect pouches. <https://www.detectachem.com/products/mobiledetect-pouches> (accessed 10 November 2020).
- Detector Electronics Corp (2014). The history of the metal detector. <https://www.metaldetector.com/learn/metal-detector-history/history-of-the-metal-detector> (accessed 31 March 2020).
- Doty, K.C. and Lednev, I.K. (2018a). Differentiation of human blood from animal blood using Raman spectroscopy: A survey of forensically relevant species. *Forensic Science International* 282: 204–210.
- Doty, K.C. and Lednev, I.K. (2018b). Raman spectroscopy for forensic purposes: Recent applications for serology and gunshot residue analysis. *TrAC Trends in Analytical Chemistry* 103: 215–222. <https://doi.org/10.1016/j.trac.2017.12.003>, (2017).
- Doty, K.C., McLaughlin, G., and Lednev, I.K. (2016). A Raman “spectroscopic clock” for bloodstain age determination: the first week after deposition. *Analytical and Bioanalytical Chemistry* 408 (15): 3993–4001. <https://doi.org/10.1007/s00216-016-9486-z>.
- Doty, K.C., Muro, C.M., and Lednev, I.K. (2017). Predicting the time of the crime: bloodstain aging estimation for up to two years. *Forensic Chemistry* 5: 1–7.
- Drug Identification Bible (2015). 2014–2015 ed. Amera-Chem Inc.
- Drugs.com (2020, March 2). Pill Identifier. <https://www.drugs.com/imprints.php> (accessed 1 April 2020).
- Federal Bureau of Investigation (n.d.). Rapid DNA: general information. <https://www.fbi.gov/services/laboratory/biometric-analysis/codis/rapid-dna> (accessed 3 April 2020).
- Federal Rules of Evidence (2014). Rule 702. Testimony by Expert Witnesses.

- Feine, I., Gafny, R., and Pinkas, I. (2017). Combination of prostate-specific antigen detection and micro-Raman spectroscopy for confirmatory semen detection. *Forensic Science International* 270: 241–247. <https://doi.org/10.1016/j.forsciint.2016.10.012>.
- Fikiet, M.A. and Lednev, I.K. (2019). Raman spectroscopic method for semen identification: Azoospermia. *Talanta* 194: 385–389.
- Forensic Technology Center of Excellence (2018). *Landscape Study of Field Portable Devices for Chemical and Presumptive Drug Testing*. National Institute of Justice, Office of Investigative and Forensic Sciences: U.S. Department of Justice.
- Frye v. United States (1923). 293 F. 1013 (D.C. Cir.).
- Fujihara, J., Fujita, Y., Yamamoto, T. et al. (2017). Blood identification and discrimination between human and nonhuman blood using portable Raman spectroscopy. *International Journal of Legal Medicine* 131: 319–322. <https://doi.org/10.1007/s00414-016-1396-2>.
- Fujihara, J., Nishimoto, N., and Yasuda, T. (2018). Discrimination between infant and adult bloodstains using micro-Raman spectroscopy: A preliminary study. *Journal of Forensic Sciences* 64 (3): 698–701. <https://doi.org/10.1111/1556-4029.13904>.
- Furton, K.G. and Harper, R.J. (2004). Detection of ignitable liquid residues in fire scenes: accelerant detection canine (ADC) teams and other field tests. In: *Analysis and Interpretation of Fire Scene Evidence* (eds. J.R. Almirall and K.G. Furton), 75–96. CRC Press.
- Gabrielson R., and Sanders, T. (2016). How a \$2 roadside drug test sends innocent people to jail. *The New York Times* (7 July). <https://www.ny-times.com/2016/07/10/magazine/how-a-2-roadside-drug-test-sends-innocent-people-to-jail.html> (accessed 31 October 31 2020).
- Jeong, S. (2017). Man spends three months in jail after false positive on police drug test. *Cable News Network* (28 June). <https://www.cnn.com/2017/06/28/us/drug-test-drywall-positive-arrest-trnd/index.html> (accessed 28 April 2017).
- Jones, A.W. (1996). Measuring alcohol in blood and breath for forensic purposes – a historical review. *Forensic Science Review* 8 (1): 13–44.
- Kammrath, B.W., Leary, P.E., and Reffner, J.A. (2017). Collecting quality infrared spectra from microscopic samples of suspicious powders in a sealed cell. *Applied Spectroscopy* 71 (3): 438–445. <https://doi.org/10.1177/0003702816666286>.
- Karahacane, D.S., Dahmani, A., and Khimeche, K. (2019). Raman spectroscopy analysis and chemometric study of organic gunshot residues originating from two types of ammunition. *Forensic Science International* 301: 129–136. <https://doi.org/10.1016/j.forsciint.2019.05.022>.
- Kelly, J. (2008). False positives equal false justice. *Marijuana Policy Project*. <https://www.mpp.org/issues/criminal-justice/false-positives> (accessed 28 April 2018).
- Khandasammy, S.R., Rzhevskii, A., and Lednev, I.K. (2019). A novel two-step method for the detection of organic gunshot residue for forensic purposes: fast fluorescence imaging followed by Raman microspectroscopic identification. *Analytical Chemistry* 91 (18): 11731–11737. <https://doi.org/10.1021/acs.analchem.9b02306>.
- Kirk, P.L. (1953). *Crime Investigation: Physical Evidence and the Police Laboratory*. Interscience Publishers, Inc.
- Leary, P.E. (2014). Counterfeiting: A challenge to forensic science, the criminal justice system, and its impact on pharmaceutical innovation (order no. 3623631). ProQuest Dissertations & Theses A&I (1550892703). <http://unh-proxy01.newhaven.edu:2048/login?url=https://search-proquest-com.unh-proxy01.newhaven.edu/docview/1550892703?accountid=8117> (acessed 31 October 2020).
- Leary, P.E., Dobson, G.S., and Reffner, J.A. (2016). Development and applications of portable gas chromatography-mass spectrometry for emergency responders, the military, and law-enforcement organizations. *Applied Spectroscopy* 70 (5): 888–896. <https://doi.org/10.1177/0003702816638294>.
- Leary, P.E., Kammrath, B.W., and Reffner, J.A. (2018). *Field-Portable Gas Chromatography-Mass Spectrometry. Encyclopedia of Analytical Chemistry*. Wiley <https://doi.org/10.1002/9780470027318.a9583>.

- Leary, P.E., Kammrath, B.W., Lattman, K.J., and Beals, G.L. (2019). Deploying portable gas chromatography-mass spectrometry (GC-MS) to military users for the identification of toxic chemical agents in theater. *Applied Spectroscopy* 73 (8): 841–858. <https://doi.org/10.1177/0003702819849499>.
- Lieblein, D., McMahon, M.E., Leary, P.E. et al. (2018). A comparison of portable infrared spectrometers, portable Raman spectrometers, and color-based field tests for the on-scene analysis of cocaine. *Spectroscopy* 33 (12): 2–8.
- López-López, M., Delgado, J.J., and García-Ruiz, C. (2013). Analysis of macroscopic gunshot residues by Raman spectroscopy to assess the weapon memory effect. *Forensic Science International* 231 (1–3): 1–5. <https://doi.org/10.1016/j.forsciint.2013.03.049>.
- McCrone, W.C. (1957). *Fusion Methods in Chemical Microscopy*. Interscience Publishers, Inc.
- McLaughlin, G., Sikirzhytski, V., and Lednev, I.K. (2013). Circumventing substrate interference in the Raman spectroscopic identification of blood stains. *Forensic Science International* 231: 157–166.
- McLaughlin, G., Doty, K.C., and Lednev, I.K. (2014a). Discrimination of human and animal blood traces via Raman spectroscopy. *Forensic Science International* 238: 91–95.
- McLaughlin, G., Doty, K.C., and Lednev, I.K. (2014b). Raman spectroscopy of blood for species identification. *Analytical Chemistry* 86 (23): 11628–11633.
- McLaughlin, G. and Lednev, I.K. (2015). In situ identification of semen stains on common substrates via Raman spectroscopy. *Journal of Forensic Sciences* 60 (3): 595–604. <https://doi.org/10.1111/1556-4029.12708>.
- McLaughlin, G., Fikiet, M.A., Ando, M. et al. (2019). Universal detection of body fluid traces in situ with Raman hyperspectroscopy for forensic purposes: evaluation of a new detection algorithm (HAMAND) using semen samples. *Journal of Raman Spectroscopy* 50 (8): 1147–1153. <https://doi.org/10.1002/jrs.5621>.
- Mistek, E., Halamkova, L., Doty, K.C. et al. (2016). Race differentiation by Raman spectroscopy of a bloodstain for forensic purposes. *Analytical Chemistry* 88: 7453–7456.
- Moquin, K., Higgins, A.G., Leary, P.E., and Kammrath, B.W. (2020). Optimized explosives analysis using portable gas chromatography-mass spectrometry for battlefield forensics. *Current Trends in Mass Spectrometry* 18 (2): 10–17.
- Muro, C.M. and Lednev, I.K. (2017). Race differentiation based on Raman spectroscopy of semen traces for forensic purposes. *Analytical Chemistry* 89 (8): 4344–4348. <https://doi.org/10.1021/acs.analchem.7b00106>.
- Muro, C.K., Doty, K.C., Fernandes, L.D.S., and Lednev, I.K. (2016). Forensic body fluid identification and differentiation by Raman spectroscopy. *Forensic Chemistry* 1: 31–38. <https://doi.org/10.1016/j.forc2016.06.003>.
- Muro, C.K., Fernandes, L.D.S., and Lednev, I.K. (2016). Sex determination based on Raman spectroscopy of saliva traces for forensic purposes. *Analytical Chemistry* 88: 12489–12493.
- Oliveira, V.D.S., Honorato, R.S., Honorato, F.A., and Pereira, C.F. (2018). Authenticity assessment of banknotes using portable near infrared spectrometer and chemometrics. *Forensic Science International* 286: 121–127. <https://doi.org/10.1016/j.forsciint.2018.03.001>.
- Peralta, E. (2011). Thinking it was Cocaine. N.C. Police Jail Man for Cheese and Tortilla Dough. *National Public Radio* (16 May). [https://www.npr.org/sections/thetwo-way/2011/05/16/136359770/thinking-it-was-cocaine-n-c-police-jail-man-for-cheese-and-tortilla-dough?ft=1&f=1001&sc=tw&utm\\_source=twitterfeed&utm\\_medium=twitter](https://www.npr.org/sections/thetwo-way/2011/05/16/136359770/thinking-it-was-cocaine-n-c-police-jail-man-for-cheese-and-tortilla-dough?ft=1&f=1001&sc=tw&utm_source=twitterfeed&utm_medium=twitter) (accessed 28 April 2018).
- Planchet, J. (2017). Why handheld narcotics analyzers are worth the Investment. *PoliceOne* (16 May). <https://www.policeone.com/emerging-tech-guide/articles/why-handheld-narcotics-analyzers-are-worth-the-investment-kpECJMUBzrdQiqTy> (accessed 2 April 2020).
- Report: Cocaine charges against Georgia Southern QB Shai Werts dropped ahead of LSU game (2019). *The Advocate* (8 August). [https://www.theadvocate.com/baton\\_rouge/sports/article\\_55065ff6-ba4e-11e9-9b24-ab98e21113fa.html](https://www.theadvocate.com/baton_rouge/sports/article_55065ff6-ba4e-11e9-9b24-ab98e21113fa.html) (accessed 2 April 2020).
- Rodrigues, A.R.R., Melquiades, F.L., Appoloni, C.R., and Marques, E.N. (2019). Characterization of Brazilian banknotes using portable X-ray fluorescence and Raman spectroscopy. *Forensic Science International* 302: 109872. <https://doi.org/10.1016/j.forsciint.2019.06.030>.

- Rosenblatt, R., Halámková, L., Doty, K. et al. (2019). Raman spectroscopy for forensic bloodstain identification: method validation vs. environmental interferences. *Forensic Chemistry* 16: 100175. <https://doi.org/10.1016/j.forc.2019.100175>.
- Schlagetter, T. and Glynn, C.L. (2017). The effect of fabric type and laundering conditions on the detection of semen stains. *International Journal of Forensic Sciences* 2 (2): 000122.
- Schlagetter, T., Kammerath, B., and Glynn, C.L. (2017). The use of Raman spectroscopy for the identification of forensically relevant body fluid stains. *Spectroscopy* 32 (12): 19–22.
- Schweir, R. (2015). The “drunk-o-meter”: Indiana’s Pioneering Contribution to DUI Investigations. *Indiana Legal Archive* (17 January). <http://www.indianalegalarchive.com/journal/2015/1/16/the-drunk-o-meter-indianas-pioneering-contribution-to-enforcing-duiwi-laws> (accessed 31 October 2020).
- Sensidyne® (n.d.). *Colorimetric Gas Detector Tube Handbook*. Sensidyne®.
- Sikirzhyskaya, A., Sikirshytksi, V., and Lednev, I.K. (2012a). Advanced statistical analysis of Raman spectroscopic data for the identification of body fluid traces: semen and blood mixtures. *Forensic Science International* 222: 259–265.
- Sikirzhyskaya, A., Sikirshytksi, V., and Lednev, I.K. (2012b). Raman spectroscopic signature of vaginal fluid and its potential application in forensic body fluid identification. *Forensic Science International* 216 (1–3): 44–48.
- Sikirzhyskaya, A., Sikirshytksi, V., and Lednev, I.K. (2012c). Multidimensional Raman spectroscopic signature of sweat and its potential application to forensic body fluid identification. *Analytica Chimica Acta* 718: 78–83.
- Sikirzhyskaya, A., Sikirshytksi, V., and Lednev, I.K. (2017). Determining gender by Raman spectroscopy of a bloodstain. *Analytical Chemistry* 89 (3): 1486–1492. <https://doi.org/10.1021/acschem.6b02986>.
- Sikirzhyskaya, A., Sikirshytksi, V., McLaughlin, G., and Lednev, I.K. (2013). Forensic identification of blood in the presence of contaminations using Raman microspectroscopy coupled with advanced statistics: effect of sand, dust, and soil. *Journal of Forensic Sciences* 58 (5): 1141–1148.
- Sikirshytksi, V., Virkler, K., and Lednev, I.K. (2010). Discriminant analysis of Raman spectra for body fluid identification for forensic purposes. *Sensors* 10 (4): 2869–2884.
- The Crown Prosecution Service (2019, October 9). *Expert Evidence* (9 October). [www.cps.gov.uk/legal-guidance/expert-evidence](http://www.cps.gov.uk/legal-guidance/expert-evidence) (accessed 1 April 2020).
- Virkler, K. and Lednev, I.K. (2008). Raman spectroscopy offers great potential for the nondestructive confirmatory identification of body fluids. *Forensic Science International* 181 (1–3): e1–e5.
- Virkler, K. and Lednev, I.K. (2009a). Raman spectroscopic signature of semen and its potential application to forensic body fluid identification. *Forensic Science International* 193: 56–62.
- Virkler, K. and Lednev, I.K. (2009b). Blood species identification for forensic purposes using Raman spectroscopy combined with advanced statistical analysis. *Analytical Chemistry* 81 (18): 7773–7777.
- Virkler, K. and Lednev, I.K. (2010a). Raman spectroscopic signature of blood and its potential application to forensic body fluid identification. *Analytical and Bioanalytical Chemistry* 396 (1): 525–524.
- Virkler, K. and Lednev, I.K. (2010b). Forensic body fluid identification: the Raman spectroscopic signature of saliva. *The Analyst* 135: 512–517.
- Visotin, A. and Lennard, C. (2016). Preliminary evaluation of a next-generation portable gas chromatograph mass spectrometer (GC-MS) for the on-site analysis of ignitable liquid residues. *Australian Journal of Forensic Sciences* 48: 203–221. <https://doi.org/10.1080/00450618.2015.1045554>.
- Wigmore, J.G. and Langille, R.M. (2009). Six generations of breath alcohol testing instruments: changes in the detection of breath alcohol since 1930. An historical overview. *Canadian Society of Forensic Science Journal* 42 (4): 276–283. <https://doi.org/10.1080/00085030.2009.10757614>.
- World Drug Report (2019). United Nations publication, Sales No. E.19.XI.9.

**7**

## Military Applications of Portable Spectroscopy

*Alan C. Samuels*

*US Army Combat Capabilities Development Command, Chemical Biological Center, Aberdeen Proving Ground, MD, USA*

### 7.1 Introduction

The intent of this chapter is to convey a snapshot of current and evolving spectroscopic methods and instrumentation that are in use by the military. The notion of “portability” in a military context is loosely defined as transportable on a moveable platform, to include a vehicle, broadening the field of instrumentation under consideration to include several larger instruments than most of the “handheld” technologies discussed in much of these volumes. While there are handheld technologies that are very important to small technical teams and special operations personnel, there are also important on-the-move sensing and mobile sensing applications that warrant discussion in the context of military applications.

This chapter will review the current state of the art in the application of numerous optical spectroscopy instrumentation and methods for military operations. An important area of emphasis is the use of hyperspectral imaging technology for threat detection applications. Spectroradiometry, the spectrally resolved sensing approach for detection of hazardous vapors at distance, continues to play a significant role in early warning for chemical agent attacks. Infrared and Raman spectroscopy technologies are the “go to” capabilities in the toolbox when technical forces and special operators encounter unknown and potentially hazardous liquids and solids on their missions. Additionally, Raman spectroscopy has emerged as rapid, noncontact detection capability for locating and identifying contaminants on surfaces. Raman spectroscopy also affords some capacity to assess the likelihood that a sample contains pathogens. Fluorescence continues to serve as an invaluable early “trigger” in biodefense systems, affording a first indication of an anomalous population of fluorescent particles that would be expected in the instance of a biowarfare incident.

Chemical and radiological sensors are increasingly being integrated onto unmanned robotic ground and aerial platforms, with the vision of a remote-controlled sensor serving as the initial entry system for uncovering threats and revealing hazardous situations before a manned team enters the scene, or in large-scale operations prior to the entry of a maneuver force into a geographic area that is held by an adversary. Lately, the development of advanced analytics to enable the fusion of disparate data to include contextual information with the raw sensor response has emerged as a new paradigm for threat sensing systems, enabling the bona fides of individual sensing modalities to be exploited to best advantage while suppressing the nuisance of false-positive detection events.

This chapter will focus on the applications of optical spectroscopy methods in military operations and by military specialty units that provide support to a domestic response authority when called upon to do so by local authorities under the circumstance of a domestic incident. While the workhorse of the vapor sensing capability set in the military today is the ion mobility spectrometer (IMS) by virtue of its small size, sensitivity, and relative reliability, detailed discussions of the underlying ion mobility measurement science are outside the scope of this chapter.

For a detailed discussion of IMS, see the chapter in Volume 1 by DeBono and Leary. However, in discussions of a system-of-systems approach toward the exploitation of networked and mobile sensors, IMS technologies play a significant role as the principal mature individual sensing modality that contributes to the whole. Similarly, the foundational analytical tools afforded by the mass spectrometry community play a critical role in the confirmatory analysis and definitive identification and attribution of the use of hazardous materials by an adversary in a conflict zone. Mass spectrometry tools are habitually used by highly technical military units with extensive training and augmented by civilian and contracted expertise afforded by both department of defense and a plurality of other government agencies. The application and practical use of the many varieties of mass spectrometric instrumentation by the military, while crucial to the definitive analysis of samples from a conflict zone or domestic incident scene, is beyond the scope of this chapter. For a detailed discussion of GC-MS, MS, and high-pressure MS, see the chapters in Volume 1 by Leary et al., Snyder, and Blakeman and Miller, respectively.

This chapter will discuss the spectroscopic methods that have found utility in military missions and discuss the common pitfalls that operators encounter so that the strengths and limitations afforded by the technology may be better appreciated.

## 7.2 Visible/Near-Infrared Hyperspectral Imaging for Bulk Explosive Material Detection and Camouflage Defeat Applications

Substantial use of hyperspectral imaging sensor systems were appreciated during the recent conflicts in Iraq and Afghanistan in support of the search for illicit homemade explosive operations. The Airborne Cueing and Exploitation System Hyperspectral (ACES Hy) platform was integrated onto an MQ-1 Predator drone and is widely credited with the discovery of hundreds of thousands of pounds of ammonium nitrate and related energetic materials and related explosive preparations that were used by the Taliban, ISIS, and other adversaries and insurgents to fabricate improvised explosive devices [1, 2]. The ACES Hy spectrometer is an evolution of the US Army's Compact Airborne Spectral Sensor (COMPASS) visible through very near-infrared (Vis/VNIR, 0.4–2.5 μm) hyperspectral imaging system [3]. Spectral data are captured in an overflight by “pushbroom” operation, which develops a hypercube by sweeping a line imager along one dimension of the focal plane array while dispersing the spectrum of each element of the line in the second dimension. As the aircraft travels, successive lines are developed to construct a three-dimensional hypercube (two spatial dimensions and one spectral dimension).

## 7.3 Infrared Spectroradiometry for Remote Hazardous Vapor Detection and Early Warning

The threat of large-scale use of chemical agents as a weapon on the battlefield, while prohibited by most modern nations under international treaty agreements and the Chemical Warfare Convention, remains a significant concern. The recent evidence of the shelling of populated areas in the Syrian conflict with nerve and blister agents by the Syrian authority demonstrates the willingness of modern state actors to take full advantage of the impact these weapons can have on an adversary.

An adversary may execute an attack involving chemical vapors upwind of a concentration of troops to produce and sustain disproportionate effects and to affect degradation of combat power as a consequence of the implementation of chemical protective posture (i.e. protective respirators and overgarments). Open-path or remote sensing technologies play an important role in the reduction of casualties inflicted by off-target chemical agent attack situations and can afford sufficient early warning of such situations to enable a maneuver force to avoid the hazard rather than increase protective posture.

The principal approach toward remote sensing as applied to chemical agent vapor detection is passive infrared spectroradiometry. This environmental analysis technology takes advantage of three coincidental characteristics that coexist when a toxic agent vapor plume is released in the environment: (i) the environment radiates thermal infrared photons in the long-wave infrared as a function of the blackbody radiance (the Planck function) that characterizes all matter, (ii) the atmosphere is transparent to the long-wave infrared radiation, and (iii) most toxic chemicals used for chemical warfare are organic compounds that exhibit characteristic vibrational “fingerprints” manifest as radiant absorption or emission when the temperature of the plume differs from that of the background scene (terrestrial objects or the sky). The exploitation of these circumstances to affect remote sensing of chemical species is an established discipline [4–6].

A plurality of circumstantial factors contribute to the efficacy of the spectroradiometry remote sensing approach, and the contributions of these factors to the usable signal emitted or absorbed by the chemical species define the reliability of the approach. The first factor is the noise-equivalent spectral radiance, or NESR, which defines the lower limits of sensitivity of a sensor due to its intrinsic optical and thermal detector characteristics. The second factor is the thermal contrast, or  $\Delta T$ , between the plume radiance and the background radiance ( $B$ ) that enter the optical sensor’s aperture. The third factor is the solid angle that is realized by the plume in the scene considered by the optical sensor’s aperture or its instantaneous field of view (IFOV),  $\theta$ . The solid angle,  $\Delta\Omega = \pi\sin^2(\theta/2)$ , describes the area of the scene encompassed by the sensor’s IFOV, and the solid angle of the plume,  $\Delta\Omega_{\text{plume}}$ , represents the portion of the sensor’s IFOV that contains the chemical vapor plume. Another dimension of the plume character that contributes to its detectability by a remote optical sensor is the “column content” or concentration–path length product ( $C \times L$ ) of the chemical vapor in the IFOV. Finally, the absorption cross section,  $\alpha(\lambda)$ , or mass extinction coefficient as a function of wavelength ( $\lambda$ ), of the molecular species, an intrinsic property afforded by the likelihood and energetic character of vibrational transitions of a given species, defines the degree to which the signal realized by the sensor is detectable and can be reliably assigned to the spectral fingerprint of that species. All of these factors are captured in the radiance equation:

$$\text{signal} = [B(T) - B(T - \Delta T)]\alpha(\lambda)CL \times \Delta\Omega_{\text{plume}} \quad (7.1)$$

When the background scene radiance consists of terrain, trees, buildings, or other terrestrial objects, the thermal contrast is typically a negative quantity because the plume signal is colder than the background temperature. In this case, the signal is resolved as absorbance or an attenuation on the scene radiance. When the background scene consists of a clear, cloudless sky, then the sensor is staring into space, and the signal is resolved as emission, or an additive signal on top of the scene radiance. The Implications of Equation (7.1) are Illustrated in Figure 7.1.

A common fallacy related to the concept of employment of the spectroradiometric technology in remote sensing is that the main purpose of the sensing modality is to detect hazardous threat agents at range. While the technology does deliver in its capacity to do just that, the real advantage of the remote sensing concept lies in its ability to sweep out a large sector of real estate all around the protected area. Notwithstanding the advent of sensors on autonomous, unmanned platforms as an emerging concept of employment for threat agent sensing, spectroradiometry affords the most extensive and persistent capacity to continuously monitor large areas for the emergence of a threat plume. Unmanned systems have limited mission time and typically carry air-sampling point sensors, thus limiting the spatial coverage that they can provide.

## 7.4 Infrared and Raman Spectroscopy for Condensed Phase Analysis (Energetics, Chemical Agents, Biological Agents)

Advances in optical engineering have led to miniaturization of both infrared and Raman spectroscopy systems. For detailed discussions of infrared and Raman technologies, see chapters in Volume 1 by Rathmell et al. and

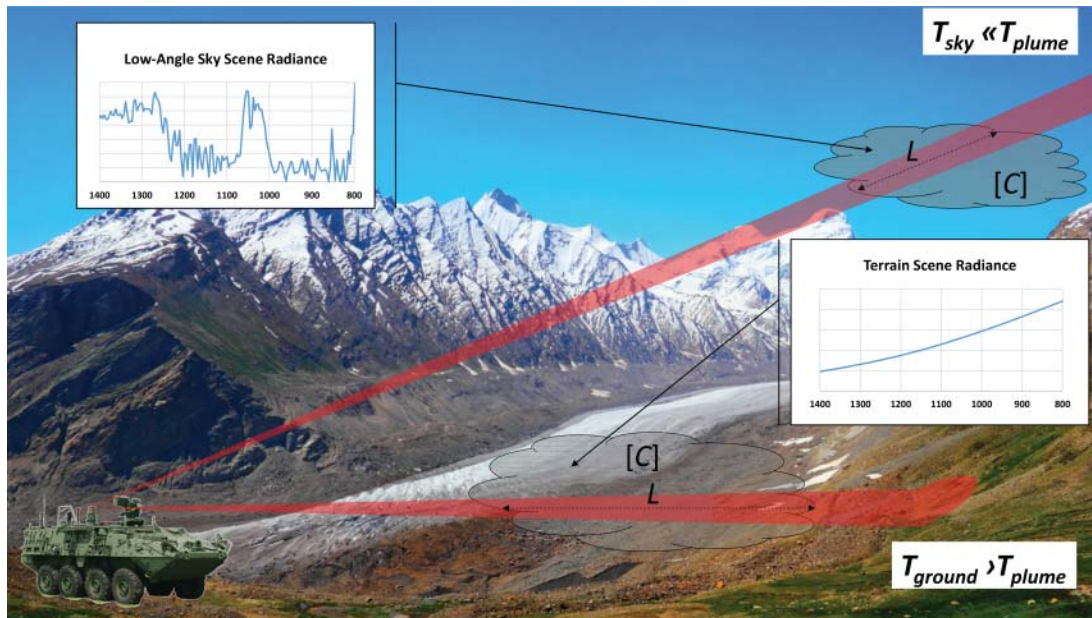


**Figure 7.1** Characteristics of a chemical vapor plume in the scene of a remote sensing spectroradiometer that give rise to its performance in detecting the plume. When the background consists of clear sky radiance, the plume signature is an emission term added onto the scene radiance because the air/plume temperature is greater than the temperature of the cold sky background. When the background consists of terrain features, then the plume signature is an attenuation on the radiance observed from the terrain features because the air/plume temperature is less than the temperature of the terrain feature. *Source:* Natalia Davidovich/Shutterstock.com; U.S. Army.

Schiering and Stein, respectively. Chemical reconnaissance teams and Weapons of Mass Destruction Civil Support teams are issued and trained in the use of the Thermo FirstDefender portable Raman spectrometer and the TruDefender portable attenuated total reflection (ATR) Fourier transform infrared spectrometer (ATR-FTIR) for the identification of unknown substances encountered on their missions. The technologies afford complementarity in capability to exploit vibrational spectroscopy to interrogate an unknown condensed phase (solid or liquid) material (Figure 7.2). Often, these systems are the “go to” technology for preliminary investigations of “white powder” incidents. The FirstDefender affords a compact Raman laser source coupled to the detector by a fiber optic, allowing operators to “point and shoot” the instrument directly at the unknown substance. Measurements are possible through some glass or polymer containers to capture the Raman spectrum of the contents of the container. Additionally, Raman measurements are typically unaffected by the presence of moisture or even liquid water embedded in or mixed with the analyte. The TruDefender allows for the measurement of condensed phase samples by a complementary vibrational spectroscopy measurement method. The benefits of measuring with both Raman and FTIR-ATR spectroscopy are twofold: (i) the methods corroborate a given detection result, and (ii) the shortcomings of the two approaches are in general mutually exclusive. Raman measurements can be complicated or obfuscated by the presence of a highly absorbing matrix that limits the scattered light from some samples, and sample autofluorescence can obscure the Raman signal, rendering identification of the unknown substance difficult or ineffective. Infrared measurements, on the other hand, are indifferent to the presence of autofluorescence, and the ATR method is less impaired by an absorbing matrix, but the presence of significant amounts of moisture in the sample can lead to a false reading.

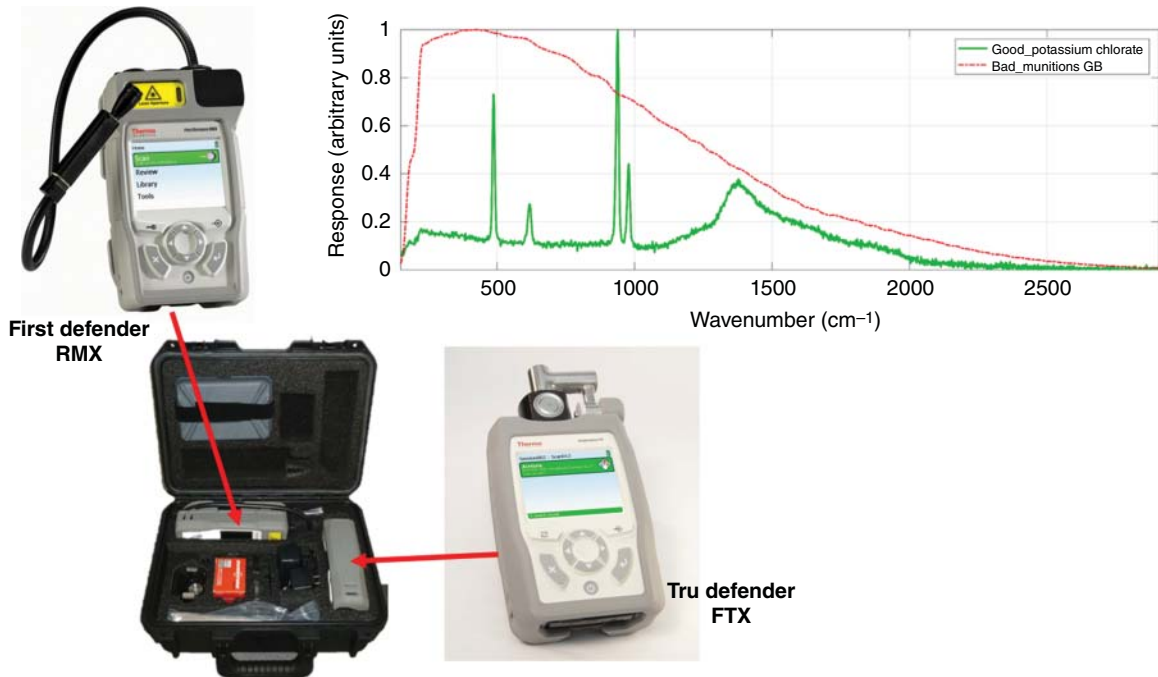


**Figure 7.2** FirstDefender portable Raman spectrometer and TruDefender portable FTIR-ATR spectrometer for presumptive identification of condensed phase materials [7]. The inset shows “good” (green trace) and “bad” (red trace) results from FirstDefender Raman measurements. The “good” spectrum has clearly resolved Raman absorption features, whereas the “bad” spectrum is a broad, featureless trace with no identifying spectral lines. This can be caused by the presence of a highly fluorescent matrix. *Source:* Thermo Fisher Scientific.

## 7.5 Raman Spectroscopy for Surface Contamination Detection

Many chemical warfare agents present as persistent surface contact hazards and are used in operational settings to deny key terrain. Detection and mapping of the contaminated areas in such circumstances becomes an operational imperative. Both Raman and infrared are capable of extracting chemical signatures from such condensed phase contaminants as noted in the previous section; however, the surface itself presents a particularly challenging backdrop for the recovery of reliable vibrational spectra of the target compounds. The surface affords a host of vibrational spectra intrinsic to its material composition, as well as other potentially frustrating signals that can obscure the spectra of the target species. In the case of infrared spectroscopy, surfaces frequently present Reststrahlen features, caused by variations in refractive index [8], sometimes leading to unreliable detection results. In the case of Raman spectroscopy, the aforementioned fluorescence signal often occurs in environmental settings to obscure or suppress the vibrational fingerprint of the contaminants of concern. The use of very short wavelength laser sources (the “solar blind” region) for Raman spectroscopy has been shown to mitigate the fluorescence signal by operating below the fluorescence wavelength of the environmental species, affording a clean Raman signal for detection [9]. The implementation of solar blind ultraviolet Raman spectroscopy for surface contamination detection enables on-the-move sensing of contaminants on operational surfaces at relevant operational speeds of travel (Figure 7.3). This technology has been implemented on both manned and unmanned reconnaissance vehicles for the detection and mapping of surface contamination.

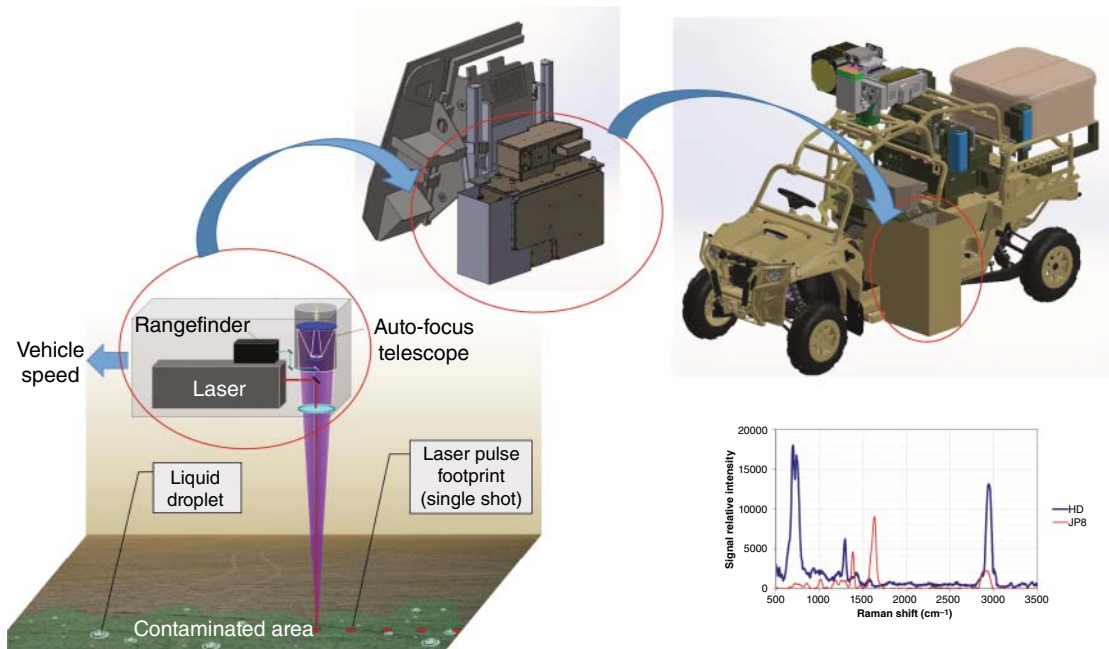


**Figure 7.3** Ultraviolet Raman spectroscopy for the detection of surface contamination implemented on a robotic, unmanned ground vehicle.

## 7.6 Raman Spectroscopy for Presumptive Biological Hazard Classification and Early Warning of a Biowarfare Agent Attack

Raman spectroscopy has also been applied to the early presumptive detection of bioaerosol threat agents. An aerosol collector has been engineered to deliver a sample of particles from the environment onto an aluminized reflective tape, which is periodically advanced to the stage of a Raman chemical imaging system for rapid, non-destructive interrogation. The Raman chemical image is analyzed by advanced signal processing integrated onto the Resource-Effective Biological Sensor (REBS) to recognize the constituent Raman features associated with bio-threat agents. When a presumptive identification result occurs, the sample can be recovered from the surface of the tape for further analysis by molecular techniques to verify the presence of a pathogen in the sample (Figure 7.4). The REBS automates the process by punching out the segment of the tape on which the suspected threat agent was discovered [10–12].

## 7.7 Fluorescence Spectroscopy as a Biological Detection “Trigger”

The Raman and molecular methods discussed in the previous section, while collectively yielding high confidence in the detection and identification of biothreat agents that present as aerosols, are latent processes that take from several minutes (in the case of Raman analysis) to an hour or more in the case of molecular assays. In order to provide early warning in the event of a bioaerosol attack, a more immediate analytical approach can be realized using fluorescence spectroscopy [13–19]. Biothreat agents consist of viral or microbial pathogens or proteinaceous toxins, all of which have proteins in common. Two key amino acids, tyrosine and tryptophan, are strong fluorophores, affording the fluorescent characteristic that tags a particle containing proteinaceous matter as a possible threat agent. Biothreat sensors have been engineered to interrogate sampled aerosol particles in real time using integrated

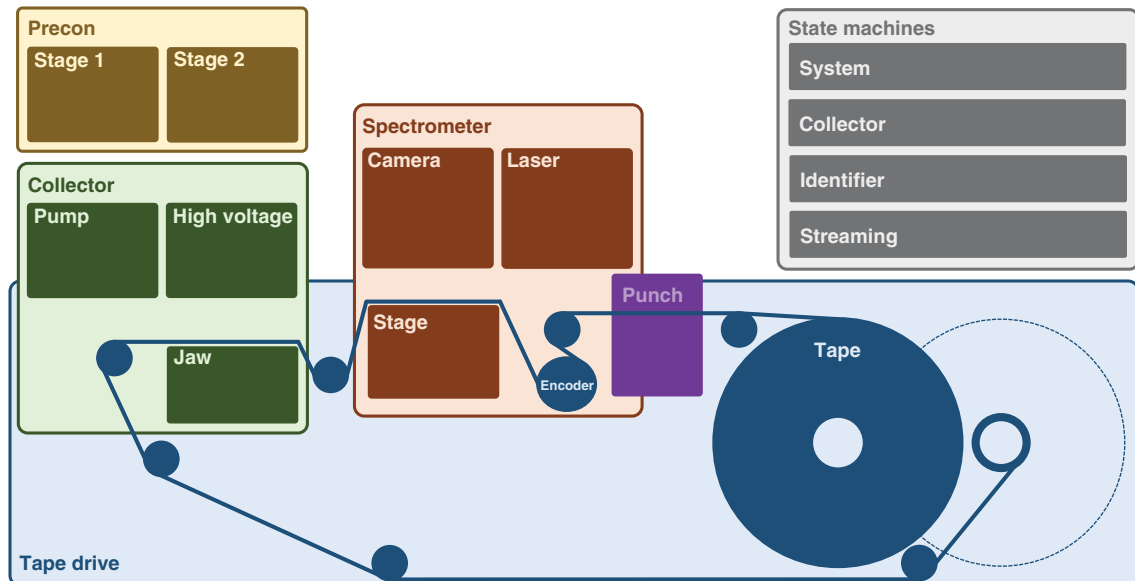


**Figure 7.4** The Resource-Effective Biological Sensor consists of an aerosol collection component that impacts particles onto an aluminized tape, which is then advanced to deliver the sample to a Raman chemical imaging microscope. On identification of a suspect biothreat agent by the Raman spectral analysis algorithm, the tape is then advanced again to a hole punch that deposits a chit containing the suspect biothreat agent into a sample container for further analysis by molecular assays. *Source:* Bartko [10].

diode light sources coupled with multichannel photometric detectors that characterize the particle fluorescence characteristics as well as the particle size distribution of the sampled aerosol particles. Two such analyzers have been developed to automatically classify bioaerosol particles as “threat like” based on these metrics and immediately deliver a warning signal when they are present (Figure 7.5). The FLIR IBAC™ uses ultraviolet laser-induced fluorescence to discriminate biological organisms from background particles, reliably detecting biological agents at concentrations below 100 agent-containing particles per liter of air (ACPLA) in less than 60 seconds with high confidence and low false alarm rates. The system alarms automatically upon detection, can be configured to collect and preserve samples for confirmatory analysis, and supports remote monitoring and transmission of spectral data to command and control centers. The TacBio sensor incorporates ultraviolet laser diodes and photomultiplier detectors configured in an integrated aerosol optical chamber designed for low-cost, high-performance production. These presumptive biological detection sensors are sometimes referred to as “trigger” detectors, as they are implemented in a biodetection system as the first stage that provides immediate notification while activating a downstream analytical procedure that includes sampling a larger volume of the suspected threat aerosol onto a collection filter for molecular analysis to confirm the presence of a biothreat agent, usually by a manually manipulated assay.

## 7.8 Networked Multimodal Sensors and Data Analytics and the Future

The military applications of portable spectroscopy discussed in this chapter illustrate the diversity of the threat space presented by chemical and biological threat agents and homemade explosives. The specific spectroscopic technologies, employment considerations, and analytic methodologies applied by circumstance have been discussed. The complexity in the breadth and diversity of the threat agents coupled with the challenges imposed on their reliable detection by background clutter in diverse battlefield environments and urban settings dictate



Instantaneous biological analyzer and collector (IBAC)

Tactical biodetector (TacBio)

**Figure 7.5** The FLIR IBAC (left) [20] and TacBio (right) [21] bioaerosol “trigger” sensors rely on the presence of proteins in biothreat agents to provide an immediate response to the presence of a possible bioaerosol. Since the fluorescence property of the particles is insufficiently specific to biothreat agents to yield a high confidence threat identification, these sensors serve as the first stage in a tiered biothreat agent detection and warning framework that involves collecting particles for subsequent analysis using more specific molecular methods. *Source:* (left) FLIR Technologies, Inc.; (right) Cabalo et al. [21].

that no single sensor modality or analytical approach suffices to address the problem. Modernization efforts aimed at improving the reliability of the various sensor modalities and their concepts of employment are focusing on the implementation of advanced signal processing and machine learning approaches that exploit correlation and covariance in the data from a plurality of sensors. The use of artificial intelligence routines has also appreciated a rapidly accelerating reduction to practice, with promising performance demonstrated in the application of expert systems for improved confidence threat sensing by incorporating automated recognition of contextual circumstances that are consistent with the threat situation surrounding an adversary’s employment of chemical, biological, or homemade explosive threats.

## References

- 1 Brown, Jarvis D. (2019). Honoring the contributions of the ACES HY sensor, 23 January 23. [https://www.militarynews.com/...ws/honoring-the-contributions-of-the-aces-hy-sensor/article\\_6a282fdc-1f3e-11e9-bb14-b7a54bd785ff.html](https://www.militarynews.com/...ws/honoring-the-contributions-of-the-aces-hy-sensor/article_6a282fdc-1f3e-11e9-bb14-b7a54bd785ff.html) (accessed 31 January 2020)
- 2 Ziph-Schatzberg, L., Wiggins, R., Woodman, P., Saleh, M., Nakanishi, K., Soletsky, P., Goldstein, N., Fox, M., and Tannian, B. (2018). Compact visible to extended-SWIR hyperspectral sensor for unmanned aircraft systems (UAS). *Proceedings of SPIE 10644, Algorithms and Technologies for Multispectral, Hyperspectral, and Ultraspectral Imagery XXIV*, 106441G (8 May 2018). <https://doi.org/10.1117/12.230561e5>.
- 3 Christopher, S., Edwin, W., Mary, W., David, D. (2001). Compact Airborne Spectral Sensor (COMPASS). *Proceedings of SPIE 4381, Algorithms for Multispectral, Hyperspectral, and Ultraspectral Imagery VII*, (20 August 2001); <https://doi.org/10.1117/12.437000>.
- 4 Hanst, P.L. and Hanst, S.T. (1994). Gas measurement in the fundamental infrared region. In: *Air Monitoring by Spectroscopic Techniques* (ed. M.W. Sigrist). New-York, NY: Wiley.

- 5 Griffith, D.W.T. and Jamie, I.M. (2000). Fourier transform infrared spectrometry in atmospheric and trace gas analysis. In: *Encyclopedia of Analytical Chemistry* (ed. R.A. Meyers). Chichester: Wiley.
- 6 Griffiths, P.R. and deHaseth, J.A. (1986). *Fourier Transform Infrared Spectroscopy*. Wiley.
- 7 Joint Program Executive Office for Chemical Biological Radiological and Nuclear Defense, Product Manager, Dismounted Reconnaissance Sets, Kits, and Outfits, Aberdeen Proving Ground, MD. <https://asc.army.mil/web/portfolio-item/jpeo-cbd-dismounted-reconnaissance-sets-kits-and-outfits-dr-sko/> Accessed on 1/4/21.
- 8 Adachi, S. (1999). The Reststrahlen region. In: *Optical Properties of Crystalline and Amorphous Semiconductors*. Boston, MA: Springer [https://doi.org/10.1007/978-1-4615-5241-3\\_2](https://doi.org/10.1007/978-1-4615-5241-3_2).
- 9 Ray, M.D., Sedlacek, A.J., and Wu, M. (2000). Ultraviolet mini-Raman lidar for stand-off, in situ identification of chemical surface contaminants. *Review of Scientific Instruments* 71: 3485. <https://doi.org/10.1063/1.1288255>.
- 10 Bartko, A. P. Personal communication. Battelle Memorial Institute, Columbus, OH. [www.battelle.org](http://www.battelle.org).
- 11 Ronningen, T.J., Schuetter, J.M., Wightman, J.L. et al. (2014). Raman spectroscopy for biological identification. In: *DNA Amplification and Sequencing, Optical Sensing, Lab-On-chip and Portable Systems*, 313–333. Woodhead Publishing <https://doi.org/10.1533/9780857099167.3.313>.
- 12 Ross, B. B., Bartko, A. P. (2016). Line light source for Raman or other spectroscopic system. US Patent 9,389,121, 2016.
- 13 Kaye, P.H., Stanley, W.R., Hirst, E. et al. (2005). Single particle multichannel bio-aerosol fluorescence sensor. *Optics Express* 13 (10): 3583–3593. <https://doi.org/10.1364/OPEX.13.003583>.
- 14 Reyes, F.L., Jeys, T.H., Newbury, N.R. et al. (1999). Bio-aerosol fluorescence sensor. *Field Analytical Chemistry and Technology* 3: 240–248. [https://doi.org/10.1002/\(SICI\)1520-6521\(1999\)3:4/5<240::AID-FACT3>3.0.CO;2-%23I](https://doi.org/10.1002/(SICI)1520-6521(1999)3:4/5<240::AID-FACT3>3.0.CO;2-%23I).
- 15 Pöhlker, C., Huffman, J.A., and Pöschl, U. (2012). Autofluorescence of atmospheric bioaerosols – fluorescent biomolecules and potential interferences. *Atmospheric Measurement Techniques* 5: 37–71.
- 16 Sivaprakasam, V., Huston, A.L., Scotto, C., and Eversole, J.D. (2004). Multiple UV wavelength excitation and fluorescence of bioaerosols. *Optics Express* 12 (19): 4457–4466. <https://doi.org/10.1364/OPEX.12.004457>.
- 17 Cheng, Y.S. (1999). Detection of bioaerosols using multiwavelength UV fluorescence spectroscopy. *Aerosol Science and Technology* 30 (2): 186–201. <https://doi.org/10.1080/027868299304778>.
- 18 Pan, Y.-L., Eversole, J.D., Kaye, P.H. et al. (2007). Bio-aerosol fluorescence. In: *Optics of Biological Particles*, NATO Science Series, vol. 238 (eds. A. Hoekstra, V. Maltsev and G. Videen). Dordrecht: Springer [https://doi.org/10.1007/978-1-4020-5502-7\\_4](https://doi.org/10.1007/978-1-4020-5502-7_4).
- 19 Jonsson, P. and Kullander, F. (2014). Bioaerosol detection with fluorescence spectroscopy. In: *Bioaerosol Detection Technologies, Integrated Analytical Systems* (eds. P. Jonsson et al.), 111–141. New York: Springer-Verlag.
- 20 Corte, K. FLIR Systems, Inc., Arlington, VA. [www.flir.com](http://www.flir.com).
- 21 Cabalo, J., DeLucia, M., Goad, A., Lacis, J., Narayanan, F., Sickenberger, D. (2008). Overview of the TAC-BIO detector. *Proceedings of SPIE 7116, Optically Based Biological and Chemical Detection for Defence IV*; 71160D (2 October 2008). <https://doi.org/10.1117/12.799843>

## 8

# Applications of Ion Mobility Spectrometry

Pauline E. Leary<sup>1</sup> and Monica Joshi<sup>2</sup>

<sup>1</sup>Federal Resources, Stevensville, MD, USA

<sup>2</sup>Department of Chemistry, West Chester University of Pennsylvania, West Chester, PA, USA

## 8.1 Introduction

No conversation on portable spectrometers is complete without a discussion about ion mobility spectrometers. They have long been used in various law enforcement, military, and security settings for field detection of chemical threats such as explosives, drugs, chemical warfare agents (CWAs), and toxic industrial chemicals (TICs) (Eiceman and Stone 2004; Ewing et al. 2001; Mäkinen et al. 2010; National Institute of Justice 2000; Verkouteren and Staymates 2010). Unlike traditional laboratory instruments that were made field-portable by miniaturization such as laser-induced breakdown spectroscopy (LIBS) systems for elemental spectroscopy and infrared and Raman spectroscopies for molecular spectroscopy, ion mobility spectrometers were first introduced as a portable technique.

Ion mobility spectrometers are the ideal portable instrument. Benchtop models offer small footprints that are lightweight and can operate on battery power. Models miniaturized even further are handheld or wearable. Some systems have been ruggedized to meet aggressive military standards for deployment, and modern systems have low power and minimal consumable requirements. The analysis itself is typically completed in seconds per sample and performed under ambient pressure. Probably, the most important reason for the success of ion mobility spectrometry (IMS) as a field technique is the high level of specificity and low picogram-level sensitivity to chemicals of interest. The analysis can be targeted toward a group of chemicals by programming reference parameters that are compared against the experimental result. This results either as an audible alarm or in a simplified red (fail) or green (pass) output that can be interpreted by field operators without a technical background. All these reasons have made IMS a technique of choice for field screening of chemical threats in various military, security, and law enforcement settings.

IMS is an analytical technique in which an analyte, if not already in the gas or vapor phase, is converted to the gas phase, ionized, and then characterized based upon the size, shape, and collision cross section of the ions. Ionization generally occurs by atmospheric pressure chemical ionization (APCI) in the presence of reactant ions that can be optimized to cause selective ionization of the target species. Various IMS technologies exist to create and separate ions. This chapter focuses specifically on the applications of portable IMS. The reader is directed to the chapter in volume 1 of this text by DeBono and Leary for a comprehensive discussion of IMS instrumentation and technology.

Ion mobility spectrometers are typically used to analyze chemicals in the solid and vapor states of matter. Based on the type of sample introduction system used, instruments are classified into two types: (i) *particle detection instruments* and (ii) *vapor detection instruments*. Particle detection instruments identify traces of particles recovered from the test sample by swabbing its surface. The traces collected are then converted within the ion mobility

spectrometer to the gas phase using thermal desorption. The vaporized particles formed at the inlet during thermal desorption are then directed into the ionization chamber of the system using air flow. Vapor detection instruments, on the other hand, collect gases or vapors directly from the environment for analysis. Air containing the target analyte is usually directly sampled at the inlet and directed into the ionization chamber of the system using air flow. The choice of instrument used depends on the set of target substances. If the target substance has an appreciable vapor pressure and is present in the air at sufficient concentration, then a vapor detection system may be used. If not, a particle detection system may be used. Once the sample is introduced into the ionization chamber, the subsequent analysis steps for both particle and vapor detection systems are equivalent.

The first step in the analysis after sample introduction and vaporization is ionization. Radioactive ionization sources were the traditional sources of choice due to their low maintenance and long-term stability. Nonradioactive sources including corona discharge sources have become more popular in recent years as they are not subject to regulatory requirements for radioactivity and can be readily deployed throughout the world. The most common IMS technology in commercial instruments used for the field applications discussed in this chapter is the drift tube technology. In this technique, the ions formed are introduced into the instrument's drift region in bundles known as ion swarms using an electronic ion shutter. The ions are accelerated through the drift region by an electric field. Deceleration of the ions occurs in the drift region due to collisions with neutral drift gas molecules that flow in the opposite direction of the ion swarm. At equilibrium, each ion achieves a constant drift velocity, which is defined as the time it takes for an ion to travel the distance of the drift tube between the ion shutter (usually a gating grid) and the ion detector. This time is referred to as drift time. A Faraday plate is generally used to detect the ions. Figure 8.1 shows a schematic of a drift tube ion mobility spectrometer.

IMS systems operate at ambient pressure and frequently use purified and dried air from the environment as the drift gas. Drift velocity of an ion can vary with changes in temperature and pressure. To account for these variations and standardize across instruments, the drift velocity is corrected for temperature and pressure inside the drift tube and is reported as the reduced mobility of the ion. For day-to-day operational variations within an instrument, the drift time and reduced mobility are referenced to an internal calibrant.

Ions of different masses and structure have different reduced mobilities and, when analyzed under the same conditions, exhibit different drift times. For a specific IMS method, factors that impact drift time including ionization conditions, temperature, electric field strength, data processing settings, and ion shutter characteristics are set the same. Therefore, the drift times of two different analytes measured using the same method can be used for identification. Figure 8.2 shows a simple ion mobility spectrum with the calibrant peak and two analyte peaks.

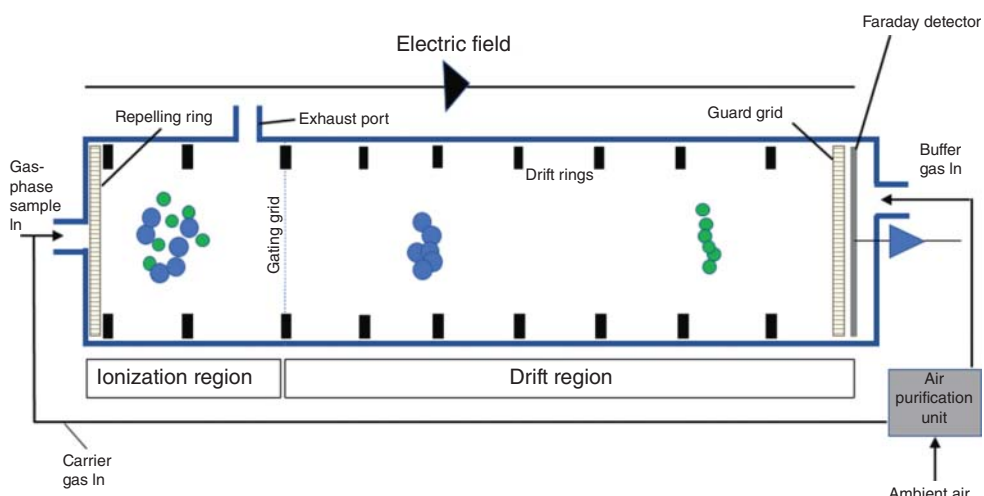
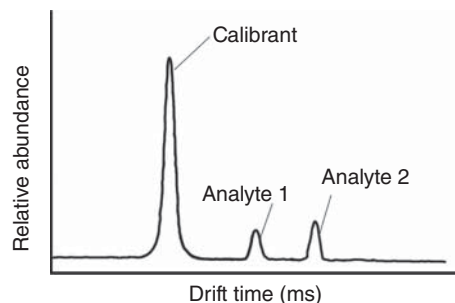


**Figure 8.1** Schematic of drift tube IMS where the sample is brought in with a clean carrier flow.

**Figure 8.2** Ion mobility spectrum of two-component sample.



IMS instruments are generally programmed to produce a positive indication of a substance or “alarm” if a peak is detected above a preset threshold for size and shape in the programmed drift time window. The drift time of the analyte peak is compared with the drift time of the calibrant peak to generate the normalized reduced mobility value that is used for identification. The drift time is the measured value, but the positive identification is reported based upon the reduced mobility. Reduced mobilities of ions of many target chemicals are very well characterized.

The operating parameters of an instrument such as the temperatures of the inlet and the drift tube are optimized to detect the ions of a set of target analytes. Historically, commercial instruments were programmed to detect either positively or negatively charged ions during a given analysis. Negative mode was used for explosives; positive mode was used for drugs and CWAs. A challenge to this approach was that the selection of a single ion-type mode limited the range of analysis and excluded certain compounds that may be of interest. For example, triacetone triperoxide (TATP) is an explosive that produces positive ions. Most other explosives produce negative ions. Therefore, an IMS instrument programmed to detect explosives and operating in the negative mode would fail to detect TATP traces present in a sample. To address this limitation, dual-tube instrument designs became available around the year 2005. For these systems, a single sample is vaporized at the inlet and then split into two: one-half of the vaporized sample is analyzed in one drift tube programmed in the negative mode, and the other half of the vaporized sample is analyzed in a second drift tube programmed in the positive mode. Alternatively, the second tube could be programmed in the same ion-type mode but using different reactant ions to detect different target chemicals. Results from both tubes are generated from a single sample giving a more thorough analysis. More modern instruments have improved electronics and instrument configurations enabling fast switching of polarities. This allows for simultaneous detection of both types of ions using a single drift tube (Bruker 2020a; Smiths Detection 2017a; Zhou et al. 2015) However, temperature of the drift tube is a compromise that can impact sensitivity. Explosives tend to generate better results when drift tube temperature is lower, while drugs tend to generate better results when drift tube temperature is higher. Selection of the optimal tube temperature for these single-tube, dual-mode systems is critical. Historically, inlet temperatures were constant, too, but some systems currently available offer variable-temperature-inlet desorption profiles, which can significantly improve analytical results. Practically, instruments that can detect both polarities simultaneously are potentially more beneficial due to their ability to detect an increased breadth of chemical threats.

Commercially available portable IMS systems do not generally offer a front-end separation mechanism, and both the target analyte and the sample matrix are introduced to the system during analysis. Sample overload and unwanted contamination from sample matrix for both vapor and particle detection systems are primary reasons IMS systems need to be routinely cleaned by bakeout and other cleaning procedures. Bakeout for IMS systems is a term that typically refers to a process where the temperature of the drift tube and other system components are increased for a specified time period to allow contaminants and other debris to volatilize and pass through the system. Although the bakeout procedures are usually automatic, they are routine maintenance requirements that cause system downtime. In addition, if the IMS systems get contaminated or overloaded at the scene where analysis is required, it may need to go out of operation while a bakeout is performed. Instrument vendors design systems to minimize contamination from sample matrix and overload. The use of low-thermal-mass inlets and

contactless desorption for particle detection systems are useful for this purpose. For some vapor detection systems, the sampling cycling time, which usually is preset for a specified time period, will automatically stop the sampling but allow the IMS analysis to continue.

In this chapter, we discuss the crucial role of trace chemical detection that IMS plays in various military, security, and law enforcement settings. Though there are other niche applications of IMS, this chapter is focused on those commercial applications where IMS has thrived as a portable trace chemical threat detector.

## 8.2 Applications

### 8.2.1 Military Applications – Chemical Warfare Agents and Toxic Industrial Chemicals

#### 8.2.1.1 Background

Chemical attacks have been and continue to be a threat to militaries across the world. Not only is the threat real in war zones, but also these substances have been used by terrorist organizations and by tyrannical governments on their own citizens (Hoffman et al. 2007; OPCW Confirms Use of Sarin and Chlorine in Ltamenah, Syria, on 24 and 25 March 2017 2018; Schwirtz 2018; Sircany and Kourdi 2018). Interestingly, military preparedness significantly improved as a result of lessons learned after a CWA attack on the general public by domestic terrorists in the Tokyo subway system in 1995 (Hyams et al. 2002).

A chemical agent can be defined as a chemical substance that is intended for use in military operations to kill, seriously injure, or incapacitate primarily through its physiological effects (United States Department of Defense 2018). When these toxic chemicals and their precursors are prohibited under the Chemical Weapons Convention (CWC) (Convention on the Prohibition of the Development, Stockpiling and Use of Chemical Weapons and Their Destruction 2005), they can be defined as CWAs (United States Army, Marine Corps, Navy, Air Force 2005). CWAs include choking, nerve, blood, blister, and incapacitating agents. Compared with conventional weapons, relatively small amounts of modern chemical agents may cause high numbers of casualties; therefore, CWAs have been classified as weapons of mass destruction (WMD) (Szinicz 2005).

Modern CWAs are different from their historical brethren, especially in that design and synthesis of these agents has become standard practice. Substances can be designed to circumvent detection capabilities and treaties like the CWC (Mirzayanov 2009). They can be tailored to meet toxicological goals, and storage, transport, and delivery methods can be optimized (Leary et al. 2019). CWAs can be deadly in and of themselves, but it is the method and accuracy of their delivery that determines the severity of their damage (The Deputy Assistant to the Secretary of Defense for Chemical and Biological Defense 2001).

While chemical agents in the form of CWAs are a significant concern to military organizations, so, too, are TICs. Industrial chemicals are produced in large quantities and stored and transported across the world for various industrial purposes. TICs are those industrial chemicals that when released into the atmosphere can have severe toxic effects on people and the environment. Examples include ammonia, chlorine, hydrogen chloride, hydrogen cyanide, and phosgene. The Occupational Safety and Health Administration (OSHA) of the US Department of Labor classifies TICs into two groups based on the type of risk they pose, i.e. chemical and physical hazards (Occupational Safety and Health Administration n.d.). Those that are chemical hazards include chemicals that are carcinogenic, corrosive, or irritants. Chemicals causing physical hazards include those that are very reactive, explosive, or flammable. In general, because of the abundance of their production and ease of access, especially to terrorist organizations, TICs may be used in a chemical attack.

CWAs and TICs can cause acute and long-lasting toxic effects and even death within minutes for some substances. Immediate and reliable detection and identification of these substances at very low levels is very important. From a security perspective, IMS systems have been used for perimeter and personal monitoring. Detection and identification downrange is also critical (Ludwig et al. 1994).



**Figure 8.3** Images of the M8A1 (a), M22 ACADA (b) CAM in use (c), ICAM (d). *Source:* Top images courtesy of the United States Army; bottom images used with permission. © Smiths Detection.

### 8.2.1.2 Historical Development

Military interest in IMS began in the 1960s with defense organizations seeking methods for detecting CWAs and other vapors of interest. Some of the IMS systems ultimately deployed include the M8A1 automatic chemical agent detection and warning system, the chemical agent monitor (CAM), the improved chemical agent monitor (ICAM), the M22 automatic chemical agent detector (ACADA), and the Joint Chemical Agent Detector (JCAD). The following paragraphs present the history of IMS in the detection of CWAs and TICs. It is interesting to note how the IMS technology grew out of the increasing demands for ruggedness and portability. Figure 8.3 shows some of the historical instruments used by the military for CWA and TIC detection.

The M8A1 (Intellitec, FL) was an automatic chemical agent detection and warning system that was standardized by the US Department of Defense in 1981 and used by the US Army and US Air Force during the 1991 Gulf War for the detection of nerve agents and inhalable aerosols (Law Enforcement and Corrections Standards and Testing Program 2000; Smart 2009). More than 40,000 M8A1 systems have been fielded by the US Army and many foreign countries (Committee for an Assessment of Naval Forces's Defense Capabilities Against Chemical and Biological Warfare Threats, Naval Studies Board 2004). The system included the M43A1 IMS detector coupled with

the M42 remote alarm unit. A continuous air pump drew air past the radioactive  $^{241}\text{Am}$  ionization source, and a small percentage of the air sampled was ionized. The difference in ion current when the nerve-agent-contaminated air passed through the detector as compared with when clean air passed through the detector triggered an alarm in the remote alarm unit (Preparedness Directorate Office of Grants and Training 2007). The system offered a response time of less than one second and could detect CWAs such as tabun, sarin, and soman with a sensitivity of 0.1–0.2 mg/m<sup>3</sup> and VX with a sensitivity of 0.4 mg/m<sup>3</sup> (National Institute of Justice 2000).

The M8A1 was replaced by the M22 ACADA. The M22 ACADA started as a program in the 1970s and was standardized in 1997 for use by the US military including the Army, Navy, Air Force, and Marine Corps (Headquarters, Departments of the Army, Air Force, Marine Corps and Navy 1998; Smart 2009). It was also used by the Ministry of Defense in the United Kingdom, the Canadian Department of National Defence, the Australian Army, and militaries of other nations including some in the Middle East (National Institute of Justice 2000). The system was an advanced point-sampling chemical agent alarm system. It simultaneously detected both nerve and blister agent vapors and was suitable for monitoring collective protective shelters. It was significantly more sensitive than the M8A1 alarm and less responsive to interferences (Smart 2009). It offered a visible and audible warning with a response time of less than one second. It detected tabun at 0.001 ppm, sarin and soman at 0.002 ppm, VX at 0.0009 ppm, distilled mustard (HD) and nitrogen mustard (HN) at 0.015 ppm, and Lewisite at 0.01 ppm. It also detected TICs including chlorine, hydrogen cyanide, and phosgene (National Institute of Justice 2000). A primary benefit of this system over its predecessor was that it could be linked to other systems such as the multipurpose integrated chemical agent detector (MICAD) to support battlefield automation systems (Appendix D: Detecting and Monitoring Chemical Agents 2000). The system included the base IMS detector unit (M88) and power supply as well as the M42 remote alarm (Smart 2009). The M8A1 (including the M42 remote alarm) and the M22 ACADA (without the M42 remote alarm and power supply) each weighed approximately 10–12 lbs. They were classified as handheld stationary and fixed-site detection systems, respectively (Headquarters, Departments of the Army, Air Force, Marine Corps and Navy 1998; National Institute of Justice 2000).

The urgent need for a lightweight handheld chemical detector and the movement to microprocessors was reflected in the development of the CAM (Graseby Dynamics, now Smiths Detection, Edgewood, MD, USA), which was standardized by the US military in 1988. The electronics for this system were upgraded in the improved CAM known as the ICAM, which was standardized by the US military in 1993 (Smart 2009). Both the CAM and ICAM used timing and microprocessor techniques to reject interference (Appendix D: Detecting and Monitoring Chemical Agents 2000). These instruments weighed approximately 4 lbs and were classified as handheld portable devices. They detected G- and H-series agents as well as VX with sensitivity at about 0.02 ppm in the vapor phase and response times of one minute or less (National Institute of Justice 2000). Though the units both offered the same external design and used the same radioactive ionization source, the ICAM was superior to the CAM because of its increased reliability, lowered maintenance costs, and reduced need for depot repair (Smart 2009). During the peak of their use in the early to late 1990s, at least 31 countries were using these instruments with over 62,000 units deployed (Preparedness Directorate Office of Grants and Training 2007).

It seems the most successful IMS deployed to the US Department of Defense is the Joint Chemical Agent Detector (JCAD) M4A1 (United States Army n.d.). This system was optimized for the detection of CWAs and TICs. JCAD M4A1 was intended to support the various mission requirements of the US Joint Forces. These include interior detection for both tracked and wheeled vehicles, fixed- and rotary-winged aircraft interior detection during ground and airborne operations, shipboard interior and exterior detection, fixed-site chemical agent detection, personal detection to be carried by an individual soldier or for advanced warning, and chemical agent surveys of personnel equipment and cargo. Prior to the development of JCAD M4A1 using IMS technology, the JCAD program was based upon surface acoustic wave technology (SAW). This was ultimately abandoned in favor of development and production of the JCAD M4A1 system as a nonradioactive source IMS. Exact sales figures are not known, but initial projections for the JCAD established a US Joint Forces requirement for 257,135 systems (Laljer 2003).

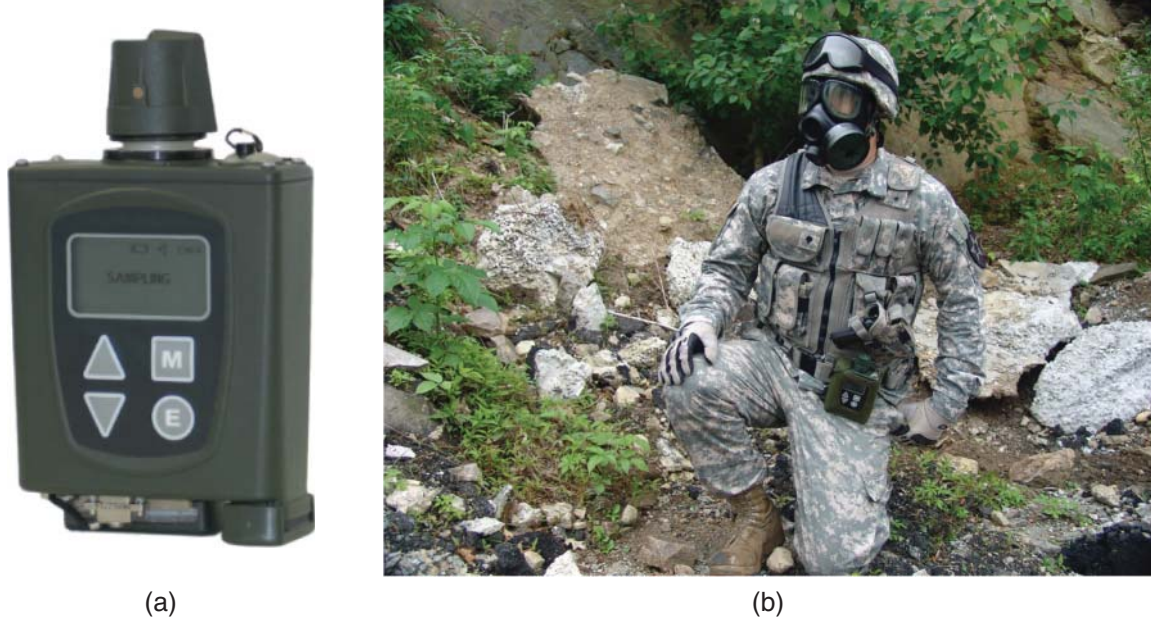


**Figure 8.4** The LCD 3.3 (a) and the LCD 3.3 (b) as worn hands-free by a military officer. *Source:* Images used with permission. © Smiths Detection.

The JCAD M4A1 is a variant of the Smiths Detection LCD 3.3, an advanced warning device that alarms to gas and vapor threats detected at or below levels that are immediately dangerous to life and health (IDLH). It can also be used as a screening and survey device. The system offers a combined CWA and TIC detection library and can run for up to 75 hours of continuous use from a single set of commercial AA batteries. It weighs 1.3 lbs including batteries and responds to nerve, blood, blister, and choking agents, as well as a selected library of TICs. It can be worn and integrated into vehicle systems, or onto robots with an auto inlet module accessory to provide remote and automatic operation. The unit can be fitted with a survey nozzle to aid in the detection of residual persistent contamination while in survey mode (Smiths Detection 2017b). Figure 8.4 shows images of the Smiths Detection LCD 3.3 and its use as a hand-free wearable detector.

While initial JCAD M4A1 (and predecessor) deployments focused on vapor-phase threats, attempts were underway to extend the capabilities of the JCAD M4A1 systems to low volatility compounds, explosives, and pharmaceutical-based compounds without any modification to existing JCAD M4A1 hardware (Smiths Detection Inc. 2018). This would allow the system to detect solid and liquid substances in the field. In October 2020, Smiths Detection Inc. announced it will initiate manufacturing of the Solid Liquid Adapter (SLA) for the US Department of Defense. JCAD fitted with an SLA (JCAD-SLA) gives the operator the ability to both test for illicit drugs, including opioids such as fentanyl, and detect explosive compounds – without compromising the conventional CWA detection capability of the JCAD (Smiths Detection 2020).

In addition to the JCAD M4A1, there are other IMS systems available for the analysis of CWAs and TICs. Many of them are marketed to first responders. One system of note is the Bruker RAID-XP (Billerica, MA, USA). The instrument combines the detection of CWAs and TICs with the detection of gamma radiation. The IMS options available are the  $^{63}\text{Ni}$  radioactive source in the RAID-XP and a nonradioactive high-energy photoionization (HEPI) source RAID-XP<sub>NR</sub> (Bruker 2020b). More instruments are adding this dual capability as radioactive materials are becoming an increasing threat in military zones. Another IMS system of note is the Hardened MobileTrace® (Rapiscan Systems, Torrance, CA, USA). This system is designed for both particle and vapor detection methods and can detect CWAs, TICs, explosives, precursors, explosive taggants, and narcotics (Rapiscan Systems 2019).

The evolving needs of the military continue to drive advances in capabilities and performance of IMS systems. Vendors of this technology are improving ease of use and deployment by eliminating radioactive ionization sources, extending capabilities to detect substances in all phases of matter, and increasing the breadth of target analytes to include substances such as fentanyl and its analogues. IMS systems continue to provide critical safety and security capabilities within military operations.

## 8.2.2 Aviation Industry – Explosive Detection and Identification

### 8.2.2.1 Background

The development of explosive detection capabilities using IMS has been heavily supported by the demands of the aviation industry. It is interesting to note, though, that the earliest adopters of IMS systems for explosive detection were groups including the Ministry of Defence in the United Kingdom and the Israel Defense Forces (L. Kim, Personal Communication, 26 March 2020). Infiltration of IMS systems into the aviation industry for explosive detection began soon after. In 1996, the Federal Aviation Administration of the US Department of Transportation established the qualification process for checkpoint screening (Kraus 2008). Then, in November 2001, the Aviation and Transportation Security Act was signed into law in the United States, and the Transportation Security Administration (TSA) was created to oversee security in all modes of transportation (United States Transportation Security Administration n.d.).

The need for explosive detection within the aviation industry was precipitated by a number of incidents including three high-profile terrorist attacks. These three attacks remain the deadliest terror attacks in the histories of Canada, the United Kingdom, and the United States. The bombing of Air India flight 182 occurred on 23 June 1985. This flight was en route to Heathrow Airport in London from Montréal–Mirabel International Airport in Canada when it blew up off the coast of Ireland killing all 329 people on board. It was the largest mass killing in Canadian history. A second bombing within the aviation industry occurred in the United Kingdom on 21 December 1988 when Pan Am flight 103 exploded killing all 259 people on board and 11 people on the ground in Lockerbie, Scotland. This flight took off from Heathrow Airport and was en route to New York's John F. Kennedy Airport. Then, on 11 September 2001, a series of coordinated terrorist attacks against the United States were carried out using four commercial flights. American Airlines flight 11 and United Airlines flight 175 were hijacked and crashed into the north and south towers of the World Trade Center in New York City. American Airlines flight 77 was hijacked and crashed into the Pentagon. United Airlines flight 73 was hijacked and flown toward Washington, DC, but crashed into a field near Shanksville, Pennsylvania. In total, 2977 people died as a direct result of these 4 hijackings and subsequent crashes, and thousands more were injured.

Though these three terrorism events were years apart, they clearly showed there was a need within the industry for explosive screening. By the time of the Air India crash, IMS was already establishing itself as a fast, reliable, and sensitive technique for the detection of chemical threats as discussed in the timeline of military use above. The technology was transitioned to the aviation industry relatively quickly for trace explosive detection. Since its introduction for this purpose in the early 1990s, it has been a mainstay in airports across the world.

### 8.2.2.2 Detection of Explosives

The detection of explosives by IMS is based on the premise that explosives leave particulate residues on surfaces through either direct or secondary contact. These residues are invisible to the naked eye but can be collected by swiping the surface of the contaminated article (Theisen et al. 2004). Therefore, many of the IMS instruments used for explosive detection are based on particle detection methods. The swipes used to collect the explosive particulate matter may be made of cellulose, Nomex- or Teflon-coated fiberglass, or other proprietary material. The swipe is then introduced into the desorber region of the IMS where the explosive particles are heated, vaporized, and transferred into the ionization region. The analysis time per sample is as little as seven seconds, and an alarm that is color-coded red is returned when explosives are present. In airport security checkpoints, travelers' luggage and other possessions are swiped and analyzed by IMS to screen for explosive residues. Travelers may also be tested as

part of random screening or as a follow-up to luggage screening. IMS systems deployed routinely at airports can detect explosive traces at sub-nanogram levels.

It is important to note that a big challenge to explosive detection is the evolving nature of these threats. When IMS systems first entered the market for explosive detection, threats for detection and identification tended to be military and/or commercial explosives such as Semtex, TNT, and dynamite. Today, homemade explosives are commonly used by terrorist organizations in improvised explosive devices. Detection and identification of these evolving threats can be challenging, and algorithms used to identify them are continually updated to verify the most current threats are reliably detected and identified.

### 8.2.2.3 Regulation

The process used to deploy IMS systems at airports is vastly different from other industries because the air travel industry is subject to several significant security regulations. These regulations are regional; therefore, the final choices for viable detectors are governed by a variety of organizations such as the TSA in the United States, the Department for Transport (DfT) in the United Kingdom, Transport Canada in Canada, the European Civil Aviation Conference (ECAC) in Europe, and the Civil Aviation Administration of China (CAAC) in China. Each of these governing bodies has its own set of directives and criteria by which it chooses the instruments to be deployed within its country's airports.

Screening of passengers and their checked baggage at airports was first introduced and widely adopted right after 9/11. The qualification processes to provide explosive trace detection systems in this environment is quite extensive. Regulators test these systems to qualify/approve them to be used for passenger screening (including checked baggage) and for air cargo applications. Depending upon whether the system can meet the specific requirements established for each application, it may be approved for passenger screening, air cargo screening, or for both.

In the United States, TSA has established and maintains a list of technologies and specific equipment recommended to be used to maintain aviation security. TSA's Air Cargo Screening Technology List (ACSTL) is a document that serves as an official guide for regulated parties to use when procuring screening equipment under TSA-approved security programs (Transportation Security Administration 2020). The document classifies technologies into five qualification groups – non-computed tomography (non-CT) transmission X-ray devices, explosive trace detection (ETD) devices, electronic metal detection (EMD) devices, explosive detection systems (EDS), and carbon dioxide (CO<sub>2</sub>) monitors. IMS systems are contained in the ETD group of technology.

In each of these qualification groups, the instruments are further classified into three groups – Qualified, Approved, and Grandfathered. Qualified Technology are systems that have undergone a formal TSA-sponsored test process and are deemed qualified for screening operations. When procuring an instrument from the ACSTL, regulated parties are encouraged to select a device from the Qualified Technology section. Approved Technology are systems that have been conditionally approved for screening operations and are currently undergoing or are scheduled for field test activities. These devices have up to 36 months from the date added to the Approved Technology section to successfully pass TSA's suitability-based field test activities. If a device is unable to pass field test activities within the prescribed 36 months, it will be removed from the Approved Technology section. Due to this fact, regulated parties who procure a device from the Approved Technology section do so at their own risk. Grandfathered Technology are systems that are currently qualified to screen cargo but have a stated expiration date. This allows regulated parties who are using the Grandfathered Technology an opportunity to gradually phase out the device and transition to devices listed in the Qualified or Approved sections.

The ACSTL is routinely reviewed and updated to meet the latest security directives and needs. In the February 2020 release of the 11.2 version, no ETD detectors are listed as Qualified Technology. One IMS system is listed as Approved Technology, and four IMS systems are listed as Grandfathered Technology (Transportation Security Administration 2020). These instruments are shown in Table 8.1, and images are shown in Figure 8.5.

Most of the IMS instruments used in the aviation industry are portable benchtop units. These benchtop systems have continued to be the mainstay of explosive detection at security checkpoints. The requirements for hand-held or wearable instruments, as was for military use, are not mandatory for the aviation industry. Sensitivity to

**Table 8.1** ETD systems listed on the ACSTL, version 11.2.

Technology status	Manufacturer	IMS model
Approved/Grandfathered	Smiths Detection	IONSCAN 600
Grandfathered	L3 Security & Detection Systems (now Leidos)	QS-B220
Grandfathered	Rapiscan Systems	Itemiser DX
Grandfathered	Smiths Detection	IONSCAN 500DT

explosives, particle detection, and high throughput, which are standard in portable benchtop units, are the primary requirements within the aviation industry. Table 8.2 lists the general specifications of the Smiths Detection IONSCAN 600 IMS unit, which is listed in the Approved Technology section of the ACSTL for ETDs.

In 2004, the TSA began testing trace particle detectors that became known as trace portals and commonly referred to as “puffer” machines (Elias 2009; Transportation Security Administration 2004). These instruments were large walk-through portals that puffed air on the person being screened. The particles dislodged from the person and their clothing during this puff and were then directed into an on-board IMS unit. The IMS units used in these portals were very similar in design to the benchtop units within the industry. However, these instruments were prone to false positives from interferences and contamination due to the numerous particles collected from people and suffered long downtimes for repair. Therefore, after evaluation of the field reports, the TSA began phasing out the devices in 2008 from the over 37 US airports where they had been deployed (Elias 2009).

## 8.2.3 Correctional Facilities

### 8.2.3.1 Background

Contraband in prisons is an item that may pose a threat to the security of the prison, or the physical and mental welfare of the inmates, staff, or visitors. Prison contraband generally includes drugs, alcohol, weapons, cellphones, and tools. Though different jurisdictions define contraband items differently, illicit drugs are always included. Drugs in prisons, apart from the obvious safety risks, can cause severe health and addiction issues in inmates.

A primary aim of drug interdiction units in correctional facilities is to mitigate the problem of illicit drugs by preventing entrance of these substances into the prison. Various creative ways are used to smuggle in this contraband. Drugs are often thrown over prison walls into open yards. They are sometimes disguised or concealed within innocuous packages. Increasingly, drones have been used to deliver drugs into prisons (Vandam et al. 2018).

There are two critical supply routes that are very difficult to control and warrant trace chemical detection. The first and main route is through visitors delivering them to an inmate during a contact visit (Standing Committee on Public Safety and National Security 2018). The second is through prison mail. Ion mobility spectrometers are a critical component used in correctional facilities across the world for screening within these two supply routes.

To prevent drug infiltration by contact visitors, portable benchtop IMS instruments configured to detect and identify drugs are placed in the front entrances to prisons. These systems are like those used in the aviation industry and shown in Figure 8.5. Incoming visitors are noninvasively searched for traces of drugs on their person or their belongings (Johnson and Dastouri 2011; Standing Committee on Public Safety and National Security 2018). Sampling is similar to the methods used in airport security checkpoints. Traces of drugs detected on a person, when swiped and analyzed in the ion mobility spectrometer, indicate primary or secondary contact with an illicit drug and will warrant further search and questioning of the individual. Based on a physical search of belongings, a consideration of the history of positive detections on the individual, and the threat assessment interview with prison staff, the visitor may be (i) denied access to the facility, (ii) denied a contact visit, (iii) allowed a restricted visit, or (iv) allowed a contact visit (Standing Committee on Public Safety and National Security 2018).



**Figure 8.5** ACSTL Approved and Grandfathered Technology Explosive Trace Detectors. Images of the Smiths Detection IONSCAN 600 (a) and IONSCAN 500DT (c) (Source: Images used with permission. © Smiths Detection); Leidos B220 HT (b) (Source: Image used with permission of Leidos).

**Table 8.2** Technical specifications for the Smiths Detection IONSCAN 600.

General specifications	
Detector type	Nonradioactive IMS source
Sampling	Trace particle sampling using single-use swabs with either manual or wand collection
Calibration	Automatic internal self-calibration
Alarm method	Substance identification with configurable audio alarm
Consumables	Cost-effective single-use swabs and verification pen
Connectivity	Ethernet, 4 USB 2.0 (standard, 2 front/2 back)
Weight	Non-printer version: 23.8 lbs (10.8 kg) Integrated printer version: 25.3 lbs (11.5 kg)
Battery	One hour full of operation, hot swappable for extended operating time
Analysis time	Less than 8–12 seconds
Warm-up time	Less than 10 minutes
Data display	9" high-resolution, antireflective, color touch screen
Dimensions (W × D × H)	Non-printer version: 14.8 × 12.0 × 12.9 in. (37.7 × 30.4 × 32.7 cm) Integrated printer version: 15.1 × 15.6 × 14.8 in. (38.3 × 39.5 × 37.7 cm)
Operating temperature	14–122 °F (−10 to +50 °C)
Operating altitude	Up to 10 000 ft (3 048 m)
Operating humidity	0–95% noncondensing
Explosive detection	Military, commercial, and HMEs including RDX, TNT, PETN, NG, AN, UN, HMTD, TATP, EGDN, Tetryl, HMX, and others
Narcotics detection	Amphetamine, buprenorphine, carfentanil, cocaine, fentanyl, methamphetamine, morphine, THC, and others
Storage capacity	250 000 samples
Printer	Integrated printer (option at time of order only) or external USB printer
Power	100–240 V AC, 50–60 Hz
Safety	No hazardous parts and tamper-proof casing

Instruments are also placed in mailrooms where incoming prison mail is screened for traces of drugs (Butler 2003). This route of supply is common for some of the more potent drugs that can be impregnated into paper or concealed in innocuous liquids. The person receiving the paper can then use these drug-impregnated papers as rolling paper for tobacco or may inconspicuously suck on the paper to release the drug orally. The drugs concealed in liquids such as prayer oils, fragrances, and lotions can be spiked onto regular paper or tobacco by the inmate prior to smoking. To detect these drugs, correctional facilities swab the mail and analyze by IMS instruments to detect the drugs. The inmate is denied the mail if it is determined to contain drug substance. It is important to note that delivery of drugs through prison mail has become so prolific that to mitigate this supply route, the US Bureau of Prisons recently determined they would send all mail to a central location where it is scanned and delivered to the inmates electronically (Balsamo 2019). State prisons such as the Pennsylvania Department of Corrections have also adopted this policy (Pennsylvania Department of Corrections n.d.).

### 8.2.3.2 Evolution in Drugs of Abuse and Challenges to Detection

The detection of drugs of abuse within correctional facilities is not without its challenges. The four drugs that have traditionally been the most common ones detected in bulk or trace samples are (i) Δ9-tetrahydrocannabinol (THC), (ii) cocaine, (iii) heroin, and (iv) methamphetamine. Although IMS detection of THC can be challenging (Verkouteren and Staymates 2010), the other three are routinely detected at low limits of detection using this method. More recently, though, an abundance of novel psychoactive substances (NPSs) have flooded the market. Proliferation of NPSs is even more pronounced in correctional facilities (Vandam et al. 2018). From a detection perspective, these substances and other designer drugs can be challenging. Generally, there is nothing about them that specifically prevents their detection using either IMS or other traditional screening and identification techniques. The reason they can be considered difficult and present challenges is because they are constantly changing. For this reason, library comparison data and other match criteria to drug standards are not sufficiently established, either by the detection equipment vendor and/or the relevant legal and regulatory authorities, to support identification of the “new” drug substance. In any given year, there are 15 or more drugs in a given NPS category that gain prominence. Of these, one or two will be most commonly present in all seized samples. For example, 5F-ADB and FUB-AMB were the most common synthetic cannabinoids found in seized synthetic cannabinoids in the year 2018 (National Forensic Laboratory Information System 2018). In 2015, however, XLR-11 and AB-CHMINACA were the most common.

The proliferation of NPSs and other designer drugs grew out of the need to circumvent legal restrictions placed on established drugs of abuse. If a substance has not been characterized and become regulated by legal authorities such as the Drug Enforcement Administration in the United States, they are not illegal. In prisons, while physical searches of inmate cells often lead to confiscation of suspected contraband, NPSs frequently go undetected using routine methods for detection including IMS. In these instances where IMS systems are used, algorithms for detection of the NPS have not usually been updated to include these substances. In many instances, prison staff are certain there is contraband present due to the behavior of the inmate or other scene information, but they are not able to prove drugs are present due to deficiencies in the current detection capability for the specific target substance. The 2018 study by the European Monitoring Centre for Drugs and Drug Addiction (EMCDDA) about NPSs in prisons considers synthetic cannabinoids the most common NPSs in prisons across Europe (Vandam et al. 2018). This study highlights the need to couple detection methods such as IMS with appropriate training of prison staff and increased interdiction efforts.

Programming new threats into an existing IMS method can be challenging. Ion mobility spectrometers are usually deployed with a “method” programmed into the system to detect a specific set of chemicals. The method is not necessarily optimized for a specific chemical, but rather for a set of chemicals. Method settings such as inlet and drift tube temperatures, ionization conditions, data processing, and detection algorithms are optimized for this set of chemicals. As new chemicals are added to the method, the detection performance for the other substances already programmed into the method can be impacted. In some instances, the addition may cause a decrease in the detection limits of existing chemicals due to signal quenching resulting from the presence of the new substance. In other instances, an increase in the signal of an existing chemical may occur. As a result, the criteria used in the algorithm to identify a specific chemical may need to be changed in order to allow for reliable detection of the new chemical while maintaining the ability to reliably detect the chemicals already in the method. Deployed IMS methods do their best to strike an optimal balance for all substances detected, and the addition of new substances to the method can upset this balance.

It is also important to note that data collection in the anticipated deployed environment is critical to achieving reliable detection. Rigorous validation is required prior to programming the detection algorithm for field-deployed IMS units so that the system generates an alarm when the substance is present, but not when the substance is not present. There are very few studies presenting IMS parameters for NPSs. Joshi et al., Armenta et al., and Yanini et al. have presented parameters for NPSs, primarily the cathinones and cannabinoids (Armenta et al. 2014; Joshi et al. 2014; Yanini et al. 2018). Metternich et al. present an IMS study based on synthetic cannabinoid materials

and tested it against materials seized from prisons in Germany (Metternich et al. 2019). Though these literature sources present some guidance for correctional facilities for new substances, they are not tested in the field conditions of correctional facilities. Most state correctional facilities work directly with the IMS manufacturers to get the instrument models and parameters needed for the drugs that are prevalent in their facilities. Frequently, this is not ideal, especially considering the rapidly evolving nature of the drugs of abuse. Uniform standardized parameters for all prison facilities do not exist, and generally, there is a lack of shared knowledge across states and instrument manufacturers. This has precipitated other issues, because the methods are not tested rigorously before deployment and are being field-tested as part of the routine screening.

The circumstances of expanding the detection algorithms to include NPSs as they become a threat have caused correctional facilities to face new challenges to IMS screening, i.e. increased alarm rates (Johnson and Dastouri 2011; Melamed 2018; Standing Committee on Public Safety and National Security 2018; Yanini et al. 2018). When a visitor tests positive for an illicit drug substance regardless of whether or not they have had direct contact with an illicit substance, they are put through an additional interrogation, or may lose visiting privileges with the inmate. In recent years, correctional facilities in Canada and the United States where some NPSs have been programmed into the IMS units have had an increased number of positive alarms. Some causes for such alarms include low threshold levels set for the alarms, or the probability of secondary contact with the drug substance. When there are low thresholds set for alarms, contamination from environmental exposure to such low levels of drugs may become a problem. For instance, it has been reported that a majority of US currency is contaminated by cocaine at levels detectable by desktop ion mobility spectrometers (Biello 2009). In states such as New York, Massachusetts, and Maryland, some visitors have filed legal suits against the correctional system over claimed false-positive results (Lyon 2019). A review conducted by the Correctional Service Canada (CSC) affirms the value of the use of IMS in prisons but admits that there is a need to balance the sensitivity level and need for trace detection (Standing Committee on Public Safety and National Security 2018). The conversation about the viability of IMS in screening visitors at prisons will continue. In the meantime, there is a need to address the gap between research and practice with IMS and the gap in communication between different correctional systems.

### 8.2.4 Other Applications

The three major applications discussed above have specific types of target compounds of interest that are effectively detected at relevant levels using IMS: one for CWAs and TICs, one for explosives, and one for illicit drugs. There are, however, several other security industries and scientific disciplines where IMS has value in detection and identification of a range of chemical substances. Some of these applications are discussed briefly here.

#### 8.2.4.1 Forensic Science

Chemical identification of trace amounts of material is an important capability in the field of forensic science. When traces of foreign material are detected on an object or person, it implies that these traces transferred either by direct contact or by secondary transfer with the object or person. The transfer of material between two objects or people is a foundational principle of forensic science set forth by Edmond Locard and is known as Locard's Exchange Principle (De Forest et al. 1983). Transfer evidence can be used to establish the elements of a crime. Due to the sensitivity of IMS, it can be used to detect and identify trace levels of transfer evidence. For example, IMS may be used to detect traces of drugs when a location is suspected of being a clandestine drug lab, but the drug substance has been removed from the scene, and no visible amount of drug remains present. IMS analysis of different locations at the suspected lab may be used to establish that drugs were once present at the location.

Drug interdictions at sea are another example where this type of analysis of residual material can be important. Drug smugglers aboard a vessel may sometimes, as law enforcement approaches, jettison the drugs to get rid of the evidence and avoid prosecution. In these instances, chemical detection of trace amounts of drugs on surfaces aboard the vessel can be used to establish that drugs were previously present. The US Coast Guard seizes

a significant amount of cocaine (United States Coast Guard, 2019), and IMS limits of detection for cocaine are in the single-nanogram range. Therefore, IMS analysis can provide useful information about the history of the vessel when traces that are invisible to the naked eye are detected but no bulk substance is recovered.

IMS may also be used to detect trace amounts of explosive residues at the scenes of bombings or other explosive events. IMS can detect and identify nanogram amounts of explosive material and, therefore, can be used at scenes of explosions and bombings to search for explosive materials not consumed during the explosive event.

Although the primary value of IMS is its ability to detect and identify trace amounts of material, IMS is also a useful tool for the analysis of bulk substances such as seized drug substances. The Scientific Working Group for the Analysis of Seized Drugs (SWGDRUG) in its mission to improve the quality of the forensic examination of seized drugs identifies and recommends best practices for drug evidence analysis. Within their recommendations, SWGDRUG provides categories for different methods of analysis for drugs based upon the method's highest potential level of selectivity. Category-A techniques provide the highest level of selectivity through structural information, Category-B techniques provide an intermediate to high level of selectivity through physical/chemical characteristics without structural information, and Category-C techniques achieve a low level of selectivity but provide general or class information. Current SWGDRUG recommendations identify IMS as Category-B technique. In accordance with the SWGDRUG recommendations, IMS can, therefore, be successfully incorporated into an analytical scheme when coupled with at least one other test result such as that from an infrared or Raman spectrometer (Scientific Working Group for the Analysis of Seized Drugs 2019).

#### 8.2.4.2 Emergency Response

IMS may be used by emergency response personnel to detect and identify trace amounts of dangerous chemicals such as fentanyl. Fentanyl is a synthetic opioid that has been on the market in therapeutic dosage forms such as low-dose intravenous solutions since the 1960s. In recent years, though, powder forms of this dangerous drug have found their way into the hands of drug abusers with fatal consequences. Exposure to response personnel has become more common since the rise of fentanyl and its analogs as drugs of abuse (The National Institute for Occupational Health and Safety [NIOSH] 2020). Airborne particles at overdose scenes can cause exposure by inhalation. This is of particular concern as the lethal dose of these drugs can be as little as 2 mg (United States Drug Enforcement Administration 2018). IMS has been shown to be a viable screening technique to detect fentanyl at the scene to protect personnel from exposure when responding to the scene and while handling evidence (Sisco et al. 2017). It has also been used to verify that no drug substance is present after decontamination of a hazardous scene.

#### 8.2.4.3 Border Protection

Border protection agencies such as the US Customs and Border Protection play an important role in the protection of a nation from dangerous people and materials. They must also enhance a nation's global economic competitiveness by enabling legitimate trade and travel (U.S. Customs and Border Protection n.d.). This requires not only that methods used to screen people and materials be thorough but also that they achieve answers quickly so that extensive delay in the flow of people and goods does not occur. These organizations use multiple tools to interdict any number of illicit substances. Canine detection, X-ray and other imaging techniques, and IMS systems are all used to screen people and cargo for illicit substances. These methods work relatively quickly and can even be used in concert with each other when appropriately deployed. For instance, if an illicit substance is detected during a screening using X-ray equipment, further interrogation of the shipment using IMS may occur. IMS instruments are used for the detection of trace residues on surfaces that might indicate illicit contraband such as drugs and explosives concealed within the shipment. IMS has been demonstrated to be an effective screening method to help stem the entry of fentanyl across the US borders (Forbes et al. 2019). In addition, IMS systems have been used for decades by border protection agencies in other countries including Canada, Australia, France, South Korea, and Hong Kong (L. Kim, Personal Communication, 26 March 2020).

#### 8.2.4.4 Critical Infrastructure

Critical infrastructure describes the physical and cyber systems and assets that are so vital to a nation that their incapacity or destruction would have a debilitating impact on the physical or economic security or public health or safety of a country. The US Department of Homeland Security has identified 16 different critical infrastructure sectors (United States Department of Homeland Security n.d.). In some instances, regulations require that these locations are physically protected against threats. For instance, the US Nuclear Regulatory Commission (NRC) requires that nuclear facilities including nuclear reactors, fuel cycle facilities, and spent fuel storage and disposal facilities are physically protected against sabotage, theft, diversion, and other malicious acts. To achieve this goal, the NRC and its licensees use a graded approach for physical protection, consistent with the significance of the facilities or material to be protected. In so doing, the NRC establishes the regulatory requirements and assesses compliance, and licensees are responsible for providing the protection (United States Nuclear Regulatory Commission, n.d.). It is common for critical infrastructure systems to deploy IMS systems as part of their security protocol.

### 8.3 Conclusion

Clearly, the value of IMS lies in its ability to detect and identify invisible traces of target compounds in the air, on surfaces, and on people. Due to their many desirable features including portability, ease of deployment, fast analysis times, sensitivity, and selectivity to target substances, IMS systems are commonly deployed to protect both military and civilian populations. The development of these systems was fueled by the needs of the military and the aviation industries, but their value is not limited to these users. IMS systems are routinely deployed to protect critical infrastructure sites including government and nuclear facilities, chemical and other industrial plants, and transportation systems. Their value to the field of forensic science is rooted in the need for practitioners within this discipline to understand the transfer of trace amounts of material between two objects or people to help establish the elements of a crime.

Ion mobility spectrometers, however, are not without limitations. The detection capabilities can be critically impacted by sample matrix. This can complicate field analyses when sample matrices, such as those that may be recovered on the surface swipes, are complex. End users in the field rely on preprogrammed detection algorithms established by the vendor. This can cause both false positives from the matrix or false negatives when emerging threats are not incorporated into the detection algorithm. End users choose IMS instruments because they are very sensitive to specific classes of compounds. However, the instruments may get contaminated or overloaded. Although this is not usually detrimental to the detector in the long term, it can cause downtime or may even render the detector useless at a scene until the system is cleared of the substance. All these factors need to be considered by end users when these systems are being chosen for deployment.

Portable technologies have become more prevalent in recent years. This is evident in the breadth of technologies presented in the chapters of this text. Techniques that provide structural information of the chemical such as mass spectrometry and Raman spectroscopy have successfully been miniaturized and joined ion mobility spectrometry as on-site threat detectors. Each technique has its own advantages and disadvantages. This allows users to add multiple techniques to their detection capabilities and leverage their individual strengths. Ion mobility spectrometers, due to their many advantages and history of their expansion to different sectors as shown here, will continue to improve and evolve to meet new chemical challenges and the need for field detection of chemical threats.

## References

- National Research Council (2000). Appendix D: detecting and monitoring chemical agents. In: *Strategies to Protect the Health of Deployed U.S. Forces: Detecting, Characterizing, and Documenting Exposures* (eds. T.E. McKone, B.M. Huey, E. Downing and L.M. Duffy), 197–211. Washington, D.C.: National Academies Press.
- Armenta, S., Garrigues, S., de la Guardia, M. et al. (2014). Detection and characterization of emerging psychoactive substances by ion mobility spectrometry. *Drug Testing and Analysis* 7 (4) <https://doi.org/10.1002/dta.1678>.
- Balsamo, M. (2019). Federal prison system is photocopying inmate mail to curb drug smuggling. The Associated Press (21 October). <https://www.nj.com/news/2019/10/federal-prison-system-is-photocopying-inmate-mail-to-curb-drug-smuggling.html> (accessed 19 March 2020).
- Biello, D. (2009). Cocaine contaminates majority of U.S. currency. Scientific American (16 August). <https://www.scientificamerican.com/article/cocaine-contaminates-majority-of-american-currency> (accessed 19 March 2019).
- Bruker (2020a). *RAID-S2plus Technical Details*. Bruker <https://www.bruker.com/products/cbrne-detection/ims/raid-s2plus/technical-details.html> (accessed 20 February 2020).
- Bruker (2020b). *Technical Details: RAID-XP Combined Sensors for Radiological Detection and CWA's*. Bruker <https://www.bruker.com/products/cbrne-detection/ims/raid-xp/technical-details.html> (accessed 8 October 2019).
- Butler, R.F. (2003). *Mailroom Scenario Evaluation, Final Report*. United States Department of Justice <https://www.ncjrs.gov/pdffiles1/nij/grants/199048.pdf> (accessed 19 March 2019).
- Committee for an Assessment of Naval Forces's Defense Capabilities Against Chemical and Biological Warfare Threats, Naval Studies Board (2004). *Naval Forces' Defense Capabilities Against Chemical and Biological Warfare Threats*. Washington, D.C.: The National Academies Press.
- Organisation for the Prohibition of Chemical Weapons (2005). *Convention on the Prohibition of the Development, Stockpiling and Use of Chemical Weapons and Their Destruction*. Organisation for the Prohibition of Chemical Weapons [https://www.opcw.org/sites/default/files/documents/CWC/CWC\\_en.pdf](https://www.opcw.org/sites/default/files/documents/CWC/CWC_en.pdf) (accessed 14 June 2018).
- De Forest, P.R., Gaensslen, R., and Lee, H.C. (1983). *Forensic Science: An Introduction to Criminalistics*. New York: McGraw-Hill, Inc.
- Eiceman, G. and Stone, J. (2004). Ion mobility spectrometers in national defense. *Analytical Chemistry* November: 390A–397A.
- Elias, B. (2009). *Airport Passenger Screening: Background and Issues for Congress*. Congressional Research Service <https://fas.org/sgp/crs/homesec/R40543.pdf> (accessed 19 March 2019).
- Ewing, R., Atkinson, D., Eiceman, G., and Ewing, G. (2001). A critical review of ion mobility spectrometry for the detection of explosives and explosives related compounds. *Talanta* 54 (3): 515–529. doi: [https://doi.org/10.1016/S0039-9140\(00\)00565-8](https://doi.org/10.1016/S0039-9140(00)00565-8).
- Forbes, T.P., Lawrence, J., Verkouteren, J.R., and Verkouteren, R.M. (2019). Discriminative potential of ion mobility spectrometry for the detection of fentanyl and fentanyl analogues relative to confounding environmental interferents. *Analyst* 144 (21): 6391–6403. <https://doi.org/10.1039/C9AN01771B>.
- Headquarters, Departments of the Army, Air Force, Marine Corps and Navy (1998). Technical Manual, Operator's Unit and Maintenance Manual for Alarm (March). Chemical Agent, Automatic: M22.
- Hoffman, A., Eisenkraft, A., Finkelstein, A. et al. (2007). A decade after the Tokyo Sarin attack: a review of neurological follow-up of the victims. 172 (6): 607–610.
- Hyams, K., Murphy, F., and Wessely, S. (2002). Responding to chemical, biological, or nuclear terrorism: the indirect and long-term health effects may present the greatest challenge. *Journal of Health, Politics, Policy and Law* 27 (2): 273–291. <https://doi.org/10.1215/03616878-27-2-273>.
- Johnson, S. and Dastouri, S. (2011). *Use of Ion Scanners in Correctional Facilities: An International Review*. Correctional Services Canada <https://www.csc-scc.gc.ca/005/008/092/rr11-01-eng.pdf> (accessed 19 March 2019).

- Joshi, M., Centroni, B., Camacho, A. et al. (2014). Analysis of synthetic cathinones and associated psychoactive substances by ion mobility spectrometry. *Forensic Science International* 244: 196–206. <https://doi.org/10.1016/j.forsciint.2014.08.033>.
- Kraus, T.L. (2008). *The Federal Aviation Administration: A Historical Perspective, 1903-2008*. Washington, DC: United States Department of Transportation [https://www.faa.gov/about/history/historical\\_perspective](https://www.faa.gov/about/history/historical_perspective) (accessed 30 March 2020).
- Laljer, C. (2003). Joint Chemical Agent Detector (JCAD): the future of chemical agent detection. *Proceedings SPIE, Chemical and Biological Sensing IV* 5085 <https://doi.org/10.1117/12.508515>.
- Law Enforcement and Corrections Standards and Testing Program (2000). *Guide for the Selection of Chemical Agent and Toxic Industrial Material Detection Equipment for Emergency First Responders*, vol. 2. National Institute of Justice <https://www.ncjrs.gov/pdffiles1/nij/184450.pdf> (accessed 21 February 2020).
- Leary, P.E., Kammerath, B.W., Lattman, K.J., and Beals, G.L. (2019). Deploying portable gas chromatography-mass spectrometry (GC-MS) to military users for the identification of toxic chemical agents in theater. *Applied Spectroscopy* 73 (8): 841–858. <https://doi.org/10.1177/0003702819849499>.
- Ludwig, H.R., Cairelli, S.G., and Whalen, J.J. (1994). *Documentation for Immediately Dangerous to Life or Health Concentrations (IDLHs)*, 1–7. Cincinnati: United States Department of Health and Human Services <https://www.cdc.gov/niosh/idlh/pdfs/1994-IDLH-ValuesBackgroundDocs.pdf> (accessed 21 February 2020).
- Lyon, E. (2019). Problems with ion scanners used to detect drugs on prison visitors. *Prison Legal News* 30 (8): 18.
- Mäkinen, M.A., Anttalainen, O.A., and Sillanpää, M.E. (2010). Ion mobility spectrometry and its applications in detection of chemical warfare agents. *Analytical Chemistry* 82 (23): 9594–9600. <https://pubs.acs.org/doi/10.1021/ac100931n> (accessed 26 December 2018).
- Melamed, S. (2018). Are Pa. Prisons' drug screenings plagued by false positives? The Philadelphia Inquirer (3 October). <https://www.inquirer.com/philly/news/pennsylvania-department-of-corrections-sci-phoenix-ion-scanners-k2-20181003.html> (accessed 19 March 2020).
- Metternich, S., Zörntlein, S., Schönberger, T., and Huhn, C. (2019). Ion mobility spectrometry as a fast screening tool for synthetic cannabinoids to uncover drug trafficking in jail via herbal mixtures, paper, food, and cosmetics. 11 (6): 833–846. <https://doi.org/10.1002/dta.2565>.
- Mirzayanov, V.S. (2009). *State Secrets: An Insider's Chronicle of the Russian Chemical Weapons Program*. Denver: Outskirts Press, Inc.
- National Forensic Laboratory Information System (2018). *NFLIS-DRUG 2018 Annual Report*. Diversion Control Division of the United States Drug Enforcement Administration <https://www.nflis.deadiversion.usdoj.gov/DesktopModules/ReportDownloads/Reports/NFLIS-Drug-AR2018.pdf> (accessed 19 March 2020).
- National Institute of Justice (2000). *Guide for the Selection of Chemical Agent and Toxic Industrial Material Detection Equipment for Emergency First Responders*. Rockville, MD: The Law Enforcement And Corrections Standards and Testing Program.
- Occupational Safety and Health Administration (n.d.). *Toxic Industrial Chemicals (TICs) Guide*. United States Department of Labor <https://www.osha.gov/SLTC/emergencypreparedness/guides/chemical.html> (accessed 21 February 2020).
- OPCW Confirms Use of Sarin and Chlorine in Itamenah, Syria, on 24 and 25 March 2017 (2018). Organization for the Prohibition of Chemical Weapons. <https://www.opcw.org/news/article/opcw-confirms-use-of-sarin-and-chlorine-in-itamenah-syria-on-24-and-25-march-2017>.
- Pennsylvania Department of Corrections (n.d.). *Pennsylvania Department of Corrections*. How to Send Mail. <https://www.cor.pa.gov/family-and-friends/Pages/Mailing-Addresses.aspx> (accessed 30 October 2020)
- Preparedness Directorate Office of Grants and Training (2007). *Guide for the Selection of Chemical Detection Equipment for Emergency First Responders*, 3e. United States Department of Homeland Security.
- Rapiscan Systems (2019). *Technical Details: Hardened Mobile Trace*. Rapiscan Systems <https://www.rapiscansystems.com/en/products/hardened-mobiletrace> (accessed 8 October 2019).

- Schwartz, M. (2018). U.S. accuses Syria of new chemical weapons use. The New York Times (23 January). <https://www.nytimes.com/2018/01/23/world/middleeast/syria-chemical-weapons-ghouta.html> (accessed 31 January 2018)
- Scientific Working Group for the Analysis of Seized Drugs (2019). Scientific Working Group for the Analysis of Seized Drugs (SWGDRUG) Recommendations, Version 8.0. <http://swgdrug.org/approved.htm> (accessed 17 May 2020)
- Sirgany, S., & Kourdi, E. (2018). Dozens injured in toxic gas attack on Aleppo, Syria, reports say. CNN Middle East (26 November). <https://www.cnn.com/2018/11/25/middleeast/syria-gas-attacks/index.html> (accessed 29 November 2018).
- Sisco, E., Verkouteren, J., Staymates, J., and Lawrence, J. (2017). Rapid detection of fentanyl, fentanyl analogues, and opioids for on-site or laboratory based drug seizure screening using thermal desorption DART-MS and ion mobility spectrometry. *Forensic Chemistry* 4: 108–115. <https://doi.org/10.1016/j.frc.2017.04.001>.
- Smart, J.K. (2009). *Chemical and Biological Detectors, Alarms and Warning Systems*. Aberdeen Proving Ground: U.S. Army Research, Development and Engineering Command.
- Smiths Detection (2017a). *Technical Information - IONSCAN 600 Explosives and Narcotics Trace Detector*. Hemel Hempstead: Smiths Detection.
- Smiths Detection (2017b). *Technical Information: LCD 3.3 Compact, Wearable CWA Identifier and TIC Detector*. Smiths Detection <https://www.smithsdetection.com/products/lcd-3-3> (accessed 7 October 2019).
- Smiths Detection Inc (2018). *Develop Enhanced Chemical Explosives Detection Capability for United States Department of Defense*. Edgewood, MD: Smiths Detection <https://www.smithsdetection.com/press-releases/smiths-detection-inc-to-develop-enhanced-chemical-explosives-detection-capability-for-us-department-of-defense> (accessed 25 September 2019).
- Smiths detection Inc. (2020). *Smiths Detection Inc. Receives a \$90.8M IDIQ Contract to Manufacture Joint Chemical Agent Detector (JCAD) Adapter for US Department of Defense*. Edgewood, MD: Smiths Detection <https://www.smithsdetection.com/press-releases/smiths-detection-inc-receives-a-90-8m-idiq-contract-to-manufacture-jcad-adapter-for-us-department-of-defense/> (accessed 12 February 2021).
- Standing Committee on Public Safety and National Security (2018). *Interim Report: Use of Ion Mobility Spectrometers by the Correctional Service of Canada*. House of Commons, Parliament of Canada [https://www.ourcommons.ca/content/Committee/421/SECU/Reports/RP9998633/421\\_SECU\\_Rpt25\\_PDF/421\\_SECU\\_Rpt25-e.pdf](https://www.ourcommons.ca/content/Committee/421/SECU/Reports/RP9998633/421_SECU_Rpt25_PDF/421_SECU_Rpt25-e.pdf) (accessed 19 March 2020).
- Szinicz, L. (2005). History of chemical and biological warfare agents. *Toxicology* 214: 167–181.
- The Deputy Assistant to the Secretary of Defense for Chemical and Biological Defense (2001). *Chemical and Biological Defense Primer*. United States Department of Defense Chemical and Biological Defense Program <https://www.hsdl.org/?view&did=1504> (accessed 2 January 2019).
- The National Institute for Occupational Health and Safety (NIOSH). (2020). *Preventing Emergency Responders' Exposures to Illicit Drugs*. <https://www.cdc.gov/niosh/topics/fentanyl/risk.html> (accessed 30 October 2020).
- Theisen, L., Hunnum, D.W., Murray, D.W., and Parmeter, J.E. (2004). *Survey of Commercially Available Explosives Detection Technologies and Equipment 2004*. United States Department of Justice.
- Transportation Security Administration. (2004). *Five Airports to Serve a TSA Test Bed for Explosives Trace Detection*. <https://www.tsa.gov/news/releases/2004/06/17/five-airports-serve-tsa-test-bed-explosives-trace-detection-portals> (accessed 30 October 2020).
- Transportation Security Administration (2020). *TSA Air Cargo Screening Technology List (ACSTL), Version 11.2*. Transportation Security Administration [https://www.tsa.gov/sites/default/files/non-ssi\\_acstl.pdf](https://www.tsa.gov/sites/default/files/non-ssi_acstl.pdf) (accessed 19 March 2020).
- U.S. Customs and Border Protection (n.d.). Mission Statement of U.S. Customs and Border Protection. <https://www.cbp.gov/about> (accessed 30 October 2020).
- United States Army (n.d.). *Joint Chemical Agent Detector (JCAD) M4A1*. United States Army Acquisition Support Center <https://asc.army.mil/web/portfolio-item/cbd-joint-chemical-agent-detector-jcad-m4a1> (accessed 26 September 2019).

- United States Army, Marine Corps, Navy, Air Force (2005). Potential Military Chemical/Biological Agents and Compounds, Multiservice Tactics, Techniques and Procedures.
- United States Coast Guard (2019). *Review of U.S. Coast Guard's Fiscal Year 2018 Drug Control Performance Summary Report*. Office of the Inspector General of the United States Department of Homeland Security <https://www.oig.dhs.gov/sites/default/files/assets/2019-03/OIG-19-27-Mar19.pdf> (accessed 30 October 2020).
- United States Department of Defense (2018). *DOD Dictionary of Military and Associated Terms*. Washington, D.C.: United States Department of Defense.
- United States Department of Homeland Security (n.d.). *Critical Infrastructure Security*. Official Website of the United States Department of Homeland Security. <https://www.dhs.gov/topic/critical-infrastructure-security> (accessed 30 October 2020).
- United States Drug Enforcement Administration (2018). *Photo Illustration of 2 Milligrams of Fentanyl, A Lethal Dose in Most People*. United States Drug Enforcement Administration. <https://www.dea.gov/galleries/drug-images/fentanyl> (accessed 20 March 2020).
- United States Nuclear Regulatory Commission (n.d.). *Nuclear Security – Physical Protection*. United States Nuclear Regulatory Commission <https://www.nrc.gov/security/domestic/phys-protect.html#Fixed%20Site> (accessed 15 January 2020).
- United States Transportation Security Administration (n.d.). *Transportation Security Timeline*. Transportation Security Administration <https://www.tsa.gov/timeline> (accessed 30 March 2020).
- Vandam, L., Borle, P., Montanuri, L. et al. (2018). *New Psychoactive Substances in Prison: Results from an EMCDDA Trendspotter Study*. Lisbon: European Monitoring Centre for Drugs and Drug Addiction <https://doi.org/10.2810/7247>.
- Verkouteren, J.R. and Staymates, J.L. (2010). Reliability of ion mobility spectrometry for qualitative analysis of complex, multicomponent illicit drug samples. *Forensic Science International* 206 (1–3): 190–196.
- Yanini, Á., Esteve-Turrillas, F.A., de la Guardia, M., and Armenta, S. (2018). Ion mobility spectrometry and high resolution mass-spectrometry as methodologies for rapid identification of the last generation of new psychoactive substances. *Journal of Chromatography A* 1574: 91–100. <https://doi.org/10.1016/j.chroma.2018.09.006>.
- Zhou, Q., Peng, L., Jiang, D. et al. (2015). Detection of nitro-based and peroxide-based explosives by fast polarity-switchable ion mobility spectrometer with ion focusing in vicinity of Faraday detector. 5 (10659): 1–8. <https://doi.org/10.1038/srep10659>.

## 9

# Portable Spectroscopy in Hazardous Materials Response

David DiGregorio

*Hazardous Materials Emergency Response, Massachusetts Department of Fire Services, Stow, MA, USA*

## 9.1 The Hazmat Clinician

Hazardous materials or hazmat response is a unique discipline. Just like a firefighter trains in various techniques to extinguish fires and save lives or a medical clinician spends years studying the systems of the human body and must continue to keep abreast of changes in techniques and procedures, hazmat technicians must constantly train and hone their skills to successfully mitigate a potentially dangerous scene. How does a hazmat technician decide what tactics, techniques, and procedures to use that could result in the least amount of harm? The incident commander (IC) must coordinate with the hazmat team and approve the objectives for each specific incident and clearly relay relevant information to all responders at the scene and must inform all stakeholders affected by the incident.

As a former practicing medical clinician, I see significant parallels between the hazmat scene mitigation and the treatment of an emergency room patient, whether that be one patient or a mass casualty event. This may sound like a stretch, but as you read on, I believe you will see the similarities between the two events. As mentioned earlier, one must immediately begin setting the goals for the specific event, keeping in mind the stakeholders involved.

When a patient enters the emergency department, the variables are numerous. Is the patient conscious, and if so, can they communicate? If not, was the individual accompanied by someone able to convey what has happened prior to the event, during the event, and any pertinent information that has occurred since the initial event had taken place until the time you are presented with this person? What are the pertinent positive factors that have occurred? As importantly, what are the pertinent negatives?

Pertinent positives include what you see, signs and symptoms of injury, allergies, medications, past medical history (if known), last known oral intake, and the events leading up to the injury or illness. In the medical field, this mnemonic is called a SAMPLE history. Pertinent negatives can be derived from these factors and help direct your treatment goals. If there was no specific trauma that would have caused a head or neck injury, the clinician must check the unconscious patient more carefully using X-rays, MRI, or ultrasound. Hopefully, readers could begin to see how a similar approach can be used during a hazmat event.

Not every instrument or technology is pertinent to every situation, and to employ unnecessary techniques is often a waste of valuable time and effort. In medicine, specifically in the emergency room, an important tenet is to first “rule out the bad stuff,” which refers to a cause of severe damage or death. Once complete, the clinician can “diagnose and mitigate this event.” It is no different in hazmat.

### 9.1.1 Collecting Information

Many believe that gathering data begins with the arrival at the scene. Although much helpful information can be collected at the scene, the hazmat technician is often not the first responder. The hazmat scene is a dynamic one, and factors change rapidly. Information that can be gathered prior to the arrival of the hazmat team is often extremely helpful. The ability to speak to those responders first on the scene is invaluable. The type of information they may be able to provide include

- Victim signs and symptoms.
- Unusual odors.
- Clouds or mists.
- Approximate time of release or incident.
- Initial readings (multi-gas, thermal imaging, etc.).
- Flame or smoke color.
- Information gathered from employees with regard to chemicals used, firsthand account of the event.
- Bystander accounts.
- Initial mitigation steps.

Often, first responders can begin by gathering information such as Safety Data Sheets and blueprints of the building and collecting keys and passes to enable hazmat entry personnel access to restricted areas if required. Good communication with those on the scene should happen well before the team's arrival, if possible.

## 9.2 Defining the Mission: Meeting with the IC

There are several missions that may be asked of the hazmat team when arriving at the scene. Most often, the IC is a member of the local fire department, which responds to such incidents; this is not always the case. If the scene involves a criminal matter, law enforcement may have significant input in the type of sampling needed and how these samples will be taken. Often a collection of substances in question must be acquired and packaged for a crime laboratory or public health laboratory prior to any substances being used for on-scene sampling, detection, and identification. This must be established early on as it may require more stringent chain-of-custody procedures and the ruling out of any unexpected hazards such as radiation or energetic materials.

If working for the local fire department, the hazmat team must determine the incident commander's priorities. Some ICs have a wealth of experience working with hazmat teams and are confident in making decisions during calls involving hazardous materials. Others may be reluctant to make these calls and will require more guidance. Often in these cases and if manpower allows, assigning a liaison to the IC is prudent. This individual can serve as a conduit from the hazmat team to IC staff to explain operational details in depth when required. In either case, the hazmat team will advise and make recommendations on an action plan for the IC's approval.

Team leadership must determine the desired outcome of the incident at hand. Is the goal of the team and the IC to decrease or eliminate the hazard, causing the least amount of harm? Is the objective to identify the product that is causing the hazardous situation, or is that factor known? As stated earlier, is the team expected to collect and provide samples for a confirmatory laboratory, whether for law enforcement, or public health or is identification a task expected from the hazmat team itself? How specific must the team be with its results? Often, detection of a product, e.g. an unknown gas, is specific enough to determine later if mitigation actions have lowered the harm to safe levels. Is cleanup of the scene an expectation of the IC? If so, is that a capability of your hazmat team? If not, the IC will most often look to you for ideas and recommendations to mitigate and recover the scene. To prevent confusion, the answers to these and many other questions must be determined prior to establishing a plan of attack and communicating that plan with your team.

### 9.2.1 Assigning Roles

Roles are assigned upon arrival, often by the team leader aide. For larger events, roles are divided into the following groups:

- Command and Staff
  - Team Leader
  - Entry Leader
  - Decontamination Team Leader
  - Team Leader Aide
  - Safety Officer
  - Liaison
- Planning
  - Situation Unit
  - Communications Unit
  - Documentation Unit
- Operations
  - Entry Group
  - Decontamination Group
  - Area Monitoring Group (as needed)
- Logistics\*

### 9.2.2 Site Setup

After positions are assigned, members of the team get to work and contribute. Scene setup, to include establishing the decontamination line and delineating hot, warm, and cold zones, conducting research on potentially hazardous products, readying the entry and backup teams, and meeting with other agencies and industry experts are all important and most often conducted early on. The United States Environmental Protection Agency (EPA) defines the three most frequently identified zones (US Environmental Protection Agency 2017) as follows:

1. The exclusion zone (or hot zone) is the area with actual or potential contamination and the highest potential for exposure to hazardous substances.
2. The contamination reduction zone (or warm zone) is the transition area between the exclusion and support zones. This area is where responders enter and exit the exclusion zone and where decontamination activities take place.
3. The support zone (or cold zone) is the area of the site that is free from contamination, and that may be safely used as a planning and staging area.

### 9.2.3 Information Sharing

#### 9.2.3.1 Communication Board

Once the IC goals have been established, these goals must be communicated with the team as they arrive on the scene. Members of the team may be arriving at different times, and preparation may already be underway. It doesn't make sense to have to stop operations to communicate the basic information associated with the incident each time a new member arrives. A good method of conveying information to the team is by using a whiteboard or communications board. This device should be placed in an area that will be seen by arriving members as they check into the scene. This allows for important information to be disseminated quickly to the team; more detailed

---

\* These assignments may differ from team to team.



**Figure 9.1** Hazmat Communications board on the scene to keep all personnel informed in real time. *Source:* Randy Quarles.

information can be conveyed later. The team leader should assign a team member to update information on the communication board as it changes or as more information is obtained (Figure 9.1).

Information that may be detailed on the communications board include:

- Chemical characteristics
- Packaging
- Decontamination
- Personal protective equipment (PPE)
- Command assignments
- Incident information
- Unit assignments
- Tactical goals
- Communications
- Staging
- Weather

#### 9.2.3.2 Initial Brief

Whether a relatively minor or routine hazmat event or a large-scale or multidisciplinary response, communicating the plan to all team members is paramount to a successful outcome. This begins at the outset during the initial

team officers brief involving representation from command and staff and occurs prior to any operational tasks being conducted. This briefing often includes:

- Review of incident strategy
- Review of the situation
  - Type of release
  - Chemical information
  - Site layout and description
  - Weather information
  - Hazards
  - Health effects of exposure
  - Hot and warm zones specifications
- Review of the Hazmat Action Plan
- Review of the Site Safety Plan
- Review of the Rapid Intervention Team (RIT) Plan
- Scope of operations and expected roles of the operational units

Once this briefing concludes, each group leader conducts a back brief to members of their sections to ensure that all team members understand the mission.

## 9.3 Hazmat Huddle or Pre-Entry Brief

Some team leaders will conduct a pre-entry brief to reiterate the downrange plan. Routes of entry and egress are clarified. Decontamination procedures are reviewed. Hand signals and communications checks are conducted prior to entry into the hot zone. Tasks such as reconnaissance, detection, sampling, air monitoring, identification and/or mitigation are reviewed. This leads us to the discussion of selecting the appropriate technologies for the mission at hand.

### 9.3.1 Selecting Technologies

Various technologies have been discussed in great detail throughout the two volumes of this text. Each has its own unique abilities and limitations. No one instrument exists that can provide all of the answers needed or wanted at a hazmat incident. Selecting an inappropriate technology for the scenario at hand can lead to confusion or frustration, prolonging the incident and perhaps causing damage to the instrument itself or harm to the technician. Discussion must take place prior to deploying these various technologies downrange as to what the expected outcomes may be and how they relate to the mission goals. Some technology is suited to classify the type of substance at hand. Others may detect the presence of something other than normal background, and others can identify the specific compound or material. Each has its place in the realm of hazmat response. The educated hazmat technician knows the capabilities of the available technology and deploys them in a complementary fashion to accomplish the mission.

### 9.3.2 Know What's Out There

According to the US Department of Transportation Pipeline and Hazardous Materials Safety Administration, in 2017, there were a reported 3391 incidents of hazmat spills during transit. This does not take into account the many industrial and residential accidents that take place every day. Nor does it account for nefarious acts where

a hazmat team may be asked to identify unknown substances. How does a hazmat response team begin to decide what technologies and equipment to purchase and carry on their vehicles with limited space?

If you had five technologies to carry with you into the hot zone, knowing nothing else, what would you choose? I have heard this question asked several times in different ways over the years and have heard many answers, and although there may be some slight differing of opinions, the following seems to be the consensus opinion of many:

- pH paper
- LEL (lower explosive limit) sensor
- Oxygen sensor
- Photoionization detector
- Radiation monitor/detector

With all of the hundreds, perhaps thousands of instruments, technologies, and gadgets out there, why do the majority usually settle on the list above? It comes down to our earlier discussion; rule out the “bad stuff” and then continue the mission. So, how do we break this down into something more palatable? Of the millions of chemicals that exist, what are we really responding to? According to *Hazardous Materials Monitoring and Detection Devices, Hawley, Third Edition* (Hawley 2020), the top 10 bulk chemicals released during transportation in 2017 are shown in Table 9.1. According to the same publication, the top 20 chemicals released within the United States are shown in Table 9.2.

Knowing that the listed chemicals are the most frequently encountered during hazmat incidents, we can look at the commonalities of each. Many of these chemicals are in the same chemical “families,” and thus have many similarities with regard to behaviors. Learning the behaviors of each family and understanding the capabilities of the monitoring equipment available makes choosing these technologies less daunting.

Taking a closer look at the lists above, we can see that many, if not all, present hazards that can be placed in just a few groupings. At the risk of oversimplifying this concept, each fit into one of the following, as shown in Figure 9.2; fire hazard, corrosive hazard, and toxic hazard. I have included radiological hazards as a separate category. Response to potential energetic, radiological, or nuclear hazards involves its own set of skills and equipment but should be considered or ruled out on most calls.

Getting back to the five technologies that most would choose to take downrange, the reason now becomes clearer. Let’s discuss the capabilities and limitations of each of these technologies and how they can be deployed to identify the hazards above.

- Fire



- Corrosive



- Toxic



- Radiation



**Figure 9.2** Hazmat risks of concern.

**Table 9.1** Top 10 bulk chemicals released during transportation in 2017.

**Top 10 bulk chemicals released (2017)**

---

- Flammable liquids
- Sodium hydroxide
- Hydrogen peroxide
- Acetone
- Potassium hydroxide
- Corrosive liquids (acids)
- Alcohols
- Methanol
- Caustic liquids (bases)
- Ethanol

---

**Table 9.2** Top 20 chemicals released within the United States.

**Top 20 chemicals released within the United States**

---

- Ammonia
- Benzene
- Butadiene
- Chlorine
- Combustible liquids (including various oils)
- Crude oil
- Ethyl alcohol
- Ethylene glycol
- Flammable liquids
- Gasoline
- Hydrochloric acid
- Hydrogen cyanide
- Hydrogen sulfide
- Methane
- Methanol
- Propane
- Refrigerant gases
- Sodium hydroxide
- Sodium hypochlorite
- Sulfuric acid

---

### 9.3.3 pH Paper

pH paper is a rapid and fairly accurate technology to measure “corrosiveness.” The Occupational Safety and Health Administration (OSHA) definition of a corrosive is a chemical that produces destruction of skin tissue, namely visible necrosis through the epidermis and into the dermis, in at least one of three tested animals after exposure up to a four-hour duration (Occupational Safety and Health Administration ). Corrosives can also damage or even destroy metal. Most corrosives are either acids or bases.

pH paper alone can determine whether we are dealing with an acid or base. Although it does not have the capability of positively identifying a specific chemical, acids and bases have a pH value. Many chemicals can be ruled in or ruled out using a single piece of pH paper. Ammonia tends to have a pH of approximately 13, while hydrofluoric acid has a pH of 0–1. This is easily distinguishable. Sodium hydroxide or lye also has a pH of 13, so other methods would have to be used to distinguish between ammonia and lye.

Knowing the pH can be important because corrosives can destroy skin tissue. pH can help determine the proper level of PPE needed to keep those in the hot zone safe. It can also play a role in determining which technologies to take downrange and which should be kept away. Due to the destructive nature of corrosives, some instruments and sensors may become damaged or inoperable if exposed to these substances, and consideration must be given to this issue.

### 9.3.4 LEL Sensors

Mixtures of flammable gases or vapors with air will combust only when they are within particular concentration ranges. When a gas is present at a concentration below its LEL or lower flammability limit (LFL), it is considered too lean a mixture to burn and cannot be ignited. At concentrations above its upper explosive limit (UEL), the fuel/air mixture is too rich to burn and not ignite (DeHaan and Icove 2012). LEL sensors are used to determine the flammability of the gas in the environment in which it is found. Thus, the LEL sensor is used to determine the fire risk. There are several types of LEL sensors with varying sensor types. Sensitivity of these different sensors varies, and each has advantages depending on the environment in which they are deployed. The operator should be familiar with the LEL’s capabilities and limitations.

Zero percent LEL represents a combustible gas-free environment, whereas one hundred percent LEL represents an atmosphere in which gas is at a lower flammable limit. OSHA and the EPA have established action levels for first responders and are, for the most part, well accepted. These values are summarized in Table 9.3.

Flammables and combustibles are the leading category of hazardous materials released in the United States. The use of the LEL sensor as an initial entry tool, taking into account its limitations, is commonplace with most fire departments and hazmat teams across the country.

### 9.3.5 Oxygen Sensors

Oxygen is necessary to sustain human life. It is also necessary to allow for most hazmat monitors to function correctly. The human body functions best at 21% oxygen in most cases, barring some respiratory conditions. This

**Table 9.3** OSHA and EPA recommended action levels for first responders based upon %LEL.

Level (% of LEL)	Action
<10% (EPA)	Continue to monitor with caution
10–25% (EPA)	Continue to monitor but use extreme caution, especially as higher levels are found
>10% (OSHA)	Requires evacuation
>25% EPA	Explosive hazard: evacuate

**Table 9.4** Effects on the body at various oxygen breathing levels (European Industrial Gases Association AISBL 2018).

Oxygen percent at sea level (atmospheric pressure = 760 mmHg)	Effects
20.9	Normal (below 19.5% is considered oxygen deficient)
19.5–10	Increased breathing rates; accelerated heartbeat; and impaired attention, thinking, and coordination
10–6	Nausea, vomiting, lethargic movements, and perhaps unconsciousness
<6	Convulsions, then cessation of breathing, followed by cardiac standstill (death). These symptoms can occur immediately.

1. Adapted from Title 29 of the U.S. *Code of Federal Regulations*, Parts 1910 and 1926 (United States Department of Labor, Occupational Safety and Health Administration 2012).
2. These indications are for a healthy average person at rest. Factors such as individual health (being a smoker), degree of physical exertion, and high altitudes can affect these symptoms and the oxygen levels at which they occur.
3. A hazardous atmosphere oxygen concentration range as defined by OSHA is outside the range of 19.5 and 23.5% (United States Department of Labor, Occupational Safety and Health Administration 2012).
4. While the percentage of oxygen does not change with altitude, the partial pressure of the atmosphere decreases, which creates physiological effects similar to oxygen deficiency. These effects increase at higher altitudes. Working at altitudes above 2 438 m (8 000 ft) can have similar effects to working in a 15% oxygen atmosphere and working at altitudes of 4267 m (14 000 ft) can have effects similar to a 12% oxygen atmosphere. Precautions such as supplemental oxygen and acclimatisation shall be taken when working at altitudes to protect the employees against the effects of altitude sickness and other physiological effects similar to those experienced with decreasing oxygen concentrations. Consult knowledgeable medical and safety professionals regarding the specific precautions to take when working at high altitudes.

is normally the percentage of oxygen in air. The minimum prolonged oxygen concentration for human survival is 19.5%. As oxygen levels decrease, survivability follows (see Table 9.4).

If oxygen is below 21% in the environment, another gas is displacing that oxygen. The percentage of the decrease in oxygen is directly related to what is displacing it; a 1% drop in oxygen concentration from 20.9 to 19.9% would indicate that 50 000 parts per million (ppm) of a contaminant is present. Thus, for every 0.1% drop in oxygen displayed on the meter, 5000 ppm of something has entered the atmosphere. The contaminant, at this level, could be potentially dangerous or even deadly if toxic.

An increase in oxygen level is also important to know. Oxygen is needed for combustion. An oxygen-enriched environment (one over 20.9%) indicates an oxidizing agent may be present, indicating an increase in fire hazard.

### 9.3.6 Photoionization Sensors

Most often, oxygen sensors are included in a series of sensors assigned to one meter. A four-gas or five-gas meter, often known as a multi-gas meter, contains sensors for multiple common gases of concern. Many of these instruments employ photoionization sensors as they are very effective in detecting volatile organic compounds (VOCs) - those compounds that are carbon-based chemicals that easily evaporate into the air. Along with carbon, they contain elements such as hydrogen, oxygen, fluorine, chlorine, bromine, sulfur, and nitrogen. VOCs are commonly referred to as solvents, a common hazard. The most common sensors in these instruments include an LEL sensor, an oxygen ( $O_2$ ) sensor, a carbon monoxide sensor (CO), and a hydrogen sulfide sensor ( $H_2S$ ). An HCN (hydrogen cyanide) sensor is typically added as part of the five-gas meter array. These gases are often monitored within confined space environments. These instruments allow for the replacement of sensors as needed and the swapping of various sensors based on the mission.

### 9.3.7 Radiation Monitors/Detectors/Identifiers

All hazmat teams should include some type of instrument capable of detecting and measuring radiation. Members should be monitored for accumulated dose if a release or transmission of ionizing radiation is suspected. Some teams will have the ability to detect and identify radioisotopes within the environment. Although identification is important, this task is often assigned to specially trained technicians within the state. Early detection by local first responders and/or hazmat teams is paramount to rapid response and determination of a successful mitigation plan.

Each of these technologies provides the hazmat team with crucial information. As was stated previously, many, if not all, of the “bad” things that can cause injury and property damage can be detected with the five technologies discussed. Often, detection of the problem is not enough. Identification and mitigation strategies are expected from the hazmat teams. The next several pages will discuss how more advanced technologies can be deployed in a hazardous environment to obtain vital data. For a thorough description of many of these technologies, see Volume 1 of this text, Chapter 3 by Schiering and Stein for a discussion of portable FT-IR, Chapter 6 by Rathmell, Bingemann, Zieg and Creasey for a discussion of portable Raman, Chapter 14 by Snyder for a discussion of portable MS, Chapter 15 by Leary, Kammrath and Reffner for a discussion of portable GC-MS, chapter 16 by Blakeman and Miller for a discussion of portable HPMS, and Chapter 17 by DeBono and Leary for a discussion of portable IMS.

### 9.3.8 Scenario

A good way to show how to develop a strategy is by applying a strategy used at a previous hazmat incident and going through the rationale for that strategy. At this previous incident, a local fire department has called for a hazmat response to a home with two deceased individuals. There is a white/brown powder in a large baggie broken on the floor by the bed and containers of unknown substances in the basement. Some appear to be liquids and some powders. Two local law enforcement officers have been transported to a medical treatment facility after investigating the residence with complaints of dizziness, lightheadedness, dry mouth, and palpitations. The home has been cordoned off and awaits your response. As the team leader, you meet with the IC, and he requests that the product be identified and possibly neutralized prior to re-occupancy. Your team has the following technologies:

- High pressure mass spectrometry (HPMS)
- Raman
- Fourier-transform infrared (FT-IR)
- Colorimetrics (gas detection tubes, test strips, direct-read instruments)
- Biological testing (immunoassay)
- Ion mobility spectrometry (IMS)
- Gas chromatography-mass spectrometry (GC-MS)
- Multi-gas meter
- Pancake radiological meter and dosimeter
- Thermal imager
- pH paper

What do you and your team do?

Is having this array of technologies a benefit or a hindrance? That is dependent upon the team’s knowledge base of each technology and its strengths and weaknesses. Carrying all of these instruments downrange would be cumbersome and counterproductive.

A sample plan should be developed prior to sending the entry team into the hot zone. Zones need to be established. The level of PPE to include respiratory protection must be determined. Decontamination procedures should be discussed, approved, and delineated to the decontamination team as well as the entry and RIT teams. Are all plans consistent with the IC’s goals and requests?

Other considerations: Is this incident associated with a crime? Will the results of the testing of this sample be used for prosecution? If so, will this be a local, state, or federal case? Who makes this determination in your

jurisdiction, and is there a concern with the possible “destruction” of evidence? Will a sample need to be packaged for a confirmatory laboratory analysis? Does this take precedence over field sampling?

In most cases, confirmatory testing must be performed by a fixed facility laboratory. Do you have joint protocols with these laboratories about how the sample must be packaged, what screening must take place prior to the lab accepting the sample? Has your team considered chain-of-custody issues? These are a few of the many questions that should be asked prior to sampling and field testing.

At this incident, the State Police would like to pursue prosecution and request a sample be sent to the State Crime Laboratory. They are also requesting field sampling and testing to be conducted if there is enough product in the vehicle to provide the lab with a sample and concurrently conduct field testing.

After the initial site is set up, the leadership team is reconvened to discuss the Hazmat Action Plan and Site Safety Plan. IC goals are reiterated, where section leaders discuss their responsibilities with each other. Other contributing agencies discuss concerns and plans. Once all factors are considered, and the Hazmat Action Plan is approved by the IC, section leaders discuss the responsibilities and tasks within their section with those assigned.

Lastly, a pre-entry brief is conducted to review overall downrange operations. Can all of these tasks be completed in one entry, or will tasks such as screening, sample collection, and testing be split into multiple entries? Based on the answers to these questions, instrument selection is determined. The team decides that since the substances remain unknown, and the officers became symptomatic after a fair amount of time in the home, the initial entry team will conduct a reconnaissance in level B PPE with self-contained breathing apparatus (SCBA). Combinations of PPE are generally classified into four levels, ranging from the most protective (Level A) to the least protective (Level D). These levels consist of a combination of protective equipment and clothing that help reduce respiratory, eye, skin, and other types of exposures (Hazwoper Training 2019). One of the goals of the initial entry team is to rule out hazards to decrease the level of PPE required. The initial entry team most often conducts a full assessment of the extent of the hazards, allowing the team to develop an entry and mitigation plan for subsequent entry teams. Ensuing teams may conduct other tasks such as sampling, neutralizing hazardous materials, or shutting down processes to lessen the hazard release. Pictures will be obtained and reviewed upon return to develop a sample collection and testing plan.

The team decides that the initial entry team will carry a multi-gas detector to rule out toxic compounds, determine O<sub>2</sub> levels and flammability hazards. They also carry radiological monitoring equipment and pH paper, both wet and dry, to rule out any threat of ionizing radiation and corrosivity, respectively. Lastly, they will carry a camera with a secure digital (SD) card, enclosed in a protective casing, to capture pictures of potential sampling sites.

Readings were as follows:

- Radiation: background
- LEL: no change from background
- O<sub>2</sub>: 21.9%
- All other sensor readings are within normal limits

Upon return, the pictures are reviewed, and a sampling plan is discussed. The decision is made that although the substances remain unknown, PPE to include respiratory protection can be decreased to splash protection with P100 cartridges. The P100 particulate cartridge filters at least 99.97% of airborne particles and is strongly resistant to oil. The mask with the P-100 cartridge tends to be far less cumbersome and provides longer stay time than the SCBA. The entry team is briefed on the priority of sampling: first is the white powder in the bedroom, and second is the liquids in the refrigerator in the basement. If there are other samples of opportunity that are discovered, this information is to be radioed back to the entry team leader before sampling takes place.

Now that the environment has been cleared of explosive or energetic hazards as well as any radiation hazard that may cause the responders immediate harm, the team must determine which technologies will accomplish the mission. What considerations must go into choosing the instruments to take into the hot zone? Let's discuss this decision process in detail for choosing each of the technologies listed above.

## 9.4 HPMS

### 9.4.1 Advantages

HPMS is relatively new to field sampling. In the hazmat community, HPMS typically refers to a mass spectrometer that operates at modest pressures, almost at atmospheric pressure. For a thorough review of HPMS instrumentation and technology, please see the chapter by Blakeman and Miller in volume one of this text. HPMS also has a high sensitivity, capable of measuring some substances at the parts-per-billion level in the vapor phase at the nanogram level for particles. It offers vapor, solid, and liquid analysis. Even though HPMS does not offer separation capabilities on the front end, it sometimes has the ability to “see” small concentrations of product hidden within larger bulk substances depending upon the ionization response of the sample matrix. Field users can analyze in different modes of operation to include drugs, explosives/energetics, chemical weapons, weapons of mass destruction, and precursors to include fourth-generation agents (FGAs). Start-up is relatively fast and easy, which is important in hazmat response. The analysis is quick, and the interface with the results screen is relatively uncomplicated.

### 9.4.2 Disadvantages

One of the first aspects of the HPMS that hazmat teams will note is that it is currently one of the more expensive technologies available. Teams with a limited budget must consider this. Although extremely sensitive and accurate, the limited library for toxic industrial chemicals (TICs) and toxic industrial materials (TIMs) may deter some teams from purchasing if there is a need to cover a broader base of substances. Due to the intricate technology being “shrunk down” for field use, this technology can still be rather bulky. There are specific nuances to operating and maintaining the instrument for peak performance. Although this can be handled at the user level, care must be taken to consistently train with this technology to take full advantage of its powerful applications. This technology is considered to be destructive as a small sample is required for sampling. Although a minute amount, this aspect should be cleared with law enforcement if the sample will be used for evidence in the future.

## 9.5 Raman Spectroscopy

### 9.5.1 Advantages

There are several manufacturers of field Raman technology. For a thorough review of Raman instrumentation and technology, please see the chapter by Rathmell et al. in volume one of this text. Most manufacturers have taken into account size and ergonomics to allow for ease of use in the field. Many of the Raman technology manufacturers have included a vast library of TICs and TIMs, as well as energetics and weapons of mass destruction (WMD) agents and precursors. The use of Raman is relatively easy, a point-and-shoot technology. Raman is a very good technology to identify pure products or products in mixtures with concentrations over 7–10%. Products packaged in clear bottles or bags can be identified without opening the container by aiming the laser into the contents of the container. This capability is especially important to responders that are concerned about exposure to unidentified substances. The laser depth can be adjusted to better “focus” on the sample to improve results. Certain Raman systems, using especially offset Raman spectroscopy (SORS), can detect product through opaque packaging by taking into account the packaging material in its process and subtracting it from the results. Raman is considered a nondestructive technology and is often preferred by law enforcement. Another advantage of this technology is that it does not recognize water, which can significantly interfere with other technologies. Most instruments are user-friendly, and “button-ology” can be easily taught. Lastly, most Raman instruments include a delayed laser analysis option, allowing the user to step away prior to activation to increase safety.

### 9.5.2 Disadvantages

Raman technology involves the use of a laser, which, if pointed in the direction of the eye, can cause eye injury. As mentioned above, mixtures tend to be an issue with Raman; chemicals may not be detected if less than 7–10% of the total sample concentration. Another issue with this technology stems from the heat generated from the laser. Dark materials have the possibility of igniting through heat absorption from the laser. This is especially problematic with flammable or energetic materials; thus, it is best not to use Raman with darker colored materials. It is always good practice to separate a small amount of product from the original source when focusing the laser at the sample, if possible. If ignition does occur, the likelihood of significant damage is lessened by using a smaller sample size. Some samples also fluoresce, which can challenge the identification capability of the Raman. The fluorescence interference may result from the analyte or impurities in the sample matrix. This can make identification with the Raman delayed, if not impossible. Some manufacturers have decreased the occurrence of fluorescence significantly using a 1064 nanometer (nm) excitation laser rather than the more typical 532 or 785 nm systems.

## 9.6 Fourier-Transform Infrared Spectroscopy (FT-IR)

### 9.6.1 Advantages

Similar to Raman technology, manufacturers of portable FT-IR systems have catered to the hazmat community and designed much of their products to suit field use. Please see Chapter 3 by Schiering and Stein in volume one of this text for a thorough review of FT-IR instrumentation and technology. Ergonomics, button size, weight of the product, and ease of use have all been considered. Some instruments are designed for solid and liquid use; others are focused on the identification of gases. Many of these instruments have ample libraries, and the user should compare the needs of their department with the library's capabilities. FT-IR works best to identify organic solvents, chemical weapons, many TICs, explosives, and drugs. Materials that fluoresce that tend to cause issues with Raman technology are not an issue with FT-IR.

### 9.6.2 Disadvantages

Like Raman technology, FT-IR does not identify compounds if the concentration of the total product is less than ~7–10%. FT-IR can usually differentiate between products if the concentration of each is above 10%. Compounds containing water will generate a water spectrum that may “mask” other substances within the compound, similar to the way fluorescence masks other substances in the Raman. FT-IR requires that a small portion of the product be placed on the instrument for identification. Although the analysis doesn't degrade or decompose the sample, the samples are not usually recovered post-analysis for hazmat teams. Thus FT-IR in hazmat is considered a “destructive” method of identification.

## 9.7 IMS

### 9.7.1 Advantages

IMS systems are usually used in hazmat environments to detect gas-phase threats. For a thorough review of IMS instrumentation and technology, please see the chapter by DeBono and Leary in volume one of this text. A common theme with many of the previously mentioned technologies like Raman and FT-IR is the extent of the substances in the libraries. Raman and FT-IR instruments usually offer extensive libraries of chemicals and products that can be matched against samples analyzed at a scene. IMS works the same in that it matches the data from the sample

analyzed at the scene and compares it to libraries to provide a “match,” but the onboard libraries for IMS systems are much more limited. Most IMS detectors will only alarm to a limited number of substances (usually on the order of about 40 or 50 chemicals at most). Hazmat teams must consider their needs and their mission and compare it to the abilities of the specific instrument. Some IMS instruments are focused on chemical warfare agents (CWAs), while others have a more in-depth TICs and TIMs library. Other IMS technologies incorporate a sensor array. Knowing the capabilities of the instrument is paramount to the unit’s success. IMS tends to be high in sensitivity, with some instruments manufactured with the ability to “sniff” out abnormalities in the environment and lead the user to the source through visual and audible prompts. IMS can be a good complement to photoionization detectors. Some IMS detectors classify products within families or groups. This can be extremely helpful to the technician in the field to narrow down possible hazards as well as provide pertinent negatives. As an example, IMS can determine the presence of an organophosphate. Another instrument may have the ability to determine whether it is sarin, soman, or a common pesticide, but for immediate information for the IC and medical providers, the general organophosphate result may be sufficient initially.

### 9.7.2 Disadvantages

Some chemicals do not generate good IMS results. Usually, vendors will provide a list of the chemicals their system is capable of detecting. The IMS type of ionization method is one of the primary factors that will determine the effectiveness of the system for a specific chemical. In addition, the sample matrix, which is difficult or even impossible in hazmat environments to control, can also challenge IMS detection results. It must be understood that IMS is a presumptive method and should be used for detection and classification rather than for identification of chemicals or products. IMS instruments are limited because they have focused libraries; this must be considered. False positives can be an issue as substances with similar chemical components as those programmed to detect in the library may cause the instrument to alarm.

## 9.8 GC-MS

### 9.8.1 Advantages

GC-MS has been a gold standard for chemical detection in fixed facility labs for several years. For a thorough review of GC-MS instrumentation, technology, and applications, please see the chapter by Leary et al. in volume one of this text. Attempts have been and continue to be made to “ruggedize” these instruments for field use with varied success. A primary limitation is that these systems require a vacuum for operation, and pumps required to achieve the necessary vacuum can be logistically problematic. GC-MS will identify, not just detect, components of a product at low concentrations (ppm levels). This can be an advantage or disadvantage based on the knowledge base of the user. The GC-MS can identify chemicals in liquid, solid, and vapor phases. The primary requirement for successful analysis using GC-MS is that the chemical must have an appreciable vapor pressure at the column temperature. Most GC-MS systems offer an extensive chemical library and can complement other detectors used in the field. Newer systems have taken into account the need for users to operate the instrument in PPE. Larger screens and more convenient controls are helpful.

### 9.8.2 Disadvantages

Although manufacturers have come a long way in making the field GC-MS more user-friendly, the bottom line is that as a best practice, this instrument requires consistent training by members dedicated to learning the science

and techniques associated with GC-MS. The instrument does best when operated often. The “art” and science of interpreting chromatograms and spectra and understanding the nuances of this technology is one that requires time and practice. The benefits may be worth the purchase for those teams that can dedicate staffing in this way. Cost is another factor to consider. Often these instruments are too expensive for the team to invest in this one technology.

## 9.9 Colorimetrics

### 9.9.1 Advantages

One underutilized technology on many hazmat teams is colorimetric tubes. Often, this technology allows the user to classify the family of the chemical that is present rather than specifically identifying the hazard, although there are cases where this technology will identify the hazard if present. Many times, multiple tubes are used to accomplish this task. Each tube has a very specific set of instructions that must be followed for accurate results. The use of multiple tests can rule out specific hazards, allowing the team to make decisions on PPE, ventilation, etc. If present, generalized concentrations of substances can be determined.

### 9.9.2 Disadvantages

Colorimetric tubes are very environmentally sensitive. Changes in temperature and humidity can play a significant role in the accuracy of these instruments. The user MUST pay close attention to the instructions on each tube, as they all vary significantly from tube to tube. Also, color interpretation can be subjective. Some vendors have tried to remove this subjectivity by offering electronic readers to interpret the color. This technology performs better with higher vapor pressures. Each tube is specific for the gas or vapor that it was designed to detect. Mixtures can cause issues, and cross sensitivities are not uncommon. Using the hand pump can be both labor-intensive and time-consuming, depending upon which substance is being tested. Automatic pumps are sold for some systems that significantly decrease these factors.

## 9.10 Warranties and Reachback

When a hazmat response team is considering the purchase of various technologies, certainly for the more expensive and technical pieces of equipment, one should consider purchasing extended warranties with reachback. Components of these instruments can be extremely expensive to repair, and although “ruggedized,” the rigors of response can cause unforeseen or unpreventable damages. Extended warranties tend to cover most, if not all, repairs unless due to negligence.

Reachback is often an option that can be purchased with the warranty. Spectra and other technical data gathered by such technologies as GC-MS, HPMS, FT-IR, and Raman can be downloaded to a universal serial bus (USB) drive and sent to the manufacturer for further analysis. This can be done to bolster confidence with results gathered in the field. In other cases, the instrument itself may not “see” a product within the spectra due to other components overshadowing the chemical of concern. Detection algorithms used in field-deployed systems are designed to minimize false results. However, sometimes data interpretation by a scientist skilled in the art of the technology can provide better results. Scientists from the manufacturer, who are experts at interpreting spectral results, are on call to provide further analysis. A consideration when inquiring about reachback is availability. Hazardous materials incidents happen every day of the week at any time of the day, regardless of holidays, weather,

etc. Twenty-four-hour per day, seven-day per week reachback can be expected from some manufacturers. Another consideration when comparing different manufacturers is their willingness to work with your team to improve existing technology. Accepting feedback from first responders to improve response is a sign of a great future partnership with the manufacturer.

## 9.11 Pitfalls

### 9.11.1 Watch Your Units

Much of the technology discussed is extremely accurate and extremely sensitive. It is crucial to understand the correct units of measurement when reporting results to team leaders or other stakeholders at an incident. Parts per million and parts per billion could mean the difference between evacuation and safety. Microrem, millirem, and rem all have very different action levels and responses. LEL monitors require correction factors depending upon which gas it is exposed to and which gas it has been calibrated to. These correction factors must be considered to report accurate results.

### 9.11.2 Cross Sensitivities

Many sensors in various instruments have cross sensitivities to chemicals other than those they were built to alarm. Simple Green, a cleaning product, has been known to alarm as a nerve agent. Weaker pesticides have been mistaken for nerve agents as well. RAE Technical Note 114, Sensor Specifications and Sensitivities (RAE Systems 2018), lists all of the sensors that RAE Systems manufactures and gives known sensitivities for each. This type of technical resource is very helpful. The user must take these cross sensitivities into account prior to reporting “definitive” findings.

## 9.12 Complimentary Technologies

As stated above, no one instrument can produce all of the answers for the hazmat team. As shown, each has its strengths and weaknesses. Those who are selecting instruments for purchase and deciding which to bring into the hot zone must consider how these technologies complement each other for the best results. Raman technology and FT-IR are not mutually exclusive. On the contrary, each has its advantages and disadvantages and can be powerful tools in identifying hazardous materials. HPMS or GC-MS would rarely be the first instrument downrange. Other “classifying” technologies may be prudent to use on initial entry. The use of pH paper to detect or rule out corrosives may save the user money and aggravation as strong corrosives can impair or destroy other technologies.

## 9.13 An Introduction to the Scientific Working Group for the Analysis of Seized Drugs (SWGDRUG)

The mission statement of SWGDRUG, which is comprised of a core committee of approximately 20 international members, is as follows: “SWGDRUG works to improve the quality of the forensic examination of seized drugs and to respond to the needs of the forensic community by supporting the development of internationally accepted minimum standards, identifying best practices within the international community, and providing resources to help laboratories meet these standards” (Scientific Working Group for the Analysis of Seized Drugs 2019).

SWGDRUG lists the following objectives to define the purposes and nature of the organization (Scientific Working Group for the Analysis of Seized Drugs 2020):

- Specifying requirements for forensic drug practitioners' knowledge, skill, and abilities.
- Promoting professional development.
- Providing a means of information exchange within the forensic science community.
- Promoting ethical standards of practitioners.
- Recommending minimum standards for drug examinations and reporting.
- Providing resources and tools.
- Establishing quality assurance requirements.
- Considering relevant international standards.
- Seeking international acceptance of SWGDRUG recommendations.

## 9.14 SWGDRUG Recommendations: How They Related to the Hazmat Field

Many scientists and technicians working in laboratories such as the state public health labs within the Laboratory Response Network, State Police Crime and Forensic Labs, and others, operate sophisticated equipment within their facilities to identify chemical or biological agents submitted to them through various means. Until relatively recently, these technologies were unavailable to first responders due to size and sensitivity to the elements. Today, many of these technologies have been reduced to handheld instruments and ruggedized for first responder use. While their limits of detection and sampling and other accessories may be more limited, the fundamental technologies of field-deployed systems are usually the same as their laboratory versions.

With that said, laboratories have developed guidance documents such as that of the SWGDRUG in order to standardize how they analyze samples to assure defendable results. It stands to reason that if these standards are successful in the laboratory setting, many of these same standards could be adopted for the use of these instruments in the field setting. The SWGDRUG recommendations, although specifically for the processing of seized drug samples, provide guidelines for the use of various technologies based on their sensitivity and specificity. Many of the technologies discussed within their standards are being deployed every day by hazmat teams around the

<b>Category A</b>  (Selectivity through structural information)	Infrared spectroscopy
	Mass spectrometry
	Nuclear magnetic resonance spectroscopy
	Raman spectroscopy
	X-ray diffractometry
<b>Category B</b>  (Selectivity through chemical and physical characteristics)	Capillary electrophoresis
	Gas chromatography
	Ion mobility spectrometry
	Liquid chromatography
	Microcrystalline tests
	Supercritical fluid chromatography
	Thin layer chromatography
	Ultraviolet/visible spectroscopy
	Macroscopic examination (cannabis only)
	Macroscopic examination (cannabis only)
<b>Category C</b>  (Selectivity through general or class information)	Color tests
	Fluorescence spectroscopy
	Immunoassay
	Melting point
	Pharmaceutical identifiers

**Figure 9.3** Categorization by SWGDRUG based upon technology selectivity.

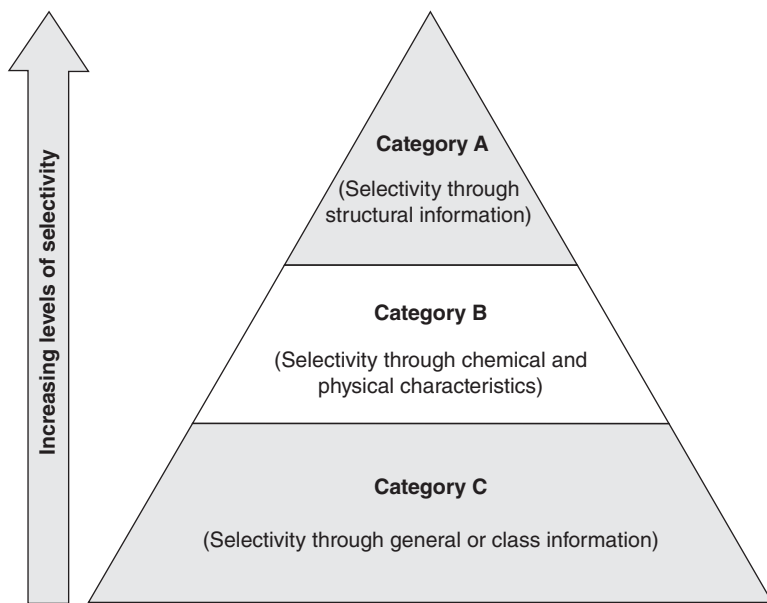


**Figure 9.4** Hierarchy of SWGDRUG-recommended method categories.

country, and the adoption of relevant components of the SWGDRUG guidance may be very beneficial to the hazmat community.

SWGDRUG ranks techniques of analysis based upon their selectivity potential and is shown in Figure 9.3. Figure 9.4 shows the selectivity hierarchy. SWGDRUG guidance recommends that laboratories adhere to the following minimum standards when using these different methods of analysis:

When a validated Category A technique is incorporated into an analytical scheme, at least one other technique (from either Category A, B, or C) shall be used.

When a Category A technique is not used, at least three different validated techniques shall be employed. Two of the three techniques shall be based on uncorrelated techniques from Category B.

Many hazmat teams have purchased technologies from each of the categories listed in the table above. Based on these recommendations, if applied correctly, these guidelines will produce the best results.

## 9.15 Ancillary Equipment

Although many would not consider cameras, drones, and robotics hazmat-specific equipment, this chapter would not be complete without mentioning each of these as a potential part of hazmat response. When discussing emerging trends in hazmat response, many point toward remote monitoring and detection as the next frontier. There are teams around the country that have instituted each to varying degrees with success. Like all new technology, training and consistent use are paramount to a successful drone or robotics program.

Drones are fast becoming commonplace in the hazmat world. Whether assessing a rollover on the highway or measuring oxygen and LEL levels indoors, drones have been used to accomplish these tasks with growing success. Infrared technology and sensors are now being implemented with drone technology to decrease the burden on hazmat teams by conducting reconnaissance.

Robotics, in similar ways, are breaking their way into hazmat tactics, techniques, and procedures. Cameras, sensors, and infrared technologies can be attached to a robot to conduct hot zone operations. The ability to open doors, climb stairs, and navigate through and over various terrains make it a useful addition to the hazmat mission.

Significant enhancements in downrange camera systems is a technology that many teams are considering. Live feed to a command post is now a reality. Issues with connectivity and distance have been improved dramatically. The ability to allow vetted personnel access to live, hot zone operations through encrypted transmissions is a game-changer in the field. Law enforcement or scientists can have access to video, allowing them to advise on sampling needs and procedures. The fog of being downrange in cumbersome PPE that often impairs vision can be aided by unimpaired eyes.

There is no clear-cut recipe for choosing which instruments and technologies to purchase and, further, which to take into the hot zone on any given incident. This decision-making process comes from experience and consistently keeping abreast of changes in the field. Hazardous materials technology can be compared to information technology regarding shelf life. New methods are being developed and tested every day. Building a rapport with the manufacturers of the various technologies serves to improve the products that are being used and, more importantly, contributes to the safety of the responders and the communities for which they serve.

## Acronyms, Abbreviations, and Mnemonics

CWA	chemical warfare agent
EPA	Environmental Protection Agency
GC-MS	gas chromatography–mass spectrometry
Hazmat	hazardous materials response
HPMS	high pressure mass spectrometry
IC	incident commander
IMS	ion mobility spectrometry
LEL	lower explosive limit
LFL	lower flammability limit
nm	nanometer
OSHA	Occupational Safety and Health Administration
pH	quantitative measure of the acidity or basicity of aqueous or other liquid solutions
PPE	personal protective equipment
ppm	parts per million
RIT	Rapid Intervention Team
SCBA	self-contained breathing apparatus
SD	secure digital
SAMPLE	Signs and symptoms of injury, Allergies, Medications, Past medical history (if known), Last known oral intake, and the Events leading up to the injury or illness
SWGDRUG	Scientific Working Group for the Analysis of Seized Drugs
TIC	toxic industrial chemical
TIM	toxic industrial material
UEL	upper explosive limit
USB	universal serial bus
WMD	weapon of mass destruction

## References

- DeHaan, J.D. and Icove, D.J. (2012). Combustion properties of liquid and gaseous fuels. In: *Kirk's Fire Investigation* (eds. J.D. DeHaan and D.J. Icove), 88. Pearson Education, Inc.
- European Industrial Gases Association AISBL. (2018). *Hazards of Oxygen-Deficient Atmospheres, Doc 44/18*. European Industrial Gases Association. <https://www.eiga.eu/index.php?eID=download&t=f&f=3509&token=4f84c3906146bcfb0c22fa32e4726ac882af2ad1> (accessed 19 November 2020).
- Hawley, C. (2020). *Hazardous Materials Monitoring and Detection Devices*, 3ee. Jones & Bartlett Learning, LLC.
- Hazwoper Training (2019). *Personal Protective Equipment (PPE) Levels*. Hazwoper Training <http://hazwoperhazmattraining.com/blog/personal-protective-equipment-ppe/levels-of-personal-protective-equipment-ppe> (accessed 25 November 2019).
- Occupational Safety and Health Administration (n.d.). *Appendix A to §1910.1200 – HEALTH HAZARD CRITERIA*. United States Department of Labor Occupational Safety and Health Administration. <https://www.osha.gov/dsg/hazcom/hazcom-appendix-a.html> (accessed 16 May 2020)
- RAE Systems (2018). *Sensor Specifications and Cross-Sensitivities, Technical Note TN-114*. RAE Systems [https://www.raesystems.com/sites/default/files/content/resources/Technical-Note-114\\_updated\\_03-26-2018.pdf](https://www.raesystems.com/sites/default/files/content/resources/Technical-Note-114_updated_03-26-2018.pdf) (accessed 17 May 2020).
- Scientific Working Group for the Analysis of Seized Drugs (2019). *Recommendations of the Scientific Working Group for the Analysis of Seized Drugs*. Scientific Working Group for the Analysis of Seized Drugs [http://swgdrug.org/Documents/SWGDRUG%20Recommendations%20Version%208\\_FINAL\\_ForPosting\\_092919.pdf](http://swgdrug.org/Documents/SWGDRUG%20Recommendations%20Version%208_FINAL_ForPosting_092919.pdf) (accessed 17 May 2020).
- Scientific Working Group for the Analysis of Seized Drugs (2020). *SWGDRUG Objectives*. SWGDRUG <http://swgdrug.org/objectives.htm> (accessed 17 May 2020).
- United States Department of Labor, Occupational Safety and Health Administration (2012). Appendix A to §1910.1200 – Health Hazard Criteria. United States Department of Labor Occupational Safety and Health Administration, Occupational Safety and Health Standards, Toxic and Hazardous Substances. <https://www.osha.gov/dsg/hazcom/hazcom-appendix-a.html> (accessed 1 December 2020).
- United States Environmental Protection Agency (2017). *Emergency Response, Safety Zones*. United States Environmental Protection Agency <https://www.epa.gov/emergency-response/safety-zones> (accessed 29 January 2020).

## 10

### Toward Clinical Applications of Smartphone Spectroscopy and Imaging

William J. Peveler<sup>1</sup> and W. Russ Algar<sup>2</sup>

<sup>1</sup>School of Chemistry, University of Glasgow, Joseph Black Building, University Avenue, Glasgow, UK

<sup>2</sup>Department of Chemistry, University of British Columbia, Vancouver, British Columbia, Canada

Smartphones and their built-in camera technology have become globally ubiquitous in the last 20 years. The potential for this technology to provide portable data capture, computing, and analysis in the chemical and biological sciences has been rapidly taken up. A huge number of research-stage and commercialized devices now incorporate sensors into smartphones and smartphones into sensors. In particular, there has been great interest in utilizing smartphone-based devices in clinical settings and for mobile health (mHealth), with the aim of improved democratization of evidence-based medical practice via better point-of-care (PoC) testing in resource-limited settings [1, 2]. A search on Web of Science for “(smartphone\* AND clinic\*) OR mHealth” found 12847 publications between 2007 and the end of 2020, with 2570 publications in 2020 alone. The clinical tests developed typically use the smartphone to analyze, via optical or electrochemical methods, a portable and low-complexity assay for one or more biomarkers in a patient sample. In this chapter, we focus on optical smartphone platforms that are under development and have potential to impact clinical medicine. Electrochemical platforms have been reviewed elsewhere [3].

The “biomarkers” for which detection and quantification are needed include proteins, nucleic acids, and small molecules, as well as whole cells and infectious organisms (e.g. viruses, bacteria, parasites). However, smartphone optics are optimized for taking selfies and not for molecular diagnostics [4, 5]. Therefore, good smartphone-enabled testing relies on ingenuity in the chemistry and biology of the assays, their incorporation into a simple and portable device, and their integration with the smartphone optical capabilities. Compared with ground-up development of a custom, dedicated device for a biomarker assay, the advantages of building around a smartphone are a multitude of out-of-the-box, instrument-like features: a built-in power supply to run peripheral devices like optical sensors and light sources, processing power to run programs and analyze results, and wireless/network connectivity to distribute results, add geolocation metadata, and connect to remote databases. Smartphones are also ubiquitous and familiar, being carried by people around the world for both professional and personal use.

In the following sections, we briefly revisit how a smartphone camera can be used for optical measurements, including spectroscopy, and how the use of peripherals enables the creation of spectroscopic devices that can measure clinical samples. We then discuss types of clinical samples, the biomarker content to be analyzed by smartphone spectroscopy and imaging, and present selected examples of developments in this area over the last decade. Finally, we conclude with a perspective on what might be next for smartphone spectrometers and imagers, both in and out of the clinic.

## 10.1 Smartphone Imaging and Spectroscopy Capabilities: An Overview

### 10.1.1 Hardware

The detailed technical aspects of smartphone spectroscopy and imaging have been covered by Scheeline in Volume 1, Chapter 9. To avoid repetition, we only briefly outline the aspects essential to discussion of the diagnostic technologies that follow.

Smartphone-based imaging systems and spectrometers utilize the camera chip of the smartphone as an optical detector for measurements of light intensity and color [6]. The use of these complementary metal-oxide-semiconductor (CMOS) sensor chips enables measurement of light in the photoresponse range of silicon (ca. 400–1100 nm). The silicon pixels are generally overlaid with red (R), green (G), and blue (B) filters to obtain RGB images that mimic those perceived by the human eye. A typical “Bayer” filter configuration has twice as many green pixels as red or blue pixels (Figure 10.1a). Between different smartphones, the choice of R, G, and B filter materials and differences in the relative gain applied to each channel create slight differences in the wavelength ranges detected in each channel, the overlap between the channels, and the sensitivities in each channel (Figure 10.1b) [7, 9]. An infrared (IR) filter is also normally included to restrict imaging to the visible

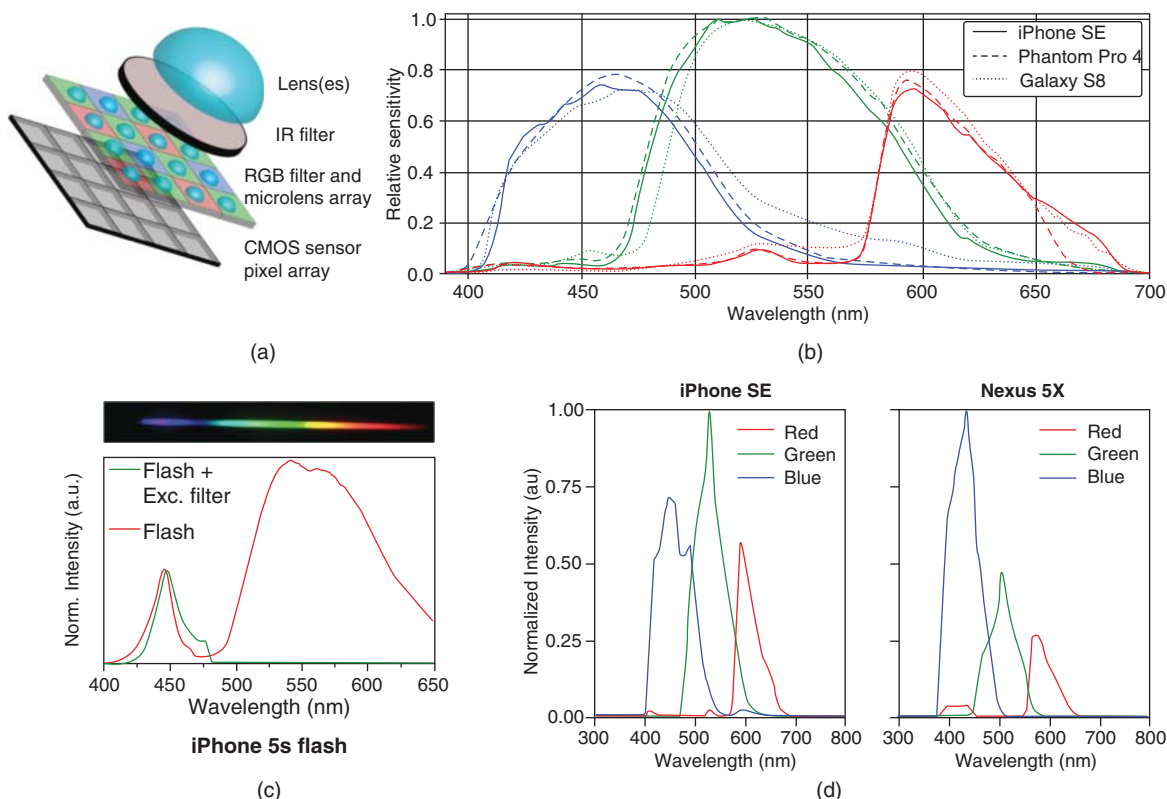


**Figure 10.1** (a) Schematic of a CMOS smartphone camera showing the key components. (b) Similar and differing RGB sensitivities in two smartphones (iPhone, Galaxy) and a drone-mounted camera device (Phantom) extracted from RAW imaging of a monochromated white light source. *Source:* Burggraaff et al. [7]. (c) Spectrum of a smartphone flash used to excite photoluminescence (*Source:* Adapted with permission from Petryayeva and Algar [8]. © 2016, Springer Nature), overlaid with diffraction grating image of the flash, showing the two clear regions in the blue and green-red. (d) Greatly differing RGB response of two brands of smartphone from JPG imaging of a monochromated white lamp source (10 nm increments), highlighting the need for ratiometric analysis of RGB images. *Source:* Shah et al. [9]. American Chemical Society.

region (<700 nm). Several companies now provide after-market modification of phones to remove this filter, enabling near IR (NIR) imaging out to 1050 nm [10]. As different brands of phone manufacturer experiment with IR imaging for facial recognition (particularly Apple's Face ID), inbuilt IR-responsive sensors will possibly become more widespread, as existing plug-in IR imaging technologies are already finding applications in the clinic (e.g. IR thermal imaging on a phone to measure loss of blood flow in acute limb ischemia, [11] analysis of lateral-flow assays (LFAs) by thermometry [12]).

The smartphone's onboard image capture software tends to undertake heavy processing of the image, balancing colors and intensities to produce a lifelike image output (e.g. as a compressed JPG file) to match what the user sees. This is particularly prevalent in modern smartphones, where images from multiple cameras are sometimes combined, digital zoom is applied, and auto adjustment of focus, shutter speed, and ISO (sensor gain) is used. Given the foregoing, it has become apparent that smartphone imaging in a research context benefits from the use of the RAW images created by the CMOS sensor, with none of this post-processing applied. RAW imaging (e.g. a DNG file format) is important for obtaining linear optical responses to light intensity, minimizing crosstalk between color channels, and for achieving similar results between different smartphone cameras (Figure 10.1d) [7]. The implementation of the SPECTACLE database (<http://spectacle.ddq.nl>) will provide a resource for locating comparative data on device cameras.

In front of the CMOS sensor is a collection of fixed focusing optics, which combine with sensor control to enable a degree of near and far focusing. The most recent models of phone are now starting to contain periscope optics, adding a degree of true optical zoom, greatly increasing the quality of imaging that is possible.

A final optical component of note on the smartphone is the flash module. This module can be used to provide illumination and, in some cases, photoexcitation to the bioassay under interrogation. These flash units consist of one or more broadband white light-emitting diodes (LEDs) that can be triggered synchronously or asynchronously ("torch mode") with the camera. By applying additional band-pass filters or dispersive monochromation (e.g. using a grating) to the flash, different illumination wavelengths in the visible range can be achieved for exciting bioassays (Figure 10.1c).

To extend the capabilities of the smartphone into the clinic, peripherals and add-ons are often necessary to improve the optical measurement capabilities of the phone and hold all the components and sample in alignment [13]. For example, to illuminate samples with blue or ultraviolet (UV) light, additional LED arrays can be powered by the phone (or a separate battery), or laser diodes can provide a more intense illumination source. In each of these cases, the camera on the phone is still used to capture optical information. However, further examples exist where the full optical setup (both illumination and detection) are "outboard," with the smartphone only providing data logging and processing [14–16]. Such devices are not integrated smartphone spectrometers and are outside the scope of this chapter.

To create the peripherals and integrated optical benches for smartphones, fast and cheap 3D printing (additive manufacturing) of plastic components has been hugely important, allowing for the rapid prototyping of many combinations of phone, custom-designed sample holders, and attachment points and mounts for off-the-shelf optical components (lenses and objectives, LEDs, filters, etc.) The phone itself can provide low-voltage battery power to a range of lighting, heating, and mechanical parts (e.g. motors) while simultaneously imaging.

### 10.1.2 Types of Optical Measurements

Smartphone optical imaging and measurement systems have been used to measure a wide variety of different optical processes that can be applied in bioassays.

The simplest measures are those of absorption and/or scattering. There is an increase or decrease in the intensity of light incident on the camera sensor that is related to a change in the optical properties of the sample (Figure 10.2a) [18, 19]. Broadband white light can be used to illuminate the sample, and absorption at particular wavelengths monitored with the CMOS chip, using the RGB filters inbuilt, or absorption at particular targeted

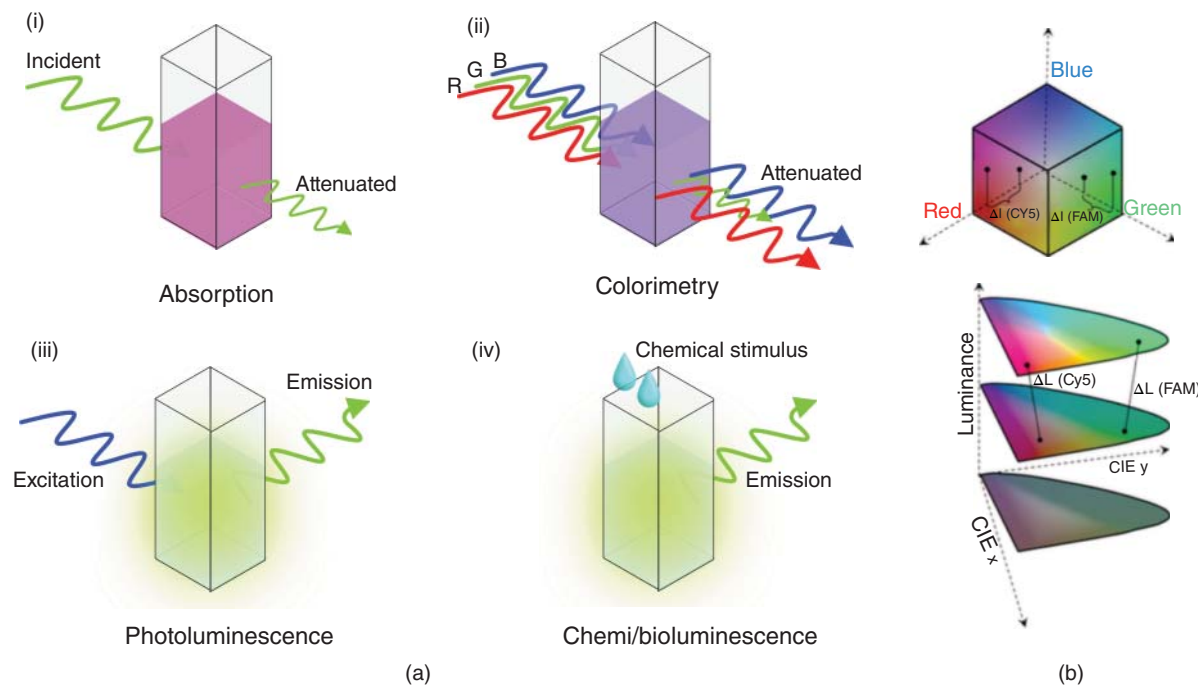


**Figure 10.2** (a) Possible optical measures made by a smartphone including absorption of (i) a single color (or broadband absorption and scattering of white light, not shown), (ii) colorimetry (i.e. absorption of part of an incident broadband white light spectrum), (iii) luminescence stimulated by photoexcitation, and (iv) chemiluminescence or bioluminescence triggered by reagent addition. (b) RGB (top) colors can be interconverted into other color schemes. Here, the luminance of two dyes (FAM and Cy5) are plotted in color space as their brightness increases. Source: Priye et al. [17]. © 2018, American Chemical Society.

wavelengths can be measured using filter sets and/or single-color LEDs. Absorption spectroscopy in this format can measure single analytes in solution or on paper test strips with relative ease and is hugely important in enzyme-amplified assays such as an enzyme-linked immunosorbent assay (ELISA); [20] however, multiplexing at more than two wavelengths can be difficult if the spectra of the absorbing species are not well separated [21]. It is often simpler to separate the absorbing species in space, for example, in a 96-well plate, where multiple different sample absorptions can be measured simultaneously at single or multiple wavelengths. If the change in absorption can be measured rapidly, then binding or reaction kinetics can also be followed as a time-dependent response curve [22, 23]. Advances in photonic and plasmonic materials with strong and well-defined light absorbing characteristics have greatly increased the power of absorption spectroscopy methods [19, 24].

A change in the color of a sample (a shift in the absorption wavelength) can also be instructive (Figure 10.2a), and smartphones are well suited to colorimetric analysis [25, 26]. RGB pixel values in an image taken under white light can be computed, enabling measurement of a difference vector from starting point to end point for correlation with a clinical result [27, 28]. Such RGB color analysis has been widely applied to paper-based assays, for example, pH and glucose sensing in routine urine testing [26]. High degrees of multiplexing can be achieved, as described above, via analyzing distinct colorimetric tests in multiple regions of an image [29]. RGB values for an image can also be converted into hue, saturation, and luminance (HSL) and other color quantification schemes to isolate particular color changes (Figure 10.2b).

Luminescence intensity and color has also been extensively leveraged in smartphone spectroscopy and imaging for clinical sensing (Figure 10.2a). Photoluminescence (PL) uses an excitation wavelength to stimulate materials

that label the biomarkers under study. This excited label (typically a small-molecule dye or luminescent nanoparticle) then relaxes to emit a second, shifted wavelength of light that is detected by the CMOS detector. At the simplest level, the luminescence intensity is linearly correlated with the amount of biomarker present in the sample. The exciting light required to generate PL can come from the smartphone camera flash or a compact LED or laser source.

PL can be rapid (on the order of nanoseconds, as with fluorescence) or much longer lived (microseconds up to milliseconds, or even a few seconds, as with phosphorescence). The former is bright but can run into challenges from sample or test “autofluorescence” (*vide infra*) and may require filter components to block the excitation light from reaching the camera. Phosphorescence is typically much weaker in intensity, but its long-lived emission enables the removal of background autofluorescence by time-gated data collection (*vide infra*) and may eliminate background from excitation light.

It is also possible to stimulate light emission using chemical means via chemiluminescence or bioluminescence, where optical excitation is replaced by a chemical trigger for emission (Figure 10.2a) [30–32]. This luminescence is instrumentally simpler to generate, requiring no external excitation light, eliminating any autofluorescence from sample or background, and potentially increasing assay sensitivity [32]. However, the reagents required can be more prone to degradation, and so consideration must be given to this in assay designs for remote usage where cold chain transport may be an issue. The signal is also time dependent, unlike steady-state PL measurements, and so the reaction rate, development time, ambient temperature, and other factors will influence the quantitative capabilities of any assay.

No matter the luminescence mechanism, a huge amount of recent research has advanced and expanded the labels available to assay builders and designers, particularly with smartphone and other portable spectroscopies in mind. For example, the advent of luminescent nanoparticle technologies, such as quantum dots (QDs) [8, 33], upconverting nanoparticles (UCNPs) [34], conjugated polymer nanoparticles [35, 36], and other materials with bright and tunable emission, and a wide range of bioconjugation chemistry have led to a wealth of highly sensitive and multiplexed assays. A detailed discussion of this field and how it has advanced smartphone spectroscopy and imaging is beyond the scope of this chapter, but reviews of this topic are available [4].

Resolution of multiplexed luminescent signals is usually achieved using color discrimination (RGB). A single excitation wavelength is often used to simultaneously excite a number of different color emissions (especially with QD labels or UCNPs) [37–39]. Another dimension can potentially be added by using discreet excitation/emission pairs (e.g. with an array of different color excitation LEDs or laser diodes) to target specific fluorophores. To go beyond RGB demixing of images, smartphone spectrometers incorporating diffraction gratings have been used, as discussed in detail in Volume 1, Chapter 9, to give a full spectrum across the visible wavelengths. This spectrum can then be deconvoluted into the separate signal contributions. [40, 41]

## 10.2 Clinical Biomarkers Targeted for the Smartphone

For smartphone-based optical tools, such as smartphone spectrometers, to be useful in the clinic, they must measure some aspect of the patient’s physiology with adequate sensitivity and specificity. Research has largely focused on the optical detection and measurement of key biomarkers of health/disease in blood, saliva, urine, sweat, tears, and other bodily fluids (Table 10.1). These biomarkers can be ions, small molecules, proteins including enzymes, and nucleic acids (deoxyribonucleic acid [DNA] and ribonucleic acids [RNAs], including microRNAs) [68]. Assays for these targets can be run by the clinician, or potentially by the patient, and read with the smartphone. Spectroscopy determines the outcome of the biomarker test (positive/negative) and quantifies the biomarker where possible/appropriate.

Smartphone applications have, in part, focused on emulating and automating existing clinical biomarker tests and panels that are normally performed in hospitals and pathology laboratories on expensive benchtop instruments, for example, complete blood counts, cholesterol levels, and metabolic panels measuring liver, pancreas, and

**Table 10.1** A nonexhaustive selection of the clinically relevant biomarkers that can currently be measured with smartphone tools, labeled by their biomarker type, source, and clinical application.

Biomarker	Source	Class	Relevance	Recognition element	Concentration range	Example(s)
Human serum albumin (HSA)	Blood	Protein	Kidney function, liver function	Antibody, specific dye binding	mg/mL	[42]
Prostate specific antigen (PSA)	Blood	Protein	Prostate cancer	Antibody	ng/mL	[43]
Mucin	Blood	Protein (glycosylated)	Some cancers	Reactive nanoparticle	ng/mL	[44]
Human epidermal growth factor receptor 2 (HER2)	Cells	Protein (membrane bound)	Breast cancer	Cell surface marker labeled with anti-HER2 antibody	N/A	[37]
Epithelial cell adhesion molecule (EpCAM)	Cells	Glycoprotein (membrane bound)	CTCs and tumorigenicity	Cell surface marker labeled with antibody	N/A	[45]
Tumor necrosis factor $\alpha$ (TNF- $\alpha$ )	Blood	Protein	Inflammatory response	Antibody	pg/mL	[46]
Human epididymis protein 4 (HE4)	Urine	Protein	Ovarian cancer	Antibody	pM or ng/mL	[20]
Thrombin	Blood	Protein (enzyme)	Clotting disorders	Model peptide	- <sup>a)</sup>	[47]
Lipase	Blood, saliva	Protein (enzyme)	Pancreatitis	Model fatty acid ester	U/L	[22]
Cardiac troponin I (cTnI)	Blood	Protein	Myocardial infarction	Antibody	pg/mL	[48]
B-type natriuretic peptide (BNP)	Blood	Protein	Heart failure	Antibody	pg/mL	[49]
Interleukin 1 receptor ST2 (ST2)	Blood	Protein	Heart failure	Antibody	ng/mL	[49]
C-reactive protein (CRP)	Blood	Protein	Inflammation	Antibody	$\mu$ g/mL	[50]
Human chorionic gonadotropin (hCG)	Urine	Protein (hormone)	Pregnancy	Antibody	mIU/mL	[51]
Fetal fibronectin (fFN)	Cervical secretion	Protein	Preterm birth risk	Antibody	ng/mL– $\mu$ g/mL	[52]
Thyroid stimulating hormone	Blood	Protein (hormone)	Thyroid activity, some cancers	Antibody	mIU/L	[24]

Cortisol	Saliva, blood	Small molecule (hormone)	Stress, anxiety, depression	Antibody	ng/mL	[30]
Phenylalanine	Blood	Small molecule	Phenylketonuria	Enzyme	µg/mL	[52]
Glucose	Blood, urine, tears	Small molecule	Diabetes	Enzyme	mg/mL	[27, 53]
Cholesterol	Blood	Small molecule	Blood cholesterol, risk factor in cardiovascular disease	Enzyme	mg/mL	[32]
Vitamin D	Blood	Small molecule	Vitamin levels	Antibody	ng/mL	[54]
Chloride ( $\text{Cl}^-$ )	Blood	Ion	Cystic fibrosis	Reactive dye	mg/mL	[55]
p24 capsid protein	Blood	Viral protein	HIV	Antibodies	- <sup>b)</sup>	[56]
Nucleoprotein	Blood, nasal secretion	Viral protein	Flu	Antibodies	- <sup>b)</sup>	[9, 57]
Hepatitis surface antigen (HBsAg)	Blood	Viral Protein	Hepatitis B	Antibody	- <sup>b)</sup>	[56]
Raised IgM or IgG	Blood	Antibody to virus	Measles	Recombinant target	- <sup>b)</sup>	[58, 59]
Raised IgM or IgG	Blood	Antibody to virus	Mumps	Recombinant target	- <sup>b)</sup>	[58, 59]
Raised IgG	Blood	Antibody to virus	Ebola	Recombinant target	- <sup>b)</sup>	[60]
Virus glycoprotein (gG), antigen, DNA	Blood	Viral protein or nucleic acid	Herpes	Antibody, complementary primer	- <sup>b)</sup>	[58, 59]
DNA	Blood	Viral nucleic acid	Zika	Complementary primers	- <sup>b)</sup>	[17, 31, 61]
DNA	Blood	Viral nucleic acid	Dengue	Complementary primers	- <sup>b)</sup>	[61]
DNA	Blood	Viral nucleic acid	Chikungunya	Complementary primers	- <sup>b)</sup>	[17, 61]
DNA	Blood	Bacterial nucleic acid	Gonorrhea	Complementary primers	- <sup>b)</sup>	[17]
Whole cell, DNA	Blood	Bacterial surface glycoproteins or nucleic acid	<i>E. coli</i>	Antibody, complementary primer	- <sup>b)</sup>	[62, 63]

(Continued)

**Table 10.1** (Continued)

Biomarker	Source	Class	Relevance	Recognition element	Concentration range	Example(s)
Whole cell, DNA	Blood	Bacterial surface glycoproteins or nucleic acid	<i>S. aureus</i> (e.g. sepsis)	Antibody, complementary primer	- <sup>b)</sup>	[64]
Whole cell, DNA	Blood	Bacterial surface glycoproteins or nucleic acid	Salmonella	Antibody, complementary primer	- <sup>b)</sup>	[62, 65]
Whole parasite, DNA	Blood	Surface proteins or nucleic acid	Malaria	Antibody, complementary primer	- <sup>b)</sup>	[66, 67]

Clinically relevant concentration ranges were obtained from the literature and the units standardized where possible. Only the approximate order of magnitude is reported to highlight the range of analytical requirements for clinical applications of smartphone assays. Readers are advised to consult the most recent literature for more precise clinical ranges and thresholds for particular biomarkers of interest.

- a) Levels of thrombin in blood increase dramatically when clotting is triggered, as prothrombin is converted into thrombin, reaching an estimated (but variable) final concentration of c 1 IU/mL.
- b) These biomarkers are indicative of infection or disease, and so their presence/absence is measured rather than necessarily a concentration range. For these applications, limit of detection and detection accuracy become key clinical criteria.

kidney function. These tests constitute assays for lipoproteins, glucose, serum albumin, and a range of other common ions, small molecules, and serum proteins and enzymes (e.g. assays for aspartate transaminase (AST)/alanine aminotransferase (ALT) to measure liver injury and function [69]). In each of these cases, quantification of the biomarker against a normal reference range is the target outcome, ideally with multiplexing of the different assays to increase throughput and efficiency. By creating portable smartphone tools for the analysis, these routine tests can be performed more often (several times a day rather than only in a surgery visit), giving clinicians better longitudinal data and, in more remote or rural settings around the world, increase access to basic healthcare services [70, 71].

A second clinical application of smartphone optics focuses on the detection of rare biomarkers that normally exist in the blood (or other body fluids) at very low levels (or are absent), but their increased level indicates a potentially severe condition or presence of a pathogen. Examples include the detection of prostate-specific antigen (PSA) as a marker for prostate cancer, cardiac troponin I (cTnI) as an indicator of cardiac tissue damage, and therefore myocardial infarction (MI), HIV p24 protein, or circulating nucleic acids (DNA or RNA) from bacterial or viral infections. Here, the focus is on achieving very low limits of detection for single or few highly specific analytes.

Biomarker recognition is most often enabled by complementary antibodies, binding proteins or peptide sequences, enzymes, and complementary nucleic acid sequences or aptamers. Common detection and amplification configurations are shown in Figure 10.3.

In the following sections, we discuss how the detection and measurement of these markers with clinical utility is being implemented with optical methods based on minimalist, portable smartphone systems. Outside the laboratory are challenges of assay and instrumentation sensitivity, of transporting and manipulating reagents, and of sample separation, labeling, and washing arise. Therefore, to target the desired biomarkers in a smartphone assay, it is therefore not always possible or desirable to adapt an assay directly from the clinical laboratory. To address some of these challenges, assays have been translated to the smartphone by reengineering the assays themselves, performing them on new substrates such as paper, or incorporating them into self-contained devices such as microfluidic chips.

We have elected to distinguish those assays that use minimal reagents and are more suited to a low-cost PoC setting from others that use solution processing to handle samples, often coupled with more advanced microfluidics. Finally, we will examine examples of (spectral/wavelength selective) imaging on a smartphone platform for biomedical and clinical application.

### 10.3 Toward Clinical Applications of the Smartphone in Low-Cost and Point-of-Care Settings

The distinct advantage to creating a smartphone imaging or spectrometric analysis platform is portability and reduction in instrumentation cost. To this end, smartphones have become deeply intertwined with the movement to create low-cost, rapid, PoC, or near-patient diagnostic testing for use in resource-limited settings. In order to process and analyze biomarkers in clinical samples in a PoC setting, assays have been reformatted to operate on planar substrates rather than in bulk solution, for example, paper in the format of dot blots [72] and colorimetric dipsticks [73], lateral-flow assays, [74] or wax-in-paper microfluidics [75].

Paper devices such as the lateral flow test (illustrated in Figure 10.3a) allow for separation and labeling of a biomarker in a rapid and reasonably efficient format, often based on a sandwich immunoassay, and have proved very attractive in a range of clinical applications for detecting proteins [76]. It is also possible to detect and quantify DNA or RNA with complementary strands [77] and even small molecules using aptamer technology [78, 79]. By incorporating a colored bead, gold nanoparticle, or luminescent dye or nanoparticle on the labeling antibody or nucleic acid, color or luminescence are generated at the test line, normally increasing in intensity with increasing

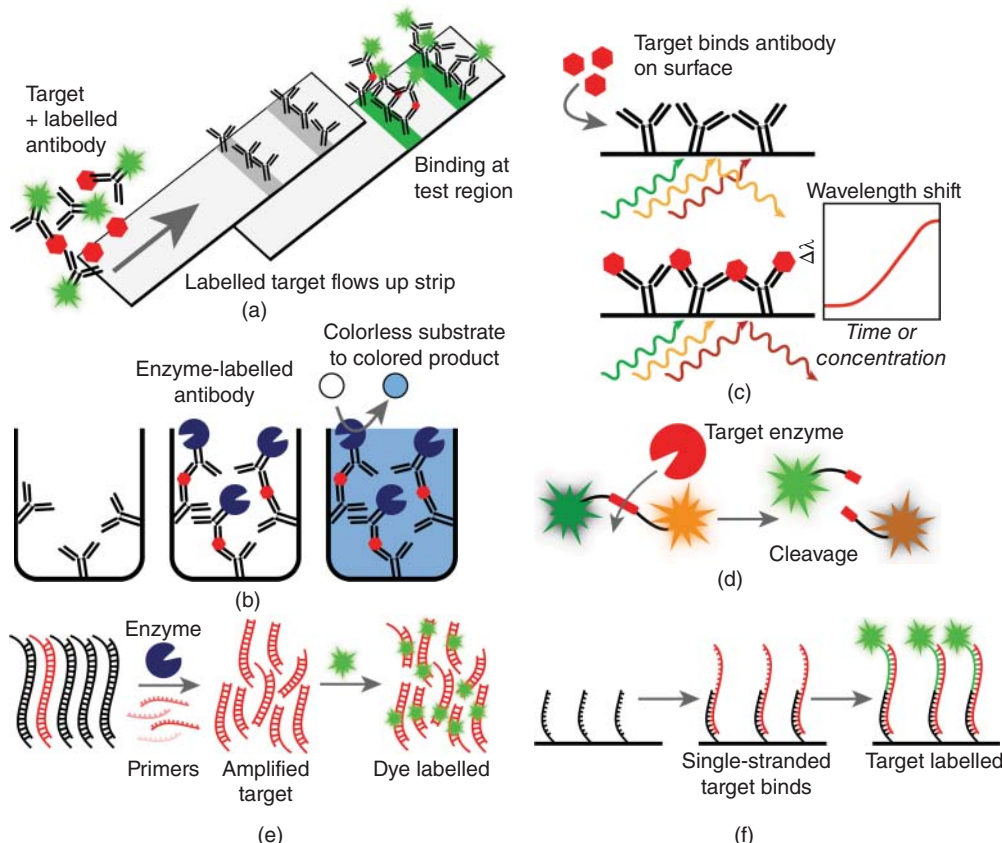


**Figure 10.3** Common target biomarker detection schemes. (a) Lateral flow assay. The target is labeled with a colored or luminescent antibody label and flows up the test strip to bind at the target region. Unbound antibodies bind at a control line, regardless of the presence of the target to confirm the test has worked and is negative. (b) Enzyme-linked immunosorbent assay (ELISA). The target is sandwiched in an antibody pair where one half is labeled with an enzyme. The linked enzyme acts on the added substrate to catalyze production of a strongly colored product, amplifying the target binding. (c) Label-free measurement. The target biomarker binds at antibodies bound on an optically active surface (e.g. a gold surface) changing the refractive index at the surface, measurable as a shift in wavelength of reflected light. (d) Enzyme sensing. Catalytic cleavage of a designed, labeled peptide strand, triggering a luminescence color change. (e) Nucleic acid sensing. The target strand is amplified using primers, restriction enzymes, and polymerase enzymes to generate a large amount of amplified material that is then labeled with a nonspecific dye to generate a fluorescent or color change. (f) Amplified target nucleic acids can also be bound as single-nucleotide strands to a matching strand on a surface and then further labeled with a fluorescent strand for detection.

analyte concentration and hence increasing label binding. Lateral flow tests have been particularly studied for the detection of infectious disease in resource-limited settings, due to their low cost and short time to result [74, 80]. By coupling, the readout with the capabilities of the smartphone to collate and transmit data, the spread of an infection can be monitored in near real time; this proved to be useful, for example, in the 2014–2016 Ebola crisis [60].

Most lateral flow devices detect a single analyte and so use a calibrated color or luminescence intensity measurement at the test and control line for quantification of the biomarker. Colorimetric sensitivity can also be enhanced by tuning the test illumination. Ozcan demonstrated that, because gold nanoparticles strongly absorb and scatter light of a particular wavelength (tuned by changing their size), illuminating a gold nanoparticle-labeled LFA in reflection or transmission mode with the matched wavelength (here 565 nm) increased the limits of detection [81]. With this device, HIV and malaria assays were successfully read, and metadata on test location was also collected.

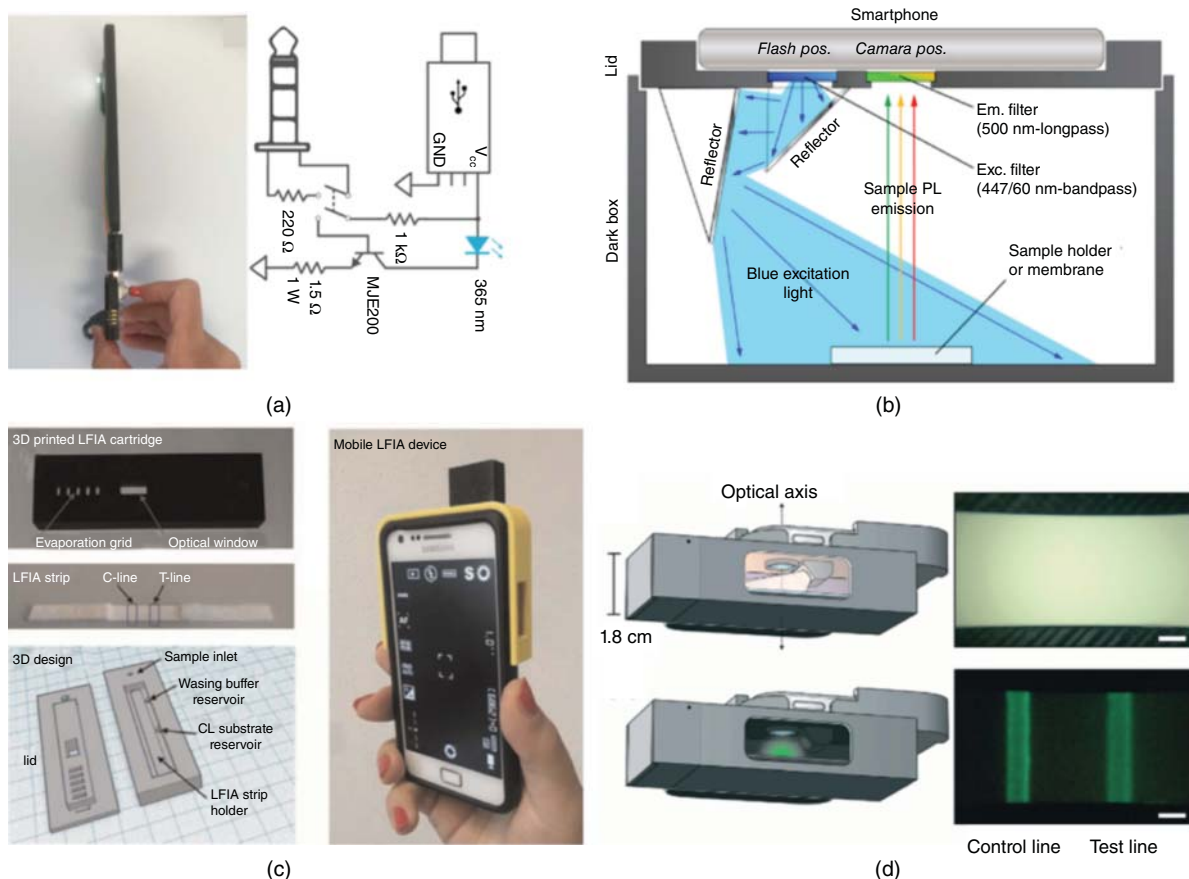


**Figure 10.4** (a) A simple UV LED and camera trigger for fluorescent LFA imaging with R/B ratiometric imaging. *Source:* Adapted with permission from Shah et al. [9]. © 2018, American Chemical Society. (b) Using the smartphone camera flash to excite luminescent nanoparticles on an LFA with filtered blue light and measuring their emission across the green-red visible spectrum. *Source:* Gupta et al. [35]. © 2019, American Chemical Society. (c) Removing the need for photoexcitation using a chemiluminescent (CL) LFA that can be imaged by smartphone. *Source:* Reprinted from Zangheri et al. [30]. © 2015, Elsevier. (d) Removing LFA paper autofluorescence using smartphone flash excitation to trigger a phosphorescent label that can be imaged hundreds of milliseconds after the autofluorescence has decayed. *Source:* Reproduced from Paterson et al. [51] with permission from The Royal Society of Chemistry.

This modality is well suited to reading a number of commercially available diagnostic assays based on binding gold nanoparticles.

Luminescence offers benefits of increased sensitivity over colorimetric imaging but requires a slightly more sophisticated optical set up. The removal of background light by enclosure in a dark box or sample holder is the norm, and an excitation source of a suitable wavelength for the lumiphore is required, often a UV or blue LED (Figure 10.4a) or laser diode or even filtered light from the phone flash (Figure 10.4b) [70]. The materials used to construct these assays can be selected to ensure sensitive transduction by a smartphone, often incorporating nanomaterials as discussed above, such as brightly fluorescent QDs or UCNPs to take advantage of their unique properties, for colorimetric or luminescent sensing [71].

However, fluorogenic paper assays also suffer from the drawback of autofluorescence from the paper substrate in the green part of the spectrum. Autofluorescence can cause substantial background noise and lower limits of detection [82]. Indeed, Shah and Yager carried out a full study of different kinds of papers for smartphone assays, including a proof-of-concept influenza (influenza A nucleoprotein) LFA and a nucleic acid assay for *Staphylococcus*

*aureus* [57]. They concluded that the autofluorescence commonly found was in the blue-green region of the spectrum (400–500 nm) and had a short luminescence lifetime (<5 ns). They also reported that spectral information alone was not enough to choose the best paper for an assay and the imaging system and fluorescent label must also be considered. To assist in future development of paper assays for smartphone spectrometry, they have made their full dataset public.

The same authors later demonstrated that a very simple method to work around the background fluorescence induced in paper is simply to use the red channel in a Bayer-filtered CMOS sensor. They demonstrated this with a red-emitting QD LFA for influenza A nucleoprotein, excited by an external 365 nm LED powered from the smartphone, on both Nexus 5X and iPhone SE systems (Figure 10.4a) [9]. Ratiometric quantification between the R and B channels was used to correct for the brightness of the excitation source, and a limit of detection on the order of 1–2 fmol of influenza nucleoprotein was achieved.

To remove the need for an excitation source that might trigger autofluorescence, bioluminescent or chemiluminescent LFAs have been developed, where the test and control lines generate luminescence in the presence of a chemical or biological (enzyme) species. In an early example, Roda and coworkers produced a simple chemiluminescent assay for measuring salivary cortisol (a small-molecule steroid hormone that acts as a marker of stress and anxiety). The small-molecule nature of the target necessitated a competition binding assay, where less peroxidase-labeled antibody binds to the test line with increasing biomarker concentration. The test and control lines are then developed with peroxide and luminol to generate blue chemiluminescence over about 20–30 minutes. Cortisol levels between 1 and 100 ng mL<sup>-1</sup> could be quantified, with a limit of detection (LOD) of 0.3 ng mL<sup>-1</sup> (Figure 10.4c) [30].

Willson and coworkers presented an alternative approach to overcoming the background fluorescence found on luminescent LFAs: engineering of the luminescent nanoparticles used for their human chorionic gonadotropin (hCG) (i.e. pregnancy) assay [51]. By using strontium aluminate phosphor nanoparticles that exhibit persistent luminescence (long-lived phosphorescence) to tag their label antibodies, the LFA can be run and placed in a small dark box attached to the phone (iPhone 5S). The smartphone's torch and flash modes (broadband white light, unfiltered) were used to irradiate the sample for ~3 seconds, and video was captured during and after irradiation, enabling the phosphor lines to be imaged in the 100 ms after the illumination is ended (Figure 10.4d). Repeated cycles over 60 seconds were run and integrated to obtain quantitation of the luminescence from the test and control lines. The LOD for hCG was 45 pg mL<sup>-1</sup>, significantly improving on the current standard tests with LODs of above 450 pg mL<sup>-1</sup>. This LOD was achieved with a very minimalist smartphone setup, and the technique could be simply extended in the future by incorporating multicolor phosphors or by tuning the phosphors to better suit the wavelengths in the smartphone flash for even brighter phosphorescence.

A final approach to avoid autofluorescence is to apply *upconversion*, which is the use of long-wavelength (IR) light to stimulate visible emission from an anti-Stokes process. This concept has been demonstrated for the rapid detection of heart failure, where sensitive detection and short time to accurate diagnosis are of the essence [83]. A smartphone was used to read out a two-color upconversion LFA for two proteins, brain natriuretic peptide (BNP) and protein ST2 [49]. Xu and coworkers labeled the reporter antibodies with UCNPs, which were excited with a 980 nm laser diode built into a compact housing upon which the smartphone sat (three models tested). The use of two colors enabled unequivocal identification of each biomarker and ensured that any crosstalk between testing regions was identified. The LODs were <10 ng mL<sup>-1</sup> for ST2 and <50 pg mL<sup>-1</sup> for BNP, well below the clinical thresholds for heart failure.

### 10.3.1 Alternatives to LFAs

In paper-based clinical assays, the lateral flow method is the most widely adopted and practically applied technique. However, several variations of this format are possible with a smartphone camera. Dot blots and “vertical flow” assays enable the capture, washing, and labeling of a target at a single point [84]. Reactions

(e.g. enzyme-catalyzed hydrolysis) can also be performed on a localized reporter, changing its optical properties as measured by the smartphone (*vide infra*). Finally, paper can be used as a microfluidic channel that supports mixing, separation, and multiple reaction steps beyond what is possible by lateral flow. Channels are typically patterned in the paper via photolithography or wax printing (also known as  $\mu$ -PADs or micro-paper-based analytical devices) [65].

Petryayeva and Algar demonstrated a single-step smartphone assay for the enzyme thrombin, using QD sensors immobilized on a paper-in-PDMS (polydimethylsiloxane) chip [47]. This assay was excited with external 470 nm LEDs and imaged with an iPhone 5s, using time-lapse imaging to capture enzyme kinetics at the paper surface, versus a reference spot. Judicious choice of QD and filter set enabled the measurement of the enzyme in whole blood, with detection limits of 18 NIH units  $\text{mL}^{-1}$ . Such a device could have clinical applications for measuring clotting disorders or the efficacy and dosing of some anticoagulant medications. The authors later showed that the camera flash could also be used as an excitation source for such an enzyme assay, negating the need for the external LED array (Figure 10.4b) [8].

Building on work by Petryayeva et al. [85], Krull and Noor demonstrated ratiometric color smartphone imaging of a luminescent nucleic acid dot-blot assay, measuring changes in the G and R channels based on Förster resonance energy transfer (FRET) from a green QD donor to a red emitter that bound when the target strand was present [72]. An iPad was used for imaging with an external UV lamp source for excitation and a limit of detection of 450 fmol of target nucleic acid even in complex matrices such as serum. Although not a fully integrated smartphone platform, this technique demonstrated the feasibility of nucleic acid detection on paper assay formats with a portable device. If coupled with *in situ* nucleic acid amplification, the approach would have prospective clinical application in a variety of nucleic acid assays for infectious disease.

Erickson and coworkers took a different approach to the dot blot, using absorption rather than luminescence to quantify the amount of vitamin D present in a serum sample [54]. Their test strip contained the vitamin, which then underwent a competitive binding assay (necessary for small molecules, which cannot bind antibodies in a sandwich configuration) with Au nanoparticles labeled with anti-vitamin D antibodies mixed with the serum sample. If the vitamin concentration in the serum was high, the binding of nanoparticles to the test strip was low. The test strip was then further developed with a silver salt, increasing the contrast at any bound Au nanoparticles. The test strip was placed in an integrated smartphone peripheral in front of a 592 nm LED, and the camera of the phone detected the absorption of light by the test strip, versus a reference, with lower concentrations of vitamin D causing greater absorbance by the test, due to the increased nanoparticle/silver deposition. Nanomolar quantities of vitamin D were detectable in serum, in the clinical range required for measuring vitamin D deficiency.

## 10.4 Toward Clinical Applications in Primary Care or Pathology Laboratory Settings

Most standard pathology laboratory assays requested and performed in hospitals are “wet.” That is, they take a liquid input (e.g. whole blood, serum, sputum, urine), mix it with a set of reagents in solution, and measure the optical output as a change in color or luminescence. Many of these assays have been ported onto smartphone imaging and spectroscopy tools and have been enabled by using innovative miniaturization and microfluidic techniques to handle the liquid reagents. Although this type of biomarker assays becomes harder to handle and operate in resource-limited settings, these assays often enable higher sensitivities and greater flexibility in measurement techniques than the minimalist paper devices described above. They are suitable for primary care applications such as general practitioner clinics and traveling doctors.

As an early example of translating a standard clinical biomarker assay to a phone, Ozcan and coworkers demonstrated detection of serum albumin in urine using a luminescent intensity assay on a smartphone [42]. The device consisted of two disposable plastic chambers, one reference and one sample, excited with a 532 nm 5 mW laser

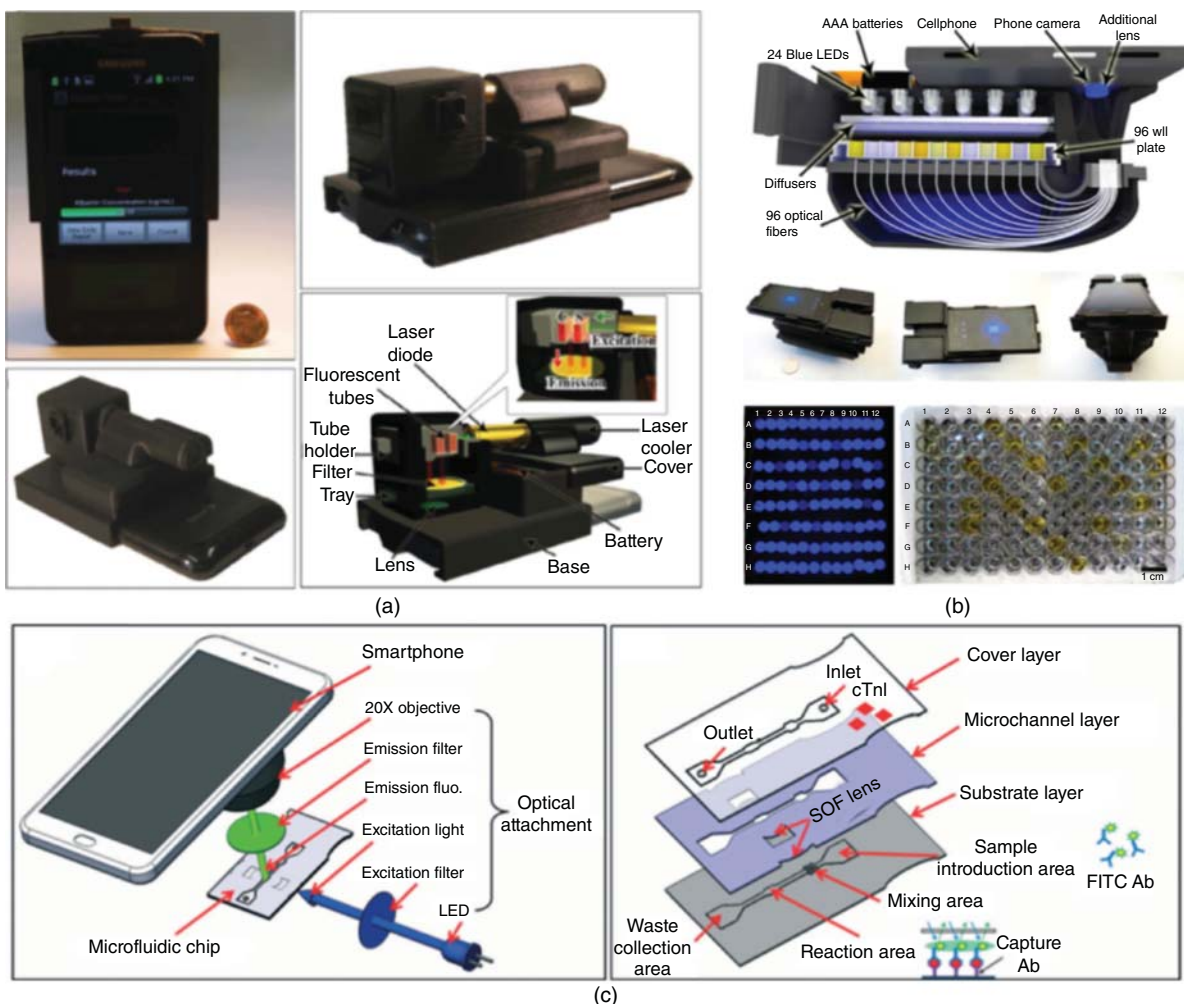


**Figure 10.5** (a) A smartphone peripheral for analyzing HSA in urine with fluorescence of the probe stimulated by a laser diode. *Source:* Reproduced from Coskun et al. [42]. With permission from The Royal Society of Chemistry. (b) A compact 96-well plate reader on a smartphone, using LED excitation and an optical fiber for each well to obtain a dot matrix representing absorption of light in each well. *Source:* Berg et al. [59]. (c) A self-contained microfluidic assay for a biomarker of heart disease with inbuilt microlenses (SOF lens) to focus LED light on a readout zone, where fluorescence intensity is read by the smartphone camera. *Source:* Liang et al. [48]. © 2019, Royal Society of Chemistry of Chemistry.

diode (Figure 10.5a). The greater the concentration of albumin present in the urine sample added to the reagents, the stronger the red fluorescence measured by the camera. The test has clinical potential for daily monitoring elevated levels of urinary albumin in cases of kidney dysfunction and had a clinically relevant detection limit of ca.  $10 \mu\text{g mL}^{-1}$  in urine versus a clinical norm of  $<30 \mu\text{g mL}^{-1}$  with a linear response up to elevated levels of  $>200 \mu\text{g mL}^{-1}$ . The authors posited that such a scheme could be easily multiplexed with another color fluorophore for detecting an additional biomarker.

In another example of noninvasive biomarker detection, Zhang et al. demonstrated chloride monitoring in arm sweat, using a fluorescence quenching assay [55]. Such an assay is used to screen for those suffering from cystic

fibrosis, who have much higher than normal levels of chloride. The assay was performed by adding a sweat sample into cuvette containing a solution of a small molecular probe with a high specificity for chloride. The cuvette was set against the smartphone camera and excited with a UV LED to generate emission at 440 nm. Emission was quenched by elevated chloride levels, as measured at the CMOS sensor. The test had a linear range of 0.8–200 mM and its diagnostic power was tested in a 10-patient cohort. Although there is no internal reference in this assay, it could easily be added as the technique is developed.

In a final example of single-biomarker cuvette assays on a smartphone, Ghosh and coworkers demonstrated the sensing of mucin in plasma, as a potential cancer biomarker [44]. Overexpression of mucin MUC1 has been associated with colon, breast, ovarian, lung, and pancreatic cancers, although here the authors used the porcine protein as a model analyte. Spiked plasma samples were combined with a solution containing a novel luminescent gold nanomaterial, which was excited at 310 nm with an external LED. Increasing luminescence of the nanoparticles with increasing concentration of mucin was observed. The phone image was analyzed in the hue/saturation/value (HSV) color space as an alternative to RGB, with an increasing “value” (darkness of the hue) being well correlated with increasing biomarker.

#### 10.4.1 Multiplexed and Microfluidic Liquid Systems

In contrast to the single-biomarker assay examples described above, clinical assays performed in pathology laboratories are often based on high-throughput 96-well-plate ELISA formats or continuous-flow auto-analyzer systems. These assays can also be ported to a smartphone system. For example, Vashist et al. demonstrated the reading of a colorimetric 96-well-plate assay for C-reactive protein (a biomarker of inflammation) using a large dark box and two smart devices: one underneath the plate (an iPad, iPad mini, or iPhone 5s) with a white screensaver to provide uniform transmitted illumination and a smartphone with camera at the top of the box to image the transmitted light [86]. The assay was analyzed with three different phones (Samsung Galaxy S3 mini, iPhone 4, and iPhone 5s), giving similar results for all with LODs of ca. 1 ng mL<sup>-1</sup> in plasma and whole blood [50].

A similar approach has been demonstrated by Li and coworkers, using LED back panels rather than another smart device and installed a prism-containing top lid that enabled more wells to be read at once by the phone close to the plate, shrinking the device dramatically. [58] The device was used to implement 12 infectious disease ELISA assays including herpes, measles, mumps, and others. The same group also incorporated gratings into the optical path to read spectral information rather than just RGB coordinates, albeit only eight wells at a time, increasing the time required to read a plate [87].

Ozcan and coworkers demonstrated a rather more compact, albeit more complex, smartphone-based colorimetric/absorption spectroscopy 96-well-plate reader (Figure 10.5b) [59]. In the sample holder, each of the 96 wells was illuminated by an array of 464 nm blue LEDs. Under each well, a fiber optic collected the transmitted light and transferred it to the smartphone camera, creating a dot array on the CMOS sensor that was analyzed for intensity to measure light absorption per well. This device effectively enabled multiplexing through spatial separation of the well regions and was used to undertake standard clinical ELISA assays for measles, mumps, and herpes viruses at US Food and Drug Administration (FDA)-approved threshold levels with over 99% accuracy.

These approaches using standard labware are very flexible and will be applicable to a wide variety of standard assays. However, to miniaturize smartphone clinical diagnostics further, microfluidics has been utilized to detect a range of clinically important analytes.

Focusing again on the clinical problem of rapid and accurate detection of heart failure, Ning and coworkers constructed a microfluidic chip containing a sandwich immune assay for cTnI, a very sensitive marker of cardiac injury, and particularly MI [48]. The reagents for the assay were contained within the chip, and the added serum sample provided the liquid needed to drive the assay via capillary action. The serum mixed with a fluorescein-conjugated label antibody that bound to any cTnI present and, in turn, formed a sandwich in a readout zone under the smartphone camera (Figure 10.5c). The camera detected the intensity of green (530 nm)

fluorescence from the fluorescein dye excited by blue (490 nm) LEDs. The chip contained built-in microlenses to tightly focus excitation light from LEDs at the readout zone, improving the amount of dye that can be detected and giving an LOD of  $94 \text{ pg mL}^{-1}$ . Although the clinical threshold for possible MI is  $14 \text{ pg mL}^{-1}$ , this route shows promise with further optimization and is attractive due to its self-contained approach and fast running (12 minutes).

Reis and coworkers have developed a range of assays based in microcapillary films (MCFs). These transparent films contain 10 parallel microfluidic channels that can be preloaded with reagents and pumped with sample and development solutions. The group devised a diagnostic test for PSA, a marker of prostate cancer, as a sandwich assay in the MCF. The assay was read either by an absorption measurement using a 450 nm LED behind the MCF or using a fluorescent assay with a 365 nm light source in front of the film [43]. In each case, the smartphone camera was used to capture data in the appropriate color channel. The multiple channels potentiate highly multiplexed measurements on small volumes of sample, [88] and, in this case, LODs of 148 and  $8 \mu\text{M}$  of PSA were recorded by absorbance and fluorescence, respectively. The technology is versatile as, for example, the same system has also been used to measure *Escherichia coli* with a smartphone [63] and can be applied to simultaneous detection of BNP and cTnI as markers of heart failure (albeit with a compact digital camera and not yet attempted on a smartphone) [89].

#### 10.4.2 Nucleic Acid Testing on a Smartphone

A key method of detecting infectious disease and measuring pathogen load in a patient is nucleic acid testing. This method enables discrimination between pathogen DNA/RNA and human genomic material, but, given the relative amounts of material present in a sample, selective amplification of pathogen nucleic acids via either a thermal cycling method (polymerase chain reaction [PCR]) or an isothermal method (rolling circle amplification [RCA] or loop-mediated isothermal amplification [LAMP]) is necessary. The resulting amplified nucleic acids are labeled to give an increasing fluorescent signal with increasing copy number (concentration) and time. These techniques have been applied to in-solution and on-paper detection of a wide range of clinical markers for infectious diseases such as malaria [77]. However, they require not just illumination for fluorescent measurement of the output, but also a thermal treatment to power the analysis *in situ*.

Although it is, in theory, possible to use the smartphone battery to power a thermal element, researchers have often elected to use an external power source to provide a stable and long-lived output over ca. one hour. As another strategy, Liu and coworkers have developed a device they call a “Smart Cup” (Figure 10.6a). It consists of a commercial Thermos® cup body that houses the thermal regulation system, a microfluidic chip for processing the sample, and a holder containing excitation and emission filter sets to enable quantitative luminescence imaging with phone flash excitation. Heating is chemical rather than electronic, provided by a one-time-use Mg—Fe alloy pouch (of the type used in self-heating meals) mounted in a heat sink phase-change material. On addition of a small amount of water to the pouch, this system generates a relatively constant  $68^\circ\text{C}$  over two hours to power the LAMP reaction [90]. The microfluidic chip contains three independent channels for multiplexing or replicate analysis and can filter and concentrate the sample as it is loaded. Primers and fluorescent dye or bioluminescence reagents (requiring no external excitation) are added, and the chip is sealed and heated in the Smart Cup. The smartphone can then follow amplification in real time with the increasing fluorescent or bioluminescent signal and has been used to detect <100 copies of HSV-2, Zika, and HIV with LAMP assays in saliva, urine, and blood in under one hour. The authors also used the smartphone’s location services to geolocate the test result [31].

Meagher and coworkers developed a LAMP assay for Zika, dengue, and chikungunya viruses with a multicolor output, excited with broadband white light and readable by smartphone with a set of optical filters [61]. A heat block, powered by an external 5 V battery, controlled by Bluetooth from the phone was used to perform the LAMP assay in standard PCR tubes or 96-well plates (Figure 10.6b), and up to four different color LAMP assays were readable by the filter setup, with the authors finding this approach more effective for detecting luminance intensity

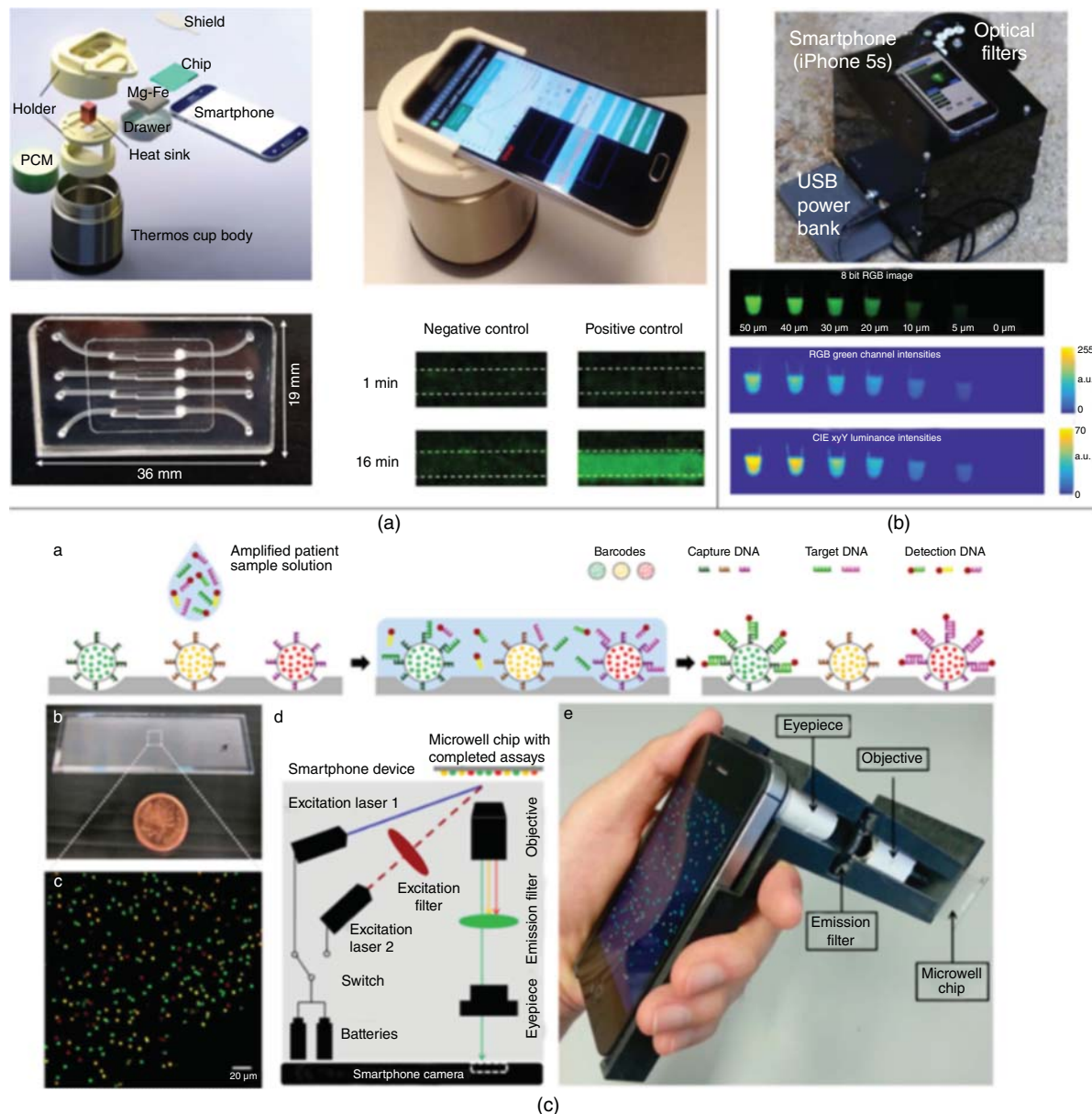


**Figure 10.6** (a) The “Smart Cup” in exploded view and assembled. A close-up of the LAMP assay chip with four channels and the developing bioluminescence signal over 16 minutes to detect Zika. *Source:* Song et al. [31]. © 2018, American Chemical Society. (b) A smartphone LAMP assay containing a heating tray for PCR tubes read by smartphone using CIE xyY luminance rather than RGB. *Source:* Adapted with permission from Priye et al. [17]. © 2018, American Chemical Society. (c) QD-doped bead barcoding for multiplexed nucleic acid detection, with detection enabled by a second dye label. The barcodes are located and read out with one laser and a set of emission filters, and the label read out with a second laser wavelength. A smartphone microscope reads and counts the barcoded beads to give a clinical result. *Source:* Adapted with permission from Ming et al. [38]. © 2015, American Chemical Society.

changes than simple RGB imaging with the phone. The same group revisited this problem, using smartphone imaging with transformation into the CIE *xyY* color space from RGB to detect Zika and chikungunya, as well as gonorrhea down to 3.5 copies in a 10 µL sample volume (ca. 350 copies mL<sup>-1</sup>) [17].

The group of Chan demonstrated an alternate, highly multiplexed approach to nucleic acid detection combining spectroscopic and spatial resolutions of barcoded microparticles (based on ratiometric mixing of QDs inside the microparticle) [38]. The seven different barcoded beads were arrayed on a glass slide, and each was coated to detect nucleic acids from four types of influenza, HIV, HBV, or HCV, along with a positive and negative control. Target nucleic acids in a patient sample were isothermally amplified (off the smartphone) and added to the microarray of barcoded beads, where the target binds to the matched bead and is then further labeled with a second fluorescent strand (bearing Alexa Fluor 647 dye) (Figure 10.6c). The array was imaged with the smartphone camera coupled to a microscope objective (160–200×) and long-pass emission filter to remove excitation light. Additional band-pass filters were then inserted to read different portions of the emission spectrum and interpret the barcodes. Excitation was provided by a violet (405 nm) laser diode to read the location and color of the microparticle barcodes. A set of three images using the different band-pass filters was collected to read the color of each barcoded particle (green/yellow/red) in the field of view. A second 650 nm laser diode and fourth band-pass filter were used to read whether the labeled strand was present on each microparticle. This system can analyze between 1000 and 2000 barcoded particles in a sample to statistically probe if the target is present above a threshold concentration. This assay was validated with clinical HIV and HBV samples with less than 1000 copies mL<sup>-1</sup> of viral DNA detectable [38]. The authors envisioned creating a fully integrated device capable of running the sample purification and nucleic acid amplification, similar to the examples above, before mixing with the barcodes and reading with the smartphone device. The authors clinically validated their barcoding technology for HBV, testing for four regions of the virus genome to achieve 90% sensitivity at the clinical threshold of 2000 IU mL<sup>-1</sup> (72 patients) [91].

#### 10.4.3 Beyond Standard Absorption/Emission Assays

The group of Cunningham have pioneered the combination of smartphone spectroscopy and photonic crystal (PC) materials to create sensitive “label-free” analyzers for clinical applications (Figure 10.7a) [19]. Their photonic materials block one wavelength (565 nm) very selectively (a narrow peak with a full width at half maximum of ca. 5 nm) when irradiated with broadband white light. When the light passing through this PC is incident on a diffraction grating, the smartphone CMOS sensor sensitively registers a narrow absence/dark band in the diffracted white light. The wavelength position of the PC absorption is very sensitive to surface absorption, and so, by coating the surface with suitable antibodies, a peak wavelength shift (PWS) can be effected, which is further shifted when the antibodies bind a target biomarker.

This work was incorporated into a “TRI” device capable of three modalities of data collection: grating-enabled measurements on PCs and measuring colorimetric absorption and fluorescence emission spectra (Figure 10.7a) [52]. The camera flash provided broadband white light for absorption assays and a green laser diode providing more intense focused light for photoexcitation of luminescence. The assays themselves were contained in a 3D-printed plastic/PDMS liquid cell holder that can be scanned through the instrument, enabling multiple different assays to be measured in sequence. This TRI tool was utilized to perform a dual biomarker test for fetal fibronectin (fFN) as an indicator of preterm birth using a commercial ELISA kit in the TRI tool and a luminescence assay for phenylalanine as a marker for phenylketonuria in serum. LODs in each case were clinically relevant, although dynamic range was a concern raised by the authors [52].

An alternative photonic material in a label-free smartphone assay was demonstrated by Buscaglia et al. using the principle of reflective phantom interference (RPI) sensing (Figure 10.7b) [56]. A flat substrate cast from a fluoropolymer was refractive index matched to water. On this surface, 200 µm-diameter spots of different antibodies were immobilized. The surface was then placed in an aqueous solution at 45° to incoming white light from the flash and the smartphone camera. The carbonaceous materials (antibodies in this case) deposited altered the

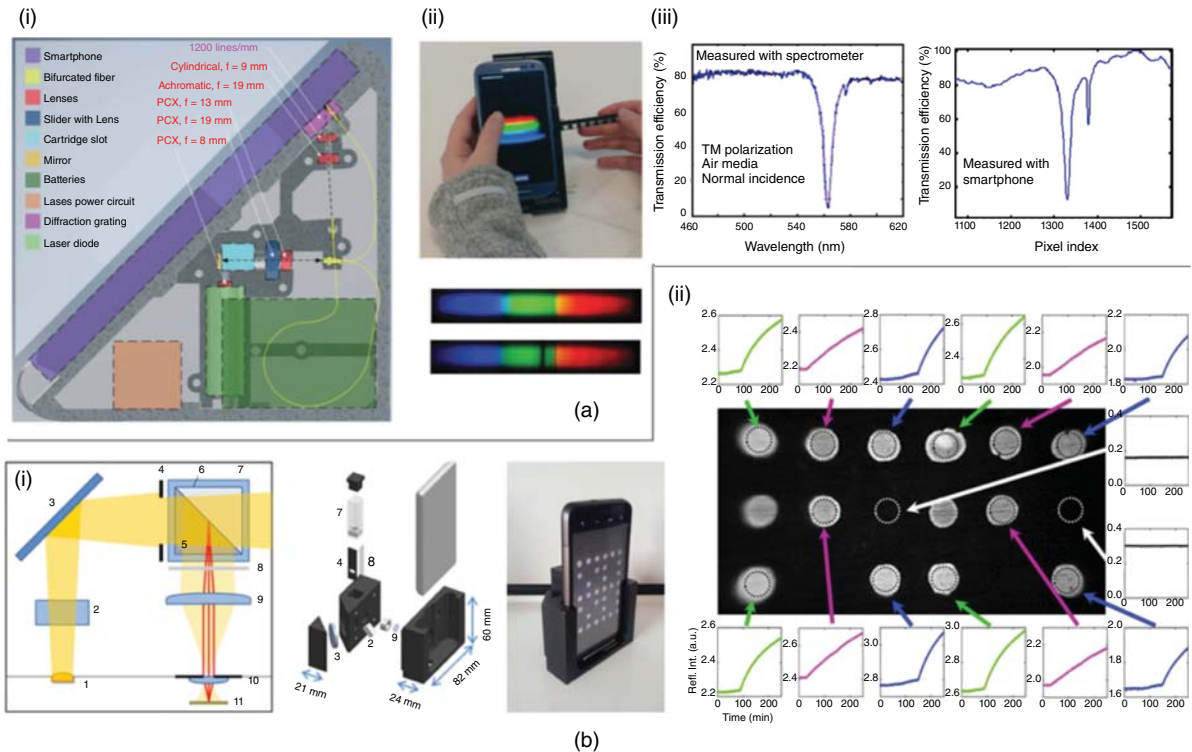


**Figure 10.7** (a) (i) The TRI system using a smartphone, laser diode, and grating for reading absorption, emission, and photonic crystal sensors. (ii) The grating readout from white light and a photonic crystal sensor with (iii) sharp absorption at 565 nm. Source: Reproduced from Gallegos et al. [41] and Long et al. [52]. With permission from The Royal Society of Chemistry. (b) Reflective phantom interference sensing based on light scattering changes at each spot on a photonic chip material. The phone flash is used for broadband light excitation of the chip at  $45^\circ$  to the camera. (ii) The intensity at each point can be read over time to measure binding kinetics. Source: Adapted from Giavazzi et al. [56]. © 2014, Elsevier.

reflectivity at each spot because of their substantially different refractive index versus the surface and solvent, and the intensity of the reflection at each spot was measured by the camera. The intensity of the spot changed as more carbonaceous material is deposited. If the target biomarker was present in a sample added to the device, it would bind to the surface antibody, depositing more material at antibody spot. The rate of binding was estimated from the change in spot intensity over time, generating a kinetic binding curve corresponding to the biomarker concentration. Given the number of spots in the field of view (18), multiplexing is theoretically possible. This system was tested against the p24 HIV antigen in serum with an LOD of  $100\text{ ng mL}^{-1}$ ; however, this value was limited by reaction kinetics, and the authors propose that with faster binding antibodies, LODs of  $<100\text{ pg mL}^{-1}$  may be possible. Detection of Hepatitis B surface antigen was also demonstrated in diluted serum [56].

The group of Swager demonstrated a simple and elegant enzyme sensor based on simple absorption/scattering spectroscopy using the ambient light sensor of a smartphone, rather than the CMOS chip. Their assay consisted of biphasic oil/perfluorous droplets in water, stabilized by a surfactant, to create a droplet lens array. When an enzyme was introduced that degraded the surfactant, the droplet optical properties changed, leading to decreased or increased light scattering, which was recorded in against a background of ambient light. Assays were created for amylase, lipase, and sulfatase activity, with kinetics followed in real time over 30 minutes on the smartphone [22].

## 10.5 Microscopy and Imaging on the Smartphone and the Potential Clinical Applications

The examples above have focused on testing for a biomarker in a sample to infer some information of clinical diagnostic value. However, simply measuring the intensity and color of a signal does not fully utilize the imaging capabilities of a CMOS sensor (i.e. spatial resolution). For the examples presented to this point, imaging has been utilized to enable multiplexing via the localization of signals in multiple regions of a 96-well plate or other samples arrays. However, by incorporating powerful objective lenses into smartphone-based devices, for example, as Chan did to achieve highly multiplexed measurements on barcoded microbeads, [38] it also becomes possible to image structures of biological interest and perform on-phone microscopy combined with colorimetric or spectroscopic analysis, which is promising for several emerging and potential future clinical applications.

Smartphone microscopy has been well developed, with many commercial devices now available for bright-field imaging. Fluorescence and dark-field microscopies extend the capabilities and sensitivities possible, [92] and research has been driven by the group of Ozcan who have, for example, created compact systems capable of imaging labeled single viruses or nanoparticles (e.g. human cytomegalovirus [HCMV], ca. 150–300 nm in diameter). For this work they applied smartphone-based fluorescence microscopy with a relatively high-power external laser diode (75 mW) but minimal optics (without a bulky objective lens in this case) to achieve localization of small objects (Figure 10.8c) [94]. Similar devices have been used for clinical virus load counting in influenza [95].

By using the RGB channels of the CMOS sensor, it becomes possible to then multiplex these fluorescence microscopy measurements. Tran and Algar recently demonstrated clinical potential for this type of instrumentation (Figure 10.8a) [37]. They constructed a magnetic pull-down assay that separated SK-BR3 breast cancer cells from a mixed population, based on attachment of hybrid QD/magnetic nanoparticle materials using HER2 immunostaining. Imaging was performed using standard cell counting slides incorporated into a 3D-printed peripheral device, with an adjustable stage for focusing, and a 405 nm laser diode powered by the phone USB port. Magnetic capture rates were ca. 70%, and different colors of QDs were identifiable by RGB image analysis on the CMOS smartphone sensor for potential multiplexing.

Weissleder, Lee, and coworkers recently demonstrated an imaging platform capable of imaging cells tagged with UCNPs [45]. Similarly to the phosphor and UCNPs containing LFA examples above (e.g. Figure 10.4d), a pulsed excitation source, this time an IR laser, enabled time-gated, background-free smartphone imaging of samples tagged with the UCNPs, with multiple images accumulated and integrated to improve sensitivity. With this system, human cervical cells from a Pap smear test were antibody labeled and imaged to assess the risk of cervical cancer through surface expression of EpCAM, CD44, or Trop2 markers, and by using multiple color UCNPs, multiplexing could be introduced in future [45].

RGB imaging coupled with microscopy has also been applied to enable differential phase contrast (DPC) microscopy for improving clarity of hard-to-see features in bioimaging scenarios, for example, transparent cells against a light background. Joo and coworkers constructed a color-coded (structured) LED array of red, green, and blue LEDs that simultaneously illuminate a sample and enable “single-shot” (simultaneous) capture of light-field, dark-field, and DPC images by splitting out the R, G, and B channels (Figure 10.8b) [93]. The technique was demonstrated by imaging endothelial cells and *Caenorhabditis elegans* worms and could have clinical applications in cell morphology analysis in cancer biopsies or parasite detection.

A final example of smartphone wide-field luminescence imaging, rather than microscopy, was demonstrated by Wu and coworkers, who implanted glucose-sensitive luminescent polymer nanoparticles under the skin of a mouse [53]. The nanoparticles luminesced at 700 nm in response to elevated (1–20 mM) glucose concentration, and this subdermal luminescence was bright enough to be monitored in real time over 60 minutes using the signal ratio between the red and blue channels in the acquired image under external UV illumination. The clinical applications of this technology in glucose monitoring would reduce the need for finger-stick blood sampling

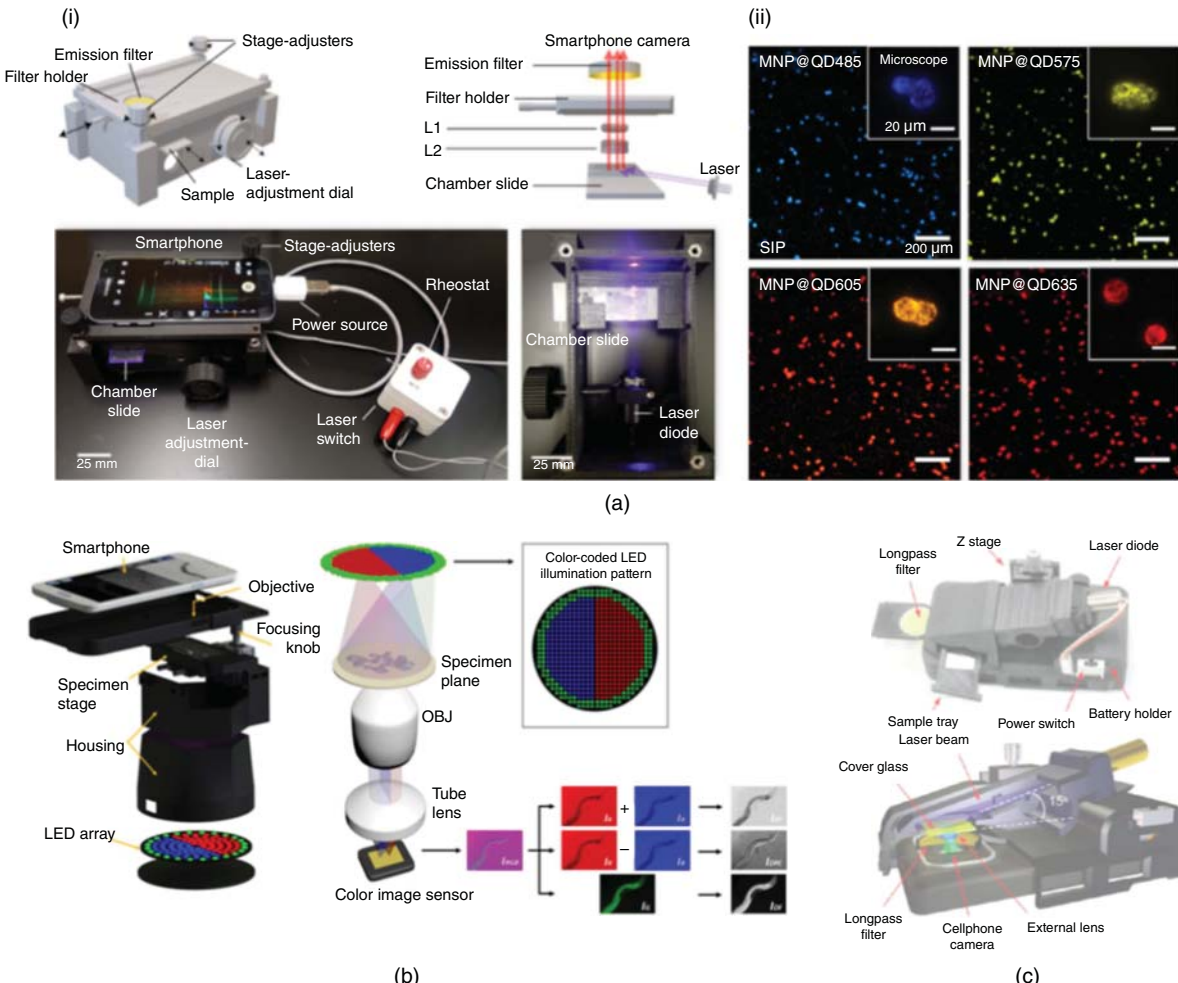


**Figure 10.8** (a) Smartphone-based imaging and cell counting using QD-based labels excited with a laser diode, powered by the smartphone: (i) device design and (ii) images of cells labeled with different colors of QD-based labels. *Source:* Adapted with permission from Tran et al. [37]. © 2019, American Chemical Society. (b) Light-field, dark-field, and differential phase contrast microscopies using structured multicolor illumination, acquired in a single smartphone image and separated using RGB analysis. *Source:* Adapted with permission from Jung et al. [93] licensed under CC BY 4.0. (c) A multipurpose fluorescence microscope on smartphone, capable of resolving structures of 150 nm with laser excitation, including larger viruses, using oblique excitation. *Source:* Adapted with permission from Wei et al. [94]. © 2013, American Chemical Society.

methodologies that are currently common, but the requirement for a powerful and potentially harmful external UV illumination would need to be eliminated before practical application is feasible.

## 10.6 Optical Measurements with Smartphones in the Clinic: An Outlook

As the above examples illustrate, smartphone cameras can be readily manipulated to read and even perform complete clinical assays for a wide variety of biomarkers in multiple different formats, in both resource-limited and near-patient settings. The use of the built-in CMOS sensor(s) to measure light intensity and color is augmented by peripheral optical devices to align samples, lenses, filters, and additional illumination sources, often with support

from rapid and inexpensive 3D printing. The computational power on the phone enables these images to be analyzed locally and a rapid result delivered. The wireless capabilities of the smartphone and ubiquity of wireless networks (even in less developed nations) allow for assay outcome, geolocation, and other reference data to be posted to external databases for further analysis.

However, challenges for smartphones in a clinical setting still remain, particularly if they are to be widely applied in rural or resource-limited settings. These challenges are likely to be solved by advances in the peripheral devices and bioassays rather than phone technology. First among these challenges is the need for sample collection and processing – a particularly important issue with blood. Blood provides the best average representation of human internal physiology in a sample, containing hundreds of useful biomarkers, but whole blood is viscous and optically dense, making it challenging for handling and optical analysis. Therefore, the removal of blood cells to create plasma or serum will often be required before analysis can be performed, requiring either an external preparation step off-phone or integrated filtering in the peripheral device. This separation is achievable with plasma separation membranes or application of microfluidics, but has not yet been routinely incorporated into clinically oriented smartphone devices.

A second challenge is assay reagent transport and storage to perform clinical tests on a smartphone. Many of the assays described in this chapter are self-contained and simply require a sample to be added (e.g. many of the LFAs); however, other assays require several additional solutions to be made up and added along with the sample to develop a result, increasing the difficulty of transport and storage, particularly if these reagents require refrigeration. Several groups are now tackling this challenge by reengineering reagents to be stable for long periods under ambient conditions. For example, Chan et al. have preformulated the reagents required for the QD-barcoded nucleic acid assay into tablets that can be dissolved to give the assay solutions. [96]

A final challenge to consider is safe and environmentally friendly sample disposal. Paper assays have been designed that can be safely burned after reading with the phone; however, plastic microfluidics and other contaminated plastic waste present a bigger disposal challenge, and their reusability should be a consideration going forward.

Beyond these open challenges, it is also of interest to look to the future and examine what other technologies will come to impact on the next generation of portable clinical smartphone tools.

Smartphones enable portable measurement of parameters of clinical relevance, but a new generation of “wearables” is now entering the market with the potential for clinical exploitation. Indeed, smartwatches are already capable of blood flow measurements, including a basic electrocardiogram technology and pulse oximetry, as well as heart rate measurements, using spectroscopic techniques of reflected/absorbed light measurements across multiple wavelengths. Smart contact lenses are in their infancy [97] but can perform basic on-board assays, albeit largely electrochemical. Spectroscopy will be much more challenging to achieve in these smaller platforms. However, thanks to ever-shrinking LED and photodetector chip technology [98], there is now the possibility of spectrometers that one can swallow in a lab-in-a-pill or capsule-endoscopy format for spectroscopic examination of the digestive tract [99].

While RGB-filtered CMOS technology is well integrated into smartphone cameras, and focusing optics are an area of ongoing improvement [100], optical sensing technology is still evolving, and as these more advanced photon manipulating and measuring technologies shrink and become cheaper, they may jump from the optical bench to the portable device. One example is the improvements in single-photon avalanche diode (SPAD) arrays that may lead to miniaturized luminescence lifetime imaging chips, resulting in improved sensitivity (single photon counting), the possibility to measure changes in luminescence lifetime (e.g. fluorescence quenching) independently of label concentration, and multiplex measurements in both the wavelength and luminescence lifetime domains. There would also be the potential to perform basic fluorescence lifetime imaging microscopy on a smartphone. A second example is the shrinking of tunable optical filters, based on liquid crystal tunable filters (LCTFs), which work as a tunable band-pass filter, allowing for selective monochromation of incoming or outgoing light,

and would greatly increase the versatility of portable spectrometers, enabling multispectral imaging (3–10 color channels) as an alternative to dispersive spectroscopy, as well as switchable IR filtering and imaging [101, 102].

Another interesting partner technology to smartphone diagnostics is the possibility of incorporating them into drone (unmanned aerial vehicle [UAV]) technology to remotely access the hardest-to-reach areas and enable transport of bulkier and more complex clinical systems. Ugaz and coworkers have already demonstrated a smartphone-enabled PCR system for DNA/RNA detection and analysis in infectious disease monitoring. The whole apparatus is mounted on a drone, where elements of the drone's drive system can be used in parts of the assay protocol, as a centrifuge for sample purification, and the processed sample is then input to the PCR reaction and read by a smartphone in flight [64].

A final consideration in the future development of smartphone spectrometers is the rise of advanced machine learning and computer vision to further improve assay analysis and ease of assay development. Such tools can, at a basic level, enable advanced, automated correction for a “wonky” sample holder or a change in background lighting [103]. At a higher level, machine vision can interpret dense information from massively multiplexed assays of several different types in a short pace of time or analyze complex stacked colored or luminescent microscopy images to assist data the interpretation by a clinician [104–106]. Such “artificial intelligence-based” tools are still in their relative infancy and require a great deal of processing power to achieve their full potential. However, improving camera technology, with ever increasing onboard processing power on phones, will likely enable progression of machine vision tools from selfie filters to clinical diagnostics in the coming years.

In many futuristic sci-fi classics, medics are armed with small touchscreen devices that can rapidly determine what is wrong with a patient – the tricorder from Star Trek being arguably the most famous of these. As smartphones and telecommunications networks near ubiquity and the possibilities of optical attachments grow, such devices begin to look more and more plausible in a clinical medicine setting. Although many challenges remain, we hope this overview has provided a flavor of the future possibilities of smartphone-enabled optical measurements and spectroscopy in the clinic and inspires research that further develops the portable and robust clinical assays and assessments that are needed every day around the world.

## References

- 1 Yager, P., Domingo, G.J., and Gerdes, J. (2008). Point-of-care diagnostics for global health. *Annu. Rev. Biomed. Eng.* 10 (1): 107–144.
- 2 Wood, C.S., Thomas, M.R., Budd, J. et al. (2019). Taking connected mobile-health diagnostics of infectious diseases to the field. *Nature* 566 (7745): 467–474.
- 3 Sun, A.C. and Hall, D.A. (2019). Point-of-care smartphone-based electrochemical biosensing. *Electroanalysis* 31 (1): 2–16.
- 4 Petryayeva, E. and Algar, W.R. (2015). Toward point-of-care diagnostics with consumer electronic devices: the expanding role of nanoparticles. *RSC Adv.* 5 (28): 22256–22282.
- 5 Malekjahani, A., Sindhwan, S., Syed, A.M., and Chan, W.C.W. (2019). Engineering steps for mobile point-of-care diagnostic devices. *Acc. Chem. Res.* 52 (9): 2406–2414.
- 6 Swager, T.M. (2018). Sensor technologies empowered by materials and molecular innovations. *Angew. Chemie Int. Ed.* 57 (16): 4248–4257.
- 7 Burggraaff, O., Schmidt, N., Zamorano, J. et al. (2019). Standardized spectral and radiometric calibration of consumer cameras. *Opt. Express* 27 (14): 19075.
- 8 Petryayeva, E. and Algar, W.R. (2016). A job for quantum dots: use of a smartphone and 3D-printed accessory for all-in-one excitation and imaging of photoluminescence. *Anal. Bioanal. Chem.* 408 (11): 2913–2925.
- 9 Shah, K.G., Singh, V., Kauffman, P.C. et al. (2018). Mobile phone ratiometric imaging enables highly sensitive fluorescence lateral flow immunoassays without external optical filters. *Anal. Chem.* 90 (11): 6967–6974.

- 10 Smartphone NIR Technical Notes. [https://bit.ly/eigen\\_imaging\\_IR](https://bit.ly/eigen_imaging_IR) (accessed 24 December 2019).
- 11 Peleki, A. and da Silva, A. (2016). Novel use of smartphone-based infrared imaging in the detection of acute limb Ischaemia. *EJVES Short Reports* 32: 1–3.
- 12 Wang, Y., Qin, Z., Boulware, D.R. et al. (2016). Thermal contrast amplification reader yielding 8-fold analytical improvement for disease detection with lateral flow assays. *Anal. Chem.* 88 (23): 11774–11782.
- 13 Alawsi, T. and Al Bawi, Z. (2019). A review of smartphone point-of-care adapter design. *Eng. Reports* 1 (2): e12039.
- 14 Stedfeld, R.D., Tourlousse, D.M., Seyrig, G. et al. (2012). Gene-Z: a device for point of care genetic testing using a smartphone. *Lab Chip* 12 (8): 1454–1462.
- 15 Ye, J., Li, N., Lu, Y. et al. (2017). A portable urine analyzer based on colorimetric detection. *Anal. Methods* 9 (16): 2464–2471.
- 16 Guo, T., Patnaik, R., Kuhlmann, K. et al. (2015). Smartphone dongle for simultaneous measurement of hemoglobin concentration and detection of HIV antibodies. *Lab Chip* 15 (17): 3514–3520.
- 17 Priye, A., Ball, C.S., and Meagher, R.J. (2018). Colorimetric-luminance readout for quantitative analysis of fluorescence signals with a smartphone CMOS sensor. *Anal. Chem.* 90 (21): 12385–12389.
- 18 Chen, Y., Fu, Q., Li, D. et al. (2017). A smartphone colorimetric reader integrated with an ambient light sensor and a 3D printed attachment for on-site detection of zearalenone. *Anal. Bioanal. Chem.* 409 (28): 6567–6574.
- 19 Inan, H., Poyraz, M., Inci, F. et al. (2017). Photonic crystals: emerging biosensors and their promise for point-of-care applications. *Chem. Soc. Rev.* 46 (2): 366–388.
- 20 Wang, S., Zhao, X., Khimji, I. et al. (2011). Integration of cell phone imaging with microchip ELISA to detect ovarian cancer HE4 biomarker in urine at the point-of-care. *Lab Chip* 11 (20): 3411–3418.
- 21 Macias, G., Sperling, J.R., Peveler, W.J. et al. (2019). Whisky tasting using a bimetallic nanoplasmonic tongue. *Nanoscale* 11 (32): 15216–15223.
- 22 Zarzar, L.D., Kalow, J.A., He, X. et al. (2017). Optical visualization and quantification of enzyme activity using dynamic droplet lenses. *Proc. Natl. Acad. Sci.* 114 (15): 3821–3825.
- 23 Guner, H., Ozgur, E., Kokturk, G. et al. (2017). A smartphone based surface plasmon resonance imaging (SPRI) platform for on-site biodetection. *Sensors Actuators B Chem.* 239: 571–577.
- 24 You, D.J., Park, T.S., and Yoon, J.-Y. (2013). Cell-phone-based measurement of TSH using Mie scatter optimized lateral flow assays. *Biosens. Bioelectron.* 40 (1): 180–185.
- 25 Il Hong, J. and Chang, B.-Y. (2014). Development of the smartphone-based colorimetry for multi-analyte sensing arrays. *Lab Chip* 14 (10): 1725–1732.
- 26 Shen, L., Hagen, J.A., and Papautsky, I. (2012). Point-of-care colorimetric detection with a smartphone. *Lab Chip* 12 (21): 4240–4243.
- 27 Wang, T.-T., Lio, C.k., Huang, H. et al. (2020). A feasible image-based colorimetric assay using a smartphone RGB camera for point-of-care monitoring of diabetes. *Talanta* 206: 120211.
- 28 Jalal, U.M., Jin, G.J., and Shim, J.S. (2017). Paper–plastic hybrid microfluidic device for smartphone-based colorimetric analysis of urine. *Anal. Chem.* 89 (24): 13160–13166.
- 29 Li, Z., Askim, J.R., and Suslick, K.S. (2019). The optoelectronic nose: colorimetric and fluorometric sensor arrays. *Chem. Rev.* 119 (1): 231–292.
- 30 Zangheri, M., Cevenini, L., Anfossi, L. et al. (2015). A simple and compact smartphone accessory for quantitative chemiluminescence-based lateral flow immunoassay for salivary cortisol detection. *Biosens. Bioelectron.* 64: 63–68.
- 31 Song, J., Pandian, V., Mauk, M.G. et al. (2018). Smartphone-based mobile detection platform for molecular diagnostics and spatiotemporal disease mapping. *Anal. Chem.* 90 (7): 4823–4831.
- 32 Roda, A., Michelini, E., Cevenini, L. et al. (2014). Integrating biochemiluminescence detection on smartphones: mobile chemistry platform for point-of-need analysis. *Anal. Chem.* 86 (15): 7299–7304.

- 33** Hildebrandt, N., Spillmann, C.M., Algar, W.R. et al. (2016). Energy transfer with semiconductor quantum dot bioconjugates: a versatile platform for biosensing, energy harvesting, and other developing applications. *Chem. Rev.* 117 (2): 536–711.
- 34** Chen, G., Qiu, H., Prasad, P.N., and Chen, X. (2014). Upconversion nanoparticles: design, nanochemistry, and applications in theranostics. *Chem. Rev.* 114 (10): 5161–5214.
- 35** Gupta, R., Peveler, W.J., Lix, K., and Algar, W.R. (2019). Comparison of semiconducting polymer dots and semiconductor quantum dots for smartphone-based fluorescence assays. *Anal. Chem.* 91: 10955–10960.
- 36** Yu, J., Rong, Y., Kuo, C.-T. et al. (2016). Recent advances in the development of highly luminescent semiconducting polymer dots and nanoparticles for biological imaging and medicine. *Anal. Chem.* 89 (1): 42–56.
- 37** Tran, M.V., Susumu, K., Medintz, I.L., and Algar, W.R. (2019). Supraparticle assemblies of magnetic nanoparticles and quantum dots for selective cell isolation and counting on a smartphone-based imaging platform. *Anal. Chem.* 91 (18): 11963–11971.
- 38** Ming, K., Kim, J., Biondi, M.J. et al. (2015). Integrated quantum dot barcode smartphone optical device for wireless multiplexed diagnosis of infected patients. *ACS Nano* 9 (3): 3060–3074.
- 39** Lee, J., Bisso, P.W., Srinivas, R.L. et al. (2014). Universal process-inert encoding architecture for polymer microparticles. *Nat. Mater.* 13 (5): 524–529.
- 40** Wang, L.-J., Chang, Y.-C., Ge, X. et al. (2016). Smartphone optosensing platform using a DVD grating to detect neurotoxins. *ACS Sensors* 1 (4): 366–373.
- 41** Gallegos, D., Long, K.D., Yu, H. et al. (2013). Label-free biodetection using a smartphone. *Lab Chip* 13 (11): 2124–2132.
- 42** Coskun, A.F., Nagi, R., Sadeghi, K. et al. (2013). Albumin testing in urine using a smart-phone. *Lab Chip* 13 (21): 4231–4238.
- 43** Barbosa, A.I., Gehlot, P., Sidapra, K. et al. (2015). Portable smartphone quantitation of prostate specific antigen (PSA) in a fluoropolymer microfluidic device. *Biosens. Bioelectron.* 70: 5–14.
- 44** Dutta, D., Sailapu, S.K., Chattopadhyay, A., and Ghosh, S.S. (2018). Phenylboronic acid templated gold nanoclusters for Mucin detection using a smartphone-based device and targeted cancer cell theranostics. *ACS Appl. Mater. Interfaces* 10 (4): 3210–3218.
- 45** Huang, C.-H., Il Park, Y., Lin, H.-Y. et al. (2019). Compact and filter-free luminescence biosensor for mobile in vitro diagnoses. *ACS Nano* 13 (10): 11698–11706.
- 46** Michelini, E., Calabretta, M.M., Cevenini, L. et al. (2019). Smartphone-based multicolor bioluminescent 3D spheroid biosensors for monitoring inflammatory activity. *Biosens. Bioelectron.* 123: 269–277.
- 47** Petryayeva, E. and Algar, W.R. (2015). Single-step bioassays in serum and whole blood with a smartphone, quantum dots and paper-in-PDMS chips. *Analyst* 140 (12): 4037–4045.
- 48** Liang, C., Liu, Y., Niu, A. et al. (2019). Smartphone-app based point-of-care testing for myocardial infarction biomarker cTnI using an autonomous capillary microfluidic chip with self-aligned on-chip focusing (SOF) lenses. *Lab Chip* 19 (10): 1797–1807.
- 49** You, M., Lin, M., Gong, Y. et al. (2017). Household fluorescent lateral flow strip platform for sensitive and quantitative prognosis of heart failure using dual-color Upconversion nanoparticles. *ACS Nano* 11 (6): 6261–6270.
- 50** Vashist, S.K., Marion Schneider, E., Zengerle, R. et al. (2015). Graphene-based rapid and highly-sensitive immunoassay for C-reactive protein using a smartphone-based colorimetric reader. *Biosens. Bioelectron.* 66: 169–176.
- 51** Paterson, A.S., Raja, B., Mandadi, V. et al. (2017). A low-cost smartphone-based platform for highly sensitive point-of-care testing with persistent luminescent phosphors. *Lab Chip* 17 (6): 1051–1059.
- 52** Long, K.D., Woodburn, E.V., Le, H.M. et al. (2017). Multimode smartphone biosensing: the transmission, reflection, and intensity spectral (TRI)-analyzer. *Lab Chip* 17 (19): 3246–3257.

- 53 Sun, K., Yang, Y., Zhou, H. et al. (2018). Ultrabright polymer-dot transducer enabled wireless glucose monitoring via a smartphone. *ACS Nano* 12 (6): 5176–5184.
- 54 Lee, S., Oncescu, V., Mancuso, M. et al. (2014). A smartphone platform for the quantification of vitamin D levels. *Lab Chip* 14 (8): 1437–1442.
- 55 Zhang, C., Kim, J.P., Creer, M. et al. (2017). A smartphone-based chloridometer for point-of-care diagnostics of cystic fibrosis. *Biosens. Bioelectron.* 97: 164–168.
- 56 Giavazzi, F., Salina, M., Ceccarello, E. et al. (2014). A fast and simple label-free immunoassay based on a smartphone. *Biosens. Bioelectron.* 58: 395–402.
- 57 Shah, K.G. and Yager, P. (2017). Wavelengths and lifetimes of paper autofluorescence: a simple substrate screening process to enhance the sensitivity of fluorescence-based assays in paper. *Anal. Chem.* 89 (22): 12023–12029.
- 58 Wang, L.-J., Naudé, N., Demissie, M. et al. (2018). Analytical validation of an ultra low-cost mobile phone microplate reader for infectious disease testing. *Clin. Chim. Acta.* 482: 21–26.
- 59 Berg, B., Cortazar, B., Tseng, D. et al. (2015). Cellphone-based hand-held microplate reader for point-of-care testing of enzyme-linked Immunosorbent assays. *ACS Nano* 9 (8): 7857–7866.
- 60 Brangel, P., Sobarzo, A., Parolo, C. et al. (2018). A serological point-of-care test for the detection of IgG antibodies against Ebola virus in human survivors. *ACS Nano* 12 (1): 63–73.
- 61 Priye, A., Bird, S.W., Light, Y.K. et al. (2017). A smartphone-based diagnostic platform for rapid detection of Zika, chikungunya, and dengue viruses. *Sci. Rep.* 7: 44778.
- 62 Cheng, N., Song, Y., Zeinhom, M.M.A. et al. (2017). Nanozyme-mediated dual immunoassay integrated with smartphone for use in simultaneous detection of pathogens. *ACS Appl. Mater. Interfaces* 9 (46): 40671–40680.
- 63 Alves, I.P. and Reis, N.M. (2019). Microfluidic smartphone quantitation of *Escherichia coli* in synthetic urine. *Biosens. Bioelectron.* 145: 111624.
- 64 Priye, A., Wong, S., Bi, Y. et al. (2016). Lab-on-a-drone: toward pinpoint deployment of smartphone-enabled nucleic acid-based diagnostics for mobile health care. *Anal. Chem.* 88 (9): 4651–4660.
- 65 Park, T.S., Li, W., McCracken, K.E., and Yoon, J.-Y. (2013). Smartphone quantifies Salmonella from paper microfluidics. *Lab Chip* 13 (24): 4832–4840.
- 66 Xu, G., Nolder, D., Reboud, J. et al. (2016). Paper-origami-based multiplexed malaria diagnostics from whole blood. *Angew. Chemie Int. Ed.* 55 (49): 15250–15253.
- 67 Scherr, T.F., Gupta, S., Wright, D.W., and Haselton, F.R. (2016). Mobile phone imaging and cloud-based analysis for standardized malaria detection and reporting. *Sci. Rep.* 6: 28645.
- 68 Vignaux, J.-J. and André, A. (2018). Biomarkers in precision medicine: the era of omics. In: *Digital Medicine* (ed. A. André), 59–69. Cham: Springer International Publishing.
- 69 Vella, S.J., Beattie, P., Cademartiri, R. et al. (2012). Measuring markers of liver function using a micropatterned paper device designed for blood from a Fingerstick. *Anal. Chem.* 84 (6): 2883–2891.
- 70 Neuta, I.H., Neumann, F., Brightmeyer, J. et al. (2019). Smartphone-based clinical diagnostics: towards democratization of evidence-based health care. *J. Intern. Med.* 285 (1): 19–39.
- 71 Aydindogan, E., Guler Celik, E., and Timur, S. (2018). Paper-based analytical methods for smartphone sensing with functional nanoparticles: bridges from smart surfaces to global health. *Anal. Chem.* 90 (21): 12325–12333.
- 72 Noor, M.O. and Krull, U.J. (2014). Camera-based ratiometric fluorescence transduction of nucleic acid hybridization with reagentless signal amplification on a paper-based platform using immobilized quantum dots as donors. *Anal. Chem.* 86 (20): 10331–10339.
- 73 Woodburn, E.V., Long, K.D., and Cunningham, B.T. (2019). Analysis of paper-based colorimetric assays with a smartphone spectrometer. *IEEE Sens. J.* 19 (2): 508–514.
- 74 Banerjee, R. and Jaiswal, A. (2018). Recent advances in nanoparticle-based lateral flow immunoassay as a point of care diagnostic tool for infectious agents and diseases. *Analyst* 143: 1970–1996.

- 75 Akyazi, T., Basabe-Desmonts, L., and Benito-Lopez, F. (2018). Review on microfluidic paper-based analytical devices towards commercialisation. *Anal. Chim. Acta* 1001: 1–17.
- 76 Gong, X., Chang, J., Cai, J. et al. (2017). A review for fluorescent lateral flow Immunochromatographic strip. *J. Mater. Chem. B* 393: 569.
- 77 Reboud, J., Xu, G., Garrett, A. et al. (2019). Paper-based microfluidics for DNA diagnostics of malaria in low resource underserved rural communities. *Proc. Natl. Acad. Sci.* 116 (11): 4834–4842.
- 78 Kaiser, L., Weisser, J., Kohl, M., and Deigner, H.-P. (2018). Small molecule detection with aptamer based lateral flow assays: applying aptamer-C-reactive protein cross-recognition for ampicillin detection. *Sci. Rep.* 8: 5628.
- 79 Frohnmyer, E., Tuschel, N., Sitz, T. et al. (2019). Aptamer lateral flow assays for rapid and sensitive detection of cholera toxin. *Analyst* 144 (5): 1840–1849.
- 80 Pilavaki, E. and Demosthenous, A. (2017). Optimized lateral flow immunoassay reader for the detection of infectious diseases in developing countries. *Sensors* 17 (11): 2673.
- 81 Mudanyali, O., Dimitrov, S., Sikora, U. et al. (2012). Integrated rapid-diagnostic-test reader platform on a cellphone. *Lab Chip* 12 (15): 2678.
- 82 Ulep, T.-H. and Yoon, J.-Y. (2018). Challenges in paper-based fluorogenic optical sensing with smartphones. *Nano Converg.* 5: 14.
- 83 Hu, J., Cui, X., Gong, Y. et al. (2016). Portable microfluidic and smartphone-based devices for monitoring of cardiovascular diseases at the point of care. *Biotechnol. Adv.* 34 (3): 305–320.
- 84 Joung, H.-A., Ballard, Z.S., Ma, A. et al. (2019). Paper-based multiplexed vertical flow assay for point-of-care testing. *Lab Chip* 19 (6): 1027–1034.
- 85 Petryayeva, E. and Algar, W.R. (2013). Proteolytic assays on quantum-dot-modified paper substrates using simple optical readout platforms. *Anal. Chem.* 85 (18): 8817–8825.
- 86 Vashist, S.K., van Oordt, T., Schneider, E.M. et al. (2015). A smartphone-based colorimetric reader for bioanalytical applications using the screen-based bottom illumination provided by gadgets. *Biosens. Bioelectron.* 67: 248–255.
- 87 Wang, L.-J., Chang, Y.-C., Sun, R., and Li, L. (2017). A multichannel smartphone optical biosensor for high-throughput point-of-care diagnostics. *Biosens. Bioelectron.* 87: 686–692.
- 88 Castanheira, A.P., Barbosa, A.I., Edwards, A.D., and Reis, N.M. (2015). Multiplexed femtomolar quantitation of human cytokines in a fluoropolymer microcapillary film. *Analyst* 140 (16): 5609–5618.
- 89 Pivetal, J., Pereira, F.M., Barbosa, A.I. et al. (2017). Covalent immobilisation of antibodies in Teflon-FEP microfluidic devices for the sensitive quantification of clinically relevant protein biomarkers. *Analyst* 142 (6): 959–968.
- 90 Liao, S.-C., Peng, J., Mauk, M.G. et al. (2016). Smart cup: a minimally-instrumented, smartphone-based point-of-care molecular diagnostic device. *Sensors Actuators B Chem.* 229: 232–238.
- 91 Kim, J., Biondi, M.J., Feld, J.J., and Chan, W.C.W. (2016). Clinical validation of quantum dot barcode diagnostic technology. *ACS Nano* 10 (4): 4742–4753.
- 92 Orth, A., Wilson, E.R., Thompson, J.G., and Gibson, B.C. (2018). A dual-mode mobile phone microscope using the onboard camera flash and ambient light. *Sci. Rep.* 8: 3298.
- 93 Jung, D., Choi, J.-H., Kim, S. et al. (2017). Smartphone-based multi-contrast microscope using color-multiplexed illumination. *Sci. Rep.* 7: 7564.
- 94 Wei, Q., Qi, H., Luo, W. et al. (2013). Fluorescent imaging of single nanoparticles and viruses on a smart phone. *ACS Nano* 7 (10): 9147–9155.
- 95 Minagawa, Y., Ueno, H., Tabata, K.V., and Noji, H. (2019). Mobile imaging platform for digital influenza virus counting. *Lab Chip* 19 (16): 2678–2687.
- 96 Udugama, B., Kadhireesan, P., Samarakoon, A., and Chan, W.C.W. (2017). Simplifying assays by tabletting reagents. *J. Am. Chem. Soc.* 139 (48): 17341–17349.

- 97 Park, J.-U.J., Kim, J., Kim, S.-Y. et al. (2018). Soft, smart contact lenses with integrations of wireless circuits, glucose sensors, and displays. *Sci. Adv.* 4 (1): eaap9841.
- 98 Yang, Z., Albrow-Owen, T., Cui, H. et al. (2019). Single-nanowire spectrometers. *Science* 365 (6457): 1017–1020.
- 99 Kalantar-zadeh, K., Ha, N., Ou, J.Z., and Berean, K.J. (2017). Ingestible sensors. *ACS Sensors* 2 (4): 468–483.
- 100 Park, J.-S., Zhang, S., She, A. et al. (2019). All-glass, large metalens at visible wavelength using deep-ultraviolet projection lithography. *Nano Lett.* 19 (12): 8673–8682.
- 101 Kim, S., Cho, D., Kim, J. et al. (2016). Smartphone-based multispectral imaging: system development and potential for mobile skin diagnosis. *Biomed. Opt. Express* 7 (12): 5294–5307.
- 102 Kim, S., Kim, J., Hwang, M. et al. (2019). Smartphone-based multispectral imaging and machine-learning based analysis for discrimination between seborrheic dermatitis and psoriasis on the scalp. *Biomed. Opt. Express* 10 (2): 879.
- 103 Carrio, A., Sampedro, C., Sanchez-Lopez, J.L. et al. (2015). Automated low-cost smartphone-based lateral flow saliva test reader for drugs-of-abuse detection. *Sensors* 15 (11): 29569–29593.
- 104 Rivenson, Y., Ceylan Koydemir, H., Wang, H. et al. (2018). Deep learning enhanced mobile-phone microscopy. *ACS Photonics* 5 (6): 2354–2364.
- 105 Liu, X., Faes, L., Kale, A.U. et al. (2019). A comparison of deep learning performance against health-care professionals in detecting diseases from medical imaging: a systematic review and meta-analysis. *Lancet Digit. Heal.* 1 (6): e271–e297.
- 106 De Fauw, J., Ledsam, J.R., Romera-Paredes, B. et al. (2018). Clinically applicable deep learning for diagnosis and referral in retinal disease. *Nat. Med.* 24 (9): 1342–1350.

## 11

### Applications of Portable and Handheld Infrared Spectroscopy

*John A. Seelenbinder<sup>1</sup> and Christina S. Robb<sup>2</sup>*

<sup>1</sup>*PointIR Consulting LLC, Watertown, CT, USA*

<sup>2</sup>*The Connecticut Agricultural Experiment Station, New Haven, CT, USA*

Handheld and portable instrument development has been one of the largest areas of growth for infrared spectroscopy for several years. Technology developments (discussed in Volume 1, Chapter 3 by Schiering) have driven the introduction of new handheld and portable instruments, but as with all instrumentation, the advancements have been propelled by an application need. Handheld and portable infrared spectrometers are used in a wide range of applications in many different industries. They are used to measure solids, liquids, and gases. They measure both neat and mixed materials. Handheld and portable instruments are used for sample identification, classification, and quantitative measurements. Similar to laboratory spectroscopy, the universal measurement capabilities of infrared spectroscopy have led to a wide variety of applications.

Though the industries and sample types vary, there are a set of common benefits, or drivers, which all portable applications share. These drivers provide advantages for handheld and portable measurements, which lead to their adoption and success. They provide real advantages to the consumers of the analytical information. These advantages are not typically in analytical accuracy or sensitivity (though at times they can be) but are often more practical. Handheld and portable measurements may provide more safety, better efficiency, cost savings, or sample preservation. While the science of analytical chemistry always works for higher selectivity and sensitivity, the preference in industry for one technique over another often comes down to these practical factors.

Since the range of applications for portable and handheld infrared instruments is quite large, there are many ways of grouping the applications. This chapter groups applications by the need that drives those applications to be made with portable instruments. Three primary drivers of handheld and portable infrared applications have been identified:

1. Rapid response
2. Dispersed samples
3. Nondestructive measurement

Rapid response is one of the hallmarks of portable instrumentation. Measuring samples where they occur provides nearly instantaneous answers when compared with transporting samples to a separate laboratory, even if the laboratory is in close proximity. Furthermore, infrared measurements are relatively fast; it is not uncommon to have an answer in less than a minute. The increased speed along with infrared's ability to identify materials based on their molecular structure makes handheld and portable infrared systems a key tool for identification of unknown materials in forensics, military, and hazardous-materials (hazmat) response applications (Volume 2, Chapters 6, 7 and 9).

In a similar way, portable instrumentation allows efficient measurement of samples that are spread out over a large physical area. Here, the quantitative capabilities of portable infrared spectrometers are used to

determine concentration profiles, saving time and money over conventional sample collection and laboratory analysis.

And finally, handheld infrared spectrometers allow measurement of large or complex-shaped objects wherever they exist, allowing for true nondestructive analysis. The chemical identification and quantification provided by infrared measurement complements and extends the primarily physical measurements made by ultrasound and other conventional nondestructive assessment techniques.

For each application, there are other needs and drivers that contribute to the success of the application. Cost, efficiency, analytical accuracy, and precision all contribute to the success of any one application. The identified analytical drivers, though, provide the impetus for portable and handheld measurement and provide the advantage that pushes these measurements out of the lab.

## 11.1 Rapid Response

Emergency responders use portable and handheld vibrational spectrometers for the identification of unknown materials. Measurement of samples on site provides quick answers that allows fast remediation and improves public safety. This industry was the primary driver that led the development and expansion of portable infrared instruments; nearly 20 years after the first use, it remains one of the largest markets for portable and handheld vibrational spectroscopic instrumentation. Large-scale adoption and use was sparked by the postal-based anthrax attacks that occurred on media organizations and political figures in 2001.

It may come as a surprise to most analytical chemists, but prior to 2001, few hazmat or other emergency response teams used instrumental methods to identify unknown materials. Teams would typically use nonspecific combustion gas or photoionization detector (PID) meters to determine if dangerous gases were present. If an unknown solid or liquid was found, teams would try to identify it by labels, shipping documents, or other documentation. The anthrax attacks, though, posed a new problem. In response to the initial attacks, many government agencies published warnings related to “unknown white powders.” As media coverage of the attacks and subsequent warnings increased, emergency responders faced an increasing number of calls reporting suspicious white powders. With no way to identify the found materials and determine the danger of the suspected material, responders were left with no choice but to restrict access to buildings until laboratory tests could be completed. Nearly all the samples found were innocuous; however, the potential danger of weaponized anthrax made rapid identification critical. The cost associated with restricting access to buildings and infrastructure was enormous. In an often-repeated story, a responder was told by a supervisor on a white powder call, “Please be quick. I have the airport terminal shut down and it’s costing \$1000 per minute...”

In the months following the initial anthrax attacks, first responders began to use portable instrumentation, such as SensIR Technologies TravelIR and Thermo Nicolet CompoundID instruments originally designed for industrial applications [1]. Using a diamond attenuated total reflection (ATR) sample interface and paired with appropriate spectral libraries, these instruments allowed emergency responders to identify samples on-site. Although infrared spectroscopy cannot accurately identify bacillus anthracis (the pathogen in the biological weapon anthrax), the infrared instruments could identify many of the materials being found, providing a rapid solution to most “white powder” calls [2]. Shortly afterward, SensIR (now Smiths) developed the first portable instrument specifically targeted at the homeland security market [3, 4]. The SensIR HazMatID was a fully self-contained, battery-operated, Fourier transform infrared (FTIR) spectrometer with a diamond ATR sample interface. It included an integrated touchscreen computer complete with appropriate spectral libraries. The method-driven software was easy to use and specifically designed for identification of unknowns. The instrument was fully waterproof and allowed decontamination, which was critical for its success in the marketplace. Once the instrumentation was fielded in civilian emergency response teams, they quickly applied it to other situations where the identification of an unknown material was needed. Currently, both handheld and portable instruments using both infrared and Raman spectroscopy are used for this application [5]; infrared systems have also been developed for gas-phase identification [6, 7]. Small, handheld systems provide sample identification in a small,

easy-to-carry package; slightly larger, portable systems have larger screens and controls that some users find easier to operate when wearing protective gear [8–10].

The basic application of both handheld and portable infrared and Raman spectrometers in emergency response is the identification of unknown solids and liquids through spectral measurement and automated comparison with a predefined spectral library. Infrared instruments designed for this application typically use an FTIR spectral engine and a diamond ATR sample interface. These systems are used by both civilian and military emergency response teams worldwide. Often the systems are used by civilian hazmat response teams in the fire and police protective services. Users are typically hazmat specialists, but not typically chemists. User-friendly software dedicated to identification of materials allows the systems to be successfully used with minimal training. Military use is slightly different where the focus is on the identification of chemical weapons, explosives, and hazardous industrial chemicals. The use of infrared spectroscopy for sample identification in emergency response scenarios has relied on three technological advancements: diamond ATR, suitable spectral libraries, and ruggedized construction suitable for difficult operating conditions.

Diamond ATR has been an enabling technology for sample identification by infrared spectroscopy. It provides consistent sample measurement with little user interaction; furthermore, the diamond crystal interface is durable as it is scratch, chemical, and shock resistant. It provides a consistent pathlength that produces a uniform absorbance intensity for most samples. The user simply needs to ensure that the sample is in good contact with the diamond interface, using a press with solids or simply covering the crystal for liquids. The consistent absorbance intensity leads to accurate library searching for most materials.

Hand in hand with the diamond ATR, appropriate spectral libraries allow emergency responders to identify samples without spectral interpretation. A large effort was made in the years following the initial adoption of infrared in emergency response to build libraries of ATR infrared spectra composed of materials that responders were likely to encounter. Today, large libraries exist that cover a range of chemicals, including both known hazards and common products. Libraries are included with instruments, or can be purchased, which contain spectra of explosives (including homemade or improvised explosives), illegal drugs, chemical weapons, pesticides, pharmaceuticals, household products, toxic industrial chemicals, and common white powders. Given the high signal to noise and repeatability of ATR measurements, library matches with a correlation of 0.95 or higher are easily obtained if the sample is present in the library. These large spectral libraries, paired to method-driven software that automatically conducts a library search, allow nonexpert users in emergency response units the ability to quickly identify samples. One area where standard correlation-based library searches fail, though, is in the analysis of mixtures. Unfortunately, many consumer products are mixtures of several components. If the sample is a mixture and the mixture is present in the library at roughly the same ratio, it can be identified with a correlation algorithm. In an emergency response scenario, though, one must assume that the unknown sample could be anything; therefore, having every possible mixture contained in a library is impossible. Several groups have developed advanced multivariate algorithms to address the mixture analysis issue, with a great deal of success (discussed in Volume 2, Chapter 1). Today it is common for commercially available portable or handheld infrared spectrometers designed for the hazmat market to incorporate a mixture analysis algorithm [11]. These are implemented differently; however, it is common for the software to alert the user that a mixture may be present and present proposed constituents of the mixture. Usually a measure of the probability of those components being part of the mixture is presented as well. The algorithms are usually limited to three or four components, with the most consistent results being obtained with binary mixtures.

Another feature offered by most handheld and portable instrument companies in the hazmat marketplace that enables the successful use of the technology is technical and application support services that are available 24 hours a day, seven days a week. Through these services, customers have access to infrared spectroscopic experts who can guide the user through sample measurement problems, address technical support issues, and even evaluate sample data for the customer via phone and email. The ability to quickly send data to a qualified spectroscopist gives emergency responders the confidence required to use the instruments in the field.

Ruggedized construction is the third technological breakthrough that has enabled portable and handheld instrument to succeed in the material application space [12]. This includes waterproof enclosures, nonhygroscopic optics, diode reference lasers, and shock and vibration resistance. Hazmat teams require instruments that can be taken to the sample location in a restricted area referred to as the “hot zone.” Any item leaving the “hot zone” must be decontaminated including any instrumentation; decontamination often involves washing off any visible contamination and immersing items in bleach to ensure any material is removed. Therefore, portable and handheld spectrometers used by hazmat teams must be waterproof and resistant to bleach as well as solvents, acids, bases, and other chemicals that may get spilled on the system during use. In addition to the waterproof outer enclosure, these systems must survive in any climatic condition, including high humidity. Traditional laboratory FTIR spectrometers use hygroscopic optics; the key to the development of portable systems suitable for hazmat was zinc selenide (ZnSe) optics that provide excellent optical performance and are unaffected by atmospheric or liquid water. When combined with the durable and easy-to-use diamond ATR and method-driven software, these ruggedized systems require little maintenance, allowing operation and upkeep by nonspecialists.

Another application where a fast, on-site analysis provides meaningful sample identification is at scene presumptive testing of confiscated illegal drugs. Presumptive tests provide law enforcement officials probable cause for the arrest of persons possessing materials suspected to be drugs. Currently, there are a number of test kits available that provide colorimetric tests for certain drug substances [13]. There has been a great deal of interest in replacing presumptive tests with portable instrumentation to reduce subjectivity, improve false positive rates, and provide reviewable results. In an economic study, Menking-Hoggatt [14] calculated that the use of portable instrumentation to test and identify confiscated drugs on-site or at the time of booking could save up to \$10 000 per case, and providing other advantages such as increased prosecution accuracy and public trust. To provide these benefits, on-site measurement would need to obtain the level of accuracy and precision required of laboratory testing. This high bar is not currently achievable, but there is motivation to improve and adopt these techniques. Early technical studies [15] found it difficult to use handheld and portable infrared and Raman instruments due to low concentrations of drug compounds in street-confiscated samples; however, more recent studies show additional promise in the areas of narcotics [13, 16] and new synthetic psychoactive substances [17].

A comparison study was conducted by Lieblein et al. evaluating the efficacy of handheld infrared and Raman instruments to colorimetric tests for on-scene determination of cocaine [13]. The researchers tested laboratory-generated samples of cocaine mixed with excipients including lidocaine, mannitol, caffeine, artificial sweetener, and baby formula in concentrations representative of street-confiscated samples. The handheld infrared and Raman systems correctly identified cocaine in all samples down to 25% concentrations. In some excipients (lidocaine for infrared and artificial sweetener for Raman), the limit of detection was as low as 5%. When compared with color-based techniques, the researchers found that both portable infrared and portable Raman instruments provided advantages (see Table 11.1). Advanced mixture analysis algorithms used in the tested infrared and Raman instruments provided lower limits of detection as compared with the correlation algorithms used in previous studies [15]. In the colorimetric test, lidocaine is an interferent causing false positive; for other excipients, the limit of detection was 10%. The authors did note that detection required manual spectral interpretation at lower concentrations. Despite the higher capital costs, handheld infrared and Raman spectrometers were found to offer good value over the long term compared with colorimetric tests, as well as providing more consistent results with fewer false positives. In another study, Mainali et al. demonstrated a different data analysis technique to identify cocaine in low-concentration street-seized samples measured on a portable infrared spectrometer with an ATR sample interface [16]. The novel analysis used a focused peak picking routine combined with an expert system that predicted the probability of the sample containing cocaine based on the presence and intensity of peaks found. This technique was found to be independent of the adulterants and diluents present, allowing for easy field use.

New synthetic drugs, such as synthetic cannabinoids and synthetic cathinones, have been a growing concern over the past 10–15 years. These new psychoactive substances present a legal and enforcement challenge as manufacturers continually change formulations making detection and prosecution difficult. Harkai and Pütz

**Table 11.1** A favorable comparison of portable infrared and Raman spectroscopies to conventional color-based field tests for cocaine.

Parameter	Color-based	Portable IR	Portable Raman
Complexity	Easy to use	Easy to use	Easy to use
Training	1 day, a component of narcotics training	1 day	1/2 day
Sample consumption	Destructive	Nondestructive	Nondestructive
Time for analysis	1–3 minutes	1–3 minutes	1–3 minutes
Versatility	Each test is specific for a drug class, thus different illicit drugs require separate tests	Capable of identifying a large range of compounds in a mixture	Capable of identifying a large range of compounds in a mixture
Objectivity	Subjective: based on perception of color	Objective	Objective
Limit of detection	10%	5–25%, depending on the adulterant	5–25%, depending on the adulterant
Specificity	Prone to false positives and negatives	No false positives or negatives reported	No false positives or negatives reported, however fluorescence of adulterants and dark-colored samples prohibit illicit drug identification
Chain of custody corroboration	No	Yes	Yes
Safety	Testing requires exposure to unknown chemicals	Testing requires exposure to unknown chemicals	Reduction of exposure to unknown chemicals because of analysis through containers
Cost	\$2–5 per single-use test; >\$30 000 per year	\$25 000–\$65 000 per instrument, no consumables	\$12 500–\$25 000 per instrument, no consumables

Source: Lieblein et al. [13]. © 2018 MJH Life Sciences.

[17] published a study that compared handheld infrared and Raman spectrometers for the field identification of confiscated materials containing new psychoactive substances. The authors first built a library containing known synthetic cannabinoids and cathinones on both the infrared and Raman instruments and then searched spectra measured of the confiscated materials using available library mixture search algorithms. The authors found advantages in the use of infrared, especially for dark samples where absorption of the Raman laser led to thermal degradation of materials. Raman systems were found to offer advantages in measuring confiscated samples through plastic bags or other clear containers. In the end, a combination of both handheld infrared and Raman instrumentation was recommended to meet the different needs of new psychoactive substance identification.

For hazardous or illegal materials, portable and handheld infrared spectroscopy provides valuable identification quickly and on-scene. These tools are simple enough to be used by nonchemists with minimal training and provide accurate identifications in the majority of situations. In these cases, the fast identification provided by portable and handheld instruments ensures public safety, advances military operations, and allows fast, efficient resolution for forensic cases. All of these measurements could certainly be conducted in a lab, but speed of analysis provided by portable systems makes them the clear choice for emergency response, military, and illicit drug identification.

## 11.2 Dispersed Samples

Another group of applications that benefit from the use of portable and handheld measurements are those where samples are dispersed over a large area. In some cases, dispersed samples could be collected and analyzed in a

laboratory, such as soil or mineral samples; other dispersed samples are difficult to bring into the lab such as air pollution or motor vehicle emissions. Typically, these samples are located over a large geographical area, and often data is represented as a data map where both the location and concentration of the desired analyte provide meaningful information. Portable and handheld infrared spectrometers provide many advantages for dispersed samples. Field measurement of samples can often be conducted more efficiently. Collection, documentation, transportation, and measurement are all time-consuming activities for laboratory analysis of field samples. Users still need to identify samples and measure and document the results in the field; however, portable instruments eliminate the transportation time and cost and avoid backlogs in the laboratory. Handheld instruments can often make measurements *in situ* without sample collection further increasing efficiency. In addition, users can often generate more meaningful data maps by dynamically modifying sample spacing. This measurement-guided mapping allows additional data points in information-rich areas and fewer data points where they are not needed. Instead of working on a fixed grid, dynamic data collection can optimize the number of samples needed and reduce the overall data collection time and cost.

The contamination of soils with petroleum exemplifies some of the advantages handheld infrared measurement brings to dispersed samples. Handheld infrared spectroscopy has been successfully used to measure hydrocarbon contamination in soil. In the event of petroleum product spill, soil can become contaminated, negatively impacting human and soil health. The contamination can migrate through the soil, spreading as a plume. To properly remediate the site, the concentration of total petroleum hydrocarbons (TPH) or total recoverable hydrocarbons (TRH) in the soil must be determined spatially across the contamination area. Conventional analysis involves physically collecting samples at the site, transporting the samples to an off-site laboratory, and analyzing the samples with a published methodology. The current gold standard method for laboratory analysis is gas chromatography paired with either a flame ionization detector or mass spectrometer (GC/FID or GC/MS). The current process is both time consuming and expensive; as an example, authors reported that *in situ* field measurement with portable infrared spectroscopy can provide reduced analytical costs of 8- to 10-fold [18, 19]. Field measurement also reduces time; a dozen samples can be analyzed in only two hours in the field but would take up to five workdays with off-site laboratory analysis [18]. Handheld measurement also offers reduced consumable use, lower energy consumption, the elimination of hazardous solvents for extraction, and decreased hazardous waste generation.

Infrared spectroscopy with a diffuse reflectance sample interface has been shown to provide accurate measurement of hydrocarbons in soil, providing the specificity to distinguish petroleum hydrocarbons from other soil components. With recent advancements in handheld FTIR instrumentation, field measurement of TPH (or TRH) in soils has become a successful application. In a study by Khudur and Ball [18], a handheld infrared instrument was shown to be very accurate compared with conventional laboratory GC/MS measurements in a large-scale study of bioremediated and weathered soils with both moderate and heavy contaminations. Handheld infrared measurements correlated to the GC/MS values with a correlation factor  $R^2 = 0.998$ . Accurate predictions were made of TPH concentrations in the range from 100 to 100 000 mg/kg.

In a separate study by Ng et al. [20], the performances of field portable and benchtop mid-infrared (MIR) spectrometers both using diffuse reflectance sample interfaces were compared for the analysis of TRH from petroleum-contaminated soils. Both spiked laboratory samples and field-contaminated samples were included in the study. The handheld and benchtop FTIR systems were found to have similar spectral features with slightly different absorbance values due to optical difference between the two systems. Individually calibrated, the handheld systems ( $R^2 = 0.71$ ) provided predictions that were more accurate than laboratory-based analysis ( $R^2 = 0.53$ ). In addition to the ability to determine TRH accurately, this study also considered other factors that are relevant to remediation such as soil texture, hydrocarbon loss due to degradation, and organic matter addition (Table 11.1).

Finally, in one of the more complicated studies by Webster et al. [19], a handheld FTIR spectrometer with a diffuse reflectance interface was shown to accurately predict TPH in three different soil types. The soils were Italian carbonate-dominated clay spiked with diesel fuel at concentrations 0–60 000 mg/kg, Australian

kaolinite-dominated clay spiked from an actual diesel spill site with concentrations from 0 to 40 000 mg/kg, and a Nigerian loam soil spiked with diesel fuel with concentrations ranging from 0 to 30 000 mg/kg. This study attained partial least squares regression (PLSR) predictions with an  $R^2$  of 0.99 and a root mean square error of prediction (RMSEP) of 200 mg/kg for TPH concentrations ranging from 0 to 3000 mg/kg, regardless of the soil type tested. A large TPH concentration range (0–60 000 mg/kg) for each soil type was investigated for prediction models:  $R^2$  of 0.99 and RMSEP of 1255 mg/kg were attained.

The above studies demonstrate the predictive capabilities of handheld infrared for the direct measurement of TPH in soil; implementation of this technology has also been shown to provide increased information and cost savings over conventional laboratory analysis. As an example, in a case study presented by Ziltek, the RemScan™ handheld infrared was used for both the initial quantitation and validation of remediation on a diesel fuel spill site [21]. Using a single instrument, over 200 samples per day were measured, allowing the entire validation to be completed in four days, compared with several weeks if done by conventional laboratory analysis. Figure 11.1a shows the handheld measurement being made, and Figure 11.1b shows the close correlation between the conventional laboratory measurements and the handheld data. The time savings alone reduced the cost of remediation by an estimated \$30 000. Another case study demonstrated the use of handheld infrared on a transformer remediation site where the on-site measurements demonstrated that all the affected soil was removed, allowing backfilling on the same day [22]. A third case study demonstrated the use on a large site of over 4 km<sup>2</sup> where the handheld infrared was used to define areas of high contamination, verify that excavated areas were free of contamination, and sort contaminated material by TPH concentration for efficient disposal [23].

Similar to the soil contamination work above, portable and handheld infrared spectroscopy has also been used extensively to monitor soil health for agriculture. Traditional soil sampling and analysis is a slow, intensive, and expensive process but one that is routinely performed. Soil is a complex and dynamic matrix; researchers are interested in a range of measurable soil properties. The ability to accurately characterize the chemical components of soil is the heart of precision agriculture; it also affects numerous agriculture-related issues ranging from understanding climate change to achieving food security.

MIR spectroscopy is an established technique for soil analysis. It provides a chemical fingerprint of both mineral and organic components; therefore, many soil properties or analytes can be simultaneously determined from a single spectrum. Handheld MIR systems enable the leap from the laboratory to the field [24, 25]. The great potential advantage of using portable MIR for soil analysis is that it presents no barrier to extensive data collection; the costs per sample are very low, it can be performed very quickly, and data can be measured and analyzed in a single field visit. Handheld MIR is a potentially transformative technology for soil analysis. Portable spectrometers can provide insight into site-specific issues such as troubleshooting poor crop yield areas to enhancing global knowledge by providing more accurate soil mapping. There are challenges for portable MIR systems to meet; the ability to determine soil samples in the native state means that unlike in the laboratory setting, the sample is not milled and cannot be extensively dried.

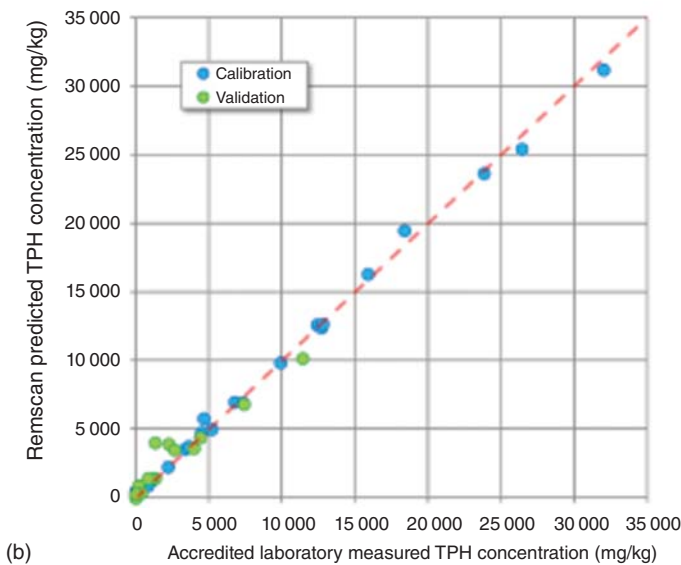
Several studies illustrate the interest and progress in this area [26–32]. The assessment of handheld instruments to benchtop models for soil analysis has numerous variables to consider, there are multiple vendors producing instruments of varying technical specifications, field samples are not in the same condition as laboratory-prepared samples, and different approaches for developing calibration models exist.

Comparisons of handheld MIR systems to laboratory systems for prediction of soil parameters have been performed [26–27]. Huetengs et al. [26] studied the prediction accuracy of calibrations for soil organic carbon (SOC), nitrogen, clay, sand, and pH in soils using both handheld and laboratory MIR instruments. This study found that the handheld system had comparable prediction accuracy to the laboratory spectrometer with a diffuse reflectance sample interface; only when equipped with an integrating sphere did the laboratory spectrometer clearly outperform the handheld systems. In a second study, Huetengs et al. [28] compared calibrations of SOC between portable near-infrared (NIR) and handheld MIR spectrometers. The results indicated that increased sample preparation improved all measurements; calibrations of dried and ground samples were 1.8 times more accurate than those



(a)

Comparison of RemScan data to laboratory data for TPH



(b)

**Figure 11.1** Handheld measurement of TPH in soil (a) and validation data comparing handheld FTIR results to a standardized laboratory measurement (b). Source: Figures courtesy of Ziltek [21].

of samples measured *in situ* with no preparation. In all cases, though, handheld MIR spectrometers with diffuse reflectance sample interface provided the most accurate prediction of SOC. Soriano-Disla et al. [27] conducted a large study comparing the prediction accuracy of 17 different soil properties between laboratory and handheld infrared systems with portable and handheld NIR systems; properties tested included bulk density, saturated moisture, drained upper limit moisture, organic carbon, total carbon, total nitrogen, electrical conductivity, cation exchange capacity, exchangeable calcium, magnesium, sodium, potassium, exchange sodium percentage, sand

silt, and clay. The study found similar performance between the handheld MIR and laboratory instruments. The portable NIR instrument performed sufficiently in about half of the analytes, while the handheld NIR did not provide accurate predictions. These studies demonstrate that sample preparation can cause distinct differences in the prediction accuracy between field and laboratory measurements; only when sample preparations are kept consistent can field and laboratory measurement be compared.

Several other studies of soil chemistry relevant to the agricultural field by handheld and portable infrared spectroscopy have been conducted. Forrester et al. [29] developed a method to predict the phosphorous buffering index (PBI) in Australian soils using handheld MIR spectrometer with a diffuse reflectance sample interface, predicting concentrations using PLSR models. The study used over 600 soil samples encompassing different land use, climate, and geographic regions. Both highly fertilized and unfertilized samples were included. PLSR models were developed for use with portable MIR based upon spectral data from unground samples. Two concentration ranges were studied: 0–150 units and 0–800 units. The method did not accurately predict available (Colwell) phosphorous, but it could accurately predict PBI, with the best predictions in the lower concentration range.

Soriano-Disla et al. [30] also developed a method for the prediction of total cyanide in soil using handheld MIR with a PLSR calibration. The method was able to very accurately determine cyanide in field soils within the range 0–611 mg kg<sup>-1</sup> (with a root mean square error of cross validation [RMSECV] of 21 mg kg<sup>-1</sup>). The handheld MIR instrument matched the benchtop model and a portable MIR spectrometer. Cyanide was most accurately determined in ground samples: satisfactory results (with increased error) were still attained for wet samples. The method had the capability of determining several kinds of cyanide complexes. The CN frequency is in an area of the infrared spectrum with no other absorbances allowing for easy speciation and good performance in the presence of moisture.

Saline content in soil is a concern for many arid and semiarid regions, leading to soil degradation and unproductive farmland. Monitoring salt content in soil can facilitate understanding the extent of salinization, environmental contributions, and possible remediation strategies. Handheld NIR and handheld MIR spectrometers were evaluated for the prediction of total salt-specific ion concentration in soils in a study by Peng et al. [31]. Soil samples from four regions in Xinjiang, China, were collected, and ion concentration was measured using conventional techniques; a separate portion of each sample were kept for spectral measurement. From the 261 original samples, two thirds were used for calibration and one third for validations. The study found good performance for all ions except potassium, with the handheld MIR spectrometer outperforming the handheld NIR system. The paper concluded that handheld infrared spectroscopy could be a valuable tool for assessing soil salinity in many regions.

As stated above, soil is a complex matrix and the species of interest can exist in many forms. Enhanced data analysis can benefit this complicated system, similar to the way advanced mixture analysis benefits sample identification in hazmat or forensic response. Martinez-Espana et al. [32] studied the benefit of advanced algorithms by comparing machine learning techniques to the standard statistical PLSR method; machine learning techniques investigated included random forest (RF), M5 rules (regression rules with the M5 technique), Gaussian process regression (GPR), bagging, and the decision tree (DT) techniques. These were applied to portable MIR data of 458 soil samples for the prediction of silt, clay, cation exchange capacity, exchangeable sodium, and total carbon and nitrogen values. The initial assessment of the techniques focused upon the standard deviation (STD) and the RMSEP: the result was that RF was the best model for silt, and everything else was most accurately determined by GPR. A direct comparison to PLSR also determined that GPR was the best overall technique for the soil properties except for silt that was still best predicted by the RF technique. The accuracy of GPR with respect to the other techniques was confirmed by further statistical validation using the Wilcoxon test. This study shows that although the standard statistical approach of PLSR yields good results for some analytes, soil systems often present more variables in both sample matrix and soil chemistry than can be effectively modeled with that technique. In these cases, more accuracy can be gained by using modern machine learning techniques that can correlate concentrations to subtle changes in the data set.

The ultimate dispersed samples are gases, of course. Portable infrared spectroscopy systems provide gas identification and quantitation in real time, at the site of interest. They have been successfully used for pollution studies [33], hazmat identification [6, 7], and industrial hygiene [34]. An emerging application of portable infrared gas analysis is monitoring the evolution of greenhouse gases from various sources. Using a portable FTIR with a photoacoustic detector, researchers have determined the concentration and identification of gases evolving from various agriculture and livestock conditions [35–37]. In a series of studies conducted at Texas A&M University by Storlien et al., evolved gases from sorghum and other plants grown for biofuel production were determined. The goal of the work is to understand what factors contribute to greenhouse gas emissions from these plants and develop growing strategies to minimize emissions such that biofuels can offer a net reduction in greenhouse gas emissions [35]. Similarly, the Allerton Project, an agricultural research facility in Leicestershire, UK, has studied the evolution of both carbon dioxide ( $\text{CO}_2$ ) and nitrous oxide ( $\text{N}_2\text{O}$ ) from croplands using various farming practices [36]. In both of these studies, portable measurement provides increased accuracy and specificity by measuring the gases evolved from true field conditions; transportation of soil samples creates a further disturbance causing inaccurate results. In the field of livestock production, Preston et al. have studied the relationship between feedstocks and greenhouse gas production in goats and cattle [37–42]. Portable infrared with photoacoustic detection allowed both identification and quantitation of multiple gases including  $\text{CO}_2$  and methane produced by test subjects fed specific diets compared with controls. This research has led to a further understanding of the relationship between ruminant nutrition and methane emission.

A slightly different take on dispersed samples is the growing need to determine authenticity in a wide variety of products. From food to fuel and pharmaceuticals to plastics, the ever-growing issues of counterfeit or mislabeled products force additional testing to ensure authenticity. Adulteration is a similar concern, where undesired components are added to a product, typically for economic gains. Authenticity, counterfeiting, and adulteration are big concerns for the pharmaceutical industry, where several portable analytical methods, including infrared and Raman, have been implemented [43]. These issues affect other areas as well and examples in the food industry will be given here. These are dispersed samples as counterfeits or adulterants can be introduced at multiple points along a supply chain. In many cases, the most effective testing options occur at the point of distribution, opening the door to handheld and portable measurement. Handheld and portable infrared spectroscopies' identification and chemical fingerprinting capabilities are uniquely suited to handle many authenticity and adulteration issues.

The potential dangers of adulterated foods gained prominence in 2008 when adulterated milk powder sickened 294 000 people in China [44]. The resulting crisis led to the development of several sensitive analytical methods for the detection of melamine, the main adulterant; most of the test methods were laboratory based. In a recent article by Limm et al. [44], a portable infrared spectrometer including a multireflection diamond ATR with a nontargeted mathematical approach was used to detect adulteration. Melamine is a well-known adulterant in protein-based food products due to its interference in commonly used protein concentration tests. Although this is an important adulterant to measure, Limm et al. make the argument that other adulterants may be present; therefore, they developed nonspecific test methods using a soft independent modeling of class analogs (SIMCA) classification that identify spectra that are atypical compared with spectra of authentic milk protein. The method was able to identify with 100% accuracy samples with as little as 0.3% melamine. The authors point out that these results are comparable with laboratory measurements by NIR and Raman, but the portable infrared with ATR sample interface can be used at distribution points as needed.

Most counterfeits are economically motivated. With respect to food, often a regional or specialty product is targeted by counterfeiters because these products generate a premium price. Portable infrared spectroscopy can play a role in evaluating the authenticity of foods. As an example, Maurer et al. [45] compared laboratory and portable infrared spectrometers to distinguish vegetable oils high in omega-3 fatty acids (see Figure 11.2). The authors found accurate classification using SIMCA with both laboratory and handheld systems, both using ATR sample interfaces. In addition to classification, models were also developed to calculate food oil performance parameters, such free fatty acid values and oxidative efficiency. In a similar study, Schotts et al. [46] demonstrated the ability to

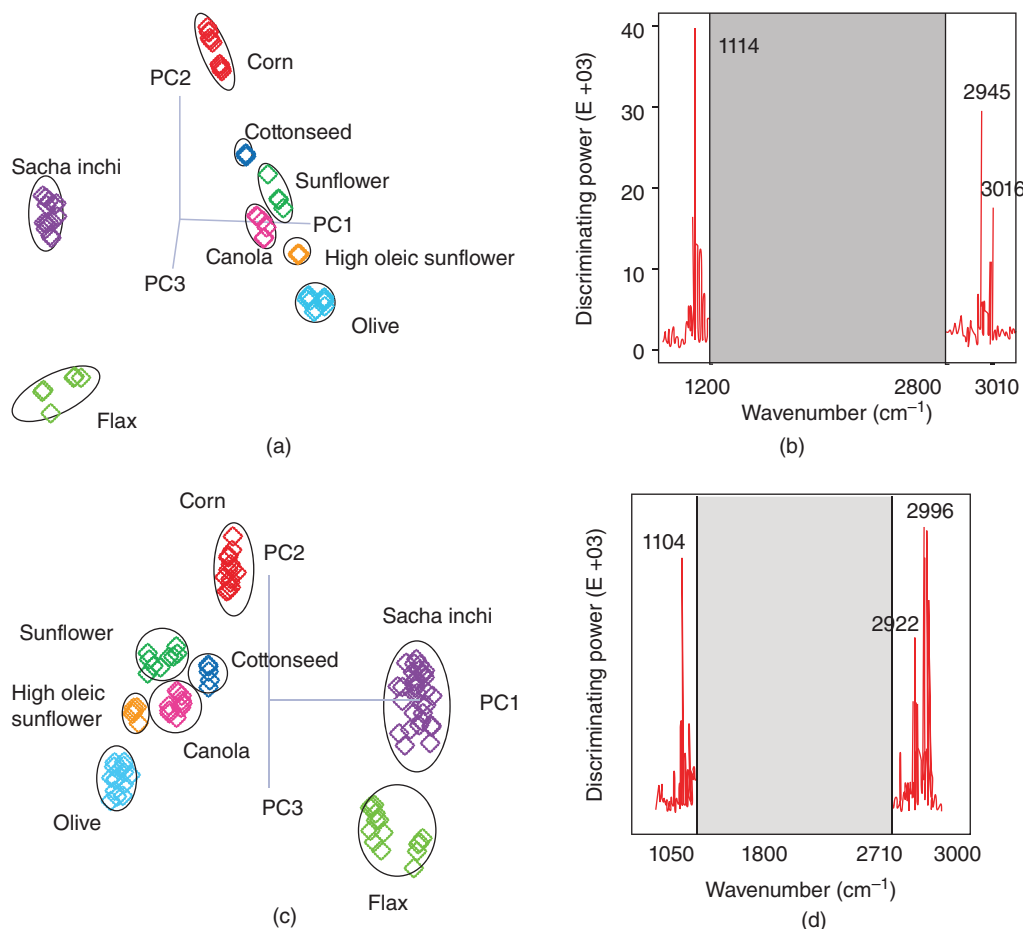


**Figure 11.2** Results by Maurer et al. of SIMCA analysis showing the classification Sacha Inchi oil compared to other more common flour products. 3D projection plot and SIMCA discrimination plots are shown for data sets from both benchtop (a and b) and handheld (c and d) infrared spectrometers. Source: Maurer et al. [45]. © 2012, Elsevier.

distinguish three sources of Andean flour, which have health benefits but limited production, from more common flour such as soy, wheat, barley, and corn. Using a SIMCA model on data collected using a portable FTIR with a diamond ATR sample interface, the researchers were able to identify mixtures, where pure Andean flours had been modified with less expensive flour products. Additionally, models were developed to determine protein and fat content using the same spectra. In addition to contamination and origin validation, differentiation between organic and nonorganic butter has also been demonstrated using portable infrared spectroscopy with a multireflection ATR sample interface. Pujolras et al. [47] found a significant difference in the trans-fat content of organic butter compared with nonorganic butter. The measurement of these differences by portable infrared spectroscopy and classification using SIMCA analysis was shown. The resulting model provided 100% correct classification of the butters tested. As in the other authentication papers, a multivariate quantitative model was developed as well to measure a key performance parameter of the samples, in this case trans fat. The combination of classification and quantitation in this work, as well as the two previous examples, provides users both authenticity assurance and key quality parameters in a single measurement, at any point in the distribution chain, demonstrating the value portable measurement can bring to the food industry.

### 11.3 Nondestructive Testing

Infrared spectroscopy has long been considered a nondestructive measurement technique. Infrared light does not have sufficient energy to cause chemical reactions, and it cannot damage samples. Although infrared light is nondestructive, prior to the advent of handheld instrumentation, large or fragile samples could not typically be measured in a laboratory instrument without removing a small sample. Handheld infrared instruments, though, allow for the nondestructive measurement of large, fragile, or irreplaceable samples. Their compact size and non-contact or minimal contact sampling optics allow measurement of complex objects without the removal of the sample, allowing the full promise of nondestructive testing to be realized.

Four applications of nondestructive analysis stand out as prime examples: thermal damage of aerospace composites, coatings analysis, art conservation, and archeology (the latter two are discussed in Volume 2, Chapters 21 and 22). For aerospace composites, small, handheld infrared instruments allow *in situ* measurement of oxidative thermal damage to composite materials. The nondestructive nature allows structures to be evaluated and then repaired if necessary. Coatings can be identified for validation or quantitatively measured for quality control as prepared on the surface of interest. In art conservation, infrared spectra can be used to determine authenticity of artwork, evaluate degradation, and monitor restoration processes in real time. Measurement of the art without sampling by handheld instrumentation preserves the value and allows for more frequent measurement throughout restoration processes. Handheld infrared measurement has similar advantages for archeology as well. Historical sites have been conserved and preserved with various methods for many years. Modern archeologists often need to evaluate what has been added or modified at a site in order to determine the best preservation techniques to use going forward. Here, nondestructive infrared analysis can provide valuable identification tools to aid in this process.

Evaluation of thermal damage in composite materials is an ever-present need for the aircraft industry. Composites offer advantages in both strength and weight over conventional aluminum construction; however, damage mechanisms are different between the two materials. Structural components of composites (typically fiberglass or carbon fiber/graphite) are not damaged by low thermal loads, but the resins in composites can be thermally damaged, resulting in a measurable decrease in strength. Furthermore, aerospace materials can experience various thermal events, such as lightning, engine fires, or electrical issues. Particularly important is the identification of incipient heat damage [48]. This is damage to the resin of the composite material that happens prior to the formation of charring, cracks, or delamination; it is invisible to conventional nondestructive techniques, such as ultrasound, but it can be detected using molecular spectroscopy. Infrared measurement of incipient thermal damage of composites was first studied by Oak Ridge National Laboratory in 1990 [49]. The intent of the study was to evaluate spectroscopic tools for the measurement of thermal oxidation of epoxy/carbon composites. One of the tools evaluated was infrared spectroscopy using a diffuse reflectance sample interface. The study used a conventional laboratory spectrometer (no portable instruments were available at the time) with specially designed sample optics allowing the evaluation of large samples outside of the instrument sample compartment. Although limited in real-life applications, the study demonstrated that infrared spectroscopy could be used to monitor thermal damage of composites and set the stage for further developments.

As more composites were used in commercial and military airplanes, the need for thermal damage analysis grew. Prior to the development of handheld instrumentation, various means of measuring composite samples using conventional laboratory spectrometers were considered including different means of mounting benchtop spectrometers and fiber-optic sample interfaces. When handheld infrared spectrometers with the appropriate reflection sampling optics became available in 2008, the aircraft industry moved quickly to adopt this technology.

Currently, both aircraft manufacturers and service organizations use handheld FTIR spectrometers with diffuse reflectance sample interfaces to monitor composite thermal exposure [50, 51]. Prediction of exposure is typically calculated using multivariate data analysis techniques. A large study was conducted by A2 Technologies (now Agilent Technologies), the Boeing Corporation, the University of Delaware, and Sandia National Laboratory on

the use of handheld FTIR for thermal damage evaluation funded by a grant from the Federal Air Administration [48]; the program was later transferred to and finished by the University of Washington Materials Science and Engineering department [52]. The study focused on two different epoxy/carbon composites. A test matrix was developed where composite samples were exposed to eight temperature points from 162 to 280° centigrade for hold times from 30 minutes to 8.5 hours. In total, samples for 40 different temperature/time points were generated; from each temperature/time point, samples were generated from physical testing and two different infrared measurements. Each of the sample points was evaluated using a gold standard physical test, short beam shear, to determine the reduction in strength versus an undamaged sample. Samples for infrared analysis were separated into two groups. The first group was measured in the resin-rich state as a part would come from the mold; the second group was abraded with sandpaper to remove the resin-rich layer and expose the fibers below. Resin-rich samples represent parts that are used unpainted, while the sanded samples represent parts that were painted, but the paint was removed to analyze the composite material underneath. Infrared spectra were also collected for both the resin-rich and sanded specimens at each of the sample points using an A2 Technologies (now Agilent) Exoscan handheld FTIR with a diffuse reflectance sample interface. Four complete data sets, two composites each resin rich and sanded, containing both the handheld infrared and physical test data were therefore obtained. Handheld infrared spectra show the changes that are observed with increasing thermal exposure including a growing carbonyl band at  $1720\text{ cm}^{-1}$  due to surface oxidation as well as changes in sulfone cross-linking as seen in the region between 1350 and  $1300\text{ cm}^{-1}$  (Figure 11.3).

In order to demonstrate the efficacy of predicting thermal damage, each data set was divided into a calibration and validation set. In each case, a partial least squares (PLS) method was developed to predict the resulting short beam shear strength value of the composite after the given thermal exposure. Accurate predictions were demonstrated in all cases, though the relative error of the methods varied by composite type and between resin-rich and sanded samples. Overall, the relative error for the methods ranged from 5.9 to 11.4% with the resin-rich samples generally having a lower relative error. As an example, a calibration for resin-rich samples of one epoxy had a relative error of 5.9%, while the calibration for sanded samples of the same composite had a relative error of 7.4%.

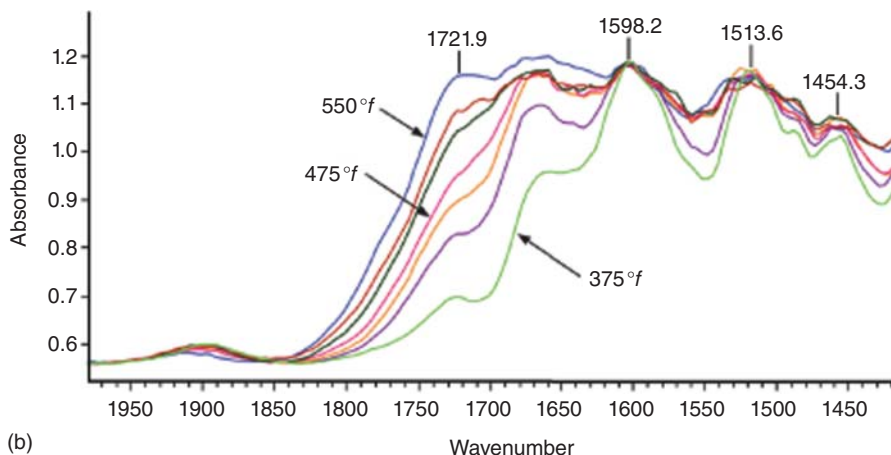
In the second report [52], Howie et al. demonstrated the use of handheld infrared spectrometers in repair scenarios. Handheld mapping studies were conducted on panels that were damaged over a finite location. The infrared results detected changes in the composite prior to any detected changes with ultrasonic testing. Locally heated samples were sectioned, and the infrared spectra were found to correlate well with the damage measured on the sectioned samples through interlaminar sheer physical testing. In addition to the epoxy work cited above, Toivola et al. [53] have also studied the measurement of thermal damage on bis-imide (BMI) carbon composites. BMI has superior high-temperature performance to epoxy. Toivola demonstrated that handheld infrared spectroscopy could also be used to predict thermal damage on BMI composites with similar accuracy to epoxy composites.

Airbus has also used handheld infrared spectroscopy as a nondestructive measurement technique for composites. In a paper presented at the 7th International Symposium on NDT in Aerospace, authors from Airbus Group Innovation, the Technical University of Munich, and the Bundeswehr Research Institute for Materials, Fuels and Lubricants discuss the use of handheld infrared for the measurement of composite thermal degradation, water uptake, and hydraulic fluid contamination [54]. The study by Heckner et al. correlated the spectra measured using a handheld FTIR with diffuse reflectance interface to an interlaminar sheer physical measurement. The study found good correlation through the use of a PLS algorithm for resin-rich samples. Similar to other studies, abraded samples were more difficult to model but still provided sufficient information for testing. In addition to the quantification of thermal degradation, the study also successfully used a principal component analysis (PCA) to classify the sample spectrum, ensuring the correct model (resin rich vs. abraded) was applied.

The study also used handheld infrared spectroscopy with a diffuse reflectance sample interface to nondestructively measure water uptake on composite parts [54]. Composites can absorb over 1% by weight water in humid environments. The absorbed water can adversely affect composite-to-composite bonding in subsequent assembly steps, determining the amount of water absorbed by composite parts is critical to ensure quality bonds. In this



(a)



(b)

**Figure 11.3** Nondestructive measurement of thermal damage on a composite part (a) and spectral changes corresponding to thermal oxidation of an epoxy composite (b). *Source:* Higgins [51]. Reproduced with Permission of Agilent Technologies, Inc.

study, composite samples were exposed to humid atmospheres; the absorbed water content was determined gravimetrically. Handheld infrared spectra of those same samples were subsequently measured. Correlation was found between the absorbed water content and both the OH stretching frequency at  $3660\text{ cm}^{-1}$  and the HOH deformation at  $1670\text{ cm}^{-1}$ . A PLS model was developed to predict the water content from the collected infrared spectra. The model was considered accurate for water determination with RMSEP of 0.11 for concentrations ranging from 0 to 1.2% water.

Finally, Heckner's study also evaluated the use of handheld infrared spectroscopy of the determination of hydraulic fluid contamination of composite parts [54]. In repair scenarios, contamination of the composite part is a grave concern as bonding repairs are not typically successful on contaminated surfaces. Composite samples were immersed in water solutions containing increasing amounts of aircraft hydraulic fluid prior to being measured by handheld FTIR with a diffuse reflectance sample interface. The work found a correlation between a band near  $1730\text{ cm}^{-1}$  and the amount of hydraulic fluid to which the sample was exposed. In this case, the

handheld FTIR instrument allows for measurement of contamination on aircraft parts at the repair site without the need for complicated cleaning or extraction procedures. In almost all cases, measurements conducted to evaluate composite parts for potential repair must be nondestructive to be of value to aircraft repair facilities. Handheld infrared spectroscopy has met those needs in several cases.

Similar to composites, the nondestructive chemical evaluation of coatings by infrared spectroscopy is an area of great interest to advanced materials manufacturers and users. Modern coatings serve to protect advanced materials from moisture, corrosive environments, ultraviolet (UV) damage, and abrasion. Coating identification and qualification is critical to ensure products meet their desired usage specifications. Conventional coating analysis is conducted through destructive testing of either a first article or witness panels. Handheld infrared spectroscopy can be used to nondestructively measure coated materials to verify coating authenticity and qualify correct coating application, allowing for 100% inspection of coated items to ensure proper performance.

As an example, the identification and classification of coatings by nondestructive analysis is demonstrated in an application note by Agilent Technologies [55]. As the note demonstrates, typical library searching using spectral correlation analysis can distinguish between different types, such as acrylic versus polyurethane, but it does not have the specificity required to distinguish between similar coating formulations. The note goes on to demonstrate that formulations can be distinguished using a partial least squares discriminant analysis (PLS-DA); coatings are divided into groups that are given an identification index. Five different PLS-DA models were created, allowing the classification of eight different formulations of polyurethane coatings to be identified correctly (see Figure 11.4).

In addition to coating identification, qualification of proper coating application is also important to ensure coating performance. Modern high-performance coatings are typically composed of a variety of organic and inorganic compounds with a cured polymeric binder. Two-part coatings must be mixed at the right ratio to ensure proper cure and the correct surface texture. An application note by Agilent Technologies describes the use of handheld FTIR using a specular reflectance sample interface to quantify the mix ratio of the two-component system in post cured polyurethane coatings [56]. Coatings were measured at ratios of 2.5:1, 3.0:1, and 4.0:1 with 3:1 being the ideal mix ratio. High or low mix ratios of this coating system led to poor surface quality. A quantitative PLS algorithm was developed that predicted the ratio with a relative error of 1.3%, allowing measurement to the manufacturer's recommendation of  $\pm 5\%$ . This test allowed for nondestructive quality control of the coating process.

Nondestructive analysis by handheld FTIR has found strong support in the archeology and art conservation communities as well. Although working on objects on the opposite end of the historical timeline compared with composites and coatings, the need for information about the molecular content of the sample without modifying or damaging the artwork or historical relic being measured is critical; in many cases, historical sites are protected by law, preventing even microscopic samples from being removed [55]. Handheld and portable infrared and Raman systems provide nondestructive analysis of art and archeological sites for both research and preservation.

Both handheld and portable infrared and Raman spectroscopy instruments are used to determine the composition and aging of archeological sites. Several studies of paintings in the historical structures of Pompeii have been published [57–59]. In each of these studies, handheld instruments were used to identify colorants and binders nondestructively. Madariaga et al. [58] used handheld infrared and Raman spectroscopies in combination with handheld X-ray fluorescence (XRF) to identify both colorants and waxes used as preservation treatments. Chemical evidence was found of both early degradation caused by acidic volcanic gases and continued degradation caused by acidic pollution from nearby cities (see Figure 11.5). In a similar study, Hernanz et al. [60] used handheld infrared spectrometers with diffuse reflectance sample interfaces as a supporting technique to studies using handheld Raman, handheld XRF, and portable confocal Raman for the measurement of open-air rock paintings on the Iberian Peninsula. The work identified mineralogy of pigments used even in the presence of crusts formed by weathering. Infrared was particularly useful in cases where strong fluorescence hinders Raman measurements. Handheld infrared has also been applied to the measurement and characterization of historical artifacts. In a study published by Maguregui et al. [59], handheld FTIR with a diffuse reflectance sample interface

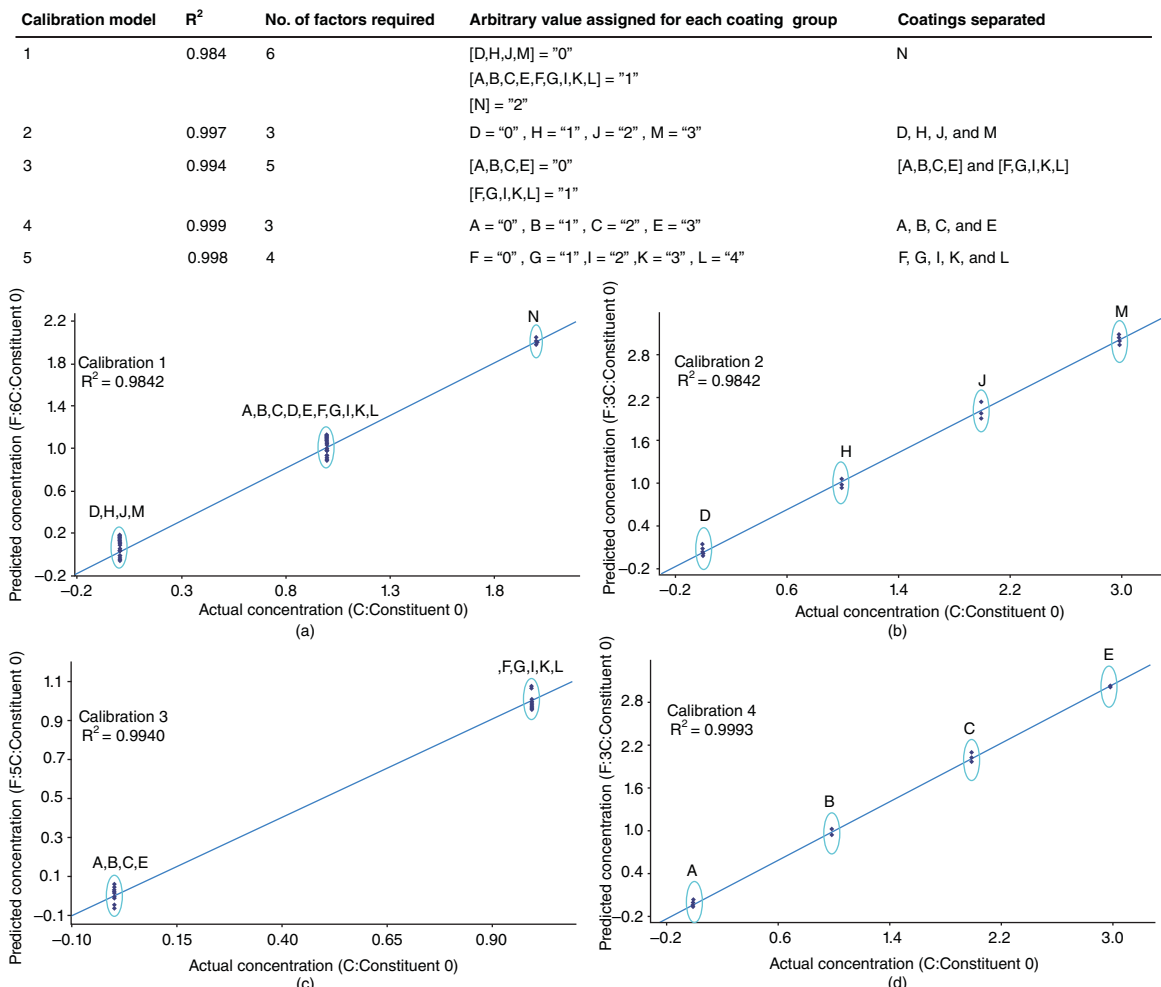


**Figure 11.4** Classification of five different acrylic coatings using a partial least squares discriminant analysis (PLS-DA). Source: Mainali and Tang [55]. Courtesy of Agilent Technologies, Inc © Agilent Technologies, Inc.

was used to distinguish between lacquers used during restorations (nitrocellulose) and those used in the original manufacture of historical Japanese armor. These pieces were too large to measure in a conventional laboratory system, but the handheld instrument allowed easy, nondestructive measurement even on complex surfaces. In another study, Veneranda et al. [61] showed the use of a laboratory calibration for semiquantitative determination of iron oxide minerals used on a portable infrared spectrometer using an ATR sample interface. The relative concentration of oxides, especially lepidocrocite and akageneite that are indicative of accelerated corrosion, was used to calculate a protection availability index (PAI). The mobile system was able to predict PAI, allowing conservators to monitor corrosion on and preserve iron antiquities.

Handheld infrared spectroscopy provides the flexibility required to measure valuable sample in their native condition, providing users with meaningful information about the sample's condition. It provides molecular chemical information about the sample that is unique among other nondestructive analysis techniques. Whether the sample is an aerospace composite or a historical artwork, handheld infrared can be used for meaningful, nondestructive, chemical analysis.

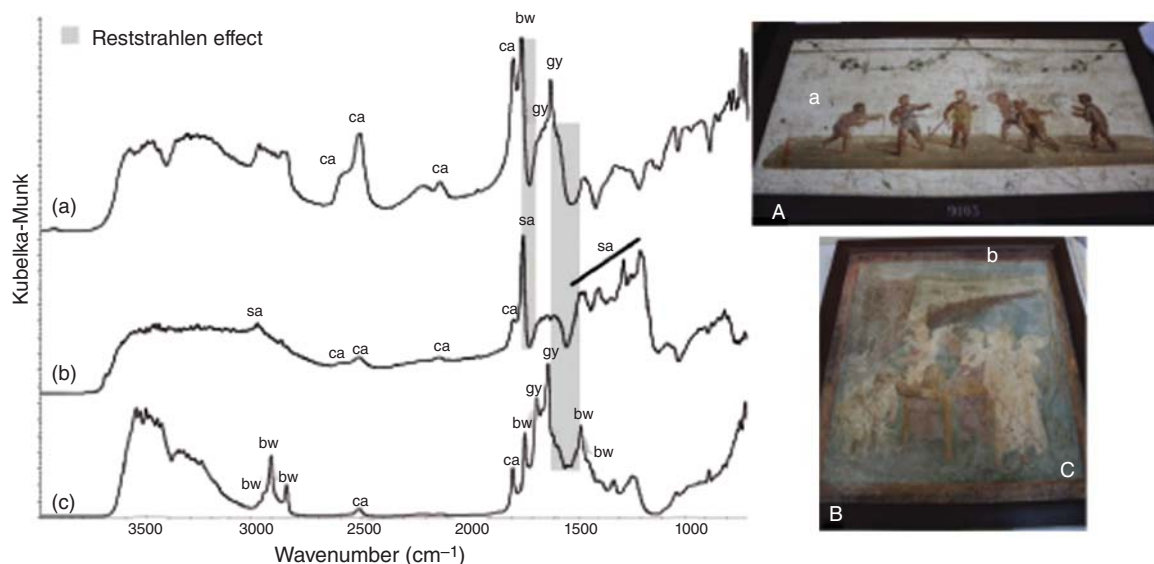


**Figure 11.5** Diffuse reflectance spectra measured nondestructively of wall paintings in historic Pompeii showing identification of beeswax (bw), sandarac (sa), calcite (ca), and gypsum (gy). *Source:* Reprinted with Permission from Sage Publications, Madariaga et al. [58]. © 2016, SAGE Publications.

## 11.4 Conclusion

Portable and handheld infrared instruments provide a wide range of important chemical analysis over a wide variety of applications. Successful portable or handheld measurements can be divided into the areas of rapid response, dispersed samples, and nondestructive testing. Making these measurements on-site where the sample occurs drives the success for each of these applications.

Measurements on-site allow for rapid response to emergency, military, or forensic situations, providing accurate chemical identification in an easy-to-use format. The identification provided improves public safety and security in the fast time frame required. In a similar way, portable systems allow efficient data collection of samples over a large area, whether environmental, agricultural, or consumer products. The efficiency provided by the on-site measurement allows for large-scale testing, further improving the conclusions that can be drawn from the results. In addition, handheld instruments that can effectively measure samples in their native state without sampling or damage provide information not previously obtainable on large or valuable samples. The unique ability to take the instrument to the sample has enabled these portable and handheld infrared applications, providing measurement where not previously possible.

## References

- 1 Burgess, D.S. (2000, July). Portable spectrometer reduces mill downtime. *Photonics Spectra* [https://www.photonics.com/Articles/Portable\\_Spectrometer\\_Reduces\\_Mill\\_Downtime/p5/v014/i59/a6607](https://www.photonics.com/Articles/Portable_Spectrometer_Reduces_Mill_Downtime/p5/v014/i59/a6607) (accessed 11 February 2020).
- 2 Ong, K.Y., Baldauf, F.C., Carey, L.F., and Amant, D.C. (2003). Domestic preparedness program: evaluation of the TravelIR HCI™ HazMat chemical identifier. In: *Aberdeen Proving Ground Research and Technology Directorate ECBC-TR*, August 2003, pp. 1–32.

- 3 Norman, M.L., Gagnon, A.M., Reffner, J.A. et al. (2004, March). An FTIR point sensor for identifying chemical WMD and hazardous materials. In: *Chemical and Biological Point Sensors for Homeland Defense*, vol. 5269, 143–149. International Society for Optics and Photonics <https://doi.org/10.1117/12.515881>.
- 4 Mukhopadhyay, R. (2004, October). Product review: portable FTIR spectrometers get moving. *Analytical Chemistry* 76 (19): 369A–372A. American Chemical Society. <https://doi.org/10.1021/ac041652z>.
- 5 Department of Homeland Security System Assessment and Validation for Emergency Responders (SAVER) Program (2016, June). Portable infrared spectroscopy chemical detectors assessment report. [https://www.dhs.gov/sites/default/files/publications/Portable-Infrared-Spectroscopy-Chemical-Detectors-ASR\\_0616-508.pdf](https://www.dhs.gov/sites/default/files/publications/Portable-Infrared-Spectroscopy-Chemical-Detectors-ASR_0616-508.pdf) (accessed 28 March 2020).
- 6 Levy, D. and Diken, E.G. (2010). Field identification of unknown gases and vapors via IR spectroscopy for homeland security and defense. *IEEE Sensors Journal* 10 (3): 564–571. <https://doi.org/10.1109/JSEN.2009.2038540>.
- 7 Doherty, W.J. III, Falvey, B., Vander Rhodes, G. et al. (2013, May). A handheld FTIR spectrometer with swapable modules for chemical vapor identification and surface swab analysis. In: *Next-Generation Spectroscopic Technologies VI*, vol. 8726, 87260T. International Society for Optics and Photonics <https://doi.org/10.1117/12.2015295>.
- 8 Smiths detection webpage. <https://www.smithsdetection.com/products/hazmatid-elite> (accessed 26 March 2020).
- 9 ThermoFisher webpage. <https://www.thermofisher.com/order/catalog/product/TRUDEFENDERFTX#/TRUDEFENDERFTX> (accessed 26 March 2020).
- 10 Redwave Technology webpage. <http://www.redwavetech.com/products/threatid> (accessed 26 March 2020).
- 11 Arnó, J., Andersson, G., Levy, D. et al. (2011, May). Advanced algorithms for the identification of mixtures using condensed-phase FT-IR spectroscopy. In: *Next-Generation Spectroscopic Technologies IV*, vol. 8032, 80320Z. International Society for Optics and Photonics <https://doi.org/10.1117/12.883886>.
- 12 Arnó, J., Cardillo, L., Judge, K. et al. (2012, May). Advances in handheld FT-IR instrumentation. In: *NEXT-GENERATION SPECTROSCOPIC TECHNOLOGIES V*, vol. 8374, 837406. International Society for Optics and Photonics <https://doi.org/10.1117/12.921052>.
- 13 Lieblei, D., McMahon, M., Leary, P., and Kammrath, B. (2018). A comparison of portable infrared spectrometers, portable Raman spectrometers, and color-based field tests for the on-scene analysis of cocaine. *Spectroscopy* 33 (12): 20–28.
- 14 Menking-Hoggatt, K. (2017). The Economic Benefits of Portable Instrumentation on the Criminal Justice System: A Comprehensive Return-on-Investment Analysis. Graduate Theses, Dissertations, and Problem Reports. 6217. <https://researchrepository.wvu.edu/etd/6217> <https://doi.org/10.33915/etd.6217>.
- 15 Valussi, S. and Underhill, M. (2006, September). Raman and infrared techniques for fighting drug-related crime: a preliminary assessment. In: *Optics and Photonics for Counterterrorism and Crime Fighting II*, vol. 6402, 64020I. International Society for Optics and Photonics <https://doi.org/10.11117/12.689099>.
- 16 Mainali, D. and Seelenbinder, J. (2016). Automated fast screening method for cocaine identification in seized drug samples using a portable Fourier transform infrared (FT-IR) instrument. *Applied Spectroscopy* 70 (5): 916–922. <https://doi.org/10.1177/0003702816638305>.
- 17 Harkai, S. and Pütz, M. (2015). Comparison of rapid detecting optical techniques for the identification of New Psychoactive Substances in ‘Legal High’ preparations. *Toxichem Krimtech* 39: 229–238.
- 18 Khudur, L.S. and Ball, A.S. (2018). RemScan: A tool for monitoring the bioremediation of Total Petroleum Hydrocarbons in contaminated soil. *MethodsX* 5: 705–709. <https://doi.org/10.1016/j.mex.2018.06.019>.
- 19 Webster, G.T., Soriano-Disla, J.M., Kirk, J. et al. (2016). Rapid prediction of total petroleum hydrocarbons in soil using a hand-held mid-infrared field instrument. *Talanta* 160: 410–416. <https://doi.org/10.1016/j.talanta.2016.07.044>.

- 20 Ng, W., Malone, B.P., and Minasny, B. (2017). Rapid assessment of petroleum-contaminated soils with infrared spectroscopy. *Geoderma* 289: 150–160. <https://doi.org/10.1016/j.geoderma.2016.11.020>.
- 21 RemScan used in Rapid Response to Diesel Spill. Z010-03 07/20. <https://ziltek.com/uploads/Z010-03-RemScan-Case-Study-1-RemScan-used-in-Rapid-Response-to-Diesel-Spill.pdf>.
- 22 Rapid Validation of an Excavation Pit using RemScan. Z012-03 07/20. <https://ziltek.com/wp-content/uploads/2019/09/Z012-02-RemScan-Case-Study-3-Rapid-Validation-of-an-Excavation-Pit-using-RemScan.pdf> (accessed 20 March 2020).
- 23 RemScan Success in Qatar. Z013-02 07/20. <https://ziltek.com/wp-content/uploads/2019/08/Z013-01-RemScan-Case-Study-4-Suez.pdf> (accessed 20 March 2020).
- 24 Robertson, A.H.J., Shand, C., and Perez-Fernandez, E. (2016). The application of Fourier transform infrared, near infrared and X-ray fluorescence spectroscopy to soil analysis. *Spectroscopy Europe* 28 (4): 9–13.
- 25 Robertson, A.H.J., Hill, H.R., Main, A.M. (2013). Analysis of Soil in the Field using Portable FTIR. International Workshop Soil Spectroscopy: the present and future of Soil Monitoring FAO HQ. [www.fao.org/fileadmin/user\\_upload/GSP/docs/Spectroscopy\\_dec13/AHJbutton.pdf](http://www.fao.org/fileadmin/user_upload/GSP/docs/Spectroscopy_dec13/AHJbutton.pdf) (accessed 21 March 2020).
- 26 Hutengs, C., Ludwig, B., Jung, A. et al. (2018). Comparison of portable and bench-top spectrometers for mid-infrared diffuse reflectance measurements of soils. *Sensors* 18 (4): 993.
- 27 Soriano-Disla, J.M., Janik, L.J., Allen, D.J., and McLaughlin, M.J. (2017). Evaluation of the performance of portable visible-infrared instruments for the prediction of soil properties. *Biosystems Engineering* 161: 24–36. <https://doi.org/10.1016/j.biosystemseng.2017.06.017>.
- 28 Hutengs, C., Seidel, M., Oertel, F. et al. (2019). In situ and laboratory soil spectroscopy with portable visible-to-near-infrared and mid-infrared instruments for the assessment of organic carbon in soils. *Geoderma* 355: 113900. <https://doi.org/10.1016/j.geoderma.2019.113900>.
- 29 Forrester, S.T., Janik, L.J., Soriano-Disla, J.M. et al. (2015). Use of handheld mid-infrared spectroscopy and partial least-squares regression for the prediction of the phosphorus buffering index in Australian soils. *Soil Research* 53 (1): 67–80. <https://doi.org/10.1071/SR14126>.
- 30 Soriano-Disla, J.M., Janik, L.J., and McLaughlin, M.J. (2018). Assessment of cyanide contamination in soils with a handheld mid-infrared spectrometer. *Talanta* 178: 400–409. <https://doi.org/10.1016/j.talanta.2017.08.106>.
- 31 Peng, J., Ji, W., Ma, Z. et al. (2016). Predicting total dissolved salts and soluble ion concentrations in agricultural soils using portable visible near-infrared and mid-infrared spectrometers. *Biosystems Engineering* 152: 94–103. <https://doi.org/10.1016/j.biosystemseng.2016.04.015>.
- 32 Martínez-España, R., Bueno-Crespo, A., Soto, J. et al. (2019). Developing an intelligent system for the prediction of soil properties with a portable mid-infrared instrument. *Biosystems Engineering* 177: 101–108. <https://doi.org/10.1016/j.biosystemseng.2018.09.013>.
- 33 Daham, B., Andrews, G. E., Li, H., Ballesteros, R., Bell, M. C., Tate, J., & Ropkins, K. (2005). *Application of a portable FTIR for measuring on-road emissions* (No. 2005-01-0676). SAE Technical Paper. <https://doi.org/10.4271/2005-01-0676>.
- 34 Gas Analysis Improves Container Safety. <https://www.gasmet.com/cases/gas-analysis-improves-container-safety> (accessed 21 March 2020).
- 35 Monitoring Greenhouse Gases from Biofuel Crops. <https://www.gasmet.com/cases/monitoring-greenhouse-gases-from-biofuel-crops> (accessed 20 March 2020).
- 36 Bussell, J., Stoate, C. The Allerton Project Research into Sustainable Agriculture with Gasmet Gas Analyser. <https://www.gasmet.com/cases/the-allerton-project-research-into-sustainable-agriculture-with-gasmet-gas-analyser> (accessed 20 March 2020).
- 37 Managing Livestock Diets to Reduce Greenhouse Gas Emissions. <https://www.gasmet.com/cases/managing-livestock-diets-to-reduce-greenhouse-gas-emissions> (accessed 20 March 2020).
- 38 Binh, P.L.T., Preston, T.R., Duong, K.N., and Leng, R.A. (2017). A low concentration (4% in diet dry matter) of brewers' grains improves the growth rate and reduces thiocyanate excretion of cattle fed cassava pulp-urea

- and “bitter” cassava foliage. *Livestock Research for Rural Development* 29: 104. <http://www.lrrd.org/lrrd29/5/phuo29104.html> (accessed 25 March 2020).
- 39 Duy, N.T. and Khang, D.N. (2016). Effect of coconut (*Cocos nucifera*) meal on growth and rumen methane production of Sindhi cattle fed cassava (*Manihot esculenta*, Crantz) pulp and Elephant grass (*Pennisetum purpureum*). *Livestock Research for Rural Development* 28 (11) <http://www.lrrd.org/lrrd28/11/duy28197.html> (accessed 4 March 2020).
- 40 Inthapanya, S. and Preston, T.R. (2015). Effect of source of supplementary dietary protein and feed offer level (ad libitum or restricted) on feed intake, digestibility and N balance in local “Yellow” cattle fed rice straw treated with urea as basal diet. *Livestock Research for Rural Development* 27: 45. <http://www.lrrd.org/lrrd27/3/sang27045.htm> (accessed 23 March 2020).
- 41 Keopaseuth, T., Preston, T.R., and Tham, H.T. (2017). Cassava (*Manihot esculenta* Cranz) foliage replacing brewer’s grains as protein supplement for Yellow cattle fed cassava pulp-urea and rice straw; effects on growth, feed conversion and methane emissions. *Livestock Research for Rural Development* 29 (2) <http://www.lrrd.org/lrrd29/2/toum29035.html> (accessed 4 March 2020).
- 42 Phongphanith, S. and Preston, T.R. (2018). Effect of rice-wine distillers’ byproduct and biochar on growth performance and methane emissions in local “Yellow” cattle fed ensiled cassava root, urea, cassava foliage and rice straw. *Livestock Research for Rural Development* 28: 178. <http://www.lrrd.org/lrrd28/10/seng28178.html> (accessed 1 April 2020).
- 43 Thayer, A.M. (2012). Finding fakes. *Chemical & Engineering News* 90 (33): 11–15.
- 44 Limm, W., Karunathilaka, S.R., Yakes, B.J., and Mossoba, M.M. (2018). A portable mid-infrared spectrometer and a non-targeted chemometric approach for the rapid screening of economically motivated adulteration of milk powder. *International Dairy Journal* 85: 177–183. <https://doi.org/10.1016/j.idairyj.2018.06.005>.
- 45 Maurer, N.E., Hatta-Sakoda, B., Pascual-Chagman, G., and Rodriguez-Saona, L.E. (2012). Characterization and authentication of a novel vegetable source of omega-3 fatty acids, sacha inchi (*Plukenetia volubilis* L.) oil. *Food Chemistry* 134 (2): 1173–1180. <https://doi.org/10.1016/j.foodchem.2012.02.143>.
- 46 Shotts, M.L., Pujolras, M.P., Rossell, C., and Rodriguez-Saona, L. (2018). Authentication of indigenous flours (Quinoa, Amaranth and kañiwa) from the Andean region using a portable ATR-Infrared device in combination with pattern recognition analysis. *Journal of Cereal Science* 82: 65–72. <https://doi.org/10.1016/j.jcs.2018.04.005>.
- 47 Pujolras, M.P., Ayvaz, H., Shotts, M.L. et al. (2015). Portable infrared spectrometer to characterize and differentiate between organic and conventional bovine butter. *Journal of the American Oil Chemists’ Society* 92 (2): 175–184. <https://doi.org/10.1007/s11746-015-2591-x>.
- 48 Rein, A. (2014). Advanced Fourier Transform Infrared Spectroscopy for Analyzing Damage in Aircraft Composites. *Federal Aviation Association Technical Report*. <http://www.tc.faa.gov/its/worldpac/techrpt/tc14-26.pdf> (accessed 18 March 2020).
- 49 Janke, C.J., Muhs, J.D., Wachter, E.A. et al. (1990). *Composite Heat Damage Spectroscopic Analysis* (No. ORNL/ATD-42). TN (USA): Oak Ridge National Lab <https://www.osti.gov/servlets/purl/5588643> (accessed 20 March 2020).
- 50 Seelenbinder, J. (November 2015). *Composite Heat Damage Measurement using the Handheld Agilent 4100 ExoScan FTIR*. Agilent Technologies, Inc., Publication Number 5990-7792EN <https://www.agilent.com/cs/library/applications/5990-7792EN.pdf>. (accessed 10 March 2020).
- 51 Higgins, F. (March 2014). *Non-Destructive Evaluation of Composite Thermal Damage with Agilent’s New Handheld 4300 FTIR*. Agilent Technologies, Inc., Publication Number 5991-4037EN <https://www.agilent.com/cs/library/applications/5991-4037EN.pdf> (accessed 10 February 2020).
- 52 Howie, T., Tracey, A., and Flinn, B. Composite thermal damage measurement with handheld fourier transform infrared spectroscopy. *Federal Aviation Association Technical Report* TC-15/51. <http://www.tc.faa.gov/its/worldpac/techrpt/tc15-51.pdf> (accessed 12 February 2020).

- 53** Toivola, R., Afkhami, F., Baker, S. et al. (2018). Detection of incipient thermal damage in carbon fiber-bismaleimide composites using hand-held FTIR. *Polymer Testing* 69: 490–498. <https://doi.org/10.1016/j.polymertesting.2018.05.036>.
- 54** Heckner, S., Geistbeck, M., Grosse, C. U., Eibl, S., & Helwig, A. (2015). FTIR spectroscopy as a nondestructive testing method for CFRP surfaces in Aerospace. In *7th International Symposium on NDT in Aerospace; German Society for Non-Destructive Testing*. Bremen, Germany. <http://2015.ndt-aerospace.com/Portals/aerospace2015/BB/tu1a3.pdf> (accessed 15 March 2020).
- 55** Mainali, D. and Tang, L. *Positive and Nondestructive Identification of Acrylic-based Coatings*. Agilent Technologies, Inc. Publication Number 5991-5965EN. <https://www.agilent.com/cs/library/applications/5991-5965EN.pdf> (accessed 12 February 2020).
- 56** Tang, L. (August 2017). *Rapid Quantification of the A:B Mix-Ratio of a 2K Industrial OEM PU Paint Prior to Autoclave Thermal Activation*. Agilent Technologies, Inc Publication number: 5991-8323EN. [https://www.agilent.com/cs/library/applications/4300\\_5991-8323\\_FTIR\\_2K\\_paint\\_cure\\_mix\\_ratio.pdf](https://www.agilent.com/cs/library/applications/4300_5991-8323_FTIR_2K_paint_cure_mix_ratio.pdf) (accessed 12 February 2020).
- 57** Marcaida Ormazabal, I. (2019). Analytical chemistry to decipher the colors of Pompeii before and after the 79AD Mount Vesuvius eruption. University of the Basque Country (EPV/EHU) Thesis. [https://addi.ehu.es/bitstream/handle/10810/39975/TESIS\\_MARCAIDA\\_ORMAZABAL\\_IKER.pdf?sequence=1&isAllowed=y](https://addi.ehu.es/bitstream/handle/10810/39975/TESIS_MARCAIDA_ORMAZABAL_IKER.pdf?sequence=1&isAllowed=y) (accessed 17 March 2020).
- 58** Madariaga, J.M., Maguregui, M., Castro, K. et al. (2016). Portable Raman, DRIFTS, and XRF analysis to diagnose the conservation state of two wall painting panels from Pompeii deposited in the Naples National Archaeological Museum (Italy). *Applied Spectroscopy* 70 (1): 137–146. <https://doi.org/10.1177/0003702815616589>.
- 59** Maguregui, M., Knuutinen, U., Trebolazabala, J. et al. (2012). Use of in situ and confocal Raman spectroscopy to study the nature and distribution of carotenoids in brown patinas from a deteriorated wall painting in Marcus Lucretius House (Pompeii). *Analytical and Bioanalytical Chemistry* 402 (4): 1529–1539. <https://doi.org/10.1007/s00216-011-5276-9>.
- 60** Hernanz, A., Ruiz-López, J.F., Madariaga, J.M. et al. (2014). Spectroscopic characterisation of crusts interstratified with prehistoric paintings preserved in open-air rock art shelters. *Journal of Raman Spectroscopy* 45 (11–12): 1236–1243. <https://doi.org/10.1002/jrs.4535>.
- 61** Veneranda, M., Aramendia, J., Bellot-Gurlet, L. et al. (2018). FTIR spectroscopic semi-quantification of iron phases: A new method to evaluate the protection ability index (PAI) of archaeological artefacts corrosion systems. *Corrosion Science* 133: 68–77. <https://doi.org/10.1016/j.corsci.2018.01.016>.

## 12

# Spectra Transfer Between Benchtop Fourier-Transform Near-Infrared and Miniaturized Handheld Near-Infrared Spectrometers

*Uwe Hoffmann<sup>1</sup>, Frank Pfeifer<sup>2</sup> and Heinz W. Siesler<sup>2</sup>*

<sup>1</sup>*nir-tools, Essen, Germany*

<sup>2</sup>*Department of Physical Chemistry, University of Duisburg-Essen, Essen, Germany*

### 12.1 Introduction

The qualitative identification or discrimination of different chemical materials and the quantitative determination of chemical or physical material properties based on their near-infrared (NIR) spectra have become widely used techniques for industrial quality and process control and are usually carried out in combination with multivariate calibration methods like principal component analysis (PCA) or partial least squares (PLS) regression, respectively. Depending on the complexity of the material under investigation, the necessary calibration methods may require analytical procedures with 30 up to several hundred reference samples involved. For the PLS regression evaluation procedure, the properties of interest of these reference samples have to be determined independently, and their NIR spectra have to be measured in order to develop the calibration. This is usually a very time-consuming and costly procedure, particularly if complicated reference methods are involved. Furthermore, the calibration set has to be representative for the whole expected sample population, which might be a difficult situation to fulfill, if the origin of the samples is an industrial process in which the extremes of the population occur at rare intervals. Thus, the greater the complexity of this process, the more valuable is a resulting calibration model that provides fast and accurate analytical results. However, due to aging or exchange of important hardware components (source, detector, etc.) or the replacement of the complete instrument, the differences in spectral response can lead to erroneous predictions by using the primary calibration over time. To avoid recalibration and to retain the calibration model that was developed with the data of the original instrument (from now on called the “master instrument”) for further reliable predictions, these differences have to be estimated and corrected. Thus, the extensive discussions and proposals for the transfer of spectral data and calibrations between different spectrometers come as little surprise even in the early phase of industrial applications of NIR spectroscopy. Several different approaches have been described in the literature already in the 1990s, with the common objective to measure only a few – identical – samples before and after the change in spectral response or on the master and a “target” instrument and to develop a correction procedure based on the differences of the spectra or predicted values of these samples. Generally, these approaches cover three groups of correction procedures:

1. Correcting the predicted values [1, 2]
2. Correcting the spectra [3–7]
3. Correcting the calibration models [1, 3]

The applicability of a certain algorithm, however, depends on several criteria. For example, the corrections of the calibration models are only developed for the classical least squares (CLS) and the inverse least squares (ILS)

algorithms, which are, however, rarely used as calibration methods for condensed phase samples. The correction of predicted values is restricted to applications where calibration models are already developed and where the reference values of the sample properties of interest are known. Furthermore, the method described by Bouveresse [2] corrects only linear deviations.

The most frequently applied method corrects the spectra, because the algorithms do not depend on the calibration methods and reference values. But these algorithms have been developed under different aspects of expected instrument change. For example, Shenk's patented algorithm [4, 5] is applicable for the standardization of instruments of the same type with the same spectral resolution. The differences between the master and the target instrument are assumed to be a wavelength shift and a linear deviation in intensity. Two other methods for the correction of spectra are the direct standardization (DS) [3, 6, 7] and the piecewise direct standardization (PDS) [3]. For these algorithms, restrictions of applicability are not explicitly given, but due to the use of multilinear methods for the development of the standardization models, the correction of nonlinear intensity shifts is limited by a multilinear approximation.

For the PDS method described by Wang [3], it is assumed that the wavelength/wavenumber scales of the master and the target instrument are the same, at least in the spectral range to be transferred. Furthermore, the spectral information of a certain data point of the master spectrum is reflected by a narrow spectral window of the target instrument where the central datapoint of this window has the same data point number as the currently investigated master data point. The PDS generates a transfer matrix, which can be used to transfer any spectrum measured on the target to make it compatible to the calibration model developed on the master. It will be shown later that for this work, the "target to master" transfer had to be inverted into a "master to target" transfer.

The reference sample set, which is used for the transfer of a calibration, has to represent the whole expected sample population. Two different algorithms for the selection of these standardization samples have been described:

1. Selection based on leverages [3].
2. Selection based on interpoint distances (Kennard and Stone algorithm) [1, 8, 9].

Excellent and most comprehensive review articles on standardization and calibration transfer practices and instrument differences in spectroscopy are available in the literature [10–12]. Thus, in lieu of delving deeper into the theory of the subject, in what follows, the focus will be on the actual topic of this chapter, the practical aspects of spectra transfer between benchtop and handheld instruments.

With the increased interest in commercializing cost-effective, handheld NIR spectrometers for field applications, it is desirable to utilize spectral data that have already been acquired on standard samples with benchtop instruments. Such data may have been taken over a long period of time and have generally been time consuming to generate from the start. By transferring the data from the benchtop to the handheld instrument, one can significantly shorten the model development time and accelerate the adoption of the handheld device for on-site field use. In many cases, the benchtop instrument – usually a Fourier-transform near-infrared (FT-NIR) spectrometer – is regarded as a "gold standard," in particular due to the laser referencing of its wavelength scale.

The aim of this chapter is to demonstrate the transfer of spectra that have been measured on two different laboratory FT-NIR spectrometers to the format of handheld instruments based on a linear variable filter (LVF) monochromator (see Figure 12.1), by measuring only a few samples with both spectrometer types. Thus, despite the extreme differences in spectral range and resolution (see Figure 12.2), spectral data sets that have been collected and quantitative as well as qualitative calibrations that have been developed thereof, respectively, over a long period on a laboratory instrument can be conveniently transferred to the handheld system without the requirement for elaborate complete rescanning of spectra. Thus, the necessity to prepare completely new calibration samples and the effort required to develop calibration models when changing hardware platforms is minimized.

The transfer procedure applied for the described case studies is based on PDS that was, however, originally developed to standardize spectrometers of the same design [1–3, 13–16].

**Figure 12.1** The spectrometers involved in the spectra transfer procedure. (a) Bruker MPA FT-NIR spectrometer, (b) Bruker VECTOR 22/N FT-NIR spectrometer, (c) VIAVI MicroNIR LVF NIR spectrometer.

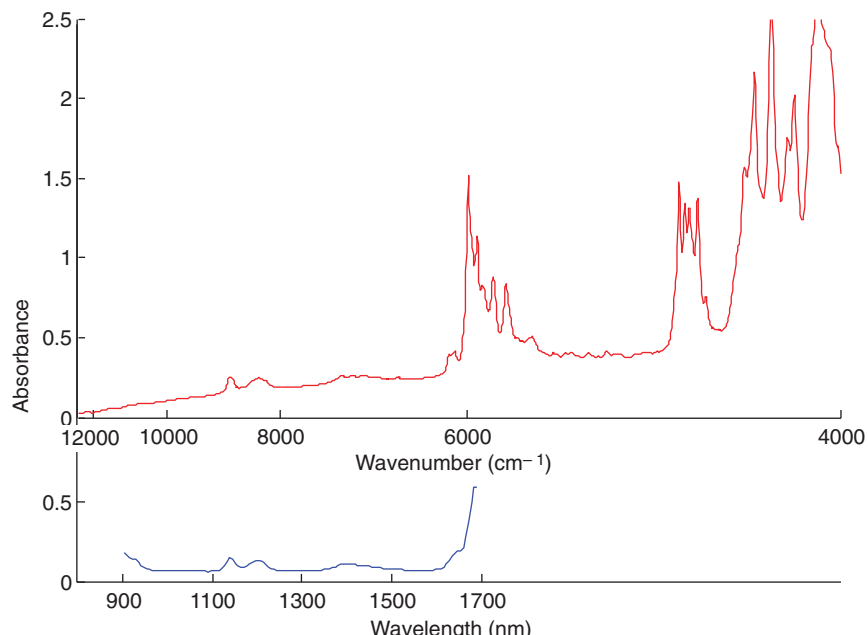
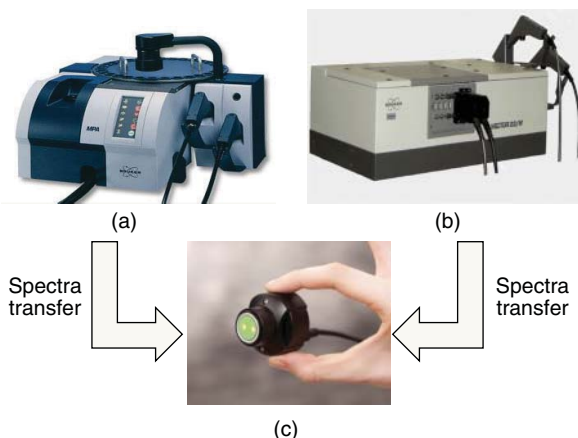


**Figure 12.2** Comparison of NIR transmission spectra (path length 2 mm) measured of a liquid mixture of benzene/cyclohexane/ethylbenzene 40 : 30 : 30%(v/v/v) on the benchtop master (red) and the handheld target (blue) spectrometer.

In principle, the two transfer directions “target to master” and “master to target” are possible. While the first approach yields a transfer matrix that is used to make the target spectra – measured for prediction – compatible to the master calibration, the second approach can be used to transfer the entire calibration spectral set measured on the master to the target format, so that a stand-alone calibration for the target can be developed from these transferred calibration spectra.

Concerning the two spectrometer pairs (see Figure 12.1a/c and b/c) discussed in this work, the master spectrometers had a much higher spectral resolution than the target instrument so that a transfer “target to master” seems to be unsuitable and the transfer direction had to be inverted. Consequently, the following description of the original PDS algorithm [3] will also be given in “master to target” direction (Figure 12.3).

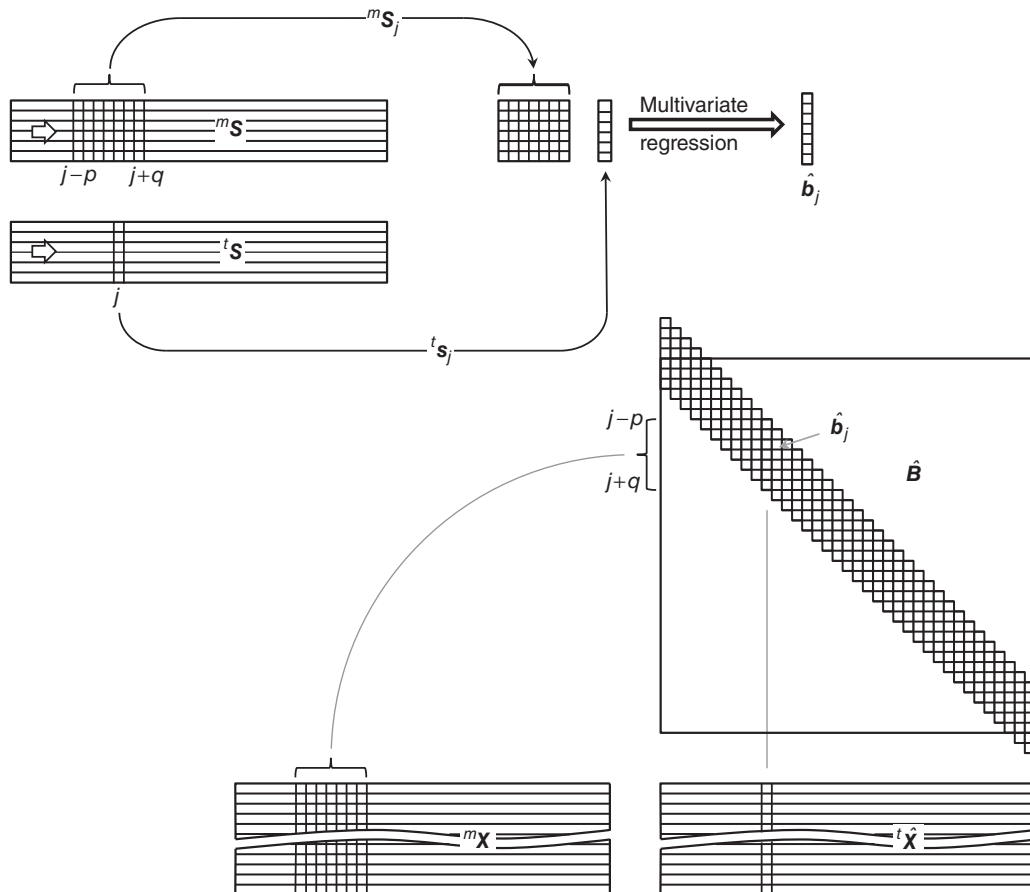


**Figure 12.3** Generation and application of the transfer matrix  $\hat{\mathbf{B}}$  in the PDS procedure described by Wang [3] for identically constructed spectrometers (the symbols correspond to the symbols in the text). Source: Based on Wang et al. [3].

In particular, the wavelength/wavenumber scales of the master and target instruments were identical, which led to an algorithm where a transfer matrix  $\hat{\mathbf{B}}$  was derived by shifting a data point window of range  $j-p$  to  $j+q$  over the master spectra and calculating multivariate regression vectors  $\hat{\mathbf{b}}_j$  for each of these windows. The vector of reference values (comparable to component concentrations in quantitative calibration models) is given by the spectral intensities of the target spectra at the corresponding data point  $j$ . Finally, the transfer of spectra measured on the master was performed by multiplying the master spectra  ${}^m\mathbf{X}$  by the transfer matrix  $\hat{\mathbf{B}}$ . Ideally, the resulting spectral matrix  ${}^t\hat{\mathbf{X}}$  should be identical to the spectral matrix of the same sample set but measured on the target.

In the present situation (Figure 12.4), the data point assignment is more complex, because the handheld target and the benchtop FT-NIR master spectrometers cover different wavelength (wavenumber) scales of 904–1690 nm ( $11\,062$ – $5917\text{ cm}^{-1}$ ) and 2500–800 nm ( $4000$ – $12\,493\text{ cm}^{-1}$ ), respectively (Figure 12.2). Under these conditions, corresponding wavelengths/wavenumbers instead of corresponding data point indices have to be handled.

The principle of the PDS is preserved, but in contrast to the procedure shown in Figure 12.3, the window in the master spectrum is not simply constructed by adding a left wing of length  $p$  and a right wing of length  $q$  to the data point  $j$ . Instead, the master data point with the most similar wavelength  $\lambda_j$  was assigned to  $j$ . Consequently, also the spectral window around  $\lambda_j$  was defined in terms of a wavelength range ( $\lambda_j - \delta_l$  to  $\lambda_j + \delta_u$ ). This generalized window

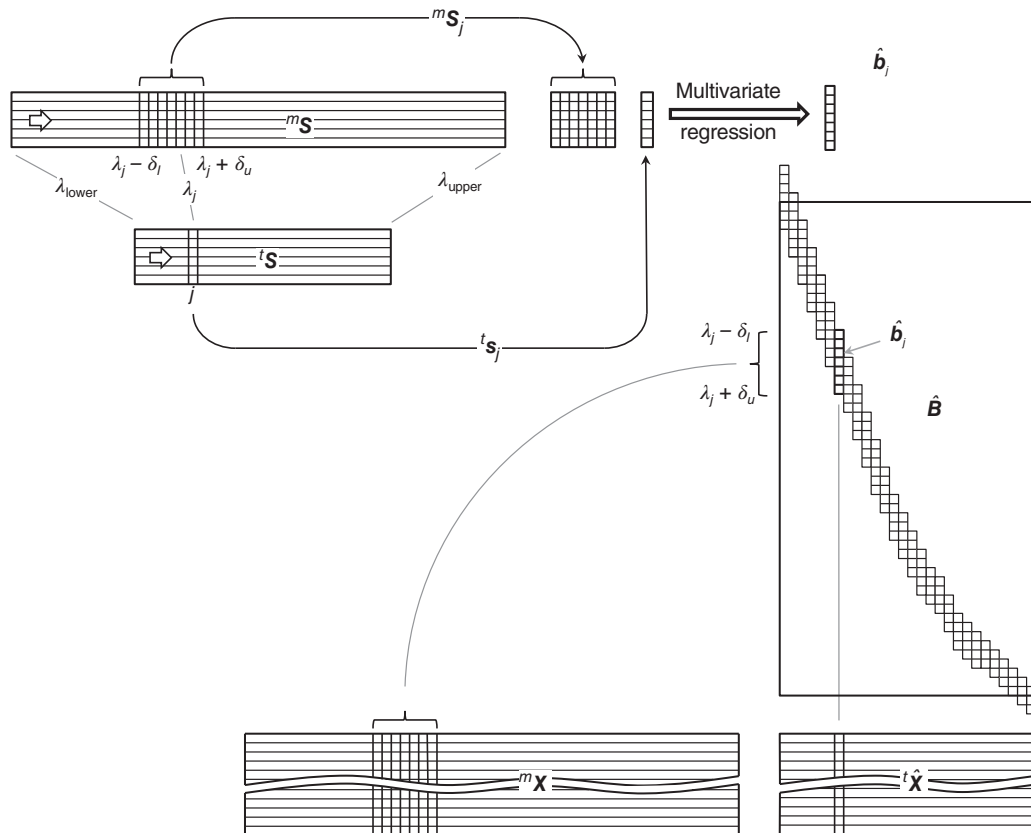


**Figure 12.4** Generation and application of the transfer matrix  $\hat{B}$  in the PDS procedure described in the present chapter for instruments with different wavelength scales and spectral resolutions (the symbols correspond to the symbols in the text).

assignment leads to the fact that neither the width nor the shift of the master window is necessarily constant for each step of the data point  $j$  in the target.

The enabling procedure is a window assignment matrix (Figure 12.5a) that is passed to the transfer function. Therefore, the window assignment matrix can be freely constructed, and since spectra measured on the master cover a much larger spectral range compared with the spectra of the target instrument (Figure 12.2), one gains the additional advantage that ranges of the master spectra that are outside the target spectrum could be used.

The assignment matrices developed for the spectra transfers in this work are based on the assumption that each window of the master spectrum contains sufficient information to predict the intensity of the corresponding data point of the target because they reside in the same spectral region. This window assignment is as similar as possible to the original PDS [3], and furthermore, the construction of the window assignment matrix can be automated by a parametrizable function.

However, there is no restriction concerning the construction of the assignment matrix. The spectral range of the master could be extended over the whole spectrum, and any arbitrary spectral data point set of the master spectrum could be assigned to a given data point of the target spectrum irrespective of whether or not they form a coherent data point set of the master instrument.

Using this more general approach, it should also be possible to predict the intensities of target data points by assigning additional or different spectral ranges. This could probably improve the results, or in case that the spectral ranges of the master and the target do not overlap, it would actually be the only possibility to perform a spectra

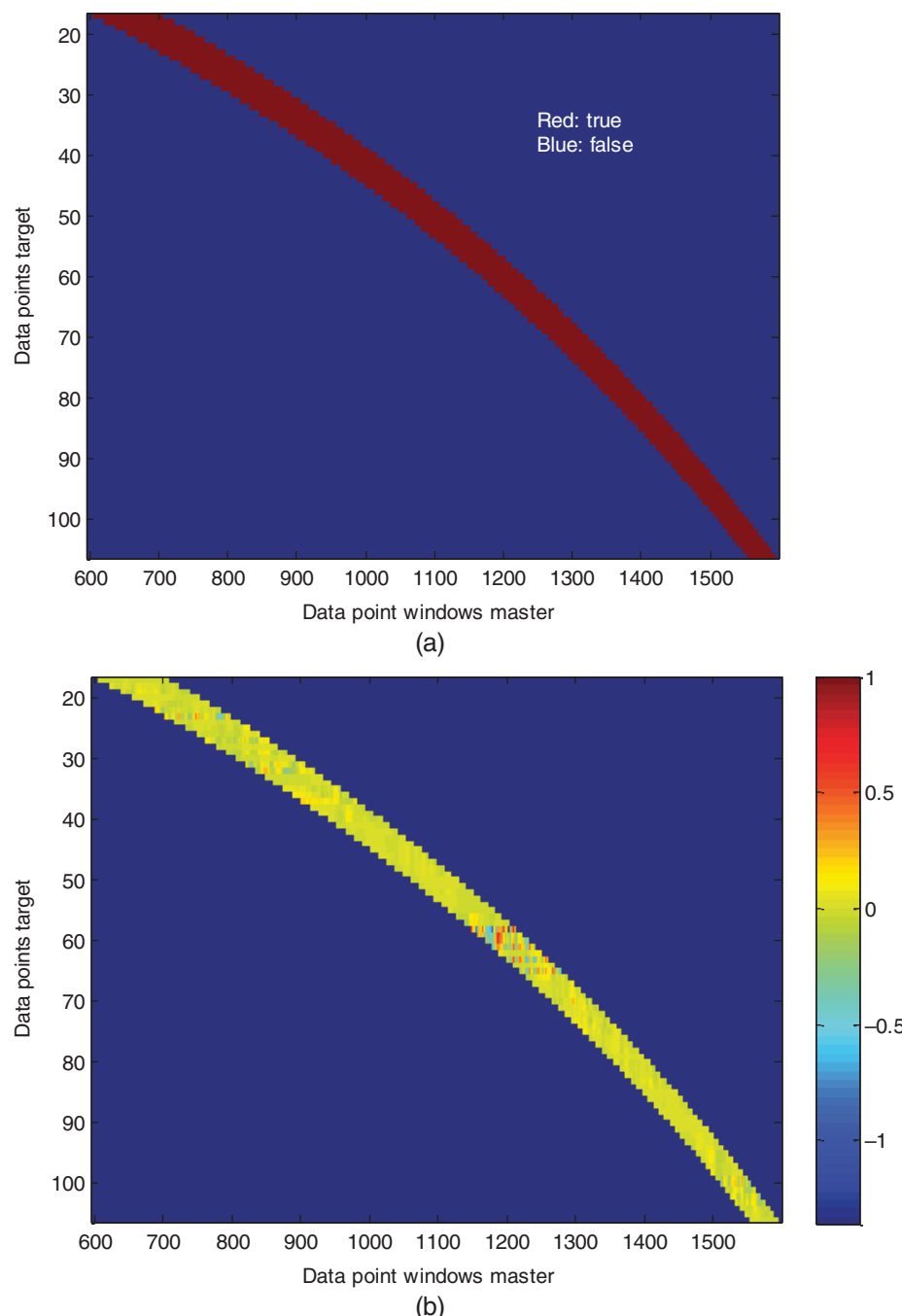


**Figure 12.5** (a) PDS window assignment matrix for the transfer of the spectra of the three-component mixtures of organic solvents. (b) B-coefficient matrix ( $\hat{\mathbf{B}}$ ) from PLS at each individual data point of the target (nonzero within the master windows, zero outside the master windows (the color scale refers to the trace of the master windows only)).

transfer. The problem using this approach, however, is that the master ranges have to be selected individually for each data point of the target, requiring an automatic variable selection for the generation of the assignment matrix.

The procedure of generalized PDS applications and the diagnostic routines to prove the successful transfer will be exemplarily discussed for the quantitative case study of the transmission spectra of 25 liquid mixtures of benzene, cyclohexane, and ethylbenzene of varying composition. To demonstrate the success of the transfer for a qualitative application example, the diffuse reflection spectra of six different commodity polymers (polyethylene [PE], polypropylene [PP], poly(vinyl chloride) [PVC], poly(ethylene terephthalate) [PET], polystyrene [PS], and polycarbonate [PC]) of varying morphology have been used in a chemometric discrimination model [17].

## 12.2 Experimental Details

### 12.2.1 Materials

#### 12.2.1.1 Three-Component Mixtures of Organic Solvents

Twenty-five mixtures of the three organic solvents benzene (>99%) (J.T. Baker, B.V., Deventer, The Netherlands), cyclohexane (>99%), and ethylbenzene (>98%) (both Fluka Chemie AG, Buchs, Switzerland) were prepared with compositions (%(v/v/v)) given in Table 12.1.

#### 12.2.1.2 Polymer Samples

Six different types of polymers in different physical forms (plates, powders, granules, films, fibers) have been chosen for the investigations: PE, PP, PVC, PS, PET, and PC.

### 12.2.2 Instrumentation

#### 12.2.2.1 Spectrometers Used for Three-Component Mixtures of Organic Solvents

The target instrument was a MicroNIR 1700 spectrometer (Viavi Solutions, formerly JDSU, Santa Rosa, CA, USA), based on a LVF monochromator with a spectral range of 950–1650 nm (data point interval 6.2 nm) and a spectral resolution of <1.25% of the center wavelength (< 12.5 nm at 1000 nm). It was used in the transmission mode with a quartz cuvette of 2 mm path length. The integration time was 5000 ms, and 50 scans were accumulated per spectrum. A Bruker MPA FT-NIR spectrometer (Bruker Optik GmbH, Ettlingen, Germany) equipped with a light fiber coupled 2 mm path length transmission probe (Hellma GmbH & Co. KG, Müllheim, Germany) served as master instrument with a spectral range of 4000–12 493 cm<sup>-1</sup> (data point interval 3.86 cm<sup>-1</sup>), and spectra were measured with a spectral resolution of 8 cm<sup>-1</sup> by coadding 32 scans. It should be kept in mind for further discussion that the x-axis of the FT-NIR master instrument is linear in wavenumbers. Thus, converting its x-axis into wavelength units makes it nonlinear (non-equidistant) in wavelength. Three replicate spectra were measured of each sample on the master and the target instrument, and for further data processing, the three spectra were averaged after baseline correction.

#### 12.2.2.2 Spectrometers Used for the Measurement of the Polymer Samples

As target instrument, a different MicroNIR 1700 spectrometer (VIAVI Solutions, Santa Rosa, CA, USA) was used in the diffuse reflection mode. Here too, the integration time was 5000 ms, and 50 scans were accumulated per spectrum. A Bruker VECTOR 22/N FT-NIR spectrometer equipped with a light fiber coupled diffuse reflection probe (Bruker Optik GmbH, Ettlingen, Germany) served as master instrument with a spectral range of 4000–12 493 cm<sup>-1</sup> (data point interval 3.86 cm<sup>-1</sup>), and the spectra were measured with a spectral resolution of 8 cm<sup>-1</sup>, and 32 scans were coadded. Each polymer sample was measured five times on the target instrument, and finally, in total, 150 diffuse reflection spectra (PE, 40; PP, 20; PVC, 35; PS, 15; PET, 25; and PC, 15) were available. Only PE, PP, and PVC were measured on the master instrument to provide spectral sets for subsequent application of the transfer procedure. Here too, for further processing, the replicate spectra were averaged after baseline correction.

**Table 12.1** Composition (%(v/v)) of the investigated three-component mixture samples.

Sample	Benzene (%(v/v))	Cyclohexane (%(v/v))	Ethylbenzene (%(v/v))
1	95	5	0
2	90	5	5
3	80	10	10
4	70	15	15
5	60	20	20
6	50	30	20
7	40	30	30
8	30	40	30
9	20	40	40
10	10	50	40
11	5	60	35
12	10	70	20
13	10	80	10
14	5	90	5
15	0	90	10
16	25	25	50
17	20	20	60
18	20	10	70
19	5	15	80
20	0	10	90
21	5	0	95
22	50	50	0
23	50	0	50
24	0	50	50
25	5	95	0

### 12.2.3 Data Evaluation

All PLS models for the prediction of the concentration of the organic solvents and the PCA models for the discrimination of the commodity polymers were developed with the Unscrambler™ software (version X 10.3; CAMO AS, Norway). The Mahalanobis distance plots for the identification of the polymers and the software for the transfer algorithm were developed by U. Hoffmann using MATLAB (version R2011a, The MathWorks, Inc., Natick, MA, USA).

## 12.3 Results and Discussion

### 12.3.1 Application of PDS to the Spectra of the Three-Component Mixtures of Organic Solvents

To make the master spectra comparable with the target spectra, the wavenumber scale of the master was converted into a wavelength scale, and subsequently, the spectra of both instruments were pretreated as follows:

- (a) The original replicate spectra of each sample were baseline corrected, averaged, and truncated to the selected wavelength range (980–1580 nm).
- (b) The resulting 25 spectra sets obtained for both instruments were then split up into 10 transfer spectra, selected according to the Kennard and Stone algorithm [8], and 15 reference spectra (Figure 12.6a and b). In Table 12.2, the different spectra sets and their role in the transfer procedure have been summarized.

**Table 12.2** Definition of the different spectra sets and their role in the described transfer procedure.

	Master	Target	Transferred
<b>Transfer spectra</b>	Will be used for the construction of the B-matrix and should be representative for the calibration sample set	Same sample set as selected for the master transfer spectra	
	Members of the master calibration spectra set (if available)	Part of the target calibration spectra set	
<b>Reference spectra</b>	Will be transferred with the B-matrix and correspond in subsequent applications to the calibration spectra set that has to be transferred	Are used in the present study for the comparison with the transferred spectra, but are not required in subsequent applications	Result from application of B-matrix to the reference spectra measured on the master instrument and act as transferred calibration set

For the generalized PDS algorithm, the following input is required: a certain (preferably small) number of pretreated transfer spectra measured on the master instrument, in the present case 10 spectra (Figure 12.6a); the same number of pretreated transfer spectra (of the same samples) measured on the target spectrometer (Figure 12.6b); and a matrix (type logical, i.e. only the values true and false are defined) that assigns the master windows to the corresponding target data points.

The window assignment matrix for the transfer of the three-component mixtures is shown in Figure 12.5a. Each line in this matrix assigns a window of the master spectrum (red = true) to the corresponding data point of the target spectrum by adding a certain interval (in the present case about  $\pm 20$  nm) to the wavelength at each data point of the target. This wavelength interval is searched in the master spectrum, and the corresponding data points are set to true in this matrix.

The function to create the matrix shown in Figure 12.5a requires the following input parameters: wavelength scale of the master, lower and upper limit of the selected wavelength range of the master, wavelength scale of the target, lower and upper limit of the selected wavelength range of the target, and left and right interval of the window in the master spectrum around the corresponding data point of the target ( $\pm 20$  nm).

The width of the resulting window in data point units varies, while the window is shifted over the selected range because in contrast to the target instrument, the wavelength scale of the master is not equidistant (see above).

The PDS procedure performs an individual PLS model for each transferred target data point. Since each of these models yields a B-vector, the compilation of these vectors results in the B-matrix shown in Figure 12.5b, which is finally used to perform the transfer by multiplication with the spectra of the master instrument.

### 12.3.2 Diagnostic Procedures for the Transferred Spectra of the Three-Component Mixtures of Organic Solvents

The transfer procedure requires several parameters to control the particular functions. To compare the performance of different parameter settings, the following diagnostic method is provided: after the transfer has been

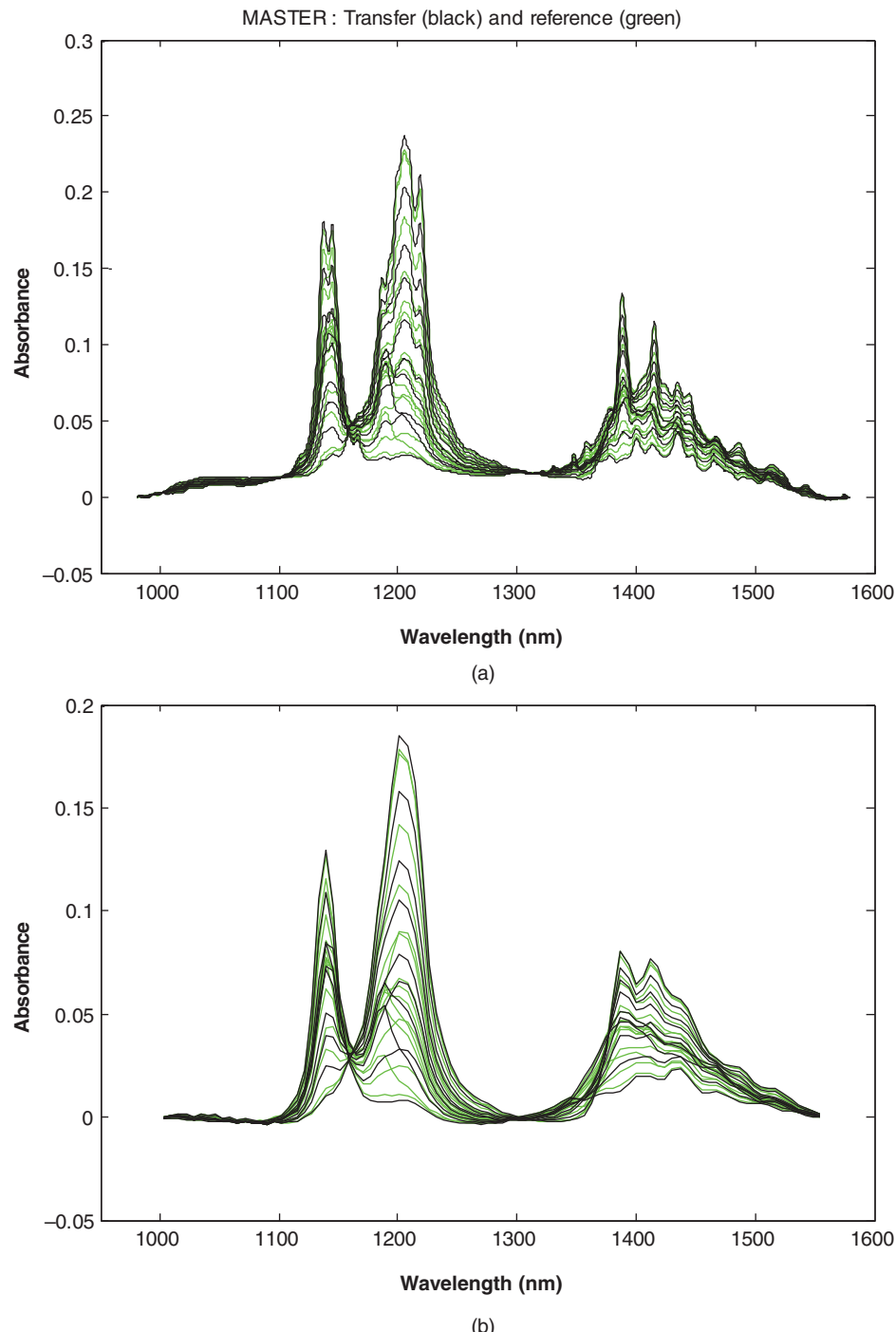


**Figure 12.6** (a) 10 transfer (black) and 15 reference (green) spectra measured on the benchtop spectrometer (master) after baseline correction (two points: 980/1580 nm) and wavelength range selection (980–1580 nm). (b) 10 transfer (black) and 15 reference (green) spectra measured on the handheld spectrometer (target) after baseline correction (two points: 1000/1560 nm) and selection of the 1000–1560 nm wavelength range (the master wavelength range [Figure 12.6a] has been extended for 20 nm on each side in order to avoid the cutoff of the first and last windows during further processing).

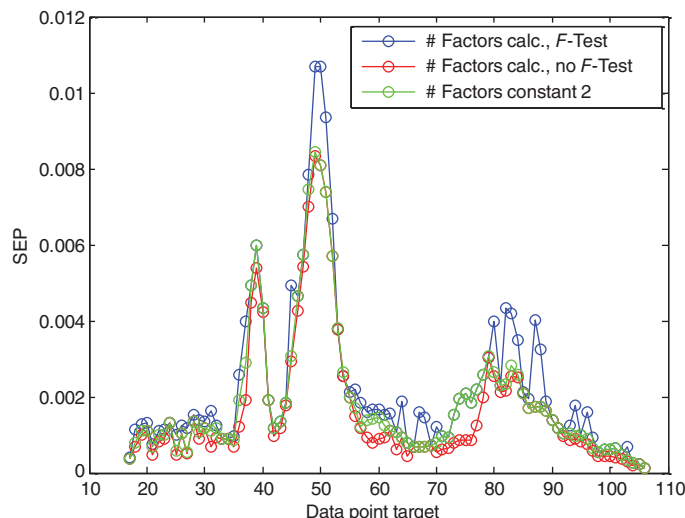


**Figure 12.7** SEP at the individual target data points depending on the three different methods to find the optimum number of factors for the PLS model (see text).

carried out, the entire variable set of the current MATLAB session is saved to a MAT-file. For diagnostics, several of these files can be read, and a preselected set of variables can be evaluated. Thus, for example, the number of PLS factors at each individual data point can be determined by three different methods:

1. Finding the minimum of standard error of prediction (SEP) versus number of factors.
2. Using an *F*-test to find the first SEP that is insignificantly larger than the minimum.
3. Definition of a user-selected number of factors that is constant for all data points.

The different effects on the SEP at each individual data point for these three parameter settings are shown in Figure 12.7.

### 12.3.3 Development of Test Calibrations with the Transferred Spectra of the Three-Component Mixtures of Organic Solvents and Prediction of Measured Target Spectra

The quality of spectral transfer is demonstrated in Figure 12.8; it shows the overlay of an original spectrum, which was measured on the target instrument, with the corresponding spectrum of the same sample transferred from the master to the target format by applying the B-matrix to the master spectrum.

However, as a more objective diagnostic tool, cross-validated PLS-1 calibrations were developed for each of the three organic solvents with the 15 master spectra (reference set) that were transferred to the target format (Figure 12.9), and based on these calibrations, the three components were then predicted for the 15 baseline-corrected spectra measured on the target instrument (Table 12.3). It should be emphasized that the last mentioned 15 spectra were not involved in the transfer procedure and furthermore they represent in a realistic case the unknown samples that have to be predicted with a calibration based on transferred spectra (Table 12.2). It is worth noting that the PLS-1 calibrations (based on two factors) for the three solvents obtained with the spectra transferred to the target format (Figure 12.9) actually yielded better cross-validation results than the PLS-1 calibration models (also based on two factors) developed with spectra of the same sample set in the same spectral range but measured directly on the handheld instrument (Table 12.4a). Listed in Table 12.4b are the cross-validation results for the PLS-1 calibrations (based on three factors) obtained with master spectra of the same samples and in the same spectral range.

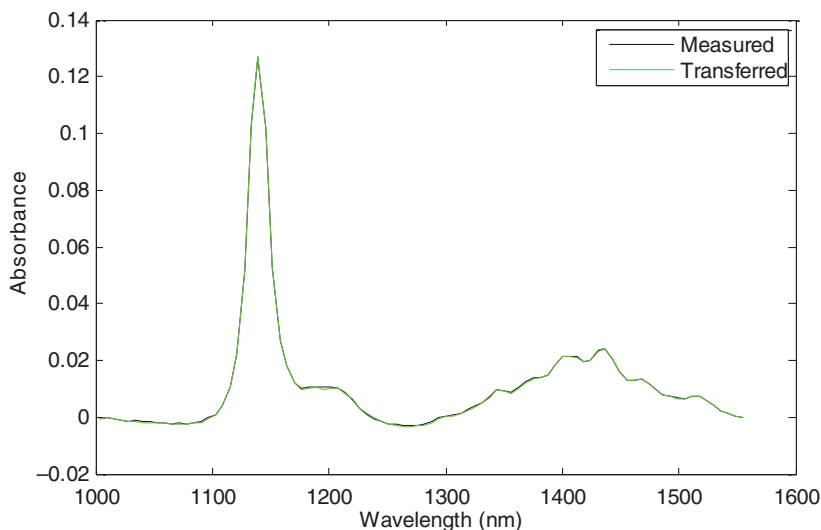


**Figure 12.8** Overlay of a spectrum of a liquid mixture of cyclohexane/benzene/ethylbenzene (Table 12.1, sample 7) measured on the target instrument (black) and the corresponding spectrum after transfer from the master to the target format (green).

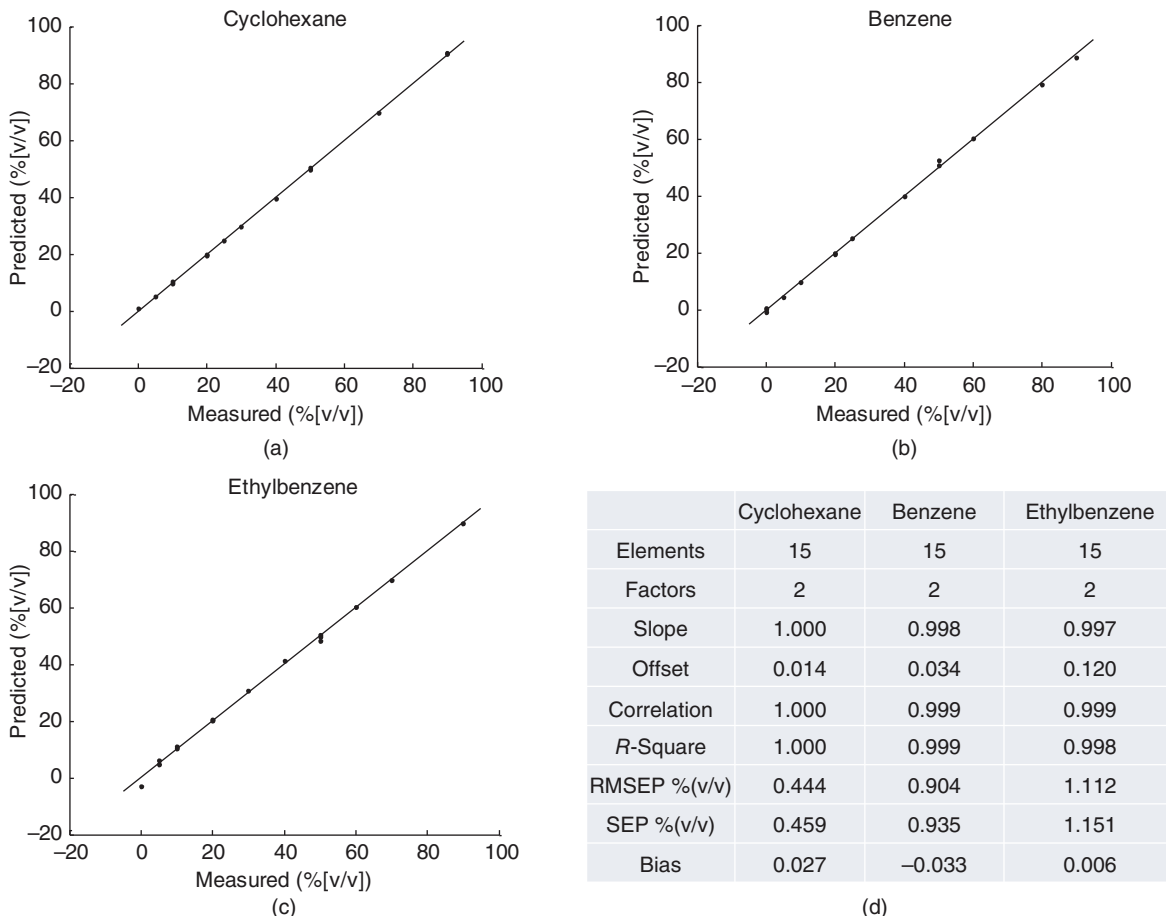


**Figure 12.9** Measured/predicted plots of the PLS-1 models for the three components of the organic solvent mixtures based on the 15 master spectra (reference set) after transfer to the target format: (a) cyclohexane, (b) benzene, (c) ethylbenzene, and (d) corresponding cross-validation results.

**Table 12.3** Comparison of predicted and reference concentrations of cyclohexane/benzene/ethylbenzene for the 15 baseline-corrected spectra measured on the target instrument (see text).

Sample	Cyclohexane predicted (%(v/v))	Cyclohexane reference (%(v/v))	Benzene predicted (%(v/v))	Benzene reference (%(v/v))	Ethylbenzene predicted (%(v/v))	Ethylbenzene reference (%(v/v))
2	5.08	5.00	88.59	90.00	6.34	5.00
3	11.56	10.00	76.48	80.00	11.96	10.00
5	21.88	20.00	58.11	60.00	20.01	20.00
7	30.68	30.00	40.55	40.00	28.77	30.00
9	40.30	40.00	20.34	20.00	39.36	40.00
12	71.05	70.00	10.47	10.00	18.48	20.00
14	91.30	90.00	4.57	5.00	4.14	5.00
15	91.19	90.00	-0.67	0.00	9.48	10.00
16	25.11	25.00	24.52	25.00	50.38	50.00
17	20.74	20.00	19.93	20.00	59.33	60.00
18	11.00	10.00	19.47	20.00	69.54	70.00
20	11.05	10.00	-0.31	0.00	89.27	90.00
22	48.31	50.00	54.17	50.00	-2.49	0.00
23	0.84	0.00	48.64	50.00	50.53	50.00
24	50.79	50.00	0.47	0.00	48.75	50.00

### 12.3.3.1 Identification of Different Polymer Classes by Their NIR Spectra

In this second case study, the priority objective of the investigations was to clarify whether the potential of identification or discrimination of different classes of polymers by NIR spectroscopy is retained by the transfer of the spectra from the master to the target format. For this purpose, exemplarily, the spectra of those three current classes of polymers (PE, PP, and PVC) were chosen, which are most difficult to discriminate. They were measured on the master and target instrument, respectively (Figure 12.10), whereas the other three classes (PS, PET, and PC) were measured on the target instrument only. For the first three mentioned commodity polymers (PE, PP, PVC), it should then be tested whether PCA models developed with transferred spectra can be applied to discriminate the spectra measured on the target instrument from the other polymer classes. Due to the influence of the different physical forms of the polymers on the scatter effects, a multiplicative scatter correction (MSC) was applied before further processing of the spectra.

In analogy to the previous quantitative case studies, the available master and target spectra for PE, PP, and PVC were split up in transfer/reference spectra sets (PE, 16/24; PP, 8/12; PVC, 14/21). Then, the transfer spectra sets of the master and target instrument were applied to generate the transfer matrix ( $B$ -matrix), and subsequently, the transfer was applied to both, the transfer and the reference spectra set of the master instrument. Here, too, a good agreement between the original spectra of the master instrument and the spectra transferred to the target format has been achieved as exemplarily demonstrated in Figure 12.11 for PE.

### 12.3.4 Development of PCA Model for PE as Performance Tests for the Spectra Transfer

In what follows, the performance test is only described for PE, and for further information on PP and PVC, the interested readers are referred to the original literature [17]. The spectra of all polymer classes measured on the

**Table 12.4** Cross-validation results for the three solvents of the PLS-1 calibrations (two factors) developed with spectra measured on the target instrument (A) and analogous results of the PLS-1 calibrations (three factors) developed with spectra measured on the master instrument (B).

	Cyclohexane	Benzene	Ethylbenzene
<b>A</b>			
Elements	15	15	15
Slope	0.998	0.998	0.996
Offset	0.084	0.071	0.111
Correlation	0.999	0.999	0.999
R-square	0.998	0.998	0.998
RMSEP (%v/v)	1.380	1.186	1.304
SEP (%v/v)	1.393	1.196	1.316
Bias	6.197e-05	0.011	0.007
<b>B</b>			
Elements	15	15	15
Slope	0.999	0.999	0.998
Offset	0.039	0.032	0.042
Correlation	1.000	1.000	0.999
R-square	1.000	1.000	0.998
RMSEP (%v/v)	0.361	0.375	0.655
SEP (%v/v)	0.363	0.378	0.661
Bias	0.022	0.002	-0.025

target instrument were pretreated by MSC, i.e. the individual spectra were fitted to the mean spectrum of PE (Figure 12.12). The transfer and reference spectra of PE, measured on the master instrument and transferred to the target format, were then applied as modeling spectra for the PCA model to identify PE (black symbols in Figure 12.13). Together with the reference spectra of PE measured on the target instrument (red symbols in Figure 12.13), the target spectra of the five other polymer classes were then subjected to this PCA model to discriminate PE from the rest of the polymers (other colors in Figure 12.13). The discrimination efficiency is demonstrated by the Mahalanobis distances [18], a measure that can be obtained by projecting the relevant spectrum onto the corresponding PCA model, for a selected number of factors. As can be derived from Figure 12.13, a Mahalanobis distance threshold of MD = 4 for PE ensures a secure identification and discrimination relative to each other (PP and PVC) and to the other polymer classes (PC, PET, and PS).

## 12.4 Summary of Transfer Strategy

### 12.4.1 Transfer of Spectra for Quantitative Applications

In commercial applications, a set of spectra measured on a laboratory instrument (master) will be available that has been used to develop a chemometric calibration for the quantitative evaluation of the component of interest.

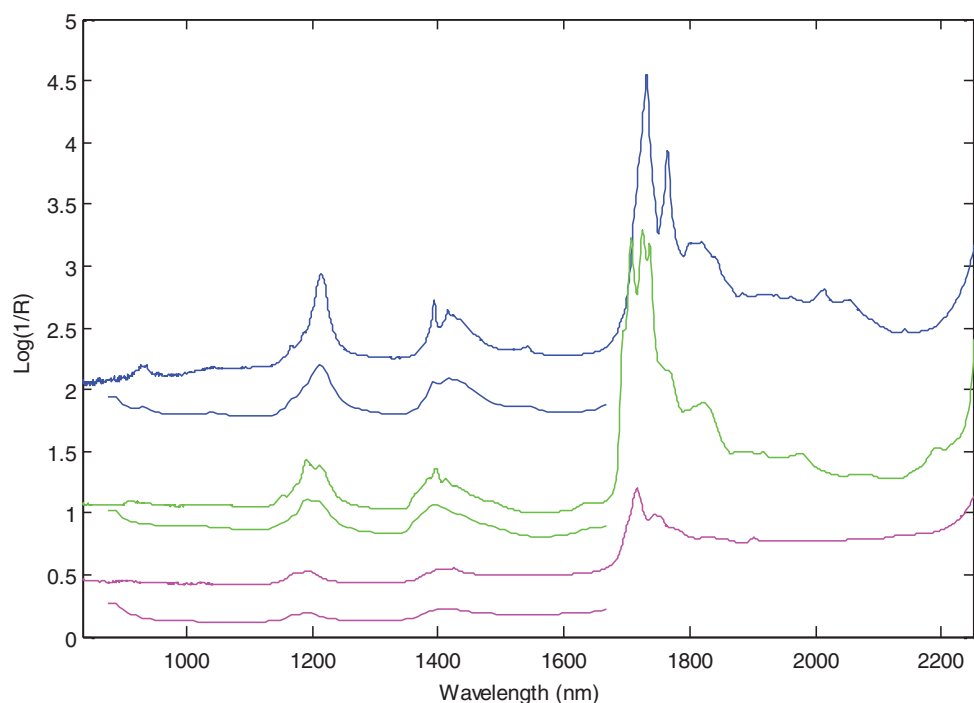


**Figure 12.10** Selected original spectra of PE (blue), PP (green), and PVC (magenta), measured on the benchtop master (top) and the handheld target (bottom) instrument.

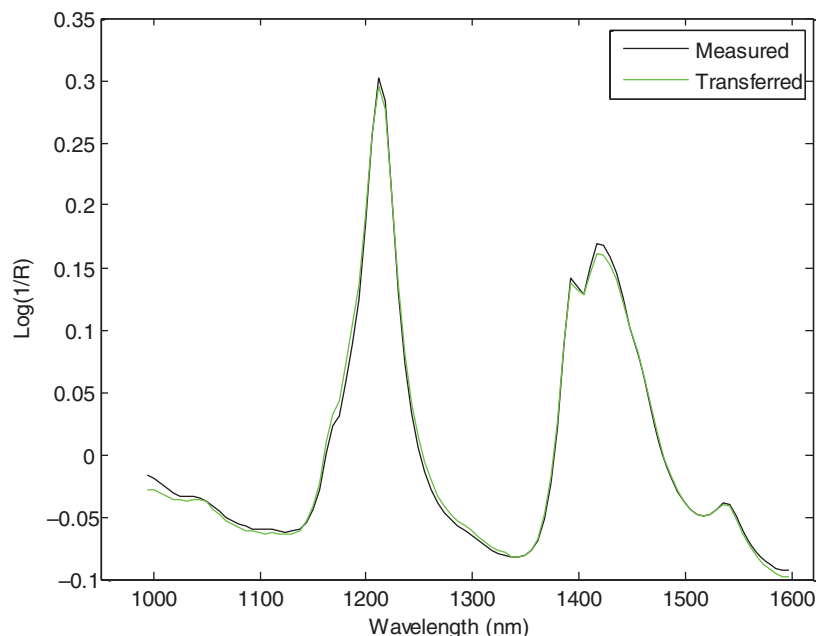


**Figure 12.11** Overlay of the spectrum of a polyethylene sample measured on the target instrument (black) and the spectrum of the same sample after transfer from the master to the target format (green).

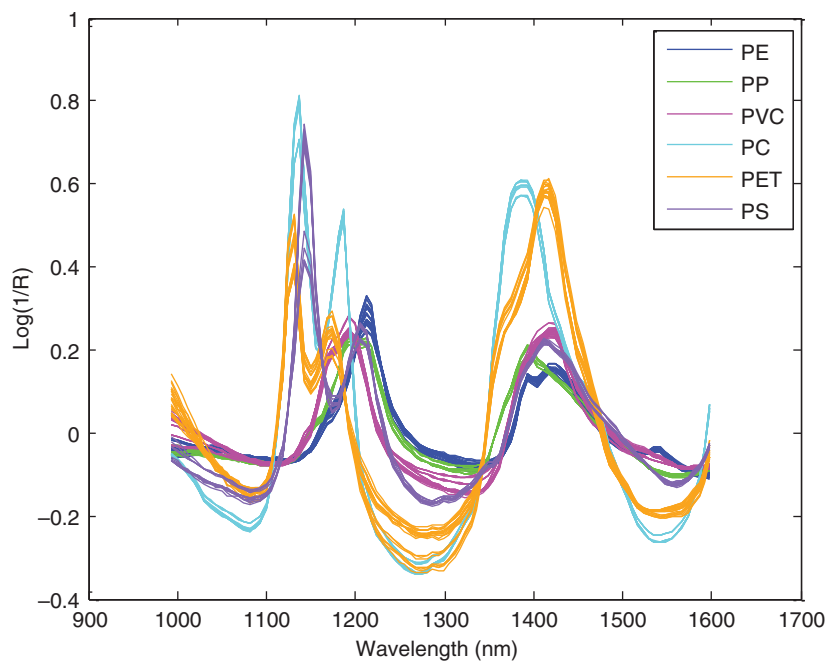


**Figure 12.12** Spectra of all polymer classes measured on the target instrument and pretreated by MSC (i.e. fitted to the mean spectrum of polyethylene) (see text).

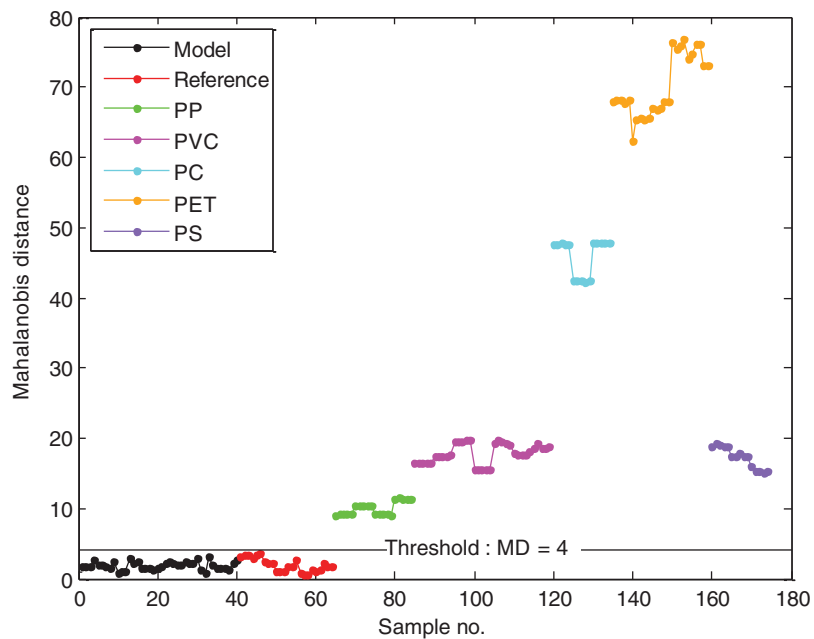


**Figure 12.13** Mahalanobis distances for the PCA model (for four factors) developed for the identification of PE.

For the transfer of this spectral (master) data set to the target format of a handheld instrument, the following steps will have to be applied:

1. If storage samples are available for the calibration set, select a small subset (~10–20) of master spectra from the calibration set that represents its spectral variance. Then, the corresponding samples have to be measured only on the target instrument. In case no storage samples are available, new samples, which cover the spectral variance as close as possible, have to be measured on both spectrometers.
2. After appropriate spectral pretreatment, use the corresponding transfer set measured on both instruments to create the transfer matrix. Subsequently, transfer all the spectra of the master calibration set to the target format.
3. Develop a PLS calibration for the target instrument for the component of interest with the transferred calibration set of the master instrument.
4. Predict any future samples measured on the target instrument with this calibration.

#### 12.4.2 Transfer of Spectra for Qualitative Applications

In reality, a set of spectra of a certain class of compound measured on a laboratory instrument (master) will be available that can be used to develop a multivariate model for the qualitative identification or discrimination of this product from other products. For the transfer of this spectral data set from the benchtop spectrometer (master) to the format of the handheld instrument (target), the following steps will have to be applied:

1. If storage samples are available for the calibration set, select a small subset (~10–20) of master spectra from the calibration set that represents its spectral variance. The corresponding samples have to be measured only on the target instrument. In case no storage samples are available, new samples, which cover the spectral variance as close as possible, have to be measured on both spectrometers.
2. After appropriate spectral pretreatment, apply the PDS algorithm to the transfer sets measured on both instruments and use the resulting matrix to transfer all the spectra measured so far on the master instrument to the target format.
3. Develop the previously used identification or discrimination model for the compound of interest with the transferred reference and transfer sets of the master instrument, and subject any future samples measured on the target instrument to the prediction with this qualitative model.

### 12.5 Conclusions

Based on a quantitative case study and a qualitative application example, it has been demonstrated that the proposed transfer algorithm for spectra measured on a laboratory instrument to the format of a handheld spectrometer provides spectral data that yield quantitative prediction data and allow qualitative classification comparable with the originally available data set. The transfer method approach will help save significant time and cost in adopting the miniature NIR spectrometers in a wide range of applications by leveraging existing calibration and classification models developed with the high-end, high-resolution instruments.

### References

- 1 Bouveresse, E. and Massart, D.L. (1996). Standardisation of near-infrared spectrometric instruments: a review. *Vib. Spectrosc.* 11 (1): 3–15.
- 2 Bouveresse, E., Hartmann, C., Massart, D.L. et al. (1996). Standardization of near-infrared spectrometric instruments. *Anal. Chem.* 68 (6): 982–990.

- 3 Wang, Y., Veltkamp, D.J., and Kowalski, R.B. (1991). Multivariate instrument standardization. *Anal. Chem.* 63 (23): 2750–2756.
- 4 Shenk, J.S. and Westerhaus, M.O. (1993). Comments on standardisation: part 2. *NIR News* 4 (5): 13–15.
- 5 Shenk, J.S. and Westerhaus, M.O. (1989). US Pat. No. 4 866 644, September 12, 1989.
- 6 Forina, M., Drava, G., Armanino, C. et al. (1995). Transfer of calibration function in near-infrared spectroscopy. *Chemom. Intel. Lab. Syst.* 27 (2): 189–203.
- 7 Forina, M., Armanino, C., and Giangiacomo, R. (1992). *Near Infra-red Spectroscopy: Bridging the Gap between Data Analysis and NIR Applications* (eds. K.L. Hildrum, T. Isaksson, T. Naes and A. Tandberg), 91. Chichester: Ellis Horwood.
- 8 Kennard, R.W. and Stone, L.A. (1969). Computer aided design of experiments. *Technometrics* 11 (1): 137–148.
- 9 Bouveresse, E. and Massart, D.L. (1996). Improvement of the piecewise direct standardization procedure for the transfer of NIR spectra for multivariate calibration. *Chemom. Intell. Lab. Syst.* 32 (2): 201–213.
- 10 Fearn, T. (2001). Standardisation and calibration transfer for near infrared instruments: a review. *J. Near Infrared Spectrosc.* 9 (4): 229–244.
- 11 Pierna, J.A.F., Vermeulen, P., Lecler, B. et al. (2010). Calibration transfer from dispersive instruments to handheld spectrometers. *Appl. Spectrosc.* 64 (6): 644–648.
- 12 Workman, J.J. Jr. (2018). A review of calibration transfer practices and instrument differences in spectroscopy. *Appl. Spectrosc.* 72 (3): 340–365.
- 13 Wang, Y. and Kowalski, B.R. (1992). Calibration transfer and measurement stability of near- infrared spectrometers. *Appl. Spectrosc.* 46 (5): 764–771.
- 14 Kowalski, B.R., Veltkamp, D.J., and Wang, Y. (1995). US Pat. No. 5 459 677, 1995.
- 15 Feudale, R.N., Woody, N.A., Tan, H. et al. (2002). Transfer of multivariate calibration models: a review. *Chemom. Intel. Lab. Syst.* 64 (2): 181–192.
- 16 Sulub, Y., LoBrutto, R., Vivilecchia, R., and Wabuyele, B.W. (2008). Content uniformity determination of pharmaceutical tablets using five near-infrared reflectance spectrometers: a process analytical technology (PAT) approach using robust multivariate calibration transfer algorithms. *Anal. Chim. Acta* 611 (2): 143–150.
- 17 Hoffmann, U., Pfeifer, F., Hsuing, C., and Siesler, H.W. (2016). Spectra transfer between a Fourier transform near-infrared laboratory and a miniaturized handheld near-infrared spectrometer. *Appl. Spectrosc.* 70 (5): 852–860.
- 18 Ritchie, G.E., Mark, H., and Ciurczak, E.W. (2003). Evaluation of the conformity index and the Mahalanobis distance as a tool for process analysis: a technical note. *AAPS PharmSciTech* 4 (2): 109–118.

# 13

## Applications of Handheld Near-Infrared Spectrometers

Hui Yan<sup>1</sup> and Heinz W. Siesler<sup>2</sup>

<sup>1</sup>School of Biotechnology, Jiangsu University of Science and Technology, Zhenjiang, China

<sup>2</sup>Department of Physical Chemistry, University of Duisburg-Essen, Essen, Germany

### 13.1 Introduction

Miniaturization of vibrational spectrometers started more than two decades ago, but only within the last decade have real handheld Raman, mid-infrared (MIR), and near-infrared (NIR) spectrometers become commercially available and utilized for a broad range of analytical applications [1–4]. While the weight of handheld Raman and MIR spectrometers is still in the  $\geq 1$  kg range, the miniaturization of NIR instruments has advanced down to weights of  $< 100$  g, and developments are underway to integrate them into mobile phones [5, 6]. Furthermore, Raman and MIR handheld spectrometers are still in the price range of several tens of thousands of US dollars (USD), whereas miniaturized NIR systems have already reached the  $< 1000$  USD level. In view of the high price level of Raman and MIR instruments, the acquisition of these systems will be restricted to industrial, military, and homeland security applications, as well as public use by first responders, customs, or environmental institutions, whereas due to the further reduction of costs by high-volume manufacturability, the acquisition of NIR systems can be considered in the near future for private use in everyday life applications by a nonexpert user community. Therefore, this chapter will focus on state-of-the-art miniaturized NIR spectrometers and their applications to practical analytical problems.

The bright future and significant growth rate predicted by marketing companies for the segment of miniaturized spectrometers has, unfortunately, also led to negative commercial developments in this field of instrumentation. Therefore, this chapter will be clear about the exaggerated claims of some direct-to-consumer companies regarding the performance of their “NIR scanners” with “cloud evaluation of big data” but will also point out where the authors believe handheld NIR spectroscopy can offer a better analytical alternative than current methods.

### 13.2 Instrumentation

Generally, recent progress in NIR spectrometer miniaturization has taken advantage of new microtechnologies such as micro-electro-mechanical systems (MEMS), micro-opto-electro-mechanical systems (MOEMS), and linear variable filters (LVF), and despite the drastic reduction of spectrometer size and weight, good qualitative and quantitative calibration results have been achieved for a broad range of applications. In what follows, the basic instrumental principles of the four different types of NIR spectrometers, which we have used for the application examples discussed in this chapter, will be described (Figure 13.1).

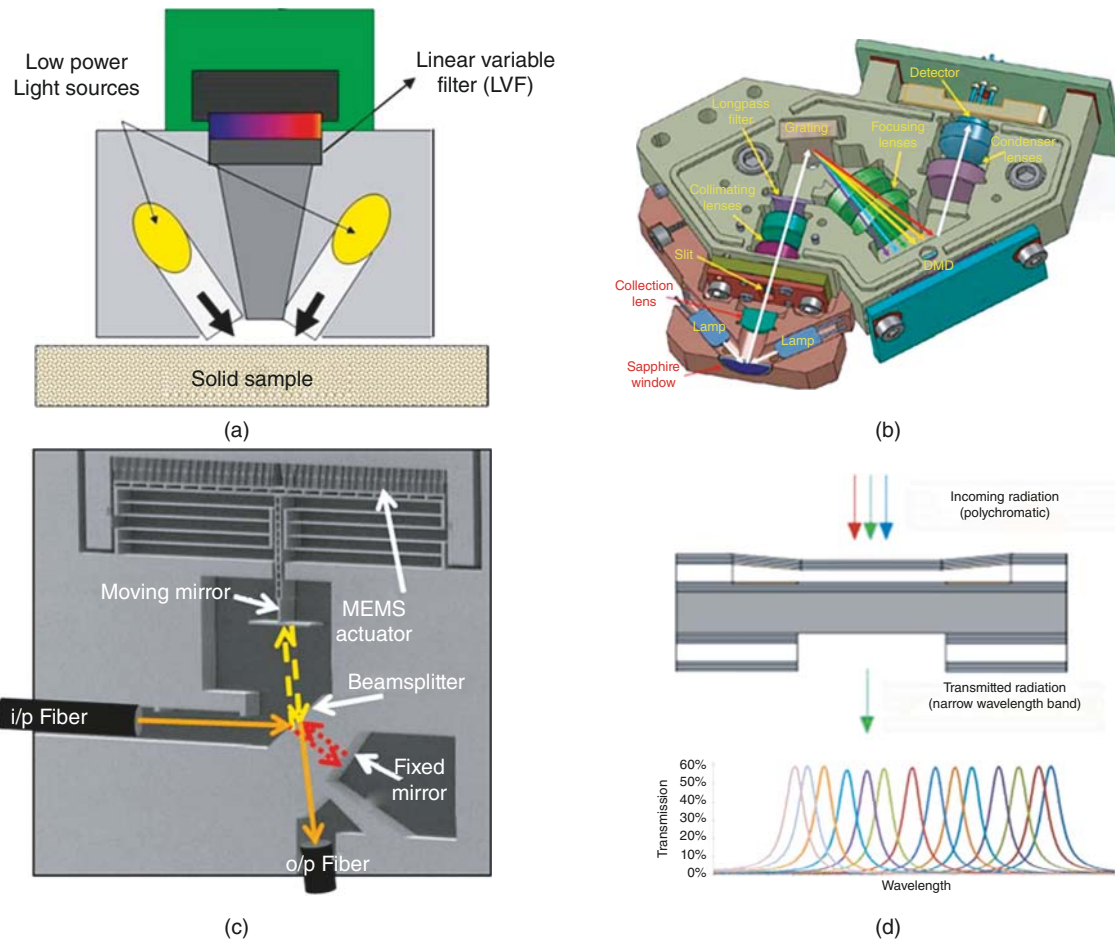


**Figure 13.1** The optical schemes of the handheld NIR spectrometers used for the discussed application examples: (a) VIAVI MicroNIR 1700, linear variable filter (LVF); (b) DLP NIRscan Nano EVM with Texas Instruments digital micromirror device (DMD<sup>TM</sup>); (c) Si-Ware Systems, MEMS-based FT-NIR spectrometer; (d) Spectral Engines NIR spectrometer with Fabry–Perot tunable filter.

Based on the type of detector, handheld NIR spectrometers can be classified in the two categories of array detector and single-detector instruments [7]. One of the earliest, if not the first commercial, very lightweight, handheld (<100 g) NIR spectrometer, the MicroNIR 1700 (VIAVI, formerly JDSU, Santa Rosa, CA, USA), has an array detector that covers the wavelength range from 908 to 1676 nm and uses an LVF as a monochromator. It has been used for many applications ranging from the authentication of seafood and determination of food nutrients to the analysis of hydrocarbon contaminants in soil and authentication, and quantitative determination of pharmaceutical drugs [8–11]. However, in the NIR where indium gallium arsenide (InGaAs) is the preferred detector material, the price for a single detector is much lower compared with an array detector, and in an attempt to further reduce the hardware costs, new developments focus on systems with single detectors. Thus, the DLP NIRscan Nano EVM (Dallas, TX, USA), for example, is based on Texas Instruments' digital micromirror device (DMD<sup>TM</sup>), in combination with a grating and a single-element detector, and also covers the wavelength range from 900 to 1701 nm. Recently, a MEMS-based FT-NIR instrument, which contains a single-chip Michelson interferometer with a monolithic opto-electro-mechanical structure, has been introduced by Si-Ware Systems (Cairo, Egypt). Contrary to most other handheld spectrometers, this FT-NIR instrument can scan spectra over the longer wavelength range from

1298 to 2606 nm. Finally, Spectral Engines (Helsinki, Finland) has developed miniaturized NIR spectrometers that are based on a scanning Fabry–Perot etalon, which acts as a tunable wavelength filter. In order to cover the NIR wavelength region 1350–2450 nm, however, four spectrometers are required.

### 13.3 Applications

Although handheld NIR spectrometers can be applied for a broad range of industrial raw material quality control applications [12–15], the present chapter is targeted at in-the-field and practical, everyday life, on-site applications. In these days, fraud and adulteration have become frequent problems, ranging from life science materials (foods, pharmaceuticals) to everyday life materials such as textiles, and the progress in miniaturization and increasing affordability of handheld NIR spectrometers make them an attractive identification and authentication tool for customer protection. Some of the following application examples will not only demonstrate the potential of handheld NIR spectroscopy for this purpose but also suggest everyday life applications. The descriptions of these examples also describe the efforts involved in generating robust calibrations or classifications, including the use of validation sample sets, replicate measurements of samples, choices of variable selection algorithms, and spectral preprocessing procedures. In view of the aggressive commercials of some companies, however, we will also report unsuccessful experiments, in order to put any exaggerated expectations into perspective.

## 13.4 Qualitative Applications of Handheld NIR Spectrometers

### 13.4.1 Authentication and Identification of Textiles

In recent publications [16], the potential of handheld NIR spectroscopy for the identification of textile materials was investigated in some detail. Depending on the raw material (natural, e.g. silk, cashmere, etc., or synthetic, e.g. acrylics, polyamides, polyesters, etc.), the price varies considerably, and this situation is regularly misused by untrustworthy businessmen to sell textile products for unrealistic prices to credulous customers. Mercerization of cotton, for example, gives the fibers a glossy appearance and feel, which can be used to make a counterfeit silk carpet – one that can deceive a nonexpert. However, such an attempted deception can be readily detected by a visual comparison of reference spectra with the spectrum recorded on site by handheld NIR spectroscopy (Figure 13.2). In combination with material-specific, easy-to-use evaluation algorithms, handheld NIR sensors integrated into mobile phones could, therefore, be used in the future by nonexperts to identify or authenticate a product of interest rapidly.

In order to explore the potential of handheld NIR for more comprehensive identification of unknown textiles, 72 samples based on nine different classes of natural and synthetic materials (silk, wool/cashmere, cotton, acrylics, elasthane, Kevlar, Nomex, polyester, polyamide-6/polyamide-66) were also investigated in this work [16]. For this purpose, the NIR spectra of the 72 samples were measured in diffuse reflection with the four instruments shown in Figure 13.1, and 48 samples were randomly selected as a calibration set, and the residual 24 samples were used to test the identification performance of the calibration models. In Figure 13.3, the NIR spectra measured with the four different instruments for exemplary representatives of the synthetic (polyester) and natural (silk) classes, respectively, are shown. The principal component analysis (PCA), in combination with soft independent modeling of class analogies (SIMCA), and the evaluation of the mean Euclidian distances in the PCA score plots then provided a suitable analytical tool for the assignment of the different types of textile classes and a ranking of the identification performance of the different handheld instruments, respectively. Due to the coverage of the largest and most important spectral range (blue spectra in Figure 13.3), the best discrimination capability was demonstrated for the FT-NIR spectra of the MEMS Michelson interferometer-based instrument, followed

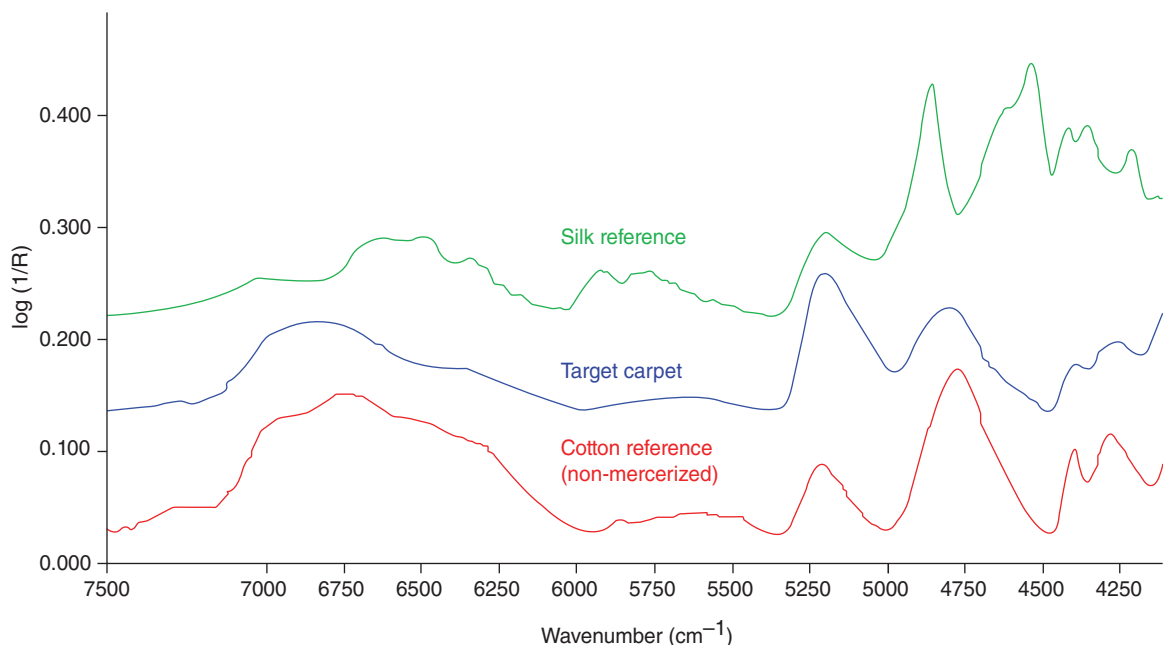


**Figure 13.2** Rapid identification of the material utilized for the manufacture of a carpet based on visual inspection of NIR spectra recorded with a handheld NIR instrument.

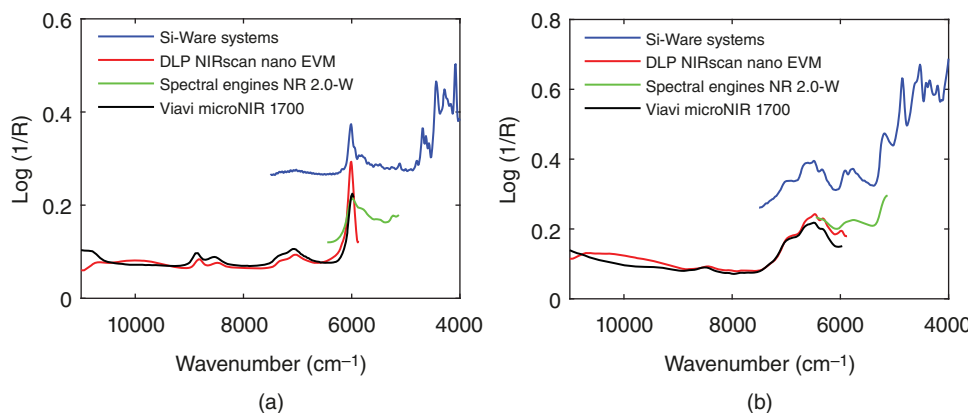


**Figure 13.3** NIR spectra of selected representatives of the investigated textile species ((a) polyester, (b) silk) measured with the four different handheld spectrometers.

by spectra measured with the DMD (red spectra) and the LVF (black spectra) spectrometers, and lastly with the instrument based on a Fabry–Perot tunable filter (green spectra).

Notwithstanding the comparatively low analytical performance of this last-mentioned instrument, it is presented under the brand name X-Spect by different websites and videos as the “scanner of the future,” used to not only measure nutritional parameters (see below) but also identify contaminations of textiles that allow one to choose the relevant program of a washing machine in a “smart home.” However, the present authors, using the handheld FT-NIR spectrometer that had provided the best identification performance in the textile investigations discussed above, were not really successful in duplicating these claims. Neither red wine nor coffee stains

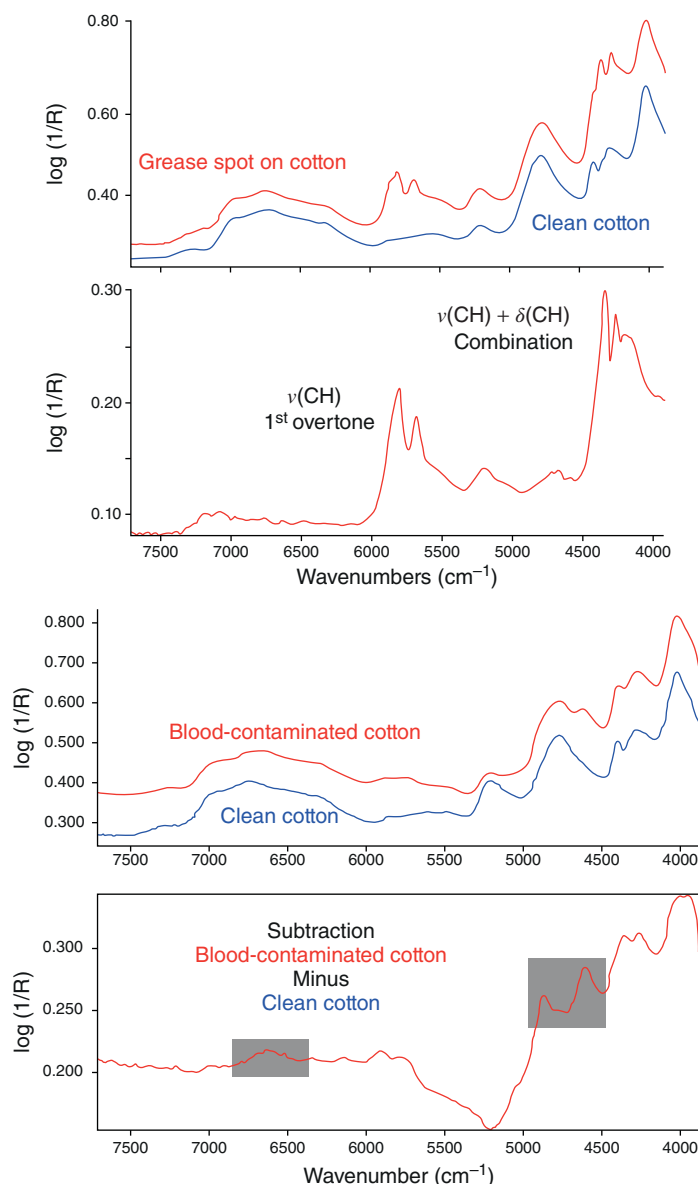


**Figure 13.4** Identification of cotton contaminations by difference spectroscopy. (a) NIR spectra of clean and grease-contaminated cotton (top), difference spectrum contaminated minus clean cotton (bottom); (b) NIR spectra of clean and blood-contaminated cotton (top), difference spectrum (bottom).

on cotton – as claimed in the videos – could be identified by difference spectroscopy (contaminated textile minus clean textile), because the spectral footprints of these contaminants were not characteristic enough for identification purposes, despite the larger available wavelength range. Although not really relevant for the control of a washing machine, but rather indicative of its excessively high sugar content, the stain of a Red Bull drink on cotton could be unambiguously detected by the corresponding carbohydrate absorption bands in the difference spectrum. Successful identification of contaminations with grease and blood on cotton, however, has been reported recently [17]. While in the first case the absorptions of the grease-specific C–H overtone and C–H combination bands could

be isolated by difference spectroscopy (Figure 13.4a, bottom), in the case of the bloodstain, the protein-specific N–H first overtone, and amide I and amide II combination bands in the 6600 and 4500–5000 cm<sup>-1</sup> wavenumber regions, respectively, can be used to identify the type of contamination (Figure 13.4b, gray-shaded wavenumber regions).

### 13.4.2 Identification of Polymers for Recycling Purposes

The performance comparison of the different handheld NIR spectrometers, reported above for textile materials, has also been conducted for polymer recycling applications [18]. Here too, PCA calibration models based on the diffuse reflection spectra measured with the four handheld instruments were developed, and subsequently, unknown test samples were predicted (Figure 13.5). The samples were the five polymer commodities – polyethylene (PE), polypropylene (PP), polystyrene (PS), polyvinylchloride (PVC), and poly(ethyleneterephthalate) (PET) – in different physical forms (pellets, films, plates, fibers, powders). Despite

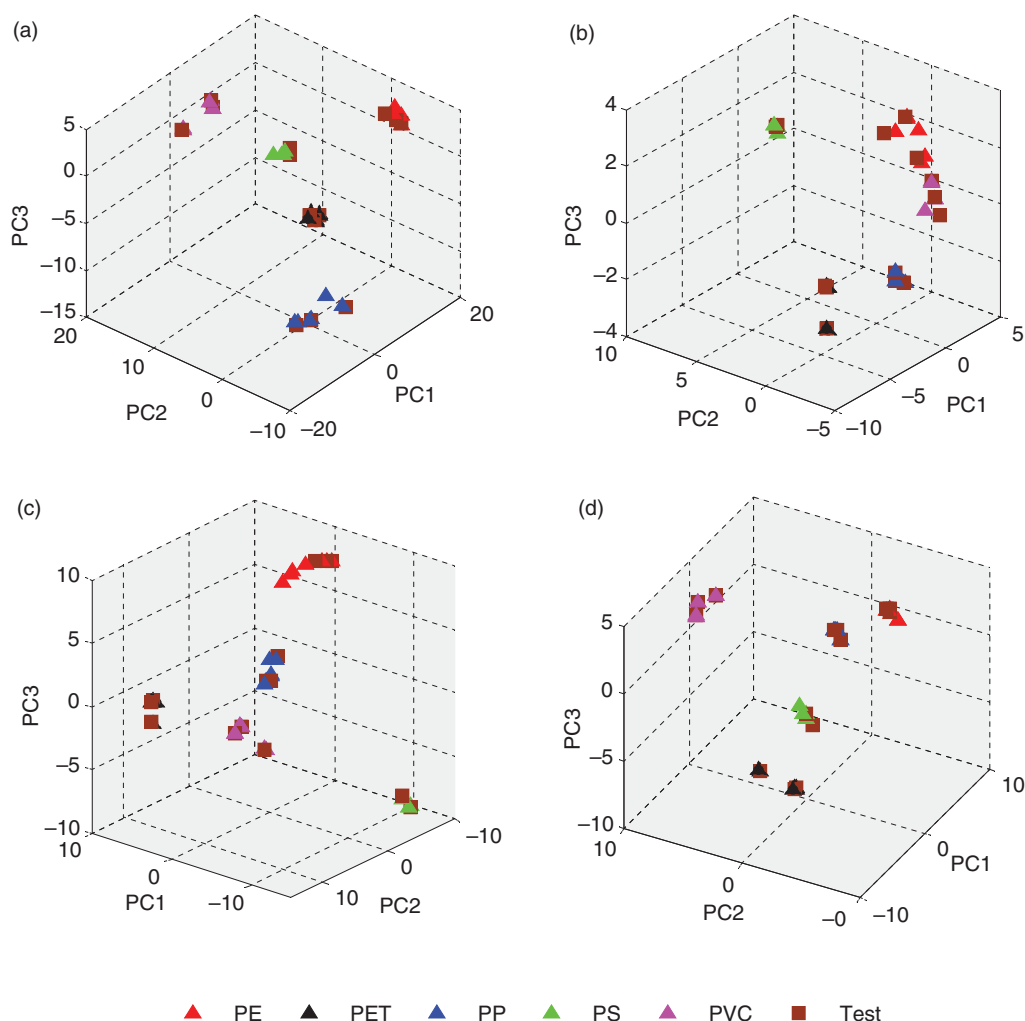


**Figure 13.5** 3D PCA score plots based on the calibration spectra of the five polymer commodities and the corresponding test samples measured with the four different instruments: (a) Si-Ware Systems, (b) Spectral Engines NR 2.0 W, (c) DLP NIRscan Nano EVM, and (d) Viavi MicroNIR 1700.

the significant differences in wavenumber range and spectral resolution, the prediction performance of the four spectrometers for the test samples was almost comparable. Thus, with the exception of the Fabry–Perot tunable filter-based instrument, which basically covers only the first overtone region of  $\nu(\text{CH})$  vibrations ( $5300\text{--}6200\text{ cm}^{-1}$ ) and could not discriminate PE and PVC (Figure 13.5b), all samples were correctly identified by the PCA models developed on the basis of the instrument-specific spectra. Interestingly, in a further step of developing a SIMCA model, even the PCA problem case of PE and PVC discrimination could be solved.

### 13.4.3 Identification of the Geographic Origin of a Traditional Chinese Plant Root

As a counterpart to the textile and polymer applications discussed in the preceding sections, a case study in the field of traditional Chinese medicines (TCMs) will be outlined in this section. *Radix Pseudostellariae* is the dried root of a plant of *Pseudostellaria heterophylla* (Miq.) Pax et Hoff of *Caryophyllaceae* and has been widely applied in China as a kind of TCM and high-value food [19]. This plant root has many claimed pharmacological effects for the improvement of immunity, antistress, anti-fatigue, etc. Due to different climatic conditions and soil types, however, the quality of *Radix Pseudostellariae* varies greatly. Thus, the geographic origin is not only a critical index for the quality valuation based on the Pharmacopoeia of the People's Republic of China but also the consumers' concerns [20]. Although the identification of the geographic origin of *Radix Pseudostellariae* by benchtop NIR spectroscopy has been reported [21], for obvious reasons, this approach is not feasible for on-site determination. Instead, this is a typical example that demonstrates the flexibility of handheld NIR spectrometers for in-the-field applications.

For this study, a total of 300 dried *Radix Pseudostellariae* samples were collected from the main Chinese medicinal material production bases in Anhui, Fujian, and Guizhou provinces. Two hundred of these samples were randomly selected as a calibration set for model development, and the rest were used as a test set to validate the accuracy of the calibration models. The MicroNIR 1700 (Viavi, Santa Rosa, CA, USA) was used to collect the diffuse reflection spectra of the samples (Figure 13.6). Each individual spectrum was the average of 50 scans over the wavelength range of 891–1670 nm, and a certified 99% Spectralon™ reflectance standard (Labsphere Inc., North Sutton, USA) was used to measure the reference spectrum. After each measurement, the sample was rotated by approximately  $120^\circ$ , and the average of three spectra was used as the final raw spectrum for further processing.

In Figure 13.7, the raw spectra of the calibration set are shown. The three main absorption bands at 1450, 980, 1190 nm can be assigned to the first and second overtones of the  $\nu(\text{OH})$  absorption, respectively, and the second overtone of the  $\nu(\text{CH})$  absorptions. The spectral pretreatment methods of autoscaling, first derivative, standard normal variate (SNV), and their combinations were tested. Ultimately, SNV plus first derivative (with a Savitzky–Golay smoothing procedure of five data points and a second-order polynomial) turned out as the spectral pretreatment yielding the best calibration performance. Then, the competitive adaptive reweighted sampling (CARS) [22] and

**Figure 13.6** Sample presentation for a *Radix Pseudostellariae* specimen.



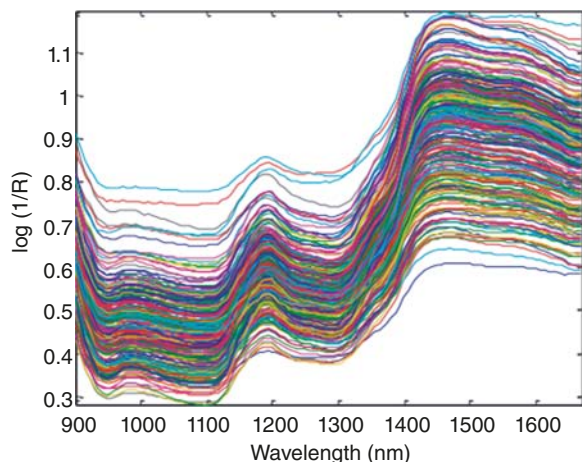


**Figure 13.7** Raw NIR spectra of the *Radix Pseudostellariae* calibration set.

**Table 13.1** Comparison of calibration performance for identification of the geographic origin of *Radix Pseudostellariae* with different wavelength selection methods.

Geographical origin	Wavelength selection technique	Factors	Hit rate (%)		
			Calibration set	Cross-validation set	Test set
Fujian	CARS	7	90.9	90.2	92.1
	RF	6	95.0	93.2	94.3
Anhui	CARS	7	95.7	93.7	93.4
	RF	7	96.2	91.7	93.4
Guizhou	CARS	7	95.5	91.5	95.5
	RF	7	96.6	93.2	95.5

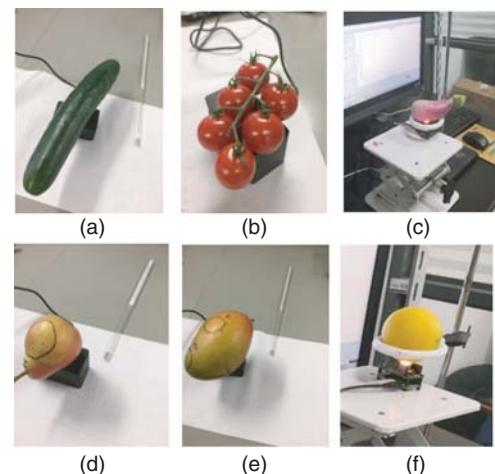
random frog (RF) [23] algorithms were applied for wavelength selection, to improve the identification accuracy of the partial least squares regression discriminant analysis (PLS-DA) model.

As shown in Table 13.1, the RF algorithm yields a better wavelength optimization than the CARS. For the *Radix Pseudostellariae* from Fujian province, the prediction hit rates were 95.0, 93.2, and 94.3% for the calibration set, cross-validation set, and test set, respectively; the analogous figures for samples from the Anhui province were 96.2, 91.7, and 93.4%, and samples from Guizhou were predicted with hit rates of 96.6, 93.2, and 95.5%. Lin et al. [21] also reported similar NIR spectroscopic investigations with a benchtop instrument combined with support vector data description (SVDD), however, with a somewhat lower identification hit rate of 92.5% for a test set. Nevertheless, both studies demonstrate that handheld NIR spectroscopy can be used for rapid on-site identification of the geographic origin of *Radix Pseudostellariae*.

#### 13.4.4 Measurement of Fruit and Vegetable Freshness

The freshness of fruits and vegetables is an important consumer-relevant everyday life issue. In order to test the feasibility of monitoring this parameter, time-dependent NIR spectroscopic measurements of selected fruits and vegetables were conducted with a handheld FT-NIR spectrometer (Figure 13.8) during storage at room temperature and in a refrigerator, respectively, and subsequent evaluation of the spectroscopic data by PCA. Contrary to what some manufacturers of handheld NIR spectrometers claim, however, no day-to-day trend in spectral changes

**Figure 13.8** Investigated vegetables (a) cucumber, (b) cherry tomatoes, and (c) radish and fruits (d) pear, (e) mango, and (f) lemon.



could be detected due to decreasing freshness. Only a small proportion of the investigated fruits and vegetables (cherry tomatoes, radishes, and lemons) provided rudiments of discrimination trends that allowed – at best – to discriminate fresh material from material that had been stored at least several days. As an example, the raw and pretreated (first derivative + SNV) spectra of lemons, measured during storage for 11 days at 20 °C, are shown with their corresponding PCA 3D score plot for the days 1, 7, and 11 in Figure 13.9. In view of these rather poor results, we would certainly not categorize the evaluation of freshness as a viable application for handheld NIR spectroscopy.

#### 13.4.5 Authentication of Fish

To conclude the section on qualitative applications with a successful case study, the authentication of fish shall serve as an example. A report on one of the largest surveys conducted to date about seafood fraud revealed that one-third of seafood species purchased at restaurants and grocery stores in cities across the United States were mislabeled [24]. The study was conducted by Oceana, a nonprofit international advocacy group, over a period of two years from 2010 to 2012, when over 1200 samples were collected from 674 retail outlets in 21 US states. Deoxyribonucleic acid (DNA) testing was performed on all the fish samples to identify the fish species and uncover mislabeling. Similar conclusions could be drawn from a previous Congressional Research Service Report regarding combating fraud and deception in seafood marketing [25]. As a typical example, the aquaculture catfish (*Pangasius*, Vietnam) and the tilapia (Victoria Lake, Africa) have become popular, relatively low priced edible fish in numerous countries, but have come under criticism for their extensive treatment with pesticides and antibiotics and as ecologically harmful, belonging to the 100 most dangerous alien species. Thus, it would be desirable if these fish can be unambiguously identified and discriminated in their whole fish or fillet form from any other high-quality species.

In this respect, handheld NIR spectroscopy has been demonstrated as an extremely valuable analytical tool to authenticate whole fish or fish fillets of superior species from cheaper substitutes [9, 26]. As a typical example, the measurement setup for a handheld FT-NIR spectrometer, the diffuse reflection spectra (including the truncation limits for calibration use), and the 2D (PC1/PC2) score plot of the PCA model derived from 40 spectra each of samlet and salmon trout species are shown in Figure 13.10a–c. These results give hope that in the near future the situation regarding commercial fraud in seafood marketing can be alleviated significantly, because in view of the flexibility of the experimental setup with handheld instruments, not only corporate enforcement bodies but also customers would have a very fast on-site measurement tool at hand to distinguish lower quality from superior quality seafood in mislabeling attempts.

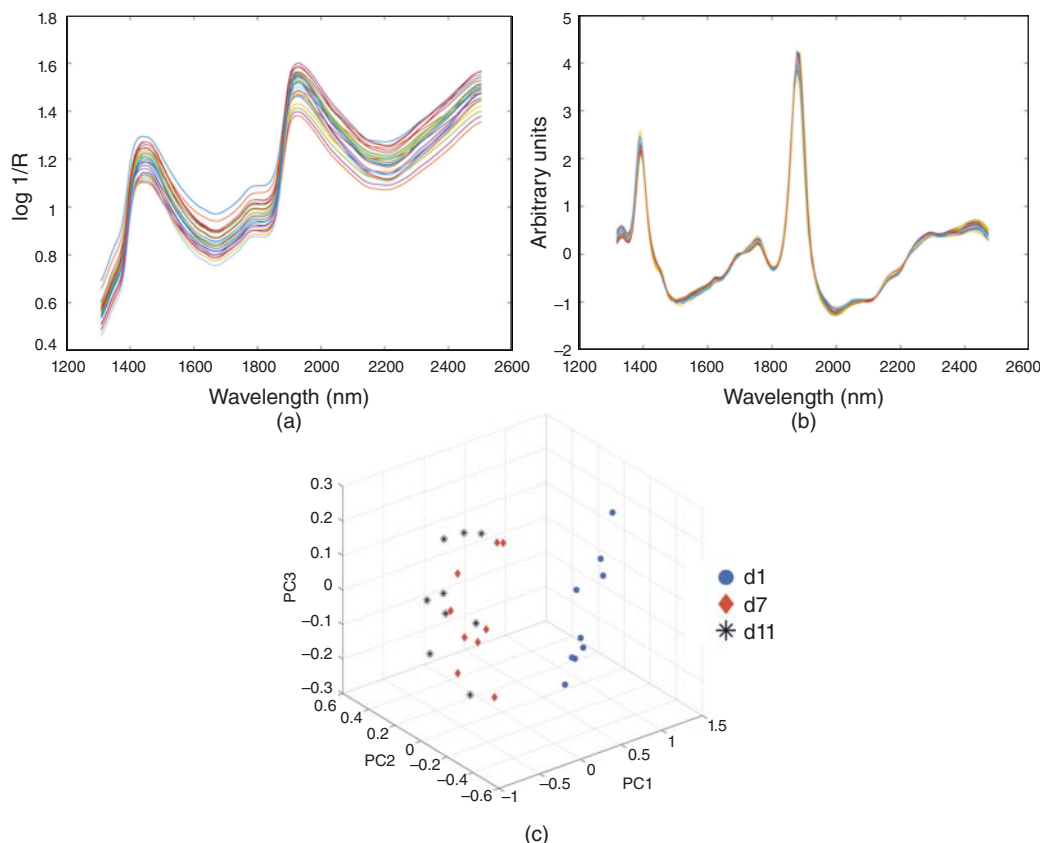


**Figure 13.9** Raw NIR spectra (a), first derivative + SNV pretreated and truncated (1309–2503 nm) NIR spectra (b), and PCA 3D score plot (c) for the lemons stored for 11 days at 20 °C.

## 13.5 Quantitative Analyses with Handheld NIR Spectrometers

### 13.5.1 Determination of Soluble Solids Content in Apples

In this example, a method for the rapid and nondestructive quantitative analysis of soluble solids content (SSC [ $^{\circ}$ Brix]) in apples was conducted with the DLP NIRScan Nano EVM. A total of 90 Fuji apples were purchased from the local supermarket (Zhenjiang, Jiangsu, China). The SSC was measured using a portable refractometer (WZ-103, TOP Instrument Co. Ltd, Zhejiang, China) based on National Standard Methods GB 12295-90. On the equator of each apple, a point was selected, and the diffuse reflection NIR spectrum was recorded (Figure 13.11). The spectral range was 900–1650 nm, and 32 scans were coadded. After each measurement, the sample was rotated approximately 120°, and the average of the three spectra was used as the final raw spectrum. For the reference measurement, a certified 99% Spectralon™ reflectance standard (Labsphere Inc., North Sutton, NH, USA) was used.

The detailed statistical results of the SSC in the calibration and test sets are shown in Table 13.2. The range, mean, and standard deviation of the calibration set were 9.10–17.80, 14.34, and 1.49  $^{\circ}$ Brix, respectively. Therefore, the samples collected as a calibration set have significant differences, which is beneficial for the calibration and the prediction of unknown samples. The statistical parameters for the test set (30 samples) were similar to that for the calibration set, indicating that the test set was suitably selected for the validation of the calibration model.

The raw spectra of the calibration set are shown in Figure 13.12. The most prominent absorption bands can be assigned to the second overtones of the  $\nu(\text{O-H})$  (950 nm) and  $\nu(\text{C-H})$  (1180 nm) stretching vibrations and the first

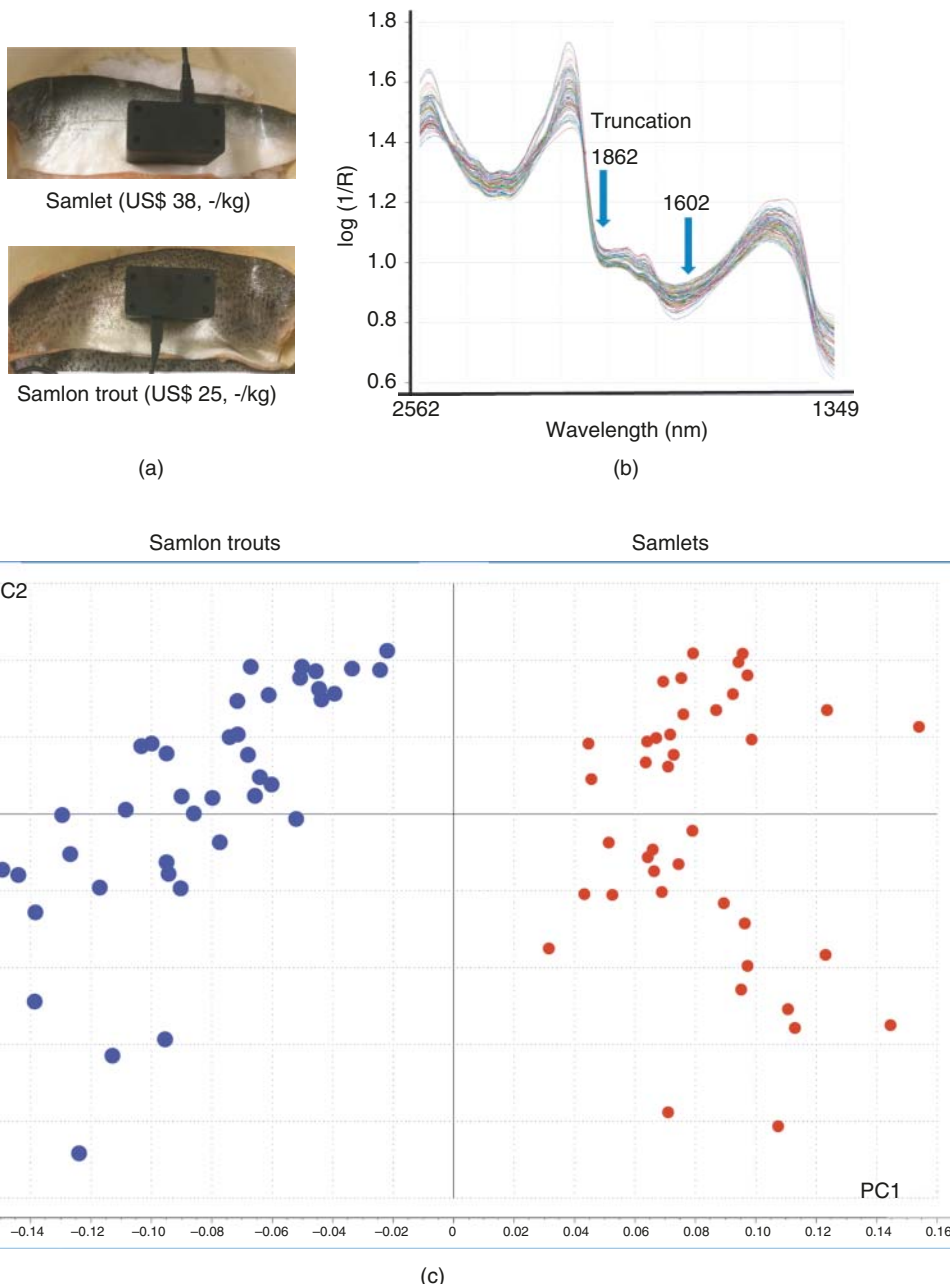


**Figure 13.10** Experimental measurement setup (a), diffuse reflection spectra after EMSC (including truncation limits for calibration use) (b), and 2D (PC1/PC2) score plot (c) based on the PCA of 40 calibration spectra each of the investigated samlets and salmon trouts.

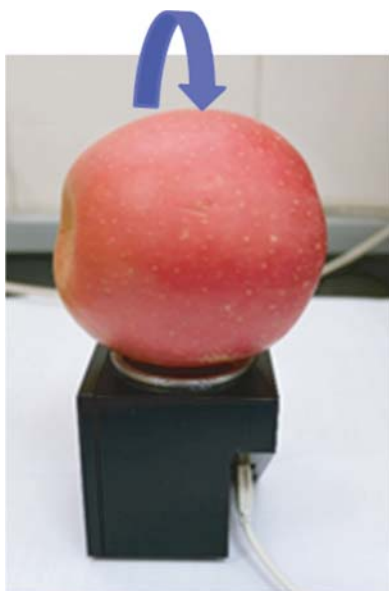


**Figure 13.11** Sample presentation for the measurement of diffuse reflection NIR spectra of an apple.

**Table 13.2** Statistical parameters of SSC ( $^{\circ}$ Brix) in the calibration and test set (CV: coefficient of variation).

	Calibration	Test
Sample number	60	30
Range (SSC, $^{\circ}$ Brix)	9.10–17.80	10.50–17.70
Mean (SSC, $^{\circ}$ Brix)	14.34	14.37
Standard deviation	1.49	1.45
CV (%)	10.39	10.06

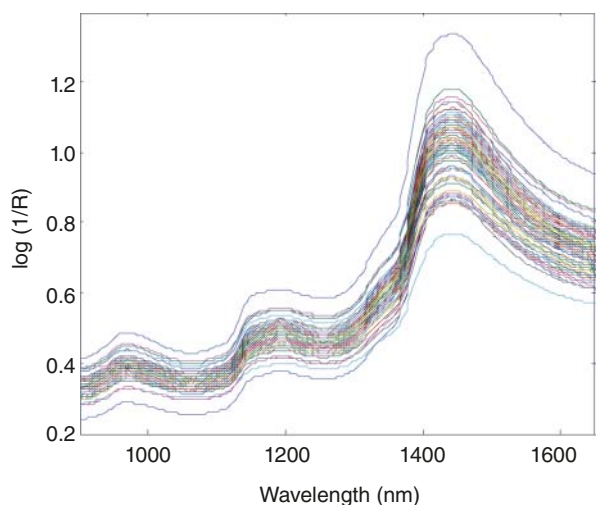


**Figure 13.12** The raw NIR spectra of the calibration set of the investigated apples.

**Table 13.3** Statistical parameters for the calibrations based on different variable selection techniques (the technique yielding the best results is shown in bold).

Methods	LVs	SVs	RMSEC	R <sub>C</sub>	RMSECV	R <sub>CV</sub>	RMSEP	R <sub>P</sub>
PLS	7	209	0.4990	0.9412	0.7310	0.8716	0.6748	0.8847
RF-PLS	9	50	0.3678	0.9685	0.5157	0.9373	0.5388	0.9285
<b>CARS-PLS</b>	<b>6</b>	<b>20</b>	<b>0.3950</b>	<b>0.9636</b>	<b>0.4870</b>	<b>0.9442</b>	<b>0.5575</b>	<b>0.9223</b>
UVE-PLS	6	99	0.4717	0.9477	0.6418	0.9013	0.6308	0.9019

overtone of the  $\nu(\text{O-H})$  (1450 nm) stretching vibration. After pretreatment of the spectra by first derivative (with a Savitzky–Golay smoothing procedure with a five data point window and a second-order polynomial) and SNV, the CARS, RF, and uninformative variable elimination (UVE) wavelength selection techniques were used for the optimization of the calibration performance. The comparison of the results is summarized in Table 13.3.

Interestingly, the calibrations with selected wavelength variables showed better performance compared to the PLS model that used all wavelength variables. The number of variables selected by UVE, RF, and CARS was 99, 50, and 20, respectively. The variables selected by CARS yielded the best calibration performance (see bold symbols in Table 13.3) and are shown in detail in Figure 13.13. The values of root-mean-square error of calibration (RMSEC), root-mean-square error of cross-validation (RMSECV), and root-mean-square error of prediction (RMSEP) were 0.3950, 0.4870, and 0.5575 °Brix, respectively, and the corresponding parameters of R<sub>C</sub>, R<sub>CV</sub>, and R<sub>P</sub> were 0.9636, 0.9442, and 0.9223, respectively. The scatter plot for the actual versus predicted SSC values is shown in Figure 13.14, which demonstrates that the predictive ability of the CARS-PLS calibration model was excellent.

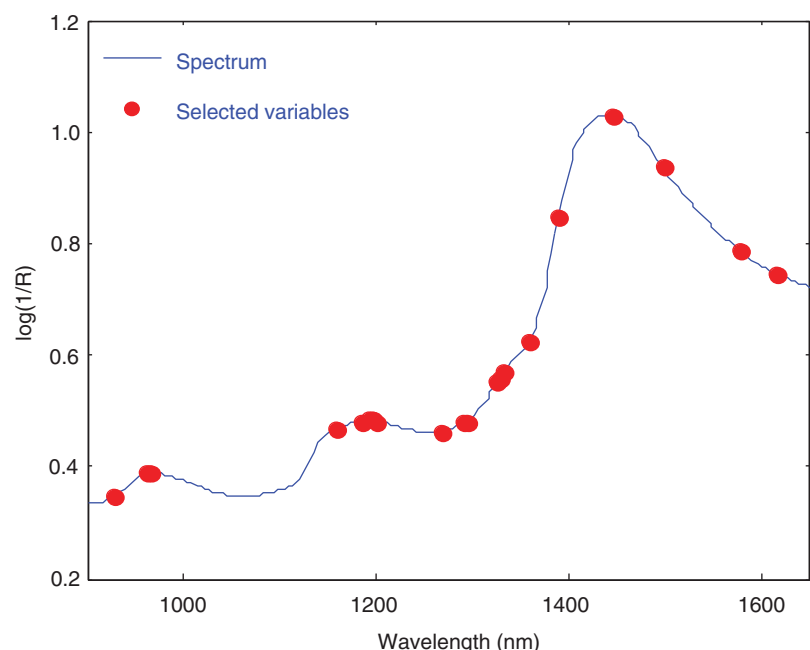


**Figure 13.13** The distribution of the 20 wavelength variables selected by CARS for the determination of the SSC (°Brix).

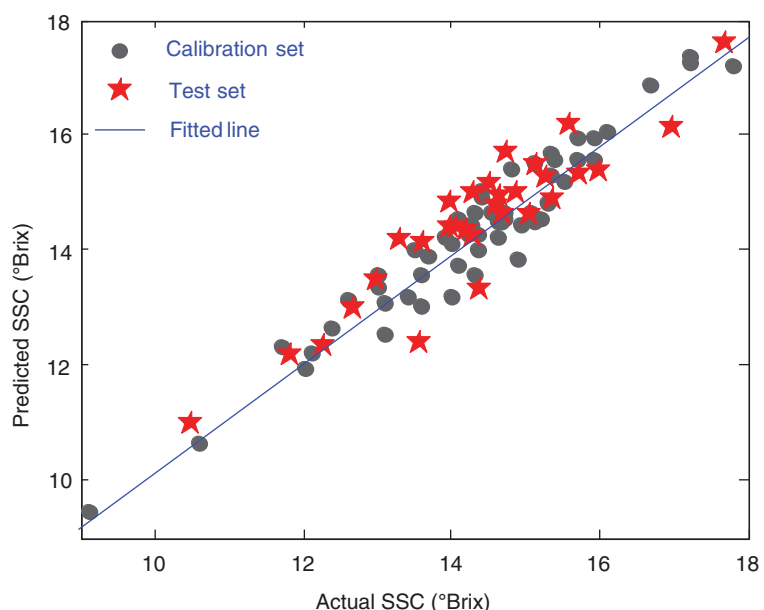


**Figure 13.14** Actual/predicted scatter plot of the CARS-PLS calibration for SSC (°Brix).

### 13.5.2 Quantitative Determination of the Ingredients in Caryophylli Flos

*Caryophylli flos*, commonly known as cloves, are the dried buds of the Myrtaceae plant (*Syzygium aromaticum* (L.) Merrill et L.M. Perry). It has a planting history of over 1000 years and shows a wide range of applications in the food and pharmaceutical industries. It is a natural, non-harmful preservative and flavoring substance applied in food products [27]. In addition, *caryophylli flos* has antioxidant, antibacterial, antipyretic, analgesic, and anti-inflammatory pharmacological effects [27–30].

The main active ingredients in *caryophylli flos* are eugenol, beta-caryophyllene, and eugenyl acetate [31], which are strongly related to the quality of *caryophylli flos*. The content of eugenol, which dictates the quality of the *caryophylli flos*, must be not less than 11 % (w/w) based on the Pharmacopoeia of the People's Republic of China [20]. The commonly used method for the determination of the three ingredients in *caryophylli flos* is gas chromatography (GC) [20]. However, because of the time-consuming analysis and high cost, the GC method is not necessarily the technique of choice. The main objective of this application example was, therefore, to investigate the feasibility of a faster and simpler determination of the three main ingredients in *caryophylli flos* by handheld NIR spectroscopy.

Samples (dried buds of *caryophylli flos*) were acquired from two of the largest traditional Chinese medicine markets, Bozhou city (Anhui, China) and Yulin city (Guangxi, China). A total of 104 batches of *caryophylli flos* were collected, originating from Indonesia, Madagascar, the Philippines, Somalia, and Malaysia. Before scanning, *caryophylli flos* samples were pulverized to powders by a pulverizer and passed through a 40-mesh sieve. The reference values were determined by the GC method.

The DLP NIRScan Nano EVM (Texas Instruments, Dallas, TX, USA) was used to collect the NIR spectra of samples. A 1.5–2 cm powder layer was placed in a cup with a 1 mm-thick quartz window in the bottom, through which the diffuse reflectance spectra were recorded. Each individual spectrum was the average of 32 scans, with 209 wavelength variables over the wavelength range 909–1649 nm. A certified 99% reflection standard (Labsphere, North Sutton, NH, USA) was used to measure the reference spectrum. After each measurement, the sample cup was rotated by 120°, and the average of three spectra was used as the final raw spectrum.

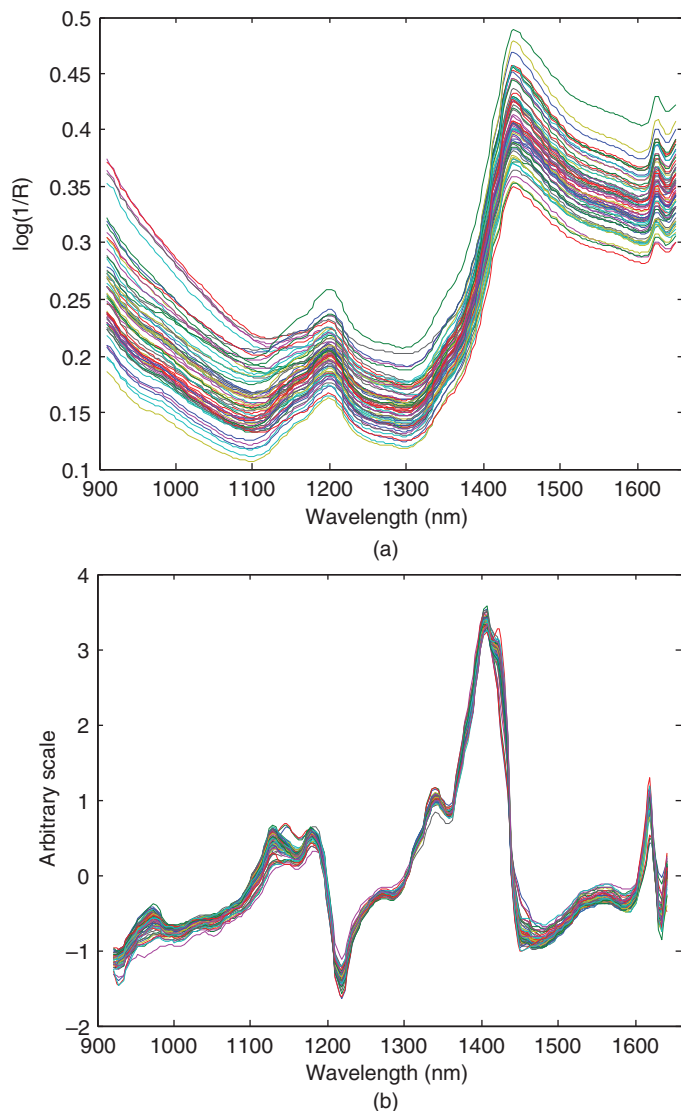


**Figure 13.15** NIR spectra of caryophylli flos, (a) raw data, (b) pretreated by first derivative and SNV.

The raw NIR spectra of the samples are shown in Figure 13.15a. The band at about 1200 nm belongs to the second overtone of  $\nu(\text{C-H})$  stretching vibrations, and the band at about 1450 nm is the first overtone of the  $\nu(\text{O-H})$  stretching vibration. Different spectral pretreatments showed significant effects on the calibration results. The combination of the first derivative followed by SNV (Figure 13.15b) yielded the best performance for the calibration of eugenol and beta-caryophyllene, while the optimum results for eugenol acetate were achieved by pretreatment in the reversed sequence (SNV followed by first derivative). The CARS wavelength selection method was applied because it showed a distinct increase in predictive accuracy [32]. The number of variables retained for modeling was 38, 15, and 36 for eugenol, beta-caryophyllene, and eugenyl acetate, respectively, which is a significant reduction compared with the original 209 variables of the raw spectra (Figure 13.16). Although the selected variables differ for the three compounds, the majority were located in two wavelength ranges: 1320–1500 and 1560–1660 nm. The range 1320–1500 nm is characteristic of the  $2\times\nu(\text{CH}_2) + \delta(\text{CH}_2)$  combination band and the first overtone of the

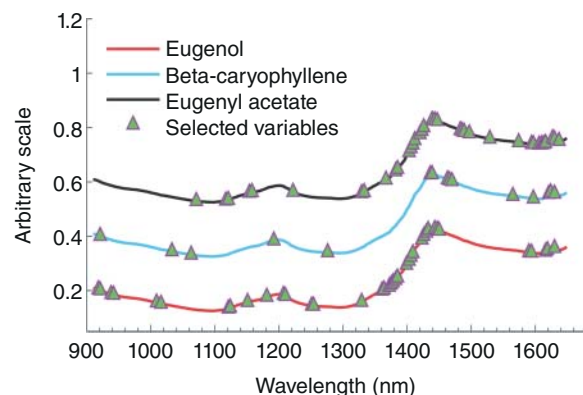


**Figure 13.16** Wavelength variables selected for the calibration of eugenol, beta-caryophyllene, and eugenyl acetate by the CARS method.

**Table 13.4** Statistical parameters of the PLS calibrations for the different ingredients with the CARS-selected wavelength variables.

Ingredients	Selected variables	Factors	SEP (% (w/w))			$R^2$		
			Calibration	CV	Test	Calibration	CV	Test
Eugenol	38	5	0.46	0.58	0.60	0.955	0.93	0.89
Beta-caryophyllene	15	7	0.11	0.14	0.14	0.89	0.85	0.86
Eugenyl acetate	36	5	0.30	0.36	0.38	0.89	0.86	0.80

$\nu(\text{O-H})$  stretching vibration, whereas the 1560–1660 nm range encompasses primarily the first overtone regions of the  $\nu(\text{N-H})$  and  $\nu(\text{C-H})$  stretching vibrations. Thus, the chosen wavelength variables cover absorption regions of chemical functionalities that are contained in the compounds under quantitative investigation.

The results of the PLS calibration statistics for the different ingredients are summarized in Table 13.4. The ratios of standard error of prediction to standard deviation (RPDs) for eugenol, beta-caryophyllene, and eugenyl acetate were 4.7, 3.0, and 3.6, respectively. In summary, these results indicate that the expected accuracy of the predictions based on the PLS calibrations is suitable for the quantitative determination of the three ingredients and the substitution of the GC method by the faster handheld NIR spectroscopic approach.

The reference versus predicted scatter plots for the calibration, cross-validation, and test sets of the three ingredients are shown in Figure 13.17a–c. These graphs basically reflect the statistical parameters of the different calibration models outlined in Table 13.4. Thus, the PLS calibration models for beta-caryophyllene and eugenyl acetate have somewhat lower prediction performance compared with the PLS model for eugenol.

### 13.5.3 Quantitative Determination of Active Ingredients in Pharmaceutical Formulations

The main reason for the inclusion of this case study as a separate section is to compare the performance of handheld NIR spectrometers based on different instrumental principles for a quantitative application example [10], in analogy to Sections 13.4.1 and 13.4.2 for qualitative discrimination purposes. A critical analysis of the reasons for differences in prediction accuracy will then contribute toward guidelines regarding the selection of the most suitable instrument for a specific analytical task.

Within the scope of process analytical technology (PAT), NIR spectroscopy has become an indispensable tool for pharmaceutical production and quality control [33–36]. Whether it is qualitative NIR investigations for the identity control of incoming raw materials, or quantitative analysis of the final pharmaceutical formulations,

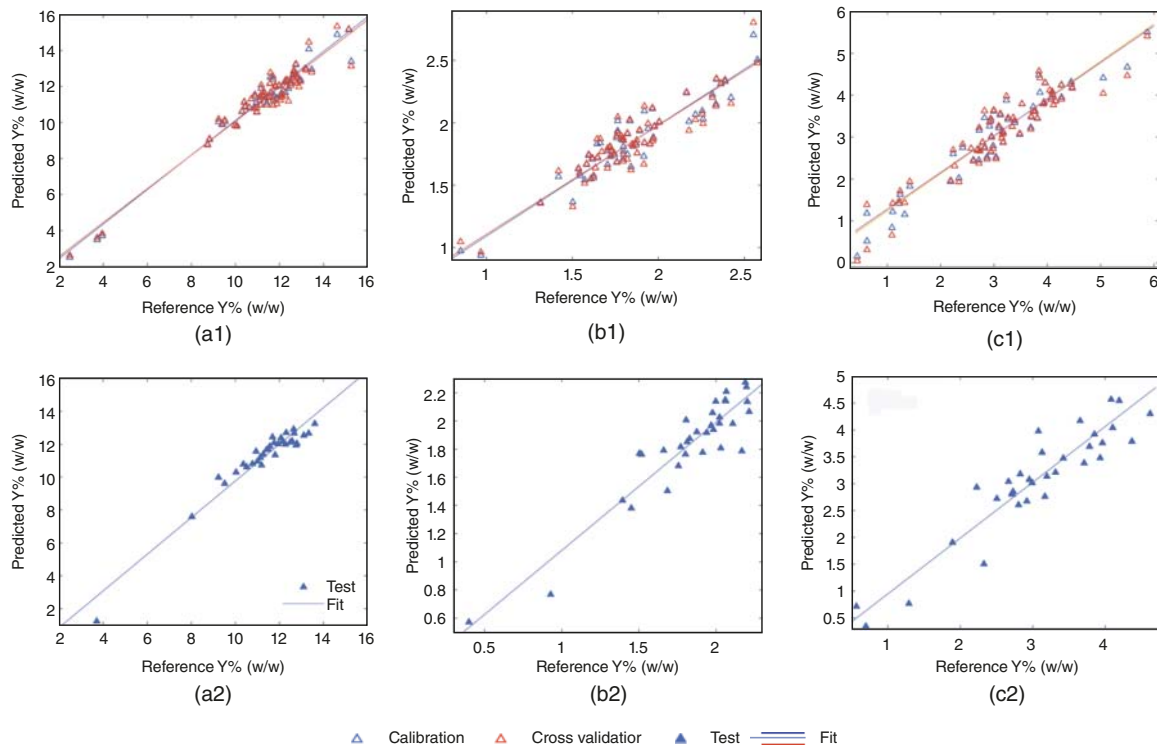


**Figure 13.17** Reference versus predicted scatter plots for the calibration, cross-validation, and test sets of eugenol (a1, a2), beta-caryophyllene (b1, b2), and eugenyl acetate (c1, c2).

both applications are essential steps in the pharmaceutical process chain [37–41]. Because the majority of pharmaceutical analyses are still performed in the quality control laboratory remotely from the production facility, the availability of results is delayed, which limits the frequency of analyses and the optimization of the production process. Novel handheld instrumentation, capable of performing a rapid on-site analysis of process samples, shows promise as a critical tool to further advance the effectiveness of quality control in the pharmaceutical industry.

In the quantitative case study under discussion, the investigated solid drug formulations consisted of mixtures of the three crystalline active ingredients acetylsalicylic acid (ASA), ascorbic acid (ASC), and caffeine (CAF) with the two amorphous excipients: cellulose (CE) and starch (ST) [10]. A set of 34 samples (10 g each) was prepared by weighing varying amounts of the three active ingredients in the min/max concentration range 15.08/24.84% (w/w) ( $\Sigma$  60.00% (w/w)) with equal amounts (40.00% (w/w)) of a 1:3 (w/w) mixture of cellulose and starch into cylindrical flat bottom vials with plastic stoppers. Another 16 samples were prepared as a test set, in the same concentration range, to control the prediction performance of the calibration models. Selected statistical parameters of the content of active ingredients in the calibration and test set samples are summarized in Table 13.5. Each sample was homogenized by mixing for 120 s at 2000 rpm in a SpeedMixer<sup>TM</sup> (Hauschild & CoKG, Hamm, Germany) based on a dual asymmetric centrifuge (DAC) principle.

The NIR spectra of the calibration and test samples were measured in diffuse reflection after transferring the solid formulations from the glass containers into a Petri dish ( $\varnothing$  6.0 cm) that was rotated on a platform at 2 rpm to average any residual heterogeneities. This sample presentation geometry is exemplarily shown for the Si-Ware Systems FT-NIR spectrometer in Figure 13.18. The reference measurements were performed with a 99% Spectralon<sup>TM</sup> reflectance standard (Labsphere Inc., North Sutton, NH, USA). In the first step, the wavelength scale

**Table 13.5** Selected statistical parameters of the active ingredient contents in the calibration and test set samples.

Statistical parameters	ASA % (w/w)			ASC % (w/w)			CAF % (w/w)		
	Total	Cal.	Test	Total	Cal.	Test	Total	Cal.	Test
Mean	20.14	20.22	19.99	20.11	20.20	19.93	19.74	19.83	19.56
Max	24.84	24.84	24.17	24.70	24.70	24.36	24.78	24.78	24.13
Min	15.93	15.93	15.98	15.08	15.08	15.36	15.09	15.09	15.39
Range	8.91	8.91	8.19	9.62	9.62	9.00	9.69	9.69	8.74
Std. dev.	2.53	2.59	2.48	2.89	2.96	2.83	2.79	2.86	2.71
Variance	6.40	6.68	6.15	8.35	8.74	8.02	7.76	8.16	7.33

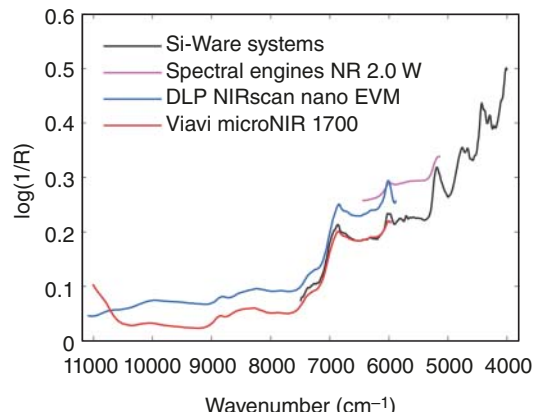
**Figure 13.18** Sample presentation geometry for the measurements of the pharmaceutical formulations with the Si-Ware Systems FT-NIR spectrometer.

of the spectra was transformed into wavenumbers, because, despite being an FT-NIR spectrometer, Si-Ware's software reports the data on a wavelength scale. In Figure 13.19, the NIR spectra measured with the four different handheld NIR spectrometers are compared for sample 1. From inspection of these spectra, several features can be noted:

- The Si-Ware Systems spectrometer covers the largest wavenumber range encompassing the important CH and NH combination region ( $4000\text{--}4800\text{ cm}^{-1}$ ), the OH combination region (at about  $5200\text{ cm}^{-1}$ ), and the CH, NH, and OH first overtone regions ( $5400\text{--}7300\text{ cm}^{-1}$ ).
- The NIR spectra recorded with the Spectral Engines NR 2.0 W instrument covers only the  $\nu(\text{CH})$  first overtone range and a small part of the OH combination region.
- The spectra recorded with the DLP NIRscan Nano EVM and Viavi MicroNIR 1700 instruments are similar and comprise the  $\nu(\text{OH})$  and  $\nu(\text{NH})$  first and second overtones and the  $\nu(\text{CH})$  second overtone and combination regions.

Before further pretreatment, the noisy spectral regions of the different spectrometers were truncated, and the following wavenumber ranges were used for quantitative evaluation: Si-Ware Systems,  $7504\text{--}4001\text{ cm}^{-1}$

**Figure 13.19** NIR spectra of sample #1 measured with the four different handheld NIR spectrometers.



(1330–2500 nm); Spectral Engines NR 2.0-W, 6451–5128 cm<sup>-1</sup> (1550–1950 nm); DLP NIRscan Nano EVM, 11101–5879 cm<sup>-1</sup> (900–1701 nm); and Viavi MicroNIR 1700, 11012–5966 cm<sup>-1</sup> (908–1676 nm). Then, the SNV method was applied as a scatter correction procedure, and the calibration sets were tested for outliers that were subsequently excluded from calibration development. Calibration statistic parameters,  $R^2$ , RMSECs, and RPDs, were used to evaluate the calibration performance, and results can be comparatively categorized:

1. All four instruments provide the best (and comparable) calibration results for CAF. With average values for RMSE (0.589 % (w/w)) and RPD (4.56) and correlations between 0.94 and 0.99, this active ingredient can be predicted in unknown samples with good performance.
2. In contrast to the results for CAF, the calibration parameters of the other active ingredients vary depending on the instrument in use.
3. Although the calibration results for ASA and ASC are of slightly lower quality compared with CAF, the best overall results were achieved with the LVF spectrometer.
4. Second in calibration performance – with only slightly worse results for ASC – is the spectrometer based on the digital micromirror device.
5. Although still within the range of applicability for quantitative analysis, the lowest overall performance – with significantly lower prediction capabilities for either ASA or ASC – was shown by the instruments based on the Michelson interferometer and the Fabry–Perot tunable filter.

The instrument-specific calibration statistics parameters for the three active ingredients are summarized in Table 13.6 and clearly support the above conclusions. Thus, the following trend of the different instruments regarding their quantitative analytical performance for the investigated pharmaceutical formulation was obtained: linear variable filter > digital mirror device > Fabry–Perot tunable filter > Michelson interferometer.

The consistently good results for the prediction of CAF by all instruments can be explained by inspection of Figure 13.20. In all instrument-specific wavenumber ranges, CAF has dominating absorption bands. This effect is also reflected by inspection of the instrument-specific CAF calibration loading plots of the first four factors (not shown here) that explain between 88 and 98 % of the variance. The superior performance of the linear variable filter and digital mirror device spectrometers for the prediction of ASC and ASA, relative to the Fabry–Perot tunable filter instrument, is based on the comparatively narrow spectral range of the latter spectrometer that contains only a few characteristic absorption features of these analytes. Surprisingly, the FT-NIR instrument, which had the largest spectral range, showed a lower performance for ASC compared with all other instruments. Reasonable explanations could be the rather small spectral contributions of this active ingredient in the available wavenumber range (Figure 13.20) and the low S/N ratio (2820:1) of the spectra measured with this instrument. Having said that, interestingly, in Sections 3.1.1 and 3.1.2 and in very recent publications [16, 18], it was demonstrated that

**Table 13.6** The statistical parameters of the instrument-specific calibration models for the three active ingredients.

Spectrometers	Ingredients	Data sets	Outliers	Factors	RMSE (% w/w)	Bias (% w/w)	Slope	Offset (% w/w)	Correlation	RPD
Si-Ware Systems	ASA	Calibration	4	6	0.52	0.00	0.96	0.81	0.98	3.12
		Validation	4	6	0.83	-0.02	0.94	1.23	0.95	
		Test	3	6	1.05	0.18	0.88	2.55	0.90	
	ASC	Calibration	3	4	1.19	0.00	0.82	3.58	0.91	2.16
		Validation	3	4	1.37	0.00	0.81	3.96	0.88	
		Test	2	4	2.17	0.61	0.85	3.64	0.76	
	CAF	Calibration	2	5	0.45	0.00	0.97	0.52	0.99	4.21
		Validation	2	5	0.68	0.01	0.96	0.79	0.97	
		Test	1	5	0.73	-0.15	1.01	-0.35	0.96	
Spectral Engines NR 2.0 W	ASA	Calibration	3	5	0.85	0.00	0.88	2.35	0.94	2.33
		Validation	3	5	1.11	0.02	0.85	3.09	0.90	
		Test	2	5	1.66	1.03	1.23	-3.63	0.94	
	ASC	Calibration	2	4	0.77	0.00	0.93	1.50	0.96	3.22
		Validation	2	4	0.92	0.01	0.91	1.84	0.94	
		Test	3	4	1.34	-0.33	1.25	-5.49	0.95	
	CAF	Calibration	2	6	0.51	0.00	0.96	0.73	0.98	4.03
		Validation	2	6	0.71	-0.04	0.95	0.97	0.96	
		Test	0	6	0.52	0.18	0.96	0.90	0.98	
DLP NIRscan NANO EVM	ASA	Calibration	3	5	0.54	0.00	0.95	0.97	0.98	3.70
		Validation	3	5	0.70	0.00	0.93	1.34	0.96	
		Test	3	5	1.10	0.21	0.95	1.26	0.90	
	ASC	Calibration	4	3	0.72	0.00	0.94	1.29	0.97	3.22
		Validation	4	3	0.92	-0.03	0.89	2.16	0.95	
		Test	0	3	0.86	0.12	0.87	2.67	0.95	
	CAF	Calibration	1	6	0.39	0.00	0.98	0.39	0.99	5.40
		Validation	1	6	0.53	-0.02	0.95	1.03	0.98	
		Test	1	6	0.85	0.06	0.97	0.61	0.94	
Viavi MicroNIR 1700	ASA	Calibration	5	5	0.57	0.00	0.95	0.98	0.98	3.65
		Validation	5	5	0.71	0.03	0.92	1.65	0.96	
		Test	2	5	0.70	-0.11	1.11	-2.29	0.97	
	ASC	Calibration	4	3	0.55	0.00	0.96	0.73	0.98	4.55
		Validation	4	3	0.65	-0.02	0.96	0.83	0.97	
		Test	0	3	0.79	-0.03	0.92	1.59	0.96	
	CAF	Calibration	2	5	0.48	0.00	0.97	0.57	0.99	4.61
		Validation	2	5	0.62	-0.08	0.96	0.64	0.98	
		Test	0	5	0.53	0.02	0.92	1.56	0.98	

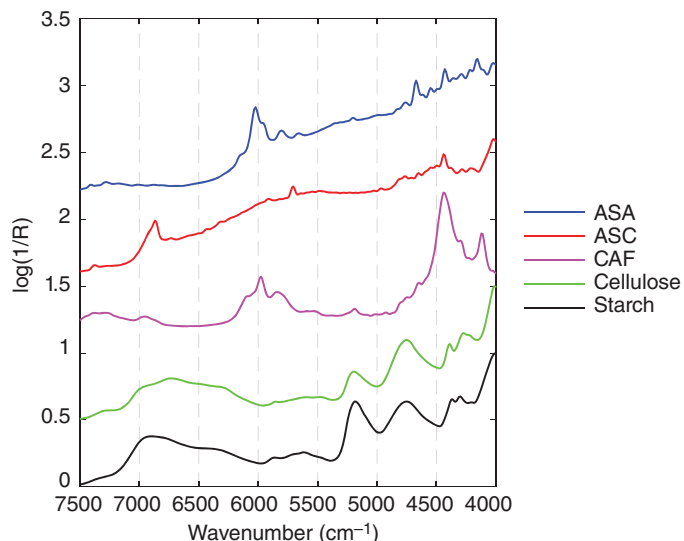


**Figure 13.20** Offset NIR spectra of the five pure ingredients recorded with the Si-Ware Systems FT-NIR spectrometer.

in comparative qualitative investigations of polymers and textiles with the same four spectrometers, the FT-NIR instrument yielded the best identification and discrimination results by PCA and SIMCA.

#### 13.5.4 Quantitative NIR Spectroscopic Analysis of Hydrocarbon Contaminations in Soil

The contamination of soil with hydrocarbons (diesel, oil, gasoline) due to accidents or leakages is a widespread phenomenon with potential health risks. Until several years ago, no technique has been available for fast on-site identification and quantitative determination of these contaminants. Such data, however, would be necessary for the assessment of decontamination measures to be taken for the area under consideration, either by excavation or a biotechnical approach. In 2010, diffuse reflection measurements were conducted with one of the first – although comparatively heavy – portable NIR spectrometers (Phazir™, see below) for the qualitative and quantitative analysis of hydrocarbon contaminations in different types of soil, and calibration models (PCA and PLS) for gasoline, diesel, and oil contaminations in soil were published in 2013 [11]. Almost at the same time, the application of handheld FT-IR spectroscopy for diffuse reflection measurements of total petroleum hydrocarbon (TPH) content in soil was commercialized [42]. Notwithstanding its market success, the reasons why the NIR spectroscopic approach should be favored over the MIR technique are manifold:

1. The weight and the price of present handheld NIR systems are only a fraction of this portable FT-IR system.
2. The advertisement for the FT-IR system trivializes the experimental effort to a “pull-the-trigger” technique that provides, within seconds, TPH contaminations down to – in our opinion – unrealistically low ppm levels.
3. Additionally, major doubts are appropriate regarding the applicability of a universal calibration for unknown soil samples.

Thus, we deem it justified to outline the performance of handheld NIR spectroscopy for the qualitative identification of hydrocarbon contaminations, as well as their quantitative determination in soil, as a more realistic alternative to the handheld FT-IR approach. For a detailed account of the investigations, the interested reader is referred to the original literature reference [11].

For the preparation of calibration and test samples, the standard soil types 2.1 and 2.4 (Landwirtschaftliche Untersuchungs- und Forschungsanstalt [LUFA], Speyer, Germany) were used, because they represent the

extremes of silty sand and clayey loam, respectively. Homogeneous diesel/oil contaminated soil samples (concentration range from 0 to 13% (w/w)) were prepared by dissolving the corresponding amounts of sulfur-free diesel (Aral AG, Bochum, Germany) and oil (Aral Tronic 15W-40 SAE, Aral AG, Bochum, Germany) in methylene chloride ( $\text{CH}_2\text{Cl}_2$ ) and saturating the adequate amount of soil with this solution. Then, the methylene chloride was completely evaporated at 60 °C in a drying oven, and the contaminated soil samples were transferred into a Petri dish for further spectroscopic investigations.

Due to the volatility of gasoline, the sample preparation and spectra acquisition for the calibration development was different from the experimental procedure applied for oil and diesel contamination. For the preparation of gasoline (Aral Super, RON 95, Aral AG, Bochum, Germany)-contaminated soil calibration samples, a certain amount of soil was directly placed into a Petri dish and loaded with excess gasoline [ $>11%$  (w/w)] and homogenized. During evaporation of the gasoline, fast, repeated weighing and spectra measurement steps were performed in short time intervals in order to collect spectral calibration data in the 0–11% (w/w) gasoline concentration range. Spectra of two such measurement series were combined for the development of a PLS calibration model.

The NIR measurements were conducted with the Phazir™ portable NIR spectrometer (Thermo Fisher Scientific Inc., formerly Polychromix, Tewksbury, USA) (Figure 13.21), in diffuse reflection mode, by coadding 64 scans for a spectrum. As an example, Figure 13.22 highlights the spectral changes resulting from the increase of diesel contamination (between 0.23 and 4.85% (w/w)) in soil type 2.1, which were eventually used as the basis for the development of quantitative calibration models. Contrary to gasoline, for diesel and oil, three replicate measurements were made for each sample and subsequently averaged in order to compensate for heterogeneities. The Phazir™ spectrometer is no longer the instrumental state of the art (primarily due to the comparatively large weight and price of the system), but analogous investigations have also been successfully performed with the LVF-based VIAVI MicroNIR 1700 handheld spectrometer [43].

Data pretreatment and calibration development by PCA for qualitative discrimination and cross-validated PLS for quantitation of the hydrocarbon contaminations were performed using the Unscrambler™ (v. 9.7, CAMO Software AS, Oslo, Norway) software. A set of approximately 200 samples, with a representative variation of their composition, was used for the development of a cross-validated PLS calibration model, and as a performance test, a set of samples with varying contamination concentrations across the calibration range was used as “unknowns” to predict their hydrocarbon content and compare it with their reference values. Outliers in the calibration sample

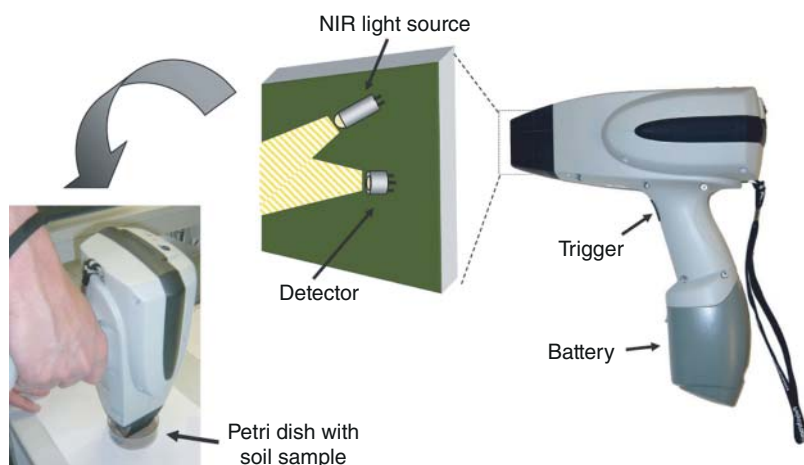
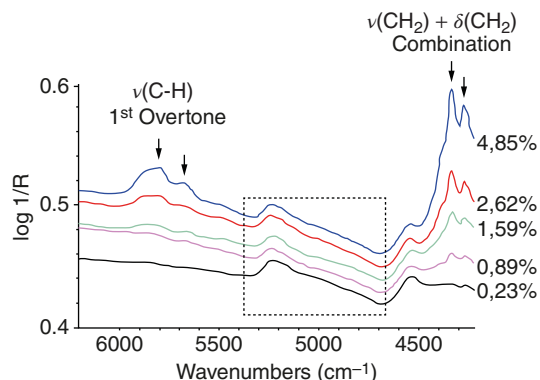


**Figure 13.21** Source and detector geometry of the Phazir NIR spectrometer (right) and diffuse reflection measurement of a soil sample in a Petri dish (left).

**Figure 13.22** Spectral changes observable in differently diesel-contaminated (0.23–4.85% (w/w)) soil 2.1 samples (--- box: water absorption region, that is truncated before PCA and PLS calibration).



set were determined by the so-called “influence plot” provided by the Unscrambler™ software. The calibration and prediction results for oil contamination in standard soil type 2.1 will be discussed in some detail.

Prior to the quantitative determination of hydrocarbon contamination, however, an identification step is required. In this context, PCA was applied to the NIR spectra of contaminated soil samples in order to explore whether such a procedure is a feasible analytical route for discrimination of different hydrocarbons. Figure 13.23 shows the NIR spectra of differently hydrocarbon-contaminated [approx. 3% (w/w)] and uncontaminated standard soil type 2.1. Visual inspection of these spectra readily allows the discrimination of gasoline contamination, whereas oil and diesel are more difficult to differentiate. In the 3D PCA score plot (Figure 13.24), however, based on the second derivative spectra and removal of the water absorption region ( $5523\text{--}4513\text{ cm}^{-1}$ ), the uncontaminated and the three contaminated soils were readily distinguished and identified. From further investigations of a series of samples with different concentrations of diesel and oil in standard soil type 2.1, the threshold value of contamination level for reliable differentiation of these two hydrocarbons was assessed at >1% (w/w).

The quantitative results shown in the following section are based on a cross-validated PLS model for oil contamination in soil type 2.1, followed by a prediction of an “unknown” test sample set. For this purpose, 199 samples with a contamination range of 0–13% (w/w) were used. The best calibration results were achieved by applying the second derivative, truncating the wavenumber region to  $6133\text{--}4224\text{ cm}^{-1}$  and eliminating the water absorption region ( $5523\text{--}4513\text{ cm}^{-1}$ ). In Figure 13.25, the second derivative calibration spectra (before elimination of the

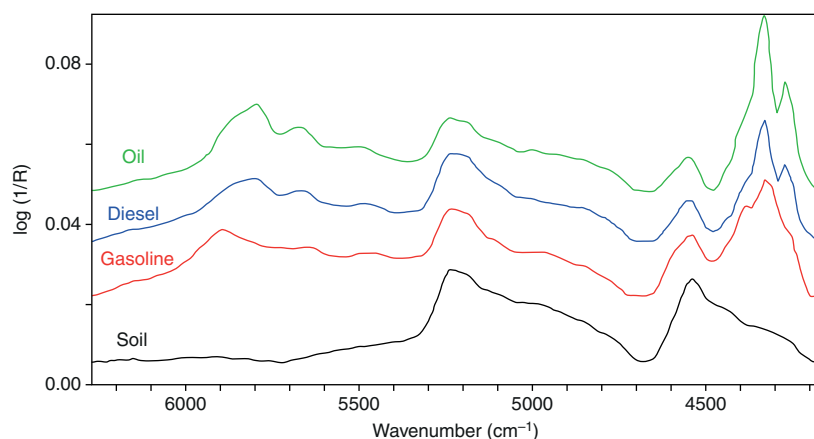


**Figure 13.23** NIR spectra of diesel-, oil-, and gasoline-contaminated (app. 3% (w/w)) and uncontaminated soil type 2.1 samples.

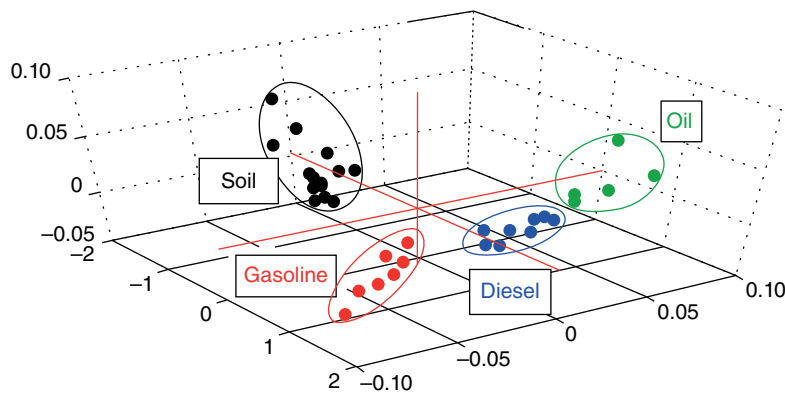


**Figure 13.24** 3D PCA score plot derived from the second derivative NIR spectra of differently hydrocarbon-contaminated and uncontaminated soil type 2.1.

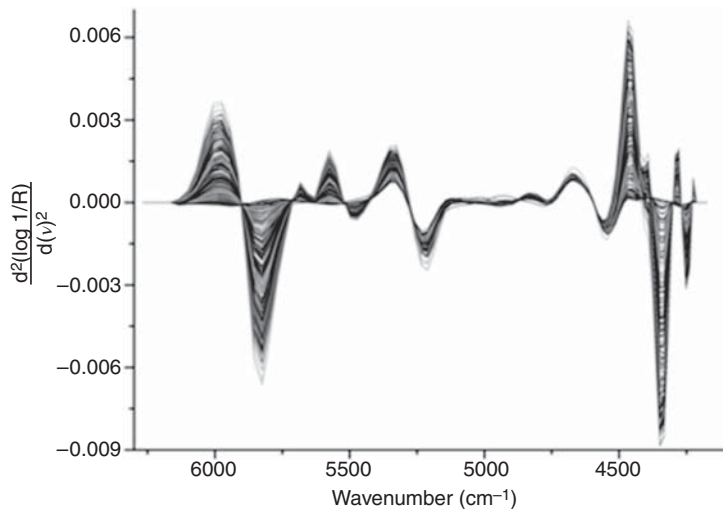


**Figure 13.25** Second derivative NIR spectra of oil-contaminated soil type 2.1 calibration samples before truncation of the water absorption region.

water region) are shown. For the final calibration model based on two factors, eight outliers were removed, and the actual versus predicted plot with the calibration and cross-validation parameters of the PLS model is shown in Figure 13.26.

In summary, the investigations have shown that based on diffuse reflection measurements with a handheld NIR spectrometer, hydrocarbon contaminants (gasoline, diesel, and oil) in the soil can be qualitatively discriminated and quantitatively determined with RMSECV values between 0.3 and 0.5% (w/w). This approach can serve as proof of concept to replace conventional separation methods, in the case of hazardous incidents with high contamination concentrations, by on-site investigations, for a fast assessment of decontamination measures and effective monitoring of their success.

Finally, it is worth mentioning that the attempt to develop calibrations for oil and diesel by combining the spectral data for different soil types had to be abandoned after it was realized that these calibrations yielded

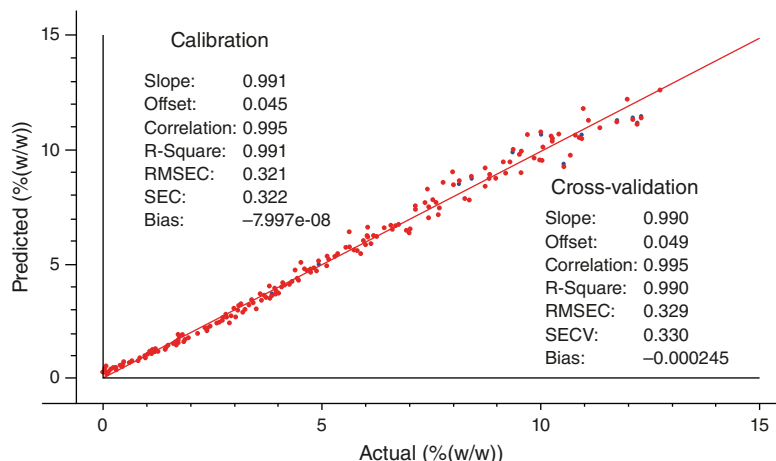


**Figure 13.26** Actual versus predicted cross-validation plot of the PLS calibration model (two factors) for oil contamination in soil type 2.1 based on second derivative NIR calibration spectra after elimination of eight outliers and truncation of the water absorption region ( $5523\text{--}4513\text{ cm}^{-1}$ ).

unacceptable deviations in the hydrocarbon concentration range <3% (w/w). Thus, in conclusion, it has to be clearly stated that neither the detection of the low ppm levels of hydrocarbon contamination nor the universal calibration claimed for the portable FT-IR technique could be achieved.

### 13.5.5 Quantitative Determination of Nutritional Parameters

This specific topic is included as a final section in this chapter because it is regularly used as a most misleading advertising point by direct-to-consumer companies regarding the performance of their “NIR scanners” with “cloud evaluation of big data.” In almost identical approaches, these companies demonstrate in their videos point-and-shoot measurement procedures of food products with their handheld instruments, disregarding any provisions for the representativity of their measurements regarding sample-to-instrument distance and elimination of sample heterogeneities. Furthermore, the subsequent demonstration of an instantaneous “cloud evaluation” of their spectral data not only neglects the influence of these experimental shortcomings on prediction accuracy but also, in general, hides the fact that reliable results for nutritional parameters require extensive calibration data based on sound data acquisition procedures and reference analyses.

Nevertheless, with the availability of miniaturized spectrometers weighing <100 g and with prices in the range of <USD 1000 level, the stage is set for NIR spectroscopy to become the technique of choice for food and beverage testing, not only in industry but also for consumer applications. In order to put into perspective the exaggerated claims of the abovementioned companies, the following case study will demonstrate realistic analytical data derived from PLS calibration models for six different nutritional parameters (energy, protein, fat, carbohydrates, sugar, and fiber) derived from the NIR spectra of pasta/sauce blends recorded with a handheld instrument. Because the detailed data of this project are available from a very recent publication [44], only a short summary of the results will be presented here in order to provide the reader an insight into the essential measurement efforts and data evaluation requirements to achieve meaningful data of the nutritional parameters under investigation for the described popular type of meal.

For each pasta/sauce-type blend, five different combinations (ranging from 0 to 50% (w/w) sauce addition) were investigated. The pasta/sauce mixtures were prepared “ready to eat” on a plate, and the NIR spectra were recorded

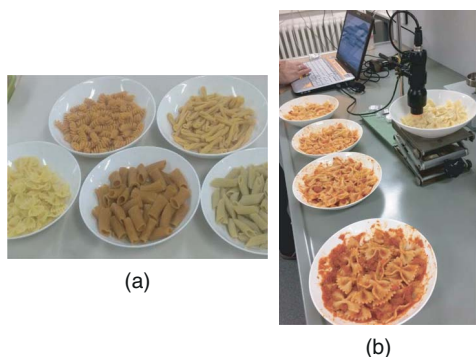


**Figure 13.27** The different particle shapes of the investigated pasta (a) and the experimental setup for the measurements of different pasta/sauce blends with the LVF NIR spectrometer.

at room temperature ( $22 \pm 1^\circ\text{C}$ ) at a distance of 1–2 mm above the sample surface at five different positions of the plate in order to compensate inevitable compositional and surface heterogeneities of the investigated pasta shapes (Figure 13.27a and b). The NIR spectra were measured in diffuse reflection with a Viavi MicroNIR 1700 handheld spectrometer. Five replicate spectra were recorded with an integration time of 8.8 ms by averaging 1000 scans in the wavelength range of 908–1676 nm. As a reference, the 99% Spectralon reflectance standard (Labsphere Inc., North Sutton, NH, USA) was used.

Five kinds of commercial pasta and five commercial tomato sauces were used for the preparation of the samples. Both, the kinds of pasta and the sauces were carefully selected to represent a large variety of nutritional parameters and shapes, in order to develop representative chemometric PLS models for the individual parameters of energy, fat, protein, carbohydrates, sugar, and fiber. The nutritional parameter values of the calibration mixtures were calculated from the package labels of the pasta and sauces according to the mixture compositions and are summarized in Table 13.7. Before mixing, the dry pasta was cooked by boiling in water for 10 minutes, and after draining, they were put on the plate, and the sauces were added. In total, 125 plates were prepared, and five replicate spectra were measured for each plate yielding 625 NIR spectra for further processing and analysis. For the separation of the available pasta/sauce mixtures into calibration and test samples, the 125 samples were arranged by increasing order of the respective parameter, and one sample was removed randomly from each consecutive

**Table 13.7** Nutritional parameter values calculated for 100 g of dry pasta and 100 g of sauce.

Sample	Energy (kcal)	Carbohydrate (g)	Fat (g)	Fiber (g)	Protein (g)	Sugar (g)
<b>Pasta</b>						
1	374.00	75.00	1.80	3.00	13.50	3.00
2	347.00	69.00	2.10	4.00	12.00	6.00
3	360.00	61.00	2.80	6.50	21.00	3.40
4	335.00	47.40	2.90	12.00	25.00	1.80
5	348.00	45.10	7.30	14.00	21.00	2.90
<b>Sauce</b>						
1	97.00	6.80	7.70	1.80	3.40	5.00
2	136.00	8.60	11.30	2.00	3.00	6.50
3	74.00	6.60	4.70	2.10	1.50	4.80
4	91.00	6.00	7.40	1.40	1.50	5.40
5	33.00	4.80	0.90	1.00	1.00	3.90

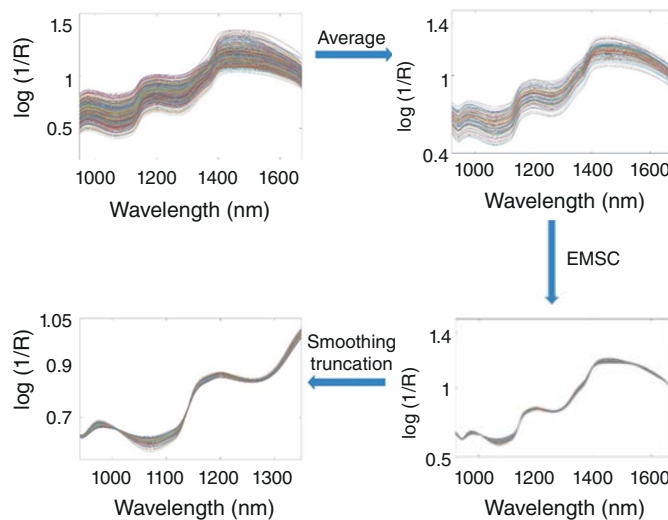


**Figure 13.28** The sequence of spectra pretreatments before model development (truncation: 950–1350 nm).

group of five samples. The 100 remaining samples were used as a calibration set, whereas the 25 removed samples were used as a test set. Individual PLS calibrations with leave-one-out cross-validation were then developed for the different nutritional parameters with MatLab software (version R2016a, The MathWorks, Inc., Natick, MA, USA) and the PLS toolbox (version 8.6., Eigenvector Inc., Manson, WA, USA). The test set samples were finally used for an additional validation step and the demonstration of the predictive capability for “unknown” samples. The spectral pretreatment sequence applied before PLS model development is summarized in Figure 13.28. The choice of the number of latent variables (factors) is a critical point in PLS model development and should always be based on the relation to other statistical parameters such as RMSEC and RMSECV [45]. In the present case, eight factors were chosen for energy, carbohydrate, sugar, fiber, and protein, respectively, and only seven factors for fat, because the graphs of the RMSEs versus the number of latent variables flatten out beyond these numbers of latent variables. The comparatively high number of factors can be readily explained by the complexity of the samples, which were prepared with five different types of pasta with varying shapes and sauces with considerable variations of ingredients (vegetables, cheese, etc.). Furthermore, residual amounts of water lead to hydrogen bonding interactions with carbohydrates, sugars, fibers, and proteins. In Figure 13.29, the scatter plots of the predicted versus actual concentrations are shown for the calibration and test set samples for all nutritional parameters, with a linear regression fit, and the content ranges and selected calibration parameters such as RMSEC, RMSECV, RMSEP, bias, slope, offset, and correlation have been summarized in Table 13.8. The RPD was also included to estimate how well the calibration model can predict compositional data. Generally, the RMSEs and RPDs shown in Table 13.8 furnish evidence that, at best, medium quality calibrations have been achieved that can be used for screening purposes of the nutritional parameters under investigation. For an overview of the test set prediction results compared with the reference values, the interested reader is referred to the original literature [44].

Predictions for energy and carbohydrate of the test set samples were obtained with  $R^2_{\text{Cal}}$  0.85–0.89, respectively, and average relative prediction errors of 2.7 and 6.38%(w/w), respectively. Protein had an  $R^2_{\text{Cal}}$  of 0.87 and an average relative prediction error of 8.3%(w/w). The calibrations for sugar and fat led to average relative prediction errors of 11.4 and 16.1%(w/w), respectively. The largest average relative prediction error of 18.2%(w/w) was obtained for the fiber calibration model. This observation is not really unexpected in view of the overlap of the structural characteristics of this component with carbohydrates and sugar. The method described, using a miniaturized spectrometer and PLS calibration models to quantify nutritional parameters of pasta/sauce mixtures, is simple, fast, and nondestructive. The achieved calibration results provide an overview of the realistically

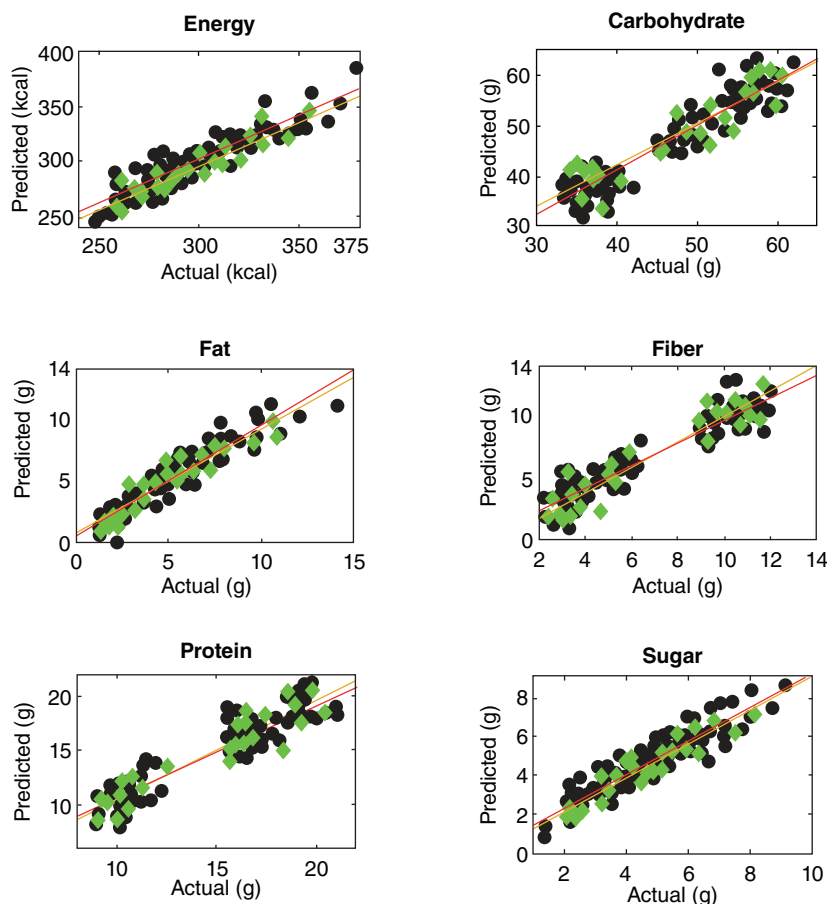


**Figure 13.29** Scatter plots of predicted versus actual content of the respective nutritional parameter per serving (calibration fit (yellow), prediction fit (red), calibration samples (black), and predicted test set samples (green)).

expectable prediction accuracy to quantify energy, carbohydrate, fat, fiber, protein, and sugar by the application of handheld NIR instruments. However, the results also demonstrate that the “cloud-derived” concentration data reported by several direct-to-consumer companies in commercial videos and advertising papers are far beyond any realistic accuracy achievable with their relatively simple food scanners.

## 13.6 Conclusions

The objective of this chapter is to turn readers’ attention to the realistic potential of state-of-the-art handheld NIR spectrometers for qualitative and quantitative quality control. For this purpose, concrete examples have been selected because we are firmly convinced that in the near future these miniature handheld spectrometers will enable a nonexpert population of users, in new measurement environments, to gain significant benefits. Thus, we can foresee the use of such instruments beyond police and customs forces, first responders, food inspection agents, or military personnel. Why shouldn’t customer-affordable, miniaturized spectrometers – especially if they have been integrated into mobile phones and equipped with user-friendly evaluation software – gain widespread

**Table 13.8** Content range and statistical parameters obtained for the individual PLS models of the nutritional parameters.

Parameter	Energy	Carbohydrate	Fat	Fiber	Protein	Sugar
# LVs	8	8	7	8	8	8
RMSEC	11.15 <sup>a</sup>	2.97 <sup>b</sup>	0.83 <sup>b</sup>	1.10 <sup>b</sup>	1.36 <sup>b</sup>	0.65 <sup>b</sup>
RMSECV	13.10 <sup>a</sup>	3.43 <sup>b</sup>	0.94 <sup>b</sup>	1.27 <sup>b</sup>	1.56 <sup>b</sup>	0.74 <sup>b</sup>
RMESEP	10.64 <sup>a</sup>	3.59 <sup>b</sup>	0.95 <sup>b</sup>	1.11 <sup>b</sup>	1.39 <sup>b</sup>	0.61 <sup>b</sup>
Content Range	248.67–378.54 <sup>a</sup>	33.55–62.13 <sup>b</sup>	1.34–14.06 <sup>b</sup>	2.23–12.03 <sup>b</sup>	8.89–21.67 <sup>b</sup>	1.34–9.15 <sup>b</sup>
R <sup>2</sup> Cal	0.85	0.89	0.91	0.89	0.87	0.86
R <sup>2</sup> CV	0.80	0.85	0.88	0.85	0.83	0.82
R <sup>2</sup> Pred	0.86	0.85	0.89	0.90	0.86	0.88
RPD	2.02	2.54	2.77	2.45	2.26	2.19
Slope CV	0.85	0.89	0.91	0.89	0.87	0.86
Offset CV	43.12 <sup>a</sup>	5.21 <sup>b</sup>	0.46 <sup>b</sup>	0.73 <sup>b</sup>	1.92 <sup>b</sup>	0.62 <sup>b</sup>
Slope Pred	0.80	0.83	0.84	0.99	0.91	0.87
Offset Pred	55.0 <sup>a</sup>	8.81 <sup>b</sup>	0.75 <sup>b</sup>	0.37 <sup>b</sup>	1.40 <sup>b</sup>	0.38 <sup>b</sup>

<sup>a</sup>=kcal; <sup>b</sup>=g.

public adoption for on-site quality control and protection against product counterfeiting? Black market goods like bastard amber, fake ivory, and “silk” shirts made from nylon could be consigned to the past, together with the issues we now have with food quality, adulteration, and authentication, as well as healthcare technology.

Despite these positive future prospects, let us end with some words of caution. If the interest of readers in handheld NIR spectrometers has been sparked, they should make sure to critically scrutinize the technical background of new, elaborately advertised products – particularly those “scanners” offering food and life science applications – because many of these appear to lack feasibility.

## Acknowledgments

The authors gratefully acknowledge experimental assistance of Yichao Xu, Yue Ma, and Cheng Guo (School of Biotechnology, Jiangsu University of Science and Technology); Damir Sorak, Lars Herberholz, Sylvia Iwascek, Sedakat Altinpinar, and Frank Pfeifer (Department of Physical Chemistry, University of Duisburg-Essen, Germany); and Marina D. G. Neves (Institute of Chemistry, University of Campinas, Brazil) and instrumental support by Nada O’Brien (previously JDSU, Santa Rosa, CA, USA), Ahmed Korayem (Si-Ware Systems, Cairo, Egypt), and Janne Suhonen (Spectral Engines, Helsinki, Finland).

## References

- 1 Sorak, D., Herberholz, L., Iwascek, S. et al. (2012). New developments and applications of handheld Raman, mid-infrared, and near-infrared spectrometers. *Applied Spectroscopy Reviews* 47 (2): 83–115.
- 2 Crocombe, R.A. and Druy, M.A. (2016). *Applied Spectroscopy Special Issue: Portable and Handheld Spectroscopy*. Thousand Oaks, CA: Sage publications INC 2455 Teller RD.

- 3 Guillemain, A., Dégardin, K., and Roggo, Y. (2017). Performance of NIR handheld spectrometers for the detection of counterfeit tablets. *Talanta* 165: 632–640.
- 4 Soriano-Disla, J.M., Janik, L.J., and McLaughlin, M.J. (2018). Assessment of cyanide contamination in soils with a handheld mid-infrared spectrometer. *Talanta* 178: 400–409.
- 5 Yan, H., Lu, D.-L., Chen, B., and Hansen, W.G. (2014). Development of a hand-held near infrared system based on an Android OS and MicroNIR, and its application in measuring soluble solids content in Fuji apples. *NIR News* 25 (4): 16–19.
- 6 Pügner, T., Knobbe, J., and Grüger, H. (2016). Near-infrared grating spectrometer for mobile phone applications. *Applied Spectroscopy* 70 (5): 734–745.
- 7 Wolffenduttel, R.F. (2005). MEMS-based optical mini-and microspectrometers for the visible and infrared spectral range. *Journal of Micromechanics and Microengineering* 15 (7): 145.
- 8 Jantra, C., Slaughter, D.C., Liang, P.-S., and Pathaveerat, S. (2017). Nondestructive determination of dry matter and soluble solids content in dehydrator onions and garlic using a handheld visible and near infrared instrument. *Postharvest Biology and Technology* 133: 98–103.
- 9 O'Brien, N., Hulse, C.A., Pfeifer, F., and Siesler, H.W. (2013). Near infrared spectroscopic authentication of seafood. *Journal of Near Infrared Spectroscopy* 21 (4): 299–305.
- 10 Yan, H. and Siesler, H.W. (2018). Quantitative analysis of a pharmaceutical formulation: Performance comparison of different handheld near-infrared spectrometers. *Journal of Pharmaceutical and Biomedical Analysis* 160: 179–186.
- 11 Altinpınar, S., Sorak, D., and Siesler, H.W. (2013). Near infrared spectroscopic analysis of hydrocarbon contaminants in soil with a hand-held spectrometer. *Journal of Near Infrared Spectroscopy* 21 (6): 511–521.
- 12 So, C.-L., Via, B.K., Groom, L.H. et al. (2004). Near infrared spectroscopy in the forest products industry. *Forest Products Journal* 54 (3): 6–16.
- 13 da Silva, V.H., da Silva, J.J., and Pereira, C.F. (2017). Portable near-infrared instruments: Application for quality control of polymorphs in pharmaceutical raw materials and calibration transfer. *Journal of Pharmaceutical and Biomedical Analysis* 134: 287–294.
- 14 Sun, L., Hsiung, C., Pederson, C.G. et al. (2016). Pharmaceutical raw material identification using miniature near-infrared (MicroNIR) spectroscopy and supervised pattern recognition using support vector machine. *Applied Spectroscopy* 70 (5): 816–825.
- 15 Dos Santos, C.A.T., Lopo, M., Páscoa, R.N., and Lopes, J.A. (2013). A review on the applications of portable near-infrared spectrometers in the agro-food industry. *Applied Spectroscopy* 67 (11): 1215–1233.
- 16 Yan, H. and Siesler, H.W. (2018). Identification of textiles by handheld near infrared spectroscopy: Protecting customers against product counterfeiting. *Journal of Near Infrared Spectroscopy* 26 (5): 311–321.
- 17 Hui, Y. and Siesler, H.W. (2018). Handheld Raman, mid-infrared and near infrared spectrometers: State-of-the-art instrumentation and useful applications. *Spectroscopy* 33 (11): 6–16.
- 18 Yan, H. and Siesler, H.W. (2018). Identification performance of different types of handheld near-infrared (NIR) spectrometers for the recycling of polymer commodities. *Applied Spectroscopy* 72 (9): 1362–1370.
- 19 Liu, X.H., Han, L., Wang, L.J., and Fu, X.S. (2010). Study on quality standards of *Pseudostellaria heterophylla*. *China Pharmacy* 21 (19): 1769–1771.
- 20 Pharmacopoeia Committee of People's Republic of China (2010). *Caryophylli Flos. Pharmacopoeia of People's Republic of China*, 1<sup>st</sup> ed. Beijing: China Medical Science Press.
- 21 Lin, H., Zhao, J., Chen, Q. et al. (2011). Discrimination of Radix Pseudostellariae according to geographical origins using NIR spectroscopy and support vector data description. *Spectrochimica Acta, Part A: Molecular and Biomolecular Spectroscopy* 79 (5): 1381–1385.

- 22 Li, H.-D., Xu, Q.-S., and Liang, Y.-Z. (2018). libPLS: An integrated library for partial least squares regression and linear discriminant analysis. *Chemometrics and Intelligent Laboratory Systems* 176: 34–43.
- 23 Yun, Y.-H., Li, H.-D., Wood, L.R. et al. (2013). An efficient method of wavelength interval selection based on random frog for multivariate spectral calibration. *Spectrochimica Acta, Part A: Molecular and Biomolecular Spectroscopy* 111: 31–36.
- 24 Warner, K., Timme, W., Lowell, B., and Hirschfield, M. (2013). *Oceana Study Reveals Seafood Fraud Nationwide*. Washington, DC: Oceana.
- 25 Buck, E.H. *Seafood Marketing: Combating Fraud and Deception 2007*. Washington, DC: Congressional Research Service, Library of Congress.
- 26 O'Brien, N.A., Hulse, C.A., Siesler, H.W. and Hsiung, C. (2016). Viavi Solutions Inc, assignee. Spectroscopic characterization of seafood. United States patent US 9,316,628. 19 April 2016.
- 27 Çoban, Ö.E. and Patir, B. (2013). Antimicrobial and antioxidant effects of clove oil on sliced smoked *Oncorhynchus mykiss*. *Journal für Verbraucherschutz und Lebensmittelsicherheit* 8 (3): 195–199.
- 28 Fu, Y., Chen, L., Zu, Y. et al. (2009). The antibacterial activity of clove essential oil against *Propionibacterium acnes* and its mechanism of action. *Archives of Dermatology* 145 (1): 86–88.
- 29 Siddiqua, S., Anusha, B.A., Ashwini, L.S., and Negi, P.S. (2015). Antibacterial activity of cinnamaldehyde and clove oil: effect on selected foodborne pathogens in model food systems and watermelon juice. *Journal of Food Science and Technology* 52 (9): 5834–5841.
- 30 Yamahara, J., Kobayashi, M., Saiki, Y. et al. (1983). Biologically active principles of crude drugs. Pharmacological evaluation of cholagogue substances in clove and its properties. *Journal of Pharmacobio-Dynamics* 6 (5): 281–286.
- 31 Nikousaleh, A. and Prakash, J. (2016). Antioxidant components and properties of dry heat treated clove in different extraction solvents. *Journal of Fisheries Science and Technology* 53 (4): 1993–2000.
- 32 Li, H., Liang, Y., Xu, Q., and Cao, D. (2009). Key wavelengths screening using competitive adaptive reweighted sampling method for multivariate calibration. *Analytica Chimica Acta* 648 (1): 77–84.
- 33 Ciurczak, E.W. and Drennen, J.K. (2002). *Pharmaceutical and Medicinal Applications of Near-Infrared Spectroscopy*. Marcel Dekker Inc: New York, USA.
- 34 Luypaert, J., Massart, D.L., and Heyden, Y.V. (2007). Near-infrared spectroscopy applications in pharmaceutical analysis. *Talanta* 72 (3): 865–883.
- 35 Roggo, Y., Chalus, P., Maurer, L. et al. (2007). A review of near infrared spectroscopy and chemometrics in pharmaceutical technologies. *Journal of Pharmaceutical and Biomedical* 44 (3): 683–700.
- 36 Mantanus, J. (2012). *New Pharmaceutical Applications Involving Near Infrared Spectroscopy as a PAT Compliant Process Analyzer*. Belgium: University of Liege.
- 37 Guo, C., Luo, X., Zhou, X. et al. (2017). Quantitative analysis of binary polymorphs mixtures of fusidic acid by diffuse reflectance FTIR spectroscopy, diffuse reflectance FT-NIR spectroscopy, Raman spectroscopy and multivariate calibration. *Journal of Pharmaceutical and Biomedical* 140: 130–136.
- 38 Fuenffinger, N., Arzhantsev, S., and Gryniewiczruzicka, C. (2017). Classification of ciprofloxacin tablets using near-infrared spectroscopy and chemometric modeling. *Applied Spectroscopy* 71 (8): 1927–1937.
- 39 Kandpal, L.M., Park, E., Tewari, J., and Cho, B.K. (2015). Spectroscopic techniques for nondestructive quality inspection of pharmaceutical products: a review. *Journal of Biosystems Engineering* 40 (4): 394–408.
- 40 Patlevic, P., Dorko, F., Sj, P. et al. (2013). False drugs - How to reveal them? *Chemicke Listy* 107 (1): 37–43.
- 41 Rajalahti, T. and Kvalheim, O.M. (2011). Multivariate data analysis in pharmaceuticals: a tutorial review. *International Journal of Pharmaceutics* 417 (1): 280–290.
- 42 Instant and accurate TPH soil measurement [Internet]. Ziltek.com. 2020. <https://ziltek.com/remscan/> (accessed 20 November 2019).

- 43** O'Brien N.A., Hulse C.A., Friedrich D.M., Van Milligen F.J., von Gunten M.K., Pfeifer F., et al. (2012). Miniature near-infrared (NIR) spectrometer engine for handheld applications. *Proceedings of SPIE; 2012: International Society for Optics and Photonics*.
- 44** Neves, M.D., Poppi, R.J., and Siesler, H.W. (2019). Rapid determination of nutritional parameters of pasta/sauce blends by handheld near-infrared spectroscopy. *Molecules* 24 (11): 2029.
- 45** Fearn, T. (2002). Assessing calibrations: SEP, RPD, RER and  $R^2$ . *Nir News* 13 (6): 12–14.

## 14

# X-Ray, LIBS, NMR, and MS Applications in Food, Feed, and Agriculture

Krzysztof Bernard Bęć, Justyna Grabska and Christian Wolfgang Huck

*Institute of Analytical Chemistry and Radiochemistry, Leopold-Franzens University, Innrain 80–82, CCB-Center for Chemistry and Biomedicine, Innsbruck, Austria*

### 14.1 Introduction

Spectroscopic methods of qualitative and quantitative analysis have profound practical importance in food and agriculture. There exist subtle differences among the problems typically encountered in analytical routines between these two sectors, but the advantages of the methodologies described in this chapter are equally meaningful in both fields. Analytical tasks in food science and technology, regardless of whether the food industry, governmental agencies, or academic laboratories are considered, are expected to determine food composition and characteristics to ensure the quality and safety of the food supply. It is mandatory by legal regulations to perform analysis of food products throughout the production process, from raw material to the final product after its delivery to the market. This includes the chemical composition and physical properties of food items. The result of the analysis should be sufficient to determine the nutritional value of the product, its functional characteristics, and market acceptability. The specific nature of the food supply chain puts particular importance on the rapidness, precision, and robustness of the analysis. The prominence of the method's reliability ensured through proper validation is stressed. Through these lenses, conventional methods for determining food chemical and physical properties become hardly suitable for the needs of the modern global market. The traditional approaches of analytical chemistry are time-consuming, and what is critical, are mostly limited to laboratory use. The quality data from items analyzed in food and agriculture are typically obtained through time-consuming, inflexible, and destructive (wet chemical) conventional methods. These conventional methods do not meet today's requirements for rapid, on-site, analytical routine. In contrast, spectroscopic and spectrometric methods are capable of high-throughput yet low sample volume, rapid, often non- or minimally-invasive analysis, and, in certain cases, remote measurement as well. Furthermore, as it will be emphasized in this chapter, the challenges met in the food and agriculture areas imply a particular set of advantages for the application of portable spectroscopy and spectrometry.

#### 14.1.1 Issues in Quality Control of Food

The problem of maintaining the quality and safety of food is an active topic in public debate. To some extent, this results from consumers' desire for quality food, which grows rapidly on a global scale, including the developing countries. This desire, motivated by increased awareness about positive health benefits, creates an economically-stimulated driver for efficient and accurate quality control methods applicable to raw materials and finished products. Due to obvious reasons, foods are ubiquitous products that feature particularly complex and

vulnerable production and supply chains (DeKieffer 2006; Charlebois and MacKay 2010; Holbrook 2013). The quality and safety of food may become easily compromised at each of these stages. With an accelerating increase in world trade, emerging new markets, and the thriving internationality of food supplies, food safety becomes crucial. Recent years have brought numerous food safety incidents, causing severe concerns in governments and regulatory authorities (Kjærnes 2012). Most of the safety incidents have been unintentional, resulting from the hastening food trade imposing difficulties in proper control of the quality. However, others were deliberate and economically motivated food frauds driven by a steady increase in food prices all around the world (DeKieffer 2006; Charlebois and MacKay 2010; Holbrook 2013; Evershed and Temple 2016). Food fraud can generally be understood as a collective term that includes the deliberate substitution, addition, tampering, or misrepresentation of foods and food-related items. This includes food ingredients, food packaging, and among others, false or misleading statements describing the product, issued to deliver an economic gain. The mechanism may include substituting, diluting, or modifying any of the physical or chemical inherent properties of the raw material or food product. Ultimately, adulteration or fraud compromises the identity of the food item in terms of purity and/or originality of any of the ingredients.

Food production and supply chain suffer from intrinsic vulnerability to contamination (Jacquet and Pauly 2008; Rovina and Siddiquee 2015). Numerous safety incidents (e.g. recent 2017 fipronil scandal resulting from insecticide contamination in eggs; Munoz-Pineiro and Robouch 2018) induced reworking and redesigning safety procedures and improving quality assurance of dairy products throughout the entire world (Huck et al. 2016). Further, these incidents had an impact on the global food industry and economy, creating an economic driver for adopting new methods (Le Vallée and Charlebois 2015). Food safety creates a challenge for the techniques used for quality control, with on-site capability being one of the most substantial requirements. The prerequisites for the most feasible analytical tool-of-choice are mainly determined by its ability to perform straightforward, noninvasive quality assessments for a wide range of both raw and final products while maintaining high performance, low limit of detection (LOD), reliability and reproducibility, and possibly achieving low total cost of its implementation, so that its wide utilization can be achieved. Rapid on-site analysis is crucial for foods, as most food items need to be distributed quickly to ensure freshness, despite the complexity of the supply chain. These prerequisites strongly promote the application of rugged, transportable sensors and analyzers based on spectroscopic and spectrometric techniques. Concerning the discussed portable techniques, chemical analysis by nuclear magnetic resonance (NMR) relaxometry and mass spectrometry (MS), and elemental analysis by X-ray fluorescence (XRF) or laser-induced breakdown spectroscopy (LIBS) (e.g. detection of heavy metals, assessment of nutrient elements, etc.) show high potential for application in food-related issues.

### 14.1.2 Challenges in the Agricultural Sector

The agriculture sector remains in a relatively close connection with the food area. However, additional problems are faced here due to the particular characteristics of agri-food products and systems (Cozzolino 2012). The applications are considerably more diverse, as they include a wider scope of samples, both organic and inorganic, and a notable broader range of encountered problems (e.g. soil, water, widely understood examination of raw materials including dry matter and moisture analysis, feed, plants, crops, flock, detection and control of pests, and diseases, etc.) (Cozzolino et al. 2015). These add up to the analysis of quality parameters, for instance, protein or sugar content in agricultural products during harvest or post-harvest, which is an issue comparable to those commonly encountered in the food sector. Nonetheless, far-reaching similarities can be identified between these two sectors, at least from the point of view of the prerequisites for general characteristics of the analytical tool of choice. Modern farming increasingly demands easy and on-site deployable, cost-effective and rapid, chemical-free, and nondestructive physicochemical methods of analysis that can be operated by untrained personnel. In recent years, considerable attention is given to researching efficient solutions, mostly the development of sensors and analytical methods, to improve agricultural production and processes at the farm level (Cozzolino et al. 2015). This aligns with the contemporary shift toward precision agriculture (Finger et al. 2019). Primarily, there appears a need

for monitoring changes of physical and chemical nature occurring in crops throughout the lifecycle of the plant. This yields the capability to establish the optimum harvest time, bringing benefits to crop quality and improving agronomic management routines, directly resulting in increased profitability.

Further, diagnostics of crops and related factors (e.g. soil, cultivation conditions), and detection and control of contaminants and environmental pollutants, demonstrate the significant potential of spectroscopic and spectrometric analysis methods in agriculture. The potential savings and improved quality are accompanied by the environmentally-friendly (reagentless) nature of the monitoring technologies based on portable spectroscopy and spectrometry. Therefore, studies emphasize the significance of the low-cost, low-power, multifunctional sensor technologies applied for monitoring intensively-cultivated crops (Ruiz-Altsent et al. 2012). Nonetheless, one needs to understand the limits of this technology. The process of their integration with the existing routines should preferably be stimulated and controlled in close cooperation with academic research institutes (Cozzolino et al. 2015).

In response to the threats discussed here, proactive legal regulations relevant to the chemical analysis of foods are issued in most countries, often within international agreements. In the US, the Food and Drug Administration (FDA) is the primary agency responsible for regulating food safety. Issues in controlling food quality are a major concern for governmental administration, standard-setting, and legislation institutions in the European Union (EU) as well. Examples of such activities include the EU Food Fraud Network (FFN) coordinating the efforts of EU countries against possible intentional violations of the food chain law. ([https://ec.europa.eu/food/safety/food-fraud/ffn\\_en](https://ec.europa.eu/food/safety/food-fraud/ffn_en) [accessed 12 February 2020]). Presently, a major focus in food safety and transparency is the automation in data collection for the individual product or lot to be traced at any stage of the food supply chain (Montet and Ray 2017). Legislation and standardization describing the analytical methods applied in these fields are equally important in establishing novel approaches and instrumentation.

## 14.2 Applications of Transportable Spectroscopy and Spectrometry in Food, Feed, and Agriculture

Atomic and molecular spectroscopy and spectrometry are extremely potent tools in agro-food analysis. The last decade brought a remarkable leap with the introduction of portable instrumentation, enabling practical applications. Such sensors enable rapid elemental and molecular analysis of the sample on-site, a factor of critical importance in this sector. Wide deployment of portable spectrometry is an essential gain given the contemporary demands arising in this field of application. Despite the practical potential of portable techniques, one needs to consider their limitations as well. Primarily, lower reliability, sensitivity, and susceptibility to inaccurate measurement may become apparent in certain roles. In other cases, such as NMR, most of the available portable devices yield a significantly reduced information on the sample in physicochemical sense. While *qualitative* assessment, or “yes/no” type of answer, is regarded as reliable when using portable instruments, more challenging *quantitative* analyses are also being developed. This is a promising area, as quantitative methods for agro-food analyses are often already successfully implemented on benchtop instruments.

In this chapter, it is assumed that the reader is familiar with the physical principles, laboratory applications, and data-analytical approaches corresponding to the physicochemical methods of analysis that are overviewed here. On the other hand, the fundamental information corresponding to the underlying technology, design, and engineering principles utilized in transportable instrumentation is provided in other chapters of this book (see the references in each section below). Nonetheless, a brief outline of the essential information is included here, with the intent to describe the strengths and limitations of these techniques in the particular application field. This chapter deals with the food and agriculture-related applications of portable (i.e. transportable, field-portable, or fieldable, including briefcase-like, handheld, and miniaturized) instrumentation using the principles of XRF, LIBS, NMR, and MS techniques.

### 14.2.1 X-Ray Fluorescence (XRF)

Portable XRF instrumentation is perfectly suited, although perhaps somewhat undervalued, to perform rapid elemental analysis of food- and agriculture-related raw materials and final products. In the past, this technology was routinely employed in environmental applications, for example, for the detection of metal particulates in soil or, after filtration, in the air as well; in geology for precious-metal identification, and in the recycling industry interested in alloy identification (Palmer et al. 2009; the chapter 19 by Piorek in this volume)). Although XRF is unable to match the sensitivity of the “gold standard” methods such as inductively coupled plasma-mass spectrometry (ICP-MS) capable of sub-ppm level performance, it features a set of advantages critical for applications in the food and agriculture sectors. These include the ability to perform high throughput, rapid in situ analysis with minimal sample preparation, which yields a definitive identification of toxic elements, and their accurate quantification. Some of the previous issues faced in portable XRF instrument applications in analytical chemistry have been covered in focused review articles, e.g. by Palmer et al. (2009) and Bosco (2013).

The XRF technique can be straightforwardly applied to the analysis of trace elements in food items, where it has demonstrated high potential and was adopted relatively early, e.g. as summarized by Palmer et al. (2009) (Figure 14.1). As outlined earlier, the suitability of portable instrumentation adds significantly to the general value of the XRF methodology. For instance, the feasibility of applying portable XRF for assessing trace elements in rice, as raw material and resulting products, was explored by Fleming et al. (2015). The method was compared with the ICP-MS approach in the detection of arsenic (As), manganese (Mn), iron (Fe), nickel (Ni), copper (Cu), and zinc (Zn) in a selection of rice samples. ICP-MS was used as the reference method for determining the elemental composition of the sample after microwave-digestion. A comparison of the results for these two methods showed a linear relationship, with a significant correlation for As, Mn, Fe, Cu, and Zn. An exception was noted for Ni, as

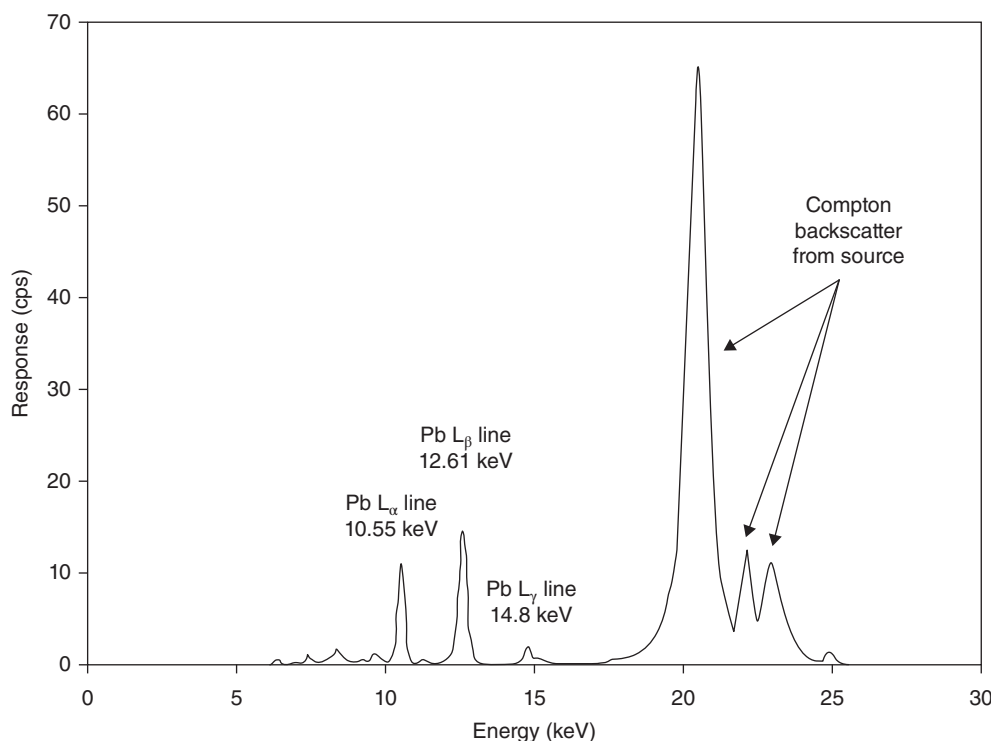


**Figure 14.1** XRF spectrum of 1% lead in chocolate obtained with the portable Niton XLi analyzer. Source: Palmer et al. (2009). © 2009, American Chemical Society.

no significant correlation between XRF amplitude and ICP-MS concentration was observed for this element. This fact highlights the possible issue with portable XRF, as other studies also signaled a varying level of XRF sensitivity toward particular elements in practical applications.

The XRF approach can be used as a highly sensitive yet quick and easily applicable on-site quantitative method for determining the total content of a given element in foods. An example of such application, using a portable analyzer, was provided by Sánchez-Pomales et al. (2013) in their study of silver (Ag) concentration in liquid dietary supplements. Reliable detection and accurate quantitation of Ag content in nano-based liquid dietary supplements were achieved by portable XRF. The developed method achieved a detection limit of 3 ppm and a quantitation limit of 10 ppm, and suitability over a broad linear range from the detection limit to 10 000 ppm (1%). Although the performance level is inferior to that achievable by, e.g. ICP-MS, it is still suitable for fast screening. The accuracy in quantitation of Ag was also maintained in the presence of potentially interfering palladium (Pd) and cadmium (Cd). The results were validated against ICP-MS analysis and using a series of silver nitrate ( $\text{AgNO}_3$ ) standards. As assessed, a good correlation was observed between the total Ag concentration obtained in XRF and ICP-MS analyses, demonstrated by the percentage differences between the average values remaining under 15%.

In the elemental analysis of foods, the detection of toxic elements is critically important. The available early laboratory-based radioisotope-induced X-ray fluorescence spectrometry (RXRFS) instruments, employing isotope sources, occupied the niche for rapid, nondestructive detection of heavy metals (e.g. Cd, lead (Pb)) and other toxic elements in food-related items (Anderson et al. 1995; Anderson and Cunningham 1996; Anderson 2003). Despite the compatibility of RXRFS instrumentation with the concept of portability, the decay of the source over time, and regulatory issues related to the use of radioactive material, were major disadvantages. The advent of miniaturized X-ray tubes and cooled Si-PiN (silicon PiN) diode detectors (Pantazis et al. 2010) was a breakthrough (see Chapter 19, Volume 1), and a new generation of instrumentation was developed, eliminating isotope sources while also providing superior levels of sensitivity and LOD. These newer-generation instruments are well-suited for screening a variety of raw materials and food products (Potts and West 2008). For example, Anderson (2009) showed that they are capable analyzers for screening foods, thin films, and ceramic glazes for toxic elements. Quantification of Pb content in thin films and ceramic glazes was possible with high accuracy. LOD values of 0.2–15 and  $2 \mu\text{g cm}^{-2}$  were achieved for the Pb element in thin films and glazes, respectively. The LOD obtained for Cd in thin films was  $15 \mu\text{g cm}^{-2}$ . Hence, the sensitivity and LOD of newer XRF instrumentation were superior to those obtained with the conventional RXFRS analysis, together with a much more rapid analysis time totaling 0.5–1 minute (vs. 3–10 minutes required in the isotope-source-based RXFRS). This instrumentation was found capable of screening foods for toxic elements (e.g. Cu, As, Pb). The analysis was often possible without removing samples from their original polymer or aluminum (Al) containers (Anderson 2009).

The detection of heavy metals and toxic elements in foods is an evolving direction of research. Recently, Byers et al. (2019) reported on their study on portable XRF techniques employed for quantification of heavy metals in vegetables at very low LODs. They evaluated the general potential and application details of wavelength dispersive XRF (WD-XRF) and energy dispersive XRF (ED-XRF) portable instruments. The reported LODs (in  $\mu\text{g g}^{-1}$ ) achieved by WD-XRF for chromium (Cr), Ni, Pb, and Y were: 0.6, 0.4, 0.3, and 0.3, respectively. The analysis by ED-XRF yielded LODs (in  $\mu\text{g g}^{-1}$ ) of 2.3, 0.3, 1.4, and 1.5, for respectively, Cr, Ni, Pb, and yttrium (Y). Quantification of Pb and other heavy metals in dried and wet plant tissue imposes certain difficulties, e.g. those related to water content and the matrix effects (mostly carbon matrix), for the analysis performance to reach the regulatory levels. It was noted that the effects of carbon matrix specific to vegetable sample on metals quantitation by XRF have rarely been considered before. In addition, standard factory calibrations are typically optimized for non-carbon matrices.

Byers et al. (2019) have successfully minimized the influences from the carbon matrix on their analysis. It was accomplished by wavelength optimization to eliminate peak overlaps and by controlling the enhancement factor resulting from the matrix. The validity of the calibration was verified by analyzing the vegetables cultivated in metals-rich garden soil. The quantitative models based on WD-XRF spectra could be reliably calibrated for dried

vegetables. A relatively lower precision and accuracy of the analysis based on the portable ED-XRF was observed. A superior level of robustness in the case of the WD-XRF approach was confirmed, although its limitation to fixed laboratory-based analysis should be noted. Nonetheless, concentrations of heavy metals in raw consumable vegetable tissues, which are good examples of wet and coarsely-homogenized samples, were successfully quantified with portable ED-XRF. Authors emphasized the need for maintaining proper control over the measurement conditions, e.g. sample thickness adequate to retain all source and characteristic X-rays, interfering X-rays generated by the shielding/housing, influences of the random variations in the energy, current, filter, count time, atmosphere, and management of the matrix effects as they are manifested in the spectra. This demonstrates a considerable room for improvement for the method's robustness. Nonetheless, when these crucial parameters are maintained, WD-XRF and portable ED-XRF instrumentation can be used for rapid quantitative analysis of heavy metals in vegetable samples, with LODs matching the regulatory thresholds. These methods can also be applied to coarsely-homogenized wet raw materials with lower water content, e.g. grains and legumes, and prepared foods. However, the performance of the analysis, expressed in root mean square error (RMSE) and LOD values, of a dry-weight basis was found to be under a strong influence of the measurement time and water content that are the current limits of this technology. Future research is anticipated to be directed at solving these issues.

In agriculture, the XRF technique can be utilized to monitor the elemental composition of water and soil. Considering the increasing environmental pollution, an analytical approach capable of rapid on-site elemental analysis of soil and water would be an invaluable tool in modern agriculture. So far, the approaches to soil analysis by portable XRF instruments are relatively better developed than those focused on water.. The analysis of metal contamination of soil by portable XRF technique was established early, at least for relatively heavy contamination scenarios. Among others, these correspond to the urban expansion into traditional agricultural lands. Rapid urbanization causes increasing appearances of peri-urban agricultural areas. It stimulates the need for a quick and flexible, on-site capable analytical approach that would be more effective than the time-consuming and cost-prohibitive traditional methods for assessing environmental quality. The study by Weindorf et al. (2012) examined the potential of portable XRF spectrometry for assessing the environmental quality of sugarcane fields in proximity to industrial complexes. The achieved correlation between XRF measurement and the certified National Institute of Standards and Technology (NIST) standards indicated that the technique is suitable for accurate identification of most heavy metals in soil. The XRF analysis provided results of the quality comparable to that of traditional laboratory analysis. The best achieved LODs (in  $\text{mg kg}^{-1}$ ) reported by Weindorf et al. (2012) were: 10 000 for lighter elements (phosphorus [P], sulfur [S], chlorine [Cl], argon [Ar]), 250 for intermediate ones (potassium [K], calcium [Ca]), and five for heavier elements (Fe, Cu, and Zn). Further, the elevated elemental concentrations of Cu, Pb, and Zn elements found can be attributed to anthropogenic activities. In addition, XRF proved to be superior in certain ways to the reference method, laboratory-based ICP analysis. It was concluded that the extent of the detrimental effect that field moisture conditions have on the elemental analysis is relatively lesser for XRF as compared with the laboratory ICP analysis. In such case, XRF analysis more accurately represents the true in-field elemental concentrations. The conclusions drawn by Weindorf et al. (2012) suggest that petroleum refineries and chemical plants elevate the concentrations of Cu, Mn, Pb, and Zn in soil. On the other hand, the increasing concentration of other trace elements, specifically Pb and Zn, should be primarily attributed to the intensified anthropogenic activities associated with urbanization, e.g. traffic and residential construction.

Portable XRF enables rapid and flexible tools for the determination of trace elements in the soil as well with the purpose of screening potentially polluted areas. The statistical treatment of the measured data, e.g. by hierarchical cluster analysis (HCA), or analysis of variance (ANOVA) algorithms, enables the detection of anomalous concentrations of elements, with the additional information on the spatial distribution of the soil pollution level. As early as in 2010, Peinado et al. (2010) applied portable XRF for rapid in situ soil analysis for traces of potentially toxic elements (As, Pb, Zn, and Cu). The analysis was carried out around the perimeter of an abandoned mining site. Statistical treatment of the measured data-enabled examination of the spatial distribution of these trace elements' anomalous quantities. The study indicated that As, Pb, Zn, and Cu elements exceeded the background values of the soils in the adjacent area accordingly, as concentrations exceeded the intervention thresholds both

for agricultural as well as natural levels, with 89% and 67% of the samples found above these limits, respectively. The study resulted in far-reaching insights as well: the resolved spatial distributions implied that water and wind erosion are the main mechanisms of dispersion of the trace elements in the soil.

Proximal sensing and rapid quantitative assessment of elemental constituents are feasible by portable XRF analyzers in agricultural soil and vegetable-based biomass. As demonstrated by Sacristán et al. (2016), Cu concentration could be successfully determined through rapid proximal analysis of agricultural soil and lettuce (*Lactuca sativa* L.) using a portable XRF spectrometer. The approach was found adequate for the screening purposes for Cu contamination in biomass assays, comprising Cu contaminated agricultural soil and lettuce. It was confirmed that portable XRF analysis is capable of reliably assessing soil contaminated with Cu and potentially other heavy metals. The analogous analysis performed for plant material could not match a similar level of accuracy. Nonetheless, the potential use of this technique as the first pass screening to assess the Cu concentration in plants was noted. In such a role, the rapid analysis, cost-effectiveness, and minimal sample preparation were recognized as notable advantages. On the other hand, the analytical performance could probably be improved by fine-tuning the data-analytical approaches, e.g. by using multivariate statistics.

The suitability of XRF analysis for vegetables and agricultural plants is continuously improved. For example, nutrition assessment in sugarcane using XRF sensors has been demonstrated by Guerra et al. (2018). This is an essential parameter of sugarcane, an important crop of the tropical regions that strongly contributes to the establishment of precision agriculture and economic boost for the corresponding countries. In the study, the authors employed a portable ED-XRF device to evaluate *in situ* the nutrition value, understood as K, Ca, S, and silicon (Si) contents, of fresh sugarcane leaves. The reference analysis was carried out in the laboratory by a benchtop ED-XRF instrument on the same leaf fragments after drying and further by ICP-atomic emission spectroscopy (ICP-AES) after microwave-assisted acid digestion. These were found to remain in a good agreement with the validated comparative method, as evidenced by the correlation coefficients of a linear regression (intensities of X-ray characteristic emission lines against reference elemental mass fractions) between 0.9575 (Ca) and 0.9851 (Si). The established LODs were fully satisfactory and significantly lower than the critical nutrient levels. It was suggested that Mn analysis might become feasible upon improvements in the data analysis procedures. The method developed provides an advantage over the conventional approaches, offering a rapid evaluation of the nutritional profile of plants while avoiding time-consuming steps, such as drying, grinding, weighing, and acid digestion.

Irrigation has profound importance in agriculture, and the ability to monitor the quality of water is essential for modern agriculture. Among other properties, water salinity is a key feature dictating the usefulness of a water source. Conventional approaches to the analysis of salinity are mostly based on electrical conductance (EC). This method provides only the total effective salinity with no information on the elemental composition. Hence, no distinction of the presence of particularly dangerous cations in water is possible. No feasible methodologies existed before capable of quick screening of water samples against heavy metals and/or other pollutants.

In contrast, the XRF approach is capable of elemental data analysis of soil, sediment, and other matrices. However, one should acknowledge the limitations of handheld XRF devices in analyzing elements lighter than Si. Therefore, assessment of several elements (e.g. sodium [Na], lithium [Li], Al, magnesium [Mg]) with essential importance to plant growth (Gransee and Führs 2013) and human health (Negrel et al. 2017) is not feasible. Further, its applicability to moist samples is still limited, as shown by Weindorf et al. (2014) in the case of a moisture-laden soil. Therefore, efforts have been made to develop an XRF-based methodology feasible for *in situ* elemental moist soil analysis. Recently, Pearson et al. (2017) successfully attempted to adopt a portable XRF instrumentation to perform elemental analysis of water samples and to predict water EC. The assessment of the method's feasibility was based on 256 water samples acquired from 10 different countries. In addition to portable XRF, ICP-AES and digital salinity bridge techniques were used to provide reference data. As a proof of concept, the study demonstrated an easily accessible protocol for quantifying water EC by analyzing Cl, K, and Ca contents by portable XRF. Although there is no clear correlation between the EC values and K and Ca contents, an acceptable prediction accuracy for water EC was obtained despite the matrix effects, leading to absorption and secondary fluorescence. However, the need for establishing more effective XRF spectra preprocessing methods was concluded, as

EC predictability based on XRF spectral bands parameters was limited. The study indicated that the effectiveness of portable XRF notably varies for different elements.

Nonetheless, the methods were found sufficient for predicting water EC via quantifying Cl element (total Cl content) in water samples, yielding  $R^2(\text{VAL})$  of 0.77 with RMSE of  $0.95 \log \mu\text{S cm}^{-1}$ . As an advantage over the salinity assessment via the conventional method of measuring electrical conductivity, this approach of portable XRF measurement also yields information that can help identify certain types of salts dissolved in the analyzed water sample. Moreover, even if only an indirect correlation with the matrix effect is effectively determined, the results obtained by Pearson et al. (2017) confirmed the potential of the portable XRF approach for further development in this direction. It seems feasible that improved methods for XRF spectra were preprocessing, alongside factory calibration of the portable XRF toward such applications (i.e. “water mode”), may bring the instrumentation nearer the practical application for analyzing water salinity in agriculture.

Interestingly, developments in portable XRF sensing techniques employed for elemental analysis of soil have received support from military applications. For example, the feasibility of this technology was evaluated in fast screening for depleted uranium (DU) contamination in soil. Armor-penetrating munitions is a concerning DU pollution source, as this weaponry is used during peacetime for testing and training purposes. Easy and rapid screening methods are needed to prevent prolonged exposure to DU. In the investigation carried out by Proctor et al. (2020), through direct comparisons with the reference analysis (ICP–MS after acid digestion), it was found that portable XRF spectrometry is an effective approach to locate/measure/detect DU at levels of interest to military operators. In this study, the detrimental effect of soil moisture on the elemental analysis was manifested as the underestimation of the uranium concentration.

Portable XRF methodologies for soil analysis are undergoing continuous development. For example, a recent investigation by Rawal et al. (2019) was aimed at the determination of soil base saturation percentage (BSP). This property plays an important role in the taxonomic classification of soil and the evaluation of soil fertility. Traditional methods for the determination of BSP are destructive, labor-intensive, time-consuming, and tend to underestimate the true cation exchange capacity (CEC). The methodology developed by Rawal et al. (2019) accomplished a successful prediction of BSP for 300 soil samples from active agricultural lands in the US (Colorado, California, Minnesota, Nebraska, Oklahoma, and Texas), using an Olympus Vanta portable XRF analyzer to assess the contents of Mg, K, and Ca. The quantified elements were claimed as representative of the BSP index available from reference laboratory analysis. Quantification of heavy metals in soil is also of high importance for ecological risk assessment. The global expansion of greenhouse cultivation results in accelerated accumulation of heavy metals in agricultural soils that developments stimulated by the agricultural sector’s needs augment similar research performed for environmental studies. In particular, high-throughput and efficient ways of analysis enabled by portable XRF techniques bring substantial benefits to large-scale soil analysis. As outlined by Wan et al. (2019), rapid analytical methods are essential for efficient large-area assessment of soils toward environmental quality and protection of human health. Analysis of heavy metal contamination by portable XRF enables rapid landscape-scale reconnaissance, surface surveys, and sediment tracing without the need to perform sample pretreatments or complex chemical analyses.

One should note that the progress achieved in environmental research brings a direct positive impact on the development of the methodology for the agriculture sector’s needs. As argued by Ravansari et al. (2020) in their comprehensive review article focused on portable XRF technology for environmental assessment, despite the general potential and applicability of portable XRF spectrometry, considerable challenges still exist in this field. The performance of this technique depends on a number of factors giving rise to elementally dependent disparities in accuracy and precision. The sources of interfering variability include sample heterogeneity, instrument stability, and instrumental drift, effects of protective coatings, incident X-rays, varying analysis times, sample thickness, sample width, analyte interferences, detector resolution, or power source fluctuations, among others. Detrimental effects arising from water content and organic matrix (carbon, oxygen) require further attention. One should note that the typical variability in organic matter and water content in soil can also affect the sample’s density, a

phenomenon often not properly taken into account in analyses. The resulting fluctuating sample critical thickness affects the effective analyzed sample volume. Supplemented by the differences in the characteristic fluorescence energy between elements, this effect may compromise the representative character of the whole sample. Further considerations should be aimed at the data-analytical methods to properly account for these effects. A systematic approach to these issues can successfully mitigate the outlined vulnerabilities, granting high accuracy of portable XRF spectrometry.

### 14.2.2 Laser-Induced Breakdown Spectroscopy (LIBS)

LIBS belongs to the family of atomic emission spectroscopic techniques (Markiewicz-Keszycka et al. 2017). By focusing a pulsed laser beam on a microscopic spot at the sample surface, a plasma is generated from a small volume of the sample material. Upon the subsequent expansion, the plasma cools down, and the electromagnetic radiation is emitted. This emission spectrum contains characteristic lines from the excited species (atoms, ions) that constitute the plasma (Hahn and Omenetto 2010). Therefore, LIBS delivers information on the elemental composition of the sample. In practical applications, LIBS enables rapid multi-elemental analysis with no or minimal sample preparation, in a reagent-free and minimally intrusive manner (Hahn and Omenetto 2012). The recent development of portable LIBS instruments (see Chapter 13, Volume 1), their capability of remote sensing at low running cost, ease of use in identifying materials, and their elemental analysis make LIBS a promising analytical technique for the food and agriculture sectors. These advantages have been recognized and the technique has progressed over the past decade with a number of applications developed intending to replace the traditional time-consuming analytical methods for assessing the quality and composition of foods and agriculture-related materials and products. LIBS technology is suitable for in- and on-line applications and potentially applicable in the process control in the food industry as well. Despite considerable advantages of LIBS technology, several limitations and challenges remain in food and agriculture-related sample analyses. Those include matrix effects resulting from the complex composition of the typical samples (e.g. carbon matrix) or moisture content, which create a need for applying spectral preprocessing methods, model calibration, and further enhancements of the instrumentation. Improvements are needed that correspond to instrument stability, self-absorption, line broadening, strong matrix effects, and the baseline/background effects. Compared with XRF, which also an elemental analysis technique, LIBS avoids the issues and safety considerations due to X-ray radiation. The total energy delivered to the sample is low, as the laser energy is focused on a microscopic spot, and it employs widely available and low cost optical spectroscopic components. However, this feature makes LIBS less suitable for the analysis of imperfectly homogenous samples, as the information is collected from a small sample spot. Sample homogenization or multi-spot measurements may be necessary for certain applications of this technique. LIBS enables a relatively faster and potentially more cost-effective analysis. On the other hand, reliability of LIBS analysis is more susceptible to moisture and surface contamination. The performances of these two techniques distinctively differ depending on the element's mass. LIBS is uniquely suitable for the analysis of light elements (including beryllium or Li), while XRF is suited for sensing heavy elements. This leads to a reduced sensitivity of LIBS analysis toward minor mineral elements and heavy metals in low concentrations, particularly for the samples that feature a complex organic matrix.

On the other hand, the spot-focused sensing nature of the LIBS technique makes it easily implementable in imaging instrumentation. Spatially-resolved elemental distribution in the sample may be obtained using a motorized translational stage. Recently, the instrumental development aimed at the LIBS imaging direction progressed notably stimulated by the needs for an examination of biological tissues, as demonstrated by the breakthroughs accomplished over the past decade (e.g. Kaiser et al. 2012; Gimenez et al. 2016). Potent capabilities of this technique were demonstrated (Kaiser et al. 2012; Gimenez et al. 2016), e.g. successful mapping of the accumulation of Pb, Mg, and Cu in plant material, multi-elemental imaging with direct detection and quantification of elements in murine kidney tissues, etc. The accomplishments in the field of bioanalytical applications provide promising

prospects for adoption in food and agriculture-related areas as well. As a relatively new technique, the design of handheld LIBS instrumentation is progressing rapidly. Further advances of the general capacity of this technique will come from the adoption of new chemometric and data-analytical methods.

Although not as well established in the food sector as XRF technology, LIBS applications in foods have become more widespread recently, e.g. Andersen et al. 2016; Bilge et al. 2016; Cama-Moncunill et al. 2017; Casado-Gavalda et al. 2017. LIBS analyses for trace elements and elements fundamental for human diet and health, including quantitative analyses aided by chemometrics, may be noted (Sezer et al. 2017). In particular, the detection of toxic elements and their amounts is crucial for food safety and quality. However, in this role, the capability of XRF as the competitive method for the detection of heavy metals is noteworthy. Nonetheless, a notable increase in applications of LIBS in agriculture-related basic research and applications occurred in the last few years (Nicolodelli et al. 2019). Portable LIBS technology has found utilization in routine analyses in practical agriculture (Sezer et al. 2017). Similar to XRF, the potential of the portable LIBS technique has mostly been found in the examination of soils and fertilizers (Nicolodelli et al. 2019). As early as in 2008, Ferreira et al. (2008) demonstrated the suitability of portable LIBS instrumentation to perform a quantitative analysis of copper concentration in soil with the aid of an artificial neural network (ANN) as the calibration method. The study established a method for Cu content prediction with a LOD of  $2.3 \text{ mg dm}^{-3}$  and a mean squared error (MSE) of  $0.5 \text{ mg}^2 \text{ dm}^{-6}$ . The study evidenced that an efficient calibration is significantly more difficult for direct solid analysis because of the effect of complex matrix typical for soil. Further, key difficulties in the quantitative analysis were identified as low sensitivity and low spectral resolution, which in the case of multiple emission lines decreased the ability of some detectors to elucidate the lines of interest in the LIBS spectrum.

Despite difficulties that this technique has in analyzing heavy metals, attempts have been made to develop a method for quantitative analysis of Pb content in soil and plants by portable LIBS instrumentation. LIBS was deemed useful in the case of phytoremediation, in which plants remove/transfer or contain the contaminant. In the study by Barbaieri et al. (2011), the LIBS technique was evaluated in analyzing Pb concentration in soil and phytoremediant plant samples from phytoremediation experiments. The performance of LIBS was found satisfactory against the reference method, atomic absorption spectroscopy (AAS). LIBS analysis was deemed suitable for pre-screening of contaminated sites, as the sensitivity of the analysis was sufficient for delimitation of areas with metal concentration exceeding the legal limits, which could be designated for further analysis by other methods. Therefore, the methodology based on a transportable LIBS analyzer was suggested as a viable semi-analytical tool capable of rapid, low-cost analysis, applicable for any solid matrix (e.g., rocks, soils, plants), with no need for laborious and time-consuming preparations.

The development of on-site quantitative elemental analysis of soil, including heavy metals, by portable LIBS instrumentation, has continued. For example, El Haddad et al. (2013) stressed the importance of pretreatment algorithms and data-analytical methods to mitigate the problems arising in LIBS measurements from the saturation and matrix effects. In their study, they achieved an error of prediction lower than 20% for Al, Ca, Cu, and Fe for on-site quantitative LIBS analysis of soils. This performance level was accomplished with the use of a transportable LIBS system and an artificial neural network (ANN) method employed in the quantitative data work-up to mitigate the matrix effects and the nonlinear behavior of the calibration. Recently, the conditions for accurate determination of nitrogen (N) in soil by portable LIBS were investigated by Yan et al. (2018). They examined the effects of sample pretreatment and particle size, as well as evaluated the potential implementation of the LIBS analyzer in the form of a robotic-borne remote sensor. The latter solution could be used for automatic agricultural soil analysis.

Furthermore, such an analyzer would be suitable for determining soil N on Mars during expeditions aimed to assess the planet's future habitability. The analyzer employed a miniaturized LIBS system with an neodymium-doped yttrium aluminum garnet (Nd:YAG) laser (1064 nm emission wavelength) and 25 mJ energy per pulse. One of the aims of the study was to assess the effects of sample preparation on the N quantification in soil. As an alternative for pelletization, milling the sample to yield particle size lower than 100  $\mu\text{m}$  was assessed as being suitable for a remote rover-based analytical platform. Smaller particles yield more uniform ablation

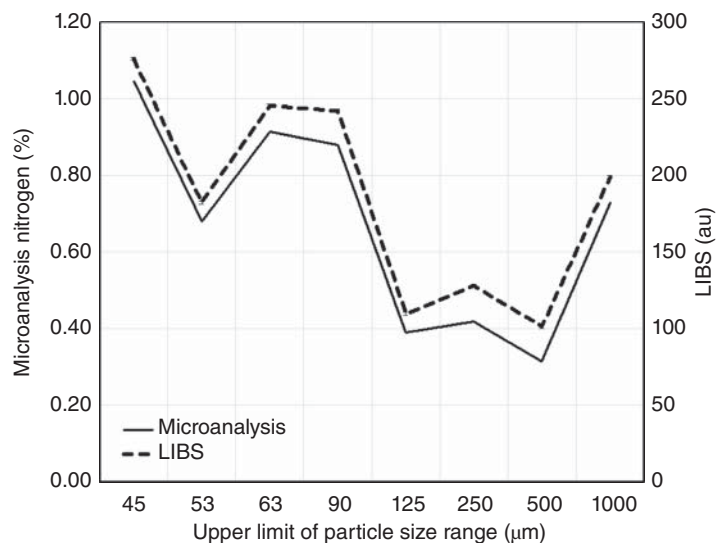


**Figure 14.2** Comparison between the response from a portable LIBS system at 746.83 nm and nitrogen concentration determined by microanalysis for pellets containing soil particles in different size ranges. Source: Yan et al. (2018). © 2018, Royal Society of Chemistry.

craters with fewer fractures, which improves spectra quality. LIBS performance in determining nitrates in soil was similar to the reference microanalysis by ion chromatography and colorimetric analysis (Figure 14.2). The analysis of the total N content by LIBS followed similar trends to quantitative results obtained by microanalysis.

Recently, a handheld LIBS spectrometer was successfully employed for nutrient detection in soil in the study by Erler et al. (2020). An in-field spatially differentiated determination of various soil parameters was achieved, giving the total mass fractions of the major nutrients (Ca, K, Mg, N, P) and the trace nutrients (Mn, Fe). A representative LIBS spectrum of a soil sample acquired in this study is presented in Figure 14.3. Further relevant soil parameters not directly related to one element, humus content, and soil pH value, as well as plant-available P content, were successfully determined as well. The methodology employed various multivariate regression methods for calibration and prediction to mitigate the noticeable impact of the soil matrix, and the best prediction results were obtained for Ca, K, Mg, and Fe. The performance was lower in the case of Mn due to a much lower concentration level, while the analysis of N and P content deviated because of the low atomic number and very weak intensities of the corresponding emission lines, and those nutrients could only be determined *qualitatively* with the handheld instrument. Multivariate analysis was deemed much more capable of accounting for matrix

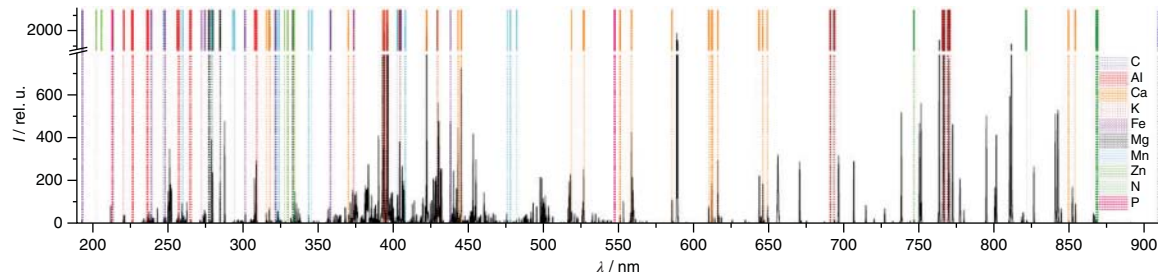


**Figure 14.3** Representative laser-induced breakdown spectroscopy (LIBS) spectrum of a soil sample studied by Erler et al. (2020), lines of the elements investigated is marked by colored lines (labels on the right). Source: Erler et al. (2020). Licensed Under CC BY 4.0.

effects and enabled creating more robust (i.e. universal) calibration models. Handheld LIBS instrumentation easily delivers spatially differentiated sensor information, a critical advantage in modern precision agriculture (Erler et al. 2020).

Over the past decade, the potential of portable LIBS technology has been recognized in agriculture and food-related sciences. In the former sector, analytical methodologies aimed at elemental analysis of soil are relatively well-established at the moment, including continuing research on improved quantitative approaches. A number of studies demonstrated the potential of portable LIBS to perform analyses of plant materials as well. LIBS exemplifies good applicability for major and minor nutrient analyses, particularly for lighter elements. Current research and development mostly aim at improving various performance factors of the LIBS technique. A notable progress has been achieved in enhancing LOD against some elements, mitigating the matrix effect, improving the spectra quality, e.g. signal intensity, leading to a better signal-to-noise ratio. Adoption of new spectra pretreatments and chemometric methods has improved the analytical performance of the technique. The fundamental development of LIBS instrumentation is noteworthy; implementation of novel technologies such as double-pulse (DP)-LIBS, femtosecond (fs)-LIBS, micro-LIBS, nanoparticle-enhanced LIBS, and 3D elemental imaging systems may stimulate the progress of the portable instrumentation as well (Nicolodelli et al. 2019). The advance achieved in portable LIBS technology in agricultural applications, alongside developments stimulated by the metallurgical industry, creates promising prospects for the applicability of this technique in other fields. It should be anticipated that, in the forthcoming years, portable LIBS will be increasingly more used in the food sector, in which the potential of this technique may not yet been fully acknowledged.

### 14.2.3 Nuclear Magnetic Resonance

The NMR technique falls into two broad classes: chemical shift analysis and relaxometry. Practical miniaturization of NMR instrumentation became possible mostly in the latter form (Capitani et al. 2017). However, promising developments in the compact technology falling into the former class should be noted (see the last paragraph in this Section). Implementation of NMR relaxometry (NMRR) refers to the study and/or measurement of the relaxation of the nuclear spin systems, which rate depends on the dynamics (i.e. mobility) of the molecular environment and the external magnetic field. The relaxation rate is a function of the fluctuating local magnetic field highly specific to the dynamics of a given molecular composition, thus yielding a fingerprint of the sample. In relaxometry, instead of an entire NMR spectrum, only relaxation time as one specific parameter is measured. Unlike in NMR spectroscopy (refer to Chapter 20, Volume 1), low homogeneity fields are used. NMR relaxation phenomenon is characterized by relaxation times of, respectively, longitudinal relaxation  $T_1$  and transverse relaxation  $T_2$ . Note, there exist fundamental differences in the quality of information available in portable NMR relaxometry compared with benchtop instrumentation. Because of a strongly inhomogeneous magnetic field in the case of the former, the NMR signal decays rapidly. It is only registered as an echo with no direct availability of free induction decay (FID) signal.

Further, the property of such field includes a strong gradient; this results in molecular diffusion effects (stronger for smaller molecules), causing an apparent shortening and artifacts in the measured  $T_2$ . Moreover, further effects appear (mixing of  $T_1$  and  $T_2$ ; early echo effect) that make only an effective  $T_{2\text{eff}}$  directly available. The average measured  $T_{2\text{eff}}$  can be divided into intermediate and the longest components,  $T_{2a}$  and  $T_{2b}$ , respectively (Capitani et al. 2017). The physical principle of NMR relaxometry enabled designing miniaturized sensors for analyzing in situ the matrices in a nondestructive manner. In contrast to the benchtop instruments capable of using a strong magnetic field gradient, the inhomogeneous magnetic field is more suitable for portable NMR devices but limits the spectrum of their applications. The development of powerful, rare-earth-based, permanent magnets (Casanova et al. 2008) has enabled the development of increasingly smaller NMR instruments, both those measuring chemical shifts and relaxometers. The most common portable sensors incorporate the unilateral principle with an open geometry of the magnet. The so-called “single side” instruments feature the magnet fixed to one side, followed

by the open space for sample interrogation. Single-sided sensors are more suitable for miniaturization and convenient in practical use, as easy sample access is provided. However, the field inhomogeneity markedly lowers their sensitivity and robustness. These portable instruments are incapable of measuring the FID and instead rely on registering the echo signal. Nonetheless, various analytical methods have been successfully developed based on those devices, which found numerous practical applications.

In the food sector, the portable low-field proton NMR relaxometers are extensively used for noninvasive analysis of foods (e.g. Bruker minispec ProFiler, <https://www.bruker.com/products/mr/td-nmr/minispec-profiler.html>). As proton analyzers, these instruments are sensing C–H, N–H, and O–H functional groups abundant in major chemical constituents of foods. In particular, the relaxation parameters and amplitude of the NMR signals are sensitive probes of the diffusion and movement of H<sub>2</sub>O molecules, thus they deliver information on water content in food-related items. Moisture analysis can be performed instantaneously and without sample pretreatment. Other typical applications include the analysis of oil content in food emulsions and solid fat content (Capitani et al. 2017). Once developed, these methods can be easily transferred to quality control applications as standard protocols.

The advent of low-field NMR sensors provided a breakthrough for food sciences applications. Their portability and straightforward sample examination process are particularly important for rapid, high-throughput analysis of foods, including packaged items, in industrial environments. The analysis yields information on the compositional analysis and structural characterization (e.g. matrix properties such as intermolecular interactions and local chemical environment; Bertocchi and Paci 2008; Hatzakis 2019) of food materials. Recently, the performance of these devices has progressed, particularly in the area of quality control, owing to unilateral magnets, yielding higher sensitivity and shorter analysis times. Further, applications developed for monitoring cultivation processes such as ripening, growth rate of fruits, and drying process, are known (Capitani et al. 2017).

The study by Guthausen et al. (2004) serves as an example of the early adoption of a portable NMR analyzer for quality control of foods. Fat content is one of the most important quality parameters of most food products, particularly highly processed ones. Several destructive techniques are used in conventional food analytical routines to determine the amount of fat in a given product. As demonstrated by Guthausen et al. (2004), a dedicated portable NMR analyzer was capable of quantifying the fat content in a packaged product in a nondestructive manner. The study evaluated two different methods suitable for elucidating useful information from low-field NMR measurements. The first one, proposed as a diffusion-weighted method, took advantage of the distinctively different diffusion coefficients  $D$  between fat ( $9.8 \times 10^{-12} \text{ m}^2 \text{ s}^{-1}$ ) and water ( $2.3 \times 10^{-9} \text{ m}^2 \text{ s}^{-1}$ ). The diffusion coefficient corresponds to the echo time  $\tau$ . Fat and water content in the sample were then determined from transverse magnetization decay (Guthausen et al. 2004), which is influenced by relaxation processes and diffusion. The second approach was a more routine relaxation time method, as the relaxation times for water and fat markedly differ and can be used to differentiate these two constituents. The former approach was based on the fact that diffusion coefficients of fat and water molecules are different by more than an order of magnitude; the corresponding analysis yielded correlation coefficient  $R = 0.996$  against the fat content known from reference measurements. The latter adopted the differences between the relaxation times of these two species; the obtained correlation coefficient was 0.991. However, the diffusion-weighted approach was developed for specific experimental circumstances and deemed not transferrable to the devices operating with homogeneous fields. The authors concluded that the obtained linear correlation allowed a straightforward application of single-sided NMR devices for fat analysis in foods.

The portable NMR method for analysis of fat content in foods has continued to be developed and applied. For instance, Veliyulin et al. (2005) developed the method for rapid, minimally intrusive determination of fat content in live Atlantic salmon. A mobile low-field NMR analyzer was calibrated against a set of reference samples (fish oil in agarose) and used for fat determination in anesthetized fish specimens, with the total time of analysis of 20 seconds per fish. For the purpose of evaluating the method, the results from the NMR analysis were validated against reference destructive measurement of the fat content obtained from the same fish specimen. A significant

correlation of  $R = 0.92$  with the reference data was observed. The authors concluded that the mobile NMR sensor is suitable for nondestructive fat content analysis in Atlantic salmon. Recently, Nakashima (2019) reported that a surface scanner utilizing this technology is applicable to nondestructive quantification of lipid and water in meat block samples of farmed bluefin tuna (*Thunnus thynnus*).  $^1\text{H}$  NMR relaxation measurements of the fresh meat block samples were performed at room temperature with 70 seconds per sample. The developed method yielded prediction errors of 3.7 g/100 g and 2.7 g/100 g for the lipid and water weight fractions, respectively. Therefore, the method demonstrates room for further improvements in terms of accuracy. However, it was noted that the effective sensing depth reached 3 cm beneath the sample surface. Consequently, a nondestructive quantification of lipid and water in intact meat blocks is possible, with effective sensing beneath the package, thick scales, skin, and subcutaneous fat (Veliyulin et al. 2005). Therefore, quality control of the whole intact tuna blocks in markets and seafood factories was shown as feasible with a portable NMR analyzer.

Agricultural applications of portable NMR analyzers are progressing as well. For example, the technique's sensitivity toward water content may be successfully employed for controlling drying processes. In particular, the drying of fruits is a critical conservation measure, and their moisture may highly influence the post-harvest processing and storage. Moreover, the dryness of such products is an important quality standard. Monitoring the water content in fruits is critical for optimizing the drying process to minimize the thermal damage and the loss of fruit's quality. Fruits with high sugar content are relatively more resistant to losing moisture, for example, pears with their relatively high sugar concentration (60–75 g of carbohydrates per 100 g of dry fruit). In the study by Adiletta et al. (2015), the effect of the drying process of pear (*Pyrus communis*) samples was explored using an analytical method based on portable NMR instrumentation. This technique enabled elucidating the water transport mechanism and drying kinetics in pears undergoing the drying process at 50 °C. The  $^1\text{H}$  NMR relaxation time enabled measuring the moisture profile during the 30 hours of sample drying time. Those nondestructive measurements were found to be in an excellent correlation ( $R^2 = 0.978$ ). The reference results on the drying kinetics data obtained by standard weight measurements were performed for the selected sample sections: exterior, intermediate, and central section of a fruit. Here, a portable NMR analyzer enabled exploring the drying kinetics and elucidating the effect of drying on the textural and physical structure of pear fruits. However, it may be noted that the approach proposed by Adiletta et al. (2015) required rather time-extensive measurements, and future development of a more rapid analysis would be a major improvement.

The ability of the portable NMR technique to sensitively screen water-related molecular properties of the sample was employed by Capitani et al. (2013) to follow the metabolic features of kiwifruits. The study focused on profiling of aqueous extracts of Zespri Gold (*Actinidia chinensis*) and CI.G cultivar, which are a controlled cross-breed from different species of *A. deliciosa*. The water state (understood as the differences in relaxation dynamics of water resulting from the local chemical environment) of the outer pericarp of entire kiwifruits was monitored over the season. Interestingly, the portable low-field  $^1\text{H}$  NMR device supplemented the benchtop high-field NMR spectrometer yielding appropriate  $^1\text{H}$  NMR spectrum in this study. Through comparison with the reference benchtop NMR data, it was noted that  $T_2$  relaxation time was registered shorter on the portable analyzer as the result of the inhomogeneous field that it generates. The authors successfully interpreted the collected data; the average  $T_{2a}$  relaxation time was assigned to proton dynamics in the cytoplasm and extracellular space, while  $T_{2b}$  was ascribed to protons in the vacuole. Those relaxation times lengthened with the season-wise progressing sample measurements. The corresponding spin population increased with the season for the former, while it decreased with the season for the latter. The  $T_2$  relaxation times were found highly sensitive to the kiwifruit developmental stage from October to February.

In contrast, constant values were observed for the measurements performed before October. However, the ratio between the spin populations was deemed sensitive to the kiwifruit developmental stage over the whole season. The results were compared with the data on Hayward cultivar of kiwifruits published earlier in the literature (Capitani et al. 2010). Metabolic profiling confirmed the more rapid maturation of the Zespri cultivar compared with the two other varieties (Capitani et al. 2010, 2013). A portable NMR analyzer is capable of determining in situ

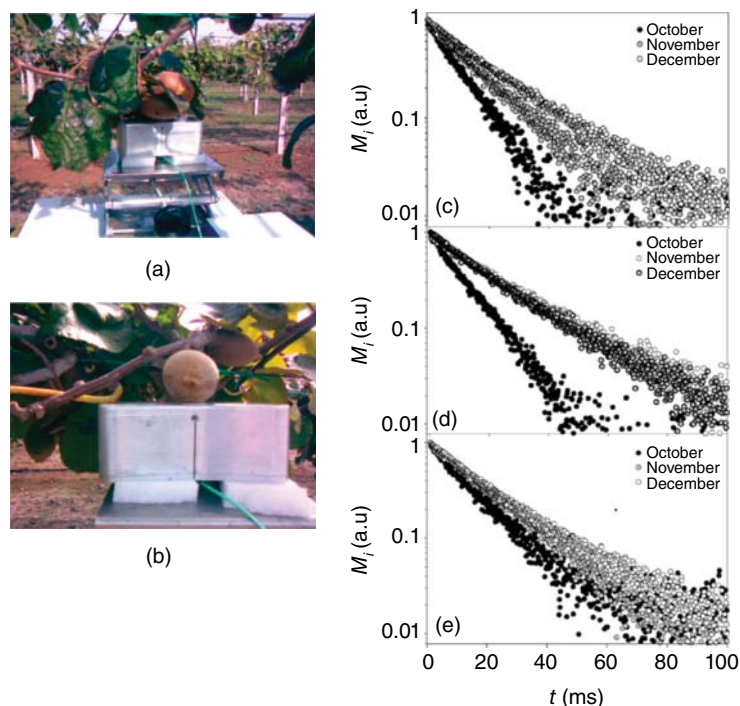


**Figure 14.4** Measurements in the field on entire kiwifruits attached to the tree with a portable unilateral NMR instrument (a, b). CPMG decays were measured in October, November, and December on Hayward (c), Zespri (d), and Cl.GI (e) kiwifruits (a.u. = arbitrary unit). *Source:* Reprinted with permission from Capitani et al. (2013). © 2013, American Chemical Society.

the water state of entire, live kiwifruits attached to the plants or detached from the plants (Figure 14.4). The technique enables straightforward and rapid analysis of the kiwifruit developmental stage. The information on fruit metabolism is available as well. It can be elucidated from the relaxation dynamics of water in the analyzed fruits, as it depends on the metabolites present in the sample. Noteworthy, benchtop NMR spectroscopy is an established technology in food-related metabolomics (Tomassini et al. 2013). Still, the use of unilateral NMR devices is somewhat limited in this field. Further improvements of the instrumentation and data analytical methods will be required to expand their utilization to a broader range of food matrices and to develop protocols for online inspections for monitoring quality and food processes. Nonetheless, it should be anticipated that portable NMR techniques would become increasingly popular in the forthcoming decade. Developments of portable NMR techniques progressing in other fields bring potential benefits for agricultural applications as well. For instance, a portable low-field  $^1\text{H}$  NMR analyzer with a unilateral, small-sized permanent magnet was successfully employed to *in situ* assessment of moisture protective properties of woods coated with various types of commercial paints. Development of low-cost, portable NMR sensors is a continuing trend in the current decade (e.g. Pourmand et al. 2011; Kerr et al. 2019).

Attention should be given to agricultural applications of compact benchtop NMR spectrometers. For example, Pinter et al. (2014) developed an approach to track factory relevant tomato paste spoilage. The sample was successfully interrogated in bulk, in large metal-lined totes of  $1000 \text{ dm}^3$  capacity. A single-side sensor with a reduced magnetic field monitored the relaxation properties of sterile and unsterile samples. An increase in  $T_1$  values for the unsterile samples was concluded as a practically useful marker of tomato paste spoilage. More importantly, the developed method was described as fully compatible with downsized portable sensors, which could be used in industrial applications (Pinter et al. 2014).

It is noteworthy that currently, the development of portable NMR instrumentation is at its peak. Extremely compact, high-performing, and easy-to-use sensors appear on the market, such as WaveGuide Formula (1.4 kg weight, operating with various pulse sequences). In a laboratory-scale, benchtop high-field NMR spectrometers yield an outstanding level of sensitivity and chemical specificity highly suitable for testing and controlling food authenticity. In addition to relaxometers, compact NMR spectrometers have been developed (Blümich 2016). This technology has been made available very recently and is not yet fully adopted for practical routines in the food and agriculture sectors. Nonetheless, promising progress in this technology (Zalesskiy et al. 2014) may bring new opportunities for applications in food and agriculture-related sciences in the near future. Additionally, the magnetic resonance imaging (MRI) technique is applicable in the laboratory for spatially-resolved measurement of foods (Guthausen 2016). As a quality control analysis, it can assess the defects, internal structure, and other quality-related parameters (Patel et al. 2015). Low-field MRI systems have been used in foodstuff investigations (Oztop et al. 2014). While still being far from implementable in an on-site deployable, portable format, the MRI technology progresses presently (Federal Drug Association announcement) (<https://www.fdanews.com/articles/195877-hyperfines-bedside-mri-system-nabs-510k-clearance> accessed 15 February 2020), bringing the concept of portable MRI closer to reality.

#### 14.2.4 Mass Spectrometry

MS is a highly potent technique for molecular analysis with a number of practical advantages for applications within the food and agriculture sectors (Ellis et al. 2015). As a targeted analytical method, MS offers superior sensitivity and chemical specificity. Highly sensitive (sub-mg concentrations) and accurate identification and quantification of known molecules within complex matrices, typically found in food and agriculture items, is feasible. On top of very low detection limits and rapid analysis, the technique stands out due to wide molecular applicability, with suitability toward small and large organic, inorganic, volatile, nonvolatile, single-analyte molecules as well as complex mixtures. For those reasons, MS is established as the gold standard analytical method in the agri-food field, often coupled to chromatographic techniques to provide fingerprinting capability. Coupled MS techniques (e.g. liquid chromatography–MS (LC–MS) and gas chromatography–MS (GC–MS)) and MS/MS substantially reduce the need for sample preparation and enhance the selectivity for both qualitative and quantitative analysis of analytes present in complex matrices. Matrix assisted laser desorption ionization-time of flight MS (MALDI-TOF MS) systems are used to detect pollutants, toxins, and biomolecules in agro-food items, with the ability of direct profiling and imaging of the sample. Some MS methods have the fingerprinting capability on their own, using a direct sample acquisition by MS instrument without any prior chromatographic separation (Ellis et al. 2007). For instance, MS fingerprinting by means of direct infusion (i.e. injection) mass spectrometry (DIMS) was employed by Howlett et al. (2014) for the characterization of a foodborne pathogen *Campylobacter jejuni*. In another form, a fingerprint-capable desorption electrospray ionization (DESI) technique was used to examine melamine migration into foods from tableware (Mattarozzi et al. 2012). Laboratory scale MS is an established and matured technique, particularly potent in analyzing and authenticating food adulteration and contamination. However, the detection of nontarget or unknown molecules remains a challenge for MS analysis performed in complex matrixes of agro-food items. In such cases, relying on databases of chemical ingredients and contaminants increases the chance for successful identification. An exhaustive overview of state-of-the-art lab-scale MS is available from Ellis et al. (2012) and Bowers and Taylor (2017). Given the physicochemical potential of MS, a strong stimulus for development toward instrument miniaturization was noticed over the past two decades (Ellis et al. 2015). The last decade witnessed a continued progress in the level of portability of the MS instrumentation, with the appearance of handheld devices weighing less than 4 kg (Ouyang and Cooks 2009), implementation of low-temperature plasma, paper spray compact, or low-power pumping systems (Ellis et al. 2015). Miniature mass spectrometers are described in Chapter 14, and portable GC–MS in Chapter 15, Volume 1.

In the past three years, there has been a notable increase in the literature pertaining to MS in food safety and quality analysis. Rapid, reliable, and accurate MS techniques for detection, identification and quantification of analytes in food samples are very useful for food safety and quality control applications. Some exhaustive overviews of the applications of MS in food safety and quality analysis are available in focused reviews (Wang et al. 2013). The development of simple, robust, and reliable portable MS instrument for *in situ*, rapid, accurate identification, and quantification of compounds in food samples remains an active field. Repeatedly occurring large-scale food counterfeits and rapidly increasing food-adulteration hazards have led to focused developments of analytical methods for screening against unwanted contents in foods. The research aimed at that direction, detection, and quantification of melamine contamination has attracted particular attention in the past decade. Efforts were made to adopt a compact MS technology for direct analysis of melamine in complex matrices of foods. For example, Huang et al. (2010) developed an analytical approach to this problem based on a portable mass spectrometer using a low-temperature plasma ambient ionization source. This type of source enables small size and low power consumption in a portable MS instrument and translates to direct sampling without any sample pretreatment. The key modification of this design vs. the standard discontinuous atmospheric pressure interface (DAPI) was the supplementary pumping that increased the ion transfer efficiency. Thus, atmospheric pressure ion sources could be directly connected to the MS system. The method was aimed at the determination of melamine content in whole milk and related materials. Straightforward detection of melamine contamination in whole milk, fish, milk powder, and other complex matrices without sample pretreatment was enabled accordingly. The performance of the analysis included LOD of 250 ng/mL in whole milk, notable below the regulatory levels (e.g. 1 µg/mL in the US; 2.5 µg/mL in the EU), a linear dynamic range of 0.5–50 µg/mL with the relative standard deviation of 7.6–16.2% with a very good time-to-result ratio of two samples per minute. In conclusion, portable MS enabled a rapid, sensitive, and highly specific quantitative analysis of melamine content with performance fully suiting regulatory levels. Thermally-assisted desorption and ionization of the analyte offer considerable advantages in practical applications for food analysis.

Analysis and discrimination of microorganisms *in situ* are prominently important for assessing the quality of food and agriculture items. However, the conventional biochemical techniques such as enzyme-linked immunosorbent assay (ELISA) or polymerase chain reaction (PCR) are particularly inefficient and time-consuming and troublesome for application *in situ*. With a potential benefit to agri-food applications, methods for the characterization of bacteria colonies were developed based on a miniaturized benchtop spectrometer using the principle of paper spray MS (PS-MS) ionization (Pulliam et al. 2016). The compact instrument used in this study (Mini 12; Li et al. 2014) weighs under 4 kg and has MS/MS capability. Although not fully autonomous, this spectrometer is miniaturized, with the need to be interfaced with an ambient ionization source. Because of the very compact dimension, it may be considered transportable/shareable between laboratories, which increases its practical value.

Further, it accomplishes the highly desired ability to perform analysis with no sample pretreatment and to operate by untrained personnel (Li et al. 2014). In the study by Pulliam et al. (2016), MS analysis in the negative ion mode was performed using the miniaturized MS system operating in the full scan mode to speciate bacteria and the MS/MS mode lipid identification. Negative ion mode was chosen because the authors were examining phospholipids; however, positive ion mode analysis of lipids has been previously demonstrated. In addition, a fully suited benchtop MS utilizing the linear ion trap MS working principle was used for comparative measurements. Noteworthy, the miniaturized device was capable of performing the same scan functions as its full-scale benchtop counterpart. Therefore, valuable comparative observations were made. Eight species of bacteria were analyzed in their study; *B. subtilis*, 3 Gram-positive species (*S. aureus*, *S. epidermidis*, *S. agalactiae*) and 4 Gram-negative species (*P. aeruginosa*, *E. coli*, *A. baumannii*, and *A. lwoffii*). *B. subtilis* was used to establish the mass range of the compact MS system, and the phospholipid profiles for Gram-positive and Gram-negative bacteria were established. Tandem MS/MS technique is highly potent in compound identification and quantitative performance due to noise

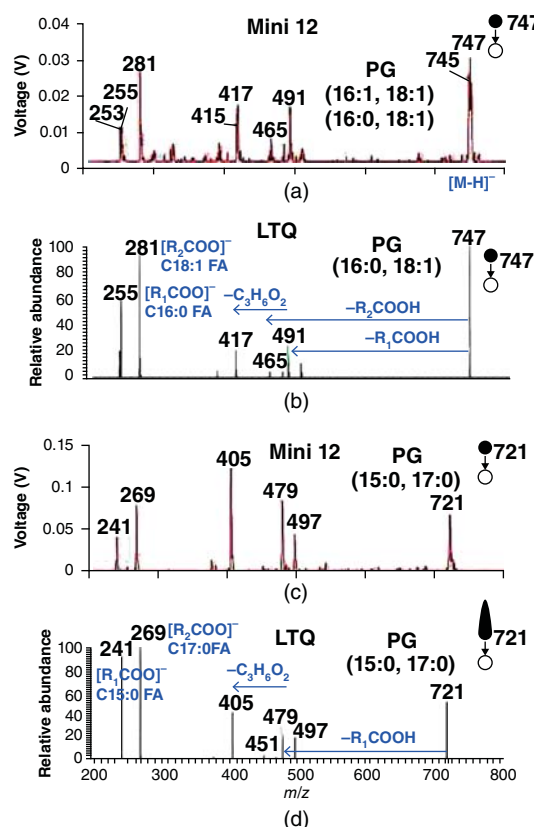


**Figure 14.5** Negative ion mode MS/MS of  $m/z$  747 in *P. aeruginosa* and  $m/z$  721 in *S. aureus* using paper spray and: (a, c) miniature mass spectrometer; (b, d) benchtop linear ion trap mass spectrometer. Source: Pulliam et al. (2016). © 2016, Royal Society of Chemistry.

reduction and quantitation. Retaining these capabilities by the compact MS analyzers is a substantial goal for their wider applicability, and the ability to have this capability in a transportable format would be highly desirable.

In the study by Pulliam et al. (2016), the MS/MS measurements in negative ion mode performed on the compact device were compared with the reference results from the benchtop spectrometer. For example, they compared MS/MS product ion spectra of  $m/z$  747 in *P. aeruginosa*, and  $m/z$  721 in *S. aureus*, corresponding to the two typical phosphoglycolipids (PGs) observed from these microorganisms (Figure 14.5). The primary peaks were measured similarly in both mass and intensity on both instruments. The quantitative comparison between the peak intensities measured on different instruments requires tuning of collision energy, activation time, and pressure. The tandem MS/MS spectra of a lipopeptide (surfactin) produced by *B. subtilis* and most of the high mass fragments of surfactant were relatively similar as well. The study by Pulliam et al. (2016) confirmed that highly compact benchtop MS spectrometers are capable of sensing meso-sized molecules through a reproducible analysis of lipids in bacteria. Despite smaller day-to-day variations, the distinct differences in the lipid profiles obtained from the investigated bacteria species were observed. Hence, these accomplishments demonstrated a high potential for direct analysis of microorganisms by compact MS instrumentation for environmental protection, food safety, or agriculture. Although this was performed for relatively high concentrations of bacteria, research needs to be continued to enable many future many applications in low-level bacteria scenarios. Future directions may also involve developing an effective in situ MS analysis of bacteria using miniaturized benchtop devices without the burden of culturing the specimen.

Other application fields, such as environmental research and ecology, continue to drive the development of portable MS analytical methodologies. These applications have similar requirements to those faced in agriculture sciences. For example, herbicide content is an important quantity from the point of view of environmental

monitoring and in assessing the safety of agro-food items. An effective herbicide analysis can be performed with a miniaturized MS system combined with electrospray ionization (ESI), via an analysis of polar and thermally labile organic compounds, in low sample volumes of 20–30 µL (Janfelt et al. 2012). The device was designed to operate without pumps and supplementary sheath gases to achieve field deployability. Further, the unit features a capillary spray cell directly compatible with micro-extraction techniques for sample pre-concentration. The instrument proved capable of detecting common herbicides (Atrazine, Prometryne, Terbutryne, and Triadimefone) at LODs of 1 mg/L and quantitative reproducibility of ±30%. It may also be possible to use portable MS systems to help understand plant physiology by evaluating plant-insect communication mechanisms. An efficient, sensitive, and nonintrusive collection and analysis of chemical cues from plants *in situ* is indispensable for such investigations. Research into this direction may be advanced by employing portable MS analyzers, as demonstrated by Beck et al. (2015). They employed a handheld, portable GC-MS system to discriminate between mechanically damaged and undamaged flower heads of yellow starthistle (*Centaurea solstitialis*). The method was developed to be applicable not only for a potted plant but in a natural plant environment scenario as well. The portable GC-MS system, using a needle trap adsorbent technology, was employed to identify and analyze biomarker volatiles of varying yellow starthistle with respect to different treatments. In total, 31 biomarker volatiles were distinguished from the four treatments during rapid analysis that took less than three minutes per single GC-MS run. Principal Component Analysis (PCA) classification distinguished four distinct groups corresponding to the four batches – damaged and undamaged potted plants and damaged and undamaged natural plants. Damage-specific biomarkers were identified in the process. Hence, the developed method successfully distinguished the treatments based on volatile biomarker profiles measured by a portable GC-MS system.

Portable MS technology can be made efficient and accurate for the analyses of various plant products. As recently evidenced by Jjunju et al. (2019), a portable MS system coupled to a direct inlet membrane (DIM) probe may be applied to a direct *in situ* analysis of essential fragrant oils. The active fragrant compounds, which are commonly used in the formulation of flavors and fragrances (3-methylbutyl acetate, 2-methyl-3-furanthiol, methyl butanoate, and ethylmethyl sulfide), were measured in real time (Figure 14.6). The study confirmed that this instrumentation could detect the traces of the active fragrant compounds in complex raw products, such as mixtures of essential fragrant oils *in situ*. The method achieved very low LOD in the (<2.5 pg) and very good linearity with a relative standard deviation of 5–7% for the studied active fragrant compounds. The identification of the fragrance's active compounds in essential oil samples (banana, tangerine, papaya, and blueberry muffin) was possible by comparison with a standard fragrance compound mixture analyzed by GC-MS and compared with the NIST standard reference library. Therefore, a route for rapid qualitative and quantitative analysis of essential fragrant oils *in situ* by means of a portable MS instrument was established.

### 14.3 Current Developments, Remaining Challenges, and Future Prospects

It is widely understood that the agro-food sector benefits enormously from the new generation of portable spectroscopy and spectrometry instruments. The current portable technology offers a major advantage over the conventional approaches in terms of in-field deployability. However, other significant values of novel sensors need to be acknowledged: speed, flexibility, and low cost of analysis. Future evolution is likely to be aimed at ease-of-operation, with the ultimate goal of minimal user involvement, enabling widespread applications with no reliance on trained personnel. The progress in miniaturization technology of the instrumentation is noteworthy, with considerable successes in the development aiming to implement the “spectrometer chip” concept. The major breakthroughs required to make this concept a reality have been accomplished, e.g. for optical spectroscopy (FT-IR sensors; Sieger and Mizaikoff 2016) as well as for NMR (Zaleskiy et al. 2014). This trend will likely continue in the forthcoming decade. Some optical spectroscopy technologies have currently achieved a smartphone-level of deployability (Rateni et al. 2017; McGonigle et al. 2018). While the techniques described

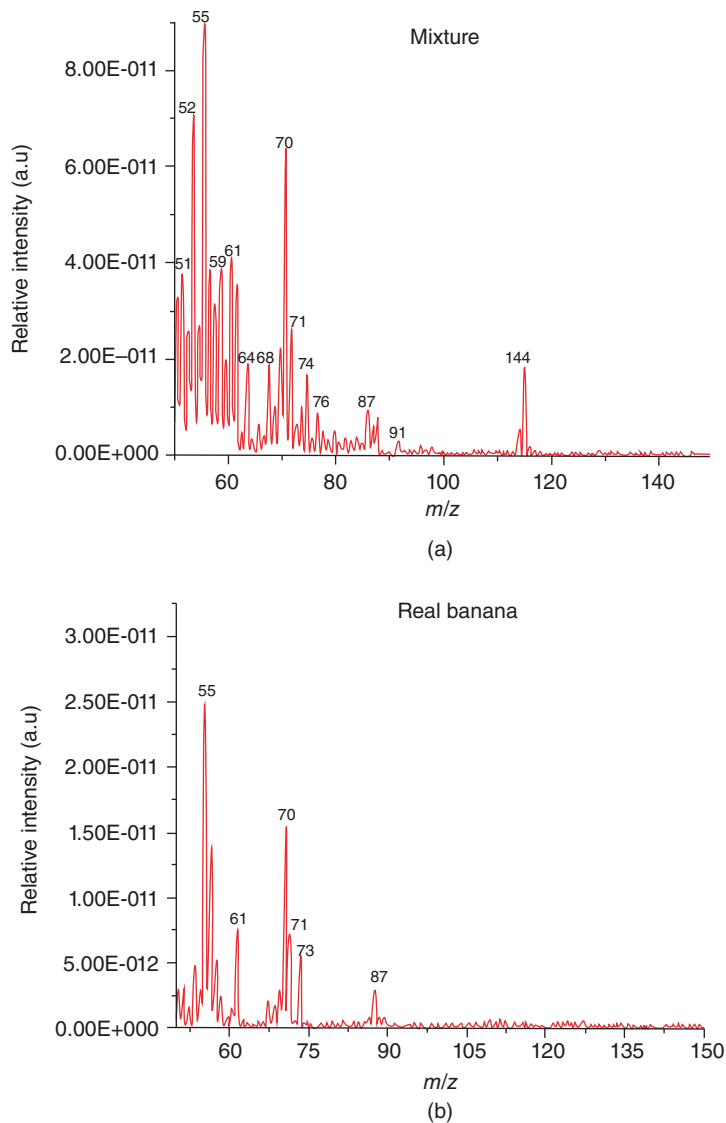


**Figure 14.6** In situ analysis of standard model compounds in an artificial; (a) mixture of 3-methylbutyl acetate, 2-methyl-3-furanthiol, methyl butanoate, and ethylmethyl sulfide in equal volumes of 10 ppm (v/v) using a direct membrane probe coupled to a portable mass spectrometer. Approx. 5  $\mu$ L of the mixture was deposited in the flask and left for two hours. The headspace vapor of the mixture was detected using a portable mass spectrometer coupled to a direct membrane probe and (b) shows the mass spectrum of the real banana headspace vapor measured using a DIM probe with a portable mass spectrometer. Source: Ijjunju et al. (2019). Licensed Under CC BY 4.0.

in this chapter are not quite there yet, nonetheless, the breakthroughs in the hardware layer have been made. Currently, the refinements of the instrumentation, its optimization, and miniaturization are still ongoing.

Further progress in the application field depends strongly on establishing cost-effective, self-sustained, integrated, miniaturized spectroscopic/spectrometric sensors. At the same time, developments in data-analytical methods, user-friendly algorithms, and interfaces accessible for nonspecialist personnel are essential for a variety of on-site applications. Continuing advancement into these research directions is essential, enabling the

development of “universal techniques,” which will be routinely used by nonspecialists within a wide range of applications outside of laboratories, such as in agriculture or food production and supply chains.

## 14.4 Concluding Remarks

The significance of maintaining the quality and safety of agro-food raw materials and products is indisputable, as they have a worldwide market reach. Yet, despite a dense network of regulatory and legal measures, recent years have seen increasingly frequent compromises of food safety, resulting in loss of health or life, and in many cases, significant economic damage. The risks of accidental contamination are present at all stages of food production and supply chain. Further, multiple examples of money-driven (i.e. criminal) intentional counterfeiting and adulteration of foods are known. Therefore, it is becoming challenging to maintain the geographic origin and purity of food products that reach the market. Food quality relies on the prevalence of quality control procedures at multiple stages of supply and delivery. To ensure consumer safety, physicochemical methods of analysis, deployable on-field, and capable of rapid, sensitive, and reliable analysis are indispensable.

Consequently, there is a great demand from the society and agro-food industries for these analytical methods to be deployable in-field for routine testing. Further, nondestructive techniques that do not compromise the market value of a product are preferred. Those qualities are featured in the modern technology of portable spectroscopy/spectrometry which underwent a leap in development in the past decade. Consequently, applications of portable spectroscopy and spectrometry thrived in this sector. In this chapter, we discussed numerous examples of analytical methods developed on the basis of portable XRF, LIBS, NMR, and MS instrumentation for solving the major issues faced in agricultural and food-related analyses. Those include direct food adulteration, pesticide/herbicide control, contamination by heavy metals and toxic elements, quantification of macro- and micro-nutrient and nutrition value, soil, and water quality assessment for agriculture, to name a few. While the instrumentation currently continues its rapid development, the future progress will rely relatively more on making this technology more accessible for nonspecialized personnel. Well-designed software and integrated data-analytical methods should unveil a spectrum of new applications in the food and agriculture-related fields.

## References

- Adiletta, G., Russo, P., Proietti, N. et al. (2015). Characterization of pears during drying by conventional technique and portable non invasive NMR. *Chemical Engineering Transactions* 44: 151–156.
- Andersen, M.B.S., Frydenvang, J., Henckel, P., and Rinnan, Å. (2016). The potential of laser-induced breakdown spectroscopy for industrial at-line monitoring of calcium content in comminuted poultry meat. *Food Control* 64: 226–233.
- Anderson, D.L. (2003). Multielement analysis of housewares and other food-related items by a 241Am radioisotope X-ray fluorescence transportable spectrometer and handheld analyzers. *Journal of AOAC International* 86: 583–597.
- Anderson, D.L. (2009). Screening of foods and related products for toxic elements with a portable X-ray tube analyser. *Journal of Radioanalytical and Nuclear Chemistry* 282: 415–418.
- Anderson, D.L. and Cunningham, W.C. (1996). Nondestructive determination of lead, cadmium, tin, antimony, and barium in ceramic glazes by radioisotope X-Ray fluorescence spectrometry. *Journal of AOAC International* 79: 1141–1157.
- Anderson, D.L., Cunningham, W.C., Lindstrom, T.R., and Olmez, I. (1995). Identification of lead and other elements in ceramic glazes and housewares by  $^{109}\text{Cd}$ -induced X-ray fluorescence emission spectrometry. *Journal of AOAC International* 78: 407–412.

- Barbaifieri, M., Pini, R., Ciucci, A., and Tassi, E. (2011). Field assessment of Pb in contaminated soils and in leaf mustard (*Brassica juncea*): the LIBS technique. *Chemistry and Ecology* 27: 161–169, Supplement.
- Beck, J.J., Porter, N., Cook, D. et al. (2015). In-field volatile analysis employing a handheld portable GC–MS: emission profiles differentiate damaged and undamaged yellow starthistle flower heads. *Phytochemical Analysis* 26: 395–403.
- Bertocchi, F. and Paci, M. (2008). Applications of high-resolution solid-state NMR spectroscopy in food science. *Journal of Agricultural and Food Chemistry* 56: 9317–9327.
- Bilge, G., Sezer, B., Eseller, K.E. et al. (2016). Determination of whey adulteration in milk powder by using laser induced breakdown spectroscopy. *Food Chemistry* 212: 183–188.
- Blümich, B. (2016). Introduction to compact NMR: a review of methods. *Trends in Analytical Chemistry* 83: 2–11.
- Bosco, G.L. (2013). Development and application of portable, handheld X-ray fluorescence spectrometers. *Trends in Analytical Chemistry* 45: 121–134.
- Bowers, M.T. and Taylor, S. (2017). Recent advances and development trends in miniature mass spectrometry. *International Journal of Mass Spectrometry* 422: 146–147.
- Byers, H.L., McHenry, L.J., and Grundl, T.J. (2019). XRF techniques to quantify heavy metals in vegetables at low detection limits. *Food Chemistry: X* 1: 100001.
- Cama-Moncunill, X., Markiewicz-Keszycka, M., Dixit, Y. et al. (2017). Feasibility of laser-induced breakdown spectroscopy (LIBS) as an at-line validation tool for calcium determination in infant formula. *Food Control* 78: 304–310.
- Capitani, D., Mannina, L., Proietti, N. et al. (2010). Monitoring of metabolic profiling and water status of Hayward kiwifruits by nuclear magnetic resonance. *Talanta* 82: 1826–1838.
- Capitani, D., Mannina, L., Proietti, N. et al. (2013). Metabolic profiling and outer pericarp water state in Zespri, CIGI, and Hayward kiwifruits. *Journal of Agricultural and Food Chemistry* 61: 1727–1740.
- Capitani, D., Sobolev, A.P., Di Tullio, V. et al. (2017). Portable NMR in food analysis. *Chemical and Biological Technologies in Agriculture* 4: 17.
- Casado-Gavalda, M.P., Dixit, Y., Geulen, D. et al. (2017). Quantification of copper content with laser induced breakdown spectroscopy as a potential indicator of offal adulteration in beef. *Talanta* 169: 123–129.
- Casanova, F., Blümich, B., and Perlo, J. (2008). *Single-Sided NMR*. Springer Science & Business Media.
- Charlebois, S. and MacKay, G. (2010). *World Ranking: 2010 Food Safety Performance*. Regina/Saskatchewan: Johnson-Shoyama graduate school of public policy.
- Cozzolino, D. (2012). Recent trends on the use of infrared spectroscopy to trace and authenticate natural and agricultural food products. *Applied Spectroscopy Reviews* 47: 518–530.
- Cozzolino, D., Porker, K., and Laws, M. (2015). An overview on the use of infrared sensors for in field, proximal and at harvest monitoring of cereal crops. *Agriculture* 5: 713–722.
- DeKieffer, D. (2006). Trojan drugs: counterfeit and mislabeled pharmaceuticals in the legitimate market. *American Journal of Law & Medicine* 32: 325–349.
- El Haddad, J., Villot-Kadri, M., Ismaël, A. et al. (2013). Artificial neural network for on-site quantitative analysis of soils using laser induced breakdown spectroscopy. *Spectrochimica Acta B* 79–80: 51–57.
- Ellis, D.I., Dunn, W.B., Griffin, J.L. et al. (2007). Metabolic fingerprinting as a diagnostic tool. *Pharmacogenomics* 8: 1243–1266.
- Ellis, D.I., Brewster, V.L., Dunn, W.B. et al. (2012). Fingerprinting food: current technologies for the detection of food adulteration and contamination. *Chemical Society Reviews* 41: 5706–5727.
- Ellis, D.I., Muhamadali, H., Haughey, S.A. et al. (2015). Point-and-shoot: rapid quantitative detection methods for on-site food fraud analysis – moving out of the laboratory and into the food supply chain. *Analytical Methods* 7: 9401–9414.
- Erler, A., Riebe, D., Beitz, T. et al. (2020). Soil nutrient detection for precision agriculture using handheld laser-induced breakdown spectroscopy (LIBS) and multivariate regression methods (PLSR, lasso and GPR). *Sensors* 20: 418.

- Evershed, R. and Temple, N. (2016). *Sorting the Beef from the Bull: The Science of Food Fraud Forensics*. London, UK: Bloomsbury Sigma.
- Ferreira, E.C., Milori, D.M.B.P., Ferreira, E.J. et al. (2008). Artificial neural network for cu quantitative determination in soil using a portable laser induced breakdown spectroscopy system. *Spectrochimica Acta B* 63: 1216–1220.
- Finger, R., Swinton, S.M., El Benni, N., and Walter, A. (2019). Precision farming at the nexus of agricultural production and the environment. *Annual Review of Resource Economics* 11: 313–335.
- Fleming, D.E.B., Foran, K.A., Kim, J.S., and Guernsey, J.R. (2015). Portable X-ray fluorescence for assessing trace elements in rice and rice products: comparison with inductively coupled plasma-mass spectrometry. *Applied Radiation and Isotopes* 104: 217–223.
- Gimenez, Y., Busser, B., Trichard, F. et al. (2016). 3D imaging of nanoparticle distribution in biological tissue by laser-induced breakdown spectroscopy. *Scientific Reports* 6: 29936.
- Gransee, A. and Führs, H. (2013). Magnesium mobility in soils as a challenge for soil and plant analysis, magnesium fertilization and root uptake under adverse growth conditions. *Plant and Soil* 368: 5–21.
- Guerra, M.B.B., Adame, A., de Almeida, E. et al. (2018). In situ determination of K, Ca, S and Si in fresh sugar cane leaves by handheld energy dispersive X-ray fluorescence spectrometry. *Journal of the Brazilian Chemical Society* 29: 1086–1093.
- Guthausen, G. (2016). Analysis of food and emulsions. *Trends in Analytical Chemistry* 83: 103–106.
- Guthausen, A., Guthausen, G., Kamrowski, A. et al. (2004). Measurement of fat content of food with single-sided NMR. *Journal of the American Oil Chemists' Society* 81: 727–731.
- Hahn, D.W. and Omenetto, N. (2010). Laser-induced breakdown spectroscopy (LIBS), part I: review of basic diagnostics and plasma—particle interactions: still-challenging issues within the analytical plasma community. *Applied Spectroscopy* 64: 335A–336A.
- Hahn, D.W. and Omenetto, N. (2012). Laser-induced breakdown spectroscopy (LIBS), part II: review of instrumental and methodological approaches to material analysis and applications to different fields. *Applied Spectroscopy* 66: 347–419.
- Hatzakis, E. (2019). Nuclear magnetic resonance (NMR) spectroscopy in food science: a comprehensive review. *Comprehensive Reviews in Food Science and Food Safety* 18: 189–220.
- Holbrook, E. (2013). Dining on deception: the rising risk of food fraud and what is being done about it. *Risk Management* 60: 28–31.
- Howlett, R.M., Davey, M.P., Quick, W.P., and Kelly, D.J. (2014). Metabolomic analysis of the food-borne pathogen campylobacter jejuni: application of direct injection mass spectrometry for mutant characterisation. *Metabolomics* 10: 887–896.
- Huang, G., Xu, W., Visbal-Onufraik, M.A. et al. (2010). Direct analysis of melamine in complex matrices using a handheld mass spectrometer. *Analyst* 135: 705–711.
- Huck, C.W., Pezzei, C.K., and Huck-Pezzei, V.A.C. (2016). An industry perspective of food fraud. *Current Opinion in Food Science* 10: 32–37.
- Jacquet, J.L. and Pauly, D. (2008). Trade secrets: renaming and mislabeling of seafood. *Marine Policy* 32: 309–318.
- Janfelt, C., Græsbøll, R., and Lauritsen, F.R. (2012). Portable electrospray ionization mass spectrometry (ESI-MS) for analysis of contaminants in the field. *International Journal of Environmental Analytical Chemistry* 92: 397–404.
- Jjunju, F.P.M., Giannoukos, S., Marshall, A., and Taylor, S. (2019). In-situ analysis of essential fragrant oils using a portable mass spectrometer. *International Journal of Analytical Chemistry* 2019: 1780190.
- Kaiser, J., Novotný, K., Martin, M.Z. et al. (2012). Trace elemental analysis by laser-induced breakdown spectroscopy – biological applications. *Surface Science Reports* 67: 233–243.
- Kerr, J.D., Balcom, B.J., McCarthy, M.J., and Augustine, M.P. (2019). A low cost, portable NMR probe for high pressure, MR relaxometry. *Journal of Magnetic Resonance* 304: 35–41.
- Kjærnes, U. (2012). Ethics and action: a relational perspective on consumer choice in the European politics of food. *Journal of Agricultural and Environmental Ethics* 25: 145–162.

- Le Vallée, J.C. and Charlebois, S. (2015). Benchmarking global food safety performances: the era of risk intelligence. *Journal of Food Protection* 78: 1896–1913.
- Li, L., Chen, T.-C., Ren, Y. et al. (2014). Mini 12, miniature mass spectrometer for clinical and other applications. Introduction and characterization. *Analytical Chemistry* 86: 2909–2916.
- Markiewicz-Keszycka, M., Cama-Moncunill, X., Casado-Gavalda, M.P. et al. (2017). Laser-induced breakdown spectroscopy (LIBS) for food analysis: a review. *Trends in Food Science & Technology* 65: 80–93.
- Mattarozzi, M., Milioli, M., Cavalieri, C. et al. (2012). Rapid desorption electrospray ionization-high resolution mass spectrometry method for the analysis of melamine migration from melamine tableware. *Talanta* 101: 453–459.
- McGonigle, A.J.S., Wilkes, T.C., Pering, T.D. et al. (2018). Smartphone spectrometers. *Sensors* 18: 223.
- Montet, D. and Ray, R.C. (eds.) (2017). *Food Traceability and Authenticity: Analytical Techniques*. CRC Press.
- Munoz-Pineiro, M.A., Robouch, P. (2018). Fipronil in Eggs: Factsheet – December 2017, European Commission. <https://ec.europa.eu/jrc/en/publication/brochures-leaflets/fipronil-eggs-factsheet-december-2017> (accessed 30 April 2020).
- Nakashima, Y. (2019). Nondestructive quantification of lipid and water in fresh tuna meat by a single-sided nuclear magnetic resonance scanner. *Journal of Aquatic Food Product Technology* 28: 241–252.
- Negrel, P., Reimann, C., Ladenberger, A., Birke, M. (2017). Distribution of lithium in agricultural and grazing land soils at European continental scale (GEMAS project). *Geophysical Research Abstracts*, vol. 19, EGU2017-15340, 2017EGU General Assembly 2017. *19th EGU General Assembly, EGU2017* (23–28 April 2017). Vienna, Austria. p. 15340.
- Nicolodelli, G., Cabral, J., Menegatti, C.R. et al. (2019). Recent advances and future trends in LIBS applications to agricultural materials and their food derivatives: an overview of developments in the last decade (2010–2019). Part I. soils and fertilizers. *Trends in Analytical Chemistry* 115: 70–82.
- Ouyang, Z. and Cooks, R.G. (2009). Miniature mass spectrometers. *Annual Review of Analytical Chemistry* 2: 187–214.
- Oztop, M.H., Bansal, H., Takhar, P. et al. (2014). Using multislice-multi-echo images with NMR relaxometry to assess water and fat distribution in coated chicken nuggets. *Food Science and Technology* 55: 690–694.
- Palmer, P.T., Jacobs, R., Baker, P.E. et al. (2009). Use of field-portable XRF analyzers for rapid screening of toxic elements in FDA-regulated products. *Journal of Agricultural and Food Chemistry* 57: 2605–2613.
- Pantazis, T., Pantazis, J., Huber, A., and Redus, R. (2010). The historical development of the thermoelectrically cooled X-ray detector and its impact on the portable and handheld XRF industries. *X-Ray Spectrometry* 39: 90–97.
- Patel, K.K., Khan, M.A., and Kar, A. (2015). Recent developments in applications of MRI techniques for foods and agricultural produce – an overview. *Journal of Food Science and Technology* 52: 1–26.
- Pearson, D., Chakraborty, S., Duda, B. et al. (2017). Water analysis via portable X-ray fluorescence spectrometry. *Journal of Hydrology* 544: 172–179.
- Peinado, F.M., Morales Ruano, S., Bagur González, M.G., and Molina, C.E. (2010). A rapid field procedure for screening trace elements in polluted soil using portable X-ray fluorescence (PXRF). *Geoderma* 159: 76–82.
- Pinter, M.D., Harter, T., McCarthy, M.J., and Augustine, M.P. (2014). Using NMR to screen for spoiled tomatoes stored in 1000 L, aseptically sealed, metal-lined totes. *Sensors* 14: 4167–4176.
- Potts, P.J. and West, M. (eds.) (2008). *Portable X-Ray Fluorescence Spectrometry: Capabilities for In Situ Analysis*. London: Royal Society of Chemistry.
- Pourmand, P., Wang, L., and Dvinskikh, S.V. (2011). Assessment of moisture protective properties of wood coatings by a portable NMR sensor. *Journal of Coating Technology and Research* 8: 649–654.
- Proctor, G., Wang, H., Larson, S.L. et al. Rapid screening for uranium in soils using field-portable X-ray fluorescence spectrometer: a comparative study. *ACS Earth and Space Chemistry* 2020, 4: 211–217.
- Pulliam, C.J., Wei, P., Snyder, D.T. et al. (2016). Rapid discrimination of bacteria using a miniature mass spectrometer. *Analyst* 141: 1633–1636.
- Ratnai, G., Dario, P., and Cavallo, F. (2017). Smartphone-based food diagnostic technologies: a review. *Sensors* 17: 1453.
- Ravansari, R., Wilson, S.C., and Tighe, M. (2020). Portable X-ray fluorescence for environmental assessment of soils: not just a point and shoot method. *Environment International* 134: 105250.

- Rawal, A., Chakraborty, S., Li, B. et al. (2019). Determination of base saturation percentage in agricultural soils via portable X-ray fluorescence spectrometer. *Geoderma* 338: 375–382.
- Rovina, K. and Siddiquee, S. (2015). A review of recent advances in melamine detection techniques. *Journal of Food Composition and Analysis* 43: 25–38.
- Ruiz-Altisent, M., Ruiz-Garcia, L., Moreda, G.P. et al. (2012). Sensors for product characterization and quality of specialty crops—a review. *Computers and Electronics in Agriculture* 74: 176–194.
- Sacristán, D., Viscarra Rossel, R.A., and Recatalá, L. (2016). Proximal sensing of Cu in soil and lettuce using portable X-ray fluorescence spectrometry. *Geoderma* 265: 6–11.
- Sánchez-Pomales, G., Mudalige, T.K., Lim, J.-H., and Linder, S.W. (2013). Rapid determination of silver in nanobased liquid dietary supplements using a portable X-ray fluorescence analyzer. *Journal of Agricultural and Food Chemistry* 61: 7250–7257.
- Sezer, B., Bilge, G., and Boyaci, I.H. (2017). Capabilities and limitations of LIBS in food analysis. *Trends in Analytical Chemistry* 97: 345–353.
- Sieger, M. and Mizaikoff, B. (2016). Toward on-chip mid-infrared sensors. *Analytical Chemistry* 88: 5562–5573.
- Tomassini, A., Capuani, G., Delfini, M., and Miccheli, A. (2013). Chemometrics in food chemistry: NMR-based metabolomics in food quality control. In: *Chemometrics in Food Chemistry* (ed. F. Marini). Elsevier Inc.
- Veliyulin, E., van der Zwaag, C., Burk, W., and Erikson, U. (2005). In vivo determination of fat content in Atlantic salmon (*Salmo salar*) with a mobile NMR spectrometer. *Journal of the Science of Food and Agriculture* 85: 1299–1304.
- Wan, M., Hu, W., Qu, M. et al. (2019). Application of arc emission spectrometry and portable X-ray fluorescence spectrometry to rapid risk assessment of heavy metals in agricultural soils. *Ecological Indicators* 101: 583–594.
- Wang, X., Wang, S., and Cai, Z. (2013). The latest developments and applications of mass spectrometry in food-safety and quality analysis. *Trends in Analytical Chemistry* 52: 170–185.
- Weindorf, D.C., Zhu, Y., Chakraborty, S. et al. (2012). Use of portable X-ray fluorescence spectrometry for environmental quality assessment of peri-urban agriculture. *Environmental Monitoring and Assessment* 184: 217–227.
- Weindorf, D.C., Bakr, N., and Zhu, Y. (2014). Advances in portable X-ray fluorescence (PXRF) for environmental, pedagogical, and agronomic applications. *Advances in Agronomy* 128: 1–45.
- Yan, X.T., Donaldson, K.M., Davidson, C.M. et al. (2018). Effects of sample pretreatment and particle size on the determination of nitrogen in soil by portable LIBS and potential use on robotic-borne remote Martian and agricultural soil analysis systems. *RSC Advances* 8: 36886–36894.
- Zalesskiy, S.S., Danieli, E., Blümich, B., and Ananikov, V.P. (2014). Miniaturization of NMR systems: desktop spectrometers, microcoil spectroscopy, and “NMR on a chip” for chemistry, biochemistry, and industry. *Chemical Reviews* 114: 5641–5694.

## 15

### Portable Near-Infrared Spectroscopy in Food Analysis

*Ellen V. Miseo, Felicity Meyer\* and James Ryan*

*TeakOrigin, Inc., Waltham, MA, USA*

#### 15.1 Introduction

The world food supply has become very complicated. For most consumers, food is no longer produced close by and provided to the consumer the day it is picked. Therefore, many consumers do not understand where their food comes from: a local small family farm, a large agricultural operation in their own country, or a different country. In addition, consumers in developed countries have lost the concept of seasonality and expect to be able to get what they want when they want it. Both factors have led to a food supply that is treated as an industrial operation.

This industrialization has led to a food system that rivals any modern production and distribution system that the modern world could envision. With this type of supply chain, food products, especially produce, need to be durable to survive industrial harvesting, storage, and transportation. To achieve this durability, new cultivars have been bred to withstand the abuse of the supply chain. In many cases, produce is picked unripe and subjected to treatments during shipping and storage to enhance [1–3] or retard ripening or decomposition [4–7]. This is an area of such intense work that there is a peer-reviewed journal *Postharvest Biology and Technology* (Elsevier), one of whose aims is to publish research on storage, treatment, and packaging as they impact fresh fruits and vegetables.

This intense focus on breeding, shipping, and storage has negatively impacted the consumers' perception of foods and may have impacted the nutritional quality. Again, this is an area of intense academic study [8–12]. Many questions arise from this: If a food is subjected to this extended supply chain, does it retain its nutrients? Is it as tasty as if it were picked yesterday? And if every retailer's produce is in the same supply chain, are you getting your money's worth if you pay more from a premium retailer?

Consumers are increasingly confused and continue to demand transparency. This has led to an increase of true farmers' markets (where the farmer is actually bringing their product into urban areas), community-supported agriculture, and urban farms. One of the fallouts of this increasing confusion is the consumer's reliance on the term "organic," where it is implied that you are getting a healthier, more nutritious, and tastier product, but again, research has not confirmed this [13–16].

Finally, as the world population grows, minimizing the waste of edible food becomes more and more important. Some estimates indicate that 30–40% of food in the developing and developed world are lost to waste [17]. To make matters worse, in the developed countries, the biggest losses come from sources in the supply chain. These include food not meeting cosmetic standards, waste and loss at the processing or storage steps on the way to the consumer, and finally postconsumer waste [18, 19] where the purchased foods are not used before they become inedible [20, 21].

\* Present address: SmartLabs, Boston, MA, USA

Tools and methods are required to address these issues, but these tools need to be nondestructive, easy to use, and fast. In addition, they need to tell us something valuable about the food and not just make a measurement because the measurement is easy to do. Optical spectroscopy comes to the rescue.

## 15.2 Spectroscopy

Optical spectroscopy can cover the wavelength region from 200 nm to greater than 25  $\mu\text{m}$ , with near-infrared (NIR) occupying a small portion of this range. NIR spectroscopy has been used since the 1960s to analyze foods, based on the pioneering work of Karl Norris, who is considered the father of this field [22], and will be the focus of this chapter due to its ubiquitous use in the food industry. NIR originally required large complicated instrumentation [23], but with the revolution in technology, the size of these instruments has decreased significantly, while their capabilities have increased (see the chapter by Grüger in volume 1 and the chapters by Siesler and colleagues in this volume). NIR instruments, with adequate performance for food analysis, are now available at the price point of a good laptop and are the size of a computer mouse.

### 15.2.1 Spectral Range

The spectral range covered by an instrument is commonly defined by the wavelength of light and the limits of the detector used, but the terms used to describe those regions can vary based on the technical background of the user. This situation can cause enormous confusion. It is generally agreed that the NIR starts at 700 nm, and chemists define it as ending at 2500 nm ( $4000 \text{ cm}^{-1}$ ). The region from 1100 to 2500 nm is considered by chemists to be the most useful, because this is where the first and second overtones of the X-H vibrations are located [24, 25]. Terms that have been used to describe this region of the spectrum also include the “lead sulfide region” reflecting the first detectors used to interrogate this region (as well as wavelengths as long as 3300 nm).

The shortwave near-IR (sometimes abbreviated as SWIR or SWNIR) is typically defined as 700–1100 nm and has been called the “silicon region,” again to reflect the detectors used. Unfortunately, the term visible and near-infrared (VNIR) is also used, and this refers (by most definitions) to the 400–1100 nm region, which causes confusion about what is being measured. The hyperspectral community has complicated the discussion of regions of the spectrum and prediction of food parameters by referring to the VNIR, which in many articles is actually the visible and very-near-infrared, using silicon cameras that are robust and reasonably priced [26, 27]. However, these instruments do not deliver significant chemical composition data.

With the development of “big data” concepts, instrument developers, who are not skilled in spectroscopy, rely on the assumption that by having very large numbers of spectra, predictions of some quantity of a dataset are possible, whether or not the measurements being made are actually valid. In these cases, they are relying on large numbers of spectra to attempt to correct for the lack of information in this region.

For prediction of chemical composition (identity and quantity), the first and second overtone regions of the NIR spectrum have proven to be most useful in foods. In particular, since many foods are >85% water, the 1000–1700 nm region is the most useful for foods that are high in moisture. Since water is such a strong absorber in the infrared (IR) in general, interference of the highly absorbing water band at approximately 1950 nm [28] will mask the chemistry. Lower water content foods, such as coffee and olive oil, can be examined in the 1700–2500 nm region [29]. For classification, which uses the spectrum to sort different types of similar objects, shorter wavelength data may prove useful, depending on the system.

In recent years, a new class of spectrometer has emerged: very low cost and targeted directly to consumers. Most of these are based on silicon material detectors, covering at best from 400 to 1100 nm, but in practice often a more limited spectral range. The purveyors of some of these devices are playing fast and loose with the definitions of the NIR, as discussed by You et al. [30]. In addition, these companies publish very preliminary data to the nonfood and

non-spectroscopy communities. At times, the experimental data reported in their publications cannot be replicated in independent experiments (for instance, in our laboratory results).

Since a consumer judges the quality of foods by their appearance, using visible region spectral data is also valuable. Some compositional differences, such as the amount of lycopene in tomatoes [31, 32], can also be predicted in this region of the spectrum and are therefore discussed further below.

### 15.3 Analysis, Sampling, and Detection Limits

A trained analytical chemist understands the concepts of representative sampling, as well as detection limits. In making a spectroscopic measurement in foods, both concepts are crucial. All solid foods are to some extent heterogeneous, and sampling a heterogeneous material is a science in itself, with introductory analytical chemistry texts going into great detail on this topic [33, 34]. Therefore, when making a spectroscopic measurement, the user needs to take into consideration the heterogeneity of the sample.

Let us look at a blueberry muffin, as shown in Figure 15.1. Sample variability can exhibit itself within a sample, sample to sample, lot to lot, etc. Each of these sources of variability will impact the analyses. If you take a standard recipe for blueberry muffins, it contains butter, sugar, flour, eggs, milk, and blueberries. The nutritional information, calculated from software based on the ingredients, gives a fat content of 9%, carbohydrates of 42%, and sugars of 25%.

Most blueberries are larger than 5 mm in diameter. If the spectrometer is interrogating a spot comparable in size to that (neglecting for the moment the question of depth penetration into the sample) and you sample where a blueberry is, you will obtain a lower fat content, because blueberries do not contain fat. Conversely, if you sample in the pastry area, the measured fat will be higher than the reported value, because the values are for the *entire* recipe. If the butter was not mixed properly, there could be measurements where the fat would be even higher because of poor mixing. Clearly also, just on a visual basis, the outer surface of the muffin – the crust – is different from the interior. If you then look at muffin-to-muffin variability, your values will be different. No one is going to count the blueberries in a muffin, but a larger number of blueberries in one muffin versus another will impact the fat values.

Instrument manufacturers that produce NIR instruments for food composition take great care to ensure that a representative sample is examined. Sample preparation, large “spot sizes”, sample spinners, and integrating

**Figure 15.1** Blueberry muffin illustrating the heterogeneity of the sample as well as the difficulties to obtain a representative spectral signature. *Source:* Picture courtesy of Eric Crocombe.



**Table 15.1** Typical limits of detection in mixtures without any sample preparation.

Spectral range	Typical path length	Typical detection limits
Mid-infrared (MIR)	10 μm to 1 mm	0.1% in a sample
Near-infrared (NIR)	1–5 mm	1% in a sample
UV/Vis	10 mm	0.1% in an average absorber

Most foods are high in water and may require very short path lengths, which will impact these estimated detection limits.

spheres have all been used in laboratory instruments to assure the spectrum is collected from a representative area. Most handheld instruments do not provide any mechanism for ensuring a representative sample, or tacitly assume the user is experienced and recognizes the problem. It is up to the user to take care when collecting spectra. Trained researchers and analytical instrument manufacturers are realistic about what can be detected by the optical techniques. Developers who believe they have invented the latest and greatest device that will solve the problems of the world are not. Although this review focuses on NIR spectroscopy for food analysis, it is instructive to examine Table 15.1, which shows detection limits for a variety of spectroscopic techniques without sample preparation or enrichment.

### 15.3.1 Reference Analysis

Much of the use of NIR spectroscopy in the food area is on complicated matrices. The spectra have poorly defined features, and the interactions among components in a matrix can impact the spectrum. Because of this, it is usually impossible to make a simple calibration curve from a known component to predict the concentration. It is critical to conduct the proper reference analyses on the samples, to understand the concentrations of the analyte or analytes of interest, and to generate a valid calibration that can predict a parameter of the sample from the spectrum. Unfortunately, many new to the spectroscopy area miss this critical aspect and use reported values from databases, or the literature, as the known values for analytes.

### 15.3.2 Class vs. Specific Analysis

In this day of increasingly sophisticated separation techniques, coupled with equally sophisticated identifications, the analytical chemist has come to assume that to quantify materials, they need to be separated, identified, and quantified [35–38]. But is this always necessary?

Many compounds that are important in foods are part of a class of chemicals with similar structures. Examples of this include carotenoids, where α- and β-carotene are important in carrots, lycopene in tomatoes, and lutein in spinach. As shown in Figure 15.2, these compounds all have very similar structures. In the NIR, these isoprenoid structures exhibit nearly identical spectra due to their very similar structures. In some cases, these materials would be well below the detection limit of NIR spectroscopy and have interferences in the visible region from other components of a sample, such as chlorophyll. But by analyzing these materials without separation [39], as a collection of materials, they can be correlated with spectral information derived from the field instruments.

For samples where one compound predominates (such as lycopene in tomatoes), this translates into a reasonable measure of that particular compound. In other samples such as broccoli, where β-carotene, lutein, and zeaxanthin all contribute to the total carotenoid content, this strategy will account for most of the carotenoid content in the material.

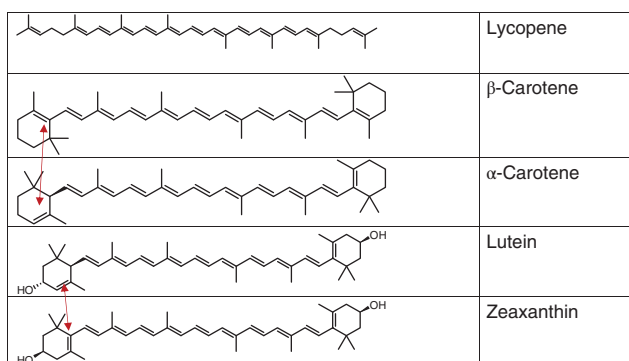


**Figure 15.2** Structure of typical carotenoids found in foods illustrating the similarity in structure.  $\alpha$ - and  $\beta$ -carotene differ by the position of the double bond as do lutein and zeaxanthin.

### 15.3.3 Make Sure You Are Measuring What You Think You Are Measuring

Since, in general, the spectroscopic measurement is correlated with some measurable analytical quantity, the user needs to be sure that the quantity they are measuring is actually what they think it is. A very good example of this is the °Brix measurement of fruit juices. Although the scientific community describes this measurement as total dissolved solids (which will change the refractive index of a solution), the produce community equates this measurement with sweetness – this is not true.

Degrees Brix (°Brix) is a method of defining the sucrose content of an aqueous solution [40]. It was developed as a scale that measured the relative density of a sucrose solution, originally with a hydrometer. It was also recognized that by dissolving different materials in water, the refractive index changed, so that at the same concentration, solutions of different common food materials in water show different refractive indices. For example, a 20% solution of sucrose (table sugar) has a refractive index of 1.3639, while a 20% solution of fructose (fruit sugar) has a refractive index of 1.3633. Since a refractive index measure of °Brix is designed for sucrose, a mixture of sucrose and fructose (as found in a fruit juice) will give an inaccurate value. Citric acid, a common fruit acid, behaves the same way. When dissolved in water at a 20% concentration, it has a refractive index of 1.3589. Most fruits have a number of acids such as citric, malic, and tartaric acid, all of which behave in a similar manner.

Although the analytical chemistry and food communities recognize these differences and the impact on a measurement, it is obvious that the broader engineering community does not recognize that making a measurement does not equate with making a meaningful measurement, as seen in this article from IEEE Spectrum Magazine [41]. This is one of the major problems regarding food spectroscopy as practiced by non-spectroscopists, especially in the NIR. Although you can make a measurement, you need to make sure the measurement means something. Established spectroscopic instrument companies, who have been providing tools to the food industry for many years, understand the constraints and operate within them. Some of the new entries into the market are making wide claims and either do not understand what they believe they are measuring or are simply relying on “big data” to try to make up for deficiencies in the data their devices provide.

### 15.3.4 Optical Considerations

To the analytical chemist/spectroscopist, sampling has two distinct meanings. The first is getting a true representation of the sample as described above. The second is how you get the light to the sample and back from the sample.

In the simplest implementation of an analysis, to obtain a representative sample, the material is homogenized, and an aliquot is taken and analyzed, ideally in transmission. If transmission is not an option, the sample may be

examined in reflection mode, probably using an integrating sphere to collect all the scattered light and to eliminate the stray light.

The optical configurations described above probably assume a destructive sample preparation. One of the major benefits of using NIR is the ability to probe the sample *in situ*. But how do you account for the natural inhomogeneity of the samples? In our laboratory, the method used is to collect multiple spectra at many points on the sample and use the average of those measurements as a representative sample. For an item like a peach, up to 30 spectra will be taken from a sample, at different places on the surface, either using a fiber optic probe or direct contact with the optical window on the device, depending on the instrument design.

For very small produce like berries or grapes, a sample spinner, where the samples are typically placed in a dish and rotated through the optical beam while spectra are collected, is used. In both these sampling configurations, the user has to be aware of and careful to control for the impact of extraneous scattered light. This is usually addressed using some sort of shield that mitigates ambient light.

### 15.3.5 Calibration and Validation Samples

Any measurement system needs to be tested to make sure it is delivering an appropriate answer. The calibration and validation samples need not be complex, but must be appropriate for the application. For example, in the NIR, there are National Institute of Standards and Technology (NIST) standards that can be used to measure wavelength position and photometric accuracy. NIST standards, or NIST-traceable standards, tend to be expensive and may be fine for a recalibration of a device upon service, but they may not be appropriate for field use. A sample that is consistent and delivers interpretable data is appropriate. For field measurements, ceramic reflectance standards such as AluWhite98 [42] may be appropriate. For NIR wavelength position, there are limited field standards, although thick samples (greater than 1 cm) of polystyrene, polyethylene, or polypropylene may be appropriate.

But, as mentioned above, those standards must be appropriate for the analysis. In the small, inexpensive instrument area, that does not always happen. In this author's lab, we purchased an inexpensive NIR (900–1700 nm) spectrometer from a distributor. The device came with "calibration standards" that were white balance photographic cards, made of a polymeric material, and were completely useless since the spectrum of the polymer was visible. Grayscale standards are appropriate in the NIR, but they must be in a matrix that does not have a NIR spectrum.

### 15.3.6 Quality Control Analysis

No true analytical chemist believes that one measurement represents the exact composition of a sample. In good analytical practice, replicate measurements and samples, as well as quality control samples like blanks, spikes, and standards, are also necessary. In the discussion above, we described spinning or rotating a sample to get more representative spectra of the samples. In a field situation, this may be the best that can be accomplished given the use case constraints.

But before defining that sampling strategy, good practice necessitates looking at the repeatability and the reproducibility for the analysis. The repeatability tests the measurement device and the reproducibility: the inter-operator variability. Using standards, these measurements are made, and then, the range and variability of the values are examined. A broad range of results obtained on the same sample, in the same way, by the same operator, indicates that the measurement device is at fault. Since more than one operator is likely to be taking measurements, the reproducibility needs to be defined. Again, running multiple samples and determining if there is an operator bias are important.

### 15.3.7 Data Interpretation

One of the major reasons the NIR region of the spectrum was neglected in the early years of development of instrumentation is because the data is difficult to interpret. Figure 15.3 shows the spectrum of solid, crystalline sucrose from the visible through to the mid-infrared (MIR). All the spectra presented are auto-scaled to the strongest band in that region, and it should be noted that the path length differs substantially across the spectral ranges.

As the spectra show, in the MIR (Figure 15.3a), the absorbances are sharp and well defined, and using well-understood interpretation rules, the material can be identified. In the NIR (Figure 15.3b and c), the spectral features are due to overtones of X-H vibrations, where X is usually carbon, oxygen, or nitrogen. These overtones tend to be weaker bands than fundamentals, by at least an order of magnitude, and because of highly overlapping components, and being in a condensed phase, the bands are much broader, and therefore, features are less well separated in the spectrum. The weakening of the features, as well as the increasing overlap in the spectral signatures, is shown in Figure 15.4. These issues make interpretations based on first principles very difficult.

To counter these difficulties, the standard approach to data interpretation is chemometrics [43], which can be defined as using standard mathematical and statistical techniques and applying them to analytical chemistry problems. These techniques arose in the early 1970s as the power of computers were applied to chemical measurement. In the NIR, the most used approaches are multivariate data analysis, classification pattern recognition, and clustering. Although anecdotal, our extensive review of the NIR food literature indicates that probably 90% of the analysis of foods in the NIR relies on chemometrics.

The chemometric approaches used in food analysis are typically either to classify materials into categories, for example, tea authentication or chicken parts identification [44, 45], or to quantify components in a spectroscopically complex matrix [46]. The chemometric approaches both for classification and quantitation are

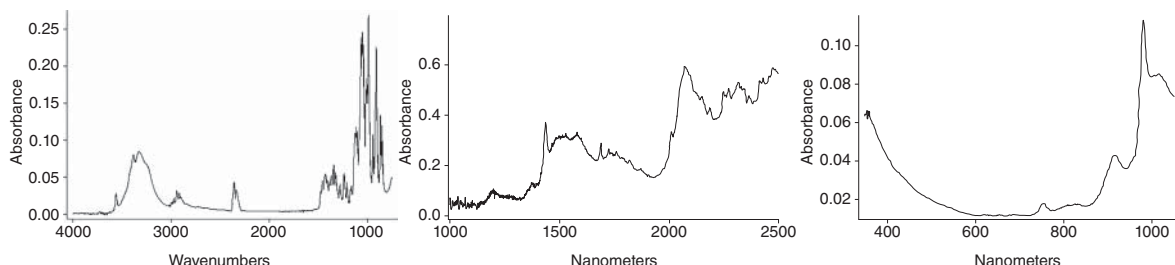
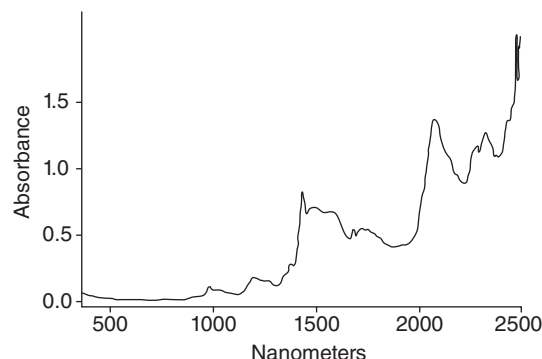


**Figure 15.3** (a) Mid-infrared spectrum of sucrose illustrating the sharp well-defined bands indicative of fundamental vibrations. Collected using attenuated total reflection on an FTIR. (b) Near-infrared spectrum of sucrose illustrating the broad bands indicative of overtone vibrations. Collected in diffuse reflection on an FTIR. (c) Very near IR and visible spectrum of sucrose. Collected in diffuse reflection using a polychromator instrument.

**Figure 15.4** Spectrum of sucrose from 375 to 2500 nm showing the substantial change in intensity of the features. The path length on this sample was approximately 5 mm.



the subjects of a large number of reviews in the literature. For a review of these principles and approaches, see the book *Chemometrics in Analytical Spectroscopy* [47].

## 15.4 Use of Portable Near-Infrared Instruments in Food Analysis

Although food systems are the bulk of NIR spectroscopy practices [48], food applications that involve handheld or portable devices are much less common in the literature. A recent review discusses applications of handheld or portable NIR across the food industry [49, 50], but the bulk of the reviews concentrate on more traditional laboratory-based instruments. In the meat industry, there are specific reviews concentrating on handheld instruments [51, 52].

### 15.4.1 Agricultural Products

Based on the literature, apples are the most examined category of fruit in NIR spectroscopy. Many of these studies are aimed at determining quality parameters such as dry matter or sugars. Unfortunately, most of these studies rely on laboratory-based instruments. Many of these laboratory instruments are Fourier transform in nature and can collect data from the entire NIR region [53–59]. When handheld or portable instruments are used, we are again faced with the problem of how the spectral range is defined and the real information content of the measurement.

In the literature, handheld or portable instruments fall into three categories, entirely home built, put together from spectrometer components, or purpose-built handheld instruments that are applied to a problem.

Home-built instruments in the food literature appear to be more a demonstration of the ability to build something that can be used in the food space [59–64]. For these instruments, the analysis is on fruit and mainly in an “it can be done” vein. The second category uses component spectrometers such as those available from companies like Ocean Optics (now Ocean Insights) and Avantes. Again, these appear to be a proof of concept, and the samples examined are fruits such as apples, blueberries, or citrus, to prove that the technique works [63, 65–70].

True applications to measure relevant parameters usually rely on either general purpose instruments, designed to apply to many industries such as the Thermo Scientific microPHAZIR [71–78] or the Viavi MicroNIR [76, 79–84]. Another general purpose instrument that has been used as a handheld in the food area is from Panalytical’s ASD [85, 86], although this instrument does not appear to be as widely used for food analysis as the other two devices. Our laboratory has only identified one vendor, Felix Instruments, which sells a handheld NIR instrument directly aimed at the food space [87–92].

An instrument based on the Texas Instruments Digital Light Processor has been examined by various groups for food analysis [93–98]. These devices, in a package approximately the size of a computer mouse, have been shown to have spectroscopic performance as good or better than dispersive instruments using 1D image sensors and typically in larger form factors with higher price points.

Finally, the SCiO from Consumer Physics has received an enormous amount of popular press coverage [41], and some investigators have used or evaluated this device for agricultural analysis [99–103]. Many of these analyses are simple classifications, and according to those investigators, it has mixed performance. Agricultural products that have been examined using the SCiO include rice [102], fruit [88, 99, 104], and grains [78, 100]. In some studies, the SCiO was initially praised for its design and general ease of use. However, upon further investigation, the SCiO produced models with very poor performance [101], particularly in models aiming to quantify analytes. Consumer-aimed devices such as the SCiO may be capable of screening and “quick and dirty” quality control, but they have not reached the level of performance seen in other handheld and portable spectrometers.

Some of the articles cited so far are attempts to compare the performance of a set of the devices mentioned above [88, 101, 105–107]. As expected, these tests are more rigorous, and the more expensive devices produced by

companies in the spectroscopy business appear to perform better. Specific applications have spanned a number of foods and food types. In the next section, we discuss particular categories of foods and what is representative in the current literature.

### 15.4.2 Produce

NIR spectroscopy has been used as a tool to predict quality parameters as well as classify various fruits. As portable instruments have emerged, they have allowed for determination of maturity and optimal harvest times in the field, prediction of shelf life during harvest, seedling screening in research areas, classifying storage conditions in the supply chain, and identification of specialty products. Table 15.2 summarizes fruit applications using portable Visible/NIR (Vis/NIR) or NIR spectroscopy. Fruit categories are as follows: citrus (mandarin, orange), tropical (kiwi, mango, pineapple), and stone fruit (apricot, cherry, nectarine, peach, plum).

### 15.4.3 Dairy

Milk and milk products have generated a lot of interest because of major newsworthy issues with contamination and adulteration [133, 134]. Many of the concerns can be addressed using spectroscopy. Portable NIR devices were used to make calibration models for protein, fat, solids-not-fat [135], and fatty acid composition [136] in

**Table 15.2** NIR applications for analysis of fresh produce.

Analysis	Applications
Soluble solids or °Brix	Apple [53, 60, 63, 69, 70, 77, 90, 108, 109], blueberry [65, 110], citrus [66, 111–113], grape [72, 114, 115], pear [62, 116, 117], stone fruit [67, 80, 92, 97, 118–120], strawberry [121], tropical fruit [83, 91, 122], spinach [123, 124], sugar beet [125] summer squash [126]
Sucrose	Sugar beet [125]
Moisture or dry matter	Apple [88, 90, 109], stone fruit [80, 88, 92, 118], tropical fruit [83, 88, 91, 122]
Acidity (titratable, pH)	Apple [59, 63, 69, 127], citrus [66, 112, 113], stone fruit [67, 120], strawberry [121], tropical fruit [83], spinach [123, 128], sugar beet [125], summer squash [126]
Polyphenols (phenols, anthocyanins, flavonoids)	Apple [63, 77], blueberry [65, 110], grape [84, 115]
Carotenoids	Apple [63], banana [129]
Ascorbic acid	Apple [63], blueberry [65], citrus [66], spinach [124]
Color or chlorophyll	Apple [59, 63, 70], citrus [66], strawberry [121], spinach [128]
Mechanical (firmness)	Apple [53, 63, 109], blueberry [65], pear [116], stone fruit [67, 118–120], strawberry [121], tropical fruit [83]
Maturity	Apple [89], blueberry [64, 65, 110], citrus [112, 130], stone fruit [97], tropical fruit [91]
Defect classification	Apple (sunscald) [131], blueberry (insect infestation) [132], stone fruit (peach damage) [80]
Storage conditions	Apple [81, 89], stone fruit [118]
Cultivar classification	Stone fruit [67, 118]
Specialty	Apple [81]
Nitrate level (“safety”)	Spinach [123, 124], summer squash [126]

raw milk. A recent review article covered two applications of portable NIR to measure fat, protein, and lactose in milk [137]. The presence of lactose in lactose hydrolyzed milk was classified using portable NIR spectroscopy [138], and several groups claimed to distinguish organic from conventional milk [139, 140]. Contamination of milk is an issue that has been widely investigated, and handheld Vis/NIR spectroscopy has been used to determine melamine content in milk [141] while a portable visible light-emitting diode (LED) photometer was used to determine the concentration of urea in cow and goat milk [142].

#### 15.4.4 Meat, Poultry, and Fish

There has been much discussion in the press about authenticity, product quality, and contamination in the meat and fish supply [143]. Handheld or portable devices can be used to create classifiers that distinguish classes of chicken parts and ground meat [44], to determine the species of a whole or minced cut of meat [144], to flag adulterated products such as veal sausages made with pork meat or fat [145], or to discriminate Atlantic cod from haddock in fillet or ground patty form [146]. Chemometric models can also be built using spectral data from these devices to classify the quality of a product such as ultimate pH, shear force, and intramuscular fat content in lamb loin [147]. Quantitative models predict parameters for pork (including protein, water, nitrogen, and intramuscular fat) [148], sodium chloride in tuna [149], or to authenticate Iberian acorn-fed pork by its fatty acid content [150]. A recent review article covered numerous applications related to poultry, including identifying unwholesome or contaminated carcasses, classifying samples with wooden breast defect, and predicting quality parameters such as pH<sup>51</sup>, while another review article described portable NIR applications to evaluate meat quality [151].

#### 15.4.5 Sweeteners

NIR spectroscopy has been used in several applications related to sweeteners and sugar products. Two groups reported using portable NIR spectrometers to predict the Pol value (sucrose concentration of the juice) in sugarcane stalks, to evaluate quality, and potentially to influence breeding management and harvest schedules [152, 153]. Handheld devices were used to determine the main carbohydrate content in syrups and verify the composition criteria for reformulated syrups [74, 154]. Total sucrose and total sugar contents were predicted in infant cereals using handheld NIR and portable MIR spectrometers [155].

#### 15.4.6 Processed Foods

Although the potential for portable instruments seems to be very large in the processed food areas, there are very few published applications. Food processors are the target markets for the traditional instrumentation companies, and penetration of handheld devices into these markets is impacted not only by decades of research into NIR food applications but also by a need to shrink instrument footprints and develop user-friendly methods for food labs. For example, in a brief examination of the literature collected by these authors, over the past 10 years, there were over 40 references on NIR analysis used on apples. But when the examination concentrates on handheld or portable instruments, only four of those references are pertinent, and all were published within the past three years.

For “minimally” or “moderately” processed foods, there has been a recent growing body of research focused on authentication or classification of dissimilar or adulterated product. These foods include roasted and ground coffee, teas, rice, grains with and without husks, flour, and other similar products. These foods are ideal candidates for handheld, portable spectrometers as they both are generally uniform in their natural state and are prone to adulteration or contamination with difficult-to-distinguish material after they have been processed (e.g. dried, ground, etc.).

Specifically, there has been promising results in detecting adulteration in coffee [79, 156], grains and flour [101, 102, 157], fats [158, 159], and honey [160]. These studies focus primarily on distinguishing between high

quality product and that cut with lower quality product or foreign matter, presumably to increase profit margins. Undesirable processing methods can also be distinguished in high value goods, as demonstrated by Zhang et al. in processing of Chinese herbals [161].

The materials outlined below are particularly good candidates for NIR applications, due to their low water content, as compared with fresh produce. Nevertheless, sampling and processing methods can still reduce model integrity in authentication and quantitative determinations. Because these samples are processed, key analytes may be degraded or changed. This results in poorly performing chemometric models, or even samples that are no longer representative of the initial analysis of the unprocessed material. For example, in total antioxidant capacity (TAC) in a variety of gluten-free grains, unmilled samples showed higher concentrations than the milled aliquots, potentially due to loss in material (i.e. husks) and overall degradation of antioxidants during the milling process [101]. Table 15.3 summarizes a handful of minimally and moderately processed foods, the investigated application, and instrument used, if specified by the authors.

**Table 15.3** Portable NIR applications for minimally and moderately processed foods.

Category	Subcategory	Analyte and/or application	Instrument
Tea and Coffee	Matcha tea [93]	Authentication and quality (polyphenols and amino acids)	Portable NIR (not specified)
	Congou black tea [162]	Quality (phenolic compounds)	Portable NIR (not specified)
	Coffee [163]	Roasting quality	Viavi MicroNIR
	Coffee [156]	Bean quality and roasting quality	Aurora NIR
Herbs	<i>Verbena officinalis</i> [71]	Quality (to determine ideal harvest time), prediction of verbenalin and verbascoside	microPHAZIR™ RX Analyzer
	Radix paeoniae alba (Chinese herbals) [161]	Classification (processed with sulfur fumigants v. sun-dried) and quality	Vis-NIR (Specim Corp, INFINITY 3-1 detector/VI0E spectrometer)
Grasses	Sugarcane [152]	Pol (sucrose concentration of juice)	Portable NIR (not specified)
	Sugarcane [164]	Fiber contents	Visible-shortwave near-infrared (Vis/SWNIR) (not specified)
Rice	Rice [102]	Authentication (country of origin, import v. local) and quality (grade) classification	SCiO
	Hybrid rice [157]	Authentication and quality (chlorophyll content of plant)	Ocean Optics USB4000
Beans	Common beans ( <i>Phaseolus vulgaris L.</i> ) [165]	Characterization, quality (determination of protein, starch, amylose)	Portable NIR and MIR systems (not specified)
Fats + oils	Virgin olive oil [158], extra virgin olive oil [166]	Authentication of quality (free acidity) Authentication and discrimination	Battery-operated portable spectrometer (not specified)
	Sunflower oil [159]	Adulteration (w. mineral oil)	Portable NIR (not specified)
Misc.	Syrup [154]	Classification; quality (glucose, fructose, sucrose concentration), authentication	Portable NIR (not specified)
	Syrup [74]	Quality (carbohydrates)	microPHAZIR GP 4.0

In addition to maintaining integrity of the sample quality, it is also important to remember *sampling* quality. While Zhang et al. were able to measure both chlorophyll levels in leaves and discriminate between hybrid varietals of rice with good results, distinguishing between which rice plants had been fertilized with different concentrations of nitrogen fertilizer proved more difficult. The author notes that all samples were collected in the same year and from the same paddy, which could potentially limit the robustness of their model. The model lacks the diversity to appropriately predict chlorophyll level or varietal type, and the authors propose future analysis from other regions and in different seasons to increase the robustness of the model [157]. In a similar vein, Plans et al. illustrated that while developing classification and quality-related models for common beans, cross contamination during rapid data collection, as well as the presence of packaging, strongly interfered with model performance [165]. In short, while these methods are largely nondestructive, they are not necessarily nondestructive to sealed packaging or the initial state of the food in question.

## 15.5 Summary

Although one might expect to see more information in the literature applying handheld, portable or miniature NIR instruments in the food area, the hardware technology is moving faster than the application areas. For established instrument companies such as Thermo Fisher Scientific, Malvern Panalytical, or even Viavi, the instrumentation and technologies are within the realm of the food and spectroscopic communities. For small device manufacturers, they are either addressing a niche or are not entirely familiar with the problems the industry is facing and, therefore, have not created solutions using their devices.

As the technology develops and the developer and user communities become more closely aligned, this disconnect should change, providing the industry access to small, portable, simple-to-use devices that will provide an answer in near real time.

## References

- 1** Façanha, R.V., Spricigo, P.C., Purgatto, E., and Jacomino, A.P. (2019). Combined application of ethylene and 1-methylcyclopropene on ripening and volatile compound production of 'Golden' papaya. *Postharvest Biology and Technology* 151: 160–169.
- 2** Huang, J.-Y., Xu, F., and Zhou, W. (2018). Effect of LED irradiation on the ripening and nutritional quality of postharvest banana fruit. *Journal of the Science of Food and Agriculture* 98 (14): 5486–5493.
- 3** Duan, J., Wu, R., Strik, B.C., and Zhao, Y. (2011). Effect of edible coatings on the quality of fresh blueberries (Duke and Elliott) under commercial storage conditions. *Postharvest Biology and Technology* 59 (1): 71–79.
- 4** Sun, X., Baldwin, E., and Bai, J. (2019). Applications of gaseous chlorine dioxide on postharvest handling and storage of fruits and vegetables – a review. *Food Control* 95: 18–26.
- 5** Aguirre-Joya, J.A., Ventura-Sobrevilla, J., Martínez-Vazquez, G. et al. (2017). Effects of a natural bioactive coating on the quality and shelf life prolongation at different storage conditions of avocado (*Persea americana* mill.) cv. Hass. *Food Packaging and Shelf Life* 14: 102–107.
- 6** Burg, S.P. and Burg, E.A. (1966). Fruit storage at subatmospheric pressures. *Science* 153 (3733): 314–315.
- 7** Zheng, X., Ye, L., Jiang, T. et al. (2012). Limiting the deterioration of mango fruit during storage at room temperature by oxalate treatment. *Food Chemistry* 130 (2): 279–285.
- 8** Koyuncu, M.A. and DİLMAÇÜNAL, T. (2010). Determination of vitamin C and organic acid changes in strawberry by HPLC during cold storage. *Notulae Botanicae Horti Agrobotanici Cluj-Napoca* 38 (3): 95–98.
- 9** Lado, J., Gurrea, A., Zacarías, L., and Rodrigo, M.J. (2019). Influence of the storage temperature on volatile emission, carotenoid content and chilling injury development in star ruby red grapefruit. *Food Chemistry* 295: 72–81.

- 10** Napolitano, A., Cascone, A., Graziani, G. et al. (2004). Influence of variety and storage on the polyphenol composition of apple flesh. *Journal of Agricultural and Food Chemistry* 52 (21): 6526–6531.
- 11** Awad, M.A. and de Jager, A. (2003). Influences of air and controlled atmosphere storage on the concentration of potentially healthful phenolics in apples and other fruits. *Postharvest Biology and Technology* 27 (1): 53–58.
- 12** Bunea, A., Andjelkovic, M., Socaciu, C. et al. (2008). Total and individual carotenoids and phenolic acids content in fresh, refrigerated and processed spinach (*Spinacia oleracea* L.). *Food Chemistry* 108 (2): 649–656.
- 13** Bourn, D. and Prescott, J. (2002). A comparison of the nutritional value, sensory qualities, and food safety of organically and conventionally produced foods. *Critical Reviews in Food Science and Nutrition* 42 (1): 1–34.
- 14** Zhao, X., Rajashekhar, C.B., Carey, E.E., and Wang, W. (2006). Does organic production enhance phytochemical content of fruit and vegetables? Current knowledge and prospects for research. *HortTechnology* 16 (3): 449–456.
- 15** Da Cunha, D.T., Antunes, A.E.C., Da Rocha, J.G. et al. (2019). Differences between organic and conventional leafy green vegetables perceived by university students: vegetables attributes or attitudinal aspects? *British Food Journal* 121 (7): 1579–1591.
- 16** Dangour, A., Dodhia, S., and Hayter, A. (2009). Nutritional quality of organic foods: a systematic review. *The American Journal of Clinical Nutrition* 90 (3): 680–685.
- 17** Godfray, H.C.J., Beddington, J.R., Crute, I.R. et al. (2010). Food security: the challenge of feeding 9 billion people. *Science* 327 (5967): 812–818.
- 18** Parfitt, J., Barthel, M., and Macnaughton, S. (2010). Food waste within food supply chains: quantification and potential for change to 2050. *Philosophical Transactions of the Royal Society, B: Biological Sciences* 365 (1554): 3065–3081.
- 19** van Giesen, R.I. and de Hooge, I.E. (2019). Too ugly, but I love its shape: reducing food waste of suboptimal products with authenticity (and sustainability) positioning. *Food Quality and Preference* 75: 249–259.
- 20** Wilson, N.L.W., Rickard, B.J., Saputo, R., and Ho, S.-T. (2017). Food waste: the role of date labels, package size, and product category. *Food Quality and Preference* 55: 35–44.
- 21** Gunders, D. and Bloom, J. (2017). *Wasted: How America is Losing up to 40 Percent of its Food from Farm to Fork to Landfill*. Natural Resources Defense Council New York.
- 22** McClure, W.F. (2003). 204 years of near infrared technology: 1800–2003. *Journal of Near Infrared Spectroscopy* 11 (6): 487–518.
- 23** McClure, W.F. (1987). Near-infrared instrumentation. In: *Near-Infrared Technology in the Agricultural and Food Industries* (eds. P. Williams and K. Norris), 109–127. St. Paul, MN: American Association of Cereal Chemists, Inc.
- 24** Osborne, B.G. (1986). *Near Infrared Spectroscopy in Food Analysis*, 200. Longman Scientific and Technical.
- 25** Murray, I. and Williams, P.C. (1987). Chemical principles of near-infrared technology. In: *Near-Infrared Technology in the Agricultural and Food Industries* (eds. P. Williams and K. Norris). American Association of Cereal Chemists.
- 26** Romaniello, R. and Baiano, A. (2018). Discrimination of flavoured olive oil based on hyperspectral imaging. *Journal of Food Science and Technology* 55 (7): 2429–2435.
- 27** Barreto, A., Cruz-Tirado, J.P., Siche, R., and Quevedo, R. (2018). Determination of starch content in adulterated fresh cheese using hyperspectral imaging. *Food Bioscience* 21: 14–19.
- 28** Pontes, M.J.C., Santos, S.R.B., Araújo, M.C.U. et al. (2006). Classification of distilled alcoholic beverages and verification of adulteration by near infrared spectrometry. *Food Research International* 39 (2): 182–189.
- 29** Lee, C., Polari, J.J., Kramer, K.E., and Wang, S.C. (2018). Near-infrared (NIR) spectrometry as a fast and reliable tool for fat and moisture analyses in olives. *ACS Omega* 3 (11): 16081–16088.
- 30** You, H.; Kim, Y.; Lee, J. H.; Choi, S. (2017). In classification of food powders using handheld NIR spectrometer. *2017 Ninth International Conference on Ubiquitous and Future Networks (ICUFN)* (4–7 July 2017). pp. 732–734.

- 31** Ncama, K., Magwaza, L., Asanda, M., and Samson, T. (2018). Application of visible to near-infrared spectroscopy for non-destructive assessment of quality parameters of fruit. *Infrared Spectroscopy-Principles, Advances, and Applications* IntechOpen: 2018.
- 32** McGoverin, C.M., Weeranantanaphan, J., Downey, G., and Manley, M. (2010). Review: the application of near infrared spectroscopy to the measurement of bioactive compounds in food commodities. *Journal of Near Infrared Spectroscopy* 18 (2): 87–111.
- 33** Skoog, D.A., West, D.M., Holler, F.J., and Crouch, S.R. (2013). *Fundamentals of Analytical Chemistry*. Cengage Learning ISBN-13: 9780495558286.
- 34** Harvey, D. (2016). *Analytical Chemistry 2.1*, 1122. DePauw University.
- 35** Oliver, J. and Palou, A. (2000). Chromatographic determination of carotenoids in foods. *Journal of Chromatography A* 881: 543–555.
- 36** Sikorska-Zimny, K., Badełek, E., Grzegorzecka, M. et al. (2019). Comparison of lycopene changes between open-field processing and fresh market tomatoes during ripening and post-harvest storage by using a non-destructive reflectance sensor. *Journal of the Science of Food and Agriculture* 99 (6): 2763–2774.
- 37** Reque, P.M., Steffens, R.S., Jablonski, A. et al. (2014). Cold storage of blueberry (*Vaccinium spp.*) fruits and juice: anthocyanin stability and antioxidant activity. *Journal of Food Composition and Analysis* 33 (1): 111–116.
- 38** You, Q., Wang, B., Chen, F. et al. (2011). Comparison of anthocyanins and phenolics in organically and conventionally grown blueberries in selected cultivars. *Food Chemistry* 125 (1): 201–208.
- 39** Fish, W.W. (2012). Refinements of the attending equations for several spectral methods that provide improved quantification of β-carotene and/or lycopene in selected foods. *Postharvest Biology and Technology* 66: 16–22.
- 40** Nielsen, S.S. (2010). *Food Analysis*. Springer.
- 41** Perry, TS. What happened when we took the SCiO food analyzer grocery shopping. IEEE Spectrum Magazine, online (March 2017). <https://spectrum.ieee.org/view-from-the-valley/at-work/start-ups/israeli-startup-consumer-physics-says-its-scio-food-analyzer-is-finally-ready-for-prime-timeso-we-took-it-grocery-shopping> (accessed 19 July 2019).
- 42** Buz, J., Ehlmann, B., Kinch, K. et al. (2019). Photometric characterization of Lucideon and avian technologies color standards including application for calibration of the Mastcam-Z instrument on the Mars 2020 rover. *Optical Engineering* 58 (2): 027108.
- 43** Gemperline, P. (2006). *Practical Guide to Chemometrics*. CRC press.
- 44** Nolasco Perez, I.M., Badaró, A.T., Barbon, S. et al. (2018). Classification of chicken parts using a portable near-infrared (NIR) spectrophotometer and machine learning. *Applied Spectroscopy* 72 (12): 1774–1780.
- 45** Firmani, P., De Luca, S., Bucci, R. et al. (2019). Near infrared (NIR) spectroscopy-based classification for the authentication of Darjeeling black tea. *Food Control* 100: 292–299.
- 46** Dardenne, P., Simnaeve, G., and Baeten, V. (2000). Multivariate calibration and chemometrics for near infrared spectroscopy: which method? *Journal of Near Infrared Spectroscopy* 8 (4): 229–237.
- 47** Adams, M.J. (2004). *Chemometrics in Analytical Spectroscopy*, 2nde, 224. London: Royal Society of Chemistry.
- 48** Strategic Directions International (February 2019). *SDi Global Assessment Report 2019*. Los Angeles, CA: Strategic Directions International. <https://strategic-directions.com/product/the-2020-global-assessment-report-the-analytical-and-life-science-instrumentation-industry> (accessed 12 November 2020).
- 49** Santos, C.A.T.d., Lopo, M., Páscoa, R.N.M.J., and Lopes, J.A. (2013). A review on the applications of portable near-infrared spectrometers in the agro-food industry. *Applied Spectroscopy* 67 (11): 1215–1233.
- 50** Ellis, D.I., Muhamadali, H., Haughey, S.A. et al. (2015). Point-and-shoot: rapid quantitative detection methods for on-site food fraud analysis—moving out of the laboratory and into the food supply chain. *Analytical Methods* 7 (22): 9401–9414.
- 51** Perez, I.M.N., Cruz-Tirado, L.J.P., Badaró, A.T. et al. (2019). Present and future of portable/handheld near-infrared spectroscopy in chicken meat industry. *NIR News* 30 (5–6): 26–29.

- 52 Shotts, M.-L. (2018). *The New Generation of Handheld Vibrational Spectroscopy Devices; Applications for Authentication of High Valued Commodities*. The Ohio State University.
- 53 Guozhen, Z. and Chunna, T. Determining sugar content and firmness of 'Fuji' apples by using portable near-infrared spectrometer and diffuse transmittance spectroscopy. *Journal of Food Process Engineering* 0 (0): e12810.
- 54 Fan, S., Li, J., Xia, Y. et al. (2019). Long-term evaluation of soluble solids content of apples with biological variability by using near-infrared spectroscopy and calibration transfer method. *Postharvest Biology and Technology* 151: 79–87.
- 55 Giovanelli, G., Sinelli, N., Beghi, R. et al. (2014). NIR spectroscopy for the optimization of postharvest apple management. *Postharvest Biology and Technology* 87: 13–20.
- 56 Liu, Y. and Ying, Y. (2005). Use of FT-NIR spectrometry in non-invasive measurements of internal quality of 'Fuji' apples. *Postharvest Biology and Technology* 37 (1): 65–71.
- 57 Liu, Y., Ying, Y., Yu, H., and Fu, X. (2006). Comparison of the HPLC method and FT-NIR analysis for quantification of glucose, fructose, and sucrose in intact apple fruits. *Journal of Agricultural and Food Chemistry* 54 (8): 2810–2815.
- 58 Liu, Y.-d. and Ying, Y.-b. (2004). Measurement of sugar content in Fuji apples by FT-NIR spectroscopy. *Journal of Zhejiang University* 5 (6): 651–655.
- 59 Das, A.J., Wahi, A., Kothari, I., and Raskar, R. (2016). Ultra-portable, wireless smartphone spectrometer for rapid, non-destructive testing of fruit ripeness. *Scientific Reports* 6.
- 60 Temma, T., Hanamatsu, K., and Shinoki, F. (2002). Development of a portable near infrared sugar-measuring instrument. *Journal of Near Infrared Spectroscopy* 10 (1): 77–83.
- 61 Yang, B., Guo, W., Li, W. et al. (2019). Portable, visual, and nondestructive detector integrating Vis/NIR spectrometer for sugar content of kiwifruits. *Journal of Food Process Engineering* 42 (2): e12982.
- 62 Yu, X., Lu, Q., Gao, H., and Ding, H. (2016). Development of a handheld spectrometer based on a linear variable filter and a complementary metal-oxide-semiconductor detector for measuring the internal quality of fruit. *Journal of Near Infrared Spectroscopy* 24 (1): 69–76.
- 63 Beghi, R., Spinardi, A., Bodria, L. et al. (2013). Apples nutraceutic properties evaluation through a visible and near-infrared portable system. *Food and Bioprocess Technology* 6 (9): 2547–2554.
- 64 Beghi, R., Giovenzana, V., Spinardi, A. et al. (2013). Derivation of a blueberry ripeness index with a view to a low-cost, handheld optical sensing device for supporting harvest decisions. *Transactions of the ASABE* 56 (4): 1551–1559.
- 65 Guidetti, R., Beghi, R., Bodria, L. et al. (2009). *Prediction of Blueberry (Vaccinium Corymbosum) Ripeness by a Portable VIS-NIR Device*, 877–886. Leuven, Belgium: International Society for Horticultural Science (ISHS).
- 66 Xudong, S., Hailiang, Z., and Yande, L. (2009). Nondestructive assessment of quality of Nanfeng mandarin fruit by a portable near infrared spectroscopy. *International Journal of Agricultural and Biological Engineering* 2 (1): 65–71.
- 67 Camps, C. and Christen, D. (2009). Non-destructive assessment of apricot fruit quality by portable visible-near infrared spectroscopy. *LWT - Food Science and Technology* 42 (6): 1125–1131.
- 68 Sun, H.; Peng, Y.; Li, P.; Wang, W (2017). A portable device for detecting fruit quality by diffuse reflectance Vis/NIR spectroscopy. *Proceedings of SPIE 10217, Sensing for Agriculture and Food Quality and Safety IX*, 102170T (1 May 2017), pp 102170T-102170T-6. <https://doi.org/10.1117/12.2262526>
- 69 Bennedsen, B.S. (2004). Near infrared (NIR) technology and multivariate data analysis for sensing taste attributes of apples. *International Agrophysics* 2000: 203–211.
- 70 Guo, Z., Huang, W., Peng, Y. et al. (2016). Color compensation and comparison of shortwave near infrared and long wave near infrared spectroscopy for determination of soluble solids content of 'Fuji' apple. *Postharvest Biology and Technology* 115: 81–90.

- 71** Pezzei, C.K., Schönbichler, S.A., Kirchler, C.G. et al. (2017). Application of benchtop and portable near-infrared spectrometers for predicting the optimum harvest time of *Verbena officinalis*. *Talanta* 169: 70–76.
- 72** Urraca, R., Sanz-Garcia, A., Tardaguila, J., and Diago, M.P. (2016). Estimation of total soluble solids in grape berries using a hand-held NIR spectrometer under field conditions. *Journal of the Science of Food and Agriculture* 96 (9): 3007–3016.
- 73** Wiedemair, V. and Huck, C.W. (2019). Investigating the total antioxidant capacity of gluten-free grains with miniaturized near-infrared spectrometer. *NIR News* 30 (5–6): 35–38.
- 74** Henn, R., Kirchler, C.G., and Huck, C.W. (2017). Miniaturized NIR spectroscopy for the determination of main carbohydrates in syrup. *NIR News* 28 (2): 3–6.
- 75** Sánchez, M.-T., Torres, I., de la Haba, M.-J. et al. (2019). Rapid, simultaneous, and in situ authentication and quality assessment of intact bell peppers using near-infrared spectroscopy technology. *Journal of the Science of Food and Agriculture* 99 (4): 1613–1622.
- 76** Entrenas, J.-A., Pérez-Marín, D., Torres, I. et al. (2019). Safety and quality issues in summer squashes using handheld portable NIRS sensors for real-time decision making and on-vine monitoring. *Journal of the Science of Food and Agriculture* 99 (15): 6768–6777.
- 77** Schmutzler, M. and Huck, C.W. (2016). Simultaneous detection of total antioxidant capacity and total soluble solids content by Fourier transform near-infrared (FT-NIR) spectroscopy: a quick and sensitive method for on-site analyses of apples. *Food Control* 66: 27–37.
- 78** Ayvaz, H., Plans, M., Towers, B.N. et al. (2015). The use of infrared spectrometers to predict quality parameters of cornmeal (corn grits) and differentiate between organic and conventional practices. *Journal of Cereal Science* 62: 22–30.
- 79** Correia, R.M., Tosato, F., Domingos, E. et al. (2018). Portable near infrared spectroscopy applied to quality control of Brazilian coffee. *Talanta* 176: 59–68.
- 80** Du, X.-l., Li, X.-y., Liu, Y. et al. (2019). Genetic algorithm optimized non-destructive prediction on property of mechanically injured peaches during postharvest storage by portable visible/shortwave near-infrared spectroscopy. *Scientia Horticulturae* 249: 240–249.
- 81** Buccheri, M., Grassi, M., Lovati, F. et al. (2019). Near infrared spectroscopy in the supply chain monitoring of Annurca apple. *Journal of Near Infrared Spectroscopy* 27 (1): 86–92.
- 82** Malegori, C., Nascimento Marques, E.J., de Freitas, S.T. et al. (2017). Comparing the analytical performances of micro-NIR and FT-NIR spectrometers in the evaluation of acerola fruit quality, using PLS and SVM regression algorithms. *Talanta* 165: 112–116.
- 83** Marques, E.J.N., de Freitas, S.T., Pimentel, M.F., and Pasquini, C. (2016). Rapid and non-destructive determination of quality parameters in the ‘Tommy Atkins’ mango using a novel handheld near infrared spectrometer. *Food Chemistry* 197: 1207–1214.
- 84** Baca-Bocanegra, B., Hernández-Hierro, J.M., Nogales-Bueno, J., and Heredia, F.J. (2018). Feasibility study on the use of a portable micro near infrared spectroscopy device for the “in vineyard” screening of extractable polyphenols in red grape skins. *Talanta* 192: 353–359.
- 85** Bonifazi, G., Gasbarrone, R., and Serranti, S. (2019). *Dried Red Chili Peppers Pungency Assessment by Visible and near Infrared Spectroscopy*, vol. 10986. SPIE.
- 86** Diao, H., Wu, Y.M., Yang, Y.H. et al. (2016). Study on the determination of the maturity level of tobacco leaf based on in-situ spectral measurement. *Spectroscopy and Spectral Analysis* 36 (6): 1826–1830.
- 87** Subedi, P.P. and Walsh, K.B. (2020). Assessment of avocado fruit dry matter content using portable near infrared spectroscopy: method and instrumentation optimisation. *Postharvest Biology and Technology* 161: 111078.
- 88** Kaur, H., Künnemeyer, R., and McGlone, A. (2017). Comparison of hand-held near infrared spectrophotometers for fruit dry matter assessment. *Journal of Near Infrared Spectroscopy* 25 (4): 267–277.

- 89 McCormick, R. and Biegert, K. (2019). Monitoring the growth and maturation of apple fruit on the tree with handheld Vis/NIR devices. *NIR News* 30 (1): 12–15.
- 90 Zhang, Y., Nock, J.F., Al Shoffe, Y., and Watkins, C.B. (2019). Non-destructive prediction of soluble solids and dry matter contents in eight apple cultivars using near-infrared spectroscopy. *Postharvest Biology and Technology* 151: 111–118.
- 91 dos Santos Neto, J.P., de Assis, M.W.D., Casagrande, I.P. et al. (2017). Determination of ‘palmer’ mango maturity indices using portable near infrared (VIS-NIR) spectrometer. *Postharvest Biology and Technology* 130: 75–80.
- 92 Escribano, S., Biasi, W.V., Lerud, R. et al. (2017). Non-destructive prediction of soluble solids and dry matter content using NIR spectroscopy and its relationship with sensory quality in sweet cherries. *Postharvest Biology and Technology* 128: 112–120.
- 93 Wang, J., Muhammad, Z., He, P. et al. (2019). Evaluating matcha tea quality index using portable NIR spectroscopy coupled chemometric algorithms. *Journal of the Science of Food and Agriculture* 99: 5019–5027.
- 94 Dong, A.; Wang, W.; Zhao, X.; Chu, X.; Wang, B.; Bai, X.; Qin, H.; Jiang, H.; Jia, B.; Yang, Y.; Kimulia, D. (2018). Identification of fiber added to semolina by near infrared (NIR) spectral techniques. *2018 ASABE Annual International Meeting*, ASABE: St. Joseph, MI. p 1.
- 95 Sheng, R., Cheng, W., Li, H. et al. (2019). Model development for soluble solids and lycopene contents of cherry tomato at different temperatures using near-infrared spectroscopy. *Postharvest Biology and Technology* 156: 110952.
- 96 Jianqiang, Z., Panpan, Y., Weijuan, L. et al. (2019). Rapid and automatic classification of tobacco leaves using a hand-held DLP-based NIR spectroscopy device. *Journal of the Brazilian Chemical Society* 30 (9): 1927–1932.
- 97 Wang, T., Chen, J., Fan, Y. et al. (2018). SeeFruits: design and evaluation of a cloud-based ultra-portable NIRS system for sweet cherry quality detection. *Computers and Electronics in Agriculture* 152: 302–313.
- 98 Dong, A., Wang, W., Zhao, X. et al. (2018). Rapid classificataion of corn varieties by using near infrared spectroscopy. In: *2018 ASABE Annual International Meeting*, 1. St. Joseph, MI: ASABE.
- 99 Li, M., Qian, Z., and East, A.R. (2018). *Does Consumer-Scale Near-Infrared (NIR) Spectroscopy Provide Opportunities for Kiwifruit Quality Measurement?* 481–488. Leuven, Belgium: International Society for Horticultural Science (ISHS).
- 100 Kosmowski, F. and Worku, T. (2018). Evaluation of a miniaturized NIR spectrometer for cultivar identification: the case of barley, chickpea and sorghum in Ethiopia. *PLoS One* 13 (3): e0193620.
- 101 Wiedemair, V. and Huck, C.W. (2018). Evaluation of the performance of three hand-held near-infrared spectrometer through investigation of total antioxidant capacity in gluten-free grains. *Talanta* 189: 233–240.
- 102 Teye, E., Amuah, C.L.Y., McGrath, T., and Elliott, C. (2019). Innovative and rapid analysis for rice authenticity using hand-held NIR spectrometry and chemometrics. *Spectrochimica Acta Part A: Molecular and Biomolecular Spectroscopy* 217: 147–154.
- 103 Zhao, T., Koumis, A., Niu, H. et al. (2018). Onion irrigation treatment inference using a low-cost hyperspectral scanner. In: *SPIE Asia-Pacific Remote Sensing*, 7. SPIE.
- 104 Lee, S.; Noh, T. G.; Choi, J. H.; Han, J.; Ha, J. Y.; Lee, J. Y.; Park, Y. (2017). NIR spectroscopic sensing for point-of-need freshness assessment of meat, fish, vegetables and fruits. *Proceedings of SPIE 10217, Sensing for Agriculture and Food Quality and Safety IX*, 1021708 (1 May 2017). <https://doi.org/10.1117/12.2261803>.
- 105 Entrenas, J.-A., Pérez-Marin, D., Torres, I. et al. (2019). Safety and quality issues in summer squashes using handheld portable NIRS sensors for real-time decision making and for on-vine monitoring. *Journal of the Science of Food and Agriculture* 99 (15): 6768–6777.
- 106 Wiedemair, V., Mair, D., Held, C., and Huck, C.W. (2019). Investigations into the use of handheld near-infrared spectrometer and novel semi-automated data analysis for the determination of protein content in different cultivars of *Panicum miliaceum* L. *Talanta* 205: 120115.

- 107** Yan, H.; Siesler, HW. (2018). Hand-held near-infrared spectrometers: State-of-the-art instrumentation and practical applications. *NIR News.* 0960336018796391.
- 108** Qi, S., Oshita, S., Makino, Y., and Han, D. (2017). Influence of sampling component on determination of soluble solids content of Fuji apple using near-infrared spectroscopy. *Applied Spectroscopy* 71 (5): 856–865.
- 109** Kumar, S., McGlone, A., Whitworth, C., and Volz, R. (2015). Postharvest performance of apple phenotypes predicted by near-infrared (NIR) spectral analysis. *Postharvest Biology and Technology* 100: 16–22.
- 110** Ribera-Fonseca, A., Noferini, M., and Rombolá, A.D. (2016). Non-destructive assessment of highbush blueberry fruit maturity parameters and anthocyanins by using a visible/near infrared (Vis/NIR) spectroscopy device: a preliminary approach. *Journal of Soil Science and Plant Nutrition* 16: 174–186.
- 111** Masithoh, R.E., Ron, H., and Kawano, S. (2016). Determination of soluble solids content and titratable acidity of intact fruit and juice of Satsuma mandarin using a hand-held near infrared instrument in transmittance mode. *Journal of Near Infrared Spectroscopy* 24: 83–88.
- 112** Torres, I., Sánchez, M.-T., de la Haba, M.-J., and Pérez-Marín, D. (2019). LOCAL regression applied to a citrus multispecies library to assess chemical quality parameters using near infrared spectroscopy. *Spectrochimica Acta Part A: Molecular and Biomolecular Spectroscopy* 217: 206–214.
- 113** Antonucci, F., Pallottino, F., Paglia, G. et al. (2011). Non-destructive estimation of mandarin maturity status through portable VIS-NIR spectrophotometer. *Food and Bioprocess Technology* 4 (5): 809–813.
- 114** Xiao, H., Sun, K., Sun, Y. et al. (2017). Comparison of benchtop Fourier-transform (FT) and portable grating scanning spectrometers for determination of total soluble solid contents in single grape berry (*Vitis vinifera* L.) and calibration transfer. *Sensors* 17 (11): 2693.
- 115** Leiqing, P. A. N.; Hui, X.; Ke, S. U. N.; Kang, T.U. (2018). Development and application of a portable specialized visible and near-infrared detective instrument for grape quality. *2018 ASABE Annual International Meeting*, ASABE: St. Joseph, MI. p 1.
- 116** Wang, J., Wang, J., Chen, Z., and Han, D. (2017). Development of multi-cultivar models for predicting the soluble solid content and firmness of European pear (*Pyrus communis* L.) using portable Vis-NIR spectroscopy. *Postharvest Biology and Technology* 129: 143–151.
- 117** Li, J., Wang, Q., Xu, L. et al. (2019). Comparison and optimization of models for determination of sugar content in pear by portable Vis-NIR spectroscopy coupled with wavelength selection algorithm. *Food Analytical Methods* 12 (1): 12–22.
- 118** Pérez-Marín, D., Paz, P., Guerrero, J.-E. et al. (2010). Miniature handheld NIR sensor for the on-site non-destructive assessment of post-harvest quality and refrigerated storage behavior in plums. *Journal of Food Engineering* 99 (3): 294–302.
- 119** Pérez-Marín, D., Sánchez, M.-T., Paz, P. et al. (2009). Non-destructive determination of quality parameters in nectarines during on-tree ripening and postharvest storage. *Postharvest Biology and Technology* 52 (2): 180–188.
- 120** Christen, D., Camps, C., Summermatter, A. et al. (2012). *Prediction of the Pre- and Postharvest Apricot Quality with Different Vis/Nirs Devices*, 149–153. Leuven, Belgium: International Society for Horticultural Science (ISHS).
- 121** Sánchez, M.-T., De la Haba, M.J., Benítez-López, M. et al. (2012). Non-destructive characterization and quality control of intact strawberries based on NIR spectral data. *Journal of Food Engineering* 110 (1): 102–108.
- 122** Walsh, K.B., Golic, M., and Greensill, C.V. (2004). Sorting of fruit using near infrared spectroscopy: application to a range of fruit and vegetables for soluble solids and dry matter content. *Journal of Near Infrared Spectroscopy* 12 (3): 141–148.
- 123** Entrenas, J.-A., Pérez-Marín, D., Torres, I. et al. (2020). Simultaneous detection of quality and safety in spinach plants using a new generation of NIRS sensors. *Postharvest Biology and Technology* 160: 111026.

- 124 Pérez-Marín, D., Torres, I., Entrenas, J.-A. et al. (2019). Pre-harvest screening on-vine of spinach quality and safety using NIRS technology. *Spectrochimica Acta Part A: Molecular and Biomolecular Spectroscopy* 207: 242–250.
- 125 Pan, L., Lu, R., Zhu, Q. et al. (2015). Measurement of moisture, soluble solids, sucrose content and mechanical properties in sugar beet using portable visible and near-infrared spectroscopy. *Postharvest Biology and Technology* 102: 42–50.
- 126 Torres, I., Sánchez, M.-T., Entrenas, J.-A. et al. (2019). Monitoring quality and safety assessment of summer squashes along the food supply chain using near infrared sensors. *Postharvest Biology and Technology* 154: 21–30.
- 127 Jha, S.N. and Ruchi, G. (2010). Non-destructive prediction of quality of intact apple using near infrared spectroscopy. *Journal of Food Science and Technology* 47 (2): 207–213.
- 128 Sánchez, M.-T., Entrenas, J.-A., Torres, I. et al. (2018). Monitoring texture and other quality parameters in spinach plants using NIR spectroscopy. *Computers and Electronics in Agriculture* 155: 446–452.
- 129 Davey, M.W., Saeys, W., Hof, E. et al. (2009). Application of visible and near-infrared reflectance spectroscopy (Vis/NIRS) to determine carotenoid contents in banana (*musa spp.*) fruit pulp. *Journal of Agricultural and Food Chemistry* 57 (5): 1742–1751.
- 130 Torres, I., Pérez-Marín, D., De la Haba, M.-J., and Sánchez, M.-T. (2017). Developing universal models for the prediction of physical quality in citrus fruits analysed on-tree using portable NIRS sensors. *Biosystems Engineering* 153: 140–148.
- 131 Grandón, S., Sanchez-Contreras, J., and Torres, C.A. (2019). Prediction models for sunscald on apples (*Malus domestica* Borkh.) cv. Granny Smith using Vis-NIR reflectance. *Postharvest Biology and Technology* 151: 36–44.
- 132 Peshlov, B.N., Dowell, F.E., Drummond, F.A., and Donahue, D.W. (2009). Comparison of three near infrared spectrophotometers for infestation detection in wild blueberries using multivariate calibration models. *Journal of Near Infrared Spectroscopy* 17 (4): 203–212.
- 133 Henn, R., Kirchler, C.G., Grossgut, M.-E., and Huck, C.W. (2017). Comparison of sensitivity to artificial spectral errors and multivariate LOD in NIR spectroscopy – determining the performance of miniaturizations on melamine in milk powder. *Talanta* 166: 109–118.
- 134 Karunathilaka, S.R., Yakes, B.J., He, K. et al. (2018). Non-targeted NIR spectroscopy and SIMCA classification for commercial milk powder authentication: a study using eleven potential adulterants. *Heliyon* 4 (9): e00806.
- 135 de la Roza-Delgado, B., Garrido-Varo, A., Soldado, A. et al. (2017). Matching portable NIRS instruments for in situ monitoring indicators of milk composition. *Food Control* 76: 74–81.
- 136 Llano Suárez, P., Soldado, A., González-Arrojo, A. et al. (2018). Rapid on-site monitoring of fatty acid profile in raw milk using a handheld near infrared sensor. *Journal of Food Composition and Analysis* 70: 1–8.
- 137 Holroyd, S.E. (2013). The use of near infrared spectroscopy on Milk and Milk products. *Journal of Near Infrared Spectroscopy* 21 (5): 311–322.
- 138 de Lima, G.F., Andrade, S.A.C., da Silva, V.H., and Honorato, F.A. (2018). Multivariate classification of UHT milk as to the presence of lactose using benchtop and portable NIR spectrometers. *Food Analytical Methods* 11 (10): 2699–2706.
- 139 Liu, N., Parra, H.A., Pustjens, A. et al. (2018). Evaluation of portable near-infrared spectroscopy for organic milk authentication. *Talanta* 184: 128–135.
- 140 van Ruth, S. and Liu, N. (2019). How organic is organic milk? Can we have a quick check? *NIR News* 30 (2): 18–21.
- 141 Cattaneo, T.M.P. and Holroyd, S.E. (2013). The use of near infrared spectroscopy for determination of adulteration and contamination in milk and milk powder: updating knowledge. *Journal of Near Infrared Spectroscopy* 21 (5): 341–349.
- 142 Suarez, W.T., de Alvarenga Junior, B.R., de Oliveira Krambeck Franco, M. et al. (2017). In situ determination of urea in milk employing a portable and low-cost LED photometer. *Food Analytical Methods* 11: 1149–1154.

- 143** Evershed, R. and Temple, N. (2016). *Sorting the Beef from the Bull: The Science of Food Fraud Forensics*. Bloomsbury Publishing.
- 144** Wiedemair, V., De Biasio, M., Leitner, R. et al. (2018). Application of design of experiment for detection of meat fraud with a portable near-infrared spectrometer. *Current Analytical Chemistry* 14 (1): 58–67.
- 145** Schmutzler, M., Begovic, A., Bohler, G., and Huck, C.W. (2015). Methods for detection of pork adulteration in veal product based on FT-NIR spectroscopy for laboratory, industrial and on-site analysis. *Food Control* 57: 258–267.
- 146** Grassi, S., Casiraghi, E., and Alamprese, C. (2018). Handheld NIR device: a non-targeted approach to assess authenticity of fish fillets and patties. *Food Chemistry* 243 (Supplement C): 382–388.
- 147** Knight, M.I., Linden, N., Ponnampalam, E.N. et al. (2019). Development of VISNIR predictive regression models for ultimate pH, meat tenderness (shear force) and intramuscular fat content of Australian lamb. *Meat Science* 155: 102–108.
- 148** Wenxiu, W.; Yankun, P.; Hongwei, S.; Long, L. (2017) Real-time detection of intact pork freshness based on near infrared spectroscopy. *2017 ASABE Annual International Meeting*, 1.
- 149** Pochanagone, S. and Rittiron, R. (2019). Rapid detection of infrared inactive sodium chloride content in frozen tuna fish for determining commercial value using short wavelengths. *Journal of Near Infrared Spectroscopy* 27 (6): 424–431.
- 150** Garrido-Varo, A.; Riccioli, C.; Fearn, T.; Pedro, E. D.; Pérez-Marín, DC. (2019). Miniature near infrared spectroscopy spectrometer and information and communication technologies to guarantee the integrity of the EU high added-value “acorn Iberian pig ham” (IP). *Proceedings of the SPIE 10665, Sensing for Agriculture and Food Quality and Safety X*, 106650M (7 June 2018). <https://doi.org/10.1117/12.2299641>.
- 151** Prieto, N., Pawluczyk, O., Dugan, M.E.R., and Aalhus, J.L. (2017). A review of the principles and applications of near-infrared spectroscopy to characterize meat, fat, and meat products. *Applied Spectroscopy* 71 (7): 1403–1426.
- 152** Maraphum, K., Chuan-Udom, S., Saengprachatanarug, K. et al. (2018). Effect of waxy material and measurement position of a sugarcane stalk on the rapid determination of pol value using a portable near infrared instrument. *Journal of Near Infrared Spectroscopy* 26 (5): 287–296.
- 153** Taira, E., Ueno, M., Saengprachatanarug, K., and Kawamitsu, Y. (2013). Direct sugar content analysis for whole stalk sugarcane using a portable near infrared instrument. *Journal of Near Infrared Spectroscopy* 21 (4): 281–287.
- 154** Henn, R., Schwab, A., and Huck, C.W. (2016). Evaluation of benchtop versus portable near-infrared spectroscopic method combined with multivariate approaches for the fast and simultaneous quantitative analysis of main sugars in syrup formulations. *Food Control* 68: 97–104.
- 155** Lin, C.-A., Ayvaz, H., and Rodriguez-Saona, L.E. (2014). Application of portable and handheld infrared spectrometers for determination of sucrose levels in infant cereals. *Food Analytical Methods* 7 (7): 1407–1414.
- 156** Tugnolo, A., Beghi, R., Giovenzana, V., and Guidetti, R. (2019). Characterization of green, roasted beans, and ground coffee using near infrared spectroscopy: a comparison of two devices. *Journal of Near Infrared Spectroscopy* 27 (1): 93–104.
- 157** Zhang, H., Duan, Z., Li, Y. et al. (2019). Vis/NIR reflectance spectroscopy for hybrid rice variety identification and chlorophyll content evaluation for different nitrogen fertilizer levels. *Royal Society Open Science* 6 (10): 191132.
- 158** Grossi, M., Palagano, R., Bendini, A. et al. (2019). Design and in-house validation of a portable system for the determination of free acidity in virgin olive oil. *Food Control*.
- 159** Picouet, P.A., Gou, P., Hyypio, R., and Castellari, M. (2018). Implementation of NIR technology for at-line rapid detection of sunflower oil adulterated with mineral oil. *Journal of Food Engineering* 230: 18–27.
- 160** Guelpa, A., Marini, F., du Plessis, A. et al. (2017). Verification of authenticity and fraud detection in south African honey using NIR spectroscopy. *Food Control* 73: 1388–1396.

- 161** Zhang, H.M., Wu, T.X., Zhang, L.F., and Zhang, P. (2016). Development of a portable field imaging spectrometer: application for the identification of sun-dried and sulfur-fumigated Chinese herbals. *Applied Spectroscopy* 70 (5): 879–887.
- 162** Zareef, M., Chen, Q., Ouyang, Q. et al. Rapid screening of phenolic compounds in congou black tea (*Camellia sinensis*) during in vitro fermentation process using portable spectral analytical system coupled chemometrics. *Journal of Food Processing and Preservation* 0 (0): e13996.
- 163** Baqueta, M.R., Coqueiro, A., Março, P.H., and Valderrama, P. (2019). Quality control parameters in the roasted coffee industry: a proposal by using MicroNIR spectroscopy and multivariate calibration. *Food Analytical Methods* 13: 50–60.
- 164** Phuphaphud, A., Saengprachatanarug, K., Posom, J. et al. (2019). Prediction of the fibre content of sugar-cane stalk by direct scanning using visible-shortwave near infrared spectroscopy. *Vibrational Spectroscopy* 101: 71–80.
- 165** Plans, M., Simó, J., Casañas, F. et al. (2013). Characterization of common beans (*Phaseolus vulgaris* L.) by infrared spectroscopy: comparison of MIR, FT-NIR and dispersive NIR using portable and benchtop instruments. *Food Research International* 54 (2): 1643–1651.
- 166** McReynolds, N., Auñón Garcia, J.M., Guengerich, Z. et al. (2016). Optical spectroscopic analysis for the discrimination of extra-virgin olive oil. *Applied Spectroscopy* 70 (11): 1872–1882.

## 16

### Handheld Raman, SERS, and SORS

Michael Hargreaves

*Rigaku Analytical Devices Inc, Wilmington, MA, USA*

#### 16.1 Introduction

Raman spectroscopy application areas continue to expand, as this analytical technique may be applied to a wide variety of fields, including safety and security, pharmaceuticals, and narcotics screening. Portable Raman spectrometers have seen widespread deployment by the military, homeland security, and major pharmaceutical companies, mainly because of their high chemical specificity, which allows robust identification (ID) and verification. Other chapters in these volumes discuss in detail the technologies used in portable Raman instruments (Rathmell et al.), construction of libraries and databases (Schreyer), ID algorithms (Zhang, Lee, and Schreyer), and pharmaceutical counterfeiting (Leary, Crocombe, and Kalyanaraman), so these topics will only be touched on lightly. This chapter discusses the various variants, applications, and technologies of the latest portable Raman spectrometers that enable robust field ID of chemicals of interest to the military, hazardous materials (hazmat), law enforcement, and pharmaceutical companies for raw material ID and anti-counterfeit activities. In particular, the approaches to current challenges that portable Raman faces in the field (standoff detection, sample heating, fluorescence, through-package measurement, low-level detection in mixtures) are described.

Figure 16.1 highlights several of the available handheld Raman devices currently available on the market, spanning conventional, spatially offset Raman spectroscopy (SORS), and standoff devices.

#### 16.2 Raman Spectroscopy: Sampling Techniques, Technologies, and Considerations

Since the Raman effect is a scattering process, sampling for Raman spectroscopy is straightforward [1–3]. However, compared with mid-infrared spectroscopy, it is a weak effect so that for successful measurement, an efficient sampling geometry and collection optics are critically required [2–4]. The scattering nature of the technique implies that the requirements for sample handling and preparation are minimal and often noncontact is feasible, and this is the major and often cited advantage of Raman spectroscopy over other techniques and technologies [1–13]. Another significant advantage that Raman spectroscopy has compared, especially with mid-infrared spectroscopy, is that glass, which is a very strong absorber of mid-infrared radiation, is a relatively weak Raman scatterer, enabling facile collection of Raman spectra from glass vessels. A second major advantage that Raman spectroscopy has compared with mid-infrared spectroscopy is that water, a very strong absorber of mid-infrared radiation, is a relatively weak Raman scatterer, enabling collection of spectra from wet samples and aqueous



**Figure 16.1** (From top left) B&W TEK (Tactic ID 1064), Agilent (Resolve), Pendar Technologies (X10), and Rigaku Analytical Devices (CQL ResQ). Source: Reproduced with Permission, Courtesy of: B&W TEK Inc, Agilent Technologies Inc, Pendar Technologies Inc, Rigaku Analytical Devices Inc.

solutions. Finally, the combination of these advantages, coupled with the use of a laser as the exciting source (as compared with a large-area incandescent source used in mid-infrared spectroscopy), facilitates the study of small samples. Therefore, over the last decade, Raman spectroscopy has moved to the forefront as a technique for criminalistic and forensic analyses applications and studies related to art and archaeology specimen conservation and authenticity.

The main sampling categories for Raman spectroscopy may be considered as (i) *conventional* using either a 180° (sometimes referred to as *backscattering*) or a 90° sampling geometry, (ii) *Raman microspectroscopy* based on integrating Raman spectroscopy and optical microscopy for high lateral and depth spatial resolution studies, and (iii) *remote or noninvasive* sampling via a fiber-optic probe [1]. The most common and convenient configuration for handheld Raman spectroscopy is the 180° geometry.

**Table 16.1** List of common pure chemical explosives and their suitability for examination with Raman spectroscopy.

Type	Examples	Raman
Low explosives	Gunpowder	Y <sup>a</sup>
	Metal powders	N
	Smokeless powders	Y <sup>a</sup>
High explosives (primary)	Lead azide	Y
	Lead styphnate	Y
	Lead picrate	Y
	Mercury fulminate	Y
	Nitroglycerin	Y
	Nitrocellulose	Y
	TATP	Y
	HMTD	
High explosives (secondary)	TNT	Y
	EDGN	Y
	PETN	Y
	RDX	Y
	HMX	Y

Y = Yes – this analyte may be identified. N = No – this analyte cannot be identified.

a) Some handheld system manufacturers claim the ability to scan these materials.

The challenges in collecting Raman spectra are well known [1]. Raman scattering is a very weak phenomenon, several orders of magnitude less than Rayleigh (elastic, i.e. with no shift from the wavelength of the exciting radiation) scattering, which occurs simultaneously. This has placed extreme demands on spectrometer design to manage both the intensity of the Rayleigh scattering returned to the spectrometer and the resulting “stray light” within the spectrometer. Fluorescence is a much stronger effect than Raman scattering, and fluorescence from even minor components or contaminants in a sample can obscure and prevent the collection of a useful Raman spectrum. While the shape of broadband fluorescence can be modeled and mathematically “subtracted” or removed, its shot noise contribution will remain and in extreme cases will totally obscure the Raman spectrum. Fluorescence is reduced with long wavelength excitation, due to the relative absence of electronic transitions in the near infrared (NIR), but the intensity of Raman scattering is proportional to  $\nu^4$ , where  $\nu$  is the exciting frequency, so that a penalty is paid (in terms of system sensitivity, limit of detection (LOD), and general applicability). Lastly, because it is necessary to detect low very light levels, sensitive detectors are used, but NIR detectors (e.g. using indium gallium arsenide [InGaAs]) have significantly higher data noise (higher dark current) than visible and shortwave NIR detectors (charge-coupled detectors [CCD] and complementary metal–oxide–semiconductor [CMOS]), based on silicon as a detector material. The performance characteristics of the sensor types, leads to compromises which can impact feasibility of applications and require trade-offs to be made to yield acceptable performance for in-field applications [14]. Moving to shorter excitation wavelengths, ultraviolet (UV) excitation promises Raman and fluorescence spectra separated in wavelength space or the absence of fluorescence for many samples with excitation at wavelengths shorter than 250 nm. While detection will be more sensitive than in the NIR, UV Raman systems are challenging to move and deploy today and do not permit measurement of spectra through barrier layers, even glass.

Laboratory Fourier transform (FT-) Raman instruments, developed in the mid-1980s, employed 1064 nm excitation to minimize fluorescence and had the throughput and multiplex advantages of the interferometer to compensate partially for both the  $\nu^4$  loss and increased detector noise. In the 1990s, 785 nm excitation and CCD detection

emerged as the best compromise for many applications, and these components are especially amenable to use in a miniature spectrometer [7, 8]. In the mid-2000s, dispersive-based 1064 nm excitation systems started to become available, as InGaAs sensors matured to a point of being viable, both for economic and performance reasons. However, 1064 nm excitation instruments typically require more laser power at the sample and longer collection times; one study estimated that factor was about 40 [15].

Ongoing developments seek to address consequences of the challenges listed above and provide portable Raman systems capable of standoff detection, reduced sample heating and fluorescence, and through-package measurement. For standoff detection, a large deep-UV excitation system has been developed, and recently a cordless drill sized instrument with excitation in the visible portion of the spectrum. For sample heating, the laser beam can be defocused on the sample, but this leads to collection inefficiencies. Alternatively, the excitation and collection spot can be moved around rapidly, so that there is a minimal dwell time at each spot. For fluorescence avoidance, there has been a trend toward longer wavelength excitation (1064 nm), as well as schemes to model or “subtract” the fluorescence contribution via shifting the excitation wavelength slightly. Through-package measurement has been addressed by the development of SORS.

### 16.3 Handheld Raman Devices

Raman spectroscopic applications have been slowly emerging for many decades. Due to the relatively weak Raman scattering effect, it has taken time for the hardware to progress to a level that allows these measurements to offer a practical advantage for many analytical applications, especially in the field. As such, Raman spectroscopy has only seen widespread use outside research laboratories over the last decade or so. More recently, some of the advances that have made portable Raman spectrometers possible are the introduction of miniature laser diode sources, miniaturized spectrographs, and microprocessor instrument control.

The revolution of handheld Raman devices that began about a decade ago continues apace. The shift to a longer wavelength excitation region beyond 1  $\mu\text{m}$  allowing a reduction in fluorescence has significantly improved capabilities, permitting samples that may not give a spectrum at 785 nm to now be identified (see Figure 16.2). The move from the laboratory to the field now facilitates ID, verification, and screening of a multitude of chemicals at the sample site across a wide range of applications.

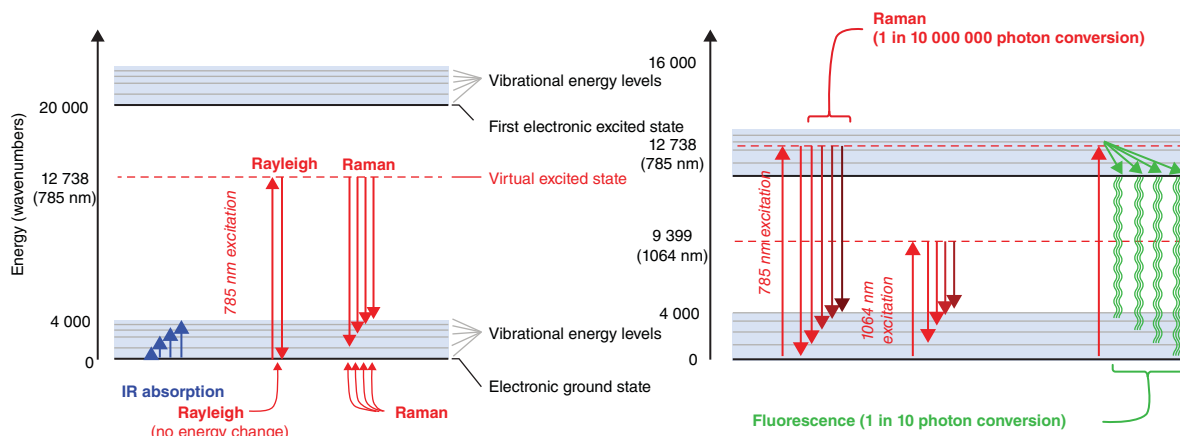


**Figure 16.2** Impact of different laser excitations on causing fluorescence. Source: Hargreaves, M. D. (2014). Handheld raman spectrometers and their applications. Encyclopedia of Analytical Chemistry, 1–16.

## 16.4 Sample Considerations

There are several practical aspects of Raman analysis that should be considered because they ultimately govern the applicability of handheld Raman technologies. It is important to note that many materials that cannot be identified by Raman spectroscopy are amenable to ID by Fourier transform infrared (FT-IR) spectroscopy, and vice versa. For this reason, these methods are frequently deployed together to provide complementary results and a more complete understanding of the sample.

### 16.4.1 Fluorescence

Some materials can be very difficult to identify with Raman systems due to overwhelming fluorescence. Strongly colored materials are particularly problematic in this regard with 785 nm excitation, but they are less problematic at 1064 nm. The trade-off in moving to 1064 nm excitation is that the lower performance of InGaAs-based detectors required for this excitation frequency, when compared with the CCD detectors used in 785 nm systems, requires longer collection times. In addition, intensity of Raman scattering is proportional to  $\nu^4$ , where  $\nu$  is the exciting frequency. This also leads to longer collection times. In some application cases simply having the ability to collect a useful spectrum using 1064 nm excitation, even if sampling takes a long time, outweighs the reduction in spectral performance compared with the inability to collect a Raman spectrum at 785 nm. A shift in excitation further into the red, past 1  $\mu\text{m}$ , will reduce, but not eliminate completely, fluorescence and luminescence.

Surface-enhanced Raman spectroscopy (SERS) is also used in field instruments to reduce fluorescence and permit detection of substances of interest in complex and fluorescing mixtures. This is discussed in more detail in the following section. A laboratory time-gated Raman spectrometer recently became available, and this is another approach to mitigate or avoid fluorescence. However, this technology is complex, and it is unlikely to be available in a handheld form factor for many years.

Raman spectroscopy has the advantage of being noncontact and capable of performing analysis of materials contained in transparent containers (e.g. glass bottles, plastic bags). Although some thick containers can be challenging for Raman spectroscopy and fluorescent containers (e.g. green glass wine bottles) even more so, today's Raman spectroscopic devices coupled with the appropriate signal processing often have little difficulty providing ID in conditions that were historically challenging.

### 16.4.2 Sample Heating

In addition to the fluorescence considerations noted above, very darkly colored, thermally sensitive materials, such as gunpowder, may even burn when measured by Raman spectroscopy using high-power excitation. Systems like one offered by Metrohm use rastering of the laser to spread the laser power across a larger area rather than performing a point measurement. This reduces heat buildup, diminishing the risk of sample degradation or ignition. Fluorescence is not a limitation in mid-IR spectroscopy, nor is there an ignition risk for dark materials from laser heating, but there is potential for issues with mid-IR when utilizing ATR (attenuated total reflectance) accessories, whereby pressure is applied to samples and care should be taken when sampling as some samples are pressure sensitive.

### 16.4.3 Through-Package Measurement

Handheld Raman instruments can obtain spectra of samples contained in optically transparent (clear glass and plastic) containers, and this represents a major advantage of this technique over mid-infrared spectroscopy. SORS can be used to scan samples in translucent (opaque) or highly fluorescent packaging, and is described in detail in the following section. It is in active use in the Agilent Resolve handheld spectrometer (see Figure 16.1), a new

system targeted for pharmaceutical verification, the Vaya handheld device, and the RapID trolley device for raw material verification, as well as the Insight100 Bottle Liquid Screener (BLS).

## 16.5 Usability Considerations

With handheld devices, a unique emphasis needs to be placed on interaction design, human factors, ruggedness, and embedded software intelligence, which allow nonspecialist users to employ the technology in the field to reliably analyze pure and mixed samples with little to no spectroscopic training. Handheld Raman devices are often taken by nonscientific operators into the field in full personal protective equipment (PPE). Little interaction is required, such as pushing buttons or touch displays, all which are possible in hazmat level-A gear (self-containing breathing apparatus and totally encapsulating chemical-protective [TECP] suit) or explosive ordnance disposal (EOD) bomb suits. Workers in the pharmaceutical raw-material-receiving warehouses may use handheld Raman devices for extended periods of time requiring, not only reasonable battery life but also ergonomic design. Some active pharmaceutical ingredients (APIs) are highly potent, and exposures to bulk material could be hazardous, and so protective equipment can be necessary in that environment as well.

Another important consideration is instrument maintenance and robustness. Ideally, the instruments should also be sealed and waterproof and allow for complete submersion into a cleaning solution to allow for decontamination. Finally, the instruments must be field hardened: they need to be able to withstand the knocks and bumps of an active life, whether that is being transported over a mountain range or used for eight hours every day in a warehouse. Some manufacturers test their devices to the US military standard, the latest revision being MIL-810H,<sup>1</sup> and IP68 penetration standard.<sup>2</sup>

## 16.6 Surface-Enhanced Raman Spectroscopy (SERS)

The portability of modern Raman instrumentation makes Raman spectroscopy an attractive technique for the detection of low concentration analytes in forensic applications, such as detection of bulk seizures of samples, and for roadside testing. However, where detection of trace amounts of drugs is important, for example, in the analysis of fentanyl street samples, or body fluids such as saliva and urine, or in the detection of trace amounts of drugs in fingerprints or on banknotes, the use of Raman scattering is limited both by the inherent lack of sensitivity and by fluorescence interference. SERS can be used to overcome these disadvantages, increase scattering efficiencies by several orders of magnitude, and quench fluorescence from the target analyte or an impurity in the sample [16].

A limitation of Raman scattering is fluorescence from the analyte or from impurities within the sample (e.g. in street heroin), which often interferes with the measurement. This can be addressed using SERS. SERS involves the adsorption of an analyte on a suitable surface (e.g. roughened gold, silver, or copper) [17, 18] and analysis of the adsorbed analyte using a Raman spectrometer. The exciting laser radiation excites a surface plasmon, a collective oscillation of electrons activated by transfer of energy from the laser, and the effective formation of the plasmon is dependent on the nature of the substrate and the frequency of the laser [18]. Silver and gold have reasonable chemical stability, with suitable surface electron structures to create a plasmon with resonances which overlap with the NIR lasers most commonly used to in handheld Raman spectrometers. The enhancement process, which can be many orders of magnitude, involves transfer of incident energy to the surface to form the plasmon, followed by the transfer of energy from the plasmon to the analyte to facilitate the Raman process. This is followed by transfer of energy, reduced or increased by the amount of one vibration, and back to the plasmon and emission of the wavelength-shifted radiation from the surface as enhanced Raman scattering [19]. Adsorption of a molecule to

1 <https://en.wikipedia.org/wiki/MIL-STD-810>

2 [https://en.wikipedia.org/wiki/IP\\_Code](https://en.wikipedia.org/wiki/IP_Code)

the surface usually quenches fluorescence very efficiently, so SERS measurements can be made with fluorescent samples provided the fluorophore is very close to the surface [20].

Roughness is required to create a component of the plasmon that oscillates perpendicular to the surface plane and gives scattering. In addition, the dimensions of the roughness features can also be used to control plasmon properties to maximize the enhancement and maximize the coupling to the laser excitation frequency. The plasmon properties required for SERS are now well understood, but the fundamental nature of the actual adsorbate site at the molecular level on a rough surface is more difficult to probe and consequently less understood, with several possible mechanisms hotly debated. In practice, for molecules containing an aromatic ring and adsorbing effectively, enhancements of approximately  $10^6$  are commonly observed.

Colloids are also an attractive substrate for SERS, as they are relatively simple to make and provide a fresh surface for each analysis, reducing interference from contaminants, which can be a problem due to the high sensitivity of the technique. They are relatively inexpensive and can be made into test kits. In addition, they are more readily adapted to work with solution assays, making them similar to other test kits used in the field.

Whichever substrate is chosen, one major consideration is to ensure that the analyte is adsorbed effectively and evenly as a very thin layer on the surface. In the case of colloid, this is determined by the nature of the surface and the analyte and must be controlled through the surface chemistry. However, due to the very high enhancement factors, if the analyte is not fluorescent, good signals can still be obtained even if the analyte only adsorbs weakly. With solid substrates, one commonly used approach is to place a drop of analyte onto the substrate, dry it out, and record the SERS spectrum. SERS requires that the sample is adsorbed very close to the surface, with about 90% of the signal said to come from the first layer [19].

SERS is a useful technique for drug detection and ID, since it has the potential to enable the development of rapid, sensitive, and molecularly specific methods of qualitative analysis while overcoming the inherent lack of sensitivity obtained with conventional Raman spectroscopy. One of the main issues with the detection of drugs of abuse by SERS is that the species involved do not tend to have chemical groups that bind strongly to the metal surfaces routinely used for SERS analysis to give the necessary sensitivity required. In addition, many SERS substrates give irreproducible enhancement, making repeat measurements or quantitation difficult or impossible, so at present this is qualitative only: a detection and ID method.

A great amount of research and development are required to release commercial SERS kits. There are now several vendors of SERS test kits or substrates, and several companies are developing cost-effective SERS substrates for use in a multitude of applications. The commercial SERS kits that are available are mostly directed toward the screening or ID of street narcotic samples.

Typically, SERS spectra of a given compound are less well defined and have a different spectrum than conventional Raman spectra of that compound. While the spectra of most SERS data can be similar to the non-surface-enhanced spectra, there are often differences in the number of modes present; most often SERS spectra have less bands. Additional modes not found in the traditional Raman spectrum can be present in the SERS spectrum, while other modes can disappear. When molecules are adsorbed on to a roughened SERS surface, the symmetry can change, slightly modifying the symmetry of the molecule, which can lead to differences in mode selection. SERS spectra of very similar molecules can have indistinguishable spectra from one another, which results in less specificity and “grouping” of chemicals into result screens. This requires that SERS-specific spectra are collected and are part of an onboard spectral library. Shown in Figure 16.3 are several spectra of synthetic cannabinoids and fentanyl derivatives, highlighting that they are different but less “information-rich” compared with conventional Raman spectra. The spectra shown at the top of Figure 16.3 are synthetic cannabinoids. They have a similar building blocks with various naming conventions, with many being from the John W. Huffman (JWH) group. Over time, various analogues and derivatives have arrived on the street, often with simple modifications, such as adding halogens to various parts of the molecular structures or joining similar building blocks together in an often-predictable manner.

Thermo Scientific uses SERS to aid in the ID of narcotics via their “Type-H” kit. This kit utilizes a SERS substrate in a stick format for ID of street heroin, fentanyl, sprayed (on leaf) synthetic cannabinoids, and some low dose

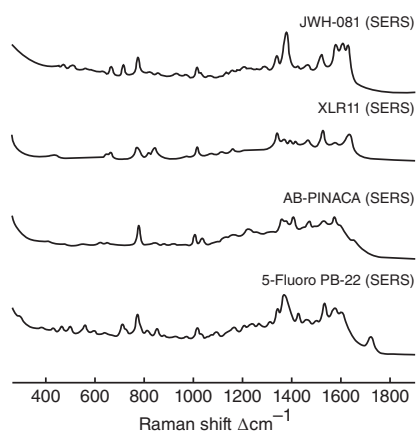


**Figure 16.3** SERS spectra of synthetic cannabinoid and fentanyl derivatives (785 nm excitation). *Source:* Courtesy of Thermo Fisher Scientific Inc.

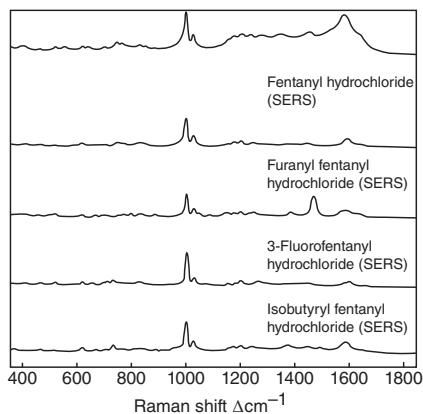
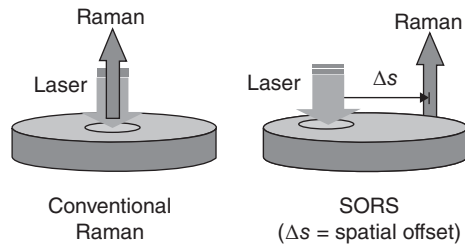


**Figure 16.4** Top: Thermo Scientific Type-H SERS test kit. *Source:* Thermo Fisher Scientific. Bottom: Metrohm Heroin ID kit. *Source:* Reproduced with Permission, Courtesy of Metrohm AG.

**Figure 16.5** Comparison of conventional backscattering Raman spectroscopy and the SORS configuration. Source: Modified from Professor Matousek images.



pills, including alprazolam, clonazepam, diazepam, and oxycodone. Figure 16.4 indicates the use of the Type-H kit. Metrohm also offers a SERS-based test kit that employs a paper-based substrate, where the active surface is printed onto the test strip.

## 16.7 Spatially Offset Raman Spectroscopy (SORS)

Conventional Raman spectroscopy is well suited to probing transparent or semitransparent containers. However, when it comes to characterizing the content of translucent (diffusely scattering) [21] bottles or highly fluorescing packaging (e.g. green glass bottles or paper envelopes), its applicability can be reduced. The principal challenge is the photon diffusion process; this prevents or limits the use of conventional Raman confocal-type spectroscopic methods. In those optical schemes, the laser is focused at a spot (at the surface of a solid or within the body of a liquid), and the collection optics are focused at the same spot. This standard arrangement has a direct line of sight of the probed content for the clean separation of Raman signals of the container and its content(s).

Photon propagation in diffusely scattering media, in the absence of significant absorption, is dominated principally by diffuse scattering [21], a process resulting in a random-walk-like motion of photons in the medium. There are two main consequences of this process; the photons are fast diffusing away from the interaction zone on their way to deeper zones, and their directionality is randomized, preventing the collection of direct-line-of-sight optical images. As noted above, this is required, for example, by conventional confocal Raman microscopy, thereby rendering it inapplicable in these situations. An alternative way of stating this is that, because of scattering by the barrier material, it is not possible to focus the laser beam at a point on or within the sample, not to collect light from such a point efficiently. An additional damaging process can be the presence of strong Raman and/or fluorescence signals originating from surface layer (e.g. packaging), adding additional noise to the Raman spectrum of the content (due to photon shot noise), and reducing the technique's sensitivity [22, 23].

Advances in deep Raman probing of diffusely scattering media have overcome these restrictions and widened the applicability of Raman spectroscopy to these types of samples. The key technique in this area is SORS [21, 24], which permits the interrogation of these diffusely scattering packaging and containers. SORS is based on collecting Raman signals from regions that are laterally offset from the point of laser illumination on the sample surface (see Figure 16.6 in this chapter). The SORS spectra contain different relative contributions from the surface (e.g. packaging) and subsurface (e.g. powder content), due to the wider spread of photons emerging from deeper layers at the sample surface [21]. Consequently, the method provides access to Raman spectra containing a varying degree of surface and subsurface content at different spatial offsets, with the subsurface Raman signal diminishing more slowly than that of the surface layer. This variation permits the complete separation of the measured Raman signals into pure components: one belonging to the surface and one to the subsurface layer (content), and this separation can be accomplished using several processing methods. For a two-layer sample, which is the case of a container and its content, a simple scaled subtraction of SORS spectra acquired at two different spatial offsets, for example, at zero and nonzero spatial offsets, cancels the residual surface component within the spatially offset spectrum to satisfactorily render the pure subsurface spectrum [21]. For a multilayer system, or sample with an unknown number of layers, multivariate statistical data analysis techniques can be used. In both cases, the process can be automated. In addition to the ability to separate layers from each other, SORS can also effectively suppress

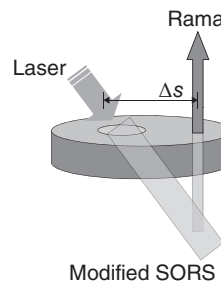


**Figure 16.6** Tilting the incident laser beam facilitates simultaneous capability to probe transparent and diffusely scattering containers with a single fixed SORS geometry. Source: Modified from Professor Matousek images.

Raman, interfering fluorescence signals originating from the surface layers. This provides an additional powerful feature benefiting noninvasive measurements.

The choice of spatial offset for particular experimental conditions is governed by a compromise between the need for introducing appreciable change to relative intensity of the surface and subsurface layers in SORS spectra, calling for larger spatial offsets, and the need for acquiring a sufficiently good-quality Raman spectrum of the sublayer, which diminishes in intensity with increasing spatial offset. In many practical applications, these dependencies are not strong functions of the spatial offset, and it is possible to find a spatial offset where both the conditions are adequately satisfied for a range of experimental parameters. For example, when probing the wide range of plastic containers typically used in the packaging industry, a single spatial offset can typically be found, enabling the use of the technique without adjusting the spatial offset from sample to sample.

The technique can also be made compatible with probing transparent containers, traditionally accessible to the conventional Raman approach, with an added benefit of suppressing fluorescence if present from the packaging material (e.g. that originating from green glass). This can be accomplished simply by adjusting the angle of the laser beam entering the sample, enabling the laser beam to intersect the Raman collection zone placed below the surface of the containers (e.g. below the surface of the glass bottle) (see Figure 16.6). In such case when the instrument is presented with a diffusely scattering sample, the configuration behaves entirely as a SORS device as laser photons quickly “forget” their original directionality, which is fast randomized through the diffusion process.

Such a configuration has an extra advantage in situations where transparent fluorescing containers are present (e.g. green glass), as such fluorescence can be effectively suppressed if it originates from the container, due to the fact that the laser beam intersects the container material spatially offset, out of sight of the Raman collection system. It has been demonstrated that such a single experimental configuration with a fixed spatial offset (10 mm) and laser beam angled at 45° could be effectively used to probe a wide range of containers, both diffusely scattering and transparent [25]. In this application, also an automated separation of the surface and subsurface layers was used to mimic closely practical conditions. However, it should be noted that if fluorescence originates from the probed medium (content), it cannot be eliminated by these means.

The general applicability of the SORS technique is limited to samples that do not exhibit strong absorption, in particular within the surface layer. For instance, black containers are problematic. In addition, samples that exhibit excessive fluorescence originating from the content itself are also problematic. In both these cases, the restrictions can be reduced or eliminated by using laser excitation in the NIR region of the spectrum. In practical settings, to minimize the effect of fluorescence, the majority of SORS systems operate with 830 nm laser excitation wavelength, minimizing the degree of exciting fluorescing electronic states while still permitting the use of the effective CCD detection technology (i.e. silicon-based detectors). In situations where fluorescence is still an issue, a move to even longer laser excitation wavelength (e.g. to 1064 nm) can still be beneficial, [26] and such SORS technology has been developed. Another limitation, in common to other optical spectroscopies, is the restriction of the method to nonmetallic containers, as metals do not permit the transport of electromagnetic energy through their bulk at thicknesses typically found in metal containers and packaging. This restricts the



**Figure 16.7** Agilent Raman SORS spectrometers – resolve highlighting the ability to scan through opaque packaging and containers. Source: Reproduced with Permission, Courtesy of Agilent Technologies Inc.

use of optical spectroscopy to a first layer screening modality, requiring further invasive checks on packages that cannot leverage the benefits of Raman spectroscopy, in either conventional backscatter or SORS forms. The SORS technique and its wider applications have been reviewed elsewhere [22, 27–29].

“Yellow Palm Oil Containers” (Figure 16.7 – right) present a challenge for security professionals. Their barrier, commonly colored polyethylene, provides both a Raman signal and a source of fluorescence that could hinder ID of the contents using conventional Raman optical systems. Furthermore, the expected contents of a benign sample in this case would be palm oil, a material that exhibits fluorescence and similar Raman characteristics to high-density polyethylene (the barrier). The automated SORS system on Resolve removes the influence of the barrier and enables the user to ID the contents, whether benign or a “threat.” SORS does not require any prior knowledge of the barrier, and it can also be a combination of materials, such as multiple layers of plastic packaging of different types. SORS effectively removes the signal that originates from the barrier, regardless of its composition.



**Figure 16.8** Pendar Technologies X10 standoff handheld Raman spectrometer, highlighting the standoff applications of their product. *Source:* Reproduced with Permission, Courtesy of Pendar Technologies Inc.

## 16.8 Standoff

The next advancement in handheld Raman devices has already arrived. The ability to collect data a distance away from a sample, or at a stand-off, has been a capability wish for several years for several user groups, especially the military dealing with suspected improvised explosive devices (IEDs). There are now a few different companies offering standoff capabilities. There are several different ways to achieve this, either through the use of a fiber, light-pipe (probe), or true standoff (i.e. free-space optics). The first truly handheld standoff device was recently launched by Pendar Technologies. The Pendar X10 device is capable of measurements at 3 ft (1 m) and can collect data through transparent barriers (such as glass and plastic; see Figure 16.8). An alternative approach has been released by Metrohm, where they have several accessories for their MIRA based product, including a ball (contact) probe and a small telescope accessory, offering users a short standoff capability (see Figure 16.9). Other vendors with backpack and transportable products have longer-range standoff devices, and this is surely going to be an area of future development and advancement.

## 16.9 Technology Combinations

There are several practical aspects that ultimately govern the applicability of handheld technologies, including Raman and FT-IR. Some materials that may be challenging to identify by Raman are amenable to ID by FT-IR, and vice versa. For example, some materials can be very difficult to identify with Raman systems due to overwhelming fluorescence, depending on the laser excitation wavelength used. Strongly colored materials are particularly problematic in this regard with 785 nm excitation, although several handheld and portable systems are now commercially available with 1064 nm excitation, which reduces the issue of fluorescence. In some application cases, the ability to collect a Raman spectrum using 1064 nm excitation outweighs the reduction in spectral performance issues, especially in the field of safety and security applications. A shift in excitation further into the red, past 1  $\mu\text{m}$  (1000 nm), reduces, but does not eliminate, fluorescence.

Tactically, Raman has the advantage of being noncontact and capable of performing analysis of materials contained in transparent containers (e.g. glass bottles, plastic bags). The laser excitation in a Raman instrument presents a sample ignition risk from overheating, while an FT-IR instrument, with an ATR sample interface head, requires intimate sample contact and pressure on the sample, presenting some risk when handling



**Figure 16.9** Metrohm MIRA handheld Raman spectrometer and accessories, highlighting the standoff applications of their product. Source: Reproduced with Permission, Courtesy of Metrohm AG.

pressure-sensitive energetic materials. Although some thick containers can be challenging for Raman and fluorescent containers (e.g. green glass wine bottles) even more so, today's Raman devices, coupled with the appropriate signal processing, often have little difficulty providing unequivocal ID in historically challenging conditions. To address these limitations, Thermo Scientific developed a handheld instrument combining a Raman and an FT-IR spectrometer (Figure 16.10).

An alternative to combining Raman and FT-IR is to combine Raman with another complementary technique. Rigaku has released an add-on capability that uses DetectaChem's wet-chemistry colorimetric technology. It employs test kits using well-known reagents to react with target chemicals, and change color, to indicate their presence: these test kits are "swipe cards" with reagent pouches, and crushing the pouch releases the reagents, generating a characteristic color, if the target material is present. The Rigaku CQL combines a DetectaChem application that can read and scan the swipe cards and provide additional supporting information. In some cases, the use of the colorimetric kits may also afford ID of lower concentration targets. Figure 16.11 shows the result screen for fentanyl, with a corroborating fentanyl result with the QuickDetect capability, reenforcing the ID.

## 16.10 Leveraging Data

In addition to the analytical capability of handheld Raman instruments, several devices also provide additional information to help their operators arrive at decisions based on the chemical information obtained from the samples they are measuring. This aspect can be most important, as the operators may not have knowledge of



**Figure 16.10** Gemini Analyzer, highlighting Raman and FT-IR measurement modes. Source: Reproduced with Permission, Courtesy of Thermo Fisher Scientific Inc.

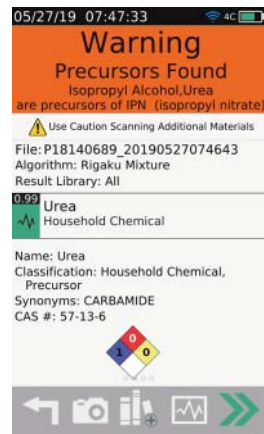


**Figure 16.11** Rigaku CQL ResQ and DetectaChem test kit and result. Source: Reproduced with Permission, Courtesy of Rigaku Analytical Devices Inc., DetectaChem Inc.



the chemicals or understand what those chemicals may be being used for or what they make when combined. There are several different aspects to this additional information, which may be in the form of chemical hazard information (i.e. Safety Data Sheets (SDS)), National Fire Protection Association (NFPA) or hazard symbols, to in-built programs that can take the results from the devices and provide additional information to the user. There are several manufacturers that provide this additional information, and several also allow operators to use other third-party programs to monitor results and provide actionable information (Figure 16.12).

**Figure 16.12** Rigaku CQL ResQ “4C” result monitoring. Source: Reproduced with Permission, Courtesy of Rigaku Analytical Devices Inc.



## 16.11 Military Identification Applications

### 16.11.1 Explosives

Explosives are widely employed in a variety of commercial uses including industrial demolition, controlled cutting and earth moving in construction, explosive charges in airbags, and pyrotechnic bolts and fasteners. Explosives are also used as weapons, both as part of military ordnance and for acts of terrorism.

A range of technologies can be employed to detect the presence of explosives with moderate to high sensitivity. As with all analytical technologies, there is an inevitable trade-off between sensitivity, selectivity, portability, and breadth of applicability (the number of analytes that can be measured).

An explosive is a substance capable of undergoing violent reaction or decomposition to produce heat, gas, and rapid expansion of matter. In order for combustion to occur, the material must contain both an oxidizer and a fuel. Explosives can be pure materials containing an oxidizer and fuel in the same molecule (e.g. trinitrotoluene) or mixtures of two or more components that separately provide an oxidizer and fuel (e.g. ammonium nitrate and fuel oil [ANFO]). Often, the materials making up an explosive mixture are not explosive in isolation.

### 16.11.2 Raman Spectroscopy Explosive Identification Capabilities

Table 16 outlines the respective suitability of Raman spectroscopy for the most common pure explosive materials. Likewise, Figure 16.13 demonstrates Raman spectra for several of these materials.

Raman instruments are routinely used for solid and liquid analyses in the field, as discussed in previous sections of this chapter. While most pure explosives can be measured with either Raman or FT-IR spectroscopy, some materials are better suited for measurement by a particular technique [30–38]. For reasons of color, mid-IR spectroscopy often performs better for particularly darkly colored materials such as gunpowder and smokeless powders.

Improvised explosives such as triacetone triperoxide (TATP), methyl ethyl ketone peroxide (MEKP), and hexamethylene triperoxide diamine (HMTD) are all identifiable by Raman (see Figures 16.8 and 16.10). Raman spectroscopy is often tactically preferred due to the pressure sensitivity of these types of materials, which make contact and pressure with an FT-IR-ATR element problematic, but care should be taken to minimize transfer of heat to the sample during sampling using Raman. Many portable Raman systems offer a scan delay to allow safer analysis of energetic materials.

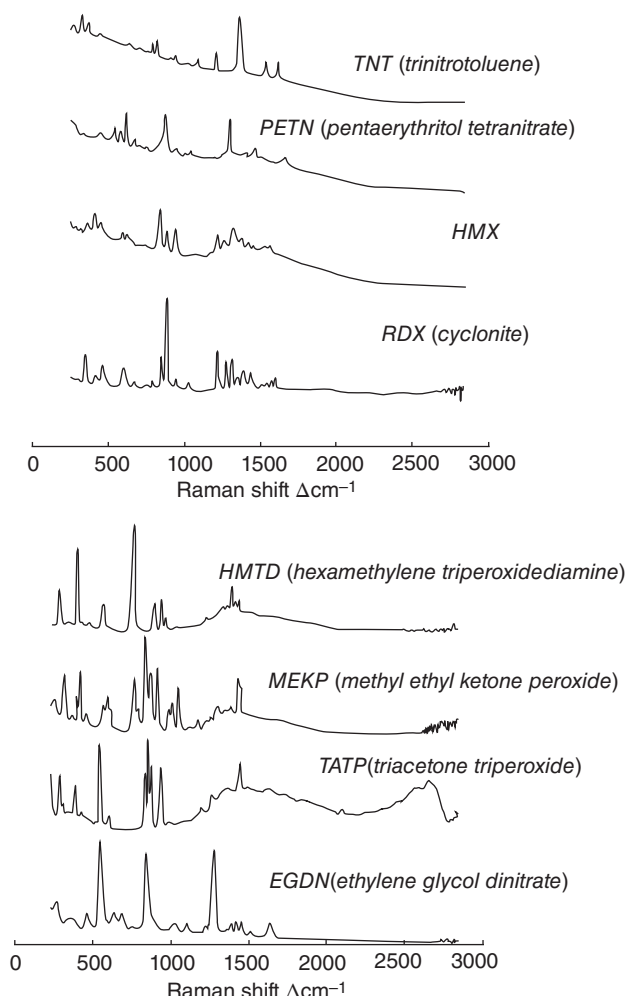


**Figure 16.13** Raman spectra of some common explosives. (TATP, triacetone triperoxide; RDX is an explosive nitroamine; PETN, pentaerythritol tetranitrate; and HMX, an explosive nitroamine) (785 nm excitation). Source: Courtesy of Thermo Fisher Scientific Inc.

Though ID of pure explosives is certainly an important facet of explosives prohibition, explosive precursor mixture components are also equally important to consider. Table 16.2 summarizes the applicability of Raman spectroscopy for common explosive precursors and ingredients; Figure 16.14 highlights spectra for several of these materials.

As is the case with finished explosives, precursor materials are often well suited to measurement by Raman spectroscopy. Raman spectroscopy is an excellent tool for the inorganic materials, enabling clear and unique ID of chlorates/chlorites/hypochlorites, chromates, permanganates, and inorganic nitrates, which are prevalent in IEDs. Water-laden samples such as acids, and particularly hydrogen peroxide, are excellent Raman scatterers but difficult to identify with mid-IR (FT-IR) spectroscopy due to heavy interference from water. Materials such as sulfur and phosphorus are often used as sensitizers, and their most active vibrational modes (i.e. fundamentals) fall below the range typically covered by mid-IR FT-IR spectrometers. As such, it is easier to identify these materials using Raman spectroscopy because of the ability to see the low wavenumber bands to approximately  $200\text{ cm}^{-1}$  Raman

**Table 16.2** Common synthetic agents and mixture components and applicability for examination by Raman spectroscopy (these considerations are dependent on laser excitation and, while general true, are dependent on specific systems).

Oxidizers	Raman	Fuels	Raman
Sodium chlorate	Y	Gasoline/petrol	Y
Potassium chlorate	Y	Diesel/fuel oil	Y
Ammonium perchlorate	Y	Kerosene	Y
Calcium hypochlorite	Y	Carbon	N
Ammonium nitrate	Y	black/charcoal	Y
Potassium nitrate (saltpeter)	Y	Sugar	Y
Hydrogen peroxide	Y	Wax	N
Barium peroxide	Y	Vaseline	Y
Potassium permanganate	Y	Dextrin	N
Nitric acid	Y	Shellac	Y
	Y	Rosin	Y
	Y	Alcohols	Y
		Glycols	

Y = Yes – this analyte may be identified. N = No – this analyte cannot be identified.

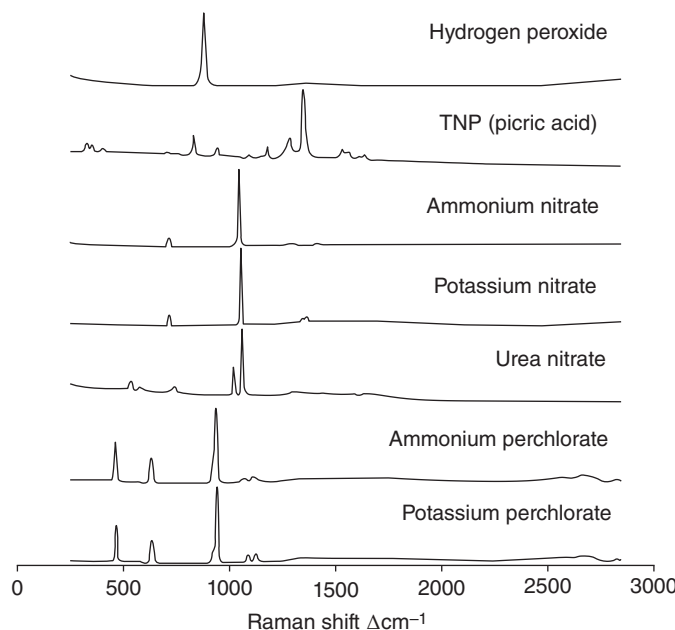


**Figure 16.14** Raman spectra of common explosive precursors and ingredients (785 nm excitation). Source: Courtesy of Thermo Fisher Scientific Inc.

shift, close to the laser filter cutoff. (Handheld Raman devices normally do not have filters as close to the laser line, e.g. 5–10  $\text{cm}^{-1}$  Raman shift, as are found on benchtop Raman systems, which enable phonon-mode work.)

In addition to pure explosives, precursors, and mixture components, it is important to consider finished explosive mixtures. Explosive mixtures are composed of distinct substances and are formulated in varying proportions. Some commercial explosives mixtures include C-4, Semtex, and Detasheet. Many commercial explosives contain plastics



**Figure 16.15** Handheld Raman instrument measurement homemade explosive (TATP) and ammonium nitrate. *Source:* Reproduced with Permission, Courtesy of Rigaku Analytical Devices Inc.

and dyes that tend to fluoresce with 785 nm excitation Raman spectroscopy. As such, several of these materials are often more practical to measure with FT-IR spectroscopy (Figure 16.15).

## 16.12 Pharmaceuticals

There are two main application areas for handheld Raman in the pharmaceutical area: raw material ID and anti-counterfeit screening (see the chapter by Leary, Crocombe, and Kalyanaraman). Raw material testing and verification is a key step in the manufacturing of pharmaceutical formulations. It is a critical part of the quality control process, and it has a significant impact on consumer safety, as well as speed and cost of production.

Handheld Raman instruments have been deployed all over the world with many of the major pharmaceutical manufacturers, ensuring the correct materials are entering into the manufacturing process, including APIs, excipients, and drug products. Chemical identity testing of pharmaceutical materials is one of the most widely utilized forms of analysis in the development, manufacturing, and distribution of pharmaceutical products and materials, including ID within packaged units.

One of the major advantages of using Raman spectroscopy for the chemical ID of pharmaceutical materials, as compared with other techniques including mid-infrared (FT-IR) and NIR spectroscopies, is that Raman spectroscopic analysis does not require sample preparation for subsequent analysis (which is also true of solid samples with NIR – but liquid samples are more challenging). Raman spectra may be acquired on neat material, as well as through packaging enclosures including glass vials, plastic bags, and sealed blister packs (commonly used in the pharmaceutical space; an example of scanning is seen in Figure 16.16) [39]. This lack of sample preparation allows Raman spectroscopy to be a very flexible technique in a multitude of testing environments that require routine chemical identity testing of liquids and solids. A new device, a handheld device from Agilent, called Vaya adds SORS in a handheld device for pharmaceutical analysis, further enabling users to scan through opaque barriers such as plastic and paper as well as container types conventional Raman can scan, reducing the need to remove samples into amenable containers for verification (Figure 16.16)

A stumbling block in the use of Raman spectroscopy has been the perceived lack of acceptance of the technique by regulatory bodies. Raman spectroscopy is incorporated into the US Pharmacopeia (USP), being referenced in Spectroscopy and Light Scattering, Chapter 851.<sup>3</sup> More recently, a separate USP chapter has been devoted to Raman spectroscopy: Chapter <1120>. Raman Spectroscopy.<sup>4</sup>

Raman spectroscopy can be used for chemical ID of pharmaceutical materials (API, excipients, drug product) after it is demonstrated that Raman is suitable for the intended application (validation). Figure 16.17 indicates the excellent selectivity handheld Raman devices can have for relevant pharmaceutical chemicals.

Many of the papers demonstrating the use of Raman spectroscopy for pharmaceutical analysis use laboratory benchtop dispersive or FT-based systems. As we have seen, during the past decade, significant improvements have been made in the design, hardware miniaturization, and efficiency of lasers, spectrographs, and detectors utilized

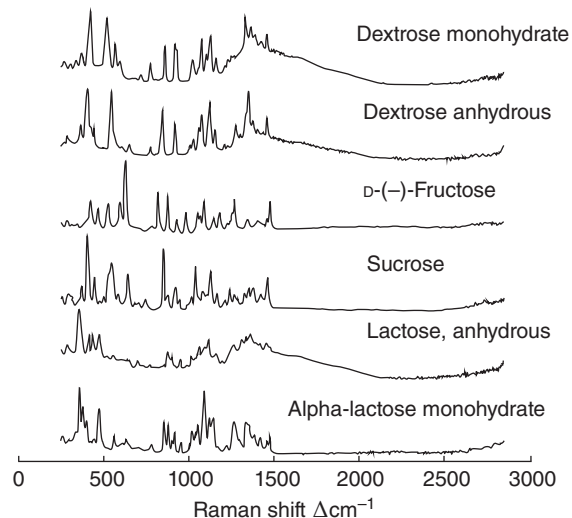
<sup>3</sup> [http://www.pharmacopeia.cn/v29240/usp29nf24s0\\_c851.html](http://www.pharmacopeia.cn/v29240/usp29nf24s0_c851.html) (accessed October 2019).

<sup>4</sup> [http://www.pharmacopeia.cn/v29240/usp29nf24s0\\_c1120.html](http://www.pharmacopeia.cn/v29240/usp29nf24s0_c1120.html) (accessed October 2019).



**Figure 16.16** Left: Handheld Raman device verifying the contents of opaque colored packaging. Right: Handheld Raman device scanning a colored sample. Source: Reproduced with Permission, Courtesy of Agilent Technologies, Inc, B&WTek (Metrohm AG).

**Figure 16.17** Raman spectra of several sugars using 785 nm excitation. Source: Courtesy of Thermo Fisher Scientific Inc.



for Raman spectroscopy [13]. These advancements have led to the development of handheld Raman spectrometers that approach the performance characteristics of some laboratory-based systems [40]. Additionally, these same handheld Raman spectrometers have incorporated 21 Code of Federal Regulations (CFR) Part 11 compliant software, permitting the use of these instruments in Current Good Manufacturing Practice (cGMP) settings. The advent of the handheld Raman spectrometer now allows the pharmaceutical scientists to bring the laboratory to the sample, no matter where the sample may reside: loading dock, warehouse, cGMP laboratory, pharmacy, or makeshift counterfeit location.

Counterfeiting of prescription drugs is a growing problem, especially in second- and third-world locations [41]. The US Food and Drug Administration (FDA) have been working on anti-counterfeiting measures to fight this mounting problem. For example, the FDA has introduced guidance on the use of identifiers (physical-chemical identifiers [PCID]) to make it more difficult for counterfeiters to duplicate genuine drug products and also to make it easier to confirm the authenticity of the drug [42]. The World Health Organization (WHO) has established the International Medical Products Anti-Counterfeiting Taskforce. Although the application of Raman spectroscopy

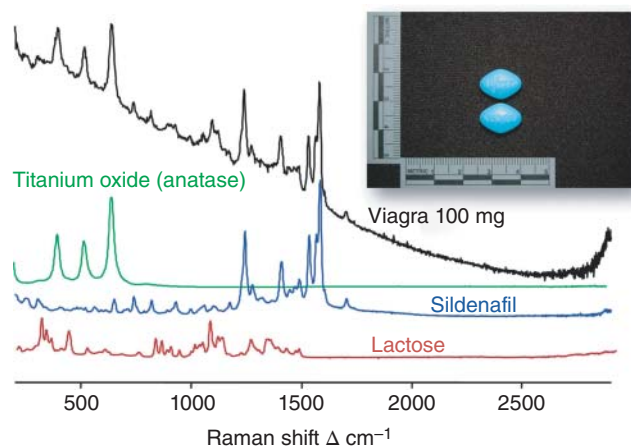


**Figure 16.18** Authentic Viagra spectrum, sildenafil citrate, titanium dioxide, and lactose (785 nm excitation). *Source:* Reproduced with Permission, Courtesy of Thermo Fisher Scientific Inc. The image, shape and trademark of Viagra are the property of Pfizer Inc.

for the analysis of counterfeit drugs is still a developing application, there has been a significant increase in the number of papers in the literature, discussing the utility of this technique [43–52].

Raman spectroscopy has been used extensively to study counterfeit pharmaceuticals and is especially well suited to analyze oral dosage forms. For example, it can be used to detect different solid-state forms of an API, such as polymorphs and amorphous versus crystalline drug [52]. Raman spectroscopy is a particularly useful analytical technique for pharmaceutical products because little to no sample preparation is required and it is a nondestructive technique, meaning that intact dosage forms can be often measured and then utilized for additional analyses.

An additional advantage is that many APIs are aromatic compounds, which is in contrast to the majority of pharmaceutical excipients. This affords distinction in the spectrum between the API bands and the excipient bands, because while excipients like cellulose are weak Raman scatterers, aromatic and conjugated molecules tend to be strong scatterers.

An example of a pharmaceutical formulation and the spectral breakdown of its components is shown in Figure 16.18. The API, sildenafil citrate, has sharp features, well differentiated from the other excipients, in this case lactose and titanium dioxide. The active ingredients, in small-molecule medicine, as discussed above, are typically aromatic compounds that lend themselves to Raman spectroscopy. In some instances, fluorescence can have an impact on the ability of a device to identify counterfeits. Different laser excitations can, in some instances, have a favorable impact on the ability to identify counterfeits, and Figure 16.19 shows the authentic and counterfeit spectra using 785 and 1064 nm excitations. The Raman spectrum at 1064 nm reduces the fluorescent interference, enabling the clear differentiation, but it should be noted that for this particular matrix, this is also feasible at 785 nm. The use of multivariate analysis techniques permits the use of 785 nm systems, reducing the practical cases where 1064 nm is fundamentally required to where overwhelming fluorescence is experienced. However, if there are no Raman spectral features visible with 785 nm excitation, an instrument employing longer excitation wavelength must be used.

### 16.13 Narcotics

These compounds are reasonably complex molecules that yield characteristic fingerprint spectra. However, in some cases, given their very similar molecular structures, they can yield very visually similar vibrational spectra,

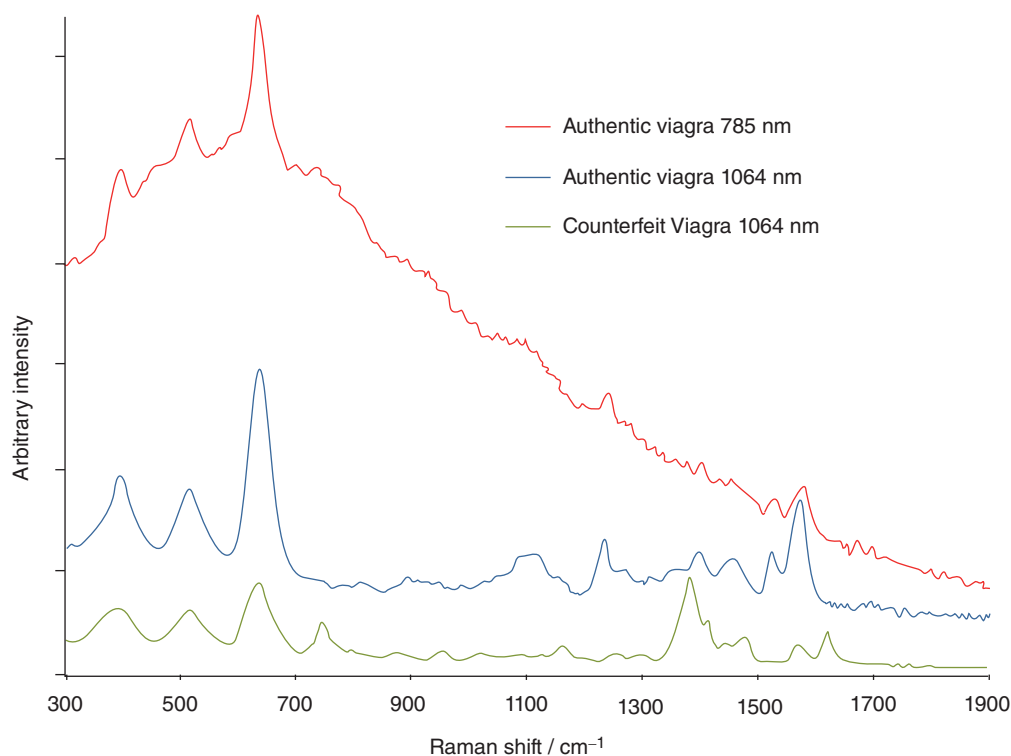


**Figure 16.19** Authentic Viagra spectrum (785 nm), authentic Viagra spectrum (1064 nm), and counterfeit Viagra spectrum (1064 nm). Source: Courtesy of Rigaku Analytical Devices Inc.

but distinguishable by chemometric methods (see the chapter on ID and confirmation algorithms by Zhang, Lee, and Schreyer for handheld spectrometers) [53–56]. The addition of cutting agents, and the concentration of the “active” component, can lead to a complex spectral interpretation task. Generally, vibrational spectroscopy has an LOD of around 5–10%, which can be higher or lower depending on the application and analytes in question, but practically the lowest LOD achievable with conventional backscatter Raman is around 1–2% and is normally higher for handheld devices, typically >5%. This may be higher depending on the Raman cross section of the analyte of interest and the Raman cross sections of the other items present in the mixture.

The types of drugs of abuse are growing rapidly: new threats are emerging, the so-called synthetic narcotics. These include such chemicals as mephedrone and “Spice,” classified as controlled substances in several countries over the last few years.<sup>5</sup> In numerous regions of the world, they are becoming a significant problem. This highlights one very important issue: as quickly as chemicals are outlawed, the supplier synthesizes another similar molecule, and so the threats can change very rapidly. The ability to identify and screen is therefore very important, as the drug investigation and crime laboratories are almost always dealing with long case backlogs (Figure 16.20).

While the chemical structure of many drugs of abuse are similar, there are also differences, which allow ID and discrimination of these closely related compounds, which may be important if different laws apply to each narcotic in a country. Subtle differences, especially in complex mixtures, can be challenging to solve by vibrational spectroscopy techniques, given the complexity of having several spectral components superimposed and possible chemical interactions, which may give rise to band shifts and band shape changes. What makes vibrational

<sup>5</sup> [http://www.emcdda.europa.eu/edr2019\\_en](http://www.emcdda.europa.eu/edr2019_en)

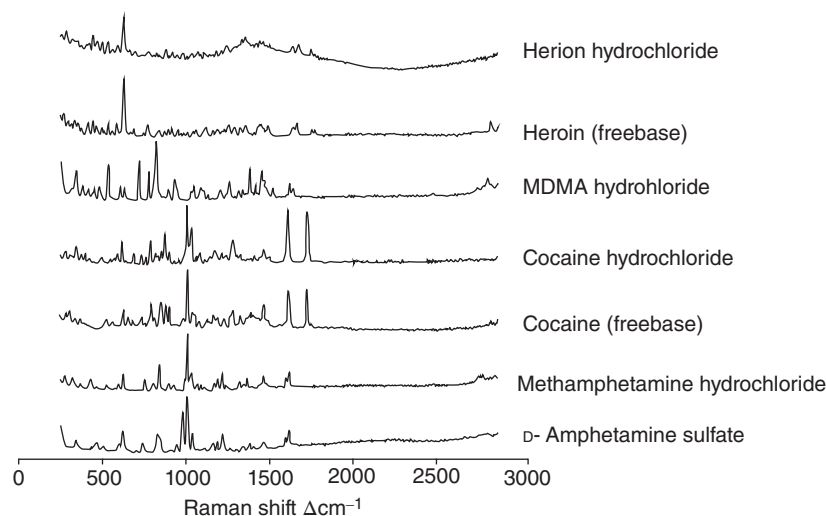


**Figure 16.20** Raman spectra of common narcotics using 785 nm excitation. Source: Courtesy of Thermo Fisher Scientific Inc.



**Figure 16.21** A B&WTek 1064 nm excitation TacticID identifying a brown-colored heroin sample. Source: Reproduced with Permission, Courtesy of B&WTek (Metrohm AG).

spectroscopy so powerful and useful in this field are the following attributes: the ability to quickly collect spectra and perform an ID in a nondestructive manner, the selectivity and specificity of Raman spectroscopy, and the handheld and portable nature of the instruments, allowing them to be taken to the point of need.

In this rapidly changing landscape, the ID of narcotics is an ever more complicated challenge, and handheld Raman devices are ideally positioned to help. Not only can Raman spectroscopy identify the well-known and common narcotics such as amphetamine, cocaine, heroin, and methamphetamine, but also it can be used to identify emerging narcotic threats, such as cathinones, synthetic cannabinoids, phenethylamines (2Cs), and phenethylamine derivatives. Synthetic cannabinoids are also referred to as “Spice,” and as an example, many new synthetic cannabinoids are monitored by European Union (EU) Early Warning System (<sup>6</sup>as of 2018 >700 novel psychoactive substances [NPS]). Phenethylamine derivatives, NBOMe, are referred to as N-BOMBs. Spectra of common narcotics are shown in Figure 16.21), highlighting the spectral differences between them. Note the difference in the Raman spectra of cocaine freebase and cocaine HCl.

This highlights one very important issue: as quickly as chemicals are outlawed, the supplier changes to another similar molecule, and so the threats can change very rapidly. The ability to identify or screen is therefore very

<sup>6</sup> <http://www.emcdda.europa.eu/publications/topic-overviews/eu-early-warning-system>

**Figure 16.22** The result from a handheld Raman spectrometer after scanning a rum bottle. Source: Reproduced with Permission, Courtesy of HazmatLINK Ltd.



important, as the drug investigation laboratories are almost always dealing with long backlogs, and anything to reduce the number of samples or shorten the analysis time would be highly welcomed.

There are several practical aspects that govern applicability of narcotics ID by Raman spectroscopy. Some materials that cannot be identified by Raman spectroscopy, because of fluorescence at the specific excitation wavelength, are amenable to ID by mid-IR spectroscopy, and vice versa. Some street sample materials are particularly problematic in this regard when using laser excitation at a shorter wavelength than 1  $\mu\text{m}$ , due to either the molecular structure, matrix materials, or degradation of the components. The move to instruments using 1064 nm excitation has permitted the ID of colored samples, including street heroin, which can be challenging for 785 nm excitation devices (see Figure 16.21), and this highlights the ability of 1064 nm handheld devices to identify street heroin samples directly without the need of an SERS test kit.

The ability of Raman to be able identify targets in a matrix is especially important where a target may be mixed or dissolved. An example of this is the mixing of cocaine in an alcohol. This method has been used by criminals in the past to smuggle narcotics. Raman is especially useful to screen for narcotics in water and alcohols, providing the concentration is high enough (when smuggling, concentration is not normally an issue; see Figure 16.22).

In the real world, unfortunately, it is rare to find street narcotic samples that are pure, i.e. one component. It is also important to consider that the drugs may degrade over time, depending on the storage conditions. This is most likely in border and custom points where the drugs are being smuggled in or out of a country. The handheld Raman spectrometers described here do not survey a large area; however, they analyze a small area (less than 1  $\text{mm}^2$ ) of a sample at a close range (<1 cm). Therefore, a suspicious package or container must first be identified by other technologies or personnel.

## 16.14 Novel Psychoactive Substances (NPS)

There are several new classes of narcotics that have made a dramatic appearance, especially in Europe: this latest challenge for law enforcement is fentanyl and new synthetic derivatives. Other psychoactive targets include cathinones, synthetic cannabinoids, NBOMe (NBOMBs), and phenethylamine (2Cs).

The term “bath salts” refers to an emerging family of drugs containing one or more synthetic chemicals related to cathinone, an amphetamine-like stimulant found naturally in the khat plant. Bath salts typically take the form of a white or brown crystalline powder and are sold in small plastic or foil packages labeled “not for human consumption,” sometimes also marketed as “plant food” – or, more recently, as various cleaning solutions. They are sold online and in drug paraphernalia stores under a variety of brand names.

Cathinone derivatives include a variety of chemical compounds including cathinone, methcathinone, mephedrone, flephedrone (4-fluoromethcathinone), methylone, and several others (Figure 16.23).

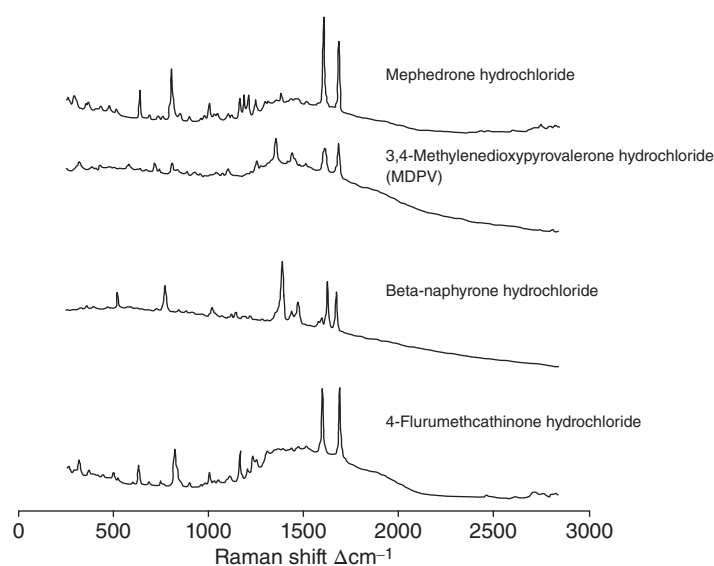


**Figure 16.23** Raman spectra of cathinones using 785 nm excitation. Source: Courtesy of Thermo Fisher Scientific.

Synthetic cannabinoids, commonly known as “synthetic marijuana,” “K2,” or “Spice,” are often sold in legal retail outlets as “herbal incense” or “potpourri.” Synthetic cannabinoids are man-made chemicals, functionally like  $\Delta^9$ -tetrahydrocannabinol (THC), the active principle of cannabis, are applied (often sprayed) onto plant material, and are then marketed as a “legal” high. Like THC, they bind to the same cannabinoid receptors in the brain (cannabinoid receptor agonists) and were developed over the past 40 years as therapeutic agents, often for the treatment of pain. However, it proved difficult to separate the desired properties from unwanted psychoactive effects. There are now many different molecules covered under the umbrella of synthetic cannabinoid, and this continues to grow. One major group is the “JWH” cluster, named after the organic chemist John W. Huffman. Many other different chemicals have joined this group with many different naming conventions. Figure 16.24 has

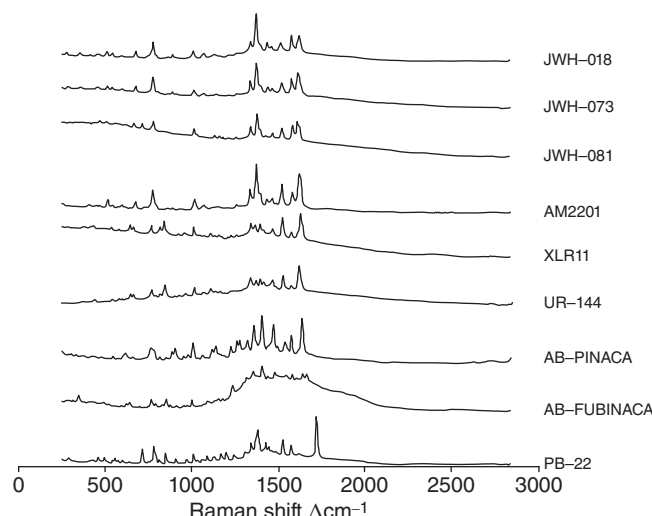


**Figure 16.24** Raman spectra of several synthetic cannabinoids using 785 nm excitation. Source: Courtesy of Thermo Fisher Scientific.



**Figure 16.25** A handheld Raman instrument (TruNarc) identifying two fentanyl samples. *Source:* Reproduced with Permission, Courtesy of Thermo Fisher Scientific Inc.

spectra for just eight different chemicals, highlighting the ability of Raman to differentiate between them. In some cases, there only minimal molecular differences (i.e. between JWH-018 and AM-2201 – its fluorinated analogue).

The latest challenge for law enforcement is fentanyl and its ever-increasing number of analogues or derivatives. Fentanyl is a synthetic opioid that is 80–100 times stronger than morphine, and in recent years, there has been a massive increase in the amount of fentanyl and its derivatives in circulation.<sup>7,8</sup> Several fentanyl spectra are shown in Figure 16.25. Fentanyl and its derivatives present the same challenge to identify as any other novel chemical, but the safety aspects are quite different. Due to this, it is preferable to identify the suspicious material

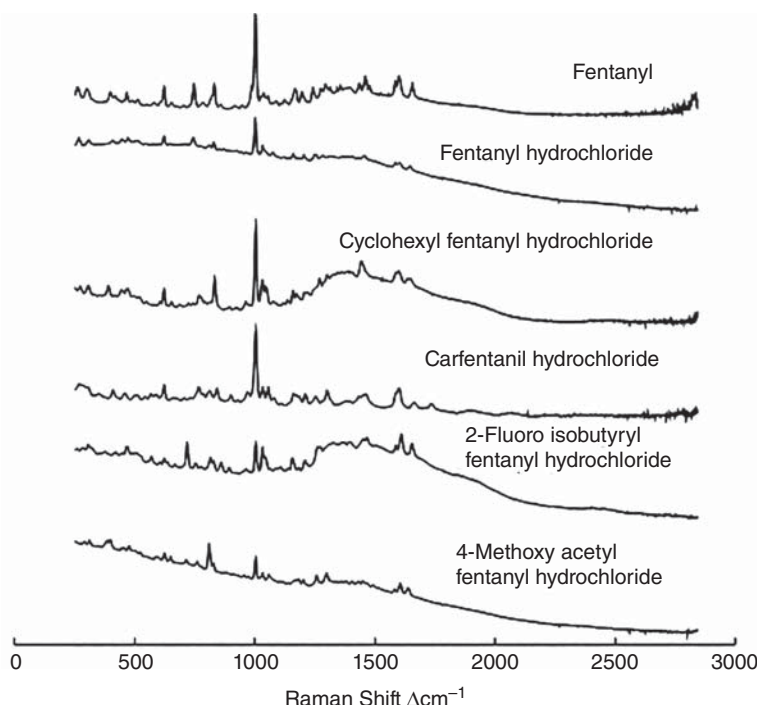


**Figure 16.26** Raman spectra of several fentanyl derivatives using 785 nm excitation. *Source:* Courtesy of Thermo Fisher Scientific.

7 <http://www.emcdda.europa.eu/publications/drug-profiles/fentanyl>

8 <https://www.dea.gov/factsheets/fentanyl>

without removing opening any packaging because of concerns about personnel exposure. The challenge, however, is the low concentration of fentanyl present in street samples. As is the case for any narcotic, they are found in much higher concentration when being shipped (smuggled) to their destination, and once there, they are mixed with other narcotics or benign cutting agents. As has been discussed earlier in this chapter, various companies have SERS-based kits that are designed to screen for and identify narcotics and that can provide an additional capability on top of conventional Raman spectroscopy. In Figure 16.26, two different samples of Fentanyl were identified.

## 16.15 Summary

Handheld Raman spectroscopy devices have matured to become a major tool for the identification, verification, and authentication of chemicals all over the world. Raman instruments are actively used by the military for ID of explosives and their precursors, law enforcement for ID of narcotics and their precursors, and the pharmaceutical industry for material verification and anti-counterfeit activities. These applications are currently the largest areas for handheld Raman instruments.

Over the next few years, with advancements in software, onboard data storage, and computational capabilities, more instruments will offer standoff capability, and further advances of the instruments themselves and the sampling devices, such as SERS kits, will enable handheld Raman spectrometers and their users to move further into increasingly more challenging applications.

## Acknowledgments

The author wishes to thank Richard Crocombe for thoughtful discussion during development of this chapter and Keith Carron (Metrohm), Melissa Gelwicks (Metrohm), Jennifer Lynch (Rigaku), Christopher Langford (Rigaku), Robert Stokes (Agilent), Fred Prulliere (Agilent), Romain Blanchard (Pendar) and Michael Stephens (Thermo Fisher Scientific) for the information provided and permission to use the information and images.

## Images

All images are produced with Permission, Courtesy of their respective Copyright holders – as identified in the figures.

## References

- 1 McCreery, R.L. (2000). *Raman Spectroscopy for Chemical Analysis*. New York: John Wiley.
- 2 Popp, J. (2006). Wolfgang Kiefer “Raman Scattering Fundamentals”. John Wiley & Sons Ltd: Encyclopaedia of Analytical Chemistry.
- 3 Hendra, P.J. (2002). Sampling Considerations for Raman Spectroscopy. In: *Handbook of Vibrational Spectroscopy*, vol. 2 (eds. J.M. Chalmers and P.R. Griffiths), 1263–1288. Chichester: John Wiley & Sons Ltd.
- 4 Smith, E. and Dent, G. (2005). *Modern Raman Spectroscopy – A Practical Approach*. Chichester: John Wiley & Sons Ltd.

- 5 Crocombe, R.A. (2008). Miniature optical spectrometers: there's plenty of room at the bottom. Part 1, background and mid-infrared spectrometers. *Spectroscopy* 23 (1): 38–56.
- 6 Crocombe, R.A. (2008). Miniature optical spectrometers: follow the money. Part II: the telecommunications boom. *Spectroscopy* 23 (2): 56–69.
- 7 Crocombe, R.A. (2008). Miniature optical spectrometers: part III: conventional and laboratory near-infrared spectrometers. *Spectroscopy* 23 (5): 40–50.
- 8 Crocombe, R.A. (2008). Miniature optical spectrometers: the art of the possible. Part IV: new near-infrared technologies and spectrometers. *Spectroscopy* 23 (6): 26–37.
- 9 Williamson, J.L., Bowling, R.J., and McCreery, R.L. (1989). Near-infrared Raman spectroscopy with a 783-nm diode laser and CCD array detector. *Appl. Spectrosc.* 43: 372–375.
- 10 Wang, T. and McCreery, R.L. (1989). Evaluation of a diode laser/charge coupled device spectrometer for near-infrared raman spectroscopy. *Anal. Chem.* 61: 2467–2651.
- 11 Denson, C., Pommier, C.J.S., and Denton, M.B. (2007). The impact of array detectors on raman spectroscopy. *J. Chem. Educ.* 84: 67.
- 12 Pelletier, M.J. (1999). Raman instrumentation”, Chapter 2. In: *Analytical Applications of Raman Spectroscopy* (ed. M.J. Pelletier). Oxford, UK: Blackwell Science.
- 13 Adar, F. (2001). Evolution and revolution of raman instrumentation – application of available technologies to spectroscopy and microscopy”, Chapter 2. In: *Handbook of Raman Spectroscopy* (eds. I.R. Lewis and H.G.M. Edwards). New York: Marcel Dekker.
- 14 Carron, K. (2005). *Raman Spectroscopy, Instrumentation, Encyclopaedia of Analytical Science*, 2ee (ed. P. Worsfold), 94–104. Elsevier, Oxford: Alan Townshend and Colin Poole.
- 15 Christesen, S.D., Guicheteau, J.A., Curtiss, J.M., and Fountain, A.W. III, (2016). Handheld dual-wavelength Raman instrument for the detection of chemical agents and explosives. *Opt. Eng. (Bellingham, WA, U. S.)* 55: 074103.
- 16 Fleischmann, M., Hendra, P.J., and McQuillan, A.J. (1974). *Chem. Phys. Lett.* 26 (2): 163.
- 17 Smith, W.E., White, P.C., Rodger, C., and Dent, G. (2001). Raman and surface enhanced resonance raman scattering: applications in forensic science, Chapter 18. In: *Handbook of Raman Spectroscopy* (eds. I.R. Lewis and H.G.M. Edwards), 733–748. New York: Marcel Dekker, Inc.
- 18 Vo-Dinh, T. and Stokes, D.L. (2002). SERS-based Raman Probes. In: *Handbook of Vibrational Spectroscopy*, vol. 2 (eds. J.M. Chalmers and P.R. Griffiths), 1302–1317. Chichester: John Wiley & Sons Ltd.
- 19 Campion, A. and Kambhampati, P. (1998). Surface-enhanced Raman scattering. *Chem. Soc. Rev.* 27: 241.
- 20 Faulds, K., Barbagallo, R.P., Keer, J.T. et al. (2004). SERRS as a more sensitive technique for the detection of labelled oligonucleotides compared to fluorescence. *Analyst* 129: 567.
- 21 Matousek, P., Clark, I.P., Draper, E.R.C. et al. (2005). Subsurface Probing in Diffusely Scattering Media Using Spatially Offset Raman Spectroscopy. *Appl. Spectrosc.* 59: 393.
- 22 Everall, N., Hahn, T., Matousek, P. et al. (2001). Picosecond time-resolved raman spectroscopy of solids: capabilities and limitations for fluorescence rejection and the influence of diffuse reflectance. *Appl. Spectrosc.* 55: 1701.
- 23 Matousek, P. (2007). Deep non-invasive Raman spectroscopy of living tissue and powders. *Chem. Soc. Rev.* 36: 1292.
- 24 Matousek, P., Morris, M.D., Everall, N. et al. (2005). Numerical Simulations of subsurface probing in diffusely scattering media using spatially offset Raman spectroscopy. *Appl. Spectrosc.* 59: 1485.
- 25 Eliasson, C., Macleod, N.A., and Matousek, P. (2007). Noninvasive detection of concealed liquid explosives using Raman spectroscopy. *Anal. Chem.* 79: 8185.
- 26 Macleod, N.A. and Matousek, P. (2008). Deep noninvasive Raman spectroscopy of turbid media. *Appl. Spectrosc.* 62: 276A.

- 27** Macleod, N.A. and Matousek, P. (2008). Emerging non-invasive Raman methods in process control and forensic applications. *Pharm. Res.* 25: 2205.
- 28** Matousek, P. and Stone, N. (2009). Emerging concepts in deep Raman spectroscopy of biological tissue. *Analyst* 134: 1058.
- 29** Matousek, P. and Parker, A.W. (2006). Bulk Raman analysis of pharmaceutical tablets. *Appl. Spectrosc.* 60: 1353.
- 30** Hargreaves, M.D., Green, R.L., Jalenak, W. et al. (2012). Handheld Raman and FT-IR spectrometers, in infrared and Raman spectroscopy. In: *Forensic Science* (eds. J.M. Chalmers, H.G.M. Edwards and M.D. Hargreaves). Chichester, UK: John Wiley & Sons,Ltd.
- 31** Lewis, I.R., Daniel, N.W. Jr., and Griffiths, P.R. (1997). Interpretation of Raman spectra of nitro-containing explosive materials. Part II: the implementation of neural, fuzzy, and statistical models for unsupervised pattern recognition. *Appl. Spectrosc.* 51: 1868–1879.
- 32** Daniel, N.W. Jr., Lewis, I.R., and Griffiths, P.R. (1997). *Mikrokim. Acta [Suppl.]* 14: 281–282.
- 33** Cheng, C., Kirkbride, T.E., Bachelder, D.N. et al. (1995). In situ detection and identification of trace explosives by Raman microscopy. *J. Forensic Sci.* 40: 31–37.
- 34** Griffiths, P.R., Lewis, I.R., Chaffin, N.C. et al. (1995). Remote characterization of materials by vibrational spectrometry through optical fibers. *J. Mol. Struct.* 347: 169.
- 35** Keto, R.O. (1986). Improved method for the analysis of the military explosive. Composition C-4. *J. Forensic Sci* 31: 241–249.
- 36** Bartick, E.G. and Merrill, R.A. (1993). *Proceedings of the International Symposium on the Forensic Aspects of Trace Evidence*. Washington, DC: U.S. Government Printing Office.
- 37** Lewis, I.R., Daniel, N.W. Jr., Chaffin, N.C. et al. (1995). Raman spectroscopic studies of explosive materials: towards a fieldable explosives detector. *Spectrochimica Acta Part A* 51: 1985–2000.
- 38** McNesby, K.L., Wolfe, J.E., Morris, J.B., and Pesce-Rodriguez, R.A. (1994). Fourier transform Raman spectroscopy of some energetic materials and propellant formulations. *J. Raman Spectrosc.* 25: 75.
- 39** Bugay, D.E. and Brush, R.C. (2010). Chemical identity testing by remote-based dispersive raman spectroscopy. *Appl. Spectrosc.* 64: 5.
- 40** Eckenrode, B., Bartick, E.G., Harvey, S.D. et al. (2001). *Forensic Sci. Commun.* 3.
- 41** World Health Organization (2018). *Substandard and Falsified Medical Products*, 31 January 2018. WHO <https://www.who.int/news-room/fact-sheets/detail/substandard-and-falsified-medical-products> (accessed 9 March 2018).
- 42** The World Health Organization (2010). *Counterfeit Medicines: A Public Health Challenge*. WHO <http://www.who.int/mediacentre/factsheets/fs275/en/index.html> (accessed 27 January 2010).
- 43** de Veij, M., Vandenabeele, P., Hall, K.A. et al. (2007). Fast detection and identification of counterfeit antimalarial tablets by Raman spectroscopy. *J. Raman Spectrosc.* 38: 181–187.
- 44** Dowell, F.E., Maghirang, E.B., Fernandez, F.M. et al. (2008). Detecting counterfeit antimalarial tablets by near-infrared spectroscopy. *J. Pharm. Biomed. Anal.* 48: 1011–1014.
- 45** de Peinder, M., Vredenbregt, M.J., Visser, T., and de Kaste, D. (2008). Detection of Lipitor counterfeits: a comparison of NIR and Raman spectroscopy in combination with chemometrics. *J. Pharm. Biomed. Anal.* 47: 688–694.
- 46** Ricci, C., Eliasson, C., Macleod, N.A. et al. (2007). Characterization of genuine and fake artesunate anti-malarial tablets using Fourier transform infrared imaging and spatially offset Raman spectroscopy through blister packs. *Anal. Bioanal. Chem.* 389: 1525–1532.
- 47** Vredenbregt, M.J., Blok-Tip, L., Hoogerbrugge, R. et al. (2006). Screening suspected counterfeit Viagra and imitations of Viagra with near-infrared spectroscopy. *J. Pharm. Biomed. Anal.* 40: 840–849.
- 48** Ricci, C., Nyadong, L., Yang, F. et al. (2008). Assessment of hand-held Raman instrumentation for in situ screening for potentially counterfeit artesunate antimalarial tablets by FT-Raman spectroscopy and direct ionization mass spectrometry. *Anal. Chim. Acta* 623: 178–186.

- 49** de Veij, M., Deneckere, A., Vandenabeele, P. et al. (2008). Detection of counterfeit Viagra with Raman spectroscopy. *J. Pharma. Biomed. Anal.* 46: 303–309.
- 50** Kwok, K. and Taylor, L.S. (2012). Raman spectroscopy for the analysis of counterfeit tablets. In: *Infrared and Raman Spectroscopy in Forensic Science* (eds. J.M. Chalmers, H.G.M. Edwards and M.D. Hargreaves). John Wiley & Sons, Ltd: Chichester, UK.
- 51** Vehring, R. (2005). Red-excitation dispersive Raman spectroscopy is a suitable technique for solid-state analysis of respirable pharmaceutical powders. *Appl. Spectrosc.* 59: 286–292.
- 52** Pratiwi, D., Fawcett, J.P., Gordon, K.C., and Rades, T. (2002). Quantitative analysis of polymorphic mixtures of ranitidine hydrochloride by Raman spectroscopy and principal components analysis. *Eur. J. Pharm. Biopharm.* 54: 337–341.
- 53** Varmuza, K., Karlovits, M., and Demuth, W. (2003). *Anal. Chim. Acta* 490: 313–324.
- 54** Brown, C.D. and VanderRhodes, G.H. (2007). *US Patent 7 (254)*: 501.
- 55** Green, R.L. and Brown, C.D. (2008). *Pharm. Tech.* 32 (3): 148–163.
- 56** Green, R.L., Hargreaves, M.D., and Gardner, C.M. (2013). Performance characterization of a combined material identification and screening algorithm. *Proc SPIE 8726 Next-Generation Spectrosc. Technol. VI*: 87260F.

## Abbreviations and Acronyms

21 CFR Part 11	The section of the US Code of Federal Regulations dealing with electronic records and electronic signatures
ANFO	Ammonium nitrate fuel oil
API	Active pharmaceutical ingredient
ATR	Attenuated total reflectance
CCD	Charge-coupled detector
cGMP	Current Good Manufacturing Practice
EGDN	Ethylene glycol dinitrate
EOD	Explosive ordnance disposal
FDA	Food and Drug Administration
FT-IR	Fourier transform infrared spectroscopy
HMTD	Hexamethylene triperoxide diamine
HMX	Explosive also known as octogen and cyclotetramethylenetrinitramine
ID	Identification
IED	Improvised explosive device
InGaAs	Indium gallium arsenide
IP68	International Protection Code (68 refers to the level)
LOD	Limit of detection
MEKP	Methyl ethyl ketone peroxide
MDPV	Methylenedioxypyrovalerone
MIL-STD-810G/H	United States Military Standard (for operation in harsh environments)
NIR	Near infrared
NPS	Novel psychoactive substance
ORS	Orbital Raster Scanning
PETN	Pentaerythritol tetranitrate
PPE	Personal protective equipment
RDX	Research Department Formula X (explosive) – also known as cyclonite
SERS	Surface-enhanced Raman spectroscopy

SORS	Spatially offset Raman spectroscopy
TATP	Triacetone triperoxide
TECP	Totally encapsulating chemical protective
THC	Tetrahydrocannabinol
TNT	Trinitrotoluene
USP	US Pharmacopeia
WHO	World Health Organization

## 17

### Portable Raman Spectroscopy in Field Geology and Astrobiology Applications

H.G.M. Edwards<sup>1</sup>, J. Jehlička<sup>2</sup> and A. Culka<sup>2</sup>

<sup>1</sup>Centre for Astrobiology and Extremophiles Research, School of Chemistry and Biosciences, Faculty of Life Sciences, University of Bradford, Bradford, West Yorkshire, UK

<sup>2</sup>Institute of Geochemistry, Mineralogy and Mineral Resources, Charles University, Faculty of Science, Prague 2, Czech Republic

#### 17.1 Introduction

Before the advent of miniaturized portable, handheld instrumentation, the standard approach for the analytical interrogation of geological specimens was the removal of selected samples from the site for analysis in the laboratory. This often involved the taking of hundreds of samples, and their proper curation and storage at the site, and then in the laboratory. The drive for on-site rapid detection and identification procedures started with the adoption of such miniaturized instruments for forensic crime scene work centered on drugs and explosives and their chemical precursors, and the discovery of makeshift laboratories whose purpose was initially unknown at the scene. This was reinforced by demand for a reliable instrument that could detect important classes of chemicals for in-field use by military, paramilitary, and counterinsurgency task forces. The range of portable Raman instrumentation developed for these specific tasks has now been transposed into several other fields including biomedicine, clinical trials, disease detection, art forensics, archeological excavations, manuscript pigment characterization, and museology. All of these have a classic common theme – namely, the avoidance of sample excision and destructive testing analyses, and with the consequent provision of rapid analytical information at source.

The practical application of miniaturized, portable Raman spectrometers in the molecular characterization of minerals, rocks, and associated natural compounds in the field and the assessment of the data obtained from analogous specimens in laboratory environments will be reviewed and discussed in this chapter. The advantages of the acquisition of Raman spectroscopic data *in situ* in field applications and coverage of potential pitfalls and problems experienced in the use of miniaturized instrumentation in these applications will first be highlighted for a range of geological sites and situations. Protocols for acquiring data outdoors and under outcrop conditions in zones including altered rocks, hot and cold deserts, high altitudes and solar radiation environments are presented mainly for geoscience applications in the first part of this chapter. Similar scenarios and testing of high relevance for the emerging astrobiology field will be introduced in the second part of the chapter. There, other accents are given to biomarkers and their detection by Raman spectroscopic approaches. A particular feature of the use of Raman spectroscopic instrumentation in these environments is the capability to detect the presence of extremophilic biological and biogeological materials arising from organisms that have modified their geological niche environments. The detection of key biomolecular Raman spectral signatures in these stressed terrestrial geological environments has paved the way for the adoption of miniaturized Raman spectrometers for suites of analytical instrumentation on space missions dedicated to the search for extant or extinct life on planetary surfaces and subsurfaces, particularly the forthcoming ExoMars 2022 and Mars 2020 missions, which were both originally scheduled to be launched in July 2020. In March 2020 the European Space Agency announced that they were

postponing the launch of the ExoMars mission for two years for unavoidable reasons related to communications issues, but Mars 2020 launched from Cape Canaveral on 30 July 2020. Both of these missions have Raman spectrometers, which will be deployed on Martian surface rovers, known as Rosalind Franklin and Perseverance for ExoMars 2022 and Mars 2020, respectively, and both will provide screening devices for the molecular interrogation of minerals and rock specimens. The remote characterization of the mineralogy of a planetary surface and subsurface and the detection of spectroscopic signatures of extinct or extant life poses a major challenge for analytical science which builds upon the use of geological miniaturized instrumentation in terrestrial environments and affords what is undeniably one of the most extreme applications of these scenarios.

## 17.2 Dawn of Portable Raman Spectrometers

Miniaturized/portable Raman spectrometers started to be commercially available roughly 10 years ago. They were introduced on the market as easy-to-operate analytical tools suitable for state organizations such as firefighters, customs officers, and police forces, for the rapid identification of unknown and possibly illicit and dangerous substances, such as drugs or explosives. However, their potential outside of their original intended usage was soon realized. Studies that started to report the results and experiences obtained with these miniaturized instruments in the field quickly followed. For the purpose of this chapter, a focus is set on the mineralogical or geological applications of these instruments. Since no previous experience in applications in the geosciences was available, these initial studies involved common minerals, often in ideal form, such as samples taken from mineralogical expositions etc. This way a baseline knowledge or estimate of possible scientific outcome that could be expected from this kind of novel analytical instrumentation was being established. Progressively, the portable Raman spectrometers were involved in studies including less ideal, real-world mineralogical and geological samples. Studies involving samples of very fine crystallinity producing complex mineral assemblages at outcrops or in underground mine galleries that were analyzed *in situ* are examples of much more challenging applications with respect to the instrumental, practical, and operational considerations. On the other hand, the technological progress in the field resulted in a much broader selection of portable Raman spectrometers in the year 2020, and majority of these new types of instruments provide data of significantly improved quality and thus scientific value. Following paragraphs will provide a chronological overview of scientific research that was conducted using the portable spectrometers in the mineralogical applications, to show what kind of samples or settings were investigated and provide summary of both the results and also challenges.

Possibly the first study of clearly mineralogical application was published by Jehlička et al. (2009a), which reported the Raman spectra of a range of important minerals taken *in situ* by two portable spectrometers with 785 nm excitation, the only excitation source available in the first generation of the commercial Raman spectrometers. Tested minerals – calcite, quartz, andradite, tremolite, anglesite, wulfenite, almandine, barite and realgar – yielded Raman spectra that allowed their unambiguous identification. The number of detected Raman bands, as well as their wavenumber positions, were compared to the data obtained using a fully fledged laboratory instrument, which has become a standard for this type of studies. For these early miniaturized Raman spectrometers, the stability of the Raman band positions, and the appearance of the Raman spectra in general, needed to be compared to the Raman spectra of the fully fledged laboratory instruments. Additionally, practical considerations such as the necessity of shielding the analyzed samples from the sunlight were discussed.

A follow-up study by the same authors described the detection of gypsum, barite, and anglesite, all simple sulfate minerals, under suitable field conditions, using again a 785 nm excitation-equipped portable instrument. The authors noted an excellent reliability and satisfactory spectral resolution for this specific instrument; both of these parameters are crucial, especially when the minerals from similar groups are analyzed and need to be unambiguously discerned or differentiated from one another. This will become more obvious when additional reports dealing with even more similar sulfates are discussed further in this chapter. The authors also stressed that this

kind of approach (*in situ* spectroscopic analyses) opens up a completely new field, which is dramatically different from the classical field work being practiced in the geosciences (Jehlička et al. 2009b).

After establishing that portable Raman spectrometers provided good tools for *in situ* identification of the relatively common minerals, Jehlička et al. (2009c) used similar instrumentation for analyses of selected organic minerals. This small and heterogeneous group includes minerals in the form of salts of organic acids, or in the form of higher polycyclic hydrocarbons. These phases can be unambiguously described by their exact chemical composition and ordered structure, having been formed by geological processes. Therefore, they are classified as minerals, as opposed to, for example, fossil resins (amber, copal), which do not fulfill the required conditions of exact chemical composition and structure. Good-quality spectra of whewellite, mellite, and idrialite were acquired both under laboratory conditions and under outdoor conditions with the portable Raman spectrometer equipped with 785 nm excitation. The authors comment that with a good shielding against stray light and proper positioning of the samples, the spectral quality of *in situ* outdoor measurements was comparable to those obtained from indoor analyses. Additionally, the light yellowish or white color of the samples in this study positively affected the resulting Raman spectra.

Jehlička et al. (2011) provided a critical study where two portable Raman spectrometers equipped with near-infrared (NIR) excitation (785 nm) were tested on a selection of minerals ranging from light to dark colored (Figure 17.2b). They ascertained that these portable spectrometers can be used for an unambiguous discrimination of a number of light-colored minerals from different parts of the mineralogical system. On the other hand, dark-colored green, black, and metallic minerals pose an ultimate challenge, and it is commonly not possible to acquire any usable Raman spectra from these minerals due to effects such as absorption, reflection, and fluorescence. The main technical limitations of these portable spectrometers included the limits on both ends of spectral range, which did not permit the collection of spectra outside the ca. 200–3000 cm<sup>-1</sup> region, where important lattice modes (low Raman shift) and –OH stretching vibrations (high Raman shift) occur in minerals. Recurring issues of maintaining a good and constant focus during the *in situ* analyses when the instruments are handheld, in often-difficult positions for longer periods, were also discussed.

A comparison study that featured two miniaturized Raman spectrometers, one with 532 nm excitation and second with dual excitation option at 532 and 1064 nm for the indoor analyses of various hydrated sulfates, with a relevance to the Martian studies, was performed. Miniaturized Raman spectrometers with the then new green (532 nm) excitation wavelength provided better results than the 1064 nm excitation for the identification and description of minerals such as simple hydrated magnesium sulfates, as well as copiapite, coquimbite, jarosites and others (Culka et al. 2014). At that time the spectral range was not broad enough to cover the spectra at high wavenumber shift, where the stretching vibrations of water and hydroxyl groups are located. This region is important for additional information that allows for a better discrimination between hydrated sulfates, for example.

Complex silicate minerals from the zeolite group and beryllium-containing silicate minerals were also studied using the portable Raman spectrometers. Jehlička et al. (2012), and Jehlička and Vandenabeele (2015), investigated the rapid and unambiguous discrimination among these visually similar, mostly white, zeolite minerals. Portable instruments equipped with NIR excitation 785 nm, and green excitation 532 nm, as well as a dual excitation 532/785 nm-equipped spectrometer were used for analyses of thomsonite, stilbite, natrolite, beryl, chrysoberyl, euclase, phenacite, bavenite, and milarite. Portable instruments equipped with the NIR excitation wavelength provided good-quality spectra, sufficient for the unambiguous identification of these species. Spectrometers equipped with the green excitation wavelength performed significantly worse on these kind of samples, both in the number of detected Raman bands and in the intensity of the fluorescence background.

Olcott Marshall and Marshall (2013) identified carbonaceous matter from an Ordovician age stromatolite, sampled from the Gunter Sandstone Member of the Gasconade Dolomite in Reynolds County, Missouri, using an instrument with 785 nm excitation. D and G bands of disordered carbonaceous material were identified at the characteristic wavenumber positions of 1280 and 1540 cm<sup>-1</sup>, respectively, in addition to a 464 cm<sup>-1</sup> Raman band of

quartz. However, the carbonaceous matter has been historically studied using the shorter wavelength excitations, for example 514.5 nm, which is known to provide the best results.

Crupi et al. (2014) analyzed fragments of meteorites SaU 008, Allende, DaG 400, and NWA 869 nondestructively using a portable X-ray fluorescence analyzer (Alpha 4000 by Innov-X), and also using a 785 nm excitation portable Raman spectrometer. They reported the identification of the following minerals in the samples using portable Raman: pyroxene in SaU 008, olivine and graphite in Allende, calcite and plagioclase in DaG 400, and olivine in the NWA 869 meteorite, respectively.

Marshall and Olcott Marshall (2015) studied samples consisting of various types of gypsum minerals from a Martian analogue site at the gypsiferous Blaine Formation, Lone Peak Mountain, Oklahoma. They used an instrument with 785 nm excitation, and noted that for the minerals containing elevated concentrations of transition metals such as chromium and manganese (as were reported from the Gale Crater on Mars), the adoption of NIR excitation might be better, because it provides spectra with less fluorescence. However, the ExoMars 2022 and Mars 2020 mission rovers will be equipped with a green excitation laser and ultraviolet (UV) excitation laser, respectively.

The mineral composition of sulfate deposits at Dalangtan Playa on the Tibetan Plateau was investigated by Kong et al. (2014). For these in situ analyses they used a portable instrument with 532 nm excitation. In freshly uncov-ered layered sediments formed after desiccation of sulfate brines, they identified the following important hydrated magnesium sulfates – hexahydrite, pentahydrite, starkeyite, sanderite, and kieserite – and plotted their distribution with increasing depth of the samples. Kieserite, identified in samples closest to the surface, is magnesium sulfate monohydrate, and is produced here as a dehydration product of hexahydrite, while other minerals of the series are considered to be intermediate products. The stability and distribution of these hydrated magnesium sulfates provide invaluable information applicable to the Martian deposits of similar minerals. The potential for the outdoor analyses of complex assemblages of secondary sulfate minerals was also evaluated. Other sites rich in sulfur and sulfate-rich rocks – Solfatara volcano (Italy) were suggested as excellent fields for testing of mobile analytical tools including Raman spectroscopy, very NIR (VNIR) spectroscopy and other techniques (Flahaut et al. 2019).

Secondary sulfate minerals that are appearing in their natural settings (see Figure 17.2a) at an outcrop of a former pyritic shales mine at Valachov, Czech Republic, were studied by Košek et al. (2017a). They used two portable spectrometers equipped with 532 and 785 nm excitations and reported that they provided unambiguous in situ analysis and discrimination among these finely crystalline whitish to yellowish materials, predominantly hydrated iron sulfates, identifying minerals such as rozenite, melanterite, fibroferrite, copiapite, and jarosite, all of which were previously described to occur at the locality. Among notable issues found during this study, the authors commented that the area from which the signal is collected using the portable instruments is much larger than that sampled in laboratory benchtop instruments, which means that for these complex natural mineral assemblages the signal of more than one mineral is often recorded. This needs to be taken into consideration, especially for the structurally similar sulfate minerals that can have Raman bands at close wavenumber positions.

Another intriguing setting that has been studied from a mineralogical perspective is burning coal heaps. In this special environment, secondary minerals are being formed from the primary carbonaceous-matter-enriched mate-rial, as a product of the interaction of high temperatures inside the heap, and precipitation that infiltrates from the surface. A portable Raman spectrometer with 785 nm excitation was used to record the Raman spectra of phases such as elemental sulfur, sal-ammoniac, and sulfates, both hydrated and anhydrous, by Košek et al. (2017b). The portable instrumentation that allows for the in situ analyses of often-unstable high-temperature mineral phases (see Figure 17.2d) proved a powerful tool for the fast mineral discrimination in these settings.

In the similar theme of application of a portable spectrometer in more challenging settings, Culka et al. (2016) reported an investigation of secondary arsenate minerals analyzed in situ at two localities of their occurrence in the contaminated soils near Kaňk in the Kutná Hora mining district, in the central part of the Czech Republic, and in the Lehnschafter gallery (see Figure 17.2c) of a former silver mine in Mikulov, in the Krušné Hory mountains, in the northwest part of the Czech Republic. Over 600 years of mining history at both locations has provided a

plentiful supply of a rich secondary mineralization of arsenate minerals. Using two portable instruments equipped with 785 and 532 nm excitations, the authors reported that several important secondary arsenate minerals were unambiguously detected *in situ*: bukovskýite, kaňkite, parascorodite, and scorodite were identified from Kaňk near Kutná Hora, while kaňkite, scorodite, and zýkaite were identified at the old silver mine at Mikulov. While the performance of both instruments allowed for the acquisition of good spectral data, the environmental conditions (more specifically when close to a 100% relative humidity) in the former silver mine caused the spectrometer with 785 nm excitation to stop functioning, which necessitated its subsequent repair. Such extreme conditions definitely pose significant limitations on the use of these portable instruments.

Lalla et al. (2016) investigated the “Los Azulejos” site at Cañadas Caldera in Tenerife Island, with its alteration processes and mineralogy, which could be considered as a Martian analog. Using a Raman portable spectrometer with 532 nm excitation, they were able to identify only a few minerals *in situ*: quartz, anatase, and feldspar; however a much more detailed mineralogical assemblage was revealed by micro Raman studies on collected samples in the laboratory.

An advanced *in situ* Raman spectroscopic study involving the identification of minerals was organized in speleothems in Spain, namely the El Soplao Cave (Cantabria, N Spain) and in the Gruta de las Maravillas (Aracena, SW Spain). The authors used a Raman instrument with a 785 nm excitation, and identified common speleothem minerals, such as calcite and aragonite, as well as the bedrock minerals, dolomite and quartz. Additional minerals identified included the magnesium carbonates hydromagnesite, and huntite, and several oxides in the colored cave ornaments, cuprite for blue, goethite for red-brown, and birnessite for the black pigments. Moreover, gypsum was identified as the probable product of oxidation of small amounts of pyrite in this calcium-rich environment (Gázquez et al. 2017).

As the number of types of portable spectrometers that have been available on the market increased, with a greater variability in both excitation and overall instrument specifications and design, a comparison of their performance in the mineralogical application was appealing. An extensive comparative study was therefore published by Jehlička et al. (2017a), in which a total of seven portable Raman spectrometers (see Figure 17.1a–f) were employed for field analyses of varieties of beryl minerals. A range of natural and cut samples of beryl mineral varieties were analyzed, and it was documented that the performance of the portable instrumentation is quite variable, and that generally the newly available portable Raman spectrometers performed rather well, sometimes comparably to the laboratory equipment. The parameters used for comparison were the number of detected bands and their wavenumber shifts from the expected correct values as determined in the laboratory. The overall best performance was achieved by the two most novel (freshly available on the market at the time) portable spectrometers, one equipped with 532 nm excitation and the other with a newly implemented sequentially shifted excitation (SSE). This study illustrated that the quality of data coming from these latest additions to the field of portable Raman spectrometers is significantly higher, and in some applications it even sufficiently approaches the quality of data of classical benchtop laboratory spectrometers.

A novel technological improvement in the field of miniaturized Raman spectrometers was introduced in 2016 with the appearance of the portable Raman spectrometer featuring the combination of two laser wavelengths (853 and 785 nm) operated in the SSE mode. This instrument was designed to minimize or eliminate laser-induced fluorescence (LIF) using the different behavior of fluorescence features and genuine Raman bands in the Raman spectra. A slight change (<1 nm) in the excitation wavelength causes a relative shift of Raman bands in the spectral space, while the fluorescence features remain at fixed positions. This enables the instrument to “compute” the final spectrum from the six raw spectra by subtracting the fluorescence features. This process is generally rather effective; however in some cases, for example for samples exhibiting very strong or unusual shaped fluorescence features, it introduces the so-called “artifact” bands, or significantly modifies the shape of the existing Raman bands.

Several studies with mineralogical or geological focus were published, in which authors tried to ascertain the feasibility of this new improvement (portable SSE Raman spectrometer: PSSERS) that promised to mitigate one



**Figure 17.1** Examples of miniaturized Raman spectrometers. Bruker Bravo (a), DeltaNu Inspector Raman/RockHound (b), EnSpectr RaPort (c), Rigaku FirstGuard (d), Ahura/Thermo Scientific First Defender XL (e), Ahura/Thermo Scientific First Defender RM (f), Enwave EZRaman-I Dual (g), B&W TEK i-Raman EX (h).

of the main problems in natural samples, which is LIF. Thus the ability of the instrument to remove fluorescence from the Raman spectra of natural samples of minerals such as anhydrite, apatite, and zircon was investigated by Culka and Jehlička (2018). Raman spectra of these minerals contain a typical fluorescence pattern caused mostly by the presence of the rare earth elements (lanthanides) in their crystal lattices. This fluorescence takes the form of relatively narrow bands, which resemble closely genuine Raman bands. Removal of this type of fluorescence is possible, but sometimes new artifact bands inevitably appear in the Raman spectra of the most problematic samples.

A set of 42 loose gemstones and other cut minerals frequently encountered within gemmology or related works-of-art was analyzed using the PSSERS in Culka and Jehlička (2019). The recorded spectra were generally of very good quality, but again instrument artifact bands appeared in the spectra of some typically problematic minerals such as apatite and fluorite, as well as, for example, diopside. This is again a result of the fluorescence removal process, for samples which exhibit a complex and strong fluorescence pattern. A slight limitation for some samples might also be the spectral range of the instrument, which does not cover the higher wavenumber region of the OH stretching vibrations on one side and the low-wavenumber region, where lattice modes occur, on the other.

This instrument was also tested on materials that have naturally broad Raman bands, such as carbonaceous matter. Jehlička et al. (2017b) showed that care must be taken when interpreting the SSE Raman spectra of G and D bands of these carbonaceous materials, because the fluorescence-removal process noticeably alters the shape of

these bands. The authors stress that the raw data need to be accessed when visually “suspicious” bands appear in the Raman spectra of not just carbonaceous matter. As mentioned earlier in this chapter, in Jehlička et al. (2017a) this PSSERS was a part of a comparison study along with seven other miniaturized instruments. On the test set of beryl minerals, and their emerald and aquamarine varieties, PSSERS achieved results of the highest overall quality of Raman spectra, together with another novel 532 nm excitation spectrometer, demonstrating the big progress of quality of data obtainable from this new instrumentation.

Malherbe et al. (2019) evaluated the 785 nm excitation portable Raman spectrometer for in-the-field measurements of minerals in preparation for space missions. Minerals such as quartz, barite, calcite, dolomite, sphalerite, and amorphous carbon were identified at the Snailbeach mine locality. They noted the strong, sharp, band-shaped fluorescence signal in the Raman spectrum of calcite. This can compromise the detection of a carotenoid pigment as a biomarker, whose key Raman bands are located in the same spectral region between 1000 and 1800 cm<sup>-1</sup>.

The same instrument was evaluated for use in the exploration of pegmatite dikes at Wekusko Lake, Manitoba by Benn et al. (2019). Studies involving pegmatite-type mineralization are empowered by the recent high demand for lithium (and especially its usage in lithium-ion batteries), which naturally occurs in pegmatitic micas. In this short study, the authors reported the *in situ* Raman spectra of muscovite as one of the important mica minerals.

The previous paragraphs present an overview of the applications of portable Raman spectrometers with a focus to in-field geoscience studies. The miniaturized Raman spectrometers were firstly developed and produced with intention to be operated in completely different tasks, such as those encountered for example by firefighters, police, and customs officers. The typical application for the miniaturized Raman spectrometers was to serve as tools for *in situ* identification of unknown substances such as drugs, explosives, and similarly looking materials or possibly their respective mixtures. Some of the models were equipped with a vial holder or compartment to accommodate the usually-tested sample types that can be generally called “white powders.” Analysis using Raman spectroscopy is known to be very suitable for this kind of samples, rapidly yielding the results, especially with the built-in databases of the most common substances of abuse etc.

Nevertheless, the idea to employ this analytical technique for fast, nondestructive *in situ* analysis in other fields such as geoscience or cultural heritage meant that substantially different types of samples were to be analyzed and frequently also in diametrically different settings. Therefore, the initial goal was the evaluation of the technical and spectroscopic performance of the small systems in these applications. A succinct description of variability among the different types of miniaturized Raman spectrometers might be in place for a better understanding of the strong and weak points of this type of instrumentation. Examples of several types of instruments are shown in Figure 17.1, and demonstrate the degree of variability. There are several important parameters that can influence both the handling and operation of the instrument, and the quality of data it provides.

Firstly, the excitation wavelength selection greatly determines the outcome for specific sample types. The possible choices of excitation are rather limited for the miniaturized instruments. The pioneering models of miniaturized instruments utilized exclusively NIR 785 nm excitation (see Figure 17.1b, e, f, g), probably for technological reasons, but the safety perspective also could play a role. The next common excitations were a 532 nm green laser (utilized in instruments shown in Figure 17.1c, d, g), and to a lesser degree 1064 nm infrared laser (instrument depicted in Figure 17.1h). Lastly, an SSE using the combination of a 785 nm laser and an 853 nm laser was implemented relatively recently in portable Raman spectrometers (see Figure 17.1a). The reviewed studies showed that the 785 nm excitation provided arguably the most solid results for the mineralogical applications such as fast and unambiguous discrimination of light-colored minerals of different chemistry. The 532 nm excitation may introduce higher occurrence of fluorescence, and on the other hand, the SSE was tested as a relatively effective tool for fluorescence removal from spectra acquired on geological samples.

The second important characteristic to consider is the combination of size and weight of the miniaturized instruments. These determine among other things the user experience during prolonged data acquisition in complicated settings (i.e. natural outcrops), or even the effort to physically move the spectrometers to a distant location for *in situ* analysis, when on foot. The miniaturized instruments range in sizes from palm (weight less than 1 kg,

see Figure 17.1f), handheld (weight 1–3 kg, see Figure 17.1a–e) to portable suitcase-sized (weight 10–20 kg, see Figure 17.1g,h) or even bigger and heavier transportable instrument not discussed here. The acquisition of spectra using the heavier instruments is facilitated by the fact that they use optical fibers to connect their probe heads, but generally, and not surprisingly, the lighter the instrument the easier the manipulation over the long periods for the operator. The weight of the instrument thus plays a significant role for the in situ analyses when the instrument is actually handheld, during the data acquisition. Every slight movement caused by excessive weight influences the stability of the location and focus of the laser spot.

The third parameter which also greatly influences the user experience and can have impact on the resulting data, is the type or shape of the probe head of each miniaturized instrument. As mentioned previously, the heavier instruments are equipped with the probe head connected to the body of the spectrometer with fiber optics typically of several meters long. This setting (see Figure 17.1g, h) is probably the best with regard to positioning at the measured spot; on the other hand, it requires two people actively cooperating during the analysis, the second person operates the laptop PC. The smaller instruments can be generally divided into two groups; one features spectrometers with some kind of cone-shaped probe head with a narrowing tip (see Figure 17.1b, d, e, f), the other group includes spectrometers equipped with flat probe head (see Figure 17.1a, c). The tip-pointed probe head provides a significant advantage over the flat probe head for the geological applications *sensu lato*. It allows for a much better control of the exact position and focus of the analyzed spot, and moreover, frequently it provides the access to the parts of sample that have complex morphology or surface in the first place (natural outcrops, complex works-of-art). Some example illustrations of the advantage of the tip probe head for the access to analyzed samples are shown in Figure 17.2, as opposed to the difficulty of positioning of the completely flat probe head on uneven



**Figure 17.2** Examples of analytical applications. Secondary sulfates at Valachov, Czech Republic (a), granulite and pegmatite at Vlastějovice quarry, CR (b), secondary arsenate minerals in old silver mine at Mikulov, CR (c), secondary minerals at Heřmanice coal dump, CR (d), emerald-bearing rocks at Habachtal, Austria (e), gemstones adorning Torah shield in Jewish Museum in Prague, CR (f), snow algae at Luční hora, CR (g), extremophilic colonizations in rocks in Negev Desert, Israel (h).

surface of a rock outcrop (see Figure 17.2h). In some cases, it is more feasible to position a small object to be analyzed directly on top of the flat probe head while the instrument is positioned stationary on the level ground.

Some of the other testing evaluation was much more connected to establishing the molecular spectroscopic training for the detection of pure organic compounds and their mixtures, and also mixtures of biomarkers in mineral matrices of relevance for their astrobiology context. Not all compounds studied can be considered as true biomarkers, and some were chosen because they belonged to a group of chemicals with some similarities to those tentatively suggested as existing on some of planets and satellites of our solar system, for example, polycyclic aromatic hydrocarbons, carboxylic acids, and nitrogen-containing compounds of different chemistry. Testing was carried out under high-mountain and cold environmental conditions, which enabled the basic technical properties of these small spectroscopic devices to be evaluated for an important class of compounds that exist in the geological record. Some field applications of portable Raman spectrometers have a similar focus in establishing the molecular signatures of biomarkers of extremophiles, mainly pigments, collected in the frame of Earth-based planetary analogue sites, some examples of which are described later.

The testing of different portable Raman spectrometers has been performed outdoors under harsh, ambient conditions – at low temperatures, involving measurements in glaciated areas and in snow, in dark and damp cave environments or in dry and hot desert zones. Some studies are dedicated to the evaluation of the performances of miniaturized Raman spectrometers under these extreme conditions. These studies showed that Raman spectrometers can be applied on-site, under relatively low temperature conditions and outdoors in inaccessible mountain areas. The motivation for these studies comprised the necessity of research and geological survey of these remote areas, with a focus on the discovery and understanding of the formation of deposits of ores or other natural resources. Additionally, there are major consequences for their planned use for remote instrumentation in planetology and space research, as well as astrobiology. The first studies of this type used pure chemicals in different admixtures. Samples of powders of amino-acids ( $\text{l}$ -alanine,  $\beta$ -alanine,  $\text{l}$ -asparagine,  $\text{l}$ -aspartic acid,  $\text{l}$ -glutamic acid,  $\text{l}$ -glutamine, glycine,  $\text{l}$ -methionine,  $\text{l}$ -proline,  $\text{l}$ -serine,  $\text{l}$ -threonine,  $\text{l}$ -tryptophan and  $\text{l}$ -tyrosine) (Culka et al. 2010; Jehlička et al. 2010a, b) and nitrogen containing organics (formamide, urea, 3-methylpyridine, aniline, indene, 1-[2aminoethyl]piperazine, benzofuran, indoline) were brought to Alpine glacier zones (Pitztall, 2860 m,  $-15^\circ\text{C}$ ) (Jehlička et al. 2010c; Jehlička and Culka 2010). Here, two portable instruments equipped with 785 nm excitation, namely Ahura (Wilmington, USA) and Delta Nu (Laramie, USA), were used to collect the Raman signatures. The performance of both the spectrometers was excellent, and the wavenumbers of the strongest and medium-intensity bands corresponded well with their characteristic reference values ( $\pm 3 \text{ cm}^{-1}$ ). It was shown that the derived Raman spectra could be used without any additional spectral manipulation. There are some minor differences observed between the Raman spectra from both instruments and the effects and influence of the positioning and immobilization of the instrument and sample during acquisition of the spectra were documented and discussed.

More complex samples were prepared as mixtures of organics with mineral powders and other measurements focused on obtaining Raman spectral signatures through transparent minerals, such as gypsum (Culka et al. 2011, 2012). Detecting low concentrations of biomarkers in the frame of host mineral matrices for future use in search for life space missions seems to be the important challenge for instrumentation in the astrobiology area. Some studies have focused on aminoacids. Other studies show the advantage of excitation close to the resonance Raman conditions to obtain strong signals, as experienced for example in the case of  $\beta$ -carotene (Vítek et al. 2011). Vandenabeele et al. (2012) have discussed in detail the analytical aspects connected to the dispersion of molecular species in the frame of granular matrices, and limits of Raman spectroscopy for their detection and quantitative analysis.

Transportable Raman spectrometers are sometimes equipped with less common excitation wavelengths: this is the case of the Advantage DeltaNu system having a 1064 nm diode laser, and more recently also the BWTek instrument. Vítek et al. (2012a, b) demonstrated the good performance of this transportable system for detecting organic minerals and also fossil resins. Clearly, the strongest bands are correctly recorded, but better spectra are nevertheless obtained applying a laboratory 1064 nm excitation FT-Raman spectrometer.

### 17.2.1 The Exploration of Mars: A Raman Spectral Chronicle for the ExoMars 2022 and Mars 2020 Missions

The application of Raman spectroscopic techniques to the characterization of the protective biochemicals used in the survival strategies of extremophilic organisms in terrestrially stressed environments (Wynn-Williams and Edwards 2000a, b), coupled with the palaeogeological recognition that early Mars and Earth had maintained similar planetary environments under which Archaean cyanobacteria could have developed (McKay 1997), has driven the proposal for the adoption of Raman spectroscopy as novel analytical instrumentation for planetary exploration (Dickensheets et al. 2000; Edwards and Newton 1999; Ellery and Wynn-Williams 2003). As stated earlier, the application of remote, miniaturized analytical spectroscopic instrumentation affords an example of the extension of geological terrestrial prospecting to one of the most extreme environments. The European Space Agency/Roscosmos (ESA/Roscosmos) has announced that a miniaturized Raman spectrometer, operating in the visible region of the electromagnetic spectrum at 532 nm, would form part of the Pasteur analytical life-detection protocol in the 2022 ExoMars mission for the search for traces of life on Mars in the AURORA program. That instrument is selected for the first-pass analytical interrogation of specimens from the Martian surface and subsurface (accessed by a 2 m drill) aboard the *Rosalind Franklin* rover vehicle, confirming that Raman spectroscopy will perform a key role for the molecular analytical protocols aboard the ExoMars 2022 rover vehicle. Also, NASA has announced that a Raman spectrometer (SHERLOC), operating in the deep UV region at 249 nm, will be part of the scientific instrumentation aboard its Mars 2020 mission, which was launched in 2020 (Abbey et al. 2017; Beegle et al. 2015). These comprise the first two planetary missions wherein analytical Raman spectroscopy will be utilized for the molecular characterization of Martian geology and biogeology dedicated to a search-for-life scenario; undoubtedly, the catalyst and ongoing major driving force for this unique application of portable Raman instrumentation has been the growth of terrestrial field geological experiments carried out *in situ* on generically described terrestrial Mars analogue sites. As noted recently, the European Space Agency has now decided to postpone its ExoMars 2020 to 2022, but the NASA Mars 2020 mission went ahead in July 2020. Both missions have a suite of dedicated geophysical and spectroscopic instrumentation, several components of which are complementary to the delivery of the mission objectives. NASA has stated the four goals for its Mars Exploration Program are (1) the determination of whether life ever arose on Mars, (2) to characterize the Martian climate, (3) to characterize the Martian geology, and (4) to prepare for human exploration of Mars. To deliver these it will be necessary to identify past geological environments capable of sustaining microbial life and the characterization of rocks that are known to be capable of preserving their relict biosignatures. An important aspect of the Mars 2020 mission is to acquire rock, drill cores and regolith samples and to store them in tubes in a “depot cache” system for their collection and return to Earth on a later mission. During the mission, instrumentation will also use MOXIE apparatus to evaluate the production of oxygen from the predominantly carbon dioxide Martian atmosphere (approximately 96% CO<sub>2</sub>) and to derive more information about Martian weather patterns, seasonal changes, and dust production to assist in the future human exploration missions.

Clearly, from these mission objectives, it is seen that the most important scientific discovery in a future space mission would be the furnishing of indisputable evidence from chemical analytical instrumentation for the presence of life signatures on another planet, and whether these arise from extant or extinct sources. However, this idea generates two very important questions: namely, how do we define life, and how would we then recognize it or its residues, which themselves may have been significantly degraded due to the influence of extreme environmental conditions in the planetary geological record using remote analytical instrumentation? The precise definition of life is actually rather elusive (Bedau 2010; Benner 2010; Tirard et al. 2010): the NASA definition of life is “A self-sustaining system capable of Darwinian evolution.” This incorporates a molecular genesis with replicative procedures and avoids several pitfalls of alternative definitions that have been based upon the ability of the system to reproduce (Cleland and Chyba 2002). The presence of extraterrestrial life, its origin, survival, and evolution, is the medium of astrobiology (or exobiology). Clearly, current studies of terrestrial life and its evolution, from the

earliest prebiotic beginnings on a formative Earth some four billion years (Gya) ago, is of direct relevance to the current astrobiological search for the emergence of life on other planets and their moons.

Fundamentally, the three questions addressed by astrobiology are: how did life begin and evolve, does life exist elsewhere, and what is the future of life on Earth and beyond? It is, therefore, the function of analytical astrobiology to apply the principles of chemical, biomolecular, morphological, and microbiological analyses to these three baseline questions. Terrestrial chemical and biomolecular instrumental analyses associated with living organisms can inform remote extraterrestrial exploration missions envisaged by the inclusion of analytical instrumentation on planetary spacecraft, landers, and rover vehicles. The key question here, of course, is what biochemical species truly define the presence of extinct or extant life, be this terrestrial or extraterrestrial, and can we recognize such biomarkers in the extreme environments that we would expect to find on missions to our neighboring planets and planetary moons, such as Mars, Titan, and Europa? Although the accent is upon astrobiological themes, these are inexorably encompassed in the characterization of the geological extraterrestrial environments upon which the preservation of life and its associated biosignatures is dependent; the instrumentation on the Mars rover vehicles, therefore, is dedicated to the identification of suitable mineralogy and geology capable of sustaining microbial life and the preservation of its relevant biosignatures, through instruments on the Mars 2020 mission such as SHERLOC, SuperCam, PIXL, and MASTCAM-Z.

### 17.2.2 The Spectroscopic Detection of Life Signatures on Mars

It is appropriate to consider some of the scientific parameters that will need to be evaluated for the detection of life signatures using remote robotic analytical instrumentation, specifically in both the ExoMars 2022 and Mars 2020 missions: primarily, the selection criteria for an analytical astrobiological mission such as ExoMars 2022 need to consider the following questions:

- What organisms could have existed and have survived the current and past extremes of environment on Mars?
- What type of geological protective niches are to be found that may conceal the traces of relict or extant life on Mars, bearing in mind the hostile environment now experienced at the planetary surface? Does this imply that a subsurface interrogation is desirable or mandatory?
- What signatures would these organisms have left in such environments as indicators of their presence and how can we recognize them using remote spectroscopic instrumentation?
- What molecules, if detected by remote planetary instrumentation interrogating surface and subsurface specimens, could be considered as constituting a proof that life exists or once existed on Mars?
- Are there terrestrial Mars analogue sites that could be used as “models” for the refinement of spectral data that can be utilized as evidential confirmation of the presence of biosignatures on Mars?

### 17.2.3 The Historical Mars

From the birth of our solar system some 4.6 Gya, the terrestrial geological record suggests that microbial autotrophic ecosystems already existed on Earth from 4.0 to 3.8 Gya. There is now much evidence that early Earth and early Mars were indeed very similar in their physicochemical composition; since Mars is significantly smaller than Earth, it is therefore likely that planetary cooling occurred more rapidly than it did on Earth as proposed by McKay (1997). The planet was probably more temperate and wet, and since there is geological evidence that life had already started on Earth during this period, it seems reasonable to conclude that life could have possibly started on Mars. By Epoch IV (ca. 1.5 Gya to present), however, catastrophic environmental changes on Mars would have compromised the survival of organisms on the Martian surface, and it is possible that the Martian analogues of our own terrestrial extremophiles could therefore have been the last survivors of life on Mars, through their environmental adaptation of Martian geological niche sites.

### 17.2.4 The Analytical Astrobiology of Mars and the Role of Raman Spectroscopy

The detection of biomolecular markers in geological substrates, or the subsurface regolith of Mars, is a primary goal for astrobiology (Edwards 2004; Edwards et al. 2005); the evolutionary pressure of environmental stresses on the surface of Mars, especially the high levels of low-wavelength high-energy damaging UV radiation, low temperatures, extreme desiccation, chemical toxicity, and hypersalinity would have demanded protective strategies adopted by biological organisms to promote the origin, survival, and evolution of microbial life (Cockell and Knowland 1999). However, the UV radiation protection afforded to subsurface organisms by the iron (III) oxide on the surface regolith, acting as a low-wavelength filter, has been proposed as a key factor for the maintenance of biomolecular activity in the immediate Martian subsurface (Clark 1998), as the same UV and low-wavelength electromagnetic radiation generates hydroxyl radicals and peroxides, which would certainly inhibit the survival of complex biomolecules in the surface oxidation zone. The complex chemical systems comprising terrestrial soils, bitumens, and kerogens found in our own planetary lithology would not be expected to occur to the same wide-ranging extent on the surface of Mars, although niche environments favorable to their survival may still occur (Edwards et al. 2010; Jehlička et al. 2010a, b; Marshall et al. 2010; Pullan et al. 2008).

However, it is believed that Mars might still preserve a chemical record of early life in rocks and sediments from the Noachian era, which overlaps the terrestrial Archaean geological history, from about 3.8 Gya. The search for extinct or extant life on Mars must therefore center upon the identification and recognition of specially protected niche geological sites, firstly, in regions where they were generated and, secondly, where these biomolecular signatures would be well preserved, especially in lacustrine or deltaic sedimentary deposits, laid down when Mars had surface water and fluvial activity. The fundamental analytical approach to the astrobiological instrumental interrogation of Mars must then consider the spectral detection of key molecular biomarkers, probably within rocks and certainly in subsurface terrain, perhaps even in these ancient lacustrine sediments (Bishop et al. 2004; Doran et al. 1998), which will necessitate the deployment of remote analytical sensors with preset protocols and an established database recognition strategy for minerals, biologically modified geological strata, and biomolecular residues. Examples from the appropriate terrestrial analogue sites could therefore include carbonates, carbonated hydroxyfluoroapatite, gypsum, calcium oxalates, porphyrins, carotenoids, scytonemin, and anthraquinones (Edwards 2010; Wynn-Williams and Edwards 2002). Clearly, the identification and selection of terrestrial Mars analogue sites (Bishop et al. 2004; Pullan et al. 2008) will be a critical and fundamental step in the development of the analytical astrobiology missions for Mars, with a two-pronged experimental concept: the understanding of the type of geological formations that have been colonized by extremophilic organisms in terrestrial “limits of life” situations, and the deployment of novel miniaturized analytical instrumentation, which can reveal the presence of the key signatures of extinct and extant life in micro-niches in the geological record (Bishop et al. 2004; Doran et al. 1998; Edwards 2010; Edwards et al. 1997; Treado and Truman 1996; Wynn-Williams 1991, 1999; Wynn-Williams and Edwards 2002).

The application of Raman spectroscopic techniques has been already been demonstrated to be successful, through the direct characterization of the signatures of biomolecules, and their modified structures situated in the terrestrial geological record, which does not involve either the physical or the chemical separation of the organic and inorganic components. Some of these terrestrial Mars analogue sites have been described here, and the data obtained from them using laboratory-based Raman spectroscopic techniques and more recently, mobile spectrometers, including prototype versions of the flight model destined for the ExoMars 2022 mission, have advanced our understanding of extremophile behavior significantly. The detection capability of the Raman spectroscopic instrumentation for biomarker spectral signatures has assisted in the development of a spectral database of recognizable spectral band wavenumbers that can positively identify the presence of biomolecules and associated cyanobacterial colonies in terrestrial geologies of relevance to Mars.

In a special issue of the *Philosophical Transactions of the Royal Society*, in a year that celebrated its 350th anniversary as the longest-running scientific journal, several articles highlighted the role of Raman spectroscopy in the

characterization of biosignatures of extremophilic colonization of geological substrates in a range of stressed terrestrial environments (Brier et al. 2010; Carter et al. 2010; Edwards 2010; Edwards et al. 2010; Jehlička et al. 2010b; Jorge-Villar and Edwards 2010; Marshall and Olcott Marshall 2010; Rull et al. 2010a, b; Sharma et al. 2010; Varnali and Edwards 2010; Vítek et al. 2010). These articles address the detection of geological and biogeological spectral markers that are relevant to space missions, and give a very good appreciation of the Raman spectroscopic requirements that will be essential for the construction of a relevant spectral database (Jorge-Villar and Edwards 2005) for the ExoMars 2022, and other space missions that have a Raman spectrometer aboard their rover vehicles.

### 17.2.5 Spectral Biosignatures and Biomarkers

A Raman spectral biosignature is a unique band from a compound that has been synthesized **exclusively** by biological organisms, henceforth known as a *biomarker*, and which ideally is relatively stable under niche astrogeological conditions. Ambiguous and indefinite biomarkers do exist, however, and unfortunately are frequently incorrectly cited in the literature as genuine, despite the realization that these can be synthesized both biotically and abiotically under planetary surface and subsurface conditions, or in an interstellar medium. Examples of these potentially false biomarkers include n-alkanes, polycyclic aromatic hydrocarbons, N-heterocycles, aminoacids, kerogens, urea and carbon. A further subset of biogeomarkers, or biominerals, can be identified from terrestrial geological niches where they are produced as geologically altered material as a result of biological colonization that has interacted with the prevailing geology. For instance, a calcite matrix, in the presence of oxalic acid produced from the Krebs metabolic cycle of lichen colonies, results in the formation of whewellite and weddellite, both of which are hydrated calcium oxalates (mono- and di-hydrate, respectively). Evidence of these biominerals in biologically inactive geological strata is deemed terrestrially to be indicative of the presence of extinct biological colonization.

True biomarkers, which have been characterized Raman spectroscopically are actually rather limited in number and comprise: scytonemin (and its family of methylated and methoxylated derivatives), carotenoids, carotanes (degraded and hydrogenated carotenoids), trehalose (a polysaccharide water replacement molecule for biological cells at low temperatures), chlorophyll (the photosynthetic pigment), porphyrins, phycocyanins (radiation protective accessory pigments), deoxyribonucleic acid (DNA) and ribonucleic acid (RNA), hopanoids and hopanes, terpenoids and sterols (and their degraded steranes). The thermal diagenesis of complex biomolecules above 200 °C results in decomposition products such as polycyclic aromatic hydrocarbons and disordered carbon; although these strictly cannot in themselves be considered as spectroscopic biomarkers for unambiguous diagnostic purposes; nevertheless, their presence in association with other organic molecules could be considered as reliable potential indicators of once extant, or extinct, life.

In terrestrial Mars analogue sites the prime objective is the identification of a suite of spectroscopic molecular biomarkers whose remote detection on a planetary surface or subsurface would positively and unambiguously indicate the presence of extinct or extant life; we need to also narrowly permit the definition of life as essentially cyanobacterial, which represents the earliest identifiable Archaean life forms on the emerging planetary and oceanic Earth, some 3.8 Gya. From spectroscopic and microbiological analytical studies of terrestrial cyanobacteria, it has been possible to isolate several biomolecules, which truly can be considered as key spectroscopic biomarkers, from which we can construct a Raman spectroscopic database that will act as a true standard of assessment for the presence of life in the biogeological record. Such a definitive list of biomarkers for analytical astrobiology could be: *bio-organic molecules: scytonemin, carotenoids, carotanes, trehalose, phycocyanins, hopanoids; and bioinorganic molecules: whewellite, weddellite, aragonite, mellite, vaterite, chlorophyll*.

Westall et al. (2015) have recently published an elegant paper that critically describes the type of biosignature that might be expected to be detected on Mars in search-for-life experiments, concentrating upon chemolithotrophic and anaerobic life development in an extended Martian environment: they recognize that the search for life on Mars will present a particular challenge analytically because of the difficulty in detecting biosignatures from organic molecules in the prevailing hostile environments there. This work extends that of Farmer and Des Marais

(1999), Westall and Cavalazzi (2011), and Summons et al. (2011) on the potential for the preservation of organic biomolecules in the Martian regolith. The general conclusion is that organic molecules would not be preserved on the Martian surface, due to the extremely intense low-wavelength radiation, and especially because of the presence of perchlorates and peroxides created in the surface regolith. However, Freissinet et al. (2015) detected low levels in the ppb range of chlorobenzene and C<sub>2</sub>–C<sub>4</sub> chloroalkanes in the mudstone drill holes of Gale Crater, using the NASA Mars *Curiosity* Rover MSL science laboratory Gas Chromatography-Mass Spectrometry (GCMS) instrument, which they have attributed to the reaction of chlorine produced at the surface of Mars with organic carbon deposits – and it was concluded that the complete destruction of organics, at or near the surface of Mars, was not a sine qua non. In a similar experiment, also at Gale Crater, Webster et al. (2015) detected the presence of methane and discussed its possible abiotic or biotic origins. In the only Martian rocks currently available for analysis in terrestrial laboratories, namely Martian meteorites, there have been several reports of the detection of carbon and/or carbonaceous materials, which are indicative of the possible existence in the past of subsurface organic-bearing materials on Mars (Grady et al. 2004; Lin et al. 2014; Steele et al. 2012).

In one of the most recent reports of the analyses of the *Curiosity* rover data, Webster et al. (2018) have detected a strong seasonal variation in the concentration of methane in the Martian atmosphere, by tunable laser spectroscopy, over a five-year period, ranging from 0.24 to 0.65 ppb, with an average value of  $0.41 \pm 0.16$  ppb, which they have ascribed to small localized sources of methane release from subsurface reservoirs. In a paper immediately following in the same journal, Eigenbrode et al. (2018) reported further data from the 3.5 billion-year lacustrine sedimentary Murray formation at Pahrump Hills in the Gale Crater on Mars, using the GCMS instrument in the Sample Analysis at Mars (SAM) suite on *Curiosity*: they have identified complex aromatic and aliphatic organic molecules in the pyrolysis products released between 500 and 820 °C, including thiophenic acid, to which they attribute its sulfurization as a survival protection.

A very important requirement fulfilled by Raman spectroscopy in the analysis of potential biomarkers is the ability to differentiate between the key molecular species on the basis of their characteristic spectral signatures; this is not only manifest in the discrimination between the relevant organic components of the complex protective biochemical, comprising the stressed biological colonies and the minerals of the geological host matrix, but also the identification of the different types of biomarker, such as carotenoids, several of which appear in the biogeological studies enumerated above.

#### 17.2.5.1 Raman Spectroscopy on the ExoMars 2022 Mission

Although, as stated earlier, the ExoMars 2020 mission is now postponed until 2022, the ExoMars Raman spectrometer (RLS: PI, Fernando Rull, University of Valladolid, Spain) uses a Raman laser excitation wavelength of 532 nm in order to optimize the range of accessible biominerals and biological molecular targets, in a compromise between a potentially strong fluorescence background emission against an increased Raman spectral intensity, with the proviso that laser diodes could be commercially sourced to fit the mass and power requirements of the mission. A laser spot diameter of 50 µm was chosen to balance the requirements of transect sampling of powdered specimens, with grain sizes between 20 and 200 µm, against excessive heating of the sample. It is anticipated that around 400 sample points will be interrogated during the mission. The UK flight-like ExoMars 2022 prototype instrument (Edwards et al. 2012) operates with a similar system, autofocus at each position. This flight-like prototype, and a similar related commercially available, portable system with 532 nm excitation, has been used to interrogate a variety of biogeological Mars analogue specimens (Edwards et al. 2014).

#### 17.2.5.2 Raman Spectroscopy on the NASA Mars 2020 Mission

The NASA Raman spectrometer on the Mars 2020 mission is known as SHERLOC (Scanning Habitable Environments with Raman and Luminescence for Organics and Chemicals: PI Luther Beegle, NASA/JPL, Pasadena), and is comprised of deep UV neon-copper hollow-cathode laser excitation at 249 nm, which is designed to demonstrate induced fluorescence from elemental carbons and aromatic compounds, and the interrogation of pre-resonance

Raman spectra in the range 250–270 nm (Abbey et al. 2017; Beegle et al. 2015; Eshelma et al. 2019). With an instrument mass of 1.61 kg, and a laser spot size of 50 µm, it is planned to undertake rastering experiments on selected powdered samples. A feature of the Mars 2020 rover is the facility for caching specimens of the Martian regolith, at several points on its transect route, which will be collected by future Mars mission landers. The Mars 2020 rover will be the heaviest planned space rover vehicle on Mars, at 1050 kg, some 3.5 times heavier than the ESA/Roscosmos ExoMars 300 kg rover, named *Kazachok* (little Cossack), and significantly heavier than *Curiosity*, which was 900 kg in mass.

Both the Mars 2020 and ExoMars 2022 missions were originally scheduled to launch for Mars in July 2020, during the favorable Mars launch window between 17 July and 5 August 2020: the Mars 2020 mission landing site is in Jezero Crater (Western Isidis Basin, 18.379° N and 77.579° E) whereas that of ExoMars 2022 was in Oxia Planum (18.275° N and 335.368° E). Both are ancient geologically lacustrine deltaic sites containing old river channels and outflows, with considerable sedimentary depths of smectic clays and silicates, which are predicted to potentially harbor residual chemical traces of extinct or extant Martian life. The predicted landing date for the Mars 2020 mission is February 2021, after a seven-month journey from Earth and insertion into the Mars orbit.

Although the SHERLOC instrument is a dedicated Raman instrument on Mars 2020, which will have UV-Raman dedicated excitation at 249 nm, another Raman instrument is included in the SuperCam instrument package mentioned earlier, with a pulsed 532 nm wavelength laser. This is a different concept altogether and comprises a miniaturized time-resolved Raman spectrometer (TRRS) (Angel et al. 2012; Garsda et al. 2015; Blacksberg et al. 2016), which is designed to circumvent the LIF that is generated from geological materials, especially those comprising clays with rare earth elements, which fluoresce strongly under visible excitation (Misra et al. 2016; Perez et al. 2016; Wiens et al. 2017). Also, organic- and biomolecules generate short-lived fluorescence, which can be addressed by the use of TRRS and pulsed laser excitation, which will be required to achieve good spectral quality. From an earlier paper advocating optical heterodyne spectroscopy (Gomer et al. 2011) with gated detection, which reduces the need for a narrow spectrometer slit, and resulting in the maximum throughput of low-light intensities, a recent paper (Egan et al. 2020) has developed this into a miniaturized one-mirror, one-grating spatial heterodyne spectrometer for remote Raman sensing, which lends itself to application in planetary science.

### 17.2.6 Terrestrial Extremophilic Sites: Mars Analogues

Although it is appreciated that the environmental conditions on Mars are probably much more extreme than any found on Earth, the search for life signatures in the Martian regolith inherently depends upon the identification of specific biomarkers that have been produced by the extremophilic colonization of comparator terrestrial geological niche environments that are to be found in terrestrial Mars analogue sites. A comprehensive list of these sites that have been investigated by Raman spectroscopy is now emerging from the literature, and a wide range of instrumentation and protocols has been adopted for spectroscopic site investigation, from the sampling of specimens for study in the laboratory using benchtop instrumentation, to the adoption of in-field miniaturized spectroscopic instrumentation for the direct interrogation of specimens *in situ* where appropriate.

Several of these sites and their associated Raman spectroscopic measurements have been described in detail in a special issue (Jehlička and Edwards 2014) of the *Philosophical Transactions of the Royal Society* published in 2014, and edited by the present authors, in which some 15 papers on the Raman spectroscopy of extremophiles in several Mars analogue sites have been collected and described. This will provide the reader with a good summary of the type of information and spectral data that emerge from such experiments for the identification of biogeomarkers and biomarker molecules, along with associated geomarkers in real bio-geo systems. This will be seen to be vital for the diagnostic ability of analytical spectroscopy in furtherance of the search for life experimental scenarios, and for the remote planetary instrumentation envisaged for forthcoming decades, particularly in advance of proposed human space missions in our solar system.

### 17.2.6.1 The Atacama Desert

The Atacama Desert has been described as one of the oldest and driest deserts on Earth, with a superficial covering that can be compared to the Martian one during its transit to desertification (Dose et al. 2001; Wierzchos et al. 2011). The Atacama Desert is an excellent extremely dry area for learning about survival of extremophilic microorganisms of various phylae (lichens, cyanobacteria, algae) in different rocks and surface soil crusts. Several studies focus on such environments in astrobiological context. How to learn about detecting traces of life in rocks? How to deepen knowledge of different mineralogical niches hiding extremophile life? Is Raman spectroscopy well adopted for this as suggested in two next missions to Mars? Several studies used laboratory-based Raman microspectrometric instrumentation to gather details on biomarkers, pigments, as well as mineralogy of selected specimens (e.g Villar et al. 2005). However, Vitek et al. (2012a) applied 1064 nm excitation in a miniaturized system to detect biosignatures of epilithic lichen species, and for a preliminary survey of endolithic microbial communities in halite pinnacles from the Atacama Desert. In another study, it was shown that portable Raman devices are well adapted for analysis and detection of pigments of different chemistry in rock specimens (halite); 532 nm excitation was suggested as preferential to 785 nm excitation for bulk analysis for organic spectral signatures, due to its exceptional sensitivity toward carotenoids, while 785 nm excitation was preferred for detection of scytonemin directly on the rock without any pretreatment (Vitek et al. 2012b). As documented before, the precise focusing on the particular cell aggregates became a key requirement for obtaining any signal. Comparisons show both excellent results obtained on rock specimens and powdered samples. Other sites investigated include several dry saline lakes in California (Deep Springs Lake, Owens Lake, Searles Lake). Again also here the detection of carotenoid signals in evaporitic specimens may be achieved without any advanced handling, and proved to be stable through replicated measurements (Vitek et al. 2014). This was confirmed for studying the powdered and homogenized samples, and also for the direct analyses on the rocks containing homogeneous spatial distribution of microbial cells. On the other hand, the original spatial distribution of microbes at micrometric level within the rocks is lost through homogenization, and this may cause a decrease in the intensity of the Raman signal. Few other studies report on the application of portable or transportable Raman devices to study pigments in other dry extreme native environments. Miralles et al. (2012) have shown how portable Raman spectrometers (785 nm) can be used for detection of biomolecules including pigments of lichens (Tabernas, Spain). However, in their study, the instrument did not enable detection of carotenoids (nor other UV-protective pigments) of cyanobacteria.

### 17.2.6.2 Salterns

Saltern ponds allow the study of halophilic ecosystems, which develop under different salinities in individual sites. Bottom gypsum crust with stratified microbial communities colored by the presence of different types of cyanobacteria, and purple sulfur bacteria, were sampled from the bottom of an evaporation pond in Eilat (Israel). Massive blocks of crystalline gypsum crusts with well-developed colonizations were obtained, Raman spectra were recorded from small pieces (millimeter diameter) of colored crystalline material. It was found that a handheld Raman spectrometer can record spectra of carotenoids occurring in microorganisms in a solid natural mineral matrix. Cyanobacteria of the Halothece-type colonize the superficial part of the mat, and are the cause of the orange coloration; below, a layer of green filamentous *Phormidium*-type cyanobacteria can be found, and finally, a bright red-purple layer of anoxygenic phototrophs is present in the deeper parts. It was shown previously that myxoxanthophyll and echinenone (and minor amounts of chlorophyll a, phaeophytin, zeaxanthin, and canthaxanthin) are present in the orange parts of the mat (Oren et al. 1995). Myxoxanthophyll, echinenone, and phycocyanin (with minor contributions of phaeophytin-a and chlorophyll-a) dominate the green layer, and spirilloxanthin and bacteriochlorophyll-a are the main pigments of the halophilic anoxygenic phototrophs in the deeper red layer. Raman bands at 1510, 1152, 1006 cm<sup>-1</sup> and 1513, 1153, 1005 cm<sup>-1</sup> were recorded in different parts of the orange layer, and the green colonization is characterized by Raman bands at 1509, 1150, and 1003 cm<sup>-1</sup>. Chlorophyll-a and phycocyanin, expected in the green layer, were not detected with the green excitation used in this study (Jehlička and Oren 2013). These pigments

can potentially be identified using other excitations (785 nm). Unfortunately, the native samples from the gypsum mats investigated contain polysaccharide slime, which induces important fluorescence using the 785 nm lasers, prohibiting recording faint signals of the pigments. Raman spectra of the red layer contain major bands at 1510, 1151, and 1004 cm<sup>-1</sup>. Because of the colonization of the red layer by *Ectothiorhodospira/Halorhodospira* and *Halochromatiumlike* purple sulfur bacteria, spirilloxanthin-like carotenoids are expected to occur in these parts of the mat. In fact, the main Raman bands recorded on the cultivated strain of *Ectothiorhodospira* are 1510, 1149, and 1002 cm<sup>-1</sup>, which is very close to those of the red layer gypsum; these bands correspond to spirilloxanthin (Jehlička and Oren, 2013).

#### 17.2.6.3 Snow Algae

Isolated snowfields in high mountains or snowfields in the frame of glaciers are a specific environment for psychophilic extremophilic microorganisms. These are not considered Martian analogues (probably because they are not considered to be geological environments), however even on Mars extensive water ice deposits in the form of polar ice caps are present. Moreover, there are other candidates for search for life in our solar system, the so-called icy worlds. These are moons of giant planets such as Europa, Enceladus, or Titan, whose surface is covered mostly with water ice. On Earth during the spring or summer months the snow algae in some localities reach the phase in their life cycle when they start to accumulate substantial amounts of UV-protecting carotenoid pigments and can be observed as reddish coloration of snow, the prominent “red snow” phenomenon. Jehlička et al. (2016) performed in situ analyses of snow algae in the snowfields at Luční hora, Krkonoše, Czech Republic, and at the Rettenbach Glacier, Austria during the spring and early summer. At this time of the year, the algae *Chloromonas nivalis* and *Chlamydomonas nivalis* (Chlamydomonadales, Chlorophyta) produce the UV-protecting secondary carotenoid pigment astaxanthin, in addition to other carotenoids, such as β-carotene utilized in the process of photosynthesis. A handheld Raman spectrometer equipped with 532 nm excitation was used for the analyses, and enabled the acquisition of resonance Raman spectra of carotenoid pigments. The downshift of the ν<sub>1</sub>(C=C) band was documented between the flagellate and cyst forms of *Chloromonas nivalis*, illustrating the increased concentration of the pigment astaxanthin present.

## 17.3 Conclusions

In summary, this chapter has reviewed the application of miniaturized Raman spectroscopic instrumentation for terrestrial geological field applications, which has demonstrated the feasibility of analyzing materials in situ and without the need for removal of specimens to study using laboratory fixed-base instrumentation. The ability to recognize the presence of materials of special interest has been well promoted in the area of forensic crime scene investigation where the advance warning of hazardous compounds and precursors for the synthesis of drugs, chemical warfare nerve agents, and explosives is vital for ensuing strategies for their containment. The adoption of such instrumentation for geological sites in inaccessible terrestrial areas is exemplified in hot and cold desert areas, several of which are regarded by astrobiologists and planetary geologists as comprising Mars analogue sites for the evaluation and development of the flight-like prototype Raman instruments, which will eventually be part of the analytical instrumental suites aboard planetary rover vehicles. This aspect of remote sensing instrumentation undoubtedly represents the most challenging application for remote Raman spectroscopy in future unmanned space missions to Mars, the first of which, NASA Mars 2020, has departed in July 2020 and is scheduled to arrive on Mars in early 2021. Originally, an ESA/Roscosmos mission, ExoMars 2020, was due to launch at the same time but setbacks have caused its rescheduling to 2022. Both missions have dedicated miniaturized Raman spectrometers aboard, which are designed to examine the surface and subsurface geology of the Martian rocks and regolith – in addition, the Mars 2020 mission will have a cache store for Martian specimens, including subsurface drill cores, which will be housed and saved for collection in a future NASA mission to Mars. Already, space agencies are planning more experiments involving advanced instrumentation, some including Raman spectroscopic techniques, for missions to the Moon, Venus, and the Jupiter satellites.

## Glossary

<b>Abiotically</b>	Abiotic process or material is a natural process or product of a process that does not involve a biological organism. However, even relatively complex organic compounds are known to be created abiotically in nature.
<b>Anoxygenic</b>	Means being or carrying out photosynthesis in which oxygen is not produced as a by-product.
<b>Archean</b>	Archean eon means the oldest eon of the Earth's history. It is one of the four geologic eons of Earth history, occurring between 4 and 2.5 billion years ago. During the Archean, the Earth's crust had cooled enough to allow the formation of continents and life began its development. By the end of the Archean c. 2.5 billion years ago, plate tectonic activity may have been similar to that of the modern Earth.
<b>Astrogeological</b>	Astrogeology or planetary geology studies geology of the solid bodies in the solar system such as terrestrial planets, moons, asteroids, etc.
<b>Autotrophic</b>	Autotroph is any organism capable of self-nourishment by using inorganic materials as a source of nutrients and using photosynthesis or chemosynthesis as a source of energy, as most plants and certain bacteria and protists, an organism that manufactures its own food from inorganic substances, such as carbon dioxide and ammonia. Most autotrophs, such as green plants, certain algae, and photosynthetic bacteria, use light for energy.
<b>Biotically</b>	Biotic process or material is a natural process or product of a process that involves a biological (living) organism.
<b>Chemolithotrophic</b>	Chemolithotrophic organisms obtain energy by the oxidation of suitable inorganic compounds such as reduced iron compounds, ammonia, nitrites, sulfides or elemental sulfur. They do not need a light source for this process. They can either fix carbon dioxide or use other source of carbon for biosynthesis.
<b>Deltaic</b>	Derived from the river delta, a body of sediment, which is deposited by the river where it reaches its mouth, and enters into sea or lake, for example, where it loses capability to transport sedimentary material. Typically used in a connection with the environment or sediment.
<b>Epilithic</b>	Means growing on the surface of rock without penetrating the rock substrate.
<b>Extremophilic</b>	Extremophilic organisms, i.e. extremophilic cyanobacteria. Organisms which cope with extremely hot (thermophiles), sour (acidophiles) or salty (halophiles) conditions, toxic substances like heavy metals also do them good and even give them energy.
<b>Lacustrine</b>	Denotes the environment within a lake; in a geological context the sedimentary rocks formed from sedimentation in the lake; these sediments are typically finer grained when compared to the deltaic sediments.
<b>Lithology</b>	Is a description of the rock type(s) at a given locality (outcrop). This description can be based on observation of physical properties of rocks by a geologist and typically leads to the classification of rocks into one of three major rock types: sedimentary, igneous, or metamorphic.
<b>Noachian</b>	A time period in the geological history of Mars. It occurred approximately between 4.1 and 3.7 billion year ago. A warmer and wetter period, with formation of water bodies, weathering, and extensive volcanic activity.
<b>Ordovician</b>	The Ordovician is a geologic period and system, the second of six periods of the Paleozoic Era. The Ordovician spans 41.6 Mya from the end of the Cambrian Period 485.4 Mya years and ended with the Ordovician–Silurian extinction events, about 443.8 Mya, which

	wiped out 60% of global marine genera. The Ordovician is best known for its diverse marine invertebrates, including graptolites, trilobites, brachiopods, and the conodonts.
<b>Palaeogeological</b>	Relates to palaeogeology. Palaeogeology is a branch of geoscience concerned with the study of geologic features exposed at the surface during a past epoch or period but now buried beneath rocks formed in subsequent time. If the map depicts the geological structure of the earth's surface during a period of geological past, it is called a palaeogeological map.
<b>Pegmatitic</b>	Relates to pegmatite, which is an igneous rock, formed underground, with interlocking crystals usually larger than 2.5 cm in size, which is an exceptionally coarse-grained igneous rock. Most pegmatites are composed of quartz, feldspar, and mica, having a similar composition as granite. Pegmatitic mica is a mica commonly occurring in pegmatites.
<b>Phototrophs</b>	Are those organisms that obtain their energy from sunlight, typically through photosynthesis.
<b>Regolith</b>	Regolith is the unconsolidated material above bedrock and comprises in situ and transported materials that have usually undergone some degree of weathering. It is present on Earth, the Moon, Mars, some asteroids, and other terrestrial planets and moons.
<b>Scytonemin</b>	Is a secondary metabolite and an extracellular sheath pigment synthesized by many strains of cyanobacteria (i.e. Nostoc, Scytonema, Calothrix, Lyngbya). This is a symmetrical indole alkaloid composed of fused heterocyclic monomers, connected through a carbon–carbon bond with a molecular weight of about 544 Da. It acts as protective compound against short-wavelength solar UV radiation.
<b>Smectic</b>	Smectites belong to a group of clay minerals, hydrated aluminum phyllosilicates, that form during weathering (in the presence of water) of other silicates rich in magnesium and iron such as olivine. They are an important part of soils on Earth and were also found on Mars.
<b>Speleothems</b>	(“Cave deposits”) are cave formations, secondary mineral deposits formed in a cave. Speleothems typically form in limestone, dolomite, marble, and less commonly gypsum solutional caves (it means formed in the soluble material).

## Acknowledgement

AC and JJ were partially supported by institutional funding from the Center for Geosphere Dynamics (UNCE/SCI/006) and by the Czech Science Foundation(GACR project no. 21-03322S).

## References

- Abbey, W., Bhartia, R., Beegle, L. et al. (2017). Deep UV Raman spectroscopy for planetary exploration: the search for *in situ* organics. *Icarus* 290: 204–214.
- Angel, S.M., Gomer, N.R., Sharma, S.K. et al. (2012). Remote Raman spectroscopy for planetary exploration: a review. *Applied Spectroscopy* 66: 137–150.
- Bedau, A. (2010). An Aristotelean account of minimal chemical life. *Astrobiology* 10: 1011–1020.
- Beegle, L., Bhartia, R., White, M. et al. (2015). SHERLOC: Scanning habitable environments with Raman and luminescence for organics and chemicals. *IEEE Aerospace Conference Proceedings*, June 2015, AERO.2015.7119105.

- Benn, D., Linnen, R., and Martins, T. (2019). Evaluating portable Raman spectrometers for use in exploration of pegmatite dikes, Wekusko Lake, Manitoba. *The Canadian Mineralogist* 57: 711–713.
- Benner, S.A. (2010). Defining life. *Astrobiology* 10: 1021–1030.
- Bishop, J.L., Aglen, B.L., Pratt, L.M. et al. (2004). A spectroscopic and isotopic study of sediments from the Antarctic dry valleys as analogues for potential palaeolakes on Mars. *International Journal of Astrobiology* 2: 273–287.
- Blacksberg, J., Alerstam, E., Maruyama, Y. et al. (2016). Miniaturised time-resolved Raman spectrometer for planetary science based on a fast single photon avalanche diode detector array. *Applied Optics* 55: 739–748.
- Brier, J.A., White, S.N., and German, C.R. (2010). Mineral-microbe interactions in deep-sea hydrothermal systems: a challenge for Raman spectroscopy. *Philosophical Transactions of the Royal Society A* 368: 3067–3086.
- Carter, E.A., Hargreaves, M.D., Kee, T.P. et al. (2010). A Raman spectroscopic study of a fulgurite. *Philosophical Transactions of the Royal Society A* 368: 3087–3098.
- Clark, B.C. (1998). Surviving the limits to life at the surface of Mars. *Journal of Geophysical Research* 103: 28545–28556.
- Cleland, C.E. and Chyba, C.F. (2002). Defining life. *Origins of Life and Evolution of Biospheres* 32: 387–393.
- Cockell, C.S. and Knowland, J.R. (1999). Ultraviolet screening compounds. *Biological Reviews* 74: 311–345.
- Crupi, V., Giunta, A., Kellett, B. et al. (2014). Handheld and non-destructive methodologies for the compositional investigation of meteorite fragments. *Analytical Methods* 6: 6301.
- Culka, A. and Jehlička, J. (2018). Sequentially shifted excitation: a tool for suppression of laser-induced fluorescence in mineralogical applications using portable Raman spectrometers. *Journal of Raman Spectroscopy* 49: 526–537.
- Culka, A. and Jehlička, J. (2019). A database of Raman spectra of precious gemstones and minerals used as cut gems obtained using portable sequentially shifted excitation Raman spectrometer. *Journal of Raman Spectroscopy* 50: 262–280.
- Culka, A., Jehlička, J., and Edwards, H.G.M. (2010). Acquisition of Raman spectra of amino acids using portable instruments: outdoor measurements and comparison. *Spectrochimica Acta A* 77: 978–983.
- Culka, A., Jehlička, J., Vandebaele, P. et al. (2011). The detection of biomarkers in evaporite matrices using a portable Raman instrument under alpine conditions. *Spectrochimica Acta A* 80: 8–13.
- Culka, A., Jehlička, J., and Strnad, L. (2012). Testing a portable Raman instrument: the detection of biomarkers in gypsum powdered matrix under gypsum crystals. *Spectrochimica Acta A* 86: 347–350.
- Culka, A., Košek, F., Drahota, P. et al. (2014). Use of miniaturized Raman spectrometer for detection of sulfates of different hydration states – significance for Mars studies. *Icarus*: 440–453.
- Culka, A., Kindlová, H., Drahota, P. et al. (2016). Raman spectroscopic identification of arsenate minerals *in situ* at outcrops with handheld (532 nm, 785 nm) instruments. *Spectrochimica Acta A* 154: 193–199.
- Dickensheets, D.L., Wynn-Williams, D.D., Edwards, H.G.M. et al. (2000). A novel miniature confocal Raman spectrometer system for biomarker analysis on future Mars missions after Antarctic trials. *Journal of Raman Spectroscopy* 31: 633–635.
- Doran, P.T., Wharton, R.A.J., des Marais, D.J. et al. (1998). Antarctic palaeolake sediments and the search for extinct life on mars. *Journal of Geophysical Research, Planets* 103: 28481–28488.
- Dose, K., Bieger-Dose, A., Ernst, B. et al. (2001). Survival of microorganisms under the extreme conditions of the Atacama Desert. *Origins of Life and Evolution of Biospheres* 31: 287–303.
- Edwards, H.G.M. (2004). Raman spectroscopic protocol for the molecular recognition of key biomarkers in astrobiological exploration. *Origins of Life and Evolution of Biospheres* 34: 3–11.
- Edwards, H.G.M. (2010). Raman spectroscopic approach to analytical astrobiology: the detection of key geological and biomolecular markers in the search for life. *Philosophical Transactions of the Royal Society A* 368: 3059–3066.
- Edwards, H.G.M. and Newton, E.M. (1999). Applications of Raman spectroscopy for exobiological prospecting. In: *The Search for Life on Mars* (ed. J.A. Hiscox), 75–83. London: British Interplanetary Society.
- Edwards, H.G.M., Russell, N.C., and Wynn-Williams, D.D. (1997). Fourier-transform Raman spectroscopic and scanning electron microscopic study of cryptoendolithic lichens from Antarctica. *Journal of Raman Spectroscopy* 30: 685–690.

- Edwards, H.G.M., Moody, C.D., Jorge Villar, S.E. et al. (2005). Raman spectroscopic detection of key biomarkers of cyanobacteria and lichen symbiosis in extreme Antarctic habitats: evaluation for Mars lander missions. *Icarus* 174: 560–571.
- Edwards, H.G.M., Sadooni, F., Vítek, P. et al. (2010). Raman spectroscopy of the Dukhan sabkha: identification of geological and biogeological molecules in an extreme environment. *Philosophical Transactions of the Royal Society A* 368: 3099–3108.
- Edwards, H.G.M., Hutchinson, I.B., and Ingleby, R. (2012). The ExoMars Raman spectrometer and the identification of biogeological spectroscopic signatures using a flight-like prototype. *Analytical and Bioanalytical Chemistry* 404: 1723–1731.
- Edwards, H.G.M., Hutchinson, I.B., Ingleby, R. et al. (2014). Biomarkers and their Raman spectroscopic signatures: a spectral challenge for analytical astrobiology. *Philosophical Transactions of the Royal Society A* 372: 20140193.
- Egan, M.J., Acosta-Maeda, T.E., Angel, S.M. et al. (2020). One mirror, one grating spatial heterodyne spectrometer for remote sensing Raman spectroscopy. *Journal of Raman Spectroscopy* 51 <https://doi.org/10.1002/jrs5788>.
- Eigenbrode, J.L., Summons, R.E., Steele, A. et al. (2018). Organic matter preserved in 3 billion-year-old mudstones at Gale crater, Mars. *Science* 360: 1096–1101.
- Ellery, A. and Wynn-Williams, D.D. (2003). Why Raman spectroscopy on Mars? A case of the right tool for the right job. *Astrobiology* 3: 565–579.
- Eshelma, E., Malaska, M., Manatt, K. et al. (2019). *In Situ* organic detection in subsurface ice using deep UV fluorescence spectroscopy. *Astrobiology* 19: 771–784.
- Farmer, J.D. and des Marais, D.J. (1999). Exploring for a record of ancient Martian life. *Journal of Geophysical Research* 104: 26977–26995.
- Flahaut, J., Bishop, J.L., Silvestro, S. et al. (2019). The Italian Solfatara as an analog for Mars fumarolic alteration. *American Mineralogist* 104: 1565–1577.
- Freissinet, C., Glavin, D.P., Mahaffy, P.R. et al. (2015). Organic molecules in the Sheepbed mudstone, Gale crater, Mars. *Journal of Geophysical Research Planets* 120: 495–514.
- Garsda, P.J., Acosta-Maeda, T.E., Lucey, P.G. et al. (2015). Next generation laser-based standoff spectroscopic techniques for Mars exploration. *Applied Spectroscopy* 69: 173–192.
- Gázquez, F., Rull, F., Sanz-Arranz, A. et al. (2017). *In situ* Raman characterization of minerals and degradation processes in a variety of cultural and geological heritage sites. *Spectrochimica Acta A* 172: 48–57.
- Gomer, N.R., Gordon, C.M., Lucey, P.G. et al. (2011). Raman spectroscopy using a spatial heterodyne spectrometer. Proof of concept. *Applied Spectroscopy* 65: 849–857.
- Grady, M.M., Verchovsky, A.B., and Wright, I.P. (2004). Magmatic carbon in Martian meteorites: attempts to constrain the carbon cycle on Mars. *International Journal of Astrobiology* 3: 117–124.
- Jehlička, J. and Culka, A. (2010). Raman spectra of nitrogen-containing organic compounds obtained using a portable instrument at –15 degrees C at 2860 m above sea level. *Journal of Raman Spectroscopy* 41: 537–542.
- Jehlička, J. and Edwards, H.G.M. (2014). Raman spectroscopy meets extremophiles on earth and Mars: studies for successful search of life. *Philosophical Transactions of the Royal Society A* 372: 20140207.
- Jehlička, J. and Oren, A. (2013). Use of a handheld Raman spectrometer for fast screening of microbial pigments in cultures of halophilic microorganisms and in microbial communities in hypersaline environments in nature. *Journal of Raman Spectroscopy* 44: 1285–1291.
- Jehlička, J. and Vandenebeele, P. (2015). Evaluation of portable Raman instruments with 532 and 785-nm excitation for identification of zeolites and beryllium containing silicates. *Journal of Raman Spectroscopy* 46: 927–932.
- Jehlička, J., Vítek, P., Edwards, H.G.M. et al. (2009a). Application of portable Raman instruments for fast and non-destructive detection of minerals on outcrops. *Spectrochimica Acta A* 73: 410–419.
- Jehlička, J., Vítek, P., Edwards, H.G.M. et al. (2009b). Fast detection of sulphate minerals (gypsum, anglesite, baryte) by a portable Raman spectrometer. *Journal of Raman Spectroscopy* 40: 1082–1086.

- Jehlička, J., Vítek, P., Edwards, H.G.M. et al. (2009c). Rapid outdoor non-destructive detection of organic minerals using a portable Raman spectrometer. *Journal of Raman Spectroscopy* 40: 1645–1651.
- Jehlička, J., Vandenabeele, P., Edwards, H.G.M. et al. (2010a). Raman spectra of pure biomolecules obtained using a hand-held instrument under cold, high-altitude conditions. *Analytical and Bioanalytical Chemistry* 397: 2753–2760.
- Jehlička, J., Edwards, H.G.M., and Culka, A. (2010b). Using portable Raman spectrometers for the identification of organic compounds at low temperatures and high altitudes: exobiological applications. *Philosophical Transactions of the Royal Society A* 368: 3109–3125.
- Jehlička, J., Culka, A., and Edwards, H.G.M. (2010c). Raman spectra of nitrogen-containing organic compounds obtained in high altitude sites using a portable spectrometer: possible application for remote robotic titan studies. *Planetary and Space Science* 58: 875–881.
- Jehlička, J., Culka, A., Vandenabeele, P. et al. (2011). Critical evaluation of a handheld Raman spectrometer with near infrared (785 nm) excitation for field identification of minerals. *Spectrochimica Acta A* 80: 36–40.
- Jehlička, J., Vandenabeele, P., and Edwards, H.G.M. (2012). Discrimination of zeolites and beryllium containing silicates using portable Raman spectroscopic equipment with near-infrared excitation. *Spectrochimica Acta A* 86: 341–346.
- Jehlička, J., Culka, A., and Nedbalová, L. (2016). Colonization of snow by microorganisms as revealed using miniature Raman spectrometers - possibilities for detecting carotenoids of psychrophiles on Mars? *Astrobiology* 16: 913–924.
- Jehlička, J., Culka, A., Bersani, D. et al. (2017a). Comparison of seven portable Raman spectrometers: beryl as a case study. *Journal of Raman Spectroscopy* 48: 1289–1299.
- Jehlička, J., Culka, A., and Košek, F. (2017b). Obtaining Raman spectra of minerals and carbonaceous matter using a portable sequentially shifted excitation Raman spectrometer - a few examples. *Journal of Raman Spectroscopy* 48: 1583–1589.
- Jorge-Villar, S.E. and Edwards, H.G.M. (2005). Raman spectroscopy in astrobiology. *Analytical and Bioanalytical Chemistry* 384: 100–113.
- Jorge-Villar, S.E. and Edwards, H.G.M. (2010). Raman spectroscopy of volcanic lavas and inclusions of relevance to astrobiological exploration. *Philosophical Transactions of the Royal Society A* 368: 3127–3136.
- Kong, W.G., Zheng, M.P., Kong, F.J. et al. (2014). Sulfate-bearing deposits at Dalangtan playa and their implication for the formation and preservation of Martian salts. *American Mineralogist* 99: 283–290.
- Košek, F., Culka, A., Drahota, P. et al. (2017a). Applying portable Raman spectrometers for field discrimination of sulfates: training for successful extraterrestrial detection. *Journal of Raman Spectroscopy* 48: 1085–1093.
- Košek, F., Culka, A., and Jehlička, J. (2017b). Field identification of minerals at burning coal dumps using miniature Raman spectrometers. *Journal of Raman Spectroscopy* 48: 1494–1502.
- Lalla, E.A., Sanz-Arranz, A., Lopez-Reyes, G. et al. (2016). Raman-Mössbauer-XRD studies of selected samples from “Los Azulejos” outcrop: a possible analogue for assessing the alteration processes on Mars. *Advances in Space Research* 57: 2385–2395.
- Lin, Y., Goresy, A.E., Hu, S. et al. (2014). NanoSIMS analysis of organic carbon from the Tissint Martian meteorite: evidence for the past existence of subsurface organic-bearing fluids on Mars. *Meteoritics and Planetary Science* 49: 2201–2218.
- Malherbe, C., Hutchinson, I.B., McHugh, M. et al. (2019). Minerals and microstructure identification using Raman instruments: evaluation of field and laboratory data in preparation for space mission. *Journal of Raman Spectroscopy* <https://doi.org/10.1002/jrs.5685>.
- Marshall, C.P. and Olcott Marshall, A. (2010). The potential of Raman spectroscopy for the analysis of diagenetically transformed carotenoids. *Philosophical Transactions of the Royal Society A* 368: 3137–3144.
- Marshall, C.P. and Olcott Marshall, A. (2015). Challenges analyzing gypsum on Mars by Raman spectroscopy. *Astrobiology* 15: 761–769.
- Marshall, C.P., Edwards, H.G.M., and Jehlička, J. (2010). Understanding the application of Raman spectroscopy to the detection of traces of life. *Astrobiology* 10: 229–243.

- McKay, C.P. (1997). The search for life on Mars. *Origins of Life and Evolution of Biospheres* 27: 263–289.
- Miralles, I., Jorge-Villar, S.E., Canton, Y. et al. (2012). Using a mini-Raman spectrometer to monitor the adaptive strategies of extremophile colonizers in arid deserts: relationships between signal strength, adaptive strategies, solar radiation, and humidity. *Astrobiology* 12: 743–753.
- Misra, A.K., Acosta-Maeda, T.E., Sharma, S.K. et al. (2016). “Standoff biofinder” for fast, noncontact, nondestructive, large-area detection of biological materials for planetary exploration. *Astrobiology* 16: 715–729.
- Olcott Marshall, A. and Marshall, C.P. (2013). Field-based Raman spectroscopic analyses of an Ordovician stromatolite. *Astrobiology* 13: 814–820.
- Oren, A., Kühl, M., and Karsten, U. (1995). An endoevaporitic microbial mat within a gypsum crust: zonation of phototrophs, photopigments, and light penetration. *Marine Ecology Progress Series* 128: 151–159.
- Perez, R., Pares, L., Newell, R., Robinson, S. et al. (2016). The SuperCam instrumento on the NASA 2020 Mars missión – optical design and performance. *International Conference on Space Optics ICSO-2016*(eds. B. Cugny, N. Korafolios, and Z. Sodnik). *Proceedings SPIE*, 10562; 105622K/1–9.
- Pullan, D., Hofmann, B.A., Westall, F. et al. (2008). Identification of morphological biosignatures in Martian analogue field specimens using *in situ* planetary instrumentation. *Astrobiology* 8: 119–156.
- Rull, F., Delgado, A., and Martinez-Frias, J. (2010a). Micro-Raman spectroscopic study of extremely large atmospheric ice conglomerations (megacryometeors). *Philosophical Transactions of the Royal Society A* 368: 3145–3152.
- Rull, F., Munoz-Espadas, M.J., Lunar, R. et al. (2010b). Raman spectroscopic study of four Spanish shocked ordinary chondrites: canellas, Olmedilla de Alarcon, Reliegos and Olivenza. *Philosophical Transactions of the Royal Society A* 368: 3153–3166.
- Sharma, S.K., Misra, A.K., Clegg, S.M. et al. (2010). Time-resolved remote Raman study of minerals under supercritical CO<sub>2</sub> and high temperatures relevant to Venus exploration. *Philosophical Transactions of the Royal Society A* 368: 3167–3191.
- Steele, A., McCubbin, F.M., Fries, M.D. et al. (2012). Graphite in the Martian meteorite Allan Hills 84001. *American Mineralogist* 97: 1256–1259.
- Summons, R., Amend, J.P., Bish, D. et al. (2011). Preservation of Martian organic and environmental records. *Astrobiology* 11: 157–181.
- Tirard, S., Morange, M., and Lazcano, A. (2010). The definition of life: a brief history of elusive scientific Endeavour. *Astrobiology* 10: 1003–1009.
- Treado, P.J. and Truman, A. (1996). Laser Raman spectroscopy. *Point Clear Exobiology Instrumentation Workshop*(eds. T.J. Wdowiak, and D.G. Agresti) (1996), pp. 7–10. Birmingham, AL, USA: University of Alabama Press.
- Vandenabeele, P., Jehlička, J., Vítek, P. et al. (2012). On the definition of Raman spectroscopic detection limits for the analysis of biomarkers in solid matrices. *Planetary and Space Science* 62: 48–54.
- Varnali, T. and Edwards, H.G.M. (2010). *Ab initio* calculations of scytonemin derivatives of relevance to extremophile characterisation by Raman spectroscopy. *Philosophical Transactions of the Royal Society A* 368: 3193–3204.
- Villar, S.E.J., Edwards, H.G.M., and Seaward, M.R.D. (2005). Raman spectroscopy of hot desert, high altitude epilithic lichens. *Analyst* 130: 730–737.
- Vítek, P., Edwards, H.G.M., Jehlička, J. et al. (2010). Microbial colonization of halite from the hyper-arid Atacama Desert studied by Raman spectroscopy. *Philosophical Transactions of the Royal Society A* 368: 3205–3221.
- Vítek, P., Edwards, H.G.M., Jehlička, J. et al. (2011). Evaluation of portable Raman instrumentation for identification of β-carotene and mellitic acid in two-component mixtures with halite. *Spectrochimica Acta A* 80: 32–35.
- Vítek, P., Ali, E.M.A., Edwards, H.G.M. et al. (2012a). Evaluation of portable Raman spectrometer with 1064 nm excitation for geological and forensic applications. *Spectrochimica Acta A* 86: 320–327.
- Vítek, P., Jehlička, J., Edwards, H.G.M. et al. (2012b). The miniaturized Raman system and detection of traces of life in halite from the Atacama desert: some considerations for the search for life signatures on Mars. *Astrobiology* 12: 1095–1099.

- Vítek, P., Jehlička, J., Edwards, H.G.M. et al. (2014). Miniaturized Raman instrumentation detects carotenoids in Mars-analogue rocks from the Mojave and Atacama deserts. *Philosophical Transactions of the Royal Society A* 372: 20140196.
- Webster, C.R., Mahaffy, P.R., Atreya, S.K. et al. (2015). Mars methane detection and variability at Gale crater. *Science* 347: 415–417.
- Webster, C.R., Mahaffy, P.R., Atreya, S.K. et al. (2018). Background levels of methane in Mars' atmosphere show strong seasonal variation. *Science* 360: 1093–1096.
- Westall, F. and Cavalazzi, B. (2011). Biosignatures in rocks. In: *Encyclopaedia of Geobiology* (eds. V. Thiel and J. Reitner), 189–201. Berlin: Springer.
- Westall, F., Foucher, F., Bost, N. et al. (2015). Biosignatures on Mars: what, where and how? Implications for the search for Martian life. *Astrobiology* 15: 1–32.
- Wiens, R.C., Maurice, S., and Perez, F.R. (2017). The SuperCam remote sensing instrument suite for the Mars 2020 rover: a preview. *Spectroscopy* 22: 50–55.
- Wierzchos, J., Camara, B., De Los Ríos, A. et al. (2011). Microbial colonization of Ca-sulfate crusts in the hyperarid core of the Atacama Desert: implications for the search for life on Mars. *Geobiology* 9: 44–60.
- Wynn-Williams, D.D. (1991). Cyanobacteria in deserts-life at the limit? In: *The Ecology of Cyanobacteria: Their Diversity in Time and Space* (eds. B.A. Whitton and M. Potts), 341–366. Dordrecht, The Netherlands: Kluwer Academic Press.
- Wynn-Williams, D.D. (1999). Antarctica as a model for ancient mars. In: *The Search for Life on Mars* (ed. J.A. Hiscox), 49–57. London: British Interplanetary Society.
- Wynn-Williams, D.D. and Edwards, H.G.M. (2000a). Antarctic ecosystems as models for extraterrestrial surface habitats. *Planetary and Space Science* 48: 1065–1075.
- Wynn-Williams, D.D. and Edwards, H.G.M. (2000b). Proximal analysis of regolith habitats and protective biomolecules *in situ* by laser Raman spectroscopy: overview of terrestrial Antarctic habitats and Mars analogs. *Icarus* 144: 486–503.
- Wynn-Williams, D.D. and Edwards, H.G.M. (2002). Environmental UV-radiation: biological strategies for protection and avoidance. In: *Astrobiology: The Quest for the Origins of Life* (eds. G. Horneck and C. Baumstark-Khan), 245–260. Berlin: Springer-Verlag.

## 18

# Hyperspectral Proximal Sensing Instruments and Their Applications for Exploration Through Cover

*Carsten Laukamp, Monica LeGras and Ian Christopher Lau*

*CSIRO Minerals Resources, Australian Resources Research Centre, Kensington, WA, Australia*

## 18.1 Introduction

Field and drill core hyperspectral sensing technologies can be used to cost-effectively and objectively characterize mineralogy, which can then be turned into higher level geoscience products (e.g. bedrock lithology and regolith stratigraphy, Laukamp et al. 2015a; alteration mineral patterns, Burley et al. 2017). Large amounts of data can be quickly collected to (i) identify mineralogical trends (e.g. vectoring toward mineral deposits during exploration), and (ii) map mineralogical domains, aiding ore body knowledge. Objective sample and drill core logging data derived from hyperspectral sensing technologies increases the reliability of the lithological logging codes, which can be extremely subjective, especially in regolith environments (i.e. unconsolidated rock material atop bedrock). It also allows geologists to undertake resource modeling from the collected spectral data.

The aim of this chapter is to provide examples for applying field and drill core hyperspectral sensing technologies to exploration and mining challenges. For this, technical specifications of currently available hyperspectral field and drill core sensors are summarized, and important considerations for the acquisition of high-quality data described. This is followed by brief case studies that describe experiences with these instruments in real-life situations, and demonstrate their huge potential for applications in exploration through cover.

Reflectance spectroscopy has been used for characterizing rock-forming minerals since the mid-twentieth century (e.g. Hunt and Turner 1953; Keller et al. 1952), and progressed due to increased interest in remote sensing and space exploration (e.g. Lyons 1962). Numerous published summaries of mineral reflectance spectra have demonstrated the potential for rapid mineral characterization using reflectance spectroscopy (e.g. Bishop et al. 2008; Clark et al. 1990; Hunt 1977). However, the last comprehensive summary of infrared functional groups of minerals was published by Farmer in 1974. The advent of commercially available handheld spectrometers, such as the Portable Infrared Mineral Analyzer (PIMA, Integrated Spectronics Pty Ltd.) and Analytical Spectral Devices FieldSpec (“ASD”, now Malvern Panalytical) in the 1990s was a major game changer for the exploration and mining industry, as it enabled real-time mineralogical analysis in the field and on mine sites. This was followed by the development of hyperspectral drill core sensors in the early 2000s (e.g. Schodlok et al. 2016), which are now successfully utilized by industry and government agencies (Huntington 2016). The increasing availability of portable and desktop Fourier transform infrared (FTIR) spectrometers at commercial laboratories across the world complements the large fleet of hyperspectral proximal sensing instruments.

Handheld and drill core hyperspectral technologies acquire reflectance spectra in different wavelength regions. Hence, an understanding of which mineral groups are active in each wavelength range is paramount. A summary of commonly commercially available hyperspectral proximal sensing instruments shows that most sensors cover the visible–near infrared (VNIR) to shortwave infrared (SWIR) wavelength ranges from 350 to 2500 nm (28 570 to

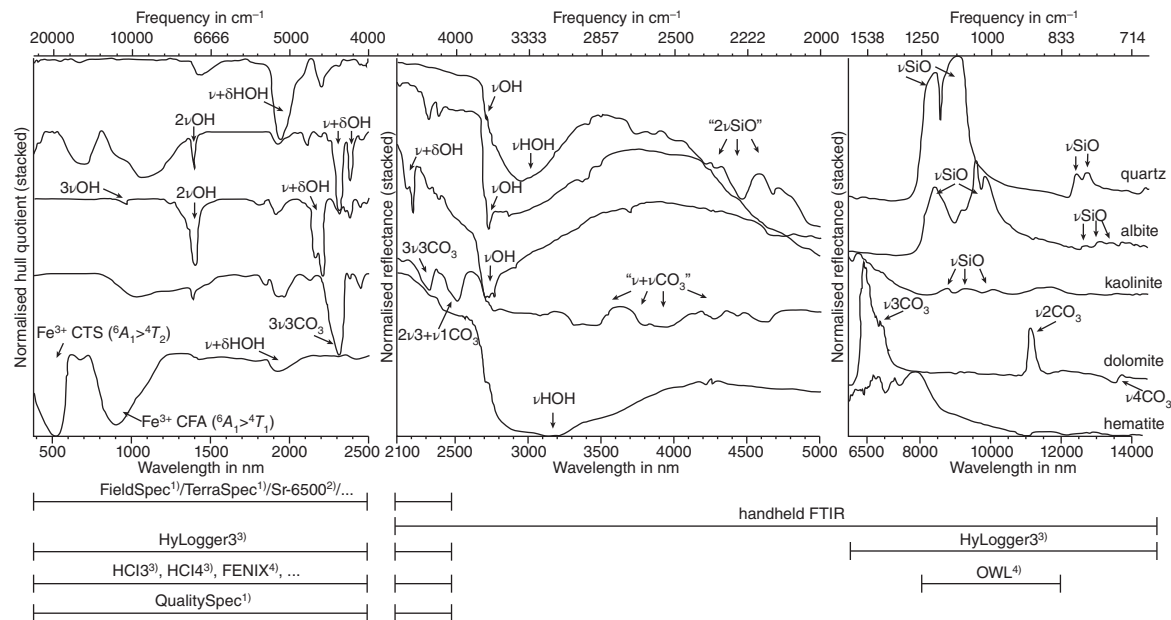


**Figure 18.1** Reflectance spectra of major rock-forming minerals in the 380–14 500 nm wavelength region ( $26\ 315\text{--}690\ \text{cm}^{-1}$ ) and wavelength coverage of example hyperspectral proximal sensing instruments (1) Malvern Panalytical, (2) Spectral Evolution, (3) Corescan Pty Ltd., (4) Specim, Spectral Imaging Ltd). Top left reflectance spectra were collected using a TerraSpec3. Top middle and top right reflectance spectra were collected using a handheld FTIR. Minerals from top to bottom are: quartz (LB1; pulverized; Lucky Bay, Western Australia); albite (Z49149; granules; location unknown); kaolinite (KGa-1b; powder; Georgia, U.S.A.); dolomite (MT8327; granules; Thornwood, New York, U.S.A.); hematite (C1; powder; synthetic). Infrared functional groups:  $\nu$  – fundamental stretching mode;  $2\nu/3\nu$  – first/second overtone of fundamental stretching mode;  $\delta$  – fundamental bending mode;  $\nu+\delta$  – combination band. Electronic absorptions: CFA – crystal field absorption; CTS – charge transfer absorption.

4000 cm<sup>-1</sup>) (Figure 18.1). However, nominally anhydrous silicates, for example, are only active in the mid-wave infrared (MIR; 2500–6000 nm; 4000–1667 cm<sup>-1</sup>) and thermal infrared (TIR; 6000–15 000 nm; 1667–667 cm<sup>-1</sup>) wavelength regions. In addition, certain mineral assemblages produce spectral signatures where major mineral components overlap considerably. An example is the combined SWIR spectral signatures of white mica and chlorite, which can mimic a spectral signature reminiscent of carbonates (see the discussion and figure later in this chapter). In this case, the addition of spectral information from the TIR wavelength region, where carbonates and sheet silicates can be easily discriminated, is required (Lampinen et al. 2019). In summary, the right hyperspectral sensor must be chosen to address the respective mineral exploration or mining challenge.

## 18.2 Field VNIR-SWIR Sensors

Field spectroradiometers covering the VNIR (350–1000 nm; 28 570–10 000 cm<sup>-1</sup>) and SWIR (1000–2500 nm; 10 000–4000 cm<sup>-1</sup>) target the mineral-specific absorption features active in this wavelength range, which are due to (i) electronic (charge transfer and crystal field absorptions) and/or (ii) vibrational absorption bands (largely combination and overtone bands of hydroxyl groups or carbonate complexes). The spectral resolution and signal-to-noise ratio (SNR) of common commercially available field spectrometers (Table 18.1) are comparable, and allow a fast characterization of minerals that are active in the respective wavelength ranges (Chang and Yang 2012). For the latest published overview of field hyperspectral sensors, the reader is referred to Milton et al. (2009).

**Table 18.1** Technical specifications of selected VNIR-SWIR field spectrometers often used for exploration and mining.

	PIMA (portable infrared mineral analyzer) <sup>a</sup>	FieldSpec/ TerraSpec 4 Standard-Res	FieldSpec/ TerraSpec 4 Hi-Res	TerraSpec halo mineral identifier	SR-6500	PSR+ 3500
Wavelength range	SWIR: 1300–2500 nm	VNIR-SWIR: 350–2500 nm				
Spectral resolution [values in nm]	600 channels at resolution	3 at 700; 10 at 1400; 10 at 2100	3 at 700; 8 at 1400; 8 at 2100	3 at 700; 9.8 at 1400; 8.1 at 2100	1.5 at 700; 3 at 1500; 3.8 at 2100	3 at 700; 6 at 1500; 6 at 2100
Measurement	Contact only	Viewing and contact probe		Contact only	Viewing and contact probe	
Weight	2.5 kg	5.44 kg	5.44 kg	2.5 kg	3.5 kg	3.5 kg
Company	Integrated Spectronics Pty Ltd.	Malvern Panalytical			Spectral evolution	

a) (No longer commercially available).

Preconditions for acquiring high-quality VNIR-SWIR reflectance spectra are the correct setup (including allowing time for the instrument to warm up and stabilize), and frequent calibration. A sintered polytetrafluoroethylene (PTFE, a.k.a. Spectralon™, National Institute of Standards and Technology [NIST]-traceable standard) is widely used as a white reference, and allows a straightforward comparison of reflectance spectra that relies on the concept of a reflectance factor introduced by Nicodemus et al. (1977). The reflectance factor is described as the “ratio of the radiant flux actually reflected by a sample surface to that which would be reflected into the same reflected-beam geometry by an ideal (lossless) perfectly diffuse (Lambertian) standard surface irradiated in exactly the same way as the sample.” Frequent calibration with a clean white reference (minimum every 10 minutes or less) is fundamental for achieving useable data. In the laboratory, the user also must take ambient lighting into account. For example, fluorescent lights will produce distinct mercury absorption lines in the VNIR that may significantly impact on the mineral spectral signature. This may be more evident when the sample surface is uneven and the measurement window cannot be completely filled by the sample. The reader is referred to Malthus et al. (2019) and Milton et al. (2009) for the workflow of collecting VNIR-SWIR reflectance spectra outdoors, and to Lau et al. (2017) as well as Ben Dor et al. (2015) for measurements in the laboratory.

There are no specific sample requirements other than that the analyzed material is dry, and nothing is between the sample material and the sensor (e.g. sample bag). Water is VNIR-SWIR active, and produces additional absorptions in the MIR, which will increasingly reduce the reflectance values from 1600 nm ( $6250\text{ cm}^{-1}$ ) to longer wavelengths (Figure 18.2). A VNIR-SWIR reflectance spectrum of a wet kaolinite (a 1:1 layer type, planar hydrous phyllosilicate; Guggenheim et al. 2006) shows the significant impact water has on the overall spectral shape and intense absorption bands at around 1400 nm ( $7143\text{ cm}^{-1}$ ) and 1900 nm ( $5265\text{ cm}^{-1}$ ). The hydroxyl-related combination bands of kaolinite in the SWIR at 2160 nm ( $4630\text{ cm}^{-1}$ ) and 2206 nm ( $4533\text{ cm}^{-1}$ ), which are commonly used for estimating kaolinite abundance, display a significantly different intensity when comparing the dry and wet sample measurements. As water is a major component of Earth’s atmosphere, measurements that utilize the sun as a source of electromagnetic radiation to illuminate the sample surface will render the 1400 and 1900 nm wavelength ranges useless. An example is the use of VNIR-SWIR sensors for ground validation of remote sensing

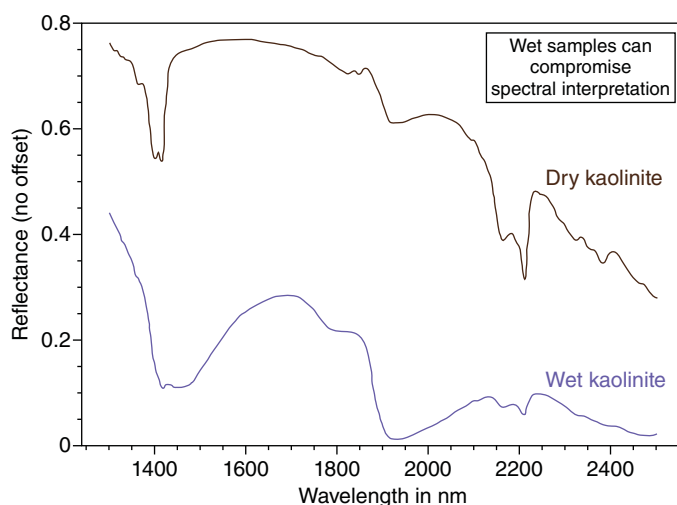


**Figure 18.2** VNIR-SWIR reflectance spectra of dry kaolinite and wet kaolinite, showing the significant impact of water on the spectral signature. Major water-related absorption features at around 1450 and 1950 nm result in broad troughs overlapping with the kaolin-related hydroxyl absorptions at around 1400 and 2200 nm. In addition, the major water-related absorption features in the mid-wave infrared at around 3000 nm result in an overall lower reflectance, especially toward the longer wavelengths in the SWIR.



**Figure 18.3** Examples for measuring surface samples in the field using a TerraSpec (Malvern-Panalytical) VNIR-SWIR field spectroradiometer. The left image (a), taken in the Mount Isa Inlier in Queensland, shows the researcher carrying the field spectrometer in a backpack and field viewing probe attached to monopod, which allows the researcher to acquire measurements over larger area, without being compromised by shadowing. The right image (b), taken in the Rocklea Inlier, Western Australia, shows the use of a contact probe that is attached to the end of monopod and allows reflectance measurements with minimal atmospheric impact. *Source:* Carsten Laukamp.

data, which may require the acquisition of a circa 1 m<sup>2</sup> surface area (including vegetation) attached to a telescope stick if no special fore-optics are used (Figure 18.3).

Good-quality reflectance spectra can be acquired from rock samples, but also rock chips and soils or powders. However, grain size differences can impact the VNIR-SWIR spectral signatures significantly. This is evident in hemispherical reflectance measurements of a set of quartz–kaolinite mixtures, using 11 different quartz grain size fractions (38–1000 µm) and kaolinite standard KGa-1b (<2 µm). Reflectance spectra spanning the 2000–16 000 nm (5000–625 cm<sup>-1</sup>) wavelength range were obtained by Laukamp et al. (2018) from the mineral mixtures using a Bruker Vertex FTIR equipped with an integrating sphere (A 562-G, Bruker) and HgCdTe (MCT) detector. Albeit quartz is not infrared-active in the SWIR, a specific range of quartz grain sizes has a substantial impact on the intensity of these kaolinite-related absorptions, with finer quartz grain sizes having the least, and grain size ranges between 125 and 1000 nm having the largest, impacts (Figure 18.4).

VNIR-SWIR field sensors are versatile, easy to use and complement other field instruments such as portable X-ray fluorescence (pXRF). However, an appropriate measurement setup and workflow is required, designed for the respective sample material. A recent review about using VNIR-SWIR reflectance spectroscopy in digital soil mapping (pedometrics) was given by Fang et al. (2018), summarizing recent efforts for predicting soil organic carbon (SOC), pH and moisture using partial least squares regression (PLSR) from spectral measurements on soils. Noble et al. (2019) combined a whole suite of field sensors, including reflectance spectroscopy, applied to green-fields exploration in Western Australia and developed a workflow called UltraFine+™ that provides a wide range of data to support mineral exploration using soil and regolith samples, including 40 elements, spectral mineralogy, particle size distribution, pH, and specific surface area.

In addition to mineralogical analysis of regolith materials (e.g. Lau et al. 2003), applications of VNIR-SWIR sensors include, for example, characterization of iron oxides (Cudahy and Ramanaidou 1997) and Cu-ore from oxidized zones of ore deposits (e.g. atacamite, antlerite; Laukamp et al. 2015b), as well as hydroxylated silicates (e.g. Al-clays: Bishop et al. 2008, Doublier et al. 2010, Yang et al. 2011; amphiboles: Laukamp et al. 2012; calcsilicates: Roache et al. 2011; White et al. 2017; chlorites: McLeod et al. 1987) and sulfates (e.g. alunite: Chang et al. 2011), and carbonates (Gaffey 1986). Example case studies are given further below. A less-known application of VNIR

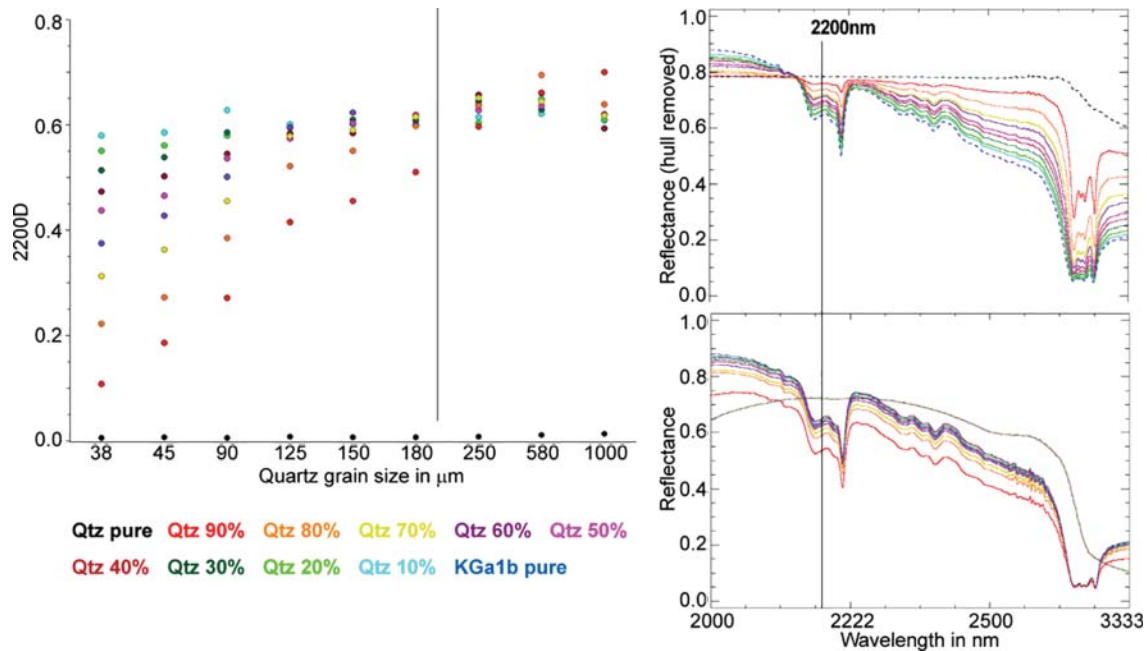


**Figure 18.4** Reflectance spectra of quartz–kaolin mixtures in the 2000–3333 nm wavelength range.

reflectance spectroscopy is the mapping of rare earth elements (REEs). Apart from  $\text{La}_2\text{O}_3$ ,  $\text{Lu}_2\text{O}_3$ , and  $\text{CeO}_3$ , REEs show diagnostic absorption features in the VNIR (White 1967). Rowan et al. (1986) described a detection limit of 300 ppm for successful identification of Nd using hyperspectral data. However, electronic absorption bands of ferric iron and other transition metals can mask REE-related absorption features. A recent review of VNIR and SWIR reflectance spectra of REE-fluorcarbonates is given in Turner et al. (2014).

### 18.3 Field and Laboratory Fourier Transform Infrared Spectrometers

Laboratory-based FTIR spectroscopy is commonly applied for mapping and characterizing minerals that are active in the mid- (MIR) to far-infrared (FIR) wavelength range (ca. 2500–20 000 nm; 4000–500  $\text{cm}^{-1}$ ). Almost all mineral groups show distinct absorption features in this wavelength range, arising from fundamental bending and stretching vibrations of chemical bonds or groups of atoms forming covalent bonds, and lattice vibrations (Chukanov 2014; Farmer 1974). However, in the case of mineral mixtures, as represented in rock and regolith samples, sulfides and oxides exhibit weak absorptions when compared to silicates, carbonates and sulfates (Iglesias et al. 2013). The great variety of iron oxides in natural samples, such as those from regolith and iron ore deposits, represented by variations in goethite, hematite, and magnetite, result in broad absorption peaks in the 17 000–20 000 nm wavelength range ( $588\text{--}500\text{ cm}^{-1}$ ), which do not enable the discrimination of the various mineral species.

Laboratory-based FTIR has been successfully used for quantitative phase analysis of ore material in mining operations (e.g. bauxite, Konrad et al. 2015) and quantifying deleterious minerals (e.g. kaolinite). Recently, portable instruments that do not require liquid nitrogen for their detector cooling have become commercially available, enabling data acquisition to be undertaken in locations away from laboratories, such as at exploration camps and drill core sheds. Handheld FTIR spectrometers (pFTIR) are equipped with measurement interfaces for diffuse reflectance infrared Fourier transform spectroscopy (DRIFT) or infrared attenuated total reflectance spectroscopy

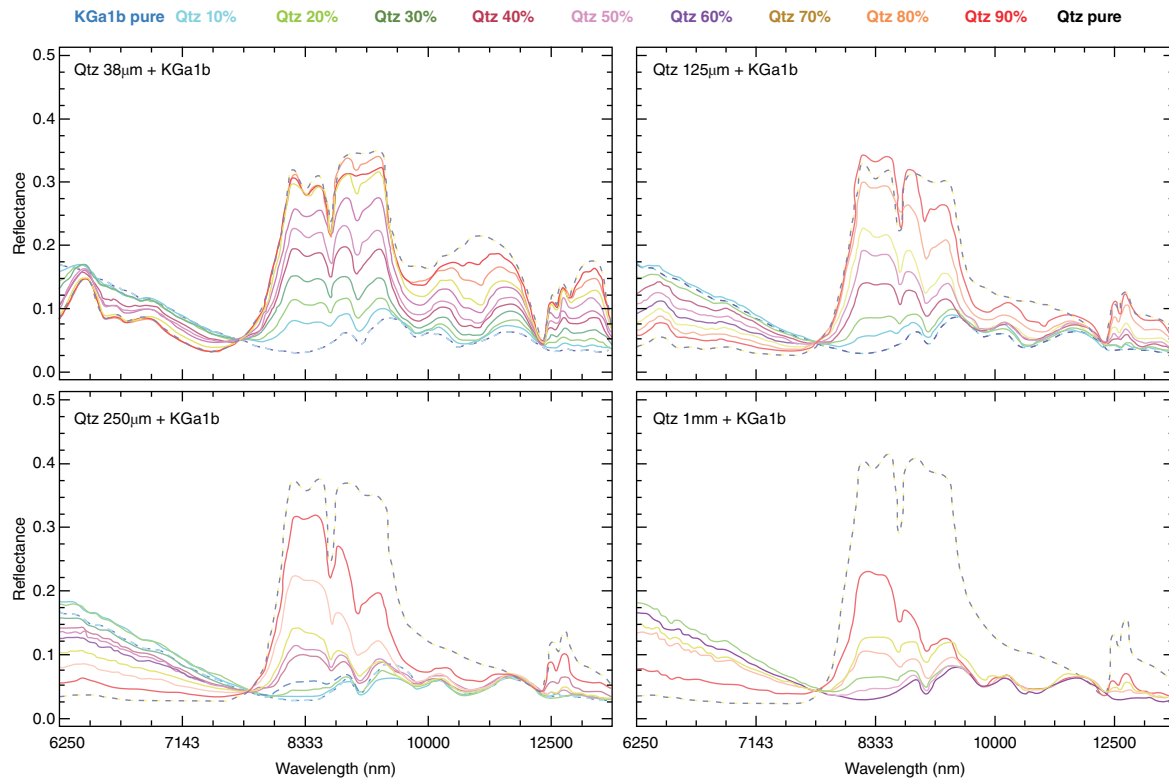


**Figure 18.5** MIR to FIR reflectance spectra of mixtures of kaolin standard KGa1b ( $2\text{ }\mu\text{m}$ ) and a range of quartz grain sizes ( $38, 125, 250$ , and  $1000\text{ }\mu\text{m}$ ) showing the impact of volume scattering on the spectral signatures. The coarse-grained pure quartz sample (bottom right) shows the primary and secondary reststrahlen bands of quartz between  $8000$  and  $10\,000\text{ nm}$  and  $12\,500$ – $13\,000\text{ nm}$ , respectively. Successive replacement of quartz by kaolin shows the gradually decreasing intensity of quartz absorption peaks and relative increase of the kaolin-related absorption peaks in the  $8500$ – $11\,000\text{ nm}$  wavelength range. In samples containing fine-grained quartz (top left), the kaolin-related absorption peaks are masked by intense volume scattering features between  $10\,000$  and  $12\,000\text{ nm}$ . In the latter case, the presence of kaolin is only indicated by the trough at around  $9300\text{ nm}$ , overprinting the reststrahlen band of quartz.

(IR-ATR), which allow collection of data with minimal sample preparation. Powder samples need to be pressed before pFTIR measurement to reduce the impact of volume scattering on the MIR to FIR spectral signatures. Gentle pressing of powder samples in sample holders with a glass slide does not remove the impact of grain size and the resulting volume scattering on the spectral signature (Figure 18.5).

Because all silicates, carbonates, and sulfates display characteristic combinations of absorption peaks in the TIR, FTIR data are a cost-effective method for rapid characterization of the respective mineral species in the field. Furthermore, after calibration with independent analytical methods, such as quantitative X-ray diffractometry (QXRD) or Quantitative Evaluation of Materials by Scanning Electron Microscopy (QEMSCAN®), modal mineral abundances can be achieved. For example, LeGras et al. (2018) used handheld FTIR data to characterize and quantify lithium-bearing minerals in samples derived from Western Australian and West African lithium–cesium–tantalum (LCT) pegmatites. Furthermore, they calibrated the FTIR reflectance spectra with whole-rock geochemistry, achieving a standard error of better than  $0.07\%$  for Li. This highlights the usefulness of handheld FTIRs for Li-exploration, as both the Li content as well as the Li-bearing mineral can be quantified in the field using the same instrument.

## 18.4 Hyperspectral Drill Core Sensing

The first trials of acquiring reflectance spectra from drill cores were undertaken by Kruse (1994) who employed a PIMA instrument to collect SWIR spectra in 10 mm steps down and across drill core samples to create a hyperspectral image. Currently commercially available hyperspectral drill core sensors can be classified into two main categories, represented by (i) line profilometers (e.g. Schodlok et al. 2016) and (ii) imaging techniques (e.g. HCI3, Corescan Pty Ltd.; Specim, Spectral Imaging Ltd.; HySpex, Norsk Elektro Optikk). A list of hyperspectral drill core sensors currently employed by service providers and geological surveys is provided in Table 18.2. In the case of line profilometers, reflectance spectra are collected in steps along the central line of a drill core. Imaging spectrometers provide hyperspectral imagery of the drill core down to sub-mm pixel size. An example is shown in Figure 18.6, where the hyperspectral imagery clearly highlights prehnite veins in a muscovite  $\pm$  biotite/chlorite matrix of an altered tonalite. Typically, only the VNIR, SWIR, and/or thermal infrared TIR (ca. 6000–14 500 nm; 1667–690 cm<sup>-1</sup>) or parts of the TIR (i.e. long-wave infrared, LWIR: 8000–12 500 nm; 1250–800 cm<sup>-1</sup>) wavelength regions are acquired simultaneously or in stages (Figure 18.1). In addition to the hyperspectral data, these systems also collect high-resolution RGB imagery and employ laser profilometer data to measure the morphology of the drill core. Throughput ranges from about 200 to 500 m of drill core per day, largely depending on the required amount of sample preparation (e.g. vacuuming drill core, turning depth markers away from sensors). Apart from drill core, these hyperspectral systems are also used to collect reflectance spectra from chips or even pulp samples.

Hyperspectral drill core sensors are increasingly used by researchers and industry. The high density of hyperspectrally derived mineralogy helps to map out gradients of mineral chemistry and relative mineral abundance in detail, unraveling trends that could not be otherwise recognized. Recent examples for applications include the mapping of hydrothermal alteration footprints associated with orogenic gold deposits (Arne et al. 2016; Wang et al. 2017), sediment-hosted gold and base metal deposits (Lampinen et al. 2019; Wells et al. 2016), Ni sulfides (Burley et al. 2017), volcanic hosted massive sulfide (VHMS, Duuring et al. 2016), and iron oxide copper gold (IOCG, Mauger et al. 2016) deposits as well as resource characterization of Ni-Co laterites (Cracknell and Jansen 2016). Analysis of hyperspectral data from single drill cores can provide important background information prior to commencement of drilling programs (Gordon et al. 2016).

Regional- or continental-scale hyperspectral drill core data collections, such as that published by the National Virtual Core Library (NVCL; Huntington 2016), provide detailed insights into the complexity of mineral assemblages that are usually missed in conventional sporadic sampling. These larger drill core data sets enable mapping the extent of diagenetic overprints (i.e. non-hydrothermal alteration up to 1 kb between 100 and 300 °C), such as in the McArthur Basin (Smith and Bottrill 2017), but also of regional metamorphism and hydrothermal alteration, such as in the Central Lachlan Orogen (Downes et al. 2016). Beyond hydrothermal mineral systems, hyperspectral drill core data have provided useful insights into the understanding of hydrocarbon systems (Ayling et al. 2016; Hill and Mauger 2016).

## 18.5 Data Processing

The vast amount of hyperspectral data that can be collected rapidly with hyperspectral proximal sensing technologies requires bulk processing. For example, the Australian State and Territory Geological Surveys have collected VNIR-SWIR-TIR reflectance spectra from over 3000 drill cores (as of June 2019) in the frame of the government-funded NVCL, delivering c. 24.7 million single measured drill core and chips samples during the June 2017–June 2019 timeframe alone. These precompetitive data are publicly available via AuScope's Discovery portal (<http://portal.auscope.org>).

Common methods for processing hyperspectral data include (i) matching algorithms, (ii) end member unmixing, (iii) single or multiple absorption feature extraction methods, and (iv) Gaussian deconvolution. All of these

**Table 18.2** Specifications of hyperspectral drill core sensing systems.

	Imaging			Line profiling			
	HCI3 (Corescan)	Fenix (Specim)	Owl (Specim)	HyLogger3 <sup>a</sup> (Corescan/CSIRO)			
Wavelength range	VNIR-SWIR: 350–2500 nm	VNIR: 400–1000 nm	SWIR: 970–2500 nm	LWIR: 7700–12 000 nm	VNIR: 380–1000 nm	SWIR: 1000–2500 nm	TIR: 6000–14 500 nm
Spectral resolution	ca. 4	3.3 nm	12 nm	100 nm	4 nm	4 nm	25 nm
Spatial resolution	0.5 px <sup>2</sup> (note that images are down sampled 5 × 5 for interpretation)	0.64 mm	2 mm	1.7 mm	10 mm across track × 14 mm along track @ 4 mm sampling interval		
RGB image resolution	50 mm				10 mm across track × 18 mm along track @ 8 mm sampling interval		
Scan rates	200–1000 m per day	for single core box: 15 s	for single core box: 20 s	for single core box: 17 s	0.1 mm		
Output data format	All	BIL image file format (“band interleaved by line”), compatible with ENVI/Evince compatible					

a) HyLogger3 is not commercially available, but Corescan is currently developing a new model “HyLogger4,” which will also collect data in the mid-wave infrared wavelength range.

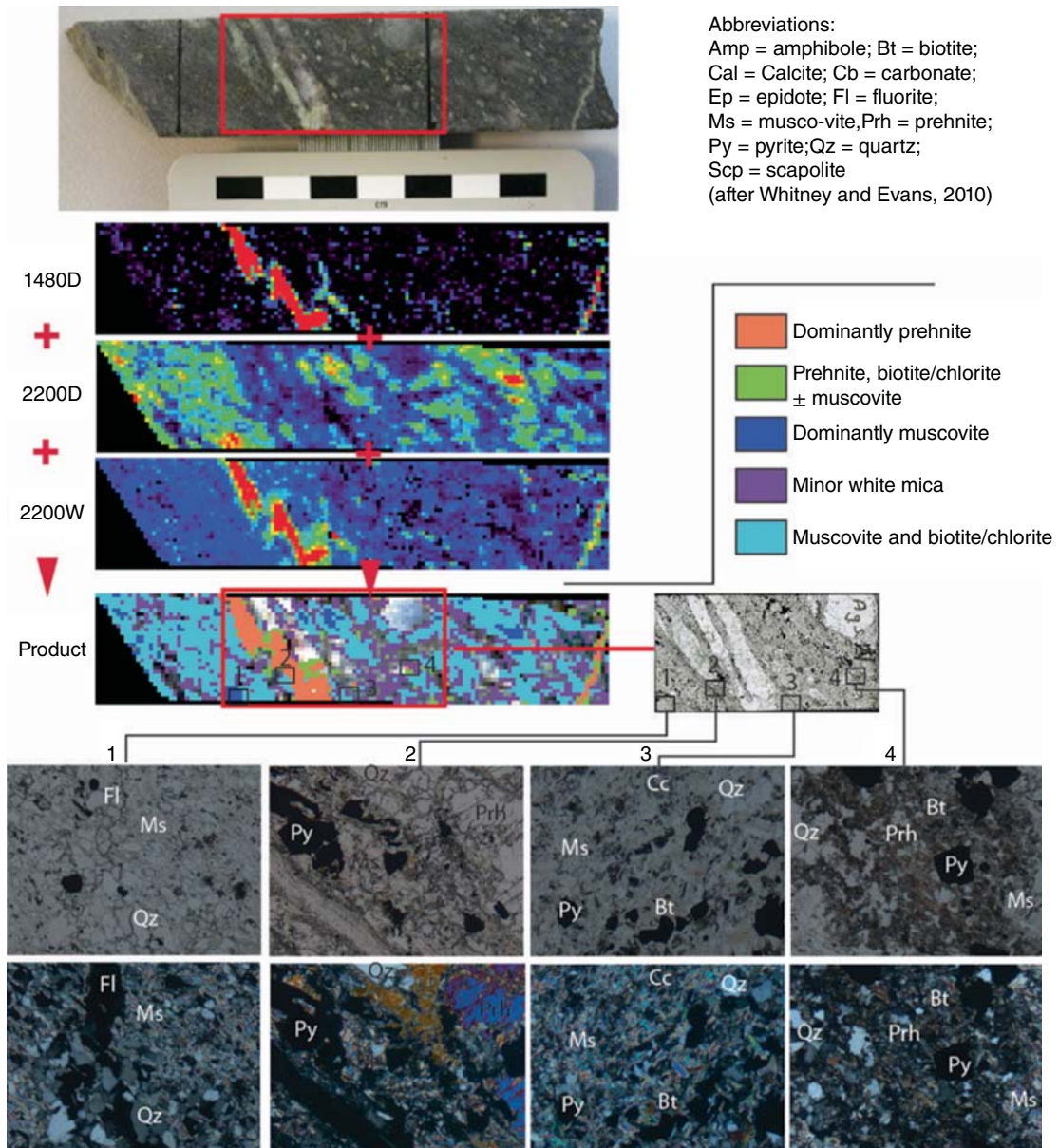


**Figure 18.6** A sample with porphyritic texture (referred to as tonalite) was scanned with the HySpex' SWIR imaging spectrometer. Various absorption spectra related to wavelength positions (e.g. 2200 W) and/or depth (e.g. 1480D and 2200D) were used to identify mineral trends. The final product was then compared to a thin section (red box) in the microscope and SEM for data validation.

methods can be compromised by various effects that alter the spectral signatures, such as grain size variation, moisture content and surface roughness.

Matching algorithms aim to model the measured reflectance spectra by combining a suite of reference library spectra. For example, “The Spectral Assistant” (TSA, Berman et al. 2017) algorithm, which is inbuilt in CSIRO’s The Spectral Geologist Software package (<https://research.csiro.au/thespectralgeologist>), uses a spectral reference

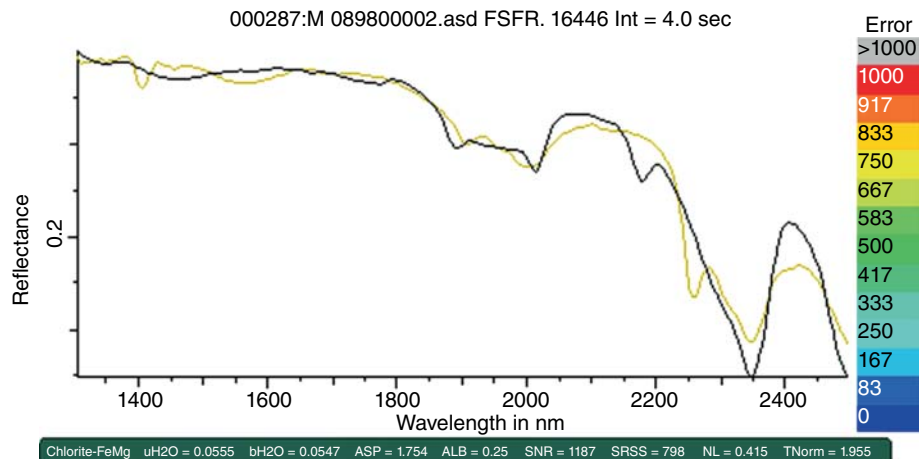


**Figure 18.7** Reflectance spectrum of a rock sample containing carbonate (calcite) as major SWIR-active mineral (black line) overlain by modeled SWIR reflectance spectrum (dark yellow line) that suggests the presence of chlorite. For the modeling, a mixture of up to three minerals was considered, based on a SWIR spectral reference library containing over 250 single mineral species.

library to match the unknown spectral signature against a single reference spectrum, or to create a simulated mixture of two or more spectra (Figure 18.7). Many providers of hyperspectral proximal sensing instruments also offer automated interpretation of mineral assemblages by means of matching algorithms inbuilt in the handheld spectrometer or the acquisition software. However, all automated mineral interpretations rely heavily on the composition and quality of the underlying spectral library. Also, if a mineral present in the rock is not active in the measured wavelength range, the mineral matching algorithm cannot report it. Automated algorithms always provide an answer about minerals present, but require careful evaluation by experienced geologists.

Aside from the challenge of understanding and removing background effects that have different physical causes throughout the full visible and infrared reflectance spectrum, overlapping absorption bands between different mineral groups and species cause difficulties with developing automated unmixing algorithms. A common example for the latter is the combined SWIR spectral signatures of white mica and chlorite or chlorite alone, which can mimic a spectral signature reminiscent of carbonates (Figure 18.7).

A less computing-intensive alternative to mineral matching algorithms are single- and multiple-feature extraction methods (Laukamp et al. 2010), which target mineral-specific absorption features. Absorption feature extraction methods use the relative intensity (depth in volume-scattering dominated wavelength ranges from the VNIR to MIR; height in surface-scattering dominated wavelength ranges from the MIR to FIR), wavelength position, full-width at half-maximum (FWHM), or slopes of absorption features. The absorption intensity, relative to the background continuum, is assumed to be proportional to the mineral content (Clark et al. 1990). The wavelength position of the absorption feature provides information about the composition of the mineral, the geometry of the absorption feature (FWHM and asymmetry) about the disorder. Multiple absorption features are used for each mineral to resolve ambiguities regarding mixtures with other minerals or materials. An example using Al-clays is shown in Figure 18.8. All AlOH-bearing minerals display strong absorptions in the 2160–2450 nm wavelength range ( $4630\text{--}4082\text{ cm}^{-1}$ ). To distinguish the Al-smectite, white mica, kaolin, and pyrophyllite groups, the combined presence or absence of the respective diagnostic absorption features can be used to quickly map the different minerals in large data sets. Absorption feature extraction methods enable the determination of other parameters that are important for understanding geological systems, for example, the illite spectral maturity index (Doublier et al. 2010). It should be noted that most of the absorption features that can be observed in VNIR-SWIR reflectance spectra collected with handheld and drill core hyperspectral sensors are composites of two or more absorption

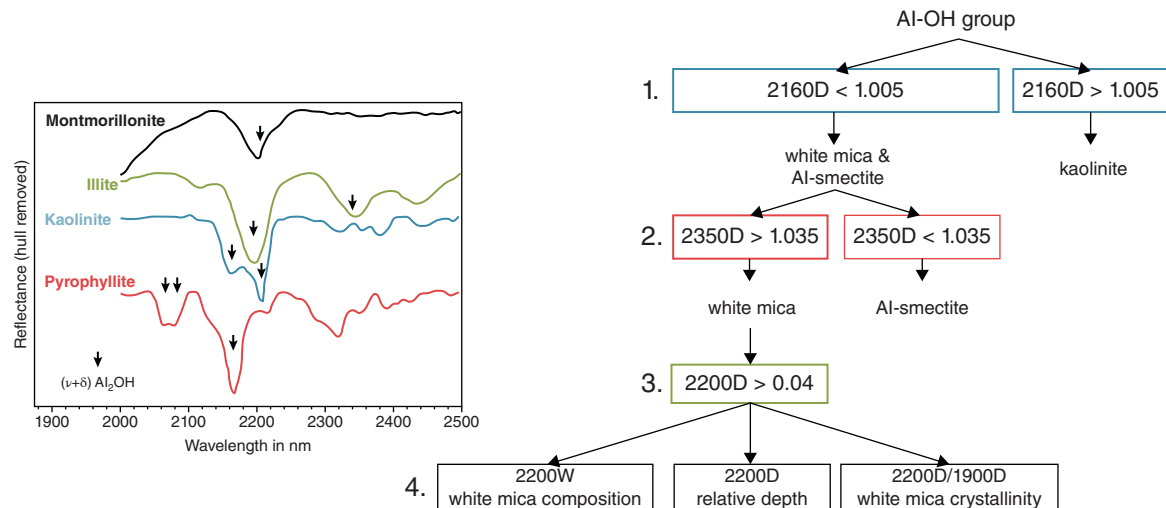


**Figure 18.8** Left: Hull-quotient removed, stacked reflectance spectra of (from top to bottom) Al-smectite, white mica, kaolin, and pyrophyllite in the 1900–2500 nm wavelength range. Black arrows highlight the hydroxyl-related combination bands. Right: Decision tree that allows the discrimination of Al-clays. Precondition for application of this decision tree is the presence of an absorption feature at around 2200 nm, where D stands for depth and W the wavelength of the absorption feature. The values represent the cut-off values.

bands (i.e. electronic or vibrational modes). Gaussian deconvolution allows the decomposition of the single modes (e.g. Laukamp et al. 2012).

### 18.5.1 Spectral Reference Libraries

Publicly available spectral reference libraries of rock forming minerals in reflectance mode are crucial for the processing of the voluminous hyperspectral data sets. Example spectral reference libraries are provided by the United States Geological Survey (USGS) (Clark et al. 2007), JPL (Grove et al. 1992) and CSIRO (<http://mineralspectrallibraries.csiro.au>). Emission spectra of natural and artificial mineral samples are available from Johns Hopkins University (JHU: Salisbury et al. 1991) and Arizona State University (ASU: Christensen et al. 2000; Salisbury et al. 1991). Libraries of transmission spectra, such as the large spectral library of over 3300 samples compiled by Chukanov (2014), can help to characterize spectral signatures that are not covered in the online spectral libraries. However, conversion of emission and transmission spectra to reflectance spectra, for comparison with data collected in the field and laboratory using reflectance and emission measurements, is not straightforward and can lead to misinterpretations.

## 18.6 Applications

### 18.6.1 Field Spectrometer Data for Ground Validation of Remote Sensing Data

Field spectrometers, especially VNIR-SWIR sensors, are frequently used for independent verification of remotely sensed surface reflectances (e.g. from satellites, aircraft, helicopters, or drones) and their uncertainties. This provides a link between remote sensing products and measurements made on the ground (Malthus et al. 2019). For this, reflectance spectra are collected along field traverses or selected measurement sites, both predetermined on the base of remote sensing and other geospatial, geochemical, or geological maps. A recommendation for a standardized workflow of vicarious calibration of remotely sensed data is given in Malthus et al. (2019).

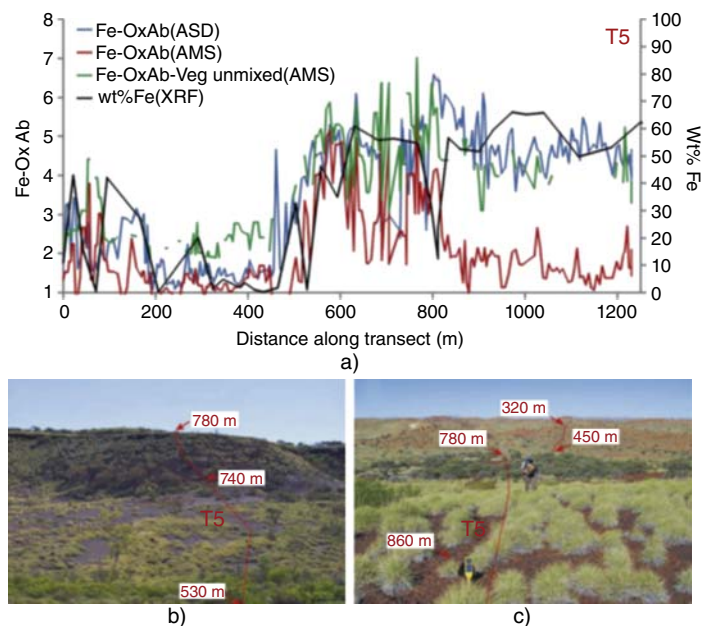


**Figure 18.9** (a) wt.% Fe (from pXRF) and Fe-(oxyhydr-)oxide (Fe-Ox) abundance (from airborne hyperspectral “AMS” data and VNIR-SWIR field spectrometer “ASD” data) as a function of distance along transect 5 which goes from south to north. Both the original and the vegetation unmixed (Veg unmixed) Fe-Ox abundance from airborne hyperspectral data are shown. (b) Picture of transect 5, looking north, showing the 530–780 m section. The lack of vegetation in this section results in a close alignment of the airborne (AMS) and ground (ASD) Fe-Ox abundance. (c) Picture of transect 5, looking south, showing the 780–860 m section. The abundance of vegetation in this section causes a strong discrepancy between the AMS (without vegetation unmixing) and ASD Fe-Ox abundance. *Source:* Haest et al. (2013).

Beyond verification of surface mineralogy unmixed from the remote sensing spectra, the ground validation also helps to improve the remote sensing products, by, for example, providing data for unmixing green and dry vegetation from mineral maps. Haest et al. (2013) validated quantitative iron (oxyhydr-)oxide (Fe-Ox), AlOH-clay, and carbonate abundance maps of the Rocklea Dome in Western Australia derived from airborne hyperspectral data against field transect data, including ~5500 VNIR-SWIR spectra and ~300 pXRF measurements (Figure 18.9). The ground validation enabled Haest et al. (2013) to (i) unmix the green and dry vegetation from the mineral maps, resulting in improved geological mapping, and (ii) estimate the average error on the airborne mineral abundance estimates. The improved mineral maps highlighted some areas that appear sub-economic from the airborne Fe-Ox abundance map without vegetation removal but show as potentially economic channel iron deposit (CID) resources when the influence of vegetation cover is unmixed from the airborne hyperspectral data.

In another case study area in the Western Australian Capricorn Orogen, Lampinen et al. (2017, 2019), used a field spectrometer and X-ray diffraction (XRD) data to link mineral maps generated from spaceborne multispectral data with drill core hyperspectral data. Reflectance spectra collected with the field spectrometer rarely represent reflectance spectra of “fresh” (i.e. unweathered rocks), which are commonly used in mineral exploration to develop mineral systems models (McCuaig and Hronsky 2014). By linking hyperspectrally derived subsurface mineralogy with surface mineralogy derived from field spectrometer data, Lampinen et al. (2017, 2019) were able to characterize the unweathered alteration mineral assemblages associated with the formation of the Abra Pb-Zn-Ag deposit, which are characterized by variations in abundance and mineral chemistry of white mica, chlorite, and carbonate, as well as their weathered equivalents. The weathering of altered rocks resulted in the destruction of chlorite and carbonate, leaving white mica and its compositional variations behind as the only alteration pattern

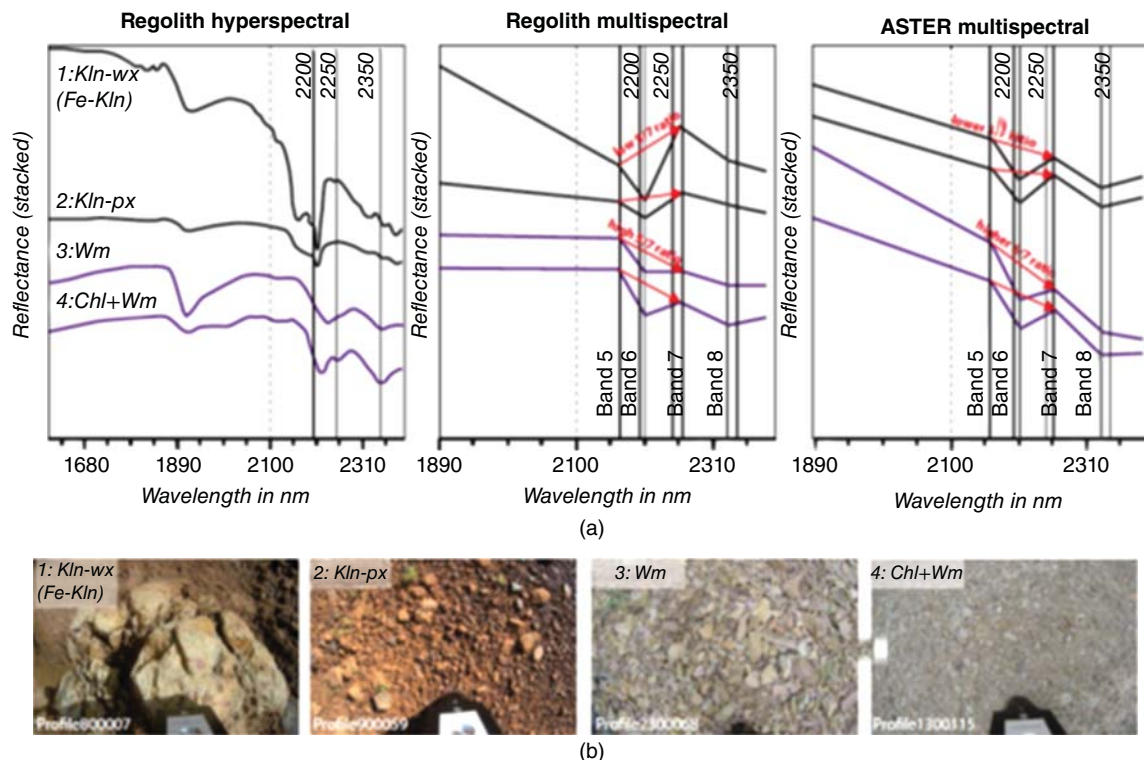


**Figure 18.10** Examples of spectral features for regolith sample kaolinites, white mica, and chlorite + white mica (from left to right). (a) Hyperspectral resolution, down sampled multispectral and ASTER data extracted from the sample coordinates; (b) sample photos, where the contact probe having a ~50 mm body width is presented for scale. Abbreviations: Chl = chlorite, Kln-wx = well-ordered kaolinite, Kln-px = poorly ordered kaolinite, and Wm = white mica. Source: Lampinen et al. (2017).

that is detectable at the surface. Lampinen et al. (2017) then resampled the hyperspectral field spectrometer data to multispectral resolution, and used a combination of spaceborne multispectrally derived white mica composition maps and airborne potassium radiometric data to map out the extents of alteration minerals at the surface related to base metal-mineralization at 250 m depth (Figure 18.10).

### 18.6.2 Mapping Physicochemical Gradients in Mineral Systems

Mineral footprints of hydrothermal alteration systems often display variations in mineral chemistry. The wavelength positions of absorption features can be used to trace exchange vectors of solid solutions between end members of mineral groups. The different infrared wavelength regions allow a detailed characterization of different vibrational modes that change their frequency depending on the respective mineral compositions. A summary of exchange vectors commonly tracked in mineral exploration is provided in Table 18.3.

An example of SWIR-active exchange vectors is represented by white micas, which are indicators for hydrothermal alteration processes in a wide range of mineral systems. Compositional zoning of white micas in hydrothermal deposits is manifested in a change of the Tschermak composition ( $\text{Al}^{\text{IV}}\text{Al}^{\text{VI}}\text{Si}^{\text{IV}}_{-1}[\text{Fe},\text{Mg}]^{\text{VI}}_{-1}$ ) Duke (1994), which impacts on the wavelength position of the major SWIR-active hydroxyl-related combination band at around 2200 nm ( $4545 \text{ cm}^{-1}$ ). Trends observed in lode gold deposits range from distal high-Al/low-Si micas (e.g. muscovite; short wavelength) to low-Al/high-Si micas (e.g. phengite; long wavelength) proximal to the ore

**Table 18.3** Exchange vectors in rock-forming minerals and their expression in wavelength shifts of mineral-diagnostic absorption features ( $\nu$  – fundamental stretching vibration,  $\delta$  – fundamental bending vibration,  $\nu+\delta$  – combination band,  $2\nu$  – first overtone).

Mineral group	Exchange vector	Common name	Band assignment	Lower limit [nm]	Upper limit [nm]
White mica $KAl^{VI}_2Al^{IV}Si_3O_{10}(OH)_2$	Tschermark Substitution $Al^{VI}Al^{IV}[Mg,Fe]^{VI}_{-1}Si^{IV}_{-1}$	“AlOH”	$\nu + \delta(Al,Mg,Fe^{2+},\dots)_2OH$	2185 ([VI]Al-rich)	2215 ([VI]Al-poor)
Chlorite (Mg, Fe) $Al^{VI}_2Al^{IV}_4Si_6O_{20}(OH)_{16}$	MgFe <sub>-1</sub>	“FeOH”	$\nu + \delta(Mg,Fe^{2+},\dots)_2OH$	2248 (Mg-rich)	2261 (Fe <sup>2+</sup> -rich)
Alunite (K, Na) $Al_3(SO_4)_2(OH)_6$	NaK <sub>-1</sub>	n.a.	$2\nu M_n OH, \nu + 2\delta H_2O$ (Na/K)	1473 (K-rich)	1491 (Na-rich)
Garnet (ugrandite series): grossular: $Ca_3M_2(SiO_4)_3$ with M = Cr, Al, Fe <sup>3+</sup>	$AlFe^{3+}_{-1}$ $Fe^{3+}Cr_{-1}$	n.a.	$\nu_3 Si-O$ (asymmetric stretch)	11 628 (Al-rich; grossular)	12 118 (Fe <sup>3+</sup> -rich; andradite)
Plagioclase $NaAlSi_3O_8$ (Albite) – $CaAl_2Si_2O_8$ (Anorthite)	NaCa <sub>-1</sub> , SiAl <sub>-1</sub>	n.a.	$\nu Si-O$	15 440 (Na-rich; albite)	16 160 (Ca-rich; anorthite)

References: white mica: Vedder and McDonald (1963); chlorite: McLeod et al. (1987); alunite: Bishop and Murad (2005); garnet: Geiger et al. (1989), McAloon and Hofmeister (1995); plagioclase: Thompson and Wadsworth (1957).

(e.g. Kanowna Belle, Western Australia) or distal to the ore (e.g. Ann Mason porphyry Cu–Mo deposit, Nevada USA) (Wang et al. 2017). In the VHMS system of Panorama (Western Australia), white micas formed as a result of upwelling hydrothermal fluids at temperatures of 175–325 °C (Van Ruitenbeek et al. 2012). Numerous reasons for the zoning of white micas in different hydrothermal systems are discussed in literature (e.g. Wang et al. 2017), such as pH and concentration of ferrous iron and potassium in the hydrothermal fluids, or temperature (e.g. muscovite = low-T recharge zones vs. phengite = high-T hydrothermal fluids).

The TIR provides opportunities for mapping exchange vectors in nominally anhydrous silicates (e.g. garnets, feldspars, pyroxenes), as well as carbonates (Green and Schodlok 2016), and phosphates. Garnets are common components of high-temperature mineral systems, such as the skarn-hosted Cu–Zn–Mo deposit of Antamina, Peru, where grossular ± andradite were described as the major garnet phases in endoskarn (*sedimentary* protolith – original, unmetamorphosed rock), whereas the exoskarn (*igneous* protolith) was dominated by andradite ± uvarovite. Using hyperspectral TIR drill core data, the garnet-related  $SiO_4$  tetrahedra stretching modes between 10 000 and 12 000 nm (1000–833  $cm^{-1}$ ), shifting toward shorter wavelengths with increasing grossular component of the ugrandite series (i.e. increasing Al/Fe) could be observed (Laukamp et al. 2014). Tracking the compositional changes of the garnets helped to distinguish the Cu–Zn from the Mo-dominated parts of the ore body.

### 18.6.3 Modeling Geochemical Indices from Hyperspectral Data

Hyperspectral reflectance spectra contain information about molecules or elements present in the measured sample. A direct link between hyperspectral and geochemical data can be drawn in many cases. For example, potassium in a granite is predominantly contained within micas and K-feldspars. Hyperspectral data collected in wavelength regions where these mineral groups are active (i.e. white mica: 2190–2450 nm; 4566–4082  $cm^{-1}$  and 8000–10 000 nm; 1250–1000  $cm^{-1}$ ; compared to K-feldspar: 8000–10 000 nm; 1250–1000  $cm^{-1}$ ) often show a strong correlation with potassium derived from whole-rock geochemistry.

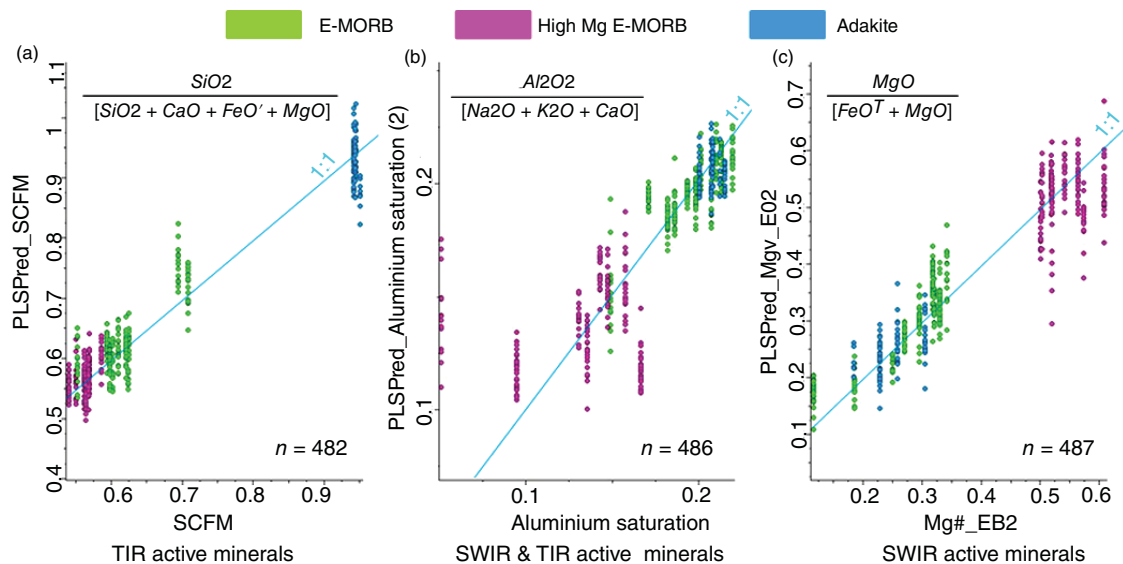


**Figure 18.11** Geochemical indices calculated from whole-rock geochemistry (x-axis) plotted against modeled geochemical indices using a PLS-algorithm (y-axis), colored by rock types (green = E-MORB; pink = high Mg E-MORB; blue – adakite). From left to right (1) SCFM ( $\text{SiO}_2 / (\text{SiO}_2 + \text{CaO} + \text{FeO}' + \text{MgO}$ ; Source: Based on Walter and Salisbury 1989) showing 482 sample points,  $r^2 = 0.972$ , (2) Aluminum saturation index ( $\text{Al}_2\text{O}_3 / (\text{Na}_2\text{O} + \text{K}_2\text{O} + \text{CaO})$ , 486 sample points,  $r^2 = 0.812$ ; Source: Based on Zen 1986) and (3) the Mg# ( $\text{Mg}/(\text{Mg} + \text{Fe})$ ; Source: Based on Miyashiro 1975), 487 sample points,  $r^2 = 0.937$ .

PLSR methods can be applied to model geochemical indices from hyperspectral data by using geochemical analyses for calibration. For example, as part of the Eucla basement stratigraphic drilling program conducted by the Geological Survey of Western Australia (GSWA; Spaggiari and Smithies 2015), hyperspectral VNIR-SWIR and TIR reflectance spectra were collected from drill core using a HyLogger3 located at the GSWA's drill core library in Carlisle, Western Australia. Drill cores were sourced from the Western Australian portion of the Great Australian Bight and Eucla Basins, where Cretaceous and Cenozoic sediments cover a vast area of Precambrian crust. Three geochemical indices, that are commonly used to characterize basement lithologies, were modeled (Figure 18.11): (i) the magnesium number-Mg# ( $\text{Mg}/(\text{Mg} + \text{Fe})$ ; Miyashiro 1975), (ii) the aluminum saturation index ( $\text{Al}_2\text{O}_3 / (\text{Na}_2\text{O} + \text{K}_2\text{O} + \text{CaO})$ ; Zen 1986) and (iii) silicon, calcium, iron, magnesium index-SCFM ( $\text{SiO}_2 / (\text{SiO}_2 + \text{CaO} + \text{FeO}' + \text{MgO})$ ; Walter and Salisbury 1989). The example from the Great Australian Bight and Eucla Basins showed that modeled geochemical indices allow a more detailed characterization of basement rock types (Figure 18.12). This could potentially reveal information critical for exploration, which would have been missed by conventional, sparse geochemical sampling. Furthermore, scalars developed from the XRF and spectral data for modeling geochemical indices in one drill core could, in many cases, be successfully applied to the spectral data of other drill cores from the same geological province to estimate the geochemistry.

## 18.7 Summary

This overview of handheld and drill core spectral sensing technologies and their applications aimed to demonstrate their effectiveness in characterizing rock-forming minerals and vector minerals important for mineral systems analysis and regolith analysis. Furthermore, the integration of visible and infrared spectroscopic data with geochemical data was addressed, as well as a discussion on the potential for modeling geochemical indices from the spectral data.

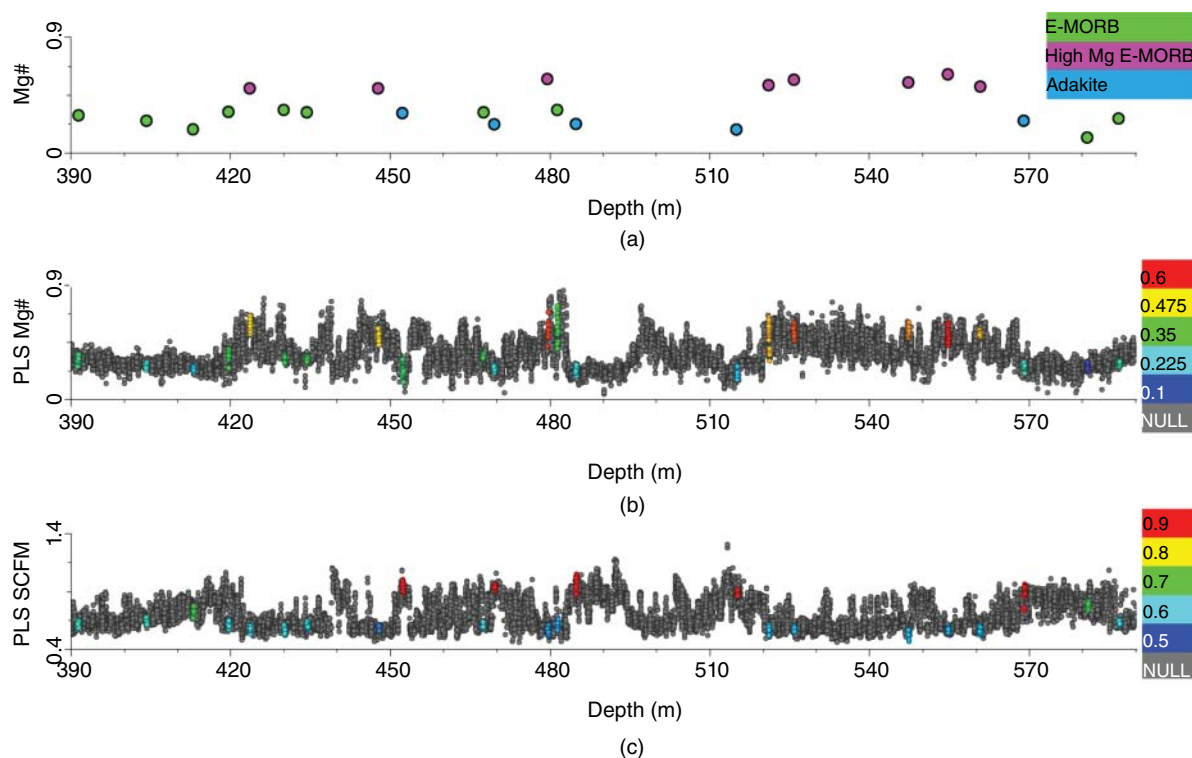


**Figure 18.12** Downhole plots of (a) Mg# ( $Mg/[Mg+Fe]$ ; Source: Based on Miyashiro 1975) calculated from whole-rock geochemistry (y-axis) down hole (x-axis), colored by rock type and (b and c): modeled geochemical indices (colored by actual values calculated from whole-rock geochemistry) show trends within basement rock types and across lithological boundaries (x-axis = depth; y-axis = modeled geochemical index). (b) Mg#, showing 487 sample points,  $r^2 = 0.937$ ; (c) SCFM ( $SiO_2/(SiO_2+CaO+FeOt+MgO)$ ; Source: Based on Walter and Salisbury 1989) showing 482 sample points,  $r^2 = 0.972$ .

Handheld spectrometers have been successfully used for many years in the resources sector for mineral characterization. In mineral exploration, typical applications range from mapping alteration mineral assemblages associated with hydrothermal ore deposits, to ground validation of multi- and hyperspectral remote sensing imagery collected for regional exploration. The advent of drill core hyperspectral sensing technologies expedites the applications that handheld spectrometers were engineered for, resulting in cost-effective, objective collection of considerable data volumes of mineralogy and related geoscience data.

Most commonly used handheld and drill core hyperspectral sensors still rely on reflectance measurements of the VNIR and SWIR, enabling the characterization of, for example, iron oxides, hydroxylated silicates, sulfates and carbonates, based on absorptions related to their respective electronic and vibrational modes. However, handheld FTIRs and inclusion of MIR and TIR in drill core sensing systems have seen an increased interest in utilizing visible and infrared spectroscopy by the resources sector, mainly because more minerals can now be cost-effectively characterized by means of the mid- to long-wave infrared wavelength regions. FTIRs collecting the MIR and TIR can detect spectral signatures related to the vibrational modes of nominally anhydrous silicates (e.g. quartz, feldspar, garnet) and heavy minerals (e.g. zircon, rutile, ilmenite). Furthermore, the lower frequency regions provide additional information about hydroxylated silicates, sulfates, and carbonates, enabling the informed user to acquire large amounts of spatially contiguous datasets of almost all major rock-forming minerals. The choice of handheld or drill core spectral sensing instrument depends on the expected mineral assemblage and/or the mineral group or species of interest. If nominally anhydrous silicates are important for addressing the respective exploration

or mining challenge, only MIR or TIR technologies will be useful. Also, it should be considered whether new spectrometers are required for the task at hand. For example, the wavelength range collected by all currently commercially available VNIR-SWIR spectrometers ends at 2500 nm ( $4000\text{ cm}^{-1}$ ). However, a major absorption feature of carbonates is located at around 2500 nm (Gaffey 1986), which would suggest that these handheld instruments should encompass the wavelengths up to ca. 2600 nm ( $3846\text{ cm}^{-1}$ ).

The hyperspectral data that can be collected with a wide range of technologies can be used to identify mineralogical and geochemical gradients that are commonly observed in mineral systems, including the regolith. When applied during the exploration phase, host minerals that potentially downgrade the resource can be identified, as well as deleterious minerals that may compromise the value of a prospective deposit, allowing explorers to make better decisions. In the mine site, handheld instruments can be used for identifying deleterious minerals that cause problems during the processing of ore and mapping the distribution of minerals that cause geotechnical issues. Dalm et al. (2014) demonstrated the potential of reflectance spectroscopy for sorting copper ore on conveyor belts using the SWIR-active combination bands characteristic of hydroxylated mineral species typically found in porphyry Cu deposits. During exploration and mining, companies can save on the costs of expensive laboratory analysis, and improve targeting for future sampling, by recognizing the potential for extrapolating expensive geochemical data to the thousands of hyperspectral measurements that can be acquired from scanning drill core in a matter of days.

The examples presented provide a brief overview of the many applications that are possible for field and drill core spectral sensing for the resources sector. The increasing use of reflectance spectroscopy in the areas of exploration through to the mining stage has uncovered knowledge gaps that have to be addressed by both background research as well as applied research. Examples include: (i) cross-calibration of different field and drill core spectral sensors (e.g. mine face, drilling extracted material [chips, core, and powders] and conveyor belt sensors in mine sites); (ii) Publicly available spectral reference libraries of rock-forming minerals and mineral mixtures (VNIR to FIR); and (iii) vibrational and electronic processes of minerals, including ab initio quantum mechanical modeling of spectral signatures of rock-forming minerals and conversion into reflectance spectra.

## Acknowledgements

HyLogger data in the presented case studies were provided by the AuScope and CSIRO-funded National Virtual Core Library.

## References

- Arne, D., House, E., Pontual, S. et al. (2016). Hyperspectral interpretation of selected drill cores from orogenic gold deposits in Central Victoria, Australia. *Australian Journal of Earth Sciences* 63 (8): 1003–1025.
- Ayling, B., Huntington, J., Smith, B. et al. (2016). Hyperspectral logging of middle Cambrian marine sediments with hydrocarbon prospectivity: a case study from the southern Georgina Basin, northern Australia. *Australian Journal of Earth Sciences* 63 (8): 1069–1085.
- Ben Dor, E., Ong, C., and Lau, I.C. (2015). Reflectance measurements of soils in the laboratory: standards and protocols. *Geoderma* 245–246: 112–124. ISSN 0016-7061, doi:<https://doi.org/10.1016/j.geoderma.2015.01.002>.
- Berman, M., Bischof, L., Lagerstrom, R. et al. (2017). A comparison between three sparse unmixing algorithms using a large library of shortwave infrared mineral spectra. *IEEE Transactions on Geoscience and Remote Sensing* 55 (6): 3588–3610.
- Bishop, J.L. and Murad, E. (2005). The visible and infrared spectral properties of jarosite and alunite. *American Mineralogist* 90: 1100–1107.

- Bishop, J., Lane, M., Dyar, M. et al. (2008). Reflectance and emission spectroscopy study of four groups of phyllosilicates: smectites, kaolinite-serpentines, chlorites and micas. *Clay Minerals* 43: 35–54.
- Burley, L.L., Barnes, S.J., Laukamp, C. et al. (2017). Rapid mineralogical and geochemical characterisation of the fisher east nickel sulphide prospects, Western Australia, using hyperspectral and pXRF data. *Ore Geology Reviews* <https://doi.org/10.1016/j.oregeorev.2017.04.032>.
- Chang, Z. and Yang, Z. (2012). Evaluation of inter-instrument variations among short wavelength infrared (SWIR) devices. *Economic Geology* 107: 1479–1488.
- Chang, Z., Hedenquist, J.W., White, N.C. et al. (2011). Exploration tools for linked porphyry and epithermal deposits: example from the Mankayan intrusion-centered cu-au district, Luzon, Philippines. *Economic Geology* 106: 1365–1398.
- Christensen, P.R., Bandfield, J.L., Hamilton, V.E. et al. (2000). A thermal emission spectral library of rock-forming minerals. *Journal of Geophysical Research* 105: 9735–9739.
- Chukanov, N.V. (2014). *Infrared Spectra of Mineral Species*. Springer.
- Clark, R.N., King, T.V., Klejwa, M. et al. (1990). High spectral resolution reflectance spectroscopy of minerals. *Journal of Geophysical Research - Solid Earth* 95: 12653–12680.
- Clark, R. N., Swayze, G. A., Wise, R. et al. (2007). USGS digital spectral library splib06a. USGS Data Series 231. <https://doi.org/10.3133/ds231>.
- Cracknell, M.J. and Jansen, N.H. (2016). National virtual core library HyLogging data and Ni-co laterites: a mineralogical model for resource exploration, extraction and remediation. *Australian Journal of Earth Sciences* 63 (8): 1053–1067.
- Cudahy, T. and Ramanaidou, E.R. (1997). Measurement of the hematite:goethite ratio using field visible and near-infrared reflectance spectrometry in channel iron deposits, Western Australia. *Australian Journal of Earth Sciences* 44: 411–420.
- Dalm, M., Buxtin, M.W.N., Ruitenbeek, F.J.A. et al. (2014). Application of near-infrared spectroscopy to sensor based sorting of a porphyry copper ore. *Minerals Engineering* 58: 7–16.
- Doublier, M.P., Roache, T., and Potel, S. (2010). Short wavelength infrared spectroscopy: a new petrological tool in low- to very low-grade pelites. *Geology* 38: 1031–1034.
- Downes, P.M., Tilley, D.B., Fitzherbert, J.A. et al. (2016). Regional metamorphism and the alteration response of selected Silurian to Devonian mineral systems in the Nymagee area, central Lachlan Orogen, New South Wales: a HyLogger™ case study. *Australian Journal of Earth Sciences* 63 (8): 1027–1052.
- Duke, E.F. (1994). Near infrared spectra of muscovite, Tschermak substitution, and metamorphic reaction progress: implications for remote sensing. *Geology* 22: 621–624.
- Duuring, P., Hassan, L., Zelic, M. et al. (2016). Geochemical and spectral footprint of metamorphosed and deformed VMS-style mineralization in the Quinns District, Yilgarn Craton, Western Australia. *Economic Geology* 111: 1411–1438.
- Fang, Q., Hong, H., Zhao, L. et al. (2018). Visible and near-infrared reflectance spectroscopy for investigating soil mineralogy: a review. *Journal of Spectroscopy* <https://doi.org/10.1155/2018/3168974>.
- Farmer, V.C. (1974). *The Infrared Spectra of Minerals*. Mineralogical Society of Great Britain and Ireland.
- Gaffey, S.J. (1986). Spectral reflectance of carbonate minerals in the visible and near infrared (0.35–2.55 µm): calcite, aragonite and dolomite. *American Mineralogist* 71: 151–162.
- Geiger, C.A., Winkler, B., and Langer, K. (1989). Infrared spectra of synthetic almandine-grossular and almandine-pyrope garnet solid solutions: evidence for equivalent site behaviour. *Mineralogical Magazine* 53: 231–237.
- Gordon, G., McAvaney, S., and Wade, C. (2016). Spectral characteristics of the Gawler range Volcanics in drill core Myall Creek RC1. *Australian Journal of Earth Sciences* 63 (8): 973–986.
- Green, D. and Schodlok, M.C. (2016). Characterisation of carbonate minerals from hyperspectral TIR scanning using features at 14 000 and 11 300 nm. *Australian Journal of Earth Sciences* 63 (8): 951–957.

- Grove, C. I., Hook, S. J., Paylor, E. D. (1992). Laboratory reflectance spectra of 160 minerals, 0.4 to 2.5 micrometers. *NASA Jet Propulsion Laboratory report*. JPL Publication 92-2, 405pp.
- Guggenheim, A., Adams, J.M., Bain, D.C. et al. (2006). Summary of recommendations of nomenclature committees relevant to clay mineralogy: report of the association internationale pour l'étude des argiles (AIPEA) nomenclature committee for 2006. *Clays and Clay Minerals* 54 (6): 761–772.
- Haest, M., Cudahy, C., Rodger, A. et al. (2013). Unmixing vegetation from airborne visible-near to shortwave infrared spectroscopy-based mineral maps over the Rocklea dome (Western Australia), with a focus on iron rich palaeochannels. *Remote Sensing of Environment* 129: 17–31.
- Hill, A.J. and Mauger, A. (2016). HyLogging unconventional petroleum core from the Cooper Basin, South Australia. *Australian Journal of Earth Sciences* 63 (8): 1087–1097.
- Hunt, G.R. (1977). Spectral signatures of particulate minerals in the visible and near infrared. *Geophysics* 42 (3): 501–513.
- Hunt, J.M. and Turner, D.S. (1953). Determination of mineral constituents of rocks by infrared spectroscopy. *Analytical Chemistry* 25: 1169–1174.
- Huntington, J. (2016). Uncovering the mineralogy of the Australian continent: the AuScope National Virtual Core Library. A national hyperspectrally derived drill-core archive. *Australian Journal of Earth Sciences* 63 (8): 923–928.
- Iglesias, M.L., Laukamp, C., Alves Rolim, S.B. et al. (2013). Thermal infrared spectroscopy and geochemical analyses of Volcanic rocks from the Paraná Basin (Brazil), 13th International Congress of the Brazilian Geophysical Society & EXPOGEf, Rio de Janeiro, Brazil (26–29 August 2013).
- Keller, W.D., Spotts, J.H., and Biggs, D.L. (1952). Infrared spectra of some rock forming minerals. *American Journal of Science* 250: 453–471.
- Konrad, F., Stalder, R., and Tessadri, R. (2015). Quantitative phase analysis of lateritic bauxite with NIR-spectroscopy. *Minerals Engineering* 77: 117–120.
- Kruse, F. (1994). Identification and mapping of mineral sin drill core using hyperspectral image analysis of infrared reflectance spectra. *International Journal of Remote Sensing* 17: 1623–1632.
- Lampinen, H., Laukamp, C., Occhipinti, S. et al. (2017). Delineating alteration footprints from field and ASTER SWIR spectra, geochemistry and gamma-ray spectrometry above regolith covered base metal deposits - an example from Abra, Western Australia. *Economic Geology* 112: 1977–2003.
- Lampinen, H., Laukamp, C., Occhipinti, S. et al. (2019). Mineral footprints of the paleoproterozoic sediment-hosted Abra Pb-Zn-cu-au deposit Capricorn orogen, Western Australia. *Ore Geology Reviews* 104: 436–461.
- Lau, I.C., Cudahy, T.J., Heinson, G. et al. (2003). Practical applications of hyperspectral remote sensing in regolith research. In: *Advances in Regolith* (ed. I.C. Roach), 249–253. CRC LEME.
- Lau, I.C., Ong, C., Laukamp, C. de Caritat, P., Thomas, M. (2017). The acquisition and processing of voluminous spectral reflectance measurements of soils and powders for national datasets. *IGARSS Texas, USA* (23–28 July 2017), 3pp.
- Laukamp, C., Cudahy, T., Caccetta, M. et al. (2010). The uses, abuses and opportunities for hyperspectral technologies and derived geoscience information. *AIG Bulletin* 51: 73–76.
- Laukamp, C., Termin, K.A., Pejcic, B. et al. (2012). Vibrational spectroscopy of calcic amphiboles - applications for exploration and mining. *European Journal of Mineralogy* 24: 863–878.
- Laukamp, C., Windle, S., Yang, K. et al. (2014). Skarn gangue mineral assemblage characterisation using SWIR-TIR-spectroscopy. Geological Society of Australia, AESC, Abstract No 110 of the 22nd Australian Geological Convention, Newcastle, Australia (7–10 July 2014).
- Laukamp, C., Salama, W., and González-Álvarez, I. (2015a). Proximal and remote spectroscopic characterisation of regolith in the Albany-Fraser Orogen (Western Australia). *Ore Geology Reviews* 73 (3): 540–554.
- Laukamp, C., McFarlane, A., Montenegro, V. et al., (2015b). Rapid resource characterisation of Cu-chlorides and sulphates in porphyry Cu deposits using reflectance spectroscopy. *SGA 2015, Nancy, France* (24–27 August 2015).

- Laukamp, C., Lau, I.C., Stolf, M. et al. (2018). Impact of grain size variations of quartz on estimation of kaolinite content from infrared spectral signatures. *IMA 2018*, Melbourne, Australia (13–17 August 2018).
- LeGras, M., Laukamp, C., Otto, A. et al. (2018). Measuring lithium-bearing minerals with infrared reflectance spectroscopy. *AGCC 2018*, Adelaide, Australia (14–18 October 2018).
- Lyons, R. J. P. (1962). Evaluation of infrared spectrophotometry for compositional analysis of lunar and planetary soils. *NASA contractor report, part II*.
- Malthus, T.J., Ong, C., Lau, I. et al. (2019). *A Community Approach to the Standardised Validation of Surface Reflectance Data. A Technical Handbook to Support the Collection of Field Reflectance Data. Release Version 1.0*. Australia: CSIRO. ISBN: 978-1-4863-0991-7.
- Mauger, A.J., Ehrig, K., Kontonikas-Charos, A. et al. (2016). Alteration at the Olympic dam IOCG–U deposit: insights into distal to proximal feldspar and phyllosilicate chemistry from infrared reflectance spectroscopy. *Australian Journal of Earth Sciences* 63 (8): 959–972.
- McAlloon, B.P. and Hofmeister, A.M. (1995). Single-crystal IR spectroscopy of grossular-andradite garnets. *American Mineralogist* 80: 1145–1156.
- McCuaig, C.T. and Hronsky, J.M.A. (2014). The mineral system concept: the key to exploration targeting. *Applied Earth Science* 126 (2): 77–78.
- McLeod, R. L., Gabell, A. R., Green, A.A. et al. (1987). Chlorite infrared spectral data as proximity indicators of volcanogenic massive sulphide mineralization. *Pacific Rim Congress '87*, Gold Coast, Queensland (26–29 August 1987).
- Milton, E.J., Schaepman, M.E., Anderson, K. et al. (2009). Progress in field spectroscopy. *Remote Sensing of Environment* 113 (Supplement 1): S92–S109.
- Miyashiro, A. (1975). Volcanic rock series and tectonic setting. *Earth and Planetary Science* 3: 251–269.
- Nicodemus, F.F., Richmond, J.C., Hsia, J.J. et al. (1977). Geometrical considerations and nomenclature for reflectance. In: *National Bureau of Standards Monograph*, vol. 160, 20402. Washington D.C: U.S. Govt. Printing Office.
- Noble, R., Lau, I., Anand, R. et al. (2019). Application of ultrafine fraction soil extraction and analysis for mineral exploration. *GEEA* <https://doi.org/10.1144/geochem2019-009>.
- Roache, T.J., Huntington, J.F., and Quigley, M.A. (2011). Epidote-Clinozoisite as a hyperspectral tool in exploration for Archean gold. *Australian Journal of Earth Sciences* 58 (7): 813–822.
- Rowan, L.C., Kingston, M. J., Crowley, J.K. (1986). Spectral Reflectance of Carbonatites 745 and Related Alkalic Igneous Rocks: Selected Samples from Four North American Localities. *746 Economic Geology* 81: 857–871.
- Salisbury, J.W., Walter, L.S., Vergo, N. et al. (1991). *Infrared (2.1–25 μm) Spectra of Minerals*. Baltimore and London: The Johns Hopkins University Press.
- Schodlok, M.C., Whitbourn, L., and Huntington, J. (2016). HyLogger-3, a visible to shortwave and thermal infrared reflectance spectrometer system for drill core logging: functional description. *Australian Journal of Earth Sciences* 63 (8): 929–940.
- Smith, B.R. and Bottrill, R. (2017). Are spatial mineralogical variations in the Bessie Creek Sandstone, McArthur Basin evidence for variable provenance, diagenesis or hydrothermal alteration? *Annual Geoscience Exploration Seminar (AGES) Proceedings*, Alice Springs, Northern Territory (28–29 March 2017). Northern Territory Geological Survey, Darwin. 100–105.
- Spaggiari, C. V. and Smithies, R. H. (2015). Eucla basement stratigraphic drilling results release workshop: extended abstracts. *GSWA record 2015/10*.
- Thompson, C.S. and Wadsworth, M.E. (1957). Determination of the composition of plagioclase feldspars by means of infrared spectroscopy. *American Mineralogist* 42: 334–341.
- Turner, D.J., Rivard, B., and Groat, L.A. (2014). Visible and short-wave infrared reflectance spectroscopy of REE fluorcarbonates. *American Mineralogist* 99: 1335–1346.

- Van Ruitenbeek, F.J.A., Cudahy, T.J., van der Meer, F.D. et al. (2012). Characterization of the hydrothermal systems associated with Archean VMS-mineralization at panorama, Western Australia, using hyperspectral, geochemical and geothermometric data. *Ore Geology Reviews* 45: 33–46.
- Vedder, W. and McDonald, R.S. (1963). Vibrations of the OH ions in muscovite. *The Journal of Chemical Physics* 38: 1583–1590.
- Walter, L. and Salisbury, J. (1989). Spectral characterization of igneous rocks in the 8 to 12 µm region. *Journal of Geophysical Research* 94 (B7): 9203–9213.
- Wang, R., Cudahy, T., Laukamp, C. et al. (2017). White mica as a hyperspectral tool in exploration for sunrise dam and Kanowna belle gold deposits, Western Australia. *Economic Geology* 112: 1153–1176.
- Wells, M., Laukamp, C., and Hancock, L. (2016). Reflectance spectroscopic characterisation of mineral alteration footprints associated with sediment-hosted gold mineralisation at Mt Olympus (Ashburton Basin, Western Australia). *Australian Journal of Earth Sciences* 63 (8): 987–1002.
- White, W.B. (1967). Diffuse-reflectance spectra of rare-earth oxides. *Applied Spectroscopy* 21: 167–171.
- White, A., Laukamp, C., Stokes, M. et al. (2017). Vibrational spectroscopy of calc-silicate minerals applied to low-grade regional metabasites. *Geochemistry: Exploration, Environment, Analysis* 17: 315–333.
- Yang, K., Huntington, J.F., Gemmell, J.B. et al. (2011). Variations in composition and abundance of white mica in the hydrothermal alteration system at Hellyer, Tasmania, as revealed by infrared reflectance spectroscopy. *Journal of Geochemical Exploration* 108: 143–156.
- Zen, E.-A. (1986). Aluminium enrichment in silicate melts by fractional crystallization: some mineralogic and petrographic constraints. *Journal of Petrology* 27: 1095–1117.

# 19

## Handheld X-Ray Fluorescence (HHXRF)

*Stanislaw Piorek*

*Rigaku Analytical Devices, Wilmington, MA, USA*

### 19.1 Introduction – X-Ray Fluorescence

Handheld X-ray fluorescence (HHXRF) spectrometry belongs to the family of atomic emission spectroscopic methods. It is an emission spectroscopic technique that utilizes the physical principles of interaction of gamma or X-rays with matter. When a beam of low-energy (usually less than 100 keV) gamma or X-rays is directed toward the sample material, the beam photons may either be scattered off the sample, or they may excite the sample atoms. It is that latter form of interaction that is of analytical value for an XRF spectrophotist.

The excited state of the atom is achieved when the incident quanta of radiation have high enough energy to remove an electron from one of the inner energy shells of the atom. The vacancy created is filled almost instantly (in less than  $10^{-16}$  seconds) by an electron from any of the higher energy shells. In the process, the electron filling the vacancy on the lower energy shell sheds the excess energy, which most of the time is released by the atom in the form of an X-ray photon (see Figure 19.1).

The energy of that photon is unique, or “characteristic,” to any given element and therefore it can be used to identify the presence of the element in the sample (Figure 19.2). On the other hand, the emitted number of photons characteristic of a given element is – in turn – representative of the quantity of atoms (concentration) of that element in the sample. Thus X-ray fluorescence (XRF) spectrometric analysis is both a qualitative and a quantitative elemental analytical technique. It is worth noting that it is this interaction of the external radiation with inner energy shells of an atom that distinguishes XRF from other atomic spectroscopies described in this book. The inner energy shell interaction is also the reason the XRF is an elemental method; the energy of characteristic X-rays is not affected by the chemical state of the atom. The XRF method obtained its name after the fluorescence phenomena observed in visible range of electromagnetic radiation; however, here the characteristic X-ray radiation emitted by excited atoms ceases immediately after the exciting radiation stops.

The end “product” of XRF is called an X-ray spectrum of the sample. Figure 19.3 shows an example of a spectrum obtained by exciting a sample of 316-grade stainless steel. It is a histogram of the number of counts of X-rays of specific energy recorded as a function of their energy. There are number of peaks in the spectrum, and their centroids represent characteristic X-ray energies of the elements present in the sample. The magnitude of each characteristic energy peak represents the quantity of each element in the sample.

XRF analysis offers a unique combination of features and one of the most valuable ones is its truly nondestructive character. Not only is the sample preserved in an unaltered state after the analysis, but very often – and this is where small, HHXRF analyzers enter the scene – the analysis may be performed on the object “as is,” *in situ*, without the need to deface or destroy it. Additionally, the same sample may be analyzed repeatedly, the feat not possible with classical wet chemistry or inductively coupled plasma (ICP) methods. This single property of XRF spectrometry is undoubtedly responsible for most of its widespread acceptance, especially in its “handheld” embodiment.

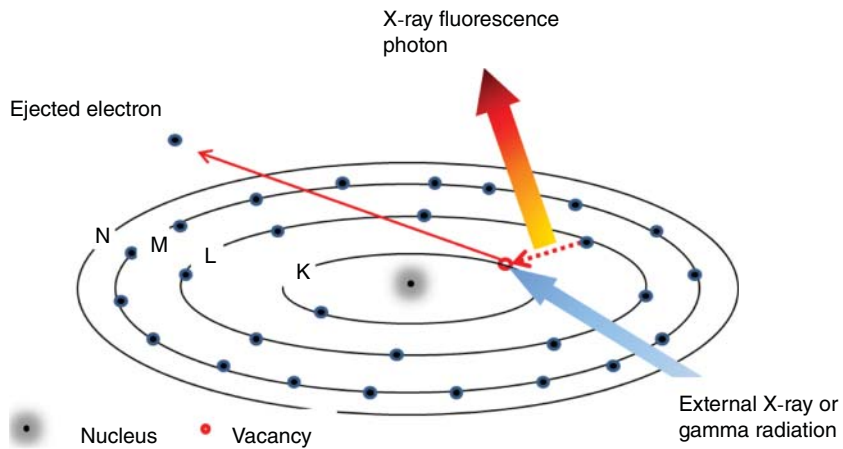


**Figure 19.1** A diagrammatic illustration of the X-ray fluorescence process in an atom.

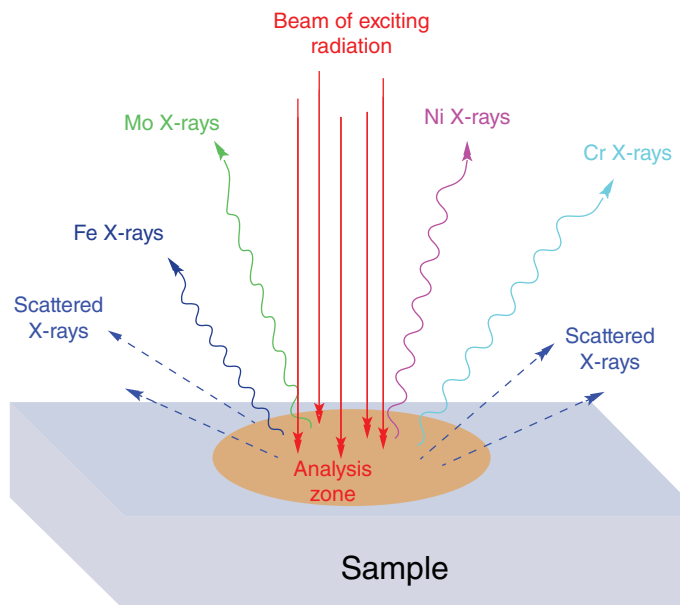


**Figure 19.2** A diagrammatic illustration of X-ray fluorescence from a sample.

XRF is truly a multielemental technique, since in a single measurement many elements can be determined simultaneously and within wide concentration and elemental ranges, from single mg/kg to 100%, and from Mg to U, respectively. It is a fast analytical method able to provide “on-the-spot” results in seconds. Finally, XRF features so-called “standardless” calibration via the Fundamental-Parameters (FP) approach, the property which allows for very robust, versatile calibrations and easy operation.

The advantages of XRF analysis were known for decades; however, only the technological improvements of the last decade or two made it possible to fully realize their potential. The advent of HHXRF analyzers set a new paradigm for analysis. So much so that HHXRF analysis is now a method of choice for such applications as alloy identification and sorting, screening an environment for toxic metals, analysis of minerals and ores, testing consumer goods for compliance with pertinent norms and regulations. It is estimated that over the last 15 years or so,

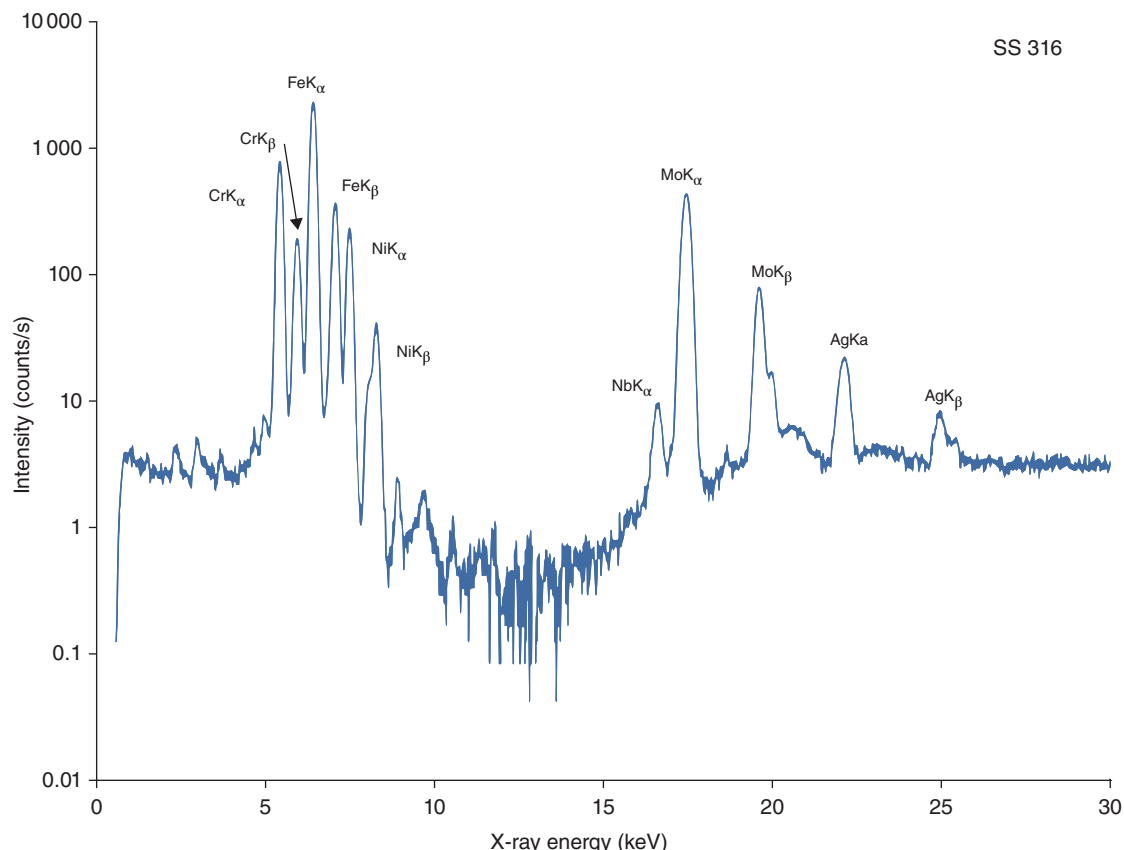


**Figure 19.3** A XRF spectrum of Stainless Steel 316 with the major element peaks marked. Note that the ordinate (y-axis) is on a logarithmic scale.

about 70 000 to 80 000 HHXRF analyzers have been placed in service worldwide, with several thousand entering global market every year.

This chapter is devoted to the development and present state of HHXRF spectrometers. Discussion of their features and performance is illustrated by typical applications served by these instruments. Finally, an attempt is made to outline the directions of future development of this versatile method.

## 19.2 How Did We Get Here – Evolution of a Handheld XRF Analyzer

Classical XRF analysis is realized either as wavelength-dispersive (WDXRF) or an energy-dispersive (EDXRF) based method [1]. Historically, the former was developed first. The WDXRF spectrometer utilized a high-power X-ray tube as the source of exciting radiation, and a gas-filled proportional counter coupled with relatively large, bulky goniometers for wavelength (energy) dispersion. When in the mid-1970s small semiconductor detectors became commercially viable, the bulky goniometer and gas-filled detector were replaced by high-resolution Si(Li) or Ge(Li) detectors, paving the road for EDXRF spectrometers. Additionally, availability of small size radioisotope capsules created an opportunity for their use as excitation sources. They were not only orders of magnitudes smaller in size than any X-ray tube, they also did not need any power to operate and thus created an opening for battery-operated systems. Consequently, during the period from the late sixties to mid-seventies a battery-powered,

truly portable XRF (pXRF) spectrometer was designed to initiate migration of XRF spectrometry from the lab into the field [2]. Thus, HHXRF spectrometry is EDXRF spectrometry practiced with the use of HHXRF analyzers. It is worth noting that the XRF practiced with HHXRF analyzers has been frequently called in literature FPXRF (field-portable XRF), HHpXRF (handheld portable XRF) or pXRF, the last two acronyms being favored by the scientific community in Europe.

The initial push for the development of a pXRF analyzer came from geologists and prospectors. They realized the benefits of generating quantitative, multielemental results in real time, on the site, rather than sending samples to laboratory and waiting for weeks for the results.

The early design pXRF spectrometers of the nineteen seventies and eighties were quite heavy, two-component systems, weighing anywhere from 5 to 10 kg. Figure 19.4 shows an example of such system. A handheld probe with a gas-filled proportional X-ray detector and isotope source would be connected via a cable to a backpack-sized electronics box hosting a power supply, multichannel analyzer, and a computer that converted the probe signal into elemental concentrations. While somewhat bulky and not very convenient to use, those first portable analyzers gained attention and recognition from governmental bodies in charge of environmental protection. It was the period of time when governments in the United States and in Europe started the massive effort of cleaning natural environments polluted by decades of uncontrolled industrial activities that had released hazardous and toxic elements into the soil, water, and air. Responsible regulatory agencies realized that the use of pXRF spectrometry equipment for field, on-site, assessment of contamination levels can drastically reduce the costs and time of cleanup and remediation efforts. Thus the synergy of the available technology with the urgent need for intensive testing culminated in development by the US Environmental Protection Agency (EPA) of the first ever standard test method for soil screening for metallic contaminants using pXRF, in which the acronym FPXRF – for field-portable XRF – was introduced [3, 4]. Soon after, FPXRF was adopted by metals and alloys recycling industries, followed by metal manufacturing and fabrication. Since that time, alloy scrap sorting became the most important application for FPXRF and consequently for HHXRF analyzers [5–7].

During the next decade, pXRF analyzers underwent drastic reductions in size and weight. The metamorphosis was enabled by the progress made in miniaturization of electronics, which gave us laptop computers. Gas-filled detectors were replaced by tiny silicon diodes, and postal stamp-sized advanced microprocessors could not only operate the analyzer, but also execute complex analytical programs. Thus, in the year 1995 the very first, truly handheld, one-piece XRF analyzer was introduced by Niton LLC as Model XL-300. The  $20 \times 8 \times 5$  cm box, shown in



**Figure 19.4** Portable XRF analyzer with gas-filled proportional detector in probe.

**Figure 19.5** A first, truly handheld XRF analyzer from Niton Corporation with isotope source and silicon diode detector.

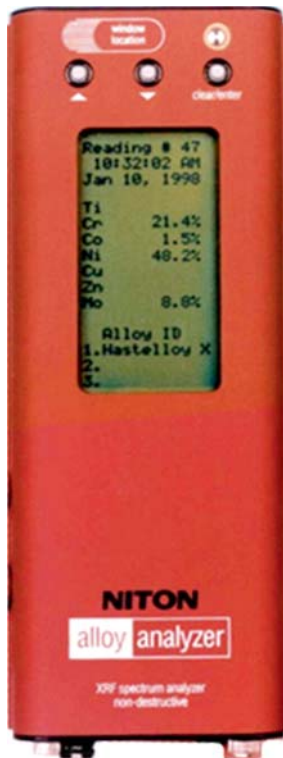


Figure 19.5, contained a multichannel analyzer, radioisotope sources, silicon p-i-n detector and a battery that could sustain continuous operation for up to eight hours. The results and X-ray spectrum were displayed on a  $5 \times 7$  cm LCD. Weighing less than 1.2 kg, this instrument started a new era for XRF spectrometry analysis [8, 9]. Just a few years later, in 2002, the first ergonomically designed HHXRF analyzer, with miniature X-ray tube replacing isotopes as excitation source was unveiled, removing the last obstacle to further progress and growth of HHXRF. Since then several tens of thousands of HHXRF analyzers have been placed in use worldwide for alloy identification and sorting, soil screening for metals and for screening electronic, consumer products and childrens' toys for compliance with pertinent regulations.

## 19.3 Contemporary HHXRF Analyzer: Construction and Operation

While the physical principles of XRF spectrometry are the same for all instruments the HHXRF analyzer is not just a miniaturized laboratory system. HHXRF analyzers are designed for ruggedness, immunity to environmental conditions, ease of operation, and yet for excellent analytical performance. Last but not least, it is a purpose-designed instrument, which should not be used as a general application instrument. These analyzers are very often operated by nonscientist personnel to perform routine analysis in field using simple, preprogrammed analytical models. With this in mind we will describe essential components and their functions in HHXRF analyzer.

### 19.3.1 Main Functional Blocks of a HHXRF Analyzer

Any XRF analyzer, handheld included, must possess three basic components that are: a source of radiation to excite characteristic X-rays from the sample, detector of X-ray radiation and associated electronics with data processing capabilities, and a means for reproducible presentation of the sample for analysis. The specific arrangement of these three elements depends on the environment and primary application for which the analyzer is designed.

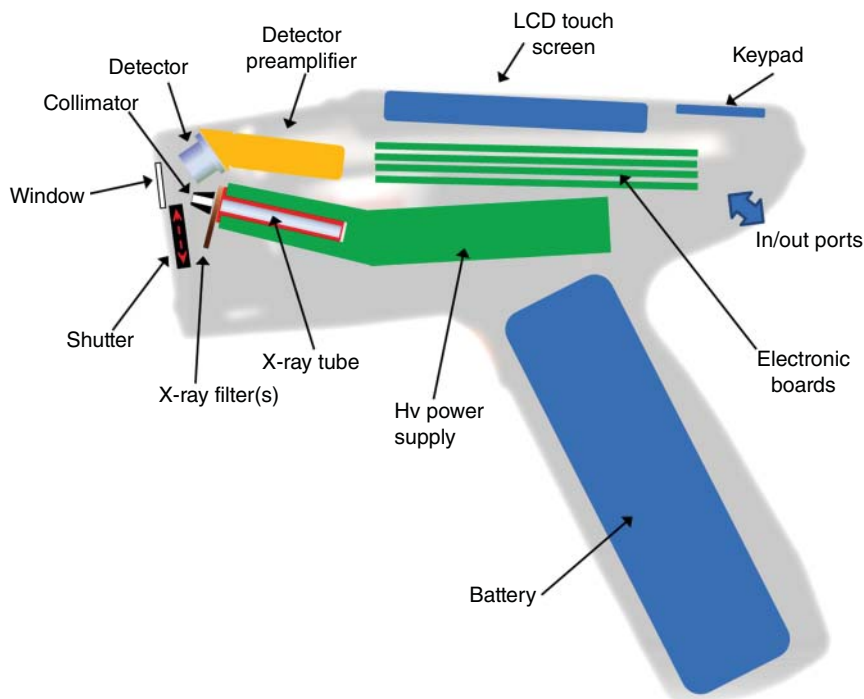


**Figure 19.6** Basic internal structure of a HHXRF analyzer.

The layout of components in a typical HHXRF analyzer is shown in Figure 19.6. Following the practice of good ergonomic design, the analyzer is usually given a shape of a handheld drill. As a rule, battery is held in the grip, which provides counterweight to the front of instrument. The front of the instrument houses the X-ray tube and detector, both positioned as close as possible to the inspection plane of the instrument. The inspection plane is a flat plate in the very front of the instrument with a small, usually round, opening or window, which is placed against the tested sample during the measurement. Through this window, the X-ray tube illuminates the sample, and the detector collects characteristic X-rays of elements from the sample. For protection, the window is sealed with a thin polyester film, which is transparent for X-rays.

The basic configuration of the analyzer is complemented by a digital signal processor (DSP), multichannel analyzer (MCA), and touch-screen liquid crystal display (LCD), which allows the user to operate the instrument. The analyzer is controlled by a microprocessor, which also executes analytical programs.

#### 19.3.1.1 Excitation source

All HHXRF analyzers use miniature X-ray tubes to excite the characteristic X-rays of the sample. These are typically end-window, transmission-anode-type tubes [10, 11]. The anode of such tubes is made of 250- $\mu\text{m}$  thin beryllium foil, coated on the inside with a thin film of target material such as silver, tungsten, palladium, rhodium, or molybdenum. The anode serves also as an exit port of radiation emitted by the tube, which consists of bremsstrahlung continuum and characteristic X-rays of the anode material. Tube dimensions may vary from 8 to 15 mm in diameter and 25 to 50 mm in length. Figure 19.7 shows an early design miniature X-ray tube used in many HHXRF analyzers. The tube is powered by a high-voltage (HV) power supply, which can polarize the tube between 5 and 50 kV DC, and operate it at anode current varying from 40 to 100  $\mu\text{A}$ , for the total power of a few Watts. The tube and its HV power supply are usually integrated into a single, well-isolated, block. X-ray tubes for HHXRF spectrometry are described in detail in the chapter by Cornaby in Volume 1.

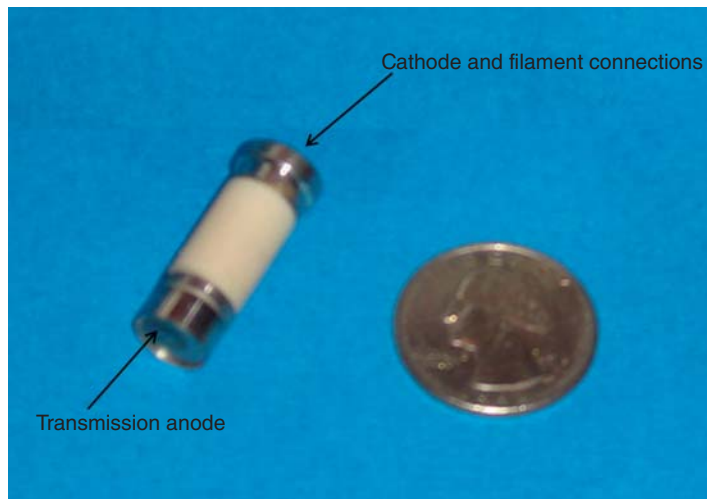


**Figure 19.7** Miniature X-ray tube shown next to a “US quarter” coin.

### Primary Filters

The X-ray beam emitted directly from the tube is not very useful due to the high background from the tube’s bremsstrahlung (see Figure 19.8). To reduce the background, a filter in a form of thin, pure metal foil is placed between the tube anode and a sample. Figure 19.8 shows spectra of X-rays as emitted by the silver anode tube, one without a primary filter and another with a molybdenum filter placed directly over the tube anode. The molybdenum filter significantly reduces the intensity of tube X-rays below 15 keV, thus enabling analysis of elements whose X-ray energies fall in that region.

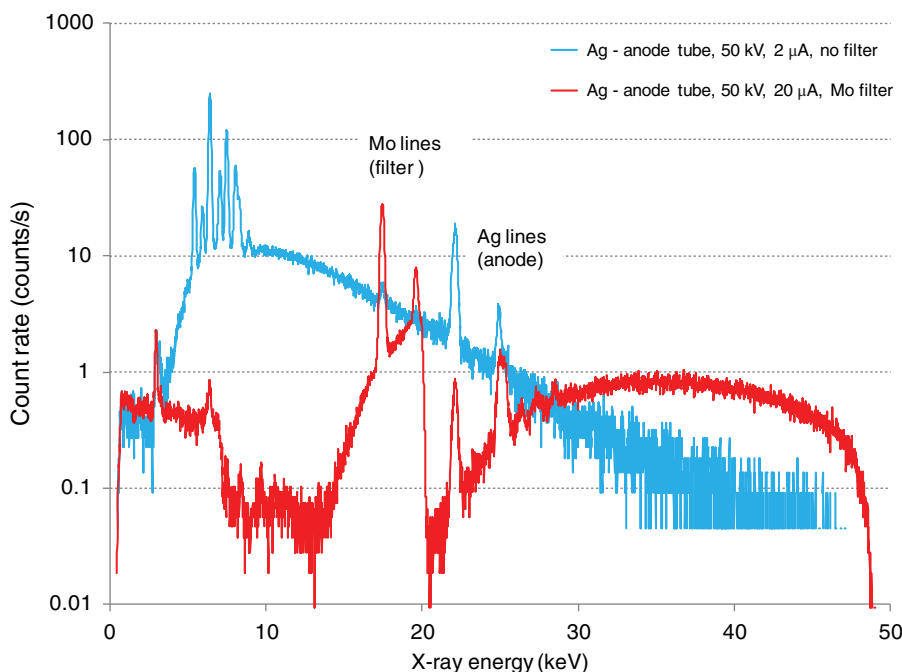


**Figure 19.8** Unfiltered (blue) and filtered (red) X-ray spectra of X-ray tube with silver anode.

### Radioactive Isotope Sources

Some older models of HHXRF analyzers used radioisotope sources to excite the fluorescent X-rays in the object being analyzed. Specifically, the analyzers designed solely for the purpose of measurement of lead in applied paint use almost exclusively radioisotopes, with  $^{153}\text{Gd}$  being the source of choice. This is because this isotope emits gamma radiation at 97 and 103 keV, which is very well suited to excite K-alpha X-rays of lead. This subject will be discussed separately in Section 19.5.4. The main advantage of isotope sources is that they do not need power to operate. On the other hand, their usefulness is limited by half-life time, which for some is rather short (see  $^{153}\text{Gd}$ , and  $^{109}\text{Cd}$  in Table 19.1), which means one must replace them. Additionally, the photon output of radioisotope sources is several orders of magnitude lower than that from X-ray tubes. Regulations governing use of isotopes are also much more restrictive when compared to X-ray tubes.

Figure 19.9 shows an example of sealed radioisotope capsule, while Table 19.1 lists radioisotope sources that have been used with portable and HHXRF analyzers.

#### 19.3.1.2 Detector

A detector used in HHXRF analyzer is either a silicon p-i-n diode or – nowadays more often – a silicon-drift detector (SDD) [12, 13]. Both are in the simplest terms reversely polarized, about 0.5 mm thin diodes, mounted on a tiny Peltier pile (a cooler), and enclosed in a small metal capsule about 15 mm in diameter and about 8–10 mm high (Figure 19.10). The capsule has a round window sealed by thin (few micrometers) beryllium foil. X-rays can pass through this window, and are then absorbed in the bulk of the diode. When an X-ray photon strikes the detector, it ionizes atoms of silicon along its path, and creates a charge, the magnitude of which is directly proportional to the photon's energy. Photons of different energies will create different charges. This is how the silicon diode sorts – or disperses – the photons by their energies. The number of photons, characteristic of a given element, counted over measurement time, is representative of the number of atoms of this element in the sample. Both detectors are cooled down to  $-25\text{ }^{\circ}\text{C}$  by Peltier pile, so the instrument can operate at room temperature and feature very good energy resolution. The advantage of a SDD is its ability to operate at an order of magnitude higher pulse frequencies (count rates) than the p-i-n diode. The charges generated in the detector by X-rays are converted by a dedicated charge-sensitive preamplifier to voltage pulses of only millivolt amplitudes.

**Table 19.1** Radioisotope sources in use with portable and HHXRF analyzers.

Isotope	Emitted Radiation	Energies (keV)	Half-life time	Typical applications	Notes
$^{55}\text{Fe}$	X-rays	5.9 and 6.5	2.7 y	XRF	
$^{244}\text{Cm}$	X-rays	15.8 to 17.9	18.1 y	XRF	Emits neutrons
$^{109}\text{Cd}$	X-rays	22.1 and 24.9	1.26 y	XRF	
$^{241}\text{Am}$	$\gamma$ radiation	59.5	432.2 y	XRF	
$^{153}\text{Gd}$	$\gamma$ radiation	97.4 and 103.2	241.6 d	XRF	



**Figure 19.9** Example of radioisotope source capsule for use in HHXRF analyzer.  
Source: Copyright Eckert & Ziegler AG.

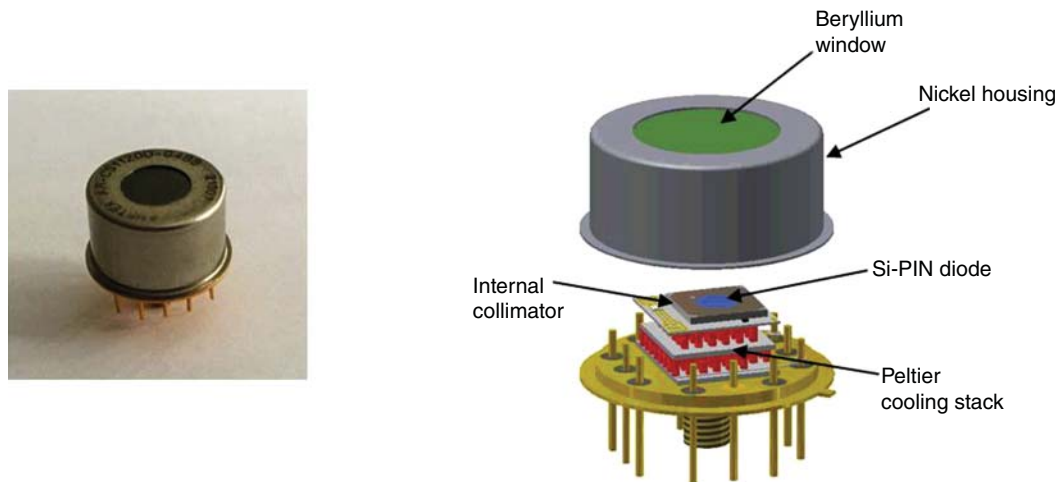


**Figure 19.10** Anatomy of Silicon Diode p-i-n detector.

An important detector parameter is its active area, and that can vary from a few  $\text{mm}^2$  to  $50 \text{ mm}^2$ . The larger the detector active area the larger the étendue – the area \* solid angle product from which the detector can collect X-rays, which translates into better analytical sensitivity and lower detection limits.

It is worth noting here that the detector in HHXRF analyzer is its most fragile component in terms of resistance to shock or vibrations. Detector technologies for HHXRF are described in detail in the chapter by Stratilatov in Volume 1.

#### 19.3.1.3 Spectrum Analyzer

The stream of millivolt pulses generated by the detector preamplifier is further amplified, shaped and digitized by a DSP, and then passed to an MCA, which sorts and arranges them into a histogram, which is called an X-ray spectrum. Figure 19.11 shows an X-ray spectrum of soil (NIST 2710). The graph in the figures shows how many photons per second (ordinate) of given energy (abscissa) were registered by the system over a certain period of time.

The peak of intensity that occurs at characteristic X-ray energy emitted by a particular element tells us how much of that particular element is in the sample. Visual inspection of the spectrum displayed on instrument's LCD screen provides the user with immediate feedback about the quality of the measurement as well as with clues about why the measurement might not be good. The spectrum of sample is the only source of information from

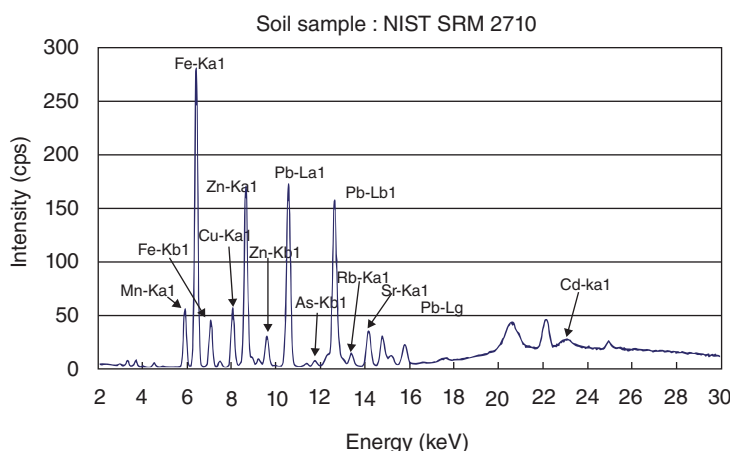


**Figure 19.11** X-ray spectrum of Certified Reference Material, NIST 2710, soil contaminated with metals.

which analytical algorithms can extract the information about elemental composition, and the quality of the spectrum directly affects the analytical performance of the analyzer. The better the energy resolution of the detector, the better are peaks in the spectrum separated from each other, which improves accuracy of analysis. Good energy resolution of the detector must be matched with the multichannel analyzer, which should have at least 4096 channels. The overall performance of the spectrometer is the aggregated sum of performances of all its components.

#### 19.3.1.4 Electronics

All electrical and moving mechanical parts of an analyzer are controlled by an on-board computer, powered by a fast microprocessor, which also supports complex analytical algorithms. The challenge for all electronic circuits in the analyzer, with miniature X-ray tube in close proximity, is to be immune to the high level of electromagnetic noise generated by the HV power supply of the X-ray tube. This is especially true for the detector and its preamplifier. An X-ray tube generates not only X-rays, but also a considerable amount of heat, which has to be dissipated in order to secure stability of operation of all the electronic circuits. There is nothing trivial in making a very sensitive detector, cooled to  $-25^{\circ}\text{C}$  to reduce its noise, to operate next to the noise generating X-ray tube/HV assembly routinely warming up to  $50^{\circ}\text{C}$  while operating!

#### 19.3.2 Operation

To perform the measurement, one needs to place the front plate of the analyzer in direct contact with the object to be tested, making sure that the object completely covers the measuring window of the analyzer. Next, the actual measurement is initiated either by push button or by a trigger for a period of time long enough to satisfy precision requirements of the test, remembering that longer measurement times improve the precision of the measurements. During that time period, the analyzer continuously acquires the X-ray spectrum (or spectra) of the object under test. After the measurement is completed, the results of the quantitative determination of elements in the sample are reported on the display, and also stored in the instrument's memory, along with associated X-ray spectra. Additionally, depending on the specific application, the numerical results of elemental concentrations may be further processed and converted by the analyzer software into a specific result or decision communicated to the operator, such as "alloy grade" or "pass/fail" determination.

Real embodiments of some commercially available HHXRF analyzers are shown in Figure 19.12. Typical features of contemporary HHXRF analyzer are listed in Table 19.2 They reflect the present state of the art of the commercially available HHXRF analyzers.



**Figure 19.12** Selection of commercially available HHXRF analyzers (from left: X-MET 8000 from Hitachi, Spectro Sort from Ametek and X-250 from SciAps). Sources: Image courtesy of Hitachi High-Tech Corporation; Photo courtesy of SPECTRO Analytical Instruments GmbH. All rights reserved; SciAps, Inc.

### 19.3.3 Typical Technical Specifications

**Table 19.2** Typical specifications and features of the contemporary HHXRF analyzer.

<b>Mechanical</b>	<b>Dimensions:</b> about 10 × 10 × 4 in. (250 × 250 × 100 mm) <b>Weight:</b> <3.0 lbs (<1.3 kg)
X-ray engine	X-ray source: End window transmission Ag, Au, or W anode X-ray tube, 50 kV maximum, 100 µA maximum, (2–3 W total power); primary beam may be modified by multi-position filter and various diameter collimators Detector: Large-area silicon-drift detector (FWHM < 165 eV), 180 000 counts/s throughput
Analyzer	Usually a 4096-channel analyzer supported by dedicated DSP and central processor, run by a proprietary operating system at frequency of 500 MHz or higher
Power	Li-ion battery, 7.4 V DC, 7.8 Ah
Display/user Interface	Adjustable angle, color touch-screen display, keypad for the most often used, routine commands
Analytical	Elemental range: from Mg to U (>25 elements depending on the application) Concentration Range: mg/kg to 100% Analytical Programs: – Fundamental Parameters Based – Compton Normalization – Empirical (User Application) Standard Calibrations: alloys, precious metals, soils and mining, RoHS, plastics, toys and consumer goods, plastics, coatings Sample type: solids, powders, liquids, thin films
Data handling	Data entry: via touch-screen keyboard and/or wireless, remote bar code reader Data storage: internal memory for several thousand readings with spectra Data transfer: via a proprietary PC-based program using either USB, Bluetooth, or RS-232 communications Data integrity and safety: encrypted, password protected
Additional features and optional useful accessories	Internal CCD camera He purge for improved light element detection Portable test stand Welding mask (to limit the viewing area of instrument to the width of the weld joining two metals)

## 19.4 Calibration Methods

The results of measurements are derived from the X-ray spectra of the sample using either an empirical calibration or one based on the FP approach. Each method requires the net X-ray intensities of analytes to be extracted from the X-ray spectra of samples. The methods of spectrum deconvolution that can be used to obtain net X-ray intensities are described in chapter 4 of reference [1]. All HHXRF analyzers are equipped with programs providing such

function. A thorough treatment of the calibration methods can also be found in reference [1] (chapters 5 and 6), while here we provide only short descriptions.

### 19.4.1 Empirical Calibration Curve

Empirical calibration requires the availability of a number of samples with known concentrations of analytes, and with their matrix characteristics as close as possible to that of the unknown samples. Stated in the simplest way, empirical calibration method relies on algebraic equation(s) that correlate analyte concentration in a sample with its measured X-ray intensity. The coefficients of such equation are determined by least squares regression. One needs to keep in mind that empirically derived calibration equations are valid only for the concentration ranges of analytes covered by the set of calibration samples, and only for the type of calibration samples used. For example, the calibration derived for alloys of iron must not be used for copper alloys or for liquid samples, etc. On the other hand, if the calibration set represents well the compositions of unknown samples, empirical calibration may be the most accurate one of all methods. Within the class of empirical calibrations two methods have been useful for handheld instruments: Compton Normalization [14] and Multiple Linear Regression of Lucas-Tooth and Price [15].

*Compton Normalization Method:* Compton Normalization [14] is used predominantly when relatively small concentrations of elements are analyzed in a relatively light, relatively uniform matrix. An example may be analysis of sub-percent concentrations of iron, zinc, or calcium in cellulose, in liquid, or in soil. The general form of the calibration equation is as follows:

$$C_j = A_j + B_j \cdot \left( \frac{I_j^{\text{net}}}{I_{\text{Compt}}} \right) + \dots + D_j \cdot \left( \frac{I_j^{\text{net}}}{I_{\text{Compt}}} \right)^2 \quad (19.1)$$

where:

- $C_j$  is the concentration of element  $j$
- $I_j^{\text{net}}$  and  $I_{\text{Compt}}$  are intensities of analyte  $j$  and Compton scatter, respectively, and
- $A_j, B_j, D_j \dots$  are coefficients derived via least square fit.

Usually, the second-order term in Eq. (19.1) may be omitted. The calibration equation contains only the terms involving net intensity of an analyte in question ratioed to that of the Compton scatter; it is the ratioing to Compton scatter intensity,  $I_{\text{Compt}}$ , through which absorption matrix effects are corrected in this calibration model. After a suite of calibration samples is measured, the intensities of the analyte and Compton scatter, along with the concentrations of the analyte, are used to determine the coefficients  $A_j, B_j, D_j$  via least squares regression.

This method will fail if the X-ray absorption edge of another element present in sample in appreciable concentration falls between the X-ray energy of an analyte and the energy of the Compton-scattered peak.

*Multiple linear regression:* The Compton Normalization method does not correct for significant variations of concentrations of analytes and matrix of samples. In such instances a multiple linear regression should be employed. A calibration expression for analyte  $j$  has a generic form of Eq. (19.2):

$$C_j = A_j + I_j^{\text{net}} \left[ 1 + \sum_{i=1}^n K_{ji} I_i^{\text{net}} \right] + \left( \frac{I_j^{\text{net}}}{I_{\text{Compt}}} \right). \quad (19.2)$$

where:

- $C_j$  is concentration of element  $j$
- $I_j^{\text{net}}, I_i^{\text{net}}$ , and  $I_{\text{Compt}}$  are intensities of analyte  $j$ ,  $i$ , and Compton scatter, respectively, and
- $A_j, K_{ji}$  are coefficients derived via least square fit.

This equation represents the intensity-based correction of matrix effects, since the correction terms are all expressed by the net intensities of elements measured in the sample, rather than by their concentrations. This method is also referred to as the “intensity correction method of Lucas-Tooth and Price,” who were first to propose it [15, 16]. The last term in Eq. (19.2) is a familiar Compton Normalization term from Eq. (19.1).

To calibrate the analyzer for  $n$  analytes one needs a set of  $n^2$  analyzed standards with concentrations known for all analytes. The set must cover expected concentration ranges for all analytes and be otherwise as similar as possible to unknown samples to be tested. Calibration standards must not be obtained by serial dilution. Net intensities of all elements present in samples, that is those of the analytes and those of the other elements, must be extracted from spectra and used along with their corresponding elemental concentrations in a multiple linear regression fit.

#### 19.4.2 Fundamental Parameters-Based Calibration (FP)

This is the most versatile calibration approach, allowing for analysis of unknown samples within a wide concentration range from mg/kg to 100%. The FP-based calibration is predicated on the system of exact equations correlating measured intensities of the analytes with their concentrations via the use of fundamental laws, principles, and physical constants governing interaction of X-rays with matter. Those equations are by their nature transcendental, and as such can only be solved numerically by iteration, a computationally intensive process. This is why this method became available in handheld and portable instruments only after miniature, yet very powerful, micro-processors became available. The FP-based calibration works extremely well in well-defined applications such as metal alloys. On the other hand it is also an excellent tool for the initial, approximate assessment of elemental composition of the sample.

For the sake of completeness and also to illustrate the calculational complexity of this approach, the formal FP equation for the analyte  $i$  is shown below:

$$I_f = G \times I_0 \times \varepsilon_{K,L} \times \omega_{K,L} \times \frac{\tau_{i,E} \times w_i}{\frac{\mu_1}{\sin \varphi_{in}} + \frac{\mu_2}{\sin \varphi_{out}}} \times \left(1 - \frac{1}{j_{K,L}}\right) \times \left[1 - e^{-\left(\frac{\mu_1}{\sin \varphi_{in}} + \frac{\mu_2}{\sin \varphi_{out}}\right)m}\right] \quad (19.3)$$

with:  $\mu_1 = \sum_{i=1}^{i=n} w_i \cdot \mu_{i/E}$  and  $\mu_2 = \sum_{i=1}^{i=n} w_i \cdot \mu_{i/K,L}$ ,

where:

- $I_f$  is the net intensity (an actual measured signal) of characteristic X-rays of series  $K$  or  $L$  of element  $i$  excited by external source of energy  $E$ , in (counts/s)
- $I_0$  is the intensity of exciting radiation of energy,  $E$ , in (counts/s)
- $G$  is the geometry of measurement coefficient
- $\varepsilon_{K,L}$  is the detector efficiency for X-rays of  $K$ - or  $L$ -series of element  $i$
- $\omega_{K,L}$  is the fluorescence efficiency for  $K$ - or  $L$ -series of characteristic radiation of element  $i$
- $j_{K,L}$  is a ratio (jump factor) of photoelectric absorption coefficient just above to that of just below the absorption edge for an element  $i$ , for  $K$ - or  $L$ -series
- $\tau_{i,E}$  is the photoelectric absorption coefficient for element  $i$  at energy  $E$
- $\mu_1$  is the total mass absorption coefficient of the sample for exciting radiation of energy  $E$ , in ( $\text{cm}^2/\text{g}$ )
- $\mu_2$  is the total mass absorption coefficient of the sample for analyte  $K$ - or  $L$ -series X-rays, ( $\text{cm}^2/\text{g}$ )
- $m$  is the mass per unit area of the sample, ( $\text{g}/\text{cm}^2$ )
- $w_i$  is the weight fraction (concentration – an unknown to be determined) of analyte,  $i$ , in sample
- $\varphi_{in}$  and  $\varphi_{out}$  are the angle of incidence of exciting radiation and angle of emission of fluorescent radiation from sample, respectively.

Since the unknown weight fraction,  $w_i$ , is also present in expressions for  $\mu_1$  and  $\mu_2$ , we now can see why the equation cannot be solved for  $w_i$  algebraically, but only by using the iterative approach.

A detailed discussion of the FP method and its various modifications can be found in reference [1].

## 19.5 The Most Important Applications for HHXRF Analyzers

### 19.5.1 Alloy Analysis and Identification

The unique synergy of features offered by XRF analysis on one hand, and analytical requirements of application on the other hand, are the reasons why analysis of alloys became a flagship application for HHXRF. As a matter of fact, it is estimated that about 70% of all HHXRF analyzers deployed are used for analysis of alloys.

Alloys are tested for elemental composition almost at every stage of their life cycle. However, the HHXRF analyzers are used primarily for sorting of metal alloy scrap and for the so-called “positive materials identification” – PMI for short.

Alloy scrap is sorted for its value, which is a function of an alloy's elemental composition; a piece of an ordinary construction steel is worth much less than the equivalent mass of stainless steel or nickel-based alloy. On the other hand, since alloy scrap is used in production of new alloys, its composition must be ascertained before it can be added to the melt for a new alloy in order for the latter to maintain its final, specified composition.

Parts and components made of alloys, which are incorporated into critical industrial structures such as refinery pipelines, chemical plant installations, nuclear power plants, airplanes, etc. are subject to mandatory verification testing before being put in use. Many of these industries require also mandatory 100% testing after assembly of the object, a PMI process.

Alloys are a perfect medium for XRF analysis. With the few well-known exceptions, metallic alloys can be considered as homogeneous, solid solutions. The X-rays of all alloying elements (those that account for at least 99.5% of the whole alloy) are easily measurable, which allows for very accurate and precise analysis using a standardless, FP approach. HHXRF analyzers are routinely employed for analysis and sorting of stainless and low-alloy steels, high-temperature steels, tool steels, nickel and cobalt-based alloys, brasses and bronzes, titanium alloys, a number of aluminum alloys and precious metals.

Analysis of alloys involves determination of elemental composition of an alloy followed by identification of its grade designation. To determine the alloy grade, its measured elemental concentrations are compared with tables of specifications of alloy grades [17]. The alloy being tested is assigned the grade designation whose specifications are matched by the concentrations in the analyzed alloy. Most routine analyses can be performed within one to five seconds. Figure 19.13 shows readout screens from an HHXRF analyzer displaying the results of analysis of a very common grade of stainless steel, SS321. The analysis was performed using a Fe/Al primary beam filter with a silver anode tube, powered to 50 kV of high voltage. During measurement, the analyzer continuously updates the screen with the most recent analysis results.

The two screens are the consecutive time snapshots recorded during a single measurement of the sample. The left screen shows the results after just 0.2 seconds from the start of test. Concentrations of the four elements are displayed along with their errors at two standard deviations level. The lines above show that, based on these results, the grade of the alloy tested may be either stainless steel SS321 or stainless steel SS304, with the preference given to the former because its so-called “match number” of 1.1 is smaller than 1.4 for the latter. The right screen shows the results when this measurement was continued until 1.1 seconds elapsed from the start. Three more elements appeared in the result table, Mn, Nb, and Ti, because after longer measurement time the X-ray intensities of these three elements were measured with better precision and sensitivity, which allowed them to be quantified. Specifically, the detection and quantification of titanium concentration resulted in an unambiguous determination of the alloy grade as SS321 with a 0.0 match number. As a matter of fact, it is the 0.3% of titanium that differentiates these two popular steels, SS304 containing none.

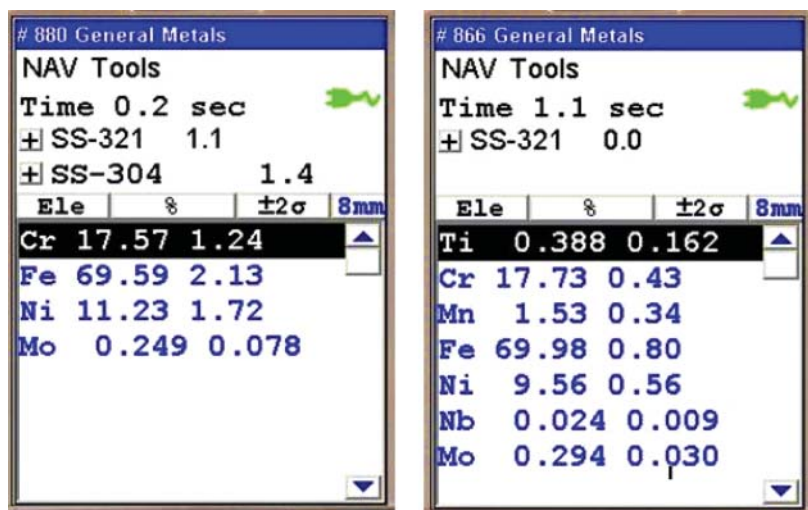


Figure 19.13 Screen shots showing analysis of grade SS321 stainless steel.

On one hand, this example illustrates the real challenges of alloy sorting and identification, which often depend on small concentration differences, while on the other hand it shows the power and capabilities of the contemporary HHXRF analysis.

Additional excitation conditions may be used if needed; for example, low concentrations of such elements as Ca, S, Ti, V, and Cr may be better analyzed with 20 kV excitation, and the very light elements such as Mg, Al, and Si may benefit from the use of a helium purge. Stainless steel SS303 differs from SS304 by only 0.12% sulfur. Yet, when scale and debris is removed from the surface of the analyzed alloy, the sulfur signal from 0.15% S in SS303 is intense enough to enable an HHXRF analyzer to positively distinguish these two alloys from each other.

Another useful observation we can make from the results shown in Figure 19.13 is that the error of measurement is reduced as measurement time gets longer. This is a known, universal feature of the EDXRF; for every fourfold increase of measurement time we gain a twofold reduction of measurement error.

This is illustrated in the Figure 19.14, which shows how the scatter (a measure of precision) of the measured concentrations of nickel in steel SS304 decreases with time. It is evident that extending the measurement time past five seconds is not justified, since it does not appreciably reduce the precision of the measurement, a practical illustration of the law of diminished returns.

#### 19.5.1.1 Typical Performance

Typical performance data to be expected when analyzing alloys with a HHXRF analyzer are listed in Table 19.3. The data were obtained for 60 seconds measurement time per primary filter. Detection limits for light elements can be improved using the HHXRF analyzer with a He purge option.

One must remember that the performance quoted above is valid for a flat, clean surface of tested alloy sample. The sample must not be covered by any paint, rust, scale, or oily residue, especially if analysis involves light elements such as Mg, Si, Al, and S. On the other hand, certain alloys exhibit significant local composition non-homogeneities which, when not accounted for, will lead to grossly inaccurate results. Figure 19.15 shows two examples. The left image is of an aluminum–silicon alloy with 17.6% of Si content. The large, irregular “silverish” shapes visible in the left part of the image are crystallites of silicon, which at high concentrations does not “dissolve” in aluminum, but precipitates as pure silicon. It is clear that when analyzer collects the X-rays from areas rich in such crystallites, it will produce an artificially high silicon concentration. Knowing that, the user may take

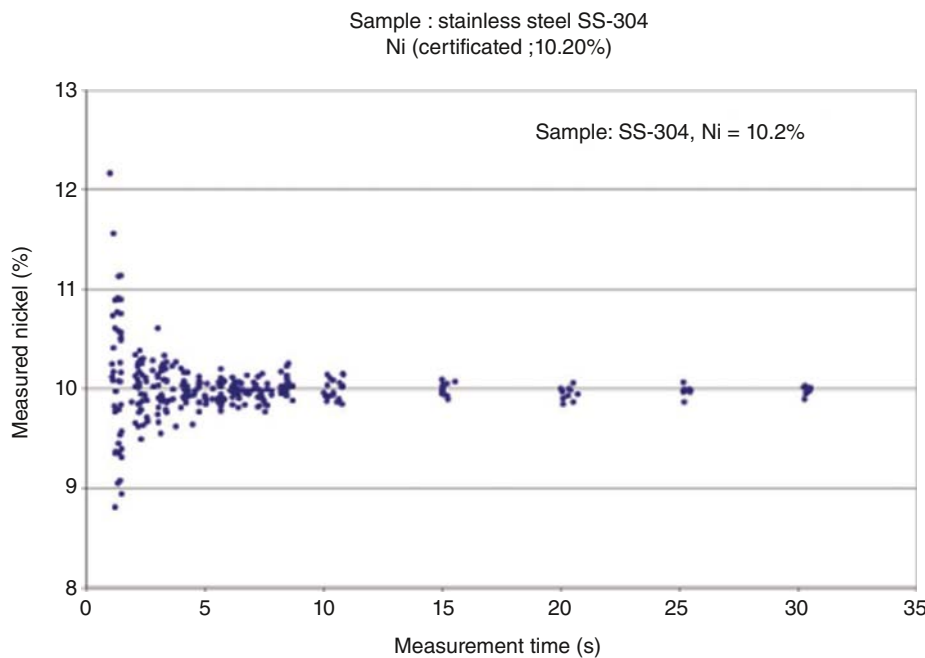


**Figure 19.14** Diminishing scatter of test results as function of measurement time.

a number of measurements moving the analyzer over the area of the sample and this way, by averaging, mitigate the effect of this metallurgical non-homogeneity.

The right image in Figure 19.15 shows a surface of copper-leaded bronze, containing 6.3% of lead. The dark, thickening veins are due to undissolved lead whose atoms, being much larger than copper's, have difficulty fitting into the copper matrix crystalline structure. However, since lead is also a very soft metal, grinding copper-leaded bronze to clean its surface for analysis will result in smearing the lead over the alloy surface, which will result in inflated concentration of lead. Therefore, one should use a lathe to clean the surface of this type of alloy. A similar effect can be expected with other copper alloys, such as brass (70% Cu, 30% Zn), and bronzes containing other soft metals, such as bismuth.

A more thorough overview of HHXRF application for analysis of alloys can be found in reference [18].

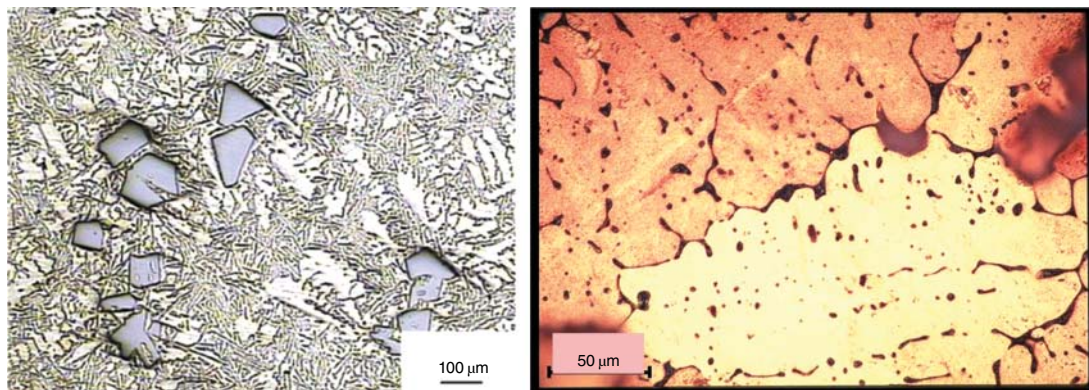


**Figure 19.15** Heterogeneity of alloys may adversely affect analytical results.

**Table 19.3** Example of limits of detection in alloys achievable with HHXRF analyzer.

Alloying element	Limits of detection for 60 s measurement time (mg/kg)			
	Al-base	Ti-base	Fe-base	Cu-base
Sb	20	35	50	70
Sn	15	30	50	70
Pd	15	20	40	55
Ru	15	15	20	20
Mo	N/A	15	15	15
Nb	N/A	15	15	15
Zr	N/A	15	15	15
Bi	15	15	15	30
Pb	15	15	40	35
Se	N/A	15	20	20
W	20	75	120	100
Zn	15	20	40	220
Cu	25	40	70	N/A
Ni	30	75	100	110
Co	30	70	500	110
Fe	50	175	N/A	175
Mn	70	160	160	175
Cr	50	160	35	65
V	20	550	25	40
Ti	20	N/A	30	30
S	N/A	N/A	250	N/A
P	N/A	N/A	N/A	N/A
Si	400	320	900	350
Al	N/A	N/A	4750	1300
Mg	4000	1500	N/A	N/A

### 19.5.2 Soil Screening for Heavy Metals

In this section, we discuss the applications that constitute the second largest – after alloy testing – use of HHXRF analysis.

No other application highlights all the benefits of a HHXRF better than screening soil for metals during cleanup and remediation of hazardous waste sites. Usually, not much, if any, reliable information is available about a site contaminated with hazardous waste, especially an old site. The first step in the long and costly process of site cleanup is site assessment, which always involves the task of testing the soil for contaminants.

The goal is to characterize the polluted site as to contaminant(s) type, location, spatial distribution, and concentration(s). The traditional approach relies on following random or predetermined grid patterns for extracting soil samples, and sending them to the laboratory for analysis. Such a method is not effective, and at the same time slow and very expensive.

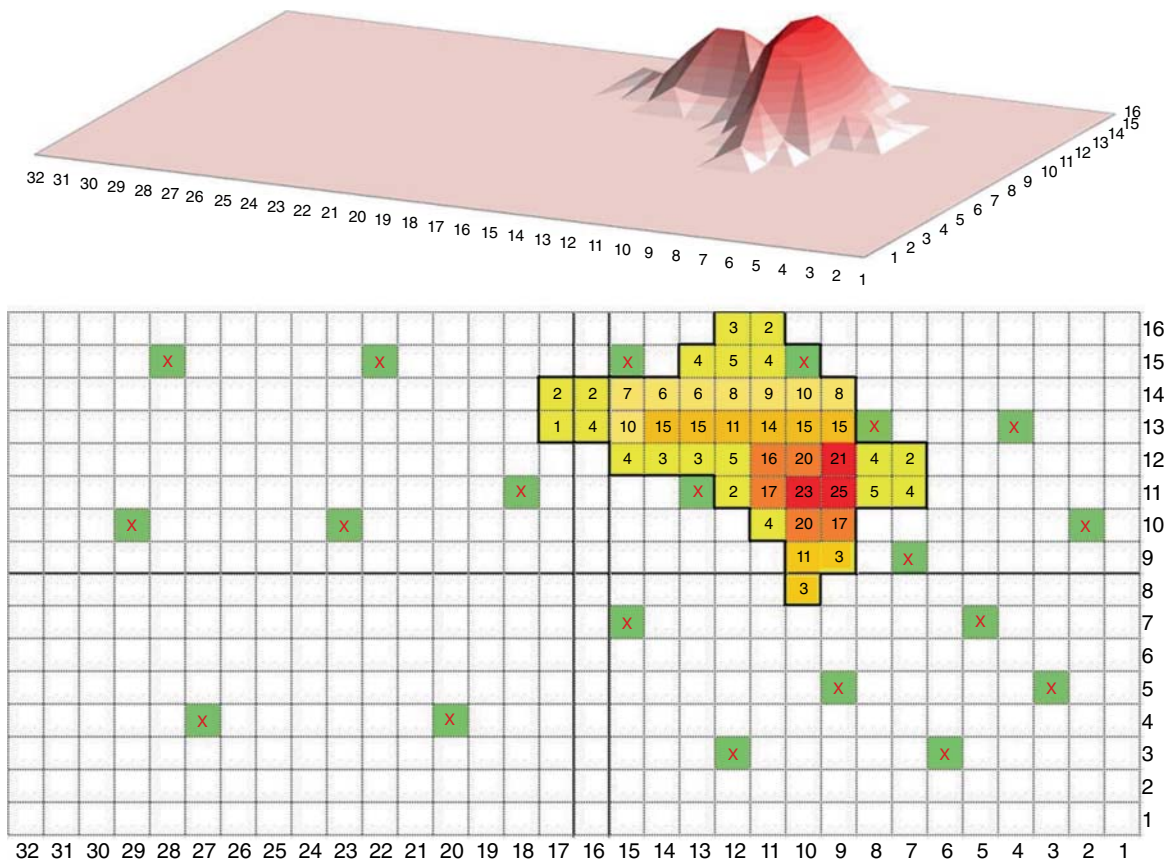


**Figure 19.16** 3D graph of hypothetical contaminated site (a), and map of contaminant concentration (b). The numbers in colored squares indicate the relative level of contaminant in arbitrary units. Green squares indicate randomly selected locations from which samples might be collected for traditional, laboratory analysis.

Figure 19.16 shows a map of a hypothetical contaminated site with a marked plume of inorganic contaminant. Each square of the grid is 5 m on the side, so the total dimension of the site is a 160 by 80 m rectangle, almost twice the size of a football field. Should we collect a sample from each square of the grid, we would end up with 512 samples of soil to be sent for laboratory analysis. Not only would it be prohibitively expensive but we would have to wait several weeks for the results. A seemingly better approach would be to collect a smaller number of samples from randomly selected squares, say a total of 20 samples from locations marked with a red X. Unfortunately, after weeks of waiting, the results of laboratory analyses would not reveal the location of the plume because random sampling just missed it.

Alternatively, an operator using a HHXRF analyzer would be able to perform in situ measurements at all 512 locations and accomplish the task in a day or two. The analyses would not only provide results for a number of elements, but since many of HHXRF instruments are GPS-enabled, the results would be stored with physical coordinates for automated mapping. Arguably, while the in situ measurements, performed directly on the surface of soil, may not be very accurate, they will nevertheless show trends of elemental concentrations and will allow delineating locations with elevated levels of contaminants.

The approach described here has been thoroughly researched [3, 19–24] and was adopted as the so-called “screening method” for metals in soil in the EPA Test Method 6200 [4]. The method provides the procedure for analyzing soil for metals by placing a handheld instrument directly on the soil surface. It also recognizes the fact that the degree of preparation of soil sample affects the representativeness and accuracy of XRF analysis. The undisturbed soil measured “as is” is a very non-homogeneous medium and, therefore, one cannot expect the XRF results to be representative of the average, bulk concentration. Unfortunately, many users tend to forget this and make unsubstantiated claims that the results obtained by XRF in situ do not agree with the results of laboratory analyses and, therefore, the XRF results must be wrong. The reality is that the soil sample analyzed by a laboratory is very different from the soil sample analyzed in situ by XRF. While the former is typically a 1–2 g aliquot withdrawn from about 250 g of dried, ground, and homogenized soil, the latter represents a few grams of an undisturbed, “as is” surface soil. If the XRF analyses are performed on soil samples that are given the same degree of preparation as those for the laboratory analysis, the agreement between the methods is excellent [23, 24].

A larger number of measurements, even with a relaxed accuracy of “screening,” provides reliable information about the presence and spread of contaminant and its relative concentration distribution throughout the investigated site [25]. Based on such information, it is possible to devise a precise plan for more accurate testing of the site within the contaminated range, accompanied if necessary by confirmatory laboratory analysis of selected samples.



**Figure 19.17** Soil screening in situ with HHXRF analyzer. Source: BartCo/Getty Images.

Having the ability to quickly and reliably pinpoint contaminated areas allows for timely and cost-effective decontamination, without the risk of disturbing areas free of contaminants. Additionally, the ability to perform in situ analysis, directly on the soil surface, allows for real-time verification of effectiveness of decontamination efforts at every phase of the process.

The added value of using HHXRF for soil screening is its nondestructive character, which means that soil samples, once measured, can be archived for future reference or re-testing should the need arise. This is extremely important in situations involving litigation, as practically all environmental cleanups are.

Most recently the International Standard Organization also published its own test method for screening soils for metals with portable or HHXRF instruments [26].

#### 19.5.2.1 Typical Performance

Figure 19.18 shows typical limits of detection achievable with an HHXRF analyzer in a 60-second measurement time, using a silver anode tube at 50 kV. The limits of detection (LOD) are calculated as three standard deviations of element concentration, as measured in silica matrix (blue color) or in certified reference material sample with low concentrations of the analytes (red color). As can be seen, the LODs stay on average at the 10–20 mg/kg level, which is more than sufficient as typical “action levels” to which the contaminants need to be reduced are specified at 100 mg/kg or higher.

The LOD values reported in Figure 19.18 are valid for homogeneous, dry, finely ground material presented for analysis in a cup with an X-ray transparent window. An aliquot of material in a cup must form a layer thick enough that it can be considered infinitely thick for characteristic X-rays of analytes: approximately a 15 mm thick layer is sufficient for X-ray energies up to about 20 keV.

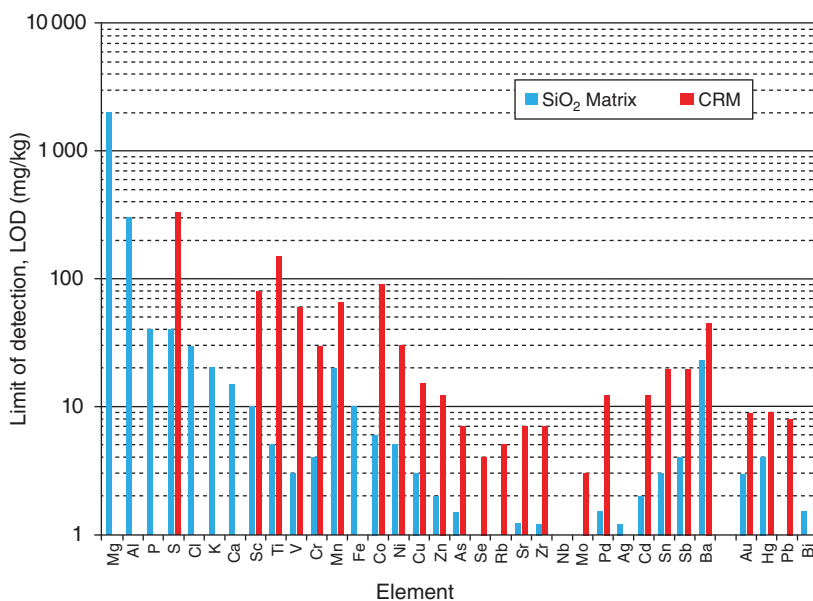


**Figure 19.18** Typical limits of detection for elements in soil matrix, achievable with contemporary handheld XRF analyzer.

### 19.5.3 Screening Electronic, Consumer Products and Children Toys for Compliance

HHXRF analyzers have proven themselves very useful in screening various consumer products for compliance with the regulations which limit the content of certain elements or substances known to be harmful for humans or the environment in those products.

#### 19.5.3.1 Electronic and Consumer Products

The European Council Directive [27], commonly known as the “RoHS” Directive, which went into effect in June of 2006, limits concentrations of lead, mercury, hexavalent chromium, and brominated flame retardants in electronic products entering the European market to less than 0.1% and that of cadmium to less than 0.01%. In the reality of global economy and trade, the directive has worldwide reach, and pretty much all countries in the world adopted the essence of the directive in their jurisdictions.

XRF cannot distinguish hexavalent and trivalent chromium, but it does provide the total concentration of chromium. Thus, if the measured concentration of total chromium is below the permissible limit, so is the amount of hexavalent chromium. Similarly, XRF cannot speciate brominated flame retardants. However, since all brominated flame retardants in order to be effective contain at least 50% of elemental bromine, if XRF analysis shows total bromine to be less than 0.05%, one may conclude the product meets compliance requirements.

The XRF method detection limits are low enough to assure reliable measurement and decision-making, even considering the fact of enormous diversity and non-homogeneity of composition designed into these products. Consequently, XRF analysis has been adopted by the electronics industry as a method of choice for screening their products for the presence of the restricted substances named above, and the International Electrotechnical Commission developed a test method for screening electronic products using XRF [28].

HHXRF is predominantly used to screen electronic products, preferably in their undisturbed state. The attribute of nondestructiveness of the HHXRF analysis is a very important factor because products passing the compliance test are not defaced and, therefore, can be put to use or sold.

Typical limits of detection expected when using HHXRF to analyze polymers and electronic alloys are listed in Table 19.4. The elements that must be tested for compliance are highlighted. The data in the table were determined using an Ag anode tube with Mo primary filter powered to 50 kV and using 30 seconds acquisition time. The lead content of tin (in the so-called “lead-free solder”) can be reliably analyzed way below 1000 mg/kg of compliance threshold. Printed circuit boards (PCBs) are often screened for halogens such as chlorine and bromine, which are each limited to less than 900 mg/kg.

An updated version of the “RoHS” Directive broadened its scope to practically any consumer product that contains any type of electronics. This way, fancy tennis shoes with built-in lights blinking during walking or a talking doll are considered electronic products and must comply with the directive.

#### 19.5.3.2 Testing Toys and Children Articles for Lead and Other Toxic Elements

While children’s toys and consumer products designed for children are tested for a number of elements, it is because of devastating consequences of lead poisoning in children that lead has always been the main target of testing. More recently, high percent concentrations of lead have been identified in paints applied to toys and in materials used for toys and children’s articles. In the fall of 2007, tens of thousands of toys imported from China were sequestered by US Customs after tests revealed high concentrations of lead in them. The lead was found not only in paints used on toys, but also in substrate materials. Consequently, the U.S. Congress passed in 2008 a law that bans lead in paint applied to toys at 90 mg/kg, and in any other materials used for children’s products

**Table 19.4** Limits of detection (LODs) for elements typically in electronic products or materials.

Limits of detection for 30 s measurement time (mg/kg)						
	Polymer matrix			Metal matrix		
Element	PE	PVC	Element	Cu	Zn	Sn
Ba	100	N/A	Ba	150	150	1400
Sb	22	25	Sb	60	65	300
Sn	18	20	Sn	65	70	N/A
<b>Cd</b>	<b>13</b>	<b>15</b>	<b>Cd</b>	<b>35</b>	<b>35</b>	<b>220</b>
Bi	5	20	Bi	65	400	90
<b>Pb</b>	<b>5</b>	<b>15</b>	<b>Pb</b>	<b>75</b>	<b>80</b>	<b>120</b>
<b>Br</b>	<b>3</b>	<b>8</b>	<b>Br</b>	<b>25</b>	<b>110</b>	<b>35</b>
Se	3	20	Ag	A/S	A/S	A/S
As	3	18	In	40	40	250
<b>Hg</b>	<b>6</b>	<b>30</b>	<b>Hg</b>	<b>150</b>	<b>1200</b>	<b>165</b>
Au	8	40	Pd	22	25	40
Zn	12	70	Au	250	7000	250
Cu	12	60	Pt	350	1000	250
Ni	12	75	Zn	300	N/A	130
Fe	20	120	Cu	N/A	160	250
<b>Cr</b>	<b>12</b>	<b>20</b>	Ni	175	75	600
V	200	1100	Co	75	80	450
Ti	10	50	Fe	115	100	750
<b>Cl</b>	<b>40</b>	<b>N/A</b>	<b>Cr</b>	<b>30</b>	<b>25</b>	<b>110</b>

Elements in **bold font** are restricted under the directive. A/S means application specific.

at 100 mg/kg [29]. Again, XRF analysis using handheld instruments has been found by regulatory and enforcing bodies as the most practical screening tool for lead testing in toys and children products as is shown in Figure 19.19 [30, 31]. Field Inspectors from the Consumer Products Safety Commission in the United States use a number of HHXRF analyzers for screening toys and children products for lead at ports of entry to the United States [32, 33]. Many countries announced that they also will use pXRF analyzers for screening consumer products and toys for the presence of heavy metals.

The analytical performance of HHXRF analyzers, when applied to testing bulk materials used for children's products, is the same as listed in Table 19.4. On the other hand, when analyzing lead in a thin layer of applied paint, the most useful and meaningful approach is to measure lead based upon its areal mass in units of  $\mu\text{g}/\text{cm}^2$ . One can expect from the typical HHXRF analyzer a lower LOD for lead of about 0.2–0.3  $\mu\text{g}/\text{cm}^2$ . For a paint of 1.4  $\text{g}/\text{cm}^3$  density and 50  $\mu\text{m}$  thick, this would translate into a mass fraction of lead in paint of 30–45 mg/kg. In other words, any paint with lead detected at an areal mass greater than 0.7  $\mu\text{g}/\text{cm}^2$  should be considered as potentially exceeding the regulatory limit.

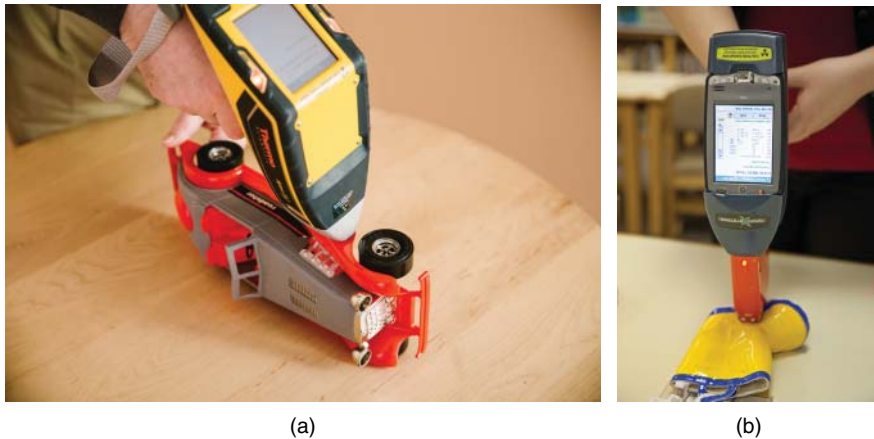


**Figure 19.19** (a, b) Testing toys for lead with a handheld XRF analyzer. Source: Richard A. Crocombe; Jim West / Alamy Stock Photo.

ASTM has developed a Standard Test Method to address just the problem of lead in paint on toys using XRF analyzer [34].

#### 19.5.4 Testing for Presence of Lead in Household Paint

Historically, the main source of lead poisoning in children has been household lead contained in wall paint. Lead pigments, such as lead chromate ( $PbCrO_4$ ) or lead carbonate ( $PbCO_3$ ) are added to paint to speed up drying and increase the adherence and durability of paint layers. Unfortunately, lead in paint is especially hazardous to small children, whose developing bodies are very susceptible to lead poisoning. Lead causes irreversible damage to the brain and nervous system, manifesting itself by learning and comprehension difficulties, stunted growth, kidney damage, and delayed development. Small children, especially those below three years of age, are notorious for putting their toys and any other objects they play with in their mouths. They also can be exposed by eating lead-based paint chips, chewing on objects painted with lead-based paint, or swallowing house dust or soil that contains lead. To address the problem of lead in household paint, many countries banned the use of leaded paint in residential applications. In the United States, lead-based paint was banned by U.S. Congress in 1971 [35]. XRF analysis was determined early on as the preferred test method for detecting lead in applied paint, and the areal mass of lead equal to  $1\text{ mg/cm}^2$  was established as the maximum permissible federal level of lead in applied paint. HHXRF analyzers designed specifically for testing lead in household paint are exceptional in the fact that they use  $^{109}\text{Cd}$  or  $^{57}\text{Co}$  radioisotopes as sources of exciting radiation. These instruments can quantify an areal mass of lead down to  $0.05\text{ mg/cm}^2$  in 5–30 seconds of test time.

Figure 19.20 shows a handheld analyzer specifically designed to test lead in applied paint. It uses  $^{57}\text{Co}$  isotope rather than the less-energetic  $^{109}\text{Cd}$ . A cadmium source can only effectively excite lead L-series X-rays, which fall between 10 and 14 keV. These X-rays are often totally absorbed by the outer layer of paint, often containing barium compounds, which are very strong absorbers of lead L-series X-rays. A  $^{57}\text{Co}$  source with over 100 keV photons can easily excite K-series X-rays of lead, which do not suffer from absorption like those of the L-series.

#### 19.5.5 Other Applications

##### 19.5.5.1 Mining and Minerals

The mining industry has benefited from the development of the field-portable and HHXRF analysis. All mining operations are preceded by prospecting and exploration phases, and it is in prospecting and early stage exploration



**Figure 19.20** Pb200i, Lead in Paint Analyzer from Viken Detection. *Source:* © Viken Detection.

in which the HHXRF analyzer is the most useful to geologists looking for new, mineral-rich, ore deposits [36, 37]. The ability to use XRF on site allows the prospector not only to assess ore grade and make proper decisions in real time, but also to select more representative samples for laboratory analysis [38]. On-site measurements, especially on unaltered surface of rock or soil, may not provide representative results for reasons discussed in Section 19.5.2.1. Nevertheless, high spatial frequency of the field tests outweighs higher uncertainties of the individual results to the extent that the *in situ* XRF can be up to three times more cost-effective than the *ex situ* method (such as atomic absorption spectroscopy (AAS) or ICP) at characterizing the site or body of ore [39].

The expected limits of detection reported in Figure 19.18 will generally also apply for ores and minerals. However, there is a subtle difference. In analysis of soil for contaminants the emphasis is placed on accurate determination of contaminants, while less attention is paid to matrix elements such as iron, aluminum, or silicon. When analyzing ores and rocks, all elements may be equally important for grading the ore (on average about 30 elements are critical for geologist to assess the ore). Specifically, the economic quality of many ores very much depends on accuracy of determination of such abundant elements as magnesium, aluminum, silicon, phosphorus, potassium, or calcium. Unfortunately, the X-ray energies of these light elements are easily absorbed in the ore matrix, and additionally by air in the gap between the detector and sample surface. Therefore, they are difficult to measure, despite the fact that they are present at high concentrations. However, if an air gap in the close-coupled geometry of measurement in HHXRF analyzer can be maintained at less than about 5 mm, the absorption of light element's X-rays by air between the detector and sample can be effectively reduced to the levels allowing quantification down to magnesium without the need for vacuum or helium flush. A recently introduced model of HHXRF analyzer is said to be able to analyze magnesium in soil/ore down to 2000 mg/kg, and in 30 seconds measurement time to determine uranium in ore down to 10 mg/kg [40].

Prospecting operations usually take place in remote, difficult-to-access locations. Therefore, in order to increase the accuracy of the on site analysis, prospectors are willing to carry specially designed, miniaturized, battery-operated equipment for sample preparation, along with the HHXRF analyzer. A small grinding drill and press allows the prospector to prepare a homogeneous, free from particle-size effects, sample in the form of a powder or pellet, thus improving the accuracy and representativeness of ore analysis [41].

Despite the challenges, HHXRF analysis offers a number of distinct advantages for the mining industry such as: real-time geochemistry, on-site delineation and mapping of prospect ore boundaries, on-site analysis of light elements, ore grade control, drill core analysis [42–44], and elemental analyses required at all stages of the mining process.

### 19.5.5.2 Art and Archaeometry

Archaeometry evolved from archaeology to become a separate scientific discipline, which deals with the application of various scientific techniques to the analysis and dating of archaeological materials. During the last decade, HHXRF analysis became one of the favorite analytical techniques of archeologists, conservationists, museum curators, and historians of art. The factors driving its popularity are its portability and truly nondestructive character of analysis.

HHXRF analysis is mainly used for rapid analysis of all kinds of historical artifacts and objects found at archaeological excavation sites. They represent metallic alloys, ceramics, glass, pigments, wood, and fabrics. Historical artifacts are unique, one-of-a-kind, objects which must be preserved rather than deliberately defaced or altered for analysis. This is why XRF analysis of historical artifacts is, as a rule, qualitative and, at best, only semiquantitative. Nevertheless, even qualitative XRF analysis provides a vast amount of information about the object, which allows establishment of provenance, dating, and – if needed – designing proper restoration procedures. A number of examples of investigations of elemental composition of archeological and cultural heritage objects using handheld and portable XRF can be found in journals such as *Archaeometry*, *X-Ray Spectrometry*, and *Journal of Archeological Science*, to name a few, and in many dedicated books chapters [45, 46]. See also the chapters by Pozzi and Donais in this volume.

Special attention is devoted to analysis of objects made of obsidian [47]. This volcanic glass was very much praised by ancient humans as material for very sharp tools and also for jewelry. Elemental analysis of obsidian artifacts allows for the study of migration and trade routes of our ancestors [48].

Metallic objects such as coins and bronze sculptures are often investigated using HHXRF. An example of the in situ analysis of a bronze monument of a Slovenian Poet, France Prešeren (1800–1849) with a HHXRF is presented in reference [49]. It was found that composition of tin-lead bronze was not consistent between different sections of the monument, with tin content varying as much as from 5 to 10% absolute, implying the possibility of different sources of material and/or evidence of repairs performed on the monument.

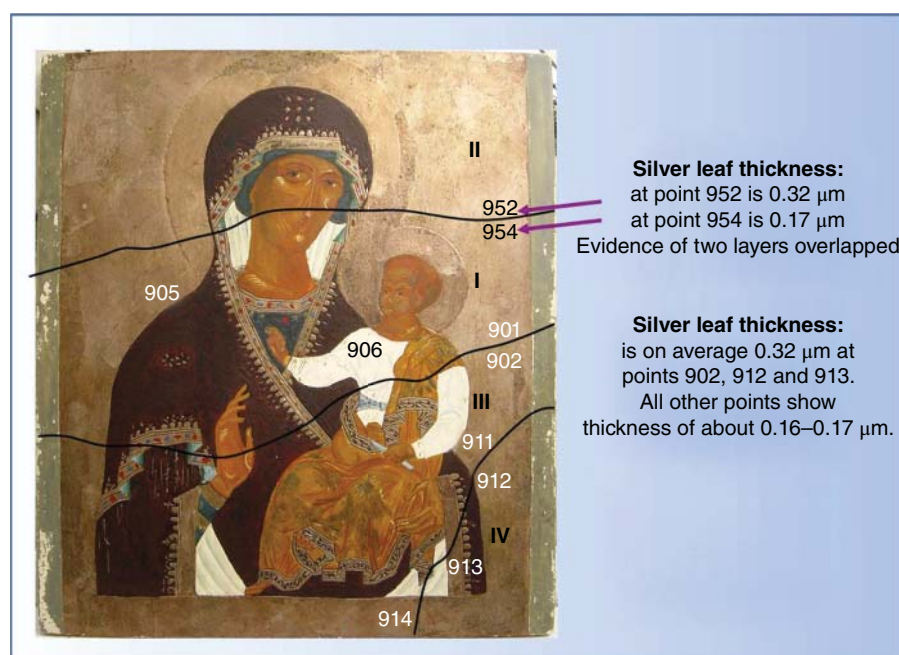


Figure 19.21 Sixteenth-century icon from the Bieszczady region of Poland; a study of the silver leaf background.

Another interesting, and yet simple example of, an HHXRF application is shown in Figure 19.21 [50]. Here, an HHXRF analyzer was used to measure thickness of silver leaf foil used as a background for the sixteenth-century icon painting. After verifying that the leaf was indeed silver, the instrument was calibrated with thin film standards to read thickness of silver layers in  $\mu\text{m}$ . By taking measurements at numbered locations, it was found that the thickness of silver leaf was either  $17 \pm 2$  or  $34 \pm 2 \mu\text{m}$ , with the latter results originating always at the edge of area. Based on that, it has been concluded that most likely a sheet of silver marked as I was applied by the painter first to the wooden board, then either II or III, and then IV.

Many museums have to deal with residues of pesticides present on artifacts of an organic nature, such as feathers, cloth, wood, samples of old wall paper. Historically, pesticides were applied to those objects to prevent their destruction by insects. Some of these collections are to be returned to their original owners like Indian Tribes, who will use them in their rituals. HHXRF is used to monitor for the presence of arsenic (dominant component in older pesticides) in those objects before they can be released [51–54].

An excellent source on HHXRF applications in art and archaeology is a book by A.N. Shugar and J.L. Mass [55].

## 19.6 Remarks on Safety When Using HHXRF

HHXRF analyzers, whether isotope or X-ray tube based, are subject to strict regulations aimed to limit accidental exposure of humans to radiation. Those regulations are less stringent for X-ray tube devices since once the instrument is powered off, X-ray tube cannot emit any radiation. The analyzers are perfectly safe if operated according to manufacturers' instructions and for the purpose they were designed. A HHXRF analyzer is by its design and mode of operation a so-called "open beam" device. When the analyzer is measuring a sample, the X-ray beam, whether from the X-ray tube or radioisotope, is contained only by the sample itself. Therefore, it is mandatory that the operator of such analyzer is trained on proper operation of the instrument and all safety precautions. For example, when working with the analyzer, the operator must not use the instrument in such a manner that the X-ray beam is directed at him/herself or any other person.

The radiation safety issues that concern pXRF instruments with miniature X-ray tubes are addressed in the international standard developed by International Electrotechnical Commission (IEC) [56]. However, ultimately the ownership and operation of these devices are governed by state and local safety laws and regulations, which always take precedence over other rules. It is the responsibility of the user of the device to comply with such laws and regulations.

## 19.7 Summary and Possible Future Developments for HHXRF

The performance of the present-day HHXRF analysis in many instances rivals that expected of the stationary, laboratory EDXRF equipment. It represents a good balance between uncompromised analytical performance and portability, ruggedness, nondestructiveness, speed, and versatility. These features have been recognized by a broad spectrum of users, representing mostly the various branches of industry, but also research and academia. As it is often the case, the success of HHXRF has created new avenues for the use of the XRF method. A number of less visible applications emerged, such as detecting counterfeit currency and fake jewelry, quality control of thickness of various coatings on various substrates [53], detection of counterfeit medication and dietary supplements, and so on.

Contemporary HHXRF analyzers are often equipped with wireless and GPS capabilities, which make them very practical, real-time, remote location data-collecting probes. Efforts have been initiated to develop new X-ray sources with promise to be even smaller and less power hungry than the existing miniature X-ray tubes [57], but they have not materialized yet.

More and more emphasis is being placed on the user software to make the use of the instrument easier, such as through voice commands. Another improvement track is focused on making the user software “smarter,” which not only generates numerical results, but will also make a proper decision, based on the result. In the drive to make instruments smaller, lighter, and smarter, there are ideas to make HHXRF analyzers trimmed down to just a small sensor generating X-ray spectrum of sample, which would be sent via internet to some central location where sophisticated software would analyze it and feedback the results to the user.

One of the older trends pursued was “hyphenation” or “hybridization” of the HHXRF with another “handheld” analytical technique(s) the results of which when combined would provide more complete description of the object tested. For example, combining elemental composition data from XRF with molecular data from NIR or Raman spectra would provide both elemental and mineralogical information about analyzed rock in the field [58].

Whatever the outcome of the efforts mentioned here, one thing is certain: that the use of HHXRF will increase and that users will find and develop new applications.

## Acronyms and Abbreviations

A/S	Application Specific
ASTM	American Society for Testing and Materials
CCD	Charge-coupled device
DSP	Digital signal processor
EDXRF	Energy-dispersive X-ray fluorescence
EPA	US Environmental Protection Agency
FPXRF	Field-portable X-ray fluorescence
FWHM	Full-width at half-maximum
HHXRF	Handheld X-ray fluorescence
HHpXRF	Handheld portable X-ray fluorescence
ICP	Inductively coupled plasma
LCD	Liquid crystal display
LODs	Limits of detection
MCA	Multichannel analyzer
pXRF	Portable X-ray fluorescence
p-i-n	p-type-intrinsic-n-type silicon diode
PMI	Positive Material Identification
PCB	Printed circuit board
RoHS	Restriction of Hazardous Substances
SDD	Silicon-drift detector
WDXRF	Wavelength dispersive X-ray fluorescence
XRF	X-ray fluorescence

## References

- 1 Van Grieken, R.E. and Markowicz, A.A. (eds.) (2002). *Handbook of X-Ray Spectrometry: Methods and Techniques*, 2ed. Marcel Dekker.
- 2 Rhodes, J.R. and Rautala, P. (1983). Application of a microprocessor-based portable XRF analyzer in mineral analysis. *Int. J. Appl. Radiat. Isot.* 34 (1): 333–343.

- 3 Piorek, S. (1990). XRF technique as a method of choice for on-site analysis of soil contaminants and waste material. In: *Advances in X-Ray Analysis*, vol. 33, 639–645. New York: Plenum Press.
- 4 US-EPA Method 6200 (2007). *Field Portable X-ray Fluorescence Spectrometry for the Determination of Elemental Concentrations in Soil and Sediment..* Rev. 0, February 2007, SW 846. EPA [www.epa.gov/osw/hazard/testmethods/sw846/pdfs/6200.pdf](http://www.epa.gov/osw/hazard/testmethods/sw846/pdfs/6200.pdf) (accessed 14 April 2020).
- 5 Piorek, S. and Rhodes, J.R. (1986). Application of a microprocessor based portable analyzer to rapid, non-destructive alloy identification. *Proceedings of International Conference and Exhibit*, ISA 86 Houston, TX (13–16 October 1986), paper 86-2839, pp. 1355–1368. Instrument Society of America.
- 6 Berry, P.F. and Voots, G.R. (1989). On-site verification of alloy materials with a new field-portable XRF analyzer based on a high-resolution HgI<sub>2</sub> semiconductor X-ray detector. In: *Non-Destructive Testing* (Proceedings of the 12th World Conference on Non-Destructive Testing, Amsterdam, The Netherlands (23–28 April 1989) (eds. J. Boogaard and G.M. Van Dijk), 737–742. Amsterdam: Elsevier Science Publishers.
- 7 Piorek, S. (1989). Modern alloy analysis and identification with a portable X-ray analyzer. In: *Advances in X-Ray Analysis*, vol. 32, 239–250. New York: Plenum Press.
- 8 Piorek, S. (1994). Principles and applications of man-portable X-ray fluorescence spectrometry. *Trends in Analytical Chemistry* 13 (7): 281–286, *invited paper*.
- 9 Piorek, S. (1997). Field-portable X-ray fluorescence spectrometry, past, present and future. *Field Analytical Chemistry and Technology* 1 (6): 317–329. (*invited technology review paper*).
- 10 Reyes-Mena, A., Moras, M., Jensen, C. et al. (2004). Characterization techniques for miniature low-power X-ray tubes. *Advances in X-Ray Analysis* 47: 85–90.
- 11 Jensen, C., Elliott, S.M., Liddiard, S.D. et al. (2004). Improvements in low power, end-window, transmission-target X-ray tubes. *Advances in X-Ray Analysis* 47: 64–69.
- 12 XR-100CR Additional Performance Spectra and Detector Properties. <https://www.amptek.com/-/media/ametekamptek/documents/products/xr100cr.pdf> (accessed 13 November 2020).
- 13 Lechner, P., Fiorini, C., Longoni, A. et al. (2004). Silicon drift detectors for high resolution, high count rate X-ray spectroscopy at room temperature. *Advances in X-Ray Analysis* 47: 53–58.
- 14 Andermann, G. and Kemp, M.W. (1958). Scattered X-rays as internal standards in X-ray emission spectroscopy. *Analytical Chemistry* 30: 1306.
- 15 Lucas-Tooth, H.J. and Price, B.J. (1961). A mathematical method for investigation of inter-element effects in X-ray fluorescent analysis. *Metallurgia* 64 (383): 149–161.
- 16 Lucas-Tooth, H.J. and Pyne, C. (1964). The accurate determination of major constituents by X-ray fluorescence analysis in the presence of large interelement effects. *Advances in X-ray Analysis* 7: 523–541.
- 17 SAE International (2017). *Metals and Alloys in the Unified Numbering System*, 13ed. Warrendale, PA: SAE International <https://www.sae.org/publications/books/content/hs-1086/2017> (accessed 13 November 2020).
- 18 Piorek, S. (2008). “Alloy identification and analysis with a field-portable XRF analyzer”, Chapter 6. In: *Portable X-ray Fluorescence Spectrometry* (eds. P.J. Potts and M. West), 98–140. Cambridge, UK: The Royal Society of Chemistry.
- 19 Piorek, S. (June 1998). Determination of metals in soil by field-portable XRF spectrometry, unit 3B.1. In: *Current Protocols in Field Analytical Chemistry* (ed. V. Lopez-Avila), 3b.1.1–3B.1.18. John Wiley & Sons.
- 20 Piorek, S. (1997). On-site, in-situ characterization of contaminated soil and liquid hazardous waste with field portable X-ray analyzer – a cost effective approach. In: *Field Screening Europe* (eds. J. Gottlieb, H. Hötzl, K. Huck and R. Niessner). Springer, Dordrecht. [https://doi.org/10.1007/978-94-009-1473-5\\_76](https://doi.org/10.1007/978-94-009-1473-5_76).
- 21 Piorek, S., Pasmore, J., Piorek, E., Kahn, M.R. (1995). Significance of field portable X-ray fluorescence spectrometry for expedited site characterization and risk assessment. Presented at International Symposium and Trade Fair on the Clean-up of Manufactured Gas Plants, Prague, Czech Republic (19–21 September 1995), published in *Land Contamination and Reclamation* 3 (4): 17–19.

- 22** Piorek, S. (1994). Modern, PC based, high resolution portable EDXRF analyzer offers laboratory performance for field, in-situ analysis of environmental contaminants. *Proceedings of the 1994 Symposium on Radiation Measurements and Applications*, Ann Arbor, Michigan (16–19 May 1994), in NIM, Section A 353: 528–533.
- 23** Shefsky, S. (1995). Lead in soil analysis using the NITON XL. *International Symposium on Field Screening Methods for Hazardous Wastes and Toxic Chemicals (A&WMA VIP-47)*, Las Vegas (22–24 February 1995), pp. 1106–1117.
- 24** Shefsky, S. (1997). Comparing field portable X-ray fluorescence (XRF) to laboratory analysis of heavy metals in soil. Presented at the *International Symposium of Field Screening Methods for Hazardous Wastes and Toxic Chemicals*, Las Vegas, Nevada, USA (29–31 January 1997). <https://citeseerx.ist.psu.edu/viewdoc/download?doi=10.1.1.204.7887&rep=rep1&type=pdf> (accessed 13 November 2020).
- 25** Kalnicky, D.J. and Singhvi, R. (2001). Field portable XRF analysis of environmental samples. *Journal of Hazardous Materials* 83 (1–2): 93–122.
- 26** ISO 13196 (2013). *Soil Quality – Screening Soils for Selected Elements by Energy-dispersive X-ray Fluorescence Spectrometry using a Handheld or Portable Instrument*. Geneva, Switzerland: International Organization for Standardization <https://www.iso.org/standard/53490.html> (accessed 13 November 2020).
- 27** EUR-Lex (2017). Directive 2011/65/EU of the European Parliament and of the Council of 8 June 2011 on the restriction of the use of certain hazardous substances in electrical and electronic equipment <http://data.europa.eu/eli/dir/2011/65/2020-09-01> (accessed 13 November 2020).
- 28** International Standard IEC 62321. Electrotechnical products – determination of levels of six regulated substances (lead, mercury, cadmium, hexavalent chromium, polybrominated biphenyls, polybrominated diphenyl ethers), Edition 1.0, 2008-12, IEC Central Office, 3, rue de Varembe, Geneva, Switzerland. <https://webstore.iec.ch/publication/6834> (accessed 13 November 2020).
- 29** U.S. Congress, 110th. Public Law 110-314: Consumer Product Safety Improvement Act of 2008. Washington, D.C., 14 Aug 2008. (H.R. 4040).
- 30** Test Method: CPSC-CH-E1001-08.3 Standard Operating Procedure for Determining Total Lead (Pb) in Children's Metal Products (Including Children's Metal Jewelry), Revision 1, 15 November 2012. [https://www.cpsc.gov/s3fs-public/pdfs/blk\\_media\\_CPSC-CH-E1001-08\\_3.pdf](https://www.cpsc.gov/s3fs-public/pdfs/blk_media_CPSC-CH-E1001-08_3.pdf) (accessed 13 November 2020).
- 31** Test Method: CPSC-CH-E1002-08.3 Standard Operating Procedure for Determining Total Lead (Pb) in Nonmetal Children's Products, Revision 1, 15 November 2012. [https://www.cpsc.gov/s3fs-public/pdfs/blk\\_pdf\\_CPSC-CH-E1002-08\\_3.pdf](https://www.cpsc.gov/s3fs-public/pdfs/blk_pdf_CPSC-CH-E1002-08_3.pdf) (accessed 15 November 2020).
- 32** Consumer Product Safety Commission. CPSC's National Product testing and Evaluation Center. <https://www.youtube.com/watch?v=2weOcnXZ2xU> (accessed 13 November 2020).
- 33** Cobb, D. (August 2009). "Study on the Effectiveness, Precision and Reliability of X-ray Fluorescence Spectrometry and Other Alternative Methods for Measuring Lead in Paint." U.S. CPSC, Gaithersburg, MD. <https://www.cpsc.gov/s3fs-public/pdfs/leadinpaintmeasure.pdf> (accessed 13 November 2020).
- 34** ASTM (2015). F3078-15, "Standard Test Method for Identification and Quantification of Lead in Paint and Similar Coating Materials using Energy Dispersive X-ray Fluorescence Spectrometry (EDXRF)". ASTM International, West Conshohocken, PA, USA. [www.astm.org](http://www.astm.org) (accessed 13 November 2020).
- 35** U.S. Congress, 91st. Public Law 91-695: Lead-based paint poisoning prevention act. Washington, D.C., 13 Jan 1971. (H.R. 19172).
- 36** Peter, J. M., Chapman, J. B., Mercier-Langevin, P. et al. (2010). Use of portable x-ray fluorescence spectrometry in vectoring for base metal sulfide exploration. *TGI-3 Workshop: Public Geoscience in Support of Base Metal Exploration*, Vancouver, BC, Canada (22 March 2010), pp. 3–6. [https://www.researchgate.net/publication/257503026\\_Use\\_of\\_Portable\\_X-ray\\_Fluorescence\\_Spectrometry\\_in\\_Vectoring\\_for\\_Base\\_Metal\\_Sulfide\\_Exploration](https://www.researchgate.net/publication/257503026_Use_of_Portable_X-ray_Fluorescence_Spectrometry_in_Vectoring_for_Base_Metal_Sulfide_Exploration) (accessed 13 November 2020).
- 37** Chapman, J. B., Peter, J. M., Layton-Matthews, D., and Gemmell, J. B. (2010). Portable XRF and laser-ablation ICP-MS as vectoring tools in base metal exploration. *TGI-3 Workshop: Public Geoscience in Support of*

- Base Metal Exploration*, Vancouver, BC, Canada (22 March 2010), pp. 7–10. [https://www.researchgate.net/publication/257503740\\_Portable\\_XRF\\_and\\_laser-ablation\\_ICP-MS\\_as\\_vectoring\\_tools\\_in\\_base\\_metal\\_exploration\\_examples\\_from\\_the\\_Kidd\\_Creek\\_Mine\\_area](https://www.researchgate.net/publication/257503740_Portable_XRF_and_laser-ablation_ICP-MS_as_vectoring_tools_in_base_metal_exploration_examples_from_the_Kidd_Creek_Mine_area) (accessed 13 November 2020).
- 38 Houlahan, T., Ramsay, S., and Povey, D. (2003). Use of field portable X-ray fluorescence spectrum analyzers for grade control – a presentation of case studies. *Proceedings of the 5th International Mine Geology Conference*, Bendigo, Victoria (17–19 November 2003). Australasian Institute of Metallurgy, pp. 377–385.
- 39 Taylor, P.D., Ramsey, M.H., and Potts, P.J. (2004). Balancing measurement uncertainty against financial benefits: comparison of in situ and ex situ analysis of contaminated land. *Environmental Science and Technology* 38 (24): 6824–6831.
- 40 Bauer, M. (2020). Exploring new frontiers of in situ geochemical analysis. Application Note, Thermo Fisher Scientific, Tewksbury, MA, USA. <https://www.thermofisher.com/us/en/home/industrial/spectroscopy-elemental-isotope-analysis/portable-analysis-material-id/portable-mining-exploration-solutions/portable-hard-rock-mining-analysis.html> (accessed 7 February 2020).
- 41 Berry, P.F., Furuta, T., and Rhodes, J.R. (1968). Particle size effects in radioisotope X-ray spectrometry. *Advances in X-Ray Analysis* 12: 612–632.
- 42 Tohyama, S. (22 March 2010). *Mapping Elemental Concentrations with HHXRF Analyzer on the Surface of Drill Core*. Billerica, MA, unpublished Internal Report: Thermo-Fisher Niton LLC.
- 43 Ge, L., Lai, W., and Lin, Y. (2005). Influence of and correction for moisture in rocks, soils and sediments on *in situ* XRF analysis. *X-Ray Spectrometry* 34 (1): 28–34.
- 44 Rothwell, R.G. (ed.) (2006). *New Techniques in Sediment Core Analysis*. London: Geological Society, Special Publication No. 267.
- 45 Liritzis, I. and Zacharias, N. (2012). Portable XRF of archeological artifacts: current research, potentials and limitations. In: *X-Ray Fluorescence Spectrometry (XRF) in Geoarcheology* (ed. M.S. Shackley), 109–142. Springer.
- 46 Gigante, G.E., Ridolfi, S., Ricciardi, P., and Colapietro, M. (2005). Quantitative analysis of ancient metal artefacts by means of portable energy-dispersive X-ray fluorescence spectrometers: a critical review. In: *Cultural Heritage Conservation and Environmental Impact Assessment by Non-Destructive Testing and Micro-Analysis* (eds. V. Grieken and Janssens), 1–9. London: Taylor & Francis Group.
- 47 Frahm, E. (Winter 2017). First hands-on tests of an Olympus Vanta portable xrf analyzer to source armenian obsidian artifacts. *International Association for Obsidian Studies (IAOS) Bulletin* 58: 8–23.
- 48 Frahm, E. (2017). First Hands-On Test of an Olympus Vanta Portable XRF Analyzer to Source Armenian Obsidian Artifacts. IAOS Bulletin, No. 58, Winter, pp. 2–23.
- 49 Piorek, S. and Richter, A. (2007). Nondestructive investigation of metallic artifacts with a handheld, small spot, x-ray fluorescence alloy analyzer. Poster presented at “METAL 2007” Conference, Amsterdam, Holland (1–21 September 2007).
- 50 Piorek, S. (2011). Nondestructive investigation of objects of art and natural heritage with a handheld, ‘small-spot’ XRF analyzer (some practical tips). Handheld XRF Workshop, ICDD Headquarters, Newton Square, PA (11–13 October 2011).
- 51 Podsiki, C. (2009). XRF applications on native American collections. Presentation at Symposium org. by School for Advanced Research, Indian Arts Research Center, Santa Fe, NM (28 May 2009). [http://findebookee.com/x/xrf\\_file\\_locator: sarweb.org/media/files/cheryl\\_podsiki\\_presentation.ppt](http://findebookee.com/x/xrf_file_locator: sarweb.org/media/files/cheryl_podsiki_presentation.ppt) (accessed 1 July 2013).
- 52 Odegaard, N., Smith, D. R., Boyer, L. V. and Anderson, J. (2013). Use of handheld XRF for the study of pesticide residues on museum objects. The Society for the Preservation of Natural History, *Collections Forum*, Vol. 20, No. 1–2, pp. 42–48. [https://www.researchgate.net/publication/236336185\\_Use\\_of\\_handheld\\_XRF\\_for\\_the\\_study\\_of\\_pesticide\\_residues\\_on\\_museum\\_objects](https://www.researchgate.net/publication/236336185_Use_of_handheld_XRF_for_the_study_of_pesticide_residues_on_museum_objects) (accessed 13 November 2020).
- 53 Piorek, S. (2008). Coatings, paints and thin film deposits. In: *Portable X-ray Fluorescence Spectrometry* (eds. P.J. Potts and M. West), 56–82. Cambridge, UK: The Royal Society of Chemistry.

- 54** Block, C.N., Shibata, T., Solo-Gabriele, H.M., and Townsend, T.G. (July 2007). Use of handheld X-ray fluorescence spectrometry units for identification of arsenic in treated wood. *Environmental Pollution* 148 (2): 627–633.
- 55** Shugar, A.N. and Mass, J.L. (eds.) (2012). *Handheld XRF for art and archaeology*. Leuven, Belgium: Leuven University Press.
- 56** “Nuclear instrumentation – Portable X-ray fluorescence analysis equipment utilizing a miniature X-ray tube”, International Standard IEC62495, Edition 1.0, April 2011, International Electrotechnical Commission, Geneva, Switzerland.
- 57** Camara, C.G., Escobar, J.V., Hird, J.R., and Puttermann, S.J. (October 2008). Correlation between nanosecond X-ray flashes and stick-slip friction in peeling tape. *Nature* 455 (23): 1089–1092.
- 58** Hamilton, M. A., Piorek, S., and Crocombe, R. A. (2015). Sample Analysis. US Patent 8,982,338 B2 (17 March 2015).

# 20

## XRF and LIBS for Field Geology

Bruno Lemi  re<sup>1</sup> and Russell S. Harmon<sup>2</sup>

<sup>1</sup>BRGM, Orleans, France

<sup>2</sup>Department of Marine, Earth & Atmospheric Sciences, North Carolina State University, Raleigh, NC, USA

### 20.1 Introduction

As technology for chemical analysis in the laboratory has progressively advanced, so has the interest in its application outside the laboratory. One of the long-standing needs of the geosciences community is instrumentation for *in situ* chemical analysis that is suitable for routine use in the field. Requirements for such include the analyzer being readily portable; lightweight so as to facilitate use by an individual; ruggedized and robust for use in the harsh environments in which geological materials need to be analyzed; simple to use; and capable of identifying the widest range of elements over a short acquisition time. Different forms of spectroscopy and spectrometry are presently utilized for in-field portable chemical analyzers in five typical-use cases (Croccombe 2018), each defined by a question:

- Detection: Is something present?
- Confirmation: Is this what I think it is?
- Classification: What group does this belong to?
- Identification: What is this?
- Quantification: How much of this is present?

X-ray fluorescence spectrometry (XRF) and laser-induced breakdown spectroscopy (LIBS) are both analytical techniques for elemental analysis that meet the criteria for use by geoscientists in the field under ambient environmental conditions, and can be used to answer the questions related to the five typical-use cases, all of which are routinely asked during geological fieldwork. For example, use of a field-portable instrument for chemical analysis allows an exploration geologist to gain a real-time understanding about the geochemistry of an ore prospect, and thus streamline field survey operations, and facilitate decisions about which samples to collect for further laboratory analyses. Both of these capabilities provide a considerable saving of time and cost. Similarly, in-field analysis permits an environmental geologist to rapidly delineate the extent of soil contamination by toxic metals across an area, or determine the efficacy of an environmental remediation action to clean up a contaminated site.

In this chapter, field-portable X-ray fluorescence spectroscopy is designated *pXRF* (although sometimes referred to in the literature as *FPXRF*, or *hhXRF* for handheld XRF). By contrast, current instrumentation for field-portable LIBS has two forms, lightweight LIBS systems consisting of multiple parts that can be readily transported to the field designated *fpLIBS* and handheld instruments designated as *hLIBS*. The sections that follow consider *pXRF* first for chronologic reasons only, as *pXRF* preceded *fpLIBS* and *hLIBS* by about 20 years. At present, there has been little simultaneous use of both techniques, but there can be no doubt that this situation will soon change.

**Table 20.1** Performance comparison of *pXRF* and *hLIBS* ( $Z$  = atomic number).

Performance criterion	<i>pXRF</i>	Requirements	<i>hLIBS</i>	Requirements
Light elements ( $Z < 13$ )	No	—	Yes	Matrix-matched calibration
Lighter elements ( $13 < Z < 17$ )	Possible	SDD detector, sample palletization	Yes	Matrix-matched calibration
Transition and alkali earth elements ( $19 < Z < 28$ )	Yes	Calibration	Yes	Matrix-matched calibration
Heavier elements ( $29 < Z < 92$ ), concentrations above 1000 ppm	Yes	Calibration	Yes	Matrix-matched calibration
Heavier elements ( $29 < Z < 92$ ), concentrations of 20–1000 ppm (may vary according to element)	Yes	Soil calibration	Yes	Matrix-matched calibration
Heavier elements ( $29 < Z < 92$ ), concentrations of 5–20 ppm (may vary according to element)	Yes	Compton calibration	Yes	Matrix-matched calibration
Heavier elements ( $29 < Z < 92$ ), concentrations under 5 ppm (may vary according to element)	Not possible with standard software	Specific signal processing	With difficulty	Matrix-matched calibration
Large measurement area (>5 mm)	Standard	—	Yes	Through multiple spots or grids on sample surface
Small measurement area (<5 mm)	Possible to 3 mm	Beam collimation	Yes	By raster over multispot grid
Spot measurement area (<1 mm)	No	—	Yes	—

XRF analysis is chiefly used for solid material analysis, whereas LIBS can analyze material in all physical states (gas, liquid, and solid), although containerization is required for gas or liquid analysis by LIBS. The technologies used in *pXRF* are described by Cornaby and Stratilatov (Vol 1, Chapters 18 and 19), and *hLIBS* instrumentation by Day (Vol 1, Chapter 13). The use of ultraviolet (UV)–visible spectroscopy and Raman spectroscopy in geochemistry is discussed in the respective chapters by Laukamp et al. (Vol. 2, Chapter 18) and Edwards et al. (Vol. 2, Chapter 17).

Handheld instruments for energy-dispersive XRF have been commercially available since the early 1990s. Their state of technological development is presently mature (e.g. Lemi  re 2018; Young et al. 2016), much more so than for handheld LIBS, which only was realized some 20 years later (Connors et al. 2016). However, both types of handheld analyzers have found widespread application across a broad spectrum of user communities, including the geosciences, with each instrumentation type having particular advantages and disadvantages (Table 20.1).

The essential components of a handheld XRF system, the X-ray tube and silicon drift detector (SDD), are comparatively expensive compared to the low-cost lasers and detector/spectrometers used in handheld LIBS analyzers. There is the additional complication that XRF instrumentation is burdened with licensing requirements, special operating precautions, and operator safety training because of its open-beam X-ray source, which can also result in restrictions for transportation. These restrictions are still applicable in many countries, despite the implementation of safety systems preventing X-ray emission when no sample is detected. It is these radiation safety regulations that limit the ultimate performance of open-beam and unshielded handheld XRFs analyzers, as typically the upper limit for voltage is 50 kV and the upper power limit of X-ray sources is 4 W (Young et al. 2016). A handheld LIBS instrument does not emit ionizing radiation; so no special operation restriction is required, except the use of an

eye-safe laser, or a locking system that will prohibit the laser from firing unless the analyzer is in physical contact with a sample. Handheld XRF analyzers also have intrinsic limitations because of the low beam energies utilized, which means that the returning secondary X-rays also have lower energies that make the detection and measurement of the lighter elements difficult. Thus, handheld XRF analyzers are unable to measure elements of low atomic number, typically those lighter than Al. They are not currently able to reliably quantify Mg (Hall et al. 2011; Horta et al. 2015) or detect Na due to the severe drop in fluorescence yield with decreasing atomic number and the absorption of fluorescent X-rays by air (Jenkins 1999; Ravansari et al. 2020). Rare earth elements (REEs) are challenging, due to the difficult separation of element lines in the spectrum (Gallhofer and Lottermoser 2018; Simandl et al. 2014). Other known limitations include the inability to quantify reliably Au, Hg, and Pt group elements (PGEs), but these are related to heterogeneous distribution in small-volume samples, or nugget effects rather than true analytical limitations. LIBS, in principle, can detect any element of the periodic table, but is particularly suited for analysis of light elements with low ionization potentials (particularly, H, Li, B, Be, and Na), is satisfactory for the metallic elements in the middle of the periodic table, but far less efficacious for elements of high ionization potential (e.g. S, P, F, Cl, and Br). LIBS is also a significantly faster analytical technique than XRF, with an analysis complete in seconds rather than minutes and, therefore, is arguably the more expedient detector for the presence of an element in a material. However, quantification is much less problematic for XRF analysis, which unlike LIBS does not require a set of closely matrix-matched standards for quantitative analysis (Harmon et al. 2013). Handheld XRF and LIBS provide very different areas of interrogation; a typical XRF analyzer will nondestructively interrogate the integrated composition of an area of a few millimeters diameter to a few hundred microns depth (Piorek 2008; Ravansari et al. 2020), compared to the area  $\sim$ 100  $\mu\text{m}$  diameter and a few 10s of micron depth excavated from a solid material by the LIBS ablation process (Cremers and Radziemski 2013; Harmon et al. 2019). Unlike its XRF counterpart, handheld LIBS analyzers have the ability to use its laser to “clean” the surface of a material prior to analysis, e.g. remove a thin contaminant or alteration layer on a rock or mineral, or to specifically analyze that layer. Then, continued firing of the laser will allow penetration through the layer into the sample for analysis of the pristine sample. Because it is possible to raster the laser beam across a sample surface in small steps, microscale compositional mapping is also possible by handheld LIBS (Harmon et al. 2019).

Neither commercial *pXRF* nor *hLIBS* analyzers necessarily require extensive sample preparation when used in the field, to provide valuable information (screening, mapping, decision helping). However, in many instances, a careful sample preparation for *pXRF* analysis can provide significant advantages, such as better accuracy, and better consistency between field analysis and standard laboratory results (Hall et al. 2011, 2014) or access to lighter elements (Si, Al, P). However, fast results obtained on unprepared sample can justify alone the use of *pXRF* or *hLIBS* for field screening or decision-making. Sample concentration, and/or separation may be required for the analysis of specific mineral phases and preparation of pellets in the field can facilitate soil analysis. It seems that the slow acceptance of *pXRF* for mineral exploration, for example, resulted from unsatisfactory comparisons with absolute concentrations determined by laboratory analyses (Durance et al. 2014).

## 20.2 X-Ray Fluorescence Spectroscopy (XRF)

### 20.2.1 Background

The first applications of commercial *pXRF* date from the early 1990s as a detection device for Pb in paint in housing and the development and early application of *pXRF* has been summarized by Bosco (2013). The multielement capabilities of these instruments were soon recognized and tested for environmental applications (Bernick et al. 1995). Pioneer applications in fieldwork for mineral exploration began shortly thereafter in Russia (Konstantinov and Strujkov 1995) and China (Ge et al. 1997), but it took several additional years before geological applications were described in the international literature (e.g. Ge et al. 2005; Houlahan et al. 2003).



**Figure 20.1** Chemical investigation of an outcrop with *pXRF* as employed in mineral exploration or field geology situations. Such pictures can be found in many advertisements, and misleadingly suggest that proper analyses can be done this way.

The first commercial *pXRF* instruments were based on radionuclide sources for X-rays, and then on miniaturized X-ray tubes after 2000 (Bosco 2013). The transition to X-ray tubes significantly reduced the regulatory constraints for use of the technology and facilitated widespread application. Most of the development since then has been focused on the improvement of detectors, with silicon drift detectors (SDDs) replacing traditional Si-PIN diode detectors. Current devices for geoscience applications are “top-of-the-range” *pXRF* models, as opposed to the less-expensive instruments used for metal recycling or positive metal identification. Most current *pXRF* instruments share 50 kV tubes, SDD detectors, and less critical components, such as inboard GPS and CCD cameras.

Field use of *pXRF* tends to take two forms: rapid measurements of solid geological media for decision-making purposes, and more careful analyses on properly prepared samples, which can be used as substitutes to laboratory analyses. The most popular image of *pXRF*, and maybe the most uninformative and confusing one, shows a geologist with an XRF spectrometer in a holster along his leg, ready to answer any question about the composition of an unknown rock or soil (Figure 20.1). But, part of the story may be the inappropriate comparison of handheld analyzer performance in the field with that at a near-site test facility (Figure 20.2), where much better analytical conditions can be achieved without losing too much of the benefit of real-time analysis. During an analytical campaign, the geologist can readily return to a field site to make additional analyses, taking into account the information obtained in the test facility.

### 20.2.2 Qualitative Versus Quantitative Analysis

Due to its ease of use and multielement capabilities, *pXRF* has been used in almost all field situations where the chemical composition of a solid geological material is required. However, the reliability of the results can be extremely variable, particularly in regard to the “point-and-shoot” approach, compared to the analysis of carefully



**Figure 20.2** A typical near-site setting for *pXRF* analysis using a portable analyzer with PC control, permitting longer measurements, performed in indoor conditions with AC power and temperature control. The room may be in a field camp laboratory (above), office, or hotel room. Note that the *pXRF* instruments are shown here used in test stands, providing closed-beam operation.

prepared samples using an appropriate set of standards (Figure 20.3). The type of measurement depends on the requirements and objectives of the user.

#### 20.2.2.1 Qualitative Analysis

Quantitative analysis is not required for all applications, as in many instances a simple identification of elements present in sample will be sufficient. In this situation, *pXRF* provides a quick answer about whether an element of interest is present at concentrations above limit of detection (LOD). From such knowledge, an experienced geologist or geochemist can identify the presence of a mineral or infer a particular rock type based on the presence or absence/scarcity of several elements. If the geologist has other indices for identification, such elemental information will help the decision. For example, the identification of a rock type may allow determination of a specific Formation or Group in a stratigraphic sequence with abnormal contacts, or allow a lava to be placed within a particular magmatic series. Mineral identification also allows hydrothermal alteration or metamorphic zones to be recognized. In this type of application, *pXRF* is not used as an instrument for precise determination of elemental abundance, but instead as a decision aid for the trained geologist or geochemist. Of course, measurements for such applications should be recorded and geolocated for traceability but not necessarily mapped or further processed.

#### 20.2.2.2 Quantitative Analysis

Due to its capability for multielement analysis, *pXRF* is able to provide information on both major and trace element concentrations. In many situations, it is desirable to obtain highly accurate abundance data instead of just an indication of elemental presence or absence. In these instances, the geologist expects to have a preview of subsequent results from laboratory analysis, but at the site of interest in the field within minutes. The data quality provided by the *pXRF* can be highly variable (Lemière 2018; Ravansari et al. 2020), as determined by such factors as:

- Sample surface condition.
- Sample grain size, texture, porosity, and homogeneity.
- Sample moisture content.

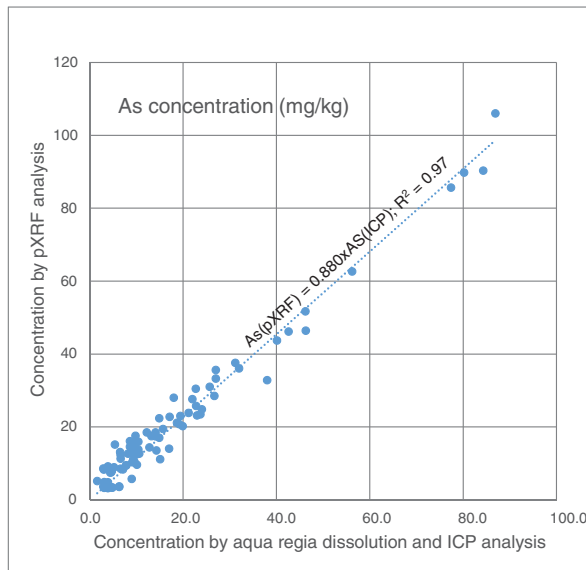


**Figure 20.3** Comparison of *p*XRF analysis for As in soil samples near a Sb deposit with that by laboratory analysis via total sample dissolution by aqua regia digestion and subsequent measurement by inductively coupled optical spectrometry.

- Interfering or shielding elements, especially for high Fe abundances.
- Matrix composition variability.

Most documented cases (see e.g. Caporale et al. 2018; Hall et al. 2011, 2014; Ravansari et al. 2020; VanCott et al. 1999) demonstrate that a careful, laboratory-ready preparation of samples, including milling and drying prior to analysis, provides the best consistency between *p*XRF and standard laboratory analysis (Figure 20.3). It must not be forgotten that a *p*XRF is not a magical “black box”; rather, it is an analytical instrument and as such will yield much better results if laboratory QA/QC procedures are applied to its use. Even in the field, the geoscientist must be a chemist.

The regular use of certified reference materials (CRMs) for standardization and blanks within the sequence of analysis for a sample series is thus desirable. However, *p*XRF is a matrix-sensitive technique and matching CRMs are not always available. In such situations, the prior preparation of project-specific SRMs (Standard Reference Materials) may be necessary if quantitative analysis is required, and spiking these with different amounts of the critical elements of interest is necessary for the development of robust calibrations.

Besides this good practice, it is essential to have a small percentage of the field samples analyzed later by a qualified laboratory, using total digestion methods and adequate techniques for the concentration range of interest. In most cases, the relationship between *p*XRF and laboratory analysis is acceptably linear, with biases typically in the 5–30% range (Hall et al. 2013; Rouillon et al. 2016; Simandl et al. 2014; Young et al. 2016). Such linearity allows screening and ranking samples, drawing maps, and defining thresholds based on the in-field analysis. The user can then adjust the *p*XRF measurements accordingly during later data processing, or develop a custom calibration, if the matrix variability of the project area is not very high, and if data are used for on-site decision-making.

The observed bias of 13% between the *p*XRF and laboratory ICP analysis for the example shown in Figure 20.3 is within the range typically observed. This may reflect either calibration differences, or differences between a purely physical analysis (*p*XRF) and the analysis of a digestate. The  $R^2$  value for the observed covariation is considered acceptable, taking into consideration the difference between methods, and between sample volumes analyzed. However, the comparison between *p*XRF measurements and laboratory analyses by wet chemical techniques can be misleading in some situations, as refractory elements may be only partly dissolved by commonly used digestion

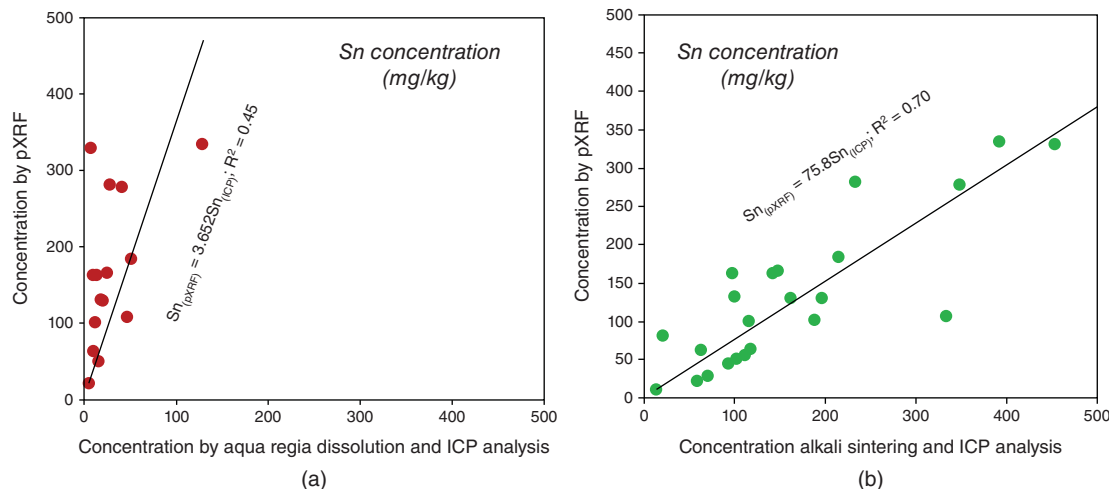


**Figure 20.4** (a) Comparison between pXRF for soil samples near a W-Sn deposit with that by laboratory analysis via total sample dissolution by aqua regia digestion and subsequent measurement by inductively coupled optical spectrometry. (b) Comparison between pXRF for soil samples near a W-Sn deposit with that by laboratory analysis via total sample dissolution by alkali sintering and subsequent measurement by inductively coupled optical spectrometry.

techniques, especially aqua regia. For example, the much higher concentrations observed by pXRF relative to ICP analysis than aqua regia digestion approach to sample digestion shown in Figure 20.4 are not overestimated, but closer to the true concentrations. A correct control should be based on laboratory XRF or another physical method, or at least on a total digestion method, such as alkali sintering. It should be remembered that the bias coefficient is not a constant between analytical methods, as pXRF is a matrix-dependent technique. Thus, a user should not use such coefficient to correct analyses without an understanding of laboratory preparation methods and precise laboratory controls.

A third example comes from the study of Ross et al. (2014a, 2014b) from comparative pXRF and laboratory analysis of samples from a Zn–Cu exploration project (Figure 20.5). Three pXRF analyzers were used to collect more than 2000 pXRF measurements in the pXRF soil mode for a sediment standard, and >12 000 pXRF measurements made in the “mining plus” mode for 6942 m of unmineralized rock cores that ranged in composition from mafic to felsic volcanic and intrusive, lithologies. The study concluded that pXRF is quite precise for a number of elements, but not very accurate using factory calibrations. For example, the  $1\sigma$  precision for one instrument tested on a basaltic core was observed to be better than 5% for Al, Ca, Fe, K, Mn, S, Si, Ti, Zn, and Zr. But the same instrument tested on a range of volcanic and intrusive core samples yielded the following average systematic errors: Al = -23%, Ca = -4%, Fe = +1%, K = -9%, Mg = -17%, Mn = -15%, P = +218%, Si = +4%, Ti = -23%, Cu = +220%, Zn = +151%, and Zr = +17%. These systematic errors can largely be removed by the application of correction factors, which are unique to each pXRF analyzer and each project.

An important aspect of quantitative analysis by pXRF is the careful selection of the calibration mode. Two main modes are available on most pXRF instruments: fundamental parameters for the “Mining” or “Geochem” modes and Compton normalization for the “Soil” mode. The former is typically used when interested in major element abundances or ore-grade elemental concentrations, whereas the latter is used for trace level elemental concentrations in more general sample matrices. This approach overcomes the “broken line” calibration issues observed for very large concentration ranges described by Hall et al. (2014). The “Soil” mode is mainly used for the analysis of elemental constituents present at low concentrations, whereas the quantification of high or contrasted concentrations is better achieved using the “Mining” mode. The hybrid “Geochem” mode provides semiquantitative

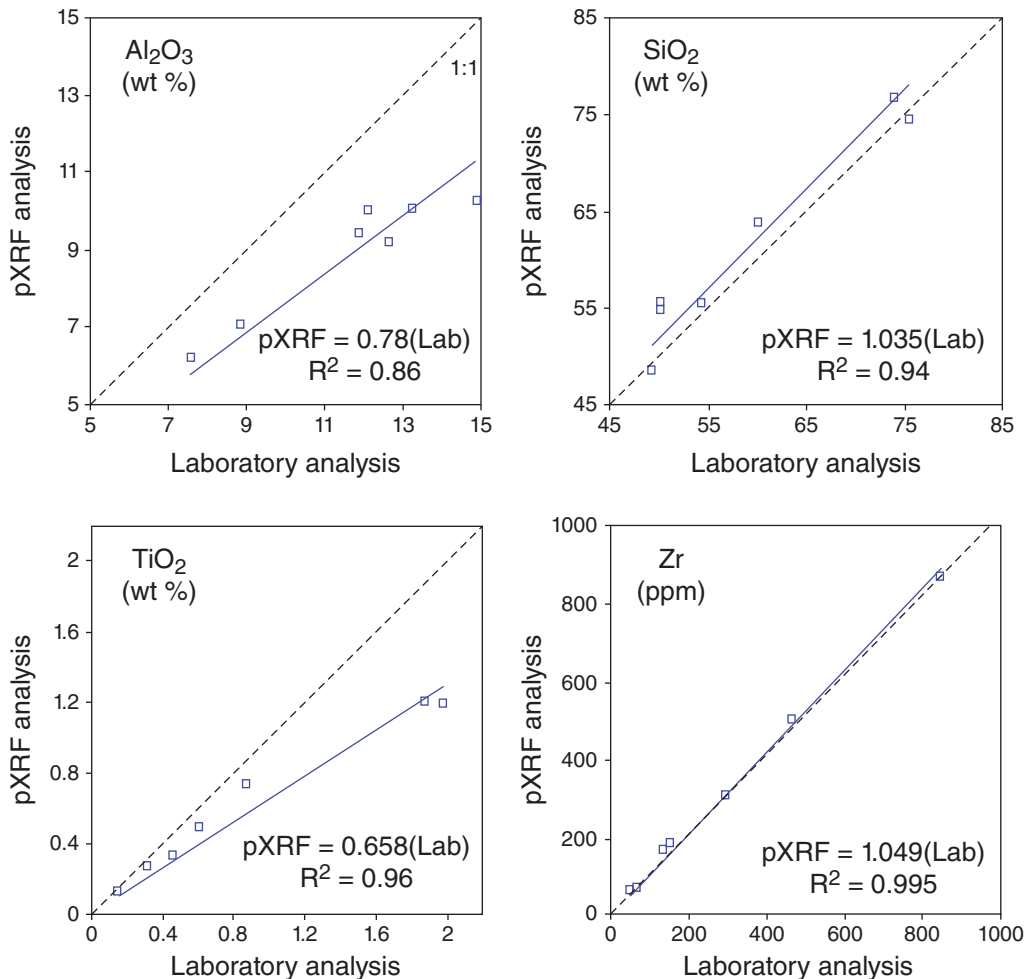


**Figure 20.5** Comparison of *pXRF* and laboratory wavelength dispersive XRF analysis for Al, Si, Ti, and Zr on samples from the Matagami rock core. Modified from Ross et al. (2014b).

information over a larger concentration range. Some elements may be available through only one mode, according to the manufacturer's calibration scheme

### 20.2.3 Applications of *pXRF* in Field Geology

#### 20.2.3.1 *pXRF* in Mineral Exploration

The analytical performance of *pXRF* for Pb, Zn, Cu, and As was observed to be promising since its commercial introduction, and was soon after tested in exploration (Konstantinov and Strujkov 1995). A surprisingly small number of papers have been written on these tests (Houlihan et al. 2003), while the same elements have been successfully analyzed for environmental studies (Bernick et al. 1995; Kalnicky and Singhvi 2001). It seems that the slow acceptance of *pXRF* for mineral exploration resulted from unsatisfactory comparisons with absolute concentrations determined by laboratory analyses. The exploration community was used to absolute accuracy and did not immediately recognize the potential of what can be biased but sensitive and reproducible measurements

(Durance et al. 2014). Later, better documented case studies helped *pXRF* to play a larger role in geochemical surveys (Burley et al. 2017; Marquis 2019; Peter et al. 2010; Simandl et al. 2014), or in prospect evaluation (Bosc and Barrie 2013; Marquis 2019). By now, it is an analytical tool in common use by most mineral exploration companies.

Specific applications utilizing *pXRF* were developed for particular media, such as till (Plourde et al. 2013; Sarala 2016) or regolith soil (Gazley et al. 2017). These proved to be efficient in locating targets and delineating anomalies, even near or below the analyzer lower analytical limit, commonly referred to as the limit of detection – LOD (Potts 2012). The explanation for this is that *pXRF* is still a sensitive technique for elemental detection, even when instrumental limitations preclude any accuracy in abundance determination.

The precious metals Au and Ag, the metals Bi, Hg, and Tl together with the platinum group elements are among the most desirable elemental commodities, as well as critical elements (Hayes and McCullough 2018), and they are within the elemental range of *pXRF*. However, two reasons preclude using *pXRF* for their exploration:

- Their low abundance in most media lies below the LOD in most cases.
- These elements are prone to high matrix heterogeneity and nugget effects, resulting in poor reproducibility and false positives or negatives.

Some attempts have been made to overcome this limitation (Bolster and Lintern 2018), but there are, until now, few demonstrated success stories. Thus, most of the use of *pXRF* in gold or PGE exploration is based on the identification of pathfinder elements, those non-valuable elements that are associated or correlated with commodity elements, spatially or due to genetic processes, but easier to analyze. A typical example is As for Au prospecting.

Moving exploration results to the feasibility stage may be another challenge, as they need to be supported by official standards to be acceptable, and reporting is controlled by JORC<sup>1</sup> or NI 43-101<sup>2</sup> regulations. *pXRF* data may be suitable if obtained under strict QA/QC conditions (Arne et al. 2014; Arne and Jeffress 2014; Stoker and Berry 2015).

### 20.2.3.2 *pXRF* in Lithological Applications

*pXRF* is able to analyze lithology-related elements (Ca, Fe, K, Ti, Zr, Rb, Ba, Sr) in rocks, soil or stream sediment. However, the important lighter rock-forming elements Si, Al are not easy to analyze in field conditions without prepared samples, and Mg can be observed by *pXRF*, but its abundance not reliably determined.

Lithological applications of *pXRF* are widespread and varied. Some examples include geological mapping of poor outcrops or deep alteration profiles (Benn et al. 2012; Durance et al. 2014), recognition of geological units with specific geochemical characteristics without macroscopic differences, the identification and discrimination of volcanic units, and the mapping and monitoring of drill core with fast identification of drilled sequences and decision support to continue or stop drilling. Marsala et al. (2012) used *pXRF* to integrate mineralogy and chemostratigraphy into real-time formation evaluation. Gazley et al. (2011) employed *pXRF* analysis to reconstruct metabasalt stratigraphy at the Plutonic Gold Mine, Western Australia. A similar application by McNulty et al. (2018) used traditional volcanic geochemistry diagrams to recognize volcanic sequences affected by hydrothermal alteration.

Rock identification by *pXRF* is often used in tracing the provenance of archaeological items (Giménez et al. 2017; Richards 2019; Donais et al. this volume). The nondestructive character of *pXRF* is essential for this application.

Absolute accuracy is not needed for such applications so the use of portable analyzers whose results are reliable, but not always consistent with laboratory results unless calibrated, is entirely appropriate for the needs of the study. The determination of geochemical patterns and their spatial distribution is the primary objective in such

<sup>1</sup> The Australasian Code for Reporting of Exploration Results, Mineral Resources and Ore Reserves (“the JORC Code”) is a professional code of practice that sets minimum standards for Public Reporting of mineral exploration results, mineral resources, and ore reserves.

<sup>2</sup> National Instrument 43-101 (the “NI 43-101” or the “NI”) is a national instrument for the Standards of Disclosure for Mineral Projects within Canada. The Instrument is a codified set of rules and guidelines for reporting and displaying information related to mineral properties owned by, or explored by, companies which report these results on stock exchanges within Canada.

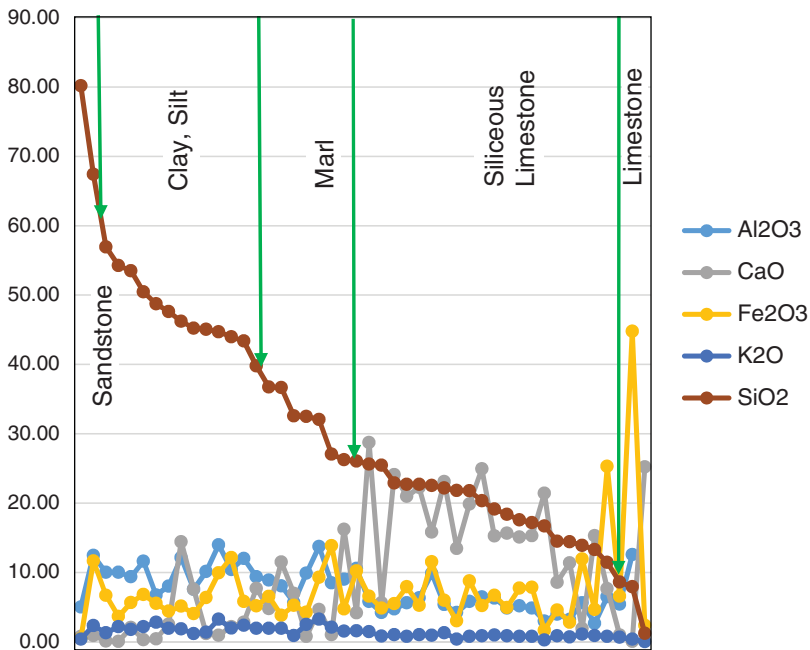


**Figure 20.6** Variations of major element composition of soil and source formation main lithology measured by *pXRF*.

applications. Sensitivity to minor element variations is an important asset of *pXRF*, but attention needs to be paid to reproducibility. In these use cases, it is essential to compare data for geologically similar types of material such as soil, sediment, rock outcrop, or drill core. Otherwise, data must be processed separately if different types of media are analyzed. Two examples of such applications from the authors' experience include:

- The recognition of dolomitic and marl facies in a limestone sequence from soil analyses (Figure 20.6). This analysis was carried out during a post-mining survey in the Pallières-Carnoulès mining area, southern France, while establishing a baseline geochemical map for potential environmental impact assessment.
- Localization of heavy minerals-enriched horizons in a sandstone sequence, from direct measurements on drill hole cores and cuttings. This survey was aimed at locating the potential sources of radioactive contamination (U-Th-Ra) of deep groundwater, which could be demonstrated as being Naturally Occurring Radioactive Minerals (NORMs). Figure 20.7 is extracted from the original full log, on a section of the drill hole. The two left columns portray the cuttings-based lithology. The Th, U, and K columns on the left side of the figure illustrate the abundances of these elements estimated from the gamma-ray logging of the borehole. The eight columns on the right, from Ca to Zr, are *pXRF* measurements performed on cuttings milled on the drill site. The main intervals of heavy mineral enrichment, located between 130–135 and 200–203 m, are clearly visible in *pXRF* measurements (Fe, Th, U, Ti, Zr) and correlate well with the Th gamma signal, with limited depth shift of the cuttings compared to the downhole spectral log.

### 20.2.3.3 Field Mineralogy

The mapping of hydrothermal alteration is usually based on mineral assemblages, and the preferred on-site technique in exploration is handheld near-infrared (*hNIR*) spectroscopy (Laukamp, this volume). However, hydrothermal alteration is rarely isochemical, and alteration zones can be represented by depletion or enrichment zones in reactive elements within a given lithogeochemical unit.

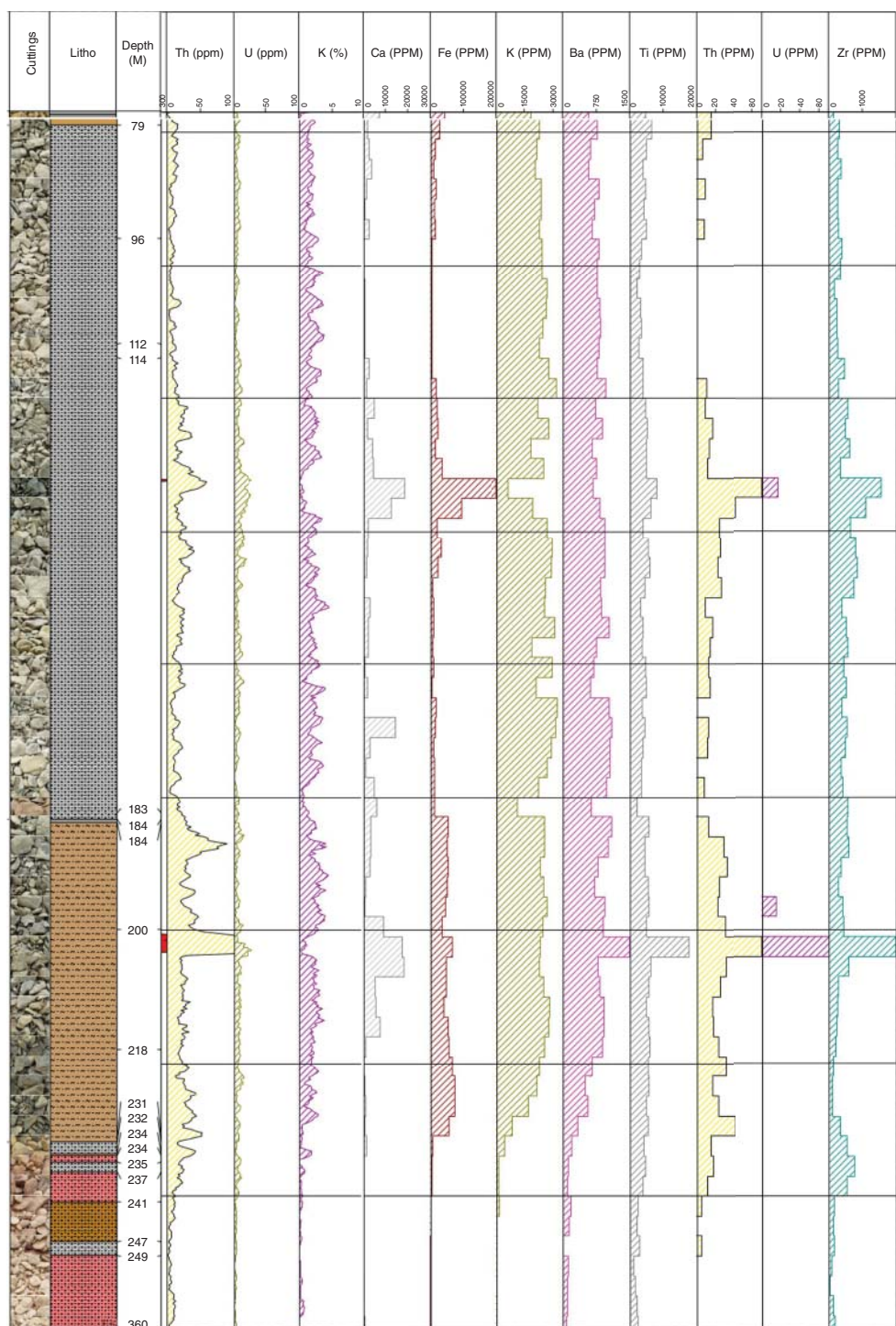


**Figure 20.7** Variations of gamma-ray spectrometry compared to formation lithology and major and trace element composition of drill cuttings measured on site by pXRF.

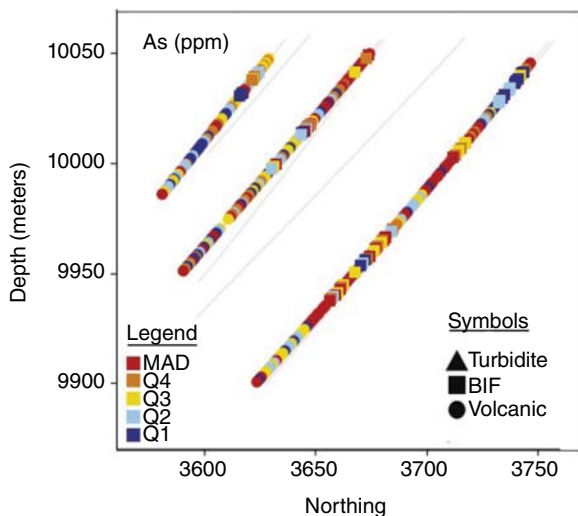


**Figure 20.8** Unprocessed *pXRF* analyses for As concentration plotted along the F Zone drill fan in the Meliadine gold district, Nunavut, Canada. Anomalous As concentrations, defined as median absolute deviations (MAD) for As. MAD outliers are co-spatial with BIF-hosted replacement-style gold mineralization and also extend into hanging wall and footwall rocks devoid of gold. Q1 = are values from the data minimum to the lower hinge; Q2 are As values from the lower hinge to the median, and Q3 are As values from the median to the upper hinge; and Q4 are As values from the upper hinge to the maximum. Modified from Lawley et al. (2015).

For instance, in porphyry copper or epithermal systems, the potassic zone is characterized by K enrichment, or at least conservation, while Ca, Mg, and Na are significantly depleted, with Si, A, and/or Ti comparatively enriched due to mass leaching. In the advanced argillic zone, K becomes depleted and Si, Al, and Ti are further enriched. Although Na is not accessible to *pXRF*, and Mg is difficult to analyze, Ca and K are readily analyzed, and mapping of these two elements may allow delineation of alteration zones in situations where original rock composition is not too heterogeneous.

The Meliadine Gold District is a gold deposit hosted in an Archean banded iron formation of the Rankin Inlet Greenstone Belt in northern Canada. Here, the BIF-hosted replacement-style gold mineralization and auriferous greenstone-hosted quartz ( $\pm$ ankerite) veins cut mafic volcanic rocks, interflow volcanoclastic rocks, and turbidite successions characterized by multiple alteration zones (silicification, sulphidization, sericitization, carbonatization, chloritization) adjacent to the deposit. In an earlier case study, Lawley et al. (2015) performed more than 1000 *pXRF* analyses of selected drill core surfaces for which whole rock analyses were available. Guides to extent of auriferous mineralization comprise chemical patterns of hydrothermal alteration, spatially associated with anomalous concentrations of the pathfinder elements As, Te, Bi, and Sb (Figure 20.8).

Pathfinder anomalies are defined with threshold concentrations for each element, while hydrothermal patterns are based on element ratios. Typically, arsenopyrite is accompanied by a sulfide mineral assemblage consisting of pyrrhotite and arsenian pyrite accompanied by lesser amounts of chalcopyrite, galena, and sphalerite; with the sulfidized samples denoting anomalous sulfur concentrations that are an Au vector. Combining both approaches in a vectoring guide requires a multivariate processing, in order to overcome the imprecision of boundaries between barren and mineralized rock. The accuracy and precision of *pXRF* on drill core surfaces was observed to be sufficient to map these hydrothermal geochemical patterns.

Several alteration zones are observed around the large Ni-Cu-PGE deposit of Kevitsa – serpentinitization, pervasive amphibole replacement, and epidote alteration. These were characterized by *pXRF* at both deposit and individual veins and selvages by Le Vaillant et al. (2016) on a suite of more than 5500 altered samples. A careful investigation of matrix heterogeneity was performed, using multiple shoots near the same point, and results were averaged to recognize alteration zones and interpret element mass transfer at the deposit.

Geothermal field alteration was recognized by Mauriohooho et al. (2016) using composite samples of more than 300 drill hole cuttings. These were cleaned, dried, and lightly milled, as required, and then analyzed by *pXRF*. Lithological boundaries were recognized through alteration using less mobile elements Y and Zr, whereas

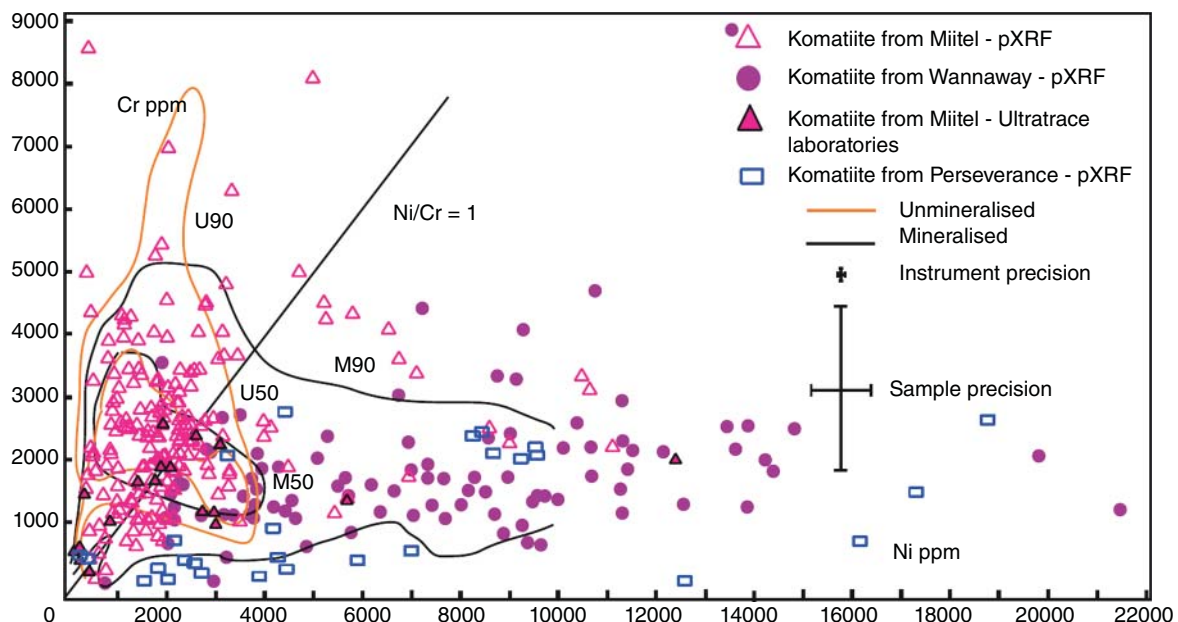


**Figure 20.9** *pXRF* analyses of komatiites from units associated with nickel sulfide ores in the Yilgarn Craton of Western Australia. From Le Vaillant et al. (2014).

alteration defines formation boundaries and identifies subunits. The mobile elements Rb, Ba, Ca, and K correlate with alteration zones. Other potentially mobile elements that can be analyzed by *pXRF* include Rb, Sr, Si, and Fe.

Hughes and Barker (2017) mapped adularia alteration zone related to vein Au-Ag mineralization in an andesite body based on the K/Al ratios measured by *pXRF*. The success of this application, which was verified using XRD, can be attributed to the homogeneity of the andesite body and the chemical contrast of the alteration zone.

Carbonate vein composition determined by *pXRF* has been used as a vectoring guide to mineralization. One difficulty encountered was the lack of suitable CRMs. Andrew and Barker (2018) developed a method for determining carbonate vein chemistry based on *pXRF* analysis, and matrix-matched CRMs that was applied as vectoring guide to elemental concentration at the Mount Isa Pb-Zn ore deposit in Northwest Queensland, Australia. A rigorous procedure of Quality Analysis/Quality Control (QA/QC) was employed to develop linear calibration equations for mineralization-related elements Mg, S, Mn, Fe, Zn, Sr, and Pb. Although difficulties were encountered with the low concentrations of some elements in commercially available CRMs, this case study demonstrated that *pXRF* can also be used to identify veins with multiple generations of carbonate infill.

Barnes et al. (1995, 2004) have demonstrated that the potential of komatiites for nickel sulfide mineralization can be assessed using discriminant diagrams based on trace element contents (e.g. Cr, Ni, Ti, Zr, Co). Based on this approach, Le Vaillant et al. (2014) used *pXRF* to measure these elements and others in 75 samples from three komatiite units associated with nickel sulfide ores in the Yilgarn Craton of Western Australia (Figure 20.9). A total 670 analyses were performed on cut and polished cores, and compared with laboratory XRF data on discriminant diagrams used in exploration for komatiite-hosted nickel sulfides (Cr versus Ni and Ni/Ti versus Ni/Cr). This study demonstrated that *pXRF* analysis is a viable tool for rapid assessment of the Ni-sulfide potential of komatiites, provided that strict control protocols are followed. As Ni/Ti and Ni/Cr ratios are preserved during moderate weathering, the element-ratio approach is applicable to samples from percussion drilling in weathered terrains, without needing completely fresh bedrock samples for analysis (Barnes et al. 2014).

#### 20.2.3.4 Soil Characterization and Sediment Analysis

Soil geochemical characterization is typically undertaken for several purposes (Weindorf et al. 2012d):

- Recognition of the relationships between soil and bedrock composition.
- Determination of soil chemical properties and spatial heterogeneities as regards cultivation or vegetal growth character (Sharma et al. 2014, 2015; Wang et al. 2015; Weindorf et al. 2012b, 2012c; Melo de Lima et al. 2019).
- Determination at the field scale of trace elements concentrations, with relevance to precision agriculture, in order to rectify elemental deficiencies or toxicities (Adler et al. 2020; Wan et al. 2019).
- Identification and mapping of soil environmental contamination (Kim et al. 2019; Swift 1995; Weindorf et al. 2012a), for instance at abandoned mine sites (Chakraborty et al. 2017; Oyourou et al. 2019).

Environmental contamination detection and mapping was among the first geoscientific applications of *pXRF* (Argyraiki et al. 1997; Bernick et al. 1995; Kalnicky and Singhvi 2001; Piorek 1994a, 1994b), as the instrument was first designed for Pb detection. Early successes were reported for Pb (Argyraiki et al. 1997; Shefsky 1997), Zn, Cu (Bernick et al. 1995), and As, insofar as Pb content is not large (Bernick et al. 1995), and ensured the use of *pXRF* for environmental investigations. Some elements cannot be monitored by *pXRF* because their critical concentration or baseline abundance is below the lower analytical level for *pXRF*. This is the same situation for Cd. However, Cd anomalies recorded by *pXRF* are usually true positives and can be used for mapping purposes. Furthermore, Cd and Zn are usually correlated, and high Zn concentrations recorded by *pXRF* may be used as a sample-screening criterion for analyzing Cd in the laboratory. The toxic elements Hg and Tl are also on the priority list for environmental and health contaminants, but should not be monitored using *pXRF* only, for the same reasons as Au or PGEs in exploration (Section 20.2.3.1).

Soil science and agricultural applications came later, as there were no major drivers for implementing expensive *pXRF* use in these areas. This situation changed radically with the emergence of precision agriculture and technology improvement for light elements (Al, Si, P, S) analysis by *pXRF* (Pelegrino et al. 2019; Wan et al. 2019). The implementation of *pXRF* sensors on agricultural machinery, along with Fourier transform infrared spectroscopy (FTIR) and LIBS, might become popular in the near future.

#### 20.2.3.5 Sediments

Besides being media of interest for agriculture, and hosts for contamination by industrial pollution, sediments are also of particular interest in the context of mineral exploration. Analysis by *pXRF* can be readily applied to the historic practice of stream sediment surveys for vectoring to new mineralization (Agnew 2004; Cohen and Bowell 2014; Farahbakhsh et al. 2019; Hale and Plant 1994; Moon and King 2015). It has the benefits of faster and more efficient application than laboratory analysis, as immediate decisions can be taken on site during a sampling campaign. As in many other applications, a careful selection and processing of the samples is required and consideration of sediment grain size, moisture, and content of organic matter is required.

For example, Luck and Simandl (2014) used *pXRF* at the Lonnlie carbonatite complex, a Nb prospect in the alkali-line province of British Columbia in westernmost Canada, to determine the best size fraction of stream sediments to analyze in carbonatite-related indicator mineral surveys. Precise results (generally <5% RSD) were obtained for key pathfinder elements that included Nb, Ta, La, Ce, Pr, Nd, Y, P, Sr, Ba, Th, and U. Results from laboratory sieving observed the highest abundances in the finer size fractions. Samples upstream from the Lonnlie deposit display higher concentrations of the carbonatite pathfinder elements than samples downstream of the deposit, suggesting the presence of other source(s) farther upstream (Figure 20.10).

*pXRF* has proven to be a particularly efficient tool for environmental investigations at active, historic, or abandoned mine sites. Examples include allowing immediate monitoring following a dam-break event (Guerra et al. 2017) and high-density mapping and dynamic sampling (Byrne et al. 2018). Stream sediment surveys can be used to rapidly assess the extent of mining contamination, especially at abandoned sites. Lemière and Laperche (2018)

**Figure 20.10** Comparative abundances of U, Th, and Pb in stream sediment samples and their geographic distribution relative to the Lonnie carbonatite. Source: Modified from Luck and Simandl et al. (2014).

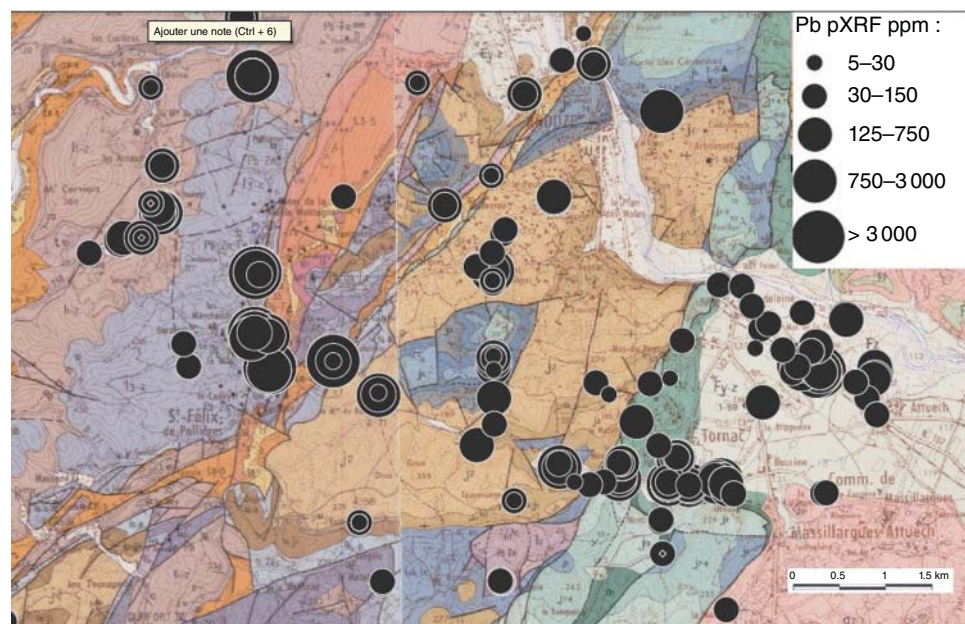
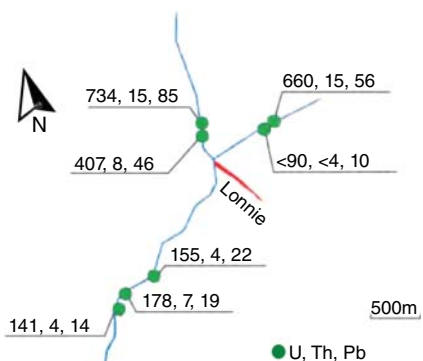


**Figure 20.11** Distribution of Pb in stream sediment samples in drainage downstream abandoned mines, Pallières district. Modified from Lemière and Laperche (2018).

used *pXRF* analysis to measure the extent of pollution from unmanaged mine waste deposits and delineate a zone of potential impact (Figure 20.11).

#### 20.2.3.6 Hydrogeological and Hydrogeochemistry Applications

Literature references on hydrogeological applications, such as aquifer or aquitard characterization, are limited. This suggests that *pXRF* is not yet routinely used for drill-hole logging of groundwater wells. This is probably based more on habit rather than on a lack of interest, as lithological identification is readily accomplished by *pXRF*. Major element logging could include Ca (for carbonates), K and Al (for clays), Si (for sand), and Ti and Zr (for heavy mineral sands).

Despite the need for chemical analysis in water resources evaluation and quality determination, hydrochemical and environmental surveying is a challenge for *pXRF* because of the typically low solute contents of most natural waters. However, two recent studies demonstrated the potential of *pXRF* for the analysis of waters with relatively high metal loadings, provided that a robust procedure is used for sample preparation. Zhou et al. (2018) determined

the in situ concentrations of the toxic metals Cu and Pb in polluted water by *pXRF*. The penetration depth of X-rays in water was observed to be between 2 and 4 mm. *pXRF* results were found to be comparable with the certified concentrations of prepared solutions, and the minimum respective detectable concentrations of 21 and 28 ppm were determined for Cu and Pb. Field *pXRF* measurements also demonstrated linear correlation with laboratory analyses. Pearson et al. (2013) analyzed 390 waters samples from leaching columns of mine tailings in South Africa containing high levels of metals to examine the potential predictive ability of *pXRF*, demonstrating differential effectiveness in elemental quantification. Using multiple beams produced stronger correlations to ICP relative to the use of a single-beam *pXRF* analysis. This study indicated the need for a *pXRF* “Water Mode” calibration for future examination of polluted or contaminated waters.

Tighe et al. (2020) described a novel method for quickly and quantitatively measuring aqueous lead in drinking water. The procedure uses an activated carbon felt to capture and concentrate Pb from tap water. Analysis of a 2 L volume of tap water by *pXRF* documented quantitative measurement of aqueous lead in drinking water down to concentration around 15 ppb. The method was also demonstrated to be reliable for detecting Ca and other divalent metals in drinking water including Fe, Mn, Cu, and Zn. Nissinen et al. (2018) used nanosilica filters for a similar purpose, with encouraging results for Cu, Zn, Ni, Mn, U, and Pb. Under currently available technology, water analysis by *pXRF* is not possible by direct measurement, but may be considered using a calibrated sorption process on a filter. This is a potential breakthrough for research.

#### 20.2.3.7 Rock and Soil Mechanics Applications

Similarly, literature references to the use of *pXRF* application in rock and soil mechanics are limited. Sadeghiamirshahidi and Vitton (2019) used *pXRF* in a soil mechanics study to recognize gypsum composition.

#### 20.2.4 Summary and Concluding Remarks

In the last decade, *pXRF* has gained extensive recognition in many areas of the geosciences as a field geoscientist’s tool. Moving from a qualitative, decision-aid role toward a quantitative tool for in-field analysis tool was slower, but was demonstrated to be effective whenever attention was paid to sample preparation and to QA/QC protocols. The geoscience world, and especially the mining industry, was properly skeptical about the excessive claims by instrument manufacturers, who let prospective customers imagine that “point-and-shoot” measurements could provide analytical results comparable to those made in the laboratory. Supporting this idea, the images in most advertisements displayed a mining geologist analyzing a rock face or an unprepared soil surface, which resulted in valuable instruments not being used since they did not provide the same high-accuracy abundance measurements as the laboratory. The acceptance by industry was, therefore, slower than the technical improvement of the instruments by the commercial sector.

As a decision aid or diagnostic instrument, *pXRF* has achieved its place in the geologist’s toolbox, because it is helps to address certain uncertainties associated with geochemical fieldwork and been demonstrated to be a money-saving tool. For example, *pXRF* analysis of drill core on site to conclude a drill hole as soon as it reaches the footwall of a deposit or *pXRF* analysis of stream sediments during an exploration campaign can identify the small creek delivering the strongest metal signal to the river, thus narrowing the soil sampling grid where it matters most, without waiting for next year’s sampling campaign.

The benefit of on-site sample assessment by *pXRF* has been frequently overlooked, though it was identified soon after the introduction of commercial instruments (Crume 2000). Even when priority is given in a project to laboratory analysis, on-site sample screening by *pXRF* prior to shipping can result in a large cost savings. This is the case when reporting based on *pXRF* analyses only is not yet acceptable by regulatory authorities (environmental monitoring) or by investors (mineral exploration). The biggest benefit is, however, the possibility of making real-time decisions, which can provide a time and money saving during exploration operations.

## 20.3 Laser-Induced Breakdown Spectroscopy (LIBS) for Field Geology

### 20.3.1 Background

LIBS is a convenient, versatile, and reliable form of analytical atomic spectrometry for material compositional analysis. It is ideally suited for the real-time chemical analysis of geological materials in the field under ambient environmental conditions because the small number of constituent components needed for a LIBS system (laser, optics for light transmission, a spectrograph-detector system, and computer for signal processing and system control) can be comfortably fit into a compact device as described by Day (Vol. 1, Chapter 13). Advantages of LIBS include its ability to rapidly analyze material in any state – solid, liquid, or gas, with little-to-no sample preparation. Due to the fact that LIBS atomic emission from all elements occurs within the spectral range between 200 and 900 nm (Cremers and Radziemski 2013), information can be readily obtained on both the chemical species present in a sample and their abundance by monitoring the position and intensity of emission lines in the LIBS optical spectrum. Different geological materials can be readily recognized through their elemental composition or discriminated through spectral matching against pre-established databases and chemometric analysis (e.g. Gottfried 2013). Quantitative elemental abundances can be readily achieved for many elements down to the 10s of ppm level or below using calibration curves generated from matrix-matched standards (Harmon and Russo 2014), or through calibration-free methodologies (Corsi et al. 2006).

LIBS sampling is highly spatially resolved, as the high-temperature plasma forms over a limited area of 10 µm to more than 100 µm, so that only a small amount of material (typically sub-mg) is ablated, vaporized, and dissociated into a mixture of free electrons and weakly ionized molecular, atomic, and ionic species by each laser shot. As the plasma rapidly cools, species' recombination, de-excitation, and the release of energy occurs as photons when electrons return to lower energy levels. This produces sharp emission lines at discrete wavelengths (Figure 20.12). LIBS also affords analysis at high spatial resolution for: (i) chemical analysis at spatial scales <10 µm for the in situ analysis of individual particles or inclusions; (ii) the analysis of thin crusts, coatings, or surface alteration

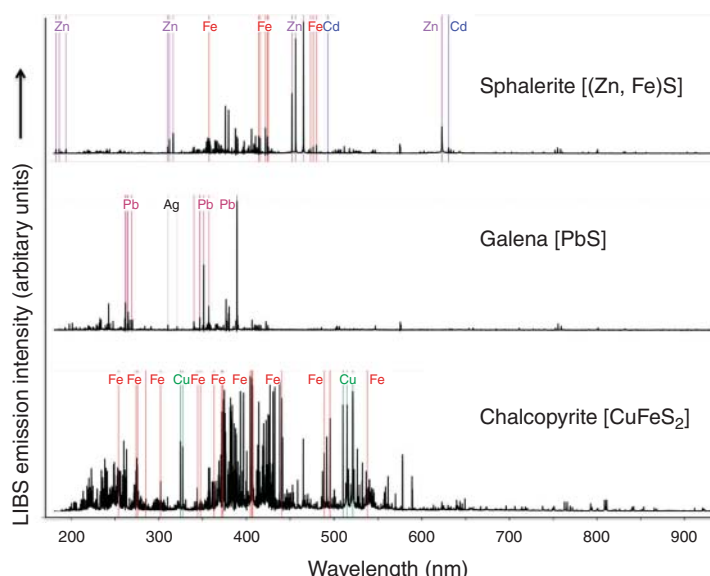


**Figure 20.12** LIBS emission spectra acquired on an unprepared surface of drill core for three minerals of economic importance – sphalerite [(Zn, Fe)S], galena [PbS], and chalcopyrite [CuFeS<sub>2</sub>] using a SciAps Z-300 handheld LIBS analyzer. Modified from Harmon et al. (2019).

zones without substrate interference; and (iii) stratigraphic compositional analysis of a sample by depth profiling as sequential ablation forms a crater that progressively bores down into a sample with successive laser shots and (iv) and lateral raster mapping that can be used for the rapid examination of microscale elemental distributions across the surface of a rock, drill core, or mineral.

### 20.3.2 Qualitative Versus Quantitative Analysis by LIBS

#### 20.3.2.1 Qualitative Analysis

LIBS has been widely used for qualitative compositional analysis since excited electrons for all elements emit photons at specific wavelengths over the 190–900 nm spectral range that typically is fully or partially monitored in LIBS analysis. Most elements have multiple emission lines, so a typical broadband LIBS emission spectrum for most geological materials consists of hundreds to thousands of spectral lines. The wavelength of a spectral line in the LIBS emission identifies the chemical species present; the intensity of the emission lines is proportional to its abundance in the LIBS plasma. Generally, elements on the left side of the periodic table have relatively low ionization energy, display strong emission and, therefore, can be detected at very small abundances. By contrast, nonmetallic elements on the right side of the periodic table with high ionization potentials are more challenging to determine by LIBS and, consequently, have much higher limits of detection (Harmon and Russo 2014). Thus, the metal elements of the three sulfide minerals are readily manifested in the three LIBS spectra of Figure 20.12, but the S lines between 921.3 and 923.8 nm are only apparent in the chalcopyrite spectrum. The constituent elements present in different kinds of geological samples can be ascertained by comparing the peaks in a LIBS emission spectrum with established spectral databases such as the one maintained by the US National Institute of Science and Technology (Reader et al. 1980; Kramida et al. 2018), or available online (see e.g. Atom Trace A.S.; <https://www.atomtrace.com/elements-database/>). Such qualitative LIBS can also be particularly useful in *geochemical fingerprinting*, as shown by Hark and Harmon (2014), where the objective is to ascertain what elements are present in a sample, without knowing exactly how much of the element is present.

#### 20.3.2.2 Quantitative Analysis

Like all analytical methodologies, optimal conditions for quantitative analysis depend on the nature of the sample, the purpose of the analysis, and critically the availability of calibration or reference materials. Quantitative analysis using LIBS is possible because elemental abundances in the sample are proportional to their line intensities from the plasma emission based on two assumptions: (i) that the contents of an element in the plasma and in the sample are proportional, and (ii) that the emission line intensity of an atomic or ionic species of an element in the LIBS spectrum is likewise representative of the concentration of the corresponding element in the plasma (Cremers and Radziemski 2013). Even though these assumptions may be satisfied, emission-line intensity also depends on several other interrelated factors. These include laser-pulse characteristics, material characteristics, degree of laser-material coupling and the environmental conditions of the analysis, and the complication encountered with quantitative LIBS, whether using laboratory or portable instruments, is the phenomena known as matrix effects (Harmon et al. 2013).

Matrix effects can be grouped into two types, chemical and physical. First, because of the high density of material in the LIBS plasma, the physical character and bulk chemical composition of the sample being analyzed will affect the concentration of an element present in the plasma. For example, an element present at equal concentration in different host materials may exhibit different LIBS emission intensities (Anzano et al. 2006; Eppler et al. 1996; Hahn and Omenetto 2012). Chemical matrix effects are a consequence of one element interfering with the emission behavior of another. Typically, this happens when there is a species present in the sample that inhibits the ionization of another species of much lower ionization potential. For example, the emission for an ionized species in the plasma will be different for a material that contains a very easily ionizable element compared to another that does not. This is because the readily ionizable species elevates the plasma density and, therefore, decreases

the concentration of the other ionic species in the plasma at the same laser energy (Eppler et al. 1996). Physical matrix effects are more complex and difficult to ameliorate than chemical ones. Such effects occur during the ablation step of the LIBS process because of material differences in such properties as the thermal conductivity, specific heat, and latent heat of vaporization that influence the quantity of mass ablated. Samples with the same concentration of an element in a different host material may produce different emission intensity because of the change in the amount of sample ablated. For example, the silicate minerals feldspar and mica, because of their difference in crystal structure and hardness, will yield a different amount of material ablation per laser shot without any change in the character of the laser ablation pulse. Also, factors related to sample character and intrinsic variability, such as degree of sample crystallinity, grain size, hardness, coherence, and induration, that produce variable surface textures, will directly affect the degree of laser energy coupling, the laser pulse energy distribution within the material, and the consequent extent of material ablation. As a result, there will be a different degree of laser energy coupling to samples having different degrees of transparency to the laser light, a rough versus smooth surface, different grain sizes, or variable moisture contents, which can generate a large shot-to-shot variation in the emission signal. Thus, for quantitative LIBS using handheld analyzers, it is essential to have standards that are very closely matrix-matched to the type of samples being analyzed, so that calibration curves are developed for the element in the material of interest, and then LIBS measurements for the unknown samples are acquired under the same experimental conditions (see, e.g. Arca et al. 1997; Barrette and Turmel 2001; Rosenwasser et al. 2001).

In the ideal situation, LIBS can provide quantitative analysis using any suitable emission wavelength when matrix-matched reference materials exist (see e.g. Anzano et al. 2006). This becomes much more problematic when reference materials do not exist (e.g. Eppler et al. 1996), as spectral emission intensity is influenced not only by the elemental concentration in the sample but also by both the laser operational parameters (energy, power density, wavelength) and the physical nature of the sample (e.g. Liu et al. 2005; McMillan et al. 2006; Rauschenbach et al. 2008). For quantitative analysis, it is also necessary to know how much mass is sampled by each laser pulse. This can be achieved by using an internal standard simultaneously measuring the elemental emission of interest along with that from a common matrix element (Harmon et al. 2013), assuming that the desired element will exhibit the same mass-ablation-rate behavior in both the sample and the internal standard. The spatial distribution of the element in the internal standard must be homogeneous, and the internal standard and analyte must be equally affected by the ablation, which can be particularly problematic for geological samples, which frequently are not elementally homogeneous at the microscale.

Univariate or multivariate and linear or nonlinear models can be used to calibrate LIBS analysis (e.g. Ferreira et al. 2008, 2011). Univariate and linear models may be suitable in most cases, but multivariate models, such as partial least square regression (PLSR), support vector machine (SVM), and artificial neural network (ANN) approaches may also be used when the intensity of a single emission line does not reflect the variation of an element concentration, because of self-absorption, weak signal, or interference by lines of other elements.

### 20.3.3 Geological Applications of LIBS

As described in the published literature, much of which has been described in review papers by Harmon et al. (2013); Hark and Harmon (2014), Senesi (2014), and Qiao et al. (2015), LIBS analysis is applicable to the wide variety of materials that a geologist or geochemist can encounter in the field. Gases, such as those emanating from volcanic edifices or geothermal fields, can be directly analyzed by forming the plasma within the gaseous environment of interest. Analysis of liquids of all types is accomplished by focusing the laser on the surface of the liquid or within the body of the liquid below its surface. Fine-grained rocks and minerals are analyzed by focusing the laser on the surface of the sample.

The basic differences between LIBS analysis in the laboratory, which commonly uses bespoke instrumentation that may be reconfigured from experiment to experiment, and the current generation of handheld LIBS analyzers

relate to laser energy, firing rate, and spectral analysis; see the chapter by Day (Vol. 1, Chapter 13). As described by Cremers and Radziemski (2013), typical laboratory LIBS systems employ high-power flashlamp-pumped, Q-switched Nd-YAG lasers that produce up to 400 mJ pulse energy with adjustable pulse width and laser firing rate, although excimer, and CO<sub>2</sub> lasers are also in use, and detectors (PMT, APD, PDA, IPDA, CCD, or ICCD) coupled to high-resolution spectrographs or spectrometer stacks so that a large wavelength range can be observed at high resolution. By contrast, handheld LIBS analyzers have been developed utilizing compact detector-spectrometer combinations and diode-pumped solid-state lasers with low pulse energy (microjoules to millijoules) fired at a very high repetition rate (5–10 kHz).

Most of the geological and environmental materials analyzed to date in the laboratory can be undertaken in the field using commercial handheld LIBS analyzers, and the different analytic approaches used to process LIBS analyses in the laboratory can be implemented for applications using handheld LIBS analyzers. Some of these applications include (i) quantitative elemental analysis of water and ice, volcanic glass, minerals, and fine-grained rocks; (ii) the qualitative analysis of many different types of geomaterials for chemical fingerprinting for gemstone analysis, ore analysis, soil and sediment analysis and contaminant identification; analysis of shale, hydrocarbon, and coal analysis, the analysis of carbonate fossils, concretions, speleothems, and coatings; analysis of extraterrestrial materials; and (iii) microscale geochemical mapping and imaging.

#### 20.3.4 Field-Portable and Handheld LIBS

Senesi reviewed the state of field-portable LIBS instrumentation in 2017. Significant technical advances have been made since that time, with field-portable and handheld LIBS analyzers presently being marketed by more than half-a-dozen commercial manufacturers.

The first initiatives to take LIBS out of the laboratory and into the field utilized the *LIBS-in-a-box* approach that simply compressed the components of a simple laboratory LIBS apparatus into a briefcase size box that could be transported to the site of sample analysis (Castle et al. 1998; Palanco et al. 2003; Wainner et al. 2001; Yamamoto et al. 1996). Such man-portable systems typically used a Q-switched Nd-YAG laser operated at its fundamental wavelength of 1064 nm to deliver a short-duration pulse of low energy, a gated detector and spectrograph/spectrometer array, and a fiber optic cable to both deliver the laser light to the sample and then collect the resultant plasma emission.

The portable LIBS instrument developed at the US DOE Los Alamos National Laboratory was used to measure Ba, Be, Pb, and Sr in soil (Yamamoto et al. 1996), with quantitative results produced similar to those obtained by a conventional LIBS apparatus and by XRF. A similar field-portable LIBS system sponsored by the US Army Research Laboratory (Harmon et al. 2005, 2006) consisted of a laser-bearing sample probe with an optical fiber for laser light transmission and plasma signal collection and a central detector-analyzer unit housing the spectrometer-detector, timing, power, and data acquisition and analysis equipment in a companion aluminum case, with data stored in a palmtop-type personal computer. This man-portable analyzer exhibited similar performance to a laboratory LIBS system with regard to the quantification of Pb in soil over a 0.05–1 wt. % concentration range.

Subsequent portable LIBS devices followed the concept of having an optical probe and a hardware unit as two separate components. Initial backpack LIBS designs (Cuñat et al. 2008; Harmon et al. 2006) used a hand-operated wand containing the laser and fiber optic cable for light delivery and acquisition, with the detector, spectrometer, and data processing hardware, and control apparatus integrated into the backpack unit. Rakovský et al. (2012) made a next major step forward toward today's commercial handheld LIBS analyzers by placing the laser and optical elements within a drill-shaped box that was connected by an umbilical containing the optical fiber to a second box containing the spectrometer, batteries, system control apparatus, and data processing computer.

Further development of small and compact LIBS analyzers was strongly driven during the first decade of the current millennium by the selection of LIBS as one of the technologies to be contained in the *ChemCam* system

designed by NASA to analyze the elemental composition of soils and rocks on the surface of Mars by the Curiosity rover (Weins et al. 2013; <https://pds-geosciences.wustl.edu/missions/msl/chemcam.htm>). Then, the first truly handheld LIBS analyzer was introduced to the commercial market in 2013 and described in the literature shortly thereafter (Connors et al. 2016). Although the development of portable LIBS instrumentation for geological application continues in research laboratories (e.g. Guo et al. 2019; Kumar et al. 2018; Meng et al. 2017), commercial handheld analyzers are now the preferred solution to the long-standing latent need for a technology capable of rapid chemical analysis outside the laboratory. Designed to utilize recent advances in optics, compact laser sources, miniaturized high-resolution spectrometers, microelectronics, and computers, several manufacturers are presently producing lightweight handheld LIBS analyzers that are battery-powered and can be used continuously for several hours. It is expected that this trend will continue and incorporate new component technology (e.g. Alvarez-Llamas et al. 2018) as it is developed.

This current generation of handheld instruments offers real-time spectral display plus many features present in laboratory systems, including variable gating, gas purging, sample rastering, video targeting, and on-board chemometric analysis. Used in combination with an on-board Global Positioning System (GPS) capability and with wireless data transmission, handheld LIBS analyzers are expected to realize widespread utilization for real-time geochemical analysis in the field in the future, particularly given the LIBS capability to detect and analyze the light elements ( $Z < 14$ ) not possible by handheld XRF. Typical limits of detection for handheld LIBS analyzers are higher than for laboratory instrumentation (see e.g. Michaud et al. 2019), but nonetheless quite acceptable for a wide variety of geological field applications.

#### 20.3.4.1 Field-Portable LIBS

Over the past few years, there has been a slow but growing uptake of handheld LIBS within the geological and environmental science communities. The paragraphs that follow summarize these applications as examples of the broad potential of this technology for the analysis of geological materials.

In 2005, Harmon et al. used a battery-powered, suitcase-type LIBS system to analyze metal contamination in unconsolidated and low-permeability carbonate-rich lacustrine and fluvial lakebed sediments and alluvial fan deposits of sand, silt, and clay at a military facility in the arid setting in northeastern California. This location east of the Sierra Nevada mountains had been contaminated during the 1940s to mid-1950s by the demilitarization of small arms ammunition by burning. Ash and solid furnace residues were buried locally at shallow depths in the soil around the furnace, resulting in strongly metal-contaminated soil. The LIBS survey recognized distinctly elevated and highly variable concentrations of Pb, Cu, and Zn across the furnace site compared to background soil levels. That same year, Cuñat et al. (2005) used a mobile LIBS system to analyze surface alteration layers on  $\text{CaCO}_3$  speleothems at nine locations within the interior of the Nerja Cave in Spain. The alteration layers were observed to be enriched in Si, Al, and Fe, elements not present in the calcite matrix of the speleothems. Four years later, Cuñat et al. (2009) used a backpack-type field-portable LIBS system to analyze Pb in road sediments.

Rakovský et al. (2012) demonstrated that a *fpLIBS* instrument could be used to analyze geological samples in the field. Two applications were demonstrated – the recognition of tephra layers in lacustrine sediments and fossilization processes in ammonites, using a bespoke portable LIBS system that placed the laser and optical elements within a drill-shaped box that was connected by an umbilical containing the optical fiber and wires to power and control the laser. This umbilical was connected to a second box containing a small spectrometer, system control and data processing computer, and batteries. Geochemical signatures were obtained for a tephra layer from the Lacher See volcano in Germany intercalated with lacustrine chalk sediments of the Jura region of France. A clear difference in Al, Ca, Ti, Ba, and Na abundances was observed through the sediment profile. The fossilization process in ammonites in the sediment section was also examined. Emission intensity depth variations for Fe, Ca, and Al, as well as ratios of Fe/Ca and Al/Ca, provided information about ammonite pyritization. The negative correlation observed between Ca and Fe is compatible with the replacement of Ca by Fe during the pyritization process.

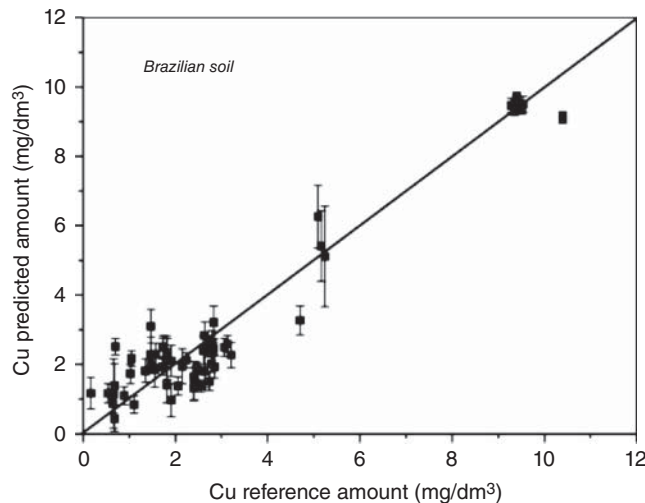


**Figure 20.13** Calibration curve for Cu derived for Brazilian soils by an artificial neural network approach. Modified from Ferreira et al. (2008).

Ferreira et al. (2008) utilized a *fpLIBS* analyzer, with spectral data processed through an artificial neural network, to develop a quantitative calibration for Cu in soil based upon analysis of 59 Brazilian soils of known copper content that contained different proportions of sand, silt, and clay. Sixty single-shot LIBS broadband spectra between 190 and 400 nm were collected at different locations on each pellet and then averaged to obtain single emission intensity values for the Cu atomic emission lines at 324.7 and 327.4 nm. Using this approach, the resultant calibration curve (Figure 20.13), with mean standard error estimated from a 10-fold cross validation methodology, was considered to be independent of soil matrix. Both simple linear regression and a wrapper approach were employed to select the set of wavelengths for learning by an artificial neural network procedure, with cross-validation applied for verification of prediction accuracy after the ANN training. The overall limit of detection (LOD) determined was  $2.3 \text{ mg dm}^{-3}$  of Cu.

Volcanic rocks were analyzed *in situ* in the field in Iceland by Roux et al. (2015) using a *hLIBS* instrument custom-made in a hand drill shape by the Laboratory Interdisciplinaire Carnot de Bourgogne (ICB), with analysis of spectral data undertaken on a laptop computer using a software package developed at the ICB. An analysis of 19 atomic lines for Al, Ba, Ca, Cr, Cu, Fe, Mg, Mn, Na, Si, Sr, and Ti, with discrimination based upon principal component analysis was performed successfully for 21 volcanic rocks belonging to three different magmatic series (Figure 20.14), with only the altered sample from Group 1 (#15) incorrectly assigned to Group 2.

A year later, Connors et al. (2016) offered the first description in the published literature of a commercial *hLIBS* instrument to analyze different types of geological materials. The SciAps Z-500 analyzer, and its recently introduced Z-300 companion instrument, has two data processing capabilities that are particularly oriented to geochemical analysis. For qualitative analysis, the GeoChem Pro operation mode can identify the spectral peaks of specific elements and generate elemental concentration maps based upon the relative intensities of these peaks across a raster pattern. The *GeoChem* mode of operation is used for quantitative analysis, based upon either calibration curves loaded at the factory or from custom calibrations generated by the user using the SciAps proprietary *Profile Builder™ PC* software, which allows conversion of elemental concentrations to oxides in user-selectable units of measurement of wt. % or ppm. Application notes available on the SciAps website (<https://www.sciaps.com/resource-library/application-notes/>) illustrate how the SciAps Z-series LIBS analyzers can be used for the detection in soil of toxic elements like Be, for use by the mineral exploration community for the

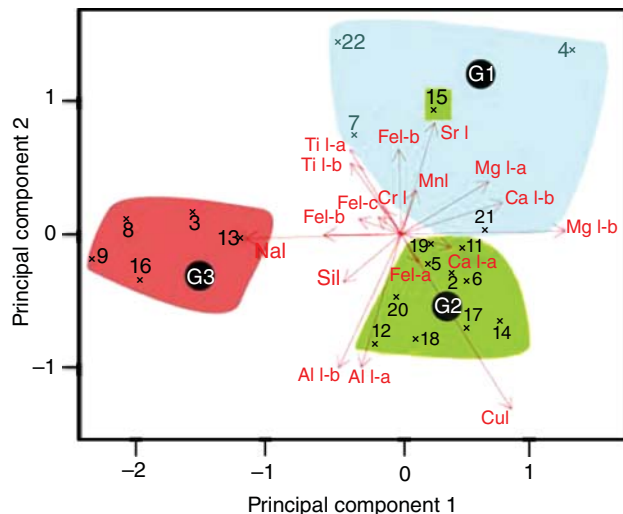


**Figure 20.14** Principal component (PC) plots for Icelandic volcanic rocks based upon 19 spectral emission lines analyzed in the samples belonging to series A. The first PC explains 48.7% of the observed variance and the second PC another 18.7%. The red lines in the figure indicate the loadings for the specified spectral emission line. Modified from Roux et al. (2015).

detection, localization, and/or quantification of Li, Au, and base metals (Cu, Zn, Pb), and for the quantification of C in soil that is of particular interest to the agricultural and climate research communities.

Harmon et al. (2017) used the SciAps *hLIBS* analyzer for the rapid identification and discrimination of a wide spectrum of geological material types that included carbonate minerals of different composition, modern carbonate platform sediments, and lithified carbonate rocks; the silicate mineral garnet, which is a *pathfinder mineral* in kimberlite exploration; the oxide mineral pair columbite–tantalite, which is a common *conflict mineral*; and native gold of different provenance. The distinct chemical features within the different sample suites samples analyzed, i.e. the spectral differences in minor and trace contents between similar samples, were identified through principal component analysis and then partial least squares discriminant analysis was used to distinguish and classify the samples within each suite with excellent discrimination for all sample types. This study demonstrates how handheld LIBS analysis can be used to distinguish between similar samples based on broadband LIBS spectra, which can be considered comprehensive *geochemical fingerprints* of the different types of geological sample types analyzed. This study also illustrates how handheld LIBS could be used for real-time chemical analysis in the field for element or mineral identification and applications such as stratigraphic correlation, provenance determination, and natural resource exploration via spectral matching with a predetermined and assembled spectral library for materials of interest.

For the carbonate muds, *hLIBS* analysis was undertaken for six carbonate platforms around the world – the Alacran Reef, Mexico; Yucatan Shelf, Mexico; Crooked–Acklins Platform, Bahamas; Platform, Turks and Caicos; Maupiti Atoll, French Polynesia; and Nonouti Atoll, Republic of Kiribati. These locations are characterized by mud samples from shallow water (<11 m) that have distinct physical, chemical, and biological character. Classification success for discrimination of the six sample suites was 96.3% (Figure 20.15). The spectral loadings from the LIBS analysis documented that Sr, Ca, and Mg are the main compositional components contributing to the discrimination. Interestingly, the 288.16 nm line for Si was prominent in the LIBS spectra of the Yucatan Shelf mud fractions, most likely identifying a biosiliceous component (i.e. radiolaria, diatoms, and/or sponge spicules), but largely absent from the muds accumulating on the other five locations, most likely due to upwelled, nutrient-rich water at this site. That the six carbonate mud localities also group well by ocean basin implies that water chemistry may influence the composition of carbonate at both the local and the regional spatial scales.

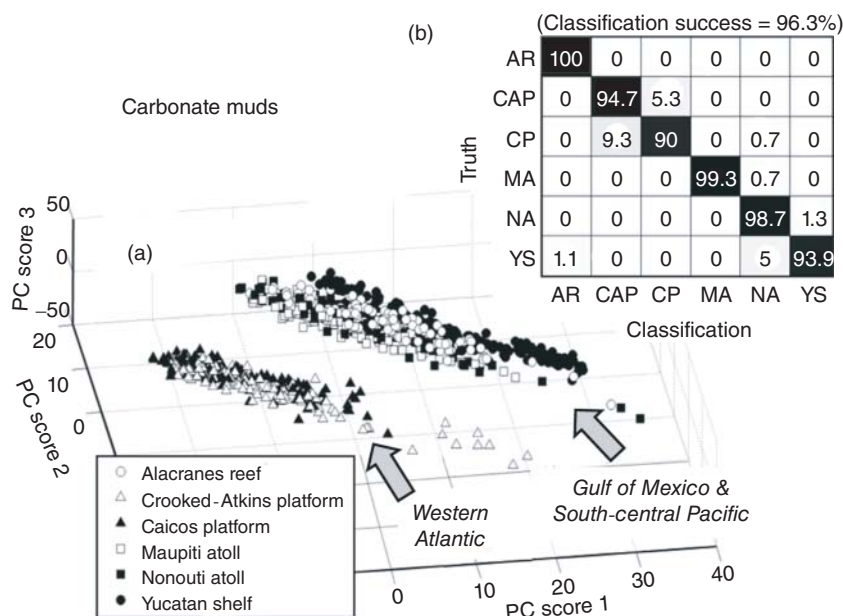


**Figure 20.15** Principal component analysis (PCA) score plot (a) and partial least squares-discriminant analysis (PLS-DA) classification matrix (b) for carbonate muds from the south-central Pacific Ocean (PAC: Maupiti Atoll and Nonouti Atoll), western Atlantic Ocean (ATL: Caicos Platform and Crooked-Acklins Platform) and Gulf of Mexico (GM: Alacran Reef). The classification matrix (b) is a bivariate plot that portrays the reclassification of the observations, where each entry in the matrix indicates the percentage of spectra identified as belonging to the column class, when in fact they are actually members of the row class, which shows that >93% LIBS spectra acquired over the spectral range from 180 to 675 nm range by *hLIBS* analysis were successfully discriminated. The fact that the Atlantic and Pacific localities group together in the PCA plot (a) also implies that seawater chemistry likely influences the composition of carbonate mud deposits at the ocean basin spatial scale as well as at the local scale. Modified from Harmon et al. (2017).

Harmon et al. (2017) also analyzed native gold from 18 placer locations in New Zealand, Australia, and the United States (Alaska, Idaho, California, Colorado, Virginia and North Carolina) plus samples of pure gold and silver (Figure 20.16). Notably, in a first experiment, samples were consolidated into 11 groups based on geological affinity and samples from these domains were differentiated by *hLIBS* analysis with an overall success of 92.5%, based solely on silver and gold content. Using the full LIBS spectrum of each sample, the most important spectral lines for the PLSDA discrimination, in terms of loading values, were the prominent emission lines Au lines at 523.0, 583.7, and 479.2 nm, plus the Ag lines at 546.5, 520.9, 328.1, and 338.2 nm.

In 2017, de Vallejuelo et al. (2017) combined in situ measurement using a *fpLIBS* analyzer, and chemometric data processing, using principal component analysis of complete LIBS spectra, after outlier identification and removal by a k-nearest neighbor approach, to assess water quality in the urban Deba River catchment in the Gipuzkoa province of northern Spain during large rainfall events (Figure 20.17). Measurements were performed on suspended particulate matter samples collected every two hours during five storm events, at an automatic water sampler at three stations. This particulate matter consisted of colloids and particles of different sizes, including heterogeneous aggregates of mineral, organic, and biological phases. After baseline correction and mean centering of the LIBS spectra, principal component analysis focused on the spectral range between 198 and 552 nm revealed the toxic elements Pb, Cr, Ni, and Cu in the suspended matter as important discriminant variables. Additional principal component analysis was able to differentiate between monitored localities and the timing of the storm event. The environmental risk of these riverine pollutants was assessed through correlation

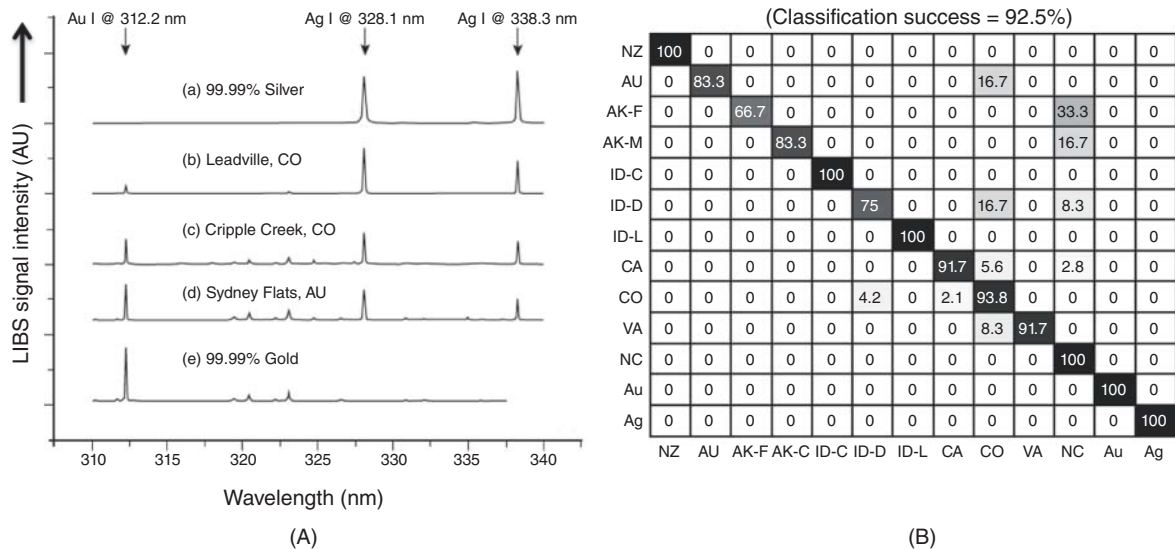


**Figure 20.16** (a) *h*LIBS emission spectra acquired between 305 and 345 nm for pure silver (a); placer gold samples from Leadville, Colorado (b); Cripple Creek, Colorado (c); Sydney Flats, Australia (d); and pure gold showing relative spectral intensities of the 312.2 nm Au line and 328.1 and 338.3 nm Ag lines. (b) PLSDA classification matrix for placer gold samples by location based only on the 16 most prominent gold and silver spectral lines (Legend: NZ = Naseby, Central Otago Goldfield, New Zealand; AU = Sydney Flats, Bendigo Goldfield, Victoria, Australia; AK-F = Fortymile District, Alaska, USA; AK-M = Mastodon Creek, Circle District, Alaska, USA; ID-C = Coeur D'Alene District, Idaho (USA); ID-D = Dry Creek, Elmore County, ID (USA); ID-L = Loon Creek District, Custer County, ID (USA); CA = Mother Lode Gold District, CA (USA), CO = Colorado Mineral Belt (USA); VA = Virginia Pyrite Belt (USA); NC = Carolina Slate Belt (USA); Au = pure gold, and Ag = pure silver). Modified from Harmon et al. (2017).

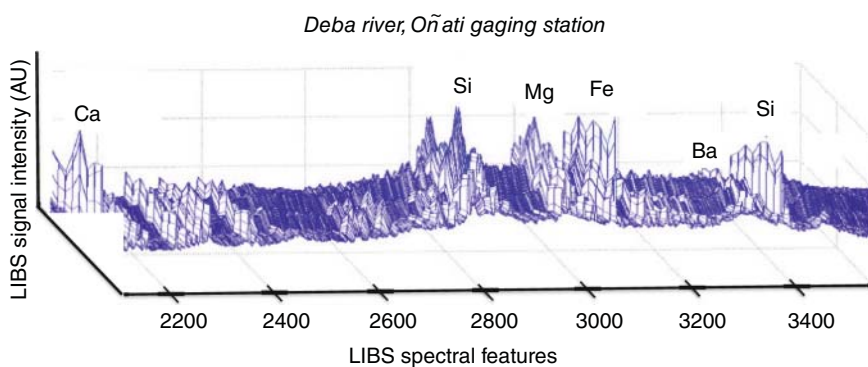


**Figure 20.17** Composite plot of *fp*LIBS spectra of suspended particulate matter as sampled at the Oñati gaging station on the Deba River in the Gipuzkoa province of northern Spain collected at two-hour intervals during a high flow event. The first spectra of the time series is at the back, of the plot, with the spectra for each successive two-hour interval shown progressively toward the front. The large peaks for Ca, Si, Mg, Fe, and Ba document the greater levels of suspended particulate matter in runoff during the middle of the storm event. Modified from de Vallejuelo et al. (2017).

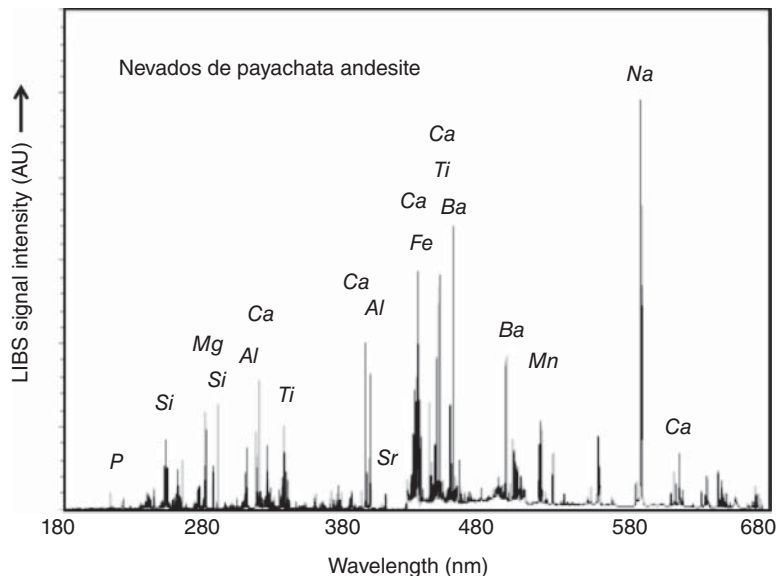


**Figure 20.18** Broadband LIBS spectrum collected with a *hLIBS* analyzer for an andesite lava from the Nevados de Payachatas volcanic complex in North Chile. The most intense emission lines for the elements present in the LIBS spectra are identified; other emission lines not labeled are lower intensity lines of the same elements or very low intensity lines of minor and trace elements. The *hLIBS* analyzer had a spectral range of 180–675 nm, so K with primary emission lines at 766.5 and 769.9 nm does not appear in the LIBS spectrum. From Harmon et al. (2018) used with permission. Modified from Harmon et al. (2018).

between variables representing the different sources (urban/municipal contamination, anthropogenic activities, etc.) of the contaminant elements.

Meng et al. (2017) described a mobile LIBS system based around the integration of a hemispherical spatial confinement cavity to provide spatial confinement thought to significantly enhance plasma radiation and improve the strength and stability of the LIBS emission. The handheld part includes the laser head, spatial confinement cavity, focusing lens and optical fibers, with the laser power supply, spectrometer, and computer located in a mobile cabinet. This system was demonstrated for heavy metal analysis of pellets prepared from contaminated soil collected from two depths around a smelter in a mining industrial city close to the Yangtze River in southern China. Semiquantitative measurement was demonstrated using the calibration curve method, with LODs obtained for Pb, Cu, and Zn below the 10 ppm level needed for rapid screening of soil heavy-metal pollution. Given the rapid and continuing technical progress being made by the manufacturers of commercial *hLIBS* analyzers, there is unlikely to be a market for such bespoke LIBS systems.

Harmon et al. (2018) compared broadband LIBS emission spectra for fresh and unaltered volcanic samples (Figure 20.18) of varying age and composition from two tectonic settings by *hLIBS* analysis. The different volcanic sources were differentiated through multivariate chemometric analysis after the chemical characteristics of the different volcanic regions and centers were distinguished. Classification and discrimination were accomplished successfully using a pattern recognition approach. Novel use of similarity analysis, a technique not previously utilized to evaluate the quality of LIBS spectral data, indicated that it is necessary to capture the full spectral heterogeneity of different sample types in order to maximize performance of chemometric classifiers.

Senesi et al. (2018a) used a *hLIBS* instrument to compositionally interrogate and discriminate an actual iron meteorite from a suspected meteorite fragment labeled as a “meteor-wrong” and a pig iron product. A calibration-free approach was used to quantify the major element contents of Fe, Ni, and Co plus the trace elements Ga and Ir in the iron meteorite, and Fe, Mn, Si, and Ti in the other two fragments. As the LIBS

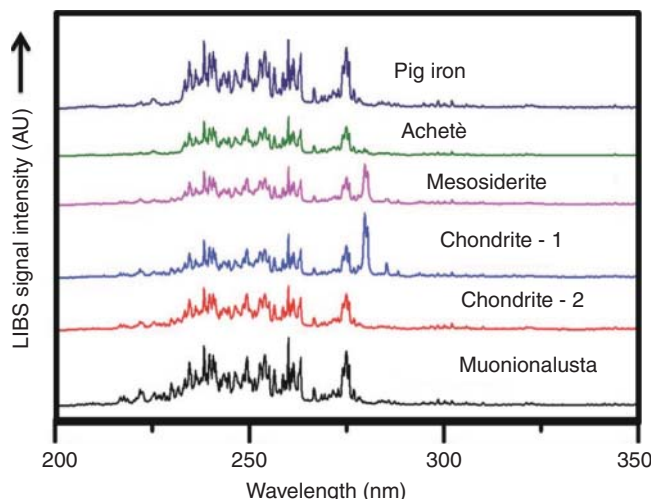


**Figure 20.19** Emission spectra acquired by a *hLIBS* analyzer over a spectral range of 200–350 nm for five iron meteorites and manufactured “pig iron” that provide a *spectral fingerprint* for each sample. Modified from Senesi et al. (2018a).

quantitative data were only partially satisfactory for the identification and classification of metallic objects of extraterrestrial origin with respect to human artifacts, improvements of the handheld LIBS instrument were deemed necessary to increase analytical sensitivity.

In a second meteorite application, Senesi et al. (2018a) used the same *hLIBS* analyzer to investigate meteorite classification based on the integration of automated feature selection and supervised learning using a fuzzy-rule-based classifier to discriminate among iron, stone, stony-iron meteorites and “meteor-wrongs,” terrestrial samples often mistaken for meteorites (Figure 20.19). This successful effort was able to classify correctly 25 of 26 samples, whereas only 18 samples were correctly discriminated by partial least squares discriminant analysis.

In another application of *hLIBS*, Senesi et al. (2018a) analyzed a limestone fragment from a block of the masonry of Castello Svevo, Bari, Italy, which has been subject to strong surface degradation characterized by a black surface crust layer. The broadband emission spectra acquired provide a *geochemical fingerprint* of the samples, which contained Al, C, Ca, Fe, K, Mg, Na, and Si, with Ca, C, and Mg characterizing the unaltered limestone, whereas Al, Fe, and Si are the major constituents of the alteration crust. Figure 20.20 shows a portion of the emission spectra between 230 and 270 nm, illustrating the compositional difference between the pristine limestone and the altered surface crust. A calibration-free CF-LIBS approach was used to test the possibility to obtain a suitable quantitative composition of the main elements present in the sample.

Gómez-Nubla et al. (2018) acquired LIBS emission spectra between 200–400 and 600–950 nm for weathered terrestrial analogs to meteorites, in this case impact glasses from meteorite impacts in Libyan desert of western Egypt and from the south of Queenstown on the West Coast of Tasmania using a *fpLIBS* analyzer (Figure 20.21), and developed a statistical methodology for the quantitative analysis of Si, Al, Mg, Ca, Ba, Na, and Fe. The predictive performance of a PLS regression model was used to evaluate LIBS spectral data for discrimination of the impact glasses from black steel slag residues. Analytical results obtained were in good agreement with the range of compositions measured by XRF analysis.

The mineral fluorite ( $\text{CaF}_2$ ) is a primary source for the F used to manufacture hydrofluoric acid. Typically, this fluorite is a by-product of the mining and processing of metallic ores that is recovered by a froth flotation process. Foucaud et al. (2019) used a *hLIBS* analyzer to quantify the F content of rock samples from the tungsten ore deposit at Tabuaço in northern Portugal containing fluorite ( $\text{CaF}_2$ ), scheelite ( $\text{CaWO}_4$ ), and various silicate minerals. Rock powders exhibiting a range of fluorine from 1.5 to 40.7 wt. %, in which F was predominantly

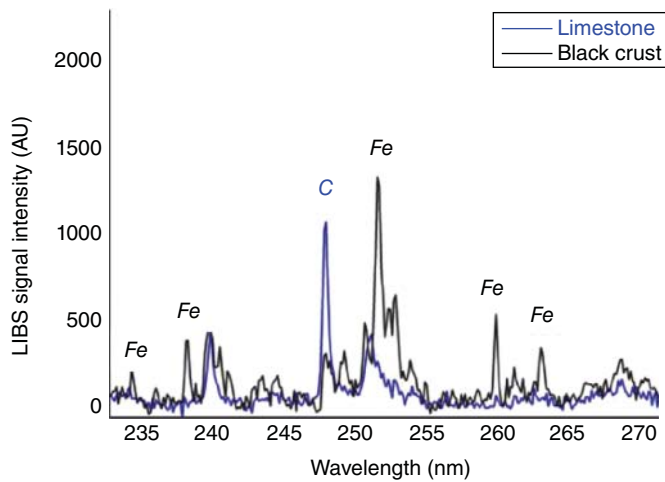


**Figure 20.20** Emission spectra acquired by a *hLIBS* analyzer spectra between 230 and 270 nm for secondary black crust and limestone block. Modified from Senesi et al. (2018b).

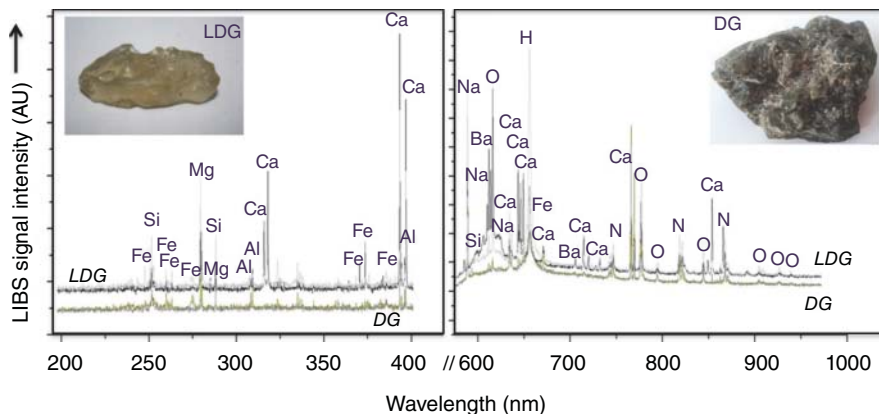


**Figure 20.21** LIBS emission spectra acquired by a *hLIBS* analyzer over the spectral ranges of 200–400 and 600–1000 nm for meteorite impact glasses from the desert of eastern Libya and western Egypt (LDG) and from the south of Queenstown on the West Coast of Tasmania (DG). Modified from Gómez-Nubla et al. (2018).

present in fluorite, were pressed into pellets and *hLIBS* analyses made at nine separate spots by measuring the two CaF molecular bands situated between 529–543 and 590–606 nm (Figure 20.22). LIBS emission intensities over these two spectral regions were normalized, averaged over several ablated zones, and correlated with the fluorine content determined F contents determined using the F-ion sensitive electrode method. It was observed that a matrix effect strongly impacted the measured LIBS intensities, which displayed a non-linear relationship with measured F contents. This necessitated the development of nonlinear univariate models that were calculated on 27 training samples and validated on 9 test samples. Although nonlinear models fitted the experimental data adequately, a multivariate approach using both CaF molecular bands was adopted to address the matrix effect. A linear, quadratic formula was generated from the multivariate regression that predicted F contents with  $R^2 = 0.94$  and a mean average error of 2.18 wt. % F.

Harmon et al. (2019) demonstrated, through a review of previously published research and new results, how LIBS can be used in the context of mineral exploration through qualitative element detection for geochemical

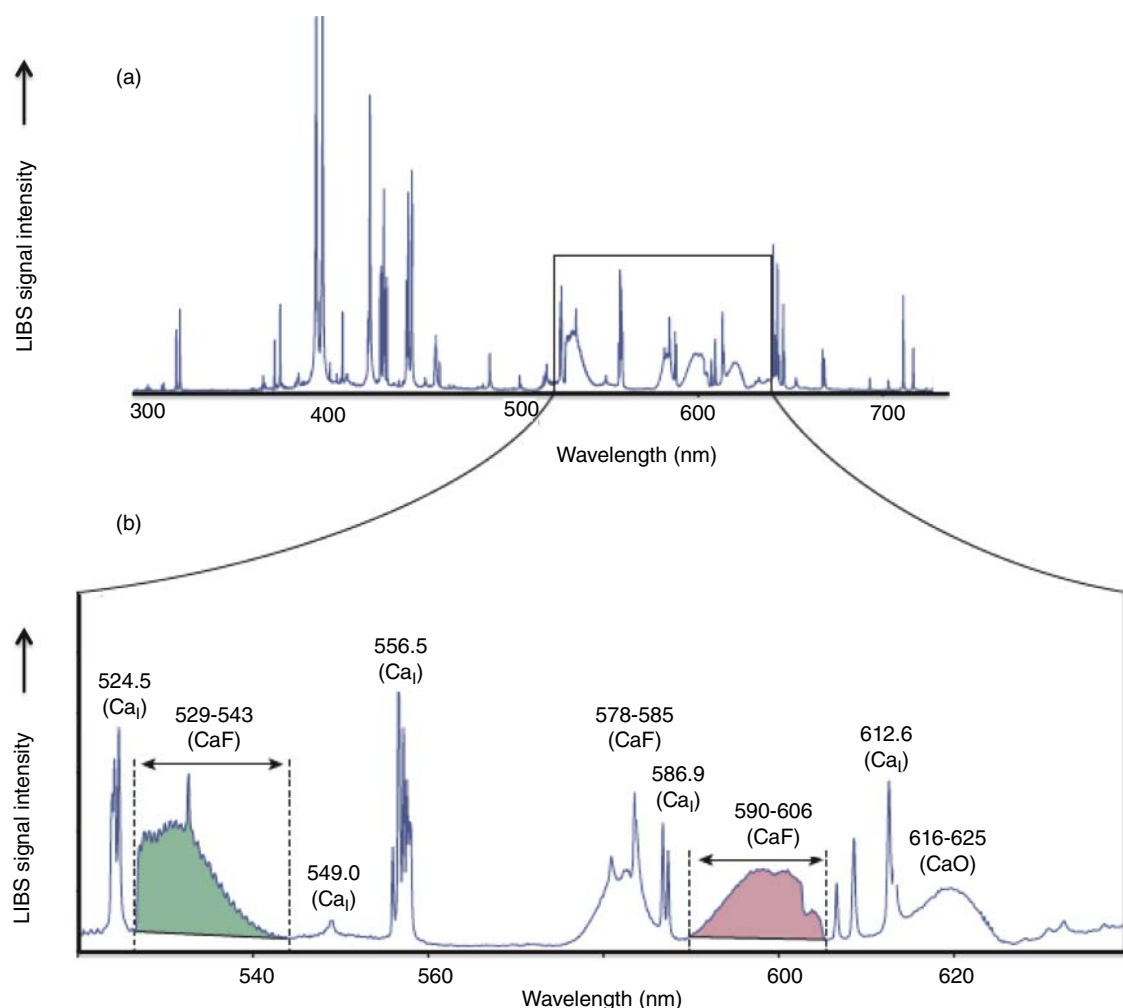


**Figure 20.22** Broadband LIBS emission spectrum for pressed powder pellet acquired using a *hLIBS* analyzer for a sample assaying at 14.73% F (a) and the spectral region between 520 and 640 nm that contains the atomic lines for  $\text{Ca}_\text{I}$  and the  $\text{CaF}$  and  $\text{CaO}$  molecular bands (b). The  $\text{CaF}$  molecular bands denoted in green and pink are those for the spectral ranges and their baselines used in the calibration for F content. Modified from Foucaud et al. (2019).

fingerprinting, sample classification, and discrimination, quantitative geochemical analysis, and in situ geochemical imaging using the raster capability of the *hLIBS* analyzer. The capability of LIBS for micromapping was demonstrated for a set of gold-bearing veins from the MacLellan gold deposit, Lynn Lake, Manitoba, Canada for which LIBS spectra were acquired in Ar on unprepared surface of a cut drill core. As illustrated in Figure 20.12, many of the minerals associated with gold in these veins have characteristic LIBS spectra. Handheld LIBS can, thus, be used to define the spectral fingerprint of the different vein suites and their hydrothermally altered halo in the field and directly on sawed core surfaces. Gold-bearing vein mineralogy can be complex including quartz ( $\text{SiO}_2$ ), calcite ( $\text{CaCO}_3$ ), arsenopyrite ( $\text{FeAsS}$ ), pyrrhotite ( $\text{Fe}_{1-x}\text{S}$ ), sphalerite ( $[\text{Zn}, \text{Fe}]\text{S}$ ), and rare galena ( $\text{PbS}$ ). Geochemical imaging of the core surface clearly demonstrates how qualitative LIBS spectra can be used to differentiate the complex mineralogy of the vein at the microscale (Figures 20.23). This study demonstrated that LIBS is ideally suited for field exploration programs that would benefit from rapid chemical analysis under ambient

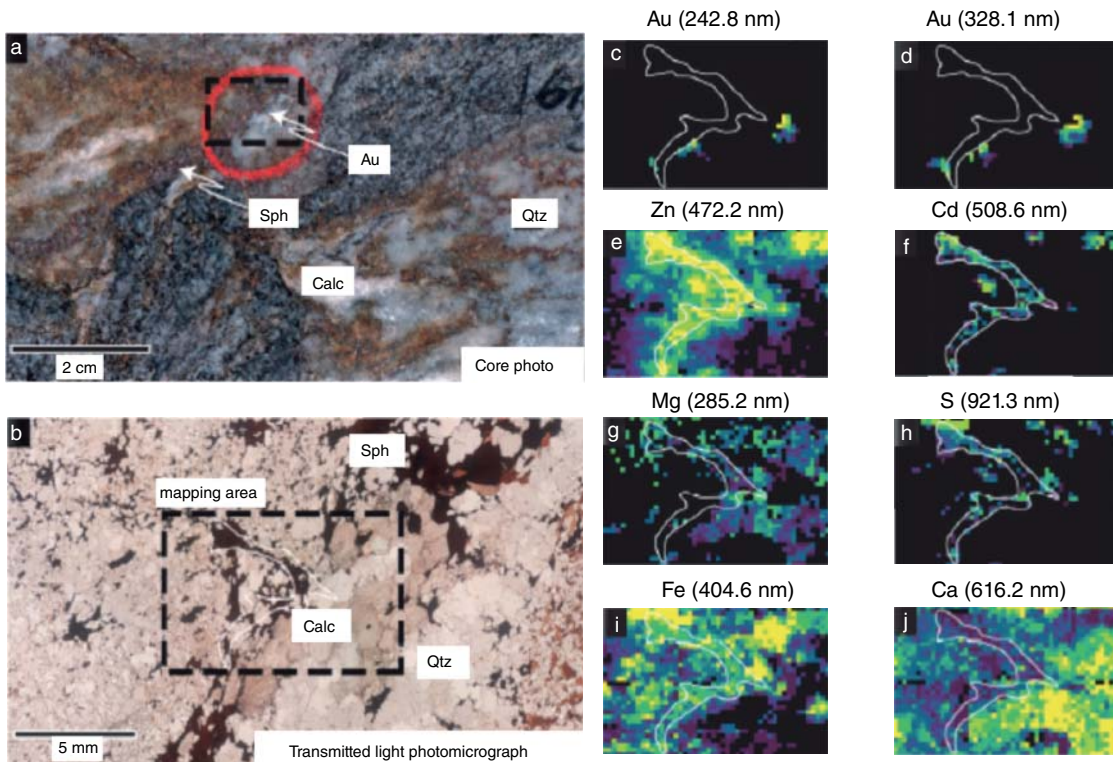


**Figure 20.23** (a) Metal-hosting quartz vein from the MacLellan deposit at Lynn Lake in Manitoba, Canada. The *hLIBS* mapping area comprises quartz (Qtz), calcite (Calc), arsenopyrite (Asp), pyrrhotite (Po), and sphalerite (Sph); (b) transmitted light photomicrograph of the mapping area; (c–j), *hLIBS* results for Au (c), Ag (d), Zn (e), Cd (f), Mg (g), S (h), Fe (i), and Ca (j) displayed as relative wavelength intensities (%) with warm colors indicating higher concentrations and cool colors denoting lower concentrations. Each mineral phase identified within the mapping area can be identified based on its LIBS spectral signature and some prior knowledge of the main mineral-forming elements. Minor to trace elements associated with each mineral can be used to support mineral identification (g). Geochemical imaging is also effective at mapping the distribution of minute minerals of significant economic interest, including native Au inclusions. *Source:* Modified from Harmon et al. (2019).

environmental conditions. LIBS data can be acquired *in situ*, facilitating the interpretation of geochemical data in a mineralogical context, which is important for unraveling the complex geological history of most ore systems.

Yant et al. (2019) described work of the Project Exploration Science Pathfinder Research for Enhancing Solar System Observations (ESPRESSO) team to use *hLIBS* analysis in the context of human space exploration to answer specific geological questions at field analogue sites. The elemental composition was measured for sequences of ash/pyroclastic material at the Kilbourne Hole maar and basaltic material/surface coatings in inflation domes in the Potrillo Volcanic Field in southern New Mexico. Three distinct color layers within the ~3.5 m sequence of a lava flow were measured using the default calibrations of the handheld LIBS analyzer. Then, the underlying portion of the lava flow was analyzed after removal of the superficial layer to determine if distinct compositions could be detected among surface coatings and the underlying rock with respect to the surface. The data acquired were used to evaluate the capacity of such field-portable instruments to solve meaningful geochemical questions and assess the relationship of chemistry to both outcrop-scale compositional spatial variability and small-scale sedimentological heterogeneity (ash, lithics, xenoliths, diagenetic components, etc.).

Erler et al. (2020) considered the application of handheld LIBS to precision agriculture. The total mass fractions of the major nutrients Ca, K, Mg, N, P and the trace nutrient Mn and Fe, together with agriculturally important

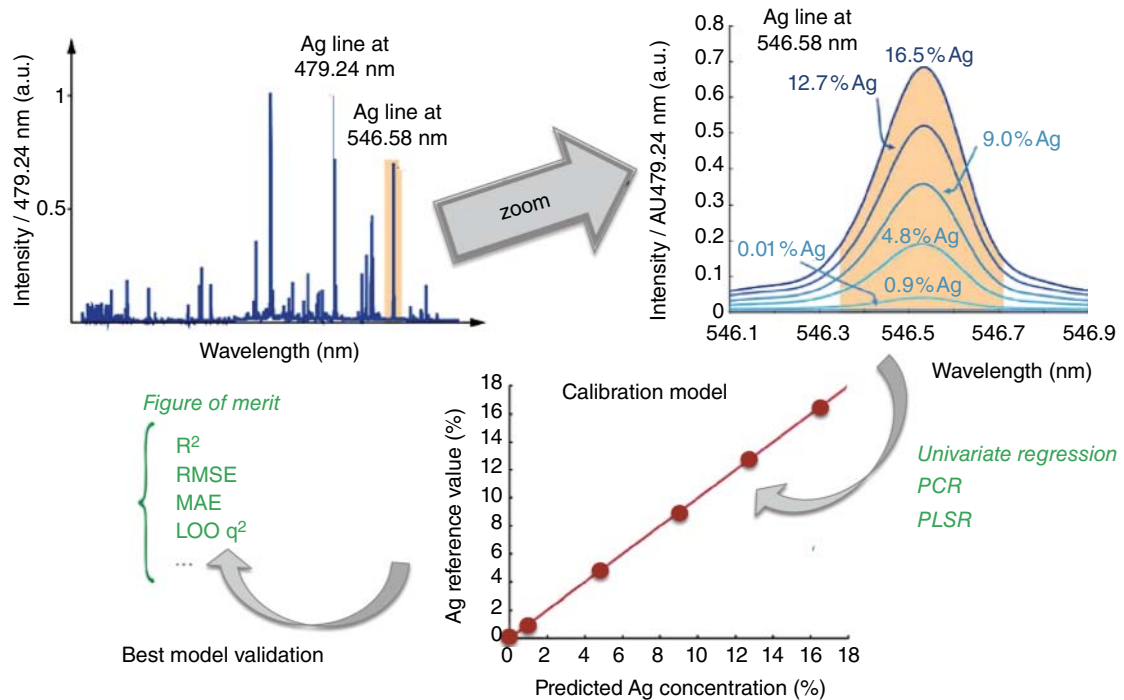


**Figure 20.24** Three-step schema illustrating the LIBS spectral analysis approach used for regression modeling of *hLIBS* spectra for Ag calibration. Modified from Pochon et al. (2020).

soil parameters (humus content, soil pH value, and plant-available P content) were spatially resolved for topsoil (0–30 cm) consisting of sand, loamy sand, and sandy loam derived from calcareous glacial till from 69 locations in two agricultural fields near Wilmersdorf, Germany through laboratory measurement of pressed soil pellets. Because quantification by LIBS depends strongly on the soil matrix, three different multivariate regression methods were characterized and compared. Lasso and GPR were observed to yield better regression results than PLSR.

Pochon et al. (2020) used a *hLIBS* analyzer to acquire emission spectra between 190 and 625 nm to determine the silver content in samples of natural gold from French Guiana. A three-step procedure was developed that used univariate and multivariate regression modeling to evaluate calibration models for Ag quantification. A quadratic univariate model having a correlation coefficient ( $R^2$ ) of 0.99 and a mean average error of 0.36 wt. % Ag for concentration prediction was selected for its good predictive ability (Figure 20.24). Statistical comparisons of the LIBS analyses for five populations of French Guiana gold suggest that it is possible to match gold samples coming from the same source.

### 20.3.5 Summary and Concluding Remarks

As noted by Senesi (2017), *hLIBS* is a very promising analytical tool for use in geological field investigations, but the technique is still advancing technologically and has not yet been used widely in the field. Necessary improvements include the realization of much lower limits of detection, from 100's and 10's of ppm for some elements, to ppm and sub-ppm levels for all common elements, and improvements in analytical precision. Current calibrations for commercial instruments are not sufficiently robust and not designed specifically for the analysis of different kinds of geological material types. Nor are user interfaces yet designed specifically for geological or environmental applications. In particular, more work is required to understand and define the best operational parameters for analysis of the broad spectrum of geological materials encountered in the field, to develop material-specific

analysis protocols, and to define best practices for determining trace element concentrations, with handheld LIBS instrumentation. Two particular needs in this context are the robust matrix-matched calibrations for different types of geological materials needed for their quantitative analysis by LIBS, and large broadband spectral libraries for geochemical fingerprinting of geological materials in the field in real time.

## 20.4 Current Potential and Future Developments of Field-Portable XRF and LIBS

Both pXRF and *hLIBS* analyzers can be utilized effectively by trained geologists and environmental scientists with an adequate background in geochemistry. The best commercial instruments presently available are reliable and able to provide quality data, insofar as the user keeps in mind that their use requires the same care and QA/QC protocols that would be used in the laboratory. For *pXRF*, absolute accuracy is not routine using the on-board calibrations provided by the commercial manufacturers and may need significant additional calibration work, whereas calibration using matrix-matched standards to the specific type of material being analyzed is essential for *hLIBS*. Having arrived earlier to the market and today in more widespread use, *pXRF* has generated a larger publication base, particularly as regards field studies, with hundreds of scientific papers and reports in the literature. However, *hLIBS* is not less technically advanced than *pXRF* and its publication base is expanding rapidly. Advances are still being made in the miniaturization and performance of X-ray tubes, and also with SDDs, with novel or improved applications of *pXRF* as a result. *hLIBS* technology is also improving, while new applications are continually being developed and described. Each of these two tools has its particular advantages, such as the low limits of detection of base metals by *pXRF* and the capability of *hLIBS* for light element analysis and surface micromapping. Together, *pXRF* and *hLIBS* provide a powerful complementary capability for rapid chemical analysis in the field. The chemical information that can be obtained by the field user with the current generation of *pXRF* and *hLIBS* analyzers is not necessarily of the same precision and accuracy as that available from time-consuming and costly laboratory techniques such as AAS, XRF, ICPOES, LAICPMS, SEM, or EM analysis, but is suitable for an ever-increasing number of geological applications. For large campaigns of systematic measurements, such as analysis of a large soil grid, *pXRF* is presently the preferred tool, as it will need less rigorous calibration and less geochemical interpretation than *hLIBS*, but this situation is likely to change in the near future.

Both technologies are continuously improving, and each new generation of instruments offers significantly better performance. In an analogy to portable computers or smartphones, *pXRF* and *hLIBS* spectrometers today become outdated before the end of their operational life. However, they still can offer valuable services while using an up-to-date model for more advanced applications. We do not see a predictable end to this continuous improvement process, unless a new technology makes both obsolete.

The common attribute of both *pXRF* and *hLIBS* is that they actually offer significant improvement to the cost, quality, and efficacy of geochemical surveys, when compared with the traditional “sample-now/analyze-later” strategy. First, rapid in-field analysis ensures testing for sample representativeness, homogeneity, anomaly recognition on site, prior to sample collection and shipping. Second, samples can be screened for compositional variation, which reduces the number of repetitive barren samples that might be collected and allows focus on the most important parts of concentration ranges and verification of the most significant anomalies. The result of such a screening process is minimizing the cost of sample shipment to the analytical laboratory, as well as optimizing cost and analysis performed in the laboratory. Third, the use of field-portable instruments allows dynamic sampling and, thus, encourages the field geologist to expand an investigation in areas where anomalies are observed and map them without having to wait for laboratory results or return to field area after laboratory analysis. For exploration or environmental projects, the time benefit can be in weeks or months, and the savings are not only in the logistics and field campaigns but also in the cost of the subsequent laboratory work.

Another benefit of in-field analysis is “*Fitness or Suitability for Purpose*” (Ramsey and Boon 2012). Both *pXRF* and *hLIBS* have very low operational costs. Most of the cost is the initial investment for the instrumentation and the time of the operator. This typically results in the generation of substantially larger data sets than would be acquired by laboratory analysis. The result of this is a much denser spatial coverage of a study area. Even if the intrinsic quality of each field analysis is lower than that of a high-quality laboratory analysis, the amount of relevant information contained in the whole data set has the potential to be much higher. Therefore, the quality of global data set will often be much better, as there is less chance for overlooking a significant geochemical observation. In terms of project decision-making, the level of confidence attributable to the data set can be higher than the one of a high-quality laboratory data set with far less samples.

While much attention has been given to the development and improvement of both *pXRF* and *hLIBS*, it has become obvious with use that the utility of both instrument types can be enhanced with state-of-the-art data processing through the application of chemometrics and the techniques of machine learning and artificial intelligence (e.g. Gottfried 2013; Kaniu and Angeyo 2015; Panchuk et al. 2018). The widespread use of *pXRF* and *hLIBS* chemical analyzers for field use presents an opportunity for the co-processing of their respective data streams or even the integration of the technologies to generate significantly greater analytical capability than currently possible with either analyzer individually (Hark et al. 2019; Lemière and Uvarova 2019). This reason alone portends a bright future for the rapid, *in situ* analysis of natural materials in the field under ambient environmental conditions.

## Geological and Geochemical Glossary

Adularia	A variety of orthoclase feldspar ( $KAlSi_3O_8$ ) that commonly forms colorless to white prismatic, twinned crystals in low-temperature felsic crystalline rocks, typical of hydrothermal alteration around some ore bodies.
Amphibole	An common group of silicate minerals consisting of double chains of $SiO_4$ tetrahedra, linked at the vertices and generally containing ions of iron and/or magnesium in their structures.
Andesite	A volcanic rock of intermediate composition having between 57 and 63% $SiO_2$ and containing plagioclase feldspar and one or more mafic minerals.
Ankerite	A carbonate mineral of the group of rhombohedral carbonates with general formula: $Ca(Fe, Mg, Mn)(CO_3)$ related to dolomite [ $CaMg(CO_3)_2$ ] but with iron replacing part of the magnesium; also typical of hydrothermal alteration around some ore bodies.
Archean	One of the four geologic eons of Earth history, occurring from 4.0 to 2.5 billion years ago.
Argillic Zone	Hydrothermal alteration of wall rock in which clay minerals including kaolinite, smectite, and illite are formed from the alteration of feldspar and amphibole by low-temperature acidic groundwater.
Arsenopyrite	The sulfide ore of arsenic having the formula $FeAsS$ that commonly occurs as silver-white to steel-gray crystals. It occurs frequently in association with gold deposits.
Banded Iron Formation	A chemically precipitated sediment, typically consisting of thin layers of iron and chert, chalcedony, jasper, or quartz that occur on all the continents and usually are more than 1.7 billion years old.
Carbonatite	A type of igneous rock consisting of greater than 50% carbonate minerals. It commonly hosts highly desirable commodities, such as REEs, Nb, Ta, U, Th, Zr, and other rare elements.

Chalcopyrite	A sulfide ore of copper having the formula CuFeS <sub>2</sub> that commonly has a brassy to golden yellow color.
Certified Reference Material	A reference material whose composition has been analyzed by a metrologically valid analysis procedure, and that is accompanied by a certificate that provides the value of the specified property, its associated uncertainty, and a statement of metrological traceability.
Chemostratigraphy	The study of the chemical variations vertically within sedimentary sequences.
Columbite-Tantalite	A mineral group that is an ore of niobium and tantalum having the general formula (Fe, Mn)(Nb, Ta) <sub>2</sub> O <sub>6</sub> commonly found in granitic pegmatites.
Conflict mineral	A mineral having commercial value that is mined illicitly and used to influence and finance armed conflict, human rights abuses, and violence.
Diagenetic	The process by which sediment undergoes chemical and physical changes during its lithification to a rock.
Dolomite	A carbonate mineral having the formula CaMg(CO <sub>3</sub> ) <sub>2</sub> .
Epidote	A complex sorosilicate mineral commonly present as a result of replacement in regionally metamorphosed rocks of low-to-moderate grade having the chemical formula Ca <sub>2</sub> Al <sub>2</sub> (Fe <sup>3+</sup> ;Al)(SiO <sub>4</sub> )(Si <sub>2</sub> O <sub>7</sub> )O(OH).
Epithermal	Mineral veins and ore deposits formed from waters at shallow depth under conditions in the lower ranges of temperature and pressure.
Facies	The particular character of a rock as expressed by its formation, composition, and fossil content.
Felsic	A silicate mineral, magma, or igneous rock that is enriched in the lighter elements such as silicon, oxygen, aluminum, sodium, and potassium.
Galena	The sulfide ore of lead having the formula PbS.
Geochemical Fingerprint	A chemical signal, usually an association of elements, that provides information about the origin, formation, and/or environment of a geological sample.
Kimberlite	An igneous rock, which sometimes contains diamonds.
Komatiites	A mantle-derived volcanic rock crystallized from a lava low in silica, potassium, and aluminum but having an extremely high magnesium content.
Lacustrine	Relating to, formed in, living in, or growing in lakes.
Limit of Detection	The limit of detection can refer to either the “Lower Detection Limit” or the “Lower Determination Limit.” The former is the lowest quantity that can be determined with >50% confidence between the presence or absence of an element, whereas the latter is the lowest quantity that may be quantified with less than 30% uncertainty. Typically, the latter is 2× or 3× the former.
Lithics	Pieces of other rocks that have been eroded down to small sizes.
Maar	A broad, low-relief volcanic crater caused by a magmatic eruption into the water-saturated zone just below the Earth’s surface.
Mafic	A silicate mineral, magma, or igneous rock that is rich in magnesium and iron.
Magmatic Series	A series of chemical compositions that describes the evolution of a mafic as it fractionally crystallizes to become a felsic magma.
Marl	A calcium carbonate or lime-rich mud or mudstone that contains variable amounts of clays and silt.
Metabasalt	An amphibole-bearing rock produced from a basalt by metamorphism.
Radiolaria	Protozoa of diameter 0.1–0.2 mm that produce intricate silica skeletons.

Regolith	The layer of loose, heterogeneous superficial deposits covering solid rock.
Porphyry Copper	Copper (and often Mo, Ag, Au) ore bodies that are formed from hydrothermal fluids that originate from a voluminous magma chamber several kilometers below the Earth's surface. Some of the largest ore bodies belong to this group. They have characteristic hydrothermal alteration mineral zones, largely used for their exploration.
Pyroclastic	A sedimentary clastic rock composed solely or primarily of volcanic materials.
Pyrrhotite	A nonstoichiometric sulfide ore mineral of iron having the composition $\text{Fe}(1-x)\text{S}$ , where $x$ can vary up to 0.2.
Scheelite	A primary ore mineral for tungsten having the chemical formula $\text{CaWO}_4$ .
Selvage	A zone of altered rock at the edge of a rock mass. Recognition of hydrothermal alteration is a guide to mineralization.
Sericitization	A process of hydrothermal alteration in which plagioclase feldspar within a rock is converted to the fine-grained white mica sericite. Often used as a guide to locate ore bodies.
Serpentinization	A low-temperature metamorphic process occurring within the oceanic crust along the boundaries of tectonic plates in which ultramafic rocks from the Earth's mantle are oxidized and hydrated.
Spelothem	The $\text{CaCO}_3$ deposits that form in caves.
Sphalerite	The sulfide ore mineral of zinc having the composition $(\text{Zn}, \text{Fe})\text{S}$ .
Spicule	The structural elements present in most sponges.
Standard Reference Material	A reference material that has been sufficiently well characterized, typically by comparison to a certified reference material, to be fit-for-purpose in calibrating analytical measurements.
Tephra	Fragmental material produced by a volcanic eruption.
Turbidite	A deposit formed by the gravity flow of sediment off the continental shelf to the deep ocean floor.
Xenolith	A fragment of a pre-existing rock that becomes enveloped in a larger rock during the latter's development and solidification.

## Acronyms and Abbreviations

AAS	Atomic Absorption Spectroscopy
ANN	Artificial Neural Network
APD	Avalanche Photodiode
BIF	Banded Iron Formation
CCD	Silicon Charge Coupled Detector
CRM	Certified Reference Material
EM	Electron Microscope
GPR	Gaussian Process Regression
GPS	Global Positioning Satellite
ICCD	Intensified Charge Coupled Detector
ICPOES	Inductively Coupled Plasma–Optical Emission Spectroscopy
IPDA	Intensified Photodiode Array
LAICPMS	Laser Ablation-Inductively Coupled Plasma–Mass Spectrometry
Lasso	Least Absolute Shrinkage and Selection Operator

Nd-YAG	Neodymium Yttrium Aluminum Garnet (type of laser)
PDA	Photodiode Array
PLSR	Partial Least Square Regression
PGE	Platinum Group Elements
PMT	Photomultiplier Tube
REE	Rare Earth Elements
QA/QC	Quality Assurance/Quality Control
SDD	Silicon Drift Detector
SEM	Scanning Electron Microscope
Si-PIN	A Silicon P-type–Intrinsic–N-type Diode
SVM	Support Vector Machine

## References

- Adler, K., Piikki, K., Söderström, M. et al. (2020). Predictions of Cu, Zn, and Cd concentrations in soil using portable X-ray fluorescence measurements. *Sensors* 20: 474.
- Agnew, P.D. (2004). Applications of geochemistry in targeting with emphasis on large stream and lake sediment data compilations. In: *Predictive Mineral Discovery Under Cover: Society of Economic Geology Symposium*, Perth, WA. Littleton, CO: The Society of Economic Geologists.
- Alvarez-Llamas, C., Roux, C., and Musset, O. (2018). A compact, high-efficiency, quasi-continuous wave mini-stack diode pumped, actively Q-switched laser source for laser-induced breakdown spectroscopy. *Spectrochimica Acta Part B: Atomic Spectroscopy* 148: 118–128.
- Andrew, B.S. and Barker, S.L.L. (2018). Determination of carbonate vein chemistry using portable X-ray fluorescence and its application to mineral exploration. *Geochemistry: Exploration, Environment, Analysis* 18: 85–93.
- Anzano, J.M., Villoria, M.A., Ruiz-Medina, A., and Lasheras, R.J. (2006). Laser-induced breakdown spectroscopy for quantitative spectrochemical analysis of geological materials: Effects of the matrix and simultaneous determination. *Analytica Chimica Acta* 575: 230–235.
- Arca, G., Ciucci, A., Palleschi, V. et al. (1997). Trace element analysis in water by the laser-induced Breakdown spectroscopy technique. *Applied Spectroscopy* 51: 1102–1105.
- Argyraiki, A., Ramsey, M.H., and Potts, P.J. (1997). Evaluation of portable X-ray fluorescence instrumentation for in situ measurements of lead on contaminated land. *Analyst* 122: 743–749.
- Arne, D.C. and Jeffress, G.M. (2014). Sampling and analysis for public reporting of portable X-ray fluorescence data under the 2012 edition of the JORC code. *Sampling 2014 Conference*, Perth, WA, Australia. VIC, Australia: The Australasian Institute of Mining and Metallurgy.
- Arne, D.C., Mackie, R.A., and Jones, S.A. (2014). The use of property-scale portable X-ray fluorescence data in gold exploration: advantages and limitations. *Geochemistry: Exploration, Environment, Analysis* 14: 233–244.
- Barnes, S.J., Lesher, C.M., and Keays, R.R. (1995). Geochemistry of mineralised and barren komatiites from the Perseverance nickel deposit, Western Australia. *Lithos* 34: 209–234.
- Barnes, S.J., Hill, R.E.T., Perring, C.S., and Dowling, S.E. (2004). Lithogeochemical exploration for komatiite-associated Ni-sulfide deposits: Strategies and limitations. *Mineralogy and Petrology* 82: 259–293.
- Barnes, S.J., Fisher, L.A., Anand, R., and Uemoto, T. (2014). Mapping bedrock lithologies through in situ regolith using retained element ratios: a case study from the Agnew-Lawlers area, Western Australia. *Australian Journal of Earth Sciences* 61: 269–285.
- Barrette, L. and Turmel, S. (2001). On-line iron-ore slurry monitoring for real-time process control of pellet making processes using laser-induced breakdown spectroscopy: graphitic vs. total carbon detection. *Spectrochimica Acta Part B: Atomic Spectroscopy* 56 (6): 715–723. [https://doi.org/10.1016/S0584-8547\(01\)00227-0](https://doi.org/10.1016/S0584-8547(01)00227-0).

- Benn, C., Jones, N., Weeks, D. et al. (2012). Lithological discrimination in deeply weathered terrains using multielement geochemistry – an example from the Yanfolila gold project, Mali. *Explorer* 156: 1–8.
- Bernick, M.B., Kalnicky, D.J., Prince, G., and Singhvi, R. (1995). Results of field-portable X-ray fluorescence analysis of metal contaminants in soil and sediment. *Journal of Hazardous Materials* 43: 101–110.
- Bolster, S. and Lintern, M. (2018). Low level gold determinations using pXRF: Towards a new paradigm in gold exploration. AIG WA Exploration Geochemistry Seminar – 3 December 2018, Burswood on Swan, Western Australia. Australian Institute of Geoscientists.
- Bosc, R. and Barrie, C.T. (2013). Douvray porphyry copper deposit mineral resource estimate. Somine Project, Northeast mineral district, Republic of Haiti. NI 43-101 Technical Report, MAJESCOR Resources Inc., ON, Canada. doi: 10.13140/2.1.2535.8086.
- Bosco, G. (2013). Development and application of portable, hand-held X-ray fluorescence spectrometers. *Trends in Analytical Chemistry* 45: 121–134.
- Byrne, P., Hudson-Edwards, K.A., Bird, G. et al. (2018). Water quality impacts and river system recovery following the 2014 Mount Polley mine tailings dam spill, British Columbia, Canada. *Applied Geochemistry* 91: 64–74.
- Burley, L.L., Barnes, S.J., Laukamp, C. et al. (2017). Rapid mineralogical and geochemical characterisation of the Fisher East nickel sulphide prospects, Western Australia, using hyperspectral and pXRF data. *Ore Geology Reviews* 90: 371–387.
- Caporale, A.G., Adamo, P., Capozzi, F. et al. (2018). Monitoring metal pollution in soils using portable-XRF and conventional laboratory-based techniques: Evaluation of the performance and limitations according to metal properties and sources. *Science of the Total Environment* 643: 516–526.
- Castle, B.C., Knight, A.K., Visser, K. et al. (1998). Battery powered laser-induced plasma spectrometer for elemental determinations. *Journal of Analytical Atomic Spectrometry* 13: 589–595.
- Chakraborty, S., Man, T., Paulette, L. et al. (2017). Rapid assessment of smelter/mining soil contamination via portable X-ray fluorescence spectrometry and indicator kriging. *Geoderma* 306: 108–119.
- Cohen, D.R. and Bowell, R.J. (2014). Exploration geochemistry. In: *Treatise on Geochemistry* (eds. H.D. Holland and K.K. Turekian), 623–650. Netherlands: Elsevier.
- Connors, B., Somers, A., and Day, D. (2016). Application of handheld laser-induced breakdown spectroscopy (LIBS) to geochemical analysis. *Applied Spectroscopy* 70 (5): 810–815.
- Corsi, M., Cristoforetti, G., Hidalgo, M. et al. (2006). Double pulse, calibration-free laser-induced breakdown spectroscopy: a new technique for in situ standard-less analysis of polluted soils. *Applied Geochemistry* 21: 748–755.
- Cremers, D.A. and Radziemski, L.J. (2013). *Handbook of Laser-Induced Breakdown Spectroscopy*, 407. Chichester: Wiley.
- Crocombe, R.A. (2018). Portable spectroscopy. *Applied Spectroscopy* 72: 1701–1751.
- Crume, C. (2000). The business of making a lab field-portable. In: *Environmental Testing and Analysis*. Burbank, CA, USA: The Target Group.
- Cuñat, J., Palanco, S., Carrasco, F. et al. (2005). Portable instrument and analytical method using laser-induced breakdown spectrometry for in-situ characterization of speleothems in karstic caves. *Journal of Analytical Atomic Spectrometry* 20: 295–300.
- Cuñat, J., Fortes, F.J., Cabalín, L.M. et al. (2008). Man-portable laser-induced breakdown spectroscopy system for in-situ characterization of karstic formations. *Journal of Analytical Atomic Spectrometry* 62: 1250–1255.
- Cuñat, J., Fortes, F.J., and Laserna, J.J. (2009). Real time and in situ determination of lead in road sediments using a man-portable laser-induced breakdown spectroscopy analyzer. *Analytica Chimica Acta* 633: 38–42.
- de Vallejuelo, S.F.O., Gredilla, A., Gomez-Nubla, L. et al. (2017). Portable laser induced breakdown spectrometry to characterize the environmental impact of potentially hazardous elements of suspended particulate matter transported during a storm event in an urban river catchment. *Microchemical Journal* 135: 171–179.
- Durance, P., Jowitt, S.M., and Bush, K. (2014). An assessment of portable X-ray fluorescence spectroscopy in mineral exploration, Kurnalpi Terrane, Eastern Goldfields Superterrane, Western Australia. Institute of Materials, Minerals

- and Mining and The AusIMM. *Applied Earth Science (Transactions of the Institutions of Mining and Metallurgy: Section B)* 123: 150–163.
- Eppler, A.S., Cremers, D.A., Hickmott, D.D., and Koskelo, A.C. (1996). Matrix effects in the detection of Pb and Ba in soils using laser-induced breakdown spectroscopy. *Applied Spectroscopy* 50: 1175–1181.
- Erler, A., Riebe, D., Beitz, T. et al. (2020). Soil nutrient detection for precision agriculture using handheld laser-induced breakdown spectroscopy (LIBS) and multivariate regression methods (PLSR, Lasso and GPR). *Sensors* 20: 418. <https://doi.org/10.3390/s20020418>.
- Farahbakhsh, E., Chandra, R., Eslamkish, T.R., and Müller, D. (2019). Modeling geochemical anomalies of stream sediment data through a weighted drainage catchment basin method for detecting porphyry Cu-Au mineralization. *Journal of Geochemical Exploration* 204: 12–32.
- Ferreira, E.C., Milori, D.M., Ferreira, E.J. et al. (2008). Artificial neural network for Cu quantitative determination in soil using a portable laser induced breakdown spectroscopy system. *Spectrochimica Acta Part B* 63: 1216–1220.
- Ferreira, E.C., Milori, D.M.B.P., Ferreira, E.J. et al. (2011). Evaluation of laser induced breakdown spectroscopy for multielemental determination in soils under sewage sludge application. *Talanta* 85: 435–440.
- Foucaud, Y., Fabre, C., Demeusy, B. et al. (2019). Optimisation of fast quantification of fluorine content using handheld laser induced breakdown spectroscopy. *Spectrochimica Acta Part B* 158: 105628. <https://doi.org/10.1016/j.sab.2019.05.017>.
- Gallhofer, D. and Lottermoser, B.G. (2018). The influence of spectral interferences on critical element determination with portable X-ray fluorescence (pXRF). *Minerals* 8: 320.
- Gazley, M.F., Vry, J.K., du Plessis, E., and Handler, M.R. (2011). Application of portable X-ray fluorescence analyses to metabasalt stratigraphy, Plutonic Gold Mine, Western Australia. *Journal of Geochemical Exploration* 110: 74–80.
- Gazley, M.F., Bonnett, L.C., Fisher, L.A. et al. (2017). A workflow for exploration sampling in regolith-dominated terranes using portable X-ray fluorescence: comparison with laboratory data and a case study. *Australian Journal of Earth Sciences* 64 (7): 903–917.
- Ge, L., Zhimin, C., Chuanmin, S. et al. (1997). The applications of XRF and micro-gold analysis techniques to gold exploration in Tibet. *Geology and Prospecting*: 1997–1905.
- Ge, L., Lai, W., Lin, Y. and Zhou, S. (2005). In situ applications of FPXRF techniques in mineral exploration. *In Situ Applications of X-Ray Fluorescence Techniques*. IAEA-TECDOC-1456: 61–120. International Atomic Energy Agency, Vienna International Centre, Vienna, Austria.
- Giménez, J., Sánchez, J.A., and Solano, L. (2017). Identifying the Ethiopian origin of the obsidian found in Upper Egypt (Naqada period) and the most likely exchange routes. *The Journal of Egyptian Archaeology* 103: 349–359.
- Gómez-Nubla, L., Aramendia, J., de Vallejuelo, S.F.O., and Madariaga, J.M. (2018). Analytical methodology to elemental quantification of weathered terrestrial analogues to meteorites using a portable Laser-Induced Breakdown Spectroscopy (LIBS) instrument and Partial Least Squares (PLS) as multivariate calibration technique. *Microchemical Journal* 137: 392–401.
- Gottfried, J.L. (2013). Chemometric analysis in LIBS. In: *Handbook of Laser-Induced Breakdown Spectroscopy* (eds. D.A. Cremers and L.J. Radziemski), 223–255. Chichester: Wiley.
- Guerra, M.B.B., Teaney, B.T., Mount, B.J. et al. (2017). Post-catastrophe Analysis of the Fundão tailings dam failure in the Doce River system, Southeast Brazil: Potentially toxic elements in affected soils. *Water, Air, & Soil Pollution* 228: 252.
- Guo, G., Niu, G., Lin, Q. et al. (2019). Compact instrumentation and (analytical) performance evaluation for laser-induced breakdown spectroscopy. *Instrumentation Science & Technology* 47: 70–89.
- Hahn, D.W. and Omenetto, N. (2012). Laser-induced breakdown spectroscopy (LIBS), part II: review of instrumental and methodological approaches to material analysis and applications to different fields. *Applied Spectroscopy* 66: 347–419.
- Hale, M. and Plant, J.A. (eds.) (1994). Drainage geochemistry. In: *Handbook of Exploration Geochemistry*, vol. 6, 766. Amsterdam: Elsevier.

- Hall, G., Buchar, A. and Bonham-Carter, G. (2011). Quality control assessment of portable XRF analysers: development of standard operating procedures, performance on variable media and recommended uses. *Canadian Mining Industry Research Organization (Camiro) Exploration Division*, Project 10E01 Phase I Report. CAMIRO Mining Division, ON, Canada.
- Hall, G., Page, L. and Bonham-Carter, G. (2013). Quality control assessment of portable XRF analysers: development of standard operating procedures, performance on variable media and recommended uses. Phase II. *Canadian Mining Industry Research Organization (Camiro) Exploration Division*, Project 10E01 Phase I Report. CAMIRO Mining Division, ON, Canada.
- Hall, G.E.M., Bonham-Carter, G.F., and Buchar, A. (2014). Evaluation of portable X-ray fluorescence (pXRF) in exploration and mining: Phase 1, control reference materials. *Geochemistry: Exploration, Environment, Analysis* 14: 99–123.
- Hark, R.R. and Harmon, R.S. (2014). Geochemical fingerprinting using LIBS. In: *Laser-Induced Breakdown Spectroscopy* (eds. S. Musazzi and U. Perini), 309–348. Berlin, Heidelberg: Springer.
- Hark, R.R., Throckmorton, C.S., Harmon, R.S. et al. (2019). Signal Processing of Handheld LIBS-Raman-XRF Multisensor Data for Soil Analysis: (abstract) SciX 201 Symposium. CA: Palm Springs.
- Harmon, R.S., DeLucia, F.C., Mizolek, A.W. et al. (2005). Laser-induced breakdown spectroscopy (LIBS) – An emerging field-portable sensor technology for real-time, in-situ geochemical and environmental analysis. *Geochemistry: Exploration, Environment, Analysis* 5: 21–28.
- Harmon, R.S., DeLucia, F.C., McManus, C.E. et al. (2006). Laser-induced breakdown spectroscopy—An emerging chemical sensor technology for real-time field-portable, geochemical, mineralogical, and environmental applications. *Applied Geochemistry* 21: 730–747.
- Harmon, R.S., Hark, R.R., Throckmorton, C.S. et al. (2017). Geochemical fingerprinting by handheld laser-induced breakdown spectroscopy. *Geostandards and Geoanalytical Research* 41: 563–584.
- Harmon, R.S., Russo, R.E., and Hark, R.R. (2013). GEOLIBS – a review of the application of laser-induced breakdown spectroscopy (LIBS) for geochemical and environmental analysis. *Spectrochimica Acta, Part B: Atomic Spectroscopy* 87: 11–26.
- Harmon, R.S. and Russo, R.E. (2014). Laser-induced breakdown spectroscopy. In: *Treatise on Geochemistry, Analytical Geochemistry and Inorganic Instrumental Analysis*, vol. 15 (ed. W. McDonough), 245–272. Amsterdam: Elsevier.
- Harmon, R.S., Throckmorton, C.S., Hark, R.R. et al. (2018). Discriminating volcanic centers with handheld laser-induced breakdown spectroscopy (LIBS). *Journal of Archaeological Science* 98: 112–127.
- Harmon, R.S., Lawley, C.J., Watts, J. et al. (2019). Laser-induced breakdown spectroscopy—an emerging analytical tool for mineral exploration. *Minerals* 9: 718.
- Hayes, S.M. and McCullough, E.A. (2018). Critical minerals: a review of elemental trends in comprehensive criticality studies. *Resources Policy* 59: 192–199.
- Horta, A., Malone, B., Stockmann, U. et al. (2015). Potential of integrated field spectroscopy and spatial analysis for enhanced assessment of soil contamination: a prospective review. *Geoderma* 241–242: 180–209.
- Houlihan, T., Ramsay, S. and Povey, D. (2003). Use of field portable X-ray fluorescence spectrum analyzers for grade control – a presentation of case studies. *Proceedings of the 5th International Mine Geology Conference*. Australasian Institute of Metallurgy: pp. 377–385.
- Hughes, R. and Barker, S.L.L. (2017). Using portable XRF to infer adularia halos within the Waihi Au-Ag system, New Zealand. *Geochemistry: Exploration, Environment, Analysis* 18: 97–108.
- Jenkins, R. (1999). *X-ray Fluorescence Spectrometry*, vol. 2, 232. New York: Wiley.
- Kalnicky, D.J. and Singhvi, R. (2001). Field portable XRF analysis of environmental samples. *Journal of Hazardous Materials* 83: 93–122.
- Kaniu, M.I. and Angeyo, K.H. (2015). Challenges in rapid soil quality assessment and opportunities presented by multivariate chemometric energy dispersive X-ray fluorescence and scattering spectroscopy. *Geoderma* 241: 32–40.

- Kim, H.R., Kim, K.H., Yu, S. et al. (2019). Better assessment of the distribution of As and Pb in soils in a former smelting area, using ordinary co-kriging and sequential Gaussian cosimulation of portable X-ray fluorescence (PXRF) and ICP-AES data. *Geoderma* 341: 26–38.
- Konstantinov, M.M. and Strujkov, S.F. (1995). Application of indicator halos (signs of ore remobilization) in exploration for blind gold and silver deposits. *Journal of Geochemical Exploration* 54: 1–17.
- Kumar, N., Lan, Y.J., Lu, Y. et al. (2018). Development of a micro-joule portable LIBS system and the preliminary results for mineral recognition. *Optoelectronics Letters* 14: 401–404.
- Lawley, C.J.M., Dubé, B., Mercier-Langevin, P. et al. (2015). Defining and mapping hydrothermal footprints at the BIF-hosted Meliadine gold district, Nunavut, Canada. *Journal of Geochemical Exploration* 155: 33–55.
- Lemière, B. (2018). A review of applications of pXRF (field portable X-ray fluorescence) for applied geochemistry. *Journal of Geochemical Exploration* 188: 350–363.
- Lemière, B. and Laperche, V. (2018). Application of pXRF to environmental investigations and geochemical baseline of abandoned mines. *Resources for Future Generations Conference*, Vancouver, BC (16–21 June 2018), Conference Proceedings, Paper #1702.
- Lemière, B. and Uvarova, Y.A. (2019). New developments in field portable geochemical techniques and on-site technologies and their place in mineral exploration. *Geochemistry: Exploration, Environment, Analysis* 20: 205–216. Published Online. <https://doi.org/10.1144/geochem2019-044>.
- Le Vaillant, M., Barnes, S.J., Fisher, L. et al. (2014). Use and calibration of portable X-Ray fluorescence analysers: application to lithogeochemical exploration for komatiite-hosted nickel sulphide deposits. *Geochemistry: Exploration, Environment, Analysis* 14: 199–209.
- Le Vaillant, M., Barnes, S.J., Fiorentini, M.L. et al. (2016). Effects of hydrous alteration on the distribution of base metals and platinum group elements within the Kevitsa magmatic nickel sulphide deposit. *Ore Geology Reviews* 72: 128–148. <https://doi.org/10.1016/j.oregeorev.2015.06.002>.
- Liu, H.C., Mao, X., Mao, S. et al. (2005). Particle size dependent chemistry from laser ablation of brass. *Analytical Chemistry* 77: 6687–6691.
- Luck, P. and Simandl, G.J. (2014). Portable X-ray fluorescence in stream sediment chemistry and indicator mineral surveys, Lonnie carbonatite complex, British Columbia. *Geological Fieldwork 2013*, British Columbia Ministry of Energy and Mines, British Columbia Geological Survey Paper 2014-1: pp. 169–182.
- Marquis, P. (2019). Unravelling the geological model using XRF multi-element geochemistry at the Birimian-age Bomboré Gold Deposit, Burkina Faso. *AME Roundup 2019: Elements for Discovery*, Vancouver, BC (31 January 2019). CO, USA: The Society of Economic Geologists, Inc.
- Marsala, A.F., Loermans, T., Shen, S. et al. (2012). Portable energy-dispersive X-ray fluorescence integrates mineralogy and chemostratigraphy into real-time formation evaluation. *Petrophysics* 53: 102–109.
- Mauriohooho, K., Barker, S.L.L., and Raeb, A. (2016). Mapping lithology and hydrothermal alteration in geothermal systems using portable X-ray fluorescence (pXRF): a case study from the Tauhara geothermal system, Taupo Volcanic Zone. *Geothermics* 64: 125–134.
- McMillan, N.J., McManus, C.E., Harmon, R.S. et al. (2006). Laser induced breakdown spectroscopy analysis of complex silicate minerals – Beryl. *Analytical and Bioanalytical Chemistry* 385: 263–271.
- McNulty, B.A., Fox, N., Berry, R.F., and Gemmell, J.B. (2018). Lithological discrimination of altered volcanic rocks based on systematic portable X-ray fluorescence analysis of drill core at the Myra Falls VHMS deposit, Canada. *Journal of Geochemical Exploration* 193: 1–21.
- Melo de Lima, T., Weindorf, D.C., Curi, N. et al. (2019). Elemental analysis of Cerrado agricultural soils via portable X-ray fluorescence spectrometry: inferences for soil fertility assessment. *Geoderma* 353: 264–272.
- Meng, D., Zhao, N., Ma, M. et al. (2017). Application of a mobile laser-induced breakdown spectroscopy system to detect heavy metal elements in soil. *Applied Optics* 56: 5204–5210.
- Michaud, D.D., Rollossen, L.M., Ytsma, C.R., and Dyar, M.D. (2019). Limits of Detection for Minor and Trace Elements Using SciAps Z-300 Portable LIBS. *Lunar & Planetary Institute Abstracts* 2132: 1079.

- Moon, C.J., and King, A. (2015). Geochemical exploration for tin deposits: application of conventional and novel techniques in Cornwall, England. *27th IAGS Symposium*, Tucson, AZ (20–24 April 2015),, ON, Canada: The Association of Applied Geochemists.
- Nissinen, T., Tiilonen, T., Riikonen, J. and Lehto, V.P. (2018). On-site analysis of metal concentrations of natural waters. *13. Geokemian Päivät 2018 – 13th Finnish Geochemical Meeting 2018*, 28–30.11.2018 Oulun yliopisto, Linnanmaa – University of Oulu, Finland.
- Oyourou, J.N., McCrindle, R., Combrinck, S., and Fourie, C.J.S. (2019). Investigation of zinc and lead contamination of soil at the abandoned Edendale mine, Mamelodi (Pretoria, South Africa) using a field-portable spectrometer. *Journal of the Southern African Institute of Mining and Metallurgy* 119: 55–62.
- Palanco, S., Alises, A., Cuñat, J. et al. (2003). Development of a portable laser-induced plasma spectrometer with fully-automated operation and quantitative analysis capabilities. *Journal of Analytical Atomic Spectrometry* 18: 933–938.
- Panchuk, V., Yaroshenko, I., Legin, A. et al. (2018). Application of chemometric methods to XRF data – a tutorial review. *Analytica Chimica Acta* 1040: 19–32.
- Parsons, C., Grabulosa, E.M., Pili, E. et al. (2013). Quantification of trace arsenic in soils by field-portable X-ray fluorescence spectrometry: considerations for sample preparation and measurement conditions. *Journal of Hazardous Materials* 262: 1213–1222.
- Pelegrino, M.H.P., Weindorf, D.C., Silva, S.H.G. et al. (2019). Synthesis of proximal sensing, terrain analysis, and parent material information for available micronutrient prediction in tropical soils. *Precision Agriculture* 20: 746–766.
- Peter, J.M., Chapman, J.B., Mercier-Langevin, P., Layton-Matthews, D., Thiessen, E., and McClenaghan, M.B. (2010). Use of portable x-ray fluorescence spectrometry in vectoring for base metal sulfide exploration. *Targeted Geoscience Initiative 3 Workshop: Public Geoscience in Support of Base Metal Exploration*, Vancouver, BC (22 March 2010). Vancouver, BC: Geological Association of Canada.
- Piorek, S. (1994a). Modern, PC based, high resolution portable EDXRF analyzer offers laboratory performance for field, in-situ analysis of environmental contaminants. *Nuclear Instruments and Methods in Physics Research Section A: Accelerators, Spectrometers, Detectors and Associated Equipment* 353: 528–533.
- Piorek, S. (1994b). Principles and applications of man-portable X-ray fluorescence spectrometry. *TRAC Trends in Analytical Chemistry* 13: 281–286.
- Piorek, S. (2008). Alloy identification and analysis with a field-portable XRF analyser. In: *Portable X-ray Fluorescence Spectrometry, Capabilities for in Situ Analysis* (eds. P.J. Potts and M. West), 98–140. Cambridge: RSC Publishing.
- Plourde, A.P., Knight, R.D., Kjarsgaard, B.A., Sharpe, D.R. and Lesemann, J.-E. (2013). Portable XRF spectrometry of surficial sediments, NTS 75-I, 75-J, 75-O, 75-P (Mary Frances Lake – Whitefish Lake – Thelon River area), Northwest Territories. *Geological Survey of Canada, Open File Report 7408*. Natural Resources Canada, ON, Canada.
- Pochon, A., Desaulty, A.M., and Bailly, L. (2020). Handheld laser-induced breakdown spectroscopy (LIBS) as a fast and easy method to trace gold. *Journal of Analytical Atomic Spectrometry* <https://doi.org/10.1039/c9ja00437h>.
- Potts, P.J. (2012). *A Handbook of Silicate Rock Analysis*, 622. Springer Science & Business Media.
- Qiao, S., Ding, Y., Tian, D. et al. (2015). A review of laser-induced breakdown spectroscopy for analysis of geological materials. *Applied Spectroscopy Reviews* 50: 1–26.
- Rakovský, J., Musset, O., Buoncristiani, J. et al. (2012). Testing a portable laser-induced breakdown spectroscopy system on geological samples. *Spectrochimica Acta Part B: Atomic Spectroscopy* 74: 57–65.
- Ramsey, M.H. and Boon, K.A. (2012). Can in situ geochemical measurements be more fit-for-purpose than those made ex situ? *Applied Geochemistry* 27 (5): 969–976.
- Rauschenbach, I., Lazic, V., Pavlov, S.G. et al. (2008). Laser induced breakdown spectroscopy on soils and rocks: Influence of the sample temperature, moisture and roughness. *Spectrochimica Acta Part B* 63: 1205–1215.
- Ravansari, R., Wilson, S.C., and Tighe, M. (2020). Portable X-ray fluorescence for environmental assessment of soils: Not just a point and shoot method. *Environment International* 134: 105250.

- Reader, J., Corliss, C.H., Wiese, W.L., and Martin, G.A. (1980). *Wavelengths and Transition Probabilities for Atoms and Atomics Ions*, NSRDS-NBS 68. Washington: US Government Printing Office.
- Richards, M.J. (2019). Realising the potential of portable XRF for the geochemical classification of volcanic rock types. *Journal of Archaeological Science* 105: 31–45.
- Rosenwasser, S., Asimellis, G., Bromley, B. et al. (2001). Development of a method for automated quantitative analysis of ores using LIBS. *Spectrochimica Acta Part B* 56: 707–714.
- Ross, P.-S., Bourke, A., and Fresia, B. (2014a). Improving lithological discrimination in exploration drill-cores using portable X-ray fluorescence measurements: (1) testing three Olympus Innov-X analysers on unprepared cores. *Geochemistry: Exploration, Environment, Analysis* 14: 171–185.
- Ross, P.-S., Bourke, A., and Fresia, B. (2014b). Improving lithological discrimination in exploration drill-cores using portable X-ray fluorescence measurements: (2) applications to the Zn-Cu Matagami mining camp, Canada. *Geochemistry: Exploration, Environment, Analysis* 14: 187–196.
- Rouillon, M., Taylor, M.P., and Dong, C. (2016). Reducing risk and increasing confidence of decision making at a lower cost: In-situ pXRF assessment of metal-contaminated sites. *Environmental Pollution* 214: 255–264.
- Roux, C.P., Rakovsky, J., Musset, O. et al. (2015). In situ Laser Induced Breakdown Spectroscopy as a tool to discriminate volcanic rocks and magmatic series, Iceland. *Spectrochimica Acta Part B* 103: 63–69.
- Sadeghamirshahidi, M. and Vitton, S.J. (2019). Mechanical properties of Michigan Basin's gypsum before and after saturation. *Journal of Rock Mechanics and Geotechnical Engineering* 11: 739–748.
- Sarala, P. (2016). Comparison of different portable XRF methods for determining till geochemistry. *Geochemistry: Exploration, Environment, Analysis* 16: 181–192.
- Senesi, G.S. (2014). Laser-Induced Breakdown Spectroscopy (LIBS) applied to terrestrial and extraterrestrial analogue geomaterials with emphasis to minerals and rocks. *Earth-Science Reviews* 139: 231–267.
- Senesi, G.S. (2017). Portable hand held laser-induced breakdown spectroscopy (LIBS) instrumentation for in-field elemental analysis of geological samples. *International Journal of Earth & Environmental Sciences* 146 <https://doi.org/10.15344/2456-351X/2017/146>.
- Senesi, G.S., Manzari, P., Tempesta, G. et al. (2018a). Handheld laser induced breakdown spectroscopy instrumentation applied to the rapid discrimination between iron meteorites and meteor-wrongs. *Geostandards and Geoanalytical Research* 42: 607–614.
- Senesi, G.S., Manzini, D., and De Pascale, O. (2018b). Application of a laser-induced breakdown spectroscopy handheld instrument to the diagnostic analysis of stone monuments. *Applied Geochemistry* 96: 87–91.
- Sharma, A., Weindorf, D.C., Man, T. et al. (2014). Characterizing soils via portable X-ray fluorescence spectrometer: 3. Soil reaction (pH). *Geoderma* 232–234: 141–147.
- Sharma, A., Weindorf, D.C., Wang, D., and Chakraborty, S. (2015). Characterizing soils via portable X-ray fluorescence spectrometer: 4. Cation exchange capacity (CEC). *Geoderma* 239–240: 130–134.
- Shefsky, S. (1997). Sample handling strategies for accurate lead-in-soil measurements in the field and laboratory. Presented at the *International Symposium of Field Screening Methods for Hazardous Wastes and Toxic Chemicals*, Las Vegas, Nevada, USA, 29–31 January 1997.
- Simandl, G.J., Stone, R.S., Paradis, S. et al. (2014). An assessment of a handheld X-ray fluorescence instrument for use in exploration and development with an emphasis on REEs and related specialty metals. *Mineralium Deposita* 49: 999–1012.
- Stoker, P. and Berry, M. (2015). *Reporting of pXRF Data in Compliance with the JORC Code*. Brisbane: Australian Institute of Geoscientists Friday Seminar Series [https://www.aig.org.au/wp-content/uploads/2015/11/pXRF2015\\_02\\_Stoker.pdf](https://www.aig.org.au/wp-content/uploads/2015/11/pXRF2015_02_Stoker.pdf).
- Swift, R.P. (1995). Evaluation of a field-portable X-ray fluorescence spectrometry method for use in remedial activities. *Spectroscopy* 10: 31–35.
- Tighe, M., Bielski, M., Wilson, M. et al. (2020). A sensitive XRF screening method for lead in drinking water. *Analytical Chemistry* <https://doi.org/10.1021/acs.analchem.9b05058>.

- VanCott, R.J., McDonald, B.J., and Seelos, A.G. (1999). Standard soil sample preparation error and comparison of portable XRF to laboratory AA analytical results. *Nuclear Instruments and Methods in Physics Research A* 422: 801–804.
- Wainner, R.T., Harmon, R.S., Mizolek, A.W. et al. (2001). Analysis of environmental lead contamination: Comparison of LIBS field and laboratory instruments. *Spectrochimica Acta Part B* 56: 777–793.
- Wan, M., Hu, W., Qu, M. et al. (2019). Application of arc emission spectrometry and portable X-ray fluorescence spectrometry to rapid risk assessment of heavy metals in agricultural soils. *Ecological Indicators* 101: 583–594.
- Wang, D., Chakraborty, S., Weindorf, D.C. et al. (2015). Synthesized use of VisNIR DRS and pXRF for soil characterization: Total carbon and total nitrogen. *Geoderma* 243–244: 157–167.
- Weindorf, D.C., Zhu, Y., Chakraborty, S. et al. (2012a). Use of portable X-ray fluorescence spectrometry for environmental quality assessment of peri-urban agriculture. *Environmental Monitoring and Assessment* 184: 217–227.
- Weindorf, D.C., Zhu, Y., McDaniel, P. et al. (2012b). Characterizing soils via portable x-ray fluorescence spectrometer: 2. Spodic and Albic horizons. *Geoderma* 189–190: 268–277.
- Weindorf, D.C., Zhu, Y., Haggard, B. et al. (2012c). Enhanced pedon horizonation using portable X-ray fluorescence spectrometry. *Soil Science Society of America Journal* 76: 522–531.
- Weindorf, D.C., Bakr, N., and Zhu, Y. (2012d). Advances in portable X-ray fluorescence (PXRF) for environmental, pedological, and agronomic applications. *X-Ray Spectrometry* 41: 304–307.
- Wiens, R.C., Maurice, S., Lasue, J., Forni, O., Anderson, R.B., Clegg, S., Bender, S., Blaney, D., Barraclough, B.L., Cousin, A., and Deflores, L. (2013). Pre-flight calibration and initial data processing for the ChemCam laser-induced breakdown spectroscopy instrument on the Mars Science Laboratory rover. *Spectrochimica Acta Part B: Atomic Spectroscopy* 82:1 –27.
- Yamamoto, K.Y., Cremers, D.A., Ferris, M.J., and Foster, L.E. (1996). Detection of metals in the environment using a portable laser-induced breakdown spectroscopy instrument. *Applied Spectroscopy* 50: 222–233.
- Yant, M.H., Lewis, K.W., Parker, A.H. et al. (2019). Project ESPRESSO: exploration roles of handheld LIBS at the potrillo volcanic field. *LPI* 2132: 2645.
- Young, K.E., Evans, C.A., Hodges, K.V. et al. (2016). A review of the handheld X-ray fluorescence spectrometer as a tool for field geologic investigations on Earth and in planetary surface exploration. *Applied Geochemistry* 72: 77–87.
- Zhou, S., Yuan, Z., Cheng, Q. et al. (2018). Rapid in situ determination of heavy metal concentrations in polluted water via portable XRF: using Cu and Pb as example. *Environmental Pollution* 243 (Pt B): 1325–1333. <https://doi.org/10.1016/j.envpol.2018.09.087>.

## 21

### Portable Spectroscopy for Cultural Heritage

#### Applications and Practical Challenges

*Federica Pozzi<sup>1</sup>, Adriana Rizzo<sup>1</sup>, Elena Basso<sup>1</sup>, Eva Mariasole Angelin<sup>2</sup>, Susana França de Sá<sup>2</sup>, Costanza Cucci<sup>3</sup> and Marcello Picollo<sup>3</sup>*

<sup>1</sup>*Department of Scientific Research, The Metropolitan Museum of Art, New York, NY, USA*

<sup>2</sup>*Department of Conservation and Restoration and LAQV-REQUIMTE, NOVA School of Science and Technology, NOVA University Lisbon, 2829-516 Monte da Caparica, Portugal*

<sup>3</sup>*"Nello Carrara" Institute of Applied Physics - National Research Council (IFAC-CNR), Via Madonna del Piano 10, 50019 Sesto Fiorentino (Florence), Italy*

#### 21.1 Introduction

Decades of technological advances in instrumental analysis have transformed many techniques from laboratory innovations to customary analytical tools with increasing applicability to the study of cultural heritage objects. In particular, enduring research in the field of miniaturization has given rise to new generations of mobile, portable, and handheld spectrometers that have deeply altered the way in which scientists approach the analysis of materials in artifacts of archaeological, historical, and artistic significance.

Among the portable techniques developed over the years, some are widely used in the cultural heritage field and commonly found in museums' laboratories; others, on the other hand, are still under study and appear to be mostly available in university research facilities. The first set of techniques, which includes X-ray fluorescence (XRF) spectroscopy, fiber optic reflectance spectroscopy (FORS), Raman spectroscopy, and Fourier-transform infrared (FTIR) spectroscopy, among others, constitutes the focus of the present chapter. Due to the impossibility to carry out a comprehensive review of all portable equipment currently in use, nuclear magnetic resonance (NMR), laser-induced breakdown spectroscopy (LIBS), and laser-induced fluorescence (LIF), as well as other techniques belonging to the latter group, will not be discussed here.

X-ray-based techniques are among the most commonly used analytical tools in conservation science. Especially in archaeology- and conservation-related contexts, portable and handheld XRF spectrometers have rapidly become a must-have thanks to their relatively low cost, movability and non invasiveness, and immediate response in terms of results. The last 10 years have witnessed an exponential technological advancement for what concerns XRF analyzers, with many new devices becoming commercially available alongside improved versions of already known ones. Among these, portable equipment that combines XRF with other techniques, such as Raman spectroscopy or X-ray diffraction, has been successfully launched onto the market (Alberti et al. 2017; Barbi et al. 2014; Sarrazin et al. 2009). Compact, portable mapping systems have been also developed, bringing XRF to a significantly higher level of potential and applicability (Alfed et al. 2011; Mosca et al. 2016; Ruberto et al. 2016). In the field of cultural heritage research, the development of movable instruments has greatly contributed to fulfill the requirements and challenges specifically related to the analysis of objects that cannot be moved from museum galleries, storages, and conservation studios (Uhlir et al. 2012). The multiple applications of handheld XRF to a variety of archaeological, historical, and artistic artifacts, extensively described in the literature, were recently the subjects of a dedicated

book (Shugar and Mass 2012) and of a comprehensive review (Crocombe 2013). The majority of articles, however, focus on case studies. Notably, the inclusion of portable XRF mapping systems in the array of techniques available to conservation scientists is reflected in the literature by an increasing number of elemental mapping studies of inaccessible or unmovable objects, which often revealed details of the works that would otherwise remain unveiled (Galli et al. 2017; Mosca et al. 2016).

Considerable progress has been made in recent years in the subject of ultraviolet–visible–infrared (UV–Vis–IR) spectroscopy due to the development of new detectors, new sources, new accessories, and improved types of instruments. UV–Vis–near IR reflectance spectroscopy has been widely used as a noninvasive method for the study of cultural heritage materials for several decades. In particular, FORS, introduced in the 1980s, allows the acquisition of hundreds of reflectance spectra *in situ* in a short time, contributing to the identification of artists' materials (Bacci et al. 1987, 1991, 1993). Due to its noninvasive nature and portability of the available devices, FORS data are useful for the identification of pigments, dyes, chromophores, and alteration products by matching the unknown spectrum collected from the object to a suitable spectral database (<http://fors.ifac.cnr.it>). Moreover, FORS can be used to complement other noninvasive techniques, most notably XRF, as well as FTIR and Raman spectroscopies (Aceto et al. 2012; Appolonia et al. 2009; Picollo et al. 2011). FORS has also proven very useful in extending the relevance of local data obtained through microanalyses to a broader scale across a work of art. In recent years, FORS was also applied in the 2000–2500 nm region to the characterization of binding media specifically on illuminated manuscripts, thus opening new opportunities to this technique for the investigation of artworks and artists' materials (Delaney et al. 2014; Ricciardi et al. 2012).

Relentless research in the field of Raman spectroscopy for cultural heritage using mobile, portable, and handheld instrumentation has resulted in a rich body of literature on the topic. Most publications to date describe the analysis of specific types of artifacts or classes of materials; however, many reviews and articles offer a critical evaluation of various spectrometers, highlighting the unique features that are particularly beneficial for cultural heritage studies (Lauwers et al. 2014; Vandenabeele et al. 2004; Vandenabeele et al. 2007a, b, 2014). Some works trace the history of mobile Raman equipment and discuss the technique's main drawbacks and advantages (Colomban 2012), while others are devised as surveys of applications to the scientific analysis of artworks and museum objects (Vandenabeele et al. 2007c; Vandenabeele and Donais 2016). In some instances, Raman spectroscopy has been combined with other laser-based techniques, such as LIBS and LIF spectroscopy, in the form of mobile equipment (Osticioli et al. 2009). In addition, a handful of Raman studies carried out with the aid of movable instrumentation focuses on the assessment of certain materials' conservation state or degradation processes (Aramendia et al. 2014; Gomez-Laserna et al. 2013, 2015; Maguregui et al. 2008). The performances of portable Raman instrumentation have been also compared with those of mobile FTIR to monitor the conservation treatment of monument plaster surfaces using various classes of polymeric consolidants and protectives (Conti et al. 2013).

Among the portable equipment for noninvasive vibrational spectroscopy, most used in cultural heritage research along with Raman is reflection FTIR spectroscopy. This technique works in spectral ranges of the mid-IR (MIR, 4000–400 cm<sup>-1</sup>) and near-IR (NIR, 14 000–4000 cm<sup>-1</sup>) (Bitossi et al. 2005; Brunetti et al. 2016; Madariaga 2015; Picollo et al. 2014), with some instruments able to work across both ranges (ca. 7000–400 cm<sup>-1</sup>). Some publications have also reported analysis performed with minimally invasive attenuated total reflection (ATR)-FTIR spectroscopy (Bressan et al. 2019; Nel et al. 2010; Noake et al. 2017). MIR is the range most commonly investigated, as fundamental bands and features in the fingerprint region are easily interpreted, also by comparison with data obtained from objects and references using benchtop instrumentation. On the other hand, the weak overtones and combination bands for C–H, O–H, and N–H detected in the NIR range have been used in the identification of certain materials, and to study oxidation processes and the effect of conservation treatments (Kissi et al. 2017; Parkin et al. 2013; Trafela et al. 2007). As opposed to reflection FTIR techniques, high-quality spectra can be obtained by NIR regardless of the materials' surface topography, producing useful data for quantitative measurements. However, spectra may be difficult to interpret without complex statistical treatments based on models

specifically created from large spectra sets. Portable reflection FTIR spectroscopy techniques (external and diffuse modes) in the MIR range are, therefore, preferred as *in situ* complement to elemental and other spectroscopic analysis as they provide information on organic materials, organometallic complexes, and MIR-active inorganic molecules. Mid-FTIR portable techniques have been applied to cultural heritage for over 20 years (Casini et al. 2005; Fabbri et al. 2001; Williams 1996), and in the past decade their application to this field has seen an exponential growth due to the availability of compact and handheld spectrometers (Arrizabalaga et al. 2014; Cucci et al. 2016a; Ford et al. 2019; Invernizzi et al. 2017; Leung Tang et al. 2016; Rifkin et al. 2016; Saviello et al. 2016). Data can be acquired on multiple areas within the same object, with the only limitation dictated by the instrument's interface accessibility to the surface chosen for analysis. The use of tripods with geared head for tilting and precise positioning, as well as video camera, have also contributed to a wider applicability of this technique in the field. Reflection FTIR spectroscopy is primarily a surface analysis technique, thus it is particularly suited for the identification of pure materials, mixtures, coatings, for the study of surface phenomena such as natural aging, as well as of contributions from environmental factors and conservation treatments (Carretti et al. 2005; De Luca et al. 2015; Ford et al. 2019; Legan et al. 2020; Leung Tang et al. 2016; Manfredi et al. 2015; Miliani et al. 2012; Nodari and Ricciardi 2019; Ormsby et al. 2009; Picollo et al. 2014; Rosi et al. 2019).

## 21.2 Instrumentation

### 21.2.1 XRF

All XRF analyses discussed in this chapter were performed at The Morgan Library & Museum and New York Public Library, New York, using two different spectrometers available at The Metropolitan Museum of Art (MMA): an XGLab Elio XRF system and a Bruker/Keymaster Tracer III-V™ instrument. The Elio XRF analyzer has a high-resolution, large-area silicon drift detector with 130 eV at manganese (Mn) K $\alpha$  with 10 kcps input photon rate (high-resolution mode), and 170 eV at Mn K $\alpha$  with 200 kcps input photon rate (fast mode). The system is equipped with changeable filters, and a rhodium (Rh) transmission target with 50 kV maximum voltage and 4 W maximum power. The size of the analyzed spot is 1 × 1 mm. This instrument is also equipped with a portable 2D mapping system to obtain scans of flat objects or surfaces. The translator stage can cover a maximum area of 10 × 10 cm with a step of 10  $\mu$ m. The Bruker/Keymaster Tracer III-V™ XRF analyzer is equipped with a Peltier-cooled advanced high-resolution silver-free Si-PIN detector with a 0.2  $\mu$ m beryllium (Be) window and average resolution of approximately 142 eV for the full-width at half-maximum of the Mn K $\alpha$  line. The system includes changeable filters, and a Rh transmission target with maximum voltage of 45 kV and tunable beam current of 2–25  $\mu$ A. The size of the analyzed spot is approximately 3 × 4 mm.

### 21.2.2 FORS

FORS measurements were acquired at the Institute of Applied Physics “Nello Carrara” of the National Research Council of Italy (IFAC-CNR), Florence, by means of two Zeiss systems. The first is composed of two single-beam Zeiss spectroanalyzers, models MCS501 UV-NIR (190–1015 nm range) and MCS511 NIR 1.7 (900–1700 nm range), mounted on two different chassis. The other is equipped with two single-beam Zeiss spectroanalyzers, models MCS601 UV-NIR (190–1015 nm range) and MCS611 NIR 2.2WR (910–2200 nm range), housed together in a compact and portable framework for *in situ* analysis. The data acquisition step was 0.8 nm/pixel for the 1024-element silicon photodiode array detector (MCS501/MCS601), and 6.0 nm/pixel for the 256-element InGaAs diode array detector (MCS511/MCS611). Radiation between 320 and 2700 nm, provided by a voltage-stabilized 20 W halogen lamp (module Model CLH500 and CLH600, respectively), was conveyed to the object by means of a quartz optical fiber bundle that also transported the reflected radiation back to the detectors. The sampled area was smaller than

the fiber's approximate 2 mm diameter, and acquisition time for each spectrum was less than 1 s. The spectrometers were calibrated using a white Spectralon® 99% reflectance standard. Two probe heads with 0°/45°/45° and 8°/8° geometries were adopted to avoid specular reflectance.

### 21.2.3 Raman

All Raman measurements described in this chapter were performed at the Brooklyn Museum, The Morgan Library & Museum, and New York Public Library using a Bruker Bravo handheld Raman spectrometer available at the MMA. This system is equipped with a charge-coupled device detector, provides a spectral resolution of 10–12 cm<sup>-1</sup>, and features double laser excitation (785 and 853 nm, Duo LASER™). In this configuration, spectra are collected in the OPUS software (Bruker Optics) within two separate spectral ranges, i.e. 170–2200 cm<sup>-1</sup> and 1200–3200 cm<sup>-1</sup>, each obtained with one of the two sources. Data acquisition exploits a sequentially shifted excitation (SSE™) algorithm that allows for automatic fluorescence removal (Pirzer and Sawatzki 2008; Shreve et al. 1992), followed by merging of spectra obtained in the two spectral ranges at different excitation wavelengths. The output laser power is ≈50 mW for both lasers and spot diameter ≈1 mm. Measurements were typically collected by positioning the spectrometer at a 1–2 mm distance from the artwork, but space was increased on a case-by-case basis to prevent potential alteration or thermal damage on particularly sensitive substrates and objects. The number of scans and integration time were adjusted within the 1–20 and 200–1000 ms ranges, respectively, according to the color and Raman response of the different areas examined. A more detailed description of this system, along with information on data collection and post-processing, can be found in a previous publication (Pozzi et al. 2019).

### 21.2.4 FTIR

The MIR reflection measurements presented here were performed by using two portable FTIR spectrometers: a Bruker Optics Alpha system and a handheld Agilent 4300. Comparative data with both instruments were collected at the Department of Conservation and Restoration, NOVA School of Science and Technology of NOVA University Lisbon (DCR FCT NOVA), Portugal. Measurements solely with the Bruker Alpha were also acquired at the MMA. The Alpha acquires in situ, noncontact external reflection (ER) measurements, and is equipped with a silicon carbide (SiC) Globar source and temperature-stabilized deuterated tri-glycine sulfate (DTGS) detector. Measurements were performed by positioning the samples or objects in front of the instrument's external reflectance module, and centering the area of interest to the 6-mm diameter spot. At the MMA, positioning of the area of interest was optimized using an integrated video camera controlled by the IC capture 2.4 software. The specified working optical layout for reflection measurements is 22°/22°. Experimental parameters were as follows. DCR FCT NOVA: spectral range 4000–650 cm<sup>-1</sup>, 8 cm<sup>-1</sup> resolution, 128 scans for both background (gold flat mirror) and samples. MMA: spectral range 7000–375 cm<sup>-1</sup>, 4 cm<sup>-1</sup> resolution, 64 scans. Data manipulation was carried out with the OPUS software (Bruker Optics). In situ diffuse reflection (DR) measurements were performed using the handheld Agilent 4300, equipped with wire wound IR source and a thermoelectrically cooled DTGS detector, coupled to a diffuse reflectance sampling module with a 10-mm diameter of the measurement area. The diffuse reflectance sampling module imparts the infrared beam normal to the sample and collects the diffusely reflected radiation at a range of angles from 24 to 60° from normal. Acquisition parameters in DR were the same as for ER for analysis performed at DCR FCT NOVA. A coarse silver reference cap was used for the background calibration every 10 minute. The data were converted and processed to spectral graphs using OMNIC (Thermo Electron Corp.) and OriginPro 8 (Origin-Lab Corp.) softwares, with no baseline correction or normalization, unless otherwise specified. The reflectance IR spectra are reported as apparent absorption spectra ( $A' = \log(1/R)$ ; R = reflectance). Kramers–Kronig (KK) transform was applied to the ER spectra with the aim to correct spectral distortions by using the OMNIC or OPUS softwares.

## 21.3 Applications to Cultural Heritage Research

The application of XRF, FORS, Raman, and FTIR spectroscopies to the analysis of artworks and cultural heritage materials will be described in the following paragraphs, along with the techniques' main advantages and drawbacks, through the presentation and critical discussion of series of case studies that the authors of this chapter have worked on in recent years.

### 21.3.1 Elemental Spectroscopy

#### 21.3.1.1 XRF

XRF spectroscopy is widely used in the cultural heritage field to provide answers to object-related questions raised by conservators and curators in a totally noninvasive way. Aspects most typically investigated with this technique include the materials constituting an object (e.g. metal alloys, glass, glazed ceramics, stones and gemstones, as well as inorganic pigments); the provenance of certain types of artifacts made, for instance, of obsidian, turquoise, glass, and ceramics; the possible presence of contaminants or harmful elements; the nature of degradation patinas formed on an object's surface; and the technique used to create photographs. When noninvasive analysis is the only available option, along with the great advantages offered by the XRF technique, its drawbacks, extensively discussed in the literature (Brunetti et al. 2016; Shugar and Mass 2012), must be also taken into account. Among the main limitations are the heterogeneity of the materials under investigation, which often generates ambiguous results; the often uneven morphology of the surface analyzed; the presence of complex layering; and the thinness of some types of objects such as photographs, prints, and drawings that do not meet the infinite thickness requirement. XRF is one of the analytical techniques used at the MMA on a daily basis for the scientific investigation of artifacts of archaeological, historical, and artistic relevance. The case studies reported in the following paragraphs refer to a series of research projects carried out within the Network Initiative for Conservation Science (NICS), a program designed to offer access to the MMA's scientific expertise and resources to a core group of partner institutions in New York City.

Dating to the end of the nineteenth century is a group of 157 photographs made during the 1894–1897 Jackson–Harmsworth expedition to Franz Josef Land that, in the early 1900s, the New York Public Library assembled into one album. Gifted from publishing houses and spanning a 30-year period of exploration, the majority of these photographs has been heavily retouched with overpainting and masking, as well as drawn and collaged elements (Cronin and Keister 2020). XRF analysis of these objects was conducted with a portable Elio analyzer in order to assess the possible presence of silver halide residues that would indicate incomplete processing and, thus, support the hypothesis that the preliminary photographs, which are small and in poor condition, may have been printed on site in the Arctic. In addition, examination of the main overpainted areas aimed to identify the pigments used as retouching materials in the improved positives and compare them with those listed in nineteenth-century photographic publications. Despite visual examination of the preliminary photographs undoubtedly suggesting that silver (Ag) could be present, XRF found this element in only trace amounts even on maximum density areas. Possible reasons for this include the extremely thin nature of the silver-bearing layer within the prints, which makes the detection of Ag-K lines difficult and requires the Ag-L lines to be measured instead; and the overlapping of Ag-L lines with the L lines of argon from the air, combined with the fact that conducting measurements in helium atmosphere upon connection to a gas tank can be problematic when working in the field. Silver, on the other hand, was more easily detected on maximum density areas of the improved photographs (Figure 21.1). Surprisingly, minor amounts of gold were ubiquitously identified, suggesting that, if these photographs were printed in the Arctic, Jackson and his expedition were also gold toning them. Barium was also detected in all the photographs examined, confirmed by the presence of K $\alpha$  and K $\beta$  lines as well as L lines, leading to rule out the presence of titanium, whose K lines interfere with barium L lines. Barium, in this case, is indicative of the presence of a baryta layer, composed of a mixture of barium sulfate and

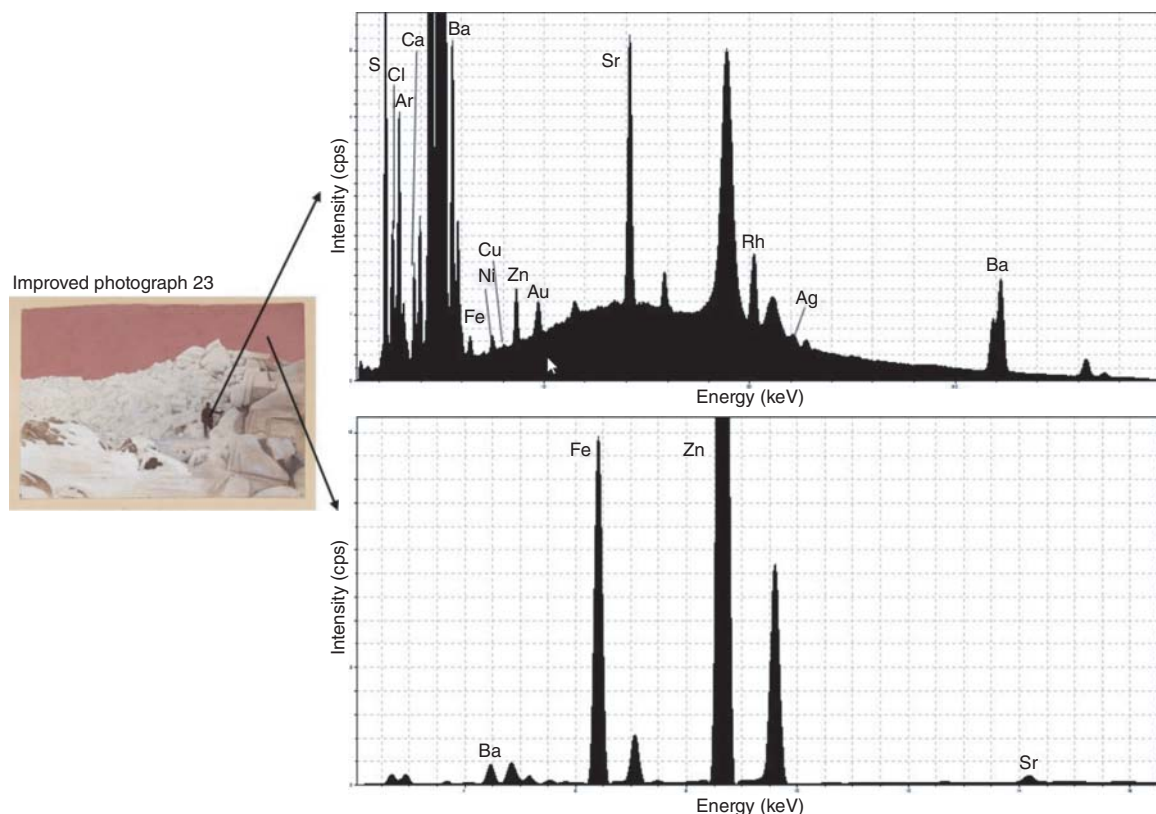


**Figure 21.1** Left, *Sea ice crushed up by pressure on the shore at Cape Flora, MFY+ 96-4073, Plate 023*, from the *Arctic Exploration* album. The Miriam and Ira D. Wallach Division of Art, Prints and Photographs, Photography Collection. The New York Public Library, Astor, Lenox and Tilden Foundations. Right, XRF spectra of a maximum density region (top) and of the pink sky (bottom). Source: Reproduced with permission of the New York Public Library, New York.

gelatin that provides an opaque white surface to the photographic paper, enabling the printing of a more sharply detailed image. For what concerns the retoucher's palette, the array of colors analyzed included white, black, as well as various shades of gray, blue, pink, and purple. White areas were found to contain high amounts of zinc, likely indicating the use of zinc white. XRF data revealed that this material was employed on colored areas, too, though in mixtures with other pigments. The detection of iron in pink shades, for instance, suggested the additional presence of iron oxides/hydroxides (Figure 21.1). Moreover, results showed that a combination of these white and red pigments with a calcium- and phosphorus-containing black, likely bone or ivory black, was used to obtain purple colors, while gray-blue was achieved as a mixture of white and black only. Even if not entirely conclusive, analysis with portable XRF offered essential insights into the photographic techniques used at the end of nineteenth and early twentieth centuries; as described in the following, some of these results were further clarified and confirmed by Raman analysis.

A second case study regards a collaborative project carried out with The Morgan Library & Museum on late Coptic manuscripts that are mostly dated to the ninth and tenth centuries and were discovered in the Fayum Oasis near Hamouli, Egypt, in 1910. Upon excavation, the manuscripts, written on parchment, were promptly sent to the Vatican Library for restoration, but the intervention performed there was never recorded (Southworth and Trujillo 2016, p. 89). The main purpose of XRF analysis, in this case, was to determine the elemental composition of inks and pigments. However, ink lines in these manuscripts are usually less than 2 mm wide, thus of a significantly

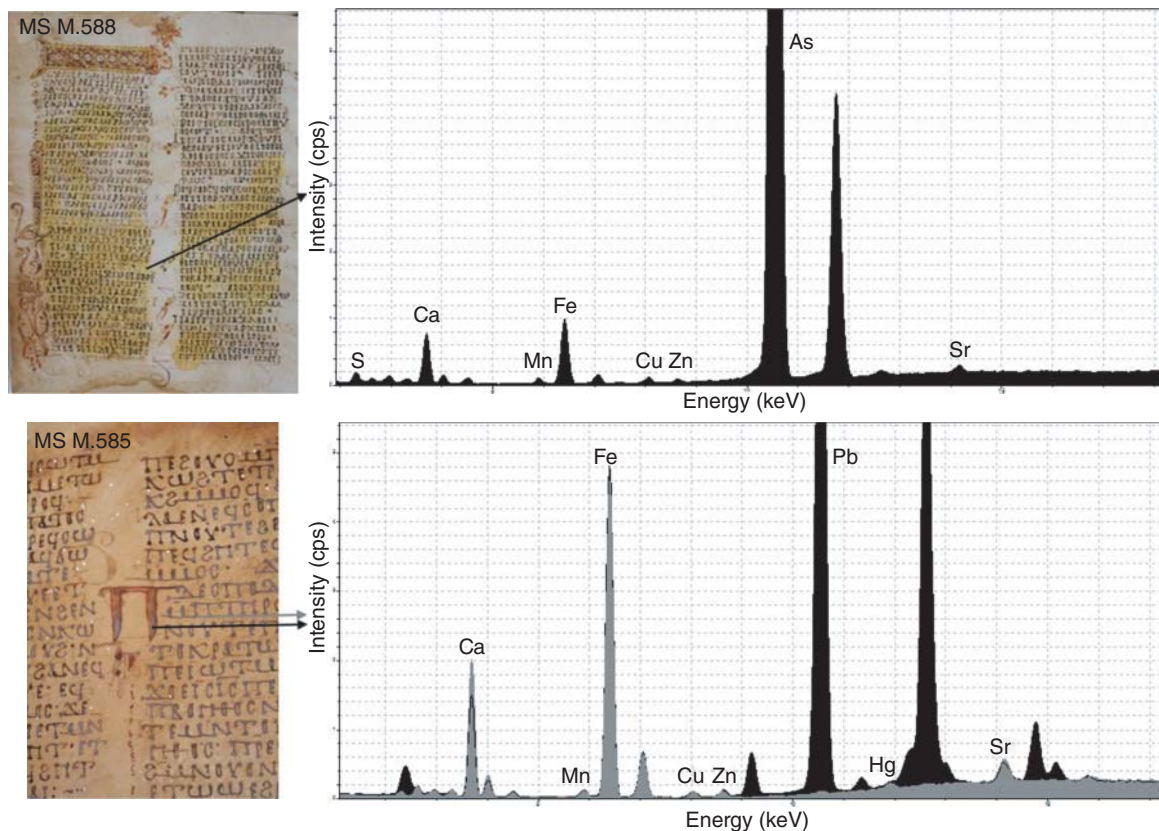


**Figure 21.2** Left, manuscripts MS M.588 and MS M.585. Purchased for J. Pierpont Morgan (1837–1913) in 1911. The Morgan Library & Museum. Right, XRF spectra of a yellow stain on MS M.588, folio 8v (top), and of an ink line (gray spectrum) and degraded area of the “pi” letter (black spectrum) on MS M.585, folio 7r (bottom). Source: Reproduced with permission of The Morgan Library & Museum, New York.

smaller size than the spectrometer’s  $3 \times 4$  mm aperture. As a result, the signal from the parchment support yielded a strong background that interfered with the inherently weak response of the thin ink lines. Moreover, the lack of a camera or laser indicator poses an additional challenge for the operator to correctly align the X-ray beam onto the location of interest. While the analysis of inks proved problematic, relatively large colored areas could be examined more effortlessly. In particular, XRF analysis of what appears to be a yellow stain covering the lettering in one of the manuscripts (Figure 21.2), initially thought to be made of an organic colorant, resulted in the detection of the  $K\alpha$  and  $K\beta$  lines of arsenic along with weak signals for sulfur, which is indicative of the presence of orpiment. Minor peaks also observed in that spectrum were attributed to iron, manganese, copper, and zinc, as well as calcium, likely due to the interference from the ink and parchment, respectively. Figure 21.2 also reports another example of the XRF data obtained from one of the Coptic manuscripts examined. In that case, visual examination suggested that a “pi” capital letter on one of the pages might have been drawn and colored with ink, while the lower part of two internal red areas appeared to have degraded to a dark gray metallic color. Spectra associated with those regions (reported in black in Figure 21.2) were compared with data from the writing ink (reported in gray in the same image). The two spectra show a very good match in the energy range between 2.5 and 9 keV, where the signals of iron, along with weak peaks for manganese, copper, and zinc, are related to the use of an iron gall ink. However, the spectrum collected from the metallic gray on the right stroke of the “pi” letter displays an additional intense lead signal, which might be linked to the presence of a red lead pigment that has degraded overtime. Such a degradation

process involving red lead is explained in the literature as related to the formation of a patina of galena, or lead(II) sulfide, upon reaction of the lead oxide with vermillion (Miguel et al. 2009), whose presence in traces has been in fact hypothesized thanks to the identification of a shoulder to the L $\beta$  lines of lead at 11.9 keV.

### 21.3.2 Electronic Spectroscopy

#### 21.3.2.1 FORS

In the UV, Vis, NIR spectral ranges, electronic and vibrational transitions can be observed. In the latter case, the observed transitions are caused by multiple (overtones) or combination of the fundamental transitions, which are commonly observed in the MIR region. The electronic transitions between the electronic energy levels determine absorption bands in the UV, Vis, NIR regions. As a rule, the absorption bands of inorganic pigments are related to ligand-field (d-d transitions), charge transfer (CT), and valence–conduction band transitions, while for organic materials delocalized molecular orbital (MO) band transitions are involved (Burns 1993; Nassau 1983). Noninvasive UV–Vis–NIR FORS may be used as contactless or contact technique. It is based on the analysis of the radiation diffused by the surface under examination in the 200–2500 nm range when compared with a highly reflecting reference standard, such as 99% Spectralon® targets. The reflectance spectrum of the analyzed surface is then generally reported as the percentage of reflected radiation as a function of the wavelength. The main problem faced in the identification of unknown compounds, however, lies in the creation and availability of a suitable spectral database of artists' materials to be used for comparison purposes. Indeed, the interpretation of spectra is usually conducted by correlating the unknown data to a suitable reference library. Reference spectra can be acquired, for example, on mock-up paintouts prepared by reproducing as closely as possible the pictorial materials and techniques used by artists in a certain period. For instance, the first database created and hosted by IFAC-CNR, named "Fiber Optics Reflectance Spectra (FORS) of Pictorial Materials in the 270–1700 nm range," is a collection of reflectance spectra in the 270–820, 350–1000, and 980–1700 nm ranges (<http://fors.ifac.cnr.it>) (IFAC-CNR 2016). One issue with UV–Vis–NIR FORS lies in the fact that it does not yield as accurate results when complex mixtures are investigated: in these cases, the position of the absorption bands may be shifted by a few nanometers or be reduced in intensity. In addition, the effect of yellowing of the binder/vehicle or of the varnish may cause their curve inflection points to move, particularly when the pigments or dyes are present in low concentrations. Furthermore, not all the pigments can be identified, because some materials have extremely similar reflectance spectra: among these, cadmium red and vermillion (Thoury et al. 2011).

An example of application of FORS to support the conservation treatment of a painting titled *Pascolo a Pietramala* (c. 1889) by Telemaco Signorini, from the Galleria di Arte Moderna, Palazzo Pitti, in Florence, is presented in the following (Bacci et al. 2009). This project focused on the study of the blue portion of the artist's palette using noninvasive UV–Vis–NIR FORS in the 350–1700 nm range. Signorini (Florence, 1835–1901), one of the most relevant Italian painters of the second half of the nineteenth century, was particularly famous among his colleagues for his way of depicting dark details and shadows by using primarily blue colors. Hence, an in-depth study of the blue pigments he used was undertaken by initially preparing linseed oil mock-up paintouts upon selection of the following powdered pigments: Prussian blue; synthetic ultramarine blue; cerulean blue; Thénard blue; basic lead carbonate; and zinc oxide. The pure powdered blues and their mixtures with the two white pigments were dispersed in a linseed oil binding medium onto rectangular pieces of canvas with a cardboard support (3 × 5 cm) on a kaolinite and titanium dioxide (rutile) ground. It is worth noticing that the spectral features of Prussian blue drastically changed when the reflectance spectra of its mixtures with the white pigments were compared with those acquired on its masstone mock-up paintout. This incongruity is due to the fact that the strong absorption band in the Vis–NIR regions between 400 and 1000 nm, attributed to a homonuclear intervalence charge transfer transition between Fe<sup>2+</sup> and Fe<sup>3+</sup> (metal to metal charge transfer, MMCT), is extremely intense, almost resembling the reflectance spectrum of a black pigment in the Vis. The spectral features of the other three blue

pigments, on the other hand, were not affected by the presence of the two whites, even when the concentration of the blue colors in the mixture was very low. Data recorded on several spots of the painting showed that the artist used three different blue pigments, namely Prussian blue, ultramarine blue, and cobalt blue. In addition, a careful comparison of the FORS spectra revealed that the strong absorption band centered at about 700 nm due to Prussian blue had shifted in the painting's spectra compared to those taken from the mock-up paintouts. This discrepancy was probably due to the different ages of the binding media and related yellowing of the material examined.

Another interesting application of FORS, in conjunction with XRF, involved a technical study of the *Graduale n. 558* by Beato Angelico (c. 1400–1455), one of the most important artists of the fifteenth century. His amazing talent was celebrated in 2007–2008 with a special exhibition titled “*Fra Giovanni Angelico. Pittore miniatore o miniatore pittore?*” held at the San Marco Museum in Florence. On this occasion, the techniques and materials used by the artist in the creation of manuscripts and panel paintings were investigated and compared. The main goal of this study, in the context of the exhibition, was the analysis of materials – with a special focus on pigments and dyes – used by Angelico to produce illuminated manuscripts and, in particular, one of his most beautiful pieces of the permanent collection of the San Marco Museum: the above-mentioned *Graduale n. 558* (Picollo et al. 2011; Scudieri and Picollo 2017). Assignments were made using both the primary and first derivative reflectance spectra. Given the thinness of the paint layers and the presence of overtone bands in the NIR associated with the vellum substrate, the interpretation of spectra required particular care. However, the NIR region was found to be particularly useful for the identification of some pigments, as well as gypsum. FORS measurements, due to the limitation in spectral sensitivity of the device (900–1700 nm), did not provide any additional information on the materials used to prepare the parchment but, based on FORS data, the use of calcium sulfate bi-hydrated (gypsum) or calcium sulfate hemi-hydrated (plaster of Paris) in the ground layer could be ruled out (Bacci et al. 2007). It appears that gypsum was present only as a preparatory layer for the application of the gold leaves in mixture with iron oxide (hematite) pigments. As revealed by FORS spectra collected on about 30 different areas of the *Graduale*, the painted blue areas were made with ultramarine blue (*lapis lazuli*). This pigment was also used in combination with a red lake pigment in different relative proportions to depict violet-purple details. Azurite, on the other hand, was used only for the watermarked letters.

One of the most recent applications of FORS in the art conservation field consists in the challenging identification of contemporary artistic materials. In this case, the materials used by self-taught artist Fernando Melani (1907–1985), one of the precursors of the Poor Art artistic movement in Italy, were studied (Carlesi et al. 2013). Here, FORS was used in conjunction with FTIR for the analysis of 15 powder compounds collected from a paint box found in the attic of the artist's home-studio in Pistoia, and one of his artworks, named by Melani himself with its inventory number N. Inv. 2625 (1981) (Figure 21.3). Results showed that the artist used traditional inorganic pigments, such as chrome yellow, Mars yellow, Mars red, ultramarine blue, Prussian blue, and vermillion, as well as modern organic pigments, such as arylide yellows (PY1 and PY3), toluidine red (PR3), Victoria Blue B (PB26), and phthalocyanine blue (PB15). He also employed calcite and barite as fillers and extenders. Moreover, sulfur and abrasive powders were also found, thus confirming Melani's use of a large variety of nonconventional artists' materials. In particular, data obtained on a straw paper artwork labeled N. Inv. 2625 (1981) revealed that two of the yellow pigments detected, arylide yellow PY3 and chrome yellow, matched those found in the artist's paint box. This study confirmed the potential of FORS for the analysis of contemporary artists' materials and artworks, due to the fact that it does not require sampling, the acquisition of spectra is rapid, and can be performed with or without touching the surface of the object that is being analyzed (Figure 21.3). In some cases, however, it is necessary to integrate FORS with other analytical techniques, such as FTIR, Raman, XRF, and others, to achieve conclusive identification of the materials. Nevertheless, FORS can also be used as a valuable preliminary tool to locate areas for micro-sampling or to extend local data from microanalyses to a broader scale, thus minimizing the need for sample removal.

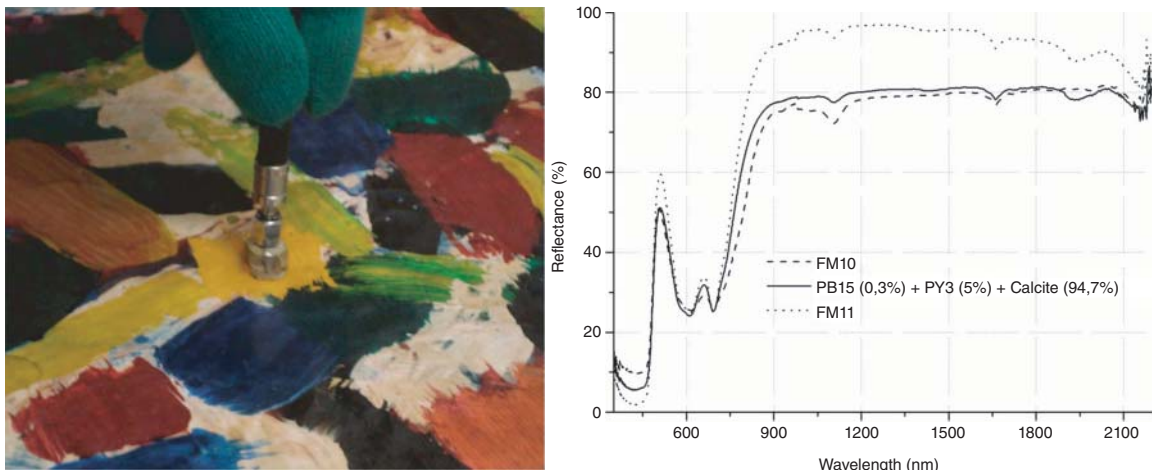


**Figure 21.3** Left, FORS 8°/8° probe head used to acquire reflectance spectra on a painting by Fernando Melani. Right, FORS spectra of two of Melani's green powdered pigments (FM10 and FM11) compared with a mixture of phthalocyanine blue, PY3, and calcite in powder made at the IFAC laboratory to simulate the composition of FM10 and FM11. The painting under study is *Opera n. inv. 2625* (1981), acrylics on paper, 68.8 × 83 cm; Pistoia, Casa-studio Fernando Melani. Source: Reproduced with permission of the Municipality of Pistoia.

### 21.3.3 Vibrational Spectroscopy

#### 21.3.3.1 Raman

Works on paper such as prints and photographs constitute some of the most fragile art forms, whose handling requires great caution and care. When dealing with such delicate artworks, noninvasive analysis performed *in situ* with portable equipment is typically preferred to more intrusive approaches that involve sampling. Recent work carried out at the MMA has demonstrated the great potential of handheld Raman spectroscopy for the noninvasive analysis of pigments on paper. The latest examples of application focused on objects in the holdings of several prestigious New York City museums, with whom MMA scientists collaborated as part of NICS.

Among these collaborative projects is the examination of a selection of block books from The Morgan Library & Museum, most of which are attributed to the Netherlands and Germany and dated to ca. 1460–1480. Block books are multipage works produced entirely from hand-colored woodcuts, with both text and images carved in relief in a single block. Handheld Raman analysis of such unusual objects revealed that their color palette, similar to that found in manuscript illuminations, includes mineral pigments that are consistent with those detected on coeval hand-colored relief prints at the National Gallery of Art, Washington D.C. (Fletcher et al. 2009). In detail, vermillion and red lead are predominant in most orange and red tones of both the imagery and lettering, applied individually or, more often, as mixtures. The typical signals of iron(III) oxide, or red ochre, were also observed in two cases, combined with those of vermillion or red lead to depict a figure's robe and the flames of hell. Interestingly, yellow areas on three different books were printed using distinct yellow pigments, i.e. orpiment, lead tin yellow (type I) (Figure 21.4), and yellow ochre. Although green areas generated featureless spectra likely due to unsuitable laser excitation, partially successful results were achieved for the blue colors, some of which gave rise to the main band of azurite at  $400\text{ cm}^{-1}$ . As expected, natural dyes – mostly cochineal and brazilwood – yielded no results when analyzed with the handheld Raman spectrometer and could be only identified by surface-enhanced Raman spectroscopy (SERS) on a benchtop instrument equipped with a 20× microscope objective and 488 nm excitation. The *in situ*, noninvasive characterization of the printing inks, displaying a great variety of black, gray, and brown shades and various opacity, also proved particularly challenging. Indeed, only the typical fingerprint of amorphous carbon was detected using the Bravo spectrometer even in the case of brown inks that were found by

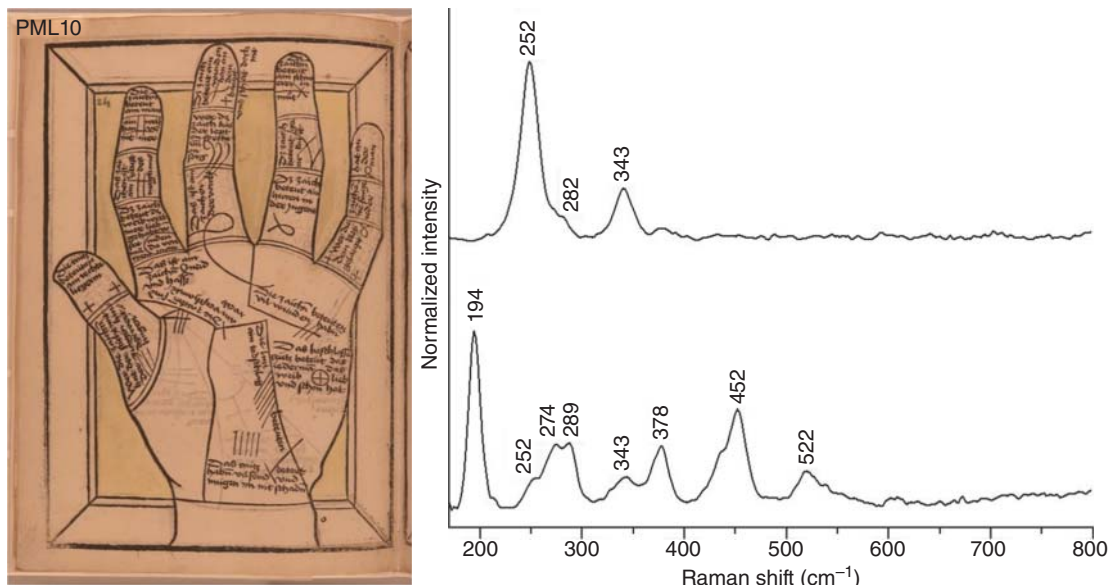


**Figure 21.4** Left, block book PML10. Purchased with the Bennett collection, 1902. The Morgan Library & Museum. Right, Raman spectra collected from two areas of the yellow background of PML10, plate 12, showing the characteristic bands of vermilion (top) and lead tin yellow type I (bottom). *Source:* Reproduced with permission of The Morgan Library & Museum, New York.

XRF spectroscopy to contain iron. This was likely due to the impossibility of adjusting the laser power, automatically set at ~50 mW, which may cause thermal degradation of particularly sensitive or delicate materials such as iron gall inks. Defocusing the laser beam by manually increasing the working distance did not help overcome the issue, as the Raman response of the analyte under study got unduly reduced. In addition, the absence of a camera, also typical in portable equipment, prevented precise focusing especially in the case of very thin ink lines, leading, as a result, to a severe interference from the paper substrate in the Raman spectra.

A second case study is related to the analysis of a selection of photographs from Arctic expeditions belonging to the New York Public Library, already described above. Noninvasive analysis with handheld Raman spectroscopy revealed that the variety of pigments used in the color retouches is relatively limited. In detail, white regions and accents in the snow banks were found to be mostly painted with zinc white; this pigment was also employed in the most intense pink tones of the sky in combination with iron(III) oxide. Gray retouches gave rise to two broad bands at approximately 1325 and 1590 cm<sup>-1</sup>, attributable to a carbon-based black; the detection of calcium and phosphorus in a microscopic sample removed from this area by means of scanning electron microscopy coupled with energy-dispersive X-ray (SEM/EDS) spectroscopy enabled to further specify the identity of this pigment as bone or ivory black. Normally, the differentiation between carbon black and bone or ivory black can be accomplished with Raman thanks to the observation of a 960 cm<sup>-1</sup> band in the spectrum of the latter, assigned to the P-O stretching of orthophosphate ions in the calcium phosphate. However, such band is usually more clearly visible when using green wavelengths and in fact, in the present analysis, it likely went undetected due to the scarce flexibility of the portable equipment used in terms of available excitation wavelengths. Interestingly, mixtures of all the pigments listed above, i.e. zinc white, iron(III) oxide, and carbon-based black, were found to be responsible for the purple color of the sky in certain photographs, while bluish tones appeared to have been obtained as a combination of just white and black. In addition to the characterization of pigments, Raman analysis was also crucial to confirm, in some of these objects, the presence of a baryta layer.

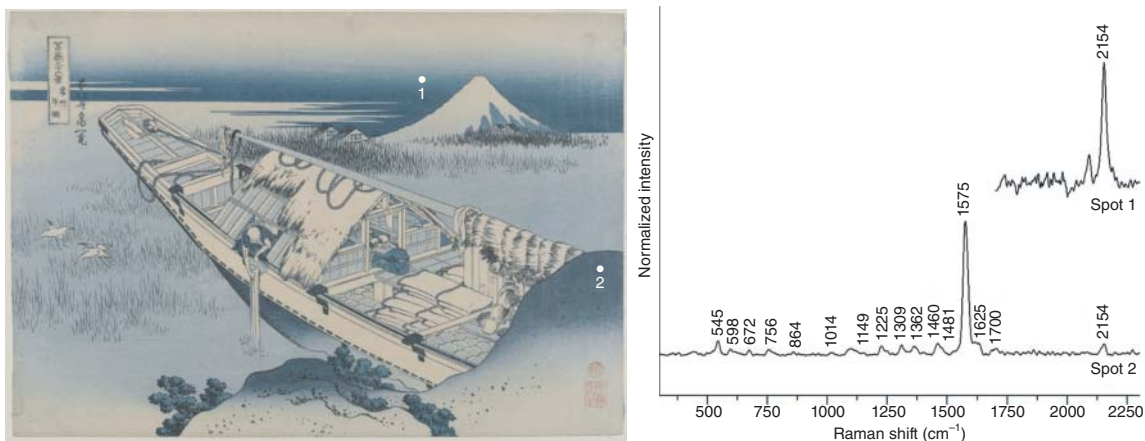


**Figure 21.5** Left, Katsushika Hokusai (Japanese, 1760–1849). *View of Fuji from a Boat at Ushibori* from “Thirty-Six Views of Fuji,” 1834. Woodblock color print, 10 3/8 × 15 1/4 in. (26.4 × 38.7 cm). Brooklyn Museum, gift of Louis V. Ledoux, 47.47. Right, Raman spectra collected from two blue areas of the print, displaying the typical spectral features of Prussian blue alone (top) and with indigotin (bottom). Source: Reproduced with permission of the Brooklyn Museum, New York.

Another project carried out within the NICS program involved the examination of two Japanese prints, i.e. Eisen Keisai’s *View of Shogetsu Pond* (1829) and Katsushika Hokusai’s *View of Fuji from a Boat* (1834), in the collection of the Brooklyn Museum. This project was proposed as part of a broader investigation aimed at testing the response of various blue pigments when analyzed by means of a wide range of imaging techniques, with a special focus on multiband reflectance image subtraction (MBRIS) (Bradley et al. 2020). In that context, Raman spectroscopy was employed as a complementary technique to substantiate or challenge materials characterization performed by MBRIS and FORS. Initial testing of *View of Shogetsu Pond*, one of the earliest known *aizuri-e*, entirely printed in blue, led conservators to believe that the print was executed exclusively in Prussian blue; however, subsequent imaging results suggested that an indigotin-based pigment may also have been used. Scientific analysis by means of handheld Raman spectroscopy detected both colors, individually or in combination, on various areas of the two prints (Figure 21.5). While indigotin yielded well-resolved data, the Raman spectrum of Prussian blue, whose most intense signal is located at  $2154\text{ cm}^{-1}$ , appeared quite noisy even upon application of a series of manipulations to the raw data to improve spectral quality (Pozzi et al. 2019).

Aside from the advantages and drawbacks highlighted thus far, in general, one of the key issues of portable Raman instrumentation lies in the ability to reach stable placement of the system. Given the relatively modest size and flat nature of most of the works examined in the case studies presented above, measurements could be acquired by positioning the equipment either on a table or on wooden supports assembled for this specific purpose, with the objects placed on an easel or frame and held upright with pins. As for most similar systems, the handheld instrument used here does not require complex alignment procedures, but rather a simple calibration with calcite and polystyrene that must be repeated every few weeks. Another benefit of the equipment employed in this study that equates it to benchtop instrumentation lies in its ability to acquire data down to  $170\text{ cm}^{-1}$ , thanks to the recent implementation of an extended spectral range. Furthermore, the high fluorescence emission of most organic molecules or compounds embedded in complex matrices, which often hampers the detection and identification of weak Raman scatterers, is automatically corrected by SSE (Pirzer and Sawatzki 2008; Shreve et al. 1992). As shown in the analysis of the Japanese prints and thoroughly explained elsewhere (Pozzi et al. 2019), in cases when the use of this patented method of fluorescence mitigation yields to the creation of artifacts, relying on the manual application of a series of manipulations to the raw data might provide better quality results.

### 21.3.3.2 FTIR

Within cultural heritage materials, synthetic polymers can present serious conservation challenges (Bressan et al. 2019; Lavédrine et al. 2012; Quye et al. 2011; Shashoua 2009; van Oosten 2015). Environmental factors can affect their longevity, and after degradation starts, rarely conservation treatments are capable of returning the polymer to its original condition. Noninvasive and noncontact reflection FTIR spectroscopy has found increasing application to survey plastic heritage collections so that conservation treatments, preservation, storage, display, or use can be strategized (Cucci et al. 2016a; Lazzari et al. 2011; Picollo et al. 2014; Rosi et al. 2016; Saviello et al. 2016; Toja et al. 2012; Williams 1996).

Within reflection MIR spectroscopy devices, both ER and DR modes are used depending on the optical geometry of the acquisition interface and information desired from the material. Two types of reflection known as surface reflection ( $R_S$ ) and volume reflection ( $R_V$ ) can take place when an IR beam strikes on the surface of a bulk material (Brimmer et al. 1986; Vincent and Hunt 1968). The external mode is associated to more superficial analysis, as it measures mainly  $R_S$ , the part of the radiation that is directly reflected without entering the sample, according to the Fresnel's equations. The diffuse mode is characterized rather by a volume investigation, as it should measure  $R_V$ , after the IR beam is reflected upon being partially absorbed, refracted, transmitted, and scattered by the particles in the medium, according to the Kubelka–Munk model. The extent of  $R_S$  and  $R_V$  measured depends on the geometry of acquisition and analyte properties, including concentration, surface morphology (topography and texture), and infrared optical constants (mainly refractive-( $n$ ) and absorption-( $k$ ) indexes) (Körtum 1969). In addition,  $R_S$  and  $R_V$  show an angular distribution, and their reflectance response can include specular and/or diffuse components, depending on the characteristics of the material being analyzed. Whereas the specular component is detected in the incident plane at the same angle of the incident beam (the angles are equal), the diffuse component is associated to all the other cases (the angles do not agree). The geometrical layout of the detection system determines whether specular and/or diffuse components can be read from both ER and DR modes.

Portable IR reflection spectroscopy was recently employed at DCR FCT NOVA for the study of over 200 historical plastic objects gathered from various private collections and plastic industries, as part of a research project titled “The Triumph of Bakelite – Contributions for a History of Plastics in Portugal.” The project’s main goal was to contribute to a comprehensive history of the plastics industry in the country, based on both documentary and material sources, as well as oral testimonies collected during the investigation. IR analysis aimed to assess the polymer nature and condition of the whole set of historical objects gathered within the first two years of the project, so that a selection (and adequate conservation treatment, when necessary) could be studied for inclusion in a 2019 exhibition entitled “Plasticity – A History of Plastics in Portugal,” held at the Museum of Leiria, Portugal. On the occasion of that material survey, two portable FTIR instruments were used and their performance compared when applied to the analysis of certain materials. Here we present a case study involving the characterization of polyethylene (PE), in which data acquired in ER mode (Alpha) and DR mode (handheld Agilent 4300) from reference samples of PE (unaged and uncolored) and from an historical 1960s plastic bottle are compared to demonstrate the power of reflection spectroscopy for analysis of plastic materials regardless of the acquisition mode. In the discussion of this case, it is important to note that, in the ER configuration, all IR beams reflected from a material’s surface are collected and  $R_S$  is the main contribution observed. The DR geometry detects both surface and volume reflections, but excludes the specular component. With this later module, the IR beam is mostly all transmitted because  $\Theta_i = 0^\circ$ , thus, for the Fresnel equation (Schrader 1995) for an air–plastic interface ( $n_{\text{air}} = 1$ ;  $n_{\text{plastic}} = 1.5$ ), the total percentage of reflectance (R%) and transmittance (T%) is respectively 4% and 96%. The different optical geometries of the ER and DR modules are mirrored in the collected reflectance spectra for the PE reference. Compared to an ATR spectrum, reflectance spectra feature more bands; the fundamental bands are distorted with change in maximum, shape, and relative intensity (Figure 21.6). These resulting reflection profiles are modeled according to the extent of the  $R_S$  and  $R_V$  contributions. The  $R_S$  gives rise to derivative-like spectral features and/or inverted bands (*reststrahlen* effect), respectively found for bands with  $k < 1$  (following the anomalous dispersion of  $n$ ) and for strong oscillators with  $k \gg 1$  (strong absorbance coefficient). For pure organic polymers, the presence

of *reststrahlen* bands is not common due to their low  $k$  index, i.e. the average  $k$  for a reasonably strong absorption of an organic molecule is about 0.1 (Kattner and Hoffmann 2002). *Reststrahlen* bands, however, can be common in the presence of some inorganic additives, which make the bulk optically dense, increasing their absorbance coefficient (Miliani et al. 2012). The  $R_V$  gives rise to differences in terms of broadening and relative band intensities by the contribution of the diffuse reflection (Griffiths and De Haseth 2007; Korte and Roeseler 2005; Miljkovic et al. 2012). As shown in Figure 21.6, the DR spectrum shows more intense bands, but a lower signal/noise ratio. This is due to the higher penetration depth of the IR beam, thus to a higher contribution of the volume reflection, and to the detection of a lower portion of the reflected radiation (i.e. the information is collected only between 24° and 60° from normal). The ER spectrum is less noisy since all components are equally collected at all angles. In

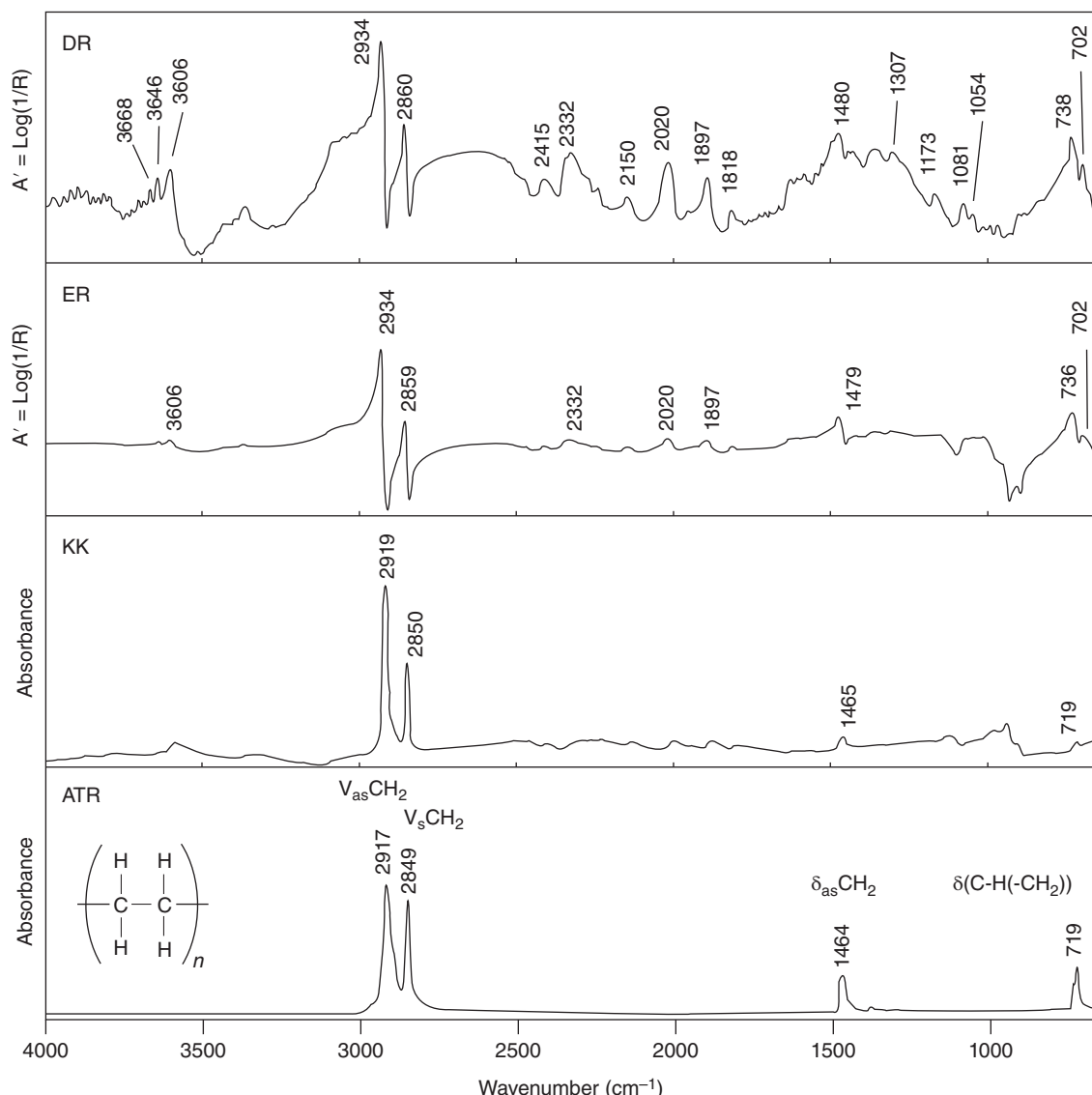


**Figure 21.6** FTIR spectra of a PE reference sample collected with several acquisition modes. From top to bottom: DR, ER, KK transform of the ER spectrum, and ATR.

both reflectance spectra, all fundamental bands of PE appear as derivative-shaped bands. Due to their characteristic profile, these bands can be used as markers to identify PE. Also, regions showing overtones and combination bands are found (2500–1800 cm<sup>-1</sup> range), which might be associated with the semi-crystallinity of PE spherulites (Gedde and Mattozzi 2004; Woo and Lugito 2015). The KK transform algorithm can be used to make reflectance spectra more comparable with those acquired in transmission or ATR modes, correcting distortions arising from  $R_S$  reflection (Lucarini et al. 2005) by turning derivative-shaped bands into absorption bands (Figure 21.6). However, this algorithm is not always suitable for application over the entire reflectance spectrum, as *reststrahlen* bands, such as those of PE between 1200 and 800 cm<sup>-1</sup> and regions assigned to combination/overtones bands, appearing as absorption bands in the reflectance spectrum, are transformed into new derivative-shaped profiles. Analysis in ER and DR of the historic plastic bottle (purple body and red lid) shows comparable results to that of the PE references, highlighting the importance of creating spectral databases for correct data interpretation (Figure 21.7). In addition, not only ER and DR enable the identification of polymers by assigning their corresponding IR marker bands, but these two methods also display a higher sensitivity compared to ATR. ER and DR show more visible differences between the body and lid, especially in the 2500–2100 cm<sup>-1</sup> and 1400–800 cm<sup>-1</sup> regions, compared to ATR spectra collected from the same parts. In summary, both ER and DR modules have proven equally powerful for the identification and study of historic plastics. Owing to the noninvasive approach offered by the two devices, both ER and DR interfaces enabled a complete overview of the molecular characterization of the historical plastic,

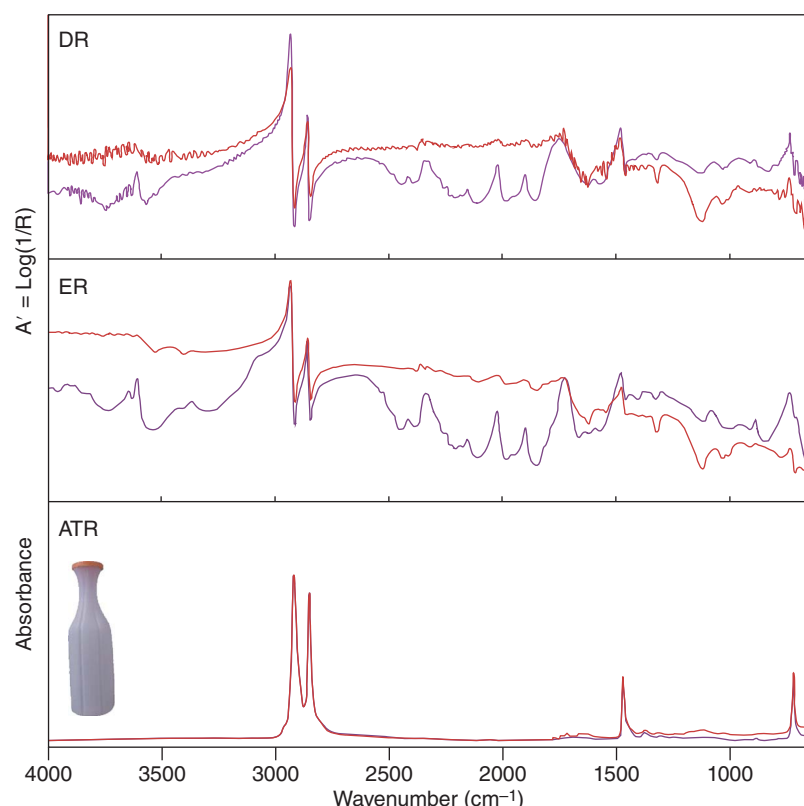


**Figure 21.7** FTIR spectra of a PE historical bottle collected with several acquisition modes. From top to bottom: DR, ER, and ATR. Purple and red spectra represent the body and lid of the bottle, respectively. Inset, historical purple plastic bottle donated to DCR FCT NOVA by Isabel Florentino, Portugal.

as many areas of the object were analyzed without compromising its physical integrity and with no limitations correlated to micro-sampling (required in transmission) or pressure (required in ATR).

In a second case study, the materials of an evening dress dated to 1967 and designed by Dran Hamilton, American, were studied at the MMA, as part of an ongoing survey of vinyl and imitation leather used in the MMA's Costume Institute (CI) collection from the 1960s to the contemporary age. Polyvinyl chloride (PVC)-based vinyl and thermoplastic polyurethane elastomers (TPU) employed in imitation leather present serious conservation issues. In particular, glossy surfaces could be greatly affected by migration of chemical components to the surface (e.g. additives, including phthalate plasticizers in PVC and adipic acid in TPU) (Shashoua 2009; Tüzüm Demir and Ulutan 2013). The dress is composed of a striped medium-gloss black and white bodice and a glossier black skirt. Analysis at the CI had the Alpha reflectance interface orthogonal to the surface of the dress by means of a tripod. In this way, the dress could rest on its storage board without being handled. Optimal positioning with the material surface could be ensured by moving the board and the instrument interface by way of a mount and tripod gear. The bodice was cut from an individual piece of black and white striped material, with the black stripes tapered into straps. Even if representative of the same plastic-coated fabric, the reflectance spectra obtained from the black and white stripes from the bodice overall appear different, affected by the reflectance properties of the individual substrate (Figure 21.8). The spectrum from the black stripe shows most prominent interference as *reststrahlen* bands between 800 and 100 cm<sup>-1</sup>, while that of the white stripe is affected by high reflectivity as well as scattering of the white substrate, and appears more complex. Nevertheless, although weaker, characteristic features for PVC were distinctive enough also in the spectrum of the white stripe, which could be easily compared to that obtained from a contemporaneous medium-gloss white PVC used in a pair of gloves by French designer André Courrèges, whose surface had been also analyzed by FTIR upon removal of a microscopic sample (Figure 21.8). The spectrum of the glossier black is less affected by interference from the substrate and represents rather a refractive index (*n*) spectrum, because of the low *k*, the thickness of the coating, and higher gloss. Here, the KK algorithm (4000–1040 cm<sup>-1</sup>) could be successfully applied to convert inverted peak into

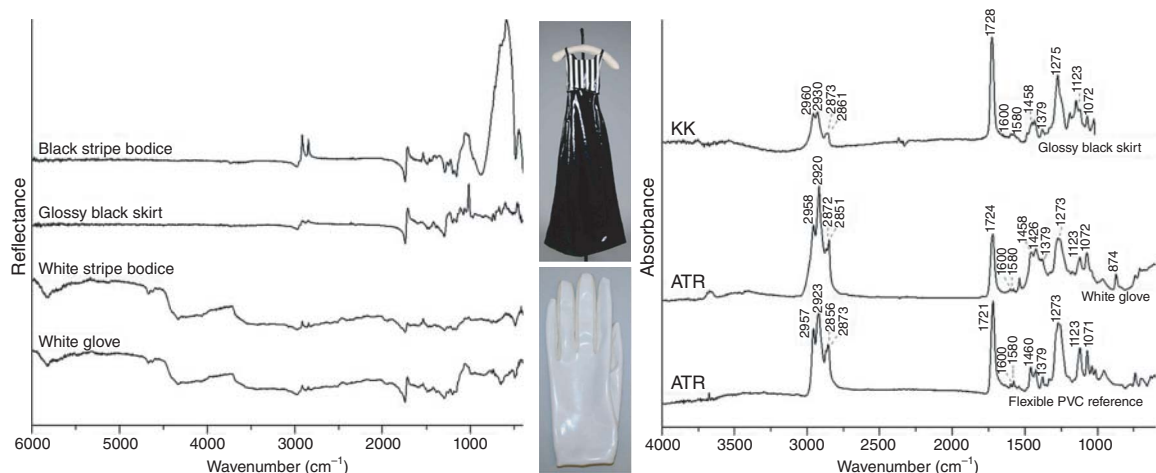


**Figure 21.8** Left, from top to bottom, raw ER spectra obtained from the medium-gloss black stripe of the bodice, the glossy black skirt, the white stripe of the bodice (all from MMA dress 2009.300.7948, Brooklyn Museum Costume Collection at The Metropolitan Museum of Art, gift of the Brooklyn Museum, 2009; gift of Dran Hamilton, 1978), and the medium-gloss white PVC coating from the white gloves (MMA 1979.329.9, gift of Bernice Chrysler Garisch, 1979). Right, from top to bottom, KK transform spectrum of the glossy black skirt compared with ATR spectra of the medium-gloss white PVC coating from the gloves and flexible PVC ResinKit™ 29 reference, plasticized with bis(2-ethylhexyl) phthalate (Tüzüm Demir and Ulutan 2013). Bands at 1426 and 874 cm<sup>-1</sup> in the white substrate of the glove are assigned to inorganic carbonate stretching from calcium carbonate. Source: Reproduced with permission of The Metropolitan Museum of Art, New York.

absorption bands, which can easily match the spectrum of a flexible PVC reference. Also, from both the ER and KK-transformed spectra it is possible to clearly discern the phthalate plasticizer (inverted bands centered at around 2920 and 2850  $\text{cm}^{-1}$  for aliphatic CH stretch, and 1728 and 1270  $\text{cm}^{-1}$  for C=O ester stretch).

As seen in the latter case study, an advantage of reflection FTIR, depending on the instrument's detection geometry and optical properties of the material surface, is the detection of coatings. The ability of portable reflection FTIR to detect plastic coatings on fashion fabrics with different gloss, color and reflective background, had been previously tested at the MMA on dated swatch fabrics in the American quarterly periodical "American Fabrics" (AF 1946–1975), later called "American Fabrics and Fashions" (AFF 1975–1986). The manufacturers' material swatches in this periodical are described in their characteristics, use, and sometimes compositions, and represent a valuable source of dated reference materials of this kind for multi-analytical studies, as well as can inform on their deterioration. Reflectance FTIR spectroscopy was used to create a database of these swatches, and also detected composition mislabeling/omissions. As an example, the material "Accordion" (Hicks 1983, p. 12), a black swatch with stripes embossed with blue-colored metallic foil-transfer, created by New York-based designer Scott Simon for use in fashion accessories as well as home furnishing and wall covering, is described as 100% polyurethane skin on sateen. Surface analysis by ER indicates a coating of cellulose nitrate (Figure 21.9), an information omitted from the description. Cellulose nitrate coatings are still popular in the creation of glossy surface (e.g. patent leather and imitation leather) and their detection on fashion objects bears implications for storage and display of the works (Quye et al. 2011).

In the case of organic coatings on metallic substrates, the differences between acquiring in ER or DR modes could be drastic. Organic coatings on metallic substrates, including fashion garments and accessories studied at the MMA, showed that the ER geometry of the Alpha is suited for this type of analysis, as specular radiation is collected. However, signal from clear, transparent films over highly reflective, polished surfaces can saturate the detector, preventing interpretation, unless it is matched with spectra from similar surfaces, where samples were analyzed for absorption FTIR, thus further confirming the importance of creating spectral databases for reflection FTIR techniques, regardless of the quality of the signal obtained for purely qualitative purposes.

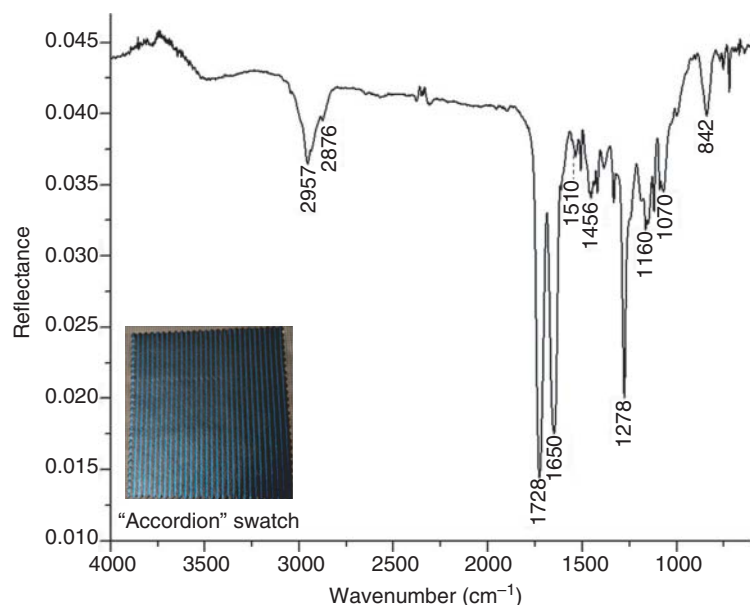


**Figure 21.9** Raw ER spectrum obtained from the surface of the "Accordion" fabric swatch, appearing as if acquired in transmittance because of the high specular reflection from the substrate including the colored metallic foil. Characteristic bands for cellulose nitrate are marked. Photographic credit: Adriana Rizzo.

In summary, FTIR reflection techniques can give information on the coating only, or on coating and substrate, depending on the instrument geometry and optical properties of the surfaces examined. Therefore, when using this technique to survey plastic heritage collections, the analyst should always take into account that the spectrum obtained may not be representative of the bulk of the object. If the bulk is not easily accessible for noninvasive analysis, sampling may be required for full material characterization. In that case, a portable ATR attachment or complementary instrumentation could be used for the *in situ* characterization of the material.

## 21.4 Conclusions

Benefits and drawbacks of portable XRF, FORS, Raman, and FTIR equipment have been described in a large body of literature, and are also detailed in Volume 1 of this book (reference chapters by Cornaby, Stratilatov, Creasy, Schiering). Compactness, light weight, and user-friendliness are some of the characteristics that are typically numbered among the main advantages of the movable, portable, and handheld versions of these techniques. Particularly desirable for the field of cultural heritage research is the fact that portable instrumentation represents a truly safe and efficient alternative to the removal of samples, which in many cases is severely limited, if not entirely forbidden, due to authorization or conservation-related issues. Furthermore, by enabling the operator to easily transport them and collect data in the field in a timely manner, transportable instruments have opened up viable roads for the scientific investigation of invaluable objects that cannot be moved from museum galleries, storage facilities, and conservation laboratories, and would not otherwise be accessible for analysis. Limitations and drawbacks are mainly related to a scarce flexibility in terms of spectral acquisition settings, to the spectral interpretation of the complex signals obtained, and to the intrinsic complexity of the materials that constitute artworks and ancient artifacts. Most of these challenges, however, may be overcome by a complementary use of several of these techniques, which generally enables to identify a wide range of inorganic and organic materials.

Without doubt, the commercial offerings of portable spectroscopy equipment have expanded the possibilities for the analysis of objects of archaeological, historical, and artistic significance in the field. Imaging spectroscopy of cultural heritage, with the attainment of chemical distribution maps of materials within the artwork examined, using portable dedicated cameras as well as sophisticated imaging systems, is greatly expanding the resources available to the analyst for *in situ*, noninvasive measurements. Multispectral and hyperspectral imaging equipment is currently used with dedicated optics and detecting systems to acquire high-resolution spectral data, generally in the visible and near-IR regions, from flat surfaces and three-dimensional objects (Brunetti et al. 2016; Casini et al. 2005; Cucci et al. 2016b; Delaney et al. 2016; Liang 2012; Liang et al. 2014; Palomar et al. 2019; Pouyet et al. 2017; Wijsman et al. 2018). The instrumental setups are typically borrowed from commercial systems or customized in house, and their specifications and wide range of applications would deserve discussion in another chapter. As for now, they have shown great promise as screening techniques that are complementary to those described in this chapter, also informing on potential sampling areas for more in-depth and localized analysis.

## Acknowledgments

Part of this research (XRF and Raman case studies) was made possible by the Network Initiative for Conservation Science (NICS), a Metropolitan Museum of Art program. Support for NICS was provided by a grant from The Andrew W. Mellon Foundation. The authors are grateful to Tuesday A. Smith, intern in the MMA's Department of Scientific Research during summer 2019 and Barnard College undergraduate, for contributing to the ER-FTIR survey of garments and accessories at the MMA CI from which two examples were drawn for this chapter, as well as to former CI conservator Sarah Scaturro for supporting this survey. The authors are also thankful to Isabel Florentino for granting access to her historical collection of Portuguese plastic objects for analysis with portable FTIR

spectroscopy instrumentation. Part of this research was also supported by Fundação para a Ciência e Tecnologia, Ministério da Educação e da Ciência (FCT/MCTES), Portugal, through doctoral program CORES-PD/00253/2012 and PhD grant PB/BD/114412/2016, as well as by “The Triumph of Bakelite – Contributions for a History of Plastics in Portugal” project (PTDC/IVC-HFC/5174/2014) and the Associate Laboratory for Green Chemistry – LAQV, financed by Portuguese funds from FCT/MCTES (UID/QUI/50006/2019). The authors would like to also acknowledge Carlo Sisi, former director of the Galleria di Arte Moderna di Palazzo Pitti, Florence, who kindly gave permission to carry out scientific analysis, and conservator Muriel Vervat for supporting work on Signorini’s *Pascolo a Pietramala* painting. Measurements on Melani’s materials and artwork were made under the auspices of the Pistoia City Council and within the “Preventive Conservation of Contemporary Art” project (COPAC, 2011–2013) financed by Regione Toscana (Tuscany, Italy). Finally, a special thanks to Magnolia Scudieri, former director of the Museum of San Marco, for introducing the authors to the fascinating world of Beato Angelico.

## References

- Aceto, M., Agostino, A., Fenoglio, G. et al. (2012). First analytical evidences of precious colourants on Mediterranean illuminated manuscripts. *Spectrochimica Acta Part A: Molecular and Biomolecular Spectroscopy* 95: 235–245. <https://doi.org/10.1016/j.saa.2012.04.103>.
- Alberti, R., Crupi, V., Frontoni, R. et al. (2017). Handheld XRF and Raman equipment for the in situ investigation of Roman finds in Villa dei Quintili (Rome, Italy). *Journal of Analytical Atomic Spectrometry* 32: 117–129. <https://doi.org/10.1039/C6JA00249H>.
- Alfed, M., Janssens, K., Dik, J. et al. (2011). Optimization of mobile scanning macro-XRF systems for the in situ investigation of historical paintings. *Journal of Analytical Atomic Spectrometry* 26: 899–909. <https://doi.org/10.1039/COJA00257G>.
- Appolonia, L., Vaudan, D., Chatel, V. et al. (2009). Combined use of FORS, XRF and Raman spectroscopy in the study of mural paintings in the Aosta Valley (Italy). *Analytical and Bioanalytical Chemistry* 395: 2005–2013. <https://doi.org/10.1007/s00216-009-3014-3>.
- Aramendia, J., Gomez-Nubla, L., Castro, K. et al. (2014). Spectroscopic speciation and thermodynamic modeling to explain the degradation of weathering steel surfaces in SO<sub>2</sub> rich urban atmospheres. *Microchemical Journal* 115: 138–145. <https://doi.org/10.1016/j.microc.2014.03.007>.
- Arrizabalaga, I., Gómez-Laserna, O., Aramendia, J. et al. (2014). Applicability of a Diffuse Reflectance Infrared Fourier Transform handheld spectrometer to perform in situ analyses on Cultural Heritage materials. *Spectrochimica Acta Part A: Molecular and Biomolecular Spectroscopy* 129: 259–267. <https://doi.org/10.1016/j.saa.2014.03.096>.
- Bacci, M., Baldini, F., Carlà, R. et al. (1991). A color analysis of the Brancacci Chapel frescoes. *Applied Spectroscopy* 45 (1): 26–31. <https://doi.org/10.1366/0003702914337713>.
- Bacci, M., Baldini, F., Carlà, R. et al. (1993). A color analysis of the Brancacci Chapel frescoes: Part II. *Applied Spectroscopy* 47 (4): 399–402. <https://doi.org/10.1366/0003702934335074>.
- Bacci, M., Cappellini, V., and Carlà, R. (1987). Diffuse reflectance spectroscopy: an application to the analysis of art works. *Journal of Photochemistry and Photobiology, B: Biology* 1: 132–133.
- Bacci, M., Magrini, D., Picollo, M. et al. (2009). A study of the blue colors used by Telemaco Signorini (1835–1901). *Journal of Cultural Heritage* 10 (2): 275–280. <https://doi.org/10.1016/j.culher.2008.05.006>.
- Bacci, M., Picollo, M., Trumy, G. et al. (2007). Non-invasive identification of white pigments on 20th century oil paintings by using fiber optic reflectance spectroscopy. *Journal of the American Institute for Conservation* 46 (1): 27–37. <https://doi.org/10.1179/019713607806112413>.
- Barbi, N., Alberti, R., Bombelli, L. et al. (2014). A non-invasive portable XRF system for cultural heritage analyses. *Microscopy and Microanalysis* 20 (3): 2020–2021. <https://doi.org/10.1017/S1431927614011830>.

- Bitossi, G., Giorgi, R., Mauro, M. et al. (2005). Spectroscopic techniques in cultural heritage conservation: a survey. *Applied Spectroscopy Reviews* 40 (3): 187–228. <https://doi.org/10.1081/ASR-200054370>.
- Bradley, L., Ford, J., Kriss, D. et al. (2020). Evaluating multiband reflectance image subtraction for the characterization of indigo in Romano-Egyptian funerary portraits. In: *Mummy Portraits of Roman Egypt: Emerging Research from the APPEAR Project* (eds. M. Svboda and C.R. Cartwright). Los Angeles: J. Paul Getty Museum.
- Bressan, F., Hess, R.L., Sgarbossa, P. et al. (2019). Chemistry for audio heritage preservation: a review of analytical techniques for audio magnetic tapes. *Heritage* 2 (2): 1551–1587. <https://doi.org/10.3390/heritage2020097>.
- Brimmer, P.J., Griffiths, P.R., and Harrick, N.J. (1986). Angular dependence of diffuse reflectance infrared spectra. Part I: FT-IR spectrogoniophotometer. *Applied Spectroscopy* 40 (2): 258–265. <https://doi.org/10.1366/0003702864509619>.
- Brunetti, B., Miliani, C., Rosi, F. et al. (2016). Non-invasive investigations of paintings by portable instrumentation: the MOLAB experience. In: *Analytical Chemistry for Cultural Heritage* (ed. R. Mazzeo), 41–75. Cham, Switzerland: Springer [https://doi.org/10.1007/978-3-319-52804-5\\_2](https://doi.org/10.1007/978-3-319-52804-5_2).
- Burns, R.G. (1993). Mineralogical applications of crystal field theory. In: *Cambridge Topics in Mineral Physics and Chemistry*, 2nde, vol. 5. Cambridge: Cambridge University Press.
- Carlesi, S., Bartolozzi, G., Cucci, C. et al. (2013). The artists' materials of Fernando Melani: a precursor of the Poor Art artistic movement in Italy. *Spectrochimica Acta Part A: Molecular and Biomolecular Spectroscopy* 104: 527–537. <https://doi.org/10.1016/j.saa.2012.11.094>.
- Carretti, E., Rosi, F., Miliani, C. et al. (2005). Monitoring of pictorial surfaces by mid-FTIR reflectance spectroscopy: evaluation of the performance of innovative colloidal cleaning agents. *Spectroscopy Letters* 38 (4-5): 459–475. <https://doi.org/10.1081/SL-200062901>.
- Casini, A., Bacci, M., Cucci, C. et al. (2005). Fiber optic reflectance spectroscopy and hyper-spectral image spectroscopy: two integrated techniques for the study of the Madonna dei Fusi. In: *Optical Methods for Arts and Archaeology*, vol. 5857 (eds. R. Salimbeni and L. Pezzati), 58570M. International Society for Optics and Photonics, 177–184.
- Colomban, P. (2012). The on-site/remote Raman analysis with mobile instruments: a review of drawbacks and success in cultural heritage studies and other associated fields. *Journal of Raman Spectroscopy* 43 (11): 1529–1535. <https://doi.org/10.1002/jrs.4042>.
- Conti, C., Striova, J., Aliatis, I. et al. (2013). Portable Raman versus portable mid-FTIR reflectance instruments to monitor synthetic treatments used for the conservation of monument surfaces. *Analytical and Bioanalytical Chemistry* 405 (5): 1733–1741. <https://doi.org/10.1007/s00216-012-6594-2>.
- Crocombe, R.A. (2013). Handheld spectrometers: the state of the art. In: *Next-Generation Spectroscopic Technologies VI*, vol. 8726, 87260R. International Society for Optics and Photonics.
- Cronin, E. and Keister, J. (2020). Polar expeditions: a photographic landscape of sameness? *Proximity and Distance in Northern Landscape Photography: Contemporary Criticism, Curation and Practice* 171: 35.
- Cucci, C., Bartolozzi, G., Marchiafava, V. et al. (2016a). Study of semi-synthetic plastic objects of historic interest using non-invasive total reflectance FT-IR. *Microchemical Journal* 124: 889–897. <https://doi.org/10.1016/j.microc.2015.06.010>.
- Cucci, C., Delaney, J.K., and Picollo, M. (2016b). Reflectance hyperspectral imaging for investigation of works of art: old master paintings and illuminated manuscripts. *Accounts of Chemical Research* 49 (10): 2070–2079. <https://doi.org/10.1021/acs.accounts.6b00048>.
- Delaney, J.K., Ricciardi, P., Deming Glinsman, L. et al. (2014). Use of imaging spectroscopy, fiber optic reflectance spectroscopy, and X-ray fluorescence to map and identify pigments in illuminated manuscripts. *Studies in Conservation* 59 (2): 91–101. <https://doi.org/10.1179/2047058412Y.0000000078>.
- Delaney, J.K., Thoury, M., Zeibel, J.G. et al. (2016). Visible and infrared imaging spectroscopy of paintings and improved reflectography. *Heritage Science* 4 (1): 6. <https://doi.org/10.1186/s40494-016-0075-4>.
- De Luca, E., Bruni, S., Sali, D. et al. (2015). In situ nondestructive identification of natural dyes in ancient textiles by reflection Fourier transform mid-infrared (FT-MIR) spectroscopy. *Applied Spectroscopy* 69 (2): 222–229. <https://doi.org/10.1366/14-07635>.

- Fabbri, M., Picollo, M., Porcinai, S. et al. (2001). Mid-infrared fiber optics reflectance spectroscopy: a non-invasive technique for remote analysis of painted layers. Part II – statistical analysis of spectra. *Applied Spectroscopy* 55 (4): 428–433. <https://doi.org/10.1366/0003702011952181>.
- IFAC-CNR (2016). *Fiber Optics Reflectance Spectra (FORS) of Pictorial Materials in the 270-1700 nm Range*. Istituto di Fisica Applicata “Nello Carrara” - National Research Council (IFAC-CNR) <http://fors.ifac.cnr.it> (accessed 7 November 2019).
- Fletcher, S., Glinsman, L., and Oltrogge, D. (2009). The pigments on hand-colored fifteen-century relief prints from the collections of the National Gallery of Art and the Germanisches Nationalmuseum. *Studies in the History of Art* 75: 276–297.
- Ford, T., Rizzo, A., Hendricks, E. et al. (2019). A non-invasive screening study of varnishes applied to three paintings by Edvard Munch using portable diffuse reflectance infrared Fourier transform spectroscopy. *Heritage Science* 7: 84. <https://doi.org/10.1186/s40494-019-0327-1>.
- Galli, A., Caccia, M., Alberti, R. et al. (2017). Discovering the material palette of the artist: a p-XRF stratigraphic study of the Giotto panel ‘God the Father with Angels’. *X-Ray Spectrometry* 46: 435–441. <https://doi.org/10.1002/xrs.2751>.
- Gedde, U.W. and Mattozzi, A. (2004). Polyethylene morphology. In: *Long Term Properties of Polyolefins. Advances in Polymer Science*, vol. 169 (ed. A.C. Albertsson), 29–74. Berlin, Heidelberg: Springer <https://doi.org/10.1007/b94176>.
- Gomez-Laserna, O., Arrizabalaga, I., Prieto-Taboada, N. et al. (2015). In situ DRIFT, Raman, and XRF implementation in a multianalytical methodology to diagnose the impact suffered by built heritage in urban atmospheres. *Analytical and Bioanalytical Chemistry* 407 (19): 5635–5647. <https://doi.org/10.1007/s00216-015-8738-7>.
- Gomez-Laserna, O., Olazabal, M.A., Morillas, H. et al. (2013). In-situ spectroscopic assessment of the conservation state of building materials from a Palace house affected by infiltration water. *Journal of Raman Spectroscopy* 44 (9): 1277–1284. <https://doi.org/10.1002/jrs.4359>.
- Griffiths, P.R. and De Haseth, J.A. (2007). *Fourier Transform Infrared Spectrometry*, 2nde. New York: Wiley.
- Hicks, S. (ed.) (1983). *American Fabrics and Fashions Magazine* 128. New York: Doric Publishing Company.
- Invernizzi, C., Daveri, A., Vagnini, M. et al. (2017). Non-invasive identification of organic materials in historical stringed musical instruments by reflection infrared spectroscopy: a methodological approach. *Analytical and Bioanalytical Chemistry* 409 (13): 3281–3288. <https://doi.org/10.1007/s00216-017-0296-8>.
- Kattner, J. and Hoffmann, H. (2002). External reflection spectroscopy of thin films on dielectric substrates. In: *Handbook of Vibrational Spectroscopy*, vol. 2 (eds. J.M. Chalmers and P.R. Griffiths), 1009–1027. Chichester, UK: Wiley <https://doi.org/10.1002/0470027320.s2204>.
- Kissi, N., Curran, K., Vlachou-Mogire, C. et al. (2017). Developing a non-invasive tool to assess the impact of oxidation on the structural integrity of historic wool in Tudor tapestries. *Heritage Science* 5: 49. <https://doi.org/10.1186/s40494-017-0162-1>.
- Korte, E.H. and Roeseler, A. (2005). Infrared reststrahlen revisited: commonly disregarded optical details related to  $n < 1$ . *Analytical and Bioanalytical Chemistry* 382 (8): 1987–1992. <https://doi.org/10.1007/s00216-005-3407-x>.
- Körtum, G. (1969). *Reflectance Spectroscopy: Principles, Methods, Applications*. New York: Springer Verlag.
- Lauwers, D., Hutado, A.G., Tanevska, V. et al. (2014). Characterisation of a portable Raman spectrometer for in situ analysis of art objects. *Spectrochimica Acta Part A: Molecular and Biomolecular Spectroscopy* 118: 294–301. <https://doi.org/10.1016/j.saa.2013.08.088>.
- Lavédrine, B., Fournier, A., and Martin, G. (2012). *Preservation of Plastic Artefacts in Museum Collections*. Paris: Comité Des Travaux Historiques et Scientifiques (CTHS).
- Lazzari, M., Ledo-Suárez, A., López, T. et al. (2011). Plastic matters: an analytical procedure to evaluate the degradability of contemporary works of art. *Analytical and Bioanalytical Chemistry* 399 (9): 2939–2948. <https://doi.org/10.1007/s00216-011-4664-5>.
- Legan, L., Leskovar, T., Črešnar, M. et al. (2020). Non-invasive reflection FTIR characterization of archaeological burnt bones: reference database and case studies. *Journal of Cultural Heritage* 41: 13–26. <https://doi.org/10.1016/j.jculher.2019.07.006>.

- Leung Tang, P., Alqassim, M., Nic Daéid, N. et al. (2016). Nondestructive handheld Fourier transform infrared (FT-IR) analysis of spectroscopic changes and multivariate modeling of thermally degraded plain portland cement concrete and its slag and fly ash-based analogs. *Applied Spectroscopy* 70 (5): 923–931. <https://doi.org/10.1177/0003702816638306>.
- Liang, H., Lucian, A., Lange, R. et al. (2014). Remote spectral imaging with simultaneous extraction of 3D topography for historical wall paintings. *ISPRS Journal of Photogrammetry and Remote Sensing* 95: 13–22. <https://doi.org/10.1016/j.isprsjprs.2014.05.011>.
- Liang, H. (2012). Advances in multispectral and hyperspectral imaging for archaeology and art conservation. *Applied Physics A* 106 (2): 309–323. <https://doi.org/10.1007/s00339-011-6689-1>.
- Lucarini, V., Saarinen, J.J., Peiponen, K.-E. et al. (2005). *Kramers-Kronig Relations in Optical Materials Research*, Springer Series in Optical Sciences, vol. 110. Berlin: Springer.
- Madariaga, J.M. (2015). Analytical chemistry in the field of cultural heritage. *Analytical Methods* 7 (12): 4848–4876. <https://doi.org/10.1039/C5AY00072F>.
- Maguregui, M., Sarmiento, A., Martinez-Arkarazo, I. et al. (2008). Analytical diagnosis methodology to evaluate nitrate impact on historical building materials. *Analytical and Bioanalytical Chemistry* 391 (4): 1361–1370. <https://doi.org/10.1007/s00216-008-1844-z>.
- Manfredi, M., Barberis, E., Rava, A. et al. (2015). Portable diffuse reflectance infrared Fourier transform (DRIFT) technique for the non-invasive identification of canvas ground: IR spectra reference collection. *Analytical Methods* 7 (6): 2313–2322. <https://doi.org/10.1039/C4AY02006E>.
- Miguel, C., Claro, A., Pereira Gonçalves, A. et al. (2009). A study on red lead degradation in a medieval manuscript Lorvão Apocalypse (1189). *Journal of Raman Spectroscopy* 40: 1996–1973. <https://doi.org/10.1002/jrs.2350>.
- Miliani, C., Rosi, F., Daveri, A. et al. (2012). Reflection infrared spectroscopy for the non-invasive in situ study of artists' pigments. *Applied Physics A* 106 (2): 295–307. <https://doi.org/10.1007/s00339-011-6708-2>.
- Miljkovic, M., Bird, B., and Diem, M. (2012). Line shape distortion effects in infrared spectroscopy. *Analyst* 137 (17): 3954–3964. <https://doi.org/10.1039/C2AN35582E>.
- Mosca, S., Frizzi, T., Pontone, M. et al. (2016). Identification of pigments in different layers of illuminated manuscripts by X-ray Fluorescence mapping and Raman spectroscopy. *Microchemical Journal* 124: 775–784. <https://doi.org/10.1016/j.microc.2015.10.038>.
- Nassau, K. (1983). *The Physics and Chemistry of Color, the Fifteen Causes of Color*. New York: Wiley <https://doi.org/10.1002/col.5080120105>.
- Nel, P., Lonetti, C., Lau, D. et al. (2010). Analysis of adhesives used on the Melbourne University Cypriot pottery collection using a portable FTIR-ATR analyzer. *Vibrational Spectroscopy* 53 (1): 64–70. <https://doi.org/10.1016/j.vibspec.2010.01.005>.
- Noake, E., Lau, D., and Nel, P. (2017). Identification of cellulose nitrate based adhesive repairs in archaeological pottery of the University of Melbourne's Middle Eastern archaeological pottery collection using portable FTIR-ATR spectroscopy and PCA. *Heritage Science* 5 (1): 3. <https://doi.org/10.1186/s40494-016-0116-z>.
- Nodari, L. and Ricciardi, P. (2019). Non-invasive identification of paint binders in illuminated manuscripts by ER-FTIR spectroscopy: a systematic study of the influence of different pigments on the binders' characteristic spectral features. *Heritage Science* 7 (1): 7. <https://doi.org/10.1186/s40494-019-0249-y>.
- Ormsby, B., Kampasakali, E., Miliani, C. et al. (2009). An FTIR-based exploration of the effects of wet cleaning treatments on artists' acrylic emulsion paint films. *e-Preservation. Science* 6: 186–195.
- Osticioli, I., Mendes, N.F.C., Nevin, A. et al. (2009). A new compact instrument for Raman, laser-induced breakdown, and laser-induced fluorescence spectroscopy of works of art and their constituent materials. *Review of Scientific Instruments* 80 (7): 076109. <https://doi.org/10.1063/1.3184102>.
- Palomar, T., Grazia, C., Cardoso et al. (2019). Analysis of chromophores in stained-glass windows using Visible Hyperspectral Imaging in-situ. *Spectrochimica Acta Part A: Molecular and Biomolecular Spectroscopy* 223: 117378. <https://doi.org/10.1016/j.saa.2019.117378>.

- Parkin, S.J., Adderley, W.P., Young, M.E. et al. (2013). Near infrared (NIR) spectroscopy: a potential new means of assessing multi-phase earth-built heritage. *Analytical Methods* 5 (18): 4574–4579. <https://doi.org/10.1039/C3AY40735G>.
- Picollo, M., Aldrovandi, A., Migliori, A. et al. (2011). Non-invasive XRF and UV-VIS-NIR reflectance spectroscopic analysis of materials used by Beato Angelico in the manuscript graduate N. 558. *Revista de Historia da Arte, série W* 1: 219–227.
- Picollo, M., Bartolozzi, G., Cucci, C. et al. (2014). Comparative study of Fourier transform infrared spectroscopy in transmission, attenuated total reflection, and total reflection modes for the analysis of plastics in the cultural heritage field. *Applied Spectroscopy* 68 (4): 389–396. <https://doi.org/10.1366/13-07199>.
- Pirzer, M. and Sawatzki, J. (2008). Method and device for correcting a spectrum. US Patent 7, 359,815 B2, filed 21 February 2006 and issued 15 April 2008.
- Pozzi, F., Basso, E., Rizzo, A. et al. (2019). Evaluation and optimization of the potential of a handheld Raman spectrometer: in situ, noninvasive materials characterization in artworks. *Journal of Raman Spectroscopy* 50 (6): 861–872. <https://doi.org/10.1002/jrs.5585>.
- Pouyet, E., Devine, S., Grafakos, T. et al. (2017). Revealing the biography of a hidden medieval manuscript using synchrotron and conventional imaging techniques. *Analytica Chimica Acta* 982: 20–30. <https://doi.org/10.1016/j.aca.2017.06.016>.
- Quye, A., Littlejohn, D., Pethrick, R.A. et al. (2011). Investigation of inherent degradation in cellulose nitrate museum artefacts. *Polymer Degradation and Stability* 96 (7): 1369–1376. <https://doi.org/10.1016/j.polymdegradstab.2011.03.009>.
- Ricciardi, P., Delaney, J.K., Facini, M. et al. (2012). Near infrared reflectance imaging spectroscopy to map paint binders in situ on illuminated manuscripts. *Angewandte Chemie International Edition* 51 (23): 5607–5610. <https://doi.org/10.1002/anie.201200840>.
- Rifkin, R.F., Prinsloo, L.C., Dayet, L. et al. (2016). Characterising pigments on 30 000-year-old portable art from Apollo 11 Cave, Karas Region, southern Namibia. *Journal of Archaeological Science: Reports* 5: 336–347. <https://doi.org/10.1016/j.jasrep.2015.11.028>.
- Rosi, F., Cartechini, L., Monico, L. et al. (2019). Tracking metal oxalates and carboxylates on painting surfaces by non-invasive reflection mid-FTIR spectroscopy. In: *Metal Soaps in Art* (eds. F. Casadio, K. Keune, P. Noble, et al.), 173–193. Cham, Switzerland: Springer [https://doi.org/10.1007/978-3-319-90617-1\\_10](https://doi.org/10.1007/978-3-319-90617-1_10).
- Rosi, F., Daveri, A., Moretti, P. et al. (2016). Interpretation of mid and near-infrared reflection properties of synthetic polymer paints for the non-invasive assessment of binding media in twentieth-century pictorial artworks. *Microchemical Journal* 124: 898–908. <https://doi.org/10.1016/j.microc.2015.08.019>.
- Ruberto, C., Mazzinghi, A., Massi, M. et al. (2016). Imaging study of Raffaello's "La Muta" by a portable XRF spectrometer. *Microchemical Journal* 126: 63–69. <https://doi.org/10.1016/j.microc.2015.11.037>.
- Sarrazin, P., Chiari, G., and Gailhanou, M. (2009). A portable non-invasive XRD-XRF instrument for the study of art objects. *Advances in X-Ray Analysis* 52: 175–186.
- Saviello, D., Toniolo, L., Goidanich, S. et al. (2016). Non-invasive identification of plastic materials in museum collections with portable FTIR reflectance spectroscopy: Reference database and practical applications. *Microchemical Journal* 124: 868–877. <https://doi.org/10.1016/j.microc.2015.07.016>.
- Schrader, B.e. (1995). *Infrared and Raman Spectroscopy: Methods and Applications*. VCH Verlagsgesellschaft <https://doi.org/10.1002/9783527615438>.
- Scudieri, M. and Picollo, M. (2017). Fra Angelico and his circle: the materials and techniques of book illumination. In: *Art and Science (Manuscript in the Making)*, vol. 1 (eds. S. Panayotova and P. Ricciardi), 96–108. London: Harvey Miller Publishers.
- Shashoua, Y. (2009). *Conservation of Plastics – Materials Science, Degradation and Preservation*. Oxford: Elsevier. Reprinted.

- Shreve, P., Cherepy, N.J., and Mathies, R.A. (1992). Effective rejection of fluorescence interference in Raman spectroscopy using a shifted excitation difference technique. *Applied Spectroscopy* 46 (4): 707–711. <https://doi.org/10.1366/0003702924125122>.
- Shugar, A.N. and Mass, J. (eds.) (2012). *Handheld XRF for Art and Archaeology*. Leuven, BE: Leuven University Press.
- Southworth, G. and Trujillo, F. (2016). The coptic bindings collection at the Morgan Library & Museum: history, conservation, and access. *The Book and Paper Group Annual* 35: 89–95.
- Thoury, M., Delaney, J.K., de La Rie, E.R. et al. (2011). Near-infrared luminescence of cadmium pigments: in situ identification and mapping in paintings. *Applied Spectroscopy* 65 (8): 939–951. <https://doi.org/10.1366/11-06230>.
- Toja, F., Saviello, D., Nevin, A. et al. (2012). The degradation of poly(vinyl acetate) as a material for design objects: a multi-analytical study of the effect of dibutyl phthalate plasticizer. Part 1. *Polymer Degradation and Stability* 97 (11): 2441–2448. <https://doi.org/10.1016/j.polymdegradstab.2012.07.018>.
- Trafela, T., Strlič, M., Kolar, J. et al. (2007). Nondestructive analysis and dating of historical paper based on IR spectroscopy and chemometric data evaluation. *Analytical Chemistry* 79 (16): 6319–6323. <https://doi.org/10.1021/ac070392t>.
- Tüzüm Demir, A.P. and Ulutan, S. (2013). Migration of phthalate and non-phthalate plasticizers out of plasticized PVC films into air. *Journal of Applied Polymer Science* 128 (3): 1948–1961. <https://doi.org/10.1002/app.38291>.
- Uhlir, K., Frühmann, B., Buzanich, G. et al. (2012). A newly developed, portable, vacuum-chamber equipped XRF-instrument, designed for the sophisticated needs of the Kunsthistorisches Museum, Vienna. *IOP Conference Series: Materials Science and Engineering* 37: 012008. <https://doi.org/10.1088/1757-899X/37/1/012008>.
- Vandenabeele, P., Castro, K., Hargreaves, M. et al. (2007a). Comparative study of mobile Raman instrumentation for art analysis. *Analytica Chimica Acta* 588 (1): 108–116. <https://doi.org/10.1016/j.aca.2007.01.082>.
- Vandenabeele, P. and Donais, M.K. (2016). Mobile spectroscopic instrumentation in archaeometry research. *Applied Spectroscopy* 70 (1): 27–41. <https://doi.org/10.1177/0003702815611063>.
- Vandenabeele, P., Edwards, H.G.M., and Jehlicka, J. (2014). The role of mobile instrumentation in novel applications of Raman spectroscopy: archaeometry, geosciences, and forensics. *Chemical Society Reviews* 43: 2628–2649. <https://doi.org/10.1039/C3CS60263J>.
- Vandenabeele, P., Edwards, H.G.M., and Moens, L. (2007b). A decade of Raman spectroscopy in art and archaeology. *Chemical Reviews* 107 (3): 675–686. <https://doi.org/10.1021/cr068036i>.
- Vandenabeele, P., Tate, J., and Moens, L. (2007c). Non-destructive analysis of museum objects by fibre-optic Raman spectroscopy. *Analytical and Bioanalytical Chemistry* 387 (3): 813–819. <https://doi.org/10.1007/s00216-006-0758-x>.
- Vandenabeele, P., Weis, T.L., Grant, E.R. et al. (2004). A new instrument adapted to in situ Raman analysis of objects of art. *Analytical and Bioanalytical Chemistry* 379 (1): 137–142. <https://doi.org/10.1007/s00216-004-2551-z>.
- van Oosten, T. (2015). *PUR Facts: Conservation of Polyurethane Foam in Art and Design*. Amsterdam: Amsterdam University Press.
- Vincent, R.K. and Hunt, G.R. (1968). Infrared reflectance from mat surfaces. *Applied Optics* 7 (1): 53–59. <https://doi.org/10.1364/AO.7.000053>.
- Wijsman, S., Neate, S., Kogou, S. et al. (2018). Uncovering the Oppenheimer Siddur: using scientific analysis to reveal the production process of a medieval illuminated Hebrew manuscript. *Heritage Science* 6: 15. <https://doi.org/10.1186/s40494-018-0179-0>.
- Williams, R.S. (1996). On-site non-destructive Mid-IR spectroscopy of plastics in museum objects using a portable FTIR spectrometer with fiber optic probe. *MRS Proceedings* 462: 25–30. <https://doi.org/10.1557/PROC-462-25>.
- Woo, E.M. and Lugito, G. (2015). Origins of periodic bands in polymer spherulites. *European Polymer Journal* 71: 27–60. <https://doi.org/10.1016/j.eurpolymj.2015.07.045>.

## 22

### Portable Spectroscopy for On-Site and In Situ Archaeology Studies

Mary Kate Donais<sup>1</sup> and Peter Vandenabeele<sup>2</sup>

<sup>1</sup>Saint Anselm College, Manchester, NH, USA

<sup>2</sup>Gent University, Gent, Belgium

#### 22.1 Introduction

The technological advances in, and increased availability of, portable instruments has had a significant and positive impact on archaeometry research. Devices such as ground-penetrating radar and global positioning systems (GPS) have been used at archaeological sites for many years, and thus portable measurement devices are familiar both to project directors and research team members. Other more sophisticated measurement techniques, however, have in the past required sample collection and analyses with laboratory-based equipment. Now, with many of those larger instruments shrunk into smaller, portable, and often handheld packages, archaeologists and cultural heritage researchers can easily bring the equipment to the sample, instead of the sample to the equipment.

Advantages to the integration of portable instrument-based measurements for work within the archaeology and cultural heritage fields are many. First and foremost, chemical characterization is now achievable for objects that are impossible to move to a laboratory, and/or cannot be sampled. For some situations sample collection is possible but not preferred, and can therefore now be eliminated through the application of portable techniques. With the time required to plan and execute sample collection removed from the research team's duties, more time is available for well-planned and careful data collection at the site; this can and often does lead to increased confidence in the conclusions drawn from the data.

Certainly, there are some disadvantages to using portable equipment at site. Transportation of the instrument can be challenging, and at times costly. The instrument must be kept secure from theft and damage. Powering the instrument through electrical cords and/or batteries can be difficult depending on the site's infrastructure. Planning archaeometric measurements around other site activities is necessary to maximize the overall work achieved within a research campaign, while also ensuring the safety of personnel. Note that safety is related to both the instrument itself (e.g. use of dosimeters to monitor X-ray radiation exposure), and physical location of the object(s) to be analyzed (e.g. use of a hardhat in a cave, or scaffolding at an elevated height).

This chapter serves as an update to a 2016 review of mobile spectroscopic instrumentation for archaeometry [1]. The chapter content will be limited to only portable applications outside of controlled laboratory settings, and at site locations. Therefore, measurements using portable instruments within a museum setting will not be discussed here; see the chapter by Pozzi (Vol. 2, Chapter 21) for this type of application. The scope of the chapter will instead cover work done at archaeological excavations (both *in situ* and at field labs), and at cultural heritage sites (e.g. buildings, churches, monuments). Specific to the research discussed in this chapter, people are sometimes confused about the terms "nondestructive" and "noninvasive" analyses. Nondestructive investigations refer to studies where the objects or samples are not consumed during the analysis: they are still available for

further investigations with other techniques. One can sample an art object and investigate this sample with several nondestructive techniques. Noninvasive investigations, on the other hand, imply that no sampling is performed or, in other words, the artifacts are analyzed directly. This direct analysis can eventually be performed in situ, which literally means “on site.” For the latter, mobile instrumentation is required. In situ analysis implies that the spectrometer(s) are brought to the artifacts as emphasized in this chapter, instead of transporting the artworks, which is not addressed here.

Measurement techniques covered in our review will include the following: molecular and vibrational spectroscopies – Raman spectroscopy, Fourier transform infrared (FTIR) spectroscopy, fiber optic reflectance spectroscopy (FORS), and diffuse reflectance infrared Fourier transform spectroscopy (DRIFTS); atomic techniques – X-ray fluorescence (XRF) spectrometry and laser-induced breakdown spectroscopy (LIBS); and other less frequently reported techniques such as spectrofluorimetry. The choice of technique(s) for a particular study is largely dictated by the cultural object(s) themselves that are under investigation and the research questions being asked. Molecular and vibrational spectroscopy techniques are applied to characterize compounds within a sample, such as identification of red ochre ( $\text{Fe}_2\text{O}_3$ ) for a red pigment on a wall painting via Raman spectroscopy. Atomic techniques are instead used to characterize elements in a sample; XRF spectrometric detection of Fe for the wall painting pigment example. Using both molecular and atomic instrumental methods within one study can lead to more definitive conclusions when data are in agreement such as in the examples above. Metallic objects such as jewelry made from gold or silver, coins, or lead pipes are best studied via atomic techniques. Characterization of wood, organic pigments (contain no metals), and food residues is instead best addressed through molecular and/or vibrational spectroscopy analyses.

In the 2016 review, a separate section on multi-technique approaches was included. With more and more research teams having ready access to at least two or more mobile instruments for their archaeometry work, many studies in the past five years would be included under the multi-technique umbrella. Therefore, a separate section on multi-technique approaches is not included in this chapter.

The chapter concludes with a case study on construction mortars for a stone tower analyzed via portable X-ray fluorescence spectrometry. The mortar elemental compositions for two different construction phases for the tower are compared to each other, as well as to Roman wall mortars in the region. This case study illustrates the care taken in planning a campaign, documentation of data collection, and the use of chemometrics to group and classify data. The end result is connecting the chemistry to the archaeology, drawing conclusions with a higher confidence that would likely not be possible through archaeology alone.

## 22.2 Molecular and Vibrational Spectroscopic Analysis

Molecular spectroscopic techniques are frequently applied in cultural heritage research; the most frequently applied techniques, using mobile instrumentation, are Raman spectroscopy and infrared spectroscopy.

### 22.2.1 Raman Spectroscopy

Shortly after the introduction of confocal micro-Raman spectroscopy, this technique started to grow to become a widespread approach in the analysis of art objects. The technique has been largely appreciated for its speed of analysis, the ability to obtain molecular spectra at a micrometer scale and – provided the laser power is kept sufficiently low – its nondestructive character [2].

One of the first applications of micro-Raman spectroscopy on artworks was the direct analysis of medieval manuscripts, where a manuscript was positioned under the microscope of a laboratory Raman instrument [3]. However, for large manuscripts this approach was not convenient, and in that period the focus of research was rather on proving the applicability of the method and reducing the sample size [4]. With the introduction of fiber optics probe heads, the direct analysis of large paintings became within reach [5], and thanks to further

miniaturization of the Raman spectrometers, designated mobile Raman instrumentation applicable for archaeometric studies could be developed [6]. Commercial instruments that initially were developed for forensics, pharmaceutical analysis, and even astrobiology [7], were in a later stage adapted for the study of artistic or archaeological objects. This opened the doors to a broad range of archaeometric applications of mobile, portable and handheld Raman instruments [8].

As mobile Raman spectrometers became commercially available, the number of mobile Raman studies rose. These include the direct analysis of precious objects inside museums. For example, a mobile Raman instrument, equipped with a fiber optics probe head, was used to study the blue arsenic and cobalt containing decorations on European porcelain artifacts with the results compared to antique Chinese porcelains [9]. Other research that clearly illustrates the importance of mobile instrumentation includes the direct investigation of wall paintings. Moreover, several studies have been performed on the analysis of rock art. In these cases, the instrumentation had to be brought to places that were often difficult to access.

Not only are many studies aimed at identifying the different artists' materials, many *in situ* research campaigns examine, as well, the degradation under different local influences. As an example, during one campaign, deterioration processes were studied on Patagonian rock art paintings on 16 open-air shelters [10]. Different degradation products were identified and related to the ecological environment present: forests, ecotones, or steppes. Raman spectra were recorded with different laser wavelengths (785 or 532 nm lasers) to deal with interferences caused by fluorescence.

Another recent study [11] revealed how *in situ* Raman spectroscopy can be used to examine salt formation on Pompeian wall paintings. Not only unprotected paintings from rain but also the protected ones were damaged. Even after recent restoration, the salt efflorescence (coating caused by the migration of a salt to the surface of a porous material) returned and was analyzed with Raman spectroscopy. The study helped determine that water entering the building stones from the outside induced the efflorescence on the inside of the building.

The technique can also be applied on (historical) construction materials and their decorations. The *in situ* Raman spectroscopic examination of the marble capitals (the top section of a column) of the Alhambra complex in Granada (Spain), is illustrative for this [12, 13]. This study was not only able to identify degradation products, like tin oxide and weddellite (a mineral form of calcium oxalate), but it was even possible to examine controversial nineteenth century restorations.

It must be said that, when possible, it can be very useful to have two Raman instruments available, equipped with different lasers (i.e. excitation wavelengths). This was for instance the case when studying the corrosion of metallic objects under the influence of marine aerosols [14]. On the one hand, this can help to avoid absorption or interference from fluorescence, while on the other hand this might be of use due to the resonance Raman effect: if the laser wavelength corresponds with the energy of electronic transitions in the analyte molecule, the transition is favored and the resulting Raman signal is very intense. This was clearly observed when analyzing a glyph (a hieroglyphic character or symbol) made of coral in the museum *Quinta das Cruzes* in Funchal (Madeira, Portugal) [15]. When using a red 785 nm laser, the spectrum was dominated by the Raman bands of calcium carbonate; when working in resonance mode using a green (532 nm) laser, however, the spectrum clearly showed the Raman bands of a carotenoid.

Recently, Jehlička [16] made a comparison between the performances of seven mobile Raman spectrometers during fieldwork for the investigation of beryl (mineral of beryllium aluminum cyclosilicate) samples. An approach that was more dedicated toward cultural heritage research was made by Rousaki et al. [17]. We speak of mobile instruments, as they are designed for mobile use [1, 18]. Typically these instruments are equipped with batteries, allowing for fieldwork.

For cultural heritage research, two main instrument design types are distinguished: the portable instruments that typically are equipped with a fiber optics probe head(s), and the smaller handheld instruments. (Portable Raman instrumentation, and the use of SERS with those instruments, is covered by Hargreaves, Vol. 2, Chapter 16.) In many cases, the portable instruments are better suited for these investigations, as the small probe head allows

for focusing on small details. Positioning handheld instruments is often more difficult, and works only for analyzing larger, relatively homogeneous zones. If inhomogeneous areas or small details are involved, it is impossible to know whether detail or inhomogeneity is studied – especially since the laser spot size can typically be sub-millimeter. Moreover, handheld instruments usually do not have the possibility to change objective lenses, and as a consequence the working distance and laser spot size is fixed. Many handheld spectrometers have a fixed focal plane, which corresponds with the instrument touching the object, an approach which is not ideal when analyzing brittle artworks. Generally speaking, the use of fiber optics probe heads is more convenient when analyzing artworks, especially if good-quality positioning equipment is available. Unfortunately, instrument manufacturers tend to pay little attention to the latter, and it seems that it is to the laboratories to set this up.

Recently, a new handheld Raman spectrometer was introduced on the market (Bruker Bravo [19]), which might be of special interest in some cases for cultural heritage research [20–22]. This instrument has at least two favorable properties: it is a dual laser system and it is equipped with the sequentially shifted excitation algorithm [23, 24]. Basically the latter is an effective way of eliminating the fluorescence background by recording a series of spectra with slightly different excitation wavelengths. Next the spectra are subtracted from each other, and the resulting (first derivative) spectra are reconstructed by integrating the curve-fitted spectra. Moreover, the spectra recorded with both lasers are also merged. Although this procedure is very successful in mitigating fluorescence, in some cases artifacts are introduced in the spectra.

One very promising Raman spectroscopy approach for the analysis of cultural heritage is the implementation of surface-enhanced Raman spectroscopy (SERS). By using metallic nanoparticles, it is possible to obtain an intense Raman spectrum, which is especially helpful when studying weak scatterers or fluorescent molecules. The approach has recently been extensively reviewed [25]. Although the approach has been successfully applied in cultural heritage research [26–28], the application of silver nanoparticles directly on the artwork is often a limitation. Most SERS studies are performed on samples, as the application of the silver colloid may stain the artifact. Recently a handheld Raman spectrometer was used for the study of fading felt-tip pen inks [29]. The group was able to identify the organic colorants in a series of commercial inks, as well as in pen ink, used by the celebrated Italian film director Federico Fellini. To develop the SERS effect, it was necessary to leave a drop of Ag nanoparticles on the ink surface. To avoid this, the use of tip-enhanced Raman spectroscopy (TERS) [30] could be a favorable approach, although little has been explored to date. It has been used for the study of indigo and iron gall inks on documents [31]. This approach will likely find more applications in cultural heritage research in the near future.

Spatially offset Raman spectroscopy (SORS), on the other hand, is a technique that allows one to retrieve subsurface Raman signals [32]. The method is based on a spatial offset between the laser source and the analyzed zone; see Hargreaves (Vol. 2, Chapter 16). When moving toward micro-SORS, it is possible to probe layers of a few micrometers thickness, which has successfully been applied for the investigation of cultural heritage [33, 34]. Three possible micro-SORS approaches can be distinguished: full micro-SORS, defocusing micro-SORS, and fiber optics micro-SORS [35–38]. The potential of the technique for mapping the study of overpaintings [39] and mapping experiments [40] has been demonstrated. Probe heads for mobile SORS experiments have been developed [41]. Recently, a promising alternative for probing underlying layers was proposed: frequency offset Raman spectroscopy (FORS) [42], which relies on a material's different scattering properties at different optical wavelengths. Although promising, the setup of the optical pathway is not straightforward.

In many studies on cultural heritage materials, it is of the utmost importance to minimize the (risk of) damage while maximizing the information that can be obtained. Therefore, often complimentary analytical approaches are used together. Raman spectroscopy, being a molecular spectroscopic technique, is frequently combined with an element-specific analytical approach, such as X-ray fluorescence spectroscopy (XRF) [43–47]. A nice overview of the use of complementary analytical techniques for the investigation of wall paintings is given by Costantini et al. [48]. Another example combining Raman spectroscopy with other in situ methods was the research of a precious cork model of the Roman pantheon [49]. In this case, Raman spectroscopy was combined with handheld XRF and different imaging techniques (macrophotography, UV-fluorescence photography, and computed tomography

or CT-scanning) to obtain information on the structure and materials used in this model. The potential of a combination of both techniques for the use in underwater archaeology has been clearly demonstrated [50]: with XRF it is possible to identify the elemental composition of metal artifacts, while Raman spectroscopy is used to study the molecular basis of the corrosion. The combined approach is frequently used for the analysis of building and painting materials on archaeological sites [51, 52], or in a museum context [15]. Next to the combination with XRF, Raman spectroscopy has also been used along with laser-induced breakdown spectroscopy (LIBS) [53–56].

### 22.2.2 Fourier Transform Infrared Spectroscopy (FT-IR)

Infrared reflectography is a well-known approach for imaging the underdrawings and/or other layers below the visual surface in paintings [57, 58], and is usually a broad-band (very low resolution) technique, applied to whole objects in a museum setting. As such, it is not discussed further in this chapter. As an analytical/spectroscopic method in cultural heritage research, FT-IR spectroscopy is frequently used, though mainly when investigating samples (i.e. portions of an object) [59, 60]. A spectral database of natural organic products used in cultural heritage can be of huge interest [61]. An excellent review on the application of infrared spectroscopy for cultural heritage research – in the lab as well as using mobile instrumentation – was recently published [62].

Most modern laboratory infrared instruments use the Fourier transform (FT) technique, and require liquid nitrogen-cooled detectors. One approach to set up the interface between the object of art and the spectrometer is the use of an attenuated total reflection (ATR) crystal. In that case, the ATR crystal is brought into contact with the artifact and the electromagnetic radiation is guided through the crystal. This approach has successfully been applied for the *in situ* analysis of plastics in contemporary art [63]. The same analytical approach has been used for the analysis of objects made of paper [64]. Despite these successes, the need for intimate contact between the probe and the surface of the artifact seems to hamper the wide application of ATR-FTIR. The use of specular reflection FT-IR has been proposed as an alternative approach, and was proven to be successful for the analysis of photographs and other cultural heritage objects [65].

DRIFTS (diffuse reflectance) is also a frequently used spectroscopic approach [66]. DRIFTS applications for archaeology and cultural heritage have increased in recent years and often utilize portable equipment [43]. FORS also is more frequently used within archaeometric research campaigns as evidenced by these examples [67, 68]. A very rare plant extract pigment, folium, was identified in the illustrations of a liturgical book via ultraviolet visible FORS in combination with spectrofluorimetry data [67]. DRIFTS spectroscopy has also been used in combination with a portable LIBS approach to identify mineral pigments [69]. In this book, portable FT-IR instrumentation is described in the chapter by Schiering (Vol. 1, Chapter 3), and its general applications in the chapter by Seelenbinder (Vol. 2, Chapter 11).

Some groups prefer to focus on the near-infrared (NIR) spectral region. The use of NIR spectroscopy in these investigations might be practical but has the disadvantage that the spectra are difficult to interpret, and often require statistical processing. The feasibility of *in situ* visible near-infrared fiber optics reflectance spectrometry (Vis-NIR-FORS), in combination with a statistical approach, has been proven successful for the analysis of restoration products [70].

## 22.3 Atomic Spectroscopic Analysis

### 22.3.1 X-Ray Fluorescence Spectrometry

A common use of portable XRF spectrometry for *in situ* measurements is for pigment identification. Using the well-documented chronology of historic pigments from ancient to modern times, pigments can often be identified with high degrees of confidence via only elemental analysis, and definitively if a molecular technique such as Raman spectroscopy is also used in the study. Pigment analysis typically requires only qualitative evaluation of

spectral data, and thus can be one of the least complex applications of portable XRF spectrometry for cultural heritage work. In addition to pigment identity, previous conservation efforts and environmental damage can often be detected. A number of particularly interesting examples of pigment analyses for archaeology and cultural heritage purposes are described below, with a number of others found in the literature [45, 71, 72].

The polychrome (use of multiple colors) carpentry at the fifteenth-century Casa de Pilatos of Seville was analyzed at over 50 points on doors and ceilings [73]. A number of pigment mixtures were identified such as vermillion (mercuric sulfide) with lead oxide, iron oxides with lead oxide, red ochre (ferric oxide) with orpiment (an arsenic sulfide mineral,  $\text{As}_2\text{S}_3$ )/realgar (another arsenic sulfide mineral,  $\alpha\text{-As}_4\text{S}_4$ , often found together with orpiment), and vermillion with realgar. Environmental effects on pigments were documented: light conversion of orpiment to realgar; blackening of some samples by formation of lead sulfide through reaction with atmospheric hydrosulfuric acid; and conversion of copper carbonate to black copper sulfide, also through reaction with atmospheric hydrosulfuric acid. And the use of a modern green pigment for repaint was observed. Pigments on statues, pottery, and fresco were analyzed by both portable and 2D mapping XRF spectrometry at the ruins of the Villa dei Qunitili [44]. Of particular interest in this study was to compare results for intact fresco to items stored in the excavation warehouse. Various shades of reds, browns, and yellows were verified via 2D mapping, including ochres (a family of earth mineral pigments ranging in color from yellow to purple), with minium (also known as red lead or lead tetroxide), as detected by elevated lead together with iron. Comparisons of this and other data allowed the research team to ascribe the correct original positioning of frescos in the warehouse to specific areas of the villa. Lastly, a sarcophagus in the Sts. Mark, Marcellian, and Damascus catacombs in the San Callisto complex in Rome was analyzed via multiple techniques, including portable XRF spectrometry in an attempt to identify polychromy (the art of painting in many colors) no longer visible by the naked eye [68]. The high humidity, low temperatures, and elevated carbon dioxide levels in the catacombs made these measurements especially challenging for both analysts and instrumentation. Both vermillion and lead white were identified through single spot XRF spectrometry measurements with FORS, and multispectral photography adding significantly to the body of work.

Paper, parchment, and inks are another area of archaeometry research worth noting, with a limited number having been reported in recent years. There is obvious overlap between these studies, and those discussed in the previous paragraph when the paper object is illuminated or contains both text and painted illustrations and decorations. Inks, like pigments, have their own documented history that can be associated with specific time periods and geographic locations. One study of particular note is that by Aceto et al. [67], in which the different hands that contributed to the composition of a fourteenth-century breviary (liturgical book) were evaluated. Through point analyses of the iron gall inks in the *Breviario di San Michele della Chiusa* liturgical book, and subsequent principal component analysis, six different scribes with all but two using partially or fully different inks were identified. The inks used by the *Breviario* scribes also were compared to inks on other regional manuscripts; four of the *Breviario* scribes were identified as likely being from outside the abbey scriptorium.

Rock analysis is another application for portable XRF spectrometry. In some cases the rocks themselves are the specific focus of the work, such as in the case of volcanic rocks for provenance purposes [74], and obsidian igneous rocks used to produce wall mirrors [47]. Or in other instances, the rock material is in the context of rock art with applied pigments. The rock material and rock art at six sites in the Atacama Desert region of Northern Chile were characterized for their elemental makeup [75]. High levels of iron were found in both the pigments and rock, which made identification of the pigment themselves challenging. Arsenic was found in only the pigment areas and not the rocks, which lead the authors to conclude it was in the pigment binder or thinner as arsenic is commonly found in regional waters. Evidence of chemical decomposition from rock weathering and groundwater mobilization in the form of gypsum (calcium sulfate hydrate) exterior coatings was also found. Paleolithic paint palettes in the La Garma Cave (Northern Spain) were explored by both synchrotron and in situ XRF spectrometry measurements [76]. Semiquantitative results were analyzed via principal component analysis to compare pigments in the same color group from different graphical units and galleries to assess artistic phases to the paintings.

Building materials includes mortars, stone, brick, and tiles. Studies on building materials via portable techniques such as XRF spectrometry can have a number of goals including phasing (determining objects that are associated to the same time period) and identification of different material types within one structure [77], documentation of damage, and characterization for conservation purposes among others. In situ measurements, with portable XRF spectrometry together with DRIFTS and Raman spectroscopy, were used to characterize the origin, mechanism, and severity of damage to the Guevara Palace in the village of Segura in Basque Country, northern Spain [43]. No toxic metals pollutants were identified via the study.

Metals, including gilding (application of a thin layer of decorative metal such as gold), are another common application of portable XRF spectrometry, although not without its challenges, due to the corrosion layers and surface contamination often present on metallic objects. (See the chapter by Piorek, Vol. 2, Chapter 19, for a detailed discussion of the analysis of metals by portable XRF spectroscopy.) In the previously discussed Casa de Pilatos study [73], the authors also examined areas of gilding and determined some to be gold, with others to be a copper/zinc brass alloy, or a copper/zinc/lead bronze alloy. Mazzinghi et al. [78] focused only on the gilding of the Crocifissione con Santi at the Dominican Monastery of San Marco in Florence for their study. Data interpretation of the point analyses on five halos was challenged by surface cracks and correct identification of original areas versus previous conservation efforts.  $K_{\alpha}/K_{\beta}$  and  $L_{\alpha}/L_{\beta}$  ratios were used to evaluate signal depths with higher ratios indicative of more shallow layers. Preparation and gilding layers were identified as well as approximate gilding thicknesses. Lastly, archaeological slags (waste separated from metals during the refining process) were prepared and analyzed on site via portable XRF spectrometry to better understand the original ore sources and production techniques, such as technology choice and fuel source [79]. In-house matrix-matched calibration standards were used to generate semiquantitative results. Groupings identified through the at-site analyses agreed with the conclusions drawn from previously collected inductively coupled plasma optical emission spectroscopy data.

### 22.3.2 Laser-Induced Breakdown Spectrometry (LIBS)

LIBS is applied less frequently for in situ field archaeology compared to the more established elemental analysis technique of XRF spectrometry. This is due no doubt to the only more recent availability of commercial portable and handheld LIBS instruments, described in the chapter by Day (Vol. 1, Chapter 13). Considering its shorter analysis times and potential for collecting more data during a field campaign, the use of LIBS may increase in the coming years if it is accepted as a reliable technique for cultural heritage work, despite its micro-destructive nature. Note also that portable XRF cannot be used for low-atomic number elements (typically lighter than silicon), but that LIBS performs well for those elements.

As noted in the previous section, elemental analysis of pigments is common within cultural heritage research, and a number of multi-technique studies that include LIBS for pigment characterization have been reported in recent years. One application of note reported the analyses of painted carved stone doorways at rural churches in Crete [54]. Quick assessment of pigment identities was achieved based on visual color, specific elements present, and the relative strengths of spectral lines paired and verified with Raman data if possible. Of particular interest in this study was the presence of chromium, only detectable in the first laser pulse but not subsequent pulses, likely due to chromium yellow (lead(II) chromate) applied only in a thin layer as an intervention or chromium in a modern restoration adhesive. LIBS and Raman spectroscopy (as noted earlier in the chapter) were also applied to characterize two murals at Pompeii [47]. First, specific pigments on the murals such as red and yellow ochre were verified, along with the mortar binder material as calcium carbonate. A second aspect of this study was to investigate environmental degradation pathways specific to visible damage on the murals, such as the white crusts on the mural surface, identified as solubilization/recrystallization of the mortar binder. Two wall mirrors also found at Pompeii were examined in a multi-technique approach equally incorporating LIBS, Raman spectroscopy, and XRF spectrometry to both identify the mirror materials and better understand environmental damage [46]. LIBS results, supported by Raman results, led to the conclusion that the mirror matrix was obsidian igneous rock.

Calcium and sulfur in white crusts on the mirror were determined to be from past restorations with a filling material containing gypsum that likely underwent a lixiviation/recrystallization process. Yellow crusts, identified as goethite (an iron oxyhydroxide mineral that is part of the ochre family) mixed with gypsum, were instead caused by iron from a different type of filling mortar.

Characterization and laser cleaning of building materials, such as limestones, via LIBS was successfully demonstrated by Senesi et al. [80]. The entrance gate of Castello Svevo (Bari, Italy) showed evidence of environmental pollution as black crusts, cracks, spalling (cracks from water entering the material), corrosion, and fractures. Three different cleaning procedures were evaluated with the LIBS results playing a key role in optimization. In addition, detected elements were determined to be related to soil and dust deposition and atmospheric pollution.

LIBS has also been applied to extreme-conditions archaeology for underwater elemental characterization of archaeological shipwrecks. A multi-pulse LIBS with a handheld probe and main unit connected with a long umbilical cord was developed to operate at depths up to 50 m [81]. Gas delivered through the cord removes water from the sample surface. After concretion (hard outermost) layers were removed from a metal cannon using established protocols, a trained diver used the handheld probe to collect 100 point analyses at five adjacent positions. Iron was verified as the main elemental component of the cannon; effective removal of the concretion was verified by lack of calcium and magnesium signal. Later work by the same group involved development and successful application of a linear discriminant analysis method for the sorting of materials found in a shipwreck by type: alloy, metal, ceramic, or marble [82].

### 22.3.3 Other Analysis Approaches

Spectrofluorimetry [66]: A laser-induced fluorescence system capable of hyperspectral imaging was used to identify previous restoration areas on fresco in a catacombs complex [45]. A collection of multispectral photography techniques including ultraviolet fluorescence, visible-induced luminescence, near infrared, and infrared false colors were used to locate areas of trace pigments and previous conservation treatments on a sarcophagus [67].

## 22.4 Case Study – Characterization of a Multiphased Stone Tower in Monterubliaglio, Umbria (Italy) by Portable X-ray Fluorescence Spectrometry

### 22.4.1 Archaeological Settings

Excavations have been conducted at the Coriglia, Castel Viscardo excavation site (Umbria, Italy) by Saint Anselm College faculty and students under the auspices of the Soprintendenze per I Beni Archeologici dell’Umbria and the Parco Archeologico e Ambientale dell’Orvietano since 2006. Previous archaeometric studies at Coriglia by this research group include examination of mortars [83], fresco pigments [84], glasses [85], and hypocaust and floor tiles [86].

The town of Monterubliaglio is located to the south, and up a significant hill, from Coriglia. Members of the Saint Anselm College excavation team visit Monterubliaglio each day for lunch breaks and casual exploration of the town. A friendly relationship has developed over the years between the town and the excavation participants. A stone tower located in the town square, and shown in Figure 22.1, was the focus of this study; equipment and a researcher collecting data can be seen in the photo. By visual inspection, the tower has two construction phases, one corresponding to the lower portion of the tower from its base to approximately 75 cm in the vertical direction, and the other starting from approximately 75 cm to the tower’s full height. Considering the proximity of Monterubliaglio to Coriglia, it is possible that the tower’s lower construction phase is related to Coriglia. Two goals were put forth for this study: (i) to verify through chemical analyses that the tower is of two construction phases; (ii) to explore whether the lower construction phase is related to construction at Coriglia. Both of these goals were approached



**Figure 22.1** Multi-phased tower in Monterubbiaglio.

using portable XRF spectrometry analyses of the mortars' elemental compositions and statistical evaluation of the resulting data.

#### 22.4.2 The Town and the Tower

The tower was part of the castle that was in the possession of the Monaldeschi della Cervara family from 809 until 1698. The tower itself is documented in titles, as well as management notes kept in the Monaldeschi family archives in the city of Orvieto, beginning in 809. Under the Monaldeschi the tower was repaired 29 times. All repairs indicate repointing of the quoins (masonry blocks at the corner of a wall), as well as around windows. The records indicate that the base of the tower was in good shape in 809 and was recognized as an old Roman tower of unspecified date. The most extensive repair of the tower was reported in 1299, when Cardinal Theudoric received the tower as part of his inheritance and built a defensive wall into the base of the tower, as well as modified the upper portions of it to be suitable to survive a cannonade. He also expanded the piazza at the base of the tower (fundò la torre de Monterubbialio), which would indicate work on the substructure of the tower below its Roman phase. The tower remained untouched until some unspecified repairs noted in 1589. The tower and castle then passed to the current family whose archives are closed to the public. The next major event in its history was during

the Second World War when the castle was bombed by the allies during the 1944 campaign up the Paglia and Tiber valleys. There was substantial damage to the defensive walls, the castle itself, as well as minor damage to the upper portion of the tower, but the lower sections remained intact.

### 22.4.3 Methods

#### 22.4.3.1 Portable X-Ray Fluorescence Spectrometer

The XRF data for this study were collected in two phases: (i) analyses of the upper and lower mortars on the north and west faces of the tower as phase one; (ii) repeat analyses of the upper and lower mortars on the north and west faces of the tower, plus analyses of mortars at the Coriglia and Sant'Ansano excavation sites as phase two. Sant'Ansano is an additional excavation site studied by our research team and is located three kilometers to the north of Coriglia. A Bruker AXS Tracer III-SD (Kennewick, WA) portable energy dispersive XRF spectrometer was used for the first phase of the study; a Bruker AXS Tracer III-V (Kennewick, WA) portable energy dispersive XRF spectrometer was used for the second phase. Both instruments utilize an Rh target X-ray tube excitation source, with a 40 kV maximum voltage and an elliptical spot size of approximately three by four millimeters. The Tracer III-SD has a 10 mm<sup>2</sup> X-Flash silicon drift detector, whereas the Tracer III-V has a Si-PIN diode detector. (See the chapters by Cornaby and Stratilatov, Vol. 1, Chapters 18 and 19 for details of X-ray sources and detectors in these instruments.) Both instruments were operated in the field using rechargeable Li-ion batteries and a laptop for instrument control and data storage. The instrument conditions and data collection settings used with the Tracer III-SD were as follows: fluorescence signal collected for 120 seconds for each analysis with three repeat analyses at each location, 40 kV X-ray tube energy, 21 µA tube current, and the Bruker green filter composed of 0.006 in Cu, 0.001 in Ti, and 0.12 in Al. The instrument conditions and data collection settings used with the Tracer III-V were as follows: fluorescence signal collected for 180 seconds for each analysis with two repeat analyses at each location, 40 kV X-ray tube energy, 8.0 µA tube current, and the Bruker yellow filter composed of 0.001 in Ti and 0.012 in Al.

#### 22.4.3.2 Quality Control and Data Evaluation

Three quality control materials, NIST SRM 1881a Portland Cement, NIST SRM 1886a Portland Cement, and a calcium carbonate sample were analyzed prior to each mortar type, and at periodic intervals within each data set. The control materials data were examined to evaluate changes in instrument signal over time, with minimal drift being observed. Spectral data were exported as .pdz files, corrected for live time using the Bruker S1PXRF software, and then exported as individual .txt files. A Microsoft Excel macro was used to create one spreadsheet for each phase of the study from the individual .txt files. Data from the spreadsheets were imported into The Unscrambler X multivariate data analysis software (Camo Software, Woodbridge, NJ), for evaluation consisting of transposition, derivatization, and principal component analysis (PCA).

#### 22.4.3.3 In Situ Data Collection

Flat and smooth sampling locations on the tower mortar larger than the analyzer spot size were found for each analysis. For the upper mortar, small inclusions were visually observed in the mortar and were avoided as sampling locations so as to improve precision among sampling locations. The sampling locations were cleaned with a plastic brush to remove loose debris, scraped with a trowel if necessary to remove lichen or other contamination, and then brushed clean again. The chosen sampling locations were marked with an arrow, and a digital photograph was taken, as shown in Figure 22.2a for the lower mortar, and Figure 22.2b for the upper mortar, to document the work.

Details pertaining to each analysis location including vertical and horizontal distance on the wall, GPS location, and digital picture number, were recorded on data acquisition sheets in a binder. With the instrument window positioned directly on the cleaned sampling location, the XRF signal was then collected while holding the instrument securely and steadily with both hands. The XRF data file names were then recorded onto the data sheets, and the next analysis location was processed. Data also were collected for the three quality control materials noted



**Figure 22.2** (a) (left) of lower mortar analysis locations marked with arrows and (b) (right) of upper mortar analysis locations.

earlier in the “Methods” section. These analyses were conducted prior to each data set (typically three to four hours of field work), at least once during the analyses, and at the conclusion of the data set so that all mortar data were bracketed; the control material data were then examined for consistency throughout the study sample set to ensure data validity. Additional details pertaining to the in situ data collection protocols used for this study have been reported elsewhere [87].

Two faces of the tower were analyzed for this study, one facing north toward the Coriglia excavation site and the other facing west. Twelve analysis locations on the lower mortar, and twelve locations on the upper mortar, were analyzed on the north face. Five analysis locations on the lower mortar and five locations on the upper mortar were analyzed on the west face. Fewer locations were chosen on the west face due to physical space constraints. As noted earlier, each location was analyzed in triplicate. This provided a total of 51 analyses for each mortar type for a total of 102 analyses.

A reanalysis of the tower mortars was conducted in phase two to verify the phase one results; 6 analysis locations on the lower mortar, and 6 on the upper mortar, were examined on the north and west faces, for a total of 24 locations in duplicate, and 48 analyses total. Analyses were also conducted during phase two on wall mortars at the Coriglia and Sant’Ansano excavation sites, to which the lower tower mortar data were compared. At Sant’Ansano the eastern apse was analyzed at 18 locations and the western apse was analyzed at 13 locations for a total of 31 locations and 62 analyses. At Coriglia, 13 different mortared wall loci (the plural of locus, an archaeology term used to designate a unique documented feature at a site) from 5 different trenches (an archaeology term used to designate an area of excavation at a site) were examined. This provided a total of 55 locations and 110 total analyses at Coriglia.

#### 22.4.4 Results and Discussion

Data for phase one of the tower study were collected on two separate days, one day for each tower face. To ensure no day-to-day bias or tower face bias was introduced into the complete data set, the spectra were first evaluated as four separate data sets – north lower (NL), north upper (NU), west lower (WL), west upper (WU). A fully cross-validated Principal Components Analysis (PCA) was performed with centering and no weighting of the spectral data, and is provided in Figure 22.3. The first three principal components (PCs) accounted for 91.7% of the variance with the two lower mortar data sets (open symbols) clearly overlapping each other, and the two upper mortar data (filled symbols) sets doing the same. Close examination of the scores plot also reveals that north face

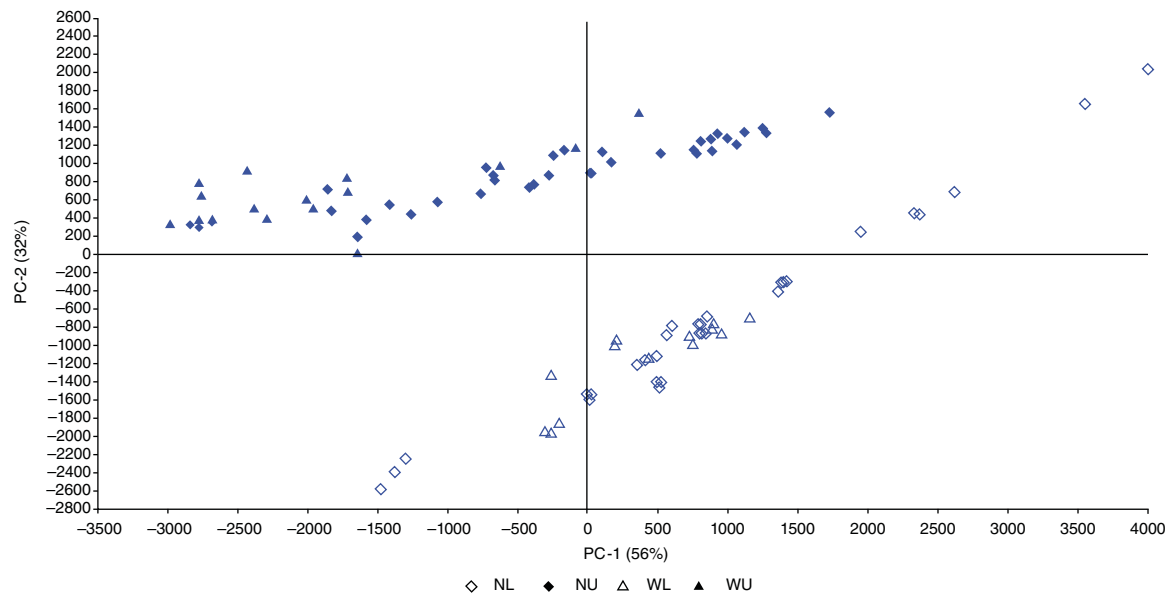


**Figure 22.3** Scores plot of XRF spectral data for the upper and lower mortars on the north and west tower faces.

data (diamonds), and west face data (triangles) are evenly distributed within the lower and upper clusters as well, showing that no elemental differences based on the wall's exposure to weathering have occurred.

Examination of the loadings plot for this PCA model indicated that PC1 is associated with differences in Sr, Rb, and Zr content, PC2 is associated with Mn, Fe, Cu, and Zn differences, and PC3 is associated with Ca differences. These differences can be readily observed in the overlapping spectral plot in Figure 22.4. The lower mortar has a significantly higher signal for Ca, whereas the upper mortar has a slightly higher signal for Fe and significantly higher signals for Sr, Rb, and Zr.

A two-way analysis of variance (ANOVA) with replicates was then performed on the spectral peak areas for the lower and upper mortars. Peak areas for Ca, Cu, Fe, Mn, Pb, Rb, Sr, Zn, and Zr were included in the calculations. A statistically significant difference was found at a 95% confidence ( $F_{\text{crit}} = 7.13$ ,  $F_{\text{table}} = 3.85$ ) for the 32 degrees of freedom indicated for the repeat measurements on the two mortar types. The scores plot resulting from the phase two tower reanalysis was extremely similar to that shown in Figure 22.3 and provided the same conclusions as those made from the phase one study, thus demonstrating reproducibility to our data collection and analysis approaches.

#### 22.4.4.1 Relating This Study to Knowledge of Ancient Mortars

As has been noted by previous researchers [88–92], ancient mortars have been demonstrated to have a great variety of compositions based on geography, application, and time period. The elemental differences observed in the tower's lower mortar and upper mortar, therefore, are not surprising. Mortar is a mixture of binder and aggregate with other possible additions depending on the desired mortar characteristics. The choices and sources of binder, aggregate, and other materials, as well as their relative ratios in the final product contribute to variations in the mortar's overall elemental composition. The three common binder types used in mortars dating up to approximately two hundred years ago are mud, gypsum, and lime. Ancient mortars in Europe are most commonly lime-based [88, 93]. The aggregate materials used in ancient mortars, usually sand and crushed rock, are considerably more diverse in composition due to variability in raw material sources. Additions of pozzolana

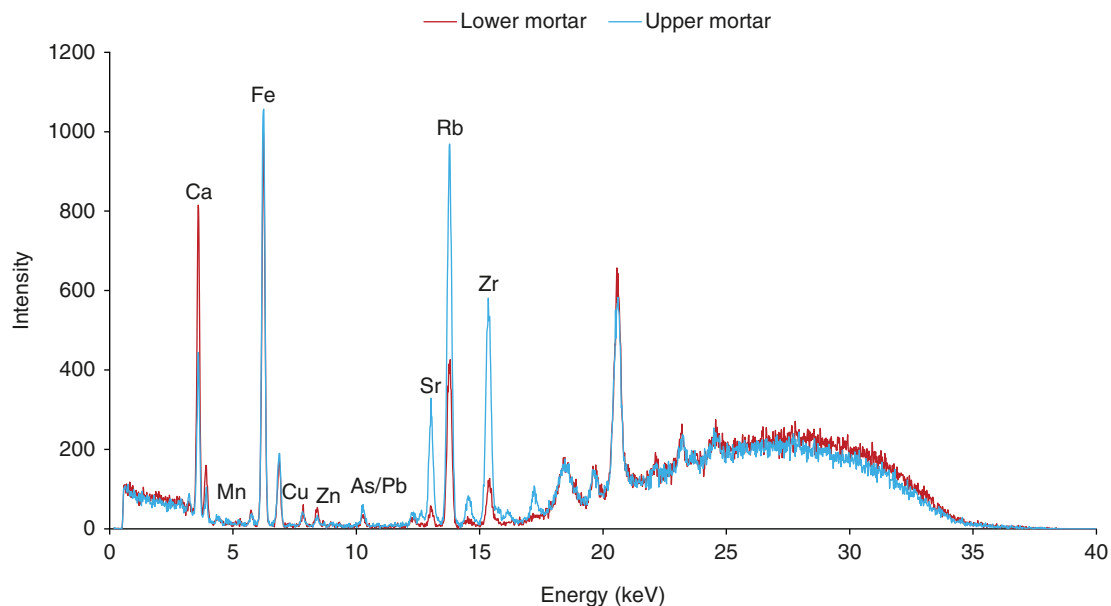


**Figure 22.4** High-voltage XRF spectra of lower mortar and upper mortar.

(a natural siliceous or siliceous-aluminous material) impart hydraulic character to mortar [94–96]. Chemical characterization of mortars are commonly used for age and provenance studies as well as for conservation efforts [91, 93, 97–103].

Calcium is the major component of mortar in various forms such as calcite, dolomite, and gypsum [83] and can account for 26–51% (as CaO) of the elemental composition [104–107]; the elevated calcium signal for the lower tower mortar indicates that non-calcium containing materials were used in higher amounts in the upper mortar, possibly as filler. This is in agreement with our visual observations of small inclusions in the upper mortar. The other elements of significant difference between the two mortars were Sr, Rb, and Zr. Sr and Rb are associated with detritic materials (eroded from rocks) added as aggregates to the mortar, whereas Zr is associated with pelitic (fine-grained sedimentary rock) materials [100].

#### 22.4.4.2 Comparison of Lower Tower Mortars to Coriglia Mortars

The Coriglia excavation site is a multi-phased site, starting in the ninth-century BCE as an iron age settlement, and continuing into the seventeenth-century CE, based on numismatic evidence. The lower portion of the Monterubbiano tower was likely constructed at the same time period as certain portions of Coriglia, particularly a number of the walls uncovered since 2006. Establishment of a relationship between the Coriglia site and the Monterubbiano tower would be of particular interest to our research, in that it would verify interactions among the peoples in this region at that time.

A fully cross-validated PCA was performed with centering and no weighting of the spectral data for the lower tower mortar and Coriglia mortars. The PCA was found to account for 92.4% of the variance within the first three PCs. Significant overlap was observed in the scores plot, shown in Figure 22.5, thus indicating similarities among the mortars at these two sites. As had been observed in phase one of the tower mortar study, elements associated with variance were Ca, Fe, Sr, Rb, Cu, Zn, Zr, and Mn. This wide spread in the Coriglia data points is not surprising, as the wall mortars examined in this study likely span structures built over an approximately four hundred years' time span, and thus would be expected to have considerable compositional variation. The lower tower data

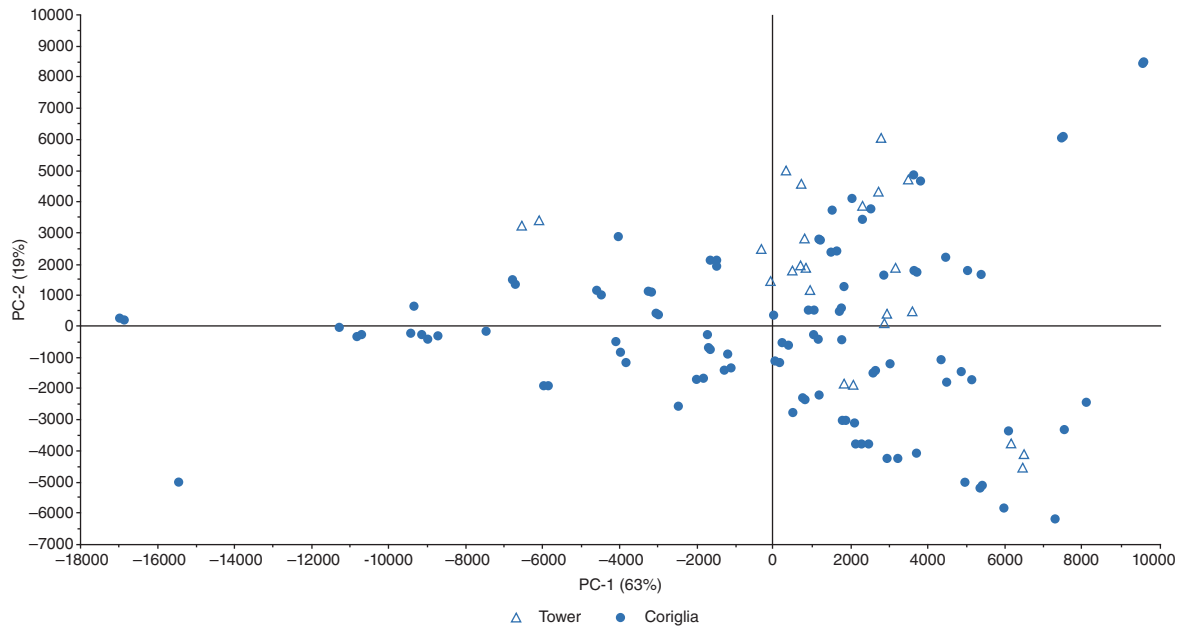


**Figure 22.5** Scores plot of XRF spectral data for the lower tower mortar and wall mortars at Coriglia.

points are clearly integrated throughout a significant portion of the Coriglia data points, allowing one to conclude an association between the two sites.

#### 22.4.4.3 Comparison of Lower Tower Mortars to Sant'Ansano Mortars

The Sant'Ansano excavation site, first explored in 2013 by our team, consists of two apsidal structures that are part of a collapsed church. A comparison was made between the lower tower mortar and the Sant'Ansano apsidal mortars. A fully cross-validated PCA was performed with centering and no weighting of the spectral data and is provided in Figure 22.6. The PCA model accounted for 96.0% of variance within the first three PCs with the same elements accounting for the variance as had been noted earlier. Most of the Sant'Ansano and tower data points are clustered separately, although a few data points appear to be outliers in this trend and overlap into the other group.

#### 22.4.5 Archaeological Implications

This evidence allows for several useful conclusions to be made about the site of Coriglia and provides practical insights into the larger world in which this study is set. Based on the analyzed data, it is now safe to say that the Roman habitation related to the site of Coriglia stretched from the top of the hill down to the site itself. While this may not have been a continuous settlement (further excavation is needed before such a claim can be substantiated), it can be concluded that construction was occurring in both locations simultaneously, using mortar produced from the same sources, and mixed the same way. This indicates that the same workmen were being used for both sites, that the same resources were being exploited for both locations, and that construction projects were happening in a relatively narrow timeframe. Furthermore, the fact that the construction of the lower tower in Monterubiaglio is closely linked to the construction of the major retaining walls at the site of Coriglia demonstrates that there may have been a construction plan that encompassed the entirety of the hillside. This suggests that the construction of the major features of the archaeological site were more intentional and part of a larger plan than previously thought, offering a new area of inquiry for future seasons of excavation.

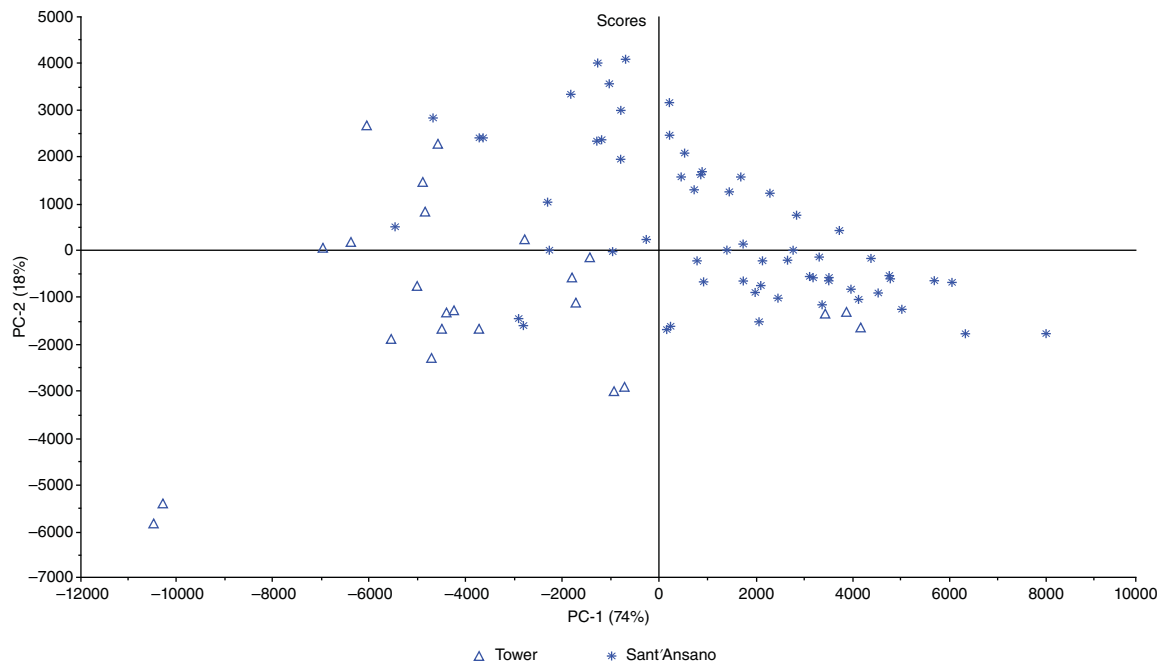


**Figure 22.6** Scores plot of XRF spectral data for the lower tower mortar and wall mortars at Sant'Ansano.

The difference between the upper tower and the mortar at Saint'Ansano can also be easily placed within assumptions that have been made about the region. As the two sites are separated by the River Paglia, which flows through the wide valley dividing these two hilltops, it has always been our assumption that the sites were part of different spheres of influence. These results have demonstrated that despite the proximity of the two sites, the mortar being used at each was made in a different manner and from different sources. As we expected for this period, it appears that these two sites were operating independently when it comes to building projects and resource exploitation. This can be explained by both the natural barriers provided by the geography and the habitation trends of the region. As excavation has revealed at Coriglia, after the sixth-century BCE, the habitation of the hillside began to restrict and retreat up toward the hilltop, mimicking other broader regional trends during this time, and through the time of the construction of the upper tower. This places the construction of the upper tower and the construction of the apse at Saint'Ansano in a period when resources were being focused internally and not externally as is seen in the different types of mortar.

The evidence gained from this study with the use of portable spectrometers has allowed the project to confirm several assumptions about the locations involved. Indeed, it allowed us to confirm that the cultural memory of the inhabitants of Monterubiaglio, who call the tower at the center of their town a Roman tower, is indeed correct. This study was also particularly effective in providing evidence to confirm our understanding of the broad trends at the site of Coriglia and the region as a whole, while also creating opportunities for more detailed research questions in the future.

## 22.5 Conclusions

This overview serves to highlight the influence portable spectroscopy has had in advancing the work conducted by both field archaeologists and cultural heritage researchers. Through the application of noninvasive and

nondestructive analysis, considerable information is gained while also preserving these valuable cultural heritage objects. As noted previously [1], Raman spectroscopy and XRF spectrometry continue to be the most commonly utilized techniques. LIBS is gaining in use, however, as additional commercial portable instruments become available. There is no doubt additional strides will be made in the future as new portable instruments become available with capabilities not yet imagined. The aesthetic beauty of the objects under investigation is appreciated to an even higher degree as we better understand the chemistry underlying their creation.

## Acknowledgements

Data for the Case Study presented in this chapter were collected by students Anthony Desmond and Bradley Duncan with the assistance of students Mariah Tamanaha, Katherine Lunny, Bonnie Etter, and Steve Sarno as participants in the Saint Anselm College field school program near Orvieto, Italy. The program is directed by Dr. David B. George. We would like to thank Bruker AXS for loan of the portable XRF instruments used in the study. We also would like to thank Claudio Bizzarri, Cody Barnett, and the Institute for Mediterranean Archaeology for their ongoing support of our archaeometric research. Lastly, William H. Ramundt (University of Buffalo) contributed significantly to connecting the XRF results to the archaeology at the sites.

## References

- 1 Vandenabeele, P. and Donais, M.K. (2016). Mobile spectroscopic instrumentation in archaeometry research. *Applied Spectroscopy* 70 (1): 27–41.
- 2 Vandenabeele, P., Edwards, H.G.M., and Moens, L. (2007). A decade of Raman spectroscopy in art and archaeology. *Chemical Reviews (Washington, DC, United States)* 107 (3): 675–686.
- 3 Clark, R.J.H. (1995). Raman microscopy: application to the identification of pigments on medieval manuscripts. *Chemical Society Reviews* 24 (3): 187–196.
- 4 Vandenabeele, P., Wehling, B., Moens, L. et al. (1999). Pigment investigation of a late-medieval manuscript with total reflection X-ray fluorescence and micro-Raman spectroscopy. *The Analyst* 124 (2): 169–172.
- 5 Vandenabeele, P., Verpoort, F., and Moens, L. (2001). Non-destructive analysis of paintings using Fourier transform Raman spectroscopy with fibre optics. *Journal of Raman Spectroscopy* 32 (4): 263–269.
- 6 Vandenabeele, P., Weis, T.L., Grant, E.R., and Moens, L.J. (2004). A new instrument adapted to in situ Raman analysis of objects of art. *Analytical and Bioanalytical Chemistry* 379 (1): 137–142.
- 7 Vandenabeele, P., Edwards, H.G.M., and Jehlicka, J. (2014). The role of mobile instrumentation in novel applications of Raman spectroscopy: archaeometry, geosciences, and forensics. *Chemical Society Reviews* 43 (8): 2628–2649.
- 8 Casadio, F., Daher, C., and Bellot-Gurlet, L. (2016). Raman spectroscopy of cultural heritage Materials: overview of applications and new frontiers in instrumentation, sampling modalities, and data processing. *Topics in Current Chemistry* 374 (5): 62.
- 9 Colombar, P., Lu, T.-A., and Milande, V. (2018). Non-invasive on-site Raman study of blue-decorated early soft-paste porcelain: the use of arsenic-rich (European) cobalt ores – comparison with huafalang Chinese porcelains. *Ceramics International* 44 (8): 9018–9026.
- 10 Rousaki, A., Vargas, E., Vázquez, C. et al. (2018). On-field Raman spectroscopy of patagonian prehistoric rock art: pigments, alteration products and substrata. *TrAC, Trends in Analytical Chemistry* 105: 338–351.
- 11 Prieto-Taboada, N., Fdez-Ortiz de Vallejuelo, S., Veneranda, M. et al. (2018). Study of the soluble salts formation in a recently restored house of Pompeii by in-situ Raman spectroscopy. *Scientific Reports* 8 (1): 1613.

- 12** Arjonilla, P., Ayora-Cañada, M.J., Rubio Domene, R. et al. (2019). Romantic restorations in the Alhambra monument: spectroscopic characterization of decorative plasterwork in the Royal Baths of Comares. *Journal of Raman Spectroscopy* 50 (2): 184–192.
- 13** Arjonilla, P., Domínguez-Vidal, A., de la Torre López, M.J. et al. (2016). In situ Raman spectroscopic study of marble capitals in the Alhambra monumental ensemble. *Applied Physics A* 122 (12): 1014.
- 14** Veneranda, M., Aramendia, J., Gomez, O. et al. (2017). Characterization of archaeometallurgical artefacts by means of portable Raman systems: corrosion mechanisms influenced by marine aerosol. *Journal of Raman Spectroscopy* 48 (2): 258–266.
- 15** Lauwers, D., Candeias, A., Coccato, A. et al. (2016). Evaluation of portable Raman spectroscopy and handheld X-ray fluorescence analysis (hXRF) for the direct analysis of glyptics. *Spectrochimica Acta A* 157: 146–152.
- 16** Jehlička, J., Culka, A., Bersani, D., and Vandenabeele, P. (2017). Comparison of seven portable Raman spectrometers: beryl as a case study. *Journal of Raman Spectroscopy* 48 (10): 1289–1299.
- 17** Rousaki, A., Costa, M., Saelens, D. et al. (2019). A comparative mobile Raman study for the on field analysis of the Mosaico de los Amores of the Cástulo Archaeological Site (Linares, Spain). *Journal of Raman Spectroscopy*: 1–11. <https://doi.org/10.1002/jrs.5624>.
- 18** Lauwers, D., Hutado, A.G., Tanevska, V. et al. (2014). Characterisation of a portable Raman spectrometer for in situ analysis of art objects. *Spectrochimica Acta A* 118: 294–301.
- 19** Bruker (Billerica, MA). Bravo handheld Raman spectrometer. <https://www.bruker.com/products/infrared-near-infrared-and-raman-spectroscopy/raman;bravo/overview.html> (accessed 15 November 2020).
- 20** Conti, C., Botteon, A., Bertasa, M. et al. (2016). Portable sequentially shifted excitation Raman spectroscopy as an innovative tool for in situ chemical interrogation of painted surfaces. *The Analyst* 141 (15): 4599–4607.
- 21** Culka, A. and Jehlička, J. (2019). A database of Raman spectra of precious gemstones and minerals used as cut gems obtained using portable sequentially shifted excitation Raman spectrometer. *Journal of Raman Spectroscopy* 50 (2): 262–280.
- 22** Culka, A. and Jehlička, J. (2019). Identification of gemstones using portable sequentially shifted excitation Raman spectrometer and RRUFF online database: a proof of concept study. *The European Physical Journal Plus*. 134 (4): 130.
- 23** Culka, A. and Jehlička, J. (2018). Sequentially shifted excitation: a tool for suppression of laser-induced fluorescence in mineralogical applications using portable Raman spectrometers. *Journal of Raman Spectroscopy* 49 (3): 526–537.
- 24** Shreve, A.P., Cherepy, N.J., and Mathies, R.A. (1992). Effective rejection of fluorescence interference in Raman spectroscopy using a shifted excitation difference technique. *Applied Spectroscopy* 46 (4): 707–711.
- 25** Analytical Methods Committee AN (2017). Surface-enhanced Raman spectroscopy (SERS) in cultural heritage. *Analytical Methods* 9 (30): 4338–4340.
- 26** Ceseratto, A., Leona, M., and Pozzi, F. (2019). Recent advances on the analysis of polychrome works of art: SERS of synthetic colorants and their mixtures with natural dyes. *Frontiers in Chemistry* 7: 105.
- 27** Fazio, A.T., López, M.M., Temperini, M.L.A., and de Faria, D.L.A. (2018). Surface enhanced Raman spectroscopy and cultural heritage biodeterioration: Fungi identification in earthen architecture from Paraíba Valley (São Paulo, Brazil). *Vibrational Spectroscopy* 97: 129–134.
- 28** Shabunya-Klyachkovskaya, E.V., Kulakovich, O.S., and Gaponenko, S.V. (2019). Surface enhanced Raman scattering of inorganic microcrystalline art pigments for systematic cultural heritage studies. *Spectrochimica Acta A* 222: 117235.
- 29** Saviello, D., Di Gioia, A., Turenne, P.-I. et al. (2019). Handheld surface-enhanced Raman scattering identification of dye chemical composition in felt-tip pen drawings. *Journal of Raman Spectroscopy* 50 (2): 222–231.
- 30** Meyer, R., Yao, X., and Deckert, V. (2018). Latest instrumental developments and bioanalytical applications in tip-enhanced Raman spectroscopy. *TrAC, Trends in Analytical Chemistry* 102: 250–258.

- 31** Kurouski, D., Zaleski, S., Casadio, F. et al. (2014). Tip-enhanced Raman spectroscopy (TERS) for in situ identification of indigo and iron gall ink on paper. *Journal of the American Chemical Society* 136 (24): 8677–8684.
- 32** Matousek, P., Clark, I.P., Draper, E.R.C. et al. (2005). Subsurface probing in diffusely scattering media using spatially offset Raman spectroscopy. *Applied Spectroscopy* 59 (4): 393–400.
- 33** Botteon, A., Colombo, C., Realini, M. et al. (2018). Exploring street art paintings by microspatially offset Raman spectroscopy. *Journal of Raman Spectroscopy* 49 (10): 1652–1659.
- 34** Conti, C., Colombo, C., Realini, M., and Matousek, P. (2015). Subsurface analysis of painted sculptures and plasters using micrometre-scale spatially offset Raman spectroscopy (micro-SORS). *Journal of Raman Spectroscopy* 46 (5): 476–482.
- 35** Conti, C., Colombo, C., Realini, M. et al. (2014). Subsurface Raman analysis of thin painted layers. *Applied Spectroscopy* 68 (6): 686–691.
- 36** Conti, C., Realini, M., Colombo, C., and Matousek, P. (2015). Comparison of key modalities of micro-scale spatially offset Raman spectroscopy. *The Analyst* 140 (24): 8127–8133.
- 37** Matousek, P., Conti, C., Realini, M., and Colombo, C. (2016). Micro-scale spatially offset Raman spectroscopy for non-invasive subsurface analysis of turbid materials. *The Analyst* 141 (3): 731–739.
- 38** Vandenabeele, P., Conti, C., Rousaki, A. et al. (2017). Development of a fiber-optics microspatially offset Raman spectroscopy sensor for probing layered materials. *Analytical Chemistry* 89 (17): 9218–9223.
- 39** Botteon, A., Conti, C., Realini, M. et al. (2017). Discovering hidden painted images: subsurface imaging using microscale spatially offset Raman spectroscopy. *Analytical Chemistry* 89 (1): 792–798.
- 40** Rousaki, A., Botteon, A., Colombo, C. et al. (2017). Development of defocusing micro-SORS mapping: a study of a 19th century porcelain card. *Analytical Methods* 9 (45): 6435–6442.
- 41** Realini, M., Botteon, A., Conti, C. et al. (2016). Development of portable defocusing micro-scale spatially offset Raman spectroscopy. *The Analyst* 141 (10): 3012–3019.
- 42** Sekar, S.K.V., Mosca, S., Farina, A. et al. (2017). Frequency offset Raman spectroscopy (FORS) for depth probing of diffusive media. *Optics Express* 25 (5): 4585–4597.
- 43** Gomez-Laserna, O., Arrizabalaga, I., Prieto-Taboada, N. et al. (2015). In situ DRIFT, Raman, and XRF implementation in a multianalytical methodology to diagnose the impact suffered by built heritage in urban atmospheres. *Analytical and Bioanalytical Chemistry* 407 (19): 5635–5647.
- 44** Alberti, R., Crupi, V., Frontoni, R. et al. (2017). Handheld XRF and Raman equipment for the in situ investigation of Roman finds in the Villa dei Quintili (Rome, Italy). *Journal of Analytical Atomic Spectrometry* 32 (1): 117–129.
- 45** Almaviva, S., Fantoni, R., Colao, F. et al. (2018). LIF/Raman/XRF non-invasive microanalysis of frescoes from St. Alexander catacombs in Rome. *Spectrochimica Acta, Part A: Molecular and Biomolecular Spectroscopy* 201: 207–215.
- 46** Veneranda, M., Fdez-Ortiz de Vallejuelo, S., Prieto-Taboada, N. et al. (2018). In-situ multi-analytical characterization of original and decay materials from unique wall mirrors in the House of Gilded Cupids, Pompeii. *Heritage Science* 6 (1): 40.
- 47** Veneranda, M., Prieto-Taboada, N., Fdez-Ortiz de Vallejuelo, S. et al. (2018). In-situ multianalytical approach to analyze and compare the degradation pathways jeopardizing two murals exposed to different environments (Ariadne House, Pompeii, Italy). *Spectrochimica Acta A* 203: 201–209.
- 48** Costantini, I., Castro, K., and Madariaga, J.M. (2018). Portable and laboratory analytical instruments for the study of materials, techniques and environmental impacts in mediaeval mural paintings. *Analytical Methods* 10 (40): 4854–4870.
- 49** Rousaki, A., Pincé, P., Lycke, S. et al. (2019). In situ and laboratory analysis on the polychromy of the Ghent Pantheon cork model by Antonio Chichi. *The European Physical Journal Plus*. 134 (8): 375.

- 50 Estalayo, E., Aramendia, J., Matés Luque, J.M., and Madariaga, J.M. (2019). Chemical study of degradation processes in ancient metallic materials rescued from underwater medium. *Journal of Raman Spectroscopy* 50 (2): 289–298.
- 51 Miriello, D., Bloise, A., Crisci, G.M. et al. (2018). Non-destructive multi-analytical approach to study the pigments of wall painting fragments reused in mortars from the archaeological site of pompeii (Italy). *Minerals*. 8 (4): 134.
- 52 Marcaida, I., Maguregui, M., Morillas, H. et al. (2018). In situ non-invasive characterization of the composition of Pompeian pigments preserved in their original bowls. *Microchemical Journal* 139: 458–466.
- 53 Aramendia, J., Gómez-Nubla, L., Fdez-Ortiz de Vallejuelo, S. et al. (2019). The combination of Raman imaging and LIBS for quantification of original and degradation materials in cultural heritage. *Journal of Raman Spectroscopy* 50 (2): 193–201.
- 54 Papliaka, Z.E., Philippidis, A., Siozos, P. et al. (2016). A multi-technique approach, based on mobile/portable laser instruments, for the in situ pigment characterization of stone sculptures on the island of Crete dating from Venetian and Ottoman period. *Heritage Science* 4: 15/1–8.
- 55 Brysbaert, A., Melessanaki, K., and Anglos, D. (2006). Pigment analysis in bronze age Aegean and Eastern Mediterranean painted plaster by laser-induced breakdown spectroscopy (LIBS). *Journal of Archaeological Science* 33 (8): 1095–1104.
- 56 Giakoumaki, A., Osticioli, I., and Anglos, D. (2006). Spectroscopic analysis using a hybrid LIBS-Raman system. *Applied Physics A* 83 (4): 537–541.
- 57 Alfeld, M. and Broekaert, J.A.C. (2013). Mobile depth profiling and sub-surface imaging techniques for historical paintings—a review. *Spectrochimica Acta B* 88: 211–230.
- 58 France, F.G. (2011). Advanced spectral imaging for noninvasive microanalysis of cultural heritage materials: review of application to documents in the U.S. Library of Congress. *Applied Spectroscopy* 65 (6): 565–574.
- 59 Veneranda, M., Aramendia, J., Bellot-Gurlet, L. et al. (2018). FTIR spectroscopic semi-quantification of iron phases: A new method to evaluate the protection ability index (PAI) of archaeological artefacts corrosion systems. *Corrosion Science* 133: 68–77.
- 60 Sarmiento, A., Pérez-Alonso, M., Olivares, M. et al. (2011). Classification and identification of organic binding media in artworks by means of Fourier transform infrared spectroscopy and principal component analysis. *Analytical and Bioanalytical Chemistry* 399 (10): 3601–3611.
- 61 Invernizzi, C., Rovetta, T., Licchelli, M., and Malagodi, M. (2018). Mid and near-infrared reflection spectral database of natural organic materials in the cultural heritage field. *International Journal of Analytical Chemistry*. 2018: 16.
- 62 Rosi, F., Cartechini, L., Sali, D., and Miliani, C. (2019). Recent trends in the application of Fourier Transform Infrared (FT-IR) spectroscopy in Heritage Science: from micro- to non-invasive FT-IR. *Physical Sciences Reviews* 4: 11.
- 63 Bell, J., Nel, P., and Stuart, B. (2019). Non-invasive identification of polymers in cultural heritage collections: evaluation, optimisation and application of portable FTIR (ATR and external reflectance) spectroscopy to three-dimensional polymer-based objects. *Heritage Science* 7 (1): 95.
- 64 Xia, J., Zhang, J., Zhao, Y. et al. (2019). Fourier transform infrared spectroscopy and chemometrics for the discrimination of paper relic types. *Spectrochimica Acta A* 219: 8–14.
- 65 McClelland, A., Bulat, E., Bernier, B., and Murphy, E.L. (2019). Specular reflection FTIR: a non-contact method for analyzing coatings on photographs and other cultural materials. *Journal of the American Institute for Conservation* 59: 1–14.
- 66 Manfredi, M., Barberis, E., Aceto, M., and Marengo, E. (2017). Non-invasive characterization of colorants by portable diffuse reflectance infrared Fourier transform (DRIFT) spectroscopy and chemometrics. *Spectrochimica Acta A* 181: 171–179.

- 67** Aceto, M., Agostino, A., Fenoglio, G. et al. (2017). Characterisation of the different hands in the composition of a 14th century breviary by means of portable XRF analysis and complementary techniques. *X-Ray Spectrometry* 46 (4): 259–270.
- 68** Iannaccone, R., Bracci, S., Cantisani, E., and Mazzei, B. (2015). An integrated multimethodological approach for characterizing the materials and pigments on a sarcophagus in St. Mark, Marcellian and Damasus catacombs. *Applied Physics A: Materials Science & Processing* 121 (3): 1235–1242.
- 69** Siozos, P., Philippidis, A., and Anglos, D. (2017). Portable laser-induced breakdown spectroscopy/diffuse reflectance hybrid spectrometer for analysis of inorganic pigments. *Spectrochimica Acta, Part B: Atomic Spectroscopy* 137: 93–100.
- 70** Odisio, N., Calabrese, M., Idone, A. et al. (2019). Portable Vis-NIR-FORS instrumentation for restoration products detection: statistical techniques and clustering. *The European Physical Journal Plus*. 134 (2): 67.
- 71** Marutoiu, C., Nica, L., Bratu, I. et al. (2016). The scientific investigation of the imperial gates belonging to Sanmihaiul Almasului wooden church (1816). *Revista de Chimie (Bucharest, Romania)* 67 (9): 1739–1744.
- 72** Calza, C., Oliveira, D.F., Freitas, R.P. et al. (2015). Analysis of sculptures using XRF and X-ray radiography. *Radiation Physics and Chemistry* 116: 326–331.
- 73** Garrote, M.A., Robador, M.D., and Perez-Rodriguez, J.L. (2017). Analytical investigation of Mudéjar polychrome on the carpentry in the Casa de Pilatos palace in Seville using non-destructive XRF and complementary techniques. *Spectrochimica Acta, Part A: Molecular and Biomolecular Spectroscopy* 173: 279–291.
- 74** Richards, M.J. (2019). Realising the potential of portable XRF for the geochemical classification of volcanic rock types. *Journal of Archaeological Science* 105: 31–45.
- 75** Sepulveda, M., Gutierrez, S., Carcamo, J. et al. (2015). In situ X-ray fluorescence analysis of rock art paintings along the coast and valleys of the Atacama Desert, northern Chile. *Journal of the Chilean Chemical Society* 60 (1): 2822–2826.
- 76** Gay, M., Alföld, M., Menu, M. et al. (2015). Palaeolithic paint palettes used at La Garma Cave (Cantabria, Spain) investigated by means of combined in situ and synchrotron X-ray analytical methods. *Journal of Analytical Atomic Spectrometry* 30 (3): 767–776.
- 77** Crupi, V., D'Amico, S., Denaro, L. et al. (2018). Mobile spectroscopy in archaeometry: some case study. *Journal of Spectroscopy* 8295291: 1–11.
- 78** Mazzinghi, A., Giuntini, L., Gelli, N., and Ruberto, C. (2016). XRF study on the gilding technique of the fresco 'Crocifissione con Santi' by Beato Angelico in the San Marco monastery in florence. *X-Ray Spectrometry* 45 (1): 28–33.
- 79** Scott, R.B., Eekelers, K., and Degryse, P. (2016). Quantitative chemical analysis of archaeological slag material using handheld X-ray fluorescence spectrometry. *Applied Spectroscopy* 70 (1): 94–109.
- 80** Senesi, G.S., Carrara, I., Nicolodelli, G. et al. (2016). Laser cleaning and laser-induced breakdown spectroscopy applied in removing and characterizing black crusts from limestones of Castello Svevo, Bari, Italy: a case study. *Microchemical Journal* 124: 296–305.
- 81** Guirado, S., Fortes, F.J., and Laserna, J.J. (2015). Elemental analysis of materials in an underwater archeological shipwreck using a novel remote laser-induced breakdown spectroscopy system. *Talanta* 137: 182–188.
- 82** López-Claros, M., Fortes, F.J., and Laserna, J.J. (2018). Subsea spectral identification of shipwreck objects using laser-induced breakdown spectroscopy and linear discriminant analysis. *Journal of Cultural Heritage* 29: 75–81.
- 83** Donais, M.K., Duncan, B., George, D., and Bizzarri, C. (2010). Comparisons of ancient mortars and hydraulic cements through in-situ analyses by portable X-ray fluorescence spectrometry. *X-Ray Spectrometry* 39: 146–153.
- 84** Donais, M.K., George, D., Duncan, B. et al. (2011). Evaluation of data processing and analysis approaches for fresco pigments by portable X-ray fluorescence spectrometry and portable Raman spectroscopy. *Analytical Methods* 3 (5): 1061–1071.

- 85 Donais, M.K., Van Pevenage, J., Sparks, A. et al. (2016). Characterization of Roman glass tesserae from the Coriglia excavation site (Italy) via energy-dispersive X-ray fluorescence spectrometry and Raman spectroscopy. *Applied Physics A: Materials Science & Processing* 122: 1051–1061.
- 86 Donais, M.K., Duncan, B., Wojtas, S. et al. (2012). Differentiation of hypocaust and floor tiles at coriglia, castel viscardo (Umbria, Italy) using principal component analysis (PCA) and portable X-ray fluorescence (XRF) spectrometry. *Applied Spectroscopy* 66: 1005–1012.
- 87 Donais, M.K. and George, D. (2012). Using portable XRF to aid in phasing, locus comparisons, and material homogeneity assessment at an archaeological excavation. In: *Handheld XRF for Art and Archaeology* (eds. A. Shugar and J. Mass), 349–377. Leuven: Leuven University Press.
- 88 Elsen, J. (2006). Microscopy of historic mortars—a review. *Cement and Concrete Research* 36 (8): 1416–1424.
- 89 Genestar, C., Pons, C., and Mas, A. (2006). Analytical characterization of ancient mortars from the archaeological Roman city of Pollentia (Balearic Islands, Spain). *Analytica Chimica Acta* 557 (1-2): 373–379.
- 90 Mertens, G., Elsen, J., Brulet, R. et al. (2009). Quantitative composition of ancient mortars from the Notre Dame Cathedral in Tournai (Belgium). *Materials Characterization* 60 (7): 580–585.
- 91 Cuevza, S., Garcia-Guinea, J., Fernandez-Cortes, A. et al. (2016). Composition, uses, provenance and stability of rocks and ancient mortars in a Theban Tomb in Luxor (Egypt). *Materials and Structures* 49 (3): 941–960.
- 92 Miriello, D., Bloise, A., Crisci, G.M. et al. (2018). New compositional data on ancient mortars and plasters from Pompeii (Campania - Southern Italy): Archaeometric results and considerations about their time evolution. *Materials Characterization* 146: 189–203.
- 93 Corti, C., Rampazzi, L., Bugini, R. et al. (2013). Thermal analysis and archaeological chronology: The ancient mortars of the site of Baradello (Como, Italy). *Thermochimica Acta* 572 (0): 71–84.
- 94 Oleson, J.P., Bottalico, L., Brandon, C. et al. (2006). Reproducing a Roman maritime structure with Vitruvian pozzolanic concrete. *Journal of Roman Archaeology* 19: 29–52.
- 95 Gotti, E., Oleson, J.P., Bottalico, L. et al. (2008). A comparison of the chemical and engineering characteristics of ancient Roman hydraulic concrete with a modern reproduction of vitruvian hydraulic concrete. *Archaeometry* 50 (4): 576–590.
- 96 Maravelaki-Kalaitzaki, P., Galanos, A., Doganis, I., and Kallithrakas-Kontos, N. (2011). Physico-chemical characterization of mortars as a tool in studying specific hydraulic components: application to the study of ancient Naxos aqueduct. *Applied Physics A: Materials Science & Processing* 104 (1): 335–348.
- 97 Szczepaniak, M., Nawrocka, D., and Mrozek-Wysocka, M. (2008). Applied geology in analytical characterization of stone materials from historical building. *Applied Physics A: Materials Science & Processing* 90 (1): 89–95.
- 98 Vendrell-Saz, M., Alarcon, S., Molera, J., and Garcia-Valles, M. (1996). Dating ancient lime mortars by geochemical and mineralogical analysis. *Archaeometry* 38 (1): 143–149.
- 99 Zacharias, N., Mauz, B., and Michael, C.T. (2002). Luminescence quartz dating of lime mortars. A first research approach. *Radiation Protection Dosimetry* 101 (1-4): 379–382.
- 100 Rampazzi, L., Pozzi, A., Sansonetti, A. et al. (2006). A chemometric approach to the characterisation of historical mortars. *Cement and Concrete Research* 36 (6): 1108–1114.
- 101 Papayianni, I., Pachta, V., and Stefanidou, M. (2013). Analysis of ancient mortars and design of compatible repair mortars: the case study of Odeion of the archaeological site of Dion. *Construction and Building Materials* 40 (0): 84–92.
- 102 Ortega, L.A., Zuluaga, M.C., Alonso-Olazabal, A. et al. (2008). Geochemical characterization of archaeological lime mortars: provenance inputs. *Archaeometry* 50 (3): 387–408.
- 103 Marra, F., D'Ambrosio, E., Gaeta, M., and Mattei, M. (2016). Petrochemical identification and insights on chronological employment of the volcanic aggregates used in ancient Roman mortars. *Archaeometry* 58 (2): 177–200.

- 104** Alvarez, J.I., Navarro, I., and Garcia Casado, P.J. (2000). Thermal, mineralogical and chemical studies of the mortars used in the cathedral of Pamplona (Spain). *Thermochimica Acta* 365 (1-2): 177–187.
- 105** Bruno, P., Calabrese, D., Di Pierro, M. et al. (2004). Chemical-physical and mineralogical investigation on ancient mortars from the archaeological site of Monte Sannace (Bari--Southern Italy). *Thermochimica Acta* 418 (1-2): 131–141.
- 106** Maravelaki-Kalaitzaki, P., Bakolas, A., and Moropoulou, A. (2003). Physico-chemical study of Cretan ancient mortars. *Cement and Concrete Research* 33 (5): 651–661.
- 107** Montoya, C., Lanas, J., Arandigoyen, M. et al. (2004). Mineralogical, chemical and thermal characterisations of ancient mortars of the church of Santa Maria de Irache Monastery (Navarra, Spain). *Materials and Structures* 37 (270): 433–439.

## 23

### The Future of Portable Spectroscopy

*Richard A. Crocombe*

*Crocombe Spectroscopic Consulting, Winchester, MA, USA*

#### 23.1 Introduction

The portable instruments described in these volumes have dramatically increased their capabilities over the past 20 years, while becoming smaller and lighter. On one hand, this is due to all the developments in consumer electronics and computing power, and on the other, to ongoing R&D, manufacturing experience and innovation in the companies producing the instruments, and these enhancements have been described in Volume 1. A continuing trend in these instruments is more precise tailoring of the instrument to the end users' exact needs. This covers every aspect of the instrument; the size, weight, and form factor; the continued shrinking size yet improved performance; the environmental and ruggedness requirements; the user interface and workflow; communications (wireless, Wi-Fi, Bluetooth); GPS (Global Positioning System); data integrity and encryption; algorithms; result reporting, etc. This chapter attempts to look forward to future developments, both instrumental and application, based on the state of the art as of early 2020.

#### 23.2 Optical Spectroscopy

In optical spectroscopy, there is a clear division in both cost and performance between silicon detectors and those used in the near-infrared (typically InGaAs), and in the mid-IR (pyroelectrics and mercury–cadmium–telluride). The very low cost of silicon-based detectors has implications in the devices available, who makes them, whom they are marketed to, and into applications like hyperspectral imaging. As an example, a color matching instrument, operating in the visible region, may retail for \$299; whereas the least expensive near-infrared instrument (1000–1700 nm) will cost upward of \$2000. Therefore, instruments marketed directly to consumers, and embedded in consumer goods, will typically use silicon-based detectors. This has important consequences for their applications, as we will see below; in some cases, consumer devices are attempting to perform analyses in the silicon detector region, which really are not applicable.

Photonic integrated circuits could potentially enable very small sensors and spectrometers, and this field has been summarized from the defense chemical and biological sensing perspective [1].

## 23.3 General Technology Improvements

### 23.3.1 Optical Filters and Array Detectors

Optical filter technology, and its application to portable spectroscopy, has been described in the chapter by Pust (Vol. 1, Chapter 7). In particular, the combination of optical filters and silicon detectors can produce very low-cost and very compact devices [2]. For instance, on their website, **ams** [3], an Austrian sensor and electronics company, describe a “Smart 18-Channel VIS+NIR Spectral ID Sensor with Electronic Shutter.” [4]. This has “18 VIS and NIR channels from 410 nm to 940 nm each with 20 nm FWHM.” For quantity 100, this is offered at \$6.84, so that it would be ideally suited for a consumer product conducting colorimetric-type analyses. Using this type of technology, the company Variable [5] offers a color matching spectrometer (“SPECTRO 1™”) [6], controlled via a smartphone, and accessing a database of paint colors from the major manufacturers. This is a good example of a specifically targeted product, performing one type of measurement only, with an associated database, and which gives very specific answers: the names and numbers of matching paints (as well as CIE and RGB data, and a graphical spectrum). Another vendor in this space, Ocean Insight, in their Pixelteq product line, offers a filter-based sensor with eight wavelength selective photodiodes in a  $9 \times 9$  mm array format, configurable in the silicon detector region [7]. One version is optimized for polymerase chain reaction (PCR) testing at the point-of-care (PoC). These are both advertised on the web as being “from \$195.” We can expect many more complete commercial products based on this type of technology, priced for the individual consumer, or incorporated in consumer products.

Ocean Insight also offers a mid-infrared spectrometer, OCEANMZ5 [8], quoted at \$7995 on the website. This instrument is based on the Pyreos PZT (lead zirconate titanate) 128-element, uncooled, piezoelectric detector array [9], in conjunction with a linear variable filter. It covers the range  $5.5\text{--}11 \mu\text{m}$  ( $1818\text{--}909 \text{ cm}^{-1}$ ), with an ATR sample interface, and an effective resolution of  $\sim 75 \text{ cm}^{-1}$  in the center of its range. Again, this illustrates the cost differential between Si-based components and instruments and those used at longer wavelengths.

“trinamiX,” a brand of BASF, developed new-generation lead sulfide (PbS) and lead selenide (PbSe) detectors, using thin-film encapsulation, suitable for surface mounting [10]. These are available as bare chips, in TO cans and as linear arrays. The PbS array operates in the range of  $1\text{--}3 \mu\text{m}$ , and is at the heart of their portable near-infrared spectrometer [11]. See below for a discussion of their analyzer, based on this technology.

As noted above (and in the chapter by Pust), the combination of silicon detector technologies and linear variable filters can produce very compact multispectral imaging instruments. These are discussed in a later section, but one recent example [12] provides single-shot acquisition of 66 spectral channels,  $400 \times 400$  pixels per channel, with a linear spectral sampling over a wavelength range of 450–850 nm. The size of the system is only  $60 \times 60 \times 28 \text{ mm}$ .

Just in these few examples, we can see the pattern laid out in Table 23.1: very low-cost devices available in the silicon detector region, but near-infrared and mid-infrared components and instruments costing at least an order of magnitude more.

### 23.3.2 Light Sources

A compact spectrometer will require a compact light source. Miniature and sub-miniature incandescent (e.g. tungsten-halogen) sources have been used in the past, from suppliers like Gilway [13]. However, a recent development is the availability of a family of near-infrared (650–1050 nm) LED-based light sources from OSRAM [14]. This is aimed at small spectrometers, and the possibility of spectrometers in smartphones.

Quantum cascade lasers (QCLs) promise a very bright, coherent, tunable infrared source. In practice, these have not been adopted rapidly as spectroscopic sources because it has taken some time to recognize their noise characteristics, and the implications for absorption spectroscopy. These noise sources include varying etalons, relative intensity noise (RIN), and speckle [15–17]. In the military and safety and security market areas, there is a clear need for remote chemical sensing and stand-off detection of explosives and related compounds [18, 19],

**Table 23.1** Spectral ranges for optical (absorption and reflectance) instruments, and their detector technologies.

Range	Name	Detector material(s)	Detector types	Molecular spectra based on	Application comments	Relative cost	Comments	Arrays
~400 to ~700 nm	Visible	Silicon	CCD, CMOS	Electronic transitions	Color matching, plant and produce color, blood oxygenation	\$		For example, smartphone cameras
~700 to ~1050 nm	Short-wave near-infrared	Silicon	CCD, CMOS	Some electronic transitions; third and fourth vibrational overtones	Third and fourth vibrational overtone bands significantly weaker and less specific than first and second	\$	Thicker silicon required for good response at longer wavelengths	
~1000 to 1700 nm	Near-infrared	InGaAs	Single point, 1D and 2D arrays	Vibrational overtones	Traditionally used in food, feed, and agriculture	\$\$\$	InGaAs significantly more expensive than Si-based detectors	128-element linear arrays available at reasonable cost
~1200 to 2500 nm	Near-infrared	Extended InGaAs	Single point, 1D and 2D arrays	Vibrational overtones and combinations	Strong water bands; best for dry samples; combination bands more specific than overtones	\$\$\$\$	Detector cooling required	2D arrays very expensive; larger arrays may be export-controlled

Note that in a handheld instrument, detector cooling not only draws power, but also generates internal heat, therefore reducing battery life and requiring thermal dissipation measures.

and both Block Engineering [20–23] and Pendar Technologies [24, 25] have recently developed QCL-based instruments for this application (see chapter by Nelson et al., Vol. 1, Chapter 10). The Block Engineering system uses external-cavity tuned QCLs, whereas Pendar Technologies' instrument is based on a “bar” of QCLs, each operating at a different wavelength [26]. These instruments are designed to be handheld.

There is ongoing work on the development of supercontinuum sources in the near-infrared, and moving to longer wavelengths [27, 28], and although these are not portable at the present time, there are continuing investigations for their applications to spectroscopy [29–33], including in the mid-infrared [34–37].

## 23.4 Raman Spectrometers

The technologies for portable Raman spectrometers have been described in these volumes in the chapters by Creasey and Hargreaves. Despite the improvements in portable Raman instruments over the past 15 years, some challenges remain, and we can look at them in the context of safety and security applications.

Every Raman spectroscopist, no matter what kind of samples he/she deal with, is aware of the potential for fluorescence inference. Excitation at 785 nm has been a good compromise between long-wavelength excitation while still using low-cost, and low-noise, silicon-based detectors. There has been a recent trend to move to 1064 nm excitation, although a penalty is paid in terms of measurement time for comparable signal-to-noise spectra [38]. Deep-UV excitation [39] is intriguing, especially for stand-off detection [40–42], but brings along its own issues, and obviously does not work with glass containers. Various shifted-excitation schemes are also in use [43, 44], and time-gating is commercially available in a laboratory instrument [45]. It is not clear if there is a “best approach,” or what a universal solution, could be.

Stand-off detection is of obvious benefit for the military and other practitioners dealing with potentially explosive or highly toxic materials. Truck- and backpack-mounted instruments have existed for some time [46–49], often using deep-UV excitation [50, 51], which has the benefit of being able to use solar-blind detectors. But this technology is still relatively immature, and has issues related to the lifetime of key components. A handheld spectrometer operating at 830 nm excitation, capable of a one meter stand-off has recently been announced [52, 53], and that represents the first true handheld instrument of this kind.

Using a Raman instrument, sample heating is a concern for potentially explosive samples, and using portable Fourier transform infrared (FT-IR) instrumentation, with diamond ATR sampling, the pressure required to obtain good spectra is also a concern. Sample heating in portable Raman instruments is being addressed in schemes involving motion of the laser spot over the sample [54].

Real-life samples are most often mixtures, and this is tackled with a combination of library and algorithm development [55] (see the chapters by Zhang and Schreyer in this book), aided by improvements in mobile processing power and memory, and also with the possibility of Wi-Fi communications and cloud processing. Finally, examination of a sample contained in packaging is desirable, in areas as different as pharmaceutical incoming raw material inspection, smuggling of contraband into prisons, and detection of potential explosives at airport checkpoints. Spatially offset Raman spectroscopy [56] (see the chapters by Creasey and Hargreaves) can address that issue for many packaging materials (not metals, though!), and other methods have been developed. So although there are still challenges for portable Raman spectroscopy, progress is being made on all fronts.

A remarkable trend in portable Raman instruments is that their size has diminished while the performance (SNR for the same collection time and resolution) has increased. The first-generation portable Raman instruments, typified by the Ahura Scientific TruDefender and TruScan, were based on a reflective Čzerny–Turner design with fiber-coupled components. Second-generation instruments, typified by the Thermo Scientific TruScan RM, eliminated fiber coupling, are significantly smaller, and are more tightly integrated, using free-space optical coupling. These instruments improved the SNR (with the same range and resolution) by about a factor of 5 over their predecessors. Now, there are even smaller instruments, a little larger than a pack of playing cards, with yet improved

SNR, possibly as much as a factor of 10, made possible via transmission grating designs [57, 58]. This leads to the possibility of even smaller instruments in the future – today, a Raman instrument about  $1'' \times 1'' \times 1''$  in size is possible. One other possibility is to use the camera in a cellphone, and a recent paper describes an effort in that area [59]. The project was called “spectrometer on a phone” (SOAP), and was designed using commercial-off-the-shelf (COTS) components. The system measured  $40 \times 40 \times 14$  mm, and was coupled directly to the cellphone detector camera optics. However, it achieved roughly only  $\sim 40\text{ cm}^{-1}$  resolution. Nonetheless, it indicates what is possible today, bearing in mind that some applications may only require low resolution (e.g.  $15\text{ cm}^{-1}$ ) in order to perform a quick screening of a sample in the field.

### 23.4.1 Airport Bottle Liquid Screening

Strictly speaking, this is not a handheld or portable spectroscopy application, but bottle liquid screening (BLS) can use many of the features noted above for portables, including spatially offset Raman spectroscopy, and faces some of the same concerns with fluorescent containers or samples: dark rum is a favorite test sample. Both Smiths Detection [60] and Cobalt Light Systems (now Agilent) [61] have Raman-based systems deployed in airports, and a completely different technology, from CEIA, using a wideband radio frequency (RF) complex impedance measurement, is also used in Europe [62]. For aviation security, every regulatory agency (DHS/TSA in the United States, CAAC in China, ECAC in Europe, DfT in the United Kingdom, and CATSA in Canada) determines what technology can be used within their own airports.

## 23.5 XRF and LIBS

Handheld XRF instruments are based on mature technologies, as can be seen in the chapters on XRF technology in this book. Recent improvements in their X-ray tubes have provided enhanced stability and beam shape and size, and enabled the size of the instruments to be reduced. The overall cost is unlikely to diminish much as the key components, X-ray tubes and detectors, especially silicon drift detectors, are also relatively expensive specialized items, available from only a few vendors. XRF is a better quantitative technique than LIBS via fundamental parameter calculations [63, 64], but requires licensing and operator safety training as an open-beam X-ray source.

LIBS is an emerging, and rapidly developing technique, but is less quantitative, although potentially faster than XRF for simple alloy identification. Although LIBS instruments do not emit ionizing radiation, they do have open-beam lasers, with consequent concerns about eye safety. LIBS addresses light elements (lighter than aluminum and silicon), an area that handheld energy-dispersive XRF (ED-XRF) will never be able to do (due to absorption of the fluorescent X-rays by air, and the dramatic drop in fluorescence yield with decreasing atomic number [65]), and that leads onto niche applications like aluminum alloy identification and lithium mining. The largest alloy market for handheld LIBS instruments is potentially for low levels of carbon in steel; this is inaccessible by handheld XRF, and therefore has been performed using large laboratory OES instruments. The “killer app” for handheld LIBS is a reliable detection limit of 100 ppm carbon (“L-grade” steel) to distinguish it from “H-grade” steel (300–350 ppm C); see the chapter by Day (Vol. 1, Chapter 13) for details. We can expect the performance of handheld LIBS instruments to improve rapidly over the next few years, driven by advances in solid-state lasers, gated detectors and the general experience of designing and manufacturing the instruments.

One recent innovation in handheld X-ray instruments, albeit not spectroscopic, is the introduction of portable backscatter imaging instruments [66–68]. The handheld X-ray imager has obvious applications in the safety and security arena, for instance for the detection of materials hidden in car and truck door panels or tires, or behind drywall.

## 23.6 GC-MS and LC-MS

GC-MS instruments are briefcase-sized and typically weigh around 30 lbs (~14 kg). A good design will be “flow-rate-matched,” just as a good optical design is throughput-matched. In other words, the flow rate in the GC column is matched to the desired operating pressure in the mass spectrometer, which is determined by the pumping speed, and therefore you cannot improve the system performance by changing one component. So shrinking the size of the system as a whole implies changing all the components, which will then have an impact on the number of ions in the mass spectrometer, and hence the signal-to-noise ratio; this in turn implies that we are unlikely to see dramatic changes in these instruments in the near future, absent a new technology being applied. In addition, the physical complexity of these instruments implies a high cost to the user, typically around \$100,000. Even with all the efforts to make these instruments easy to use, the price alone is a barrier to rapid expansion of their use.

Current development efforts, meeting the needs of the military and security sectors, are focused on ease-of-use in the field, the analysis of low-volatility compounds, and improving field sampling techniques [69]. The Novichok chemical agents, used in the Salisbury and Amesbury incidents in the United Kingdom during 2018, fall into the class of “non-traditional agents” (NTAs), and these are typically low-volatility, oily liquids. Field identification of NTAs is clearly high on the agenda. In a more general sense, real-time chemical threat confirmation in the field is required, including the ability to identify chemicals at low levels in aerosol, gas, liquid, and solid phases of matter. It is also worth noting that a field-portable liquid chromatograph is commercially available [70], measuring  $7.9 \times 9.1 \times 12.6$  in. ( $20.1 \times 23.1 \times 32.0$  cm), and weighing 16.0 lbs. (7.26 kg), and the company (Axcent Corp) has recently entered an agreement with Microsaic Systems [71], who has developed a MEMS-based quadrupole mass spectrometer [72], and employed it for liquid chromatography detection [73].

## 23.7 Ion Mobility Spectrometry (IMS) and High-Pressure Mass Spectrometry (HPMS)

In their handheld formats, neither of these techniques currently has a separations front end, so that the resulting spectra have features from all of the species present. IMS is still the dominant technique for explosives detection in aviation security, as it is fast, easy, and sensitive for this application, even though other technologies keep trying to replace it. Current research and development for these instruments focuses on non-radioactive ionization sources, algorithm refinement to minimize false positives, and reduction of their battery requirements by innovative heating approaches. Smiths Detection recently introduced an attachment to the JCAD that enables sampling of solids (for instance fentanyl and NTAs), by adding a front end thermal desorber and repackaging the instrument’s case, not requiring any change to the JCAD hardware itself.

HPMS has become a great tool for hazmat teams, specifically for fentanyl. However, because the instruments from 908 Devices currently do not have a separations front end, there is a steep learning curve for sampling, and learning how to best use the system. There is the possibility of false alarms or false negatives, both highly undesirable in a hazmat operation, which is being addressed by ongoing algorithm and library development. Smiths Detection received an award from the US Department of Defense at the end of 2018 to develop the next-generation Aerosol and Vapor Chemical Agent Detector (AVCAD). The press release states, “Being developed as the next step in miniaturised chemical detection, AVCAD will be able to detect, identify, and use wireless remote alarm capability to report the presence of traditional and advanced threat vapours and aerosols.” This will use the HPMS engine from 908 Devices. AVCAD may eventually replace the current joint chemical agent detector (JCAD) system, and Smiths Detection has shipped more than 91,000 JCAD units over the past 14 years.

## 23.8 NMR (Relaxometry, or Time-Domain NMR)

Nuclear magnetic resonance instruments can be divided into imagers (MRI), spectrometers for chemical shift measurements (conventional NMR), and relaxometers. MRI is beyond the scope of this chapter. A significant number of commercial tabletop and lab spectrometers are available today [74], and these will not be discussed further here (see the chapter by Kizzire, Vol. 1, Chapter 20). Relaxometers (or time-domain NMR) are the third class of NMR instruments, are typically used to analyze moisture and fat in samples. Relaxometers have been commercially available, in compact benchtop formats, for decades from companies like Bruker [75] and Oxford Instruments [76]. With advances in magnet and RF technologies, this type of instrument can be miniaturized, and examples are Bruker's "minispec ProFiler" [77] and Magritek's "NMR-MOUSE." [78]. A new entrant into this field is from Waveguide ("Formula™") [79], which is miniature and battery-powered, and the company's website discusses a wide range of analytical applications from food and lubricants to pharmaceuticals. This appears to be a field that could grow in technology and applications very rapidly.

## 23.9 Hyphenation

As the size of miniature spectrometers continues to shrink, the possibility of small, and portable, instruments implementing more than one technique grows correspondingly. One obvious case is a combined visible-NIR instrument, spanning ~400 to ~1700 nm; at least one such instrument is on the market today [80], and there is a European project for a portable food analyzer of this type [81]. For spectrometer designs employing single-element detectors, several vendors offer "Si over InGaAs" sandwich detectors, providing detection from ~400 to ~1800 nm.

A combined instrument can help overcome problems with individual spectroscopic techniques, for example a combined Raman/FT-IR instrument [82], used for explosives. As noted above, a Raman approach can be problematic due to sample heating (especially for dark or black samples), and an FT-IR approach (using a diamond ATR) is undesirable for pressure-sensitive materials. In the more general case, obtaining data from "orthogonal" techniques (e.g. Raman for molecular analysis and LIBS for elemental analysis) can obviously lead to enhanced data analysis.

There is continuing interest in combining XRF or LIBS with other analytical techniques, especially for planetary exploration: X-ray diffraction (XRD) and XRF [83], Raman and XRF, or Raman and LIBS. There are several groups, in Europe and the United States, working in these areas [84, 85]. Clearly, XRF or LIBS provides the elemental information, and Raman the molecular data. The next year or two should see the launch of both US and European Mars missions, with Raman and LIBS capabilities (see the discussion in the chapter by Edwards, et al, Vol. 1, Chapter 17). The combination of Raman and time-resolved laser-induced fluorescence has also been proposed [86]. Raman spectroscopy and LIBS are the preferred techniques as they can both operate with a considerable working distance (i.e. in stand-off), as opposed to energy-dispersive XRF (ED-XRF), which requires close proximity. Past examples of spectrometers on planetary missions – the ultimate in portable spectroscopy – include a GC-MS instrument on a Viking mission to Mars in the late 1970s [87], and FT-IR instruments on the two Voyager missions [88, 89], launched in late 1970s, continuing on their planetary tours throughout the 1980s [90]. There has also been considerable interest in the development of combined miniature technologies for archeometry, as summarized by Vandenabeele and Donais in 2016 [91], and in Vol. 2, Chapter 22.

The varieties of miniature technologies described in this book may enable a new generation of "hyphenated" instruments [92–94], but not just the separations-spectroscopy techniques described by Hirschfeld 40 years ago, but spectroscopy-spectroscopy techniques, enabling rapid and unequivocal identification of materials in a wide variety of environments. Table 23.2 summarizes some of these developments.

**Table 23.2** Possible portable dual-technology (“hyphenated”) instruments.

Technology 1	Technology 2	Comments	Examples
<b>Molecular</b>	<b>Other physical technique</b>		
Near-infrared	Electrochemical	Commercial product for soil analysis	[95]
Mid-infrared	Solid state	Prototype product for hazardous gases and vapors	[96]
<b>Molecular</b>	<b>Molecular</b>		
UV-visible, or visible	Near-infrared	Commercial products, and European project	[80], [81]
Raman	Mid-infrared	Hazardous solids. Good complementary functional group information. Commercial product	[82]
Raman	Near-infrared	Would both be “point-and-shoot” and NIR would give information where Raman is obscured by fluorescence. Technically possible today	
Mid-infrared	Near-infrared	Would be different optical paths. Minimal additional information. Technically possible today	
Deep UV-Raman	Fluorescence	Signal separated by wavelength in deep UV. Prototype product described in the literature	[97]
<b>Elemental</b>	<b>Molecular</b>		
LIBS	Raman (and/or laser-induced fluorescence)	Many examples aimed toward planetary exploration; also explosives detection and cultural heritage studies	[98–108]
XRF	Raman	Highly synergistic for field geology and minerals	[109]
XRF	X-ray diffraction (XRD)	Commercial product existed, as well as academic prototypes	[110–112]
XRF plus LIBS		LIBS used for light elements; lower-power X-ray tube for transition metals; small wavelength range requirement for LIBS	[113]
XRF	Visible and near-infrared	Identification of artists’ pigments	[114]
<b>Separations</b>	<b>Molecular</b>		
Gas chromatography (GC)	Mass spectrometry	Commercial products exist	[115–118]
Gas chromatography (GC)	Ion mobility spectrometry (IMS)	Commercial lab products exist; portable prototypes described in the literature	[119, 120]
Liquid chromatography (LC)	Mass spectrometry	Becoming feasible with on-chip LC technologies and MEMS MS	[121]

Source: Crocombe [15]. © 2018, SAGE Publications.

## 23.10 Smartphone Spectrometers

As noted by Scheeline (Vol. 1, Chapter 9), smartphones are attractive for portable spectroscopy for numerous reasons: the built-in 2D sensor, computing power, memory, well-understood user interface, compactness, battery-powered, and wide availability. A developer can also make use of the other capabilities or sensors in the

smartphone: time and date, global positioning system (GPS), orientation, even local temperature and weather conditions. From an optical point of view, the availability of the very small wavelength-selective devices described in these volumes enables very compact additions to the smartphone for low-resolution, colorimetric spectroscopy. That being said, the performance of the camera in the smartphone needs to be well understood, and this process is described in detail in a paper by Burggraaff et al [122].

Today, the activity in this area falls into three broad classes: research and development on clinical assays (see the chapter by Algar, Vol. 2, Chapter 10); citizen science applications organized by a scientific body [123]; and individual citizen science. Handheld instruments of this type for clinical assays have started field trials [124]. An example of citizen science project organized by a scientific body was published by Snik et al., and described an integrated smartphone spectropolarimeter developed for observations of atmospheric aerosols [125], where 3187 people made simultaneous measurements, which were compared to standard field instrumentation. That project is now being extended to develop low-cost optical sensors, methods and technologies to support water quality monitoring by regional and national agencies, under the name MONOCLE [126]. The University of Leiden appears to be the leader in this field at present, but it is likely that other universities and institutes will follow down this path. A more individual approach has been taken by the US-based Public Laboratory [127], including offering a \$9 foldable spectrometer addition for a smartphone [128].

## 23.11 Spectrometers Embedded in Consumer Goods

As noted above, spectrometers based on silicon detectors, and technologies like linear variable filters or discrete optical filters, can be very low cost, compact, and rugged. This leads to the possibility of incorporating them into consumer appliances (e.g. “white goods” like refrigerators, washing machines, and ovens) and as an adjunct, or diagnostic assistant, to personal care products. Apart from an altruistic desire to improve products, and a move toward the “smart home,” there are two possible other motivations for large companies to incorporate spectroscopic devices into consumer products: a “halo” effect, enhancing the image of a product; and the “razorblade” strategy of selling hardware at a low cost, and making money on personal care consumables. The latter strategy is used, for instance, with inkjet printers. Here is a selection of recent announcements, not all of which may be final products.

### 23.11.1 Bosch “X-Spect”

At the March 2019 Appliance World Expo in Shanghai, BSH Hausgeräte GmbH (Bosch) formally announced “an innovative laundry scanner based on sensor technology from Spectral Engines, a Finnish innovator of material sensing technologies. The two companies collaborated to create a device called X-Spect, an intelligent connected scanner for recognizing different fabric types and stains at home.” [129, 130].

*X-Spect makes common household decisions easier, safer and more exciting by providing washing and pre-treatment recommendations for any garment or stain type. After scanning the textiles, the wireless device can automatically transfer the recommended settings to BSH’s range of connected washing machines. The secret behind X-Spect is its sensor technology from Spectral Engines that determines which fabrics you are washing, and how best to get rid of any stains.*

Spectral Engines instruments use a scanning Fabry-Pérot filter (see the chapter by Grüger, Vol. 1, Chapter 5), combined with a single-element detector [131]. A typical “engine” covers a few hundred nanometers in the near-infrared region, at a resolution of about 20 nm. The “Home Connect” website states that the product is not available for purchase today.

### 23.11.2 Henkel “SalonLAB”

This was formally announced at the Consumer Electronics Show (CES) in January 2019. The SalonLAB web site [132] gives this description: “A game-changer in hair analysis: the hand-held SalonLab Analyzer measures inner hair condition, moisture level and the current hair color – providing the perfect basis for a truly personalized consultation.” And the press release [133] states, “With the first end-to-end ecosystem of connected devices that measure hair condition as well as hair color and provide hyper-personalized products and services, Henkel Beauty Care and its leading salon brand Schwarzkopf Professional are reinventing the salon experience as we know it. Henkel’s technology takes the guess work out of which products and services are best for each client’s hair by analyzing hair at the molecular level, empowering the consultation process with data-driven insights and producing on-demand, personalized care solutions.”

The device includes a visible camera with a blue LED for illumination, and also a MEMS FT-NIR from Si-Ware NeoSpectra [134].

### 23.11.3 P&G Ventures’ “Opté™”

Although it does not appear to include a spectrometer, it does include photonic components.

The website [135] states, “Opté is comprised of a Precision Wand and Precision Serum that work together to provide immediate coverage and long-term benefits. The Opté Precision Wand consist of four unique, proprietary technologies:

- **Blue LED Scan Lights** maximize contrasts in skin melanin (allowing the camera to see up to 3× more pigmentation than the human eye is capable of perceiving) to detect discolored spots that are not yet noticeable.
- **An Integrated Digital Camera** captures 200 skin images per second, providing approximately 24,000 pictures for analysis with each use.
- **The Minicomputer Precise Color Algorithm** microprocesses 70,000 lines of code to determine the size, shape, and intensity of each skin spot.

**A Micro Serum Jet Printer** with 120 thermal inkjet nozzles each thinner than a human hair, deposits 1,000 Optimizing Serum picoliter (1 billionth of a liter) droplets on each skin spot to achieve precise coverage with 99% less product than alternatives.” *Source: Procter & Gamble, Opté™ Precision Skincare System, April 19. © 2020, PR Newswire Association LLC.*

At the time this chapter was written (April 2020), the opteskin.com website was advertising the starter kit product at \$599, but it was “available soon,” and enquiries were directed to a wait list.

### 23.11.4 BASF Trinamix “Hertzstück™” Future Dining Room

Trinamix is a wholly owned subsidiary of BASF. As noted above, they have developed a new generation of lead salt infrared detectors, both single-point and linear arrays, using thin-film encapsulation, under the name Hertzstück™. From this technology, a handheld analyzer has been developed, a version of which was first shown during the 2018 London Restaurant Festival [136], where they set up a “Future Dining Room,” showcasing the near-infrared-based instrument as a food analyzer, coupled to a smartphone [137]. The detailed design of this instrument [138] has not been disclosed.

### 23.11.5 Sport Watches

Garmin [139] recently announced a sports watch, incorporating both a heart rate monitor and a pulse oximeter (various watch models from ~\$600 to ~\$1150 in the United States) [140]. This is another area we can expect to

expand, and note that skin hydration is a relatively easy near-infrared spectroscopic measurement to make [141]. (Pulse oximeters have traditionally used specific-wavelength LEDs; a stand-alone device for use in the home can be purchased for as little as \$40, and has been recommended for monitoring coronavirus symptoms.)

### 23.11.6 Automotive Odor Detector

A US patent application for “Transportation System Using Odor Preferences” was recently filed by the Ford Motor Company [142]. The intent is for a customer to obtain information about a vehicle he/she intends to use as part of a ride share system: taxi, rental car, or “transportation as a service” system (e.g. Uber). It envisages a sensor in the vehicle which could be spectrometer, a chromatograph, an optical sensor, a metal-oxide semiconductor sensor or electronic nose. Via a smartphone, the customer’s preferences would be recorded within an app, then transmitted to the vehicle’s onboard computer, which would test the odors within the vehicle, comparing them to predetermined thresholds.

## 23.12 Spectrometers Marketed Directly to Consumers

As we have seen above, using low-cost devices (silicon detectors, optical filters), some spectrometers are of low enough cost to be marketed directly to consumers. But what applications are actually possible? Everybody’s ideal would be a Star Trek-style “Tricorder” – a point-and-shoot device capable of instantly analyzing everything. While near-infrared instruments have wide applications for the identification and quantitation of many organic materials [143] those calibrations are not universal, and may only apply, for instance, for one type of vegetable, or one apple cultivar. Possible application areas for spectroscopic devices for consumers, or incorporated in products for consumers, include food, personal fitness, personal care, identification and verification of household items, etc., but each of these would need its own validated calibration or database. Some of these “desired application areas” are listed in Table 23.3.

There is a mismatch between these aspirations and the reality of analytical spectroscopy, especially for low-cost instruments marketed to and operated by nonscientists. This may seem to be an obvious statement to make, but some devices marketed to the general public seem to have been developed by people unfamiliar with fundamental concepts of analytical chemistry like limits of detection and sampling [144]. For instance, some trace detection requirements can only be met by sophisticated laboratory instruments like ICP-MS and GC/MS/MS, while the issues of how to analyze a heterogeneous sample seem to be foreign to some of these developers. However, a desire to sell to consumers leads to straightforward high-level marketing specifications: a low-cost device, a few hundred dollars at most; compact; easy to carry; and easy to use with a familiar user interface. This drives the development toward devices that use silicon-based sensors, and smartphones as their data systems, saving considerable cost and integration effort, with the assumption that “everybody has a phone.”

While there is obviously interest in the general public to be able to analyze materials, including food and medicines, there are numerous significant issues here. The first is whether there is appropriate information in the spectral region covered, most likely the silicon detector region from  $\sim 400$  to  $\sim 1050$  nm. You can obviously match colors, and you can certainly examine classes of compounds like lycopenes and carotenoids in fruits and vegetables. But general food analysis has traditionally used the near infrared, especially the 1000–1700 nm region, where overtone and combination bands are much stronger. Second, foods, in particular, are highly heterogeneous, and laboratory instruments typically employ large sample areas, often combined with sample spinners or integrating spheres for their measurements, whereas portable instrument may only interrogate a 2 mm diameter area, and rely on a contact measurement (i.e. zero working distance). Third, the interrogation of foods using a handheld instrument, especially by an untrained operator, can be highly irreproducible, giving erroneous results, due to issues like distance from the sample, angle of contact, stray light, etc. Fourth, years

**Table 23.3** “Desired applications” for spectrometers marketed directly to consumers.

Application area	Desired information	Comments
Food nutrition	What is it? Amount of fat, protein, and carbohydrate Calorie content Is it fresh?	See chapter in this book by Miseo
Food fraud	Is it genuine?	Probably possible by optical spectroscopy (NIR or Raman) for manufactured products, but note that speciation for meat or fish will typically require DNA-type analyses
Food adulteration	Is it safe? Is it contaminated?	Note that desired detection levels for pathogens, allergens, pesticide and herbicide residues, etc. are orders of magnitude below that achievable by optical spectroscopy.
Fitness	Hydration Oxygenation	Smartwatch capability
Personal care products	Which cosmetics to use? Which hair products to use? Have I enough UV protection?	See section on “Spectrometers Embedded in Consumer Goods”
Identification and verification of household products	What is this? Is it real or counterfeit?	Pharmaceuticals, fabrics, hazardous materials, recycling, gemstones, etc.
Environmental	Is this good for me and/or my children? Is it good for the environment?	Very wide range of materials to be identified, and trace detection desirable
Cannabis	Potency Hemp vs. cannabis CBD oil analysis	Some commercial instruments available, but costing more than \$10,000 Trace analyses not possible using optical spectroscopy

Note that this table does not imply these applications are possible in a handheld format, or in any small analytical instrument.

of experience in the near-infrared community have shown the need for careful and validated calibrations, to eliminate the possibility of accidental correlations when limited sample sets are used, mostly on one type of sample. Fifth, some of these new vendors seem to be relying on “crowd-sourced” data, with the dual questions of the quality of the spectroscopic measurement, and the accuracy of the metadata (identification, or quantitative information). Sixth, there seems to be a lack of understanding about the possible detection limits of optical spectroscopy in the condensed phase, with claims to detect trace amounts – e.g. allergens, pathogens, pesticide and herbicide residues. Finally, there is the question of what portion of the sample is being interrogated: just the surface, or the bulk? With all the issues noted above, and the lack (most likely) of reference analyses, the potential for “garbage-in/garbage out” analyses is extremely high. This list of caveats can go on and on, but suffice it to say this is an area of concern, with the potential to mislead the general public, even with fatal consequences. There is no universal calibration for food! The cannabis and CBD oil analysis markets bear watching, and there is potential for low cost, visible-NIR and Raman spectrometers there, for bulk component analyses (see below). Again, trace analyses for these samples remain the domain of laboratory techniques.

With all that said, there are new companies marketing devices operating in the ~400 to ~1050 nm region directly to the public, and making wide claims about their analytical capabilities. This author has even seen a claim to assay gold using a low-cost visible spectroscopy device, something that is straightforward using handheld or portable XRF, but impossible in the visible region of the spectrum! A recent paper [145], written by authors of chapters in this book, notes that, “*Opportune conditions of the contemporary market promote overly optimistic and aggressive marketing strategies, which may bring the opposite effect. At some point, the customers are likely to attempt to use NIR spectroscopy in unrealistic scenarios and fail therein. The resulting crisis of public trust in this technology may severely harm sales, and thus future development. Such scheme can, however, be avoided if a close cooperation between the vendor companies and research laboratories is maintained.*”

### 23.13 Emerging Applications for Portable Spectrometers

A theme in several chapters in this book has been that “devices drive applications, and applications drive devices”; see Seelenbinder and Robb (Vol. 2, Chapter 11). Therefore, the availability of portable spectrometers, sometimes at low cost, has lead – and is leading – to new applications. Only a few of the possibilities are highlighted here.

The legalization of cannabis in Canada (among other places), and the legalization of hemp in the United States, has spurred a demand for analysis. As noted above, trace analysis (e.g. pesticide and herbicide residues) requires a technique like laboratory GC-MS, trace heavy metals a technique like ICP or ICP-MS [146], and reference analyses of all the components, GC-FID, LC and LC-MS [147]. However, routine analysis of bulk components can be done with a portable optical technique, once the appropriate calibrations are in place [148]. A number of companies now have products in this area, using near-infrared spectroscopy. For instance, on their website, Allied Scientific in Canada offers an analyzer from GemmaCert in Israel [149] for \$3995, with an additional license fee (for a software license and updated calibrations) of \$99 per month. Other near-infrared-based instruments are offered by Sage Analytics [150] and Lightwave Science [151], for instance. Big Sur Scientific [152] uses a different approach, working in the mid-infrared [153], using ATR sampling, and a spectrometer based on Infratec’s scanning Fabry-Pérot filter, integrated with a mid-infrared detector [154]. Hemp has been legalized in the United States with the proviso that it may only legally contain up to 0.3% THC [155, 156], and therefore, for legal purposes, quick discrimination between hemp and cannabis is desirable. This can clearly be achieved using near-infrared spectroscopy, and a university has proposed a method for this using portable Raman spectroscopy [157]. Raman spectroscopy can also be used to characterize CBD oil [158].

Food, feed, and agriculture have been the largest area for applied near-infrared spectroscopy [159], and so it is not surprising to see new instruments and applications in that area, especially with the growing emphasis on “precision agriculture.” One example is Grainsense [160], part of a “SmartFarm” consortium [161], which offers a portable near-infrared spectrometer to analyze protein, moisture, carbohydrates, and oil content from crops, using a Spectral Engines device and sampling via an integrating sphere. A second example is a soil nutrient scanner from Agrocares [162]. Two current initiatives for food assurance are TeakOrigin [163] in the United States, and PhasmaFood [164] in Europe, using broadband visible-NIR spectroscopy, combined with reference analyses, to analyze produce for quality. TeakOrigin’s focus is on giving customers information about the quality of produce in a store today, and working with grocery retailers to improve that quality. PhasmaFood’s focus is on detection of food hazards, spoilage, and food fraud.

The technologies inside portable optical spectrometers – rugged, compact spectrometers, requiring little power, battery-operated, Wi-Fi-enabled, etc. – lend themselves to being adapted for process measurements, where an analyzer may be subject to vibrations, and where it may not be easy to remote an analyzer via optical fibers. Examples of this can be found in the unit processes in pharmaceutical manufacturing like bin blending, wet granulation, fluid bed drying, and pill pressing [165–168]. A variety of small analyzers have been placed on-line over the past 10 years, following the United States Food and Drug Administration’s Process Analytical Technology (PAT) initiative [169]. Ongoing developments include moves toward real-time release and continuous processing, and we can expect to see miniature spectrometers (if not portable spectrometers) employed here [170, 171].

**Table 23.4** Some commercially available small and handheld hyperspectral imagers.

Company	Type	Technology	Range	Web
BaySpec	Snapshot	IMEC sensor	600–1000 nm	<a href="http://www.bayspec.com/spectroscopy/snapshot-hyperspectral-imager/">http://www.bayspec.com/spectroscopy/snapshot-hyperspectral-imager/</a>
ChemImage	Snapshot	LCTF – liquid crystal tunable filter	900–1700 nm	<a href="http://www.chemimage.com/">http://www.chemimage.com/</a>
Corning	Pushbroom	Dispersive	450–950 nm	<a href="https://www.corning.com/au/en/products/advanced-optics/product-materials/spectral-sensing.html">https://www.corning.com/au/en/products/advanced-optics/product-materials/spectral-sensing.html</a>
Cubert	Snapshot	Continuously variable bandpass filter with a lenslet array	450–850 nm	<a href="https://cubert-gmbh.com/product/ultris-20-hyperspectral/">https://cubert-gmbh.com/product/ultris-20-hyperspectral/</a>
Delta Optical	—	LVF manufacturer	Various	<a href="https://www.deltaopticalthinfilm.com/applications/hyperspectral-imaging/">https://www.deltaopticalthinfilm.com/applications/hyperspectral-imaging/</a>
Emberion	—	Graphene and nanocrystalline photonic absorber	400–2200 nm	<a href="https://www.emberion.com/products/">https://www.emberion.com/products/</a>
Headwall	Pushbroom	Dispersive	Typically 400–1000 nm	<a href="http://www.headwallphotonics.com">http://www.headwallphotonics.com</a>
IMEC	Snapshot	Mosaic and tiled	Typically 400–900 nm	<a href="https://www.imec-int.com/en/hyperspectral-imaging">https://www.imec-int.com/en/hyperspectral-imaging</a>
Ocean Insight	Snapshot	Mosaic	Si detector; RGB + NIR	<a href="https://www.oceaninsight.com/products/imaging/multispectral/">https://www.oceaninsight.com/products/imaging/multispectral/</a>
Pacific Advanced Technology	Pushbroom	Multiplex dispersive: four-lenslet (lens + grating) array	3–5 μm	<a href="https://patinc.com/">https://patinc.com/</a>
SENOP	Snapshot	Uses VTT Technology	400–1000 nm	<a href="http://senop.fi/optronics-hyperspectral#hyperspectralCamera">http://senop.fi/optronics-hyperspectral#hyperspectralCamera</a>
Specim	Pushbroom	Dispersive	Various, 400–1000 nm	<a href="http://www.specim.fi/hyperspectral-cameras">http://www.specim.fi/hyperspectral-cameras</a>
Spectral Sciences	Hadamard	MEMS matched filter	~700–1200 nm	<a href="https://www.spectral.com/what-we-do/electro-optical-sensing-and-imaging/spectral-and-temporal-imaging/">https://www.spectral.com/what-we-do/electro-optical-sensing-and-imaging/spectral-and-temporal-imaging/</a>
Stratio	Point-by-point	?	450–1000 nm	<a href="https://beyonsense.io/">https://beyonsense.io/</a>
TruTag/HinaLea	Snapshot	Tunable Fabry-Pérot	450–850 nm	<a href="https://hinaleaimaging.com/#products">https://hinaleaimaging.com/#products</a>
Unispectral	Snapshot	Tunable Fabry-Pérot	400–1000 nm (claim)	<a href="http://www.unispectral.com/">http://www.unispectral.com/</a>
VTT	Snapshot	Tunable Fabry-Pérot	~400–650 nm for cellphone version	<a href="https://www.vttresearch.com/en/ourservices/hyperspectral-technologies">https://www.vttresearch.com/en/ourservices/hyperspectral-technologies</a>

Source: Crocombe [15]. © 2018, SAGE Publications.

## 23.14 Portable Hyperspectral Imaging

The optical technologies described in these volumes can not only be applied for single point spectroscopy, but in many cases can be utilized with two-dimensional sensors for spectroscopic imaging (see the chapters by Pust, Nelson and Laukamp for some details: Vol. 1. Chapters 7 and 10; Vol. 2, Chapter 18). Spectroscopic imaging is a huge field in and of itself, and therefore all that can be done here is to note some of the recently introduced products and described prototypes, and to indicate the directions in which these technologies could lead [172]. The key point is that in the silicon detector spectral region, extremely low-cost hyperspectral sensors are feasible. For instance, at Photonics West 2019, VTT, the Finland research and development institute, described a “cubic inch-sized” imager [173], based on their Fabry–Pérot scanning filter technology [174], covering 650–950 nm, with a  $640 \times 512$  pixel image. The previous year they projected that the cost of goods in volume could be as low as \$15 [175]. A number of articles testify to the possibilities in this area [176–179], and the marketing company Tematys [180] estimated [181] that the sales of hyperspectral instruments will increase from 3600 in 2017 to more than 9000 in 2022. This could be a significant underestimate, given the rapid developments in low-cost instruments. The small size, weight, and power consumption (SWaP) of newer instruments enables them to be mounted on small drones, e.g. quadcopters, as well as being handheld.

Clearly, the applications for hyperspectral imagers are for heterogeneous samples, but these could be applied in a wide variety of situations, from the field to home. Civilian application areas include agriculture, produce ripeness [182], geology and minerals, global change detection, meteorology, etc., and a partial list of possibilities for low-cost and portable imagers is shown in Table 23.5.

Hyperspectral imaging of food has been studied for at least fifteen years [183–185]. Contamination or adulteration of food (e.g. with allergens or pathogens) is a major consumer concern, and the goal may be to detect one

**Table 23.5** Possible application areas for low-cost portable and handheld spectroscopic imaging.

Field	Government	Factory	Retail	Medical	Home and consumer
Precision farming	Precision farming	Mineral processing	Fruit and vegetable	Environmental	Precision farming
Plant and crop health	Plant and crop health	Environmental	Pharmaceutical	Hazardous materials	Plant and crop health
Fruit and vegetable	Environmental	Emissions	—	Narcotics	Fruit and vegetable
Field geology	Emissions	Hazardous materials	—	Pharmaceutical	Environmental
Mining	Hazardous materials	Pharmaceutical	—	Diagnosis	Hazardous materials
Drilling	Safety and security	Chemical	—	Clinical assays	Pharmaceutical
Mineral processing	Airport screening	Composites	—	Surgery	Chemical
Environmental	Law enforcement	Structured materials	—	Tissue oxygenation	Composites
Emissions	Narcotics	Failure analysis	—	Tissue hydration	Structured materials
Hazardous materials	—	Recycling	—	Skin conditions	Recycling
Safety and security	—	—	—	—	Tissue oxygenation
—	—	—	—	—	Tissue hydration
—	—	—	—	—	UV protection
—	—	—	—	—	Skin conditions

small particle in a large sample. In a bulk measurement, the overall proportion of the contaminant may be too small to detect against the spectrum of the bulk material. However, Lewis and co-workers [186] pointed out that the question of detection limits in hyperspectral imaging becomes dependent on particle statistics rather than weight percentage. For instance a  $640 \times 480$  array contains 313,600 pixels, and if one particle of peanut is present, and fits into a pixel, then it could be detected spectroscopically, and the “detection limit” would improve as the number of pixels increases. The detection limit will also depend on the strength of the bands from the contaminant, and this, in turn, depends on the spectral region in which the imager operates. For the visible and near-infrared regions, the band strength drops by about an order of magnitude with each increasing vibrational overtone. Therefore, the lowest-cost hyperspectral imagers, operating in the silicon detector region, and able to detect the third or fourth overtones only, will have significantly poorer detection limits than their counterparts operating at longer wavelengths in the InGaAs detector region. In addition, if the contaminant is homogeneously dispersed, then hyperspectral imaging does not deliver any advantage over single point spectroscopy. There have been a number of studies on particulate contamination on foods [187–193], but there is a considerable time lag between laboratory demonstration and commercial deployment in the field, so it remains to be seen what the utility of very low-cost hyperspectral imagers will be for this application.

### 23.15 Biological Analyzers

This chapter is being written in April 2020, in the midst of the coronavirus pandemic. A recent online article in the Boston Business Journal [194] listed more than two dozen Massachusetts companies that are working on COVID-19 tests and treatments. If we extrapolate that to the whole world, there must be hundreds of companies, institutes, and universities working in this area. It therefore goes without saying that we can expect rapid progress in fast DNA analysis and in virus detection and tests in general. These are references to some very recent papers and announcements [195–199].

### 23.16 Algorithms, Databases, and Calibrations

The challenge of constantly updating a database is most obvious in the case of street narcotics. In the case of opioids, illicit synthetic chemists are creative, and new derivatives have to be obtained by law enforcement before they and their spectra can be added to the database. So it is a constant struggle, and “unknowns” will always be detected. The problem was described in a news magazine article [200], focusing on Thermo Fisher Scientific’s portable Raman spectrometer, the “TruNarc.” This is not just an issue for Thermo: other instrument companies working in this space are facing the same issues [201]. Nonetheless, today, the best general-purpose field analytical tool for this application is a portable Raman spectrometer. With the very powerful (and dangerous) fentanyl derivatives coming onto the street today, possibly in very low concentrations, a mass spectrometry-based portable solution (IMS, HPMS, or GC-MS) may be required.

For portable optical instruments, continuing additions to spectral libraries and improvements in algorithms are significant [202]. In particular, algorithms to determine the components in mixtures are important, and also minimizing false positives and false negatives. For many customers, especially those in regulated industries and law enforcement, fleet management of their instruments is essential so that each instrument is operating with known algorithms, libraries, and related databases. For instruments sold to the general public, the ability to move calibrations and databases from one instrument (with its own wavelength or mass scale and resolution) to another will be increasingly important. There is a large literature on this topic, summarized in a recent review article [203]. Finally, it should be realized that for a well-defined application, a broad spectral range is not always required, nor is particularly high resolution. An application may be proven on a more general purpose instrument, but deployed on one with limited specifications [2].

## 23.17 Conclusions

To sum up, portable and handheld spectroscopy is a rapidly growing area, with instruments spanning the electromagnetic spectrum from the X-ray region to the mid-infrared, and ranging in techniques from GC-MS to NMR relaxometry. Instruments are becoming smaller, lighter, and more capable, and combined spectroscopic techniques are clearly feasible. But manufacturers still have to understand the basic analytical spectroscopy concepts of sampling, heterogeneity, detection limits, signal-to-noise, etc., especially as they apply to instruments sold to the general public. We can expect to see some very small spectrometers, and even hyperspectral imagers, which would be easily “wearable” or capable of being mounted on a drone. As the price and size of these instruments is reduced, they will be incorporated in “white goods” as analyzers, used in the personal care realm, available for “citizen science,” and also sold directly to the general public.

## Acknowledgements

The author acknowledges many useful conversations with his co-editors, Pauline Leary and Brooke Kammrath.

## Acronyms and Abbreviations

ATR	Attenuated total reflectance
AVCAD	Aerosol and vapor chemical agent detector
CAAC	Civil Aviation Administration of China
CATSA	Canadian Air Transport Security Authority
CBD	Cannabidiol
CCD	Charge coupled detector
CES	Consumer Electronics Show
CIE	Commission Internationale de l'Eclairage
CMOS	Complementary metal oxide semiconductor
COTS	Commercial off the shelf
DfT	Department for Transport (UK)
DHS/TSA	Department of Homeland Security/Transportation Security Administration
ECAC	European Civil Aviation Conference
ED-XRF	Energy-dispersive X-ray fluorescence
GC	Gas chromatography
GC-FID	Gas chromatography – flame ionization detector
GC-MS	Gas chromatography – mass spectrometry
HPMS	High-pressure mass spectrometry
ICP-MS	Inductively coupled mass spectrometry
InGaAs	Indium–Gallium–Arsenide
JCAD	Joint chemical agent detector
LC	Liquid chromatography
LED	Light emitting diode
LIBS	Laser-induced breakdown spectroscopy
MEMS	Micro electro mechanical machines
MRI	Magnetic resonance imaging
NIR	Near infrared

NMR	Nuclear magnetic resonance
NTA	Non-traditional agent
OES	Optical emission spectroscopy
PCR	Polymerase chain reaction
PZT	Lead zirconate tantalate
QCL	Quantum cascade laser
RGB	Red green blue
RIN	Relative intensity noise
SNR	Signal-to-noise ratio
TD-NMR	Time-domain nuclear magnetic resonance
THC	Tetrahydrocannabinol
TO	Transistor outline (a form of electronics packaging)
XRF	X-ray fluorescence

## References

- 1 Chandrasekar, R., Lapin, Z.J., Nichols, A. et al. (2018). Photonic integrated circuits for Department of Defense-relevant chemical and biological sensing applications: state-of-the-art and future outlooks. *Optical Engineering* 58 (2): 020901.
- 2 Vunckx, K., Geelen, B., Munoz, V.G., Lee, W., Chang, H., Van Dorpe, P., Tilmans, H.A.C., Nam, S.H., Lambrechts, A. (2020). Towards a miniaturized application-specific Raman spectrometer. Proceedings of SPIE 11421, Sensing for Agriculture and Food Quality and Safety XII, 1142108 (22 April 2020).
- 3 ams (Premstaetten, Austria). "About ams". <https://ams.com/as7265x#tab/shop-now> (accessed 18 April 2020).
- 4 ams (Premstaetten, Austria). "AS7265x Smart Spectral Sensor". <https://ams.com/as7265x#tab/shop-now> (accessed 18 April 2020).
- 5 Variable (Chattanooga, TN, USA). <https://www.variableinc.com/index.html> (accessed 18 April 2020).
- 6 Variable (Chattanooga, TN, USA). "SPECTRO 1™ BY VARIABLE™". <https://www.variableinc.com/spectro.html> (accessed 18 April 2020).
- 7 Ocean Insight (Orlando, FL). PCR Fluorescence Sensor. <https://www.oceaninsight.com/products/imaging/multi-band-sensor/pixelsensor/pcr-fluorescence-sensor/> (accessed 18 April 2020).
- 8 Ocean Insight (Orlando, FL). Mid-IR Spectrometers. <https://www.oceaninsight.com/products/spectrometers/mid-ir/> (accessed 20 April 2020).
- 9 Pyreos (Edinburgh, Scotland). Linear array components – spectrometer on a chip. <https://pyreos.com/linear-arrays> (accessed 18 April 2020).
- 10 trinamiX (Ludwigshafen am Rhein, Germany). trinamiX IR Detectors. <https://trinamix.de/ir-detectors/> (accessed 18 April 2020).
- 11 trinamiX (Ludwigshafen am Rhein, Germany). trinamiX Mobile IR Spectroscopy Solutions. <https://trinamix.de/nir-spectroscopy/mobile-spectroscopy-solution/> (accessed 18 April 2020).
- 12 Hubold, M., Berlich, R., Gassner, C., Brüning, R., Brunner, R. (2018). Ultra-compact micro-optical system for multispectral imaging. *Proceedings of SPIE 10545, MOEMS and Miniaturized Systems XVII*, 105450V (22 February 2018). <https://doi.org/10.1117/12.2295343>.
- 13 Gilway (International Light Technologies, Peabody, MA). Subminiature T-¾ and T-1 NDIR Lamps. <https://www.intl-lighttech.com/specialty-light-sources/subminiature-t-34-and-t-1-ndir-lamps> (accessed 18 April 2020).
- 14 OSRAM (Munich, Germany). Near-Infrared (NIR) Spectroscopy. <https://www.osram.com/os/applications/mobile-competence/mobile-competence-spectroscopy.jsp> (accessed 18 April 2020).
- 15 Crocombe, R.A. (2018). Portable spectroscopy. *Applied Spectroscopy* 72 (12): 1701–1751.

- 16** Schwaighofer, A., Montemurro, M., Freitag, S. et al. (2018). Beyond fourier transform infrared spectroscopy: external cavity quantum cascade laser-based mid-infrared transmission spectroscopy of proteins in the amide i and amide II region. *Analytical Chemistry* 90: 7072–7079.
- 17** Lindner, S. et al. (2020). External cavity quantum cascade laser-based mid-infrared dispersion spectroscopy for qualitative and quantitative analysis of liquid-phase samples. *Applied Spectroscopy* 74: 452–459.
- 18** Miles, J., Muir, M.F., Scully, S.W.J., Hunter, I., McIlroy, C., Cunningham, J.E., Robinson, C.V., Howle, C.R.. (2020). Towards standoff photothermal spectroscopy of CBRNE hazards using an ultra-fast tunable QCL. *Proceedings of SPIE 11416, Chemical, Biological, Radiological, Nuclear, and Explosives (CBRNE) Sensing XXI*, 114160A (24 April 2020). <https://doi.org/10.1117/12.2558085>
- 19** DeWitt, K.. (2020). Key advancements from the SILMARILS program in chemical sensing and hyperspectral imaging. *Proceedings of SPIE 11390, Next-Generation Spectroscopic Technologies XIII*, 113900P (24 April 2020). <https://doi.org/10.1117/12.2559019>
- 20** Block Engineering (Southborough, MA). Welcome to Block Engineering. <http://www.blockeng.com/> (accessed 30 April 2018).
- 21** Kotidis, P., Deutsch, E.R., Goyal, A. (2015). Standoff detection of chemical and biological threats using miniature widely tunable QCLs. *Proceedings of SPIE 9467, Micro- and Nanotechnology Sensors, Systems, and Applications VII*, 94672S (10 June 2015). <https://doi.org/10.1117/12.2178169>.
- 22** Kelley, D.B., Wood, D., Goyal, A.K., Kotidis, P. (2018). High-speed and large-area scanning of surfaces for trace chemicals using wavelength-tunable quantum cascade lasers. *Proceedings of SPIE 10629, Chemical, Biological, Radiological, Nuclear, and Explosives (CBRNE) Sensing XIX*, 1062909 (16 May 2018). <https://doi.org/10.1117/12.2304387>.
- 23** Wood, D., Kelley, D.B., Goyal, A.K., Kotidis, P. (2018). Mid-infrared reflection signatures for trace chemicals on surfaces. *Proceedings of SPIE 10629, Chemical, Biological, Radiological, Nuclear, and Explosives (CBRNE) Sensing XIX*, 1062915 (16 May 2018). <https://doi.org/10.1117/12.2304453>.
- 24** Pendar Technologies (Cambridge, MA). Pendar Technologies home. <http://www.pendartechnologies.com/> (accessed 30 April 2018).
- 25** Witinski, M.F., Blanchard, R., Pfluegl, C. et al. (2018). Portable standoff spectrometer for hazard identification using integrated quantum cascade laser arrays from 6.5 to 11 μm. *Optics Express* 26: 12159–12168.
- 26** Lee, B.G., Belkin, M.A., Pflugl, C. et al. (2009). DFB Quantum Cascade Laser Arrays. *IEEE Journal of Quantum Electronics* 45: 554–565.
- 27** Alfano, R.R. (2016). *The Supercontinuum Laser Source: The Ultimate White Light*, 3rde. New York: Springer.
- 28** Islam, M.N. (2017). Infrared super-continuum light sources and their applications. In: *Raman Fiber Lasers*, Springer Series in Optical Sciences, vol. 207 (ed. Y. Feng), 117–203. Berlin-Heidelberg: Springer International Publishing. Chapter 4.
- 29** Kilgus, J., Müller, P., Moselund, P.M., and Brandstetter, M. (2016). Application of supercontinuum radiation for mid-infrared spectroscopy. *Proceedings of SPIE* 9899: 98990K-1.
- 30** Michaels, C.A., Masiello, T., and Chu, P.M. (2009). Fourier Transform Spectrometry with a Near-Infrared Supercontinuum Source. *Applied Spectroscopy* 63: 538–543.
- 31** Ringsted, T., Dupont, S., Ramsay, J. et al. (2016). Near-infrared spectroscopy using a supercontinuum laser: application to long wavelength transmission spectra of Barley endosperm and oil. *Applied Spectroscopy* 70 (7): 1176–1185.
- 32** Gasser, C., Kilgus, J., Harasek, M. et al. (2018). Enhanced mid-infrared multi-bounce ATR spectroscopy for online detection of hydrogen peroxide using a supercontinuum laser. *Optics Express* 26: 12169–12179.
- 33** Borondics, F., Jossent, M., Sandt, C. et al. (2018). Supercontinuum-based Fourier transform infrared spectro-microscopy. *Optica* 5: 378–381.
- 34** Kilgus, J., Duswald, K., Langer, G., and Brandstetter, M. (2018). Mid-infrared standoff spectroscopy using a supercontinuum laser with compact Fabry-Pérot filter spectrometers. *Applied Spectroscopy* 72: 634–642.

- 35** Liu, Q., Ramirez, J.M., Vakarin, V. et al. (2018). Mid-infrared sensing between 5.2 and 6.6  $\mu\text{m}$  wavelengths using Ge-rich SiGe waveguides. *Optical Materials Express* 8: 1305–1312.
- 36** Moselund, P.M., Bowen, P., Huot, L. et al. (2018). Compact low-power mid-IR supercontinuum for sensing applications. *Proceedings of SPIE* 10540: 105402I.
- 37** Zorin, I., Kilgus, J., Duswald, K. et al. (2020). Sensitivity-enhanced fourier transform mid-infrared spectroscopy using a supercontinuum laser source. *Applied Spectroscopy* 74: 485–493.
- 38** Christesen, S.D., Guicheteau, J.A., Curtiss, J.M., and Fountain, A.W. III, (2016). Handheld dual-wavelength Raman instrument for the detection of chemical agents and explosives. *Optical Engineering* (Bellingham, WA, U. S.) 55: 074103.
- 39** Asher, S.A. (1993). UV Raman spectroscopy. *Analytical Chemistry* 65: 59A-66. and 201A-210A.
- 40** Hug, W.F., Reid, R.D., Bhartia, R., Lane, A.L.. (2009). Performance status of a small robot-mounted or hand-held, solar-blind, standoff chemical, biological, and explosives (CBE) sensor. *Proceedings of SPIE* 7304, *Chemical, Biological, Radiological, Nuclear, and Explosives (CBRNE) Sensing X*, 73040Z (8 May 2009). <https://doi.org/10.1117/12.817881>.
- 41** Tuschel, D.D., Mikhonin, A.V., Lemoff, B.E., and Asher, S.A. (2010). Deep ultraviolet resonance Raman excitation enables explosives detection. *Applied Spectroscopy* 64: 425–432.
- 42** Hopkins, A.J., Cooper, J.L., Profeta, L.T.M., and Ford, A.R. (2016). Portable deep-ultraviolet (DUV) Raman for standoff detection. *Applied Spectroscopy* 70: 861–873.
- 43** Shreve, A.P., Cherepy, N.J., and Mathies, R.A. (1992). Effective rejection of fluorescence interference in Raman spectroscopy using a shifted excitation difference technique. *Applied Spectroscopy* 46: 707–711.
- 44** Zhao, J., Carrabba, M.M., and Allen, F.S. (2002). Automated fluorescence rejection using shifted excitation Raman difference spectroscopy. *Applied Spectroscopy* 56: 834–845.
- 45** Timegate Instruments (Oulu, Finland). <https://www.timegate.com/> (accessed 18 April 2020).
- 46** Carter, J.C., Angel, S.M., Lawrence-Snyder, M. et al. (2005). Standoff detection of high explosive materials at 50 meters in ambient light conditions using a small Raman instrument. *Applied Spectroscopy* 59: 769–775.
- 47** Fountain, A.W. III,, Christesen, S.D., Guicheteau, J.A. et al. (2009). Long range standoff detection of chemical and explosive hazards on surfaces. *Proceedings of SPIE* 7484: 748403-1–748403-11.
- 48** Pacheco-Londoño, L.C., Ortiz-Rivera, W., Primera-Pedrozo, O.M., and Hernández-Rivera, S.P. (2009). Vibrational spectroscopy standoff detection of explosives. *Analytical and Bioanalytical Chemistry* 395: 323–335.
- 49** Hernández-Rivera, S.P., Pacheco-Londoño, L.C., Ortiz-Rivera, W. et al. (2011). Remote Raman and infrared spectroscopy detection of high explosives. Chapter 10. In: *Explosive Materials: Classification, Composition and Properties* (ed. T.J. Janssen). Nova Science Publishers, Inc.
- 50** Wu, M., Mark Ray, K., Fung, H. et al. (2000). Stand-off detection of chemicals by UV Raman spectroscopy. *Applied Spectroscopy* 54: 800–806.
- 51** Gaft, M. and Nagli, L. (2008). UV gated Raman spectroscopy for standoff detection of explosives. *Optical Materials* 30: 1739–1746.
- 52** Pendar Technologies (Cambridge, MA). Pendar technologies X10. <https://www.pendar.com/products/pendar-x10/> (accessed 18 April 2020).
- 53** Blanchard, R. and Vakhshoori, D. (2020). Standoff detection of chemicals using infrared hyperspectral imaging and Raman spectroscopy. *SPIE Proceedings 11416, Chemical, Biological, Radiological, Nuclear, and Explosives (CBRNE) Sensing XXI*; 114160C (24 April 2020). <https://doi.org/10.1117/12.2558806>.
- 54** Watson, W., Buller, S. and Carron, K. (2019). US Patent 10,473,522 B2, issued 12 November 2019.
- 55** For instance:Yaghoobi, M., Wu, D., Clewes, R.J., and Davies, M.E. (2016). Fast sparse Raman spectral unmixing for chemical fingerprinting and quantification. *Proceedings of SPIE* 9995: 99950E.
- 56** Matousek, P., Clark, I.P., Draper, E.R.C. et al. (2005). Subsurface probing in diffusely scattering media using spatially offset Raman spectroscopy. *Applied Spectroscopy* 59: 393–400.

- 57 Creasey, D., Sullivan, M., Paul, C., and Rathmell, C. (2018). Extending Raman's reach: enabling applications via greater sensitivity and speed. *Proceedings of SPIE* 10490: 104900V.
- 58 Owen, H. (2002). Volume phase holographic optical elements. In: *Handbook of Vibrational Spectroscopy*, vol. 1 (eds. J.M. Chalmers and P.R. Griffiths). Chichester: Wiley.
- 59 Bonvallet, J., Auz, B., Rodriguez, J., and Olmstead, T. (2018). Miniature Raman spectrometer development. *Proceedings of SPIE* 10490: 104900W.
- 60 Smiths Detection (Edgewood, MD). Smiths Detection Awarded Approximately \$7 Million Contract for Bottled Liquid Scanners. <https://www.smithsdetection.com/press-releases/smiths-detection-awarded-approximately-7-million-contract-bottled-liquid-scanners/> (accessed 21 April 2020).
- 61 Agilent Insight200M. [https://www.agilent.com/cs/library/brochures/5991-8866EN\\_Insight\\_200M\\_brochure.pdf](https://www.agilent.com/cs/library/brochures/5991-8866EN_Insight_200M_brochure.pdf) (accessed 21 April 2020).
- 62 Costruzioni Elettroniche Industriali Automatismi S.p.A. (CEIA, Province of Arezzo, Italy). <https://www.ceia.net/security/product.aspx?a=EMA%20series> (accessed 21 April 2020).
- 63 Markowicz, A.A. (2008). Quantification and correction procedures. In: *Portable X-ray Fluorescence Spectrometry, Capabilities for In Situ Analysis* (eds. P.J. Potts and M. West), 13–38. Cambridge, UK. Chapter 2: RSC Publishing.
- 64 Piorek, S. (2008). Alloy identification and analysis with a field-portable XRF analyzer. In: *Portable X-ray Fluorescence Spectrometry, Capabilities for In Situ Analysis* (eds. P.J. Potts and M. West), 98–140. Cambridge, UK. Chapter 6: RSC Publishing.
- 65 Jenkins, R. (1999). *X-Ray Fluorescence Spectrometry*, 2nde, 6–7. Chichester, UK: Wiley-Interscience.
- 66 Viken Detection (Burlington, MA). 'HBI-120 Handheld X-Ray Imager. <https://www.heuresistech.com/hbi120> (accessed 20 April 2020).
- 67 Rapiscan/AS&E (Billerica, MA). MINI Z®, Handheld Z Backscatter® imaging system for detecting drugs and contraband. <https://www.rapiscansystems.com/en/products/ase-mini-z> (accessed 20 April 2020).
- 68 Videray (Boston, MA). The first generation of true inspection technology. <https://videray.com/> (accessed 20 April 2020).
- 69 Leary, P.E. et al. (2019). Deploying portable gas chromatography–mass spectrometry (GC-MS) to military users for the identification of toxic chemical agents in theater. *Applied Spectroscopy* 73 (8): 841–858.
- 70 Axcend Corp, (Provo, Utah, USA). HPLC Anywhere®. <https://www.axcendcorp.com/> (accessed 20 April 2020).
- 71 Microsaic Systems (Woking, UK). Real-time point-of-need mass spectrometers for optimized productivity. <https://www.microsaic.com/> (accessed 20 April 2020).
- 72 Malcolm, A. et al. (2010). Miniature mass spectrometer based on a microengineered quadrupole filter. *Analytical Chemistry* 82: 1751–1758.
- 73 Malcolm, A. et al. (2011). A miniature mass spectrometer for liquid chromatography applications. *Rapid Communications in Mass Spectrometry* 25: 3281–3288.
- 74 Blümich, B. (2016). Miniature and tabletop nuclear magnetic resonance spectrometers. In: *Encyclopedia of Analytical Chemistry*. Chichester, UK: Wiley.
- 75 Bruker (Billerica, MA). Time-Domain (TD) NMR. <https://www.bruker.com/products/mr/td-nmr.html> (accessed 20 April 2020).
- 76 Oxford Instruments (Oxford, UK). MQC+ benchtop Nuclear Magnetic Resonance (NMR) analyser. <https://nmr.oxinst.com/mqc> (accessed 20 April 2020).
- 77 Bruker (Billerica, MA). Minispec ProFiler. <https://www.bruker.com/products/mr/td-nmr/minispec-profiler.html> (accessed 20 April 2020).
- 78 Magritek (Wellington, New Zealand). NMR-MOUSE. <http://www.magritek.com/products/nmr-mouse/> (accessed 20 April 2020).
- 79 WaveGuide (Cambridge, MA). WaveGuide Formula™. <https://waveguidecorp.com/> (accessed 20 April 2020).

- 80** BaySpec (San Jose, CA). “Breeze”. <https://www.bayspec.com/spectroscopy/breeze-smart-palm-spectrometer/> (accessed 18 April 2020).
- 81** PhasmaFOOD (European consortium). Food sensing device. <https://phasmafood.eu/> (accessed 18 April 2020).
- 82** Thermo Fisher Scientific (Tewksbury, MA). Gemini. <https://www.thermofisher.com/us/en/home/industrial/spectroscopy-elemental-isotope-analysis/portable-analysis-material-id/chemical-explosives-narcotics-identification/gemini-ftir-ftir-raman-handheld-analyzer.html> (accessed 18 April 2020).
- 83** Olympus (Waltham, MA). TERRA portable XRD. <https://www.olympus-ims.com/en/xrf-xrd/mobile-benchtop-xrd/terra/#!> (accessed 2 July 2018).
- 84** Clegg, S.M., Wiens, R., Misra, A.K. et al. (2014). Planetary geochemical investigations using Raman and laser-induced breakdown spectroscopy. *Applied Spectroscopy* 68 (9): 925–936, and references therein.
- 85** Moros, J., ElFaham, M.M., and Laserna, J.J. (2018). Dual-spectroscopy platform for the surveillance of mars mineralogy using a decisions fusion architecture on simultaneous LIBS-Raman data. *Analytical Chemistry* 90: 2079–2087.
- 86** Wiens, R.C. et al. (1780). OrganiCam: A lightweight time-resolved fluorescence imager and Raman spectrometer for Mars cave or icy-world surface organic characterization. 51st Lunar and Planetary Science Conference (2020), paper 1780.
- 87** Mukhopadhyay, R. (2007). The viking GC/MS and the search for organics on Mars. *Analytical Chemistry* 79: 7249–7256.
- 88** Borman, S.A. (1981). Voyager infrared spectrometer. *Analytical Chemistry* 53: 1544A–1553A.
- 89** Hanel, R.A. et al. (1980). Infrared spectrometer for Jupiter. *Applied Optics* 19: 1391–1400.
- 90** Maguire, W.C., Hanel, R.A., Jennings, D.E. et al. (1981). C<sub>3</sub>H<sub>8</sub> and C<sub>3</sub>H<sub>4</sub> in Titan’s atmosphere. *Nature* 292: 683–686.
- 91** Vandenabeele, P. and Donais, M.K. (2016). Mobile spectroscopic instrumentation in archeometry research. *Applied Spectroscopy* 70: 27–41.
- 92** Sweedler, J.V. (2002). The continued evolution of hyphenated instruments. *Analytical and Bioanalytical Chemistry* 373: 321–322.
- 93** Hirschfeld, T. (1980). The Hy-phenated methods. *Analytical Chemistry* 52: 297A.
- 94** Hirschfeld, T. (1985). Instrumentation in the next Decade. *Science* 230: 286–291.
- 95** SoilCares (Wageningen, The Netherlands). <http://www.soilcares.com/en/products/scanner/> (accessed 18 April 2020).
- 96** Doherty, W., Falvey, B., Vander Rhodes, G. et al. (2013). A handheld FTIR spectrometer with swappable modules for chemical vapor identification and surface swab analysis. *Proceedings of SPIE* 2013: 8726.
- 97** Hug, W., Bhartia, R., Sijapati, K. et al. (2014). Improved sensing using simultaneous deep-UV Raman and fluorescence detection. *Proceedings of SPIE* 9073: 83581A-1-9.
- 98** Wiens, R.C., Sharma, S.K., Thompson, J. et al. (2005). Joint analyses by laser-induced breakdown spectroscopy (LIBS) and Raman spectroscopy at stand-off distances. *Spectrochimica Acta A* 61: 2324–2334.
- 99** Sharma, S.K., Misra, A.K., Lucey, P.G. et al. (2007). Combined remote LIBS and Raman spectroscopy at 8.6 m of sulfur-containing minerals, and minerals coated with hematite or covered with basaltic dust. *Spectrochimica Acta A* 68: 1036–1045.
- 100** Dreyer, C.B., Mungas, G.S., Thanh, P., and George Radziszewski, J. (2007). Study of sub-mJ-excited laser-induced plasma combined with Raman spectroscopy under Mars atmosphere-simulated conditions. *Spectrochimica Acta B* 62: 1448–1459.
- 101** Ancillotti, L., Castelluci, E.M., and Beucci, M. (2005). A combined Raman-LIBS spectrometer: toward a mobile atomic and molecular analytical tool for in situ applications. *Proceedings of SPIE* 5850: 182–189.
- 102** Courrèges-Lacoste, G.B., Ahlers, B., and Pérez, F.R. (2007). Combined Raman spectrometer/laser-induced breakdown spectrometer for next ESA mission to Mars. *Spectrochimica Acta A* 68: 1023–1028.

- 103** Escudero-Sanz, I., Ahlers, B., and Courrèges-Lacoste, G.B. (2008). Optical design of a combined Raman–laser induced-breakdown-spectroscopy instrument for the European Space Agency ExoMars Mission. *Optical Engineering* 47: 033001.
- 104** Moros, J., Lorenzo, J.A., Lucena, P. et al. (2010). Simultaneous Raman spectroscopy–laser-induced breakdown spectroscopy for instant standoff analysis of explosives using a mobile integrated sensor platform. *Analytical Chemistry* 82: 1389–1400.
- 105** Misra, A.K., Sharma, S.K., Acosta, T.E., and Bates, D.E. (2011). Compact remote Raman and LIBS system for detection of minerals, water, ices, and atmospheric gases for planetary exploration. *Proceedings of SPIE* 8032: 80320Q.
- 106** Osticioli, I., Mendes, N.F.C., Nevin, A. et al. (2009). A new compact instrument for Raman, laser-induced breakdown, and laser-induced fluorescence spectroscopy of works of art and their constituent materials. *The Review of Scientific Instruments* 80: 076109.
- 107** Allen, A. and Angel, S.M. (2018). Miniature spatial heterodyne spectrometer for remote laser induced breakdown and Raman spectroscopy using Fresnel collection optics. *Spectrochimica Acta B* 149: 91–98.
- 108** Abedin, M.N., Bradley, A.T., Sharma, S.K. et al. (2015). Mineralogy and astrobiology detection using laser remote sensing instrument. *Applied Optics* 54: 7598–7611.
- 109** Hamilton, M.A., Piorek, S. and Crocombe, R.A. (2015). Sample Analysis. US Patent 8,982,338 B2 (17 March 2015).
- 110** Olympus “Terra Portable XRD”. <https://www.olympus-ims.com/en/xrf-xrd/mobile-benchtop-xrd/terra/> (accessed 18 April 2020).
- 111** Vaniman, D.T., Bish, D., Guthrie, G. et al. (1999). Process monitoring and control with CHEMIN, a miniaturized CCD-based instrument for simultaneous XRD/XRF analysis. *Proceedings of SPIE* 3769: 243–251.
- 112** Marinangeli, L., Pompilio, L., Baliva, A. et al. (2015). Development of an ultra-miniaturised XRD/XRF instrument for the in situ mineralogical and chemical analysis of planetary soils and rocks: implication for archaeometry. *Rendiconti Lincei. Scienze Fisiche e Naturali* 26: 529.
- 113** Sackett, D.W. (2018). Combined handheld XRF and OES systems and methods. US patent 10,012,603 B2 (3 July 2018).
- 114** Delaney, J.K., Conover, D.M., Dooley, K.A. et al. (2018). Integrated X-ray fluorescence and diffuse visible-to-near-infrared reflectance scanner for standoff elemental and molecular spectroscopic imaging of paints and works on paper. *Heritage Science* 6: 31.
- 115** Inficon Hapsite. <https://products.inficon.com/en-us/nav-products/product/detail/hapsite-er-identification-system/> (accessed 18 April 2020).
- 116** PerkinElmer Torion T9. <https://www.perkinelmer.com/product/torion-t-9-portable-gc-ms-instrument-ntsst090500> (accessed 18 April 2020).
- 117** Smiths Detection Guardion. <https://www.federalresources.com/product smiths-detection-guardion-e-package-green/> (accessed 18 April 2020).
- 118** FLIR (Wilsonville, Oregon). Griffin G510. <https://www.flir.com/products/griffin-g510/> (accessed 18 April 2020).
- 119** Synder, A.P., Harden, C.S., Brittain, A.H. et al. (1993). Portable hand-held gas chromatography/ion mobility spectrometry device. *Analytical Chemistry* 65: 299–306.
- 120** Dworzanski, J.P., McClenen, W.H., Cole, P.A. et al. (1997). Field-portable, automated pyrolysis-GC/IMS system for rapid biomarker detection in aerosols: A feasibility study. *Field Analytical Chemistry and Technology* 1: 295–305.
- 121** Axcent Corporation (Provo, UT). Axcent® and Microsaic Systems Enter a Worldwide Integration and Joint Marketing and Sales Agreement. <https://www.axcentcorp.com/2020/02/27/axcent-and-microsaic-systems-enter-a-worldwide-integration-and-joint-marketing-and-sales-agreement/> (accessed 12 November 2020).

- 122** Burggraaff, O., Schmidt, N., Zamorano, J. et al. (2019). Evangelos Spyarakos, and Frans Snik, “Standardized spectral and radiometric calibration of consumer cameras”. *Optics Express* 27 (14): 19075–19101.
- 123** For instance, the University of Leiden Citizen Science Lab. <https://www.universiteitleiden.nl/en/citizensciencelab> (accessed 19 April 2020).
- 124** Snodgrass, R., Gardner, A., Semeere, A. et al. (2018). A portable device for nucleic acid quantification powered by sunlight, a flame or electricity. *Nature Biomedical Engineering* 2: 657–665.
- 125** Snik, F., 3187 iSPEX citizen scientists et al. (2014). Mapping atmospheric aerosols with a citizen science network of smartphone spectropolarimeters. *Geophysical Research Letters* 41: 7351–7358.
- 126** MONOCLE (Plymouth, UK). Citizen Science. [https://monocle-h2020.eu/Citizen\\_science](https://monocle-h2020.eu/Citizen_science) (accessed 19 April 2020).
- 127** Public Lab (Cambridge, MA). Public Laboratory. <https://publiclab.org/> (accessed 19 April 2020).
- 128** Public Lab (Cambridge, MA). Public Lab Spectrometry. <https://publiclab.org/wiki/spectrometry> (accessed 19 April 2020).
- 129** Spectral Engines (Helsinki, Finland). Spectral Engines and BSH have developed a textile scanner for making laundry easier. <https://www.spectralengines.com/news/a-textile-scanner-for-making-laundry-easier> (accessed 19 April 2020).
- 130** BSH Group (Stuttgart, Germany). Home Connect. <https://www.home-connect.com/is/en/connected-household/x-spect#!> (accessed 19 April 2020).
- 131** Spectral Engines (Helsinki, Finland). Home page. <https://www.spectralengines.com/> (accessed 19 April 2020).
- 132** Henkel – Schwarzkopf Professional (Düsseldorf, Germany). SALONLAB. <https://www.salonlab-server.de/en-GB/> (accessed 19 April 2020).
- 133** Henkel (Düsseldorf, Germany). Henkel Beauty Care revolutionizes personalized hair care with new, cutting-edge digital technology. <https://www.henkel-northamerica.com/spotlight/2018-03-01-henkel-beauty-care-revolutionizes-personalized-hair-care-with-new-cutting-edge-digital-technology-827002> (accessed 19 April 2020).
- 134** NeoSpectra (La Canada, CA). Si-Ware NeoSpectra is First Spectrometer Built Into Beauty Product. <https://www.neospectra.com/si-ware-neospectra-is-first-spectrometer-built-into-beauty-product/> (accessed 19 April 2020).
- 135** Opteskin (Santa Monica, CA). Your skin optimized. <https://www.opteskin.com/> (accessed 19 April 2020).
- 136** London Restaurant Festival (London, UK). Home page. [http://www.londonrestaurantfestival.com/about\\_us/#](http://www.londonrestaurantfestival.com/about_us/#) (accessed 18 April 2020).
- 137** BASF (Ludwigshafen, Germany). “Hertzstück™ Future Dining Room. <https://www1.bASF.com/hertzstueck/article.hertzstueck-future-dining-room.en.html> (accessed 18 April 2020).
- 138** trinamiX (Ludwigshafen am Rhein, Germany). trinamiX Mobile IR Spectroscopy Solutions. <https://trinamix.de/nir-spectroscopy/mobile-spectroscopy-solution/> (accessed 12 November 2020).
- 139** Garmin (Schaffhausen, Switzerland). Garmin fēnix® 6 Pro and Sapphire. <https://buy.garmin.com/en-US/US/p/641479/#specs> (accessed 19 April 2020).
- 140** For reviews, see. T3 Smarter Living (Bath, UK). Garmin Fenix 6 Pro review. <https://www.t3.com/us/reviews/garmin-fenix-6-pro-review> and Wearable (London, England), “SpO<sub>2</sub> and pulse ox wearables: Why blood oxygen is the big new health metric. <https://www.wearable.com/wearable-tech/pulse-oximeter-explained-fitbit-garmin-wearables-340>
- (accessed 19 April 2020).
- 141** Michael Attas, E. et al. (2002). *Skin Hydration Images from Near-Infrared Reflectance Spectra*, 32–36. American Clinical Laboratory.
- 142** Yeung, J., Macneille, P., Makke, O. et al. US Patent Application 2020/0111189A10, “Transportation System Using Odor Preferences”, published 9 April 2020.
- 143** Burns, D.A. and Ciurczak, E.W. (2007). *Handbook of Near-Infrared Analysis*, 3rde. Boca Raton, FL: CRC Press.

- 144 IUPAC (1990). Nomenclatures for sampling in analytical chemistry. *Pure and Applied Chemistry* 62 (6): 1193–1208.
- 145 Beć, K.B., Grabska, J., Siesler, H.W., and Huck, C.W. (2020). Handheld near-infrared spectrometers: where are we heading? *NIR News*, first published 13 April. doi: <https://doi.org/10.1177/0960336020916815> (accessed 19 April 2020).
- 146 Nie, B., Henion, J., and Ryona, I. (2019). The role of mass spectrometry in the cannabis industry. *Journal of the American Society for Mass Spectrometry* 30 (5): 719–730.
- 147 Brown, A.K., Xia, Z., Bulloch, P. et al. (2019). Validated quantitative cannabis profiling for Canadian regulatory compliance - Cannabinoids, aflatoxins, and terpenes. *Analytica Chimica Acta* 1088: 79–88.
- 148 Sánchez-Carnerero Callado, C., Núñez-Sánchez, N., Casano, S., and Ferreiro-Vera, C. (2018). The potential of near infrared spectroscopy to estimate the content of cannabinoids in Cannabis sativa L.: a comparative study. *Talanta* 190: 147–157.
- 149 Allied Scientific (Gatineau, PQ, Canada). “GemmaCert Cannabis Analyser. <https://alliedscientificpro.com/shop/product/gc200-gemmacer-cannabis-analyser-24069> (accessed 21 April 2020).
- 150 Sage Analytics (Los Altos, CA). The Profiler II (HSE). <https://sageanalytics.com/products/#mini> (accessed 21 April 2020).
- 151 Lightwave Science (Eugene, OR). “Cannalyzer-420. <https://lightwavescience.com/#price> (accessed 21 April 2020).
- 152 Big Sur Scientific (Capitola, CA). home page. <https://bigsurscientific.com/> (accessed 21 April 2020).
- 153 Smith, B.C. (2019). Quantitation of Cannabinoids in dried ground hemp by mid-infrared spectroscopy. *Cannabis Science & Technology* 2 (6).
- 154 Infratec (Dresden, Germany). Tunable Detectors. <https://www.infratec.eu/sensor-division/fpi-detectors/> (accessed 21 April 2020).
- 155 115th United States Congress, Senate Bill S.2667. Hemp Farming Act of 2018. <https://www.ams.usda.gov/sites/default/files/HempExecSumandLegalOpinion.pdf> (accessed 12 November 2020)
- 156 Agricultural Marketing Service, USDA (Washington, DC). Establishment of a Domestic Hemp Production Program, 84 FR 58522 (58522-58564). <https://www.federalregister.gov/documents/2019/10/31/2019-23749/establishment-of-a-domestic-hemp-production-program> (accessed 21 April 2020).
- 157 Sanchez, L., Filter, C., Baltensperger, D., and Kurouski, D. (2020). Confirmatory non-invasive and non-destructive differentiation between hemp and cannabis using a hand-held Raman spectrometer. *RSC Advances* 10: 3212–3216.
- 158 Hanif, M.A., Nawaz, H., Naz, S. et al. (2017). Raman spectroscopy for the characterization of different fractions of hemp essential oil extracted at 130°C using steam distillation method. *Spectrochimica Acta Part A: Molecular and Biomolecular Spectroscopy* 182: 168–174.
- 159 Roberts, C.A., Workman, J. Jr., and Reeves, J.B. III, (eds.) (2004). *Near Infrared Spectroscopy in Agriculture*. Madison, WI: American Society of Agronomy.
- 160 Grainsense (Oulu, Finland). “The GrainSense Analyzer. <https://www.grainsense.com/> (accessed 21 April 2020).
- 161 Spectral Engines (Helsinki, Finland). SmartFarm – concepts and collaboration for better future farms. <https://www.spectralengines.com/news/spectral-sensors-enable-future-farm-digitalization> (accessed 21 April 2020).
- 162 Agrocares (Wageningen, The Netherlands). Precision farming technology with global impact. <https://www.agrocares.com/en> (accessed 21 April 2020).
- 163 TeakOrigin (Waltham, MA). “How Nutritious are the Foods We Buy and Eat?. <https://www.teakorigin.com/> (accessed 21 April 2020).
- 164 PhasmaFOOD (European consortium). Food sensing device. <https://phasmafood.eu/> (accessed 18 April 2020).
- 165 Guenard, R. and Thurau, G. (2010). Implementation of process analytical technologies, Chapter 2. In: *Process Analytical Technology*, 2nde (ed. K.A. Bakeev). Chichester, UK: Wiley.

- 166** Smith-Goettler, B. (2010). On-Line PAT applications of spectroscopy in the pharmaceutical industry, Chapter 13. In: *Process Analytical Technology*, 2nde (ed. K.A. Bakeev). Chichester, UK: Wiley.
- 167** Romía, M.B. and Bernárdez, M.A. (2010). NIR spectroscopy in pharmaceutical analysis: off-line and at-line PAT applications, Chapter 14. In: *Process Analytical Technology*, 2nde (ed. K.A. Bakeev). Chichester, UK: Wiley.
- 168** Avila, C.R. et al. (2020). Process monitoring of moisture content and mass transfer rate in a fluidised bed with a low cost inline MEMS NIR sensor. *Pharmaceutical Research* 37: 84.
- 169** United States Food & Drug Administration Guidance Document (Washington, DC). "PAT — A Framework for Innovative Pharmaceutical Development, Manufacturing, and Quality Assurance, Guidance for Industry, October 2004. <https://www.fda.gov/regulatory-information/search-fda-guidance-documents/pat-framework-innovative-pharmaceutical-development-manufacturing-and-quality-assurance> (accessed 21 April 2020).
- 170** Ciurczak, E.W. (2019). NIRS is having a renaissance; but not all the pieces are moving at the same speed. *NIR News* 30 (3): 12–14.
- 171** Ciurczak, E.W. (2018). *What's new in NIR?* 30–34. *American Pharmaceutical Review*.
- 172** Hagen, N.A. and Kudenov, M.W. (2013). Review of snapshot spectral imaging technologies. *Optical Engineering* (Bellingham, WA, U.S.) 52 (9): 090901.
- 173** Näsilä, A., Holmlund, C., Briede, E. et al. (2019). Cubic-inch MOEMS spectral imager. *Proceedings of SPIE MOEMS and Miniaturized Systems XVIII* 10931: 109310F.
- 174** Guo, B., Näsilä, A., Trops, R. et al. (2018). Wide-band large-aperture Ag surface-micro-machined MEMS Fabry-Perot interferometers (AgMFPIs) for miniaturized hyperspectral imaging. *Proceedings of SPIE* 10545: 105450U.
- 175** Näsilä, A., Trops, R., Stuns, I. et al. (2018). Hand-held MEMS hyperspectral imager for VNIR mobile applications. *Proceedings of SPIE* 10545: 105450R.
- 176** Stiephenhofer, P. Hyperspectral imaging is conquering the industry. *Photonics Views* 2020 (2): 23–25.
- 177** Daukantas, P. (2020). Hyperspectral imaging meets biomedicine. *Optics & Photonics News* 31 (4): 32–39.
- 178** Keen, C.E. (2020). Smartphone camera enables hyperspectral imaging for skin analysis. *Physics World* <https://physicsworld.com/a/smartphone-camera-enables-hyperspectral-imaging-for-skin-analysis/> (accessed 21 April 2020).
- 179** Selci, S. (2019). The future of hyperspectral imaging. *Journal of Imaging* 5: 84–92.
- 180** Tematys (Paris, France). Hyperspectral And Multispectral Imaging: Applications And Market Trends. <https://tematys.fr/Publications/en/18-latest-reports> (accessed 30 July 2018).
- 181** Bouyé, C., Robin, T., and d'Humières, B. (2018). Spectral imaging spreads into new industrial and on-field applications. *Proceedings of SPIE* 10539: 1053918.
- 182** Logan, R.D., Scherrer, B., Senecal, J., Walton, N.S., Peerlinck, A., Sheppard, J.W., Shaw, J.A. (2020). Hyperspectral imaging and machine learning for monitoring produce ripeness. *Proceedings of SPIE* 11421, *Sensing for Agriculture and Food Quality and Safety XII*, 114210O (22 April 2020).
- 183** Gowen, A.A., O'Donnell, C.P., Cullen, P.J. et al. (2007). Hyperspectral imaging - an emerging process analytical tool for food quality and safety control. *Trends in Food Science & Technology* 18: 590–598.
- 184** Wu, D. and Sun, D.-W. (2013). Advanced applications of hyperspectral imaging technology for food quality and safety analysis and assessment: a review — part I: fundamentals. *Innovative Food Science and Emerging Technologies* 19: 1–14.
- 185** Wu, D. and Sun, D.-W. (2013). Advanced applications of hyperspectral imaging technology for food quality and safety analysis and assessment: a review — part II: applications. *Innovative Food Science and Emerging Technologies* 19: 15–28.
- 186** Lewis, E.N., Kidder, L.H., Lee, E., and Haber, K.S. (2005). Near-infrared spectral imaging with focal plane array detectors. In: *Spectrochemical Analysis using Infrared Multichannel Detectors* (eds. R. Bhargava and I.W. Levin), 25–55. Oxford, UK: Blackwell Publishing. Chapter 2.

- 187 Fernández Pierna, J.A., Dardenee, P., and Baeten, V. (2010). In-house validation of a near infrared hyperspectral imaging method for detecting processed animal proteins (PAP) in compound feed. *Journal of Near Infrared Spectroscopy* 18: 121–133.
- 188 Fernández Pierna, J.A., Vermeulen, P., Amand, O. et al. (2012). NIR hyperspectral imaging spectroscopy; chemometrics for the detection of undesirable substances in food and feed. *Chemometrics and Intelligent Laboratory Systems* 117: 233–239.
- 189 Feng, Y.-Z., ElMasry, G., Sun, D.-W. et al. (2013). Near-infrared hyperspectral imaging and partial least squares regression for rapid and reagentless determination of Enterobacteriaceae on chicken fillets. *Food Chemistry* 138: 1829–1836.
- 190 Manley, M. (2014). Near-infrared spectroscopy and hyperspectral imaging: non-destructive analysis of biological materials. *Chemical Society Reviews* 43: 8200–8214.
- 191 Pierna, J.A.F., Vincke, D., Dardenne, P. et al. (2014). Line scan hyperspectral imaging spectroscopy for the early detection of melamine and cyanuric acid in feed. *Journal of Near Infrared Spectroscopy* 22: 103–112.
- 192 Mishra, P. et al. (2015). Detection and quantification of peanut traces in wheat flour by near infrared hyperspectral imaging spectroscopy using principal-component analysis. *Journal of Near Infrared Spectroscopy* 23: 15–22.
- 193 Caporaso, N., Whitworth, M.B., and Fisk, I.D. (2018). Near-Infrared spectroscopy and hyperspectral imaging for non-destructive quality assessment of cereal grains. *Applied Spectroscopy Reviews* 53 (8): 667–687.
- 194 Boston Business Journal. <https://www.bizjournals.com/boston/news/2020/04/16/these-mass-companies-are-developing-covid-19.html> (accessed 21 April 2020).
- 195 Moor, K., Terada, Y., Taketani, A. et al. (2018). Early detection of virus infection in live human cells using Raman spectroscopy. *Journal of Biomedical Optics* 23 (9): 097001.
- 196 Xu, H. et al. (2020). An ultraportable and versatile point-of-care DNA testing platform. *Science Advances* 6: eaaz7445.
- 197 Ghosh, S., Aggarwal, K., U, V.T. et al. (2020). A new microchannel capillary flow assay (MCFA) platform with lyophilized chemiluminescence reagents for a smartphone-based POCT detecting malaria. *Microsystems & Nanoengineering* 6: 5.
- 198 BioOptics World 2020. Health Canada approves fast, portable COVID-19 test. <https://www.bioopticsworld.com/biophotonics-tools/article/14174260/spartan-bioscience-receives-health-canada-approval-for-fast-portable-covid19-test> (accessed 26 April 2020).
- 199 Martinelli, F. et al. (2020). Application of a portable instrument for rapid and reliable detection of SARS-CoV-2 infection in any environment. *Immunological Reviews* 00: 1–7.
- 200 Bloomberg (2017). <https://www.bloomberg.com/news/articles/2017-12-21/this-handheld-device-detects-opioids-it-s-not-always-right> (accessed 21 April 2020).
- 201 Rigaku. <https://www.rigaku.com/press/rad/fentanyl-and-B&WTek> <http://bwtek.com/news/major-fentanyl-and-heroin-update-now-available-for-tacticid-handheld-id-instruments/> (accessed 21 April 2020).
- 202 DeWitt, K. (2020). Algorithm and system advancements to enable infrared standoff trace detection. *Proceedings of SPIE 11392, Algorithms, Technologies, and Applications for Multispectral and Hyperspectral Imagery XXVI*, 113920L (24 April 2020).
- 203 Workman, J.J. Jr., (2018). A review of calibration transfer and instrument differences in spectroscopy. *Applied Spectroscopy* 72: 340–365.

## Index

### Symbols

<sup>1</sup>H 312-313, 383  
<sup>109</sup>Cd 429-430, 445  
<sup>153</sup>Gd 429-430  
 21 CFR Part 11 (section of the US Code of Federal Regulations) 15, 365  
 241Am 164, 430  
 244Cm 430  
 3D Printing 201, 220  
<sup>55</sup>Fe 430  
<sup>57</sup>Co 445  
<sup>63</sup>Ni 165  
 9/11 2, 131, 140, 167

### a

Ablation 309, 459, 474-475, 491  
 Accuracy 21-22, 47, 68, 70, 162, 193, 206, 213, 227-228, 230, 233-236, 239, 273-274, 281-282, 291, 294, 301, 303-307, 312, 330, 432, 441, 446, 457, 462-463, 466, 470, 176, 486, 556  
 Acetone 130, 184  
 Activation 190, 316  
**Adulteration, Authenticity, Contamination and Counterfeits**  
 Acrylic 241-242, 269, 508  
 Adulterants 67-68, 135, 230-231, 236  
 Antibiotic 114  
 Antimalarial 114  
 Authentic 86, 89-91, 95-98, 100-108, 110-111, 113, 116, 236, 366-367  
 Authenticity 97, 105, 236-238, 241, 314, 334, 348, 365  
 Contaminant 56, 69, 149, 153, 186, 268, 271, 287, 290, 301, 308, 314-315, 349, 353, 426, 438, 442, 446, 457, 468, 474, 480, 503, 560  
 Contamination 11, 44, 46-47, 49, 71, 88, 136, 142, 153-154, 161, 165, 168, 172, 181, 230, 232-233, 237, 239-241, 270-272, 287-291, 300, 304-307, 314-315, 333-334, 426, 455, 464, 468, 475, 480, 529, 532, 559-560  
 Cotton 134, 269-271  
 Counterfeit 4, 44, 49, 85-117, 128, 137-138, 141, 236, 269, 296, 315, 320, 347, 364-367, 372, 448, 556  
 Counterfeit Drugs 86, 89-91, 95-96, 101, 106, 108, 111-112, 115-116, 118-121, 123, 128, 137-138, 366

Counterfeit Medicine 118-123  
 Counterfeit Pharmaceuticals 85-117, 364-367  
 Diabetes 114  
 Food 333-335, 559-560  
 Meat 334  
 Melamine 56, 236, 314-315, 334  
 Milk 333-334  
 Silk 269-270  
 Soil 192, 287-291, 304-307, 455, 468, 473, 479  
 Statin 114-115  
 Textile 20, 269-273, 287, 553  
 Vaccine 114  
 Viagra 86, 88-89, 95, 366-367  
 Water 454  
 Wool 269  
 Aerosol 154-155, 163, 525, 550, 553, 561  
 Aerospace Composites 238  
**Agriculture**  
 Agricultural 45, 55, 101, 235-236, 300, 304-306, 308, 310, 312-313, 325, 332-333, 468, 477, 485  
 Agriculture 44, 233, 236, 299-311, 313-316, 325, 468, 484, 547, 558-559  
 Crop Quality 301  
 Crops 300-301, 558  
 Feed 44-45, 55-58, 60, 81, 196, 299-301, 303, 305, 307, 309, 311, 313, 315, 547, 558  
 Precision Agriculture 233, 300, 305, 310, 468, 484, 558  
 AI (Artificial intelligence) 309, 412  
 AIMS (Aspiration Ion Mobility Spectrometry) 308, 325  
 Airborne 150, 164, 173, 189, 413-414  
 Airport 4-5, 9, 27, 166-168, 228, 548-549, 559  
 Alarm 1, 27, 29, 128, 135, 155, 159, 161, 164-166, 170-172, 191-192, 194, 550  
 Allergen 556, 559  
 ALS (Alternative Light Source) 68  
 Ambient Light 24-25, 81, 217, 330  
 Amino Acids 155, 335  
 Anode 428-429, 433, 437, 443-444  
 APCI (Atmospheric Pressure Chemical Ionization) 159  
 Applications, Role of 1-16  
 Applications of Ion Mobility Spectrometry 159-174  
 Aptamer 207

- Army Research Laboratory 474  
 Array Detector 268, 373, 501, 546  
 Artificial neural network 29, 308, 473, 476, 489  
 Artwork 238, 241-242, 500, 502-503, 507-508, 516, 524, 526  
 Ascorbic acid 283, 333  
 Assignment Matrix 253-255, 257  
 ASTM (American Society for Testing and Materials) 47, 55, 67, 135, 445  
 Astrobiology 377-378, 380, 382, 384-390, 392, 394, 525  
 Atmospheric Pressure Interface 315  
 Atomic Spectroscopy 423  
 ATR (Attenuated Total Reflection) 11, 13, 46, 49, 66, 68-69, 73, 76, 80, 93-97, 117, 128, 133, 135, 143, 151-153, 228-230, 236-237, 242, 358, 361, 407, 500, 511-514, 516, 527, 546, 548, 551, 558, 561  
 Aviation 140, 166-168, 174, 549-550, 561  
 Aviation Security 167, 549-550
- b**
- Baby Formula 132-133, 230  
 Background Fluorescence 210  
 Backlog 232, 367, 369  
 Backscatter 302, 357, 367, 549  
 Bacteria 69, 199, 315-316, 392-394  
 Bakeout 161  
 Baseline correction 55-56, 69, 255, 258, 478, 502  
 Battery 103, 107, 159, 165, 170, 201, 212, 214-215, 217, 219, 228, 288, 335, 352, 383, 425, 427-428, 433, 448, 474-475, 523, 525, 532, 547, 550-552, 558  
 Battlefield 150, 164  
 Benzene 67-69, 185, 251, 255-256, 260-262  
 Beryl 379, 381, 383, 525  
 Bias 13, 61, 80, 140, 260, 262, 286, 291, 293, 330, 460-461, 533  
 Biological 132, 134, 142, 149, 152, 154-155, 162, 188, 195, 199, 210, 218, 228, 307, 374, 377, 388-390, 394, 477-478, 545, 560  
 Biomass 305  
 Biomolecule 314, 388-392  
 Bleach 230  
 Blood 125-127, 141, 162, 165, 201, 203-207, 211, 213-214, 218, 220, 271, 547  
 Blood Flow 201, 220  
 Bluetooth 214, 434, 545  
 Body fluids 207, 352  
 Boiling Point 109  
 Bootstrapping 29  
 Border Protection 173  
 Bottle Liquid Screening 549  
 Breath alcohol 127-130, 141  
 Bremsstrahlung 428  
 Buffer Gas 160
- c**
- CO<sub>2</sub> (Carbon Dioxide) 19-39  
 CAAC (Civil Aviation Administration of China) 167, 549, 561  
 Canadian 164, 166, 561  
 Capillary 141, 143, 195, 213, 317  
 Capillary Electrophoresis 141, 143, 195
- Carbohydrate 8, 56, 271, 291-294, 312, 327, 334-335, 556, 558  
 Carbon 1-2, 69-70, 109, 126-127, 167, 187, 233-236, 238-239, 303, 306-307, 331, 363, 383, 386, 389-390, 394, 405, 472, 508-509, 528, 549  
 Carbon Nanotubes 69  
 Carotenoid 328-329, 333, 383, 388-390, 392-393, 525, 555  
 Carrier 11, 15, 107, 160  
 Cathode 390, 429  
 CCD (Charge-Coupled Device) 19, 25, 349, 351, 356, 373, 433, 458, 474, 489, 547, 561  
 CE (Capillary Electrophoresis) 141, 143, 283, 470, 535, 554, 561  
 Cell 128-130, 140, 171, 199, 204-206, 216, 218-220, 317, 389, 392  
 Cellphone 168, 212, 219, 549, 557  
 Cellulose 94, 132, 166, 283, 287, 366, 434, 511  
 Ceramic 303, 330, 447, 503, 530  
 Ceramic Glaze 303  
 Certified Reference Materials 460  
 Charge Coupled Device 373  
 Charge Transfer 402, 506
- Chemical, Biological and Nerve Agents**
- Anthrax 2, 131-132, 134, 228  
 Bacillus 133, 228  
 Bacillus Anthracis 228  
 Bioaerosol 154-155  
 Biological Agent 151-152, 155, 195  
 Biodefense 149  
 Biodetection 134, 155  
 Biothreat 154-155  
 Biowarfare 149, 154  
 Blister Agent 150, 164  
 CBRNE (Chemical, Biological, Radiological, Nuclear, and Explosives) 52  
 Chemical Agent 149-152, 162-164, 373, 550, 561  
 Chemical Biological 149  
 Choking Agent 165  
 CWA (Chemical Warfare Agent) 2, 15, 35, 153, 159, 161-165, 172, 191  
 CWC (Chemical Weapons Convention) 162  
 ECAC (European Civil Aviation Conference) 167, 549, 561  
 Incapacitating Agent 162  
 JCAD (Joint Chemical Agent Detector) 163-165, 550, 561  
 Mass Casualty 179  
 Novichok 550  
 Nerve Agent 163, 194, 393  
 White Powder 2, 7, 29, 128, 131-134, 152, 189, 228-229, 383  
 WMD (Weapons of Mass Destruction) 162, 190  
 Chemical Characterization 523  
 Chemical Industry 65-81  
 Chemiluminescence 202-203, 210
- Chemometrics and Spectral Processing**
- Algorithm 1-8, 10-11, 13, 15, 19-40, 43-62, 68-70, 92, 95, 104, 132, 135-136, 155, 167, 171-172, 174, 193, 229-231, 235, 239, 241, 249-252, 256-257, 269, 274, 304, 308, 318, 347, 367, 408, 410-411, 416, 432, 502, 513-514, 526, 545, 548, 550, 554, 560  
 Calibration Model 8, 233, 242, 249-250, 252, 259, 269, 272-273, 276, 279, 282-283, 286-288, 290-291, 293, 310, 333, 434, 485

- Calibration Transfer 44, 250  
 CART (Classification and Regression Trees) 48, 142  
 Chemometrics 33, 45, 67, 98, 100, 117, 308, 331-332, 487, 524  
 Classification Algorithm 29  
 Cluster-Analysis Algorithm 8  
 Conditioning 21-22, 26  
 Confirmation Algorithm 19-39, 367  
 Confirmatory 12, 107, 111, 133, 135-136, 139, 143, 150, 155, 180, 188, 441  
 Correlation-Coefficient 7  
 Data Conditioning 21-22, 26  
 Data Processing 160, 171, 255, 408, 411, 428, 460, 474-476, 478, 487  
 Database 2, 6, 8, 16, 30-31, 37-38, 45-46, 86, 95, 141, 201, 388-389, 472, 500, 506, 515, 527, 546, 555, 560  
 Databases 1-3, 15, 37, 133, 199, 220, 314, 328, 347, 383, 473-474, 513, 515, 560  
 Deconvolution 44, 48, 408, 412, 433  
 Derivative filter 26  
 Detection Algorithm 4, 27, 135, 171-172, 174, 193  
 Discriminant Analysis 241-242, 274, 477-478, 481, 530  
 Expert System 230  
 False Negative 61, 141, 174, 550, 560  
 False Positive 34, 54, 61, 135, 168, 174, 192, 230-231, 465, 550, 560  
 First-Order Derivative 58  
 HCA (Hierarchical Cluster Analysis) 48, 56, 304  
 HQI (Hit Quality Index) 19, 28-31, 34-37, 46, 48  
 Identification Algorithm 19-39  
 ILS (Inverse Least Squares) 249  
 KNN (K-Nearest Neighbors) 29, 33  
 Mahalanobis Distance 31, 35, 48, 256, 262  
 Master to Target 250-251  
 MCR (Multivariate Curve Resolution) 67-68  
 MCR-ALS (Multivariate Curve Resolution with Alternating Least Squares) 68  
 Multivariate Analysis 310, 366  
 Multivariate Regression Vectors 252  
 MSC (Multiplicative Scatter Correction) 117, 261-262, 264  
 Neural Network 29, 33, 68, 308, 475, 476, 489  
 Non-Recursive Filter 26  
 PCA (Principal Components Analysis) 43, 48, 56-58, 68, 95, 98-100, 103-107, 117, 239, 249, 256, 261-262, 269, 272-277, 287-290, 317, 480, 532-536  
 PCR (Principal Component Regression) 43, 48-49, 214-215, 315, 546  
 Piecewise Direct Standardization 250  
 PLS (Partial Least Squares) 58, 60, 67-68, 70, 239-242, 249, 254, 256-257, 259-260, 262, 265, 274, 279-280, 282, 287-293, 414-415, 478, 481  
 PLSR (Partial Least Squares) 43, 48-49, 58, 60, 69, 233, 235, 249, 405, 473, 481, 485  
 Polynomial Fit 55-56  
 Polynomial Least-Squares Filter 26  
 Predictive Model 55, 58, 61  
 Preprocessing 31, 44-45, 55-56, 58-59, 69, 77-79, 269, 306-307  
 Pretreatment 44, 55, 98, 103-107, 265, 273, 279, 281, 284, 288, 293, 306, 308, 310-311, 315, 392  
 Precision 21-22, 39, 68, 228, 230, 233, 299-300, 304-306, 310, 432-433, 438, 461, 466-468, 484-486, 532, 554, 558-559  
 Probability 29, 34-37, 46, 48, 93, 172, 229-230  
 Qualitative Algorithm 39  
 Quantitative Algorithm 26, 33  
 Quantitative Calibration 252, 267, 288, 476  
 Reference Library 37-38, 47, 317, 410-412, 506  
 Regression Coefficients 32  
 RMSEC (Root Mean Square Error of Calibration) 60, 279, 285, 291, 293  
 RMSECV (Root Mean Square Error of Cross-Validation) 60, 235, 279, 290, 293  
 RMSEP (Root Mean Square Error of Prediction) 60, 233, 235, 240, 260, 262, 279, 293  
 ROC (Receiver-Operator Characteristic) Curve 39  
 Regression 19, 31-33, 43, 45, 48, 55, 57-58, 60, 67-68, 233, 235, 249, 252-253, 274, 293, 305, 309, 405, 416, 434-435, 473, 476, 481-482, 485, 489  
 Search Algorithm 2, 7, 69, 132, 135, 231  
 Second-Order Derivative 55  
 SIMCA (Soft Independent Modeling of Class Analogies) 43, 48, 236-237, 269, 273, 287  
 Smoothing 26, 58, 105-106, 273, 279, 293  
 SNV (Standard Normal Variate) 55-56, 58-59, 103-105, 117, 273, 275-276, 279, 281, 285  
 Statistical inference 34-36  
 Stepwise Regression 32  
 SVM (Support Vector Machine) 29, 473  
 Target to Master 250-251  
 Spectral Libraries 1, 46, 128, 133, 135-136, 138, 228-229, 412, 486, 560  
 Spectral Library 7, 69, 132, 136, 229, 353, 411-412, 477  
 Spectral Subtraction 31-32, 39, 73  
 Spectral Transfer 249-265  
 SEP (Standard Error of Prediction) 259-260, 262, 282  
 Transfer Matrix 250-253, 261, 265  
 Validation 7-8, 29, 34, 38, 46, 48, 58, 60-61, 79, 98, 105, 117, 143, 171, 233-235, 237-239, 259-260, 262, 269, 274, 276, 279, 282-283, 286, 290-291, 293, 299, 330, 364, 404, 410, 412-413, 417, 476, 485  
 Chlorobenzene 390  
 Chlorophyll 328, 333, 335-336, 389, 392  
 Cholesterol 203, 205  
 Chromatogram 108-112, 140, 192  
 Chromatography 5, 19-20, 69, 90-91, 107, 117, 136, 141, 143, 188, 195, 232, 280, 309, 390, 550, 552, 561  
 Chromophore 500  
 Citizen 112, 115, 162, 553, 561  
**Clinical**  
 Antibody 204-208, 210-211, 213, 216-218  
 Antigen 204-205, 207, 217  
 Bioassay 201, 220  
 Bioconjugation 203  
 Bioluminescence 202-203, 214-215  
 Biomarker 199, 203-204, 206-208, 210-213, 216-220, 317, 377, 383, 385, 387-392  
 Biomarker Assay 199, 211, 213  
 Clinical 7, 199-220, 377, 553, 559

**Clinical (contd.)**

Clinical Applications 199-220  
 Clinical Assay 210, 213, 219, 553, 559  
 Clinical Samples 199, 207  
 Disease 117, 203, 205-206, 208, 211-214, 300, 377  
 Ebola 205, 208  
 HSL (Hue, Saturation, Luminance) 202  
 HSV (Hue, Saturation, Value) 213-214  
 Immunoassay 141, 188, 195, 207  
 LAMP (loop-mediated isothermal amplification) 47, 105, 107, 200, 211, 214-215, 268, 501  
 Lateral Flow Assay 201, 208  
 Lipoproteins 207  
 Molecular Diagnostics 199  
 Parasites 199  
 Recombinant Target 205  
 Serum Albumin 207, 211  
 Cloud 33-34, 37-38, 67-68, 180, 267, 291, 294, 548  
 CMOS (Complementary Metal-Oxide-Semiconductor) 200-201, 203, 210, 213, 216-220, 349, 547, 561  
 Coating 5, 33, 71-73, 75, 90, 92-93, 108, 216, 238, 241-242, 306, 433, 448, 471, 474, 484, 501, 514-516, 525, 528

**Color**

- Color Analysis 202
- Color Discrimination 203
- Color Matching 545-547
- Color tests 12, 126, 195
- Colorimetric 12, 126-127, 134-135, 139, 141, 188, 193, 202, 207-209, 213, 216, 218, 230, 309, 359, 546, 553
- Colorimetric tests 12, 126, 139, 141, 202, 230
- Combination Band 1, 8-9, 31-34, 37-38, 49, 58, 60, 67-68, 70, 73, 93-95, 103, 105, 114, 139, 189, 201, 216, 231, 237, 241, 249, 268-269, 271-273, 281, 284, 289, 291, 347, 357-358, 381, 383, 402, 404, 407, 412, 414-415, 423, 474-475, 500, 504, 506-507, 509-510, 513, 527, 546-548, 551, 555
- Combustible 27, 185-186
- Composite Material 238-239
- Conservation 94, 238, 241, 312, 348, 466, 499-503, 506-507, 511, 514, 516, 528-530, 535
- Consumer Appliances 553
- Consumer Goods 2, 16, 425, 433, 545, 553, 556
- Consumer Products 229, 427, 443-446, 546, 553
- Contact Lenses 220
- Containers 13, 45, 49, 94, 128, 133, 136, 139, 152, 188, 231, 283, 303, 355-359, 364, 550-551
- Contaminant 56, 69, 149, 153, 268, 271, 287, 290, 301, 314-315, 349, 353, 426, 438, 439-442, 446, 468, 503
- Contaminated Soil 232, 288-290, 380, 475, 480
- Continuous Processing 558
- Correction Factor 194, 461
- Correctional Facilities 168, 170-172
- Corrosive 67, 162, 184-186, 194, 241
- Cosmic ray 21, 26
- COTS (Commercial Off-The-Shelf) 549, 561
- Count 23-25, 50-51, 110, 203, 215, 304, 327, 423, 425, 430, 433, 436
- Counterions 47, 50-51
- COVID-19 (Coronavirus Disease of 2019) 86, 115, 117, 560

**Crowd-Sourced Data** 9

Crude Oil 67, 185  
 Crystallinity 378, 412, 473, 513

**Cultural Heritage**

- Archaeological 447, 463, 499, 503, 516, 523, 525, 527, 529-530, 536
- Archaeology 348, 447, 448, 499, 523-524, 526-530, 532-534, 536
- Archaeometry 448-449, 523-524, 528
- Art 4, 20, 66, 71, 94, 149, 192-193, 238, 241, 267, 288, 294, 314, 348, 373, 377, 382, 384, 432, 443, 448, 487, 499-501, 504, 507-508, 514, 516, 524-525, 527-528, 545
- Art Conservation 94, 238, 241, 507
- Brooklyn Museum 502, 510, 514
- Cement 532
- Chrome Yellow 507
- Coins 447, 524
- Cultural Heritage 383, 447, 499-516, 523-529, 537, 552
- Dye 134, 202-205, 207-208, 214-216, 364, 500, 506-508
- Excavations 377, 523, 530
- Fresco 528, 530
- Glyph 525
- Illuminated Manuscript 500, 507
- Iron Gall 505, 509, 526, 528
- Lacquers 140, 241
- Lapis Lazuli 507
- Marble 525, 530
- Metropolitan Museum of Art 499, 501, 514, 516
- Museum 384, 447, 448, 499-502, 504-505, 507-511, 514, 516, 523, 525, 527
- Morgan Library 501-502, 504-505, 508-509
- Mortar 524, 529-537
- New York Public Library 501-504, 509
- Obsidian 447, 503, 528, 529
- Ochre 508, 524, 528-530
- Painting 241, 447, 506-508, 534-528
- Parchment 504-505, 507, 528
- Pigment 8, 133, 241, 377, 381, 383, 385, 389, 392-393, 445, 447, 500, 503-510, 524, 527-530, 552
- Pompeii 241, 529
- Porcelain 525
- Plaster 500, 507
- Prussian Blue 506-507, 510
- Red Ochre 508, 524, 528
- Restoration 238, 242, 447, 499, 502, 504, 525, 527, 529-530
- Topography 500, 511
- Varnish 506
- Vermilion 506-509
- Yellow Ochre 508, 529
- Cuvette 12, 213, 255
- CV (Compensation Voltage) 98-100, 103, 117, 278, 282
- Cyanobacteria 386, 389, 392, 394
- Cyclohexane 251, 255-256, 260-262

**d**

Dark Current 24, 349  
 DART (Direct Analysis in Real Time) 91, 117, 142-143

- Data Collection 2, 20-23, 25-26, 37, 55, 58, 95, 125, 171, 203, 216, 232-233, 301, 336, 408, 502, 523-524, 532-534  
 DC (Direct Current) 132, 166, 374, 428, 433  
 Decontamination 173, 181-183, 188, 228, 230, 287, 290, 352, 442  
 Deep Learning 38  
 Department for Transport 167, 563  
 Deployment 5, 9, 11, 13, 16, 29, 33, 66, 95, 104, 114, 159, 165, 172, 174, 301, 347, 388, 560  
 Deposition 141, 211, 530  
 Depth Penetration 93, 327  
 DESI (Desorption Electrospray Ionization) 91, 117, 314  
 Desorption 91, 109, 117, 159-162, 314-315  
 Detection Limit 5-6, 44, 69-70, 107, 135, 142, 171, 211-212, 303, 314, 327-329, 331, 406, 431, 437, 443, 488, 449, 556, 560-561  
 DHS (US Department of Homeland Security) 549, 561  
 Diamond 13, 69, 228-230, 236-237, 490, 533, 548, 551  
 Diamond ATR 69, 228-230, 236-237, 548, 551  
 Diesel 26, 67-68, 70, 139, 232-233, 287-290, 363  
 Diffraction Grating 200, 203, 216-217  
 Diffuse Reflectance 67, 69-70, 73, 232-235, 238-241, 280, 373, 406, 502, 524, 527  
 Diffuse Reflection 133, 255, 269, 272-273, 275-278, 283, 287-288, 290, 292, 331, 502, 512  
 Diluents 230  
 DIMS (Differential IMS) 314  
 Dispersed Sample 227, 231-233, 235-237  
 Distance metrics 28, 31, 35, 48  
 DLP (Digital Light Processor) 268, 270, 272, 276, 280, 284-286  
 DMD (Digital Micromirror Device) 268, 270  
**DNA (Deoxyribonucleic acid)**  
 DNA 142, 203, 205-207, 214-216, 275, 389, 556, 560  
 DNA Detection 215  
 DNA Profile 142  
 Rapid DNA 142  
 Drift Gas 160  
 Drift Tube IMS 160  
 Drone 150, 168, 196, 200, 412, 559, 561  
**Drugs, Narcotics and Pharmaceuticals**  
 Acetylsalicylic acid 283  
 Active Pharmaceutical Ingredient 90, 111, 117, 352  
 Amphetamine 170, 368, 369  
 Antibiotic 114  
 Antimalarial 114  
 API (Active Pharmaceutical ingredient) 90-91, 93-94, 97, 103, 111, 117, 352, 364, 366  
 Avastin 115-116  
 Bath Salts 136, 369  
 Blister Pack 94-95, 364  
 Cannabinoid 136, 171, 230-231, 353-354, 368-370  
 Cannabis 195, 370, 556, 558  
 Carfentanil 14, 135, 170, 371  
 Cathinone 136, 143, 171, 230-231, 368-370  
 CBD (Cannabidiol) 556, 558, 561  
 cGMP (Current Good Manufacturing Practice) 365  
 Clandestine Laboratories, ("Clan Labs") 136, 139-140  
 Cocaine 103, 115, 134-135, 170-173, 230-231, 368-369  
 Contraband 168, 171, 173, 548  
 Counterfeit Drugs 137-138  
 Counterfeit Pharmaceuticals 85-117  
 Cutting Agent 7, 367, 372  
 Diabetes 114  
 Drugs 4, 12, 14-16, 86, 89-91, 93, 95-96, 101, 106-108, 111-116, 128, 134-137, 139, 141, 143, 159, 161, 168, 170-173, 190-191, 194, 229-231, 268, 352-353, 365-367, 369, 377-378, 383, 393  
 Excipients 7, 51, 93-96, 100, 103, 230, 283, 364, 366  
 Fentanyl 14, 88, 111-112, 128, 135-136, 166, 170, 173, 352-354, 359, 369, 371-372, 550, 560  
 Hemp 556, 558  
 Heroin 6, 14, 111, 115, 135-137, 171, 352-354, 368-369  
 Illicit Drugs 14, 128, 134-136, 141, 168, 172  
 Lidocaine 230  
 Magnesium Stearate 22-23  
 Methamphetamine 141, 170-171, 368  
 Mephedrone 367, 369-370  
 NAFDAC (National Agency for Food and Drug Administration and Control – Nigeria) 112-115  
 Narcotics 4, 7, 12, 44, 126, 165, 170, 230-231, 347, 353, 366-369, 372, 559-560  
 NPS (Novel Psychoactive Substances) 171, 211, 368-372  
 Pharmaceutical 4, 7, 11, 13, 20, 22, 28, 34, 38, 43-48, 50, 85-117, 126, 137-138, 141, 165, 195, 229, 236, 268-269, 280, 282-285, 347, 352, 364-366, 372, 374, 525, 548, 551, 556, 558-559  
 Pharmacopoeia 273, 280  
 Polymorph 50-51, 90, 136, 366  
 Polymorphic 47, 90, 93  
 Polymorphism 47, 50, 90  
 Psychoactive substances 4, 171, 230-231, 368-372  
 Spice 367-368, 370  
 Statin 114-115  
 Street Drug 4, 14  
 SWGDRUG (Scientific Working Group for the Analysis of Seized Drugs) 173, 194-196  
 THC ( $\Delta 9$ -tetrahydrocannabinol) 170-171, 370, 558  
 Traditional Chinese Medicines 273  
 USFDA (US Food and Drug Administration) 103  
 USP (US Pharmacopeia) 47-49, 55, 95, 364  
 Vaccine 114  
 DTGS (Deuterated Triglycine Sulphate) Detector 502  
 Dustproof 2  
 Dynamic Range 216, 315
- e**
- Ease of Use 14, 43-44, 135, 166, 190-191, 307, 332, 458  
 ED-XRF (Energy-Dispersive X-Ray Fluorescence) 303-305, 425, 438, 448, 449, 551, 561  
 Efflorescence 525  
 Electric Field 160  
 Electrochemical 129-130, 199, 220, 552  
 Electrode 482  
 Electron 352, 407, 423-424, 471-472, 489, 502, 509  
 Electronic Spectroscopy 506  
 Electrophoresis 141, 143, 195  
 Electrospray 91, 117, 314, 317

- Element Abundance 461  
 ELISA (Enzyme-Linked Immunosorbent Assay) 202, 208, 213, 216, 315  
 Emerging Application 236, 558  
 Emission Line 24, 305, 308-309, 471-473, 476-478, 480  
 Emission Wavelength 308, 473  
 Empirical 33, 434  
 Energy-Dispersive 425-426, 456, 509, 549, 551, 561  
 Environmental Analysis 151  
 Environmental Contamination 468  
 Enzyme 202-205, 207-208, 210-211, 217, 315  
 EPA (US Environmental Protection Agency) 181, 186, 426, 441  
 Epoxy 238-240  
 Equilibrium 65, 109, 160  
 Essential Oil 317  
 Etalon 269, 546  
 étendue 431  
 Euclidean Distance 7  
 Eugenol 280-283  
 Excitation Wavelength 202-203, 349-350, 356, 358, 366, 369, 379, 381, 383, 385, 390, 502, 509, 525-526
- Explosives**  
 ANFO (Ammonium Nitrate-Fuel Oil) 138, 361  
 Cellulose Nitrate 515  
 Dynamite 167  
 Energetics 151-152, 190  
 Explosive 2, 4-5, 12, 14-15, 19-20, 26-27, 34, 44, 51, 53-54, 67, 94, 128, 135, 138-139, 141, 150, 155, 159, 161-162, 165-170, 172-173, 184, 186, 189-191, 229, 349, 352, 358, 361-364, 372-374, 377-378, 383, 393, 546, 548, 550-552  
 Explosive Residues 166, 173  
 HME (Homemade Explosive) 170  
 HMTD (Hexamethylene Triperoxide Diamine) 139, 170, 349, 361-362  
 HMX (1,3,5,7-tetranitro-1,3,5,7-tetrazoctane) 170, 349, 362  
 IED (Improvised Explosive Device) 138, 358, 362  
 NG (Nitroglycerin) 6, 128, 143, 170, 204-205, 210, 213, 217, 232, 315  
 Peroxide 20, 54, 68, 184, 210, 361-363, 388, 390  
 RDX (Research Department Formula X - Cyclonite) 170, 349, 362  
 SEMTEX (plastic explosive containing RDX and PETN) 167, 363  
 Tannerite 138  
 TATP (Triacetone triperoxide) 138, 161, 170, 349, 361-362, 364  
 Tetryl 170  
 TNT (Trinitrotoluene) 167, 170, 349, 362
- f**  
 Fabry-Perot 268-270, 273, 285, 553, 557-559  
 FBI (US Federal Bureau of Investigation) 132, 142-143  
 FDA (US Food and Drug Administration) 15, 47, 112, 213, 301, 365  
 Fiber 67, 80, 109, 125, 132, 141, 152, 212-213, 217, 238-239, 255, 268-269, 272, 291-294, 330, 335, 348, 358, 374, 384, 474-475, 480, 499, 501-502, 506, 524-527, 548, 558  
 Fiber-Optic Probe 348  
 Field 1, 3, 5, 7, 11-14, 20, 23, 26, 30, 34, 38-39, 44, 46-47, 66-70, 80, 86, 89-95, 97, 101, 103, 105-109, 111, 116, 125-128, 130-143, 149, 151, 159-160, 165-168, 171-172, 174, 179, 188-193, 195-196, 203, 216-219, 229-233, 235-236, 250, 267, 269, 273, 299, 301, 304, 306, 308-318, 326, 328, 330, 333, 347, 349-353, 358, 361, 368, 377-386, 388, 390-394, 401-403, 405-407, 412-414, 426-427, 440, 446, 449, 455-460, 462-464, 466, 468, 470-489, 499-501, 503, 506-507, 516, 523, 529, 532-533, 537, 545, 549-553, 559-560  
 Figure of Merit 485  
 Filament 429  
 Fingerprint Region 500  
 Finite impulse response (FIR) filter 26  
 First Overtone 77, 272-273, 281-282, 284, 415  
 Flammable 139-140, 162, 184-186, 191  
 Fleet Management 11, 560  
 Flow 45, 160, 173, 201, 207-208, 210-211, 213, 220, 479, 484, 489, 537, 550  
 Fluorescence Interference 142, 191, 352  
 Flux 404  
 Foam 73, 76-77  

**Food and Beverage**  
 Alcohol 127-130, 139, 141, 168, 184-185, 363, 369  
 Apple 276-280, 332  
 Artificial Sweetener 133, 230  
 Beer 45  
 Beverage 291  
 Blueberry 317, 327, 333  
 Brix 276, 278-280, 329, 333  
 Caffeine 230, 283  
 Cereal 334  
 Citric Acid 329  
 Citrus 332-333  
 Coffee 270, 326, 335  
 Dairy 300, 333-334  
 Diet 236, 308  
 Fat 8, 45, 58, 132, 237, 271, 291-294, 311-312, 327, 333-335, 553, 556  
 Flour 7, 56, 58-59, 134, 237, 327, 334  
 Food 3, 8, 16, 44-45, 55, 58, 71, 101, 103, 112, 213, 233, 236-237, 268-269, 273, 280, 291, 294, 299-305, 307-311, 313-317, 325-330-336, 365, 369, 394, 524, 547, 551, 554-556, 558-560  
 Food Adulteration 314-315, 556  
 Food Applications 315, 332, 334  
 Food Fraud 300-301, 556, 558  
 Food Hazard 558  
 Food Quality 299  
 Fruit 274-275, 311-313, 325, 329, 332-333, 555, 559  
 Fish 275, 311, 315, 334, 556  
 Glaze 303  
 Glucose 202, 205, 207, 218, 335  
 Honey 134, 334  
 Lactose 7, 333, 365-366  
 Lamb 334  
 Lipid 312, 315-316  
 Lycopene 327-329, 555

- Mannitol 7, 230  
 Milk 236, 315, 327, 333  
 Milk Powder 236, 315  
 Nutritional Parameters 270, 291-293  
 Nutrient 268, 300, 305, 309-310, 325, 394, 477, 484, 558  
 Palm Oil 357  
 Pork 334  
 Rice 302, 334-336  
 Soluble Solids 276, 333  
 Stearic acid 22-23  
 Sugarcane 304-305, 334, 335  
 Tartaric Acid 329  
 Tomato 8-9, 275, 292, 313, 327-328  
 Tryptophan 155, 385  
 Vegetable Oil 67-68, 236
- Forensics**  
 Booking Station 142  
 Chain of Custody 4, 126, 231  
 Crime Scene 125-126, 135, 140-143, 377, 393  
 Daubert 126  
 Fingerprints 125, 151, 352, 479  
 Forensic 1, 4, 12, 44, 46, 86, 90, 103, 117, 125-128, 130-143, 171-174, 194-195, 227, 231, 235, 348, 352, 373-374, 377, 393, 525  
 Forensic Applications 125-143  
 Forensic Analysis 140, 142, 348  
 Forensic Science 1, 12, 86, 117, 125-143, 172, 174, 194, 373-374  
 Frye 126  
 Gunshot residue 126, 141  
 Hair 125, 554, 556  
 Human Hair 554  
 Semen 125  
 Urine 202-205, 211-212, 214, 352  
 FORS (Fiber Optic Reflectance Spectroscopy) 499-501, 503, 506-508, 510, 516, 524, 526-528  
 Fossil 379, 385, 474, 488  
 Fourier Transform 11, 19, 21, 66-67, 95, 101, 117, 132, 143, 152, 228, 332, 349, 351, 374, 401, 406-407, 468, 499-500, 524, 527, 548  
 Fourth Overtone 8, 560  
 Frequency 12, 44, 88, 105, 117, 132, 235, 240, 283, 349, 351-353, 402, 414, 417, 433, 446, 526, 549  
 FRET (Fluorescence Resonant Energy Transfer) 211  
 FTIR (FT-IR, Fourier Transform Infrared) 7, 9-11, 13, 19, 21, 27, 31, 49-50, 55, 66-74, 80, 94-97, 117, 128, 132-133, 135, 140-141, 143, 152-153, 228-230, 232, 234, 236-241, 287, 291, 317, 331, 351, 358-362, 364, 374, 401-402, 405-407, 417, 468, 499-503, 507, 511-516, 524, 527, 548, 551  
 FTIR (Fourier Transform Infrared) Spectrometer 27, 67, 70-71, 230, 232, 238, 406, 502  
 FTIR (Fourier Transform Infrared) Spectroscopy 406, 500-501, 503, 511, 515-516  
 Fuel 26, 67-69, 129-130, 138, 174, 186, 232-233, 236, 239, 361, 363, 529  
 Fundamental 20, 33, 44, 73, 93-95, 131, 195, 301, 308, 310, 317, 331, 353, 362, 372, 388, 402, 404, 406, 415, 424, 434-437, 461, 474, 500, 506, 511, 513, 549, 555
- Fundamental Parameters 33, 434-437, 461  
 Future 16, 46, 66, 116, 140-142, 155, 190, 193, 210, 218, 220, 265, 267, 269-270, 275, 294, 304, 308, 312, 314, 316-317, 336, 358, 385-387, 391, 393, 425, 442, 448, 468, 470, 475, 486-487, 489, 526, 536-537, 545-560  
 FWHM (Full-Width at Half-Maximum) 411, 433, 546
- g**  
**Gases and Vapors**  
 Argon 503  
 Carrier Gas 11, 15, 160  
 Chlorine 162, 164, 185, 187, 306, 390, 444  
 Gas Analysis 139, 236  
 Gas Detection 128, 188  
 Greenhouse Gases 236  
 Helium 438, 446, 503  
 Vapor Sampling 14  
 Volatile Analytes 109  
 Gasoline 67-68, 70, 80, 126, 136, 139, 185, 287-290, 363  
 Gated Detector 474, 549  
 Gating 160, 475, 548  
 Gaussian 235, 408, 412, 489
- GC (Gas Chromatography)**  
 GC (Gas Chromatography) 5, 19-20, 91, 107, 117, 136, 143, 188, 195, 232, 280, 390, 552, 561  
 GC Column 550  
 GC-MS (Gas Chromatography-Mass Spectrometry) 128, 136-137, 139-141, 143, 188, 390, 550-552, 558, 560-561
- Geology, Mineralogy and Mining**  
 Carbonaceous 216-217, 379-380, 382-383, 390  
 Carbonates 70, 381, 388, 402, 405-407, 411, 415, 417, 469, 487  
 ChemCam 474-475  
 Chlorate 51-52, 54, 153, 362-363  
 Chlorite 362, 402, 405, 408, 410-411, 413-415  
 Clay 9, 232-233, 235, 391, 405, 411-413, 464, 469, 475-476, 487-488  
 Coal 380, 384, 474  
 Conflict Mineral 477, 488  
 Dolomite 69, 379, 381, 383, 402, 487-488, 535  
 Drill Core 386, 393, 401, 406, 408-409, 411, 413, 415-417, 446, 463-464, 466, 470-472, 483  
 Extremophiles 377, 385, 387, 391  
 Extremophilic 377, 384, 386, 388-389, 391, 393-394  
 Feldspar 381, 415, 417, 473, 487, 489  
 Field Geology 13, 377-394, 455-456, 458, 460, 462, 464, 466, 468, 470-486, 488, 552, 559  
 Gemstone 382, 384, 474, 503, 556  
 Geochemical 412, 415-417, 463-464, 466, 468, 470, 472, 474-477, 481-484, 486-488  
 Geochemical Fingerprinting 486  
 Geochemical Fingerprints 477  
 Geolocation Metadata 199  
 Geology 13, 302, 377-378, 380, 382, 384, 386-390, 392-394, 455-456, 458, 460, 462, 464, 466, 468, 470-486, 488, 552, 559  
 Geoscience 377-379, 383, 401, 417, 455-456, 458, 470, 475  
 Grain Size 390, 405-407, 410, 549, 468, 473

**Geology, Mineralogy and Mining (contd.)**

Gypsum 378, 380-381, 385, 388, 392-393, 470, 507, 528, 530, 534-535  
 Hydrothermal Alteration 408, 414, 459, 463-464, 466, 487, 489  
 Hydroxides 70, 504  
 Kaolinite 70, 233, 402, 404-406, 412, 414, 487  
 Lithological 401, 417, 463, 466, 469  
 Mars 390-393  
 Metamorphic Zones 459  
 Meteorite 380, 390, 480-482  
 Mica 383, 402, 410-415, 473, 489  
 Mineral 4-6, 69-70, 232-233, 242, 307, 335, 377-385, 388, 390, 392, 401-408, 410-417, 424, 446, 457-549, 462-464, 466, 468-474, 476-479, 481-484, 487-489, 508, 525, 527-528, 530, 552, 559  
 Mineralogy 377-378, 381, 387, 392, 401, 405, 408, 413, 417, 463-464, 483  
 Mining 3, 70, 304, 380, 401-403, 406, 433, 448, 461, 464, 468, 470, 480-481, 549, 559  
 Nitrate 26, 51-54, 138, 150, 309, 333, 361-364, 515  
 Ore 70, 385, 401, 405-406, 414-415, 417, 424, 445, 446, 455, 461, 463, 467, 474, 481, 484, 487-489, 529  
 Oxides 70, 242, 381, 405-406, 417, 476, 504, 528  
 Pathfinder Element 463, 466, 468  
 Pathfinder Mineral 477  
 Phosphate 23, 415, 509  
 Phyllosilicate 70, 404  
 Polycyclic Aromatic Hydrocarbons 385  
 Porphyry 415, 466, 489  
 Prospecting 386, 445, 446, 463  
 Prospector 426, 446  
 Quartz 49, 255, 280, 378, 380-381, 383, 402, 405-407, 410, 417, 466, 483-484, 487, 501  
 Regolith 13, 386, 388, 390-391, 393, 401, 405-406, 414, 416, 463, 489  
 Shale 380, 474  
 Silicate 70, 379, 391, 402, 405-407, 415, 417, 473, 477, 481, 487-488  
 Sulfates 70, 378-380, 405-407, 417  
 Sulfide 126, 185, 187, 317-318, 326, 394, 406, 408, 466-467, 472, 487-489, 506, 528, 546  
 Sulfur 138, 187, 288, 335, 362, 380, 392-394, 438, 466, 505, 507, 530  
 Weddellite 389, 525  
 Volcanic 241, 394, 408, 447, 461, 463, 466, 473-474, 476-477, 480, 484, 487-489, 528  
 Zeolite 379  
 Geographic Origin 273-274  
 Glass 13, 27, 49, 66, 94, 125, 129, 133, 152, 216, 219, 283, 347, 349, 351, 355-356, 358-359, 364, 407, 447-448, 474, 481-482, 503, 530, 548  
 Gold Standard 192, 232, 239, 250, 302, 314  
 Grain 5, 8, 304, 332, 334, 390, 405-407, 410, 459, 468, 473  
 Grating 67, 101, 200-201, 203, 213, 216-217, 268, 391, 549, 557  
 Ground Validation 404, 412-413, 417  
 Guard Grid 160

***h***

Hadamard 557  
 Handheld Near-Infrared Spectrometers 267-295  
 Handheld Raman 347-372  
 Handheld XRF 423-449

**Hazardous Materials (HazMat) and Emergency Response**

Emergency Responder 228-229  
 Emergency Response 132, 173, 179, 228-229, 231  
 First Responder 14, 44, 47, 98, 107, 132, 134-135, 165, 180, 186-187, 193, 195, 228, 267, 294  
 Hazardous 1, 4, 7, 47, 51-52, 67, 93-94, 98, 107, 128, 139, 149-151, 170, 179-184, 186-190, 192-194, 196, 228-229, 231-232, 290, 347, 352, 393, 426, 438, 445, 552, 556, 559  
 Hazardous Materials 4, 7, 128, 150, 179-196, 228-229, 347, 559  
 Hazardous Materials Response 179-197  
 Hazmat 4, 11, 132, 179-180, 182-196, 228-230, 235-236, 347, 352, 550  
 Hot Zone 11, 181, 183, 186, 188-189, 194, 196, 230  
 Reachback 9, 11, 193  
 Threat Identification 138, 174  
 TICs (Toxic Industrial Compound) 159, 162-165, 172, 190-192  
 TIMs (Toxic Industrial Material) 190, 192

Hemispherical Reflectance 405  
 Herbicide 316-317, 556, 558  
 Herbicide Residue 556, 558  
 HHXRF (Hand Held X-Ray Fluorescence) 423-434, 436-440, 442-450, 457  
 Hollow-Cathode Laser 390  
 Homemade 14, 138, 150, 155, 167, 229, 364  
 Homogeneity Field 310  
 HPMS (High Pressure Mass Spectrometry) 20, 128, 136, 143, 188-190, 193-194, 550, 560-561  
 Human 27, 86, 88, 125, 131, 179, 186, 200, 204, 210, 214, 218, 220, 232, 305-306, 308, 352, 369, 386, 391, 481, 484, 488, 554  
 Humidity 20, 23, 26, 76-77, 106-107, 170, 193, 230, 381, 528  
 Hyperspectral Imaging 142, 149-150, 401-418, 518, 532, 547, 559-560

***i***

ICE (US Immigration and Customs Enforcement) 393, 474, 504  
 ICP (Inductively Coupled Plasma) 302-306, 423, 446, 462-463, 470, 555, 558, 561  
 Identification 1, 3-4, 6-8, 11-14, 16, 19-22, 24, 26-28, 30-39, 43-46, 49, 52-53, 57, 86, 90-92, 95-96, 98, 103, 105, 107-108, 110-111, 116-117, 125-126, 128, 132-139, 141-142, 150, 152-155, 160-162, 166-167, 170-172, 174, 180, 183, 187-188, 191-192, 210, 227-231, 235-236, 238, 241, 249, 256, 261-262, 265, 269-274, 287, 289, 302, 304, 314-315, 317, 328, 331, 333, 347, 361, 363, 374, 377-381, 383, 387-391, 406, 424, 427, 436-438, 455, 458-459, 463, 468-469, 474, 477-478, 481, 484, 500-501, 506-507, 510, 513, 524, 527-529, 549-552, 555-556  
 Ignitable Liquid 126, 128, 139  
 IM (Ion Mobility) 5-6, 15, 19-20, 128, 135, 139, 143, 149-150, 159-168, 170-174, 188, 191-192, 550, 552, 560

Images 10, 163, 165, 167, 169, 200-201, 203, 216, 218-220, 355-356, 372, 409, 470, 508, 554  
 IMS (Ion Mobility Spectrometry) 5-6, 15, 19-20, 128, 135, 139, 143, 149-150, 159-168, 170-174, 188, 191-192, 550, 552, 560  
 In Situ Monitoring 65  
 Industrial Hygiene 236  
**Infrared**  
 Infrared 2, 6, 12, 19-21, 23, 26-27, 38, 43, 65-66, 70-71, 86, 92, 95, 101, 117, 127, 143, 149-153, 159, 173-174, 188, 191, 195-196, 200, 227-242, 249-250, 252, 254, 256, 258, 260, 262, 264, 267-268, 270, 272, 274, 276, 278, 280, 282, 284, 286, 288, 290, 292, 294, 325-326, 328, 330-336, 347-349, 351, 364, 373-374, 380, 383, 401-409, 411, 414, 416-417, 464, 468, 449-500, 502, 511, 524, 527, 530, 545-548, 552-556, 558, 560-561  
 Infrared Detector 554, 558  
 Infrared Spectrometer 152, 227-230, 232, 236-239, 241-242, 249-250, 252, 254, 256, 258, 260, 262, 264, 267-268, 270, 272, 274, 276, 278, 280, 282, 284, 286, 288, 290, 292, 294, 373, 406-407, 546, 558  
 Infrared Spectroradiometry 150-151  
 Infrared Spectroscopy 6, 20, 23, 65-66, 95, 143, 153, 191, 195, 227-242, 325-326, 328, 330, 332, 334, 336, 347-348, 351, 417, 468, 524, 527, 558  
 InGaAs (Indium Gallium Arsenide) Detector 68, 560  
 Ink 4, 86, 504-505, 508-509, 526, 528  
 Instrument Standardization 61  
 Integrating Sphere 233, 330, 405, 555, 558  
 INTERPOL (International Criminal Police Organization) 85, 117  
 Ion Detector 160  
 Ion Mobility Spectrometry, Applications of 159-174  
 Ion Trap 136-137, 315-316  
 Ionization Potential 457, 472  
 Ionizing Radiation 187, 189, 456, 549  
 IP68 (Ingress Protection) 352  
 Ischemia 201  
 ISO (International Standards Organization) 201

**j**

Jewelry 449-448, 524

**l**

Laser Excitation 219, 350, 353, 356, 358, 363, 366, 369, 390-391, 502, 508  
 Laser-Induced Fluorescence 155, 381-382, 391, 499-500, 530, 551  
 LC (Liquid Chromatography) 90-91, 117, 141, 143, 314, 550, 552, 558, 561  
 LIBS (Laser Induced Breakdown Spectroscopy) 2, 5-6, 13, 20, 33, 140, 159, 299-301, 307-310, 455-458, 460, 462, 464, 466, 468, 470-489, 499, 524, 527, 529-530, 549, 551-552, 561  
 Life Science 90, 231, 269, 377  
 Limit Of Detection 44, 133, 143, 206, 210-211, 230-231, 349, 444, 459, 463, 476, 488

Linear Variable Filter 250, 267-268, 285, 546, 553  
 Liquid Chromatography 90, 117, 141, 143, 195, 550, 561  
 LOD (Limit Of Detection) 128, 133, 135, 143, 210, 213-214, 216-217, 300, 303-305, 308, 310, 315, 317, 349, 367, 443, 444, 446, 444, 459, 463, 476, 480  
 Longpass Filter 219, 268

**m**

Magnetic Field 310, 313  
 Malaria 86-87, 206, 208, 214  
 Matrix Effects 303-305, 307-308, 310, 434, 472-473  
 Matrix-Matched 456-457, 467, 471, 473, 486, 529  
 Matrix-Matched Calibration 456, 529  
 Median filter 26  
 Membrane 69, 204, 209, 220, 317-318  
 MEMS (Micro-Electro-Mechanical-Systems) 102-103, 117, 267-269, 550, 552, 554, 557, 561  
 Metadata 199, 208, 556

**Metals**

Alloy 2-3, 5-6, 13, 33, 214, 302, 424, 427, 432-433, 436-439, 443, 447, 503, 529-530, 549  
 Alloy Identification 33, 302, 424, 427, 549  
 Alloy Sorting 33, 438  
 Barium 363, 445, 503  
 Beryllium 307, 379, 428, 430-431, 501, 525  
 Brass 436, 438, 529  
 Bronze 436, 438, 449, 529  
 Cadmium 444, 445, 506, 545  
 Copper 5, 13, 302, 305, 308, 352, 408, 434, 438, 466, 476, 488-489, 505, 528-529  
 Gold 3, 69, 192, 207-209, 213, 232, 239, 250, 302, 312, 314, 352, 408, 414, 463, 466, 477-479, 483, 485, 487, 502-503, 507, 524, 529, 558  
 Heavy Element 307  
 Heavy Metal 3, 300, 303-308, 394, 438, 446, 480, 558  
 Iron 5, 13, 70, 87, 242, 302, 308, 380, 388, 394, 405-406, 408, 413, 415-417, 434, 446, 466, 480-481, 487-489, 504-505, 507-509, 526, 528, 530, 535  
 Lead 3, 9, 66, 71, 80, 88, 91, 108, 115, 125-126, 139, 153, 171, 180, 183, 192, 220, 227, 229, 249, 253, 293, 302-303, 307-308, 326, 349-351, 353, 367, 394, 412, 434, 444, 445, 447, 470, 488, 505-506, 508-509, 523-524, 528-529, 546, 549, 551, 553-555, 558-559  
 Molybdenum 428  
 Nickel 5, 13, 302-303, 431, 437-438, 467  
 Palladium 428  
 PGE (Platinum Group Metals) 457, 463, 466, 468  
 Platinum Group Element 463  
 Rare Earth Element 382, 391, 405, 457  
 Steel 1, 70, 423, 425, 437-438, 481, 487, 549  
 Titanium 366, 436-437, 503, 506  
 Transition Metal 380, 406  
 Uranium 70, 306, 446  
 Microcapillary films 214  
 Microfluidic 207, 211-214, 220  
 Microscope 70, 155, 215-216, 219, 410, 489, 508, 524  
 Microscopy 138, 218-220, 348, 355, 373-374, 407, 509

**Military**

- IED (Improvised Explosive Device) 138, 358, 362
- MIL-STD (Military Standard) 352
- Military Applications 4, 149-150, 152, 154-155, 162, 306
- Minimally-Invasive Analysis 299
- Mislabeled 111, 236, 275
- Mixture Analysis 7, 32, 34, 36, 38, 44, 48-49, 135-136, 229-230, 235
- Mobile Health 199
- MOEMS (Micro-Opto-Electro-Mechanical-Systems) 103, 117, 267
- Moisture 45, 47-48, 53-54, 58, 65, 76, 101, 152-153, 234-235, 241, 300, 304-307, 311-313, 326, 333, 405, 410, 460, 468, 473, 551, 554, 558
- Molecular Assay 154-155
- Morphology 218, 255, 384, 408, 503, 511
- Multispectral Imaging 546

**n**

- Nanoparticle 69-70, 203-204, 207-210, 213, 218, 310, 526
- National Research Council of Italy 501
- NDT (Nondestructive Test) 239
- NMR (Nuclear Magnetic Resonance) 68, 79, 299-301, 310-314, 317, 499, 551, 561
- Nondestructive 92, 103, 128, 154, 190, 227-228, 231, 238-242, 276, 293, 300, 303, 310-312, 326, 336, 366, 368, 383, 423, 442, 447, 463, 523-524
- Non-invasive 212, 300, 311, 348, 356, 374, 500, 503, 506, 508-509, 511, 513, 516, 523-524, 537
- Non-scientist 93, 95, 116, 125, 131, 427, 555
- Nucleic Acid 214-216

**o**

- Oak Ridge National Laboratory 238
- OES (Optical Emission Spectroscopy) 2, 549
- Oil 13, 67-69, 80, 138, 170, 185, 189, 217, 236-237, 287-291, 311, 317, 326, 335, 357, 361, 363, 506, 556, 558
- Operator Bias 330
- Optical Emission 2, 489, 529
- Optical Fiber 212, 374, 384, 474-475, 480, 501, 558
- Optical Filter 214, 220, 546, 553, 555
- Origin Validation 237
- OSHA (US Occupational Safety and Health Administration) 162, 184, 186-187
- Overtone 8, 49, 58, 60, 67, 70, 73, 77, 93-94, 103, 271-273, 276, 279, 281-282, 284, 289, 326, 331, 402, 415, 500, 506-507, 513, 547, 555, 560
- Oxidation 68, 129-130, 238-240, 381, 388, 394, 500
- Oxygen sensor 184, 186-187

**p**

- Packaging 44, 49, 86, 90-96, 100, 105-106, 115, 182, 190, 300, 325, 336, 351, 355-357, 364-365, 372, 548
- Paint 3, 9-10, 13, 125, 141, 239, 313, 430, 437, 443, 444, 457, 507, 528, 546

PAT (Process Analytical Technology) 45, 92, 103, 117, 282

Pathogen 149, 154-155, 207, 214, 228, 314, 556, 559

Pattern Recognition 331, 374, 480

Peak Picking 230

Peltier 430, 501

Personal Care 16, 553, 555-556, 561

Pesticides 194, 229, 275, 449

Petrochemical 65, 67

Phenylalanine 205, 216

Phosphorus 139, 362, 446, 504, 509

Photoionization Detector 184, 192, 228

Photoionization Sensor 187

Photometric Accuracy 330

Photonic Integrated Circuits 545

Phytoremediation 308

PIN (p-type-intrinsic-n-type) Diode Detector 303, 458, 532

**Plastics and Polymers**

- ABS (Acrylonitrile-Butadiene-Styrene) 59, 69
- PE (polyethylene) 72, 255, 261-264, 272-273, 444, 511-513
- PET (polyethylene terephthalate) 69, 71-73, 75, 255, 261-262, 264, 272
- Poly(ethylene terephthalate) 255
- Poly(vinyl chloride) 255
- Polycarbonate 255
- Polyester 72, 269-270, 428
- Polyethylene 49, 69, 72, 95, 255, 263-264, 272, 330, 357, 511
- Polymer 69, 71-73, 78, 81, 109, 152, 203, 218, 255-256, 261-262, 264, 272-273, 287, 303, 330, 443-444, 511, 513
- Polymeric films 71
- PP (polypropylene) 255, 261-264, 272
- Polypropylene 72, 255, 272, 330
- Polystyrene 24-25, 69, 255, 272, 330, 510
- Polyurethane 73, 76, 241, 514-515
- PS (polystyrene) 69, 255, 261-262, 264, 272, 315
- PVC (polyvinylchloride) 69, 255, 261-264, 272-273, 444, 514-515
- SAN (Styrene-Acrylonitrile) 69, 507, 528-529
- SB (Styrene-Butadiene) 69, 439, 443, 444, 462, 468
- Plasmon 352-353
- Plume 151-152, 232, 440
- PPE (Personal Protective Equipment) 1-2, 9-10, 93, 117, 182, 186, 188-189, 192-193, 352
- Presumptive 12, 89, 126, 128, 134-135, 141, 153-155, 192, 230
- Presumptive Identification 126, 128, 154
- Prison 135, 168, 170-172, 548
- Probe 12, 66-67, 80-81, 212-213, 216, 255, 311, 317-318, 330, 348, 353, 356, 358, 373, 384-385, 403, 405, 414, 426, 448, 474, 502, 508, 524-527, 530
- Protein 8, 45, 56-61, 101, 132-133, 155, 199, 203-207, 210, 213, 236-237, 272, 291-294, 300, 333-335, 556, 558
- Proximal Sensing 305, 401-402, 404, 406, 408, 410-412, 414, 416
- Pulse Oximeter 554-555
- Pulse Oximetry 220
- Pure material 5-7, 30, 37-38, 49, 361, 501
- Pyroelectric 545
- PZT (Lead Zirconate Tantalate) 546

**q**

QA/QC (Quality Assurance\Quality Control) 11, 460, 463, 467, 470, 486  
 QC (Quality Control) 11, 13, 34, 44-45, 65, 92, 238, 241, 269, 282-283, 294, 299-300, 311-312, 314-315, 330, 332, 364, 448, 462, 465, 472, 469, 488, 532  
 Quantum Dot 203, 210-211

**r**

R&D (Research and Development) 3, 65-66, 547  
 Radiation Monitor 184, 187  
 RAW ("Digital Negative" File Format) Image 201  
 Raw material 4, 11-13, 20, 22, 28, 34, 43, 92, 95, 103, 108, 269, 282, 299-300, 302-304, 347, 351, 364, 534, 548  
 Raw Material Identification 11-13, 43, 92, 95, 103  
 Reaction Monitoring 65-66, 78  
 Real-Time Release 557  
 Reference Sample 249-250, 261, 311, 511-512  
 Reflectance Standard 273, 276, 283, 292, 330, 504  
 Reflection Probe 255  
 Refractive Index 13, 153, 208, 216-217, 329  
 Region 8, 12, 25, 31, 55, 58-60, 67, 69-71, 73, 75, 93, 98, 101-102, 112, 115, 153, 160, 166, 200-202, 208, 210, 213, 216, 218, 235, 239, 253, 269, 272-273, 282, 284, 289-291, 305, 326-328, 331-332, 336, 350, 355-356, 367, 379, 382-383, 386, 388, 401-402, 408, 414-415, 417, 429, 449, 460-461, 475, 480, 482-483, 500, 504-507, 509, 513, 516, 524, 527-528, 535, 537, 545-546, 553, 555, 558-561  
 Representative Sample 327-330, 446  
 Residual solvent 91, 107-109  
 Resource-limited settings 199, 207-208, 211, 220  
 Reststrahlen Band 407, 512-514  
 RIN (Relative Intensity Noise) 546  
 RMID (Raw Material identification) 11, 13, 43  
 Robotics 196  
 RoI (Return on Investment) 11, 15

**s**

Salinity 235, 305-306, 392  
 Sample Collection 6, 108-110, 189, 220, 227, 232, 486, 523  
 Sample Heating 94, 347, 350-351, 548, 551  
 Sample Matrix 5-6, 135, 161, 174, 190-192, 235, 461  
 Sample Preparation 11-15, 65, 69-70, 91, 108-109, 111, 128, 133, 233, 235, 288, 302, 305, 307-308, 314, 327-328, 330, 364, 366, 407-408, 446, 457, 470-471  
 Sample Spinner 327, 330, 555  
 Sediment 305-306, 380, 388, 394, 408, 416, 461, 463-464, 468-470, 474-475, 477, 487-489  
 SEIRS (Surface Enhanced Infrared Spectroscopy) 6  
 Selectivity 22, 44, 47, 50-54, 56-57, 61, 173-174, 195-196, 227, 314, 361, 364, 368  
 Sequentially Shifted Excitation 381, 383, 502, 526  
 SERS (Surface Enhanced Raman Spectroscopy) 6, 14, 45, 69, 128, 142-143, 347-348, 350-356, 358, 360, 362, 364, 366, 368-370, 372-374, 508, 525-526  
 Si Detector 557

**Silica**

70, 442, 490  
 Silicon Detector 545-546, 553, 555, 559-560  
 Silicon Drift Detector 456, 458, 501, 532, 549  
 Silicone 65, 69, 71, 73  
 Skin Hydration 555  
 Smart Home 270, 553  
 Smartphone 199-220  
 Smartwatch 220, 556  
 Sniffer 27, 139-140  
 SNR (Signal to Noise Ratio) 1, 6, 22-25, 46, 402, 411, 548-549  
 Soil Health 232-233  
 Solar-Blind 548  
 SPAD (Single-Photon Avalanche Diode) 220  
 Spatial Heterodyne 391  
 Spatial Resolution 216, 218, 348, 471  
 Specificity 44, 47, 105-106, 130, 134, 159, 195, 203, 213, 231-232, 236, 241, 314, 347, 353, 368  
 Speckle 456  
 Spectral Resolution 1, 33, 67-68, 81, 105, 136, 250-251, 253, 255, 273, 308, 378, 402-403, 504  
 Spectrofluorimetry 524, 527, 530  
 SPME (Solid-Phase Microextraction) 108-111, 117, 136, 140  
 Sport Watch 554  
 Standoff Detection 347, 350  
 Starch 47-48, 283, 287, 335  
 Stratigraphic Sequence 459  
 Stratigraphy 401, 463  
 Stray Light 330, 349, 379, 555  
 Styrene 69  
 Supply Chain 86, 91, 112, 115-116, 236, 299-301, 325, 333  
 Swipe Cards 359

**t**

Technical Support 9, 11, 229  
 Telescope 154, 358, 404  
 Terrorism 138, 166, 361  
 Terrorist 134, 138, 162, 166-167  
 Thermal Desorption 159  
 Thermometry 201  
 Thin Films 33, 303, 433  
 Tissue 87, 184, 186, 207, 303-304, 307-308, 374, 559  
 Tissue Hydration 559  
 Tissue Oxygenation 559  
 TLC (Thin Layer Chromatography) 69, 91-92  
 Toxic 15, 139, 151, 159, 162, 184-186, 189-190, 229, 302-304, 308, 394, 424, 426, 443, 455, 468, 470, 476, 478, 529, 548  
 Toxic Element 302-304, 308, 426, 443, 468, 476, 478  
 TPH (Total Petroleum Hydrocarbons) 232-234, 287  
 Trace Detection 6, 167, 172, 557-558  
 Transmission Grating 549  
 Transmission Probe 255  
 TRH (Total Recoverable Hydrocarbons) 232  
 True-Positive Rate 39  
 TSA (US Transportation Safety Administration) 166-168, 410, 549, 561  
 Tyrosine 155, 385

**U**

Underwater 527, 530  
Unmix 413  
Unmixing 408, 411, 413  
Upconversion 210  
US Customs and Border Protection 173  
US Postal Service 132  
UV (Ultra-Violet) 12, 65, 68, 141, 201, 209, 211, 213, 218-219, 241, 328, 349-350, 380, 391-393, 456, 500-501, 506, 526, 548, 552, 556, 559  
UV Protection 556, 559

**V**

Verification 16, 22-23, 43, 45-46, 49-50, 91-92, 125, 170, 347, 350, 352, 364, 372, 412-413, 436, 442, 476, 486, 555-556  
Virus 205, 216, 218, 560  
VOCs (Volatile Organic Compounds) 107-109, 187

**W**

Water Vapor 46, 66  
Wavelength-Dispersive 425  
WD-XRF (Wavelength-Dispersive X-ray Fluorescence) 303-304, 425  
White Goods 553, 561  
WHO (World Health Organization) 85, 109, 113-116, 118, 365, 376

**X**

X-ray Detector 426  
X-ray Filter 2, 428  
X-Ray Fluorescence 1, 19, 53, 71, 140, 302-303, 380, 405, 423-451, , 455-469, 499, 524, 526-527, 530, 532, 561